
THIRD RECENT ADVANCES IN QUANTITATIVE REMOTE SENSING

Auditori de Torrent, Spain
27 September – 1 October 2010

Editor

José A. Sobrino
Global Change Unit
Universitat de València, Spain

Published by
Publicacions de la Universitat de València.
C/del Batxiller, 1-1
46010 València
publicacions@uv.es

THIRD RECENT ADVANCES IN QUANTITATIVE REMOTE SENSING

Edited by
José A. Sobrino
Universitat de València, Spain

Typesetting: G. Sòria, J. C. Jiménez-Muñoz, J. Cuenca, V. Hidalgo, B. Franch, R. Oltra-Carrió, C. Mattar and Y. Julien,

Copyright © 2010 by the Authors

All rights reserved. This book or parts thereof may not be reproduced in any form or by any means, electronic or mechanical, including photocopying, recording or any information storage and retrieval system now known or to be invented, without written permission from the authors.

ISBN: 978-84-370-7952-3
Depósito legal: V-4572-2010
Printed in Spain by Guada Impresores

Preface

The Third International Symposium on Recent Advances in Quantitative Remote Sensing, was held in Torrent, Spain from September 27 to October 1, 2010. It was sponsored and organized by the Global Change Unit (GCU) from the Image Processing Laboratory (IPL), University of Valencia (UVEG), Spain. Other sponsors include:

- City Council of Torrent (Spain);
- National Aeronautics and Space Administration (NASA);
- European Space Agency (ESA);
- Consellería de Empresa, Universidad y Ciencia de la Generalitat Valenciana (Spain);
- Ministerio de Ciencia e Innovación (MICINN), Spain.

This Symposium addressed the scientific advances in quantitative remote sensing in connection with real applications. Its main goal was to assess the state of the art of both theory and applications in the analysis of remote sensing data, as well as to provide a forum for researcher in this subject area to exchange views and report their latest results. In this book 154 of the 263 contributions presented in both plenary and poster sessions are arranged according to the scientific topics selected. The papers are ranked in the same order as the final programme.

To conclude, I would particularly like to thank the participants who have contributed to constructive discussions and the members of the International Scientific Committee, who greatly contributed to select the papers presented at the Symposium providing an attractive scientific programme. The symposium took place in Torrent in excellent conditions thanks to the UVEG, City Council of Torrent, NASA, ESA, MICINN and Consellería de Empresa, Universidad y Ciencia de la Generalitat Valenciana for their material and financial support. The success is also due to the efforts made by the Organizing Committee: by the chairperson Pilar Gómez-González, and by the members Juan Carlos Jiménez, Guillem Sòria, Juan Cuenca, Victoria Hidalgo, Belén Franch, Rosa Oltra, Cristian Mattar, Yves Julien, and also by the collaboration of Paula Zapata. Many thanks to all of them.

José A. Sobrino
Symposium Chairperson
Global Change Unit,
Universitat de València

Valencia, November 2010

International Scientific Committee:

Chairperson:

J. A. Sobrino University of Valencia, Spain

Members:

G. Asrar	WMO, Switzerland
F. Baret	INRA, Avignon, France
M. Berger	ESA/ESRIN, Italy
S. Briggs	ESA/ESRIN, Italy
G. Chehbouni	IRD, France
A. P. Cracknell	University of Dundee, UK
J. Font	ICM-CSIC, Spain
A. Gillespie	University of Washington, USA
R. O. Green	NASA, JPL, Pasadena, USA
G. Gutman	NASA, Washington, D. C., USA
A. Huete	University of Arizona, USA
Y. Kerr	CESBIO, Toulouse, France
Z.-L. Li	LSIT, Strasbourg, France
S. Liang	University of Maryland, USA
M. Menenti	Delft University of Technology, The Netherlands
J. Moreno	University of Valencia, Spain
F. Nerry	LSIT, Strasbourg, France
A. Oliso	INRA, Avignon, France
E. Oriol-Pibernat	ESA/ESRIN, Italy
F. Prata	NILU, Norway
J. Privette	NOAA, USA
S. Quegan	University of Sheffield, UK
M. Rast	ESA/ESRIN, Italy
A. Royer	University of Sherbrooke, Canada
J. Shi	ICISS, UCSB, USA
Z. Su	ITC, Enschede, The Netherlands
E. Vermote	University of Maryland, USA
Z. Wan	UCSB, USA
J. P. Wigneron	INRA, Bordeaux, France
Y. Yu	NOAA, USA
P.J. Zarco-Tejada	IAS, CSIC, Spain

Organizing Committee:

Chairperson:

P. Gómez-González Symposium, Torrent, Spain

Members:

J. Cuenca	University of Valencia, Spain
B. Franch	University of Valencia, Spain
M. V. Hidalgo	University of Valencia, Spain
J. C. Jiménez-Muñoz	University of Valencia, Spain
Y. Julien	University of Valencia, Spain
R. Oltra-Carrió	University of Valencia, Spain
C. Mattar	University of Valencia, Spain
G. Sòria	University of Valencia, Spain

CONTENTS

Preface

iii

How Powerful are Radiative Transfer Models of the Land Surface? Applications and Challenges H. Bach	1
Modelling reflectance of partially submerged canopies M.E. Beget, C.M. Di Bella, F. Baret, and J.-F. Hanocq	6
Approximating the average daily surface albedo with respect to soil roughness and latitude J. Cierniewski, A. Karnieli, K. Kuśnierek, and I. Herrmann	10
Aerosols characterization in the Western Mediterranean (Málaga, Spain) I. Foyo-Moreno, I. Alados, H. Lyamani, F.J. Olmo, and L. Alados-Arboledas	16
Comparison of current methods to determine the downwelling atmospheric irradiance in the thermal infrared V. García-Santos, M. Mira, E. Valor, V. Caselles, C. Coll, J.M. Galve, and L. Martinez	21
Incomplete temperature/emissivity separation in ASTER standard products AST08 and AST05 A. R. Gillespie, E. A. Abbott, L. Gilson, G. Hulley, J.-C. Jiménez-Muñoz, and J. A. Sobrino	27
Atmospheric heating rates related with the vertical distribution of aerosol single scattering albedo in a desert dust situation J.L. Gómez-Amo, A. di Sarra, D. Meloni, M. Cacciani, M.P. Utrillas and J.A. Martínez-Lozano	33
Evaluation of MODIS atmospheric profiles product for atmospheric correction in the thermal infrared domain J. C. Jiménez-Muñoz, J. A. Sobrino, C. Mattar, B. Franch, G. Sòria, V. Hidalgo, R. Oltra-Carrió, and Y. Julien	39
Vegetation Radiative Transfer Modeling Based on Virtual Flux Decomposition: FDM A. Kallel	44
Surface temperature downscaling from multi-resolution instruments based on MAP criterion and Markov models A. Kallel, C. Ottlé, S. Le Hégarat-Masclé	50
Estimating forest parameters from top of atmosphere multi-angular radiance data using coupled radiative transfer models V. C. E. Laurent, W. Verhoef, J. G. P. W. Clevers, M. E. Schaepman	56
D-PROSPECT: A Model to Simulate Leaf Optical Properties Spectra of Double Surfaces J. Li, and Q. Liu	62
Analysis of uncertainties in the estimation of vineyard biophysical variables from canopy reflectance using 3D architecture models R. López-Lozano, F. Baret, B. Tisseyre, E. Lebon, H. Poilvé, and J. Rousseau	67
Vegetation Cover Method Emissivity Dependencies on Atmosphere and Multispectral Vegetation Index L. Martínez, V. Caselles, E. Valor, F. Pérez, and V. García-Santos	72
The far-infrared: prospective of remote sensing applications O. Pancrati, J.-P. Blanchet, A. Royer, F. Châteauneuf, T. Ayash, Y. Blanchard, L. Garand	77
Aerosol size distributions retrieved from star-photometry by King inversion method D. Pérez-Ramírez, H. Lyamani, F. J. Olmo, F. Navas-Guzmán, and L. Alados-Arboledas	83
Proposal of a simple model for the characterization of aerosols in relation to the dominant air masses S. Segura, V. Estellés, M. P. Utrillas, A. R. Esteve, and J. A. Martínez-Lozano	89

Soil moisture retrieval from geostationary satellite data using combined daily evolution of surface temperature and net surface shortwave radiation	94
X. N. Song, P. Leng, Z. L. Li, X. T. Li, and X. H. Li	
Consistency of vegetation estimates from SEVIRI/Meteosat observations and operational algorithms	99
A. Verger, F. Baret, F. J. García-Haro, F. Camacho, and J. Meliá	
Significant improvements in the AATSR land surface temperature algorithm	105
O. Zeller, J. Remedios, A. J. Prata	
Estimation of surface soil moisture from combined solar shortwave radiation and surface temperature	111
X. Zhang, J. Wang, and Z.-L. Li	
Thermal Infrared Imaging of Weathering Changes of Mauna Ulu Basalts, Hawai'i	117
E. A. Abbott, A. R. Gillespie, and A. B. Kahle	
Geological classification of volcano Teide by hyperspectral and multispectral satellite data	123
S. Amici, A. Piscini, M. F. Buongiorno and D. Pieri	
Storage of Hyperspectral Sensor Images, Sources of Error and Footprint Analysis	127
A. Cristo, R. Pérez, P. Martínez, M. Koch, T. Schmid, L. Hernández and J. Merino	
Discrimination of Cruciferous Weeds in Wheat Crops Using Quickbird Satellite Image	133
A.I. De Castro, M. Jurado-Expósito, M.T. Gómez-Casero, D. Gómez-Candón, J.J. Caballero-Novella and F. López-Granados.	
Determinación de la Contaminación Producto de la Actividad Minera, Utilizando Sensores de Alta Resolución Espectral, en Huancavelica	138
M.Y. Díaz Núñez, Y. Loaiza., M.A. Miranda Peña and M. Caycho.	
Spectral characteristics of soil and vegetation in saline wetlands, NE Spain	143
M. Domínguez, B. Mougenot and C. Castañeda	
Using hyperspectral images to study regeneration of burned areas	149
F. González-Alonso, M. Huesca, S. Merino de Miguel, S. Martínez, J.M.Cuevas and A. Calle	
Noise in emissivity images obtained from the ASTER Temperature and Emissivity Separation (TES) algorithm: a case study of airborne imagery and implications for ASTER	154
J. C. Jiménez-Muñoz, J. A. Sobrino and A. R. Gillespie	
Independent component analysis application to multispectral sensors	158
F. J. Mesas-Carrascosa, I.L. Castillejo-González, A. García-Ferrer Porras and M. Sánchez de la Orden.	
Preliminary applications of a land surface temperature retrieval method to IASI and AIRS data	163
X. OuYang, G. Kang, F. Zeng and Z.-L. Li	
Operational cloud masking scheme for marine AHS and CASI imagery	169
I. Pérez González, E. de Miguel Llanes, C. Robles González and J.A. Gómez Sánchez	
Spatial and Temporal VIS/SWIR/TIR Spectral Variability of Natural Desert Surfaces	175
D. Sabol, F. A. Kruse, Z. Aslett, T. Minor, Ch. Kratt, J. Taranik and T. Morkin.	
Application of imaging spectroscopy to map indicator plant species for wetland degradation in the National Park of Las Tablas de Daimiel, Spain	181
T. Schmid, H. Feilhauer, U. Faude, S. Cirujano, R. Sánchez, M.J. Sierra, M. Rodríguez and S. Sánchez	
Study of Air and Land Surface Temperature Differences from EOS-MODIS and Ground Data	187
R. Niclòs, J. A. Valiente, M. J. Barberà and M. J. Estrela	
Validation of Split-Window Algorithms for Estimating Sea Surface Temperature on the Coast of Northern Chile	193
J.C. Parra, L. Morales, J. A. Sobrino and J. Romero	

Compensation for subpixel roughness effects in thermal-infrared images I. Danilina, A. R. Gillespie, L. Balick, A. Mushkin, M. Smith and D. Blumberg	196
Field measurements and modelling of diurnal cycles of land surface temperature at Gobabeb, Namibia F.M. Göttsche, F.S. Olesen, and A. B. Unkelbach	202
Consistent and accurate LAI, FAPAR and FCOVER global products: principles and evaluation of GEOV1 products F. Baret, M. Weiss, R. Lacaze, F. Camacho, P. Pacholczyk, H. Makhmara and B. Smets	208
Assessment of evapotranspiration and biomass of irrigated grasslands in South-Eastern France from FORMOSAT-2 images used in a crop model D. Courault, R. Hadria, F. Ruget, A. Olioso, B. Duchemin, O. Hagolle and G. Dedieu	214
Testing In-Scene Atmospheric Corrections of Hyperspectral Thermal Data from Nadir- and Oblique-Viewing Geometries M. R. Smith, A. R. Gillespie, H. Mizzon, L. K. Balick, J. C. Jiménez-Muñoz and J. A. Sobrino	220
Mapping vegetation density properties in a river floodplain and agricultural ecosystems using CHRIS-PROBA data J. Verrelst, E. Romijn, L. Kooistra, J.P. Rivera, L. Alonso and J. Moreno.	225
Retrieval of atmospheric and land surface parameters using neural network technique from the satellite based thermal infrared hyperspectral data N. Wang, F. Zeng, B.H. Tang and Z.-L. Li	231
Satellite Constellation For Crop Monitoring: Formosat-2, Deimos-DMC, Landsat 5TM and 7ETM+ A. Calera, M. Odi, C. Martínez-Beltrán, I. Campos and J. González-Piqueras	237
Applying VENUS bands for agriculture I. Herrmann, A. Pimstein, A. Karnieli, D. J. Bonfil, Y. Cohen, and V. Alchanatis	243
Assessment of the Land Cover Classification Accuracy of Venus and Sentinel-2 Image Time Series with respect to Formosat-2 J. Inglada, O. Hagolle and G. Dedieu	247
Use of Dense Time Series of High Resolution Images for Change Detection and Land use Classification J. Inglada, B. Beguet, J.-F. Dejoux, C. Marais-Sicre, D. Ducrot, M. Huc, O. Hagolle, F. Baup and G. Dedieu,	251
Exploring the potential of crop specific green area index time series to improve yield estimation at regional scale G. Duveiller, A. de Wit, L. Kouadio, B. Djaby, Y. Curnel, B. Tychon and P. Defourny	256
Quantitative remote sensing with off-the-shelf instruments on a small UAV U. Kirchaessner, U. Putze, M. von Schoenermark	262
Potential of multi-directional spectral data collected with a digital aerial frame camera to retrieve forest canopy characteristics T. Koukal and W. Schneider	268
Modeling thermal infrared directional anisotropy over a mature pine forest M. Mira, J.-P. Lagouarde, C. Moisy, D. Guyon, B. Kurz, J. Ogée, P. Moreau	274
Coupling of a Limited Area Atmospheric Model with a sequential MSG-derived LST Assimilation scheme for the production of a two-years meteorological dataset L. Campo, F. Castelli, D. Entekhabi and F. Caparrini	280
Application of the Maximum Cross-Correlation technique to sequential ocean thermal imagery in the Cape Blanc region P. Castellanos, J. L. Pelegrí, D. Baldwin, W. J. Emery and A. Hernández-Guerra	286
Multisensor and multitemporal image fusion methods to improve remote sensing image classification D. Ducrot, A. Masse, C. Marais-Sicre, J. F. Dejoux and F. Baup	292

A Multi Sensor Approach to Land Surface Temperature	298
S. C. Freitas, I. F. Trigo, J. Macedo, C. Barroso and R. Silva	
Automatic detection of field furrows and features from Very High Resolution optical imagery	304
S. Le Hégarat-Masclé and C. Ottlé	
Contribution of high resolution satellite imagery to water erosion prediction in Lokna sub-catchment within Plava watershed (Russia)	310
C. Ottlé, O. Evrard, N. Lio Soon Shun, S. Le Hégarat-Masclé and V. Belayev	
New Hyperspectral Unmixing Techniques in the Framework of the Earth Observation Optical Data Calibration and Information Extraction (EODIX) Project	315
A. Plaza, J. Plaza, I. Dópido, G. Martín, M.-D. Iordache and S. Sánchez	
Air temperature mapping using ground and satellite data in the context of a heat wave monitoring and warning system in the Valencia region	321
J.A. Valiente, R. Niclòs, M.J. Barberá, M.J. Estrela and J. Miró	
Fusion of MODIS and VEGETATION observations for improved consistency and continuity of LAI product time series	326
A. Verger, F. Baret and M. Weiss	
Integrating multi-source data into land surface model for an improved state estimation through data assimilation	332
K. Wang, Z.-L. Li and R. Tang	
Analysis of temperature maps of water bodies obtained from ASTER TIR images	338
F. Despini and S. Teggi	
Retrieving crop specific green area index from remote sensing data when the spatial resolution is close to the target field size	343
G. Duveiller, M. Weiss, F. Baret, A. de Wit and P. Defourny	
Land surface heterogeneity and appropriate spatial resolution of remote sensing imagery	349
C. Li, X. Wang, L. Ma and S. Qiu	
The effect of spatial resolution in remote sensing of water stress using optical and thermal imagery	355
L. Suárez, P. J. Zarco-Tejada, J. A. J. Berni, V. González-Dugo, E. Fereres and D. Goldammer	
Spatial scaling in the remote sensing retrieval	358
H. Wu, B.-H. Tang and Z.-L. Li	
A new empirical expression to relate aerodynamic and surface temperatures for use within single-source energy balance models	364
G. Boulet, A. Olioso, P. Béziat, V. Rivalland, J. Chirouze, E. Ceschia and G. Chehbouni	
Relation between CO₂ measured by MOPITT sensor, and large fires emissions in the most affected regions in the world	370
A. Calle, J. L. Casanova, J. Sanz, P. Salvador and F. González-Alonso	
Using MODIS-LAI images on the spatio-temporal functioning of a Mediterranean forest in Tunisia: impact on water budget estimations	376
H. Chakroun, F. Mouillot and M. Nouri	
Application of canopy radiant temperature in the estimation of gross primary productivity	382
L. Chen, J. Yan, Y. Gao and H. Tao	
Performance assessment of four surface energy budget models, forced with in-situ and ASTER surface temperature, against eddy covariance and scintillometer data in temperate and semi-arid regions	388
J. Chirouze, G. Boulet, P. Béziat, L. Jarlan, R. Fieuzal, J. Garatuza-Payan, C. Watts, J.C. Rodríguez, J. Ezzahar, S. Er-raki and G. Chehbouni	

Land surface temperature representativeness and its relationship with soil moisture through an energy water balance model	393
C. Corbari, J. A. Sobrino, M. Mancini and V. Hidalgo	
Canopy water content retrieval from CHRIS/PROBA data using neural networks training with radiative transfer model simulations	399
J. Cernicharo, F. Camacho, A. Verger and E. López-Baeza	
Monitoring soil and vegetation fluxes of carbon and water at the global scale: the land carbon core information service of GEOLAND2	405
J.-C. Calvet, C. Albergel, G. Balsamo, M. Balzarolo, A. Barbu, S. Boussetta, A. Cescatti, F. Chevallier, N. Delbart, J. de Vries, L. Kullman, S. Lafont, J.-F. Mahfouf, F. Maignan, D. Papale and C. Szczpta	
LAI remote sensing products and simulated LAI: an intercomparison over FRANCE	411
S. Lafont, Y. Zhao, M. Weiss, J.-C. Calvet, P. Peylin and P. Ciais	
Geoland2 – Towards an operational GMES Land Monitoring Core Service. First results of the Biogeophysical Parameter Core Mapping Service	416
R. Lacaze, G. Balsamo, F. Baret, J.-C. Calvet, F. Camacho, R. D'Andrimont, S. Freitas, P. Pacholczyk, H. Poilvé, B. Smets, K. Tansey and W. Wagner	
The YLCD method: Monitoring vegetation from annual behaviour of NDVI and LST time series	422
Y. Julien, J. A. Sobrino, C. Mattar, J. C. Jiménez-Muñoz, G. Sòria, V. Hidalgo, B. Franch, R. Oltra-Carrió and J. Cuenca	
FAPAR over Europe for the past 29 years: A temporally consistent product derived from AVHRR and VEGETATION Sensors	428
M. Weiss, F. Baret, H. Eerens and E. Swinnen	
Interannual vegetation dynamics over Morocco through the NDVI/AVHRR from 1982 to 2008: linkages with climate signals and potential for seasonal prediction	434
L. Jarlan, F. Driouech, Y. M. Tourre, B. Duchemin, J. Abaoui, M. Le Page, H. Kharrou, A. Ouldbba, A. Mokssit and G. Chehbouni	
Long term observations of active volcanoes: Orbital missions and growing remote sensing archives	440
D. Pieri and M. F. Buongiorno	
MISTIGRI, a microsatellite project associating high spatial resolution and high revisit frequency in the Thermal InfraRed	444
J. P. Lagouarde, M. Bach, J. A. Sobrino, G. Boulet, X. Briottet, S. Cherchali, B. Coudert, I. Dadou, G. Dedieu, P. Gamet, O. Hagolle, F. Jacob, F. Nerry, A. Oliso, C. Ottlé, V. Pascal, J.L. Roujean and F. Tintó García-Moreno	
Validating satellite land surface temperature product using ground data: quantifying the site-to-pixel scaling uncertainty	450
Y. Yu, J.L. Privette and M. Chen	
Landsat ETM+ Thermal Band Calibration	456
J. A. Barsi, B. L. Markham, J. R. Schott, S. J. Hook and N. G. Raqueno	
Monitoring the spectral accuracy of AHS images	461
E. de Miguel, R. Rodríguez and O. Gutiérrez de la Cámara	
Relationship between evapotranspiration and rainfall variability in the Doñana region, Spain	466
M. García, N. Fernández and M. Delibes	
A remote sensing study of forests to estimate biophysical indicators and monitor CO2 fluxes in Spain: the ARTEMIS project	471
M.A. Gilabert, F. Maselli, B. Martínez, A. Moreno, F. Camacho, M. Chiesi, F.J. García-Haro, J. Meliá, A. Pérez-Hoyos and A. Verger	
Global Evapotranspiration for the 1981-2001 period from PAL database	477
V. Hidalgo, J. A. Sobrino, J. C. Jiménez Muñoz, Y. Julien, C. Mattar, B. Franch, G. Sòria, R. Oltra-Carrió and J. Cuenca	

Multi-scale estimation of vegetation and soil moisture in a Mediterranean wooded grassland (dehesa) using optical sensors	483
G. Mendiguren, M. P. Martín, D. Riaño, F. J. Martínez, J. Pacheco and L. Vilar	
Daily photosynthetic active radiation (PAR) images to estimate carbon fluxes at regional scale: A case study in Spain	489
A. Moreno, M. A. Gilabert and B. Martínez	
Remote sensing-based evapotranspiration estimates under semi-arid conditions. Comparing METRIC, MSSEBS, STSEB and HidroMORE	495
E. Rubio, R. G. Allen, A. Calera, V. Caselles, J. Colin, A. Osann, M. Menenti, J. M. Sánchez, M. Tasumi, E. Torres and R. Trezza	
Comparison of two models of evapotranspiration estimation using remote sensing and ground data collected at an agriculture experimental station	501
R. Tang, Z.-L. Li, Y. Jia, X. Sun and J. Lou	
Land surface soil moisture retrieval from temporal change of land surface temperature: a sensitivity study	507
W. Zhao and Z.-L. Li	
Assimilation of CYCLOPES LAI product within the SURFEX platform over France	513
A. L. Barbu, J.-C. Calvet and S. Lafont	
Application of remote sensing and GIS techniques on QUICKBIRD images to locate and distinguish wild pear (<i>Pyrus bourgeana</i>) in Sierra Morena (Cordoba, Andalusia, Spain)	518
S. Arenas, G. Sòria, C. Mattar, V. Hidalgo, R. Oltra-Carrió, B. Franch, Y. Julien, J. C. Jiménez-Muñoz, J. A. Sobrino, J. F. Haeger and D. Jordano	
Analysing wildfires in Valencia with the Haines Index and monitoring the natural regeneration with MODIS data	524
M. J. Barberà, R. Niclòs, M. J. Estrela and J. A. Valiente	
A New tool for information extraction and mining from satellite imagery available from Google Maps engine	529
S. Bernabé and A. Plaza	
MODIS-based remote sensing monitoring of the spatiotemporal patterns of China's grassland vegetation growth	535
X. Bin, Y. Xiuchun, T. Weiguo, M. Jianming, Y. Zhi, L. Haiqi, Q. Zhihao, L. Haiyan, J. Yunxiang, L. Jinya, Z. Xiaohua and L. Zhaoliang	
Application of artificial neural networks to the prediction of forest fire danger using MODIS data	540
M. Bisquert, E. Caselles, J. M. Sánchez, V. Caselles and E. Rubio	
Monitoring natural and anthropized vegetation trends using remotely sensed LAI MODIS in semi-arid region. Study case of agricultural systems of northwest Senegal	545
C. Bobée, C. Ottlé, F. Maignan and M. Ndiaye	
Discrimination of olive groves through object-based hierarchy classifications	551
I. L. Castillejo-González, A. García-Ferrer Porras, F. J. Mestas-Carrascosa, M. Sánchez de la Orden and F. López-Granados	
Monitoring water bodies over whole Africa in near real time: detection algorithms and preliminary results	557
R. D'Andrimont, J.-F. Pekel, E. van Bogaert and P. Defourny	
Land cover classification in Spain from seasonal trajectories of MODIS data	562
F. J. García-Haro and A. Pérez-Hoyos	
Assessment of vegetation response to climate variability in Spain	568
F. J. García-Haro, A. Moreno, A. Pérez-Hoyos, M. Gilabert, J. Meliá, F. Belda, D. Poquet, B. Martínez and A. Verger	

Synergy of ECOCLIMAP land cover and LSA SAF vegetation parameters F. J. García-Haro, A. Verger, J. L. Roujean, F. Camacho and J. Meliá	574
Global vegetation monitoring with NOAA-AVHRR data between 1981 and 2001 Y. Julien, J. A. Sobrino, F. González-Alonso, C. Mattar, J.-C. Jiménez-Muñoz, G. Sòria, V. Hidalgo, B. Franch, R. Oltra-Carrió and J. Cuenca	580
Pastoruri glacier cover mapping from Landsat and ASTER imagery J. J. Pasapera-Gonzales, C. Villon-Reinoso, R. D. Moreno, D. Pareja-Quispe, J. C. Jiménez-Muñoz, C. Mattar and J. A. Sobrino	586
Ecosystem functional characterization in the Iberian Peninsula A. Pérez-Hoyos, F. J. García-Haro, B. Martínez and M. A. Gilabert	591
Spatiotemporal dynamic of French forest phenology from MODIS and GLOBCARBON products J.-C. Samalens, D. Guyon, N. Bories, C. Moisy, J.-P. Wigneron	597
Dynamic mapping of cropland areas in Sub-Saharan Africa using MODIS time series C. Vancutsem, J.-F. Pekel and F. Kayitakire	603
A new 300 m vegetation map for Central Africa based on multi-sensor times series A. Verhegghen and P. Defourny	608
Size matters: the effect of urban vegetation patch size on surface temperature patterns along a urban-to-rural gradient in NW Argentina A. Gioia, L. Paolini, A. Malizia, R. Oltra-Carrio and J. A. Sobrino	614
Large-scale climatic influence on Sahelian vegetation dynamics S. Huber and R. Fensholt	616
Monitoring and forecasting the Urban Heat Island phenomenon in ten european cities: the UHI project P. Manunta, M. Viel, G. Ceriola, I. A. Daglis, K. De Ridder, T. Giannaros, I. Keramitsoglou, B. Maiheu, D. Melas, E. Montero Herrero, M. Paganini, M. Palacios, A. Radius, T. Sapage, M. Tamame and H. Tambuyzer	620
Characterization of marine benthic habitats located at the Puerto Morelos Reef National Park, México incorporating remote sensing data P.A. Zapata –Ramírez, H. Hernández – Nuñez, P. Blanchon and J.A Sobrino	626
Wheat yield monitoring in southern Spain using a series of satellite images F. Muñoz-Padilla, M.P. González Dugo, F. Mansilla, J. Domínguez and P. Gavilán	632
Surface urban heat island monitoring. The case study of Madrid (Spain), Athens (Greece) and San Miguel de Tucumán (Argentina) R. Oltra-Carrió, J. A. Sobrino, G. Sòria, J. C. Jiménez-Muñoz, C. Mattar, V. Hidalgo, B. Franch, Y. Julien and J. Cuenca.	638
Spatial distribution of air temperature measured in the framework of the DESIREX 2008 and Thermopolis 2009 Urban Heat Island Campaigns G. Sòria, J. A. Sobrino, J. C. Jiménez-Muñoz, R. Oltra-Carrió, C. Mattar, V. Hidalgo, B. Franch, Y. Julien and J. Cuenca	644
Generation of continuous rasters of climatological variables using geographic weighted regression L. Morales, J. C. Parra and J. Espinosa	649
STRS (Spectro-Temporal Reflectance Surfaces): a new conceptual framework for the integration of remote sensing data from multiple different sensors G. Villa, J. Moreno, A. Calera, J. Amorós, G. Camps, E. Domenech, P. Escobar, J. Garrido, J. González-Matesanz, L. Gómez-Chova, S. Luaces, J. A. Martínez, S. Molina, J. C. Ojeda, J. J. Peces, N. Plaza, A. Porcuna, J. A. Tejero and N. Valcarcel	654
Quality assessment of the first version of Geoland-2 biophysical variables produced at global scale F. Camacho, J. Cernicharo, F. Baret, R. Lacaze and M. Weiss	660

The GLOBCORINE land cover map – a joint EEA-ESA initiative for operational land cover mapping at pan-european scale	666
S. Bontemps, P. Defourny, E. van Bogaert, J.-L. Weber and O. Arino	
European Space Agency campaign activities in support of Earth Observation Projects	672
R. Bianchi, M. W. J. Davidson, C. Bouzinac and D. Schuettmeyer	
First evaluation of SMOS observations and Level-2 products over agricultural sites in temperate regions	678
J-P Wigneron, Y. Kerr, A. Mialon, N. Novello, F. Cabot, S. Delwart, F. Demontoux, M. J. Escorihuela, P. Ferrazzoli, A. Govind, J. P. Grant, D. Guyon, E. Jacqueline, H. Lawrence, E. Lopez-Baeza, A. Mahmoodi, C. Mattar, S. Mecklenburg, C. Moisy, S. Monerris, R. Rahmoune, P. Richaume, P. de Rosnay, C. Rüdiger, K. Saleh, M. Schwank, J. Sobrino and P. Waldteufel	
Satellite (Modis) against ground-based (Aeronet) AOD-ångström for various aerosol case studies over southwestern Spain: a complement to the previous evaluation of climatologies	684
Y.S. Bennouna, V.E. Cachorro, C. Toledano, A. Berjón, D. Fuertes, R. Gonzalez, R. Rodrigo, B. Torres and A. de Frutos	
Calibration of thermal infrared radiometer by optimization of spectral filter function	690
G. Brogniez, P. François and B. Damiri	
Consistency assessment of FVC and LAI operational products over Africa	694
F. Camacho, J. Cernicharo, J. García Haro, A. Verger and J. Meliá	
Integration of MSG-derived solar radiation maps with ground observations with a statistical copula model	700
L. Campo and F. Castelli	
Land surface temperature: towards the ideal dataset	706
E. Comyn-Platt, J.J. Remedios, E.J. Good, R. Saunders	
Cross-calibration of CBERS-02B/CCD with Terra/MODIS	712
C. Gao, X. Jiang, X. Li and X. Li	
Study of Remote Sensing Validation System	718
X. Jiang, X. Song, Z.-L. Li, X. Li, X. Xi, Z. Li and X. Li	
Cross-calibration of HJ-1 CCD with Terra Modis on Dunhuang observations	722
L. Ma, S. Qiu, X. Wang and L. Tang	
Evaluation of land surface temperature and emissivities retrieved from MSG-SEVIRI data with modis land surface temperature and emissivity products	728
Y.-G. Qian and Z.-L. Li	
First results towards building up a reliable in-situ measurements database for LST algorithms validations using modular WSN: Northern Morocco campaigns case study	734
N. Raissouni, J. A. Sobrino, A. Chahboun, N. Ben Achhab, M. Lahraoua, and A. Azyat	
Using several water vapor MODIS-NIR algorithms for retrieval of the surface water vapor pressure in the Iberian Peninsula. First results	740
C. Recondo, E. Pendás and R. Aguirre	
Validation of Imaging Infrared Radiometer (IIR) onboard CALIPSO during the CIRCLE-2 and VALIDATION-CALIPSO campaigns	745
O. Sourdeval, G. Brogniez, P. Dubuisson, F. Parol, L. Labonnote and J. Pelon	
Subsidence determination in the city of Valencia and its surroundings using RADAR interferometry	751
J. M. Delgado, F. Cian, A. B. Ruescas, F. Sarti, M. Datcu and R. Capilla	

Numerical modeling of the L-Band emission and scattering of a rough soil layer covered with a grass litter layer- consideration of Moisture and Temperature gradients	756
F. Demontoux, H. Lawrence, J.-P. Wigneron, A. Mialon, C. Duffour, A. Kruszwski, V. L. Mironov, L. G. Kosolapova and Y. Kerr	
Comparison between SMOS and VUA soil moisture products	760
D. Leroux, Y. Kerr, R. de Jeu, E. Wood and B. Berthelot	
Synergy of SMOS Microwave Radiometer, Thermal data and Vegetation Index for monitoring the water status of forest and natural vegetation	766
C. Mattar, J. A. Sobrino, J. P. Wigneron, Y. Kerr, A. Al-Bitar and N. Novello	
Sampling strategy for the validation of SMOS surface soil moisture at the Valencia Anchor station. Campaigns of 2008, 2009, 2010.	772
C. Millán-Scheiding; M. C. Antolín; E. Carbó; E. López-Baeza	
Application of GNSS-R Data Over the Valencia Anchor Station Site During the SMOS Validation Rehearsal Campaign 2008	776
A. Buil, V. Gomez Rubio, F. Fabra, E. Cardellach, A. Rius, C. Millan, E. Lopez-Baeza	
Estimation of TVDI (Temperature Vegetation Dryness Index) and its relation to soil moisture in the framework of the SMOS validation campaigns in the Valencia Anchor Station	780
M.A.Coll, E.López-Baeza	
Impact of atmospheric effects on the land surface brightness retrieval from AMSR-E data over the China continent	784
S. Qiu, Z. Liu and Z.-L. Li	
Characterization of sunflower, cotton and maize THROUGH AERIAL lidar data	789
E. Aguirre-Lora, I.L. Castillejo-González, A. García-Ferrer, F.J. Mesas-Carrascosa, J.E. Meroño de Larriva and M. Sánchez de la Orden	
Atmospheric aerosol characterization by lidar depolarization profiles	795
J.A. Bravo-Aranda, F. Navas-Guzmán, M.J. Granados and L. Alados-Arboledas	
Evaluation of fluorescence estimation using different methodologies at airborne and in situ level	801
B. Franch, J. A. Sobrino, V. Hidalgo, J. C. Jiménez-Muñoz, G. Soria, Y. Julien, R. Oltra-Carrió, C. Mattar and J. Cuenca	
Characterization of middle- and high-altitude clouds over Évora (Portugal)	807
J. L. Guerrero-Rascado, M. J. Costa, J. Preißler, F. Wagner and A. M. Silva	
Global Climatology of the of the Aerosol Extinction-to-Backscatter Ratio from Direct Irradiance Values of the AERONET Network	813
R. Pedrós, V. Estellés, J. L. Gómez-Amo, M. P. Utrillas and J. A. Martínez-Lozano	
Technological solutions of ScanEx company for remote sensing data acquisition and processing	819
D.Fedotkin and I.Farutin	
Defining the revisit frequency for the MISTIGRI project of a satellite mission in the thermal infrared	824
J.-P. Lagouarde, A. Olios, G. Boulet, B. Coudert, S. Dayau, S. Castillo, M. Weiss, J.-L. Roujean, E. Delogu and N. Puche	
Challenges and Solutions on the Development of the Ingenio/SEOSAT Mission Primary Payload	830
D. Zorita, J. I. Bueno, C. Miravet, L. Pascual, G. Taubmann, J. Azcona, J. M. Arroyo, I. Monasterio, U. García, J. Martín, J. Muñoz, A. López, J. Eguía, S. Jarabo, R. García, R. Navarro, T. Belenguer, L. M. González, C. Pastor, D. Arrazola, I. Cabeza and A. Marini	
Spanish National Remote Sensing Program, a way to achieve massive use of remote sensing data	834
J.J. Peces, G. Villa, A. Arozarena, J.A.Tejeiro, E. Domenech and N. Plaza	
Thermal Airborne Spectrographic Imager for Temperature and Emissivity Retrieval	840
L. Pipia, F. Pérez, A. Tardà, L. Martínez, V. Pala and R. Arbiol	

Spectral Measurements of Photosynthetic Efficiency	845
E. M. Middleton, Y.-B. Cheng, K. F. Huemmrich, Q. Zhang, P. K. E. Campbell, L. A. Corp, W. P. Kustas and H. A. Margolis	
Estimation of gross ecosystem production by hyperspectral measurements in terrestrial ecosystems	851
M. Rossini, M. Meroni, M. Migliavacca, S. Cogliati, L. Busetto, E. Cremonese, M. Galvagno, B. Gioli, F. Magnani, F. Miglietta, U. Morra di Cella, C. Siniscalco and R. Colombo	
Modelling vegetation fluorescence from single leaves and the canopy, observed on the ground and from space	857
W. Verhoef	

AUTHOR INDEX	863
---------------------	------------

FIGURES IN COLOUR

How Powerful are Radiative Transfer Models of the Land Surface? Applications and Challenges

Heike Bach

VISTA Remote Sensing in Geosciences GmbH,

Gabelsbergerstrasse 51, 80333 München, Germany

Email: bach@vista-geo.de

ABSTRACT - The application of radiative transfer (RT) models that allow the simulation of the reflectance on the land surface depending on surface properties and observation geometry has been evolving during the last years. Such applications start with sensitivity studies. Depending on the land surface property of interest the RT model simulates the change in spectral reflectance for this variable. The spectral ranges or indices with highest sensitivity can thus be selected. RT models that consider the anisotropy of the surface can be used to better understand the BRDF of the land surface. This allows the correction of the influence of variable observation geometries on the measured signal. RT models can use turbid media approximations or ray tracing techniques. In the examples presented here, the SLC (Soil-Leaf-Canopy) model, an extended version of the SAIL model family, is used. An application case of SLC is the simulation of realistic scenes of future optical sensors allowing tests of data processors and end-to-end mission performance. When the RT models are inverted, they are used for land surface parameter retrieval. A further step in such an inversion is that even the land use can be classified by testing for which land use the inversion provides a best result. The most complex application is the coupled ecosystem and reflectance modelling. By using data assimilation techniques the coupled land surface models are able to simulate also the spatial distribution of the carbon cycle in a realistic way.

1 INTRODUCTION

Common approaches to estimate vegetation parameters from optical remotely sensed data can be classified into explicit and implicit methods.

Implicit methods such as empirical or statistical approaches attempt to obtain a relationship between a vegetation parameter of interest (e.g. LAI measured in situ) and the leaf or canopy reflectance, or some form of vegetation index. The accuracy of the measurements and the range of conditions that were taken into account for the establishment of a relationship determine to a large extent the validity and transferability of the relationship (Sims and Gamon, 2002). Traditional techniques of linking spectral information to the variable of interest are Simple Regression or Multiple Regression techniques. More recent approaches include Artificial Neural Networks, Partial Least Squares Regression (PLS) and Modified PLS. A fundamental problem however of these implicit methods is their lack of generality, as they are mostly restricted to the prevailing conditions of the conducted study. For direct large-scale operational use and the application to different conditions or phenological seasons they are recognized as being inadequate (Houborg et al. 2007, Meroni et al. 2004).

Explicit methods are physically based approaches involving the use of radiative transfer or canopy reflectance models. Using physical laws, they attempt

to provide an accurate description of the transfer and interaction of radiation at the soil surface, inside the leaves and the canopy. The complexity of these models ranges from simple non-linear to complex radiative transfer models in realistic three-dimensional vegetation canopies. A lot of studies at leaf scale use the model PROSPECT (Jacquemoud and Baret, 1990). For simulations on canopy scale, leaf scale models are often coupled with canopy scale radiative transfer models, like KUUSK (Kuusk, 1998). Most studies operate with the SAIL (Scattering by Arbitrarily Inclined Leaves) model developed by Verhoef (1985) or modified versions of the SAIL model such as SLC (Verhoef and Bach, 2007).

Figure 1 illustrates the application of implicit, statistical approaches in comparison to modelling approaches as a result of a recent literature review conducted by VISTA that compiled 140 peer-reviewed papers dealing with hyperspectral approaches for agricultural applications. Obviously the simple statistical approaches still dominate in agricultural research. Transferable, generally applicable or automated procedures for agricultural information retrieval from optical data require however the application of RT models. The state of the art in the forward mode of these models is already well developed. The fact that these models are still not widely used (see Fig. 1) might be caused by their complex nature. Easy to use and user friendly model tools might be a solution to overcome this acceptance

problem. Also, reliable inversion schemes are still sometimes lacking.

This paper tries to demonstrate the large potential of RT models for a wide range of applications in order to give motivation for their more intensive use.

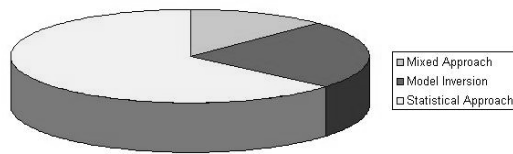


Figure 1: Application of statistical approaches versus RT modelling approaches based on a literature review

2 APPLICATIONS OF RT MODELS

The examples shown here are using the SLC land surface reflectance model. SLC stands for “Soil Leaf Canopy” and is a recent extension of SAIL to account for heterogeneous canopies by allowing the simulation of two spatial layers with different optical properties. Leaf transmittance and reflectance are simulated with the PROSPECT approach. Incomplete vegetation coverage of the canopy is considered in SLC by applying a non-linear mixing of background and vegetation cover. Additionally, a flexible soil background model is integrated in SLC that also considers soil BRDF and moisture effects. (Verhoef and Bach, 2003 and 2007)

2.1 Sensitivity studies

Sensitivity studies using RT models can be used to define the best set of spectral bands for multispectral acquisitions. Depending on the land surface property of interest (e.g. LAI, albedo, moisture) the RT model simulates the change in spectral reflectance for this variable and the spectral ranges with the highest response can be selected. These simulations also help to define the most sensitive spectral indices from hyperspectral data (Haboudane et al. 2002) which can be related for example to chlorophyll or water content.

Sensitivity studies of the retrieval performance are further possible. They allow e. g. analysing the impact of the spectral configuration of a sensor on the uncertainty of parameter retrieval. Spectral signatures are simulated with SLC for a large set of combinations of land surface properties (variable LAI, leaf chlorophyll content and fraction of dead leaves in the canopy). The RT model is then inverted using these simulated spectra as input and the retrieved land surface properties compared to the ones used as input. This pure model approach allows a systematic

accuracy assessment of the parameter retrieval. When different optical sensors are simulated, their retrieval performance can be compared.

Figure 2 shows results for such an assessment for the retrieval of LAI using simulated LANDSAT TM data (top) and RapidEye data (bottom) as scenario. Mean values and the standard deviation of inverted LAI values based on hundreds of simulation runs were calculated for the respective LAI input. The 6 optical Landsat TM bands covering the visible to shortwave infrared (SWIR) obviously allow an accurate retrieval of the LAI. Up to an LAI of 5 the theoretical retrieval accuracy is excellent. RapidEye has 5 bands but is limited to the visible and near infrared spectral range.

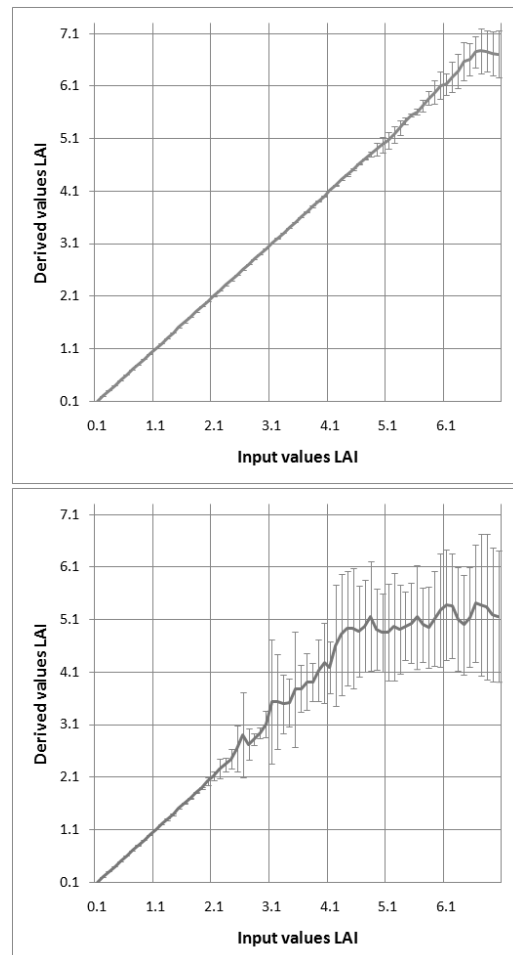


Figure 2: Accuracy assessment of parameter retrieval for LAI based on simulated reflectances of different sensors (top: Landsat TM, bottom: RapidEye)

This sensitivity study illustrates that parameter retrieval of LAI is less accurate for RapidEye. This can be explained by the missing of SWIR bands which causes an increase in retrieval error already with LAI values of 3. The RT simulation thus allows studying and assigning uncertainty values for the inversion process depending on sensor characteristics.

2.2 Improved understanding of the spectral BRDF

RT models that consider the anisotropy of the surface can be used to better understand the BRDF of the land surface. The BRDF describes the deviation from an ideal reflector for which reflectance is the same for each observation angle. Knowledge of the BRDF enables the correction of the influence of variable observation geometries on the measured signal. This is of special importance if sensors with pointing capabilities (like SPOT) or wide swaths (for example Sentinel 3) are used.

Bach et al. 2006 showed that sensors like CHRIS allow deriving typical BRDF features from reflectance measurements of 5 observation angles. These features can be related to the phenological development of the observed crop. It could be shown that the BRDF effect increases when a wheat crop matures. This BRDF behaviour could be simulated with SLC by changing the average leaf inclination angle which again was in agreement with field observations since the dominance of stems and heads increases with maturity,

while the leaf area reduces due to crumbling of the dry leaves. As a result, the RT model can be optimised for wheat by considering the phenological status of the crop. Using the correct average leaf angle is a basis for accurate leaf area determination.

2.3 Parameter retrieval of bio-geophysical information

In order to use physically based models for the retrieval of vegetation characteristics from observed reflectance data, they have to be inverted. For model inversion, different techniques have been proposed. The most dominant are numerical optimization methods, look-up table (LUT) approaches, artificial neural networks and recently support vector machines regression. A drawback of the numerical optimization approach is that it cannot always guarantee a stable and optimum inversion, as the search algorithm may get trapped in local minima before reaching the global minimum. Look up tables on the other hand are limited by the available computer memory, since their sizes increase fast with increasing number of variables and smaller increments.

2.4 Model-supervised land use classification

A further step in such a parameter retrieval is that even the land use can be classified by testing for which land use class - which is characterised with a land use specific parameter set and valid ranges for dynamic

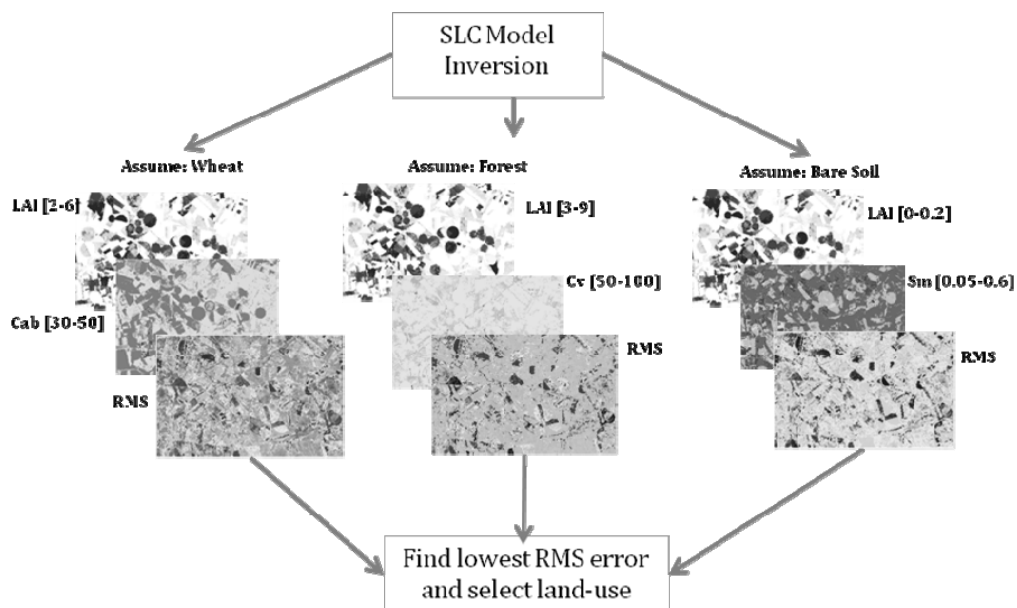


Figure 3: Concept of model-supervised land use classification

variables like LAI - the inversion provides a best result. Using multitemporal evaluations and knowledge on crop phenological developments, very detailed classifications are possible in an unsupervised way. Thus the RT model based approach opens up new automatic land cover classification possibilities.

SLCCLASS (Migdal et al., 2010b) aims at such an automated land-use classification. It is an unsupervised classification system that allows for a direct allocation of the spectral information to meaningful land-use classes, and also for a combined retrieval of land-use and canopy variables like leaf area index, chlorophyll content and fraction of dead leaves. This means that the classification is based on the physical principles behind the spectral behaviour of the different land-use classes expected in the region and is independent of subjective decisions about class membership by the user.

The inversion of the model allows for each land-use class only specific ranges for selected canopy parameters. A priori knowledge about the phenological status of the crops in the target area at the time of image acquisition is used to constrain the parameter space. In a first step, the best fitting variable combination for each land-use is found using the RMS error as a best fit criterion. In a second step from the resulting RMS values of all the land-use classes the lowest overall RMS error is selected (compare Fig. 3). This land-use class is the one that fits best to the measured value. This is done for all pixels in the image, resulting in a mono-temporal land-use classification. Certainly the accuracy of the classification increases when repeating the procedure on multitemporal acquisitions and making use of the typical temporal phenological dynamics.

2.5 Scene simulations of future sensors

The approach of parameter retrieval is adaptable to different sensors. That makes it almost universally applicable. It can even be used to simulate sensors that are still in the planning phase. Scene simulations of future sensors help to optimize the technical specifications of the sensor, test the level 1 and 2 processors, allow checking of the end-to-end mission performance and can provide first test data for the science community.

The approach (Verhoef and Bach, 2007) uses textural files of bio-geophysical information retrieved from existing satellites and allows the simulation of realistic scenes with new spectral features like ENMAP (hyperspectral) (Migdal et al. 2010a) or new observation geometries like Sentinel 3 (large swath).

2.6 Coupled ecosystem and reflectance modelling

Coupled ecosystem and reflectance modeling gives the opportunity to simulate not only singular satellite image acquisitions but also their temporal dynamic change. Land surface variables, like leaf area index are updated daily using a crop growth model and the daily change of soil moisture which results from water balance simulations. These two variables have the most influence on the change of spectral reflectance with time.

Whenever a satellite acquisition is possible the measured reflectance signatures can be used to update the simulated variables. Figure 4 illustrates such a data assimilation process.

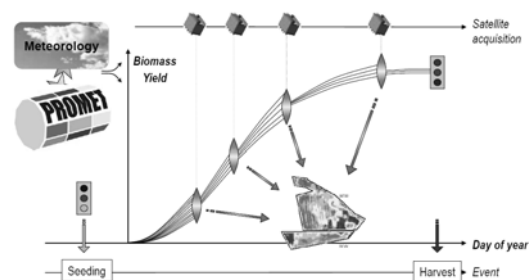


Figure 4: Concept of data assimilation of crop variables derived from remote sensing in a crop growth model

Migdal et al. (2009) could demonstrate how such a data assimilation improved the spatial simulation of crop growth and thus of the carbon cycle.

3 CHALLENGES

Besides these applications, recent challenges for the application of RT model shall also be highlighted. The optimum selection of the plant pigments in the leaf model is still not perfectly solved. The inversion techniques have challenges connected to the ill-posedness of the inversion problem and the a priori information that is required for stable inversion results. Also the computational performance of the inversion still requires improvements. The integration of the fluorescence signal in the RT simulation is recently evolving, but needs application tests. Further, the coupled ecosystem and RT modelling is in a starting phase and assimilation techniques into process models are presently central research topics.

4 REFERENCES

- Bach, H., Begiebing, S., Verhoef, W., 2006, Application of the canopy reflectance model SLC for parameter retrieval of wheat based on CHRIS and AVIS data, *Proceedings RAQRS'2006, Second Recent Advances in Quantitative Remote Sensing* (ed. J. Sobrino), pp.278-283.
- Haboudane, D., Miller, J. R., Tremblay, N., Zarco-Tejada, P. J. and Dextraze, L., 2002, Integrated narrow-band vegetation indices for prediction of crop chlorophyll content for application to precision agriculture, *Remote Sensing of Environment*, 81, pp. 416-426.
- Houborg, R., Soegaard, H. & Boegh, E., 2007, Combining vegetation index and model inversion methods for the extraction of key vegetation biophysical parameters using Terra and Aqua MODIS reflectance data, *Remote Sensing of Environment*, 106, pp. 39–58.
- Jacquemoud, S. and Baret, F., 1990, PROSPECT: a model of leaf optical properties spectra, *Remote Sensing of Environment*, 34, pp.75-91.
- Kuusk, A., 1998, Monitoring of vegetation parameters on large areas by the inversion of a canopy reflectance model, *International Journal of Remote Sensing*, 19(15), pp. 2893–2905.
- Meroni, M., Colombo, R. & Panigada, C., 2004, Inversion of a radiative transfer model with hyperspectral observations for LAI mapping in poplar plantations. *Remote Sensing of Environment*, 92, pp. 195–206.
- Migdall, S., Bach, H., Bobert, J., Wehrhan, M. & Mauser, W., 2009, Inversion of a canopy reflectance model using hyperspectral imagery for monitoring wheat growth and estimating yield, *Precision Agriculture*, 10, pp.508-524.DOI 10.1007/s11119-009-9104-6.
- Migdall, S., Bach, H., Kaufmann, H., 2010a, Simulation of EnMAP-like Hyperspectral Images Based on Textural Information and a Radiative Transfer Approach; *Proc. 'Hyperspectral 2010 Workshop'*, Frascati, Italy, 17–19 March 2010, ESA SP-683.
- Migdall, S., Hausknecht, B., Bach, H., 2010b, SLCCCLASS – a model-based unsupervised land-use classification system; *Proceedings ESA Living Planet Symposium*, Bergen, 2010, in print
- Sims, D. and Gamon, J., 2002, Relationships between leaf pigment content and spectral reflectance across a wide range of species, leaf structures and developmental stages. *Remote Sensing of Environment*, 81, p. 337–354.
- Verhoef, W. and Bach, H., 2007, Coupled soil–leaf–canopy and atmosphere radiative transfer modeling to simulate hyperspectral multi-angular surface reflectance and TOA radiance data. *Remote Sensing of Environment*, 109, 166–182.
- Verhoef, W. and Bach, H., 2003, Simulation of hyperspectral and directional radiance images using coupled biophysical and atmospheric radiative transfer models, *Remote Sensing of Environment*, 87, pp.23-41.
- Verhoef, W., 1985, Earth observation modeling based on layer scattering matrices. *Remote Sensing of Environment*, 17, pp.165–178.

Modelling reflectance of partially submerged canopies

M.E. Beget^{a1}, C.M. Di Bella^{a2}, F. Baret^{b3}, J.-F. Hanocq^{b4}

^aCNIA-INTA, Hurlingham, Buenos Aires, Argentina; ^bINRA EMMAH UMR1114, Avignon Cedex 9, France

¹mbeget@cnia.inta.gov.ar, ²cdibella@cnia.inta.gov.ar, ³baret@avignon.inra.fr,

⁴hanocq@avignon.inra.fr

ABSTRACT - Flooded areas, such as natural grasslands, wetlands and rice crops are an important source of ecosystem goods and services and remote sensing techniques provide valuable tools to characterize them at different temporal and spatial scales. Radiative transfer models inversion is one of the available methodologies for biophysical variables estimation. However, particularly situations, as flooded environments, require special attention using remote sensing as water modifies the spectral response of vegetation covers. The aim of this paper was to develop a radiative transfer model for partially submerged vegetation called SAILHFlood. The model simulates reflectance for a partial or totally submerged canopy from vegetation variables, water level, acquisition geometry and soil reflectance. The model is based on SAILH, and includes two layers, one emerged vegetation layer, and one submerged vegetation layer below, for which the attenuation of radiation by water is considered. Additional inputs from SAILH model are submerged and emerged leaf area index and water level. The model validation was performed comparing results to those obtained in controlled experiment. Simulated data fitted measured data satisfactorily and even better if considering MODIS sensor bands. The root mean square error (RMSE) obtained was 0.067, and the spectral angle was 0.31 radians. The model could be applied to the diversity of vegetation flooded situations, both to understand spectral behavior of these environments under different scenarios and to estimate vegetation variables from model inversion. Further work will be addressed in field validation over natural flooded areas and rice crops for both direct and inverse mode.

1 INTRODUCTION

Radiative transfer modelling techniques had been developed and improved for more than two decades, in contribution to the understanding of biophysical processes that determine canopy reflectance.

One of the most popular canopy reflectance model, the *SAILH* model, was developed by Verhoef (1984, 1985) and improved by Kuusk (1995). It has been widely used in combination with a leaf optical properties model (PROSPECT) for vegetation characterization (Jacquemoud *et al.* 2009). *SAILH* model is based on Suits model (1972). Suits model describes scattering and extinction of four upward and downward fluxes assuming plant canopy as turbid medium. Relations between fluxes are expressed as four linear differential equation system, with nine coefficients which give solution to the radiative transfer equation.

Top of canopy reflectance is described as a function of canopy architecture (leaf area index, leaf angle distribution and relative leaf size), configuration geometry (sun and sensor position) and leaf and soil optical properties.

Although the *SAILH* model was improved to cover several aspects of vegetation it had not yet included the presence of surface water. Considering the importance of the flooded areas, such as natural grasslands, wetlands and rice crops, in the provision of ecosystem goods and services, there was the concern of extending the modeling to these systems. Modelling in flooded environments requires special attention as water modifies the spectral response of vegetation covers. The aim of this paper was to develop a radiative transfer model for partially submerged vegetation called SAILHFlood.

2 MATERIALS AND METHODS

2.1 Model description

SAILHFlood is composed of stacked horizontal layers (Figure 1). Bottom layer is considered a lambertian soil and above it, there is a layer of submerged vegetation, where energy propagation medium is water. Top layer consists of the portion of the vegetation that is above the water surface, emerged vegetation. The surface water is considered as an interface that interacts with energy fluxes by changing

their direction due to the difference in refractive indices of both media (Hecht 2000).

Emerged vegetation reflectance is computed by *SAILH* model (see Verhoef 1984, 1985). Interface reflectance matrix is considered as the background reflectance matrix, since upward incoming radiation is the downward radiation reflected by soil and transmitted upward by the submerged vegetation and by the interface. *LAI* used for computation of coefficients that provide solution to the radiative transfer equation is only the emerged. Air-water interface is not considered as a layer itself because of its negligible thickness. Although its effect is exclusively associated to change in fluxes direction by Snell's Law due to the shift of propagation medium.

Submerged vegetation layer receives direct and diffuse fluxes transmitted downward by the emerged vegetation layer and by the interface. They become incident fluxes for the submerged vegetation and layer reflectance is computed considering soil as background. Reflectance and transmittance coefficients of scattering matrix are modified taking account of water optical properties.

Model inputs are *SAILH* model inputs and additionally, submerged and emerged leaf area index and water level.

From additive method (van de Hulst 1980; Cooper *et al.* 1982) is it possible to calculate reflectance of top of one layer stacked of finite height. This method supposes canopy total reflectance is the sum of vegetation layer reflectance and soil reflectance after a number of interactions between vegetation and soil (Kallel *et al.* 2007). This proceed was used to compute reflectance of top of canopy considering emerged vegetation layer (VE), air-water interface (I), submerged vegetation layer (VS) and soil (S). Following the additive method, from bottom to top layer, layer reflectance matrices are defined as:

$$\begin{aligned} R_t^{VS+S} &= R_t^{VS} + T_u^{VS} (Y - R_t^{VS} R_b^{VS})^{-1} R_t^S T_d^{VS} \\ R_t^{I+VS+S} &= R_t^I + T_u^I (Y - R_t^{VS+S} R_b^I)^{-1} R_t^{VS+S} T_d^I \\ R_t^{VE+I+VS+S} &= R_t^{VE} + T_u^{VE} (Y - R_t^{I+VS+S} R_b^{VE})^{-1} R_t^{I+VS+S} T_d^{VE} \end{aligned} \quad (1)$$

Reflectance and transmittance matrices are represented as *R* and *T* respectively, sub-indices *t* and *b* represent top and bottom reflectance, respectively, and *u* and *d* represent upward and downward flux transmittance, respectively. *Y* means identity matrix. Top of emerged canopy reflectance $R_t^{VE+I+VS+S}$ equals total canopy reflectance.

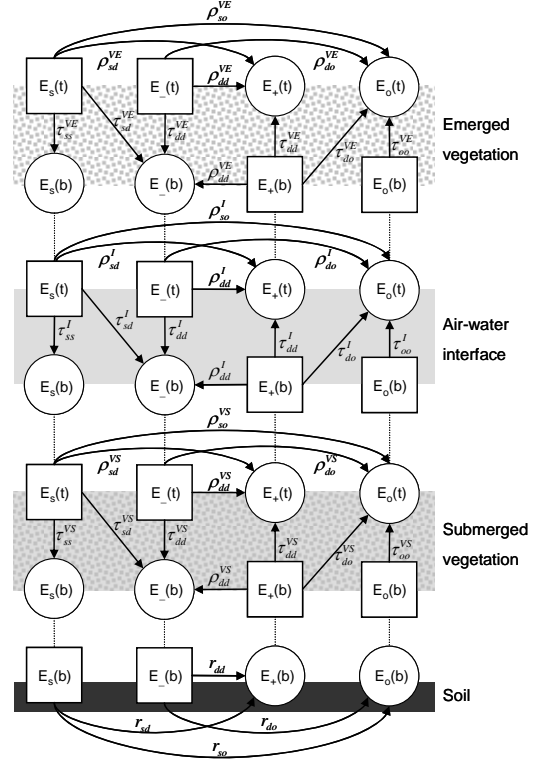


Figure 1. Downward and upward flux interaction for the combination of soil, submerged vegetation and emerged vegetation layer of *SAILHFlood* model. Squares and circles represent incidents and outwards fluxes respectively (*E_o* direct solar irradiance, *E₋* diffuse downward irradiance, *E₊* diffuse upward irradiance, *E_o* radiance in the observer radiation). Reflectance and transmittance coefficients show fluxes interactions. Sub-indices indicate incident and outward flux type: direct solar (*s*), in the observer direction (*o*), or diffuse (*d*). Soil reflectance coefficients are denoted by *r*.

2.2 Experimental design

One experiment was setup to test model performance. Shoots of *Pittosporum tobira* L. were collected outside on the trees and ‘planted’ in an artificial soil to simulate a canopy of 12 cm height. In order to represent flooded situations, ‘plants’ were inside a container. Five leaf area index levels were generated ‘planting’ an increasing density of shoots over the substrate (*LAI*= [0.7 1.2 1.7 3.5 5.2]).

Reflectance measurements were performed indoor using a 2000 watts halogen projector plugged into a stabilized power source and placed at 10-15 m from the ‘canopies’ to get better collimated light beam over the sampled area. Reflected radiation measurements were acquired with an ASDFieldSpec©

spectroradiometer equipped with a 8° FOV lens in the 400-2400 nm range with a 1 nm of spectral sampling interval. Calibrations were made frequently using a Spectralon Labsphere® reference panel to get absolute reflectance values.

Measurements were made for three incidence angles ($\theta_s = [8^\circ \ 30^\circ \ 60^\circ]$) for 9 viewing zenith angles ($\theta_v = [-60^\circ \ -45^\circ \ -30^\circ \ -15^\circ \ 0^\circ \ 15^\circ \ 30^\circ \ 45^\circ \ 60^\circ]$) in the principal plane (relative azimuth angle, $\phi_s - \phi_v = 0^\circ$). Measurements were replicated 30 times from which the average was computed. The series of directional measurements were achieved over the 5 canopies with different LAI with 3 depths of water ($h = [0 \ 5 \ 13\text{cm}]$) resulting in 15 canopy cases.

2.3 Data comparison

Model evaluation was performed through the comparison of simulated data to measured data. Data were compared by terms of root mean squared error (*RMSE*, Equation 2) and spectral angle (*SA*, Equation 3):

$$RMSE = \sqrt{\frac{1}{N} \sum_{i=0}^{N-1} (\overline{R_{sim}} - R_{meas})^2} \quad (2)$$

where R_{sim} and R_{meas} are simulated and measured spectra, respectively, and N the spectral bands considered. The spectral angle between two spectra is the difference angle between two vectors in m -dimensional space, where m is the number of available spectral bands. The vectors are given by the reflectance value of the first spectrum in the bands i and j ($x1, y1$) and the reflectance value of the second spectrum in bands i and j ($x2, y2$). The spectral angle is calculated in radians as:

$$SA = \cos^{-1} \left(\frac{sim(\lambda) \cdot meas(\lambda)}{\|sim(\lambda)\| \cdot \|meas(\lambda)\|} \right) \quad (3)$$

where λ is the wavelength range for m band, and $sim(\lambda)$ y $meas(\lambda)$ are simulated and measured spectra respectively. *RMSE* values give idea of similarity in the magnitude of reflectance, while *SA* is associated to similarity in shape of spectra.

3 RESULTS AND DISCUSSION

The model validation was performed comparing results to those obtained in the controlled experiment. Simulated data fitted measured data satisfactorily. The averaged root mean square error (*RMSE*) obtained for

hyperspectral bands was 0.067, and the spectral angle was 0.31 radians. The correlation (86%) and *RMSE* obtained between simulated and observed data are comparable with those obtained by other authors. Model performed better considering *MODIS* sensor bands (Figure 2).

While *SAILHFlood* model incorporates two new variables to the *SAILH* model (water level and submerged leaf area index), it did not show an increase in error with respect to the simulations without the presence of water.

In general, simulated reflectance was more similar to measured in terms of magnitude than shape. Although several authors used *SA* as a methodology to compare spectra in satellite images classification or model inversion (Debba *et al.* 2005; Yebra *et al.* 2008), we found no threshold decision value to be compared with those found in this case. Results indicated that the simulated spectra show greater similarity to those observed in terms of shape, were those for the partially submerged canopies and those without water (water level 5 and 0 cm respectively). No flooded situation also showed lower values of *RMSE*, resembling more on the magnitude of spectra. In contrast, in the case of completely submerged canopies, the spectra were more similar in magnitude but variable in terms of similarity in shape.

Model performance was not related to the magnitudes of the input variables. That is, the *RMSE* was not related to leaf area index, observation and illumination zenith angles or water level. This becomes important for application of model inversion to diversity of flooded vegetation situations and available sensors.

4 CONCLUSIONS

A radiative transfer model for partially submerged vegetation called *SAILHFlood* was developed and successfully tested on *MODIS* bands. The model could be applied to the diversity of vegetation flooded situations, both to understand spectral behavior of these environments under different scenarios and to estimate vegetation variables from model inversion. Further work will be addressed in field validation over natural flooded areas and rice crops for both direct and inverse mode.

5 ACKNOWLEDGMENTS

This work was supported by projects PICT 32415 (ANPCyT) and AERN4-AERN4642 (INTA) and by INRA EMMAH.

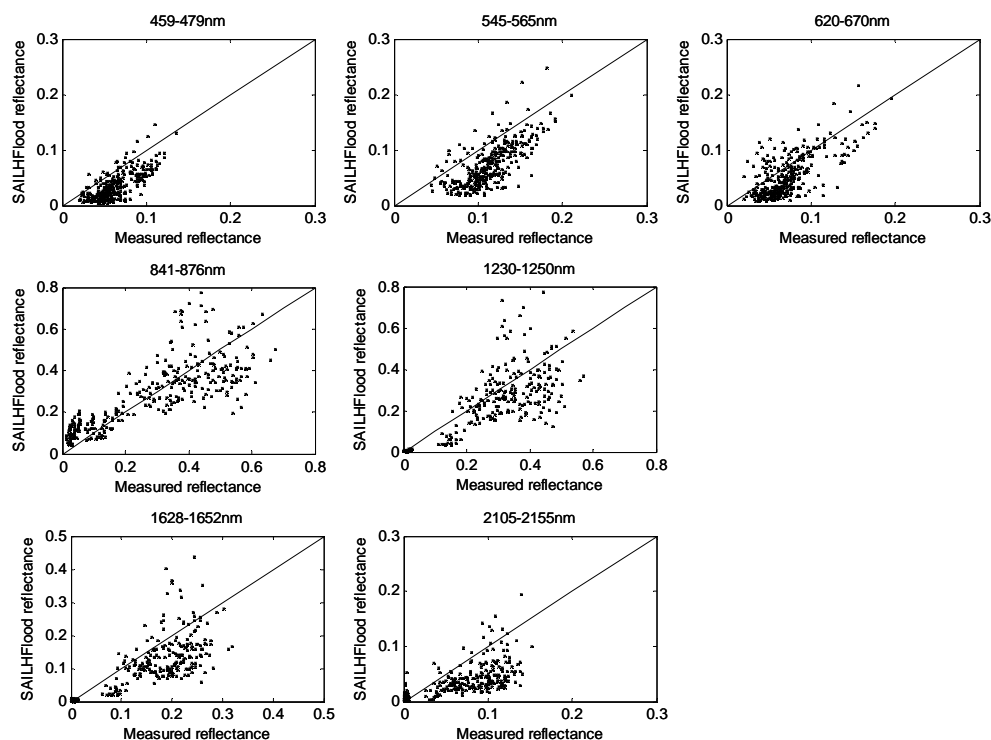


Figure 2. Comparison between modelled by SAILHFlood and measured reflectance for MODIS bands. Spectral response for MODIS bands were calculated from measured hyperspectral data (400-2400 nm).

6 REFERENCES

- Debba, P., van Ruitenbeek, F.J.A., van der Meer, F.D., Carranza, J.M. and Stein, A., 2005. Optimal field sampling for targeting minerals using hyperspectral data. *Remote Sensing of Environment* 99, 373-386.
- Hetch, E., 2000. *Óptica*. Pearson (Ed.). 720 pp.
- Jacquemoud, S., Verhoef, W., Baret, F., Bacour, C., Zarco-Tejada, P.J., Gregory, P., Asner, François, C., Ustin, S.L. 2009. PROSPECT+SAIL models: A review of use for vegetation characterization. *Remote Sensing of Environment*, 113, S56-S66.
- Kallel, A., Le Hégarat-Masclé, S., Ottlé, C. and Hubert-Moy, L. 2007. Determination of vegetation cover fraction by inversion of a four-parameter model based on isoline parametrization. *Remote Sensing of Environment*, 111, 553-566.
- Kuusk, A., 1985. The hot spot effect of a uniform vegetative cover. *Sovietic Journal of Remote Sensing* 3, 645-658.
- Suits, G. H., 1972. The calculation of the directional reflectance of a vegetative canopy. *Remote Sensing of Environment*. 2, 117-125.
- van de Hulst, H. C. (1981). Light scattering by small particles. New York: Dover Publications, Inc.
- Cooper, K., Smith, J. A. and Pitts, D., 1982. Reflectance of a vegetation canopy using the adding method. *Applied Optics*, 21(22), 4112-4118.
- Verhoef, W., 1984. Light scattering by leaf layers with application to canopy reflectance modeling: the SAIL model. *Remote Sensing of Environment*, 16, 125-141.
- Verhoef, W., 1985. Earth observation modeling based on layer scattering matrices. *Remote Sensing of Environment*, 17, 165-178.
- Yebra, M., Chuvieco, E. y Riaño, D. (2008b). Estimation of live Fuel Moisture Content from MODIS images for fire risk assessment. *Agricultural and Forest Meteorology*, 148: 523-536.

Approximating the average daily surface albedo with respect to soil roughness and latitude

Jerzy Cierniewski^{1*}, Arnon Karnieli², Krzysztof Kuśnierek¹ and Ittai Herrmann²

¹ Institute of Physical Geography and Environmental Planning, Adam Mickiewicz University, 61-680 Poznań, Poland

² The Remote Sensing Laboratory, Jacob Blaustein Institutes for Desert Research, Ben Gurion University of the Negev, Israel

*Corresponding author: ciernje@amu.edu.pl

ABSTRACT The current study explores the diurnal of blue-sky albedo (α) of soils under clear sky condition with respect to the surface roughness. Three roughness levels were examined – smooth, moderate, and rough – on the same loessial soil material, located on cultivated and uncultivated areas in the Negev Desert, Israel. The α of the surfaces was measured by an albedometer LP PYRA 06 in a spectral range of 0.335-2.200 μm . Roughness was measured using a Konica-Minolta VIVID-910 laser scanner. The relation between α of the surfaces and the solar zenith angle, determined in the measuring experiment, enabled us to predict the diurnal α variation of the surfaces during the whole year at given latitude between 75° S to 75° N. Also calculated the optimal time (T_o) for measuring the soil albedo, acquired by its instantaneous observation, is defined as the best represented time for the daily averaged value, within an error lower than $\pm 2\%$. The measured data show that the optimal time for evaluating the average daily soil albedo $\bar{\alpha}$ falls at different time depending on the roughness of the studied soil surfaces. The strongly defined time for evaluation of the average daily soil surface albedo of different roughness limits possibilities of the data achievement by remote sensing satellites along one of their sun-synchronous orbits.

1 INTRODUCTION

Surface albedo is the ratio, expressed as a fraction or percentage, of the amount of outgoing electromagnetic radiation reflected by the earth's surface to the amount incident upon it. Year-around variations of soils albedo values, generated by the hemispherical-directional reflectance model, from midday to sunset under clear sky conditions in different latitudes, are presented in Cierniewski and Gdala (2010). These data are predicted for virtual surfaces representing the smooth, moderately and very rough soils, located between 75° S to 75° N latitude. As supplementary material to the Cierniewski and Gdala (2010) results, the objective of the current letter is to explore the relation between the broad band blue-sky soil albedo and the solar zenith angle, based on field measurements under clear sky conditions.

2 METHODS

Measurements were conducted on soil surfaces in the Israeli Negev desert, near Sede Boker in Israel (30°51'26"N, 34°47'09"E). The area is characterized by loessial substrate (Issar *et al.*, 1984). Specifically, the study was carried out over uncultivated and cultivated fields with three levels of surface roughness

– smooth, moderately rough (after shallow plowing), and very rough (after deep plowing) (figure 1).

The blue-sky albedo of the soil surfaces was measured by an albedometer LP PYRA 06 in a spectral range of 0.335 - 2.200 μm . The instrument, consists of two, down-facing and up-facing, LP PYRA 03 pyranometers, was installed at 2 m above the ground. Data were recorded by a Campbell Scientific 21x datalogger.

Surface roughness of the three surfaces was measured by using a Konica-Minolta VIVID-910 laser scanner. The scanner was placed on a tripod that was moved around to read a 1 m² plot from four different directions. Due to the scanner's working conditions, the 3D measurements were conducted at night using fluorescent lamp.

The textural composition of the soil surface material was analyzed in laboratory using a hydrometer, the organic carbon content by Walkley Black's method, calcium carbonate equivalent by Piper's method and the total "free" iron oxide by CDB method of Mehra and Jackson (Sparks *et al.*, 1996).

3 RESULTS AND THEIR DISCUSSION

Soil properties that significantly influence the reflectance features are very similar for all the tested surfaces (table 1).

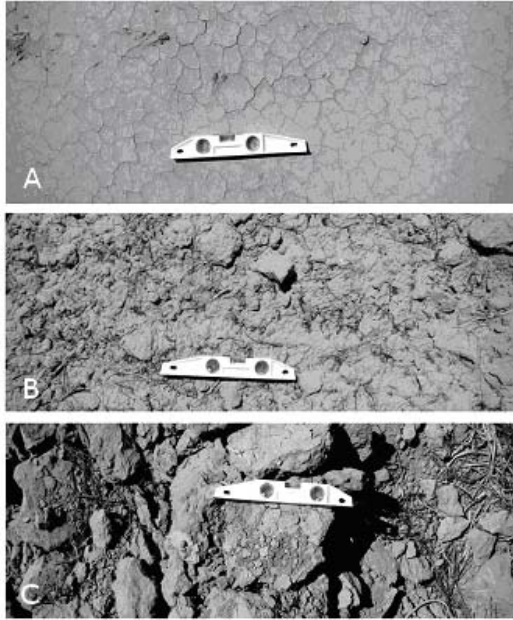


Figure 1. View of the tested soil surfaces - (A) smooth, (B) moderately rough, (C) rough. A level of 30 cm for referencing.

DEM of all of the surfaces, computed from the 3D scanner data with 1 mm horizontal and vertical spatial resolution, was used to quantitatively characterize the shape of the studied surfaces using the following indices: the height standard deviation (HSD), the ratio of the total surface area to the total projected area (RTS), the height variogram range (RHV), and sill parameters (SHV) (table 2).

Table 1. Properties of the tested soils with the smooth (S), moderately rough (M) and very rough (R) surfaces.

Soil properties	S	M	R
Sand (2-0.05mm) (%)	45	46	48
Silt (0.05-0.002mm) (%)	45	42	40
Clay (<0.002mm) (%)	10	12	12
Organic carbon (%)	0.5	0.87	0.92
CaCO ₃ (%)	30.7	30.1	28.1
Fe ₂ O ₃ (%)	1,48	1,51	1.52
Munsell dry color	10YR7/4	10YR7/4	10YR7/4

Table 2. Values of shape indices for the studied surfaces: smooth (S), moderately rough (M), and very rough (R).

Shape indices	S	M	R
HSD (mm)	0.54	10.43	46.73
RTS	1.01	1.2	1.72
RHV (mm)	101.69	572.57	1017.35
SHV (mm ²)	0.3	101.34	1017.35

The measurements of the blue-sky albedo of the surfaces were carried out on August 8-12, 2008 under clear sky conditions from local noon to sunset in one minute intervals. Variation of the measured blue-sky albedo α as the function of the solar zenith angle θ_s is presented in figure 2.

The measured albedo data are demonstrated on the background of the analogous relation, but predicted by the hemispherical-directional reflectance model using the virtual surfaces discussed in Cierniewski and Gdala (2010). The measured curves behave in a similar way, but their distributions are not as parallel as the modeling ones.

The soil albedo distribution measured for the moderately rough surfaces is treated in the further analysis as the base pattern to compare modeling and measured effects of soil surface roughness on the optimal time for the average daily soil albedo approximation. The authors showed that the roughness of the virtual surfaces does not influence the optimal time T_o of the average daily soil albedo approximation. To show how the measured soil albedo distributions in the θ_s function, different from their modeling equivalents, can change the previous findings concerning the T_o of soil surfaces in context of their roughness, the same procedure was used. The optimal time T_o was re-calculated in 5 minutes intervals and 5° latitude increments in the Northern (NH) and Southern Hemispheres (SH) between the latitude L angles of 75° for the same four dates of 2000 year: 21 March, 16 April, 07 May, 22 June. Figure 3 shows that the optimal time calculated for the real surfaces depends on their roughness. The differences in the optimal time between the extremely rough and smooth surfaces, are expressed as relative to the optimal time for the moderately rough one.

In Cierniewski and Gdala (2010), the optimal time for achieving the average daily soil albedo for surfaces in the latitude function was considered with its accuracy error ε lower than $\pm 2\%$ as the required accuracy for global climate modeling, determined by Sellers *et al.* (1995).

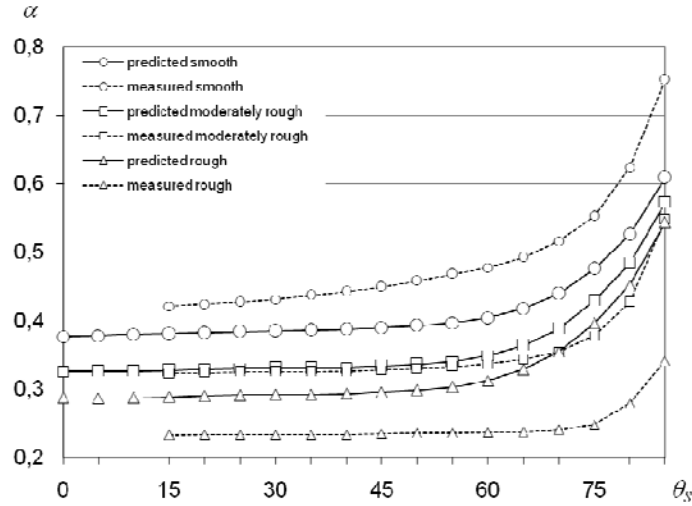


Figure 2. Variation of the blue-sky albedo α in the function of the solar zenith angle θ_s , measured and predicted by the hemispherical-directional reflectance model.

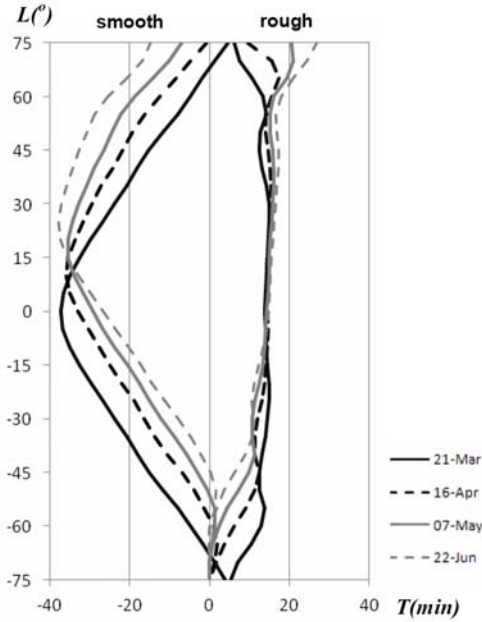


Figure 3. The intervals of the optimal time T for the real smooth and rough soil surfaces in respect to the moderately rough one in the latitude L function in the afternoon for the chosen days. Negative values of the L concern the Southern Hemisphere.

It was further evaluated if achievement of the average daily albedo for the rough and smooth surfaces may be assessed with the ε lower than $\pm 2\%$ using the optimal time adequate for the moderately rough surface. The graphs in figure 4 show the To distribution calculated for the moderately rough

surfaces in the L function with its $\pm 2\%$ error lines. The adequate distributions for the smooth surface To_S and the very rough one To_R complete the graphs to check whether they do not exceed the acceptable lines of $\pm 2\%$ error specified for the moderately rough surface. The optimal time for the very rough surface To_R does not exceed these $\pm 2\%$ error limits for all the tested dates. The To_S distribution predicted for the smooth surface does not exceed $\pm 2\%$ error limits only in certain latitude ranges. In the SH they are located at the L lower than -35° , -30° , -20° , and -15° for 21 March, 16 April, 07 May, and 22 June, respectively. In the NH those ranges are located at the L higher than 35° , 45° , 50° , and 60° for the same dates, respectively. It was found that the maximum ε associated with the To_S distribution does not exceed 3% (Fig. 4).

As in Cierniewski and Gdala (2010), it was considered what practical notes follow the acceptable time intervals for evaluation of the average daily albedo $\bar{\alpha}$ of soil surfaces with their various roughness levels by satellite technology in a wide latitude range of the Earth.

A remote sensing satellite on a typical sun-synchronous orbit with its 98-minutes period was analyzed, assuming for simplification that the satellite crosses the equator exactly at the optimal time for the four chosen dates for the moderately rough surface. It was judged as a representative soil surface for their wide roughness range. It was determined from which part of that orbit, expressed by the length of the latitude range, the remote sensing satellite can collect the $\bar{\alpha}$ with its acceptable $\pm 2\%$ error.

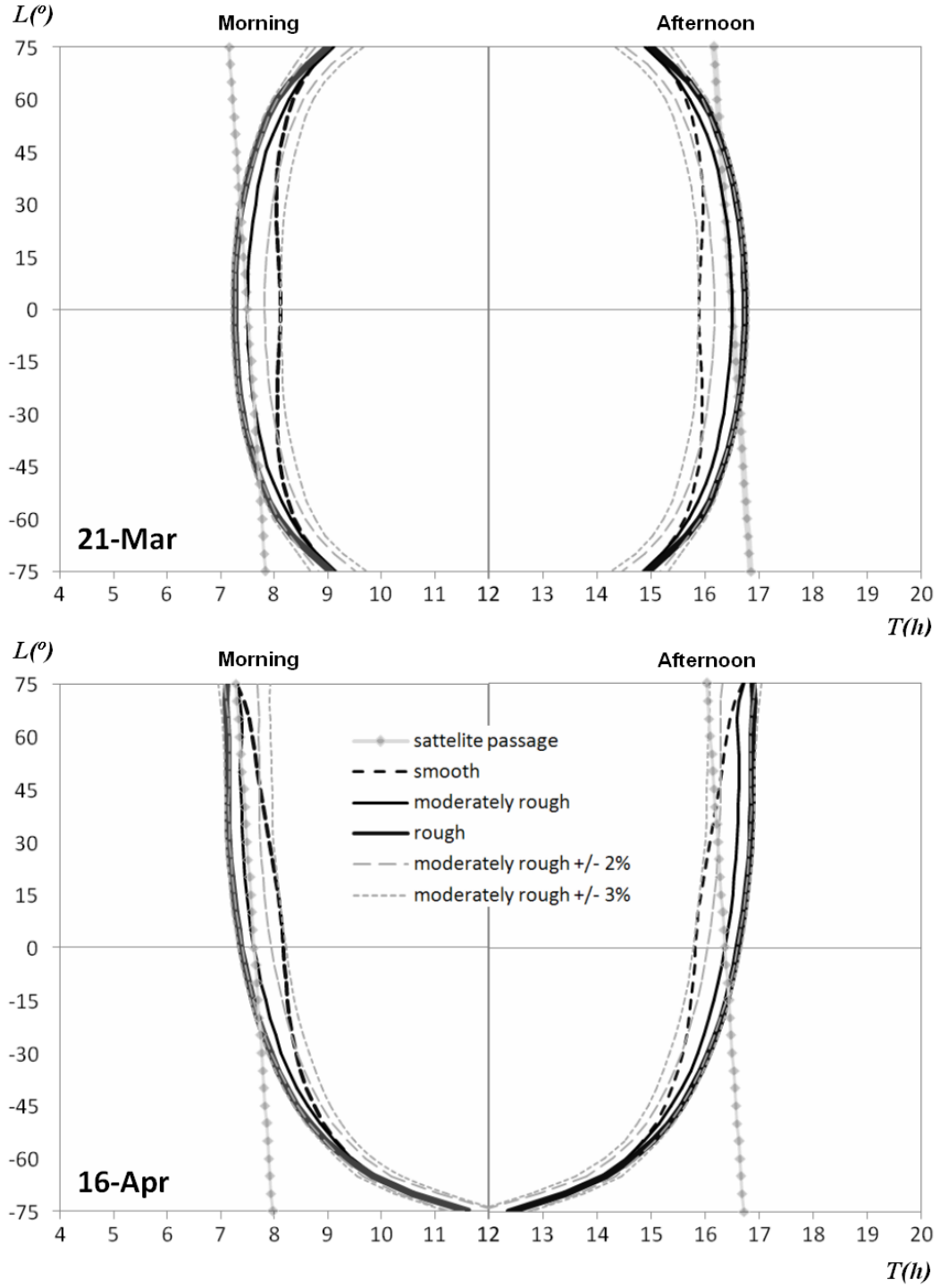


Figure 4. The optimal time of the daily soil albedo for various soil roughness when for the chosen dates the average daily soil surface albedo $\bar{\alpha}$ varying with the latitude L is available to assess with their error ε lower than $\pm 2\%$ and $\pm 3\%$. The dotted lines imagine the time of the remote sensing satellite passage crossing the equator exactly at the optimal time for the latitude $L = 0^{\circ}$.

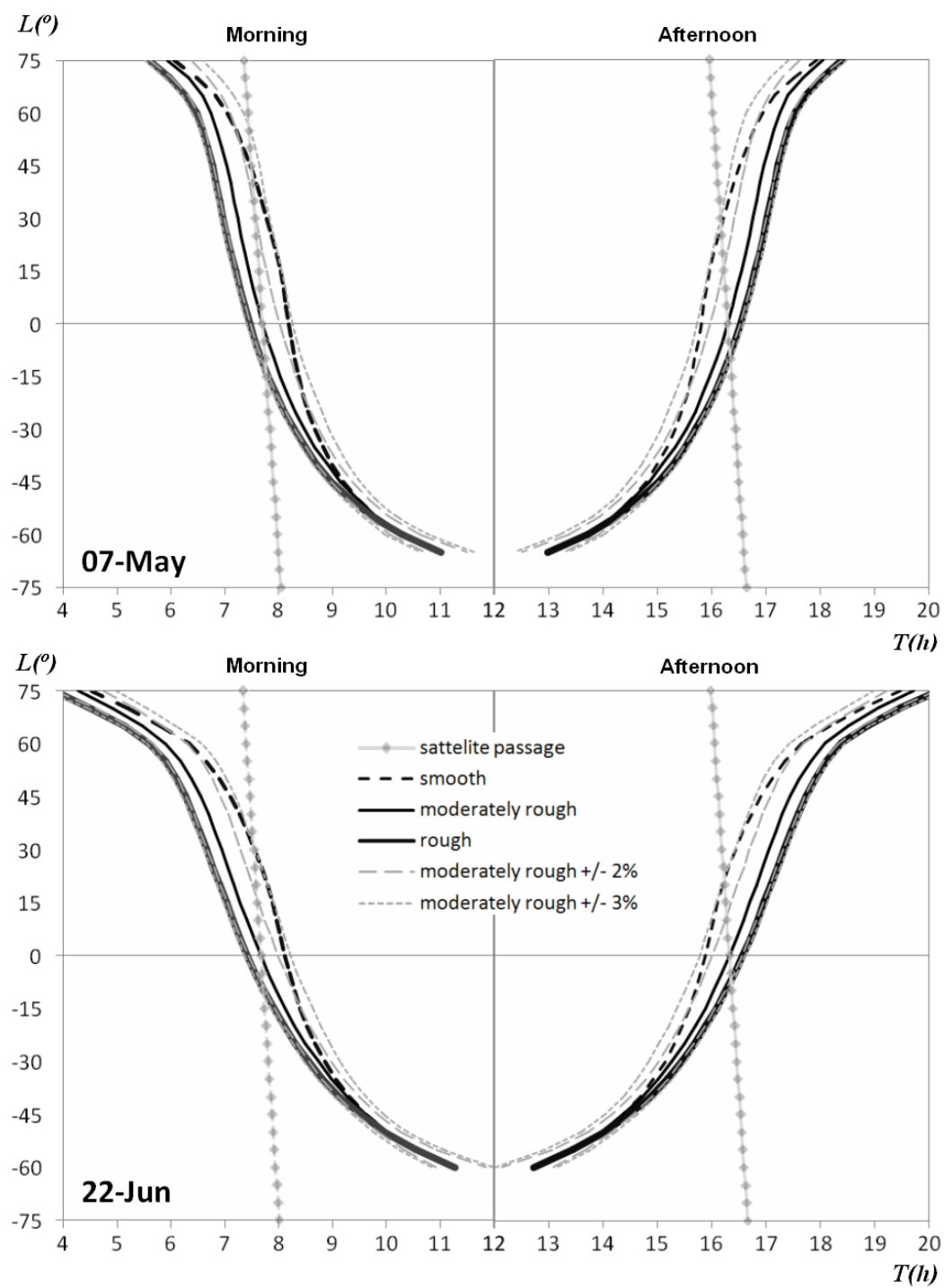


Figure 4. Continued.

Results of the assessment are also presented in figure 4. This length of the orbit part is described between intersection points of two kinds of lines: the dotted one, defining the time of the satellite passage at various latitude L , and the dashed lines, describing limits of the acceptable $\pm 2\%$ error. The higher the convergence of the two kinds of the lines, the higher the orbit part length sought for the analyzed dates. The results obtained in this paper are not significantly different in comparison to Cierniewski and Gdala (2010) (table 3).

Table 3. The length of a remote sensing satellite orbit at which it can collect the average daily $\bar{\alpha}$ albedo of soil surfaces with its $\pm 2\%$ error.

Date	Morning		Afternoon	
	Measured	Predicted	Measured	Predicted
21-Mar	70°	60°	70°	60°
16-Apr	>95°	>90°	40°	20°
07-May	45°	25°	25°	15°
22-Jun	25°	20°	15°	10°

4 CONCLUDING REMARKS

The distribution of the soil albedo data as a function of the solar zenith angle obtained directly by the field measurements are not parallel such as the modeling ones. The measured curve of the extremely rough surface almost does not raise at the θ_s angles lower than 75°, while the curve of the extremely smooth one increases at all the analyzed θ_s range, especially strongly at the θ_s angles higher than 65°. The measured albedo distribution for the moderately rough surface is similar to the distribution predicted by the model using the virtual surface, however, its increase is noticed at θ_s higher than 57°.

The measured data show that the optimal time To for evaluation of the average daily soil albedo $\bar{\alpha}$ falls at different time depending on the roughness of the studied soil surfaces. In the afternoon, the To_S for the smooth soil surface falls earlier than for the moderately rough To_M , whereas for the very rough one To_R it falls later than for To_M . In the morning this trend is reversed. In a certain latitude ranges, the interval between To_S and To_M does not exceed 40 minutes, while among To_R and To_M 15 minutes. It was found that at the optimal time predicted for the moderately rough surface To_M , taking into consideration its $\pm 2\%$ error, is also available to achieve the average daily albedo $\bar{\alpha}$ for very rough surfaces. Achievement at the same time To_M $\bar{\alpha}$ for the smooth surface in a wide latitude range is available with the higher error reaching $\pm 3\%$.

The strongly defined time for evaluation of the average daily soil surface albedo of different roughness limits possibilities of the data achievement by remote sensing satellites. Overall, the measured albedo distribution in relation to the modeling one provides an slight increase of the length of a remote sensing satellite orbit at which it can collect the average daily $\bar{\alpha}$ albedo of soil surfaces with its acceptable $\pm 2\%$ error for all chosen dates. The highest length of the orbit part, calculated by the measured data such as modeling one, was specify as no shorter than 90°. It was predicted for the date of 16 April morning, whilst the shortest length, reaching only about 15°, is expected for 22 June afternoon.

5 ACKNOWLEDGEMENT

This work was carried out within the framework of the projects 2 P04E 030 29 and NN 306013637, supported by the Polish Ministry of Science and Higher Education and by the "Sixth EU Framework Programme – Transnational Access implemented as Specific Support Action - Dryland Research " (Number of the EC contract 026064). The authors wish to thank Aleksander Goldberg for his help in the field measurements.

6 REFERENCES

- Cierniewski, J. and Gdala, T., 2010, Calculating the optimal time when albedo approximates its daily average: an example using soil surfaces with various roughnesses at different latitudes. *International Journal of Remote Sensing*, 31, 2697-2708.
- Sellers, P.J., Meeson, B.W., Hall, F.G., Asrar, G., Murphy, R.E., Schiffer, R.A., Bretherton, F.P., Dickinson, R.E., Ellingson, R.G., Field, C.B., Huemmrich, K.F., Justice, C.O., Melack, J.M., Roulet, N.T., Schimel, D.S. and Try, P.D., 1995, Remote Sensing of the land-surface for studies of global change: models-algorithms-experiments. *Remote Sensing of Environment*, 51, 3-26.
- Issar, A., Karnieli, A., Bruins, H.J. and Gilead, I., 1984, The quaternary geology of Sede-Zin, Negev, Israel. *Israel Journal of Earth Science*, 33, 34-42.
- Sparks, D.L., Page, A.L., Helmke, P.A., Loeppert, R.H., Soltanpour, P.N., Tabatabai, M.A., Johnston, C.T. and Summer, M.E. (Ed.), 1996, *Methods of Soil Analysis. Part 3. Chemical Methods* (Madison, WI: Soil Science Society of America and American Society of Agronomy).

Aerosols characterization in the Western Mediterranean (Málaga, Spain)

I. Foyo-Moreno^{1,2}, I. Alados³, H. Lyamani^{1,2}, F.J. Olmo^{1,2} and L. Alados-Arboledas^{1,2}

¹*Applied physic Department. Science Faculty. University of Granada. Fuentenueva s/n, 18071, Granada. Spain*

²*Andalusian Center for Environmental Research. Av. del Mediterráneo s/n. 18006. Granada. Spain*

³*Applied physic Department. Science Faculty. University of Málaga. Campus de Teatinos s/n, 29071, Málaga. Spain*

ifoyo@ugr.es; alados@uma.es; hlyamani@ugr.es; olmo@ugr.es; alados@ugr.es

ABSTRACT. *This paper presents the first attempts to study and characterize the atmospheric aerosol at the city of Malaga, Spain, a coastal location in the Western Mediterranean. We have analyzed the seasonal variation of the aerosol radiative properties in this place. The study uses measurements gathered from February 2009 to February 2010 using a CIMEL sun/sky photometer included in RIMA, Iberian network of sun-photometers included in AERONET (<http://www.rima.uva.es/RIMA/>). We show the seasonal evolution of the aerosol optical depth (AOD), the Angström exponent (α), the single scattering albedo (ω_0), the asymmetry parameter (g) and the columnar size distributions ($v(r)$) at different wavelengths. Our results evidence the significant Saharan dust influence over our station, especially during the summer, and also the anthropogenic influence during all seasons.*

1 INTRODUCTION

The role of atmospheric aerosols on climate is very important by its direct and indirect effects; the direct effects altering the radiation budget and the indirect effects affecting on cloud properties. On other hand, the high spatial and temporal variability of aerosols imply a high uncertainty about it. So, to reduce these uncertainties, efforts have been made over the last years to better characterize the aerosols. In fact, the Mediterranean area has been repeatedly suggested as one of the areas where aerosols are expected to play a significant effect (Tragou and Lascaratos, 2003).

Ground-based remote sensing of aerosols is ideal for the reliably and continuously derivation of aerosol columnar radiative properties in key locations around the world. Besides, the ground based aerosols data are required to validate satellite data. Many aerosols ground-based observations network have been established in order to understand the optical and radiative properties of aerosols and indirectly to evaluate their effect on climate (i.e., AERONET).

To determine the influence of aerosols on climate different columnar aerosol radiative properties like aerosol optical depth, Angström exponent, size distribution, single scattering albedo and asymmetry parameter are required.

The aerosol optical depth (AOD) is representative of the airborne aerosol loading in the atmospheric column and is important for the identification of aerosol source regions and aerosol evolution (Liu et al., 2008).

The Angstrom exponent (α) is defined by the spectral dependence of the aerosol optical depth (Angstrom turbidity formula, Angström, 1929) and is related to the particles size (Shifrin, 1995). Large values of α indicate the prevalence of fine particles, while low values are related with the presence of coarse particles such as desert dust, marine aerosols, etc (Dubovik et al., 2002).

The single scattering albedo (ω_0) represents a key parameter in describing the aerosol radiative properties; it is defined as ratio between the aerosol scattering and extinction coefficients. So, this parameter is a common measurement of the relative contribution of absorption and is an important variable in assessing the climatic effects of atmospheric aerosol (Dubovik et al., 2002). Hansen et al. (1997) suggest that the effect of aerosol could shift from cooling to warming if the ω_0 goes below a critical value that they estimated as 0.86.

The asymmetry parameter (g) is a useful parameter to characterize the relative importance of forward-to backward aerosol scattering. So, this parameter represents an estimation of the asymmetric distribution

of the scattered radiation. For symmetric scattering, g is considered to be 0 and for a purely forward scattering is taken as 1. For a cloudless atmosphere g ranges from 0.1 -very clean conditions- to 0.75 in polluted zones.

Also, the relationship between the columnar volume aerosol size distribution ($v(r)$) and AOD is important for climate forcing studies (Liu et al., 2008).

This work contributes to the understanding of atmospheric aerosol properties for a particular region. We present results on atmospheric aerosol radiative properties measured at Málaga (Spain) from February 2009 to February 2010.

In section 2 we will describe the instrumentation used and we will give a brief description of the experimental site. The section 3 contains the results and discussion, and finally we present some concluding remarks in section 4. Acknowledgement and references are included in sections 5 and 6, respectively.

2 INSTRUMENTATION AND EXPERIMENTAL SITE

Columnar atmospheric aerosol characterization has been done at Málaga (36.72°N, 4.5°W, 40 m a.s.l.), a coastal location in the Western Mediterranean, by means of a sun-photometer CE-318-4 (CIMEL Electronic, France), which is the standard sun/sky photometer used in the AERONET network. The measurement device is operated by the Atmospheric Physics Group of the Andalusian Center for Environmental Studies (GFAT_CEAMA) in the framework of RIMA and AERONET networks, following the data quality criteria used in AERONET network (i.e. Holben et al., 1998; Smirnov et al., 2000; <http://aeronet.gsfc.nasa.gov/>). The instrument makes direct Sun irradiance measurements with a 1.2° full field of view at 340, 380, 440, 670, 870, 940, and 1020 nm. Also, the instrument is able to make sky radiances, both in almucantar and principal plane, at 440, 670, 870 and 1020 nm. More details about CIMEL CE-318-4 can be found in Holben et al. (1998).

The Ångström exponent was computed from AOD values at 440 and 870 nm. A flexible inversion algorithm, developed by Dubovik and King (2000) is used to retrieve columnar aerosol volume size distributions, single scattering albedo and asymmetry parameter from direct-sun and diffuse-sky radiance measurements. A brief discussion on the accuracy of individual retrievals is reported in Dubovik et al. (2002). Cloud-screened retrievals (level 1.5) are used in this study (Smirnov et al., 2000).

The analysed period ranges from February 2009 to February 2010. The study area is located in the

Mediterranean coast and due to its proximity to the African Continent, is frequently affected by intrusions of Saharan air masses. In the study area both anthropogenic and natural particles are present.

The annual averaged rainfall at Málaga is 524 mm, and the annual averaged temperature is 18.0 °C, being the averaged maximum temperature 22.9 °C and the averaged minimum temperature 13.1 °C. The annual averaged relative humidity is about 66%, being the climate subtropical wet Mediterranean (www.aemet.es).

3 RESULTS AND DISCUSSION

Figure 1 shows the seasonal averages of AOD(λ) during the analyzed period, including the standard deviation values. We can observe a clear annual pattern with larger values in summer (0.22 ± 0.11 at 440nm and 0.14 ± 0.07 at 870 nm), indicating larger aerosol load, and lower in winter (0.14 ± 0.08 at 440nm and 0.07 ± 0.051 at 870 nm). Similar patterns have been found at other Mediterranean sites: at Évora (Portugal), AOD values ranges from 0.23 ± 0.18 during summer 2002 at 440 nm and 0.11 ± 0.14 at 873 nm (Elias et al., 2006). Also, similar values occurred at Granada (Spain) for 440 nm: 0.23 ± 0.10 and 0.16 ± 0.08 in summer and winter, respectively (Lyamani et al., 2010).

According to Figure 2, α also presents a seasonal cycle: larger values in spring and winter (close to 1.0 ± 0.4) and lower values in summer (0.7 ± 0.3), indicating an increase in coarse particles fraction in summer. At Granada, for all seasons, the α values are slightly higher than Málaga indicating the predominance of larger particles at Málaga respect to Granada, probably due to the local pollution at Granada and the presence of marine aerosol at Málaga. At Évora the averages values during summer 2002 and 2003 were higher (1.2 ± 0.4 and 1.4 ± 0.4).

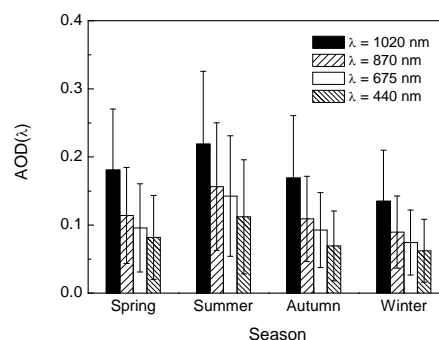


Figure 1. Seasonal averages of AOD for the analysed period. The error bars are standard deviations.

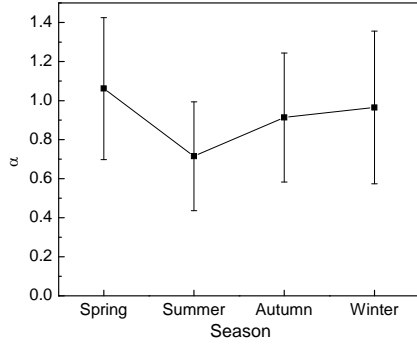


Figure 2. Seasonal averages of α for the analysed period. The error bars are standard deviations.

Figure 3 shows the seasonal average of $\omega_0(\lambda)$. The seasonal average values shows low sensitivity to wavelengths, with the highest average in the spring months (0.91 ± 0.04 at 670 nm), indicating a predominance of scattering over absorption, and the lowest value in winter season (0.83 ± 0.13 at 670 nm). These values are higher than found at Granada (0.70 ± 0.06 and 0.66 ± 0.063 at 670 nm), although the extreme values at Granada are encountered for different seasons (Lyamani et al., 2010). The higher values at Málaga indicate minor presence of absorbing particles compared to Granada.

Figure 4 shows the results for $g(\lambda)$, with the highest average values in summer season (0.69 ± 0.03 at 670 nm) and the lowest values in winter (0.65 ± 0.04 at 670 nm). This pattern is similar to the pattern followed by $AOD(\lambda)$ and opposite to that showed by α . The results show the predominance of large particles during the dry summer months due to the contribution of local particles, regional mineral and marine particles. Additionally, during summer season Málaga presents high frequency of long range transport events from the Sahara desert. Following Hess et al. (1998), these values are typical of locations with moderate contamination. Similar values are encountered at Armilla, a location close to Granada (Spain), with an average value of 0.67 ± 0.3 at 670 nm (Lyamani et al., 2004).

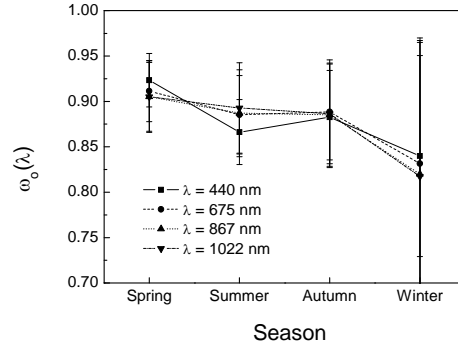


Figure 3. Seasonal averages of ω_0 for the analysed period. The error bars are standard deviations

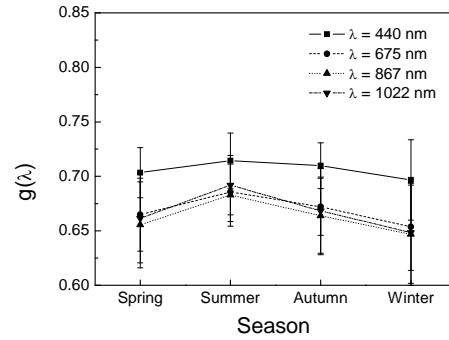


Figure 4. Seasonal averages of g for the analysed period. The error bars are standard deviations

Figure 5 shows the volume size distribution seasonal averages for the analyzed period. The distributions were found to be bimodal, with fine mode ($r < 0.5 \mu\text{m}$) and coarse mode ($r > 0.5 \mu\text{m}$). The seasonal evolution of the fine mode shows radius close to $0.13 \mu\text{m}$. In winter the radius are slightly displaced to a higher value ($0.15 \mu\text{m}$). The coarse modes show radius around $2.5 \mu\text{m}$ in summer and close to $5 \mu\text{m}$ in winter. This last radius increase may be related to the growth of hygroscopic particles due to the high relative humidity values showed in winter season.

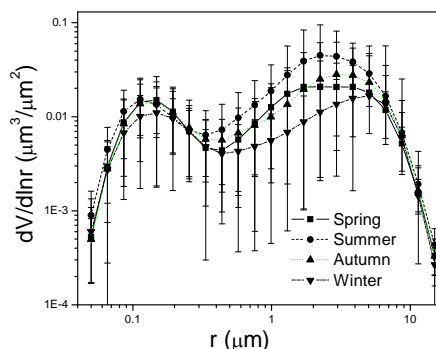


Figure 5. Seasonal averages of $v(r)$ for the analysed period. The error bars are standard deviations.

Figure 5 also shows a seasonal pattern. It is evident the seasonal change in the coarse mode, with larger contribution during summer. On the other hand, the fine mode, with radii lower than $0.5 \mu\text{m}$, does not present this marked variation. This could indicate a constant fine mode aerosol load along the year, probably due to the heavy traffic at Málaga during all seasons. It is interesting to note that the climate of Málaga is characterized by long, hot, dry summers and very mild rainy winters, so Málaga has attracted many thousands of tourists making it one of Europe's favourite holiday destinations. Also Málaga is surrounded with industrial estates.

4 CONCLUSIONS

We have analyzed the aerosol radiative properties to characterize the aerosol load at a coastal location (Málaga, Spain), from February 2009 to February 2010. The instrument used is a sun-photometer CE-318-4 (CIMEL Electronic, France), which is the standard sun/sky photometer used in the AERONET network.

The radiative parameters analyzed are the aerosol optical depth (AOD), Angström exponent (α), single scattering albedo (w_0), asymmetry parameter (g) and volume size distribution ($v(r)$).

The AOD and α parameters have shown seasonal cycles at all wavelengths, with larger AOD values in summer and lower in winter. The α seasonal values presents larger values in winter than in summer, indicating larger aerosol load in summer associated to the higher frequency of dust events occurred in these months.

Single scattering albedo also presents a seasonal cycle, with largest values in spring, showing a predominance of scattering over absorption specially in this season. The minimum values in winter can be associated to the anthropogenic activities.

Asymmetry factor presents the largest values in summer and the lowest values in winter, indicating larger particles in summer.

The volume size distributions showed a bimodal structure for all seasons with a seasonal pattern for coarse mode. The coarse mode is larger in summer, associated with the Saharan dust events and local mineral resuspension due to the anthropogenic activities. On the other hand, the fine particles mode does not present this marked seasonal variation, indicating an almost constant contribution in the fine particles along the year, taking into account that Málaga is a holiday destination and with industrial estates in the surroundings.

From our study it is evident the significant Saharan dust influence over our station, especially during the summer, and also the anthropogenic influence during all seasons.

5 ACKNOWLEDGEMENTS

This work is supported by Spanish Ministry of Science through grant CGL2007-28871-E/CLI and projects CGL2007-66477-C02-01 and CSD2007-00067; by Autonomous Government of Andalusia through the projects P08-RNM-3568 and P06-RNM-01503, by EARLINET-ASOS project (EU-CA.025991 ,RICA), and framework of RIMA.

6 REFERENCES

- Angström, A., 1929. On the atmospheric transmission of sun radiation and on dust in the air. *Geografiska Annaler* **11**, 156–166.
- Dubovik, O., Holben, B., Eck, T.F., Smirnov, A., Kaufman, Y.J., King, M.D., Tanré, D. and Slutsker, I., 2002, Variability of absorption and optical properties of key aerosol types observed in worldwide locations. *Journal of the Atmospheric Sciences*, **59**, 590–608.
- Dubovik, O., King, M.D., 2000. A flexible inversion algorithm for retrieval of aerosol optical properties from Sun and sky radiance measurements. *Journal of Geophysical Research*. **105**, 20673–20696.
- Elias, T., Silva, A. M., Belo, N., Pereira, S., Formenti, P., Helas, G., and Wagner, F., 2006, Aerosol extinction in a remote continental region of the Iberian Peninsula during summer, *Journal of Geophysical Research*, **111**, 25679-25720, doi:10.1029/2005JD006610.
- Hansen, J., Sato M., Ruedy R., Lacis A., Asamoah K., Beckford K., Borenstein S., Brown E., Cairns B., Carlson B., Curran B., de Castro S., Druryan L.,

- Etwarrow P., Ferede T., Fox M., Gaffen D., Glascoe J., Gordon H., Hollandsworth S., Jiang X., Johnson C., Lawrence N., Lean J., Lerner J., Lo K., Logan J., Luckett A., McCormick M.P., McPeters R., Miller R.L., Minnis P., Ramberran I., Russell G., Russell P., Stone P., Tegen I., Thomas S., Thomason L., Thompson A., Wilder J., Willson R., and Zawodny J., 1997: Forcings and chaos in interannual to decadal climate change. *Journal of Geophysical Research*, **102**, 25679-25720, doi:10.1029/97JD01495.
- Hess M., Koepke, P. and Schult., 1998, Optical properties of aerosols and clouds: the software package OPAC, *Bulletin of the American Meteorological Society*, **79**, 831–845.
- Holben, B.N., Eck, T.F., Slutsker, I., Tanre, D., Buis, J.P., Setzer, A., Vermote, E., Reagan, J.A., Kaufman, Y.J., Nakajima, T., Lavenue, F., Jankowiak, I. and Smirnov, A., 1998, AERONET—a federated instrument network and data archive for aerosol characterization. *Remote Sensing of Environment*, **66**, 1–16.
- Liu, J., Zheng Y., Li, Z. and Wu, R., 2008, Ground-based remote sensing of aerosol optical properties in one city in Northwest China. *Atmospheric Research*, **89**, 194-205.
- Lyamani H., Olmo, F.J. and Alados-Arboledas, L., 2004, Long-term changes in aerosol radiative properties at Armilla (Spain), *Atmospheric Environment*, **38**, 5935-5943.
- Lyamani H., Olmo, F.J. and Alados-Arboledas, L., 2010, Physical and optical properties of aerosols over an urban location in Spain: seasonal and diurnal variability, *Atmospheric Chemistry and Physics*, **10**, 239-254.
- Nakajima, T., Tonna, N., Rao, R., Boi, P., Kaufman Y.J. and Holben B., 1996, Use of sky brightness measurements from ground for remote sensing of particulate polydispersion, *Applied Optics*, **35**, 2672-2686.
- Shifrin K.S., 1995, Simple relationships for the Angström parameter of disperse system. *Applied Optics*, **34**, 4480–4485.
- Smirnov, A., Holben, B.N., Eck, T.F., Dubovik, O. and Slutsker, I., 2000, Cloud screening and quality control algorithms for the AERONET database. *Remote Sensing of Environment*, **73**, 337–349.
- Tragou, E. and Lascaratos A., 2003, The role of aerosols on the Mediterranean heat budget, *Journal of Geophysical Research*, **108**, NO. C2, 3025, doi:10.1029/2001JC001258.
- Yu X., Zhu, B. and Zhang, M., 2009, Seasonal variability of aerosol properties over Beijing, *Atmospheric Environment*, **43**, 4095-4101.

Comparison of current methods to determine the downwelling atmospheric irradiance in the thermal infrared

V. García-Santos¹, M. Mira¹, E. Valor¹, V. Caselles¹, C. Coll¹, J.M. Galve¹ and L. Martinez²

¹Department of Earth Physics and Thermodynamics, University of Valencia. C/ Dr. Moliner 50, 46100, Burjassot, València, Spain

²Remote Sensing Area, Institut Cartogràfic de Catalunya. Parc de Montjuïc s/n, 08038, Barcelona, Spain

vicente.garcia-santos@uv.es

ABSTRACT - Ground measurements of land surface temperature (LST) are necessary for the validation of LST products derived from thermal infrared (TIR) remote sensing data. In the validation campaigns, one important factor to take into account is the downwelling hemispheric irradiance ($F_{\text{HEM}}^{\downarrow}$), which has to be measured near-simultaneously to the surface temperature measurements. Direct measurements of $F_{\text{HEM}}^{\downarrow}$ with a radiometer involve the measurement of sky radiances from all zenithal and azimuthal directions, and the integration over the upper hemisphere. Such measurements are time-consuming and are not useful because atmospheric conditions may change during the measurement process. Several methods to accurately determine $F_{\text{HEM}}^{\downarrow}$ in a short period of time are analyzed in this paper to evaluate which is the most suitable: the diffusive approximation, the use of a TIR diffuse reflectance panel, and the simulation of $F_{\text{HEM}}^{\downarrow}$ values by means of a radiative transfer code using both radiosounding data measured at the study area, and atmospheric profiles from the National Center for Environment Prediction. The results show that the fastest and most reliable method to obtain $F_{\text{HEM}}^{\downarrow}$ is to make measurements with a diffuse reflectance panel at zenith angles from nadir to 50°, at any azimuthal angle, and keeping a distance of about 80-90 cm between the panel and the radiometer.

1 INTRODUCTION

Accurate land surface temperatures (LSTs) measurements using thermal infrared data needs to take into account two important factors: land surface emissivity (ϵ_{sur}) and the downwelling radiance coming from the surroundings and the atmosphere reflected by the surface. The radiative transfer equation of the land-leaving radiance from an area (L_{sur}) at surface level is:

$$L_{\text{sur}} = \epsilon_{\text{sur}} B(LTS) + (1 - \epsilon_{\text{sur}}) \frac{F_{\text{HEM}}^{\downarrow}}{\pi} \quad (1)$$

where B is Planck's function for a blackbody emitting at the LST, this procedure assumes a Lambertian behavior of the surface following Kirchhoff's law and $F_{\text{HEM}}^{\downarrow}$ is the downwelling irradiance.

The term $F_{\text{HEM}}^{\downarrow} / \pi$ is called hemispheric downwelling radiance ($L_{\text{HEM}}^{\downarrow}$) and can be written as:

$$L_{\text{HEM}}^{\downarrow} = \frac{\int_0^\pi \int_0^{2\pi} L^{\downarrow}(\theta, \varphi) \sin \theta \cos \theta d\theta d\varphi}{\int_0^\pi \int_0^{2\pi} \sin \theta \cos \theta d\theta d\varphi} \quad (2)$$

where $L^{\downarrow}(\theta, \varphi)$ is the downwelling radiance at the zenithal and azimuthal direction (θ, φ). To correct the L_{sur} measurements in equation (1) for the emissivity effect and get accurate LST values, it is needed to measure $F_{\text{HEM}}^{\downarrow}$ in addition to ϵ_{sur} . The most exact way to obtain $L_{\text{HEM}}^{\downarrow}$ is to measure the radiance from all possible zenithal and azimuthal directions, $L^{\downarrow}(\theta, \varphi)$, and integrate these measurements in the upper hemisphere according with (2). Since take these measurements is a very time-consuming process which is critical with skies partially cloudy and changing. It is necessary alternative faster methods.

2 ALTERNATIVE METHODS

2.1 Diffusive Approximation

Proposed by Kondratyev (1969), this method needs homogeneous atmospheric conditions (cloudy or cloudless skies). A single radiance measurement of the sky at an effective zenithal angle gives $L_{\text{HEM}}^{\downarrow}$:

$$L_{\text{HEM}}^{\downarrow} = L_{\text{sky}}^{\downarrow}(\theta_{\text{eff}}) \quad (3)$$

In this study we choose an effective zenithal angle of 54°.

2.2 Alternative Diffusive Approximation

A modification of this method, was proposed by Rubio *et al.* (1997), suggesting take measurements of the sky at 0° and multiplying this value by a factor γ :

$$L_{HEM}^{\downarrow} = \gamma L_{sky}^{\downarrow}(0^{\circ}) \quad (4)$$

Values of γ vary from 1.1 to 1.7. This version of the diffusive approximation is more practical in the field, since it is not needed an accurate measurement of the viewing zenithal angle. These techniques are very fast but both of them require homogeneous atmospheric conditions (complete cloud cover or completely clear skies), and do not consider the possible radiative contribution of the surrounding elements. According with García-Santos *et al.* (2010), γ vary linearly with the wavelength and the water vapor content (W). Then it is necessary an indepent measuement of W to carry out this method.

2.3 Atmospheric Profiles

An alternative way to obtain L_{HEM}^{\downarrow} is introducing an atmospheric profile, acquired with a radiosonde launched concurrently to the surface measurements, in a radiative transference code (RTC) such as MODTRAN 4v3r (Berk *et al.* 1999). If there are not radiosondes available, another possibility is to use atmospheric profiles resulting from reanalysis techniques, provided by weather forecast centers such as the National Center for Environmental Prediction (NCEP). These profiles need to be interpolated temporally and spatially at the time and place of the measurements (Kalnay *et al.* 1995) using the coordinates of the desired zone and the central hour of the measurement session. Simulation procedures present also some drawbacks: radiosondes are not always available, and the NCEP profiles are predicted from data obtained from spatial and temporal interpolation, whereas the atmospheric conditions can be different in the region nearest to the interest zone, and changing with time.

2.4 Diffuse Reflectance Panel

The last possibility proposed is the use of a diffuse reflectance panel with Lambertian behavior, which allows obtaining L_{HEM}^{\downarrow} measuring the reflected radiance by the panel from any viewing direction. This panel can be used under any atmospheric condition, and it takes into account the radiative contribution of the surroundings elements in addition to the atmosphere.

The objective of the present work is to compare all the previous methods and assess which of them could be the most suitable. With this aim a simple

experimental setup was designed allowing us to obtain radiance measurements, both from a golden diffuse reflectance panel at different combinations of zenithal and azimuthal angles, and also with both diffusive approximation methods on cloudless days. Simulated values of L_{HEM}^{\downarrow} calculated from introducing atmospheric profiles provided by different sources into a RTC were also included.

3 INSTRUMENTATION

3.1 Multispectral Radiometer

At the present study was used a radiometer CIMEL Electronique (CE312-1) (Brogniez *et al.* 2003), which is a multi-spectral sensor that measures the radiance emitted by a surface in the TIR region (8-14 μm). This radiometer is composed composed of an optical head, which points to the surface, and a data-logger joined to the optical head, responsible for registering the measurements. The CE312-1 has four filters that allow us to measure in a wide spectral interval (channel 1: 8.0 μm -13.3 μm), and three narrow spectral intervals within the wide channel (channel 2: 11.5 μm -12.4 μm ; channel 3: 10.2 μm -11.3 μm ; channel 4: 8.3 μm -9.3 μm). The field of view (FOV) of the optical head is 10°.

A previous calibration of the CE312-1 shows a linear relationship between the black-body and the radiometer with an uncertainty for the channels 1 to 4, in units of $\text{mWm}^{-2}\text{sr}^{-1}\text{cm}$, of: ± 0.0019 , ± 0.02 , ± 0.01 and ± 0.02 , respectively (or equivalently: ± 0.013 K, ± 0.012 K, ± 0.011 K and ± 0.03 K, in the radiative temperature).

3.2 Diffuse TIR Reflectance Panel

The diffuse reflectance panel used in this work corresponds to the model Infragold Reflectance Target IRT-94-100 from Labsphere®. It is a gold rugged surface with dimensions of 25.4 x 25.4 cm^2 and a height of 1 cm. This panel has a high reflectivity in the TIR region, with values of 0.923, 0.925, 0.925 and 0.918, respectively, for CE312-1 channels 1 to 4, with an error of ± 0.009 . Consequently, following Kirchhoff's law the emissivities of the panel in each channel are 0.077, 0.075, 0.075 and 0.082, respectively.

4 METHODOLOGY

An experiment was conducted on 28th May of 2009 in order to compare the different procedures to determine L_{HEM}^{\downarrow} in a large and flat area of rice fields of the Albufera of Valencia, Spain, to minimize the effect of the surroundings. The site is located at 39° 15' 53"N, 0° 18' 15"W. This day the sky was completely clear

assuring a minimal variation of $L_{\text{HEM}}^{\downarrow}$ during the measurement process. The measurements were performed following the next procedure. One radiometer was fixed in a goniometer taking angular measurements over the panel from 0° to 65° zenithal angles, at intervals of 5° . Three consecutive readings at each angle were made, calculating the average value. Each zenithal sweep was made for two different azimuthal angles (0° , respect to the complementary solar plane and 90° , on the corresponding perpendicular), were chosen only two azimuthal angles because the time of measurements session was close to an hour, exactly the time consumed by a radiosonde launched concurrently to the measurements. Simultaneously, another identical radiometer took readings vertically from the sky to obtain the radiance $L^{\downarrow}(0^\circ)$, required in Eq. (4) and sometimes this radiometer was placed measuring $L^{\downarrow}(54^\circ)$ according with Eq. (3), to get a value of $L_{\text{HEM}}^{\downarrow}$ according to the diffusive approximation. The experimental setup can be seen in Figure 1.

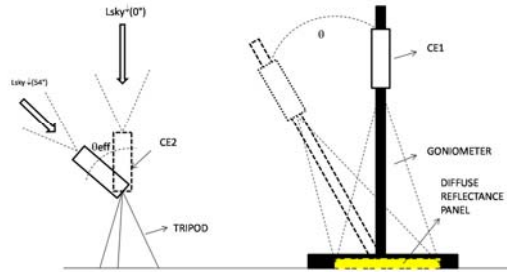


Figure 1: Experimental assembly used to perform the angular measurements over the diffuse reflectance panel, with the CE312-1, here called CE1, and the sky, with another radiometer called CE2.

In the case of the alternative diffusive approximation method proposed by Rubio *et al.* (1997) an adequate value of the γ coefficient must be set, since it depends on the channel and also on W . To this end, a previous simulation study (García-Santos *et al.* 2010) was carried out using the radiosonde data contained in the Cloudless Land Atmosphere Radiosonde (CLAR) database (Galve *et al.* 2008), which spans a W interval from 0.02 to 5.61 cm. For each of these radiosondes, the parameters W , $L^{\downarrow}(0^\circ)$ and $L_{\text{HEM}}^{\downarrow}$ were obtained by simulation, from both radiance the γ coefficient was derived according with Eq. (4). Finally it was obtained a linear relationship between γ and W using these data for the 4 channels of the CE312-1:

$$\gamma_{ch1} = -0.04W + 1.43 \quad (5)$$

$$\gamma_{ch2} = -0.09W + 1.61 \quad (6)$$

$$\gamma_{ch3} = -0.09W + 1.73 \quad (7)$$

$$\gamma_{ch4} = -0.03W + 1.44 \quad (8)$$

A radiosonde was launched to get an atmospheric profile concurrent to the radiance measurements. This radiosonde provides values of pressure (in mbar), atmospheric temperature (in K) and relative humidity (in %). From that profile it was derived an W of 1.3 ± 0.2 cm, which allowed calculating the coefficient using Eqs. (5) to (8), for the CE312-1 channels 1 to 4, yielding 1.38, 1.49, 1.61 and 1.40, respectively. Additionally $L_{\text{HEM}}^{\downarrow}$ values were calculated using atmospheric profiles into the MODTRAN 4v3r code (Berk *et al.* 1999). The profiles came from two different sources. One was the profile acquired concurrently with the radiosonde mentioned above. The other one was a profile provided by NCEP reanalyses interpolated spatially and temporally at the place and time of the radiance measurements. In both cases the profiles were processed with a RTC, which provided $L^{\downarrow}(\theta, \phi)$ values for the zenithal angles 0.0° , 11.6° , 26.1° , 40.3° , 53.7° , 65.0° , 70.0° , 75.0° , 80.0° , 87.0° and 89.0° , $L_{\text{HEM}}^{\downarrow}$ was calculated introducing these values into eq. (2).

5 RESULTS

Figure 2 shows the results of the comparison for all the different methods to obtain $L_{\text{HEM}}^{\downarrow}$ at the four spectral channels of the CE 312-1 thermal radiometer. L_{panel} is the direct measurement of $L_{\text{HEM}}^{\downarrow}$ obtained from the panel. L_{desc} is the direct measurement of $L_{\text{HEM}}^{\downarrow}$ obtained from the panel correcting its emissivity effect. The uncertainty assigned at each channel of both parameters is: $\pm 1.2(\text{CH1})$, $\pm 1.8(\text{CH2})$, $\pm 1.9(\text{CH3})$ and $\pm 1.2(\text{CH4})$ mWm⁻²sr⁻¹cm. L_{Kond} is the average value of the continuous measurements of $L_{\text{HEM}}^{\downarrow}$ by means of diffusive approximation proposed by Kondratyev (1969). The uncertainty assigned at each channel is: $\pm 0.3(\text{CH1})$, $\pm 0.6(\text{CH2})$, $\pm 0.4(\text{CH3})$ and $\pm 0.2(\text{CH4})$ mWm⁻²sr⁻¹cm. L_{Rubio} is the average value of the continuous measurements of $L_{\text{HEM}}^{\downarrow}$ by means of diffusive approximation proposed by Rubio *et al.* (1997). The uncertainty assigned at each channel is: $\pm 2(\text{CH1})$, $\pm 3(\text{CH2})$, $\pm 3(\text{CH3})$ and $\pm 2(\text{CH4})$ mWm⁻²sr⁻¹cm. L_{Radio} is the simulated value of $L_{\text{HEM}}^{\downarrow}$ obtained from introducing the atmospheric profile retrieved by the radiosonde

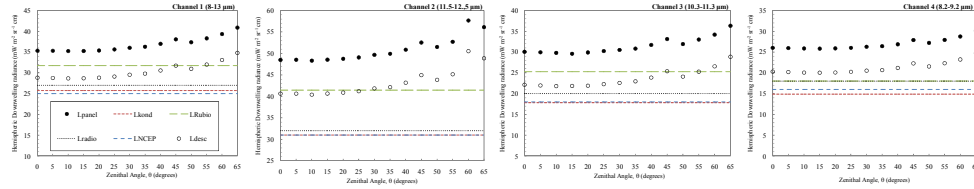


Figure 2. Radiance measurements as a function of the observation angle, using the goniometer setup for the 4 channels of the CE312: Direct measurements from the panel (L_{panel}); measurements corrected for the panel's emissivity (L_{desc}); values of radiance calculated from the diffusive approximation, eq.(3), from radiance measurements of the sky at 54° , (L_{Kond}) and values of radiance calculated by eq.(4) from radiance measurements of the sky at 0° , (L_{Rubio}); simulated values obtained from NCEP profiles (L_{NCEP}); and from radiosonde made at the same place and time of the measurements (L_{radio}), introduced in a RTC.

into the RTC. The uncertainty assigned at each channel is: ± 2 (CH1), ± 4 (CH2), ± 3 (CH3) and ± 2 (CH4) $mWm^{-2}sr^{-1}cm$. L_{NCEP} is the simulated value of L_{HEM} obtained from introducing the atmospheric profile retrieved by the NCEP database into the RTC. The uncertainty assigned at each channel is: ± 2 (CH1), ± 4 (CH2), ± 3 (CH3) and ± 2 (CH4) $mWm^{-2}sr^{-1}cm$.

5.1 Radiative effect of the panel's emissivity

The results for L_{panel} show that the panel presents a near Lambertian behavior, since the measured radiance is almost constant with viewing angle. The increase of radiance at 45° and 60° is probably due to the measurement of the reflected radiance coming from the radiometer itself, known as Narcissus effect. For these angles the radiometer is placed closer to the panel to assure that the field of view lies within the panel area. This means that for measuring the sky radiance with the panel, the most adequate viewing angles are those within 30° and 40° , to minimize the Narcissus effect and observe the largest panel's area possible. It can be also observed in Figure 2 that there is a significant difference between L_{panel} , and the values provided by the other approaches considered (L_{radio} , L_{Kond} , L_{Rubio} and L_{NCEP}). This can be attributed to the contribution of the panel, since it is not a perfect reflector, its emissivity being different from 0 (Korb *et al.* 1996). Thus, this effect must be corrected for taking into account that the radiance measured over the panel is given by:

$$L_{panel} = \varepsilon_{panel}B(LTS) + (1 - \varepsilon_{panel})L_{desc} \quad (9)$$

where T_{panel} is the temperature of the panel, ε_{panel} is its emissivity for a given channel, and L_{desc} is the hemispheric radiance of the surroundings and the atmosphere, which is actually what we want to measure. Inverting Eq. (9), this last term can be calculated obtaining the downwelling radiance corrected for the panel emissivity effect:

$$L_{desc} = \frac{L_{panel} - \varepsilon_{panel}B(T_{panel})}{1 - \varepsilon_{panel}} \quad (10)$$

To obtain the radiance in Eq. (10) T_{panel} must be known to calculate Planck's function, $B(T_{panel})$; therefore it is necessary to have an independent estimation of this temperature. A contact thermometer, with a precision of ± 1 K, was used to take measurements of the panel on five different points on its surface and taking the average value. The measurement error of panel temperature implies an error in L_{desc} for channels 1 to 4 of the CE312-1 of: ± 0.12 , ± 0.14 , ± 0.13 and ± 0.12 $mWm^{-2}sr^{-1}cm$, respectively, which correspond to an error in terms of temperature of: 0.2, ± 0.2 , ± 0.3 and ± 0.3 K, respectively.

If the effect of the panel emissivity is ignored (considering it to be zero), there is an overestimation of the downwelling radiance for the channels 1 to 4 of: +7, +9, +9 and +6 $mWm^{-2}sr^{-1}cm$, respectively, as can be seen in the graphs of Figure 2. In terms of atmospheric temperature this means differences of: +10, +10, +15 and +10 K, respectively, for channels 1 to 4. An alternative way to see the effect of ignoring the emissivity of the panel is to calculate the difference in terms of LST obtained from eq. (1), when we substitute, the measurement taken directly from the panel (L_{panel}) or the value corrected for the panel emissivity (L_{desc}) for a given value of surface brightness temperature. This temperature difference, $\Delta T = LST_{ign} - LST_{corr}$ (difference between the temperature, if the panel's emissivity is ignored, and the temperature, if this emissivity is considered and corrected), is shown in Figure 3, for the case of a surface whose brightness temperature is 303 K and for different values of surface emissivity. The difference increases when the surface emissivity decreases, and for an emissivity of 0.9 temperature differences for channels 1 to 4 of: +0.4, +0.5, +0.5 and +0.4 K, respectively, can be seen. However, for surface

emissivities larger than 0.94, the effect of the panel emissivity is not significant. In any case, when the emissivity effect is corrected, a better agreement between the measurements of the panel and the other approaches (diffusive approximation and use of atmospheric profiles) is obtained, as can be observed in Figure 2 in the angular interval between 0° and 50° . Beyond 50° there is still a radiance increase related to the Narcissus effect as explained above. However, there is still a radiance difference that could be due to two sources. On the one hand, the contribution of the used goniometer; in this case it would be needed to use a material with a lower emissivity to minimize its radiative contribution. On the other hand, the panel is also accounting for the contribution of surrounding elements (experimenters, instrumentation, etc.), which is not possible with the other methodologies, but which in fact should be considered since this contribution do affect ulterior LST measurements.

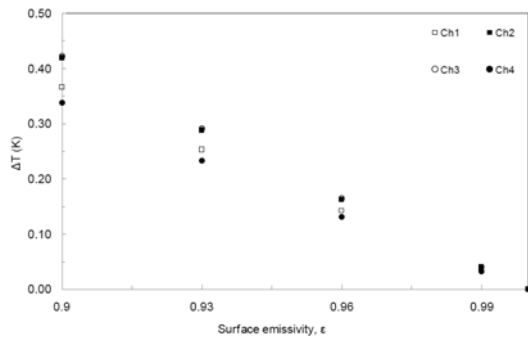


Figure 3. Systematic error in the retrieved LST from a surface, whose brightness temperature is 303 K, if we neglect the effect of emissivity of the panel, depending on the value of surface emissivity.

6 CONCLUSIONS

The hemispheric downwelling radiance ($L_{\text{HEM}}^{\downarrow}$) in the thermal infrared is a parameter which has a big importance in field radiometry. Some different methods exist to obtain $L_{\text{HEM}}^{\downarrow}$. It is possible to determine the irradiance by two ways, the first one by means of direct measurements either pointing to the sky, in the so called diffusive approximation method, or pointing to a diffuse panel with a high reflectivity value in the TIR. The second way to obtain $L_{\text{HEM}}^{\downarrow}$ is introducing an atmospheric profile in a RTC obtaining the radiance by simulation procedures. In this study, a profile obtained from a radiosonde launched concurrently to the measurements in the interest zone, and another provided by NCEP reanalyzes, were used. In the present study it has been carried out a comparison of these different methods already in use to obtain $L_{\text{HEM}}^{\downarrow}$, since to date no evaluation has been

made to determine which of them could be the most suitable. Analyzing the results obtained from the comparison of the four different methods, the first conclusion extracted is that the uncertainties in all the techniques are very similar for the four spectral channels of the radiometer. These uncertainties vary in an interval, in terms of hemispheric downwelling radiance, from ± 1.5 to $\pm 4 \text{ mWm}^{-2}\text{sr}^{-1}\text{cm}$, or equivalently from ± 1.3 to $\pm 3.2 \text{ K}$ in the atmospheric radiative temperature. Although it is worth noting that the lowest uncertainty corresponds to the in situ measurements method. The comparison of the different methods proposed here concludes that the most suitable of them is the use of a diffuse reflectance panel, since that method offers two key advantages over the others. The first one is that the panel can be used under any atmospheric condition, including heterogeneous skies, which are problematic for the diffusive approximation method. The second advantage is that the panel takes into account the radiative contribution of the surrounding elements (trees, experimenters, instrumental, etc.), which doesn't occur either in the case of the simulation methods or the diffusive approximation.

7 REFERENCES

- Berk, A., Anderson, G. P., Acharya P. K., Chetwynd J. H., Bernstein L. S., Shettle, E. P., Matthew M. W. and Adler-Golden, S. M., 1999, MODTRAN 4 user's manual. *Air Force Research Laboratory, Space Vehicles Directorate*, Air Force Materiel Command, Hascom AFB, MA, 95.
- Brogniez, G., Pietras, C., Legrand, M., Dubuisson P., and Haeffelin, M., 2003, A high-accuracy multiwavelength radiometer for in situ measurements in the thermal infrared. Part II: Behavior infield experiments. *Journal of Atmospheric and Oceanic Technology*, 20, 1023-1033.
- Galve, J.M., Coll, C., Caselles, V., and Valor, E., 2008, An atmospheric Radiosounding Database for generating land Surface Temperature Algorithms. *IEEE Transactions on Geoscience and remote Sensing*, 46, 1547-1557, DOI:10.1109/TGRS.2008.916084.
- García-Santos, V., Galve, J. M., Valor, E., Caselles, V., and Coll, C., 2010, Determination of atmospheric water vapour content from direct measurements of radiance in the thermal infrared region. *International Journal of Remote Sensing* (In Press).
- Kalnay, E., Kanamitsu, M., Kistler, R., Collins, W., Deaven, D., Gandin, L., Iredell, M., Saha, S., White, G., Woollen, J., Zhu, Y., Chelliah, M.,

- Ebisuzaki, W., Higgins, W., Janowiak, J., Mo, K. C., Ropelewski, C., Wang, J., Leetmaa, A., Reynolds, R., Jenne, R., and Joseph, D., 1995, NCEP/NCAR 40 Year Reanalysis Project. *Bulletin of the American Meteorological Society*, 437-471.
- Kondratyev, K.Y., 1969, Radiation in the Atmosphere. *New York and London: Academic Press.*
- Korb, A.R., Dybwad, P., Wadsworth W., and Salisbury, J.W., 1996, Portable Fourier transform infrared spectroradiometer for field measurements of radiance and emissivity. *Applied Optics*, 35, 1679-1692.
- Rubio, E., Caselles V., and Badenas, C., 1997, Emissivity Measurements of Several Soils and Vegetation Types in the 8-14 μm Wave Band. *Remote Sensing of Environment*, 59, 490-521.

Incomplete temperature/emissivity separation in ASTER standard products AST08 and AST05

Alan R. Gillespie^{1*}, Elsa A. Abbott², Laura Gilson¹, Glynn Hulley², Juan-C. Jiménez-Muñoz³, and José A. Sobrino³

1. University of Washington, Seattle, WA, USA.

2. Jet Propulsion Laboratory, Pasadena, CA, USA.

3. University of Valencia, Burjassot, Spain.

*Corresponding author email: arg3@uw.edu

ABSTRACT –Temperature T and emissivity ε are independent variables, yet the shape and values of ε spectra retrieved from ASTER thermal-infrared data are incorrectly sensitive to T . Sources of this error include both electronic striping and atmospheric compensation. Spatial filtering and upgrading the atmosphere compensation algorithm to use water-vapor scaling should be considered in making AST05 and AST08.

1. INTRODUCTION

Emissivity ε and temperature T are independent, yet in the standard products for the Advanced Spaceborne Thermal Emission and Reflection radiometer (ASTER), ε appears to decrease with T . The result is to distort spectra in AST05, the standard emissivity product made using the Temperature/Emissivity Separation TES algorithm (Gillespie et al., 1998). Inaccuracies of radiant temperatures for lakes, calculated using the known emissivity spectrum of water and Planck's Law instead of TES, are reported by Hook et al. (2007) to be no larger than estimated by Gillespie et al. (1998) before launch. Finding the cause of the AST05 distortion is necessary if this problem is to be fixed.

Calculating apparent ε' is essentially a ratioing operation:

$$\varepsilon'(\lambda) = \frac{L'(\lambda, T)}{L_{BB}(\lambda, T)} \quad (1)$$

where λ is wavelength, L' is measured spectral radiance and L_{BB} is radiance for a blackbody having the same T . $\varepsilon'(\lambda)$ recovered for different scene elements for compositionally identical targets can vary with L (and T) if $L' = aL + b$ (L is the true value), as can happen if residual calibration and/or atmospheric terms persist in the data, or if there is electronic noise. In this case,

$$\varepsilon_i = \frac{(a_i L_i(T) + b_i)}{L_{BB,i}(T_m)}, \quad T_m = F^{-1} \left(\frac{L'_{ref}(T)}{\varepsilon_{ref}} \right) \quad (2)$$

Where i and ref are image and reference channels, ε_{ref}

is the ε at $i=ref$, F^{-1} is the inverse Planck function, and T_m is the recovered model temperature. Even if $b=0$, ε' is the ratio of Planck functions at different temperatures scaled by a , warping the spectrum.

Four possible sources of error could link ε and T : 1) TES; 2) atmospheric compensation; 3) calibration; and 4) radiometric striping (Jiménez-Muñoz et al., 2010). In this paper we document the sensitivity of ε to T and test ASTER data over homogeneous targets of known ε – lakes – for each possible source. For case (1) we calculate ε as in equation (2) to separate T and ε and compare with AST05. In case (2), we calculate ε spectra for lakes having the same and different surface temperatures from the same image strip and the same radiometric calibration. In case (3), we calculate spectra for lakes from different images. In case (4), we compare spectra for individual adjacent pixels with the same calibration and atmosphere but visibly affected and unaffected by striping. The main focus of the paper is on the spectral shape of the AST05 standard product.

2. APPROACH

2.1 Test sites

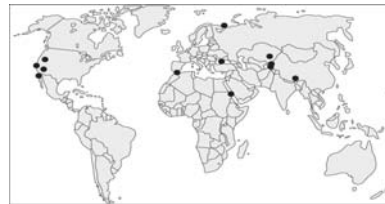


Figure 1. Location of studied water sites.

We used lakes at different elevations and geographic locations (Fig. 1) to document the relationship between ε and T , and to test for the source of connection between ε and T recovered from ASTER data. Data were averaged for regions no larger than 10×10 pixels on a side (some samples were smaller due to lake dimensions). T_m values calculated this way agree with surface data (Hook et al., 2007) and also AST08 values (Sabol et al., 2009), within the accuracy limits suggested by Gillespie et al. (1998). Multi-pixel samples are commonly used in validation experiments to minimize random measurement errors. Lake Tahoe (Fig. 2), instrumented by Hook et al. (2007), was a main site for study.

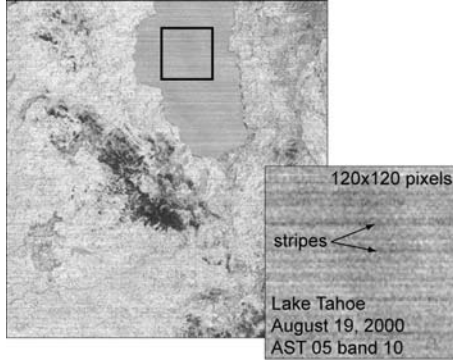


Figure 2. Lake Tahoe study site (California, USA), made from AST05 band 10, contrast-stretched to show detail. Inset shows boxed area in the lake, and the electronic striping.

2.2 ASTER

ASTER, onboard NASA's Terra satellite, includes five TIR image channels (8.3, 8.6, 9.1, 10.6, 11.2 μm) with 90-m resolution and 0.25 K NEAT_{300K}. Striping is not removed. Data are calibrated and atmospherically corrected using MODTRAN 3.5 driven by reanalyzed radiosonde profiles (NCAR/NCEP) resampled to degree grids and 6-hr intervals. MODTRAN is code used to predict atmospheric transmissivity and path radiance (Abreu, and Anderson, 1996). The radiosonde data cannot capture heterogeneity in the boundary layer, and the 1-km DEM used by ASTER imperfectly represents terrain.

2.3 Calculations

Planck's Law, used to relate L to ε and T , is under-determined. The TES algorithm uses an empirical scaling relationship between spectral contrast and minimum emissivity to remove the indeterminacy and separate T and ε by inversion of Planck's Law. TES is used for making the standard products AST05 (surface emissivity) and AST08 (surface temperature) from ASTER images after calibration and atmospheric

correction. We used TES standard products to document the undesired sensitivity of ε to T .

The emissivity spectrum of water is known from laboratory measurements. This information can be used to eliminate the indeterminacy of the inverse Planck's Law, allowing calculation of a model T_m from measured, calibrated and atmospherically corrected values of L available as the AST09T "land-leaving radiance" standard product. The first step is to correct AST09T to "ground-emitted radiance" L_g by compensation for reflected down-welling sky irradiance L_\downarrow :

$$L_{g_i} = L_{AST09_i} - \frac{1-\varepsilon_i}{\pi} L_\downarrow \quad (3)$$

L_\downarrow is available as a layer in the AST09T standard product. Below, we refer to ε calculated using L_g as ε_{AST09} .

We used a reference channel (ASTER band 13) to calculate T_m because it has the least sensitivity to atmospheric transmissivity and path radiance, and used this T_m in Planck's Law to find L_{BB} , and ε_i for the other four ASTER channels. Thus,

$$L_{BB_{13}} = \frac{L_{13}}{\varepsilon_{13}}; \quad (4)$$

$$T_m = c_2^{-1} \lambda / \ln \left(L_{BB_{13}}^{-1} c_1 \lambda^{-5} \pi^{-1} + 1 \right)$$

as in equation (2), and

$$\varepsilon_i = \frac{L_i}{L_{BB,i}(T_m)} \quad (5)$$

where c_1 and c_2 are known constants. Finally, we normalize ε_{AST09} to the laboratory value for water,

$$\varepsilon_{AST09_i} = \frac{\varepsilon_i}{\varepsilon_{13}} \quad (6)$$

Discrepancies between laboratory and AST05 values for ε_i are used to document the existence of an undesired linkage between AST05 and AST08. Discrepancies between AST05 and ε_{AST09T} indicate a problem with the TES algorithm; and discrepancies between ε_{AST09T} and the laboratory water spectra indicate a problem with the AST09T input data.

3. RESULTS

3.1 Agreement of TES results and ε_{AST09}

Normalized ε spectra from AST05 and ε_{AST09} have the same shape, as shown in Figure 3. Therefore TES

does not warp spectra, although it is known to introduce scaling errors to the un-normalized spectra (Gillespie et al., 1998; Hook et al., 2007). This finding allows us to use AST05 or ϵ_{AST09} . Scatter in the emissivity spectra is less for ϵ_{AST09} (Fig. 3b) than for AST05 (Fig. 3a) because ϵ_{13} is known independently in calculating ϵ_{AST09} .

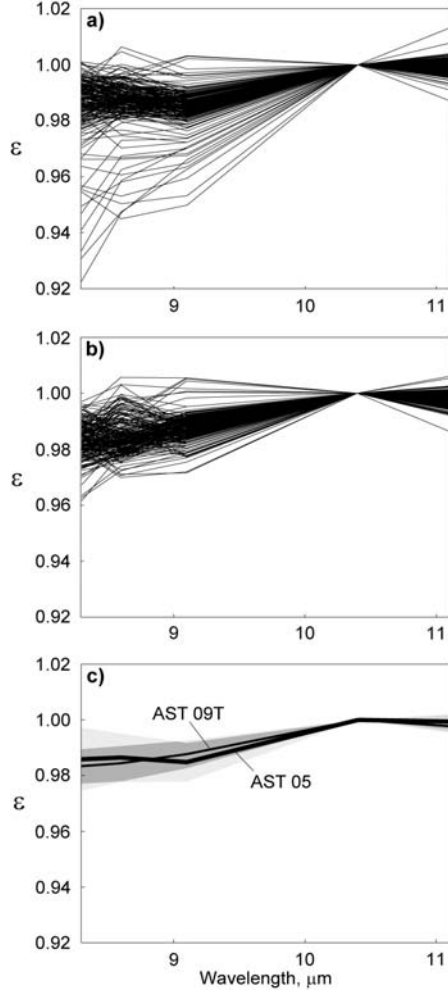


Figure 3. Emissivities for the global data set of 229 multi-pixel water samples. a) ϵ from AST05. b) ϵ from AST09T. c) Mean spectra (solid lines) compared. Shaded areas represent $\pm 1\sigma$.

3.2 Emissivity as a function of temperature

We found that AST05 emissivities varied with the AST08 temperatures for image sub-samples from the lakes and ocean sites shown in Figure 1. To test if this relationship was due to an error in TES, we recalculated the values from the AST09T data, as discussed in §2.3 (Fig. 4). Values of ϵ_{AST09} systematically decreased with T_m about 0.01 over 33 K

for ASTER bands 10 – 12; band 14 showed no significant trend. The different trends show that the spectra change shape systematically with temperature.

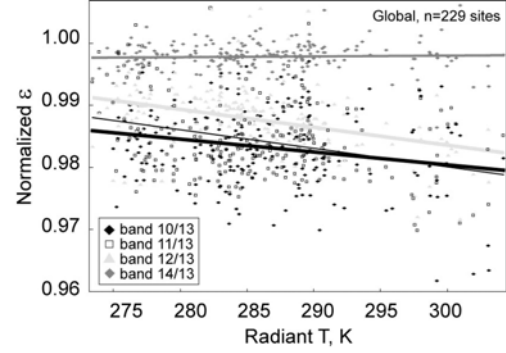


Figure 4. ϵ_{AST09} calculated independently of TES decrease with T_m : $\frac{\Delta \epsilon_{12}}{\Delta T_m} \approx -0.001 K^{-1}$.

As predictable from the reduced spectral contrast at lower temperatures in Figure 4, TES recovers spectra accurately for cold surfaces. Figure 5 presents ϵ_{AST09} spectra for lake ice at 273 K, renormalized to ice emissivities such that accurate recovery gives $\epsilon_i = 1$. The scatter about unity in each channel is about the value (± 0.15) predicted by Gillespie et al. (1998).

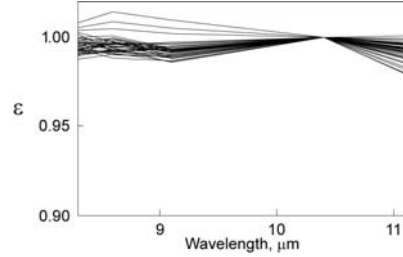


Figure 5. AST05 data of lake ice normalized to the emissivity of ice (*speclib.jpl.nasa.gov*).

3.3 ε in the same lake, same image

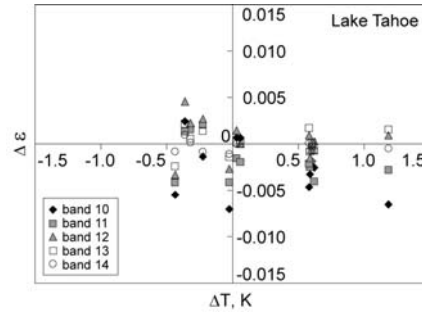


Figure 6. ϵ_{AST09} differences for 12 pairs of sites from the same lake in the same image. Random measurement errors should cause an error in $\Delta \epsilon$ of ~ 0.002 K (1 standard error).

In Figure 6 we compare sample pairs from Lake Tahoe to determine differences between samples when temperatures were similar and calibrations identical. Each sample was averaged from a 10x10 pixel area, as it would be in a validation experiment, and each pair was from the same image up to ~10 km apart. Surface water temperatures were measured directly from buoys in the lake (Hooke et al., 2007). Except for band 10, $|\Delta\epsilon| < 0.005$ K. This is only slightly greater than the 95% expectation of ± 0.004 K, but less than the scatter for the data clouds from Figure 4, even at the same temperature. No trend with ΔT was evident. Band 10 was the most sensitive to atmospheric water vapor.

3.4 ϵ_{AST09T} as a function of air mass

Figure 7 shows spectra for water measured 70 s apart through different air masses. Lake Tahoe is at 1825 m elevation and 530 km NNW of the sea-level site. Although water temperatures were similar ($\Delta T = 1$ K) the optical path lengths and atmospheric corrections were different. The scaling of the spectra depended on spectral contrast or curvature (Gillespie et al., 1998).

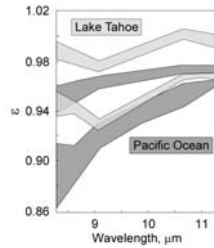


Figure 7. AST05 un-normalized ϵ spectra for 44 individual stripe-free pixels from Lake Tahoe (light, $T=289$ K) and 18 from the Pacific Ocean (dark, $T=288$ K). Shaded areas show the range. For each site the upper envelope is for striping-free pixels, and the lower is for 16 (Tahoe) and 22 (ocean) pixels affected by striping.

Figure 7 shows that mean $\Delta\epsilon_{10}$ and $\Delta\epsilon_{13}$ values between sites (unstriped data) were $10 \times$ greater than expected from $NE\Delta T$ (0.004). Band 10 was the most variable, as might be observed if there were different atmospheric-correction errors at the two sites.

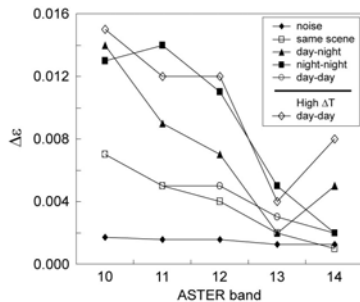


Figure 8. $\Delta\epsilon$ for Lake Tahoe image pairs, 10X10 pixel averages including contributions from stripes. All pair images were acquired within 2 months of each other. “Noise” is calculated from ASTER precision.

If we examine pair-wise differences for the same site measured at different times (Fig. 8), we see a great range of $\Delta\epsilon$ values, with the greatest in band 10. This variability exceeds what can be expected from calibration errors (e.g., Hook et al., 2007). Therefore another factor such as atmospheric temperature and humidity, or striping, must be important in controlling $\Delta\epsilon$.

3.5 Changing atmospheric compensation

To evaluate the role of atmospheric compensation algorithms in producing errors in emissivity recovery, we compared the standard AST05 (from land-leaving radiances calculated with MODTRAN 3.5 alone) to AST05 made from improved atmospheric corrections. MODTRAN 5.2 is a newer version, and “WVS” is an algorithm that adjusts atmospheric humidity profiles using the water-vapor scaling method of Tonooka et al., (2001, 2005) (Fig. 9a).

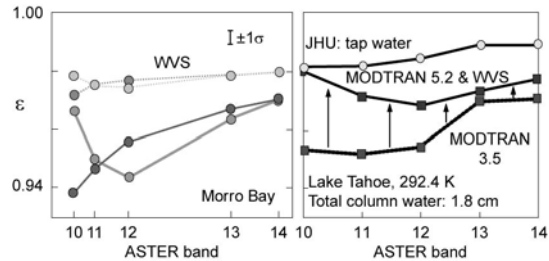


Figure 9. The effect of atmospheric compensation algorithms on AST05 ϵ . **a)** Mean ϵ spectra. The darker gray symbols refer to MODTRAN 3.5, labeled WVS if used in combination with water-vapor scaling. The lighter gray symbols refer to MODTRAN 5.2. **b)** AST05 data (“MODTRAN 3.5”) and AST05 made with MODTRAN 5.2 and WVS, compared to laboratory water spectrum (speclib@jpl.nasa.gov).

Although changing MODTRAN versions has an obvious effect, especially on ϵ_{10} , it is the addition of the WVS code that makes the greatest improvement. Figure 9b shows, for Lake Tahoe data, that MODTRAN 5.2 with WVS most closely approaches the known spectrum for water. The shape of the spectrum, however, is still significantly in error. This residual may be due to errors in characterizing the atmosphere with resampled radiosonde data, even combined with satellite estimates of total column water, rather than algorithm errors.

3.6 Sensitivity of ϵ to atmospheric parameters

Correctly retrieved, ϵ is a surface characteristic that is independent of the atmosphere. In this section, the

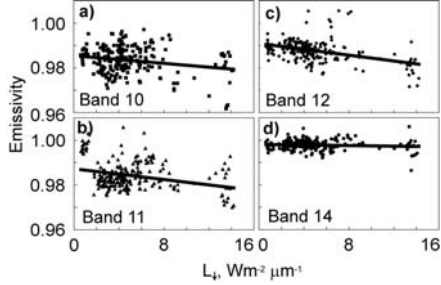


Figure 10. ϵ_{AST09} covaries with AST09T values of L_{\downarrow} for Lake Tahoe data.

erroneous sensitivity of ϵ to down-welling irradiance is examined. L_{\downarrow} is one of the AST09T products. Plotting ϵ_{AST09} against L_{\downarrow} (Fig. 10) shows that it decreases with L_{\downarrow} enough to explain much of the T/ϵ dependency. This is only an indirect relationship, because L_{\downarrow} and the more significant path radiance are correlated. L_{\downarrow} is also correlated with air temperature, because warm air can hold more absorbing/emitting water vapor than cold air can. This predicts a weaker correlation with water temperature, shown in Figure 11, because both water and air temperature fluctuate seasonally. Figure 10 thus implies that ϵ decreases with T because the atmosphere correction, and the uncorrected residual, increases with air temperature.

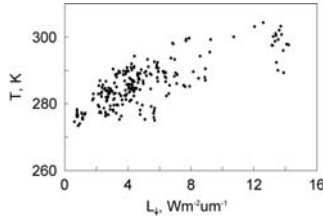


Figure 11. AST09T values of L_{\downarrow} covary with AST08 water temperatures T .

3.7 Striping

Figure 7 showed that for two images from the same orbit, individual striped pixel spectra were distinctly different from unstriped spectra, although neither were accurate. Figure 12 shows that striped emissivity data not completely unrelated to the scene, but are related to unstriped data through a linear equation having non-zero gains and offsets (a and b in equation 2). Therefore, it is possible that striping is causing or contributing to the linkage of ϵ and T .

4. DISCUSSION

4.1 Cause of the linkage

The experiments presented above were designed to determine the cause of the sensitivity of ϵ to T in ASTER standard product AST05. Sabol et al. (2009)

found no sign of error in TES. Our experiment likewise eliminated the role of TES by showing that ϵ calculated independently agreed with AST05 calculated by TES (Fig. 3).

Yet, ϵ varied with T in the global data for which calibration, atmospheric correction, and striping all differed (Fig. 4). Reducing scene T to ~ 273 K (Fig. 5) greatly increased accuracy, implicating atmospheric compensation as an important cause of error. In part, this is because calibration coefficients are determined at higher temperatures and can be expected to perform best at those radiance levels, and less well at lower temperatures, opposite of what we observed.

Isolating spectra for individual pixels affected and not affected by striping, but all at the same temperature and calibrated using the same coefficients, shows that affected spectra are less accurate than unaffected spectra (Fig. 7). Striping is therefore a source of error, especially in the averaged spectra used in validation studies.

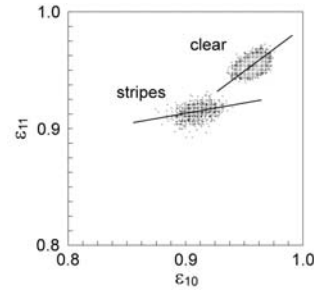


Figure 12. Variation diagram relating ϵ_{11} to ϵ_{10} for data from the Salton Sea, California. “Clear”: no stripes.

Figure 12 is a variation diagram plotting the correlation of individual pixel emissivities in bands 11 and 10. The clusters for pixels differently affected by striping are ellipses with similar eccentricities (scatter) about semi-major axes differently oriented. The semi-major axes define linear transformations (equation 2) relating ϵ_{11} to ϵ_{10} . It is clear that a significant additive coefficient (axis intercept) in equation 2 is involved as well as a gain (a). Therefore, admixing striping can artifactually link ϵ and T . However, that does not preclude errors in atmosphere compensation from doing the same thing.

4.2 Atmospheric compensation effects

It appears that this is indeed the case, because the pixel spectra unaffected by stripes from Figure 7 are different for Lake Tahoe and the Pacific Ocean, and the main difference between the two images – the calibration is identical and the temperatures are within 2 K – lies in the amount of atmosphere and especially humidity between the scene and sensor. This provides

the opportunity for different residuals to affect the land-leaving radiance data after atmospheric compensation. Figure 6 suggests that different air masses over water at the same T decrease accuracy. Figures 10 and 11 demonstrate the ε does covary with L_{\downarrow} , and therefore with the more important factors of transmissivity and path radiance. L_{\downarrow} predictably increases with surface temperature (and, presumably, air temperature).

4.3 Can the linkage be broken?

Figure 9 establishes that improving the atmosphere compensation algorithm will decrease but not eliminate inaccuracy, confirming that in AST05 atmosphere compensation is a problem. Were MODTRAN 5.2 to be used in conjunction with the WVS algorithm in creating the AST09T land-leaving radiance data, the accuracy of the AST05 would likely be improved.

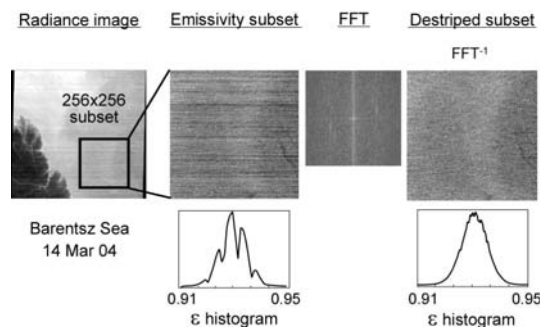


Figure 13. Striping can be reduced by Fast Fourier Filtering, shown for ASTER Band 10. FFT is the transform, and FFT^{-1} is the inverse transform (spatial image) after suppression of striping spikes and streaks.

For some experiments such as product validation, simply editing stripes would improve accuracy. However, the AST05 product would still be adversely affected. Figure 13 shows that, at least for water sites, striping can be simply reduced by standard Fourier filtering, with significant improvement of emissivity histograms. Filtering artifacts such as ringing may pose a problem over scenes containing high-frequency detail, such as shorelines. Careful study may be required before filtering can be used in producing a standard produced automatically.

5. CONCLUSIONS

The ASTER AST05 standard surface emissivity product is less accurate than predicted due to striping and to residual errors in atmosphere compensation that distort the emissivity spectra. The errors increase with increasing surface temperature.

Were MODTRAN 5.2 to be used in conjunction with the WVS algorithm in creating the AST09T land-

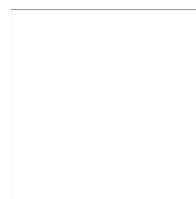
leaving radiance data, the accuracy of the AST05 would likely be improved. Were striping to be reduced, the overall accuracy of AST05 would be improved further. Together, these improvements may increase product accuracy enough to match the TES performance standards estimated by Gillespie et al. (1998). However, reduced errors due to mischaracterization of the atmospheric temperature and relative humidity profiles will probably persist.

6. REFERENCES

- Abreu, L. W. and G. P. Anderson, 1996. The MODTRAN 2/3 Report and LOWTRAN 7 Model. Prepared by Ontar Corporation for PL/GPOS.
- Gillespie, A. R., S. Rokugawa, T. Matsunaga, J. S. Cothren, S. J. Hook, and A. B. Kahle, 1998. Temperature and Emissivity Separation from Advanced Spaceborne Thermal Emission and Reflection Radiometer (ASTER) Images. *Institute of Electrical and Electronics Engineers (IEEE) Transactions on Geoscience and Remote Sensing* 36, 1113-1126.
- Hook, S. J., R. G. Vaughan, H. Tonooka and S. G. Schladow, 2007. Absolute Radiometric In-Flight Validation of Mid Infrared and Thermal Infrared Data From ASTER and MODIS on the Terra Spacecraft Using the Lake Tahoe, CA/NV, USA, Automated Validation Site. *IEEE Transactions Geoscience and Remote Sensing* 45, 1798-1807.
- Jiménez-Muñoz, J.-C., J. A., Sobrino, and Gillespie, A. R., 2010. Noise in emissivity images obtained from Temperature and Emissivity Separation (TES) algorithm: A case study of airborne imagery and implications for ASTER. *Proceedings of the Conference on Recent Advances in Quantitative Remote Sensing III (RAQRS III)*, University of Valencia, Spain, Sept. 27-Oct. 1, this volume.
- Sabol, D. E. Jr., A. R. Gillespie, E. A. Abbott, and G. Yamada, 2009. Field Validation of the ASTER Temperature-Emissivity Separation Algorithm. *Remote Sensing of Environment* 113, 2328-2344.
- Tonooka, H. 2005. Accurate atmospheric correction of ASTER thermal infrared imagery using the water vapor scaling method. *IEEE Transactions on Geoscience and Remote Sensing* 43 (12), 2778-2792.
- Tonooka, H., 2001. An atmospheric correction algorithm for thermal infrared multispectral data over land—a Water-Vapor Scaling method. *IEEE Transactions on Geoscience and Remote Sensing* 39 (3), 682-692.

7. ACKNOWLEDGMENTS

This work was done under contract to NASA.



Atmospheric heating rates related with the vertical distribution of aerosol single scattering albedo in a desert dust situation

J.L. Gómez-Amo^a, A. di Sarra^b, D. Meloni^b, M. Cacciani^c, M.P. Utrillas^a and J.A. Martínez-Lozano^a

^a Solar Radiation Group, University of Valencia, Spain.

^b ENEA Climatic Laboratory, S. Maria di Galeri, Rome, Italy.

^c Dpt. Physics. "La Sapienza" University of Rome, Italy.

jlgomez@uv.es

ABSTRACT The aim of this study is to characterize the sensitivity of the atmosphere to changes in the vertical distribution of aerosol absorption, taken into account through the aerosol single scattering albedo (SSA). The reaction of the atmosphere is measured in terms of the vertical variation of the Earth-Atmosphere radiative fluxes. The case study represents a real atmospheric situation with a desert dust layer (DDL) in the mid troposphere over an urban Boundary Layer (BL) observed at Rome on 20 June 2007. A moderately high aerosol optical depth (AOD), 0.292 at 550nm and low Angström exponent of 0.30 were measured. The case was reconstructed with a radiative transfer model where the SSA of the BL aerosol was varied from a highly absorbing aerosol type (urban) to a highly scattering one (clear marine). The SSA of the DDL is determined keeping fixed the measured SSA of the whole atmospheric column. The simulations show notable changes in the surface and top of the atmosphere (TOA) aerosol radiative forcing (ARF) and the atmospheric heating rates depending on the BL aerosol properties. The changes at the surface are by 6-19 Wm⁻², varying with solar zenith angle while the ARF differences at TOA are between 1-5 Wm⁻² when urban and clear marine BL aerosol were used, showing a smaller dependency on solar zenith angle. A increase of heating in the BL occurs when absorbing particles are present, with significative differences which depend on the aerosol type used in the BL.

1 INTRODUCTION

Aerosol affects the energy budget in the Earth-Atmosphere system directly by extinction and absorption of solar radiation, and indirectly by affecting cloud processes. The aerosols may change the radiative forcing at the surface, at the TOA and within the whole atmospheric column. Shortwave fluxes are strongly affected by changes in the aerosol properties. The aerosol absorption (Stier et al. 2007; Kim et al. 2005; Ramana and Ramanathan, 2006) which is essentially controlled by the presence of black and organic carbon from biomass burning, combustion processes, and dust transport, is one of the key parameter in the climate. Usually the aerosol absorption is taken into account through the aerosol single scattering albedo, which is the ratio between the aerosol scattering and extinction. SSA measurements are generally affected by large uncertainties. The SSA for the whole atmospheric column is retrieved by a combination of sun photometry and inversion methods with uncertainties of 0.03-0.07, taking the higher values when AOD becomes smaller (Dubovik et al. 2000; Meloni et al., 2006). The SSA at the surface is obtained by a combination of scattering and absorption coefficients measured by nephelometers and

aethalometers, respectively. This method presents uncertainties around 0.06 and depends on the relative humidity and other corrections (Richiazzi et al., 2006). The values measured at the surface are often assumed to be representative for the SSA of the boundary layer aerosols, which are considered to be well mixed.

Vertical information on the aerosols properties is interesting for an accurate estimation of the radiation field in the whole atmospheric column, altering the vertical distribution of the heating rates (Guan et al., 2010). The heating rate (heating or cooling) may be produced by aerosol layers and influence the suppression or enhancement of cloud formation, and the atmospheric stability (Ackerman et al., 2000).

The presence of desert dust is fairly common in the Mediterranean region. The changes in the optical properties of the dust layer due to the long range transport and its different state of mixture within the boundary layer yield a large variability in the SSA (di Sarra et al., 2008; Di Biagio et al., 2009; Meloni et al., 2007). The dust transport in the Mediterranean exhibits a peculiar vertical distribution (Di Iorio et al., 2009) that has an effect on the radiative fluxes (Meloni et al., 2005). Frequently, a relatively large dust concentration occurs in the mid troposphere, and is decoupled from the boundary layer. In these cases the

aerosol of the two layers may display totally different optical properties.

The aim of this study is to characterize the sensitivity of the atmosphere to changes in the vertical distribution of aerosol absorption, taken into account though the aerosol single scattering albedo (SSA). The reaction of the atmosphere is measured in terms of the vertical variation of the Earth-Atmosphere radiative fluxes and heating rate profiles. Observed column integrated aerosol optical properties and vertical distribution are used as input data to the MODTRAN (MODerate spectral resolution atmospheric TRANsmision) radiative transfer code. Simulations are performed for aerosols with varying absorption properties in the boundary layer, when a dust layer is present in the free troposphere.

2 METHODOLOGY

The aerosol radiative forcing (ARF) is defined as the change in net radiative flux produced by aerosols at a fixed altitude in the atmosphere:

$$ARF = (F^\downarrow - F^\uparrow) - (F^{0\downarrow} - F^{0\uparrow}) \quad (1)$$

where F^\downarrow and F^\uparrow are the downward and upward radiative fluxes with aerosol, respectively, and $F^{0\downarrow}$ and $F^{0\uparrow}$ are the same fluxes in an aerosol-free atmosphere. The ARF at the ground level is the difference between net (downward minus upward) irradiances for an atmosphere with aerosol and without aerosol. At the top of the atmosphere ARF is defined as the upward component without aerosol minus the upward component with aerosol. The difference between TOA and surface forcing is the atmospheric forcing, which represents the amount of energy trapped within the atmosphere due to the presence of absorbing particles. The heating rate ($\partial T/\partial t$) is determined by the vertical gradient of the net radiative flux as in the equation (2),

$$\frac{\partial T}{\partial t} = -\frac{g}{C_p} \frac{\partial F_{net}}{\partial p} \quad (2)$$

where T is temperature, t is time, g is the gravity acceleration, C_p is the specific heat of dry air at constant pressure, and $\partial F/\partial p$ is the gradient of the net radiative flux with the pressure.

3 OBSERVATIONS AND MODELLING

3.1 Observations

The case study represents a real atmospheric situation with a desert dust layer (DDL) in the troposphere over an urban Boundary Layer (BL) up to 1-km altitude observed at Rome on 20th June 2007. The vertical profile of the extinction coefficients reveals the presence of aerosol particles from the ground up to 4

km (Fig. 1). A moderate high Aerosol Optical Depth (AOD) of 0.292 at 550nm and low Angström Exponent (AE) of 0.30 were measured (Table 1), suggesting the presence of large particles. Such a low value of AE is not usual in Rome, and is generally associated with dust events. Trajectory analysis confirms that aerosols in the free troposphere were transported from the Sahara desert. Surface chemical analysis of trace components supports the presence of urban aerosol species in the boundary layer.

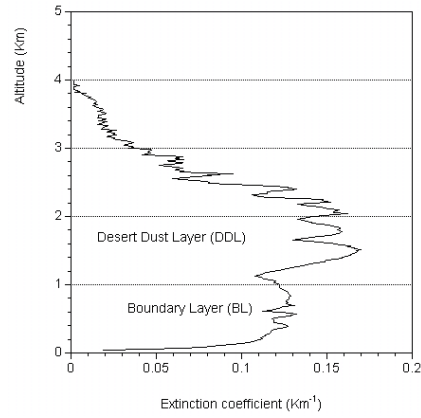


Fig. 1. Aerosol extinction profile from lidar measurements at Rome on 20 June 2007

3.2 Modelling

The radiative transfer code MODTRAN version 4.2 (Berk et al., 1998) was used to reproduce the atmospheric structure, composition and radiative fluxes simulating the irradiances at different altitudes in the atmosphere over the spectral range 0 - 50 cm^{-1} using a maximum spectral resolution of 2 cm^{-1} . The discrete ordinate algorithm (Stamnes et al., 1998) with 16 streams was selected to solve the radiative transfer equation including multiple scattering. Radiative fluxes are integrated over the shortwave spectral region (280-2800 nm). The model has been modified to vary the thickness and the optical properties of the aerosol layer with respect to the prescribed scheme, following Stone et al. (2007, 2008). Furthermore it is also possible to introduce the experimental aerosol extinction profile from lidar measurements.

For the purpose of the analysis, we assume that the layer above 1 km altitude is constituted of desert dust, while a different aerosol type is present in the boundary layer, which is assumed to extend from the surface to 1 km (where the aerosol extinction displays a relative minimum). The aerosol type in the boundary layer is varied with the aim of investigating the sensitivity of the radiative fluxes and heating rates to changes in SSA (Gómez-Amo et al., 2010).

Table 1. Aerosol optical properties used in the simulations: HL (homogeneous aerosol layer), ABL (Urban aerosols in the boundary layer), and SBL (clean marine aerosols in the boundary layer).

λ (nm)	HL Measured		ABL (Absorbent Boundary Layer)				SBL (Scattering Boundary Layer)			
	AOD	SSA	Urban BL		Desert Dust		Clear Marine BL		Desert Dust	
	AOD	SSA	AOD	SSA	AOD	SSA	AOD	SSA	AOD	SSA
415	0.318	0.76	0.190	0.83	0.130	0.66	0.140	0.99	0.178	0.58
550	0.292	0.81	0.134	0.82	0.157	0.80	0.134	0.99	0.157	0.66
863	0.253	0.92	0.077	0.77	0.175	0.98	0.126	0.99	0.127	0.85
AE	0.309		1.257				0.147			

The optical properties of the boundary layer aerosol type are taken from the Optical Properties of Aerosols and Clouds (OPAC) database (Hess et al. 1998). Once the aerosol in the boundary layer is fixed, we used the following relationships to retrieve the spectral optical properties of desert dust:

$$AOD_{T\lambda} = AOD_{BL\lambda} + AOD_{FT\lambda} \quad (3)$$

$$SSA_{T\lambda} AOD_{T\lambda} = SSA_{BL\lambda} AOD_{BL\lambda} + SSA_{FT\lambda} AOD_{FT\lambda}$$

In order to analyze the role of the aerosol SSA vertical profile on shortwave fluxes and heating rate we defined three different cases. Only the spectral absorption coefficients are varied among the three cases, while the spectral extinction coefficients and asymmetry parameters are kept fixed. In the first case, defined as homogeneous layer (HL), the measured SSA is assumed through out the atmospheric column. In the second case, identified as absorbing boundary layer aerosols (ABL), the boundary layer is characterized by urban aerosols; in the third case, defined as scattering boundary layer aerosols (SBL), it is characterized by clean marine particles. The optical properties of the desert dust layer for cases ABL and SBL are changed as explained above. Thus, the column optical properties are always the same in all calculations, and only the vertical distribution of SSA is varied. Using these boundary layer aerosol types the most wide range of aerosol absorption is covered. Data are summarized in Table 1 (Gómez-Amo et al., 2010).

The three cases are thus relative to an homogeneous layer (HL), a highly absorbing layer below and a mainly scattering layer above (ABL), and a scattering layer below and an absorbing layer above (SBL).

4 RESULTS

ARF at the surface, TOA, and in the atmosphere together with the atmospheric heating rates were calculated for the three cases using 10 values of the solar zenith angle, SZA (SZA= 10, 20, 30, 40, 50, 60, 65, 70, 75, 80°).

4.1 Shortwave aerosol radiative forcing

The vertical variation of aerosol absorption through the SSA produces large variations in the diffuse fluxes at both the surface and TOA. These variations are opposite in sign when ABL and SBL were used. The BL role in the determination of the diffuse flux is larger for large particles when the forward scattering is dominant. The SBL case shows an increase of diffuse irradiances at both the surface and TOA with respect to the HL case, indicating that there is a net loss of energy in the atmosphere. Conversely, the ABL case yields a reduction of the diffuse flux at both the surface and TOA. These differences in the diffuse fluxes cause important differences in the ARF among the three cases. The differences in ARF with respect to HL are larger for highly scattering BL.

At the surface, the increase of absorption in BL (ABL case) produces an increase in the surface ARF with respect to HL (up to -106 Wm^{-2} at $\text{sza} = 60^\circ$), while the presence of a scattering BL (SBL case) produces a large decrease of ARF (up to -87 Wm^{-2} at $\text{sza} = 60^\circ$) with respect to the ARF obtained when HL is used (102 Wm^{-2}). The forcing at the surface usually presents a minimum between 40 and 60° zenith angle (Meloni et al., 2005) followed by an increase for SZA larger than 60° . When the scattering BL (SBL) is used, the minimum shifts towards larger solar zenith angles. Conversely, the ARF remains constant with SZA up to 50° if ABL is used. The differences among the three cases decrease with solar zenith angle due to the increase of the photon path length inducing a great reduction of ARF. The difference HL-ABL varies from 6 to 1 Wm^{-2} from 10° to 80° solar zenith angle. The differences are much larger but opposite in sign when HL-SBL are considered, reaching a maximum of 19 Wm^{-2} at 10° SZA, and a minimum of 6 Wm^{-2} at 80° .

The ARF at TOA is negative for all cases inducing an increase of solar radiation scattered back to space. The ARF decreases up to 75° , where it displays a minimum for all cases. The effect of introducing two aerosol layers with different absorption properties has a large impact on the TOA ARF, especially for the SBL case. The absolute ARF is larger for SBL than for HL with

differences of about 5 Wm^{-2} for all SZA range. The ARF for ABL is close to HL, with differences less than 1 Wm^{-2} for all SZA.

The atmospheric ARF is directly related to the aerosol absorption, and is larger for ABL (85 Wm^{-2}) than for HL (80 Wm^{-2}) and SBL (60 Wm^{-2}) at a solar zenith angle of 60° .

The absolute differences HL-ABL and HL-SBL are always larger at the surface than at TOA. Nevertheless, the relative differences are larger at TOA than at the surface. The HL-ABL relative differences are -4 and 12% at the surface and TOA, respectively. In case of HL-SBL the differences are 15 and -63% at the surface and TOA, respectively.

A detailed explanation of the ARF behaviour and the differences among the three considered cases can be found in Gómez-Amo et al. (2010).

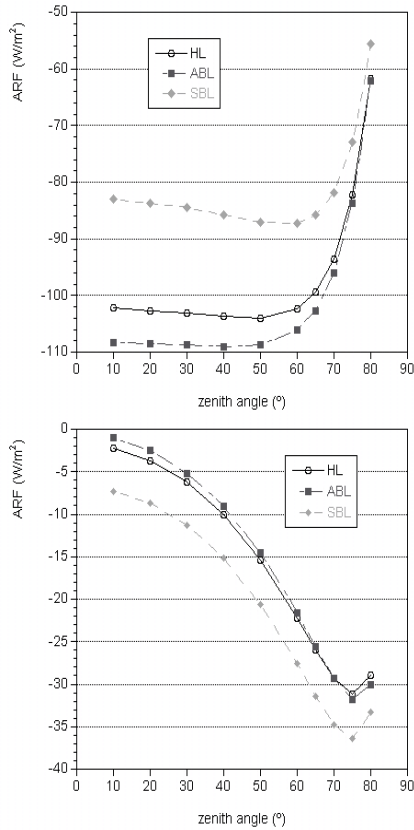


Fig. 2. Aerosol radiative forcing at the surfaces (a) and at Top of the atmosphere (b). for the three cases: HL, ABL and SBL.

4.2 Atmospheric heating rates

The variation of the atmospheric heating rates among the three cases (HL, ABL, SBL) considered in this work are shown in Fig. 3 (a and b) for 20 and 60° SZA respectively.

In general the atmospheric heating rate increases with height inside the BL, from ground to 1-km altitude. The heating reaches the maximum value at the base of DDL, and remains almost constant inside of DDL region, between 1-2 km height, where the aerosol extinction coefficient reaches the highest values. Furthermore, a slight decrease of the heating rate is observed above 2 km, as the aerosol extinction coefficient diminishes. This behaviour is similar for all cases (HL, ABL and SBL) and for all solar zenith angles analyzed, and can be considered independent of the boundary layer aerosol type used in the simulations.

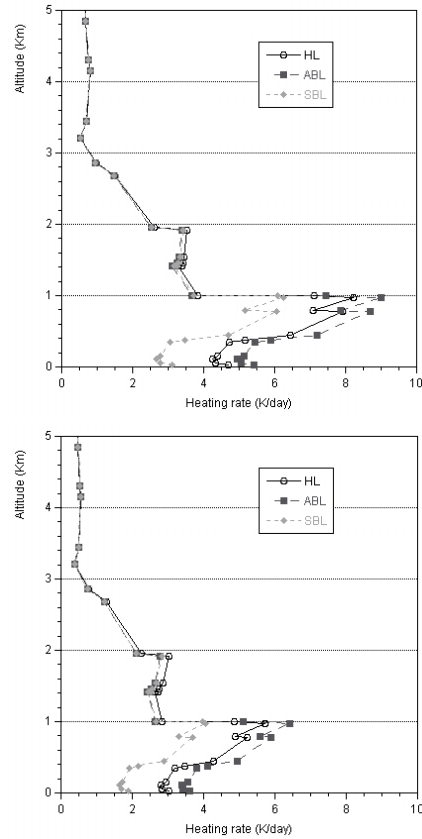


Fig. 3. Atmospheric heating rate profiles for the three cases: HL, ABL and SBL at a) sza = 20° and b) sza = 60° .

The most important effects in the atmospheric heating rate are observed inside of the BL itself, where the largest differences among the three cases were observed. The heating increases as the BL absorption increases. The surface heating is 3.1, 4.7 and 5.4 K/day for SBL, HL, and ABL, respectively at 20° solar zenith angle. The heating rate increases up to 1-km height, where a maximum value is observed for the three cases. The heating rate values are of 6.2, 8.2 and

9.0 K/day for SBL, HL, and ABL, respectively at the bottom of the DDL at 20° zenith angle. The difference between HL and ABL cases is 0.7K/day and displays a small variation by about 0.01 K/day in the whole boundary layer. Conversely, the difference between HL and SBL increases with altitude from 1.6 K/day at the surface to 2 K/day at the top of the boundary layer. The differences among the three cases disappear inside the DDL, where the heating rate values remains almost constant with altitude in the 1-2 km height range. The variations in the atmospheric HR inside of the DDL are smaller than those observed in BL, with changes by less than 0.2 K/day between the three cases. The changes in the aerosol absorption in the boundary layer have negligible effects on the DDL heating rates. The strongest DDL heating occurs for the measured SSA value, due to an excess of absorption in this layer.

These results are different from those reported by Guan et al. (2010), who reported an increase of aerosol heating rate inside the dust layer itself. In that case they considered the aerosol heating rate, which takes into account only the aerosol effect, instead of the atmospheric heating rate that we used here. The constant atmospheric heating rate observed in Fig. 3 (a and b) in the first kilometer of the DDL could be due to an inverse behaviour of both, the aerosol and the water vapour effects, which yield a net compensation in the atmospheric heating rates. If this is the case, the aerosol heating rate must increase (Guan et al., 2010) while the water vapour heating rate decreases due to the water vapour decrease with height. In fact, the relative humidity is high, about 60-80%, in the first 500 meters above the surface, and decreases with altitude up to 17% at 2 km. (Fig. 4).

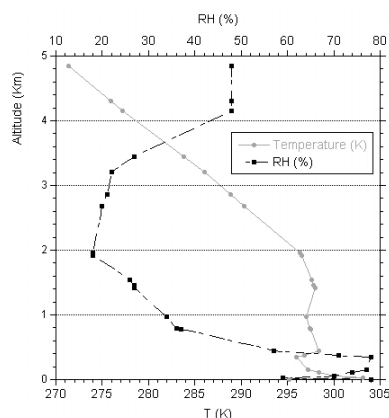


Fig. 4. Atmospheric profiles for Temperature (T) and Relative Humidity (RH) from radio sounde measurements on 20 June, 2007 at Pratica di Mare (Roma).

5 CONCLUSIONS

The aerosol radiative forcing strongly depends on the aerosol SSA vertical distribution, with differences up to 19 Wm⁻² among the studied cases at the surface, and up to 5 Wm⁻² at TOA. These changes are about 15% and 63% of the surface and TOA aerosol radiative forcing, respectively. The largest differences were observed when the scattering BL was used, with a net loss of energy yielding a cooling effect on both, surface and TOA ARF, with respect to HL. Conversely, the absorbent BL produces stronger heating than HL at both the surface and TOA.

Changes in the vertical distribution of the aerosol absorption have the largest impact on atmospheric heating rates inside the BL region. The atmospheric heating rate reaches the maximum intensity just at the bottom of DDL, and it is reduced drastically inside of DDL where it keep invariable between 1-2 km and it is continuously reduced as the altitude increases above 2 km. The largest differences were observed for the scattering BL case, where the surface heats less than in the HL and ABL cases. The differences between HL-ABL cases display a small variation in the boundary layer, about 0.01 K/day, while the differences between HL-SBL increase with height inside the boundary layer. The heating in the DDL region is very similar in the three cases, with variations less than 0.2 K/day. In this region the heating rate is larger for HL than for ABL and SBL, due to an excess of absorption in this layer.

6 REFERENCES

- Ackerman, A. S., Toon, O. B., Stevens, D. E., Heymsfield, A. J., Ramanathan, V., Welton, E. J., 2000, Reduction of Tropical Cloudiness by Soot, *Science* 288, 1042-1047.
- Berk, A., G.P. Anderson, P.K. Acharya, M.L. Hoke, J.H. Chetwind, L.S. Bernstein et al., 1998, MODTRAN4 Version 3 Revision 1 User's Manual Tech. rep., Hanscom Air Force Base, MA, USA: Air Force Research Laboratory.
- Di Biagio, C., di Sarra, A., Meloni, D., Monteleone, F., Piacentino, S. and Sferlazzo, D., 2009, Measurements of Mediterranean aerosol radiative forcing and influence of the single scattering albedo, *J. Geophys. Res.*, 114, D06211, doi: 10.1029/2008JD011037.
- Di Iorio, T., di Sarra, A., Sferlazzo, D. M., Cacciani, M., Meloni, D., Monteleone, F., Fuà, D. and Fiocco G., 2009, Seasonal evolution of the tropospheric aerosol vertical profile in the central Mediterranean and role of desert dust, *J. Geophys. Res.*, 114, D02201, doi:10.1029/2008JD010593.

- di Sarra, A., Pace, G., Meloni, D., De Silvestri, L., Piacentino, S., and Monteleone, F., 2008, Surface shortwave radiative forcing of different aerosol types in the central Mediterranean, *Geophys. Res. Lett.*, 35, L02714, doi:10.1029/2007GL032395.
- Dubovik, O., Smirnov, A., Holben, B. N., King, M. D., Kaufman, Y.J., Eck, T. F. and Slutsker, I., 2000, Accuracy assessments of aerosol optical properties retrieved from AERONET sun and sky-radiance measurements, *J. Geophys. Res.*, 105, 9791-9806.
- Gómez-Amo, J.L., di Sarra, A., Meloni, D., Cacciani, M., Utrillas, M.P., 2010, Sensitivity of shortwave radiative fluxes to the vertical distribution of aerosol single scattering albedo in the presence of a desert dust layer. *Atmos. Env.* 44, 2787-2791.
- Guan, H., Schmid, B., Bucholtz, A., Bergstrom, R., 2010, Sensitivity of shortwave radiative flux density, forcing, and heating rate to the aerosol vertical profile, *J. Geophys. Res.*, 115, D06209, doi: 10.1029/2009JD012907.
- Hess, M., Koepke, P., Schult, I., 1998, Optical properties of aerosols and clouds: the software package OPAC. *Bull. Amer. Meteorol. Soc.* 79, 831-844.
- Kim, D. H., Sohn, B. J., Nakajima, T. and Takamura, T., 2005, Aerosol radiative forcing over east Asia determined from ground-based solar radiation measurements, *J. Geophys. Res.*, 110, D10S22, doi:10.1029/2004JD004678.
- Meloni D., di Sarra, A., Biavati, G., DeLuisi, J.J., Monteleone, F., Pace, G., Piacentino, S. and Sferlazzo, D., 2007, Seasonal behavior of Saharan dust events at the Mediterranean island of Lampedusa in the period 1999-2005, *Atmos. Environ.*, 41, 3041-3056.
- Meloni, D., di Sarra, A., di Iorio, T., Fiocco, G., 2005, Influence of the vertical profile of Saharan dust on the visible direct radiative forcing. *Journal of Quantitative Spectroscopy & Radiative Transfer*, 93, 397-413.
- Meloni, D., di Sarra, A., Pace, G. and Monteleone, F., 2006, Optical properties of aerosols over the central Mediterranean. 2. Determination of single scattering albedo at two wavelengths for different aerosol types, *Atmos. Chem. Phys.*, 6, 715-727.
- Pace, G., di Sarra, A., Meloni, D., Piacentino, S. and Chamard, P., 2006, Aerosol optical properties at Lampedusa (central Mediterranean). 1. Influence of transport and identification of different aerosol types, *Atmos. Chem. Phys.*, 6, 697-713.
- Ramana, M. V., and Ramanathan, V. 2006, Abrupt transition from natural to anthropogenic aerosol radiative forcing: Observation at the ABC-Maldives Climate Observatory, *J. Geophys. Res.*, 111, D20207, doi:10.1029/2006JD007063.
- Ricchiazzi, P., Gautier, C., Ogren, J. A. and Schmid, B., 2006, A comparison of aerosol optical properties obtained from in situ measurements and retrieved from Sun and sky radiance observations during the May 2003 ARM Aerosol Intensive Observation Period, *J. Geophys. Res.*, 111, D05S06, doi:10.1029/2005JD005863.
- Stamnes, K., Tsay, S. C., Wiscombe, W. and Jayaweera, K., 1988, Numerically Stable Algorithm for Discrete-Ordinate-Method Radiative Transfer in Multiple Scattering and Emitting Layered Media, *Appl. Opt.*, 27, 2502-2509.
- Stier, P., Seinfeld, J. H., Kinne, S. and Boucher, O. 2007, Aerosol absorption and radiative forcing, *Atmos. Chem. Phys.*, 7, 5237-5261.
- Stone, R.S. Anderson, G.P., Andrews, E., Dutton, E. G., Shettle E.P. and Berk, A., 2007, Incursions and radiative impact of Asian dust in northern Alaska. *Geophys. Res. Lett.*, doi: 10.1029/2007GL029878.
- Stone, R.S. Anderson, G.P., Shettle, E.P., Andrews, E., Loukachine, K., Dutton, E. G., Schaaf, C. and Roman III, M.O., 2008, Radiative impact of boreal smoke in the Arctic: observed and modeled. *J. Geophys. Res.*, 113, doi: 10.1029/2007JD009657.

Evaluation of MODIS atmospheric profiles product for atmospheric correction in the thermal infrared domain

J. C. Jiménez-Muñoz, J. A. Sobrino, C. Mattar, B. Franch, G. Sòria, V. Hidalgo, R. Oltra-Carrió, and Y. Julien

Global. Change Unit, Image Processing Laboratory, University of Valencia; P.O. Box 22085, E-46071 Valencia SPAIN

Email: jcjm@uv.es

ABSTRACT- *In this work we analyze the results obtained when MODIS atmospheric profiles product (MOD07) is used in the atmospheric correction of Thermal Infra-Red (TIR) data for Land Surface Temperature (LST) retrieval purposes. LST retrievals from Landsat5-TM and Terra-ASTER TIR data after atmospheric correction using MOD07 were compared to the ones obtained when local soundings are considered. Analysis was focused on imagery acquired in July 2004 and 2005 over an agricultural area in Spain. LST was retrieved from TM data using a single-channel algorithm, whereas the Temperature and Emissivity Separation (TES) algorithm was applied to ASTER data (in this last case surface emissivities were also retrieved). The difference between MOD07- and local sounding-based corrections provided Root Mean Square Errors (RMSE) below 0.8 K. Therefore, MOD07 product provides useful atmospheric information at higher spatial resolution (5 km) than other infrared soundings or reanalysis-based products, although its use is limited from 2000 to present. The feasibility of applying TES algorithm to MODIS data using atmospherically corrected data in a pixel-by-pixel basis is also discussed.*

1 INTRODUCTION

The removal of the atmospheric perturbation introduced in the signal registered by remote sensing sensors is one of the key elements in order to obtain accurate geo/biophysical products for Earth Observation purposes. The relationship between Top Of Atmosphere (TOA) signal and ground-level signal is given by the Radiative Transfer Equation (RTE). In the case of Thermal Infra-Red (TIR) data scattering processes are commonly neglected and only atmospheric absorption is considered. In general terms, conversion from TOA to ground-level signal is referred as Atmospheric Correction or Compensation (AC). When the AC is addressed directly from inversion of the RTE, one needs to compute the different atmospheric parameters involved. In the case of TIR region (see Eq. 1, spectral notation omitted), these parameters are: atmospheric transmissivity (τ) and atmospheric up-welling (L_u) and down-welling (L_d) radiances. Land Surface Temperature (LST or T_s) retrieval from TIR data also requires the knowledge of surface emissivity (ε).

$$L_{TOA} = \varepsilon \tau B(T_s) + (1 - \varepsilon) \tau L_d + L_u \quad (1)$$

Computation of atmospheric parameters requires the knowledge of vertical distribution for some

meteorological variables (atmospheric profile) to be introduced into a Radiative Transfer Code (RTC). Spectral outputs are then averaged according to the system spectral response of a given sensor band.

Since in most cases local soundings are not available, it is important to assess the feasibility of using other external sources of atmospheric profiles for accurate AC of TIR imagery. This work focuses on profiles extracted from MODIS Atmospheric Profiles Product (MOD07), which provides daily atmospheric profiles (day and night) at 5 km spatial resolution and at a world-wide scale since year 2000. MOD07 values for a single pixel centered at the study area have been compared to local soundings for two test dates, and differences in the AC of TIR imagery (ASTER and L5/TM) when using both sources have been calculated. MODTRAN-4 RTC (Berk et al., 1999) has been used in this analysis. Maps of atmospheric parameters at continental scale (Iberian Peninsula) were also created by application of MODTRAN-4 at every single MOD07 pixel.

More details related to this work can be found in Jiménez-Muñoz et al. (2010), in which the comparison is extended to Reanalysis-based products and AC is performed also to VNIR-SWIR data.

2 METHODS

The study area is located in the agricultural area of Barrax (Albacete, Spain: 39° 3' N, 2° 6' W, 700m; see Fig. 1). Dates considered in this study were 18-July-2004 and 13-July-2005, as part of two field campaigns (SPARC and SEN2FLEX, respectively) organized by European Space Agency (ESA).

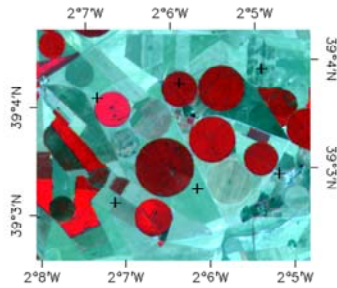


Figure 1. The Barrax test area (RGB composition from ASTER VNIR data).

Local soundings (Vaisala RS80) were compared to MODIS atmospheric product MOD07 at 5x5 1-km pixel resolution with height, air and dew temperatures at 20 pressure levels (see Fig. 2).

LST was retrieved from Landsat/TM data using the single-channel algorithm proposed by Jiménez-Muñoz et al. (2009), using input ε obtained from NDVI approaches (Sobrino et al., 2008). LST and ε was retrieved from ASTER data using the Temperature and Emissivity Separation (TES) algorithm (Gillespie et al., 1998).

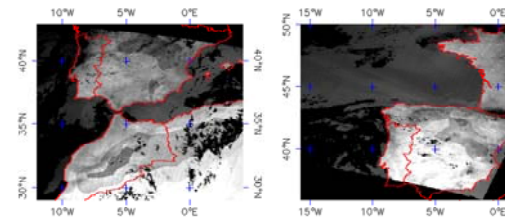


Figure 2. Spatial coverage of MOD07 products in 2004 (left) and 2005 (right).

MODIS products MOD02 (at-sensor radiances) and MOD11 (LST and emissivity) were also used in the analysis of TES results when the algorithm is applied to MODIS, as will be explained below.

3 RESULTS FROM MOD07

Air and dew temperature values extracted from MOD07 pressure levels (pixel centred at Barrax coordinates) were compared to profiles provided by

local soundings. Figures 3 and 4 show the results obtained in the comparison for 2004 and 2005 test cases, respectively. Air temperature profiles show a good agreement between MOD07 and local sounding values, with slight differences at first levels (approximately between 1000 and 700 hPa). Higher differences were found in the case of dew temperatures. A similar general tendency is observed for MOD07 and local soundings, but significant discrepancies are revealed in the region between 700 and 400 hPa.

Since MOD07 provides atmospheric profiles at pixel level (5-km), atmospheric parameters involved in the atmospheric correction can be spatialized. For this purpose MOD07 profiles at every single pixel were introduced to MODTRAN-4 radiative transfer code and then spectral magnitudes were averaged to ASTER and TM bands. Results are presented in Figures 5 and 6, respectively.

LST was retrieved from ASTER and Landsat5/TM data using both MOD07 and local soundings for atmospheric correction. A significant agreement was found in this comparison, with a bias (MOD07-SOUND) of (-0.6 ± 0.5) K in the case of ASTER and (0.6 ± 0.1) K in the case of TM. Band emissivities retrieved from ASTER provided bias of 0.03 for bands 10 to 12 (located in 8-9.3 μm) and bias below 0.008 for bands 13 and 14 (10-12 μm).

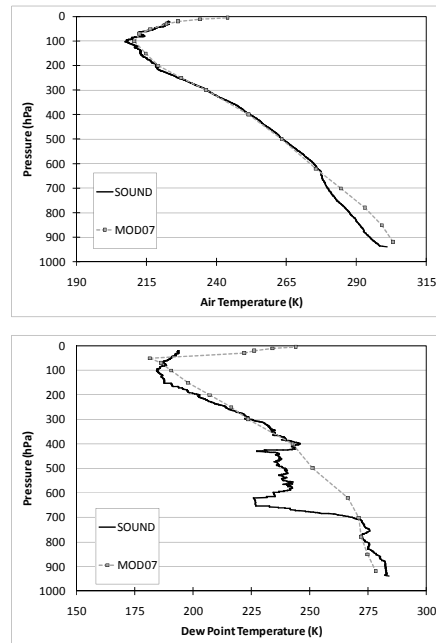


Figure 3. Air (top) and dew (bottom) temperature profiles extracted from local soundings (SOUND) and MOD07, 18th July, 2004 (11:00 UTC).

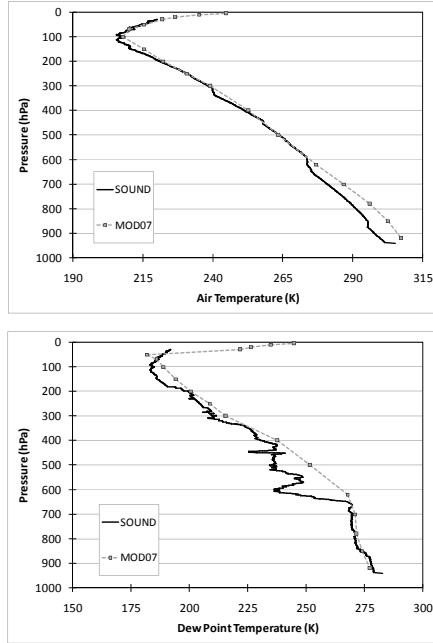


Figure 4. Air (top) and dew (bottom) temperature profiles extracted from local soundings (SOUND) and MOD07, 13rd July, 2005 (11:45 UTC).

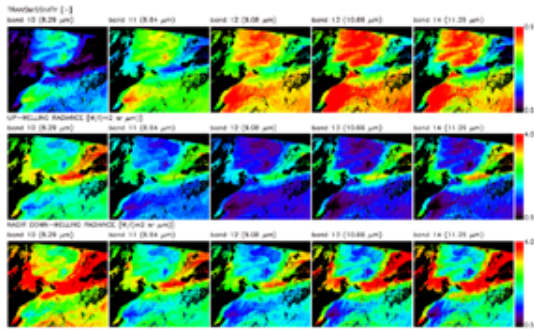


Figure 5. Atmospheric parameters obtained from MOD07 for ASTER TIR bands (18-July-2004, 11:00 UTC).

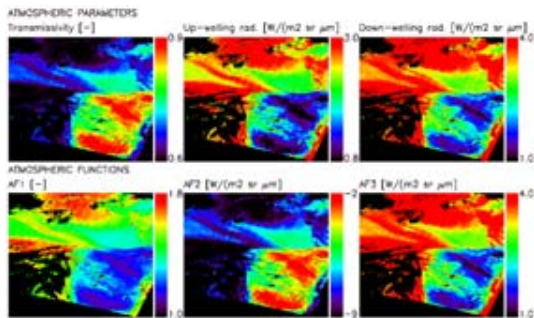


Figure 6. Atmospheric parameters obtained from MOD07 for Landsat5/TM band 6 (13-July-2005, 11:45 UTC).

4 TES RESULTS FROM MODIS DATA

Despite that surface emissivities can be obtained from different approaches in which TIR data are not used (e.g. NDVI or classification-based approaches), it has been recognized that only surface emissivities retrieved from the TIR data itself are useful for land cover characterization and change (French et al., 2008; French and Inamdar, 2010). TES algorithm developed for ASTER TIR data (Gillespie et al., 1998) allows the retrieval of both surface temperature and emissivity from multispectral TIR data (at least 3 bands). TES algorithm can be applied to MODIS sensor, since it has 3 TIR bands in the atmospheric window (bands 29, 31 and 32, with effective wavelengths of 8.54, 11.02 and 12.04 μm). TES algorithm has been partially applied to MODIS data in French et al. (2008) and French & Inamdar (2010) (they applied NEM module and not the complete TES algorithm). Hulley et al. (2010) applied the complete TES algorithm to MODIS data and compared the results with the MODIS LST product (MOD11) over the Namib Desert. They found in general a good agreement between both LST retrievals.

TES algorithm has been applied to MOD02 at-sensor radiances (1km) using atmospheric parameter maps for MODIS bands 29, 31 and 32 obtained from MOD07 products (5km). LST and ϵ retrievals were compared to MOD11v5 product (only bands 31 and 32 are used in the product). Figure 7 shows the results obtained for the test date on 18 July 2004. Maps of TES derived LST and emissivities (bands 29, 31 and 32) are presented respectively in Figs. 4d to 4g. Differences (TES retrievals minus MOD11) for emissivities at bands 31 and 32 and LST are presented in Figs. 4h, 4i and 4j, respectively. Differences over the Iberian Peninsula and Northern Morocco, Argelia and Tunisia, which are areas with mixed to high vegetation cover (see NDVI in Fig. 4c) show an acceptable agreement, typically within ± 0.015 for ϵ and ± 1.5 K for LST. However, huge differences have been found in the Sahara Desert (> 6 K), the MOD11 product providing lower LST values. This result could be due to the different emissivity values retrieved with TES in comparison to the values extracted from MOD11 (differences up to 0.06 for band 31 and up to 0.02 for band 32), and also to a higher water vapor content (> 2 cm) over North Africa in comparison to the Iberian Peninsula (< 2 cm) (see water vapor map in Fig. 4b). Huge differences have been also found at the edges of the image, which can be attributed to an angular effect (see MODIS view angle map in Fig. 4a). A deeper analysis is required to assess which product (TES or MOD11) provides more accurate values.

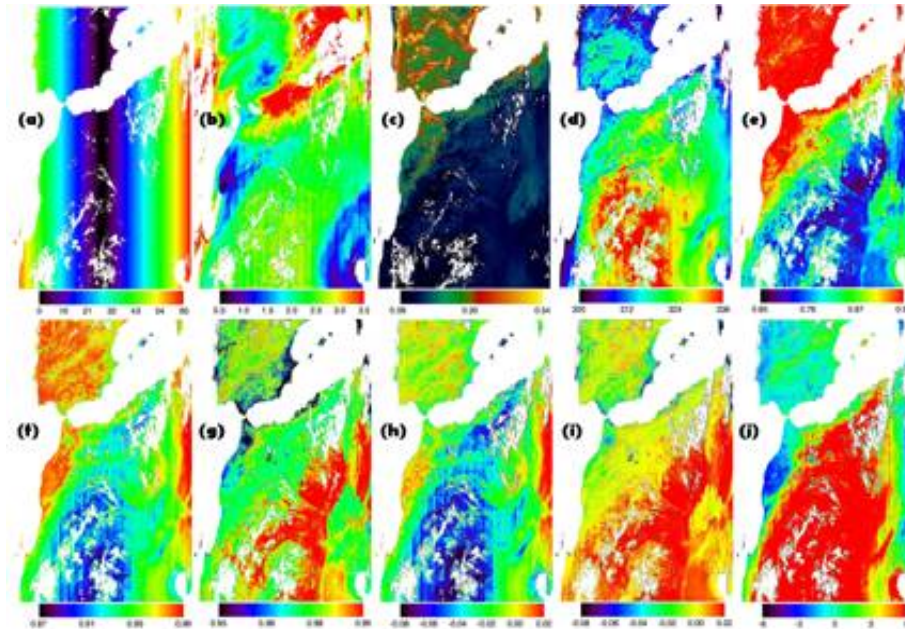


Figure 7. Retrievals from MODIS data acquired on 18 July 2004 (1km): a) view angle in degrees, b) water vapor in cm (MOD05), c) NDVI from TOA reflectances (MOD021KM), d) TES-LST e) TES- ϵ at b29 (8.5 μ m), f) TES- ϵ at b31 (11 μ m), g) TES- ϵ at b32 (12 μ m), h) TES minus MOD11 ϵ at b31, i) TES minus MOD11 ϵ at b32, j) TES minus MOD11 LST.

5 CONCLUSIONS

MODIS atmospheric profiles product (MOD07) provides data accurate enough to perform atmospheric corrections of TIR imagery, at least for the test cases analysed in this paper. Spatial resolution of MOD07 products (5km) is higher than Reanalysis-based products or retrievals from infrared soundings currently operative, so it can be used in atmospheric corrections of both high resolution (~100m) and low resolution (> 1km) sensors. In the case of low resolution sensors, corrections can be performed almost in a pixel-by-pixel basis. This is useful to apply algorithms such as TES, which allows retrievals of LST and surface emissivities from TIR data. Very few works have reported accuracies of TES algorithm applied to low resolution data, so further research is required in this topic.

6 REFERENCES

- Beck, A., Anderson, G. P., Acharya, P. K., Chetwynd, J. H., Bernstein, L. S., Shettle, E. P., Matthew, M. W., and Adler-Golden, S. M., 1999, MODTRAN4 User's Manual. Air Force Reserach Laboratory, Hanscom AFB, MA.
- French, A. N., Schmugge, T. J., Ritchie, J. C., Hsu, A., Jacob, F., and Ogawa, K., 2008, Detecting land cover change at the Jornada Experimental Range, New Mexico with ASTER emissivities. *Remote Sensing of Environment*, 112, 1730-1748.
- French, A. N., and Inamdar, A., 2010, Land cover characterization for hydrological modelling using thermal infrared emissivities. *International Journal of Remote Sensing*, 31(14), 3867-3883.
- Gillespie, A., Rokugawa, S., Matsunaga, T., Cothren, J. S., Hook, S., and Kahle, A. B., 1998, A temperature and emissivity separation algorithm for advanced spaceborne thermal emission and reflection radiometer (ASTER) images. *IEEE Transactions on Geoscience and Remote Sensing*, 36(4), 1113-1126.
- Hulley, G. C., Hook, S. J., Baldrige, A. M., 2010, Investigating the effects of soil moisture on thermal infrared land surface temperature and emissivity using satellite retrievals and laboratory measurements. *Remote Sensing of Environment*, 114(7), 1480-1493.
- Jiménez-Muñoz, J. C., Cristóbal, J., Sobrino, J. A., Soria, G., Ninyerola, M., and Pons, X., 2009, Revision of the single-channel algorithm for land surface temperature retrieval from Landsat

- thermal-infrared data. *IEEE Transactions on Geoscience and Remote Sensing*, 47(1), 339-349.
- Jiménez-Muñoz, J. C., Sobrino, J. A., Mattar, C., and Franch, B., 2010, Atmospheric correction of optical imagery from MODIS and Reanalysis atmospheric products. *Remote Sensing of Environment*, 114(10), 2195-2210.
- Sobrino, J. A., Jiménez-Muñoz, J. C., Soria, G., Romaguera, M., Guanter, L., Moreno, J., Plaza, A., and Martínez, P., 2008, Land surface emissivity retrieval from different VNIR and TIR sensors. *IEEE Transactions on Geoscience and Remote Sensing*, 46(2), 316-327.

Vegetation Radiative Transfer Modeling Based on Virtual Flux Decomposition: FDM

Abdelaziz Kallel,

High Institute of Electronic and Communication of Sfax, 3000 Sfax, Tunisia

abdelaziz@aai.ee

ABSTRACT -The hot spot effect, is treated in classical RTM by increasing the reflectance value at the first collision of incident photons leading to energy conservation law violation. To overcome this shortcoming, we propose in this paper a new model called the Flux Decomposition Model (FDM) and based on the Kallel et al. approach (AddingSD) which propose a formulation showing that the hot spot could be viewed as an increase of the posterior gap probability. The formalism is based on a decrease of the vegetation density and is called "the effective vegetation density". Thus, inspired from this idea, in our study, energy conservation is achieved using the same effective density to estimate the upward diffuse radiance distribution provided by the first collision of the solar irradiance (L_+^1) as well as the diffuse fluxes created by L_+^1 scattering. Finally, to solve the RT equations, L_+^1 is divided into virtual sub-fluxes having simple expressions, allowing the division of the problem into a finite number of sub-problems, each one corresponding to a given sub-flux easily solved based on SAIL++ formalism. Simulation tests show that the proposed model conserves energy. Compared to 3-D models in the ROMC/RAMI 3 database, our model performs similarly. Finally, compared to AddingSD, the running time is drastically reduced from about 15 minutes to a few milliseconds.

1 INTRODUCTION

In addition to the empirical methods based on various vegetation indices (e.g., NDVI, EVI) (Kallel et al., 2007), many methods and algorithms have been developed in order to understand the relationships between the vegetation features (namely amount and structure) and the amount of sunlight reflected in the visible and near- to middle-infrared spectral domains. This research field is known as passive optical remote sensing and is based on the radiative transfer (RT) theory.

The RT theory was first proposed by Chandrasekhar (1950) to study radiation scattering in conventional media. Such an assumption appears rudimentary for modeling the reflectance of a vegetation canopy since the size of vegetation elements cannot be assumed null. Among others, Kuusk (1991) proposed the extension of this theory to the discrete canopy case by taking into account the hot spot effect. His approach suffers from a severe shortcoming: compared to the turbid case, it increases only the reflectance created by the first collision of the incident radiation by leaves. As this increase is not followed by the decrease of the other fluxes, it leads to a violation of the energy conservation law (Kallel et al., 2008).

Among the fast vegetation RTM describing the turbid case, we can cite SAIL++ (Verhoef, 1998) which is a

1-D model providing accurate Bidirectional Reflectance Distribution Function (BRDF) and Bidirectional Transmittance Distribution Function (BTDF) estimation for the homogeneous turbid canopy case. In the discrete case, Kallel et al. (2008) propose AddingSD which is based on the adding method (Van de Hulst, 1980) dividing a thick layer into thin sublayers for which the adding operators (reflectance and transmittance operators) are computed, and to obtain the original thick layer operators, thin sublayers are concatenated using the adding-doubling principle. In this model, the hot spot effect is shown as a local reduction in vegetation density, called 'effective vegetation density'. All scattering parameters are estimated using the same effective vegetation density, thus enabling energy conservation. Despite its good performance, AddingSD still suffers from a relatively long running time.

In this study, we propose to benefit from both the rapidity of the SAIL++ and the hot spot modeling in the AddingSD.

2 THEORETICAL BACKGROUNDS

In this section, we first present a new formulation of SAIL++ model allowing second to define our new model based on the processing of the collision of direct fluxes with vegetation.

2.1 SAIL++ model reformulation

The formalism shown in this subsection is an extension of the original SAIL++ formalism (Verhoef, 1998) to the continuous case.

The SAIL++ equations are written in the continuous case as

$$\frac{dE_s(z, \Omega_s)}{dz} = kE_s(z, \Omega_s), \quad (1)$$

$$\frac{dL_+^1(z, \Omega_+)}{dz} = [s \circ E_s(z, \Omega_s)](\Omega_+) - [\Lambda \circ L_+^1(z)](\Omega_+). \quad (2)$$

$$\frac{dL_+^\infty(z, \Omega_+)}{dz} = [B' \circ L_+^1(z)](\Omega_+) + [B \circ L_-(z)](\Omega_+) - [A \circ L_+^\infty(z)](\Omega_+), \quad (3)$$

$$\frac{dL_-(z, \Omega_-)}{dz} = -[s' \circ E_s(z, \Omega_s)](\Omega_-) + [A \circ L_-(z)](\Omega_-) - [B \circ L_+^1(z)](\Omega_-) - [B \circ L_+^\infty(z)](\Omega_-), \quad (4)$$

$$\frac{dE_o^+(z, \Omega_o)}{dz} = wE_s(z, \Omega_s) + [v \circ L_-(z)] + [v' \circ L_+^1(z)] + [v' \circ L_+^\infty(z)] - KE_o^+(z, \Omega_o), \quad (5)$$

$$\frac{dE_o^-(z, \Omega_o)}{dz} = -w'E_s(z, \Omega_s) - [v' \circ L_-(z)] - [v \circ L_+^1(z)] - [v \circ L_+^\infty(z)] + KE_o^-(z, \Omega_o), \quad (6)$$

where E_s is the solar incident flux, L_- is the downward hemispherical distributions of diffuse radiance, L_+^1 , L_+^∞ are the upward hemispherical distributions of diffuse radiance created by the first collision and multiple collision of the incident flux with the vegetation, E_o^+ , E_o^- are the upward and downward radiances in the source direction, Ω_s , Ω_- , Ω_+ and Ω_o are the orientation of E_s , L_- , L_+ (L_+^1 or L_+^∞) and E_o (E_o^+ or E_o^-), respectively, and k , s , s' , Λ , A , B , w , w' , v , v' and K are the generalized Suits scattering terms (Suits, 1972). Moreover, each Suits parameter (X) can be decomposed as

$$X = d_L P_\chi X_o, \quad (7)$$

with d_L the average density of leaf area per unit volume, P_χ the probability of finding foliage and X_o a scattering parameter depending only on the leaf distribution and the solar and sensor orientations, but not the foliage density. X_o is the normalized parameter corresponding to X .

Applied to E_s , s and s' give respectively

$$\begin{aligned} [s \circ E_s(\Omega_s)](\cdot) &= \pi^{-1} w(\Omega_s \rightarrow \cdot) E_s, \\ [s' \circ E_s(\Omega_s)](\cdot) &= \pi^{-1} w'(\Omega_s \rightarrow \cdot) E_s, \end{aligned} \quad (8)$$

where w and w' are the bidirectional scattering terms when the input and the output flux directions are in the same and opposite hemispheres, respectively.

Applied to a radiance distribution (L), the operator B gives

$$[B \circ L](\cdot) = \pi^{-1} \int_{\Pi} w'(\Omega \rightarrow \cdot) L(\Omega) \cos(\Omega) d\Omega. \quad (9)$$

As in the original SAIL++ version (Verhoef, 1998), A can be divided into two terms

$$A = \Lambda - B', \quad (10)$$

where Λ and B' are respectively the extinction and the scattering terms.

Since the extinction of L_- is given by

$$\frac{dL_-(z, \Omega_-)}{dz} = \kappa L_-(z, \Omega_-). \quad (11)$$

Therefore, applied to a radiance distribution L , the operator Λ can be defined as

$$\begin{aligned} [\Lambda \circ L](\Omega' = (\theta', \phi')) \\ = \int_{\Pi} \frac{\delta(\theta') \delta(\phi')}{\cos(\theta') \sin(\theta')} \kappa(\Omega) L(\Omega) \cos(\theta) d\Omega. \end{aligned} \quad (12)$$

Applied to a radiance distribution (L), B' gives

$$[B' \circ L](\cdot) = \pi^{-1} \int_{\Pi} w(\Omega \rightarrow \cdot) L(\Omega) \cos(\Omega) d\Omega. \quad (13)$$

Applied to a radiance distribution (L), v and v' give respectively

$$\begin{aligned} v \circ L &= \int_{\Pi} w(\Omega \rightarrow \Omega_o) L(\Omega) \cos(\Omega) d\Omega, \\ v' \circ L &= \int_{\Pi} w'(\Omega \rightarrow \Omega_o) L(\Omega) \cos(\Omega) d\Omega. \end{aligned} \quad (14)$$

2.2 Flux decomposition

As in AddongSD, we will use the effective vegetation density approach, too. However, it will be applied only for the incident flux and the fluxes created by its scattering. Nevertheless, energy conservation will be maintained by increasing the first order scattered flux by E_+^1 and decreasing the fluxes created by E_+^1 scattering.

2.2.1 Taylor decomposition of L_+^1

Figure 1 shows two points $M(x, y, z)$ and $N(x', y', t)$ in a vegetation layer assumed a homogeneous discrete medium such that $t < z$. The elementary volume at M is viewed from N within an elementary solid angle $d\Omega$ with $\Omega = (\theta, \phi)$. A direct flux, called $E_s(0)$, present above the vegetation layer having as direction $\Omega_s = (\theta_s, 0)$ passes through the vegetation from the top to N without a collision. By assuming a constant extinction k along the path, E_s at altitude t is

$$E_s(t) = E_s(0)\exp(kt). \quad (15)$$

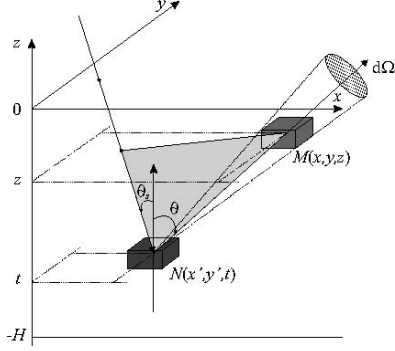


Figure 1 A vegetation layer located from altitude 0 to $-H$ and assumed a discrete medium. Two points $M(x, y, z)$ and $N(x', y', z)$ are located in the layer. The elementary volume at M is viewed from N under an elementary solid angle ($d\Omega$) with a polar angle θ . A direct flux with zenith angle θ_s collides with vegetation in an elementary volume at point N , is then reflected in the solid angle $d\Omega$ and reaches point M without collision. The downward and upward paths are correlated from altitude z to t as shown by the gray triangle linking the two paths.

Then the light is scattered in an elementary volume at N with an elementary thickness dt . The bidirectional scattering parameter under the vegetation (assumed homogeneous) is called w depending on the source and observation directions but not on the position under the vegetation. The scattered radiance in the direction $d\Omega$ called ($dL_+^1(N, \Omega)$) is

$$dL_+^1(N, \Omega) = E_s(t)\pi^{-1}w(\Omega_s \rightarrow \Omega)dt. \quad (16)$$

$dL_+^1(N, \Omega)$ travels from N to M without collision. By assuming a constant extinction κ along the path and without taking into account the dependency between paths, the radiance reaching M called $dL_+^{1*}(N \rightarrow M, \Omega)$ is

$$\begin{aligned} dL_+^{1*}(N \rightarrow M, \Omega) &= dL_+^1(N, \Omega)\exp[\kappa(t-z)], \\ &= E_s(0)\exp[(k+\kappa)(t-z)] \\ &\quad \times \exp(kz)\pi^{-1}w(\Omega_s \rightarrow \Omega)dt. \end{aligned} \quad (17)$$

Since the medium is assumed discrete, the hot spot effect representing the dependency between downward direct fluxes and diffuse fluxes at N has to be taken into account from depth t to z . Using Kuusk (1991)'s model, the radiance reaching M ($dL_+^1(N \rightarrow M, \Omega)$) is given versus $dL_+^{1*}(N \rightarrow M, \Omega)$ as

$$dL_+^1(N \rightarrow M, \Omega) = dL_+^{1*}(N \rightarrow M, \Omega)C_{HS}(\Omega_s, \Omega, t-z), \quad (18)$$

C_{HS} the correction factor,

$$C_{HS}(\Omega_s, \Omega, t-z) = \exp\left[\frac{\sqrt{k\kappa}}{b}(1 - \exp[b(t-z)])\right], \quad (19)$$

where b is a function of the vegetation features, the different solid angles and the hot spot factor d defined as the ratio between the leaf radius and the layer height (Kuusk, 1991).

According to Eqs. (17) (18), the radiance $dL_+^1(N \rightarrow M, \Omega)$ is written versus $E_s(0)$ as

$$\begin{aligned} dL_+^1(N \rightarrow M, \Omega) &= E_s(0)\exp[(k+\kappa)(t-z)] \\ &\quad \exp\left[\frac{\sqrt{k\kappa}}{b}(1 - \exp[-b(z-t)])\right] \\ &\quad \exp(kz)\pi^{-1}w(\Omega_s \rightarrow \Omega)dt. \end{aligned} \quad (20)$$

Eq. (20) has a complex expression, in particular its extinction is not linearly dependent on the depth $z-t$ (C_{HS}) enabling a classical way to solve the RT problem. To overcome such a disadvantage, we propose to decompose L_+ into virtual subfluxes having simple expressions of the extinction,

$$dL_+^1(N \rightarrow M, \Omega) = \sum_{n=0}^{\infty} (-1)^n a_n dL_+^{1,n}(N \rightarrow M, \Omega), \quad (21)$$

where

$$\begin{aligned} dL_+^{1,n}(N \rightarrow M, \Omega) &= E_s(0)\exp[(k+\kappa_n)(t-z)] \\ &\quad \times \exp(kz)\pi^{-1}w(\Omega_s \rightarrow \Omega)dt, \end{aligned} \quad (22)$$

$$\begin{aligned} a_n &= \frac{(k\kappa)^{n/2}}{n!b^n} \exp\left[\frac{\sqrt{k\kappa}}{b}\right], \\ \kappa_n &= \kappa + nb. \end{aligned} \quad (23)$$

As the vegetation is homogeneous, $dL_+^1(N \rightarrow M, \Omega)$ can be written simply as $dL_+^1(t \rightarrow z, \Omega)$. Thus, $L_+^1(z, \Omega)$ is obtained by integration of dL_+^1 over the depth $[-H, z]$

$$L_+^1(z, \Omega) = \int_{t=-H}^z dL_+^1(t \rightarrow z, \Omega) \quad (24)$$

Based on (7), L_+^1 can be written as

$$L_+^1(z, \Omega) = \sum_{n=0}^{+\infty} (-1)^n a_n L_+^{1,n}(z, \Omega), \quad (25)$$

where

$$\begin{aligned} L_+^{1,n}(z, \Omega) &= E_s(0) \frac{1 - \exp[-(k+\kappa+nb)(H+z)]}{k+\kappa+nb} \\ &\quad \times \exp(kz) \frac{w(\Omega_s \rightarrow \Omega)}{\pi}. \end{aligned} \quad (26)$$

2.2.2 Application of the effective vegetation density approach

The hot spot effect can be treated as an increased posterior gap probability which, in turn, results from a

reduction in vegetation density. In particular, it is possible to use the concept of ‘effective vegetation density’ to describe the phenomenon. In this subsection, we propose to derive this density for $L_+^{1,n}, \forall n \in N$, and to use it further to derive the equations of fluxes created by $L_+^{1,n}$ scattering. Moreover, based on AddingSD approach, it is possible to show that the effective density application leads to conserve energy.

In Eqs. (17) (22), the difference between $dL_+^{1*}(N \rightarrow M, \Omega)$ and $dL_+^{1,n}(N \rightarrow M, \Omega)$ is the value of the extinction in the direction Ω (κ and κ_n respectively). According to AddingSD approach, the variation in the extinction factor is linked to the variation of the collision probability locally around M . In other words, a decrease in the probability of finding foliage at M decreases P_χ , accordingly. In particular, according to Kallel et al. (2008)

$$\left. \begin{aligned} \kappa &= d_L P_\chi(M) \kappa_o \\ \kappa_n &= d_L P_{\chi,n}(N \rightarrow M, \Omega) \kappa_o \end{aligned} \right\} \quad (27)$$

$$\Rightarrow P_{\chi,n}(N \rightarrow M, \Omega) = \frac{\kappa_n}{\kappa} P_\chi(M),$$

with $P_{\chi,n}(N \rightarrow M, \Omega)$ the a posteriori probability of finding vegetation at M for the radiance $dL_+^{1,n}$, and κ_o the normalized extinction factor [as explained in Eq. (7), it is independent on vegetation density].

Now, due to the homogeneity of the vegetation layer, $P_\chi(M)$ is a constant (does not depend on M), thus according to Eqs. (27), $P_{\chi,n}(N \rightarrow M, \Omega)$ depends neither on N nor M . It will be simply called $P_{\chi,n}$. Then, based on L_+^1 differential equation derivation [cf. Eq. (2)] and replacing κ by κ_n , we obtain,

$$\frac{dL_+^{1,n}(z, \Omega)}{dz} = [s \circ E_s(z, \Omega_s)](\Omega) - d_L P_{\chi,n} [\Lambda_0 \circ L_+^{1,n}(z)](\Omega), \quad (28)$$

where Λ_0 is the normalized scattering term corresponding to Λ [cf. Eq. (10)]. It leads to the following important result linking the differentiation of L_+^1 to $(L_+^{1,n})_{n \in N}$:

$$\frac{dL_+^1(z, \Omega)}{dz} = [s \circ E_s(z, \Omega_s)](\Omega) - d_L \sum_{n=0}^{+\infty} (-1)^n a_n P_{\chi,n} [\Lambda_0 \circ L_+^{1,n}(z)](\Omega). \quad (29)$$

2.2.3 Dependency on $L_+^{1,n}$

In this subsection, we propose a modification to the reformulated SAIL++ equation set, presented in Subsection 2.1, in order to take into account the effective vegetation density values in the expressions of L_- , L_+^∞ , E_o^+ and E_o^- that depend on $L_+^{1,n}$ scattering.

First, let us derive the angular differentiation of E_o^+ that depends only on $L_+^{1,n}$ [$d^2 E_o^+(L_+^{1,n}, z, \Omega \rightarrow \Omega_o)$]. Compared to the dependency on L_+ in classical SAIL++ equations, P_χ has to be replaced by $P_{\chi,n}$. Thus,

$$\frac{d[d^2 E_o^+(L_+^{1,n}, z, \Omega \rightarrow \Omega_o)]}{dz} = w_n(\Omega \rightarrow \Omega_o) L_+^{1,n}(z, \Omega) \cos(\theta) d\Omega, \quad (30)$$

where

$$w_n(\Omega \rightarrow \Omega_o) = d_L P_{\chi,n} w_0(\Omega \rightarrow \Omega_o), \quad (31)$$

with w_0 the normalized scattering parameter corresponding to w' [cf. Eq. (6)].

Then, the angular differentiation of E_o^+ which depends only on L_+^1 [$d^2 E_o^+(L_+, z, \Omega \rightarrow \Omega_o)$] is obtained by summing the contribution of the set $(L_+^{1,n})_{n \in N}$

$$\frac{d[d^2 E_o^+(L_+, z, \Omega \rightarrow \Omega_o)]}{dz} = d_L \sum_{n=0}^{+\infty} (-1)^n a_n P_{\chi,n} L_+^{1,n}(z, \Omega) \cos(\theta) d\Omega. \quad (32)$$

The integrated value of $d^2 E_o^+(L_+, z, \Omega \rightarrow \Omega_o)$ over all possible values of Ω (the upper-hemisphere) noted $E_o^+(L_+, z, \Omega_o)$ is [cf. Eqs. (5)(14)]

$$\frac{dE_o^+(L_+, z, \Omega_o)}{dz} = d_L \sum_{n=0}^{+\infty} (-1)^n [a_n P_{\chi,n} v'_0 \circ L_+^{1,n}(z)], \quad (33)$$

with v'_0 the normalized scattering parameter corresponding to v' [cf. Eq. (5)].

Next, by integrating the dependency on E_s , L_- and L_+^∞ , the original reformulated SAIL++ Eq. (5) becomes

$$\frac{dE_o^+}{dz} = w E_s + v \circ L_- + v' \circ L_+^\infty + d_L \sum_{n=0}^{+\infty} (-1)^n [a_n P_{\chi,n} v'_0 \circ L_+^{1,n}(z)] - K E_o^+. \quad (34)$$

Similarly, Eqs. (4), (3) and (6) become respectively

$$\begin{aligned}
\frac{dL}{dz} &= -s' \circ E_s + A \circ L_- - B \circ L_+^\infty \\
&\quad - d_L \sum_{n=0}^{+\infty} (-1)^n [a_n P_{\chi,n} B_0 \circ L_+^{1,n}(z)], \\
\frac{dL_+^\infty}{dz} &= 0 \circ E_s + B \circ L_- - A \circ L_+^\infty \\
&\quad + d_L \sum_{n=0}^{+\infty} (-1)^n [a_n P_{\chi,n} B_0' \circ L_+^{1,n}(z)], \\
\frac{dE_o^-}{dz} &= -w' E_s - v' \circ L_- - v \circ L_+^\infty \\
&\quad - d_L \sum_{n=0}^{+\infty} (-1)^n [a_n P_{\chi,n} v_0 \circ L_+^{1,n}(z)] + K E_o^-,
\end{aligned} \tag{35}$$

with 0 the vacuum operator.

To derive the BRDF values, L_- , L_+^1 and L_+^∞ in Eqs. (29) (34) (35) have to be discretized over the hemispheres as described in (Verhoef, 1998).

3 VALIDATION

This section is dedicated to the validation of our model. In particular, our model is compared to the references simulations of the ROMC database.

The RADIation transfer Model Intercomparison (RAMI) exercise (Pinty et al., 2001) (Widlowski et al., 2006) proposes some protocols to benchmark radiative transfer models applied to plant canopies covering soil surfaces. Recently, a RAMI On-Line Model Checker (ROMC) was set up in order to evaluate model performances by comparing it to RAMI third phase exercise reference simulations. As reference, RAMI 3 uses simulation results of 3-D models since ground truth data are not available for this phase.

To validate our model, we propose to compare FDM performances to SAIL++ based on the ROMC exercise.

The present study deals only with homogenous vegetation assumed a discrete medium. Also, we only present the results relative to the purist corner case. We test the eighteen experiences possible, corresponding to three values of LAI: 1, 2 and 5, three values of solar zenith angle: 0° , 30° and 60° , and two leaf distributions: planophile and erectophile. ROMC proposes eleven experiments (BRDF and directional-hemispherical terms). However, to be short, we present only some recapitulative results dealing with the global (vegetation and soil background) BRDF in the principle and cross planes.

Figure 1 shows FDM and SAIL++ (noted SPP) model simulation results of the BRDF function of the ROMC simulations for the eighteen ROMC simulations. Figure 1.a and Figure 1.b show the results corresponding to the principle and cross planes. By comparison between models, we see that FDM curves

are closer to the diagonal which is confirmed by the total RMSE that is equal to 0.74% and 0.66% for FDM in the principle and cross planes, respectively, whereas the SAIL++ RMSE are 2.43% and 2.55% for the principle and cross planes, respectively. Moreover, the points corresponding to SAIL++ are in the most of case higher than the diagonal which is not the case for FDM confirming that SAIL++ does not conserve energy.

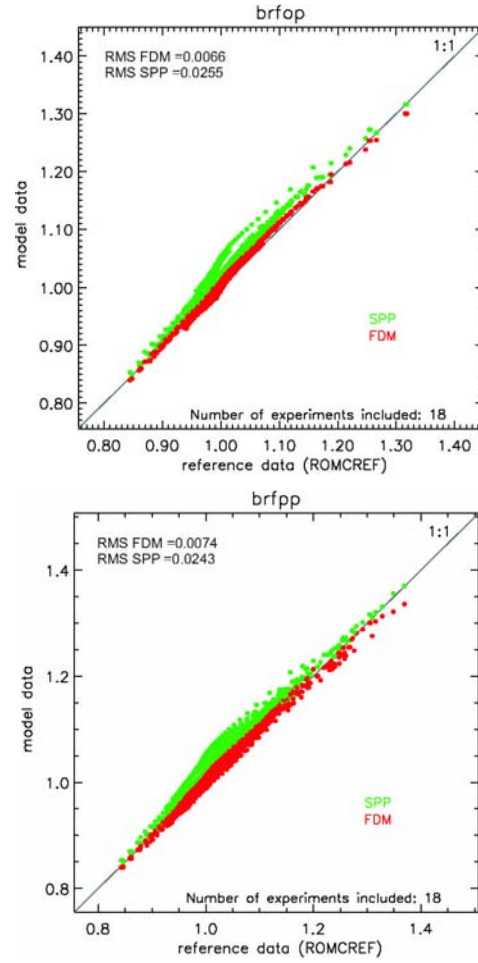


Figure 2. FDM and SAIL++ (noted SPP) model simulation results of the BRDF at the principle (a) and cross (b) planes function of the ROMC ones for the eighteen ROMC simulations.

4 CONCLUSIONS

The goal of this article was to derive a new method for computing canopy reflectance so that it both conserves energy and surmounts the assumption that diffuse fluxes E_+ / E_- are isotropically distributed over hemispheres. To achieve this object, we benefited

from two existent models: (i) SAIL++ that overcomes the isotropy assumption and is very fast since it is based on Discrete Cosine Transformation. However, this model does not conserve energy in the discrete case; (ii) AddingSD which also overcomes the isotropy assumption and allows to conserve energy based on the effective vegetation density approach. However, the running time of AddingSD is relatively high. Our new model was based on injecting the effective vegetation density approach in SAIL++, and therefore, benefited from both energy conservation and a short running time. The procedure was as follows. First, the radiance distribution created by direct solar light scattering upwards from vegetation, L_+^1 , was computed by taking into account the hot spot effect. Second, according to the effective density approach, the hot spot effect corresponded to a local vegetation density variation. Therefore, the diffuse fluxes and radiances in the observation direction (created by L_+^1 scattering) have had to be estimated using the same density achieving consequently energy conservation. Third, since the computation in the latter step was too laborious, L_+^1 was decomposed into virtual subfluxes using Taylor series. Such subfluxes have a simpler expression, and were interpreted each one as a virtual direct solar flux. The provided fluxes, radiances and BRDF/BTDF by the virtual flux scattering were estimated using the SAIL++ formalism. Finally, compared to ROMC database references, our model gave accurate results.

5 REFERENCES

- Chandrasekhar, S., 1950, Radiative Transfer (Dover, New-York).
- Kallel, A., Le Hégarat-Masclé, S., Ottlé, C., Hubert-Moy, L., 2007, Determination of vegetation cover fraction by inversion of a four-parameter model based on isoline parametrization, *Rem. Sens. Env.*, **111**(4), pp. 553–566.
- Kallel, A., Verhoef, W., Le Hégarat-Masclé, S., Ottlé, C., Hubert-Moy, L., 2008, Canopy Bidirectional Reflectance Calculation based on Adding method and SAIL formalism: AddingS/AddingSD, *Rem.Sens. Env.*, **112**(9), pp. 3639–3655.
- Kuusk, A., 1991, The hot spot effect in plant canopy reflectance, in: Myneni, R. B., Ross, J. (Eds.), *Photon vegetation interactions. Applications in optical remote sensing and plant ecology*, (Berlin: Springer), pp. 139–159.
- Pinty, B., Gobron, N., Widlowski, J., Gerstl, S., Verstraete, M., Antunes, M., Bacour, C., Gascon, F., Gastellu, J., Goel, N., Jacquemoud, S., North, P., Qin, W., Richard, T., 2001, The RAdiation transfer Model Intercomparison (RAMI) Exercise, *Journal of Geophysical Research*, **106**, pp. 11937–11956.
- Suits, G. H., 1972, The calculation of the directional reflectance of a vegetative canopy, *Rem. Sens. Env.*, **2**, pp. 117–125.
- Van de Hulst, H. C., 1980, Multiple Light Scattering: Tables, Formulas, and Applications (Academic press, Inc., New York).
- Verhoef, W., 1998, Theory of Radiative Transfer Models Applied to Optical Remote Sensing of Vegetation Canopies, Ph.D. thesis, Agricultural University (Wageningen, The Netherlands).
- Widlowski, J.-L., Taberner, M., Pinty, B., Bruniquel-Pinel, V., Disney, M., Fernandes, R., Gastellu-Etchegorry, J.-P., Gobron, N., Kuusk, A., Lavergne, T., Leblanc, S., Lewis, P., Martin, E., Mottus, M., North, P. J. R., Qin, W., Robustelli, M., Rochdi, N., Ruiloba, R., Soler, C., Thompson, R., Verhoef, W., Verstraete, M. M., Xie, D., 2006, The third RAdiation transfer Model Intercomparison (RAMI) exercise: Documenting progress in canopy reflectance modelling, *Journal of Geophysical Research*, **112**.

Surface temperature downscaling from multi-resolution instruments based on MAP criterion and Markov models

Abdelaziz Kallel¹, Catherine Ottlé², Sylvie Le Hégarat-Masclé³,

¹High Institute of Electronics and Communication of Sfax, 3000 Sfax, Tunisia

²LSCE/IPSIL, Centre d'Etudes de Saclay, Orme des Merisiers 91191, Gif-sur-Yvette, France

³IEF/AXIS, Université de Paris-Sud 91405, Orsay Cedex, France

abdelaziz@aai.ee

ABSTRACT- *The aim of this work is the development of a downscaling method to assess intra-pixel surface temperature based on the combined use of both spatial and temporal high resolution measurements. The purpose is to estimate the surface temperature of each component of a mixed pixel observed at high temporal frequencies, using regular observations at high spatial resolution, and provided the precise knowledge of the intra-pixel composition. To infer intra-pixel information from these measurements, statistical inversion methods can be used. But, such a problem is ill-posed when only one low resolution measurement is used to estimate several high resolution unknowns, called 'endmembers' in the following. Thus to be solved, constraints from a priori information are needed in the inversion process. The inversion is performed at the low resolution pixel scale and is constrained by two types of information: (i) a first guess sub-pixel temperature derived from a Land Surface Model; (ii) the surface temperature temporal dependency from times t to $t+1$. In addition, we assume known the low resolution pixel composition from a high resolution land cover map. As a result, the MAP estimator gives the a posteriori most likely endmember temperatures, given the observed low resolution temperatures the pixel composition, the first guess value, and the a priori temporal distribution. Method performances are checked on simulated data and its accuracy versus the observation errors and the number of endmembers is studied.*

1 INTRODUCTION

Since the early 1970's, many space-borne remote sensors have been launched providing continuous measurements of surface radiometric properties at global scale such as the brightness temperature in the Thermal Infra-Red (TIR) domain. Such measurements allow the estimation of the Land Surface Temperature (LST) which can help to better understand the surface-atmosphere water and energy transfers. Indeed, LST is one of the key parameters giving access to the biophysical exchanges between the soil, the biosphere and the atmosphere.

LST is the result of a coupled soil-vegetation-atmosphere system; its diurnal variations may be very large, depending on solar radiation, vegetation coverage and moisture availability. Its spatial variability is lower when looking to the neighboring at mesoscale (for a given type of vegetation), result of the assumed atmosphere homogeneity at those scales as well as the relative stationarity of the soil and vegetation properties. The pixel size of existing TIR space instruments is typically kilometric when providing frequent observations with hundred meters pixel resolution, for the poor revisiting ones. As an

example, Meteosat/SEVIRI instrument has a minimum resolution of $3km*3km$ at the equator but provides observations each 15 minutes. On the opposite, TERRA/ASTER shows a spatial resolution of $60m$ with a revisit capability of about two weeks. Given the fact that for many applications, the diurnal variations of the surface temperature is fully informative, the inverse problem is the following: how to downscale the low resolution measurements to estimate the surface temperature at both high temporal and spatial resolutions? Such a problem is ill-posed because of its under-determination. It can however be solved by adding other types of information: for example a priori estimation of the unknowns and/or spatial and/or temporal constraints.

LST prior estimations may be provided by Land Surface Models (LSM) often called also Soil-Vegetation-Atmosphere Transfers (SVAT) models (Ottlé and Vidal-Madjar, 1994) (Coudert et al., 2006). Such models allow to represent the energy and matter exchanges in the biosphere-atmosphere continuum as well as the surface states or variables (temperature, soil moisture in particular).

This study focuses on the development and validation of a downscaling method at the pixel scale, for estimating sub-pixels LST from an integrated

measurement. The method is based on *a priori* knowledge of the sub-temperatures provided by a LSM, and on adding temporal constraints on consecutive measurements, permitting to increase the accuracy of the inversion process. A land cover map at high spatial resolution is required that provides the composition of the coarse resolution pixel to downscale. The chosen approach is based on Bayesian modeling, the low resolution/high repetitively data are assumed to be Gaussian-Markov field (Besag, 1997) (Geman and Geman, 1984) (Guyon, 1993). In particular the temperature temporal evolution is assumed to be a Markov chain with dependency parameters estimated using a LSM. The resolution of the inverse problem (to find the sub-temperatures given the satellite observations) is based on the maximization of the *a posteriori* probability (MAP criterion). Some assumptions on the surface temperature permitted to linearize the least-square inversion problem allowing a direct and fast inversion.

The article is divided up as follows. The downscaling method is first presented with the theoretical background of our model (Section 2). Then, validation and performance results are shown and compared (Section 3). Finally, we present our main conclusions (Section 4).

2 DOWNSCALING APPROACH

Our problem consists of estimating sub-pixel temperatures given pixel temperatures, pixel land cover compositions and *a priori* information about the temperature temporal distribution. According to the *Maximum A Posteriori* criterion our algorithm will provide the *a posteriori* most likely sub-temperatures given the observation, the pixel composition and all the *a priori* information.

We firstly present our global model, then we introduce the Markov assumptions, and finally we derive the solution.

2.1 Model assumptions

The assumptions about our data are the following:

- N is the number of classes, representing the different land cover types: vegetation, soil, forest and urban areas;
- The studied area is covered by K thermal infrared coarse resolution pixels [i.e., MeteoSat Second Generation (MSG) pixels];
- T_d is the number of data per day.

The *a priori* information is provided by the land surface model as follows. We assume that we know a reliable meteorological forcing for variables such as temperature, precipitation, wind, vapor pressure, etc, and we also know a range of soil and vegetation parameters. The land surface model is therefore run

many times varying the soil and vegetation parameters. In particular, the temperature is estimated for each class ($i \in \{1, \dots, N\}$) and acquisition time ($t \in \{1, \dots, T_d\}$). The model first guess is obtained averaging all the simulated temperature values for each couple (i, t) . The first guess temperature will be called in the following $T_{bi}(t)$. Other statistics are also

carried out like the standard deviation (sdv), $\sigma_i(t)$ and the correlation between two temporal consecutive realizations (at times t and $t+1$) noted $cor_i(t, t+1)$.

We also assume that the class i , at pixel $k \in \{1, \dots, K\}$ and time t temperature ($T_i^k(t)$) follows a Gaussian distribution, with mean and sdv equal respectively to $(T_{bi}(t), \sigma_i(t))$. Moreover, to simplify, we will assume in the following that at each time t , the temperature of each class i does not vary from a pixel to another (i.e., $\forall k, k', T_i^k(t) = T_i^{k'}(t)$). Therefore, the superscript k will be removed from the temperature expression.

For temperature estimation at coarse resolution, we assume the linear mixing model. Each coarse resolution pixel k temperature ($T_{br}^k(t)$) is equal to a linear combination of the different class temperatures weighted by their proportions within pixel, noted α_i^k

($\sum_{i=1}^N \alpha_i^k = 1$). To obtain linear equation, we assume in this study, that the low resolution temperature of pixel k at time t ($T_{br}^k(t)$) can be written as the weighted sum of the entity temperatures $T_{br}^k(t) = \sum_{i=1}^N \alpha_i^k T_i(t)$ (Liu et al., 2006). According to Liu et al. (2006), using this linear approximation model, the error for a plain surface is around $0.2K$. Finally, assuming an additive white noise, the low resolution pixel temperature is linked to the class temperatures as follows:

$$T_{br}^k(t) = \sum_{i=1}^N \alpha_i^k T_i(t) + \xi_k(t), \quad (1)$$

with $\xi_k(t)$ a white centered Gaussian noise with a sdv value equal to $\sigma'_k(t)$. We assume also that the noise is independent from one pixel to another and from one acquisition time to another:

$$\begin{aligned} \forall (k, k') \in \{1, \dots, K\}^2, (t, t') \in \{1, \dots, T_d\}^2 \\ / (k, k') \neq (t, t') \Rightarrow E[\xi_k(t) \xi_{k'}(t')] \approx 0, \end{aligned} \quad (2)$$

where E represents the mathematical expectation of a random variable. In the following, σ' is assumed to be constant: independent from pixel and time of acquisition.

Now, let $T = \{T_i(t), i \in \{1, \dots, N\}, t \in \{1, \dots, T_d\}\}$ and $T_{br} = \{T_{br}^k(t) / k \in \{1, \dots, K\}, t \in \{1, \dots, T_d\}\}$. We need an estimator of T^* given T_{br} . The MAP estimator consists in optimizing T such that its probability given T_{br} is maximal,

$$\begin{aligned} T^* &= \operatorname{argmax}_T P(T | T_{br}), \\ &= \operatorname{argmax}_T \frac{P(T_{br} | T)P(T)}{P(T_{br})}, \\ &= \operatorname{argmax}_T P(T_{br} | T)P(T), \end{aligned} \quad (3)$$

$P(T_{br})$ is removed because it is a constant for the maximization of $P(T | T_{br})$.

2.1 Probability modeling

In the following we derive $P(T_{br} | T)$ and $P(T)$ expressions successively.

From (2) and since $\xi_k(t)$ is independent relatively to pixel and acquisition time,

$$\begin{aligned} P(T_{br} | T) &= \prod_{k=1}^K \prod_{t=1}^{T_d} P(T_{br}^k(t) | T_i(t), i \in \{1, \dots, N\}), \\ &= \frac{\exp \left\{ - \sum_{t=1}^{T_d} \sum_{k=1}^K \frac{(T_{br}^k(t) - \sum_{i=1}^N \alpha_i^k T_i(t))^2}{2\sigma'^2} \right\}}{(\sqrt{2\pi}\sigma')^{KT_d}}. \end{aligned} \quad (4)$$

In the following, the temperatures of the different vegetation classes are assumed being independent. However, for each class i , the temperature $T_i = \{T_i(t), t \in \{1, \dots, T_d\}\}$ is assumed to follow a Multivariate Gaussian distribution, satisfying some dependencies in time (Guyon, 1993). In fact, as the temperature of each endmember (i, k) depends on its physical features which do not change from acquisition time t to $t+1$, thus the temperatures could not vary randomly from time t to $t+1$. Therefore, we assume that each endmember temperature is correlated from a time t to $t+1$ building therefore a temporal Markov chain.

$$P(T_i(t) | T_i(t'), t' \leq t) = P(T_i(t) | T_i(t-1)). \quad (5)$$

It follows that:

$$\begin{aligned} P(T_i) &= P(T_i(1)) \prod_{t=2}^{T_d} P(T_i(t) | T_i(t-1)), \\ &= P(T_i(1)) \prod_{t=2}^{T_d} \frac{P(T_i(t), T_i(t-1))}{P(T_i(t-1))}, \\ &= \prod_{t=2}^{T_d-1} P(T_i(t))^{-1} \prod_{t=2}^{T_d} P(T_i(t), T_i(t-1)). \end{aligned} \quad (6)$$

As T_i follows a Multivariate Gaussian distribution, $(T_i(t), T_i(t-1))$, denoted $T_i(t, t-1)$, follows a bivariate Gaussian distribution. In the following, the joint mean value vector is noted $T_{bi}(t, t-1) = (T_{bi}(t), T_{bi}(t-1))$, and the covariance matrix is noted $\Sigma_i(t, t-1)$.

$$\begin{aligned} P(T_i(t, t-1)) &= \frac{1}{2\pi |\Sigma_i(t, t-1)|^{1/2}} \\ &\quad \exp \left(-\frac{1}{2} (T_i(t, t-1) - T_{bi}(t, t-1))' \right. \\ &\quad \left. [\Sigma_i(t, t-1)]^{-1} (T_i(t, t-1) - T_{bi}(t, t-1)) \right). \end{aligned} \quad (7)$$

Since the class temperatures are independent,

$$\begin{aligned} P(T) &= \prod_{i=1}^N P(T_i), \\ &= \prod_{i=1}^N \left[\prod_{t=2}^{T_d-1} P(T_i(t))^{-1} \prod_{t=2}^{T_d} P(T_i(t, t-1)) \right], \\ &= \frac{1}{Z} \exp \left[-\frac{1}{2} \sum_{i=1}^N \left(\sum_{t=2}^{T_d} (T_i(t, t-1) - T_{bi}(t, t-1))' [\Sigma_i(t, t-1)]^{-1} \right. \right. \\ &\quad \left. \left. (T_i(t, t-1) - T_{bi}(t, t-1)) - \sum_{t=2}^{T_d-1} \frac{(T_i(t) - T_{bi}(t))^2}{\sigma_i(t)^2} \right) \right], \end{aligned} \quad (8)$$

where Z is a constant term.

According to Eqs. (4) (8):

$$P(T_{br} | T)P(T) = \frac{1}{Z'} \exp[-U(T)], \quad (9)$$

where Z' is a probability normalization term given by

$$Z' = (\sqrt{2\pi}\sigma')^{KT_d} Z \quad (10)$$

and

$$\begin{aligned} U(T) &= \frac{1}{2\sigma'^2} \sum_{t=1}^{T_d} \sum_{k=1}^K \left(T_{br}^k(t) - \sum_{i=1}^N \alpha_i^k T_i(t) \right)^2 \\ &\quad + \frac{1}{2} \sum_{i=1}^N \left(\sum_{t=2}^{T_d} (T_i(t, t-1) - T_{bi}(t, t-1))' [\Sigma_i(t, t-1)]^{-1} \right. \\ &\quad \left. (T_i(t, t-1) - T_{bi}(t, t-1)) - \sum_{t=2}^{T_d-1} \frac{(T_i(t) - T_{bi}(t))^2}{\sigma_i(t)^2} \right). \end{aligned} \quad (11)$$

2.3. Optimal temperature derivation

According to Eqs. (3) and (9), and since Z' is a constant for the maximization,

$$T^* = \operatorname{argmin}_T U(T). \quad (12)$$

The minimum is obtained for null derivatives,

$$\nabla U(T) = 0 \Rightarrow \forall (i, t) \in \{1, \dots, N\} \times \{1, \dots, T_d\}, \frac{\partial U(T)}{\partial T_i(t)} = 0. \quad (13)$$

Then,

$$\begin{aligned}
& \frac{1}{\sigma_i^2} \sum_{k=1}^K \alpha_i^k \left(\sum_{j=1}^N \alpha_j^k T_j(t) \right) \\
& + [1 - \delta(t-1)] [\Sigma_i(t, t-1)]^{-1}(2) T_i(t, t-1) \\
& + [1 - \delta(t-T_d)] [\Sigma_i(t+1, t)]^{-1}(1) T_i(t+1, t) \\
& - [1 - \delta(t-T_d) - \delta(t-1)] \frac{T_i(t)}{\sigma_i(t)^2} \\
& = \frac{1}{\sigma_i^2} \sum_{k=1}^K \alpha_i^k T_{br}^k(t) \\
& + [1 - \delta(t-1)] [\Sigma_i(t, t-1)]^{-1}(2) T_{bi}(t, t-1) \\
& + [1 - \delta(t-T_d)] [\Sigma_i(t+1, t)]^{-1}(1) T_{bi}(t+1, t) \\
& - [1 - \delta(t-T_d) - \delta(t-1)] \frac{T_{bi}(t)}{\sigma_i(t)^2}.
\end{aligned} \tag{14}$$

where δ is the Kronecker function [$\delta(x)=1$ if $x=0$ and 0 otherwise], for a given matrix C and number k , $C(k, \cdot)$ is the row k of C ,

Writing Eq. (14) for each triplet (i, t) , we obtain a system of linear equations to solve:

$$AT = X. \tag{15}$$

The solution is finally given by

$$T = A^{-1}X. \tag{16}$$

3 RESULTS AND DISCUSSION

In this section, we present the validation of our approach using simulated data over the 'la Crau' region in South-East France. This area has been chosen due to the big diversity of the encountered cultures as well as the observed high water and thermal contrast. As a priori data (ground measurements), we have at our disposal meteorological forcing data as well as vegetation and water parameter variation ranges for three successive days starting from July 25th, 2006. Coarse resolution temporal image series provided from the sensor SEVIRI was acquired during July 26th. The image spatial and temporal resolutions are $3 \times 5 \text{ km}^2$ and one acquisition by fifteen minutes, respectively. On the same day at 10:47, a high resolution ASTER image was also acquired. Its spatial resolution is 90 m . A valid land cover map derived from ASTER image classification is also provided for our study. The land cover map considers six classes (water, rice, salines, forest, cultures and bare soils). Figure 1 shows successively the ASTER image, the SEVIRI image and the land cover map. The SEVIRI image has been processed in order to remove pixels (black pixels) containing water or cloud biasing the surface temperature estimation.

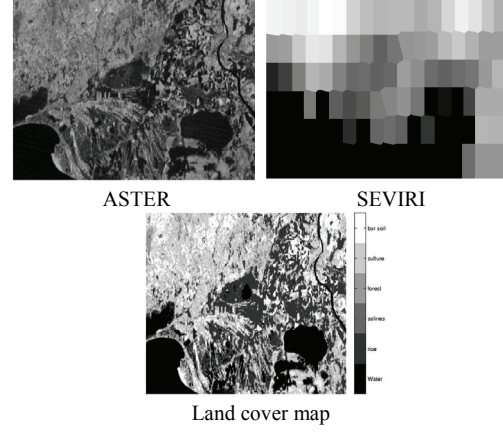


Fig. 1. Satellite images and land cover map of the la Crau area.

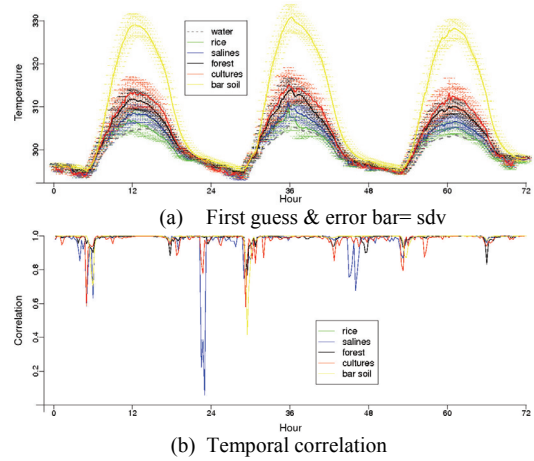


Fig. 2. Temperature statistics for the six vegetation classes. In the first subfigure the first guess variation is plotted as well as an error bar corresponding to the std value. In the second subplot, the temporal correlation is between times t and $t+1$.

Using the meteorological forcing and the different ranges of the surface parameters, the SETHyS model was run many times providing two thousand simulations for each land cover class except the water for which the temperature is approximated by the atmospheric temperature. Applying statistic metrics over these simulations, the first guess temperatures as well as the temporal correlations (between a measurement time t and $t+1$) were obtained. Fig. (2) shows such a statistics. In particular, Fig. (2).b shows that the correlations between class temperatures from time t to $t+1$ are in general very close to 1, demonstrating the strong inter-dependency (in other words, a time step of fifteen minutes is sufficiently small to not see a temperature variation, proving therefore the adequacy of such a time step). However,

at noon and early in the morning, the correlation decreases and the surface temperature becomes almost a random variable.

Now, when the temporal dependency is not taken into account the inversion is referred as or the ‘first order method’ (since it does not take into account the second order dependency between temperatures).

The improvement (Imp) of the Markov model in respect to the classical method will be computed as

$$Imp = \frac{RNCE_C - RNCE_M}{\max\{RNCE_C, RNCE_M\}}, \quad (17)$$

with $RNCE_C$ and $RNCE_M$ corresponding to the estimation Root Mean Square Error (RMSE) using respectively the classical method and the Markov model. Note that, $Imp > 0$ means that Markov model improves the results; conversely $Imp < 0$ reflects a performance decrease.

The actual endmember temperatures are chosen as one among the SEtHyS simulations. In particular, only one random simulation is attributed for all the endmembers belonging to a given land cover class. The coarse resolution satellite observations are simulated using Eq. (1).

In order to understand the difference between the first order method and the Markov one, we propose the comparison between them when only two endmembers (rice and salines) and two pixels are considered. Fig. 3 shows such an example of temperature downscaling. Three methods are then compared: using only the first guess, the classical method and the Markov model. Moreover, to quantify the estimation quality, Tab. 1 shows the $RMSE$ corresponding to each estimation method, for each endmember and both of them together. In addition, the improvement of the Markov approach compared to the classical one (Imp) is shown. As the model standard deviation is too small at night (cf. error bars in Fig. 2.a), the actual simulation curves and the first guess ones are close at night. Conversely, the difference becomes large at noon. Moreover, Fig. 3.a shows that salines actual curve is closer to the first guess than the rice one, the corresponding $RMSE$ are 1.34 and 2.26, respectively. When the classical downscaling method is applied and the satellite coarse resolution observations are taken into account, the results are enhanced and the majority of the method points are between the curves first guess and the actual curves, the global $RMSE$ is reduced from 1.86 to 1.57.

When the dependency between two successive temperatures is taken into account in the Markov case, the estimation results become very close to the actual ones. The total $RMSE$ is reduced to 0.59. In particular the improvements corresponding to the rice and salines rise up to 78.8% and 40.7%, respectively. The relative low Imp value corresponding to the salines is

due to the fact that the Markov model fails to correct the estimation at noon the first simulated day. Such a result could be explained by the relative low temporal correlation of the salines [cf. Fig. 3.b] reducing the interest of the Markov model.

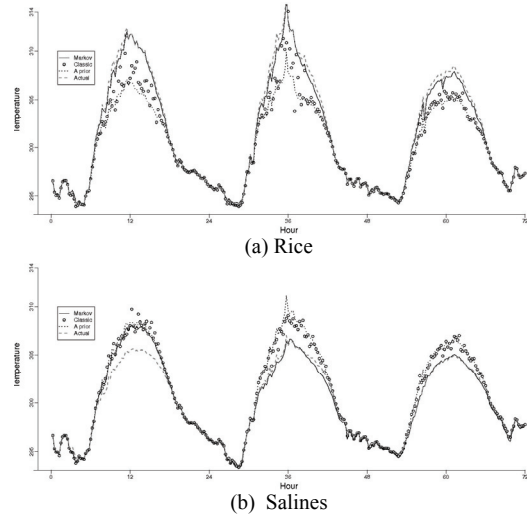


Fig. 3. Temperature downscaling using Markov model, classical method and a priori model. The used parameters are: pixel number=2, endmember number=2 (rice & salines) and $\sigma' = 3$. Pixel compositions are (0.37, 0.63) and (0.28, 0.72).

Tab. 1. Statistic related to temperature downscaling of Fig. 3. Imp in the fourth column represents the enhancement with respect to the classical method [cf. Eq. (17)].

	A priori RMSE	Classical RMSE	Markov RMSE	Imp
Rice/Salines	1.86	1.57	0.59	62.4
Rice	2.26	1.84	0.39	78.8
Salines	1.34	1.23	0.73	40.7

Fig. 4 shows the Markov model estimation performances in terms of $RMSE$ and Imp versus the pixel number and the observation error σ' . Fig. 4 shows that the $RMSE$ increases with σ' . Moreover, as the increase of the pixel number is an increase of the information quantity, thus the estimation $RMSE$ decreases with the pixel number. In particular, for fifteen pixels and $\sigma'=0.25$, the $RMSE$ reaches 0.2. Conversely, for only one pixel and $\sigma'=5$, $RMSE=1.1$, which is close to the *a priori* ($RMSE=1.2$). Furthermore, when only one pixel is used the estimation, accuracy remains low ($RMSE>1$) for smaller σ' values. Indeed, only one pixel is not enough to inverse five temperatures. Moreover, the improvement with respect to the classical approach is low in this case ($Imp<10\%$). Particularly, when $\sigma'=5$, the improvement equals -3%, which means that for very noisy data, the Markov approach cannot improve the results. Then, Imp increases with the pixel number

and σ' , reaches 43% for a number of pixels and σ' equal to 12 and 0.25, respectively. In fact, the classical downscaling temporal variation curves become closer to the actual ones relative to the pixel number and σ' . Thus by smoothing their fluctuation the Markov improvement impact increases. However, in the particular case where the number of pixels and σ' are equal to 15 and 5, respectively, and compared to the case (12, 0.5), the improvement decreases slightly from 43% to 37%. This behavior is due to the observation high accuracy leading to the decrease of the classical method curve fluctuation and therefore the decrease of the Markov improvement.

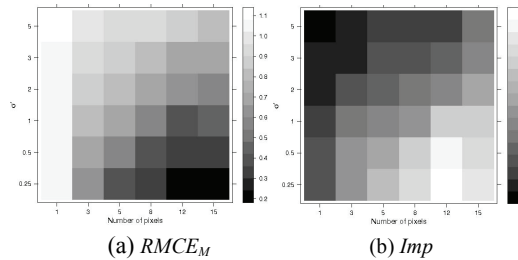


Fig. 4. Markov approach estimation $RMCE_M$ and Imp function of the pixel number and σ' . The used parameters are: endmember number=5 (rice, salines, forest, cultures, bar soil) and random pixel compositions.

4 CONCLUSIONS

In order to monitor highly variable surface physical process a downscaling method of the surface brightness temperature measured by a low spatial resolution sensor was proposed in this article. The problem consists of estimating a sub-pixel temperature which is an ill-posed problem since only one observation is used to estimate a few endmember temperatures. The solution that we present here consists of adding *a priori* information concerning each endmember temperature statistics. Indeed, each endmember temperature temporal variation is assumed a Markov chain with mean values and dependency between successive measurements are given based on statistics over the SVAT model SEtHyS. Each vegetation class spatial distribution is assumed stationary.

In order to estimate the *a posteriori* most likely sub-pixel temperature given the satellite observations, the MAP criterion has been used. The obtained problem corresponds to a minimization of a quadratic form. Then by differentiation, the problem becomes linear and therefore simple to solve.

The model performances are tested using simulated data. The simulated database is obtained using the SEtHyS model and observation obtained assuming Gaussian noise. The model robustness to noise level is studied in many cases by varying the

pixel number and the observation noise. Compared to the results of the case when the temperature temporal dependency is not taken into account, our model shows overall better performances.

References

- Ottlé, C. and Vidal-Madjar, D., 1994, Assimilation of soil moisture inferred from infrared remote sensing in a hydrological model over the HAPEX-MOBILIHY region, *Journal of hydrology*, **158**, pp. 241–264.
- Coudert, D., Ottlé, C., Boudevillain, B., Demarty, J. and Guillevic, P., 2006, Contribution of thermal infrared remote sensing data in multiobjective calibration of a dual source svat model, *Journal of hydrometeorology*, **7**, pp. 404–430.
- Besag, J., 1974, Spatial interaction and the statistical analysis of lattice systems, *Journal of the Royal Statistical Society, Series B*, **36**, pp. 192–236.
- Geman, S., and Geman, D., 1984, Stochastic relaxation, Gibbs distribution and Bayesian restoration of images, *IEEE Trans. On Pattern Analysis & Machine Intelligence*, **6**, pp. 721–74.
- Guyon, X., 1993, *Champs aléatoires sur un réseau*. (Masson).
- Liu, Y., Hiyama, T., and Yamaguchi, Y., 2006, Scaling of land surface temperature using satellite data: A case examination on ASTER and MODIS products over a heterogeneous terrain area, *Rem. Sens. Env.*, **105**, pp. 115–128.

Estimating forest parameters from top of atmosphere multi-angular radiance data using coupled radiative transfer models

Valérie C.E. Laurent¹, Wout Verhoef², Jan G.P.W. Clevers¹, Michael E. Schaepman³

¹ Centre for Geo-Information, Wageningen University, the Netherlands

² Faculty of Geo-Information Science and Earth Observation (ITC), University of Twente, the Netherlands

³ Remote Sensing Laboratories, University of Zurich, Switzerland

valerie.laurent@wur.nl, verhoef@itc.nl, jan.clevers@wur.nl, michael.schaepman@geo.uzh.ch

ABSTRACT – Traditionally, the estimation of forest parameters using physically-based canopy radiative transfer models (RT) requires correcting the remote sensing data to top-of-canopy (TOC) level by inverting an atmosphere RT model. By coupling the same canopy and atmosphere models, it is possible to simulate the top-of-atmosphere (TOA) radiance and to work directly with the measured TOA radiance data, thus avoiding the correction to TOC level. Many studies discussed the increased potential of multiangular data for parameter estimation, especially for forests, which have strong directional properties. These studies, however, were based on TOC data. In this study, we investigate the potential of multiangular data at TOA level, based on a case study for three Norway spruce stands in the Czech Republic, using multi-angular CHRIS data and the coupled SLC-MODTRAN model. The coupled model provided satisfactory TOA simulations of spectral and angular signatures, and the dimensionality of the parameter estimation problem increased with increasing angular sampling. Canopy cover, fraction of brown material, leaf chlorophyll and leaf dry matter content were estimated using all possible angular combinations. No combination was best for all parameters.

1 INTRODUCTION

Traditionally, the estimation of forest parameters requires correcting the remote sensing data to top-of-canopy (TOC) level. This requires inverting an atmosphere radiative transfer (RT) model, which adds errors to the data that will be used for the inversion of the canopy RT model. By coupling the same canopy and atmosphere models, it is possible to simulate the top-of-atmosphere (TOA) radiance and to work directly with the measured TOA radiance data, thus avoiding the correction to TOC level. Many studies discussed the increased potential of multiangular data for parameter estimation (Kempeneers et al., 2008; Weiss et al., 2000), especially for forests (Huber et al., 2010), which have strong directional properties. These studies, however, were based on TOC data. This study coupled the SLC soil-leaf-canopy (Verhoef and Bach 2007) and the MODTRAN4 atmosphere (Berk et al., 2003) radiative transfer models to estimate forest parameters from multi-angular TOA radiance data. The study focused on three Norway spruce stands in the Czech Republic.

2 MATERIALS AND METHODS

2.1 Study area and data

The study area is located in a rather flat area in Eastern Czech Republic, at the Bily Kriz experimental

research site in the Moravian-Silesian Beskydy Mountains, (18.54°E, 49.50°N; altitude 936 m above sea level). A detailed description of the environmental conditions can be found in (Kratochvilová et al., 1989). The forest area is dominated by montane Norway spruce (*Picea abies* (L.) Karst.). Three stands of different ages and structures were selected for the study (Table 1): YOUNG, OLD1 and OLD2. The data were collected in the first half of September 2006.

A set of multi-angular data was acquired on September 12th, 2006, by CHRIS (Compact High Resolution Imaging Spectrometer) on board of the PROBA (Project for On Board Autonomy) satellite platform. Only four images covered the study area. Their acquisition geometry is shown in Figure 1. The images were acquired in chlorophyll mode (mode 4), resulting in 18 spectral bands in the range 485-802 nm at a spatial resolution of 17 m. The images were radiometrically calibrated by the data provider and were further de-striped, geo-corrected and orthorectified using nearest neighbor interpolation. Band 15, centered at 761 nm, was not used because it sampled one of the oxygen absorption features and was very noisy. An AISA (Airborne Imaging Spectroradiometer) Eagle image with 40 cm pixel size was acquired on September 14th, 2006. It was atmospherically corrected using ATCOR4.

The plant area index (PAI), defined as half of the total plant area (needles and non photosynthetic plant material) per unit of ground surface area (Chen, 1996),

Table 1. Stand characteristics and model inputs (DBH: diameter at breast height, LIDF: leaf inclination distribution function, Sph: spherical).

Stand		YOUNG	OLD1	OLD2
Age (years)		29	100	75
Density (trees/ha)		1450	160	420
DBH (cm)		14	53	37
Canopy	PAI	8.88	5.73	7.35
	fB	0.13	0.23	0.4
	D	0	0	0
	Hot	0.01	0.01	0.01
	LIDF	Sph	Sph	Sph
	Cv	0.9	0.55	0.7
	Zeta	0.34	0.24	0.26
Needle	Cab ($\mu\text{g}/\text{cm}^2$)	55	60	65
	Cw (cm)	0.02	0.02	0.02
	Cdm (g/cm^2)	0.04	0.04	0.04
	Cs	0	0	0
	N	2.7	2.5	2.3
Bark	Cab ($\mu\text{g}/\text{cm}^2$)		10	
	Cw (cm)		0	
	Cdm (g/cm^2)		0.5	
	Cs		15	
	N		10	

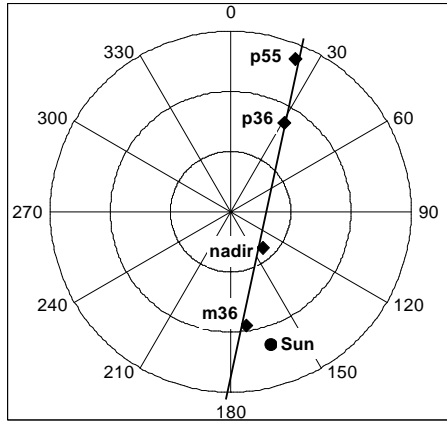


Figure 1: Polar view of the geometry of the CHRIS acquisition.

was estimated in each stand by three methods: LAI-2000 plant canopy analyzer, hemispherical photograph, and TRAC (Tracing Radiation and Architecture of Canopies) (Homolová et al., 2007). The obtained values were averaged to one PAI value for each stand. The crown cover (Cv) was estimated by classifying the AISA image (Lukeš, 2009).

Ten sample trees in the YOUNG stand and 20 in the OLD1 stand were selected for canopy and needle measurements. Only canopy measurements were made in the OLD2 stand. Canopy structure measurements included tree height, crown radius, and crown length.

The spectral properties of the main background

components (soil, humus, litter, understory species) and of the bark were measured in the field at 1 nm resolution with an ASD spectro-radiometer.

2.2 Radiative transfer models

The Soil-Leaf-Canopy (SLC) model was used to simulate the four top-of-canopy (TOC) reflectance components of the stands. It couples:

- 4SOIL: soil reflectance model which was not used in this study,
- PROSPECT: leaf optical properties model (Jacquemoud and Baret, 1990), modified to include brown pigments (Cs) (Verhoef and Bach, 2003),
- 4SAIL2: canopy reflectance model which includes the crown clumping effect thanks to the introduction of two additional inputs: crown cover (Cv) and tree shape factor (Zeta) defined as the crown diameter divided by the height of the crown centre above ground (Verhoef and Bach, 2007). 4SAIL2 also allows mixing green and brown leaves in the canopy by using the fraction of brown material (fB) and the dissociation factor (D). The brown leaves were used for the bark.

The MODTRAN4 model was used for the atmosphere. The following options were selected: DISORT algorithm with 8 streams, medium speed correlated-k option with 17 values, and 5 cm^{-1} database.

2.3 Calculation of the TOA radiance

The 4-stream RT theory provides a simple but accurate framework for radiative transfer modeling. We use subscripts to indicate the direction of the radiation: *s* for the sun direction, *o* for the observer direction and *d* for diffuse hemispherical radiation. When ignoring the adjacency effect, the TOA radiance L_o can be calculated as (Laurent et al., Submitted):

$$L_o = L_{atm} + \frac{G_{ssdo}r_{sd} + G_{sddo}r_{dd}}{1 - r_{dd}\rho_{dd}}, \quad (1)$$

$$+ \frac{G_{sdoo} + G_{mult}r_{sd}}{1 - r_{dd}\rho_{dd}}r_{do} + G_{ssoo}r_{so}$$

where L_{atm} is the atmospheric path radiance, the r terms are the reflectance factors of the canopy, ρ_{dd} is the spherical albedo of the atmosphere, and the G terms are atmospheric gain factors for the double pass in the atmosphere. The G factors were calculated from the total path radiance, the sunlight ground-reflected radiance, and the total ground-reflected radiance outputs of three MODTRAN runs for Lambertian surfaces (Laurent et al., Submitted). Canopy reflectances and G factors were resampled to the

CHRIS bands using Gaussian approximations of the sensor response functions.

2.4 Model parameterization

The background signature was calculated as the average of the signatures of the background components, weighted by their fractional area. The PROSPECT model was used to simulate the optical properties of the needles and bark material. It was not designed for that, so it was optimized to match the measured bark signature, and the parameters for the needles were tuned using the four angular measurements at TOA level, together with the D parameter (Table 1).

The same atmospheric properties were used for the four images. The urban aerosol type was chosen in MODTRAN because of the dominant north wind blowing from an industrial zone and high air concentration of SO₂. The visibility was chosen as the smallest value (100 km) for which the simulated L_{atm} was smaller than all radiances in all CHRIS images.

2.5 Local sensitivity analysis

A local sensitivity analysis (LSA) was performed based on the Jacobian values. For each observation direction o , the Jacobian matrix \mathbf{J}_o is the matrix of the partial derivatives of the model output L_o with respect to each input parameter p_k , normalized assuming a uniform distribution over its potential variation range:

$$\mathbf{J}_o = [j_{o,i,k}]_{1 \leq i \leq n_b, 1 \leq k \leq n_p}, \quad (2)$$

with $j_{o,i,k} = \frac{\partial L_o(\theta_o, \lambda_i)}{\partial p_k},$

where n_b is the number of bands and n_p is the number of parameters. The hotspot parameter (hot) was changed by 0.005 because of its very small value.

We note Θ the ensemble of the observation directions used in the multi-angular analysis. The Jacobian matrices for o in Θ were vertically stacked into the matrix \mathbf{J} .

Only the most influent parameters can be estimated. To evaluate the influence of each parameter, the indicator α_k was defined as:

$$\alpha_k = \sqrt{\frac{\sum_{o \in \Theta} \sum_{i=1}^{n_b} w_i j_{o,i,k}^2}{\sum_{o \in \Theta} \sum_{i=1}^n w_i}}, \quad (3)$$

where the w terms are the weights that were introduced to account for the irregular spectral

distance of the CHRIS bands:

$$\begin{cases} w_1 = (\lambda_2 - \lambda_1) \\ w_i = (\lambda_{i+1} - \lambda_{i-1})/2, \quad 2 \leq i \leq n-1. \\ w_n = (\lambda_n - \lambda_{n-1}) \end{cases} \quad (4)$$

To allow easier comparison between stands, the α values were normalized (α_{norm}).

A Singular Value Decomposition (SVD) was then applied to \mathbf{J} , yielding the singular matrix \mathbf{S} . \mathbf{S} relates the transformed output differences $\mathbf{U}^T \Delta \mathbf{L}$ to the transformed parameter variations $\mathbf{V}^T \Delta \mathbf{p}$ as:

$$\mathbf{U}^T \Delta \mathbf{L} = \mathbf{S} \mathbf{V}^T \Delta \mathbf{p}, \quad (5)$$

where $\Delta \mathbf{L}$ is the stacked vector of model output differences for o in Θ and $\Delta \mathbf{p}$ is the vector of normalized parameter variations. Because \mathbf{S} is diagonal and \mathbf{U}^T and \mathbf{V}^T are orthonormal, there is a one-to-one relationship between $\Delta \mathbf{L}$ and $\Delta \mathbf{p}$. Therefore, the rank of \mathbf{S} is the dimensionality of the estimation problem. The rank of \mathbf{S} was taken as the number of singular values needed to reach 95% of the sum of all singular values.

2.5 Parameter estimation

The cost function χ was defined using the same structure as the α indicator:

$$\chi = \sqrt{\frac{\sum_{o \in \Theta} \sum_{i=1}^{n_b} w_i (\Delta L_o(\lambda_i))^2}{\sum_{o \in \Theta} \sum_{i=1}^n w_i}}. \quad (6)$$

The look-up table (LUT) method was chosen because of its ability to find the global minimum of the cost function. The free parameters in the LUT were chosen based on the results of the LSA.

3 RESULTS AND DISCUSSION

3.1 Simulations

The TOA simulations were satisfactory. The χ values for $\Theta = \{\text{m36, nadir, p36, p55}\}$ were: 5.9 mW/(m².sr.nm) for the YOUNG stand, 9.5 for the OLD1 stand, and 7.6 for the OLD2 stand.

Figure 2 presents the spectral simulation results for the YOUNG stand. The monoangular χ values were smaller in the forward than in the backward direction ($\Theta_{\text{nadir}} = -16^\circ$). The signatures were overestimated in the nadir, p36, and p55 directions and underestimated in the m36 direction. This might be due to the leaf angle distribution function or to the

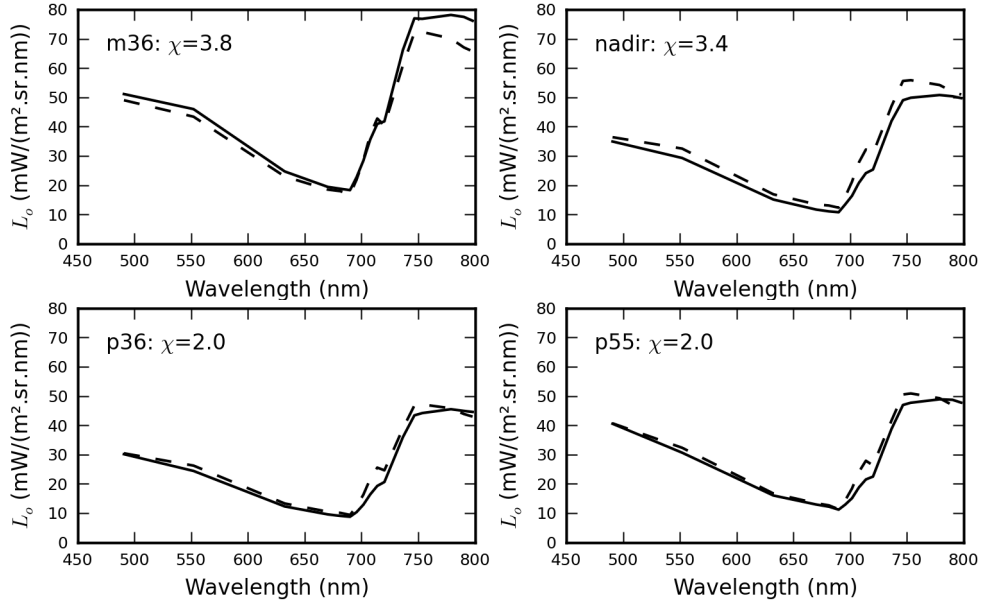


Figure 2. Spectral simulations (dashed lines) and CHRIS measurements (solid lines) of the TOA radiance for the four available images for the YOUNG stand

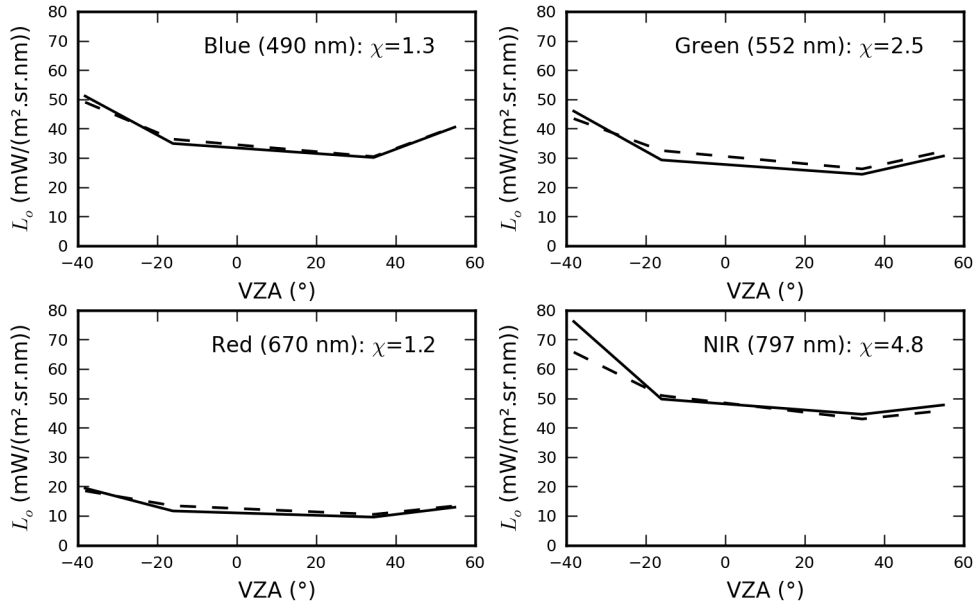


Figure 2. Angular simulations (dashed lines) and CHRIS measurements (solid lines) of the TOA radiance for four selected wavelengths for the YOUNG stand

assumption of constant atmospheric parameters for the four angles.

The angular results for the YOUNG stand are shown in Figure 3. Both the simulations and the measurements present the bowl shape expected for dense coniferous forests (Verrelst et al., In press). The

χ values were smallest in the visible domain, especially in the blue and red band where the radiance is lowest, and larger in the NIR band, where the radiance is highest. This may be due to the atmospheric path radiance which is most important in the visible and accounts for the most part of the

radiance, with only a small part coming from the canopy. Thus, inaccuracies in the canopy reflectance were less important in the visible domain. On the contrary, the atmospheric path radiance is very small in the NIR domain, and inaccuracies at the canopy level fully translated to TOA level.

Similar trends were observed for the OLD1 and OLD2 stands, but with higher χ values. This may be due to the lesser quality of the field data for these stands.

3.2 Local sensitivity analysis

For each angular combination, the α_{norm} values were averaged over the three stands (not shown). All combinations presented similar influence profiles, except for the hotspot parameter. Hot was most influent for m36 ($\alpha_{norm} = 0.33$) and nadir (0.14) and was not influent for the forward angles (<0.04). For the multiangular combinations, its influence depends on which angles were used (e.g. 0.22 for four angles). For the other parameters, the most influent were fB (0.18-0.22), Cv (0.14-0.22), needleCdm (0.14-0.17), LIDFa (0.09-0.17), and needleCab (0.06-0.08). The bark ($\alpha_{norm} < 0.03$) and atmosphere ($\alpha_{norm} < 0.04$) parameters were least influent.

The importance of the hotspot parameter is due to the wide angular area of influence caused by the very high PAI of the three stands. The m36 image is close to the hotspot, and the nadir image is close to the principal plane (relative azimuth = 25°). The value of 0.01 for forests is well known. The LIDFa parameter was also very influent, but for coniferous stands, we cannot assume any other leaf distribution than spherical.

The local dimensionality values obtained from the SVD are presented in Table 2. For each combination, the three stands had very similar values, with the YOUNG stand having slightly smaller dimensionality.

The dimensionality increases when using more angles in the combination, thus showing the increasing information content when increasing the angular sampling.

Table 2. Dimensionality

	YOUNG	OLD1	OLD2
nadir	3	3	3
m36	3	3	3
p36	3	3	3
p55	4	4	4
nadir_m36	4	4	4
nadir_p36	4	5	5
nadir_p55	5	5	5
m36_p36	4	4	4
m36_p55	4	5	5
p36_p55	5	5	5
nadir_m36_p36	5	5	5
nadir_m36_p55	5	6	6
nadir_p36_p55	5	6	6
m36_p36_p55	5	6	6
4 angles	5	6	6

3.3 Parameter estimation

Based on the dimensionality results, it was decided to have four free parameters in the LUT. The four parameters which were most influent and also most relevant for applications (forest health, fuel moisture, carbon stock...) were used: fB, Cv, needleCdm, and needleCab. fB and Cv were sampled from 0 to 1 in steps of 0.1, Cab from 0 to 100 in steps of 5, and Cdm from 0 to 0.05 in steps of 0.005.

The estimation results for the YOUNG stand are presented in Table 3. In all cases, only one solution was found in the LUT. No combination provided the best estimates for all parameters. Some combinations, however, were able to provide good estimates for two parameters. The best estimates for Cv were obtained

Table 3. Parameter estimates for the YOUNG stand (best estimates in bold).

	Cv	fB	Cab (g/cm ²)	Cdm (g/cm ²)	χ	# solutions
nadir	0.8	0.0	75	0.050	1.044	1
m36	1.0	0.2	50	0.025	1.672	1
p36	0.9	0.1	75	0.045	0.960	1
p55	0.8	0.2	75	0.030	0.982	1
nadir_m36	0.6	0.0	55	0.025	1.689	1
nadir_p36	0.7	0.0	75	0.040	0.722	1
nadir_p55	0.8	0.1	75	0.040	0.762	1
m36_p36	0.7	0.2	50	0.015	1.673	1
m36_p55	1.0	0.4	50	0.005	1.749	1
p36_p55	0.9	0.1	75	0.045	0.710	1
nadir_m36_p36	0.7	0.0	60	0.035	1.377	1
nadir_m36_p55	0.8	0.2	60	0.025	1.620	1
nadir_p36_p55	0.8	0.1	75	0.040	0.618	1
m36_p36_p55	0.9	0.4	55	0.005	1.469	1
4 angles	0.8	0.2	60	0.025	1.270	1

by combinations including p36, best estimates for Cab using m36 and best estimates for Cdm using nadir, and the best estimates of fB used only nadir and forward angles, similar to Cdm. The m36 angle was only used for the Cv and Cab estimates. It is interesting to note that the nadir angle was not used in the combinations providing the best Cv and that the combination using the four angles did not provide the best estimate for any parameter.

The results for the OLD1 and OLD2 stands were different, but similarly to the YOUNG stand, it was not possible to distinguish a single combination providing the best estimates.

5 CONCLUSION

The coupled SLC-MODTRAN model was able to provide satisfactory simulations of the TOA radiance of the coniferous stands. Despite the simplicity of SLC, the brown material and crown clumping features adequately mimicked the stand structures, also when seen from multiple observation directions.

The SVD is a very interesting tool to assess the dimensionality of the estimation problem and to get insight in the influence of the parameters, thus being of great interest for steering the inversion process. The multiangular SVD proved that the dimensionality increases with increasing number of angles at TOA level. In the future, the LUT will be extended to more parameters to make full use of the extra information provided by the multiangular data.

6 ACKNOWLEDGEMENT

The data collection was conducted under ESA/PECS project No. 98029 and provided by the Institute of Systems Biology and Ecology, Academy of Sciences of the Czech Republic. The authors wish to thank Petr Lukeš and Lucie Homolová for their help with the data and Allard de Wit for his assistance with model implementation and LUTs.

7 REFERENCES

- Berk, A., Anderson, G.P., Acharya, P.K., Hoke, M.L., Chetwynd, J.H., Bernstein, L.S., Shettle, E.P., Matthew, M.W., and Adler-Golden, S.M. 2003, MODTRAN4 Version 3 Revision 1 User's manual. (p. 97): Airforce Research Laboratory, Hanscom, MA, USA.
- Chen, J.M., 1996, Optically-based methods for measuring seasonal variation of leaf area index in boreal conifer stands. *Agricultural and Forest Meteorology*, 80, 135-163.
- Homolová, L., Malenovský, Z., Hanuš, J., Tomášková, I., Dvořáková, M., and Pokorný, R., 2007, Comparison of different ground techniques to map leaf area index of Norway spruce forest canopy. In M.E. Schaepman, S. Liang, N.E. Groot & M. Kneubühler (Eds.), *10th ISPMSRS*. Davos, Switzerland: Intl. Archives of the Photogrammetry, Remote Sensing and Spatial Information Sciences.
- Huber, S., Koetz, B., Psomas, A., Kneubühler, M., Schopfer, J., Itten, K., and Zimmermann, N.E., 2010, Impact of multiangular information on empirical models to estimate canopy nitrogen concentration in mixed forest. *Journal of Applied Remote Sensing*, 4.
- Jacquemoud, S., and Baret, F., 1990, PROSPECT: A model of leaf optical properties spectra. *Remote Sensing of Environment*, 34, 75-91.
- Kempeneers, P., Zarco-Tejada, P.J., North, P.R.J., de Backer, S., Delalieux, S., Sepulcre-Canto, G., Morales, F., van Aardt, J.A.N., Sagardoy, R., Coppin, P., and Scheunders, P., 2008, Model inversion for chlorophyll estimation in open canopies from hyperspectral imagery. *International Journal of Remote Sensing*, 29, 5093-5111.
- Kratochvilová, I., Janouš, D., Marek, M., Barták, M., and Řiha, L., 1989, Production activity of mountain cultivated Norway spruce stands under the impact of air pollution. I. General description of problems. *Ekológia*, 8, 407-419.
- Laurent, V.C.E., Verhoef, W., Clevers, J.G.P.W., and Schaepman, M., Submitted, Estimating forest parameters from top-of-atmosphere radiance satellite measurements using coupled radiative transfer models. *Remote Sensing of Environment*.
- Lukeš, P., 2009, Retrieval of canopy cover of the Norway spruce stands in the Bily Kriz area (CZ) from classification of AISA Eagle data. Personal communication.
- Verhoef, W., and Bach, H., 2003, Simulation of hyperspectral and directional radiance images using coupled biophysical and atmospheric radiative transfer models. *Remote Sensing of Environment*, 87, 23-41.
- Verhoef, W., and Bach, H., 2007, Coupled soil-leaf-canopy and atmosphere radiative transfer modeling to simulate hyperspectral multi-angular surface reflectance and TOA radiance data. *Remote Sensing of Environment*, 109, 166-182.
- Verrelst, J., Clevers, J.G.P.W., and Schaepman, M.E., In press, Merging the Minnaert- k Parameter With Spectral Unmixing to Map Forest Heterogeneity With CHRIS/PROBA Data. *IEEE Transactions on Geoscience and Remote Sensing*.
- Weiss, M., Baret, F., Myneni, R.B., Pragnère, A., and Knyazikhin, Y., 2000, Investigation of a model inversion technique to estimate canopy biophysical variables from spectral and directional reflectance data. *Agronomie*, 20, 3-22.

D-PROSPECT: A Model to Simulate Leaf Optical Properties Spectra of Double Surfaces

Jing Li, Qinhuo Liu, and Qiang Liu

State Key Laboratory of Remote Sensing Science, Jointly Sponsored by the Institute of Remote Sensing Applications of Chinese Academy of Sciences and Beijing Normal University.

lijing@irsa.ac.cn

ABSTRACT (OF 200-250 WORDS)-The difference of optical properties between leaf upper and lower surfaces has been described by Woolley in 1971. The different leaf models have been developed to account for the optical properties of the dorsiventral leaf, including Yamada and Fujimura's model, QSPECT, and DLM. It is needed to make a better balance between the model complexity and its accessibility. This paper proposes a leaf model, D-PROSPECT, which is capable of simulating the leaf reflectance and transmittance of double surfaces in the 350-2500nm domain. The double N-layers model structure is suggested in D-PROSPECT instead of a pile of N homogeneous layers in PROSPECT to represent the leaf asymmetric layer structure. Two parameters, W_{ab} and W_w , are introduced into D-PROSPECT model to represent the fraction of chlorophyll concentration and leaf water content between leaf upper and lower layers. The method to determine W_{ab} and W_w is proposed. The sensitivity analysis proves that D-PROSPECT model has the capability to simulate the reflectance and transmittance of leaf both surfaces, which fits with the experiment results.

1 INTRODUCTION

The difference of optical properties between leaf upper and lower surfaces has been described by Woolley in 1971. The different leaf models have been developed to account for the optical properties of the dorsiventral leaf, including Yamada and Fujimura's model, QSPECT, and DLM. It is needed to make a better balance between the model complexity and its accessibility.

The assumption that the leaf upper and lower surfaces have the same optical properties is widely used in leaf and canopy reflectance models, such as in PROSPECT and SAIL models. The PROSPECT leaf model simulates one reflectance and one transmittance for both of leaf upper and lower surfaces. The SAIL canopy model calculates the scattering efficiency factors with leaf reflectance and transmittance, no matter the scattering happens on leaf upper or lower surface.

However the reflectance of leaf upper and lower surface is not necessarily equal to each other. Previous research pointed out that according to the experiment results the optical properties of leaf upper and lower surfaces have significant difference in some wavelength, especially for some dicotyledonous leaves. We have also done experiments to measure the reflectance and transmittance of the double surfaces of cotton leaves from five sample cotton plants by the Li-Cor 1800-12s integrating sphere attached to the spectroradiometer of ASD company. The experimental

results show that (1) for the mature leaf there is obvious reflectance difference between upper and lower leaf surfaces in 350nm - 700nm and 1350nm - 2500nm domain, and the largest difference reaches about 10 percent, (2) for the new leaf on the top layer of the plant the reflectance has small difference between the upper and lower leaf surfaces, (3) the transmittance of both leaf surfaces has no obvious difference. Figure 1 shows the measured reflectance of upper surface and lower surface of a mature cotton leaf.

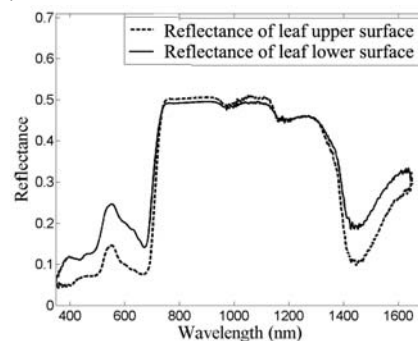


Fig. 1. Measured reflectance of upper surface and lower surface of cotton leaf

Thus the assumption that leaf upper and lower surfaces have the same reflectance is not always true, especially for some dicotyledonous leaves. The reflectance models with such an assumption can not accurately simulate the leaf or canopy reflectance for

those species in the theoretical basis. Therefore it is necessary to take into account the difference between leaf upper and lower surface.

PROSPECT is an accurate, invertible and widely-used leaf model. It used the assumption and simulates one reflectance for both of leaf surfaces. In this letter, a radiative transfer model, D-PROSPECT was developed to simulate the reflectance and transmittance of leaf upper and lower surfaces based on PROSPECT leaf model.

2 LEAF STRUCTURE AND MODEL STRUCTURE

Before constructing the leaf model it is required to know the reason that leads to the reflectance difference between leaf upper and lower surface. We started analyzing from the leaf structure. Figure 2 shows the structure of a dicotyledonous leaf.

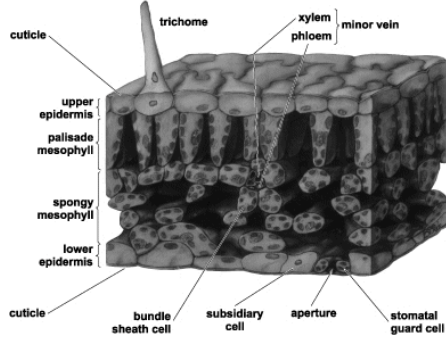


Fig. 2. Structure of a dicotyledonous leaf (<http://content.answers.com/main/content/img/McGrawHill/Encyclopedia/images>)

A typical dicotyledonous leaf has an obvious layer structure. It includes four layers of upper epidermis, palisade mesophyll, spongy mesophyll, and lower epidermis. The water, chlorophyll and pigment features distribute in the palisade mesophyll and spongy mesophyll. The research of Terashima & Saeki concluded that photosynthetic properties of chloroplasts differ spatially and that this variation results in more efficient light utilization within the leaf. This efficient way decides that the distribution of chlorophyll and leaf water can not be well-proportioned within the leaf. The recent imaging technique measured the distribution of leaf water and chlorophyll inside the leaf. The results show that for a typical *Acer platanoides* sun leaf the chlorophyll and leaf water distribute more in the palisade mesophyll, which is close to the leaf upper surface, than in the spongy mesophyll, which is close to the leaf lower surface. This asymmetric distribution of leaf water and chlorophyll inside the leaf challenges the symmetric model structure of PROSPECT.

PROSPECT leaf model is based on Allen's "Plate

model". It inherits the model structure from "Plate model" as stacking elementary layers. A leaf is then assumed to be composed of a pile of N homogeneous layers. But the homogeneous characteristic can not describe the distribution variation of chlorophyll and leaf water inside the leaf. This model does not work when taking into account the difference of leaf both surfaces.

Figure 3 is a simplified two-layer inhomogeneous pile. Two layers have unequal reflectance and transmittance as ρ_1, τ_1 and ρ_2, τ_2 . The figure shows the ray schematic illustration of reflectance ρ^+ and transmittance τ^+ of upper surface, and also ρ^- , τ^- of lower surface. Equation (1) gives their calculation. It is concluded that the difference between ρ_1 and ρ_2 , τ_1 and τ_2 results in difference between ρ^+ and ρ^- , but none for τ^+ and τ^- .

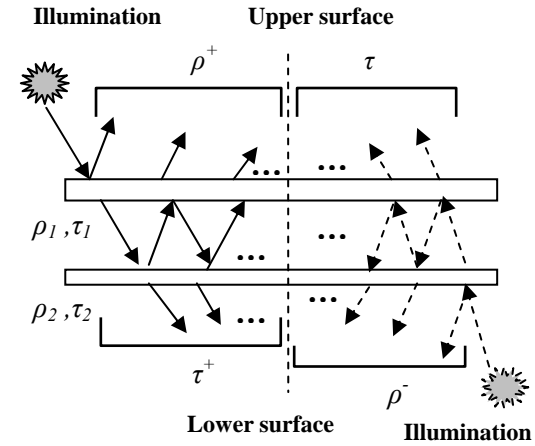


Fig. 3. Ray schematic illustration of ρ^+, τ^+ (solid line) and ρ^-, τ^- (dotted line) in a two-layer inhomogeneous pile

The mechanism in figure 3 proves that the layers inside the leaf with different optical properties results in the reflectance difference of leaf both surfaces. It also gives a likely solution to the new model structure.

$$\begin{aligned}\rho^+ &= \rho_1 + \frac{\tau_1^2 \rho_2}{1 - \rho_1 \rho_2} & \rho^- &= \rho_2 + \frac{\tau_2^2 \rho_1}{1 - \rho_1 \rho_2} \\ \tau^+ &= \frac{\tau_1 \tau_2}{1 - \rho_1 \rho_2} & \tau^- &= \frac{\tau_1 \tau_2}{1 - \rho_1 \rho_2}\end{aligned}\quad (1)$$

3 D-PROSPECT

3.1 Theory

D-PROSPECT is based on PROSPECT model. The basic theory is similar, but two modifications were implemented in D-PROSPECT. The first one is on the model structure. To describe the difference of optical properties between leaf layers we change the model

structure from a pile of N homogeneous layers in PROSPECT into a pile of double N-layers in D-PROSPECT. Inside each of N-layers the elementary layers are homogeneous, but the elementary layers from different N-layers have different optical properties. Still the void area index (VAI) is used to describe the leaf internal structure, given by $VAI = N - 1$.

The second modification is introducing two parameters W_{ab} and W_w into D-PROSPECT to describe the fraction of concentration of chlorophyll and leaf water between upper and lower N-layers. W_{ab} and W_w range from -1 to 1. $W_{ab} = -1$ means that all the chlorophyll distribute in upper N-layers. $W_{ab} = 0$ means that the chlorophyll has well-proportioned distribution in upper and lower N-layers. And $W_{ab} = 1$ means that all the chlorophyll distribute in lower N-layers. -1 and 1 refers to an extreme situation and generally can not happen in real world. W_w has the similar meaning as W_{ab} .

Based on above two modifications the computation of leaf reflectance and transmittance in D-PROSPECT is a little different with PROSPECT. The double N-layers in D-PROSPECT can be treated as inhomogeneous two-layer pile as figure 3. Then the reflectance and transmittance of leaf upper surface and lower surface can be calculated as Eq. (1). In this case ρ_1 , τ_1 and ρ_2 , τ_2 are the reflectance and transmittance of upper N-layers and lower N-layers respectively.

As PROSPECT model, D-PROSPECT keeps Ω to describe the incoming beam penetrates the leaf with incident directions within a solid angle Ω . Therefore for illuminated N-layers the reflectance and transmittance are represented as $R_{N,\alpha}$ and $T_{N,\alpha}$, and for the shade N-layers as $R'_{N,90}$ and $T'_{N,90}$. When calculating ρ^+ and τ^+ , the upper N-layers are illuminated, and when calculating ρ^- and τ^- , the lower N-layers are illuminated. The calculation of $R_{N,\alpha}$ and $T_{N,\alpha}$ can be referred to Eq. (7) and (8) in Jacquemoud (1990), and the calculation of $R'_{N,90}$ and $T'_{N,90}$ referred to Eq. (9) in Jacquemoud (1990). Based on Eq. (1) the transmittance of leaf upper surface and lower surface are supposed to be equal, therefore the output of D-PROSPECT consists of the reflectance of leaf upper surface ρ^+ , the reflectance of leaf lower surface ρ^- , and the leaf transmittance τ .

3.2 Fitting of parameters

When calculating $R_{N,\alpha}$, $T_{N,\alpha}$, $R'_{N,90}$ and $T'_{N,90}$, it requires four parameters: an incidence angle α , a refractive index n , a transmission coefficient θ , and N . The solution of α continues to use 59° as in PROSPECT. The refractive index n also can be referred to the refractive index in PROSPECT. The transmission coefficient θ is related to the absorption coefficient k . Equation (2) and (3) give the calculation

of k_1 for upper N-layers and k_2 for lower N-layers in D-PROSPECT. And then based on Eq.(11) in Jacquemoud (1990) θ_1 for upper N-layer and θ_2 for lower N-layer are calculated.

where $K_{cab}(\lambda)$, $K_{cw}(\lambda)$, and $K_i(\lambda)$ are respectively the spectral specific absorption coefficient relative to chlorophyll, leaf water, and the other leaf component i . C_{ab} , C_w and C_i are the content of chlorophyll, leaf water, and the other component i per unit leaf area respectively. W_{ab} and W_w are the fractions of chlorophyll concentration and leaf water content between upper and lower N-layers. $k_e(\lambda)$ is the term as defined in PROSPECT.

W_{ab} and W_w are newly introduced into leaf model. They describe the grade of the asymmetric distribution of chlorophyll and leaf water inside the leaf vertical profile. They ranged from -1 to 1 generally depending on the plant species and on the leaf development. They can be measured by the imaging technique [6]. They can also be determined indirectly by measuring leaf reflectance and transmittance. For each plant type, we adjusted the W_{ab} at the wavelength where the absorption of chlorophyll is maximum (about 670nm in red) by minimizing

$(R^+ - R_{sim}^+)^2 + (R^- - R_{sim}^-)^2 + (T - T_{sim})^2$, where R^+ , R^- and T are experimental data for reflectance of leaf upper surface, reflectance of leaf lower surface and transmittance, and R_{sim}^+ , R_{sim}^- and T_{sim} are simulated by D-PROSPECT. W_w is determined at the wavelength where the absorption of leaf water is maximum (about 1450nm in microwave infrared). For cotton leaf, W_{ab} and W_w are respectively 0.4 and 0.3.

N in D-PROSPECT has a different meaning from that in PROSPECT. But the determination method is similar. For each plant type, we adjusted the parameter N at the wavelength where the absorption is minimum (near infrared) by minimizing

$(R^+ - R_{sim}^+)^2 + (R^- - R_{sim}^-)^2 + (T - T_{sim})^2$. Since the wavelength to determine N is where the absorption of chlorophyll and leaf water is minimum, the determination of N is hardly affected by their concentration or their distribution fraction. Therefore for one plant type the number of the total layers in D-PROSPECT and in PROSPECT is equal. The determination of W_{ab} and W_w are not affected by each other, but they are affected by N . Hence N should be determined ahead of W_{ab} and W_w .

D-PROSPECT is developed based on PROSPECT. PROSPECT is included in D-PROSPECT as a special case. When both of W_{ab} and W_w equal to 0, D-PROSPECT is equivalent to PROSPECT and is capable of calculating leaf which is modeled as a compact single layer, such as corn.

$$k_1(\lambda) = (K_{Cab}(\lambda) * (1 + W_{Cab}) * Cab + K_{Cw}(\lambda) * (1 + W_{Cw}) * Cw + \sum K_i(\lambda) * Ci) / 2 * N + k_e(\lambda) \quad (2)$$

$$k_2(\lambda) = (K_{Cab}(\lambda) * (1 - W_{Cab}) * Cab + K_{Cw}(\lambda) * (1 - W_{Cw}) * Cw + \sum K_i(\lambda) * Ci) / 2 * N + k_e(\lambda) \quad (3)$$

4 ANALYSIS AND DISCUSSION

The advantage of D-PROSPECT is to simulate the reflectance and transmittance of leaf upper and lower surface. In the following analysis we compared the simulation of PROSPECT and D-PROSPECT, and then made the sensitivity analysis to W_{ab} and W_w in D-PROSPECT.

4.1 Comparison of PROSPECT and D-PROSPECT

D-PROSPECT outputs reflectance and transmittance for double surfaces of a leaf, instead for only one surface in PROSPECT. Figure 4 shows the simulation results from PROSPECT and D-PROSPECT with the same inputs. The concentration of chlorophyll C_{ab} , content of leaf water C_w and content of dry matter C_m are respectively 55, 0.01 and 0.005. W_{ab} , W_w and VAI in D-PROSPECT are set to be 0.4, 0.3 and 1. VAI in PROSPECT is 2.

From this figure we can see that leaf reflectance simulated by PROSPECT is always between reflectance of leaf upper surface and lower surface simulated by D-PROSPECT in the 350nm – 2500nm domain. In the absorption domains of chlorophyll and leaf water the reflectance of upper surface and lower surface has obvious difference. While in near infrared where the absorption is minimum the reflectance of both surfaces are almost equal.

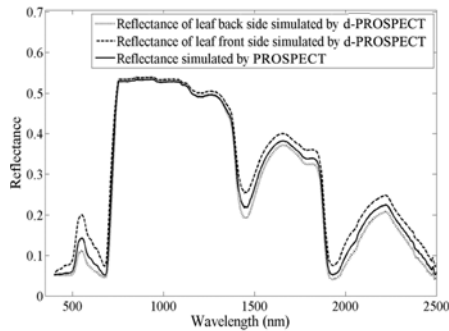


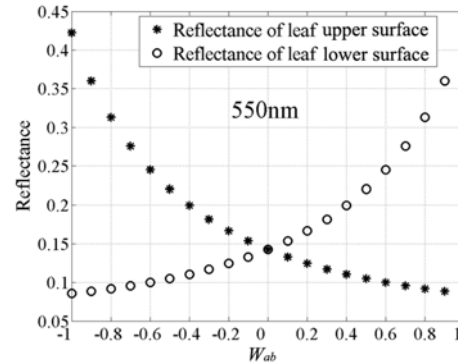
Fig.4 Reflectance simulated by PROSPECT and D-PROSPECT

4.2 Sensitivity Analysis of W_{ab} and W_w

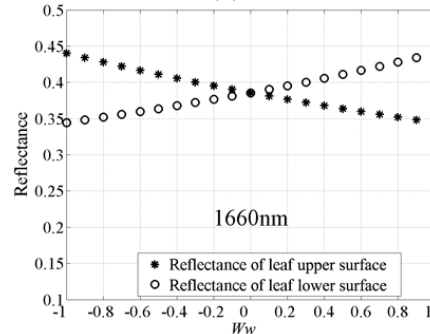
W_{ab} and W_w describe the grade of the asymmetric distribution of chlorophyll and leaf water in leaf vertical profile. W_{ab} has an influence on the reflectance of double surfaces in the chlorophyll absorption domains (350nm – 750nm), and W_w in the absorption domains of leaf water (1200nm - 2500nm). In the following analysis we simulated the reflectance of leaf

upper and lower surfaces in 550nm with W_{ab} ranging from -1 to 1, and in 1660nm with W_w ranging from -1 to 1, and in 1660nm with W_w ranging from -1 to 1 using D-PROSPECT, as shown in figure 5. The model inputs are the same with the simulation in figure 4.

$W_{ab} > 0$ means that the chlorophyll distributing in palisade mesophyll is more than in spongy mesophyll. In this case the reflectance of leaf upper surface is smaller than that of the lower surface. It is reversed for $W_{ab} < 0$. $W_{ab} = 0$ means that the chlorophyll has a well-proportioned distribution within leaf, and the reflectance of leaf upper and lower surfaces are equal to each other. And in this case D-PROSPECT is equivalent to PROSPECT. W_w has the similar meaning as W_{ab} . W_{ab} has a more significant influence on reflectance than W_w . When $W_{ab} = 0.4$ the reflectance difference of leaf upper and lower surfaces is about 10 percent in 550nm, and only 4 percent in 1660nm when $W_w = 0.4$.



(a)



(b)

Fig. 5. Simulated reflectance of leaf upper and lower surfaces (a) at 550nm with W_{ab} ranging from -1 to 1, (b) at 1660nm with W_w ranging from -1 to 1.

5 CONCLUSION

In this letter, a leaf radiative transfer model, D-PROSPECT, has been developed based on PROSPECT model to simulate the leaf optical properties spectra of upper and lower surfaces. The analysis showed that the asymmetric leaf structure causes the difference of optical properties of leaf upper and lower surfaces. The introduction of the double N-layer structure and the parameters W_{ab} and W_w in D-PROSPECT succeeds in depicting their causality. The new model, D-PROSPECT, is able to simulate the difference of optical properties between leaf upper and lower surface.

D-PROSPECT improves the simulation accuracy of leaf optical properties spectra. It is possible to couple D-PROSPECT with canopy model, such as SAILH, to improve the simulation accuracy in canopy level. Therefore, to modify the canopy radiative transfer model to take into account the different optical properties of leaf upper and lower surface in canopy radiative transfer process, and is our next work.

6 REFERENCES

- S. Jacquemoud, and F. Baret, 1990, PROSPECT : A Model of Leaf Optical Properties Spectra. *Remote Sens. Environ.*, vol. 34, pp. 75-91.
- W. Verhoef, 1984, Light Scattering by Leaf Layers with Application to Canopy Reflectance Modeling: The SAIL Model. *Remote Sens. Environ.*, vol. 16, pp. 125~141.
- J. T. Woolley, 1971, Reflectance and Transmittance of Light by Leaves. *Plant Physiol.*, Vol. 47, 656-662.
- J. Stuckens, W. Verstraeten, S. Delalieux, R. Swennen, and P. Coppin, 2009, A dorsiventral leaf radiative transfer model: Development, validation and improved model inversion techniques. *Remote Sens. Environ.*, vol. 113, pp. 2560~2573.
- K. Ma, F. Baret, P. Barroy, and L. Bousquet, 2007, A leaf optical properties model accounting for differences between the two faces. *10th International Symposium on Physical Measurements and Signatures in Remote Sensing*, 2007. ISPMRS07.
- International Society for Photogrammetry and Remote Sensing. Y. L. Tang, X. Z. Wang, J. F. Huang, W. Z. Kong, and R. C. Wang, 2003, The Hyperspectra and their Red Edge Characteristics of Cotton(I), *Cotton Science*, vol. 15, pp. 146-150. [唐延林, 王秀珍, 黄敬峰, 孔维姝, 王人潮, “棉花高光谱及其红边特征(I)”. *棉花科学*, 15 卷, 146-150, 2003.]
- I. Terashima and T. Saeki, 1985, A new model for leaf photosynthesis incorporating the gradients of light environment and of photosynthetic properties of chloroplasts within a leaf. *Annals of Botany*, vol. 56, pp. 489-499.
- D. C. McCain, J. Croxdale, and J. L. Markley, 1993, The spatial distribution of chloroplast water in *Acer platanoides* sun and shade leaves. *Plant, Cell and Environment*, vol. 16, pp. 727-733.

Analysis of uncertainties in the estimation of vineyard biophysical variables from canopy reflectance using 3D architecture models

R. López-Lozano^{1*}, F. Baret¹, B. Tisseyre², E. Lebon³, H. Poilvé⁴, J. Rousseau⁵,

¹ Institut National de la Recherche Agronomique, UMR EMMAH. Site Agroparc, 84914 Avignon Cedex 9 France

² Montpellier SupAgro, UMR ITAP, 2 Place Viala, 34060 Montpellier Cedex 2 (France)

³ Institut National de la Recherche Agronomique, UMR LEPSE, 2 Place Viala, 34060 Montpellier Cedex 2 (France)

⁴ Infoterra France, Parc Technologique du Canal, 15 Avenue de l'Europe, 31520 Ramonville Saint-Agne (France)

⁵ Institut Coopératif du Vin, La Jasse Maurin, 34970 Lattes (France)

* Contact details: email raul.lopez@avignon.inra.fr Phone: +33 432 72 24 18

ABSTRACT Vineyards are discontinuous and structured canopies that constitute an important challenge in the estimation of canopy biophysical variables from remote sensing observations. The role of canopy architectural variables such as row dimensions, planting pattern or rows direction jointly with soil reflectance should be adequately studied when canopy reflectance is used to estimate variables such as Leaf Area Index (LAI), the fraction of intercepted photosynthetically active radiation (fIPAR) or the effective leaf surface.

In the present work, a sensitivity analysis is carried out based on a dataset of virtual 3D vineyard canopies representing a wide range of architectures typical of Mediterranean conditions. Canopy reflectance is simulated from the 3D scenes and the resulting Look Up Table (LUT) is used to analyze the estimation errors in canopy biophysical variables and the contribution of canopy architecture. Several scenarios of a priori knowledge on canopy architecture are considered, and a special attention is paid to the influence of sun-target-sensor geometry on the error structure. The estimation errors will be also analyzed comparing the target biophysical variables, which allow describing the influence of canopy architecture in the relationships between each variable and canopy reflectance in vineyards.

1 INTRODUCTION

The estimation of biophysical parameters in structured discontinuous canopies represents an important challenge in remote sensing studies. The methods commonly used to estimate leaf area index (LAI) or the fraction of photosynthetically active radiation (fIPAR) are based on the assumption of homogeneous distribution of foliage within the canopy. Thus reflectance models as SAILH (Verhoef, 1984) or MCCRM (Kuusk, 1995) are based on this turbid medium assumption to predict canopy reflectance from biophysical variables. The MCCRM model can include leaf clumping in the distribution of foliage in the canopy, but cannot describe a preferential direction (planting pattern), as it happens in row crops.

Although many studies have dealt with the use of ray tracing techniques in clumped canopies as forests (North, 1996; Kotz et al., 2004) the application of these techniques in row crops needs of further effort.

Some studies as Zarco-Tejada et al., 2005 or Zarco-Tejada et al., 2009 have successfully used reflectance modelling in orchard canopies, but they observed leaf-scale variables such as leaf chlorophyll content or fluorescence, and not structural parameters such as LAI or fIPAR.

The present paper studies the estimation capabilities of different biophysical parameters commonly used in viticulture to describe crop development from reflectance observations through a simulation study. A database of vineyard canopy reflectance was created using a couple of architecture+ray tracing models and is used to assess the uncertainties in the estimation of LAI, day-integrated fIPAR, Exposed Leaf Surface (ELS) and vine porosity, with special attention in the contribution of observational parameters..

2 METHODS

2.1 Vineyard architecture modelling

A simple geometrical model was proposed to describe actual vineyard architecture (Figure 1). Vines

are represented as infinite parallelepipedic rows described by a height H , a width W and leaf density determined by canopy the leaf area density (LAD, leaf surface per row volume).

The placement of the rows in the scene is given by the distance between rows $-D_{rows}-$ and the height of the trunks $-H_{trunk}-$ which describes the height of the first wire in the trellis system. The distance between trunks in the same row is determined by D_{plants} .

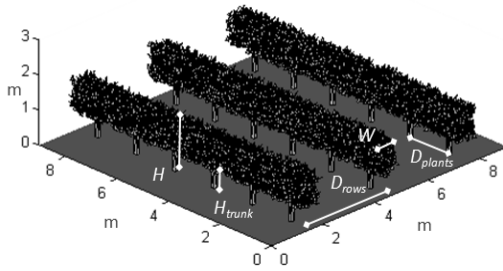


Figure 1. An example of a vineyard scene.

A dataset of architectures was simulated using the proposed 3D model, representing the range of variation of actual vineyards in France (Table 1). To reduce the number of parameters, the vine dimensions are all normalized by the distance between rows.

Table 1. Input parameters and values to the proposed 3D architecture model

Parameter	min	max	steps
W/D_{rows}	0.20	0.80	0.20
$(H-H_{trunk})/D_{rows}$	0.30	0.90	0.20
H_{trunk}/D_{rows}	0.30	0.40	0.10
LAD (m^2/m^3)	3	12	3

2.2 Reflectance modelling

Canopy reflectance was calculated over the virtual scenes generated following the experimental plan described in Table 1 using the PARCINOPY ray-tracing code (Chelle, 1997). Red and near infrared bands of Formosat-2 sensor were simulated. Leaf and trunk optical properties were measured from field samples collected during the summer 2009 at Piolenc site (SE France). Reflectance and transmittance were thus determined in the samples using a FieldSpec Pro spectrometer (ASD Inc, USA) coupled with an integrating sphere (LiCor, USA).

Eighteen different sun positions were also included to analyse the contribution of observational parameters in the uncertainties of the estimation of vine parameters. Three sun zenith angles: 22°, 30° and 44° were selected representing the possible values during the day in the field at summer on mid-latitudes.

At the same time, six different sun azimuth angles relative to rows direction were also considered (0°, 10°, 20°, 30°, 45° and 90°) representing the range of possible situations in the field. Sensor position was fixed at zenith, where the greatest the effect of leaf clumping at canopy scale is expected, and thus the effect of canopy architecture in the relation between reflectance and biophysical parameters becomes more evident.

A clay soil spectrum was introduced in the simulations. However to include a variation in the soil brightness, the slope of the linear function between soil reflectance and canopy reflectance was calculated for each one of the reflectance simulations in the red and NIR bands. This slope was determined from the mean fluxes that PARCINOPY provides as outputs, jointly with canopy BRDF, which allows recalculating canopy reflectance assuming different values of soil reflectance.

2.3 Biophysical parameters calculation.

Day-integrated fIPAR was simulated directly from the scenes calculating monodirectional gap fraction (P_0) following the method proposed by Lopez-Lozano et al. (2009) at directions corresponding to sun positions between dawn and sunset in time steps of 10 minutes, and taking as reference the day of year 201 (when vine leaf area reaches to maximum). Monodirectional P_0 was then integrated in the day using a $\cos(\theta_s)$ weight function, where θ_s is sun zenith angle along the day.

Vineyard porosity ($P_{0,h}$) is a widely used parameter in precision viticulture to describe leaf area density within the vines. It corresponds to the horizontal gap fraction of a single row, and it's usually measured in the field processing a horizontal digital photograph of a single row (Espinosa et al., 2010). $P_{0,h}$ was extracted directly from the 3D scenes calculating monodirectional P_0 at $\theta_s=90^\circ$ in a single row.

ELS is also a commonly used parameter used in viticulture to describe the effective leaf area exposed to sun illumination (Acevedo-Opazo et al., 2010). It's calculated following the expression:

$$ELS = (W + 2H) * (1 - P_{0,h}) \quad [1]$$

ELS thus integrates the vine dimensions and a variable closely related to LAD. Finally, LAI was calculated directly from the simulates scenes;

2.4 Look-up table generation and treatment

Canopy reflectance and biophysical parameters resulting from simulations were stired in a look-up table (LUT). The LUT was then interpolated at steps of 0.025 in W/D_{rows} , $(H-H_{trunk})/D_{rows}$ and H_{trunk}/D_{rows} and 0.1 m^2/m^3 in LAD using a spline function. The

accuracy of interpolation was tested against an independent dataset of random architectures.

The RMSE between simulated and interpolated reflectance was 0.0019 and 0.0049 in the red and near infrared bands, which can be considered satisfactory, as well as the interpolation between soil and canopy reflectance (see section 2.1). Also, fIPAR, ELS and $P_{0,h}$ were interpolated with a RMSE of 0.0037, 0.009 and 0.006 respectively.

2.5 Estimation of biophysical parameters from reflectance

100 architectures were randomly selected to represent observation datasets. The vineyard dimensions were selected randomly within the limits of actual vineyards in Mediterranean regions. LAD was selected randomly, within the limits established according to the vineyard width. In actual vineyards, LAD results from the trellis system, and is thus dependent of vine width: wider rows present lower leaf density while thinner rows are usually denser.

For each one of the architectures selected reflectance was simulated with PARCINOPY code, as well as fIPAR, ELS, LAI and $P_{0,h}$. Then 50 synthetic observations for each architecture were created, contaminating the original reflectance with a Gaussian noise with a standard deviation of 0.013 and 0.016 in the red and NIR bands. For each of the 50 synthetic observations, the minimum RMSE against simulated reflectance in the LUT was searched, accounting for a variation of ± 0.1 in soil brightness. The distribution of the LUT outputs for the observations were computed, and the estimated values of fIPAR, LAI, ELS and $P_{0,h}$ for each architecture were selected from the most frequent interval of the distributions.

3 RESULTS AND DISCUSSION

3.1 Contribution of observational parameters in the estimation of biophysical parameters.

The results of biophysical parameters estimation depending on sun position at the moment of data acquisition are shown in the Figure 2. As it can be appreciated, the effect of the sun azimuth relative to rows reveals as a key variable determining the degree of uncertainty in the estimations.

Generally speaking, the best estimations are achieved when sun is illuminating perpendicular to rows (relative azimuth of 90°), and the shadow is thus projected in the inter-row space. The RMSE of LAI reaches in these conditions 0.50 with a variation coefficient of 30.6. Conversely when sun illuminates almost parallel to rows (10° - 20°) from the row directions the error increases substantially, and the estimation produces unsatisfactory results with RMSE higher than 2.

ELS and, mainly, day-integrated fIPAR also show the same trend. In the fIPAR, the differences in the estimations depending on sun position are especially important (Figure 3), with good agreement between estimated and observed fIPAR in perpendicular illumination and large errors when sun is parallel to rows.

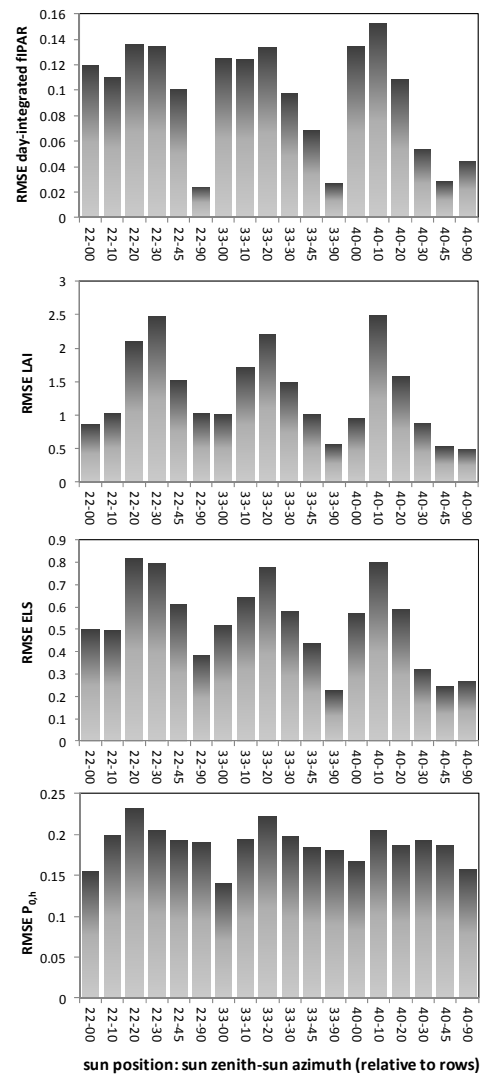


Figure 2. RMSE in the estimation of fIPAR, LAI, ELS and $P_{0,h}$ under different sun position.

This is a consequence of the higher sensitivity of canopy reflectance to changes in leaf area when the shadows of the vines are projected in the inter-row space: these changes are translated in changes on the

fraction of shaded soil. That enhances the link between canopy reflectance and the parameters of interest. Conversely, when sun is illuminating at 10° - 20° from the rows direction, the fraction of shaded soil remains almost constant, which makes difficult the determination of vine parameters.

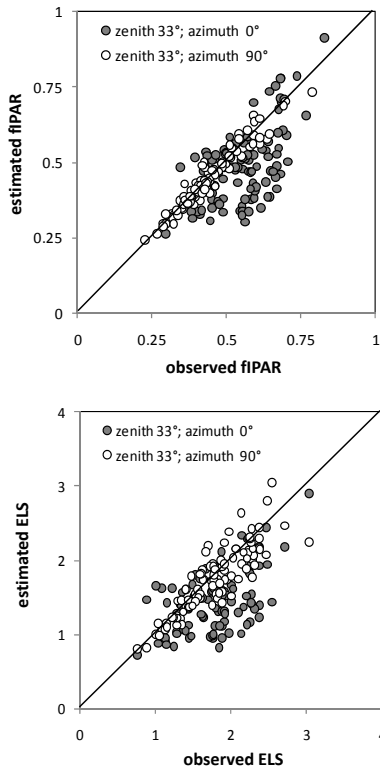


Figure 3. Scatter plot of observed versus estimated fIPAR and ELS in two different sun positions. Solid line is 1:1 line.

3.2 Suitability of the different biophysical parameters in vineyard monitoring from reflectance.

The canopy reflectance of vineyard canopies is mainly sensitive to changes in the volume of the row. This is in agreement with the findings of 3.1 section: the fraction of shaded soil in the inter-row space is determined mainly by the row volume, and less by the leaf area density within this volume. As a consequence, the parameters that are closely related to changes in row volume will be estimated with low uncertainties. This is the case, for example, of fIPAR (Figures 2 and 3), with a RMSE 0.027 and a variation coefficient of 6% or the ELS with an error of 0.22 and a variation coefficient of 12%.

However LAI and porosity provides significantly higher errors. In the case of LAI the results (Figure 4)

shows a non-biased but scattered relation between the observed and estimated value. This is consequence of the low sensitivity of changes in leaf area within the row, which mainly determines LAI. The estimation of $P_{0,h}$ provides even worse results (Figure 4).

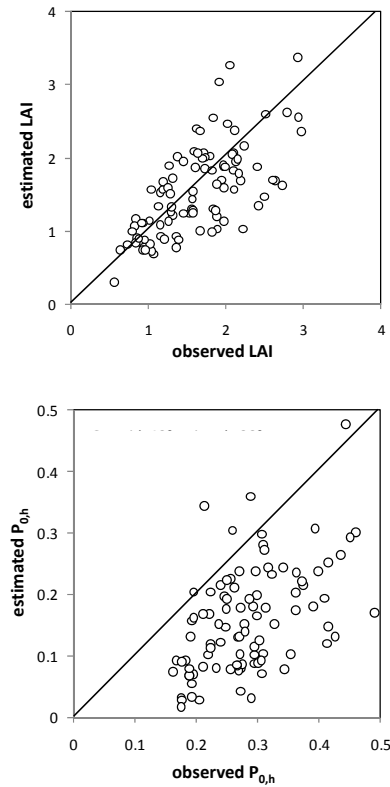


Figure 4. Scatter plot of observed versus estimated LAI and $P_{0,h}$ in sun zenith 40° and azimuth 90° relative to rows. Solid line is 1:1 line.

This low sensitivity of canopy reflectance to LAI is linked also to the saturation effect observable in homogeneous canopies when LAI reaches values higher than 4 (Baret & Guyot, 1991). In the case of vineyard canopies, this effect can be observed at lower LAI values, due to the high local leaf density in the row, as a result of the trellis system. Moreover, the fraction of canopy occupied by the row is relatively low (usually 30-60%), which reduces the impact of moderate to low changes of leaf area in canopy reflectance.

4 CONCLUSIONS

In the present work, a simulation study have been carried out to describe the uncertainties in the estimation of different biophysical parameters (fIPAR,

Leaf Area Index, Exposed Leaf Surface and row porosity) on vineyard canopies from reflectance measurements.

The reflectance simulations carried out over a wide range of vineyard architectures by means of a 3D model coupled with a ray-tracing code have highlighted the important contribution of observational parameters in the uncertainties of fIPAR, LAI, ELS and porosity estimation;

More specifically, the sun position at the moment of reflectance data acquisition plays a key role to increase the accuracy of the methods proposed. When sun illuminates perpendicular to rows direction and thus row shadow is projected in the inter row space, the sensitivity of canopy reflectance to variations in vine dimensions or leaf area is enhanced, since changes are also translated in the fraction of shaded soil, which contributes greatly to soil reflectance.

As a consequence, the biophysical variables associated to changes in the row volume such as ELS and fIPAR yield the best results and the lowest uncertainties. Conversely, the parameters linked to leaf density within the rows such as LAI and the vine porosity produced worse results, due to the saturation effect at high local LAI values within the row.

The observational parameters constitute, at the light of the results presented here, an important factor to account for in the estimation of biophysical parameters of row canopies from remote sensing. Moreover, biophysical parameters based in the estimation of row volume such as ELS or fIPAR appear more robust to monitor vineyard development and status than those targeting the leaf area density (LAD, LAI, vine porosity...).

Although the present work has been focused in vineyard canopies, it can be extrapolated to the rest of row crops, mainly those presenting a highly clumped leaf distribution. However, future works should evaluate the validity of the theoretical findings presented in this study.

5 ACKNOWLEDGEMENTS

This work is a results of the Vinnotec project (Qualimed Pole of Languedoc Roussillon region—France).

6 REFERENCES

Acevedo-Opazo, C., Tisseyre, B., Taylor, J. A., Ojeda, H. and Guillaume, S., 2010, A model for the spatial prediction of water status in vines (*Vitis vinifera* L.) using high resolution ancillary information. *Precision Agriculture*, **11**, 358-378.

Baret, F. and Guyot, 1991, Potentials and limits of vegetation indices for LAI and APAR assessment. *Remote Sensing of Environment*, **35**, 161-173.

Chelle, M., 1997, Développement d'un modèle de radiosité mixte pour simuler la distribution du rayonnement dans les couverts végétaux. PhD. Dissertation. Université Rennes I, 154 pp

Espinosa, M., Acuña, E., Espinosa, M., Barrera, J., 2010, Commercial digital camera to estimate postharvest leaf area index in *Vitis vinifera* L. cv. Cabernet Sauvignon on a vertical trellis, *Chilean Journal of Agricultural Research*, **70**, 315-322.

Kötz, B., Schaepman, M., Mosdorf, F., Bowyer, P., Itten, K. And Allgöwer, B., 2004, Radiative transfer modelling within a heterogeneous canopy for estimation of forest fire fuel properties. *Remote Sensing of Environment*, **92**, 332-344.

Kuusk, A., 1995, A Markov chain model of canopy reflectance. *Agricultural and Forest Meteorology*, **76**, 221-236.

López-Lozano, R., Baret, F., García de Cortázar, I., Bertrand, N. and Casterad, A., 2009, Optical geometric configuration and algorithms for LAI indirect estimates under row canopies: The case of vineyards. *Agricultural and Forest Meteorology*, **149**, 1307-1316.

North, P.R.J., 1996, Three-dimensional forest light interaction using a Monte Carlo method. *IEEE Transactions on Geoscience and Remote Sensing*, **34**, 946-956.

Verhoef, W., 1984, Light scattering by leaf layers with application to canopy reflectance modelling: The SAIL model. *Remote Sensing of Environment*, **16**, 125-141

Zarco-Tejada, P; J., Berjón, A., López-Lozano, R., Miller, J. R., Martín, P., Cachorro, V., González, M. R. and de Frutos, A., 2005, Assessing vineyard condition with hyperspectral indices: Leaf and canopy reflectance simulation in a row-structured discontinuous canopy. *Remote Sensing of Environment*, **99**, 271-287.

Zarco-Tejada, P. J., Berni, J. A. J., Suárez, L., Sepulcre-Cantó, G., Morales, F. and Miller, J. R., 2009, Imaging chlorophyll fluorescence with an airborne narrow-band multispectral camera for vegetation stress detection. *Remote sensing of Environment*, **113**, 1262-1275.

Vegetation Cover Method Emissivity Dependencies on Atmosphere and Multispectral Vegetation Index

¹L. Martínez, ²V. Caselles, ²E. Valor, ¹F. Pérez, ²V. García-Santos

¹Remote Sensing Area, Institut Cartogràfic de Catalunya.

Parc de Montjuïc s/n, 08038 Barcelona, Spain

²Department of Earth Physics and Thermodynamics, University of Valencia,
Dr. Moliner 50, 46100 Burjassot (València), Spain

Lucas.Martinez@icc.cat

ABSTRACT - This work studies the effect caused on land surface emissivity (LSE) by the lack of atmospheric correction of the optical images used to calculate a multispectral vegetation index. Previous works of the authors pointed out that improved thermal emissivity is calculated with the Vegetation Cover Method (VCM) by means of atmospherically corrected optical images. Now, the Second Simulation of the Satellite Signal in the Solar Spectrum (6S) radiative transfer code is used to simulate common atmospheric situations. Atmosphere type, aerosol model and total load, illumination and observation geometries and spectral range are taken into account. The described atmosphere simulation data are applied to a set of spectral configurations from AVHRR, MODIS and MERIS satellite sensors. In addition, vegetation and soil samples from ASTER spectral library version 2.0 are used to compute the effect of the atmosphere on the estimation of the vegetation cover, using the Normalized Difference Vegetation Index (NDVI) and the thermal emissivity, when top of the atmosphere (TOA) reflectances are used in relation to bottom of the atmosphere (BOA) reflectances. For a pure landscape the thermal (8-13 μm) emissivity error varies between -0.0009 and +0.0014 (which represents a systematic error of approximately -0.05K to +0.07K). The results for a mixed landscape show the combined effect of the spectral mixing of soils along with the atmosphere effect. The impacts of both vegetation cover and thermal emissivity are then larger than previously. In this case, the thermal emissivity error varies between -0.02 and +0.05 (which represents a systematic error of approximately -1.0K to +2.5K).

1 INTRODUCTION

Land surface temperature (LST) is a key parameter for most Earth environmental models. Many sensors on board satellites provide the radiance emitted from the surface at local, regional or even global scales. However, this radiance is affected by three main effects which must be compensated in order to obtain the temperature: atmospheric, emissivity and angular effects. The planet atmosphere disturbs the radiation emitted from the surface to the sensor acting as an emitting and absorbing body. Emissivity is the physical property which defines the capacity of a body to emit radiation at a given temperature in relation to the perfect emitter with emissivity equal to 1. Land surfaces are not perfect emitters, their emissivity must be known. Due to the directional nature of radiance measurements on heterogeneous and rough surfaces, we also must account for the angular effects.

Land surface emissivity (LSE) measurement by remote sensing has the drawback that the temperature and the emissivity cannot be simultaneously calculated because the number of unknown variables is always

higher than the number of measurements. Several methods have been proposed in order to obtain the LSE from space. The vegetation cover method (VCM) algorithm developed by Valor and Caselles (1996) relates the data taken in the solar spectrum to the thermal infrared region through the vegetation cover of the surface. The solar radiation data is related to vegetation cover by means of the normalized difference vegetation index (NDVI) described by Rouse et al. (1973). Therefore, the methodology relates vegetation index to emissivity estimations. It is based on the relationship between emissivity in the thermal infrared and the NDVI suggested by Van de Griend and Owe (1993). As a consequence, it is expected that the determination of thermal emissivity may be affected to a certain extent by the interaction of the atmosphere with the solar radiation (Martinez et al., 2008), which is the subject of this work.

The atmospheric effect in the solar spectrum is sometimes not significant (Song et al., 2001), but this is not the general case. Vegetation indexes decrease the influence induced by the atmosphere, but the scattering effects from atmospheric aerosols still can

affect the top of the atmosphere (TOA) reflectances (Kaufman and Tanre, 1992). There are many procedures described in the literature for obtaining bottom of the atmosphere (BOA) reflectances on multispectral satellite sensors. The most accurate are those based on the use of a radiative transfer code (Bolle and Langer, 1991). One of the most popular codes is the Second Simulation of the Satellite Signal in the Solar Spectrum (6S), described by Vermote et al. (1997).

The aim of this study is to measure the influence of the atmospheric correction on the estimate of thermal emissivity with the VCM. First, the 6S code is used to compute a radiative transfer database at high spectral resolution. Next, this database is applied to a set of mixed ground-vegetation spectra and then vegetation cover is computed from them to AVHRR, MODIS and MERIS channels by using NDVI. Then, thermal emissivity values for the 8-13 μ m region are computed and compared with the original ones. Finally, temperature differences are estimated when TOA reflectances are used instead of BOA reflectances with the VCM.

2 METHODOLOGY

2.1 Vegetation Cover Method

The vegetation cover method is a model for calculating the LSE of a pixel that provides the effective emissivity of an heterogeneous and rough surface for a given i th band, ε_i , as:

$$\varepsilon_i = \varepsilon_{iv} \cdot P_v + \varepsilon_{ig} \cdot (1 - P_v) + 4 \cdot \langle d\varepsilon_i \rangle \cdot P_v \cdot (1 - P_v) \quad (1)$$

where ε_{iv} represents vegetation emissivity in the i th band, P_v is the fractional vegetation cover, ε_{ig} is bare soil emissivity in the i th band, and $\langle d\varepsilon_i \rangle$ is the cavity term for the same band related to the radiance indirectly emitted through internal reflections occurring between vegetation walls and the ground (Valor and Caselles, 1996). Emissivity values for vegetation and bare soil are obtained from Salisbury and D'Aria (1992) database. The cavity term is a mean cavity term for several kinds of vegetation types (Table 1).

Emissivity values for the 8-13 μ m region	
ε_{iv}	0.985 \pm 0.005
ε_{ig}	0.93 \pm 0.03
$\langle d\varepsilon_i \rangle$	0.03 \pm 0.02

Table 1 Values for the VCM coefficients in the 8-13 μ m region.

The determination of the fractional vegetation cover is calculated using the NDVI, with the following expression (Valor and Caselles, 1996):

$$P_v = \frac{\left(1 - \frac{NDVI_g}{NDVI_v}\right)}{\left(1 - \frac{NDVI_g}{NDVI_g}\right) - K \cdot \left(1 - \frac{NDVI_g}{NDVI_v}\right)} \quad (2)$$

where $NDVI_g$ and $NDVI_v$ represent the minimal and maximum values of the NDVI image respectively, which, provided that the area is large enough, will correspond with areas with no vegetation (bare soil) and with full vegetation coverage.

The K parameter for a multispectral set of bands is calculated as (Valor and Caselles, 1996):

$$K = \frac{\rho_{nir-v} - \rho_{red-v}}{\rho_{nir-g} - \rho_{red-g}} \quad (3)$$

where ρ_{nir-v} and ρ_{red-v} are the reflectances in the near infrared (AVHRR band 2, MODIS band 2, MERIS band 13) and in the red (AVHRR band 1, MODIS band 1, MERIS band 8) for the area with full vegetation cover, ρ_{nir-g} and ρ_{red-g} the reflectances in the near infrared and in the red for the area without vegetation (bare soil).

2.2 Mixed pixels

A mixed pixel reflectance without considering neither internal reflections occurring inside the rough surface, nor the effect of shadows is expressed as

$$\rho_i = \rho_{iv} P_v + \rho_{ig} (1 - P_v) \quad (4)$$

where ρ_i is the pixel reflectance measured in the i th band, and ρ_{iv} and ρ_{ig} are the vegetation and bare soil reflectances for the same band. P_v is the fractional vegetation cover that ranges from 0 to 1 in order to represent all the possible mixed vegetated landscapes.

2.3 Atmospheric simulations database

Considering the interaction phenomena described in Staenz and Williams (1997), it is possible to express the TOA radiance L_i^* , when observing an horizontal surface, for a given i th band, as

$$L_i^* = A_i \frac{\rho_i}{(1 - \langle \rho_{ie} \rangle S_i)} + B_i \frac{\langle \rho_i \rangle}{(1 - \langle \rho_{ie} \rangle S_i)} + L_{ia} \quad (5)$$

where ρ_i is the BOA reflectance of the surface, $\langle \rho_{ie} \rangle$ is the BOA reflectance of the neighbourhood, S_i is the atmospheric albedo, L_{ia} is the radiance backscattered to the sensor, and A_i and B_i are coefficients related to the direct and diffuse radiance (all for the i th band).

The parameters A_i , B_i , S_i and L_{ia} characterize both observation and illumination geometries and the atmospheric conditions for the i th band. Their values

depend neither on the observed surface reflectance, nor on the neighbourhood's. Thus, they are calculated from the magnitude L_{ig} , which is the radiance entering the sensor from the observed surface, and the magnitude L_{ip} , which is the radiance entering the sensor from the neighbourhood of the observed surface and backscattered by the atmosphere towards the sensor. If the surface has a uniform reflectance, those magnitudes for the i th band are:

$$L_{ig} = A_i \frac{\rho_i}{1 - \rho_i S_i} \quad L_{ip} = B_i \frac{\rho_i}{(1 - \rho_i S_i)} + L_{ia} \quad (5)$$

Both L_{ig} and L_{ip} are obtained by means of the 6S radiative transfer code working on direct form. The values of A_i , B_i , S_i and L_{ia} are directly obtained by solving the corresponding equations systems. The radiative transfer simulations are performed using the atmospheric and geometric data in Table 2 at 6S maximum spectral resolution (2.5nm of spectral sampling between 250 and 4000nm). A Look Up Table system is calculated and stored in a database. Consequently, atmospheric simulation is possible on the spectra by using equation 5 with the adequate set of A_i , B_i , S_i and L_{ia} parameters and the hypothesis of a uniform reflectance environment, so that in equation 5 $\langle \rho_{ie} \rangle$ is be equal to ρ_{ic} .

6S Radiative Transfer Parameters Values	
Atmospheric model	US standard 62, Tropical, Mid-latitude winter, Mid-latitude summer, Sub-arctic summer & Sub-arctic winter
Aerosol model	Continental, maritime & urban
Aerosol concentration (meteorological vis km)	7.5, 15, 30, 60 & 120
Solar zenith angle (zenith=0°)	0, 30, 45, 60 & 75
Sensor zenith angle (zenith=0°)	0, 15, 30, 45 & 60
Azimuth difference	0, 45, 90, 135, 180, 225, 270 & 315

Table 2 Geometric and atmospheric values for the 6S radiative transfer simulations (total 18,000).

3 DATASET

The Second Simulation of the Satellite Signal in the Solar Spectrum radiative transfer code is used to simulate the atmosphere. Atmosphere type, aerosol model and total load, illumination and observation geometries, and spectral range are taken into account when computing simulations. The described

atmosphere simulation database is applied to a set of spectral configurations from different satellite sensors (AVHRR, MODIS and MERIS) by means of their red and near infrared spectral sensitivities.

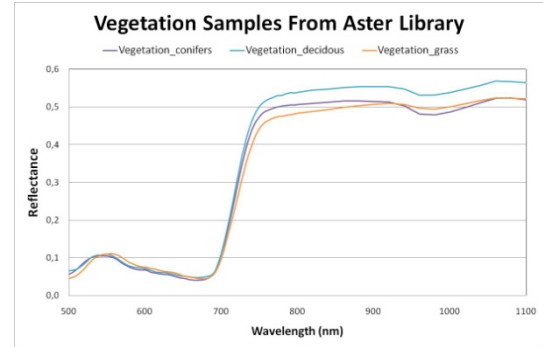


Figure 1 Vegetation samples from Aster spectral library used to characterize the vegetation covers.

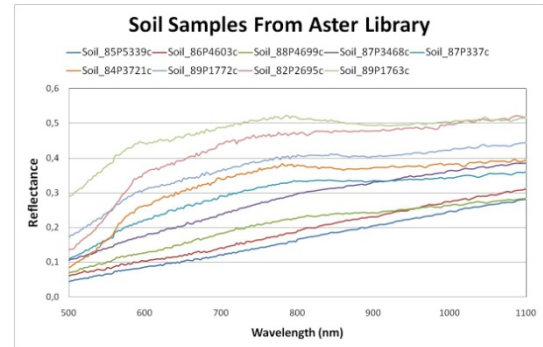


Figure 2 Soil samples from Aster spectral library used to characterize the soil covers.

Three vegetation samples (Figure 1) and nine soil samples (Figure 2) from ASTER spectral library version 2.0 (Baldrige et al., 2009) are combined by using the Equation 4 with several P_v values to compute up to 1,200 different mixed vegetation-soil samples. Each reflectance sample and the atmospheric simulation are also computed at 2.5nm of spectral sampling between 250 and 4000nm.

4 RESULTS

Differences are computed in two ways: pure landscape and mixed landscape. When all 1,200 different mixed vegetation-soil samples are taken into account, the results are representative of a mixed landscape. Then a single spectrum is chosen as pure soil, and another one, as pure vegetation. Otherwise, a pure landscape is represented if only the mixed spectra coming from a pure ground sample and a pure vegetation sample are considered each time to find the pure soil and the pure vegetation.

First, the results for a pure landscape (Table 3) show that the atmosphere effect only slightly impacts the estimation of the vegetation cover. In this case, the vegetation cover error ΔP_v varies between -0.010 and +0.016. Furthermore, the thermal (8-13 μm) emissivity error $\Delta \varepsilon$ varies between -0.009 and +0.0015 (which, according to Becker (1987), represents a systematic error of approximately -0.05K to +0.08K) when TOA reflectances are used instead of BOA reflectances.

Pure landscape and atmosphere			
	AVHRR	MODIS	MERIS
ΔP_v mean	0.002	0.002	0.002
ΔP_v max	0.016	0.016	0.016
ΔP_v min	-0.010	-0.010	-0.009
$\Delta \varepsilon$ mean	0.0001	0.0001	0.0001
$\Delta \varepsilon$ max	0.0014	0.0014	0.0014
$\Delta \varepsilon$ min	-0.0009	-0.0009	-0.0008

Table 3 Differences in fractional vegetation cover P_v and thermal emissivity ε (8-13 μm) for a pure landscape and atmosphere (Results are TOA values minus BOA values).

Mixed landscape and atmosphere			
	AVHRR	MODIS	MERIS
ΔP_v mean	0.112	0.112	0.117
ΔP_v max	0.438	0.442	0.427
ΔP_v min	-0.247	-0.248	-0.212
$\Delta \varepsilon$ mean	0.0074	0.0073	0.0071
$\Delta \varepsilon$ max	0.0502	0.0501	0.0493
$\Delta \varepsilon$ min	-0.0199	-0.0198	-0.0171

Table 4 Differences in fractional vegetation cover P_v and thermal emissivity ε (8-13 μm) for a mixed landscape and atmosphere (Results are TOA values minus BOA values).

Mixed landscape without atmosphere			
	AVHRR	MODIS	MERIS
ΔP_v mean	0.170	0.161	0.150
ΔP_v max	0.509	0.486	0.457
ΔP_v min	-0.022	-0.023	-0.011
$\Delta \varepsilon$ mean	0.0089	0.0086	0.0079
$\Delta \varepsilon$ max	0.0567	0.0546	0.0518
$\Delta \varepsilon$ min	-0.0056	-0.0055	-0.0052

Table 5 Differences in fractional vegetation cover P_v and thermal emissivity ε (8-13 μm) for a mixed landscape without atmosphere (Results are TOA values minus BOA values).

Next, the results for a mixed landscape (Table 4) show the combined effect of the spectral mixing of several soils along with the atmosphere effect. The impacts on both vegetation cover and thermal emissivity ε are then larger than previously. Now, the

vegetation cover P_v error varies between -0.25 and +0.44. Besides, the thermal emissivity error varies between -0.02 and +0.05 (which, according to Becker (1987), represents a systematic error of approximately -1.0K to +2.6K) when TOA reflectances are used instead of BOA reflectances.

Thus, previous results on Tables 3 and 4 indicate that there is an important dependence of the final emissivity values on the soil type. This fact is related to the sensitivity of the NDVI to the soil brightness. This hypothesis is confirmed by the results of Table 5, where only the pure original vegetation and soil samples are analyzed without considering atmospheric effects. The results show that even without the influence of the atmosphere there is an important impact of the soil on both the vegetation cover P_v and the thermal emissivity (the same order of magnitude than for a mixed landscape and atmosphere). The vegetation cover P_v error varies between -0.023 and +0.51. Besides, the thermal emissivity error varies between -0.006 and +0.06 (which, according to Becker (1987), represents a systematic error of approximately -0.3K to +3.0K).

Next, the variations in vegetation index and fractional vegetation cover show a decrease when using MERIS sensor compared to MODIS (which, in turn, are smaller than in AVHRR results). This behavior seems to be correlated to the bandwidth of the sensors in such a way that, the narrower the bandwidth is, the less error is produced in vegetation index and fractional vegetation cover.

Finally, it should be considered that other vegetation indexes different from NDVI could yield smaller differences in the emissivity with the VCM.

5 CONCLUSIONS AND FUTURE WORK

This work studies the influence of the atmosphere (simulated with 6S over a mixed ground-vegetation set of spectra) on the estimate of thermal emissivity (8-13 μm region) with the VCM for AVHRR, MODIS and MERIS.

The vegetation proportion shows a substantial increase when using BOA reflectances instead of TOA reflectances. The spectral mixing of several soils increases this systematic error due to NDVI sensitivity to background soil brightness. Nonetheless, the atmosphere effect impacts only a few tenths of Kelvin on the measurement of the temperature. However, the spectral mixing of several soils increases this systematic error to a few Kelvin.

Future work will focus on multispectral vegetation indexes that are less sensitive to the background soil. Additionally, these emissivity and temperature results would be compared to real data.

6 ACKNOWLEDGMENTS

This work is financed by the Spanish *Ministerio de Ciencia e Innovación* (grant of V. Garcia-Santos). The study is carried out under the ESA EO Campaigns Project ID number 6432. Comments and suggestions from ICC and UV colleges have also been very useful.

7 REFERENCES

- Baldrige, A.M., Hook, S.J., Grove, C.I., and Rivera, G., 2009, The ASTER spectral library version 2.0, *Remote Sensing of Environment*, **113**, 711-715.
- Becker, F., 1987, The impact of spectral emissivity on the measurement of land surface temperatures from a satellite, *International Journal of Remote Sensing*, **8**, 1509-1522.
- Bolle, H.J., and Langer, I., 1991, Echival Field Experiment in a Desertification-Threatened Area (EFEDA). Field Experiment Plan. Meteorological Institute, Free University of Berlin, Germany.
- Kaufman, Y. J., and Tanre, D., 1992, Atmospherically resistant vegetation index (ARVI) for EOS-MODIS, in Proc. IEEE Int. Geosci. and Remote Sensing Symp. '92, IEEE, New York, 261-270.
- Martinez, L., Caselles, V., Pala, V., Valor, E., 2008, Emissivity errors in the vegetation cover method caused by the lack of atmospheric correction, *International Journal of Remote Sensing*, **29**, 1825-1832.
- Rouse, J. W., Haas, R. H., Schell, J. A., and Deering, D. W., 1973, Monitoring vegetation systems in the great plains with ERTS, *Third ERTS Symposium, NASA SP-351*, **1**, 309-317.
- Salisbury, J.W., and D'Aria, D.M., 1992, Emissivity of terrestrial materials in the 8-14 μm atmospheric window. *Remote Sensing of Environment*, **42**, 83-106.
- Stanz, K., and Williams, D.J., 1997, Retrieval of Surface Reflectance from Hiperespectral Data Using a Look-up Table Approach. *Canadian Journal of Remote Sensing*, **23**, 354-368.
- Song, C., Woodcock, C.E., Seto, K.C., Lenney, M.P., and Macober, S.A., 2001, Classification and change detection using Landsat TM data: when and how to correct atmospheric effects?, *Remote Sensing of Environment*, **75**: 230-244.
- Valor, E., and Caselles, V., 1996, Mapping land surface emissivity from NDVI: application to european, african and south american areas. *Remote Sensing of Environment*, **57**, 167-184.
- Van de Griend, A.A., and OWE, M., 1993, On the relationship between thermal emissivity and the normalized difference vegetation index for natural surfaces, *International Journal of Remote Sensing*, **14**: 1119-1131.
- Vermote, E., Tanré, E.D., Deuzé, J.L., Herman M., and Morcrette, JJ, 1997, Second simulation of the satellite signal in the solar spectrum, 6S: an overview. *IEEE Transactions on Geoscience and Remote Sensing*, **35**, 675-686.

The far-infrared: prospective of remote sensing applications

Ovidiu Pancrati¹, Jean-Pierre Blanchet², Alain Royer³, François Châteauneuf¹, Tarek Ayash², Yann Blanchard³, Louis Garand⁴

¹INO (Institut National d'Optique), Québec, Canada, ² University of Québec at Montréal (UQAM), Montréal Canada, ³ University of Sherbrooke, Sherbrooke, Canada, ⁴ Environment Canada, Dorval, Canada

Email addresses: Ovidiu.Pancrati@ino.ca, Blanchet.Jean-Pierre@uqam.ca, Alain.Royer@usherbrooke.ca, Francois.Chateauneuf@ino.ca, tarek.ayash@utoronto.ca, Yann.Blanchard@usherbrooke.ca, Louis.Garand@ec.gc.ca

ABSTRACT: *The far-infrared (FIR) region of electromagnetic radiation spectrum, commonly defined between 15.4 μm and 100 μm wavelength, is responsible for more than 40 % (Kratz, 2001) of longwave radiation escaping from the Earth's atmosphere-surface system. Despite its importance in Earth's radiative balance, the far-infrared remains relatively unobserved, mostly due to instrumental limitations. Strong atmospheric absorption dominated by the water vapor rotational spectrum is also an issue for FIR remote sensing applications. However, radiative transfer simulations show that certain conditions (cold and dry specific polar atmospheres) can induce the appearance of semitransparent micro-windows in the FIR. The spectral radiances within so called "dirty window" (18 to 25 μm) are sensibly affected by the atmospheric water amount. For space-borne applications, the surface and boundary level contribution will be completely attenuated by the strong absorption of lower atmospheric levels, producing then a real interest for upper-troposphere and stratosphere studies. These studies revealed some potential remote sensing applications, such as atmospheric water and clouds studies and atmospheric sounding possibilities. Recently, new advancements in sensor developments enable FIR observation, opening new possibilities for climate studies and for atmospheric remote sensing in the upper troposphere. This paper presents results obtained during FIR exploration in the framework of a future Canadian space mission dedicated to polar ice clouds and water vapor remote sensing called TICFIRE (Thin Ice Clouds in Far Infra Red Experiment).*

1 INTRODUCTION

Water vapor is a major atmospheric greenhouse compound, and its understanding is far from being complete due to uncertainties in its spatial and temporal distribution. Moreover, the far-infrared part of the spectrum is dominated by spectral features of rotational bands of atmospheric water vapor. The far-infrared plays then a key role in cooling rate throughout the troposphere (Clough et al, 1992). Energetic absorption/emission phenomena are strongly related to water vapor radiative impact. Indeed, the upwelling thermal radiation presents high sensitivities induced by humidity perturbations in the upper troposphere. Thus, uncertainties in water vapor distribution throughout the atmosphere and the associated FIR radiative forcing and feedbacks critically affect the forecast prediction and climate change studies. Far-infrared measurements are therefore clearly needed for a better understanding of the global energy budget. However, there's not yet any operational FIR space-borne mission dedicated to Earth direct observations. Recent investigations from the scientific community evidence the importance of this part of the spectrum and open new satellite

prospective. Thus, three Fourier transform spectrometers were developed for experimental testing of FIR capabilities and to prove the necessary technologies for future space-borne measurements. For instance, the Tropospheric Airborne Fourier Transform Spectrometer (TAFTS) or the Radiation Explorer in the Far InfraRed (REFIR) took part in FIR dedicated field campaigns. More recently, FIRST (*Far-Infrared Spectroscopy of the Troposphere*) instrument was successfully used in balloon-borne measurements (Mlynchak et al, 2006), FIRST is a precursor mission for studying atmospheric radiation and climate, cirrus, and water vapor for the upper troposphere in FIR.

This study concerns a list of potential remote sensing applications in the FIR (water vapor detection, atmospheric sounding and ice cloud effect) that will be analyzed theoretically by means of radiative transfer modeling. The lack of operational space-based measurements in the FIR was used as an opportunity for a new process-oriented mission on a micro-satellite platform with respect to the targeted remote sensing applications. The main findings will be summarized in Conclusions section.

2 WATER VAPOR EFFECT

Water is the leading material acting on the radiation balance in the atmosphere. It determines the fate of storm activities through the generation of thermal imbalances responsible for establishing the circulation. Atmospheric water is also modulated by anthropogenic emission of greenhouse gases and particulates through cloud nucleation and alteration of precipitation efficiency. Since water vapor is the strongest greenhouse gas on Earth, it plays a leading role in several feedback processes in the atmosphere (clouds, radiation, precipitation) and at the surface (snow, sea ice, soil moisture), especially at the high latitudes. As a major greenhouse gas, knowledge of the temporal and spatial distribution of water vapor in Polar Regions is an essential input for forecast models and climate model validation (Delamere et al. 2010). However, ground based measurements of water vapor are typically sparse in the Arctic. Satellite based remote sensing measurements try to fill these gaps with techniques presenting different advantages and limitations. Nevertheless, all these techniques commonly face the problems of detection of small water amounts, as it is generally the case of dry Arctic atmospheric conditions.

Atmosphere simulations were performed with the radiative transfer code MODTRAN5 in order to study the water vapor effect in the FIR. First simulation results show a strong atmospheric absorption, for MODTRAN built-in standard atmospheres

(McClatchey et al. 1972). Moreover, as expected, the atmospheric absorption increases with model humidity abundance (Figure 1). These spectra contain some useful preliminary information. First, we observe that the atmospheric transmittance in 18-25 μm region (so called “dirty infrared window”) increases when the water content decreases. If the tropical atmosphere is completely opaque in FIR, continental model US Standard 1976 and Sub-Arctic Winter model present drier and colder conditions, which will increase transparency.

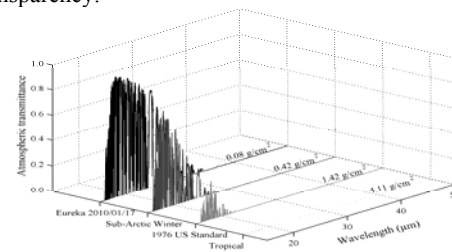


Figure 1. Total atmospheric transmittance for an Arctic experimental profile compared with three standard atmospheres, characterized by superior water amount and temperature.

Taking into account a more realistic Arctic atmosphere built from an experimental balloon-sounding profile measured in polar winter conditions at Eureka weather station (79°59'N, 85°56'W, 2010/01/17 at 00Z), the transmittance could even reach 90 % around 20 μm .

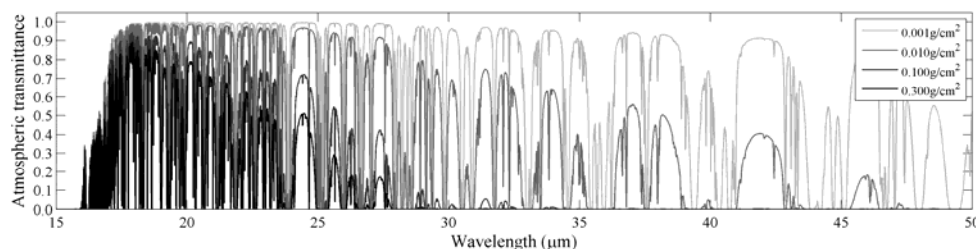


Figure 2. Transmittance spectra for total atmospheric columns computed with Modtran5 radiative transfer code. The considered atmospheric model was Sub-Arctic Winter, with different water content values within the range 0.001 and 0.3 g/cm^2

Further simulations performed under dry polar conditions show a strong sensitivity to water content, especially for low concentrations. Figure 2 contains some spectra of total atmospheric transmittance covering the 15 – 50 μm region.

Additional tests showed that, when viewed from satellite, the atmosphere becomes opaque at a certain vertical level depending mostly on water content (Figure 3). This could be an interesting feature for upper-troposphere and stratosphere studies, because any surface and boundary level contribution will be completely attenuated by strong absorption of lower

atmospheric levels. The absorption features could also be used for appropriate selection of “semi-transparent” bands.

Some early stage studies performed at INO demonstrate that the FIR simulated radiances are highly sensitive to water content variations, even more at weak values. The simulations were made considering nadir viewing of a snow surface at 257 K with the Eureka profile. Figure 4 shows how the brightness temperature will be affected by $\pm 10\%$ variation around weak water amounts. Figure 4 shows the real potential of water remote sensing in FIR,

especially when compared to PCW 8.3-8.7 μm channel dedicated to total water retrieval.

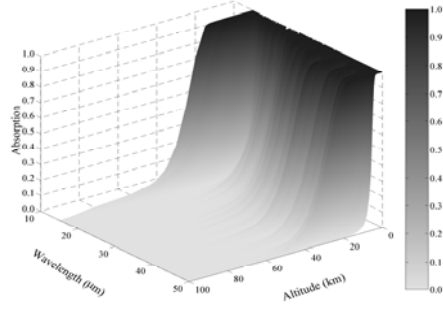


Figure 3. Atmospheric vertical absorption for realistic polar winter atmosphere

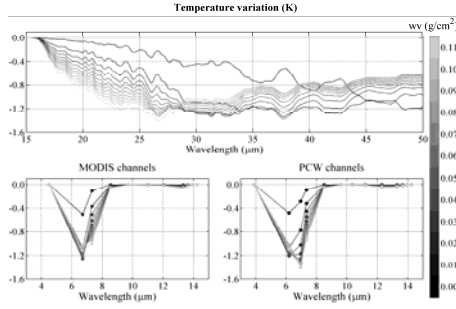


Figure 4. Brightness temperature variations for $\pm 10\%$ variations around weak water amount values expressed by the color bar scale. Upper graph represents this variation over the FIR spectral domain; the dots in lower graphs contain the variation observed over the infrared channels of MODIS (Moderate Resolution Imaging Spectroradiometer) and future PCW (Polar Communication and Weather) mission.

All these results consolidate the prospective of water vapor remote sensing in extreme Arctic conditions, where “classic” instruments operate at their performance limits. Further tests will contribute to elaborate inversion retrieval algorithms and their sensitivity.

3 ATMOSPHERIC SOUNDING POSSIBILITIES

The new generation of space-based instruments such as AIRS (*Atmospheric InfraRed Sounder*) or IASI (*Infrared Atmospheric Sounding Interferometer*) represents major advances in the atmospheric sounding capabilities (Chahine et al, 2001). The measured hyperspectral radiances were used in various inversion algorithms in order to vertically solve, at high resolution, the profiles of atmospheric temperature and gas concentration (H_2O , CO_2 , O_3), as well as cloud and surface properties. The global coverage of this information and its assimilation in forecast operational schemes have lead to a sensibly improvement of weather prediction and climate observations (Goldberg et al, 2003).

All these instruments cover the mid and thermal infrared, therefore the need to explore the sounding possibilities in the far-infrared appeared naturally in the special context of complete transparency of the high troposphere and stratosphere. The characteristic property making a certain band interval to perform atmospheric sounding is contained in its jacobian matrix defined as derivatives with respect to the state vector. Jacobians for selected FIR channels were computed using a simplified strategy involving the radiative transfer code MODTRAN. Even if line-by-line models insure more sensitive jacobian studies than radiative transfer models (Garand et al., 2001), MODTRAN with its last version at 0.1 cm^{-1} spectral resolution could be used in a first approach. The upwelling FIR radiance in nadir direction was simulated under the following conditions:

- 2 standard atmospheres: Sub-Arctic Winter (SAW) and US Standard 1976 (USS), plus the Eureka experimental profile
- default humidity (0.42 g/cm^2 for SAW and 1.42 g/cm^2 for USS) and 25 % reduced values (0.105 g/cm^2 for SAW and 0.355 g/cm^2 for USS)
- Gaussian filters with 1 cm^{-1} full width at half maximum and central wavelength scanning the 15 - 50 μm spectral interval

For radiometric signals expressed in terms of brightness temperature, the jacobian is defined by the variation of the channel brightness temperature ΔT_B caused by the variation of the atmospheric component X at vertical level z (equation 1).

$$J(z) = \left. \frac{dT_B}{dX} \right|_z \quad (1)$$

Simplified formulations (equations 2 and 3) were employed for jacobian computation for temperature and gas concentration respectively, at each vertical level z .

$$J_T(z) = \frac{T_B(T(z) + \Delta T(z)/2) - T_B(T(z) - \Delta T(z)/2)}{\Delta T(z)} \quad (2)$$

with $\Delta T(z) = 1\text{K}$.

$$J_Q(z) = T_B(Q(z) + \Delta Q(z)) - T_B(Q(z) - \Delta Q(z)) \quad (3)$$

where $Q(z)$ is the mass mixing ratio at level z and its variation $\Delta Q(z)$ is considered as 10% perturbation around $Q(z)$ value. Some of the main results are summarised in Figure 5. As expected, some FIR channels are suitable for atmospheric sounding. Figure 5a contains temperature Jacobians computed for 4 different channels, but with the same atmospheric conditions (SAW model with 0.42 g/cm^2 water amount).

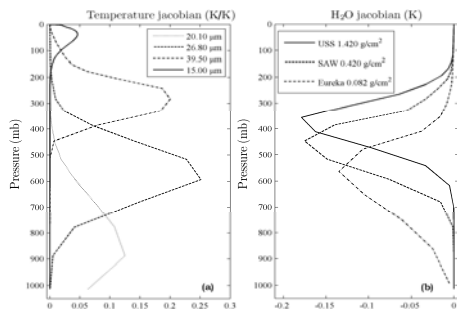


Figure 5. (a) sensitivity of the temperature jacobian at different vertical levels for different channels; (b) atmospheric water amount affects the vertical distribution of jacobians.

The peaks indicating vertical sensitivity allow to select FIR channels appropriate for upper troposphere and stratosphere sounding. Besides vertical levels commonly available from classic sounders (at 900 mb, 600 mb, 300 mb), a possible improvement could be the sensitivity of some FIR channels to high stratospheric levels (around 50 mb), beyond the 100 mb limit of thermal IR instruments for humidity sensing.

Water vapor amount affects the vertical resolution of humidity profile (see Figure 5b). Computed water vapor Jacobians present peaks related to different humidity conditions of considered atmosphere. The difference between the observed maximum for typically continental atmosphere (USS) and theoretic Arctic profile (SAW) is around 100 mb and increases to 200 mb if applied to an experimental Arctic atmosphere.

Finally, atmospheric sounding in the FIR appears very promising, subject to instrumental capacity to deliver appropriate radiometric sensitivity. Simulations performed for radiometric signal integrated over large FIR bands confirm some of these properties observed at high spectral resolution.

4 THIN ICE CLOUDS IMPACT

Recent studies express the continuous growth of interest from the scientific community in FIR application on ice clouds. The theoretical study lead by Yang et al. (2003) demonstrates the feasibility of FIR measurements in quantification of optical thickness of thin cirrus clouds. Stackhouse and Stephens (1991) pointed out the radiative processes occurring in whole cloud depth. Combining FIR predominant emission (heating) of radiation with thermal infrared absorption (cooling) could be a key issue in determining important parameters like clouds time evolution and their radiative effect in the atmosphere.

Space-based CloudSat-CALIPSO measurements combined to ground observations at Eureka emphasise

the interaction between manmade pollution (mostly sulfate) in the formation of thin ice cloud and their significant impact on climate (Girard et al, 2007; Grenier et al, 2009). It was shown that very extensive thin ice clouds (TIC) are dominant in the cold regions and can be classified with roughly the same proportion in two broad categories:

- TIC1: none precipitating fine crystals ($< 30 \mu\text{m}$) visible by lidar measurements only.
- TIC2: precipitating large ice crystals ($> 30 \mu\text{m}$), with sub-categories TIC2a and TIC2b whether detectable by lidar or radar measurements, and TIC2c characterised by a cloud ice/liquid mixed phase.

The first type cools the upper troposphere (7 – 9 km typically) and warms the lower regions by strengthening the downward atmospheric radiation component. On the contrary, the TIC2 type cools the bulk of the troposphere deeply and effectively leads to water precipitation, which dehydrates and cools the air. This generates available potential energy which directly feeds the storm development. The occurrence of TIC2 to the expense of TIC1 is enhanced significantly by ice inhibition from acid coating (mostly anthropogenic) on ice forming nuclei. As a consequence, direct radiative cooling from the body of the clouds and the water vapor concentration from precipitation by these clouds are profoundly altered. These have been shown from model simulation to induce very significant cool biases in the Polar temperature trend and largely explaining cold winter anomalies observed in recent decades. These anomalies alter the atmospheric circulation and storm activity at our mid latitudes.

The large particle size of these thin ice clouds and their occurrence in Arctic environment consolidate the idea to push the remote sensing methods toward the far-infrared. For that, the radiometric signature was investigated using a complex simulation scheme implying the following inputs:

- aerosol and cloud profiles from CALIPSO/CloudSat
- ECMWF (*European Center for Medium range Weather Forecasting*) information on surface and atmospheric profiles
- ice crystals properties database, kindly shared by Yang et al (2003)

Thermal and far-infrared radiances were simulated with MODTRAN code in order to evaluate TIC radiative forcing, well visible in FIR (Figure 6), and the sensitivity to ice particle size and shapes (Figure 7). These results offer the possibility to differentiate certain particle shapes and sizes, which will be concretized soon with inversion algorithms.

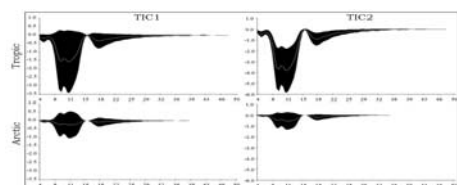


Figure 6. Spectral variation of TIC radiative forcing (in $\text{W m}^{-2} \text{sr}^{-1} \mu\text{m}^{-1}$), represented as variations around their mean value.

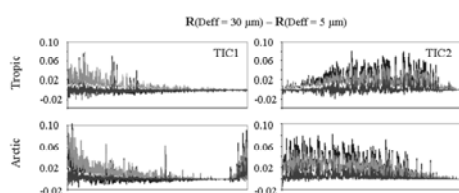


Figure 7. Computed radiance difference in FIR 22.5 – 27.5 μm band for particle sizes of 30 μm and 5 μm effective diameters. Several particle shapes were considered: aggregate, bullet rosette, droxtal, hexagonal plates, solid and hollow columns. The abscise axis is occurrence number.

Knowledge of cloud phase is an also an important component in correctly modeling cloud microphysical and optical properties. Assuming an incorrect phase can lead to errors up to 100% in particle size and optical thickness, resulting in errors of 5-20% in the amount of modeled downwelling radiation reaching the surface. Determining cloud phase is especially difficult in the Arctic, where the underlying snow-covered surface, persistent temperature inversions, and long periods of polar night make satellite retrievals very difficult. Turner et al. (2003) compares the different absorption by liquid water and ice cloud particles in thermal and far-infrared observations. The absorption properties in the spectral region between 11 and 19 μm cause clouds composed of liquid water droplets to emit different amounts of radiation than clouds composed of ice particles. Thus, far-infrared observations can help to resolve ambiguities and improve infrared cloud phase detection.

5 POTENTIAL TECHNICAL DESIGN FOR FUTURE FIR SPACE MISSION

The continuous evolution in sensor developments enables now relatively low cost space-borne missions in order to fill an important gap in the far-infrared range where most of the Earth's atmosphere thermal cooling originate and yet unobserved from satellites. All the theoretical findings in FIR remote sensing helped us to propose TICFIRE as micro-satellite mission with following scientific objectives:

- monitoring of the formation of cold anomalies in Polar Regions and globally near the tropopause from FIR emissions
- characterization of sub-visible cloud types and properties in extreme cold regions.

- improvement of water vapor concentration measurements in the low limit (less than 0.2g/cm^2 columnar amount) where cold climate is most sensitive.

The proposed technical design is based on state-of-the-art uncooled microbolometers technology available at INO and extending well into the far-infrared region up to 50 μm . To meet the science objectives, the proposed payload is a nadir multi-band radiometer working in the thermal and far-infrared spectral range, along with a limb-looking IR camera for retrievals of cloud top vertical profile (Figure 8). A pointing mechanism will allow in-flight radiometer characterisation by successive radiometric measurements of the control blackbody and deep space. Six pushbroom line arrays will collect information consistent with six narrowband channels selected in conformity with scientific objectives: 7.9-9.5 μm , 10-12 μm , 12-14 μm , 16-18.5 μm , 22.5-27.5 μm and 30-50 μm .

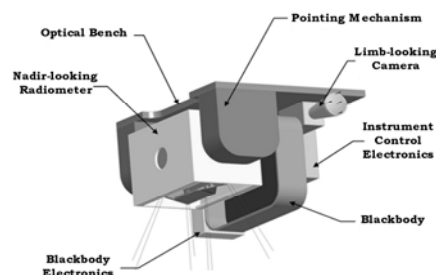


Figure 8. The payload for TICFIRE (Thin Ice Clouds in Far Infra Red Experiment) mission

Pixel designs will be tailored to address the specific needs of the mission in terms wavelength range, pixel size and thermal response time. To maintain the radiometric calibration and minimize the need for frequent radiometric calibration, the focal plane arrays are temperature-controlled at a temperature around their natural temperature of operation using a simple one stage thermo-electric cooler.

These measurements will allow for retrieval of the water vapor concentration profiles above the cloud tops and will permit to monitor more closely the drying rate of the atmosphere. To achieve the required degree of signal within sufficiently narrow spectral intervals and to allow adequate profiling capability, a relatively long integration time over the same scene is required. This technical concept should be adequate to retrieve water vapor, TIC types, light precipitation, cloud optical depth, to discriminate liquid and ice cloud phases, and to provide possible cross calibration with similar space missions such as MISTIGRI (*MicroSatellite for Thermal InfraRed Ground Surface Imaging*) or PREMIER (*PRocess Exploration through Measurements of Infrared and millimetre-wave Emitted Radiation*). TICFIRE will also provide on a

global scale a needed contribution in calibrated radiance assimilation near the IR maximum emission to improve weather forecast. Therefore, TICFIRE is a science-driven mission with a strong operational component.

6 CONCLUSIONS

The study emphasizes that FIR measurements are needed for a better understanding of complex Earth's energy processes and its climate. Observed radiances could provide important information concerning the key role played by water vapor and ice clouds in atmosphere energy budget and climate change. This will certainly lead to a sensible improvement in atmospheric modeling and weather prediction.

The strong atmospheric absorption in the FIR depends on atmospheric water content. FIR simulated radiances are highly sensitive to water content variations, even more at weak values; in these conditions, the FIR is more sensitive to water vapor than the thermal IR.

FIR measurements offer a good prospective for upper-troposphere and stratosphere studies, where the atmosphere is quasi-transparent and the surface and lower levels contribution is completely attenuated. Thus, the FIR measurements could provide useful input for forecast modeling, which often overestimate the water concentration at higher altitudes. Moreover, an adequate FIR technique will increase the precision of water vapor remote sensing in extreme polar conditions, where the classic methods operate at their performance limits.

Interesting properties useful in atmospheric sounding were found by exploring a large ensemble of narrow FIR channels.

Ice cloud super micron particles are highly sensitive to FIR radiation. Arctic atmospheres become colder with the formation of super-micron ice crystals inducing atmospheric dehydration effects. Since the FIR signal is dependent on shape/size of ice particles, it could be used to study these phenomena. Cloud phase detection and studies on precipitation initiation using refractive index contrast should also be considered as potential applications in the FIR.

FIR space missions are now possible due to recent advances in sensor technology. A relatively low power and volume instrument is proposed to exploit for the first time the remote sensing capabilities in the FIR from space. Thus, INO is proud to contribute to sensor development and to support science team efforts for the future TICFIRE space mission

7 ACKNOWLEDGMENTS

This study was supported by the Canadian Space Agency who funded the TICFIRE mission definition concept study.

8 REFERENCES

- Chahine, M. T. et al., 2001, AIRS Level 2 Algorithm Theoretical Basis Document Version 2.2, JPL D-17006.
- Clough, S. A. et al., 1992: Line-by-line calculations of atmospheric fluxes and cooling rates: application to water vapor, *Journal of Geophysical Research*, **97**, pp. 15761-15785.
- Delamere, J. S. et al., 2010, A far-infrared radiative closure study in the Arctic: Application to water vapor, *Journal of Geophysical Research*, **115**, D17106.
- Garand L. et al., 2001, Radiance and Jacobian intercomparison of radiative transfer models applied to HIRS and AMSU channels, *Journal of Geophysical Research Atmosphere*, **106** (D20), pp. 24017-24031.
- Girard, E. and A. Stefanof, 2007, Assessment of the dehydration-greenhouse feedback over the Arctic during February 1990., *International Journal of Climatology*, **27**, No. 8, pp. 1047-1058.
- Goldberg, M. D. et al., 2003, AIRS near real-time products and algorithms in support of operational numerical weather prediction, *IEEE Transactions on Geoscience and Remote Sensing*, **41**, pp. 379–389.
- Grenier, P. et al., 2009: Study of polar thin ice clouds and aerosols seen by CloudSat and CALIPSO during midwinter 2007, *Journal of Geophysical Research*, **114**, D09201.
- Kratz, D. P., 2001: High-resolution modeling of the far-infrared. *SPIE Proceedings*, **4485**, 171-180.
- McClatchey, R. A., et al., 1972, Optical properties of the atmosphere., Air Force Cambridge Research Labs., AFCRL-72-0497
- Mlynczak, M. G. et al., 2006, First light from the Far-Infrared Spectroscopy of the Troposphere (FIRST) instrument, *Geophysical Research Letters*, **33**, L07704.
- Stackhouse, P.W., Jr., and G.L. Stephens, 1991, A theoretical and observational study of the radiative properties of cirrus clouds: results from FIRE 1986. *Journal of the Atmospheric Sciences*, **48**, pp. 2044-2059.
- Tobin, D. C. et al., 1999: Downwelling spectral radiance observations at the SHEBA ice station: water vapor continuum measurements from 17 to 26 microns, *Journal of Geophysical Research*, **104**, pp. 2081-2092.
- Turner, D.D. Et al., 2003: Cloud Phase Determination Using Ground-Based AERI Observations at SHEBA, *Journal of Applied Meteorology* **42**(6), pp. 701-715.
- Yang, P. et al., 2001, Radiative Properties of cirrus clouds in the infrared (8–13 μ m) spectral region, *Journal of Quantitative Spectroscopy and Radiative Transfer*, **70**, pp. 473–504.

Aerosol size distributions retrieved from star-photometry by King inversion method.

*D. Pérez-Ramírez^{1,2}, H. Lyamani^{1,2}, F.J. Olmo^{1,2}, F. Navas-Guzmán^{1,2} and L. Alados-Arboledas^{1,2}

¹Centro Andaluz de Medio Ambiente. Av. del Mediterráneo s/n. 18006-Granada. Spain.

²Dpto. de Física Aplicada. Universidad de Granada. 18071-Granada. Spain

Email address: *dperez@ugr.es

Knowledge of aerosol microphysical properties is essential to understand the role of atmospheric aerosols in climate change. Passive remote sensing allows for the retrieval of columnar aerosol size distributions from spectral measurements of aerosol optical depth by the application of numerical methods. These techniques are widely applied to sun photometers. However, night-time retrievals require the use of star photometers. The Atmospheric Physics Group of the University of Granada, GFAT, operates a star photometer with channels at 380, 436, 500, 670, 880 and 1020 nm in Granada (South-eastern Spain, 37.16° N, 3.60° W, 680 m a.s.l.). The GFAT also operates a sun photometer CIMEL CE-318 with filters at similar wavelengths. Columnar aerosol size distributions can be retrieved by the well-know inversion code developed by King et al. (1978). In this work, we present day and night aerosol size distributions and effective radius retrievals for different aerosol load and characteristics. The analyses and discussions include the use of backward-trajectories (air masses information) and synoptic conditions.

1. INTRODUCTION

The importance of atmospheric aerosols for the Earth's climate has been widely recognized. They affect solar radiation and hence climate directly by absorbing and scattering radiation back to space, but also indirectly by acting as cloud condensation nuclei [Forster et al., 2007]. In this sense several efforts have been made to estimate the aerosol perturbation of the Earth radiation budget [e.g. Charlson et al. 1992; Haywood and Schulz, 2007; Forster et al., 2007]. Estimations of the aerosol radiative properties need the knowledge of aerosol microphysical properties as a key factor. In particular, the aerosol size distribution can be measured directly in situ or retrieved by remote sensing techniques.

Passive remote sensing techniques allows for the retrieval of an effective aerosol size distribution for the whole atmospheric column. In particular, using sun photometry it is possible to retrieve columnar aerosol size distributions in the interval radius from 0.04 to 10 μm approximately from direct irradiance and sky radiance measurements [Dellago and Horvath 1993; Nakajima et al., 1996; Dubovik and King, 2000; Olmo

et al., 2006]. At night time we can use a star photometer to acquire measurements of spectral Aerosol Optical Depth ($\text{AOD}(\lambda)$), and thus we can retrieve columnar aerosol size distributions using inversion codes. In this work we propose to use the King et al. (1978) inversion code. This code has been well tested in the literature [e.g. King et al., 1978; González-Jorge and Ogren, 1996; Alados-Arboledas et al., 2003; Lyamani et al., 2005], and only requires spectral $\text{AOD}(\lambda)$ as inputs.

This paper presents one week of night columnar aerosol size distributions and day-night effective radius evolutions under different aerosol types. We also use air masses and synoptic information to characterise aerosol features.

2. INSTRUMENTATION AND EXPERIMENTAL SITE.

In order to obtain a characterization of the columnar aerosol optical properties during the day time, we have used a sun photometer CIMEL CE-318-4. The instrument makes direct Sun irradiance measurements with a 1.2° full field of view at 340, 380, 440, 670, 870, 940, and 1020 nm. Furthermore, the instrument is able to make sky radiances both in almucantar and principal plane. More details about

CIMEL CE-318-4 can be found in Holben et al. (1998).

For night time columnar aerosol characterization we have used the star photometer EXCALIBUR (iTec Astronómica S.L.). Details of this instrument can be found in Pérez-Ramírez et al. (2008a, b). Basically, the instrument consists of a telescope that collects the parallel incident light rays from the required star. Later, the starlight passes through a 10-filter wheel, where it has been set up seven narrow band filters at 380, 436, 500, 670, 880, 940 and 1020nm. Once the starlight is spectrally separated and it reaches the CCD camera, which is the detector device. On the other hand, an external wide field CCD camera is employed to assure a correct pointing for a given star. The instrument also has software that is able to minimize errors associated to the CCD camera, and also to focus the telescope and to reduce the background light associated to the measurements.

Both instruments operate in the Andalusian Center for Environmental Research (CEAMA) located in the city of Granada (37.16°N, 3.60°W, 680 m a.s.l.; south-east of Spain). Granada is a medium-sized city situated in a natural basin surrounded by mountains. The study area is about 200 km away from the African continent and approximately 50 km away from the western Mediterranean basin. Due to its location in the Iberian Peninsula, the study area is affected by air masses coming from the Atlantic Ocean, from the European and African continents and from the Mediterranean Sea. In addition the city is affected by local anthropogenic pollution due mainly to domestic heating and traffic emissions [Lyamani et al., 2010].

3. INVERSION METHOD TO OBTAIN COLUMN AEROSOL SIZE DISTRIBUTION

From spectral measurements of solar or star extinction values we can obtain AOD(λ) values following the procedures described by Alados-Arboledas et al. (2003) for sun photometry data, and by Pérez-Ramírez et al. (2008a) for star photometry data. The spectral variation of AOD(λ) is produced through attenuation by aerosol and is mainly determined by the columnar aerosol size distribution. If we assume that the atmospheric particles can be modelled by equivalent spheres of known refractive index 'm', we can write:

$$AOD(\lambda) = \int_{r_1}^{r_2} \pi r^2 Q_{ext}(x, \lambda, m) n_c(r) dr \quad (1)$$

Where $Q_{ext}(r, \lambda, m)$ is the extinction efficiency factor from Mie theory for a complex refractive index 'm',

and $n_c(r)$ is the unknown columnar aerosol size distribution, i.e., the number of particles per unit area per unit radius 'r' interval in a vertical column through the atmosphere, and r_1 and r_2 are the lower and upper limits of integration, which are established considering particle sizes that contribute significantly to the integral of equation 1. These limits are closely related to $Q_{ext}(r, \lambda, m)$. For the inversions using AOD(λ) measurements in the range 380-1020 nm, we use $r_1 \approx 0.06 \mu m$ and $r_2 \approx 4 \mu m$, although there is not a fixed criterion for these values [King et al., 1978; González-Jorge et al., 1996; Alados-Arboledas et al., 2003; Martínez-Lozano et al., 1999; Lyamani et al., 2005]. An expression for $n_c(r)$ cannot be written analytically as a function of AOD(λ), and thus a numerical approach must be followed. In this work we use the King et al. (1978) inversion code. The Atmospheric Physics Group of the University of Granada (GFAT) has used previously this last code for sun photometers, obtaining successful results for different aerosol loads and aerosol characteristics [Alados-Arboledas et al., 2003; Lyamani et al., 2005].

4. PREVIOUS CONSIDERATIONS TO INVERSION

The inversion method proposed by King et al. (1978) requires the aerosol refractive index as input. In this work we take advantage of more sophisticated inversion methods based on sky radiance measurements and applied to sun photometer CIMEL. In particular, we use the Nakajima et al. (1996) code. Further developments of this last code [Olmo et al., 2006] allows for the retrieval of aerosol refractive index during day time. This refractive index is used as input for the King et al. (1978) inversion code during day time. For the night time, the aerosol refractive index is interpolated between the values obtained the day before and after.

However, the inhomogeneity of the day time sky radiance makes Nakajima et al. (1996) method fail. The simulations carried out by King et al. (1978) for a Junge size distribution shows that the shape of the retrieved aerosol size distribution does not change significantly by varying the aerosol refractive index, and thus they proposed a fixed value of $m = 1.45 - 0i$. Similar studies [D'Almieda et al., 1991; Cachorro and Frutos 1994; Kaufman et al., 1994; Martínez-Lozano et al., 1999] obtained the same results, and they proposed an aerosol refractive index of $m = 1.5 - 0.0i$. Thus, when the day time sky radiance inversion method has not been possible, we use the refractive index $m = 1.5 - 0.0i$ proposed in the bibliography.

The King et al. (1978) inversion method requires fixing interval radius for carrying out the inversions. For the spectral range used we acquired AOD (380-

1020 nm). On the other hand, the kernels functions of equation 1 limit the maximum and minimum interval radius between 0.06 and 4.00 μm , approximately [King et al., 1978]. However, according to King et al. (1978), for a set of AOD(λ) values over a given spectral range, the inversion does not necessarily follow that the upper and lower radius limits are fixed. On the other hand, to avoid the loss of accuracy in going from an integral to a finite sum, we have used 15 intervals of radius as proposed by González-Jorge and Ogren (1996).

The inversion algorithm based on King et al. (1978) method implemented in the GFAT retrieve aerosol size distributions varying the minimum radius r_1 between 0.06 and 0.2 μm , and the maximum radius r_2 between 1 and 4 μm . Once we have calculated the aerosol size distributions for all the intervals of radius, the measured spectral AOD(λ) used as input are compared with the calculated AOD(λ)' by equation 1, using Mie extinction efficiency parameters and the aerosol size distribution retrieved. The final retrieve aerosol size distribution is the one that minimizes such differences.

From the aerosol size distribution, microphysical parameters can be retrieved such as total number of particles, total volume and total surface. But in this work we focus on the effective radius, r_{eff} , given by:

$$r_{\text{eff}} = \frac{\int_0^{\infty} r^3 n_c(r) dr}{\int_0^{\infty} r^2 n_c(r) dr} = \frac{3V}{S} \quad (2)$$

5. PRELIMINARY RESULTS AND DISCUSSION

In this section we show columnar aerosol size distributions and r_{eff} evolution. The study period is from 29th July 2007 to 4th August 2007. During this period, the study area was affected by a large aerosol load, with different types of particles. Table 1 shows day and night mean values of AOD (440 nm) and Ångström parameter, α (computed from 380 to 880 nm). During the 29th and 30th July we obtained large values of AOD (mean value 0.30 ± 0.05), and α parameter (mean value 1.39 ± 0.19). The backward-trajectories from HYSPLIT model [Draxler and Rolph, 2003] for every day and night of this period (graphs not shown), indicates air mass stagnation. In addition, some fires at Guadalquivir valley (Andalusian) during 28th-31st July were detected (maps.geog.umd.edu/). These atmospheric situations can explain the values obtained for AOD(λ) and α . On 1st July, both AOD(λ) and α decrease, and the air masses come from Tropical zone. However on 2nd – 4th August the AOD(λ) values

increase (up to 0.49 ± 0.04 at 440 nm) and the α parameter decrease sharply (values till 0.24 ± 0.05). The backward-trajectories revealed African air masses that carried large amount of dust particles. This has been checked by MODIS (<http://modis.gsfc.nasa.gov/>) and TOMS (<http://jwocky.gsfc.nasa.gov/>) satellite images (graphs not shown). This dust particles made AOD(λ) increase and α decrease.

DATE	AOD(440nm)	α
30 th July-Day	0.29 ± 0.03	1.34 ± 0.09
30 th -31 st July-Night	0.32 ± 0.08	1.60 ± 0.40
31 st July-Day	0.30 ± 0.06	0.66 ± 0.05
31 st July-1 st August-Night	0.38 ± 0.02	0.62 ± 0.10
1 st August-Day	0.30 ± 0.06	0.57 ± 0.06
1 st -2 nd August-Night	0.27 ± 0.04	0.67 ± 0.16
2 nd August-Day	0.44 ± 0.06	0.39 ± 0.08
2 nd -3 rd August-Night	0.43 ± 0.02	0.40 ± 0.05
3 rd August-Day	0.40 ± 0.04	0.41 ± 0.03
3 rd -4 th August-Night	0.46 ± 0.03	0.45 ± 0.05
4 th August-Day	0.49 ± 0.04	0.24 ± 0.05
4 th -5 th August-Night	0.46 ± 0.02	0.34 ± 0.05

Table 1: Day and night mean values and its associated standard deviations of AOD (440 nm) and α for the study period.

Figure 1 shows AOD (440 nm) from 30/07/2007 12:00 UTC to 31/07/2007 12:00 UTC. There is an increase in AOD (440 nm) up to 0.46 ± 0.02 around 22:21 UTC. Later, AOD (440 nm) decreases till 0.20 ± 0.02 at the end of the night. It is remarkable the apparent continuity between day and night AOD(λ) values.

On the other hand, figure 2 shows the columnar volume aerosol size distributions ($v_c(r) = (4/3)\pi r^3 n_c(r)$) at night from 30th to 31st July 2007. Before 22:00 UTC, it is observed an increase in aerosol concentration, and it is also remarkable that such increase is larger for particles with radius lower than 0.3 μm . After 22:00 UTC, we observe a decrease in aerosol concentration for all radiuses. The evolution of aerosol size distributions agree with AOD(λ) and α values for this night. The predominance of fine particles, and the use of information of the backward-trajectories, reveals that these large values of aerosol load could be associated to smoke particles, to dense pollution plumes, or to a mixture between both situations.

The backward-trajectories change modified the aerosol load and the particles characteristics. Figure 3 shows the day-night evolution of AOD (436 nm) from 03/08/2007 12:00 UTC to 04/08/2007 12:00 UTC. This figure reveals a continuous increase in AOD at 440 nm during the night, from 0.41 ± 0.02 up to 0.57 ± 0.02 . It is again observed an apparent continuity

between day and night AOD (440 nm) values. On the other hand, figure 4 shows the columnar volume aerosol size distributions from 3rd to 4th August 2007 night. These size distributions reveal the predominance of particles with radius larger than 0.3 μm . In addition, the aerosol size distributions show an increase of large particles during the night, which agrees with the increase in AOD (440 nm). The information of the backward-trajectories revealed north-African air masses, which according to satellite images (graphs not shown) transported high amount of coarse particles. The dust particles over our station explain the large aerosol load for these days. Similar day time results has been obtained in our station for Saharan dust outbreaks using the King et al. (1978) inversion method [Lyamani et al., 2005].

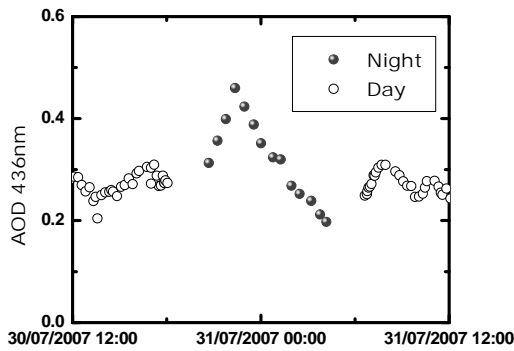


Figure 1: AOD (436 nm) evolution from 30/07/2007 12:00 UTC to 31/07/2007 12:00 UTC.

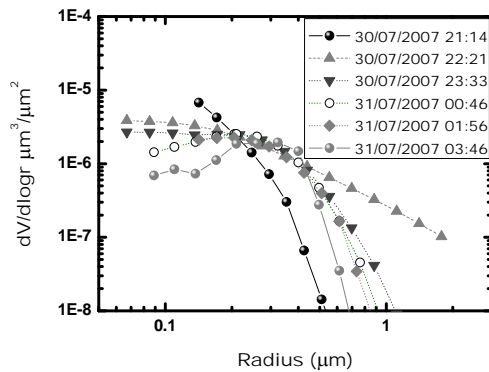


Figure 2: Columnar volume aerosol size distributions retrieved by King et al. (1978) inversion method at night from 30th to 31st July 2007.

Figure 5 shows the day-night time evolution of r_{eff} for the study period. The r_{eff} evolution shows values lower than 0.2 μm on 30th and 31st July, which

is quite related to the air masses stagnation over the Iberian Peninsula that favour anthropogenic aerosol accumulation (mainly constituted by small particles). In Alados-Arboledas et al. (2010) we detected fresh biomass burning with r_{eff} around 0.18 μm , and thus the active fires detected near our station during this period could also explain the low values of r_{eff} . On the other hand, the 1st August and the night from 1st to 2nd August we obtained r_{eff} values slightly larger than 0.2 μm , which might suggest a mixture of fine and coarse particles. This result could be associated to the changes in the synoptic conditions. However, during 2nd of August, r_{eff} increase continuously, reaching values up to 0.4 μm . This increase is larger in the night from 3rd to 4th August, where r_{eff} values up to 0.5 μm were obtained. These last values agree with those obtained previously in Lyamani et al. (2005, 2006) for Saharan dust outbreaks at day time.

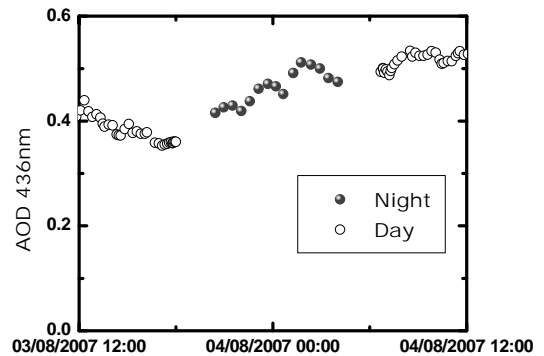


Figure 3: AOD (436 nm) evolution from 03/08/2007 12:00 UTC to 04/08/2007 12:00 UTC.

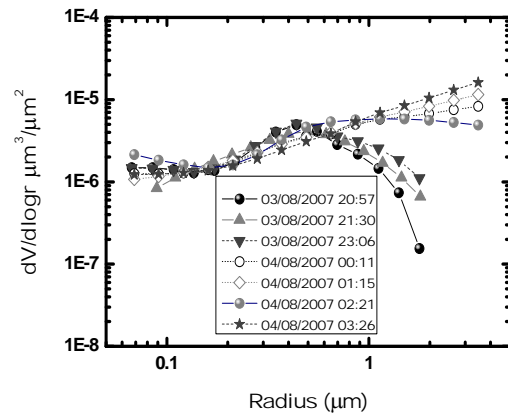


Figure 4: Columnar volume aerosol size distributions retrieved by King et al. (1978) inversion method at night from 30th to 31st July 2007.

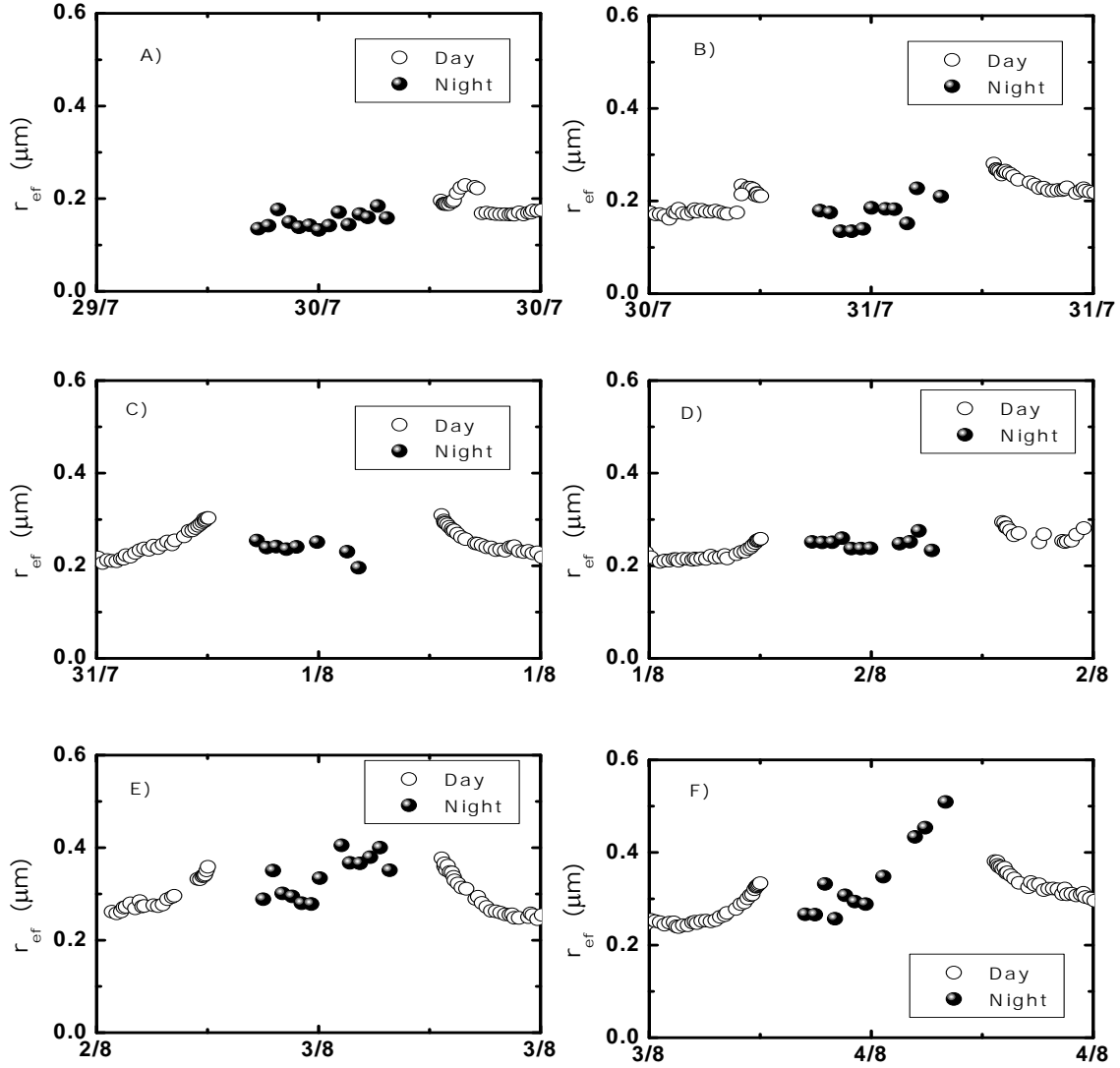


Figure 5: r_{eff} day/night time evolution in the period from 29th July to 4th August 2007.

The most remarkable result from figure 5 is the apparent continuity in the day-night evolution. This continuity has been observed in different aerosol loads and synoptic conditions, and thus gives more feasibility to our purpose of continuously monitoring the aerosol microphysical properties.

ACKNOWLEDGMENTS

This work has been supported by Spanish Ministry of Science through grant CGL2007-28871-E/CLI and projects CGL2007-66477-C02-01 and

CSD2007-00067; by Autonomous Government of Andalusia through the projects P08-RNM-3568 and P06-RNM-01503, and by EARLINET-ASOS project (EU-CA., 025991, RICA). The authors would like express their gratitude to the NASA/Goddard Space Flight Center, NOAA Air Resources Laboratory (ARL), Naval Research Laboratory for use of the HYSPLIT transport and dispersion model. We would like to express our gratitude to the University of Maryland Fire Information for Resource Management System (FIRMS).

REFERENCES

- Alados-Arboledas, L., et al., 2003, Aerosol size properties at Armilla, Granada (Spain). *Quarterly Journal of the Royal Meteorological Society*, **129**, 1395-1413.
- Alados-Arboledas, L., et al., 2010, Optical and microphysical properties of fresh biomass burning aerosol retrieved by Raman-Lidar, and star and sun photometry. *Geophysical Research Letters*, submitted.
- Cachorro, V. E., and Frutos, A. M., 1995, A revised study of the validity of the general Junge relationship at solar wavelengths: Application to vertical atmospheric aerosol layer studies. *Atmospheric Research*, **39**, 113-126.
- Charlson, R. et al., 1992. Climate forcing by anthropogenic aerosols. *Science*, **255**, 423-430.
- D'almeida, G. A., Keopke, P., and Shettle E. P., 1991, Atmospheric aerosol: Global climatology and radiative characteristics. (Edited by A. Deepak Hampton, Virginia: A. Deepak Publishing).
- Dellago, C., and Horvath, H., 1993, On the accuracy of the size distribution information obtained from light extinction and scattering measurements, I, Basic considerations and models. *Journal of Aerosol Science*, **24**, 129-141.
- Draxler, R., and Rolph, G., 2003, HYSPLIT (Hybrid Single-Particle Lagrangian Integrated Trajectory) Model access via NOAA ARL READY Website (<http://ready.arl.noaa.gov/HYSPLIT.php>). NOAA Air Resources Laboratory.
- Dubovik, O., and King, M.D., 2000, A flexible inversion algorithm for retrieval of aerosol optical properties from sun and sky radiance measurements, *Journal of Geophysical Research*, **105**, 20673-20696.
- Foster, P. et al., 2007. Climate Change 2007: The Physical Science Basis. (Cambridge University Press, NY, USA).
- González-Jorge E., and Ogren, J.A., 1996, Sensitivity of retrieved aerosol properties to assumptions in the inversion of spectral optical depths. *Journal of the Atmospheric Sciences*, **53**, 3669-3683.
- Haywood, J. and Schulz, M., 2007. *Geophys. Res. Lett.*, **34**, L20701, doi:10.1029/2007GL030749.
- Holben, B.N., et al., 1998, AERONET - A Federated instrument network and data archive for aerosol characterization. *Remote Sensing of Environment*, **66**, 1-16.
- Lyamani, H., et al., 2005, Saharan dust outbreak over southeastern Spain as detected by sun photometer. *Atmospheric Environment*, **40**, 7276-7284.
- Lyamani, H., et al., 2006, Atmospheric aerosol during the 2003 heat wave in southeastern Spain II: Microphysical columnar properties and radiative forcing. *Atmospheric Environment*, **40**, 6465-6476.
- Lyamani, H., Olmo, F.J., and Alados-Arboledas, L., 2010, Physical and optical properties of aerosols over an urban location in Spain: seasonal and diurnal variability. *Atmospheric Chemistry and Physics*, **10**, 239-254.
- Martinez-Lozano, J.A., et al., 1999, Retrieval of the aerosol size distribution from spectroradiometer measurements at coastal site in the Mediterranean Sea. *International Journal of Remote Sensing*, **20**, 2167-2182.
- Nakajima, T., et al., 1996, Use of sky brightness measurements from ground for remote sensing of particulate polydispersions. *Applied Optics*, **35**, 2672-2686.
- Kaufman, Y. J., et al., 1994, Size distribution and scattering phase function of aerosol particles retrieved from sky brightness measurements. *Journal of Geophysical Research Letter*, **99**, 10341-10356.
- King, M.D., et al., 1978, Aerosol size distributions obtained by inversion of spectral optical depth measurements. *Journal of the Atmospheric Science*, **35**, 2153-2167.
- Olmo, F.J., et al., 2006, Preliminary results of a non-spherical aerosol method for the retrieval of the atmospheric aerosol optical properties. *Journal of Quantitative Spectroscopy & Radiative Transfer*, **100**, 305-314.
- Pérez-Ramírez, D., et al., 2008a, Development and calibration of a star photometer to measure the aerosol optical depth: Smoke observations at a high mountain site, *Atmospheric Environment*, **42**, 2739-2745.
- Pérez-Ramírez, D., et al., 2008b, Sun/star photometry to derive the aerosol optical depth. *International Journal of Remote Sensing*, **29**, 5113-5132.

Proposal of a simple model for the characterization of aerosols in relation to the dominant air masses.

S. Segura, V. Estellés, M.P. Utrillas, A.R. Esteve, J.A. Martinez-Lozano
*Grupo de Radiación Solar, Departamento de Física de la Tierra y Termodinámica.
Facultad de Física. Universidad de Valencia. SPAIN*
sara.segura@uv.es

ABSTRACT- *In this work we present a simple model which allows us to obtain easily the character of the dominant air mass for any location in the Northern Hemisphere at any time. Specifically, this study is done for the characterization of the air masses arriving at Valencia, Spain, during the years 2008 and 2009. Their analysis and classification is done depending on their trajectories over pre-defined source regions in the Northern Hemisphere. These trajectories are simulated by the Hybrid Single-Particle Lagrangian Integrated Trajectory Model (HYSPLIT) and then classified by a program implemented by us. In order to verify the results of our classification, we will compare them with the African intrusions predicted for Valencia for those two years by the Ministerio de Medio Ambiente y Medio Rural y Marino (MARM) in collaboration with the Centro Superior de Investigaciones Científicas (CSIC). The importance of this work is that this model which we present can be used later either in the selection of the optimal aerosol model for atmosphere correction or to classify and understand other atmospheric properties observed at ground level.*

1 INTRODUCTION

In many applications, including remote sensing of natural parameters, is useful to have a good knowledge not only of the quantity of atmospheric aerosols but also of their type, since their radiative properties, and therefore the effects in the radiative fluxes we observe, depend of their highly variable nature. In the particular case of atmospheric correction, the user needs to select an aerosol model; the criterion followed is usually based in the surface properties of the area where the image has been acquired. This criterion would be enough if the dominant aerosol in a specific location and time was of local type; however aerosols are usually generated in source regions located faraway. We can find examples of this remote transport of aerosols in the Iberian Peninsula during summer months, when the load of mineral dust is advected from North Africa.

An air mass is traditionally defined as a volume of air whose physical properties, especially the temperature and humidity, remain relatively constant across areas of hundreds of thousand squares kilometers [Barry and Chorley, 1998]. Air masses acquire their properties by interaction with the surfaces above which they are found, whenever they must remain stationary for a certain length of time.

In order to create a simple model to characterize the dominant air masses arriving at any location at any time, our study consisted in the analysis and classification of the air masses depending on their backward trajectories over pre-defined source regions

in the Northern Hemisphere, specifically we studied those which arrived at Valencia, Spain. In these region, the Sahara desert constitutes a first order source region, originating dust intrusions in the Peninsula. We will study those intrusions with our model and compare the results with the reports given by the Ministerio de Medio Ambiente y Medio Rural y Marino (MARM) in collaboration with the Centro Superior de Investigaciones Científicas (CSIC-MARM).

This new model results from the modification and improvement of a previous one [Estellés *et al.*, 2007] to which greater flexibility and precision has been added, so it can be more interesting for remote sensing applications.

2 METHODOLOGY

The characterization of the air masses is done considering three different factors. The first of them is the trajectory they follow in the atmosphere and, therefore, the sources they cross in their way. The other two factors are related to the fact that the aerosols behaviour in the atmosphere is not constant, but depending of time and height.

2.1 Air Mass Classification and Meshing

The paths followed by the air masses arriving at Valencia are given by their back trajectories at three different heights (500 m, 1500 m, and 3000 m a.g.l.) and for a flight time of 5 days. The model used for calculating those back trajectories is the Hybrid

Single-Particle Lagrangian Integrated Trajectory Model (HYSPLIT) developed by NOAA [Draxler and Rolph, 2003]. This model combines a Lagrangian approximation for resolving the air mass transport with an Eulerian approximation for the diffusion of pollutants.

Air masses can be classified, with respect to the source region, in terms of two basic parameters: temperature and surface type. The temperature allows the differentiation between arctic (AR), polar (PO) and tropical (TR) depending on the latitude where the air masses are originated. The arctic masses are originated in the highest latitudes in very cold environments, the polar masses in high latitudes of Canada, northern Atlantic and northern Europe, and the tropical masses in warmer regions at lower latitudes, in the Atlantic ocean, Mediterranean Sea or the African continent. On the other hand, the surface type of the region may be continental (c) or maritime (m) in case they have been developed over continental or oceanic surfaces, respectively [Barry and Chorley, 1998].

Two of the main sources of cold air in our hemisphere are the continental anticyclonic weather systems from northern Canada, of continental polar type (cP), and the Arctic Basin, of continental Arctic type (cA). These masses originate over huge extensions of snow, especially in winter, so they are cold and dry, and therefore very stable near the surface. The warm air masses originate in the subtropical high pressure cells and the extensive continental zones, especially in summer. These tropical air masses (T) can be divided into maritime (mT), when they come from the Atlantic Ocean, and continental (cT), if their origin is the north of Africa. The mT air masses are characterised by high temperature and humidity, stability and low cloudiness, except when they are displaced towards higher latitudes, where they are cooled from below, especially in spring. Generally the Mediterranean, although a relatively warm and small sea, enclosed between two important continental surfaces, can impose its own specific imprint on the polar air masses that stagnate above it.

Since the HYSPLIT model allows the possibility to obtain the air mass trajectory quantitatively, a simple classification model was implemented that would permit the backward trajectories to be described using simple basic indexes, and would assign the primary and secondary characteristics of the air masses. By performing this classification automatically it would be possible to apply objective criteria and also to study the sensitivity of the classification to different input parameters of the HYSPLIT model.

Figure 1 shows the meshing of the Northern Hemisphere, which is done to get a characterization of

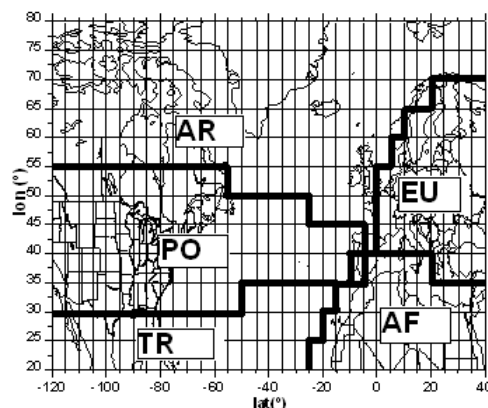


Figure 1. Meshing of the Northern Hemisphere with the different classification.

the air masses based in the trajectories they follow in the atmosphere. Thus, the Northern Hemisphere is divided in cells of 5° of longitude by 5° of latitude, and to each cell we assign a different aerosol type depending on the previous definitions as well as other factors related to the physics of aerosols. The types were defined as follows:

European (EU) type is defined by continental polar air masse, including the northern Mediterranean coast. Given its basically continental character it is expected that these air masses would transport mineral particles - originating in the soil - but its differential characteristic actually is the load of urban aerosol, including smoke and soot so the size distribution would possess a well developed accumulation mode and a relatively low single scattering albedo.

African (AF) type is characterized by tropical continental air masses, with a significant load of mineral dust due to the Sahara desert and the low pressure cells generated in summer by the intense sunshine, which cause the incorporation of dust into high altitude atmospheric layers from where they are transported to other latitudes.

Tropical (TR) type, consists of maritime air masses located to the west of Africa. Due to the global easterly circulation below 30° the air masses were predicted to possess a certain mineral footprint due to aerosols transported from the desert towards America before being partially deflected towards our region. The air was expected to be warm and moist.

Polar (PO) type comes from the region of the Atlantic located between average latitudes (between 30° and 60°) which would have an intermediate character between the maritime air masses of the tropics and the Arctic. These are polar maritime air masses generated by the movement of continental ones

coming from North America, with an occasional residue of anthropogenic aerosols.

Artic (AR) type is defined by the back trajectories originating in Canada or in the Arctic basin, with associated air masses of type mA or mP, according to the exact place of its origin. This type also includes air masses generated in the sea to the south of Iceland. Given the time taken to cross the ocean, their continental memory would be very vague.

To complement these definitions, another regional class was defined (O type), characterized by those masses whose maximum distance travelled during the five days of the back trajectory was less than 600 km from the measurement station. This class is generally indicative of synoptic conditions of weak pressure gradients and thus stationary air masses. They do not possess any clear relationship with the other five cases, since they usually loitered around the arrival point, passing consecutively through different sectors.

2.2 Index definition

The aerosols behaviour in the atmosphere is not constant; it varies with time and height. To make an approximation of the character of a given back trajectory, a percentage index was defined, ζ_i , where i corresponds to a given sector: EU, AF, TR, PO or AR. These indices were obtained by dividing the number of hours spent by the air mass moving across each sector i (t_i) by the total travel time (T), being in this case 120 hours. Both time factors are weighted by two factors that account for the life time of the aerosol and the layer height from the ground. The definitions of the indices take the next form:

$$\zeta_i(\%) = \frac{\tilde{t}_i}{T} 100 \quad (1)$$

where the temporal sums are given by:

$$\tilde{t}_i = \sum_{k=1}^3 \sum_{j=1}^N w(h_{jk}) w(t_{jk}) \Delta t_i \quad (2)$$

$$T = \sum_{i=1}^5 \sum_{k=1}^3 \sum_{j=1}^N \Delta t_i \quad (3)$$

being $w(h_{jk})$ the height weighting factor given by a first exponential function:

$$w(h_{kj}) = \exp\left(-\frac{h_{kj}}{S_H}\right) \quad (4)$$

and $w(t_{kj})$ the temporal weighting factor given by a second exponential function:

$$w(t_{kj}) = \exp\left(-\frac{t_{kj}}{S_T}\right) \quad (5)$$

In the equations above, \tilde{t}_i is the weighted sum of the time spent by the three back-trajectories in sector i , being Δt_i the time step (one hour). On turn, \tilde{T} is the sum in hours, of the total time for the three backward trajectories. In the weighting functions, h_{kj} and t_{kj} are respectively the height above ground level and the remaining time for the arrival at our site, for each point j of each trajectory k . S_H and S_T are the scale factors related to the boundary layer and the mean life time of the aerosols, and their values were set to 2000 m and 120 hours respectively.

The first weighting function tries to take into account that the concentration of aerosols is higher in the lower layers where the most interaction with the surface is produced. The second weighting function has been introduced for accounting for the fact that when an air mass formed over a source region moved over a surface with different characteristics, the initial identity of the air mass starts to be lost as particles from the origin sector are being removed and the particles from the transit region are being incorporated. Since the average life time of particles in the troposphere is between 5 and 10 days, during the time of calculation the backward trajectories a significant part of the initial characteristics of the air masses will be lost.

We then have a set of five ζ_i percentage indices (equation 1) that describe the character of the air masses as a function of five basic classes. It is interesting to apply these indices to the identification of the primary and secondary classes of air masses. In order to assign a definitive character to each group of back trajectories in practice we would consider an air mass of a purely class if the i index ζ_i possessed a value greater than 75%. Otherwise it would be considered as mixed and composed of all those classes with indices greater than 20%.

In this work, we will only focus in the dust intrusions from the Sahara desert in Valencia, thus means the air masses our program will classificate as purely African class. We will compare the results with the predictions obtained from the CSIC-MARM in

<http://www.calima.ws/episodiosocurridos.html> for dust intrusions which happened in 2008 and 2009.

In order to complement our results, we will combine the classification obtained with our program with the TOMS (Total Ozone Mapping Spectrometer) aerosol Index (AI) distribution. The TOMS aerosol index is a measure of how much the wavelength dependence of backscattered UV radiation from an atmosphere containing aerosols differs from that of a pure molecular atmosphere. With the maps obtained from the TOMS' web where we can check if dust aerosols are presented over the Iberian Peninsula.

3 RESULTS

We ran our program and analysed the classification of the air masses arriving at Valencia for two years, 2008 and 2009. The results obtained for each year are shown in Figures 2 and 3. In both figures we represent the number of successful classifications, as compared with the CSIC reported intrusions. The number of days per month are represented as triangles; these are considered our monthly references. The other two lines correspond to the results obtained using just the classification method (squares, TT) or combining the classification method with the TOMS aerosol index (solid dots, T).

In both graphics we can see how the coincidences of our model with the real predictions improve when we combine both the classification method with the TOMS Aerosol Index. If we only employed our classification method, the number of coincident days would reduce to around 80%. The results improved when we combined it with the TOMS Aerosol Index, getting a coincidence higher than 86%. However, the number of matches decreases in summer months, especially in summer, when the number of dust intrusions in Valencia increases.

After a deeper analysis of the unsuccessful cases, we concluded that these were mostly related to the meshing coarseness (mainly over the Iberian Peninsula) or simulated HYSPLIT trajectories far from African influence. Therefore, the present analysis can be improved by increasing the resolution of the mesh and the definition of improved weighting factors; however, the improvement will be limited by the HYSPLIT backward trajectories accuracy (or associated input meteorology data). Current work is being devoted to analyse these possible discrepancy sources.

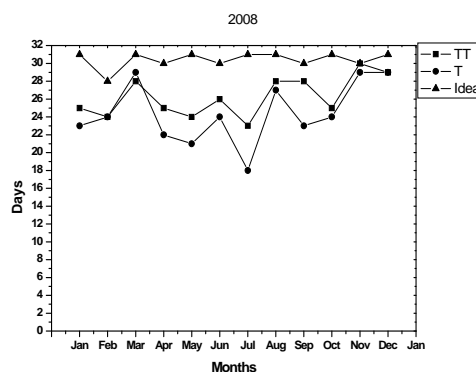


Figure 2. Number of successful identifications obtained for the year 2008.

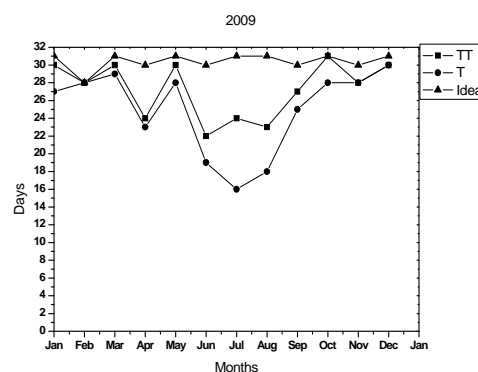


Figure 3. Number of successful identifications obtained for the year 2009.

4 CONCLUSIONS

We have developed a very simple tool in order to automatically classify the air masses depending on their trajectory over different world areas. As a mean of validation, we employed the confirmed dust intrusions reported by CSIC-MARM to check if our classification CAN successfully identify cases of African air masses.

Our results showed a good agreement with other reported cases; moreover, the consideration of the TOMS Aerosol Index improved the identification of these dust cases.

Nevertheless, the results are not conclusive because some refinements should be done. The misidentified cases were related to: coarseness of the classification method, excessive weighting factors, and also, HYSPLIT simulations with trajectories far from the

African area. This third problem may be caused by the meteorological data employed, whose spatial resolution is not good to detect African trajectories coming from the Mediterranean Sea.

5 ACKNOWLEDGEMENTS

This research was funded by the Ministry of Science and Innovation (MICINN) of Spain through the project CGL2009-07790 and the Valencian Autonomous Government through the project PROMETEO-2010-064. The collaboration of S. Segura was possible thanks to a collaboration fellowship from the MICINN.

6 REFERENCES

Barry, R. G., and R. J. Chorley (1998), *Atmosphere, weather and Climate*, 7th ed., Routledge, Boca Raton, Fla.

CSIC-MARM (2004)
<http://www.calima.ws/episodiosocurridos.html>
(Acces on Sep 2010)

Draxler, R. R., and G. D. Rolph (2003), HYSPLIT (Hybrid Single-Particle Lagrangian Integrated Trajectory), Air Resour. Lab, Natl. Oceanic Atmos. Admin., Silver Spring, Md. (Available at <http://ready.arl.noaa.gov/HYSPLIT.php>)

Estellés, V., J. A. Martínez-Lozano, M. P. Utrillas (2007), Influence of fair mass history on the columnar aerosol properties at Valencia, Spain, *J. Geophys. Res.*, *112*, D15211, doi: 10.1029/2007JD008593.

Soil moisture retrieval from geostationary satellite data using combined daily evolution of surface temperature and net surface shortwave radiation

X.N. Song¹, P. Leng¹, Z.L. Li^{2,3}, X.T. Li⁴, X.H. Li¹

¹ College of Resources and Environment, Graduate University of Chinese Academy of Sciences, Beijing 100049, China

² Key Laboratory of Water Cycle and Related Land Surface Processes, Institute of Geographical Sciences and Natural Resources Research, Chinese Academy of Sciences, Beijing, 100101, China

³ TRIO/LSIIT (UMR7005 CNRS)/ENSPS, Bld Sebastien Brant, BP10413, 67412 Illkirch, France

⁴ Remote Sensing Center, China Institute of Water Resources and Hydropower Research, Beijing 100048, China
songxn@gucas.ac.cn

ABSTRACT - Soil moisture is a key parameter in water balance, and it performs as the core and link in the atmosphere-vegetation-soil-groundwater system. Soil moisture directly affects the accuracy of model during simulation and prediction. surface temperature and surface net shortwave radiation data have been firstly simulated with Common Land Model (CoLM) to establish daily variation model of land surface temperature and net surface shortwave radiation.. Then, on the basis of the heat transfer theory, a relationship model between the daily evolution of surface temperature and net surface shortwave radiation has been developed and a relationship between soil moisture content and surface temperature-net surface shortwave radiation has been built and validated using the simulated data. In addition, with the data simulated by CoLM at different spatial resolutions, a similar relationship model between soil moisture and surface temperature-net surface shortwave radiation was always existed. In order to demonstrate the feasibility of soil moisture estimation method developed in this work, we have finally applied this method to the European continent with geostationary satellite MSG-SEVIRI (METEOSAT Second Generation-Spinning Enhanced Visible and InfraRed Imager) data, the results show that our method can produce quantitatively soil moisture content in a regional scale although many problems still have to be solved before it will be used operationally. This study provides an important parameter for hydrology, climate and land surface model, and it also has a certain scientific and practical significance in the research of water cycle, water balance and climate study.

1 INTRODUCTION

Soil moisture is a significant parameter in water balance, as well as in hydrological, climate, ecological and land surface models (Li, et al., 2007; Robock, et al., 2000; Gerten, et al., 2005). Although soil moisture can be measured by some conventional methods, it can be only on behalf of the content in a very small range because soil moisture is influenced by spatial heterogeneity of soil properties, terrain, vegetation, evaporation and other relevant factors. The precision of soil moisture estimation in regional scale has been a focus and difficulty of study. As the development of remote sensing technology, with the advantages of high speed, low cost and a wide range, it is possible to estimate soil moisture in the large area.

The methods for soil moisture estimation using

remote sensing vary with different wave bands. The more common remote sensing methods for estimating soil moisture are use of thermal infrared bands, which is due to the development of land surface temperature inversion algorithms. There are mainly two methods, one is the thermal inertia method and the other is the canopy temperature-vegetation index method. The thermal inertia method shows a high precision in low vegetation cover or bare soil area. While in the high vegetation cover area, the combination of temperature and vegetation index or the temperature difference between canopy and atmosphere is used to estimate soil moisture. Canto-Sepulcre (Sepulcre, et al., 2006) monitored the crop water potential by the difference between air and canopy temperature calculated using the airborne hyper-spectral data. In addition, it is of high precision to estimate soil moisture using microwave remote sensing, which is less affected by

weather. It is one of most common methods in soil moisture estimation (Del, et al., 2003) at present. The methods to estimate soil moisture using microwave remote sensing include active microwave remote sensing, passive microwave remote sensing and combination of active and passive microwave remote sensing. The passive remote sensing method has made great progress. Recently, there are many space-borne microwave radiometers applied to soil moisture research, as well as a serial of typical models and algorithms are set up. Although the development of soil moisture inversion methods using microwave remote sensing is rapid, there are still many restrictions to precision, such as low resolution and frequency, land surface roughness and vegetation cover.

Soil moisture is closely related to some factors, such as land surface temperature, net surface shortwave radiation and vegetation cover. Considering the temporal variation between soil moisture and these factors, it will help to improve the accuracy of soil moisture estimation while introducing these parameters to the soil moisture estimation models or establishing new soil moisture estimation models using them. In recent years, with the development of China's FengYun satellites, Japan's MTSAT satellites and Europe's METEOSAT Second Generation, 48-96 high quality multi-spectral and multi-temporal data can be acquired, and the corresponding products, such as land surface temperature and surface shortwave radiation, can also be found according to relevant organizations or websites. It may be a good way to improve the precision of soil moisture estimation with multi-temporal land surface temperature and net shortwave radiation from geostationary satellite data.

2 DATA SOURCES

Data to drive the CoLM mainly contains solar radiation, solar longwave radiation, precipitation, air temperature at reference height, wind speed, wind direction, atmospheric pressure on surface and specific humidity at reference height. All these data are with a time step of 30 minutes.

Satellite data used in the paper are land surface temperature and down welling surface shortwave radiation of MSG (Meteosat Second Generation). MSG is a new multi-spectral and multi-temporal geostationary satellite developed by the European Space Agency and EUMETSAT (European Meteorological Satellite Organization). Its main load is the SEVIRI (Spinning Enhanced Visible and Infrared Imager), which has 12 spectrum channels. Spectrum characteristics of each channel are showed in Table1. Land surface temperature and down welling surface shortwave radiation are divided into four pieces: Europe, North Africa, South Africa and South America, and they are stored as the HDF5 data format. Particularly, a time

step of 15 and 30 minutes is for land surface temperature and down welling surface shortwave radiation separately. In the paper, our research area is located in the latitude from 43.02E to 59.92E and longitude from 36.27N to 43.95N, which is a rectangle of 100 × 150 pixels in the Europe area.

3 METHODS

3.1 Land surface temperature

The method to retrieve land surface temperature from MSG-SEVIRI data is a universal split-window put forward by Wan and Dozier (Wan, et al., 1996; Sobrino, et al., 2004; Jiang, et al., 2006). In the algorithm, land surface temperature is described as the following formula.

$$T_s = (A + A_1 \frac{1-\varepsilon}{\varepsilon} + A_2 \frac{\Delta\varepsilon}{\varepsilon^2}) \frac{T_{10.8} + T_{12.0}}{2} + (B_1 + B_2 \frac{1-\varepsilon}{\varepsilon} + B_3 \frac{\Delta\varepsilon}{\varepsilon^2}) \frac{T_{10.8} - T_{12.0}}{2} + C \quad (1)$$

Where, $T_{10.8}$ ($\varepsilon_{10.8}$) and $T_{12.0}$ ($\varepsilon_{12.0}$) are the brightness temperatures (emissivities) of two MSG/SEVIRI infrared channels respectively, with the wavelength of 10.8 and 12.0 μm .

$$\varepsilon = 0.5 \varepsilon_{10.8} + \varepsilon_{12.0}, \quad \Delta\varepsilon = \varepsilon_{10.8} - \varepsilon_{12.0} \quad (2)$$

Land surface emissivity is an important parameter in the retrieving of land surface temperature. Estimation of land surface emissivity for thermal infrared bands of SEVIRI relies on the VCM (vegetation coverage method), and the pixel effective emissivity is obtained by combining the area of vegetated and exposed soil. It follows as:

$$\varepsilon_i = \varepsilon_{i,v} FVC + \varepsilon_{i,s} (1 - FVC) \quad (3)$$

Where, $\varepsilon_{i,v}$ and $\varepsilon_{i,s}$ are vegetation and soil - emissivity respectively of channel i, FVC is the fractional vegetation cover.

3.2 Surface shortwave radiation

The down welling surface shortwave radiation flux (DSSF) refers to the radiative energy per time and surface unit in the wavelength interval [0.3 μm , 4.0 μm] arriving at the Earth's surface. The method for DSSF retrieval that is implemented in the LSA SAF system largely follows previous developments achieved at Météo-France in the framework of the OSI SAF. The DSSF is approximated as:

$$S^\downarrow = S_0 v(\tau) \cos \theta_s \tau \quad (4)$$

Where, S_0 is the solar constant, θ_s is the solar zenith angle, and τ is an effective transmittance of the

atmosphere or cloud-atmosphere system. The factor $\nu(t)$ is defined as:

$$\nu(t) = 1 + 0.33 \cos(2\pi / 365) \quad (5)$$

Where, t refers to the of Julian day of the year.

For the effective transmittance, τ , different expressions are used depending on whether a given pixel is marked as clear or cloudy. For the clear sky, τ is described as:

$$\tau = \tau_A + \sum_{n=1}^{\infty} \tau_A (\alpha_S \alpha_A)^n = \frac{\tau_A}{1 - \alpha_S \alpha_A} \quad (6)$$

For the cloudy day, τ is defined as:

$$\tau = \frac{\tau_A \tau_C}{1 - \alpha_S \tau_{bc} \alpha_C} \quad (7)$$

Where, τ is effective transmittance. τ_A represents the transmittance of atmosphere and quantifies the contribution to surface flux by the direct radiation as well as the diffuse radiation after scattering by the atmosphere. τ_C is cloud transmittance. τ_{bc} is atmospheric transmittance between surface and the cloud. α_S is surface albedo. α_A is spherical albedo of the atmosphere. α_C is cloud albedo.

The specification of parameters can be found in the User's Manual (User manual, 2006). According to the validation report (Validation report-DSSF.2008) of DSSF, when considering all data points irrespective of the method applied, the bias values for the monthly statistics are within $\pm 5\%$ in the majority of cases.

3.3 Relationship model for soil moisture estimation

Land surface temperature and net surface radiation flux are very important surface parameters. Soil moisture, land surface temperature and net surface radiation are closely related. In this paper, net surface shortwave radiation is replaced by surface shortwave radiation.

Common land model (CoLM) has become one of the most common land surface models. The model performs a relatively high accuracy in the simulation of snow cover, soil moisture, sensible heat flux, latent heat flux, and so on, driven by VALDAI and ABRACOS data (Fang, et al., 2010). In the paper, the grid size of CoLM is set as the range of the study area.

The paper is focus on the method research, and the CoLM always shows a high accuracy, thus the output data of the CoLM are considered to be the "accurate value". Both the establishment and validation of soil moisture estimation model are based on these data.

As we know, both of land surface temperature

and surface shortwave radiation show a function of time, and they can be described by a sine curve. With the daily evolution of soil moisture, land surface temperature and surface shortwave radiation, a 3D model is established between soil moisture and land surface-surface shortwave radiation shown in Fig.1.

The fitting curved surface can be described as:

$$SM(T_s, S^\downarrow) = -0.0066T_s^2 + 3.8101T_s + 3.5443 \times 10^{-7} S^{\downarrow 2} - 5.0489 \times 10^{-5} S^\downarrow - 544.8359 \quad (8)$$

($R^2 = 0.988$)

Where, $SM(T_s, S^\downarrow)$ refers to soil moisture (Kg/m^2),

T_s is land surface temperature (K) and S^\downarrow is surface shortwave radiation (W/m^2).

A further study shows that a similar relation model always exists between soil moisture and land surface temperature-surface shortwave radiation simulated by CoLM with different spatial resolutions.

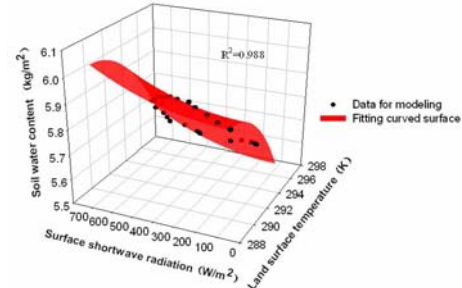


Figure 1. Fitting curved surface between soil moisture and land surface temperature-surface shortwave radiation

4 RESULTS

In the paper, land surface temperature and surface shortwave radiation products of MSG are used to cut out the research area from 10:00 to 12:30 on the 6th, September, 2010. Fig.2 and Fig.3 show the distribution of land surface temperature and surface shortwave radiation separately.

After that, soil moisture can be estimated using the relationship model shown in formula (8) inputting land surface temperature and surface shortwave radiation. The final soil moisture inversed is shown in Fig.4.

Generally, with the raise of land surface temperature, soil moisture decreases in the morning. The results from 10:00 to 12:30 demonstrate the variation. The average soil water content in Fig. 5 is 5.441 Kg/m^2 by statistic analysis and the value simulated is 5.434 Kg/m^2 . The bias between them is 0.007 Kg/m^2 . For other scales, the method can also be used by setting different grid size of CoLM to acquire other time serial soil moisture, land surface temperature and surface shortwave radiation.

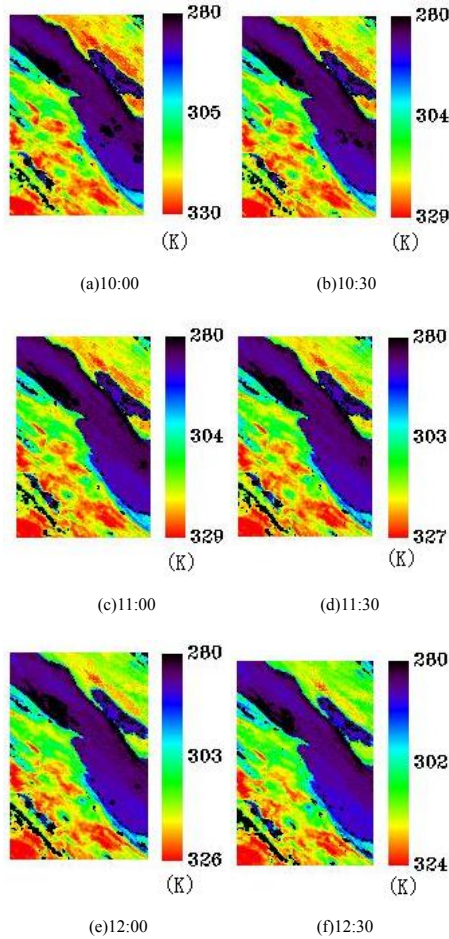


Figure 2. Time serial land surface temperature

5 CONCLUSIONS

First in the paper, CoLM is used to simulate soil moisture, land surface temperature and surface shortwave radiation of the study area. Considering the daily evolution characteristic of land surface temperature and surface shortwave radiation, a relationship model between soil moisture and land surface temperature-surface shortwave radiation is established. Then it is found that a similar relation model always exists, which should be regarded as the objective law of physics.

After that, land surface temperature and surface shortwave radiation products of MSG-SEVIRI are used to estimate soil moisture in regional scale. A statistic result and validation with the data simulated show that the method for soil moisture estimation is feasible and can also be used to estimate surface soil moisture in different scales.

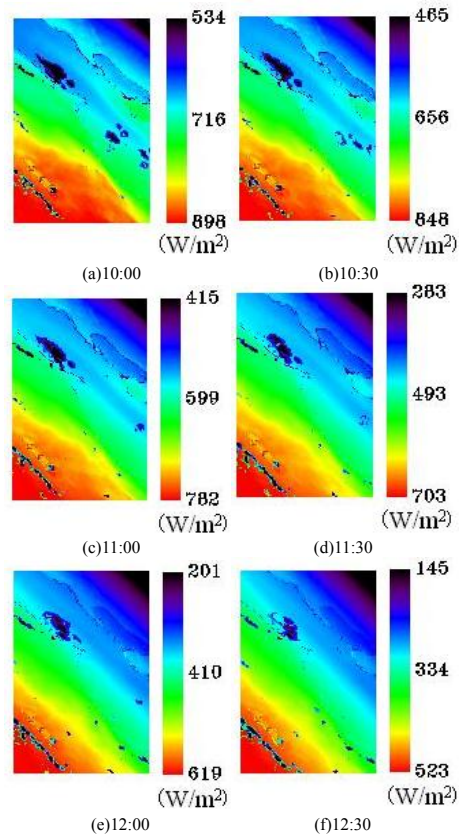


Figure 3. Time serial surface shortwave radiation

6 ACKNOWLEDGEMENTS

This work is supported in part by international cooperation in science and technology projects: Qinghai-Tibet Plateau soil moisture inversion using optical remote sensing and water balance simulation (0819), the CAS Knowledge Innovation Program: soil moisture inversion of watershed scale based on remote sensing (XMX280722), and the specific research of IWHR: soil moisture inversion based on spaceborne active microwave remote sensing.

The authors would like to thank MSG-SEVIRI products from EUMETSAT and CoLM code from Professor Yongjiu Dai.

7 REFERENCES

- Del Frate, F., Ferrazzoli P., and Schiavon G., 2003, Retrieving soil moisture and agricultural variables by microwave radiometry using neural networks [J]. Remote Sensing of Environment, 84, 174–183.

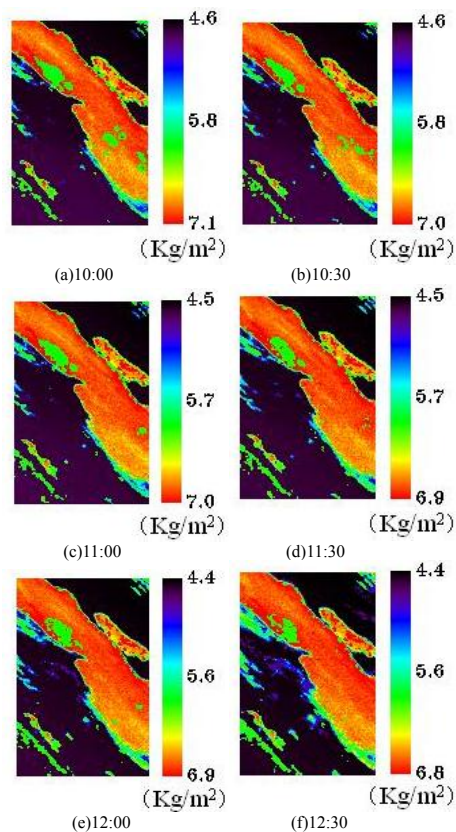


Figure 4. Soil moisture inverted

Down-welling surface short-wave radiation flux. 2006, User Manual.

<https://landsaf.meteo.pt/algorithms.jsp?selta b=1&starttab=0>.

Fang Y.L., Sun S.F., Li Q., et al., 2010, The optimization of parameters of land surface model in arid region and the simulation of land-atmosphere interaction [J] (in China). Chinese Journal of Atmospheric Sciences, 34(2), 290-306.

Jiang G.M., Li Z.L., Françoise N., 2006, Land surface emissivity retrieval from combined mid-infrared and thermal infrared data of MSG-SEVIRI [J]. Remote Sensing of Environment, 105, 326–340.

Gerten D., Hoff H., Bondeau A., et al., 2005, Contemporary "green" water flows: Simulations with a dynamic global vegetation and water balance model [J]. Physics and Chemistry of the Earth, 30, 334–338.

Sepulcre-Cantó G., Zarco-Tejada P.J., 2006, Jiménez-Muñoz J.C., et al.. Detection of water stress in an olive orchard with thermal remote sensing imagery[J]. Agricultural and Forest Meteorology,

136(1-2), 31-44.

Sobrino J.A., Romaguera M., 2004, Land surface temperature retrieval from MSG1-SEVIRI data [J]. Remote Sensing of Environment, 92, 247–254.

Land surface temperature, 2008, User Manual. <https://landsaf.meteo.pt/algorithms.jsp?selta b=0&starttab=0>.

Li H.R., 2007, Study on the Different Land Data Assimilation Algorithms [D] (in China). PhD Thesis Lan Zhou University, 1-2.

Robock A., Vinnikov K. Y., Srinivasan G., et al., 2000, The global soil moisture data bank [J]. Bulletin of the American Meteorological Society, 81(6), 1281-1299.

SAF for Land Surface Analysis, 2008, Validation report-DSSF. <https://landsaf.meteo.pt/algorithms.jsp?selta b=1&starttab=0>.

Wan, Z., Dozier J., 1996, A generalized split-window algorithm for retrieving land surface temperature from space[J]. IEEE Trans. Geosci. Remote Sens, 34, 892-905.

Consistency of vegetation estimates from SEVIRI/Meteosat observations and operational algorithms

A. Verger^{(1,2)*}, F. Baret⁽²⁾, F. J. García-Haro⁽¹⁾, F. Camacho⁽³⁾ and J. Meliá⁽¹⁾

(1) *Departament de Física de la Terra i Termodinàmica, Universitat de València. C/ Dr. Moliner, 50. 46100 Burjassot (València), Spain*

(2) *INRA, Université d'Avignon. UMR114, EMMAH, Domaine Saint-Paul, Site Agroparc, 84914 Avignon, France*

(3) *EOLAB. Parc Científic Universitat de València. C/ Catedràtic José Beltrán, 2. 46980 Paterna (València), Spain*

Email addresses: aleixandre.verger@uv.es; baret@avignon.inra.fr; j.garcia.haro@uv.es; fernando.camacho@eolab.es; joaquin.melia@uv.es

ABSTRACT - This investigation focuses on the influence of retrieval algorithms on satellite estimation of leaf area index (LAI), fraction of vegetation cover (FVC) and fraction of the photosynthetically active radiation (FAPAR). Two operational algorithms were compared: (i) a statistical algorithm based on the use of probabilistic mixture modelling and semi-empirical relationships which is implemented in EUMETSAT/LSA SAF. And (ii) a physical algorithm based on the inversion of a radiative transfer model with neural networks which is used operationally in FP5/CYCLOPES. The two considered algorithms were applied over red, near infrared and middle infrared top of the canopy bidirectional reflectance (BRDF) measurements provided by the Spinning Enhanced Visible and Infrared Imager (SEVIRI) instrument onboard the Meteosat Second Generation satellite. The analysis over Europe for the year 2008 shows an overall good agreement between the LAI, FVC and FAPAR estimates indicating the consistency of the LSA SAF and CYCLOPES operational approaches. However, significant discrepancies were found for LAI estimates of forest biomes. Problematic areas with high BRDF uncertainties were also identified.

1 INTRODUCTION

The monitoring of earth surface dynamic processes requires global observations of the structure and the functioning of vegetation. Leaf area index (LAI), fraction of green vegetation cover (FVC) and fraction of absorbed photosynthetically active radiation (FAPAR), controlling the exchanges of energy, water and carbon dioxide between the land surface and the atmosphere, have been recognized as fundamental terrestrial state variables in the context of the global change sciences. FVC, LAI and FAPAR variables have been derived at both regional and global scales in near real time from several remote sensing sensors in the context of different operational initiatives. The EUMETSAT Satellite Application Facility on Land Surface Analysis (LSA SAF) aims to provide land products, including FVC, LAI and FAPAR, from observations provided by the Spinning Enhanced Visible and Infrared Imager (SEVIRI) radiometer embarked on the Meteosat Second Generation platform. Similar products are also provided by FP5 CYCLOPES, ESA MERIS, ESA GLOBCARBON or NASA MODIS.

Despite the multiplicity of available products, recent validation studies (eg. Garrigues et al., 2008; McCallum et al., 2010) have already outlined that the current biophysical satellite products do not show the expected levels of consistency and agreement. Discrepancies among products are mainly determined by (i) differences and uncertainties in input data, (ii) algorithm influence and (iii) differences in the definition and properties of products.

This research aimed to evaluate the influence of retrieval algorithm on the differences of biophysical products. The consistency among biophysical estimates of two different operational algorithms applied to the same input data was assessed. The physical approach used in CYCLOPES was compared with the statistical approach implemented in the LSA SAF system. Both algorithms were applied to bidirectional reflectance data from SEVIRI/Meteosat over Europe for the year 2008.

2 DATA AND METHODS

2.1 SEVIRI/Meteosat data

SEVIRI/Meteosat encompasses unique spectral characteristics (12 channels) and accuracy, with a spatial resolution (sampling distance) from 3 km at

nadir up to 12 km in northern latitudes and an imaging-repeat cycle of 15 minutes (Schmetz et al., 2002). Inputs for deriving LAI, FVC and FAPAR are atmospherically corrected cloud-screened TOC k_i parameters of a parametric BRDF (Bi-directional Reflectance Distribution Function) model (Roujean et al. 1992) in three SEVIRI channels: red (0.6 μm), NIR (0.8 μm) and SWIR (1.6 μm). BRDF k_i parameters are derived from the albedo algorithm (Geiger et al., 2008) and are available as internal products in the LSA SAF system. In order to reduce the sensitivity of the resulting estimates to reflectance outliers and generate a BRDF product with high temporal resolution on a daily basis, a recursive temporal composition scheme with a characteristic time scale of five days has been implemented in the LSA SAF system. Atmospheric correction, BRDF model inversion and temporal composition algorithms are described in Geiger et al. (2008).

2.2 LSA SAF algorithm

The LSA SAF FVC algorithm relies on the use of nadir-zenith normalized reflectances (k_0 BRDF parameter) in the red, NIR and SWIR SEVIRI spectral channels and an optimized Spectral Mixture Analysis (García-Haro et al., 2008) method in which endmember signatures are no longer treated as constants, but they are represented by multi-modal probability density functions.

The LAI product is obtained directly from the FVC product using the semi-empirical relationship proposed by Roujean and Lacaze (2002). A cover-dependent empirical clumping index for each of the GLC2000 classes has been adopted based on POLDER/ADEOS estimations (Chen et al., 2005). The clumping is assumed for simplicity to be homogeneous within each vegetation cover type.

Daily FAPAR is retrieved using the statistical relationship with the Renormalized Difference Vegetation Index (RDVI) developed by Roujean and Bréon (1995). RDVI is calculated from visible and near infrared spectral reflectance values in an optimal angular geometry in the solar principal plane close to the backscattering direction ($\theta_s=45^\circ$, $\theta_v=60^\circ$ and $\phi=0^\circ$) which allows minimizing the effect of soil reflectance. The FAPAR-RDVI relationship was determined based on simulations of the SAIL (Verhoef, 1984) radiative transfer model.

Since 2005, FVC, LAI and FAPAR are routinely produced in near-real-time by the LSA SAF operational system and are currently available from LSA SAF website (<http://landsaf.meteo.pt>) or via EUMETCast. LSA SAF SEVIRI products have been validated through an intercomparison with other programs (PARASOL, CYCLOPES, TERRA,

ENVISAT) and very limited concomitant ground truth data set (e.g., Camacho et al., 2010; LandSAF, 2008).

2.3 Radiative transfer-neural network (NN) algorithm

The physical method which constitutes the basis of the FP5/CYCLOPES (Baret et al., 2007) and ESA/MERIS (Bacour et al., 2006) operational algorithms was here considered. This approach relies on training neural networks over radiative transfer model simulations comprising top-of-canopy reflectances and the corresponding canopy variables. The widely used PROSAIL radiative transfer model, which is a combination of the SAIL (Verhoef, 1984) canopy reflectance model and the PROSPECT (Jacquemoud and Baret, 1990) leaf optical properties model, was used to generate the training dataset for input variables varying within their definition intervals according to the distributions reported by Baret et al. (2007). The networks were defined and trained independently for each canopy variable. A perceptron of one hidden layer of five tangent sigmoid transfer functions was considered. The input reflectances in each neural network were made of the three SEVIRI spectral channels in the acquisition geometry considered by the LSA SAF algorithm: ($\theta_s=0^\circ$, $\theta_v=0^\circ$, $\phi=0^\circ$) for FVC and LAI, and ($\theta_s=45^\circ$, $\theta_v=60^\circ$, $\phi=0^\circ$) for FAPAR. The k_i BRDF parameters were used to compute the reflectances in each specific geometry.

Several validation studies showed some saturation in the LAI estimated with this neural network approach starting from LAI values around 4 (Bacour et al., 2006; Weiss et al., 2007 and Garrigues et al., 2008). It is also recognized that CYCLOPES FVC product systematically underestimates as compared to ground measurements and similar satellite products, with maximum values around 0.7 (Verger, 2008). To mitigate drawbacks of the considered CYCLOPES based approach, two modifications were here proposed to the Baret et al. (2007) original algorithm. The range of LAI in the training dataset was enlarged from 0 – 6 to 0 – 8. The vCover parameter forcing the pixel to be heterogeneous (fraction vCover of pure vegetation and (1-vCover) of pure bare soil) was not considered in this study. The resulting modified radiative transfer-neural network (NN) algorithm was already validated over an agricultural area using CHRIS/PROBA observations and concurrent ground measurements of LAI, FVC and FAPAR (Verger et al., 2010).

3 RESULTS AND DISCUSSION

3.1 Spatial consistency

The analysis of FVC, FAPAR and LAI maps of NN and LSA SAF (left graphs in Figure 1) reproduce similarly the spatial pattern of vegetation in Europe.

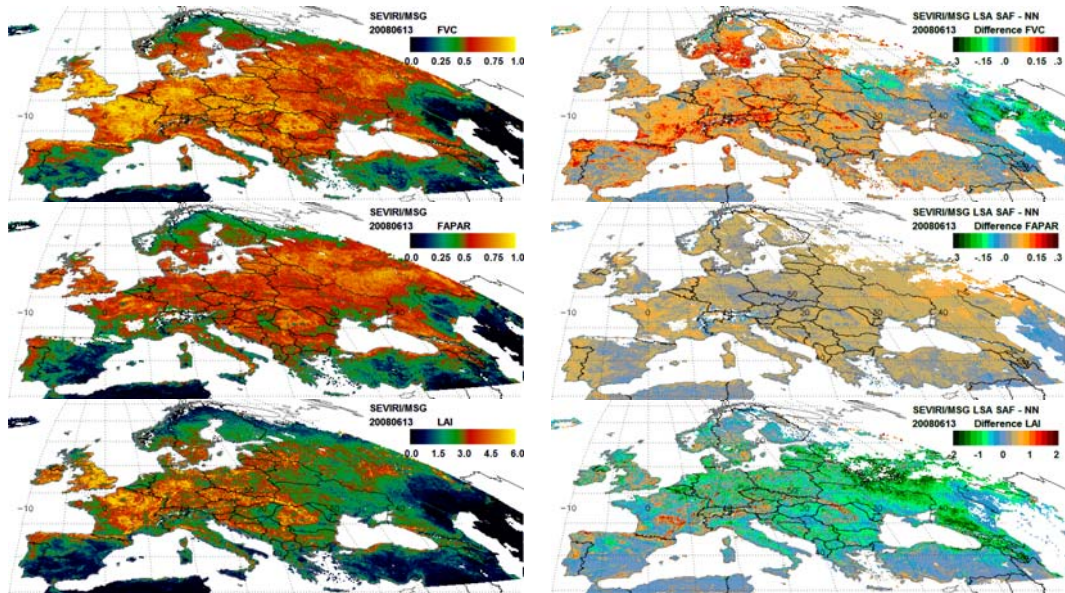


Figure 1. Left: LSA SAF FVC, FAPAR and LAI maps of Europe for the date 2008/06/13. Right: maps of differences of the comparison of LSA SAF and neural network (NN) FVC, FAPAR and LAI estimates.

Absolute differences between estimates of the two algorithms are lower than 0.1 FVC, 0.05 FAPAR and 1 LAI for most part of Europe (right graphs of Figure 1). Major differences (depicted in red and dark green) appear over areas where the quality of SEVIRI BRDF data is affected by high viewing angles, topographic effects and permanent clouds.

Comparison of NN and LSA SAF FVC and FAPAR estimates (Figure 2) show a very good agreement: RMSE lower than 0.09 (0.05) for FVC (FAPAR), correlation coefficient (R^2) higher than 0.95, slopes of the linear regression close to 1 and offsets about 0 which indicate practically no bias. The FAPAR agreement was already expected due to the similarities of NN and LSA SAF FAPAR retrieval algorithms. Both algorithms are based on statistical relationships (a neural network and a vegetation index relationship, respectively) calibrated with SAIL model simulations. More interesting is the case of FVC. The NN FVC estimates show a reliable range of variation (0 - 0.9) and a better agreement with the LSA SAF products than the CYCLOPES products (LandSAF, 2008; Verger, 2008) which justifies a posteriori the proposed modifications in the NN approach.

The largest discrepancies between the two considered algorithms are found for LAI estimates. The comparison per classes (Figure 3) shows that the

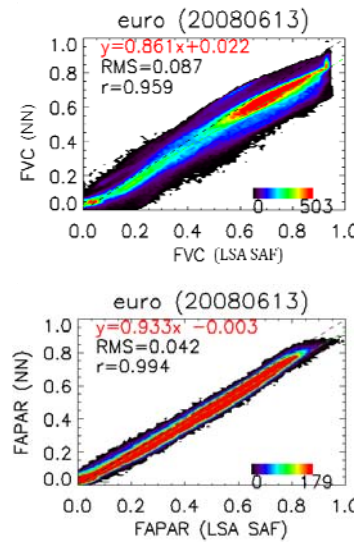


Figure 2. Density scatter plots of neural network (NN) and LSA SAF FVC and FAPAR estimates of Europe for the date 2008/06/13.

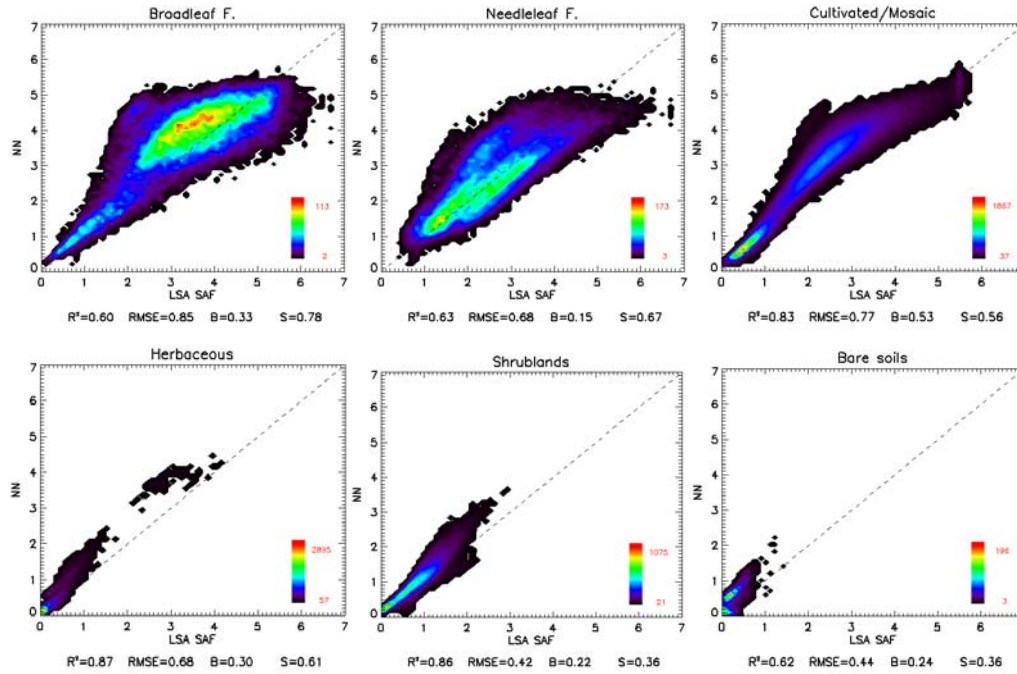


Figure 3. Density scatter plots of the biome class comparison of NN and LSA SAF LAI estimates of Europe for the date 2008/06/13.

differences in terms of RMSE range between 0.4 for shrubs up to 0.9 for broadleaf forest. Important inconsistencies between NN and LSA SAF LAI exist for forest biomes: most of the contribution to the total RMSE comes from the random fluctuations (S) which results in low correlation (R^2 around 0.6). A positive bias is systematically observed which indicates that NN LAI overestimates as compared to LSA SAF LAI. NN and LSA SAF LAI discrepancies can partially be explained due to saturation effects of the reflectance signal with LAI and differences in the clumping representation.

3.1 Temporal consistency

Temporal consistency was evaluated over a selection of control areas (Figure 4): Jarvselja (Estonia) corresponds to a boreal mixed forest including both conifers (different kinds of pines and spruces) and deciduous (birch, aspen, alder) but being birch (*Betula pendula*, *Betula pubescens*) the most widespread species; Puechabon (France) evergreen Mediterranean forest is largely dominated by trees of *Quercus ilex*; Sonian (Belgium) deciduous broadleaf forest consists mainly of European beeches (*Fagus sylvatica*) and oaks (*Quercus*); Bonassai (Sardinia) is a broadleaf cropland area. For the sake of brevity, only LAI is here considered for illustrating temporal consistency of LSA SAF and NN estimates (similar results were observed for FVC and FAPAR).

Temporal profiles show high temporal consistency between NN and LSA SAF LAI estimates that generally reproduce adequately the expected seasonality of vegetation with smooth gradual variations. High temporal continuity is observed due to the 15-minutes imaging-repeat cycle of SEVIRI/Meteosat. Most of artifacts and missing data in temporal profiles appear in wintertime because of larger uncertainties of the reflectance data as a combination of multiple effects, such as higher cloud occurrence, larger shadows and traces of snow cover.

LAI estimates capture reasonably well the beginning of the growing season at the Sonian deciduous forest. Larger differences appear at the end of the growing season when neither NN nor LSA SAF LAI profiles reproduce the expected rapid decrease in vegetation amount.

Some inconsistencies appear in the Jarvselja site during the wintertime when NN delivers unstable results and an unexpected seasonality. This can be explained due to uncertainties in the input data were not considered in the NN algorithm. Note that in this period LSA SAF LAI is unprocessed because a threshold based on the error of k_t BRDF data is used in the LSA SAF algorithm to mask unreliable inputs (e.g. presenting large errors or unidentified residual snow).

At Bonassai agricultural site NN and LSA SAF LAI estimates follow very similar seasonal trajectories

which are mainly controlled by water irrigation management.

LAI estimates reproduce reliable approximately flat profiles over Puechabon site where minimal seasonality is expected since evergreen oaks determine the major contribution to the whole ecosystem function.

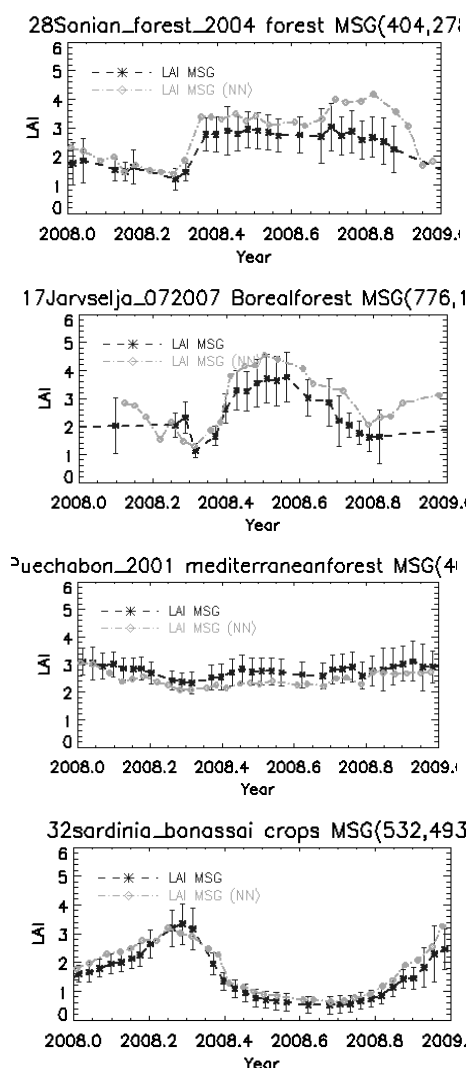


Figure 4. Temporal profiles of NN and LSA SAF LAI estimates over four validation sites.

4 CONCLUSIONS

The comparative analysis of neural networks (NN) and LSA SAF FVC, FAPAR and LAI estimates from SEVIRI/Meteosat observations show a significant

good agreement over Europe for the year 2008. An overall high spatial consistency between estimates is found. Problematic areas were identified at high latitudes due to angular viewing effects, cloud cover and snow traces. High uncertainties were also found at high altitudes due to topographic effects. Differences are lower than 0.1 for FVC, 0.05 for FAPAR and 0.8 for LAI in terms of RMSE. However, high inconsistencies are found for LAI in forest biomes (differences up to 0.9 in terms of RMSE and correlation coefficient around 0.6). Saturation of reflectance with LAI and differences in the clumping representation can partially explain these differences.

NN and LSA SAF estimates show high temporal consistency and generally reproduce the expected phenology of land surfaces. Main artefacts appear in winter time due to uncertainties in the BRDF input data.

Alternative angular configurations will be tested in a forthcoming study to improve the performances of biophysical estimates over problematic areas with high BRDF uncertainties.

5 ACKNOWLEDGMENTS

This study was supported by LSA SAF/EUMETSAT project. Alexandre Verger is funded by a postdoctoral contract within the VALi+d program (FUSAT, GV-20100270).

6 REFERENCES

- Bacour, C., Baret, F., Béal, D., Weiss, M., and Pavageau, K. (2006). Neural network estimation of LAI, FAPAR, fCover and LAIxCab, from top of canopy MERIS reflectance data: principles and validation. *Remote Sensing of Environment*, 105:313–325.
- Baret, F., Hagolle, O., Geiger, B., Bicheron, P., Miras, B., Huc, M., et al. (2007). LAI, FAPAR and fCover CYCLOPES global products derived from VEGETATION. Part 1: Principles of the algorithm. *Remote Sensing of Environment*, 110, 275–286.
- Camacho-de Coca, F., García-Haro, F. J., Verger, A. and Melia, J. (2010). Consistency assesment of FVC and LAI operational products over Africa. *This issue*.
- Chen, J. M., C. H. Menges, S. G. Leblanc, (2005), Global mapping of foliage clumping index using multi-angular satellite data, *Remote Sensing of Environment*, 97: 447 – 457.
- García-Haro, F.J., Camacho, F., and Meliá. (2008). Product user manual (PUM) vegetation parameters (FVC, LAI, FAPAR).

- SAF/LAND/UV/PUM-VEGA/2.1. 53pp. (Document online at <http://landsaf.meteo.pt>)
- Garrigues, S., Lacaze, R., Baret, F., Morisette, J. T., Weiss, M., Nickeson, J. E., Fernandes, R., Plummer, S., Shabanov, N.V., Myneni, R., Knyazikhin, Y., Yang, W. (2008). Validation and intercomparison of global leaf area index products derived from remote sensing data. *Journal of Geophysical Research*, 113, G02028. doi: 10.1029/2007JG000635.
- Geiger, B., Carrer, D., Franchistéguy, L., Roujean, J.L., Meurey, C. (2008). Land surface albedo derived on a daily basis from Meteosat second generation observations. *IEEE Transactions on Geoscience and Remote Sensing*. 46(11):3841-3856.
- Jacquemoud, S., & Baret, F. (1990). PROSPECT: A model of leaf optical properties spectra. *Remote Sensing of Environment*, 34, 75–91.
- LandSAF (2008). Validation Report of vegetation products (FVC, LAI, FAPAR) SAF/LAND/UV/VR VEGA/2.1, 91 pp. (Document online at <http://landsaf.meteo.pt>).
- McCallum, I., Wagner, W., Schmullius, C., Shvidenko, A., Obersteiner, M., Fritz, S., Nilsson, S. (2010). Comparison of four global FAPAR datasets over Northern Eurasia for the year 2000. *Remote Sensing of Environment*, 114(5):941-949.
- Roujean, J. L. and Bréon, F. M. (1995). Estimating PAR absorbed by vegetation from bidirectional reflectance measurements. *Remote Sensing of Environment*, 51: 375-384.
- Roujean, J. L., and Lacaze, R. (2002). Global mapping of vegetation parameters from POLDER multiangular measurements for studies of surface-atmosphere interactions: A pragmatic method and its validation. *Journal of Geophysical Research*, 107D, 10129–10145.
- Roujean, J. L., Leroy, M., and Deschamps, P. Y. (1992). A bidirectional reflectance model of the Earth's surface for the correction of remote sensing data. *Journal of Geophysical Research*, 97(D18), 20455–20468.
- Schmetz, J., Pili, P., Tjemkes, S., Just, D., Kerkmann, J., Rota, S., and Ratier, A. (2002). An introduction to Meteosat Second Generation (MSG), *Bulletin of the American Meteorological Society*, 83 (7) (2002), pp. 977–992.
- Verger, A. (2008). Analysis of operational algorithms for the estimation of vegetation biophysical parameters from satellite data. (In Catalan/English). PhD Dissertation. University of Valencia. 307 pp.
- Verger, A., Baret, F., and Camacho, F. (2010). Optimal modalities for radiative transfer-neural network estimation of canopy biophysical characteristics: Evaluation over an agricultural area with CHRIS/PROBA observations, *Remote Sensing of Environment*, doi: 10.1016/j.rse.2010.09.012
- Verhoef, W. (1984). Light scattering by leaf layers with application to canopy reflectance modeling: The SAIL model. *Remote Sensing of Environment*, 16, 125–141.

Significant improvements in the AATSR land surface temperature algorithm

O. Zeller⁽¹⁾, J. Remedios⁽¹⁾, A. J. Prata⁽²⁾

⁽¹⁾EOS, University of Leicester, University Road, Leicester LE1 7RH, UK; oz5@le.ac.uk

⁽²⁾ Climate and Atmosphere Department, Norwegian Institute for Air Research, Kjeller, Norway
fred.prata@nilu.no

ABSTRACT The operational land surface temperature (LST) algorithm for AATSR data depends on auxiliary data characterizing the land surface and vegetation fraction. In the Leicester version of the algorithm, the data have been replaced by new fields with a much better resolution, much more closely matching that from the AATSR orbit grid. The new auxiliary data are introduced and tested for their suitability for the AATSR LST retrieval. The tests show the comparison between the structures of the maps from AATSR data and from the auxiliary data, and the comparison between the operational and new LST. It is shown that the AATSR geolocation appears to be shifted by 1 pixel forward along-track and 1 pixel to the right across-track with respect to Globcover. Representation of land surface structure in the new LST is shown to be much improved. A correction of the shift leads to further improvements in accordance with expectations.

1 INTRODUCTION

Land surface temperature (LST) derived operationally from Advanced Along-Track Scanning Radiometer (AATSR) satellite data (nadir resolution of 1 km) is based so far on the brightness temperature from two channels and on pre-derived coefficients with dependences on auxiliary data such as the land surface type (biome) and the fractional vegetation cover, both with a resolution of 0.5° (~55 km) (Dorman, et al., 1989). The somewhat coarse horizontal resolution of the auxiliary data results in discontinuities (jumps) of the LST product at the edge of the 0.5° bins where land surface type, fractional vegetation or both change significantly. In addition, the biome maps and vegetation covers are based on data for the 1980s rather than 2000s; the operational auxiliary data utilise the Dorman and Sellers (DS) biome maps, based on data from the early to mid-1980s, and the fractional vegetation that is derived for 1987 and 1988. Therefore, investigations were made with new auxiliary data at 1 km resolution or less replacing the previous data. Several classifications of landcover types (biomes) and fractional vegetation are described in (Veal, 2008). Here, land cover biome data from Globcover and vegetation fraction from CYCLOPES (Carbon cYcle and Change in Land Observational Products from an Ensemble of Satellites) have been selected because of their global coverage and high resolutions of 1/360° (~300 m) and 1/112° (~1 km), respectively.

The LST retrieval is based on a split window algorithm for two nadir channels only analogous to N2 SST retrieval (Prata, 2002):

$$LST = a_{f,i,pw} + b_{f,i}(T_{11} - T_{12})^{p(\theta)} + (b_{f,i} + c_{f,i})T_{12} \quad (1)$$

T_{11} and T_{12} are the AATSR nadir brightness temperatures (BT) at 11 and 12 micron channel; $a_{f,i,pw}$, $b_{f,i}$, $c_{f,i}$ are retrieval coefficients depending on: surface type (i), fractional vegetation cover (f), precipitable water (pw), and time of day (currently for lakes only); and $p(\theta)$ is a function depending on the satellite zenith view pointing angle.

Section 0 of this article describes the new AATSR auxiliary data. In Section 0, the geolocation accuracy of the Globcover biome and the AATSR BT is examined. Finally, an analysis of the LST over UK is reported in Section 0.

2 NEW AUXILIARY DATA FOR THE AATSR LST ALGORITHM

As mentioned, new auxiliary data with clearly higher resolution than those of the operational LST retrieval have been chosen. This section concentrates on the auxiliary data description of the land surface type data from Globcover and of the fractional vegetation cover data from CYCLOPES.

2.1 A Globcover-derived new biome map for AATSR

The Globcover (GC) product has been derived using measurements made by MERIS (Medium Resolution Imaging Spectrometer). The result is based on surface

reflectance resulting in a land cover map with a pixel resolution of $1/360^\circ$ (~ 300 m at the equator). Details about the Globcover product are described in (Bicheron, et al., 2008). However, the definition of the surface type for Antarctica is completely ignored as only the land surface between 65°S and 85°N has been mapped. Because of this and in order to fit the GC data better for that for AATSR measurements, the following changes from the original GC product have been performed (Zeller, 2010, submitted):

- Reduction of the grid resolution from $1/360^\circ$ to $1/120^\circ$
- GC biome type 220 (GC220, permanent snow and ice) added over land south of 65°S using the AATSR land sea mask
- Distinction between inland water such as rivers and lakes as well as near coastal water (both GC210) and ocean water (set to GC0) in order to obtain LST retrievals only for the GC210 water body type

The global data set of Globcover covers the time range between December 2004 and June 2006 (Arino, et al., 2007). For the LST algorithm, the mean biome map for this time range has been chosen. The data set consists of 22 land cover types for the global mode.

The left panel of figure 1 presents the biome map for Australia from Dorman and Sellers (DS) used for the operational LST algorithm and the right panel that from Globcover for the new LST algorithm. Apart from the substantially higher resolution of the Globcover data, there are considerable differences of the land cover between the two biomes. For example, the north of Australia is dominated by trees with groundcover in the D&S biome map (DS6), but by shrubs in the Globcover map (GC130). There are also differences of the desert-like area situations (DS11 and GC200) within the outback. But the maps show also common features like evergreen broadleaved forest at the north east coast (DS1, GC40) and the cropland areas in the south of Australia (DS12,

GC14). Different calculations of the biome, but also land surface changes like desertification within the last 20 years could be the reason for the differences as the DS biome is based on data of the early 1980s and the Globcover data from approximately 2005.

2.2 Fractional vegetation cover

The CYCLOPES project has provided a global database of the fractional vegetation (FV) cover and other vegetation indices for the time range 1998 – 2007. This product database relies upon the normalized nadir reflectance in the red, NIR and SWIR wavebands. The spatial grid resolution is at $1/112^\circ$ (≈ 1 km), and the temporal resolution at 10 days resulting into 36 global maps per year. A detailed description of the algorithms of this database is described in (Baret, et al., 2007) and of the validation in (Filloi, et al., 2006.).

Comparisons between the FV cover data (SiB/ISLSCP – Simple Biosphere Model / International Satellite Land-Surface Climatology Project) used for the operational LST retrieval and those from CYCLOPES reveal large differences in magnitude a in some regions. The following reasons could explain the differences:

- Variations of the fractional vegetation due to climatic or anthropogenic changes (annual rainfall rate, de- and reforestation, urbanization etc.), as the SiB/ISLSCP data are based on observation data from the early 1980, can explain these differences in parts.
- Different methods of derivation between operational and new FV data
- Strong orientation of the SiB/ISLSCP FV to the DS biome map causing unrealistic FV gradients
- Inadequate SiB/ISLSCP FV data coverage at all coastal regions giving rise to incorrect FV values, especially for regions with high

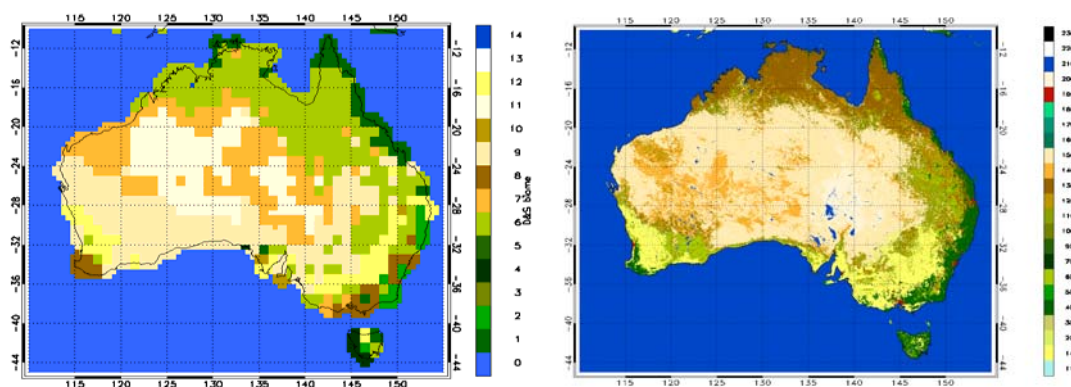


Figure 1: left: Global auxiliary biome map for the operational AATSR LST retrieval from based on (Dorman, et al., 1989); right: Globcover biome map for Australia as the new biome map for the LST retrieval.

vegetation density, and therefore to biases in the LST retrieval up to several Kelvin (Zeller, 2010, submitted).

The new FV data are a clear improvement of the FV data coverage. However, some data gaps especially over the inner tropical convergence zone may be due to persistent cloud coverage of the concerning region within the associated 10-day-time range.

A comparison between the CYCLOPES FV and the AATSR BT map show a good agreement between both structures. This agreement is confirmed by a similar agreement between the structures of CYCLOPES FV and the Globcover biome maps. In contrast to the FV and biome data for the operational LST algorithm, the new auxiliary data are independent of each other.

3 GEOLOCATION ACCURACY BETWEEN GLOBCOVER AND AATSR BT MAP

The Globcover biome has been tested for its suitability. A comparison with the AATSR brightness temperature reveals a good agreement with the structures of BT and the Globcover biome maps. However, a more precise investigation of the structures of the AATSR BT and the biome map of Globcover reveals a shift of mostly ~ 1 km between the two systems. For such a test, a small area with a size of ca. $0.1^\circ \times 0.1^\circ$ is chosen containing a clear BT contrast. Such a contrast occurs preferably on lakes with the surrounding land. A further requirement is a lake with no significant change of the water surface area which occurs at lakes with steep shores or with artificial water level regulation.

As an example, the AATSR BT of Lake Sempachersee in Switzerland during day-time is shown in a range between $47.10 - 47.20^\circ \text{N}$ and $8.10 - 8.24^\circ \text{E}$ (figure 2, left panel). The right panel of figure 2 presents the associated Globcover map with

GC210 (blue) for the water surface of the lake. The BT within the lake is clearly lower than the surrounding area, but the panels also show, that the lake in the Globcover is situated slightly northeast of the BT response. Related to the AATSR orbit grid coordinates, the BT structure is shifted 1 pixel (≈ 1 km) forward and 1 pixel to the right in swath direction.

The geolocation accuracy has been checked for other areas distributed all over the Earth as well as for day and night conditions. Comprehensive investigations show that the shifts are in most cases ca. 1 pixel forward and 1 pixel to the right as the result for Lake Sempachersee shows (Zeller O., 2010). This indicates generally exact geolocation accuracy of both instruments, but with a slight error of the AATSR view direction resulting into the mentioned shift. Slight shift fluctuations may be due to inaccuracies in the land surface mapping resulting in the resolution of 1 km, but also to changes in the land surface like lake area changes.

A further investigation contains the temporal characteristics of the shift. A record of 37 AATSR BT maps between 2002 and 2010 as well as 28 ATSR2 between 1995 and 2002 has been compared with the associated Globcover map. Table 1 shows an extract of this record for the years 1999 – 2005.

The shifts of the AATSR BT maps show a reasonable regularity with values similar or equal to the above mentioned. There is also no temporal trend of the shift strength. The regularity of the shifts related to the AATSR-orbit grid suggests a reanalysis of the AATSR geolocation. A general correction of the shift might not remove all shifts, but it should contribute to a clear improvement of the congruency between the structures of the Globcover and the AATSR BT maps. In Section 4, an example of improvement of the LST

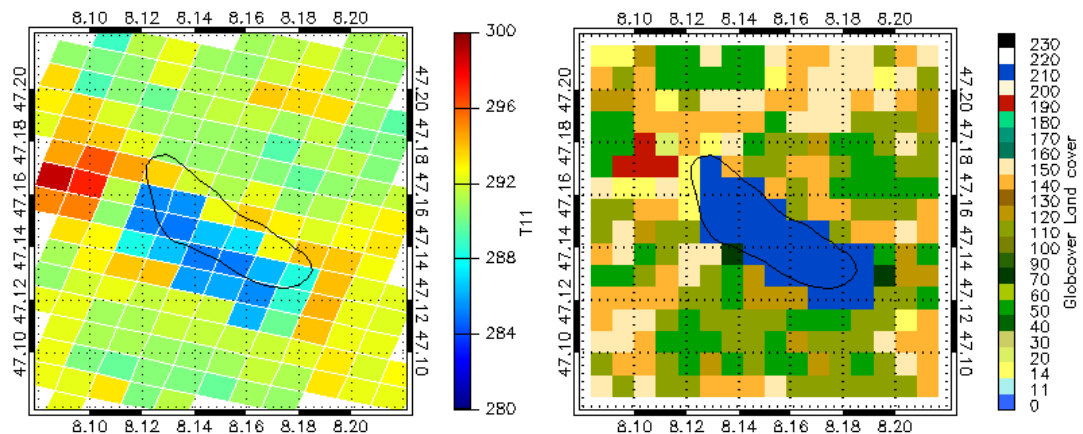


Figure 2: left: Pixels of the day-time AATSR brightness temperature at $11 \mu\text{m}$ for Lake Sempachersee from 5th May 2008; black solid line show the coast line from NGDC NOAA. Right: associated Globcover map.

Table 1: Shift of the AATSR and **ATSR2** BT response to the situation of Lake Sempachersee from 1998 – 2006; F = forward and R = right to the swath direction.

Date	Sat No	Orbit No	Shift ATSR2 / AATSR	
			along	across
8 th Sep 2005	18426	336	1F	1R
20 th Jun 2005	17281	193	1F	1R
2 nd Apr 2005	16150	064	1F	0-1R
7 th Sep 2004	13187	107	1F	1R
7 th Jun 2004	11870	293	1F	1-2R
1 st Apr 2004	10912	337	0F	2R
26 th Jun 2003	06903	336	1F	1R
1 st Apr 2003	05672	107	0-1F	1R
18th Aug 2002	38309	379	1-2F	1-2R
18 th Aug 2002	02437	379	1F	1R
15th Aug 2002	38266	336	1-2F	1-2R
15 th Aug 2002	02394	336	1F	0-1R
12th Jun 2002	37350	422	1F	1-2R
3rd Apr 2002	36348	422	1F	1R
5th Jun 2001	32025	107	2F	1R
20th Jun 2000	27015	107	5F	0
8th Apr 2000	25970	064	1-2F	1R
11th Sep 1999	22964	064	1F	1R
23rd Jun 1999	21819	422	4F	0
3rd May 1999	21089	193	0	1R
1st Apr 1999	20631	236	0-1F	1R

due to shift correction is shown.

The shifts of the ATSR2 BT structures to those from Globcover are less regular. The shifts are mostly low with 0-1 pixels to forward and 0-1 pixels to the right of the swath direction until 1999. In 1999 and 2000, two cases of very large shifts about 4-5 pixels in forward directions occurred which could be due to a timing error. Especially since 2001 the shifts became larger due to a failure of one gyro of the ERS satellite. In 2002, there are two cases of ATSR2 and AATSR flights over the lake under clear sky conditions. The BT shift of ATSR2 is slightly larger with values of 1-2 pixels forward and to the right than that from AATSR. Based on the results, a simple shift geolocation correction is not suggested for the moment for ATSR2 data due to strong irregularities.

4 LST MAP OVER UK

In this section, the day-time LST over UK is presented for 15th July 2006 as an example for a hot

summer day. To analyze the result, the mean LST for each in UK occurring Globcover biome is shown and its difference after shift correction.

Figure 3 (a) shows the map of the new AATSR LST product over UK after shift correction of 1 pixels to the left and 1 pixel back, and (b) the associated Globcover biome map. The red areas (GC190) of panel (b) represent the urban built areas, the yellow regions (GC14) the croplands, the orange ones (GC140) the grasslands, and the green areas different types of forest (e.g. GC70) or mixed vegetation containing forest and grassland (GC110). The urban areas are mostly at the same place as the LST maxima in panel (a). This is in agreement with the expectations of urban heat islands especially at hot summer days.

As a further investigation, means of the LST for each Globcover biome have been calculated. Thereby, pixels of LST values of less than 290 K have been eliminated from the mean calculation in order to avoid cloud contamination occurring over most parts of Scotland. Additionally, only LST means calculated from at least 2000 valid pixels are accepted in order to have a reliable record. Panel (c) from figure 3 shows the LST means in dependence on the Globcover biomes. As expected, the mean LST of the urban regions (GC190) has the highest value followed by the croplands. The also woodless grassland (GC140) and sparsely vegetated region (GC150) have slightly lower LST than the croplands as the crops are mainly in the low East of England whereas the natural woodless areas occur in parts in the mountainous regions with lower temperatures. The LST of the woody regions is clearly lower in good agreement with expectations.

Panel (d) of figure 3 shows the LST difference for each Globcover biome between the shift corrected and the uncorrected LST. By far the strongest LST difference has been obtained for GC210 (inland and near coastal water) with a value of approximately -3 K. The shift correction contributes strongly to a better spatial coincidence between the shorelines and the BT response. Thus, the water bodies are clearly less contaminated by the much higher land BT values resulting into a considerably lower mean LST. The other differences are much smaller with values below 1 K. Nevertheless, the difference for urban areas is slightly positive with 0.6 K indicating a better congruency of the urban areas (GC190) and the heat island signed by the BT maxima.

Generally the new LST from the Leicester algorithm represents well the land structure over UK, especially the urban areas. A correction of the geolocation shift contributes to further improvement.

5 CONCLUSION

New auxiliary data for the AATSR LST algorithm

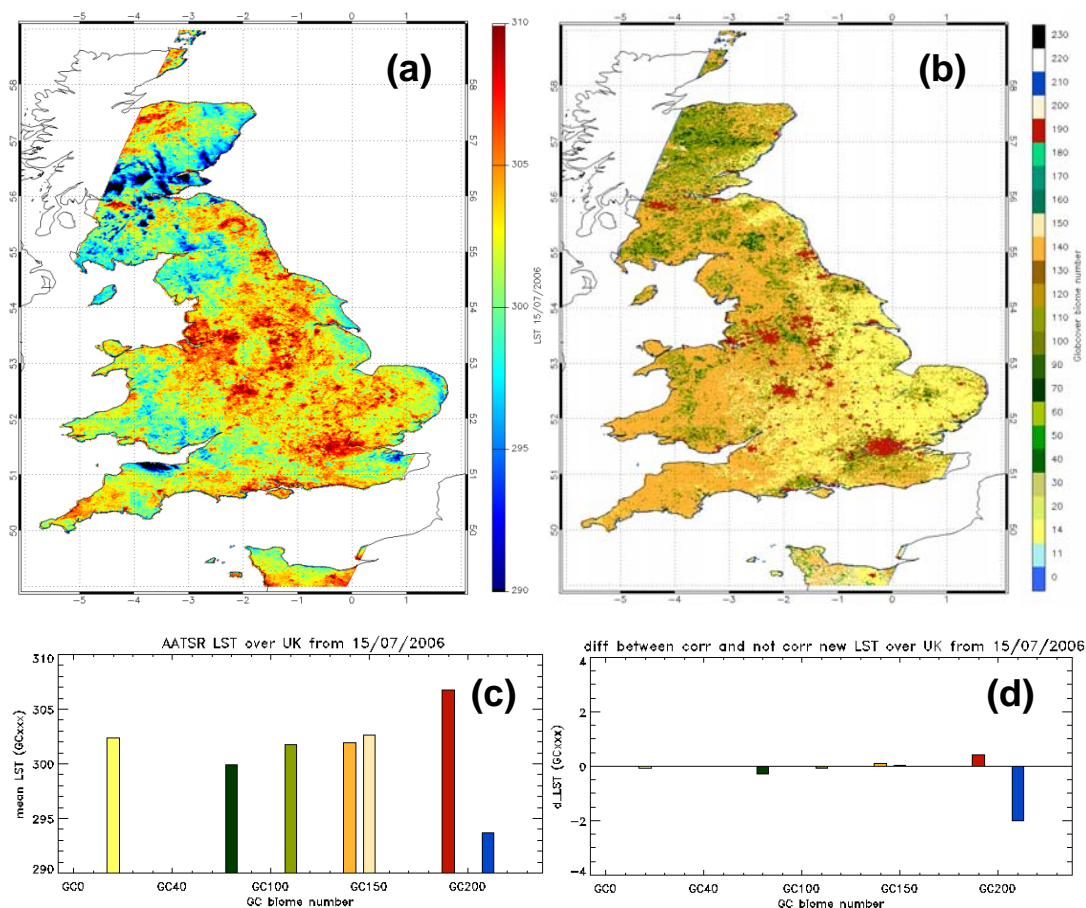


Figure 3: (a) New AATSR LST over UK from 15th July after shift correction of the Globcover biome map of 1 AATSR pixel forward and 1 pixel right to the swath direction; (b) associated GC biome map after mentioned shift correction; (c) Mean LST for UK in dependence on the GC biome type, in order to avoid cloud contamination, only LST ≥ 290 K have been taken account for the mean calculation; (d) Difference of the mean LST with and without shift correction.

with a resolution similar to that from AATSR orbit grid (~ 1 km) have been tested for their suitability. The structures of both fractional vegetation and land surface type maps are in good agreement with maps of the AATSR brightness temperature, but there is also a slight shift (1 pixel forward along-track and 1 pixel to the right across-track). Comprehensive investigations show that the shift in the geolocation between the AATSR BT and the Globcover structure is regular enabling a general correction whereas the shifts of the ATSR2 BT have some irregularities. A map of the new LST product over UK during a summer day represents the urban heat islands very well. The mean LST for each Globcover biome is in good agreement with the expectations whereas a correction of the shift geolocation gives rise to further improvement of the LST.

Based on the results, some important points of future work are listed:

- New biome map was required and has been implemented.
- A land surface emissivity map is currently being developed (similar work on-going at Met Office).
- We will generate new AATSR coefficients and conduct further LST validation on different sites
- We will link SEVIRI data to AATSR data in order to achieve consistent data sets.

6 REFERENCES

Arino O. [et al.] GlobCover – A global land cover service with MERIS [Conference]// ESA Envisat Symposium. - Montreux (Switzerland) : [s.n.], 2007. - http://dup.esrin.esa.it/files/project/131-176-131-25_2007510152516.pdf.

- Baret F. [et al.] LAI, FAPAR, and FCover CYCLOPES global products derived from Vegetation. Part 1: principles of the algorithm [Journal] // Remote Sensing of Environment. - 2007. - Vol. 110. - pp. 305-316.
- Bicheron P. [et al.] Globcover - Products Description and Validation Report [Online]. - 2008. - http://postel.mediasfrance.org/IMG/pdf/GLOBCOVER_Products_Description_Validation_Report_I2.1.pdf.
- Dorman J. L. and Sellers P. J. A global climatology of albedo, roughness length, and stomatal resistance for atmospheric general circulation models as represented by the simple biosphere model (SiB) [Journal] // J. Appl. Meteorol.. - 1989. - Vol. 28. - pp. 833-855.
- Fillol E. [et al.] Cover fraction estimation from high resolution SPOT HRV&HRG and medium resolution SPOT-VEGETATION sensors. Validation and comparison over South-West France. [Conference] // Proceedings of Second Recent Advances in Quantitative Remote Sensing Symposium. - 2006 - pp. 659-663.
- Noyes E. J. Technical Assistance for the validation of AATSR land surface temperature products [Report] / University of Leicester contractual report to ESA. - February 2006. - contract number 19054/05/NL/FF.
- Prata A. J. Land Surface Temperature Measurement from Space: AATSR Algorithm Theoretical Basis Document [Report]. - [s.l.] : CSIRO report, 2002.
- Veal K. L. Preparation for the generation of new biome classification and fractional vegetation auxiliary data sets [Report]. - [s.l.] : Contract Extension Task 2 Report, February 2008, 2008. - ESA Contract Number: 19054/05/NL/FF.
- Zeller O. AATSR Land Surface Temperature, Phase 1 Summary Report [Report]. - 2010, submitted. - ESA Contract: ESRIN/21915/08/I-OL.
- Zeller O. J. Remedios, E. Comyn-Platt and A. Prata Significant improvements in the AATSR land surface temperature algorithm [Conference] // ESA living planet symposium. - Bergen, Norway : [s.n.], 2010.

Estimation of surface soil moisture from combined solar shortwave radiation and surface temperature

Xiaoyu Zhang¹, Jiao Wang¹ and Zhao-Liang Li^{2,3}

1. School of Environment and Resources, Shanxi University, Taiyuan, Shanxi, China

2. LREIS, Institute of Geographical Sciences and Natural Resources Research, China

3. LSIT, UdS, CNRS; Bld Sebastien Brant, BP10413, 67412 Illkirch, France

E-mail address: zhang_xyhz@sxu.edu.cn

ABSTRACT With the launch of more and more high temporal resolution of geostationary metrological satellites such as MSG, it is urgent to estimate surface soil moisture from these data. In order to meet this demand, this study aims to estimate surface soil moisture from combined diurnal evolution cycle of both shortwave radiation and surface temperature. On the basis of the energy balance and some plausible assumptions, the linear relationship between the temporal variation of shortwave radiation and that of surface temperature is derived by the linearization of surface temperature with a Taylor series. On the basis of this linear relationship, a model is developed to estimate surface soil moisture from combined solar shortwave radiation and surface temperature. The results show that: (1) the approximate linear relationship between shortwave radiation and surface temperature exists from one hour after sunrise to the noon and from the time at which the surface temperature reaches its maximum to time of sunset; (2) the fitted parameters (slope and offset) display some relations with surface soil moisture; (3) the time range from one hours after sunrise to the noon is more appropriated to obtain soil moisture than that from the time at which the surface temperature reaches its maximum to time of sunset. In the end, MSG/SEVIRI data are used to map regional soil moisture and preliminary results are analyzed.

1 INTRODUCTION

Surface soil moisture (SSM) is an important variable in describing water and energy exchanges at the land surface/atmosphere interface. SSM is also the basic condition to the growth of crops. At the same time, it is a vital state variable in hydrology and climate land models.

The retrieval of SSM from satellite data is a challenging problem due to the confounding influences of kinds of variables on the satellite data (Wagner et al., 2007). Quantitative remote sensing is the process of inferring surface parameters by measuring of the upwelling electromagnetic radiation from the land surface. Estimating SSM with remote sensing technology makes great progresses thanks to more and more sensors development. Determination of SSM from satellite data mainly lies on four aspects. First, SSM can be derived using visible and near-infra spectrum.. Reginato et al. (1977) suggested to retrieve SSM using near-infra reflectance. Whiting et al., (2004) proposed to estimate SSM from soil reflectance curve using a fitted Gaussian function. Second, rapid progress in the use of thermal infrared techniques for SSM retrieval have been made since

1974. Schmer and Werner (1974) established a positive correlation between SSM and surface radiation temperatures with field test data. Idso et al (1975) estimated soil moisture using the diurnal changes of surface temperature. Pratt and Ellyett (1979) studied the method of deriving SSM using thermal inertia model. Cai et al. (2007) calculated the thermal inertia using the difference between daily maximum and minimum surface temperatures and estimated SSM. Third, many approaches have been developed to retrieve SSM from microwave radiometric measurements (Schmugge, and Jacson, 1994). Last, total moisture stored in the root zone can be estimated by assimilating time series of surface soil moisture data in Soil - Vegetation - Atmosphere Transfers models (Demarty et al., 2005).

With the launch of more and more fine temporal resolution of geostationary metrological satellites such as MSG, this paper aims to propose a method to estimate SSM from combined solar shortwave radiation and surface temperature. First, On the basis of the energy balance and some plausible assumptions, the linear relationship between the temporal variation of shortwave radiation and that of surface temperature is derived by the linearization of surface temperature

with a Taylor series; Then, these assumptions and the linear relationship are examined using simulated data from Alex Model (Norman et al., 1997) and field measurement data; Third, the relationship between slope of linear equation and SSM is studied; Finally, the method is applied to MSG data to map regional SSM.

2 METHOD

In the absence of horizontal advection, the surface energy balance can be mathematically expressed to:

$$R_n - H - LE - G = 0 \quad (1)$$

where: R_n is the net radiation, H is sensible heat flux, LE is latent heat flux, G is soil heat flux(G) which is the heat energy used for warming or cooling substrate soil volume.

Generally, regional-scale G can be described as

$$G = C_G R_n \quad (2)$$

where C_G is constant.

Formula (1) can also be rewritten as:

$$(1 - C_g)(S \downarrow - S \uparrow + L \downarrow - L \uparrow) - H - LE = 0 \quad (3)$$

where $S \downarrow$ is the solar global radiation, $S \uparrow$ is the reflected solar radiation, $L \uparrow$ is surface upwelling longwave radiation, $L \downarrow$ is downward atmospheric longwave radiation.

Taking into account

$$\begin{aligned} S \downarrow - S \uparrow &= (1 - A)S \downarrow \\ L \uparrow &= \varepsilon \sigma T^4 + (1 - \varepsilon)L \downarrow \end{aligned} \quad (4)$$

and assuming that

$$H + LE = c \times S \downarrow + d \quad (5)$$

where A is surface albedo, c and d are constants, ε is surface emissivity, T is surface temperature, by combining equations (3)-(5), one can get:

$$T = \left(\frac{L \downarrow}{C_G} + \frac{d}{\varepsilon \sigma (1 - C_G)} + \frac{1 - A + c}{\varepsilon \sigma (1 - C_G)} S \downarrow \right)^{\frac{1}{4}}$$

Linearizing surface temperature T with a Taylor series around $S \downarrow = 0$ yields:

$$T(S \downarrow) = T(0) + \frac{dT(0)}{dS \downarrow} (S \downarrow - 0) = T(0) + \frac{dT(0)}{dS \downarrow} S \downarrow \quad (6)$$

with

$$\begin{aligned} T(0) &= \left(\frac{L \downarrow}{C_G} + \frac{d}{(1 - C_G) \varepsilon \sigma} \right)^{\frac{1}{4}} \\ \frac{dT(0)}{dS \downarrow} &= \frac{1}{4} \left(\frac{L \downarrow}{C_G} + \frac{d}{(1 - C_G) \varepsilon \sigma} \right)^{-\frac{3}{4}} \left(\frac{1 - A + c}{\varepsilon \sigma (1 - C_G)} \right) \end{aligned} \quad (7)$$

therefore

$$T(S \downarrow) = \text{offset} + \text{slope} \times S \downarrow \quad (8)$$

with

$$\text{offset} = T(0)$$

$$\text{slope} = \frac{dT(0)}{dS \downarrow}$$

It should be noted that $L \downarrow$ is generally not constant and varies with air temperature and air humidity. Because the second term in the first parentheses in equation (7) is much larger than the first term, slope and offset can be thought as constant, and T is linearly proportional to $S \downarrow$.

As A , ε , c and d in equation (7) are all the function of SSM and soil texture, slope and offset are therefore both related to these two factors and can be used to infer SSM. Moreover, since linearizing surface temperature T is around $S \downarrow = 0$, equations (6) and (8) are only valid around sunrise or sunset. Considering severe atmospheric influence around sunrise, the time range from one hour after sunrise to one hour before the noon or from the time at which surface temperature reaches its maximum to sunset are used to fit equation (8) and subsequently to estimate SSM.

3 RESULTS AND DISCUSSIONS

3.1 Data

Two kinds of data were used to develop the SSM retrieval method. One is data simulated by ALEXI model which is originally called the Two-Source Time-Integrated Model (TSTIM), this model was an extension of the earlier Two-Source Model (TSM) developed by Norman et al. (1995). Another is data measured in-situ at HAPEX-Sahel experiment in Niger from August until October, 1992.

A time series of surface temperature and solar short-wave radiation data are simulated under a wide variety of land surface and atmospheric conditions using ALEX model. Atmospheric forcing

data come from field measurements at YuCheng experiment station, ShanDong Province, in China.

In this study, volumetric soil moisture varies from 0% to 40% at 5% interval. The soil texture parameters include the volume fraction of solid material varying from 10% to 90% at 10% interval, the volumetric fraction of sand and the volumetric fraction of clay ranging from 0% to 100% at 10% interval, according to the international soil texture classification system.

HAPEX-Sahel (Hydrological and Atmospheric Pilot Experiment in the Sahel) is an international land-surface-atmosphere observation program that was undertaken in western Niger, in the west-African Sahel region.. We select the site located at latitude 13.530N, longitude 2.500E because soil water was measured in the site. The land use type in this site is savanna consisting of scattered shrubs with an undergrowth of several species of grasses and herbs.

3.2 Results and Discussions

Considering the influence of atmosphere, the data from one hour after sunrise to 11h (local solar time) in the morning and from the time at which surface temperature reaches its maximum to sunset in the afternoon are used to validate the assumptions made previously.

Figure 1 compares the surface temperature simulated by ALEX model with that estimated using equation (6). The result shows that the estimated surface temperature is closer to the simulated temperature, the scatter plot is near the 1:1 line and RMSE is low than 1K. This demonstrates that the linear relationship between surface temperatures and shortwave radiation described by equations (6) and (8) is valid and the sum of sensible and latent heat fluxes could be approximated by a linear function of the solar global radiation. The linear relationship from the morning is better than that from the afternoon.

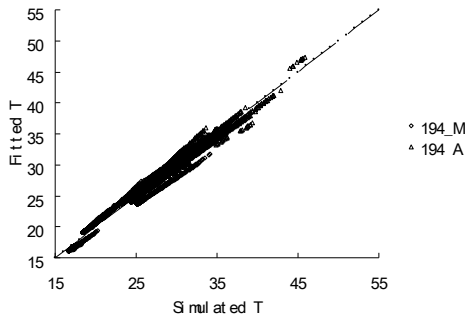


Figure 1: Comparison of model fitted surface temperature with simulated temperature (M: morning; A: afternoon)

The relations between slope and offset, between slope and SSM are examined and depicted in figure 2. As shown from this figure, these relations depend on the different surface and atmospheric conditions (1-4 denotes different soil texture) and can be expressed as a logarithmic form:

$$SSM = a \ln(\text{Slope} * 1000) + b \quad (9)$$

$$\text{offset} = a_{s_o} \ln(\text{slope} \times 1000) + b_{s_o} \quad (10)$$

where a , b , a_{s_o} , b_{s_o} are constants, and they are function of soil texture for a given atmospheric condition. Moreover, as shown in figures 3 and 4, the coefficients a , b , a_{s_o} , b_{s_o} are linearly related each other as .

$$b_{s_o} = -2.9892 * a_{s_o} + 17.838 \quad (11)$$

$$b = -3.01 * a + 0.725 \quad (12)$$

$$a = -0.3718 * a_{s_o} - 7.0813 \quad (13)$$

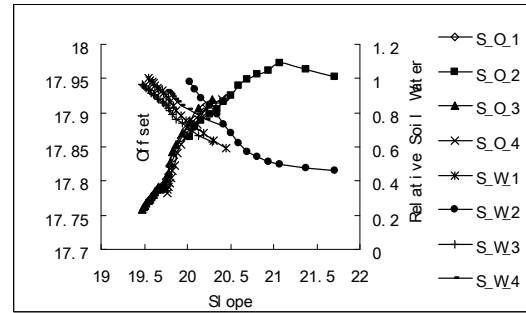


Figure 2: Relationships between slope in equation (8) and soil moisture (S_W) , and between slope and offset(S_O)

According to equation (8), the coefficients slope and offset can be obtained by fitting global radiation and surface temperature measured by satellite, SSM can therefore be estimated using equations (9), (10), (12) and (13).

Figure 5 displays the comparison of SSM estimated using equations (8)-(13) with the actual SSM. The results show that the estimated SSM is closer to the actual value and the result from the morning shows better than that from the afternoon.

Similarly, field measurement data (Hapex-Sahel) are used to validate the proposed method. From figure 6, we also find the relation between a_{s_o} and b_{s_o} can be depicted as linear form, equations (9-13) are therefore used to

calculate SSM, the results are showed in figure 7. From the figure, a similar trend between measured SSM and estimated SSM can be found, the difference of absolute value is more obvious, this may due to the fact that the coefficient between a_{s_o} and b_{s_o} from field measured data are different from that from simulated data. This needs a further study.

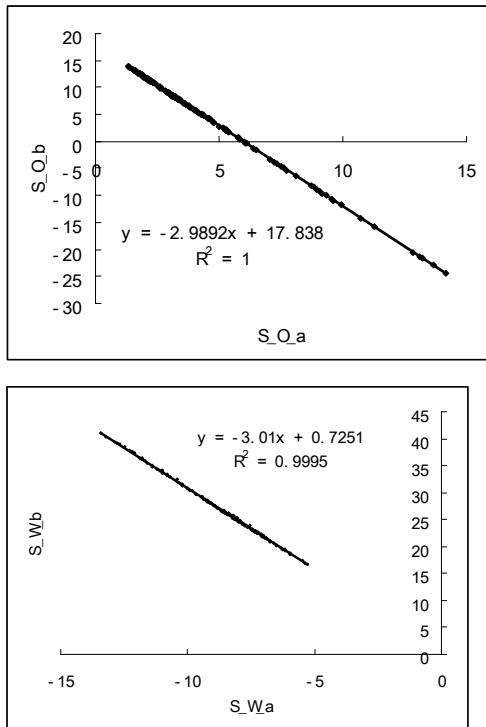


Figure 3: The relation between a and b (up) and that between a_{s_o} and b_{s_o} (down)

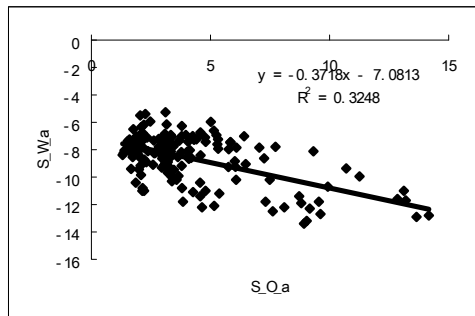


Figure 4: The relationship between a and a_{s_o}

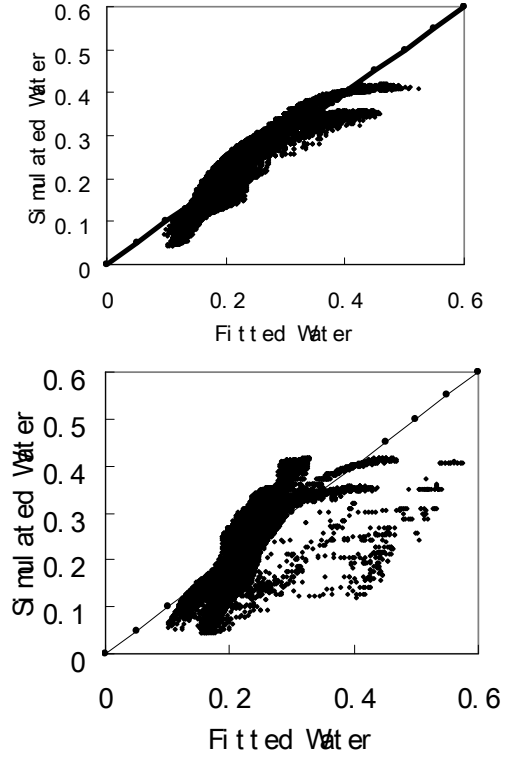


Figure 5: Comparison of the estiated SSM (fitted water) with the actual SSM (simulated water) (up figure for morning time;down figure for afternoon time)

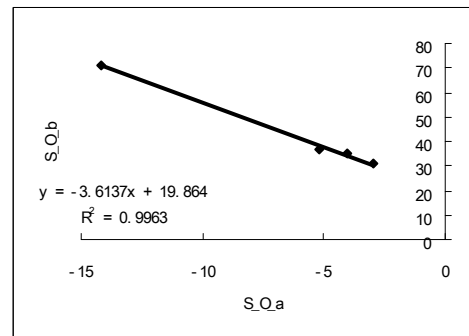


Figure 6: The relation between a_{s_o} and b_{s_o} from field measurement

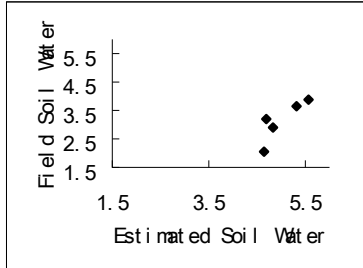


Figure 7: Comparison of measured Soil Water and estimated Soil Water from Hapex-sahel experiment data

4. APPLICATION

MSG-SEVIRI level 1.5 image data are used to calculate SSM. The spatial resolutions at nadir are 3 km for the visible and thermal infrared channels. SEVIRI Pre-processing Tools (SPT) which are provided by EUMETSAT are used to extract the images of channels 1, 2, 3, 7, 9 and 10 for the studied areas.

The retrieval of surface temperature is accomplished by the method proposed by Jiang et al (2006) and Jiang and Li (2006). Broad Albedo is obtained from the narrow band Albedo using the following conversion formula:

$$Albedo_B = 0.007 * Albedo_{band1} + 0.505 * Albedo_{band2} + 0.269 * Albedo_{band3} \quad (14)$$

where $Albedo_B$, $Albedo_{band1}$, $Albedo_{band2}$ and $Albedo_{band3}$ are broad band Albedo, band1-band3 narrow band Albedo, respectively.

Bi-direction reflectance (BRDF) of VIS-NIR range can be obtained with satellite data, and are narrow band Albedo is derived based on BRDF model which is consist of RossThick-LiSparseR kernel.

SSM is estimated after getting surface temperature and shortwave radiation. As is shown earlier, the relation between slope and SSM is different under different environmental conditions. However, according to the simulated data, the relationship between slope and offset obtained from surface temperature and shortwave radiation exhibits logarithmic equation under similar atmospheric conditions. Based on this, a 25*25 moving window is used to find out the similar atmospheric condition, if the slope and offset from these pixels in 25*25 windows shows logarithmic form, then we think these pixels are under same condition, and continue to enlarge the window until

the form is destroyed. After that, SSM can be estimated with equations (9-13).

The linear relationship between a_{s-o} and b_{s-o} obtained from slope-offset in different window is displayed in figure 8. Based on the equations (9-13), SSM are estimated and mapped in figure 9. From figure 9, we can see that the relative surface soil water can reach 50% in August in this region.

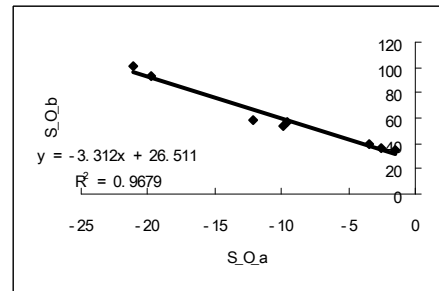


Figure 8: The relation between a_{s-o} and b_{s-o}

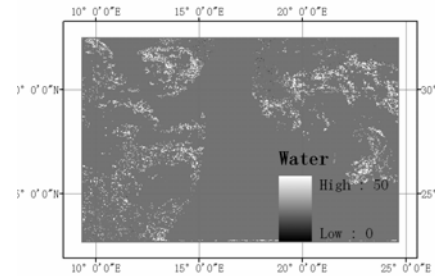


Figure 9: Relative surface soil moisture map derived from MSG data

5 CONCLUSIONS

In this paper, we addressed a method to retrieve surface soil moisture with multi-temporal geostationary meteorological satellite data. Validation is accomplished with ground measurement and data simulated from ALEX model.

The results show (1) the relation between surface temperature and shortwave radiation can be expressed to a linear form and the relationship in the morning shows better than that in the afternoon. (2) The slope of the linear equation displays logarithmic form with surface soil water depending on surrounding factors and soil water can be

estimated by the relation between the parameters depicting slope and offset and the parameters depicting slope and water. (3) Estimation of surface soil water is closer to real value using data from 1 hour after sunrise to 11 than using data from the time at which surface temperature reaches its maximum to sunset.

As a whole, the method proposed in this paper can derive SSM, at the same time, the linear fitting is much stable than nonlinear fitting, but the relationship between the slope and offset is affected by atmospheric condition. The proposed method can be used in no or less cloudy circumstance. How to overcome the influence of surrounding factor to estimation of SSM is a further work.

6 REFERENCES

- Cai, G., Xue, Y., Hu, Y., Wang, Y., Guo, J., Luo, Y., Wu, C., Zhong, S. and Qi, S., 2007, Soil moisture retrieval from MODIS data in Northern China Plain using thermal inertia model, *International journal of remote sensing*, 18(16):3567-3581.
- Demarty J., Ottle C., Braud, I., Olioso, A., Frangi, J. P., Gupta, H. V., and Bastidas, L. A., Constraining a physically based soil-vegetation-atmosphere transfer model with surface water content and thermal infrared brightness temperature measurements using a multiobjective approach, *Water Resources Research*, 2005, 41, W01011
- Idso, S. B., Schmugge, T. J., Jackson, R. D., and Reginato, R. J., The utility of surface temperature measurements for the remote sensing of surface soil water status. *Journal of geophysical research*. 1975, 80(21):3044-3049Y.
- Jiang, G.-M., Li, Z.-L., Francoise, N., 2006, Land surface emissivity retrieval from combined mid-infrared and thermal infrared data of MSG-SRVIRI. *Remote sensing of environment*, Vol. 105, Num. 4, pp 326-340 .
- Jiang, G.-M., and LI, Z.-L., 2006, Land surface temperature retrieval from MSG-SEVIRI and AATSR data and comparisons with the MODIS land surface temperature products over the Barrax site in Spain, 2nd International Symposium on Recent Advances in Quantitative Remote Sensing: RAQRS'II, pp 782-787
- Norman, J. M., Kustas, W. P., and Humes, K. S., 1995, A two-source approach for estimating soil and vegetation energy fluxes from

observations of directional radiometric surface temperature. *Agricultural and Forest Meteorology*, 77,263-293.

- Pratt, D. A., and Ellyett, C. D., 1979, The thermal inertia approach to mapping of soil moisture and geology. *Remote Sensing of Environment*, 8: 151-168.
- Reginato, R. J., Vedder, J. F., Idso, S. B., Jackson, R. D., Blanchard, M. B., and Goettelman, R. An evaluation of total solar reflectance and spectral band ratioing techniques for estimating soil water content. *Journal of geophysical research*, 1977, 82(15): 2101-2103.
- Schmer, F. A., and Werner, H. D., Remote sensing techniques for evaluation of soil water conditions, *Trans. Amer. Soc. Agri. Eng.* 17(2):310-314
- Schmugge, T. J., and Jackson T. J., Mapping surface soil moisture with microwave radiometers. *Meteorol Atmos Phys*, 1994,54: 213-223.
- Wagner, W., Naeimi, V., Scipal, K., Jeu, R., and Martinez-Fernandez, J., 2007, Soil moisture from operational meteorological satellites. *Hydrogeology Journal*, 15: 121-131
- Whitting, M., Li, L., AND Ustin, S. L., Predicting water content using Gaussian model on soil spectra. *Remote sensing of environment*, 2004, 89: 535-552.

7 ACKNOWLEDGEMENT

This work was supported by the National Natural Science Foundation of China under Grant 40971199.

Thermal Infrared Imaging of Weathering Changes of Mauna Ulu Basalts, Hawai'i

Elsa A. Abbott^{1*}, Alan R. Gillespie², Anne B. Kahle^{1**}

1. Jet Propulsion Laboratory, Pasadena, CA, USA.

2. University of Washington, Seattle, WA, USA.

*Corresponding author email: elsa.abbott@jpl.nasa.gov; ** Now retired.

ABSTRACT - Basaltic pahoehoe lavas weather and are chemically altered on time scales of days to millennia following their eruption. Continuing eruptions of Pu'u 'O'o, near Mauna Ulu, since 1983 offer an opportunity to study the effects of a persistent dousing of lavas by acidic rain and air (vog). The surface composition of basalt, including alteration products, can be detected in the thermal infrared (TIR: 8-12 μm). The ASTER imager on NASA's Terra spacecraft, with five 90-m TIR bands, offers an opportunity to study the weathering over the 11-yr period since launch in late 1999. ASTER AST05 emissivity images of Mauna Ulu flows for 2000-2002 and 2007-2009 were analyzed and compared to laboratory hemispheric reflectance spectra. Systematic changes in emissivity were observed, especially with exposure to vog. Weathering rates quantified spectrally are helpful in assessing long-term environments on volcanoes.

1. INTRODUCTION

Kahle et al. (1988), Farr and Adams (1984) and Abrams et al. (1991) have shown that basaltic lavas in a tropical environment weather measurably in decades to centuries and visibly in centuries. Important processes include oxidation, devitrification, leaching, accretion of silica rinds, as well as mechanical spalling and colonization by lichens. Spectral changes have been summarized by Kahle et al. (1988), Farr and Adams (1984) and Crisp et al. (1990). Weathering is driven by wetting, but near active vents acidic vapors from cracks, fumaroles and skylights locally accelerate different reactions (Africano and Bernard, 2000). This can happen near the time of lava emplacement or at any time thereafter, even at some distance from the source of the acidic vapor. Downwind from vents, H_2SO_4 is created from erupted SO_2 and H_2O and envelops larger tracts of lavas (Realmuto et al., 1992). Important reaction products can be measured with TIR spectroscopy from space. Spectroscopically important processes on the lavas are given in Table 1.

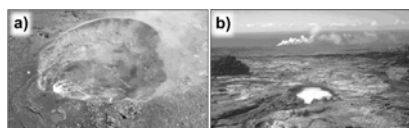


Figure 1. Pu'u 'O'o test area (Fig. 2). **a)** Vent, 0.25 km across, emitting SO_2 -rich vapors ('vog'). **b)** Glowing skylight, ~10 m across, center, between vent and ocean (ocean-entry steam plume in the distance). Images are from http://hvo.wr.usgs.gov/kilauea/update/archive/2006/Jun/20060630-1723_CCH_large.jpg and hvo.wr.usgs.gov/gallery/erupt/2553008_caption.html.

In this study we use multispectral thermal-infrared (TIR) ASTER images of active volcanoes on the "Big Island" of Hawai'i to study spectral emissivity changes in lavas erupted ~40 years ago from Mauna Ulu and the related changes in surface composition. To test the role of vapor emanations in altering basalt surfaces, we sampled flows at different distances from active vents and skylights, and compared them to samples from older flows that have had decades to centuries to weather far from active vents.

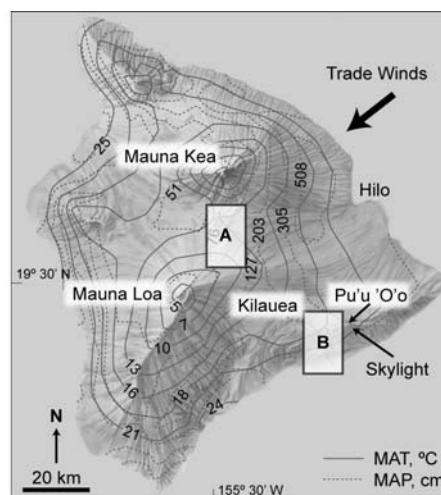


Figure 2. MODIS image showing study sites (boxed) on Hawai'i. Detailed site maps are shown in Fig. 3. Contour lines show mean annual temperature (MAT: Oregon Climate Service and NOAA) and precipitation (MAP) after Davis and Yamanaga (1973). Base map by Dorothy Nelson.

Table 1. Alteration/weathering processes, TIR spectral features, and location of band centers.

Process	Physical effect	Spectral effect	μm	Time scale
Degassing ^a	Roughness increase	Contrast loss	7-14	Days - weeks
Quenching ^b	Disorder	Broad band	10.1 – 10.3	Minutes
Acidic vapors ^{c,d}	Cation leaching, sulfate incrustation	Silica/glass \pm sulfate bands	9.1	Days - years
Hydration ^b	Glass polymerization	Broad bands shift to shorter wavelength	9.2, 10.5	Years - centuries
Crystallization ^d	Growth of quartz	Reststrahlen band	8.1	Years - centuries
Devitrification ^e	Hydration	Loss of broad bands	9-11	Decades - millennia
Tephra dissolution ^{e,f}	Silica rind	Opal band, obscuration of basalt features	8.1, 9.1	Decades - centuries
Spalling ^c	Loss of glass coat	Reduction of broad bands	9-11	Hours - centuries
Oxidation ^g	Fe hydroxides	Contrast loss, hiding of basalt features	7-14	Centuries - millennia

a) Peterson & Tilling, 1980

b) Crisp et al., 1990

c) Realmuto et al., 1992

d) Vaughan et al., 2005

e) Kahle et al., 1988

f) Farr & Adams, 1984

g) Abrams et al., 1991

2. APPROACH

We chose three locations on Hawaii for study (Figs. 2, 3). The main area was the 1970-74 Mauna Ulu flows, adjacent to and different distances from the Pu'u 'O'o vent (area #2) active since 1977. The older historic and prehistoric flows in the Mauna Loa – Mauna Kea saddle (area #3, >75 yr) were also studied for comparison to weathering away from active vents.

Samples were repeatedly collected from flows in the three areas. Samples were investigated with laboratory spectral hemispherical reflectance measurements (Fig. 4), made with a Nicolet FTIR spectrometer mounted with a gold Labsphere sphere. The data were converted to emissivity using Kirchhoff's Law, and convolved to simulate ASTER TIR bands 10-14. Spectral features and changes in them over time were identified in the lab spectra.

ASTER is an imaging system launched in the Landsat sun-synchronous polar orbit on NASA's Terra satellite 19 December 1999 and functioning since then. The TIR bands are at wavelengths 8.125-8.475, 8.475-8.825, 8.925-9.275, 10.25-10.95, and 10.95-11.65 μm

(bands 10 – 14). The TIR spatial resolution is 90 m and the $\text{NEAT}_{300\text{K}}$ is about 0.25 K.

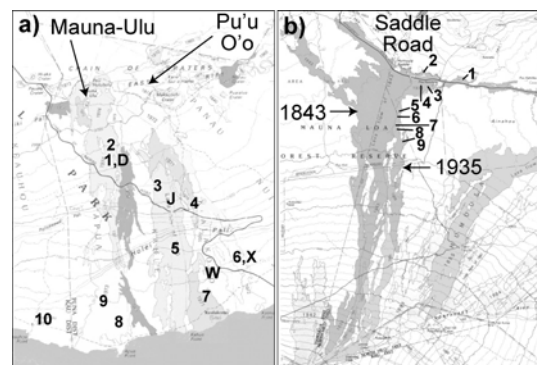


Figure 3. Black/white version of detailed flow maps at sample sites (see color supplement). a) Mauna Ulu study area showing sample sites #1-10 and D, J, W, X and Pu'u 'O'o. b) Mauna Loa-Mauna Kea saddle area showing sample sites (#1 – 9) on the 1935 and 1843 flows. After U.S. Geologic Survey (1986).

Examination of the laboratory spectra in Figure 4 shows a range of features that should also be detectable in the lower-resolution ASTER emissivity data.

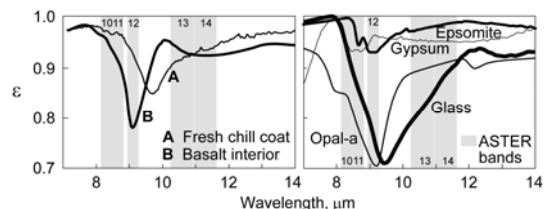


Figure 4. Thermal emissivity spectra calculated from hemispherical reflectivity measurements using Kirchhoff's Law (<http://speclib.jpl.nasa.gov>). a) Basalt lava. "A" – lava interior (Ward_basalt_35_solid). "B" – fresh chill coat, Pu'u 'O'o skylight (Fig. 1). b) Lava constituents "O" – opal-a (Kraft et al., 2003). "G" – Glass (Kraft et al., 2003). "G" – gypsum, 0-45 μm (SO-2B). "E" – epsomite, coarse powder (USGS).

ASTER emissivity images (standard product AST05) were collected for Pu'u 'O'o (active), Mauna Ulu (30-40 yr) and the historic Mauna Loa flows (65-165 yr) for two time periods, 2000-2002 and 2007-2009. Emissivities were depicted in false-color images for spatial context and compared to lab spectra collected for the same sites. Principal-component analysis (PCA) was used to identify the inherent dimensionality of the spectra, which indicates how many endmembers are needed to capture the information from the scene. Systematic changes for bands 10, 12, and 14 from Mauna Ulu were displayed in trajectories in an emissivity ternary diagram and compared to weathering trajectories for older Mauna Loa flows identified by Kahle et al. (1988). For each

ASTER band at selected sites from each study area, the difference between the averages of all 2000-2002 and all 2007-2009 spectra was plotted.

3. RESULTS

3.1 Spectral data and images

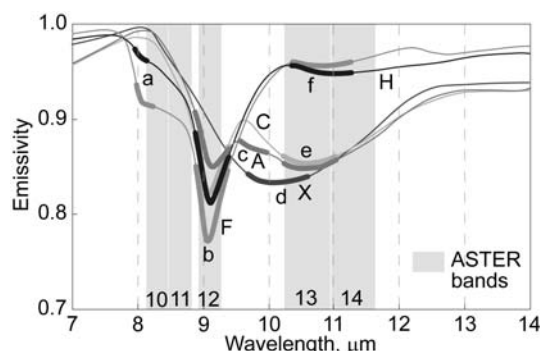


Figure 5. Averaged and redrafted 'type' spectra of Mauna Ulu flows capture the gamut of variability. Capital letters identify sub-samples from site W, Fig. 3a. Lower-case letters *a-f* identify spectral features discussed in text §4.1.

Over 100 laboratory spectra were measured on 30 samples taken from the 14 locations on the Mauna Ulu flows (Fig. 3a), plus 5 locations on Pu'u 'O'o flows. Although these spectra were all made for visually and compositionally similar rocks, they fell in only a few classes. Samples from site 'W' display the same spectral variability as the samples from all the Mauna Ulu flows (Fig. 5). These five classes consistently show combinations of six distinct features: *a-c*, sharp bands at lower wavelengths; and *d-f*, broad bands at longer wavelengths. Interpretations of these spectral features are given in §4.1. The spectral variation suggests that ASTER TIR images can be used to recognize associated flow units in the field.

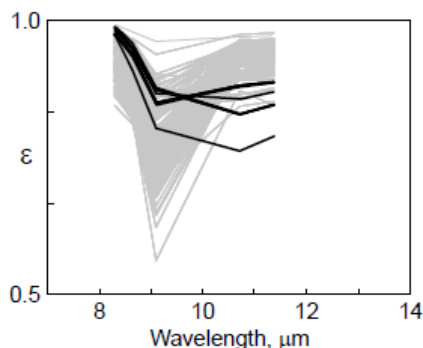


Figure 6. The gamut of 100 ASTER ϵ spectra simulated from the laboratory spectra of samples from Pu'u 'O'o and Mauna Ulu flows.

Figure 6 shows simulated ASTER spectra calculated from all the laboratory data (§2). Although the spectral detail of the full-resolution spectra has not been captured in the five ASTER bands, features *b* and *d* or *e* appear to be dominant. The simulations confirm that major spectral distinctions can be made in the images.

Figure 7 presents false-color ASTER images of the Mauna Ulu and Pu'u 'O'o areas, showing that the lavas there, similar in bulk composition, do have different surface spectra. Sites on the Mauna Ulu flows are above and below the cliffs, or pali. Two main spectral types are evident, as predicted from Figure 6. In the false-color images they appear blue and red (see §4.1). The blue areas are largely above the pali and are dominated by spectral features *d-f*; the reddish areas are dominated by *a* and *b* or by *b* (more magenta). Most color unit boundaries coincide with flows, but within flows there are irregular red – blue transitions, and on the coastal plain below the pali diffuse reddish areas transgress flow boundaries.

At Pu'u 'O'o we could select sites only at the eastern edge of the flow field due to the constant re-paving of the surface as the eruption progressed. Since this part of the flow field is upwind of the Pu'u 'O'o vent, we selected six sites, on both sides of several relatively long-lasting tube systems with their vents and skylights dissecting the area of study. In the Pu'u 'O'o image (Fig. 7b) the same two spectral groups can be seen as for Mauna Ulu, even though the Pu'u 'O'o flows are much younger. Magenta Cluster 1 and blue Cluster 2 are grouped by distance and direction from the lava tubes, with Cluster 1 being downwind from skylights. There is also a diffuse magenta area on the coastal plain downwind (east) from the complex of Pu'u 'O'o flows. In general, downwind sites were more changed than upwind sites.

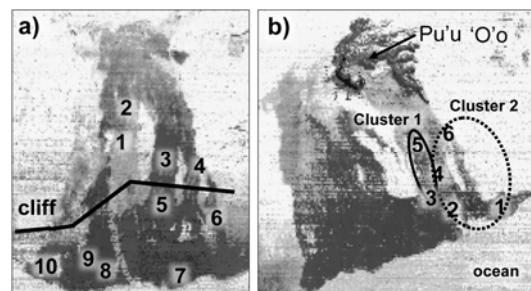


Figure 7. Recent flows, black/white version of ASTER emissivity AST05 ϵ image, RGB = bands 14, 12, 10. For image locations: see Figure 2 (see color supplement). a) Mauna Ulu, showing sample sites above and below the cliff or pali. b) Pu'u 'O'o, showing sample sites from two spectral groups of lava – Cluster 1 (red) and Cluster 2 (blue).

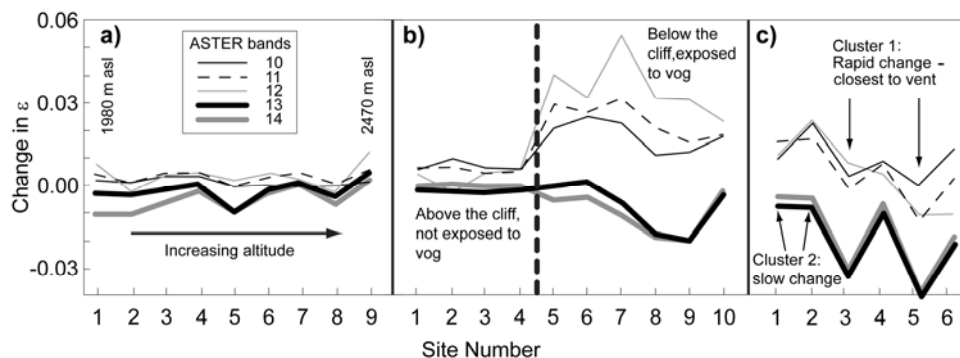


Figure 8. Spectral change in AST05 (2000-2002 minus 2007-2009) at three volcanoes. a) Mauna Loa (Kahle et al., 1988), showing little change. b) Mauna Ulu, showing change only where exposed to vog. c) Pu'u 'O'o, showing change downwind from skylights.

3.2 Spectral change

Images acquired in 2000-2002 and 2007-2009 were compared in order to assess the nature and rate of spectral change in the young Mauna Ulu and Pu'u 'O' flows relative to the older Mauna Loa flows studied by Kahle et al. (1988). Data from Mauna Loa (Fig. 8a) showed little change during this 7 yr period, independent of spectral band and altitude (and therefore, MAP and MAT: Fig. 1).

In contrast, data from Mauna Ulu (Fig. 8b) and Pu'u 'O'o (Fig. 8c) showed much greater change. At Mauna Ulu, sites 1 – 4 were unchanged, whereas sites 5 – 10, below the pali, decreased by as much as $\Delta\epsilon=0.05$ in bands 10 – 12, and bands 13 – 14 increased by <0.02 . The 'change' sites were the ones most exposed to vog from Pu'u 'O'o.

At Pu'u 'O'o', change was mainly an increase in $\Delta\epsilon$ as much as 0.03 for bands 13 and 14. Change was at sites downwind from skylights were venting of volcanic gases was strongest. In contrast to Mauna Ulu, even at 'change' sites, ϵ at ASTER bands 10 – 12 remained constant or even increased (i.e., the depth of the Reststrahlen bands lessened).

Investigation of the ASTER emissivity images shows little emissivity change for the lavas in the Mauna Loa saddle area, confirming the conclusions from Figure 8a. This area is free of acid fumes (vog) from the ongoing eruption at Pu'u 'O'o, but is subject to weathering from rain and physical changes such as spalling of glassy chill coats.

The Mauna Ulu flows lie partly in the direct path of the vog from Pu'u 'O'o. The flows began at an elevation of about 1000 m and, about halfway to the sea, flowed over the pali before spreading on the coastal plain and entering the ocean, creating additional plumes of acidic vapors. The dominant trade-wind direction causes the vog to stay below the pali most of the time. The average annual rainfall from top to bottom of these flows differs by only a few

cm. However, there is a stronger east-west gradient of about 100 cm/yr across the Mauna Ulu - Pu'u 'O'o' study areas (Fig. 1).

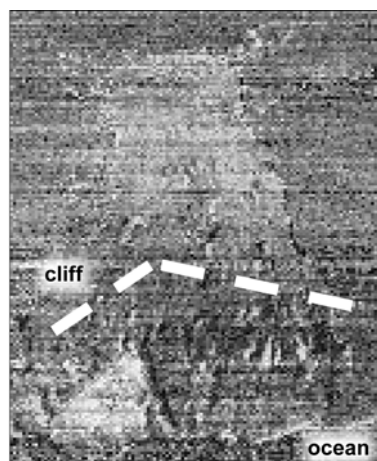


Figure 9. Black/white version of temporal ratio image, Mauna Ulu, 2008 ÷ 2000. In the color version (see supplement) RGB=bands 14, 12, 10. Dark gray (blue), no change; midgray near Mauna Ulu (green) and dark gray near coast (red) change.

3.3 Inherent dimensionality

The eigenvalues times 10^5 for ASTER bands 10-14 are 71, 17, 2, 0, and 0. Therefore, the intrinsic dimensionality of the ASTER data is 3, and only three bands are needed to capture most of the spectral image variance. This is consistent with the low number of 'type' spectra and deep spectral features.

4. DISCUSSION

4.1 Spectral features

Six spectral features in two classes were identified in Figure 5. The first group is probably due to opal-a (a)

and glass with sheet-like order (*b*), and possibly phenocrysts (*c*). Feature *c* is distinct in the laboratory spectra, but too subtle to influence the ASTER images. The second group, at longer wavelengths, is due to glass, with increasing chain-like order shifting the band to longer wavelengths (Crisp et al., 1990) who suggested that etching by acidic fumes could result in the depolymerization. The *a* feature (opal-a) appears to result from increasing degree of crystallization over time within the amorphous silica coating that develops on Hawai'ian basalts as they weather, perhaps due to the accumulation and leaching of windblown tephra and dust (Farr and Adams, 1984).

In the false-color images pixels dominated by *b* will appear magenta (low green) and pixels dominated by *a* and *b* will appear red. Pixels dominated by *d*, *e* or *f* will appear in difference shades of blue and cyan, depending on how much *b* is present.

Reddish tones thus indicate devitrified glass, or a silica coating (Kahle et al., 1988). Blue or green tones may indicate flows with glassy surfaces or chill coats intact. Thus, in Figure 7 most of the Mauna Ulu flows have little of their original glassy surfaces intact. The youngest (western) Pu'u 'O'o flows have glassy surfaces, whereas the older (eastern) flows and those nearest the vent have been devitrified. Below the pali, where exposure to vog is maximum, conversion of blue glassy lavas to reddish lavas is common.

4.2 Weathering

One of the remarkable features of the Hawai'ian lavas is that the spectral changes accompanying rapid alteration near active vents are the same or similar as changes due to slower weathering. Figure 10 shows a false-color ASTER image of flows weathering on Mauna Loa, upwind from recent volcanic activity. The spectral features increase with lava age (Kahle et al. (1988)). The younger (1935) lavas appear blue; older (1843) flows appear magenta or red.

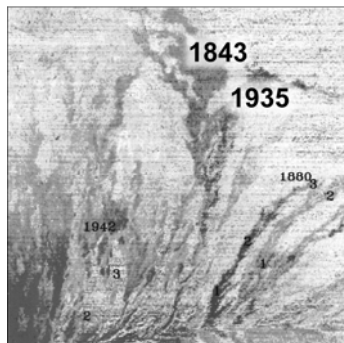


Figure 10. Black/white version of AST05 image showing saddle flows, Mauna Loa. RGB=bands 14,12,10 (color: see supplement). Lighter gray (red) 1843 flow; darker gray (blue) 1935 flow. Numbers show sample sites.

Upon cooling of the lava, their spectra exhibit a broad feature *d* that in older flows has split into two features, *b* and *e*. Feature *b* becomes more dominant, and the peak positions more separate, as weathering progresses (Kahle et al., 1988). Subsequently, feature *a* appears as a shoulder on *b*. As weathering continues lava surfaces are coated with FeOx and spectral contrast is lost.

The first change, loss of the broad feature *d*, is probably due to hydration and depolymerization of glass. Feature *b* probably results from the development of sheet structure in the glass. It also increases as amorphous silica rinds thicken, then decreases due to spalling (Kahle et al., 1988). Feature *a* appears to arise spontaneously due to increasing order within the silica rind. Figure 11 shows the progressive change in these features in the spectra of lava flows of different ages from the saddle area.

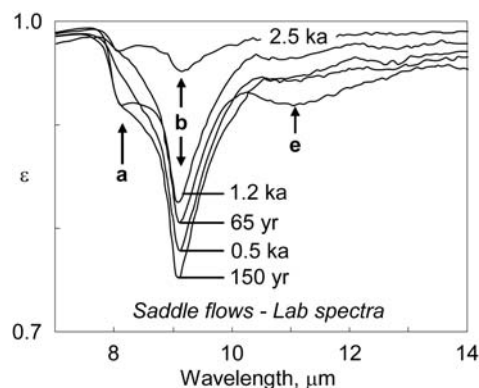


Figure 11. Spectra of Mauna Loa 1843 and 1935 flows showing spectral effects of weathering (Kahle et al., 1988).

4.3 Spectral variation and trajectories

The low inherent dimensionality of the ASTER lava images suggests that the spectral variability can be displayed in a false-color image, or displayed on a ternary diagram. Because the important component of the variability is spectral shape rather than overall amplitude, the variability is dominated by spectral angle rather than length, only the normalized emissivity values (sum to unity) need be displayed. In Figure 12 most of the basalt spectra, with the exception of the oxidized lavas, are shown to fall on two mixing lines with the weathering progression always toward more-ordered glass and a silica rind. The mixing lines connect spectral endmembers describing fresh lava (*A* and *B*) with altered or weathered lava *C*. *A* is the position for lavas covered by glassy chillcoats; *B* is the position for lavas lacking such coats. *C* is the position of lavas with silica rinds. Except for FeOx (*D*), long-term weathering and short-term alteration have similar spectral signatures.

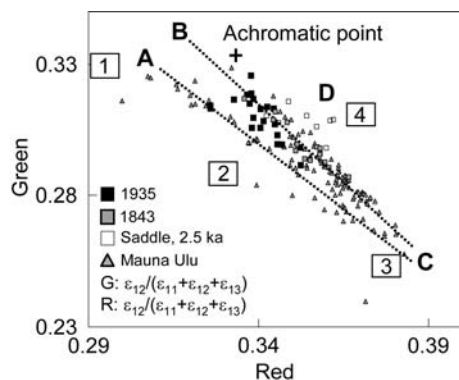


Figure 12. Ternary diagram of normalized red (R) and green (G) emissivity components. Boxes show where pixels plot that appear blue (1), purple (2), magenta (3), and brown (4) in the false-color images.

Extreme spectra from the perimeter of the mixing cluster are shown in Figure 13. The ability to image subtle or invisible changes in lava composition that occur over a wide range of time scales increases our ability to map in volcanic terrain. In particular, mapping alteration products that develop on short time may give us better insights into volcanic processes around active vents.

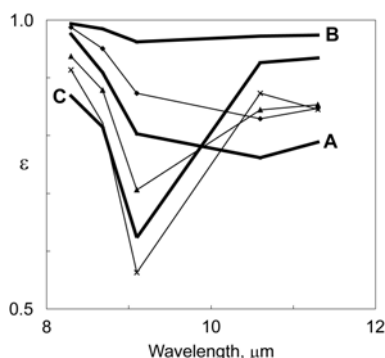


Figure 13. Extreme spectra from the perimeter of the mixing cluster of Fig. 12. Letters refer to ternary diagram. A=fresh chill coat; B=fresh basalt; C=silica rind.

5. CONCLUSIONS

Basaltic lavas may be spectrally altered soon after eruption due to outgassing, especially near fumaroles, causing cation leaching, sulfate dissolution and silica enrichment and the spalling of chill coats. In contrast, longer-term weathering results in devitrification, the conversion of silica to opal or chalcedony and accretion and spalling of silica rinds. Weathering and alteration spectra are similar and are both dominated by changes in glass and silica for the first ~100 years. Alteration due to reaction with H_2SO_4 from vog has spectral effects within years of exposure.

6. REFERENCES

- Abrams, M., E. Abbott, and A. Kahle, 1991. Combined use of visible, reflected and thermal infrared images for mapping Hawaiian lava flows. *Journal of Geophysical Research* 96, 475-484.
- Africano, F. and A. Bernard, 2000. Acid alteration in the fumarolic environment of Uso Volcano, Hokkaido, Japan. *Journal of Volcanol. Geotherm. Research* 97, 475-495.
- Crisp, J., A. Kahle, and E. Abbott, 1990. Thermal infrared spectral character of Hawaiian basaltic glasses. *Journal of Geophysical Research* 95, 21,657-21,669.
- Farr, T.G., and J.B. Adams, 1984. Rock coatings in Hawaii. *Geological Society of America Bulletin* 95, 1077-1083.
- Kahle, A. B., A.R. Gillespie, E.A. Abbott, M.J. Abrams, R.E. Walker, G. Hoover and J.P. Lockwood, 1988. Relative dating of Hawaiian lava flows using multispectral thermal infrared Images: A new tool for geologic mapping of young volcanic terranes. *Journal of Geophysical Research* 93, 15239-15251.
- Kraft, M.D., J.R. Michalski and T.G. Sharp, 2003. Effects of pure silica coatings on thermal emission spectra of basaltic rocks: Considerations for Martian surface mineralogy. *Geophysical Research Letters* 30, 2288, doi:10.1029/2003GL018848.
- Peterson, D.W. and R.I. Tilling, 1980. Transition of basaltic lava from pahoehoe to aa, Kilauea Volcano, Hawaii – Field observations and key factors. *Journal of Volcanology and Geothermal Research* 7, 271-293.
- Realmuto, V.J., K. Hon, A.B. Kahle, E.A. Abbott and D.C. Pieri, 1992. Multispectral thermal infrared mapping of the 1 October 1988 Kupaianaha flow field, Kilauea volcano, Hawaii. *Bulletin of Volcanology* 55, 33-44.
- Davis, D.A., and G. Yamanaga, 1973. Water resources summary, Island of Hawaii. U.S. Geological Survey, Hawaii Division of Water and Land Development, Department of Land and Natural Resources Report R47, 42 pp.
- U.S. Geological Survey, 1986. Hawaii Volcanoes National Park and Vicinity, Hawaii, 1:100,000 scale topographic map. 19155-D3-PF-100.
- Vaughan, R. G., S.J. Hook, W.M. Calvin and J.V. Taranik, 2005. Surface mineral mapping at Steamboat Springs, Nevada, USA, with multi-wavelength thermal infrared images. *Remote Sensing of Environment* 99, 140-158.

7. ACKNOWLEDGMENTS

This work was done under contract to NASA. We are grateful to Madam Pele for support in the field.

GEOLOGICAL CLASSIFICATION OF VOLCANO TEIDE BY HYPERSPECTRAL AND MULTISPECTRAL SATELLITE DATA

Stefania Amici¹, Alessandro Piscini¹, M. F. Buongiorno¹ and David Pieri²,

¹*Istituto Nazionale di Geofisica e Vulcanologia, Rome, Italy*

²*Jet Propulsion Laboratory, Pasadena, California USA*

stefania.amici@ingv.it

ABSTRACT Tenerife is the central island of Canarian archipelago (Spain) and has developed within the complex formed by the rifts associated with the Teide-Pico Viejo (T-PV-Lat 28° 16' 30" Lon 16°38' 42") stratovolcanoes that reach a height of 3718 mASL, 7500m above the ocean floor. It is an active, though currently quiescent shield volcano, which last erupted in 1909. In the framework of the European Project FP6 PREVIEW-EURORISK (PREvention, Information and Early Warning pre-operational services to support the management of risks) (<http://www.preview-risk.com/>), we undertook a field campaign on Pico de Teide from the 16th and 24th of September 2007. In situ reflectance spectra have been acquired on the Pico de Teide in an area also known as Las Canadas Caldera (LCC). Test sites were selected for cal/val activities and to study the geological setting of Pico the Teide volcano by image spectroscopy. The collected spectral library represents the “ground truth” and has been used for the supervised classification on multispectral (ASTER) and hyperspectral (EO1-Hyperion) data. In this work we report on the first classification mapping carried out on Teide Volcano utilizing remote sensing. Methods used to process and to classify the data are discussed, and a comparison with existing geological maps is presented-

1 INTRODUCTION

Tenerife Island is the central island of the Canary Islands archipelago and Volcano Teide (Pico del Teide) is its dominate feature.

The sub-aerial history of the island began in the late Miocene Plio-Quaternary and post-shield volcanism on Tenerife and has been characterized by the cyclic development of petrologically evolved eruptive centers. Recent eruptive activity on Tenerife (e.g., 200 ka to present) has also been described and characterized (Carracedo, 2007).

Until now, however, no spectroscopic characterization of the Teide volcanic has been available. In 2007, a remote sensing data validation campaign, funded by the European Community under the PREVIEW FP6 project was carried out, accomplishing multiple aims.

Field Reflectance and spectra were acquired in area of interest (Figure 1, right), representing a ground truth library for scientific investigation (Figure 1, left).

Using a ground truth library, a geological map of Volcano Teide was created from ASTER and EO-1 Hyperion remote sensing data.

2 METHODS

2.1 Image processing

For spectral analyses reported here, an ASTER AST_07 Surface Reflectance product, acquired

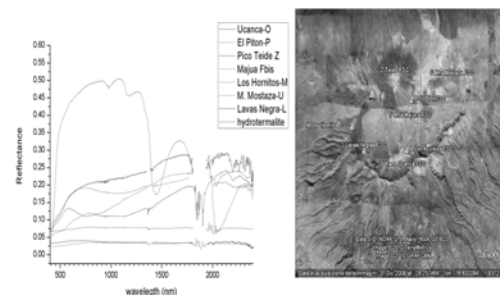


Figure 1. Ground true reflectance spectra acquired by FieldSpec (left). The position of the points are located on Google Earth™ by their latitude and longitude.

on August 4, 2007 (Figure 2, left) (Abrams, 2000) and NASA EO1-Hyperion L1R-Data (“At-Sensor Radiance”) from November 13, 2003 (figure 3), were utilized (Fujisada, 1995). Hyperion surface reflectance was retrieved, for meaningful bands (196 of 242), using the Fast Line-of-sight Atmospheric Analysis of Spectral Hypercubes (FLAASH) (EO-1 User Guide, 2003), and Minimum Noise Fraction-Image (MNF) was applied for data dimensionality estimation and noise reduction, thereby de-correlating useful information and separating noise (Green et al, 1988).

The training suite (18 classes) was selected by using both “ground truth” acquired during field campaign and visual selection. The ground truth

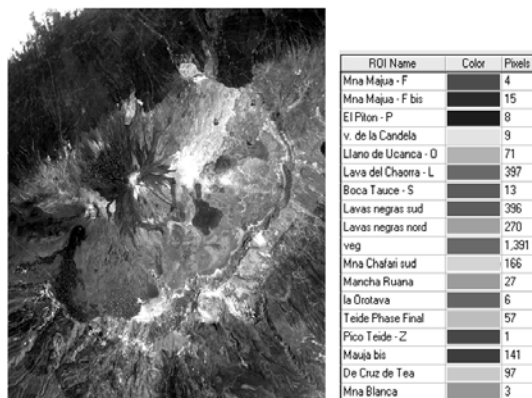


Figure 2. Ground Truth Class Training Set and description table for ASTER.

classes are a suite of 8 reflectance spectra (Figure 1, left) in the range 0.35-2.5 μ m acquired by a portable ASD FieldSpec® spectrometer. Ten spectra were chosen by visual inspection with reference to geological map. Training datasets (tables in Figure 2 and Figure 3) for classification were selected in the following way: beginning with ground truth measurements we first generate the 18 classes, populating them by using a growing sampling algorithm. Classes obtained in this manner were then sub-sampled by using a stratified random sampling method.

2.2 Classification Methodologies

In this work we applied two ENVI® supervised classification methods, Spectral Angle Mapper (SAM) and Support Vector Machine (SVM).

SAM is a physically based classification algorithm that compares the spectral similarity between surface reflectance image spectra and reference spectra, treating them as vectors in a space with the dimensionality equal to the number of bands (Jenson, 2005). The SVM classifier (Figure 4) is derived from statistical learning theory. It separates classes with a decision surface that maximizes the margin between the classes (Fooy and Mathur, 2004).

3 RESULTS AND DISCUSSION

Our best classification results were obtained with SVM classification on both images. Classification accuracies were estimated with confusion matrices: an overall accuracy of 96.8284% and K coefficient of 0.9574 for ASTER and an overall accuracy of 85.7787% and a K coefficient of 0.84 for EO1-Hyperion were achieved. When considering the Producer Accuracy for each class, we noticed that it is

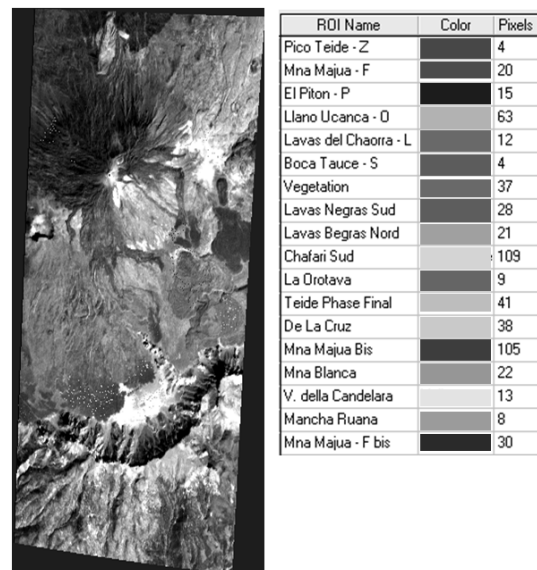


Figure 3. True Class Training Set and description table for EO-1 Hyperion.

more than 90% for ASTER, except for classes as indicated in Figure 4.

Instead, Hyperion classification has lower Producer Accuracy values with the exception of classes El Piton and Mna Majua F Bis. Furthermore, three classes—Boca Tauce, La Orotava and Pico Teide—have not been classified. This probably occurred because the scene was strongly affected by system-induced radiometric interference. The classification maps for produced from ASTER and Hyperion data, obtained by using the SVM method, (represented in Figure 5 (left) and Figure 5 (right) respectively) have been compared to the geological map of Volcano Teide (Figure 6) (Amici, 2010). They clearly demonstrate good correspondence among the classes and the geological units.

Class	Prod. Acc. (Percent)	
	ASTER	Hyperion
Mna Majua - F	92.5	50.74
Mna Majua - F bis	48.03	65.13
El Piton - P	2.6	49.67
v. de la Cand	96.7	84.5
Llano de Ucan	97.88	95.53
Lava del Chao	96.12	79.31
Boca Tauce -	45.86	0
Lavas negras S	96.27	79.36
Lavas negras N	94.67	88.79
veg	99.49	89.57
Mna Chafari s	95.85	96.98
Mancha Ruana	93.66	48.81
la Orotava	40	0
Teide Phase F	96.13	91.85
Pico Teide -	100	0
Mauja bis	99.08	97.81
De Cruz de Te	97.23	87.47
Mna Blanca	0	84.02

Figure 4. SVM classification producer accuracy both for ASTER and Hyperion

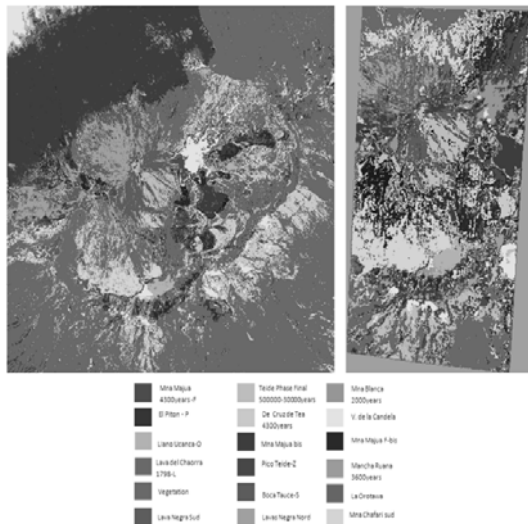


Figure 5. ASTER (left) and EO-1 Hyperion (right) SVM classification map and class description (bottom)

4 CONCLUSIONS

We report here on the first spectral characterization of Teide Volcano carried out using combined in situ field and satellite hyperspectral and multispectral data. The central part of Teide was classified utilizing the both SAM and SVM supervised methods. Comparisons between the classification images obtained by using the SVM method with both Hyperion and ASTER data and the Teide Volcano geological map show good formal statistical correspondence between the classes and the geological units. Also a good qualitative visual correspondence between the classes and the geological units is evident.

In regard to data quality, it is not surprising that best classification results were obtained from Hyperion images having high Signal-to-Noise Ratios. In all cases, pre-processing improved classification results.

The classification results obtained from ASTER and Hyperion data appear promising, and confirm the utility of both as effective tools for volcanological mapping.

5 ACKNOWLEDGEMENT

We would like to acknowledge the efforts of the INGV-Teide campaign field team, including M. Musacchio, V. Lombardo, S. Corradini, and M.I. Pannaccione Apa. We acknowledge the kind assistance of the Director of "Planificación y Operaciones de Emergencias," Dr. Fernando Clavijo Redondo, and Dr. Sergio Barrera Rodriguez, Dirección General de Seguridad y Emergencias, Gobierno de Canarias, both of whom made possible our fieldwork campaign throughout the Teide Volcano Natural Park on Tenerife Island. We thank the European Community which provided funds for the Preview project, and we thank the NASA ASTER and Hyperion spacecraft teams for their data acquisitions and processing. This work was carried out, in part, under contract to the NASA Earth Surface and Interior Program at the Jet Propulsion Laboratory of the California Institute of Technology.

6 REFERENCES

Abrams, M., 2000, "The Advanced Thermal Emission and Reflection Radiometer (ASTER): data products for the high spatial resolution imager on NASA's Terra platform," International Journal of Remote Sensing, 21(5), pp. 847-859.

Amici S., 2010, Calibration and Validation (CAL/VAL) of Remote Sensing Data and

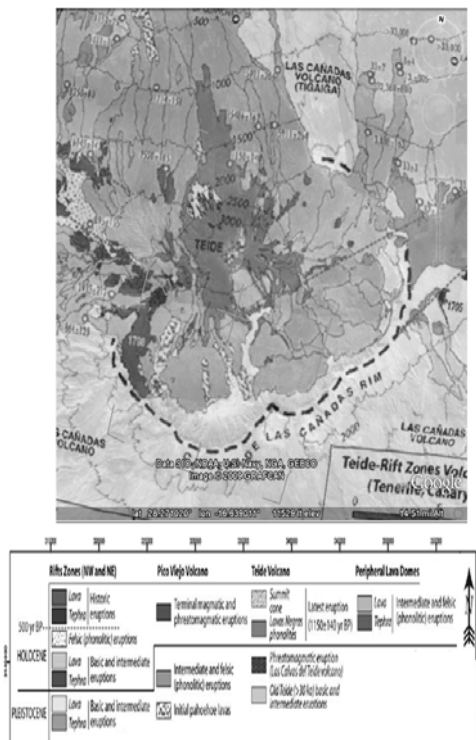


Figure 6. Teide Geological map.

- Spectral Characterization of Volcanic rocks, PhD Thesis, University of Parma.
- Carracedo, J.C., Rodríguez Badio, E., Guillou, H., Paterne, M., Scaillet, S. F.J., Pérez Torrado Paris, R., Fra-Paleo, U., Hansen, A., 2007 “Eruptive and structural history of Teide Volcano and rift zones of Tenerife, Canary Islands,” *GSA Bulletin*; September/October 2007; v. 119; no. 9/10; p. 1027–1051; doi: 10.1130/B26087.1
- EO-1 User Guide, 2003, USGS Earth Resources Observation System Data Center (EDC).
- Foody, G.M. and Mathur, A. 2004, “A Relative Evaluation of Multiclass Image Classification by Support Vector Machines,” *IEEE Transactions on Geoscience and Remote Sensing*, Vol. 42, pp. 1335-1343.
- Fujisada, H., 1995, “Design and performance of ASTER instrument,” *Proceedings of SPIE*, 2583, pp. 16-25.
- Green, A.A., Berman, M., Switzer, P. & Craig, M.D., 1988. A Transformation for Ordering Multispectral Data in Terms of Image Quality with Implications for Noise Removal. *IEEE Transactions on Geoscience and Remote Sensing*, 26(1), pp. 65-74.
- Jensen, J.R., 2005, *Introductory Digital Image Processing: A Remote Sensing Perspective*, 3rd ed.: Pearson Prentice Hall, Upper Saddle River, NJ, 526 p.

Storage of Hyperspectral Sensor Images, Sources of Error and Footprint Analysis

¹A. Cristo, ¹R. M. Pérez, ¹P. Martínez, ²M. Koch, ³T. Schmid, ¹L. M. Hernández, ¹J. Merino

1. Escuela Politécnica de Cáceres, Universidad de Extremadura, Avda. Universidad s/n 10071, Cáceres (Spain)

2. Center for Remote Sensing, Boston University, 725 Commonwealth Avenue, Boston, MA (USA)

3. CIEMAT, Avda. Complutense 22, 28040, Madrid (Spain)

pablomar@unex.es

ABSTRACT—Remotely sensed hyperspectral images are obtained by sensors carried on different kinds of platforms. These platforms are subject to influences that affect the real spatial coordinates where the spectrometer data have been measured. As a result, geometric corrections are required to produce spatially corrected images for data fusion. This paper analyses the sensor's data acquisition process and the effective spatial distribution of the centers of the real measurement for a set of AVIRIS images. In addition, an experiment has been carried out by using the AVIRIS Ivanpah low altitude image. This high spatial and spectral resolution image has been used as a reference image. The spatial location of the pixels of this image has been obtained from the GLT and IGM files provided by JPL. The synthetic spectral signatures for some spatial locations have been simulated for the same sensor at a higher altitude. These data have been obtained from the reference image taking into account the exact spatial location of the simulated pixel and the spatial overlapping between the footprints of this pixel on the pixels of the reference image. Results have been compared with the real data measured on the same scene by the same sensor. It shows that the level of accuracy depends on the precision with which the pixel position and its spectral information is obtained and preserved by the sensor. In this case, the positioning errors are very important especially in quantitative image processing, where sub-pixel analysis is one of the most commonly used techniques.

1 INTRODUCTION

Nowadays, there are a lot of applications that makes ample use of the enormous amount of Earth observation information collected every day, for instance, the study of changes on the Earth's surface. However, one of the main problems with this kind of study is the difficulty faced when comparing time image sequences of a certain region, due to the fact that the acquisition conditions may not be exactly the same, for example, due to variations in weather conditions or instrument calibration, or modifications in the trajectory and height of the plane that carries the sensor.

A number of generic formats to collect all these generated data exist (Mather, 2004), and the efforts of the CEOS (Committee on Earth Observation Satellites) to develop standardized formats are very promising. These include the HDF format, designed by NASA, which is becoming a standard.

Although a great service is already provided to the user community by standardizing formats, any new formats should also facilitate the comparison of images taken by different sensors under different acquisition scenarios. In addition, new data formats should make on board processing easier by

introducing real time algorithms (Du, 2003). However, on board processing requires that data structures integrate the spatial information provided by the positioning hardware with the continuous flow of spectral information provided by the different instruments carried on the platform (Martínez, 2005).

The original data collected by remote sensing instruments are in L0 format. They are usually pre-processed before being delivered to the user. Image pre-processing includes several operations such as noise reduction, radiance conversion, and geometric correction (Mather, 2004). A geometric correction is necessary to generate a map projection of the L0 image by removing any pixel misalignment.

When acquiring an airborne image it is necessary to take into account that the platform can be subjected to movements, so a GPS (Global Positioning System) / INS (Inertial Navigation System) system can be helpful to restore the data according to the location of the measurements. In this way, a geo-correction process like the one in Figure 1a) is required. Figure 1b) and 1c) are zoomed in regions of the geo-corrected image used in this work, with the latter one representing a synthetic image that will be useful to illustrate the concepts explained in the remaining article.

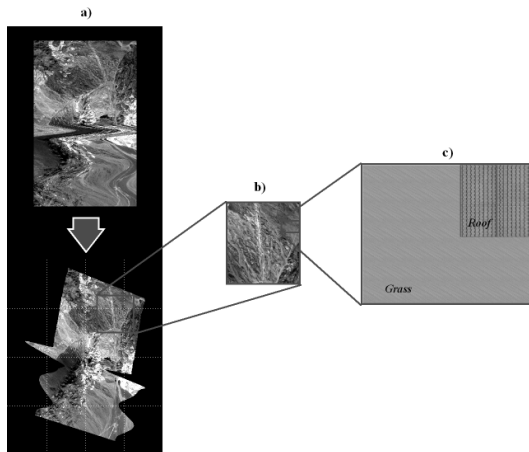


Figure 1. Image acquisition at different levels.

From the user's point of view geo-corrected images are easier to understand and to compare with maps or other images. L0 images, on the contrary, can be difficult to analyze and interpret by human experts. In this context, the geo-correction procedure can be viewed as creating an interface that makes images more easily readable by the analyst. On the other hand, geo-correction procedures require extensive computer resources and introduce spatial and spectral data errors in the very first stages of the image processing work flow.

From the machine's point of view it is possible to process the L0 image using conventional digital image analysis techniques, and leaving the geo-correction procedure at the very end of the image processing chain, when human intervention is required to conduct image comparison and visual analysis. The advantage of this schema is that more accurate image processing can be performed because the real spatial and spectral information as measured by the sensor is being used.

Therefore, new image formats should take this schema into account by using the original spectral and spatial data contained in the same file. At the same time these new formats need the development of new image processing algorithms or the modification of existing ones for processing this kind of files.

The positioning errors become especially obvious in hyperspectral image processing, where sub-pixel analysis is one of the most commonly used techniques. The level of accuracy achieved by this kind of analysis directly depends on the precision with which the pixel position and its spectral information is obtained and preserved by the sensor. This means that it is not possible to carry out an accurate sub-pixel analysis if the precise pixel position is not exactly known. In addition, the same pixel of the geometrically corrected image may correspond to two

different measurements performed by the sensor. Furthermore, one of the measurements may have been deleted during the resampling process, and thus, some of the information of the original data may have been lost, average out or, in the worst scenario, even be false information, contributing thus, to a loss of accuracy in the sub-pixel analysis. For all these reasons, the optimal data format must preserve the precision of both spatial and spectral information.

1.1 Airborne Hyperspectral Images

Hyperspectral sensor systems record the Earth's surface by building a bi-dimensional L0 image cube containing each measured band. In this case the airborne sensor captures an image, the random movement of the platform causes the real position of the centroids of the acquired pixels not to match any regular scene pattern. Figure 2 shows an example of how a sensor takes the measurements when it is subjected to these platform movements. In this figure, the circles represent the integration area of the pixel's Ground Instantaneous Field Of View (GIFOV) (Mather, 2004). These measurements are placed according to their relative position in the L0 matrix without considering their real spatial location. Because of the pixel-spacing irregularity, L0 images always give the sensation of being distorted to human eyes.

Figure 3 shows the ground-truth image that corresponds to the area where the real spatial locations of the pixels' centroids were obtained from measurements by the GPS/INS system on board the platform.

In both figures (Figure 2 and Figure 3), the integration area of the measurements' target aim have been indexed for easier identification.

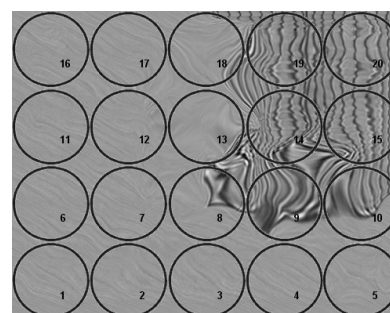


Figure 2. L0 image showing the visual deformation of the scene.

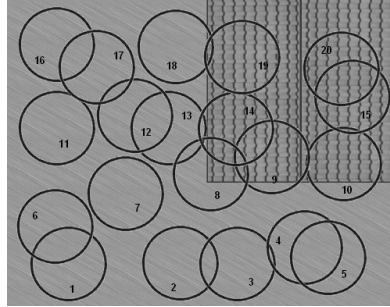


Figure 3. Pixel integration areas projected over the ground-truth image showing the real distribution of the measurements.

The spatial position of the pixel centroids in one image would not match the centroids in another image acquired over the same area, even if both were collected with the same sensor, altitude and platform. This can be largely attributed to the randomness of the platform movements during image acquisitions (Boardman, 1998). Although both images could enclose the same region and have the same spatial and spectral resolutions, the exact location of each pixel as measured by the sensor would be different from one image to the other.

Figure 4 shows how important performing these corrections on a scene is and the great impact they can have on subsequent sub-pixel analysis. In order to show the effects that geo-correction procedures can have on measurement displacements, a grid has been superimposed that corresponds to the ground truth pixel distribution and reflects the real spatial location of surface features. The grid cells have been numbered consecutively starting from the lower left corner.

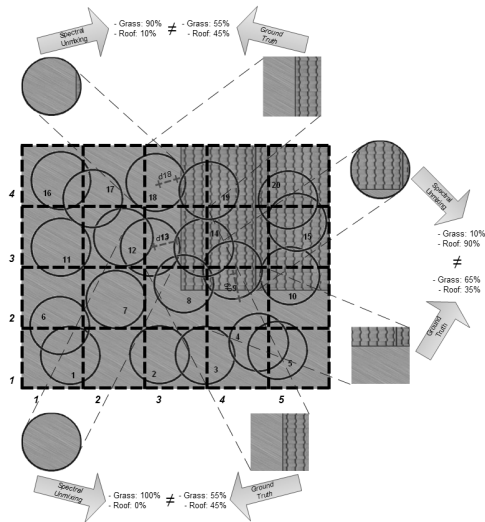


Figure 4. Erroneous unmixing results caused by geo-correction-induced displacements.

As can be observed, measurement 13 was obtained over an area covered by grass only. This means that the spectral composition that can be derived from this measurement by spectral unmixing should be 100% grass and 0% of other constituents. However, the spectral composition in grid cell (3,3) of the ground truth image, where measurement 13 is being placed after geo-correction, is in reality 50% of grass and 45% of roof material and therefore, does not correspond to the new assigned spectrum of 100% grass. This discrepancy is due to the fact that measurement 13 has been displaced by a distance of d13 from its real location, and with it the spectral information has been relocated.

Obviously, this relocation problem affects not only a single pixel but most of the pixels in the geo-corrected image. For instance, measurement 18 has a composition of 90% of grass and 10% of roof and will replace (after geo-correction) the real composition of 55% of grass and 45% of roof at pixel position (4,3). Another example is measurement 9 with its surface composition of 10% of grass and 90% of roof that will substitute the real composition of 65% of grass and 35% of roof at pixel (2,4).

2 METHODOLOGIES

New data structures are needed to optimize the way in which Earth surface information is currently being stored. The main aspects that need to be improved in current formats are: spatial and spectral information preservation; minimization of the image size, avoidance of duplicated information storage; and optimization of image processing in super-computer systems in order to facilitate the distribution of pieces of information.

In order to improve the performance of current formats according to the above listed requirements, we propose a data structure called Diffused Matrix (DMF) (Chaves, 2007; Cristo, 2009; Martínez, 2010).

This data structure is based on a measurement record (DMR), which stores information pertaining to each one of the actual measurements taken by the sensor. This information includes the UTM location of the pixel, and its spectrum (Figure 5).

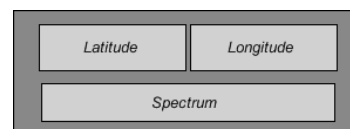


Figure 5. A DMR structure.

The DMR records will be placed in a grid called DMF matrix, according to their respective UTM location. This matrix is a regularly spaced grid that is indexed in

N/S direction with respect to the latitude and longitude and in which the size of the elemental cell must be determined from the uncertainty of the pixel position due to the platform movements. A first approach consists of selecting a size in which each cell has at least one real value (DMR). Using this scheme, it is possible to place each one of the DMRs in a specific cell depending on its UTM location. In this way, each measurement is automatically spatially placed in its respective cell, allowing real time image processing, without the necessity of running first a geo-correction phase.

One aspect that has to be taken into account is that spatially very close measurements may occur, meaning that more than one measurement may represent the same cell area (this situation occurs more often when the matrix resolution decreases, that is, when the cell size increases). In these cases, instead of averaging or substituting that particular cell, the DMR data structure will store all the corresponding real values. Therefore, as seen in Figure 6, each matrix cell will be a pointer to a list of DMRs. This enables the user to always work with the real values, and it facilitates changing the image scale without losing information. This makes it possible to process the data even in extreme situations, for example when handling a maximum resolution image, which has a maximum of DMR in each cell, or a minimum matrix with a single cell that stores all the image data.

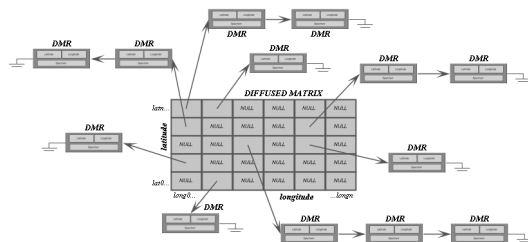


Figure 6. Structure of the Diffused Matrix (DMF).

There is only one case where the average spectrum of two measurements would be calculated, storing only one measurement, and that is when both measurements are within the aiming uncertainty (Δlat , Δlong) provided by the GPS/INS positioning system. When this situation happens, calculating an average does not imply an information loss but a noise reduction.

Similarly, it is also possible to find cells with no values in the Diffused Matrix, because the sensor did not take any measurements in that specific spatial interval. These cells are excluded while processing the diffused matrix.

3 RESULTS

In order to test the location accuracy improvement when working with the DMF version of the scene in regards to the geo-corrected version, three images of the same scene were used. The first one belongs to an acquisition in a low altitude flight, and due to this, it could be considered as ground-truth. The other two images belong to an acquisition of the same scene in a higher altitude flight, being one of them in DMF format (built from the L0 and IGM files) and the other one geo-corrected (using a conventional geo-correction from the L0 and IGM files). The abundances of the three images were extracted using Linear Spectral Unmixing (LSU). Then, the abundance values for the DMF and the geo-corrected versions of the scene (high altitude) were compared to the abundance values of the ground-truth (low altitude), according to the spatial location of the measurements, provided by the Diffused Matrix and the geo-corrected image.

Figure 7 shows the whole process in a schema for a better comprehension.

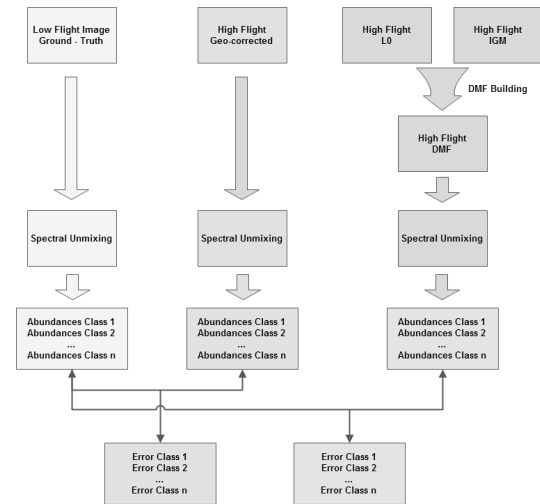


Figure 7. Schema showing the methodology used to test the accuracy.

Firstly, a scene of the Ivanpah Lake, California (USA) acquired by the AVIRIS sensor was used. Figure 8 shows the L0 (Figure 8a) and the geo-corrected (Figure 8b) versions of the higher altitude images, just for better visual identification. Five classes were considered for the abundance extraction: Desert, Lake Sand, Road, Water and Vegetation.

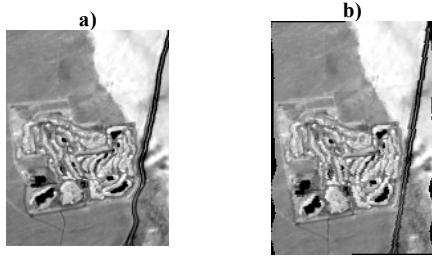


Figure 8. L0 and geo-corrected versions of the Ivanpah Lake scene.

Table 1 presents the abundance errors obtained by the DMF and geo-corrected versions with regard to the ground-truth. The error results indicate that, because the DMF always stores the real location of the measurements as provided by the GPS/INS system, the obtained DMF accuracy is better than the one obtained by the geo-corrected version (the errors committed are smaller), especially for the classes represented by few pixels such as Road, Water and Vegetation, where more accuracy is needed.

	Geo-corrected	DMF
Desert	0.361	0.322
Lake Sand	0.502	0.315
Road	0.243	0.080
Water	0.196	0.037
Vegetation	0.310	0.083

Table 1. Accuracy results for the Ivanpah Lake dataset.

In order to support the obtained results, the accuracy of the DMF was tested using a different scene acquired by a different sensor. In this case, the region of Barrax, Valencia (Spain) obtained by the AHS sensor. Figure 9 shows the L0 (Figure 9a) and the geo-corrected (Figure 9b) versions of the higher altitude images, just for a better identification. Nine classes were considered for the abundance extraction: Roof, Building, Road, Sand Road, Crop1, Crop2, Crop3, Crop4, and Crop5.

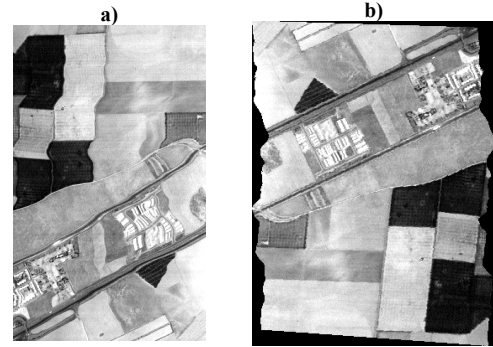


Figure 9. L0 and geo-corrected versions of the Barrax scene.

Table 2 presents the abundance errors obtained by the DMF and geo-corrected versions with regard to the ground-truth. In this case, the abundance error difference is not as high as in the previous case, because the platform was more stable. In spite of this, the accuracy obtained by the DMF version is still better than the one obtained by the geo-corrected version.

	Geo-corrected	DMF
Roof	0.033	0.022
Building	0.016	0.012
Road	0.064	0.038
Sand Road	0.096	0.061
Crop1	0.119	0.048
Crop2	0.240	0.029
Crop3	0.333	0.187
Crop4	0.234	0.087
Crop5	0.130	0.064

Table 2. Accuracy results for the Barrax dataset.

4 CONCLUSIONS

This work presents a study of the spatial errors produced by hyperspectral sensors due to the movements the platform and the subsequent pixel displacements that occur when geo-correcting the resultant image. To solve this problem, a new data structure called Diffused Matrix (DMF) that enables improved data storage of airborne hyperspectral images has been designed. This DMF provides several advantages over conventional formats. For example invalid or averaged pixels are discarded, which reduces the margin of processing error of this kind of images considerably. To test its accuracy, an experiment consisting of determining the errors committed by spectral unmixing in a geo-corrected

image and in its analog in DMF with regard to the ground-truth has been developed. Results, carried out for two different sensors and two different scenes, have shown that the accuracy achieved by the DMF data structure is much better than the errors obtained when working with geo-corrected images, because more accurate spatial locations are being considered.

5 ACKNOWLEDGEMENTS

The authors would like to thank Robert O. Green and the AVIRIS team for their support with the AVIRIS images, and José Moreno and the AHS team for his support with the AHS images.

6 REFERENCES

- Boardman, J.W., 1998, Precision geocoding of low-altitude AVIRIS data: lessons learned in 1998, *8th Annual JPL Airborne Geoscience Workshop*, Pasadena, CA, USA.
- Chaves, J.M., Vega, M.A., Martínez, P., Sánchez, J.M., Gómez, J.A., 2007, Diffuse Matrix: An optimized data structure for the storage and processing of hyperspectral images, *SIGMAP 2007*, Ed. INSTICC, Barcelona, Spain.
- Cristo, A., Martínez, P., Valencia, D., Hernández, L.M., Pérez, R.M., Plaza, A., Plaza, J., Aguilar, P.L., 2009, Análisis del funcionamiento de la Matriz Difusa para el tratamiento de imágenes hiperespectrales, *GlobalGeo, Geomatic & Telematic International Show. International Geomatic Week*, Barcelona, Spain.
- Du, Q., Ren, H., 2003, Real time linear discriminant analysis to target detection and classification in hyperspectral imagery, *Pattern Recognition*, 36, 1-12.
- Martínez, P., Hermosel, D., Green, R.O., Plaza, J., Pérez, R.M., 2005, An improved data structure for AVIRIS-type imaging spectrometer measurements, *13th JPL Airborne Earth Science Workshop*, Pasadena, CA, USA.
- Martínez P., Cristo, A., Koch, M., Pérez, R.M., Schmid, T., Hernández, L.M., 2010, Diffused Matrix Format: A new storage and processing format for airborne hyperspectral sensor images, *Sensors*, 10(5), 4996-5013.
- Mather, P.M., 2004, Computer processing of remotely sensed images, 3rd edition, *Wiley and Sons Ltd.*, West Sussex, 2004.

Discrimination of Cruciferous Weeds in Wheat Crops Using Quickbird Satellite Image

A.I. De Castro, M. Jurado-Expósito, M.T. Gómez-Casero, D. Gómez-Candón, J.J. Caballero-Novella and F. López-Granados.

Instituto de Agricultura Sostenible (IAS)-CSIC. Córdoba.

anadecastro@ias.csic.es

ABSTRACT-Weeds seriously impair crop development and yield. Herbicides are commonly applied over the entire agricultural fields although weeds are spatially distributed in patches. To reduce the consumption of herbicides, applying them only where weeds patches occur, it is necessary to develop accurate weed maps. A Multispectral (Blue, Green, Red, NIR) QuickBird image (2.4 m pixel size) was taken in April 2009 in an area located in the province of Cordoba (southern Spain) naturally and highly infested by cruciferous weeds. Multispectral bands and vegetation indices were subjected to analysis of variance (ANOVA) and means were separated at the 0.01 level of significance by LSD to determine the potential of QuickBird imagery for mapping cruciferous weeds in wheat. Accuracy of weed maps was also evaluated according to different patch size. Our results showed significant differences between wheat and cruciferous spectral values. Cruciferous patches were efficiently discriminated with the four bands and RVI, DVI and NIR/B vegetation indices. These results were affected by the infested patch size, showing the biggest differences from 12 m² patch size. A supervised classification was carried out with those bands and vegetation indices that provided the best results in the statistics analysis. The results show the availability of QuickBird imagery for the discrimination of cruciferous weeds.

1 INTRODUCTION

Cruciferous weeds, *Diplotaxis* spp. (generally *D. virgata* Cav. DC. and *D. muralis* L.) and *Sinapis* spp., (generally *S. arvensis* L. and *S. alba* L.) are very competitive broadleaf species and infest frequently cereal and legume crops. These weeds are distributed in patches and produce high yield losses in wheat (Mas and Verdú, 2003), lentils (McDonald et al., 2007) and peas (Miller et al., 2006). Winter crop weeds are commonly kept under control with pre-sowing herbicides incorporated in cereals and pre-emergence herbicides in legumes, however these herbicides do not provide an adequate control of cruciferous. There are specific and expensive herbicides that can be applied in post-emergence in cereals, but there is not any post-emergence herbicide for legume crops and then, cruciferous weeds must be controlled by tillage or weeding hoe.

The classical sunflower-wheat Andalusian rotation is being substituted by sunflower-legume-wheat rotation, therefore, cruciferous infestations are present in two of the crops of this rotation. Weeds populations tend to be distributed in stripes along the direction of cultivation, and aggregated or patchy (Jurado-Expósito et al 2003), although herbicides are commonly applied over the entire agricultural field. As a rationale consequence, site-specific weed

management (SSWM) can be used to apply any of the control measures available (herbicide, tillage) only to weed patches and/or to adjust application to weed density, the economic threshold or weed species composition (López-Granados, 2010). Accurate, appropriate and timely weed maps are the key components required in order to take full advantage of site-specific herbicide applications, avoiding over-applications and excess (Lamb and Brown, 2001). Detection and mapping of late-season weeds infestation with remote sensing is very feasible when spectral differences between crops and weeds are greatest and before crops and weeds have both reached the same phenological stage. Thus, late-season weed detection maps can be used to design SSWM to apply in-season post-emergence herbicides, in case of adequate pre-emergence control was not achieved, or in subsequent years, taking into account the fact that weed infestations can be relative stable in location from year to year (Jurado-Expósito et al., 2004). Thus, the capacity to discriminate problematic weeds at advanced phenological stage could reduce herbicide use and control costs. Multispectral aerial imagery have been used to accurately map late infestations of wildoat (*Avena sterilis*), canarygrass (*Phalaris brachystachys*) and ryegrass (*Lolium rigidum*) in wheat (López-Granados et al., 2006); corn caraway (*Ridolfia segetum*) in sunflower (Peña-Barragán et al., 2007; Gutiérrez et al., 2008); foxtail (*Setaria faberi*),

velvetleaf (*Abutilon theophrasti*) and other weeds in soybean (Gibson et al., 2004; Gray et al., 2008; Koger et al., 2003). These papers concluded this tool have enormous potential for discriminating weeds and crops.

In previous research, cruciferous patches were efficiently discriminated (> 85% overall accuracy) using high resolution aerial imagery (0.25 m of pixel) and supervised classification methods based on bands and vegetation indices (De Castro et al., 2009).

The objectives of this contribution are: 1) to determine the potential of QuickBird multispectral satellite image for discriminating and mapping cruciferous weeds, and 2) to evaluate the influence of the patch size for further development of herbicide treatment maps for site specific weed management.

2 MATERIALS AND METHODS

2.1 Study area and QuickBird image.

A Multispectral (Blue, B: 450-520 nm; Green, G: 520-600 nm; Red, R: 630-690; NIR: 760-900 nm) QuickBird image (2.4 m pixel size) was taken in April (spring in our conditions) 2009, in an area located in the province of Cordoba (southern Spain) where most of the wheat fields were naturally and highly infested by cruciferous weeds. At timing when satellite image was taken, the fields were visited to collect and georeference training points (TPs) and ground truth points (GTPs) of cruciferous-free wheat and weed-infested patches in order to carry out, substantiate and validate the classification procedure. In that moment, the wheat showed the typical green colour of vegetative growth stage and the cruciferous weeds showed an intensive yellow colour corresponding to flowering growth stage. TPs and GTPs were taken with a differential global positioning system (DGPS) TRIMBLE PRO- XRS provided with TDC-1 unit (centimeter precision; Trimble, Sunnyvale, CA, USA).

Multispectral bands and vegetation indices and ratios derived from them (NDVI, RVI, DVI, R/B, B/G, NIR/B and NIR/G), were subjected to analysis of variance (ANOVA) and means were separated at the 0.01 level of significance by LSD test using JMP 8.0.2 (SAS Institute Inc., Campus Drive, Cary, NC, USA 27513) for discriminating cruciferous.

Accuracy of weed maps was also evaluated according to different patch size. Cruciferous patches were grouped into three classes taking into account the size: small, medium and large (Table 1).

Table 1. Cruciferous patch size.

Class	Patch size	Number pixels
Small	5.76 - 11.52 m ²	One or two
Medium	17.24 - 23.04 m ²	Three or four
Large	28.8 - 40.32 m ²	Five, six or seven

Δ NDVI= (NIR-R)/(NIR+R) Normalized Difference Vegetation Index; RVI= (NIR/R) Ratio Vegetation Index; DVI= (NIR-R) Difference Vegetation Index.

2.2 Classification Images

A supervised classification based on vegetation indices was carried out with those bands and vegetation indices that provided the best results in the statistics analysis. Boundary Digital Values Intervals (BDVIs) defined each region in an iterative way, based on the information provided by the TPs of each land use, established according to the statistical value obtained from the training pixels (mean and deviation), adding and reducing the standard deviation to the average. The selected BDVIs were those that better discriminated the two classified regions, providing the highest statistical accuracy. Every vegetation index or wavebands image was classified by grouping the BDVI that better characterized each land use.

ENVI 4.6 software was used to process, analyze the image and create classified maps. From those maps can be estimate the surface occupied by both land use (cruciferous patches and wheat) and to developed site specific cruciferous management program.

2.3 Accuracy assessments.

In order to quantify the coincidence between the ground-truth and the classified map a confusion matrix was performed. The confusion matrix provides the Overall Accuracy (OA), Kappa coefficient (K) and the User Accuracy (A) of the classification. The OA is the averaged accuracy index of each land use, and indicates the global success of the classification. The optimal value for each map was the one yielding the highest overall accuracy in its confusion matrix analysis. Kappa coefficient is defined to measure the difference between on-ground data and that predicted by chance using a random classification. User accuracy is defined as being the percentage of classified pixels of each land cover that coincide with the verified ground-truth map, and indicates its correct assessment. OA and per-class accuracy have been standardized in 85% and 70%, respectively, for minimum accepted values (Thomlinson et al., 1999;

Foody, 2002) and Kappa coefficient values greater than 0.80 (Landis and Kock, 1977).

3 RESULTS

Cruciferous patches were successfully discriminated from wheat and differences in digital values between both land uses were statistically significant in any of the bands or Vegetation Index analyzed (Table 2). For example, mean values of R for cruciferous and wheat were 138.57 and 116.70, and for the DVI index were 652.16 and 588.77, respectively. The major differences were obtained with the **four bands** and **RVI, DVI, R/B** and **NIR/B** vegetation indices.

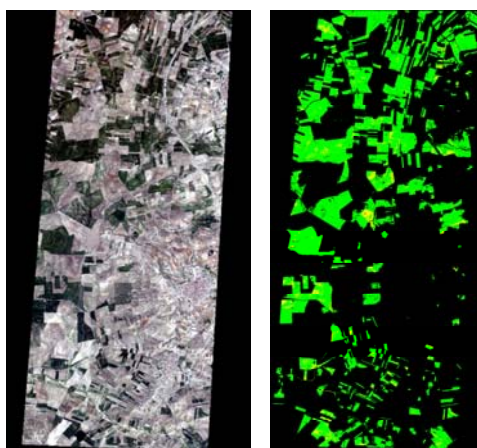


Figure 1. QB Image and QB Classified Image

The classification maps were affected by the infested patch size, showing that whereas **NIR, DVI** and **NIR/B** were able to discriminate wheat from any of the weed patch size, the rest of the bands or vegetation indices classified only cruciferous patch size equal or higher than 3 pixels (from medium patch size) (Table 3). For example, wheat can be potentially separated from small, medium and large cruciferous patch size when mean digital values in the NIR waveband are 705.47 for wheat, and 760.31, 806.76 and 870.67 for small, medium and large patch size, respectively. It is important to point out that the **G** waveband can discriminate wheat from small, and medium-large patch size.

Both results could have environmental and economical implications in terms of site-specific weed management and reducing herbicide use since farmers usually only apply herbicides when weed aggregates are bigger than 12 m².

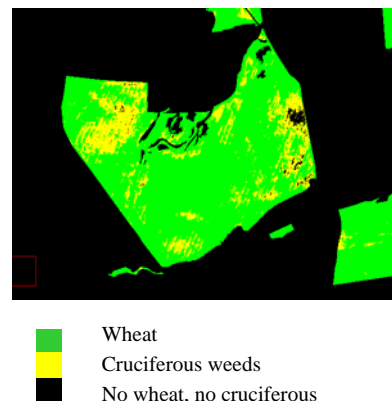


Figure 2. Detail of the QB Image and QB Classified Image.

In Table 4 are shown the selected intervals providing the highest overall accuracy and the classification statistics obtained in the Confusion Matrix (OA and User Accuracy) for DVI ratio and the surface occupied by both land use (cruciferous patches and wheat).

Table 4. Boundary Digital Values selected and Classification Statistics obtained in the Matrix Confusion with DVI ratio.

	BDVIs	OA%	A%	Area (ha)
Cruciferous	711-934	80.59	79.14	2,356
Wheat	330-710		81.09	167.5

The A% values results upper than 70%, as minimum accepted value showed by Thomlinson et al., (1999) and Foody (2002), show the availability of QuickBird imagery for the discrimination of cruciferous weeds.

An essential parameter in remote sensing is to select the suitable pixel size based on the inherent properties of the input data, *i.e.*, what is the smallest discernable feature at any given spatial resolution and the accuracy at which it is mapped. Hengl (2006) discussed the rules of thumb to find the right pixel size to help inexperienced users select the appropriate spatial resolution. He concluded that at least four pixels are required to detect smallest objects and at least two pixels to represent the narrowest objects, being objects the smallest size area that we map (weed plants or weed patches in our case). However, our results show that NIR waveband, and DVI and NIR/B vegetation ratios were able to successfully detect one object whether its size is one or two pixels (5.46 – 11.2 m²) in a Quick Bird Image (Table 3). Although the Anova analysis showed that the classification

accuracy increased when the patch size is integrated at least by three or four pixels.

4 CONCLUSIONS

The substantial differences in spectral response between wheat and cruciferous weeds for the visible range and NIR, and for RVI, DVI and NIR/B ratios proved the potential of QuickBird imagery for weed mapping and further site-specific herbicide treatments.

The classification maps were affected by the infested patch size, showing the best discrimination when the patch size is integrated at least by three pixels (12 m²). Although, NIR, DVI and NIR/B were also able to discriminate wheat from any of the weed patch size analyzed. These results are very interesting from an agronomy point of view, since farmers usually only apply herbicides when weed aggregates are bigger than 12 m². This has relevant environmental and economical implications in terms of site-specific weed management and reducing herbicide.

5 ACKNOWLEDGEMENTS

This research was partially funded by the Spanish Ministry of Science and Innovation (FEDER, R+D project AGL-2008-04670-CO3-03). The research of Ana Isabel de Castro was supported by CSIC-JAEPre-Preddoctoral Program (also co-financed by FEDER funds).

Table 2. Spectral wavebands and vegetation index mean values for cruciferous weeds and wheat

	B	G	R	NIR	NDVI	RVI	DVI	B/G	R/B	R/G	NIR/B	NIR/G
Cruciferous	181.53 a	264.85 a	138.57 a	790.3 a	0.70 a	5.81 a	652.16 a	0.74 a	0.76 a	0.52 a	4.36 a	3.00 a
Wheat	173.21 b	232.37 b	116.70 b	705.47 b	0.71 b	6.19 b	588.77 b	0.75 b	0.67 b	0.50 b	4.09 b	3.06 b

Table 3. Spectral wavebands and vegetation index mean values for wheat and small, medium and large cruciferous patch size.

	B	G	R	NIR	NDVI	RVI	DVI	B/G	R/B	R/G	NIR/B	NIR/G
Small	180.39 a	260.79 b	136.32 b	760.31 c	0.69 b	5.68 b	624.00 c	0.69 b	0.75 b	0.52 a b	4.22 c	2.93 c
Medium	182.44 a	268.47 a	141.37 a	806.76 b	0.70 b	5.83 b	665.39 b	0.68 c	0.77 a	0.52 a	4.44 b	3.02 b c
Large	183.16 a	269.20 a	137.64 a b	870.67 a	0.72 a	6.35 a	733.03 a	0.68 b c	0.75 a b	0.51 b c	4.74 a	3.23 a
Wheat	173.21 b	232.37 c	116.70 c	705.47 d	0.71 a	6.19 a	588.77 d	0.75 a	0.67 c	0.50 c	4.09 d	3.06 b

For each column and land use, mean values followed by the same letter are not statistically different at P= 0.01

6 REFERENCES

- De Castro A.I., Jurado-Expósito M., Peña-Barragán J.M., García Torres and López-Granados, F., 2009, Clasificación de *Diploaxis virgata* y *Sinapis arvensis* en trigo, habas y guisantes mediante imágenes aéreas. Proceedings of the XII Congresso SEMh/ XIX, XIX Congresso ALAM, II Congresso IBCM. Lisboa, on 10 November-13 November 2009. Vol II: pp. 579-582. (Ed.) ISA press.
- Foody, G.M., 2002, Status of land cover classification accuracy assessment. *Remote Sensing of Environment*, **80**, 185-201.
- Gibson, K.D., Dirks, R., Medlin, C.R. and Jonston, L., 2004, Detection of weed species in soybean using multispectral digital images. *Weed Technology* **18**, 742-749.
- Gray, J.C.J., Shaw, D.R., Gerad, P.D. and Bruce, L.M., 2008, Utility of multispectral imagery for soybean and weed species differentiation. *Weed Technology* **22**, 713-718.
- Gutiérrez-Peña P.A., López-Granados F., Peña-Barragán J.M., Jurado-Expósito M. & Hervás-Martínez C., 2008, Logistic regression product-unit neural networks for mapping *Ridolfia segetum* infestations in sunflower crop using multitemporal remote sensed data. *Computers and Electronics in Agriculture* **64**, 293-306.
- Hengl, T. 2006. Finding the right pixel size. *Computers and Geosciences* **32**, 1283-1298
- Jurado-Expósito, M., López-Granados, F., García-Torres, L., García-Ferrer, A., Sánchez de la Orden, M. and Atenciano, S., 2003, Multi-species weed spatial variability and site-specific management maps in cultivated sunflower. *Weed Science* **51**, 319-328.
- Jurado-Expósito, M., López-Granados, F., González-Andujar, J.L. and García-Torres, L., 2004, Spatial and temporal analysis of *Convolvulus arvensis* L. populations over four growing seasons. *European Journal of Agronomy* **21**, 287-296.
- Koger, C.H., Shaw, D.R., Watson, C.E. and Reddy, K.N., 2003, Detecting late-season weed infestations in soybean (*Glycine max*). *Weed Technology* **17**, 696-704.
- Lamb, D.W. and Brown, R.B., 2001, Remote-sensing and mapping of weeds in crops. *Journal of Agricultural and Engineering Research* **78**, 117-125.
- Landis, J.R. and Kock, G.G., 1977, The measurement of observer agreement for categorical data. *Biometrics* **33**, 159-174.
- López-Granados, F., Jurado-Expósito, M., Peña-Barragán, J.M. and García-Torres, L., 2006, Using remote sensing for identification of late-season grass weed patches in wheat. *Weed Science* **54**, 346-353.
- López-Granados, F. Weed detection for site-specific weed management: mapping and real time approaches. 2010. *Weed Research*. In press.
- Mas, M. and Verdu, A.M.C., 2003, Tillage system effects on weed communities in a 4-year crop rotation under Mediterranean dryland conditions. *Soil and Tillage*, **74**, 15-24.
- McDonald, G.K., Hollaway, K.L. and McMurray, L., 2007, Increasing plant density improves weed competition in lentil (*Lens culinaris*). *ropping. Australian Journal of Experimental Agriculture*, **47** (1), 48-56.
- Miller, P.R., Ángel, R.E. and Holmes, J.A., 2006, Cropping Sequence Effect of Pea and Pea Management on Spring Wheat in the Northern Great Plains. *Agronomy Journal*, **98**, 1610-1619.
- Peña-Barragán, J.M., López-Granados, F., Jurado-Expósito, M. and García-Torres, L., 2007, Mapping *Ridolfia segetum* patches in sunflower crop using remote sensing. *Weed Research* **47**, 164-172.
- Thomlison, J.R., Bolstad, P.V. and Cohen, W.B. 1999. Coordinating methodologies for scaling landcover classifications from site-specific to global: steps toward validating global map product. *Remote sensing of Environment* **70**, 16-28.

DETERMINACION DE LA CONTAMINACION PRODUCTO DE LA ACTIVIDAD MINERA, UTILIZANDO SENSORES DE ALTA RESOLUCION ESPECTRAL, EN HUANCATELICA

Díaz Núñez, Mirella Y.¹, Loaiza Jordan, Yahayda¹, Miguel Miranda Peña¹ & Milagros Caycho B.²
¹Comisión Nacional de Desarrollo e Investigación Aeroespacial – CONIDA y ²Dirección General de Salud Ambiental - DIGESA.
Email: mdiaz@conida.gob.pe, mmiranda@conida.gob.pe, mcaycho@digesa.minsa.gob.pe

ABSTRACT

El estudio se realizó para determinar la viabilidad del análisis espectral en la determinación de minerales típicos de alteraciones hidrotermales y contaminación del suelo a causa de relaves mineros; ubicado en la convergencia de los distritos de Castrovirreina, Santa Ana y Pilpichaca, en la Región Huancavelica (centro del Perú). Se ha escogido utilizar datos satelitales de Aster, Hyperión y Ali por sus características espectrales, complementándose con información cartográfica y temática. Como parte del pre-procesamiento y procesamiento de las imágenes de satélite se hizo la calibración radiométrica (nivel de adquisición LIB y LIR) y corrección atmosférica (con software ACORN y Flash de ENVI). Se compararon con las firmas espectrales de la USGS (usgs_min y igcp_4) y obtenidas en campo (PIMA) vs las firmas espectrales de las imágenes para identificar y mapear utilizando técnicas de procesamiento de datos hiperespectrales. También se realizó un trabajo de campo junto a la Dirección General de Salud Ambiental - DIGESA (Lima) y la Dirección Regional de Salud Ambiental – DIRESA, cerca a las minas de San Genero, Reliquia y Caudalosa; permitiendo reconocer la caracterización de aspectos geológicos estructurales y minerales de alteración argílica y argílica avanzada (sílice-alunita); además se tomaron puntos de control GPS y muestras de agua y suelo, este último se analizó con un espectrómetro Infrarrojo de Onda Corta, permitiendo validar los resultados obtenidos de las imágenes. Logrando generar una librería espectral con 4 minerales como patrón de muestra de alteración argílica.

1 INTRODUCCION

La geología de la zona de estudio está comprendida por una secuencia de rocas sedimentarias y volcánicas que datan desde el Cretáceo inferior representado por el Grupo Gollarysquiza (Valanginiense al Aptiano) las formaciones volcánicas de edad Neógena, representado por varias formaciones volcánicas, entre la más reciente esta la Formación Astobamba (mioceno – plioceno), que aflora al NE de la Carta nacional (27M); también afloran pequeñas intrusiones de granodiorita, monzogranito y diorita, parte del batolito de la costa, que intruye una secuencia mesozoica y parcialmente las secuencias volcánicas del terciario.

En cuanto a los yacimientos minerales de la zona se puede decir que han sido controlados por dos factores: Estructural (fallamiento) y magmatismo (vulcanismo). Estos yacimientos están referidos a los cambios en mineralogía y textura de las rocas encajonantes circundantes a las estructuras mineralizadas, este tipo de alteración puede darse antes, durante o después de la deposición de los minerales metálicos.

El principal control estructural en la zona de estudio, se denominada Falla Chonta con dirección NW-SE, y que controla el emplazamiento de la mineralización filoniana polimetálica y argentífera epitermal tipo bonanza en rocas volcánicas (agrupamientos San Genero y Huachocolpa).

Las alteraciones que se observan son argílica avanzada, (sílice-alunita) dentro de un amplio halo (filico-argílico). Así de esta manera podemos definir a la alteración argílica y argílica avanzada con abundantes arcillas.

Estos eventos geológicos también dieron origen a las alteraciones más extendidas en esta área de las cuales la alteración propilítica de intensidad débil es la que rodea a las otras alteraciones. A esta alteración le sigue la argílica pura que es muy limitada y casi siempre rodea a la alteración argílica en forma de bandas muy angostas, la alteración argílica de intensidad débil a mediana forma áreas irregulares circundando a cuerpos de sílice y vetas, la argílica avanzada es restringida a un punto del área de Vulcano, la silicificación se muestra formando cuerpos vetiformes y el ensamble cuarzo-sericita más arcillas está restringida a las cajas cercanas de las vetas.

2 MATERIALES Y METODOLOGIA

Se utilizaron las siguientes imágenes multispectrales e hiperespectrales:

ASTER (Advanced Spaceborne Thermal Emission and Reflection Radiometer) a bordo del satélite TERRA, el cual cuenta con una resolución temporal de 16 días, un ancho de barrido de 60 Km². ASTER está compuesto por tres subsistemas, VNIR (Visible Near Infrared), con 3 bandas, SWIR (ShortWave Infrared), con 6 bandas y TIR (Thermal Infrared), con 5 bandas; estas características espectrales fueron diseñadas especialmente para aplicaciones geológicas.

ALI (Advanced Land Imager) a bordo satélite EO-1, con una resolución temporal de 16 días, un ancho de barrido de 36 Km², esta imagen tiene 10 bandas de las cuales la primera es pancromática (10 metros de resolución) y 9 multispectrales (6 en el VNIR y 3 en el SWIR con una resolución de 30 metros), está diseñado para reemplazar al ETM+ en futuras misiones Landsat, esta imagen viene dividida en 4 tiras, las cuales se unen basándose en los píxeles de la imagen para formar un mosaico.

Hyperion (Imaging Spectrometer) es el primer sensor hiperespectral a bordo de un satélite EO-1, con una resolución temporal de 200 días, con un ancho de barrido de 7.5 km, dispone de 220 bandas que cubren de 0.4–2.5 µm con 30 metros de resolución. Gracias a su resolución espectral capta los colores de las imágenes de la superficie de la Tierra sin dejar áreas descubiertas, se puede hacer mapeos detallados de cobertura vegetal, minerales, etc.

Se utilizó la cartografía Base a escala 1/100 000 del Instituto Geográfico Nacional - IGN, para la ubicación del área de estudio, la Geología a escala 1/100 000 del Instituto Geológico Minero y Metalúrgico – INGEMMET, para reconocer el tipo de formación del suelo, mapas de vertimientos y estaciones de monitoreo en las lagunas del distrito de castrovirreyna proporcionados por la Dirección General de Salud Ambiental – DIGESA, para ubicación y ver los posibles metales presentes en la zona de estudio.

Como patrón de muestra se utilizó las librerías espectrales del igcp264, jhu_lib; jpl_lib; usgs_min y las firmas espectrales de ASTER (jhu_desc; jpl_desc) Spectral Library V.2.0, autores A.M. Baldridge, S.J. Hook, C.I. Grove, G. Rivera, del Jet Propulsion Laboratory, quien nos proporcionó dicha información digital.

Además de las firmas espectrales obtenidas de las muestras tomadas en campo, con un espectrómetro Infrarrojo de Onda Corta (PIMA).

2.1 Pre- Procesamiento

Las características de cada imagen son esenciales a la hora de hacer una selección de cuáles usar y para qué tipo de estudio, estas características también son usadas para calibrar la imagen, por que constan de diversos valores para cada una de ellas. Se utilizó las imágenes Aster, Ali, Hyperion, las cuales se tuvieron que llevar a valores de radiancia con la siguiente fórmula matemática.

Para ASTER L1B:

Radiancia = (ND value-1) x Unit conversión Coefficient. (JPL, ASTER Handbook).

Para ALI nivel 1R: datos procesados antes del 22 de diciembre de 2004:

$L = DN / 300.0$ (EO1-DFCB-0001 Versión 4.0)

Para HYPERION:

VNIR (1-70) $L = DN / 40.0$ y
SWIR (71-242) $L = DN / 80.0$ (EO-1 User Guide v.2.3)

Una vez obtenida la Radiancia se llevó a valores a reflectancia TOA por cada banda, con la siguiente fórmula:

$$\rho = \frac{\pi \cdot L_{\lambda} \cdot d^2}{ESUN_{\lambda} \cdot \cos(\theta_s)}$$

ρ = unitless planetary reflectance

L_{λ} = Spectral radiance at the sensor's aperture

d = Earth-Sun distance in astronomical units from nautical

$ESUN_{\lambda}$ = Mean solar exoatmospheric irradiances from Table 11.3

θ_s = Solar zenith angle in degrees

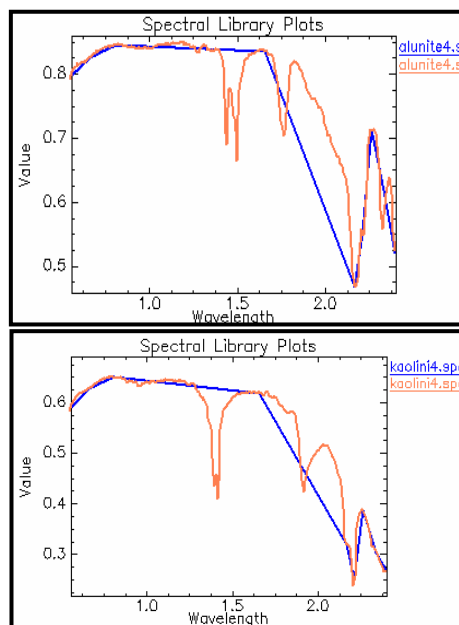
Para obtener una reflectancia de superficie, se utilizó la corrección atmosférica con el método FLAASH del Software ENVI, para esto se integraron los subsistemas VNIR y SWIR a una resolución espacial de 30m de la imagen Aster L1B, también se realizó la unión (fusión) de los subsistemas VNIR de la imagen Ali con el SWIR de la imagen Aster L1B, obteniendo valores de reflectancia TOA. Es fundamental tener las imágenes con esos valores para poder comparar las firmas espectrales de las imágenes vs. las firmas de la USGS y las firmas espectrales obtenidas de las

muestras de suelo tomadas en campo. De la imagen Hyperión se tuvo que depurar ciertas bandas que no contienen información (sin calibrar), de un total de 242 bandas se analizó 158 bandas que también se hizo la corrección atmosférica.

2.2 Procesamiento e Interpretación de Datos

Se han procesado imágenes de distintas fechas, la imagen Aster (10/09/2003), se elaboró mosaicos de las imágenes Ali (26/09/2003), y Hyperión (26/09/2003). Las diferentes combinaciones de bandas en los subsistemas VNIR, SWIR de Aster, permitió el reconocimiento preliminar de las unidades geológicas y áreas de alteración. También se hizo una fusión de la imagen Ali con la imagen Aster obteniendo así una nueva imagen de 13 bandas a 30 metros de resolución. La imagen Hyperión sirvió para corroborar los datos espectrales que se obtuvieron de las imágenes multispectrales (Ali y Aster). Además se ha realizado un control de campo, en las áreas correspondientes, en la cual se tomaron muestras de suelo cronometradas con puntos de ubicación geográfica con GPS.

Las firmas espectrales del laboratorio USGS tienen mayor detalle por lo se tuvo que se remuestrear a la longitud del espectro electromagnético de la imagen Aster, así como al de la fusión Aster-Ali, para obtener mas detalle de absorción de los minerales. También se remuestreo las firmas obtenidas con el espectrómetro a la fusión Aster-Ali e Hyperión, para un mejor análisis.



3 RESULTADOS

Se analizaron las firmas de las imágenes multispectrales e hiperespectrales, donde en el mapeo de la imagen ASTER se logró discriminar entre la respuesta espectral de las arcillas y la de los óxidos de hierro, que se pueden interpretar como alteraciones argilíticas y limoníticas respectivamente. Se ha verificado la respuesta espectral de los minerales encontrados con las firmas de la USGS de Aster, para esto se utilizó el método de análisis espectral que se lleva a cabo buscando pixel por pixel, de acuerdo a los valores del pixel y la coloración de la roca en la imagen.

3.1 Análisis de las muestras tomadas en campo

Los resultados de las muestras de suelo analizadas con el espectrómetro, nos permitió identificar algunos minerales como Caolinita, Esmeclita, Illita, Sericita, Sílice y Jarosita, para ello la muestra del suelo no debe estar húmedo o en contacto con el agua para que no se pierda las características propias del elemento; estas muestras fueron tomadas de los alrededores de la zona, y no se tuvo acceso a la toma de muestras de los relaves ya que el suelo era fangoso por el cual no se determinó los metales que estarían contenidos en estos.

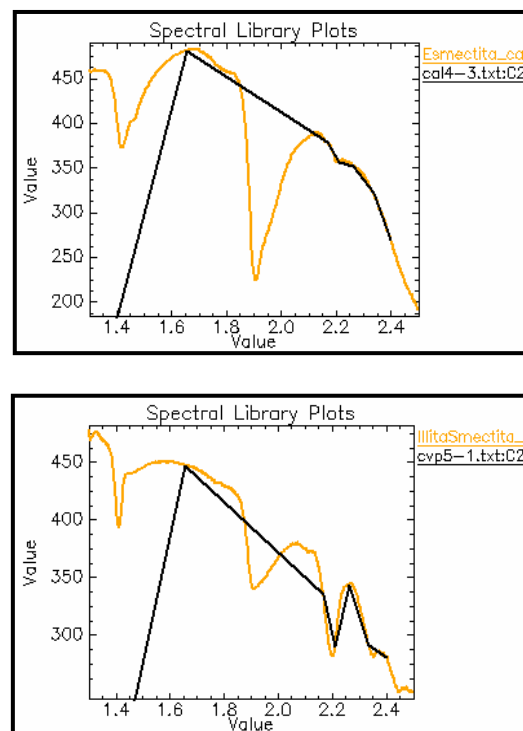


Fig.1. Firmas espectrales de la USGS (naranja) firmas remuestreadas a la imagen Aster (azul), de minerales comunes en yacimientos hidrotermales.

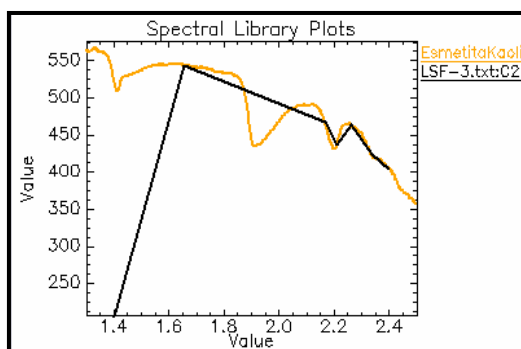


Fig.2. Firmas espectrales de las muestras de suelo analizadas con el Espectrómetro (naranja) y firmas remuestreadas a la imagen fusión Ali-Aster (negro).

permitió hacer una clasificación detallada de los minerales. En los resultados del mapeo se hallaron los siguientes minerales: Alunita, Caolinita, Caolinita-Illita, Illita, Illita-Esméctica, Esméctica-Moscovita y Moscovita, las cuales se muestran en la siguiente figura.

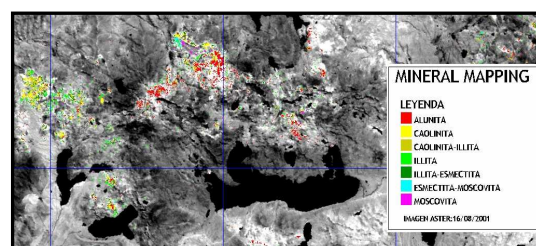


Fig.3. Imagen Aster, clasificada con el método SAM

Con los resultados del análisis del agua de las lagunas se obtuvieron los siguientes datos, el cual fueron proveídos por DIGESA, con esta información se pudo comprobar que en las aguas de las lagunas de la zona de estudio existen metales como el cobre, cadmio, cromo, hierro, manganeso, plomo y zinc, ver la siguiente figura y cuadro.



PTO	LUGAR	ESTE	NORTE	METALES ENCONTRADOS*
E-1	Laguna San Francisco	473689	8537278	COBRE, CADMIO, CROMO, HIERRO, MANGANESO, PLOMO, ZINC.
E-2	Laguna Pacococha	470518	8538034	
E-3	Laguna Orcococha	479509	8538372	
E-4	Laguna Yanacocha	483600	8540497	

* DIGESA. Encontrándose las concentraciones en algunos puntos sobre los límites permisibles de las normas ambientales.

3.2 Identificación de minerales

En la combinación RGB 987 de la imagen Aster, se identificó la firma espectral de Kaolinita+esmética, minerales indicadores de un yacimiento hidrotermal.

En el mapeo se utilizaron los métodos de clasificación supervisada Spectral Angle Mapper (SAM), que nos

También se identificó escordita un mineral que es altamente contaminante y se encuentra presente en los relaves mineros (pero falta validar).

3.3 Combinaciones de Bandas y Ratios

En la interpretación de la combinación 469, de Aster como en la fusión de Ali (Vnir)+ Aster (Swir) (ver Fig.5.a y 5.b), se muestra la diferencia de tonalidades de color en ambas imágenes, ya que en tonos rosados blanquecinos son los materiales que presentan absorción entre los rangos 1.600-2.225 μm . para Aster y para la imagen fusión Ali-Aster 0.660-2.185 μm . En la figura se observa una similar delimitación pero con distintas tonalidades de color, permitiendo interpretar distintas coberturas existentes en el área de interés.

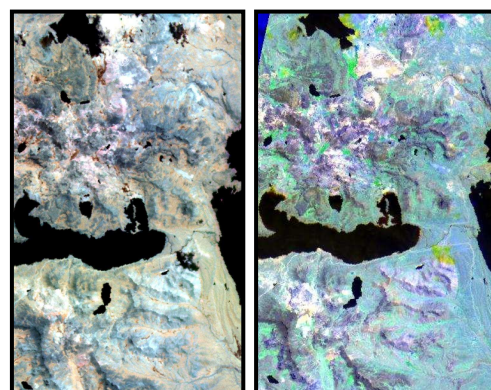


Fig.5.a Imagen Aster Fig.5.b Fusión Ali-Aster

En los ratios RGB: (b4/b5), (b4/b6), (b4/b7), se observa de color azul verdoso las áreas con presencia de alunita, Kaolinita y alunita + Kaolinita y de color verde mas oscuro las áreas de illita y/o esmética.

3.4 Librería espectral generada

Al comparar las firmas espectrales de Aster, con las firmas de las muestras de suelo, se encontró gran similitud de absorción entre los rangos 1.656-2.4 μm ., ver Fig.6a.

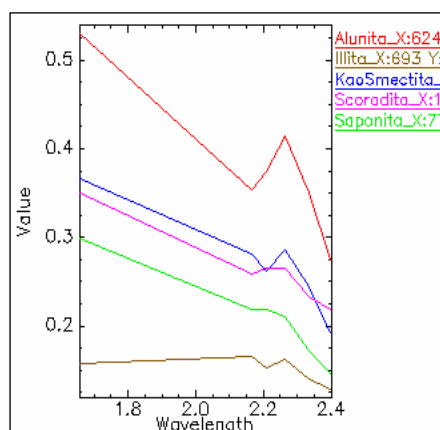


Fig. 6 a. Firmas espectral determinadas.

También se remuestreo en base a la imagen Hyperión, ver la Fig.6b, esta ultima se observa mayor detalle por sus 158 bandas que permite que las firmas espectrales estén mejor definidas que las de la Fig. 6a.

Por lo que se genero una librería espectral con 4 minerales como patrón de muestra de alteración argílica: Alunita, Illita, Kaosmectita y Saponita.

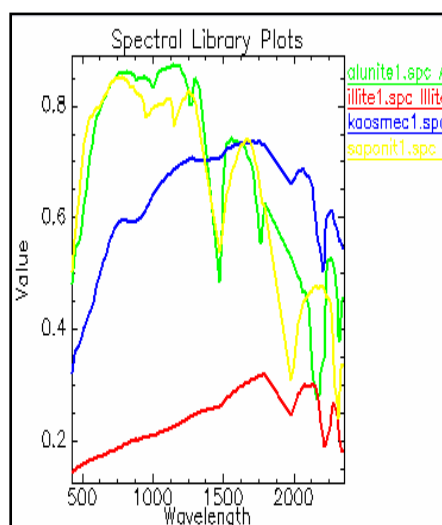


Fig.6b. Firma espectrales

4 CONCLUSIONES

Estas imágenes permitieron identificar minerales de alteraciones hidrotermales y a través de la interpretación visual se observó partículas en suspensión y relaves adyacentes en las orillas de las lagunas. Sin embargo no se llegó a determinar firmas de minerales en las lagunas, ya que éstas se encuentran en contacto con el agua, el cual cambian sus características físicas.

Se generó una librería espectral con 4 minerales como patrón de muestra de alteración argílica, así como también se identificó escoradita un mineral altamente contaminante, presente en los relaves mineros (falta validar in situ en campo).

Se realizó pruebas de la corrección atmosférica de las imágenes Aster, Ali e Hyperión con diferentes métodos usando el módulo FLAASH del software ENVI y el software ACORN, obteniendo así resultados bastantes cercanos a lo observado y comparado en las firmas espectrales del espectrómetro.

REFERENCIA

- A.M. Baldridge, S.J. Hook, C.I. Grove, G. Rivera, del Jet Propulsion Laboratory. Spectral Library V.2.0. ASTER (jhu_desc; jpl_desc).
- Bernard E. Hubbard; James K. Crowley. Mineral mapping on the Chilean-Bolivian Altiplano using co-orbital ALI, ASTER and Hyperion imagery: Data dimensionality issues and solutions. Remote Sensing of Environment. 99 (2005) 173-186.
- Hook, M.A.S.; Ramachandran, B.1999. ASTER User Handbook Version 2. Pasadena: JPL/EROS Data Center/NASA, Disponible en: http://asterweb.jpl.nasa.gov/content/03_data/04_documents/aster_user_guide_v2.pdf
- JPL. ASTER Spectral Library Version 1.2. Disponible en <http://speclib.jpl.nasa.gov>
- Richard Beck. 2003. EO-1 User Guide v.2.3. Ohio: USGS Herat Resources Observation Systems Data Center (EDC), disponible en: <http://edcsns17.cr.usgs.gov/eo1/documents/E01userguidev2pt320030715UC.pdf>
- Estudio "Caracterización con fines de Ordenamiento Territorial del Departamento de Huancavelica". www.gtci-camisea.com.pe
- Estudio "Utilización de datos Aster para el Mapeo Geológico y la Evaluación del Potencial minero en el Área de la Sierra de Aguilar, Provincia de Jujuy, Argentina".

Spectral characteristics of soil and vegetation in saline wetlands, NE Spain

M. Domínguez¹, B. Mougenot², C. Castañeda³

¹Soil and Irrigation Department (EEAD-CSIC Associated Unit) Agrifood Research and Technology Centre of Aragon, Avda. Montañana 930, 50059, Zaragoza, Spain

²Centre d'Etudes Spatiales de la Biosphère, 18 av. Eduard Belin, 31401 Toulouse cedex 9, France

³Department of Soil and Water, Estación Experimental de Aula Dei, CSIC, PO Box 13034, 50080 Zaragoza, Spain
ccastaneda@eead.csic.es

ABSTRACT -Remote sensing is helpful to identify the changes of vegetation in wetlands and to assess their degradation. In this sense, is crucial to establish a relationship between spectral data and vegetation cover, type, and phenological state. Mapping and estimating vegetation cover in arid environments is conditioned by the sparse vegetation and the influence of soil background reflectance. Moreover, the perennial plants adapted to saline environment include dry, senescent and green parts. Annual specimens are highly conditioned by local and seasonal variations.

The monitoring of the vegetation of the saline wetlands of Monegros, NE Spain, using remote sensing requires knowing the relationship between their spectral characteristics and the vegetation cover and soil conditions. For this purpose, we studied the spectral characteristics of soils and vegetation and we established the relationship between vegetation cover and spectral data collected using two spectrometers, based on discrete and continuous readings, respectively.

We conducted two field surveys in 11 wetlands. A total of 242 sites were sampled in 2007 and 2008 for their spectral study in the visible and infrared spectra. The resulting NDVI values were interpreted together with soil moisture and color data, allowing for their relationship with plant cover. The mixture of dry, senescent and green parts in the plant contribute to their spectral response. The NDVI and Brightness Index were the most suitable to discriminate vegetation and to separate soil classes. These results are essential to validate the reflectivity measured with remote sensors.

1 INTRODUCTION

A goal of European Habitats Directive is to protect the biodiversity through the conservation of habitats (Council Directive 92/43/EEC). This task requires data about the distribution of habitats and their conservation status. The Earth Observation Techniques can provide useful data for mapping habitats (Keramitsoglou et al., 2005; Boyd et al., 2006; Kobler et al., 2006) and assessing the vegetation cover (Wang et al., 2004; Xiao and Moody, 2005; Wang et al., 2007).

Mapping and estimating vegetation cover in arid areas could be difficult due to the characteristics of the vegetation and the reflectance of soil background (Huete et al., 1985; Huete and Jackson, 1987; Smith et al., 1990; Escadafal and Huete, 1991; Elmore et al., 2000). Todd and Hoffer (1998) studied the specific influence of soil background reflectance to estimate the vegetation cover. This is frequently overestimated because the high reflectivity of the soil (Xiao and

Moody, 2005) masks the weak spectral response of sparse vegetation. Huete et al. (1985) and Elmore et al. (2000) analyzed the influence of soil brightness in the NDVI at low percent cover of vegetation. Montandon and Small (2008) showed that NDVI of soils is often underestimated in areas with sparse vegetation, resulting in overestimation of the vegetation fraction. These authors suggested local estimations of NDVI for soil and vegetation avoiding the use of global values.

The fraction of green cover could be estimated through satellite imagery, aerial photography or directly by field measures. Several efforts have been made to establish a relationship between vegetation cover, type, and phenological state with satellite data (Smith et al., 1990; Zhang et al. 2007). Several techniques are applied to determine the percent cover of green fraction, senescent vegetation, and bare soil from digital ground photographs (Jonckheere et al., 2005; Laliberte et al., 2007) to classify the vegetation cover of satellite images. In this sense, Maas (1998) studied the effect of the camera point of view on the

reflectance of the vegetation, observing a decrease of reflectance as the shadow between plants increases. The aim of this work is to study the spectral characteristics of soils and vegetation and to establish the relationship between green cover and spectral data collected using proximal sensors.

2 STUDY AREA

Sebkha is a suitable term to designate some of the saline wetlands of the south of Monegros, one of the most arid regions in Europe (Herrero and Snyder, 1997). They are playa-lakes and close saline

depressions scattered in an agricultural landscape (Figure 1) in an almost flat area in central Ebro basin (NE Spain).

Saline wetlands or saladas undergo drought, waterlogging, and high salinity, crucial factors in the distribution of the vegetation. The percent cover of vegetation is heterogeneous (maximum is 75%) and includes patches of sparsely vegetated areas, densely vegetated spots, and bare areas, which exhibit frequent changes of soil surface appearance.

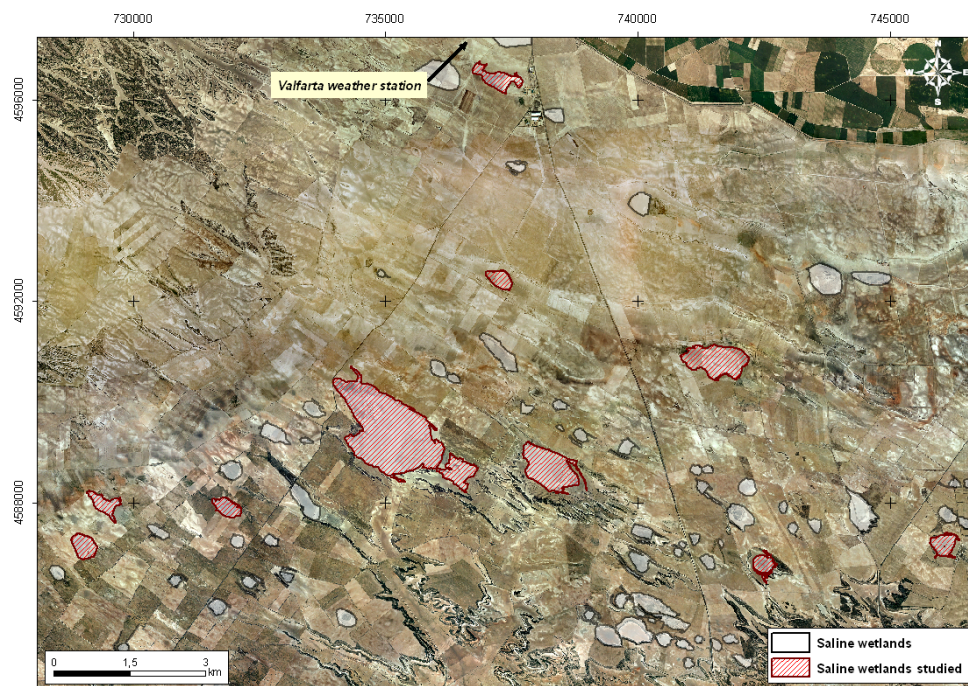


Figure 1. The saline wetlands studied in 2007 (blue striped filling), in 2008 (green striped filling), and in both years (red striped filling).

The vegetation includes endemic species and habitats protected by European laws. The most prominent halophytes are *Arthrocnemum macrostachyum* and *Suaeda vera*. Gypso-halophytic vegetation (*Lygeum spartum*) occupies high topographic positions, in the escarpments of the depressions, whereas halo-nitrophilous vegetation (*Salsola vermiculata*) can appear in the bottom. Annual halophytes such as *Halopeplis amplexicaulis* frequently pioneer the bottoms. The plants appearance depends on their phenological state and the previous rains; their greenness is always darker than that of surrounding crops, such as maize or alfalfa.

The soil surface is prone to frequent changes due to the occurrence of water, algal mats, efflorescence and salt crust.

3 MATERIAL AND METHODS

3.1 Sites selection and sampling

We conducted two field surveys, in the summer season of 2007 and 2008, based on the georeferenced database of vegetation (Domínguez et al., 2006) which fits the CORINE biotopes standard (European Commission, 1991) adapted to our region (Benito, 2010). A Quickbird image acquired in 2007 helped for the selection of sampling points in 2008.

We surveyed 11 wetlands, 10 in 2007 and 6 in 2008; 4 of them sampled in both years. Reflectivity of pure samples of soil or vegetation was recorded in 2007 campaign, at 144 points (4 to 34 points at each salada) with CropScan MSR16R multispectral radiometer (16 bands, 450-1750 nm).

A continuum spectrum (200-1100 nm) was recorded in 2008 with Ocean Optics HR2000CG-UV-NIR Spectroradiometer, along 18 transects (2 to 5 transects in each salada). From 5 to 10 points were collected in each transect, totalizing 98 sampling points. We sampled points deemed as representative of soils with different moisture and efflorescence conditions, and representative plants with different percent cover, following both the ecological and the remotely sensed approach. The readings were calibrated with a 50% (grey) Spectralon reflectance standard panel (Labsphere, Inc.). The measures were systematically collected from 11 a.m. to 15 p.m. and out of solar noon to avoid the shadows as much as possible.

3.2 Ground photographs processing and auxiliary field data.

A photograph of the ground was taken simultaneously to each spectral measure, an oblique photography in 2007, and a vertical photograph with similar field of view than the spectrometer in 2008.

The percentage of each component of our photographs was derived with Can-Eye free software developed by INRA (http://147.100.66.194/can_eye/), often used to characterize the structure of crops (Baret et al., 2004). Five classes resulted from photographs (Figure 2): green vegetation, senescent vegetation, trunks, bare soil, and mixed (i.e., shadows and pixels not included in the previous classes). Visual estimation of plant cover, Munsell soil color, and gravimetric moisture from soil surface (< 2 cm) were also recorded.

3.3 Spectral data processing

The reflectance of CropScan channels was directly analyzed. Row data from Ocean Optics were pre-processed using SAMS software (Spectral Analysis Management System, <http://www.cstars.ucdavis.edu/software-sams.htm>) developed by CSTARS (Center for Spatial Technologies and Remote Sensing, Davis, California).

The NDVI was calculated and verified according to the field data. The *fCover* (Kallel et al., 2007) or percent cover of vegetation (included yellow-green senescent parts) from photographs was related to the NDVI.

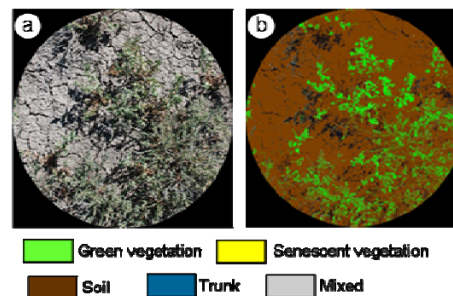


Figure 2. (a): Photograph of a sampled point (field of vision adjusted). (b): CanEye classification in five classes.

4 RESULTS

4.1 Dominant spectral features of bare soil.

The bare soil reflectivity (Figure 3) changes even in short distances, associated to the soil color and moisture and the occurrence of efflorescence, salt crust, sapropelic soil, and shadows.

Wet soil, darker than dry soil, causes a radiance absorption masking other soil characteristics. Dry soil and efflorescences dramatically increased the soil brightness.

The continuous increasing of reflectance from VIS to MIR is the spectral feature of dry soils without efflorescence. Its magnitude depends on soil color, which in turn varies with the soil composition. The high content in calcium carbonate and gypsum contributes to the bright color of the soil. The desiccation polygons decrease the reflectance due to the shadows between cracks and the dark color of the underlying soil.

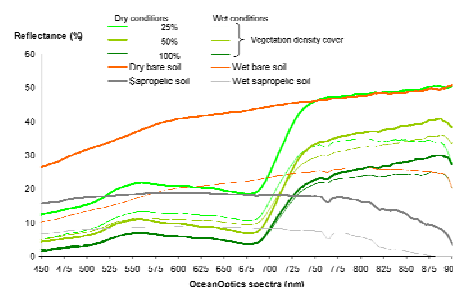


Figure 3. Reflectance of soil and vegetation (different density cover) under dry and moist conditions.

The efflorescence is a dominant factor maintaining the VIS and NIR reflectance of soils above that of other type of soils, except if saturated. In moist conditions, even a thin efflorescence increases the reflectance (overall magnitude) and dimmed the decreasing of MIR reflectance.

Salt crust yields a relatively high reflectance, rising from the visible (VIS) to the near infrared (NIR), with a strong decrease in the middle infrared (MIR) related to the occurrence of hygroscopic salts. A sapropelic layer of millimetric thickness resulting from accumulation and decomposition of organic matter under anaerobic conditions was a dominant feature producing a much lower reflectance at VIS, NIR, and MIR than any type of soil. Sapropelic soil has a distinctive spectrum of low and flat-shaped reflectance, especially between green and red (Zhang et al., 2007). The occurrence of sapropel caused a decrease of soil reflectance to the half, independently of moisture, similar to shadows effect.

4.2 Spectral characteristics of vegetation

A relative low spectral signal (reflectivity > 35%) is obtained from vegetation due to the (1) darkness of halophyte green, (2) absorption of the pigments in succulent stems (Salisbury et al. 1992), (3) variable density cover, and (4) soil moisture. VIS reflectance is < 10%, and NIR reflectance, > 10%.

The reflectance of control samples with known percent cover (0%, 25%, 50%, and 100%) confirms that the reflectance of vegetation (1) increases with the decreasing of vegetation density, though the shape of the spectral signature remains; and (2) decreases with the increasing of soil moisture, especially for low-density covers.

For different plants sampled, VIS reflectance increases with the decrease of the density cover, from 100% to 30%, producing similar spectra than bare soil. The plants sampled show a 20% difference between VIS and NIR reflectance, excepting for *Juncus maritimus*. Hypersaline plants such as *Salicornia* have a high variability of NIR and MIR reflectance because of the occurrence of efflorescence patches.

Despite the differences in color, morphology, and density cover, *L. spartum*, *Microcnemum coralloides*, and *Salsola kali* have similar spectra. The high proportion of dry and senescent vegetation for *S. vera* results in a short difference between NIR and MIR reflectance. The occurrence of moisture and organic matter in the soil, or a thin sheet of water covering the vegetation, make difficult the interpretation of the spectra.

Moisture masks the occurrence of sparse vegetation. Decaying and dry vegetation have greater influence on soil spectra than green vegetation; dead vegetation can be spectrally confused with soil because of the flat signature and the increase from VIS to MIR.

4.3 Spectral indexes and surface characteristics

The soil line (Baret et al., 2002) underestimates sparse vegetation with dark green color. Assuming a standard NDVI value of 0.2 to separate soil and vegetation, a 40% of vegetation sampled should be considered as bare soil.

The analysis of spectral data together with field photographs confirms that senescent vegetation (yellow-green colored) contribute in part to the NDVI from spectrometer.

4.3.1 NDVI versus green cover fraction (*fCover*)

Different *fCover* values were extracted with CanEye (Figure 4) by computing: (1) the pure green vegetation of control samples with known percent cover; (2) the green fraction of sampled points; (3) the green and yellow-green fraction (senescent vegetation) of sampled points, which includes dry and dead vegetation, largely represented in our sampling points.

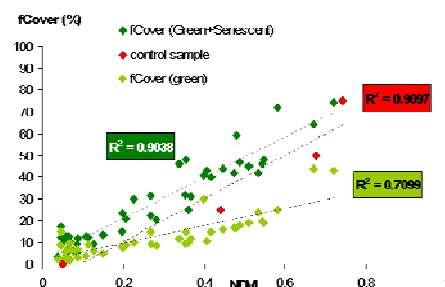


Figure 4. Regressions of *fCover* on NDVI, for control sample (in red), green (in light green) and green plus yellow-green (in dark green) fraction cover.

The first approach provides the stronger correlation between *fCover* values and NDVI ($R^2 = 0.91$), followed by that derived from the sum or green and yellow-green parts of the plant ($R^2 = 0.90$).

Spectrometer measures overestimate NDVI due to the contribution of the soil background, with a high reflectance in NIR. Ground photograph classification underestimates the *fCover*, even if computed as also the yellow-green fraction, due to (1) the masking effect of shadows, and (2) the difficulty of classifying the wide range of green and yellow-green hues in the photographs.

4.3.2 Indexes to separate vegetation and soils

The field spectral measures used to quantify the *fCover* were strongly affected by soil brightness, and for a given density of vegetation, dark soil gives lower NDVI values (Huete et al., 1985). Redness Index (Escadafal, 1993) is better adapted to arid lands, and its relationship with NDVI indicates the influence of the type of plant or the dominance of the vegetation against the soil.

S. vera and *L. spartum* were distributed in all the range while *A. macrostachyum* concentrates in two different groups: the first group, with minimum NDVI and maximum RI, corresponds to dry and dispersed shrubs; the second group, with NDVI > 0.4 and RI < 0, corresponds to dense areas and greener plants.

In contrast with RI, the Brightness Index (Escadafal and Bacha, 1996) allows to establish a reflectivity a threshold (35%) to separate bare soil and vegetation, with vegetation for BI < 35% and bare soil ranging from 35% to 50%. BI decreases with soil moisture and increases with the occurrence of efflorescence or salt crust, despite the water content of salts.

BI index also shows differences in the spectral behavior of plants. Halophytes such as *A. macrostachyum* and *S. vera* clearly differ from non halophytes. Their low chlorophyll concentration decreases the VIS reflectance absorption and the RED boundary value resulting in BI < 30%, except if efflorescence occurs. BI is very high for *L. spartum*, similar to the soil.

The proportion of shadows produced by branches and intertwines stems is an additional factor influencing BI values. *L. spartum* is less affected.

To improve separation of plant species we related BI with color index (Houssa et al., 1996). Bare soils have a wide range of BI (20%-100%) and low values of CI (< 0.15), corresponding to the Munsell colors 10YR and 2.5Y.

RI, BI, and CI indexes allow studying the influence of the type of vegetation or its dominance, and are suitable to separate soil and vegetation and to distinguish halophytes from non-halophytes. However, they are not useful to differentiate species of halophytes.

5 CONCLUSIONS

Vegetation has low reflectance < 30%, depending on the vegetation density, plant species community, phenological state, and shadows. In sparsely vegetated areas, the efflorescences and the sapropelic layer increase and decrease the reflectance, respectively.

The classification of ground photographs shows (1) the spectral confusion of dry and died vegetation with soil, and (2) the contribution of green and yellow green parts of the plant to the fraction cover and NDVI.

Field data about spectral characteristics of soil and vegetation are essential in the validation and classification of satellite images.

6 REFERENCES

- Baret, F., Jacquemond, S., and Hanocq, J.F., 2002, About the soil line concept in remote sensing. *Advances in Space Research*, **13**, 281-284.
- Baret, F. and Weiss, M., 2004, Can-Eye: processing digital photographs for Canopy structure characterization. INRA, Avignon, France. [Online] http://www.avignon.inra.fr/can_eye/page2.htm. Consulted on September 2010.
- Benito, J.L., 2010, Cartografía de los hábitats CORINE de Aragón a escala 1: 25000. II. Lista de hábitats de Aragón (versión 4.06). 87 pp. Departamento de Medio Ambiente del Gobierno de Aragón.
- Boyd, D.S., Sánchez-Hernández, C. and Foody, G.M., 2006, *International Journal of Remote Sensing*, **27**, 2631-2644.
- Domínguez, M., Conesa, J.A., Pedrol, J. and Castañeda, C., 2006, Una base de datos georreferenciados de la vegetación asociada a las saladas de Monegros. Actas del XII Congreso Nacional de Tecnologías de la Información Geográfica. Granada, Spain. ISBN: 84-338-3944-6.
- Elmore, A.J., Mustard, J.F., Manning, S.J. and Lobell, D.B., 2000, Quantifying vegetation change in semiarid environments: Precision and accuracy of spectral mixture analysis and the Normalized Difference Vegetation Index. *Remote Sensing of Environment*, **73**, 86-102.
- Escadafal, R. and Huete, A.R., 1991, Improvement in remote sensing of low vegetation cover in arid regions by correcting vegetation indices for soil "noise": C. R. *Académie des Sciences Paris*, **312**, 1385-1391.
- Escadafal, R. and Bacha, A.R., 1996, Strategy for the dynamic study of desertification. Proceedings of the ISSS International Symposium Ouagadougou, Burkino Faso, 6-10 February 1995 (Paris: Orstom Editions), pp. 19-34.
- European Commission (EU), 1991, Corine Biotopes manual. Habitats of the European Community. A method to identify and describe consistently sites of major importance for nature conservation. 426 pp. EUR 12587/3. Office for Official Publications of the European Communities. Luxembourg. ISBN: 92-826-3228-3 / 92-826-2431-5.
- Herrero, J. and Snyder, R.L., 1997, Irrigation and aridity in Aragon, Spain. *Journal of Arid Environments*, **35**, 535-547.

- Huete, A.R. and Jackson, R.D., 1987, Suitability of spectral indices for evaluating vegetation characteristics on arid rangeland. *Remote Sensing of the Environment*, **23**, 213-232.
- Huete, A.R., Jackson, R.D. and Post, D.F., 1985, Spectral Response of a Plant Canopy with Different Soil Backgrounds. *Remote Sensing of Environment*, **17**, 37-53.
- Jonckheere, I., Nackaerts, K., Muys, B. and Coppin, P., 2005, Assessment of automatic gap fraction estimation of forests from digital hemispherical photography. *Agricultural and Forest Meteorology*, **132**, 96-114.
- Kallel, A., Le Hegarat-Masclé, S., Ottle, C. and Hubert-Moy, L., 2007, Determination of vegetation cover fraction by inversion of a four-parameter model based on isoline parametrization. *Remote Sensing of Environment*, **111**, 553-566.
- Keramitsoglou, I., Kontoes, C., Sifakis, N., Mitchley, J. and Xofis, P., 2005, Kernel based re-classification of Earth observation data for fine scale habitat mapping. *Journal of Nature Conservation*, **13**, 91-99.
- Kobler, A., Dzeroski, S. and Keramitsoglou, L., 2006, Habitat mapping using machine learning-extended kernel-based reclassification of an Ikonos satellite image. *Ecological Modelling*, **191**, 83-95.
- Laliberte, A., Fredrickson, E. and Rango, A., 2007, Combining decision trees with hierarchical object-oriented image analysis for mapping arid rangelands. *Photogrammetric Engineering and Remote Sensing*, **73**, 197-207.
- Maas, S.J., 1998, Estimating cotton canopy ground cover from remotely sensed scene reflectance. *Journal Agronomy*, **90**, 384-388.
- Montandon, L.M. and Small, E.E., 2008, The impact of soil reflectance on the quantification of the green vegetation fraction from NDVI. *Remote Sensing of Environment*, **112**, 1835-1845.
- Smith, M.O., Ustin, S.L., Adams, J.B. and Gillespie, A.R., 1990, Vegetation in deserts: I. a regional measure of abundance from multispectral images: *Remote Sensing of the Environment*, 31: 1-26.
- Todd, S.W. and Hoffer, R.M., 1998, Responses of Spectral indices to variations in vegetation cover and soil background. *Photogrammetric Engineering and Remote Sensing*, **64**, 915-921.
- Wang, L., Sousa, W., Gong, P. and Biging, G., 2004, Comparison of IKONOS and Quickbird images for mapping mangrove species on the Caribbean coast of Panama. *Remote Sensing of Environment*, **91**, 432-440.
- Wang, C., Menenti, M., Stoll, M.P., Belluco, E. and Marani, M., 2007, Mapping mixed vegetation communities in salt marshes using airborne spectral data. *Remote Sensing of Environment*, **107**, 559-570.
- Xiao, J. and Moody, A., 2005, Comparison of methods for estimating fractional green vegetation cover within a desert-to-upland transition zone in central New Mexico, USA. *Remote Sensing of Environment*, **98**, 237-250.
- Zhang, Y.M., Chen, J.L., Wang, X.Q. and Gu, Z.H., 2007, The spatial distribution patterns of biological soil crusts in the Gurbantunggut Desert, Northern Xinjiang, China. *Journal of Arid Environments*, **68**, 599-610.

Using hyperspectral images to study regeneration of burned areas

F. González-Alonso (1), M. Huesca(2), S. Merino de Miguel(3), S. Martínez(4),
J.M.Cuevas(1),A. Calle(5)

¹*Remote Sensing Laboratory, CIFOR – INIA, Ctra. A Coruña, km 7.5 Madrid 28040. Spain*

²*ETSI Montes, Universidad Politécnica de Madrid, Ciudad Universitaria s/n Madrid 28040. Spain*

³*EUIT Forestal, Universidad Politécnica de Madrid, Ciudad Universitaria s/n Madrid 28040. Spain*

⁴*Consejería de Medio Ambiente y Desarrollo Rural, Junta de Castilla-La Mancha Toledo. Spain*

⁵*Departamento de Física Aplicada. Universidad de Valladolid. Spain*

Email corresponding autor: alonso@inia.es

ABSTRACT- *Recent advances in sensor technology have led to the development of new hyper-spectral instruments capable of measuring reflected radiation in a wide range of wavelengths. In this sense, it is possible to assess diverse characteristics of vegetation recovery that are only noticeable in some parts of the electromagnetic spectrum. Such technology is applied in this work for the study of a forest fire that occurred in the Rodenal of Guadalajara (Central Spain) between the 16th and 21st July, 2005. This paper focused on two objectives: (i) the development of accurate level-of-damage maps and (ii) the monitoring of post-fire vegetation recovery. Burned area was finally estimated in 12.938,5 hectares (129,4km²). Level-of-damage was estimated using the Normalized Burn Ratio (NBR). Field data was used to assess the NBR-derived severity maps resulting that the one based on the NBR1 produced the highest accuracy of 70%. Post-fire vegetation recovery was carried out using the Normalized Difference Vegetation Index (NDVI). AHS-INTA hyper-spectral images in combination with field data have been proved to be a reliable way for estimating burned area, levels of damage (severity levels), as well as, for monitoring post-fire vegetation recovery trends. The data and maps derived in this way may be very useful in order to locate priority intervention areas and plan forest restoration works.*

1 INTRODUCTION

Each year, wildfire affects millions of hectares of forests around the world. Forest fires at a local scale alter the ecosystem functionality due to the fact that fire plays an essential role in vegetation composition, biodiversity, soil erosion and water cycle. In addition, forest fires release a significant amount of greenhouse gases, particulates and aerosol emissions into the atmosphere, which significantly increases the anthropogenic CO₂ emissions. The global warming effect has been increasing the intensity and frequency of droughts in many areas, creating more destructive and frequent wildfires (Levine, 1991). This fact is especially important in the Mediterranean region where forest fires are the main cause of natural resources destruction and wildfire trends are more common and severe during years of drought. Besides, frequency and intensity of forest fires are expected to increase in the following years due to the increase of temperature and the reduction of rainfall, facts which in turn will amplify the risk of desertification in this

region (Moreno, 2007). For all these reasons, a good understanding of the forest fire phenomenon is essential nowadays.

One of the most common and useful data about a forest fire is the mapping of the affected area. On the other hand, and in order to estimate the ecological impact, it could be very interesting to be able to assess fire severity. Fire severity is a measure of the level of damage over vegetation, organic materials and soil. Besides, fire severity is a descriptive term that usually integrates physical, chemical and biological changes induced by fire (White et al., 1996). Traditionally, both burned area and fire severity had been measured using field or plane surveys. The perimeter of fire affected area is usually determined using GPS techniques. However, either burned area or fire severity can be estimated using remote sensing techniques in a very rapid, economic and effective way thanks to its spatial and temporal coverage, conveniently reducing field works (Chuvieco y Martín., 2004).

Remote sensing data have been profusely used for the assessment and mapping of burned area (Huesca et al., 2008; Merino-de-Miguel et al., 2005; Barbosa et

al., 1999). However, the determination of different levels of fire severity within a study area is not so common. Forest fire severity studies have been mainly used medium to high spatial resolution images such as Envisat-MERIS, Landsat-TM & -ETM+ and SPOT (Roldán-Zamarrón et al., 2006, Miller & Thode, 2007; De-Santis & Chuvieco, 2007). Recent advances in sensor technology had lead to the development of new hyper-spectral instruments capable of measuring reflected radiation in a wide range of wavelengths. These new systems, which register spectral information of study area in a high number of bands, make it possible to identify some vegetation characteristics that are only perceptible in certain electromagnetic spectrum regions. Remote sensing has also revealed as an useful tool for the post-fire vegetation recovery monitoring, (Díaz-Delgado et al., 1998, Riaño et al., 2002), allowing managers to take decisions for planning future works.

The objective of this work is to accurately map fire-affected area indicating different levels of fire severity, as well as to monitor vegetation recovery within the study area. This information will help managers to properly plan the needed post-fire restoration works.

2 STUDY AREA

The study area is located in the forest fire that took place in the Rodenal of Guadalajara (central Spain), between the 16th and the 21st of July, 2005. Fire started in an area called Cueva de Casares (Riba de Saelices municipality) from a barbecue.

The affected area is hilly and it was characterized by a high spatial continuity of vegetation (fuel). Besides, weather conditions were really adverse during the days the fire spread: relative air moisture was below 20%, wind speed was up to 50 km/h and temperature was over 30°C. The most important vegetation species within the study area were *Pinus pinaster* Ait. and *Cistus laurifolius* L.

3 MATERIAL AND METHODS

3.1 Material

The Remote Sensing Laboratory of CIFOR-INIA accounts for a set of four hyper-spectral images for the study area. The images were acquired by the hyper-spectral AHS (Advanced Hyperspectral Sensor) that flies onboard a CASA-C212 plane and is provided by INTA (Instituto Nacional de Técnica Aeroespacial). This sensor has 80 bands of variable width in the VIS/NIR, SWIR, MIR and TIR regions, and a spatial resolution of 3m. Several field campaigns were also carried out in order to sample any combination of level-of-damage and vegetation type (A-samples), as well as in order to define training areas for non-

affected vegetation and bare soil (B-samples). Both sets of samples were used for both training and validation purposes.

First flight was done the 6th of October 2005, just before the first autumn rainfalls and it clearly reflects the state of the study area after fire. The other flights took place the 6th of October 2006, 25th of September 2007 and 15th of September 2008.

3.2 Methods

Field trips throughout the study area took place during several days of October 2005. During the first journey we made a general survey of the study area in order to plan a sampling procedure. Sample points were of two types: A points, situated within the study area according to different levels of damage, and B points, situated outside de study area (non-affected by fire) and used to define training areas (endmembers) of non-affected vegetation and bare soil.

Between August and October 2007, a systematic sampling work was done by a company called Tragsa. It consisted of 2468 sample plots and it was given to the CIFOR-INIA by means of the Junta de Castilla-La Mancha. Besides, during 2005, 2007 and 2008, and in coordination with the flights, some spectra field campaigns were done and later used for image radiometric correction.

Hyperspectral images were radiometrically corrected by INTA (Instituto Nacional de Técnica Aeroespacial). Later on, a geometric correction was carried out using the PARGE software (PARAmetric GEocoding). For the last, an atmospheric correction was done using the ATCOR4 software. In order to get a good temporal coherence of the four hyperspectral images, a procedure of reflectance homogenization (empirical line) was done using non-variant spectra from the 2008 field campaign.

Once the images were pre-processed, first task consisted on delineating the fire-affected area. For doing so, the 2005 AHS image (the closest to the fire event) was processed using a matched filtering analysis. This method assigns a probability value to any single pixel that estimates how similar certain pixel is in comparison with an endmember collection. The later was defined using a sample of 100 pixels of the AHS image itself. The resulting image was classified using an Isodata algorithm in which the threshold values were selected in order to best fit the results.

Level-of-damage was estimated using the Normalized Burn Ratio (NBR) (Key y Benson 2002) that is calculated using pixel reflectance in the NIR (near-infrared) and SWIR (short-wave-infrared) bands.

$$NBR = (\rho_{NIR} - \rho_{SWIR}) / (\rho_{NIR} + \rho_{SWIR}) \quad (1)$$

Where, ρ_{NIR} and ρ_{SWIR} are reflectance in the near-infrared and short-wave-infrared, respectively.

This spectral index was selected for being sensible to due-to-fire changes in vegetation. This index varies between -1 (indicating high severity) and +1 (indicating low severity or non-affected vegetation). Sensor bands for NBR calculation were selected based on their lowest noise and largest variability, what resulted in the selection of band 13 (centred at 0,8µm) and bands 31, 38 and 41 (centred at 2,13, 2,22 and 2,25µm, respectively). In this sense, three severity indices (NBR1, NBR2 and NBR3) were calculated.

Post-fire vegetation recovery was carried out using the Normalized Difference Vegetation Index (NDVI) that is calculated based on red (R) and NIR reflectance values.

$$NDVI = (\rho_{NIR} - \rho_R) / (\rho_{NIR} + \rho_R) \quad (2)$$

The analysis of the NDVI evolution was completed with a more detailed analysis of the vegetation cover that was estimated using a spectral unmixing algorithm, for which pure bare soil and vegetation endmembers had been previously extracted.

4 RESULTS

4.1 Burned area mapping

Using the methodology described above, the burned area was mapping what resulted in a total area of 12.983,50 ha, which is quite closed to the figure given by the Ministry of Environment (12.887,37 ha).

4.2 Fire severity

Fire severity estimation was performed using NBR (equation 1), as described above. In this sense, we performed a statistical analysis in order to determine which bands best represent the NIR and SWIR bands for the index. The results we obtained showed the best band for representing the NIR band was band 13 (centred at 0,8 µm), while for the SWIR band there were three good options: bands 31, 38 and 41 (centred at 2,13, 2,22 y 2,25 µm, respectively). Therefore, we calculated three severity indices called NBR1, NBR2 and NBR3. Three classifications were then performed, one for each of the NBR index. Field data was used to assess the NBR-derived severity maps resulting that the one based on the NBR1 produced the highest accuracy of 70%.

Figure 1 shows the spatial distribution of fire severity within the study area using a 3-level legend. Low severity (2.544,85 ha – 19,60%) in white color, medium severity (7.286,08 ha – 56,12%) in light grey and high severity (3.152,57 ha – 24,28%) in dark grey.

Figure 2 synthesizes fire severity using the managing units, those used by the forest services. In this case, we carried out a quantitative analysis of fire severity using the mean NBR value and table 1 summarizes reached results.

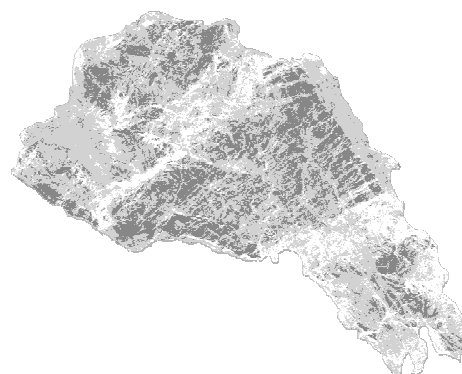


Figure 1. Fire severity levels.



Figure 2. Fire severity according to managing units.

Table 1. NBR values for each of the managing units.

ID	NAME	NBR
GU240	Navavilla y Solana de Pelancosa	0.00
GU190	Entredicho	-0.02
GU191	El Pinar	-0.02
GU126	Dehesa Común	-0.03
GU292	Sierra del Gallubar y Vigorra, Los Milagros, Vallejo del Cabrero y las Ocecillas	-0.06
GU293	El Bosque del Buen Desvío	-0.07
GU301	Dehesa de la Mata	-0.08
GU239	Los Casares	-0.11
GU150	Pinar	-0.12
GU149	Dehesa	-0.13
GU232	Dehesa Común de Solanillos	-0.13
GU298	Ceño Negrillo y la Virgen	-0.13
GU294	El Pinar	-0.15
GU296	Pinar	-0.18
GU297	La Tasuguera	-0.19
GU300	El Pinarejo	-0.27
GU299	El Pinar	-0.3

As a reference, we used the GU-240 forest unit that did not suffer from fire (NBR value of 0). The more negative the NBR value is, the high is the fire severity level. As shown in table 1, the managing units with higher severity were GU-299 and GU-300 (in the East part of the study area). Units GU-190, GU-191 and GU-126 where those with lower NBR values, and are situated to the South of the study area, closed to GU-240 (non-affected).

4.3 Vegetation recovery

Table 2 shows a summary of mean vegetation recovery level for each of the managing units, estimated using the NDVI index (equation 2), as multiplied by 100, for each of the study years.

Table 2. NDVI mean values ranging from 0 (bare soil) to 100 (complete cover vegetation).

ID	NDVI			
	2005	2006	2007	2008
GU190	19,27	26,46	31,71	46,38
GU191	20,25	24,15	24,57	42,61
GU126	19,37	33,85	35,89	47,36
GU292	14,22	15,30	26,15	43,86
GU293	19,73	43,27	50,19	63,21
GU301	16,74	25,48	29,97	45,87
GU239	16,71	30,69	33,47	50,24
GU150	15,57	34,14	39,39	51,43
GU149	18,65	54,31	55,70	70,79
GU232	15,61	32,11	34,34	50,84
GU298	14,44	24,67	26,63	44,88
GU294	11,27	19,94	31,29	45,11
GU296	12,46	33,32	41,31	55,54
GU297	10,02	20,64	32,22	47,53
GU300	7,04	20,52	27,31	43,90
GU299	8,05	27,78	28,81	45,81

Figures 3 and 4 show temporal and spatial evolution of both the NDVI and the spectral unmixing, during the period 2005 - 2008. Areas in light grey are those where either vegetation activity or vegetation cover is higher, while areas in dark grey are those where either vegetation activity is lower or we found bare soil.

Results from both analyses are very close. The areas with the highest degree of vegetation recovery are located to the North-East, while those with the lowest amount of vegetation recovery are located to the South-East. Managing units GU149, GU293 and GU296, located to the North-East showed the best vegetation recovery, mainly due to the presence of

Quercus in the area. Worst managing units in terms of vegetation state were GU126, in the East, and GU191 and GU-190 in the South.

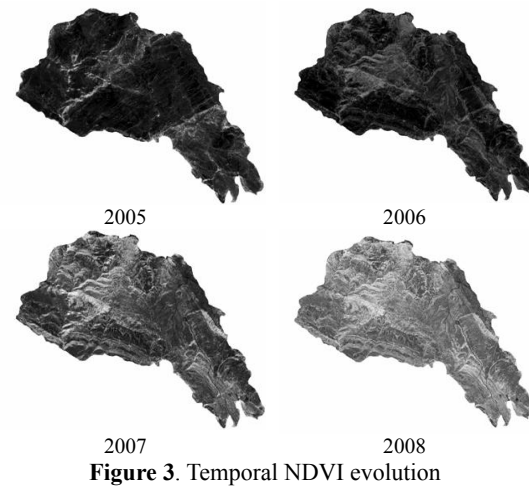


Figure 3. Temporal NDVI evolution

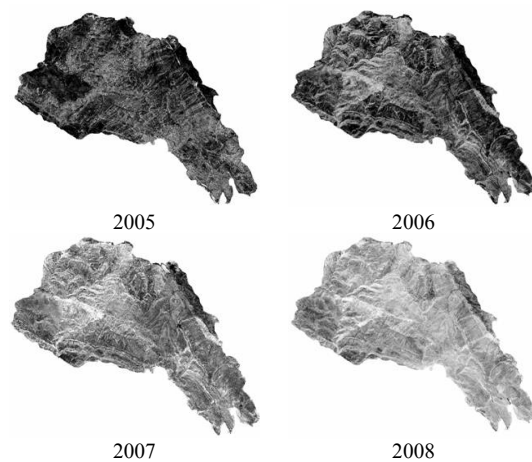


Figure 4. Spectral unmixing evolution

5 DISCUSSION

It can be observed a high accuracy in the results obtained in this work, in terms of affected area, in relation to those proposed by the Ministry of Environment.

Fire severity maps allowed us to locate the area with the highest affection in the central part of the study area and oriented SouthEast – NorthEast. Using a digital elevation model, one can observe that there is a high dependency between the level of damage and the terrain slopes. Steeper areas generally showed more damaged. This information could be really useful in order to plan future restoration works.

Finally, regeneration maps showed how vegetation is recovering during the study period (four years) after the fire. According to the results from the field surveys, best vegetation recovery occurred in those areas with a predominant presence of *Quercus* and shrubs. Vegetation recovery in areas covered by *Pinus* is observed with less accuracy due to the amount of bare soils during the first recovery stages.

6 CONCLUSIONS

One of the first needed data about a forest fire is a map of the affected area and an estimation of the level of damage caused by the fire. In the following years, it could be really interesting to know how vegetation recovers. All these three types of information are key aspects in relation to forest planning and management of the affected area. The present study shows the advantages of using hyperspectral images in order to accurately estimate each of the mentioned variables.

In relation to the capacity of the hyperspectral AHS images to map fire affected areas, we should point out its high accuracy in relation to the official figures given by the Ministry of Environment.

In relation to the capacity of the hyperspectral AHS images to map severity (level of damage), we can also confirm their optimal capabilities. The use of the NBR1 as severity index showed highly accurate results.

Finally, and in relation to the capacity of the hyperspectral AHS images to estimate degrees of vegetation recovery after fire, we can also confirm that it performed reasonably good, specially in areas dominated by *Quercus* and shrubs.

5 REFERENCES

- Barbosa, P.M.; Gregoire, J.L. and Pereira, J.M., 1999, An algorithm for extracting burned areas from time series of AVHRR GAC data applied at a continental scale. *Remote Sensing of Environment*, 69, 253-263.
- Chuvieco, E. y Martin, M.P., 2004, Nuevas tecnologías para la estimación del riesgo de incendios forestales. Consejo Superior de Investigaciones Científicas. Instituto de Economía y Geografía. 190 p.
- De Santis, A. and Chuvieco, E., 2007, Burn severity estimation from remotely sensed data: Performance of simulation versus empirical models. *Remote Sensing of Environment*, 108, 422-435.
- Díaz-Delgado, R.; Salvador, R. and Pons, X., 1998, Monitoring of plant community regeneration after fire by remote sensing. In: L. Trabaud (Ed.), *Fire management and landscape ecology* pp 315-324.
- Fairfield, WA: International Association of Wildland Fire.
- Huesca, M., González-Alonso, F., Cuevas, J.M. and Merino-De-Miguel, S., 2008, Estimación de la superficie quemada en los incendios forestales de canarias en julio de 2007 utilizando sinérgicamente imágenes MODIS y anomalías térmicas. *Investigación Agraria: Sistemas y Recursos Forestales*, 17, 308-316.
- Key, C.H. and Benson, N.C., 2005, Landscape assessment: Remote sensing of severity, the Normalized Burn Ratio. In: D. C. Lutes et al., Editors, *FIREMON: Fire effects monitoring and inventory system*, General Technical Report, RMRS-GTR-164-CD: LA1-LA51, USDA Forest Service, Rocky Mountain Research Station, Ogden, UT.
- Levine, J. S., 1991, Introduction. In: *Global Biomass Burning: Atmospheric, Climatic and Biospheric Implications*. Edited by J. S. Levine (Cambridge, USA: MIT press).
- Merino-De-Miguel, S.; González-Alonso, F.; García-Gigorro, A.; Roldán-Zamarrón, A. and Cuevas, J.M., 2005, Is it possible to timely and accurately estimate wildfire burnt areas using remote sensing techniques? En: *New Strategies for European Remote Sensing* (Oluic, Ed). Millpress, Rotterdam.
- Miller, J. D. and Thode, A. E., 2007, Quantifying burn severity in a heterogeneous landscape with a relative version of the delta normalized burn ratio (DNBR). *Remote Sensing of Environment*, 109, 66-80.
- Moreno, J.M., 2007, Cambio global e incendios forestales: Una visión desde España. 4ª Conferencia Internacional sobre Incendios Forestales, Sevilla, 22 p.
- Riaño, D.; Chuvieco, E.; Ustin, S.; Zomer, R.; Dennison, P.; Roberts, D. and Salas, J., 2002, Assessment of vegetation regeneration after fire through multitemporal analysis of AVIRIS images in the Santa Monica Mountains. *Remote Sensing of Environment*, 79, 60-71.
- Roldán-Zamarrón, A.; Merino-De-Miguel, S.; González-Alonso, F.; García-Gigorro, S. and Cuevas, J.M., 2006, Minas de Riotinto (South Spain) forest fire: burned area assessment and severity mapping using Landsat 5 - TM, Envisat - MERIS and Terra - MODIS post-fire images. *Journal of Geophysical Research*, 111, G04S11.
- White, J.D.; Ryan, K. C.; Key, C. C. and Running, S.W., 1996, Remote sensing of forest fire severity and vegetation recovery. *International Journal of Wildland Fire*, 6, 125-136.

Noise in emissivity images obtained from the ASTER Temperature and Emissivity Separation (TES) algorithm: a case study of airborne imagery and implications for ASTER

J. C. Jiménez-Muñoz¹, J. A. Sobrino¹, and A. R. Gillespie²

¹Global. Change Unit, Image Processing Laboratory, University of Valencia; P.O. Box 22085, E-46071 Valencia SPAIN

²Dpt. of Earth and Space Sciences, University of Washington, Seattle, WA, 98195-1310 USA
Email: jecm@uv.es

ABSTRACT- Emissivity images generated from the Temperature and Emissivity Separation (TES) algorithm developed for ASTER and now applied to high spatial resolution and multispectral Thermal-InfraRed (TIR) data show an undesirable noise which jeopardizes the photo-interpretation of the emissivity images, although overall the accuracy appears to be maintained within specifications (~ 0.01 - 0.02). Comparable noise is not observed in the Land Surface Temperature (LST) outputs. To improve interpretation of the emissivity images, it is desirable to filter out the noise. It is necessary first to identify the causes of such noise in order to propose effective removal techniques. It is known that instrumental noise and imperfect atmospheric correction can lead to artifacts in the emissivity images. However, most works have focused on the impact of these problems on the retrieved emissivity spectrum for an individual pixel or groups of pixels and not on the spatial analysis. In this work we used Airborne Hyperspectral Scanner (AHS) imagery (3m spatial resolution and 10 TIR bands in 8-13 μm) to investigate causes of such a noise by constructing synthetic images of LST and emissivity and then adding instrumental noise and atmospheric variation in a pixel-by-pixel basis. We also refined atmospheric correction of AHS TIR data from water vapor contents retrieved on a pixel-by-pixel basis, accounting for differences in scan angle. Implications of our findings for improvements on ASTER Standard Products are discussed.

1 INTRODUCTION

Land Surface Emissivity (LSE) provides valuable information about land cover conditions and land cover change (French et al., 2003; French and Inamdar, 2010), and it is a key variable for mineral mapping (Vaughan et al., 2003). Knowledge of LSE is also required to obtain accurate values of Land Surface Temperature (LST). The ASTER project is providing to the scientific community with Standard Products of LST (AST08) and LSE (AST05) generated with the Temperature and Emissivity Separation (TES) algorithm (Gillespie et al., 1998). These are the first existing Standard Products at high spatial resolution (90m) and with multispectral (five bands) characteristics. Different validation exercises have demonstrated that TES generally performs according to specifications (accuracies of 1.5 K for LST and 0.015 for LSE). However, an undesirable noise is observed in the LSE images which jeopardizes the photo-interpretation (visual inspection) of these products. It is important to highlight that this noise is also observed when TES or other algorithms (NEM, alpha-residuals, reference channel, etc.) are applied to other multispectral TIR sensors, i.e., the problem lies

in the data and not in the algorithm. In order to provide high-quality LSE products it is necessary to remove that noise, but it is necessary first to identify and understand its causes. Noise mainly arises due to two causes: i) instrumental noise (difficult to be removed in a systematic way especially for images acquired over land) and ii) imperfect atmospheric correction (which can be improved with corrections in a pixel-by-pixel basis). In this paper we show some examples of instrumental and atmospheric noise on emissivity images as a first step to understand the problem and to propose effective noise removal techniques. The study has been performed using Airborne Hyperspectral Scanner imagery (AHS) at 3 m spatial resolution (flight altitude around 1300m over ground level; acquisition date: 12-July-2005; acquisition time: 12:21 UTM) over an agricultural area in Spain. AHS instrument has 10 TIR bands (from 71 to 80) in the 8-13 μm spectral region. Emissivity results will be referred to AHS band 75 (10 μm).

2 SIMULATION OF RANDOM NOISE

To simulate the effect of atmospheric and instrumental noise on emissivity images, we have

constructed synthetic at-sensor radiance images taking as reference LST and LSE images obtained respectively with a split-window algorithm and the NDVI approach (see details on Sobrino et al., 2008). Simulated at-sensor values were obtained from the radiative transfer equation using single atmospheric parameters values for the whole image obtained from local soundings and MODTRAN code. Note that these simulated images are free of instrumental and atmospheric noise. In the case of atmospheric in-scene variability, we have added noise to the simulated images by assigning to each image pixel random variations of a single parameter values according to:

$$x' = x(1 + \gamma p) \quad (1)$$

where x is the atmospheric parameter (transmissivity, up-welling and down-welling), γ is a random value assigned to each pixel (ranging from -1 to +1) and p is a certain percentage of variation from the constant value x . In the case of instrumental noise, we considered the expression:

$$T'_{\text{sensor}} = T_{\text{sensor}} + \gamma \text{NEDT} \quad (2)$$

where T_{sensor} is the simulated at-sensor brightness temperature and NEDT is the Noise Equivalent Delta Temperature.

TES algorithm was applied to radiance images with the added noise. Figure 1 shows the LST/LSE images used as input to construct the synthetic images, the LST/LSE images obtained after application of TES algorithm to the real radiances and the LST/LSE images obtained after application of TES algorithm to the simulated (free of noise) images. Figure 2 shows the resulting LSE images derived with the TES algorithm applied to simulated images with added atmospheric noise for different p values (0.01, 0.02, 0.05 and 0.10) and simulated images with added instrumental noise for different NEDT values (0.1, 0.3, 0.5 and 1 K).

According to Fig. 1, LSE image obtained from TES algorithm applied to synthetic images without noise does not show noise, so TES algorithm itself is not introducing the noise observed when applied to real data. However, when the atmospheric in-scene variability or the NEDT is added (Fig. 2), the noise appears in the emissivity images. Spatial distribution of simulated noise is random, since γ parameter involved in previous equations was chosen to be random. This spatial distribution does not follow the one observed in Fig. 1 (center) for the real data, attributed to instrumental scan-line noise (striping).

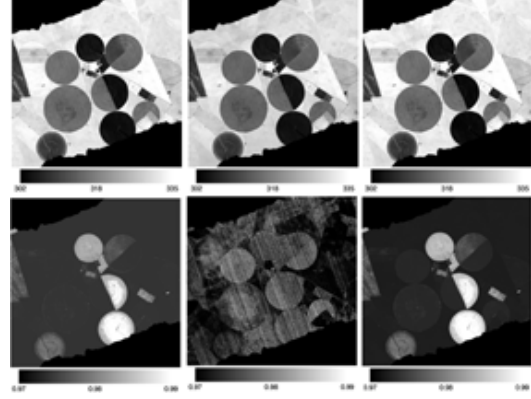


Figure 1. Land Surface Temperature (top) and Emissivity (bottom) images obtained from Split-Window and NDVI approach (left column), TES algorithm applied to real data (central column) and TES algorithm applied to simulated radiances in which in-scene atmospheric variability has not been considered.

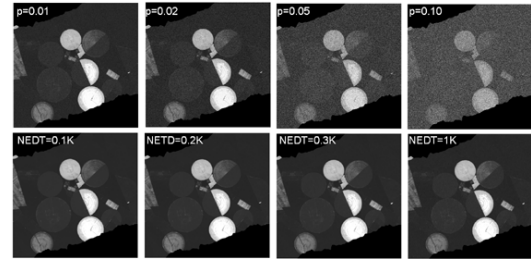


Figure 2. Land Surface Emissivity (LSE) at 10 μm (AHS band 75) obtained from TES algorithm applied to simulated images with added in-scene atmospheric variability (top) and added instrumental noise in terms of NEDT (bottom). Grayscale ranges from 0.97 (black) to 0.99 (white).

3 ATMOSPHERIC CORRECTION OF AHS

In-scene atmospheric variability can be removed using atmospheric correction procedures in a pixel-by-pixel basis. This implies that atmospheric absorbers (mainly water vapor in the case of TIR) should be known for each pixel element. Differences due to the sensor scan angle should be also corrected. Atmospheric water vapor content at pixel level was retrieved from AHS VNIR data using the ratio technique. Scan angle and water vapor images (Fig. 3) were used as input to a Look-Up-Table (LUT) generated from MODTRAN computations in order to obtain atmospheric transmissivity and up- and down-welling radiances values for each pixel. LSE retrieved with this improved approach and LSE retrieved using a single value of atmospheric parameters for the whole image is presented in Figure 3. LSE image obtained with the improved atmospheric correction shows a better contrast than the other one, showing that this

correction was better addressed, but striping is also present.

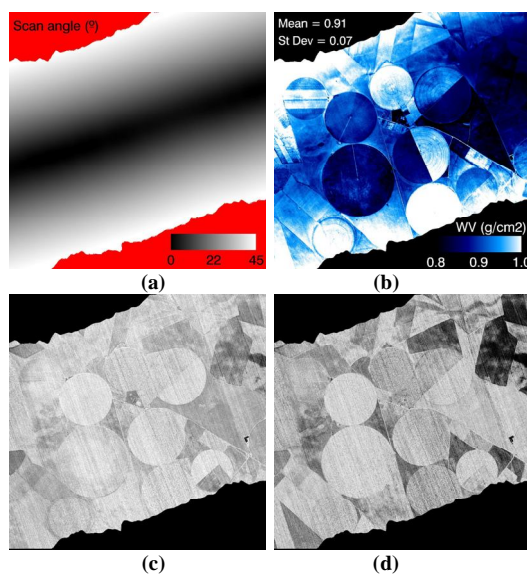


Figure 3. a) AHS scan angle, b) atmospheric water vapor content at pixel level for the flight altitude, c) LSE obtained with TES algorithm after atm corr using one single value for atmospheric parameters over the whole image and d) LSE/TES image obtained after atm corr in a pixel-by-pixel basis.

4 IMPLICATIONS FOR ASTER

Figure 4 shows an example of ASTER Standard Product of LST (AST-08) and LSE (AST-05) over the test area (18 July 2004). LSE image shows some artifacts introduced by the TES algorithm. Causes and proposed solutions for these artifacts are discussed in Gustafson et al. (2006). However, even if these artifacts are removed, noise will be still present in the LSE image because of the instrumental noise or imperfect atmospheric correction.

If successful noise removal techniques are found in the analysis of the airborne imagery, they could be extrapolated to the ASTER case in order to generate de-noised emissivity products (Gillespie et al., 2010).

5 CONCLUSIONS

Instrumental noise and imperfect atmospheric correction in the TIR spectral range leads to noisy emissivity products (hardly observed in the land surface temperature products because LST comprises most of the radiance signal, so the noise is a bigger part of the LSE data; in addition noise is not the same band to band, and LSE is the spectral magnitude, not the temperature). It seems that the spatial pattern of the

noise is governed by the instrumental noise more than the in-scene atmospheric variability. The effect of noise in AHS TIR bands was analyzed in De Miguel et al. (2010). They found that noise showed a fairly Gaussian distribution per spectral band with an amplitude which is approximately the one reported by the on-board blackbodies standard deviation, with a significant spectral and spatial (both across-track and along-track) correlation. Noise removal techniques based on Maximum (or Minimum) Noise Fractions (MNF) methods were inefficient, and due to the spatial correlation, the noise is far from being “white” and should be characterized for each individual image. For these reasons a rigorous simulation of instrumental noise is not an easy task. In this work a random variation of NEDT was added to the at-sensor temperatures as a first (and simple) approach to simulate the instrumental noise. Further research is required in this topic in order to find automatic noise removal techniques to improve the final emissivity maps.

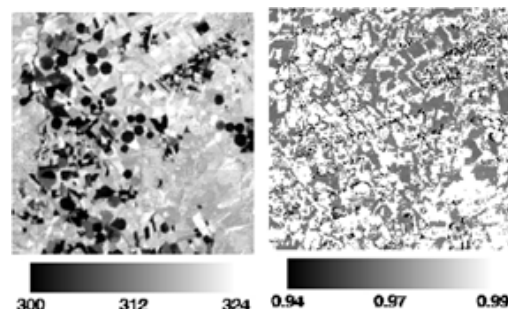


Figure 4. ASTER level 2 Standard Product of LST (AST-08) and LSE (AST-05) at band 13 (10.6µm).

5 ACKNOWLEDGEMENTS

This work was supported by European Space Agency (SEN2FLEX, project RFQ 3-11291/05/I-EC), European Union (EAGLE, project SST3-CT-2003-502057; CEOP-AEGIS, project FP7-ENV-2007-1 Proposal No. 212921; WATCH, project 036946) and Ministerio de Ciencia y Tecnología (EODIX, project AYA2008-0595-C04-01).

6 REFERENCES

De Miguel, E., García, R., and Fernández-Renau, A., 2010, The effect of noise in AHS thermal bands in the retrieval of pixel temperature. *10th Int. Symposium on Physical Measurements and Spectral Signatures in Remote Sensing – ISPRS*, Vol. XXXVI, Part 7/C50, pp. 6, Davos (CH). ISSN 1682-1777.

- French, A. N., Schmugge, T. J., Ritchie, J. C., Hsu, A., Jacob, F., and Ogawa, K., 2008, Detecting land cover change at the Jornada Experimental Range, New Mexico with ASTER emissivities. *Remote Sensing of Environment*, 112, 1730-1748.
- French, A. N., and Inamdar, A., 2010, Land cover characterization for hydrological modelling using thermal infrared emissivities. *International Journal of Remote Sensing*, 31(14), 3867-3883.
- Gillespie, A., Rokugawa, S., Matsunaga, T., Cothern, J. S., Hook, S., and Kahle, A. B., 1998, A temperature and emissivity separation algorithm for advanced spaceborne thermal emission and reflection radiometer (ASTER) images. *IEEE Transactions on Geoscience and Remote Sensing*, 36(4), 1113-1126.
- Gillespie, A. R., Abbott, E. A., Gilson, L., Hulley, G., Jiménez-Muñoz, J. C., and Sobrino, J. A., 2010, Incomplete temperature/emissivity separation in ASTER standard products AST08 and AST05. *Recent Advances in Quantitative Remote Sensing*, Torrent, Spain, Sep. 27-Oct. 1, 2010, this volume.
- Gustafson, W. T., Gillespie, A. R., and Yamada, G. J., 2006, Revisions to the ASTER temperature/emissivity separation algorithm. *Recent Advances in Quantitative Remote Sensing*, Torrent, Spain, Sep. 25-29, 2006, pp. 770-775.
- Sobrino, J. A., Jiménez-Muñoz, J. C., Soria, G., Gómez, M., Barella-Ortiz, A., Romaguera, M., Zaragoza, M., Julien, Y., Cuenca, J., Atitar, M., Hidalgo, V., Franch, B., Mattar, C., Ruescas, A., Morales, L., Gillespie, A., Balick, L., Su, Z., Nerry, F., Peres, L., and Libonati, R., 2008, Thermal remote sensing in the framework of the SEN2FLEX project: field measurements, airborne data and applications. *International Journal of Remote Sensing*, 29 (17-18), 4961-4991.

Independent component analysis application to multispectral sensors

F. J. Mesas-Carrascosa, I.L. Castillejo-González, A. García-Ferrer Porras, M. Sánchez de la Orden.

Dpto. Ingeniería Gráfica y Geomática, Universidad de Córdoba
lg2mecaf@uco.es

ABSTRACT. *Blind Source Separation (BSS) is a powerful technique used to separate signals with mixture by different methods. One of these methods is the Independent Component Analysis (ICA), which is based on three concepts: independence, normality and complexity. Such technique has been analyzed and contrasted with hyperspectral sensors in order to reduce the dimension in their number of bands to finally carry out successful classifications. In case of multispectral sensors, such techniques haven't had the same development. When compiling information, there are several factors to take into account depending on the type of pixel (pure or mixture). To do so, it is commonly used the number of classes, which are present at the area covered by such pixel, refusing other factors like the sensor design itself where bands have certain overlapping in their spectral bandwidth. The aim of the present article is to contrast whether it has sense to apply ICA techniques over multispectral sensors based on characteristics on the basis of such methods.*

1 INTRODUCTION

Independent component analysis (ICA) is a Blind Source Separation (BSS) method, which consists on separating observed data into information sources even if it is unknown how such data have been mixed. As documented in Common (1994) and Hyvärinen and Oja (2000), all this process is performed over the statistical independence concept so that the value of a set of data will not provide information regarding another set of data.

The application fields of these techniques are numerous and varied, with several studies related to the next fields: telecommunications, acoustics, economy and image processing.

In remote sensing, nearly all applications and studies developed under an ICA base are aimed at working with hyperspectral sensors in order to reduce the number of bands dimensionality (Jimenez and Landgrebe, 1999; Nascimiento and Bioucas 2005 and Wang and Chang 2006) and/or carry out non-supervised classifications (Jimenez et al 1999; Bachmann et al 2002; Shah et al, 2002 and Jimenez et al 2007), being scarce works developed over multispectral sensors (Azizi et al 2006).

ICA is often related to conventional and more standardized methods such as the principal component analysis (PCA) or the factor analysis (FA). Such relation is not as close as it may be thought because while PCA or FA are based on finding a set of uncorrelated bands, ICA goes beyond, finding a set of bands independent within each other, based on an statistical model of latent variables, which means that cannot be directly observed.

Pure pixel is defined as the pixel that only contains one class. By contrast, a mixture pixel is defined as the pixel that is composed of two or more classes. Empirical studies based on real data have proved that increasing the spatial resolution does not necessary improve a classification quality. Effects and consequences of the presence of pure or mixture pixels have been attributed to the degree of spatial resolution (Hsieh et al 2001) regardless of other considerations such as the sensor design.

The application of methods like ICA has a wider approach considering all those factors that make information not to be shown independently. For example, let's think in sensors with some kind of spectral overlapping between their bands. Undoubtedly each band will contain a certain amount of information out of the corresponding spectral interval, and therefore bands will not show themselves in their pure form.

In the first part of the present article, the concept of independence will be analyzed, as well as its characteristics and properties. All details related to the study of sensors, Ikonos, and DMC camera, will also be studied in detail. Lastly, it will be mathematically evaluated whether the use of ICA methods are valid in multispectral sensors based on the two prior sensors' data.

2 INDEPENDENCE CONCEPT AND PROPERTIES

The problem of separating information is known as BSS, and ICA is a specific method to develop it. The use of ICA techniques in multispectral sensors is schematized in the present article at Fig 1. Therefore, at first there is an amount of energy that could be

broken up into several bands –covering each of them a specific spectral width- with an ideal sensor. Bands presented in a sensor do not cover the spectral width they were designed for. Thus, it also registers information in wavelengths typical from the adjacent band, that is, bands present a spectral overlapping between them. Therefore, the information present in a band is not a source of pure information because it will contain information of the adjacent bands and hence it may be said that such information is a mixture of data as a result of different pure sources. The use of ICA techniques will aim at finding out a set of data, like bands, as much independent as possible.

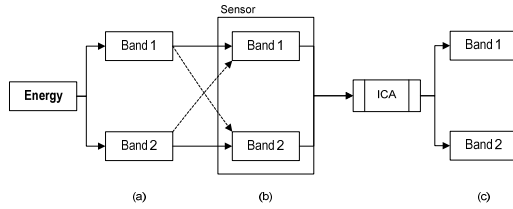


Figure 1. General schema of ICA approach. (a) Ideal bands, (b) Bands registered by a sensor with spectral overlapping between bands, (c) Set of data, like bands, as much independent as possible.

In ICA, the whole process of data separation into information sources is performed over the concept of statistical independence. Thus, if two bands were statistically independent, the value of one band would not contribute with information to the value of the other band.

ICA is based on the premise that when obtaining information, it is performed by means of different processes, thus, the original information will be statistically independent. Therefore, in case of an image, if obtaining independent signals is possible, such signals will be a result of different physical processes.

When developing ICA, three characteristics are basic: independence, normality and complexity. While a source of information is statistical independent, its possible mixtures will not be so. At the same time, such source will present a peaky histogram, so that a signal histogram –resulting from the sum of different sources-, will have a normal shape. Thus, the gaussian distribution is the natural distribution when several factors contribute to the generation of a certain property or physical attribute. The aim will consist on finding the least gaussian distribution in those factors, that will not be able to be a mixture, and therefore they will be pure information.

So, if there is a set of source signals with a certain X property and a set of signals that do not have such property, given a set of mixtures, the original ones may be extracted with as much quantity of X as

possible, taking into account that the signals obtained will be the source of information. In this stage, it is possible to substitute X for the concepts of independence, normality and complexity.

3 INDEPENDENCE AND CORRELATION

The term correlation is commonly used to express that two variables are somehow related. Thus, such concept is used to indicate whether two variables are independent or not. This statement is not certain at all. The essence of the relationship between two variables is expressed by means of the statistical independence, which is defined in terms of probability density function (fdp).

As an x variable has a fdp that is equal to p_x , a couple of variables have a joint fdp that determines the probability density associated to the couple of values of x and y.

Two variables x and y are independent only if:

$$p_{xy}(x, y) = p_x(x)p_y(y) \quad (1)$$

Thus, if two variables are independent, the joint fdp would be obtained as a result of $p_x(x) p_y(y)$.

If variables x and y are independent, the prior equation will imply that:

$$E[x^p y^q] = E[x^p] E[y^q] \quad (2)$$

If $p=1$ and $q=1$ then

$$E[x^p y^q] = E[xy] = E[x]E[y] \quad (3)$$

This will correspond to the first moment of the joint fdp p_{xy} . The mathematical expectation of $E[xy]$ matches the covariance between x and y in case of having N samples of x and y with an average that is equal to zero.

$$E[xy] = \int_x \int_y p_{xy}(x, y) xy dx dy \quad (4)$$

Covariance is a concept close to the correlation $\rho(x, y)$, which may be described as a normalized version of the covariance:

$$\rho(x, y) = \frac{E[xy]}{\sigma_x \sigma_y} \quad (5)$$

Such normalization ensures that the correlation will present values between -1 and 1. The value $\rho=1$ implies that as x increases, the variable y increases in accordance with x; the value $\rho=-1$ implies that as x decreases, the variable y decreases in accordance with x; finally, the value $\rho=0$ implies that, for example, as x

increases, the variable y does not increase or decrease in accordance with x .

As it has been previously shown, the correlation is based on the first stage of the joint fdp.

Thus, the correlation is a measure of the amount of covariance between x and y , depending on the first moment of pxy .

By contrast, the independence is a measure that depends on all pxy moments. Thus, it is a more generalized concept than the correlation.

Two signals, x and y , are statistically independent if and only if the joint fdp $pxy(x,y)$ may be expressed as the product of $px(x)$ $py(y)$. This implies that if two signals are independent, the central moment $E[xpyq]$ of their joint fdp is a product of $E[xp]E[yq]$ for every positive whole value of p and q .

Two signals are uncorrelated if the central moment of their joint fdp is equal to:

$$E[xy] = E[x]E[y] \quad (6)$$

By contrast, to make them independent it is necessary to fulfil

$$E[x^p y^q] = E[x^p]E[y^q] \quad (7)$$

4 SENSORS ANALYSIS

In order to evaluate the convenience of using ICA techniques in data registered with multispectral sensors, tests with two sensors have been performed. These two sensors have different characteristics but present relative spectral response curves, all of them overlapped with a different spatial resolution.

Therefore, the first sensor used has been an Ikonos sensor, a high resolution spatial sensor with a spatial resolution of 3.2 meters in the nadir that offers four bands in a multispectral mode and 0.82 meters in a panchromatic mode.

The second sensor used has been DMC camera of Intergraph, which contributes with four bands in a multispectral mode with a spatial resolution as a function of the performed planning flight. In this case it has been of 0.07 meters.

As shown in Figure 2, curves of spectral response of both sensors are overlapped in different levels, so that the higher the sensor's spatial resolution is, the more noticeable the overlap. Thus, the value contained in a pixel will have typical information of the band that is being analyzed with information that belongs to wavelengths of adjacent bands. Moreover, it will have to be taken into account that such pixel could cover one or more different types of covers. In any case it is shown that as a consequence of the registration of the information through a sensor with such characteristics, the information is not shown in its purest form.

5 TESTS IN MULTISPECTRAL IMAGES

Both sensors mentioned in the previous section have been used to test whether those bands registered by them are independent or not. Although both sensors present big differences in terms of design, functionality, architecture, etc., they have a high spatial resolution.

Tests have been aimed at determining that both, every band fdp and the joint fdp, have a normal behavior and thus they are the result of the sum of several origin sources. At the same time, it has been checked whether the condition (7) is true.

5.1 DMC Camera

Tests performed with this sensor have been done using a sample of a photogram taken in a flight in Arganda del Rey (Madrid, Spain) in May 2006. The Ground Sample Distance (GSD) was equal to 7 cm.

As shown in Figure 3, the four bands of DMC camera have a bell-shaped histogram. Thus, as a consequence of what it has been previously said, the joint fdp between bands does not compile the information into two perpendicular axis as expected in case of bands with a higher kurtosis value. Therefore, data normal behavior takes priority.

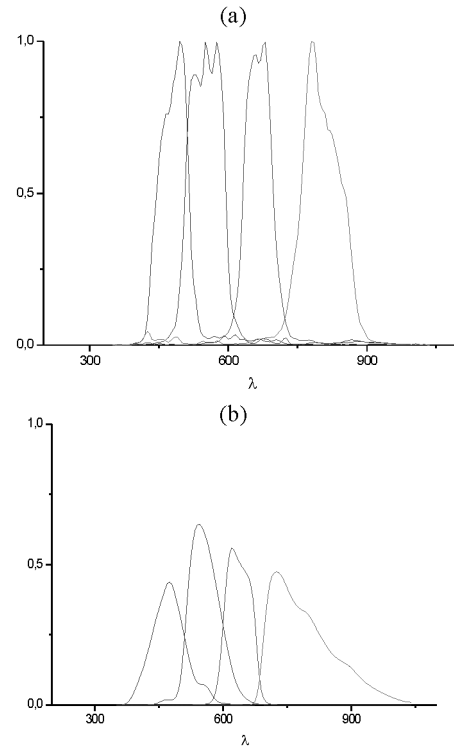


Figure 2. Graph of the relative spectral response: (a) Ikonos (b) DMC sensors.

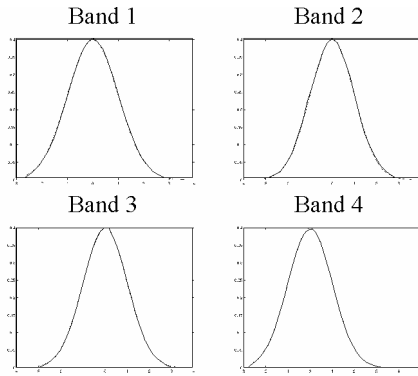


Figure 3. fdp of the image taken with a DMC camera

All these issues are shown in the results of Table 1, where everything defined in (7) is not fulfilled. Thus, it may be assumed that according to the information compiled in the four bands of the DMC camera are not independent.

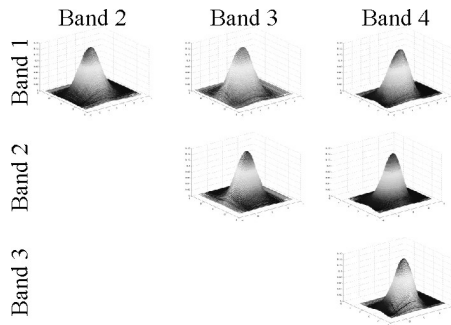


Figure 4. Joint fdp image taken with DMC camera

5.2. Ikonos sensor

Sensor of high resolution with a spatial resolution of 3.2 meters in the nadir, offering four bands in a multispectral manner and 0.82 meters in a panchromatic manner.

It has been used a 750x860 pixel fragment taken on June 2001 from a scene in Montilla (Spain). The covers that characterize the image are olive grove, bare ground and herbaceous growing.

In Figure 5, the histograms of the four bands where tests have been performed are presented. As it is shown, all of them have a normal shape, which means that, according to prior information, the result stored in each band is a result of the sum of different sources of information.

As in DMC camera, such information is confirmed when calculating the joint fdp, which is shown for each band in Figure 6.

Analytically it may be observed that, according to the results of Table 2, the four bands are a result of the sum of different sources of information when everything established in (7) is not fulfilled.

Table 1. Joint fdp of the image registered by the DMC camera

	$E[B1B2]$	$E[B1]E[B2]$	$E[B1B3]$	$E[B1]E[B3]$	$E[B1B4]$	$E[B1]E[B4]$
M 1	0,0000	0,0000	0,0000	0,0000	0,0000	0,0000
M 2	0,9992	0,9992	0,9992	0,9992	0,9992	0,9992
M 3	0,0058	0,0058	0,0245	0,0245	0,0612	0,0612
M 4	5,1360	0,0202	5,7572	-0,0208	7,4987	-0,1358

	$E[B2B3]$	$E[B2]E[B3]$	$E[B2B4]$	$E[B2]E[B4]$
M 1	0,0000	0,0000	0,0000	0,0000
M 2	0,9992	0,9992	0,9992	0,9992
M 3	0,0175	0,0175	0,0437	0,0437
M 4	5,9967	-0,0122	7,7857	-0,0796

	$E[B3B4]$	$E[B3]E[B4]$
M 1	0,0000	0,0000
M 2	0,9992	0,9992
M 3	0,1834	0,1834
M 4	8,6093	0,0817

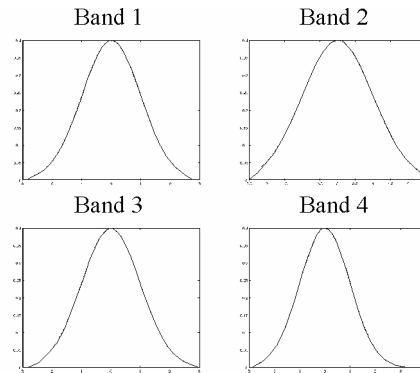


Figure 5. fdp of the image taken with a Ikonos sensor

6 CONCLUSIONS

In the present paper the most relevant aspects of ICA have been presented in order to analyze the differences between independency and correlation. To demonstrate whether the application of these methods over multispectral sensors have sense, the characteristics of both, Ikonos and DMC camera, have been exposed, though they present big differences in

terms of design, functionality, etc. By contrast, they both have overlapping bands in their bandwidth. With data from these two sensors, the fdp and the joint fdp between bands have been calculated, verifying that they are a result of different information sources. Besides testing the normal behavior of the response, it has been contrasted whether the central moment of the joint fdp is equal to the product of the central moments of each band, resulting that this relationship is not possible.

This fact demonstrates that ICA may be applied not only to hyperspectral sensors but also to multispectral, so that the latter may be improved as the hyperspectral sensors.

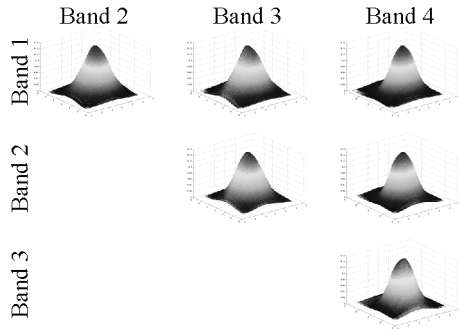


Figure 6. Joint fdp of the image registered by the Ikonos sensor

Table 2. Joint fdp of the image registered by the Ikonos sensor

	$E[B1B2]$	$E[B1]E[B2]$	$E[B1B3]$	$E[B1]E[B3]$	$E[B1B4]$	$E[B1]E[B4]$
M 1	0,0000	0,0000	0,0000	0,0000	0,0000	0,0000
M 2	0,9992	0,9992	0,9992	0,9992	0,9992	0,9992
M 3	-0,0012	-0,0012	0,0018	0,0018	0,0101	-0,0101
M 4	1,9793	0,5708	1,9081	0,5902	3,4565	0,1674

	$E[B2B3]$	$E[B2]E[B3]$	$E[B2B4]$	$E[B2]E[B4]$
M 1	0,0000	0,0000	0,0000	0,0000
M 2	0,9992	0,9992	0,9992	0,9992
M 3	-0,0003	-0,0003	0,0015	0,0015
M 4	1,4009	0,8136	2,7893	0,2307

	$E[B3B4]$	$E[B3]E[B4]$
M 1	0,0000	0,0000
M 2	0,9992	0,9992
M 3	-0,0021	-0,0021
M 4	2,7066	0,2386

7 REFERENCES

- Azizi, N., Marble, A. E., Meng, J., 2006. Projection pursuit feature analysis for pan-sharpened multispectral Ikonos imagery. Electrical and Computer Engineering, 2006. CCECE '06. Canadian Conference on, pp 1970-1973.
- Bachmann, C.M., Donato, T.F., Lamela, G.M., Rhea, W. J. Bettenhausen, M. H., Fusina, R. A., Du Bois, K. R., Porter, J. H. and Trutti, B. R., 2002. Automatic Classification of land cover on Smith Island. IEEE Transactions on Geoscience and Remote Sensing., 40, pp 2313-2330.
- Common, P. 1994. Independent component analysis, a new concept? Signal Processing, 36, pp 287-314.
- Hsieh, P., Lee, L.C. and Chen, N., 2001. Effect of spatial resolution on classification errors of pure and mixed pixels in remote sensing, IEEE Transactions on Geoscience and Remote Sensing., 39, pp 2657-2663.
- Hyvärinen, A. and Oja, E., 2000. Independent component analysis: Algorithms and applications". Neural Networks, 13, pp 411-430.
- Jimenez, L.O. and Landgrebe, D.A., 1999. Hyperspectral data analysis and supervised feature reduction via projection pursuit, IEEE Transactions on Geoscience and Remote Sensing, 37, pp 2653-2667.
- Jimenez, L.O. Morell, A. M and Creus, A., 1999. Classification of hyperdimensional data based on feature and design fusion approaches using projection pursuit, majority voting, and neural networks. IEEE Transactions on Geoscience and Remote Sensing., 37, pp 1360-1366.
- Jimenez, L. O., Cruz, E. A. and Reyes, M. V., 2007. "Unsupervised linear feature extraction methods and their effect in the classification of high dimensional data", IEEE Transactions on Geoscience and Remote Sensing, vol 45, pp 469-483.
- Nascimento, J.M.P. and Bioucas, J.M., 2005. Does independent component analysis play a role in unmixing hyperspectral data?, IEEE Transactions on Geoscience and Remote Sensing, 43, pp 175-187.
- Shah, C. A., Arora, M. K., Robila, and P. K. Varshney, 2002. ICA mixture model based unsupervised classification of hyperspectral imagery. Applied imagery pattern recognition workshop, 2002, pp 29-35.
- Wang, J. and Chang, C. 2006. Applications of independent component analysis in endmember extraction and abundance quantification for hyperspectral imagery, IEEE Transactions on Geoscience and Remote Sensing, 44,, pp 2601-2006.

Preliminary applications of a land surface temperature retrieval method to IASI and AIRS data

Xiaoying OuYang^{1,2}, Guoting Kang^{1,2}, Funian Zeng^{3,*} and Zhao-Liang Li^{2,4}

1. State Key Laboratory of Remote Sensing Science, Jointly Sponsored by the Institute of Remote Sensing Applications of Chinese Academy of Sciences and Beijing Normal University, Beijing, 100101, China

2. State Key Laboratory of Resources and Environmental Information System, Institute of Geographical Sciences and Natural Resources Research, Beijing, 100101, China

3. China Aero Geophysical Survey & Remote Sensing Center for Land and Resources, Beijing, 100083, China

4. LSIT, UdS, CNRS, Boulevard Sébastien Brant, BP10413, 67412 Illkirch, France

Author to whom correspondence should be addressed: zengfunian@agr.cn

Abstract -Land surface temperature (LST) is one of key state variables for many applications. This paper aims to apply our previously developed LST retrieval method to Infrared Atmospheric Sounding Interferometer (IASI) and Atmospheric Infrared Sounder (AIRS) data. On the basis of the opposite characteristics of the atmospheric spectral absorption and surface spectral emissivity, a 'Downwelling Radiance Residual Index' (DRRI) was recalled and improved to provide a constraint, which can be used to obtain the realistic solution for the temperature/emissivity separation. To construct an efficient DRRI, an automatic channel selection procedure was proposed, and finally 11 groups of channels have been selected within 800cm^{-1} to 1000cm^{-1} . The DRRI was tested with IASI and AIRS data. For the IASI data, the radiosonde data was used to correct for atmospheric effects and to retrieve LST, while for the AIRS data, the atmospheric profile retrieved from AIRS data itself was used to perform atmospheric corrections, and subsequently to estimate LST. Compared with Moderate Resolution Imaging Spectroradiometer (MODIS)-derived LST product, the differences between IASI and MODIS derived LSTs are no more than 2K, while the differences between AIRS and MODIS derived LSTs are less than 5K. Although the IASI-derived LST is more accurate than AIRS-derived one, the convenient retrieval of AIRS atmospheric profile made this method more applicable. Limitations and uncertainties in retrieving LST using the present method were discussed.

1 INTRODUCTION

The aim of this study is to present an inversion algorithm that retrieves land surface temperature (LST) from hyperspectral satellite measurements. We are confronted in this work with problems related to the ill-posed character of the inverse problem. The spectrally smooth emissivity (SSE) retrieval algorithm is particularly interesting to solve this kind of problem. Such an approach has already been developed by Borel (1998), for the hyperspectral thermal image data. The great advantages of SSE are the accuracy of results. The SSE algorithm uses all the channels in thermal infrared (TIR) domain in the calculations. In that case, the frequent appearances of singular value and the low efficiency in calculation with thousands of channels impede the application of SSE.

In this paper, the inversion procedure is simplified by introducing the 'Downwelling Radiance Residual Index' (DRRI) on the smoothness method. This approach may be achieved within the selected 11

group channels (a group includes one centre channel and two bilateral channels) (Wang et al., 2008) to speed up the calculation and reduce the singular points.

We present here an application to the problem of LST retrieved from Infrared Atmospheric Sounding Interferometer (IASI) and Atmospheric Infrared Sounder (AIRS) data. Previous studies have used hyperspectral simulated data (Ouyang et al., 2010), but this kind of retrieval is dependent on some assumptions (atmospheric correction is well done). To analyse the feasibility of the DRRI method on the actual data, IASI and AIRS, the newest hyperspectral thermal data, are chosen to apply this method.

This paper is organized as follows. The DRRI method is recalled in section 2.1. The channel selection procedure is presented in section 2.2. The data used in this study are described in section 3. Two application results of our DRRI method to retrieve LST from both IASI and AIRS data are presented in section 4. Conclusions and perspectives are given in section 5.

2 METHOD

2.1 Principle of the Downwelling Radiance Residual Index (DRRI)

Since the natural land surface is not a blackbody, at-ground leaving radiance therefore contains both the surface thermal emission and the reflected atmospheric downwelling radiance. If the LST is not accurately estimated, the corresponding emissivity spectrum retrieved from at-ground radiance exhibits 'downwelling radiance residual feature', namely, there are some sharp convexities or concavities caused by the atmospheric absorption lines on the estimated emissivity spectrum. This residual feature can be quantified by a Downwelling Radiance Residual Index (DRRI) and be computed with the estimated emissivity values at several groups of well-chosen channels, where the peak corresponding to strong atmospheric line absorption and valley corresponding to weak atmospheric absorption are used to depict the direction and magnitude of the downwelling radiance residual feature (Wang et al., 2008), the component DRRI is calculated by the selected channels in each group, namely:

$$DRRI_j = \left((\varepsilon_1 - \varepsilon_2) + \frac{V_2 - V_1}{V_3 - V_1} (\varepsilon_3 - \varepsilon_1) \right)^2 \quad (1)$$

where ε_1 , ε_2 and ε_3 denotes the channel emissivities at the left, middle, and right channels in each group respectively. The final DRRI is the sum of the DRRI components. According to the definition, the DRRI value is only a function of the estimated temperature and will be close to zero if this temperature approaches the actual one. The Newton-Raphson algorithm (Press et al., 2007) is employed to find LST which is the solution of equation $DRRI=0$. Once LST is determined, the land surface spectral emissivities can be easily derived from the at-ground leaving spectral radiances. More detailed information on the development of DRRI can be referred to our previous work (Wang et al., 2008; Ouyang et al., 2010).

2.2 Automatic channel selection method

Fig.1 details the process of the automatic channel selection method in DRRI construction. To analyse the characteristics of the atmospheric downwelling radiance, 1413 cloud-free atmospheric profiles extracted from Thermodynamic Initial-Guess Retrieval (TIGR) (<http://ara.lmd.polytechnique.fr/~htdocs-public/products/TIGR/TIGR.html>) database are used to simulate atmospheric downwelling spectral radiance with the hyperspectral thermal infrared atmospheric radiative transfer model (4A/OP, Operational Release

for Automatized Atmospheric Absorption Atlas) (<http://ara.lmd.polytechnique.fr/>). Selection of the channels for constructing the DRRI has to satisfy following criteria:

1. Atmospheric transmittance in the channel should be larger than 0.3. Otherwise, the atmospheric effects are so large that data measured by this channel could not contain enough information for the LST retrieval.
2. Center channel and two bilateral channels should have strong contrast in atmospheric absorption characteristics. Center channel should have relatively strong atmospheric absorption and two bilateral channels should have weaker atmospheric absorption.
3. Emissivities in these three channels (one center plus two bilateral channels) have to be on one line. That is to say that three points (three channels) constructed by wavelength and emissivity should be collinear.

Taking into account these three constraints, and examining the atmospheric downwelling spectral radiance and the emissivity spectrum, preliminary 107 groups of three channels are selected. Subsequently, all the 107 groups are further tested with simulated satellite data to find much better ones. Finally, 11 optimum groups of channels are selected to construct DRRI and to retrieve LST. Table 1 shows the central position of channels for 11 selected groups.

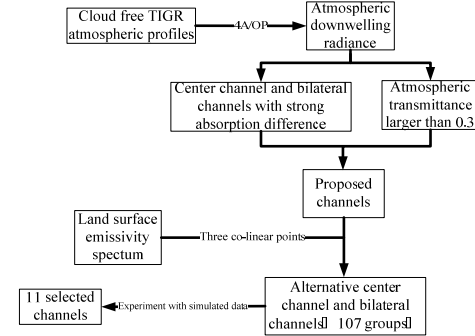


Figure 1: Automatic channel selection procedure

Table 1: Central position of channels for 11 selected groups

Left(cm ⁻¹)	Center(cm ⁻¹)	Right(cm ⁻¹)
802.25	803.25	804.25
823.75	825.25	826.25
826	827.75	830.25
831.75	840	841.25
847	849.5	851.75
851	852.5	854
920	922.25	923.75
923.75	925	926.5
947	948.25	949
975	976	976.75
976.5	977.25	978

3 DATA PROCESSES

3.1 IASI data

With 8461 spectral samples, aligned in three regions between 645.0 cm^{-1} and 2760 cm^{-1} ($15.5\mu\text{m}$ and $3.63\mu\text{m}$), with a spectral resolution of 0.5 cm^{-1} and spectral sampling of 0.25 cm^{-1} , the IASI is a high-resolution Fourier transform spectrometer as a key payload element of the METOP-A, which is one of European meteorological polar-orbit satellites funded by the European Organization for the Exploitation of Meteorological Satellites (EUMETSAT) and the European Space Agency member states and launched in 2006. IASI is expected to lead to dramatic improvements in the accuracy and height resolution of remotely sensed temperature and humidity profiles. The spatial resolution of the IASI L1C data is 12km.

The study area selection procedure and IASI level 1C data preparation process is showed in Fig. 2. The upper part is the study area selection procedure, while the bottom part is the data preparation process.

In the study area selection part, MetOp two-line element is used to match the UKMO radiosonde data acquisition times (UTC time 0000 and 1200 hour) to the IASI/MetOp-A acquisition time so that the IASI data can be corrected for atmospheric effects with simultaneous atmospheric profile. Excluding water (lake, ocean) and cloud-contaminated pixels, the satellite data at-nadir with simultaneous atmospheric profile are then selected as our study area.

In the data preparation part, the IASI L1C data selected from the upper part is put into the IDL reader package and get the measurements data record (MDR). Combined with the auxiliary data, the IASI TOA radiance could be extracted.

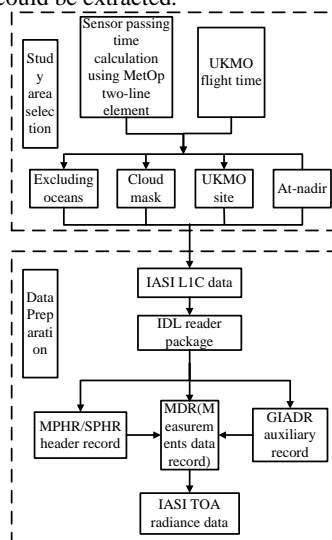


Figure 2: Study area selection and data preparation of the IASI

3.2 Radiosonde data

Accurate retrieval of LST and emissivity requires radiances at ground level, but satellites measurement is at the top of atmosphere (TOA). Therefore, the atmospheric correction has to be performed firstly. In this study, the UKMO (United Kingdom Meteorological Office) data together with 4A/OP are used to correct IASI for atmospheric perturbations. The UKMO data provide profiles of pressure, altitude, temperature and dew point temperature for 2 main UTC times 0000 and 1200 hour. they are still very coarse in temporal resolution when used to process the hyperspectral IASI data.

3.3 AIRS data

The AIRS is a facility instrument aboard the second Earth Observing System (EOS) polar-orbiting platform, Aqua. It constitutes an innovative atmospheric sounding. Global coverage of IASI data is obtained twice daily (day and night) on a 1:30pm sun synchronous orbit from a 705 km altitude.

The Aqua AIRS instrument is a ~2500 spectral channel cooled grating spectrometer with a spectral resolving power of ~1200 ($0.5\text{--}2\text{ cm}^{-1}$ spectral resolution) operating within the spectral range $650\text{--}2700\text{ cm}^{-1}$.

The level 2 cloud-cleared radiances contain calibrated, geolocated channel-by-channel AIRS infrared radiances ($\text{milliWatts/m}^2\text{cm}^{-1}\text{steradian}$) that would have been observed within each Advanced Microwave Sounding Unit (AMSU) footprint if there were no clouds in the field of view (FOV) and produced along with the AIRS standard product, as they are the radiances used to retrieve the standard product. The spatial resolution of AIRS cloud-cleared data is 0.5° .

The level 2 AIRS standard retrieval product consists of retrieved estimates of cloud and surface properties, plus profiles of retrieved temperature, water vapour, ozone, carbon monoxide and methane. Estimates of the errors associated with these quantities are also part of the standard product. This product along with 4A/OP will give the real-time atmospheric parameters of AIRS TOA data. The temperature profile at vertical resolution is 28 levels in total between 1100 mb and 0.1 mb, while moisture profile is reported at 14 atmospheric layers between 1100 mb and 50 mb. The horizontal resolution is 0.5° . An AIRS granule has been set as 6 minutes of data, 30 footprints cross track by 45 lines along track. (<http://gcmd.nasa.gov>)

3.4 MODIS LST product - MOD11B1 data

The level-3 MODIS global LST and emissivity daily data are retrieved at 6km grids in a sinusoidally projected tile by the day/night LST algorithm from

pairs of MODIS daytime and nighttime observations in seven bands under certain conditions (Wan and Li, 1997). MOD11B1 is comprised of the 6km daytime and nighttime LSTs, quality assessment, observation times, view angles, and emissivities retrieved in Bands 20, 22-23, 29, and 31-32 (Wan, 2008). Since the spatial resolution of IASI and AIRS TOA data are 12km and 0.5°, Mod11B1 data should be reprojected and resampled to the same pixel size for each data using MRT (https://lpdaac.usgs.gov/lpdaac/tools/modis_reprojection_tool)

4 RESULTS

LST were retrieved from IASI and AIRS data at nadir observation using our DRRI method. The atmospheric parameters (downwelling radiance, upwelling radiance and transmittance) are estimated with 4A/OP for a spectral range varying from 800 cm^{-1} to 1000 cm^{-1} . IASI and AIRS have different spectral resolutions, thus the spectral function response should be considered for different sensors.

4.1 LST retrieval from IASI data

The initial attempt to use the DRRI method was performed using the IASI 12km data set processed at the EUMETSAT Data Centre. Fig. 3 shows the retrieval and comparison scheme.

This study exploits one year (2008) IASI L1C data on 0h, 12h UTC when UKMO data are available. This choice of data makes the time of satellite data in accordance with the atmospheric profiles. Moreover, the IASI footprints with at-nadir view angles are selected. Meanwhile, IASI L2 data were used to remove the cloud cover data from L1C data. The UKMO atmospheric profiles together with 4A/OP were used to correct for atmospheric effects.

Four points within the image acquired on July 31, 2008 in southeast Russia (Fig. 4) were chosen as a preliminary application. Since the locations of these 4 points are all around the site where the UKMO atmospheric data were measured, the single UKMO data were used for all the four points. Fig.5 shows the atmospheric correction results, including the atmospheric upwelling and downwelling radiance, at-satellite (TOA) radiance, at-ground (including the atmospheric downwelling radiance) radiance, and the corresponding brightness temperature (BT).

Finally, DRRI method was applied to derive LST from atmospherically corrected at ground radiance. The results were compared with MODIS/MOD11B1 LST product (Table 2). The MODIS LST_6km nighttime data were integrated to 12km to meet the IASI spatial resolution, and the differences of LST are less than 2K. In general, the results show that IASI as a hyperspectral sensor could yield LST estimates using

the DRRI method while the atmospheric effects could be corrected for. However, only four points have been analyzed in this preliminary work, more cases studies have to be performed in the future.

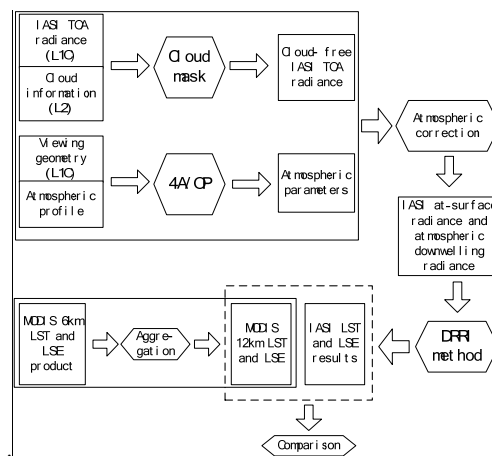


Figure 3: Procedure to retrieve LST from IASI data and to compare IASI derived LST with MODIS LST product (MOD11B1)



Figure 4: Locations of four study points and UKMO site (July 31, 2008)

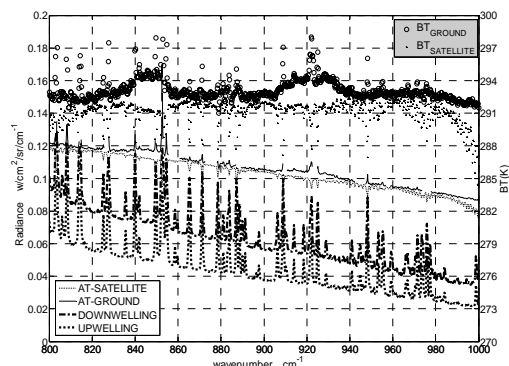


Figure 5: An example of atmospheric correction results using UKMO radiosonde data (July 31, 2008)

Table 2: IASI estimated LSTs compared with MOD11B1 values

Sites	Nadir	Dal	Dal_1	Dal_2
Estimated LST(K)	291.45	291.47	291.49	287.99
Mod11B1 (K)	292.1	290.5	290.04	290.04
Diff □K□	-0.65	0.97	1.45	-2.05

4.2 LST retrieval from AIRS data

Instead of UKMO radiosonde data used in IASI data retrieval, the AIRS retrieved profiles of atmospheric temperature and water vapor were used in the AIRS data retrieval process. Although the comparison of the IASI estimated LST results with MOD11B1 data is good as shown in table 2, the payload satellites of IASI and MODIS are not the same. This may cause a lot of problems, such as the difference of viewing zenith angle, azimuth angle and data acquisition time. These will impede the validation of IASI derived LST results. Since AIRS and MODIS are two payloads in the same satellite (Aqua), the comparison of AIRS estimated LST with MOD11B1 is more convincible. The level 2 cloud-cleared infrared radiances were used here. The spatial resolution is 0.5° , same to that of the atmospheric profiles. A granule of August 11, 2008 (granule 204) was chosen to perform the LST retrieval because this granule is all in continent near the west coast of America. Moreover, the centre place of the granule for the view zenith angle effect could be ignored. Figs.6 and 7 show the estimated atmospheric parameters from AIRS physical profile product. Fig.8 shows the land surface emissivity estimated from AIRS data. Four samples are chosen: A: 110.66W, 45.43N; B: 111.3432, 45.83N; C: 111.52W, 46.31; D: 109.46W, 46N. Table 3 shows the comparison of LST for four sites with Aqua/MOD11B1. Differences of LST are no more than 5K.

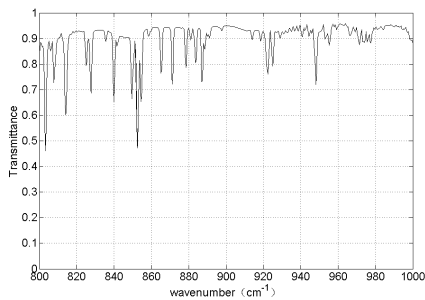


Figure 6: Example of the estimated transmittance from AIRS retrieved atmospheric profile product (Aug. 11, 2008)

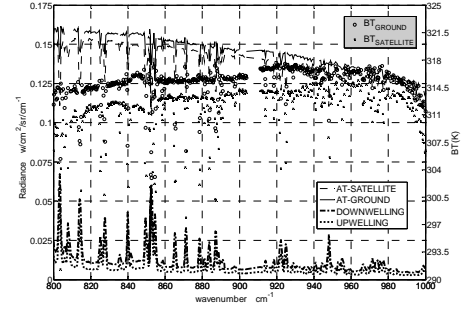


Figure 7: Example of atmospheric correction results using AIRS retrieved atmospheric profile product (Aug. 11, 2008)

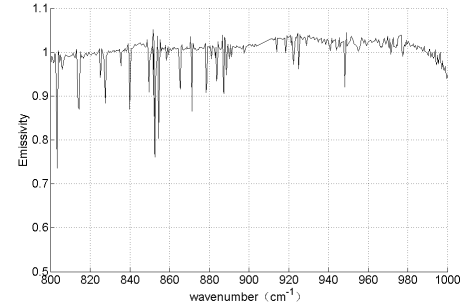


Figure 8: An example of estimated land surface emissivity using AIRS data (Aug. 11, 2008)

Table 3: AIRS estimated LSTs compared with MOD11B1 values

Sites	A	B	C	D
Estimated LST(K)	304.76	303.95	304.68	314.68
MOD11B1 (K)	299.86	302.46	307.28	311.76
Diff. (K)	4.9	1.49	-2.6	2.92

5 CONCLUSIONS

The new DRRI procedure for retrieving LST from hyperspectral satellite data is an improvement over past approaches. The main advantage is that the algorithm is fully automatic and optimal and suitable for processing the actual satellite data. The differences of IASI and MODIS derived LST are no more than 2K, while the differences of AIRS and MODIS derived LST are less than 5K. Although the AIRS data got imperfect results, the convenient retrieval of AIRS atmospheric profiles makes the DRRI method feasible for retrieving LST from the hyperspectral TIR data.

However, it should be noted that all retrievals have been done for observations at nadir in this study. Uncertainties and errors would be increased for large viewing zenith angles. Furthermore, the estimated emissivities from actual IASI and AIRS data are sometimes larger than 1 for some wavelengths. More cases studies and further work have to be performed in the future.

6 ACKNOWLEDGMENT:

This work was supported by the Hi-Tech Research and Development Program of China (863 Plan Program) under Grants 2008AA121805 and 2006AA12Z121. The authors would like to sincerely thank NOVELTIS Inc. for providing the 4A/OP model, the Laboratoire de Meteorologie Dynamique for providing the TIGR database.

7 REFERENCES

- Borel, C. C., 1998, Surface emissivity and temperature retrieval for a hyperspectral sensor, in *Proceedings of IEEE International Geoscience and Remote Sensing Symposium* (Seattle, 1998), 1, pp. 546-549.
- OuYang, X.Y., Wang, N., Wu, H., and Li, Z.-L., 2010, Errors analysis on temperature and emissivity determination from hyperspectral thermal infrared data, *Optics Express*, Vol.18, No.2, 544-550.
- Press, W. H., Flannery, B. P., Teukolsky, S. A., and Vetterling, W. T., 2007, *Numerical Recipes: The Art of Scientific Computing*, Cambridge University Press, 2007. ISBN 0-521-88068-8 (available for a fee online, with code samples [4]).
- Wang, X., OuYang, X. Y., Tang, B. H., Li, Z.-L., and Zhang, R.H., 2008, A new method for temperature/emissivity separation from hyperspectral thermal infrared data, in *Proceedings of IEEE International Geoscience and Remote Sensing Symposium* (Boston, Massachusetts, 2008), III, pp. 286-289.
- Wan, Z. M., and Li, Z. L., 1997, A physics-based algorithm for retrieving land-surface emissivity and temperature from EOS/MODIS data, *IEEE Transactions on Geoscience and Remote Sensing*, **35**, 980-996.
- Wan, Z. M., 2008, New refinements and validation of the MODIS land-surface temperature/emissivity products. *Remote Sensing of Environment*, **112**, 59-74.

Operational cloud masking scheme for marine AHS and CASI imagery

I. Pérez González, E. de Miguel Llanes, C. Robles González and J.A. Gómez Sánchez
Instituto Nacional de Técnica Aeroespacial Esteban Terradas, INTA (Spain)
crepadpo@inta.es

ABSTRACT - *EUFAr's (EUropean Facility for Airborne Research) Joint Research Activity 2 (JRA2) aims at the development of quality layers for hyperspectral data. As a consortium member, the Remote Sensing Laboratory at INTA is placing a special effort to meet the specifications agreed in the context of JRA2. In this work, we deal with the implementation of a marine cloud mask for the imagery acquired by the sensors currently operated by INTA: AHS (Airborne Hyperspectral Scanner) and CASI-1500 (Compact Airborne Spectrographic Imager).*

The scheme developed is based on the assumption that clouds can be considered as clusters of brighter and whiter pixels when compared to water pixels. Thus, a radiometric test is firstly applied to detect bright pixels, followed by a spatial uniformity test.

Results obtained with this methodology are compared to ATCOR4's, the commercial software package for airborne imagery processing.

1 INTRODUCTION

INTA's Remote Sensing Laboratory collaborates in a wide range of hyperspectral airborne remote sensing projects, from land to marine applications, thanks to the experience in acquiring, pre-processing and processing Airborne Hyperspectral Scanner (AHS) and Compact Airborne Spectrographic Imager (CASI) imagery. The marine final products nominally delivered to the end user are georeferenceable at sensor radiances (Ls) and sea surface temperature (SST), as no operational airborne imagery processing suite is accurate enough for the atmospheric correction of such a dark surface, without an exhaustive monitoring of atmospheric conditions and reference field data.

Providing the end user with a cloud mask attached to the Ls product, helps increasing the reliability of the value added products resulting from its own analysis of the imagery. Besides, this cloud mask is one of the quality layers for hyperspectral airborne imagery agreed in the context European Facility for Airborne Research-Joint Research Activity 2 (EUFAr-JRA2).

Existing algorithms for cloud masking, mainly developed for satellite imagery, rely on cloud properties such as its very high reflectance and whiteness, its differential temperature with respect to the underlying scene or the lower atmospheric path above the cloud top (see for example, Gómez-Chova, 2007 and Ackerman, 2006 and references therein). These premises do not always hold, or are

not easy to detect, on some type of clouds that can cover a representative area of airborne imagery.

The goal of this study is to find a cloud masking scheme with better sensitivity to low-reflectance clouds that frequently contaminate airborne marine imagery. Since the final product delivered to the users is Ls, the methodology must be able to work on Ls, preferably on the common spectral range spanned by AHS and CASI, the visible-near infrared region (VIS-NIR). Finally, full automatism and computational economy are an asset.

In section 2 we detail the methodology developed that best suites the previous requirements, followed by its application to various scenes in section 3, where our results are compared to those obtained by ATCOR4 (Richter, 2010), one of the reference airborne image processing suites. In section 4, results obtained and future work are discussed.

2 METHODOLOGY

The approach followed by our methodology, depicted in the flowchart of Figure 1, is to consider a cloud as a cluster of bright and white pixels. Instead of setting static thresholds for brightness and whiteness definition, an approach not feasible if we are working on Ls, and usually highly restrictive to very reflective clouds, we define brightness and whiteness relative to the darkest pixels in the scene, as will be further explained in section 2.2, assuming that a minimum percent of the image is cloud free. Marine surface processes

also characterized by an almost white spectrum, such as disperse sunglint and white cap formation, are filtered out by a spatial homogeneity test, as their spatial characteristic scale is smaller than that of the clouds.

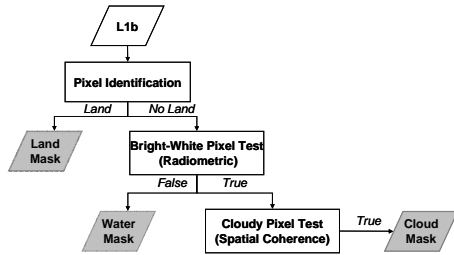


Figure 1.- Flowchart of the cloud masking scheme

2.1 Pixel identification. Land mask

A pre-processing step prior to cloud identification, masks out land or cloud over land pixels, so that the subsequent algorithm steps will only be applicable to water or cloud over water pixels. Pixels satisfying one of the conditions of Equation 1 will pertain to the Land mask (Figure 2):

$$\frac{Ls(850)}{Ls(480)} \geq 0.5 \text{ or } \frac{Ls(750)}{Ls(680)} \geq 0.95 \quad (1)$$

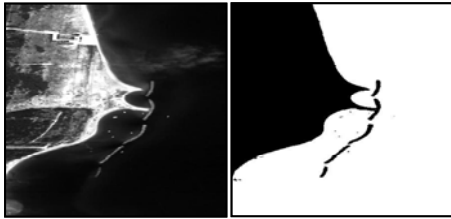


Figure 2.- Left: subset of a CASI image over the coastal area of Tenuta di San Rossore (Pisa, Italy). Right: land mask for the image on the left.

2.2 Radiometric test. Bright pixel mask

This radiometric test is designed to detect bright and white pixels over water. As previously mentioned, it works on Ls, rather than reflectances, preventing the use of static thresholds.

This test is based on two of the basic radiometric cloud properties: clouds are not only brighter than a water pixel, but they are also spectrally flat. On the other hand, the Ls of dark pixels in a marine scene, shows a continuous decrease towards the NIR. This means that when compared to a dark water pixel, a cloudy pixel will be increasingly brighter along the spectrum.

Figures 3 and 4 illustrate this fact. The plot on Figure 3 shows the Ls spectra of 6 surfaces, as registered by CASI-1500 over the coastal area of Tenuta di San Rossore (Pisa, Italy) in the framework of Sentinel 3 Experiment (Sen3Exp) carried out by the European Space Agency (ESA). Along with these signatures, a mean spectrum of the darkest pixels in the NIR (RS) is also shown in black. The *Cloud* and *White Cap* spectra are clearly brighter along the whole spectrum than RS. The shape of both Ls spectra indicates the whiteness of the surfaces, resulting from a quite uniform reflectance in all the wavelengths and the interaction of the reflected signal with the atmosphere. The *Turbid* and *Sandy* bottom spectra are also brighter than RS in the entire spectrum, but there's a significant increase in the Ls signal in the green and red with respect to the blue and NIR part of the spectrum. As for the *Coastal* and *Rocky* bottom spectra, both higher than RS in the NIR, the spectral shape of the former is dominated by pigment absorption features in the blue and green and the shape of the later, by a higher absorption in the blue.

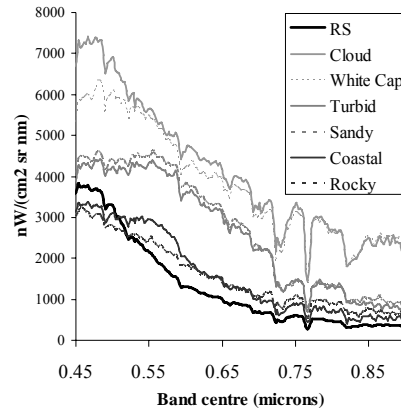


Figure 3.- CASI Ls of different targets of an image acquired over Tenuta di San Rossore, Pisa (Italy). The thick black spectrum is the mean reference spectrum (RS) obtained in step 2.2 of the masking scheme for that image.

These differential spectral responses of the various water and bottom types help discriminate when a pixel can be considered a bright and white target over the sea surface, without having to get into reflectance thresholding. In Figure 4, the ratio of each of the 6 surfaces in Figure 3 to RS is plotted. The ratio for the *Cloud* and *White Cap* spectra is greater than 1 for all the wavelengths and always increasing along the spectrum. The *Turbid* and *Sandy* surfaces ratios are also greater than 1,

but the higher reflectivity of these surfaces in the green and red with respect to the NIR is clearly highlighted here, with a local minimum at the beginning of the NIR. As for the last surfaces, their ratio is lower than 1 in the blue, with a local maximum in the green, as a consequence of pigment activity.

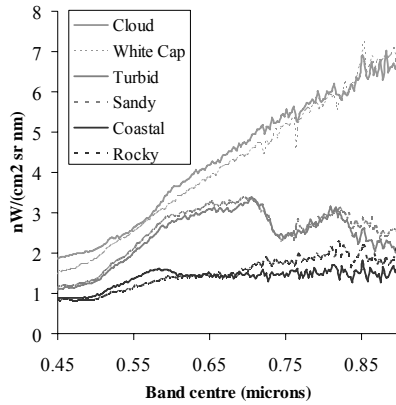


Figure 4.- Ratio of each of the spectra on the Figure 3, to RS.

The L_s spectral ratio of each of the pixels in the scene to a reference L_s spectrum retrieved from the image itself, is the basis of this radiometric test, that can be summarized in the following steps:

- a) Pixels whose L_{s850} is below the 5th percentile of the image L_{s850} are selected as dark pixels (DK)

$$L_{s850,j} \leq \text{percentile5}(L_{s850}) \quad (2)$$

- b) A mean reference spectrum (RS) is computed by averaging the L_s of DK at a set of reference bands (i)

$$RS_i = \text{mean}(DK_i) \quad (3)$$

- c) A spectral ratio (SR) is computed for each pixel by computing the ratio of its L_s to RS at the reference bands

$$SR_{i,j} = \frac{L_{s,i,j}}{RS_i} \quad (4)$$

- d) Pixels are selected into the Bright Pixel mask (BP) if they satisfy the criteria:

$$SR_{1,j} \geq 1.2 \text{ and } \frac{SR_{i+1,j}}{SR_{i,j}} \geq 1 \quad (5)$$

In step 4 (Eq.5), a relative threshold is introduced. This threshold forces bright pixels to be, at least, 20% brighter in the blue, than the dark pixels.

2.3 Spatial homogeneity test

Once the bright pixels in the scene have been identified, the discrimination of surface bright targets (white caps, boat wakes, disperse sunglint) and cloud must follow. Ideally, atmospheric absorption features would help, as the atmospheric path is larger for a signal coming from the surface than for a signal coming from an intermediate height between surface and sensor. However, using this differential absorption features is not always straightforward, due to several reasons, such as the high sensitivity of the calculation of the absorption column depth to sensor calibration and the instability of this computation over dark surfaces.

Thus, according to our definition of clouds, only those pixels in the BP mask that cluster in a minimum area, are tagged as cloud, based on the idea that a cloud has a minimum size which is larger than the surface phenomena possible in an image. The performance of the cloud mask on small clouds depends on the selection of the size of this area, that must be a compromise between performance completeness and false positive rate.

A spatial homogeneity test, Morans's I (Moran, 1950) is performed on the BP mask, to find clusters of bright pixels. In Figure 5(left), the BP mask of an area affected by disperse sunglint, shows how facets that specularly reflect the sun light fall into it. In the BP mask checked for spatial homogeneity (Figure 5, right), sunglint affected pixels have been removed from it.

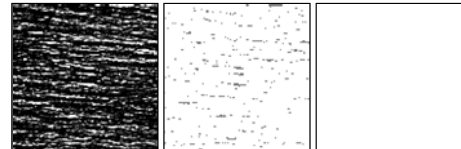


Figure 5.- Left:: CASI image subset acquired over Tenuta di San Rossore, Pisa (Italy). Centre: Same image with BP pixels in grey and water pixels in white. Right: Same image after spatial homogeneity test applied: cloud mask pixels in grey, water pixels in white. Pixel size @ nadir is 1.4x3.5m

3 RESULTS

The scheme detailed in the previous section has been applied to marine AHS and CASI imagery acquired during the summer of 2009 in the framework of SEN3EXP, covering both Case I and Case II waters.

The middle column of Figures 6 and 7 show the resulting cloud masks for coastal (Tenuta di San Rossore, top and middle panels) and oceanic (Boussole Bouy, bottom panels) waters. CASI images are given in Figure 6 and AHS images in Figure 7. Together with this cloud screening scheme results, ATCOR4's cloud masks are also shown in the right column. ATCOR4's criteria for the detection of clouds over water is:

$$\begin{aligned} 0.20 < \rho^*(\text{blue}) < 0.4, \\ \rho^*(\text{green}) < \rho^*(\text{blue}), \\ \rho^*(\text{NIR}) < \rho^*(\text{NIR}) \text{ and NSDI} < 0.2 \end{aligned} \quad (6)$$

where ρ^* indicates apparent reflectance.

The reflectance threshold in the blue region for cloud detection was set to the minimum accepted (20%) in the ATCOR4 runs.

The comparison of the two cloud masks shown in Figures 6 and 7, shows that the methodology presented here is more sensitive to lower reflectance clouds over water than the currently available at ATCOR4. Most of the cloudy pixels are masked as land by ATCOR4, only falling in the cloud category the brightest centre of a cloud (Figure 6, lower panel, right). Cloudy pixels misclassified by ATCOR4 as land, most probably fail to satisfy its criteria both for cloudy and water pixels. The better performance of our cloud masking scheme, when compared to ATCOR4, mainly stems from the fact that this processing suite is not specially devised for marine imagery processing, the minimum reflectance threshold for clouds results, thus, too high, if low reflectance clouds are to be detected.

4 DISCUSSION AND CONCLUSIONS

By relaxing the radiometric requirements and using a scene dependent threshold for the Ls in the blue region, instead of using a fixed reflectance threshold, lower brightness clouds can be detected.

Although our methodology shows a better performance for marine cloud masking, very transparent clouds are still not classified. The spatial homogeneity test applied, although successful in detecting bright surface targets, removes from the cloud mask some pixels of the border of the clouds.

Checking the spatial homogeneity of the BP mask, prevents the inclusion of other bright targets over the sea surface, such as white caps, boat wakes or sunglint contaminated pixels. Consequently, the minimum cloud size will be dependent on the characteristic size of these targets, therefore forcing to reach a compromise between performance completeness and false positive rate.

This spatial uniformity test will fail over severe sunglint regions, where the conditions of wind and solar and viewing illumination are such that a high percent of the surface pixels is contaminated by it. Although airborne data acquisition campaigns are planned to avoid these situations, they are sometimes inevitable, so a critical local viewing and illumination geometry mask for each image is recommended to be provided along with the cloud mask, in case of severe sunglint.

Further comparison of this scheme with other algorithms is planned as well its validation on new hyperspectral marine imagery.

5 ACKNOWLEDGEMENTS

This work has been developed in the framework of the Joint Research Activity 2 of the European Facility for Airborne Research. The images used in this study were acquired for the Sentinel 3 Experiment of the European Space Agency.

6 REFERENCES

- Ackerman, S. A. *et al*, 1998, Discriminating clear sky from clouds with MODIS. *Journal of Geophysical Research*, **103**, 32 139–32 140.
- Gómez-Chova, L. *et al*, 2007, Cloud-Screening Algorithm for ENVISAT/MERIS Multispectral Images. *IEEE Transactions on Geosciences and Remote Sensing*, **45**, 4104–4118.
- Moran, A.P., 1950, Notes on continuous stochastic phenomena. *Biometrika*, **37**, 17–23.
- Richter, R., 2010, Atmospheric/Topographic correction for Airborne Imagery. DLR German Aerospace Centre, Remote Sensing Data Centre.

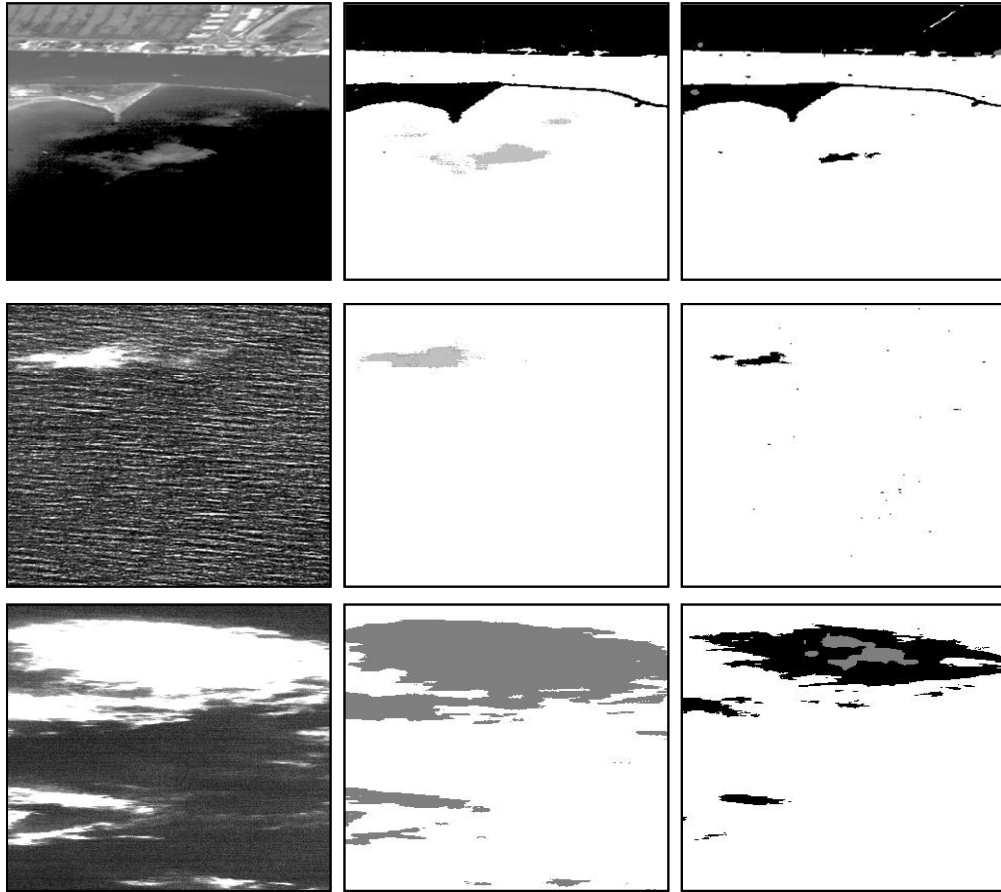


Figure 6.- Cloud masks for three marine scenes (*Top and middle panels*: coastal area off San Rossore (Pisa, Italy), *bottom panels*: oceanic waters of the Boussole Bouy (Ligurian Sea)) for CASI imagery. Left column: gray scale image of the scene. Centre column: cloud mask retrieved with our methodology. Right column: cloud mask retrieved by ATCOR4. Masking colour code is: white-water, grey-cloud, black-land. Pixel size @ nadir is 1.4x6.9m.

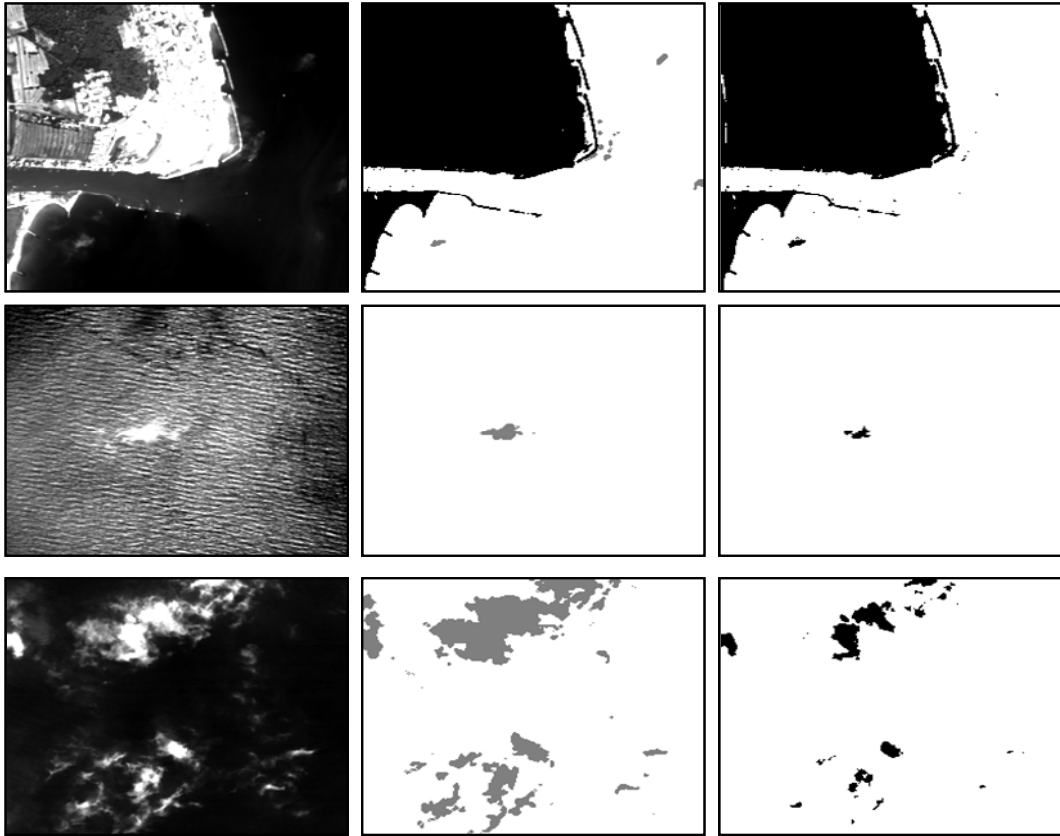


Figure 7.- Cloud masks for three marine scenes (*Top and middle panels*: coastal area off San Rossore (Pisa, Italy), *bottom panels*: oceanic waters of the Boussole Bouy (Ligurian Sea)) for AHS imagery. Left column: gray scale image of the scene. Centre column: cloud mask retrieved with our methodology. Right column: cloud mask retrieved by ATCOR4. Masking colour code is: white-water, grey-cloud, black-land. Pixel size @ nadir is 6.9m.

Spatial and Temporal VIS/SWIR/TIR Spectral Variability of Natural Desert Surfaces

Sabol, Donald E.¹, Kruse, Fred A.², Aslett, Zan², Minor, Tim¹, Kratt, Chris¹, Taranik, James², and Morkin, Todd²

1 Desert Research Institute, 2215 Raggio Parkway, Reno, Nevada, USA, 89512

2 Department of Geological Science, University of Nevada, Reno, Nevada, USA, 89557

don.sabol@dri.edu, fkruise@unr.edu, zaslett@gmail.com, tim.minor@dri.edu, Christopher.Kratt@dri.edu,

jtaranik@unr.edu, tmorkin@unr.edu

ABSTRACT - Remote sensing has been widely used for monitoring terrestrial surface changes. Typically, these changes include dramatic vegetation changes due to storms or changes in land-use, urban encroachment, or large-scale desertification. However, subtle changes can be early indicators of natural process affecting the surface. This is especially true for vegetation ecotomes that border unvegetated desert regions on the brink of survivability and are most apt to very sensitive to subtle changes in local weather; especially rainfall. In this study, we examined the compositional changes for five natural desert surfaces near Beatty, Nevada, USA over ~5 years using hyperspectral VIS/SWIR/TIR spectral data measured in the field, by aircraft, and by multispectral satellite-based ASTER data. These changes identify temporal “spectral trajectories” that are indicative of natural compositional changes in the surface over the temporal scale of the data used in the analysis. Spectral mixture analysis was performed on these data using field-measured spectral components at each site. Fractions were plotted for initial determination of spectral trajectories that indicate seasonal changes on the surface. Although visually similar, compositional trends for the five sites were different with some overlap, suggesting different natural spectral trajectories. These results are preliminary. However, once developed for a range of typical desert landscapes over a longer period of time and at a higher temporal frequency, a basic model can be produced to predict the range of variation; this will provide us a new analytical tool for identifying and separating seasonal variability from subtle long-term surface changes caused by global/regional climate changes.

1 INTRODUCTION

The spectral signature of a surface (and variance of that signature) give insights into the composition of the surface, its texture, as well as processes that cause changes on that surface. Although it is generally understood that the spectral signature of natural surfaces are both spatially and temporally variable, little has been done to examine (in the field) the full spectrum (VIS/SWIR/TIR) spatial and temporal variability of complex natural surfaces.

Spectral changes occur at different temporal scales short term (daily), intermediate (monthly /seasonally) to long term (over many years). Separating the short-term from longer-term changes may be difficult, especially when the long-term changes are slow and subtle, and when viewed in a short time series of images. This separation may be critical for early detection of long-term changes due to global / regional climate change or human encroachment.

In this paper, we present our initial results of monitoring compositional changes in five natural desert sites over ~5 years, using VIS/SWIR/TIR spectral measurements made in the field, and acquired

by airborne and satellite systems. These changes identify temporal “spectral trajectories” that are indicative of natural compositional changes in the surface over time. To monitor natural changes in surface composition, it is necessary to understand the changes at these different scales.

2 BACKGROUND

Arid and semiarid environments comprise approximately 35% of the earth’s land surface. Often, the spectral variability of these surfaces is influenced by windblown deposits and/or vegetation variability. Regional changes in the vegetation can be an important early indication of global warming-induced shifts in climate; especially in vegetation ecotomes that border unvegetated desert regions. These ecotomes tend to be on the brink of survivability and are very sensitive to subtle changes in local weather; especially precipitation fluctuations. However, quantifying the health and abundance of vegetation in these environments has been problematic because vegetation cover is sparse and surface reflectance may be dominated by soil.

The finer spectra resolution provided by hyperspectral VIS/SWIR image data may improve estimates of

green leaf area in sparsely vegetated arid environments. Hurcom and Harrison (1998) used field spectra to show the enhanced sensitivity of hyperspectral reflectance to vegetation abundance in Spain and Portugal. Spectral mixture modeling has been promoted as a method that can make effective use of the information content of multispectral and hyperspectral data (Smith et al., 1990) by decomposing each pixel into a linear combination of reference spectra, referred to as endmembers.

Non-photosynthetic vegetation in arid and semi-arid regions dominates the total vegetation signal and methods that specifically identify this component are critical for characterizing these landscapes (Okin, 2010). The subtle absorptions due to cellulose, lignin, and nitrogen may not be detectable unless there is a relatively high surface coverage of dry vegetation measured (>10%) with high spectral resolution data at a very low signal-to-noise. Fortunately, the thermal infrared (TIR) spectra of dry vegetation often exhibit a broad emissivity feature from 10.5 – 12.5 μ m (Elvidge, 1988) that can help in this separation. Green vegetation is relatively featureless across these wavelengths. Multi-temporal data may help to improve on estimations to monitor trends over time (Adams, et al., 1995; Sabol et al., 2002). However, incorporation of coincident multispectral TIR adds the capability to improve the discrimination of arid and semi-arid vegetation cover that is so strongly dominated by dry and non-photosynthetic biomass (Okin, 2010). French, et al. (2008) used both the VIS-SWIR and TIR bands of ASTER to help improve detection of vegetation in a semi-arid environment.

3 METHODS

We studied five natural desert sites near Beatty, Nevada. Multiple VIS/SWIR/TIR field spectra were measured at each site in the field (2 dates) and compared to data from nine ASTER scenes as well as two hyperspectral airborne data sets. Spectral endmembers were measured in the field (at each site) and used to model the field, hyperspectral airborne, and ASTER data using Spectral Mixture Analysis (SMA). The resulting compositions were then plotted to identify the spectral trajectories over time.

3.1 Study Sites

Five study plots of natural desert surfaces near Beatty, Nevada, USA., (Figure 1), were used for this study. Each of the plots (30m²) is representative of the much larger adjacent area (Figure 2), include:

- 1) Carbonate. Site. Composed of sparse phreatophytes growing over exposed carbonate units and soil.
- 2) Evaporites. Located on the west side of Oasis Valley, this site has a spring with some vegetation (mostly grasses), evaporites and some exposed silicified rock surfaces.
- 3) Saddle Fan. This site sits in a relatively flat saddle between two hills with exposed bedrock, consisting of sparse phreatophyte coverage over eroded, drained gravels, soils, and some bedrock.
- 4) Phreatophytes/alluvial fan. This site consists of alluvial fan material covered with creosote shrubs and sparse grass.
- 5) Volcanics. This site consists of dark volcanic rocks mixed with some lighter gravels and other alluvial units.

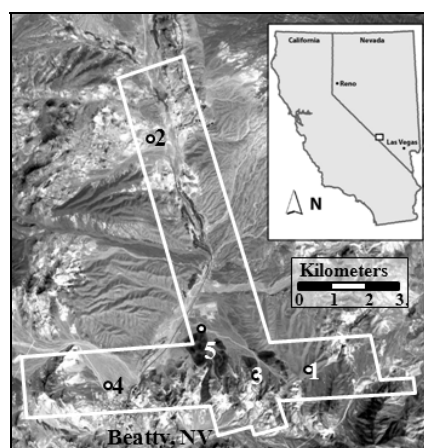


Figure 1: Location of the 5 study sites near Beatty, NV. The flight boxes for the hyperspectral data is outlined in gray. 1) Carbonate, 2) Evaporite, 3) Saddle fan, 4) Alluvial fan, and 5) Volcanic.

3.2 Field data acquisition

To allow for repeated field measurements over different seasons / years, a sampling protocol was established. Initially, the four corners of each site were located using a Trimble ProXRT gps (~30 cm accuracy) and marked with stakes. VIS/SWIR field measurements were made using an Analytical Spectral Devices (ASD) field spectrometer (0.35 – 2.5 μ m). These measurements were made on a grid of 7 X 7 sampling sites (5 meter spacing) for a total of 49 measurements (Figure 3). The thermal spectra were measured using a Designs and Prototypes Fourier Transform Infrared (D&P FTIR) spectrometer (2.0 – 16.0 μ m). Because of the length of time required to take each measurement, the sampling of the D&P was

made at 9 locations at each site (the center point, 5 meters in toward the center from each corner as well as 5 meters from the center toward the corners).

3.3 Airborne / Spaceborne Data

The VIS/SWIR hyperspectral airborne data was collected by Terra Remote Sensing on 9 April 2007, and 25 September 2007; and SpecTIR on 2-3 April 2007, and 6 August 2008. Measurements included 178 bands between 0.45 and 2.45 μm , with pixel sizes between 2.4 and 5 meters. Field calibration targets (established prior to and measured during overflight) were used to calibrate the data to reflectance. ACORN was also used to improve the atmospheric correction.

Thermal airborne data was collected by SEABASS on 16 July 2007 and 6 August 2008. This data consists of 128 bands between 7.8 – 13.4 μm with a pixel size of 5 meters.

3.3 Spectral Modeling

We used the simple SMA model (Adams et al., 2005) for this preliminary analysis.

$$R_b = \sum_{em=1}^{Ne} F_{em} R_{em,b} \quad ; \quad (1)$$

$$\sum_{em=1}^{Ne} F_{em} = 1$$

Where R_b is the reflectance for each channel (b , Ne is the number of spectral endmembers (components in the scene) and F_{em} is the fraction of endmember em . The fractions sum to one. The number of endmembers is almost always small (<6) and in natural environments often includes green vegetation, dry vegetation, soil, rock, and shade. There are several permutations of SMA that range from simple SMA that uses a single small number of

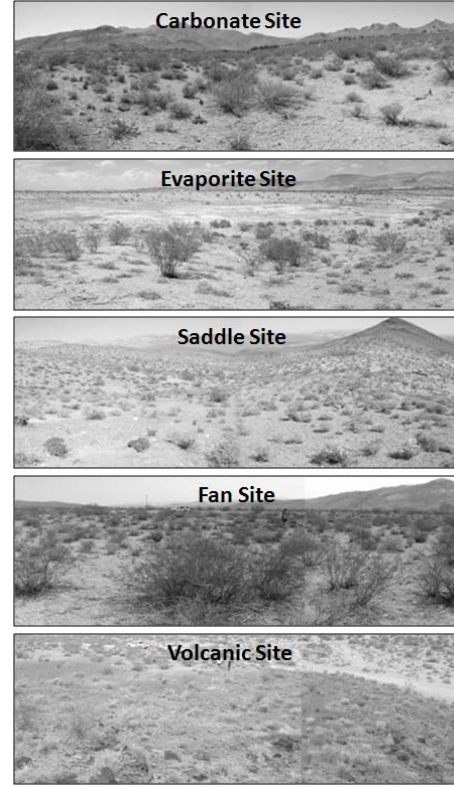


Figure 2. Photos of the study sites.

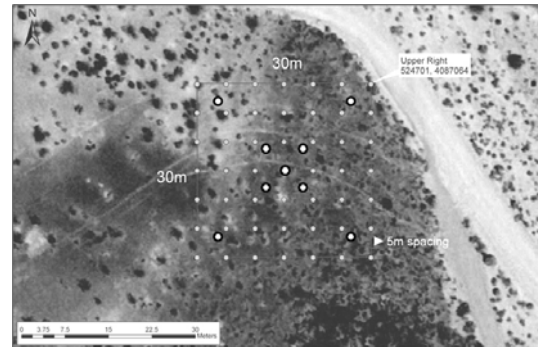


Figure 3. Site measurement protocol over the Volcanic Site. The 49 ASD measurement sites are shown as small grey circles while the 9 mFTIR sites are large white circles. The same measurement scheme was used on all 5 sites.

endmember spectra to describe the surface to complex approaches that identify different endmember spectra for each pixel (Roberts, et. al, 1998). We avoided the complex model as we were able to collect field endmember spectra from each site. Endmembers were selected from models that provided the lowest RMS error, were compositionally realistic, and required the fewest endmembers. We used the same general

approach for TIR unmixing described by Gillespie et al. (1990).

4 RESULTS / DISCUSSION

4.1 Field Spectra

The ASD field and VIS/SWIR airborne spectra are shown in Figure 4. A comparison of the May and September 2009 field spectra are quite different for three of the sites (Carbonate, Evaporite, and Saddle). While the solar illumination is different for all three sites, field observations indicate that changes in surface composition was minimal for the Carbonate site, indicating the difference is primarily due to the change in illumination. The Spring evaporite site, however, had a slightly higher evaporate crust in May than in September. In this case the spectral difference is due to both illumination and compositional differences. The difference at the Saddle site is primarily due to an increase in the dry vegetation in September over that in May. This was observed in the field as well as in the fractions from SMA. The data in Figure 4 was used in combination with the endmember spectra (Figure 5) as inputs into the SMA model to derive the spectral fractions (Figure 6). Although the spectra in Figure 5 represent all the spectra that were used as endmembers, only three to four were needed to model the data for any single date. Different spectra were needed for different dates at the same site.

4.2 Modeled Results

The fractions from the SMA results are shown plotted in ternary diagrams (by date) in Figure 6. Fractions for VIS/SWIR were determined separately from the TIR. Generally, we found that the TIR fractions for the ASTER data were most useful for detecting low fractions of green vegetation and less useful for distinguishing between soil and rock and detection of

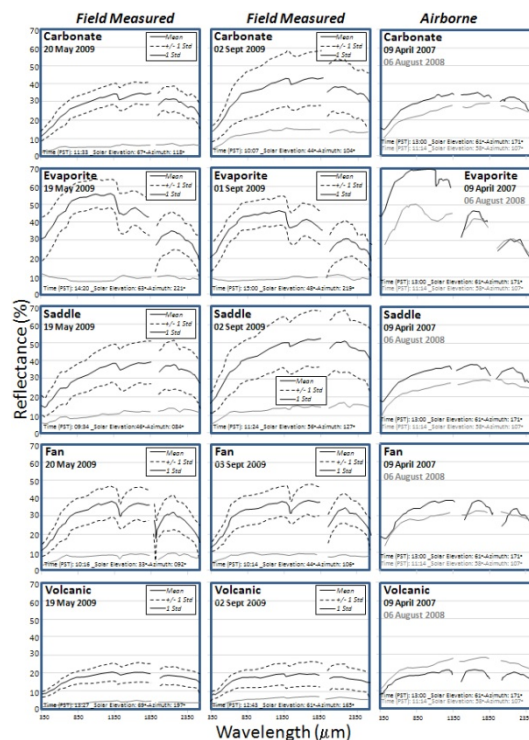


Figure 4: Field measured and hyperspectral airborne spectra for each site.

dry vegetation. This was due to the minimal bands of ASTER TIR as well as the 90meter spatial resolution. The fractions follow a general trajectory that show subtle increased green vegetation during wetter periods and an increase of dry vegetation, soil, and/or rock when dry (Figures 6&7). For the Saddle Fan, Volcanic, and Fan sites, the wetter periods are in the Spring and Fall. The carbonate site is interesting in that August and September measurements in 2008-2009 show a greater abundance of vegetation (~10%) than during those months in 2003-2007. Continued monitoring here is necessary to determine this trend continues, stays the same, or reverts back to the fractions of previous years.

The Evaporite site generally shows an increase in green vegetation in the early spring (wetter). As the temperatures rise, the vegetation dries out and stronger evaporates cover more of the surface. Later, once the surface has dried, some of the evaporate surface gives way to the underlying/wind-blown silt soil. Unfortunately, the data is lacking winter measurements that would help complete the trajectories. This is because measurements between late October and mid-March are difficult here due to cloud cover.

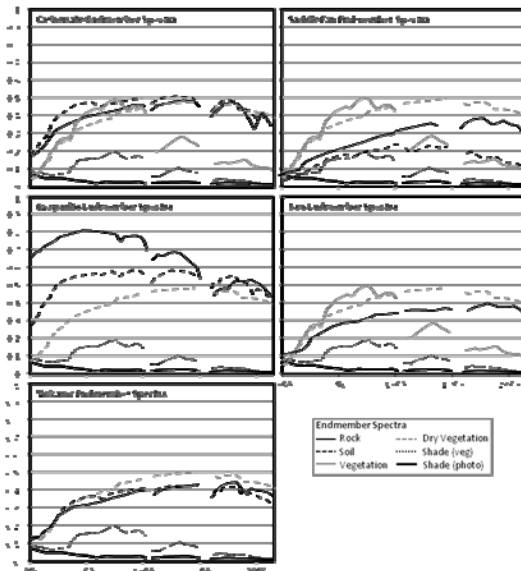


Figure 5. Best fit endmembers found to model each of the five sites (VIS/SWIR). Note that not all of the endmembers were necessarily used for any particular date.

5 CONCLUSIONS

Generalized trends in surface composition of natural desert surfaces can be identified using field, airborne, and spaceborne multispectral / hyperspectral data. The trends generally show subtle seasonal vegetation changes that appear (over the short period ~5 year observed in this study) to be seasonally cyclic. The compositional trends are different for the 5 sites, with some overlap as shown in Figure 7. A closer investigation into fractional uncertainty (measurement, modeling, etc) is yet needed to clarify the trends shown here. However, once these data are understood for a range of typical desert landscapes over a longer period of time and at a higher temporal frequency, a basic model can be produced to predict the range of variation. This would give us a new analytical tool for identifying and separating seasonal variability from subtle long-term surface changes caused by global/regional climate changes.

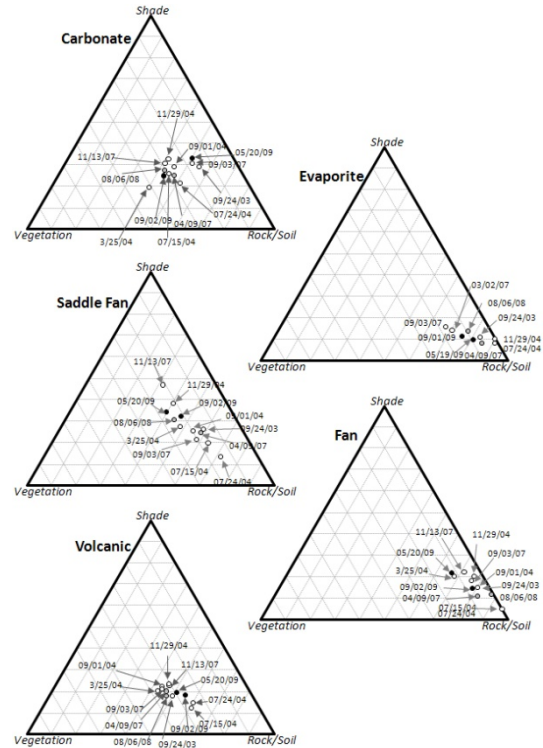


Figure 6: Fraction data from SMA plotted to the field, airborne, and ASTER data. Each point is the mean value for that particular date. Black circles = field data; Gray circles = airborne data; White circles = ASTER data. Vegetation = green and dry vegetation.

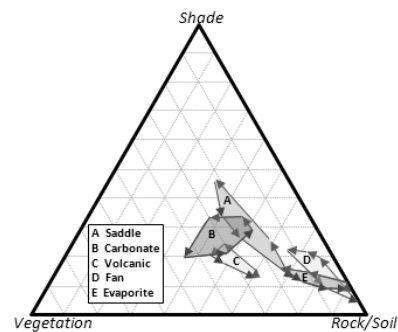


Figure 7. General compositional trends observed using field, airborne, and ASTER data. These trends are primarily seasonal and related to vegetation growth; which affects the vegetation and shade fractions. Vegetation in this figure includes green and dry vegetation.

6 REFERENCES

- Adams, J.B., Sabol, D.E., Kapos, V., Almeida, R. Filho, Roberts, D.A., Smith, M.O., Gillespie, A. (2005). "Classification of multispectral images based on fractions of endmembers: Applications to land-use change in the Brazilian Amazon." *Remote Sensing of Environment* **52**, 137-154.
- Elvidge, C. (1988). "Thermal infrared reflectance of dry plan materials: 2.5-20.0 μm ." *Remote Sensing of Environment* **28**: 265-285.
- French, A. N., T. J. Schmugge, J. C. Ritchie, A. Hsu, F. Jacob and K. Ogawa (2008). "Detecting land cover change at the Jornada Experimental Range, New Mexico with ASTER emissivities." *Remote Sensing of Environment* **112**(4): 1730-1748.
- Gillespie, A.R., M.O. Smith, J.B. Adams and S.C. Willis, (1990) "Spectral Mixture Analysis of Multispectral Thermal Infrared Images", in Abbott, E.A. (Ed.), *Proc. of the Second TIMS Workshop*, JPL Pub. 90-55, JPL, Pasadena, Calif., pp. 57- 74.
- Hurcom, S., and Harrison A., (1998). The NDVI and spectral decomposition for semi-arid vegetation abundance estimation." *International Journal of Remote Sensing* **19**(16):3109-3125.
- Okin, G. S. (2010). "The contribution of brown vegetation to vegetation dynamics." *Ecology* **91**(3): 743-755.
- Roberts, D.A., Gardner, M., Shurch, R., Ustin, S, Scheer, G., and Green, R.O. (1998). "Mapping chaparral in the Santa Monica Mountains using multiple endmember spectral mixture models." *Remote Sensing of Environment* **65**, 2675-279.
- Sabol, D.E., Gillespie, A.R., Adams, J.B., Smith, M.O., and Tucker, C.T. (2002). "Structural stage in Pacific Northwest forests estimated using simple mixing models of multispectral images." *Remote Sensing of Environment* **80**(1), 1-16.
- Smith. M.O., Ustin, S.L., Adams, J.B., and Gillespie, A.R. (1990). "Vegetation in Deserts: I. A regional measure of abundance from multispectral images." *Remote Sensing of Environment* **31**, 1-26.

Application of imaging spectroscopy to map indicator plant species for wetland degradation in the National Park of Las Tablas de Daimiel, Spain

¹Thomas Schmid, ²Hannes Feilhauer, ²Ulrike Faude, ³Santos Cirujano, ³Raquel Sánchez, ¹María José Sierra, ¹Manuel Rodríguez, ⁴Salvador Sánchez

¹CIEMAT – Avda. Complutense 22, 28040 Madrid, España. thomas.schmid@ciemat.es; mj.sierra@ciemat.es; manuel.rodriguezrastrero@ciemat.es

²Universität Bonn, Vegetationsgeographie, Geographisches Institut, Meckenheimer Allee 166, 53115 Bonn Germany. hannes@geographie.uni-bonn.de; ulrike.faude@giub.uni-bonn.de

³CSIC, Real Jardín Botánico de Madrid, Plaza de Murillo, 2, 28014 Madrid, Spain. santos@rjb.csic.es; rsanchez@rjb.csic.es

⁴CSIC, Instituto de Recursos Naturales, Serrano 115, 28006 Madrid, Spain. sanchez.carrillo@ccma.csic.es

ABSTRACT - Las Tablas de Daimiel National Park is threatened by groundwater overexploitation as a result of inappropriate agricultural and water management policies. Therefore, wetland degradation is an important issue that has to be addressed urgently. In this study, an integrated methodology is applied to map indicators for wetland degradation by combining soil characteristics and hyperspectral reflectance data of surface covers, mainly associated to vegetation. Partial least square regression and imaging spectroscopy (HyMap) was used to map soil characteristics across the wetland. Best mapping results were achieved for soil characteristics such as organic carbon and cation exchange capacity. These characteristics were related to the spatial distribution of wetland vegetation and vegetation conditions. The natural helophytic vegetation unit made up of the autochthonous vegetation (*Cladium mariscus* stands) showed the highest predicted contents in organic carbon indicating good wetland conditions with frequent flooding. However, deteriorated vegetation stands featured increased areas with low organic carbon content and this leads to areas that are most vulnerable to the degradation of the wetland. The cation exchange capacity was correlated with organic carbon and hence showed a similar spatial distribution. However, this trend changed for soils supporting halophilous vegetation and rush communities. These soils are influenced by high amounts of clay minerals in fine-textured soils originating largely from the surrounding upland soils that are managed by agricultural activity.

1 INTRODUCTION

In the semiarid region of Central Spain, wetland areas are mainly threatened by human activities causing rapid degradation with loss of wetland surface and, eventually leading to their disappearance. Activities such as intensive irrigation, overexploitation of groundwater, sewage discharge as well as altering and channeling of rivers have severely affected the wetlands and their natural functions. A combination of these activities is the major cause of wetland degradation (Cirujano, 2000).

This is the case of the National Park of Las Tablas de Daimiel (NPTD) in Central Spain, which is included

as a Biosphere Reserve in the international network of UNESCO's Man and the Biosphere Programme, and is also included on the list of the [Ramsar Convention](#). Likewise, from the [European Union](#) it was designated as [Special Protection Area](#) for Birds (SPA) under the 79/409/CEE "[Birds Directive](#)" and integrated in the [Natura 2000 Network](#).

Prior to human intervention, this wetland was surrounded by dense holm-oak (*Quercus ilex subsp. ballota*) woods and the open water bodies supported rich aquatic vegetation. Traditionally, such woodlands were replaced by rain-fed agriculture. In recent times, this traditional agriculture has been increasingly substituted by crops that require intensive irrigation.

This resulted in an overexploitation of the underlying aquifer. Furthermore, water and soil quality changed due to differences in chemical composition between groundwater and surface water supplies. This had a strong impact on wetland health contributing to the deterioration of the wetland over the past forty years. Prolonged droughts, eutrophication and contamination of water lamina, siltation, invasion of ruderal species, and loss of biodiversity lead to degradation and loss of wetland surface (Sánchez-Carrillo and Álvarez-Cobelas, 2001; Álvarez-Cobelas, *et al.*, 2001).

Earth Observation (EO) data are essential for characterizing and monitoring the evolution and condition of such wetland areas. Previous studies have been carried out where EO information from different sensors has been applied to wetlands (Schmid *et al.*, 2005, and 2010; Ríaza *et al.*, 2005).

The objective of this study is to map the spatial distribution of soil and vegetation parameters with imaging spectroscopy and to identify indicator plant species for wetland degradation. For this purpose, information on soil and vegetation properties were obtained to identify indicators (e.g., for desiccation and nutrient accumulation).

2 STUDY AREA

The national park (Figure 1) is located in the Province of Ciudad Real within the Autonomous Community of Castilla-La Mancha. This region has a Mediterranean semi-arid climate with a mean annual temperature of 13.3°C (Jan: 5.0°C; Aug: 23.4°C.), an annual precipitation of 435 mm (Jul: 6 mm; Feb: 57 mm) and an annual potential evapotranspiration of 736 mm (max. July, 135 mm) according to the local meteorological station at Las Tablas de Daimiel.

The park consists of an extended wetland area within the plain of La Mancha in Central Spain. The area is an alluvial plain ranging from 605 to 620 m a.s.l. that lies within a basin of Tertiary (limestone and calcareous clays) and Quaternary sediments. The wetland area consists of lacustrine-palustrine Holocene sediments with mud, calcareous, gypsiferous and peat facies. The soil types include (according to Soil Taxonomy 11th ed., 2010) Entisols, Inceptisols and Histosols Orders.

The wetland is located at the confluence of two rivers: 1) the Guadiana river that normally supplies fresh water, although the river has been dry during the past years; and 2) the Cigüela river with seasonal brackish water that discharges a high content of agrochemicals and urban residuals into the wetland. In the past, a further water source was the upwelling of groundwater from the underlying karstic aquifer; this is, however, not occurring nowadays as the groundwater table has dropped considerably as a result of the above mentioned overexploitation. The flood

plain covers 1750 ha, with permanent waters as well as shallow and seasonal waters. In 2009, there was a reduced water lamina of about 10 ha. The rest of the wetland area was completely dry.

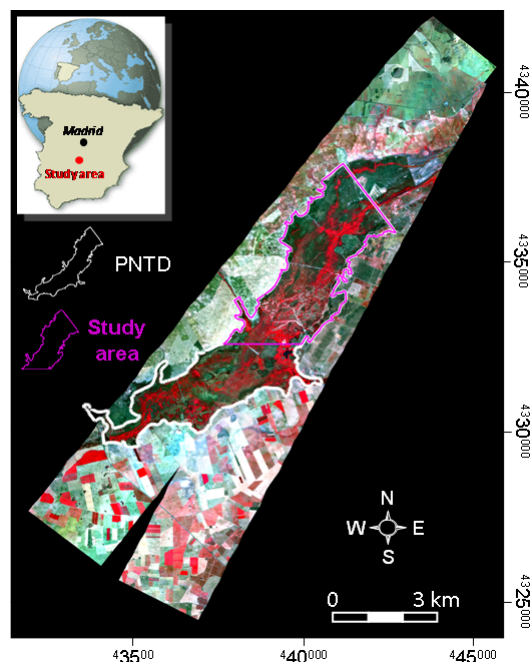


Figure 1. Study area of the Las Tablas de Daimiel wetland National Park acquired with HyMap on 12th August 2009 (false color composite using bands at wavelengths of 0.833, 0.661 and 0.558 μm in the red, green and blue channels).

A complex mosaic of plant communities includes aquatic plants (*Chara hispida*), palustrine vegetation (*Cladium mariscus*, *Phragmites australis*, *Typha domingensis*), halophytic plants in areas of temporal flooding (*Salsola vermiculata*, *Scirpus maritimus*, *Lythrum salicaria*), halophytic plants in areas rarely flooded (*Limonium carpetanicum*), and wooded areas (*Tamarix gallica*, *Tamarix canariensis*) within the wetland area.

3 MATERIALS AND METHODOLOGY

Data was acquired from various sources at different spatial scales. A field campaign was carried out in August 2009. Surface cover samples (sediment, soil, and vegetation) were taken within 35 plots representing 225 m² each. These samples were analyzed in the laboratory. Analyses included: soil color, texture, pH (1:2.5), electrical conductivity (EC, 1:5), organic matter (OM) and organic carbon (OC), calcium carbonate (CaCO₃), cation exchange capacity (CEC); sulphate (SO₄²⁻) and basic cations.

Hyperspectral data was acquired with a flight campaign on the 12th of August 2009 by the German Aerospace Center (DLR). The data was obtained with the HyMap airborne hyperspectral sensor covering an area of 79 km² in two flight lines with a spatial resolution of 5 m and 125 bands.

The pre-processing of the data included system, geometric and atmospheric corrections and was carried out by DLR. A further fine geometric calibration was carried out using 23 and 20 ground control points, obtaining an RMS error of 0.29 and 0.28 pixels for the flight lines, respectively. Digital cartographic data was included at a scale of 1:25 000 (Instituto Geográfico Nacional, 2000 and 2001). Further ancillary data was used and included geology, vegetation, and land use maps as well as meteorological data.

The vegetation map by Cirujano *et al.* (2008) was used to assign the initial selection of field plots within the study area to vegetation units. These units include natural helophytic (*Cladium mariscus*), helophytic (*Phragmites australis*), rush communities, halophilous (*Limonium carpetanicum* and *Suaeda vera*), and invasive nitrophilous vegetation (*Conyza canadensis* and *Lactuca serriola*).

The methodological procedure integrates field data, hyperspectral airborne data, and ancillary cartographic information (Figure 2).

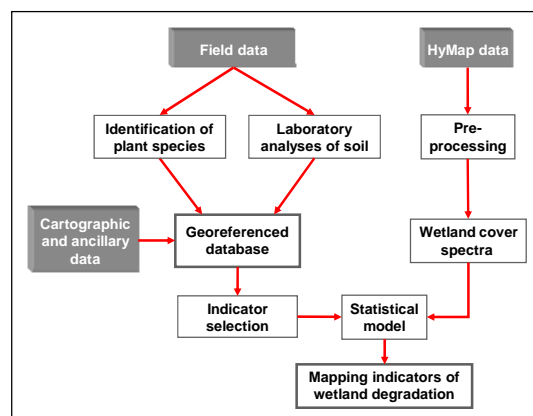


Figure 2. Methodology for mapping indicators of wetland degradation.

The two flight lines were mosaicked and resized. Furthermore, a mask was created to carry out the processing of the data solely on the study area.

The wetland indicators were spatially modeled based on the HyMap data using partial least square regression (PLSR, Wold *et al.*, 2001) and brightness-normalized partial least squares regression (bnPLSR, Feilhauer *et al.*, 2010). For each indicator, a model was generated and validated with leave-one-out cross-validation. The empirical relation from the model was

thereafter applied to the HyMap image to generate a map of individual indicators of wetland degradation.

3 RESULTS

The extensive analysis of the soil parameters for both surface (0 to 10 cm) and subsurface (20 to 30 cm) resulted in the following relations: 1) soils associated with halophilous vegetation featured fine textures, neutral to strongly alkaline pH, variable salinity and generally low content of OC; 2) soils associated with natural helophytic vegetation had loamy to coarse textures, very high content in OC, high CEC, and a pH that is strongly acid to slightly alkaline; 3) soils associated with rush communities were fine-textured, neutral to moderately alkaline, with a high variability in CaCO₃ and OC percentages; 4) soils with helophytic vegetation had notably high amounts of CaCO₃ and OC and intermediate textural, saline and pH values; 5) soils under invasive vegetation were extremely rich in CaCO₃ and markedly poor in OC, with low salinity and lowest content in SO₄²⁻.

Differences between surface samples with respect to subsurface samples showed, in general, coarser textures, lower EC, higher content in OM and OC, and lower contents in SO₄²⁻. No relevant differences were observed in pH and CaCO₃. All samples featured Ca²⁺ as the main exchangeable cation and Ca²⁺ and SO₄²⁻ as main soluble ions.

Soil characteristics included OM, OC, EC, CaCO₃, CEC, and soluble SO₄²⁻, which distinguished well the different vegetation units. Initial exploratory work with PLSR to relate these soil characteristics to the hyperspectral data for the different plots gave acceptable results for the OC, OM and CEC.

The bnPLSR model for OC (Figure 3) included 7 significant predictors and obtained a R² val of 0.56. This model was used to map OC as an indicator of wetland degradation.

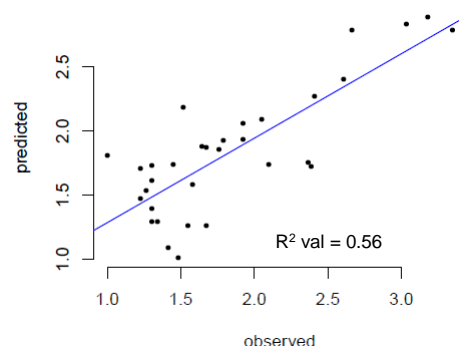


Figure 3. The bnPLSR result for OC and hyperspectral data. The values are square root transformed to achieve Gaussian distribution.

The PLSR model for CEC (Figure 4) included 13 significant predictors and exhibited a fit of R^2 val of 0.60 which was again taken as valid for mapping the CEC.

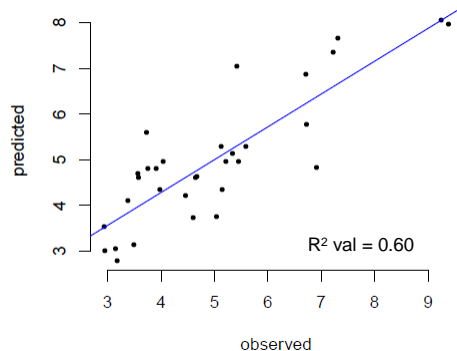


Figure 4. The PLSR result for cation exchange capacity and hyperspectral data. The values are square root transformed to achieve Gaussian distribution.

The spatial distribution of OC (Figure 5) and CEC (Figure 7) in the study area is considered an initial result. The respective soil parameters are determined from the surface reflectance that mainly is related to vegetation as well as sediment, soil, and water in decreasing extent.

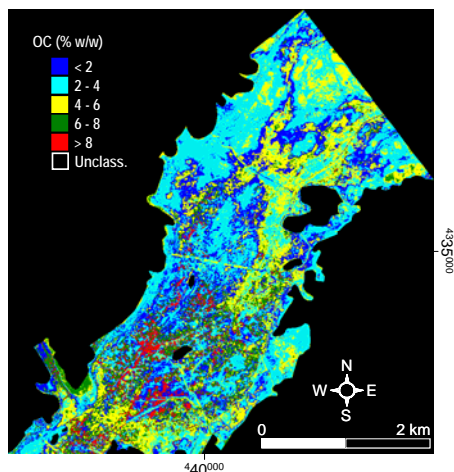


Figure 5. Spatial distribution of OC in the study area.

The surface area occupied by the different classes of OC ranged from 51 ha (1.9%) to 439 ha (16.4%) for the classes with more than 8% and between 2 and 4% of OC in the soil surface. The remaining classes of < 2%, 4 to 6% and 6 to 8% occupy a surface area of 212 ha (7.9%), 225 ha (8.4%), and 115 ha (4.3%), respectively.

The natural helophytic vegetation unit showed the highest predicted contents in organic carbon (Table 1) that were associated with 42% of pixels in classes > 6% of OC (Figure 6). This contrasts significantly with predicted values of the rest of the units in the same classes: 21% for invasive nitrophilous vegetation; 15% for helophytic; 3% for rush communities, and 2% for halophytic vegetation.

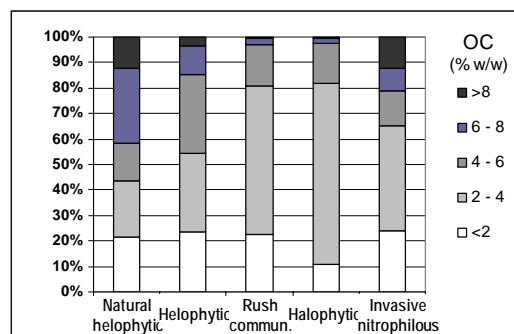


Figure 6. OC class distribution for the different vegetation units.

Measured OC values confirmed this trend in most vegetation units, except for invasive vegetation (Table 1). A tentative explanation is based on the fact that invasive vegetation spreads specially in areas (called “tablazos”) where high soil water content and low organic matter are typical features.

Table 1. Dominant predicted OC classes and average measured OC values.

Vegetation unit	Dominant predicted OC class (%w/w)	Average measured OC in vegetation plots (%w/w)
Natural helophytic	6-8	9.5
Helophytic	2-4 / 4-6	4.8
Rush communities	2-4	3.4
Halophytic	2-4	2.3
Invasive nitrophilous	2-4	1.9

High values related to the helophytic vegetation (*Cladium mariscus* stands) were concentrated in the central part of the wetland, which are an indicator of good wetland conditions. Deteriorated stands featured increased areas with low organic carbon content and this leads to areas that are most vulnerable to degradation of the wetland. As a consequence of drought conditions over several years, low OC content was found in areas where enriched CaCO_3 bottom sediments, are exposed. These areas are occupied by nitrophilous invasive vegetation and their spatial

distribution is a further indicator of degraded wetland conditions.

The surface area occupied by the classes of CEC (Figure 7) ranged from 76 ha (2.8%) to 457 ha (17.0%) for the classes with more than 40 $\text{cmol}^+ \text{kg}^{-1}$ and between 10 and 20 $\text{cmol}^+ \text{kg}^{-1}$ at the soil surface. The remaining classes of < 10, 20 to 30, and 30 to 40 $\text{cmol}^+ \text{kg}^{-1}$ occupied an area of 156 ha (5.8%), 249 ha (9.3%), and 106 ha (4.0%), respectively.

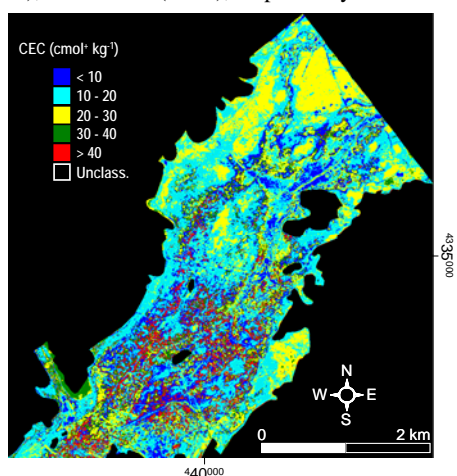


Figure 7. Spatial distribution of CEC in the study area.

In relation with CEC (Figure 8), the highest predicted values were also spatially associated with natural helophytic vegetation, showing 40% of pixels in the corresponding classes of over 30 $\text{cmol}^+ \text{kg}^{-1}$. Areas occupied by invasive and helophytic vegetation show intermediate predicted values, with 20 and 19% of the area within the classes of greater than 30 $\text{cmol}^+ \text{kg}^{-1}$. Areas occupied by rush communities and halophytic vegetation were associated with lowest predicted CEC values (6% and 3% of the area with over 30 $\text{cmol}^+ \text{kg}^{-1}$, respectively).

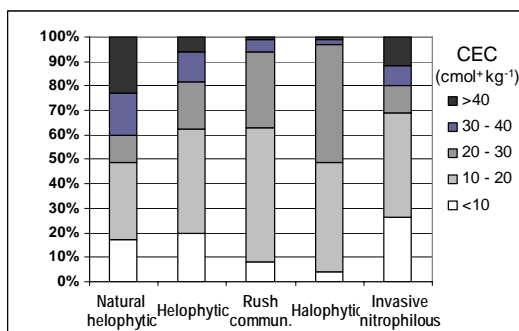


Figure 8. CEC class distribution for the different vegetation units.

Measured CEC values in field plots showed, nevertheless, significant differences in average values with respect to the predicted values (Table 2). This was especially the case for natural helophytic vegetation. The CEC distribution was related to OC content (highest in natural helophytic vegetation plots), assuming the high CEC values of organic matter (around 200 $\text{cmol}^+ \text{kg}^{-1}$). In this case, it is to mention that a qualitative relation between the predicted and measured CEC for the different vegetation units has been observed; however, a quantitative relation is still not accurate.

Table 2. Dominant predicted CEC classes and average measured CEC values.

Vegetation unit	Dominant predicted CEC class ($\text{cmol}^+ \text{kg}^{-1}$)	Average measured CEC in vegetation plots ($\text{cmol}^+ \text{kg}^{-1}$)
Natural helophytic	10-20	74.3
Helophytic	10-20	28.4
Rush communities	10-20	23.4
Halophytic	20-30	23.1
Invasive	10-20	9.7

On the other hand, CEC measured values in soils containing vegetation units with halophytic vegetation and rush communities were relatively high considering that they have some of the lowest organic carbon content. Nevertheless, the content in clay minerals in these plots (dominant clay textural classes) was the highest within the study area. These values of CEC seem to be related with the relative abundance in clay minerals instead of organic matter. The soil properties are hence determined by a high deposition of fine-textured sediments originating largely from the surrounding upland soils that are managed by agricultural activity.

4 CONCLUSIONS

The application of an integrated methodology, where data is obtained from different sources, showed that indicators for wetland degradation can be identified through the quantitative assessment of soil parameters and surface reflectance data. Identifying such indicators and relating them to plant species and soil characteristics is an attempt to determine the wetland conditions and degradation.

Several soil parameters showed good relationships to the general vegetation units. PLSR analyses showed that the most promising soil parameters are OC and CEC for a quantitative

determination of their respective contents throughout the study area.

Soils supporting natural helophytic vegetation unit showed the highest amounts of OC. The natural vegetation consists of *Cladium mariscus* stands which are an indicator of optimal wetland conditions. Deteriorated stands featured increased areas with low organic carbon content and this leads to areas that are most vulnerable to degradation of the wetland.

CEC is correlated to OC and shows a similar spatial distribution for the different vegetation units within the study area. However, this trend changes for soils supporting halophilous vegetation and rush communities due to the influence of high amounts of clay minerals in fine-textured soils originating largely from the surrounding upland soils that are managed by agricultural activity. A qualitative relation between the predicted and measured CEC for the different vegetation units has been well observed; however, a quantitative relation is still not accurate.

5 ACKNOWLEDGEMENTS

The data of this study was funded by the German Ministry of Education and Research (BMBF) within the framework of the project of the EnMAP preparatory application. The authors would like to acknowledge the support of the following: the German Aerospace Centre (DLR), Dr. Martin Bachmann, and Sebastian Weide with respect to the HyMap data supplied to the HyEurope 2009 campaign; Dr. Sebastian Schmidlein for his support regarding the collaboration between the Vegetation Geography Group at Bonn University and CIEMAT; Ana Mecó and Ángela Gumuzzio for their support in the field work; Dr. Jaime Cuevas and Dr. Ana Ruiz for their interpretation of the soil chemistry; and Carlos Ruiz de la Hermosa, Director of the Park, for supporting our work and his team for accompanying us in the field work.

6 REFERENCES

- Álvarez-Cobelas, M., Cirujano, S., and Sánchez-Carrillo, S. (2001). Hydrological and botanical man-made changes in the Spanish wetland of Las Tablas de Daimiel. *Biological Conservation* 97, 89-98.
- Cirujano, S. (2000). Flora y vegetación. In *Humedales de Ciudad Real*, (Ed. S. L. Esfagos), Talavera de la Reina, Toledo: Esfagos, pp. 124-131.
- Cirujano, S., Álvarez-Cobelas, M., Soriano, O., Alonso, J.M., Moreno, M., López, E., and Ortiz, M.J. (2008). Informe de seguimiento y monitoreo ambiental en el P. N. Las Tablas de Daimiel (2003-2007). EINTAM, Estudios Europeos de Medio Ambiente S.L. y Organismo Autónomo Parques Nacionales, 329 pp.
- Feilhauer, H., Asner, G.P., Martin, R.E., and Schmidlein, S. (2010). Brightness-normalized partial least square regression for hyperspectral data. *Journal of Quantitative Spectroscopy & Radiative Transfer*, 111, 1947-1957.
- Instituto Geográfico Nacional (2000). Mapa Topográfico Nacional de España. Map sheets 737 (I and IV), scale 1:25000. Ministerio de Fomento, Instituto Geográfico Nacional.
- Instituto Geográfico Nacional (2001). Mapa Topográfico Nacional de España. Map sheets 760 (I and II), scale 1:25000. Ministerio de Fomento, Instituto Geográfico Nacional.
- Riaza, A., García Meléndez, E., Suárez, M., and Müller, A. (2005). Mineral climate indicators in paleoflooded and emerged areas around lake marshes (Tablas de Daimiel, Spain) using hyperspectral DAIS 7915 spectrometer data. *International Journal of Remote Sensing*, 26, 4565-4582.
- Sánchez-Carrillo, S., and Álvarez-Cobelas, M. (2001). Nutrient dynamics and eutrophication patterns in a semi-arid wetland: the effects of fluctuating hydrology. *Water, air, and soil pollution*, 131, 97-118.
- Schmid, T., Gumuzzio, J., Rodríguez, M., and Koch, M. (2010). Application of hyperspectral spaceborne data to identify sensitive wetland areas of Central Spain. Proceedings of the European Space Agency (ESA) Hyperspectral Workshop held in Frascati, Italy, on 17-19 March 2010, ESA SP-683, 1-6.
- Schmid, T., Koch, M., and Gumuzzio, J. (2005). Multisensor Approach to determine changes of wetland characteristics in semiarid environments (Central Spain). *IEEE Trans. Geosci. Remote Sensing*, 43, 2516-2525.
- Wold, S., Sjöström M., and Eriksson L. (2001). PLS-regression: a basic tool of chemometrics. *Chemometrics and Intelligent Laboratory Systems*, 58, 109-30.

Study of Air and Land Surface Temperature Differences from EOS-MODIS and Ground Data

Raquel Niclòs¹, José A. Valiente¹, Maria J. Barberà¹, and Maria J. Estrela²

¹ Unidad Mixta CEAM-UVEG. Instituto Universitario Centro de Estudios Ambientales del Mediterráneo CEAM - UMH (CEAM), 14 Charles Darwin, 46980 Paterna, Spain

² Unidad Mixta CEAM-UVEG. Departamento de Geografía. Universidad de Valencia (UVEG). 28 Blasco Ibáñez, 46010 Valencia, Spain

niclos@ceam.es, josean@ceam.es, barbera@ceam.es, majoesna@uv.es

ABSTRACT – To monitor and define the climate and meteorology of a specific geographic region, knowledge of the spatial and temporal patterns of surface air temperature is essential. This work analyzed correlations between surface air temperature (T_a) and land surface temperature (LST) in Eastern Spain with the aim of establishing suitable techniques to obtain T_a maps from satellite images and geographical data. Two sources of data were used: 10-min averaged data from the meteorological station network set up by CEAM in the Valencia region and MODIS images from the EOSTerra and EOSAqua satellites. Thermal radiometers were also set up on two reference sites, and the ground-measured LSTs were used not only to analyse possible relationships between LST- T_a and solar irradiance, but also to validate the MODIS-retrieved LSTs before using them in the study. The correlations between T_a and satellite-retrieved LST were analysed in terms of the specific geographical parameters and the meteorological variables measured at the CEAM stations, which included solar irradiance, surface wind speed, and relative humidity. In addition, satellite-retrieved surface properties, such as albedo and vegetation indexes, were also considered so as to take into account the observed dependence of LST- T_a on land cover type. Finally, several expressions, both for daytime and night-time, were proposed to determine the T_a from remote sensing data (LST, vegetation indexes, and albedo) and geographical and meteorological parameters. These expressions can provide T_a data with accuracies up to $\pm 1.2K$ both for daytime and night-time.

1 INTRODUCTION

Surface air temperature (T_a), which is defined as the temperature measured at about 2m above the ground, is a key climatic and meteorological variable and allows us to quantify exchange processes at surface level. T_a is involved, for example, in the assessment of energetic fluxes, potential and actual evapotranspiration and water stress indexes, and it can be used as an input parameter in meteorological models.

T_a is usually measured from meteorological stations and thus T_a data are limited by the density and distribution of the available station network. The aim of this study is to establish relationships between ground-measured T_a , remote sensing data and geographical parameters, so as to be able to generate T_a maps. Satellite images provide spatially continuous data and can be a useful tool to solve the discontinuity problem of ground data. Thus, the present study is based in satellite images from the Moderate Resolution Imaging Spectroradiometer (MODIS) on board EOSAqua and EOSTerra satellites, meteorological data measured by the CEAM station network (www.ceam.es/ceamet) covering the Valencia region in the East of Spain, along with geographical and land cover data.

2 DATA

2.1 Remote Sensing Data

EOS-MODIS images in the summer months of 2009 were used for the study. The EOSAqua-MODIS MYD11A1 product was selected to obtain land surface temperature (LST). This product is generated daily at 1-km spatial resolution and contains LSTs (with different layers for daytime and night-time overpasses), emissivities for channels 31 and 32, acquisition time and satellite-viewing angle for each pixel, and quality flags. The EOSAqua-MODIS acquisition time over the studied area was 12-14 UTC during daytime and 1-3 UTC at night-time (around 2 hours later than the EOSTerra-MODIS acquisitions), which are closer to the times of maximum and minimum T_a values in the diurnal cycle.

The MYD13A2 product was used to obtain spectral vegetation indexes. This product contains MODIS 16-day composites both of the Normalized-Difference Vegetation Index (NDVI) and also of the Enhanced Vegetation Index (EVI) at 1-km spatial resolution (Huete et al., 2002).

Additionally, albedo (AL) values were obtained from the MCD43A3 product, which provides 16-day

composites of EOSAqua and EOSTerra MODIS at 500-m spatial resolution.

Finally, a regional land cover map was generated by means of a supervised classification method (maximum likelihood) based on a selection of representative and tested CORINE polygons as ground-truth areas and the use of spectral images of the isotropic BRDF parameter given by the MODIS 16-day MCD43A1 product (Nicolòs et al., 2010a).

2.2 Ground meteorological data

Concurrent ground-measured meteorological data were collected by the CEAM meteorological station network (see locations in Fig. 1), which is composed of 36 stations distributed throughout the Valencia region, Eastern Spain. This network systematically records data on the main meteorological variables, i.e., humidity (Hr), air temperature at 1.5-2m height (T_a), wind direction and speed (U), rainfall and solar irradiance (I), the latter at only 13 stations (Fig. 2). Data are recorded every 10 minutes and sent to the CEAM headquarters through a GPRS service.

NIST-calibrated Apogee 8-14 μ m radiometers (SI-111 & SI-112) (Theocharous et al., 2010, www.apogeeinstruments.com) were set up on two reference sites selected because of their relatively high homogeneity (Fig. 3). The ground-measured LSTs were used to analyze relationships between $LST-T_a$ and I (Nicolòs et al. 2010b). An increase in $LST-T_a$ was observed with I on both sites, but the degree of dependence was different for each site; only a slight dependence was observed at site B probably due to the low water stress and the full vegetation cover on this site (Nicolòs et al. 2010b). Additionally, ground-measured LSTs were also used to validate MODIS-retrieved LSTs before using them for the analysis.

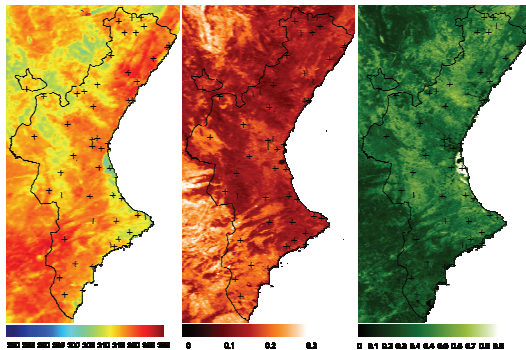


Figure 1.- From left to right, examples of: daytime LSTs (in K) retrieved from the daily 1-km MYD11A1 product (2009/07/24, 13:30-13:36UTC), albedo obtained from the 16-day 500-m MCD43A3 product (2009/07/28-2009/08/12), and NDVI obtained from the 16-day 1-km MYD13A2 product (2009/07/20-2009/08/04). Station locations are shown with +.

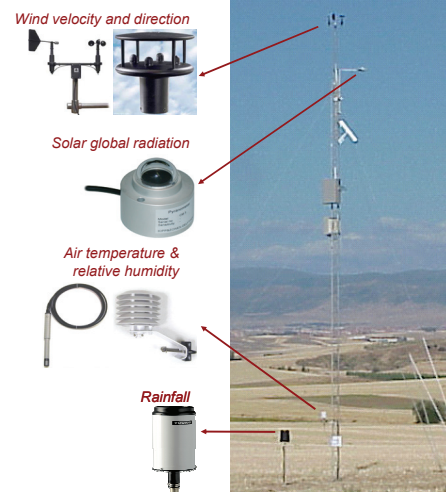


Figure 2.- Meteorological instrumentation available at the CEAM meteorological stations (www.ceam.es/ceamet).

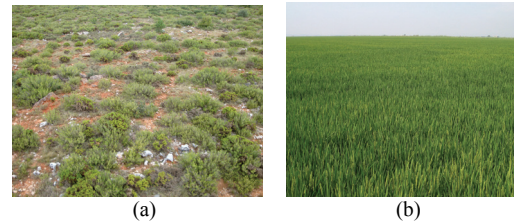


Figure 3.- Reference sites: (a) A: Mediterranean calcic thermophile shrubland, 39.224°N, -0.903°E, and (b) B: rice-crops, FVC~1 in summers, 39.274°N, -0.317°E (WGS-84).

Only MODIS LSTs collected with satellite-viewing angles lower (higher) than 40° (-40°) were finally used in the study, since MODIS LST uncertainties were shown to increase with angle (Fig. 4).

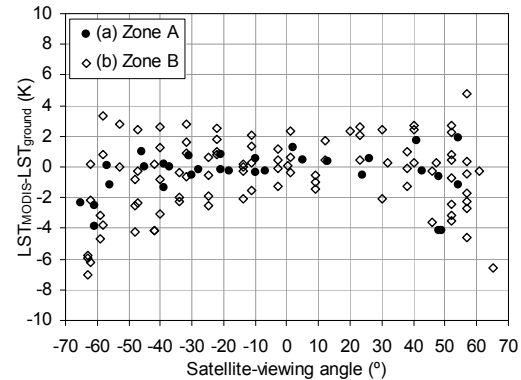


Figure 4.- Dependence of the difference between MODIS-retrieved LST and ground-measured LST on the MODIS-viewing angle.

2.3 Geographical data

Ninyerola et al. (2007) and Cristóbal et al. (2008) pointed out T_a dependences on geographical variables, such as elevation (h), latitude (Lat), continentality and terrain curvature. Zaksek and Schroedter-Homscheidt (2009) also considered the terrain curvature dependence and they introduced a term defined as the difference between the station elevation and the mean elevation within 20km vicinity (Δh). A digital elevation model (DEM) was generated by interpolating the contour lines of the 1:10000 topographic maps of the Valencia region (www.icv.gva.es). Topographic aspects and slopes (ϕ , s), distance to coast ($dist$) as a measurement of continentality, and Δh were computed from the DEM to analyse the T_a dependences on geographical data. Additionally, solar zenith and azimuth angles (z , a) were computed as a function of time and station locations. The solar azimuth angle was defined as the angle relative to the South (positive to the East).

2.4 Final database

Finally, a database of concurrent ground-measured meteorological variables (T_a , Hr , I and U), satellite-retrieved data (LST, NDVI, and AL), and geographical data (Lat , h , $dist$, Δh , ϕ , s , z , and a) were obtained during the summer months of 2009. 845 sets of concurrent data were examined to analyse T_a dependences at night-time (after removing the satellite-retrieved LSTs at angles larger than 40°). 285 sets were used to study daytime dependences due to the availability of solar irradiance measurements.

3 METHODOLOGY AND RESULTS

T_a dependences on remote sensing, meteorological and geographical data were first analysed using the abovementioned database both for daytime and night-time. Figure 5 shows examples of these dependences, e.g., T_a against LST (for both daytime and night-time), I (at daytime) and h (at night-time). More or less strong dependences of T_a were observed on: remote sensing LST, 1-NDVI and AL; ground-measured I , Hr and U ; and geographical Lat , h , $dist$, Δh , $\cos z$, and a . The T_a dependence on LST was one of the strongest.

Then, the available daytime and night-time databases were randomly split into a training dataset (with 80% of the data) and a test dataset (with 20% of the data). The first lines of Tables I and II (D.1 and N.1) show the regressions of T_a against LST (both in K) obtained for daytime and night-time, respectively, when using the corresponding training datasets. R^2 and $\sigma(T_a)$ are the coefficient of determination and the error of estimate of the regressions.

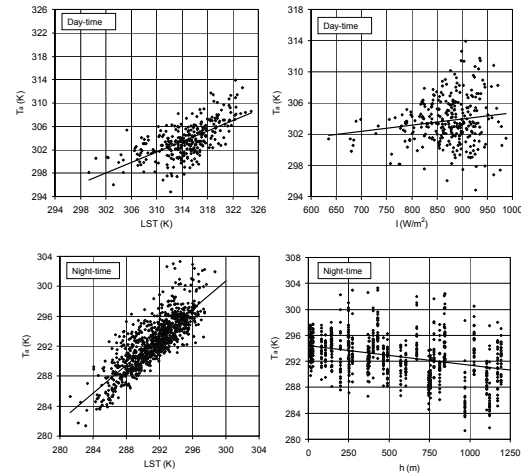


Figure 5.- Examples of the analyzed T_a dependences.

We also computed differences between T_a values calculated with the determined regression equations for the test datasets and ground-measured T_a data. Tables I and II show the biases and standard deviations, σ , of the differences, together with the root-mean-square error, RMSE, which provides an uncertainty estimate for the proposed equations since it is a quadratic sum of systematic and random errors. $\sigma(T_a)$ and RMSE values higher than $\pm 2K$ and of about $\pm 1.8K$ were obtained for the T_a linear regressions against LST at daytime and night-time, respectively.

A stepwise procedure (Draper and Smith, 1998) was applied on the training dataset to select the statistically significant terms in a multilinear regression of all the abovementioned variables, not just LST. The second lines of Tables I and II (D.2 and N.2 equations) show the multilinear regressions of T_a against the statistically significant terms selected by the stepwise procedure. D.2 and N.2 equations achieved T_a accuracies of about $\pm 1.2K$. Figure 6 shows T_a calculated with the D.2 equation against the ground-measured T_a values, for both the training and the test datasets. The agreement between the results obtained with the training and test datasets separately proves the consistency of the proposed equation. The D.3 equation in Table I replaces the I and AL terms in D.2 with a common $(1-AL)I$ term related to the surface reflection of I . However, no improvement was observed with such a term. The night-time N.2 equation in Table II includes dependences on Hr (quadratic) and U . Nevertheless, the U dependence can be removed without increasing the error (see N.3 in Table II). Figure 7 shows the N.3-calculated T_a values against the ground-measured T_a values for both the training and test datasets.

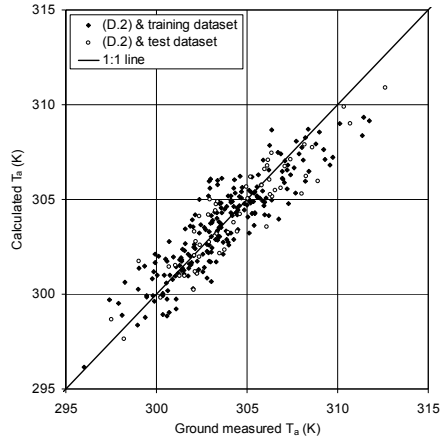


Figure 6.- Daytime D.2-calculated T_a values against ground-measured T_a data for both the training and test datasets.

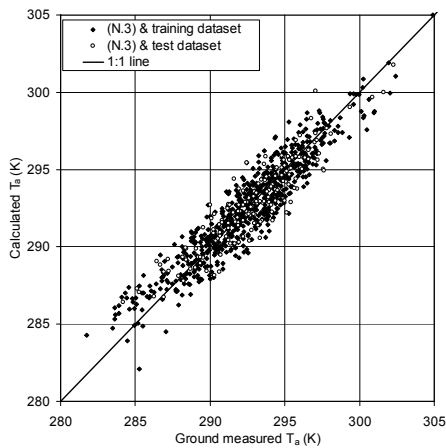


Figure 7.- Night-time N.3-calculated T_a values against ground-measured T_a data for the training and test datasets.

As H_r may be difficult to obtain without ground measurements, similar expressions without H_r terms were also tested. H_r terms in daytime D.2 and D.3 (night-time N.2 and N.3) were removed in D.4 and D.5 (N.4 and N.5) equations (see Tables I and II). Minimum errors of about $\pm 1.7K$ were obtained with the expressions without H_r terms. Nevertheless, cloudless I can be easily estimated as a function of solar angles (Iancu and Kudish, 2008) and a DEM, or simulated by using radiative transfer models.

Additionally, the daytime model proposed by Zaksek and Schroedter-Homscheidt (2009) was checked on the study region (D.6 in Table I). The D.6 results gave RMSEs higher than $\pm 3K$ on both the training and the test datasets. Figure 8 shows T_a calculated with this model and the D.2 equation against the ground-measured T_a values. Much higher discrepancies are shown for the model of Schroedter-

Homscheidt (2009) than for D.2. Better results were obtained by fitting the model coefficients on the training dataset, but T_a uncertainties higher than $\pm 2K$ were still shown (see D.7 in Table I).

A stepwise procedure was also applied to evaluate the statistical significance of the terms included in D.7. Two terms could be removed from the expression, leaving just the terms related to LST, 1-NDVI and (1-AL)I (see D.8 in Table I). Other significant terms, which were selected by the first stepwise procedure and considered in D.2, were added to D.8 with the aim of improving its results. D.9 shows the final equation, which includes a H_r term, and D.10 the same expression without the H_r term. Errors of around $\pm 1.5K$ and $\pm 1.9K$ were obtained for D.9 and D.10 equations, respectively, which did not achieve the accuracies given by D.2 and D.4.

Finally, D.2 and N.3 equations gave the lowest T_a uncertainties, which were of about $\pm 1.2K$, during both daytime and night-time. As both the training and the test datasets include data for different land cover types, D.2 and N.3 results were also analyzed against land cover. A regional land cover map (see Section 2.1) was used to distinguish the land cover types for each station, which were reclassified in 4 generic types for simplicity: shrublands, forests, croplands and urban areas. Table III shows the accuracies of D.2 and N.3 when they were applied on the training and the test datasets split into these land cover types. There are no significant differences for the different land covers. This fact proves the soundness of the proposed equations for any land cover type, which is a consequence of the inclusion of terms related to surface properties, like albedo and vegetation indexes, in the equations to determine T_a from remote sensing and geographical data.

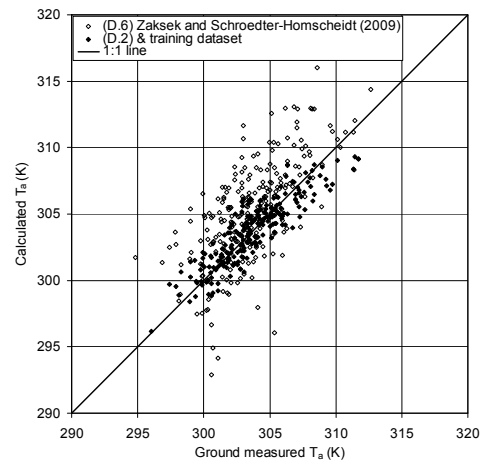


Figure 8.- Comparison of the results of the model of Zaksek and Schroedter-Homscheidt (2009) and the proposed D.2.

Table I.- Daytime proposed and tested T_a models, together with the corresponding uncertainties in K.

DAY-TIME EXPRESSIONS	Training		Test		
	R^2	$\sigma(T_a)$	bias	σ	RMSE
(D.1) $T_a=0.40LST+178.7$	0.41	2.08	-0.56	2.33	2.40
(D.2) $T_a=0.26LST-12.4(1-NDVI)-5.9I-0.102Hr-0.031Lat-0.081dist+27.0AL+260.1$	0.80	1.24	-0.21	1.24	1.26
(D.3) $T_a=0.25LST-9.3(1-NDVI)-8.8(1-AL)I-0.109Hr-0.029Lat-2.2h-0.057dist+264.6$	0.79	1.27	-0.21	1.28	1.30
(D.4) $T_a=0.47LST-18.6(1-NDVI)-6.0I-0.040Lat+1.9h-0.101dist+44.4AL+195.4$	0.67	1.59	-0.29	1.66	1.69
(D.5) $T_a=0.49LST-13.5(1-NDVI)-10.5(1-AL)I-0.037Lat-0.5h-0.056dist+194.6$	0.63	1.67	-0.31	1.72	1.75
(D.6)* $T_a=LST+1.82-10.66\cos z(1-NDVI)-0.566a-3.72(1-AL)(\cos i/\cos z+(\pi-s)/\pi)I-3.41\Delta h$		3.31	+1.83	2.83	3.37
(D.7) $T_a=0.52LST+152.7-8.6\cos z(1-NDVI)+1.4a-4.1(1-AL)(\cos i/\cos z+(\pi-s)/\pi)I-2.9\Delta h$	0.46	2.15	+0.09	2.26	2.26
(D.8) $T_a=0.52LST+152.3-8.5\cos z(1-NDVI)-5.4(1-AL)(\cos i/\cos z+(\pi-s)/\pi)I$	0.44	2.16	+0.09	2.28	2.28
(D.9) $T_a=0.23LST-9.5\cos z(1-NDVI)-2.3(1-AL)(\cos i/\cos z+(\pi-s)/\pi)I-0.115Hr-0.033Lat-2.8h-0.059dist+270.4$	0.76	1.42	+0.06	1.63	1.64
(D.10) $T_a=0.51LST-15.1\cos z(1-NDVI)-3.1(1-AL)(\cos i/\cos z+(\pi-s)/\pi)I-0.040Lat-1.0h-0.059dist+188.5$	0.61	1.84	-0.04	2.00	2.00

(6)* Zaksek and Schroedter-Homscheidt (2009), $\cos i = \cos z \cos s + \sin z \sin s \cos(a-\phi_i)$, a and s are in radians, and $\sigma(T_a)$, bias, σ , and RMSE are in K. and $\sigma(T_a)$ =RMSE on the training dataset.

Table II.- Night-time proposed T_a models, together with the corresponding uncertainties in K.

NIGHT-TIME EXPRESSIONS	Training		Test		
	R^2	$\sigma(T_a)$	bias	σ	RMSE
(N.1) $T_a=0.94LST+19.3$	0.71	1.83	+0.05	1.68	1.69
(N.2) $T_a=0.85LST+1.8(1-NDVI)-0.129Hr+0.00056Hr^2-0.009Lat-0.8h-0.009dist-10.4AL+0.04U+58.9$	0.88	1.20	-0.09	1.24	1.24
(N.3) $T_a=0.86LST+1.7(1-NDVI)-0.130Hr+0.00056Hr^2-0.009Lat-0.7h-0.008dist-10.6AL+56.1$	0.88	1.20	-0.08	1.25	1.25
(N.4) $T_a=0.92LST+2.8(1-NDVI)-0.012Lat+0.9h-0.018dist-11.4AL+0.26U+31.8$	0.76	1.69	-0.04	1.55	1.55
(N.5) $T_a=0.99LST+2.3(1-NDVI)-0.012Lat+1.3h-0.016dist-13.3AL+12.2$	0.74	1.73	-0.01	1.62	1.62

Table III.- D.2 and N.3 accuracies obtained with the training and the test datasets for different land cover types.

RMSE (K)	D.2 equation		N.3 equation	
	Training	Test	Training	Test
Shrublands	1.14	1.29	1.23	1.39
Forests	1.33	1.15	1.16	1.13
Croplands	1.48	1.25	1.16	1.08
Urban areas	1.02	1.50	1.19	1.33

4 CONCLUSIONS

Several expressions have been proposed in this work to obtain T_a from remote sensing data and geographical parameters. Linear regressions with MODIS-retrieved LST data provide T_a with errors higher than $\pm 2K$ during daytime and errors of $\pm 1.8K$ at night-time. Nevertheless, T_a errors decrease up to $\pm 1.2K$ when other remote sensing variables (NDVI and AL) and geographical and meteorological data (Lat, h, dist, I, and Hr) are considered as terms (see D.2 and N.3). Additionally, the proposed D.2 and N.3 equations are shown to work properly for any land cover type. Ninyerola et al. (2007) and Cristóbal et al. (2008) pointed out the soundness of combining remote sensing and geographical variables. Although they did not consider Hr as an input for modelling T_a , the inclusion of Hr terms improves the results; a minimum error of $\pm 1.7K$ is obtained with expressions without Hr. Finally, the model proposed by Zaksek and Schroedter-Homscheidt (2009) (D.6) shows errors

higher than $\pm 3K$, or errors higher than $\pm 2K$ when fitting the model to the training dataset.

ACKNOWLEDGEMENTS

This work was supported by the Spanish Ministerio de Ciencia e Innovación under Projects CGL2007-65774/CLI and CGL2008-04550/CLI, by CONSOLIDER-INGENIO 2010 CSD2007-00067, by the AQ2 European Social Fund, and by the European Union (Project CIRCE N.036961). Instituto Universitario CEAM – UMH is supported by the Generalitat Valenciana and Fundación BANCAJA. Moreover, we thank Jackie Scheiding for the revision and Eloi Ribeiro for his collaboration.

5 REFERENCES

- Cristóbal, J., Ninyerola, M., and Pons, X., 2008, Modeling air temperature through a combination of remote sensing and GIS data. *Journal of Geophysical Research*, **13**, D13106.
- Draper, N.R., and Smith, H., 1998, Applied Regression Analysis. Ed. Hoboken, N.J.: Wiley-Interscience, 307-312.
- Huete, A., Didan, K., Miura, T., Rodriguez, E.P., Gao, X., and Ferreira, L.G., 2002, Overview of the radiometric and biophysical performance of the

- MODIS vegetation indices. *Remote Sensing of Environment*, **83**, 195-213.
- Ilanetz, A., and Kudish, A., 2008, A method for determining the solar global and defining the diffuse and beam irradiation on a clear day. In: Modeling solar radiation at the Earth surface. Ed. Badescu, V.: Springer, 93-113.
- Niclòs, R., Estrela, M.J., Valiente, J.A., and Barberà, M.J., 2010a, "Clasificación periódica de coberturas terrestres a escala regional con imágenes MODIS". *International Review of Geographical Information Science and Technology-GeoFocus*, **10**, 1-17.
- Niclos, R., Estrela, M.J., Valiente, J.A., and Barberà, M.J., 2010b, "Análisis de correlaciones entre la temperatura del aire y la temperatura de las superficies vegetadas medida con radiometría térmica". *Revista de Teledetección*, **34**.
- Ninyerola, M., Pons, X., and Roure, J.M., 2007, Objective air temperature mapping for the Iberian Peninsula using spatial interpolation and GIS. *International Journal of Climatology*, **27**, 1231-1242.
- Theocharous, E., Usadi, E., and Fox, N. P., 2010, CEOS comparison of IR brightness temperature measurements in support of satellite validation. Part I. National Physical Laboratory (NPL) Report OP 3, 130pp.
- Zaksek, K., and Schroedter-Homscheidt, M., 2009, Parameterization of air temperature in high temporal and spatial resolution from a combination of the SEVIRI and MODIS instruments. *ISPRS Journal of Photogrammetry and Remote Sensing*, **64**, 414-421.

Validation of Split-Window Algorithms for Estimating Sea Surface Temperature on the Coast of Northern Chile.

Juan C. Parra¹, Luis Morales², José A. Sobrino³, Juan Romero⁴

¹ *Department of Physical Sciences. Universidad de La Frontera. Av. Francisco Salazar 01145, Casilla 54-D, Temuco, Chile.*

² *Department of Environmental Sciences and Renewable Natural Resources. Universidad de Chile. Casilla 1004, Santiago, Chile.*

³ *Image Processing Laboratory. Universitat de València. P.O. Box 22085. Valencia, Spain*

⁴ *Department of Electrical Engineering. Universidad de La Frontera. Av. Francisco Salazar 01145, Casilla 54-D, Temuco, Chile.*

ABSTRACT Split-Window (SW) Algorithms are presented and applied which allow sea surface temperature to be estimated using data obtained from the Advanced Very High Resolution Radiometer (AVHRR) on board the National Oceanic and Atmospheric Administration (NOAA) series of satellites. The algorithms are validated by comparison with in situ measurements from a hydrographic buoy located off the coast of northern Chile, specifically at 21° 21'S; 70° 06' W (Tarapacá Region), approximately 3 km from the coast. Of the SW algorithms implemented, the one presenting the best goodness of fit is that proposed by Sobrino and Raissouni (2000), with a mean squared error of 0.82 °K

1 INTRODUCTION

Estimating Sea Surface Temperature (SST) from infra-red thermal data has been done routinely since the beginning of the 1970s. This parameter is fundamental for climatic and meteorological studies, since the oceans, which cover 70% of the earth's surface, have an enormous heat-storing capacity, and can therefore exchange large quantities of energy with the atmosphere. Furthermore, knowledge of the sea surface temperature is very important for the verification of models of ocean circulation and many other oceanographic phenomena (Arbelo, 1997).

One of the greatest problems encountered in estimating SST from satellite data is the combined action of the disturbance generated by the atmosphere and the spatial variability of emissivity. Atmospheric disturbance is due almost entirely to the absorption and emission of thermal radiation by the water vapour content in the atmosphere (Galve et al., 2008), while emissivity is due to the heterogeneity of the elements present on the earth's surface (Morales and Parra, 2002). Consequently, proper estimation of SST from satellite data requires the correction of these effects.

One of the principle techniques available to address the problem of correcting atmospheric disturbances and emissivity is the Split-Window (SW) method, based on the differential absorption of the atmosphere in two bandwidths of the electromagnetic spectrum (McMillin, 1975). Based on this technique, a large

number of algorithms exist today which are intended for use in obtaining the land surface temperature (LST) (Vera et. al., 2010, Parra et. al., 2006, Zhihao et. al., 2001) and the SST (McClain et al., 1985; Coll et al., 1992; Coll et al., 1994; Sobrino and Raissouni, 2000).

In the present article SW algorithms are applied, compared and validated, which allow SST to be estimated using data obtained from the Advanced Very High Resolution Radiometer (AVHRR), on board the National Oceanic and Atmospheric Administration (NOAA) series of satellites.

2 MATERIALS AND METHODS

The study area is in the north of Chile, at 21° 21'S; 70° 06' W (Tarapacá Region, Chile), where there is a buoy located approximately 3 kilometres off the coast which keeps daily records of the sea surface temperature.

The SST information available covers the months between July and November 2005, and was acquired by the Laboratorio de Procesos Oceanográficos y Clima PROFC [Laboratory of Oceanographic and Climate Processes], of the Universidad de Concepción (Chile).

In addition, images from the NOAA satellite in the visible and thermal infra-red spectrum bands were used, obtained cost-free from the Comprehensive Large Array data Stewardship System (CLASS). The images, in LAC (Local Area Coverage) format, level

1B, were subjected to radiometric calibration and georeferencing. Subsequently they were subjected to rigorous selection on the basis of two criteria: (a) a maximum difference of 35 minutes between the satellite pass over the study region and the *in situ* acquisition of the SST (Donlon et al., 2006); (b) days free of cloud over the study area.

Of a total of 153 satellite images, only 13 (Table 1) met the above criteria. This shows clearly the difficulty implied in correctly validating algorithms used for estimating SST.

Fecha (GMT)	Hora de paso	Angulo de observación (°)
31/08/2005	19:09	34
09/09/2005	19:18	47
20/09/2005	19:07	33
21/09/2005	18:56	17
03/10/2005	18:35	22
11/10/2005	18:54	14
12/10/2005	18:44	05
14/10/2005	18:25	38
19/10/2005	19:17	43
28/10/2005	19:23	49
30/10/2005	19:03	29
01/11/2005	18:42	07
02/11/2005	18:32	25

Table 1. Selected dates, time of pass and angle of observation of the NOAA satellite. The time of the *in situ* measurement of the SST is 19:00 hrs (GMT) for all the samples.

Table 2 presents the mathematical structure of the SW algorithms used

Autores	Algoritmo
Mc. Clain et al. (1985)	$SST = 1.0561 T_4 + 2.542 (T_4 - T_5) + 0.888 (T_4 - T_5) (\sec \theta - 1) - 16.98$
Coll et al. (1992)	$SST = T_4 + [1.41 + 0.24 (T_4 - T_5)] (T_4 - T_5)$
Coll et al. (1994)	$SST = T_4 + [1.0 + 0.58 (T_4 - T_5)] (T_4 - T_5) + 0.51$
Sobrin y Raussouni et al. (2000)	$SST = T_4 + 1.4 (T_4 - T_5) + 0.32 (T_4 - T_5)^2 + 0.83$

Table 2. SW algorithms selected for estimating SST. T_4 and T_5 are the radiometric temperatures corresponding to channels 4 and 5 of the AVHRR-NOAA; θ is the angle of observation of the sensor.

The algorithms proposed present different variations on the classic SW equation. Indeed in the case of McClain et al. (1985), the dependence on the angle of observation of the sensor θ is specifically taken into account. This is because it has been found that the error produced in the estimation of SST increases with the angle of observation, a consequence of increased atmospheric attenuation due to the increase in the optical thickness (Arbelo, 1997).

The algorithms of Coll et al. (1992, 1994) and Sobrino and Raussouni et al. (2000) present quadratic fits in

which the coefficient A is not constant but has a linear dependency on the difference in the radiometric temperatures, i.e. $A = a_0 + a_1 (T_4 - T_5)$, while coefficient B remains constant.

The implementation of the various algorithms presented supposes the availability of information corresponding to radiometric temperature in bands 4 and 5, which was obtained from the original satellite image using the specialized software for the treatment of ENVI images, version 4.3.

3 RESULTS OBTAINED

Figure 1 presents a contrast between the SST measured *in situ* and the corresponding radiometric temperatures. As can be seen in the graph, the radiometric temperatures in bands 4 and 5 appear underestimated when compared with the surface sea temperature measured *in situ*, with differences of up to 6.7 °K.

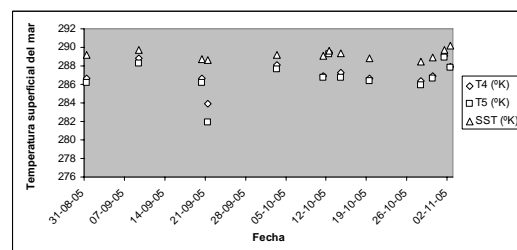


Figure 1. Surface sea temperature (SST) measured *in situ* compared with the radiometric temperatures (T_4 , T_5)

Figure 2 illustrates the SST *in situ* contrasted with the equivalent values estimated by application of the different algorithms.

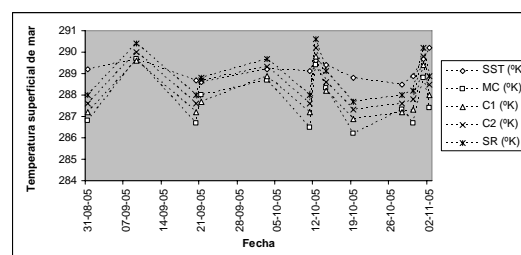


Figure 2. SST *in situ* contrasted with equivalent values by application of the different algorithms.

Table 3 shows the mean squared errors. As may be observed, the best fit is obtained with the application of the Sobrino and Raissouni (2000) algorithm.

Algoritmo	Error Cuadrático Medio (°K)
Mc <u>Clain</u> et al. (1985)	1.75
Coll et al. (1992)	1.38
Coll et al. (1994)	1.04
Sobrino y Raissouni (2000)	0.82

Table 3. Mean squared errors with the application of the various algorithms.

4 CONCLUSIONS

The SST was estimated by the application of different SW algorithms, based solely on information obtained from the sensor on board the satellite.

The results obtained indicate that the variations found between the radiometric temperature and that measured *in situ* demonstrate the effect introduced by omission of atmospheric correction. Thus the radiometric temperatures T_4 and T_5 (°K) appear to be underestimated when compared with the T_{in} (°K), with differences of up to 6.7 °K.

Of all the algorithms used, that of Sobrino and Raissouni produces the smallest mean squared error (0.82).

5 ACKNOWLEDGEMENTS

The authors wish to thank Project DI08-0029 of Universidad de La Frontera for support to the present research, and at the same time, the Laboratorio de Procesos Oceanográficos y Clima PROFCE of the Universidad de Concepción for providing the information of the SST *in situ*, and the Comprehensive Large Array data Stewardship System (CLASS) for facilitating the satellite images from the NOAA satellite cost free.

6 REFERENCES

Arbelo M. 1997. Determinación de la temperatura superficial de mar mediante la sinergia de los sensores AVHRR y TOVS. Aplicación a Canarias. Tesis Doctoral. Universidad de la Laguna, España, 207 pp.

Coll C., Casselles V., Sobrino J.A., 1992. Desarrollo de un modelo de corrección atmosférica en el término II. Aplicación a los canales y 5 del NOAA. Anales de Física, 120.132.

Coll C., Casselles V., Sobrino J.A., Valor E., 1994. On the atmospheric dependence of the Split-Window equation for land surface temperature. Intr. J. Remote Sensing, vol 15, N0 1, 105-122.

Donlon C., W. Wimmer, I. Robinson, G. Fisher, D. Poulter, G. Corlett, G. 2006. Validation of AATSR using in situ radiometers in the English channel and

bay of Biscay. Proc. Second Working Meeting MAVT-2006, SP-615, 20-24. Frascati, Italy.

Galve J.M., C. Coll, V. Caselles, E. Valor, J. M. Sánchez y M. Mira. 2008. Development and Validation of Land Surface Temperature Algorithms. Revista de Teledetección. ISSN: 1988-8740. 29: 38-44.

Morales, L., Parra, J. 2002. Estimating thermal infrared radiance emitted by the atmosphere using reanalysis data. Rev. Mex. Fis. 48: 119-121.

Mc. Clain E., Pichel W. and Walton C., 1985. Comparative performance of AVHRR based multichannel sea surface temperatures. J. Geoph. Res., C6: 11587 - 11601.

Mc. Millin, L.M., 1975, Estimation of the sea surface temperatures from two infrared window measurements with different absorption, J. Geoph. Res., 36: 5113-5117.

Parra, J., Sobrino, J., Morales, L., Castellaro, G., Uribe, J., Gaete, N. 2006. Aplicación de un Algoritmo de Split-Window para la estimación de la temperatura de la superficie terrestre desde datos AVHRR-NOAA. Agric. Téc. 66(4): 385-392.

Sobrino J.A., Raissouni N., 2000. Toward remote sensing methods for land cover dynamics monitoring: Application to Morocco. Intr. J. Remote Sensing, vol 21, N° 2, 353-366.

Vera L., J.C. Parra, L. Morales, C. Mattar y E. Jorquera, 2010. Comparative analysis of Split-Window algorithms for estimating soil temperature. R.C. Suelo Nutr. Veg. 10(1): 35-39.

Zhilhao Q., G. Dall'Olmo and A. Karnieli, 2001. Derivation of split window algorithm and its sensitivity analysis for retrieving land surface temperature from NOAA-Advanced Very High Resolution Radiometer data. J. Geoph. Res., Vol 106, N° D19, 22655-22670.

Compensation for subpixel roughness effects in thermal-infrared images

Iryna Danilina¹, Alan R. Gillespie¹, Lee Balick², Amit Mushkin^{1,3}, Matthew Smith¹, Dan Blumberg⁴

1 Department of Earth and Space Sciences, University of Washington, Seattle, WA, USA;

2 Los Alamos National Laboratory, Los Alamos, NM, USA;

3 Geological Survey of Israel, Jerusalem, IS;

4 Ben-Gurion University of the Negev, Beer-Sheva, IS

danilina@u.washington.edu

ABSTRACT - Emissivity spectra recovered from spectral radiance images may have lowered spectral contrast due to irradiance from nearby surface elements ("cavity effect"). For analysis based only on photointerpretation or Reststrahlen band identification, it is not always necessary to account for cavity effects, but for full spectral analysis it may be desirable. We present an approach to compensate thermal-infrared images for cavity radiation. This approach is based on optical estimates of subpixel surface roughness and estimation of cavity contribution for different natural surfaces using a TIR radiosity model. It was tested on tripod-mounted Telops Hyper-Cam hyperspectral thermal-infrared images of natural targets from the Mojave Desert, California (USA), along with cm-scale DEMs of similar targets measured by ground LiDAR. For remote subpixel roughness estimation, ASTER nadir- and aft-looking (27.6°) near-infrared (NIR) brightness ratios were used, as well as synthetic aperture RADAR (SAR) images calibrated to roughness RMS. The TIR compensation approach is adaptable for different spectral resolutions, including hyperspectral.

1 INTRODUCTION

Thermal-infrared (TIR) ground-leaving radiance comprises direct ground-emitted radiance and reflected radiance from the atmosphere and neighboring scene elements. The latter term reduces the apparent emissivity contrast ("cavity effect") in remotely estimated emissivity spectra because reflectivity ρ and emissivity ε are complementary (Kirchhoff's law). For an ideal cavity, approximated in Figure 1a by a mine adit (coarse scale) and in Figure 1c,d by cracks in a rock (fine scale), the radiance spectrum Figure 1b approaches that of an ideal blackbody, regardless of composition.

If roughness at either topographic or subpixel scales is not accounted for in image analysis, it is possible to confuse rough surfaces with smooth surfaces of intrinsic low ε contrast, or with mixtures of high- and low- ε contrast rocks. Uncorrected, these ambiguities can lead to uncertainty in surface compositions and abundances inferred from remotely acquired thermal images.

Cavity effects from resolved, coarse-scale topography can be corrected with a DEM and a TIR radiosity model, but effects from unresolved cavities require a more elaborate protocol because the fine-

scale roughness cannot be measured directly from remote-sensing data. Compensation for this latter effect of subpixel roughness on thermal images does not appear to have previously accomplished. Our goal in this abstract is therefore to define an approach for accounting for fine-scale cavity effects in thermal images of natural surfaces, and to test it with high-resolution field data.

2 BACKGROUND

The fundamental parameter measured in TIR remote sensing is spectral radiance L_S

$$L_S(\lambda, T) = \tau(\lambda)\pi^{-1}(\varepsilon(\lambda)M_{BB}(\lambda, T) + (1 - \varepsilon(\lambda)) * (S^\downarrow(\lambda) + R(\lambda))) + S^\uparrow(\lambda), \quad (1)$$

where L_S is measured spectral radiance at wavelength λ and surface temperature T , τ is atmospheric transmissivity, ε is the apparent surface emissivity, M_{BB} is blackbody spectral radiant exitance (defined by Planck's Law), S^\downarrow is downwelling spectral irradiance, R is the spectral irradiance from neighboring surface elements, and S^\uparrow is the path spectral radiance. τ and S^\uparrow pertain to the path between the surface and the

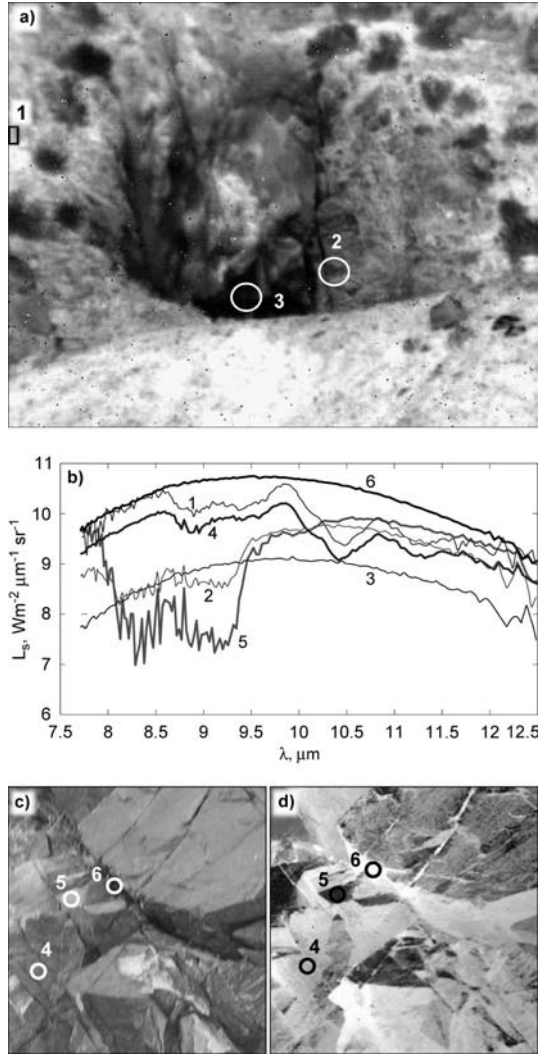


Figure 1. Telops, Inc., Hyper-Cam TIR data, Owens Valley, CA, USA (range: ~25 m). Black/white version of color figure available in Supplement as *Danilina_color Figure 1*. a) False-color image ~10 m across (RGB= 10.87, 8.59, 8.26 μm). b) Radiance spectra of schistose (1) and quartzite (2) wall rocks, the adit (3), schistose (4) and quartzite (5) parts of a 1 m rock fallen from the cliff, and deep cracks in the rock (6). c) Photo of the rock (range: ~9 m; image is ~80 cm across). d) False-color TIR image of the same rock (RGB same as in a).

spectrometer, short in field experiments; S^{\downarrow} is independent of spectrometer position.

In general, L_s is inverted to find T and apparent ϵ after model correction for τ and S^{\downarrow} . Some algorithms (Gillespie *et al.*, 1998) also correct for S^{\downarrow} , but in general R – and the cavity effect – is overlooked since there is no simple way to estimate it.

Neglecting to correct for R will lead to underestimation of contrast in recovered ϵ spectra, regardless of the scale of the roughness elements. For resolved rough topography, $(1-\epsilon)R/\pi$ can be as much as ~20% of L_s . At the finer, unresolved (subpixel) scales discussed in this paper the ratio can be as much as ~10%.

3 METHODS AND DATA

Image compensation for coarse-scale roughness uses a TIR radiosity model to calculate $R(\lambda)$. The model must account for changing illumination geometry over the course of a day, thermo-physical properties of the surface material, multiple-scattering effects, sensible heat transfer at the surface-air boundary, and downwelling sky radiation. The main driver is a DEM of the topography at the pixel scale. The problem for subpixel roughness, discussed herein, is more complex because fine-scale (cm) DEMs are commonly not available. This paper explores a possible way around this problem using remotely sensed proxies for roughness.

The image-processing model uses as input the TIR apparent emissivity image to be corrected and a co-registered image of subpixel roughness. In addition, curves or transfer functions are required for relating the contribution of cavity radiation from landscape elements of different roughnesses, calculated for the time of image acquisition using a TIR radiosity model. The processing procedure uses the roughness image to predict the amount of cavity radiation, and then to unmix it from the apparent emissivity using standard linear mixing models that have been developed and applied both to the spectral radiance data and to the emissivities. Both the roughness images and the radiosity model are discussed below.

2.1 Unresolved roughness

Estimating $R(\lambda)$ requires determining unresolved roughness, pixel by pixel. Two approaches have been used: inversion of models relating backscatter to roughness in synthetic aperture RADAR (SAR) images, and inversion of models relating reflectance lowering caused by unresolved shadows to roughness (Weeks *et al.*, 1996; Mushkin & Gillespie, 2005). The SAR approach requires accounting for soil moisture; the optical approach requires separating the darkening effects of shadowing. In either, it is necessary to calibrate the image-derived parameters to some conventional measure of surface roughness from which $R(\lambda)$ can be estimated.

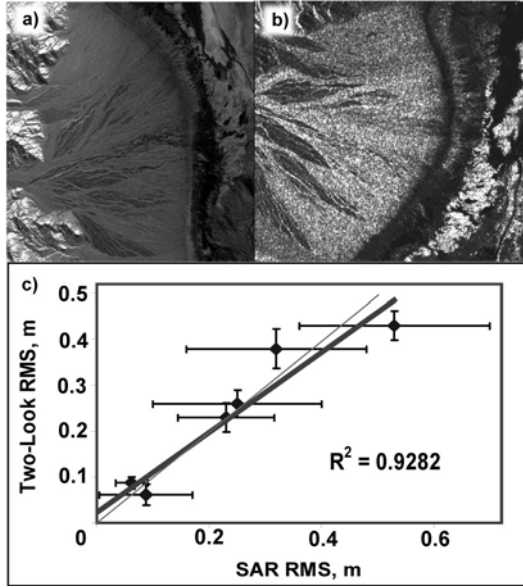


Figure 2. a) RMS roughness image derived using two-look method (Mushkin & Gillespie, 2005) for Trail Canyon fan, Death Valley, CA, USA. b) RMS roughness image derived from RADAR image (SIR-C, C band, HV polarization) of the same area. c) Correlation between mean RMS roughness for various regions of interest in the area derived using two different methods. Bold line illustrates linear trend. Thinner line illustrates actual diagonal. The error bars represent standard deviation within the regions of interest.

Mushkin and Gillespie (2005) related ASTER nadir- and aft-looking (27.6°) near-infrared (NIR) brightness ratios (two-look method) to independently measured surface topographic RMS at the cm - m (xy) scale. For calibration, the RMS roughness is calculated from fine-scale DEMs measured at test sites in the field.

We compared RMS roughness values for Trail Canyon fan, Death Valley, CA, derived using two-look method to the similar values derived from RADAR backscatter data (Greeley *et al.*, 1995), using region of interest statistics for corresponding areas. The values demonstrated good agreement (Fig. 2). Two-look results showed smaller levels of variability within samples. This is explained by the fact that ASTER NIR data don't suffer from speckle noise as much as RADAR data do. This is one of the advantages of the two-look method.

Although RMS is a commonly used statistical measure of roughness, more complete parameterizations have also shown promise: for example, fractal dimensionality (Vidal Vázquez *et al.*, 2004) in which both the slope and intercept of 2-D power spectra are employed. The parameter choice, however, doesn't influence the strategy.

2.2 TIR radiosity model

The general form of a TIR radiosity model for compositionally homogeneous Lambertian surfaces is written as:

$$B_i = \varepsilon_i M_i + (1 - \varepsilon_i) R_i, \quad i = 1, 2, \dots, n, \quad (2)$$

where B_i is radiosity (the total spectral radiant exitance, $\text{Wm}^{-2}\mu\text{m}^{-1}$) from surface element i , M_i is the thermal energy released from the surface element, R_i is irradiance on i from neighboring elements, and n is number of surface elements. The R term is given by:

$$R_i = \sum_{j=1}^n B_j F_{ij}, \quad i, j = 1, 2, \dots, n, \quad (3)$$

where F_{ij} represents fraction of radiance emitted from surface element j and incident on surface element i . F_{ij} is defined by the geometric relation between the elements, and specified by

$$F_{ij} = \frac{\cos \theta_i \cos \theta_j}{d^2 \pi} A_i, \quad (4)$$

where θ is projection angle between the normal of a surface element and line, linking the pair of elements together, A_i is the area of element i (m^2), and d is the distance between two elements (m).

In order to find R , it is necessary to estimate the surface temperature and actual emissivity fields. These are the same variables that are the ultimate goal of the analysis and are unknown, but approximate values can be estimated from L_S after correction for atmospheric effects, as is routinely done in standard T/ε separation algorithms.

An example of our radiosity model is given in Figure 3. The surface used in this example was a granite bedrock outcrop in Owens Valley, CA, USA about 1 m by 1.5 m in size.

In Figure 3b a 3-D view of the surface generated from a high-resolution DEM measured by the tripod-mounted LiDAR is rotated to match the perspective view of the surface in the photo taken in the field. The shaded relief image generated from the DEM and radiosity distribution images for different times of day are oriented such that the North direction corresponds to "up" in the Figure. Radiosity scales in the radiosity distribution images are different.

The plot of the difference between the apparent and prescribed emissivities, $\Delta\varepsilon$ (Fig. 3e), does not mimic the quasi-sinusoidal behavior of mean radiosity and mean temperature plots. The largest differences are registered in the late morning and late afternoon. In the middle of the day when the sun is high $\Delta\varepsilon$ drops

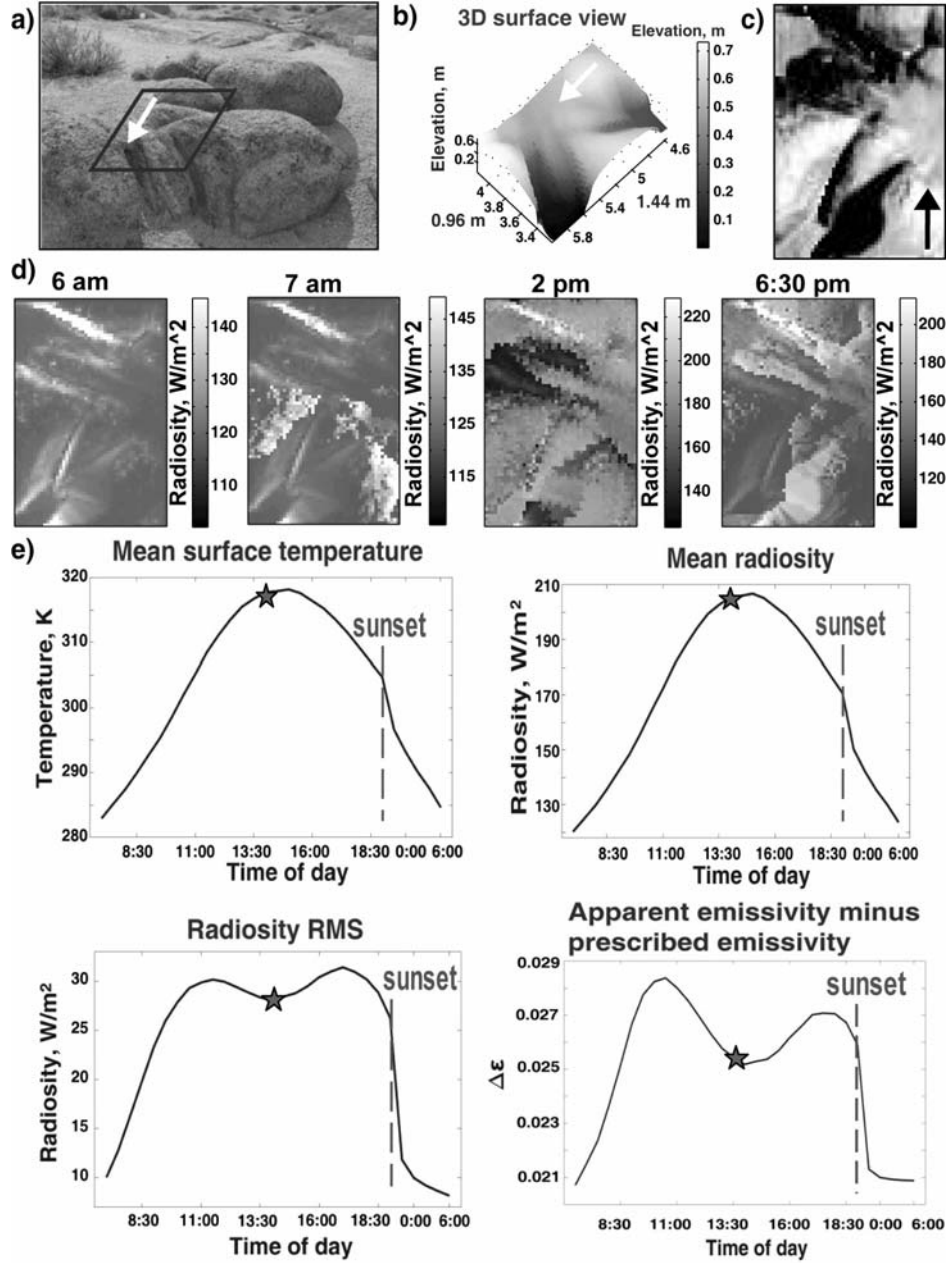


Figure 3. The radiosity model results for a granite bedrock surface from Owens Valley, CA, USA. Pixel size of the surface DEM is 0.02 cm, RMS roughness is 0.18 m, prescribed emissivity is 0.9. a) Photo of the surface. b) 3D surface view generated with Matlab. c) Shaded relief image of the surface. The arrows in a, b, and c indicate direction to the North. d) Modeled radiosity distributions at different times of day. Note the different radiosity scales for the plots. e) Modeled change of mean surface kinetic temperature, mean surface radiosity, radiosity RMS, and difference between prescribed and apparent emissivities over the course of a day. The stars indicate points on the plots that correspond to 2 pm radiosity distribution (see d). Note the difference in the time step after the sunset.

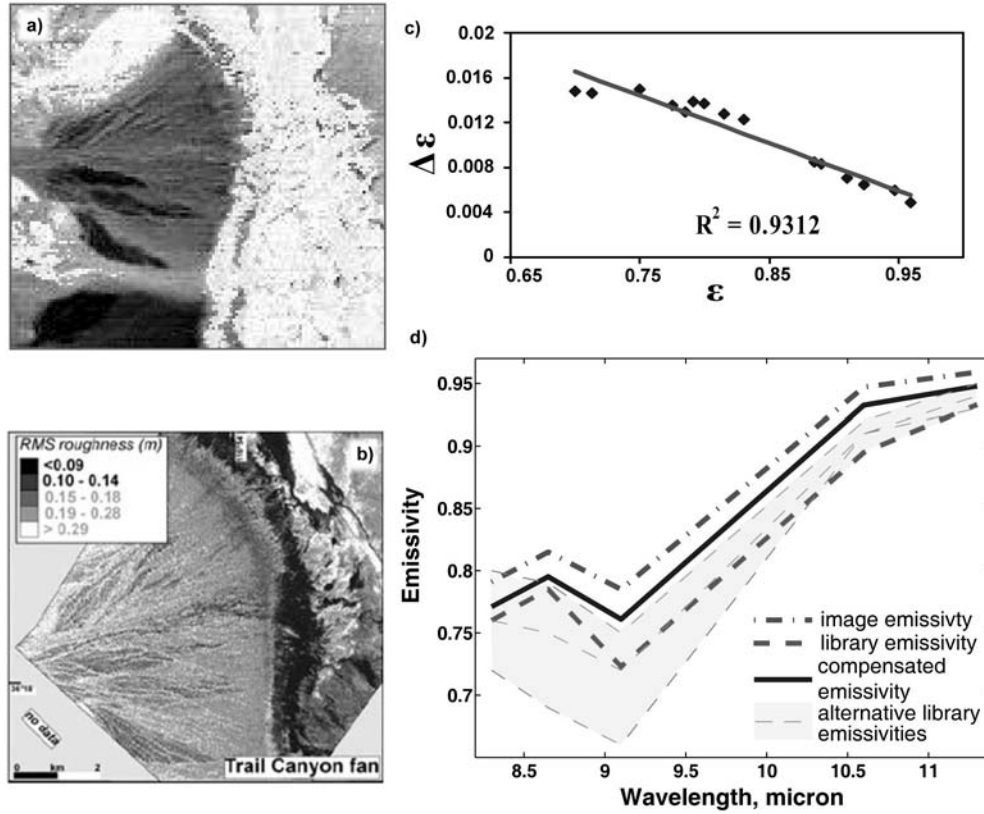


Figure 4. a) ASTER emissivity image for Trail Canyon fan, Death Valley, CA, USA ($\lambda = 8.3 \mu\text{m}$). Black/white range runs from $\epsilon = 0.72$ to 1. b) ASTER nadir- and aft-looking NIR ratio image, calibrated to RMS roughness measured at test sites (two-look method). c) Example of a generalized transfer function. It was calculated using TIR radiosity model for surfaces with RMS roughness of 0.16 m. d) Example of cavity compensation for single pixel.

by more than 10 %. This demonstrates the importance of using a TIR radiosity model to predict roughness effects for natural surfaces for any given time (e.g. the time of a satellite overflight).

For many natural surfaces for which roughness is not extreme, this approach is probably adequate. For very rough surfaces, it may be necessary to perform an iterative analysis, as has been done for correcting L_S for reflected S^{\downarrow} .

2.3 Estimating transfer functions

The roughness data and radiosity calculated for a gamut of surface DEMs can be related empirically. It is possible from the radiosity modeling to construct curves relating apparent ϵ to ϵ , as in Figure 4c. It is important that the radiosity calculations are individualized for the actual time and date of image acquisition to account for the differential solar heating of the surface.

2.4 Cavity compensation

Once R has been estimated for a roughness image such as Figure 4b, it is straightforward to subtract it from the measured L_S , after atmospheric compensation. The resulting difference is the “ground-emitted spectral radiance,” and standard methods can be used to calculate ϵ from it. It is also possible to use shortcuts, for example if curves have been calculated that relate apparent ϵ to ϵ directly (Figure 4c). Again, the roughness image must be used to select the curve for the appropriate roughness, pixel by pixel across the image.

Figure 4d demonstrates an example of an emissivity spectrum of single pixel of a smooth roughness RMS = 0.16 m) surface from Trail Canyon fan. This surface, part of a smooth “desert pavement” of the geological unit QG₂ (Hunt and Maybe, 1966), appears dark in Figure 4b. The spectrum was sampled

from the ASTER image after compensation for the cavity effect. In order to do that the appropriate transfer function estimated with TIR radiosity model (Figure 4c) was used. The compensation increased spectral contrast from 0.17 for the image spectrum to 0.19 for the compensated spectrum.

3 DISCUSSION

From the two-look data, ratio values are calculated and regressed to RMS roughness for a suite of DEMs. This enables remotely sensed ratios to be calibrated to RMS. Because a similar regression relates RMS and R , it is possible to link the regressions such that the ratio data can be expressed as R values. A drawback to this approach, however, is that in order to calculate R , it is necessary to know the temperature and emissivity of the surface – the very parameters we seek to determine. In principle, this can be done iteratively, starting from temperature and emissivity values found conventionally from the measured L_S . In practice, therefore, correction is more accurate for less rough surfaces. To avoid running the radiosity model separately for each depression angle (SAR) or viewing/illumination geometry (shadow) it will be necessary to survey carefully the gamut of natural surfaces for which the regressions have a suitable uncertainty. For example, random noise and natural DEMs sharing the same RMS value can produce different values of R (Weeks *et al.*, 1996). Characterizing the gamut of natural surfaces has not been completed.

The current requirement is that the radiosity model be run and transfer functions generated individually for different specific solar heating histories and image-acquisition times. Solution of the problem probably requires first amassing and assimilating more experience with the TIR radiosity model.

4 SUMMARY

We present a protocol for compensating remotely sensed emissivity images for the effects of surface roughness. The inputs to the model are TIR spectral radiance images (or apparent temperature and ε images), a co-registered image of surface roughness, and transfer functions generated by a TIR radiosity model. The transfer functions relate the decrease in apparent ε compared to actual ε for a given roughness. It is necessary to calibrate the remotely sensed roughness proxy to standard measures before they can be used as input to the process.

5 ACKNOWLEDGEMENT

Funded by the U. S. National Nuclear Security Administration, Office of Nonproliferation Technology Development, contract DE-FG52-08NA28772, and subcontract DE-AC52-06NA25396 with the Los Alamos National Laboratory.

6 REFERENCES

- Gillespie, A. R., Matsunaga, T., Rokugawa, S., and Hook, S. J., "Temperature and Emissivity Separation from Advanced Spaceborne Thermal Emission and Reflection Radiometer (ASTER) Images." *Institute of Electrical and Electronics Engineers (IEEE) Transactions on Geoscience and Remote Sensing* 36, 1113-1126, 1998.
- Greeley R., D. G. Blumberg, A. R. Dobrovolskis, L. R. Gaddis, J. D. Iversen, N. Lancaster, K. R. Rasmussen, R. S. Saunders, S. D. Wall, and B. White, "Potential Transport of Windblown sand: Influence of Surface Roughness and Assessment with Radar." *Desert Aeolian Processes*, ed. V. Tchakerian, Chapman and Hall, 75-99, 1995.
- Hunt, C.B., and M.R. Maybe, "Stratigraphy and Structure, Death Valley, California." *U.S. Geological Survey Professional Paper* 494-A, 1966.
- Mushkin, A., and A. R. Gillespie, "Estimating sub-pixel surface roughness using remotely sensed stereoscopic data." *Remote Sensing of Environment* 99, 75-83, 2005.
- Vidal Vázquez, E., J. G. Vivas Miranda, and A. Paz González, "Characterizing anisotropy and heterogeneity of soil surface microtopography using fractal models." *Ecological Modelling* 182, 337-353, 2004.
- Weeks, R. J., M. Smith, K. Pak, W.-H. Li, A. Gillespie, and B. Gustafson, "Surface roughness, radar backscatter, and visible and near-infrared reflectance in Death Valley, California." *Journal of Geophysical Research* 101 (E10), p. 23,077-23,090, 1996.

Field measurements and modelling of diurnal cycles of land surface temperature at Gobabeb, Namibia

Frank-M. Göttsche, Folke-S. Olesen, and Annika Bork-Unkelbach

Karlsruhe Institute of Technology (KIT), Postfach 3640, 76021 Karlsruhe, Germany

frank.goettsche@kit.edu, folke.olesen@kit.edu, annika.bork@kit.edu

ABSTRACT - Land surface temperature (LST) derived from MSG/SEVIRI data is an operational product of the Land Surface Analysis – Satellite Application Facility (LSA-SAF). The LST have a temporal resolution of 15 min, a sampling distance of 3 km at nadir, and a targeted accuracy of better than 2K. Gobabeb (Namibia) is one of KIT's four dedicated stations for LST validation. In March 2010 a field survey was performed to characterise the Gobabeb site more closely. Brightness temperatures of the land surface were measured at several locations using a mobile mast system. SAF LST and in-situ LST obtained over a period of 3 days from field measurements on the Namib gravel plain were in good agreement with each other (bias 1.0K). For the same period, the bias between SAF LST and Gobabeb main station LST was even smaller (0.4K). The bias between LST from in-situ measurements along a 40 km track and Gobabeb main station was also 0.4K (stdev 1.2K). SEVIRI's high temporal resolution can be used to interpolate missing LST, which improves temporal compositing and aids cloud screening. Here, a simple diurnal temperature cycle (DTC) model is fitted to LST from the different sources (permanent & mobile station and LSA-SAF) and the determined parameters are briefly discussed.

1 INTRODUCTION

Karlsruhe Institute of Technology (KIT) operates four permanent validation stations for LST retrieved from TIR satellite measurements. The stations are part of the Land Surface Analysis – Satellite Application Facility (LSA-SAF) supported by EUMETSAT and their main objective is to validate LST derived from the Spinning Enhanced Visible and InfraRed Imager (SEVIRI) onboard MSG. As discussed in (Trigo, 2008b) and (Yu, 2008), ground measurements have their own issues, including the following: 1) the low number and discontinuity of high-quality data sets, 2) the lack of global representativeness, and 3) the up-scaling of LST “point” measurements to satellite pixel size. Here, we compare satellite-derived LST with in situ observations collected at the Gobabeb validation site, Namibia. For thermally heterogeneous land surfaces, point 3 introduces uncertainties that are not easily quantified; however, Gobabeb is located in a homogeneous area, which greatly simplifies the upscaling (Freitas, 2010).

Using measurements from a field survey performed in March 2010, this paper investigates the representativeness of LST from Gobabeb main station for the gravel plains surrounding the station more closely.

2 GOBABEB LST VALIDATION STATION

Gobabeb LST validation station is located near “Gobabeb Training & Research Centre” (23°33'S,

15°03'E, 408 m a.s.l.). The nearby Kuiseb river forms a natural boundary between large gravel plains (>900 km²) and the sand dunes of the Namib Desert. The station's instruments are mounted to a 30m high wind profiling tower, which is located on the gravel plains 2 km north-east of the research centre. The gravel plains are covered by varying amounts of desiccated grass. The station's core instruments are “KT-15.85 IIP” IR-radiometers (self-calibrating, chopped radiometers, Heitronics). The KT-15 measure IR radiance between 9.6 μm and 11.5 μm and express the results as brightness temperatures with an absolute accuracy of 0.3°C (Theocharous, 2010). Two KT-15s are mounted next to each other at 25m height and observe neighbouring areas of the gravel surface under a view angle of 30° in north direction. Together with the full view angle of 8.5° of the KT-15 this results in a FOV of about 14m² (Figure. 1). An additional KT-15 faces the sky at 53° w.r.t. zenith and measures the channel-specific downwelling longwave radiance, which is used to correct for the reflected component in the down-looking measurements. This setup assumes isotropy over the azimuth. The long term stability of KT-15 radiometers was proven at “Evora” station, Portugal, in a one year parallel run with a self calibrating unit based on two black bodies (Kabsch et al., 2008). Furthermore, the following meteorological parameters are measured close to the ground (3m) and at the level of the down-looking KT-15 (25m): wind-speed and wind-direction (Wind Monitor 05103, Young), relative humidity and temperature (HMP 45AC, Vaisala). A net radiometer (CNR-1, Kipp &

Zonen) measures the hemispherical broadband shortwave and longwave radiation components. The station has a solar power supply and continuously logs the measurements at an interval of 1 minute. Data are transmitted to KIT in near real time via radio modem and satellite based internet link.

2.1 Converting brightness temperatures to LST

The KT-15 radiometers provide measurements as brightness temperatures assuming an emissivity of 1. Due to the small distance between the radiometers and the surface, atmospheric attenuation of the surface-leaving IR radiation can be neglected. However, the measurements contain radiance emitted by the surface (i.e. the target signal) as well as reflected downwelling radiance originating from the atmosphere:

$$R_{KT-sfc} = \varepsilon \cdot B(T_{sfc}) + (1 - \varepsilon) \cdot B(T_{sky}) \quad (1)$$

where T_{sfc} is LST, ε is the channel-specific emissivity of the surface, B is the Planck function at the KT-15's centre wavelength (10.55 μ m), and $L^\downarrow = B(T_{sky})$ is the downwelling longwave radiance convolved with the KT-15's response function. Depending on surface emissivity and on downwelling longwave radiance (e.g. a cold clear sky vs. a warm humid atmosphere), the reflection term in equation 1 can cause differences of several degrees Celsius (Schädlich, 2001). L^\downarrow is measured by the sky-facing radiometer and emissivity is taken from LSA-SAF (about 0.96 for the Gobabeb site); ASTER emissivities retrieved with the TES algorithm agree well with this (Trigo, 2008a; Gillespie, 1999; Hulley, 2008). LST is obtained from KT-15 radiances by solving equation 1 for $B(T_{sfc})$ and then solving the Planck function for T_{sfc} at the KT-15's centre wavelength.

2.2 Retrieved LST of grass and gravel

The LST for Gobabeb presented here are for "KT-15 east" (see Figure. 1), because the surface in its FOV contains more desiccated grass, and is, therefore, deemed more representative of the gravel plains, e.g. as exemplified by Figure 3, which shows an area around the temporary site "Tidbit01" on the gravel plains.

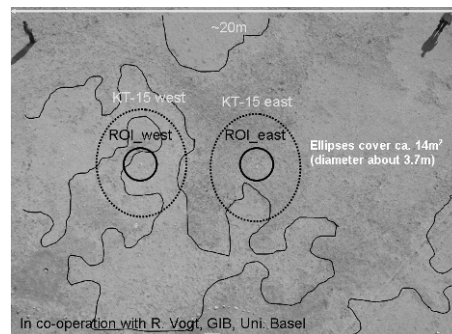


Figure. 1 FOV of the KT-15 radiometers at Gobabeb station and smaller ROI on "grass" and "gravel" used with thermal infrared camera. The hand-drawn lines outline the grass - gravel boundary.

In co-operation with Dr. Roland Vogt (University of Basel, Switzerland) visible and thermal infrared images of the area observed by the down-looking KT-15's were taken from the top of Gobabeb main tower. A visible image is shown in Figure. 1 and the variation of brightness temperature (BT) in the areas of "ROI_west" and "ROI_east" (outlined by circles) is shown in Figure 2.

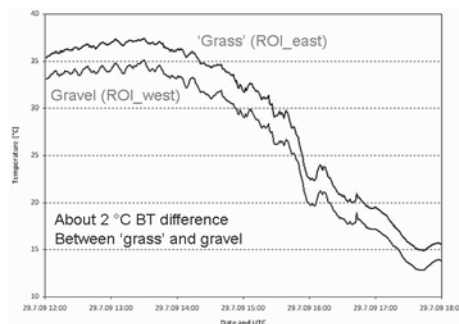


Figure 2 Temperature variation on July 29th 2009 within the ROI marked in Figure. 1 (in cooperation with Roland Vogt, University of Basel).

During the recorded period (see Figure 2) the BT for "ROI_west" (mainly gravel) is about 2 °C lower than for "ROI_east" (more desiccated grass). A similar relation is observed for the FOV of "KT-15 west" and "KT-15 east" (outlined by ellipses), but the difference is smaller due to the larger – and, therefore, less 'pure' – areas over which BT is integrated.

3 GOBABEB FIELD SURVEY 2010

Motivated by previous analyses of LST from the Gobabeb site (Freitas, 2010) as well as by the observed temperature differences between “KT-15 east” and “KT-15 west”, a field survey was performed in March 2010. The aim of the survey was to characterise the gravel plains more closely and to determine which KT-15 radiometer (or weighted average) is most representative for the gravel plains. Additional in-situ measurements with a mobile mast system were performed at various locations of the gravel plains and the retrieved LST were compared with LST from the main mast as well as with LST retrieved from MSG/SEVIRI by LSA-SAF.

3.1 Mobile Mast System

Main features of the mobile mast system (Figure 3):

- Telescopic mast (max. 14 m)
- Heitronics KT15.85 IIP radiometer (9.6-11.5 μm , ± 0.3 K accuracy)
- Full view angle: 8.5°
- Field of view from 7 m: ~ 1.1 m²
- Data logger sampling rate: 1 min

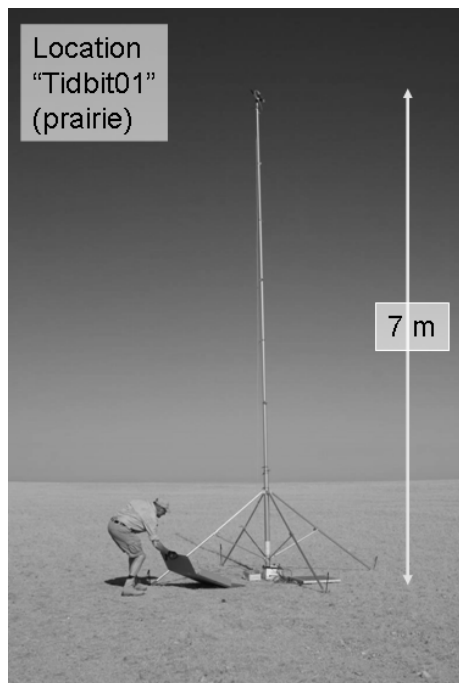


Figure 3. Mobile mast system set up at location “Tidbit01” on the gravel plains.

The KT-15 radiometer of the mobile mast system was always oriented in direction north with

viewing angle of 30° off nadir: since the Gobabeb site is located south of the Tropic of Capricorn, this avoids any shadows of the mast in the FOV of the radiometer.

3.2 Measurements at “Tidbit01” on Gravel Plain

The locations for the field measurements were chosen based on their spectral contrast from average site values in the VIS/NIR and TIR, for which Ikonos and Landsat data were used, respectively. Measurements presented here are from location “Tidbit01” on the gravel plains east of Gobabeb main station. The mobile mast system was set up for 3 days (11.-14. March 2010). BT measurements were corrected for reflected down-welling TIR radiance using sky radiance from Gobabeb main station (eq. 1). All data were resampled to MSG/SEVIRI temporal resolution (15min), but there were missing data due to power failures during night-time. Figure 4 shows the mobile station LST plotted against Gobabeb main station LST: the mobile station has a positive bias of about 1.4°C and stdev of 1.2°C , which means that the gravel plain observed at “Tidbit01” is warmer than the FOV observed by “KT-15 east”. There is a high degree of correlation between the two data sets.

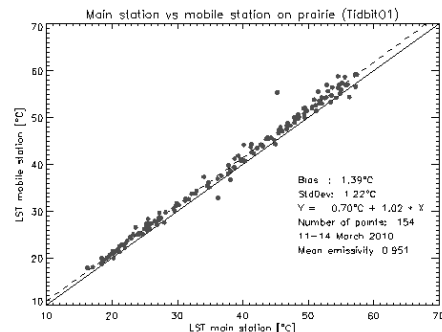


Figure 4. Plot of 3 days of LST from Gobabeb main station against LST at “Tidbit01” (mobile mast).

Figure 4 shows the LSA-SAF LST derived from MSG/SEVIRI plotted against Gobabeb main station LST: LSA-SAF LST have a positive bias of about 0.4°C and stdev is 2.0°C . The higher stdev can be explained by undetected sub-pixel clouds in the SEVIRI data. Gobabeb main station LST agree better with LSA-SAF LST than with LST obtained in-situ at “Tidbit01” with the mobile mast system. Again, there is a high degree of correlation between the two data sets.

The biases between the LST from the mobile and the main station and LST from MSG/SEVIRI are below LSA-SAF’s targeted accuracy of 2.0°C . However, the comparisons highlight the difficulty of finding

locations which are most representative for spatially coarse satellite pixel, e.g. 3 km for MSG/SEVIRI. In order to obtain a more comprehensive picture of the LST distribution over the gravel plains, in-situ LST were measured along a 40 km track.

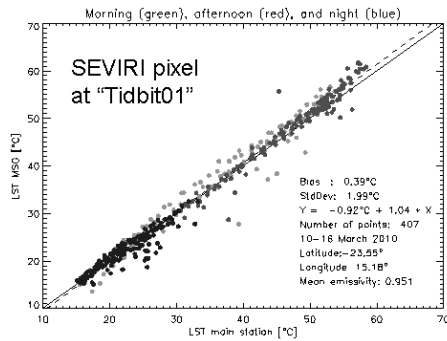


Figure 4 Plot of 3 days of LST from Gobabeb main station against SAF LST for MSG/SEVIRI pixel at “Tidbit01”

3.3 Drive across the Gravel Plain

The mobile mast was mounted to a 4WD (Figure 5). The data sampling interval was set to 15 sec and the car started at “Tidbit01” in direction north-east across the gravel plains for about 10km, turned around, and continued in direction south-west for about 30 km towards Gobabeb. The LST obtained from the 40 km drive was averaged over 1 min to match main station LST.

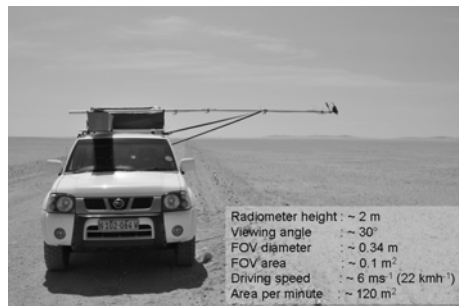


Figure 5. The 4WD with the mobile mast system on the gravel plain near Gobabeb, Namibia.

Figure 6 shows Gobabeb main station LST (line), LST obtained along the driven track (diamonds), and the 7 LSA-SAF LST falling into the measurement period (filled circles with error bars of 2 °C; LST at 10:00 UTC missing).

From Figure 6 it can be seen that even though LST from LSA-SAF are slightly warmer than Gobabeb main station LST, they are within LSA-SAF’s targeted

accuracy of $\pm 2K$. The bias between LSA-SAF LST and mobile station LST is even smaller (less than 0.5 °C): this indicates that integrating LST measurements over large areas yields LST that are more representative for LST from MSG/SEVIRI.

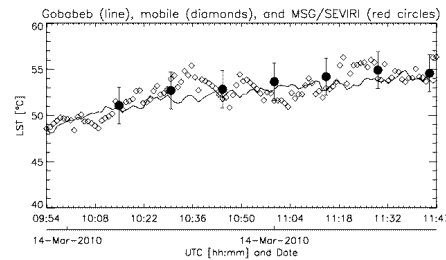


Figure 6 LST measured from moving car (distance about 40 km).

4 MODELLING OF DIURNAL LST CYCLES

The diurnal temperature cycle (DTC) model “Goe2008” (Göttsche, 2009) is applied to LST from three different sources: mobile station at “Tidbit01”, Gobabeb main station, and LSA-SAF. Compared to the first DTC model (Göttsche, 2001), the modelling of total optical thickness and relative optical air mass improves performance.

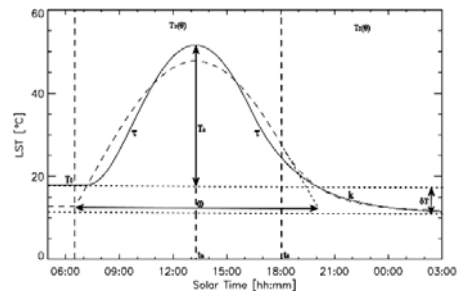


Figure 7. Diurnal temperature cycle (DTC) models Goe2001 (broken line) and Goe2008 (solid line). Parameters are given in Table 1.

The model parameters (see Table 1) summarize the thermal behaviour of the land surface and are, thus, more indicative of surface type and state (e.g. moisture) than individual LST. Figure 8 and Figure 9 show fits of the two DTC models to LST from LSA-SAF and in-situ LST at “Tidbit01”, respectively. Due to the clear atmosphere (model-determined transmissivity is about 0.8 for the three LST sources) the old and the new model perform similarly well; only in the early morning Goe2001 is about 1.5 °C too cold. LSA-SAF LST show some sub-pixel clouds around 11:00h and 18:00h UTC (Figure 8).

Table 1. Meaning of the parameters in Figure 7

Parameter	Meaning
T_o [°C]	residual temperature
T_a [°C]	temperature amplitude
t_m [solar time]	time of the maximum
t_s [solar time]	start of attenuation function
δT [°C]	$T_o - T(t \rightarrow \infty)$, where t is time
ω [hh:mm]	half-period of cosine term
k [hh:mm]	attenuation constant
τ	total optical thickness

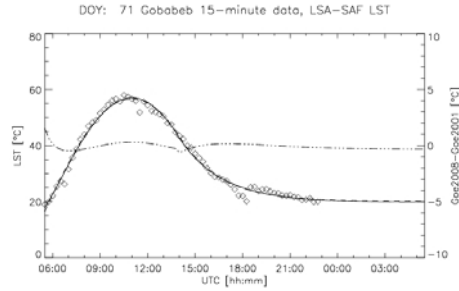


Figure 8. Fit of DTC models to LSA-SAF LST for MSG/SEVIRI pixel at "Tidbit01" (gravel plain).

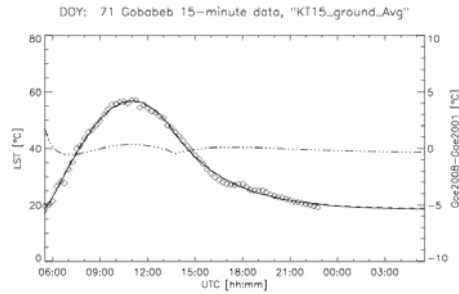


Figure 9. Fit of DTC models to LST obtained with mobile mast system at "Tidbit01" (gravel plain).

Residual temperatures, temperature amplitudes, and their respective sums – maximum temperatures of the DTC model – are listed in Table 2. While the residual (early morning) temperatures of Gobabeb main station (KT-15 East) and from LSA-SAF (pixel on the gravel plain at Tidbit01) are both about 16°C, their amplitudes differ by about 3K. The maximum temperatures of the mobile station and LSA-SAF are both higher (about 57°C) than for Gobabeb main station, which is due to their higher temperature amplitudes.

Table 2 Parameters from Goe2008 model.

Source	T_o [°C]	T_a [°C]	T_{max} [°C]
KT-15 East	16.3	38.2	54.5
Mobile Tidbit01	17.0	39.8	56.8
LSA-SAF	16.0	41.1	57.1

5 CONCLUSIONS

The results from a field survey performed in March 2010 at Gobabeb, Namibia, underline the importance of representative measurements for validating satellite-derived LST. The small areas observed by in-situ radiometers (between 1m² and 14m²) must be representative for the significantly larger areas covered by the MSG pixels of about 25km². SAF LST from MSG/SEVIRI and in-situ LST obtained from field measurements on the Namib gravel plains have a bias of 1.0K and the agreement is better than the expected accuracy of SAF LST. For the same observation period, the bias between SAF LST and Gobabeb main station LST was even smaller (0.4K). LST obtained from additional in-situ measurements made along a 40km track from a moving car yielded a bias of 0.4K w.r.t. Gobabeb main station. All biases between LSA-SAF LST and LST determined from the field measurements were within LSA-SAF's targeted accuracy of $\pm 2K$.

LST from three different sources (mobile station on gravel plain, Gobabeb main station, and LSA-SAF) were successfully fitted with a simple model of the diurnal temperature cycle. Most of the retrieved model parameters were very close to each other, e.g. time of maximum temperature and total atmospheric thickness. However, differences in temperature amplitude and residual (early morning) temperature were observed and are currently investigated.

6 REFERENCES

- Freitas, S.C., Trigo, I.F., Bioucas-Dias, J.M., and Göttsche, F., 2010, Quantifying the Uncertainty of Land Surface Temperature Retrievals from SEVIRI/Meteosat. *IEEE Transactions on Geoscience and Remote Sensing*, **48**, 523-534.
- Gillespie, A.R., Rokugawa, S., Hook, S.J., Matsunaga, T., and Kahle, A.B., 1999, Temperature / Emissivity Separation Algorithm Theoretical Basis Document, Version 2.4. Prepared under NASA Contract NAS5-31372.
- Göttsche, F.-M., and Olesen, F.-S., 2001, Modelling of diurnal cycles of brightness temperatures

- extracted from METEOSAT data. *Remote Sensing of Environment*, **76**, 337-348.
- Göttsche, Frank-M., Olesen, Folke-S., 2009, Modelling the effect of optical thickness on diurnal cycles of land surface temperature. *Remote Sensing of Environment*, **113**, 2306-2316.
- Hulley, G.C., Hook, S.J., and Baldrige, A.M., 2008, ASTER Land Surface Emissivity Database of California and Nevada. *Geophysical Research Letters*, **35**, L13401.
- Kabsch, E., Olesen, F., and Prata, F., 2008, Initial results of the land surface temperature (LST) validation with the Evora, Portugal ground-truth station measurements. *International Journal of Remote Sensing*, **29**, 5329–5345.
- Schädlich, S., Göttsche, F.-M., and Olesen, F.-S., 2001, Influence of land surface parameters and atmosphere on METEOSAT brightness temperatures and generation of land surface temperature maps by temporally and spatially interpolating atmospheric correction. *Remote Sensing of Environment*, **75**, 39-46
- Theocharous, E., Usadi, E., and Fox, N. P., 2010, CEOS comparison of IR brightness temperature measurements in support of satellite validation. Part I: Laboratory and ocean surface temperature comparison of radiation thermometers. NPL REPORT OP3, ISSN: 1754-2944, National Physical Laboratory, Teddington, UK.
- Trigo, I. F., Peres, L. F., DaCamara, C. C., and Freitas, S. C., 2008a, Thermal land surface emissivity retrieved from SEVIRI/Meteosat. *IEEE Transactions on Geoscience Remote Sensing*, **46**, 307-315.
- Trigo, I. F., Monteiro, I. T., Olesen, F., and Kabsch, E., 2008b, An assessment of remotely sensed land surface temperature. *Journal of Geophysical Research*, **113**, DOI:10.1029/2008JD010035.
- Yu, Y., Privette, J. L., and Pinheiro, A. C., 2008, Evaluation of split-window land surface temperature algorithms for generating climate data records. *IEEE Transactions on Geoscience and Remote Sensing*, **46**, 179–192.

Consistent and accurate LAI, FAPAR and FCOVER global products: principles and evaluation of GEOV1 products

F. Baret¹, M. Weiss¹, R. Lacaze², F. Camacho³, P. Pacholczyk⁴, H. Makhmara⁴ and B. Smets⁵

¹ INRA-EMMAH UMR 1114, Avignon, France

² HYGEOS/CNES/GEOLAND2, Toulouse, France

³ EOLAB, Valencia, Spain

⁴ CNES, Toulouse, France

⁵ VITO, Mol, Belgium

baret@avignon.inra.fr

ABSTRACT LAI, FAPAR and FCOVER variables are required for the monitoring, understanding and modelling of land surfaces at the global scale. While several products were already developed from the current medium resolution sensors, the few validation exercises achieved demonstrated that significant discrepancies and inconsistencies were observed. The objective of this study was to develop new global estimates of LAI, FAPAR and FCOVER that will build on the pros and minimize cons of already existing products. In a first step, the performances of the MODIS, CYCLOPES, GLOBACARBON and JRC-FAPAR products were reviewed. The MODIS and CYCLOPES products were selected since they provide higher level of consistency. These products were then fused to generate the 'best estimate' of LAI, FAPAR and FCOVER that were later scaled to better match their expected range of variation. Finally, neural networks were trained to estimate these best estimates products from SPOT-VEGETATION top of canopy directionally normalized reflectance values. Performances of the derived products called GEOV1 were evaluated, showing significant improvements as compared to previous products. These products will be extended back to 1981 using the AVHRR series of observation, and continued after the VEGETATION era thanks to AVHRR-METOP, PROBA-V and Sentinel3 future missions.

1 INTRODUCTION

The importance of continuous monitoring the Earth's surface was recently recognized by GCOS (GCOS, 2006): a set of Essential Climate Variables was identified as being both accessible from remote sensing observations and intervening within key processes. Among those related to land surfaces, LAI (Leaf Area Index) and FAPAR (Fraction of Absorbed Photosynthetic Active Radiation) may be derived from observations in the reflective solar domain. These vegetation biophysical variables play a key role in several processes, including photosynthesis, respiration and transpiration. LAI is defined as half the total developed area of leaf elements per unit horizontal ground area (Chen and Black, 1992). FAPAR is defined as the fraction of radiation absorbed by the canopy in the 400 - 700 nm spectral domain

under specified illumination conditions. It is one of the main inputs in light use efficiency models (McCallum et al., 2009). The cover fraction (FCOVER) defined as the fraction of background covered by green vegetation as seen from nadir appears also a very pertinent variable that can be used when separating the contribution of the soil from that of the canopy. Few global LAI, FAPAR and FCOVER products have already been generated from medium spatial resolution sensors such as VEGETATION, SEAWIFS, MODIS and MERIS (Table 1). Recent validation activities have shown however that significant discrepancies were existing between them as well as with ground measurements (Garrigues et al., 2008; McCallum et al., 2010; Weiss et al., 2007), calling thus for the development of new products that would reconcile these differences.

Products	LAI	FAPAR	FCOVER	Temporal frequency (days)	Time period	Projection	Reference
MODIS C5	✓	✓		8	2000-2008	Sinusoidal	(Myneni et al., 2002)
CYCLOPES V3	✓	✓	✓	10	1999-2007	Lat-lon	(Baret et al., 2007)
GLOBACARBON	✓	✓		30	1999-2007	Lat-lon	(Deng et al., 2006)
JRC-FAPAR		✓		1	1997-2006	Lat-lon	(Gobron et al., 2006)

Table 1. The currently available GLOBAL products..

The Geoland2 project (<http://www.geoland2.eu>) intends to implement a Land Monitoring Core Service that corresponds to a European contribution to GEOSS (Group of Earth Observation System of Systems). The Bio-geophysical Parameters (BioPar) service within Geoland2 aims at developing pre-operational infrastructures for providing global land products both in near real time and off-line mode with long time series. The objective of this paper is to describe the first version of Geoland2 *LAI*, *FAPAR* and *FCOVER* products that will be called GEOV1. The principles used to derive the products will first be presented. Then, the algorithm development will be described as long as some validation results.

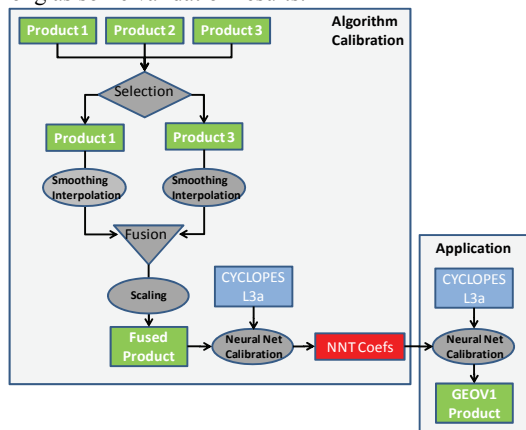


Figure 1. Schematic description of the principle used to develop the GEOV1 product.

2 ALGORITHM DEVELOPMENT

2.1 Principles

The biophysical algorithm is based on already existing products to capitalize on the efforts accomplished and get a larger consensus from the user community. Figure 1 shows the several steps used for each product. Following the published literature on products validation (Garrigues et al., 2008; Weiss et al., 2007), the best performing products were selected and combined to take advantage of their specific performances while limiting the situations where products show deficiencies. The selected products are re-projected onto the VEGETATION plate-carrée 1/12° grid, smoothed through time and interpolated at the 10 days frequency. Then the products are combined and eventually scaled to compute the fused product that is expected to provide globally the 'best' performances. The fused products are generated for 2003-2004 over the 420 BELMANIP2 set of sites (Figure 2) that is supposed to represent the possible range of surface types and conditions over the Earth (Baret et al., 2006). Neural networks are then calibrated over this set of sites to relate the fused

products to the corresponding VEGETATION L3a top of canopy directionally normalized reflectances using the CYCLOPES pre-processing algorithms (Baret et al., 2007).

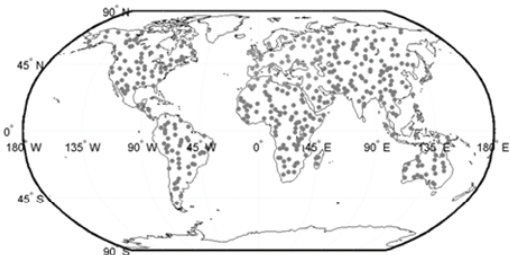


Figure 2. The 420 BELMANIP2 sites used to sample vegetation types and conditions.

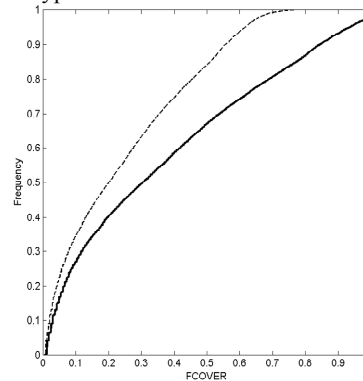


Figure 3. Cumulated frequency of *FCOVER* CYCLOPES (dashed line) and GEOV1 products as observed over the 420 BELMANIP2 sites during years 2003-2004.

2.2 Generation of the training data base

FCOVER product on one side and *LAI* and *FAPAR* products on the other will be described separately because of the differences in available products.

a) *FCOVER*

Since only the CYCLOPES products were available globally, no fusion with other products was possible. However, several evaluations have shown that CYCLOPES *FCOVER* products were suffering from a significant systematic underestimation (Verger, 2008). This was corrected for by applying a scaling factor to the CYCLOPES V3.1 products ($FCOVER_{CYCV31}$). This factor ($\frac{1}{0.6872}$) was corresponding to the inverse of the *FCOVER* value for the 99% cumulated frequency (Figure 3) that should be expected to be very close to 1.0 since it should correspond to very dense canopies:

$$FCOVER_{best} = \frac{1}{0.68} \cdot FCOVER_{CYCV31} \quad (1)$$

Where $FCOVER_{best}$ is the value that will be used for training the neural networks.

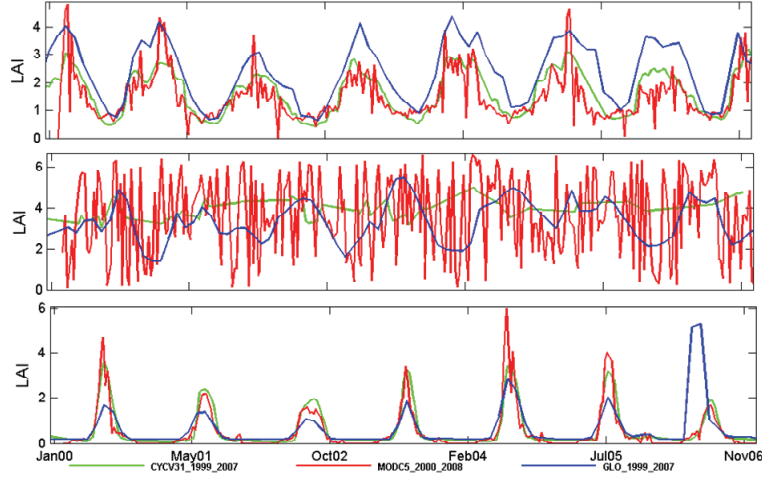


Figure 4. Example of *LAI* dynamics of CYCLOPES, MODIS and GLOBCARBON products for 3 typical sites.

b) *LAI* and *FAPAR*

The 30 days temporal sampling used for GLOBCARBON appears not very well suited to describe the seasonality of vegetation as shown in Figure 4. This is the reason why GLOBCARBON *LAI* products were not selected. Further, GLOBCARBON *LAI* products were showing a significant number of outliers. MODIS and CYCLOPES *LAI* products will therefore be selected.

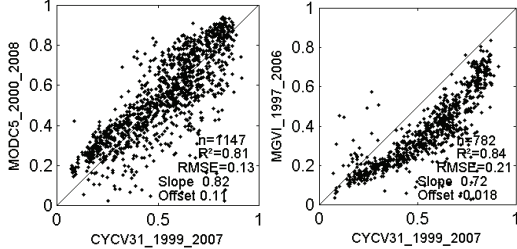


Figure 5. Scatterplot between *FAPAR* products.

JRC-*FAPAR* products derived from the SEAWIFS sensor show very similar seasonality to that of the MODIS and CYCLOPES *FAPAR* products with however generally lower values as shown in Figure 5. MODIS and CYCLOPES *FAPAR* products were showing a closer agreement, particularly for the medium to high *FAPAR* values. MODIS and CYCLOPES were thus selected to generate the *FAPAR* products. This will further provide better consistency between *LAI* and *FAPAR* products. Note that the definition of *FAPAR* products is not very different between the several products: MODIS and JRC-*FAPAR* are instantaneous black-sky at the time of satellite overpass (around 10:30), while CYCLOPES corresponds to instantaneous black-sky at 10:00 which is a good approximation of the daily integrated black-sky *FAPAR* value (Baret et al., 2007).

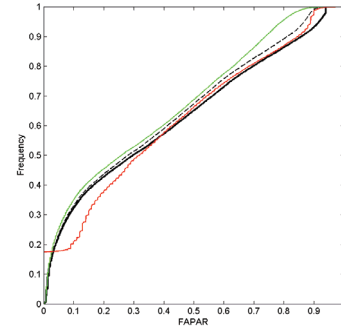


Figure 6. Cumulated frequency of *FAPAR* CYCLOPES (green line), MODIS (red line) products as observed over the 420 BELMANIP2 sites during years 2003-2004. The dashed black line corresponds to the fusion product (according to equation 3) and the solid black line to GEOV1 products.

Investigation of the relationships between MODIS and CYCLOPES *LAI* and *fAPAR* products show that:

- MODIS *FAPAR* overestimates CYCLOPES values for the lower *FAPAR* values (Figure 6).
- Fair agreement is observed for medium to high *FAPAR* values with however slightly lower values for CYCLOPES products (Figure 6).
- Fair agreement is observed between MODIS and CYCLOPES *LAI* values up to values around 3.

To benefit from the better performances observed for CYCLOPES *FAPAR* products for the lower *FAPAR* values, and for MODIS *LAI* products for the larger *LAI* values, it was proposed to average MODIS and CYCLOPES products using the following weighing factor $w = \min(1, \frac{1}{4} LAI_{CYCV31})$:

$$\begin{cases} fAPAR_{fused} = fAPAR_{MODC5} \cdot w + fAPAR_{CYCV31} \cdot (1 - w) \\ LAI_{fused} = LAI_{MODC5} \cdot w + LAI_{CYCV31} \cdot (1 - w) \end{cases} \quad (2)$$

This parallel processing of *LAI* and *FAPAR* is expected to keep a good consistency between *LAI* and *FAPAR* products. The fused *FAPAR* products showed that the maximum values are around 0.898 (Figure 6) although maximum values are expected to be close to 0.94 (Baret and Guyot, 1991). Therefore, the fused values were scaled according to:

$$fAPAR_{best} = \frac{0.94}{0.898} \cdot fAPAR_{fused} \quad (3)$$

No particular scaling was applied to *LAI* since there is no obvious maximum values to set up.

Results show that, as expected, the relationship between *LAI* and *FAPAR* was keeping very consistent as compared to the original CYCLOPES and MODIS products (Figure 7)

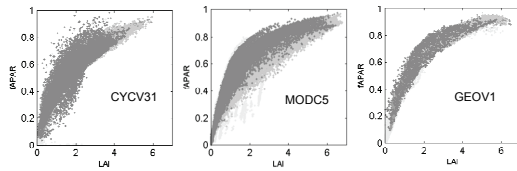


Figure 7. Relationship between *LAI* and *FAPAR* for CYCLOPES, MODIS and GEOV1 products as observed over the 420 BELMANIP2 sites during 2003-2004 period.

2.3 Training the neural networks

The training was achieved over the 420 BELMANIP2 sites for the 2003-2004 period. The spatial support was 3 x 3 pixels over each site to minimize possible geometrical problems between the several products and dates used to compute the inputs and outputs of the neural network.

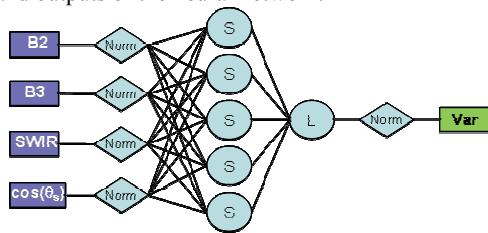


Figure 8. Structure of the neural network used to derive *LAI*, *FAPAR* and *FCOVER* from VEGETATION input reflectance.

a) Neural network architecture

A back-propagation neural network architecture was selected, with one hidden layer of 5 tangent-sigmoidal neurons and one layer with a single linear neuron (Figure 8). Inputs and outputs were normalized using the minimum and maximum values. Five networks were trained in parallel. The one providing the best performances over an independent test data set was selected.

b) Inputs

The top of canopy reflectance acquired by the VEGETATION sensor in the red (B2), near infrared (B3) and short wave infrared (SWIR) were used as inputs. The preprocessing steps are described in (Baret et al., 2007) and include cloud screening, atmospheric correction based on a climatology of aerosols, and BRDF normalization using a robust fit of the Roujean model (Hagolle et al., 2004; Roujean et al., 1992). In addition, the cosine of the sun zenith angle at the observation time is also used as input.

c) Outputs

Special attention was carried out when fusing MODIS and CYCLOPES products for the computation of the 'best' *LAI* and *FAPAR* estimates. MODIS products were re-projected to the CYCLOPES lat-lon grid. All the valid MODIS data including main, main plus saturation and back-up algorithms available within ± 10 days around the CYCLOPES date were considered. This may correspond to a maximum of three MODIS products. Then, if the difference between values at the 70% and 90% cumulated frequency was lower than 0.2 and 1.0 respectively for *FAPAR* and *LAI*, the 70% cumulated frequency value is retained for the fusion. Note that because BELMANIP2 sites are relatively homogeneous at the 10x10 pixels scale, the 70% cumulated frequency value is very close to the mean value. However, taking the 70% cumulated frequency value instead of the mean or the median value prevents from being too sensitive to possible unscreened clouds or cloud shadow that lead to lower *LAI* and *FAPAR* values.

2.4 Associated uncertainties and quality assessment

Three quality assessment criteria were provided along with the products:

- Input out of range. This represents the consistency of the measured VEGETATION input reflectances with those used in the training data base. A flag is raised when observations are outside the training definition domain. The definition domain was approximated by the convex hull formed in the reflectance feature space by the cases used in the learning process (Figure 9). When the input reflectances are outside the definition domain, a flag is raised.

Table 2. Minimum, Maximum, Resolution and Tolerance values used to raise the output of range flag.

	Unit	Min	Max	Resol.	Tol _{min}	Tol _{max}
LAI	m ² .m ⁻²	0	8.0	0.01	-0.2	7.00
FAPAR	-	0	1.0	0.01	-0.05	1.05
FCOVER	-	0	1.0	0.01	-0.05	1.05

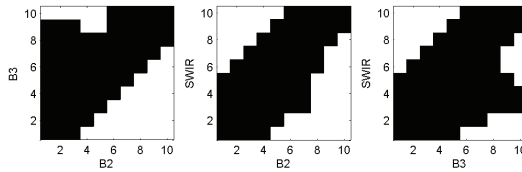


Figure 9. Definition domain of the input reflectance. The cells in black correspond to those where input reflectance were actually observed. Cells in white are outside the definition domain.

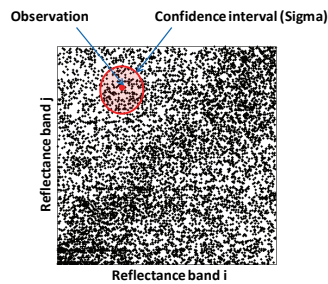


Figure 10. Scheme showing how the uncertainties attached to the products were computed.

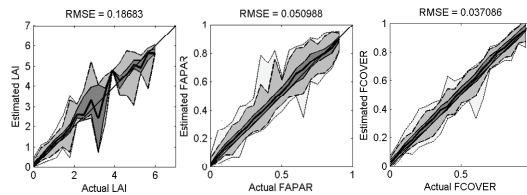


Figure 11. Relationship for *LAI*, *FAPAR* and *FCOVER* products before (actual) and after (estimated) the training process over a test dataset not used in the training process.

- Output out of range. This flag is raised only when the output is outside the output range enlarged by the tolerance values $[To_{min}, To_{max}]$ as defined in Table 2. If the outputs of the neural network falls within the $[To_{min}, Min]$ (respect. $[Max, To_{max}]$), the values are simply reset to the Minimum (respect. maximum) values.
- Estimated uncertainties. This represents the expected error expressed in RMSE between the estimated and the actual biophysical values as derived from the theoretical performances of the algorithm evaluated over an independent data set. The reflectance uncertainties are used to define a confidence interval (Figure 10). The *LAI*, *FAPAR* and *FCOVER* with corresponding reflectance inside the confidence interval are then used to compute the RMSE. A specific network is finally trained to relate the estimated uncertainties to the input reflectance and observation geometry values.

3 PERFORMANCES

3.1 Theoretical performances

Comparison between estimates by the neural network and the actual 'best' *LAI*, *FAPAR* or *FCOVER* values as evaluated over an independent test data set show very good performances without any biases (Figure 11). The scattering as measured by the RMSE is also very small.

3.2 Case studies

Three sites were selected to evaluate qualitatively the performances. An extended validation was concurrently achieved, based on quantitative metrics as proposed by CEOS (Morisette et al. 2006; Garrigues et al. 2009).

Figure 12 shows that GEOV1 products are very smooth as expected. This is due both to the quality of the pre-processing steps as well as to the properties of the neural network. The seasonality is very consistent with that of the other products. The range of variation appears quite realistic, both for the low vegetation amounts (Figure 12, left) and the larger ones (Figure 12, right). The consistency between *LAI* and *FAPAR* is also very strong (Figure 7, right) as expected.

4 CONCLUSION

The GEOV1 *LAI*, *FAPAR* and *FCOVER* products capitalize on the efforts undertaken this last decade in the development and validation of biophysical products from medium resolution observations. It results in robust, consistent and accurate estimates of these key biophysical variables that may be used for a range of applications including those targeted for the Essential Climate Variables.

These products are currently generated by VITO for open access to the user community. The VEGETATION derived time series starting in 1999 will be completed backward using the AVHRR series as processed by Vermote et al. (2010) to get a long time series of almost 30 years. Further, the sustainability of services foreseen within the Land Monitoring Core Service will be ensured by adapting the algorithm to AVHRR-METOP, PROBA-V and Sentinel 3 missions.

ACKNOWLEDGMENTS.

This study was funded partly from the GEOLAND2 FP7 European project.

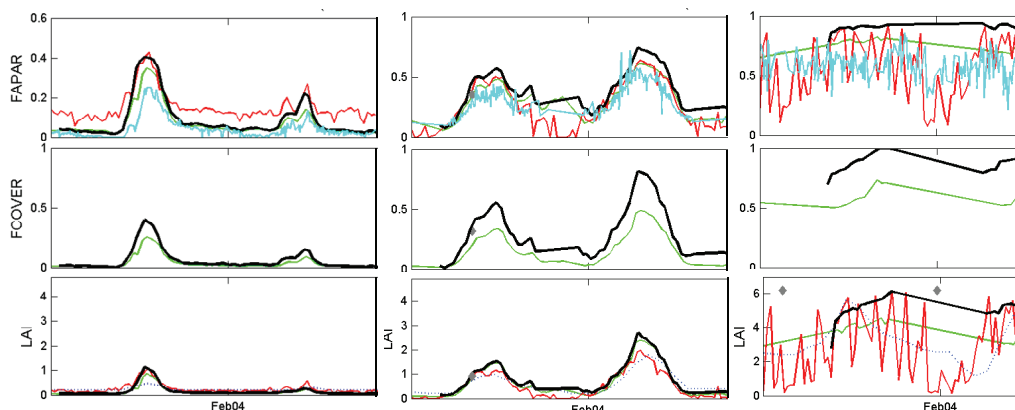


Figure 12. Temporal profiles of LAI (bottom), FAPAR (top) and FCOVER (middle) products: MODIS (red), CYCLOPES (green), GLOBACARBON (dashed blue), JRC-FAPAR (cyan) and GEOV1 (black). Gourma grassland (left 15.32°; -1.55°), Fundulea crop land (centre 44.41°; 26.58°) and Tapa evergreen broadleaf forest (right 2.87°; -54.95°) sites are presented for years 2003-2004.

REFERENCES

- Baret, F. and Guyot, G., 1991. Potentials and limits of vegetation indices for LAI and APAR assessment. *Remote Sensing of the Environment*, 35(2-3): 161-173.
- Baret, F., Hagolle, O., Geiger, B., Bicheron, P., Miras, B., Huc, M., Berthelot, B., Weiss, M., Samain, O., Roujean, J.L. et al., 2007. LAI, fAPAR and fCover CYCLOPES global products derived from VEGETATION. Part 1: Principles of the algorithm. *Remote Sensing of Environment*, 110: 275-286.
- Baret, F., Morisette, J., Fernandes, R., Champeaux, J.L., Myneni, R., Chen, J., Plummer, S., Weiss, M., Bacour, C., Garrigue, S. et al., 2006. Evaluation of the representativeness of networks of sites for the global validation and inter-comparison of land biophysical products. Proposition of the CEOS-BELMANIP. *IEEE Transactions on Geoscience and Remote Sensing*, 44(7: special issue on global land product validation): 1794-1803.
- Chen, J.M. and Black, T.A., 1992. Defining leaf area index for non-flat leaves. *Plant, Cell and Environment*, 15: 421-429.
- Deng, F., Chen, J.M., Chen, M. and Pisek, J., 2006. Algorithm for global leaf area index retrieval using satellite imagery. *IEEE Transactions on Geoscience and Remote Sensing*, 44(8): 2219-2229.
- Garrigues, S., Lacaze, R., Baret, F., Morisette, J., Weiss, M., Nickeson, J., Fernandes, R., Plummer, S., Shabanov, N.V., Myneni, R. et al., 2008. Validation and Intercomparison of Global Leaf Area Index Products Derived From Remote Sensing Data. *Journal of Geophysical Research*, 113(G02028).
- GCOS, 2006. GCOS-107. Supplemental details to the satellite based component of the "implementation plan for the global observing system for climate in support of the UNFCCC". WMO/TN N° 1338, GCOS/WMO, Geneva (Switzerland).
- Gobron, N., Pinty, B., Aussedat, O., Chen, J.M., Cohen, W.B., Fensholt, R., Gond, V., Huemmrich, K.F., Lavergne, T., Melin, F. et al., 2006. Evaluation of fraction of absorbed photosynthetically active radiation products for different canopy radiation transfer regimes: Methodology and results using Joint Research Center products derived from SeaWiFS against ground-based estimations. *Journal Of Geophysical Research-Atmospheres*, 111(D13).
- Hagolle, O., Nicolas, J.-M., Fournie, B., Cabot, F. and Henry, P., 2004. Absolute calibration of VEGETATION derived from an interband method based on the Sun glint over ocean. *IEEE Transactions on Geoscience and Remote Sensing*, 42(7): 1472-1481.
- McCallum, I., Wagner, W., Schmullius, C., Shvidenko, A., Obersteiner, M., Fritz, S. and Nilsson, S., 2010. Comparison of four global FAPAR datasets over Northern Eurasia for the year 2000. *Remote Sensing of Environment*, 114(5): 941.
- Myneni, R.B., Hoffman, S., Knyazikhin, Y., Privette, J.L., Glassy, J., Tian, Y., Wang, Y., Song, X., Zhang, Y., Smith, G.R. et al., 2002. Global products of vegetation leaf area and absorbed PAR from year one of MODIS data. *Remote Sensing of Environment*, 83: 214-231.
- Roujean, J.L., Leroy, M. and Deschamps, P.Y., 1992. A bidirectional reflectance model of the Earth's surface for the correction of remote sensing data. *Journal of geophysical research*, 97(D18): 20455-20468.
- Verger, A., 2008. Analisi comparativa d'algorismes operacionals d'estimacio de parametres biofisics de la coberta vegetal amb teledeteccio, Universitat de Valencia, Valencia (Spain), 277 pp.
- Vermote, E., Justice, C., Csiszar, I., Eidenshink, J., Myneni, R., Baret, F., Masuoka, E. and Wolfe, R., 2010. A terrestrial surface climate data record for global change studies. In: J. Sobrino (Editor), *Third International Symposium on Recent Advances in Quantitative Remote Sensing*, Torrent (Spain).
- Weiss, M., Baret, F., Garrigues, S., Lacaze, R. and Bicheron, P., 2007. LAI, fAPAR and fCover CYCLOPES global products derived from VEGETATION. part 2: Validation and comparison with MODIS Collection 4 products. *Remote sensing of Environment*, 110: 317-331.

Assessment of evapotranspiration and biomass of irrigated grasslands in South-Eastern France from FORMOSAT-2 images used in a crop model.

D. Courault⁽¹⁾, R. Hadria⁽¹⁾, F. Ruget⁽¹⁾, A. Olioso⁽¹⁾, B. Duchemin⁽²⁾, O. Hagolle⁽²⁾, G. Dedieu⁽²⁾

⁽¹⁾ INRA, UMR 1114 EMMAH, Domaine St Paul, 84914, Avignon cedex 9, France, courault@avignon.inra.fr

⁽²⁾ CESBIO, BPI 811, 18 avenue E. Belin, 31401 Toulouse Cedex 9, France

ABSTRACT- In the Mediterranean regions, there is a large spatial variability of agricultural practices, particularly for grasslands irrigated by flooding. These grasslands are harvested three times per year and produce hay of high quality, but their productions decreased significantly these last years because of the water restriction. The study objective is to develop and assess a new method based on a crop model for estimating water balance and crop yield constrained by products derived from optical remote sensing data with high spatio-temporal resolution. A great experiment was conducted over the Crau region in 2006, located in South Eastern France, including intensive ground measurements, along with more than 32 FORMOSAT-2 images. The methodology combined FORMOSAT-2 images and the STICS crop model, to estimate production, evapotranspiration and drainage of irrigated grasslands. Simple algorithms were developed to retrieve the dynamic of Leaf Area Index for each plot of the region and the main agricultural practices such as mowing and irrigation dates. This information was then used to parameterize STICS, applied at region scale to estimate the water budget associated with the biomass productions. Satisfactory results were obtained compared to ground measurements.

1 INTRODUCTION

Mediterranean region is particularly sensitive to changes in agricultural practices and land use since it is often subject to extremes climatic hazards. During these last years, severe drought conditions have reduced the stocks of water and thus have pushed the policymakers to restrict irrigation in some areas, such as in the Crau region, located in the South-Eastern France (Fig 1). About half of this region is devoted to agriculture, with permanent irrigated grasslands representing 67 % of the usable agricultural area (Mérot et al., 2008a). These grasslands are irrigated by flooding, harvested three times per year and produce a high quality hay exported all over the world (<http://www.foindecrau.com>). They are also used as sheep pasture in winter. Generally, farmers bring more water than that needed by the crop (15000 m³/ha/year to 24000 m³/ha/year), and more than 60% of this water participates to the ground-table recharge used for urban and industrial sectors (Mérot et al., 2008a). The water restrictions applied during the last dry years, affected seriously hay production in terms of yield (loss of 30% observed in 2005), and agricultural practices calendar. It is thus important to estimate accurately water needs for irrigated crops to better evaluate the future consequences of climate changes for both agricultural practices and crop production. Since several years scientists have proposed crop

models for monitoring crop and water under various environmental conditions. A lot of models were thus proposed in literature ranging from complex approaches simulating growth for different crops such as CERES (Jones et al., 2003), WOFOST (Pogacar and Kajfez-Bogataj, 2009), STICS (Brisson et al., 2003) up to whole farm optimization models such as GRAZEGRO (Barrett et al., 2005). If all these models give generally good results at field scale, issues still exist for regional applications. Indeed it's often tedious and difficult to define some key parameters describing the agricultural practices at regional scale, because of their very wide spatial variability. Some approaches proposed to use remote sensing data to inform some inputs parameters of crop models (Di Bella et al., 2005). Most of them have used vegetation indices related to Leaf Area index (LAI) (Baret et al., 2007, Jongschaap, 2006). Few have explored the possibility to derive agricultural practices (Duchemin et al., 2008). Nevertheless remote sensing data acquired at high spatial and temporal resolutions appear as an interesting tool to get information of practice modifications. A great experiment was conducted over the Crau region in 2006, including intensive ground measurements, along with FORMOSAT-2 image acquisition almost every 3 days from March to October (Courault et al., 2008). FORMOSAT-2 is a Taiwanese satellite (for more details see [//www.spotimage.fr/web/944-images-](http://www.spotimage.fr/web/944-images-)

formosat-2.php). The spatial resolution of these images was fine enough (pixel of 8m) to identify each field. The study objective was thus to evaluate the feasibility of using FORMOSAT-2 images, combined with a crop model (STICS) to estimate production, evapotranspiration and drainage of irrigated grasslands in the Crau region.

2 DATA AND MODEL

2.1 STICS crop model

STICS crop model ('Simulateur multiDisciplinaire pour les Cultures Standards') has been developed since 1996 at INRA of Avignon in France (www.avignon.inra.fr/agroclim_stics_eng). It is a crop model running at a daily time step with inputs describing climate, soil, plant and crop system (Brisson et al, 1998). STICS has a modular design. Each module deals with specific mechanisms. A first set of three modules concerns the ecophysiology of shoots, (development, vegetative growth, yield components). A second set of four modules deals with the ways in which the soil functions interact with the underground parts of plants (root growth, water balance, nitrogen balance, soil transfers). At the interface there is a module dealing with managing interactions between cultivation techniques and the soil-crop system, whether in the form of water supply, fertiliser supply or the microclimate. The phenological development of the crop is mainly controlled by canopy temperature, while the carbon balance drives biomass accumulation. STICS can either simulate LAI evolution varying according to water and nitrogen stresses, either use daily values of LAI provided as forcing inputs. The quantities/doses of water can be also imposed as an input variable or calculated by the model. The grass cutting can be achieved using two methods i) either from an imposed date ii) either from automatic computation from cumulative development units expressed in temperature. STICS was validated for various conditions and used for grasslands by (Ruget et al, 2009, 2008).

2.2 Data used

a) FORMOSAT-2 images

Thirty six FORMOSAT-2 images were acquired every 3 to 4 days over the Crau region from March to October 2006 with a constant viewing angle of 41° (fig 1). 4 spectral bands in blue, green, red and near infrared were available at 8m spatial resolution. The images were first geolocated, registered and calibrated

at CNES (Centre National d'Etudes Spatiales, France), then corrected from atmospheric effects using the multi-temporal aerosol detection method developed by (Hagolle et al, 2008).

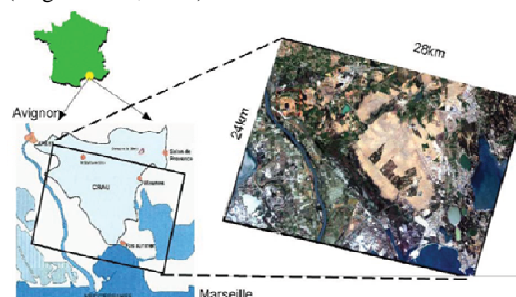


Figure 1. Location of the study area and the FORMOSAT footprint

b) Ground data

120 fields spatially distributed throughout the study area were inquired to determine agricultural practices (mowing and irrigation dates, fertilisation and productions). In addition, ground measurements were performed on a reference grassland, including classical meteorological measurements linked to a biological characterisation. LAI was estimated from hemispherical photographs, then proceeded using CAN-EYE software, http://3w.avignon.inra.fr/can_eye/page5.php, developed by Weiss and Baret at INRA Avignon. Details on these measurements can be found in (Courault et al, 2008).

3. METHODS

3.1. STICS simulations

A first step consisted in testing STICS on the reference field where numerous measurements were available.

This step is necessary to assess the accuracy of the model to simulate grassland development. Then the model was used at farm scale over 47 fields (130ha) to get evapotranspiration, drainage and biomass production maps. In this last case, a homogeneous soil type was considered for all fields with the same characteristics. The other key parameters were derived from FORMOSAT images as summarized in Table 1. In order to evaluate the contribution of these last data in STICS, simulations were compared with and without forcing from FORMOSAT data. The results of this comparison will be presented in the discussion section.

Table 1. Main inputs necessary to STICS (T: air temperature, HR: air moisture, Rg: global radiation, U: windspeed)

Input parameters	Data	Origin/value
Climatic data (daily)	Rain, T_{min} , T_{max} , U , HR, Rg	weather station on grassland
Plant (monospecific)	LAI (daily)	FORMOSAT images
	Residual LAI after cut	FORMOSAT images
	Residual dry matter after cut	Deduced from residual LAI
Agricultural practices	Mowing date	FORMOSAT images
	Irrigation date	FORMOSAT images
	frequency, dose (water)	ASA, 100 mm/event
	Nitrogen fertilisation, date, dose	Surveys: 20 May, 60 kg/ha
Soil	Layer number (2),	Soil map & soil analysis
	Depth, Texture, %stone	80 cm, 20% silt, 60% stone
	Initial Soil moisture	Measurements: 10% 20%
	Initial N_{O_3} , NH_4 , Norg contents	Analysis 80 kg/ha + knowledge f (grassland age)

3.2 Variables derived from FORMOSAT

All FORMOSAT-2 images were processed to obtain NDVI. A supervised land-use classification was made choosing 5 different dates in order to separate better the grasslands from the other land-use classes. LAI maps were obtained using the exponential law with NDVI according to eq 1. Bsaibes et al, (2009) compared different models proposed in literature. This model was calibrated over ground measurements for several crops in the Crau region and a ‘leave-one-out’ test found that this simple method gave satisfactory results compared to other methods.

$$LAI = -\left(\frac{1}{K_{LAI}}\right) \cdot \ln\left(\frac{NDVI - NDVI_{\infty}}{NDVI_s - NDVI_{\infty}}\right) \quad (1)$$

With $k=0.71$, $NDVI_{\infty}=0.89$, $NDVI_s=0.1$

A simplified approach was proposed to estimate the mowing dates from FORMOSAT images. It consisted in, first detecting the date of NDVI minimum followed by a NDVI increase for the next four image acquisitions. Then 6 days were removed from the date corresponding to this minimum because this time interval corresponded to the period needed to dry and to collect hay. The validation gave satisfactory results with high correlations between simulations and observations (fig2). This method was then applied at regional scale over more than 1500 grassland fields.

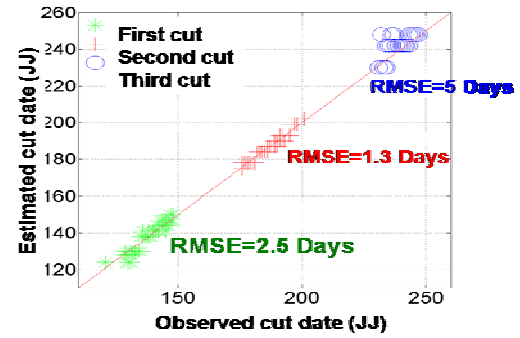


Figure 2. Correlation between mowing dates simulated from FORMOSAT and dates collected besides farmers.

In the Crau region, grasslands are irrigated from a dense channel network. There is a complex water distribution managed by different associations (called ASA), linked to each main channel. Each ASA has its own peculiarities for the irrigation frequency, for example varying from 7 to 12 days. A linear relationship was found between mowing and irrigation dates extracted from the field surveys (Courault et al, 2010). As the starting date and irrigation round were known for each ASA, the different irrigation dates could be estimated for each field. Then, water supplied at each event was set up at 100mm/day (this value was chosen from measurements performed on an experimental field by (Mérot et al., 2008b).

4. RESULTS - DISCUSSION

4.1 On the reference field

Figure 3 presents the main STICS outputs compared to the measurements over the reference grasslands. The results were globally satisfactory for the different variables. Three cycles of grassland growth appeared clearly, separated by three cut events: the first cut was on DOY 131 (11 May), the 2nd cut on DOY: 189 (7 July) and the last one on DOY: 234 (22 August). A

good agreement was observed between LAI estimated from FORMOSAT-2 with ground measurements, except for the second cycle, where the spatial variability of the measurements was the highest. Just before mowing, very high values of LAI were estimated corresponding to high NDVI values. Many authors have shown that when LAI was higher than 4, NDVI tend to saturate (Combal et al, 2003). Thus the accuracy for high LAI values can be arguable. That can explain the difference observed between simulations and measurements for these periods. The model was able to simulate correctly the biomass dynamics with the seasonal variability: the decrease in production classically observed from the first to the third cut. This was mainly explained by the variation in floristic composition which varied according to the season.

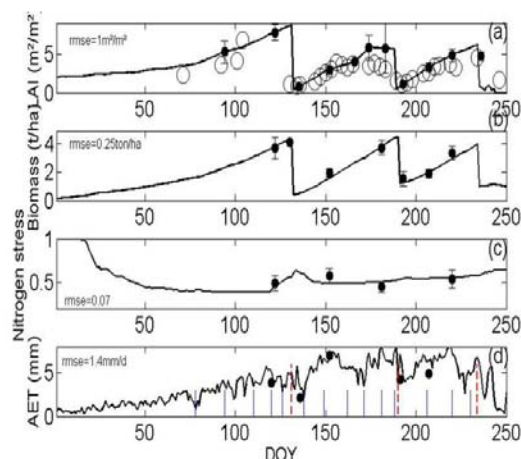


Figure 3. Comparisons between STICS simulation (continuous lines) obtained for the reference grassland with the measurements (black points: average + standard deviation) for the period: 1/1/2006 to 5/9/2006. (the circles correspond to FORMOSAT estimations in the graph (a), blue lines to the irrigation events in graph (d) and red line to the cut dates).

The total production was estimated at 13.8 ton/ha, against 12ton/ha observed, which was quite correct. Simulated evapotranspiration was 936 mm for the period from 1/1 to 5/9/2006 while irrigation by flooding provided around 2300mm. Thus, the drainage term corresponding to the water excess computed by STICS, represented almost 60% of the total water amount supplied by irrigation plus rainfall. This result was consistent with values reported in different papers by (Mérot et al, 2008a,b).

4.2. At regional scale

Figure 4 shows the maps of the total biomass and evapotranspiration computed from the 1st January to

the end of September over a specific farm in La Crau area.

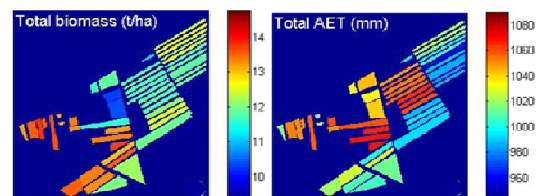


Figure 4. Total biomass and evapotranspiration simulated by STICS from 1/1 to 30/9/2006 at farm scale over 47 grassland fields (~4km²).

It appeared that even at a small spatial scale, there were a great variability for both the production, and evapotranspiration. This variability was strongly linked with the irrigation order and consequently with the order of mowing the fields. The last mowed fields could receive one or two more irrigation supplies for the same period which explained substantial differences in the order of magnitude of 105mm for cumulated evapotranspiration from one plot to another. Figure 5 shows the correlations obtained between the productions simulated at the 2nd harvest compared with the values given by the farmer. The results were globally satisfactory. A further analysis showed that the fields (50-51-52) having the lowest yields corresponded to the more recent grasslands (sown after 2000), while the oldest fields (sown before 1950) produced generally more biomass. Significant differences were also observed for the LAI between these fields. An explanation could be that the soil under the older fields is slightly deeper and more silted than those of the recent fields, because of the sediments supplied by irrigation during numerous years.

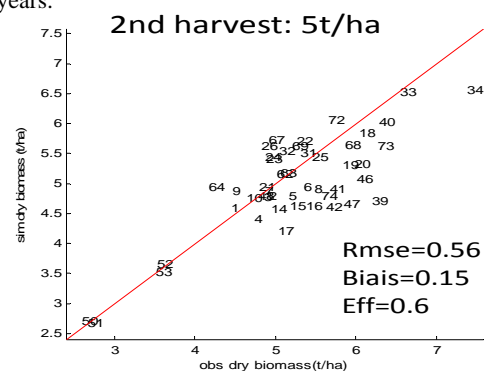


Figure 5. Comparison between production simulated for the 2nd harvest and the values given by the farmer.

In order to quantify the contribution of remote sensing to the crop model, simulations were performed according to the different cases presented in Table 2.

In the first two cases, LAI was computed by STICS, from cumulated temperatures varying according to water and nitrogen stresses. Irrigation and mowing dates were also computed automatically by the model with 2 cases for water quantity brought at each event (case 1: 20mm, case 2: 40mm). Irrigation occurred when the water stress index was below 0.8, which meant that the grasslands were globally well supplied with water. There was no water excess in these first two cases. The following cases introduced the spatial variability at different levels, only in fixing the mowing dates (case 3), or LAI, or irrigation dates, or the combination of these variables. The best results

were obtained for the biomass estimation when all the variables (LAI, mowing and irrigation dates) were forced into the model from FORMOSAT data. It appeared also that the knowledge of the variability of agricultural practices was most important than the knowledge of LAI only, which was not surprising since the agricultural practices were crucial for the vegetation development. It should be noted also that for three times less of water, simulations gave the same level production (cases 2-6).

Table 2. Different simulation cases with and without remote sensing data (forced meant computed from remote sensing data, simulated : computed by the model; for cases 1 & 2, only one simulation was performed and compared to the average of yields observed over the 47 fields surveyed the first number of the last column corresponds to the mean value of yield observed+*rmse*, for the other cases: it's *rmse* + bias, *rmse*: relative standard error.

Studied Cases		Biomass (ton/ha)	AET (mm)	Irrigation (mm)	RMSE, bias /yield obs
Input	Information source				
case 1	LAI	simulated			
	cut dates	simulated	15.9	680	16.6 - 0.42
	Irrigation	simulated (20mm)		number : 33	
case 2	LAI	simulated			
	cut dates	simulated	16.7	620	16.5 - 0.32
	Irrigation	simulated (40mm)		number : 16	
case 3	LAI	simulated			
	cut dates	forced	18.9 min-max : 10.5 - 21.6	1002 min-max : 963 - 1037	680 number : 17
	Irrigation	simulated (40mm)			1.6 - 1.1
case 4	LAI	simulated			
	cut dates	forced	15.7 min-max : 10 - 20.7	986 min-max : 940 - 1037	1500 number : 13 - 17
	Irrigation	forced (100 mm)			0.84 - 0.34
case 5	LAI	forced			
	cut dates	forced	19.9 min-max : 11.1 - 23.4	1018 min-max : 985 - 1074	660 number : 16 - 17
	Irrigation	simulated (40 mm)			1.7 - 1
case 6	LAI	forced	17.0 min-max : 11 - 21.9	1037 min-max : 996 - 1074	1500 number : 13-17

5 CONCLUSION

This study demonstrated that remote sensing data acquired at high spatio-temporal resolution could give useful information on the variability of agricultural practices at regional scale. Forcing STICS with FORMOSAT data allowed to estimate significant differences for both the biomass production (from 9 to 14t/ha), and the main water budget terms at farm scale. Simple algorithms for mapping LAI and agricultural practices easy to implement to other dataset or regions for operational applications were proposed. However, it should be noticed that only a part of the world is covered by FORMOSAT-2, but future sensors like Sentinel or Venus (Dedieu et al, 2009) would also provide similar information for the next years. Such data should help us in the assessment of modifications of farm practices due to external changes (climate or

water availability) in order to quantify the impacts on our environment.

6 Acknowledgements

This study was part of projects financed by the MIP-PACA regions in France and by the CNES (DAR 2006 TOSCA). The FORMOSAT-2 images used in this study are © NSPO (2006) and distributed by Spot Image S.A. all rights reserved. Authors thank the different institutions and farmers for surveys and measurements performed on their fields.

7 REFERENCES

Baret, F., Hagolle, O., Geiger, B., Bicheron, P., Miras, B., Huc, M., Berthelot, B., Nino, F., Weiss, M., Samain, O., Roujean, J.L., and Leroy, M., 2007. LAI, fAPAR and fCover CYCLOPES global products derived from VEGETATION - Part 1:

- Principles of the algorithm. *Remote Sensing of Environment*, **110**, 275-286.
- Barrett, P.D., Laidlaw, A.S., and Mayne, C.S., 2005. GrazeGro: a European herbage growth model to predict pasture production in perennial ryegrass swards for decision support. *European Journal of Agronomy*, **23**, 37-56.
- Brisson, N., Mary, B., Ripoche, D., Jeuffroy, M.H., Ruget, F., Nicoullaud, B., Gate, P., Devienne-Barret, F., Antonioletti, R., Durr, C., Richard, G., Beaudoin, N., Recous, S., Tayot, X., Plenet, D., Cellier, P., Machet, J.M., Meynard, J.M., and Delecalle, R., 1998. STICS: a generic model for the simulation of crops and their water and nitrogen balances. I. Theory and parameterization applied to wheat and corn. *Agronomie*, **18**, 311-346.
- Bsaibes, A., Courault, D., Baret, F., Weiss, M., Oliso, A., Jacob, F., Hagolle, O., Marloie, O., Bertrand, N., Desfond, V., and Kzemipour, F., 2009. Albedo and LAI estimates from FORMOSAT-2 data for crop monitoring. *Remote Sensing of Environment*, **113**, 716-729.
- Combal, B., Baret, F., Weiss, M., Trubuil, A., Mace, D., Pragnere, A., Myneni, R., Knyazikhin, Y., and Wang, L., 2003. Retrieval of canopy biophysical variables from bidirectional reflectance - Using prior information to solve the ill-posed inverse problem. *Remote Sensing of Environment*, **84**, 1-15.
- Courault, D., Bsaibes, A., Kpemlie, E., Hadria, R., Hagolle, O., Marloie, O., Hanocq, J.F., Oliso, A., Bertrand, N., and Desfonds, V., 2008. Assessing the potentialities of FORMOSAT-2 data for water and crop monitoring at small regional scale in South-Eastern France. *Sensors*, **8**, 3460-3481.
- Courault, D., Hadria, R., Ruget, F., Oliso, A., Duchemin, B., Hagolle, O., and Dedieu, G., 2010. Combined use of FORMOSAT-2 images with a crop model for biomass and water monitoring of permanent grassland in Mediterranean region. *Hydrol. Earth Syst. Sci.*, **14**, 1731-1744, doi:10.5194/hess-14-1731-2010.
- Dedieu, G., Karnieli, A., Hagolle, O., Jeanjean, H., Cabot, F., Ferrier, P. and Yaniv, Y., 2006 VENUS: A joint French - Israel Earth Observation scientific mission with High spatial and temporal resolution capabilities. In: J. Sobrino (Editor), Second Recent Advances in Quantitative Remote Sensing. Publicacions de la Universitat de València, 25-29 September 2006, Auditori de Torrent, Spain, pp 517-521.
- Di Bella, C., Faivre, R., Ruget, F., Seguin, B., Guerif, M., Combal, B., Weiss, A., and Rebella, C. 2004. Remote sensing capabilities to estimate pasture production in France. *International Journal of Remote Sensing*, **25**, 5359-5372.
- Duchemin, B., Hagolle, O., Mougnot, B., Benhadj, I., Hadria, R., Simonneaux, V., Ezzahar, J., Hoedjes, J., Khabba, S., Kharrou, M.H., Boulet, G., Dedieu, G., Er-Raki, S., Escadafal, R., Oliso, A., and Chehbouni, A.G., 2008. Agrometeorological study of semi-arid areas: an experiment for analysing the potential of time series of FORMOSAT-2 images (Tensift-Marrakech plain). *International Journal of Remote Sensing*, **29**, 5291-5300.
- Hagolle, O., Dedieu, G., Mougnot, B., Debaecker, V., Duchemin, B., and Meygret, A., 2008. Correction of aerosol effects on multi-temporal images acquired with constant viewing angles: Application to Formosat-2 images. *Remote Sensing of Environment*, **112**, 1689-1701.
- Jones, J.W., Hoogenboom, G., Porter, C.H., Boote, K.J., Batchelor, W.D., Hunt, L.A., Wilkens, P.W., Singh, U., Gijsman, A.J., and Ritchie, J.T., 2003. The DSSAT cropping system model. *European Journal of Agronomy*, **18**, 235-265.
- Jongschaap, R.E.E., 2006. Run-time calibration of simulation models by integrating remote sensing estimates of leaf area index and canopy nitrogen. *European Journal of Agronomy*, **24**, 316-324.
- Mérot, A., Bergez, J.E., Capillon, A., and Wery, J. 2008a. Analysing farming practices to develop a numerical, operational model of farmers' decision-making processes: An irrigated hay cropping system in France. *Agricultural Systems*, **98**, 108-118.
- Mérot, A., Bergez, J.E., Wallach, D., and Duru, M., 2008b. Adaptation of a functional model of grassland to simulate the behaviour of irrigated grasslands under a Mediterranean climate: The Crau case. *European Journal of Agronomy*, **29**, 163-174.
- Pogacar, T., and Kajfez-Bogataj, L., 2009 WOFOST: crop growth simulation model - 1st part, *Acta Agriculturae Slovenica*, **93**, pp 231-243.
- Ruget, F., Abdessemed, A., and Moreau, J.C., 2008. Impact of global climate change scenarios on alfalfa production in France. *Biodiversity and animal feed: future challenges for grassland production. Proceedings of the 22nd General Meeting of the European Grassland Federation, Uppsala, Sweden, 9-12 June 2008*, pp745-747.
- Ruget, F., Satger, S., Volaire, F., and Lelievre, F., 2009. Modeling Tillers Density, Growth, and Yield of Mediterranean Perennial Grasslands with STICS, *Crop Science*, **49**, 2379-2385.

Testing In-Scene Atmospheric Corrections of Hyperspectral Thermal Data from Nadir- and Oblique-Viewing Geometries

Matt R. Smith^{1*}, Alan R. Gillespie¹, Hugau Mizzon¹, Lee K. Balick², Juan Carlos Jiménez-Muñoz³, Jose A. Sobrino³

1.University of Washington, Seattle, WA, USA. 2.Los Alamos National Laboratory, Los Alamos, NM, USA. 3.University of Valencia, Valencia, Spain.

*Corresponding author email: matthers@uw.edu

ABSTRACT - *In-scene atmospheric correction makes use exclusively of data internal to an image in order to estimate and remove the transmissivity and path radiance terms in the radiative transfer equation. Compensating for atmospheric effects makes it easier to detect and identify surface mineralogy. ISAC is a published and widely used algorithm that uses this approach. It was developed for nadir-looking airborne images. Here we test atmospheric correction of hyperspectral images, using ISAC, for different viewing geometries: horizontal and oblique views. We find that it works well for nadir-looking and horizontal-looking geometries, but must be adapted for oblique views. For oblique views, with highly variable path lengths within a single scene, the image must be broken into sections based on similar path length, corrected individually, and reassembled.*

1 INTRODUCTION

One of the foremost problems with hyperspectral thermal imagery is atmospheric correction. Two different paths have been taken to handle this problem: model-based and in-scene correction algorithms. Model-based algorithms primarily use MODTRAN-calculated atmospheric parameter spectra and ascertain the best-fit atmosphere for the scene using large look-up tables comprised of many pre-calculated spectra (e.g. Richter and Schlapfer, 2002). In-scene corrections (those that require primarily only data from within the scene) have various forms: exploiting the inherent high-frequency nature of atmospheric absorption bands to identify and eliminate them (e.g. Borel, 1998), using known atmospheric water-vapor spectral features to reconstruct atmospheric spectra (Tonooka, 2001), and the In-Scene Atmospheric Correction algorithm [ISAC] that presumes a population of materials in the scene that approximates a blackbody to derive atmospheric parameters (Young et al., 2002). Most of these techniques, in-scene and model-based, have been devised to correct for airborne/satellite nadir viewing geometries. When correcting for side-looking or oblique-viewing geometries, previous corrections have mainly relied on MODTRAN atmospheric modeling, with the variable path lengths calculated using a digital terrain model (e.g. Richter and Schlapfer, 2002). Atmospheric corrections for side- or oblique-looking image acquisitions have not utilized in-scene atmospheric correction methods, to our knowledge.

The ISAC algorithm is the most easily applicable to a variety of scenes, since it requires the least *a-priori* knowledge of the scene. However, ISAC makes an

assumption that there is a substantial population of blackbody-like materials in the scene, an assumption that is not always possible, especially in arid landscapes.

In this paper, we apply, and adapt when necessary, the ISAC algorithm to hyperspectral thermal scenes in order to assess our ability to extract useful emissivity information from these datasets in various viewing geometries.

2 METHODS

2.1 In-Scene Correction Algorithm

ISAC is a method developed by Young et al. (2002) to determine relative atmospheric parameters (transmissivity, path radiance) using only data from within the scene. It is predicated on two main assumptions: (1) the atmosphere is homogeneous and (2) there is a population of materials that approximate blackbodies in the scene.

ISAC uses all pixels within the scene (or within the desired portion of the scene) to determine relative atmospheric parameters. The at-sensor measured radiance spectrum for each pixel is first converted to brightness temperature through the Planck equation. The highest brightness temperature is found for each pixel, as well as the band that it occurs in. The band with the highest brightness temperature is evaluated for each pixel, and the most popular high-temperature band is determined. Then, using only those pixels that share the most popular high-temperature band, a scatterplot is made for each band, plotting the measured radiance, L_s , versus the radiance of a blackbody with the same brightness temperature, $B(\lambda, T)$.

According to the radiative transfer equation,

$$L_s = \epsilon B(\lambda, T) \tau + L_u \quad (1)$$

when the blackbody radiance is plotted against the measured radiance, the slope of that line will be the surface emissivity in that band, ϵ , times the transmissivity of the intervening atmosphere, τ , and the intercept will be the atmospheric path radiance, L_u . The surface emissivity is always between 0-1, and therefore, a line that is fitted to the *top* of the data points will be a best-fit line for those data which are closest to a blackbody ($\epsilon=1$), eliminating the emissivity term from the equation, and leaving only transmissivity. The path radiance, transmissivity and emissivity terms solved in this way yield relative values, and may be converted to absolute values with additional scaling using water-vapor features. This effect will likely cause some bias when comparing laboratory mineral emissivity spectra to our retrieved relative emissivity spectra.

It is also important to note that our version of the radiative transfer equation (Eq. 1) does not include a term for sky downwelling radiance reflected from the surface. This is due to the assumption that we are finding atmospheric parameters for those pixels which are for approximately blackbody materials and, therefore, will not reflect any incident radiation.

ISAC was performed on two datasets obtained using different instruments for this exercise: The Aerospace Corporation's Spatially Enhanced Broadband Array Spectrograph System (SEBASS) and the Telops Hyper-cam. SEBASS is a pushbroom scanner that collects in 128 bands between 7.57 and 13.51 μm ($\text{NE}\Delta T \leq 0.05 \text{ K}$). Hyper-cam is a Fourier-transform Spectrometer, and can collect up to 150 bands between 7.7 – 11.5 μm ($\text{NE}\Delta T = 0.3 \text{ K}$). The Hyper-cam has been previously employed by Balick et al. (2009) to retrieve mineral emissivities for various rock types.

3 DATA AND RESULTS

3.1 Nadir views

ISAC was performed on an airborne SEBASS image – taken over Badwater Basin, Death Valley, CA (Fig. 1) – and emissivity spectra were extracted, as well as relative atmospheric parameters for the scene.

Here, as shown in Fig. 2, ISAC provided emissivity spectra that match laboratory spectra and allowed us to easily identify surface mineralogy: sulfates, clays, and quartz. However, due to some errors in the correction – possibly due to the effects of varying topography or atmosphere across the scene, or a lack of a large population of clear blackbodies – our retrieved emissivity spectra from the scene appear to contain residual atmospheric terms.

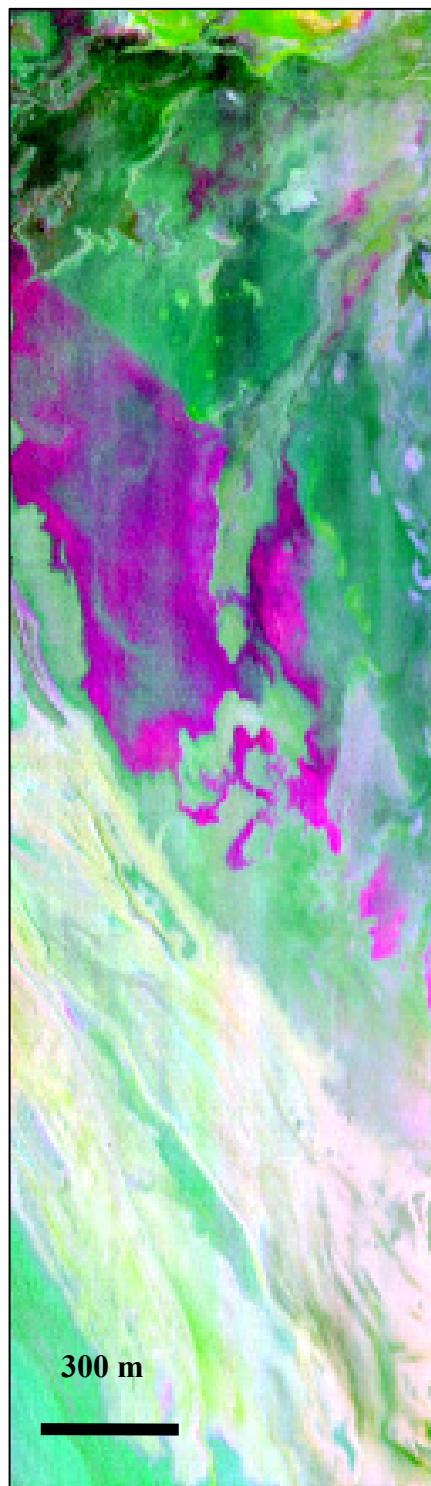


Figure 1. Airborne SEBASS image of Badwater Basin, Death Valley, CA

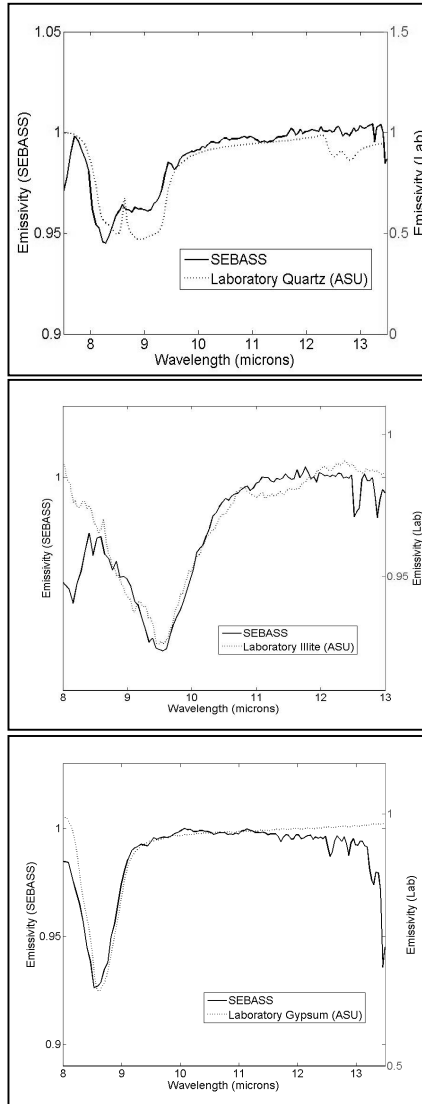


Figure 2. Comparisons of ISAC-corrected spectra versus laboratory mineral spectra for quartz (top), (phyllosilicates (middle), and anhydrite (bottom)).

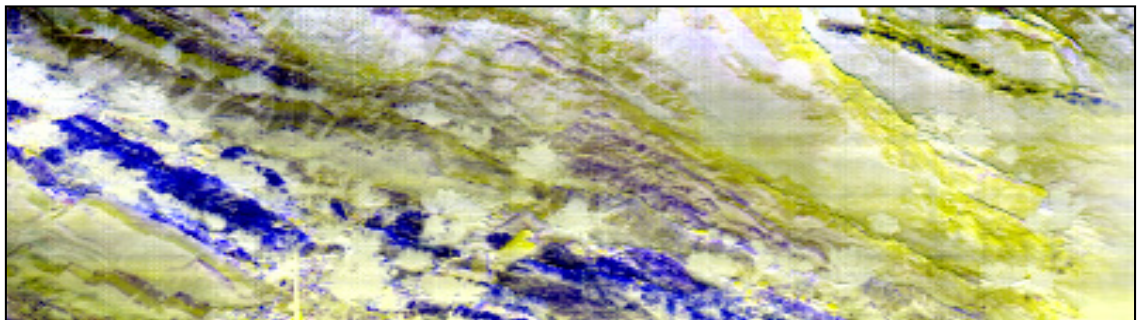


Figure 3. False color image using SEBASS of Hell's Gate, Death Valley, CA [R: 8.3 μm , G: 9.18 μm , B: 11.15 μm]

3.2 Horizontal views

Similar to nadir views, we are also able to extract useful emissivity information with ISAC on horizontal views of Hell's Gate using SEBASS data (Fig. 3); quartz and dolomite emissivity spectra were easily identified (Fig. 4).

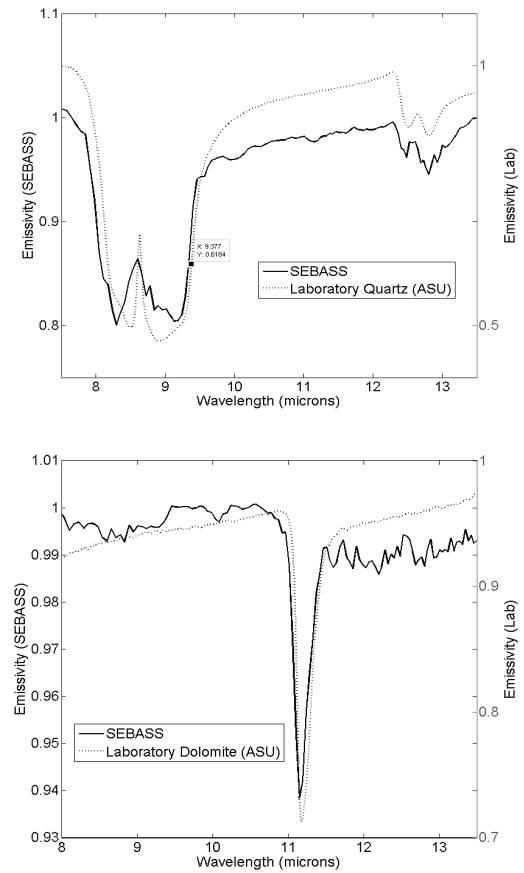


Figure 4. Comparison of ISAC-corrected emissivity spectra versus laboratory mineral spectra for quartz (top) and dolomite (bottom).

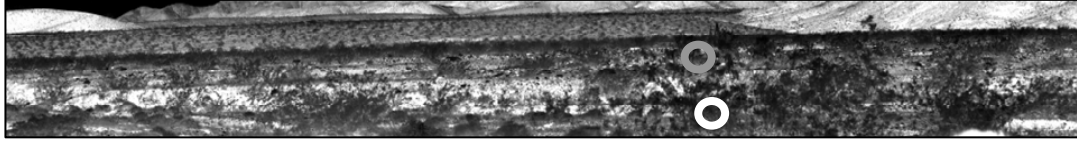


Figure 5. Panoramic SEBASS image of Corkscrew Peak, Death Valley, CA. Colored circles correspond to near-ground (white) and far-ground (grey) regions of the image used for the modified ISAC described in Sec. 3.3.

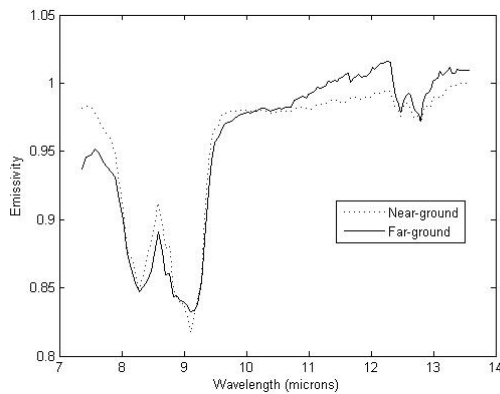


Figure 6. Corrected emissivity spectra for near-ground (white circle in Fig. 5) and far-ground (grey circle in Fig. 5). targets.

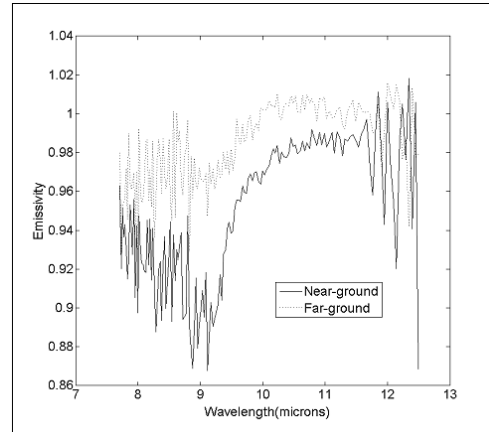


Figure 7. ISAC-corrected noisy emissivity spectra for two sections of a similar alluvial fan in Death Valley within a TELOPS Hyper-cam scene.

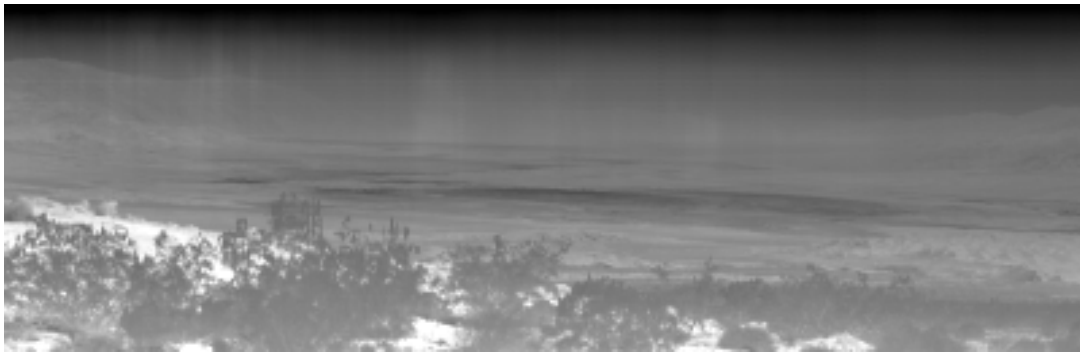


Figure 8. Panoramic SEBASS image 11.72-micron band (near a large water vapor absorption feature) of the floor of Death Valley. This image demonstrates the path length effects within oblique (slant) images.

3.3 Oblique (slant) views

Since an oblique view of the ground features a large difference in path length between the near and far-field (as seen in Figs. 8,9), we applied ISAC to two blocks of different path lengths, one each in the near- and far-ground of a SEBASS image taken from Corkscrew Peak, Death Valley, CA (Fig. 5). The recovered atmospheric parameters (transmissivity and path radiance) varied strongly between the two and surface mineralogy absorption features are apparent in our atmospheric parameters, indicating a flawed correction. However, corrected emissivity spectra (Fig. 6) are still able to show the surface mineralogical signatures. This shows that finding a blackbody in the

scene may be difficult in arid environments even when obvious blackbody analogs (bushes) are present.

ISAC, when applied to TELOPS scene of Badwater Basin, leaves a noisy emissivity spectrum, when compared with nadir- and horizontal-viewing geometries (Fig. 7). We hypothesize that this is due to one, or a combination, of the following factors:

- a. Strong variations in path length between the near- and far-field violate the assumption – necessary for ISAC – that the atmosphere is homogeneous throughout the image*

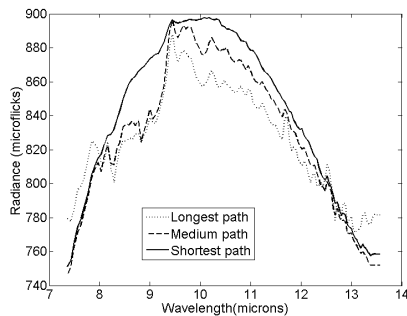


Figure 9. Three radiance spectra for three different path lengths within the same image, demonstrating the growth of atmospheric absorption features with greater path length, violating the assumption of ISAC that the atmosphere is homogeneous in the image.

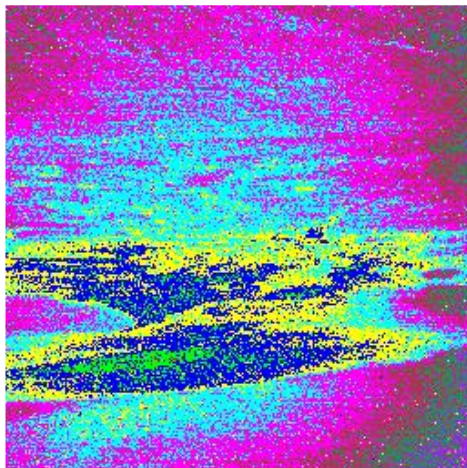


Figure 10. Ratio of 10 to 8 μm in uncorrected TELOPS radiance data. White circle indicates that radial pattern is not strictly circular, indicating some additional path length or mineralogic effects on spectra.

We do not see strong path-length dependence in the ratio of 10 to 8 μm (Fig. 10), as would be expected for a scene affected by large path length effects, these effects must not be the primary factor controlling the applicability of ISAC here. This is a surprising finding, since the atmospheric path length varies so strongly between the top and the bottom of the image.

However, when we apply a similar process to the TELOPS scene as we did to the SEBASS image – segmenting the image according to similar path length and correction each segment independently – the corrected emissivity spectra do not improve.

b. Strongly variable and non-unity emissivities in the scene can affect the measured radiance

Variable emissivities can affect the relative path length effects. For a low-emissivity surface, the

contrast between a near and far target diminishes and may affect ISAC. In Fig. 10, foreground salts (dark) display in the influence of emissivity on measured at-sensor radiance.

c Instrumental artifacts may exhibit control on scaling of measured radiance across the image

This is expressed as a sub-circular pattern within the 10 to 8 μm ratio (marked as a white circle in Fig. 10). However, since the observed pattern is not strictly circular, other factors (e.g. path length, surface characteristics) also exert an influence.

4 CONCLUSIONS

We find that ISAC is capable of correcting hyperspectral thermal imagery for atmospheric effects from nadir- and horizontal-viewing geometries. After employing ISAC, we may retrieve useful emissivity spectra from these images. However, for slant-view geometries, ISAC fails to yield useful emissivity spectra. Slant-views are complicated by the possibility of a varying atmosphere, surface emissivities or instrumental artifacts that result in vaguely radially symmetrical patterns in the image.

5 REFERENCES

- Balick, L., et al., 2009, Longwave thermal infrared spectral variability in individual rocks. *IEEE Geoscience and Remote Sensing Letters*, **6**(1), 52-56
- Borel, C. C., 1998, Surface emissivity and temperature retrieval for a hyperspectral sensor. *Geosci. and Rem. Sens. Symposium Proceedings*, **1**, 546-9.
- Richter, R. and Schlapfer, D., 2002, Geo-atmospheric processing of airborne imaging spectrometry data. Part 2: atmospheric/topographic correction. *International Journal of Remote Sensing*, **23**, 2631-2649.
- Tonooka, H., 2001, An atmospheric correction algorithm for thermal infrared multispectral data over land-a water-vapor scaling method. *IEEE Transactions on Geoscience & Remote Sensing*, **39**(3), 682-692.
- Young, S.J. et al., 2002, An in-scene method for atmospheric compensation of thermal hyperspectral data. *J. Geophys. Res.* **107**, 4774.

6 ACKNOWLEDGMENTS

The research described herein was supported by Department of Energy Grant DE-FG52-08NA28772. We thank John Hackwell and The Aerospace Corporation for the use of SEBASS hyperspectral images.

Mapping vegetation density properties in a river floodplain and agricultural ecosystems using CHRIS-PROBA data

J. Verrelst^a, E. Romijn^b, L. Kooistra^b, J.P. Rivera^a, L. Alonso^a, J. Moreno^a

^a Image Processing Laboratory, University of Valencia, Spain.

^b Centre for Geo-Information, Wageningen University, 6700 AA, Wageningen, The Netherlands

jochem.verrelst@uv.es

ABSTRACT - River floodplains in the Netherlands serve as water storage area, while at the same time they also have the function of nature rehabilitation area. Floodplain vegetation is therefore subject to natural processes of vegetation succession, which obstructs the water flow into the floodplains and increases the flood risk for the hinterland. Space-based pointable imaging spectroscopy has the potential to map and monitor the vegetation density in order to provide river managers with up-to-date information on hydraulic roughness of the vegetation. Therefore, multi-angular CHRIS/PROBA data of a river floodplain ecosystem were linked to the canopy reflectance model FLIGHT. A GUI-based toolbox was developed to streamline model inversion. Leaf area index (LAI) and fractional vegetation cover (fCover) were simultaneously computed for three main classified vegetation types 'herbaceous', 'shrubs' and 'forest' for the CHRIS viewing angles in nadir, backward (-36°), and forward (+36°) scattering direction. These variables provide continuous vegetation density information at the pixel level. Best LAI results were obtained in the nadir direction, and best fCover results in the backward scattering direction. Most sensitivity to variation in both variables was found in the backward scattering direction and the least in forward scattering direction. The proposed method enabled upscaling the vegetation density maps to the whole river basin.

1 INTRODUCTION

Climate change is expected to have a large impact on water resources and flooding risks of the main rivers in the Netherlands (Straatsma et al., 2009). General circulation models applied on the Rhine river basin predict higher winter discharge and peak flows as a result of increased winter precipitation and earlier snow-melt in the Alps (Tol et al., 2003). During the last decades, the water discharge capacity of the river system has been increased by lowering and widening of the floodplains, removal of groynes and hydraulic obstacles in the floodplains and by excavation of secondary channels (Silva et al., 2001). Concomitantly, these newly developed river floodplains, also serve as nature restoration areas, where succession of plant communities leads to highly valued ecosystems. However, floodplain vegetation causes resistance to the water flow within the river floodplains, which may lead to an increase in flooded areas (Baptist et al., 2004).

The hydraulic conductivity of a floodplain can be estimated through calculating the so-called hydraulic roughness. The hydraulic roughness indicates to what extent the water flow is obstructed and is directly related to vegetation height and density, rigidity of the stems and the presence of leaves (Duel et al., 2001). Given the tendency of plant succession to evolve towards more complex and dense plant communities, therefore, estimation of the hydraulic roughness

requires regular monitoring of the spatial distribution and structure of the floodplain vegetation.

For the rivers Rhine and Meuse in the Netherlands, ecotope maps are used for determining hydraulic roughness values, resulting in one roughness value per ecotope object. Currently, ecotope maps are based on digital false colour aerial photographs and ancillary in situ data on flood duration, management, water depth and morphodynamics (Van Velzen et al., 2003). These techniques are tedious and time-consuming and no information on spatial variability of vegetation density within the ecotopes is provided.

Alternatively, satellite remote sensing can play a major role by providing a quantifiable, spatially-explicit and replicable technique for monitoring and assessing the magnitude of vegetation density. With optical remote sensing data, vegetation properties can be characterised into a few essential structural variables such as leaf area index (LAI), and fractional vegetation cover (fCover). These variables provide continuous vegetation density information at the pixel level. Within this approach for approximating the hydraulic roughness, LAI can be considered as a measure of leaf density at the vertical extent, while fCover represents the vegetation density at the horizontal extent.

The retrieval of LAI and fCover from remote sensing data is often based on empirical relationships between spectral vegetation indices and ground-based measurements (Baret and Guyot, 1991). These relationships work well under particular viewing and

illumination geometry and for specific vegetation phenology, but they tend to produce inaccurate results when applied over a broad range of land cover types and optical and geometric conditions encountered in satellite images.

Contrary to empirical approaches, radiative transfer (RT) models take the physical features of plant canopies into account and are therefore more realistic in describing the interaction of solar radiance with vegetation components. In these RT models the spectral signal is a function of canopy geometry, defined by canopy structural variables like LAI, leaf angle distribution, fCover, etc., optical leaf and soil properties, illumination and viewing geometry. By inverting such a model against measured reflectance data, in turn, these biophysical parameters can be directly derived.

Apart from the expected enhancement of the RT modelling approach for retrieval accuracy, additional gains are to be expected with use of multiple viewing angles. Canopy reflectance measurements acquired under different observation angles have shown to yield unique information pertaining to vegetation structure (Diner et al., 2005). Reflectance data from multi-angular instruments have shown that structural variables like LAI and fCover can be more reliably estimated when combining data from multiple viewing angles than compared to conventional mono-angular data (Pocewicz et al., 2007; Chopping et al., 2006; Verhoef and Bach, 2007). Henceforth, the synergy of RT methods with multi-angular data may lead to a more robust approach to map the complex floodplain vegetation structure from space.

In this study we aim at characterizing the vegetation density of a spatially and spectrally complex river floodplain ecosystem using multi-angular CHRIS data. The objective is threefold: *i*) to develop a semi-automated and user-friendly methodology for mapping of the density variables LAI and fCover of several vegetation types in a river floodplain ecosystem using RT models; *ii*) to explore the added value of the use of the angular compound in the applied methodology; and *iii*) to assess the opportunities to upscale the methodology developed for a local floodplain to a complete river section at the regional scale.

2 MATERIALS AND METHODS

2.1 Study site

The study site is the floodplain 'Millingerwaard' ($51^{\circ} 84' \text{ N}$, $5^{\circ} 99' \text{ E}$) along the river Waal, which is the main branch of the river Rhine in the Netherlands (Fig. 1). Millingerwaard (700 ha) is one of the main floodplains of the nature reserve 'Gelderse Poort', with a total surface of 6700 hectare. Current

vegetation of the Millingerwaard floodplain consists of mixed patches and ecotones, i.e. transitions between communities with a dominance of grass, herbaceous vegetation, dwarf and tall shrubs, and a large softwood forest (Verrelst et al., 2009).

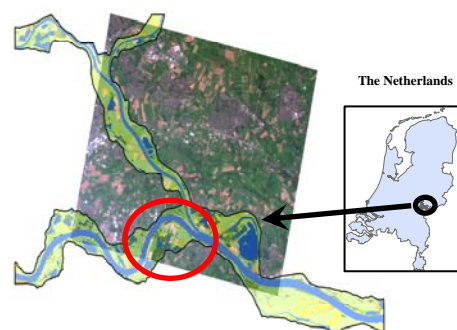


Figure 1. The study area which is located in the east of the Netherlands, indicated on the CHRIS nadir image in true colour band composition (R: 675.2 nm, G: 551.7 nm, B: 490.5 nm). The red circle represents the river floodplains of Millingerwaard. The black outlined river area overlain on the CHRIS nadir image represents the nature reserve the Gelderse Poort which was used for upscaling of the method.

2.2 Multi-angular CHRIS-PROBA data

CHRIS images for the Millingerwaard and a large part of the Gelderse Poort (Fig. 1) were acquired on 6 September 2005 in mode 3 under cloud-free conditions around solar noon. Data were available in five different nominal viewing zenith angles (VZA): nadir, $\pm 36^{\circ}$, $\pm 55^{\circ}$. The angular observations are named as such hereafter. The actual position of the sensor during the satellite overpass is shown in the polar plot of figure 2.

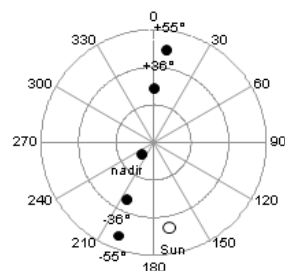


Figure 2. Polar plot showing the position of the sensor when the 5 angular CHRIS images were acquired on 6 September 2005. The solar zenith angle was 46° , the solar azimuth angle 170° .

Automatic image registration was performed according to the method of Ma et al. (2010) to reference the five separate images to each other. Geometric correction was carried out with use of 34

ground control points (GCP's) which were collected on a high spatial resolution (0.5 m) aerial photograph from early spring 2006. Because the CHRIS images were already referenced to each other, the GCP's were taken from the nadir image only and also applied to the $\pm 36^\circ$ images. A 2nd order polynomial model with nearest neighbourhood resampling technique was used for geometric correction of the 3 images which resulted in a control point error of 0.31 pixels. Atmospheric correction of the angular images was performed according to the method described by Guanter et al. (2005) using CHRIS-Box software developed as a module for the BEAM toolbox.

2.3 Land cover classification of CHRIS nadir image

Prior to vegetation density retrieval in canopies comprised of a heterogeneous mix of vegetation types, these vegetation types need to be identified so that the RT model can be parameterized accordingly. To do so, using information from the three observation angles, a map was created that included eight major land cover classes. The vegetated classes consisted of "bare and pioneer communities"; "grasses and herbaceous vegetation"; "herbaceous and low woody vegetation"; "shrubs"; and "forest". Maximum likelihood (ML) classification was performed to classify the identified land cover classes within the boundaries of Millingerwaard (Fig. 1). Following, the aerial photographs of 2006 were used as basis for selection of data-points to validate the classification result of the major land cover classes. Finally, classification accuracies were calculated. An overall accuracy of 68% was achieved.

2.4 FLIGHT model inversion to derive vegetation density properties LAI and fCover

The FLIGHT model simulates photon trajectories, starting from a solar source, through successive interactions with the vegetation, to a predetermined sensor viewing angle (North, 1996). The model incorporates the probability of free path, absorption and scattering of photons and accounts for shadowing effect, crown overlapping and multiple scattering between crowns. Within the crown, photons are scattered based on probability density functions. The individual photons are followed until they are either absorbed or exited by the canopy. The model outcome is scene top of canopy (TOC) bi-directional reflectance (BRF) values, the result of a unique stand configuration, solar illumination direction, surface reflection direction and spectral wavelength (λ).

Leaf reflectance and transmittance spectra were measured with an ASD field spectrometer during a

field campaign in 2004. Additional reflectance spectra of various bark and background types were collected in April 2009 with an ASD field spectrometer. The spectra were resampled to the configurations of the CHRIS sensor. Remaining model parameters were defined based on field measurements and ranges of variables were defined based on findings in literature.

Ground measurements for LAI and fCover were available from a field campaign that was undertaken in the Millingerwaard in July-August 2004 (Schaepman et al., 2007). The dataset consisted of thirteen sample plots of 20 m in the forest area, which were selected following a random sampling scheme with a minimum of 20 m distance from each other. Each plot was set up according to the VALERI protocol and consisted of 12 measurement points per plot. At each point within the plot one measurement in 180° upward direction and one measurement in 180° downward direction were taken with the hemispherical camera. The hemispherical photographs were processed with use of the neural network based software CAN_EYE to calculate the gap fraction and to derive the clumping factor and LAI values. (Mengesha, et al., 2005). fCover was derived from upward and downward taken hemispherical photographs with an assumption of independency between the upward gaps and downward gaps.

Model inversion is required to retrieve vegetation characteristics from reflectance data (Kimes et al., 1998). Inversion was accomplished by means of a lookup-table (LUT) approach (Schlerf and Atzberger, 2006). First a LUT containing simulated reflectance data was built by forward running of the model FLIGHT. For each combination of variables (Table 1), FLIGHT computed the TOC BRF for 18 spectral bands corresponding to the band settings of the CHRIS sensor. To estimate the LAI and fCover canopy variables, for each pixel the measured reflectance spectrum was compared to all simulated BRF spectra stored in the LUT by calculating the root mean square errors (RMSE). The minimum RMSE was then calculated to derive the set of variable combinations that yielded the closest match between the measured and simulated reflectance values. Given these combinations, pixel-by-pixel maps of LAI and fCover were derived.

Table 1. FLIGHT model parameters and variables, and input spectra.

Class name	Variables		Fixed parameters		
	Fcover	LAI (m ² /m ²)	PV	Scene	Leaf size (m)
Herbaceous	0.4-1; 0.05	1-10; 0.5	1	1D	0.027
Shrubs	0.6-1; 0.05	2.5-12; 0.5	0.7	1D	0.02
Forest	0.8-1; 0.05	2.5-12; 0.5	0.7	1D	0.02

2.5 The inversion toolbox

A secondary objective of this work was to develop a toolbox that offers the user flexibility to create its own reflectance database (DB) and then perform model inversion against measured data. The toolbox was designed so that user has the choice of coupling models at the leaf level (e.g. PROSPECT 4 or PROSPECT 5) with models at the canopy level (FLIGHT but also SAIL). A GUI was developed that facilitates the whole inversion process (Fig. 3). Internally, the simulated reflectance data is stored in a MySQL DB. The user is given the possibility to select: *i)* the image input data, *ii)* plotting options for simulated reflectance, *iii)* spectral resampling options and, *iv)* model inversion algorithms. Finally, output maps of the selected variables are provided.



Figure 3. Examples of the user interface. Left: the main panel, allowing combining a leaf model with a canopy model. Right: example of FLIGHT input panel in 1-D mode.

3 RESULTS

Through model inversion, maps of LAI and fCover results for herbaceous, shrubs and forest of the Millingerwaard were generated and mosaicked into a single map for each viewing direction (Figure 4). White parts in the maps represent areas that were not

included in one of the three vegetation classes. Large variation in retrieved LAI values could be observed within all the three classes in the river floodplain area, which reinforces the significance of quantifying density at the pixel level. Largest LAI variability was obtained in the -36° VZA, whereas, in nadir and $+36^\circ$ VZA the variation of the inverted values was considerably lower. When validating the LAI results, the retrieved LAI values fell within the same range between 2 and 5 as the LAI values obtained with the hemispherical camera. The RMSEs between both datasets were 1.17 for -36° VZA, 0.82 for nadir and 0.93 for $+36^\circ$ VZA.

The fCover maps did not show the gradual transitions of values as is the case for the LAI maps, but merely a speckled pattern appeared. Overall, the distribution and magnitude of the fCover values were the same for the nadir and -36° VZA, but slightly different for the $+36^\circ$ VZA. Similar to the patterns in the LAI maps, high fCover values were obtained for the rectangular agricultural fields and also along the dike in the south of Millingerwaard. The agricultural parcels were homogeneously covered by arable crops or grassland which led to homogeneous fCover patterns. Lower fCover values occurred in the three fCover maps just south of the river, which was covered by open herbaceous vegetation and grassland. The part west of the big lake yielded higher fCover values; here the vegetation was denser packed due to shrub encroachment. The nadir and -36° VZA yielded more fCover variability than the $+36^\circ$ VZA. The RMSEs were 0.09 for -36° VZA, 0.12 for nadir and 0.13 for $+36^\circ$ VZA.

Finally, the analysis was taken to a more general level. The complete methodology was upscaled to the

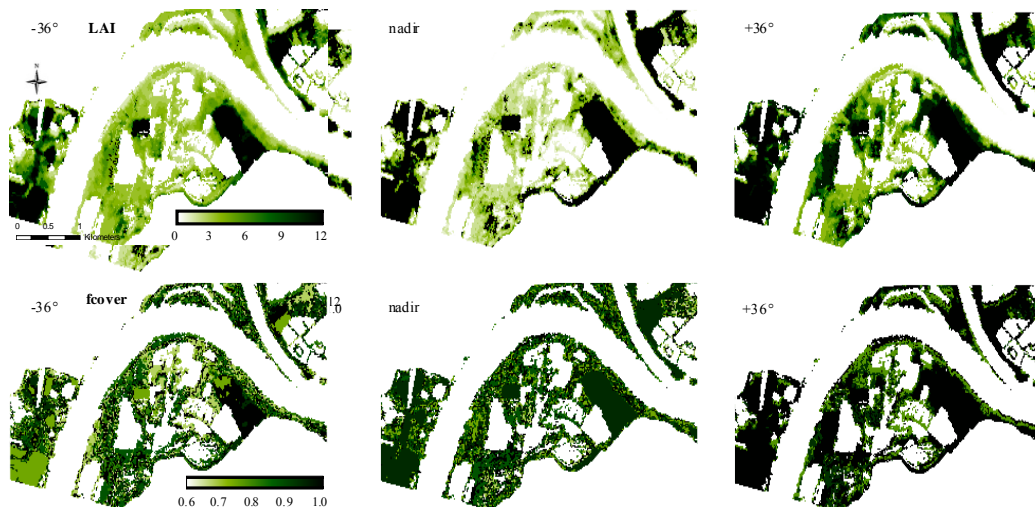


Figure 4. LAI [top] and fCover [bottom] maps of Millingerwaard for the backward scattering direction (-36° VZA) [left], the nadir direction [middle] and the forward scattering direction ($+36^\circ$ VZA) [right], derived with FLIGHT model inversion.

larger floodplain area of the Gelderse Poort nature reserve (see figure 1). This resulted in a land cover map and LAI maps and fCover maps for the three viewing angles for this area. Figure 5 shows as an example the LAI map for the -36° VZA, the viewing angle where most variability was perceived. Most natural vegetation was present in the southern part of the land cover map; in Millingerwaard and the neighbouring areas natural grasslands, shrubs, bare soil and lakes were present. To the north, the landscape was still dominated by agricultural crops and grasslands.

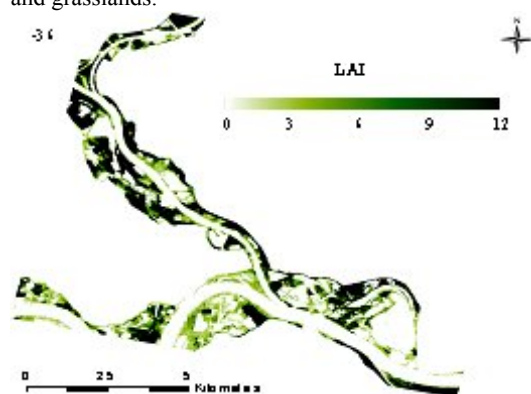


Figure 5. LAI map for the backward scattering direction (VZA -36°), derived with FLIGHT model inversion after upscaling to the Gelderse Poort area.

4 DISCUSSION

New methods are sought for automated approaches to streamline the tedious process of hydraulic roughness calculation (Van Velzen et al., 2003). The larger goal of this paper was to lay a foundation for a continuous estimation of vegetation density characterization, which is of importance for hydraulic roughness calculation. With use of the radiative transfer approach it was aimed to quantify vegetation density in terms of LAI and fCover for a river floodplain area.

LAI results provide a measure of leaf density at the vertical extent. The derived LAI maps obviously characterized the density distribution of the natural vegetation in the river floodplain ecosystem. Our results show a prominent spatial and angular variability in LAI values across the -36° , nadir and $+36^\circ$ VZAs. With respect to hydraulic roughness specifically the vegetated areas with high LAI have potential to generate a high accumulation of biomass. These are the areas that are most critical for the estimation of the hydraulic conductivity of the floodplain (Duel et al., 2001). When comparing the

LAI retrievals from the different angles, it appeared that the -36° VZA demonstrated largest variability. Particularly the important areas where vegetated material is most densely packed were best detected in this viewing configuration. An explanation for this observation is that the -36° VZA approaches the hotspot most closely, which implies the least influence of shadowing effects and therefore an enhanced richness of subtle variations in reflectance (Sandmeier and Deering, 1999). Such enhanced subtleties are assumed to be in a way related to an increased sensitivity towards structural variables (Verrelst et al., 2010), which makes this viewing angle of specific interest.

fCover results provide a measure of leaf density at the horizontal extent. The fCover maps, however, did not lead to the same gradual spatial patterns as is notable in the LAI maps. They encompassed rather speckled patterns, particularly for the natural vegetation areas. It led to quite poor validation results.

Conversely, when comparing with another study that uses CHRIS data, good fCover validation results were obtained with mapping approaches based on VI-modelling and spectral mixture analysis for homogeneous agricultural fields (Jimenez-Munoz et al., 2009). Nevertheless note that in case of a homogeneous agricultural field, a validation measurement is more likely to be valid for the whole pixel. Contrary to the latter, the Millingerwaard is a highly structurally heterogeneous floodplain ecosystem.

Eventually, however, only one spatially-explicit hydraulic roughness parameter ought to be provided to the river manager. To do so, further research would lie in combining the LAI and fCover outcomes in conjunction with other relevant allometric measurements such as vegetation height and rigidity of the stems (Duel et al., 2001) so that hydraulic roughness values can be derived. Especially the LAI outcomes from our study, which showed great variation in vegetation density, have large potential to serve as input for further water flow calculations.

5 CONCLUSIONS

The use of multi-angular CHRIS images for mapping the vegetation density of river floodplains in the Netherlands was investigated. The spatial distribution of leaf area index (LAI) and fractional vegetation (fCover) cover was estimated from the CHRIS imagery using the FLIGHT RT model. Through model inversion LAI and fCover values were pixel-by-pixel derived for the herbaceous, shrubs and forest vegetation classes, for each viewing angle separately. Although LAI retrievals matched best with validation data at nadir, most variability in LAI was

observed in the -36° VZA, the viewing angle that is closest to the solar position, followed by nadir and then $+36^\circ$ VZA. fCover retrievals led to poorer results; highest accuracies were obtained in the -36° VZA. The RT approach enabled to upscale the method to the larger floodplain area of the Gelderse Poort without introducing new assumptions.

In this paper it was demonstrated that vegetation density properties can be quantified in a semi-automatic way. A GUI-based toolbox was created to automate the inversion of the variables. The advantage of the proposed method is that hydraulic roughness values can be estimated on a pixel-basis instead of at the ecotope level, which provides more detailed information about the spatial variability within the ecotopes.

6 ACKNOWLEDGEMENTS

J. Verrelst is supported by the FP7-PEOPLE-IEF-2009 grant (Grant Agreement 252237).

7 REFERENCES

- Baptist, M.J., Penning, W.E., Duel, H., Smits, A.J.M., Geerling, G.W., Van Der Lee, G.E.M., Van Alphen, J.S.L., 2004. Assessment of the effects of cyclic floodplain rejuvenation on flood levels and biodiversity along the Rhine river. *River Research and Applications* 20, 285-297.
- Baret, F., and Guyot, G., 1991. Potentials and limits of vegetation indices for LAI and APAR assessment. *Remote Sensing of Environment* 35, 161-173.
- Chopping, M., Su, L., Laliberte, A., Rango, A., Peters, D.P.C., Kollikathara, N., 2006. Mapping shrub abundance in desert grasslands using geometric-optical modeling and multi-angle remote sensing with CHRIS/Proba. *Remote Sensing of Environment* 104, 62-73.
- Diner, D. J., Braswell, B.H., Davies, R., Gobron, N., Hu, J., Jin, Y., Kahn, R.A., Knyazikhin, Y., Loeb, N., Muller, J-P., Nolin, A.W., Pinty, B., Schaaf, C.B., Seiz, G., Strove, J., 2005. The value of multiangle measurements for retrieving structurally and radiatively consistent properties of clouds, aerosols, and surfaces. *Remote Sensing of Environment* 97 (4), 495-518.
- Duel H., Baptist M.J., Penning W.E., 2001. Cyclic Floodplain Rejuvenation: A New Strategy Based on Floodplain Measures for Both Flood Risk Management and Enhancement of the Biodiversity of the River Rhine. NCR publication 14, Delft.
- Guanter, L., Alonso, L., Moreno, J., 2005. A method for the surface reflectance retrieval from PROBA/CHRIS data over land: Application to ESA SPARC campaigns. *IEEE Transactions on Geoscience and Remote Sensing* 43 (12), 2908-2917.
- Jiménez-Munoz, J.C., Sobrino, J.A., Plaza, A., Guanter, L., Moreno, J., Martínez, P., 2009. Comparison Between Fractional Vegetation Cover Retrievals from Vegetation Indices and Spectral Mixture Analysis: Case Study of PROBA/CHRIS Data Over an Agricultural Area. *Sensors* 9, 768-793.
- Kimes, D. S., Nelson, R. F., Manry, M. T., Fung, A. K., 1998. Attributes of neural networks for extracting continuous vegetation variables from optical and radar measurements. *International Journal of Remote Sensing* 19 (14), 2639-2662.
- Ma, J., Chan, J.C.-W., Canters, F., 2010. Fully Automatic Subpixel Image Registration of Multiangle CHRIS/Proba Data. *IEEE Transactions on Geoscience and Remote Sensing* 48(7), 2829-2839.
- Mengesha, T., Schaepman, M.E., De Bruin, S., Zurita-Milla, R., Kooistra, L., 2005. Ground validation of biophysical products using imaging spectroscopy in softwood forests, *Proceedings of the VALERI Workshop* (F. Baret and M. Weiss, editors), INRA, Avignon, France, unpaginated CD-ROM.
- North, P.R.J., 1996. Three-dimensional Forest Light Interaction Model using a Monte Carlo method. *IEEE Transactions on Geoscience and Remote Sensing* 34 (4), 946-956.
- Sandmeier, S., Deering, D.W., 1999. Structure Analysis and Classification of Boreal Forests Using Airborne Hyperspectral BRDF Data from ASAS. *Remote Sensing of Environment* 69 (3), 281-295.
- Schaepman, M.E., Wamelink, G.W.W., Dobben, H.F. van, Gloor, M., Schaepman-Strub, G., Kooistra, L., Clevers, J.G.P.W., Schmidt, A.M., Berendse, F., 2007. River floodplain vegetation scenario development using imaging spectroscopy derived products as input variables in a dynamic vegetation model. *Photogrammetric Engineering and Remote Sensing* 73 (10), 1179-1188.
- Schlerf, M., Atzberger, C., 2006. Inversion of a forest reflectance model to estimate structural canopy variables from hyperspectral remote sensing data. *Remote Sensing of Environment* 100 (3), 281-294.
- Silva, W., Klijn, F., Dijkman, J., 2001. Room for the Rhine Branches in The Netherlands; What the Research Has Taught Us. WLIDelft Hydraulics: Delft; RIZA: Arnhem. Delft Hydraulics report R3294; RIZA report 2001.03.
- Straatsma, M.W., Baptist, M.J., 2008. Floodplain roughness parameterization using airborne laser scanning and spectral remote sensing. *Remote Sensing of Environment* 112, 1062-1080.
- Tol, R.S.J., Van Der Grijp, N., Olsthoorn, A.A., Van der Werff, P.E., 2003. Adapting to Climate: A Case Study on Riverine Flood Risks in the Netherlands. *Risk Analysis* 23 (3), 575-583.
- Van Velzen, E.H., Jesse, P., Cornelissen, P., Coops, H., 2003. Stromingsweerstand vegetatie in uiterwaarden, deel 1 handboek. RIZA rapport 2003.028. Arnhem: RIZA.
- Verhoef, W., Bach, H., 2007. Coupled soil-leaf-canopy and atmosphere radiative transfer modeling to simulate hyperspectral multi-angular surface reflectance and TOA radiance data. *Remote Sensing of Environment* 109 (2), 166-182.
- Verrelst, J., Geerling, G.W., Sykora, K.V. & Clevers, J.G.P.W., 2009. Mapping of aggregated floodplain plant communities using image fusion of CASI and LiDAR data. *International Journal of Applied Earth Observation and Geoinformation* 11 (1), 83-94.
- Verrelst, J., Clevers, J.G.P.W., & Schaepman, M.E. Merging the Minnaert- k Parameter With Spectral Unmixing to Map Forest Heterogeneity With CHRIS/PROBA Data. *IEEE Transactions on Geoscience and Remote Sensing* (in press).

Retrieval of atmospheric and land surface parameters using neural network technique from the satellite based thermal infrared hyperspectral data

Ning Wang^{1,2}, Funian Zeng³, Bo-Hui Tang¹ and Zhao-Liang Li^{1,4},

1. LREIS, Institute of Geographic Sciences and Natural Resources Research, Beijing, 100101, China

2. Graduate University of Chinese Academy of Sciences, China

3. China Aero Geophysical Survey & Remote Sensing Center for Land and Resources, Beijing, 100083, China

4. LSIIT, UdS, CNRS, Bld Sebastien Brant, BP10413, 67412 Illkirch, France

lizl@igsnrr.ac.cn

ABSTRACT—Land surface temperature, land surface emissivity and atmospheric profiles are all of great importance in many applications. As radiances at-satellite level depend not only on the land surface parameters (temperature and emissivity) but also on the atmospheric conditions, it is difficult to simultaneously retrieve these parameters with a high accuracy from multi-spectral radiances measured at satellite level. This work aims to establish a generalized neural network for simultaneously retrieving atmospheric profiles and surface temperature from hyperspectral thermal infrared data. The distributions of surface material, temperature and atmospheric profiles are elaborated carefully to generate the simulated data. The simulated at-sensor radiances, as the inputs of the network, are divided into two sub-ranges, one in atmospheric window and the other in water absorption band, and are subsequently transformed in the eigen-domain. The atmospheric profiles, surface temperature and emissivity are used as the outputs after the eigen-domain transformation. Comparisons of the actual and retrieved atmospheric and land surface parameters indicate that the Root Mean Square Error (RMSE) of surface temperature is around 1.6K, the RMSE of temperature profiles is around 2K in troposphere, and the RMSE of total water vapour content is around 0.3g/cm². A test of the proposed method to retrieve atmospheric and land surface parameters using actual thermal hyperspectral satellite data is carried out. The result shows that the proposed method can retrieve the atmospheric and land surface parameters with compromise accuracy. In addition, the retrieval results from the neural network can also be used as the inputs of physic-based models for improving the retrieval accuracy.

1 INTRODUCTION

Accurate retrieval of land surface temperature (LST), land surface emissivity (LSE) and atmospheric profiles of temperature and humidity are of great importance for many applications, such as global-change studies, heat-balance studies, climate research, short/medium range forecast. Though these parameters can be observed by traditional methods, satellite can monitor the surface and atmospheric conditions with higher spatial and temporal resolutions covering the whole world and provide the opportunity to promote the development of the related disciplines (Dash *et al.*, 2002). For the thermal infrared (TIR) remotely sensed radiance with emitted signals from both the surface and atmosphere, it can be used to retrieve LST, LSE, atmospheric temperature and gas content. However, the land surface and atmospheric information are coupled together in the infrared measurement, which leads to a key problem in retrieving these parameters (Ma *et al.*, 2000). Until now, great efforts have been made to retrieve geophysical properties (LST and LSE) and atmospheric parameters (atmospheric

temperature-gas content profiles) separately from multispectral TIR data. However, there are still some problems to be solved. For the retrieval of land surface properties, although the split-window technique has been developed to correct for the atmospheric influences, an exact knowledge of LSE better than 0.01 is still needed to meet the accuracy requirement of 1K in LST retrieval (Wan and Dozier, 1996). The physics-based LST retrieval algorithm can attain a high accuracy, but it requires knowing atmospheric information (Wan and Li, 1997). The retrieval of atmospheric temperature and humidity profiles from TIR data requires accurate LST and LSE. The common assumption that the surface is a black body or a gray body typically results in large retrieval errors over land surface (Li *et al.*, 2007). To improve the retrieval accuracy of atmospheric profiles, especially the near-surface profiles, better knowledge for the LST and LSE are needed. A practical idea to decouple the land surface and atmospheric information is to retrieve these parameters simultaneously (Ma *et al.*, 2002). However, to meet this goal, adequate channels with narrow band width are needed to provide enough vertical resolution,

as the sharp contribution function corresponding to each channel is required for obtaining more accurate atmospheric profiles (Chahine *et al.*, 2001).

Nowadays, hyperspectral TIR (hyper-TIR) sounding data can be obtained by several sensors such as Atmospheric InfraRed Sounder (AIRS) on EOS satellites, Interferometer Atmospheric Sounding Instrument (IASI) on METOP-A and Cross-track Infrared Sounder (CrIS) on the next generation NPOESS with thousands of channels. Undoubtedly, hyper-TIR data has its own superiority compared to the multispectral data in extracting atmospheric and land surface parameters. The narrow band width can improve the vertical resolution for atmospheric soundings. The observations measured in the atmospheric window region can provide finer land surface information. All these have been of strong impetus in remote sensing and relative disciplines. Thus, the exploration of the hyper-TIR data will become one of the hotspot in remote sensing. And there have already been some literatures on LST/LSE separation and the retrieval of atmospheric profiles using hyper-TIR data (Borel, 1997; Li, *et al.*, 2007).

The neural network (NN) technique can be used to solve the inversion problem in remote sensing discipline. Through a learning process, an NN can acquire the knowledge from its environment and store the knowledge by its interneuron connection strengths, also known as synaptic weights. In remote sensing community, NN has its own particular superiority. On the one hand, an NN represents the complex non-linear problem of a model or process, such as the relationship between the observed radiances and the surface/atmospheric parameters, which is better than that of the statistics regressions. On the other hand, it is more efficient than the physical model, obviously. The NN has been used in remote sensing since the beginning of the 1990s. After then, an increasing number of studies have been reported in the literatures spread in the remote sensing community, including land cover classification, retrieval of biophysical parameters, of atmospheric parameters, and of soil moisture/temperature, and so on. For the retrieval of atmospheric parameters, Motteler *et al.* (1995) pointed out that there exist similar performances for NN and regression in most cases, but the accuracy of NN is better than that of regression in some cases. Aires *et al.* (2002a) and Blackwell (2005) also use NN in the retrieval of atmospheric property. All these literatures showed that NN is feasible to retrieve atmospheric and surface parameters using remotely sensed TIR data.

In this work, a 'generalized' NN is proposed to retrieve atmospheric profiles, LST and LSE in the 'cloud-free' conditions using hyper-TIR data. The 'generalized' NN is designed to suit for all air mass types (tropical, mid-latitude and polar type). The NN is trained and validated using the simulated data, and is also tested with actual satellite data. The paper is

organized as follows. First, Section 2 presents the establishment of the NN. The accuracy of NN is analyzed in section 3. Section 4 introduces the test of the NN using the at-sensor data and the conclusions are drawn in section 5.

2 NEURAL NETWORK ESTABLISHMENT

2.1 Generation of the simulated data

To simulate the at-sensor hyper-TIR data, different atmospheric and land surface situations should be considered. The atmospheric condition is prepared by the thermodynamic initial guess retrieval (TIGR) database, which contains 2311 typical atmospheric profiles of temperature, moisture and ozone encountered in the whole world. TIGR supplies these profiles in 40 layers of pressures from the surface to the top of the atmosphere. Those profiles are grouped into five airmass types, where there are 872 profiles in tropical airmass, 388 in mid-latitude 1, 354 in mid-latitude 2, 104 in polar 1 and 593 in polar 2. However, only the 'cloud-free' conditions are concerned in this work. Thus, the relative humidity of each layer of the atmosphere is calculated. If the relative humidity is greater than a threshold (e.g. 90%), the corresponding atmosphere condition is regarded to be cloudy. Based on this analysis, 1413 atmosphere profiles are chosen from the 2311 profiles. The aim of our work is to establish a generalized network that can be used for various airmass types and surface conditions. Therefore, all the 'cloud-free' atmospheric profiles are used to simulate the satellite data which are then used to train the NN. Besides the atmospheric conditions, the land surface characters should also be considered. Emissivity spectra of 54 surface materials selected from the Advanced Spaceborne Thermal Emission Reflection Radiometer (ASTER) spectral library including various kinds of soils, vegetations, water, snow and ice are used to represent all kinds of surface types. The LST varies from the bottom atmospheric temperature (T_{a0})-10 K to $T_{a0}+15$ K in steps of 5 K for $T_{a0} < 280$ K, and from $T_{a0}-5$ K to $T_{a0}+20$ K in steps of 5 K for $T_{a0} \geq 280$ K, which covers the LST variance range that could be observed. The Operational Release for Automatized Atmospheric Absorption Atlas (4A/OP), a kind of atmospheric radiative transfer model, is used to simulate the at-sensor radiance. 4A/OP is a line by line model with a spectral domain from 600 to 3000 cm^{-1} and a high spectral resolution of $5 \times 10^{-4} \text{ cm}^{-1}$.

The scheme of the simulation follows that of the work of Wang *et al.* (2009). Figure 1 shows the flowchart of the at-sensor radiance simulation. To speed up the computational efficiency, for each atmospheric profile in the TIGR database, 4A/OP is run to obtain the corresponding atmospheric downwelling radiance, upwelling radiance and

transmittance. The spectral characteristic of the simulated data is similar to that of the IASI, which is a hyper-TIR sensor with a spectral resolution of 0.5 cm^{-1} and spectral sampling interval of 0.25 cm^{-1} in the spectral range from 645 to 2760 cm^{-1} . The noise equivalent temperature difference (NE Δ T) is set to be varied from 0.095 to 0.25 K at 280 K in the simulated spectral range as that shows by Aires (2002b). Finally, different combinations of the surface and atmosphere are considered to simulate the at-sensor spectral radiances on the basis of the radiative transfer equation (RTE) as follows:

$$R_{\lambda} = (\varepsilon_{\lambda} B_{\lambda}(T_s) + (1 - \varepsilon_{\lambda}) L_{\lambda, \downarrow}) \tau_{\lambda} + L_{\lambda, \uparrow} \quad (1)$$

where R is the at-sensor radiance, ε is LSE, T_s is LST, L_{\downarrow} and L_{\uparrow} denote the atmospheric downwelling and upwelling radiance, respectively, τ is the atmospheric transmittance, the subscript λ denotes the wavenumber.

The hyper-TIR data provide abundant fine spectral information on atmospheric and land surface thermal emitting characteristics, but at the same time, we have to suffer the enormous volume of data that need to be processed. Fortunately, the principal component analysis (PCA) technique can be used to compress and demoise the hyper-TIR data. Therefore, the transform coefficients of the at-sensor spectral radiances and atmospheric profiles in the eigen-domain are used in the neural network instead of using the data directly.

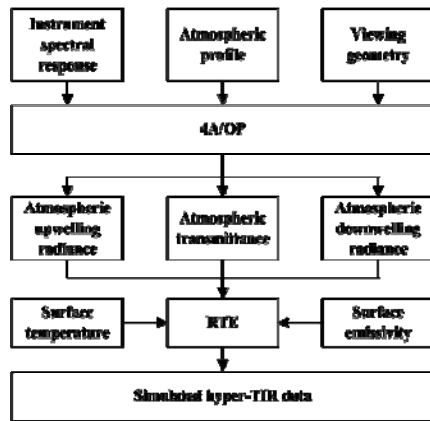


Figure 1. Flowchart of the simulation of hyper-TIR data.

2.2 Topological structure of the neural network

To establish an NN, the dimension of the input vectors, the number of hidden layers, the number of neurons in each hidden layer and the dimension of the output vectors should be specified first.

The inputs of the NN are only composed of the at-sensor radiances transform coefficients, but there are still some efforts to make the network more feasible. Since the mid-infrared spectral domain is contaminated

by the solar irradiance during the daytime. Thus, only the thermal infrared data are used (720 cm^{-1} - 1650 cm^{-1}). The observed radiances in the thermal infrared atmospheric window ($8\text{-}12 \mu\text{m}$) contain both the atmospheric and surface information, but in the water vapor absorption band ($\sim 6.25 \mu\text{m}$) only atmospheric information could be derived from the satellite observed radiances. Therefore, the whole spectrum is divided into two sub-ranges, one is from 720 cm^{-1} to 1350 cm^{-1} and the other is from 1350 cm^{-1} to 1650 cm^{-1} . In each sub-range, the eigen-vectors are calculated using the statistics information derived from the simulated data, then, the transform coefficients of the simulated data in the eigen-domain can be computed. After the analysis of the reconstruction error, 40 components in the atmospheric window and 20 components in the water absorption band are taken as the inputs of the NN.

The outputs of the network consist of the corresponding atmospheric profiles of temperature and moisture, and the land surface temperature and emissivity. As the atmospheric profiles and LSE are correlated between each layer and each channel, the PCA technique can also be used, but here the eigen-vectors are derived from the TIGR and ASTER spectral library, respectively. Finally, 15 coefficients for atmospheric temperature profile, 7 for water vapor mixing ratio profile and 20 for surface emissivity are used in the NN outputs. An additional coefficient for surface temperature is also introduced.

There is not a perfect method, yet, to determine the number of hidden layers and the number of perceptrons in each hidden layer, which are two significant parameters while establishing a network. However, Sontag (1992) demonstrated that any inverse problem may be resolved by a two-hidden-layer MLP network, because such NN can take into account discontinuities and extremely nonlinear variations in contrast to one-hidden-layer MLP. As we are facing the inverse problem when retrieve the atmospheric and land surface parameters from hyper-TIR data, the MLP with two hidden layers is chosen to model the complex relationship between the at-sensor measurements and the corresponding parameters. Then we vary the number of neurons in each layer to find where the smallest generalization error is. At last, 100 and 80 neurons are taken in the first and second hidden layer respectively. The topological structure of the NN is showed in figure 2.

After the topological structure has been determined, the net can be trained with the simulated satellite data. The conjugate gradient algorithm is adopted to optimize the training. The trained net can be then used to retrieve the atmospheric profiles and LST from the at-sensor spectral data.

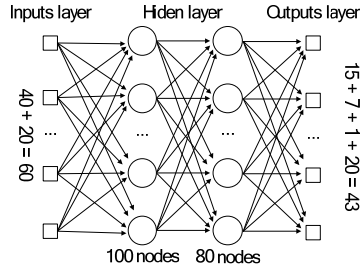


Figure 2. Topological structure of the established neural network

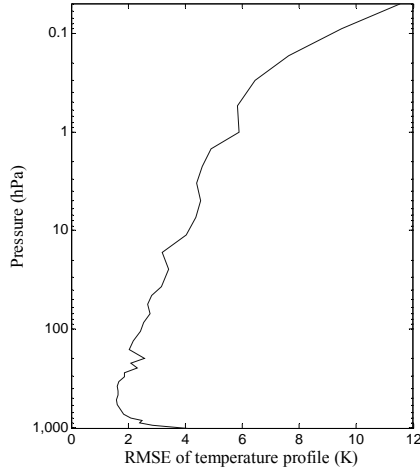


Figure 3. RMSE of atmospheric temperature profile retrieved using our NN technique

3 RETRIEVAL ACCURACY OF THE NETWORK

The simulated data with a white noise are used to validate the trained net. The results are shown in the following figures.

Figure 3 shows the Root Mean Square Error (RMSE) of the retrieved atmospheric temperature profile. From this figure, we can see that the RMSE of temperature profile is mostly around 2K in the troposphere except for that near the surface, where the errors may reach to 4K. These larger errors are possibly most caused that the atmosphere near the surface is more affected by the complex surface, and the perturbations caused by the surface that cannot be represented by the chosen eigen-vectors very well. It can also be found that the errors increasing along with the altitude beyond the troposphere. Because the selected channels are located in the atmospheric window and the water absorption bands, the peaks of the weighting function of these channels may mainly distribute in the troposphere region. Therefore, the retrieved accuracy of atmospheric temperature in the stratosphere is not high enough.

Figure 4 shows the RMSE of the retrieved atmospheric water vapor mixing ratio profile. Because the water vapor content may be varied from each other

significantly, the scatter plot of the retrieved total water content (TW) versus the actual one is shown in figure 5 and a corresponding histogram is shown in figure 6.

From these figures we can find that the retrieved error is smaller when the altitude is higher or when the actual water vapor content is less than 4g/cm^2 . This NN net underestimates the TW when the atmosphere is very wet ($\text{TW} > 4\text{g/cm}^2$). Generally, the RMSE of TW is around 0.3 g/cm^2 .

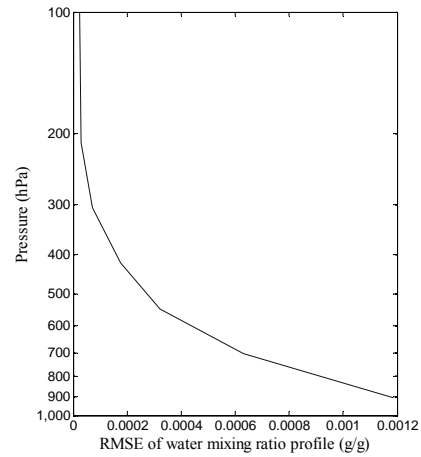


Figure 4. Same as Fig. 1 but for water mixing ratio profile

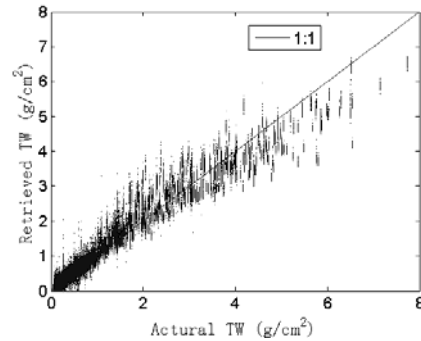


Figure 5. Comparison of the total water content (TW) retrieved using our NN technique with the actual TW

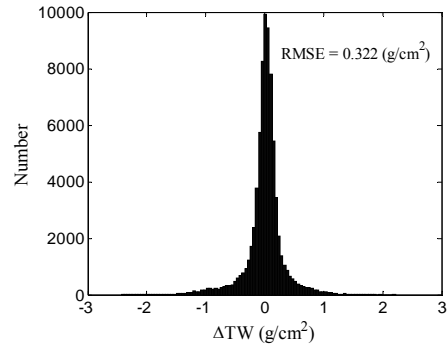


Figure 6. Histogram of the retrieved TW error

Figure 7 shows the histogram of the error of the retrieved LST. The RMSE of the retrieved LST is 1.6 K. The results are slightly worse than those obtained in

our previous paper, in which the NN net is established using the simulated data with the same airmass type (Wang *et al.*, 2009). The main reason is that the aim of the established net in this work is to suit for more generalized situation. Therefore, a large distribution range of LST may cause the difficulty in estimating. Though the accuracy is slightly lower, the established net is still or maybe more feasible when dealing with the satellite data for its global suitability.

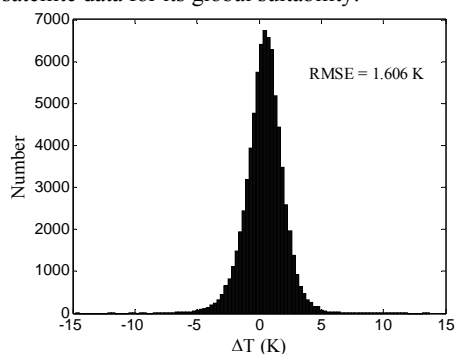


Figure 7. Histogram of LST retrieved error

4 TEST ON THE AT-SENSOR HYPER-TIR DATA

4.1 The selection of the study area

In the selection of the study area, two criteria are considered in this work, including 1) the hyper-TIR data acquired under the ‘cloud-free’ conditions and 2) the corresponding validation data acquired simultaneously with the hyper-TIR data. In this work, the validated atmospheric profiles are provided by the UK Met Office (UKMO) (available from <http://badc.nerc.ac.uk/browse/badc/ukmo-rad>). UKMO profiles are measured at 0h and 12h in UTC time everyday. However, because METOP-A, on which IASI is aboard, is a sun-synchronous orbit satellites, the two line elements (available from <http://celestrak.com/NORAD/elements/>) are used to recover the footprint of the satellite everyday during the year in 2008. Then we can select a study area with the two criteria.

The study area is located around Dalnerechensk, a town in Primorsky Krai, Russia. The radiosonde site near the town is located in 45.87N and 133.73E (Figure 8). The IASI data acquired around UTC time 12:00, July 31th, 2008. The UKMO profiles were also obtained around this time.

Figure 9 and 10 are the results of the temperature and water content mixing ratio profiles, respectively. The stars are the UKMO observed profiles and the lines are the retrieved profiles. These two figures indicate that the generalized net can obtain

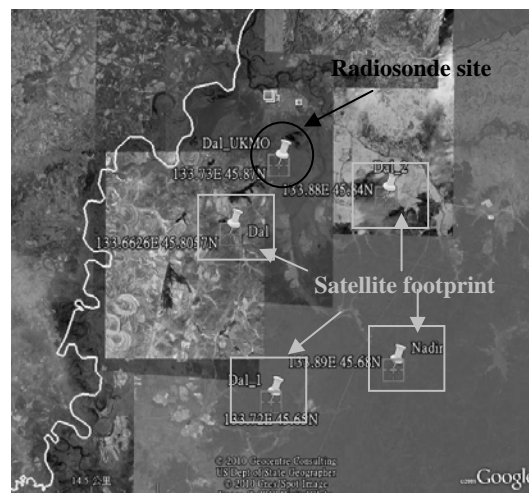


Figure 8. Study area of Dalnerechensk

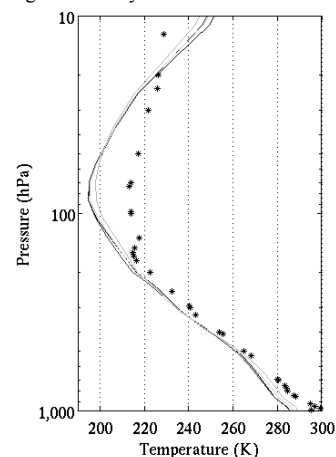


Figure 9. Results of temperature profile

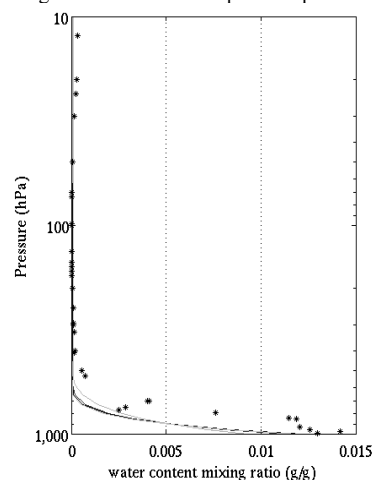


Figure 10. Results of water content mixing ratio profile

compromise results of profiles especially in the

troposphere. The LST differences were within 5K comparing with MODIS LST product. However, there may be many defects in the comparing of the results. The instrument measurement accuracy and the LST product accuracy of MODIS are not taken into account. Further validations should be taken to validate the generalized network. However, the results can be used as an initial guesses for the retrieval of atmospheric and land surface parameters with physic-based models.

5. CONCLUSION

A two-layer perception net has been constructed for retrieval of atmospheric and land surface parameters using satellite-based thermal infrared hyperspectral data in this work. The simulated satellite data were used as the inputs, and the corresponding atmospheric profiles, LST and LSE were taken as the outputs. It should be mentioned that the net we referred here is a “generalized” network. Once the net is well trained, it can be used straightforward without any needs of pre-classifying the satellite observations with other auxiliary information.

The trained net was validated with the actual satellite IASI/METOP data. The temperature profile is underestimated within 5K. The LST is overestimated by 1-5K compared with the MODIS LST products. The resultant atmospheric and land surface parameters can be used as initial guesses for the inputs of other physic-based retrieval models.

6 ACKNOWLEDGMENT:

This work was supported by the Hi-Tech Research and Development Program of China (863 Plan Program) under Grant 2006AA12Z121 and Grant 2008AA121805. The authors would like to sincerely thank NOVELTIS Inc. for providing the 4A/OP model, JPL for providing the JHU spectral library, and the Laboratoire de Meteorologie Dynamique for providing the TIGR database.

7 REFERENCES

- Aires, F., Chedin, A., Scott, N. A., and Rossow, W. B., 2002a, A regularized neural net approach for retrieval of atmospheric and surface temperatures with the IASI instrument, *Journal of Applied Meteorology*, **41**, 144-159.
- Aires, F., Rossow, W. B., Scott, N. A., and Chedin, A., 2002b, Remote sensing from the infrared atmospheric sounding interferometer instrument - 1. Compression, denoising, and first-guess retrieval algorithms, *Journal of Geophysical Research-Atmospheres*, **107**, D22, 4619.
- Blackwell, W. J., 2005, A neural-network technique for the retrieval of atmospheric temperature and moisture profiles from high spectral resolution sounding data, *IEEE Transactions on Geoscience and Remote Sensing*, **43**, 2535-2546.
- Borel, C., 1997, Iterative retrieval of surface emissivity and temperature for a hyperspectral sensor, JPL workshop/remote sensing of land surface emissivity, 1-5.
- Chahine, M., Aumann, H., Goldberg, M., McMillin, L., Rosenkranz, P., Staelin, D., Strow, L., Susskind, J., and Gunson, M., 2001, AIRS-team retrieval for core products and geophysical parameters, version2.2, Algorithm Theoretical Basis Document, 198.
- Dash, P., Gottsche, F. M., Olesen, F. S., and Fischer, H., 2002, Land surface temperature and emissivity estimation from passive sensor data: theory and practice-current trends, *International Journal of Remote Sensing*, **23**, 2563-2594.
- Li, J., Weisz, E., and Zhou, D., 2007, Physical retrieval of surface emissivity spectrum from hyperspectral infrared radiances, *Geophysical Research Letters*, **34**, L16812.
- Ma, X. L., Wan, Z. M., Moeller, C. C., Menzel, W. P., and Gumley, L. E., 2002, Simultaneous retrieval of atmospheric profiles, land-surface temperature, and surface emissivity from Moderate-Resolution Imaging Spectroradiometer thermal infrared data: extension of a two-step physical algorithm, *Applied Optics*, **41**, 909-924.
- Ma, X. L., Wan, Z. M., Moeller, C. C., Menzel, W. P., Gumley, L. E., and Zhang, Y. L., 2000, Retrieval of geophysical parameters from Moderate Resolution Imaging Spectroradiometer thermal infrared data: Evaluation of a two-step physical algorithm, *Applied Optics*, **39**, 3537-3550.
- Motteler, H., Strow, L., McMillin, L., and Gualtieri, J., 1995, Comparison of neural networks and regression-based methods for temperature retrievals, *Applied Optics*, **34**, 5390-5397.
- Sontag, E. D., 1992, Feedback stabilization using 2-hidden-layer nets, *IEEE Transactions on Neural Networks*, **3**, 981-990.
- Wan, Z. M., and Dozier, J., 1996, A generalized split-window algorithm for retrieving land-surface temperature from space, *IEEE Transactions on Geoscience and Remote Sensing*, **34**, 892-905.
- Wan, Z. M., and Li, Z. L., 1997, A physics-based algorithm for retrieving land-surface emissivity and temperature from EOS/MODIS data, *IEEE Transactions on Geoscience and Remote Sensing*, **35**, 980-996.
- Wang, N., Tang, B.-H., and Li, Z. L., 2009, Simultaneous retrieval of geophysical properties and atmospheric parameters from the infrared hyperspectral resolution sounding data using neural network technique, *IGARSS 2009*, II, 527-530.

SATELLITE CONSTELLATION FOR CROP MONITORING: Formosat-2, Deimos-DMC, Landsat 5TM and 7ETM+

A. Calera, M. Odi, C. Martínez-Beltrán, I. Campos and J. González-Piqueras
Instituto Desarrollo Regional (IDR), Grupo Teledetección y SIG, Universidad Castilla La Mancha, Albacete, Spain
Alfonso.Calera@uclm.es, MariaMagali.Odi@uclm.es, cbeltran@idr-ab.uclm.es, Isidro.Campos@uclm.es,
Jose.Gonzalez@uclm.es

ABSTRACT - Remote sensing has become a useful tool for crop monitoring. However, their performance may be limited due to a few images acquired in a temporal series either because a low temporal resolution or unsuitable atmospheric conditions. This lack of information in the temporal evolution of vegetation may be result in inaccurate crop information. Until now, a wide range of high resolution spectral sensors have been launched. To take advantage of this, this study expects to achieve the monitoring of vegetation by a satellite constellation. For this purpose, a temporal series of images of various sensors (11, 9, 6 and 2 images from Formosat-2, Deimos-DMC, Landsat 5TM and 7ETM+ respectively) were used. Six pairs of images, four synchronous and two near-synchronous were compared to evaluate the linear fit for the top of atmosphere and surface reflectances and NDVI. In general, the comparison results show a good linear fit and exhibit a good temporal stability for both, reflectances and NDVI, with R^2 ranging from 0.96 to 0.99. The comparison for the NDVI matches the 1:1 line and the correlation coefficient is better than for the reflectances. In despite of small differences, observations from different sensors can be integrated to operate as a constellation to describe the temporal evolution of vegetation.

1 INTRODUCTION

One of the main goals of Earth observation (EO) satellite systems is to monitor vegetation and its dynamics. Depending on the scale of interest, the spatial and temporal resolution provided by a single satellite is often not sufficient. This is the case of agricultural crops (irrigation or precision agriculture applications), for which remote sensing has great potential.

Crop monitoring requires high spatial resolution and frequent measurements during the whole growing season (Calera et al. 2005; Osann Jochum et al. 2006). The adequate spatial resolution can be provided by high-resolution sensors such as: Formosat-2 (8 m), Deimos- DMC 1 and 2 (20m), Landsat 5 TM and Landsat 7 ETM+ (30 m). Time series analysis is an appropriate tool for vegetation monitoring, since it may differentiate between actual changes and inter-annual variations of phenology caused by external factors, e.g. changing climatic conditions (Turner et al., 2007).

A single satellite with a 16 day time resolution (like Landsat) would provide little useful information. Moreover, cloud cover may increase the time between useful images. The critical requirement of combining high frequency with high spatial resolution has been proposed by some studies for this purpose (e.g., Moreno et al. 2002).

Intercalibration between observations of sensors aims at developing relationships that allow us to translate reflectances and spectral vegetation indices (SVI) from one sensor to another. The most frequently used SVI is the NDVI, given its relevance in describing the vegetation dynamics and exchange with the atmosphere.

Inter-sensor relationships have been the subject of many studies (Steven et al. 2003; Miura et al. 2006; Teillet et al. 2006; Van Leeuwen et al. 2006). Each work focuses on different aspects to create multi-resolution images for the analysis of bio-geophysical parameters.

The object of this paper is to assess the performance of a satellite constellation including Formosat, Landsat and Deimos imagery to monitor the temporal evolution of crops and vegetation along its growing season.

For this purpose, we performed an observational study, comparing reflectances and the Normalized Difference Vegetation Index (NDVI), for synchronous or near-synchronous image pairs to evaluate if the observations from different sensors are comparables, paying attention to the temporal behaviour of the cross-comparison. On the other hand, we display a temporal sequence of images using the NDVI to describe temporal evolution of crops and natural vegetation for the study area.

2 TEST SITE AND DATA SETS

The study area is a semi-arid plain located in Albacete (Central Spain), its altitude ranges from 650 to 800 m. This zone has got a wide range of cover types including a variety of bare soils, crops and natural vegetation, resulting in an extent NDVI values. The mean size of the plots is 4 ha (Calera, 2000), however it is also common to find crop plots larger than 100 ha.

2.1 Imagery

Images used were geometric, radiometric and atmospheric corrected by IDR-UCLM (Landsat 5 TM, Landsat 7 ETM+ and Deimos) and by CESBIO (Formosat-2) to obtain top of atmosphere (ToA) and surface (BoA) reflectances. NDVI was calculated for each sensor using the corresponding red and near infra-red bands. For the case of Deimos images no atmospheric correction for reflectances has been performed. A procedure of NDVI normalization -based on bare soil and dense vegetation has been applied to Deimos imagery.

Table 1. Pairs of sensors and acquired dates used for cross-comparison

Date	Pairs of satellites/sensors
2009/10/03	Formosat 2 / Landsat 5 TM
2009/10/19	Formosat 2 / Landsat 5 TM
2010/02/11	Deimos 1 / Formosat 2
2010/03/15-13	Deimos 1 / Landsat 7 ETM+
2010/03/30	Deimos 1 / Formosat 2
2010/05/16-17	Deimos 1 / Landsat 7 ETM+

Table 1 shows the pairs of images used to analyze the inter-sensor compatibility and continuity. Time series used to display the temporal evolution of crops and vegetation are built by 11 images from Deimos, 6 from Landsat-5 and 9 from Formosat including the images showed in the Table 1. Table 2 shows the characteristics of the satellites used in this work.

3 METHODOLOGY FOR CROSS-COMPARISON

The comparison was performed between synchronous pairs of sensors for Top Of Atmosphere (ToA) and Boton Of Atmosphere (BoA) reflectances as well as ToA and BoA NDVI. Time acquisition of images was similar for all sensors, around 10:30 am, which guaranties a similar solar illumination condition, even if view angles have been different for each sensor and acquisition.

Table 2. Characteristics of sensors used in the virtual constellation

Sensor	Return (days)	Scene (km)	Band/spectral Range (μm)	Pixel (m)
Landsat5	16	172x185	B3 0.63-0.69 B4 0.76-0.90	30
Landsat7	16	170x183	B3 0.63-0.69 B4 0.76-0.90	30
Deimos	High	600x498	B2 0.63-0.69 B3 0.77-0.90	20
Formosat2	1	24x24	B3 0.63-0.69 B4 0.76-0.90	8

3.1 Procedure for the cross-comparison.

The cross-comparison was carried out setting a grid on the study zone, bounded by the Formosat images. Both, reflectances and NDVI were aggregated to calculate the average value from the pixels contained in a grid cell, as is showed in Figure 1. Therefore, the aggregated reflectance and NDVI value is calculated as:

$$\overline{\rho_{\lambda}} = \frac{\sum \rho_{\lambda j}}{n}$$

$$\overline{NDVI} = \frac{\sum NDVI_j}{n}$$

where ρ_{λ} is the reflectance at given wavelength, n is the number of pixels aggregated.

In order to reduce the uncertainty due to the different pixel sizes and geolocation, a grid cell size of 3 x 3 pixels of the coarsest resolution sensor (90 x 90 m or 60 x 60 m for pairs with Landsat or Deimos images respectively) was defined. This cell size determines the number of pixels to be aggregated from each sensor. To increase the accuracy of the overly by the vector map of network over the raster map of image, the statistics for each grid cell was carried out with a size value of 1 m in the used Geographical Information System tool .

4 RESULTS AND DISCUSSION

The comparison between observations from pairs of sensors for reflectances and NDVI has been done using the graphic representation and calculating the linear curve fit.

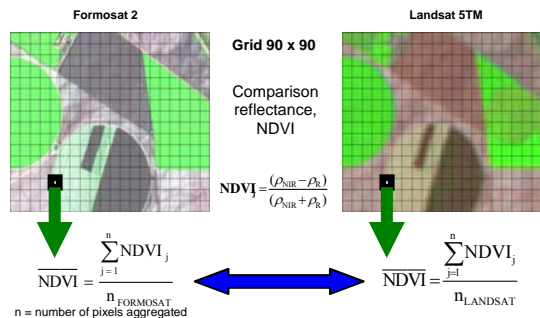


Figure 1. Methodology to compare observations from different sensors at various spatial resolution scales

Figure 2 shows the comparison between observations from Formosat and Landsat5, and from Deimos and Formosat. Table 2 and Table 3 summarize the results of the linear fit between sensor pairs for

reflectances and NDVI respectively. All of them display a good linear fit, with a correlation coefficient close to one (R^2 ranging from 0.94 to 0.99) and similar bias and gain of the linear equation. Scattering showed in the figure 2 could be due to a remaining uncertainty of geolocation, especially at the border of homogeneous plot, as well as differences of view and illumination angle. Deviation from 1:1 line could be probably due to calibration parameter, spectral band width and sensor function response differences.

The comparison between Formosat and Landsat exhibits a very good agreement, especially on NDVI cross-comparison, although slight differences on BoA reflectances could be originated by the different atmospheric corrections applied. DMC images also exhibit similar behavior, although in this case has not been evaluated the BoA reflectances.

Table 2. Linear equations for reflectances (RED and NIR) from Deimos (D), Formosat (F), Landsat 7 (L7) and Landsat 5 (L5).

Date	Pairs of sensors (dependent-independent)	REFL. RED			REFL. NIR		
		a (ToA/BoA)	b (ToA/BoA)	R^2 (ToA/BoA)	a (ToA/BoA)	b (ToA/BoA)	R^2 (ToA/BoA)
2009/10/03	F- L5	+0.01/+0.00	1.12/0.88	0.99/0.99	+0.00/-0.01	1.12/0.85	0.99/0.99
2009/10/19	F- L5	+0.00/+0.01	1.10/0.79	0.97/0.98	+0.01/+0.01	1.10/0.80	0.96/0.97
2010/02/11	D-F	+0.02/-----	0.91/-----	0.94/-----	+0.03/-----	1.02/-----	0.94/-----
2010/03/30	D-F	+0.02/-----	1.05/-----	0.96/-----	+0.06/-----	1.02/-----	0.96/-----
2010/05/16-17	F- L7	+0.01/-----	0.87/-----	0.93/-----	+0.02/-----	0.98/-----	0.88/-----

Reflectance_{dependent}=a + b*Reflectance_{independent}

Table 3. Linear equations for NDVI from Deimos, Formosat, Landsat 7 and Landsat 5.

Date	Pairs of sensors (dependent-independent)	NDVI		
		a (TOA/BOA)	b (TOA/BOA)	R^2 (TOA/BOA)
2009/10/03	Formosat- Landsat 5	-0.01/+0.02	0.98/0.94	0.99/0.98
2009/10/19	Formosat- Landsat 5	+0.02/-0.01	1.00/0.94	0.98/0.98
2010/02/11	Deimos- Formosat	+0.07/-0.05	0.89/0.96	0.96/0.96
2010/03/15-13	Deimos- Landsat 7	+0.03/+0.00	1.00/0.97	0.95/0.94
2010/03/30	Deimos- Formosat	+0.07/+0.01	0.85/0.95	0.97/0.96
2010/05/16-17	Deimos- Landsat 7	+0.06/+0.02	0.93/0.96	0.98/0.98

NDVI_{dependent}=a + b*NDVI_{independent}

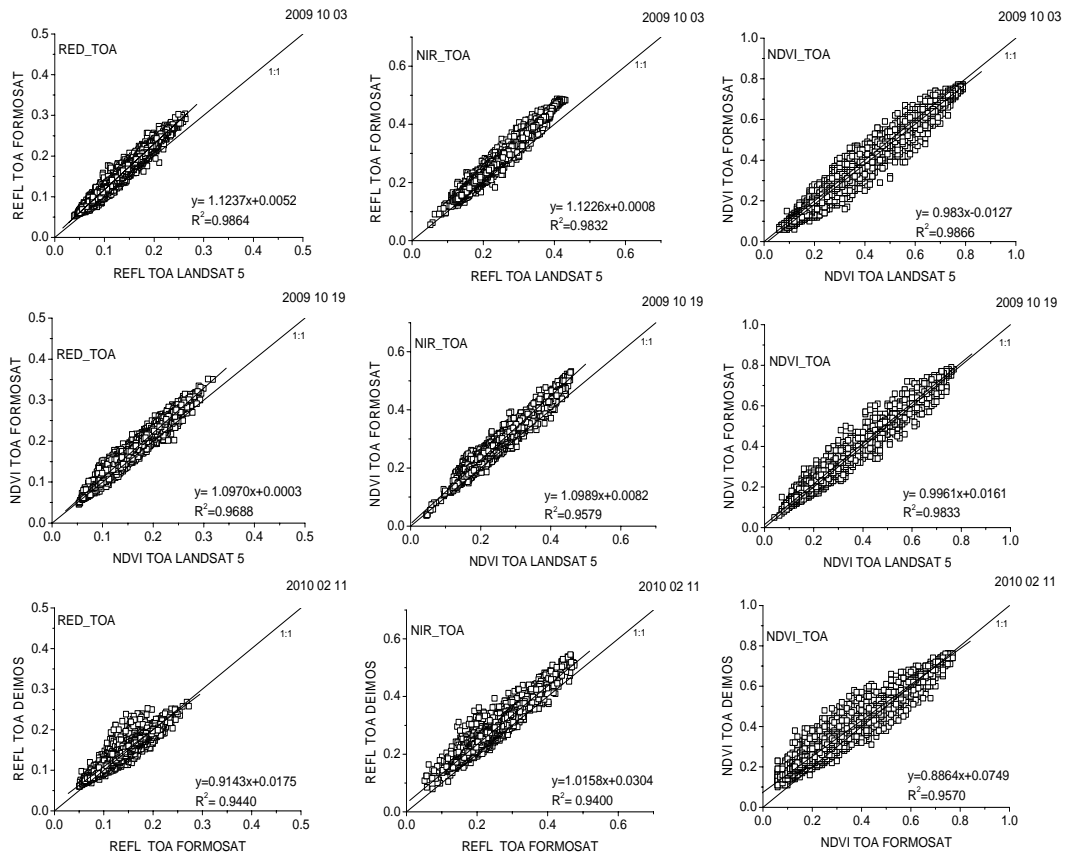


Figure 2. Interrelationships between (a) ToA Red reflectance; (b) ToA Near-infrared reflectance (NIR) and (c) ToA NDVI from selected pairs of sensors.

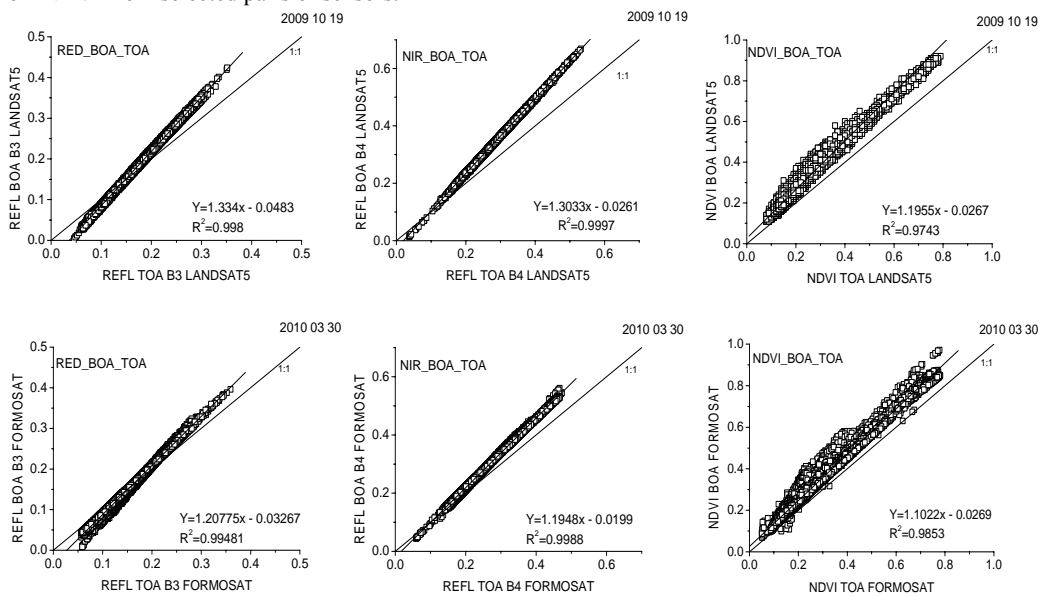


Figure 3. Interrelationships between BoA and ToA reflectances and NDVI from Landsat5 and Formosat sensors

Table 4. Comparison of reflectances ToA and BoA from Formosat, Landsat 5 and Landsat 7

Date	Sensor	REFL. RED BOA vs. TOA			REFL. NIR BOA vs. TOA		
		a	b	R ²	a	b	R ²
2009/10/03	Formosat	-0.03	1.21	1.00	-0.02	1.20	1.00
2009/10/03	Landsat 5	-0.03	1.55	1.00	-0.01	1.58	1.00
2009/10/19	Formosat	-0.03	1.20	1.00	-0.02	1.20	1.00
2009/10/19	Landsat 5	-0.05	1.33	1.00	-0.03	1.30	1.00
2010/02/11	Formosat	-0.03	1.18	1.00	-0.01	1.18	1.00
2010/03/30	Formosat	-0.03	1.21	1.00	-0.02	1.19	1.00
2010/05/16-17	Landsat 7	-0.03	1.19	1.00	-0.01	1.17	1.00

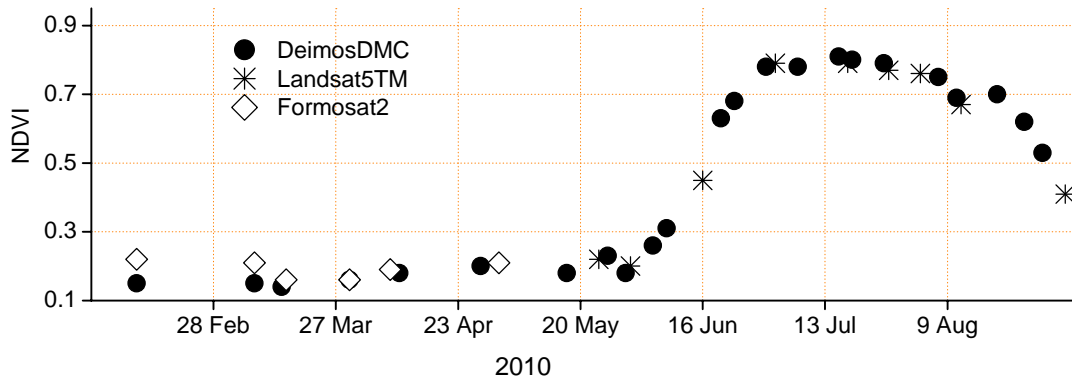


Figure 4. Temporal evolution of NDVI of an irrigated crop (corn) from Deimos, Landsat 5 TM and Formosat-2

Considering the total set of tandem images, the cross-sensor relationships exhibit a high degree of temporal stability and close to 1:1 line, see Table 3, with slight differences. Atmospherically corrected NDVI provides the better degree of temporal stability. This temporal stability on the cross-sensors relationships seems to support the assumption that it is possible to build a satellite constellation of high spatial resolution sensors, because the observations match between the used sensors.

The effect of the atmospheric correction was analyzed by comparison of ToA vs. BoA reflectances as well as NDVI. Figure 3 shows the graphics for selected dates for Formosat and Landsat5-TM and Table 4 summarizes the results. The results show that the atmospheric correction effect produced by the applied procedures can be described by a linear transformation, because the value of $R^2 = 1$. Formosat images show very similar coefficients of the linear relationships for the analyzed dates, where bias and gain coefficients are depending of the date, as is showed in Table 4.

Finally, Figure 4 shows the temporal evolution of vegetation index of an irrigated crop (corn) estimated from Deimos-DMC, Landsat 5TM and Formosat-2. Small differences may be due not only to sensor

characteristics, but also to heterogeneity of the surface and the bidirectional effects of reflectance.

5 CONCLUSIONS

Linear relationships were found for the intercalibration of reflectances and NDVI from one sensor to another. The linear equations obtained in this work are agree with the simulation-based results of Steven *et al.* (2003).

Time series using multi-sensor constellation could be a powerful tool to monitor crop development along its growing season.

6 REFERENCES

- Calera, A., 2000, Seguimiento mediante Teledetección de la cubierta vegetal de los cultivos de secano y su relación con variable climáticas en Castilla-La Mancha. PhD Thesis University of Valencia.
- Calera, A., Jochum, A.M., Cuesta, A., Montoro, A. And López Fuster, P., 2005, Irrigation management from space: Towards user-friendly products. *Irrig. Drain. Systems*, 19, 337-353.
- Chander, G., Markham, B. and Helder, L., 2009, Summary of current radiometric calibration

- coefficients for Landsat MSS, TM, ETM+, and EO-1 ALI sensors. *Remote Sensing of Environment*, 113, 893-903.
- Martínez-Beltrán, C., Jochum, M. A. Osann, Calera A. and Meliá J., 2009, Multisensor comparison of NDVI for a semi-arid environment in Spain. *International Journal of Remote Sensing*, 30:5, 1355- 1384.
- Miura, T., Huete, A. and Yoshioka, H., 2006, An empirical investigation of cross- sensor relationships of NDVI and red/near- infrared reflectance using EO- 1 Hyperion data. *Remote Sensing of Environment*, 100, 223- 236.
- Moreno, J.F., Cabeza, I., Calera, A., Jochum, A. M., Marti, J.M. and Menenti, M., 2002, Land Irrigation Support Service (LISSE), Report, ESA contract 14236/00/NL/DC. 176. Available online at: <http://io.uv.es/projects/lisse/>
- Osann Jochum, A.M., Calera, A., and Co-Authors, 2006, Operational Space-assisted Irrigation Advisory Services: Overview and lessons learned from the DEMETER project. In *Proceedings International Conference on Earth Observation for vegetation monitoring and water management*, 9-11 November 2005, Napoli (American Institute of Physics), pp. 3- 13.
- Steven, M., Malthus, T.J., Baret, F., Xu, H. and Chopping, M.J., 2003, Intercalibration of vegetation indices from different sensor system. *Remote Sensing of Environment*, 88, 412-422.
- Teillet, P.M., Barker, J.L., Markham, B.L., Irish, R.R., Fedosejevs, G. and Storey, J.C., 2001, Radiometric Cross- Calibration of the Landsat- 7 ETM+ and Landsat-5 TM sensors based on tandem data sets. *Remote Sensing of Environment*, 78, 39-54.
- Turner, B. L., II, Lambin, E. F., & Reenberg, A. (2007). The emergence of land changescience for global environmental change and sustainability. *PNAS*, 104, 20666–20671.
- Van Leeuwen, W. J.D., Orr, B.J., Marsh, S.E. and Herrmann, S.M., 2006, Multi- sensor NDVI data continuity: Uncertainties and implications for vegetation monitoring applications. *Remote Sensing of Environment*, 100, 67-81.

Applying VENμS bands for agriculture

I. Herrmann^a, A. Pimstein^b, A. Karnieli^a, D. J. Bonfil^c, Y. Cohen^d, and V. Alchanatis^d

^a *The Remote Sensing Laboratory, Jacob Blaustein Institutes for Desert Research, Ben-Gurion University of the Negev, 84990, Israel.*

^b *USDA-ARS, Hydrology and Remote Sensing Lab, Bldg. 007, BARC West, Beltsville, MD 20705, U.S.*

^c *Field Crops and Natural Resources Department, Agricultural Research Organization, Gilat Research Center, Israel.*

^d *Institute of Agricultural Engineering, Agricultural Research Organization, Volcani Center, Bet Dagan, Israel.*

ittai@bgu.ac.il , apimstein@gmail.com , karnieli@bgu.ac.il , bonfil@volcani.agri.gov.il , yafitush@volcani.agri.gov.il , victor@volcani.agri.gov.il

ABSTRACT - This study presents the Vegetation and Environmental New Micro Spacecraft (VENμS) potential spectral ability to predict leaf area index (LAI) and nitrogen (N) content in field crops. All measurements were carried out in experimental plots in the north-western Negev, Israel. All spectra were resampled to VENμS bands. Spectral (canopy level) and LAI data were obtained during four growing seasons (two of wheat and two of potato). In addition to normalized difference vegetation index (NDVI) and red-edge inflection point (REIP) computation, partial least squares (PLS) models were developed for LAI prediction. The LAI prediction for wheat alone resulted in R^2 values of 0.54 and 0.86 for NDVI and REIP, respectively, for VENμS as well as continuous spectra. Prediction by PLSR model for both crops together, resulted in R^2 values of 0.77 and 0.83 for VENμS and continuous spectra, respectively. Spectral measurements of potato leaves were obtained during two growing seasons. N measurements of leaf-%N and petiole $\text{NO}_3\text{-N}$ were performed. In addition to transformed chlorophyll absorption reflectance index (TCARI) computation, PLS models were developed. Correlation of TCARI based on continuous spectra with N content resulted in R^2 values of 0.82 and 0.66 for leaf-%N and petiole $\text{NO}_3\text{-N}$, respectively. Correlation of TCARI based on VENμS bands with N content resulted in R^2 values of 0.79 and 0.67 for leaf-%N and petiole $\text{NO}_3\text{-N}$, respectively. Therefore as presented the red-edge bands of VENμS combining its spatial and temporal resolutions should provide a powerful tool for field crops monitoring.

1 INTRODUCTION

The forthcoming Vegetation and Environmental New Micro Spacecraft (VENμS) is to be launched in 2013. This system is characterized by high spatial (5.3 m), spectral (12 spectral bands in the visible near infrared (VNIR), including 4 red-edge bands), and temporal (2 days revisit time with the same viewing angle) resolutions. The satellite will provide a 27 km swath with tilting capability, up to 30 degree along and across track that enable to detect targets at up to 360 km off-nadir.

Leaf area index (LAI) was defined by Watson (1947) as the total one-sided area of leaf tissue per unit ground surface area, leading to a dimensionless value. LAI is one of the most important variables governing canopy processes (Baret et al. 1992) and is related to leaf and canopy chlorophyll contents, photosynthesis rate, carbon and nutrient cycles, dry and fresh

biomass, and growing stages (Clevers et al. 2001, Pimstein et al. 2009). A common non-destructive surrogate for LAI, which is based on reflectance of red (R) and near infrared (NIR) bands is the normalized difference vegetation index (NDVI). However, NDVI sensitivity to LAI tends to drop at values bigger than 2 (Gitelson 2004) and therefore alternatives for predicting high values of LAI should be considered. This work focuses on the red-edge inflection point (REIP) since it is a direct outcome of spectral data that will be available by VENμS.

Nitrogen (N) is an essential element for plant growth and productivity and is frequently the major limiting factor in agricultural soils (Daughtry et al. 2000, Bonfil et al. 2004). Since N and chlorophyll contents are positively related the transformed chlorophyll absorption reflectance index (TCARI) was applied for N assessment (Cohen et al. 2009).

Therefore, VEN μ S is potentially a powerful tool for agricultural applications, including assessment of LAI and N.

2 METHODOLOGY

2.1 Study area

Wheat and potato experiments were established in the northwestern Negev, Israel. The wheat experiment took place in experimental plots of Gilat Research Center (31° 21' N; 34° 42' E). The potato experiment took place in experimental plots in commercial fields of Kibbutz Ruhama (31°28' N, 34°41' E). Both sites are on boundary between Mediterranean and semi-arid climates.

2.2 Filed measurements

The LAI wheat experiment was conducted during two winter growing seasons 2003-04 (2004) and 2004-05 (2005). The LAI potato experiment was conducted during two growing seasons in the autumn of 2006 and spring of 2007. The N potato experiment was conducted during two spring growing seasons in 2006 and 2007.

Canopy level, spectral measurements, followed by LAI measurements were obtained by Analytical Spectral Devices (ASD) FieldSpec Pro FR spectrometer and AccuPAR LP-80 ceptometer, respectively. Leaf level spectral data were obtained in the field by the mini-spectrometer HR2000 (Ocean Optics FL) and N measurements of petiole NO₃-N were performed during both growing seasons and leaf-%N data were obtained for the second season (Cohen et al. 2009).

2.3 Data analysis

The ASD spectral data range from 400 to 1000 nm and the HR2000 ranging from 400 to 900 nm. The continuous spectral data were resampled to VEN μ S bands. Vegetation indices were computed (both spectral resolutions): NDVI (Rouse et al. 1974) and REIP (Guyot et al. 1988) for LAI; and TCARI (Haboudane et al. 2002) for N, as presented in Equations 1 to 3. In Equations 1 to 3 ρ stands for reflectance value of a certain wavelength in case of a continuous spectrum or a VEN μ S band center (the entire resampled band was applied) in case of a VEN μ S spectrum, all in nm.

$$NDVI = \frac{\rho_{782} - \rho_{666}}{\rho_{782} + \rho_{666}} \quad (1)$$

$$REIP = 700 + 40 \left\{ \frac{[(\rho_{666} + \rho_{782})/2] - \rho_{702}}{\rho_{738} - \rho_{702}} \right\} \quad (2)$$

$$TCARI = 3[(\rho_{700} - \rho_{670}) - 0.2(\rho_{700} - \rho_{550}) \left(\frac{\rho_{700}}{\rho_{670}} \right)] \quad (3)$$

The indices values (both spectral resolutions) related to LAI were divided to calibration and validation in a relation of 60% and 40%, respectively. LAI predictions were obtained by NDVI and REIP. The TCARI (both spectral resolutions) was applied in order to view its correlation with N content.

For entire spectra prediction (both spectral resolutions) partial least squares (PLS) models were obtained and for LAI and N. The variable importance in projection (VIP) after Wold et al. (1993) was computed in a Matlab environment by the PLS toolbox of Eigenvector, in order to evaluate the relative importance of each wavelength in PLS models (Cohen et al. 2009). The VIP values are evaluated by "the higher the better" where the average VIP = 1 is considered to be the putative threshold.

3 RESULTS AND DISCUSSION

3.1 Vegetation indices analysis

Table 1 presents R² and root mean square error prediction (RMSEP) values of LAI predicted by NDVI and REIP, calculated for the validation subsets of both spectral resolutions. The validation was applied for three datasets: Potato; Wheat; and All data (including Potato and Wheat together). The results present that there is no advantage for the continuous over the VEN μ S spectral resolution in prediction abilities of LAI. This can be seen for example by the R² value of 0.86 in the Wheat case for the REIP in both spectral resolutions. The results also present the supremacy of the REIP method to predict LAI over the NDVI hence all R² and RMSEP values of REIP are higher and lower, respectively, than those values of the NDVI. The wheat is better predicted by both indices than the potato. This might be an outcome of the different crops properties related to plants density for a given area in the field.

Table 2 presents the R² and root mean square error of cross validation (RMSECV) values of N content correlation with TCARI. As for the LAI, there is no advantage for the continuous over the VEN μ S spectral resolution.

Table 1: Prediction quality of LAI by indices for both spectral resolutions

	VEN μ S		Continuous		VEN μ S		Continuous	
	R^2		R^2		RMSEP		RMSEP	
	NDVI	REIP	NDVI	REIP	NDVI	REIP	NDVI	REIP
Potato	0.42	0.41	0.28	0.32	0.68	0.66	0.71	0.68
Wheat	0.59	0.86	0.59	0.86	1.14	0.67	1.21	0.74
All data	0.46	0.66	0.42	0.66	1.14	0.92	1.18	0.93

Table 2: N content correlation with TCARI for both data formation

	VEN μ S		Continuous	
	R^2	RMSECV	R^2	RMSECV
Petiole (mg/kg)	0.67	Non linear	0.66	Non linear
Leaf (%)	0.79	0.2	0.82	0.2

Table 4: N content prediction by entire spectra for both data formation

	VEN μ S		Continuous	
	R^2	RMSEP	R^2	RMSEP
Petiole (mg/kg)	0.48	231	0.82	163
Leaf (%)	0.78	0.2	0.95	0.1

3.2 PLS modelling analysis

Table 3 presents the R^2 and RMSEP values of LAI predicted by the PLS models of the entire spectra of both spectral resolutions versus the observed LAI. As for the indices prediction there is no advantage for the continuous spectra over the VEN μ S spectral resolution.

Table 3: LAI prediction by entire spectra for both data formations

	VEN μ S		Continuous	
	R^2	RMSEP	R^2	RMSEP
Potato	0.64	0.52	0.52	0.54
Wheat	0.86	0.68	0.90	0.60
All data	0.77	0.70	0.83	0.63

Table 4 presents the R^2 and RMSECV values of N content prediction by the entire spectra of both spectral resolutions. For the leaf-%N content there is no advantage for the continuous over the VEN μ S spectral resolution but for the petiole NO₃-N there is an advantage for the continuous spectral resolution. Figure 1 presents the VIP values for continuous spectra PLS models of LAI and N content prediction. Also presented are the reflectance

spectrum of plant, the VIP threshold and the VEN μ S bands (the horizontal bars represents the width and location of the VEN μ S bands). For both VIP curves, LAI and N, the red-edge region (covered by four VEN μ S bands) is the most important region in the range of 400 to 900 nm. The second most important region for the LAI curve (around 550 nm) is not the same as for the N content curve (around 500 nm) but both are covered by additional VEN μ S bands.

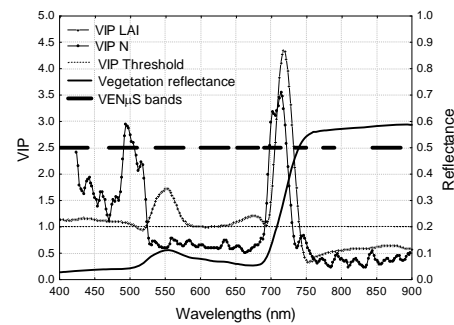


Figure 1: VIP curves for LAI and N content PLS models

4 CONCLUSIONS

After analyzing the results it can be concluded that:

- VEN μ S-based indices and entire spectra can predict LAI as good as continuous-based indices and spectra, respectively.
- REIP is significantly a better predictor of LAI for the Wheat data set.

- Leaf-%N can be predicted by VEN μ S entire spectra as good as by continuous spectra.
- The red-edge region is the most sensitive region to LAI and N content, in range of 400 to 900 nm.

Therefore the VEN μ S combining its spatial and temporal resolutions should provide a powerful tool for field crops monitoring.

5 ACKNOWLEDGEMENTS

This research was supported in part by Research Grant Award CA-9102-06 from BARD-AAFC, The United States - Israel Binational Agricultural Research and Development Fund and Agriculture and Agri-Food, Canada; the Chief Scientist of the Israeli Ministry of Agriculture, and the Israeli Ministry of Science, Culture, and Sport. The authors would like to thank Alexander Goldberg the indefatigable for his work in the field and in the lab and to express their appreciation for the vital contributions of Gadi Hadar and Ran Ferdman, the potato growers from Kibbutz Ruhama.

6 REFERENCES

- Baret, F., Jacquemoud, S., Guyot, G. and Leprieux, C., 1992, Modeled analysis of the biophysical nature of spectral shifts and comparison with information-content of broad bands. *Remote Sensing of Environment*, **41**, 133-142.
- Bonfil, D.J., Karnieli, A., Raz, M., Mufradi, I., Asido, S., Egozi, H., Hoffman, A. and Schmilovitch, Z., 2004, Decision support system for improving wheat grain quality in the Mediterranean area of Israel. *Field Crops Research*, **89**, 153-163.
- Clevers, J., G. P. W., de Jong, s., m., Ephama, G., F., Van der Meer, F., Bakker, W., H., Skidmore, A. and Addink, E., A., 2001, MERIS and the red-edge position *International Journal of Applied Earth Observation and Geoinformation*, **3**, 313-320.
- Cohen, Y., Alchanatis, V., Zusman, Y., Dar, Z., Bonfil, D., J. , Karnieli, A., Zilberman, A., Moulin, A., Ostrovsky, V., Levi, A., Brikman, R. and Shenker, M., 2009, Leaf nitrogen estimation in potato based on spectral data and on simulated bands of the VEN μ S satellite. *Precision Agriculture*.
- Daughtry, C.S.T., Walthall, C.L., Kim, M.S., de Colstoun, E.B. and McMurtrey, J.E., 2000, Estimating corn leaf chlorophyll concentration from leaf and canopy reflectance. *Remote Sensing of Environment*, **74**, 229-239.
- Gitelson, A.A., 2004, Wide dynamic range vegetation index for remote quantification of biophysical characteristics of vegetation. *Journal of Plant Physiology*, **161**, 165-173.
- Guyot, G. and Baret, F., 1988, Utilisation de la haute resolution spectrale pour suivre l'etat des couverts vegetaux, In 18 - 22 January 1988, ESA (Ed.), (Aussois: 4th International Colloquium "Spectral signatures of objects in remote sensing", 279-286.
- Haboudane, D., Miller, J.R., Tremblay, N., Zarco-Tejada, P.J. and Dextraze, L., 2002, Integrated narrow-band vegetation indices for prediction of crop chlorophyll content for application to precision agriculture. *Remote Sensing of Environment*, **81**, 416-426.
- Pimstein, A., Eitel, J.U.H., Long, D.S., Mufradi, I., Karnieli, A. and Bonfil, D.J., 2009, A spectral index to monitor the head-emergence of wheat in semi-arid conditions. *Field Crops Research*, **111**, 218-225.
- Rouse, J.W., Haas, R.H., Schell, J.A. and Deering, D.W., 1974, Monitoring vegetation systems in the Great Plains with ERTS, In December, (Goddard Space Flight Center: Third Earth Resources Technology Satellite -1, 309-317.
- Watson, D., J., 1947, Comparative physiological studies in the growth of field crops I. Variation in net assimilation rate and leaf area between species and varieties, and within and between years. *Annals of Botany*, **11**, 41-76.
- Wold, S., Johansson, E. and Cocchi, M., 1993, PLS-partial least squares projections to latent structures. In 3D QSAR in drug design: theory, methods, and applications, H. Kubinyi (Ed.), 523-550 (Leiden: ESCOM).

Assessment of the Land Cover Classification Accuracy of Venüs and Sentinel-2 Image Time Series with respect to Formosat-2

Jordi Inglada, Olivier Hagolle, Gérard Dedieu
CNES – CESBIO, UMR 5126, Toulouse, France
Jordi.inglada@cesbio.cnes.fr

ABSTRACT – *The Venüs and Sentinel-2 missions will provide high spatial, spectral and temporal resolution images which will allow for a detailed monitoring of land surfaces. In order to prepare the arrival of these new kind of data CNES/CESBIO has acquired a large amount of Formosat-2 images. These images have similar characteristics to the ones of Venüs and Sentinel-2 in terms of revisit cycle and spatial resolution. However, they lack the spectral richness that the coming systems will provide. In this paper, we try to assess the performances in vegetation land-cover classification of Venüs and Sentinel-2 with respect to Formosat-2. In order to perform a fair comparison of the different sensors, we simulate synthetic image time series starting from a real Formosat-2 time series composed by 49 images acquired over an agricultural site. These images are used to compute LAI and determine the vegetation type for each pixel and each date. These informations together with leaf pigment data are used to simulate full reflectance spectra which are then reduced using each sensor's spectral bands description. As a final step, supervised classifications are performed in order to compare the ability of each sensor to correctly discriminate the different classes of vegetation.*

1 INTRODUCTION

VENÜS (Vegetation and Environment monitoring on a New Micro-Satellite) is a superspectral sensor, dedicated to vegetation monitoring. The satellite is developed as a cooperation between France and Israel and should be launched in 2012.

VENÜS scientific objective is the provision of data for scientific studies dealing with the monitoring, analysis, and modeling of land surface functioning under the influences of environmental factors as well as human activities. To fulfill this objective, VENÜS will acquire every two days high resolution and superspectral images of predefined sites of interest all around the world. These data are acquired with constant viewing angles to minimize directional effects. The main data set characteristics are frequent (2 days), high resolution (10 meters), multispectral (11 bands) images.

Sentinel-2 polar-orbiting satellites will provide systematic global acquisitions of high-resolution multispectral imagery with a high revisit frequency. This mission is tailored towards the needs of operational land monitoring and emergency services. The Sentinel-2 mission is envisaged to fly as a pair of satellites with the first planned to launch in 2013. Each Sentinel-2 satellite carries a Multi-Spectral Imager (MSI) with a swath of 290 km. It provides a versatile set of 13 spectral bands spanning from the visible and near infrared (VNIR) to the shortwave infrared (SWIR), featuring 4 spectral bands at 10m, 6 bands at 20m and 3 bands at 60m spatial resolution.

In full operational phase, the pair of Sentinel-2 satellites will deliver data taken over all land surfaces and coastal zones every 5 days under cloud-free conditions, and typically every 15-30 days considering the presence of clouds.

In order to design and assess the processing algorithms for this new kind of high-resolution and high-revisit image time series, CNES/CESBIO has purchased several Formosat-2 time series. These data are similar to Venüs images in terms of spatial resolution, revisit cycle and constant viewing angles. However, Formosat-2 has only 4 spectral bands while Venüs will have 11. It is therefore interesting to assess the improvement, in terms of land cover classification accuracy, due to the higher spectral resolution of Venüs with respect to Formosat-2.

In this work we focus on the particular case of vegetation (crops and forests). In order to generate realistic data corresponding to the characteristics of Venüs and Sentinel-2, we will use a data base of leaf pigments and simulate reflectance full spectra.

These spectra are then convolved with the Relative Spectral Responses (RSR) of each sensor to create spectra at the sensors' resolutions. Then, these reduced spectra are used in a supervised classification framework in order to measure the classification accuracy. As the spectra for each sensor are created from the exact same full spectra, the only variation is the RSR of the sensors. This approach allows us to fairly compare the different ability of the sensors to discriminate the classes of interest.

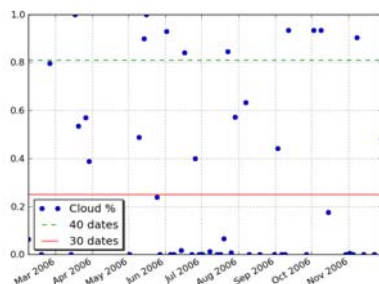
Since one of the main characteristics of the sensors we are studying is that they will provide high temporal resolution image series, we are also interested in assessing the influence of the temporal sampling. A short revisit period increases the chance of obtaining cloud-free images, however, partially cloudy images can still be used sometimes.

2 MATERIALS AND METHODS

2.1 Image time series and land-cover information

A time series of Formosat-2 images: 49 4-band (blue, green, red, near infra-red) images which have been geometrically and radiometrically corrected are available. They have a spatial resolution of 8 m. and cloud masks for each date have been obtained using the method described in (Hagolle et al. 2010).

As a matter of fact, only 10 images are completely cloud-free. The following figure presents the cloud cover for each date. The images will be sorted by cloud cover and the tests will be conducted by adding images with an number of increasing cloudy pixels. This will generate a time sampling sequence which corresponds to different acceptance thresholds for the quality of the images.



The land cover map for the whole area is also available. It has been produced using the methods described in (Idbraim et al. 2009).

2.2 Vegetation information

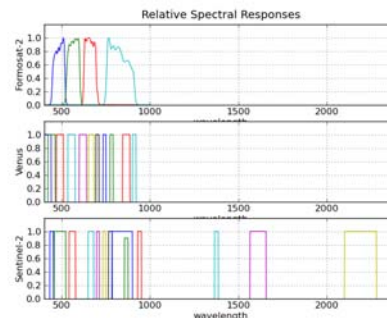
The Lopex-93 data base (Hosgood et al. 1994) is used in order to get realistic values for the following vegetation parameters:

- chlorophyll A
- chlorophyll B
- carotenoids

2.3 Spectral bands

In order to produce realistic simulations, a precise characterization of the spectral bands of the sensors is needed. In the case of Formosat-2, the real (measured) RSR are used. For Venüs and Sentinel-2, since the sensors do not exist yet, the theoretical responses are used. The SRS used in this study are presented in the

following figure:



As one can observe, Formosat-2 has 4 bands (B, G, R, NIR). Venüs has 11 different bands, which are narrow, with a fine sampling of the red edge, but lacking the SWIR. Sentinel-2 is similar to Venüs, but with a coarser sampling of the red edge but adds the SWIR.

2.4 Classification approach

The aim of this paper is not to develop a classification technique. Therefore, we will use a simple, off the shelf approach. We choose here to apply a linear Support Vector Machine (Burges, 1998).

The parameters of the classifier are optimized automatically by cross-folder validation.

Therefore, the classifier can be considered as a zero-parameter black box whose classification results can be used in order to assess the ability of a given sensor to correctly discriminate between classes of vegetation.

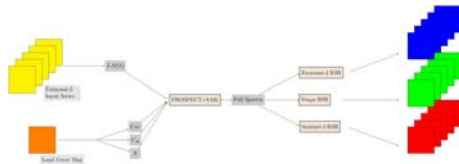
The classical metrics for classification performance are used:

1. The confusion matrix, where each element (i,j) has the value of the percentage of samples of the (true) class i assigned to the class j by the classifier.
2. The kappa coefficient which is generally thought to be a more robust measure than simple percent agreement calculation since it takes into account the agreement occurring by chance.

In this paper, only the kappa index will be used, since the results for the individual classes are not of interest for this study.

3 SIMULATIONS

The following figure presents the experimental setup used in this study.



The detailed steps of the workflow are the following:

1. The Formosat-2 time series is used to estimate the LAI for each pixel of the classes of interest.
2. Leaf pigments are obtained using the LOPEX'93 data base.
3. A land-cover map is used as input to select the pigment values for each pixel.
4. LAI and leaf pigments are used to feed the PROSPECT+SAIL (Féret et al. 2008, Jacquemoud et al. 2009) simulation code.
5. The simulated full spectra are reduced using the relative spectral responses of each sensor in order to generate the time series (Forestier et al 2009).

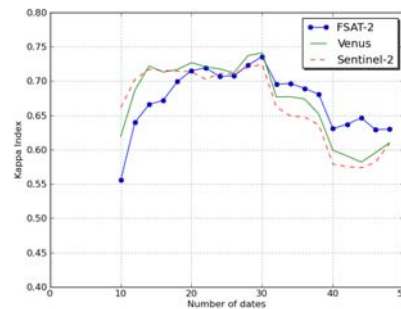
Although generic and sound the simulator presented above suffers from the following limitations:

1. Leaf pigments are constant for a given class. This gives more weight to the spectral characteristics with respect to the temporal profile.
2. No atmospheric effect is taken into account by the simulation. The relative robustness of the SWIR band (Sentinel-2) is not highlighted.
3. We perform pixel-based simulations. As a consequence, some intra-plot variabilities which can help to discriminate some classes are not taken into account.

4 RESULTS AND DISCUSSION

Using the simulation workflow described in the previous section, we will generate several time series for each sensor. These time series will consist of all the images up to a given threshold for cloud cover. The simulations start with the 10 cloud-free images, which give a relatively regular sampling of the time span considered.

The following figure presents the kappa coefficient values achieved for each sensor and for each series (number of dates used in the classification).



The figure allows to draw the following conclusions:

1. With a few images the spectral resolution makes the difference and the accuracy increases with the number of bands.
2. With many images (more than 30) cloudy images lower the accuracy and the huge amount of data makes the learning convergence difficult.
3. Venus and Sentinel-2 are equivalent starting with about 15 images.
4. Formosat-2 needs at least 20 images to give similar results, but this is difficult to obtain with a 5-day revisit cycle, given the probability of cloud cover in many areas of the globe.

5 CONCLUSIONS AND FUTURE WORK

In this paper, we presented a simulation framework which allows to compare different sensors in a realistic setting. Leaf pigment data bases and physical simulations of the plant reflectances were used in order to generate image time series representative of the phenology of several vegetation types.

This experimental setup allowed to analyze the trade-off between spectral and temporal resolutions.

However, the simulation workflow still needs improvements, such as including the temporal evolution of leaf pigments and taking into account atmospheric effects.

Future work on this topic will also include the study the use of spectral indexes (vegetation, soil, etc.) and the application of feature selection approaches in order to determine which are the most useful spectral bands.

6 REFERENCES

- Burges, C.J.C., 1998, A Tutorial on Support Vector Machines for Pattern Recognition. *Data Mining and Knowledge Discovery*, 2(2), pp. 121-167.
- Forestier, G., Inglada, J., Wemmert, C., Gancarski, P., 2009. Mining spectral libraries to study sensors'

- discrimination ability. SPIE Europe Remote Sensing, Berlin, Germany.
- Féret, J.B., François, C., Asner, G.P., Gitelson, A.A., Martin, R.E., Bidel, L.P.R., Ustin, S.L., le Maire, G., Jacquemoud, S., 2008. PROSPECT-4 and 5: advances in the leaf optical properties model separating photosynthetic pigments. *Remote Sensing of Environment*, 112, p.3030-3043.
- Hosgood, B., Jacquemoud, S., Andreoli, G., Verdebout, J., Pedrini, A., Schmuck, G., 1994. The JRC Leaf Optical Properties Experiment (LOPEX'93). Technical report, EUROPEAN COMMISSION, Directorate - General XIII, Telecommunications, Information Market and Exploitation of Research, L-2920 Luxembourg; CL-NA-16095-EN-C.
- Idbraid, S., Ducrot, D., 2009. An unsupervised classification using a novel ICM method with constraints for land cover mapping from remote sensing imagery. *International Review on Computers and Software (IRECOS)*.
- Jacquemoud, S., Verhoef, W., Baret, F., Bacour, C., Zarco-Tejada, P.J., Asner, G.P., François, C., Ustin, S.L., 2009. PROSPECT + SAIL models: a review of use for vegetation characterization. *Remote Sensing of Environment*, 113, p.56-66.

Use of Dense Time Series of High Resolution Images for Change Detection and Land use Classification

J. Inglada, B. Beguet, J.-F. Dejoux, C. Marais-Sicre, D. Ducrot, M. Huc, O. Hagolle, F. Baup, G. Dedieu,
CESBIO, UMR 5126, Toulouse, France
jordi.inglada@cesbio.cnes.fr

ABSTRACT- *In the coming years, 2 optical space-borne systems with high resolution and high temporal frequency revisit will be launched: Venus and Sentinel-2. Formosat-2 is already providing this kind of data. The availability of these data opens the opportunity for the development of new applications which require to closely monitor the temporal trajectory of the characteristics of land surfaces. In our case, we are interested in deriving land cover and change information for agricultural areas. Our long-term goal is to provide near real-time classifications of crop types, soil and crop states as well as agricultural practices. In this work we will study how a dense temporal sampling can be useful for the monitoring of such issues as the distinction of bare soils. Using a radiometric approach (reflectances of the visible and near infrared bands) we will study the possibility of identifying the soil states and the transitions from one state to another. Added to the reflectances, some indices based on spectral band combinations will also be used. We will show that soil states are difficult to identify using direct classification and optical radiometry only. However, soil state changes can be detected in some cases, but many transitions seem difficult to identify.*

1 INTRODUCTION

In the coming years, 2 optical space-borne systems with high resolution and high temporal frequency revisit will be launched: Venus and Sentinel-2. Formosat-2 is already providing this kind of data. The availability of these data opens the opportunity for the development of new applications which require to closely monitor the temporal trajectory of the characteristics of land surfaces. In our case, we are interested in deriving land cover and change information for agricultural areas. Our long-term goal is to provide near real-time classifications of crop types, soil and crop states as well as agricultural practices.

In this work we will study how a dense temporal sampling can be useful for the monitoring of such issues as the distinction of bare soils. In terms of application, this distinction needs to be done early in the season (September to November for our test site), for environmental issues (risk erosion assessment, diffuse pollution risk...) or economic issues (agricultural land surface prevision...). This means that the information which, in the case of a whole season of data, could be extracted from a phenological behavior (NDVI time series, for instance), will have to be accessed otherwise.

A very rich data set is used for the assessment and validation tasks carried out in this work. The test site is located in the South-West of France, near Toulouse and covers an area of 500 km² presenting 24 thematic

classes. This is a unique set of FORMOSAT-2 images (68 images over four consecutive years, 2006-2009) and in-situ measurements (dynamic survey of 300 fields...). The images have an original size of 4300 x 3000 pixels and have been ortho-rectified with a 8 m. ground sampling distance. They have 4 spectral bands (blue, green, red and near infra-red).

Several kinds of reference data are available in terms of thematic classes and changes occurred in terms of agricultural practices. This will allow us to validate the methodology and give some recommendations in terms of temporal sampling (image acquisition) and pertinence of the change indicators.

These data are acquired in the frame of the CESBIO's Sud-Ouest Project. The goal of this project is to contribute to the understanding and the modeling of the continental surfaces at the landscape and regional levels and to increase knowledge and develop generic methods. Yearly monitoring and regular satellite image acquisitions since 2006 have been performed. Also, 3 permanent instrumented sites are maintained.

One of the main outputs of this project is the production of land-cover maps. They are used as a means (input for models) but they are also a research goal per se. These land cover maps are produced using the techniques described in (Ibraim et al., 2009) and (Ducrot et al. 2010) using the image series for a complete season and ground reference data. The following table shows an example of map nomenclature and classification accuracy achieved by

the methodology used.

Class	accuracy
broad leaf forest	97.88
needle leaf forest	97.05
Eucalyptus	74.53
Rape	99.33
Barley	99.06
Maize	99.60
Sunflower	99.12
Sorghum	100.00
Soybean	97.36
Fallow	97.75
Grassland	95.16

2 AVAILABLE DATA

As stated in the previous section a large amount of data is available on the area of interest. For the year 2008, 11 FORMOSAT-2 images were acquired, 5 of which correspond to the period of interest for the soil work (29th August to 12th November). All images are geometrically corrected and radiometrically calibrated. Cloud screening was performed using the method described in (Hagolle et al. 2010) and atmospheric correction as described in (Hagolle et al. 2008).

Ground reference data was acquired during 7 terrain surveys during which 300 plots were revisited. This terrain surveys were synchronous with SAR acquisitions (not used in this paper). Therefore, each ground sample is associated with a confidence index depending on the time gap between the survey and the satellite acquisition.

It is interesting to note that, because if this time gap, some soil states are visible on the ground before being detected on the images.

3 PROBLEM POSITION

As stated before, the long term goal of this research is to improve real-time crop classification. Indeed, at the beginning of the agricultural season, even if the crops can not be recognized, we make the assumption that knowledge about soil work can give useful hints on the type of crop which will be grown on a given plot.

Furthermore, a map of soil states is also an interesting product by itself, since it gives information about the erosion risks, for instance.

In this framework, we define the following classes of interest:

- Crops (C): Sunflowers, which are mostly dry in September and harvested in September or October. Irrigated soybean and maize, which are green in September and begin to dry in

October (harvest in October and November).

- Inter-crop (IC): Begin after harvest. No recent or visible soil tillage. Stubble stands often right, crop residues may be visible on top soil. Some green plants can grow, like volunteers (or regrow) and weeds, if climatic conditions are favorable (rain, etc.).
- Stubble disking (SD): Superficial (5 to 15 cm) soil tillage in order to mix crop residues and soil and to destroy green vegetation (weeds). Soil surface is irregular, has some small clods and a small roughness. Stubble and crop residues are partly visible.
- Deep ploughing (DP): Mainly mouldboard ploughing between 20 to 45 cm deep. More than 95% bare soil: no visible crop residues. Visible clods and strong roughness.
- Harrowing (H): Secondary or superficial tillage. More than 95% bare soil. There are medium sized clods. Improper for seedling. Various tillage operations are possible: rotary harrowing, chiseling, superficial ploughing (less than 20 cm deep).
- Sowing preparation (SP): More than 95% bare soil. Soil ready for seedling. Regular surface. Small clods.
- Emergence (E): Germination. Plants are visible from field borders and are at cotyledons or first leaves development stages. Plant height lower than 5 cm.

Some green plants (volunteers, weeds) may be visible for the IC, SD, DP and H categories, only if climatic conditions are favorable and duration between each stage or soil tillage is sufficient. In the present paper, it was sometimes the case only in inter-crops or after stubble disking.

The aim of the work will therefore be to detect these classes on the images or to detect the transitions between them.

4 APPROACH

The existing literature about land cover map production and change detection using satellite images is very extensive. In this work, we didn't aim at making a thorough survey of the literature and we decided to use a simple approach in terms of processing. For instance we decided to use a reduced set of image features for the classification and the

change detection.

Therefore, no textural, statistical nor object-based features are used. Only radiometry features are employed. We use the 4 reflectances (blue, green, red and near infrared) available from the FORMOSAT-2 images. In order to exploit the relationships between the bands 5 spectral indices will be used. These indices are the classical NDVI and Brightness indices and the redness, color and shape indices whose formulas are given below:

$$Redness=(R-G)/(R+G) \quad (1)$$

$$Color=(R-B)/R \quad (2)$$

$$Shape=(2R-G-B)/(G-B) \quad (2)$$

These 9 features (4 reflectances and 5 indices) and their temporal evolutions are analyzed in order to find out if they can be associated with the classes of interest. It is important to note that the goal of the study is not to produce the classification or the change detection maps, but rather to understand the potential of the radiometric information for this task.

The development of a procedure for the production of soil states maps involves the tuning of the classifiers and other steps which are beyond the scope of this paper.

We analyze 2 different aspects of the radiometric measures.

1. Is there any relationship between the radiometry at a given date and the soil state?
2. Does the transition from one state to another have a particular radiometric signature?

A multivariate analysis of the different features was performed, giving no particular insight on the 2 questions listed above. Therefore it was decided to use a non-linear classifier as a performance measure for the features. This choice makes us formulate the task as a supervised classification problem. For the first point (relationship between radiometry and soil state), this is straightforward: the classes are the states and the ground reference data can be used for the supervision.

The second case is slightly more difficult. We decide to model the transitions as classes, which implies all combinations of pairs of soil states. Since the states have an order (IC, then SC, then DP, etc.) only those pairs of states are taken into account.

In order to perform the classifications, a Support Vector Machine (Burges, 1998), SVM, with a Gaussian Radial Basis Function kernel was used. The parameters of the classifier were optimized automatically by cross-folder validation.

Therefore, the classifier can be considered as a zero-parameter black box whose classification results can be used in order to obtain the answers to the 2 questions stated above.

The classical metrics for classification performance are used:

1. The confusion matrix, where each element (i,j) has the value of the percentage of samples of the (true) class i assigned to the class j by the classifier.
2. The kappa coefficient which is generally thought to be a more robust measure than simple percent agreement calculation since it takes into account the agreement occurring by chance.

5 RESULTS AND DISCUSSION

5.1 Straightforward classification

In this section, we report the results obtained using the straightforward classification approach. As described before, each soil state is considered to be a class and a SVM supervised classification is applied. The available samples are split into 75% for the training and 25% for the validation. In order to obtain a robust estimation of the performances, 20 runs with different random samplings are applied. The results presented here are the mean values of those 20 runs.

For this experiment, the 5 available images are used. That means that the same site (pixel) will be used 5 times with the corresponding soil state for each date. The fact that the same sample is used several times is not taken into account by the algorithm. Also, no consideration about the fact that the soil moisture and the weather conditions are different for each image is used. This way of proceeding will introduce a high intra-class variability, which will give us a pessimistic bound for the performances and will ensure a good generalization capability of the classifier.

The following table presents the confusion matrix obtained.

	C	IC	SD	DP	H	SP	E
C	66.4	9.54	7.08	4.67	0.35	7.53	4.43
IC	6.54	64.67	14.14	0.95	4.71	3.89	5.1
S	4.08	6.6	63.5	1.5	13.6	6.94	3.78
DP	6.36	2.76	2.64	57.54	16.51	10.53	3.66
H	1.53	1.35	6.9	20.85	44.09	23.17	2.11
SP	3.6	0.0	6.17	23.1	13.12	41.52	12.49
E	1.28	5.85	1.67	0.08	1.72	1.6	87.8

We obtain a kappa index of 0.541, which is rather low. One can observe that the crop class, which could be expected to be easy to detect is not. This is due to

the fact that several crop types are mixed and their degree of senescence varies. In the same way, IC can be confused with MT, since the amount of green vegetation before tilling varies a lot. Rather surprisingly, the emergence is correctly identified. Finally, there are many confusions between the bare soil types.

In order to go further in the analysis, we perform the same experiment again, but grouping the bare soil classes. The following confusion matrix shows that the soil classes as well as the IC and SD classes have a better recognition rate. The kappa achieved equals to 0.655.

	C	IC	SD	Soil	E
C	65.65	10.47	8.9	7.12	7.86
IC	6.19	65.22	16.16	6.23	6.2
SD	5.29	6.61	67.88	15.43	4.79
Soil	3.92	2.16	8.18	77.27	8.47
E	2.98	6.39	2.32	2.31	86.0

5.2 Change detection

In this section we investigate the possibility of detecting transitions instead of detecting soil states. The transitions are the change of a soil state between 2 image acquisitions. Therefore, a sample for the classification will be described by a vector containing the 9 radiometric features for 2 dates (that is 18 features). In a similar way to what we did for the straightforward classification, all dates will be used, which means that a given site (pixel) will be used $4+3+2+1 = 10$ times (all the pairs using the 5 dates). Of course, the most abundant classes are the “no-change” ones, where a sample remains in the same state for 2 dates. It is worth noting that the time gap between the 2 acquisitions taken into account for each individual transition can vary a lot, but is not taken into account. Again, this produces a high intra-class variability which ensures a pessimistic bound. Unfortunately, not all transition types are present in the data set. This is why the confusion matrices will not contain all the theoretically possible classes. Furthermore, the number of transitions is very low for many cases (between 12 and 50 plots; or between 1000 and 10000 pixels).

The following 3 confusion matrices summarize the results for the transitions from C (kappa=0.735), IC (kappa=0.812) and SD (kappa=0.633) respectively.

C ->	IC	SD	DP	H	SP
IC	73.49	16.23	0.03	1.07	9.18
SD	6.93	53.17	5.63	12.73	21.54
DP	0.65	2.14	83.07	3.54	10.6
H	2.47	5.93	10.7	74.97	5.93
SP	5.08	1.63	8.96	2.5	81.83

IC ->	SD	DP	H	SP
SD	75.99	11.54	10.97	1.5
DP	3.58	89.67	6.75	0.0
H	14.32	15.87	62.15	7.66
SP	0.58	0.0	2.92	96.5

SD ->	DP	H	SP	E
DP	74.1	14.02	3.2	8.68
H	23.96	32.88	28.59	14.57
SP	7.51	13.69	65.91	12.89
E	6.82	5.69	7.25	80.24

One can observe that the results are much better than for the state classification, although some of the transitions are still difficult to detect. The following table presents the best detected transitions among the cases not presented above.

Transition	DP -> H	H -> SP	H -> E	SP -> E
Accuracy (%)	97.0	88.74	87.91	96.76

As we can observe, some transitions are very well detected.

6 CONCLUSIONS AND FURTHER WORK

In this paper, we analyzed the possibility of characterizing soil states and soil work using high temporal and spatial resolution multispectral optical images.

This is an interesting application, since soil state knowledge is important for erosion risk assessment and more broadly for an improved monitoring of land cover changes in agricultural landscapes.

Using a radiometry-only approach, we found that direct detection of the soil state is difficult. However, the detection of changes between soil states due to agricultural management can be foreseen.

Even though the data set used has some limitations (only 5 images, a low number of interesting transitions, only 4 spectral bands), we claim that upcoming multi-temporal missions as for instance Venus and Sentinel 2, will allow to perform this kind of assessment with a good performance.

Some issues have to be further investigated:

- the use of other image features as textures or local statistics
- the use of ancillary data about rain events and soil type (soil texture)
- the possibility of synergy with SAR imagery.

9 REFERENCES

- Burges, C.J.C., 1998, A Tutorial on Support Vector Machines for Pattern Recognition. *Data Mining and Knowledge Discovery*, 2(2), pp. 121-167.
- Ducrot, D., Masse, A., Marais-Sicre, C., Dejoux, J-F. and Baup, F., 2010, Multisensor and multitemporal image fusion methods to improve remote sensing image classification. *3rd Recent Advances in Quantitative Remote Sensing Symposium*.
- Hagolle, O., Dedieu, G., Mougenot, B., Debaecker, V., Duchemin, B. and Meygret, A., 2008. Correction of aerosol effects on multi-temporal images acquired with constant viewing angles: Application to Formosat-2 images, *Remote Sensing of Environment*, vol. 112, no. 4, pp. 1689-1701.
- Hagolle, O., Huc, K., Villa Pascual, D., and Dedieu, G., 2010. A multi-temporal method for cloud detection, applied to FORMOSAT-2, VENUS, LANDSAT and SENTINEL-2 images. *Remote Sensing of Environment*, 114, pp. 1747-1755.
- Idbraim, S. and Ducrot, D., 2009, An unsupervised classification using a novel ICM method with constraints for land cover mapping from remote sensing imagery. *International Review on Computers and Software*

Exploring the potential of crop specific green area index time series to improve yield estimation at regional scale

Grégory Duveiller¹, Allard de Wit², Louis Kouadio³, Bakary Djaby³, Yannick Curnel^{1,4}, Bernard Tychon³ and Pierre Defourny¹

¹ *Earth and Life Institute, Université catholique de Louvain (UCL), Louvain-la-Neuve, Belgium.*

² *Centre for Geo-Information of Alterra (Alterra-CGI), Wageningen UR, Wageningen, The Netherlands.*

³ *Department of Environmental Sciences and Management, Université de Liege (ULg), Arlon, Belgium*

⁴ *Walloon Agricultural Research Centre (CRA-W), Gembloux, Belgium.*
gregory.duveiller@uclouvain.be

ABSTRACT – Crop status, such as the Green Area Index (GAI), can be retrieved from satellite observations by modelling and inverting the radiative transfer within the canopy. Providing such information along the growing season can potentially improve crop growth modelling and yield estimation. However, such approaches have proven difficult to apply on coarse resolution satellite data due to the fragmented land cover in many parts of the World. Advances in operational crop mapping will sooner or later allow the production of crop maps relatively early in the crop growth season, thereby providing an opportunity to sample pixels from medium/coarse spatial resolution data with relatively high cover fraction of a particular crop type to derive crop specific GAI time series. This research explores how to use such time series derived from MODIS to produce indicators of crop yield using two approaches over part of Belgium. The first method consists in looking at metrics of the decreasing part of the GAI curves when senescence occurs. Such metrics, like the position of the inflexion point, have been shown to be significantly correlated to yield. The second approach is to optimize the WOFOST model used in the European Crop Growth Monitoring System (CGMS) based on the GAI time series. Results show that, although the optimized model shows considerably better performance than the model running on the default parameter, the model is sometimes outperformed by the simpler metric approach. In all cases, indicators including remote sensing information provide better estimates than the average yield of previous years.

1 INTRODUCTION

Earth observation can bring valuable information for monitoring crop growth and thereby improve crop yield forecasting. Currently operational systems working over large geographic extents, such as the MARS Crop Yield Forecasting System (MCYFS), only rely on remote sensing to complement their analysis based on agro-meteorological crop growth simulations when unexpected circumstances are encountered (e.g. extreme weather conditions, unexpected agricultural practices, uncertain soil conditions, etc.). To provide a diagnostic of the deviation from normal conditions, the NDVI profile of the current year is compared to the average profile over previous years.

A finer description of the crop status can be retrieved from satellite observations in the form of biophysical variables by modelling and inverting the radiative transfer within the canopy. Providing crop specific biophysical variables such as Green Area

index (GAI) along the growing season at relevant spatial and temporal resolutions can help improve crop growth modelling either by forcing the model, by recalibrating it or by updating its temporal trajectory using assimilation techniques (Moulin et al. 1998, Dorigo et al. 2007). At field level, such approaches have long been used based on high spatial resolution imagery such as Landsat or SPOT/HRV (e.g. Bouman, 1992; Launay & Guerif, 2005; Hadria et al., 2010). To apply these techniques in an operational crop growth monitoring context, the satellite observations need to be acquired with high temporal frequency and over large geographic extents, conditions currently satisfied only by instruments with coarse pixels (e.g. MODIS or MERIS). In order to keep the information within a pixel crop specific, studies working on assimilation of such observations into crop models generally focus on landscapes with relatively homogeneous land cover (e.g. Bastiaanssen, 2003; Doraiswamy et al., 2005; Patel et al., 2006). However, spatial patterns in agricultural landscapes are generally much more

fragmented with variable requirements in terms of spatial resolution (Duveiller & Defourny 2010).

The current diversity of EO instruments, with wide swath instruments is bound to stimulate the development of techniques to produce crop maps in the current growing season. This will provide an opportunity of sampling pixels from medium/coarse spatial resolution data with a relatively high cover fraction of a particular crop type for deriving crop specific GAI time series (Duveiller et al. 2010, this issue). The aim of the research presented here is to explore two alternatives for using such time series to derive information about crop yield. The first approach consists in looking at metrics of the decreasing part of the GAI curves when senescence occurs. Such metrics, like the position (in degree-days) of the inflexion point, have been shown to be indicators of amount of grain-filling and hence relate to yield (Gooding et al. 2000). The second approach explores the compatibility with the European Crop Growth Monitoring System (CGMS) used in MCYFS. In this study, within-season updates of relevant crop parameters in the WOFOST crop model are applied to improve the crop simulations and yield forecasts.

2 STUDY SITE AND DATA

A critical aspect in relating remote sensing observations with crop specific yield is to know where the target crop has been sown in a given year. In Belgium, such information is available with the vector database of the SIGEC (*Système Intégré de Gestion et de Contrôle*) built by the government of the Walloon region. The extent of the area covered by the SIGEC database is shown on figure 1 and consists of 5 NUTS2 European administrative units for which official yield statistics are available from the EUROSTAT database of the European Commission (<http://epp.eurostat.ec.europa.eu>). All the fields covered by winter wheat were selected and rasterized to create crop masks for years 2003 to 2007.

The Earth Observation data used in this study consists of daily MODIS reflectance data from both Terra and Aqua platforms downloaded from the NASA Distributed Active Archive Center (DAAC) (<https://wist.echo.nasa.gov/api/>). Collection 5 products are used, for which atmospherically corrected reflectance is available at 250m in the red and near-infrared spectral domains. Only pixels whose observation footprint overlaps winter wheat crop masks by over 75% are retained. The methodology used to estimate this overlap, or crop specific pixel purity, is described in another study within this book (Duveiller et al. 2010, this issue). The range of selected time series ranges from 3839 to 5017 depending on the year studied.

The WOFOST crop model was implemented over the test area on a 10x10 km grid. Soil maps, weather data and crop parameters were derived from the operational MCYFS and mapped onto the model grid.

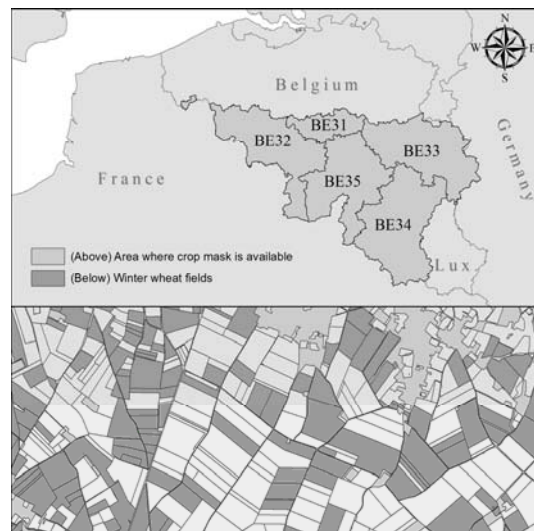


Figure 1. The study area (above) covers 5 NUTS2 administrative regions for which a winter specific crop mask can be built using the SIGEC dataset (below).

3 METHODOLOGY

3.1 Generating crop specific GAI time series

GAI is retrieved from multispectral reflectance using a neural network technique (NNT) trained over canopy radiative transfer simulations. This hybrid approach combines advantages of statistical and physical approaches in biophysical variable retrieval (Dorigo et al. 2007). The approach is based on the algorithm conceived by Baret et al. (2007) to derive the global LAI product developed within the CYCLOPES (Carbon cYcle and Change in Land Observational Products from an Ensemble of Satellites) project from SPOT/VEGETATION data. The radiative transfer model used for the simulations is PROSAIL (Baret et al. 1992), a coupling of the canopy reflectance model SAIL (Verhoef 1984) to the leaf optical properties model PROSPECT (Jacquemoud & Baret 1990). The input of the NNT is red and NIR MODIS reflectance, plus the angles describing the acquisition geometry (view and sun zenith angles and the relative azimuth angle between the imaging instrument and the sun). Once punctual GAI estimations are obtained from the individual observations of both MODIS instruments (Terra and Aqua), a temporal interpolation is applied to combine all the information together for a given spatial point. This interpolation is based on a semi-mechanistic canopy structure dynamic model (CSDM)

which relates GAI to thermal time by way of a simple mathematical relationship representing the combined effect of growth and senescence, taking the form of:

$$GAI(tt) = k \cdot [1 / (1 + \exp(-a(tt - T_0 - T_a)))^c - \exp(b(tt - T_0 - T_b))] \quad (1)$$

where a and b define the rates of growth and senescence, c is a parameter allowing some plasticity to the shape of the curve, k is a scaling coefficient and T_0 , T_a and T_b are the thermal times of plant emergence, mid-growth and mid-senescence. The driving variable, thermal time (tt), is simply the cumulated daily average temperatures above 0°C (the base temperature of winter wheat below which its growth does not progress).

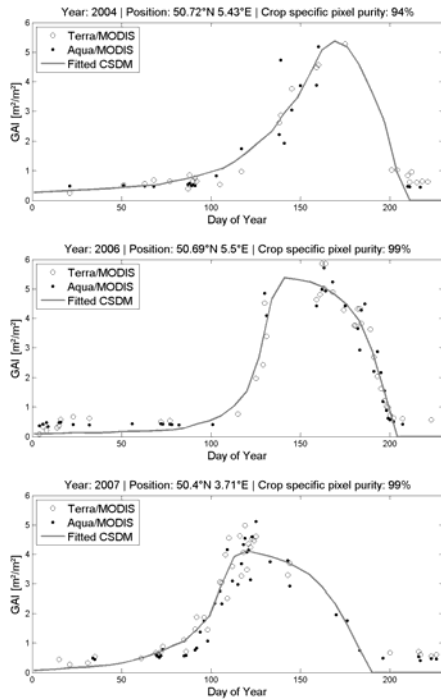


Figure 2. Examples of punctual GAI estimates from both MODIS instruments and the resulting CSDM fit for 3 different time series in different years.

The punctual GAI estimates and the CSDM fit are calculated for all selected pixel time series over the study area and for every year considered. Figure 2 illustrates the results for 3 different GAI time series selected from 3 different years, reflecting the inter-annual variability in the GAI dynamic and in MODIS data availability due to cloud cover.

3.2 Filtering out inadequate time series

Working with MODIS pixels over a fragmented agricultural landscape such as Belgium can result in noisy time series due to signal contamination from adjacent land covers. To ensure that the following processing steps relate only to GAI time series that make agronomic sense, those that do not satisfy the following criteria were discarded:

- Number of observations in growing season ≥ 9 (roughly one every 10 days)
- Maximum GAI value reached by the CSDM > 3.5
- Day of year when maximum GAI is reached by the CSDM must be between 120 and 180
- RRMSE between CSDM fit and observations (temporal consistency) $< 15\%$
- Pre-season GAI < 1.5
- Post-harvest GAI < 1.0

3.3 Calculating metrics to characterize senescence and modelling yield estimates

The method for calculating metrics from the decreasing curves of GAI and for modelling wheat yield is detailed in Kouadio et al. (2010). This approach consists of fitting two functions proposed by Gooding et al. (2000), a modified Gompertz model (Eq. 2) and a logistic model (Eq.3), on the decreasing part of the GAI curve for each point.

$$G = A * \text{EXP}[-\text{EXP}(-k*(t - m))] \quad (2)$$

$$G = A / [1 + \text{EXP}(-k*(t - m))] \quad (3)$$

where G is the GAI value, A is the initial percentage of GAI, m is the position of the inflexion point in the decreasing part of the GAI curve, k is the relative senescence rate, and t is the thermal time. Time period begins at the date where GAI equal to GAI_{\max} . At this date the time is set to 0 and then cumulated for the next days. Thermal time for each point is calculated with data from grid weather in which it falls in.

3.4 Optimizing WOFOST

Individual GAI time-series are used to optimize two important parameters in the WOFOST model. The first model parameter determines the initial amount of biomass and leaf area (TDWI). This parameter has a strong influence on the rate of increase and the maximum of GAI in the first part of the growing season. The second model parameter is the life span of leaves which determines the rate of senescence and therefore the decrease of GAI in the second part of the growing season.

For finding the optimum model fit, the Weighted Mean Absolute Error (WMAE) between the modelled

GAI (GAI_m) and the n MODIS observed GAI (GAI_o) was minimized:

$$WMAE = \frac{\sum_1^n w \cdot |GAI_o - GAI_m|}{\sum_1^n w} \quad (4)$$

The weight of a GAI observation is inversely proportional to the number of observations in a temporal window (size 11) around each observation.

The optimisation was implemented through an exhaustive search algorithm which tested all combinations of TDWI/SPAN within a specified search domain. The range of TDWI was set between 50 and 500 kg/ha in steps of 10 kg/ha while the range of SPAN was set between 20 and 50 days in steps of 1 day.

The optimization procedure was applied on all selected GAI time series and over all available years. This approach yields the joint distribution of the SPAN/TDWI parameters for the Walloon region for each year.

3.5 Aggregating towards regional level

The GAI metrics were aggregated towards NUTS regions by taking the mean value of each metric for each NUTS region for each year. Although this approach is simple, there are questions about the representativeness of this approach given that the available GAI time-series differ strongly from year to year and region to region.

Therefore, the WOFOST simulated biomass values resulting from the optimization described in section 3.4 were not directly averaged to NUTS regions. Instead, we assumed that the joint distribution of TDWI/SPAN values was representative for the entire Walloon region. Next, for each 10x10 km grid, WOFOST was applied in ensemble-mode where the TDWI/SPAN values used were sampled from the TDWI/SPAN joint distribution of each year. From the ensemble of simulated biomass values (total biomass and yield) the average values per grid were calculated and spatially aggregated to regional level using the area of wheat per 10x10 grid as weight.

This procedure was repeated for the baseline run where a single WOFOST run was executed using the default values for TDWI/SPAN.

3.6 Comparison with EUROSTAT statistics

A direct comparison with EUROSTAT yield statistics is not useful as there are substantial biases between EUROSTAT and WOFOST modelled yields. Moreover, the GAI metrics cannot be compared directly as their units deviate from the EUROSTAT

yields. All outputs are therefore treated as indicators which are used in a regression model between EUROSTAT yield as the variable to be predicted and the various indicators as explanatory variables. Table 1 lists the indicators used in the regression models with the EUROSTAT yield statistics. Note that two different WOFOST outputs (yield and total biomass) in either default or ensemble (i.e. optimized) mode are used as indicators. Note further that multiple linear regressions were not used to avoid possible collinearity problems between indicators.

Table 1. List of indicator codes and names.

Code	Indicator name
01_BE	WOFOST Total biomass – <i>Ensemble</i>
02_YE	WOFOST Yield – <i>Ensemble</i>
03_BD	WOFOST Total biomass – <i>Default</i>
04_YD	WOFOST Yield – <i>Default</i>
05_MG	M parameter in the Gompertz model
06_KG	K parameter in the Gompertz model
07_GM	GAI_{max}
08_ML	M parameter in the logistic model
09_KL	K parameter in the logistic model

4 RESULTS

Regression analysis between indicators and EUROSTAT reported yields is done separately for each NUTS region as there may be large differences between NUTS regions as a result of socio-economic conditions. Table 2 lists, for each NUTS region, the statistical properties of the 4 best predictors and the average yield as the baseline predictor (the *None* model). Note that region BE34 was due to a lack of sufficient time series in the area. The reason for this is that winter wheat is seldom cultivated in this region, and when it is, the fields used are often too small for MODIS pixels.

For region BE31, the K parameters of the Gompertz and Logistic model are the best predictors with nearly 60% of variance explained. GAI_{max} explains nearly 50%, while the Ensemble total biomass is the next best predictor with only 21%. Only the two best predictors improve beyond the average as their Leave-One-Out (LOO) error is lower than the one of the *None* model. However, none of the predictors is significant.

For region BE32, the GAI_{max} is by far the best predictor with 87% variance explained, a LOO error clearly smaller than the *None* model and a highly significant T-value. The remaining models, (K parameters of the Gompertz and Logistic model, Ensemble total biomass) show similar R^2 values but strongly varying LOO values.

For region BE33, the M parameters of the Gompertz and Logistic model are the best predictors

with 69% and 74% variance explained. The latter is significant at $\alpha=0.1$ and has a LOO lower than the *None* model. The remaining two models (Ensemble total biomass and GAI_{max}) show similar R^2 (~50%) but do not improve the LOO. Moreover the Ensemble total biomass has a negative T-value indicating that the relationship with EUROSTAT yield is negative.

For region BE35, the Ensemble total biomass is the best predictor with 75% of variance explained, an LOO clearly lower than the *None* model and a T-value significant at $\alpha=0.1$. The remaining models (M parameters of the Gompertz and Logistic model, GAI_{max}) show R^2 values ranging from 30% to 50%, but none of these models have a LOO value lower than the *None* model.

Table 2. Results from regression with EUROSTAT reported yields. SDr=Std. Dev. of the model residuals. LOO=leave-one-out error. Stud.T= Student-T statistic.

Brabant Wallon (BE31)	R^2	SDr	LOO	Stud.T
09_KL	59.5	0.08	0.10	2.10
06_KG	57.7	0.09	0.11	2.02
07_GM	50.1	0.09	0.16	1.74
02_YE	21.1	0.12	0.19	-0.90
<i>None</i>	-	0.12	0.13	-
Hainaut (BE32)				
07_GM	87.2	0.23	0.40	4.52**
09_KL	51.3	0.45	0.51	1.78
06_KG	45.9	0.48	1.22	1.60
01_BE	42.4	0.49	0.71	1.49
<i>None</i>	-	0.56	0.63	-
Liege (BE33)				
08_ML	74.1	0.25	0.40	2.93*
05_MG	68.8	0.27	0.91	2.57
01_BE	48.9	0.35	0.73	-1.69
07_GM	46.1	0.36	0.65	1.60
<i>None</i>	-	0.42	0.47	-
Namur (BE35)				
01_BE	74.8	0.26	0.36	2.98*
07_GM	49.1	0.37	1.04	1.70
05_MG	33.9	0.42	0.80	1.24
08_ML	30.5	0.43	0.75	1.15
<i>None</i>	-	0.45	0.50	-

** significant at $\alpha=0.05$

* significant at $\alpha=0.1$

5 DISCUSSIONS

The objective of our approach was to evaluate if crop specific MODIS-derived GAI time-series can be used to derive crop yield indicators that better characterize the inter-annual variability in wheat yields as reported by EUROSTAT. This objective was tested through the use of simple metrics derived directly from the GAI time-series and through assimilation of these in a biophysical model.

The results demonstrate that in all four regions indicators can be found that improve the LOO error beyond the *None* model (the baseline predictor based on the average). Region BE31 is the only region where none of the indicators has a significant T-value. However, region BE31 has very low variability in crop yield with a standard deviation of only 0.12 ton/ha.

When looking at distribution of the four best performing indicators over the regions, it is the GAI_{max} which is consistently listed among the best four. The ensemble total biomass is present in 3 out of 4 regions, with the remaining region (BE31) listing the ensemble yield.

The K parameters of the Gompertz and Logistic models are selected for regions BE31 and BE32, while the M parameters of the Gompertz and Logistic model are selected for BE33 and BE35. Conversely, the M parameters have no performance at all in regions BE33 and BE35, and similarly the K parameters not in regions BE31 and BE32. Although these indicators are among the best performing in some regions, the inconsequent behaviour of these indicators needs further investigation using a larger dataset.

Finally, the indicators which do not include any remote sensing data ('03 Total biomass – default' and '04 Yield – default') are not listed for any region showing that they are not correlated with the reported crop yield at all. This is a strong indication that the MODIS-derived GAI time-series are improving the prediction of crop yield at regional level.

6 CONCLUSIONS

The main conclusion from this work is that, for all regions studied, indicators derived from GAI time-series estimated from MODIS are generally better predictors of the EUROSTAT reported crop yield than average yield. It also shows that the WOFOST model optimized on the GAI time-series (WOFOST ensemble results) shows considerably better performance than the model running on the default parameters. Nevertheless, the WOFOST ensemble results are outperformed by more simple indicators in 3 out of 4 regions, albeit different indicators for each region.

The current analysis only spans 5 years of EUROSTAT reported yields (2003-2007) over 5

regions in Belgium. Longer time-series and more regions will be needed to confirm those results and obtain a better insight in the stability of the different indicators.

7 ACKNOWLEDGEMENTS

This research was funded by the Belgian Fond de la Recherche Scientifique-FNRS by way of a PhD grant to the first author. The research also falls in the framework of the GLOBAM project which is financed by the Belgian Scientific Policy (BELSPO) with the STEREO II programme. The authors also thank the Ministry of the Walloon Region (Belgium) for providing the SIGEC database.

8 REFERENCES

- Baret, F., Hagolle, O., Geiger, B., Bicheron, P., Miras, B., Huc, M., Berthelot, B., Nino, F., Weiss, M., Samain, O., Roujean, J. L. & Leroy, M. (2007), 'LAI, fAPAR and fCOVER cyclopes global products derived from vegetation: Part 1: Principles of the algorithm', *Remote Sensing of Environment* **110**(3), 275–286.
- Baret, F., Jacquemoud, S., Guyot, G. & Leprieur, C. (1992), 'Modeled analysis of the biophysical nature of spectral shifts and comparison with information-content of broad bands', *Remote Sensing of Environment* **41**(2-3), 133–142.
- Bastiaanssen, W. & Ali, S., 2003. 'A new crop yield forecasting model based on satellite measurements applied across the Indus Basin, Pakistan'. *Agriculture, Ecosystems & Environment*, **94**(3): 321-340.
- Bouman, B.A.M., (1992). 'Linking Physical Remote-Sensing Models with Crop Growth Simulation-Models, Applied for Sugar-Beet'. *International Journal of Remote Sensing*, **13**(14): 2565-2581.
- Doraiswamy, P., Sinclair, T.R., Hollinger, S., Akhmedov, B., Stern, A., & Prueger, J., (2005). 'Application of MODIS derived parameters for regional crop yield assessment'. *Remote Sensing of Environment*, **97**(2): 192-202.
- Dorigo, W., Zurita-Milla, R., de Wit, A., Brazile, J., Singh, R. & Schaepman, M. (2007), 'A review on reflective remote sensing and data assimilation techniques for enhanced agroecosystem modeling', *International Journal of Applied Earth Observation and Geoinformation* **9**, 165–193.
- Duveiller, G., Weiss, M., Baret, F., de Wit, A., & Defourny, P. (2010), Retrieving crop specific green area index from remote sensing data when the spatial resolution is close to the target field size, *Proceedings of the 3rd International Symposium on Recent Advances in Quantitative Remote Sensing (RAQRS'III)*, Torrent (Valencia), Spain, 2010, edited by J. Sobrino.
- Duveiller, G. & Defourny, P. (2010), 'A conceptual framework to define the spatial resolution requirements for agricultural monitoring using remote sensing', *Remote Sensing of Environment* **114**(11), 2637–2650.
- Jacquemoud, S. & Baret, F. (1990), 'Prospect: A model of leaf optical properties spectra', *Remote Sensing of Environment* **34**(2), 75–91.
- Gooding, M.J., Dimmock, J.P.R.E., France, J., & Jones, S.A., (2000) 'Green leaf area decline of wheat flag leaves: the influence of fungicides and relationships with mean grain weight and grain yield', *Annals of Applied Biology* **136**, 77–84.
- Hadria, R., Duchemin, B., Jarlan, L.; Dedieu, G., Baup, F., Khabba, S., Olioso, A. & Le Toan, T., (2010). 'Potentiality of optical and radar satellite data at high spatio-temporal resolutions for the monitoring of irrigated wheat crops in Morocco'. *International Journal of Applied Earth Observation and Geoinformation*, **12**: S32-S37.
- Kouadio, L., Duveiller, G., Djaby, B., Defourny, P., & Tychon, B. (2010) Wheat Yield Estimates at NUTS-3 level using MODIS data: an approach based on the decreasing curves of green area index temporal profiles. *Proceedings of RSPSoc2010 Annual Conference*, 1st-3rd September 2010, Cork, Ireland (Nottingham: RSPSoc), pp. 214-221.
- Launay, M. and Guerif, M., (2005). 'Assimilating remote sensing data into a crop model to improve predictive performance for spatial applications'. *Agriculture Ecosystems & Environment*, **111**(1-4): 321-339.
- Moulin, S., Bondeau, A. & Delecalle, R. (1998), 'Combining agricultural crop models and satellite observations: from field to regional scales', *International Journal of Remote Sensing* **19**(6), 1021–1036.
- Patel, N.R., Bhattacharjee, B., Mohammed, A.J., Tanupriya, B. and Saha, S.K., (2006). 'Remote sensing of regional yield assessment of wheat in Haryana, India'. *International Journal of Remote Sensing*, **27**(19): 4071-4090.
- Verhoef, W. (1984), 'Light scattering by leaf layers with application to canopy reflectance modeling: The sail model', *Remote Sensing of Environment* **16**(2), 125–141.

Quantitative remote sensing with off-the-shelf instruments on a small UAV

Ursula Kirchgaessner^a, Uwe Putze^a, Maria von Schoenermark^b

^a Institute of Space Systems, University of Stuttgart -
kirchgaessner@irs.uni-stuttgart.de, putze@irs.uni-stuttgart.de

^b Space Operations and Astronaut Training, German Aerospace Center (DLR) -
maria.schoenermark@dlr.de

ABSTRACT *The Stuttgarter Adler is a small, remote controlled aircraft which was designed as a platform for small-scale remote sensing from 100 to 300 meters above ground. Equipped with off-the-shelf cameras and a spectrometer it offers a flexible and inexpensive means to collect detailed remote sensing data in the visible and near infrared as well as in the thermal infrared range. This paper shows the capability of the platform with its VIS/NIR and thermal instrumentation to acquire remote sensing data of high resolution. A number of calibration methods have been adapted and procedures have been developed for this purpose. Digital numbers of the VIS/NIR instruments are converted to radiance values by calibration. The radiometric accuracy of the VIS/NIR cameras and of the Spectrometer with the current calibration is better than 7 percent of spectral radiance. Relative errors during calibration caused by noise range from 1 percent for the spectrometer to 2 percent for the NIR-camera. In order to derive reflectance values, the atmospheric properties are measured during image acquisition and used as input to numerical radiation transport to calculate irradiance. For geometric processing and referencing, recent developments in photogrammetric methods, based on image matching and robust bundle adjustment, have been adapted and applied to the data. Image data can be georeferenced with an accuracy of 0.02 to 0.04 metres. First steps of quality evaluation have been taken for VIS/NIR airborne data by comparison between the instruments and calculation of reflectance.*

1 Introduction

Remote sensing promises great environmental and economic benefit by means of monitoring of the environment and precision farming. However, current satellite and aerial data can satisfy the requirements of temporal and geometric resolution only at great expense. Today, unmanned aerial vehicle (UAV) technology is feasible for low-cost remote sensing, but data quality must be ensured. Several factors affect the properties of airborne platforms and the data collected using them. First of all, the platform itself and its aerodynamic properties determine the size and weight of the instrumentation, as well as possible flight paths and duration.

Equipped with off-the-shelf sensors and instruments, this platform offers the means to collect high resolution remote sensing data at low cost. The current instrumentation consists of three CCD-cameras and a spectrometer, or, alternatively, a thermal camera combined with one of the CCD-cameras.

Procedures for radiometric calibration of the instruments and correction of the data have been developed in order to calculate at-sensor radiances from digital numbers. They are based on methods developed for large airborne sensors and adapted to the presented instruments.

After initial geometric calibration of the instruments, orthorectification and georeferencing of the data is done with photogrammetric methods. Standard procedures, available in commercial software for processing of data from manned aircraft, cannot be applied easily due to the geometric properties of the implemented cameras and optics, as well as the unconventional flight block geometry. Therefore, a procedure for preprocessing has been derived from recent developments in photogrammetry.

Many methods have been suggested to refine satellite remote sensing data. These can be applied to airborne measurements as well. In order to derive spectral reflectance of surfaces from airborne measurements, incoming solar radiance is calculated numerically. The numerical calculation is based on aerosol depth and ozone column, as well as at-ground pressure and humidity.

2 Airborne Platform

In order to collect multi-angular and multi-temporal remote sensing data with great flexibility and frequency, the UAV "Stuttgarter Adler" has been developed at the University of Stuttgart during the last years. It is equipped with two electrical engines, PolyTech, 2.5 kW each, powered by lithium polymer batteries. The flight



Figure 1: Stuttgarter Adler



Figure 2: Thermal and VIS/NIR instrumentation

gear, electronics, and engines have been integrated into the wings and nacelles, leaving the fuselage for the instrumentation. For such aircraft, the total take-off mass is limited to 25 kilograms in Germany. With this limitation the payload allowance is 3 to 4 kilograms, depending on the batteries, of which two different sets are used. These permit a flight time of 15 and 25 minutes, respectively. Take off and landing require a paved or grass runway of 200 m length, the average flight speed of the aircraft is 12 m/s. Details of the airborne system and its navigation system have been described in [Schwarzbach et al., 2009].

3 Instrumentation

The payload instruments of the Stuttgarter Adler have been selected for quantitative remote sensing, considering the limitations of weight, size and cost. All instruments are commercial off-the-shelf units. Currently two sets of payload have been implemented and flown. The first set consists of three imaging instruments for the green, red and near infrared bands, along with a spectrometer covering the same wavelength region at a spectral resolution of four nanometres. The alternative payload is a thermal camera based on an uncooled microbolometer. All instruments are triggered simultaneously by a small electronics board.

Three "VC4068" industrial type cameras are mounted side by side in the aircraft. The detectors are CCD-arrays of 1280 by 1024 pixels with a dynamic range of 8 bit. The cameras are equipped with optics transmissive in the near IR and with different spectral filter in order to obtain red, green, and near infrared bands. The red and green cameras are equipped with the standard IR-blocker, but that of the NIR camera has

	VIS/NIR Cameras	Spectrometer	Thermal IR camera
Manuf./ Model:	Vision Components VC4068	Avantes AvaSpec 128	Dias Infrared Compact 320LC/50Hz
Sensor:	1280 × 1024 pixel CCD	128 pixel photo diode array	320 × 240 pixel uncooled bolometer
Dynamic Range:	8 bit	16 bit	16 bit
Channels:	green, red, NIR	VIS/NIR	TIR
Spectral ranges:	520, 630, 880 nm	500 - 1000 nm	8 - 14 µm
FWHM:	81, 135 nm	79, 6.3 nm	5.5 µm
focal length:	17.8 mm	20 mm	25 mm
Ground resolution:	10 cm	50 cm	30 cm
Swath width:	80 m	50 cm	80 m
Mass:	460 g per camera	150 g	1.6 kg

Table 1: Specification of the instruments. Ground resolution and swath width from 300m above ground.

been replaced with a glass transmissive in the IR by the manufacturer. Each camera contains its own internal memory and an interface for simultaneous triggering by the aircraft system. Aperture and focal length are fixed during image acquisition while integration time is determined and recorded for each individual image of each camera to maximise radiometric resolution but avoid saturation.

The "AvaSpec 128" spectrometer is mounted in the aircraft between two of the VC-cameras. It covers the wavelength range of 500 to 1000 nanometres in 128 continuous bands with a spectral resolution of approx. 4 nm while the FWHM of each band is 6.3 nm. Its photodetector-array offers a dynamic range of 16 bit. The settings of aperture, focal length and integration time are fixed. The spectrometer measurements are written to an external hard drive by the control electronics board also used for triggering.

The thermal camera "DIAS Pyroview 380L" is based on an uncooled microbolometer operating at maximum 50 Hz. Thermal resolution is given by the manufacturer with a noise equivalent temperature difference (NETD) of 0.11 K at 30°C at a distance of 0.4 m between camera and target [Budzier et al., 2006]. The camera is run and the data is recorded by proprietary software of the camera manufacturer which

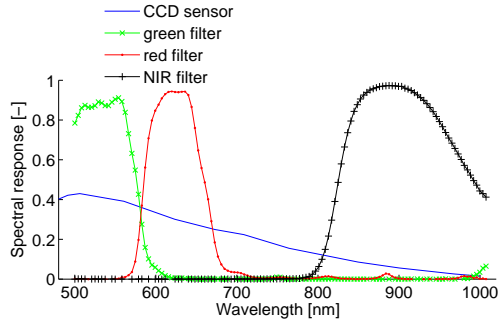


Figure 3: Sensor response and filter transmission

requires a Microsoft Windows operating system. In the aircraft, such a system is provided on a netbook-type personal computer, which satisfies the requirements of light weight and low battery consumption.

Detailed specification of the instruments are listed in table 1.

4 Calibration

4.1 Spectral calibration

The spectrometer wavelengths have been calibrated by the manufacturer using line sources at different wavelengths. The accuracy is given with 0.00 nm to 0.04 nm and the precision with ± 1.98 nm. The Full Width Half Maximum (FWHM) response of each Pixel is 6.4 nm. Hence the detector of the spectrometer has a pixel resolution of 4 nm, but the width of each channel is much larger.

The spectrometer was used to measure the transmission of the filter mounted on the VIS/NIR cameras. For the sensitivity of the CCD-sensors only a rough estimate was given, this is the largest uncertainty in the spectral calibration of the VIS/NIR cameras. The estimated sensor response and the measured filter transmission are shown in Figure 3. The total spectral response curve $R(\lambda)$ for each camera is calculated by multiplication of the corresponding filter transmission with the sensor response.

4.2 Radiometric calibration

To determine radiometric calibration factors a laboratory radiometric calibration has been performed on all VIS/NIR instruments according to [Beisl, 2006], with a calibrated integrating sphere as a source of homogeneous light. For the camera and spectrometer sensors, a linear radiometric model is assumed, where the grey values DN (digital numbers) registered by the sensors scale linearly with the incident spectral

radiance L , as well as the integration time according to

$$L = c_1 \frac{DN}{t}, \quad (1)$$

where c_1 is the radiometric gain. This equation assumes that DN is zero without illumination and that all pixels will respond equally to a certain radiance. Since this is not the case, two additional values are determined for each pixel individually.

DSNU Any CCD element will output a signal even if no illumination is present. This dark signal varies between individual elements of the same sensor, which is known as Dark Signal Non-Uniformity (DSNU). The DSNU of the instruments were obtained by taking a series of measurements with a lens cover mounted on the optics. By averaging the dark values over the series, a dark signal level was obtained for each pixel. The DSNU correction of any measurement image can then be performed by subtracting the DSNU value from the individual pixel values.

PRNU The signal response of a sensor's individual pixels varies due to manufacturing tolerances and lens effects. To compensate for this non-uniformity in signal response, the Photo Response Non-Uniformity (PRNU) is derived by illuminating the instrument with the integrating sphere. The PRNU of a sensor is defined as the ratio of the maximum value in the image to the actual pixel value of each individual pixel.

Since each pixel of the spectrometer registers a different wavelength, the PRNU is included in the radiometric gain and does not have to be determined separately.

Radiometric gain A band averaged spectral radiance L was calculated for every sensor band according to eq. 2, taking into account the spectral radiance of the integrating sphere as well as the sensitivity $R(\lambda)$ of the sensor as described in section 4.1.

$$L = \frac{\int L(\lambda)R(\lambda)d\lambda}{\int R(\lambda)d\lambda} \quad (2)$$

From this value, the radiometric gain c_1 is calculated for each camera, respectively for each pixel of the spectrometer. All calibration factors are applied during post-processing of the recorded data of each instrument in order to convert DN to spectral radiance.

Accuracy The relation between photo response and integration time was examined through measurements with variable integration times at a constant illumination by the integrating sphere. The deviation of the relation from linearity was then calculated in relation to a

	Integr Time ms	Noise DN	Noise %	Dark Signal DN
NIR	1	1.278	2.71	0.089
	2	1.722	1.94	0.094
	3	2.193	1.70	0.093
	4	2.490	1.50	0.074
red	1	1.395	1.93	0.107
	2	1.889	1.46	0.105
	3	2.354	1.26	0.107
	4	2.522	1.10	0.104
green	1	1.279	2.25	0.069
	2	1.653	1.60	0.068
	3	2.055	1.39	0.066
	4	2.402	1.24	0.064
Spectrom.300		28.755	0.09	1599

Table 2: Instrument noise at typical integration times.

linear fit At typical integration times of airborne measurements the deviation of linearity was found to be lower than 1.47%, 2.12%, and 2.06% of grey values for the green, red, and NIR camera system, respectively.

The spectral radiance calibration $L(\lambda)$ of the integrating sphere was performed by the manufacturer with an accuracy of 4% in the visual and 5% in the near infrared.

Precision The noise of the cameras and the spectrometer signal was calculated as a standard deviation over a series of images with constant illumination and integration time. The average image noise was found to be 1.60% (green), 1.46% (red), and 1.94% (NIR) of mean signal level for the cameras. The average signal noise of the spectrometer was found to be 0.09% of signal level. However, due to the low radiance of the integrating sphere in relation to an illumination by the sun, much lower signal levels and longer integration times had to be used in the lab. Therefore the noise levels during in-flight use are expected to be lower than the values obtained during calibration.

4.3 Geometry

A rough estimation of camera geometry is needed as input to geometric processing of the data, but it is determined more precisely by iteration during the bundle adjustment of the photogrammetric processing. Radiometric and geometric calibrations have been performed repeatedly. Camera geometry parameters are determined with a laboratory calibration field and associated evaluation software [Photometrix, 2004]. The estimated accuracy of image referencing is 0.3 pixels on average and the variance of focal length

is approximately 1 % for each of the VC-cameras. The cameras have proven to be sufficiently stable over time in order to allow photogrammetric processing as described in the following section.

A boresight calibration has been performed for the spectrometer, in order to determine the position of the measurement in the images. For this purpose, the spectrometer and the green camera were fixed to the frame used to mount the instruments in the aircraft. The two instruments were directed at a wall in 10 m distance, where a laser beam was pointed. The area at which the spectrometer responded to the signal, while the laser was moved across the wall, was outlined. Afterwards an image was taken with the camera. The pixels showing the outlined regions were defined as Region Of Interest (ROI), which identifies the area that the spectrometer measures. The image pixels inside the ROI are used for comparison of spectrometer and camera measurements, as described in section 7.

5 Georeferencing

A special photogrammetric workflow has been developed for orthorectification and georeferencing of the airborne images acquired with the Stuttgarter Adler. Standard procedures, which are available in commercial software for processing of image data from manned aircraft, cannot be applied easily. Partly, this is due to properties of the platform and instrumentation. The narrow viewing angle of the cameras results in uncertainty of reconstruction from stereo image pairs. The flight geometry does not satisfy standard stripes and blocks due to the relatively instable flight resulting from the small and lightweight system. More importantly, during flight the position of the aircraft is measured by means of GPS, but not its orientation. Therefore, an important requirement to the photogrammetric workflow was the possibility to process the image data without prior knowledge of exterior orientation (EO), that is orientation and position of the cameras in geographic coordinates during acquisition of each image. The structure from motion software "Bundler" [Snavely et al., 2007] has been used to calculate the relative position of the images and their matching points. From measurement of ground control points in stereo image pairs a 7-parameter-transformation from the model coordinates to the geographic coordinate system can be calculated and applied to the camera orientation. With the resulting EO in geographic coordinates, georeferenced images can be produced. Accuracy has been shown to be 0.056m and 0.048m meters horizontally and 0.38m meters vertical to the ground [Kirchgäßner et al., 2010].

Alternatively, the EO can be used as input to standard software for further processing. The above described data has been processed further in Match-AT [Sigle and Heuchel, 2001]. The achieved accuracies



Figure 4: Example of georeferenced colored infrared mosaic (NIR-Red-Green).

are 0.035m and 0.024m in horizontal directions and 0.212m vertically. Although each camera has to be processed individually for orthophotos, the processing with "Bundler" has to be run only once for each flight if the orientation is to be refined with other software. The resulting EO is sufficient as input to Match-AT in order to define flight geometry for each camera.

Finally, layer stacking and mosaicking can be used to merge the resulting orthophotos as required by each application. An example of a colored infrared georeferenced mosaic is shown in Figure 4, consisting of a detail of the overlap region of three images with the three bands acquired by the VC-cameras.

Georeferencing of the spectrometer measurements is based on the location of the ROI in the image determined by the boresight calibration described above. Projection to the ground according to the camera's EO will then deliver the coordinates of each spectrum measurement.

6 Reflectance

For many applications reflectance values are needed instead of radiances. The Biconical (or Bidirectional) Reflectance Factor (BRF) is defined by

$$R = \frac{L^\uparrow(\vartheta, \phi, \vartheta_i, \phi_i) \cdot \pi}{E^\downarrow(\vartheta_i, \phi_i)} \quad (3)$$

where the irradiance $E^\downarrow(\vartheta_i, \phi_i)$ is the sum of direct and diffuse incoming radiation. $E^\downarrow(\vartheta_i, \phi_i)$ is calculated numerically using the radiative transfer code MODTRAN4 [Berk et al., 2003]. Several atmospheric parameters are obtained during image acquisition as input to the numerical calculation. Aerosol Optical Depth (AOD) is derived from continuous measurements with a sun photometer "SP1A". Air pressure, temperature, and humidity at ground level are measured by a meteorological station or a portable instrument. Additionally, the ozone column from the instrument

TOMS [NASA, 2010] for the day of interest is entered. The atmospheric profile "Midaltitude Summer" and the aerosol model "Rural" is scaled according to these parameters and ground altitude.

In order to derive the BRF from the spectral measurements, the irradiance is convolved to the wavelengths of the spectrometer with a triangular slit function. The total width of the slit function is set to twice the FWHM of each pixel. Due to the applied slit function the resulting BRF is erroneous at wavelengths next to the strong absorption bands of oxygen at 760 nm and water vapour around 940 nm. These wavelengths must be excluded from evaluation. The wavelengths of the spectrometer usable for this method are thus from 500.1 nm to 749.3 nm, from 769.3 nm to 922.8 nm, and from 984.5 nm to 1004 nm.

7 Airborne Measurements

The first step to evaluate the airborne data is to test the consistency between instruments. In order to make spectrometer measurements comparable with the image data, the spectrometer data is averaged over the FWHM of the cameras' bands. In the case of the green band the lower boundary of the FWHM is 10 nm lower than the smallest wavelength of the spectrometer, therefore the averaging can only be applied over the available range. The resulting inaccuracy depends on the target's spectral properties but it is assumed to be negligible for natural targets. The image data is averaged over the "Region of Interest" (ROI) which includes those pixels that show the area measured by the spectrometer. The pixels in the ROI are weighted with a Gaussian function

$$h_g(n) = e^{-\frac{n^2}{2\sigma^2}}, \quad (4)$$

where n is the number of elements and σ is the standard deviation. Since the ROI is rectangular, σ and n is chosen independently for X and Y direction of the ROI in order to fit their width. To adapt σ to the size of the ROI it is set to $\frac{1}{2}n$. The middle pixel of the ROI is thus weighted with factor 1 and the corner pixels with factor 0.34.

Four examples are shown in Figure 5, where two datasets show vegetation and the other two represent bare ground. The differences between the instruments are mainly caused by the inaccuracy of the boresight calibration between the spectrometer and the cameras.

8 Conclusion

The accuracy of the resulting radiance values depends on the light source and the linear model of the measurements and is better than 7%. The precision depends on detector noise, the values are less than 3%. Accuracy of georeferencing has been shown to be 0.056 m and 0.048 m horizontally and 0.38 m vertically to the ground. Further processing with standard tools improves accuracy to better than 0.04 m horizontally.

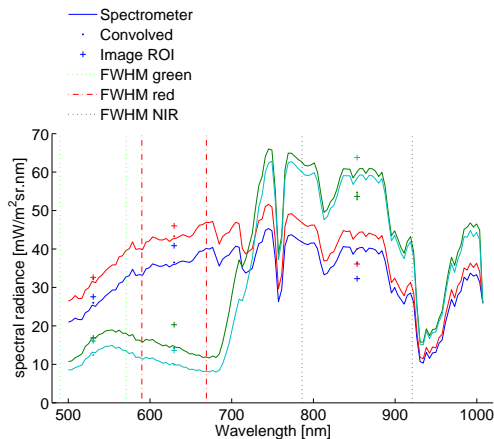


Figure 5: Example of spectrometer data with corresponding image data.

Although the data could not yet be evaluated by vicarious calibration, comparison between the VIS/NIR instruments and with atmospheric radiation transport calculations shows good results. The radiance values can be used as input to radiation transport models for vegetation.

The boresight calibration of the spectrometer has to be repeated to increase accuracy and precision of the ROI. Most importantly, the measurement has to be adapted to the depth of field of the spectrometer optics, which is focused at infinity and results in a blurring effect with calibration at only 10 m distance.

Compared to manned aircraft and satellites, the platform is very inexpensive and allows frequent measurements of the surfaces of interest.

References

- Beisl, U. Absolute spectroradiometric calibration of the ADS40 sensor. *International Archives of Photogrammetry, Remote Sensing and Spatial Information Sciences*, XXXVI (part1), on CD-ROM:5, 2006.
- Berk, A., Anderson, G. P., Acharya, P. K., Chetwynd, J. H., Bernstein, L. S., Shettle, E. P., Matthew, M., and s.m. Adler-Golden. *MODTRAN4 Version 3 Revision 1 User's Manual*. Air Force Research Laboratory, February 2003.
- Budzier, H., Krause, V., Böhmer, S., Gerlach, G., and Hoffmann, U. Fast microbolometer-based infrared camera system. In *Sensor & Test 2006 Proceedings*, pages 337–340. AMA Fachverband für Sensorik, 2006.
- Kirchgäßner, U., Putze, U., von Schönermark, M., and Haala, N. Anforderungen an die Auswertung UAV-gestützter Fernerkundungsdaten. In *DGPF Tagungsband*, 2010.
- NASA. Total ozone mapping spectrometer, 2010.
- Photometrix. Report on accuracy test of iWitness 3d measurement system. Technical report, Photometrix Pty Ltd, PO Box 3023, Kew, Vic 3101, Australia, 2004.
- Schwarzbach, M., Putze, U., Kirchgässner, U., and v. Schoenermark, M. Acquisition of high quality remote sensing data using a uav controlled by an open source autopilot. *Proceedings of the ASME 2009 International Design Engineering Technical Conferences & Computers and Information in Engineering Conference*, IDETC/CIE 2009 (DETC2009-86725), 2009.
- Sigle, M. and Heuchel, T. MATCH-AT: Recent developments and performance. *Photogrammetric Week 01*, pages 189–194, 2001.
- Snaveley, N., Seitz, S., and Szeliski, R. Modeling the world from internet photo collections. *international journal of computer vision*. 2007.

Potential of multi-directional spectral data collected with a digital aerial frame camera to retrieve forest canopy characteristics

T. Koukal, W. Schneider,
BOKU – University of Natural Resources and Life Sciences, Vienna
Institute of Surveying, Remote Sensing and Land Information
Peter-Jordan-Straße 82, A-1190 Vienna, Austria
tatjana.koukal@boku.ac.at, werner.schneider@boku.ac.at

ABSTRACT - In a previous study (Koukal and Schneider, 2009) it has been shown that the parameters of BRDF models describing individual forest plots can be estimated from digital aerial photos taken with a frame camera (Vexcel UltraCamD) with large forward and side overlap. In general, good fits could be achieved for the models under investigation. Modelled and plotted BRFs showed promising and explainable differences in forward and backward scattering depending on basic forest parameters such as tree species and age. Based on this work, the present study investigates the potential of BRDF model parameters for discriminating between different land cover types. It is assumed that the parameters derived by model inversion quantify and describe the reflectance anisotropy of surfaces and that for similar surfaces similar sets of model parameters are retrieved. The focus of the contribution is on forest cover types. Both coniferous and deciduous stands differing in age and crown cover are analysed. The variability of the estimated model parameters within and between various forest types is determined. We compare the information value of the parameters of three common semi-empirical BRDF models: RPV, Ross-Li, WAK (Dymond). Finally, the contribution quantifies the improvement of discrimination of various forest covers when directional signatures are added to the pure spectral signatures.

1 INTRODUCTION

The reflectance anisotropy of land surfaces depends on the three-dimensional structure and optical properties of the surface. It can be described by the Bidirectional Reflectance Distribution Function (BRDF). This contribution concentrates on BRDF-related effects in aerial photos of forests.

Even though automatic image analysis methods are very common for satellite imagery, difficulties arise when these methods are to be applied to aerial photos. An important reason for this is the high variability of an object's appearance introduced by different illumination-viewer-geometries within one image due to the wide field of view of aerial cameras.

However, the fact that the signatures in aerial photos are highly affected by the anisotropic reflectance properties is not only a disadvantage: it can also be seen as a source of additional information for deducing land cover (e.g. forest) parameters.

Furthermore, digital airborne imagery appears as a promising tool for studying directional reflectance characteristics of natural surfaces. Especially in the case of forest, it is impossible to perform directional measurements in the lab and special constructions such as cranes or towers are required for measurements in the field. These measurements are difficult to perform and are limited to small areas.

Therefore, aerial photos taken with a digital camera may be an interesting alternative approach.

In this study, images taken with a digital frame camera (Vexcel UltraCamD) with high forward and side overlap are used (Figure 1). The number of view directions that is a key factor in BRDF analysis depends on the forward and side overlap. In analogue aerial surveys the standard forward overlap is 60 %. This ensures that each terrain element appears on at least two images allowing stereo image analysis. Nowadays, digital aerial surveys with 80 % forward overlap are common practice. Forward overlaps of 90 % and higher are technically feasible and provide 10 view directions and more per flight line.

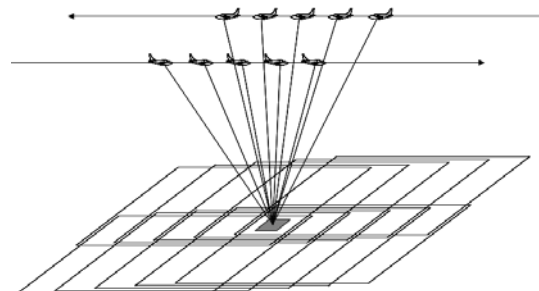


Figure 1. Directions of view on a terrain element in aerial photography with forward and side overlap

In a previous study (Koukal and Schneider, 2009) it has been shown that the parameters of semi-empirical parametric BRDF models can be estimated from digital aerial photos taken with a frame camera (Vexcel UltraCamD) with large forward and side overlap. In general, good fit could be achieved for the models under investigation. The modelled and plotted BRFs showed promising and explainable differences in forward and backward scattering depending on basic forest parameters such as tree species and age, as illustrated in Figure 2.

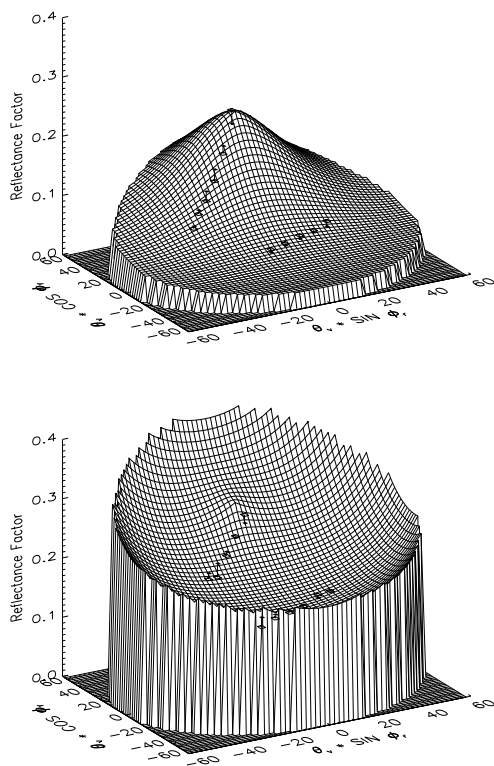


Figure 2: Bi-directional reflectance factor (BRF) in the near infrared band modelled with the RPV model for *Picea abies*, timber stage (top) and *Picea abies*, thicket stage (bottom)

Based on this work, the present study investigates the potential of BRDF model parameters for discriminating between different land cover classes. The basic assumption is that the model parameters describe the reflectance anisotropy of surfaces and that for similar surfaces similar sets of model parameters are retrieved. The focus of the contribution is on forest cover types. Both coniferous and deciduous stands differing in age and crown cover are analysed. The variability of the estimated model parameters within and between various forest types is determined and the explanatory power of the

parameters is tested. The class separability obtained with BRDF model parameters is compared with the separability obtained with pure spectral near-nadir observations. In addition, the discriminatory power of combinations of near-nadir spectral data and BRDF model parameters is investigated.

2 BRDF MODELLING

Semi-empirical parametric BRDF models predict the bidirectional reflectance factor (BRF) for arbitrary illumination-viewing geometries provided that sufficient observations (i.e. reflectance, view direction, illumination direction) are available to assess the parameters of the model. For this study the following models are chosen:

(1) Ross-Thick/Li-Sparse model (RTLS): This kernel-based model combines three kernels representing basic scattering types: isotropic scattering, volumetric scattering, and geometric-optical surface scattering. The volumetric scattering kernel is deduced from a formula by Ross (1981) (Ross-Thick kernel). The geometric-optical kernel is deduced from the model by Li and Strahler (1992) (Wanner et al., 1995). The geometric-optical kernel contains two internal parameters describing the shape of the tree crowns (oblate/round/prolate) and their relative height. The crown parameters in the best way describing the actual scene can be found by testing various sets of parameters. Both kernels, the Ross-Thick kernel and the Li-Sparse kernel, are implemented in AMBRALS, a modelling tool for the MODIS bidirectional reflectance and albedo products (Wanner et al., 1997).

(2) Rahman-Pinty-Verstraete model (RPV): The RPV model (Rahman et al. 1993) is, in contrast to kernel-driven approaches, a multiplicative semi-empirical model. It uses three parameters and combines a Lambertian term that controls the overall amplitude of the reflectance, a modified Minnaert term, and a Henvey-Greenstein function that controls the relative amount of forward and backward scattering. The RPV model is used in the retrieval of surface products from MISR data (surface BRF, albedo, LAI, FPAR) (Diner et al 2008).

(3) Dymond model (WAK): The model by Dymond et al. (2001) is a physical model that aims at reconstructing the bidirectional reflectance of homogeneous and closed vegetation canopies. Three parameters are used, one for the leaf reflectance and two to characterize the canopy phase function. The model is applicable to visible light and near-infrared light. It includes a term derived by Hapke (1981) to account for multiple scattering that is relevant in the near-infrared part of the spectrum.

3 DATA

The study is based on images taken with a Vexcel UltraCamD camera (Leberl et al., 2003). The multispectral bands (B, G, R, and NIR) without pansharping are used. Parameters of the camera relevant for this study are listed in Table 1.

Table 1: Specifications of the Vexcel UltraCamD digital aerial camera

Parameter	
FOV across track	55°
FOV along track	38°
Max. view zenith angle (diagonal)	35°
Pixel size (multi-spectral) at flying height of 3.900 m	75 cm
Radiometric resolution	12 bit

The image data were (in an approximation) radiometrically calibrated, i.e. converted to reflectance values.

The empirical line method was used (Smith and Milton, 1999). Reflectance values of reference plots were measured on the days of the image flights. Reference plots were selected for which Lambertian reflectance characteristics can be assumed, e.g. bright surfaces of concrete roads and dark surfaces of asphalt roads. The radiance values measured at these surfaces were converted to reflectance values by comparison (ratioing) with radiance values measured at a horizontal Spectralon reference panel of known reflectance. As the images used for this study were taken at different times, the differences in sun zenith angle at these times had to be taken into account. The following algorithm was used for this:

$$p_{i0} = p_i \frac{\cos \theta_{s0}}{\cos \theta_{si}} = a + b p_i \quad (1)$$

$$p = \frac{p \frac{\cos \theta_{s0}}{\cos \theta_s} - a}{b}$$

Here, p_i are the pixel values from the positions of the plots on the images and p_i are the corresponding reflectance values from the terrestrial spectro-radiometric measurements. θ_{si} is the zenith angle of the direction to the sun at the time the aerial photo showing the pixel value p_i was taken, and θ_{s0} is a standard value of the zenith angle of the sun used as a common reference: All pixel values of the plots for radiometric calibration, p_i , are converted to fictitious values p_{i0} they would have for this standard sun zenith angle. a and b are the coefficients of linear regression of the values p_{i0} to the values p_i . With this model, any pixel value p from an image taken at sun

zenith angle θ_s can be converted to the reflectance value of the corresponding surface element assuming that it has Lambertian characteristics and that it was irradiated by the sun at the standard zenith angle. $\theta_{s0} = 30^\circ$ was assumed for this work. This radiometric calibration procedure is approximative only, as it does not account for direction-dependent influences of the atmosphere. As a consequence, the BRFs obtained in this analysis include the direction-dependent influence of the atmosphere. These atmospheric effects can be expected to modify the BRFs of every land cover type in the same way (if surface-atmosphere coupling effects are neglected). Therefore, the influence of the atmospheric effects on the class separability obtained with the BRDF models should be small.

The images were taken in the Rax-Schneeberg region in the south of Lower Austria in July 2006 (sun zenith angle: 27° to 30°) with a forward overlap of $>80\%$ and a side overlap of 30% . The number of view directions per terrain element ranged from 10 to 14. It is important to point out that the angular sampling was sparse and non-systematic as the images were acquired in a standard aerial survey that was not optimized for the purpose of BRDF analysis.

Sample plots of 5 different forest cover types in terms of tree species and age (obtained from ground reference information) as well as sample plots for grassland were selected as listed in Table 2.

Table 2: Number of sample plots per class in the reference dataset

Class	
<i>Picea abies</i> , thicket stage	8
<i>Picea abies</i> , pole stage	8
<i>Picea abies</i> , timber stage	19
<i>Fagus sylvatica</i> , timber stage	12
Deciduous, thicket stage	7
Grassland	8

Criteria for the plot selection were moderate slope angles (<25 degree) to reduce effects of surface slope on the models' performance and homogeneity in terms of tree species composition, development class and crown canopy closure. Furthermore, it was important that each plot is shown on images of two neighbouring flight lines to assure that the number of observations from different points of view is sufficient for the model fitting procedure.

The plot size varied between approximately 150 m^2 to 2000 m^2 depending on the surface texture. For each plot the mean pixel value was extracted from each image on which the plot appears. Orthorectified aerial photos were used to enable automatic extraction of corresponding pixel values.

The pixel values were converted to reflectance values as described above. View and sun azimuth and zenith angles were determined corresponding to the centre of the plot.

In addition, for each plot the observation with the view direction closest to nadir was selected. With this dataset class separability without considering BRDF-related effects was studied as it is the case in, e.g., automatic mapping based on an orthophoto mosaic.

4 MODEL INVERSION AND CLASSIFICATION

The BRDF model parameters were derived by inverting the models against the multi-directional UltraCamD data for each spectral band using the Levenberg-Marquardt optimization algorithm (Markwardt, 2009).

The class separability was assessed by Linear Discriminant Analysis (LDA). LDA is a method to find a linear combination of features which separates two or more classes of objects. There are mainly two applications of LDA: firstly, it can be used to find out if there are significant differences between the classes, and to find the variables that are suitable to separate the classes. Secondly, LDA can be used to classify new objects. LDA is related to Principal Component Analysis (PCA). However, in LDA the transformation of the feature space explicitly aims at maximising the separability of the given classes, whereas in PCA the transformation is done in such a way that the resulting principal components describe the directions of maximum variance.

The number of model parameters per band is 3 (RPV, WAK) and 5 (RTLS) so that, for 4 UltraCam bands, the maximum number of features available for LDA was 12 (RPV, WAK) and 20 (RTLS). Several sets of explanatory variables were tested and evaluated: (1) sets that only contain spectral signatures (near-nadir), (2) sets that only contain BRDF model parameters, and (3) sets that contain both spectral signatures and BRDF model parameters. Band-specific and model-specific differences were investigated.

5 RESULTS

The coefficients of determination, R^2 , achieved in model inversion is similar for all models and bands and range from 0,91 to 0,97.

Table 3 summarizes the LDA classification results in terms of Overall Accuracy (OA) for different groups of explanatory variables assessed by leave-one-out cross-validation. The groups are: spectral signatures in near-nadir direction (corresponding to

“conventional” automated mapping based on an orthophoto mosaic), BRDF model parameters for the 3 models used (all parameters for single bands as well as all parameters for all bands), and spectral signatures in near-nadir direction for all bands combined with BRDF model parameters for single bands.

If only one single band is used, the classification with the BRDF model parameters outperforms the classification with the near-nadir data in 10 of 12 cases. If all 4 bands are used (4-n parameters in total, where n is the number of parameters of the BRDF model chosen, i.e. n=3 or n=5), the RPV model parameters perform clearly better (0,75) than the near-nadir spectral signature (0,67). If the spectral signature (all bands) is combined with the model parameters of one band, the classification accuracies are better in some cases (e.g. spectral signature + BRDF RPV for NIR: 0,77; spectral signature + BRDF WAK for green band: 0,79).

Concluding, with all BRDF RPV model parameters (0,75) or with the combination of spectral signatures (all bands) and BRDF WAK model parameters of the green band (0,79) higher classification accuracies can be achieved than with spectral signatures near nadir only (0,67). Although this trend does not hold for all bands and tested models, it can be concluded that directional signatures offer additional information as compared to spectral signatures and can improve the separability of forest cover types.

In Figure 3, the performance of the three models is compared. It shows the OA-differences to the near-nadir case (spectral signatures near nadir) for selected feature combinations. The RPV model performs a little better than the RTLS model and the WAK model.

There are considerable differences between the bands, particularly for the RTLS model (B: 0,36, NIR: 0,62) and the WAK model (NIR: 0,44, G: 0,66). However, the worst and best performing bands vary from model to model. Therefore, it is not possible to say in general which band is most suitable to separate the given forest cover types.

Figure 4 shows scatter plots in the discriminant function feature space and the derived class regions. The within-group variances are quite high leading to some classification errors. For some classes (e.g. grassland, *Fagus sylvatica*) the within-class variability is reduced when BRDF model parameters are used in addition to the near-nadir spectral signature.

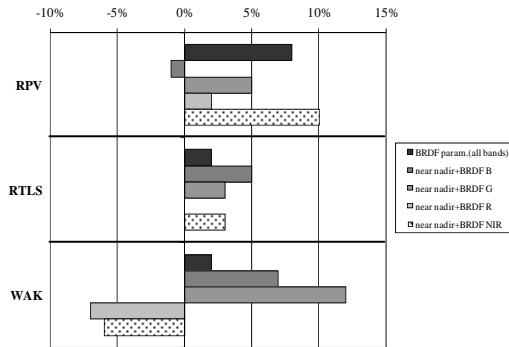


Figure 3: Overall accuracy (%) differences between near-nadir spectral signatures (all bands) and the given feature sets (positive values show improvements by the inclusion of BRDF model parameters).

Table 3: Cross-validated overall accuracy achieved by Linear Discriminant Analysis (LDA)

	B	G	R	NIR	all bands
spectral signatures near nadir (nn)	0,36	0,39	0,30	0,48	0,67
BRDF RPV parameters (all)	0,67	0,57	0,56	0,67	0,75
BRDF RTLS parameters (all)	0,36	0,43	0,57	0,62	0,69
BRDF WAK parameters (all)	0,56	0,66	0,48	0,44	0,69
spectr. sign. nn (all bands) + BRDF RPV param. (1 band)	0,66	0,72	0,69	0,77	--
spectr. sign. nn (all bands) + BRDF RTLS param. (1 band)	0,42	0,70	0,67	0,70	--
spectr. sign. nn (all bands) + BRDF WAK param. (1 band)	0,74	0,79	0,60	0,61	--

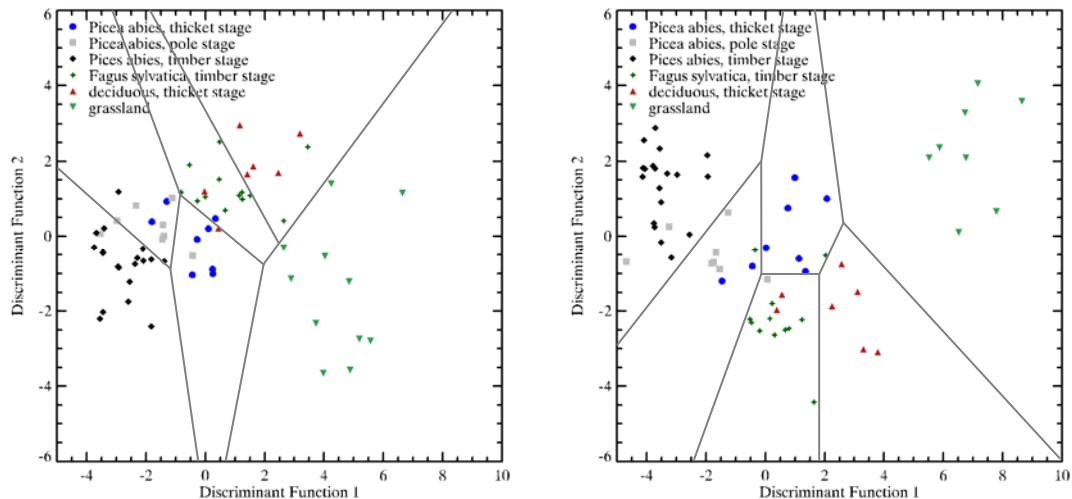


Figure 4. Distribution of sample plots in the discriminant feature space and derived class regions (left: spectral signature near nadir (4 bands), right: spectral signature near nadir (4 bands) + BRDF WAK for green band).

6 CONCLUSION

The results demonstrate that the exclusive or additional use of BRDF model parameters as features for classifications of forest types on digital aerial photos improve the classification accuracy in

comparison to the sole use of spectral features. The BRDF model parameters are determined for every cell of pixels, with a cell size chosen to comprise a certain number of trees (e.g. cell sizes of 150 m² to 2000 m²). Only the mean values of the pixels within the cells in each band are used. The method can thus be expected

to be, to a large extent, independent of the spatial resolution (scale) of the aerial photos.

The main shortcoming of this study is the small reference data set. As a consequence, the generalization error of the applied classification algorithm might be high. Furthermore, LDA instead of QDA (Quadratic Discriminant Analysis) had to be applied. With QDA maybe more significant and better results could be achieved as the assumption of equal co-variances for all classes that is made in LDA is probably not valid.

Further studies will include the analysis of larger data sets, investigations of aerial photos of different scale and of the influence of acquisition geometry on the sensitivity of the model inversion.

7 REFERENCES

- Diner, D. J., Martonchik, J. V., Borel, Ch., Gerstl, S. A. W., Gordon, H. R., Knyazikhin, Y., Myneni, R., Pinty, B. and Verstraete, M. M., 2008. Multi-angle Imaging Spectro-Radiometer - Level 2 Surface Retrieval Algorithm Theoretical Basis, Revision E. Jet Propulsion Laboratory, California Institute of Technology. <http://www-misr.jpl.nasa.gov> (accessed 25 Oct. 2009)
- Dymond, J. R., Shepherd, J. D., and Qi, J., 2001. A simple physical model of vegetation reflectance for standardising optical satellite imagery. *Remote Sensing of Environment*, 77(2), 230-239.
- Hapke, B., 1981. Bidirectional reflectance spectroscopy, 1. Theory. *Journal of Geophysical Research*, 86, pp. 3039-3054.
- Koukal, T. and Schneider, W., 2010. Analysis of BRDF characteristics of forest stands with a digital aerial frame camera. In: *The Int. Archives of the Photogrammetry, Remote Sensing and Spatial Information Sciences*, Vienna, Austria, Vol. XXXVIII, pp. 100-105.
- Leberl, F., Perko, R., Gruber, M., Ponticelli, M., 2003. The UltraCam large format aerial digital camera system. *Proceedings of the American Society for Photogrammetry and Remote Sensing Annual Convention*, Anchorage, Alaska, 5-9 May 2003, published on CD, no page numbering.
- Li, X., Strahler, A. H., 1992. Geometric-Optical Bidirectional Reflectance Modeling of the discrete crown vegetation canopy: effect of crown shape and mutual shadowing. *IEEE Transactions on Geoscience and Remote Sensing*, 30 (2), pp. 276-292.
- Markwardt, C. B., 2009. Non-linear least squares fitting in IDL with MPFIT. In: Bohlender, D. A., Durand, D., Dowler, P. (eds.), *Proceedings of Astronomical Data Analysis Software and Systems XVIII*, Quebec, Canada, ASP Conference Series, Vol. 411, Astronomical Society of the Pacific: San Francisco, pp. 251-254.
- Rahman, H., Pinty, B., and Verstraete, M. M., 1993. Coupled surface-atmosphere reflectance (CSAR) model - 2: Semiempirical surface model usable with NOAA advanced very high resolution radiometer data. *Journal of Geophysical Research*, 98: 20791-20801.
- Ross, J., 1981. *The radiation regime and architecture of plant stands*. Dr. W. Junk Publishers. The Hague.
- Roujean, J.-L., Leroy, M., and Deschamps, P.-Y., 1992. A bidirectional reflectance model of the earth's surface for the correction of remote sensing data. *Journal of Geophysical Research*, 97 (D18): 20455-20468.
- Smith, G. M., Milton, E. J., 1999. The use of the empirical line method to calibrate remotely sensed data to reflectance. *Int. Journal of Remote Sensing*, 20 (13), pp. 2653-2662.
- Wanner, W., Li, X., Strahler, A. H., 1995. On the derivation of kernels for kernel-driven models of bidirectional reflectance. *Journal of Geophysical Research*, 100 (D10), pp. 21077-21089.
- Wanner, W., Strahler, A. H., Hu, B., Lewis, P., Muller, J.-P., Li, X., Schaaf, C. L. B., Barnsley, M. J., 1997. Global retrieval of bidirectional reflectance and albedo over land from EOS MODIS and MISR data: Theory and algorithm. *Journal of Geophysical Research*, 102 (17), pp. 17143-17161.

Modeling thermal infrared directional anisotropy over a mature pine forest

M. Mira¹, J.-P. Lagouarde², C. Moisy², D. Guyon², B. Kurz², J. Ogée², P. Moreau²

¹Earth Physics and Thermodynamics Department, University of Valencia, Dr. Moliner 50, 46100 Burjassot (Spain)

²INRA, UR 1263 EPHYSE, 71 avenue E. Bourlaux, F-33140 Villenave d'Ornon (France)

Email corresponding author: lagouarde@bordeaux.inra.fr

ABSTRACT - Thermal infrared (TIR) remote sensing measurements are prone to important directional effects that need to be characterized and quantified. Over forest areas, the tree crown architecture plays a significant role, because it influences the distribution of the surface temperatures of the different elements within the tree canopy and the understory that are seen by a sensor. In the present study we model the TIR directional anisotropy over a mature Maritime pine stand, by combining a 3D canopy architecture model with a soil-vegetation-atmosphere transfer (SVAT) model that provides the surface temperature of the different elements. The 3D scene built using the POV-Ray software is validated against ground-based canopy gap fraction measurements. The microstructure effects related to the spatial distribution of needles within the shoots are introduced by adapting the parametric hot spot model of Roujean (2000). The surface temperatures of the different canopy elements and the soil are computed with the multilayer, multileaf SVAT MuSICA model (Ogée, 2000; Ogée et al., 2003). Simulated TIR directional anisotropy is then validated against airborne measurements performed at different times of the day and different dates (i.e., for different sets of solar angles). The results show that the thermal hot spot is satisfactorily reproduced and that the anisotropy is well-captured, although slightly underestimated. The generalization to other pine stands displaying different canopy structures (age, size, density of trees) is now needed before using this TIR directional anisotropy model for practical applications.

1 INTRODUCTION

Measurements of surface temperature performed in the thermal infrared (TIR) are prone to important directional anisotropy. This first depends on the canopy structure which governs (1) the temperature profiles within the vegetation through the coupled energy and radiative transfers, (2) together with the spatial distribution of the facets seen by the sensor. The directional anisotropy also depends on the solar position. Characterizing directional TIR anisotropy is necessary for different goals: the possibility of retrieving the surface temperature of the different layers within the canopy should allow to improve sensible heat flux estimations, and should facilitate the assimilation of multi-angular remotely sensed TIR data into surface models; correction and normalization of large swath satellite data are also expected for improving the analysis of temporal series, or of the spatial variability within given thermal images; finally it should help defining the specifications for future spaceborne sensors.

The study of the thermal directional anisotropy originates in the 60's. Experimental measurements of TIR directional anisotropy have been extensively performed in the past over low crops using ground

based systems and a number of models have been proposed. Less work has been made over canopies displaying important height such as forest and urban canopies, probably because of experimental difficulties. Lagouarde et al. (2000 and 2004) proposed a method based on the use of an airborne TIR camera equipped with wide-angle lenses. They report important thermal 'hot spots' both over maritime pine stands and urban canopies.

Several modelling approaches have been proposed. The simple geometrical models (Kimes, 1983, and Caselles et al., 1992) or simple multi-layer ones in which the directional temperature is computed from gap frequencies (Prévot et al., 1994) require an *a priori* knowledge of the temperature distribution within the canopy and generally suffer from too poor descriptions of the structure of the vegetation. Recent approaches based on 3D models have been proposed (Guillevic et al., 2003; Luquet et al., 2004). Kurz et al. (2006) and Kurz (2009) have proposed an approach combining a 3D canopy model and a SVAT model in the case of a maritime pine mature stand (*Pinus pinaster* Ait.). This paper presents the last improvements brought to this method, which mainly concern the 3D tree modelling and the interception simulated processes of the solar radiation within the tree canopy. The long term objective is to build a

generic model simulating the TIR anisotropy of maritime pine stands, whatever their age.

The approach is first briefly recalled. The 3D models of a pine tree and of a stand are then described. Each tree crown is modelled as a set of opaque cylinders accounting for the shoot clumps. The first simulations of Kurz et al. (2006) revealed that the initial assumption of opaque crown elements was too high a level of simplification. Kurz (2009) proposed an adaptation to take into account the contribution of needles within the shoots to the anisotropy. On these bases, we aimed to improve the simulation of directional variations in sunlit and shaded crown fractions seen in the viewing direction and on the parameterization of the size of cylinders and their location on the branches. This is described in section 3, before presenting and discussing the results of directional temperature anisotropy.

2 EXPERIMENTAL BACKGROUND

The experiment was conducted on a mature even-aged maritime pine stand (Le Bray) located in south-western France 20 km west of Bordeaux (44° 42' N, 0° 46' W). The calibration and the validation of TIR anisotropy model were based on the TIR aerial measurements performed in 1996 (Lagouarde et al. 2000) and on the directional gap fraction data of tree canopy measured in situ with DEMON instrument in 1998 (Guyon et al., 2003).

Detailed information on the structure and architecture of pine tree (length of branches, insertion angles, number of branches...) comes from destructive measurements performed at INRA in 1995 by Porté et al. (2000, 2002) and Champion et al. (1996, 2001). In 1995 the pine trees were 26 years old. Stand structure data such as tree density (e.g. 518 tree per ha in 1996), height (e.g. mean in 1996 = 17.6m) or DBH were also available in 1995, 1996 and 1998.

The understory vegetation was mainly made up of *Molinia (Molinia coerulea Moech.)* which covered completely the soil. The trees were planted by rows with a direction approximately 35° from North and a 4m spacing.

3 PRINCIPLE OF THE MODELLING APPROACH

The principle followed to simulate the brightness directional temperature $T_b(\theta_v, \varphi_v)$ is based on the aggregation of the surface brightness temperatures of the different sunlit and shaded elements of the canopy seen in the viewing direction defined by the zenith and azimuth viewing angles θ_v and φ_v for a given sun position. The anisotropy is then calculated as the difference with the nadir temperature.

A simplification consists in considering only 6 classes of elements as seen by the TIR sensor: sunlit

and shaded crowns, ground and trunks. $T_b(\theta_v, \varphi_v)$ is computed according to Eq. 1:

$$T_b(\theta_v, \varphi_v) = \sqrt[4]{\sum_{i,j} A_{i,j}(\theta_v, \varphi_v) T_{i,j}^4} \quad (1)$$

where indices i correspond to sunlit/shaded status and j to the element type respectively.

The A_{ij} fractions are estimated from images of the canopy built using the ray-tracing POV-Ray software (<http://www.povray.org/> Persistence Of Vision Ray-tracer) applied on a 3D model of the tree canopy. Images are generated for a large set of viewing directions, for a prescribed solar direction corresponding to the time of airborne acquisitions for comparison purposes. The parameters of the POV-Ray computations are selected to create schematic images of the canopy allowing easy discrimination of the different classes.

The T_{ij} were computed using the Ogée et al. (2003) MuSICA model (Multi-layer simulator of the interactions between a coniferous stand and the atmosphere). This model solves an energy budget equation for each layer of the canopy and computes the temperature of 3 classes (1, 2 and 3 years old) shaded/sunlit needles, and the temperature of the understory. In fact crown temperatures are also estimated by weighing the temperature of needles according to their respective LAI. Moreover the number of classes was reduced to 4, the trunks and the soil displaying similar temperature having finally been merged.

We worked with brightness to avoid facing the difficult problems of directional emissivity and temperature emissivity separation.

4 THE 3D MODEL

4.1 The 3D tree model

We looked for a simplified tree description combining a realistic enough representation of the tree structure and compatible with computer time constraints for POV-Ray simulations.

The trunk was modeled as a cone. The needles, shoots and small branches were concentrated within opaque cylinders placed on the 4th growth unit of main branches (or on the trunk for branches from order 1 to 4). The size of all cylinders remained constant so that two parameters only, their length and radius, suffice to describe the tree (see Figure 1).

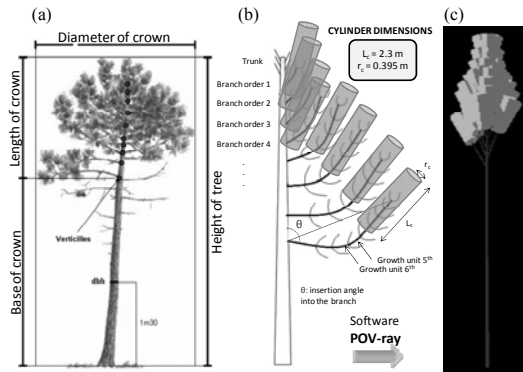


Figure 1. Example of shape of an adult pine tree (a) and principle of the simplified tree description (b) for the 3D model. Example of a POV-ray 3D modelled pine (c).

4.2 The 3D stand model

Tree dimensions were distributed according to the actual Le Bray stand structure. The trees were randomly distributed along the rows taking into account the actual variability of their distance within rows. For realism purpose, a competition effect was simulated by applying to the size of the trees a homothetic coefficient related to their distances within rows. Figure 2 displays an example of 2 simulated images of the stand viewed in 2 different directions.

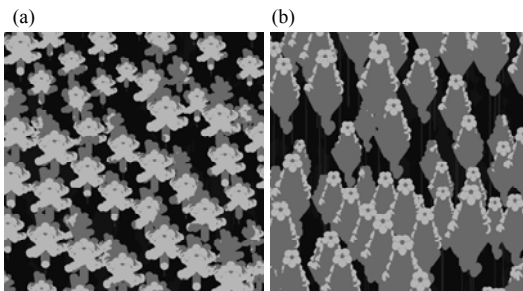


Figure 2. POV-ray simulations of the stand for a solar fixed position ($\theta_s=38.5^\circ$, $\phi_s=164.3^\circ$) and two viewing configurations: (a) $\theta_v=10^\circ$, $\phi_v=340^\circ$; (b) $\theta_v=40^\circ$, $\phi_v=340^\circ$. The four grey tones correspond to the $A_{i,j}$ fractions of sunlit and shaded elements (only crown and ground elements are simulated).

4.3. Parameterization of the tree model

The calibration of the tree model consists of determining the cylinder dimensions by minimizing errors between DEMON measurements of directional gap fraction under the tree canopy and their simulation by POV-Ray. The directional gap fraction is equal to the fraction of ground seen on the simulated image in hot spot viewing configuration, i.e. $A_{\text{sunlit,ground}}$ (with $A_{\text{shaded,ground}}=0$). The results of the calibration step were $L_c=2.3$ m and $r_c=0.395$ m (Fig. 3). The maximum

observed in figure 3 corresponds to DEMON measurement performed in the directions of rows (the sun azimuth angle of 204° indicated in fig. 3 corresponding to the 35° row direction).

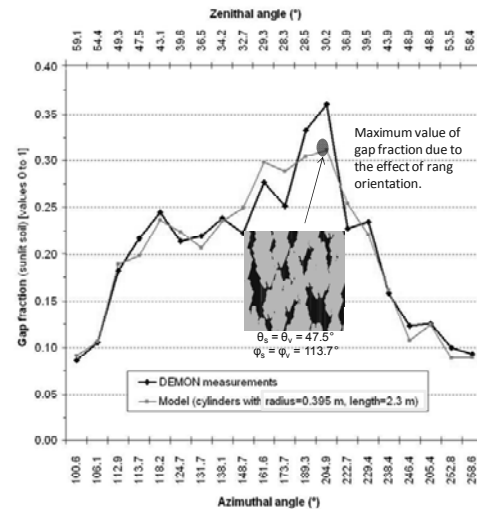


Figure 3. Modeled directional gap fraction against in situ measurements from DEMON in various zenith and azimuth angles.

The comparison between simulated and actual diameters of crowns (Fig. 4) provides additional elements of validation of the tree-stand model.

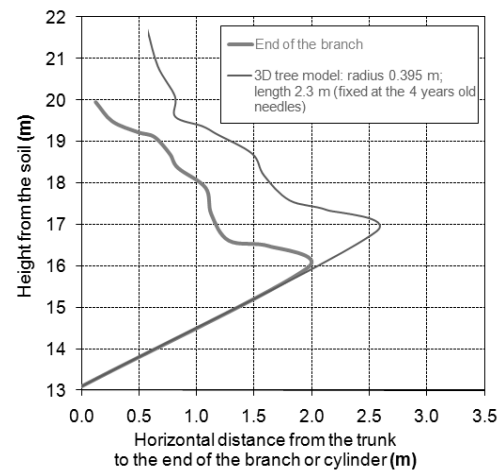


Figure 4. Shape of the crown as defined by the 3D tree model described in this work, compared with the shape of the ends of the tree branches (results for the mean 29 years-old tree in 1998).

We also tried to check if the model was able to reproduce the actual vertical LAI profile. In fact our approach does not allow one to simulate a LAI, but we considered the vertical profile of frontal area averaged in all azimuthal viewing horizontal directions of the

tree. This was normalized by its maximum value and compared against the expected vertical LAI profile (obtained from Porté et al., 2000) and similarly normalized. As shown in Figure 5, there is a relatively good agreement between these profiles despite unavoidable discrepancies due to the simplicity of our cylinder approach. Nevertheless we considered these tests were confirming the consistency of our 3D stand model.

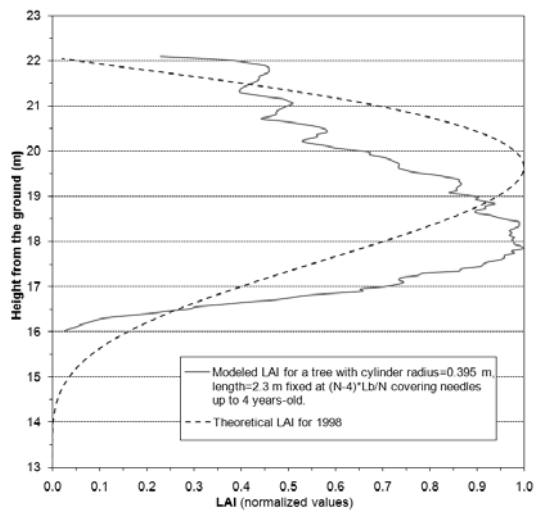


Figure 5. Comparison of LAI profiles of the modeled tree and the theoretical values obtained from horizontal area profiles (results for the mean tree in 1998, 29 years-old).

5 INTRODUCING THE IMPACT OF THE DISCRETE STRUCTURE OF CROWNS

The opaque cylinders of the 3D model only allow one to take into account the contribution of the ‘macrostructure’ (i.e. crowns and rows) of the stand to the TIR directional anisotropy. In fact, crowns have a discrete structure, and small size elements (referred to as ‘micro structures’) as needles largely contribute to the anisotropy. As a matter of fact, assuming that the surfaces of sunlit and shaded needles within crowns which effectively govern the anisotropy can be simply estimated as the sunlit and shaded surface of the envelope of crowns is too crude an approximation, and comes to ignore the diffuse nature of the media within crowns. The coefficients A_{ij} estimated at the stand scale (from images such as those presented in fig. 2) and used in the computation of the brightness temperature according to equation (1) are therefore not directly suited to compute the directional brightness temperature. They have been corrected by adapting a hot spot parameterization proposed by Roujean (2000) introducing a function F_{HS} which depends only on Sun and viewing directions:

$$F_{HS} = \sqrt{\tan^2 \theta_s + \tan^2 \theta_v - 2 \tan \theta_s \tan \theta_v \cos \varphi} \quad (2)$$

φ is the relative azimuth between Sun and viewing directions. $A_{1,1}$ and $A_{2,1}$ are replaced by $A_{1,1CORR}$ and $A_{2,1CORR}$, respectively, following:

$$A_{1,1CORR} = A_{1,1} \cdot e^{-k \cdot F_{HS}} \quad (3)$$

$$A_{2,1CORR} = A_{2,1} + A_{1,1} - A_{1,1CORR} \quad (4)$$

$$\text{with } k = \text{LAI}_c / 4 \quad (5)$$

The correction concerning the radiative transfers within crowns, LAI_c refers to their leaf area projected at ground. We therefore have $\text{LAI}_c = \text{LAI} / F_c$, F_c being the fraction cover of crowns and LAI the leaf area of the stand. As $\text{LAI} \sim 2.2$ and $F_c \sim 0.7$, we have finally $k \sim 0.8$.

6 RESULTS

TIR anisotropy airborne measurements were performed at different dates in 1995 and 1996 and different times of day to explore the impact of solar position. The experimental results revealed important hot spot effects and differences of brightness temperatures reaching 4 K between vertical and oblique measurements (up to 60°). All details can be found in Lagouarde et al. (2000). In this paper we only focused on acquisitions performed on September 9th, 1996, over the stand of Le Bray.

Figure 6 displays the comparison between airborne measured and simulated TIR directional anisotropy around 13:20, 15:00 and 17:40 local time (which corresponds to 11:20, 13:00 and 15:40 UT). In all cases, the results show that the hot spot is well-positioned (opposed to the sun position) and that the angular variations are satisfactorily simulated. The comparisons performed in the solar principal plane reveal a general agreement with measurements around the hot spot. Some discrepancies are observed for the first 2 flights for zenithal angles lower than -20°. These have been examined in details and are easily explained by experimental artefacts; as a matter of fact investigating all azimuthal directions requires flying several lines in different directions. As a consequence, time fluctuations in micrometeorological conditions (windspeed particularly) may possibly induce systematic variations in surface temperatures for some of the lines flown which in turn affect the anisotropy polar plots as those presented in fig. 6.

7 CONCLUSIONS

The TIR directional anisotropy was satisfactorily simulated over a mature pine stand at different times of a given day using a simple approach combining a

3D model of the tree and of the stand with the SVAT MuSICA model.

Regarding the macrostructure of the pine tree, a simple 3D tree model made of (1) a trunk, (2) first order branches and (3) cylinders set on them and concentrating all the crown vegetation (rest of branches from order 2 and needles) was calibrated against *gap fraction* measurements. We considered in a first step that this model was offering a good

compromise between realism and simplicity. The consistency of crown diameter and of an indicator of the vertical LAI profile against actual characteristics of the studied stand was checked. Moreover on a practical point of view, the calibration of the model was made easy by the reduced number of parameters (a unique set 2 parameters only, radius and length of cylinders).

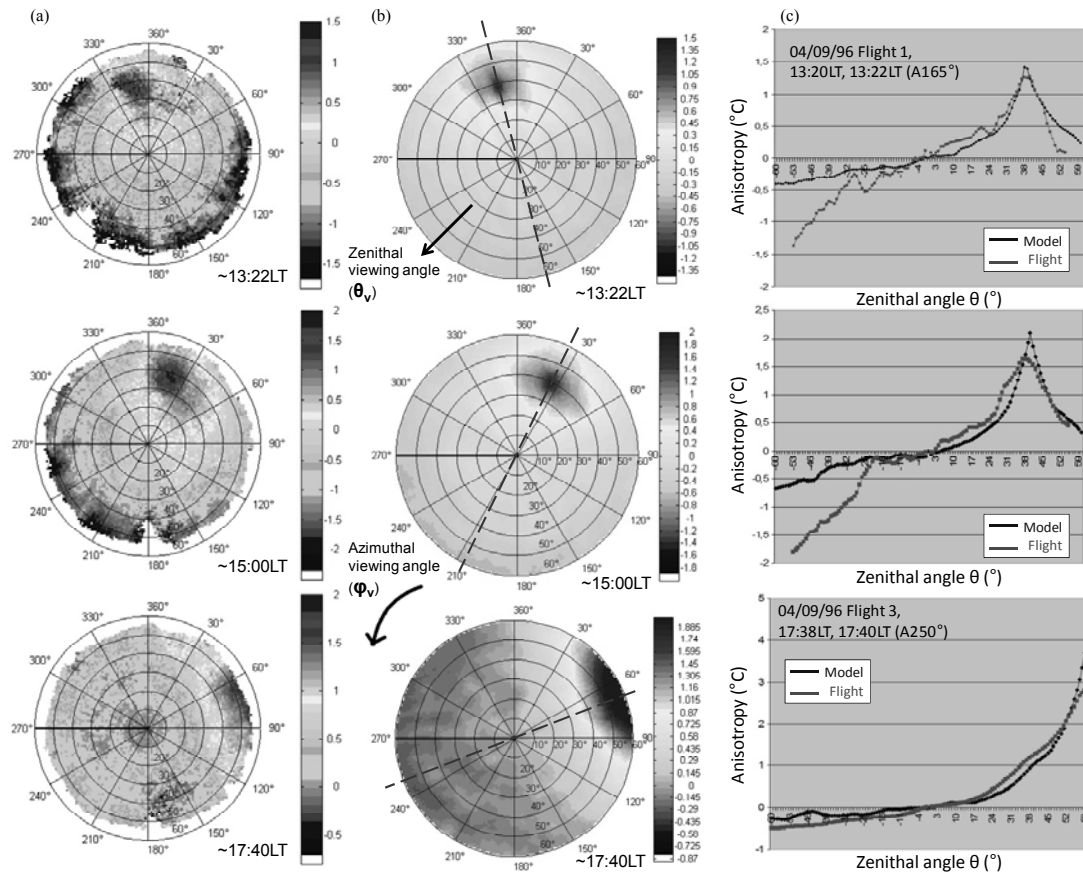


Figure 6. Comparison between (a) the anisotropy measured by airborne measurements on September 9th, 1996 over the experimental maritime pine stand of Le Bray in south-western France, and (b) the anisotropy simulated with the combined MuSICA and hot spot parameterization approach, in all azimuthal angles, and (c) in the principal solar plane.

Regarding the microstructure (needles, shoots and small branches) of the pine, the hypothesis of considering opaque cylinders was too restrictive, and a correction adapted from the parametric approach of Roujean (2000), allowed one to simulate the directional variations around the hot spot satisfactorily.

The forthcoming steps of this work consists in testing the generalization of the model to other pine stands displaying different canopy structures (age, size, density of trees). Nevertheless the geometrical description of the tree/stand model we proposed here remains very crude, and one may think it will be difficult to find simple and unique parameterizations

of the dimensions of the cylinders to prescribe them *a priori* for other stands. We could therefore suggest in a further step to test an improved and more detailed 3D model of the pine tree by using smaller cylinders (aggregating vegetation from second order branches instead of main branches) with the hope of approaching a unique elementary cylinder size more adapted to any class of stand age and structure.

8 ACKNOWLEDGMENT

The research described in this paper was carried out at INRA-Bordeaux, France. Maria Mira received a grant of the Spanish Ministry of Science and Innovation.

9 REFERENCES

- Caselles, V., Sobrino, J.A., and Coll, C., 1992, A physical model for interpreting the land surface temperature obtained by remote sensors over incomplete canopies. *Remote Sensing of Environment*, 39, 203-211.
- Champion, I., et al., 1996, Mesures de structures des pins sur des arbres de 25 ans – parcelle du Bray. *Rapport interne, INRA Bordeaux Bioclimatologie*.
- Champion, I., et al., 2001, Tree architecture in remote sensing analytical models: The Bray experiment. *International Journal of Remote Sensing*, 22(9), 1827-1843.
- Guillevic, P., Gastellu-Etchegorry, J.P., Demarty, J., Prévot, L., 2003, Thermal infrared radiative transfer within three-dimensional vegetation cover. *J. Geophysical Research-Atmosphere*, 108 (D8), doi: 10.1029/2002JD002247.
- Guyon D., Berbigier P., Courrier G., Lagouarde J.P., Moreau P., 2003. Estimation du LAI dans un écosystème cultivé de pin maritime à partir de mesures de fractions de trouées directionnelles. *Can. J. Remote Sensing*, 29: 336-348.
- Kimes, D.S., 1983, Remote sensing of row crop structure and component temperatures using directional radiometric temperatures and inversion techniques. *Remote Sensing of Environment*, 13, 33-55.
- Kurz, B., et al., 2006, Modeling directional anisotropy of thermal infrared measurements over a pine forest canopy, *Proceedings 2nd Int. Symp. 'Recent Advances in Quantitative Remote Sensing', Torrent/Valencia, Espagne, 25-29 septembre 2006*, 320-325.
- Kurz B., 2009, Modélisation de l'anisotropie directionnelle de la température de surface: application aux cas de milieux forestiers et urbains. *PhD Thesis Université de Toulouse*, 144p.
- Lagouarde, J.-P., Ballans, H., Moreau, P., Guyon, D., and Coraboeuf, D., 2000, Experimental study of brightness surface temperature angular variations of Maritime Pine (*Pinus Pinaster*) stands. *Remote Sensing of Environment*, 72(1), 17-34.
- Lagouarde, J.P., Moreau, P., Irvine, M., Bonnefond, J.M., Voogt, J.A., and Sollic, F., 2004, Airborne experimental measurements of the angular variations in surface temperature over urban areas: case study of Marseille (France). *Remote Sensing of Environment* 93, 443-462.
- Luquet, D., Vidal, A., Dauzat, J., Bégue, A., Olioso, A., Clouvel, P., 2004, Using directional TIR measurements and 3D simulations to assess the limitations and opportunities of water stress indices. *Remote Sensing of Environment*, 90 (1), 53-62.
- Ogée, J., 2000, Développement et applications du modèle MuSICA: étude des échanges gazeux d'eau et de carbone entre une pinède landaise et l'atmosphère. *PhD Thesis, Université Paul Sabatier Toulouse III*. 252 pp.
- Ogée, J., Brunet, Y., Loustau, D., Berbigier, P., Delzon, S., 2003, MuSICA, a CO₂, water and energy multilayer, multileaf pine forest model: evaluation from hourly to yearly time scales and sensitivity analysis. *Global Change Biology*, 9(5), 697-717.
- Porté, A., Bosc, A., Champion, I., and Lousau, D., 2000, Estimating the foliage area of Maritime pine (*Pinus pinaster* Ait.) branches and crowns with application to modelling the foliage area distribution in the crown. *Annals of Forest Science*, 57, 73-86.
- Porté, A., Trichet, P., Bert, D., Loustau, D., 2002, Allometric relationships for branch and tree woody biomass of Maritime pine (*Pinus pinaster* Ait.). *Forest ecology and management*, 158(1-3), 71-83.
- Prévot, L., Brunet, Y., Paw, U.K.T., and Seguin, B., 1994, Canopy modelling for estimating sensible heat flux from thermal infrared measurements. *Proc. 'Thermal remote sensing of the energy and water balance over vegetation' Workshop, La Londe-les-Maures, sept. 1993*. CEMAGREF Ed., 17-22.
- Roujean, J.-L., 2000, A parametric hot spot model for optical remote sensing applications. *Remote Sensing of Environment*, 71(2), 197-206.

Coupling of a Limited Area Atmospheric Model with a sequential MSG-derived LST Assimilation scheme for the production of a two-years meteorological dataset

Lorenzo Campo (1), Fabio Castelli (1), Dara Entekhabi (2), Francesca Caparrini (3)
(1) *Dipartimento di Ingegneria Civile e Ambientale, Università degli Studi di Firenze, Via S. Marta 3, 50139 Firenze, Italy*
(2) *Parsons Laboratory, Massachusetts Institute of Technology, Cambridge, MA 02139, USA*
(3) *Eumechanos – Via La Marmora 22, 50121 Firenze, Italy*
lcampo1@dicea.unifi.it, fabio@dicea.unifi.it, darae@mit.edu, f.caparrini@eumechanos.it

ABSTRACT - *The surface phenomena at the interface between soil and atmosphere are of great importance in the estimate of the energy budget and constitute the lower boundary condition for atmospheric models. These phenomena have been often neglected or poorly represented in the past, especially in the Global Circulation Models, while modern Limited Area Models present much more accurate modelizations that require very complex parameterization, difficult or impossible to retrieve with sufficient accuracy. In this work a variational assimilation scheme is used to assimilate Land Surface Temperature maps retrieved by MSG-SEVIRI sensor in order to produce optimal estimates of the surface energy budget in terms of sensible and latent heat fluxes patterns. This assimilation scheme, ACHAB, has then been coupled with the limited area atmospheric model RAMS replacing the surface module of the latter, LEAF-3, with the assimilation-produced surface energy fluxes. A two years long meteorological dataset (2005 – 2006) was produced on the Italian territory using this coupling framework. A control run was used in order to evaluate performances of the atmospheric model also in absence of the LST assimilation. Evaluations of the results of the coupling framework by comparison with both observations of the ground sensors network and the atmospheric soundings available in the study period are presented.*

1 INTRODUCTION

The energy and water fluxes between the land surface and the atmosphere are a fundamental component in hydrologic and meteorological applications and can improve considerably the performances in related numerical models. Such mass-energy exchanges depend on the state of soil and vegetation at the surface and their quantifications, in particular of the moisture flux (evapotranspiration). In atmospheric numerical models the heavy simplifications of these surface processes often constitutes a weakness, either in terms of not optimal reconstructions of surface variables (micrometeorological values) and in terms of surface forcing of the lower troposphere (Avissar and Pielke, 1989). On the other side, more recent atmospheric models provide a better and more accurate modelization of the surface-atmosphere interactions, that require a detailed parameterization (Vidale and Stöckli, 2005). Such parameters are often difficult or impossible to estimate in a sufficiently accurate way, leading to complex models with very poor parameterizations.

Furthermore, the measures these fluxes are very difficult to obtain, especially at temporal and spatial resolutions which are significant for the study of two-way land-atmosphere interactions such as soil moisture feedback on precipitation. A valid and largely utilized alternative is constituted by remote sensing, if necessary in conjunction with ground observed data. Spectral measurements from space borne sensors are not directly linked to heat and moisture fluxes, but they can be used to infer physical conditions at the land surface that are intimately related to the energy balance. Among these conditions is land surface temperature that is the prognostic variable for the indirect estimation of surface fluxes (Schulz, 1998). Land surface temperature (LST) can be retrieved with relatively good accuracy from satellites operating in the thermal infrared or passive microwave (Sun and Pinker, 2003).

In this study sequences of radiometric surface temperature measurements have been used as input in a data assimilation scheme in order to retrieve optimal surface states and parameters that describe energy balance at the land surface. Satellite data from SEVIRI sensor (aboard the Meteosat Second Generation,

MSG), that provides surface temperature estimates at high spatial and temporal resolutions, are used as LST input. A parsimonious 1-D multiscale variational assimilation method has been followed, based on a simplified description of the LST dynamics. This assimilation procedure has been implemented in a model (Caparrini et al., 2004), ACHAB, that has been coupled with a limited area atmospheric model, RAMS (Tremback, 1990), in order to improve performances of the latter in terms either of reconstruction of the ground variables (temperature and moisture of the air, wind velocity, etc.) and of general simulation of the atmosphere. The study interested the area of the Italian territory in a period of 2 years, from March 2005 to December 2006.

2 LST ASSIMILATION MODEL ACHAB

The estimation of heat fluxes that characterize the energy budget at the surface can be formulated with an inverse approach given a sequence of land surface temperature observations. According to the bulk parameterisation of surface exchanges (Stull, 1988), latent and sensible heat fluxes from land to the atmosphere can be calculated using surface temperature measurements and standard micrometeorological observations (air temperature, humidity, wind speed):

$$H = \rho c_p C_B |U| (T_s - T_a) \quad (1)$$

$$LE = \rho L C_B |U| (q_s - q_a) \quad (2)$$

where ρ is the air density, c_p is the specific heat at constant pressure of the air, C_B is the bulk coefficient of turbulent transfer, U is the wind velocity, L is the latent heat of evaporation, T_s and q_s are the soil surface temperature and humidity, T_a and q_a are the air temperature and humidity.

The parameters that regulate such process and that are estimated in the assimilation scheme are (Caparrini et al., 2004) the bulk transfer coefficient C_B (that characterize the *scale* of surface heat fluxes) and the evaporative fraction, EF ($= LE/(H + LE)$) which is related to soil moisture content and gives the *partition* of fluxes between latent and sensible heat.

The physical constraint of the model is constituted by the Force-Restore Equation (Dickinson, 1988) that describes the evolution of the soil surface temperature:

$$\frac{dT_s}{dt} = 2\sqrt{\pi\omega} \frac{R_n - H - LE}{P} - 2\pi\omega(T_s - T_{deep}) \quad (3)$$

where H and LE are positive upward, R_n is net surface radiation, positive downward, P is thermal inertia, T_{deep} is the deep ground temperature and it is assumed that the forcing has a dominant frequency ω (i.e. diurnal).

The assimilation scheme used in the model ACHAB (Assimilation Code for Hydrologic and Atmospheric Budget) follows the dual-source formulation in Caparrini et al., 2004. The soil-vegetation system is represented as a resistance network that includes nodes at the soil, the canopy leaves, the within canopy air and air above the canopy, as shown in figure 1.

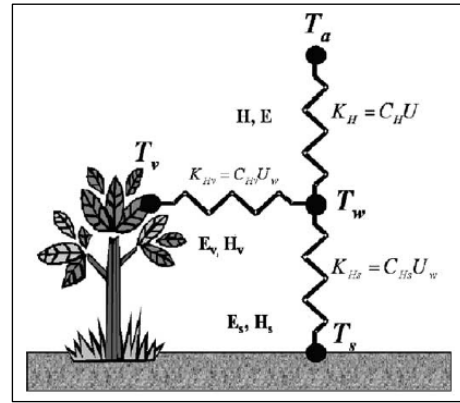


Figure 1. Schematics of dual-source (soil and vegetation) energy balance at the surface (Caparrini et al., 2004).

The force-restore governing equation is adjoint, through Lagrange multipliers, to a quadratic penalty function J which includes the parameters and forecast errors that is minimized in the assimilation algorithm. The correct values for the parameters C_{HN} and EF can be found minimizing J , thus imposing the vanishing of its first variation ($\delta J = 0$). Imposing that all the variations independently go to zero we obtain the *Euler-Lagrange* update equations.

The ACHAB model solves the Euler-Lagrange equations through an iterative procedure on monthly basis. The model worked, for each day of the period of interest, inside the diurnal temporal window at an hour timestep. Together with parameters, maps for each timestep (inside the diurnal assimilation window) and for each day were produced for surface states (temperature and humidity) and fluxes (sensible and latent heat) for both soil and vegetation.

3 ATMOSPHERIC MODEL RAMS

The Regional Atmospheric Modelling System (RAMS) is a limited area atmospheric model with complete physics and non-hydrostatic equations, developed at the Colorado State University. RAMS solves a set of equations that describe dynamics and thermodynamics of the atmosphere, mass and energy conservation and hydrometeors microphysics (Tremback, 1990).

The RAMS model can work on nested grids configuration, allowing to simulate the area of interest at very high spatial resolution without losing the information from medium- or synoptic-scale atmospheric features. The LEAF-3 surface module utilizes a detailed modelling of the interactions between the atmosphere, the soil, the vegetation, the surface water and the deep ground, taking into account the characterization of the land cover and of the health status of the vegetation. It computes the heat and humidity exchanges with the atmosphere, basically constituting the lower boundary conditions for the atmospheric grid in RAMS.

The model characterizes the surface with a global dataset of landcover, soil classes, topography and sea surface temperature at various spatial resolutions. Inside RAMS a number of numerical schemes for radiation schemes, convection, boundary conditions are available. The model was used in non-hydrostatic configuration and a set of calibration run was performed in order to retrieve the best possible configuration of the model for the domain of study.

4 DOMAIN OF THE STUDY

The domain of study was the whole Italian territory (on a grid of about 1000000 km²). The domain is characterized by presence of a numbers of mountainous regions, mainly the Appenine Mountain range and the Alps in the northern part of the country. The maximum height is reached in the Alps, at 4700 m above the sea level. The mean annual precipitation is 900 mm, the climatic condition can be considered as semi-arid with an high variability during the year; summer is hot and dry while winter is cold and rainy.

The period chosen for the analysis was 2005-2006 starting from March 2005 for a total of 22 months. The period was selected in order to observe the behavior of the coupled models in both summer (when the land-atmosphere interactions are dominated by evaporation fluxes from the surface) and winter conditions.

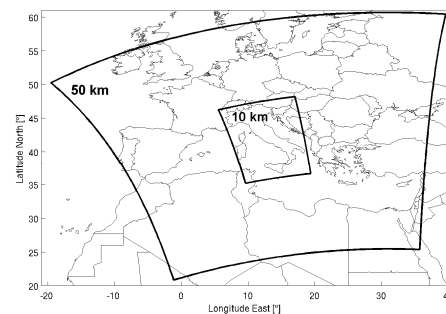


Figure 2. Grids configuration (with spatial resolution) in RAMS model.

The measures from the Italian Civil Protection ground gauges network were used to generate the forcing maps for ACHAB. Variables taken into account were air temperature, wind speed, air humidity, solar incoming radiation and deep ground temperature. Maps were obtained considering a bi-linear interpolation method of the point measures available at each time step.

5 COUPLING OF THE MODELS

The results of the assimilation procedure were replaced inside the RAMS model in order to bypass, during the diurnal window, the LEAF-3 computations.

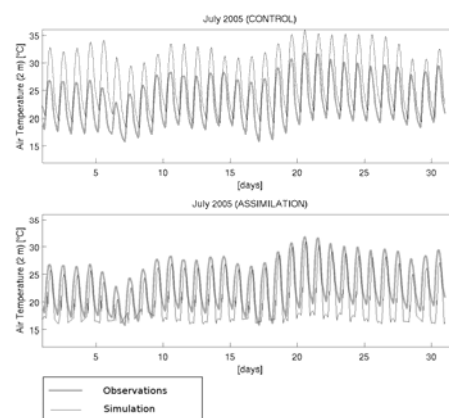


Figure 3. Comparison between average time series of the 2 m air temperature in summer period. The comparison is made between the measures (gray line) with both the control run (upper panel) and the coupled run (lower panel).

The substitution of the ACHAB products inside the atmospheric model was realized modifying the RAMS

source code and making LEAF-3 read these variables during the run.

In Figure 2 the grids used for the RAMS run are showed, the domain of the study is constituted by the nested grid, centered on Italy, that coincide with the ACHAB domain.

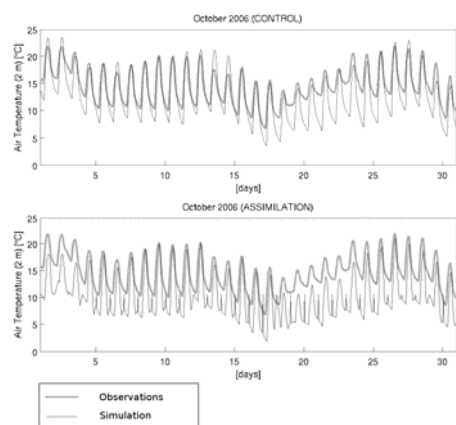


Figure 4. Comparison between average time series of the 2 m air temperature in winter period. The comparison is made between the measures (gray line) with both the control run (upper panel) and the coupled run (lower panel).

First checks on the performances of the RAMS coupled run were executed considering a comparison with the measures from the ground gauges. In figures 3 and 4 the average time series of 2 m air temperature are compared with temperatures produced in a normal RAMS run and in a run in which assimilation model products have been used, for both summer (July 2005) and winter (October 2006) periods.

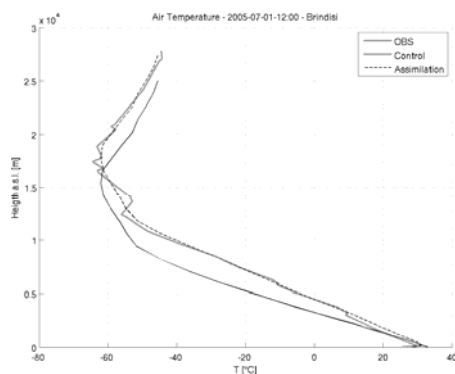


Figure 5. Comparison between the vertical profile of air temperature at the Brindisi station in summer period. Observations (gray line) are compared with

control run (continuous black line) and assimilation (dashed line).

The average of the gauged cells in the RAMS grid is compared with the average of the gauges time series. The Figure shows an improvement of the air temperature in terms of a decreasing of the positive bias (of about 3-4 °C) that normally affected the temperature produced by RAMS in summer, while a worsening is observed in winter, especially for what concerns nightly minima.

The analysis was also performed in terms of comparison between vertical atmospheric profiles. In figures 5 and 6 the soundings observed at the station of Brindisi (in southern Italy) are compared with both the simulations results in summer period, while in figures 7 and 8 the same comparison is performed for winter.

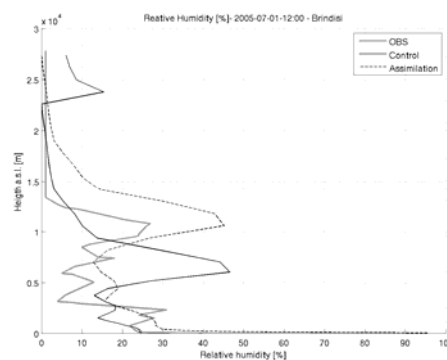


Figure 6. Comparison between the vertical profile of air humidity at the Brindisi station in summer period. Observations (gray line) are compared with control run (continuous black line) and assimilation (dashed line).

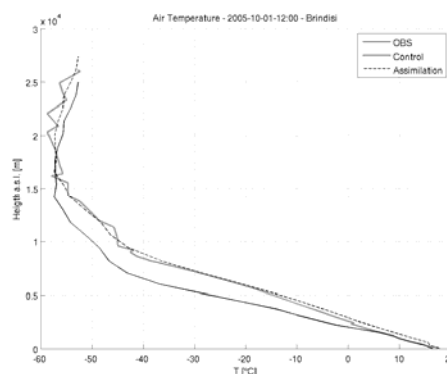


Figure 7. Comparison between the vertical profile of air temperature at the Brindisi station in winter period. Observations (gray line) are compared with

run (continuous black line) and assimilation (dashed line).

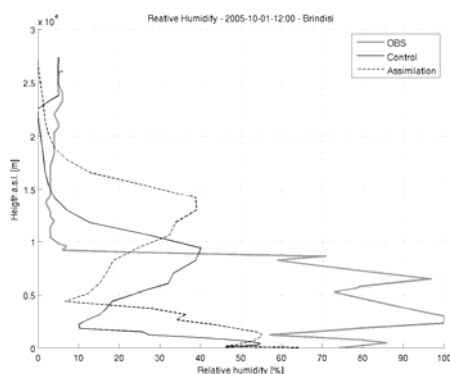


Figure 8. Comparison between the vertical profile of air humidity at the Brindisi station in winter period. Observations (gray line) are compared with control run (continuous black line) and assimilation (dashed line).

Another variable taken into consideration was the rainfall height (see figure 9): in both runs (with and without assimilation) the precipitation periods are basically the same, with no significant changes in temporal distribution, showing the dominant role of the boundary conditions in providing the availability of atmospheric moisture. On the opposite, the cumulate height shows very different behavior in summer and in winter, improving the match with the measures and significantly worsening it, respectively.

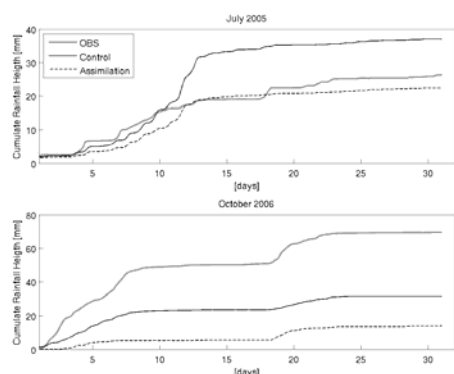


Figure 9. Observed cumulated precipitation height (gray line) compared with control run (black continuous line) and assimilation (dashed line). The comparison is shown in both summer (upper panel) and winter (lower panel).

This confirms, together with the results about the precipitation, that the coupling with the assimilation model produced strong effects on the atmospheric simulation. When the surface phenomena are dominant (summer period) improvements have been observed in both surface and atmospheric domains, while in the winter period the most part of the changes led to a worse match with the observations.

6 CONCLUSIONS

In this study a variational assimilation model, ACHAB, that uses remotely sensed maps of land surface temperature in order to characterize the surface energy budget, was coupled with a non hydrostatic limited area atmospheric model, RAMS. The results showed that the substitution of the surface energy budget of the atmospheric model led to significant improvements in RAMS performances in terms of reconstruction of the surface and atmospheric variables such as air temperature and humidity. It also led to significant changes in terms of precipitated volumes on the domain considered in the study.

The improvements, however, were registered almost only in the summer period, while the winter atmospheric and surface variables showed a significant worsening in terms of match with the available observations. While, in fact, in summer period the dominant processes that affects the planetary boundary layer are the surface exchanges of mass and energy, in winter the replacements of these fluxes was not able to positively affect the atmospheric simulation, probably also due to other dominant factor such as the atmospheric moisture advection from outside the domain.

In conclusion, the study confirmed the relevant importance represented by a correct characterization of the energy and mass land-atmosphere exchanges on the behaviour of the whole atmospheric column considered during an atmospheric simulation. On the opposite the analyses performed in winter period showed the limits of this coupling framework, leading to the necessity of further investigation for a better characterization of the winter atmospheric boundary layer processes.

7 REFERENCES

- Avissar, R. and Pielke, R. A., 1989, A Parameterization of Heterogeneous Land Surfaces for Atmospheric Numerical Models and Its Impact on Regional Meteorology. *Monthly Weater Review*, V. 117, Issue 10, pp. 2113–2136.
- Caparrini, F., Castelli, F., Entekhabi, D., 2004, Variational estimation of soil and vegetation turbulent transfer and heat flux parameters from sequences of multisensor imagery. *Water*

- Resources Research*, V. 40, W12515, doi:10.1029/2004WR003358.
- Schulz, J.-P., Dümenil, L., Polcher, J., Schlosser, C. A., Xue, Y., 1998, Land surface energy and moisture fluxes: Comparing three models. *Journal of applied meteorology*, V. 37, n° 3, pp. 288-307.
- Stull, R. N., 1988, An introduction to Boundary Layer Meteorology (Kluwer Academic Publisher, Dordrecht, The Netherlands).
- Sun, D. and Pinker, R. T., 2003, Estimation of land surface temperature from a geostationary operational environmental satellite (GOES-8). *Journal of Geophysical Research*, 108(D11), 4326, doi:10.1029/2002JD002422
- Tremback C. J., 1990, Numerical simulation of a mesoscale convective complex, model development and numerical results. Ph.D. dissertation, *Atmospheric Sciences* Paper No. 465, Colorado State University Dept. of Atmospheric Science, Fort Collins, CO 80523.
- Vidale, P. L. and Stöckli, R., 2005, Prognostic canopy air space solutions for land surface exchanges. *Theoretical and Applied climatology*, V. 80, Numbers 2-4, 245-257, doi: 10.1007/s00704-004-0103-2.

Application of the Maximum Cross-Correlation technique to sequential ocean thermal imagery in the Cape Blanc region

P. Castellanos¹, J. L. Pelegrí¹, D. Baldwin², W. J. Emery², A. Hernández-Guerra³

¹*Institut de Ciències del Mar, CSIC, Barcelona, Spain*

castellanos@icm.csic.es, pelegrí@icm.csic.es

²*Aerospace Engineering Science Department, University of Colorado, Boulder, USA*

baldwin@colorado.edu, emery@colorado.edu

³*Universidad de las Palmas de Gran Canaria, Las Palmas de G. C., Spain*

ahernandez@dfis.ulpgc.es

ABSTRACT - Sequential Advanced Very High Resolution Radiometer infrared satellite images off NW Africa during 2005 and 2006, roughly in the Cape Blanc region (14° to 26°N and from the African coast to 26°W), are analyzed with the Maximum Cross-Correlation (MCC) method. Infrared images are first geometrically corrected and accurately registered to a map grid and the advective surface velocities are then estimated from the maximum cross-correlation between pairs of time-consecutive images. The results depend on the choice of MCC parameters, specifically on the search pattern, the search area and the cross-correlation threshold. These parameters are adjusted to the study region through a sensitivity analysis which examines the statistics of the velocity component distributions. The best results are obtained by removing spurious data according to a simple criterion that both velocity components have Gaussian distributions, and after smoothing the velocity fields with a vector filter. We have analyzed 480 images and generated 106 velocity maps for the region between Cape Blanc and Cape Verde. The calculated surface circulation patterns are compared with the surface Ekman velocities, as obtained through Quikscat's wind stress and the climatological mixed-layer depth. The surface circulation responds to the seasonal winds, with initial offshore and subsequent along-shore maximum velocities occurring during persistent upwelling events. South of the Cape Verde front the flow is dominated by mesoscale structures and a mean offshore Ekman pattern predominates only during intense upwelling-favourable events.

1 INTRODUCTION

During the 1980's several studies proved there is a close correspondence between sea-surface currents derived from infrared data collected with the Advanced Very High Resolution Radiometer (AVHRR) and the velocities estimated from drifters' trajectories or measured with point current-meters (La Violette, 1984; Emery et al., 1986, 1992; Tokmakian et al., 2003). This opened up the possibility of obtaining surface velocities for any portion of the world ocean with excellent spatial and temporal coverage, limited only by the availability of satellite images with adequate sea coverage and their spatial resolution. AVHRR images are limited by meteorological factors such as atmospheric dust or clouds images, and are typically available once a day with 1 km resolution or twice daily with lower spatial resolution.

There are different quantitative methods to infer velocities from remote images, most of them based on identifying, segmenting and tracking structures (Marcello et al., 2008). The implicit hypothesis in any of these methods is that the relevant water property (temperature for infrared

images) is not modified between the consecutive images. These tracking methods also have one major practical requirement: there must be at least two good-quality images close in time, the goodness of the results depending on the temporal separation between the images and the quality of all individual figures. Other innovative attempts that aim at identifying streamlines from individual images have had substantial success (Turiel et al., 2005), but are limited by the condition that all surface features have to have a dynamic (rather than thermodynamic) origin.

The feature-tracking methods have to be carefully implemented and calibrated before they may be successfully applied to a regional ocean. This implies a proper adjustment of several parameters until the calculated current field is self-consistent and coherent with the forcing meteorological fields. Once this is attained the method will not only describe the most common current patterns but will also help understand the undergoing dynamics. A proper implementation shall provide an optimum solution and will serve to understand the method's intrinsic limitations.

2 APPLICATION OF THE MAXIMUM CROSS-CORRELATION METHOD OFF NW AFRICA

2.1 The Maximum Cross-Correlation method

The feature-tracking method we will use is the Maximum Cross-Correlation (MCC) method. It was initially developed by Leese et al. (1977) to track cloud motions and was later adapted by Ninnins et al. (1986) to detect ice motion in the Beaufort Sea and by Emery et al. (1986) to estimate surface currents from the AVHRR images in the Vancouver area. The method assumes that any thermal structure in the ocean is produced through horizontal advection. Structures may be rotated and deformed but cannot be created or destroyed. Therefore, the surface horizontal velocities may be determined by identifying the horizontal property (such as temperature) gradients and tracking their motion in time.

The MCC has been applied using thermal structures (Emery, et al., 1986, 1992, 2003; Tokmakian et al., 1990) although it is theoretically possible to use other properties, such as ocean colour (Marcello et al., 2008). It basically consists in finding out which is the maximum cross-correlation between matrixes (one matrix for each sub-area) in a pair of time-consecutive images. From image 1 (I1) at time t we extract one sub-area, or reference window RW, which is then compared with a larger area, or search window SW, in image 2 (I2) at time $t+\delta t$. The centre of the SW in I2 coincides with the centre of the RW in I1. The size of RW depends on the length of the structures in the study area, while the size of SW is a function of time lapse between the images and the expected surface currents in the region under consideration (Fig. 1).

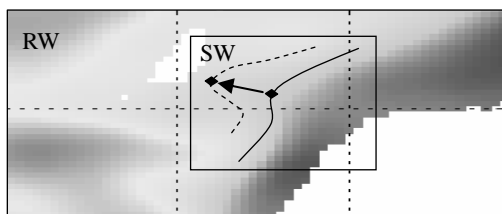


Fig. 1. Schematics of the MCC method.

We essentially followed the method as explained in Emery et al. (1992). The routines are divided into two main modules: a navigation plus georeferencing module NAV and a module to calculate the velocity MOTION. A key element of the NAV module is the algorithm for geometric corrections (Emery et al., 2003). It estimates the latitude-longitude displacement error in the image,

as well as the roll-pitch-yaw mean values, and generates a calibrated base image with the corrected position parameters which is then used for geo-reference of all other images.

The MOTION module computes the cross-correlations to estimate the displacement of the structures and then applies a coherence filter to calculate the surface velocities. In this work we have also used statistical criteria to remove spurious values and have also applied a vector smoothing filter to further correct anomalous individual values. This tracking module employs three main parameters: the size of the RW and SW and a correlation threshold CT. The RW has to be large enough to enclose a full structure but not too large to include unwanted features. The size of the SW is related to the maximum anticipated velocity in the study area, i.e. it has to be at least as large as this velocity times the time interval between the images, but it should be not too large to include undesired fortuitous high correlations. Finally, the threshold correlation sets those apparent motions taken as real. A very high correlation value ensures that a structure is properly identified but may reduce the available number of velocity vectors.

2.2 Set up for the Cape Blanc region

The images were gathered at the NOAA reception station in the University of Las Palmas. We used a simple sensitivity analysis in order to find the best combination of parameters (RW, SW and CT) for the Cape Blanc region (14° to 26° N and from the African coast to 26° W). This consisted in setting three reasonable values for each parameter and examining the output from all possible combinations. To carry out this analysis we selected two 1024×1024 pixels consecutive images of the AVHRR NOAA-16 sensor, separated by 12 hours, corresponding to 23 and 24 March 2005.

We examined those output combinations shown in Table 1. For each output we computed the fraction of valid velocity vectors, n , as compared with the total number of pixels, N (1024×1024 pixels). To assess when a velocity vector is valid we examined each velocity component as follows: (1) computed the probability density function (pdf), (2) found out the closest Gaussian distribution, (3) removed all data values beyond four standard deviations of the adjusted Gaussian distribution, (4) iterated until no further data removal was necessary. The best outputs had the largest n/N fraction. The optimum CT, SW and RW turned out to be 0.6, 22×22 and 32×32 , respectively.

RW	SW	MV	CT
18×18	22×22	50 cm/s	0.4
22×22	32×32	60 cm/s	0.6
32×32	45×45	90 cm/s	0.8

Table 1. Number of pixels for the reference window RW and search window SW, maximum velocity MV, and correlation threshold CT used for the sensitivity tests.

Figure 2 illustrates, as an example, the pdf's for both velocity components as derived from one map after applying the iterative correction procedure. When the computed pdf distribution gets close enough to a Gaussian distribution the iteration ends up.

Despite these efforts it is frequent to observe the presence of small packages of adjacent vectors, typically 4-6, with one single near-constant value. These vectors arise from fortuitous high correlations between structures that are not of dynamical origin, and cannot be removed by the above procedures. In order to minimize their effect we apply a vector smoothing routine (Astola et al., 1990) to the velocity map; by using a smoothing window of 3×3 pixels some of these small-size structures are minimized.

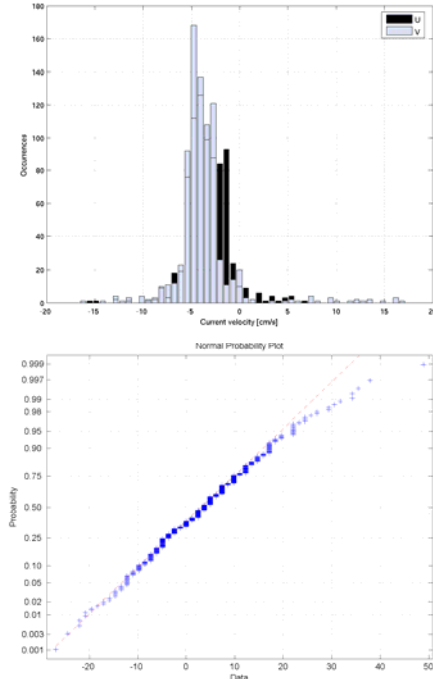


Fig. 2. Pdf distributions for both horizontal velocity components (23 Jan 2005 map) and fit to a Gaussian distribution for the u -component.

Once the method was adjusted we processed all 2005 and 2006 available images and generated a total of 106 maps (Table 2). Most maps correspond to winter and spring images as these seasons have small atmosphere-ocean heat exchange and much less cloud coverage near Cape Blanc (Schmitt et al., 1980), i.e. once cold waters reach the sea surface they warm up and extensive latent heat is released to the atmosphere. They also correspond to near adiabatic surface water parcels. Therefore, it is during this season that the large temperature gradients in the upwelling region are indeed useful are to infer near-surface motions.

year	2005	2006
processed images	317	159
generated maps	49	44
winter	24	10
spring	25	34
summer	3	1
fall	9	0
total images	480	
total maps	106	

Table 2. Number of processed images and maps.

3. SURFACE FLOW IN AN UPWELLING AREA

3.1 Upwelling dynamics

The dynamics of the Cape Blanc region is very complex, with high temporal-spatial variability. The MCC may provide very useful information to find out the scales of variability and to understand how the ocean responds to meteorological forcing. We may use the method to examine the response of the surface flow to distinct meteorological forcing in the Cape Blanc region. Before doing so, we present first a brief description of the main dynamical elements of the study region.

The mean surface flow pattern is characterized by flow convergence at the Cape Verde frontal zone, which runs from Cape Blanc to the Cape Verde Islands, of the southward flowing Canary Current and a weak northward coastal branch associated to the Guinea Dome cyclonic gyre. Over this large-scale flow we find a more variable pattern associated to intermittent upwelling. North of Cape Blanc the trade winds blow approximately parallel to the coast all year long, although with intermittent intensity that drives fluctuations in the position of the upwelling front that runs approximately parallel to shore. South of Cape Blanc wind-driven upwelling only predominates during winter. Therefore, north of Cape Blanc the

surface flow is a combination of transient offshore Ekman transport and alongshore geostrophic flow, the latter dominating in the near-steady upwelling conditions that characterize the area. South of Cape Blanc, on the contrary, upwelling is more intermittent and the most common situation is that of fluctuating offshore Ekman flow combined with mesoscalar instabilities generated near-shore or at the Cape Verde frontal zone (Pastor et al., 2008).

3.2 Transient surface velocities during upwelling

We now examine several forcing situations and the surface-flow response (Figures 3 to 6). In the top panels of these figures we show the meteorological forcing at the sea surface, expressed as the Ekman velocity. This velocity is calculated with 0.5° resolution as the Ekman transport (obtained from daily values of the microwave radar in the Quikscat satellite) divided by the climatologic depth of the surface mixed layer (from the World Ocean Atlas Data base). In the bottom panel we show the corresponding surface velocity maps, as obtained from two 1-day interval AVHRR images, with some large thick arrows superimposed solely to emphasize the most relevant features.

From Figures 3 to 6 we may appreciate that the fraction n/N is typically rather small, between 0.2 and 0.5. Most available vectors correspond to the upwelling region, in a several-hundred thick band adjacent to the coastline, and, to a lesser degree, to the Cape Verde frontal zone, located along a band between Cape Blanc and Cape Verde Islands.

Figure 3 illustrates a situation characteristic for the area, with intense offshore Ekman velocities in the coastal transition zone north of Cape Blanc. The velocity maps, however, illustrate the presence of along-shore flow that ends rather abruptly north of Cape Blanc. This corresponds to sustained wind-induced coastal upwelling, with Ekman transport building up large cross-shore pressure gradients which then drive an intense along-shore geostrophic flow (e.g. Pelegrí and Richman, 1983). The region south of Cape Blanc, with weak offshore Ekman velocities, shows no predominant flow direction, instead it presents relatively small mesoscale features (Pastor et al., 2008).

Figure 4 shows a case similar to that in Figure 3 but now with offshore Ekman velocities remaining intense as far south as half-way between Cape Blanc and Cape Verde. The along-shore flow in the northern portion remains clear until Cape Blanc, further south there is substantial eddy activity of relatively large size, in concordance with more wind-induced power transferred to the region.

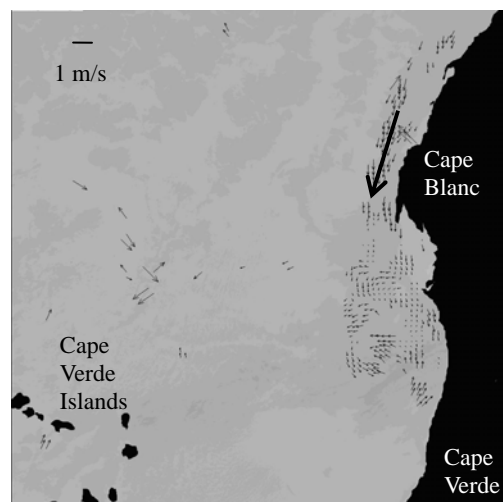
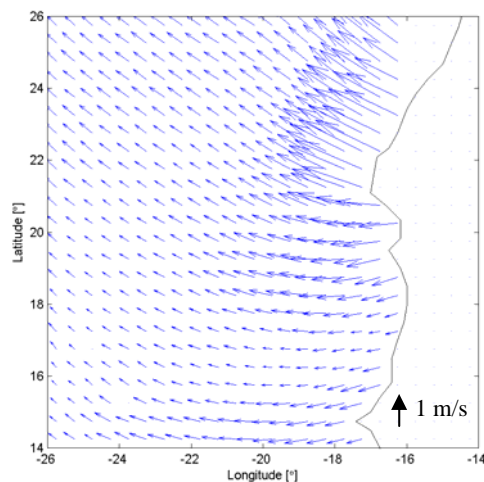


Fig. 3. Ekman and surface velocities, 24 Apr 2005.

Figure 5 shows an instance when intense cross-shore Ekman velocities weaken in the northern portion of the study area but intensify south of Cape Blanc and reach as far south as Cape Verde. In this case the flow field shows an extension of the along-shore jet into the Cape Verde frontal zone. The region south of this frontal system is dominated by Ekman offshore velocities.

Finally, in Figure 6 we present an instance when Ekman flow was much weaker in the whole domain. In this case the region south of Cape Blanc is dominated by northward flow, converging into what would constitute the Cape Blanc giant filament (e.g. Pastor et al., 2008).

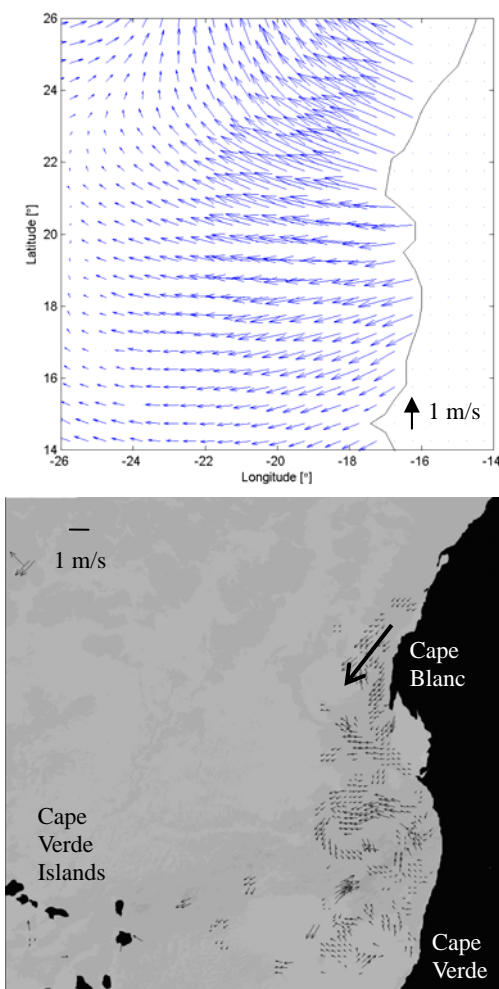


Fig. 4. Ekman and surface velocities, 5 Apr 2005.

4. CONCLUSIONS

The MCC method has been implemented for the Cape Blanc region and applied to two-years of infrared images with moderate success. Extensive cloud coverage in the upwelling region prevents obtaining information from most AVHRR images during summer and fall, and to a lesser degree from winter and spring images. During these latter seasons about one-third of the images are useful to extract velocity information.

A careful sensitivity analysis gives an optimum correlation threshold of 0.6, and search and reference windows of 22×22 pixels and 32×32 pixels, respectively. With these parameters about 20-50% of all possible velocity vectors are generated.

The removal of spurious velocity values is an important but laborious task. We have devised an

iterative procedure, which essentially computes the probability density functions of both horizontal velocity components and progressively removes observations until the re-calculated distributions are close enough to Gaussian.

Despite all these limitations, we obtain 106 surface velocity maps that help elucidate the complex surface-flow dynamics in the Cape Blanc region. The dominant pattern reflects a sequential response to surface winds. Upwelling-favourable winds induce a cross-shore surface flow followed, as cross-shore pressure gradients build up, by the intensification of the along-slope jet until Cape Blanc, where it departs southwest along the Cape Verde front. South of this front the conditions are variable, from dominant offshore flows during southward winds to northward flow as the wind relaxes, with substantial mesoscale variability.

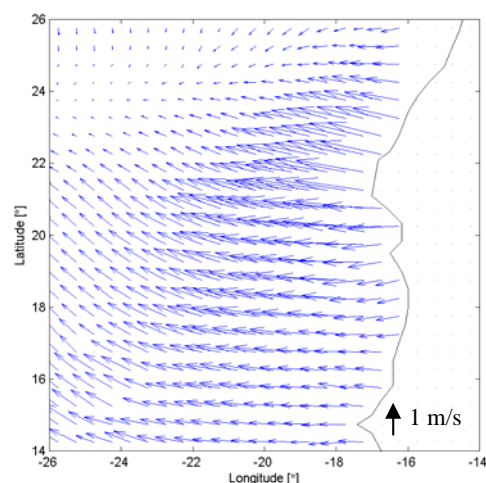


Fig. 5. Ekman and surface velocities, 21 Mar 2005.

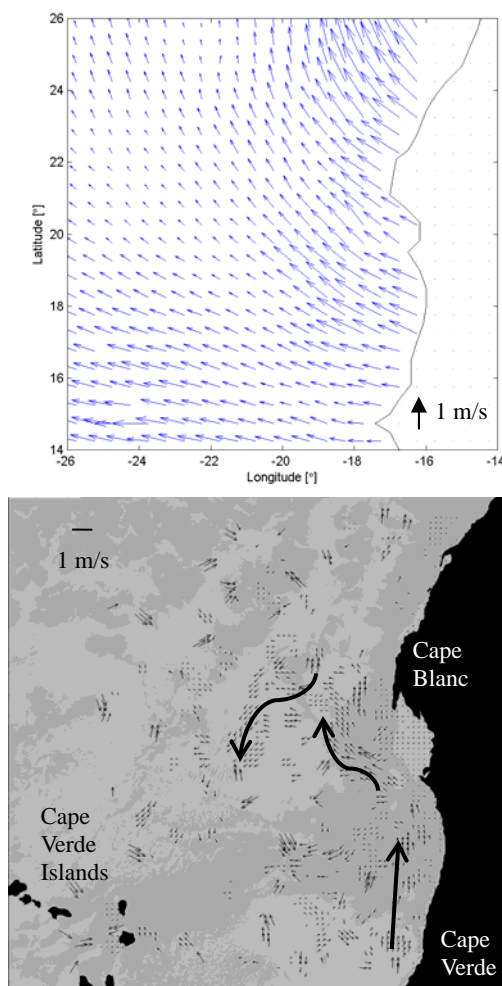


Fig. 6. Ekman and surface velocities, 23 Jan 2005.

REFERENCES

- Astola, J., Haavisto, P., and Neuvo, Y., 1990, Vector median filters. *Proceedings of the IEEE*, 78, 678-689.
- Emery, W. J., Thomas, A. C., and Collins, M. J., 1986, An objective method for computing advective surface velocities from sequential infrared satellites images. *Journal of Geophysical Research*, 91, 12865-12878.
- Emery, W. J., Fowler, C., and Clayson, A., 1992, Satellite-image-derived Gulf stream currents compared with numerical model results. *Journal of Atmospheric and Ocean Technology*, 9, 286-304.
- Emery, W. J., Baldwin, D., and Matthews, D., 2003, Maximum Cross Correlation automatic satellite image navigation and attitude corrections for open ocean image navigation. *IEEE Transactions on Geoscience and Remote Sensing*, 41, 33-41.
- La Violette, P. E., 1984, The advection of submesoscale thermal features in the Alboran Sea Gyre. *Journal of Physical Oceanography*, 14, 550-565.
- Leese, J. A., Novak, C. S., and Clark, B. B., 1971, An automated technique for obtaining cloud motion from Geosynchronous satellite data using cross correlation. *Journal of Meteorology*, 10, 118-132.
- Marcello, J., Eugenio, F., Marques, F., Hernandez-Guerra, A., and Gasull, A. 2008. Motion estimation techniques to automatically track oceanographic thermal structures in multisensor image sequences. *IEEE Transactions on Geoscience and Remote Sensing*, 46, 2743-2761.
- Ninnis, R. M., Emery W. J., and Collins, M. J., 1986, Automated extraction of pack ice motion from AVHRR imagery. *Journal of Geophysical Research*, 91, 10725-10734.
- Pastor, M. V., Pelegrí, J. L., Hernández, A., Font, J., Salat, J., and Emelianov, M., 2008, Water and nutrient fluxes off northwest Africa. *Continental Shelf Research*, 28, 915-936.
- Pelegrí, J. L., and Richman, J. R., 1993, On the role of shear mixing during transient coastal upwelling. *Continental Shelf Research*, 13, 1363-1400.
- Turiel, A., Isern-Fontanet, J., García-Ladona, E., and Font, J., 2005, Multifractal Method for the instantaneous evaluation of the Stream Function in Geophysical flows. *Physical Review Letters*, 95, 104502.
- Schmitt, R. W., Bodgen, P. S., and Dorman, C.E., 1989, Evaporation minus precipitation and density fluxes for the North Atlantic. *Journal of Physical Oceanography*, 19, 1208-1221.
- Tokmakian, R., Strub, P. T., and McClean-Padman J. 1990, Evaluation of the maximum cross-correlation method of estimating sea-surface velocities from sequential satellite images. *Journal of Atmospheric and Ocean Technology*, 7, 852-865.

Multisensor and multitemporal image fusion methods to improve remote sensing image classification

D. Ducrot, A. Masse, C. Marais-Sicre, J. F. Dejoux, F. Baup

Centre d'Etudes Spatiales de la Biosphère

18 av E.Belin - bpi 2801 - 31401 TOULOUSE cedex 9 France

danielle.ducrot@cesbio.cnes.fr, antoine.masse@cesbio.cnes.fr, claire.marais-Sicre@cesbio.cnes.fr

ABSTRACT: *As acquisition technology progresses, remote sensing data contains an ever increasing amount of information. To correctly understand the fundamental advantages of data fusion, let us list the different kinds of remote sensing data: optical and radar images, low, high and very high-resolution, multitemporal hyperspectral images, derived images, and physical or ancillary data (databases, D.E.M, G.I.S.). Data fusion is the joint use of heterogeneous images for decision-making. It is essential to group the available information from various sensor images, temporal data, expert information, etc....*

In this paper, fusion is used for improving classification at two levels: pixel by pixel or after independent "sub classification". This fusion is particularly interesting in the case of imperfect data to obtain more reliable information. Thus, it takes advantage of the best of each data type and overcomes individual limitations of each type. For example, optical and radar sensors are not sensitive to the same kind of information. We used the complementarities in these data to extract more complete information and to make a better distinction between various classes. We present some applications such as fusion between radar and optical images to detect agricultural practices on bare soil (TerraSar-X and Formosat2) which improves overall accuracy for supervised classification by 12%. Radar images lend more precision to bare soil classes and optical imagery more accuracy to active vegetation classes. We also show temporal complementarities with different dates from the same source (Formosat2).

1 FUSION DEFINITION

Fusion is the combination of heterogeneous images to support decision-making [Bloch et al, 2002, 2005]. From a mathematical point of view, fusion is applied when it is not possible to find a common metric for all the images, whatever their source. So fusion is used to blend information available from different sources: sensors, spectral or temporal data, but also external data, such as river or road maps, altitude, slope orientation (GIS), contour and texture. So we can exploit the complementarity of these data to extract more information, and provide a clearer distinction between different classes. We can decide to assign a pixel to the most reliable and accurate class possible.

In this paper, fusion is used in the sense of **classification** combination, which requires the right classification method as a first step. The applications will use multisensory and multitemporal classification from remote sensing data in a context of land use.

The various sources generally provide imperfect information i.e. uncertain, imprecise, incomplete, contradictory or inaccurate [Smets, 1999]. Fusion will use benefits of each data type to overcome the individual limitations of each one. For example, optical and radar sensors do not have the same sensitivity with the same information. Contents of parcels are more visible, sharper, and more homogenous with the optical images than in radar imaging, which is very heterogeneous due to speckle.

However, the insensitivity to weather conditions of acquisition radar remains a major advantage. So we can exploit the complementarities of these data to extract more information to better distinguish classes.

2 DIFFERENT APPROACHES

In practice, fusion is not a simple problem; it requires the use of specific methods. The main approaches to data fusion are Bayesian probabilistic methods (the oldest), fuzzy sets and possibility theory introduced by Zadeh [Zadeh 78, Dubois and Prades 93] and belief (or evidence) theory of Dempster-Schafer (first Dempster (1960) and renormalized by Shafer (1976)), widely used in image processing.

Methods implemented

A great number of tests showed that the combination of a large amount of temporal images does not necessarily give the best results [Ducrot *et al*, 1998]. We know that too much information can impair meaning and spoil the results. With specific temporal image combinations, classifications provide superior results for some classes and with other combinations, the best results for other classes. To obtain the best classification possible, the most effective solution is to merge classifications performed with various image combinations (temporal and/or different sources) chosen for their discrimination.

The fusion method is introduced in the classification and developed according to supervised or

unsupervised use. Bayesian methods are applied with different laws appropriate to each image batch and decisions made during each pixel assignment, or fusion of several classifications made independently according to their contribution to discrimination.

3 FUSION AND SUPERVISED CLASSIFICATION

For supervised classification, the fusion method which gives the best results is obtained with the use of confusion matrices for each classified image [Chust *et al.*, 2004]. These matrices, based on the proportion of Pixels Correctly Classified (PCC), can objectively quantify classification quality with mathematical and statistical criteria. Two main coefficients are calculated from these matrices: MPCC (Mean of PCC) called also Overall Accuracy and Kappa (Congalton (91)); they determine the global quality of the classification and the quality for each class.

$$MPCC = \frac{1}{n} \sum_{i=1}^n PCC(i) = \frac{1}{n} \sum_{i=1}^n \frac{m_{ii}}{m_{i.}}$$

with n = confusion matrix size, m_{ij} value at the i^{th} row and j^{th} column, $m_{i.}$ sum of row i .

The confusion matrix is computed by crossing the ground truths (lines) and classes found by the classification method (columns).

For each class, this allows the following measurements to be extracted: (1) deficit error (omission: percentage of classified sample pixels in other classes) that involves a loss $(100 - PCC)$ for this class and (2) excess error (omission: percentage of sample pixels that absorbs other classes, $100 - \text{number of incorrectly classified pixels divided by the sum of the column}$) that indicates an “over-represented” class.

3.1 Automatic and systematic measurements of image combinations

The issue to solve is the choice of the best combinations to obtain the best classification results. It is impossible to analyze each matrix manually for a lengthy time series. These combinations are selected by expert knowledge, with great uncertainty. For example, for seven dates, we get $\sum_{i=1,7} C^i_7 = 127$

possibilities. To find out the best dates for classification, it is necessary to measure the discriminatory power of these dates by calculating MPCC.

We developed an algorithm which provides, automatically and exhaustively, all confusion matrices of all possible date combinations (or spectral combinations). Thus, the choice is objective. The algorithm gives, in ascending order, the MPCC (with check and/or learning samples) of all the combinations, and confusion matrix diagonal elements in a summary table. We can also extract the best

combinations by class, which will guide us for the date combination choice to better discriminate classes.

3.2 Automatic fusion

An automatic fusion algorithm was developed. In the classification process, several classifications (called “sub classifications”) are made on n image batches; every batch contains m spectral and/or temporal images chosen according to the distinction of certain classes. An image batch is taken as a reference (the first “sub classification”), generally giving the best MPCC and kappa. Certain classes are better discriminated with other combinations, which show the relevance of merging these classified images. This principle can be applied within the classification or later in post-processing.

For two “sub classifications” with combinations of different dates, two classes can be in conflict, caused by their attribution to the same pixel. The ambiguity is removed by comparison of confusion matrices of both images which reveal the conflicts between classes.

SPOT (1)	Corn	Sunfl	ERS (2)	Corn	Sunfl
corn	50.23	30.5	corn	90.5	10.1
Sunflower	5.6	71.02	Sunfl	2.8	50

ERS (3)	Corn	Sunfl	ERS (4)	Corn	Sunfl
corn	77.53	0	corn	60.83	32.6
Sunflower	42	25	Sunfl	1.2	50.6

Table 1: confusion matrices extract (two sources)

A class can have a better score in one classification, but include other classes; it is an “over-represented” class. Thus, this class seems correctly classified (its PCC is better), but the classification loses the incorporated classes. For example, in table 1 (classification with SPOT and ERS (radar)), in the 1st classification (1) Corn is confused with Sunflower; the confusion is removed thanks to the fusion with the 2nd (2) without ambiguity. If a pixel is classified as Corn (1st classification) and Sunflower (2nd classification), the fusion with the described rules will affect it to Sunflower. Case (3), Corn seems well classified (90.5%), but it is over-represented and often replaces Sunflower (42.1%), fusion between 1st and 3rd classifications would be incorrect.

The algorithm avoids this type of confusion.

The 4th seems worst. Therefore, a fusion with this classification decreases slightly the over representation of Corn to the detriment of Sunflower.

The M_{Sk} and M_{S1} confusion matrices corresponding to classification of two sources S_k (reference source with the best global results (kappa and MPCC)) and S_1 (different combination). Sources can be different

sensors, dates (multi -spectral, -temporal, -source combinations).

S _k	i	...	j
i	m _{kii}	...	m _{kij}
...
j	m _{kji}	...	m _{kjj}

S _l	i	...	j
i	m _{lii}	...	m _{lij}
...
j	m _{lji}	...	m _{ljj}

Table 2: S_k and S_l confusion matrices

The diagonal elements m_{kii} of M_{S_k} and m_{lii} of M_{S_l}, represent the pixel percentage correctly assigned to class *i* (degree of confidence for assignment to this class) (table 2). The non-diagonal elements m_{kij} and m_{lij} are the percentage of pixels in class *i* assigned to class *j*. Example of certain rules:

If $i \cap j = \emptyset \Leftrightarrow m_{kij} = 0$ and $m_{kji} = 0$, necessary and sufficient condition, that means: no confusion between classes *i* and *j*, the confidence degree is maximum on *i* for the source S_k

Else $x \in i \cup j$, pixel $x \in S_k$

If $m_{kij} \neq 0$ **then** there is confusion between *i* and *j*, some pixels of class *i* are assigned to class *j*.

If $m_{kji} \neq 0$ **then** there is confusion between *i* and *j*, but the pixels of class *j* are assigned to class *i*.

If there is confusion between *i* and *j* in the source S_k ($i \cap j \neq \emptyset$ with a high score for m_{kij}), the source S_l can raise this ambiguity if $i \cap j = \emptyset$ in S_l or if the score is low for m_{lij}.

Let a pixel *x*, classed *i* with S_k and *j* with S_l. If the class *i* is confused with class *j* and has a poor score in M_{S_k}, *j* having a better score (low or no confusion) in M_{S_l}, the fusion facilitates class *j*, *x* is then assigned to *j*. A test is performed to minimize a possible loss in another class. To increase the overall accuracy, we introduce the notion of gain to allow the algorithm to decrease the (j,i) confusion even if the (i,j) confusion slightly increases.

3.3 Supervised fusion

Supervised fusion improves classification results by combining another classified image, best judged by the expert, after examining this classification and its confusion matrix (PCCs). Criteria are imposed by the user. Thus, the fusion concerns only certain classes chosen according to the user's knowledge

4 PROBABILISTIC MODELS: FUSION BY BAYESIAN THEORY

The widely spread probabilistic methods characterize uncertainty and, with difficulty, inaccuracy. The Bayesian method makes it possible to perform data combination in an associative way: conjunction, disjunction and averages. Fusion is carried out thanks to the Bayes rule, which requires an estimation of probability. The various terms are computed by training (supervised or random).

$$P(x \in C_i | I_1, \dots, I_l) = \frac{P(I_1, \dots, I_l | x \in C_i) P(x \in C_i)}{P(I_1, \dots, I_l)}$$

To perform data combination according to the theory of Bayes, the probability of the observation model is calculated by supposing data sources to be independent. The different sources infer different and more relevant laws according to the type of sensors. We chose the Gaussian law for optical images and the Gauss-Wishart law [Fukunaga, 1972] for radar images. It is a contextual law taking into account the pixel neighborhood with segmentation (object classification) [Ducrot et al 1998]. These laws being different, the results are no longer comparable, what involves fusion rules.

Method implemented

The process implemented consists of local decision-making first being applied to every image batch separately. We then merge the local decisions in a global decision. This type of fusion is adapted to unsupervised classifications, but requires an adjustment for correspondence to the different unsupervised sub-classification classes

A weight giving more or less credibility to each batch can be associated to these batches.

Given the inaccuracy of these data, why do we keep a single class? The difference between *n* first better measurements is unimportant. The class showing the best score is generally very close to the next classes. So, there is no valid reason to choose the 1st rather than the 2nd and so on. Several classes are thus acceptable for a pixel if their measurement shows a sufficient degree of confidence.

For every image batch, the *n* better classes are chosen, their associated measurement is kept, and the global decision is carried out for these *n* classes. For a given pixel, the measurement of the *n* classes is ordered in descending order, we would then have, for instance, [0.3865, 0.3864, 0.3862, 0.3861, 0.3858, 0.29,]. In this case, the first five classes of this image batch have very close measurements, so we can select them.

The intersection of acceptable class sets for every image batch is performed to determine the most representative class. The number of classes selected is sufficient: in our applications, an average of 6 classes are kept per image batch and per pixel.

The algorithm is more accurate and faster because it does not use all the classes for the global decision.

5 – APPLICATIONS

5-1 Fusion on a temporal series: 2008 Formosat-2 images (8m*8m) from CESBIO (Center of Spatial Study of the Biosphere) - Toulouse Southwest project

This application concerns an agricultural zone of the Toulouse Southwest (France). Nine Formosat-2 images (Taiwanese satellite, resolution 8m*8m with 4

spectral ranges: Blue (0.45 – 0.52 μm), Green (0.52 – 0.60 μm , Red (0.63 – 0.69 μm), Near Infrared (0.76 – 0.90 μm) are used.

The February image contains some clouds; the classes under clouds are mainly classified as diffuse or industrial Built or Mineral surface classes. This image was used because no spring data was available which provides optimum discrimination of the Rapeseed class.

After examining the best dates for class discrimination, “sub-classifications” with different image batches were successively completed and merged. The confusion matrix method was used.

1. The first image batch with 9 dates: 2008/02/11, 2008/06/19, 2008/10/07, 2008/31/07, 2008/21/08, 2008/25/09, 2008/06/10, 2008/10/10 and 2008/26/10.

2. Second image batch (without February): this sub classification is merged with the previous one. When pixels are classified as Built or Mineral Surface in the first sub classification, the class of the second one replaces them (figure 1). We were able to eliminate clouds blending with Mineral surfaces. This fusion provides better discrimination of the Rapeseed class as well as Built classes because, in February, the presence of many bare soil crops causes confusions between these classes and some crop classes.

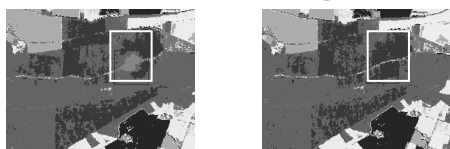


Figure 1: right, 9 date classification (grey frame: cloud corresponds to Built), left this classification merged without February classification → cloud is removed

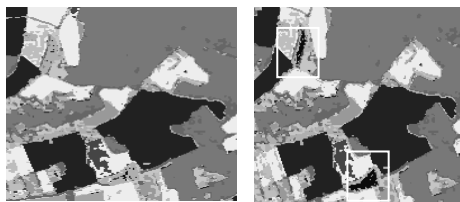


Figure 2: right, previous fusion (figure 1), left, fusion with NDVI classification; small lakes appear (dark blue), previously classified as mineral surfaces

3. The third image batch is formed with only PIR channels or NDVIs of every date. This combination improves Water, Lake or Gravel pit classes confused with roads, as well as Wheat class which present confusions with mineral class (figure 2, table 3).

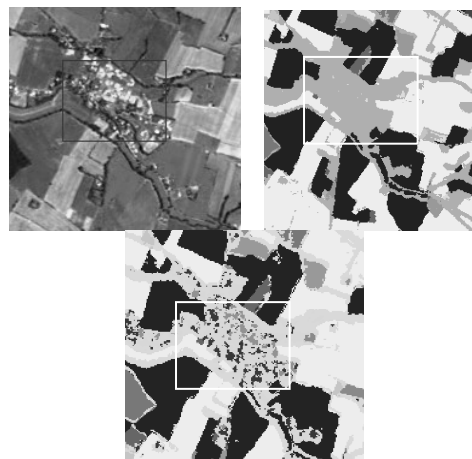


Figure 3: (a) Colored composition 08/07/10 Formosat (b) final classification (c) fusion with unsupervised classification to distinguish hedges and different stage of Built

% corrected classes	fusion final	9 dates	8 dates without february	NDVI 9dates
decideous trees	97.88	96.9	96.4	94.7
coniferous	97.05	96.82	96.15	96.79
eucalyptus.	74.53	73.84	70.41	59
wheat	97.48	96.28	92.44	71.05
rapeseed	99.33	99.11	98.05	86.63
barley	99.06	97.41	95.87	76.09
corn	99.6	99.13	98.75	90.86
sunflower	99.12	96.91	93.08	72.61
sorghum	100	98.17	97.48	96.68
soybeans	97.36	97.42	97.09	94.26
set-aside land	97.75	93.65	93.11	74.49
wild land	90.27	91.64	91.19	71.96
meadow	95.16	92.61	88.73	76.64
river	99.73	97.41	97.28	91.43
lake	99.95	99.68	99.68	94.1
built densely	96.06	96.06	94.98	93.19
built industrial	98.2	98.2	97.48	88.49
gravel pit	99.91	99.83	99.78	93.19
poplars.	98.97	97.87	98.27	96.84
diffuse built	95.47	97.46	95.29	87.5
bicultural	93.32	95.47	92.15	76.78
Sunflower particular.	100	96.91	96.74	95.37
mineral surface	99.82	99.82	99.27	93.96
Sunflower late	100	100	99.95	98.81
MPCC	96.92	96.19	94.98	86.31
Kappa	97.23	96.13	94.31	82.69

Table 3: successive improvements (from right to left) according to the steps described previously

4. A 4th step gives better accuracy for Built/mineral surface classes and hedges with unsupervised classification fusion (figure 3). Improvements are visible through the observation of the image, but they are difficult to quantify because we have no samples for their measurement.

These classifications remove a lot of confusion about certain crops (Sunflower, Corn ...). For very detailed classification, the results for land cover are highly acceptable (table 3).

5.2 - Optical / radar fusion (Spot/Radarsat) Grand Morin basin in Seine and Marne (France)

As part of a research program for the promotion of the Radarsat data (ADRO: Development and Research Opportunity application), the objective was to define an environment indicator to assess the vulnerability of the natural environment to pollution caused by human activity through land use mapping. This was established by several classifications from the following data (1) multitemporal radar data (4 unfiltered and filtered amplitude Radarsat images: 1997 June 28th, 1997 July 22nd, 1997 September 8th, 1997 November 19th); (2) optical data: SPOT image multispectral (XS), 1997 August 13th.

The area investigated is located in the Grand Morin basin in the Seine and Marne department (France) which supplies drinking water to part of the Paris region. This site is mainly fragmented agricultural terrain, with wood and forests.

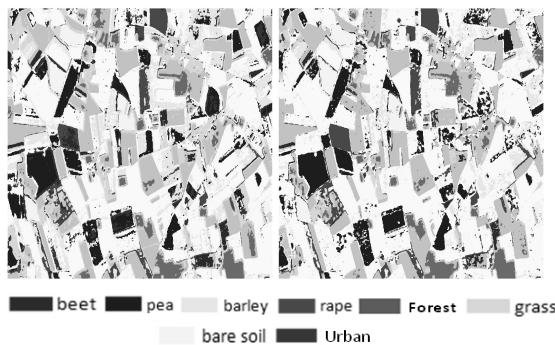


Figure 4: left, SPOT classification, right, SPOT + Radarsat fusion image

Methods and data	Gauss Spot	GW Radarsat non filtered	GW Spot + Radarsat unfiltered	gauss Spot + Pearson Radarsat unfiltered
forest	98.6	94.87	98.05	98.06
corn	85.46	80.52	99.18	97.54
wheat 1	49.55	59.89	88.87	87.79
wheat 2	86.21	62.3	88.89	90.03
barley	59.62	45.56	59.91	60.35
rape	46.02	40.15	46.02	46.02
pea 1	54.65	60.21	55.43	55.81
pea 2	79.78	70.57	80.66	82.97
beet	97.92	86.32	99.14	94.1
herb	97.09	86.25	97.43	97.44
urban	97.5	93.85	100	91
bare soil	99.56	87.49	100	96.84
mean	79.33	72.33	84.46	83.43

Table 4: percentage of corrected classified for the Spot & Radarsat classification, fusion Radarsat-Spot with two methods (GW = Gauss-Wishart is better)

The probability fusion process with the Radarsat unfiltered images, classified with the contextual Gauss Wishart law (GW), improves the results of the SPOT image (Gauss law) for the majority of the classes: approximately 5% (table 5). The display of this classification (figure 4) shows the results improved for Forest, Corn, Beet and Pea classes. Blending between the parcels of these classes is removed. The fusion eliminates pixels from Urban-mineral class (generally roads) spread across the image. Contour pixel confusion between fields and grass is reduced, thereby improving the structure of fields. This improvement is important, but does not count towards the percentage of correctly classified which is computed from samples located in the centre of parcels.

5.3 - Optical / radar fusion for the detection of agricultural practices on bare soil

The goal is to estimate the possibility of agricultural practice detection on bare soil, to take into account the soil work in modeling carbon inventories in the southwest region of Toulouse. This study is conducted with radar and optical satellite data and ground truths focusing on soil humidity and roughness. The type of the agricultural soil working plays a major role in carbon inventory on the landscape scale. Indeed, soils represent CO₂ sinks and sources. It has been shown that a ploughed ground stores 3 to 5 tons of CO₂ by hectare per year, less than slightly worked ground or direct sowing. The detection and the monitoring of the various farming practices are used to take into account their CO₂ emission and storage in complex climatic models.

The classes to be considered are as follows: (1) **Inter-crop**: begins after harvest; no recent or visible soil tillage; crop residues may be visible on soil surface; some greenery may grow, like weeds; (2) **Stubble disking**: superficial soil tillage to mix crop residues and soil (5 to 15 cm deep) and to destroy weeds; soil surface is irregular with some small clods and slight roughness, biomass may remain on the surface; (3) **Deep plowing** (20 to 45 cm deep): 95% bare soil, deeply worked with pronounced roughness (plowing), visible clods; (4) **Harrowing**: 95%, bare soil; secondary or superficial tillage, medium-sized clods, improper for seeding (5) **Sowing preparation**: 95%, bare soil, regular surface, soil ready to be sowed, fine work, small clods (6) **Emergence**: germination; plants are visible, cotyledons or first leaves development stages (5 cm height) [Inglada, 2010]. We shall add some classes corresponding to fields in active vegetation in this period: Corn, Rapeseed and Sunflower.

Fusion was performed from 08/10/10 FORMOSAT-2 optical image and 08/10/09 TerraSAR-X radar image, chosen because of a 1-day time gap.

TerraSAR-X (DLR aerospace centre and EADS Astrium) has a band X (9.65 GHz) SAR; the data is generated by a multilook process (3x3m² pixel size and a spatial resolution of 6.5*6.5 m²).

FORMOSAT-2, Taiwanese high-resolution/revisit daily (8m) satellite, can acquire any image within its coverage area every day, Blue 0.45-0.52µm, Green 0.52-0.60µm, Red 0.63-0.69µm, Near Infra Red 0.76-0.90µm, coverage 24 km X 24 km.

A mask is applied to the TerraSAR-X images to eliminate urban and forest zones, lakes, meadows and fallows. Classes are thus attributed only to agricultural zones and will differentiate bare soil types more easily

For one date, the results achieved are: with Terrassar MPCC = 41.92 %, with Formosat-2 MPCC = 76.61 %. After the fusion (using confusion matrices) we obtain MPCC = 83.16 %. The RADAR contribution is: Stubble disking 67.43%, deep plowing 91.72% Harrowing 53.52%; the optical contribution is: Sowing preparation 81.28% Emergence 93.69% Inter-crop 76.35%, Corn 92.54% Rape seed 93.3% Sunflower 96.69%

The contribution of RADAR on the optical supervised classification improves bare soil distribution classes of 12 %. The advantage of fusion in this case is to provide more precision for bare soil classes by the intervention of the RADAR and to improve active vegetation classes thanks to optical data.

4 CONCLUSION

In complex contexts involving different sensors or long temporal series, the objective was to obtain superior classification scores. The most effective solution was to perform classification fusions with diverse date combinations (image batches), selected according to discrimination of classes or sensors.

We presented two main methods: one well suited to supervised cases because it needed confusion matrices. A more general method could be adapted to unsupervised classifications, but, after each image batches classification ("sub-classification"), it involves finding correspondence between classes of these sub unsupervised classifications, which produces different labels for a same class. This type of fusion enables the law to be applied to the different image batches to be selected.

Three different applications were presented: optical temporal series, optical/radar fusion for land cover, and detection of different agricultural bare soil types. In these three cases we must obtain very precise and detailed classification. Using the fusion process developed, we achieved very satisfactory results. We used complementarities of optical and radar data to extract richer information and to obtain an enhanced distinction between the various classes.

Future objectives are to improve the unsupervised method with a Markovian model combined with the probabilistic mode to better integrate temporal changes and the problem of correspondence between classes of different sub-classifications.

REFERENCES

- Bloch I. & Maître H., 2002, Fusion d'informations en traitement d'image: spécificités modélisation et combinaison par des méthodes numériques, *Techniques de l'Ingénieur* 2002 ,TE 5 230, 1-26.
- Bloch I., 2005, Fuzzy Spatial Relationships for Image Processing and Interpretation: A Review, *Image and Vision Computing* 2005 vol. 23, 2, 89-110.
- Chust G., Ducrot D. & Pretus J. LI, 2004, Land cover discrimination potential of radar multitemporal series and optical multispectral images in a Mediterranean cultural landscape, *International Journal of Remote Sensing*, 5, 17, 3513-3528.
- Congalton R.G., 1991, A review of assessing the accuracy of classification of remotely sensed data, *Remote Sensing of Environment* 37, 35-46.
- Dubois D. & Prades H., 1993, Combination of information in the framework of possibility theory data fusion in robotics and machine intelligence, Academic Press.
- Ducrot D., Sery F., Sassier H., Goze S., Planes J.G., 1998, Classification and fusion of optical and radar satellite data for land use extraction, *Fusion of Earth Data98*, Sophia Antipolis, France, 15, 1,5-20.
- Fukunaga K., 1972, Introduction to statistical pattern recognition, *Electrical Sciences Series*, Academic press, London (UK).
- Inglada J., Beguet B., DejouxJ.-F, Marais Sicre C., Ducrot, D., Huc M. , Hagolle O. , Baup F. , Dedieu G. , 2010, Use of dense time series of high resolution images for change detection and land use classification. *In Recent Advances in Quantitative Remote Sensing*
- Shafer G., 1976, A mathematical theory of evidence, *Princeton University Press*. Princeton, NJ.
- Smets P., 1999, Imperfect Information: Imprecision, Uncertainty, *report IRIDIA July 27*
- Zadeh L.A., 1978, Fuzzy sets as a basis for a theory of possibility, *Fuzzy Sets and Systems* 1, 3-28

A Multi Sensor Approach to Land Surface Temperature

¹Sandra C. Freitas, ^{1,2}Isabel F. Trigo, ¹João Macedo, ¹Carla Barroso, ¹Ricardo Silva,

¹Instituto de Meteorologia, Rua C- Aeroporto, 1700-049 Lisboa, Portugal

² Instituto Dom Luiz/CGUL, 1749-016 Lisboa, Portugal

Sandra.coelho@meteo.pt, Isabel.trigo@meteo.pt, João.macedo@meteo.pt, Carla.barroso@meteo.pt, Ricardo.silva@meteo.pt

ABSTRACT Land Surface Temperature (LST) presents high variability in space and time, essentially due to the low thermal inertia of land surfaces and to the sensitivity of the skin temperature to local effects (such as terrain characteristics, land cover, vegetation state). The use of remotely sensed data is the only means to achieve both a large spatial coverage and its daily cycle. The latter aspect, along with an increased probability of obtaining a significant number of (clear sky) retrievals per day, constitute the main advantage of LST fields retrieved from sensors onboard geostationary satellites, when compared with those obtained from polar-orbiters. Here we will present a LST product which is the combination of retrievals from a constellation of geostationary satellites. LST is obtained from satellite sensors onboard MSG, GOES and MTSAT. Such multi-sensor LST makes use of different retrieval algorithms designed for each sensor, using brightness temperatures from infrared channels. The calibration (and verification) of the different algorithms relies on radiative transfer simulations of top-of-atmosphere brightness temperatures for the relevant channels. The simulations are performed for the database of global profiles of temperature, moisture, and ozone compiled by Borbas et al. (2005) to be representative of a wide range of atmospheric (clear sky) conditions over the whole globe. In addition, surface parameters such as skin temperatures (T_{skin}) and a landcover classification within the International Geosphere-Biosphere Programme ecosystem categories (IGBP) are assigned to each profile. The simulated data are split into two sets – one for algorithm calibration and another for the assessment of algorithm uncertainties. This also allows the quantification of the uncertainty of LST estimations, which take into account: (i) error statistics of the retrieval algorithms under different conditions; (ii) sensor noise; (iii) and a careful characterization of the uncertainty of input data, particularly the surface emissivity and forecasts of the total water vapour content. Such analysis is the basis for the assignment of error bars to estimate LST uncertainty. Finally, LST retrievals from different geostationary satellites are merged into a single field. In overlapping areas, the final LST value is an average weighted by the error bar of each LST estimation.

1 INTRODUCTION

The objective of the Land Surface Temperature (LST) product developed within the framework of Geoland-2 (the pilot project for the GMES Land Monitoring Core Service) is to increase the area coverage of the LST product currently distributed by the Eumetsat Satellite Application Facility (SAF) on Land Surface Analysis (LSA). The LSA SAF generates, archives and disseminates LST from SEVIRI (onboard MSG) with a 15-minute frequency, at the original satellite spatial resolution. A quasi-global product is obtained by merging SEVIRI- with GOES- and MTSAT-based LST produced in near real time with an hourly frequency.

LST estimations from remotely sensed data are generally obtained from one or more channels within the thermal infrared atmospheric window from 8 to 13 μm (Dash et al., 2002). Operational LST retrievals often make use of split-window algorithms (e.g., Prata, 1993; Wan and Dozier, 1996). Recent studies have

assessed the combination of middle infrared bands centred on 3.9 μm (T_{MIR}) with the split-window within the 10-to-13 μm band (T_{TIR1} and T_{TIR2} ; Sun and Pinker, 2007; Pinker et al., 2007). Although there are several caveats regarding the use of such extra channels for LST operational retrievals, they can become a very useful source of information, particularly in the absence of two T_{TIR} bands.

2 LST ALGORITHMS

Land Surface Temperature (LST) is estimated from Top-of-Atmosphere (TOA) brightness temperatures of atmospheric window channels within the infrared range. The algorithms developed for geostationary (GEO) satellites take into account the information in the available channels and are divided into three groups: (i) split-window methodologies, which make use of two adjacent window channels within the thermal infrared range (T_{TIR1} and T_{TIR2}); (ii) two-channel algorithms, which derive LST from one window channel in the thermal infrared and another in

the middle infra-red (T_{TIR1} and T_{MIR} , respectively); two-channel algorithms are used when only one thermal window channel is available and for night-time conditions, when T_{MIR} is not contaminated by solar radiation reflected by the surface; (iii) mono-channel method that corrects the TOA brightness temperature of a single channel, T_{TIR1} , for atmospheric attenuation and surface emissivity; this algorithm is used for daytime conditions, when only one thermal window channel is available. Figure 1 presents the response functions of the thermal and middle infrared channels available in GOES, MTSAT and MSG platforms.

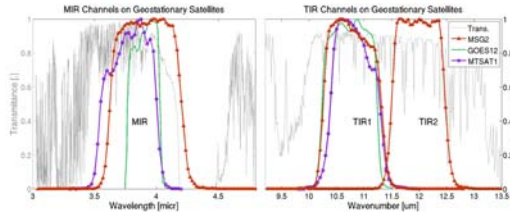


Figure 1 – Atmospheric transmittance and response functions of the thermal infrared channels of MSG, MTSAT and GOES satellites. Middle-infrared channels at left and thermal-window channels at right.

The methodologies aforementioned are based on semi-empirical formulations, where LST is expressed as a regression function of TOA brightness temperatures. To minimize LST uncertainties, the algorithms are trained for different classes of satellite zenith angle, atmospheric water vapour content, and land cover type.

2.1 Generalized Split-Window Algorithm

The LSA-SAF LST (Trigo et al., 2008) is estimated using a formulation similar to that first proposed by Wan and Dozier (1996) for AVHRR and MODIS. Thus, LST is as a function of TOA brightness temperatures of SEVIRI split-window channels (T_{TIR1} and T_{TIR2}):

$$LST = (A_1 + A_2 \frac{1-\varepsilon}{\varepsilon} + A_3 \frac{\Delta\varepsilon}{\varepsilon^2}) \frac{T_{TIR1} + T_{TIR2}}{2} + (B_1 + B_2 \frac{1-\varepsilon}{\varepsilon} + B_3 \frac{\Delta\varepsilon}{\varepsilon^2}) \frac{T_{TIR1} - T_{TIR2}}{2} + C + \Delta LST \quad (1)$$

where ε is the average of the two channels surface emissivities and $\Delta\varepsilon$ their difference ($\varepsilon_{TIR1} - \varepsilon_{TIR2}$). A_j , B_j , ($j = 1,2,3$) and C are the Generalized Split Windows (GSW) coefficients obtained by fitting equation (1) to a calibration dataset for different classes of water vapour, TCWV, and satellite zenith angle (SZA). The ΔLST is the model error. The GSW

algorithm is applied to clear sky pixels only (Freitas et al., 2010).

The calibration and verification databases of the GSW developed for SEVIRI rely on radiative transfer simulations of TOA brightness temperatures for the split-window channels. The simulations are performed for the database of global profiles of temperature, moisture, and ozone compiled by Borbas et al. (2005) for clear sky conditions, and referred to as SeeBor. The database contains over 15,700 profiles that are representative of a wide range of atmospheric (clear sky) conditions over the whole globe. In addition, surface parameters such as skin temperatures (T_{skin}) and a landcover classification within the International Geosphere-Biosphere Programme ecosystem categories (IGBP) (Belward, 1996) are assigned to each profile. Skin temperature over land surfaces corresponds to LST in SeeBor and is estimated as a function of 2m temperature (T_{2m}), and solar zenith and azimuth angles (Borbas et al. 2005). In this study, we assume that each profile corresponds to one given pixel within the Meteosat disk. Thus, for radiative simulation purposes, a Satellite Zenith Angle (SZA) chosen randomly within the $0^\circ - 80^\circ$ range is assigned to each profile, except for cases with (i) T_{skin} below 270 K, which are constrained to angles above 30° ; and (ii) $T_{skin} < 240$ K, which are allowed to be observed by a geostationary satellite with a zenith angle within 60° and 80° . This procedure ensures a realistic cover of simulated radiances for all possible viewing geometries.

The radiative transfer simulations are performed using the MODerate spectral resolution atmospheric TRANsmittance algorithm (MODTRAN4) (Berk et al., 2000). The radiance (L_v) that would be measured by each TIR channel is then estimated with MODTRAN2, for each of the surface and atmospheric conditions, and viewing geometry.

The GSW algorithm is verified against the independent subset of simulated TOA brightness temperatures (which excludes the calibration data).

2.2 Dual Algorithm

The Dual-Algorithm (DA) provides estimation of LST using measurements from (i) the middle and thermal infrared window channel (T_{MIR} and T_{TIR1}) during night-time and; (ii) a single thermal window channel (T_{TIR1}) during daytime. The reason for having two different formulations is to avoid uncertainties in LST due to solar contamination of T_{MIR} during daytime.

Following the approach presented in Sun et al. (2004), a mono-channel and a two-channel algorithm were developed for channels available onboard GOES and MTSAT. The mono- and two-channel methods are based on equations (2) and (3), and unlike the original formulations developed by Sun et al. (2004), the

coefficients depend implicitly on TCWV, satellite zenith angle and landcover classification.

I. Mono-Channel Algorithm

$$LST = A_1 + A_2 T_{TIR1} + \Delta LST \quad (2)$$

II. Two-Channel Algorithm

$$LST = B_1 + B_2 T_{TIR1} + B_3 (T_{TIR1} - T_{MIR}) + \Delta LST \quad (3)$$

where ΔLST is the model error and A_i and B_i ($i=1,2,3$) the model coefficients. As in the case of the GSW algorithm, the coefficients in equations (2) and (3) are fit to a calibration dataset for each of the 16 land-cover types within IGBP database, for 8 different classes of TCWV (up to 6 cm) and for 16 classes of SZA (up to 75°) ensuring that all ranges of atmospheric attenuation within the thermal infrared are covered. The calibration and verification databases of the DA are built independently for GOES and MTSAT imagers. They follow the same methodology described in the previous section, relying on radiative transfer simulations of TOA brightness temperatures for the middle and thermal infrared channels available onboard each sensor.

Figures 2 a) to c) show examples of the LST retrieved with the GSW algorithm, the mono-channel algorithm and the two-channel algorithm, respectively.

3 ERROR ANALYSIS

The LST product is distributed to users along with a quality flag and an uncertainty (or error bar) estimated on a pixel-by-pixel basis. The assessment of LST errors takes into account the uncertainties of the retrieval algorithm, which heavily depend on the total optical path between the sensor and the surface, essentially determined by the viewing geometry and the total water vapour content in the atmosphere and on the day/night conditions. On top of that, LST uncertainty estimates consider the propagation of input errors, namely: (i) sensor noise; (ii) uncertainties in surface emissivity (for GSW algorithm) or uncertainties on the land cover classification (in case of DA algorithm); and (iii) expected forecast errors in total column water vapour. A detailed analysis of error statistics may be found in Freitas et al. (2010). Figures 3 a) to c) show examples of the error bars associated with LST retrieved with GSW algorithm, Mono-channel algorithm and Two-channel algorithm, respectively.

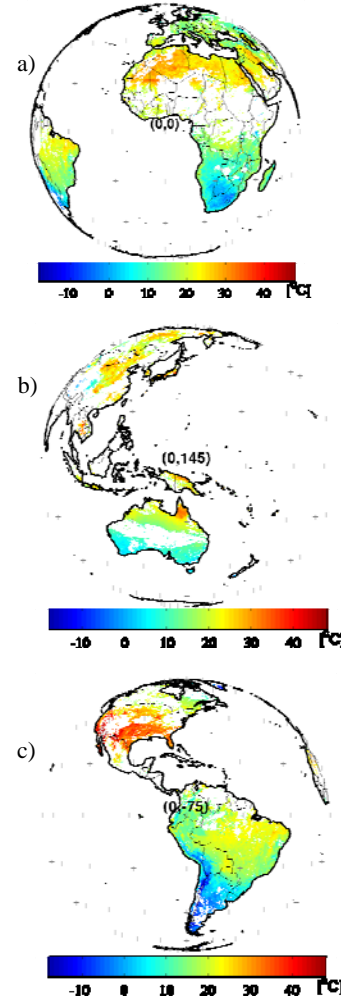


Figure 2 – LST Estimated for 21st July 2010 at 12UTC.

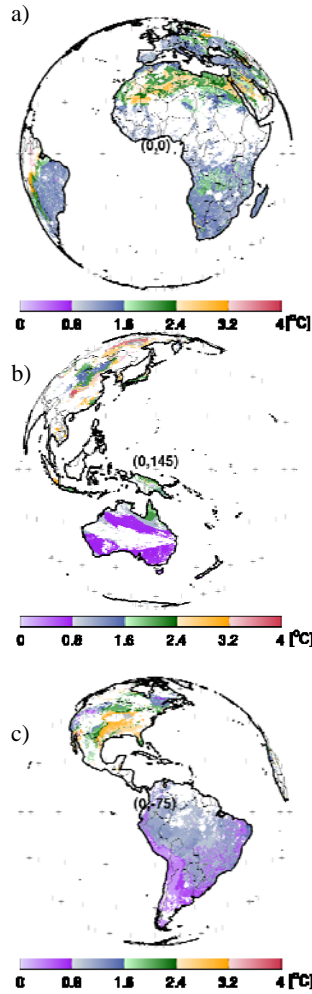


Figure 3 – Map of LST error bar [°C] for the 21st July 2010 at 12UTC.

4 ANALYSIS OF ALGORITHMS CONSISTENCY

To examine the consistency between algorithms the LST generated using GSW over MSG disk is compared with the LST from GOES, obtained with the DA, for the overlapping region. Both products were first reprojected into the *plate carrée* with 0.05° of resolution. As an example, Figures 4 and 5 show the difference between LST for GOES and MSG disks during night-time and day-time respectively, while Figures 6 and 7 present the respective scatter plots. A better agreement is observed during night-time, with the discrepancies ranging between -1°C and 1°C, while during day-time the differences may reach +4°C. This is in line with the fact that the uncertainty of the

mono-channel (used during day time) is higher than the uncertainty of the two-channel algorithm (used during night-time). Another reason might be the higher spatial and temporal variability of the surface temperature during the morning as is the case of the presented example. High discrepancies between LST values often follow the topography features since the two satellites observe the same scene from different viewing angles. This behaviour is particularly visible on the zoom box presented in Figure 8 where a longitudinal mountainous structure is identified. Due to their different satellites geometries, MSG is observing the sun-illuminated side of the mountain at 12UTC while GOES is looking at the shadowed side; this explains why LST from MSG is higher than LST measured with GOES for the Eastern oriented slopes. A further assessment of the algorithms consistency is performed by analysing the LST daily cycle and respective error bars obtained from both MSG and GOES for a specific location at the North of Brazil (Figure 7). The selected site corresponds to a flat region identified by a star in the Elevation Map (Figure 6 right panel). From Figure 7 it is clear that LST from GOES generally lies within the MSG LST error bars.

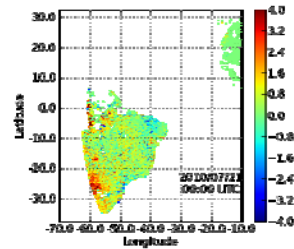


Figure 4 – Difference between LST from and MSG and GOES [°C] for 21st July 2010 at 00UTC.

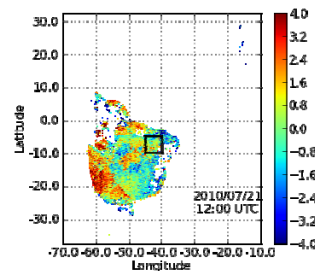


Figure 5 – Same as Figure 4 but at 12UTC.

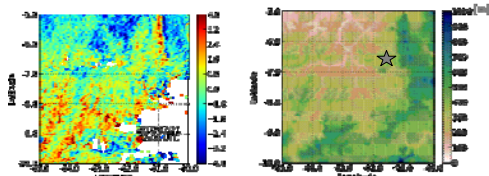


Figure 6 – Zoom over the field of differences between LST from MSG and GOES [°C] for 21st July 2010 at 12UTC (left panel) and the Elevation Map for the same geographical region (right panel).

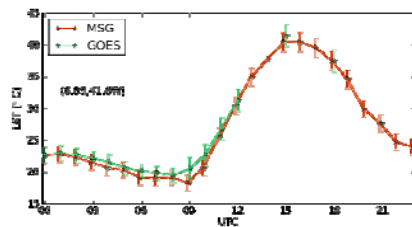


Figure 7 - LST Daily Cycle (MSG & GOES) on a specific flat region in Brazil - identified with a star in Figure 6 b).

5 DATA FUSION

The LST for GOES and MTSAT are generated for the full satellite disks every hour with a spatial resolution of 4 km at nadir. The LST estimated from SEVIRI data every 15 minutes is produced for 4 geographical areas covering the MSG disk, with a 3 km spatial resolution at sub-satellite point. All products are generated at the native Normalized Geostationary Projection (NGP) and then converted to the *plate carrée* projection using the weighted average method. Figure 8 illustrates earth disks observed by each GEO satellite in the original projection as well as the land areas (in brown) that are effectively processed. It also indicates the scanning direction and the image acquisition time of the three satellites. The better match between the times of acquisition is obtained by merging the MTSAT and GOES data for a specific reference time slot with the LSA-SAF data from the previous time slot.

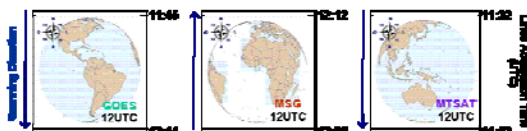


Figure 8 - Areas covered by GEO satellites and the identification of the respective direction and duration of scanning at 12UTC. From left to right: GOES, MSG and MTSAT.

The final LST product is obtained by averaging all the LST values from pixels within a grid box of 0.05° (regular in latitude and longitude). In this context all the averages are weighted by the respective error bar so that the final product is less influenced by low quality retrievals. At the end four data layers are added

to the LST product with additional information crucial for the product applications: i) the error bars in a pixel by pixel basis; ii) the mean value of the time of acquisition; iii) the fraction of pixels that were effectively processed, and iv) a quality flag with satellite information, missing data, cloudiness and land-water mask. Examples of such data layers are shown in Figures 9 a) to e).

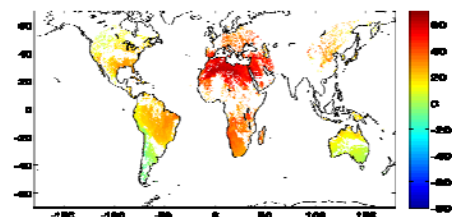


Figure 9a - Global LST product [°C] 21st July 2010 at 12UTC.

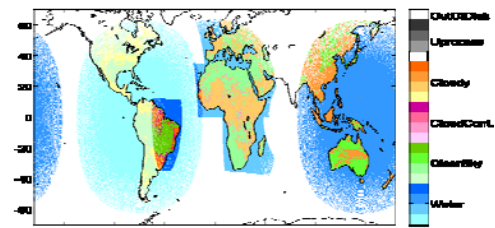


Figure 9b - Quality Flag corresponding to the LST estimate depicted in Figure 9a. Blues correspond to water pixels; greens correspond to clear sky regions; pinks correspond to could contaminated pixels; oranges correspond to cloudy areas; greys are the unprocessed pixels and white represent the out of disk areas. The 4 graded colours in each main class give information about the satellite(s). From light to dark: GOES, MSG, MTSAT and Multi-Mission.

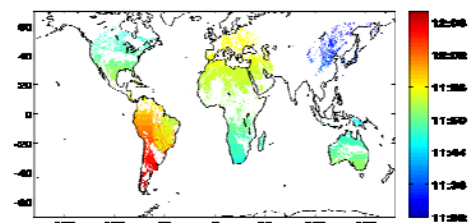


Figure 9c - Time of sensed data (HH:MM) used to retrieve the LST product depicted in Figure 9a.

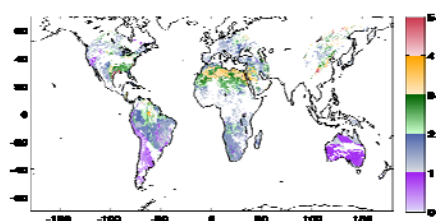


Figure 9d - Error Bars [°C] associated to the LST product depicted in Figure 9a.

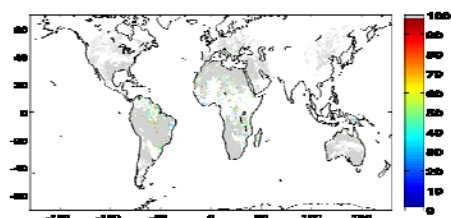


Figure 9e - Fraction of processed pixels used to retrieve the LST product depicted in Figure 9a.

6 CONCLUDING REMARKS

In the framework of the Geoland2 project a quasi-global LST product has been developed and it is now available since August 2009. The product is derived from a constellation of 3 GEO satellites (MSG, GOES and MTSAT) by using different but consistent retrieval algorithms. The GSW algorithm is used in the case of MSG, which has two adjacent channels available within the thermal window channel. As for MTSAT and GOES, only one channel is available in such region, therefore an additional channel (positioned in the middle-infrared region) is used but only during the night-time to avoid the solar contamination.

Together with the LST field error bars are provided on a pixel by pixel basis. These error bars are retrieved with a careful characterization of the algorithm uncertainties and the uncertainty of the input variables and its propagation through the LST algorithm.

Validation results of LST estimated from SEVIRI-MSG [Freitas, 2010] suggest the retrievals are generally below 2K and within the NRT estimations of error bars. Full validation of the quasi-global LST product, however, requires that such exercises be extended to LST values estimated from GOES and MTSAT.

To completely fulfil the land areas of the globe one more geostationary satellite (such as Meteosat 7) is needed to cover central Asia. In addition, a polar-orbiting satellite may be used to cover the polar regions. Therefore, the subject of future work shall be the adaptation of the LST algorithms for such satellites.

7 REFERENCES

- Belward, A. S., ed., 1996: "The IGBP-DIS global 1km land cover data set (DISCover) – proposal and implementation plans. IGBP-DIS working paper No. 13. IGBP-DIS Office, Météo-France, Toulouse, France, 61 pp.
- Berk, A., Anderson, G., Acharya, P., Ghetwynd, J., Bernstein, L., Shettle, E. Matthew M. e Adler-Golden S., 1999. *MODTRAN4 User's Manual*. Air Force Research Laboratory. Space Vehicles Directorate. Air Force Material Command. HANSCOM AFB, MA 01731-3010
- Borbas, E., S. W. Seemann, H.-L. Huang, J. Li, and W. P. Menzel, 2005: Global profile training database for satellite regression retrievals with estimates of skin temperature and emissivity. *Proc. of the Int. ATOVS Study Conference-XIV*, Beijing, China, 25-31 May 2005, pp763-770.
- Dash, P., F. M. Göttsche, F. S. Olesen and H. Fischer, 2002: "Land surface temperature and emissivity estimation from passive sensor data: theory and practice-current trends", *Int. J. Remote Sens.*, vol. 23, 2563–2594.
- Freitas, S. C., I. F. Trigo, and J. M. Bioucas-Dias, F. Göttsche, 2010: Quantifying the Uncertainty of Land Surface Temperature Retrievals from SEVIRI/Meteosat. *IEEE Trans. Geosci. Remote Sens.*, 48, doi : 10.1109/TGRS.2009.2027697.
- Trigo, I. F., I. T. Monteiro, F. Olesen, and E. Kabsch, 2008: "An assessment of remotely sensed Land Surface Temperature", *J. Geophys. Res.*, vol 113, D17108, doi:10.1029/2008JD010035.
- Prata, A. J., 1993: "Land surface temperature derived from the advanced very high resolution radiometer and the along-track scanning radiometer: 1. Theory", *J. Geophys. Res.*, vol. 98, 16,689– 16,702.
- Sun, D., R. T. Pinker, and J. B. Basara, 2004: "Land Surface Temperature Estimation from the Next Generation of Geostationary Operational Environmental Satellites: GOES M–Q", *J. Appl. Met.*, vol. 43, 363-372.
- Wan Z. E Dozier J. ,1996. A generalized split-window algorithm for retrieving land surface temperature from space. *IEEE Transactions on Geoscience and Remote Sensing*. Vol. 34. Pag. 892-905

Automatic detection of field furrows and features from Very High Resolution optical imagery

S. Le Hégarat-Masclé¹, C. Ottlé²,

(1) IEF/ACCIS, Université Paris-Sud, 91405 Orsay cedex, France

(2) LSCE-IPSL, Orme des Merisiers, 91191, Gif-sur-Yvette, France

sylvie.le-hegarat@u-psud.fr

ABSTRACT –The aim of this work is to infer surface features like furrows or gullies directly from space using high spatial resolution images such as those provided by IKONOS (pixel size $1 \times 1 \text{ m}^2$ in panchromatic mode) or WORLDVIEW instruments (pixel size $0.5 \times 0.5 \text{ m}^2$). The detection methodology includes different steps. First, a segmentation of the whole image is performed in order to label individually each agricultural field. Then, for each field, mathematical morphological processes are applied (erosion followed by functional geodesic reconstruction) in order to enhance the image contrast. Then, an automatic thresholding is applied to construct a binary image of the furrows or other singularities in the field. In order to reduce the noise due to the overlapping of the furrow and background classes, we introduce the a priori information that furrows are straight lines. Then, the Hough transform is applied to detect straight lines (using polar coordinates), and to detect the furrow direction as accumulations on the angle axis in the Hough space. Gullies and ditches would be secondly detected as unreconstructed features. The proposed method has been applied on a WORLDVIEW image acquired on the Lokna catchment within the Plava watershed in Russia (around 180 km^2) showing satisfying results. These features have then been introduced into the STREAM model to quantify the contribution of high spatial resolution imagery to water erosion prediction (see companion paper, Ottlé et al.).

1 INTRODUCTION

The context of this study is the use of Very High Resolution (VHR) imagery for the detection of erosion linear features. Water erosion is widely known as the most important factor of land degradation. In agricultural areas, erosion is mostly controlled by two parameters which are land cover and tillage practices. Tillage is indeed a key factor in water erosion processes since the furrows concentrate the water flows, especially when their direction is parallel to the main slopes (Souchère et al., 1998). Consequently, erosion monitoring requires the knowledge of such linear features. For that purpose, VHR remote sensing may be very useful, offering the possibility to map the soil properties (Vrieling et al., 2005). Such instruments give now access to centimetric scales, which are necessary to detect surface features like furrows, gullies or ditches.

The aim of this work is to develop an automatic methodology to detect and characterize linear features in a VHR image. The study is performed on a small agricultural watershed in Russia, the Lokna sub-catchment of the Plava watershed for which a WorldView1 image was acquired on 9 Sept 2009. The panchromatic image consists in surface reflectances measured in the (400-900nm) band with a 50cm pixel resolution at nadir (59cm at 25° off-nadir).

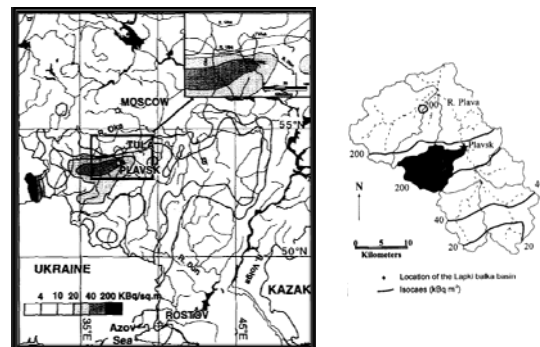


Fig. 1: Location of the Lokna

2 PROPOSED APPROACH

In this study, we propose an image processing methodology to detect the furrows field by field. Indeed, from one field to the other, the furrow direction is generally independent, but also the inter-row spacing and the contrast between the furrow pixels and those belonging to the field background. Therefore, the proposed processing is field-dependent and the first step is the segmentation of the landscape to distinguish the different fields.

In the case of the Lokna watershed, cartography of the agricultural field contours is available. However, if necessary such segmentation could be obtained from the remote sensing image, for instance using classical

algorithms such as those proposed in the ORFEO Toolbox (<http://www.orfeo-toolbox.org/otb/>).



Fig. 2: Segmentation of the Lokna site.

Even if the furrows present a pseudo periodic pattern, we do not focus on Fourier transform approach like (Chanussot et al., 2005) but we base our approach on the two following *a priori* features of furrows: (i) they are thin, (ii) they are composed of contiguous line segments. Then, the detection of the furrow direction for each field is performed in the following three main steps.

2.1 Binary image of the furrows

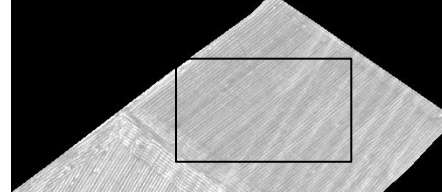
The objective is to derive a binary image, called F_b , where furrow pixels are equal to 1 and other pixels to 0. Thus the two sub-processes involved to obtain F_b are: (i) enhancement of furrow contrast on initial grey-level image, and (ii) enhanced image thresholding.

In order to straight out the furrows, we propose a grey level mathematical morphology (Serra, 1982, 1988, Dougherty, 1993, Soille, 2003) transformation to the radiometric image I , as follows:

$$F_g = I - \sup_{n \geq 0} \left\{ \left[\delta_B^I \right]^n (\varepsilon_B(I)) \right\}, \quad (1)$$

where B is a structuring element (with size related to the furrow width, namely 8-connectivity in our case), $\varepsilon_B()$ the erosion operator, and $\delta_B^I()$ the geodesic dilatation operator under I . Note that such a transformation defined a so-called ‘sharpness’ operator, close to the classical ‘top-hat like’ operator, but more precise for our purpose. In the following the resulting grey-level image F_g is called ‘grey-level image of the furrows’.

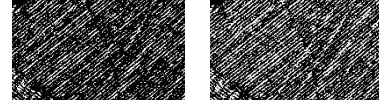
To obtain the binary image F_b from F_g , we apply an automatic thresholding process. Since ‘optimal’ grey-level threshold value may highly vary from one field to another, we rather define it assuming a given percentage p_F of furrow surface on each field (for each



Plava field n°7: WORLDVIEW data

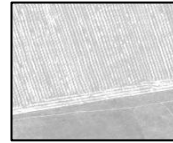


F_g $F_b / \text{Hyp } 10\%$

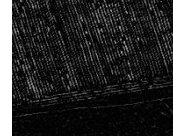


$F_b / \text{Hyp } 25\%$ $F_b / \text{Hyp } 50\%$

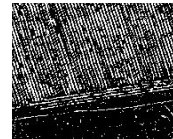
Plava field n°105



(a)



(b)



(c)

Plava field n°117



(a)



(b)



(c)

(a) Worldview data, (b) F_g , (c) $F_b / \text{hyp}.25\%$: case of a field with furrows only on a subpart

Fig. 3: Examples of the sharpness operator implementation and obtained binary images of furrows.

field, the grey-level threshold is then directly estimated from considered field histogram and p_F value).

For three cases corresponding to three examples of different furrow configurations and/or contrast, Figure 3 shows the original Worldview image I (field subparts), the F_g image, and F_b image. In order to check the result robustness versus p_F value in the first field case, three F_b images are compared that respectively correspond to three p_F assumptions,

namely 10%, 25% and 50%. Note also the ordering (inclusion relationship) between the 1-value pixel sets of the three images $F_b^{10\%}$, $F_b^{25\%}$, and $F_b^{50\%}$. In the following we focus on the $F_b^{25\%}$ image.

2.2 Field ‘Main Direction Profile’

From the previously obtained binary image of the furrows F_b , the aim is to obtain a kind of probability that a given direction (angular value in $[0, \pi]$) is the furrow direction. This latter is estimated using cumulative approach based on Hough transform interpretation.

Let us first recall the basis of the Hough transform to detect parameterized curves (Duda and Hart, 1972), namely straight lines in our case. The Hough space being those of the curve parameters, for straight lines $y = ax + b$ transform, each pixel is projected as a straight line $b = -x.a + y$ and a line is projected as a point (in this case, the Hough transform is nothing else than the linear algebra duality). Here, polar coordinates are better suited, thus we consider polar straight line parameters (θ, r) such that each pixel (x, y) in image space F_b , contributes for a value equal to $+F_b(x, y)$ ($\in \{0, 1\}$) for the points (θ, r) of the curve of equation $r = x \cdot \cos \theta + y \cdot \sin \theta$ in Hough space restricted to the $[0, \pi] \times [0, r_{\max}]$ compact H_{F_b} (r_{\max} is defined from the F_b dimensions in rows, nr_I , and columns, nc_I : $r_{\max} = \sqrt{nr_I^2 + nc_I^2}$). Then, the straight lines in F_b

can be detected as accumulating points in H_{F_b} .

In H_{F_b} , the maximum value depends on the maximum length of a F_b straight line. Therefore in the absence of normalisation the direction parallel to the longer border of the field is favoured. Now, if we consider the Hough transform of the binary mask of the field, H_{F_M} , each value $H_{F_M}(\theta, r)$ represents the maximum value in the Hough space taking into account the fact that the fields are bounded. Then, we propose to normalize the H_{F_b} pixel values as follows:

$$Hn_{F_b}(\theta, r) = \frac{H_{F_b}(\theta, r)}{H_{F_M}(\theta, r)}, \forall (\theta, r) \in [0, \pi] \times [0, r_{\max}]. \quad (2)$$

Figure 4 shows, in the case of field number 158, the different Hough transforms: of the field binary image of the furrows, of the field mask, and the normalisation result Hn_{F_b} . We note that the direction around $\pi/3$ appears with high values before normalization mainly because of the field geometry.

Finally, we state the following *a priori* hypothesis: for direction determination, the furrow length is less important than the number of furrows in a given direction. Then we define the Main Direction Profile as the function giving, for each direction (x-axis in the Hough space), the number of significant maxima. Practically, it is computed as follows: first the Hough

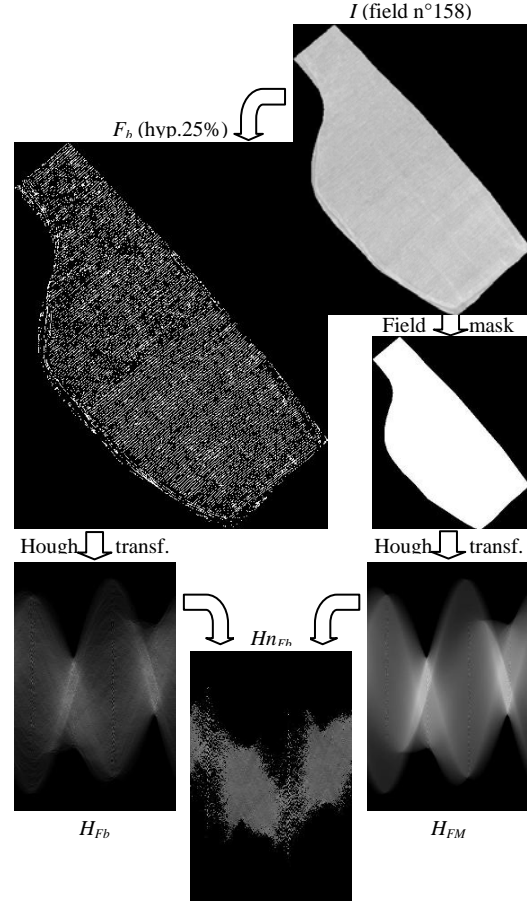


Fig. 4: Example of computation of the normalized Hough transform.

transform image is binarized to obtain an indicator function of the straight lines candidate to be furrows. Furthermore the threshold is automatically determined as the value corresponding to a given percentile of the grey level Hough transform image, namely 25% (provided that it is greater than a given ‘physical’ minimum value depending on the considered binary images of the furrows, namely 10, 20 and 30 pixels). Second, the field main direction profile is obtained integrating over the lines of the binary Hough transform image. This profile is finally smoothed (using an averaging over a sliding column ‘window’ or any low-pass filtering) accordingly to the assumed furrow direction precision (typically from few degrees to about ten degrees).

In summary, at the end of this step, a function called Main Direction Profile, representing the number of straight lines candidate to be furrows versus straight line direction is obtained. The next (and final) step of

the process consists in deriving furrow direction from this function.

2.3 Furrow direction

The number of furrows within a given field (and thus the Main Direction Profile values) depends on the length of the field in the perpendicular direction to the furrows and on the furrow spacing. Thus, once more we consider that the discriminating criterion is the 'sharpness' of a pick rather than its absolute value. Then, for each field, the sharpness profile is generated using the 'sharpness' operator defined in Section 2.1: the sharpness profile is the difference between the initial profile and the geodesic reconstruction of the eroded initial profile. The structuring element used is linear with a size related to the assumed precision of furrow direction (namely plus or minus 5° in our case).

Figure 5 shows the Main Direction Profile and the Sharpness Profile in the case of the field example presented in Figure 4. The benefit of using a sharpness criterion to flatten out the non significant main direction profile values is clearly seen.

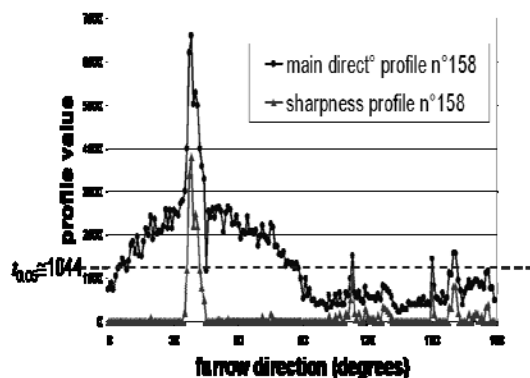


Fig. 5: Furrow direction estimation from the sharpness profile: example with one maximum around 40°.

To determine the threshold between significant and non significant sharpness values, it is assumed that in average there is a single furrow direction by field. Such an assumption is only valid when considering a large number of fields, since, depending on tillage practices (which are themselves related to land cover (cereals, vegetables, etc...)) there may be between zero and several furrow directions by field. Then Sharpness Profile threshold is derived considering global statistics on the watershed since the value corresponding to the 0.05 percentile of all Sharpness Profile values correspond to the consideration of all fields at once (as 0.05 is approximately equal to the inverse of the number of points of the Sharpness Profile, namely 180). Finally, Sharpness Profile

regional maxima exceeding the threshold are then ordered.

3 RESULTS

In this section, results are evaluated both in terms of right positives, that is to say focusing on fields with furrows, and in terms of right negatives, that is to say focusing on fields without furrows.

3.1 Performances in terms of right positives

To estimate the performances in terms of right positives, 15 test-fields were selected each of them presenting one or two furrow directions. Figure 6 compares the retrieved furrow direction to the actual one. The plotted points correspond to the furrow directions of the 15 considered fields (with field number indicated close to the point). The results show that most of the points are located close to the first bisectrix line which corresponds to an accurate estimation of furrow direction. All principal directions are well-estimated (as sharpness profile first maxima), and three out four secondary directions are also well-detected and estimated.

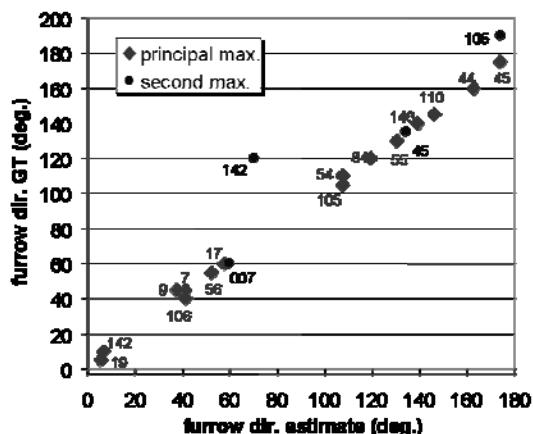


Fig.6: Actual furrow direction versus retrieved furrow direction (at most 2 directions observed).

3.2 Performances in terms of right negatives

To estimate the algorithm performances in terms of right negatives, 52 test-fields without furrow direction were selected. Figure 7 presents the estimated furrow directions (y-coordinate) for the 52 considered fields referenced by their segment number. Right negatives are points for which no furrow direction has been detected: 'bottom' value on the y-axis. False positives are points which appear with a positive y-axis value. The results show only 7 out of 52 false positives. Moreover, after visual checking, these errors may be explained in every case: e.g. by the presence of some hedges or roads in the field. For instance, on Figure 8

that shows the images of the field n°73 and n°101, we clearly see that the detected furrow directions, respectively around 15° and around 170°, are understandable even if it does not correspond to furrows.

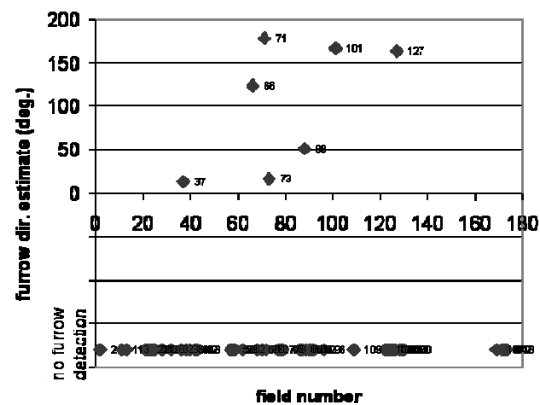


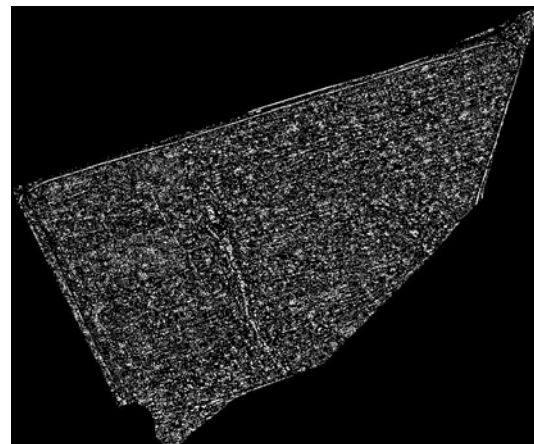
Fig.7: Identification of the false positives and true negatives.

4 CONCLUSION AND PERSPECTIVES

The methodology developed to extract automatically furrow direction from Very High Resolution imagery seems to give satisfactory results. This study demonstrates that high resolution imagery is useful for extraction of soil features that are not detectable on high resolution data e.g. SPOT or Landsat type data. The methodology has now to be validated at larger scale on different regions and applied to other instruments, i.e. IKONOS images. Meanwhile, the furrow directions obtained have been used as input to the STREAM (Sealing and Transfer by Runoff and Erosion related to Agricultural Management) expert-based runoff and erosion model (Cerdan et al., 2002, Souchère et al., 2003). This model was implemented on the Lokna watershed to predict sediment transfer (see companion's paper Ottlé et al.). The methodology will be further developed to perform an automatic segmentation of the image based on the furrow direction. Such information could be useful in particular for the fields that are actually subdivided relatively to the *a priori* field map.

5. ACKNOWLEDGEMENTS

The authors wish to thank the CNES/ORFEO program for supporting this study and for providing us with IKONOS and WORLDVIEW images on the Blosserville and Plava watersheds. The partners of the PICS (n°4946) joint programme between CNRS(France) and RFBR (Russia) are also acknowledged for providing the framework of this study.



(a)



(b)

Fig.8: Examples of fields n°73 and n°101 generating false positives.

6. REFERENCES

- Cerdan, O., Couturier, A., Le Bissonnais, Y., Lecomte, V., Souchère, V., 2002, Incorporating soil surface crusting processes in an expert-based runoff model: sealing and transfer by runoff and erosion related to agricultural management. *Catena*, 46, 189–205.
- Chanussot, J., Bas, P., Bombrun, L., 2005, Airborne remote sensing of vineyards for the detection of dead vine trees. Proceedings of IEEE IGARSS'05 - International Geoscience and Remote Sensing Symposium, July 2005, Seoul, Korea.
- Duda, R.O., Hart, P. E., 1972, Use of the Hough Transformation to Detect Lines and Curves in Pictures, *Communications of the ACM*, 15, 11-15.
- Serra, J., 1982, *Image Analysis and Mathematical Morphology*. Academic Press. London.
- Serra, J., 1988, *Mathematical morphology, Theoretical advances*. Academic Press. London.
- Dougherty, E., 1993, *Mathematical morphology in image processing*. Marcel Dekker.
- Soille, P., 2003, *Morphological image analysis, principles and applications*, 2nd edition. Springer.
- Souchère, V., King, D., Daroussin, J., Papy, F., Capillon, A., 1998. Effect of tillage on runoff direction: consequences on runoff contributing area within agricultural catchments. *Journal of Hydrology*, 206, 256–267.
- Souchère, V., Cerdan, O., Ludwig, B., Le Bissonnais, Y., Couturier, A., Papy, F., 2003. Modelling ephemeral gully erosion in small cultivated catchments. *Catena*, 50, 489–505.
- Vrieling, A., 2006. Satellite remote sensing for water erosion assessment: A review, *Catena*, 65, 2-18.

Contribution of high resolution satellite imagery to water erosion prediction in Lokna sub-catchment within Plava watershed (Russia)

C. Ottlé¹, O. Evrard¹, N. Lio Soon Shun¹, S. Le Hégarat-Masclé², V. Belayev³

(1) LSCE-IPSL, Orme des Merisiers, 91191, Gif-sur-Yvette, France

(2) IEF/ACCIS, Université Paris-Sud, 91405 Orsay cedex, France

(3) Laboratory of soil erosion and fluvial processes, Faculty of Geography, Moscow, 119991, Russia

catherine.ottle@lsce.ipsl.fr

ABSTRACT – The runoff and erosion expert-based model *STREAM* was used to understand sediment transfer across the cultivated landscape of the Plava watershed, in western Russia. This model operates at the timescale of rainfall events and requires several input data, e.g. soil and vegetation characteristics, which can be derived from remote sensing images. The purpose of this work is to evaluate the contribution of metric resolution images for the characterization of the runoff network, which is a prerequisite to predict soil erosion. A methodology presented in the companion paper (LeHégarat et al.) was developed to detect field specific features like furrows and gullies from high resolution imagery. These features can indeed modify runoff circulation within the watershed. The large scale application of this method to the Lokna sub-catchment of the Plava watershed (around 182km²) is performed using one single WorldView image acquired in April 2009. The furrows and gullies detected are used to correct the runoff network derived from topography for its further use by the *STREAM* model. Landsat imagery is used to map land cover and vegetation phenology. The contribution of remote sensing to model erosion in regions where ground-truth data are lacking is presented and discussed.

1 INTRODUCTION

Water erosion ranks among the most important factors of land degradation around the world. It becomes increasingly important and is often associated with land use change, especially deforestation and conversion to intensive agriculture. It is widely known that cultivated land suffers from erosion rates that are several orders of magnitude higher than on land under natural vegetation. These higher erosion rates are mostly due to the frequent tillage of cultivated soils, which tends to reduce the vegetation cover of the soil and to disturb its surface structure. Cultivated land is therefore particularly vulnerable to water erosion. High resolution spatial and temporal data on land use, farming practices and other erosion driving factors are therefore required before implementing efficient monitoring. In this context, remote sensing is a very useful tool since it provides regular and spatially-distributed data, which allows for instance to map the evolution of surface characteristics like vegetation cover, soil properties or tillage practices in croplands (see Vrieling, 2006, for a review). Most remote sensing studies make use of optical radiometers that provide regular measurements of the surface spectral signatures. Based on this information, land cover and its seasonal and annual variations can be assessed at

metric scales. Moreover, the most recent remote sensing instruments give now access to centimetric scales, offering the possibility to detect surface features like furrows, gullies or ditches that are likely to concentrate runoff and erosion.

The aim of this work is to use remote sensing data to derive land cover and furrows, which are two important drivers of soil erosion by water in agricultural landscapes. This information will then be used to run the *STREAM* erosion model. Our study specifically aims to quantify the contribution of very high resolution imagery to derive and characterize erosion linear features. The study is conducted in a cultivated catchment of western Russia where erosion monitoring has been performed for more than a decade. The site under study, the datasets and the model used are first described. Preliminary results of sensitivity experiments to tillage directions are then presented.

2 STUDY SITE

This study focuses on a 182-km² tributary sub-catchment of the Plava River basin (2200 km²), i.e., the Lokna River catchment (Figure 1). This sub-catchment is located in a region of Western Russia characterised by particularly high levels of contamination induced by the Chernobyl nuclear

accident that occurred on 26 April 1986. This area is located in the “Plavsk contamination hotspot” where the initial radioactive contamination exceeded 300 kBq m⁻² (Golosov et al., 1999). Bedrock consists of limestone and dolomite of Carboniferous age overlaid by a layer of Holocene loess. Soils of the catchment are mainly chernozems, with a loamy texture. The landscape morphology consists in the succession of rather flat hilltops separated from dry or wet valleys by rather steep (1–15%) and convex slopes. The sub-catchment is mainly drained by dry valleys that are locally referred to as “balkas”. Main land use on the plateaus is cropland, whereas the balka bottoms and banks are occupied by grassland.

Mean annual precipitation in this region undergoing continental climate conditions reaches 637 mm (1960–2003).

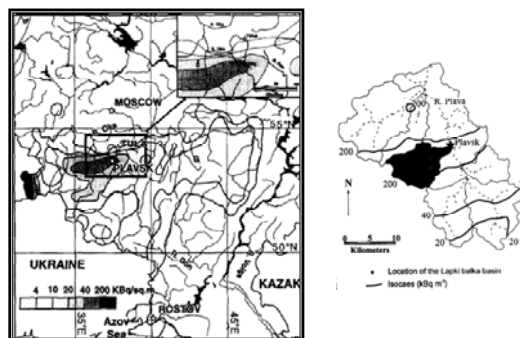


Fig. 1: Location of the Lokna sub-catchment within the Plava watershed

3 DATASETS AND MODELS

3.1 Stream model

STREAM (Sealing and Transfer by Runoff and Erosion related to Agricultural Management) is an expert-based runoff and erosion model that operates at the small catchment scale (0.1–1000 km²). It is spatially distributed, and lumped at the event-scale (Cerdan et al., 2002a). The model assumes that the following surface characteristics are the main determinants of infiltration and runoff at field scale: soil surface crusting, surface roughness, total cover of the soil (by crops and residues) and antecedent precipitation (Cerdan et al., 2002a). These characteristics are set for each field using classification rules developed by Le Bissonnais et al. (2005). A table is then used to assign a steady-state (i.e., the constant infiltration rate that is reached during prolonged rainfall) infiltration rate value to each combination of these soil surface characteristics. A runoff/infiltration balance is then computed for each pixel.

For each event, the runoff flow network is then derived by combining two models: (i) a standard topographic runoff model based on a DEM and redirecting runoff from one cell to the lowest of its eight neighbours and (ii) a tillage direction model developed by Souchère et al. (1998). Based on the infiltration/runoff balance calculated for each pixel, a programme is then run in ArcGIS to determine flow accumulation at the catchment scale (Cerdan et al., 2002a).

Interrill and concentrated erosion modules have also been integrated into STREAM. Within the interrill erosion module, a table is used to assign a potential sediment concentration value to each combination of surface characteristics (Cerdan et al., 2002b). At the catchment scale, sediment is transported in proportion to the runoff volumes computed, and is deposited as a function of topography, or vegetation cover (see Cerdan et al., 2002c for details). The module calculating gully erosion within the catchment (Souchère et al., 2003) is based on slope gradients and parameters influencing runoff velocity or soil resistance (vegetation type and cover fraction, soil roughness and surface crusting).

STREAM requires three datasets to compute runoff and erosion at any grid point of the catchment. First, a land cover dataset, associating each field of the catchment with the appropriate soil surface characteristics, is needed. Then, the slopes and the flow directions are calculated by combining the DEM of the catchment and the tillage direction model. Finally, a database characterising the simulated rainfall events must be introduced into the model (i.e., total rainfall amount (mm); total rainfall effective duration (h); total rainfall amount during the 48 h before the beginning of the event (mm); maximum 6-min rainfall intensity (mm h⁻¹)).

The originality of this study consists in using remote sensing data, and especially metric instruments, to assess land cover and tillage practices, which are key parameters to model water erosion processes.

3.2 Land cover mapping

Landsat TM imagery was used to map land cover in the Lokna catchment based on image classification methods. This radiometer measures surface reflectances in 7 spectral bands ranging from Blue to MIR with a 30m pixel resolution, and thermal infrared brightness temperatures at 60m resolution. Land cover mapping was estimated by a multi-dates and multi-bands unsupervised classification methodology (K-means). Seasonal variations of the surface spectral properties were used to discriminate between the various types of vegetation. Given the frequent cloud coverage in this region, the number of clear sky images available during the 1986–2010 period was

very low, and 2000 appeared to be the only year during which 2 images were available (24 April and 1 October). Discrimination between summer and winter crops could therefore be achieved. Various tests were done to optimize the band combinations for classification. The best results were obtained using the PIR (0.76 – 0.90 μm), MIR1 (1.55 – 1.75 μm) and MIR2 (2.08 – 2.35 μm) bands, and by prescribing a number of 13 classes which were grouped in 7 classes after the interpretation phase.

The vegetation map was obtained by analysing the temporal variations of the NDVI index (Figure 2). Prairies, summer and winter cereals could be identified, but discrimination between potatoes and sugar beets, and between legumes and summer crops could not be achieved. Fortunately, these two latter groups of cultures are characterised by similar sensitivities to water erosion. Furthermore, field surveys showed that winter crops mainly consisted of wheat, whereas maize was the most frequent summer crop.

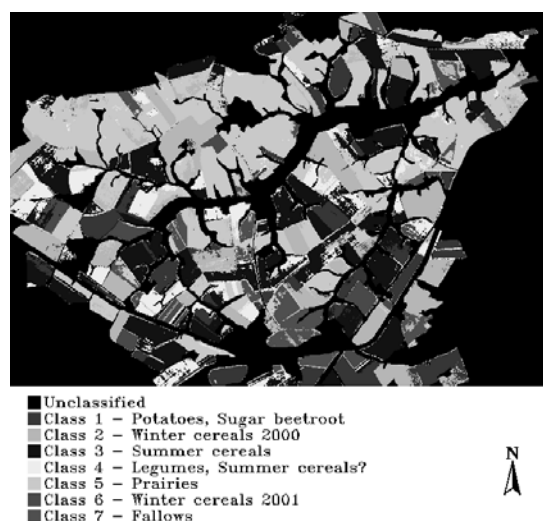


Fig. 2: Land cover map of the Lokna catchment (Year 2000)

3.3 FURROW DETECTION

Tillage directions were derived from Very High Resolution imagery, i.e., a WorldView-1 (WV1) image acquired on 9 Sept 2009. The panchromatic image consists in surface reflectances measured in the (400-900nm) band with a 50cm pixel resolution at nadir (59cm at 25° off-nadir). The methodology used to extract furrow direction is described in detail in the companion paper (LeHégarat et al., this issue).

It is based on the application of a normalized Hough transformation carried out at field scale. This method allows the detection of the main line directions in the

image ($\pm 180^\circ$). Those directions are then converted into accurate runoff directions by using the surface slopes derived from the 20-m grid cells Digital Elevation Model (DEM) available on the catchment. The method was validated using field surveys and provided the results presented in Figure 3.



Fig. 3: Furrow direction ($^\circ$) in the Lokna catchment (Year 2009)

3.4 RAINFALL DATABASE

Rainfall data in 2000 were available at a daily time step from the Mtsensk station (located at 60 km from the study site). Data from this station is representative of the weather conditions observed in Plavsk. Information on total rainfall amount and antecedent rainfall for the different events of the year were directly extracted from the database. To derive their effective duration and their maximum intensity, which are parameters required for the erosion model simulations, we constructed different scenarios to derive the temporal distribution of rainfall (Table 1).

TABLE 1. Decision rules used to derive the effective duration (D) and the maximum intensity (I-max) of different rainfall events characterised by a given rainfall amount (RA).

Type	# days	RA (mm)	D (h)	I-max (mm h ⁻¹)
Heavy storm	1	≥ 15	1	41
Storm	1	< 15	1	20
Heavy night storm	2	≥ 15	2	41
Night storm	2	< 15	6	20
Constant rain	≥ 3	n/r	6 d ¹	9

4 RESULTS

The erosion model was run for the Year 2000. The rainfall events reconstructed as detailed in section 3.4 were simulated. Significant erosion was only generated by a single storm (17 July 2000), characterised by a total rainfall amount of 35mm, a duration of 2 hours and a maximum intensity of 41 mm h⁻¹. In order to illustrate the importance of the information provided by the furrow direction derived from VHR data, we compared the quantity of eroded soil accumulated within the catchment in 2 situations:

- i) Exp1: STREAM simulation taking into account the furrow direction, gullies and roads detected using the WV1 image
- ii) Exp2: STREAM simulation relying on the prescription of these characteristics from the DEM.

4.1 Sediment transfer in the Lokna catchment

Figure 4 illustrates the sediment transfer simulated by STREAM in Exp1.

The spatial analysis of this map shows the strong relationship that exists between land cover and the occurrence of soil erosion. Erosion was only simulated on the fields covered by row crops, like maize and sugar beet. Locally, erosion rates reached up to 3 t ha⁻¹ (corresponding to sediment accumulations of up to 27 t). This would correspond to the erosion of a 0.2 mm depth soil layer for a single storm.

Overall, the simulated erosion remains rather low, compared to other regions of Europe. Nowadays, water erosion in this region of Russia would then be generated during a few heavy storms. This result can be explained by the rather high infiltration capacity of chernozem soils prescribed, the dense cover of the soil by vegetation (crops and residues) during most of the year and the generally high roughness of the soil surface. In this region characterised by mechanised agriculture, tillage erosion is hence likely the dominant erosion process. However, our current results remain mostly indicative since they only cover one year. Still, interannual rainfall variability can be particularly important. Furthermore, land cover and furrow direction were derived from images acquired during different years (2000 and 2009, respectively). They could hence lead to inconsistencies.

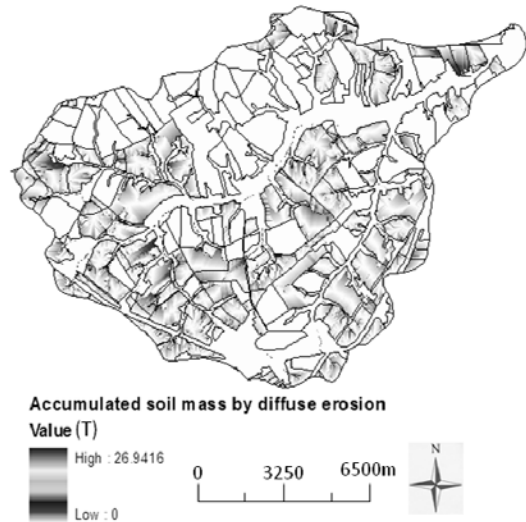


Fig. 4: Erosion simulated by STREAM in the Lokna catchment after a summer storm

4.2 Sensitivity analysis to tillage directions

Figure 5 presents detailed maps of sediment flowpaths obtained for the two simulation experiments described above, in the vicinity of fields covered by maize and located in the western part of the catchment. The impacts of the furrows directions on the runoff and sediment flows are clearly seen, especially in the case of the northern fields characterised by tillage directions of 211° and 85°, that differ significantly from the local slopes directions. These differences in the flow network, generated lower erosion rates as expected in fields characterised by furrows intersecting the main slopes. This example illustrates the potential of remote sensing to improve the quality of water erosion predictions at the catchment scale.

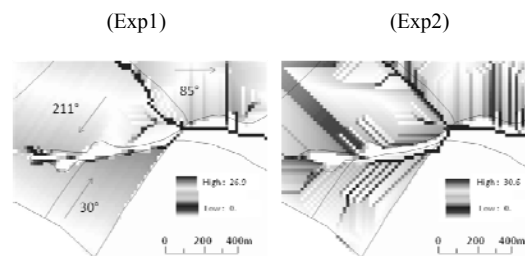


Fig. 5: Impact of furrows directions for the two simulation scenarios

5 CONCLUSIONS AND PERSPECTIVES

These preliminary results illustrate the importance of integrating detailed information on land cover, furrows imagery allowing the automatic detection of these soil characteristics was demonstrated. However, to be representative in the long term, erosion simulations will now be performed over the entire 1986-2010 period to take the rainfall interannual variability into account and to offer a way of validating the erosion predictions. STREAM outputs will indeed be compared to the erosion rates derived from Cs-137 measurements that provide a useful tool to assess soil redistribution in this catchment that was strongly contaminated by the 1986 Chernobyl accident. The use of the LANDSOIL model (<https://www.inra.fr/landsoil>), that simulates both water and tillage erosion, is also envisaged.

6. ACKNOWLEDGEMENTS

The authors would like to thank the CNES/ORFEO programme for funding this study and providing the Worldview image of the Lokna watershed. The PICS (no. 4946) joint programme between CNRS (France) and RFBR (Russia) is also acknowledged for their support.

7. REFERENCES

- Cerdan, O., Couturier, A., Le Bissonnais, Y., Lecomte, V., Souchère, V., 2002a, Incorporating soil surface crusting processes in an expert-based runoff model: sealing and transfer by runoff and erosion related to agricultural management. *Catena*, **46**, 189–205.
- Cerdan, O., Le Bissonnais, Y., Souchère, V., Martin, P., Lecomte, V., 2002b, Sediment concentration in interrill flow: interactions between soil surface conditions, vegetation and rainfall. *Earth Surface Processes Landforms*, **27**, 193–205.
- Cerdan, O., Le Bissonnais, Y., Couturier, A., Saby, N., 2002c, Modelling interrill erosion in small cultivated catchments. *Hydrological Processes*, **16** (16), 3215–3226.
- Golosov, V. N., Panin, A. V., Markelov, M. V., 1999, Chernobyl ¹³⁷Cs redistribution in the small basin of the Lokna River, Central Russia. *Physics & Chemistry of the Earth (A)*, **24** (10), 881–885.
- Le Bissonnais, Y., Cerdan, O., Lecomte, V., Benkhadra, H., Souchère, V., Martin, P., 2005, Variability of soil surface characteristics influencing runoff and interrill erosion. *Catena*, **62**, 111–124.
- Souchère, V., King, D., Daroussin, J., Papy, F., Capillon, A., 1998, Effect of tillage on runoff direction: consequences on runoff contributing area within agricultural catchments. *Journal of Hydrology*, **206**, 256–267.
- Souchère, V., Cerdan, O., Ludwig, B., Le Bissonnais, Y., Couturier, A., Papy, F., 2003, Modelling ephemeral gully erosion in small cultivated catchments. *Catena*, **50**, 489–505.
- Vrieling, A., 2006, Satellite remote sensing for water erosion assessment: A review, *Catena*, **65**, 2–18.

direction and tillage practices into the STREAM erosion model. The useful contribution of the VHR

New Hyperspectral Unmixing Techniques in the Framework of the Earth Observation Optical Data Calibration and Information Extraction (EODIX) Project

Antonio Plaza, Javier Plaza, Inmaculada Dópido, Gabriel Martín, Marian-Daniel Iordache, and Sergio Sánchez

Hyperspectral Computing Laboratory

Department of Technology of Computers & Communications

University of Extremadura, Avda. de la Universidad s/n, 10071 Cáceres, Spain

aplaza@unex.es

ABSTRACT- *The main objective of the Earth Observation Optical Data Calibration and Information Extraction (EODIX) project is to develop advanced ground segment methodologies for optical data calibration and information extraction from a broad family of imaging instruments currently in orbit. EODIX also has an important component related with advanced information extraction from remotely sensed data sets. In this paper, we describe some of the advances carried out in one of the tasks of the EODIX project, focused on the area of spectral unmixing of remotely sensed data. It is well known that most pixels in remotely sensed images are characterized by their mixed nature and can be modelled as the combination of elementary components (called endmembers) with variable per-pixel fractional abundances. The techniques described in this paper comprise several new algorithms for endmember extraction (including not only spectral information but also spatial information) and abundance estimation (with particular focus on the sparsity of the abundance estimation problem, which can be used to increase the accuracy of the estimations). The paper also describes computationally efficient implementations of some of the discussed algorithms.*

1. INTRODUCTION

Hyperspectral imaging instruments are capable of collecting hundreds of images, corresponding to different wavelength channels, for the same area on the surface of the Earth (Goetz, 1985). For instance, NASA is continuously gathering imagery data with instruments such as the Jet Propulsion Laboratory's Airborne Visible-Infrared Imaging Spectrometer (AVIRIS), able to record the visible and near-infrared spectrum (wavelength region from 0.4 to 2.5 micrometers) of the reflected light of an area 2 to 12 kilometers wide and several kilometers long using 224 spectral bands, thus allowing spectral signature-based analyses as shown by Fig. 1. On the other hand, Fig. 2 illustrates the problem of mixed pixels challenging hyperspectral data interpretation.

Spectral mixture analysis (or spectral unmixing) has been an alluring exploitation goal since the earliest days of imaging spectroscopy (Keshava and Mustard, 2002). No matter the spatial resolution, in natural environments, spectral signatures in hyperspectral data are invariably a mixture of the signatures of the various materials found within the spatial extent of the ground instantaneous field view. The mixing systematics can be inherently linear or nonlinear. On the one hand, the linear model assumes that pure

spectral components (*endmembers*) are sitting side-by-side within the field of view of the imaging instrument, as illustrated in Fig. 3(top). On the other hand, the nonlinear model assumes that multiple scattering effects dominate the interaction between incident radiation and the response measured at the imaging spectrometer, as illustrated in Fig. 3(bottom). The linear model is generally adopted in practice due to its simplicity and independence of physical properties, but it may provide more accurate results (Keshava and Mustard, 2002).

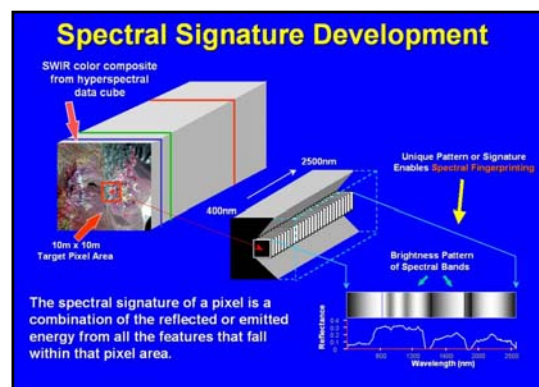


Figure 1. The concept of hyperspectral imaging.

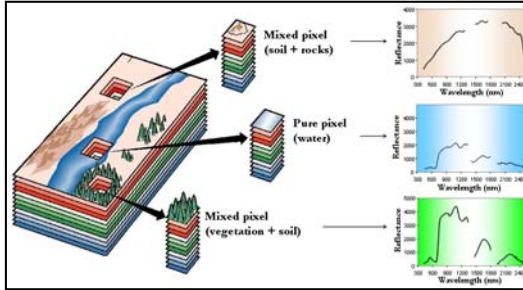


Figure 2. Problem of mixed pixels.

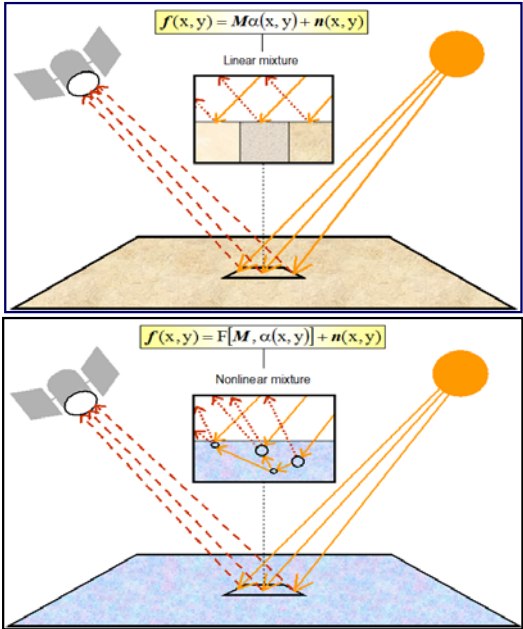


Figure 3. Linear (top) vs nonlinear (bottom) unmixing.

In the context of linear spectral unmixing, the estimated endmember fractional abundances are often required to satisfy two constraints. First, all abundances must be non-negative. Second, the sum of abundances for a given pixel must be unity. However, it is the derivation and validation of the correct suite of endmembers that has remained a challenging and elusive goal for the past several years. Several approaches have been developed for this purpose over the last few years. Many available approaches have been focused on analyzing the data in spectral terms only (Chang, 2003), i.e. trying to find the endmembers as the extreme pixels (corners) in the multi-dimensional data cloud. Examples of this convex geometry-based approach to identification of image endmembers include the pixel purity index (PPI) algorithm, the orthogonal subspace projection (OSP), the N-FINDR algorithm, or the iterative error analysis (IEA) algorithm, among others (Plaza et al., 2009).

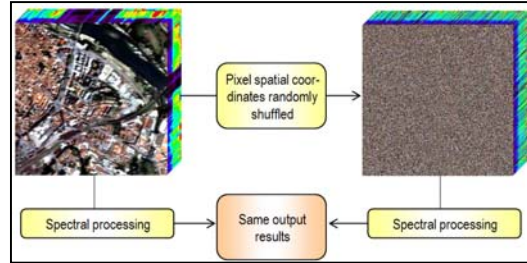


Figure 4. Importance of using spatial information.

Although these methods have shown considerable promise, they are exclusively based on the spectral information of the data. However, most endmember extraction algorithms could benefit from an integrated framework in which both the spectral information and the spatial arrangement of pixel vectors are taken into account. An example is given in Fig. 4 in which the spatial locations of pixel vectors in an urban hyperspectral scene are randomly shuffled. In this case, the application of convex geometry-based endmember extraction in the original scene and the one without spatial correlation would be the same, meaning that the rich spatial information available was not taken into account during the endmember searching process.

In this paper, we address new trends in spectral unmixing specifically developed in the framework of the Earth Observation Optical Data Calibration and Information Extraction (EODIX) project. These comprise the incorporation of spatial constraints into spectral unmixing, the use of spectral unmixing for feature extraction purposes, and the use of sparse regression-based approaches to spectral unmixing. Experimental results using a real hyperspectral data set are given at the end of the paper for illustration purposes. Combined, these topics reflect the maturity of a field that currently represents one of the most active research areas in hyperspectral image analysis.

2. INCORPORATION OF SPATIAL INFORMATION INTO SPECTRAL UNMIXING

We have recently developed a region-based spatial preprocessing technique for endmember extraction algorithms intended to exploit spectral information more effectively by adequately incorporating spatial context. Our proposed approach first adaptively searches for spectrally pure and spatially homogeneous regions by using a hybrid procedure that combines unsupervised clustering and orthogonal subspace projections, thus selecting a set of representative regions in spatial-spectral terms. This spatial preprocessing is followed by a standard endmember extraction process using the pixels located in such regions, providing a set of spatially

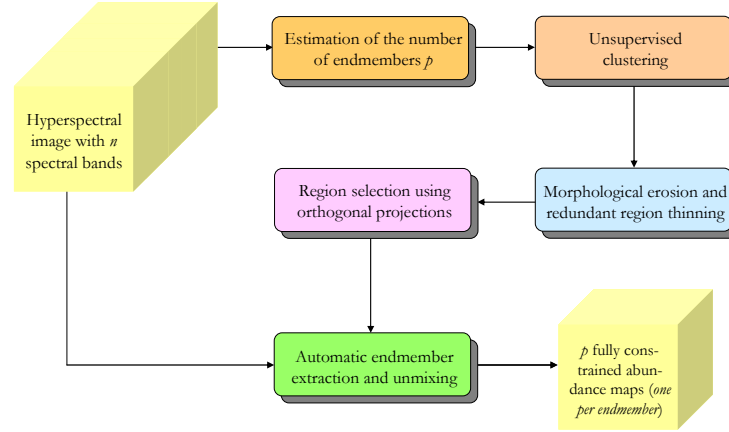


Figure 5. Region-based spatial preprocessing for endmember extraction.

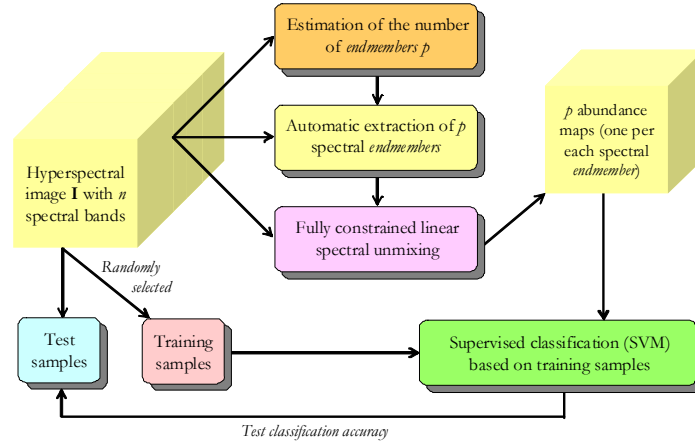


Figure 6. Spectral unmixing for feature extraction prior to supervised classification.

representative endmembers with the potential to accurately characterize large homogeneous areas in the original hyperspectral scene (Martin and Plaza, 2010). The concept of region-based spatial preprocessing, illustrated in Fig. 5, can be readily combined with algorithms that use only the spectral information contained in the original hyperspectral data set, as it is the case of the N-FINDR (Winter, 1999) in Fig. 7.

3. USING SPECTRAL UNMIXING FOR FEATURE EXTRACTION PURPOSES

Recently, we have developed a new strategy for feature extraction prior to supervised classification of hyperspectral data which is based on spectral unmixing concepts (Rojas et al., 2010). This unmixing-based feature extraction approach presents some distinctive features with regards to classic approaches commonly used in the framework of classification (such as principal component analysis) or unmixing (such as the minimum noise fraction):

- First, it provides additional information for classification in hyperspectral analysis scenarios with moderate spatial resolution, since the sub-pixel composition of training samples can be used as part of the learning process of the classifier.
- Second, it can effectively model the non-stationary behavior of the spectral signatures of land-cover classes in the spatial domain of the scene, since (possibly disjoint) regions belonging to the same class are represented by the same spectral signature, and the variations related with different cover proportions or illumination conditions are modeled via the abundance estimation process inherent in spectral unmixing.
- Third, the components estimated by the proposed feature extraction strategy exhibit physical meaning as opposed to those obtained by principal component analysis or the minimum noise transform.

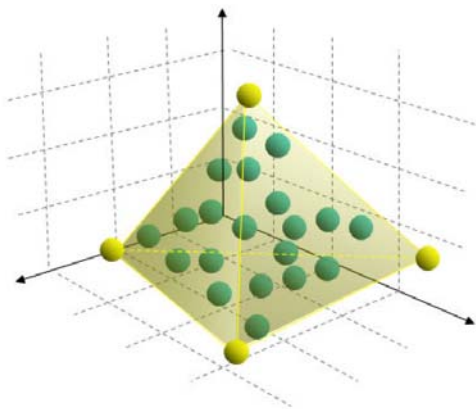


Figure 7. The N-FINDR algorithm inflates a simplex with maximum volume using the pixels available in the input hyperspectral data. After a random initialization, it tries all pixels in each endmember position until the combination with maximum volume is found.

- A final advantage of the proposed approach is that it does not penalize classes which are not relevant in terms of variance or signal-to-noise ratio (SNR).

The proposed unmixing-based feature extraction strategy has been implemented in the form of a standard unmixing processing chain prior to supervised classification using a traditional method such as the support vector machine (SVM) as illustrated in Fig. 6, and also as a modified unmixing chain in which spatial information is used to guide the selection of endmembers to spatially relevant areas by means of a spatial preprocessing framework in Fig. 8.

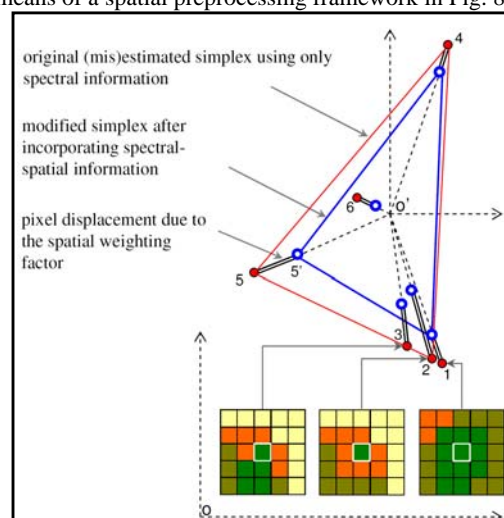


Figure 8. Spatial preprocessing to guide endmember extraction to spatially representative areas.

4. SPARSE HYPERSPECTRAL UNMIXING

The spectral unmixing problem has been recently been approached in a semi-supervised fashion, by assuming that the observed image signatures can be expressed in the form of linear combinations of a number of pure spectral signatures known in advance (e.g., spectra collected on the ground by a field spectro-radiometer). Unmixing then amounts to finding the optimal subset of signatures in a (potentially very large) spectral library that can best model each mixed pixel in the scene (Iordache et al., 2010). In practice, this is a combinatorial problem which calls for efficient linear sparse regression techniques based on sparsity-inducing regularizers, since the number of endmembers participating in a mixed pixel is usually very small compared with the (ever-growing) dimensionality and availability of spectral libraries to spatially relevant areas (Bioucas-Dias and Plaza, 2010).

5. PARALLEL IMPLEMENTATION OF A FULL HYPERSPECTRAL UNMIXING CHAIN

The unmixing techniques introduced in previous sections can be extremely time consuming when applied to real hyperspectral data sets. At the same time, these techniques exhibit inherent parallelism at multiple levels: across pixel vectors (coarse grained pixel-level parallelism), across spectral information (fine grained spectral-level parallelism), and even across tasks (task-level parallelism). As a result, they map nicely to massively parallel systems such as graphics processing units (GPUs) or field programmable gate arrays (FPGAs). The latter are particularly suitable to on-board processing due to low power consumption and tolerance to radiation in space. We have developed parallel implementations of a full hyperspectral unmixing chain for both types of platforms: GPUs (Sanchez et al., 2010) and FPGAs (Gonzalez et al., 2010). These platforms are respectively illustrated in Figs. 9 and 10.



Figure 9. NVidia commodity graphic processing unit.

6. CONCLUSION AND SUMMARY

In this paper, we have described several new techniques for spectral unmixing of hyperspectral data developed in the framework of the Earth Observation Optical Data Calibration and Information Extraction (EODIX) project, comprising new methods for endmember extraction (including not only spectral information but also spatial information) and abundance estimation (with particular focus on the sparsity of the abundance estimation problem, which can be used to increase the accuracy of the estimations). The paper also described computationally efficient implementations of some of the discussed algorithms. Although the techniques have been functionally described, experimental evidence of their success can be found in the provided references. We would like to emphasize that this work is part of a much larger strive to fully incorporate the advantages that can be obtained by spectral unmixing into the analysis of remotely sensed hyperspectral data sets. In this regard, complementary lines of research that we are planning to address in the near future comprise the refinement of some of the presented techniques (most notably, the inclusion of spatial information into sparse unmixing methods) and also the development of additional parallel implementations for some of the discussed algorithms, which are often dominated by regular computations.

7. ACKNOWLEDGEMENT

This work has been supported by the European Community's Marie Curie Research Training Networks Programme under reference MRTN-CT 2006-035927, Hyperspectral Imaging Network (HYPER-I-NET) coordinated at University of Extremadura (UEX) by Antonio Plaza. Daniel Iordache is sponsored by a research fellowship associated to this project. This work has also been supported by the Spanish Ministry of Science and Innovation (EODIX project, reference AYA2008-05965-C04-00) coordinated at University of Valencia by José Sobrino and at UEX by Antonio Plaza. Inmaculada Dópido, Gabriel Martín and Sergio Sánchez are sponsored by research fellowships associated to this project. Funding from Junta de Extremadura (local government) under project PRI09A110, coordinated at UEX by Javier Plaza, and from the European Cooperation in Science and Technology (COST) programme through the project entitled Open European Network for High Performance Computing on Complex Environments (ComplexHPC) coordinated at UEX by Antonio Plaza and led by Emmanuel Jeannot at INRIA, are also very gratefully acknowledged.

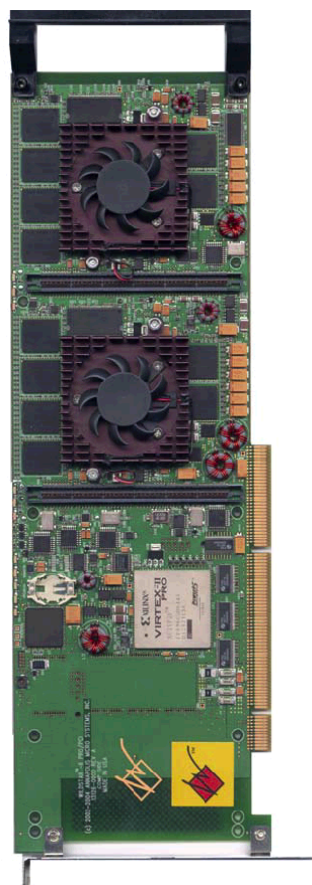


Figure 10. Xilinx field programmable gate array.

8. REFERENCES

- Bioucas-Dias, J., and Plaza, A., 2010, Hyperspectral unmixing: geometrical, statistical and sparse regression-based approaches. *Proceedings of SPIE*, in press.
- Chang, C.-I., 2003, *Hyperspectral Imaging: Techniques for Spectral Detection and Classification* (New York, USA: Kluwer).
- Goetz, A., 1985, Imaging spectrometry for Earth remote sensing. *Science*, 228, 1147–1153.
- Gonzalez, C., Resano, C., Mozos, D., Plaza, A., and Valencia, D., 2010, FPGA implementation of the pixel purity index algorithm for remotely sensed hyperspectral image analysis. *EURASIP Journal on Advances in Signal Processing*, 969806, 1–13.
- Iordache, M. D., Bioucas-Dias, J., and Plaza, A., 2010, Sparse unmixing of hyperspectral data. *IEEE*

- Transactions on Geoscience and Remote Sensing*, under review.
- Keshava, N., and Mustard, J. F., 2002, Spectral unmixing. *IEEE Signal Processing Magazine*, 19, 44–57.
- Martin, G. and Plaza, A., 2010, Region-based spatial preprocessing for endmember extraction and spectral unmixing. *IEEE Geoscience and Remote Sensing Letters*, under review.
- Plaza, A., Benediktsson, J. A., Boardman, J., Brazile, J., Bruzzone, L., Camps-Valls, G., Chanussot, J., Fauvel, M., Gamba, P., Gualtieri, J. A., Marconcini, M., Tilton, J. C., and Trianni, G., 2009, Recent advances in techniques for hyperspectral image processing. *Remote Sensing of Environment*, 113, 110–122.
- Rojas, M., Dopido, I., Plaza, A., and Gamba, P., 2010, Comparison of support vector machine-based processing chains for hyperspectral image classification. *Proceedings of SPIE*, 7810, 1–10.
- Sanchez, S., Paz, A., Martin, G., and Plaza, A., 2010, Parallel unmixing of remotely sensed hyperspectral images on commodity graphics processing units. *Concurrency and Computation: Practice & Experience*, under review.
- Winter, M. E., 1999, N-FINDR: An algorithm for fast autonomous spectral endmember determination in hyperspectral data. *Proceedings of SPIE*, 3753, 266–277.

Air temperature mapping using ground and satellite data in the context of a heat wave monitoring and warning system in the Valencia region

J.A. Valiente (1), R. Niclòs (1), M.J. Barberá (1), M.J. Estrela (2) and J. Miró (1)

(1) Unidad Mixta CEAM-UVEG, Instituto Universitario Centro de Estudios Ambientales del Mediterráneo CEAM - UMH, 14 Charles R. Darwin, 46980 Paterna, Spain

(2) Unidad Mixta CEAM-UVEG, Departament de Geografia de la Universitat de València (UVEG), 28 Blasco Ibáñez 28 Av., 46010 Valencia, Spain

josean@ceam.es

ABSTRACT -A heat-wave monitoring and warning system has been implemented by the Fundación CEAM since the 2006 summer to alert local authorities in the Valencia region. This region, which is located in Eastern Spain, is prone to undergo the effects of heat-wave incursions during summer. Typically, summer maximum daily temperatures are usually above 30 °C in most of the territory, while 20 °C minimum temperatures are common for a significant number of days during the hot season. The complex topography and the distinct coastal proximity for each of the individual areas make noticeable temperature differences throughout the region. For this reason, the alert system contemplates the region as divided into 30 thermoclimatic areas. Each of the thermoclimatic areas has been defined according to its homogeneous response to the different synoptic situations and air mass advections that yield heat-wave incursions over the territory. Different warning thresholds were determined for each of the thermoclimatic areas in base to a statistical analysis spanning 50 years of data, thus deriving what temperatures may be taken as usual during summer and what other temperatures may be taken as upper or lower limits when a normal variability of temperatures is considered. Three warning levels have been adopted: moderate, high and extreme, depending on how thresholds may be exceeded by the forecasted temperatures.

In this study, the spatial distribution of air temperature, the one which is measured at about 2-m above ground, is generated and studied for days of the 2009 summer campaign that presented any of the heat-wave warning levels. The air temperature mapping uses 10-min averaged data from an automatic meteorological station network that the Fundación CEAM has set up in the Valencia region. Several spatial interpolation methodologies are used, specifically those that make use of the Land Surface Temperature and Fraction of Vegetation Cover products available from the Land Surface Analysis Satellite Applications Facility (LSA SAF). The combination of these satellite data products with the meteorological network data enables the mapping of air temperature throughout the Valencia region.

1 INTRODUCTION

Summer temperatures are of special interest because of the economic, social and environmental impacts derived from their hypothetical increase as reported by the IPCC (2007). The extreme heat wave occurring during 2003, in which maximum air temperature records were registered during a very lasting episode, has increased the scientific interest for this type of phenomena (Rodríguez Ballesteros, 2004; Rodríguez Puebla et al., 2004). Some current studies are able to relate an increase in the mortality index with the severity and length of heat wave episodes (Kalstein, 1989; Raso, 1999). On the other hand, the spatial distribution of the air temperature is important to assess the extent of the heat wave over a specific area. Spatial distribution methods for air temperature mapping encounter most important problems such as highly varying densities of weather stations, complex

topography, lack of elevated measurements, changing conditions seasonally and daily, among others.

2 HEAT WAVE PATTERNS

2.1 Synoptic classification

The analysis of the meteorological patterns that promote the Valencia region to undergo a heat wave episode leads to eight types of different synoptic situations, each of them yielding a different heat spread over the territory. The historical high temperature peaks occurring during summers from the period 1955-2005 are the basis of this synoptic analysis. The first type encountered corresponds to a frame where an Atlantic depression placed to the NW of the Iberian Peninsula favours either westerly winds or weak breezes over the Valencia region while a tropical continental air clamp yields North-African air advection over the region. Episodes tend to last for

two days and affect coastal areas mainly, being temperatures slightly fresher inland.

The second type of synoptic pattern is determined by a North-to-South trough situated to the West of the Iberian Peninsula, being this influenced by a flat low that may develop into a thermal low during daytime with gentle breezes and occasional westerlies. Warm continental air from Algeria is advected from South to North of the Eastern part of the Peninsula. This type of pattern commonly persists for 2 to 3 days, producing an intense and widespread heat wave episode due to the Saharan air origins. Temperatures are higher inland and at mid-elevation areas such as the Turia and Vinalopo valleys and Xàtiva and Orihuela plains.

The third type is characterised by a marked tropical continental air advection from Morocco with a SW-NE component over the Valencia region. Distant low pressures are placed in the North Atlantic, sea breezes are reduced and the Iberian thermal low develops weakly. These events may spread over 7 days, affecting the whole Valencia region, more specifically the interior and Southern parts. As an example for this type of episodes, Figures 1 and 2 are the corresponding synoptic charts for the 500 hPa geopotential, surface pressure and air temperature at 850 hPa, respectively, from Wetterzentrale Karlsruhe.

The fourth type of pattern is dominated by a very wide tropical continental air from the North of Africa spreading over the whole Iberian Peninsula. The Iberian thermal low develops but sea breezes are weak, and frontal lows are distant over the Atlantic. Typically, the episodes last only for 2 days, affecting coastal areas, well-oriented valleys and highlands in a lesser extent. The South part of the region and the interior areas are the most affected in contrast.

The fifth type of situations are determined by a marked tropical continental air clamp from the interior of Algeria –Saharan origin- into the Eastern part of the Iberian Peninsula primarily due to a strong and isolated cold air depression being placed to the North of the Canary Islands. Sea breezes are weak with a noticeable South component. These situations tend to persist for 2 or 3 days, uniformly affecting the whole Valencia region with higher temperatures in the interior and slightly lower temperatures in coastal areas due to the presence of sea breezes.

The sixth type of synoptic frame comes from the presence of a small but very active cyclone travelling through the Bay of Biscay and bringing up a frontal system over the Northern part of Spain. A subtle warm air clamp is formed ahead the frontal system resulting in a strengthening of westerlies over the Valencia region and the appearance of the Föhn effect at coastal areas. The episodes typically persists for one day, being the littoral part and the lowlands the most affected areas.

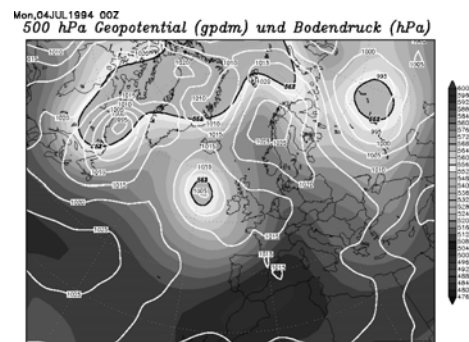


Fig 1. Typical synoptic chart of the 500 hPa geopotential and surface pressure for the type 3 episodes (Wetterzentrale Karlsruhe).

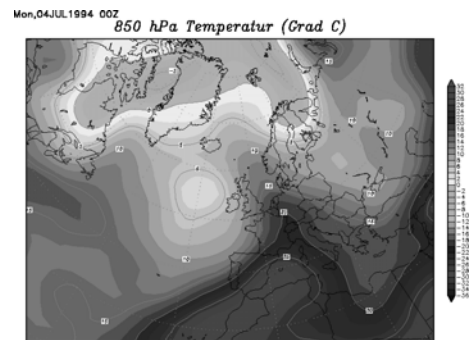


Fig 1. Typical synoptic chart of the air temperature at 850 hPa for the type 3 episodes (Wetterzentrale Karlsruhe).

The seventh type of episodes is a transition from the fourth to the second types. The presence of a large crest of tropical continental air over Northern Africa makes Saharan air to penetrate towards the South-East of the Iberian Peninsula when a slight trough wave is formed over the Atlantic in front of Portugal coast. This disposition can stay for 2-4 days causing high temperatures over the whole region, specially where sea breezes are less effective. Minimum temperatures are significantly high at the littoral edge and coastal lowlands, while maximum temperatures are higher inland and inner lowlands.

The eighth and last type of synoptic situation is governed by a tropical continental air clamp from the interior of Morocco towards the British Isles when placed between two cold troughs: one over the Atlantic and the other over the Italian Peninsula. Due to the establishment of sea breezes, highest temperatures are reached in the interior of the Valencia region and its midway parts from the coastal areas. However, minimum temperatures at night are high at the littoral margin due to the ending of sea breezes. Typically, this situation can prevail for 2 days.

2.2 Thermoclimatic division

Additionally, an analysis of the different geographic conditions that are met in the Valencia region has led to a division of the territory into 30 thermoclimatic areas. Temperature data were collected from a 281-station data base covering the 1955-2005 year period. Local temperature patterns reproduced from the daily maximum and minimum temperatures during each heat wave episode were analysed in terms of topographical features, slope orientations, dominant wind fluxes in relation to coastal breezes, inland continental effects and distance to the coast line highlighting the characteristic humid climate of the region. Figure 3 is an example pattern of the maximum and minimum temperatures reproduced from the daily maximum and minimum temperatures during each heat wave episode that took place on July 4th 1994 and which may be considered as type 3 in the synoptic chart classification. The analysis reveals that the Valencia region can be divided into 30 areas of homogeneous response to the different 8 types of heat wave episodes (fig. 4). Summer daily maximum temperatures are easily above 30 °C while summer minimum temperatures at night can be as much as 20 °C. However, normal summer temperatures attained at one of the areas may be considered as exceptional if they were registered at another area. The division of the region into 30 thermoclimatic areas allows the definition of different temperature thresholds for each area emphasizing the singular response of these areas to each type of the heat wave episodes.

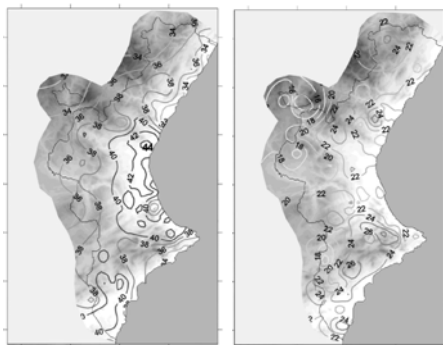


Fig 3. Spatial distribution of the daily maximum and minimum temperatures on July 4th 1994 (type 3 in the synoptic classification).

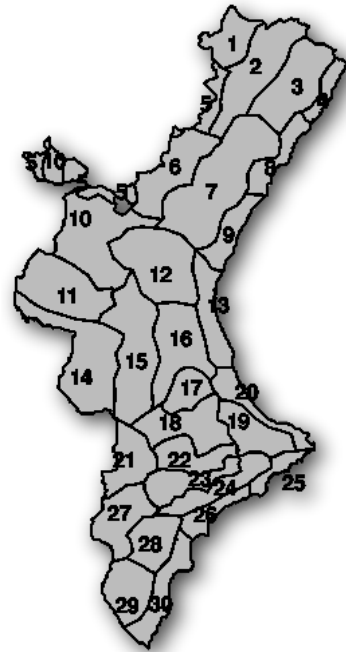


Fig 4. The Valencia region divided into the 30 thermoclimatic areas.

3 HEAT WAVE FORECAST

3.1 Atmospheric modelling

The mesoscale numerical model RAMS (Regional Atmospheric Modelling System) is used for a 72-h air temperature forecasting. This effective software, designed for the study from the regional to the local scales, has been improved with the addition of the local topography, land use and land cover of the Valencia region. The algorithm is initialized using various sources: global meteorological modelled data, sea surface temperature fields and in situ meteorological data from an automatic network deployed in the Valencia region. The model output is configured to provide high spatial resolution at 24 vertical levels, two daily simulations (00-12 UTC) extending for 96 hours and air temperature each hour at each grid point. Maximum and minimum temperatures are then selected for a day output at each of the grid points (fig. 5).

obtained lapse rate at certain specific mountain stations. Lastly, the temperature at any location can be estimated by adding the influence of elevation and LST back into the interpolated detrended temperature values. Figure 8 is an example of the resulting air temperature spatial distribution from this procedure.



Fig 7. From left to right, air temperature mapping using a simple interpolation scheme over detrended ground meteorological data for 23 July 2009 16:00 and 24 July 2009 06:00.

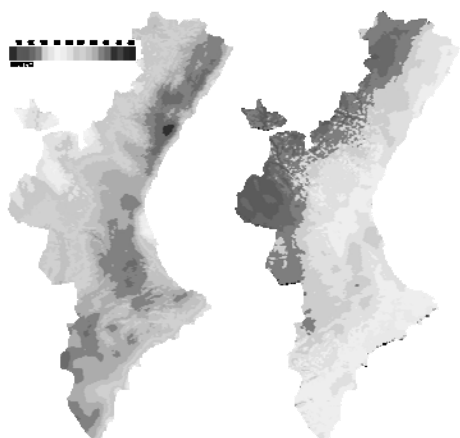


Fig 8. From left to right, air temperature mapping using a simple interpolation scheme over detrended ground meteorological data incorporating LST satellite data for 23 July 2009 16:00 and 24 July 2009 06:00.

5 CONCLUSION

The combination of satellite data products with the meteorological network data enables an improved

retrieval of the spatial distribution of the air temperature throughout the Valencia region when compared to the alert level fields from a heat wave warning system. If meteorological network data are used alone, air temperature maps lack of the severity of the heat wave affecting particular thermoclimatic areas.

6 ACKNOWLEDGEMENTS

This work was supported by the Spanish Ministerio de Ciencia e Innovación under Projects CGL2007-65774/CLI, CGL2008-04550/CLI, by CONSOLIDER-INGENIO 2010 CSD2007-00067, by the AQ2 European Social Fund, by the European Union (Project CIRCE N.036961) and by the Consellería de Sanidad (Dirección General de Salud Pública) under contract T5893000 "Meteorología Ambiental (CSISP)". Instituto Universitario CEAM-UMH is supported by the Generalitat Valenciana and Fundación BANCAJA.

7 REFERENCES

- Raso-Nadal, J. M., 1999, Temperaturas extremas y mortalidad en Barcelona. I Congreso de la Asociación Española de Climatología, Barcelona, 459-468.
- Rodríguez-Ballesteros, C., 2004, Carácter extremo del verano de 2003 en España peninsular e Islas Baleares. XXVIII Jornadas Científicas, La Meteorología y el Clima Atlántico, AME, Badajoz.
- Rodríguez-Puebla, C, Frias, M. D, Encinas, A. H., 2004, Relaciones entre los extremos de temperatura máxima y patrones de circulación en el Atlántico Norte. XXVIII Jornadas Científicas, La Meteorología y el Clima Atlántico, AME, Badajoz.
- IPCC. 2007, Climate Change 2007: Impacts, Adaptation and Vulnerability. Working Group II Contribution to the Intergovernmental Panel on Climate Change Fourth Assessment Report. Summary for Policymakers. IPCC.
- Kalstein, L. S., Davis, R .E., 1989, Weather and human mortality: an evaluation of demographic and interregional responses in the United States, *Ann. Assoc. Am. Geograph.*, 79(1), 44-64.

Fusion of MODIS and VEGETATION observations for improved consistency and continuity of LAI product time series

A. Verger^{(1,2)*}, F. Baret⁽²⁾ and M. Weiss⁽²⁾

(1) *Departament de Física de la Terra i Termodinàmica, Universitat de València. C/ Dr. Moliner, 50. 46100 Burjassot (València), Spain*

(2) *INRA, Université d'Avignon. UMR114, EMMAH, Domaine Saint-Paul, Site Agroparc, 84914 Avignon, France*

* aleixandre.verger@uv.es

ABSTRACT - The generation of continuous land surface products from remote sensing observations is key to many environment applications. Nevertheless satellite products are often affected by poor quality or missing data due to instrumentation problems, cloud cover or snow cover. An innovative multi-sensor fusion approach for improving spatio-temporal continuity, consistency, temporal smoothness and accuracy of satellite products is here presented. The approach is based on the use of neural networks and temporal fitting techniques. It is applicable to any optical sensor and satellite product. In this study, the potential of this technique was demonstrated for restoring missing and low quality data in the MODIS leaf area index (LAI) product over the BELMANIP sites in the 2001-2003 period. MODIS and VEGETATION reflectance data were used. The developed FUSION LAI product showed an overall good agreement with the MODIS LAI standard product but resulted more continuous (reduction of 90% of the invalid LAI values), stable (smoother temporal evolution with a reduction of artefacts), consistent (improved monitoring of vegetation dynamics) and accurate (better agreement with ground measurements). The proposed approach thus provides products more appropriate for environmental prediction.

1 INTRODUCTION

Moderate resolution sensors are expected to provide reliable and continuous observations for monitoring spatial and temporal variations of land surface characteristics, including leaf area index (LAI), at regional to global domains. Different LAI products are currently available, each of them being derived from a unique sensor. However, the full potential of remote sensing systems is often hampered by poor quality or missing data caused by atmospheric conditions such as cloud cover, dust and aerosols, as well as by sensor-related artefacts and algorithm retrieval failure. This limits the use of satellite products in ground surface process simulation, climatic modelling and global change researches.

Several mathematical filters have been proposed to fill gaps in remotely sensed data (e.g. Chen et al., 2004). Nevertheless, temporal (spatial) reconstruction techniques are very limited if observations are missing or noisy for long periods (large regions). Fusion of data from different satellite systems typically provides more observations of the surface within a given period, increasing the availability and quality of cloud-free data in regions with a diurnal variability of cloud. The multi-sensor fusion thus appears as an appealing strategy to fully harness the potential of current Earth observation programs and to fulfil user requirements

in terms of spatio-temporal continuity, consistency and quality of satellite products.

This research introduces a multi-sensor fusion approach based on the use of neural networks and temporal fitting techniques. It is a generic approach applicable to any satellite dataset. In this study, it is applied for improving MODIS LAI product using reflectance data from VEGETATION and MODIS sensors. The performance of the approach for restoring the spatial and temporal distribution of seasonal LAI trends is demonstrated based on the evaluation of continuity, consistency and accuracy of the original and fused products.

2 DATA AND METHODS

2.1 Satellite products

The satellite dataset is composed of VEGETATION (from the CYCLOPES program) and MODIS nadir directional normalized reflectances, as well as MODIS LAI product. Satellite products were extracted in a three-year period (2001 to 2003) over the 3 km x 3 km BELMANIP sites (Baret et al., 2006).

VEGETATION/SPOT5 reflectance products are available at <http://postel.mediasfrance.org>. They correspond to 1/112° resolution (about 1 km at the equator) and are projected in plate-carrée. The temporal sampling interval is 10 days, and the

temporal window is 30 days, with gaussian weighting that puts more emphasis on observations close to the centre of the window (Baret et al., 2007).

MODIS/TERRA products were downloaded from <http://edcdaac.usgs.gov>. They correspond to 1 km spatial resolution and are in a sinusoidal projection system. Nadir BRDF-Adjusted Reflectance Product (MOD43B4) collection 4 provides atmospherically corrected, cloud-free, normalized reflectance values for each of the MODIS spectral bands at the mean solar zenith angle of each 16 day period. Collection 5 of MODIS LAI product (MOD15A2) was used in this study. The main MODIS LAI retrieval algorithm relies on a radiative transfer model which ingests red and near infrared bidirectional reflectance factor values, their uncertainties, view-illumination geometry, and eight biome land cover types (Myneni et al., 2002). The model is inverted with a Look-Up-Table specific per biome type. MODIS LAI value corresponds to the maximum daily fraction of absorbed photosynthetically active radiation (FAPAR) value in an 8-day compositing period. The MODIS LAI product was filtered attending to information of their quality flag and only the values generated by the main algorithm were included in our dataset.

Both VEGETATION and MODIS products have approximately 1 km sampling interval while their projection systems differ. For the synergic use of both products over the same support area, the same projection system has to be used that should ideally keep the size of the sites independent from its location. The MODIS sinusoidal projection system was selected because it ensures more consistency of the area of individual pixels between sites. VEGETATION products were therefore reprojected into MODIS projection system using a bi-cubic resampling method (Reichenbach and Geng, 2003).

2.2 Algorithm description

A three-step algorithm was developed for generating the 8-day FUSION LAI products. First, neural networks were used to estimate consistent LAI products based on existing MODIS LAI products and reflectance data from both MODIS and VEGETATION sensors. Second, a temporal smoothing method was applied to the neural network estimates. Third, a gap-filling procedure was applied to the smoothed time series.

(1) *The neural networks LAI estimation.* The versatility and performance of neural networks to learn a particular LAI product from several input reflectance products was demonstrated in Verger et al. (2008). Training networks over MODIS LAI data base but with input reflectances coming from both MODIS and VEGETATION allows estimating new LAI products

with a high consistency with original MODIS LAI. The inputs of the neural networks were the reflectances in the red, near infrared and short wave infrared and the sun zenith angle. As the original MODIS LAI product is biome class dependent, networks were trained per classes. MODIS land cover (MOD12Q1 yearly product) was used for biome class distinction (Friedl et al., 2002). Seven main biomes were considered: shrubs, savanna, grasses and cereal crops, broadleaf crops, needleleaf forest, deciduous broadleaf forest and evergreen broadleaf forest.

(2) *The temporal smoothing method.* An adaptive Savitzky-Golay (SG) filter (Chen et al., 2004) was designed for smoothing LAI data. SG was selected because it can capture subtle and rapid changes in the time series. As the SG-filtering, our approach uses local polynomial functions in fitting. A minimum of 6 observations centered on the date of the data being smoothed within a 128-day period was set as a requisite for fitting original data. The proposed algorithm allows flexibility in the time window which can be variable and asymmetric. A time window providing 3 observations at each side of the date being smoothed was selected.

(3) *The gap filling method.* A simple linear interpolation was applied to fill the gaps in the smoothed data series. A local moving window of 128-day period was considered. To improve the efficiency of gap-filling, an iterative process (n=2 iterations) was considered.

3 RESULTS AND DISCUSSION

3.1 Continuity

The continuity of LAI products was evaluated by characterizing the spatio-temporal distribution of gaps (Figure 1).

The original MODIS product presents a high rate of invalid data (34%). Uncertainties or invalid data in daily reflectances during the 8-day composition period of MODIS LAI leads a gap in the LAI product. Note that the MODIS back-up LAI product was not here considered. Loss of temporal continuity in LAI products (Figure 1) is mostly observed in the equator due to persistence of clouds and at high latitudes in wintertime partially because of larger uncertainties of reflectance data as a combination of multiple effects, such as persistence of snow cover, high cloud occurrence, long periods of darkness, effects of shadows at high illumination zenith angles, but also to the limitations of BRDF modelling and data processing.

The FUSION product presents practically no gap (the fraction of invalid data is 4%). The FUSION product provides a valid data if a valid reflectance

value is provided by VEGETATION or MODIS at the considered date or within the gap filling time window. Gaps in the FUSION product are mostly located in the equator latitudes where polar satellites are mainly affected by multi-temporal noise and long duration gaps (Figure 1). Conversely, for high latitudes very few gaps are observed since the VEGETATION and MODIS reflectance product patterns are complementary: gaps at northern (southern) latitudes are mostly present in VEGETATION (MODIS) product.

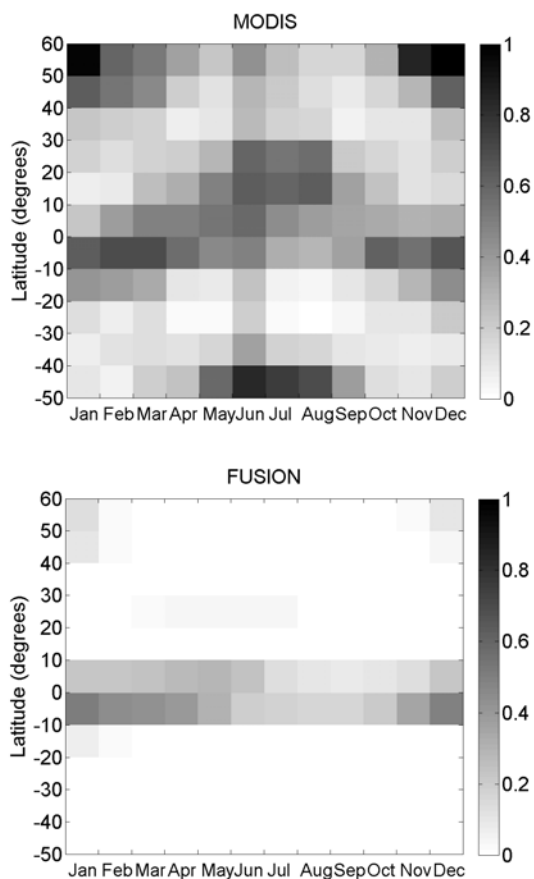


Figure 1. Fraction of invalid data as a function of the latitude and the date of acquisition for the original MODIS LAI product and the FUSION LAI product. Evaluation over the BELMANIP sites during the period 2001–2003.

3.2 Consistency

The FUSION product was compared with the original MODIS LAI product at pixel scale and the closest temporal date (Figure 2). A set of $n=1400$ samples

(pixel*date) made of 200 randomly selected samples of each of the 7 biomes were considered for the comparison.

A very high consistency (correlation coefficient, R^2 , higher than 0.8) and overall differences lower than 0.6 LAI in terms of root mean square error (RMSE) are found between FUSION and MODIS LAI products (Figure 2). Bias is not significant (lower than 0.1). The observed scattering, can be explained by different factors: (i) Outliers in the original satellite products due to residual clouds and atmospheric correction uncertainties; (ii) Inaccuracies in the land cover map which affect both the LAI retrieval and product comparison; (iii) Inconsistencies in the comparison due to the spatial and temporal differences between products; (iv) Limitations of MODIS and FUSION retrieval algorithms.

Main features of temporal signatures are illustrated by the temporal profiles of LAI over the central pixel of a selection of three BELMANIP sites (Figure 3): Hombori (Mali) classified as grasses & cereal crops by MODIS land cover corresponds to a grassland area dominated by annual herbaceous layer on sandy soil (90%); Puechabon (France) classified as savana but being an evergreen Mediterranean forest largely dominated by trees of *Quercus ilex*; Sinop-MatoGrosso (Brazil) evergreen broadleaf forest is an Amazonian evergreen ecotonal forest (transition between rain forest and tropical savanna), with a relatively closed canopy around 30 m.

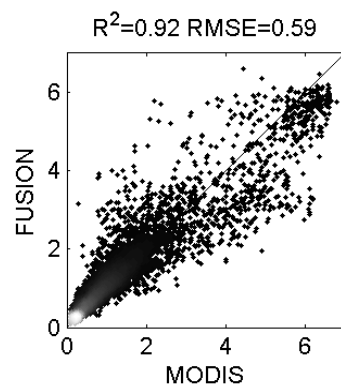


Figure 2. Comparison between FUSION and original MODIS LAI products for $n=1400$ samples uniformly distributed per biomes.

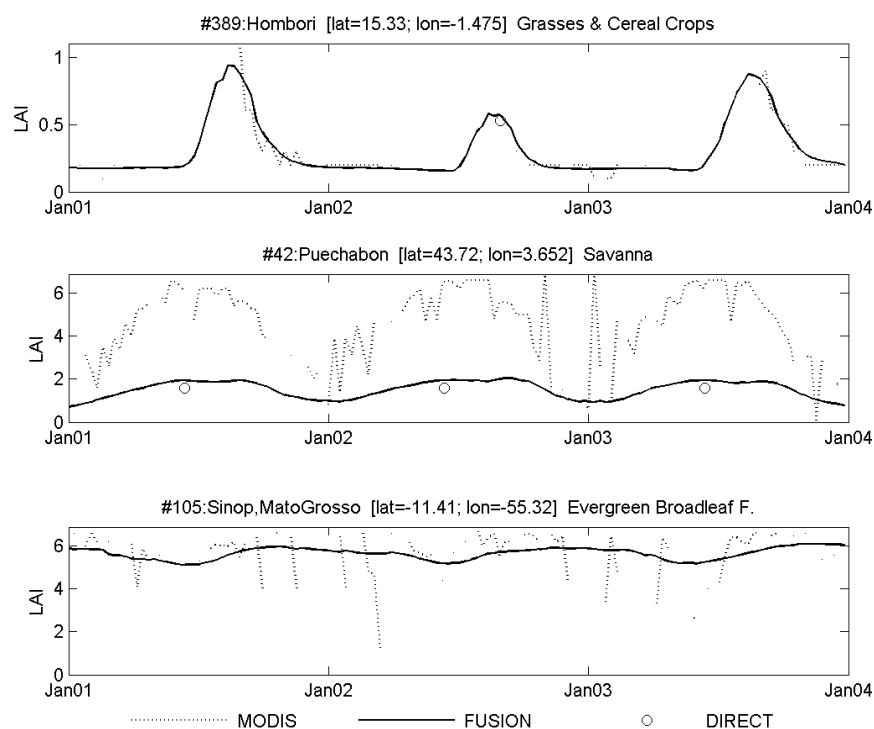


Figure 3. Temporal evolution of the original MODIS and the developed FUSION LAI products for the period 2001–2003 over the central pixel of Hombori (Mali), Puechabon (France) and Sinop-Mato Grosso (Brazil) BELMANIP sites.

Hombori site, in the Sahelian zone, is characterized by a pronounced rainfall cycle being water availability the most important determinant for vegetation growth. The rainy season lasts from July to September and determines the growing of grass vegetation with maximum values of LAI. Following this, there is a sharp decline in LAI because grass vegetation is all absent in the dry-season severe drought conditions. Vegetative growth was much more intense in 2001 and 2003 than 2002 because the year 2002 was an extremely dry year with rainfall below 50% of normal. LAI patterns of the original MODIS and developed FUSION LAI products show a good agreement and reproduce reasonably well intra-annual and interannual variations in rainfall (Figure 3). But a high rate of invalid data is observed in the original MODIS product. Discontinuities during the wet season may be explained due to the presence of clouds. Conversely discontinuities in the dry season may indicate some problems of the MODIS main algorithm to locate a solution. The FUSION product exhibits continuity for the whole period 2001–2003 taking benefit of the higher rate of valid data of the composited VEGETATION and MODIS reflectances as compared to MODIS LAI with a shorter composition period. Further the FUSION LAI agrees

well with the available ground measurement (w3.avignon.inra.fr/valeri).

Puechabon site is expected to present minimal seasonality since evergreen oaks determine the major contribution to the whole ecosystem function. However MODIS LAI exhibits an anomalous high seasonality and a shaky evolution (Figure 3). Further it significantly overestimates ground measurements (w3.avignon.inra.fr/valeri). FUSION product reproduces a reliable approximately flat temporal profile with a minimal decrease in vegetation amount after summer stress when understorey vegetation is likely to be dry. And it shows a good agreement with available ground measurements.

Despite of the enormous difficulties to retrieve LAI over the Sinop Amazonian forest as shown the many artefacts and discontinuities in the MODIS product (Figure 3), the proposed FUSION product captures fairly accurately the expected seasonality and magnitude of LAI. LAI values were estimated from ground measurements of the extinction of photosynthetic photon flux density by the canopy as a maximum of 4.5–5 during the wet season (January) and a minimum of 4–4.5 during the dry season (July) (Vourlitis et al., 2001). Pinto-Junior et al. (2010) reported LAI, estimated by micrometeorological data,

reaches maximum values of 6 which agree with the FUSION product in the wet season.

3.3 Direct validation

MODIS and FUSION LAI products were compared with direct ground measurements of LAI resulting from several international field campaigns in sites globally distributed (Garrigues et al., 2008). To increase the statistical significance of the validation exercise, some ground measurements performed out of the 2001-2003 period over forest sites almost invariant from year to year were considered for the validation of LAI products. Validation of LAI products was achieved using mean values over $3 \text{ km} \times 3 \text{ km}$ areas (typical size of validation sites) and considering the closest date to the field campaigns. We used for the validation only the sites where data of the two considered satellite products were simultaneously available at the date of ground measurements acquisition. The number of samples of the ground dataset was 68.

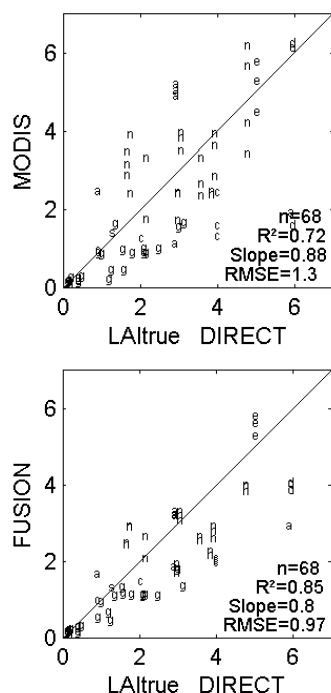


Figure 4. Comparison of the original MODIS and the FUSION products with ground measurements of LAI. Letter markers correspond to different biome classes: shrubs (s), savanna (a), grasses and cereal crops (g), broadleaf crops (b), needleleaf forest (n), deciduous broadleaf forest (d) and evergreen broadleaf forest (e).

Differences of products with ground measurements were quantified by the correlation coefficient (R^2), the slope of a zero-offset linear

regression and the RMSE error. Results (Figure 4) show that the FUSION product agrees better than the MODIS product with the ground measurements, scoring a lower RMSE value (RMSE=0.97 for FUSION and RMSE=1.3 for MODIS) and a higher correlation ($R^2=0.85$ for FUSION and $R^2=0.72$ for MODIS). Note however that the slope of the linear regression between ground measurements and satellites products is slightly closer to the unity for MODIS (slope=0.88 for MODIS and slope=0.8 for FUSION). The FUSION product seems to underestimate high LAI values but no firm conclusion can be drawn due to the low number of measurements.

4 CONCLUSIONS

This research introduced an innovative approach based on the use of neural networks and temporal fitting techniques. The algorithm ingests data from multiple satellite sensors for covering gaps or low quality data in a mono-sensor product. It is a generic approach applicable to any satellite dataset. In this study, it was applied for improving MODIS LAI product using reflectance data from VEGETATION and MODIS sensors.

The performance of the approach for restoring the spatial and temporal distribution of MODIS LAI trends is demonstrated based on the evaluation of the fraction of gaps in the original and in the developed product. The original MODIS product presents a relatively high rate of invalid data (34%) due to the shorter composition period but also to the failure of the main algorithm to provide a solution in sub-optimal conditions with high uncertainties in input data. The FUSION product (fraction of invalid data of 4%) benefits from the use of wide composited reflectances, the spatio-temporal complementarities of VEGETATION and MODIS data patterns, and the gap filling approach. But residual gaps persist in the equator revealing the difficulties to monitor these particular areas due to persistent cloudiness.

The analysis of temporal profiles shows that the MODIS original product presents some artefacts and inconsistencies. The proposed fusion approach seems to smooth out efficiently most part of the instabilities through the use of composited reflectances, neural network training and temporal smoothing techniques.

The validity and accuracy of the developed FUSION product was evaluated both indirectly through the intercomparison with the original MODIS product and through direct comparison with ground data. The intercomparison analysis shows that differences in LAI products are within 0.6 LAI in terms of RMSE. Direct validation shows that the FUSION product agrees better than the MODIS product with ground measurements of LAI, scoring a

RMSE value within 1.0 and a correlation coefficient higher than 0.8.

Our results show the high potential of the proposed multi-sensor fusion approach for improving the performance of satellite products in terms of continuity, consistency and accuracy.

5 ACKNOWLEDGMENTS

MODIS products are generated under NASA support and provided by LPDAAC. VEGETATION products are generated under EU/FP5 CYCLOPES project and provided by the POSTEL/MEDIAS-France. Alexandre Verger is funded by a postdoctoral contract within the VALi+d program (FUSAT, GV-20100270).

6 REFERENCES

- Baret, F., Hagolle, O., Geiger, B., Bicheron, P., Miras, B., Huc, et al. (2007). LAI, fAPAR and fCover CYCLOPES global products derived from VEGETATION. Part 1: Principles of the algorithm. *Remote Sensing of Environment*, 110, 275–286.
- Baret, F., Morisette, J., Fernandes, R., Champeaux, J., Myneni, R., Chen, J., et al. (2006). Evaluation of the representativeness of networks of sites for the global validation and intercomparison of land biophysical products: Proposition of the CEOS-BELMANIP. *IEEE special issue: Validation and accuracy assessment of global products*, 44(7):1794–1803.
- Chen, J., Jönsson, P., Tamura, M., Gu, Z., Matsushita, B., & Eklundh, L. (2004). A simple method for reconstructing a high quality NDVI time-series data set based on the Savitzky–Golay filter. *Remote Sensing of Environment*, 91(3–4), 332–344.
- Garrigues, S., Lacaze, R., Baret, F., Morisette, J. T., Weiss, M., Nickeson, J. E., et al. (2008). Validation and intercomparison of global leaf area index products derived from remote sensing data. *Journal of Geophysical Research*. 113, G02028, doi:10.1029/2007JG000635.
- Myneni, R., Hoffman, S., Knyazikhin, Y., Privette, J., Glassy, J., Tian, Y., Wang, Y., Song, X., Zhang, Y., Smith, G., Lotsch, A., Friedl, M., Morisette, J., Votava, P., Nemani, R., and Running, S. (2002). Global products of vegetation leaf area and fraction absorbed PAR from year one of MODIS data. *Remote Sensing of Environment*, 83:214–231.
- Pinto-Júnior, O. B., Sanches, L., Lobo, F. A., Brandão, A. A. and Nogueira, J. S. (2010). Leaf area index of a tropical semi-deciduous forest of the southern Amazon Basin. *International Journal of Biometeorology*, DOI: 10.1007/s00484-010-0317-1.
- Reichenbach, S. E., & Geng, F. (2003). Two dimensional cubic convolution. *IEEE Transactions on Geoscience and Remote Sensing*, 12, 857–865.
- Verger, A., Baret, F., and Weiss, M. (2008). The performances of neural networks for deriving LAI estimates from existing CYCLOPES and MODIS products. *Remote Sensing of Environment*, 112:2789–2803.
- Vourlitis, G.L., Priante-Filho, N., Hayashi, M.M.S., Nogueira, J.S., Caseiro, F.T. and Campelo, J.H. (2001) Seasonal variations in the net ecosystem CO₂ exchange of a mature Amazonian tropical transitional forest (cerradão). *Functional Ecology*, 15, 388–395.

Integrating multi-source data into land surface model for an improved state estimation through data assimilation

Kun Wang¹, Zhao-Liang Li^{1,2,*}, Ronglin Tang^{1,2,3}

1. LREIS, Institute of Geographical Sciences and Natural Resources Research, CAS, Beijing, 100101, China

2. LSIIT, UdS, CNRS; Bld Sebastien Brant, BP10413, 67412 Illkirch, France

3. Graduate University of Chinese Academy of Sciences, CAS, Beijing 100049, China

*lzl@igsnnr.ac.cn

ABSTRACT -On the basis of the Ensemble Kalman Filter (EnKF) and the Common Land Model (CoLM), land surface temperature (LST) and sensible heat flux data assimilation schemes are developed separately and examined with the data acquired at Yucheng experiment station (Longitude: 116.6E; Latitude: 36.93N) in Shandong, China. The predictions of ground temperature, latent and sensible heat fluxes by assimilating different observation sources are compared with surface measurements. Results show that these two data assimilation schemes can both improve the estimation of ground temperature and sensible heat fluxes. The root mean squared error (RMSE) in the comparison between simulated and in-situ sensible heat flux decreases more evidently with assimilation of large aperture scintillometer (LAS) data than with assimilation of MODIS LST. On the contrary, assimilating MODIS LST improves the prediction of ground temperature greatly than the assimilation of LAS data. In addition, integrating multi-source data (LAS and MODIS LST) simultaneously into the land surface model would become more efficient and robust to improve the predictions of latent and sensible heat fluxes.

1 INTRODUCTION

Latent (LE) and sensible (H) heat fluxes are the two key variables in the water and energy balance of land surface processes and the accurate estimation of energy partitioning into H and LE have attracted great attention in meteorology, oceanography, hydrology and agriculture (Courault et al., 2005), and would improve the forecasts of climate models as the lower boundary (Pitman, 2003). Integrating remotely sensed data into land surface model by using data assimilation technique to improve the prediction of LE and H becomes one of the promising directions (Boni et al., 2001; Caparrini et al., 2004). In the data assimilation process, the uncertainties of the land surface model and observations can be fully considered; the state variables are adjusted with the observations being assimilated. The Ensemble Kalman Filter (EnKF) (Evensen, 1994) method is one of the most popular data assimilation techniques in various studies (Pipunic et al., 2008). However, most studies focus on the assimilation of soil moisture content (Reicher et al., 2002; Kumar et al., 2008), although both the LE and H fluxes are influenced indirectly. Assimilation of the observed variables of the heat fluxes directly, such as LE and H, would be more efficient to improve LE and H prediction. A few examples can be found for the H and LE assimilations (Williams et al., 2009). Additionally, a great deal of work has been conducted

for the estimations of LE and H fluxes using remotely sensed data, especially for evapotranspiration (ET) mapping from satellite data on a regional scale (Li et al., 2009). MODIS land surface temperature products (e.g. MOD11A1) are often assimilated to improve the prediction of heat fluxes (Xu et al., 2009).

In this work, a data assimilation scheme for energy partitioning is developed. Two kinds of data sources are assimilated into the land surface model. The predictions of LE, H and ground temperature from the assimilation results are compared with the in-situ measurements.

2 DATA, MODEL AND METHOD

2.1 Data

The experimental data used in this work are from Yucheng station (Longitude: 116.6E; Latitude: 36.93N) in Shandong Province in China from January to July, 2009. The meteorological data required include atmospheric pressure, air temperature, wind speed, specific humidity, precipitation, indirect radiation, and longwave radiation. The eddy covariance measured latent and sensible heat fluxes and ground surface temperature are used to validate the simulation results.

Additionally, sensible heat flux estimated from the 10-min averaged signals measured by the large aperture scintillometer (LAS) and MOD11A1 products obtained from Land Processes Distributed Active

Archive Center (<https://lpdaac.usgs.gov/>) are assimilated into the land surface process model, respectively. The LAS is installed at Yucheng station with a length path of 1240 m along northeast-southwest direction. The zone between transmitter and receiver was mainly covered with agriculture crops. MOD11A1 data are the daily land surface temperature at 1 km resolution with the satellite overpassing at 10:30 AM.

2.2 Model and Method

The chosen data assimilation technique is the Ensemble Kalman Filter (Evensen, 1994). The EnKF is widely applied in the land data assimilation (Li et al., 2007). The land surface model used in this work is the Common Land Model (CoLM). The detailed description about the assimilation method and the model operator is shown in the related references (Evensen, 2003; Dai et al., 2001).

3 RESULTS

The CoLM model and assimilation system were run from January to July, 2009. We mainly compared the simulations from April to July to validate the performance of assimilation scheme.

3.1 Generation of initial ensembles

The generation of the ensembles in the ensemble Kalman data assimilation scheme is an important issue. Disturbing the forcing climate data to drive the model is one way to solve this issue (Pauwels et al., 2007). In this work, by adding random perturbations with zero mean and a standard deviation to the spin-up initial soil temperature values, initial ensembles were generated. The standard deviation of the random perturbation was set to 0.2K. The initial value of soil moisture and temperature were both from the observations.

3.2 Configuration of parameters in the assimilation scheme

Model errors, which are mainly related to the prediction of soil temperature in ten layers, were specified by analyzing the differences between the simulations and observations. Considering that they would decrease with the assimilation, model errors were specified as smaller static values. Here, the temperature errors induced by the model were limited within $\pm 2K$. The measurement noise was regarded to be invariable. As to the sensible heat flux measured by LAS, the errors were less than $10 Wm^{-2}$; for the MODIS LST, the accuracy is better than 1K in the range from 263K to 322K (Wan et al., 2004). All above errors were produced by adding a zero mean Gaussianly distributed random number to the corresponding variables.

In order to compare the assimilation results of data from different data sources, two assimilation scenarios were designed. When sensible heat flux is assimilated, all the calculations were done according to Pipunic et al. (2008), although the observation operator needs not to be explicitly solved. To the remotely sensed data, MODIS LST, which is a hybrid temperature of canopy and ground temperature, the observation operator is constructed by linearly regressing ground temperature observations to MODIS LST:

$$T_s = 0.6027 * T_g + 122.8 + \varepsilon \quad (1)$$

where T_s , T_g is the hybrid temperature and ground temperature, respectively, ε is the observation error item, $\varepsilon \sim N(0, R)$, R is the standard deviation of the Eq. (1).

3.3 Impact of the number of ensemble members

The number of ensemble members is one of the most important parameters in the EnKF data assimilation method. In order to test the sensitivity of the simulations to the ensemble size, the total sum of root mean square error (RMSE) of the three variables (H, LE and LST) in the data assimilation runs were compared for the ensemble size of 5, 10, 20, 30, 50 members (Figs. 1-2). Considering the computation efficiency and performance of assimilation scheme, 5 is the suitable number of ensemble for this system.

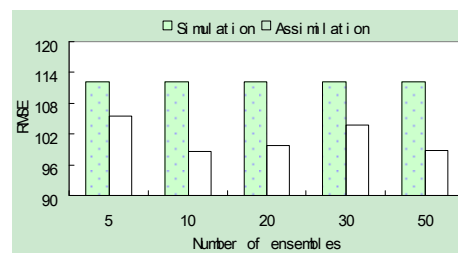


Fig.1 Impact of the ensemble size on the assimilation of sensible heat flux measured by LAS

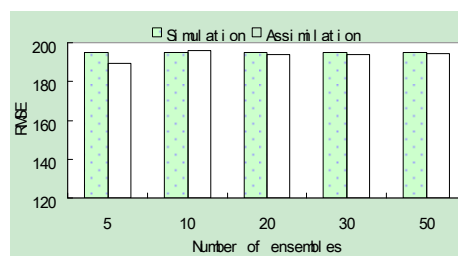


Fig.2 Impact of the ensemble size on the assimilation of MODIS LST data

3.4 Assimilation of sensible heat flux measured by LAS

In the first scenario, sensible heat flux obtained from LAS was assimilated into the model in a 30-min time step. We analyzed the influence of assimilation on the estimation of sensible heat flux, latent heat flux, and ground temperature. The mean bias error (ME) and RMSE were adopted to assess the performance of assimilation system (Table 1). Fig. 3 shows the 10-day assimilation results of ground temperature, sensible and latent heat fluxes by assimilating H flux data from May 24 to June 2. We can find that the assimilation curves of sensible heat flux and ground temperature are obviously closer to the observations than the simulation results. As for the comparison of ground temperature, ME and RMSE decrease significantly with assimilation. By contrast, for latent heat flux, ME and RMSE increase slightly when assimilating H flux

from LAS into the model.

3.5 Assimilation of MODIS LST

Secondly, MODIS LST was assimilated about once per two days. The 10-day simulations of three state variables by assimilating MODIS LST products from May 21 to May 30 are shown in Fig. 4. One can see that the estimation of the ground temperature is improved more obviously than other two variables. The error statistics of several variables are also listed in Table 2. The statistic results indicate that ME and RMSE of sensible heat flux and ground temperature decrease greatly with the assimilation of MODIS LST. However, as the effective observation frequency of MODIS LST data was decreased due to the cloud contamination, the performance of the data assimilation system was influenced.

Table 1 The error statistics of sensible and latent heat flux, ground temperature by assimilating LAS data from May 24 to June 2, 2009

	Sensible Heat Flux(Wm ⁻²)		Latent Heat Flux(Wm ⁻²)		Ground Temperature(K)	
Average Error	Simulation	Assimilation	Simulation	Assimilation	Simulation	Assimilation
	4.87	-5.29	1.70	2.02	2.15	0.33
RMSE	41.69	33.34	67.98	70.34	2.44	1.71

Table 2 The error statistics of sensible and latent heat flux, ground temperature by assimilating MODIS LST products from May 21 to May 30, 2009.

	Sensible Heat Flux(Wm ⁻²)		Latent Heat Flux(Wm ⁻²)		Ground Temperature(K)	
Average Error	Simulation	Assimilation	Simulation	Assimilation	Simulation	Assimilation
	25.15	19.42	-36.77	-39.37	3.32	2.26
RMSE	89.14	82.27	101.97	103.85	3.80	2.97

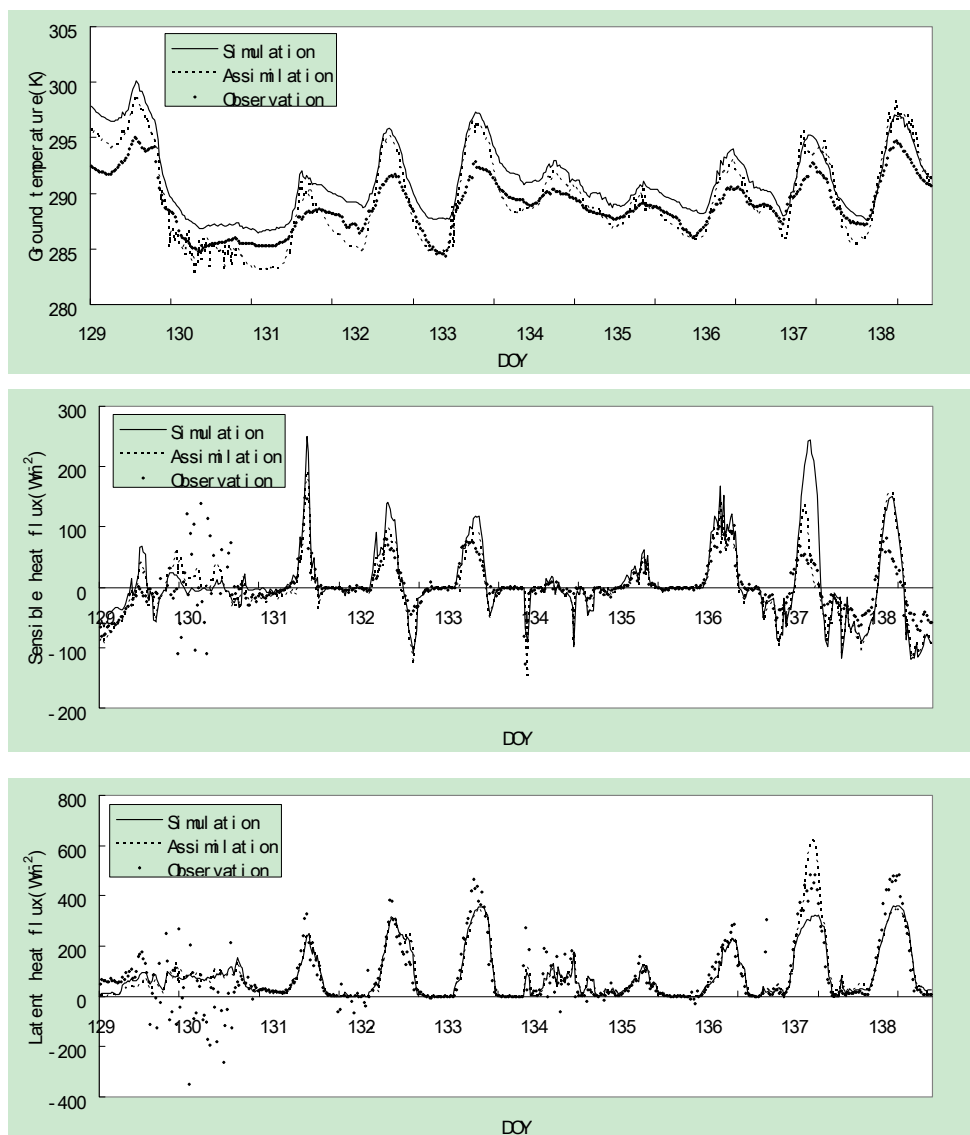


Fig. 3 Comparisons of observations to estimates from simulation and LAS data assimilation from May 24 to June 2, 2009

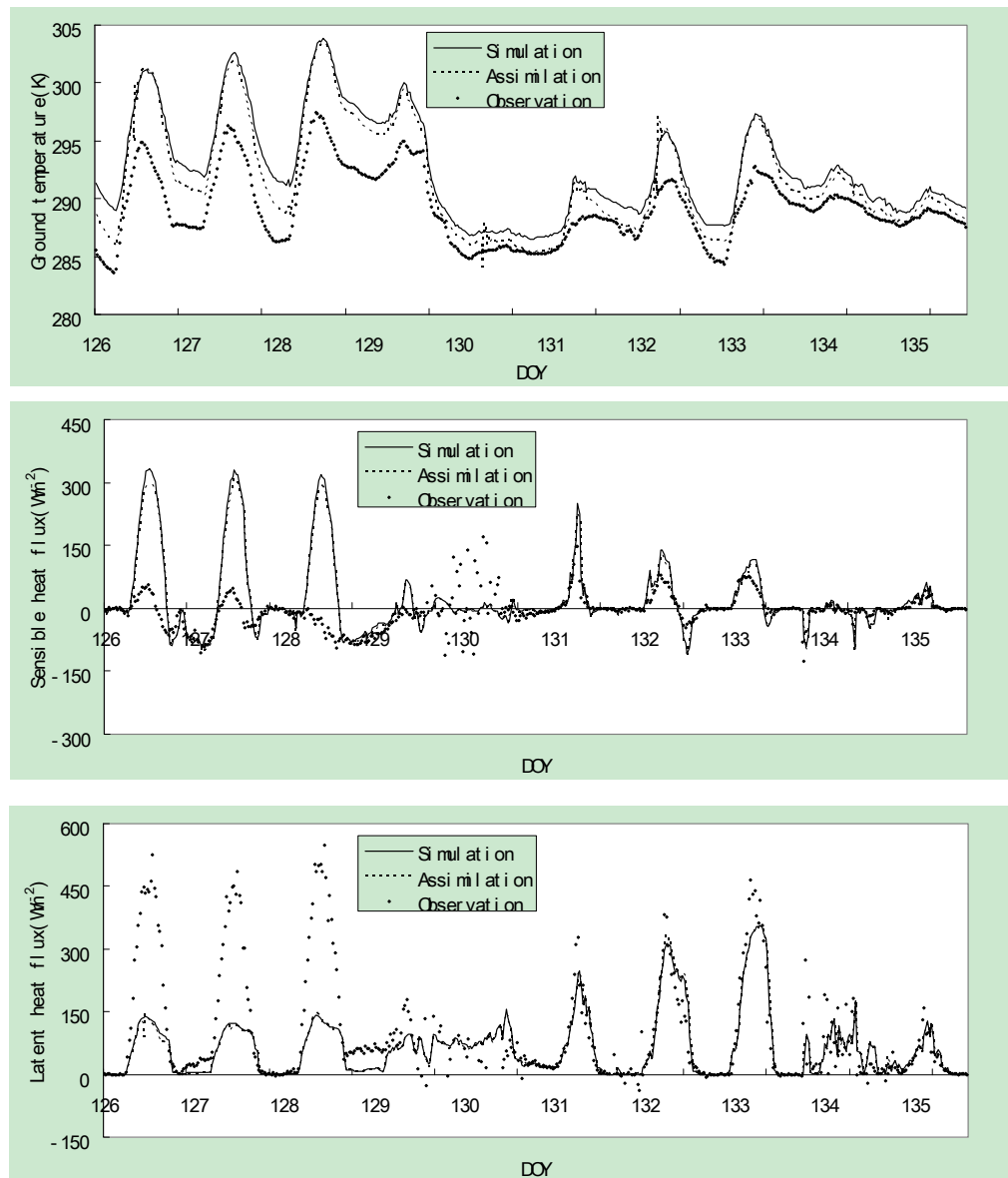


Fig. 4 Comparisons of observations to estimates from simulation and MODIS LST data assimilation from May 21 to May 30, 2009

4 CONCLUSIONS

In this paper, we developed a land data assimilation system to improve the predictions of soil surface temperature, sensible and latent heat fluxes. Different data sources (MODIS LST and sensible heat flux data from LAS) were assimilated into the Common Land Model using the ensemble kalman filter technique. Two assimilation experiments were used to evaluate the performance of the system. The estimations of energy partitioning and ground

temperature after assimilation were compared to the model simulation results.

The accuracy of the predicted ground temperature, latent and sensible heat flux with assimilation showed different variations. Except for the prediction of latent heat flux, the assimilation results of sensible heat flux and ground temperature were both obviously improved than the simulations whatever types of data sources were used. In general, assimilating remotely sensed data and LAS data into land surface model is a practical way to improve the

land surface process forecast. Furthermore, integrating multi-source data (LAS, remote sensing and ground experiments) simultaneously into the land surface model may produce better results.

5 ACKNOWLEDGMENT

This work was partly supported by the National Natural Science Foundation of China under Grant 40871169 and by the State Key Laboratory of Resource and Environment Information System under Grant 088RA400SA.

6 REFERENCES

approaches, *Irrigation and Drainage Systems*, **19**, 223-249.

Dai, Y., Zeng, X., and Dickinson, R. E., cited 2001, The Common Land Model: Documentation and user's guide. [Available online at <http://climate.eas.gatech.edu/dai/clmdoc.pdf>.]

Evensen, G., 1994, Sequential data assimilation with a non-linear quasi-geostrophic model using Monte Carlo methods to forecast error statistics, *Journal of Geophysical Research*, **99**, 10143-10162.

Evensen, G., 2003, The Ensemble Kalman Filter: theoretical formulation and practical implementation, *Ocean Dynamics*, **53**, 343-367.

Li, X., Huang, C., Che, T., et al., 2007, Development of a Chinese land data assimilation system: its progress and prospects, *Progress in Natural Science*, **17**, 881-892.

Li, Z., Tang, R., Wan, Z., Bi, Y., et al., 2009, A Review of Current Methodologies for Regional Evapotranspiration Estimation from Remotely Sensed Data. *Sensors*, **9**, 3801-3853.

Kumar, S. V., Reichle, R. H., Peters-Lidard, C. D., et al., 2008, A Land Surface Data Assimilation Framework using the Land Information System: Description and Applications, *Advances in water resources*, **31**, 1419-1432.

Pauwels, V. R. N., Verhoest, N. E. C., De Lannoy, G. J., et al., 2007, Optimization of a coupled hydrology-

Boni, G., Entekhabi, D., Castelli, F., 2001, Land Data Assimilation with Satellite Measurements for The Estimation of Surface Energy Balance Components and Surface Control on Evaporation, *Water Resources Research*, **37**, 1713-1722.

Caparrini, F., Castelli, F., Entekhabi, D., 2004, Estimation of Surface Turbulent Fluxes through Assimilation of Radiometric Surface Temperature Sequences, *Journal of Hydrometeorology*, **5**, 145-159.

Courault, D., Seguin, B. and Olioso, A., 2005, Review on estimation of evapotranspiration from remote sensing data: From empirical to numerical modeling crop growth model through the assimilation of observed soil moisture and LAI values using an Ensemble Kalman Filter, *Water Resources Research*, **43**, W04421, doi:10.1029/2006WR004942.

Pipunic, R. C., Walker, J. P. and Western, A., 2008, Assimilation of remotely sensed data for improved latent and sensible heat flux prediction: A comparative synthetic study, *Remote Sensing of Environment*, **112**, 1295-1305.

Pitman, A. J., 2003, The evolution of, and revolution in, land surface schemes designed for climate models, *International journal of climatology*, **23**, 479-510.

Reichle, R. H., Walker, J. P., Koster, R. D. and Houser, P. R., 2002, Extended versus Ensemble Kalman Filtering for Land Data Assimilation, *Journal of Hydrometeorology*, **3**, 728-740.

Wan, Z., Zhang, Y., Zhang, Q., & Li, Z. -L., 2004, Quality assessment and validation of the MODIS global land-surface temperature. *International Journal of Remote Sensing*, **25**, 261-274.

Williams, M., Richardson, A. D., Reichstein, M., Stoy, P. C., et al. 2009, Improving land surface models with FLUXNET data, *Biogeosciences Discussion*, **6**, 2785-2835.

Xu, T., Liu S., Qin, J., Liang, S., 2009, Estimation of sensible and latent heat flux by assimilating MODIS LST products, *Journal of Remote Sensing*, **13**, 989-998.

Analysis of temperature maps of water bodies obtained from ASTER TIR images

Francesca Despini^{a*}, Sergio Teggi^a

^a *Department of Mechanical and Civil Engineering, University of Modena and Reggio Emilia.*

*francesca.despini@unimore.it,

ABSTRACT *The ASTER sensor is, currently, the main radiometer that acquires information in the Thermal Infrared (TIR) region with a spatial resolution of 90 m. The purpose of this work is to develop a working methodology for the analysis of water temperature obtained from ASTER images. Images were initially processed with an algorithm that improves spatial resolution from 90 m to 30 m using information drawn from the Visible-Near infrared (VNIR) ASTER bands. Then data were analyzed and classified with an object-oriented approach. Specific procedures were developed in order to automate the monitoring process and to better interpret and display water temperature of the analyzed images. The studies were performed both on images at 90 m and at 30 m (computed with the algorithm for improving the spatial resolution). In this way it was possible to test the effectiveness and validity of the algorithm. For example, watercourses in the image at 90 m were barely visible while in the image at 30 m can be easily analyzed.*

This study is not concluded: the procedures will be soon applied to a wider range of case studies. Thus it will be possible to verify the versatility of the procedures themselves, and the advantages from the use of the algorithm for improving the spatial resolution.

1 INTRODUCTION

Localized increases in temperature in water bodies, such as lakes, rivers and seas, may have significant adverse effects on the ecosystem of the water body itself. Thermal pollution of water has in fact a double effect, being able to influence life in water bodies either directly, by varying the temperature, and indirectly going to affect a number of parameters, including density, salinity, degree of oxygenation, which in turn affect the existing ecosystem.

Spaceborne and airborne remote sensing is a very useful tool for the thermal mapping of coastal waters and rivers. Many sensors acquire information in the thermal infrared bands in order to obtain the surface temperature. Current satellite sensors are: MODIS, with 16 bands in the TIR with a spatial resolution of 1 km, AVHRR, with 2 bands in the TIR with a spatial resolution of 1 km, ATSR, with three bands in the TIR with a spatial resolution of 1 km, ASTER, with 5 bands in TIR with a spatial resolution of 90 m.

The main limiting factor of these sensors is the spatial resolution. In fact, if the spatial resolution is greater than 100 meters, the sensors are not useful for the detection and characterization of thermal plume caused by human activities in coastal areas or along river stretches. Regarding the sensors with spatial resolutions of less than 100 m, different applications can be found in the literature [Kay et al., 2005], [Ritchie et al., 2003], [Wu et al., 2007].

Today, the satellite sensor with the best spatial resolution is ASTER (Advanced Spaceborne Thermal Emission and Reflection Radiometer), which is located on the polar satellite *Terra*. This sensor has 14 spectral bands, 5 in the VNIR and 9 in the TIR. The spatial resolution of the VNIR bands varies between 15 m and 30 m, while in the TIR bands, as mentioned above, is 90 m [NASA, 2004].

The use of ASTER images brings considerable advantages because of the low cost of data, but would not allow a detailed mapping of coastal areas and water bodies since the resolution is still too low. It has therefore been developed within the Faculty of Engineering of the University of Modena, an algorithm That improve spatial resolution from 90 m to 30 m using information from the ASTER VNIR bands [Teggi, In press].

The main purpose of this work is a detailed thermal map of temperature, for the monitoring of industrial discharges to ensure compliance with the limits imposed by Italian law (D. Lgs. 152, 2006, Part III Annex 5).

Another objective is to test the effectiveness and validity of the algorithm applied to images.

2 METHODOLOGY

2.1 Data set

Two images were analyzed in this study. The first image is from the Venice Lagoon. It has been acquired

the 5 September 2007 from the ASTER sensor. This image include also the industrial area of Porto Marghera. The second image is from the Delta of the river Po. It has been acquired the 22 August 2008 from the ASTER sensor. The main branch of the Po has a width varying from 200 m to 600 m, while the main branches forming the delta of the river down even a few tens of meters.

These images have allowed us to study both the plume temperature both the rivers and channels, thus representing a good starting point for the analysis of the thermal pollution but also for testing the validity of the algorithm.

2.2 Pre-processing

The image was initially processed by an algorithm that improve spatial resolution in the ASTER TIR bands from 90 to 30 meters, using information from the Visible-Near Infrared (VNIR) ASTER bands. This algorithm has been developed starting from the TsHARP algorithm proposed by Agam et al. [2007], which is applicable to soils. Our algorithm is applicable to “coastal” pixels of the image acquired by ASTER in the TIR bands. A TIR pixel is classified as “coastal” (the adjective “coastal” is probably used improperly) if the sub-pixels, with a size of 30 m that compose it, are partially on water and partially on land. The algorithm is based on two assumptions:

- a) Hp1: There is a good degree of correlation between the radiance emitted in the TIR by the pixels of the image with a set of variables obtainable from ASTER VIS-NIR images at spatial resolutions of 15 m or 30 m;
- b) Hp2: The correlation assumed in Hp1 is invariant to small changes of scale, such as for the ratio 3:1 (e.g. 90 m: 30 m).

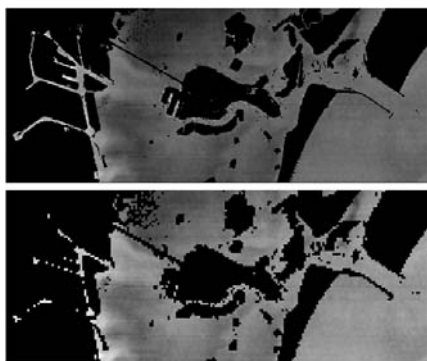


Figure 1- Venice image divided into water and not-water at 30 m (above) and 90 m (below)

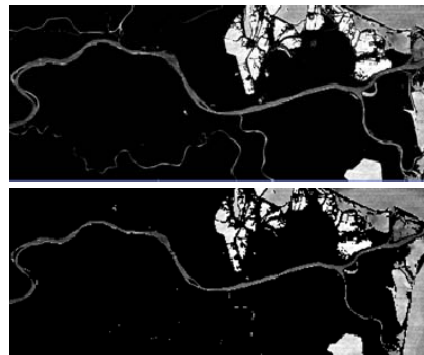


Figure 2- Po River image divided into water and not-water at 30 m (above) and 90 m (below)

This algorithm is still experimental. The detailed explanation of the algorithm, which also includes the validation of results, is beyond the purpose of this work and can be found in the work of Teggi [In Press].

2.3 Elaborations

The plume of water temperature were studied for both images in order to test the validity of the algorithm. Also for both images were then studied river stretches for the extraction of temperature profiles. In this way it could verify compliance with legal limits.

Temperature measurement was provided by MAV (Magistrato delle Acque di Venezia) for the image of Venice. These measures have helped to make a first validation of the data. Regarding the image of the Po delta we have no data on the ground. But the location of industrial plants have been checked to see if it corresponded to a rise in temperature.

2.3.1 Water Temperature

For both images (the Venice Lagoon and the Po Delta) very similar procedures were used. To observe the trend of the temperature of water bodies throughout the area, the images were segmented and classified into temperature using the software Definiens Developer 7.0. This procedure was repeated for both spatial resolutions, 30 and 90 m in order to highlight the differences and advantages of using the algorithm. Figure 3 shows the image of the Venice Lagoon classified with a spatial resolution of 30 m and 90 m.

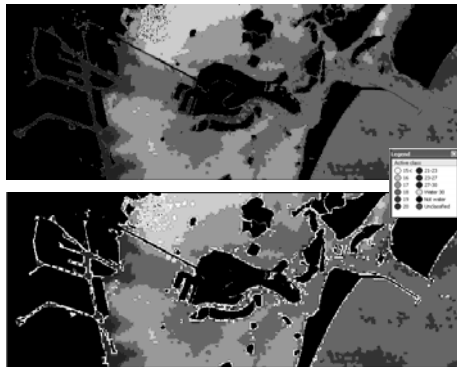


Figure 3-Venice image classified at 30 m (above) and 90 m (below)

Table 1 shows the areas (km²) of the main classes identified. The class "Water 30" is very important. In fact, it contains those pixels and those objects that in the image with spatial resolution of 90m would be classified as soil, while the image at 30m are classified as water. In Figure 3 these items are highlighted in white. Along the coast the application of the algorithm can effectively improve the image classification.

Table 1- Main classes identified on the Venice image

Class	Area (km ²)	
	30 m	90m
Water	78.5835	78.5835
Water at 30 m (but not at 90 m)	0	8.9496
Not water	5.3721	5.3676
Unclassified	52.1694	52.1739
Total area	136.125	136.125

Thanks to point measurements provided by the MAV it was possible to make a validation of satellite data. Figure 4 shows the location of measuring stations on land.



Figure 4- Ground measurements of the Venice Lagoon(MAV)

In Table 2 we see the comparison between the temperature measured on the ground and by satellite. The measures are not equal because the satellite measures the temperature of water film while the ground thermometer is placed a few centimeters below the surface. But they have the same trend, and this is

really important. In this way it is possible to detect temperature trends from satellite, and then to monitor the critical points with ground measurements.

Table 2-Satellite and ground measurements

ID	ASTER image				Ground Data
	Min Temp (°C)	Max Temp (°C)	Mean Temp (°C)	Std. Dev.	Temp (°C)
Ve-1	17.57	17.86	17.76	0.10	21.17
Ve-2	15.96	16.21	16.11	0.08	18.72
Ve-4	17.90	18.09	17.99	0.07	20.92
Ve-5	19.99	20.78	20.40	0.23	23.05

For the image of Po have been applied the same procedures as the image of the Venice lagoon (obviously with different segmentation parameters). The color white highlights what at 90 m is identified as "not-water" while at 30 m is "water" (Figure 5).

Figure 5- PoDelta image classified at 30 m (above) and 90 m (below)

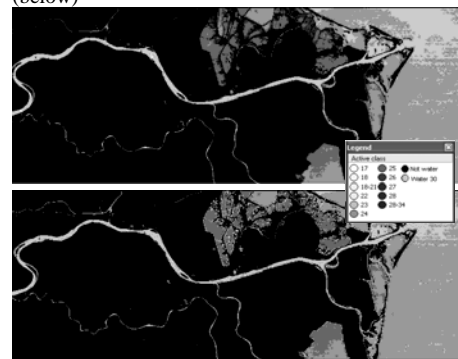


Table 3 shows areas of different classes. The secondary river branches are not identified in the image at 90m.

Table 3- Main classes identified on the Po image

Class	Area (km ²)	
	30 m	90m
Water	229.4289	205.3674
Water at 30 m (but not at 90 m)	0	24.0615
Not water	519.1812	519.1812
Total area	748.6101	748.6101

2.3.2 Canals

Channels and river stretches were analyzed in both images.

Regarding Venice were taken into account the channels of the industrial area of Porto Marghera. The channel is divided into sections normal to the axis (Figure 6) , thus it is possible to calculate the average

temperature of these sections. The image at 90 m does not allow the study of channels.

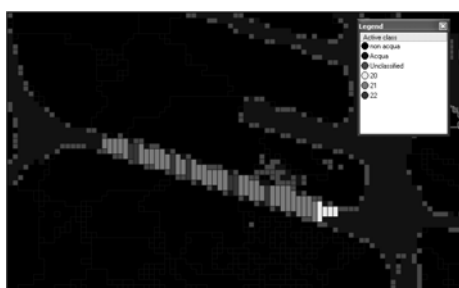


Figure 6- Segmentation and classification of a channel of Porto Marghera

It was thus possible to extract the temperature profile along the channel (Figure 7) and some statistical parameters (Table 4) calculated in sections. Note from Table 4 that the maximum temperature in the sections is less than the legal limit of 30 °C.

Table 4- Statistical parameters calculated on the axis of the channel

Mean Temp (°C)	Std Dev. Temp	Min Temp (°C)	Max Temp (°C)
21.10	0.38	19.89	21.72

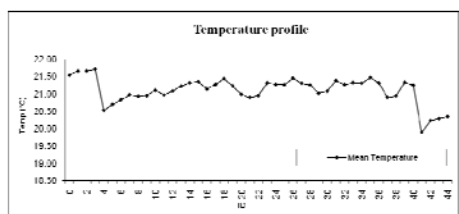


Figure 7- Temperature profile along the axis of the channel

Regarding the Po image, we studied in detail the river branches that had the higher temperatures. The river has been segmented into sections normal to the axis as required by Italian law (Figure 8).

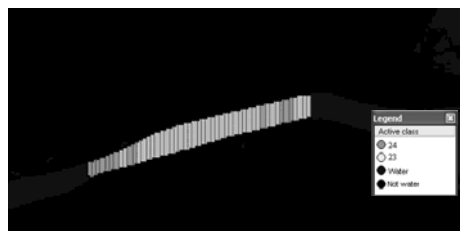


Figure 8- Segmentation and classification of a branch of the river Po

In Table 5 we show some statistical parameters calculated in order to verify compliance with the legal limits. In Figure 9 we see the temperature profile along

the axis or the river. The limit value of 30°C for the max temperature is respected.

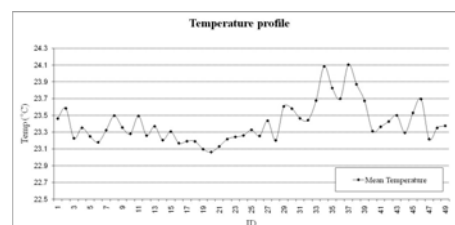


Figure 9- Temperature profile along the axis of the channel

Table 5- Statistical parameters calculated on the axis of the channel

Mean Temp (°C)	Std. Dev. Temp	Min Temp (°C)	Max Temp (°C)
23.41	0.23	23.06	24.11

3 CONCLUSIONS AND FUTURE DEVELOPMENTS

Automated procedures (easy to apply) have been developed to study the temperature of water bodies. Using this procedures, statistical parameters and graphs are extracted easily to verify compliance with the legal limits. Furthermore with maps of temperature, industrial discharges can be identified (especially in channels).

It has been tested the effectiveness and validity of the algorithm. It greatly improves the image particularly in rivers and along the coast.

A critical aspect is the lack of ground truth data in the Po image: it has however been requested, thus as soon as possible we will proceed to the comparison.

The procedures will be soon applied to a wider range of images: the purpose is to study the effectiveness of the algorithm in the analysis of rivers of various widths [Cherkauer *et al*, 2005]

4 ACKNOWLEDGEMENT

We would like to thank the Ministero delle Infrastrutture e dei Trasporti – Magistrato delle Acque di Venezia – through its dealer Consorzio Venezia Nuova.

5 REFERENCES

- N. Agam, W. P. Kustas, M.C. Anderson, F. Li and C.M.U. Neale. A vegetation index based technique for spatial sharpening of thermal imagery. *Remote Sensing of Environment*, 107(4):545-558, 2007.
- K. A. Cherkauer, S. J. Burges, R. N. Handcock, J. E. Kay, S. K. Kampf, and A. R. Gillespie. Assessing

- satellite-based and aircraft-based thermal infrared remote sensing for monitoring pacific northwest river temperature. *Journal of the American Water Resources Association*, 41(5):1149-1159, 2005.
- J. E. Kay, S. K. Kampf, R. N. Handcock, K. A. Cherkauer, A. R. Gillespie, and S. J. Burges. Accuracy of lake and stream temperatures estimated from thermal infrared images. *Journal of the American Water Resources Association*, 41(5):1161-1175, 2005.
- J. C. Ritchie, P. V. Zimba, and J. H. Everitt. Remote sensing techniques to assess water quality. *Photogrammetric Engineering and Remote Sensing*, 69(6):695-704, 2003.
- NASA (2004). ASTER (Advanced Spaceborne Thermal emission and Reflection Radiometer). URL:<http://asterweb.jpl.nasa.gov>, last visited 01/09/10, 2004.
- S. Teggi. Temperature of coastal waters and of watercourses from ASTER images. *Italian Journal of Remote Sensing*, In Press.
- C. Wu, Q. Wang, Z. Yang, and W. Wang. Monitoring heated water pollution of the dayawan nuclear power plant using tm images. *International Journal of Remote Sensing*, 28(5):885-890, 2007.

Retrieving crop specific green area index from remote sensing data when the spatial resolution is close to the target field size

Grégory Duveiller¹, Marie Weiss², Frédéric Baret², Allard de Wit³ and Pierre Defourny¹

¹ *Earth and Life Institute, Université catholique de Louvain (UCL), Louvain-la-Neuve, Belgium.*

² *Environnement Méditerranéen et Modélisation des Agro-Hydrosystèmes (EMMAH), INRA-UMR 1114, Avignon, France.*

³ *Centre for Geo-Information of Alterra (Alterra-CGI), Wageningen UR, Wageningen, The Netherlands.*

gregory.duveiller@uclouvain.be

ABSTRACT – Remote sensing observations can be used to estimate biophysical variables, such as the Green Area Index (GAI), which is a key variable in the photosynthetic processes of the canopy. For crop growth monitoring, high observation frequency is mandatory, especially when anomalies due to climatic variability must be detected. Wide geographic coverage is a further requisite to monitor specific crops at regional/continental scales. Nowadays, the instruments satisfying these requirements have coarse spatial resolutions for which crop specific GAI retrieval approaches have proven difficult to apply due to the fragmented land cover of many parts of the world. This paper demonstrates how it is possible to characterize the regional crop specific GAI dynamics using MODIS imagery by controlling the degree at which the observation footprints of the coarse pixels fall within the crop-specific mask delineating the target. This control is done by filtering out less reliable GAI estimations in both the spatial and temporal dimensions using thresholds on 3 proxy variables: pixel purity, observation coverage and view zenith angle. The discrepancies in results between using MODIS or SPOT/HRV 20m imagery to estimate the median GAI of winter wheat all along growing over a 40 by 40 km study region can be reduced to an RMSE of 0.055 by choosing adequate thresholds.

1 INTRODUCTION

The surface of green foliage is the main interface between atmosphere and vegetation, thereby governing the exchanges of energy, water and carbon. The total green leaf surface of a canopy is often quantified by a dimensionless variable called Leaf Area Index (LAI). LAI is defined as half the total developed area of green leaves per unit of ground horizontal surface area (Chen & Black 1992). This biophysical variable relates both to the structure and the functioning of a vegetation canopy, reason why it can be found as a state variable within crop growth models. Providing LAI estimation along the growing season at relevant spatial and temporal resolutions can assist and potentially improve modelling approaches by either forcing the model or by controlling its temporal trajectory using assimilation techniques (Dorigo et al. 2007, Moulin et al. 1998). Note that for cereal crops, photosynthesis is not limited to the leaves, and therefore it is more appropriate to use the term of Green Area Index (GAI) instead of LAI. Due its synoptic spatial coverage, much expectation is given to GAI estimations from satellite remote sensing to improve land surface modelling over large

geographic extents. However, satellite remote sensing is intrinsically confronted to a trade-off between spatial, temporal, spectral and radiometric resolution. The high observation frequency necessary to detect anomalies due to climatic variability comes to the expense of coarser observation supports, which in turn results in measuring a signal originating from a larger and potentially more heterogeneous area. Although technological improvements are bound to provide finer spatial resolution data with more frequent revisit times, coarse instruments will retain a valuable interest since they provide a long time record. Medium or moderate spatial resolution instruments, best represented by MERIS on-board of ENVISAT and MODIS on-board of Terra and Aqua platforms, offer an interesting combination of spatial and spectral resolutions with high repetitivity, but their spatial resolutions (pixel size ranging from 250 to 300m) is still of the same order of magnitude as the size of the crop fields in many agricultural landscapes around the world (Duveiller & Defourny 2010).

Methods to tackle this problem of monitoring heterogeneous landscapes include downscaling coarse spatial resolution time series using unmixing-based data fusion (Zurita-Milla et al. 2009) or using

geostatistics to correct the scaling bias induced by the landscape fragmentation (Garrigues et al. 2006). However, a simpler approach which is less prone to modelling errors is to concentrate the attention to a selection of pixels whose observational footprint falls within the target crop specific fields. A common misconception is that the observational footprint is the geometric projection of a rectangular pixel onto the Earth's surface (Cracknell 1998). The footprint rather depends on the instrument's point spread function (PSF), which describes how the electromagnetic radiation coming from a point source is spread over the image plane as it is recorded by an imaging instrument. By modelling the PSF and convolving it over a crop specific mask, Duveiller & Defourny (2010) derived pixel purity, a variable defining the proportion of signal encoded in a pixel which originates from the target crop, and which can assist in selecting pixels with high support-target adequacy. However, the task is compounded when attempting to use MODIS imagery due to the complexity of its observation support: (i) it is twice as large across track than along track; (ii) it varies along the swath within a single image; and (iii) it varies from image to image. The reasons for this complexity involve the whiskbroom scanning configuration of MODIS combined with specific gridding artefacts (Tan et al. 2006, Wolfe et al. 1998). Some observation geometry variables, such as the View Zenith Angle (VZA) or the observational coverage (*obsco*), can provide information on the target-pixel adequacy. The objective of this study is to see how GAI estimations from MODIS imagery can be improved by screening estimations in both space and time according to 3 proxy variables: pixel purity, observation coverage and view zenith angle. By doing so, we hope to characterize the GAI dynamic for a specific crop, winter wheat, at a regional scale.

2 STUDY SITE AND DATA

The study site is a 40 by 40 km area located in the Danube Plain, centred on Fundulea (Romania, around 44.41°N, 26.58°E). This agricultural landscape is dominated relatively large fields (15 to 40 ha) of winter cereals (wheat and barley) alternating with summer crops (such as maize and sunflower). In 2001, the study site was intensely revisited by SPOT satellites (20m spatial resolution) thanks to the ADAM project (all data is available at <http://kalideos.cnes.fr/>). The time series of images captures radiance in the green, red, near-infrared domain (NIR) and sometimes the shortwave infrared wavelengths (SWIR) domain. The images have been accurately calibrated both radiometrically and geometrically by CNES (Centre National d'Etudes Spatiales, Toulouse, France). Top-of-canopy (TOC) reflectance was obtained after

applying atmospheric correction using the SMAC model (Rahman & Dedieu 1994) with aerosol characteristics measured with an automated sun-photometer on the ground. For the present experiment, a subset of 16 images were selected which were acquired between DoY (day-of-year) 60 and DoY 180, i.e. during the winter wheat growing season. For this same time frame, daily MODIS data was downloaded from the NASA Distributed Active Archive Center (DAAC) (<https://wist.echo.nasa.gov/api/>). MOD09 collection 5 products are used, for which atmospherically corrected reflectance is available at 250m in the red and near-infrared spectral domains. Information of VZA and *obsco* were also obtained in the same grid.

3 METHODOLOGY

3.1 Neural network RTM inversion

GAI is retrieved from multispectral reflectance using neural network techniques (NNT) trained over canopy radiative transfer simulations. This hybrid approach combines advantages of statistical and physical approaches in biophysical variable retrieval (Dorigo et al. 2007). The approach is based on the algorithm conceived by Baret et al. (2007) to derive the global LAI product developed within the CYCLOPES (Carbon cYcle and Change in Land Observational Products from an Ensemble of Satellites) project from SPOT/VEGETATION data. The radiative transfer model used for the simulations is PROSAIL (Baret et al. 1992), a coupling of the canopy reflectance model SAIL (Verhoef 1984) to the leaf optical properties model PROSPECT (Jacquemoud & Baret 1990). Back-propagation neural networks with two hidden layers of respectively 5 and 1 neurons are employed. The required input values are VZA, the sun zenith angle, the relative azimuth angle and the top of canopy reflectance in the different bands (2 for MODIS and 3 or 4 for SPOT depending on the availability of the SWIR band).

3.2 Modelling the spatial response of MODIS

The net spatial response of an imaging instrument can be modelled by taking into account its different components: the electronic PSF, the detector PSF, the image motion PSF and the optical PSF (Schowengerdt 2007). For the MODIS PSF model used in this paper, the electronic components is neglected the sake of simplicity. The detector is modelled by a uniform square pulse function. While the along-track image motion can be disregarded for MODIS, the across-track must be taken into account since the integration time corresponding to image motion as the rotating mirror scans the Earth is nearly a whole detector width (Schowengerdt 2007). The detector and image motion

PSFs can be combined into a scan PSF which is modelled as triangular PSF in the along-scan direction and as a rectangular PSF in the along-track direction. Finally, the optical component is assumed to have a Gaussian behaviour. The net PSF is a convolution of all components as resumed by the following equation:

$$PSF_{net} = PSF_{det} * PSF_{IM} * PSF_{opt} \quad (1)$$

PSF_{net} must further be rotated according to the angle between the ground track of the satellite and the north-south direction since this angle varies according to the mean latitude of the observed area.

3.3 Matching SPOT and MODIS GAI

In order to compare the GAI obtained from MODIS to the GAI obtained from SPOT, the latter product has to be upscaled using the MODIS spatial response model. The change in support is realized by applying a bi-dimensional convolution of the spatial response model over the target GAI map obtained from a SPOT image:

$$GAI_S^*(x,y) = GAI_S(x,y) * PSF_{net} \quad (2)$$

The resulting image $GAI_S^*(x,y)$ is a grid with the same extent and pixel size as the original GAI map $GAI_S(x,y)$. Every (x,y) pixel of $GAI_S^*(x,y)$ indicates the GAI that can be expected when estimated with a MODIS observation support whose centroid falls at that (x,y) coordinate. This operation can also be applied to crop the crop specific mask to result in a crop specific pixel purity map. This map indicates the purity of MODIS observations with respect to our target crop: winter wheat. The geolocation position of MODIS pixels is used to retrieve the corresponding pixel purity. All pixels having crop specific pixel purity below 75% are screened out. For the remaining ones, the GAI values from each of the 16 GAI_S^* convolved maps is extracted and concatenated to form an ensemble of time series which will be denoted TS_{sim} . These time series simulate the MODIS GAI product if its original observations were all acquired at nadir. A second ensemble of time series, TS_{obs} , simply consists of the MODIS GAI estimations obtained from authentic MODIS observations obtained with variable acquisition conditions (i.e. VZA and *obscov*).

3.4 Matching SPOT and MODIS GAI in time

For proper comparison, it is not only necessary to match GAI estimations in space but also in time. To do so, either set of time series (TS_{obs} or TS_{sim}) is temporally interpolated semi-mechanistic canopy structure dynamic model (CSDM). Such model relates

GAI to thermal time by way of a simple mathematical relationship representing the combined effect of growth and senescence, taking the form of:

$$GAI(tt) = k \cdot [1 / (1 + \exp(-a(tt - T_0 - T_a)))^c - \exp(b(tt - T_0 - T_b))] \quad (3)$$

where a and b define the rates of growth and senescence, c is a parameter allowing some plasticity to the shape of the curve, k is a scaling coefficient and T_0 , T_a and T_b are the thermal times of plant emergence, mid-growth and mid-senescence. The driving variable, thermal time (tt) or cumulated growing degree-days, is calculated in the following way:

$$tt = 0.5(T_{min} - T_{max}) - T_{base} \quad (4)$$

based on the daily minimum (T_{min}) and maximum (T_{max}) air temperatures recorded at the Fundulea meteorological station. T_{base} is the temperature below which the process of interest, in this case winter wheat growth, does not progress. The base temperature used here for winter wheat is 0°C and the starting date for the temperature sum is October 1, 2000.

4 RESULTS

4.1 Selecting according to VZA and *obscov*

To analyse the impact of the VZA and *obscov* variables on the quality of the GAI estimates within TS_{obs} , these will be compared to the temporal estimation of TS_{sim} . For increasing thresholds of *obscov* and decreasing thresholds of VZA, selections of fewer, but presumably more reliable estimations are made. For each selection of points, the relative root means square error (RRMSE) is calculated on the discrepancies. The result can be visualized in 2 dimensions to see the combined effect of thresholds on both VZA and *obscov* (see figure 1). The graph of RRMSE reveals that desirable points do not need to satisfy simultaneously the conditions for the two variables. In other words, if an observation has a favourable *obscov*, it can have an unfavourable VZA (and *vice versa*) and remain reliable. To illustrate the potential improvement that can be achieved by taking into account *obscov* and VZA, the dataset Z , consisting of all individual GAI estimations in TS_{obs} is stratified into different groups for which the concurrent TS_{obs} and TS_{sim} are compared. The groups are based on a single threshold for each variable, defined so that if taken by itself, at least 30% of the points remain. This yields a maximum acceptable VZA of 24° and a minimum acceptable *obscov* of 0.36. Figure 2 shows

how retaining the union of both constraints significantly filters out sub-optimal estimations.

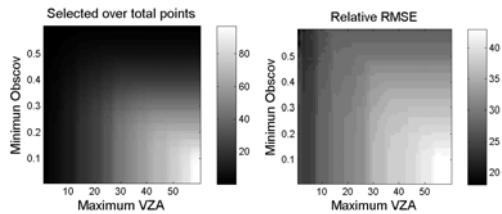


Figure 1. Effect of thresholds in VZA and *obskov* on the percentage of retained estimation (left) and the RRMSE in percent (right).

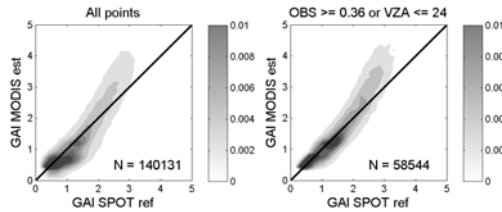


Figure 2. Contour plots of the 2-D distribution for all points (left) and for the points selected based on VZA and *obskov* thresholds.

Table 1. Comparison of the GAI temporal consistency achieved with different subset of points. The last column of the table indicates the mean number of sample points per time series. *Union* and *intersection* subset refer to the way the VZA and *obskov* constraints are combined. *Random* is a subset of randomly selected points with the same number of sample points per time series as *Union*.

Cases	RMSE	RRMSE	Mean N
<i>All points</i>	0.514	30.9%	30.3
<i>Union</i>	0.433	23.6%	13.2
<i>Intersection</i>	0.413	22.4%	7.1
<i>Random</i>	0.504	30.6%	13.2

To test if the thresholding on *obskov* and VZA improves the temporal consistency of MODIS estimates, the CSDM is fitted for all available time series using all available points (i.e. without any restrictions on either VZA or *obskov*). This temporally-smoothed GAI estimation is used as a reference, to which different sets of punctual GAI estimations are compared. The results in table 1 confirm that filtering MODIS estimations by either satisfying an *obskov* or a VZA criteria improves the temporal consistency as shown by the reduction of RRMSE. This is not merely an effect of sample number reduction as when a random sample set of

equal size is used (*Random*), the statistical indicators remain comparable to when all points are used. Furthermore, the comparison between the subsets *union* and *intersection* shows that although the temporal consistency is slightly improved for the latter, it comes at the expense of a serious reduction of observations per time series.

4.2 Validation with unconvolved GAI maps

The last question that must be addressed is how well do the MODIS GAI estimations in TS_{obs} relate to the unconvolved GAI maps, and whether they can characterize the regional GAI dynamic. Hereafter, only the temporally smoothed profile based on *Union* are used on the MODIS side. These are first compared to the punctual SPOT upscaled GAI estimations and the a series of statistical indicators (RMSE, RRMSE, the bias, the standard deviation around the bias (S) and the mean absolute error (MAE)) are displayed in figure 3. As expected, the performance is related to the date of acquisition: GAI is harder to estimate when it reaches its peak value (i.e. on DoY 123). However, the bias between MODIS and SPOT fluctuates along the season revealing shortcomings of the GAI SPOT estimation. This bias effect penalizes the performance indicated by the RMSE, and even more so for the relative RMSE (e.g. DoY = 76). However, the dispersion of the estimation characterized by CV remains relatively stable all along the season suggesting that the overall performance of the MODIS GAI is stable.

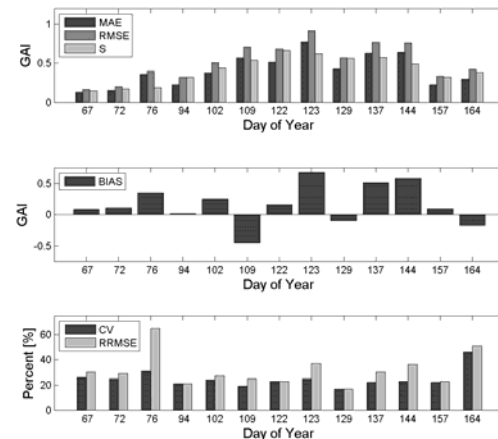


Figure 3. Statistical indicators comparing the performance of temporally smoothed MODIS GAI estimations against corresponding SPOT GAI estimations.



Figure 4. Visual assessment of the spatial correlation between the high spatial resolution GAI maps and the GAI estimations from MODIS for DoY: 94, 123 and 144 (from left to right). All GAI values use the same colour scale the goes from dark purple (GAI=0) to dark green (GAI=6) passing by a range of yellows. The images in the background are the respective Red channel of the original SPOT imagery used to derive the GAI maps.

The ensemble TS_{obs} is then compared to the distribution of all points in the fine spatial resolution GAI map falling in the winter wheat mask over the study area. Since the objective here is to assess the performance of the GAI obtained from MODIS, and not SPOT, the bias for each SPOT image is removed from the entire GAI map prior to estimating the regional dynamic. A visual assessment of the spatial correlation between the MODIS punctual GAI estimations and the corrected SPOT GAI maps is presented in figure 4. It reveals that the MODIS estimations not only grasp the inter-field dynamics reasonably well, but they can also characterize more subtle intra-field spatial differences over the larger fields. Figure 5 summarizes the comparison at regional level by showing the boxplots of the SPOT GAI distributions overlayed over the ensemble of MODIS time series.

5 DISCUSSION AND CONCLUSIONS

This paper demonstrates that crop specific GAI estimations retrieved from medium spatial resolution imagery such as MODIS are adequate to characterize crop dynamics at a regional scale. To achieve this, it is necessary to control the degree at which the observation footprints of the coarse pixels fall within the crop-specific mask delineating the target. This control is done by filtering out less reliable GAI estimations in both the spatial and temporal dimensions using thresholds on pixel purity, *obsco* and VZA. The difference in performance between MODIS and fine spatial resolution to estimate the median GAI over the 40 by 40 km study region can be

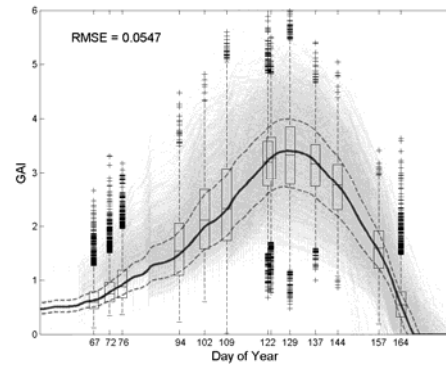


Figure 5. Boxplots of the SPOT GAI distributions overlayed over the ensemble of MODIS time series. The solid line depicts the median value of MODIS time series, while the dashed lines represent the inter-quartile range (to be compared with the boxes)

reduced to an RMSE of 0.055 by selecting appropriate filtering thresholds. The experiment has also demonstrated the possibility to retrieve coherent GAI estimates from different data with different scales using the same technique involving radiative transfer modelling and neural networks. Some shortcomings of the retrieval do exist, as revealed by the variable bias between high and medium spatial resolution estimates at the different studied dates. However, these deviations can be corrected in a fine example of instrument complementarity whereby the high temporal resolution assures the general GAI trajectory and the high spatial resolution can be used to estimate the local spatial heterogeneity.

6 ACKNOWLEDGEMENTS

This research was funded by the Belgian *Fond de la Recherche Scientifique-FNRS* by way of a PhD grant to the first author. The research also falls in the framework of the GLOBAM project which is financed by the Belgian Scientific Policy (BELSPO) with the STEREO II programme. The data used in this paper are part of the ADAM database made available by Kalideos (<http://kalideos.cnes.fr>) and the SPOT imagery have the following copyright: CNES 2001 - Distribution Spot Image.

7 REFERENCES

- Baret, F., Hagolle, O., Geiger, B., Bicheron, P., Miras, B., Huc, M., Berthelot, B., Nino, F., Weiss, M., Samain, O., Roujean, J. L. & Leroy, M. (2007), 'Lai, fapar and fcover cyclopes global products derived from vegetation: Part 1: Principles of the algorithm', *Remote Sensing of Environment* **110**(3), 275–286.
- Baret, F., Jacquemoud, S., Guyot, G. & Leprieux, C. (1992), 'Modeled analysis of the biophysical nature of spectral shifts and comparison with information-content of broad bands', *Remote Sensing of Environment* **41**(2-3), 133–142.
- Chen, J. M. & Black, T. A. (1992), 'Defining leaf area index for non-flat leaves', *Plant, Cell and Environment* **15**(4), 421–429.
- Cracknell, A. (1998), 'Synergy in remote sensing—what's in a pixel?', *International Journal of Remote Sensing* **19**(11), 2025–2047.
- Dorigo, W., Zurita-Milla, R., de Wit, A., Brazile, J., Singh, R. & Schaepman, M. (2007), 'A review on reflective remote sensing and data assimilation techniques for enhanced agroecosystem modeling', *International Journal of Applied Earth Observation and Geoinformation* **9**, 165–193.
- Duveiller, G. & Defourny, P. (2010), 'A conceptual framework to define the spatial resolution requirements for agricultural monitoring using remote sensing', *Remote Sensing of Environment* **114**(11), 2637–2650.
- Garrigues, S., Allard, D., Baret, F. & Weiss, M. (2006), 'Influence of landscape spatial heterogeneity on the non-linear estimation of leaf area index from moderate spatial resolution remote sensing data', *Remote Sensing of Environment* **105**(4), 286–298.
- Jacquemoud, S. & Baret, F. (1990), 'Prospect: A model of leaf optical properties spectra', *Remote Sensing of Environment* **34**(2), 75–91.
- Moulin, S., Bondeau, A. & Delecalle, R. (1998), 'Combining agricultural crop models and satellite observations: from field to regional scales', *International Journal of Remote Sensing* **19**(6), 1021–1036.
- Rahman, H. & Dedieu, G. (1994), 'Smac: a simplified method for the atmospheric correction of satellite measurements in the solar spectrum', *International Journal of Remote Sensing* **15**(1), 123–143.
- Schowengerdt (2007), *Remote sensing: models and methods for image processing*, 3rd edn, San Diego: Academic Press.
- Tan, B., Woodcock, C., Hu, J., Zhang, P., Ozdogan, M., Huang, D., Yang, W., Knyazikhin, Y. & Myneni, R. (2006), 'The impact of gridding artifacts on the local spatial properties of modis data: Implications for validation, compositing, and band-to-band registration across resolutions', *Remote Sensing of Environment* **105**(2), 98–114.
- Verhoef, W. (1984), 'Light scattering by leaf layers with application to canopy reflectance modeling: The sail model', *Remote Sensing of Environment* **16**(2), 125–141.
- Wolfe, R. E., Roy, D. P. & Vermote, E. (1998), 'Modis land data storage, gridding, and compositing methodology: Level 2 grid', *IEEE Transactions on Geoscience and Remote Sensing* **36**, 1324–1338.
- Zurita-Milla, R., Kaiser, G., Clevers, J., Schneider, W. & Schaepman, M. (2009), 'Downscaling time series of meris full resolution data to monitor vegetation seasonal dynamics', *Remote Sensing of Environment* **113**(9), 1874–1885.

Land surface heterogeneity and appropriate spatial resolution of remote sensing imagery

Chuanrong Li¹, Xinhong Wang^{1,*}, Lingling Ma¹, Shi Qiu²

1. Academy of Opto-Electronics, Chinese Academy of Sciences, Beijing, China

2. Laboratoire des Sciences de l'Image, de l'Informatique et de la Télédétection (UMR7005), Boulevard Sébastien Brant, BP10413, 67412 Illkirch, France

* Email: wangxinhong111@yahoo.com.cn

ABSTRACT - With the rapid development of remote sensing hardware technologies, earth observing images can be acquired in increasingly high spatial resolution. The pursuing on high resolution has become the most general expectation in the RS field. However, in order to meet the various demands of remote sensing applications, it is still worth being discussed that whether higher resolution is necessarily better. Actually, the spatial resolution should be carefully chosen according to application demands, for optimizing the balance of effectiveness and cost. In this paper the concept of "appropriate spatial resolution" is used, which should be the spatial scale with least data volume and most interested information, while not the highest precision of information. Characterization of spatial heterogeneity is the basis of analyzing spatial structure of the image under the given spatial resolution, and it is also the basis of selection of appropriate spatial resolution. For the characterization of spatial heterogeneity, the method of wavelet variance is introduced in the paper. Based on the wavelet variance method, appropriate spatial resolutions of albedo, NDVI and surface radiative temperature on the same research area are given. Results show that appropriate spatial resolutions to various retrieved physical properties are different due to different grades of spatial heterogeneity. Appropriate resolution for one quantity is probably not the appropriate resolution for another quantity. However, each geographic quantity generally has its intrinsic spatial scale feature. Proper scale range will be obtained to observe certain geographic quantity, by operation of the appropriate resolution selection.

1 INTRODUCTION

With the rapid development of remote sensing (RS) technology, RS images now can be acquired in various spatial resolutions ranging from meters to kilometers. Development of high resolution earth observation technology and its applications are getting more and more concerned by not only engineers or scientists, but also government officials. It is no doubt that high spatial resolution stands for fine detecting capability. For detailed information about land surface can be obtained, it extends RS applications to urban planning field, military reconnaissance field, etc, and greatly promotes the commercialization of earth observation technology.

However, excessively pursuing high spatial resolution may bring about some negative effects, such as increasing cost, poor spectral resolution, narrow swath and low time resolution. So, higher resolution is not necessarily better. For example, meteorological satellites are still very actively contributing to not only large scale applications, but also local RS applications, particularly in quantitative RS application field. In fact, remote sensing data in different spatial resolutions can provide multiple scaling descriptions

on surface characteristics of the Earth. When observing an interested surface feature, the viewing scale should not be too large or too small.

Then, what is the standard to choose a proper spatial resolution? In ideal state, the spatial resolution containing major information of interested objectives and deriving least data volume should be chosen, which is called "appropriate spatial resolution" (Atkinson et al, 1997). It doesn't mean the highest spatial resolution which can be found in those images covering the research area, but means the possibly largest resolution in condition of guaranteeing the primary spatial structure of the original image would be well preserved. From the perspective of quantitative RS, the appropriate resolution may be that just match the requirements of dedicated applications. Furthermore "appropriate resolution" should be a complicated function of physical variable, application type, study field, accuracy requirement, etc.

Land surface comprises elements of different natures, different aspects or different characteristics, and the characterization of these elements is not a simple thing. Heterogeneity is highly related with length of physical variable, so it could reflect the requirement of spatial resolution. Kolasa et al (1991) ever defined spatial heterogeneity through two

components: (1) The spatial variability of the surface property over the observed scene. (2) The spatial structures, also called objects or patches. They repeat themselves independently within the observed scene at a characteristic length scale (i.e. spatial scale) which represents the spatial structure extent. They can be viewed as the typical correlation area (i.e. the typical area of influence) of the surface property. Data are often distributed into independent sets of spatial structures, related to different length scales and spatial variability, being overlaid in the same region.

There has been a lot of work on the characterization of the spatial heterogeneity. Based on statistics (Ramstein et al, 1989), the concept of length scale was put forward, which is a good indicator for the spatial characterization of texture and structure through measuring the heterogeneity of land surface. Several methods have been developed to calculate length scale, including local variance (Woodcock et al, 1987), variogram (Woodcock et al, 1988a, 1988b; Garrigues et al, 2006), Fourier transform (Cosh et al, 2003) and wavelet transform (Pelgrum et al, 2000a, 2000b). The characterization of finite length scale requires a second order stationarity assumption except for wavelet transform method. Therefore wavelet analysis is the only method able to detect and properly quantify local spatial variations in the image since all of other methods rely on some stationarity hypothesis.

This paper will use wavelet analysis method to derive the length scale of land surface properties, so as to characterize the spatial heterogeneity of land surface with remote sensing data, and then the appropriate spatial resolution will be obtained. In section 2, the wavelet variance is defined to describe the spatial heterogeneity characteristics of land surface. A TM image data used in this study are described in section 3. In section 4, a series of wavelet variances is calculated based on aggregated images of different scale levels, and then they are applied in the analysis of length scale and appropriate spatial resolution. And some conclusions are drawn in section 5.

2 METHODOLOGY

2.1 Haar wavelet transform

Wavelet analysis is a tool of time-frequency analysis after Fourier analysis. Both transforms decompose data into frequencies. The Fourier transform can tell which frequencies are present in the signal but is unable to distinguish at which location a change in frequency takes place in the data. While the wavelet transform can give information on the amount of variability present at different scales. In the field of image processing, its applications have covered imaging technique, image pre-processing, image compression and transferring, image registration,

image analysis, feature extraction and pattern classification, etc.

The Haar wavelet is the first well-known wavelet which was proposed by Alfred Haar (Haar, 1910). The Haar basis is the simplest wavelet basis, which expression is as following:

$$w(l, x) \cong \frac{1}{l} \int n' H(x+z) R(z) dz \quad (1)$$

Here, l is the scaling length.

Pelgrum had carried out a test with length scales for different types of wavelets and found the Haar wavelet can produce the best results in determining the dominant length scales of an image. With a procedure of nonstandard decomposition (Stollnitz et al, 1995), the fast Haar wavelet transform can be applied to a 2-D image. After one turn of this procedure, the result is an image with four different sections: three of them are horizontal, vertical and diagonal wavelet coefficients respectively; the other one is scaling function coefficients. The next step is to apply the same procedure to the section with the scaling function coefficients until the whole image is decomposed into wavelet coefficients.

2.2 Wavelet variance and dominant length scale

Wavelet variance is a natural tool for investigating the spatial scales of variability based on wavelet transform, which gives information on the amount of variability present at different scales.

The wavelet variance $\hat{\sigma}_{f,j}^2$ is defined as:

$$\hat{\sigma}_{f,j}^2 = \frac{1}{N} \sum_{p=1}^{n_j} d_j[p]^2 \quad (2)$$

Where $\hat{\sigma}_{f,j}^2$ is the wavelet variance of data set f at scale j , and $d_j[p]$ is the wavelet coefficient at position p and scale level j . N is the number of elements in the total data set. The number of data points at scale level j is given by $n_j = N/2^j$.

The dominant length scale l_{dom} is defined as the scale for which the maximum wavelet variance is met.

2.3 Selection for appropriate spatial resolution

The standard of appropriate spatial resolution should be found upon the "length scale" which characterizes quantified feature of the surface heterogeneity. That is to say the pixel size used in observation should meet the demand of characterizing the typical length scale on the research area. Dominant length scale describes the size of dominating objects in the image. When the spatial resolution of the image is far smaller than the size of primary objects in the image, there will be strong spatial dependence between two neighbouring

pixels. As the distance of pixels increases, spatial dependence between the pixels will decrease accordingly. While the distance of pixels increases to be larger than the size of primary objects in the scene, the pixels would be consider as locating in different objects, and spatial dependence between them no longer exists. The variability of image will not be decreased even if distance between pixels continues to increases. So the dominant length scale l_{dom} can be considered as the pixel distance capable of departing data relativity.

The Shannon sampling theorem has pointed out that the proper sampling frequency of a signal must be at least twice the maximal frequency of this signal, so that the signal been sampled can be perfectly reconstructed from the samples. To retain primary spatial variety information as to certain surface feature, the spatial sampling frequency should be at least $2/l_{dom}$, and the proper pixel size should be no larger than $l_{dom}/2$, according to the Shannon sampling theorem.

3 DATA DESCRIPTION

In this paper we used a TM image required on July 6 2004, over Beijing and its outskirt. The dimension of the image is 1024 pixels by 1024 lines. Several important surface characteristic parameters were retrieved, such as surface albedo, NDVI, and surface radiative temperature, as illustrated in Fig.1. Equation (3) to (5) give the retrieving algorithms for these surface parameters. Here ρ_2 , ρ_3 , ρ_4 , ρ_5 are surface reflectance of the green, red, near infrared, shortwave infrared band, respectively. And R_6 for surface temperature retrieval is the at-satellite apparent radiance of the thermal infrared band.

$$albedo = 0.3512 \cdot \rho_2 + 0.1629 \cdot \rho_3 + 0.3415 \cdot \rho_4 + 0.1651 \cdot \rho_5 \quad (3)$$

$$NDVI = \frac{\rho_4 - \rho_3}{\rho_4 + \rho_3} \quad (4)$$

$$Ts = \frac{1260.56}{\ln(60.776/R_6 + 1)} \quad (5)$$

In the following, spatial heterogeneities of the three surface parameters will be analyzed. Some assumptions are taken for simplification in the experiments: 1) The size of image is large enough relative to the spatial feature of interest; 2) The radiometric measurement errors (due to atmospheric effect, etc.) in the remote sensing observation can be omitted, relative to the variance of surface heterogeneity; 3) The Point Spread Function (PSF) is

neglected; 4) Assuming the surface albedo, NDVI, and surface temperature images shown in Fig.1 can be considered as true value images.

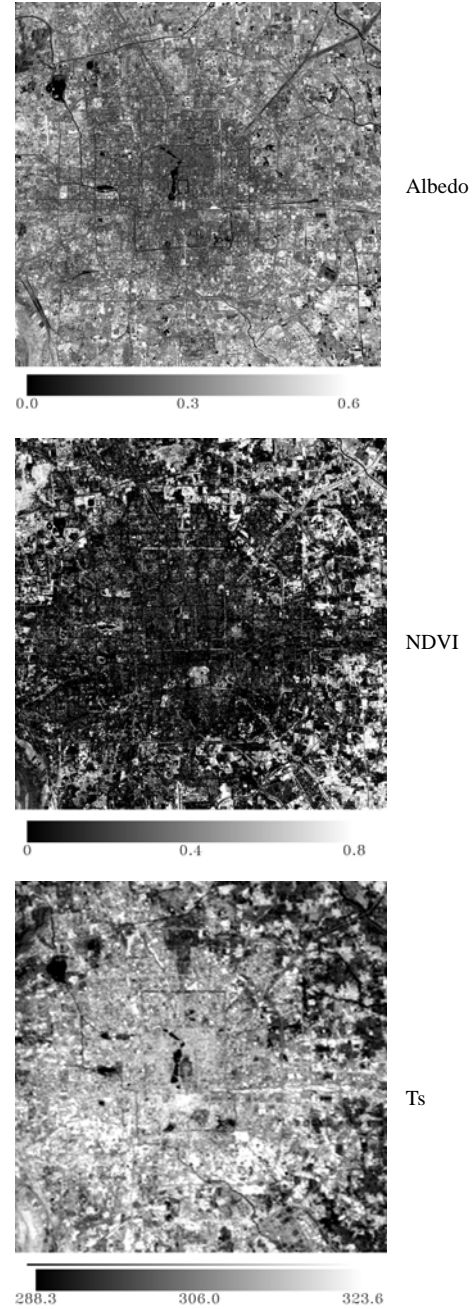


Fig.1 Several land surface parameters retrieved from the TM image

4 RESULTS

If the resolution of original image is s , and its size is $h \times h$, the highest aggregation level n will be: $n = \log_2 h$. The steps of wavelet variance analysis are as following:

(1) Calculate the proportion of the wavelet variance of each aggregation level i on the total wavelet variance, i.e. $p_i (i=1, \dots, n)$. (2) Assuming maximum of wavelet variance appears at aggregation level m , then the dominant length scale $l_{dom} = s \cdot 2^m$. (3) The percentage of spatial variability which can be obtained on the

aggregation level k will be: $\sum_{i=k}^n p_i$. (4) Then the

percentage of spatial variability which can be obtained at the dominant length scale is $\sum_{i=m}^n p_i$, which is

referred to as the wavelet variance percentage explained by $l \geq l_{dom}$. (5) Selection of the appropriate length scale l_{app} . If the wavelet variance percentage explained by $l \geq l_{dom}$ is not less than some endurable threshold (85% for example), the dominant length scale can be considered as the appropriate length scale. If the wavelet variance percentage explained by $l \geq l_{dom}$ is less than some endurable threshold, the dominant length scale will be abandoned, and the largest length scale which satisfies the endurable threshold can instead act as the appropriate length scale. (6) Determine the appropriate spatial resolution according to the appropriate length scale and Shannon sampling theorem. One half of the appropriate length scale will be considered as the appropriate spatial resolution.

The wavelet variance percentages under multiple scale levels were calculated and shown in Fig.2. The wavelet variance curve of surface albedo resembles that of NDVI, and the dominant length scales of them are both at 120 m. However, the dominant length scale of surface temperature appears at 960 m. This distinction indicates that spatial heterogeneities of surface albedo and NDVI are much more obvious than that of surface temperature. This result is in accordance with the common senses of surface albedo and NDVI, that they are both close related to the complicated surface conditions.

Table 1 lists the dominant length scale l_{dom} , 85% wavelet variance interpretable length scale $l_{85\%}$, and $l \geq l_{dom}$ interpretable wavelet variance, for each interested surface feature. The dominant length scale of radiative temperature is 960 m, which can only interpret 71.1% of the wavelet variance. It implies that only 71.1% of spatial variability information can be obtained, and 28.9% of the variability information will be lost, if using a thermal infrared band image with a 960 m spatial resolution. As can be seen that the

dominant length scale l_{dom} may not be effective enough to determine the appropriate spatial resolution, for it can not interpret enough wavelet variance. Under this circumstance, we can use the length scale which may interpret more than specified proportion (85% for example) of the wavelet variance, to determine the appropriate length scale.

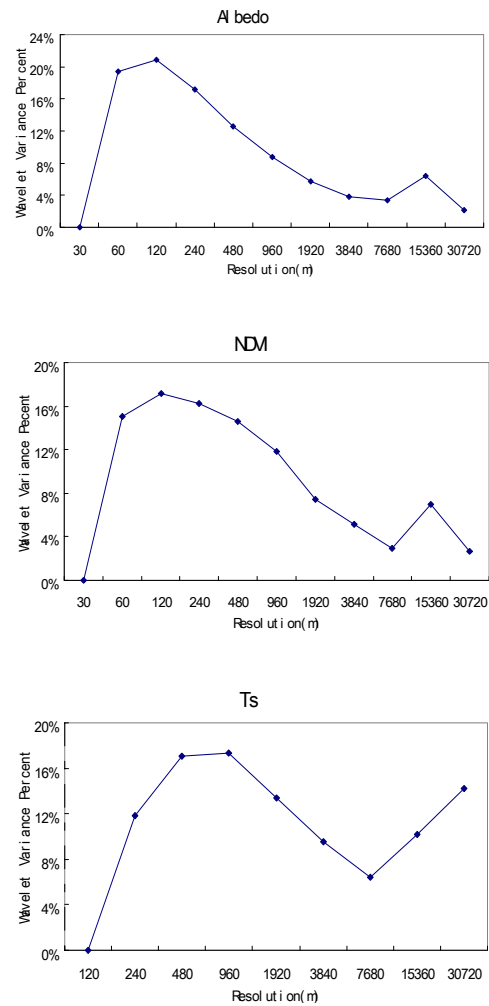


Fig.2 The wavelet variances of surface parameters as a function of spatial resolution

Nyquist – Shannon sampling theorem is used to acquire the appropriate spatial resolution as one half of the appropriate length scale. Table 2 lists the results of appropriate spatial resolution selection, for each surface parameter, based on the wavelet analysis method. The last column of the table gives spatial heterogeneity which can be preserved under the appropriate spatial resolution. As can be seen on the table, if the interested parameter is albedo, spatial

resolution of 30 m can act as an appropriate choice, in which 100% spatial variability of the original image's albedo can be captured. Similarly, 60 m resolution, 85.1% spatial variability for NDVI, and 240 m

resolution, 88.2% spatial variability for radiative temperature, respectively.

Table 1. Wavelet analysis results of surface parameters

Surface parameter	$l_{85\%}$ (m)	l_{dom} (m)	Wavelet variance percentage explained by $l \geq l_{dom}$
Albedo	60	120	80.8%
NDVI	120	120	85.1%
Ts	480	960	71.1%

Table 2. Results of appropriate resolution selection based on the wavelet analysis method

Surface parameter	Appropriate resolution (m)	Variability interpretable at appropriate resolution
Albedo	30	100%
NDVI	60	85.1%
Ts	240	88.2%

5 CONCLUSION

This work showed that wavelet transform is a useful tool to describe characteristics and quantify the spatial heterogeneity of land surface at different resolution levels. Some main viewpoints are as following:

(1) The wavelet analysis method for selecting appropriate spatial resolution has two objectives: the primary objects in the original image can be correctly identified in the appropriate resolution, and loss of spatial variability limits within certain endurable extent.

(2) Selection for appropriate resolution changes with the specific physical quantity being studied. Appropriate resolution for one quantity is probably not the appropriate resolution for another quantity. Different quantities may show various dominant spatial structures.

So when geographic model involving several different quantities is concerned, the unique appropriate resolution is usually very hard to determine. However, each geographic entity has its intrinsic spatial feature. Proper scale range will be obtained to observe certain geographic entity, by operation of the appropriate resolution selection.

6 REFERENCES

Atkinson P. M., and Curran, P. J, 1997, Choosing an appropriate spatial resolution for remote sensing

investigations. *Photogrammetric Engineering and Remote Sensing*, 63(12), pp. 1345-1351.

Cosh, M. H., and Brutsaert, W., 2003, Microscale structural aspects of vegetation density variability. *Journal of Hydrology*, 276(1-4), pp. 128-136.

Garrigues, S., Allard, D., Baret, F., and Weiss. M., 2006, Quantifying spatial heterogeneity at the landscape scale using variogram models. *Remote Sensing of Environment*, 103(1), pp. 81-96.

Haar, A., 1910, Zur Theorie der orthogonalen funktionensysteme. *Mathematische Annalen*, 69(3), pp. 331-371.

Kolasa, J., and Rollo, C., 1991, The heterogeneity of heterogeneity. In *Ecological heterogeneity*, edited by J. Kolasa & S. T. A. Pickett (New York: Springer Verlag), pp. 1-23.

Pelgrum, H., 2000, Spatial Aggregation of Land Surface Characteristic: impact of resolution of remote sensing data on land surface modelling. PhD thesis, Wageningen University, Netherlands. 2000.

Pelgrum, H., Schmugge, T., Rango, A., Ritchie, J., and Kustas, B., 2000, Length-scale analysis of surface albedo, temperature, and normalized difference vegetation index in desert grassland. *Water Resources Research*, 36(7), pp. 1757-1765.

- Ramstein, G., and Raffy, M., 1989, Analysis of the structure of radiometric remotely-sensed images. *International Journal of Remote Sensing*, 10(6), pp. 1049-1073.
- Stollnitz, E. J., DeRose, A. D., and Salesin, D. H., 1995, Wavelets for computer graphics: A primer, part 1. *IEEE Computer Graphics and Applications*, 15(3), pp. 76-84.
- Woodcock, C. E., and Strahler, A. H., 1987, The factor of scale in remote sensing. *Remote Sensing of Environment*, 21(3), pp. 311-332.
- Woodcock, C. E., Strahler, A. H., and Jupp, D. L. B., 1988, The use of variograms in remote sensing: I. Scene models and simulated images. *Remote Sensing of Environment*, 25(3), pp. 323-348.
- Woodcock, C. E., Strahler, A. H., and Jupp, D. L. B., 1988, The use of variograms in remote sensing: II. Real digital images. *Remote Sensing of Environment*, 25(3), pp. 349-379.

The effect of spatial resolution in remote sensing of water stress using optical and thermal imagery

Lola Suárez^{1,2}, Pablo J. Zarco-Tejada¹, José A. J. Berni¹, Victoria González-Dugo¹, Elias Fereres¹, David Goldhamer³

¹*Instituto de Agricultura Sostenible (IAS). Consejo Superior de Investigaciones científicas (CSIC), Córdoba, Spain*

²*Remote Sensing Laboratories (RSL), Dept. of Geography, University of Zurich, Switzerland.*

³*University of California Kearney Agricultural Center (KAC). Parlier, CA (USA)*
lsuarez@geo.uzh.ch

ABSTRACT- *Water stress detection at early stages in tablegrapes is critical to avoid negative effects on yield or quality parameters. Thermal information has been related to water stress since the late 70s. However, thermal imagery is not available at very high spatial resolution for an accurate assessment of vegetation water stress. On the contrary, there is more availability of VIS-NIR imagery at high spatial resolution. In this study, thermal imagery and the PRI optical index are used to assess water stress at high and medium spatial resolutions in a heterogeneous canopy such as a grapevine crop. The influence of the soil component within the mixed pixel is studied for both temperature and PRI. RowMCRM and DART models were used to assess the effect of soil and row orientation on PRI and temperature demonstrating water stress detection is only possible when taking into account such background and structural effects.*

1 OBJECTIVES

The objectives of this study are:

- Water stress detection in vineyards using multispectral and thermal imagery.
- Use of radiative transfer modeling to assess the influence of soil type and row orientation on PRI and temperature retrieved from imagery.

2 MATERIALS AND METHODS

2.1 Study site

The study was conducted in an experimental vineyard (cv. Thompson Seedless) located at the Kearney Agricultural Centre from the University of California. Vines were grown in a trellis system. In summer 2009 three different irrigation treatments were applied in blocks of 6-9 lines of vines: a) Sustained deficit irrigation treatment, applied to three blocks (total of 21 lines); b) Intermediate deficit irrigation, applied on three blocks (22 lines) and consisting of withholding the irrigation the two weeks prior imagery acquisition; and c) fully irrigated treatment, meeting maximum ETc. la ET del lisimetro era diferente, era un parral.

2.2 Multispectral and thermal imagery

Diurnal thermal and multispectral airborne imagery were acquired over the vineyard field in the University of California Kearney Agricultural Centre in the

summer of 2009. The multispectral camera, consisted on six independent sensors with wavelength filters at 530, 550, 570, 670, 700 and 800 nm, was calibrated in the laboratory using an integrating sphere. Atmospheric correction was performed using MODTRAN RTM code using as input data acquired in the field with a sun photometer. Spectral Information for each independent block was extracted selecting pure vegetation pixels. As a second approach, the information was extracted using rectangles comprising vegetation, soil and shadows to simulate the spectra that would be obtained from medium resolution imagery. The spectra extracted from the images were used to compute the Photochemical Reflectance Index (PRI), presented by Gamon et al. (1992) as an indicator of photosynthetic processes and light use efficiency (1). The PRI has been used as a water stress indicator in previous studies conducted on continuous (Suárez et al, 2009) and discontinuous crops (Suárez et al., 2008, 2009, 2010).

$$PRI = (R_{570} - R_{530}) / (R_{570} + R_{530}) \quad (1)$$

Where R530 and R570 are the reflectance at 530 and 570 nm respectively.

The thermal camera had an internal radiometric calibration and atmospheric calibration was conducted using a pixel-based thermal path calculation with MODTRAN RTM as explained in Berni et al (2009). As with the multispectral imagery, canopy temperature

was extracted from the image by both selecting pure vegetation pixels for each treatment and blocks comprising vegetation, sunlit and shadowed soil pixels.

2.3 Field data

At the time of the flight overpass, stem water potential, stomatal conductance and leaf PRI were measured in the field. Irrigation treatments applied lead to within-field water stress variability with leaf water potential measured ranging from -1.2 to -0.3 MPa.

2.4 Radiative Transfer Modeling

RowMCRM (Kuusk, 1995) and DART (Gastellu-Etchegory et al., 1996) radiative transfer models were used to study the effect of soil type and row orientation in the relation between high and medium spatial-resolutions for PRI and temperature. The models were used to simulate the experiment at the time of the imagery acquisition and the same scene for 3 different types of soil and 3 extra row orientations. Figure 1 shows the simulations conducted for the real orientation and for a turn of 30, 60 and 90° clockwise, leading to different shadow fractional cover.

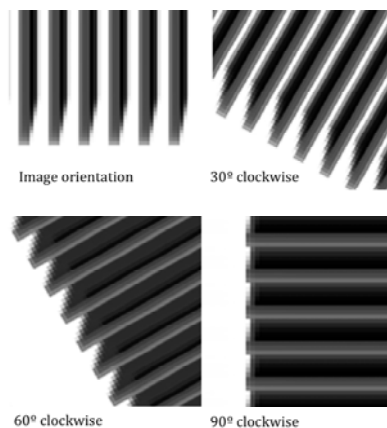


Figure 1. Simulations using DART KIM for 4 different row orientations.

3 RESULTS

3.1 Water stress detection

The relationships found for image-extracted canopy PRI and temperature with stomatal conductance and stem water potential are presented in Table 1.

Table 1. Coefficients of determination found between stem water potential (SWP) and stomatal conductance (G) and canopy PRI and temperature (K) extracted from high and medium spatial resolution imagery.

	High resolution		Medium resolution	
	PRI	T (K)	PRI	T (K)
SWP	0.46	0.86	0.50	0.66
G	0.59	0.67	0.44	0.80

3.2 Radiative Transfer Modeling

The RTM results show the effect of soil type and row orientation (Figures 2 and 3).

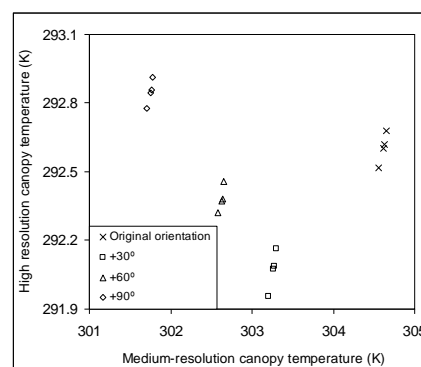


Figure 2. High versus medium resolution canopy temperature extracted from a total of 16 DART RTM simulations with 4 types of soil and 4 row orientations.

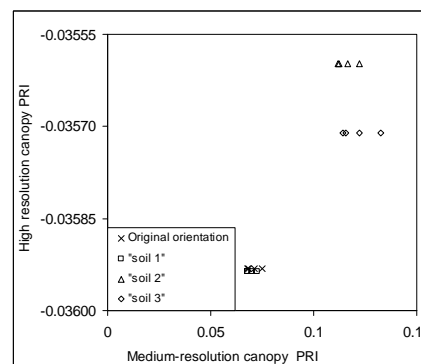


Figure 3. High versus medium resolution canopy PRI extracted from a total of 16 rowMCRM RTM simulations with 4 types of soil and 4 row orientations.

In figure 2 it can be seen how medium spatial-resolution canopy temperature is affected by the row orientation. Different row orientations brought about different percentage of shadow soil in the mixed pixel. Previous studies already show the influence of soil temperature on a mixed vegetation-soil pixel at different times of the day (Sepulcre-Cantó et al., 2006). In this case study, the relationships found for medium spatial-resolution temperature with water stress indicators are good (Table 1). Nevertheless, the fractional cover of shadowed soil is very low along the day because the rows are E-O orientated. For other orientations, the influence of soil on the mixed pixel

temperature is too high to detect small changes in canopy temperature. The results of modelling PRI for high and medium spatial-resolution show that, as temperature, the PRI computed from a mixed soil-shadow-vegetation pixel is highly affected by the soil type and fraction of shadows (Figure 3). It means that although similar coefficients of determination were found for high and medium PRI with water stress indicators, care has to be taken when having different soil types and row orientation.

4 CONCLUSIONS

Results show good relationships between water stress indicators measured in the field and PRI and canopy temperature at high and medium spatial resolutions. Nevertheless, modeling work demonstrated that the medium resolution signal is affected by soil type and row orientation. It appears that the use of temperature and PRI as indicators of vineyard water stress using medium spatial-resolution is possible for areas with homogeneous soil surface conditions and the same row orientation.

5 ACKNOWLEDGEMENTS

Financial support from the Spanish Ministry of Science and Innovation (MCI) for the projects AGL2005-04049, EXPLORA-INGENIO AGL2006-26038-E/AGR, CONSOLIDER CSD2006-67, and AGL2003 01468 is gratefully acknowledged and support provided by Bioiberica through the project PETRI PET2005-0616. Larry Williams from KAC (UC David) is acknowledged for the experiment setup and the measurements in the field. Technical support from UAV Navigation and Tetracam Inc is also acknowledged. A. Vera and D. Notario are acknowledged for measurements and technical support in the airborne campaigns.

6 REFERENCES

Berni, J.A.J., Zarco-Tejada, P.J., Suárez, L., Fereres, E. (2009). Thermal and narrow-band multispectral

remote sensing for vegetation monitoring from an Unmanned Aerial Vehicle. *IEEE Transactions on Geoscience and Remote Sensing*, 47 (3), 722-738.

Kuusk, A. (1995). A Markov chain model of canopy reflectance. *Agricultural and Forest Meteorology*, 76, 221-236.

Gamon, J.A., Peñuelas, J., Field, C.B. (1992). A narrow-wave band spectral index that tracks diurnal changes in photosynthetic efficiency. *Remote Sensing of Environment*, 41, 35-44.

Gastellu-Etchegory, J.P., Demarez, V., Pinel, V., Zagolsky, F. (1996). Modeling radiative transfer in heterogeneous 3D vegetation canopies. *Remote Sensing of Environment* 58, 131-156.

Sepulcre-Cantó, G., Zarco-Tejada, P.J., Jiménez-Muñoz, J.C., Sobrino, J.A., de Miguel, E., Villalobos, F.J. (2006). Detection of water stress in an olive orchard with thermal remote sensing imagery. *Agricultural and Forest Meteorology*, 136, 31-44.

Suárez L., Zarco-Tejada, P.J., Sepulcre-Cantó, G., Pérez-Priego, O., Miller, J.R., Jiménez-Muñoz, J.C., Sobrino, J. (2008). Assessing canopy PRI for water stress detection with diurnal airborne imagery. *Remote Sensing of Environment*, 112, 560-575.

Suárez, L., Zarco-Tejada, P.J., Berni, J.A.J., González-Dugo, V., Fereres, E. (2009). Modelling PRI for water stress detection using Radiative Transfer Models. *Remote sensing of Environment*, 113, 730-744

Suárez, L., Zarco-Tejada, P.J., González-Dugo, V., Berni, J.A.J., Sagardoy, R., Morales, F., Fereres, E. (2010). Detecting water stress effects on fruit quality in orchards with time-series PRI airborne imagery. *Remote Sensing of Environment*, 114, 1968-1986.

Spatial scaling in the remote sensing retrieval

Hua Wu¹, Bo-Hui Tang¹, Zhao-Liang Li^{1, 2,*}

1. State Key Laboratory of Resources and Environment Information System, Institute of Geographic Sciences and Natural Resources Research, CAS, Beijing, 100101, China

2. TRIO/LSIT, Bld Sebastien Brant, BP10413, 67412 Illkirch, France

lizl@igsnr.ac.cn

ABSTRACT - This paper makes an attempt to address the major scaling problems of Leaf Area Index (LAI) associated with (1) the nonlinearity in the relationships between remote sensing reflectances and the LAI products, (2) the discontinuity between contrasting cover types within a mixed pixel labelled by the dominant class and (3) only one algorithm for the dominant cover type being used. On the basis of the Taylor series expansion and following the general scaling procedure, it is demonstrated that the magnitude of the scaling effects for the nonlinearity and discontinuity situations can be expressed as a function of (1) the degree of nonlinearity quantified by its second derivative; (2) the spatial heterogeneity quantified by variances and covariance within the coarse resolution pixel; and (3) the fractions of subcomponent areas. Compared with the results before scaling, the proposed method can compensate for scaling effects due to the surface heterogeneity caused either by the density change within the same cover or by the type change between different covers. The result shows that the retrieval errors caused by scaling effects are greatly reduced, demonstrating that the proposed method is feasible and promising.

1 INTRODUCTION

Leaf Area Index (LAI) defined as the single-side leaf area per unit ground horizontal surface area can be used as an input for various land surface models such as vegetation, biogeochemical or global circulation models to provide detailed information about vegetation (Chen et al., 1997). Though it can be estimated by various retrieval model from remotely sensed data, there is a critical scaling problem in retrieval process. Generally speaking, most retrieval models and algorithms are basically derived at small scales, implying that the land surface is homogeneous. If the models and algorithms are used directly at large scales, they may cause the retrieval results unreliable (Hu and Islam, 1997; Raffy, 1992). For example, the relative scaling effect of LAI may even reach up to 50% if it is not corrected for (Chen, 1999). The application of the local-scale-validated retrieval model to the large scale data may induce a scaling effect when the model itself is nonlinear or the input parameters in a large scale pixel are heterogeneous. The scaling effect constrains the accuracy of retrieval and limits the development of remote sensing applications (Wu and Li, 2009). Thus, it becomes an emergency problem to be solved in quantitative remote sensing and attracts more and more attentions.

Raffy (1992) proposed a general method, the Computational Geometry Method (CGM), to reduce the scaling effects introduced by the heterogeneity of measurements and the nonlinearity of a retrieval model at a local scale. The method takes advantage of

the convex hull of computational geometry to determine the corrected products at large scale. Hu and Islam (1997) used textural parameters (e.g., variance and covariance) and proposed the Taylor Series Expansion Method (TSEM) to characterize the scaling effects based on the Taylor's theorem of linearizing the retrieval model around the arithmetic average of measurements. Chen (1999) proposed a different scheme, the Contextual Parameters Method (CPM) and took the contextual parameters (e.g., the fractions of subcomponents) as a bridge to quantify the scaling effects. Although these methods have already been developed, they can not reach a consensus. CGM concerns about the interval of the lower and upper bounds of the retrieval model and can not quantify the effect of the surface heterogeneity. TSEM takes into account the impact of heterogeneity within the same class and ignores the interaction between different classes. Meanwhile, CPM focuses on the effect of surface heterogeneity caused by contrasting classes on scale problem.

In order to fully demonstrate the influence of spatial heterogeneity and the model nonlinearity on the retrieval products of remote sensed data, this paper theoretically and practically analyzes the scaling problems relevant to LAI product. Section 2 is devoted to describe the scale problems due to the nonlinearity and discontinuity. On the basis of the Taylor series expansion, section 3 will propose a new scaling model to correct the scaling effects of LAI caused by the nonlinearity of the retrieval model in function of red and near infrared reflectances and the surface

heterogeneity caused either by the density change within the same cover or by the type change between different covers. Section 4 will briefly illustrate the semi-empirical LAI retrieval model and apply the proposed scaling model to multi-scale data. Finally, conclusions are given in section 5.

2 SCALING PROBLEMS DUE TO THE NONLINEARITY AND DISCONTINUITY

If LAI retrieval models validated at local scale are directly applied to large scale, what problems will be caused? Several researchers have already confirmed that the nonlinearity of remote sensing algorithm and the surface heterogeneity would result in the scaling effect problems of LAI retrieval (Hu and Islam, 1997; Garrigues et al., 2006). At the same time, the discontinuity caused either by the retrieval model itself or by the contrasting cover types would make the scale problems worse if retrieval models are various and only one model for the dominant cover type is used for a mixed pixel (Chen, 1999). To better understand such point of view, we provide figures 1 and 2 as examples to clearly show the scale problems due to the nonlinearity and discontinuity.

In figure 1, a simple case is presented where a mixed pixel is equally composed of one vegetation type with different NDVI and LAI (point A and B), and the nonlinear relationship between NDVI and LAI for spherical leaf angle distribution vegetation is assumed to be suitable for this vegetation type. Thus, the approximated LAI (point C) is estimated from the average value of NDVI of A and B and the nonlinear relationship, while the actual LAI (point D) is directly derived from the average value of LAI by its definition. Obviously, the point C and D do not converge at the same point. The difference of LAI value between C and D is due to the scaling effect caused mainly by the nonlinearity of LAI retrieval algorithm.

In figure 2, a complicated case is shown to reveal the problem of discontinuity. The mixed pixel is composed of two different vegetation types, A and B, while, vegetation A accounts for 40% and B 60%, respectively. However, they are assumed to be with different leaf angle distributions, erectophile and planophile, where horizontal leaves and vertical leaves are most frequent. Because of the discrepancy of physical properties of vegetation, the corresponding nonlinear relationship between NDVI and LAI is also different as it is shown in figure 2. The LAI retrieval model of planophile is chosen for the mixed pixel because of a larger proportion of vegetation fraction. Same as figure 1, the approximated LAI (point C) and actual LAI (point D) are estimated through the corresponding weighted average value, and the LAI scaling effect between C and D is caused by the discontinuity of LAI retrieval algorithm besides the

effect of the nonlinearity.

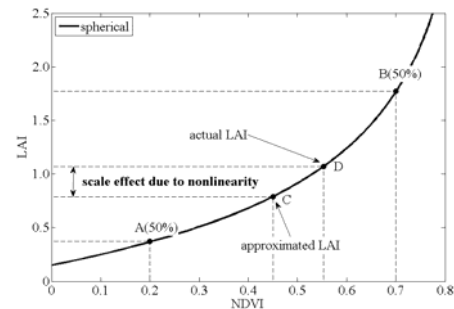


Figure 1. A nonlinear relationship between NDVI and LAI for vegetation with spherical leaf angle distribution. A mixed pixel is composed of the same vegetation type A(50%) and B(50%) with different NDVI values. The point C gives the approximated LAI using the average NDVI value for the mixed pixel and the nonlinear relationships, while the point D represents the actual LAI derived from the average value of LAI of point A and B. The difference between C and D is the scaling effect due to the nonlinearity of the retrieval algorithm.

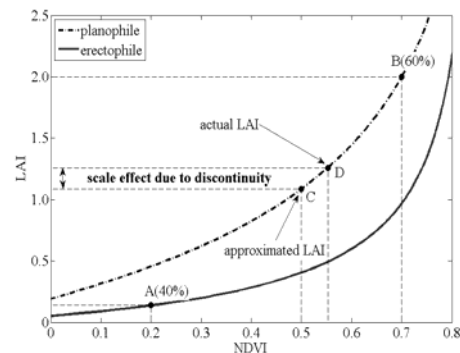


Figure 2. Relationships between NDVI and LAI for both planophile and erectophile leaf angle distribution vegetations. A mixed pixel is composed of 40% of vegetation type A (erectophile) and 60% of vegetation type B (planophile) with different NDVI values. The points C and D have the same meaning as figure 1. The difference between C and D is the scaling effect mainly due to the discontinuity of the retrieval algorithm.

Generally speaking, the case in figure 2 is more common, for example the forest and grass are mixed in one coarse resolution pixel. It is hard to imagine the LAI retrieval model of forest is also suitable for grass without any modification. Thus, these nonlinearity and discontinuity would make the scaling problem more complicated and need to be fully clarified.

3 SCALING EFFECTS AND SCALING MODEL

3.1 Scaling effects

Firstly, we need to assume that the local-scale-validated retrieval model is always valid whatever the distribution of vegetation within a large scale before

investigating the scaling effect.

By LAI definition, the exact value of LAI at large scale is the simple average of LAI at local scale within a coarse pixel and can be determined from the LAI derived from the fine resolution by:

$$LAI_{large}^{exa} = \frac{1}{N} \sum f_i(\rho_{local}^{red}, \rho_{local}^{nir}) \quad (1)$$

where N is the number of local resolution pixels within the corresponding large resolution pixel, f_i represents LAI retrieval model for vegetation type i at local scale.

As the semi-empirical LAI retrieval model at local scale, the approximated LAI at large scale can be estimated directly from the aggregated inputs according to the dominant vegetation using:

$$LAI_{large}^{app} = f_{dominant} \left(\frac{\sum \rho_{local}^{red}}{N}, \frac{\sum \rho_{local}^{nir}}{N} \right) \quad (2)$$

where $f_{dominant}$ represents LAI retrieval model for the dominant vegetation type within a mixed large scale pixel. Consequently, the scaling effect can be expressed as:

$$\delta_{scaling} = LAI_{large}^{exa} - LAI_{large}^{app} \quad (3)$$

Thus, the scaling effect of LAI described by equations (1)-(3) is owed to the nonlinearity of retrieval model, the discontinuity between contrasting cover types and the heterogeneity within one cover type. These three factors combined together determine the scaling effect.

The LAI retrieval product would be scale invariant when either the surface is homogeneous or the model is linear if the retrieval models for various vegetation types are the same. This inference has already reached a consensus by several authors (Raffy, 1992; Hu and Islam, 1997; Pelgrum et al., 2000). However, the situation becomes complicated when the retrieval models differ for different vegetation types. In such situations, linear model would also cause the scaling effect due to the fact that only one algorithm for the dominant cover type is used for a large pixel (Chen, 1999).

3.2 Scaling model

Taking sub-area of vegetation type components as weight, equation (1) can be rewritten as:

$$LAI_{large}^{exa} = \sum \omega_i LAI_i^{exa} \quad (4)$$

where ω_i is component fraction of vegetation type i and satisfies $\sum \omega_i = 1$. LAI_i^{exa} is the corresponding exact value of LAI for vegetation type i and have been

removed the scaling effect.

Hu and Islam (1997) considered the density change within the same cover and proposed a scale invariant algorithm to estimate the exact value of LAI. Assuming that reflectances vary slowly within a mixed large pixel, and the retrieval model f_i is continuous and weakly nonlinear and has continuous derivatives at least up to second orders in the interval under consideration, the exact LAI_i^{exa} at large scale can be estimated by a second order Taylor series expansion around the average vector of reflectances $\bar{\rho}_i$ of component i as:

$$\begin{aligned} LAI_i^{exa} &= f_i \left(\frac{\sum \rho_{local,i}^{red}}{N_i}, \frac{\sum \rho_{local,i}^{nir}}{N_i} \right) + \frac{1}{2} k_i V_i \\ &= f_i(\bar{\rho}_i) + \frac{1}{2} k_i V_i \end{aligned} \quad (5)$$

with

$$\begin{aligned} k_i &= \partial^2 f_i / \partial \rho^2 \Big|_{\bar{\rho}_i} \\ V_i &= \sum (\rho - \bar{\rho}_i)^2 / N_i \end{aligned} \quad (6)$$

where N_i is the number of pixels of vegetation type i within the large pixel, the term k_i is second derivative Hessian matrix and represents the effect of the nonlinearity of retrieval model, and the term V_i is the covariance matrix and reflects the heterogeneity of land surface within one vegetation type.

Consequently, the corrected LAI^{cor} at large scale can be estimated by combining equations (4)-(6) as:

$$LAI_{large}^{cor} = \sum \omega_i \left(f_i(\bar{\rho}_i) + \frac{1}{2} k_i V_i \right) \quad (7)$$

In equation (7), the scaling model combines the advantages of other models proposed by Hu and Islam(1997) and Chen(1999), and makes use of the variance, covariance and subcomponent fractions to quantify the scaling effect. Equation (7) can explain not only the heterogeneity caused by the density change within the same vegetation type, but also the heterogeneity in terms of vegetation type change. When a pixel is mixed with several vegetation types, the heterogeneity change because of the contrast between these vegetation types has a different meaning compared with the same change caused by the density within the same vegetation type. The density change for a linear retrieval algorithm will not cause scaling effect yet, while vegetation type change will do.

Because it is difficult to get the subpixel component information about the average value of reflectance, variance and covariance within a large pixel, they are replaced by the corresponding information at the large scale. Then, the scaling model for LAI can be expressed as:

$$LAI_{large}^{cor} = \sum \omega_i (f_i(\bar{\rho}) + \frac{1}{2} k_0 V_0) \quad (8)$$

where $\bar{\rho}_i$ is the average vector of reflectances within the mixed pixel and they can be estimated directly from data at large scale because of the scale invariant characteristic of reflectances (Liang et al., 2002). The term K_0 is second derivative around $\bar{\rho}_i$ and can be estimated mathematically. The term V_0 is variance (covariance) within the mixed pixel and can be estimated using the following method.

3.3 Quantification of spatial heterogeneity

In the previous sections, the scaling model has been proposed, however, it needs the spatial heterogeneity as input. The heterogeneity could be thought of as the inherent nature of land surfaces, which may be a mosaic of different cover types. It is often of great concern when deriving surface parameters using remotely sensed data. The term V_0 makes use of variance (covariance) to capture the spatial variability within a mixed pixel.

Pelgrum et al. (2000) used the wavelet variance calculated by the Haar wavelet transform as an indicator to quantify the spatial heterogeneity. The term V_0 can be estimated as:

$$V_0 = \sum_{j=1}^s \sigma_j^2 \quad (9)$$

where s is the scale level, σ_j is the wavelet variance of data set at scale j . Because this method needs the local scale data to estimate the wavelet coefficient, however, it is difficulty in obtaining both small scale and large scale remotely sensed data at the same time. Thus, Garrigues et al. (2006) further proposed a new method to estimate the spatial heterogeneity through several sample points based on the variogram. In such circumstances, the term V_0 approximately equals to the double integration of the variogram within the mixed pixel:

$$V_0 = \frac{1}{|A|^2} \int \int_A \gamma \|x - y\| dx dy \quad (10)$$

where $|A|$ is the area of pixel, γ is the variogram that could be estimated by sampling and provides the mean

characteristics of spatial heterogeneity at the image scale, and $\|x - y\|$ represents the distance between the points x and y of the pixel domain. Compared with wavelet variance method, the variogram method has probably fewer limits. The spatial heterogeneity can be estimated by several sample points.

4 APPLICATIONS

4.1 LAI retrieved model

To retrieve the LAI, a semi-empirical LAI retrieval model proposed by Baret and Guyot (1991) is used:

$$LAI = -\frac{1}{K_{NDVI}} \ln\left(\frac{NDVI - NDVI_{\infty}}{NDVI_s - NDVI_{\infty}}\right) \quad (11)$$

$$NDVI = \frac{\rho^{nir} - \rho^{red}}{\rho^{nir} + \rho^{red}}$$

where ρ^{red} and ρ^{nir} are red and near infrared reflectances, respectively, the extinction coefficient K_{NDVI} and the asymptotic value $NDVI_{\infty}$ are estimated by the combination of PROSPECT leaf optical properties model and SAIL canopy bidirectional reflectance model (Jacquemoud et al., 2009), and $NDVI_s$ is the soil NDVI value estimated from the ASTER spectral library.

For the purpose of simplicity, the scale effect of the nonlinearity and discontinuity on the LAI retrieval will be analyzed with the nonlinear relationship between NDVI and LAI of erectophile and planophile vegetation types in this paper. The corresponding biochemical and physical properties of vegetation, such as leaf structure parameter, chlorophyll content and others, are set based on some samples measured during the LOPEX'93 experiment.

4.2 Data

The data used here is extracted from high spatial resolution (10 m) SPOT-HRV scenes on June 2, 2004 in Beijing. The data is first classified based on ISODATA (Iterative Self-Organizing Data Analysis Technique) unsupervised classification to generate classification map of two supposed mixture vegetation. One stands for erectophile vegetation type and the other for planophile. The accuracy of the classification will not be discussed because it is just taken as a case study to analyze the scaling effect of LAI due to the nonlinearity and discontinuity. Then, the LAI at local scale is estimated from the proposed semi-empirical LAI retrieval model (equation (11)) with the red/near infrared reflectances and corresponding classification map. The classification map of mixture vegetation and the estimated LAI are shown in figure 3.

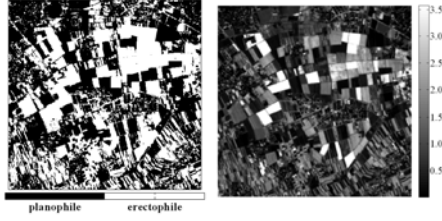


Figure 3. (a) the classification map; (b) the estimated LAI at local scale

The red and near infrared reflectances and the corresponding LAI are considered to be the ‘exact one’ or the ‘true value’ at local scale. Consequently, the local scale data are aggregated to generate the large scale data at different aggregation scales, where the subcomponent fractions are known as a priori knowledge.

4.3 Preliminary results

In order to verify the reliability of the scaling model proposed by equation (8), this scaling model is applied to the data described above. Nine different aggregation scales, 2×2 , 4×4 , 8×8 , 16×16 , 32×32 , 64×64 , 128×128 , 256×256 and 512×512 are selected to calculate the exact and approximated large-scale LAI data using equations (1) and (2). Meanwhile, the corresponding classification maps at different scales are generated based on the proportions of vegetation types. Then, the corrected LAI is estimated through equation (8).

To assess the accuracy of this correction, RMSE (root mean square error) and RE (relative error) are used to analyze the scaling performance. The RMSE and RE are defined respectively as:

$$RMSE = \sqrt{\frac{1}{N} \sum (x - y)^2}$$

$$RE = \frac{1}{N} \sum \frac{|x - y|}{y}$$
(12)

where x represents the LAI^{app} or LAI^{cor} and y represents the LAI^{exa} . The scaling performance at different aggregation scales based on the proposed method is shown in figure 4.

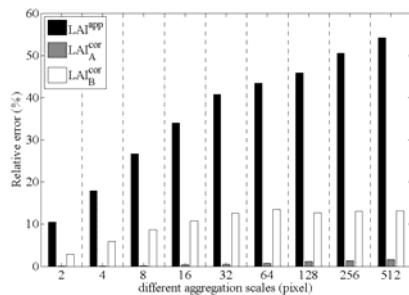


Figure 4. RE of retrieved LAI at different aggregation scales

LAI^{app} is the approximated LAI estimated using equation (2) from the aggregated inputs before scaling correction; LAI_A^{cor} and LAI_B^{cor} is the corrected LAI estimated by equation (5) and (8). In the process of correcting scaling effect, the surface heterogeneity is estimated as a priori knowledge in calculating LAI_A^{cor} and estimated through wavelet transform method in LAI_B^{cor} .

From figure 4, the scaling effect of LAI is obvious. There is a relative scaling error of about 10% on the estimation of LAI at the 2×2 aggregation scale. Because the more similar likelihood of adjacent pixels, the scaling effect here may be mainly caused by the discontinuity between contrasting covers types, which may confirm the argument of Chen (1999): the discontinuity is the main factor causing scaling effect.

When the aggregation scale increases, the more mixture of different vegetation types will happen. As a result, the scaling effect generally increases with the aggregation scale. If the scaling effect is not corrected for, the relative error of LAI would reach up to 55% at the 512×512 aggregation scale. If the subpixel component information about the average value of reflectance, variance and covariance within a large pixel is known, the proposed scaling model can well characterize the scaling effect as shown by LAI_A^{cor} . The relative error of LAI would be lower than 2% at any aggregation scale. In contrast, the method of estimating LAI_B^{cor} has less performance. It still has a relative error of about 13% at the 512×512 aggregation scale. However, the corrected LAI has a great improvement compared with the approximated LAI. The relative scaling error can decrease from about 10-55% to 3-13%.

In order to fully demonstrate the scaling result, the scatter plot between actual LAI and the estimated LAI at 32×32 aggregation scale is shown in figure 5.

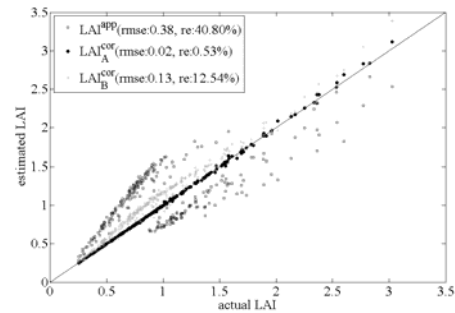


Figure 5. The scatter plot between actual LAI and estimated LAI at 32×32 aggregation scale

Obviously, both the RMSE and the relative scaling error of LAI are reduced. The corrected LAI^{cor} becomes more close to the 1:1 line compared with the approximated LAI^{app} . Due to lacking the subpixel component information, the LAI_B^{cor} is overestimated.

It implies that the scaling model proposed needs further improvement unless the subpixel component information, especially the average value and variance (covariance) in a mixed pixel can be easily estimated from remotely sensed data.

5 CONCLUSIONS

In this paper, the influence of the nonlinearity in the relationships between remote sensing reflectances and the LAI products and the discontinuity between contrasting vegetation types within a mixed pixel on the estimation of LAI are clearly analyzed. Combination of the advantages of scaling models proposed by other researchers, a new scaling model is proposed on the basis of Taylor series expansion approach with the fraction components information. However, this method must satisfy some hypotheses. The retrieval model is continuous and has at least up to second order continuous derivatives in the interval under consideration. If the retrieval model has strong nonlinearity, the approximation would not be appropriate. According to the scaling model, the scaling effects can be divided into the effects of the degree of nonlinearity and the spatial heterogeneity. The nonlinearity can be quantified by its second derivative Hessian matrix, while the heterogeneity can be quantified by variances and covariance within the mixed pixel and the fractions of subcomponent areas.

Based on the multi-scale red and near infrared reflectances and corresponding LAI, the scaling correction performance is demonstrated. The relative retrieval errors caused by scaling effects may reach up to 55% before scaling correction. Compared with the scaling results on one certain vegetation type (Wu et al, 2010), it may further reveal that the heterogeneity caused by contrasting vegetation types may be the main reason of scaling effect in a mixed pixel. Thus, it is important to collect the local scale fraction components information of vegetation for the purpose of accurate retrieving LAI products at large scales.

The final scaling result shows that the proposed method can well characterize the scaling effect and obtain more accurate LAI at large scale, demonstrating that the proposed method is feasible and promising. However, the scaling model is not mature. It would be expected that the relative scaling error could be greatly reduced if the subpixel information can be known as priority.

6 ACKNOWLEDGMENT

This work was supported by the Chinese 973 Program under Grant 2007CB714402 and the Hi-Tech Research and Development Program of China (863 Plan Program) under Grant 2008AA121805.

7 REFERENCES

- Baret, F., and Guyot, G., 1991, Potentials and limits of vegetation indices for LAI and FAPAR assessment. *Remote Sensing of Environment*, **35**, 161-173.
- Chen, J.M., Rich, P.M., Gower S.T., Norman J.M., and Plummer, S., 1997, Leaf area index of boreal forests: theory, techniques, and measurements. *Journal of Geophysical Research-Atmospheres*, **102**, 9429-29443.
- Chen, J.M., 1999, Spatial scaling of a remotely sensed surface parameter by contexture. *Remote Sensing of Environment*, **69**, 30-42.
- Garrigues, S., Allard, D., Baret, F., and Weiss, M., 2006, Influence of landscape spatial heterogeneity on the non-linear estimation of leaf area index from moderate spatial resolution remote sensing data. *Remote Sensing of Environment*, **105**, 286-298.
- Hu, Z., and Islam, S., 1997, A framework for analyzing and designing scale invariant remote sensing algorithms. *IEEE Transactions on Geoscience and Remote Sensing*, **35**, 747-755.
- Jacquemoud, S., Verhoef, W., Baret, F., Bacour, C., Zarco-Tejada, P.J., Asner, G.P., Francois, C., and Ustin, S.L., 2009, PROSPECT + SAIL models: A review of use for vegetation characterization. *Remote Sensing of Environment*, **113**, S56-S66.
- Liang, S.L., Fang, H.L., Chen, M.Z., Shuey, C.J., Walthall, C., Daughtry, C., Morisette, J., Schaaf, C., and Strahler, A., 2002, Validating MODIS land surface reflectance and albedo products: methods and preliminary results. *Remote Sensing of Environment*, **83**, 149-162.
- Pelgrum, H., Schmugge, T., Rango, A., Ritchie, J., and Kustas, B., 2000, Length-scale analysis of surface albedo, temperature, and normalized difference vegetation index in desert grassland. *Water Resources Research*, **36**, 1757-1765.
- Raffy, M., 1992, Change of scale in models of remote sensing: A general method for spatialization of models. *Remote Sensing of Environment*, **40**, 101-112.
- Wu, H., and Li, Z.L., 2009, Scale issues in remote sensing: A review on analysis, processing and modeling. *Sensors*, **9**, 1768-1793.
- Wu, H., Tang, B.H., Li, C.R., and Li, Z.L., 2010, leaf area index retrieval from remotely sensed data: scaling effect and propagation mechanisms. *IEEE International Geoscience and Remote Sensing Symposium (IGARSS2010)*, Honolulu, on 25-30 July 2010.

An empirical expression to relate aerodynamic and surface temperatures for use within single-source energy balance models

Boulet G^{1*}, Olioso A.², Béziat P.¹, Rivalland, V.¹, Chirouze, J.¹, Ceschia E.¹, Chehbouni, G.¹

¹ CESBIO UMR 5126 UPS, CNRS, CNES, IRD, Toulouse, France.

² EMMAH INRA, UPV, Avignon, France.

* Gilles.Boulet@cesbio.cnes.fr

ABSTRACT - Single-source energy balance models are simple and particularly suited to assimilate mixed pixel remote sensing data. Mixed pixels are made of a combination of two main elements, the soil and the vegetation. The use of single-source models implies that the source of convective fluxes, especially the aerodynamic temperature, is linked to the available remotely sensed surface temperature. There are many empirical relationships between both temperatures in the literature, but few that try to find objective constraints on this link. They usually modify the roughness length for thermal turbulent transport by an expression known as “radiometric k_B^{-1} ”, which depends mostly on Leaf Area Index (LAI). Acknowledging that the two temperatures should be similar for bare soil and high LAI conditions, we propose an empirical relationship between LAI and the ratio of the difference between the aerodynamic and the air temperatures and the difference between the surface and the air temperatures, also known as “ β function”. Seven datasets over agricultural areas (3 in south western France nearby Toulouse, 3 in south eastern France near Avignon, one in Morocco nearby Marrakech) are used to evaluate this new relationship. They all span the entire cropping season, and LAI values range from 0 to about 5. The new mathematical function is then compared to the β function retrieved from measured sensible heat flux and in-situ radiometric measurements as well as a two-source SVAT model (ICARE) whose parameters have been calibrated on the same datasets. Its performance in estimating the sensible heat compared to other empirical functions, either based on a “ β function” or a “radiometric k_B^{-1} ”, is also investigated. This work is carried out in the context of the preparation of the MISTIGRI satellite mission.

1 CONTEXT AND OBJECTIVES

Assessing the turbulent fluxes of latent and sensible heat at the land surface is a crucial issue for both water resource management (evapotranspiration) and meteorological forecasts. In order to compute these fluxes at a suitable spatial scale, estimation methods based on the use of remote-sensing data are favoured. There is a large panel of evapotranspiration estimation methods that use as input or constraint remotely sensed variables such as the NDVI (Courault, 2005). Evapotranspiration in potential conditions (i.e. non water limited) can be assessed with relatively good precision from in-situ (Cleugh et al., 2007) or remote-sensing derived (Venturini et al., 2008) meteorological data, and, very often, NDVI. But when water stress occurs latent and sensible heat fluxes are more difficult to assess. In those cases, there is a tight coupling between the evapotranspiration, consequently the surface temperature and remote sensing data in the Thermal Infra Red (TIR) domain is favoured (Kalma et al., 2008). Those methods often compute the instantaneous latent heat flux as the residual of the energy budget and, in most cases, an expression of the

different terms of the energy budget is proposed (Boulet et al., 2007):

$$Rn - G = H + LE \quad (1)$$

While net radiation Rn and soil heat flux G are expressed directly as a function of the surface temperature, the turbulent fluxes H (sensible heat) and LE (latent heat) depend on a mixed-surface (soil and vegetation) temperature source, the aerodynamic temperature T_0 , which represents the average temperature in the air within the canopy at the aerodynamic level, and can be significantly different from the radiometric surface temperature T_s acquired by a thermoradiometer at nadir or at a specific angle (Kustas and Anderson, 2009; Kustas et al., 2007; Stewart et al., 1994). Usually, this relationship is obtained through the use of a dual-source energy balance if both vegetation and soil bulk skin temperatures are known (Lhomme et al., 2000). For single source models, whose description of a mixed surface is more suited to assimilate surface temperature data, there is a need to develop robust yet simple methods to relate the aerodynamic temperature to the surface temperature. Many formulations exist in

the literature, and a comprehensive terminology and conversion formula is put forward by (Matsushima, 2005). Most expressions governing the relationship between the aerodynamic and the surface temperatures are improperly named “ kB^{-1} ”, and correspond somewhat to what Matsushima names “radiometric kB^{-1} ”. They represent an excess resistance when divided by the friction velocity and the van Karman constant. They’re derived according to the expected air temperature profile within the canopy, and expressed as a function of meteorological data, plant LAI and plant height. Amongst the well known formula, one can cite those from Blümel (Blümel, 1998), Massman ((Massman, 1999) revisited by (Su et al., 2001) and Lhomme (Lhomme et al., 2000). The β expression, originally proposed by (Chehbouni et al., 1997), on the other hand, is expressed in terms of the sole temperatures, independently from wind speed, and can easily be converted to a “radiometric kB^{-1} ”:

$$\beta = \frac{T_0 - T_a}{T_s - T_a} \quad (2)$$

Where T_a is the air temperature at a reference level above the canopy. The β expression entitles us to restrict the kB^{-1} to its original signification (also referred to as “aerodynamic kB^{-1} ”): the difference between the diffusion processes for momentum (and therefore the roughness length for momentum) and for heat exchange (and therefore the roughness length for heat). The first two formulations (Massman and Blümel) depend on LAI through the fraction cover of the canopy and on two difficult to assess parameters, the aerodynamic kB^{-1} for bare soil and the vegetation canopy, respectively. They thus provide a combined excess resistance which mixes both kB^{-1} factors (aerodynamic and radiometric). Since for bare soil and full cover conditions there is no real difference between both temperatures, the β formulation is fairly easily interpreted: beta values are 1 for those conditions, i.e. homogeneous surfaces, while for sparse vegetation β decreases. Factors influencing those coefficients include Leaf Area Index (LAI), and other plant geometrical features, friction velocity, time of the day and solar radiation etc. The main factor according to dual source Land Surface model outputs seems to be the Leaf Area Index. Based on ICARE SVAT model outputs (Gentine et al., 2007), we propose the following empirical relationship for β , based on a lognormal distribution:

$$\beta = 1 - \frac{a}{\text{LAI} * b * \sqrt{2\pi}} \cdot e^{-\frac{(\ln(\text{LAI}) - c)^2}{2 * b^2}} \quad (3)$$

The objective of this paper is threefold:

- 1- to retrieve β variations against Leaf Area Index for 7 experimental cultural cycles where seasonal evolution of the factors is available and LAI values range from 0 to more than 2
- 2- to compare several formula, including the new one, of $\beta(\text{LAI})$ against observed trends.
- 3- to compare the model performances in computing sensible heat flux from observed surface temperature.

2 VARIATION OF BOTH FACTORS AGAINST LAI FOR THE R3 WHEAT SITE

During the growing season 2004, a micrometeorological station equipped with standard meteorological equipment, an eddy covariance system and a thermoradiometer have been installed on a wheat plot (R3 B124 site) from January (sowing) till May (harvest). The thermoradiometer was calibrated against a black body device in actual air temperature conditions. LAI and vegetation height ranged from 0 to 4.5 and 0.8 m at maximum development.

Observed values of β were thus derived from observed sensible heat H_{obs} , surface temperature $T_{\text{s,obs}}$ and meteorological data that influence the aerodynamic resistance $r_{\text{a,obs}}$ following the Monin Obhukov Similarity Theory (MOST):

$$\beta_{\text{obs}} = \frac{r_{\text{a,obs}} H_{\text{obs}}}{\rho c_p (T_{\text{s,obs}} - T_{\text{a,obs}})} \quad (4)$$

Where ρ is the air density and c_p the specific heat. We chose the aerodynamic kB^{-1} value so that values of β are roughly equal to one for very high LAI values and for bare soils (both “aerodynamic” and “radiometric” kB^{-1} can be neglected), which is what is expected for homogeneous surfaces, as suggested both by (Massman, 1999) and (Matsushima, 2005). This of course depends tightly on the accuracy of the surface temperature measurements, and should be investigated further, but it is beyond the scope of this short paper. β values between -1 and 2 are kept (this represents >85% of all H_{obs} data for the R3 B124 dataset). Median values for each 0.5 LAI interval are shown on Figure 1a, together with β values simulated by the ICARE dual source SVAT model applied to the site without any calibration, the three expressions proposed by Blümel, Massman/Su and Lhomme as well as an interpolation along LAI values of the results

from (Matsushima, 2005) and the expression proposed in this paper (referred to from now on as “Boulet et al.”), whose a, b and c coefficients are subjectively adjusted to fit β_{obs} : a=1.7, b=c=0.8.

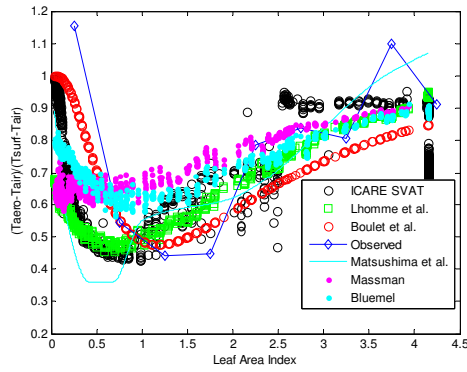


Figure 1a: $\beta(\text{LAI})$ relationships for the R3 B124 site.

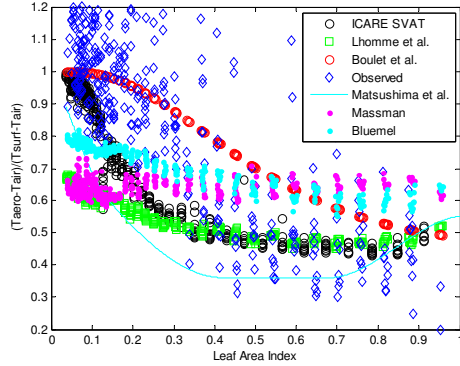


Figure 1b: idem for LAI between 0 and 1.

For well developed vegetation (say, above $\text{LAI}=2$), all expressions are very similar. For sparse and less developed vegetation however ($\text{LAI}<1$, figure 1b), there is a large difference between the Blümel, Massman/Su, Matsushima and Lhomme expressions, on the one hand, and ICARE outputs, the proposed expression and the observations, on the other. This could be explained by the fact that for those authors when LAI tends towards 0, the turbulent behavior tends to that of a smooth surface, which is rarely the case for an agricultural bare soil after ploughing. As a consequence, the sensible heat flux simulated from the different formula using the observed surface temperature (Equation 5), as one would do with remote sensing observations, is closer to the observed

for the proposed new formula compared to the three previous ones (Figure 2).

$$H = \rho c_p \beta \frac{T_s - T_a}{r_a} \quad (5)$$

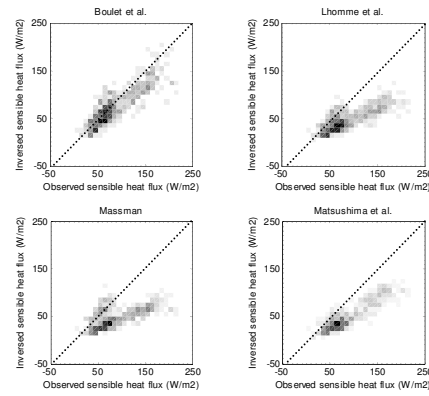


Figure 2: Scatterplots between the observed and the simulated sensible heat fluxes for the R3 B14 site. The dotted line is the 1:1 line.

3 EVALUATION FOR WHEAT AND OTHER CROPS

The different expressions for β are tested against a similar set up than for section 2, for 3 sites and for 7 experimental cultural cycles where seasonal evolution of the factors is available and LAI values range from 0 to above 2. For sites where friction velocity data was available, error bars are shown for β_{obs} , by assuming an error of 1K on T_s , 10% on friction velocity and roughness length for momentum and 10 W/m^2 for H_{obs} . Results are shown in Figure 3. For all sites sites, the new formulation fits fairly well the observed β , except for Lamasquère in 2007, which means that the calibrated values for a, b and c at the R3 B124 site are well suited for other sites. For sunflower and sorghum however (Figure 3e-f), the trend in $b(\text{LAI})$ is good but the value for a should be lower.

Since the ultimate objective of the β formulation is to provide accurate estimates of sensible heat fluxes, one needs to assess the resulting performance in using β models to simulate H . Of course the accuracy of those estimates depends primarily on the precision on surface and air temperatures, wind speed, roughness length and the validity of the MOST.

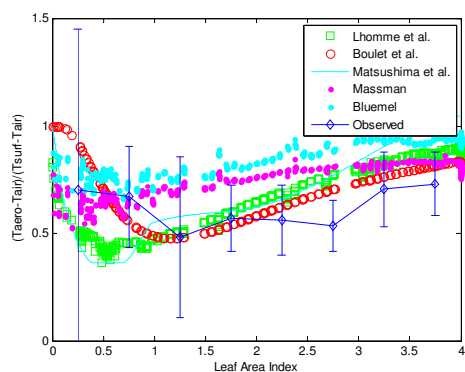


Figure 3a: $\beta(\text{LAI})$ relationships for Avignon in 2004 (Wheat).

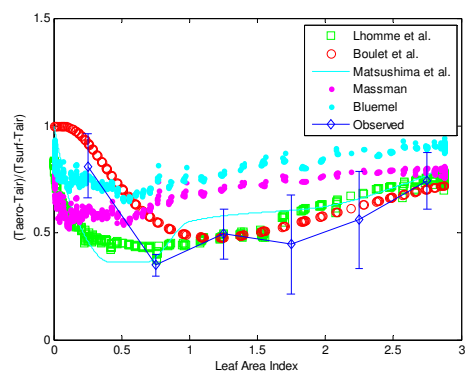


Figure 3d: $\beta(\text{LAI})$ relationships for Avignon in 2005 (Peas).

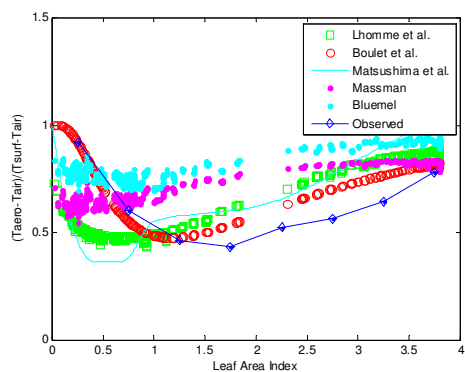


Figure 3b: $\beta(\text{LAI})$ relationships for Auradé in 2006 (Wheat).

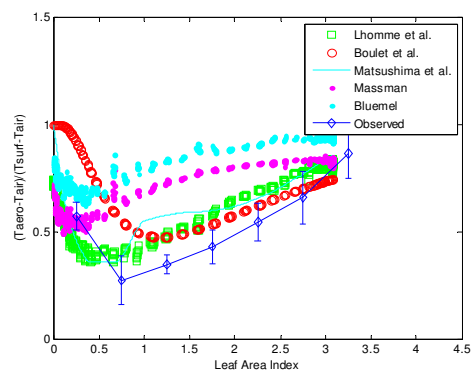


Figure 3e: $\beta(\text{LAI})$ relationships for Avignon in 2007 (Sorghum).

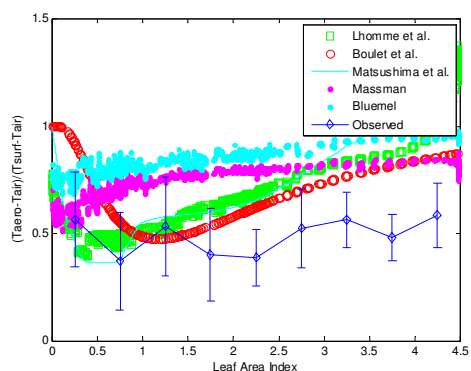


Figure 3c: $\beta(\text{LAI})$ relationships for Lamaquère in 2007 (Wheat).

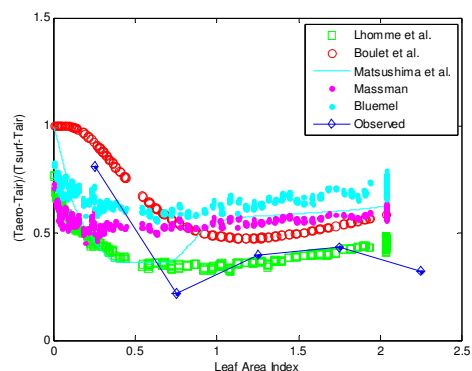


Figure 3f: $\beta(\text{LAI})$ relationships for Auradé in 2007 (Sunflower).

Estimation performance of sensible heat flux for all sites was assessed using the various β formulations. Results are shown in Table 1. All formulations perform well for some sites and much less for others, but the new formulation as the smallest number of RMSE values above 60 W/m² as well as the highest number of values under 50 W/m². Given the simplicity of this formulation and the fact that it allows tuning at least one parameter (a) to provide realistic values of the

difference between the aerodynamic and the surface temperature is an advantage. One must note that for both Blümel and Massman formulations one can adjust the poorly known values of the aerodynamic k_B^{-1} for bare soil and full cover (which are found to be close to zero here) as well as the parameter of the exponential decay of the Beer Lambert law used to convert LAI to fraction cover.

	Boulet et al.	Lhomme et al.	Matsushima	Su/Massman	Bluemel
Wheat R3 2004	52	62	76	61	57
Wheat Avignon 2004	45	46	52	50	47
Peas Avignon 2005	55	53	50	53	53
Sorghum Avignon 2007	52	54	66	54	68
Wheat Auradé 2006	45	49	66	47	54
Sunflower Auradé 2007	72	61	45	65	59
Wheat Lamasquère 2007	46	64	37	52	26

Table 1: RMSE (W/m²) between simulated and observed sensible heat fluxes (in bold: values >60 W/m², in italics: values <50 W/m²).

4 CONCLUSION

An empirical formulation of the difference between the aerodynamic and the surface temperature as a function of Leaf Area Index has been proposed, which represents in a realistic way the observed variations and leads to satisfying performances in simulating the sensible heat flux compared to other existing formulations. However, observed variations in this difference were assessed using a null aerodynamic k_B^{-1} , based on the fact that the radiometric k_B^{-1} should be close to zero for full cover. This should be investigated more thoroughly since there is no agreement on what value should be used for the aerodynamic k_B^{-1} for bare soil and fully covering vegetation, respectively (Verhoef, 1997). This work is carried out in the context of the preparation of the MISTIGRI satellite mission, which would provide daily surface temperature estimates on selected experimental sites with a one- to two- days temporal revisit and high resolution (<100m).

5 ACKNOWLEDGEMENT

Funding from the French CNES/TOSCA program is gratefully acknowledged.

6 REFERENCES

Blumel, K., 1998. Estimation of sensible heat flux from surface temperature wave and one-time-of-day air temperature observation. Bound.-Layer Meteor., 86(2): 193-232.

Boulet, G. et al., 2007. Monitoring water stress using time series of observed to unstressed surface temperature difference. Agricultural and Forest Meteorology, 146(3-4): 159-172.

Chehbouni, A. et al., 1997. Estimation of sensible heat flux over sparsely vegetated surfaces. Journal of Hydrology, 189(1-4): 855-868.

Cleugh, H.A., Leuning, R., Mu, Q.Z., Running, S.W., 2007. Regional evaporation estimates from flux tower and MODIS satellite data. Remote Sensing of Environment, 106(3): 285-304.

Courault, D., Seguin, B., Olioso, A., 2005. Review on estimation of evapotranspiration from remote sensing data: From empirical to numerical modeling approaches. Irrigation and Drainage Systems, 19(3-4): 223-249.

Gentine, P., Entekhabi, D., Chehbouni, A., Boulet, G., Duchemin, B., 2007. Analysis of evaporative fraction diurnal behaviour. Agricultural and Forest Meteorology, 143(1-2): 13-29.

Kalma, J.D., McVicar, T.R., McCabe, M.F., 2008. Estimating Land Surface Evaporation: A Review of Methods Using Remotely Sensed Surface Temperature Data. Surveys in Geophysics, 29(4-5): 421-469.

Kustas, W., Anderson, M., 2009. Advances in thermal infrared remote sensing for land surface modeling. Agricultural and Forest Meteorology, 149(12): 2071-2081.

- Kustas, W.P., Anderson, M.C., Norman, J.M., Li, F.Q., 2007. Utility of radiometric-aerodynamic temperature relations for heat flux estimation. *Bound.-Layer Meteor.*, 122(1): 167-187.
- Lhomme, J.P., Chehbouni, A., Monteny, B., 2000. Sensible heat flux-radiometric surface temperature relationship over sparse vegetation: Parameterizing B-1. *Bound.-Layer Meteor.*, 97(3): 431-457.
- Massman, W.J., 1999. A model study of $k_B(H)(-1)$ for vegetated surfaces using 'localized near-field' Lagrangian theory. *Journal of Hydrology*, 223(1-2): 27-43.
- Matsushima, D., 2005. Relations between aerodynamic parameters of heat transfer and thermal-infrared thermometry in the bulk surface formulation. *Journal of the Meteorological Society of Japan*, 83(3): 373-389.
- Stewart, J.B. et al., 1994. SENSIBLE HEAT-FLUX RADIOMETRIC SURFACE-TEMPERATURE RELATIONSHIP FOR 8 SEMIARID AREAS. *J. Appl. Meteorol.*, 33(9): 1110-1117.
- Su, Z., Schmugge, T., Kustas, W.P., Massman, W.J., 2001. An evaluation of two models for estimation of the roughness height for heat transfer between the land surface and the atmosphere. *J. Appl. Meteorol.*, 40(11): 1933-1951.
- Venturini, V., Islam, S., Rodriguez, L., 2008. Estimation of evaporative fraction and evapotranspiration from MODIS products using a complementary based model. *Remote Sensing of Environment*, 112(1): 132-141.
- Verhoef, A., de Bruin, H. A. R., and van den Hurk, B. J. J. M., 1997. Some Practical Notes on the Parameter k_B-1 for Sparse Vegetation. *J. Appl. Meteorol.*, 36: 560-572.

Relation between CO, measured by MOPITT sensor, and large fire emissions in the most affected regions in the world

A. Calle¹, J-L. Casanova¹, J. Sanz¹, P. Salvador¹ and F. González-Alonso²

¹Remote Sensing Laboratory. University of Valladolid. Spain

²CIFOR-INIA. Spain

Email: abel@latuv.uva.es

ABSTRACT - This study shows the correlation between large fires emissions and Carbon Monoxide estimated by the atmospheric sensor MOPITT (Measurements Of Pollution In The Troposphere) onboard Terra satellite. Results obtained in China, Central Africa and Amazonia forest, are shown. The CO is a very important trace gas produced by forest fire emissions and its role in the cycle of atmospheric carbon is very relevant. This study is focused on two main topics: the assessment of dispersion of CO emissions caused by large fires and the study of fires series and its CO emissions.

1. INTRODUCTION

Carbon monoxide (CO) is a trace gas located in the atmosphere mostly as the result of anthropogenic activities. Despite not being a greenhouse gas, carbon monoxide plays a significant role in the carbon cycle; it is not a direct precursor of CO₂ (dioxide of carbon), powerful greenhouse gas, but it substantially affects the budgets of OH radicals and O₃ (ozone) present in the atmosphere. The anthropogenic activities linked to CO release into the atmosphere can be divided into two well-defined groups: on the one hand, urban pollutant emissions from vehicles and other industrial processes; on the other, from fires and global biomass burning emissions.

The estimation profiles of CO and CO total column, has been identified as a very important objective in order to improve our understanding of climate global system. The EOS (Earth Observing System) Science Steering Committee has proposed: "The fate of carbon monoxide, remotely detected from space, in conjunction with a few other critical meteorological and chemical parameters, is crucial to our understanding of the chemical reaction sequences that occur in the entire troposphere and govern most of the biogeochemical trace gases" (EOS, 1987). In the same line, the WMO (World Meteorological Organization) has proposed: "Definition of trends and distributions for troposphere CO is essential. A satellite-borne CO sensor operating for extended periods could help enormously" (WMO, 1985).

Concerning CO emissions coming from biomass burning, this event accounts for about one quarter of CO emission to the atmosphere with an average of around 600 Mt CO per year (Khalil *et al.*, 1999). The occurrence of biomass burning, the fire sizes, and the fire properties, as smouldering fire or

flaming fire, vary greatly with time and space. Andreae and Merlet (2001) estimated that mean CO emission from vegetation fires in savannas and tropical forests is 342 Mt CO per year, while the total CO emission for all non-tropical forest fires is 68 Mt CO per year. Liu *et al.* (2006) have studied the emissions of forest fires in Northwest America using MOPITT (Measurements Of Pollution In The Troposphere) measurements and NOAA-AVHRR (Advanced Very High Resolution Radiometer) hot-spots.

2. OBJECTIVES

The objective is to estimate the atmospheric impact of forest fires in different pilot sites in the world by means of direct measurements. Concerning trace gases, the CO one of the main product of the biomass burning with an important role in the carbon cycle and CO₂ with a great importance related to greenhouse effect. Concerning the scale of time, the seasonal analysis is considered, for 6 years: 2003-2008, applied to China, Africa and Amazonia.

3. MOPITT SENSOR

MOPITT onboard the Terra spacecraft, is a correlation radiometer; which means that the CO profiles are retrieved using an optimal estimate of the maximum likelihood solution (Pan *et al.*, 1998). With this technique, the retrieved CO profiles depend not only on MOPITT radiance measurements, but also on the a priori CO profile and the averaging kernels. The single a priori CO profile is generated from 525 in-situ profile measurements and is used to constrain the solutions because the retrieval problem is ill posed (Liu *et al.*, 2006). Finally, The CO total column is obtained by integrating the CO mixing ratio at 35

heights from the surface to the top of the atmosphere (0.2 hPa). Validation of MOPITT CO data has been performed with various sets of correlative data and good agreement between MOPITT data and in situ aircraft measurement is found. Using this technique, the CO vertical profiles depend on the smoothing error, model parameter error, forward model error, and error due to instrument noise. Its spatial resolution is 22x22 km² at nadir by means of a swath of 640 km (3 days for global coverage).

4. METHODOLOGY

MOPITT Level 2 data show fluctuations between consecutive dates, which greatly increase the difficulty to draw conclusions from the analysis of a not large (representative) period of time. When different seasonal epochs are considered in the series and data are retrieved for different locations, revealing synoptic analyses can be carried out.

4.1. Seasonal analysis

The methodology applied to this study involved data preparation through the application of the Fourier Transform. For this reason, certain determining factors made the previous preparation of data necessary according to the following criteria:

1. The heterogeneous distribution of data has made necessary the application of spatial interpolation techniques for the retrieval of certain results. Since the location of MOPITT level 2 data was projected in longitude-latitude geographical coordinates, daily files have been projected to a grid in order to establish the Euclidean distances.
2. The cartographic projection formerly described was used to retrieve mean and maximum values in an analysis environment.
3. The application of the Fourier Transform requires the availability of continuous series of data. The Level 2 files available for the year series 2005-08 went up to 96%, 97%, 99% and 96% respectively. On the other hand, MOPITT's spatial resolution and coverage time are responsible for the temporal lack of data in each analysis zone. For this reason, in order to have continuous series available in each analysis zone, time interpolations of data have been carried out.
4. Application of the Fourier Transform and selection of the harmonics with the highest spectral energy.

The Fast Fourier Transform (FFT) is a method applied to time series data that may present certain periodicity. Its application and analysis aims at the

attainment of two objectives. In the first place, to describe the temporal behaviour of a magnitude whose data present short-term strong fluctuations which are probably caused by the noise of data. In the second place, the Fourier Transform allows us to decompose the behaviour of a variable in different terms with different weighting factors in the reproduction of the series, which can be analyzed independently in order to draw conclusions which are explained from the hidden effects caused by the variability of the original data.

The magnitude proposed in order to estimate seasonal contribution of CO is the exceeded percentage; that is, the enclosed area between synoptic curve of reference and yearly detailed curve, estimated in the fire period, Eq. 1

$$E(\%) = \left[\frac{\int_{\text{fire period}} \text{CO}_{R,Y}(t) dt}{\int_{\text{fire period}} \text{CO}_S(t) dt} - 1 \right] \times 100 \quad (1)$$

where R= Region or cluster; Y=year; S=Synoptic obtained by the main harmonic from FFT.

4.2. Single fire or cluster

The supply of CO total column emissions by a fire is estimated by means of: exceeded volume of CO concentration over the fire area. That is:

$$S = \iint_{\text{Fire area}} ([\text{CO}] - [\text{CO}]_0) dx dy \quad (2)$$

$$\text{kg of CO} = \frac{S}{N_A} 0.028 ; N_A = 6.023 \cdot 10^{23}$$

where $[\text{CO}]_0$, in eq. (2), is estimated from seasonal analysis.

5. RESULTS

5.1. Seasonal analysis in the north of China

Fig. 1 shows the results of seasonal study of CO and CO₂ in the north of China, very close to the border with Russia, where fire occurrence is strong. The bar diagram shows fire occurrence from MODIS (Giglio *et al.*, 2003; Davies *et al.*, 2009), in the period 2003-2008, overlapped in the period analyzed. In green colour, the original data of CO total column, from MOPITT, is shown; in black colour, the inverse Fourier transform by means of two main harmonics. Finally, in red colour, CO₂ values, from ENVISAT-SCIAMACHY, are averaged for each month, in the period 2003-2005.

Two main maximums, for each year, can be observed. First maximum is located in May at the end of winter season, where CO emissions are dominated by human activities and fires occurrence too. The second maximum is located in October when there is a second maximum of fires occurrence. Despite this second maximum is not so big than the first one, it's breaking the sinusoidal behaviour of CO evolution.

Daily CO total column data from MOPITT show a strong fluctuation, but the evolution of FFT curve is very clear in order to underline the maximum values in the year. Only two main harmonics of inverse FFT were used in order to extract evolution of CO total column from MOPITT; first maximum shows a correlation with the final of winter (fires and human heating activities) and the second maximum with the second maximum of fires occurrence. This explanation is very useful in order to understand results of CO₂ evolution. The first maximum of CO₂ is expected by the global behaviour of CO₂ in the Earth, explained by balance of CO₂ due to vegetations and oceans. Second maximum of CO₂ shows a good correlation with fires occurrence. This coincidence is clearer in the case of north east of China, where population density is lower than in the South-east (This results is published –in press– in the DRAGON-2, founded by ESA, midterm results proceedings). Note that the increasing value of CO₂ is clear in only three years of analysis, even when this is not the topic of this paper.

5.2. Seasonal analysis in the north of Equatorial Africa

The pattern of fire occurrence in Africa is quite different to others regions in the planet with higher population density as, for example, China (analysed in the paragraph before) or Europe. The fire occurrence, in Africa, is dominated by the displacement of ITCZ (Inter Tropical Convergence Zone). During the winter of north hemisphere, the ITCZ and, therefore, the tropical rain is located in the south of Equator; so, fire occurrence is stronger in the north of Equator.

The second part of the Fig. 1 shows the results of seasonal study of CO in the north of Equatorial Africa. The bar diagram shows fire occurrence from MODIS (Giglio et al., 2003; Davies et al., 2009), in the period 2003-2008, overlapped in the period analyzed. In green colour, the original data of CO total column, from MOPITT, is shown; in black colour, the inverse Fourier transform by means of two main harmonics (n=6 and 18). Finally, in red colour, CO values, from ENVISAT-SCIAMACHY, are averaged for each month, in the period 2003-2005, in order to compare results between MOPITT and SCIAMACHY sensors. Comparison between CO from MOPITT and SCIAMACHY are been carried out by Buchwitz et al. (2007) showing results over cities; so, this comparison over large fires, presented in this paper, is a

complementary result in order to know these source of data.

Two main maximums, for each year, can be observed. First maximum is located in the period of January and February, showing a very good correlation with fire occurrence. The second maximum, very weak, is located in August exactly when fire occurrence in the south of Equatorial Africa is stronger (see paragraph 5.3). Concerning comparison between MOPITT (daily data) and SCIAMACHY CO total column is very similar between them.

5.3. Seasonal analysis in the south of Equatorial Africa

As we have underlined in the paragraph before, the pattern of fire occurrence in Africa is dominated by the displacement of ITCZ. During the summer of north hemisphere, the ITCZ and, therefore, the tropical rain is located in the north of Equator; so, fire occurrence is stronger in the south of Equator.

The third part of the Fig. 1 shows the results of seasonal study of CO in the south of Equatorial Africa. The bar diagram shows fire occurrence from MODIS in the period 2003-2008, overlapped, in the period analyzed. In green colour, the original data of CO total column, from MOPITT is shown. Concerning Fourier transform, three main harmonics were used in order to show the seasonal evolution of CO total column (n=6, 12 and 18). Finally, in red colour, CO values, from ENVISAT-SCIAMACHY, are averaged for each month, in the period 2003-2005, in order to compare results between MOPITT and SCIAMACHY sensors.

Two main maximums, for each year, can be observed. First maximum, with the shape of a peak, is located at the end of September, showing a very good correlation with the main fire occurrence in the year. The second maximum, weaker, is located at the end of January when fire occurrence in the north of Equatorial Africa is stronger (see paragraph 5.2). Concerning comparison between MOPITT (daily data) and SCIAMACHY CO total column is very similar between them.

5.4. Seasonal analysis in the Amazonia

The pattern of fire occurrence in Amazonia is the same of the south of Equatorial Africa, due to the ITCZ behaviour. Fig. 1 shows results for Amazonia analysis. Same comments and explanations as paragraph before are suitable for Amazonia region.

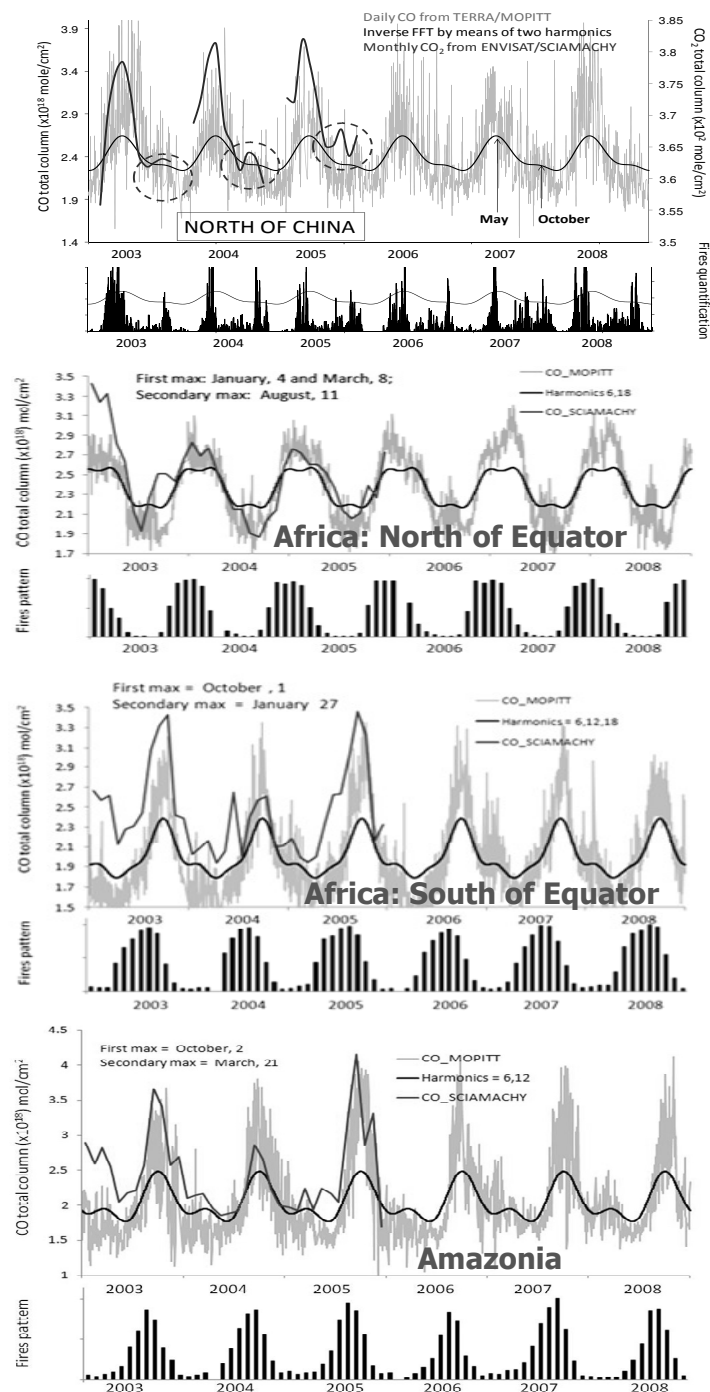


Figure 1. Results of seasonal study of CO in the north of China, Africa and Amazonia. A comparison between CO emissions, fire occurrences is shown. The bar diagram shows fire occurrence for each year. CO original values and Inverse Fourier transform is enhanced.

5.5. Single large fire in China

In this paragraph, several examples concerning fire emissions are shown. The paragraph 4.2. Methodology, and Eq. (2) explain the way to compute the total mass of CO coming from a fire or a cluster of fires, by means of $[CO]_0$ estimated in the synoptic study; this magnitude establishes the base line of the CO total column above the fire.

The Fig. 2 shows an example of analysis of a single cluster of fires, in the Heilongjiang province in the north-east of China, a province strongly affected by fires and very affected by the emissions from fires in Russia, near the border of the countries. This example corresponds to October 2004. This province shows large fires can be observed in China and Russia

very close to the border of the countries. Fig. 2, on the left, shows the cluster of Heilongjiang-China, where smoke plume can be observed in the ENVISAT-AATSR RGB image composition and on the right, fire detections algorithm applied to ENVISAT-AATSR sensor. Finally, Fig. shows the CO total column from fires, in China and Russia. On the left of Part II a two-dimensional analysis shows the gradient of spreading of CO total column by means of an iso-lines estimation of CO concentration. On the right, the estimation of total CO mass coming from fires is shown. In this example, total emissions coming from fires of China are 29.8 Kilotons of CO and fires from Russia are 37.7 Kilotons. A strong impact of Russian emission over China can be observed in the image of CO total column.

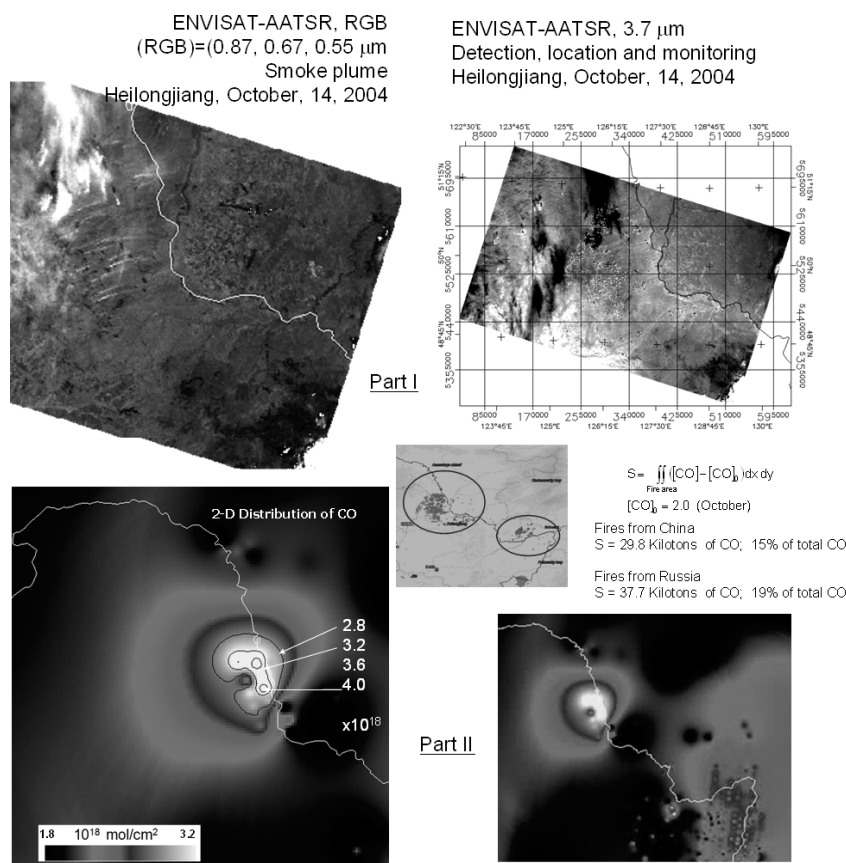


Figure 2. Analysis of a single cluster of fires, in the Heilongjiang province in the north-east of China, in October 2004. Part I, on the left, shows the smoke plume; on the right fires detection algorithm applied to AATSR sensor. Part II shows the CO total column from fires, in China and Russia, including gradient of CO spreading. (Explained in the text)

6. CONCLUSIONS

The main conclusions of this paper can be summarized as follow:

The Fourier transform is a very useful tool to analyze the seasonal behaviour of CO total column, removing the noise of data. It's useful tool in order to locate the period of maximums values and, therefore, to compare with fire occurrence.

The north of China is strongly affected by emissions from Russian forest fires. This result, confirmed by CO direct measurements, is expected from the hotspots distribution provided by MODIS data. Very close to the border of countries, Russian hotspots are more abundant than Chinese ones. In any case, CO total column behaviour is explained by human activities during winter but fires are clearly present in the maximums of CO and CO₂.

Equatorial Africa is one of the main regions of the world affected by wild fires and savannah fires. Maximums of CO and CO₂ are explained by fire occurrence. Even when ITCZ would be exactly the same on the top and bottom of Equator, the pattern of CO evolution is quite different between the north and south.

Amazonia shows exactly the same behaviour of the south of Equatorial Africa. This is an expected conclusion since the two regions are located with the same geographic latitude band.

7. ACKNOWLEDGMENTS

This work has been carried out in the framework of the Project Cat-1 ID CIP_4414 founded by ESA. Thanks to MOPITT level-2 data set, from the Atmospheric Science Data Centre of Langley ASDC User Services, NASA. Data of forest fires detections, provided by MODAPS, coming from MODIS were used. SCIAMACHY CO were provided by Michael Buchwitz from University of Bremen (Germany). Results of China were obtained in the framework of DRAGON-2 Project founded by ESA. This paper has been funded by the Junta de Castilla y León, project VA089A08 title: Seguimiento de los gases traza y emisiones de incendios forestales en la región de Castilla y León y su entorno, mediante técnicas de teledetección espacial".

8. REFERENCES

Andreae, M. O., & Merlet, P. (2001). Emission of trace gases and aerosols from biomass burning. *Global Biogeochemical Cycles*, 15, 955–966.

Buchwitz, M., de Beek, R., Bramstedt, K., No'el, S., Bovensmann, H., and Burrows, J. P. (2004). Global carbon monoxide as retrieved from

SCIAMACHY by WFM-DOAS, *Atmospheric Chemistry and Physics*, 4, 1945–1960, 2004.

Buchwitz, M., Khlystova, I., Bovensmann, H., and Burrows, J.P. (2007). Three years of global carbon monoxide from SCIAMACHY: comparison with MOPITT and first results related to the detection of enhanced CO over cities. *Atmos. Chem. Phys.*, 7, 2399–2411.

Davies, D.K., Ilavajhala, S., Wong, M.M., and Justice, C.O. (2009). "Fire Information for Resource Management System: Archiving and Distributing MODIS Active Fire Data". *IEEE Transactions on Geoscience and Remote Sensing* 47 (1):72-79.

Dils, B., De Maziere, M., Del, Müller, J.F., Blumenstock, T., Buchwitz, M., Beek, R., Demoulin, P., Duchatelet, P., Fast, H., Frankenberg, C., Gloudemans, A., Griffith, D., Jones, N., Kerzenmacher, T., Kramer, I., Mahieu, E., Mellqvist, J., Mittermeier, R.L., Notholt, J., Rinsland, C.P., Schrijver, H., Smale, D., Strandberg, A., Straume, A.G., Stremme, W., Strong, K., Susmann, R., Taylor, J., van den Broek, M., Velasco, V., Wagner, T., Warneke, T., Wiacek, A., and Wood, S. (2006). Comparisons between SCIAMACHY and ground-based FTIR data for total columns of CO, CH₄, CO₂ and N₂O. *Atmospheric Chemistry and Physics*, 6, 1953–1976, 2006

Giglio, L., J. Descloitres, et al. (2003). "An Enhanced Contextual Fire Detection Algorithm for MODIS." *Remote Sensing of Environment* 87 (2-3): 273-282.

Khalil, M. A. K, Pinto, J. P., & Shearer, M. J. (1999). Atmospheric carbon monoxide. *Chemosphere: Global Change Science*, 1, ix – xi.

Liu, J., Drummond, J.R., Jones, D.B.A., Cao, Z., Bremer, H. Kar, J. Zou, J., Nichitui, F., and Gille, J.C. (2006). Large horizontal gradients in atmospheric CO at the synoptic scale as seen by spaceborne Measurements of Pollution in the Troposphere. *Journal of Geophysical Research*, 111, D02306, doi:10.1029/2005JD006076, 2006

Pan, L., Gille, J. C., Edwards, D. P., Bailey, P. L., & Rodgers, C. D. (1998). Retrieval of tropospheric carbon monoxide for the MOPITT experiment. *Journal of Geophysical Research*, 103, 32277–32290.

Using MODIS-LAI images in the spatio-temporal functioning of a Mediterranean forest in Tunisia: impact on water budget estimations

H. Chakroun (1), F. Mouillot (2), M. Nouri (3)

(1) *Laboratory of Hydraulics and Environment Modelisation, National School of Engineering, Manar University, BP 3, 1002, Tunis, Tunisia.*

(2) *CEFE/CNRS (DREAM) Research for Development Institute (IRD, France).*

(3) *Institute for Researches in Rural Engineering, Water and Forests (INRGREF, Tunisia)*

E-mail 1: hedia.chakroun@enit.rnu.tn

ABSTRACT *The use of remote sensing data at different spatio-temporal resolutions is being common during the last decades since sensors offer many inputs to water budget estimation. Most of water balance models use the leaf area index (LAI) as a parameter for accounting water interception, evapotranspiration, runoff and available ground water. The objectives in this work are to assess the representativity level of MODIS-LAI global images of the vegetation state and the integration of these data into a water budget model. Analysis have been conducted by the exploration of weekly time series of MODIS-LAI over a year for the study region which is a forested area (northern Tunisia) extended on a band of about 20 to 30 km width along the Mediterranean coast. Profiles examinations made over homogeneous forest areas show a clear discrimination of LAI for dense deciduous areas especially in spring and summer. Profiles of dense forest over deep/shallow soils and low/high water holding capacity show a sensitivity of LAI to both characteristics with a clear discrimination of areas where the plants can extract water more easily (low tension soils). The integration of weekly LAI images into the Priestley-Taylor evapotranspiration formula and the comparison of two scenarios (LAI variable and LAI averaged over a year) show that the inclusion of temporal variability leads to actual evapotranspiration values that are quite different in the dry season, reaching 40% in terms of relative variation between "Average-LAI" and "Variable-LAI" in the case of dense forest and 70% in the case of sparse forest.*

1 INTRODUCTION

The general context of the present work is to study Mediterranean natural ecosystems vulnerability to drought and climate change by a spatial modelling of water budget at regional scale. The lack of such studies over Mediterranean areas is one of the motivations of this work. In order to contribute in these studies, there is a need to make framework simulations of water budget models using the potential of spatial data at local and regional scales. Such studies attempt to determine critical threshold of available water to ensure the viability of this forested ecosystems in North Africa. Leaf Area Index (LAI) is related to functional process rates of energy and mass exchange; it is used in satellite derived parameters for calculation of surface photosynthesis, evapotranspiration (ET) and annual net primary production (Myneni and al., 2002). Many studies reported results on integrating LAI and various vegetation indices from remotely sensed (RS) data in surface energy and water balance process-based modelling (potential and actual evapo-transpiration (PET, AET), precipitation interception and soil evaporation). These studies made use of remotely sensed data for water balance estimation and impacts on water storage, long-term

catchments and rainfall-runoff models. In the case of small areas, high and medium spatial resolution have been used (e.g. LAI from LANDSAT to account for small basins LAI variation over the, Canada, Chen et al, 2005). Global products such as MODIS are used in the case of regional studies: Li et al. (2009) used LAI-MODIS in a catchments model for runoff estimation in ungauged catchments in Australia. Guerschman et al. (2009) used the EVI (Enhanced vegetation index) and the GVM (Global Vegetation Moisture Index) from MODIS to reproduce the main spatial and temporal patterns in AET across Australia. Cleugh et al., (2007) estimated the surface conductance from MODIS-LAI products in Australia. Zhang and Vegehenkel (2006) integrated both LAI and NDVI MODIS products in soil water content and ET models in a case study in Germany. In Mediterranean ecosystems, use of MODIS images on a southern Italian forested area by Calcagno et al. (2007) pointed out generally good ET predictions especially when MODIS images are upscaled using ASTER high resolution images. Wang et al. (2007) showed a significant relation between responses of MODIS derived NDVI to root soil moisture in semi-arid and humid regions.

As summarized in Zhang and Vegehenkel. (2006), the general use of MODIS-LAI in hydrological models can be divided into : the direct estimation of

actual AET and comparison of the MODIS data to surface measurements or model-simulated values (e.g. Leuning et al. 2005, Xiao et al. 2005) and the estimation of canopy water stress (Fensholt and Sandholt, 2003). Using physical or empirical models with RS vegetation products provides estimation of spatially distributed data with a reasonable degree of accuracy at regional landscape (Guerschman et al. 2009). MODIS data can also help to identify potential model structure weakness by validation and data assimilation (Zhou et al., 2004).

The main objectives of our work consist of studying: (1) how well global satellite data such as MODIS-LAI represent the spatial heterogeneity and the seasonal functioning of natural vegetation in south Mediterranean forested areas over its gradient from 350 mm to 1000 mm annual precipitation? (2) Despite the coarse spatial resolution of MODIS-LAI (1km), could we extract parameters that would improve regional water budget modelling at a finer resolution? Answering these questions constitutes a first step for investigating the potential of global images products into spatial water budget modelling in the dense to open Mediterranean forests.

The specific objectives in this work are: (1) assessing the representativity level of MODIS-LAI global images of the vegetation status (species and density) and the sensor sensitivity to vegetation response over various topo-edaphic and climatic conditions; (2) determining the effect of the LAI dynamic on actual ET within the different seasons over a year and (3) making recommendation for improving water budget prediction.

2 STUDY SITE AND DATABASE ELABORATION

2.1 Study site

The study region belongs to the Mediterranean North African forests, it is localised at the extreme north of Tunisia. It is extended on a band of about 20 to 30 km width along the Mediterranean coast and covering 2553 km². The climate is Mediterranean with four seasons. Precipitations are concentrated in autumn and winter. Spring and summer are dry (the average precipitation of the Kroumirie region in 800 mm) with a maximum annual average of 1000 mm in Ain Draham). The landscape of the region is typically forested mountains reaching 1200 m, with homogeneous evergreen deciduous trees (43%), coniferous trees (8%) and “maquis” (Mediterranean scrubland vegetation at lower slopes of mountains) and “garrigues” (like “maquis”, but poorer vegetation on thin soils). Maquis and garrigues represent 49% of the study area (figure 1).

2.2 Time-Series MODIS-LAI analysis

MODIS images have been collected for one year (2003) on the website <https://wist.echo.nasa.gov>. These data correspond to an 8-day composite LAI products (MOD15A2). Their spatial resolution is 1km. The LAI defines an important structure property of a plant canopy which is the one-sided leaf area per unit ground area. Preliminary investigations of data were done on a 45 time-series MODIS-MODIS image set. The tiles covering North Africa region were clipped to the extent of Tunisia. The images were rectified to geographic projection by the use of MODIS reprojection tool. Next, we make a conversion from Geographic projection to Universal Transverse Mercator system (UTM, zone 32) which is the common reference system in Tunisia. Quality control of the time-series leads to replacing some data by the adjacent ones regarding the abrupt variation of LAI values within few days. In total, 6 images were replaced. Figure 2 shows a generic LAI image. The exploration of spatial variation over LAI images for a single date and the comparison to inventory ground data show that the MODIS-LAI product is important for dense evergreen forest (cork and eucalyptus) rather than for coniferous.

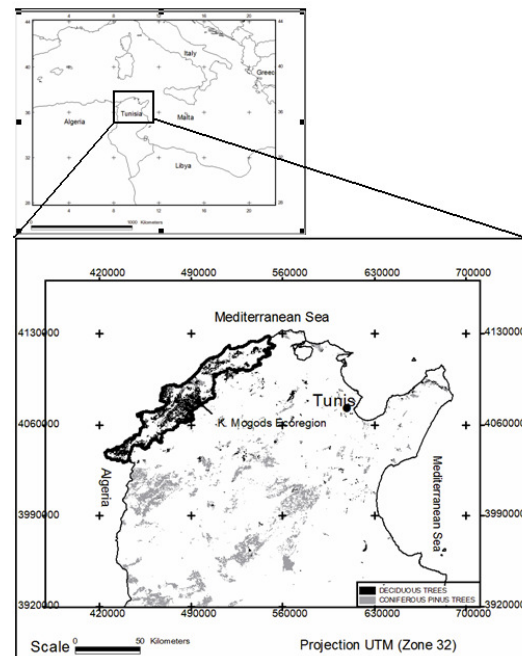


Figure 1. Forest map of Tunisia (processed from original data of Forest Department (DGF, 1995).

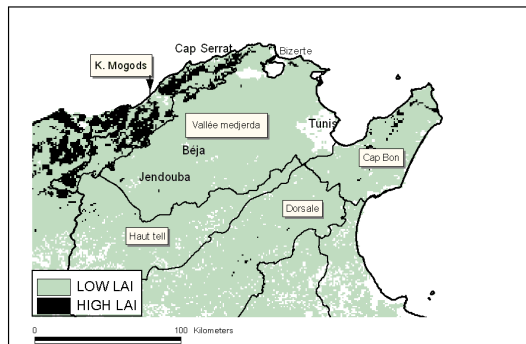


Figure 2. Example of MODIS-LAI image (Processed from original images <https://wist.echo.nasa.gov>)

2.3 Ground and climate data analysis

To assess the spatial variability of MODIS-LAI products with natural vegetation dynamic in the Mediterranean forest, we make use of the general forest inventory and the soil map both in digital format and afforded by the “Ministry of Agriculture, Water Resources and Fisheries”. Topographic characteristics of the study region are extracted from the 30m-ASTER-GDEM digital elevation model (DEM) downloaded for free from the website (<http://www.ersdac.or.jp>), georeferenced and clipped to the study region boundaries. The DEM had been validated previously by comparison to a stereoscopic DEM in sub region of the study area.

Vegetation

From the forest inventory data base is made at 1/50000 scale from plots measurements and mapping (DGF, 1995), we extract the principal forest classes present in the study region are: evergreen deciduous trees (cork oak and other oaks, eucalyptus), coniferous trees (Pines), “*Maquis*” (Mediterranean scrubland vegetation at lower slopes of mountains) and “*Garrigues*” (like maquis, but poorer vegetation on thin soils). These data are in structured vector format and projected in UTM.

Soil

The topo-edaphic characteristics of the region were studied by the soil map and the ASTER GDEM. We made processing on soil map in order to extract two characteristics that have influence on water holding capacity, namely soil depth and soil potential extraction of water. Depth values are already afforded in the soil database. For water retention estimation, we apply the method described in Saxton et al., (1986) and Saxton and Rowles (2006) where the retention potential of water by different soils is estimated from texture (sand, lemon and clay) and organic matter rates. Figures 4 and 5 illustrate the mapping of these two parameters. We note that deep soils are not

frequent in the study region; besides, the relief gradient North-East/South-West have conditioned the spatial distribution of depth and water holding capacity.

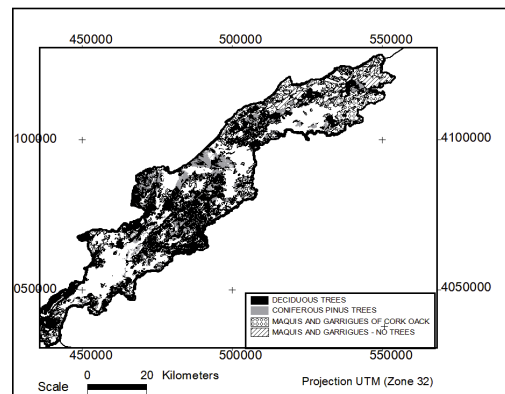


Figure 3. Natural vegetation classes in the study region processed from the Forest Inventory (DGF, 1995).

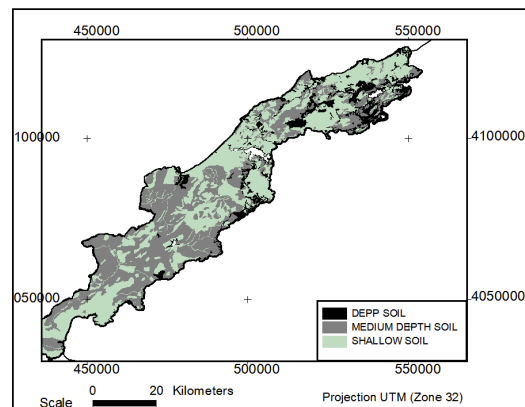


Figure 4. Soil depth map of the study region.

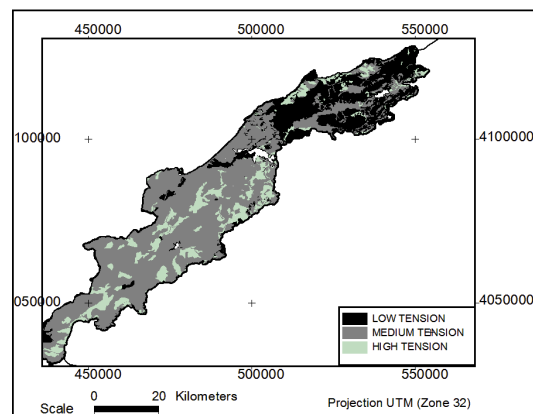


Figure 5. Soil tension map of the study region.

Climate data regionalisation

Micrometeorological data used in PET and AET calculation are daily precipitation, temperature and net radiation during 2003 over 5 meteorological stations (Beja, Ain Draham, Jendouba, Tabarka). The regionalisation of climate data requires the integration of elevation gradient, and derived parameters (slope and aspect). The ASTER-GDEM was processed to derive these two parameters. Regionalisation of these data was achieved by the inverse distance interpolation method and by the consideration of topography in temperature interpolation.

All processed and structured data in both vector and raster formats were integrated into a coherent spatial database for further processing.

3 COMBINING LAI-MODIS AND GROUND DATA

We made profiles over time to investigate the variation of LAI for the different forest/soil classes described earlier. A Profile shows mean values of reference map cells, aggregated by classes and summarized into average values and graphed simultaneously over the sequence of the time-series LAI images. The reference map cells used in this analysis are both forest classes and combination of forest/soil maps. Profiles examination of weekly LAI variation over 2003 year for each “vegetation class” (figure 6) shows:

- A seasonal variability of the LAI value is observed due to the presence of important herbaceous layer in winter (wet season). This effect was reported in other studies (Zhang and Vegehenkel, 2006; Fensholt et al, 2004).
- There is a clear discrimination of evergreen and coniferous vegetation. Highest values of LAI all over the year are observed with dense evergreen areas. Note that in both species, this discrimination is less important in wet seasons because of the presence of important herbaceous strata.

We cross inventory and soil data maps by making extraction of forest classes overlaying different soil depths and water holding capacity. For this analysis, we consider only dense forest (both evergreen and coniferous) combined with soil layers.

Profiles analysis reveal higher LAI values form medium-depth compared to shallow soils (Figure 7). We already observed that deep soils are not frequent in the study region; this is why they are not involved in this profile comparison. Figure 8 shows higher LAI values for medium-tension capacity soils compared to high-tension capacity ones. Low-tension soils are not present within region covered by dense forest concerned by this analysis, they are rather covered by

“maquis” and “garrigues”. Thus, the dynamic of LAI values over a year reveals a difference as we discriminate dense forest on deep/shallow soil and on low/medium tension soil. In this latter case, discrimination was more important. Vegetation response to sensor reported in terms of weekly LAI is influenced by underlying soils capacity of water holding (depth and tension). Similar results have been reported by Wang et al. (2007) who found correlations between NDVI-MODIS and root-zone soil moisture in semi-arid and humid regions.

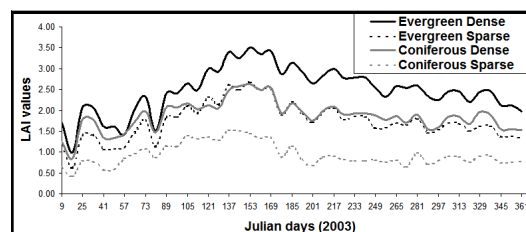


Figure 6. LAI-MODIS variation within various species and covers.

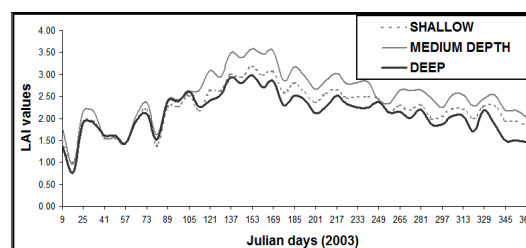


Figure 7. LAI-MODIS variation within dense deciduous forest overlaying various depth-soils.

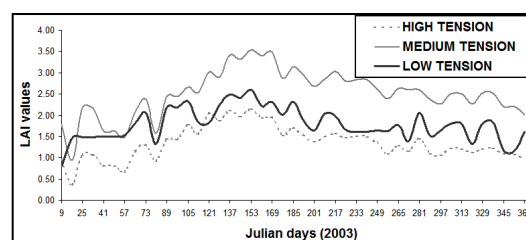


Figure 8. . LAI-MODIS variation within dense evergreen forest overlaying various water tension soils.

4 USING MODIS-LAI IN ACTUAL EVAPOTRANSPIRATION SIMULATION

The previous analyses of MODIS-LAI time series images over the Kroumirie forested region leads us to initiate an investigation of the outputs of a water budget model, particularly, the evapotranspiration component where surface conductance is determined

by the means of LAI. The PET is computed by the Priestley-Taylor equation (1), where γ is the psychrometric constant ($\text{kPa}/^\circ\text{C}$), $C_{\text{H}_2\text{O}}$ is the vaporisation latent heat ($\text{Jcm}^{-2}\text{mm}^{-1}$), Δ is the slope of the vapour pressure curve ($\text{kPa}/^\circ\text{C}$) calculated from daily temperature, R_n is the net radiation ($\text{MJ}/\text{m}^2/\text{day}$), α is the coefficient of Priestley-Taylor (1.26).

$$PET = C_{\text{H}_2\text{O}} \alpha \frac{\Delta}{\Delta + \gamma} R_n \quad (1)$$

$$AET = PET \frac{(1 - e^{-kLAI})}{\left(1 - \frac{\Psi_s}{\Psi_{\max}}\right)} \quad (2)$$

AET is given by (equation (2), where k is a coefficient assumed to remain constant while estimating AET ($k = 0.5$), the amount $(1 - e^{-kLAI})$ represents the fraction of Photosynthetically Active Radiation, Ψ_s is plant extraction potential and Ψ_{\max} is soil maximum potential (in Mpas).

PET was calculated on a daily basis then summed over a week; the weekly values of PET were next used in calculating AET assuming the factor $(1 - \Psi_s/\Psi_{\max})$ as a constant. Thus, the only effect of LAI variability is considered in this analysis. We calculate AET_{VAR} with time series LAI, and AET_{AVE} with a yearly averaged LAI. Since we do not consider the $(1 - \Psi_s/\Psi_{\max})$ factor, the comparison of the two AET calculations was done on the basis of the relative variation (equation 3). Results are represented in figure 9 for evergreen/coniferous species, and by differencing dense and sparse vegetation.

$$\Delta(AET) = \frac{AET_{\text{VAR}} - AET_{\text{AVE}}}{AET_{\text{AVE}}} \quad (3)$$

Results show that the inclusion of temporal variability leads to AET values for the dry season that are, reaching 40% less in the "Average-LAI" compared to the "Variable-LAI" for dense forest and 70% for sparse forest. LAI in open forest might be more influenced by the herbaceous seasonal dynamic. This result is important to evaluate the effect of temporal variation on the AET, and consequently on the cumulated water stress over the dry season. These results should help in refinement of regional prediction scenarios for drought in Mediterranean natural landscapes at different resolutions.

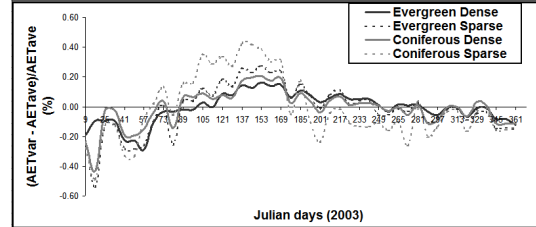


Figure 9. Relative variation of AET over a year from averaged LAI and a time-series varying LAI.

5 REFERENCES

- Calcagno et al., Distributed estimation of actual evapotranspiration through rempyte sensing techniques. (2007) *Methods and Tools for Drought Analysis and Management* Springer Netherlands, pp. 125-147.
- Chen J. M, Chen X., Ju W. and Geng X. (2005) Distribution hydrological model for mapping evapotranspiration using remote sensing inputs. *Journal of Hydrology*. 305 pp. 15-39.
- Cleugh H.A., Leuning R., Mu Q., Runnig S. X. (2007) Regional evaporation estimates from flux flow tower and MODIS satellite data. *Remote Sensing of Environment*, 106, pp. 285-304.
- DGF (1995) Results of the first National Inventory in Tunisia (*in French*). 88 p.
- Fensholt R. and Sandholt (2003) Derivation of a shortwave infrared stress index from MODIS near- and shortwave infrared data in semi arid environment. *Remote Sensing of Environment*, 87, pp. 111-121.
- Fensholt R., Sandholt and Rasmussen M.S. (2004) Evaluation of MODIS LAI, fAPAR and the relation between fAPAR and NDVI in a semi-arid environment using in situ measurements. *Remote Sensing of Environment*, 91, pp. 490-507.
- Guerschman J. P., Van Dijk A. I. J.M, Mattersdorf G., Beringer J. Hutley L.B., Leuning R., Pinpunic R. C. Sherman B. S. (2009) Scaling of potential evapotranspiration with MODIS data reproduces flux observations and catchment water balance observations across Australia. *Journal of Hydrology*. 369 pp. 107-119.
- Leuning R. Cleugh H.A., Zegelin S.J. and Hughes D. (2005) Carbon and water fluxes over a temperate Eucalyptus forest and a tropical wet/dry savanna in Australia: Measurments and comparison with MODIS remote sensing estimates. *Agricultural and Forest Meteorology*, 129, pp. 151-173.

- Li H., Zhang Y., Chiew F.H.S. and Xu S. (2009) Predicting runoff in ungauged catchments by using Xinanjiang model with MODIS leaf area index. *Journal of Hydrology*, 370, pp. 155-162.
- Myneni R., Hoffman S., Knyazikhin Y., Privette J., Glassy J. and Tian Y. Global products of vegetation leaf area and fraction absorbed PAR from year one of MODIS data. *Remote Sensing of Environment*, 83, pp. 214-231.
- Saxton K.E., W.J. Rawls, J.S. Romberger and R.I. Papendick (1986) Estimating generalized soil water characteristics from texture. *Trans. ASAE* 50, pp. 1031-1035.
- Saxton K. E. and W. J. Rowles , 2006). Soil water characteristic estimates by texture and organic matter for hydrologic solutions. *Soil Science Society American Journal* 70 (1569-1578).
- Wang X., Xie H., Guan H. and Zhou X. (2007) Different responses of MODIS-derived NDVI to root-zone soil moisture in semi-arid and humid regions. *Journal of Hydrology*, 340 P. 12-24.
- Xiao X.M., Zhang Q.Y., Hollinger D., Aber J. and Moore B. (2005) Modeling gross primary production of an evergreen needleleaf forest using MODIS and climate data. *Ecological Applications*, 15, pp. 954-969.
- Zhang Y. and Wegehenkel M. (2006) Integration of MODIS data into a simple model for the spatial distributed simulation of soil water content and evapotranspiration. *Remote Sensing of Environment*, 104, pp. 393-408.
- Zhou S.Q., Liang X., Chen J., and Gong P. (2004) An assessment of the VIC-3L hydrological model for the Yangtze River basin based on remote sensing: A case study of the Baohe River basin. *Canadian journal of Remote Sensing*, 30, pp. 840-853.

ACKNOWLEDGMENTS

This study was supported by the CORUS 2 (*Coopération pour la Recherche Universitaire et Scientifique*, Ministry of Foreign Affairs France). We are grateful to the “Ministry of Agriculture and Water Resources of Tunisia” for providing digital forest and soil data and to “NASA Earth Science Enterprise” for providing MODIS data on the web.

Application of canopy radiant temperature in the estimation of gross primary productivity

Liangfu Chen^a, Junxia Yan^{a, b, c}, Yanhua Gao^d, Jinhua Tao^a

^a State Key Laboratory of Remote Sensing Science, Jointly Sponsored by Institute of Remote Sensing Applications of Chinese Academy of Sciences and Beijing Normal University, Beijing 100101, China

^b Graduate University of Chinese Academy of Sciences, Beijing 100049, China

^c Institute of Loess Plateau, Shanxi University, Taiyuan 030006, China

^d Satellite Environment Center, Ministry of Environmental Protection, Beijing 100094, China

Email: Chen L: lfchen@irsa.ac.cn

ABSTRACT – In this study, the site measurements of canopy radiometric temperature (T_i) and photosynthetically active radiation (PAR), together with the 8-day composited Moderate Resolution Imaging Spectroradiometer (MODIS) data, of a subtropical evergreen coniferous forest ecosystem in southern China during 2005–2006 are used to estimate the seasonal variations of gross primary production (GPP) with the Production Efficiency Model (PEM). To investigate the possibility of satellite thermal infrared measurement (T_i) instead of atmospheric temperature (T_a) in the PEM model to estimate the GPP values, the T_i predicted GPP (GPP_{pred-i}) and T_a predicted GPP (GPP_{pred-a}) are used to compare the GPP values observed from eddy covariance measurements (GPP_{obs}). No significant difference is found between the relationships of GPP_{obs} and T_i and GPP_{obs} and T_a , indicating that T_i can be used to replace T_a in PEM model. There is a very strong linear relation between GPP_{pred-i} and GPP_{pred-a} ($r^2 = 0.9981$) and both the predicted GPP are highly corrected with the GPP_{obs} ($r^2 = 0.92$ and 0.91 , respectively). The annual total GPP_{pred-i} and GPP_{pred-a} values (1620.1 and 1598.6 g C m⁻² for 2005; 1703.6 and 1660.8 g C m⁻² for 2006, respectively) were slightly lower than the corresponding measurements of the flux tower GPP_{obs} (1646.8, 1867.4 g C m⁻²). The results from this study demonstrated the T_i can be potentially used to estimate ecosystem carbon fluxes instead of T_a in the PEM model.

1 INTRODUCTION

The gross primary production (GPP) of vegetation is one of the key elements that determine the strength of the carbon sink for a terrestrial ecosystem (Wu et al., 2009). Researches conducted in a variety of ecosystems have demonstrated the potential of using remote sensing-based techniques to sufficiently estimate the carbon dioxide (CO₂) exchange. However, many GPP models such as BIOME-BGC, FOREST-BGC, CASA, VPM model still require some driving parameters, such as air temperature (T_a) to be measured from ground (e.g. Running & Coughlan, 1994; Xiao et al., 2004). Since physiological activities of leaves are likely to be closer to vegetation temperature rather than T_a , thermal infrared temperature of canopy (T_i) should be a useful measurement as an index of physiological activity at top canopy, provided that leaf cover is great enough that T_i is not significantly affected by soil surface temperature (Sims et al., 2008). Besides, T_a derived from standard meteorological observations generally may not describe the spatial heterogeneity typically

encountered over larger land areas, resulting in substantial errors in the estimation of carbon exchange in an ecosystem (Prihodko et al., 1997). Yet, T_i is characterized with spatial continuity and it is available over much of the earth on a regular time basis from remote sensing satellite.

The capability of using thermal infrared data from space to infer regional and local scale evapotranspiration has been extensively studied and significant progress has been made over the past decade. The existence of an intimate relationship between crop evaporation and dry-matter accumulation was established more than 70 years ago. Dry-matter accumulation by a crop is a direct consequence of carbon assimilation (photosynthesis). A review of papers by Zelitch (1982) have shown that the existence of a close relationship between the rates of dry-matter accumulation and carbon assimilation. The pathway of carbon flow into the leaves (and other green parts) from the atmosphere was virtually identical to that of water-vapor outflow (an exception would be peristomatal transpiration) (Choudhury, 1989). Hence, there are rather conservative relationships between crop evaporation and carbon

assimilation. It is clear that if T_i can be used to estimate crop evaporation, it might be used as a model input data or as model calibration data for estimating carbon assimilation and dry-matter accumulation.

Several studies have indicated that T_i can substantially improve the GPP estimations at global or regional scales. For example, the seasonal dynamics of GPP predicted by the Temperature and Greenness (TG) model with the Enhanced Vegetation Index (EVI) and Land Surface Temperature (LST) agreed well with the measured GPP at 11 eddy correlation flux towers in a wide range of vegetation types across North America (Sims et al., 2008). Inoue et al. (2004) reported that the soil surface CO_2 flux under bare soil conditions was best correlated with the remotely sensed surface temperature, while air temperature was less well correlated and soil temperature and soil water content were poorly correlated.

CO_2 flux measurements at individual CO_2 eddy flux sites offer new opportunities to examine daily, seasonal and multiyear dynamics of the GPP at stand and ecosystem scales. The measurements can be used to validate carbon assimilations determined using remote sensing method. However, up to now, validation of T_i as an input variable instead of T_a in the satellite remote sensing based model of estimating GPP has not been conducted at any CO_2 eddy flux tower site.

In this study, the Production Efficiency Model (PEM) is selected to investigate if T_i can be used to replace T_a to accurately predict the GPP values in a subtropical coniferous ecosystem by comparing the model results with the ground measurements. Other parameters input to the PEM model include PAR (photosynthetically active radiation) from the eddy tower, the vegetation indices (the normalized difference vegetation index (NDVI) and the Land Surface Water Index (LSWI)) from MODIS sensor. The seasonal GPP simulations are conducted at a subtropical evergreen coniferous forest ecosystem in southern China over the period of 2005-2006.

2 MATERIALS AND METHODS

2.1 Brief description of the study site

The eddy flux tower site (26°44'N, 115°03'E, and elevation 102 m) is located at the Qianyanzhou Ecological Experimental Station of Chinese Ecosystem Research Network (CERN) and ChinaFLUX network in southeast China. This region is controlled with subtropical monsoon climate system, with the mean annual air temperature of 17.9°C and mean annual precipitation of 1485.1 mm (1985-2004). The artificial coniferous forest was planted in middle 1980s. The flux tower, set up in 2002, is located at the top of a hill, in a hilly

topography with a slope ranging between 2.8° and 13.5°. T_i was measured synchronously with carbon fluxes measurements using an infrared thermometer ranging from 8 to 14 μm (Model SI-212, Campbell Scientific Inc., Logan, UT, USA), which was suspended 41 m height at an angle of about 30° from horizontal. Because the forest coverage is about 90 % around the tower across the whole year, T_i is not significantly affected by soil surface temperature. The predominant species in the site was subtropical planted coniferous plantation of *Pinus massoniana* Lamb, *Pinus elliottii* Engelm, and *Cunninghamia lanceolata* Hook. More extensive description of the sites could be found in Zhang et al. (2006).

2.2 Overview of the PEM model

Several satellite-based modeling studies have used the PEM to estimate the GPP at large spatial scales (Goetz et al., 1999) and the model could be described as follows:

$$\text{GPP} = \varepsilon_g \times \text{FPAR} \times \text{PAR} \quad (1)$$

$$\varepsilon_g = \varepsilon_0 \times T_{\text{scalar}} \times W_{\text{scalar}} \quad (2)$$

where ε_g is the light use efficiency ($\mu\text{mol CO}_2/\mu\text{mol PPFD}$), and varies with the combined effects of temperature and water. PAR is the photosynthetically active radiation ($\mu\text{mol m}^{-2} \text{s}^{-1}$, photosynthetic photon flux density, PPFD); FPAR is the fraction of PAR absorbed by vegetation canopy and is estimated as a simple linear function of NDVI (Myneni and Williams, 1994) obtained from a three-dimensional radiative transfer model GeoSAIL (see Eq.(3); Huemmrich, 2001), while the NDVI is calculated from surface reflectance in the red and near-infrared (NIR) spectral bands (Tucker, 1979).

$$\text{FPAR} = 1.6579 \times \text{NDVI} - 0.3929 \quad (3)$$

$$\text{NDVI} = \frac{\rho_{\text{nir}} - \rho_{\text{red}}}{\rho_{\text{nir}} + \rho_{\text{red}}} \quad (4)$$

T_{scalar} is estimated at each time step, using the algorithms developed for the process-based biogeochemical model (Biome-BGC) by Running (1994):

$$T_{\text{scalar}} = \begin{cases} \frac{\log(T+1)}{\log(T_{\text{opt}}+1)} & \dots T < T_{\text{opt}} \\ \cos\left(\frac{T-T_{\text{opt}}}{T_{\text{max}}-T_{\text{opt}}} \times \frac{\pi}{2}\right) & \dots T \geq T_{\text{opt}} \\ 0 & \dots T < 0 \end{cases} \quad (5)$$

where T is the site-specific T_a or T_i , and T_{\max} and T_{opt} are maximum and optimal temperature for photosynthetic activities, respectively.

W_{scalar} is the indicator of water on plant photosynthesis. Xiao et al. (2004) proposed a simple approach using a water-sensitive vegetation index to estimate the seasonal dynamics of W_{scalar} :

$$W_{\text{scalar}} = \frac{1 + \text{LSWI}}{1 + \text{LSWI}_{\max}} \quad (6)$$

where LSWI is the Land Surface Water Index and LSWI_{\max} is the maximum LSWI within the growing season for individual pixels. LSWI is calculated as the normalized difference between NIR and SWIR spectral bands (Xiao et al., 2002):

$$\text{LSWI} = \frac{\rho_{\text{nir}} - \rho_{\text{swir}}}{\rho_{\text{nir}} + \rho_{\text{swir}}} \quad (7)$$

where ρ_{nir} and ρ_{swir} are reflectance data of the NIR and SWIR bands, respectively. For MODIS images, we use NIR (841-875 nm) and SWIR (1628-1652 nm) bands.

2.3 Description of field data and MODIS image acquisition

2.3.1 Field data from the CO₂ flux tower site

Daily measured net ecosystem exchange (NEE) and the derived GPP and ecosystem respiration and meteorological data during 2005-2006 were provided by researchers at Qianyanzhou tower flux station. Daily meteorological and CO₂ flux data were aggregated at the 8-day interval to be consistent with the 8-day composite MODIS images, including the 8-day sums of PAR and CO₂ flux data (see Fig. 1.)

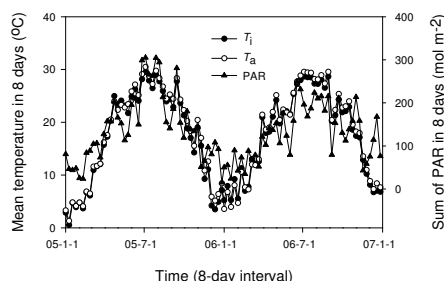


Figure 1 Seasonal dynamics of PAR and mean temperature (T_a and T_i) during 2005-2006 at the tower flux site in Qianyanzhou station.

2.3.2 The 8-day composite images of land surface reflectance from the MODIS sensor

Seven of the 36 MODIS bands are primarily designed for vegetation and land surface studies: blue (459-479 nm), green (545-565 nm), red (620-670 nm), near infrared (841-875 nm, 1230-1250 nm) and shortwave infrared (1628-1652 nm, 2105-2155 nm). The MODIS sensor acquires daily images of the globe at a spatial resolution of 250 m for red and near infrared (841-875 nm) bands, and at a spatial resolution of 500 m for blue, green, near infrared (1230-1250 nm) and shortwave infrared bands. The MODIS land Science Team provides 8-day composite products to the users. We downloaded the 8-day Land Surface Reflectance product (MOD09A1) data sets for the period of 2005-2006 from the Earth Resources Observation and Science (EROS) Data Center, US Geological Survey (<http://edc.usgs.gov/>). Reflectance values of the MOD09A1 data set from the three spectral bands red, NIR (841-875 nm) and SWIR (1628-1652 nm) were used to calculate the vegetation indices NDVI and LSWI. Based on the geolocation information (latitude and longitude) of the CO₂ flux tower site, data for vegetation indices were extracted from one MODIS pixel that is centered on the flux tower.

2.3.3 Parameterization of the model

In the PEM model, the maximum light use efficiency (ϵ_0) changes with vegetation types. Here, we used $\epsilon_0 = 0.0016 \text{ mg CO}_2 \mu\text{mol photon}^{-1}$, based on an earlier study of CO₂ fluxes at a subtropical *pinus* plantation of southeastern China (Zhang et al., 2006).

LSWI_{\max} is dependent on time and optical sensor. In this study, the mean LSWI values of individual temporal composite points were calculated at every 8 days, and the maximum LSWI value within the photosynthetically active period was used as LSWI_{\max} . We used T_{opt} of 20 °C and T_{\max} of 40 °C for this subtropical evergreen coniferous forest.

3 RESULTS

3.1 Seasonal dynamics of site-specific temperature (T_a and T_i)

The seasonal T_i and T_a vary with similar magnitude and phase (Fig. 1). They were below 10 °C in winter, increased rapidly in late March, reached its peak in early July to late August, and then declined gradually to their minimum values in winter. The values of T_i and T_a varied from -3.6 to 30.5 °C and -1.3 to 31.4 °C for 2005; from -0.07 to 31.5 °C and -2.5 to 32.5 °C for 2006, respectively. Annual mean T_i and T_a were, respectively, 16.9 ± 9.08 °C and 17.6 ± 9.04 °C for 2005; 18.36 ± 8.36 °C and 17.95 ± 7.92 °C for 2006. The mean T_i and T_a over the two years were 17.62 ± 8.71 °C and 17.78 ± 8.45 °C, respectively. No significant difference existed between the two-year

mean T_i and T_a . T_i rarely deviated from T_a by more than $\pm 2.0^\circ\text{C}$. There were significant linear relation between T_a and T_i ($r^2 = 0.99$, $p < 0.01$; Fig. 2).

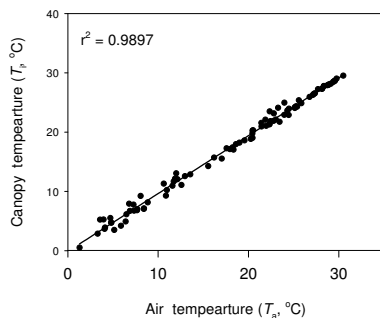


Figure 2 The linear relationship between air temperature (T_a) and canopy infrared temperature (T_i) during 2005-2006 at the tower flux site in Qianyanzhou station.

3.2 Seasonal dynamics of CO_2 fluxes during 2005-2006

The measured GPP at this forest site had a distinct seasonal cycle (Fig. 3). The GPP values were below $2 \text{ g C m}^{-2} \text{ day}^{-1}$ in winter, because low temperature inhibited photosynthetic activities of coniferous trees. It began to increase in late April and reached its peak in late June to early August. The GPP fluctuations were mostly coincidental with the fluctuations in PAR during summer season. Then it declined gradually to its lowest value in January. The seasonal dynamics of GPP could be explained in part by the seasonal dynamics of the temperature and PAR.

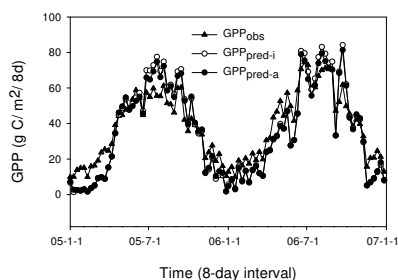


Figure 3 Seasonal dynamics of 8-day gross primary production (GPP, g C m^{-2}) during 2005-2006 at the tower flux site in Qianyanzhou station.

3.3 Analyses of the relationships between temperature (T_a and T_i) and the GPP_{obs}

As shown in Fig. 4, the seasonal dynamics of measured GPP_{obs} were highly correlated with the temperature (T_a and T_i). There is no significant

difference between the coefficients of determination of the fitted exponential equations between the GPP_{obs} and the T_a and T_i , and both variables could explain about 90% variations of the GPP_{obs} in this area. This correlation results supports the idea that canopy temperature can be used to replace air temperature to GPP to some extent.

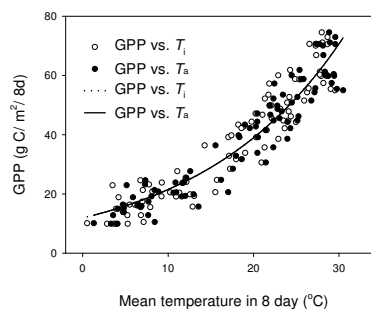


Figure 4 the quantitative relationships between the observed GPP from the tower measurements and the temperatures (T_a and T_i) during 2005-2006 at the tower flux site in Qianyanzhou station. The exponential regression models between GPP and T_i and T_a are as follows: $\text{GPP} = 10.87e^{0.0637T_i}$, $r^2 = 0.90$; $\text{GPP} = 10.455e^{0.06467T_a}$, $r^2 = 0.89$, $N = 92$.

3.4 Simulations of the PEM model

The predicted values of GPP ($\text{GPP}_{\text{pred-i}}$ and $\text{GPP}_{\text{pred-a}}$) were compared with eddy flux tower observations of GPP_{obs} at the flux site (Fig. 5). Both the $\text{GPP}_{\text{pred-i}}$ and $\text{GPP}_{\text{pred-a}}$ agreed well with the observed GPP_{obs} from the flux towers data, although the $\text{GPP}_{\text{pred-i}}$ and $\text{GPP}_{\text{pred-a}}$ values were generally lower than the GPP_{obs} in winter, and higher at the peak of the growing season (Fig. 3). A simple linear regression model showed good agreement between the GPP_{obs} and the $\text{GPP}_{\text{pred-i}}$, $\text{GPP}_{\text{pred-a}}$ ($r^2 = 0.9981$, $P < 0.01$) (Fig. 5). No significant difference was found at the coefficients of determination between the GPP_{obs} and $\text{GPP}_{\text{pred-i}}$, $\text{GPP}_{\text{pred-a}}$ ($r^2 = 0.92$, $P < 0.01$ for GPP_{obs} and $\text{GPP}_{\text{pred-i}}$; $r^2 = 0.91$, $P < 0.01$ GPP_{obs} and $\text{GPP}_{\text{pred-a}}$). This result further indicates that T_i could be used in the remote sensing GPP models as an environmental factor in calculating ecosystem carbon exchange. The annual total $\text{GPP}_{\text{pred-i}}$ and $\text{GPP}_{\text{pred-a}}$ values were 1620.1 and $1598.6 \text{ g C m}^{-2}$ in 2005; 1703.6 and $1660.8 \text{ g C m}^{-2}$ in 2006, respectively, slightly lower than the corresponding ones of the flux tower GPP_{obs} (1646.8 , $1867.4 \text{ g C m}^{-2}$ in 2005 and 2006, respectively).

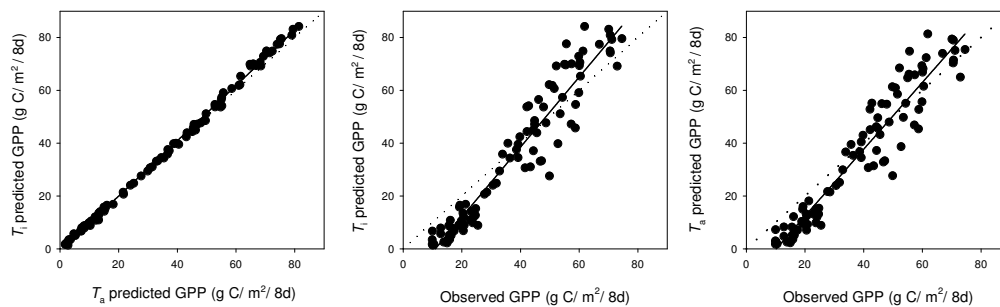


Figure 5 Comparisons between predicted GPP and observed GPP from tower data at the flux tower site in Qianyanzhou station. Solid line is regression lines between GPP_{pred-i} , GPP_{pred-a} and GPP_{obs} , and dashed line is 1:1 line.

Table 1 Comparison between the annual total value of GPP_{obs} and the corresponding ones of the predicted GPP_{pred-i} and GPP_{pred-a} in this ecosystem ($g C m^{-2}$)*

Year	GPP_{obs}	GPP_{pred-i}	GPP_{pred-a}
2005	1646.8	1620.1 (RE = 1.6 %)	1598.6 (RE = 2.9 %)
2006	1867.4	1703.6 (RE = 8.8%)	1660.8 (RE = 11.1 %)
All	1757.1	1661.9 (RE = 5.4%)	1629.7 (RE = 7.3 %)

* RE = $[(GPP_{obs} - GPP_{pre}) / GPP_{obs}] \times 100\%$.

4 CONCLUSIONS

In this study, we compared the predicted GPP (both GPP_{pred-i} and GPP_{pred-a}) with the observed GPP (GPP_{obs}) from eddy covariance determined and found that the phase and magnitude of the T_i derived GPP was very consistent with the GPP from T_a ($r^2 = 0.9981$, see Fig. 5), and they both accounts for over 90% variations of observed GPP values (GPP_{obs}). The results from this study support the hypothesis that T_i derived from thermal infrared measurement could be used to estimate ecosystem carbon fluxes instead of T_a in the PEM model. Additional studies are needed to examine the relationship between canopy infrared temperature and seasonal dynamics of GPP across the flux tower sites, and validate the capability of the PEM model of T_i as an input variable in various biomes with different vegetation coverage.

5 ACKNOWLEDGEMENTS

This study was supported financially by the National Natural Science Foundation of China (Grant No. 40871174). We thank the researchers who worked at the eddy flux tower of Qianyanzhou forest for providing multi-year CO_2 flux and climate data.

6 REFERENCES

Aber, J.D. and Federer, C.A., 1992, A generalized, lumped-parameter model of photosynthesis,

evapotranspiration and net primary production in temperate and boreal forest ecosystems. *Oecologia*, 92, 463-474

Choudhury, B.J., 1989, Estimating evaporation and carbon assimilation using infrared temperature data: vistas and modeling. In: *Theory and Application of Optical Remote Sensing*. New York: John Wiley & Sons, pp. 628-690

Goetz, S.J., Prince, S.D., Goward, S.N., Thawley, M.M., Small, J., 1999, Satellite remote sensing of primary production: an improved production efficiency modeling approach. *Ecological Modeling*, 122, 239-255

Huemmerich, K. F., 2001, The GeoSail model: a simple addition to the SAIL model to describe discontinuous canopy reflectance. *Remote Sensing of Environment*, 75, 423-431

Inoue, Y., Oliso, A. and Choi, W., 2004, Dynamic change of CO_2 flux over bare soil field and its relationship with remotely sensed surface temperature. *International Journal of Remote Sensing*, 25, 1881-1892

Myneni, R.B. and Williams, D.L., 1994, On the relationship between FAPAR and NDVI. *Remote Sensing of Environment*, 107, 510-519

Prihodko, L., Goward, S.N., 1997, Estimation of air temperature from remotely sensed surface observations. *Remote Sensing of Environment*, 60, 335-346

Running, S.W., 1994, Testing FOREST-BGC ecosystem process simulations across a climatic

- gradient in Oregon. *Ecological Applications*, 4(2), 238-247
- Sims, D.A., Rahman A.F., Cordov, V.D., El-Masri, B.Z., Baldocchi, D.D., Bolstad, P.V., Flanagan, L.B., Goldstein, A.H., Hollinger, D.Y., Misson, L., Monson, R.K., Oechel, W.C., Schmid, H.P., Wofsy, S.C., Xu, L.K., 2008, A new model of gross primary productivity for North American ecosystems based solely on the enhanced vegetation index and land surface temperature from MODIS. *Remote Sensing of Environment*, 112, 1633-1646
- Tucker, C.J., 1979, Red and photographic infrared linear combinations for monitoring vegetation. *Remote Sensing of Environment*, 8, 127-150
- Wu, J.B., Xiao, X.M., Guan, D.X., Shi, T.T., Jin, C.J., Han, S.J., 2009, Estimation of the gross primary production of an old-growth temperate mixed forest using eddy covariance and remote sensing. *International Journal of Remote Sensing*, 30, 463-479
- Xiao, X.M., Boles S., Liu J.Y., Zhang, D.F., Liu, M.L., 2002, Characterization of forest types in Northeastern China, using multi-temporal SPOT-4 VEGETATION sensor data. *Remote Sensing of Environment*, 82, 335-348
- Xiao, X.M., Hollinger, D., Aber, J.D., Goltz, M., Davidson, E.A., & Zhang, Q.Y., 2004, Satellite – based modeling of gross primary production in an evergreen needle leaf forest. *Remote Sensing of Environment*, 89, 519-534
- Zelitch, I., 1982, The close relationship between net photosynthesis and crop yield. *BioScience*, 32, 796-802
- Zhang, L.M., Yu, G.R., Sun, X.M., Wen, X.F., Ren, C.Y., Fu, Y.L., Li, Q.K., Li Z.Q., Liu, Y.F., Guan D.X., Yan J.H., 2006, Seasonal variations of ecosystem apparent quantum yield (α) and maximum photosynthesis rate (P_{\max}) of different forest ecosystems in China. *Agricultural and Forest Meteorology*, 137, 176-187

Performance assessment of four surface energy budget models, forced with in-situ and ASTER surface temperature, against eddy covariance and scintillometer data in temperate and semi-arid regions.

Chirouze J.^{1*}, Boulet G.¹, Béziat P.¹, Jarlan L.¹, Fieuzal R.¹, Garatuza-Payan J.², Watts C.³, Rodriguez J.C.³, Ezzahar J.⁴, Er-raki S.⁵, Chehbouni G.¹

¹ CESBIO UMR 5126 UPS, CNRS, CNES, IRD, Toulouse, France

² ISON, Ciudad Obregón, Sonora, Mexico

³ UNISON, Hermosillo, Sonora, Mexico

⁴ CNESTEN, Kenitra, Morocco

⁵ Université Cadi Ayyad/Institut de Recherche pour le Développement, Marrakech, Morocco

*Jonas.Chirouze@cesbio.cnes.fr

ABSTRACT – There are various types of water budget models but their use often requires a lot of input data that are difficult to estimate, at least spatially. Remote sensing data, especially the surface temperature, gives access to distributed information about the surface energy balance and water status. The MISTIGRI satellite mission is proposed with this context: to obtain high resolution thermal data (<100m) with a high temporal revisit (daily). Thus the interest of developing models which integrate such data is quite high. In this paper, four models which solve the surface energy balance equation will be compared: two single pixel models: the Surface Energy Balance System (SEBS) and the Two-Sources Energy Balance (TSEB) and two contextual models which combine remote sensing information acquired at different locations of a TIR image: the Simplified Surface Energy Balance Index (S-SEBI) and the more complex Mapping EvapoTranspiration at high Resolution with Internalized Calibration (METRIC) model. This inter-comparison is carried out for a dataset acquired in the Yaqui valley (Mexico) which has a semi-arid climate. The four models will be evaluated punctually with radiometric and eddy-covariance system data and then at a larger scale with scintillometric measurements and ASTER TIR images. Preliminary results show that the contextual models give more accurate results than the single pixel ones. However, they are very dependent on the quality of ancillary satellite data (vegetation indices, albedo), showing poor results in dry conditions (after harvesting). The single pixel models have numerous parameters whose estimation proves difficult but give more consistent results during the whole period of study.

1 INTRODUCTION

Considering the impact of current and future climatic and anthropogenic changes on the availability of water resources, particularly in arid and semi-arid zones, the optimization of water use in irrigated agriculture is an important issue. Given that irrigation uses more than 80% of the available water in these regions, assessing the evapotranspiration (ET) is a key point in water budget management.

To estimate ET at an acceptable scale (a cultivated region for example), using remote sensing data seems to be quite a valuable solution. Whereas meteorological data can be assumed as homogeneous over a small region, the surface conditions vary a lot depending on their properties (temperature, land use, vegetation cover) and are complicated to retrieve efficiently. Remote sensing data offers a large panel of spatially distributed information about the terrestrial surface like vegetation indexes (such as NDVI),

surface radiative properties (albedo, emissivity) and temperature.

Many methods based on remote sensing data in the Thermal Infra Red estimate the instantaneous latent heat flux (LE) as a residual of the surface energy balance (SEB) (Courault, 2005):

$$R_n - G - H = LE \quad (1)$$

The net radiation R_n and the soil heat flux G are usually computed as a direct function of the surface temperature but the SEB models differ mainly by their formulation of the turbulent fluxes H (sensible heat) and LE (latent heat).

In this paper we will compare the performance and philosophy of four of those methods which use distinct approaches. Two are single pixel based models which solve the SEB for each pixel independently from the others: the Surface Energy Balance System (SEBS) (Su, 2002) and the Two-Source Energy Balance

(TSEB) (Norman, 1995). The other two are contextual methods which combine remote sensing information acquired at different locations of a TIR image: the relatively simple Simplified Surface Energy Balance Index (S-SEBI) (Roerink, 2000) and the more complex Mapping EvapoTranspiration at high Resolution with Internalized Calibration (METRIC) (Allen, 2007) method.

2 DATA AND METHODOLOGY

2.1 The “Yaqui 2008” experiment

An international cooperative experiment took place in the valley of Yaqui (Sonora, México) from December 2007 to June 2008. The experimental site is a square of 4x4km located in an agricultural irrigated region of 250,000km². In this zone different types of cultures are grown: wheat, pepper, potatoes, chickpea, etc. The diversity of growing species in the area allows us to evaluate the models on homogeneous (wheat) and heterogeneous covers over the entire growing season.

A large experimental set up has been deployed over the study area. First, six micro-meteorological stations equipped with instruments measuring the turbulent fluxes (eddy-covariance system, EC), the radiative fluxes (radiometers) and conductive fluxes (heat flux plates) were installed. The net radiation is acquired with CNR1 and Q7 radiometers (Campbell). The soil heat flux is measured with two Hukseflux HFP-001 plates placed at a depth of 5cm on the top and the bottom of the furrow at each station.



Figure 1: land use of the north part of the study area

Young and CSAT3 apparatus (Campbell) were used to acquire the sensible heat flux. Finally, KH20 hygrometers (Campbell) measured the latent sensible flux. Three Large Aperture Scintillometers (LAS)

(Campbell) acquired the large scale sensible heat flux H over different types of land uses. Leaf Area Index (LAI) and crop height measurements were acquired at many locations during the growing season.

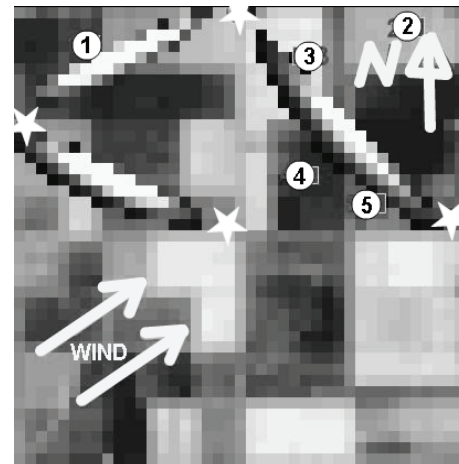


Figure 2: experimental set up. Circles from 1 to 5 are the EC stations (1 – wheat, 2 – wheat, 3 – Broccoli, 4 – Pepper, 5 – Chickpea). White stars are the LAS transmitters' positions.

2.2 The remote sensing data

We have at our disposal seven ASTER images of radiative surface temperature, from the 30th of December 2007 to the 13th of May 2008, at a resolution of 90m. Extraction of ASTER surface temperature at the EC stations coordinates shows that there is an RMSE of around 5°C with the Apogee sensor measurement at each station, but almost no bias ($B=-0.4$).

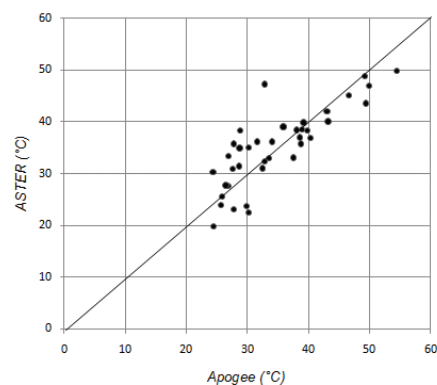


Figure 3: ASTER surface temperature versus Apogee in-situ measurements for each station

A satellite based LAI is computed from the Normalized Differential Vegetation Index (NDVI) of FORMOSAT images. Twenty six images were retrieved from November 2007 to June 2008. The

albedo is a linear combination of both reflectances from bands 3 and 4 of FORMOSAT (Courault, 2008).

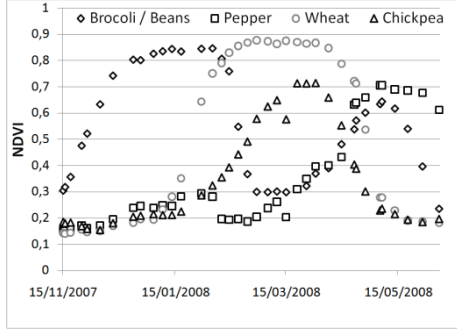


Figure 4: FORMOSAT NDVI extracted at four stations

2.3 Comparison of the methods

2.3.1 The Surface Energy Balance System (SEBS)

This single pixel one-source energy balance model considers the surface as a mixed pixel of vegetation and bare soil. In theory, the sensible heat flux H is computed as follows:

$$H = \rho C_p \frac{T_{aero} - T_a}{r_a} \quad (2)$$

With ρ the density of air, C_p its calorific capacity, T_{aero} the air temperature at the aerodynamic level, T_a the air temperature at the reference level z and r_a the aerodynamic resistance to heat transfer.

$$r_a = \frac{1}{k u_*} \left[\ln \left(\frac{z-d}{z_{oh}} \right) - \Psi_h \left(\frac{z-d}{L} \right) + \Psi_h \left(\frac{z_{oh}}{L} \right) \right] \quad (3)$$

Where $k=0.4$ is the Von Karmann constant, u_* the friction velocity, d the displacement height, z_{oh} the roughness length for heat transfer, L the Monin Obukhov length and Ψ_h the stability function for heat transfer. The temperature T_{aero} is quite difficult to assess and is often assimilated to the surface temperature. To compensate for this approximation, SEBS proposes an alternative expression based on the expected wind and temperature profile in the canopy and z_{oh} values for bare soil and full cover conditions respectively (Su, 2002).

2.3.2 The Two-Source Energy Balance (TSEB)

Instead of making assumption on the wind and temperature profiles within the canopy, this method computes separate SEBs for the soil and the vegetation (see figure 5). It distributes the net radiation between soil and vegetation depending on the LAI (see equation (6)).

$$R_{n,w} = R_n (1 - \exp(-0.45LAI)) \quad (6)$$

It also makes the strong hypothesis that vegetation evaporates at potential rate, and computes a soil evaporation residual. If this residual is negative, this means that the full transpiration is not reached, i.e.

plant suffers stress. Then vegetation water stress is again solved as a residual of the SEB by assuming that soil no longer evaporates when the vegetation and its rooting system suffers from stress.

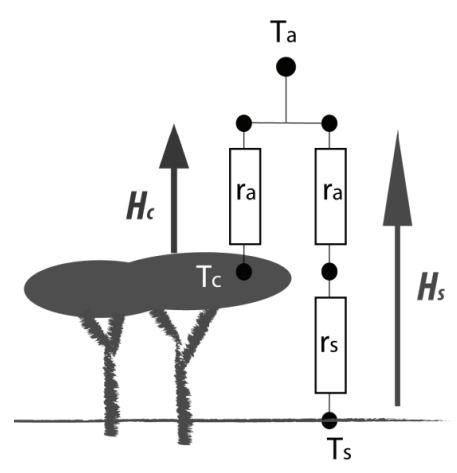


Figure 5: distribution of H fluxes for the two-source model. r_s is the aerodynamic resistance between soil and vegetation.

2.3.3 The Simplified Surface Energy Index (S-SEBI)

This method is based on the hypothesis that, given the meteorological conditions over the studied scene are homogeneous, there is a unique linear relation between surface temperature and albedo in extreme conditions for a whole satellite image (i.e. wet and dry areas, see figure 6): radiative control ($LE \sim 0$) and evaporative control ($H \sim 0$).

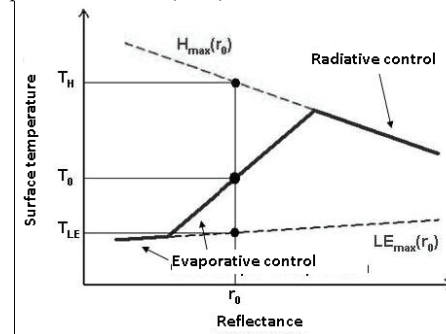


Figure 6: graphic relation between surface temperature and albedo

The user has to determine manually those two relations for each image. Then for each pixel, it computes dry and wet hypothetical temperatures, T_H and T_{LE} . The evaporative fraction is computed from those two temperatures and the surface radiometric temperature T_0 . The process is resumed in equation (7), (8) and (9).

$$T_H = a_H + b_H r_0 \quad (7)$$

$$T_{LE} = a_{LE} + b_{LE} r_0 \quad (8)$$

$$\Lambda = \frac{T_{0,max} - T_0}{T_{0,max} - T_a} = \frac{T_H - T_0}{T_H - T_{LE}} = \frac{\lambda E}{R_n - G} \quad (9)$$

2.3.4 The Mapping EvapoTranspiration at high Resolution with Internalized Calibration method (METRIC)

This contextual method is based on the hypothesis that air temperature in the first layer of atmosphere is linearly dependent on the surface temperature (see equations (10) and (11)).

$$H = \rho C_p \frac{dT}{dT_a} \quad (10)$$

$$dT = a + bT_s \quad (11)$$

In order to retrieve this relation, the user should select, similarly to S-SEBI, hot (dry) pixels and cold (wet) ones. H then dT are computed for those extremes conditions and a and b are retrieved. LE is a residual of the energy balance closure.

2.4 Methodology

In order to compare, not only the pure efficiency of the four models but also the consequences of their different structuring, the formulation of R_n and G had to be standardized for all the methods. To do that, we compared our simulated R_n and G at the pixels corresponding to the stations, with the in-situ measurements. The results are in Table 1.

	TSEB	SEBS	SSEBI	METRIC
G	94,8	100,0	96,9	63,4
Rn	81,3	81,3	85,4	101,1

Table 1: RMSE of models compared to in-situ measurements

The errors are consequent for both R_n and G . That can be partially caused by the formulation of FORMOSAT albedo we used. Indeed, those albedos were calibrated with in-situ measurements in a temperate and more complex landscape of South-Eastern France (Courault, 2008). This formulation has not been verified in our case of study so it is likely to be a source of error.

From this study, the formulations of R_n and G kept were the ones with the smallest RMSE (equations (12) and (13)).

$$R_n = (1 - \alpha) R_g + \epsilon R_{atm} + \sigma \epsilon T_0^4 \quad (12)$$

$$G/R_n = 0.05 + 0.18 \exp(-0.521 LAI) \quad \text{if } LAI \geq 0.5$$

$$G/R_n = 1.80 \frac{(T_s - 273.15)}{R_n} + 0.084 \quad \text{if } LAI < 0.5 \quad (13)$$

We will then, with this basis for the available energy $R_n - G$, compute the H and LE fluxes for the seven ASTER scenes. In order to compare them to the scintillometric data, we had to weight them with the footprints of the scintillimeters.

3 PRELIMINARY RESULTS

3.1 Comparison with the scintillometers data

The fluxes are computed for the dates where scintillometric and ASTER data are available. They go from the 2008/02/23 to the 2008/05/13 for the 20001 LAS and from the 2008/03/10 to the 2008/05/13 for the 97001 LAS.

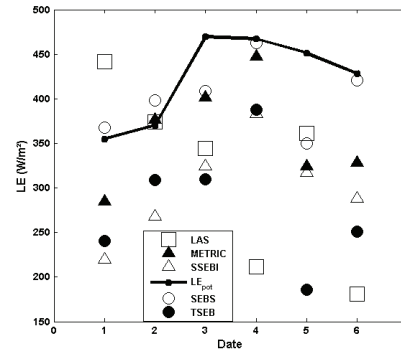


Figure 7: computed flux for the 20001 LAS (heterogeneous patch)

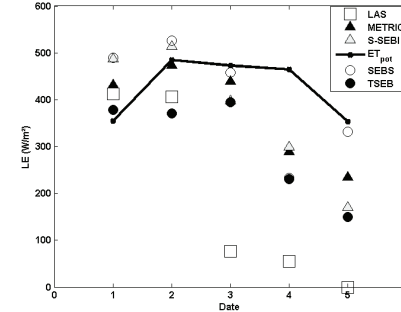


Figure 8: computed fluxes for the 97001 LAS (wheat patch)

There is a big variability in the results for 20001 LAS (north-east). SEBS and METRIC seem to be in agreement with the conditions of potential evapotranspiration for the 2nd and 3rd dates, during the growing period with a high LAI . Also, at the 5th date, we can assume that the scintillometer gives bad results. The models are in agreement with each other and over this heterogeneous patch, there should not be such a fall in LE .

Things appear to be better over the wheat field, at least during the growing period. On the contrary, the four models simulate way to high LE fluxes for the last three dates when the wheat is dry then harvested. We have yet to discover the cause of this phenomenon but, we already know that METRIC tends to simulated way to little differences between T_0 and T_a , which can explain big LE . SEBS and TSEB simulated quite high

aerodynamic resistances at the end of the study, which also leads to an over-estimation of LE .

3.2 Spatial inter-comparison

To observe the spatial variability of the models, we have made histograms of the repartition of the fluxes values on the whole northern half of the study area (figure 9).

Again the results are quite different for each model. SEBS and TSEB are both centered on a major value. It has to be expected that the two local models have, if not exactly the same, a similar behavior compared to the contextual ones. METRIC has a very poor spatial variability. All of the values are concentrated in a range of 20W/m^2 . We can assume that the retrieving of dT is quite poor. The choice of the hot and cold points on the TIR image can be questioned. S-SEBI on the contrary is the most distributed model. The linear relationship between temperature and albedo can explain a high sensibility to the change of surface properties.

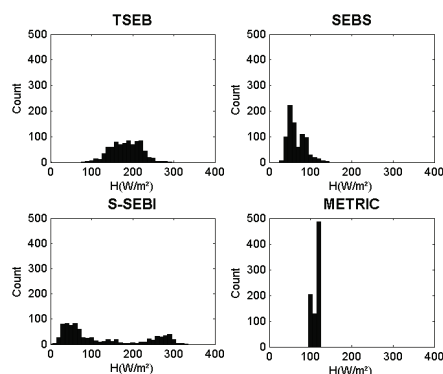


Figure 9: values histogram of H in the northern half of the study area

4 CONCLUSIONS

The four models have very different behaviors and we have yet to discover all the reasons to these divergences. Results are more consistent for well developed unstressed homogeneous crops but when stress or dry vegetation is present, the performances suffer greatly. Concerning the local models, a calibration by type of crop could bring better results.

For the contextual methods, the choice of the pixels representing extreme conditions seems to be a lead to ameliorate their estimations. More studies on the details of the methods will be conducted (e.g. new formulation of the kB^{-1} , new repartition of the net radiation in TSEB) in order to define the exact sources of error of the models. This work will later be used in order to assimilate surface temperature observations or the SEB-derived evapotranspiration into a Soil Vegetation Atmosphere Transfer model (ICARE); therefore knowing the limits of the models and performing a detailed error analysis is a crucial issue for us.

5 REFERENCES

- Allen, R.G., Tasumi, M., Trezza, R., 2007. Satellite-based energy balance for mapping evapotranspiration with internalized calibration (METRIC) - Model. *Journal of Irrigation and Drainage Engineering-ASCE*, 133(4): 380-394.
- Courault, D., Seguin, B., Olioso, A., 2005. Review on estimation of evapotranspiration from remote sensing data: From empirical to numerical modeling approaches. *Irrigation and Drainage Systems*, 19(3-4): 223-249.
- Courault, D., Bsaibes, A., Kpemlie, E., Hadria, R., Hagolle, O., Marloie, O., Hanocq, J.F., Olioso, A., Bertrand, N., Desfonds, V., 2008. Assessing the potentialities of FORMOSAT-2 data for water and crop monitoring at small regional scale in South-Eastern France. *Sensors*, 8(5): 3460-3481.
- Norman, J.M., Kustas, W.P., Humes, K.S., 1995. Source approach for estimating soil and vegetation energy fluxes in observations of directional radiometric surface temperature. *Agricultural and Forest Meteorology*. 77(3-4): 263-293.
- Roerink, G.J., Su, Z., Menenti, M., 2000. S-SEBI: A simple remote sensing algorithm to estimate the surface energy balance. *Physics and chemistry of the earth part B-Hydrology oceans and atmosphere*. 25(2): 147-157.
- Su, Z., 2002. The Surface Energy Balance System (SEBS) for estimation of turbulent heat fluxes. *Hydrology and Earth System Sciences*. 6(1): 85-99.

Land surface temperature representativeness and its relationship with soil moisture through an energy water balance model

Chiara Corbari (1), Josè A. Sobrino (2), Marco Mancini (1), M. Victoria Hidalgo (2)

(1) Department of Hydraulic, Environmental and Surveying Engineering, Politecnico di Milano, Piazza Leonardo da Vinci, 32, Milan, Italy,

(2) Global Change Unit, Image Processing Laboratory, Universitat de Valencia, Agustín Escardino 9, Paterna, Valencia, Spain

chiara.corbari@mail.polimi.it

ABSTRACT Soil moisture plays a key role in the terrestrial water cycle and is responsible for the partitioning of precipitation between runoff and infiltration. Moreover, surface soil moisture controls the redistribution of the incoming solar radiation on land surface into sensible and latent heat fluxes. Recent developments have been made to improve soil moisture dynamics predictions with hydrologic land surface models (LSMs) that compute water and energy balances between the land surface and the low atmosphere. However, most of the time soil moisture is confined to an internal numerical model variable mainly due to its intrinsic space and time variability and to the well known difficulties in assessing its value from remote sensing as from in situ measurements. In order to exploit the synergy between hydrological distributed models and thermal remote sensed data, FEST-EWB, a land surface model that solves the energy balance equation, was developed. In this hydrological model, the energy budget is solved looking for the representative thermodynamic equilibrium temperature (RET) defined as the land surface temperature that closes the energy balance equation. So using this approach, soil moisture is linked to the latent heat flux and then to LST. The relationship between land surface temperature and soil moisture is analysed using LST from AHS (airborne hyperspectral scanner), with a spatial resolution of 2-4 m, LST from MODIS, with a spatial resolution of 1000 m, and thermal infrared radiometric ground measurements that are compared with the thermodynamic equilibrium temperature from the energy water balance model. Moreover soil moisture measurements were carried out during the airborne overpasses and then compared with SM from the hydrological model. An improvement of this well known inverse relationship between soil moisture and land surface temperature is obtained when the thermodynamic approach is used. Also their spatial properties are analysed showing the capability of the model and of images at high spatial resolution to correctly catch the strong spatial variability of the area with high LST standard deviation. On the contrary coarser satellite images are able to detect only the mean LST value. The study site is the agricultural area of Barrax (Spain) that is a heterogeneous area with an alternation of irrigated and non irrigated vegetated field and bare soil. The used data set was collected during two field campaigns in July 2005 in the framework of the SEN2FLEX project and in June 2009 in the SEN3EXP project.

1 INTRODUCTION

Soil moisture is recognized as the key variable in the hydrologic water balance for operational purpose as for flash flood forecast system as well as for irrigation management in particular in presence of water scarcity [Montaldo & Albertson, 2003]. Respect to this role, it is most of the time confined to an internal numerical model variable [Dooge, 1986]. This is mainly due to its intrinsic space and time variability and to the well known difficulties in assessing its value from remote sensing as from in situ measurements [Engman & Chauhan, 1995]. These problems drove the scientific community to the use of hydrologic modelling in conjunction with remote sensing data for water content estimation at basin and

field scale through connected soil moisture variables such as land surface temperature (LST). Land surface temperature is the parameter that links the energy fluxes between the low atmosphere and the earth surface and so it becomes fundamental in the energy balance modelling to estimate the energy fluxes [Noihlan & Planton, 1989; Famiglietti & Wood, 1994]. The availability of satellite remote sensing information makes easy to retrieve LST in raster format, mainly suited for the use in conjunction to distributed model. However, some uncertainties have to be addressed concerning in particular the spatial scale of different sensors [McCabe & Wood, 2006]. In fact the definition of satellite LST over an heterogeneous area is a difficult task due to the fact that LST is a function of the surface temperature of each component of the area (bare soil or vegetation), of the occupied

percentage by each type of soil and of the scan angle of view of the satellite [Norman et al., 1995]).

A distributed hydrologic model gives the opportunity to better understand this problem of spatial scale [Anderson et al., 2004].] due to the fact that a distributed model predicts averaged variable values in each pixel. The distributed energy water balance model, FEST-EWB, has been developed grounding on the thermodynamic equilibrium temperature that is the land surface temperature that closes the energy budget [Corbari et al., 2008]. The energy balance gives the opportunity to increase the fluxes control points and so to improve the mass balance accuracy and evapotranspiration estimates. Effective evapotranspiration in a soil-vegetation-atmosphere model is not computed directly with a function in terms of soil moisture content but with soil moisture linked to land surface temperature from the closure of the energy balance.

The paper tries to assess LST and ET values and their spatial and temporal dynamic with the energy water balance model tested at field scale with fluxes measured from an eddy correlation tower and thermal infrared in situ measurements. In fact acquisition time period is critical for thermal images due to the non stable behaviour of the thermodynamic temperature, but also spatial heterogeneity induces non linear effects in land surface temperature retrieval. The spatial resolution problem, that is an important task in hydrological modelling [Blöschl & Sivapalan, 1995; Wood, 1994], is discussed and the modelled land surface temperature and evapotranspiration are compared at different spatial scales with MODIS data (1000 m spatial resolution), in situ ground measurements and AHS data (2 or 3 m).

2 HYDROLOGICAL MODEL: FEST-EWB

FEST-EWB is a distributed hydrological energy water balance model [Corbari et al., 2008] and it is developed starting from FEST-WB and the event based models FEST98 and FEST04 [Mancini, 1990; Ravazzani et al., 2008]. FEST-WB computes the main processes of the hydrological cycle: evapotranspiration, infiltration, surface runoff, flow routing, subsurface flow and snow dynamic [Corbari et al., 2009]. In FEST-EWB the energy balance module is introduced and land surface temperature is the key parameter that links the energy fluxes between the low atmosphere and the ground surface. At the ground surface, the complete energy balance equation is expressed as:

$$R_n - G - H - LE = \Delta S / \Delta t \quad (1)$$

where: R_n (Wm^{-2}) is the net radiation, G (Wm^{-2}) is the soil heat flux, H (Wm^{-2}) and LE (Wm^{-2}) are respectively the sensible heat and latent heat fluxes and $\Delta S / \Delta t$ are the energy storage terms (Wm^{-2}). All the terms of the energy balance depend on the land surface temperature and so the energy balance equation can be solved with the well known Newton-Raphson method. The terms of the energy balance equation are described in [Corbari et al., 2008].

3 DATA

3.1 The study site

The test site is located in the agricultural area of Barrax (39°3' N, 2°6' W, 700 m a.s.l) near Albacete in Spain. About 65% of cultivated lands at Barrax are dryland (67% winter cereals, 33% fallow) and 35% irrigated land (75% corn, 15% barley/sunflower, 5% alfalfa, 5% onions and other vegetables). This area was selected as a test site for a field campaign during June-July 2005 in the framework of the international project SEN2FLEX (SENtinel-2 and FLuorescence EXperiment) funded by ESA (European Space Agency). This area has a Mediterranean climate with dry summer and high temperatures. Distributed soil moisture measurements were made during the field campaign in the different type of vegetated fields and bare soil by UNINA [SEN2FLEX Final Report]. These values are used as initial condition for the modeling simulation.

3.2 Land surface temperature and evapotranspiration retrieved from AHS and MODIS

During the field campaign period from 10th to 15th July 2005, 12 daily and night overpasses of the AHS airplane were made. These images have two different spatial scale resolutions between 2 and 3 m. Land surface temperature values are obtained with the TES method [Gillespie et al., 1998], while evapotranspiration estimates are daily cumulated values obtained with the Simplified Surface Energy Balance Index (S-SEBI) model [Roerink et al., 2000]. These results are reported in [Sobrino et al., 2008]. This heterogeneous agricultural area is characterized by an alternation of irrigated and non irrigated vegetated field with different crops and bare soil and for this reason high resolution images are necessary to really understand the differences between the different fields' conditions. In particular these alternations between wet and dry area are clearly visible during the day, when the standard deviation of LST can reach very high values till 9.7 °C, while during the night the area seems to be homogeneous with a maximum standard deviation of 1.3 °C. Also if

evapotranspiration diurnal estimates are analysed, great variability is shown, as for LST.

LST products from MODIS radiometer on board of TERRA satellite, with a spatial resolution of 1 Km, are used and evapotranspiration is then retrieved (<http://ladsweb.nascom.nasa.gov/index.html>).

3.3 Micrometeorological stations

An eddy correlation tower in the vineyard field (V) measured the turbulent fluxes of sensible, latent heat and CO₂ fluxes above the canopy through the covariance between the vertical wind velocity and respectively the air temperature, the water vapour density and CO₂ density. Moreover relative humidity, air temperature, soil heat flux, soil temperature and the four component radiation sensors were mounted. The systems were installed at two different heights of 410 cm and 805 cm. The station was operated by ITC of Netherlands. Moreover the University of Castilla-La Mancha operated three agro-meteorological stations in the area providing meteorological information [SEN2FLEX Final Report].

4 ENERGY BALANCE MODEL VALIDATION

4.1 Comparison with LST from AHS and MODIS

LSTs from FEST-EWB were selected for the same instant of AHS images. The spatial resolution of AHS images has been resampled at the same spatial resolution of FEST-EWB images, equal to 10 m. LSTs from AHS are then compared with land surface temperatures simulated from FEST-EWB and a good behaviour of the model in representing the observed data is found. In particular, at this fine resolution, the model as well as the AHS is capable in representing the heterogeneity of the area that is strictly linked to vegetation type and irrigation.

Fig.1 reports the comparison between land surface temperature from AHS, FEST-EWB and MODIS for the acquisition date of 13th July at 13.46, showing a good behaviour of the model in representing the observed AHS data with a mean difference of only -0.6 °C with a standard deviation of 1.8 °C and a RMSE of 2.7 °C. Instead the MODIS coarser image does not reproduce this strong spatial heterogeneity. The lower spatial accuracy of MODIS is also evident in the frequency distribution graphs. AHS and FEST-EWB histograms (Fig.1) show similar results with a quasi bimodal distribution due to the distinction between crops and bare soil [Kustas et al., 2004]. Moreover, AHS and FEST-EWB histograms show at low temperatures, between 25 and 45°C, a lot of classes due to the presence in the fields of crop at

different growth stages and of different soil moisture conditions.

These results of land surface temperature spatial variability are similar to the ones obtained for energy fluxes.

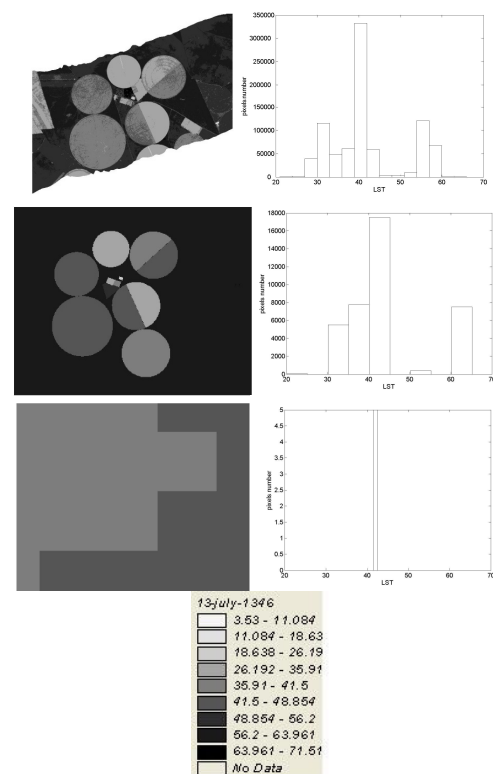


Figure 1. Comparison between LST from AHS, FEST-EWB and MODIS for 13th July at 13.46

4.2 Comparison with fluxes from the micrometeorological station

The measured net radiation, latent and sensible heat fluxes and soil heat flux are compared with the simulated fluxes and a good accuracy is reached both for the temporal dynamic and for the cumulated values. These results are confirmed from a statistical analysis looking for the minimization of the root mean square error (RMSE) and the maximization of the efficiency of the Nash and Sutcliffe index [Nash & Sutcliffe, 1970]. The net radiation is the flux with the highest efficiency, η equal to 0.99, and the lowest RMSE, equal to 30 W/m²; instead the latent heat flux has the lowest η equal to 0.78 and the highest RMSE equal to 44.4 W/m².

Fig.2 shows the distribution maps of the principal energy fluxes for the daytime image of 13th

July 13.46: net radiation, ground soil heat flux, latent and sensible heat fluxes of the diurnal image showing a strong heterogeneity in the spatial distribution. Their frequency diagrams are also reported. A quasi bimodal distribution for Rn, Le and H is evident due to the distinction between crops and bare soil (McCabe & Wood, 2006). In particular, as expected, the pixels with lower latent heat flux, typical for bare soil condition, have higher values of sensible heat flux; while viceversa for the vegetated area. Moreover the latent heat flux histogram shows at higher values, between 300 and 700 W/m², a lot of classes due to the presence in the fields of crops at different growth stages and of different soil moisture conditions. The opposite situation is present in the sensible heat flux histogram.

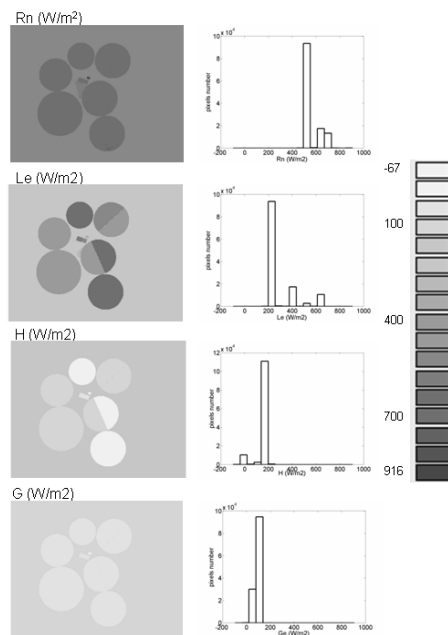


Figure.2 Distribution maps and their frequency distribution for energy fluxes from FEST-EWB at 10m for 13th July at 13.45.

4.3. Comparison with evapotranspiration from AHS and MODIS

For this agricultural area, a map of ET daily cumulated values is retrieved from AHS images for 13th July (Sobrino et al., 2008). ET from FEST-EWB was cumulated in a daily value and compared with AHS evapotranspiration (Fig.3) and statistical results show a good behaviour of the model in representing the mean observed data and the spatial variability. If the MODIS coarser image is considered, it does not catch the strong spatial heterogeneity that, on the

contrary, ET images from FEST-EWB and AHS reproduce (Fig.3). The mean value of FEST_EWB ET is equal to 4.5 mm/day with a standard deviation of 1.9 mm/day, the mean value of ET from AHS is 4.2 with a standard deviation of 1.6 mm/day while MODIS ET has a mean value of only 1.8 with a standard deviation of 0.7.

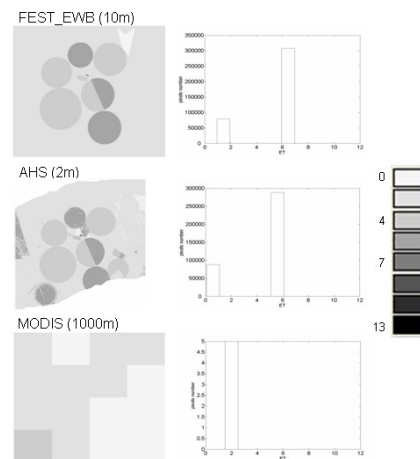


Figure.3 Comparison between FEST-EWB, AHS and MODIS daily cumulated evapotranspiration for 13th July 2005 (mm/day) and histograms.

5 RELATIONSHIP BETWEEN SM-LST-ET

Evapotranspiration is linked to land surface temperature and soil moisture through the complex system between the energy and mass balance equations in the hydrological cycle. The relationship between land surface temperature, soil moisture and evapotranspiration (Fig.4) is analysed looking for the effect of LST and soil moisture spatial variability on evapotranspiration and an inverse relationship is found.

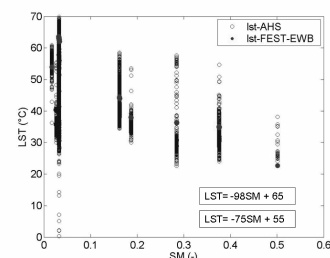


Figure.4 Relationship between modelled soil moisture and LST from FEST-EWB and AHS.

The mutual relationship between evapotranspiration values in each pixel at a define

distance can be analysed using the spatial autocorrelation function:

$$AC(d_{1,2}) = \frac{E\{[LST(X_1) - \mu][LST(X_2) - \mu]\}}{\sigma^2} \quad (2)$$

where μ is the mean, σ^2 is the variance and x_1 and x_2 are the generic positions at the distance d .

The process is considered stochastic so that the joint probability distribution does not change in time or space. Moreover the isotropy hypothesis is valid so that d is a function only of the distance between two points and not of the direction. In Fig.5 these autocorrelation functions are reported for simulated ET, SM and LST and for observed LST from AHS, and a similar behaviour is found for the different variables.

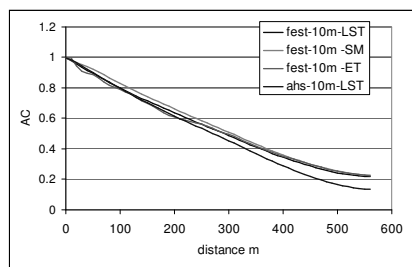


Figure.5 Autocorrelation functions for evapotranspiration, soil moisture and land surface temperature

6 CONCLUSIONS

The representativeness of land surface temperature for a distributed hydrological water balance model, FEST-EWB, has been analysed. The hydrological model performed well for the whole period of observation and was able to accurately predict energy fluxes and land surface temperature spatial and temporal distribution in comparison to in situ thermal infrared radiometric measurements, high resolution images and energy fluxes from eddy correlation tower.

The effect of LST spatial resolution is analysed for LST from AHS and MODIS images and for the hydrological model outputs. Diurnal AHS images at high spatial resolution, as well as simulated LST from hydrological model, are able to correctly catch the strong spatial variability of the area with high LST standard deviation. On the contrary, MODIS images, due to the low spatial resolution, are able to detect only the mean LST value.

Similar results on the capability to catch the field spatial variability of evapotranspiration can be

observed from ET values estimated from hydrological energy water balance model and directly from AHS images both characterized by a good agreement also when a strong ET field variance is presence, while the MODIS images do not retrieve even the mean ET values. Moreover a similar behaviour in term of spatial distribution is found between simulated ET, SM and LST and for observed LST from AHS.

6.1. Acknowledgments

This work was funded by MIUR in the framework of the Azioni Integrate Italia-Spagna project (prot. IT09G9BLE4) "Land Surface temperature from remote sensing for operative validation of an hydrologic energy water balance model" and of the ACQWA EU/FP7 project (grant number 212250) "Assessing Climate impacts on the Quantity and quality of Water".

6.2. References

- Anderson, M.C., Norman, J.M., Mecikalski, J.R., Torn, R.D., Kustas, W.P. & Basara, J.B. (2004). A multiscale remote sensing model for disaggregating regional fluxes to micrometeorological scales. *J. Hydrometeorol.*, 5, 343-363.
- Blöschl, G., & Sivapalan, M. (1995). Scale issues in hydrological modelling: a review. *Hydrol. Processes*, 9 (3-4), 251-290.
- Corbari, C., Horeschi, D., Ravazzani, G. & Mancini, M. (2008). Land surface temperature from remote sensing and energy water balance model for irrigation management. *Options Méditerranéennes*, A84, 223-234.
- Corbari, C., Ravazzani, G., Martinelli, J. & Mancini, M. (2009). Elevation based correction of snow coverage retrieved from satellite images to improve model calibration. *Hydrol. Earth Syst. Sci.*, 13, 639-649.
- Dooge, J.C.I. (1986). Looking for hydrologic laws, *Water Resour. Res.*, 22 (9) 46S-58S.
- Engman, E.T. & Chauhan, N. (1995). Status of microwave soil moisture measurements with remote sensing, *Remote Sens. Environ.*, 51, 189-198.
- Famiglietti J. S. & Wood E. F. (1994). Multiscale modelling of spatially variable water and energy balance processes. *Water Resour. Res.*, 30, 3061-3078.

- Gillespie, A., Rokugawa, S., Matsunaga, T., Cothern, J.S., Hook, S. & Kahle, A.B. (1998). A temperature and emissivity separation algorithm for advanced spaceborne thermal emission and reflection radiometer (ASTER) images. *IEEE Transactions on Geoscience and Remote Sensing*, 36, 1113–1126.
- Kustas, W. P., Li, F., Jackson, T. J., Prueger, J. H., MacPherson, J. I., & Wolde, M. (2004). Effects of remote sensing pixel resolution on modeled energy flux variability of croplands in Iowa. *Remote Sens. Environ*, 92 (4), 535–547.
- Mancini, M. (1990). La modellazione distribuita della risposta idrologica: effetti della variabilità spaziale e della scala di rappresentazione del fenomeno dell'assorbimento. PhD dissertation, Politecnico di Milano, Milan, Italy (in italian).
- McCabe, M.F. & Wood, E.F. (2006). Scale influences on the remote estimation of evapotranspiration using multiple satellite sensors. *Remote Sens. Environ.*, 105, 271-285.
- Montaldo, N. & Albertson J. D. (2003). Temporal dynamics of soil moisture variability: 2. Implications for land surface models, *Water Resour. Res.*, 39b (10), SWC 3-1: 3-13.
- Nash J. E. & Sutcliffe J. V. (1970). River flow forecasting through the conceptual models, Part 1: A discussion of principles. *J. Hydrol.*, 10 (3), 282-290.
- Noihlan J. & Planton S. (1989). A Simple parameterization of Land Surface Processes for Meteorological Models. *Mon. Wea. Rev.*, 117, 536-549.
- Norman, J.M., Kustas, W. P. & Humes, K. S. (1995). Source approach for estimating soil and vegetation energy fluxes in observations of directional radiometric surface temperature. *Agr. Forest Meteorol.*, 77, 263-293.
- Ravazzani, G., Rabuffetti, D., Corbari, C. & Mancini, M. (2008). Validation of FEST-WB, a continuous water balance distributed model for flood simulation, *Proceedings of XXXI Italian Hydraulic and Hydraulic Construction Symposium*, Perugia, Italy.
- Roerink, G., Su, Z. & Menenti, M. (2000). S-SEBI: a simple remote sensing algorithm to estimate the surface energy balance. *Physics and Chemistry of the Earth (B)*, 25, 147–157.
- SEN2FLEX Final Report (Contract n°:19187/05/I-EC 17628/03/NL/CB 17336/03/NL/CB). In *Proceedings of the SPARC*, 4–5 July, Enschede, ESA Publications Division, Noordwijk, The Netherlands.
- Sobrino, J. A., Jiménez-Muñoz, J. C., Sòria, G., Gómez, M., Ortiz, A. Barella, Romaguera, M., Zaragoza, M., Julien, Y., Cuenca, J., Atitar, M., Hidalgo, V., Franch, B., Mattar, C., Ruescas, A., Morales, L., Gillespie, A., Balick, L., Su, Z., Nerry, F., Peres, L. & Libonati, R. (2008) Thermal remote sensing in the framework of the SEN2FLEX project: field measurements, airborne data and applications. *Int. J. Remote Sens.*, 29:17, 4961-4991.
- Wood, E.F. (1994). Scaling soil moisture and evapotranspiration in runoff models. *Adv Water Resour.*, 17, 1-2.

J. Cernicharo¹, F. Camacho¹, A. Verger², E. López-Baeza²
IEOLAB. Parc Científic Universitat de València. C/ Catedrático José Beltrán, 2 46980 Paterna (Valencia). Spain.
2Departament de Física de la Terra i Termodinàmica. Universitat de Valencia. C/Dr. Moliner, 50. 46100 Burjassot (Valencia). Spain.
 jesus.cernicharo@eolab.es

1 INTRODUCTION

Information about Canopy Water Content (CWC), the total mass of liquid water in foliage per ground area (kg/m^2), is necessary to accurately retrieve soil moisture from microwave remote sensing observations. As part of the SMOS mission, the Spanish R&D MIDAS-5 project aims to develop algorithms for the estimation of CWC from satellite data.

methodology developed by Baret et al. (2007) and Verger et al. (in press), for LAI, FAPAR and FCOVER variables. The achieved performances of neural networks and look up tables were compared in terms of correlation, root mean square error and computational time.

2.1 Study area

One of the SMOS cal/val site selected over land is the Valencia Anchor Station (VAS), 10 km x 10 km, placed in the Utiel-Requena plateau in Valencia, Spain (39°34'15" N, 1°17'18" W). VAS is included in a larger region over a 125 km x 125 km footprint. Barrax cultivated site (39°30' N, 2°6' W) (figure 1) is a representative area for the whole range of CWC variation in this extended area.

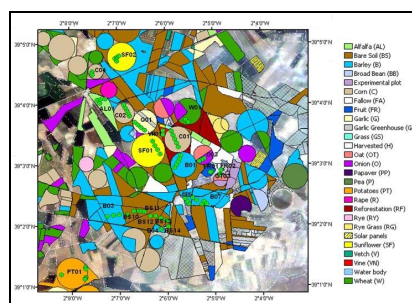


Figure 1. Land uses at Barrax area and ESUs location

2.2 Field campaign

Barrax campaign took place between 20 and 24 June 2009 as a part of SEN3EXP campaign supported by ESA for obtaining data to simulate the instruments on board Sentinel-3 satellite. In-situ vegetation characterization performed by EOLAB includes the sampling of the following variables: Leaf Area Index (LAI), Fraction of Absorbed Photosynthetically Active Radiation (FAPAR), Fraction of green Vegetation Cover (FCOVER), Fresh Weight (FW), Dry Weight (DW) and leaf area (A). LAI, FAPAR and FCOVER parameters have been obtained by using digital hemispheric photography, taking 12-15 for ESU. CWC was derived from the Leaf Area Index and the Leaf Water Content (LWC).

$$LWC = (FW - DW) / A \text{ [kg/m}^2\text{]} \quad (1)$$

$$CWC = LAI \times LWC \text{ [kg/m}^2\text{]} \quad (2)$$

In-situ values, figure 2, range between 1-1.2 kg/m² for garlic crops, and 0.05-0.1 kg/m² for vineyards and fruit trees.

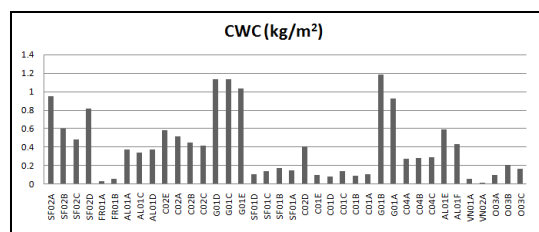


Figure 2. CWC (kg/m²) field values over different ESUs. SF (Sunflowers), FR (Fruits), AL (Alfalfa), C (Corn), G (Garlic), VN (Vineyards), O (Onion)

2.3 Simulation

Two radiative transfer models were considered: a leaf optical properties model (PROSPECT) and a turbid medium model for the canopy (SAIL).

The PROSPECT model is used to describe the leaf reflectance and transmittance that are required by SAIL. The input variables of PROSPECT are the structure variable N, the leaf chlorophyll content (Cab), the leaf water content (Cw) and the dry matter content (Cdm). The SAIL model is a 1D turbid medium radiative transfer model with three variables to describe canopy structure: the LAI, the average leaf angle of an ellipsoidal distribution function, and a hot spot parameter (Kuusk et al., 1985).

The performance of the model has been evaluated by comparing simulated reflectances using ground

data (LAI, Cw, Cab, Cdm,) and the associated CHRIS reflectances. Intercomparison, figure 3, shows reflectance deviations are lower than 0.05 over the darkest and the brightest soils of the Barrax site.

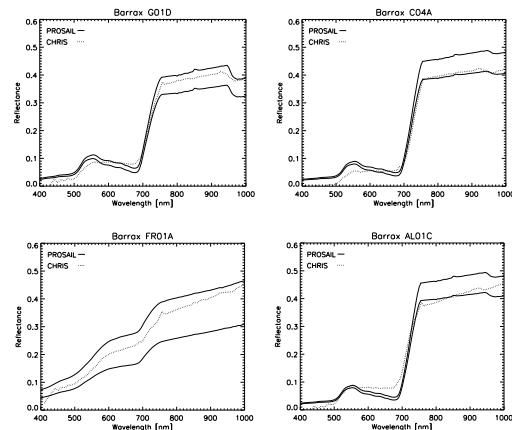


Figure 3. Simulated (model parameters were fixed according to ground measurements) and observed reflectances for garlic, corn, fruit and alfalfa ESUs.

Three different simulation datasets with 1000, 5000 and 10000 elements were generated by applying uniform and normal distributions. Model input ranges, table 1, were established according to field data. N and leaf angle variables were fixed based on mean values reported in literature. Combinations with a canopy water content greater than unrealistic 1.5 kg/m² values have been deleted so final datasets includes 586, 3621 and 7155 elements.

Table 1. Simulated databases ranges for uniform and gaussian distributions. Units: Cw (g/cm²), Cab (µg/cm²)

Input	Min	Max	Mean	Stdev
LAI	0	8	2	2
Cw	0	0.08	0.03	0.02
Cdmrel	0.05	0.50	0.22	0.08
Cab	20	50	33	5
Hotspot	0.001	1	0.1	0.3
Soil	0.7	2.3	1.4	0.3
Fixed values: N=1.5, ALA=45°				

2.4 Imagery

High resolution imagery used in this work, has been acquired by CHRIS sensor onboard PROBA-1 satellite. CHRIS image (19 June 2009) corresponds to mode 1 characterized by 62 spectral bands ranging from 405 nm to 1005 nm with a nadir ground sampling distance of 34 m. The image was re-sampled to 17 m and projected onto a reference grid using 50 ground control points ensuring about 13 m geometrical accuracy. The BEAM (WWW2) toolbox specific for

CHRIS/PROBA was used for atmospheric correction. Selection wavelengths is carried out using a compromise between minimal variability coefficient in a potatoes field and closeness to the center for bands GREEN, RED, NIR and extreme NIR, where exists a maximum sensitivity to water content. According to this criteria it has been chosen band 13 (551.9 nm), band 22 (641.8 nm), band 50 (869.1 nm) and band 61 (988.3 nm).

2.5 Inversion model

2.5.1 Neural networks

Neural networks have been increasingly used for reflectance model inversion (Bacour et al., 2006; Schlerf and Atzberger, 2006; Baret et al., 2007; Verger et al., In press) due to their ability to (i) learn complex pattern, taking into account any nonlinear complex relationship between the variables, (ii) generalize in noisy environments, which makes NNTs robust solutions in the presence of incomplete or imprecise data and (iii) incorporate a priori knowledge and realistic physical constraints into the analysis (Mas and Flores, 2008). These advantages make neural networks potentially more accurate than other estimation techniques.

Neural network retrieval approach is based on the methodology developed by Baret et al., 2007, for deriving biophysical variables from VEGETATION data and Verger et al. (in press), from CHRIS data. Training databases and structural parameters which are evaluated to optimize the results corresponds to the distribution functions, number of simulations, noise influence, number of hidden layers, numbers of neurons, activation functions and separated or jointly outputs.

No consensus exists on the way to extract the NNT solution (Verger et al., in press). The proposed method consists in training 10 networks in order to select the one providing the best performance over the datasets. Three iterations were carried out to evaluate the consistency and stability of the networks. Training datasets were randomly split into three subsets (Baret et al., 2007): the first one made of half the cases was used to adjust the network according to its error during the training, while the two others quarters of the cases were used respectively to halt training when generalization stops improving, and to test the network performance. The selected cost function corresponds to the minimum root mean square error between the simulated values and the network output. The Levenberg-Marquardt minimization algorithm was used because of its efficient convergence performance.

2.5.2 Look up tables

Look up table is conceptually a simple technique to overcome limitations from iterative inversion methods. It is a fast method which provides a control scenario on the input parameters to be searched for and allows the identification of ambiguous situations where there are several set of input parameters which can produce a modeled result that agrees with the observations within a tolerance (Yebara et al., 2008).

Simulated dataset is used to find the sets of inputs variables which provide the closest estimate of reflectance. This inversion is performed for each pixel of the CHRIS image by using a merit function which implies minimizing the quadratic distance between the observed and simulated reflectances. These results are compared with neural networks approach in statistical terms (correlation, root mean square error, bias) and computational time.

3 RESULTS

3.1 Neural networks

In a first step, the influence of the distribution (uniform or normal) and the number of elements of the simulated dataset in the network performance was evaluated. The training is carried out by applying three activation functions combination: hyperbolic tangent in hidden layers, and hyperbolic tangent, linear or saturated linear in the output layer. Initial structural conditions correspond to 5 neurons in the hidden layer and separated training for each variable (Verger et al., in press). No significant differences were obtained for different distribution functions (uniform, normal) and number of elements (586, 3621, 7155). Tangent-tangent combination (Vohland and Mader, 2007), showed in table 2, offers the best performance with ground data (minimum RMSE) and a greater stability between the three repetitions (mean RMSE).

Table 2. Minimum and averaged rmse for the best combination according different activation functions. Tang(tangent), Lin(linear), Slin(Saturated linear)

	Tang-Tang		Tang-Lin		Tang-Slin	
RMSE	Min	Mean	Min	Mean	Min	Mean
LAI	0.48	0.54	1.01	1.72	0.51	0.54
CWC	0.17	0.19	0.21	0.23	0.20	0.22

From the properties of the best network ($RMSE_{LAI} = 0.48$, $RMSE_{CWC} = 0.17 \text{ kg/m}^3$), a new exercise is performed by adding different noise levels to the simulated reflectances in order to include instrumental noise and radiometric and atmospheric uncertainties (Verger et al., in press). Networks reach a

new minimum RMSE for both variables by using an additive 4% noise level (Table 3).

Table 3. Minimum and mean RMSE by applying different noise levels to the simulated reflectances.

Noise level	LAI			CWC		
	2%	4%	6%	2%	4%	6%
Min RMSE	0.52	0.47	0.52	0.21	0.16	0.17
Mean RMSE	0.53	0.52	0.59	0.23	0.19	0.19

The structure of networks (number of hidden layers, number of neurons and number of outputs per network) were also evaluated. Concurrent estimation of the two variables with a single network provides poorer performances ($RMSE_{LAI}=0.91$, $RMSE_{CWC}=0.23$ kg/m^2). Optimal structure in the case of LAI corresponds to 1 hidden layer with 5 neurons, as was concluded in Verger et al., in press. For CWC variable, table 4, one hidden layer with 5 or 2 neurons provides the best performances.

Table 4. Minimum and mean RMSE for the Canopy Water Content estimates according to different hidden layers and number of neurons.

Neurons	1 hidden layer				2 h. layers	
	2	5	8	11	5-2	8-5
Min RMSE	0.16	0.16	0.23	0.22	0.18	0.20
Mean RMSE	0.20	0.19	0.25	0.24	0.19	0.21

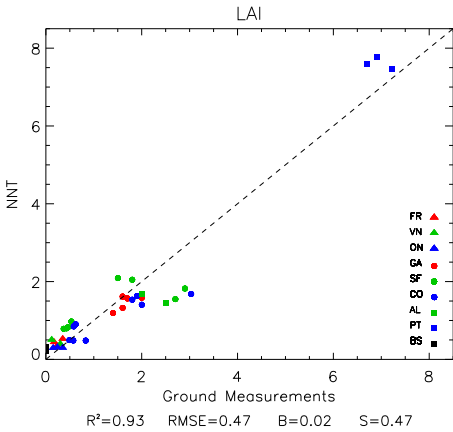


Figure 4. Comparison of NNT estimates with ground data for LAI.

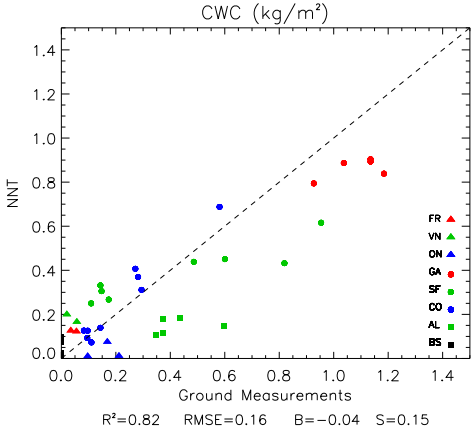


Figure 4 (cont.). Comparison of NNT estimates with ground data for CWC.

Comparison of the optimal neural networks (i.e. networks trained separately for each variable, 1 hidden layers and 5 neurons) Cw and LAI estimates with ground measurements are shown in figure 4. Results indicate correlations $R^2_{LAI}=0.93$ and $R^2_{CWC}=0.82$ and errors $RMSE_{LAI}=0.47$ and $RMSE_{CWC}=0.16$ kg/m^2 . CWC and LAI biophysical maps derived from neural network are shown in figure 5. Maximum LAI and CWC values correspond to potatoes and pea crops. White areas correspond to pixels where CHRIS image shows negative reflectance values due to atmospheric correction errors.

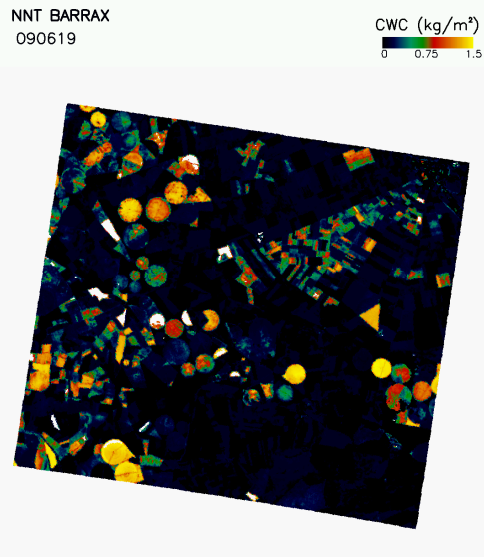


Figure 5. CWC derived map from neural network training and CHRIS data.

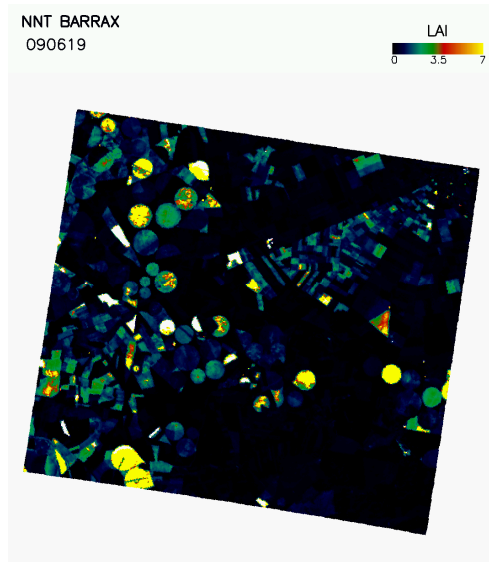


Figure 5 (cont). LAI derived map from neural network training and CHRIS data.

3.2 Look up tables

The minimisation procedure has been carried out for the six simulated datasets according different distributions functions and number of simulations. Results, table 5, show 1000 fewer elements dataset offers poor results. No significative influence has been observed between normal and gaussian distributions.

Table 5. RMSE between LUT and ground data for different distributions functions and number of simulations. U (Uniform), G (Gaussian), A (586 elements), B (3621 elements), C (7155 elements)

	A-U	B-U	C-U	A-G	B-G	C-G
LAI	1.14	0.63	0.63	0.58	0.66	0.54
CWC	0.32	0.25	0.25	0.24	0.22	0.25

The comparison with ground data for the best configuration, figure 6, show the following results: $R^2=0.91$ and $RMSE=0.54$ for LAI, and $R^2=0.64$ and $RMSE=0.22$ kg/m^2 for CWC.

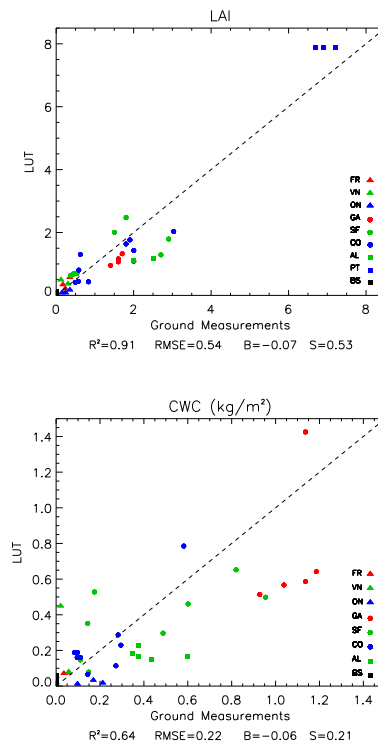


Figure 6. Comparison for classes between in-situ and LUT derived data

3.3 Intercomparison

Statistical and computational time results for the best performances obtained from the both inversion methods are showed in table 6. Neural networks approach improves all statistical indicators with a significant reduction in the computational time. Differences between both derived CWC maps, figure 7, are negative for vegetation areas generally ranging from 0.2 to 0.35 kg/m^2 values.

Table 6. Intercomparisons between NNT and LUT best performances. Ctime (Computational time).

	LAI		CWC	
	NNT	LUT	NNT	LUT
R2	0.93	0.91	0.82	0.64
RMSE	0.47	0.54	0.16	0.22
Bias	0.02	-0.07	-0.04	-0.06
Slope	0.47	0.53	0.15	0.21
Ctime	<1'	291'	<1'	161'

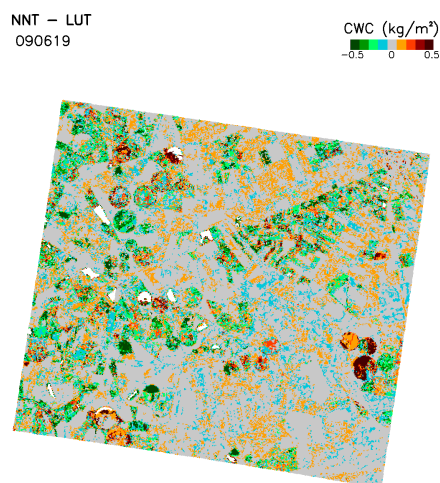


Figure 7. Differences between NNT and LUT CWC derived maps.

4 CONCLUSIONS

This study is focusing on the PROSAIL radiative transfer model inversion to estimate LAI and CWC over a cultivated area from CHRIS/PROBA top of canopy reflectances. Two different tools have been evaluated to approach the inversion process: neural networks and look up tables. Several elements have been evaluated to optimize the performance with ground data: the distribution function and the size of the simulated dataset for both approaches, and in the case of neural networks, the influence of noise and the network architecture.

Best results obtained from NNTs correspond to the following properties: one hidden layer, 5 neurons (also 2 in the case of CWC), tangent activation functions in hidden and output layers, independent training for each variable and incorporation of additive noise. The different distributions and size of the training dataset analysed in this study were not significant to achieve better performances. Stability of the network approach was quantified by carrying three executions showing RMSE deviations up to 0.05 (LAI) and 0.03 (CWC). On the other hand, for the LUT approach, a reduced number of elements provides poorer performances while the distribution function of the simulated dataset has a minor influence.

Neural networks ($R^2_{LAI}=0.93$ and $RMSE_{LAI}=0.47$, $R^2_{CWC}=0.83$ and $RMSE_{CWC}=0.16$) achieve better correlation and lower root mean square error than LUT approach ($R^2_{LAI}=0.91$ and $RMSE_{LAI}=0.54$, $R^2_{CWC}=0.84$ and $RMSE_{CWC}=0.22$) and a significant reduction in computational time requirements. The statistics of the comparison of satellite estimates with ground measurements show a better agreement for

LAI than for CWC. This may be partially explained due to the measurement in-situ protocol for CWC presents greater errors than for LAI. Furthermore, CHRIS sensor extreme wavelengths have a reduced sensibility to water content. Further studies should therefore concentrate on training the network with SWIR reflectances, where the sensibility to water content variation increases.

5 REFERENCES

- Bacour, C., Baret, F., Béal, D., Weiss, M., Pavageau, K., 2006. Neural network estimation of LAI, FAPAR, fCover and LAIxCab, from top of canopy MERIS reflectance data: principles and validation. *Remote Sensing of Environment*, 105:313–325.
- Baret, F., Hagolle, O., Geiger, B., Bicheron, P., Miras, B., Huc, M., et al. (2007). LAI, FAPAR and fCover CYCLOPES global products derived from VEGETATION. Part 1: Principles of the algorithm. *Remote Sensing of Environment*, 110: 275–286.
- Kuusk, A., 1985. The hot spot effect of a uniform vegetative cover. *Remote Sensing of Environment*, 3, 645– 658.
- Schlerf, M., Atzerberger, C., 2006, Inversion of a forest reflectance model to estimate structural canopy variables from hyperspectral remote sensing data. *Remote Sensing of Environment*, 100, pp. 281–294.
- Mas, J. F. and Flores, J. J.(2008) 'The application of artificial neural networks to the analysis of remotely sensed data', *International Journal of Remote Sensing*, 29: 3, 617 — 663
- Yebra, M., Chuvieco, M., Riaño, D., 2008. Estimation of live fuel moisture content from MODIS images for fire risk assessment. *Agricultural and Forest Meteorology*, 148, 523-536.
- Verger, A., Baret, F., Camacho, F., in press. Optimal modalities for radiative transfer-neural network estimation of canopy biophysical characteristics: evaluation over an agricultural area with CHRIS/PROBA observations. *Remote Sensing of Environment*.
- Vohland, M. and Mader, S., 2007: Numerical minimisation and artificial neural networks: Two different approaches to retrieve parameters from a canopy reflectance model. Proc. of the 5th EARSeL Workshop on Imaging Spectroscopy, Bruges, 23-25 April 2007.

Monitoring soil and vegetation fluxes of carbon and water at the global scale: the land carbon core information service of GEOLAND2

Calvet J.-C.⁽¹⁾, C. Albergel⁽¹⁾, G. Balsamo⁽²⁾, M. Balzarolo⁽³⁾, A. Barbu⁽¹⁾, S. Boussetta⁽²⁾, A. Cescatti⁽⁴⁾, F. Chevallier⁽⁵⁾, N. Delbart⁽⁵⁾, J. de Vries⁽⁶⁾, L. Kullmann⁽⁷⁾, S. Lafont⁽¹⁾, J.-F. Mahfouf⁽¹⁾, F. Maignan⁽⁵⁾, D. Papale⁽³⁾, C. Szczypta⁽¹⁾

(1) CNRM-GAME (Meteo-France, CNRS), Toulouse, (2) ECMWF, Reading, (3) University of Tuscia, Viterbo, (4) JRC-IES, Ispra, (5) LSCE (CEA, CNRS), Gif-sur-Yvette, (6) KNMI, De Bilt,

(7) OMSZ, Budapest

jean-christophe.calvet@meteo.fr, clement.albergel@meteo.fr,
gianpaolo.balsamo@ecmwf.int, manuela.balzarolo@unitus.it, alina.barbu@cnrm.meteo.fr,
souhail.boussetta@ecmwf.int, alessandro.cescatti@jrc.ec.europa.eu,
frederic.chevallier@lsce.ipsl.fr, nicolas.delbart@lsce.ipsl.fr, jdevries@knmi.nl,
kullmann.l@met.hu, sebastien.lafont@cnrm.meteo.fr, jean-francois.mahfouf@meteo.fr,
fabienne.maignan@lsce.ipsl.fr, darpap@unitus.it, camille.szczypta@cnrm.meteo.fr

ABSTRACT- A global component of the “Land Monitoring Core service” (LMCS) is being developed in the framework of the GEOLAND2 European project (FP7, 2008-2012). Land Data Assimilation Systems (LDAS) for the carbon and water cycles have been proposed as a core activity of the LMCS Global component and are developed by the Land Carbon Core Information Service (LC-CIS) of GEOLAND2. Both water and carbon terrestrial cycles require a similar data assimilation approach in which a model is constrained by as many relevant data as possible. Indeed, water and carbon cycles are closely linked and it is possible to build an integrated LDAS which includes all the processes. The advantage of that is that consistency can be achieved across a range of products based on satellite data. The LC-CIS performs modelling and data assimilation tasks, associated to a verification component based on in situ observations. Data assimilation is developed on the model of atmosphere/marine GMES core services. The LC-CIS links the LMCS to the atmosphere component of GMES using the existing infrastructure/tools developed by meteorological services (ECMWF and national meteorological services).

1 INTRODUCTION

The vegetation/land component of GMES is called “Land Monitoring Core service” (LMCS). The GEOLAND2 European project (FP7, 2008-2012) is a demonstrator of the evolution of the LMCS, including the consolidation of prototype services and the test of their operational capacity. In particular, the perimeter of the LMCS is extended, with a global component (biogeophysical parameters), and thematic core information services. The main mission of the land carbon core information service (LC-CIS) of GEOLAND2 is to assess the impact of weather and climate variability on terrestrial biospheric carbon fluxes, in the context of international conventions. The LC-CIS aims at monitoring the global terrestrial carbon fluxes and setting-up pre-operational infrastructures for providing global products, both in near-real-time and off-line mode. A multi-model carbon accounting system is developed, coupled with

satellite data assimilation schemes. Emphasis is put on validation (in-situ data), with downscaling on reference European countries (France, the Netherlands, Hungary). The C-TESSEL and SURFEX modelling platforms (of ECMWF and Meteo-France, respectively) are used for production. The ORCHIDEE modelling platform (LSCE) is used for benchmarking and validation purposes. The ECMWF reanalysis (ERA-Interim) will be used to build a global 20-y climatology of carbon and water fluxes, LAI and vegetation biomass, in order to rank the near-real time simulations. Gradually, EO data will be integrated in the modelling platforms, in order to improve the atmospheric constraint on the model (e.g. downwelling solar radiation from the EUMETSAT’s Land-SAF), analyse soil moisture and vegetation biomass (e.g. assimilate the EUMETSAT’s ASCAT soil moisture product and MODIS and/or SPOT/VGT LAI estimates). Finally, satellite data will be used for model verification (e.g. land surface temperature).

2 DESCRIPTION OF THE LC-CIS

2.1 A global land data assimilation system

GEOLAND2 intends to constitute a major step towards the implementation of the GMES Land Monitoring Core Service (LMCS). The three components (Local, Continental, and Global) of the LMCS are addressed. The architecture of GEOLAND2 is made of two different layers, the Core mapping Services (CMS) and the Core Information services (CIS). The Land Carbon CIS (LC-CIS) is one of the global CIS of GEOLAND2. LC-CIS aims at setting-up pre-operational infrastructures for providing regional (France, the Netherlands, Hungary) and global variables related to the terrestrial carbon cycle, in near real time, for describing the continental vegetation state (LAI and biomass), the surface fluxes (carbon and water), and the associated soil moisture. These variables are produced daily by models able to assimilate in situ and satellite data. This land data assimilation system (LDAS) will be implemented gradually during the GEOLAND2 time frame (2008-2012).

The key daily products of LC-CIS are:

- Global daily estimates of analysed: LAI, soil moisture, carbon flux, water flux, vegetation biomass, carbon storage (ECMWF ; CTESSEL model (Voogt et al. 2006); spatial resolution similar to the operational NWP ECMWF model, i.e. 16km in 2010)
- Focus on European test countries: France, the Netherlands, Hungary (Meteo-France, KNMI, OMSZ, respectively ; SURFEX modelling platform including the ISBA-A-gs model ; spatial resolution ranging from 1km to 10km).

The LC-CIS products are analysed biophysical variables. "Analysed variables" means that they are produced by a land surface model using atmospheric information together with ancillary data on soil characteristics and land cover, able to use satellite products through direct forcing and/or data assimilation (e.g. LAI, soil moisture). The analysed variables constitute a merged product accounting for diverse sources of information and for the physics of the model. The data assimilation accounts for the uncertainties in the model simulations and in the observations, which ensures that the analysis is optimal.

2.2 Models

Vegetation has a strong impact on the exchange of energy, water and carbon between the land surface and

the atmosphere. In particular, it influences the uptake and release of carbon dioxide from and to the atmosphere through photosynthesis and respiration. In addition, the plant growth is governed by the climate. Improving the modelling of the land surface physiological processes is required to provide quantitative estimates of the surface fluxes for meteorological, hydrological and climate applications. Soil-vegetation-atmosphere transfer (SVAT) models were originally designed to simulate exchanges of matter and energy between the surface and the atmosphere, with vegetation leaf area index (LAI) as a forcing variable, rather than a prognostic state. A number of models have recently evolved to include biogeochemical processes (Foley et al., 1996; Sellers et al., 1996; Calvet et al., 1998; Pitman, 2003), in order to improve the representation of the dynamical behaviour of the vegetation. In such models, the active biomass is often represented by the amount of leaf surface area per unit ground area, expressed through LAI.

In LC-CIS, the ISBA-A-gs model of Meteo-France (Calvet et al., 1998, 2004, 2008) is used as a baseline. New developments in ISBA-A-gs are transferred to ECMWF, in the CTESSEL land surface model (Fig. 1). ISBA-A-gs is a CO₂-responsive model, which accounts for the vegetation assimilation of CO₂. It is able to simulate energy, CO₂ and water vapour fluxes at the surface-atmosphere interface. Gibelin et al. (2006) evaluated the model performances at a global scale in the context of climatologic simulations, using atmospheric forcing fields from Numerical Weather Prediction (NWP) reanalyses and observations at a 1 degree resolution. They compared 10 years of simulation of LAI with three satellite-derived LAI datasets. It was found that the ISBA-A-gs model is able to capture the general patterns of LAI observed from space and that the simulations fall within the range of variability of satellite-retrieved LAI. Brut et al. (2009), made the same exercise at the regional scale at a 8km resolution, for a 3-year period. They demonstrated the potential of LAI remote sensing products for identifying and locating models' shortcomings at a regional scale.

ISBA-A-gs contains a simplified representation of ecosystem respiration and does not simulate all the autotrophic respiration terms, nor the carbon storage. A new version of ISBA-A-gs, called ISBA-CC (Gibelin et al., 2008), has been implemented in the SURFEX modelling platform of Meteo-France. ISBA-CC simulates the main processes of the terrestrial carbon cycle, i.e. the evolution of the carbon reservoirs in the vegetation and in the soil, and the net ecosystem exchange flux components (gross primary production, autotrophic and heterotrophic respiration). The energy and carbon fluxes simulated by ISBA-CC were

validated against in situ measurements at 26 FLUXNET (www.fluxdata.org) sites located at temperate and high latitudes of the Northern Hemisphere, sampling the main biomes present in the area (Gibelin et al., 2008). It is shown that the scores obtained by ISBA-CC are similar to those obtained by the ORCHIDEE model.

2.3 Data assimilation techniques

To quantify carbon and water fluxes between the vegetation and the atmosphere in a consistent manner, land surface models now include interactive vegetation components in which the vegetation biomass is a prognostic model state, allowing the model to adapt the vegetation growth to environmental conditions. However, the quality of its performances depends on forcing data and on model parameters that generally require continuous corrections. A number of studies (Jarlan et al., 2008; Sabater et al., 2008; Rüdiger et al., 2010) have shown the potential of assimilating leaf area index and/or surface soil moisture observations to correct vegetation model states using variants of the Extended Kalman Filter (EKF). Mahfouf et al. (2009) transformed the data assimilation system used in the two previous studies to a comprehensive EKF for its operational use within the limited area numerical weather prediction (NWP) system ALADIN of Meteo-France (Bubnova et al., 1995). This new EKF version was adapted for the purpose of LC-CIS to allow the joint assimilation of remotely sensed LAI and surface soil moisture observations for the analysis of the above-ground photosynthetically active vegetation biomass and the root-zone soil moisture within ISBA-A-gs, as previously proposed by Sabater et al. (2008).

In its current form, the EKF assimilates observations over an interval of 24 hours at 6 am, when available, by analysing the initial state via the information provided by an observation at the end of the assimilation window (i.e. the observation operator contains the forward model propagation and the conversion of the model state into an observation equivalent). The propagation of the background error covariance matrix by the tangent linear forward model in the EKF allows for observations to be available less frequently than the chosen assimilation window length (thereby providing a similar solution as a variational assimilation system over a long assimilation window but without making the assumption of a perfect model). The choice of a one-day assimilation window allows the joint assimilation of LAI with other observations available more frequently (e.g. soil moisture content, screen-level observations). Rüdiger et al. (2010) show that increasing the length to 10 days (availability of satellite LAI products) leads to significantly reduced Jacobians and consequently a significant loss of the model's response at the end of

the assimilation window to the initial perturbations of the model states. Moreover, a length of ten days for an assimilation window would jeopardize near-real time applications because of the very long cut-off needed to obtain the required observations. Such window lengths also lead to questioning the linearity and perfect model assumptions, when compared to shorter windows.

2.4 Verification approaches

In situ can be used to verify the quality of the products.

For soil moisture, Rüdiger et al. (2009), Scipal et al. (2008), Albergel et al. (2009), have shown that local soil moisture observations can be used to verify low-resolution model or satellite soil moisture products. Most of the FLUXNET sites are now measuring soil water content at different depths. Meteo-France has developed a soil moisture network in southern France (SMOSMANIA, Calvet et al. (2007), Albergel et al. (2008)) now including 21 stations.

For surface fluxes, the whole system (including the generation of the atmospheric forcing) is verified against in situ local observations of eddy correlation fluxes. In SURFEX, several patches are considered, and the patch corresponding to the observed vegetation type can be selected. In CTESSEL, the number of patches is limited, and the consistency between the model vegetation type and the observed vegetation type will have to be checked. The FLUXNET sites are available in different countries, climates and for various vegetation types, but they have commonly a footprint no larger than 1km around the measurement point. A homogeneity analysis of the footprint is performed and the consistency between the modelled and observed vegetation is checked. Cluster of towers can be selected for small regions including different vegetation types, in order to perform a local scale data-driven upscaling. Validation approaches include statistical analysis of flux magnitude, daily to annual cycles, anomalies and ecosystem response functions parameters, accounting for the spatial resolution difference.

For LAI, anomaly correlation (e.g. 2003 heat wave in Europe or 2007 drought in southeastern USA) between modelled and satellite-derived LAI estimates can be used as a verification.

In situ biomass measurements are available from Luysaert et al. (2006). The data base provides estimates of carbon stocks and carbon fluxes (GPP, Reco, NPP). Existing simulations for these sites by CEA using ORCHIDEE and the CRU atmospheric forcing will be used. CEA will rerun ORCHIDEE with ERA-INTERIM (period 1989 to present) for a subset of the forest sites growing after 1989. This will permit to assess the impact of the improved atmospheric

forcing derived from ERA-INTERIM. The same simulations will be performed with ISBA-CC for benchmarking purposes.

ERA-INTERIM was GPCP corrected (GPCP uses in situ data). A comparison of various atmospheric fields (in particular precipitation) was made with higher resolution atmospheric analyses over France (8km, using a dense precipitation gauge network) by Szczypka et al. (2010).

Regarding the carbon stocks, equilibrium modelled stocks can be compared with existing/available in situ derived estimates, in a first stage. This concerns ISBA-CC, only.

3 DISCUSSION

An important aspect of the verification is benchmarking, i.e. a comparison of performance with other models and approaches. In LC-CIS, benchmarking activities include an intercomparison of CTESSEL, SURFEX and ORCHIDEE models.

Assessing the added value of the assimilation can be done by measuring its impact on the overall agreement of the model with in situ observations (fluxes, soil moisture, and, in the case of a land surface model used in a weather forecast model, on the atmospheric variables). A realistic target for an interactive vegetation model (run in open-loop mode) is to reproduce LAI climatologies (at least in areas where the model precipitation bias is not compromising vegetation growth). In presence of large anomalies (e.g. European summer 2003, US summer 2007), the interactive vegetation model is expected to capture the sign and magnitude of the LAI anomaly in seasonal integrations where the soil preconditioning is already present in the initial conditions. EO-derived vegetation variables are the main spatially available observation proxy for seasonal carbon uptake.

The choice of a relatively long assimilation window (ie. 10 days), dictated by the current availability of satellite derived LAI (operational LAI products are provided as 8 day composites), would make such surface assimilation incompatible with atmospheric data assimilation systems that have much shorter assimilation intervals (between 3h and 12 h). Mahfouf et al. (2009) transformed the 2D-VAR used in Jarlan et al. (2008) and in Sabater et al. (2008) to a comprehensive Extended Kalman Filter (EKF) for its operational use within the limited area numerical weather prediction system ALADIN of Meteo-France. This new EKF version was then adapted to allow the joint assimilation of remotely sensed LAI and surface soil moisture observations (Rüdiger et al., 2010). In its current form, the EKF assimilates observations over an interval of 24 hours at 6 am, when available, by analysing the initial state via the information provided by an observation at the end of the assimilation

interval (i.e. the observation operator contains the forward model propagation and the conversion of the model state into an observation equivalent). The propagation of the background error covariance matrix by the tangent linear forward model in the EKF is performed through the Jacobians of the forward model. This allows for observations to be available less frequently than the chosen assimilation interval length (thereby providing a similar solution as the simplified 2D-VAR over a long assimilation window but without making the assumption of a perfect model).

Addressing the weather, seasonal, and interannual climate variability of the fluxes is the primary added value of the service. In a second stage, it is expected that adaptations of the system will be needed in order to account for crop and forest harvest/fires. The verification component of LC-CIS compares the model outputs with field data concerning, in particular, carbon fluxes (tower data). It has to be recognized that the link to inventories is challenging. However, the atmospheric CO₂ represents, undoubtedly, the best observed carbon stock. The global LC-CIS CO₂ flux product will be tested in the framework of MACC to produce integrated CO₂ concentrations at a global scale. This methodology will provide a solid benchmarking ground since large inaccuracies in the prescription of land surface fluxes are likely to produce atmospheric drifts in CO₂ concentrations. The ultimate goal of a fully interactive and data-constrained carbon cycle can be progressively improved, once the land carbon component has been coupled with the MACC system.

In order to properly address the issues raised by the carbon reporting, we will explore several ways to initialize the carbon pools that will be more appropriate than performing equilibrium runs: adjusting/constraining the models to reach the carbon pools provided by aggregated in situ data or by the national inventories ; performing a statistical analysis of the difference with the carbon fluxes inferred produced by MACC from atmospheric inversions based on the atmospheric mixing ratios of CO₂ (in collaboration with MACC) ; running the model with the best-known history of climate and disturbance for the last century. The eddy-covariance flux measurements and biometric carbon pools measurements can help to verify the maps of carbon pools at the corresponding locations.

These solutions are being explored with the ORCHIDEE model and its adjoint while the first stage of the LC-CIS is being set up.

4 REFERENCES

- Albergel, C., Rüdiger, C., Pellarin, T., Calvet, J.-C., Fritz, N., Froissard, F., Suquia, D., Petitpa, A., Pignat, B. and Martin, E., From near-surface to root-zone soil moisture using an exponential filter: an assessment of the method based on in-situ observations and model simulations. *Hydrol. Earth Syst. Sci.*, **12**, 1323–1337, 2008.
- Albergel, C., Rüdiger, C., Carrer, D., Calvet, J.-C., Fritz, N., Naeimi, V., Bartalis, Z., and Hasenauer, S., An evaluation of ASCAT surface soil moisture products with in-situ observations in southwestern France, *Hydrol. Earth Syst. Sci.*, **13**, 115–124, 2009.
- Brut, A., Rüdiger, C., Lafont, S., Roujean, J.-L., Calvet, J.-C., Jarlan, L., Gibelin, A.-L., Albergel, C., Le Moigne, P., Soussana, J.-F., Klumpp, K., Guyon, D., Wigneron, J.-P., and Ceschia, E., Modelling LAI at a regional scale with ISBA-Ags: comparison with satellite-derived LAI over southwestern France, *Biogeosciences*, **6**, 1389–1404, 2009.
- Bubnová, R., Hello, G., Bénard, P., and Geleyn, J.F., Integration of the fully elastic equations cast in the hydrostatic pressure terrain-following coordinate in the framework of the ARPEGE/Aladin NWP system, *Mon. Weather Rev.*, **123**, 515–535, 1995.
- Calvet, J.-C., Noilhan, J., Roujean, J.-L., Bessemoulin, P., Cabelguenne, M., Olioso, A., and Wigneron, J.-P., An interactive vegetation SVAT model tested against data from six contrasting sites, *Agr. Forest Meteorol.*, **92**, 73–95, 1998.
- Calvet, J.-C., Rivalland, V., Picon-Cochard, C., and Guehl, J.-M.: Modelling forest transpiration and CO₂ fluxes – response to soil moisture stress, *Agr. Forest Meteorol.*, **124**(3–4), 143–156, 2004.
- Calvet, J.-C., Fritz, N., Froissard, F., Suquia, D., Petitpa, A., and Pignat, B., In situ soil moisture observations for the CAL/VAL of SMOS: the SMOSMANIA network, International Geoscience and Remote Sensing Symposium, IGARSS, Barcelona, Spain, 23–28 July 2007, 1196–1199, 2007.
- Calvet, J.-C., Gibelin, A.-L., Roujean, J.-L., Martin, E., Le Moigne, P., Douville, H., and Noilhan, J., Past and future scenarios of the effect of carbon dioxide on plant growth and transpiration for three vegetation types of southwestern France, *Atmos. Chem. Phys.*, **8**, 397–406, 2008.
- Foley, J. A., Prentice, I. C., Ramankutty, N., Levis, S., Pollard, D., Sitch, S., and Haxeltine, A., An integrated biosphere model of land surface processes, terrestrial carbon balance and vegetation dynamics, *Global Biogeochem. Cy.*, **10**, 603–628, 1996.
- Gibelin, A.-L., Calvet, J.-C., Roujean, J.-L., Jarlan, L., and Los, S. O., Ability of the land surface model ISBA-Ags to simulate leaf area index at the global scale: Comparison with satellites products, *J. Geophys. Res.*, **111**(D18), D18102, 2006.
- Gibelin, A.-L., Calvet, J.-C., and Viovy, N., Modelling energy and CO₂ fluxes with an interactive vegetation land surface model – Evaluation at high and middle latitudes, *Agr. Forest Meteorol.*, **148**, 1611–1628, 2008.
- Jarlan, L., Balsamo, G., Lafont, S., Bejaars, A., Calvet, J.-C., and Mougin, E., Analysis of leaf area index in the ECMWF land surface model and impact on latent and carbon fluxes. Application to west Africa, *J. Geophys. Res.*, **113**, D24117, 2008.
- Luysaert et al., CO₂ balance of boreal, temperate, and tropical forests derived from a global database, *Global Change Biology*, **13**, 2509–2537, 2007.
- Mahfouf, J.-F., Bergaoui, K., Draper, C., Bouyssel, F., Taillefer, F., and Taseva, L., A comparison of two off-line soil analysis schemes for assimilation of screen level observations, *J. Geophys. Res.*, **114**, D08105, 2009.
- Pitman, A. J., The evolution of, and revolution in, land surface schemes designed for climate models, *Int. J. Climatol.*, **23**, 479–510, 2003.
- Rüdiger, C., Calvet, J.-C., Gruhier, C., Holmes, T., De Jeu, R., and Wagner, W., An intercomparison of ERS-Scat and AMSR-E soil moisture observations with model simulations over France, *J. Hydrometeorol.*, **10**, 431–447, 2009.
- Rüdiger, C., Albergel, C., Mahfouf, J.-F., Calvet, J.-C., and Walker, J.P., Evaluation of Jacobians for Leaf Area Index data assimilation with an extended Kalman filter, *J. Geophys. Res.*, **115**, D09111, 2010.
- Sabater, J.M., Rüdiger, C., Calvet, J.-C., Fritz, N., Jarlan, L., and Kerr, Y., Joint assimilation of surface soil moisture and LAI observations into a land surface model, *Agric. For. Meteorol.*, **148** (8–9), 1362–1373, 2008.
- Scipal, K., Drusch, M., and Wagner, W., Assimilation of a ERS scatterometer derived soil moisture index in the ECMWF numerical weather

- prediction system, *Adv. Water Res.*, **31**, 1101-1112, 2008.
- Sellers, P. J., Randall, D. A., Collatz, G. J., Berry, J. A., Field, C. B., Dazlich, D. A., Zhang, C., Collelo, G. D., and Bounoua, L., A revised land surface parameterization (SiB2) for atmospheric GCMs, Part I : Model Formulation, *J. Climate*, **9**, 676–705, 1996.
- Szczypta, C., Calvet, J.-C., Albergel, C., Balsamo, G., Boussetta, S., Carrer, D., Lafont, S., Meurey, C., Verification of the new ECMWF ERA-Interim reanalysis over France, *Hydrol. Earth Syst. Sci. Discuss.*, **7**, 1–40, 2010, 2010.
- Voogt, M., van den Hurk, B.J.J.M., and Jacobs, C., The ECMWF land surface scheme extended with a photosynthesis and LAI module tested for a coniferous site. KNMI publication: WR-06-02, 3/1/2006, 22pp, Available at <http://www.knmi.nl/publications/showBib.php?id=4848>, 2006.

LAI remote sensing products and simulated LAI: an intercomparison over FRANCE

Sébastien Lafont¹, Yang Zhao², Marie Weiss³, Jean-Christophe Calvet¹, Philippe Peylin², Philippe Ciais²

1) CNRM-GAME, Météo-France, Toulouse, France

2) LSCE, CEA, Gif Sur Yvette, France

3) UMR1114, INRA, Avignon, France

sebastien.lafont@cnrm.meteo.fr

ABSTRACT- *The Leaf Area Index (LAI) is an important vegetation variable. It is a good measure of the amount of active vegetation and it is linked to canopy conductance, water and carbon fluxes at the interface between the atmosphere and the vegetation. In this study, we compare four different estimates of LAI over France: two LAI products derived from visible remote sensing, and simulated LAI from two land surface models. The simulated LAI is produced by the ISBA-A-gs model (developed by CNRM) and by the ORCHIDEE model (developed by LSCE). The same atmospheric forcing is used by the two models: the SAFRAN dataset, a high resolution (8-km) operational product over France. The same vegetation map is used: the ECOCLIMAP2 dataset. The LAI remote sensing products are: MODIS (Collection 5), derived from the MODIS sensors, and CYCLOPES, derived from the SPOT4/VEGETATION sensor. These products were re-projected on the grid used by the model. The study period ranges from 2000 to 2007 and allows to study the average seasonal cycle as well as the interannual variation of LAI. We analyse monthly values of LAI over the period. The average seasonal cycle over the seven years starts earlier in the ORCHIDEE simulations than in the ISBA-A-gs ones. ORCHIDEE simulates a maximum interannual variability of LAI in spring (and a small one in summer), whereas in the ISBA-A-gs simulation the maximum is in summer (with small values in spring). These differences can be explained by contrasting levels of phenology constraints used in the two models. The interannual variability of both satellite products is more complex, with a weaker seasonal cycle and contrasted spatial patterns. Finally, we compare the water and carbon fluxes simulated by the two models.*

1 INTRODUCTION

The Leaf Area Index (defined as the leaf area per unit ground area and noted LAI) is an important characteristics of the vegetation. It is a good measure of the amount of active vegetation and is linked to the canopy resistance, the water and carbon fluxes between the atmosphere and the vegetation. In recent years, a lot of effort has been dedicated to use earth observation satellite information to derive key biophysical parameters, among them LAI. In parallel to these efforts, land surface models have been improved and are now able to predict the evolution of LAI along with the natural carbon fluxes.

Comparisons with in-situ measurements are needed, in order to evaluate simulated LAI and remote sensing products (Guarrigues et al., 2008, Calvet et al., 1998), but due to the limited number of available sites, the representativeness of local observations is limited. Therefore, it is useful to compare LAI estimates over large areas. In this work, we focus on France, with a rather high spatial resolution of 8 km.

This work used the regional modelling system of the GEOLAND2 land carbon core information service described in Calvet et al. (this issue). We compare the LAI estimation of this modelling system with other sources of LAI. Four different estimates of LAI over France are considered: two LAI products derived from visible remote sensing observations, and simulated LAI estimates from two land surface models.

2 MODELS AND DATA

2.1 The ORCHIDEE model

ORCHIDEE (Krinner et al., 2005) is a process-based terrestrial biosphere model designed to simulate ecosystem, energy, water, and carbon fluxes at half-hourly to decadal time scales. ORCHIDEE contains three sub-modules, a land surface energy and water balance model SECHIBA (de Rosnay & Polcher, 1998), a land carbon cycle model STOMATE, and a dynamic model of long-term vegetation dynamics including competition and disturbances adapted from Sitch et al. (2003). In this study, the spatial distribution of vegetation types is prescribed. The spatial

heterogeneity of vegetation is described through 13 plant functional types (PFT), with 5 PFT relevant for this study.

The instantaneous energy and water balance of vegetated and non-vegetated surfaces is simulated, as well as canopy-level photosynthesis, using coupled leaf-level photosynthesis and stomatal conductance processes (Ball et al., 1987, Farquhar et al., 1980). Stomatal conductance is reduced by soil water stress (McMurtrie et al. 1990) function of soil moisture and root profiles. Two soil water reservoirs are considered, a surface reservoir which refills in response to rain events and which is brought to zero during dry periods, and a deeper soil reservoir considered as a simple bucket updated accounting for evaporation, root uptake, percolation and runoff.

2.2 The ISBA-A-gs model within SURFEX

Météo-France has developed the SURFEX platform (SURFace EXternalisée) to be used in operational NWP models, and offline for applications in hydrology and vegetation monitoring (Le Moigne et al. 2009). Over land, SURFEX includes ISBA-A-gs, a CO₂-responsive land surface model able to simulate the diurnal cycle of carbon and water vapour fluxes (Calvet et al., 1998; Calvet et al., 2004; Gibelin et al., 2006; Calvet et al. 2007). This model accounts for different feedbacks in response to changes in [CO₂], photosynthesis enhancement and transpiration reduction (fertilization and reduced transpiration effects, respectively). The model also includes an original representation of the soil moisture stress. Two different types of drought responses are distinguished for both herbaceous vegetation (Calvet, 2000) and forests (Calvet et al., 2004), depending on the evolution of the water use efficiency (WUE) under moderate stress: WUE increases in the early soil water stress stages in the case of the drought-avoiding response, whereas WUE decreases or remains stable in the case of the drought-tolerant response. ISBA-A-gs calculates interactively the leaf biomass and the LAI, using a simple growth model (Calvet et al., 1998). Gibelin et al. (2006) and Brut et al. (2009) showed that ISBA-A-gs simulates realistic LAI at regional and global scale under various environmental conditions.

2.3 CYCLOPES LAI products

The CYCLOPES project was an initiative aiming at developing and producing global surface parameters from space-borne sensors. In particular, key biophysical parameters (LAI, fAPAR and fCover) were produced for the period 1998–2007 based on the processing of SPOT/VEGETATION data (Baret et al., 2007). Top of canopy reflectance values were corrected for surface directional effects in order to

obtain normalized reflectances. A neural network was used to retrieve LAI from the normalized reflectances. The neural network was previously trained from synthetic reflectances produced by the SAIL model (Verhoef, 1985) simulating the radiation transfer within vegetation canopies. In this study, the Version 3.1 of the CYCLOPES LAI product (Postel, 2008) is used. It has a spatial resolution of 1km and is based on a temporal composite window of 10 days. The uncertainty of this LAI product is discussed by Garrigues et al., 2008.

2.4 MODIS collection 5 LAI product

The MODIS LAI retrieval algorithm relies on a stochastic radiative transfer model (Knyazikhin et al., 1998) which ingests red and infrared reflectance values, their uncertainties, and the view-illumination geometry. The algorithm uses the MODIS land cover (MOD12Q1) product (Friedl et al., 2002) as a priori information to constrain the LAI outputs. A Look-Up-Table compares observed and modelled reflectances for a suite of canopy structures and soil patterns that represents an expected range of typical conditions for a given biome type. The LAI is retrieved as the mean value from all possible solutions within a specific level of input satellite data and model uncertainties. If this algorithm fails, a back-up procedure is triggered to estimate LAI from biome specific NDVI based relationships. We used the Collection 5 version of the MODIS LAI product

Vergert et al. 2009 describe in detail the differences between the CYCLOPES and the MODIS products. Both LAI products were re-projected on the 8-km resolution model grid. The common period for the two satellite data sets is 2000–2007. This study focuses on monthly mean values. The same land cover map (ECOCIMAP2) and the same atmospheric forcing were used for the two models.

3 RESULTS

3.1 Comparison of the four LAI estimates

We have selected a period of seven years (2000–2007) for which LAI remote sensing data were available. All the LAI values were averaged on a monthly basis. Figure 1 presents the average monthly evolution of LAI over France for the two models and for the two remote sensing products. The first striking feature is that the two models present higher maximum values than the remote sensing products. Also, the start of the growing season is earlier in the ORCHIDEE simulation. ISBA-A-gs presents a leaf onset lag of about one month (as shown by the similarity of the April LAI simulated by ORCHIDEE and the May LAI simulated by ISBA-A-gs). The delay at the start of the

vegetation growing period had previously been noticed by Gibelin et al. (2006).

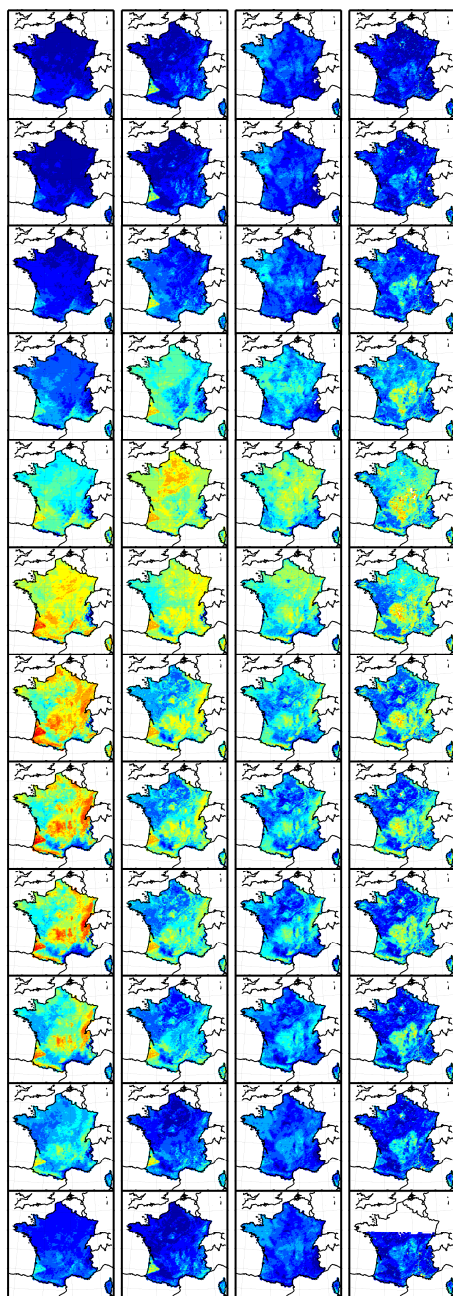


Figure 1: Monthly LAI climatology (2000-2007) derived from (from left to right) ISBA-A-gs, ORCHIDEE, CYCLOPES, MODIS. (Top) January to (bottom) December.

In summer, the maximum LAI is located over the coniferous forest of Les Landes (southwestern coast), and the minimum values are located over the

mountainous area. In contrast, the MODIS LAI maximum values are located over mountainous grassland.

There is marked differences between the two remote sensing product. For example in July, the MODIS product presents very low values over the crops areas of northern France.

Table 1: Spatial correlation (r^2) of the average monthly LAI (1994-2007) per season and for all the possible combination of the ORCHIDEE and ISBA-A-gs models (ORC, ISBA, respectively) and remote sensing (RS) CYCLOPES and MODIS products (CYC, MOD, respectively). From left to right: four model vs. RS, model vs. model, RS vs. RS comparisons.

r^2	ORC/ CYC	ORC/ MOD	ISBA/ CYC	ISBA/ MOD	ISBA/ ORC	CYC/ MOD
DJF	0.00	0.07	0.00	0.09	0.58	0.16
MAM	0.25	0.09	0.12	0.07	0.37	0.37
JJA	0.51	0.58	0.53	0.36	0.46	0.57
SON	0.17	0.22	0.25	0.18	0.43	0.42

The spatial correlation of monthly averaged LAI values depend strongly on the season. In winter and spring, only the models have a strong spatial correlation, while the correlation between model and satellite product is very low (r^2 below 0.25) whatever the model or the satellite products. These low values can be explained by the lack of spatial feature in the LAI maps, associated to disagreements between models and RS product for low LAI values.

The spatial correlation in summer (JJA) is around $r^2 = 0.5$ for all combinations (except for the ISBA vs. MODIS, presenting the lowest value). For all the seasons, the spatial correlation between models never falls below 0.37, which can be partially explained by the use of a common land cover map. The correlation between CYCLOPES and MODIS products is higher in summer and during the autumn (r^2 ranges from 0.42 to 0.57) than in winter and spring (below 0.37).

The interannual variability, expressed as the monthly coefficient of variation (CV), differs a lot from one LAI source to another (not shown). The CV reaches very high values (70 %) over a large part of France in March for the ORCHIDEE model and has very low values (10 %) in July. The ISBA model, on the other hand, has a larger variability at the end of the growing season (August and September). The RS products tend to have a lower variability (CV below 30 %). These differences between models can be explained by a more constrained phenological cycle in the ORCHIDEE model. The maximum LAI is fixed by PFT-dependent parameters. In July, most of the

vegetation types have reached the prescribed maximum LAI value, which strongly limits the possible interannual variations. In ISBA-A-gs, on the other hand, the evolution of LAI is governed by photosynthesis, which accounts for drought effects. This allows a strong interannual variability at summertime.

3.2 Analysis per vegetation type

The heterogeneity of the landscape is described in the models by a tiling scheme. This means that within a grid point, several vegetation types are considered, with their own LAI and flux values. In this study the two models use the same land cover map.

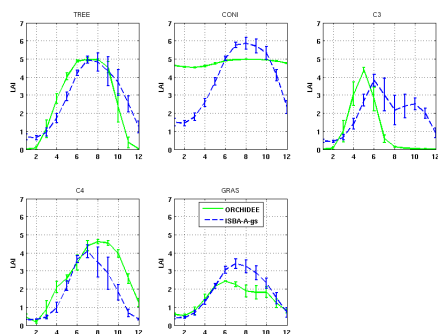


Figure 2: Average seasonal cycle of the simulated LAI (1994-2007) per vegetation type. The error bars represent the interannual variability (defined by the standard variation over the period 1994-2007). The represented vegetation types are, from left to right and from top to bottom, deciduous trees, coniferous trees, C₃ crops, C₄ crops, grasslands.

Figure 2 presents the average LAI seasonal cycle over France per vegetation type. The differences between models are directly linked to the vegetation type. There is a good agreement between ORCHIDEE and ISBA-A-gs for deciduous trees, and C₄ crops. For coniferous trees, the difference in definition of LAI appears clearly: ISBA simulates a physiologically active LAI (green LAI) which has a low value in winter. The summer values are similar for the two models. The main discrepancy concerns C₃ crops for which ORCHIDEE simulates a very sharp seasonal cycle with a maximum value in May and a leaf offset July. ISBA-A-gs simulates a later maximum (July) and a slower decline of LAI. These differences can be explained in part by the fact that the “C₃ crops” vegetation type regroups two farming practices: winter crops (sown in autumn/winter and reaching a maximum in spring) and summer crops (sown in spring and reaching a maximum in summer). It seems that ORCHIDEE simulations are closer to winter

crops, whereas ISBA-A-gs tends to simulate summer crops.

3.3 Impact on carbon fluxes

LAI is an important driving variable for carbon and water fluxes. However, air temperature and incoming radiation have also a very important influence on the fluxes. This means that despite shifts in the phenological cycle between the two models, the shift on carbon fluxes is much smaller, as can be seen in Fig. 3. The main disagreement between models is on the seasonal cycle of C₃ crops, where ORCHIDEE presents a much more intense seasonal cycle than ISBA-A-gs. The magnitude of the fluxes is similar for all the other vegetation types.

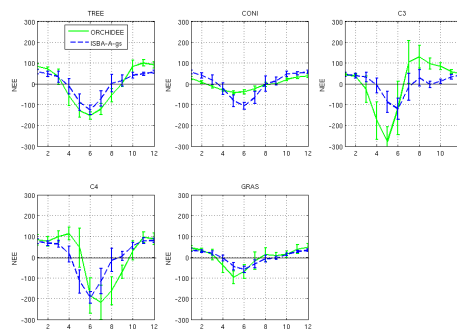


Figure 3 : Average seasonal cycle of the simulated Net carbon flux (NEE, gC/m²/month) per vegetation type. The error bars represent the interannual variability (defined by the standard variation over the period 1994-2007). The represented vegetation types are, from left to right and from top to bottom, deciduous trees, coniferous trees, C₃ crops, C₄ crops, grasslands. Negative values correspond to an uptake of carbon by the plants.

4 CONCLUSIONS

We have compared four different sources of LAI over France. The different sources shows important differences in magnitude, timing and seasonal patterns. For the models, an important part of the differences can be explained by i) the choice of a weak or a strong constraint on the phenological cycle, ii) the lack of a detailed representation of the farming practices such as crop rotation and winter vs. summer crops. For the latter point, remote sensing products may provide very useful information on the actual farming practices. The analysis of the carbon and water fluxes shows smaller differences in seasonal cycle between models. This work contributes to the evaluation of the GEOLAND2 land carbon core information service (LC-CIS) and focuses on the forward modelling component. The next step of this work is to obtain an optimum description of vegetation by combining

model results and remote sensing observations. This work is presented in Barbu et al. (this issue).

5 REFERENCES

- Ball, J., T. Woodrow, and J. Berry (1987), A model predicting stomatal conductance and its contribution to the control of photosynthesis under different environmental conditions, *Prog. Photosynthesis*, **4**, 221–224.
- Brut, A., C. Rüdiger, S. Lafont, J. Roujean, J. Calvet, L. Jarlan, A. Gibelin, and C. Albergel (2009), Modelling LAI at a regional scale with ISBA-A-gs : comparison with satellite-derived LAI over southwestern France, *Biogeosciences*, **6**, 1389–1404.
- Calvet, J., Noilhan, J., Roujean, J., Bessemoulin, P., Cabelguenne, M., Olioso, A., et al. (1998). An interactive vegetation SVAT model tested against data from six contrasting sites. *Agr. Forest Meteorol.*, **92**, 73–95.
- Calvet, J. (2000), Investigating soil and atmospheric plant water stress using physiological and micrometeorological data sets, *Agr. Forest Meteorol.*, **103**, 229–247.
- Calvet, J. (2004), Modelling forest transpiration and CO₂ fluxes response to soil moisture stress, *Agr. Forest Meteorol.*, **124**(3–4), 143–156.
- De Rosnay, P. and Polcher J. (1998) Modeling root water uptake in a complex land surface scheme coupled to a GCM. *Hydrology and Earth System Sciences* **13**(2), pp603–622
- Farquhar, G., S. von Caemmerer, and J. Berry (1980), A biochemical model of photosynthesis CO₂ fixation in leaves of C3 species, *Planta*, **149**, 78–90
- Friedl, M. A., McIver, D. K., Hodges, J. C. F., Zhang, X. Y., Muchoney, D., Strahler, A. H., et al. (2002). Global land cover mapping from MODIS: Algorithms and early results. *Remote Sensing of Environment*, **183**, 287–302.
- Garrigues, S. et al. (2008), Validation and intercomparison of global Leaf Area Index products derived from remote sensing data, *Journal of Geophysical Research - Biogeosciences*, **113**(G2).
- Gibelin, A., J. Calvet, J. Roujean, L. Jarlan, and S. O. Los (2006), Ability of the land surface model ISBA-A-gs to simulate leaf area index at the global scale: Comparison with satellites products, *Journal of Geophysical Research*, **111**(D18), 1–16.
- McMurtrie, R.E, D.A. Rook, and F. Kelliher (1990), Modelling the yield of pinus radiata on a site limited by water and nitrogen, *Forest Ecology and Management*, **30**(1–4), 381–413.
- Le Moigne, P.: SURFEX scientific documentation. Note de centre du Groupe de Météorologie à Moyenne Echelle, 87, Météo-France, CNRM, Toulouse, France, 211 pp., online available at: <http://www.cnrm.meteo.fr/surfex/>, (last access: October 2010) 2009.
- Sitch, S., et al. (2003), Evaluation of ecosystem dynamics, plant geography and terrestrial carbon cycling in the LPJ dynamic vegetation model, *Global Change Biology*, **9**, 161–185.
- Verger, A., F. Camacho, F. García-Haro, and J. Meliá (2009), Prototyping of Land-SAF leaf area index algorithm with VEGETATION and MODIS data over Europe, *Remote Sensing of Environment*, **113**(11), 2285–2297.
- Verhoef, W. (1984). Light scattering by leaf layers with application to canopy reflectance modeling: The SAIL model. *Remote Sensing of Environment*, **16**, 125–141

Geoland2 – Towards an operational GMES Land Monitoring Core Service. First results of the Biogeophysical Parameter Core Mapping Service

Roselyne Lacaze¹, Gianpaolo Balsamo², Frédéric Baret³, Jean-Christophe Calvet⁴, Fernando Camacho⁵, Raphaël D'Andrimont⁶, Sandra Freitas⁷, Philippe Pacholczyk⁸, Hervé Poilvé⁹, Bruno Smets¹⁰, Kevin Tansey¹¹, Wolfgang Wagner¹²

¹ HYGEOS, Cesbio Bpi 2108, 18 avenue E. Belin, 31401 Toulouse Cedex 9, France

² ECMWF, Shinfield Park, Reading, Berks, United Kingdom

³ INRA, EMMAH, site Agroparc, 84914 Avignon, France

⁴ CNRM/Météo-France, 42 avenue G. Coriolis, 31057 Toulouse Cedex, France

⁵ EOLAB, G.V. Marques del Turia, 20-9, 46 005 Valencia, Spain

⁶ Université Catholique de Louvain, 2 Croix du sud, B1348 Louvain-la-Neuve, Belgium

⁷ IM Portugal, Rua Cao Aeroporto de Lisboa, 1749-077 Lisboa, Portugal

⁸ CNES, 18 av. E. Belin, 31 401 Toulouse Cedex, France

⁹ Spot Image SA, 15 avenue de l'Europe, 31 522 Ramonville Ste-Agne, France

¹⁰ VITO, Boeretang 200, 2400 Mol, Belgium

¹¹ University of Leicester, LE1 7RH, Leicester, United Kingdom

¹² TU Wien, Gusshausstrass 27-29/122, 1040 Vienna, Austria

¹rl@hygeos.com, ²balsamo@ecmwf.int, ³baret@avignon.inra.fr, ⁴calvet@meteo.fr,

⁵camacho@eolab.es, ⁶dandrimont@uclouvain.be, ⁷sandra.coelho@meteo.pt,

⁸philippe.pacholczyk@cnes.fr, ⁹herve.poilve@infoterra.fr, ¹⁰bruno.smets@vito.be,

¹¹kevin.tansey@le.ac.uk, ¹²ww@ipf.tuwien.ac.at

ABSTRACT - The European GMES initiative provides a political framework for future implementations of Services Centres related to environmental applications. The FP7/geoland2 project is the last brick towards the implementation of fully mature GMES Land Services, consisting of Core Mapping Services (CMS) and Core Information Services (CIS). Its goal is to build, validate and demonstrate operational processing lines and products on a user-driven basis. The CMS produce “basic” geo-information on the land state covering a wide variety of thematic content, spatial scales from local to global, and update frequency from sub-daily to several years. Besides being a valuable information source by their own, the “basic” products are input for the Core Information Services focusing on a broad variety of thematic fields, like water quality, forest management, spatial planning, agri-environmental issues, carbon cycle analysis, supporting the European environmental policies and international treaties on climate change, food security, and sustainable development. The Biogeophysical Parameter (BioPar) CMS aims at setting-up operational infrastructures for providing regional, continental, and global variables describing the vegetation state, the radiation budget at the surface, and the water cycle, both in near real time and off-line mode. The concept, the objectives, and the structure of the BioPar CMS are introduced. Then, the first biophysical products available to the institutional users, and to the scientific community are presented.

1 INTRODUCTION

With the ongoing climate change, the pressure on nature, biodiversity and our own living conditions increases steadily. To mitigate these threats by effective counter measures and adaptation strategies, a frequent and area-wide monitoring of the environment is crucial to provide decision makers with accurate,

up-to-date information on the changing conditions of our natural resources.

The European GMES initiative provides a political framework for future implementations of Services Centres in charge of products and services related to environmental applications. The project geoland2 constitutes a major step forward in the implementation of the GMES Land Monitoring Core Service (LMCS), and addresses the 3 components (local, continental, and global) of the LMCS. The goal of geoland2 is to

build, validate and demonstrate operational processing lines and products on a user-driven basis.

Building upon the results of a series of preceding projects funded by the European Commission and the European Space Agency, geoland2 is the last brick towards the implementation of fully mature GMES Land Services, consisting of Core Mapping Services (CMS) and Core Information Services (CIS). The CMS produces “basic” geo-information on the land state covering a wide variety of thematic content, spatial scales from local to global, and update frequency from 1 day to several years, on the basis of Earth observation data. Besides being a valuable information source by their own, the mapping products are input for the Core Information Services focusing on a broad variety of thematic fields, like water quality, forest management, spatial planning, agri-environmental issues, food security, carbon cycle analysis. These CIS offer specific information for European environmental policies and international treaties on climate change, food security, and sustainable development.

2 THE BIOGEOPHYSICAL PARAMETER CORE MAPPING SERVICE (BIOPAR)

The *Biogeophysical Parameter Core Mapping Service*, named in short BioPar, is a joint venture of 13 partners: HYGEOS, CNES, INRA, Météo-France, and Spot-Image SA (France), Université Catholique de Louvain (UCL), and VITO (Belgium), Institute of Meteorology (Portugal), Vienna University of Technology (Austria), EOLAB (Spain), University of Leicester, and ECMWF (United Kingdom), and Igik (Poland).

BioPar aims at setting-up operational infrastructures for providing regional, continental, and global variables describing the vegetation state, the radiation budget at the surface, and the water cycle at any scale of interest (regional, continental, and global), both in near real time and off-line mode, and that meets the users’ needs.

2.1 The concept

The BioPar concept relies on research and development activities, shared in 3 topics (vegetation, radiation, water), and on demonstration operations, shared in NRT and off-line processing. In particular, the R&D activities focus on parameters as LAI, FAPAR, albedo, burnt areas or soil moisture, which have been identified by the WMO/GCOS in the context of UNFCCC as Essential Climate Variables (ECV). The research teams define the retrieval algorithms based upon existing and validated methodologies, improve them to match as well as possible the user requirements, and initiate innovative

actions to adapt them to the technical specificities of the next generation of sensors in order to ensure the continuity of the service. Effort will be put on the compatibility between historic and current products so that long-time series are available after the reprocessing of available EO archives. Independent teams perform the product validation, following a procedure established in close collaboration with the users and international bodies, relying on comparison with ground measurements collected over site networks, on inter-comparison with existing similar satellite products, and on data assimilation techniques, with the aim to guaranty the scientific relevancy of the BioPar products. The development teams implement the algorithms in processing lines, and generate test data sets for user evaluation. The pre-operation centers perform the pre-operational production at regional, European and global scales, in NRT and in offline mode. Finally, the resulting biogeophysical parameters are disseminated by the Spatial Data Infrastructure cross-cutting issue, in a format in accordance with the INSPIRE directive.

The BioPar CMS is a strongly user-driven service. The CMS portfolio has been designed from a careful analysis of the needs of CIS and other CMS, considered as good proxys of a large community of users including institutional users, future downstream services and the international science community. The study logic will be such that the products, their timeliness, and the R&D actions have been defined taking into account the users’ needs; the pre-operations, in NRT and in off-line mode, will start only with a user “green light”, given after they have successfully integrated test products into their current practices and working environment.

2.2 The portfolio

The BioPar CMS portfolio includes vegetation (Leaf Area Index (LAI), Fraction of Absorbed PAR, Fraction of green cover, NDVI, Dry Matter Productivity, Phenology), burnt areas, downwelling shortwave and longwave radiation fluxes, land surface temperature, surface albedo, burnt areas, soil moisture, products, provided at various spatial resolution depending on the sensor data used as input (Table 1). Most of the products will be delivered in NRT in the sense of few days (less than one week), as requested by the final users who need to know the surface conditions within a few days of delay in order to react appropriately in case of anomaly, and to anticipate and manage the potential resulting problems. Detecting anomalies by comparing the current observation with a reference requires having consistent long time series. BioPar will provide such time series for some Essential Climate Variables (LAI, FAPAR, soil moisture) taking advantage of existing EO data

archive, and developing sensor-independent methodologies.

Table 1: BioPar CMS Portfolio

Product	NRT / Off-line	Spatial Resolution	Spatial coverage	Temporal Resolution	Sensor
Continental Vegetation					
LAI, FCover, FAPAR, DMP, NDVI, Phenology	NRT	1 km	Global	10-days	VTG
Times series of vegetation products	Off-line	4 km	Global	10-days	AVHRR + VTG
Burnt areas + seasonality	NRT	1 km	global	Daily	VTG
MERIS FR biophysical variables	NRT	300 m	Europe	10-days	MERIS
HR biophysical products	Off-line	10 m	Pilot Areas	4 times/year	SPOT, RapidEye
Energy Budget					
Downwelling Shortwave Surface Flux Downwelling Longwave Surface Flux	NRT	~5 km	Global	hourly	SEGO + AVHRR
Land Surface Temperature	NRT	~5 km	Global	hourly, daily, 10-days	SEGO + AVHRR
Surface Albedo	NRT	1 km	Global	10-days	VTG
Surface Albedo	NRT	~5 km	Global	10-days	SEGO + AVHRR
Water cycle					
Water bodies + seasonality	NRT	1km, 250m	Africa	10-days	VTG, MODIS
Soil Moisture + Freeze/Thaw	NRT	0.1°	Global	Daily	ASCAT
Time series of soil moisture products	Off-line	25 km	Global	Daily	ERS-1&2 Scatt

3 THE BIOPAR PRODUCTS

3.1 LAI, FCover, FAPAR, NDVI derived from SPOT/VEGETATION sensor data

The leaf area index (LAI) is defined as half the total foliage area per unit of ground surface. The FCover is the fraction of ground unit covered by green vegetation. The FAPAR is defined as the fraction of photosynthetically active radiation absorbed by green vegetation for photosynthesis activity. The instantaneous FAPAR value at 10:00 solar time is used as a very good approximation to the daily integrated value under clear sky conditions. The Normalized Difference Vegetation Index (NDVI) corresponding to the SPOT-5/VEGETATION-2 sensor characteristics for its Red (B2) and NIR (B3) bands, is also provided.

The algorithm, defined by INRA, is detailed in Baret et al. (2010). CNES has adapted the processing line, based upon an existing chain developed previously by Medias-France in the framework of the FP5/CYCLOPES project, and has generated two years of global, 10-daily products. Before the end of the year, the processing line will run in NRT at VITO. These vegetation products are being validated by EOLAB according to the protocol defined by the Land Product Validation (LPV) group of CEOS (Morissette et al., 2006). The results of this validation are presented in Camacho et al. (2010).

The methodology is being adapted to the historical AVHRR surface reflectances made available by the LTDR project. The archive from 1981 will be processed to get a long time series (about 30 years) of vegetation variables fully consistent with the SPOT/VEGETATION products.

3.2 The set of biophysical variables derived from the FR MERIS sensor data, and HR SPOT sensor data

The MERIS Full Resolution (FR) biophysical products, and the High Resolution (HR) biophysical products, contain a set of variables including estimates of the green, brown & soil cover fractions, the LAI, the FAPAR, the chlorophyll content, a canopy shadow factor, and the water & snow cover fractions.

The baseline vegetation model developed for processing the MERIS data uses the SAIL/PROSPECT model as core component (Verhoef, 1984; Jacquemoud et Baret, 1990). This model was upgraded and completed in order to include the contribution of brown vegetation, the modelling of “rough” canopies, the computation of vegetation cover fractions in reference directional conditions, and the computation of FAPAR from the SAIL model. Then, to restore the heterogeneous nature of the MERIS pixels, a further modelling step is applied consisting in having a composite canopy model made of two components: 1) a main canopy component made of predominantly green vegetation, that may have all range of conditions from crops to forest/shrub canopies; 2) a second canopy component made of low brown vegetation, primarily designed to model either senescent crops/grasslands or bare soil conditions. Another important component of the developed model is the soil modelling, the soil reflectance being an input of the SAIL model. In this approach, the variation of soil brightness in relation with soil roughness and humidity is handled by performing an initial learning of the soil mean spectral signature in the MERIS bands at a regional level. Then, this signature is exploited through a physical model of soil variability, accounting for the soil shading and surface humidity effects. This scene model is then coupled with a model of the atmospheric transmission from Earth surface level to the sensor (Verhoef and Bach, 2003). The detection of water and snow covers is done through additional modelling of the corresponding surfaces which are combined, as linear mixture, with the standard land model.

Spot Image SA has elaborated the methodology above, developed the processing line, and ran it in off-line mode. Today, the existing MERIS FR (300m resolution) products covers some river basin across Europe (Rhine, Seine-Normandie, Guadalquivir, Adour-Garonne, Nemunas, Moselle-Sarre, Motala-Ström, Svetoji, Strymonas-Struma) for years of

major interest for the final users. The HR SPOT products cover high risk areas located in 4 river basins across Europe (Rhine, Seine-Normandie, Guadalquivir, Strymonas-Struma). They have been derived from data acquired in 2009 and 2010.

The production in NRT of the MERIS products covering the whole Europe should start before the end of 2010. These products are being validated by EOLAB, jointly with the products derived from SPOT/VEGETATION data (§3.1).

3.3 Soil Water Index (SWI) derived from ASCAT/Metop

The Soil Water Index is defined as the soil moisture content (in percent) in the soil profile. The retrieval algorithm uses an infiltration model describing the relation between Surface Soil Moisture (SSM) and profile soil moisture as a function of time. The algorithm is based on a two-layer water balance model (Wagner et al., 1999) to estimate profile soil moisture from SSM retrieved from scatterometer data. The remotely sensed topsoil represents the first layer and the second layer extends downwards from the bottom of the surface layer. In this model, the water content of the reservoir, whose depth is related to a characteristic time length (T), is described in terms of an index, which is controlled only by the past soil moisture conditions in the surface layer. A computational adaptation of the original SWI algorithm has been made based on a recursive formulation proposed by Albergel (2008). In this method, a gain factor is introduced that relates the past SWI measurements to the current measurements. The SWI processing algorithm uses ASCAT-25km SSM product as input to generate daily global SWI images, calculated for five different T values (1, 5, 10, 15, 20, 40, 60, 100) together with the respective quality flags.

The retrieval algorithm is defined by Vienna University of Technology, the processing line is developed by CNES which has also generated the SWI products over the period from 1st June 2007 to the present. In few weeks, the processing line will run in near real time at the Institute of Meteorology of Portugal. The SWI products are being validated by Météo-France and ECMWF using in-situ observations, and operational, analyzed products from models running at global and regional scale.

A second version of the product is planned in the project life, including a more accurate detection of the freeze and thaw conditions of the surface. Then, the ERS/Scat data archive will be re-processed in order to get a long time series of SWI fully consistent with the current ASCAT products.

3.4 The Surface Albedo derived from the SPOT/VEGETATION sensor data

The albedo is the fraction of the incoming solar radiation reflected by the land surface, integrated over the whole viewing directions. The BioPar albedo products include the directional albedo calculated for the local solar noon, and the hemispheric albedo, integrated over the whole illumination directions for 3 broad bands: visible [0.4, 0.7 μ m], near-infrared [0.7, 4 μ m], and the whole solar spectrum [0.3, 4 μ m]. The coefficients resulting from the inversion of a 3-kernels linear bidirectional reflectance model on the atmospherically-corrected SPOT/VEGETATION reflectances (Baret, et al. 2007) acquired during a period of 30 days are then combined with the pre-computed values of the directional kernels integrated over angular domains to estimate albedos. Finally, the broadband albedos are derived by linear relationships of spectral quantities.

This algorithm, and the processing line, have been previously set-up in the framework of the FP5/CYCLOPES project, by CNRM, and Medias-France, respectively. CNES has adapted the existing chain to the geoland2/BioPar specifications, and generated two years of global, 10-days products. Before the end of 2010, the processing line will run in NRT at VITO. These SPOT/VEGETATION albedo products are being validated by EOLAB according to the protocol defined by the Land Product Validation (LPV) group of CEOS. An inter-comparison with the other BioPar albedo product (§3.5), derived by merging geostationary and polar sensors data, will be performed.

3.5 Radiation variables derived from geostationary sensors data

The radiation variables of the BioPar portfolio (Downwelling Shortwave Surface Flux (DSSF), Downwelling Longwave Surface Flux (DSLFL), the Land Surface Temperature (LST), and the albedo) are generated by the fusion of geostationary and polar sensor data. The DSSF represents the short-wave fraction of the solar irradiance (0.3-4 μ m) reaching the soil background. The DSLFL is defined as the irradiance reaching the surface in the thermal infrared part of the spectrum (4-100 μ m). The LST is the radiative skin temperature of land surface. The albedo variables are the same as those retrieved using SPOT/VEGETATION data (§3.4).

The Institute of Meteorology of Portugal is in charge of the algorithm definition, the processing lines development, and the production in near real time of the 4 products. These radiation variables correspond to an extension of those currently produced on an operational basis by the Satellite Application Facility

on Land Surface Analysis (Trigo et al., 2010). While the latter are restricted to EUMETSAT sensors, Geoland-2 products make use of non-European geostationary satellites to increase area coverage. The description of the merging is given in Freitas et al. (2010).

The global hourly DSLF, DSSF and LST demonstration products cover one year from August 2009. They will be produced in near real time before the end of 2010. The demonstration albedo products should be available mid-2011.

3.6 Other BioPar products

The first version of the small water bodies product is derived from SPOT/VEGETATION data. The results from the fusion of two existing algorithms: the first one (Gond et al., 2004) was developed in the framework of VGT4AFRICA by the Joint Research Centre and is suited to arid and semi arid condition; the second one was developed for GlobalWatch project and was further developed in the context of Desert Locust prevention FAO product (Pekel, 2009). Both methods rely on different thresholds for the NDVI, the Normalized Difference Water Index (NDWI), the Hue (from RGB to HSV transformation) and the reflectance in the middle infra-red of SPOT/VEGETATION data. The product includes also information about the seasonality, i.e. the date of filling and the date of drying.

The Université Catholique de Louvain (UCL) is in charge of the methodology, whereas the processing line is developed and run in NRT at VITO. The SPOT/VEGETATION water bodies demonstration product are available from July 2007 to December 2008.

The second version of the product will be derived MODIS data (250m resolution) to identify smaller ponds. The methodology is described in D'Andrimont et al. (2010).

The global burnt area product derived from the daily SPOT/VEGETATION data is produced by VITO in near real time over Africa since April 2010. University of Leicester is working on the addition of a seasonality metrics (start, end and timing of maximum burning) to the improved L3JRC algorithm (Tansey et al., 2008). This upgraded version should run in near real time at global scale by the end of 2011. In parallel, the adaptation of the methodology to AATSR-like sensor data is investigated.

3.7. Product access

The near real time BioPar products are available through a web portal at the address <http://www.geoland2.eu>. A subscription is possible to get automatically the new products when available.

All information about the geoland2 project, including the description and the portfolio of various Core Mapping and Core Information Services are given in the geoland2 web site at the address <http://gmes-geoland.info>. This site contains news on the available products and direct links with the portal.

4 CONCLUSION

Geoland2 is at the mid-term of its life: the demonstration products are available, the validation exercises are in progress, and the pre-operational implementation of services has started. These efforts are focused on the implementation of the GMES Land Monitoring Core Service (LMCS), and BioPar CMS intends to bring a main brick to build the Global component of the LMCS. Through a global systematic monitoring service, the Global component of the LMCS aims to provide near real time bio-geophysical parameters at global scale, addressing primarily the 13 terrestrial ECVs, and describing the vegetation state and dynamic. The principal scope of the Global component of the LMCS is to deliver information products and services on the status and evolution of land surfaces in support to specific EU policies at international level and European commitments under international treaties and conventions, such as the three Rio conventions on Climate Change, Desertification and Biodiversity.

5. REFERENCES

- Albergel, C., Rüdiger, C., Pellarin, T., Calvet, J.-C., Fritz, N., Froissard, F., Suquia, D., Petitpa, A., Piguet, B., Martin, E., 2008. From near-surface to root-zone soil moisture using an exponential filter: an assessment of the method based on in-situ observations and model simulations. *Hydrological Earth System Science*, 12: 1323-1337.
- Baret, F., Hagolle, O. et al., 2007. LAI, fAPAR and fCover CYCLOPES global products derived from VEGETATION. Part 1: Principles of the algorithm. *Remote Sensing of Environment*, 110: 275-286.
- Baret, F., M. Weiss, R. Lacaze, F. Camacho, P. Pacholczyk, B. Smets, Consistent and accurate LAI, fAPAR and fCover global products: principles and evaluation of geoland2 products, *Proceedings of the III RAQRS held on Torrent, on 27th September – 1st October 2010, this issue.*
- Camacho, F., F. Baret, J. Cernicharo, R. Lacaze, M. Weiss, Quality assessment of the first version of geoland2 biophysical variables produced at global scale, *Proceedings of the III RAQRS held*

- on Torrent, on 27th September – 1st October 2010, this issue.
- D'Andrimont, R. J.-F. Pekel, P. Defourny, Monitoring water bodies over whole Africa at 250m resolution: multi-annual analysis of various spatio-temporal dynamics, *Proceedings of the III RAQRS held on Torrent, on 27th September – 1st October 2010, this issue.*
- Freitas, S. C., I. F. Trigo, J. Macedo, C. Barroso, R. Silva, A multi-sensor approach to land surface temperature, *Proceedings of the III RAQRS held on Torrent, on 27th September – 1st October 2010, this issue.*
- Gond, V., Bartholomé, E., Ouattara, F., Nonguierma, A., Bado, I., 2004. Surveillance et cartographie des plans d'eau et des zones humides et inondables en régions arides avec l'instrument VEGETATION embarqué sur SPOT-4, *International Journal of Remote Sensing*, 25 (5), pp. 987–1004.
- Jacquemoud, S. and Baret, F., 1990. PROSPECT: A model of leaf optical properties spectra, *Remote Sensing of Environment*, 34: 75-91.
- Morisette, J., Baret, F., Privette, J.L., Myneni, R.B., Nickeson, J., Garrigues, S., Shabanov, N., Weiss, M., Fernandes, R., Leblanc, S. et al., 2006. Validation of global moderate resolution LAI Products: a framework proposed within the CEOS Land Product Validation subgroup. *IEEE Transaction on Geoscience and Remote Sensing*, 44(7): 1804-1817.
- Pekel, J.-F., Cressman, K., Ceccato, P., Vancutsem, C., Vanbogaert, E., Defourny, P., 2009. Development and application of multi-temporal colorimetric transformation to monitor vegetation in the desert locust habitat. *Proceeding MultiTemp 2009 – The Fifth International Workshop on the Analysis of Multi-temporal Remote Sensing Images - July 28-30, 2009 - Groton, Connecticut*
- Tansey, K., Grégoire, J.-M., Defourny, P., Leigh, R., Pekel, J.-F., van Bogaert, E., and Bartholomé, E., 2008. A new, global, multi-annual (2000–2007) burnt area product at 1 km resolution, *Geoscience Research Letter*, 35, L01401, doi:10.1029 / 2007GL031567.
- Trigo, I. F., C. C. DaCamara, P. Viterbo, J.-L. Roujean, F. Olesen, C. Barroso, F. Camacho-de-Coca, D. Carrer, S. C. Freitas, J. García-Haro, B. Geiger, F. Gellens-Meulenberghs, N. Ghilain, J. Meliá, L. Pessanha, N. Siljamo, and A. Arboleda, 2010: The Satellite Application Facility on Land Surface Analysis. *International Journal of Remote Sensing*, in press.
- Verhoef, W., 1984. Light scattering by leaf layers with application to canopy reflectance modeling: the SAIL model, *Remote Sensing Environment* 16: 125-141.
- Verhoef, W. and Bach, H., 2003., Simulation of hyperspectral and directional radiance images using coupled biophysical and atmospheric radiative transfer models, *Remote Sensing Environment*, 87: 23–41.
- Wagner, W., Lemoine, G., Rott, H., 1999. A method for estimating Soil Moisture from ERS scatterometer and soil Data. *Remote Sensing of Environment*, 70: 191-207.

The YLCD method: Monitoring vegetation from annual behaviour of NDVI and LST time series

Y. Julien, J. A. Sobrino, C. Mattar, J.-C. Jiménez-Muñoz, G. Sòria, V. Hidalgo, B. Franch, R. Oltra-Carrió, J. Cuenca.

Global Change Unit, Image Processing Laboratory, Parque Científico, Universidad de Valencia, C/ Catedrático Agustín Escardino n°9, 46980 Paterna, Spain.

yves.julien@uv.es, sobrino@uv.es

ABSTRACT- *Vegetation has been traditionally monitored at global scale from remotely sensed vegetation indices. Among these indices, the Normalized Difference Vegetation Index (NDVI) has been widely used due to its simplicity, although it presents many drawbacks. Several studies have shown that monitoring Land Surface Temperature (LST) in conjunction with NDVI improved greatly the results. This work presents the YLCD (Yearly Land Cover Dynamics) method, which summarizes annual NDVI and LST behaviors in three parameters on a pixel by pixel basis. These three parameters characterize vegetation type and seasonality, and also assess the validity of the model used to describe the observed annual NDVI and LST behaviors. This method allows a clear differentiation of vegetation at both local and global scale. A classification of an agricultural area based on this method is presented, and shows good results as regards crop differentiation. This method has also been applied to Pathfinder AVHRR (Advanced Very High Resolution Radiometer) Land data (1981-2001) at global scale, and allows to evidence vegetation change hotspots such as deforestation in the tropics.*

1 INTRODUCTION

The monitoring of vegetation has come recently into focus due to the concerns about climate change. The reasons for this attention are twofold: first, vegetation is a key parameter of the climate system, which knowledge is mandatory for precise climate prediction; and second, vegetation dynamics affect atmospheric carbon sequestration, which has to be assessed by most governments in order to reach the goals they agreed in the framework of the Kyoto protocol.

Since the launch of the first satellites, earth observation has been the easiest way to monitor vegetation, due to the repeatability of the measurements as well as the access to remote areas it provides. These characteristics are all the most useful when compared with their only alternative, which consists in at the ground observations, which is tedious, spatially and temporally limited, and costly, and therefore impossible to carry out continuously.

NDVI (Normalized Difference Vegetation Index – Tucker, 1979) is a vegetation index which estimates the greenness of the vegetation, and has been widely used to monitor vegetation behavior since the 1980s (Zhou et al., 2001; Myneni et al., 1997; Julien & Sobrino, 2009a). However, several studies have evidenced a saturation of the NDVI for dense covers, which can be solved by the combined analysis of NDVI with land surface temperature (LST) (Lambin & Ehrlich, 1996; 1997; Nemani & Running, 1997).

For example, Julien & Sobrino (2006) showed that the combined analysis of NDVI and LST provided insight on vegetation change processes in Europe. Based on these findings, the YLCD (Yearly Land Cover Dynamics) method has been developed by Julien & Sobrino (2009b), in order to describe vegetation through the use of NDVI and LST. The work presented here gives an overview of the YLCD method, which is then applied to different datasets to monitor and classify vegetation.

2 DATA

Two databases have been used in this work: Pathfinder AVHRR Land (PAL) and a compilation of Landsat images for year 2009.

2.1 PAL database

PAL database (Smith et al., 1997) has been compiled by the National Aeronautics and Space Administration (NASA) and was available free of charge from their website until 2008. This database consists of images acquired by the Advanced Very High Resolution Radiometer (AVHRR) sensor, onboard NOAA (National Oceanic and Atmospheric Administration) satellites. In spite of a daily acquisition frequency of the sensor, the dataset has a temporal resolution of 10 days, because of the image compositing (accordingly to the Maximum Value Compositing or MVC method), which diminishes the contamination of the images by clouds or aerosols (Holben, 1986). The dataset extends

from July 1981 to September 2001, and for each 10-day period, 5 images are available: red reflectance (channel 1), infrared reflectance (channel 2), infrared radiometric temperatures (channels 4 and 5), and NDVI image. Images are available at 0.1 degree and eight kilometer resolution, at continental and global scale. In this work, global 10-day composites at 0.1 degree from July 1981 to September 2001 are used.

2.2 Landsat data

Landsat images have been provided by the National Geographic Institute of Spain (Instituto Geográfico Nacional- IGN). Data from Thematic Mapper (TM) sensor on board Landsat-5 platform have been used in this study. TM sensor has four spectral bands in the Visible and Near-Infrared (VNIR) range (blue, red, green and NIR, corresponding to bands 1, 2, 3 and 4), two bands in the Short-Wave InfraRed (SWIR) range (bands 5 and 7) and one band in the Thermal – InfraRed (TIR) range (band 6). Spatial resolution is 60 m for VNIR and SWIR bands and 120 m for TIR band. Bandwidths are around 0.1 μm for VNIR bands, 0.25 μm for SWIR bands and 2 μm for the TIR band. Since the Barrax site (39°3'N, 2°6'W, 700 m, located in Albacete, Spain) appears in 2 Landsat scenes (corresponding to paths 199 and 200, row 33), a total of 31 images were available from January to

December 2009, although only 16 images could be used for this study due to cloud contamination.

3 METHODOLOGY

First, NDVI is estimated for both datasets. To this end, red and near infrared channels of AVHRR and Landsat instruments using Tucker (1979). As regards LST estimation, the algorithm developed by Sobrino & Raissouni (2000) for AVHRR data, and the method developed by Jiménez-Muñoz et al. (2009) for Landsat data, for which water vapor has been extracted for the Barrax area from coincident MODIS data. Then, the YLCD approach (Julien & Sobrino, 2009b) is carried out on a yearly basis for both datasets. This YLCD approach consists in normalizing LST between 240 and 340K, and plotting the yearly behavior of a given pixel in this normalized LST and NDVI space. Then, 3 parameters are retrieved from a linear regression of this yearly behavior (see figure 1). These 3 parameters describe the vegetation type (θ), seasonality (d) and confidence in the used linear model (R^2), and are plotted in figure 2 as an IHS (Intensity Hue Saturation) composite.

Then, a maximum likelihood classification is carried out from Landsat derived YLCD parameters, using as training data half the nomenclature fields and as validating data the other half of these nomenclature

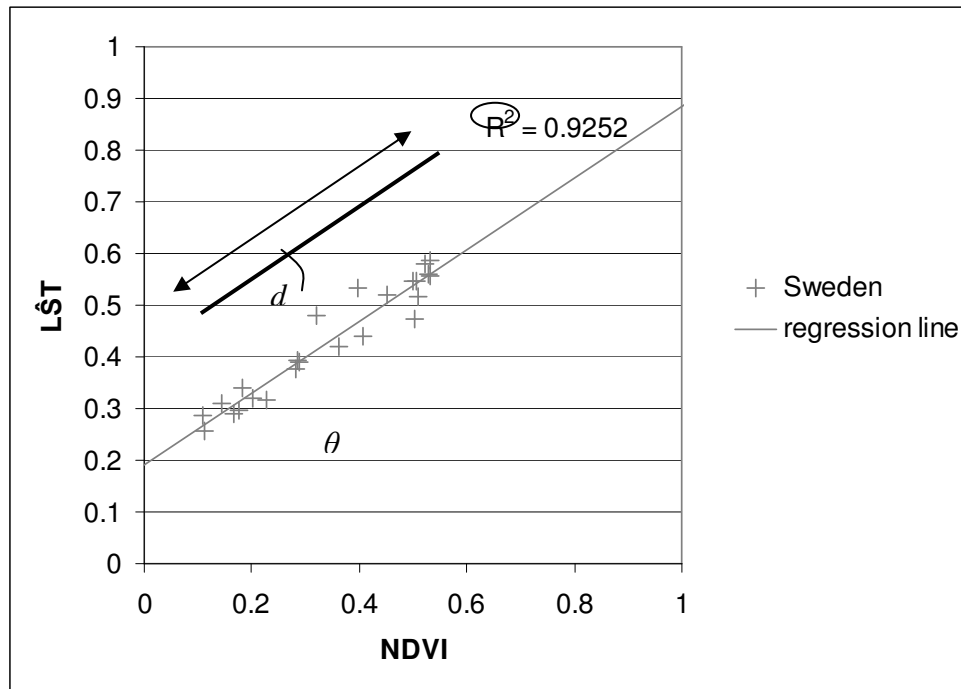


Figure 1: Chosen parameters for the YLCD method in order to describe annual vegetation behavior in terms of NDVI and normalized LST.

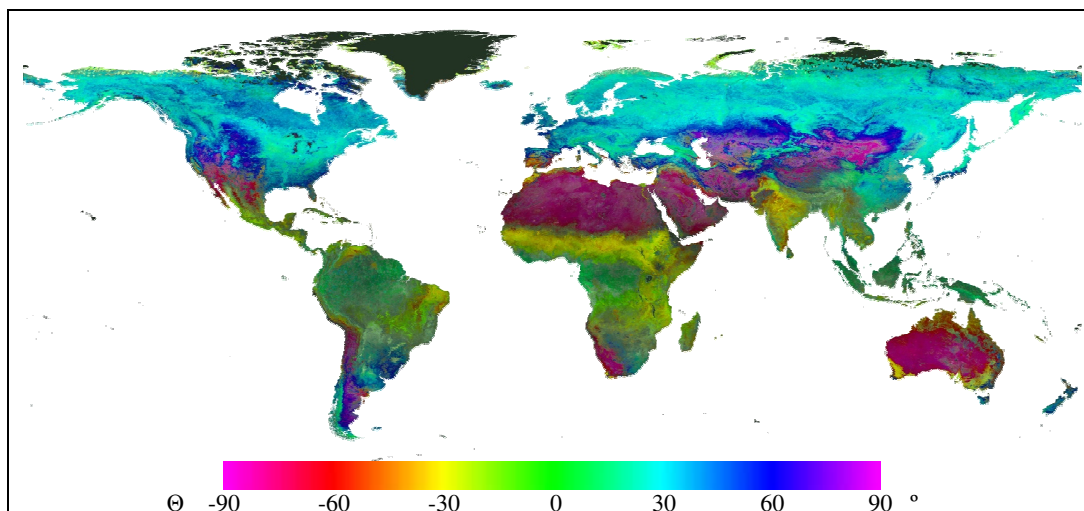


Figure 2: IHS composite (Intensity – Hue – Saturation) of global YLCD parameters for an average of the period 2000-2005. d parameter is coded as intensity, θ as hue, and R^2 as saturation. As a result, arid areas are displayed in purple ($\theta \sim \pm 90^\circ$), semi-arid areas in yellow ($\theta \sim -30^\circ$), evergreen forests in green ($\theta \sim 0^\circ$) while temperate, polar, austral and mountain vegetation appear in various shades of blue ($\theta > 0^\circ$).

fields (see figure 3a).

As regards Pathfinder AVHRR Land data, YLCD parameters are estimated for each year. Then, the presence of trend is tested for all three parameters by using the Mann-Kendall statistical framework (Hirsch & Slack, 1984; Libiseller & Grimvall, 2002), and trends for pixels which exhibit trends at 90% confidence level are retrieved by Ordinary Least Square regression. Then, pixels showing the highest trends (with an absolute value above one standard deviation) are analyzed, in order to focus on the areas undergoing land cover change which have probably been evidenced in other studies. Additionally, the YLCD parameter time series have been tested for the

influence of the orbital drift which affects all AVHRR derived LST (Price, 1991) by using the Mann-Kendall independence test. To that end, average year of satellite overpass time have been estimated for each pixel from Ignatov et al. (2004). As a result, most of the emerged areas show independence from average overpass time at 80% confidence level, with few pixels (mainly located in arid areas) having a lower confidence level (always above 50%).

4 RESULTS

The classification obtained from Landsat YLCD parameters is presented in figure 3b. This

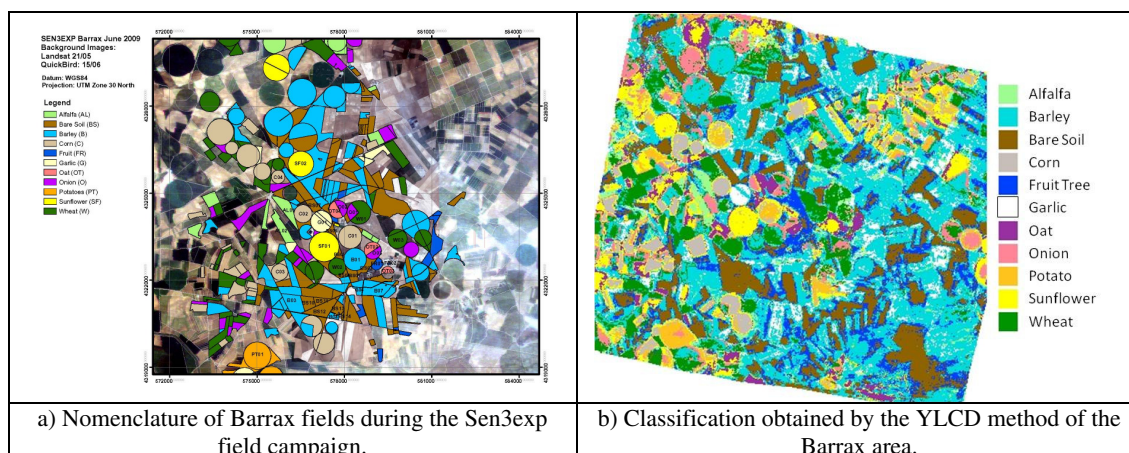


Figure 3: Nomenclature (a) and classification (b) of the Barrax (Albacete, Spain) area. The classification has been obtained by carrying out the YLCD method on one year of Landsat data from 2009.

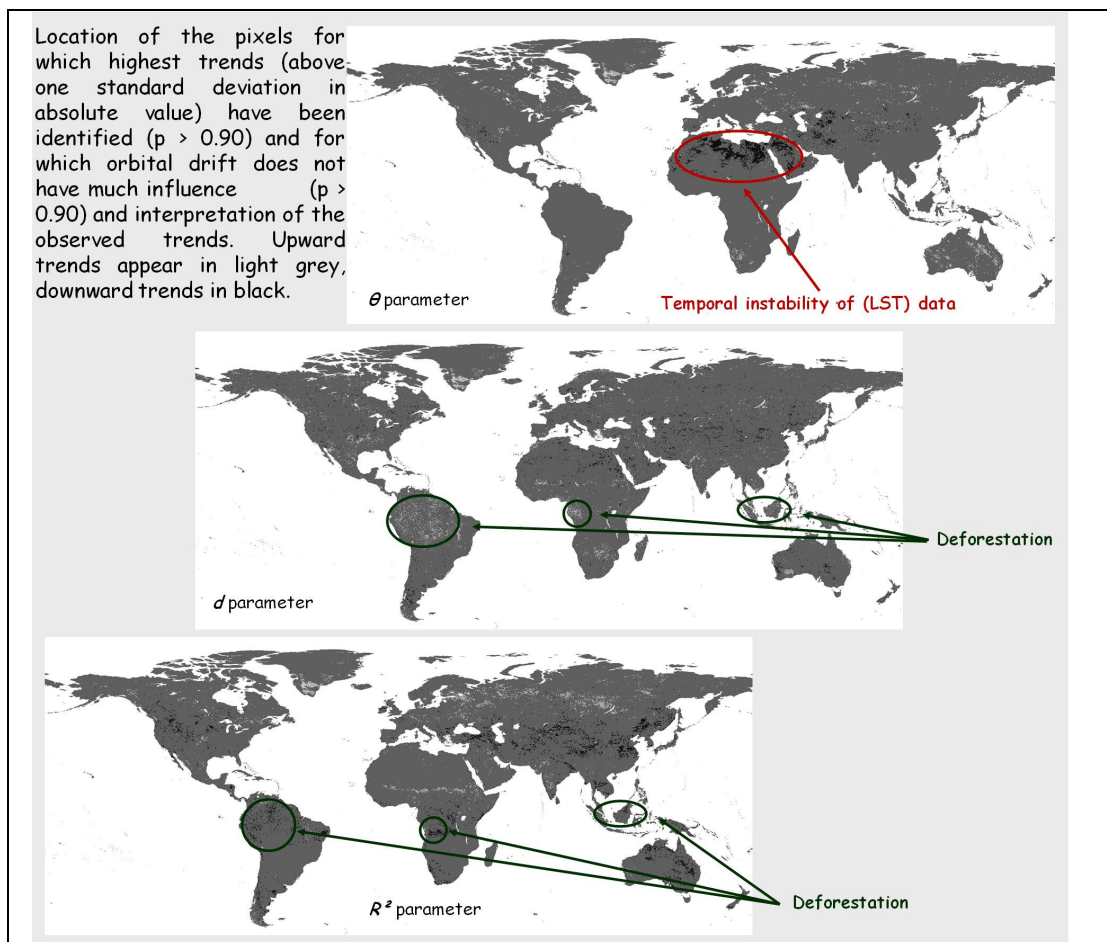


Figure 4: Identification of areas with highest trends in YLCD parameters at global scale. Deforestation in the tropics is particularly obvious, and corroborated by UNEP (2005).

classification shows an accuracy of 87%, and a kappa value of 0.85, after merging all irrigated cereal crops together (barley, oat, wheat), since their yearly NDVI and LST behavior are similar for the Barrax area. This classification shows a good correspondence with field nomenclature, except for a few fields for which corn and sunflower are sometimes misidentified.

As for the trend analysis of PAL YLCD parameters, the pixels showing the highest trends (absolute value above one standard deviation) are shown in figure 4. The pixels showing changes in θ parameters are mainly located in arid and semi-arid areas, which are due to the temporal instability of the LST signal in these areas, for which the independence of the YLCD parameters from the orbital drift is less obvious. On the other hand, changes in d and R^2 parameters are especially observed along the equator. Comparison of the pixels evidenced in UNEP (2005) report as deforestation hotspots with these higher trend

maps confirm that the areas outlined in figure 4 are undergoing deforestation.

5 CONCLUSIONS AND PERSPECTIVES

The good accuracy and kappa coefficients obtained from the Landsat YLCD derived classification show that this approach describes correctly the land cover at high spatial resolution, as suggested by YLCD derived low resolution maps (see figure 2). Additionally, study of low resolution trends in the YLCD parameters for the Pathfinder AVHRR Land database show agreement with previously reported trends. Therefore, the YLCD method is useful for the study of vegetation dynamics at both local and global scales.

The Long Term Data Record (LTDR) dataset, made available recently by NASA, provides daily AVHRR data from 1981 to 2000, for which the YLCD method could evidence changes at 0.05° spatial resolution. The authors will conduct such analysis of

the LTDR dataset in a close future. To that end, this dataset will first need to be corrected from the orbital drift, which will be carried out from an adaptation of the algorithms developed by Sobrino et al. (2008). Then, data time series will need to be reconstructed from acquisition gaps and atmospheric contamination, for which the IDR (Iterative Data Reconstruction) method developed by Julien & Sobrino (2010) will be applied. Then, the YLCD approach will be carried out, and YLCD parameter time series will be analyzed.

ACKNOWLEDGEMENTS

The authors would like to thank the LEO (Laboratory for Earth Observation) group of the University of Valencia for providing the Barrax field nomenclature image, Jordi Cristóbal (CREAF-Autonomous University of Barcelona) for assistance with Landsat radiometric calibration issues and the Instituto Geográfico Nacional (IGN, Spain) for providing Landsat imagery. The authors also wish to thank the TERMASAT project (Ministerio de Educación y Ciencia, project ESP2005-07724-C05-04), the European Union (CEOPAEGIS, project FP7-ENV-2007-1 Proposal No. 212921; WATCH, project 036946) and the Ministerio de Ciencia y Tecnología (EODIX, project AYA2008-0595-C04-01) for their financial support. Source for the PAL dataset was the Goddard Earth Sciences Distributed Active Archive Center in 2004 (data unavailable in 2008).

REFERENCES

- Hirsch, R. M. & Slack, J. R., 1984, A nonparametric trend test for seasonal data with serial dependence, *Water Resources Research*, 20, 727-732.
- Holben, B. N., 1986, Characteristics of maximum values composite images from temporal AVHRR data, *International Journal of Remote Sensing*, 1986, Vol. 7, 1417-1434.
- Ignatov, A., Laszlo, I., Harrod, E. D., Kidwell, K. B. & Goodrum, G. P., 2004, Equator crossing times for NOAA, ERS and EOS sun-synchronous satellites, *International Journal of Remote Sensing*, 2004, Vol. 25, No. 23, 5255-5266.
- Jiménez-Muñoz, J. C., Cristóbal, J., Sobrino, J. A., Soria, G., Ninyerola, M. & Pons, X., 2009, Revision of the Singl-Channel algorithm for Land Surface Temperature retrieval from Landsat thermal-infrared data, *IEEE Transactions on Geoscience and Remote Sensing*, 47(1), 339-349.
- Julien, Y., Sobrino, J. A. & Verhoef, W., 2006, Changes in land surface temperatures and NDVI values over Europe between 1982 and 1999, *Remote Sensing of Environment*, 103 (2006) 43-55.
- Julien, Y. & Sobrino, J. A., 2009a, Global land surface phenology trends from GIMMS database, *International Journal of Remote Sensing*, Vol. 30, No. 13, 3495-3513.
- Julien, Y. & Sobrino, J. A., 2009b, The Yearly Land Cover Dynamics (YLCD) method: an analysis of global vegetation from NDVI and LST parameters, *Remote Sensing of Environment*, 113 (2009) 329-334.
- Julien, Y. & Sobrino, J. A., 2010, Comparison of cloud-reconstruction methods for time series of composite NDVI data, *Remote Sensing of Environment*, 114 (2010) 618-625.
- Lambin, E. F. & Ehrlich, D., 1996, The surface temperature-vegetation index space for land cover and land-cover change analysis, *International Journal of Remote Sensing*, 1996, Vol. 17, No. 3, 163-487.
- Lambin, E. F. & Ehrlich, D., 1997, Land-cover changes in sub-Saharan Africa (1982-1991): application of a change index based on remotely sensed surface temperature and vegetation indices at a continental scale, *Remote Sensing of Environment*, 61, 181-200.
- Libiseller, C. & Grimvall, A., 2002, Performance of partial Mann-Kendall test for trend detection in the presence of covariates, *Environmetrics*, 13: 71-84.
- Myneni, R. B., Keeling, C. D., Tucker, C. J., Asrar, G. & Nemani, R. R., 1997, Increased plant growth in the northern high latitudes from 1981 to 1991. *Nature*, Vol. 386, 17 april 1997.
- Nemani, R. R. & Running, S. W., 1997, Land cover characterization using multitemporal red, near-IR, and thermal-IR data from NOAA/AVHRR, *Ecological Applications*, 7 (1), 1997, pp. 79-90.
- Price, J. C., 1991, Timing of NOAA afternoon passes, *International Journal of Remote Sensing*, vol. 12, no. 1, pp. 193-198, Jan. 1991.
- Smith, P. M., Kalluri, S. N. V., Prince, S. D. & Defries, R., 1997, The NOAA/NASA pathfinder AVHRR 8-km land data set, *Photogrammetric Engineering and Remote Sensing*, 63 (1): 12-31 jan 1997.
- Sobrino, J. A. & Raissouni, N., 2000, Toward remote sensing methods for land cover dynamic monitoring: application to Morocco,

- International Journal of Remote Sensing*, 2000, Vol. 21, No. 2, 353-366.
- Sobrino, J. A., Julien, Y., Atitar, M. & Nerry, F., 2008, NOAA-AVHRR orbital drift correction from solar zenithal angle data, *IEEE Transactions on Geoscience and Remote Sensing*, Vol. 46, No. 12, 4014-4019.
- Tucker, C. J., 1979, Red and Photographic Infrared Linear Combinations for Monitoring Vegetation, *Remote Sensing of Environment*, 8 (2), 127-150.
- UNEP, 2005, *One Planet Many People: Atlas of Our Changing Environment*, Division of Early Warning and Assessment (DEWA), United Nations Environment Programme, P.O. Box 30552, Nairobi, Kenya, <http://na.unep.net/OnePlanetManyPeople/index.php>.
- Zhou, L., Tucker, C. J., Kaufmann, R. K., Slayback, D., Shabanov, N. V. & Myneni, R. B., 2001, Variations in northern vegetation activity inferred from satellite data of vegetation index during 1981 to 1999, *Journal of Geophysical Research*, 106(D17):20069-20083.

FAPAR over Europe for the past 29 years: A temporally consistent product derived from AVHRR and VEGETATION Sensors

M. Weiss¹, F. Baret¹, H. Eerens², E. Swinnen²,

¹EMMAH UMR 1114, INRA, Avignon, France

²VITO-TAP, Mol, Belgium

marie.weiss@avignon.inra.fr, frederic.baret@avignon.inra.fr,

herman.eerens@vito.be, else.swinnen@vito.be.

ABSTRACT- *The objective of this study is to provide a consistent archive of global FAPAR maps over the past 29 years. The product must be consistent with the ones developed in the recent years that take advantages from the better capabilities of recent sensors. Among these available products, we chose the CYCLOPES FAPAR. Indeed, it has been demonstrated through global LAI and FAPAR inter-comparison and validation exercises that this product provides (i) the best RMSE when compared to ground measurements and (ii) the smoothest temporal profiles, which is expected since vegetation structure variables vary continuously with time. We therefore applied the methodology suggested by Verger et al (2008) to train a neural network using NOAA16 AVHRR or VEGETATION reflectances as inputs and the CYCLOPES FAPAR as output over the 1999-2003 period. Then, to take into account the differences of spectral response of the different AVHRR sensors, a radiative transfer model was used to compute conversion coefficients between a given AVHRR spectral band to the corresponding NOAA16. The algorithm was applied to the 1981-2008 period over Europe. Results showed good performances, especially for non forest biomes when compared to ground measurements. Temporal profiles derived for the whole period over the European BELMANIP2 sites (ensemble of 3kmx3km homogeneous areas representative of the biome distribution over the Earth), showed a very good temporal consistency without observing accident (sudden increase or decrease) when transiting from one AVHRR sensor to another.*

1 INTRODUCTION

One of the major objectives of the MARS project (Monitoring Agricultural ResourceS) is the wide-scale monitoring and forecasting of the main crop yields. To achieve this goal, several techniques and information sources are combined, mainly weather data, crop growth simulation models, GIS, statistical analyses and remote sensing. In this context, the JRC collected an extensive archive of imagery registered by the 1km-resolution sensors NOAA-AVHRR (Europe, since 1981), SPOT-VEGETATION (VGT, global, since 1998) and METOP-AVHRR (global, since 2008). Up to now, this archive was processed to produce a decadal NDVI product derived from a maximum value composite technique (Holben, 1986). However, recent decades have shown a growing tendency to infer biophysical parameters by means of model inversion techniques. Since the past ten years, new products were developed allowing a direct access to vegetation biophysical variables such as leaf area index (LAI) or the fraction of Absorbed Photosynthetic Radiation (fAPAR) that can directly be used as inputs to crop growth models. Recent studies have shown that discrepancies can be observed between products over the same area, especially

considering the level of the biophysical variable rather than its temporal profile (Garrigues et al., 2008; McCallum et al., 2010; Weiss et al., 2007). They all show, through inter comparison and validation against ground measurements, that the CYCLOPES product (Baret et al., 2007) performs well, at the global level, and especially for non forest biomes. Moreover, the CYCLOPES product is a good candidate for application such as crop growth monitoring since it provides the smoothest temporal profiles (Weiss et al., 2007). The major issue is that it is only available for the 1998-2007 period (<http://postel.mediasfrance.org/fr/TELECHARGEMENT/>)

The objective of this study is to develop a CYCLOPES light version and benefit from the available JRC archive to rapidly provide a fAPAR product over the 1981-2010 period. In practice, we followed the approach of Verger et al. (2008) who demonstrated that it is possible to estimate a biophysical state variable derived from a given sensor using the reflectances from another sensor (for the same location and time) by means of neural networks. They also showed that these estimates are accurate and free of bias. The new developed product –called CYCLight- is therefore derived from neural networks using JRC dekadal composite TOC reflectances in the

red and near infrared bands as inputs, and the CYCLOPES product as output. Following sections describe the JRC processing chain, the neural network design, as well as an evaluation of CYCLight by comparison with other existing products as well as ground measurements.

2 PRE-PROCESSING CHAIN

Although the NOAA/METOP-AVHRR and SPOT-VGT sensors have different characteristics, the pre-processing chains comprise some important common procedures. Each raw segment is geometrically corrected using orbital characteristics and geometrical modelling, and then projected in the Plate Carrée system at $1/112^\circ$ resolution ($\approx 1\text{km}$). Radiometric calibration was performed using on-board calibration lamps for SPOT-VGT while vicarious calibration coefficients estimated by Rao and Chen (1999) were used for NOAA/AVHRR sensors. For METOP, EUMETSAT uses an identical approach, to guarantee optimal agreement between the measurements of the AVHRRs on both platforms. Atmospheric correction is achieved using the SMAC algorithm (Rahman and Dedieu, 1994). Aerosols and ozone were derived from a very simple climatology (long term monthly average) while water vapour data is provided by ECMWF. Cloud/snow/ice correction is performed using band thresholding for SPOT-VGT and METOP while for NOAA, the detection is performed using sensor-specific neural networks (Swinnen et al., 2007). Then, the compositing algorithm selects the “best available” observation over the decade, *i.e.*, cloud free, good geometry and maximum NDVI value among the remaining pixels.

3 GENERATION OF THE CYCLIGHT PRODUCT

The previous steps led to data with a relatively good quality composed of top of canopy reflectances in the sensor geometrical configuration at a time step of the order of 10 days. These reflectances, as well as the associated view and solar angles will be used as inputs to the biophysical algorithm to estimate the corresponding fAPAR. As the CYCLight product is derived from CYCLOPES, fAPAR has the same definition, *i.e.* instantaneous fAPAR at 10:00AM. To keep consistency between first AVHRR sensors and recent ones, we only use the red and near infrared bands.

3.1 Building the learning database

To accurately implement the algorithm, the learning data base must be representative of both the spatial and temporal variation of the neural network reflectance inputs and fAPAR outputs. As proposed by

Verger et al (2008) and recommended by the Committee on Earth Observation System (CEOS), we used the BELMANIP2 (BENCHMARK Land Multisite Analysis and Intercomparison of Products) ensemble of sites. BELMANIP2 is an updated version of BELMANIP1 (Baret et al. 2006) which is better representative of the biome distribution at the Earth surface. As this study is reduced to Europe only, we used 51 BELMANIP2 sites, including 37 non forests, 6 deciduous broadleaf forests and 8 needle leaf forests.

BELMANIP2 sites are homogeneous, $3\text{km} \times 3\text{km}$ areas to keep consistency with product resolution, and geometric accuracy (Weiss et al., 2007). The interest of using actual data to derive CYCLight resides in the fact that the learning database is *de facto* representative of what can be found at the Earth surface. Indeed, all existing products are derived from Look-Up Techniques (eg MODIS) or neural networks (eg CYCLOPES) calibrated on synthetic data sets simulated thanks to radiative transfer models (RTM). This raises the question of its generation, and especially the distribution laws of the RTM inputs. These inputs are set arbitrarily and constrained by the low level of knowledge of these distributions at global scale. Moreover, the co-distributions of the input variables are never taken into account, which lead to a significant amount of unrealistic cases in the learning database. Besides regularization techniques that can be used to better constrained the learning dataset (Combal et al., 2002), another way to circumvent this problem, is to use actual data.

3.2 Neural network training

The neural network approach used by Verger et al. (2008) was kept since they are very computer efficient in the operational mode and therefore well adapted to process large amount of data.

The sensors used in this study have different spectral band characteristics. To keep a better consistency over the period, only the common bands are considered: red and near-infrared. NOAA/METOP (resp. VGT1/VGT2) sensors offer slight discrepancies between their band spectral responses, while their band width is much larger than VGT ones. Further, CYCLOPES data were available only for the 1999-2003 period at the time of this study and must be concomitant with the reflectance inputs for neural network learning. Therefore, to keep a sensor consistent biophysical algorithm, two neural networks were trained: one for NOAA sensors which is learned on NOAA16 reflectances (2001-2003), and one for VGT sensors (1999-2002). Then, when applying a neural network learned with a sensor to another sensor of the same family, correction coefficients between bands were computed for each sensor using radiative

transfer model simulations performed with the coupled SAIL and PROSPECT models (Jacquemoud et al., 2009). The simulation procedure is similar to the one that was used to generate the synthetic database in the learning process of CYCLOPES products. For the same set of input parameters, the reflectance is computed for each individual sensor, considering their specific spectral responses. Then red and NIR bands of each sensor is expressed as a function of the corresponding NOAA16 (Table 1) or VGT2 band ($VGT1_{RED}=1.0435VGT2_{RED}$, $VGT1_{NIR}=0.9965VGT2_{NIR}$). The RMSE (Root Mean Square Error) for the visible band is around 5.10-3, and 3.10-2 for the near infrared.

Table 1. Correction coefficients for NOAA sensors ($NOAA16_{xxx} = \alpha_{xxx} NOAA_{xxx}$)

Sensor	NOAA16	
	α_{RED}	α_{NIR}
NOAA07	0.9602	1.0311
NOAA09	0.9281	1.0274
NOAA11	0.9327	1.0279
NOAA14	0.8789	1.0098
NOAA18	1.0105	0.9973
METOP	1.0022	0.9980

The same neural network architecture as for CYCLOPES was chosen : backpropagation neural networks using one hidden layer with 5 neurons having tangent sigmoid transfer function. Inputs are composed of satellite and sun positions (sun zenith angle, view zenith angle and cosines of the relative azimuth angle) at the time of satellite overpass, as well as RED and NIR reflectances. Output is the corresponding fAPAR value.

3.3 Theoretical performances

The network theoretical performances were evaluated over the test data set. Results show that the training was quite efficient, with relatively small RMSE values (RMSE=0.05). The algorithm is unbiased as expected (Figure 3). No saturation effect is observed since the fAPAR/reflectance relationship is quite linear (as compared to LAI/reflectance relationship).

4 EVALUATION OF THE CYCLIGHT PRODUCT OVER EUROPE

To evaluate the performances of our product, we used the framework proposed in the CEOS context by Garrigues et al (2008) and Weiss et al (2007). First we present the product used for the inter comparison. Then, we perform indirect validation by computing

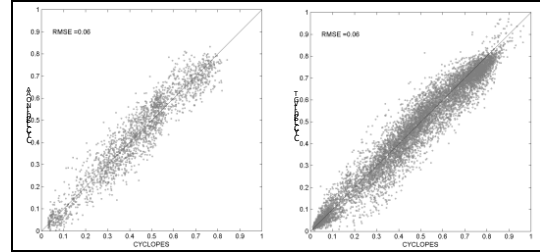


Figure 1. Neural network theoretical performances on the test data set for the NOAA (left) and SPOT-VGT (right) products.

statistics on the different product. We finally perform direct validation against ground measurements gathered by Garrigues et al (2008). A specific section is dedicated to the evaluation of the temporal continuity of the NOAA/AVHRR product over the 1981-2008 period.

The products are evaluated over the BELMANIP2 and ground validation sites (3kmx3km area) in the plate-carée projection, restrained to the European area.

4.1 Used Products

The used products are (i) CYCLOPES (CYC:1999-2003): the retrieval algorithm is based on neural networks trained on a 1D radiative transfer model simulation. The compositing is achieved at the Top Of Canopy reflectance level. The reflectance is normalized by using a kernel driven BRDF model inverted over a 30 day period using a Gaussian weighting function (Baret et al., 2007) (ii) MODIS collection5 Terra fAPAR (MOD: 2000-2010). The retrieval algorithm relies on a 3D radiative transfer model which ingests red and near infrared bidirectional reflectance factor values, their uncertainties, view-illumination geometry, and eight biome land cover types (Myneni et al., 2002). The model is inverted with a Look-Up-Table specific per biome type. MODIS LAI value corresponds to the maximum daily fAPAR value in an 8-day compositing period.(iii) the JRC fAPAR (JRC:1997-2006). The algorithm consists in two-steps where the spectral reflectances are, first rectified to minimize atmospheric and angular effects and, second, combined together as a spectral vegetation index to estimate the green fAPAR at the time of the satellite overpass(Gobron et al., 2006). Note that for 2006, we used the product derived from MERIS (Gobron et al., 1999) while we used the SeaWifs one for the other years (Gobron et al., 2006).

4.2 Product Inter-comparison

We evaluated the smoothness level of the temporal profiles since fAPAR results from incremental biophysical processes and should provide smooth

variations in time (except in extreme situations such as human intervention). We computed the difference δ between the fAPAR product value at date t , and the mean value of the same fAPAR product at date $t-\Delta t$ and $t+\Delta t$. A low δ value indicates a smooth product (Weiss et al., 2007).

Figure 2 shows that CYC is the smoothest product while CYCLIGHT-V and -A, as well as MOD present the same behaviour, except for very low fAPAR (<0.03). The “shakiest” product is the JRC one. This is mainly due to the fact that there is no compositing algorithm for this product which is provided daily. Further, MOD (8 day), CYCLIGHT-V and -A (10 days) are derived using the same compositing algorithm based on the use of the maximum fAPAR value over the period of the synthesis. On the other hand, the compositing in the CYC algorithm is performed 30 days window. Highest values of δ are generally obtained when cloud mis-detection is observed for one of the 3 dates used to compute δ . It can be noticed that this happens more frequently with CYCLIGHT-A data.

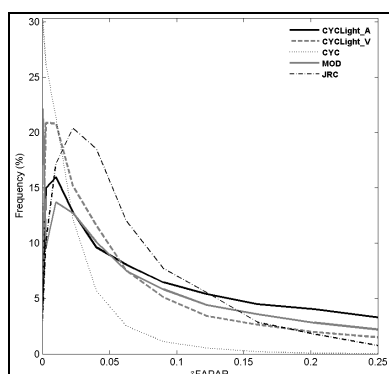


Figure 2. δ value histograms for different products, over BELMANIP2 European sites.

4.3 Scatter plots between products

To compare the consistency between the product levels, we investigated scatter plots per biomes. In order to not be contaminated by classification errors, we classified the European biome types as non forest (this includes bare soils, savannas, shrublands, crops), deciduous broadleaf forests, evergreen needleleaf forest. Products were estimated at the every 10 days (lowest frequency between all studied ones) for each site and common periods between the compared sensors.

For non forest biomes, we observe a high correlation coefficient ($R^2 \geq 0.89$) between all the products (Figure 3). CYCLIGHT_V is the closest from CYC since it is derived from the same sensor, the difference residing

in the reflectance processing chain and compositing. MODIS compared to CYCLIGHT_V also provides low RMSE (0.06, scatterplot not shown here) since the compositing algorithms are similar. CYCLIGHT_A shows some scattering as compared to CYC, which is mainly due to cloud mis-detection in the processing chain. JRC seems to under-estimate medium fAPAR values as compared to the other products. Results for forest biomes are not shown here since CYCLIGHT was mainly designed for agricultural sites and there are few BELMANIP2 European sites corresponding to forests. However, discrepancies between products are higher as already pointed out by (Garrigues et al., 2008; McCallum et al., 2010; Weiss et al., 2007).

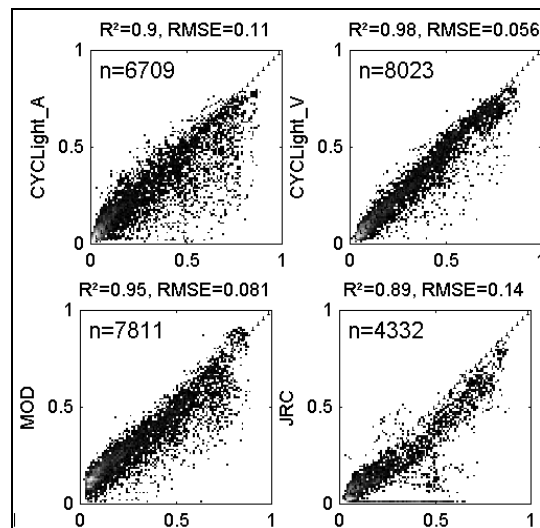


Figure 3. Scatter plots between the different products and CYCLOPES fAPAR for non forest sites. N is the number of matching points found for the comparison.

4.4 Ground Validation

We used the database gathered by Garrigues et al. (2008) over 3kmx3km ground measurement sites where indirect local measurements, derived from hemispherical images, were up scaled using high resolution images. For fAPAR and Europe, only few measured points are available (10 non forest sites, 1 deciduous broadleaf forest and one needleleaf forest). Over these two forests, the measurements were achieved at a given year and we repeated the measured value for the other years since the measurement was not performed during the growing season (of trees for DBF and understory for ENF). We therefore make the strong assumption that fAPAR does not change from one year to another for these forests.

Results (Figure 4) show the best performances for CYCLIGHT_V and CYC, with an underestimation of

high forest FAPAR values, while MOD seems to perform better on forests, as was already observed by the other validation studies. JRC underestimation found with the scatter plots is partly confirmed by the validation results, but only few points are available. CYCLight_A product performs the worst. It is mainly due to the cloud/snow mis-detection. Indeed, the number of available points for CYCLight_A (n) is higher than for the other sensor (especially for forests).

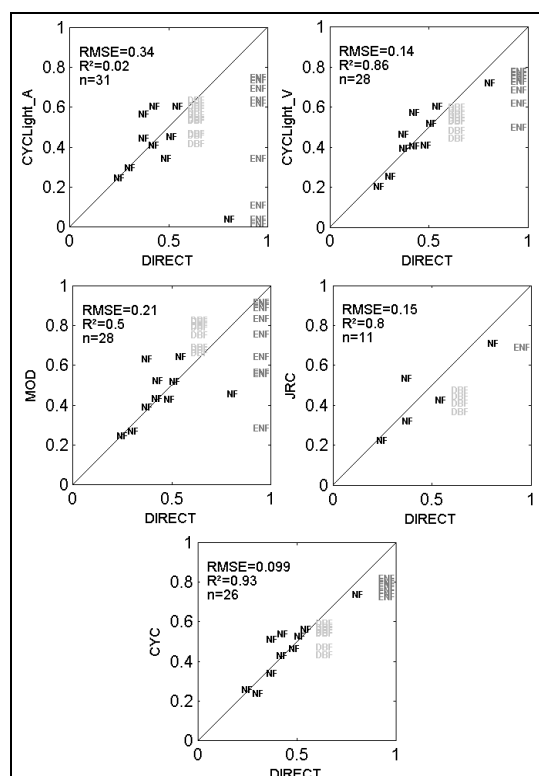


Figure 4. Comparison with ground measurements. (NF: non forest, ENF: needleleaf forest, DBF: deciduous broadleaf forest)

4.5 CYCLIGHT consistency over the 1982-2008 period

Six different AVHRR and SPOT-VGT sensors were used to generate FAPAR products over the past 28 years. Although the spectral differences were taken into account in the retrieval algorithm, other factors may influence the product value depending on the used sensor. For AVHRR (VGT), the biophysical algorithm was learned using NOAA14 (VGT2) sensor over the 2001-2003 period and a radiometric correction is applied for the other sensors. In order to check the consistency throughout the years, we computed the monthly average product over the European BELMANIP2 sites for each period

associated to a given sensor (Figure 5). We therefore assume that using a sufficiently large enough number of sites would provide a relatively stable reference across periods. As expected, the average annual profiles sites are consistent between sensors, maximum FAPAR is obtained in June since the majority of the sites correspond to non forest sites with a vegetation cycle. The standard deviation value is high, both due to the variation of FAPAR between sites and between years. However, it is of the same order from one sensor to another.

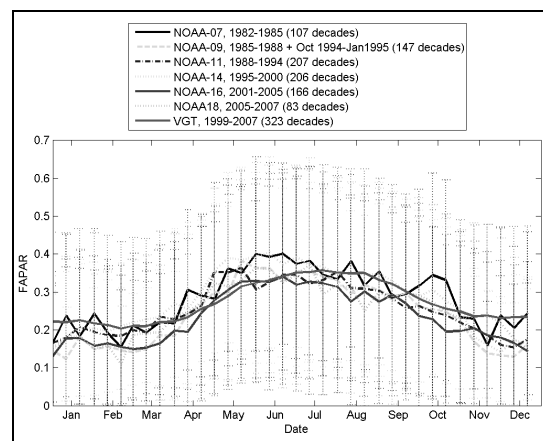


Figure 5. Average annual and standard deviation of FAPAR over the European BELMANIP2 European sites for each NOAA period and each biome type.

5 CONCLUSION

This study presents a consistent archive of fAPAR available over Europe at 1km resolution for the past 29 years. This archive will be completed for future years using METOP/AVHRR data. In order to rapidly provide the archive to the MARS community, CYCLight constitutes a light version of CYCLOPES by learning neural networks on actual data (VGT and AVHRR red and NIR reflectances and geometry as inputs, CYCLOPES FAPAR as output) over an ensemble of sites distributed over Europe and an overlapping period. The application to sensors not available during this period is performed using simple transfer coefficients between sensor spectral bands.

Results showed that the product performs quite well as compared to other existing ones. However, the quality of the product is closely linked to the quality of the input reflectances and thus, the pre-processing chain, which leads to better results for CYCLight_V as compared to CYCLight_A. These results are also limited to non forest biomes since the neural network training, as well as, the product evaluation was mainly performed on these biomes, which complies with the

objectives of the MARS project. The product is available at <http://mars.jrc.ec.europa.eu/mars>.

6 ACHNOWLEDGEMENTS

We are very grateful to the people who provided the different product extracts over the BELMANIP2 and ground validation sites: Nadine Gobron (JRC fAPAR), Greg Ederer (MODIS collection 5), as well as to the people who have contributed to ground measurements that were used in this study.

7 REFERENCES

- Baret, F. et al., 2007. LAI, fAPAR and fCover CYCLOPES global products derived from VEGETATION: Part 1: Principles of the algorithm. *Remote Sensing of Environment*, 110(3): 275-286.
- Combal, B. et al., 2002. Retrieval of canopy biophysical variables from bi-directional reflectance. Using prior information to solve the ill-posed inverse problem. *Remote Sensing of Environment*, 84: 1-15.
- Garrigues, S. et al., 2008. Validation and intercomparison of global Leaf Area Index products derived from remote sensing data. *J. Geophys. Res.*, in press: doi:10.1029/2007JG000635.
- Gobron, N. et al., 2006. Evaluation of fraction of absorbed photosynthetically active radiation products for different canopy radiation transfer regimes: Methodology and results using Joint Research Center products derived from SeaWiFS against ground-based estimations. *Journal of Geophysical Research*, 111(D13110): doi:10.1029/2005JD006511.
- Gobron, N., Pinty, B., Verstraete, M. and Govaerts, Y., 1999. MERIS Global Vegetation Index (MGVI): description and preliminary application. *International Journal of Remote Sensing*, 20(9): 1917-1927.
- Holben, B.N., 1986. Characteristics of maximum value composite images from temporal AVHRR data. *International Journal of Remote Sensing*, 7: 1417-1434.
- Jacquemoud, S. et al., 2009. PROSPECT + SAIL models: A review of use for vegetation characterization. *Remote Sensing of Environment*, 113(Supplement 1): S56-S66.
- McCallum, I. et al., 2010. Comparison of four global FAPAR datasets over Northern Eurasia for the year 2000. *Remote Sensing of Environment*, 114(5): 941-949.
- Myneni, R.B. et al., 2002. Global products of vegetation leaf area and fraction absorbed PAR from year one of MODIS data. *Remote Sensing of Environment*, 83(1-2): 214-231.
- Rahman, H. and Dedieu, G., 1994. SMAC : a Simplified Method for the Atmospheric Correction of satellite measurements in the solar spectrum. *International Journal of Remote Sensing*, 16(1): 123-143.
- Rao, C.R. and J.Chen, 1999. Revised post-launch calibration of the visible and near-infrared channels of the Advanced Very High Resolution Radiometer (AVHRR) on the NOAA-14 spacecraft. *International Journal of Remote Sensing*, 20(18): 3485-3491.
- Swinnen, E. et al., 2007. An Integrated Long Time Series of 1km Resolution NDVI for Europe from the NOAA-AVHRR and SPOT-VEGETATION Sensors. In: D.L.G.e. al (Editor), 4th International Workshop on the Analysis of Multi-temporal Remote Sensing Images, 2007 (MultiTemp 2007), Leuven, Belgium.
- Verger, A., Baret, F. and Weiss, M., 2008. Performances of neural networks for deriving LAI estimates from existing CYCLOPES and MODIS products. *Remote Sensing of Environment*, 112(6): 2789-2803.
- Weiss, M., Baret, F., Garrigues, S. and Lacaze, R., 2007. LAI and fAPAR CYCLOPES global products derived from VEGETATION. Part 2: validation and comparison with MODIS collection 4 products. *Remote Sensing of Environment*, 110(3): 317-331.

Interannual vegetation dynamics over Morocco through the NDVI/AVHRR from 1982 to 2008: linkages with climate signals and potential for seasonal prediction.

Jarlan L.^{1,2}, Driouech F.², Tourre Y.M.³, Duchemin B.¹, Abaoui J.², Le Page M.^{1,4}, H. Kharrou⁵, Ouldbba A.², Mokssit A.² and Chehbouni G.¹

¹ IRD / Centre d'Etudes Spatiales de la Biosphère, Bpi 2801, 18 avenue Edouard Belin, 31401 Toulouse Cedex 9, France ; e-mail : lionel.jarlan@cesbio.cnes.fr

² Direction de la Météorologie Nationale, Ain Chock, Face Préfecture Hay Hassani, Casablanca, Morocco

³ METEO-France, Direction de la Climatologie, 42 avenue Coriolis, 31057 Toulouse Cedex, France & LDEO of Columbia U., Palisades, NY, USA

⁴ Faculté des Sciences Semlalia, Université Cadi Ayyad, Centre Geber Salle 26, BP 2390 Marrakech, Morocco

⁵ Office Régional de Mise en Valeur Agricole du Haouz, Av Hassan II, Gueliz , BP 2411 Marrakech, Morocco

ABSTRACT The spatio-temporal variability of vegetation cover over Morocco is analyzed using the AVHRR Normalized Difference Vegetation Index (NDVI) from 1982 to 2008. Using rotated extended empirical orthogonal functions (REEOFs), dominant patterns of NDVI are isolated. Three leading modes are kept: the first mode (12.1% of total variance) is found along the Atlantic coastline, the second mode (11.9% of total variance) is in a region near the Gibraltar straight and south west of the Riff Mountains, whilst the third mode (9.8% of total variance) is found along the Mediterranean coastline. Maxima for variance explained for all modes coincide with periods when vegetation maximum development occurs, i.e., March-April. Regional signatures are used to study potential linkages between the NDVI interannual variability and that of global climate signals. This is to get a better understanding of physical mechanisms at stake and to assess potential predictors for NDVI seasonal prediction. Time-lag correlations between NDVI principal components and climate indices and fields (i.e., global sea surface temperature) are calculated. During fall, the NAO regime is found to have impacts on vegetation peaks and emergence dates over the 'Atlantic' region mode. Linkages are weaker for the 'Riff' and 'Mediterranean' modes where vegetation dynamic seems more modulated by local factors (i.e., orography, vegetation functional types) and cyclones originating from the neighbouring Mediterranean Sea. Moreover, a significant correlation is found between vegetation dynamics over Morocco and sea surface temperatures (SST) in the tropical Atlantic. Finally, lagged linkages between NDVI and climate indices and variables are used here to build a simple seasonal prediction model of NDVI, using multiple linear regression. For the 'Atlantic' mode, it is shown that the NDVI during March-April may be predicted with a reasonable accuracy using climate information from January only.

1 INTRODUCTION

Since rainfed crops and natural vegetation dynamics largely depend on climate variability (Nemani *et al.*, 2003), vegetation can be valuable integrated measure of climate impacts on land resources. Over Morocco and the southern Mediterranean countries, climate is semi-arid with high spatio-temporal variability in rainfall regimes (Bolle, 2002). The high interannual variability of rainfall amounts and the high sensitivity of ecosystems to droughts provide a unique natural environment to get a better understanding on how anomalies in the ocean-atmosphere climatic system can affect Moroccan terrestrial ecosystems. Many studies have already investigated climate effects on

land surfaces using correlation patterns based on temperature and precipitation datasets (Lamb and Pepper, 1987; Knippertz *et al.*, 2003). Nevertheless direct ecological impacts of climate variability and change, require more investigation.

The Mediterranean basin is unique in the sense that it is under the influence of the descending branch of the summer Hadley circulation and of the winter westerlies from the Atlantic Ocean (Bolle, 2002). This is a transition area in which extratropical and tropical systems might compete, with feedbacks on the occurrence of climate events modulated by the Mediterranean Sea. Parts of Morocco have suffered from a series of dry years since the late 1970s when the Atlantic multi-decadal oscillation (AMO) became

negative. These local droughts are embedded in northern hemisphere circulation and other droughts elsewhere. The recurrence of dry conditions over the Mediterranean area has been attributed to the persistence of the positive phase of the North Atlantic Oscillation (NAO, Xoplaki et al., 2002).

Vegetation cover and variability is usually monitored regionally using vegetation indices obtained from satellite such as the Normalized Difference Vegetation Index (NDVI, Tucker, 1979). This empirical index takes advantage of the strong absorption by chlorophyll in the red bands and the scattering of cellulose in the Near Infra-red (NIR). Long time-series of NDVI data are now available from the continuous acquisition of data from the AVHRR sensor on board of NOAA satellites since 1981. The quality of these observations has been questioned in the past due to satellites orbital drift. Since then several research teams have corrected the AVHRR/NDVI data and made reliable long time series of NDVI. Several studies have used NDVI to characterize the variability of active vegetation cover and studied the impact of climate variability on vegetation greenness at the continental and hemispheric spatial scales.

The objective of this study is threefold: (1) to characterize the vegetation interannual variability over Morocco at regional scales; (2) to analyse the dependency of Moroccan vegetation on the large scale ocean-atmosphere circulation systems; and (3) to evaluate the potentialities of using climate information for seasonal prediction of vegetation dynamics. The second part of the paper describes the data and the statistical methods used for NDVI analyses. The third part presents the characterization of the seasonal and interannual variability of the NDVI. In the fourth part, the linkages between NDVI variability and climate signals are analyzed and possible physical mechanisms are discussed. This analysis allowed the developing of a simple model for seasonal prediction of vegetation activity at the core of the growing season. This is presented in the fifth part of the paper. Finally, conclusions and perspectives are drawn.

2 DATA AND METHODS

2.1 The Study Region

The studied region extends from 30°N to 36°N and from 12°W to 0°. It covers the northern part of Morocco and the western part of Algeria. The land cover map displayed in Figure 1 was derived from the 1 km land surface database ECOCLIMAP (Masson et al., 2003). ECOCLIMAP initially includes 215 ecosystems composed of 12 classes with associated cover fraction. ECOCLIMAP has been re-labelled in four dominant classes through a majority filter: bare

soil, trees, grasses and crops. As such, Figure 1 illustrates roughly the overall distribution of the vegetation of Morocco with about 70% of the country dominated by bare soil including the eastern and southern desert areas and the High Atlas mountain range. The remaining 30% are composed of 6% dominated by trees, about 80% by grasses and 14% by crops following the ECOCLIMAP map. The main irrigated areas have been superimposed on Figure 1. Interesting enough, the ECOCLIMAP crops classes correspond roughly to these irrigated areas. Thus, the ECOCLIMAP grass class may include the rainfed crops. Natural vegetation is of Mediterranean type called 'maquis' in French: i.e., scrubby vegetation composed of broad-leaved evergreen. Dominating trees are green oak and parasol pine.

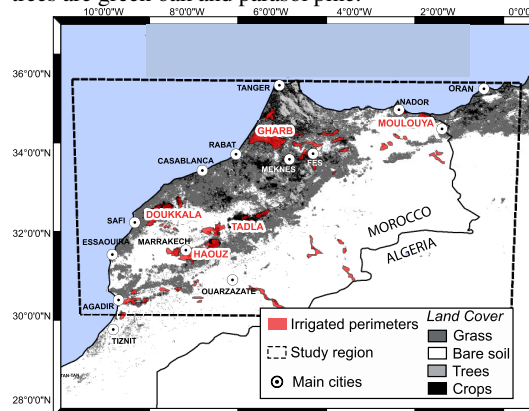


Figure 1 : Simplified land cover map derived from the land surface data base ECOCLIMAP and main irrigated areas of the country. Dotted rectangle represents the study region (30°N-36°N and 12°W-0°).

Moroccan climate is characterized by a Mediterranean climate type. The Mediterranean climate is unique as temperature and precipitation are out-of-phase. Xoplaki (2002) found that it is the October to March period which experience the highest rainfall amounts: the Mediterranean wet season. The rainy season over Morocco follows this general characteristic of the Mediterranean climate.

2.2 The NDVI data set

Vegetation cover variability using NDVI, range between 0.1 for bare soils and 0.9 for dense, photosynthetically active vegetation. The higher the NDVI value, the higher the green vegetation density. The NDVI data set used within this study is the so-called NDVI-g (version 4, Tucker et al., 2005) and derived from the AVHRR sensor on board of NOAA-7, -9, -11, -14, -16 and -17 satellites. This dataset is processed by the Global Inventory Modelling and Mapping Studies (GIMMS) team and distributed by

the Africa Data Dissemination System (ADDS available at <http://earlywarning.usgs.gov/adds/>). It covers a period from January 1982 to December 2008. Spatial resolution is 8 km. Additional details on the data processing may be found in Tucker et al. (2005).

2.3 The Climate data sets

In order to diagnose climatic factors associated with vegetation growth and identify potential predictors for the seasonal prediction model, the sea surface temperatures (SST) from Reynolds version 2 provided by NOAA is used. The analysis uses a blend of in-situ, and satellite SST merged using an optimal interpolation (OI) method. The OI SST analysis is produced weekly on a 1° grid-point system. Further details on the processing can be found in Reynolds et al. (2002). Data is available from 1982 to present;

Finally, several climatic indices are used. Ten prominent teleconnection patterns can be identified in the Northern Hemisphere throughout the year. These patterns have been presented in the literature (Barnston and Livezey 1987) together with their impact on climate. They are provided by the Climate Prediction Center (cf. The CPC web site). Only the Northern Hemisphere Teleconnection Patterns (NHTP) affecting the Atlantic Basin are selected for analysis: the NAO and the Scandinavia (SCA).

2.4 Data pre-processing

Non vegetated / Desert areas dominate over the study area (see Figure 1). A simple mask is built from raw NDVI observations in order to focus on area where vegetation develops: pixels where differences between minimum NDVI and maximum NDVI for the 26 years time series are below 0.15 are masked. The original spatial resolution of 8 km is upsampled to 48 km by a simple 6x6 moving window average. The latter is to increase the signal-to-noise ratio leading to more coherent pattern detection. For the spatio-temporal pattern detection using the REEOFs method (see below), data is aggregated to a monthly time scale (by a simple average of the initial 10-day data), de-seasonalized and detrended.

2.5 Rotated Extended Empirical Orthogonal Functions

Empirical Orthogonal Functions (EOF) is an exploratory method for data analysis aiming at summarizing the variability of a climatic data set by a small number of modes of variability and to eliminate noise. Interestingly enough, many studies have investigated the use of EOFs (with/without rotation) to characterize the spatio-temporal variability of geophysical datasets but only a few studies deal with the use of EOFs to NDVI data (Jarlan et al., 2005, Philippon et al., 2007). Conventional EOFs are very

successful in compressing the original datasets into a small number of modes capturing most of the variability but are unable to represent moving features with various phases (Venegas, 2001), such as the 'green moving wave' that could be associated to the annual propagation of the vegetation anomaly. Extended empirical orthogonal functions (EEOF) are used here for this objective. Applying a rotation to the EEOFs decomposition removes the artificial orthogonality constraint between modes and prevents from potential degenerescence between eigenvalues due to sampling errors. It also provides for more localized spatial pattern, since varimax criterion aims maximizes the local variance explained. Rotated EEOFs is applied to de-seasonalized and detrended NDVI data.

3. RESULTS AND DISCUSSION

3.1 NDVI Interannual Variability

The REEOF method is used to identify regions of coherent NDVI interannual variability over Morocco and West of Algeria. Figure 2 displays the loadings of the three REEOF leading modes shown in terms of the raw variance explained. Modes 1, 2 and 3 explain 12.1%, 11.9% and 9.8% of the monthly pre-processed 1982-2008 NDVI data, respectively. Due to rotation, spatial loadings are localized:

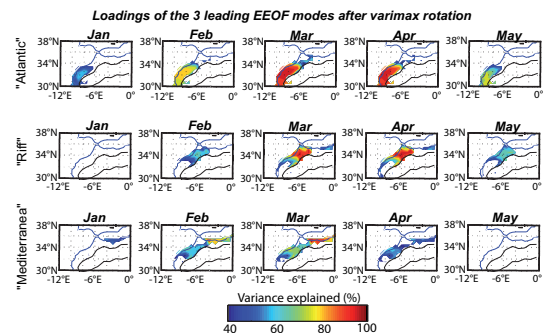


Figure 2: Loadings of rotated extended EOFs from the AVHRR/NDVI datasets over the 'Moroccan window' (30°N - 36°N and 12°W - 0°) during the 1982-2008 period for the three first modes in term of variance explained (12.1, 11.9 and 9.8 % of total variance, respectively). Mode 1 is located along the atlantic coast to the South West of the country, mode 2 occupy the Rif mountains near the Gibraltar channel and mode 3 is located along the mediterranean sea to the East. The maximum of variance explained for the three modes is around the peak of vegetation (March for mode 1 and 3 and April for mode 2).

- Mode 1 occupies a large area along the Atlantic coastline and penetrates far inland reaching the northern side of the High Atlas mountain. It is named "Atlantic" hereafter. Natural vegetation and rain-fed crops is dominant except in the vicinity of

Marrakech where irrigated areas are dense over the Haouz and Tadla regions (Figure 1).

- Mode 2 covers the northern part of the country reaching the Gibraltar straight and contains the southern side of the Riff Mountain. It is named “Riff” hereafter. Forest along the Mid-Atlas and crops along valleys dominates the Riff mode near the Gibraltar Straight.
- Mode 3 occupies a narrow band nearby the Mediterranean coastline in the northeast Morocco and northwest Algeria. It will be named “Mediterranean” hereafter and it is covered by crops and sparse natural vegetation.

The three modes show the seasonal propagation of NDVI anomaly associated to the start of the rainy season from November to May. The maximum variance explained is in March and April for the “Atlantic” and “Riff” modes and about one month earlier for the “Mediterranean” mode. This NDVI regionalization is compared to classification from Knippertz et al. (2003) who have divided the country into three climatic zones using cross-correlation of monthly precipitation from a network of 42 weather stations: ATL for the Atlantic region; MED for Mediterranean over the north-eastern Morocco and north-western Algeria; and SOA for the region south of the Atlas. NDVI modes “Atlantic” and “Riff” all together perfectly fit their “Atlantic” area and modes “Mediterranean” is very close to their “MED” region. Their SOA region is not reproduced by the NDVI REEOF as non vegetated/semi-desertic area, dominating south of the High Atlas mountains until the Sahara desert, were masked. The main difference between precipitation and NDVI spatial pattern is related to the ATL region of precipitation that is characterized by two modes of coherent vegetation variability (“Atlantic” and “Riff”). The difference between these two modes may be related to the differences in vegetation functional types. In particular, the foothills of the “Riff” region receive substantial higher rainfall amount than the Atlantic coastline, and may benefit from enhanced traditional irrigation system (the so-called “seguia”). In addition, the higher percentage of tree cover fraction in this region (Figure 1) also influence the vegetation interannual variability by contrast to the ‘Atlantic’ NDVI mode dominated by crops, mainly rain-fed, and covered with natural grasses. As a conclusion, the spatial patterns obtained from the REEOF approach applied to NDVI are consistent with the rainfall regions of Knippertz et al. (2003) and dividing their ATL region into two modes can be related to the differences in vegetation functional.

3.2 Linkages with the Northern Hemispheric Teleconnection Patterns (NHTP)

The existence of contrasted mid-latitude atmospheric large-scale patterns between dry and wet years and linkages with precipitation have been highlighted (Lamb and Pepper, 1987). As vegetation cover dynamics integrate not only precipitation (i.e., amount and distribution) and temperature variability, but is also influenced by local factors (i.e., orography, geomorphology, top-soil depth and texture, associated floristic composition, among others), the same patterns of linkages than with climate are not expected. REEOFs principal components (not shown) are correlated with NHTP indices NAO and SCA. Simple time-lag linear correlation coefficient r is used taking 3-months average indices values sliding from September to March. Only the higher correlation r (significant at the 95% using a student t-test) and the indices averaging time period are displayed in Table 1.

Table 1: Lagged correlation between REEOF principal components and the Northern Hemispheric Teleconnection Patterns (95% level significance) and time period of higher correlation.

	NAO		SCA	
	r	period	r	period
Atlantic	-0.56	NDJ	0.59	DJF
Riff			0.50	DJF
Mediterranean				

The most prominent teleconnection patterns is NAO. The principal component of the “Atlantic” mode is significantly correlated with the NDJ NAO and the correlation is of the same order than that for the NDVI peak values. This is coherent since the REEOF modes are representative of the core of the growing season. This positive correlation means that the higher the NAO index (positive phase), the lower the NDVI peak values. The linkage between precipitation and the NAO value is theoretically quasi-simultaneous whereas the smooth dynamic of the vegetation is a slow and lagged response to precipitation amount and distribution during the previous months. Over the “Riff” region, no significant correlations are found. These different behaviours between the ‘Atlantic’ and the ‘Riff’ region is to be related to differences in terms of vegetation functional type. The vegetation of the ‘Atlantic’ region dominated by rain-fed crops and annual grasses makes the NAO impacts stronger on the NDVI than for the ‘Riff’ region where the tree cover is high. The ‘Atlantic’ and ‘Riff’ modes are positively correlated with the Scandinavia (SCA) pattern. The Scandinavia pattern consists of a primary circulation center over Scandinavia, with weaker centers of opposite sign over western Europe and eastern Russia/ western Mongolia (Barnston and Livezey, 1987). The enhanced southern flow related to

the positive phase of the SCA pattern is found to induce an increase of precipitation over southern Europe. The positive correlation found with the vegetation mode may suggest a southern extension of the SCA effect onto the South Mediterranean basin through enhanced westerly flow at the southern edge of the center located over Western Europe. This enhanced precipitation would also explain the lack of correlation with the 'Mediterranean' mode located much further inside the Mediterranean basin.

Lagged correlation between PCs and SST anomaly

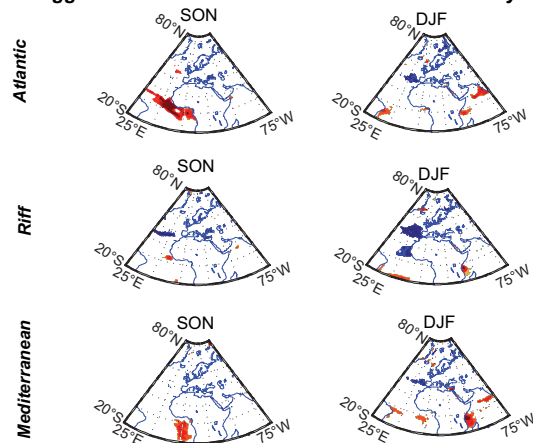


Figure 3: Correlation maps between the three first principal components of the Rotated EEOF analysis (26 yearly values) and the three month average 500hPa averaged over OND and DJF. Only significant correlation values at the 95% level (t-test) are displayed. Colorbar ranges from $r=-0.5$ (blue) to $r=0.5$ (orange).

3.3 Linkages with the tropical Atlantic

One of the potential candidates for lagged and persistent predictor is the slow SST variability. The lagged correlation maps (95% significance level) between seasonal SST and the three leading REEOF principal components are displayed in Figure 3. Whereas the highlighted linkages of vegetation variability with climate mainly concerned mid- to high- latitudes area, the striking feature of Figure 3 is the presence of an equatorial and tropical homogeneous area of significant correlation. Indeed, the vegetation interannual variability over the 'Atlantic' region is significantly correlated to the tropical SST during fall of summer/beginning of fall (SON). The 'Mediterranean' mode is also significantly correlated to the tropical SST at the same period but with weaker values. Some authors have investigated the linkage between mid-latitude and tropical climate. This linkage appears particularly important over the Mediterranean basin since we know that the winter climate is dominated by the alternation of extratropical weather regimes and subsidence of tropical dry air through the descending branch of the Hadley cell

(Bolle, 2002). Cassou et al. (2001) has shown that the observed linkages between the tropical atlantic and the mid-latitude atlantic climate could be explained by perturbation of the Hadley cell and the associated perturbation of the intensity and location of the jet stream at the mid-latitude. Knippertz et al. (2002) study three case of early autumn rain event and demonstrate that tropical West Africa and the adjacent tropical Atlantic are potential sources of moisture for Morocco. This might explain the lagged correlation pattern between 'Atlantic' and 'Mediterranean' NDVI modes and the SST anomalies located in the tropical Atlantic ocean. The 'Riff' mode is significantly correlated to SST along the Atlantic coast of Morocco and Portugal as well as locally to the west of the Mediterranean Sea during winter (Figure 3). This favors for more contribution of local rainfall rather than for a moisture transport from the tropics or the Atlantic storms.

3.4 Seasonal Prediction of NDVI principal components

Finally, a prediction of NDVI principal components is attempted from preceeding results. The Moroccan agricultural market, government agencies and decision makers would benefit grandly from early prediction of wheat yields at the regional and national level. It is hypothesized here that early predictions are possible by using large-scale climate information.

A simple multiple linear regression method is used. A pre-selection of the predictors is carried out by keeping only those indices showing a significant correlation (at the 95% level) with their associated lag. In addition to the indices, new predictors from geopotentials (not shown) and SST maps are used. For both data sets, two new predictors are built for each mode by averaging only the grid points where the correlation with the NDVI modes is significant (at the 95% level) and by separating the negative and the positive values (Figures 3). The calibration of the model is carried out using a stepwise approach: each potential predictor is added automatically one-by-one and their added value to the model performance is evaluated through a Student t-test. During a second phase, the model is validated using the so-called "leave-one-out" (loo) method: the model with the predictors kept for the stepwise approach is rebuilt n times (n is the number of years) by removing one year and predicting the value for the removed year. A new correlation r_{loo} is computed using the predicted values for the "blind" years. The lower the difference between r and r_{loo} , the better the model robustness.

Table 6 summarizes the results for the three modes. The results for the Atlantic mode supersedes largely

the ones obtained for two others regions. Indeed, the linkage between NDVI and large scale climate indices or variables has been shown to be stronger for the “Atlantic” region which is under the direct influence of the Atlantic Ocean and the NAO, than for the two other regions where linkages are altered by local factors (such as orographic influence of the Riff mountain, land cover and vicinity of the Mediterranean sea). In addition, the vegetation type of the ‘Atlantic’ region mainly composed of rain-fed crops and natural grasses may respond stronger to climate interannual variability.

Table 2: Multiple linear regression for the seasonal prediction of the NDVI principal components for the three modes: the correlation coefficients for the calibration phase r and for the validation phase r_{100} .

Modes	Calibration coefficient r	Validation coefficient r_{100}
Atlantic	0.87	0.82
Riff	0.76	0.59
Mediterranean	0.64	0.60

4 CONCLUSIONS

The interannual vegetation dynamics over Morocco has been characterized for the first time through the use of the NDVI obtained from the AVHRR sensor from 1982 to 2008. An Extended Empirical Orthogonal Function approach with a Varimax rotation criterion (REEOF) is used to identify region displaying coherent interannual variability. The first mode is located in a large band along the Atlantic coastline in the western part of the country, the second mode covers the northern part, west of the Riff mountains, whilst the third mode extends along the Mediterranean Sea to the East. These three modes are associated with specific climate conditions as already highlighted by other authors and contrasted type of vegetation. From the analyses of linkages between large scale climate signals partly governing the vegetation interannual dynamics, potential mechanisms are discussed. A strong and robust influence of the North Atlantic Oscillation on the NDVI in the ‘Atlantic’ region is highlighted through time-lag correlations with NAO indices and atmospheric variables. The intensity of the vegetation activity around the development peak in March and April and, to a lesser extent the emergence dates of the vegetation are shown of being related to the NAO fall phasing. Whereas the highlighted linkages of vegetation variability with climate mainly concerned mid- to high- latitudes area for the atmosphere, the striking result is the linkages between the ‘Atlantic’ NDVI principal component and the tropical/equatorial SST during end of summer/beginning of fall. Finally,

a simple seasonal prediction model of the NDVI principal components is built through a multiple linear regression based on the previous results. The best linear model performances are obtained for the ‘Atlantic’ area under the direct influence of the Atlantic Ocean and large scale climate mechanisms. The resulting model can predict the NDVI at the peak development of vegetation (during March April) by using only climate information as early as January.).

5 REFERENCES

- Bolle H.J., 2002, Mediterranean Climate: Variability And Trends, ISBN 978-3540438380, Springer-Verlag, 320 pp.
- Barnston A.G. and Livezey R.E., 1987, Classification, seasonality and persistence of low-frequency atmospheric circulation patterns, *Monthly Weather Review*, 115:6, pp. 1083-1126.
- Cassou C. and Terray L., 2001, Dual influence of Atlantic and Pacific SST anomalies on the North Atlantic/Europe winter climate, *Geoph. Res. Lett.*, 28, 3195-3198.
- Knippertz P., Christoph M. and Speth P., 2003, Long-term precipitation variability in Morocco and the link to the large-scale circulation in recent and future climates, *Meteorol. Atmos. Phys.*, 83, 67-88.
- Lamb P.J. and Pepler R.A., 1987, North Atlantic Oscillation: Concept and an Application, *Bulletin of the American Meteorological Society*, 68:10, pp. 1218-1225.
- Masson, V., Champeaux, J.-L., Chauvin, F., Meriguet, C. and Lacaze, R., 2003, A global database of Land Surface Parameters at 1-km Resolution in Meteorological and Climate Models. *Journal of Climate*, 16, 9, pp. 1261-1282.
- Nemani RR, Keeling CD, Hashimoto H, Jolly WM, Piper SC, Tucker CJ, Myneni RB, Running SW. 2003. Climate-driven increases in global terrestrial net primary production from 1982 to 1999. *Science* 300: 1560–1563.
- Tucker, C. J., Pinzon, J. E., Brown, M. E., Slayback, D. A., Pak, E. W., Mahoney, R., Vermote, E. F. and Saleous, N. El, 2005, An extended AVHRR 8-km NDVI data set compatible with MODIS and SPOT vegetation NDVI data, *International Journal of Remote Sensing*, 26, pp. 4485-4498.
- Venegas S., 2001, Statistical Methods for Signal Detection in Climate, Danish Center for Earth System Science (DCESS) report, Niels Bohr Institute for Astronomy, Physics and Geophysics, University of Copenhagen, Denmark.
- Xoplaki E, 2002, Climate variability over the Mediterranean. PhD thesis, University of Bern, Switzerland, http://sinus.unibe.ch/klimet/docs/phd_xoplaki.pdf.

Long term observations of active volcanoes: Orbital missions and growing remote sensing archives

David Pieri¹ and M.F. Buongiorno²,

¹ Jet Propulsion Laboratory, Pasadena, California USA

² Istituto Nazionale di Geofisica e Vulcanologia, Rome, Italy

dave.pieri@jpl.nasa.gov; fabrizia.buongiorno@ingv.it

ABSTRACT—The detection of subtle signatures of change on active volcanoes requires comprehensive compilations of long term systematic data, especially multispectral to hyperspectral data across the visible and thermal infrared spectrum, as well as systematic archives of topography. In general, the longer the time series, the better the prospective datum. Until now, such archives have not been available for individual volcanoes, or for the world's inventory of active volcanoes. With the advent of sustained, long term (>10yrs) data archives of the active volcanoes around the world (e.g., ASTER, LANDSAT), it is now possible to compile such systematic time series that hold the promise of detecting progressive changes before eruptions, if they are present, and for understanding the behavior of volcanoes over time.

1 INTRODUCTION

Timescales for the detection of changes on active volcanoes vary from very short term pre-eruptive activity bursts—from seconds to days before eruptions—to systematic changes occurring over years to decades or longer. The relationships between such timescales and underlying physical processes are at the heart of attempts at eruption prediction. Very large (10-100Tbyte) multi-sensor remote sensing data bases now permit global systematic assessments of the style and time progressions of volcanic eruptions over the last 20 to 30 years, thus making relevant a discussion of their limitations and utility for illustrating and understanding the dynamics of volcanic processes. Short term precursory changes in volcanic activity can be prompt and dramatic, and are mostly well monitored and understood by the operational community. Systematic long term changes in volcanic activity before eruptions are fundamentally more subtle, thus our experience and capabilities in their detection and quantitative analyses are far less robust. Among others, two such remote sensing archives are the LANDSAT Thematic Mapper archive at INGV (Rome) and the Advanced Spaceborne Thermal Emission and Reflection radiometer (ASTER, Pieri and Abrams, 2004) Volcano Archive at JPL (<http://ava.jpl.nasa.gov>). The former is a local archive focusing on Mt. Etna, housing all the available frames acquired since 1982 on computers of the *Istituto Nazionale di Geofisica e Vulcanologia* (INGV) in Rome, Italy. The latter is a global archive compiled at the Jet Propulsion Laboratory in Pasadena, California, USA, for all volcanoes on the Smithsonian list of volcanoes active during the Holocene epoch (GVP, 2010) for which the ASTER mission (Abrams and

Pieri, 1984) has acquired data since 1999. Currently approximately 1500 volcanoes are being monitored worldwide, with the volume of current data holdings being around 20Tb, and growing.

2 UTILITY OF ARCHIVES

2.1 Useful functions of archives

Perhaps one of the most basic functions of a remote sensing archive is to portray the geological context of the volcano and its basic activity state. This includes providing data for the mapping of the current physical geomorphology and geology of the volcano. When integrated with existing geological literature, such observations can contribute to the understanding of the volcano's geological history and its geological context. Often, from series of data taken before, during and after eruptions, the persistent character of the current eruptive phase of the volcano can be established, especially with respect to eruption volumes, possibly composition, eruption intensity and character (e.g., explosive, effusive, phreatomagmatic). Time dependence of various characteristic eruption phases can also be discerned and is important. Finally, with enough information, activity datums can be established, as well as the statistical confidence envelopes for the eruptive phenomena themselves, as well as for subtle precursor phenomena.

Of course, establishment of statistical confidence envelopes for precursor and eruptive activity is a major goal of volcano observers, and long term archives can be key in this regard with respect to thermal and geodetic data, especially when combined with in situ observations such as gas emission time series and seismic data. Remote sensing archives are now becoming robust enough to gain predictive inferences from trend (e.g., for thermal emissions—

Pieri and Buongiorno, 2010). As such, these data can substantially contribute to the mitigation of local (proximal) volcanic hazards, such as lava flows, pyroclastic flows, lahars, and debris flows. Both high resolution (e.g., for source areas) and more synoptic data (e.g., for areas of airfall deposition) can mitigate regional volcanic hazards, such as ash and gas emissions, air quality and aircraft hazards, weather and potential climate effects.

2.2 Types of Relevant Remote Sensing Data

Generally speaking, the meteorological community has had far more experience in collating and archiving data on an almost hourly basis, and disseminating it widely. Thus weather satellite remote sensing data are routinely available via government sources and commercial value-added suppliers, especially for continuing operational missions like GOES (United States), METEOSAT (Europe), and for instruments like AVHRR (US) which is now essentially iconic. Such data are typically very frequently acquired, typically once an hour. In some cases, however, a “rapid scan” mode for severe storms is available at up to 1 minute/frame intervals. Often, along with synoptic optical or radar images, data from simultaneous in situ measurements and atmospheric profiles are available.

In contrast, high spatial and high spectral remote sensing data tend to reside in balkanized libraries that are idiosyncratic in format, typically requiring an investment in time and patience that limit their usefulness. Thus our attempt at JPL and at INGV to create easily accessible, freely available compilations of images to facilitate research and, in the case of the AVA at JPL, easily accessible to the general public as well as scientific researchers.

Nevertheless, there is now a fairly large variety of microwave and multi/hyperspectral optical data at high spatial resolution (<100m/pixel), if at diverse and scattered locations. Certainly, the SRTM mission has produced a very useful radar-topography data base, available to a greater or lesser degree, worldwide. Interferometric Synthetic Aperture Radar (InSAR) data are available from US and European repositories for various specific locations around the world, especially in response to earthquake disasters. Optical data, for ASTER, is available for over 1500 volcanoes worldwide at the AVA (<http://ava.jpl.nasa.gov>) in an easy-to-download format, and in a form that is immediately compatible with display in Google Earth. More generally, ASTER, Landsat, and other land surface imaging data is available through the Land Processes Data Acquisition and Analysis Center (LPDAAC), operated by the US Geological Survey in Sioux Falls, SD, although it is up to the interested user to render it in formats suitable for Google Earth or other analysis programs.

A real challenge facing geologically oriented specialty archives, as they come online, is to integrate in situ data into their compilations in a rational factor, despite differences in physical scales of the observations, and the nature of related non-imaging data. Such data are crucial for calibration and validation of orbital or airborne remote sensing data. Relevant in situ data include geophysical measurements (e.g., seismic, geodetic, geothermal), as well as geochemical measurements (e.g., airborne and ground-based), and traditional geological field observations that involve sampling and mapping.

A brief and incomplete sample of some of the most current prominently used optical platforms would include, (a) for high spatial resolution (<100m/pixel) – Landsat (*free—widely available*); ASTER (*cheap—widely available*); (b) from the commercial satellite world—Quick Bird (*expensive-restricted*); Geo Eye (*expensive-restricted*); Ikonos (*expensive-restricted*); (c) for low spatial resolution, high time frequency multispectral data—MODIS (*free, unrestricted*); (d) for high spectral resolution data—Hyperion (*expensive-restricted, until recently*); and for (d) LIDAR altimetry—ICESat (*free-restricted*).

3 EXAMPLE OF A GLOBAL ARCHIVE

3.1 The JPL ASTER Volcano Archive (AVA)

As mentioned above, AVA was a first attempt at creating a specialty archive for ASTER holdings of over 1500 volcanoes worldwide identified by the Smithsonian Global Volcano Program (GVP) as having shown signs of activity during the Holocene epoch—basically during the last 10,000 years of geologic time.

Online since late 2007, it is a public access global volcano image archive (<http://ava.jpl.nasa.gov>) that is a dedicated *single topic archive with search tools*. AVA provides full resolution ASTER three-color composite VNIR jpgw files derived from on-demand Level L1B (geometrically rationalized). Most of the data are mostly daytime data with a full range of cloud cover. Nighttime data are now being ingested after mass download difficulties with data center have been mostly solved). The archive currently collates ASTER data for 1528 volcanoes indexed and linked to Smithsonian GVP Catalog with active Google Maps™ & Google Earth™ links.

Current plans are to continue to update archive, to improve and optimize our processing chain for data display, especially for cloudy and snowy scenes, to finish assimilating nighttime data, to add ASTER and SRTM digital elevation models for every volcano in the archive, to create volcano-specific native data sub-archives to support our ongoing international collaborations (e.g., Costa Rica, Vanuatu, Columbia,

Italy), to create global phenomena catalogs (e.g., thermal anomalies, snow/ice-burdens, topography), to support NASA sub-orbital cal/val requirements for volcanoes. Since 2007, AVA has experienced over 12M web hits, and we have served over 110,000 unique users. For general users the data are available gratis in full 4200x4800 pixel format with a spatial resolution of 15m/pixel, rendered as a three-color-composite (ASTER visible/near-IR bands 1,2, 3N) in jpeg world file (jpw) geo-located format that is compatible with one-click insertion into the Google Earth™ algorithm for 3-D projection. Scientific users, with NASA approval, can receive gratis full 15 band (including ASTER band 3B stereo) data sets for individual volcanoes.

4 EXAMPLE OF A LOCAL ARCHIVE

4.1 INGV Landsat TM Archive

A different kind of archive has been compiled at INGV-Rome: a small semi-private archive of Landsat TM data for Mt. Etna only, contains approximately 80 frames for the time period 1984 through 2003. The data are accessible by arrangement with INGV. They include LANDSAT “floating mini-frames” of Mt. Etna, and are high precision, original data, well-calibrated and optimized for scientific use, including being co-registered. As such it is a prototype for locally targeted specialty archives, and is particularly useful for hazard responders— for retrospective background studies, for longer term predictive inferences for specific volcanoes, and for forensic hazard-related applications. INGV plans to complete the archive with ASTER data.

4.2 ASI Pilot Project

In 2007 the Italian Space Agency (ASI) funded a pilot project called ASI-SRV that incorporated the Landsat TM Archive for Etna, but included far broader instrumental coverage of Italian volcanoes. The ASI-SRV goals were to develop a system based on remote sensing data to provide support to the Italian Civil Protection Department (DPC) during different volcanic activity phases, including (a) surveillance and early warning; (b) monitoring the syn-eruption phase; and (c) monitoring the post-eruption phase. The ASI project necessarily focused on the few active volcanoes in Italy that, nevertheless, seriously threaten large populations. The Campi Flegrei volcanic feature in greater Naples is characterized by persistent-to-constant low level volcanic activity, allowing the generation of products related to the syn- and post-eruptive phases. These efforts demonstrated that it was possible to provide products even when no eruptive events are occurring, using remote sensing data acquired during previous eruptive events for

retrospective studies and to inform extrapolative studies for future hazard estimates. For instance, Vesuvio and Campi Flegrei are currently in quiescent phases, and such “quiescent” products analysis can be useful, especially in the context of mapping surface deformation for purposes just mentioned.

The ASI-SRV project was laid out in three main phases. The “pre-crises” phase included (a) monitoring of surface thermal anomalies monitoring using ASTER; (b) the Volcanic Aerosol Optical Thickness (VAOT) estimation using ASTER and Hyperion; (c) fumarolic and other volcanogenic water vapor estimation using Hyperion; (d) characterizations of degassing/passively emitting SO₂ plumes with ASTER; and (e) surface deformation studies with SAR time series using ERS/ENVISAT data. During “crisis” phase, aspects include (a) calculating/estimating effusion rate using AVHRR, MODIS, and Hyperion; (b) tracking and optically characterizing ash clouds using AVHRR and MODIS; (c) investigation aerosol optical thickness at low spatial resolution using AVHRR and MODIS; (d) SO₂ plume characterization with MODIS; and (e) syn-eruptive deformation as seen by SAR interferometry utilizing ERS/ENVISAT. “Post crises” aftermath phase included (a) change detection on surface characteristics to map lava flows and their effects using high resolution imagery; and (b) assessing and mapping ash cover at high spatial resolution using Quick Bird.

5 CONCLUSIONS

To make effective use of emerging large archives containing 10's of Tb of data, a number of important points need to be recognized.

First, it is clear that the assimilation of temporally, spatially, and spectrally robust data sets is a frontier of earth science. Large archives can be used to inventory and monitor dynamic and dangerous phenomena, like volcanic activity, globally. The fusion of different types of in situ and remote sensing data to detect volcanic precursors, e.g., seismic, thermal, geodetic, optical and microwave imaging, in situ sampling, has the potential to be extremely effective. To be effective, however, long term activity datums need to be created because they are important as a gauge of waxing and waning volcanic activity. And, new information technology makes processing, archiving, and fusing terabyte to petabyte archives feasible.

Next, it has been demonstrated that minimal or no-cost data access for researchers and hazard responders, at a minimum, is critical for societal benefit and protection. It is incontrovertible that government-sponsored space borne platforms and instruments should be providing free data that is freely accessible, especially for natural hazards response and research. The inescapable lesson-learned from a number of

failed business attempts in the US and Great Britain is that cost recovery models do not work for research data. In fact, they have the opposite effect: when burdened with onerous fees, academic scientists will vote with their feet and vulnerable students will suffer.

Finally, in concert with the previous point, publicly accessible data archives are key. The internet promotes easy inspection and widest possible access by general public and researchers and that very positive aspect of the internet should be exploited to the fullest. Long term archive maintenance and data access tools should be treated as ongoing infrastructure requirements, and large central archives should support diverse distributed specialty archives with bulk download capabilities. Data format standardization is desirable, but should not impede data access.

The more freely data related to hazards and land planning are made available to the technically literate and to the general public, the more an informed electorate can make the correct decisions.

Work presented here was completed in part at the Jet Propulsion Laboratory of the California Institute of Technology, Pasadena, CA under contract to NASA.

6 REFERENCES

- Pieri, D and M Abrams, 2004, ASTER Watches the World's Volcanoes: A New Paradigm for Volcanology—Observations from Orbit, *Journal of Volcanology and Geothermal Research*, 135 (1-2): 13-28.
- Pieri, D.C., and M.F. Buongiorno, 2010, Systematic summit crater radiance increase as seen in Landsat TM data before the 1991-93 eruption of Mt. Etna, submitted to *JVGR*.
- Smithsonian GVP, 2010, <http://www.volcano.si.edu>, 2010, Worldwide Holocene Volcano and Eruption Information, the Smithsonian Institution, Washington, D.C.

MISTIGRI, a microsatellite project associating high spatial resolution and high revisit frequency in the Thermal InfraRed

J.-P. Lagouarde ⁽¹⁾, M. Bach ⁽²⁾, J.A. Sobrino ⁽³⁾, G. Boulet ⁽⁴⁾, X. Briottet ⁽⁵⁾, S. Cherchali ⁽²⁾, B. Coudert ⁽⁴⁾, I. Dadou ⁽⁶⁾, G. Dedieu ⁽⁴⁾, P. Gamet ⁽²⁾, O. Hagolle ⁽⁴⁾, F. Jacob ⁽⁷⁾, F. Nerry ⁽⁸⁾, A. Oliso ⁽⁹⁾, C. Ottlé ⁽¹⁰⁾, V. Pascal ⁽²⁾, J.L. Roujean ⁽¹¹⁾, F. Tintó Garcia-Moreno ⁽²⁾

⁽¹⁾ INRA-EPHYSE, 71 av. E. Bourlaux BP 81, F-33883 Villenave d'Ornon

⁽²⁾ CNES, 18 av. E. Belin, F-31401 Toulouse Cedex 9

⁽³⁾ UCG/IPL, Univ.Valencia P. O. Box 22085, E-46071 Valencia (Spain)

⁽⁴⁾ CESBIO (CNRS, UPS, CNES, IRD), 18 av. E. Belin, F-31401 Toulouse cedex 9

⁽⁵⁾ ONERA-DOTA, BP 74025, 2, av. E. Belin, F-31055 Toulouse cedex 4

⁽⁶⁾ LEGOS, OMP, 14 Avenue E. Belin, F-31400 Toulouse cedex

⁽⁷⁾ IRD-LISAH, 2 place P. Viala, F-34060 Montpellier cedex 1

⁽⁸⁾ LSIT/TRIO, Bd Sébastien Brant, BP 10413, F-67412 Illkirch cedex

⁽⁹⁾ INRA-EMMAH, UMR 1114, Domaine St Paul, Site Agroparc, F-84 914 Avignon Cedex 9

⁽¹⁰⁾ LSCE, Centre d'Etudes de Saclay, Orme des Merisiers, F-91191 Gif-sur-Yvette

⁽¹¹⁾ CNRM-GAME, Météo-France, 42, av. G. Coriolis, F-31057 Toulouse

lagouarde@bordeaux.inra.fr

ABSTRACT- This paper presents the MISTIGRI project of a microsatellite developed by the French space organisation CNES in cooperation with Spain. MISTIGRI is a precursor mission designed to combine a high spatial resolution (~50m) with a daily revisit in the thermal infrared (TIR). The scientific goals and expected applications of the mission are first described: they deal with (i) agriculture and hydrology, (ii) monitoring of urban areas and (iii) monitoring of coastal areas and continental waters. The spatial resolution and revisit specifications are justified. The choice of the orbit is discussed. The other mission specifications are briefly examined and rapid overviews of the instrumental concept and of the proposed mission architecture given.

1 INTRODUCTION

As it is a key signature of the surface energy budgets, the surface temperature (T_s) appears as a crucial variable to monitor and understand the interactions between the continental or maritime surfaces and the atmosphere, and their contribution to the drifts currently being observed in relation with global change (Climate Change 2007: Synthesis report IPCC). But in the field of thermal infrared (TIR) remote sensing, researchers and users have to face a dilemma between spatial and temporal resolution: systems such as AVHRR, MSG, MODIS provide daily observations at low resolution on the one hand, while systems such as Landsat or ASTER on the other hand provide high resolution images, but with poor revisit capabilities of about 2 weeks. Significant improvements in the modelling and monitoring of the surface/climate system, particularly at local scale, and in applications dealing with agriculture, hydrology, climatology...are now expected from the availability

of new spaceborne observational techniques in the thermal infrared that provide both (i) high revisit capabilities and (ii) high spatial resolution. This is the goal of the MISTIGRI (**M**icro **S**atellite for **T**hermal **I**nfrared **G**round surface **I**maging) mission initiated by CNES in collaboration with Spain, and designed to associate a resolution of 50m and a 1 or 2 day-revisit (<http://www.cesbio.ups-tlse.fr/fr/indexmistigri.html>). After a two year phase 0, the project entered a phase A (2009-mid 2011) for a possible launch in 2015.

2 SCIENTIFIC OBJECTIVES

2.1 Monitoring of energy and water budgets of the continental biosphere

The energy and water fluxes over continental biosphere govern the status of vegetation and the biogeochemical cycles (CO_2 particularly) and are strongly impacted by the interactions between the surface and the atmosphere. The first objective of

MISTIGRI is to contribute to the monitoring of the water cycle, with a particular emphasis on the assessment of the rapid changes in land surface water status (after rainfall or irrigation) at the local (field) scale. The MISTIGRI data will be used in conjunction with models with the scope of either deriving surface fluxes, or improving and developing related methodologies. Several approaches can be used to estimate the evapotranspiration (ET). Simplified algorithms based on the analysis of the relationships between T_s and albedo (or NDVI) can provide direct estimates of ET from T_s (Kalma et al., 2008) with further interpolation of ET between dates when TIR data is available to ensure a continuous monitoring of water status. Other methods are based on the use of bio-physical soil-vegetation-atmosphere transfer models (SVAT) associated to inversion (Jacob et al., 2006) and assimilation procedures (Crow et al., 2008). The expected main fields of application deal with:

- *agriculture*: monitoring of the growth, impact of agricultural practices on water use, detection of stress with application to irrigation or forest fire risk...
- *hydrology*: water budgets of watersheds, monitoring of water tables
- *biogeochemical cycles*: assessment of carbon fluxes and budgets using vegetation models.
- *meteorological forecasting*, through the improvement of the parameterization of the surface processes in the meso-scale models.

Methodological progresses are also expected from MISTIGRI data, among which the study of aggregation processes and scaling (which should in turn contribute to an improved use of the low resolution data of the global cover sensors such as AVHRR or MODIS), the determination of emissivity and temperature-emissivity separation, and the study of directional anisotropy (Lagouarde et al., 2000, Kurz, 2009)...

2.2 Monitoring of the urban environment

The climate over cities is significantly affected by a number of characteristics proper to urban areas. The three-dimensional structure of urban canopies with important heterogeneities both at local scale (heights of buildings, orientation of streets...) and at larger scale (vocation of districts: settlement, industrial, commercial...), alter the roughness of the surface and the flow within the urban atmospheric boundary layer. The use of a large panel of artificial materials with contrasted surface properties also affects the radiative transfers, while the reduction of vegetated areas and the increase of impervious surface combine to modify water cycles drastically. Human activities also contribute to urban climate by several ways:

urbanization, emission of pollutants, increase of energy consumption among others. It finally results in a strong variability of microclimates inside cities and in differences with surrounding rural climate, the well-known urban heat island phenomena.

The urban remote sensing remained focused on the description of the UHI for a long time (Arnfield, 2003), but recent progress on modeling opens new perspectives. Progress has been made not only on surface energy budgets and fluxes (Voogt et Oke, 2003) but also on the physics of the TIR signal itself: description of the directional anisotropy (Lagouarde et al., 2010), radiative transfer and aggregation processes of temperature and emissivity (Fontanilles et al., 2008). The possible fields of application of MISTIGRI deal with:

- *urban climatology and heat waves*. The increase of the frequency and intensity of heat waves expected as a consequence of the climate change makes necessary policies for mitigating their effects. A strong demand exists for building alert systems and improved urban planning.
- *urban hydrology* requires improved methodologies for a better assessment of the water budgets of urban watersheds (Carlson and Arthur, 2000) and for urban planning.
- *monitoring of urban vegetation*. Vegetation plays a significant role for hydrology (by increasing water storage capacities of ground and limiting runoff) and for the welfare and health of inhabitants (humidification of air, shading effects and reduction of temperatures...).
- *diffusion of pollutants and air quality*. The surface temperature helps to validate the atmospheric flow and diffusion models used for forecasting the extension of pollution plumes.
- *anthropogenic fluxes* (industrial activity, air conditioning or heating of buildings, transport...) can be estimated through the closure of the surface energy budgets (Pigeon et al., 2007).

2.3 Monitoring of coastal and continental waters

Many additional research fields can take benefit of MISTIGRI data (vulcanology, geology, industrial hazards...). Among those we chose to emphasise applications dealing with coastal and continental waters in this paper. Data are needed to observe submesoscale activity -1 to 100 km scale- characterized by fronts, filaments, which have a large impact on vertical transport of different properties (nutrients, CO_2 ...). In coastal area, several processes are responsible for intense and narrow SST gradients ~1 km (for instance fresh water coming from rivers or estuaries...) which have an influence on air-sea fluxes as well as winds (Chelton et al., 2007; Donlon et al.,

2009). MISTIGRI will allow one to study such fronts displaying SST signatures not detected with current low resolution satellite data. A number of applications are expected:

- coastal oceanography (internal waves, etc), sea state (storm surge, etc)
- estuary hydrology
- land and coastal ocean exchanges, and contribution to carbon, nitrogen and other biogeochemical cycles; estimates of greenhouse gas fluxes (CO_2 , N_2O , CH_4 ...) at the air-sea interfaces in coastal areas
- pollutant discharge from rivers, and exchanges (heat, pollutants...) over the tidally portion of rivers, estuaries and wetland
- coastal zone management, water quality monitoring
- algae blooms
- monitoring of halieutic resources,
- marine services

The high spatial resolution of the MISTIGRI data will also be used in a variety of applications dealing with continental waters (lakes and rivers), for instance study of confluence of rivers and lakes, monitoring of floods, thermal plumes of nuclear power plants... Surface water temperature of lakes has also been defined as Essential Climate Variable by GCOS and will be integrated in the future database (Hydrolare / Hydroweb) of the GTN-L list (Global Terrestrial Network for Lakes).

2.4 Strategy of the MISTIGRI mission

MISTIGRI is a precursor mission. Its first aim is to demonstrate the interest of combining high revisit and spatial resolution in the TIR for monitoring surface water status, and to develop the related methodologies. The strategy of the MISTIGRI mission is similar to that of Venus (<http://www.cesbio.upstlse.fr/fr/indexvenus.html>), and associates a spatial system with experimental sites monitored by scientific teams at ground. The large number of existing long term programmes and networks for monitoring climate, ecology, hydrology processes (FLUXNET, ICOS, LTER, GEWEX programmes, NEESPI...) and the persistence of the scientific questions addressed ensures that a large panel of sites will be available in the future.

3 MAIN MISSION SPECIFICATIONS

3.1 Spatial resolution

As classically for VNIR channels, the choice of the spatial resolution is first constrained by the typical size of the units or fields studied. Proposing a unique value is obviously difficult, as it depends on the type

of landscape studied. Nevertheless, we can refer to Kustas et al. (2004) who showed that a resolution lower than about 100 m was required to discriminate the contributions of 2 crops (soybean and corn) to actual evapotranspiration, in the case of Iowa plain where fields have a typical size of 100x100 m. Agam et al. (2007) confirmed this limit for agricultural applications. A similar conclusion was found by Garrigues et al. (2006) who quantified the spatial heterogeneity of the NDVI for 18 landscapes of the VALERI database (<http://w3.avignon.inra.fr/valeri/>) and similarly concluded that 'the sufficient pixel size to capture the major part of the spatial variability of the vegetation cover at the landscape scale is estimated to be less than 100m'. Another guideline is provided by an analysis of the size of fields in the case of a French typical hilly agricultural region (Gers department), according to information obtained from administration in the Common Agriculture policy framework: 75% of the surface is made of plots $\geq 150 \times 150 \text{ m}^2$, which corresponds to a typical 3x3 50 m pixel grid. We can also refer to the 100 m resolution of Landsat LDCM.

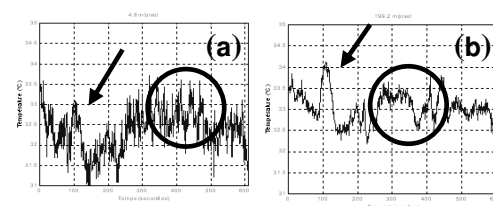


Figure 1. *Ts temporal evolution above a maritime pine stand over a 600s period at 1 Hz for 5 m (a), and 200 m (b) resolutions. Low frequency fluctuations related to convection in the PBL (arrow) are present regardless of the considered spatial resolution, whereas high frequency fluctuations are smoothed by spatial integration at pixel scale. The Y axis ranges between 31 and 35°C (after Lagouarde et al., 1997).*

A particularity of the surface temperature is to display rapid time fluctuations in relation with the turbulent nature of the atmospheric flow (with wind speed in particular). High frequency fluctuations related to the surface boundary layer flow (which correspond to small scale eddies) are partly smoothed by the spatial integration performed at the pixel scale. On the opposite the planetary boundary flow induces lower frequency fluctuations (typically a few minutes) with a characteristic size (typically the kilometer) much greater than the pixel one. These cannot be reduced and contribute to the uncertainty on instantaneous satellite Ts measurements. Experiments performed over maritime pine stands using a helicopter-borne TIR camera (Lagouarde et al., 1997) indicate that a resolution lower than ~40m is not useful (Fig. 1). A confirmation is expected soon from

recent experiments performed over a large range of surfaces (from bare soils to cities) in the South of France and from a numerical study using an improved version of the ARPS LES model. To our knowledge no similar results can be found in literature.

A resolution of about 50m finally allows one to obey the combined constraints imposed by land cover heterogeneity, minimum swath size required (25 km), and uncertainties induced by turbulence.

2.4 Revisit

The choice of the revisit is guided not only by the probability of cloudfree conditions which determines the number of data available, but also by the performances of the models used for deriving fluxes with the required accuracy. The reader will refer to a study (Lagouarde et al., 2011, same issue) presented in details in this issue, where it has been shown that a 1 day-revisit was necessary.

2.4 Spectral bands

The baseline in the TIR is a configuration of 4 bands at 8.6, 9.1, 10.3 and 11.5 μm for obtaining surface radiometric temperature and emissivity using the TES algorithm (Sobrino et al., 2005). Merging the first two bands into a single one at 8.8 μm for a better NEDT is possible and its interest for MISTIGRI is currently being evaluated.

In the Visible and Near Infrared (VNIR) range, 4 bands have been selected at 450, 670, 865 and 910 nm. with an improved resolution of $\sim 20\text{m}$. Their objectives are: registration of TIR images, detection of low clouds, estimation of the integrated water vapor content, land cover, obtaining a first guess of emissivity for TES, possible disaggregation of TIR data... Many of these objectives require VNIR imagery to be acquired simultaneously to TIR. For these reasons, using other satellites (Sentinel 2 for instance) cannot replace a VNIR instrument onboard.

4 MISSION ARCHITECTURE

The mission architecture base line has been defined by integrating as many elements having a strong heritage as possible for reducing program costs and schedule risks.

4.1 Instrument

The TIR instrument is based on the use of a 640 x 480 uncooled microbolometer array with a pixel pitch of 25 μm developed by a French company ULIS. A trade off was made leading to the selection of this detector for the TIR instrument. Although the sensitivity of micro-bolometers is less than that of

cryogenic detectors, such detectors have the main advantage of not needing a cooling system. The requirement for the swath is 25 km at least. The thermal time constant of microbolometers (9.2 ms) introduces a constraint to the satellite operation by making necessary a sampling time longer than the time constant in order to achieve a good MTF and linearity performances. This Time Delay Integration (TDI) acquisition mode requires a satellite slow down obtained by rotating the platform (varying the pitch angle) during the acquisition of the image. Moreover several lines of the array are used for each band to acquire the same line of the scene several times, thus allowing TDI-like image binning. NEDT values between 0.2 and 0.5K at 290K are finally expected.

An onboard calibration will be done using two internal blackbodies at 283 K and 313 K. This solution is preferred to blackbodies placed at the entrance of the instrument to reduce volume and to keep compatibility with the existing CNES MYRIADE platform. The goal is an absolute accuracy of 1K.

The VNIR instrument will be based on classical 1D CCD arrays, with a pushbroom classical imaging mode.

The design of the instrument results from technical studies and trade-off currently being done, and led by CNES with the support of TAS (Thales Alenia Space).

4.2 Platform

The MISTIGRI spacecraft architecture is based on the last version of the standard MYRIADE platform which allows fulfilling the mission needs with a large margin. MYRIADE is a multi-purpose flight proven platform developed by CNES in partnership with industry. It enables a total satellite mass of at least 200kg compatible with different launchers.

4.2 Orbit choice and acquisition capacity

The orbit will be Sun-synchronous to have the same overpass time. The 1 day-revisit specification imposes a one day repeat cycle orbit at an altitude of 561 km. The case of the 720 km (2 day-revisit orbit) has also been examined and is the option selected for the TIREX proposal (Sobrino et al., 2011, same issue): it requires a constellation of 2 satellites shifted by one day to fulfil the 1 day-revisit specification. Coverage and acquisition capacity are depending on the orbit choice. The coverage capacity (or potential accessibility to sites at ground) is defined by the ground area that can be seen by the satellite within the across track roll depointing limit of 30°. In the case of a 561 km altitude, the coverage is about 25% at the equator and reaches 42 % at 45° latitude. In case of the constellation at a 720 km altitude, the coverage is

pretty satisfactory: 73% at the equator latitude and up to 100 % from the 43° latitude (Fig. 2).

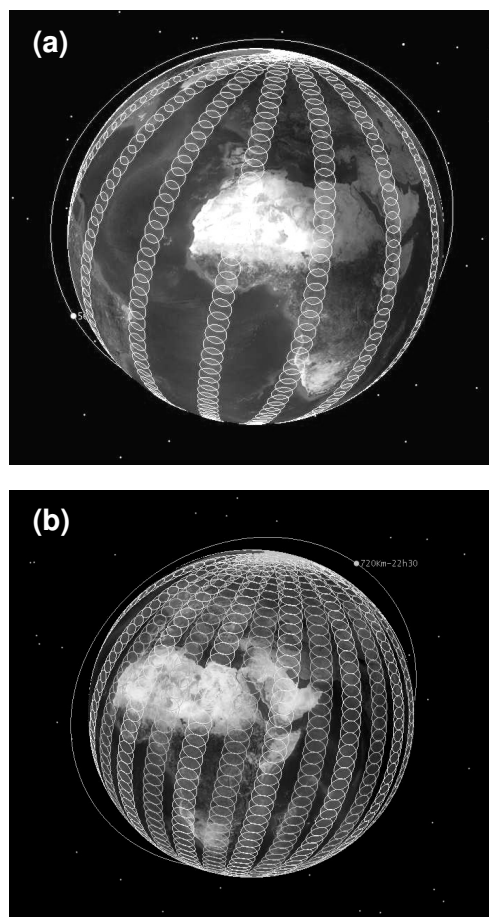


Figure 2. Potential accessibility at ground in the case of 1 satellite at 561 km (a) and of a 2 satellite-constellation at 720 km (b).

The acquisition of the sites is obtained by rotating the platform, across or along track. The acquisition capacity is therefore less than the coverage and limited by the time duration needed to achieve this rotation and by the image duration, taking into account a slow down ratio. As a consequence of the agility needs, the standard MYRIADE reaction wheels are to be replaced by more powerful wheels. A study performed at CNES has demonstrated the possibility to acquire imagery on sites in the most difficult case study of an orbit over western Europe including sites in Spain and France both sides of the track. For the 720 km altitude, the simulations show that 10 sites can be observed within a 310 s interval of time. Assuming sites spread over the land surfaces, an extension of this simulation leads to a number of 79 sites accessible on the daytime

part of the orbit, and of 157 sites for the whole orbit. For the 29 revolutions flown during the 2 day-cycle, and taking into account a 29% cover of continental surfaces, a potential of about 665 (daytime only) and 1330 sites (daytime and nighttime together) is accessible. The same computation leads to 60 (daytime) and 121 sites (whole orbit) per orbit with a 561 km altitude. For the 15 revolutions of the 1 day-cycle, about 260 (daytime) and 520 (day and night) sites can be observed with a 1 day-revisit. Despite obviously larger with the 720 km constellation, the number of potential reference sites at ground accessible with the 561 km orbit option remains quite compatible with the precursor character of the MISTIGRI mission.

The scientific data produced by the TIR and VNIR instruments are stored in the 16 Gbits Myriade Mass Memory and downloaded to a ground station located on a northern site. This location has a large visibility duration per day (~100mn) and allows to download up to 100 Gbits every day. This would also enable an additional systematic acquisition over boreal area and the constitution of an original dataset over such areas particularly affected by global change.

5 CONCLUSION

By filling the gap between high temporal /low spatial from one side and high spatial /low temporal resolutions from the other, which exists today in the context of the TIR missions, MISTIGRI is expected to bring an original information with a 1 day-revisit and ~50 m resolution. The scientific context is favourable, MISTIGRI being supported by an active scientific community having a large experience and a good maturity level in the TIR (models, experimental, spatial projects such as IRSUTE [Seguin et al., 1996] and SEXTET at CNES, PRISM and SPECTRA at ESA, FOCUS, BIRD at DLR, FUEGO in Spain...). The recent technological progress (uncooled microbolometers among others), and the fact the MISTIGRI architecture is constructed around elements having a strong heritage (platform) or being easily derived from other missions (for example the Venus ground segment) all together significantly contribute to the feasibility of MISTIGRI. Finally, dealing with the general context of global change international programs, it appears that the development or reinforcement of long term federative initiatives and programs (such as FLUXNET, ICOS, GMES...) makes urgent an innovative precursor mission in the TIR such as MISTIGRI.

6 REFERENCES

- Agam N., Kustas W.P., Anderson M.C. et al. (2007). Utility of thermal sharpening over Texas high

- plains irrigated agricultural fields., *J. Geophys. Res.*, 112, D19110, doi:10.1029/2007JD008407.
- Arnfield A.J. (2003). Two decades of urban climate research: a review of turbulence, exchanges of energy and water, and the urban heat island. *Int. J. Climatology*, 23, 1, 1-26.
- Carlson T.N. and Arthur .S.T. (2000). The impact of land use-land cover changes due to urbanization on surface microclimate and hydrology: a satellite perspective. *Global and Planetary Change*, 25, 49-65.
- Chelton, D. B., Schlax M. G., and Samelson R. M., (2007). Summertime Coupling between Sea Surface Temperature and Wind Stress in the California Current System., *J. Phys. Oceano*, 37 (3), 495-517.
- Crow, W.T., Kustas, W.P. and Prueger, J.H. (2008). Monitoring root-zone soil moisture through the assimilation of a thermal remote sensing-based soil moisture proxy into a water balance model. *Rem. Sens. Environ.*, 112(4): 1268-1281.
- Donlon C. J. et al. (GHRSSST group) (2009). "Successes and challenges for the modern Sea Surface Temperature Observing System: The Group for High Resolution Sea Surface Temperature (GHRSSST) Development and Implementation Plan (GDIP), white paper, *OceanObs09*, Venice, 45 pp.
- Fontanilles G., X. Briottet, S. Fabre, T. Trémas, (2008). Thermal infrared radiance simulation with aggregation modelling (TITAN): an infrared radiative transfer model for heterogeneous 3-D surface - application over urban areas, *Applied Optics*, Vol. 47, N° 31, pp. 5799-5810.
- Garrigues S., Allard D., Baret F., Weiss M. (2006). Quantifying spatial heterogeneity at the landscape scale using variogram models. *Rem. Sens. Envir.*, 103, 81-96.
- Jacob F., Schmugge T., Oliso A. et al. (2006). Modeling and Inversion in Thermal Infrared Remote Sensing over Vegetated Land Surfaces. *Advances in Land Remote Sensing: System, Modeling, Inversion, and Application* (ed S. Liang), 354 (Springer, on line): 245-292.
- Kalma J.D., McVicar T.R. and McCabe M.F. (2008). Estimating Land Surface Evaporation: A Review of Methods Using Remotely Sensed Surface Temperature Data, *Surveys in Geophysics*, 29(4-5): 421-469.
- Kurz B. (2009). Modélisation de l'anisotropie directionnelle de la température de surface : application au cas des milieux forestiers et urbains. *PhD thesis* Univ. Toulouse, 144p.
- Kustas W.P., Li F., Jackson T.J. et al. (2004). Effects of remote sensing pixel resolution on modelled energy flux variability of croplands in Iowa, *Remote Sens. Environ.*, 92, 535-547.
- Lagouarde, J. P., Dubreton, S., Moreau, P., and Guyon, D. (1997). Analyse de l'ergodicité de la température de surface sur des couverts forestiers à diverses résolutions spatiales. In *"7^{me} Symp. Int. on Physical Measurements and Signatures in Remote Sensing"* (G. Guyot, T. Phulpin and ISPRS eds.), 303-310. Balkema, Rotterdam (NLD).
- Lagouarde J.P., et al. (2000). Experimental Study of Brightness Surface Temperature Angular Variations of Maritime Pine (*Pinus pinaster*) Stands, *Rem. Sens. Envir.* 72, 17-34.
- Lagouarde J.-P., Hénou A., Kurz B. et al. (2010). Modelling daytime thermal infrared directional anisotropy over Toulouse city centre. *Remote Sens. Environ.* 114, 87-105.
- Lagouarde J.-P., et al. (2011). Defining the revisit frequency for the MISTIGRI project of a satellite mission in the thermal infrared. RAQRS'III Int Symp., Torrent, Spain, sept 27th - oct 1st 2010. *In this issue*.
- Pigeon G., Legain D., Durand P. and V. Masson. (2007). Anthropogenic heat release in an old European city (Toulouse, France). *Int. J. of Climatology*, 27 (14), 1969-1981.
- Seguin, B., Becker, F., Phulpin, T., Gu, X. F., Guyot, G., Kerr, Y., King, C., Lagouarde, J. P., Ottlé, C., Stoll, M. P., Tabbagh, A., and Vidal, A. (1999). IRSUTE : A minisatellite project for land surface heat flux estimation, from field to regional scale. *Remote Sensing of Environment*, 68, 357-369.
- Sobrino, J. A., and Jiménez-Muñoz, J. C., 2005, Land surface temperature retrieval from thermal infrared data: An assessment in the context of the Surface Processes and Ecosystem Changes Through Response Analysis (SPECTRA) mission, *J. Geophys. Res.*, 110, doi: 10.1029/2004JD005588.
- Sobrino J.A., et al. (2011). Overview of the thermal infrared Explorer (TIREX) mission. RAQRS'III Int Symp., Torrent, Spain, sept 27th - oct 1st 2010. *In this issue*.
- Voogt J.A., Oke T.R. (2003). Thermal remote sensing of urban climates, *Rem. Sens. Environ.*, 86, 370-384.

Validating satellite land surface temperature product using ground data: quantifying the site-to-pixel scaling uncertainty

Yunyue Yu^{*a}, Jeffrey L. Privette^b and Ming Chen^c

^aCenter for Satellite Applications and Research, NOAA/NESDIS, 5200 Auth Rd., Camp Springs, MD, USA 20746-4304.

^bNational Climatic Data Center, NOAA/NESDIS, 151 Patton Ave., Asheville, NC, USA 28801-5001.

^cI. M. Systems Group, Inc. at Camp Springs, MD, USA 20746

Email: yunyue.yu@noaa.gov

ABSTRACT - Validation of satellite land surface temperature (LST) is a significant challenge because of spectral, spatial and temporal variability of land surface emissivity. High accuracy in situ LST measurements are required for validating satellite LST products. Yet they are very hard to obtain, except at discrete points or for very short time periods (e.g., during very limited field campaigns). To compare these field-measured point data with moderate resolution (~1 km) satellite products requires quantitative estimation of the scaling uncertainty that may ultimately exceed those intrinsic measurement uncertainties of the satellite products. To date, few studies have been attempted to rigorously assess the scaling uncertainty between the satellite-derived LST and scaled in situ LST measurements. Recently, in our tasks on the U.S. Joint Polar-orbiting Satellite System (JPSS) mission and the Geostationary-orbiting Operational Environmental Satellite R series (GOES-R) mission, we developed a new method for quantitative analysis of the site-to-pixel differences. The method considers the error structures of both the satellite data and the ground data sets. It applies a linear fitting model to the “match-up” ground data for correcting the site-to-pixel differences, which are used for the satellite LST validation. In this study, high-resolution Advanced Spaceborne Thermal Emission and Reflection Radiometer (ASTER) data was used for analyzing the site-to-pixel differences at 1-km scale, which is commensurate with moderate resolution satellite data. The in situ data set was obtained from the U.S. Surface Radiation (SURFRAD) budget network. ASTER LST observations covering years from 2000 to 2009 were collected and collocated at six SURFRAD sites using a stringent match-up process. It is demonstrated that a precision range, or a conservative precision estimation of the satellite LSTs, can be determined through synthetic pixel analysis.

1 INTRODUCTION

Validation of satellite LST retrievals is usually performed with reference to ground-based observations. In reality, a satellite pixel size is generally much larger than the field of view of ground-based measurement. If the target ground site is not homogeneous enough, LST may vary significantly within the collocated satellite pixel because of relevant surface features, land cover and soil moisture variation. A direct comparison with ground-based measurement in such case may introduce significant error into the validation results. To properly validate LST product, one needs to ensure that the ground site is fairly homogeneous for representing the dominant surface type of surroundings, and quantifying the site-to-pixel difference leading to the scaling uncertainty.

In this study, we introduce a synthetic pixel analysis method to quantitatively evaluate the scaling mismatch uncertainties in the direct site-to-pixel LST

comparison. High-resolution ASTER data was used to synthesize a set of pixels at a target ground site. The synthetic pixels have a predefined scale that is commensurate with the real resolution of satellite observations to be validated, e.g., the 1-km resolution of Moderate Resolution Imaging Spectroradiometer (MODIS) data in this study. The method considers the error structures of both the satellite data and the ground data sets. It applies a linear fitting model to the co-registered “match-up” ground data for correcting the site-to-pixel differences. Example analysis was performed with four SURFRAD sites. Quantitative site-to-pixel statistics for the MODIS LST validation was achieved by 1-Km synthetic pixel analysis at the sites.

2 METHOD

An *in situ* site is considered “characterized” if we are able to provide reasonable expected values of

$$E\{T_{sat} - T_g\} \text{ and } \sigma\{T_{sat} - T_g\}, \quad (1)$$

□ ASTER 90m TIR pixels ● Ground site

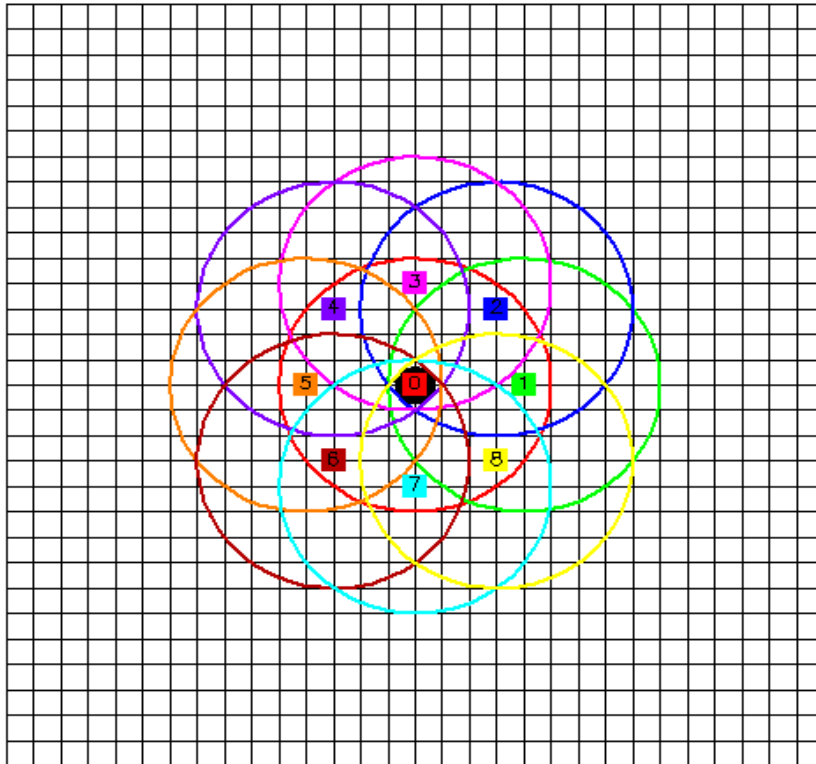


Figure 1. The large circles represent a set of moderate-resolution pixels synthesized from the high-resolution pixels (squares). Each synthetic pixel has the target ground site enclosed, but samples landscape in different directions around the ground site, counting for the possible over-passing satellite swaths. Nevertheless, the distance of every synthetic pixel center from the ground site is within the moderate-resolution pixel size (e.g., 1 Km).

where $E\{*\}$ and $\sigma\{*\}$ are the ensemble expectation and standard deviation operators, respectively; T_g denotes the LST measurement at the ground site, and T_{sat} is LST of the collocated satellite pixel. T_{sat} may be the real LST observation from a moderate resolution satellite (*i.e.*, MODIS, VIIRS, etc) or it can be the LST of a synthetic moderate resolution pixel that is aggregated from high-resolution observations. Figure 1 illustrates a conceptual model about how a set of moderate-resolution satellite pixels are synthesized from high-resolution ASTER pixels at a collocated ground site. The enclosed high-resolution ASTER pixels in Figure 1 may be taken as the sub-pixels of the corresponding moderate resolution satellite pixel for various spatial variation analyses. It is worth noting that

$$T_{sat} - T_g = (T_{sat} - T_c) + (T_c - T_g) \quad (2)$$

where T_c is the LST of the nearest sub-pixel to the ground site. Without cloud contamination, T_{sat} and T_c bear similar uncertainties of satellite radiometric measurements. The statistics of T_{sat} and T_c will be a pure measure of the contribution of landscape heterogeneity to the LST validation uncertainty. In contrast, the statistics of $T_c - T_g$, especially the bias, will contain uncertainties due to the ASTER LSTs and ground site calibration error, emissivity unknowns, etc. Therefore, we may separate site-to-pixel scaling uncertainty from measurement uncertainty with Eq (2), and perform pertinent site characterization through T_{sat} and T_c .

The simplest approach to T_{sat} estimation is to average the ASTER LST data over a circle, that is, over the size commensurate with the MODIS instant field of view (IFOV).

$$T_{sat} = \frac{1}{N} \sum \sum T_{ij}, \quad T_{ij} \in \left\{ T_{ij} \mid \|\vec{r}_{ij} - \vec{r}_c\| \leq d/2, \|\vec{r}_c - \vec{r}_o\| \leq d/2 \right\} \quad (3)$$

where T_{ij} are the ASTER pixel LST observations, r_{ij} is the ASTER pixel position vector, r_c is central position of synthetic pixel, r_o is position of ground site; d is the IFOV size which is the spatial distance between the half-power points on the band point spread function.

We assume reasonable estimates of Eq(1) can be obtained with application of Eq(2) and Eq(3) to the clear-sky sample analysis of the nine synthetic pixels of Figure 1.

3 DATA COLLECTION AND PREPROCESSING

3.1 ASTER Data

ASTER is a multispectral scanner that produces images of high spatial resolution, flying on the Terra

platform of NASA's Earth Observing System since 1999. It has five bands in the thermal-infrared (TIR) spectral range (8-12 μm) with 90-m resolution (Kahle *et al.*, 1991; Yamaguchi *et al.*, 1993). The Temperature-Emissivity-Split (TES) algorithm of ASTER produced two standard products with TIR radiometric observations, surface kinetic temperature and surface emissivity. Associated with each product is a Two-plane Quality Assurance (QA) image describing ASTER data and TES performance characteristics.

ASTER data are stored and distributed by the Land Processes of NASA's Distributed Active Archive Center. A general data inventory of all available ASTER data may be prepared with the Warehouse Inventory Search Tool (WIST), which is a client for searching and ordering earth science data from various NASA and affiliated centers (<https://wist.echo.nasa.gov/wistbin/api/ims.cgi?mode=MAINSRCH&JS=1>). To have proper data samples, we tried to include all the possible overpass clear-sky ASTER scenes of years 2000 to 2009 at our target sites. For each clear-sky scene, we collect three ASTER datasets: ASTER-08 data (surface kinetic temperature), ASTER-05 data (surface emissivity), and ASTER-04 (TIR brightness temperature).

3.2 SURFRAD Data

The SURFRAD network was established in 1993 through the support of NOAA's Office of Global Programs, and has been operational in the United States since 1995. A detailed description of the SURFRAD network and associated instrumentation can be found in Augustine *et al.* (2000; 2005). The SURFRAD data is available at <http://www.srrb.noaa.gov/surfrad/>.

SURFRAD doesn't provide LST measurements. Instead, the SURFRAD ground LSTs are estimated from the upwelling and downwelling radiation measurements by precise infrared radiometers (PIRs) in the spectral range from 3 μm to 50 μm . Following Yu *et al.*, 2008, the surface temperature, T_g , can be estimated with

$$T_g = \left[\frac{\Phi_u - (1 - \varepsilon)\Phi_d}{\varepsilon\sigma} \right]^{1/4} \quad (4)$$

where Φ_u and Φ_d are the upwelling and downwelling irradiances measured by PIRs, respectively; σ is the Stefan-Boltzmann constant which has a value of $5.67051 \times 10^{-8} \text{ Wm}^{-2}\text{K}^{-4}$; ε is the surface thermal emissivity, which is usually estimated from the measurements of several sensitive narrow bands (Seemann *et al.*, 2008; Ogawa *et al.*, 2004; Wang *et al.*, 2005). By a regression formulation (Wang *et al.*, 2005) we have

$$\epsilon = a\epsilon_{8.3} + b\epsilon_{10.8} + c\epsilon_{12.1} \quad (5)$$

where $a=0.2122$, $b=0.3859$, $c=0.4029$; $\epsilon_{8.3}$, $\epsilon_{10.8}$ and $\epsilon_{12.1}$ are the three narrow-band emissivity from the UW-Madison Baseline Fit Emissivity Database (Seemann *et al.*, 2008).

4 RESULTS AND DISCUSSION

4.1 Matched Data-Paris

Availability of the matched data pairs depends on the availability of ASTER granules, ground site measurement records and cloud conditions. We required all the ASTER pixels of a 13x13 pixel array be clear to form a 1-Km synthetic pixel. And we excluded the ASTER scene if any one of the nine synthetic pixels (see Figure 1) contains cloudy pixels. This stringent criterion may greatly reduce the sample size, but ensures the data quality on the other hand.

In earlier years of 2000-2009, some SURFRAD sites were not on operation, so there were no data records at those sites.

Table 1. Clear-sky data pairs matched at SURFRAD stati

SURFRAD Sites	Lat(N)/Lon(W)	Clear-sky Cases	Surface Type
Desert Rock, Co	36.63/116.02	46	Open Shrub Land
Bondville, IL	40.05/88.37	51	Deciduous Forest
PennState, PA	40.72/77.93	20	Crop Land
Boulder, CO	40.13/105.24	13	Grass Land
Fort Peck, MT	48.31/105.10	8	Crop Land
Soux Falls, SD	43.73/96.62	1	Mixed Forest
Goodwin Creek, MS	34.25/89.87	0	Open Shrub Land

As shown in Table 1, the available sample sizes at SURFRAD sites Fort Peck, Soux Falls and Goodwin Creek are very limited, and not enough to establish reliable statistic analysis. We performed synthetic analysis for the rest four sites, and the results are shown in the following section.

4.2 Synthetic Analysis Results

Applying Eqs (1) - (3), we obtained the following results for the four SURFRAD sites with larger sample data sizes.

Table 2 Statistical results of each SURFRAD Site characterization.ID indicates the synthetic pixel show in Figure 1; Deg gives its orientation to the site location. ID=0 is the pixel centered exactly at the site. T_a is the same to T_{sat} .

Site: Desert Rock					
Tc-Tg → Mean: 1.81 StdD: 2.46					
ID	Deg	E{Ta-Tc}	σ{Ta-Tc}	E{Ta-Tg}	σ {Ta-Tg}
0	C	-0.04	0.69	1.78	2.13
1	0	0.01	0.60	1.82	2.26
2	45	-0.08	0.61	1.74	2.20
3	90	-0.20	0.92	1.61	1.99
4	135	-0.06	0.96	1.75	2.03
5	180	0.24	0.98	2.05	2.18
6	225	0.34	0.80	2.15	2.30
7	270	0.26	0.65	2.07	2.40
8	315	0.16	0.60	1.97	2.37

Site: Boulder					
Tc-Tg → Mean: 1.81 StdD: 2.46					
ID	Deg	E{Ta-Tc}	σ{Ta-Tc}	E{Ta-Tg}	σ {Ta-Tg}
0	C	0.07	0.58	0.84	2.62
1	0	0.38	0.85	1.15	2.61
2	45	0.27	0.91	1.03	2.30
3	90	0.14	0.84	0.91	2.27
4	135	0.03	0.61	0.80	2.54
5	180	-0.10	0.61	0.67	2.64
6	225	0.00	0.69	0.77	2.75
7	270	0.10	0.70	0.87	2.80
8	315	0.25	0.70	1.02	2.70

Site: Bondville					
Tc-Tg → Mean: 1.81 StdD: 2.46					
ID	Deg	E{Ta-Tc}	σ{Ta-Tc}	E{Ta-Tg}	σ {Ta-Tg}
0	C	0.07	0.92	0.66	2.04
1	0	0.14	1.04	0.73	2.01
2	45	0.05	1.07	0.64	2.05
3	90	0.05	1.27	0.64	2.17
4	135	0.09	1.15	0.68	2.10

5	180	0.01	1.10	0.60	2.14
6	225	0.03	0.97	0.62	2.12
7	270	0.18	0.95	0.77	2.05
8	315	0.21	0.97	0.80	2.02

Site: Penn State					
T _c -T _g → Mean: 1.81 StdD: 2.46					
ID	Deg	E{Ta-Tc}	σ{Ta-Tc}	E{Ta-Tg}	σ{Ta-Tg}
0	C	0.15	1.05	-0.10	1.99
1	0	-0.18	1.13	-0.43	1.93
2	45	-0.15	1.36	-0.41	2.07
3	90	0.05	1.38	-0.20	2.19
4	135	0.16	1.07	-0.09	1.91
5	180	0.15	1.14	-0.10	1.96
6	225	0.25	1.13	-0.01	1.93
7	270	0.21	1.03	-0.04	1.91
8	315	0.06	0.99	-0.19	1.98

As shown in Table 2, the LST mean difference between the collocated central ASTER pixel (the pixel nearest to ground site) and the synthetic pixel, $T_{sat} - T_c$, is generally less than 1K, and the standard deviation of such difference is around 1K. As noted in Section 2, it is a pure measure of the contribution of landscape heterogeneity to the LST validation uncertainty. It implies that all the selected ground sites may be taken as homogeneous sites the LST calibration with 1-Km resolution. At Penn State and Bondville sites, $\sigma\{Ta-Tc\}$ appears a bit larger than most of the others. Considering that cloud contamination effects are more likely to occur at these two sites than the other two (a paper describes effect of the cloud contamination to the site data is in preparation), the larger $\sigma\{Ta-Tc\}$ would be not be surprised.

Mean difference between the ground LST and satellite LST (T_g and T_a) is generally around or less than 1K, except the Desert Rock site where the difference goes to around 2K. It is to be investigated whether such significant bias is due to emissivity uncertainty or other systematic error sources.

In comparison with the mean difference (accuracy), the standard deviations $\sigma\{T_a - T_g\}$ and $\sigma\{T_c - T_g\}$ are relatively large. Since standard deviation is the significance measure of mean difference, the large standard deviation values may degrade the reliability of the mean difference estimations. Without resorting to complicated

significance testing, we found that the estimated mean difference generally conforms to the surrounding topographic features, which in some sense indicates the reliability of our estimations.

As shown in Table 2, the directional variation of the difference between satellite LST and ground-based LST is generally not so significant, which is a good news as we do not need to worry much about possible issue due to the orientation of the satellite footprint center to the site spot.

For summarizing the results we aggregated the site characterization statistics along all the directions, and obtained the following simple linear fitting relationship for future 1-Km LST calibration at the related sites,

$$T_{sat} = T_g + C \quad (6)$$

where the offset C is determined as in Table 3.

Table 3. Site characterization statistics (aggregated).

Site	C	σ
Desert Rock, NV	1.88	2.21
Boulder, CO	0.90	2.58
Bondville, IL	0.68	2.08
PennState, PA	0.17	1.99

This is worth noting that the estimation in Tables 2 and 3 based on limited dataset size does not allow us to characterize seasonal variation of the surface heterogeneities which is more desirable than a simple mean difference. More datasets are needed for such seasonal variation study.

5 CONCLUSIONS

In this study, we developed a synthetic pixel analysis model to analyze the ground site temperature heterogeneous feature and to characterize the site-to-pixel scaling uncertainty. ASTER data are used to generate synthetic pixel data and compared to the SURFRAD site measurements. It is found that LST by SURFRAD measurements may be used as good references for the satellite LST of resolution 1-Km. In average, the site-to-pixel difference is less than 0.5 K at the scale of 1-Km with precision around 1K. Directional variations are very small as well for these sites. Directional variation of the potential sub-pixel heterogeneity is found to be consistent with the physical topographic features, even if it is small.

More datasets are needed for further investigate seasonal variation feature of the above sites, which is more desirable than a single mean difference along the year. Application of the site-to-pixel model also depends on the ASTER LST data quality.

ACKNOWLEDGMENT --The manuscript contents are solely the opinions of the authors and do not constitute a statement of policy, decision, or position on behalf of NOAA or the U. S. Government

6 REFERENCES

- Augustine, J. A., J. J. DeLuisi, C. N. Long, "SURFRAD- A National Surface Radiation Budget Network for Atmospheric Research", *Bull. Amer. Meteor. Soc.*, 81, 2341-2357, 2000.
- Augustine, J. A., G. B. Hodges, C. R. Cornwall, J. J. Michalsky and C. I. Medina, "An Update on SURFRAD- The GCOS Surface Radiation Budget Network for the Continental United States", *J. Atmos. Oceanic Technol.*, 22, 1460-1472, 2005.
- Gillespie A., Rokugawa S., et al, "A Temperature and Emissivity Separation Algorithm for Advanced Spaceborne Thermal Emission and Reflection Radiometer (ASTER) Images", *IEEE Trans. Geosci. Remote Sens.*, vol. 36, no. 4, pp. 1113-1125, 1998.
- Kahle A. B., F. Palluconi, S. Hook, V. J. Realmuto, and G. Bothwell, "The Advanced Spaceborne Thermal Emission and Reflectance Radiometer (ASTER)," *Int. J. Imaging Syst. Tech.* 3, pp. 144-156, 1991.
- Ogawa, K., and T. Schmugge, " Mapping surface broadband emissivity of the Sahara Desert using ASTER and MODIS data", *Earth Interactions*, 8, 2004.
- Salomonson, V., W. Barnes, P. Maymon, H. Montgomery, and H. Ostrow, "MODIS: advanced facility instrument for studies of the Earth as a system," *IEEE Trans. Geosci. Remote Sens.*, vol. 27, no. 2, pp. 145-153, 1989.
- Seemann, S. W., E. E. Borbas, R. O. Knuteson, G. R. Stephenson, and H-L. Huang, "Development of a global infrared land surface emissivity database for application to clear sky sounding retrievals from multispectral satellite radiance measurements", *J. Appl. Meteor. Climatol.*, 47:108-123, 2008.
- Wang, K., Z. Wan, P. Wang, M. Sparrow, J. Liu, "Estimation of land surface upwelling long wave radiation and broadband emissivity using MODIS LST products", *Journal of Geophysics Research*, 110, D11109, doi: 10.1029/2004JD005566, 2005.

Landsat ETM+ Thermal Band Calibration

Julia A. Barsi, Brian L. Markham, John R. Schott, Simon J. Hook, Nina G. Raqueno
Science Systems and Applications, Inc; NASA/Goddard Space Flight Center; Rochester Institute of Technology; NASA/Jet Propulsion Laboratory; Rochester Institute of Technology
julia.barsi@nasa.gov; brian.l.markham@nasa.gov; schott@cis.rit.edu;
simon.j.hook@nasa.gov; nina@cis.rit.edu

ABSTRACT- *Landsat-7 Enhanced Thematic Mapper+ (ETM+), launched in April 1999, has only a single thermal band. Its thermal band calibration was updated in 2000 to account for a pre-launch calibration error and until recently, the instrument was presumed to be calibrated. Two teams have made regular vicarious calibration collects in support of thermal band calibration. Rochester Institute of Technology (RIT) works primarily on the North American Great Lakes where campaigns typically capture water temperatures between 4 and 20C. The vicarious calibration team from NASA/Jet Propulsion Laboratory (JPL) has long operated automated buoys on Lake Tahoe in Northern California. The buoys operate year-round and the lake ranges between 2 and 20C. In the past two years, however, a JPL-operated station on the Salton Sea came online. The Salton Sea, located in Southern California, gets as hot as 35C. Vicarious calibration results from the Salton Sea added to the understanding of a small gain error that the previous data had suggested. With the Salton Sea data, a calibration gain error became statistically significant. This gain error means that the calibration error is dependent on target temperature. Though it causes errors as large as 1.2C at high temperatures (35C), at more usual earth temperatures (4-20C), the calibration error is within the noise of the calibration methodology (+/- 0.6K). These new data made it clear that the instrument required an adjustment to its thermal calibration coefficients. The new coefficients were generated and were implemented into the processing system on Jan 1, 2010. With the ETM+ calibration update, the RMS error of the thermal band calibration is within +/-0.6K for targets of all temperatures.*

1 INTRODUCTION

Landsat-7 was launched in 1999 and its payload consists of the Enhanced Thematic Mapper Plus (ETM+), the latest imaging instrument in the Landsat program. Landsat-7 continues to operate today, still capturing approximately 400 scenes per day. It has a 16-day repeat cycle and an 185km swath width, orbiting at 705km. The instrument is a whiskbroom scanner and the imager was affected by the failure of the Scan Line Corrector (SLC), a set of mirrors that makes the scans parallel, in 2003; this leaves gaps in the image data on both sides of the image products. However, the radiometric integrity of the data is not affected. The imager has 6 visible/near-infrared bands with a resolution of 30m, a panchromatic band with a resolution of 15m and a single thermal band with 60m resolution. Salient characteristics of the ETM+ thermal band can be found in Table 1.

The ETM+ has on-board calibrators for all bands, in order to monitor the absolute and relative calibration, as well as the stability of the instrument and to assess noise characteristics. In order to validate the on-board calibration system, there are teams on the

ground capturing vicarious calibration data for all bands. The on-board and vicarious calibration of the thermal band will be the focus of this paper.

2 ON-BOARD CALIBRATION

The on-board calibration system for the thermal band consists of a cavity blackbody held at approximately 44C and a high-emissivity shutter that drifts with the instrument ambient temperature. Both of these targets are viewed by the imager every scan of the scanning mirror when the shutter moves into the optical axis during the scan mirror's turn-around (Figure 1).

The calibration gain of the instrument is calculated from the blackbody and shutter radiances along with two calibration coefficients that represent view factors. The gain can be calculated as:

$$G = f \frac{(Q_{BB} - Q_{sh})}{(V_{BB}L_{BB} - L_{sh})} \quad (1)$$

The calibration offset was modelled during prelaunch testing and makes extensive use of internal

	Full-Width Half-Maximum bandpass [um]	Spatial Resolution [m]	NEDT [K @ 280K]	Radiometric Scaling Range [W/m2 sr um]
Landsat-5 TM	10.45 - 12.42	120	0.17-0.30	1.24 - 15.30
Landsat-7 ETM+	10.31 - 12.36	60	H: 0.22 L: 0.28	H: 3.2 - 12.65 L: 0.0 - 17.04

Table 1. Salient characteristics of the Landsat ETM+ thermal band. The same characteristics are provided for Landsat TM for comparison.

instrument components' radiances, which change temperature as the instrument warms. The effect of the components was empirically derived during the prelaunch tests (Turtle, 1999). The offset can be calculated as:

$$Q_0 = Q_{sh} - G \left[\frac{V_{sh}}{f} L_{sh} - \sum a_j L_j \right] \quad (2)$$

where:

- G external gain
- f internal/external gain ratio
- Q_{bb} response to blackbody (DN)
- Q_{sh} response to shutter (DN)
- L_{bb} blackbody radiance
- L_{sh} shutter radiance
- V_{bb} blackbody view coefficient
- V_{sh} shutter view coefficient
- Q_0 offset
- a_j view coefficient for instrument component j
- L_j radiance of instrument component j
- j components are SLC, baffle heater, primary mirror, secondary mirror, and scan mirror

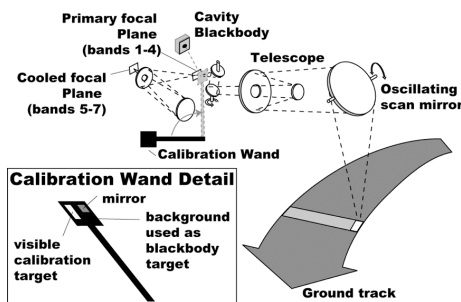


Figure 1. Optical layout of the ETM+ instrument. The calibration wand, or shutter, swings across the optical path, allowing the focal plane to see both the shutter and the blackbody.

The calibration coefficients are stored in the Calibration Parameter File (CPF), which the processing system uses in processing every scene. In this way, calibration corrections can be made easily by adjusting the necessary parameter and reprocessing the scene with the updated CPF.

The internal calibration of the instrument has been stable since launch to within 0.1%. The trended gains and offsets have shown no significant change since launch that wasn't related to a known processing change (Figure 2). Changes were made to the calibration coefficients in the CPF in December 2000

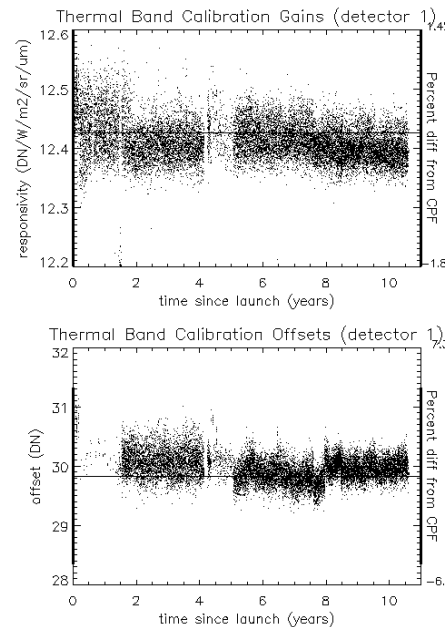


Figure 2. Calibration gains and offsets for a single detector of the ETM+ thermal band. Since the initial calibration correction in made in December 2000, the instrument gains and offsets have been stable.

to adjust for: a $0.92 \text{ W/m}^2 \text{ sr } \mu\text{m}$ calibration offset error (Barsi, 2003), which is why there are no offset data shown before about two years since launch; and to remove striping as a result of gain differences between detectors, which is why the noise in the gain trend is reduced after about two years since launch.

3 VICARIOUS CALIBRATION

Water is the primary target for thermal band calibration because it is generally homogenous, spectral uniform, and has a known and stable emissivity. Two teams are involved in the vicarious calibration of the ETM+ thermal band. Both teams have slightly different methods, but in general they both measure the surface-leaving radiance or surface temperature and predict space-reaching radiance by projecting the surface-leaving radiance through the atmospheric using a radiative transfer model and local atmospheric data (Hook, 2004), (Schott, 2001). The predicted space-reaching radiance is compared to the radiance measured by the ETM+.

The team at the Rochester Institute of Technology (RIT) has two methods of vicarious calibration. Since the launch of Landsat-7, they have been deploying on the open water and bays of Lakes Erie and Ontario. In 2003, they began collecting under Landsat-5 as well. They typically collect water temperatures between 4 and 25C. The second method involves mining the archives of the National Data Buoy Center (NDBC) for water temperatures, as recorded by buoys permanently stationed the open water around the United States. They began using this method in 2007, but with the extensive historical archive have been able to extend the calibration back to the launch of Landsat-5 in 1984. With this method, they typically see temperatures of between 4 and 20C.

The second team, the NASA/Jet Propulsion Laboratory (JPL), has installed four automated buoys on Lake Tahoe on the California/Nevada border, which have been operational since 1999. The buoys record surface temperature and surface-leaving radiance every two minutes along with local meteorological data and relay the data to JPL daily. Lake Tahoe is typically between 2 and 20C. More recently, JPL has

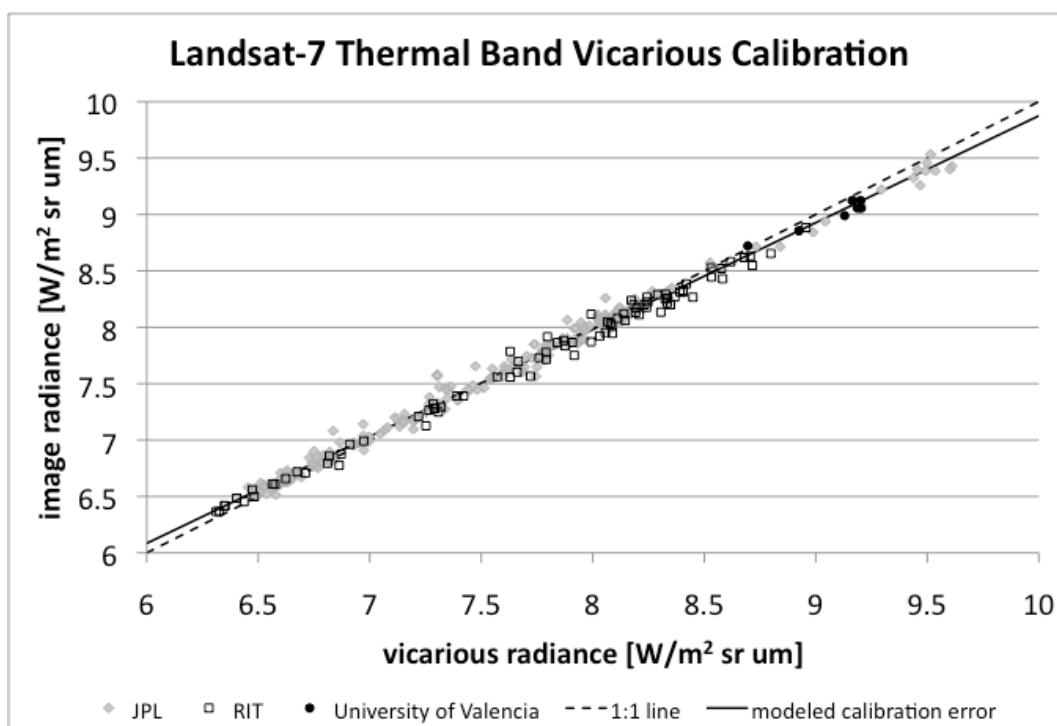


Figure 3. Combined calibration results of the ETM+ calibration teams. In a perfectly calibrated system, the data would be scattered about the 1:1 line. The data points from the Salton Sea (above $9.0 \text{ W/m}^2 \text{ sr } \mu\text{m}$) established the statistical significance of the 6% gain error. The error was confirmed by data published by the University of Valencia (Coll, 2010).

established a station on the Salton Sea in southern California. Being a desert lake, the temperatures here range between 15 and 35C. With the harsher environment, this Salton Sea station has been challenging to keep operational, but in the last two years, regular data has been collected.

Figure 3 shows the results of the collected vicarious calibration data of both teams. In a perfectly calibrated system, the data would fall on the dotted, one-to-one line. However, the RIT and JPL data acquired between 1999 and 2009 have a statistically significant slope, indicating a calibration error of 6%. The cooler data had hinted at this gain error, but the addition of the warmer Salton Sea points (above 9.5 W/m² sr um) made the slope statistically significant.

An independent confirmation of the calibration error came from the University of Valencia (Coll, 2010). Their data are also shown in Figure 3. The team was making validation measurements on a different target in a different location and seeing the same magnitude error in their relatively warm data (~9.25 W/m² sr um).

The effect of the gain error on the image data is target temperature dependent; warmer targets in the images appear cooler than they are, cooler targets in

Approximate Space-Reaching Target Radiance [W/m ² sr um]	Approximate Target Temperature [C]	Calibration Error [C @ 300K]
6.0	0	0.8
7.5	12	0.0
9.0	27	-0.7

Table 2. The estimated error in predicted target brightness temperature due to the calibration error in Landsat ETM+.

the images appear warmer than they actually are. Table 2 presents an estimate of the calibration error for targets of several temperatures.

The calibration error is corrected in the processing system by changing several calibration parameters in the CPF. The correction was implemented within the processing system on Jan 1, 2010. A sample of scenes from the JPL data set, spanning the full temperature range of the data, were reprocessed with the corrected CPF. The corrected radiances are compared to the

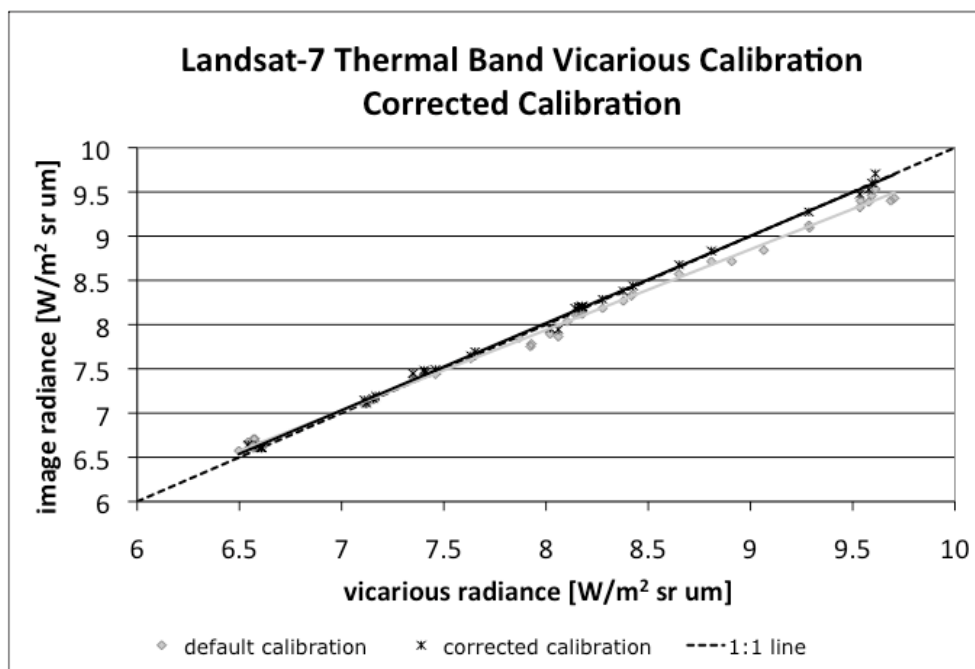


Figure 4. A comparison of a corrected data versus uncorrected (default) of a select sample of JPL data points. The corrected data line on the 1:1 line and the slope is no longer statistically significant.

original radiances in Figure 4. The slope of the corrected data is no longer statistically significant (1-sigma) and the RMSE of the sample data set is reduced from 0.91K to 0.37K.

4 CONCLUSIONS

A gain error was detected in the calibration of the thermal band of the Landsat ETM+ instrument, which affects all data acquired since launch. The 6% calibration error was found as a result the new hot-target calibration site and was confirmed by an independent calibration. The error resulted in a target temperature dependent error, where warmer targets appeared cooler than they are and cooler targets appeared warmer than they are.

The error was corrected in the US ground processing system on January 1, 2010. All data processed by the US processing system after this date will have the correction included in the calibration. Users with data processed before January 1, 2010 should reorder the data.

A similar error was detected in the Landsat-5 Thematic Mapper (TM) thermal band calibration. For more information on the TM error and the correction, see (Barsi, 2010) and (Padula, 2010).

5 REFERENCES

- Barsi, J.A., Schott, J.R., Palluconi, F.D., Helder, D.L., Hook, S.J., Markham, B.L., Chander, G. and O'Donnell, E.M., 2003, Landsat TM and ETM+ thermal band calibration. *Canadian Journal of Remote Sensing*, 29, 141-153.
- Barsi, J.A., 2010, Twenty-five years of Landsat Thermal Band Calibration. European Remote Sensing Opportunities: Systems, Sensors and Applications, Proceedings of the IGARSS Symposium held in Honolulu, HI, on 25-30 July 2010, (IEEE Geoscience and Remote Sensing Society).
- Coll, C., Galve, J.M., Sanchez, J.M., Caselles, V., 2010, Validation of Landsat-7/ETM+ Thermal Band Calibration and Atmospheric Correction with Ground Based Measurements. *IEEE Trans Geoscience and Remote Sensing*, 48, 547-555.
- Hook, S.J., Chander, G., Barsi, J.A., Alley, R.E., Abtahi, A., Palluconi, F.D., Markham, B.L., Richards, R.C., Schladow, S.G., Helder, D.L., 2004, In-flight validation and recovery of water surface temperature with Landsat-5 thermal infrared data using an automated high-altitude lake validation site at Lake Tahoe. *IEEE Trans Geoscience and Remote Sensing*, 42, 2767-2776.
- Padula, F.P., Schott, J.R., Barsi, J.A., Raqueno, N.G., Hook, S.J., 2010, Calibration of Landsat 5 Thermal Infrared Channel: updated calibration history and assessment of the errors associated with the methodology. *Canadian Journal of Remote Sensing*, **in press**.
- Schott, J.R., Barsi, J.A., Nordgren, B.L., Raqueno, N.G., de Alwis, D., 2001, Calibration of Landsat thermal data and application to water resource studies. *Remote Sensing Environment*, 78, 108-117.
- Turtle, R.R., 1999, ETM+ band 6 calibration report. PL2807E-T06298, Santa Barbara Research Center, Santa Barbara CA.

Monitoring the spectral accuracy of AHS images

Eduardo de Miguel, Rocío Rodríguez, Óscar Gutiérrez de la Cámara

Área de Teledetección - Instituto Nacional de Técnica Aeroespacial (INTA), Spain

demiguel@inta.es, crepadrc@inta.es, gutierrezcao@inta.es

ABSTRACT. The airborne sensor AHS is spectrally calibrated at the INTA calibration facility, with a resolution of 0.1 nm in the solar range and 10 nm in the thermal range. The calibration is usually performed twice a year, at the start and end of the flight campaign season. There is some uncertainty in the actual spectral position of AHS bands in operational imagery; this is due to the fact that the AHS status under flight conditions (temperature, vibrations...) could lead to small misalignments in the optics, spectrometer and focal plane impacting the bands position. Therefore, it is advisable to compute the actual spectral bands during AHS campaigns.

For the VNIR the water absorption feature around 935 nm is used. This feature causes a well defined shape on the at-sensor radiance curve even at the AHS 30 nm FWHM; we evaluate this shape for non-vegetated surfaces and compare it with a theoretical model. For the TIR the expected spectral radiance from water is used. Water was chosen due to its well known emissivity and because it is easy to locate water surfaces in most AHS images. The expected spectral radiance is estimated with MODTRAN from an initial guess of temperature and then compared with the AHS observed signal.

The application of these procedures to 2009 AHS imagery shows that the proposed methods are robust and have the required resolving power, and supports the idea that spectral position of AHS bands under flight conditions is kept within a small deviation with respect to laboratory measurements.

1 INTRODUCTION

The Airborne Hyperspectral Scanner (AHS) is an 80 bands radiometer based on a rotating mirror (i.e. a line or whiskbroom scanner), with variable FWHM (28 nm in the VNIR, 18 nm for SWIR, and 450/500 nm for TIR). It is maintained and operated by the Remote Sensing Laboratory at INTA (Spain) and it is being used in a number of remote sensing projects across Europe since 2005.

The AHS is spectrally calibrated in laboratory before and after each campaign season (typically 6 to 8 months). The calibration is performed by INTA staff using a dedicated monochromator and following a predefined procedure approved by the instrument vendor (ArgonST, USA). The expected accuracy of the spectral calibration is around 0.1 nm in the VNIR and SWIR and 10 nm in the TIR.

There is an uncertainty in the actual spectral position of AHS bands for operational campaigns. This is due to the conditions in which the instrument actually operates in-flight (temperature, vibration) and to specific stress events that the instrument is likely to suffer during the campaign season (extreme heating/cooling/humidity, or high accelerations during landing and take-off). The actual shift (if any) depends on the specific history of environmental conditions and/or stress events, and it is difficult to model it just from interpolation from pre- and post-campaign calibrations. Therefore, if the actual spectral bands in a specific dataset must be accurately

known, they must be estimated using the images themselves.

The purpose of this study is to detect this potential shift in actual, operational AHS images. Although this is a well known activity in remote sensing imagers, mainly in hyperspectral sensors (Gao, 2004; Guanter, 2006; Guanter, 2009), and it is indeed present in some processing packages like ATCOR4 (Richter, 2002), it has not been applied to AHS.

2 BACKGROUND

AHS is a whiskbroom scanner working from the visible to the thermal infrared. It is based on a single telescope and a dedicated spectrometer (Fernández-Renau, 2005). The primary optics uses a rotating mirror directing the terrain radiance to a cassegrain-type telescope with a pfund assembly. The collimated beam is directed through a single slit to the spectrometer. In the spectrometer, a combination of mirrors and dichroic filters is used to split the incoming beam to different gratings (see table 1). Each grating scatters its own subset of the incoming radiance which, after dedicated focusing optics, is recorded by an array of detectors in each focal plane. Considering this design, AHS could suffer specific spectral shifts in each port (i.e., each grating + focal plane), but also variable shifts within each port. On the other hand, problems in the primary optics could cause a shift common to all ports. In this study, and according to our experience, spectral shifts are supposed to be constant for each focal plane

Table 1. AHS ports with their nominal bandwidth

Spectral region	Spectral range (um)	Number of bands	FWHM (nm)
VNIR	0.45-1.0	20	28
SWIR	1.5-1.6	1	90
SWIR	1.9-2.5	42	18
MIR	3.0-5.0	7	300
TIR	8.0-13.0	10	500

The basic assumption in this work is that spectral features could be used to detect the spectral position in each port, even at the AHS moderate spectral resolution.

A preliminary test was used to display the feasibility of this approach in the VNIR bands. In this test, we selected an ASD-FS3 bare soil spectrum acquired simultaneously to an AHS image. The spectrum is propagated to the flight altitude using the MODTRAN interface MODO (www.rese.ch) with 2 nm resolution and resampled with the AHS nominal band set. The same location is found in the AHS image, and the observed VNIR spectrum is read and normalised. Figure 1 plots the observed and expected curves, certifying that a small shift is likely but not easy to detect.

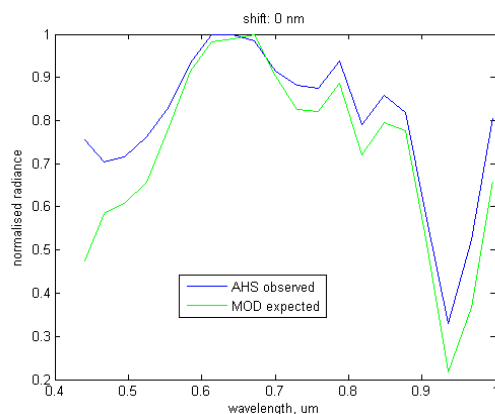


Figure 1. Expected versus observed normalised at-sensor radiance for a bare-soil target.

To complete this preliminary assessment in the VNIR, the MODO spectral at-sensor radiance is resampled with different AHS configurations, from nominal-10 nm to nominal+10 nm, in 1 nm steps. Each of these simulated spectra is compared against the AHS-observed: differences are computed and the one with the minimum RMS is selected as "correct band position" (figure 2).

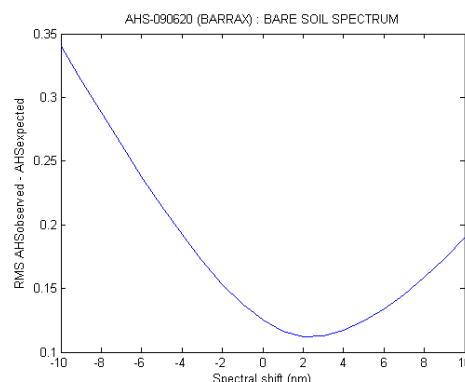


Figure 2. RMS error between (normalised) expected and observed at-sensor radiance as a function of the difference between the theoretical band center and the tested band center (i.e. *spectral shift*)

Figure 2 indicates that different spectral configurations result in different RMS errors in a systematic, coherent way; and therefore monitoring the spectral error seems fairly feasible, at least for VNIR. However, an operational procedure should be independent from ground measurements, even at the cost of some accuracy. Therefore, we chose to focus on the water absorption feature around 935 nm. This feature causes a well defined shape in the at-sensor radiance curve even at the medium spectral resolution of AHS (30 nm), and the minimum of this shape shifts with different values of the AHS band centers. Section 3 details this procedure.

For the estimation of shifts in the TIR range we could use the characteristic shape of calcite or quartzite emissivity spectra, compatible with the AHS bandwidth. However the calcite had to be discarded because its characteristic absorption is placed near AHS78, and this channel was too noisy during 2009 campaigns, which formed the bulk of the test data set for this work. Quartzite was discarded because pure pixels are too scarce to be used. Ozone absorption (Hook, 1996) was not considered because AHS is always operated at low altitude, and ozone concentration in the observation path is usually too low to be detected.

Another alternative is a full spectrum test, like the one presented for VNIR. It is proposed to evaluate the shift looking into the rather-flat spectrum from water. As seen in figure 3, the shape of the water emitted radiance is likely to depend on the specific band centers considered. In addition it is easy to find water bodies in most scenes, and no errors due to uncertainty in actual surface conditions or spectral emissivity are expected.

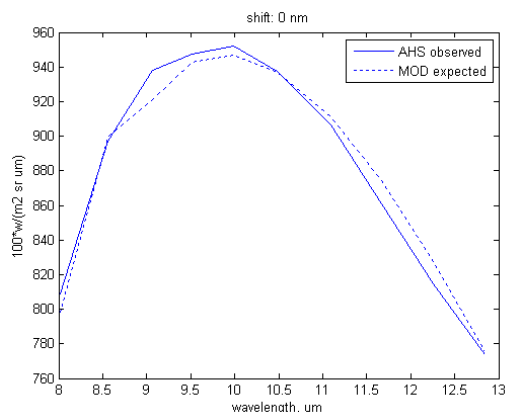


Figure 3. The at-sensor radiance over a water surface simulated by MODTRAN from ground truth data (MOD expected) plotted with the actual value recorded by AHS (AHS observed).

The following section details the automatic tests designed for VNIR and TIR.

3 METHODS

3.1 VNIR

First we estimated the theoretical shape of the water absorption region around 935 nm as seen by the AHS. We started from six ASD-FS3 spectrum from bare soil surfaces and white panels under different atmospheric conditions. The spectral at-sensor radiance of such targets was computed with MODO and resampled with three different AHS configurations, namely to those defined for the AHS images to be tested. The simulated signal was oversampled to 1 nm spectral resolution to define a fine-resolved minimum for each case. The average location of this minimum for each AHS configuration was finally annotated.

Next we open the image to be monitored, and randomly selected 512 pixels with a NIR to Red radiance ratio between 0.65 and 0.85 (an empirical threshold used to define bare soil pixels). We averaged the AHS-observed radiance and resampled it to sub-band resolution (0.025 band, i.e. 0.75 nm) using a spline interpolation.

Finally, we find the minimum of the oversampled spectra in the 0.8 to 1.0 microns and compare it with the one computed previously for the corresponding configuration. The difference between the observed and expected minimum is the estimated band shift.

3.2 TIR

As briefly outlined in section 2, a test focused in the overall shape of water emission was designed.

First the expected signal of a water surface is computed with MODTRAN from the in-situ

temperature measurements and atmospheric conditions; a small range of water temperatures and water vapour contents around the measured values is used to watch the effect of parameter uncertainty. This make the procedure valid also when no in-situ measurements, but only expected values, are available. Next, the estimated signals are resampled with different bands positions, from the nominal -160 nm to nominal +160 nm in 20 nm steps.

Each possible spectrum is compared with the AHS-measured at sensor radiance. The figure of merit to check how well both curves fit is the RMS error.

4 RESULTS

4.1 VNIR

The test was applied to a set of AHS images acquired during 2008 and 2009. Figure 4 shows the shift detected for each image. Points with the same marker symbol correspond to the same nominal band centers.

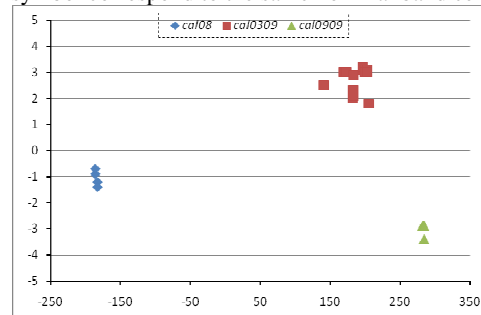


Figure 4. Estimated VNIR shift for a set of AHS images. X axis represents 2009 day-of-year. 3 series are plotted, each one corresponding to images acquired within the same flight season and therefore with the same laboratory spectral calibration (2008, March 2009 and Sept. 2009).

The figure supports the idea that shifts are detected by this procedure. Note that the value computed with different images from the same campaign season are very similar. Specially for the images acquired after the March 2009 calibration, spanning almost 3 months, there is no visible trend, i.e., the shift seems to be caused by a point event short after beginning of the flight campaign.

4.2 TIR

The TIR test was performed on two images. The first image was acquired over Athens for ESA's Thermopolis campaign (aimed to evaluate the role of remote sensing in Urban Heat Island studies). The second image corresponds to a local flight over INTA in the framework of a study on urban climate for the Spanish company INDRA. In both cases in-situ surface temperature and atmospheric water vapour measurements were made simultaneously to the image acquisition. In the Thermopolis image the ground truth

was collected by the Global Change Unit (University of Valencia) at Lake Marathonos. In the INDRA case, the target was a small pond close to INTA facilities, and the surface temperature and atmospheric conditions were measured by INTA staff. The results are shown in figures 5 and 6.

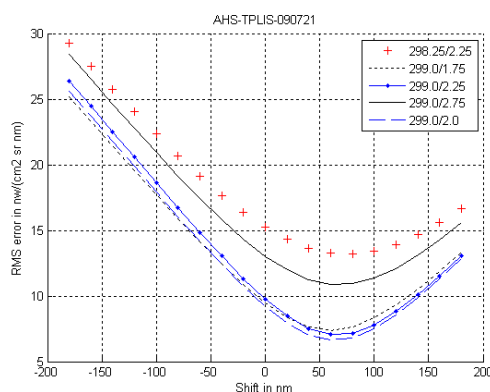


Figure 5. RMS error (in $\text{nw}/(\text{cm}^2 \text{ sr } \mu\text{m})$) between the expected signal and the observed signal for Lake Marathonos image as a function of the bandcenters, and for different atmospheric conditions and surface temperatures (see legend). The minimum error is found with a +60 nm shift with surface temperature 299 k and 2.0 gr/cm^2 atmospheric water vapour

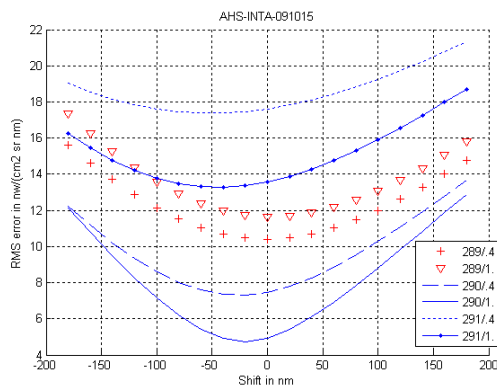


Figure 6. RMS error (in $\text{nw}/(\text{cm}^2 \text{ sr } \mu\text{m})$) between the expected signal and the observed signal for the INTA image as a function of the bandcenters, and for different atmospheric conditions and surface temperatures (see legend). The minimum error is found with a -20 nm shift with surface temperature 290 k and 1.0 gr/cm^2 atmospheric water vapour.

To assess the effect of FWHM uncertainty, a similar test was performed varying the FWHM instead of the band center. Figure 7 is a plot of the RMS error between the expected curve and the observed curve for different changes in the FWHM of all ten TIR bands. The case used is the INDRA nominal configuration (solid line in figure 6). Note that the difference in

curve-to-curve RMS (≈ 1 unit) is much smaller than those arising from shifting the band centers (≈ 8 units).

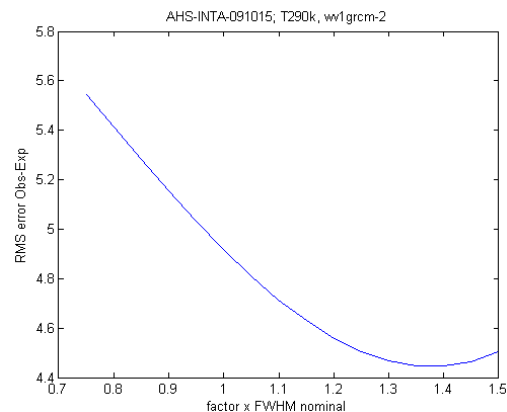


Figure 7. RMS error (in $\text{nw}/(\text{cm}^2 \text{ sr } \mu\text{m})$) for varying FWHM. FWHM factor 1.1 means an increase of 10% in the bandwidth. Curve obtained with water temperature 290 k, $\text{wv}=1.0 \text{ gr}/\text{cm}^2$, visibility 40 km, rural aerosol.

5 CONCLUSIONS

The application of the described procedures to 2009 AHS imagery shows that the proposed methods are robust and have the required resolving power, and supports the idea that spectral position of AHS bands under flight conditions is kept within a small deviation with respect to laboratory measurements.

Changes in the VNIR bands spectral position in the selected datasets are discrete, not continuous.

In the TIR region, atmospheric interference and FWHM has a second order effect in the correlation between observed and expected signals with respect to band center.

There is a correlation between changes in VNIR and TIR for the 2009 campaign, with shift being around 10% of the bandwidth in both cases. Anyhow, as this is not necessarily true always, the proposed methods work independently in each port.

6 ACKNOWLEDGEMENTS

We are very grateful to ESA and INDRA for encouraging the use of the images acquired for their projects in this study. We also acknowledge the support of the Global Change Unit from University of Valencia in all our AHS cal/val activities.

7 REFERENCES

- Fernández-Renau, A., Gómez, J. A., de Miguel, E., 2005. "The INTA AHS system". *Sensors, Systems, and Next-Generation Satellites IX*. Edited by Meynart, Roland; Neeck, Steven P.; Shimoda, Haruhisa. Proceedings of the SPIE, Volume 5978, pp. 471-478.
- Gao, B.C., Montes, M.J., Davis, C., 2004. "Refinement of wavelength calibrations of hyperspectral imaging data using a spectrum-matching

- technique". *Remote Sensing of Environment*, Vol. 90, Iss. 4, Pages 424-433.
- Guanter, L., Richter, R., Moreno, J., 2006. "Spectral calibration of hyperspectral imagery using atmospheric absorption features". *Applied Optics*, 45, 2360-2370.
- Guanter, L., Segl, K., Sang, B., Alonso, L., Kaufmann, H., and Moreno, J., 2009. "Scene-based spectral calibration assessment of high spectral resolution imaging spectrometers". *Optics Express*, 17, 11594-11606.
- Hook, S. J.; Okada, K., 1996. "Inflight wavelength correction of Thermal Infrared Multispectral Scanner (TIMS) data acquired from the ER-2". *IEEE Transactions on Geoscience and Remote Sensing*, vol. 34, issue 1, pp. 179-188.
- Richter, R., Schläpfer, D., 2002. "Geo-atmospheric processing of airborne imaging spectrometry data. Part 2: Atmospheric/topographic correction". *International Journal of Remote Sensing* 23, 2631-2649.

Relationship between evapotranspiration and rainfall variability in the Doñana region, Spain

García M., Fernández N., and Delibes, M.

(1) *Depto. de Biología de la Conservación. Estación Biológica de Doñana- CSIC.*

(2) *Americo Vespucio s/n. 41092 Sevilla, (Spain),*

Email: monicagarcia@ebd.csic.es

ABSTRACT- *Understanding how water-limited ecosystems cope with rainfall uncertainty, in particular with the rainfall component that is less predictable from year to year, can help to anticipate some of their responses to global change. In this work we propose a monitoring system to evaluate the stability to rainfall anomalies of four ecosystems with different water-use strategies in the Mediterranean region of Doñana (Spain). Time-series between 2000-2008 from MODIS and meteorological stations were used. The TVDI (Temperature Vegetation Dryness Index) was estimated as a surrogate of the ratio between actual and potential evapotranspiration deriving actual evapotranspiration from it. From the cross-correlograms of rainfall anomalies and evapotranspiration anomalies information related with ecosystem stability was extracted. In particular (i) the duration of the effects of rainfall perturbations on the ecosystem (resilience) that was found to be greater for perennial vegetation, especially xerophytic shrublands, and the resistance to change (resistance) that was lower for wetlands.*

1 INTRODUCTION

In Mediterranean ecosystems water is the main factor controlling ecosystem processes. In fact, the different vegetation types have evolved to adapt to a seasonal cycle characterized by a summer drought, predictable from year to year, and to cope with the high uncertainty of rainfall events during the rest of the year (Rambal et al., 2001). According to future climate studies rainfall uncertainty and drought are going to increase in the Mediterranean region (Chou et al. 2008).

For this reason, understanding how rainfall anomalies propagate across time and space and their persistence into biological processes (Telesca & Lasaponara 2006) might contribute to anticipating some ecosystem responses to future climate where changes in the distribution of intra-seasonal precipitation might have greater impact than changes in total annual rainfall (Weltzin et al., 2003)

In fact, ecosystem responses to rainfall in the temporal domain are not always correlated with total annual rainfall due to feedback and lagged effects (Goward & Prince, 1995). This “memory” of past events is ecosystem-specific (Schwinning et al, 2004) and is also related with their stability that can be described by two attributes, difficult to measure in practice. Resilience, that can be defined as the ability to return to its former state following a perturbation

and resistance that is the ability to avoid or resist change (Díaz., 2001).

In this work we propose a monitoring system to evaluate ecosystem resilience and resistance based on indicators from time series analyses.

We examined daily evapotranspiration as an indicator of ecosystem functioning of four ecosystems of the Mediterranean region of Doñana with contrasting water use strategies during 8 years. First, we evaluated to what extent annual and seasonal rainfall variability explain annual evapotranspiration and phenology patterns. Then, we evaluate the intra-seasonal impacts of the non-seasonal component of rainfall (hereinafter perturbations), to which ecosystems are less adapted, to assess ecosystem stability.

2 . STUDY SITE AND DATA USED

The study was performed in the Doñana region in south-western Spain (37.03°N, 6.46°W) a unique and highly biodiverse area of ~1 080 km². A rich variety of landforms and ecosystems representative of Mediterranean lowlands are present including wetlands, shrublands, grasslands, forests and agricultural areas (irrigated and non-irrigated). The climate is Mediterranean sub-humid, with mild and wet winters and dry and hot summers. Around 80% of annual rainfall concentrates between October and March with a prolonged summer drought (June to August). The Doñana region presents different protection levels but currently is subjected to human pressures modifying land use types, and groundwater

and surface hydrology threatening unique ecosystems such as the marshes or shrublands (Fernández et al, 2010). Phreatic evapotranspiration plays an important role in decreasing the net value of aquifer recharge to approximately (Trick and Custodio, 2007).

In this study satellite data from the MODIS-Terra sensor were used: Ts (Land Surface Temperature) (MOD11) (8 day average) and EVI (Enhanced Vegetation Index) (16 day composite) between 2000 and 2008. The period selected has an average annual rainfall of 535 mm, close to the long-term mean of 575 mm for the area (Trick and Custodio, 2007).

Meteorological data acquired included air temperature, wind speed, relative humidity and surface irradiance from 10 meteorological stations (Regional Government of Andalusia, RIA stations). They were averaged to be compatible with the 8-day interval of MODIS Ts and reflectance data. From the study region, a sample of pixels were selected for each vegetation type (n>6) based on homogeneity criteria regarding land cover type (> 75%) and were used to evaluate the surface fluxes at those specific sites.

3 METHODOLOGY

3.1. Estimating evapotranspiration from MODIS data

Instantaneous evapotranspiration (λEi) was estimated using the Temperature Vegetation Dryness index (TVDI) from Sandholt et al., (2002). The TVDI, based on the relationship between a vegetation index and Ts at a given date, is a simplification of the WDI (Water Deficit Index) from Moran et al., (1994).

The advantage of the TVDI is that does not require any micrometeorological data for calibration being suitable for operational purposes. Both approaches require a full range of states from full cover-high moisture to bare soil-low moisture which are present in the Doñana region along the year.

Those pixels with the lowest Ts form the “wet edge” with no water deficit while those with highest Ts form the “dry edge” where λE approaches zero. Increases in Ts are assumed to correlate linearly with turbulent fluxes. It also assumes that both soil and vegetation contribute to Ts proportionally to their cover (see Fig. 1).

One problem with triangle type models is that there is sometimes subjectivity involved in calculating wet and dry edges. We calculated systematically at each date the wet edge as the regression for quantile 5% and the dry edge as the 95% linear quantile regression.

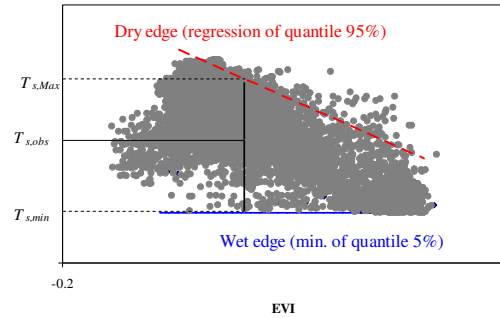


Figure 1: Example of the EVI -Ts scatterplot at DOY 209 of 2004 to estimate TVDI. The dry edge is shown in red (dashed line) and the wet edge in blue (solid line).

$$TVDI = \frac{T_{s,obs} - T_{s,min}}{T_{s,Max} - T_{s,min}} \quad (1)$$

where $T_{s,obs}$ is Ts observed at the pixel; $T_{s,min}$ the Ts at the wet edge; and $T_{s,Max}$ the Ts at the dry edge.

To obtain λEi from TVDI it was assumed that instead of TVDI being a proxy for soil moisture as in Sandholt et al., (2002) it was related with the ratio of λEd and λEpd (daily potential evapotranspiration). In this case we used λEpd from Penman-Monteith.

To obtain mean daily latent heat (λEd) from λEi it was assumed that the evaporative fraction (EF) is constant along the day, and the daily soil heat flux (Gd) is negligible (Bastiaanssen et al., 1998).

3.2. Lagged correlations between precipitation and evapotranspiration anomalies

To understand how the more erratic component of rainfall, the one associated with large-scale climate circulation, affects vegetation functioning we removed the seasonality from the signal. This also avoids obtaining spuriously high cross-correlations due to autocorrelation (Braswell et al., 1997) and allows evaluating ecosystem responses to events that are not as predictable from year to year as the seasonal cycle. Standardized precipitation anomalies (PPT_{anom}) were calculated at 4 different time scales each corresponding to antecedent rainfall accumulated during 8 days, 1 month, 3 months and 6 months. Standardized anomalies are calculated as deviations from the long-term mean divided by the standard deviation, for which they are equivalent to a z-score in case that the variables are normal.

PPT_{anom} can thus be considered as rainfall perturbations over-imposed on the seasonal rainfall signal. This rainfall component in the Doñana region should be related to inter-annual and intra-annual climatic variability of the Arctic Oscillation (AO), North Atlantic Oscillation (NAO) and Western Mediterranean Oscillation (WeMO) (Lopez-Bustins et al., 2008), overlapping with other residual non-cyclic components.

The MODIS derived evapotranspiration time series were first temporally interpolated for missing values using a cubic-spline procedure with tension 1.5. Then, Standardized evapotranspiration anomalies (ET_{anom}) were calculated at 8 day time scale. Inspection of cross-correlations between ET_{anom} and PPT_{anom} allows to evaluate for how long after the perturbation started its effects are still persisting on the functioning of vegetation (time during which there is a significant lagged correlation) and how strong its effects are (magnitude of the R coefficient) (García et al., 2010). The greater the cross-correlation is the lower is the resistance of ecosystem to change. The longer the lagged time during which cross-correlations are significant the lower is the resilience. Non-significant correlations indicate stability of the ecosystem to rainfall anomalies, and another source of disturbance should be driving the anomalies.

4 RESULTS AND DISCUSSION

4.1 Interannual variability of evapotranspiration

Figure 2 shows the 8-day time series of modelled evapotranspiration for each vegetation type. The 2004-2005 was a very dry year (169.8 mm) reflected by a drop in evapotranspiration values for all vegetation types but especially for wetlands in spring. Annual values were derived from these 8-day series to get correlations with annual and seasonal rainfall.

Linear-correlations (not lagged) at inter-annual time scales (Table 1) showed that only annual evapotranspiration from wetlands is significantly correlated with annual rainfall. In the case of xerophytic shrublands, fall rainfall has a significant role on annual ET levels.

The phenology of evapotranspiration (date of maximum evapotranspiration peak within the year) is determined by spring and annual rainfall (see Table 2) for hydrophytic shrubs, and only by spring rainfall in the case of wetlands. In both cases earlier peaks occur in drier years (positive correlation). According to the linear relationships founded, if average spring rainfall would be reduced by 50% the date of the annual evapotranspiration peak would be advanced 9 days for

hydrophytic shrublands and 6 days in the case of wetlands.

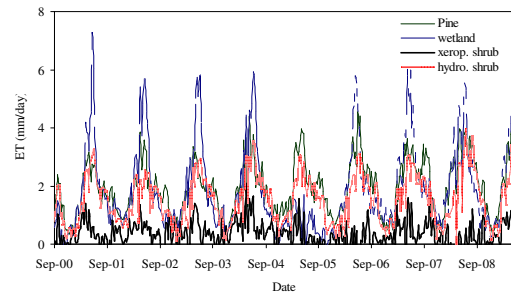


Figure 2: Time series of evapotranspiration (mm/day) derived from MODIS and meteorological data for four different vegetation types (2000-2008).

Table 1: Correlations between seasonal and annual rainfall and annual evapotranspiration. PPT_{OND} corresponds to fall rainfall, PPT_{JFM} to winter, PPT_{AMJ} to spring and PPT_{JAS} to summer. Bold figures indicate correlation significant at $p < 0.05$. $n = 8$ years

Rainfall effects on annual evapotranspiration				
	pine	wetland	Xerop. shrubs	Hydroph shrubs
PPT_{OND}	-0.55	0.46	0.72	-0.07
PPT_{JFM}	-0.34	0.27	-0.24	-0.58
PPT_{AMJ}	0.54	0.61	-0.21	0.51
PPT_{JAS}	0.33	0.74	0.09	0.5
PPT_{year}	-0.3	0.79	0.35	-0.07

Table 2: Correlations between the date of maximum annual evapotranspiration and seasonal and annual rainfall: PPT_{OND} corresponds to fall rainfall, PPT_{JFM} to winter, PPT_{AMJ} to spring and PPT_{JAS} to summer. Bold figures indicate correlation significant at $p < 0.05$. $n = 8$ years.

Rainfall effects on phenology				
	pine	wetland	Xerop. shrubs	Hydroph shrubs
PPT_{OND}	-0.08	0.4	-0.53	0.23
PPT_{JFM}	0.25	-0.37	0.0	0.51
PPT_{AMJ}	0.11	0.73	0.69	0.78
PPT_{JAS}	-0.5	0.69	0.35	0.45
PPT_{year}	0.0	0.47	-0.09	0.72

4.2. Propagation of rainfall anomalies at intra-seasonal time scales

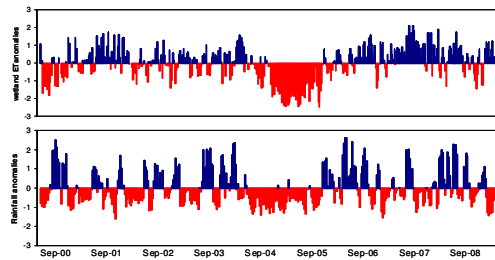


Figure 3: example of standardized evapotranspiration anomalies (upper panel) and standardized precipitation anomalies at 8-day time scale (lower panel).

Standardized precipitation anomalies (PPT_{anom}) and evapotranspiration anomalies (ET_{anom}) were cross-correlated (Figure 3). Inspection of the cross-correlograms (Figure 4) reveals that at intra-seasonal time scales the four ecosystem types tend to be more resilient to those PPT_{anom} occurring at time-scales of 8 days to 1-month. A decrease both in resilience and resistance is observed when the time scale of the anomaly increases.

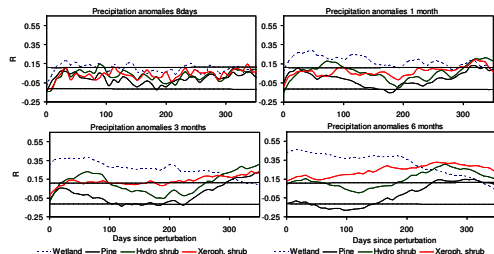


Figure 4: Cross-correlations between precipitation anomalies occurring at different time-scales and evapotranspiration anomalies. Lagged time since the beginning of the perturbation is shown in X axis. The value of R is significant ($p < 0.05$) above and below the horizontal lines.

The least resistant ecosystem type to PPT_{anom} according to our results were the wetlands (maximum lagged $R=0.46$ for 6 months antecedent rainfall) followed by xerophytic shrublands (maximum lagged $R=0.33$ for 6 months antecedent rainfall). Regarding resilience, although wetlands show a transient behaviour after rainfall perturbations, they always buffered within 1 year the effects of perturbation showing afterwards a stationary behaviour. This is reasonable as they are composed of annual plants. Their maximum response to rainfall anomalies takes place within the first month after the perturbation, while in the rest of ecosystem types the time of maximum response occur after 8 months. Thus, in

perennial vegetation (pine forests and shrubs) some of the perturbation effects propagate into the next year.

5 CONCLUSIONS

A simple monitoring system to evaluate the effect of rainfall anomalies on the functioning of vegetation is proposed and examined for four different ecosystem types in the Mediterranean region of Doñana (Spain). Evaluation of ecosystem stability in response to rainfall anomalies can be performed from inspection of cross-correlograms of rainfall and evapotranspiration anomalies. In addition, when there is a time lag between the onset of the perturbation and the response, forecasting and management actions could be considered.

Annual (12 months) and seasonal (three months) rainfall patterns explain only to some extent annual evapotranspiration in the case of wetlands and xerophytic shrublands. Pine forests and phreatophytic shrublands are not affected by interannual droughts as they can access phreatic water.

Zooming in at intra-seasonal time scales provides a better idea of the complex dynamics between rainfall and vegetation functioning. Each vegetation type is characterized by a different water-use strategy reflected in different cross-correlation patterns. According to our results, wetlands are the most resilient type but at the same time show a greater transient response, while perennial vegetation types show more resistance to change but higher persistence of effects into the next year, especially xerophytic shrublands without access to phreatic water.

From an ecological point of view and in the context of an increase in the uncertainty of rainfall as expected from global change scenarios, these analyses suggest that the long-term success in the case of pine forests and phreatophytic shrublands might depend on their capability to balance groundwater extractions and rainfall recharge while maintaining productivity levels. In the case of marshes and xerophytic shrublands their success would depend on their recovery potential after a drought sequence.

Acknowledgements

Postdoctoral financial support to MG was provided by the Dirección General de Investigación, Junta de Andalucía (Proyecto de Excelencia nr 01288). We acknowledge helpful discussions with Dr. J. Paruelo and Dr. J. Infante.

6 REFERENCES

- Bastiaanssen, W. G. M., Menenti, M., Feddes, R. A. and Holtslag, A. A. M., 1998, A remote sensing surface energy balance algorithm for land (SEBAL) - 1. Formulation. *Journal of Hydrology*, 213, 198-212.
- Braswell, B.H, Schimel, D.S., Linder, E. and Moore, B. III 1997, The response of global terrestrial ecosystems to interannual temperature variability. *Science*, 278, 870–872.
- Chou, W.W., Silver, W.L., Jackson, R.D., Thompson, A.W., and Allen-Diaz, B., 2008, The sensitivity of annual grassland carbon cycling to the quantity and timing of rainfall. *Global Change Biology*, 14 (6), 1382-1394.
- Díaz, S. 2001. Ecosystem function measurement, Terrestrial communities. In Encyclopedia of Biodiversity, vol. 2, by edited by S.A. Levin (San Diego, CA, Academic Press), pp. 321-327.
- Fernández, N., Paruelo, J.M. and Delibes, M., 2010, Ecosystem functioning of protected and altered Mediterranean environments: A remote sensing classification in Doñana, Spain. *Remote Sensing of Environment*, 114(1), 211-220.
- García, M., Litago, J., Palacios-Orueta A., Pinzón J. and Ustin S.L., 2010, Short-Term Propagation of Rainfall Perturbations on Terrestrial Ecosystems in Central California. *Journal of Applied Vegetation Science*, 13(2): 146-162
- Goward, S.N., and Prince, S.D.,1995, Transient Effects of Climate on Vegetation Dynamics: Satellite Observations, *Journal of Biogeography*, 22, 549-564.
- Lopez-Bustins J.A., Martin-Vide, J. and Sanchez-Lorenzo, A., 2008, Iberia winter rainfall trends based upon changes in teleconnection and circulation patterns. *Global and Planetary Change*, 63, 171-176.
- Moran, M.S., Kustas, W.P., Vidal, A., Stannard, D.I., Blanford, J.H. and Nichols, W.D.,1994, Use of ground-based remotely sensed data for surface energy balance evaluation of a semiarid rangeland. *Water Resources Research*, 30(5), 1339-1350.
- Rambal, S., 2001, Hierarchy and Productivity of Mediterranean-Type Ecosystems. In J. Roy, B. Saugier and H. Mooney, (Eds), *Terrestrial Global Productivity*, pp. 315-338). Academic Press.
- Sandholt, I., Rasmussen, K. and Andersen, J., 2002, A simple interpretation of the surface temperature/vegetation index space for assessment of surface moisture status. *Remote Sensing of Environment*, 79(2), 213-224.
- Schwinning, S., and Sala, O.E., 2004, Hierarchy of responses to resource pulses in arid and semi-arid ecosystems. *Oecologia*, 141 (2), 211-220.
- Telesca, L., and Lasaponara, R., 2006, Quantifying intra-annual persistent behaviour in SPOT-VEGETATION NDVI data for Mediterranean ecosystems of southern Italy. *Remote Sensing of Environment*, 101 (1), 95-103.
- Trick, T. and Custodio, E., 2004, Hydrodynamic characteristics of the western Doñana Region (area of El Abalarío), Huelva, Spain. *Hydrogeology Journal*, 12(3), 321-335.
- Weltzin, J.F., Loik, M.E., Schwinning, S., Williams, D.G., Fay, P.A., Haddad, B.M., Harte, J., Huxman, T.E., Knapp, A.K., Lin, G., Pockman, W.T., Shaw, M.R., Small, E.E., Smith, M.D., Smith, S.D., Tissue, D.T., and Zak, J.C., 2003, Assessing the Response of Terrestrial Ecosystems to Potential Changes in Precipitation. *BioScience*, 53(10), 941-952.

A remote sensing study of forests to estimate biophysical indicators and monitor CO₂ fluxes in Spain: the ÁRTEMIS project

M.A. Gilabert¹, F. Maselli², B. Martínez¹, A. Moreno¹, F. Camacho³, M. Chiesi², F.J. García-Haro¹, J. Meliá¹, A. Pérez-Hoyos¹, A. Verger¹

(1) Remote Sensing Unit, Facultat de Física, Universitat de València, Dr. Moliner, 50. 46100-Burjassot, Spain

(2) IBIMET-CNR, Via Madonna del Piano, 10. 50019-Sesto Fiorentino (FI), Italy

(3) EOLAB, Parc Científic Universitat de Valencia. 46980-Paterna, Spain

e-mail: m.amparo.gilabert@uv.es

ABSTRACT- The aim of the ÁRTEMIS project is to develop optimized remote sensing-based procedures to estimate *fAPAR* (the fraction of absorbed photosynthetically active radiation) in Spanish forests, and to monitor the CO₂ fluxes between these ecosystems and the atmosphere. At this first stage of the project, the C-Fix model is applied to estimate monthly *GPP* (gross primary production) at regional scale. The model estimates *GPP* by means of the general relation $GPP = \epsilon APAR$, where ϵ is a light use efficiency factor, and *APAR* (absorbed photosynthetically active radiation) is obtained from the product of *fAPAR* and *PAR* (photosynthetically active radiation), which in turns is obtained from temperature and precipitation data by means of an artificial neural network (ANN) procedure. The original C-Fix methodology is improved by using more abundant ancillary information and operational and robust strategies (calibrated for the study area) to derive *fAPAR* from new generation sensor facilities. The procedure is applied to forest areas in Spain by using an optimized land cover map generated from available land cover maps at coarse and medium spatial resolutions.

1 INTRODUCTION

Forests have an important role in regulating both water and carbon cycles. The necessity for monitoring and quantifying the amount of carbon accumulated within forests has recently increased in view of the application of the Kyoto Protocol and related documents.

Total forest production is generally indicated as gross primary production (*GPP*), which corresponds to the carbon entered the ecosystems and accumulated through photosynthesis. About half of *GPP* is respired by plants, thus the difference between carbon gain via *GPP* and carbon loss through plant respiration is defined as net primary production (*NPP*) (MacCallum et al., 2009). At large scales, carbon fluxes (i.e. *NPP*) cannot be directly observed. Therefore, a variety of methods have been developed to estimate them (MacCallum et al., 2009). Among all the existing models, production efficiency models (PEMs) have been developed to monitor primary production, taking advantage of satellite data. PEMs are based on the theory of light use efficiency (LUE) which states that a relatively constant relationship exists between photosynthetic carbon uptake and radiation receipt at the canopy level. PEMs typically require inputs of meteorological data (i.e. radiation, temperature and others) and the satellite-derived fraction of absorbed photosynthetically active radiation (*fAPAR*).

In this context, the ÁRTEMIS project aims to develop optimized remote sensing-based procedures to estimate *fAPAR* in Spanish forests, and to monitor the CO₂ fluxes between these ecosystems and the atmosphere. This work presents the experimental procedure to estimate monthly *GPP* because of its need for the subsequent computation of net forest carbon fluxes over Spain. To reach this objective a straightforward model (C-Fix) is applied which uses the relationship between photosynthetically active radiation absorbed by plant canopies (*APAR*) and the productivity of those canopies.

2 C-Fix MODEL

The C-Fix model is a Monteith type parametric model which accounts for the dependence of photosynthesis on vegetation type and temperature (Maselli et al., 2009). Satellite-derived *fAPAR* is combined with field based estimates of incoming solar radiation and air temperature. The C-Fix model provides estimates of monthly *GPP* and only requires the tuning of a few coefficients. In the current case, monthly *GPP* for forests ($\text{g m}^{-2} \text{month}^{-1}$, *g* refers to grams of carbon) is computed by:

$$GPP = \epsilon(T, W) \sum_{z=1}^{30} fAPAR_z PAR_z \quad (1)$$

where ϵ is the LUE coefficient for that land cover type (g MJ^{-1} (APAR)) that describes the efficiency of a plant in using radiation to produce dry matter and depends on temperature and water; $fAPAR_z$ is the daily fraction of PAR absorbed by forests; PAR_z is the daily photosynthetically active radiation ($\text{MJ m}^{-2} \text{day}^{-1}$).

3 DATA SET

3.1. Meteorological data

Daily meteorological data concerning global solar radiation, maximum and minimum temperature (T_{\max} and T_{\min}), and precipitation (P) supplied by the Spanish Meteorological Agency (AEMet) are used. The experimental dataset includes daily global radiation and temperature (and precipitation) at about 40 and 600 stations for the year 2008, respectively. Around 65% of the data, randomly distributed, are considered to train the ANN model and the rest of the data (*test data*) are used to perform validation procedures. An example of these data is presented in Figure 1.

3.2 Remote sensing data

MODIS/TERRA+AQUA reflectances at nadir sun-view geometry (MCD43A1) are used in this study to derive daily $fAPAR$ maps. These products have been downloaded from <http://edcdaac.usgs.gov>.

The MOD43B1 product provides atmospherically corrected cloud cleared BRDF data for MODIS land spectral bands. The Ross-Li kernel-driven model is used to determine the global set of parameters (k_0 , k_1 and k_2) describing the BRDF of the land surface.

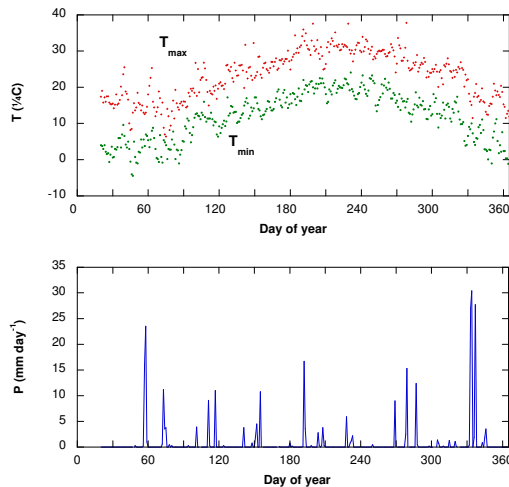


Figure 1. Example of meteorological data (Manises station, near the city of Valencia) for the year 2008. Top: maximum and minimum temperatures; bottom: precipitation.

4 DATA PROCESSING

The steps of the procedure to compute the GPP are (Maselli *et al.*, 2006): (1) Estimation of daily global radiation and PAR , (2) estimation of daily $fAPAR$ (3) estimation of the LUE coefficient (Figure 2), and (4) incorporation of optimized forest land cover information.

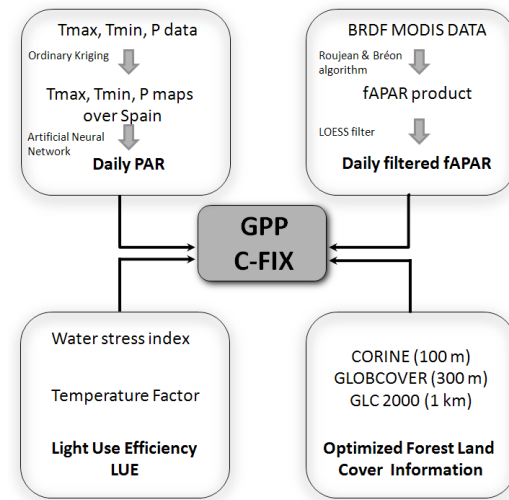


Figure 2. Methodology proposed to derive monthly GPP at 1 km for the Spanish forests.

4.1 Estimation of daily global radiation

The PAR is defined as the 46.4% of the global solar radiation (H) arriving on the surface composed between $0.4\text{--}0.7 \mu\text{m}$. H is a function of the extraterrestrial radiation (H_0) and the atmospheric constituents, represented by the total transmittance τ (Moreno *et al.*, these proceedings). In this case, daily PAR estimates are obtained by training an Artificial Neural Network (ANN), using radiation ground measurements. The inputs for this model are the maps of daily T_{\max} , T_{\min} and P derived by interpolating the observed T_{\max} , T_{\min} and P values (station data) using the ordinary kriging method.

Figure 3 shows the scatterplot of the PAR estimated vs. observed for the stations considered in the *test data*. Results have shown that the ANN approach estimates PAR more accurately than other proposed models (Moreno *et al.*, these proceedings) with a $RMSE=1.46 \text{ MJ m}^{-2} \text{day}^{-1}$ and $r = 0.93$.

Figure 4 shows an example of daily PAR at 1 km derived from the ANN method for a day of March. PAR images are rather homogeneous, showing lower values in cloudy areas.

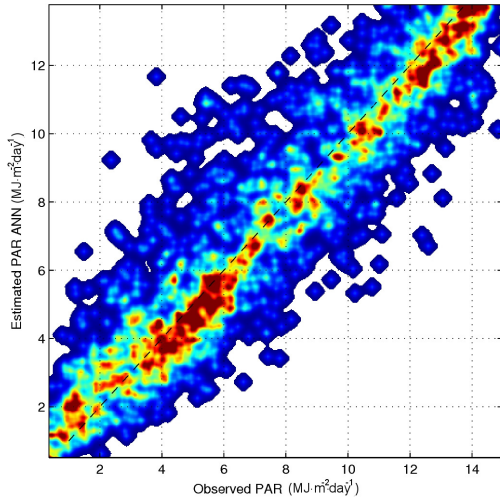


Figure 3. Scatterplot of the estimated vs. observed *PAR* with the ANN method.

4.2 Estimation of daily *fAPAR*

Daily *fAPAR* at 1 km over the Iberian Peninsula is derived by applying the algorithm from Roujean and Bréon (1995) to MODIS/Terra BRDF reflectance data.

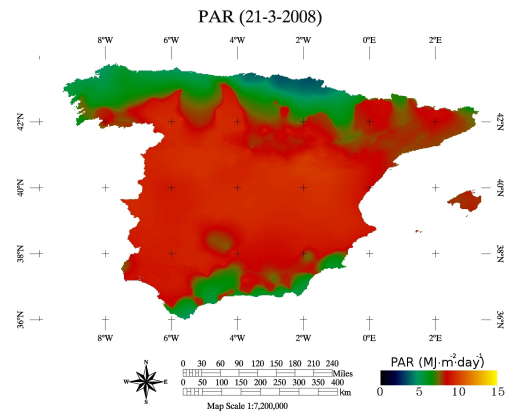


Figure 4. Example of the daily estimated *PAR* map at 1 km spatial resolution over Spain from the ANN method for 21th of March.

The algorithm used is based on a linear relationship between the vegetation index *RDVI* computed in an optimal geometry close to the backscattering direction and the daily *fAPAR*. This is an operational algorithm actually implemented on the Satellite Application Facility on Land Surface

Analysis (Land-SAF) system (García-Haro et al., 2008).

Following Roujean and Bréon (1995), the *fAPAR* is estimated from the following relationship:

$$fAPAR = 1.81 RDVI_{opt} - 0.21 \quad (2)$$

where $RDVI_{opt}$ refers to a new vegetation index (Roujean and Bréon, 1995) in the optimal geometry ($\theta_s=45^\circ$, $\theta_v=60^\circ$, $\phi=0$). To compute the *fAPAR* from remotely sensed data, it is needed first to be able to characterize the BRDF in order to compute the *RDVI* reflectance in the optimal geometry. Then, the $RDVI_{opt}$ is computed as follows:

$$RDVI_{opt} = (NDVI \times DVI)^{1/2} = \frac{NIR_{opt} - R_{opt}}{\sqrt{NIR_{opt} + R_{opt}}} \quad (3)$$

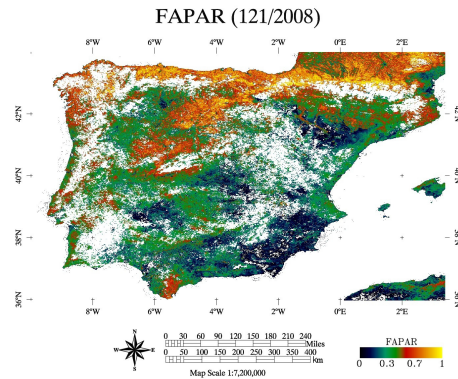
where

$$R_{opt} = k_0(R) - 0.240k_1(R) + 0.202k_2(R) \quad (4)$$

$$NIR_{opt} = k_0(NIR) - 0.240k_1(NIR) + 0.202k_2(NIR) \quad (5)$$

k_0 , k_1 and k_2 refer to the BRDF coefficients.

Figure 5 (top) shows an example of a daily *fAPAR* map derived from the above methodology belonging to the spring season. A large amount of gaps (white color) are observed for this particular. This is mainly due to atmospheric conditions (e.g., clouds and haze) or poor quality data caused by instrumentations problems. To solve this problem a simple robust method based on the LOESS (*locally weighted scatterplot smoothing*) method (Cleveland & Devlin 1988) is applied to provide a daily *fAPAR* time series without data gaps and data drop-outs.



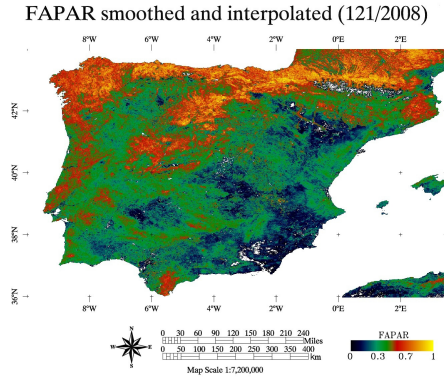


Figure 5. Original *fAPAR* estimates (top) for a day of spring, and filtered *fAPAR* (bottom) product from the LOESS approach.

LOESS consists of a low-degree polynomial function fitted to a subset of the time series. The polynomial is fit using weighted least squares. The biggest advantage of LOESS is the fact that it does not require the specification of a function to fit a model to all of the considered data. Instead only a smoothing parameter value and the degree of the local polynomial are needed. Many of the details of this method, such as the degree of the polynomial model and the weights, are flexible. In our case, the MODIS quality flag (QF) information has been taken into account in order to compute the weights associated in the LOESS filter. The equation $w=1/(QF-0.5+1)$ is used to compute the weights of the series using a polynomial of order five and a smoothing parameter of eight. Figure 5 (bottom) shows the filtered product from the LOESS approach. As can be observed the large quantity of white pixels in the original image have been properly filtered and a reliable spatial *fAPAR* distribution is obtained.

Figure 6 shows an example of the original (dash line) and filtered (hard line) *fAPAR* time series for a pixel located in Galicia (north Iberian Peninsula). It is demonstrated the ability of LOESS method to detect unlikely *fAPAR* values (data drop-outs) and provide reliable daily *fAPAR* estimates.

4.3 Estimation of LUE coefficient

The proposed C-Fix model (Equation 1) is a variant of the general formulation that includes the possible effect of water stress and temperature on photosynthesis by means of the LUE coefficient.

$$\epsilon(T, W) = \epsilon_m C_{ws} T_{cor} \quad (6)$$

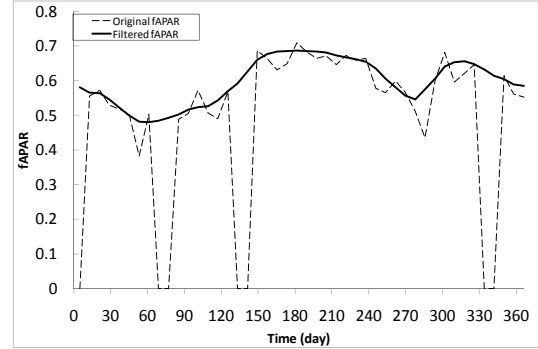


Figure 6. Original and filtered *fAPAR* time series for a pixel located in Galicia (north Iberian Peninsula).

Then, the LUE coefficient is computed as follows:

where a constant values of $1.4 \text{ gC MJ}^{-1}(\text{APAR})$ is proposed for ϵ_m . This value is consistent with those previously reported for various forest ecosystems, which generally range from 1.1 to $1.6 \text{ gC MJ}^{-1}(\text{APAR})$ (Maselli et al., 2009). C_{ws} is the water stress index obtained as:

$$C_{ws} = 0.5 + 0.5 AET/PET \quad (7)$$

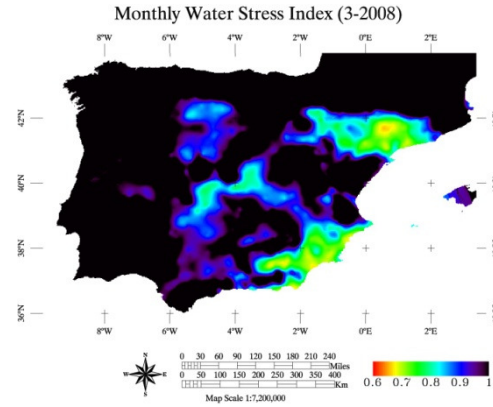


Figure 7. Monthly water stress index derived from temperature and precipitation data.

The *AET* and *PET* are the actual and potential evapotranspiration, respectively. The *PET* is computed from monthly temperature data following the Thornthwaite's approach (Jensen and Haise, 1963). For simplicity, *AET* can be assumed to equal precipitation when this is lower than *PET* over a period of two months. Figure 7 shows an example of the monthly water stress index, C_{ws} , which can vary between 0.5 (when strong water shortage reduces photosynthesis to half of its potential value) to 1 (when there is no water shortage and photosynthesis reduction).

T_{cor} is a dimensionless correction factor (computed on a monthly basis for the forests), which

depends on temperature, as suggested by Veroustraete et al. (2002),

$$T_{cor} = \left[\exp \left(C_1 - \frac{\Delta H_{a,P}}{RT} \right) \right] \left[1 + \exp \left(\frac{\Delta S - \Delta H_{d,P}}{RT} \right) \right] \quad (8)$$

where $C_1=21.77$; $\Delta H_{a,P}$ is the activation energy equal to $52\,750\text{ J mol}^{-1}$; R is the universal gas constant, equal to $8.31\text{ J K}^{-1}\text{ mol}^{-1}$; T is the monthly air temperature (K); ΔS is the entropy of the denaturation equilibrium of CO_2 equal to $704.98\text{ J K}^{-1}\text{ mol}^{-1}$; $\Delta H_{d,P}$ is the deactivation energy equal to $211\,000\text{ J mol}^{-1}$.

4.4. Optimized Forest land cover information

The land cover information is extracted from the classification proposed by Pérez-Hoyos and García-Haro (2009) (figure 8). This work evidences important inconsistencies among the most representative land cover cartographies in the Iberian Peninsula and proposes an optimized land cover map from the GLC2000 (Global Land Cover) (1 km), CORINE Land Cover (100 m) and GLOBCOVER (300 m) classifications. The broadleaved, coniferous and mixed forests as well as the sclerophyllous vegetation has been considered as forest land cover type to compute the monthly GPP.

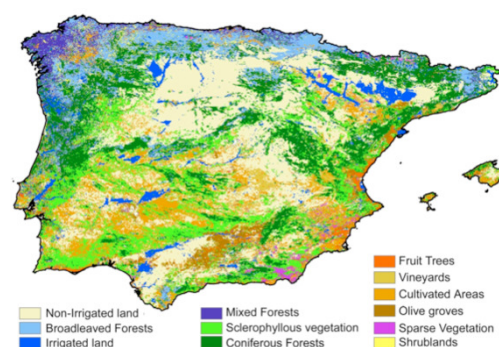


Figure 8. Optimized land cover proposed by Pérez-Hoyos and García-Haro (2009).

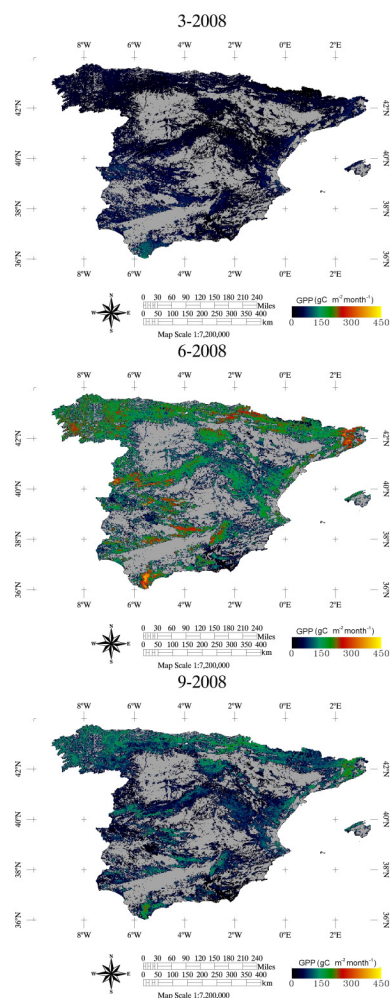
5 RESULTS

The C-Fix GPP estimates derived from the above methodology are shown in figure 9 (monthly GPP images for March, June, September, and December). The figure 9 clearly shows the different forest photosynthetic activity throughout the year, with lower values during winter time. The highest values, reached in summer time mainly in northern forests, are

compatible with the values found by other authors (Maselli et al., 2006; Veroustraete et al., 2006).

6 CONCLUSIONS

The current paper presents a complex multi-step methodology aimed at combining ground and satellite data to assess forest production patterns over the Spanish national territory. The preliminary results obtained are encouraging and generally confirm the efficiency of the approach applied. A validation exercise against ground data is however needed to quantify the actual accuracy of the methodology and its possible limitations. This exercise will be completed as soon as ground references of gross and net forest production become available.



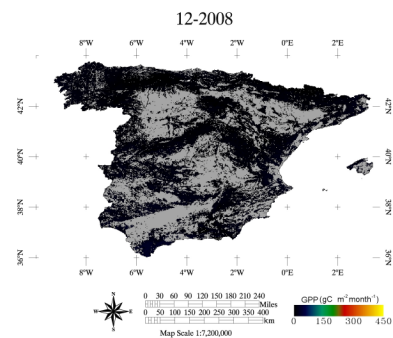


Figure 9. Examples of monthly *GPP* estimated for the different seasons. Grey: non-forestal areas, excluded from the study.

The Spanish Ministry of Science and Innovation (ÁRTEMIS CGL2008-00381) financed this study. Meteorological data were provided by the AEMet.

REFERENCES:

- Cleveland, W.S. and Devlin, S.J., 1988, Locally Weighted Regression: An Approach to Regression Analysis by Local Fitting. *Journal of the American Statistical Association*, **83**, 596-610.
- García-Haro, F. J., Camacho, F., Meliá, J., 2008, *Product user manual (PUM) vegetation parameters (FVC, LAI, FAPAR). SAF/LAND/UV/PUM-VEGA /2.1.* 53 pp. (Document online at <http://landsaf.meteo.pt>).
- Jensen, M. E., & Haise, H. R. (1963). Estimating evapotranspiration from solar radiation. *Journal of the Irrigation and Drainage Division ASCE*, **89**, 15-41.
- Maselli, F. Barbati, A., Chiesi, M., Chirici, G., Corona, P., 2006. Use of remotely sensed and ancillary data for estimating forest gross primary productivity in Italy. *Remote Sensing of Environment*, **100**, 563-575.
- Maselli, F., Papale, D., Puletti, N., Chirici, G., Corona, P., 2009, Combining remote sensing and ancillary data to monitor the gross productivity of water-limited forest ecosystems. *Remote Sensing of Environment*, **113**, 657-667.
- McCallum, I., Wagner, W., Schimullius, C., Shvidenko, A., Obersteiner, M., Fritz, S., Nilsson, S., 2009. Satellite-based terrestrial production efficiency modeling. *Carbon Balance and Management*, 4-8.
- Moreno, A., Gilabert, M.A., Martínez, B., 2010 Daily photosynthetic active radiation (PAR) images to estimate carbon fluxes at regional scale: A case study in Spain. *Proceedings of the 3rd International Symposium RAQSS*, 27 Sep-1 Oct, Torrent, Valencia (in this volume).
- Pérez-Hoyos, A. and García-Haro, F.J., 2009. Signaturas temporales para discriminar las cubiertas vegetales en la Península. *Proceedings of XIII Congreso de la AET*. Calatayud (Zaragoza), 23-26 Septiembre 2009, pp. 593-596.
- Roujean, J.L. and Bréon, F.M., 1995, Estimating PAR absorbed by vegetation from Bidirectional Reflectance Measurements. *Remote Sensing of Environment*, **51**, 375-384.
- Veroustraete, F., Sabbe, H., Eerens, H., 2002. Estimation of carbon mass fluxes over Europe using the C-Fix model and Euroflux data. *Remote Sensing of Environment*, **83**, 376-399.

Evaluation of Evapotranspiration retrieved for the 1981-2001 period from PAL database

V. Hidalgo¹, J. Sobrino¹, J.C. Jiménez-Muñoz¹, Y. Julien¹, C. Mattar¹, B. Franch¹, G. Soria¹, R. Oltra-Carrio¹, J. Cuenca¹

¹ Global Change Unit, Image Processing Laboratory, Parque Científico, Universidad de Valencia, Spain.

m.victoria.hidalgo@uv.es, jose.sobrino@uv.es

ABSTRACT- Pathfinder AVHRR Land (PAL) has been used for the retrieval of daily Evapotranspiration (ET_d) at global scale between 1981 and 2001. In this work, ET has been estimated as a residual of surface energy balance, through the use of the Evaporative Fraction (EF) concept. The PAL dataset used in this work is based of 10-day composite images with a spatial resolution of 0.1° . From this dataset, geophysical parameters such as Land Surface Temperature (LST), Normalize Difference Vegetation Index (NDVI), albedo and Land Surface Emissivity (LSE), have been estimated to retrieve net radiation flux (R_n). Additionally, fluxes at global scale are used from ERA-40 and ERA-interim database to estimate EF. Due to the different spatial resolution between PAL dataset ($0.1^\circ \times 0.1^\circ$), ERA-40 ($2.5^\circ \times 2.5^\circ$) and ERA-interim ($1.5^\circ \times 1.5^\circ$), these two land surface models have been rescaled through a cubic interpolation to 0.1° spatial resolution.

ET_d images have been compared with different flux tower data over North America (Walker Branch and Harvard). The study shows a good correlation between in situ data and fluxes estimated from AVHRR images with a RSME lower than 1 mm d^{-1} .

Additionally, we have studied the most representative soil classes for the different latitudes in terms of ET values. To complete this work, we studied the reliability of the data in the validation. The PAL dataset is a composite of 10 days, therefore the exact day is unknown for each pixel. For both station data (Walker Branch and Harvard), we consider the first day in each composition. This introduces an error around $0.3 \text{ mm} \cdot \text{d}^{-1}$ in the winter months. In the summer months this error is greatly increased, with errors of up to $2.7 \text{ mm} \cdot \text{d}^{-1}$.

1. INTRODUCTION

In the quest to accurately analyse global hydro-climate conditions as well as quantify and predict the components of the current and future global water cycles and related water resources, evapotranspiration is regarded as one of the critical fluxes.

Conventional techniques essentially provide point measurements, which usually are not representative of the regions because of the heterogeneity of land surfaces and the dynamic nature of heat transfer processes. Other techniques using remotely sensed data (Wang et al., 2007 and Song et al., 2000) have been undergoing refinement and have been provisionally analyzed at a global scale (Wang and Liang, 2008). However, data availability and sensitivity to retrieval and interpolation errors (in temperature and vegetation properties) continue to be significant issues with these sorts of techniques. As such, reliable and comprehensive direct and/or derived measurements of global or large-scale evapotranspiration remain elusive (Shlosser and Gao, 2010).

On the other hand, the study of evapotranspiration for large periods of time can be used to analyze the global water cycle for a better understanding of feedbacks in the coupled system as they affect the global water cycle and the uncertainties in coupled climate-hydrological model predictions using a combination of model ensembles and observations. The difficulty to obtain in situ data at global scale and the low temporal coverage of remote sensing data at global scale, make this work difficult to perform.

In an attempt to obtain daily evapotranspiration (ET_d) at global scale over an extended period of time, in this work, Pathfinder AVHRR Land (PAL) has been used. PAL is a large database of satellite images available which provides global images of the Earth at an $8 \cdot 8 \text{ km}$ spatial resolution, and at a 10-day temporal resolution, from July 1981 until September 2001. These images have been agreed with *ERA-40* and *ERA-Interim* data. The ERA-40 presents a time period from 1956 to 2002 and it was further replaced by the ERA-Interim (1989 to nowadays). The results obtained have been analyzed in terms of latitude as well as depending of vegetation class. In addition, we studied the reliability of the results obtained and

whether it is appropriate to use PAL dataset for the production of ET_d.

2. DATASET

2.1 Pathfinder AVHRR Land (PAL)

The NASA/NOAA-sponsored Earth Observing System Pathfinder projects produced time series of global data sets for use in climate change research. Pathfinder AVHRR Land (PAL – Smith et al., 1997) is a large database of satellite images available which provides global images of the Earth at an 0.1-0.1 degree spatial resolution, and at a 10-day temporal resolution, from July 1981 until September 2001. For each 10-day time-period four composite images are available, at visible (red — Ch1), near infrared (Ch2) and thermal infrared (Ch4 and Ch5) wavelengths, as well as an image of NDVI.

NDVI values during each 10-day period are used for the compositing technique, called Maximum Value Composition (MVC). This technique consists in selecting the highest value of NDVI during each 10-day period for each pixel, which removes most of the cloudy pixels (Holben, 1986). PAL dataset is corrected from atmospheric effects using a Rayleigh correction following the work of Gordon et al. (1988), including a correction for ozone absorption, following McPeters et al. (1993). No geometrical correction was applied to PAL dataset, for the reason that illumination and viewing angle data are not available at continental scale.

2.2 ERA-40 and ERA-Interim data

The ERA-40 reanalysis (Uppala et al., 2005) present a database of several meteorological data at global scale (2.5° x 2.5°) for forecasting and climatologic analysis. The ERA-40 data are available from 1956 to 2002 and has been upgrated with by the ERA-Interim (1989 to nowadays). Both ERA-40 and Interim data were used in this work. Despite the fact that spatial resolution are different in both reanalysis datasets (ERA-40 data presents a spatial resolution about 2.5° x 2.5° and ERA-Interim data closely 1.5° x 1.5°), both datasets were interpolated to 0.1°x0.1°. The variables used in this work are Surface Net Radiation (W·m⁻²), Surface Sensible heat flux (W m⁻²), surface latent heat flux (W·m⁻²), downwelling surface thermal radiation downwards (W·m⁻²) and Evapotranspiration (mm day⁻¹). These variables are provided four times daily (0,6,12 and 18 UTC) between 1981 and 1988 in the case of ERA-40, and from 1989 to 2001 in the case of ERA-Interim at the same time period.

3. METHODOLOGY

In this work, ET_d has been estimated as a residual of surface energy balance, and using the concept of “Evaporative Fraction” (EF) which is defined as the ratio of latent heat flux and available radiant energy. To obtain ET_d we have assumed that the evaporative fraction at daily scale is similar to the instantaneous evaporative, according to Crago (1996). On the other hand, the daily soil heat flux, G, can be approximated to 0. Thus daily evapotranspiration, can be obtained according to equation 1:

$$ET_d = \frac{EF_i \cdot Rn_d}{L} \quad (1)$$

where Rn_d is daily net radiation, EF_i is the instantaneous evaporative fraction and L is latent heat vaporization.

3.1 Net radiation

Rn_d can be obtained from remote sensing data though the instantaneous net radiation. The instantaneous net radiation, Rn_i, is obtained by equation 2;

$$Rn_i = (1 - \alpha) \cdot K_{sune} \cdot \tau \cdot \sigma \cdot \varepsilon \cdot T_s^4 + \varepsilon \cdot L^\downarrow \quad (2)$$

where α is the albedo, which is obtained as average of channels 1 and 2 of surface reflectivity. K_{sun} is the solar constant, e is the Earth orbit excentricity (in astronomical units), τ is the total transmissivity of the atmosphere, σ is the Stephan Boltzmann, ε is the surface emissivity, T_s is the land surface temperature and L^\downarrow is the incoming longwave radiation.

Total transmissivity is estimated as product of incoming transmissivity and outgoing transmissivity. Incoming transmissivity is estimated through Chavez’s method (Chavez, 1996), and the outgoing transmissivity through the average of outgoing transmissivity for all atmospheres as simulated with MODTRAN code (Berk et al. 1989).

Emissivity is obtained from the NDVI Threshold method and land surface temperature from the split window method (Sobrino and Raissouni, 2000). L^\downarrow is retrieved from ERA-40 and ERA-Interim data.

The change from instantaneous to daily values of net radiation may be carried out by using the ratio between both values ($Cd_i = Rn_d / Rn_i$) according to Sobrino et al. (2007), where Cd_i depends of the day of the year (DOY) and overpass time, t .

In this work, Cd_i was estimated by using net radiation fluxes measured in a meteorological station located in the East coast of the Iberian Peninsula. The obtained coefficients are show in equation 3.

$$Cdi = a \cdot DOY^2 + b \cdot DOY + c$$

$$a = 0.000001t^2 - 0.000026t + 0.000161 \quad (3)$$

$$b = -0.000325t^2 + 0.008465t - 0.052215$$

$$c = 0.039925t^2 - 1.009425t + 6.443925$$

3.2 Evaporative fraction

Instantaneous evaporative fraction can be written as function of daily evapotranspiration, ET_d , and daily net radiation, Rn (eq. 4).

$$EF = \frac{L \cdot ET_d}{Rn_d} \quad (4)$$

To obtain this parameter, we have used ET_d and Rn_d fluxes at global scale from ERA-40 between 1981 and 1989. From 1989 on, these fluxes are used from ERA-interim since these latter have a better spatial resolution. Due to the different scale between PAL dataset ($0.1^\circ \times 0.1^\circ$), ERA-40 ($2.5^\circ \times 2.5^\circ$) and ERA-interim ($1.5^\circ \times 1.5^\circ$), these two land surface models have been rescaled through a cubic interpolation to 0.1° spatial resolution.

4. RESULTS AND DISCUSSION

ET_d was retrieved from the PAL database from July 1981 until September 2001, by using the methodology presented above. As an example, figure 1 shows the ET_d at global scale from PAL dataset 10-day composite map on first of July of 1995. ET_d values vary between zero and 3 millimetres per day.

In order to evaluate the above methodology, we have selected 2 Ameriflux stations with a representative land cover at PAL spatial resolution (several km in all directions): Walker Branch station (35.97° N, 84.28° W) and Harvard forest station (42.53° N, 72.17° W). Figure 2 show the comparison between ET_d estimated from AVHRR, ET_d from ERA-interim and ET_d from the different Ameriflux stations during 1995. For both station, ET_d obtained from AVHRR underestimate the *in situ* data. However, in both cases, the values obtained from AVHRR data show a good correlation with *in situ* data ($0.8 \text{ mm} \cdot \text{d}^{-1}$) and an error lower that 1 millimetre per day.

A similar correlation is obtain when we compare the ET_d values from ERA-40 and ERA-interim whit *insitu* data, obtaining an error for Walker Brach station and for Harvard station of $1.7 \text{ mm} \cdot \text{d}^{-1}$ and $0.9 \text{ mm} \cdot \text{d}^{-1}$, respectively.

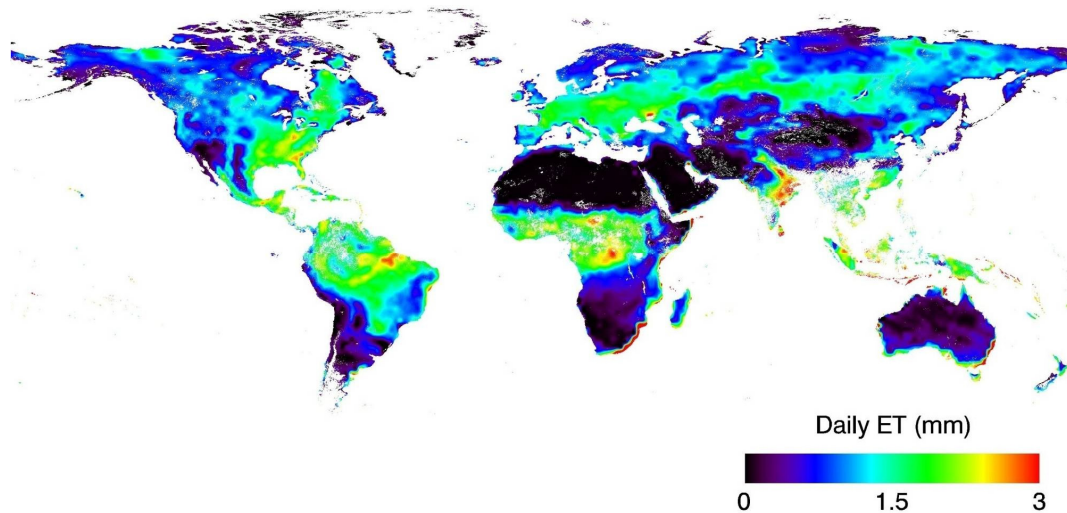


Figure 1. ET_d at global scale map for 1 July 1995 10-day composite.

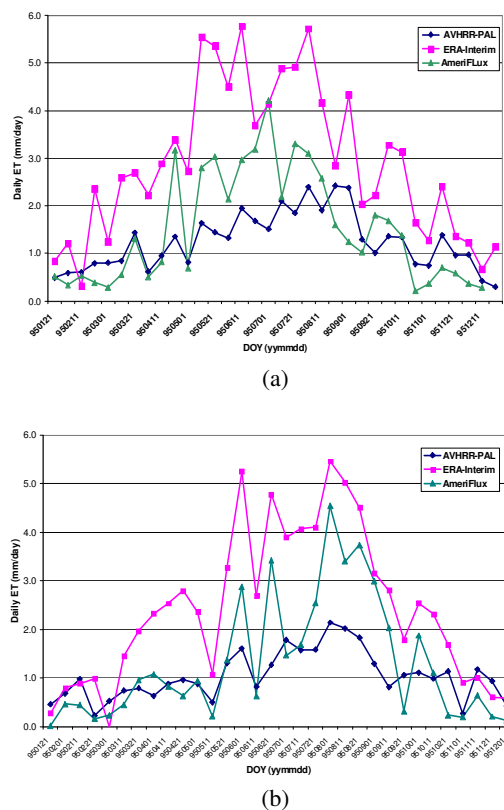


Figure 2. Comparison between ET_d estimated from AVHRR, ET_d from ERA-interim and ET_d from the different AmeriFlux stations (a) Walker Branch, (b) Harvard Forest) during the period of 1995.

The two stations used to compare *in situ* data with PAL ET_d have the similar latitude and the same type of vegetation (deciduous broadleaf forest). For a complete study over other types of vegetation, we have plotted the most representative soil class through the density of the different class of soil versus latitudes (figure 3). The four most representative vegetation types, along with the deciduous broadleaf forest have been plotted in terms of evapotranspiration for 1995 (figure 4).

For evergreen broadleaf forest we can observe similar values for 1995 (around $1.6 \text{ mm} \cdot \text{d}^{-1}$). However, for croplands and deciduous covers we can observe a yearly cycle with a maximum for the months between June and September. On the other hand, barren or sparsely vegetated classes show values around zero.

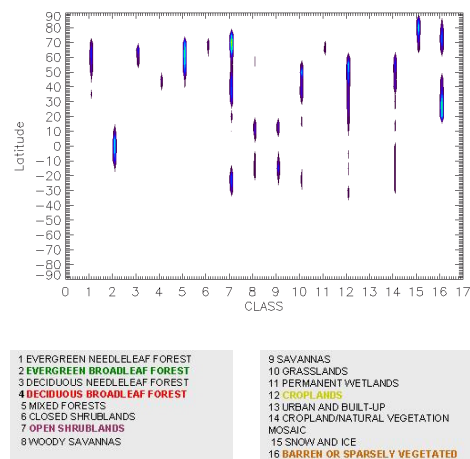


Figure 3. Density of the different vegetation class versus latitude.

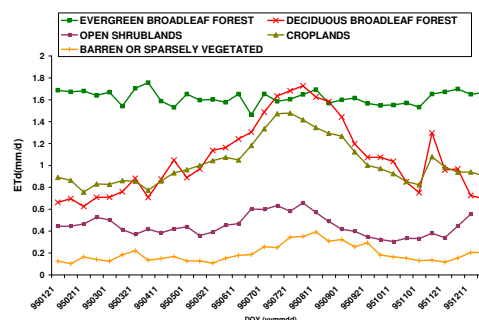


Figure 4. ET_d values for the most representative vegetation class during the period of 1995.

In addition, we have represented ET_d density versus latitude (Figure 5) for February, April, July and November of 1995. The equatorial belt (-10° to 10°) is dominated by evergreen broadleaf forest. The higher values of ET_d correspond to these latitudes, with values almost constant throughout the year corresponding to this “cloud” in the four months (figure 5).

For 20° N to 40° N latitude, land cover corresponds mainly to the desert belt with no vegetation cover. This is the reason why most ET_d values are concentrated near zero. In summer (in Northern Hemisphere) these values are higher due to the presence of the mixed forest land cover.

For higher latitudes, we can see that ET_d density is next to zero for February, and as the year advances, evapotranspiration density increases. In November this density is again close to values close to zero.

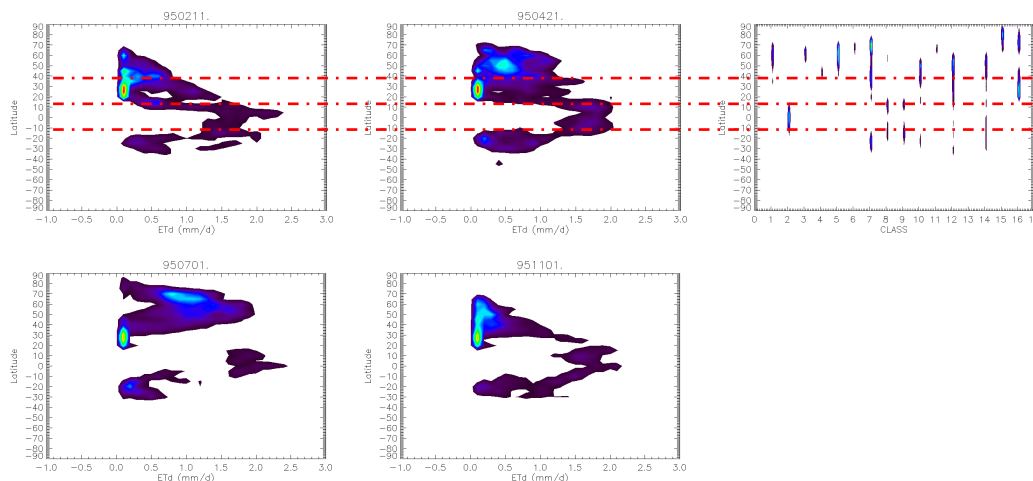


Figure 5. Relationship between ET_d density and latitude for February, April, July and November of 1995.

To complete this work, we studied the reliability of the data in the validation as the PAL dataset is a composite of 10 days, and therefore the exact day is unknown for each pixel. In previous results (Figure 2), we have obtained a good correlation between ET_d values from *in situ* data and ET_d values from PAL dataset as well as an error lower than $1 \text{ mm} \cdot \text{d}^{-1}$. The days used to this validation have been the first day of this composition of ten days. Figure 6 shows the ET_d values used in the validation, for both station, and the error made when considering this day as representative of the 10 days composite. For both station data (Walker Branch and Harvard), this error is low in the winter months, around $0.3 \text{ mm} \cdot \text{d}^{-1}$, therefore, the pixel values is representative in this case. However, in the summer months this error is greatly increased, with errors of up to $2.7 \text{ mm} \cdot \text{d}^{-1}$ so the ET_d value from the PAL dataset is not representative for these 10 days.

5. CONCLUSIONS

In this work, Pathfinder AVHRR Land (PAL) has been used for the retrieval of daily Evapotranspiration ET_d at global scale between 1981 and 2001. The results show a good correlation between ET_d values obtained from *in situ* data and PAL dataset through the methodology presented. On the other hand, for different latitudes and types of vegetation, the study shows reasonable results in terms of the annual trend of ET_d values.

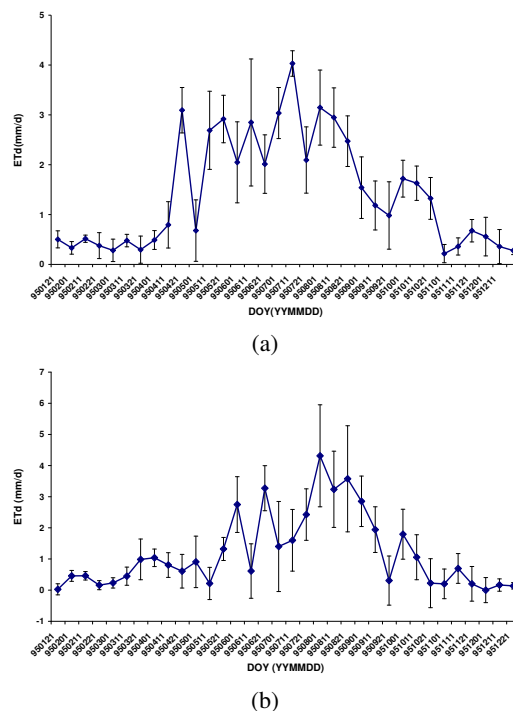


Figure 6. ET_d values from the different Ameriflux stations: a) Walker Branch, b) Harvard Forest, during the period of 1995. In this graphics it is shown the error when considering this day as representative of 10 days composite.

However, a more detailed analysis of the insitu data used for validation show that evapotranspiration retrieved through the PAL dataset is not representative of the 10 days. Therefore, despite the advantage of a database with high temporal coverage, this database is not suitable to obtain ETd.

6. ACKNOWLEDGEMENTS

The authors would like to thank the European Union (CEOP-AEGIS, project FP7-ENV-2007-1 proposal No. 212921; WATCH, project 036946) and the Ministerio de Ciencia y Tecnología (EODIX, project AYA2008-0595-C04-01) for their financial support. Source for the PAL dataset was the Goddard Earth Sciences Distributed Active Archive Center in 2004 (data unavailable in 2008).

7. REFERENCES

- Berk, A., Bernstein, L. S., & Robertson, D. C. 1989. *MODTRAN: A Moderate Resolution Model for LOWTRAN 7*, Technical Report GL-TR-89-0122
- Chavez, P.S., 1996. Image-based atmospheric correction—revisited and improved. *Photogrammetric Engineering and Remote Sensing* **62** 9, pp. 1025–1036
- Crago, R. D. (1996). Comparison of the evaporative fraction and the PriestleyTaylor alpha for parameterizing daytime evaporation,. *Water Resources Research*, 32 (5), 1403-1409.
- Gordon, H. R., Brown, J. W., & Evans, R. H. (1988). Exact Rayleigh scattering calculations for use with the Nimbus-7 coastal zone color scanner. *Applied Optics*, 27, 2111–2122.
- Holben, B. N. (1986). Characteristics of maximum values composite images from temporal AVHRR data. *International Journal of Remote Sensing*, 7, 1417–1434
- McPeters, R. D., Bhartia, P. K., Krueger, A. J., Herman, J. R., Schlesinger, B., Wellemeyer, C. G., et al. (1993). Nimbus-7 total ozone mapping spectrometer (TOMS) data products user's guide. NASA Reference Publication, vol. 1384 (April).
- Schlosser, C. Adam, Xiang Gao, 2010: Assessing Evapotranspiration Estimates from the Second Global Soil Wetness Project (GSWP-2) Simulations. *J. Hydrometeor*, **11**, 880–897.
- Sobrino, J. A., & Raissouni, N. (2000). Toward remote sensing methods for land cover dynamic monitoring: Application to Marocco. *International Journal of Remote Sensing*, 21, 353–363.
- Song, J., M. L. Wesely, M. A. LeMone, R. L. Grossman, 2000: Estimating watershed evapotranspiration with PASS. Part II: Moisture budgets during drydown periods. *J. Hydromet.*, 1, 462-473.
- Uppala, S. and Co authors. 2006. The ERA-40 reanalyses. *Quarterly Journal of the Royal Meteorological Society*. Volume 131 Issue 612, Pages 2961 – 3012.
- Wang, K., Z. Li, M. Cribb, and M. Sparrow, 2007: A simple method to estimate actual evapotranspiration from a combination of net radiation, vegetation index, and temperature, *J. Geophys. Res.*, 112
- Wang, K. and S. Liang, 2008: An improved method for estimating global evapotranspiration based on satellite determination of net radiation, vegetation index, temperature, and soil moisture, *J. Hydromet.*, 9, 712-727.

Multi-scale estimation of vegetation and soil moisture in a Mediterranean wooded grassland (dehesa) using optical sensors

^aGorka Mendiguren, ^aM. Pilar Martín, ^{a, b}David Riaño, ^aF. Javier Martínez, ^aJavier Pacheco, ^cLara Vilar

^a*Instituto de Economía, Geografía y Demografía (IEGD). Centro de Ciencias Humanas y Sociales (CCHS). Consejo Superior de Investigaciones Científicas (CSIC). Albasanz 26-28 28037 Madrid (Spain). Tel. 34-91-6022785/84*

^b*Center for Spatial Technologies and Remote Sensing (CSTARS). University of California 250-N, The Barn, One Shields Avenue Davis, CA 95616-8527 USA*

^c*Joint Research Centre of the European Commission Institute for Environment and Sustainability Land Management & Natural Hazards Unit TP 261, Via E. Fermi 2749 Ispira (VA), 21027 Italy*

gorka.mendiguren@cchs.csic.es, mpilar.martin@cchs.csic.es, david.riano@cchs.csic.es, javier.martinez@cchs.csic.es, javier.pacheco@cchs.csic.es, lara.vilar@jrc.ec.europa.eu

ABSTRACT- A multi-scale and multi-temporal approach was applied to estimate vegetation water content and soil moisture in a typical Mediterranean wooded grassland (Dehesa) using remote sensing data. A field campaign to sample vegetation water content was carried out in the test site located in NE Cáceres (Spain) from March to December 2009. Soil moisture was measured using Time Domain Reflectometry (TDR) at 4, 10 and 20 cm depths. Field spectra were acquired using ASD FieldSpec® 3 spectro-radiometer. Canopy Water Content (CWC) was estimated based on the inversion of a radiative transfer model (Trombetti et al. 2008) both for field spectra as well as from MODIS Terra satellite data. Simple regressions between vegetation, soil moisture and spectral indices were carried out. NDVI and NDW7 showed the best correlation with vegetation moisture ($R^2=0.91$ and 0.90) both from field spectra and satellite data. Correlation with soil moisture was weak for spectral indices, except for CWC estimated from MODIS data ($R^2 = 0.56$).

1 INTRODUCTION

Monitoring water fluxes between soil, vegetation and atmosphere is a key element in understanding how the ecosystem works today and also allows predicting how it will react to other climatic conditions (Cramer et al., 2001).

Remote sensing has provided valuable information for the estimation of vegetation water content (Ceccato et al., 2002a; Ceccato et al., 2002b; Gao, 1996; Tucker, 1979). In spite of the difficulty of isolating the influence of water absorption over other factors affecting plant reflectance, several studies have found good relationships between spectral indices and vegetation water content, especially in grasslands (Chuvieco et al., 2004; Danson and Bowyer, 2004; Yebra et al., 2008). Microwave remote sensing has provided useful information on soil moisture at the first centimetres of the soil surface, but in places where dense vegetation exists, this technique is less accurate (Narayan et al., 2004).

In vegetated areas, root-zone soil moisture is linked to vegetation health conditions (Song et al., 2000). In this context, some authors found good correlation between spectral indices and soil moisture conditions with statistically significant correlations R values of 0.46-0.55 (Wang et al., 2007).

The objective of this paper is to analyze the scale dependency of the relationship between spectral information acquired using a field spectro-radiometer and low resolution satellite imagery in relation to vegetation and soil moisture measured in the field.

2 METHODS

The study site is located at Las Majadas del Tietar, Cáceres (Spain). The area is a Mediterranean wooded grassland (dehesa) which is being used during the year for cow shepherding. The vegetation is mainly short pasture and holm oak trees. The mean distance between trees is 14 m. Grasslands cover 86% whereas holm oak trees (*Quercus Ilex*) cover the remaining 14% of the study area. Thirteen 25x25 m plots were randomly located for the analysis (figure 1). However,

only 6 plots, those that fall within the MODIS pixel (figure 1) were used for the regression analysis. Vegetation samples were collected every 16 days from March 1st to December 31st 2009 corresponding to the Landsat 5TM over passing. Destructive vegetation sampling of herbaceous vegetation was carried out to measure moisture content. Additionally, ASD FieldSpec® FR3 (www.asdi.com) spectro-radiometer measures were taken in the plots. MODIS Terra images (MOD09GA) were downloaded from the NASA Land Processes Distributed Active Archive Center (LPDAAC) (<https://LPDAAC.usgs.gov>).

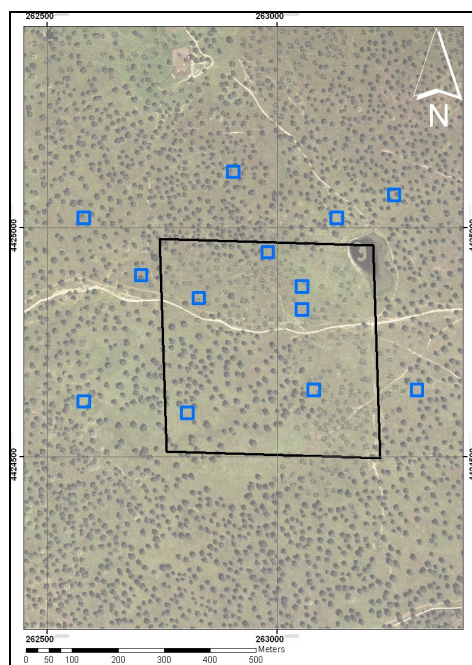


Figure 1. Sampled plots (blue dots), MODIS pixel (500 m) (black square).

Soil moisture was recorded automatically using Campbell Time Domain Reflectometry (TDR) sensors (<http://www.campbellsci.com>). TDR measures volumetric soil water content using the response of a signal to the presence of water in the pores (Cerný, 2009).

2.1 Field sampling

In each 25x25 m plot, three random points were located and vegetation samples were collected in those points using a 25x25 cm quadrant. All the plants inside the quadrangle were collected to calculate vegetation water content according to the fresh/dry weight and leaf area. Sampling was divided in three subsamples; two of them were collected inside the 25x25 cm quadrant and the other one outside. Vegetation sampled inside the quadrant was divided in live and

dead vegetation. Live vegetation samples included all plants that were rooted to the soil, while dead vegetation samples included all dead plants and litter within the quadrant. Both samples were kept in separate zip lock bags to preserve the water content until weighted. An additional live vegetation sample was collected outside the quadrant to calculate the Equivalent Water Thickness (EWT). All samples were weighted in the field using a 0.01 g precision scale and were transported to the laboratory in an iced cooler in order to preserve all the physiological properties.

In the laboratory, a small representative portion of the live vegetation sample within the quadrant was scanned to calculate leaf area index.

After this, all the samples were oven dried at 60 °C during 48 h, and dry weight was measured. Fuel Moisture Content (FMC), Equivalent Water Thickness (EWT) and Canopy Water Content (CWC) were calculated using the following equations:

$$FMC = \frac{(\text{Fresh Weight} - \text{Dry Weight})}{\text{Dry Weight}} \cdot 100 \quad (1)$$

$$EWT = \frac{(\text{Fresh Weight} - \text{Dry Weight})}{\text{Leaf Area}} \quad (2)$$

$$CWC = EWT \cdot LAI \quad (3)$$

where:

$$LAI = \frac{\text{Live vegetation sampled dry weight}}{\text{Live vegetation (subsample) dry weight}} \cdot \text{Leaf Area} \quad (4)$$

2.2 Satellite images

MODIS Terra daily surface reflectance images (MOD09GA) were downloaded for the period from March 1st 2009 to December 31st 2009. This product has seven spectral bands at 500 m spatial resolution as well as ancillary data on sensor angle and quality flags at 1 km. Band wavelengths distribution are shown in table 1.

Table 1. Terra MODIS band wavelengths distribution.

Band	Bandwidth in nm
1	620-670
2	841-876
3	459-479
4	545-565
5	1230-1250
6	1628-1652
7	2105-2155

Using a script programmed in Matlab (<http://www.mathworks.com>) image values for the pixel centred in the study area (figure 1) were

extracted. Only those images with zenith angle smaller than 20 degrees were selected. In addition, a quality check was applied using quality flag provided by the image. Only dates free of clouds or cloud shadows and also with low atmospheric aerosol content were selected for further analysis. After this process, 43 images remained out of the 305 initially downloaded.

Three spectral indexes were calculated to estimate FMC and CWC: Normalized Difference Vegetation Index (NDVI), Normalized Difference Water Index (NDWI), and NDW7:

$$NDVI = \frac{(Band\ 2 - Band\ 1)}{(Band\ 2 + Band\ 1)} \quad (4)$$

$$NDWI = \frac{(Band\ 2 - Band\ 5)}{(Band\ 2 + Band\ 5)} \quad (5)$$

$$NDW7 = \frac{(Band\ 2 - Band\ 7)}{(Band\ 2 + Band\ 7)} \quad (6)$$

where band numbers correspond to MODIS Terra sensor.

These indexes have been used by other authors to estimate vegetation water content (Chen et al., 2005; Chuvieco et al., 2004; Trombetti et al., 2008). Additionally, Canopy Water Content (CWC_{MODIS}) was obtained from MODIS images by applying an inversion of a radiative transfer model described in Trombetti et al 2008. In this model, 10 neurons were trained using a combination of 66 different combinations of MODIS spectral bands and vegetation indexes as inputs and CWC, leaf water content and LAI as outputs. (see Trombetti et al. 2008 for further details).

2.3 Field spectroscopy

Field spectroscopy measurements were acquired in the 25x25 m plots during the 2009 campaign using an ASD FieldSpec® FR3 spectro-radiometer that measures reflectance from 350 nm to 2500 nm. Those measurements were taken following two transects with direction NE-SW and NW-SE in each 25x25 m plot at the maximum sun elevation (± 2 hours from solar noon). MODIS spectral bands were simulated from the FieldSpec spectra by using average relative spectral responses (RSR) for each band as included in ENVI 4.6.1. (www.itvvis.com).

3 RESULTS

3.1 Seasonal trends for FMC, CWC, spectral variables and precipitation

Figure 2 shows the temporal evolution of the vegetation water content, precipitation and its effect on the spectral information. During the spring the vegetation water content decreases. At this time, the vegetation is still responding to rain, and some increase in the FMC and CWC of vegetation after some precipitation events can still be observed.

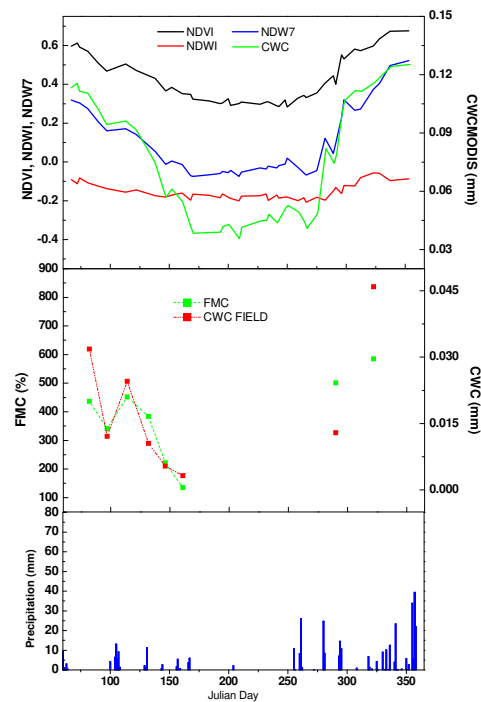


Figure 2. Seasonal trends of the variables obtained from the MODIS images (top), FMC and CWC measured in the field (middle), and precipitation (bottom).

During the summer period no field samples were collected since grassland cover is completely dry. At Julian day 275 (middle of September) vegetation showed a quick rise in the value of FMC and CWC. This was the response of the vegetation to rainfall during the previous days which suggests that the behaviour of the predominant herbaceous layer is being highly influenced by the rain. Temporal evolution of the indexes is indicating that CWC_{MODIS} response was faster than the vegetation indexes.

3.2 Correlation between FMC, CWC and spectral variables

Correlations between FMC, CWC and spectral variables were calculated for MODIS Terra (Table 2) and field spectra (Table 3).

Table 2. Correlation coefficient (R^2) between vegetation water content (FMC or CWC) and spectral variables obtained from MODIS Terra.

	FMC	CWC
CWCMODIS	0.60	0.80
NDVI	0.61	0.90
NDWI	0.49	0.75
NDW7	0.62	0.90

CWC showed higher correlation with spectral variables than FMC for both MODIS Terra and field spectra. This indicates that CWC is describing much better the vegetation water content that can be measured using satellite images than FMC. The best spectral index for CWC estimation were NDVI and NDW7 (Tables 2 and 3) but for FMC it varied.

Table 3. Correlation coefficients (R^2) between vegetation water content (FMC or CWC) and spectral variables obtained from MODIS bands simulated using field spectra (ASD FieldSpec® FR3 spectro-radiometer).

	FMC	CWC
CWC (field spectra)	0.62	0.85
NDVI	0.59	0.91
NDWI	0.40	0.87
NDW7	0.50	0.90

FMC does not take into account the LAI. This could explain observed differences in the correlation values.

3.3 MODIS and Field Spectra indexes

The indexes calculated from MODIS images and MODIS bands simulated with field spectra present some differences in their temporal evolution.

It can be appreciated in figure 3 that the performance of some indexes was very similar at both scales during the whole campaign. Only CWC MODIS and NDWI showed a significant different behaviour. In the case of the NDWI this difference is more significant in April, where field spectra NDWI showed a small increase in the value of the index that was not obtained from MODIS.

This difference is also observed in the CWC. In the case of the CWC these differences are more significant during the spring and summer seasons where CWC MODIS is suggesting and stabilisation of the index for

the summer season while the CWC calculated from field spectra still was decreasing.

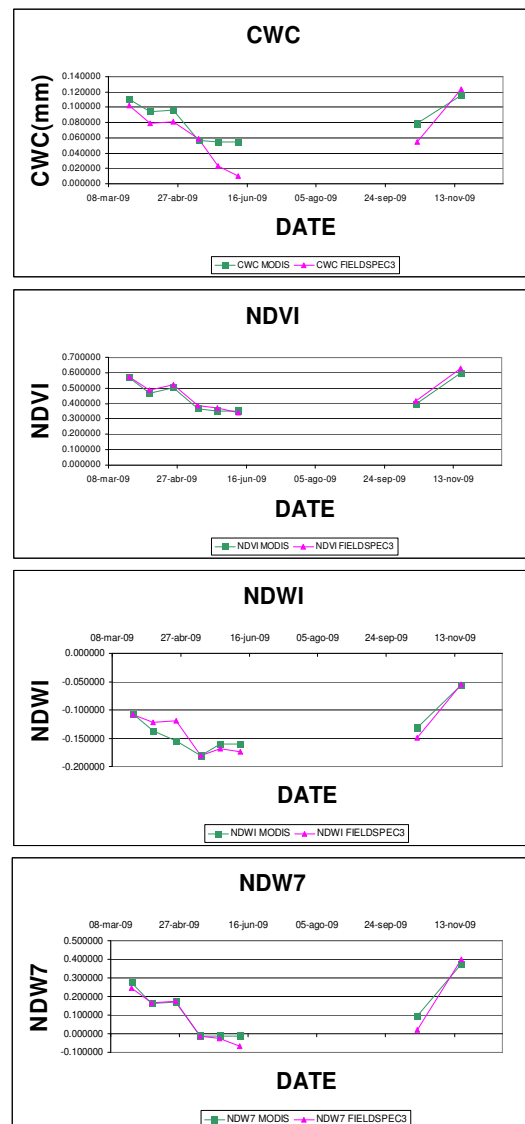


Figure 3. Temporal evolution of the indexes obtained from Terra MODIS and Fieldspec® FR3. Only days with field spectroscopy measurements are shown.

These differences in the shapes indicate that NDVI and NDW7 are not as sensible as the other indexes.

The predominant herbaceous layer seems to be controlling their values which apparently are not sensible to holm oak trees influence. The proportion of grassland and holm oak trees in the MODIS pixel is 84% grassland and 16% holm oak. MODIS CWC constant values along the end of the spring when

grassland gets dry while the trees are green could be related with the highest sensitivity of this parameter that could be able to capture the influence of trees in the whole canopy moisture content.

These differences would indicate that holm oak trees have a relevant paper in this environment, and must be taken in account in further research.

3.4 CWC, NDVI and soil moisture in the root zone

Correlation analysis was carried out between CWC, NDVI and soil moisture measured at different depths (4, 10 and 20 cm) for MODIS and field Spectra data. The study was done for a 30 days lag period between the image and the thirty previous mean values of soil moisture content obtained from the TDR at three different depths. The goal of this analysis was to observe if a time delay exist in the response of the vegetation to soil moisture conditions. The results indicated that soil moisture conditions within three days are the best correlated with spectral data.

The results shown in the table 4 indicate that highest correlation values corresponded to the deepest soil moisture measurements (TDR sensor at 20cm). This could be explained because the most superficial layer has large variations during the day, while deeper layers are more stable.

Table 4. Correlation between indexes calculated from MODIS, and field radiometry, and soil moisture at different depths. Only the NDVI and CWC correlation values are shown.

Depth	MODIS NDVI	MODIS CWC	Fieldspec NDVI	Fieldspec CWC
4 cm	0.09	0.045	0.11	0.23
10 cm	0.22	0.24	0.25	0.33
20 cm	0.41	0.52	0.40	0.36

The highest correlation value was found with MODIS, and not with field spectroscopy. This could indicate that grassland is not the only factor that has to be studied and the influence of the holm oak trees in this environment is important, even if they represent only a 14% of total cover.

4 CONCLUSIONS

The comparison between the temporal evolution of the NDVI and CWC calculated from MODIS, and with the field spectro-radiometer indicated that NDVI is being much more affected by the herbaceous layer than the CWC.

For vegetation CWC measured in the field, the highest correlations were found with NDVI (both for ASD and MODIS data). These correlations were very similar to those obtained with the NDW7. This is in agreement with other studies where good

correlations were found between FMC and the SWIR bands and also between FMC and NDVI (Chuvieco et al. 2004). As the authors indicated, the high significance of the NIR–R space to monitor changes in FMC of herbaceous plants should be related to the effects of FMC variation on grass physiological status rather than on their water content per se.

Regarding CWC estimated from MODIS and field spectra the correlation found in our study area is in agreement with the results of Trombetti et al. (2008) from grassland study sites located around the United States. In our case we could verify that correlations are higher with the CWC estimated with field spectra data than with MODIS images ($R^2 = 0.85$ vs $R^2 = 0.79$). This is a scale effect related with the potential influence of tree cover in the MODIS pixel.

Soil Moisture correlation study indicated which is the most important layer controlling the area and indicated that more factors must be studied to improve the results.

All the results obtained from the analysis indicated that holm oak trees are very important in the study area, and further research has to be carried out to include them in the analysis.

5 ACKNOWLEDGEMENTS

This study has been founded by the Spanish Ministry of Science and Innovation in the framework of the BIOSPEC Project (CGL2008-02301/CLI) and the FPI grant (BES-2009-026831) as well as by the NASA hydrology grant (NNX09AN51G).

Special thank to the colleagues from CCHS-CSIC, INIA, CEAM, University of Alcalá and University of Zaragoza that contributed to the field work.

6 REFERENCES

- Ceccato, P., Flasse, S., and Grégoire, J.-M., 2002a, Designing a spectral index to estimate vegetation water content from remote sensing data: Part 2. Validation and applications: Remote Sensing of Environment, v. 82, p. 198-207.
- Ceccato, P., Gobron, N., Flasse, S., Pinty, B., and Tarantola, S., 2002b, Designing a spectral index to estimate vegetation water content from remote sensing data: Part 1: Theoretical approach: Remote Sensing of Environment, v. 82, p. 188-197.
- Cerný, R., 2009, Time-domain reflectometry method and its application for measuring moisture content in porous materials: A review: Measurement, v. 42, p. 329-336.

- Cramer, W., Bondeau, A., Woodward, F.I., Prentice, I.C., Betts, R.A., Brovkin, V., Cox, P.M., Fisher, V., Foley, J.A., Friend, A.D., Kucharik, C., Lomas, M.R., Ramankutty, N., Sitch, S., Smith, B., White, A., and Young-Molling, C., 2001, Global response of terrestrial ecosystem structure and function to CO₂ and climate change: Results from six dynamic global vegetation models, *Global Change Biology*, Volume 7, p. 357-373.
- Chen, D., Huang, J., and Jackson, T.J., 2005, Vegetation water content estimation for corn and soybeans using spectral indices derived from MODIS near- and short-wave infrared bands: *Remote Sensing of Environment*, v. 98, p. 225-236.
- Chuvieco, E., Cocero, D., Riaño, D., Martín, P., Martínez-Vega, J., de la Riva, J., and Pérez, F., 2004, Combining NDVI and surface temperature for the estimation of live fuel moisture content in forest fire danger rating: *Remote Sensing of Environment*, v. 92, p. 322-331.
- Danson, F.M., and Bowyer, P., 2004, Estimating live fuel moisture content from remotely sensed reflectance: *Remote Sensing of Environment*, v. 92, p. 309-321.
- Gao, B.-c., 1996, NDWI--A normalized difference water index for remote sensing of vegetation liquid water from space: *Remote Sensing of Environment*, v. 58, p. 257-266.
- Narayan, U., Lakshmi, V., and Njoku, E.G., 2004, Retrieval of soil moisture from passive and active L/S band sensor (PALS) observations during the Soil Moisture Experiment in 2002 (SMEX02): *Remote Sensing of Environment*, v. 92, p. 483-496.
- Song, J., Wesely, M.L., Coulter, R.L., and Brandes, E.A., 2000, Estimating Watershed Evapotranspiration with PASS. Part I: Inferring Root-Zone Moisture Conditions Using Satellite Data: *Journal of Hydrometeorology*, v. 1, p. 447-461.
- Trombetti, M., Riaño, D., Rubio, M.A., Cheng, Y.B., and Ustin, S.L., 2008, Multi-temporal vegetation canopy water content retrieval and interpretation using artificial neural networks for the continental USA: *Remote Sensing of Environment*, v. 112, p. 203-215.
- Tucker, C.J., 1979, Red and photographic infrared linear combinations for monitoring vegetation: *Remote Sensing of Environment*, v. 8, p. 127-150.
- Wang, X., Xie, H., Guan, H., and Zhou, X., 2007, Different responses of MODIS-derived NDVI to root-zone soil moisture in semi-arid and humid regions: *Journal of Hydrology*, v. 340, p. 12-24.
- Yebra, M., Chuvieco, E., and Riaño, D., 2008, Estimation of live fuel moisture content from MODIS images for fire risk assessment: *Agricultural and Forest Meteorology*, v. 148, p. 523-536.

Daily photosynthetic active radiation (PAR) images to estimate carbon fluxes at regional scale: A case study in Spain

A. Moreno, M. A. Gilabert, B. Martínez

Remote Sensing Unit, Facultat de Física, Universitat de València, Dr. Moliner, 50.

46100-Burjassot, Spain

e-mail: alvaro.moreno@uv.es

ABSTRACT- Modeling approaches can be an efficient tool to estimate gross primary production (GPP) instead of using field-based measurements, which are expensive and time-consuming. In particular, the C-Fix model can be applied to assess vegetation photosynthesis through the general equation $GPP = \epsilon APAR$, being ϵ a light use efficiency factor, and $APAR$ the absorbed PAR (photosynthetically active radiation), which in turns can be calculated as the product of $fAPAR$ (fraction of PAR) and PAR . PAR is defined as the fraction (about the 46.4%) of the global solar radiation (H) at surface level compressed between 0.4 and 0.7 μm . The main goal of this work is to discuss available procedures to obtain daily PAR images over Spain from global solar radiation and select the most appropriate for our purposes. Two procedures based on temperature (T) and precipitation (P) station recording values are tested. The first one is based on the Bristow-Campbell (BC) empirical model, calibrated for Spain, and the second one, on an Artificial Neural Network (ANN). Daily T and P data from the AEMet for 2008 have been analyzed. Results show that the ANN approach estimates PAR more accurately than the BC model (mean rmse= 2.19 and 1.46 MJ m⁻² day⁻¹, respectively). Gamma test analysis carried out on ANN allowed us to select the optimal input variables and obtain the minimum training data length.

1 INTRODUCTION

The ultimate source of nearly all energy on the Earth is solar radiation, thanks to which life began and is maintained on this planet. Total organic material fixed by photosynthesis over a unit time is called the gross primary production (GPP).

Modeling approaches can be an efficient tool to estimate GPP . In particular, the C-Fix model (Gilabert et al., this volume) can be applied to assess vegetation photosynthesis through the general equation $GPP = \epsilon APAR$, being ϵ a light use efficiency factor, and $APAR$ the absorbed PAR (photosynthetically active radiation), which in turns can be calculated as the product of $fAPAR$ (fraction of PAR) and PAR . The PAR is defined as the 46.4% of the total solar irradiation (H) arriving on the surface composed between 0.4-0.7 μm (Iqbal, 1983).

The use of numerical techniques is an essential alternative to derive global solar radiation data. With such indirect techniques, other observed meteorological data are mathematically exploited in order to estimate solar radiation.

The solar radiation arriving on the surface of the Earth is indeed a function of its extraterrestrial value (H_0) and the atmospheric constituents (represented by their total transmittance τ). The τ can be derived applying empirical models based on available meteorological and geographical parameters such as

sunshine hours, air temperature, latitude, precipitation, relative humidity, and cloudiness. These models use the general equation:

$$\frac{H}{H_0} \propto \tau = f(\text{meteorological data}) \quad (1)$$

The daily extraterrestrial solar radiation depends on Sun-Earth astronomical relationships and solar constant (Iqbal, 1983) and can be easily derived assuming a horizontal surface.

A commonly used parameter for estimating global solar radiation is sunshine duration. Certainly, as the extinction of solar radiation due to the clouds is more important than that due to any other atmospheric constituents, the majority of solar irradiance models take into account the extinction of radiation in relation to cloud cover via the Ångström-Prescott equation (Paulescu, 2008). Particularly, Bristow & Campbell (1984) established an empirical equation for daily global solar radiation at the Earth's surface using daily air temperature amplitude, which is extensively used. Some other empirical procedures to estimate atmospheric transmittance, and then solar irradiation at the surface, offer the possibility of including other meteorological parameters via advanced non-linear approaches. That is the case of the Artificial Neural Network (ANN).

The aim of the present research is to discuss available procedures to obtain PAR on the basis of the

meteorological data and select the most appropriate for our purposes. Two procedures are quantitatively compared over Spain, the Bristow-Campbell (BC) (which uses T as input parameter) and the Artificial Neural Network (ANN) (which uses both T and P as input parameters).

2 METHODOLOGY

2.1 Study area

Spain is located in the southwestern Europe on the Iberian Peninsula (Figure 1). The study area has a temperate climate with hot and dry summers in the interior and wetter and cooler summers along the coastlines, especially along the Atlantic coast. The precipitation regime is dominated in winter by the advection of Atlantic air masses, while in summer it is determined by convective processes, which also depend on land surface conditions. In the Mediterranean coast the climate is governed by the typical Mediterranean regime, with dry and hot conditions in summer resulting from subtropical anticyclones. In this coastline, maximum rainfall occurs in autumn and spring, being complemented by intense convective precipitation events, with annual rainfall between 350 and 500 mm (Immerzeel et al., 2008).

2.2 Data

Daily meteorological data concerning maximum and minimum temperatures (T_{\max} and T_{\min} , respectively), and daily P were supplied by the Spanish Meteorological Agency (AEMet) for 2008. Around 40 stations distributed across the Spanish territory are recording radiation data, whereas 600 stations are recording T and P (see Figure 1). Around the 65% of the data, randomly distributed, were used to train the models, and 35% of the data was used for validation exercises.

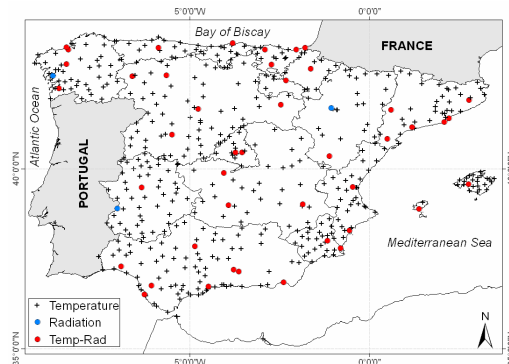


Figure 1. Study area with the location of the meteorological stations.

In this paper, an ordinary kriging procedure is used to obtain spatially continuous T and P maps over Spain (Figure 2). The daily extraterrestrial solar radiation, H_0 , depends on Sun-Earth astronomical relationships and solar constant (Iqbal, 1983).

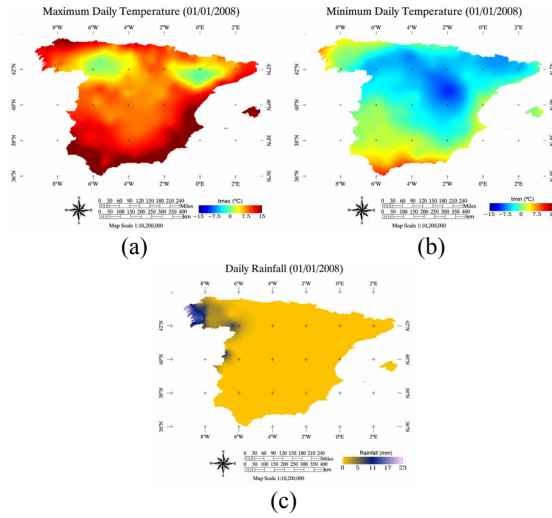


Figure 2. Example of images obtained by kriging from the meteorological stations' data obtained on 1 January 2008: (a) Maximum temperature, (b) Minimum temperature, (c) Precipitation.

2.3 Bristow-Campbell approach

Bristow & Campbell (1984) established an empirical equation for daily global solar irradiation at the Earth's surface based on the difference of daily maximum and minimum air temperatures and three empirical coefficients:

$$\frac{H}{H_0} = a \left[1 - \exp(-bD^c) \right] \quad (2)$$

being

$$D = t_{\max} - \frac{t_{\min}(j) + t_{\min}(j+1)}{2} \quad (3)$$

a , b and c are empirical coefficients, which are distinct for every location. The underlying principle of this approach is to use the diurnal temperature range as an indicator of overcast conditions that would impact on the transmittance of solar radiation through the atmosphere. In particular, the a coefficient (dimensionless) represents the atmospheric transmittance under cloudless conditions, that is, the clear sky transmittance, whereas b and c coefficients quantify the effect of the diurnal temperature range on the sky transmittance. The D parameters takes into account the minimum temperature in successive days

($j, j+1$), which seems to be a better representativeness of the minimum temperature.

The BC procedure has been particularized for the study area. As mentioned before, the empirical coefficients a , b and c in eq. (2) are distinct for every location. Therefore, instead of using the empirical values found in the literature (Ball et al., 2004), they have been calculated specifically for Spain by means of a non-linear least squares fit to the Bristow-Campbell equation (2) for each station recording solar radiation data and for every year. Table 1 shows those coefficients for the 2008.

Table 1. BC Empirical coefficients for the 2008 (a , b , and c and their respective variances).

	a (var a)	b (var b)	c (var c)
2008	0.817 (0.018)	0.0298451 (0.0000018)	1.60 (0.06)

2.4 Artificial Neural Network (ANN)

The ANNs provide a non-linear modeling method to estimate daily PAR over the data considered (T_{max} , T_{min} , P). An additional Gamma test (Remesan, 2008) has been carried out to determine the best model input combinations to achieve a particular target output. This test pointed that adding precipitation to our models will improve their accuracy.

In this work, the classical Multilayer Perceptron (MLP) has been used (Haykin, 2008). A MLP consists of a set of interconnected elementary processing units (neurons) organized into layers with no feedback or lateral connections. Each connection to a neuron has an adjustable weight factor associated with it. Every neuron carries out a non-linear transformation of its inputs defined by the following expression:

$$y = \phi \left(\sum_{i=1}^m w_i x_i + u \right) \quad (4)$$

where m is the number of inputs to the neuron, w_i are the synaptic weights (free parameters of the system), u is the bias coefficient (also to be determined), and ϕ is a non-linear function, in our case the widely used hyperbolic tangent. The weights of the connections are adjusted during the training process to achieve the desired input/output relation of the network.

It has been demonstrated that a MLP with two hidden-layers is able to model any relationship between two sets of variables. The MLP has been trained with the Levenberg-Marquardt (LM) algorithm, which is an iterative technique that locates the minimum of a function by means of a minimum

local search (Madsen et al., 2004). The approach based on MLP follows a tree-step:

1. An exhaustive initialization of the models' parameters.
2. Selection of the models that present the best performance (minimum squared error over validation data set).
3. Estimation of global solar radiation by an ANN committee (mean value of the 6 selected models).

Around 150 ANNs were trained, trying different architectures and weights initializations, to estimate the solar irradiation based on the daily temperature amplitude and daily precipitation. The final estimates of solar radiation are calculated by an ANN committee as described before.

3 RESULTS

Table 2 summarizes the outcomes obtained by the two modelling techniques over a test dataset from 2008. Table 2 shows that the non-linear approach ANN obtains more accurate estimations than the classical parametric BC model. The results point out that both the introduction of rainfall into the nonlinear model and their capability to find complex relationships between input variables can get a substantial improvement in the estimates, in comparison to the classical BC estimations.

Table 2. Mean error (ME), root mean squared error (RMSE), mean absolute error (MAE) and correlation coefficient between estimated and measured daily PAR during 2008.

	ME	RMSE ($\text{kJ m}^{-2} \text{ day}^{-1}$)	MAE	R
BC	0.23	2.19	1.49	0.84
ANN	0.01	1.46	1.06	0.93

A visual way to evaluate the quality of a model is to make scatter plots of estimated versus observed values of the parameter of interest. Figure 3 (top) shows this information: for both models the estimates distribute along the 1:1 line. However, the ANN estimates are lesser dispersed (they are then more accurate) than the BC estimates. Figure 3 (bottom) shows the temporal profile (year 2008) of the estimated and observed daily global radiation. The observed data have been retrieved from a ground station located at Manises (lat: 39° 29' 24" North, lon: 0° 27' 0" West). Again this figure shows that ANN gets a very good fit with the measured values and, in addition to this, there is a remarkable temporal consistency of the modelled profiles. It shows again

that a significant improvement has been achieved by the ANN approach.

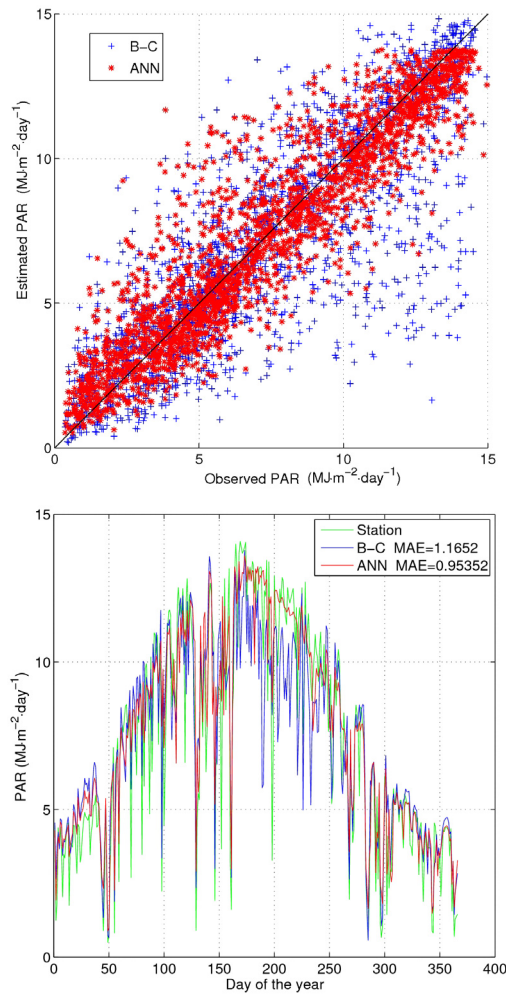


Figure 3. Performance of the models over the complete test data set from 2008 (top). Performance of the models over train and test data in the Manises ground station (bottom).

Figure 4 shows the outcomes of the residual analysis for both cases. The scatter-plots of the observed vs. residual values do not show a trend for values below 2 (predominant value). In particular, for the BC approach, high residuals are found ($>10 \text{ MJ/m}^2 \text{ day}$) for high irradiation values ($>14 \text{ MJ m}^{-2} \text{ day}^{-1}$). As the positive residual values are related to under-estimations of the model, this means that the BC approach presents a tendency to under-estimate high irradiation values.

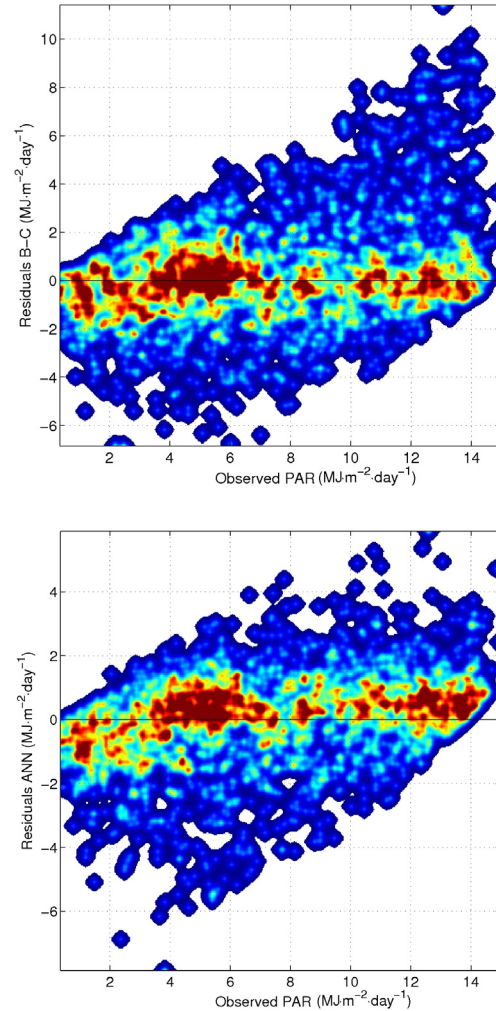


Figure 4. Observed vs. residuals for the BC (top) and ANN (bottom) approaches.

Figure 5 shows the normal probability plots. These graphs serve us to graphically assess whether the data considered could come from a normal distribution. If the data were normal, the plot should be linear. It can be observed as the residuals derived from the BC are far away from a normal distribution as compared with the ANN residuals. In the ANN case only a 20% of the data do not agree with a normal distribution.

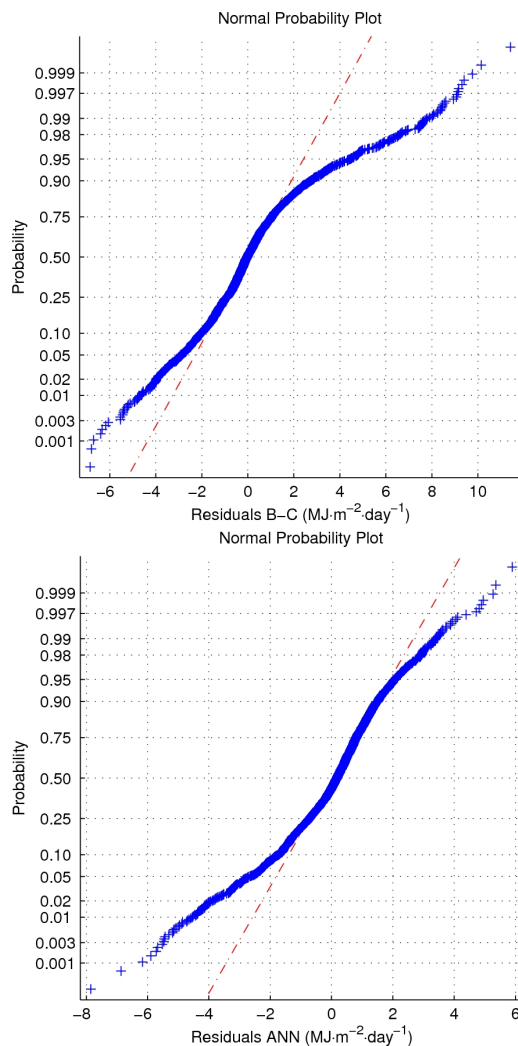


Figure 5. Normality plots for the BC (top) and ANN (bottom) approaches.

The results indicate that ANN provides us with the most accurate and lowest biased estimations of solar radiation in comparison with the BC modelling technique. They point out that both the introduction of precipitation into the nonlinear model and the model capability to find complex relationships among input variables can get a substantial improvement in the estimates. Therefore, the ANN approach has been selected to derive *PAR* maps over Spain on a daily basis, using as inputs the precipitation and temperature maps obtained by an ordinary kriging, as mentioned in section 2.

Figure 6 shows *PAR* images obtained for two particular days (at the beginning of spring and summer). Both *PAR* images are rather homogeneous,

showing lower values in cloudy areas. As expected, values are higher at the beginning of summer than three months before.

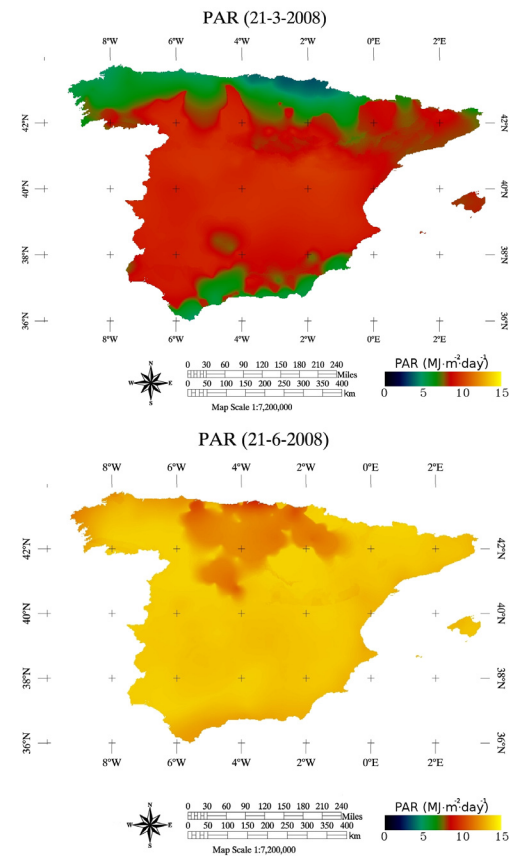


Figure 6. Example of the daily estimated *PAR* map at 1 km spatial resolution over Spain from the ANN method for two days: 21 March (top) and 21 June (bottom).

The Spanish Ministry of Science and Innovation (ARTEMIS CGL2008-00381) financed this study. Meteorological data were provided by the AEMet.

REFERENCES

- Ball, R. A., Purcell, L. C., Carey, S. K., 2004, Evaluation of solar radiation prediction models in North America. *Agronomy Journal*, **96**, 391-397.
- Bristow, K. L., and Campbell, G. S., 1984, On the relationship between incoming solar radiation and daily maximum and minimum temperature. *Agricultural and Forest Meteorology*, **31**, 159-166.

- Gilabert, M. A., Maselli, F., Martínez, B., Moreno, A., Camacho, F., Chiesi, M., García-Haro, F. J., Meliá, J., Pérez-Hoyos, A., Verger, A., 2010, A remote sensing study of forests to estimate biophysical indicators and monitor CO₂ fluxes in Spain: the ARTEMIS project. *Proceedings of the 3rd International Symposium RAQRS*, 27 Sep-1 Oct, Torrent, Valencia (in this volume).
- Haykin, S., 2008, *Neural Networks: A Comprehensive Foundation*, Prentice Hall.
- Immerzeel, W. W., Rutten, M. M., & Droogers, P., 2008, Spatial downscaling of TRMM precipitation using vegetative response on the Iberian Peninsula. *Remote Sensing of Environment*, doi:10.1016/j.rse.2008.10.004.
- Iqbal, M., 1983, An Introduction to solar radiation. In: Academic Press, New York, p. 390.
- Madsen, K., Nielsen, H. B., and Tingleff, O., 2004, Methods for non-linear least squares problems (2nd ed.), IMM, Lecture Notes, Technical University of Denmark, 58 pp.
- Paulescu, M., 2008, Solar irradiation via air temperature data, chapter 7, pp. 175-192, in Badescu, V. (Ed.), *Modeling solar radiation at the Earth's surface. Recent advances*, Springer-Verlag, Berlin.
- Remesan, R., Shamim, M. A., Han, D., 2008, Model data selection using gamma test for daily solar radiation estimation. *Hydrological Processes*, **22**, 4301-4309.

Remote sensing-based evapotranspiration estimates under semi-arid conditions. Comparing METRIC, MSSEBS, STSEB and HidroMORE

E. Rubio^{1,2}, R. G. Allen³, A. Calera¹, V. Caselles⁴, J. Colin⁵, A. Jochum^{1,6}, M. Menenti⁷, J. M. Sánchez², M. Tasumi³, E. Torres¹, R. Trezza³

1 Instituto de Desarrollo Regional, UCLM, 02071 Albacete, Spain. 2 Departamento de Física Aplicada, EIIA, UCLM, 02071 Albacete, Spain. 3 University of Idaho, Research and Extension Center, 3793 N. 3600 E., Kimberly, Idaho USA 83341. 4 Departamento de Física de la Tierra y Termodinámica, UV, Dr. Moliner, 50, 46100 Burjassot, Spain. 5 Laboratoire des Sciences de l'Image, de l'Informatique et de la Télédétection, UMR 7005 CNRS / University of Strasbourg, France. 6 ALFAclima Asesoramiento Medioambiental, Albacete, Spain. 7 Faculty of Aerospace Engineering, TU Delft, The Netherlands.

Evamaria.rubio@uclm.es

ABSTRACT - Remote sensing-based models are presently recognized better suited for mapping evapotranspiration (ET) from regions and larger geographic areas due to the spatiotemporal variability of the latent heat flux. This study compares the flux estimations of four different methods, three energy balance approaches (two one-source models and a two-source model) and a weather-based reference ET algorithm, over an agricultural landscape of Castilla-La Mancha (Spain), including Barrax pilot zone. In previous works, the models (METRIC, MSSEBS, STSEB, and HidroMORE) have shown their potential for providing reliable ET estimations and their capability for operational applications over large landscapes. Besides, they have been largely validated against in situ measurements of flux towers and weather stations. In general, this type of validations are partial and correspond to point-based comparison that does not inform us on limitations, uncertainties or biases of model-estimates for the rest of surfaces and conditions existing in the study area. Here the results of a spatial intercomparison between the flux images generated by METRIC, MSSEBS, STSEB, and HidroMORE is presented. In this comparison a Landsat-5 Thematic Mapper (TM) image acquired during the ESA SPECTRA bARRax Campaign (SPARC-2003) was used together with weather and ground vegetation data. The analysis covered the full range of surface conditions in the area (35 x 40 km²) and used field survey data on the main land uses as a basis. Data from three lysimeters were used as validation control points. Significant discrepancies between models were observed, showing the need for special care and further algorithm revision in the application of these models to large heterogeneous areas in arid and semi-arid regions.

1 INTRODUCTION

Numerous remote sensing-based algorithms are published in recent literature for estimating magnitude and trends in regional evapotranspiration (ET). Most of them focus on agricultural fields and use well-irrigated, non-stressed crops as validation targets. However, it is in arid and semi-arid regions where ET estimation has a special significance. Also, in rare occasions the whole extension of a satellite image is covered by irrigated crops. They cover a portion of the image instead whereas the rest is occupied by dry crops, forest or bare soil areas. The motivation of this work was to discuss the potential of currently-used, remote sensing-based approaches for routinely and operational estimations of ET, not only in crops but also in other land uses, where discrepancies between models may arise.

Two basic approaches can be distinguished when using remote sensing to estimate ET: land surface Energy Balance (EB) methods (Jackson et al. 1983; Norman et al. 1995; Su 2002; Allen 2007) and approaches based on FAO 56 (Allen et al. 1998) methodology (e.g., Reginato et al. 1985; Hunsaker et al. 2005; Er-Raki et al. 2007). The first algorithms consider the calculation of ET as a residual of the surface energy balance equation (EBE). A wide variety of methods can be included within this category. Basically, they differ in the manner that the sensible heat flux (H) is estimated. These models include one-source and two-source approaches. Furthermore, different one-source methods are available in the literature, depending on the criteria followed to select extreme condition pixels within an image. The FAO 56-based ET algorithms exploit the potential of remote sensing imagery to describe the actual vegetation

conditions in terms of a 'reflectance-based crop coefficient' (Bausch and Neale, 1987). These models include single-crop and dual-crop coefficient approaches (Allen et al. 1998, Allen et al. 2005). The main drawback of one-source methods is that they rely on the presence of extreme pixels ('hot' and 'cold' or 'dry' and 'wet') in the imagery (Menenti and Choudhury, 1993; Su 2002; Allen et al. 2007). Two-source models do not require this identification of extreme pixels, but atmospheric correction of images is critical (Norman et al. 1995; Sánchez et al. 2008a). The existing trade-off between spatial and temporal resolution of satellites is an additional limitation when using surface EB models as a tool for monitoring cumulated ET over large periods.

For this study we considered four different particular approaches representative of the main remote sensing-based model categories: a Multi-Scale Surface Energy Balance System (MSSEBS) (description and details in Colin et al. 2006), the Mapping ET at high resolution with internalized calibration (METRIC) procedure (description and details in Allen et al. 2007), the Simplified Two-Source Energy Balance (STSEB) method (description and details in Sánchez et al. 2008a,b) and the hydrological model HidroMORE (Rubio et al., 2004). These models were applied to an agricultural area of Castilla-La Mancha (Spanish plateau), including Barrax international pilot zone. This site was preferred for the study because of the wide variety of land uses in the area. A Landsat 5-TM image corresponding to the Golden Day July 15, 2003 was used together with weather and ground vegetation data.

Maps of the different components of the EBE were obtained for the instantaneous overpass time by applying the EB models, as well as daily ET maps through the four models. Three lysimeter systems, placed in the area, served as validation points for the non-stressed crops ET estimations. This type of validation is important since it allows us to refine the formulation of biophysical processes in models to have a greater physical realism. Nevertheless, at the same time, this type of validation is partial and corresponds to point-based comparison that do not inform us on limitations, uncertainties or biases of model-estimates for the rest of surfaces and conditions existing in a given area (Timmermans et al., 2007; Choi et al., 2009). For this reason, the model intercomparison was extended to the whole area and the different land uses.

2 STUDY SITE AND EXPERIMENTAL DATASET

The study region (90 km²) is located in La Mancha-Oriental, near Barrax and 20 km away from Albacete.

The flat morphology of this region is composed of soils poorly developed which are sparsely vegetated with Summer and Springer irrigated crops, 35%, natural vegetation, 10% and dry land uses 55% distributed in large and uniform land use units (Fig 1). Typical weather conditions correspond to Mediterranean climate for a semi-arid region with an annual rainfall of about 400 mm. In addition, this region has high continentality with high thermal oscillations during all seasons.

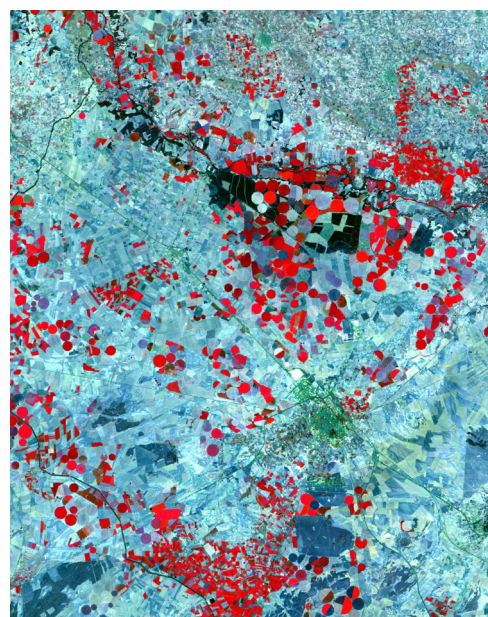


Figure 1.- False color composite of the Landsat TM-5 image (July 15, 2003) of the study area at Barrax, La-Mancha, Spain.

For this study, we selected the Landsat overpass on July 15 because it was coincident with the intensive field campaign for SPARC 2003 (Moreno et al. 2004). The SPARC experiment comprised a large variety of research activities involving numerous satellite instruments (HYMAP, ROSIS, CHRIS/PROBA, MERIS, MSG/SEVIRI, AATSR and ASTER). This framework provided us with an exhaustive ground-based dataset on soil, vegetation status (canopy height, leaf size, LAI, vegetation cover fraction, phenology, radiometric responses...), and atmospheric conditions (aerosols, optical thickness,...) which was of special interest for the generation of the inputs required by some of the approaches here tested. Additional information also used in this study were: field inventory, land-cover classification map, digital elevation model of the area (90 m resolution, from SRTM), data on the Planetary Boundary Layer description from Numerical Weather Prediction outputs, and weather data registered by several meteo-

stations distributed throughout the area that allowed the ground-based calculation of FAO Penman-Monteith (FAO PM) ETo. Notice that, in this study, the implementation of each model (METRIC, MSSEBS, STSEB and HidroMORE) to the Landsat imagery was performed by different researchers involved in this work independently, but using the above described common database.

3 RESULTS

Outputs from the three energy balance models included the instantaneous values of the EBE components (net radiation, R_n ; soil heat flux, G ; sensible heat flux, H ; and latent heat flux, LE) and the daily values of evapotranspiration, ET , from the integration of the latent heat over the day. Outputs from the hydrological model consisted of daily rather than instantaneous ET values. The comparison analysis addressed the following issues: -spatial comparison of instantaneous fluxes predicted by the three EB models; -comparison of ET estimates for the lysimeter fields predicted by the four models against

lysimeter measurements; and, -spatial comparison of the model ET estimates from the four models.

3.1 Comparison of instantaneous fluxes

Figure 2 shows the comparison of the EB terms calculated by MSSEBS, METRIC and STSEB approaches. In these histograms, which correspond to the entire area, frequencies are given as percentages. All curves show a more or less bimodal behaviour, where the larger peak corresponds to bare soil and dry or partially vegetated plots, and the smaller one corresponds to irrigated crops. Larger discrepancies in net radiation arise between the two source model, STSEB, and the one source models, METRIC and MSSEBS. Differences in soil heat flux estimations were independent of LAI for pixels with $LAI > 1$, with biases between METRIC and MSSEBS and between METRIC and STSEB of about 30 W/m^2 , and bias between MSSEBS and STSEB of about 60 W/m^2 . For pixels with $LAI < 1$ no significant differences appeared between METRIC and STSEB.

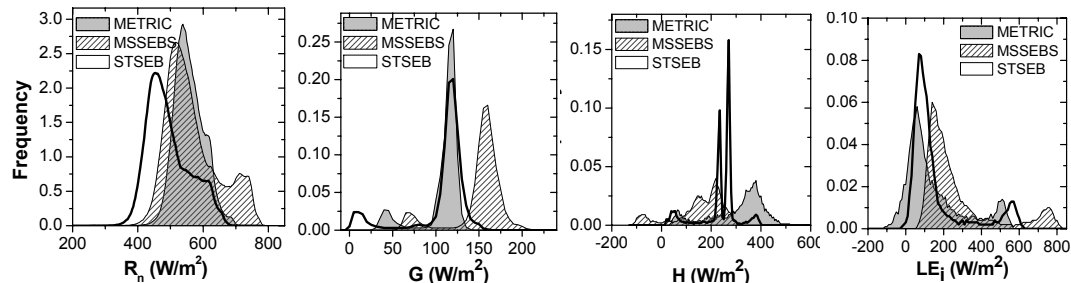


Figure 2.- Histograms of instantaneous fluxes estimates by METRIC, MSSEBS and STSEB. Shown are net radiation (R_n), soil heat flux (G), sensible heat flux (H), and latent heat flux (LE) in W/m^2 .

METRIC and MSSEBS generated similar histograms of H , spanning all over 500 W/m^2 but with significant bias, whereas the histogram of H from STSEB spanned over a slightly narrower range (less than 400 W/m^2) and provided intermediate estimates of H . Differences in H estimations by the EB models were independent of LAI for pixels with $LAI > 1$, with biases between METRIC and MSSEBS of around 150 W/m^2 , between METRIC and STSEB of about 30 W/m^2 , and between MSSEBS and STSEB of about 120 W/m^2 . For pixels with $LAI < 1$ these figures are 150 W/m^2 , 100 W/m^2 , and 80 W/m^2 respectively. According to the rationale of this work and taking into account the existing concerns on the use of one-source versus two-source models for some kinds of surfaces, one of our objectives was to identify the surface types that would present larger uncertainties when applying

an EB model regardless of the one source or two sources nature of the model. These surface types would correspond to the pixels with larger discrepancies in H between models. Thus, for each pixel we calculated the mean value of the three differences in H from the three EB models. Then, this mean discrepancy was analysed in terms of the surface type, LAI, vegetation cover and surface temperature of the pixel. Figure 3 shows the dependency of this mean discrepancy on the surface temperature for all pixels over the study area.

Largest discrepancies between the three EB models appeared for land uses 'bare soil' and 'dry crops', in particular, for 'hot' pixels with surface temperature $> 318 \text{ K}$, $LAI < 1$ and vegetation cover fraction < 0.2 . The smallest discrepancies arose for

land uses ‘vineyard’, ‘olive trees’, ‘forest’ and ‘bushes’.

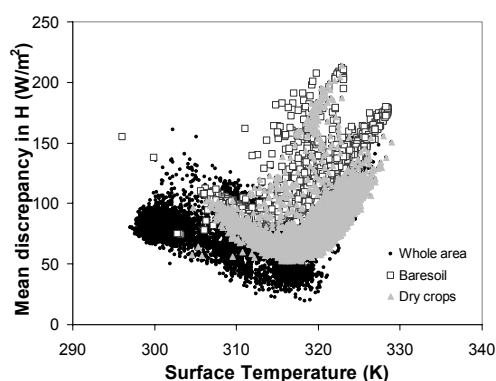


Figure 3.- Mean discrepancy (inter-model differences) in H estimates by the three EB models vs. surface temperature.

3.2 Comparison against lysimeter measurements

Data sets from three different weighing lysimeters located at Las Tiesas Experimental Farm (near Barrax test site, Spain) were thoroughly processed to obtain daily ET observations on the satellite image date (July 15, 2003). ET data from these lysimeter observations were used to compare against ET estimated by the three EB approaches (METRIC, MSSEBS, STEB) and the distributed soil water balance model, HidroMORE.

The lysimeters had between 6 and 9 m² surface area and were about 1.8 m deep. Each one of these lysimeters was placed near the centre of different fields. The crops in the lysimeter fields were: grass (*Festuca arundinacea* Schreb., cv. *Asterix*), vineyard and wheat at the end of its growing season. Model ET estimates for each one of the three lysimeter fields were extracted from the corresponding images by sampling and averaging four 25 m pixels over near the centre of these fields (2 x 2 shortwave pixels).

The comparison between ET predictions from the four models with ET derived from the three lysimeters is shown in Fig. 4. Table 1 summarizes the differences between modeled outputs and ground observations, where RMSE stands for the root-mean-square error, and Bias stands for the mean bias error.

For each one of the three lysimeter sites, the surface energy models produced similar outputs, being the RMSEs lower than 0.6 mm/day. Major discrepancies appeared between the hydrological model and the surface energy models, and between models and lysimeters (see Table 1). All models showed a negative Bias, and a RMSE of around 2 mm/day against lysimeter ET. However, prudence is required with these results due to the small size of the lysimeter fields (100 × 100 m²) in comparison with the

120 m resolution of the thermal band of Landsat 5. Thermal pixels used in the calculation of models ETs for the small lysimeter field would be affected by thermal radiance from areas outside the lysimeter field whereas lysimeter ET measurements would not be influenced.

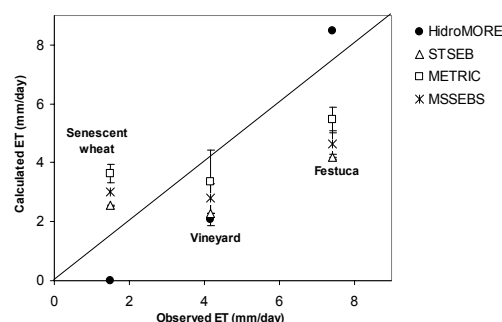


Figure 4.- Comparison of daily ET estimates from METRIC, MSSEBS, STSEB and HidroMORE vs. lysimeter measurements over Las Tiesas Experimental Farm lysimeter fields.

Table 1. Statistics of the comparison of modeled ET vs. daily ET lysimeter measurements. Bias is the mean-deviation error, and RMSE is the root-mean-square error.

	Bias (mm/day)	RMSE (mm/day)
METRIC	-0.2	1.7
MSSEBS	-0.9	2.0
STSEB	-1.3	2.2
HidroMORE	-0.8	1.6

3.3 Intercomparison of daily ET estimates

Results from the pixel-by-pixel comparison of daily ET images generated by the four models. We consider coincident results, those with differences lower than 0.6 mm/day. Table 2 contains the percentage of pixels from the ET images with not significant differences between models estimates.

Table 2. Degree of coincidence among models given as the percentage of pixels with intermodel ET difference lower than 0.6 mm/day.

	METRIC	MSSEBS	STSEB
METRIC	-		
MSSEBS	32	-	
STSEB	21	69	-
HidroMORE	24	12	2

For the instantaneous LE flux, the degree of coincidence between models (i.e. LE values with differences lower than 30 W/m^2) are smaller than for daily ET data, being about 4% for METRIC vs. MSSEBS, and MSSEBS vs. TSEBS, and 36% for

METRIC vs. TSEBS.

Finally, Figure 6 illustrates the differences between daily ET estimates generated by the four models in terms of the land use.

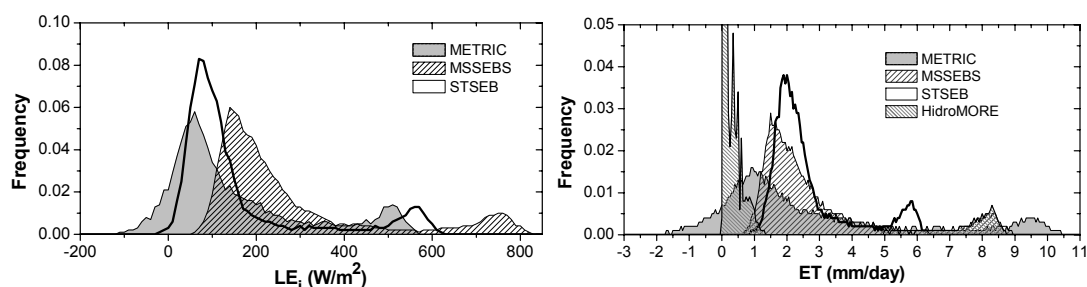


Figure 5.- (a) Histograms of instantaneous latent heat flux estimates (LE , W/m^2) by the three EB models, and (b) histograms of daily ET (mm/day) by the three EB models and the hydrological approach.

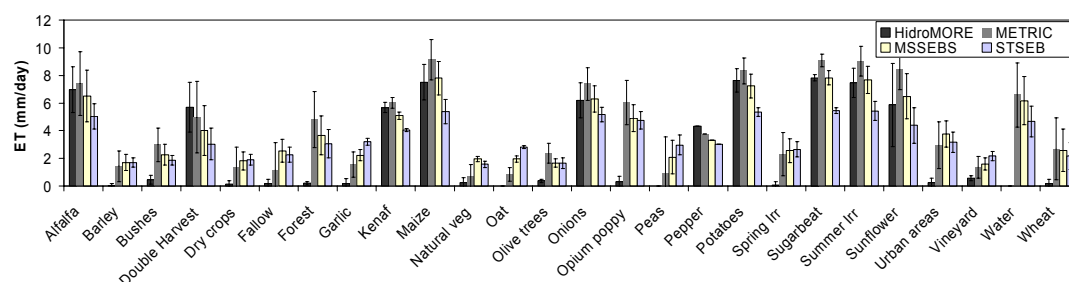


Figure 6.- Daily ET (mm/day) values for each land use in the area, generated by the three EB models and the hydrological approach.

4 CONCLUSIONS

The main conclusions from this analysis are the following: (1) Regarding the point-based validation of model estimates against lysimeter measurements the surface energy models produced similar outputs, being the RMSEs lower than 0.6 mm/day . Major discrepancies appeared between the hydrological model and the surface energy models, and between models and lysimeters (see above Table). Discrepancies (RMSE about 2 mm/day) may be due to the small size of the lysimeter fields ($100 \times 100 \text{ m}^2$). (2) With respect to the three energy balance models, MSSEBS provides larger instantaneous latent heat flux at the time of the Landsat image than METRIC and STSEB, being this difference about 200 W/m^2 . Besides the relationships amongst models are linear enough but dependent on the land use. (3) Each model is using a different time integration approach resulting on daily estimations of ET that extend in almost the same range, but also producing significant differences

in the histograms. (4) Spatial intercomparison (pixel-by-pixel) of the daily ET images generated by the four models allow us to determine the degree of coincidence between ET images. Being the most similar MSSEBS and STSEB with 69 % of estimates differing less than 0.6 mm/day . And (5), the spatial analysis of ET from surface energy models by land use reveals that larger uncertainties are for irrigated crops.

5 ACKNOWLEDGEMENTS

Financial support came from the European Commission shared-cost project DEMETER (contract EVG1-2002-00078), the Spanish Ministry (projects REN2003-02956 and ACELT), the European Space Agency technical assistance for SPectra bARrax Campaign 2003 (Ref. 18307/04/NL/FF) and the Castilla-La Mancha Consejería de Educación y Ciencia project ECOFLUX II (Ref. PCC08-0109). The authors acknowledge the Instituto Técnico Agronómico de Albacete (ITAP) for the management of the three lysimeters located in Las Tiesas and the facilities for using these field data.

6 REFERENCES

- Allen, R. G., Pereira, L. S., Raes, D. and Smith, M., 1998, *Crop Evapotranspiration, guidelines for computing crop water requirements* FAO Irrigation and Drainage Paper. FAO, Rome, Italy, 300 pp.
- Allen, R. G., Pereira, L. S., Smith, M., Raes, D. and Wright, J.L., 2005, FAO-56 Dual crop coefficient method for estimating evaporation from soil and application extensions. *Journal of Irrigation and Drainage Engineering*, **131**(1): 2-13
- Allen, R. G., Tasumi, M., and Trezza, R., 2007, Satellite-Based Energy Balance for Mapping Evapotranspiration with Internalized Calibration, METRIC)-Model. *J. Irrigation Drainage Eng.*, **133**(4), 380-394.
- Bausch, W. C. and Neale, C. M. U., 1987, Crop Coefficients Derived from Reflected Canopy Radiation: a Concept. *Transactions American Soc. Agric. Engin.*, **30**(3): 703-709
- Choi, M., Kustas, W. P.; Anderson, M. C., Allen, R. G., Li, F., Kjaersgaard, J. H., 2009, An intercomparison of three remote sensing-based surface energy balance algorithms over a corn and soybean production region (Iowa, U.S.) during SMACEX, *Agricultural and Forest Meteorology*, **149**(12): 2082-2097.
- Colin, J., Menenti, M., Rubio, E., and Jochum, A. M., 2006, A Multi-Scale Surface Energy Balance System for operational actual evapotranspiration monitoring in *Earth Observation for vegetation monitoring and water management*. American Institute of Physics Conference Proceedings, **852**, 178-184.
- Er-Raki, S., Chehbouni, A., Guemouria, N., Duchemin, B., Ezzahar, J., Hadria, R., 2007, Combining FAO-56 model and ground-based remote sensing to estimate water consumptions of wheat crops in a semi-arid region. *Agric. Water Manage.* **87**, 41-54.
- Hunsaker, D. J., Barnes, E. M., Clarke, T. R., Fitzgerald G. J., Pinter, P. J., 2005, Cotton irrigation scheduling using remotely sensed and FAO-56 basal crop coefficients. *Trans ASAE* **48**(4), 1395-1407.
- Jackson, R. D., Hatfield, J. L., Reginato, R. J., Idso, S. B., and Pinter, P. J., 1983, Estimation of daily evapotranspiration from one time-of-day measurements. *Agric. Water Manage.* **7**, 351-362.
- Menenti, M. and Choudhury, B. J., 1993, Parameterization of land surface evaporation by means of location dependant potential evaporation and surface temperature range. *Exchange Processes at the Land surface for a range of space and time scales*, Proceedings of the Yokohama Symposium (IAHS Publ. no 212).
- Moreno, J. F., et al. 2004, The SPECTRA Barrax Campaign (SPARC): Overview and first results from CHRIS data, Proceedings of the 2nd CHRIS/Proba Workshop, ESA/ESRIN, Frascati (Italy), 28-30 April 2004.
- Norman, J. M., Kustas, W. P., and Humes, K. S., 1995, A two-source approach for estimating soil and vegetation energy fluxes from observations of directional radiometric surface temperature. *Agric. For. Meteorol.* **77**, 263-293.
- Reginato, R. J., Jackson, R. D., Pinter, P. J., 1985, Evapotranspiration calculated from remote multi-spectral and ground station meteorological data. *Remote Sensing Environ.* **18**, 75-89.
- Rubio, E., Mejuto, M., Calera, A., Vela, A., Castaño, S., Moratalla, A., 2004, Validation of an Operational Model of Direct Recharge and Evapotranspiration, *Remote Sensing for Agriculture, Ecosystems and Hydrology V*, Ed.: International Society for Optical Engineering, **5232**: 351-359.
- Sánchez, J. M., Kustas, W. P., Caselles, V., and Anderson, M. C., 2008a, Modelling surface energy fluxes over maize using a two-source patch model and radiometric soil and canopy temperature observations. *Remote Sen. Environment.* **112**, 1130-1143.
- Sánchez, J. M., Scavone, G., Caselles, V., Valor, E., Copertino, V. A., and Telesca, T., 2008b, Monitoring daily evapotranspiration at a regional scale from Landsat-TM and ETM+ data: Application to the Basilicata region. *J. Hydrol.* **351**, 58-70.
- Su, Z., 2002, The energy balance system, SEBS for estimation of turbulent fluxes. *Hydrol. Earth Syst. Sci.* **6**, 85-99.

Comparison of two models of evapotranspiration estimation using remote sensing and ground data collected at an agriculture experimental station

Ronglin Tang^{1,2,3}, Zhao-Liang Li^{1,2,*}, Yuanyuan Jia⁴, Xiaomin Sun⁵, Jinyong Lou⁵

1. State Key Laboratory of Resources and Environment Information System, IGSNRR, China

2. LSIT, Uds, CNRS; Bld Sebastien Brant, BP10413, 67412 Illkirch, France

3. Graduate University of Chinese Academy of Sciences, CAS, Beijing 100049, China

4. Academy of Opto-Electronics, Chinese Academy of Sciences, Beijing 100190, China

5. Key Laboratory of Ecosystem Network Observation and Modeling, IGSNRR, China

* Author to whom correspondence should be addressed: lizl@igsnrr.ac.cn

ABSTRACT - This paper compares one- and two-source energy balance (OSEB and TSEB) models in estimating surface energy components using both Landsat TM/ETM+ data and ground measurements acquired at Yucheng station in China. Similar performance in estimating surface net radiation and soil heat flux between the TSEB and OSEB models has been observed compared with the ground measurements with Root Mean Square Difference (RMSD) within 30-34 W/m². The sensible and latent heat fluxes (H and LE, respectively) estimated from both the TSEB and OSEB models are in good agreement with those measured by ground Eddy Covariance (EC) system corrected by the residual energy correction method for energy imbalance. Cloud contamination on Julian day 218 and inaccuracy of the atmospheric and emissivity corrections on Julian day 178 contribute to the lower surface temperature retrieved from ETM+ sensor than air temperature. With data on these two days excluded, the OSEB model seems to perform better than the TSEB model due to the misuse of green leaf area index (LAI) instead of the total LAI at the maturity stage of wheat and corn. However, if we assign the total LAI to be 3 m²/m² for data at the maturity stage for both wheat (Julian day=154) and corn (Julian day=266), the TSEB model performs notably better than the OSEB model. The RMSD of the estimated H and LE in comparison with EC measurements corrected by the RE correction method is within 51 W/m² and larger than 78 W/m² for the TSEB and OSEB models, respectively, if data on Julian days 178 and 218 are excluded.

1 INTRODUCTION

Great efforts as well as progress have been made in the past decades in the estimation of evapotranspiration (ET) from remotely sensed thermal infrared data. Approaches can be roughly divided into simplified empirical regression method, one- and two-source energy balance models, spatial contexture information based surface temperature versus vegetation index triangle/trapezoid space and data assimilation method (Li et al., 2009; Kalma et al., 2008; Glenn et al., 2007). Most of those approaches rely primarily on the principle of surface energy balance equation, namely $ET = R_n - G - H$ (R_n surface net radiation, G soil heat flux, H sensible heat flux).

In the one-source energy balance (OSEB) model, land surface is treated as a big leaf and no distinction is made between sinks/sources from vegetation and soil. Sensible heat transfer is shown to be proportional to the near-surface aerodynamic and air temperature gradient.

The distinction in the various one-source energy balance models consists in the manner to parameterize the sensible heat flux. With different degree of simplifications and assumptions in the relation of inter-variables in model inputs, a series of ET estimation models have been developed in the past 30 years (Bastiaanssen et al., 1998; Su, 2001).

Two-source energy balance model (TSEB) distinguishes the surface energy transfer between soil and vegetation sub-systems. With similarly intensive ground-based measurements as in OSEB, the TSEB is able to accommodate the difference between radiometric and aerodynamic surface temperatures by incorporating the effects of view geometry from satellite/sensor to partition surface energy and temperature into sub-components of both soil and vegetation. The addition of excessive resistance into aerodynamic resistance can be also avoidable. The TSEB models have been shown to be robust for a wide range of landscape and hydro-meteorological conditions (Kustas and Norman, 1997).

The objective of this paper is to test the performances of the classic bulk transfer OSEB and the TSEB model developed by Norman et al. (1995) by comparing estimates of sensible and latent heat fluxes from Landsat satellite data to surface measurements from Eddy Covariance system (EC) at Yucheng Comprehensive Experimental Station with winter wheat-summer corn crop rotation in North China, respectively.

2 GROUND AND SATELLITE DATA

2.1 One-source energy balance model (OSEB)

In the classical one-source energy balance models, H is estimated using the following bulk transfer equation based on Monin-Obukhov similarity theory:

$$H = \rho C_p (T_{aero} - T_a) / r_a = \rho C_p \frac{T_s - T_a}{r_a + r_{ex}} \quad (1)$$

where ρ is density of air, kg/m^3 , C_p specific heat of air at constant pressure, $\text{J/(kg}\cdot\text{K)}$, T_{aero} surface aerodynamic temperature, K , T_a near surface air temperature, K , r_a aerodynamic resistance to heat transfer, s/m , T_s the remotely sensed surface temperature, K , r_{ex} the extra resistance, equivalent to $\ln(z_{om}/z_{oh})=0.15u(T_s-T_a)$, s/m , u wind speed, m/s .

Aerodynamic resistance is affected by combined factors of surface roughness, wind speed and atmospheric stability, etc. The sum of aerodynamic and excess resistance can be expressed as (Choudhury et al., 1986),

$$r_a + r_{ex} = \frac{[\ln(\frac{z_u - d}{z_{om}}) - \psi_m][\ln(\frac{z_t - d}{z_{om}}) + \ln(\frac{z_{om}}{z_{oh}}) - \psi_h]}{k^2 u} \quad (2)$$

where z_u and z_t are the reference heights at which wind speed and air temperature are measured, respectively, m , d is zero plane displacement height, m , h vegetation height, m , z_{om} and z_{oh} roughness length for momentum and heat transfer, respectively, m , ψ_m and ψ_h stability correction function of momentum and heat transfer, $k = 0.4$ von karman's constant.

2.2 Two-source energy balance model (TSEB)

In two-source energy balance models, the ensemble directional radiometric surface temperature ($T_{RAD}(\theta)$) is determined by the respective fraction of soil and vegetation viewed by a radiometer, which can be expressed as:

$$T_{RAD}(\theta) = [f(\theta)T_c^n + (1 - f(\theta))T_o^n]^{1/n} \quad (3)$$

where T_c and T_o are vegetation canopy and soil component temperatures respectively; n is usually set to 4 for 8-14 μm and 10-12 μm wavelength bands, $f(\theta)$ is the fraction of canopy in the field of view of the radiometer and can be computed by combining view zenith angle (θ), clumping factor (Ω), and fractional

vegetation cover (f_c) when assuming a clumped canopy with a spherical leaf angle distribution (Norman et al., 1995).

With assumption that the flux of soil surface (H_s) is in series with the flux of leaves of canopy (H_c), H can be expressed as two parts of energy components of soil and vegetation:

$$H = H_s + H_c \quad (4)$$

$$H_s = \rho C_p \frac{T_0 - T_{AC}}{R_s} \quad (5)$$

$$H_c = \rho C_p \frac{T_c - T_{AC}}{r_x} \quad (6)$$

where r_x and R_s are the resistance of the leaves of canopy and the resistance above the soil surface, respectively.

The other energy balance components of the whole soil and vegetation system are calculated from the following formulas:

Soil and canopy energy budgets:

$$R_{n,s} = H_s + LE_s + G \quad (7)$$

$$R_{n,c} = H_c + LE_c \quad (8)$$

Latent heat:

$$LE = LE_s + LE_c \quad (9)$$

$$LE_c = \alpha_{PT} f_g \frac{\Delta}{\Delta + \gamma} R_{n,c} \quad (10)$$

Soil heat conduction flux:

$$G = \Gamma_s R_{n,s} \quad (11)$$

where subscripts s and c are respectively indicative of soil and canopy, f_g is the fraction of LAI that is green, Γ_s is the fraction of the ratio of soil heat flux to surface net radiation at bare soil surface, α_{PT} is the Priestley-Taylor coefficient for the potentially transpiring canopy. Readers are recommended to refer to Norman et al. (1995) for comprehensive interpretation of the theory, assumption and solution of the TSEB model.

3 GROUND AND SATELLITE DATA

3.1 Ground measurements

Data collected from early May to late September 2009 over an experimental field at Yucheng Comprehensive Experimental Station (36.8291°N/ 116.5703°E, thereafter referred as Yucheng station) in China is used to drive OSEB and TSEB models and subsequently to validate the estimated R_n , G , H and LE . Yucheng station was planted by winter wheat and summer corn crop rotation. Wheat generally comes into the maturity period in early to mid June across Yucheng station and corn is seeded at mid June and harvested in early October. The soil type of this area is sandy loam and the climate is semi-humid and monsoon climate with

mean annual temperature and precipitation being 13.1 °C and 528 mm, respectively.

Meteorological variables including precipitation, air temperature, wind speed, relative humidity and atmospheric pressure are measured routinely in a 5-min interval at two levels at Yucheng station. The measurement heights of upper level and lower level instruments varied from 2.89 m and 1.63 m to 4.24 m and 2.93 m above ground on 31, July 2009. Surface 4-component radiation and soil heat flux at 5 cm soil depth, soil water content at depths of 20 cm and 40 cm below surface are also measured in a 5-min interval together with meteorological variables. 10-Hz frequency signals from Eddy covariance system are recorded by a data logger for archiving and on-line computation of the turbulence statistics and 30-min averages of H and LE with effects of fluctuations in air density corrected and data quality controlled are computed. In addition to the above data, vegetation height and leaf area index averaged from measurements sampled at 3 different sites were measured periodically every 15 and 7-8 days during the winter wheat and summer corn growth period, respectively.

3.2 TM/ETM+ data

From May to September 2009, two Landsat 5/TM (Julian days 178 and 242) and five Landsat 7/ETM+ (Julian days 122, 138, 154, 218, and 266) clear-sky scenes (Path/row: 122/34) are available from <http://glovis.usgs.gov/> website.

The calculation of L_{sensor} and T_{sensor} (radiance and brightness temperature at sensor level) from TM and ETM+ data can be referred to the work of Li et al. (2004). As no radiosounding data are available during the seven Landsat overpasses at Yucheng station, the algorithm of Jiménez-Muñoz and Sobrino (2003) requiring only the atmospheric water vapor content as input is adopted to estimate the surface temperature (T_s) from the thermal channel of ETM+ and TM. Surface emissivity is approximated by a linear weighting of assumed soil (0.96) and vegetation emissivity (0.99) based on fractional vegetation cover (Brunsell and Gillies, 2002).

4 RESULTS AND DISCUSSION

As no clumping factor (Ω) for wheat and corn was measured or derived during our study period, comparison and discussion in the TSEB model will be made with $\Omega=1$.

4.1 Energy closure analysis

A number of papers (Twine et al., 2000; Anderson et al., 2008) have reported the energy imbalance in surface energy budget measured by eddy covariance

technique ($H+LE$, is generally less than the surface available energy, R_n-G). Fig. 1 presents the closure of surface energy budget from eddy covariance measurements at Landsat overpass time during the study period at Yucheng station. Linear least squared fit of $H+LE$ to surface available energy shows a slope of 0.88 and intercept of -55 W/m^2 . The coefficient of determination is 0.665. Closure ratio (CR), defined as $(H+LE)/(R_n-G)$, approximates averagely 0.76 with the imbalanced energy (IE) equivalent to 114 W/m^2 . Data at the bottom in Fig. 2 happen on Julian day 210 with $CR=0.45$ and $IE=193 W/m^2$. This lack of closure can be possibly attributed to several factors, including measurement errors in R_n and G , inconsistent source areas between eddy covariance H , LE and surface available energy, length of sampling intervals, etc.

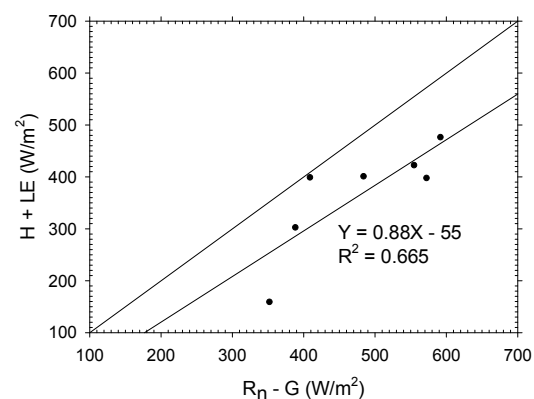


Fig. 1 Closure of surface energy balance at TM 5/ETM+ overpass time during the study period

Since the turbulent heat fluxes estimated from surface energy balance models by definition enforce energy closure among fluxes. To make sense of the comparison between model estimates of surface energy components and ground surface measurements, two approaches, namely Bowen ratio (BR) and Residual energy (RE) correction methods, are developed to correct the eddy covariance measurements (EC) to enforce energy closure (Twine et al., 2000). In the BR correction method, surface available energy is repartitioned into H and LE by conserving the measured Bowen ratio while in the RE correction method the imbalanced energy is totally assigned to LE assuming eddy covariance measured H is reliable. As there is no consensus on how to reconcile the surface energy inclosure measured by eddy covariance system, comparisons of H and LE estimated from thermal infrared data with in situ EC measurements will be performed without closure and with closure using the BR and RE correction methods in this paper.

4.2 Comparison of surface energy components

Figs. 2(a) and 2(b) illustrate the comparisons of instantaneous R_n and G estimated from the TSEB and OSEB models using both the TM/ETM+ derived surface temperatures and ground measurements. Good agreement between estimated and measured R_n is obtained in both TSEB and OSEB models with Bias and root mean square difference (RMSD) within the range of -8 W/m^2 and 32 W/m^2 for both models, respectively. The larger departure from 1:1 line in Fig. 3(a) took place on Julian days 154 and 178 with the former underestimated and the latter overestimated. Similar performances are also observed for G . Bias and RMSD are 20 (17) W/m^2 and 34 (30) W/m^2 for the TSEB (OSEB), respectively. Soil heat flux was significantly overestimated on Julian day 154 even if R_n on this day was underestimated. This is probably due to the use of much lower green leaf area index (LAI) measured during the maturity stage for wheat as total LAI (green and senescent leaves) required in the model. According to the field measurements, the green LAI measured at field decreased sharply from approximately $5 \text{ m}^2/\text{m}^2$ at the tassel stage on Julian day 115 to 0 on Julian day 158 at waxen maturity stage. Underestimate of total LAI allows more solar radiation penetrating through the canopy space to the soil surface and reflected to the atmosphere, resulting in more soil surface net radiation and soil heat flux. Overestimation of R_n by $50\text{--}60 \text{ W/m}^2$ for the TSEB and OSEB models on Julian day 178 results probably from the underestimate of T_s from ETM+ sensor. As the incident solar radiation measured at surface is used as input in both TSEB and OSEB models in this work, unless T_s is under/overestimated due to the errors in the atmospheric and emissivity corrections or cloud contamination, there should be no large difference between estimated and measured surface net radiation.

As for comparison results, both models have underestimated H with respect to the EC measurement by approximately Bias = -85 W/m^2 and overestimated LE by Bias = 176 W/m^2 . However, if the RE correction method is applied to correct EC measurements, RMSD of LE results decreases from 190 W/m^2 to 97 W/m^2 for the TSEB model and from 205 W/m^2 to 118 W/m^2 for the OSEB model. If the BR correction method is applied, the accuracy of LE is improved with RMSD of 123 W/m^2 for TSEB model and 144 W/m^2 for OSEB model but that of H is deteriorated with RMSD of 132 and 145 W/m^2 for TSEB and OSEB models, respectively. Consequently, the RE correction method yields the best agreement with the model-estimated H and LE. It is found that H estimated on Julian days 178 and 218 by both the TSEB and OSEB models is less than zero (stable atmospheric condition) while corresponding H measured by EC is 173 W/m^2 and 47 W/m^2 (unstable atmospheric condition), respectively.

On Julian day 218, global solar radiation measured on ground fluctuated slightly with high frequency (amplitude within 100 W/m^2) during the hour encompassing the satellite overpass time as a result of cloud shading, leading to the underestimation of T_s from ETM+ sensor and thereby the underestimation of H . However, there is no evidence from the global

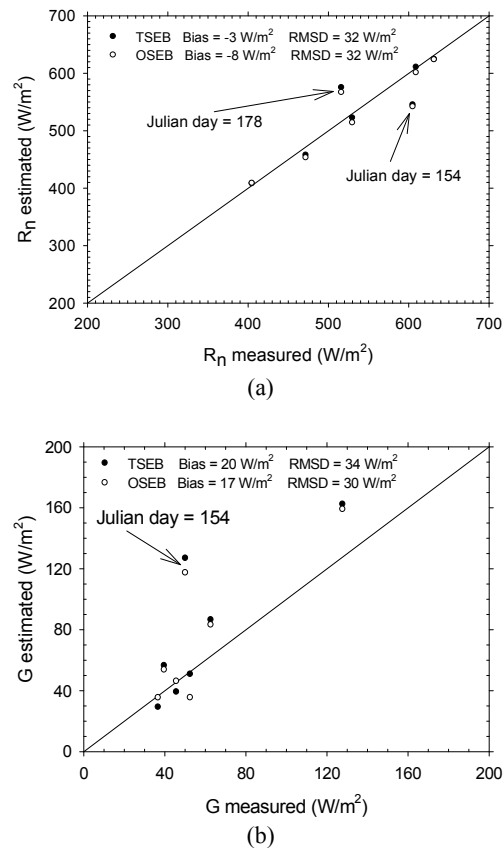


Fig. 2 Comparison of the instantaneous (a) surface net radiation and (b) soil heat flux estimated from the OSEB and TSEB models using both Landsat derived surface temperature and ground measurements

radiation measurements that underestimate of T_s and H on Julian day 178 is contaminated by cloud. This underestimation may come from the inaccuracy of atmospheric corrections in the T_s retrieval under the condition of high atmospheric water content. With data on Julian days 178 and 218 excluded, the OSEB is shown to perform better than the TSEB model in both H and LE comparison to EC measurement corrected by the RE correction method. Both Bias and RMSD have significantly decreased to -70 (-44) W/m^2 and 85 (58) W/m^2 in the TSEB (OSEB) model for the H comparison while in the LE comparison those two statistics decrease to 32 (1) W/m^2 and 60 (37) W/m^2 .

Serious underestimations of H in comparison to the measurements from EC in TSEB model correspond to data on Julian days 154 and 266, respectively (see Fig. 3a) and are likely to be caused by the use of green LAI as total LAI during the maturity stage for both wheat and corn since LAI in the TSEB model significantly determines the partition of R_n into soil and vegetation energy components and thus the H and LE .

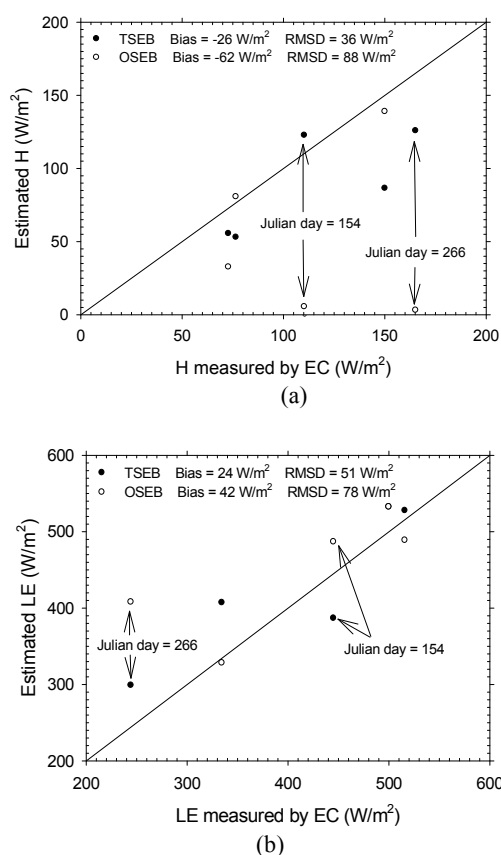


Fig. 3 Comparison of the instantaneous (a) sensible heat flux and (b) latent heat flux estimated from the OSEB and TSEB models with ground EC measurement corrected by the residual energy correction method. Data on Julian days 178 and 218 are excluded and total LAI is reassigned to be 3.0 at maturity stage for wheat and corn.

To verify whether our presumption is plausible, we assign 3 m^2/m^2 to the total LAI for Julian days 154 and 266 to recalculate the T_s from TM 5/ETM+ sensor and surface energy components in both TSEB and OSEB models. The fraction of green LAI is estimated to be the ratio of green LAI measured at field to the total LAI. T_s decreases from 302.2 K to 301.2 K on Julian days 154 and from 298.7 K to 298.0 K due to the variation of emissivity when the total LAI is reassigned. Comparisons of the estimated R_n is

improved in both the TSEB and OSEB models and the TSEB model has shown to perform better than the OSEB. Deviation in the comparison of the estimated G to surface G measurements is significantly decreased from 68 (77) W/m^2 to 4 (19) W/m^2 on Julian day 154 for the OSEB (TSEB) model. Correction to the total LAI improves the H comparison in the TSEB model but deteriorates the estimated H in the OSEB model due to the decrease of T_s retrieved from ETM+ sensor. Underestimation of H compared with EC measurement by 82 (91) W/m^2 increases further to 104 (162) W/m^2 on Julian day 154 (266) in the OSEB model whereas in the TSEB model underestimation of H by 146 W/m^2 is reduced greatly to 39 W/m^2 on Julian day 266. On Julian day 154, the TSEB model with and without corrected total LAI overestimates and underestimates the H measurements from EC by 13 W/m^2 and 99 W/m^2 , respectively. Overestimation of LE in the TSEB model by 108 W/m^2 decreases largely to 56 W/m^2 and in the OSEB model by 53 W/m^2 increases seriously to 165 W/m^2 on Julian day 266. Underestimation of LE in the TSEB by 38 W/m^2 is increased to 58 W/m^2 on Julian day 154. Estimated LE in the OSEB model increases from 397 W/m^2 to 487 W/m^2 with the EC measurements corrected by the RE correction method equal to 445 W/m^2 . RMSDs in the comparisons of H and LE to EC measurements corrected by the RE method with data on Julian days 178 and 218 excluded are 36 W/m^2 and 51 W/m^2 in the TSEB model compared with 88 W/m^2 and 78 W/m^2 in the OSEB model (Fig. 3).

Overall, taking into account the effect of senescent leaves dominating in the maturity stage in partitioning the surface energy and temperature into soil and vegetation components, estimates of soil heat flux and sensible heat flux can be improved significantly in the TSEB model. Otherwise, these two variables estimated from the TSEB model may be biased greatly to the surface measurements. For the OSEB model, soil heat flux estimation can also be improved but estimates of sensible and latent heat fluxes are likely to be deteriorated at least for the surface condition in this work.

5 CONCLUSIONS

This paper assessed the performances of two remote sensing based energy balance models, namely one- and two-source models, using ground ancillary measurements and surface temperature derived from TM/ETM+ sensor over a winter wheat and summer corn rotation region in China. Totally, data at seven TM/ETM+ overpass times undergoing the emergence to maturity growth stages for wheat/corn are used for the results analysis from late April to the end of September in 2009.

Similar performance in estimating surface net radiation and soil heat flux could be obtained between the TSEB and OSEB models with RMSD within 30-34 W/m². The OSEB model seemed to perform better than the TSEB model due to the use of green leaf area index as total leaf area index at the maturity stage of wheat and corn. However, if we considered the difference between green LAI and total LAI at the maturity stage for both wheat and corn and excluded the problematic data resulting from cloud contamination and inaccuracy of atmospheric corrections, the TSEB model would perform notably better than the OSEB model.

Acknowledgement

This work was partly supported by the National Natural Science Foundation of China under Grant 40871169 and by the State Key Laboratory of Resource and Environment Information System under Grant 088RA400SA. Mr. R. Tang is financially supported by China Scholarship Council for his stay in LSIT, France.

REFERENCES

- Anderson, M. C., Norman, J. M., Kustas, W. P., Houborg, R., Starks, P. J., and Agam, N., 2008, A thermal-based remote sensing technique for routine mapping of land-surface carbon, water and energy fluxes from field to regional scales. *Remote Sensing of Environment*, **112**, 4227–4241.
- Bastiaanssen, W. G. M., Menenti, M., Feddes, R. A., and Holtslag, A. A. M., 1998, A remote sensing surface energy balance algorithm for land (SEBAL): 1. Formulation. *Journal of Hydrology*, **212–213**, 198–212.
- Brunsell, N. A., and Gillies, R. R., 2002, Incorporating Surface Emissivity into a Thermal Atmospheric Correction. *Photogrammetric Engineering & Remote Sensing*, **68**, 1263–1269.
- Choudhury, B. J., Reginato, R. J. and Idso, S. B., 1986, An analysis of infrared temperature observations over wheat and calculation of latent heat flux. *Agricultural and Forest Meteorology*, **37**, 75–88.
- Jiménez-Muñoz, J. C., and Sobrino, J. A., 2003, A generalized single channel method for retrieving land surface temperature from remote sensing data. *Journal of Geophysical Research*, **108**, doi: 10.1029/2003JD003480.
- Kustas, W. P., and Norman, J. M., 1997, A two-source approach for estimating turbulent fluxes using multiple angle thermal infrared observations. *Water Resources Research*, **33**, 1495–1508.
- Li, F., Jackson, T. J., Kustas, W. P., Schmugge, T. J., French, A. N., Cosh, M. H., and Bindlish, R., 2004, Deriving land surface temperature from Landsat 5 and 7 during SMEX02/SMACEX. *Remote Sensing of Environment*, **92**, 521–534.
- Li, Z. -L., Tang, R., Wan, Z., Bi, Y., Zhou, C., Tang, B., Yan, G., and Zhang, X., 2009, A Review of current methodologies for regional evapotranspiration estimation from remotely sensed data. *Sensors*, **9**, 3801–3853.
- Norman, J. M., Kustas, W. P., and Humes, K. S., 1995, A two-source approach for estimating soil and vegetation energy fluxes from observations of directional radiometric surface temperature. *Agricultural and Forest Meteorology*, **77**, 263–293.
- Su, Z., 2002, The surface energy balance system (SEBS) for estimation of turbulent heat fluxes. *Hydrology and Earth System Sciences*, **6**, 85–99.
- Twine, T. E., Kustas, W. P., Norman, J. M., Cook, D. R., Houser, P. R., Meyers, T. P., Prueger, J. H., Starks, P. J., and Wesely, M. L., 2000, Correcting eddy-covariance flux underestimates over a grassland. *Agricultural and Forest Meteorology*, **103**, 279–300.

Land Surface Soil Moisture Retrieval From Temporal Change Of Land Surface Temperature: A Sensitivity Study

Wei Zhao^{1,2,3}, Zhao-Liang Li^{1,2,*}

1. State Key Laboratory of Resources and Environment Information System, Institute of Geographic Sciences and Natural Resources Research, Beijing 100101, China

2. LSIIT, UdS, CNRS, Bld Sebastien Brant, BP10413, 67412 Illkirch, France

3. Graduate University of Chinese Academy of Sciences, Beijing, 100049, China.

Email: li@lsiit.u-strasbg.fr

ABSTRACT - Land surface soil moisture (SSM) is a fundamental variable in the hydrological cycle and in any investigation of water and energy balances at the Earth's surfaces. Many efforts have been done to derive SSM from thermal infrared remote sensing data. To investigate the interaction between land surface temperature (LST) and SSM, a sensitivity study of the SSM on the diurnal cycle of surface temperature was conducted for bare soil using NOAA land surface model (LSM) and the Gaussian emulation machine for sensitivity analysis software (GEM SA). On the basis of LST and shortwave diurnal cycles, eight parameters were defined as the variable related with SSM. Sensitivity analysis (SA) was performed for both conditions with and without atmospheric variation. Results provide an insight into the relationships between these eight parameters and environmental factors including soil physical parameters, soil moisture, albedo and atmospheric parameters. Surface air temperature showed strong influence on LST especially the maximum, minimum and average temperature in daytime. For a given daily atmospheric forcing data, LST rising rate in the mid-morning normalized by absorbed shortwave radiation is the most sensitive parameter to SSM, the main effect to SSM reaches 80.72%, meanwhile, time at which daily maximum temperature occurs and daily minimum temperature are highly related to soil difference, which indicates the future direction of land surface soil moisture retrieval from LST temporal change.

1. INTRODUCTION

Land surface soil moisture content is one of the key variables in controlling the material and energy exchange between land surface and atmosphere interface. It is fundamentally important to many hydrological, biological and biogeochemical processes.

In contrast to field measurements, remote sensing methods have the advantages of low cost, large scale monitor. Many efforts have been done to investigate the possibility of surface soil moisture (SSM) retrieval from optical and microwave remote sensing data. Compared with microwave remote sensing, optical remote sensing exhibits the characteristic of higher spatial and higher spectral resolution and multi-satellite sensor availability (Verstraeten et al., 2006). Land surface temperature (LST) retrieved from thermal infrared data is the most popular and promising variable which can be used to get SSM. Many algorithms have been developed to estimate SSM with the help of LST information, such as from thermal inertia and from LST-NDVI triangle space contextual information. However, the method using the thermal inertia is only applicable in regions with little or no vegetation cover, while the use of LST-

NDVI space contextual information is only valid under the condition that both minimum and maximum surface soil wetness can be observed within the study area.

Up to now, most of SSM retrieval methods have been developed for low-earth orbiting satellites, particularly sun-synchronous polar satellites such as NOAA, MODIS. Although geostationary satellites view the Earth's surfaces with high temporal frequency (15min to 30min) and constant view angle for a given pixel, little efforts have been made to explore the possibility to retrieve SSM using the temporal variation of LST provided by geostationary satellites.

Wetzel et al. (1984) conducted a preliminary study on the sensitivity of temporal variation of LST to SSM using a boundary layer-earth's surface model, and indicated a new direction to estimate SSM from LST temporal variation observed by geostationary satellite. With the progress in the development of LST retrieval methods and the improvement of spatial resolution and frequency of geostationary satellites, it is urgent to systematically analyze the influence of SSM on LST and its temporal variation, and to develop newly appropriate methods for deriving SSM from LST temporal information.

The objective of this study is to investigate the internal connection between LST of bare surfaces and SSM using land surface model (LSM), two sensitivity analyses are conducted to study the impacts of environmental variables including SSM, albedo, soil physical and atmospheric parameters on LST value and its temporal variation

2. METHODOLOGY

2.1 Diurnal LST cycle modelling

For clear day, land surface diurnal temperature cycle (DTC) can be expressed as a harmonic variation in daytime and an exponential attenuation in night-time. The two-part semi-empirical DTC model used by Jiang et al. (2006) is applied to fit LST diurnal cycle and to define the parameters which are intuitively thought to be sensitive to SSM.

$$T(t) = \begin{cases} a + b \cos(\alpha(t - t_d)), & (t < t_s) \\ b_1 + b_2 \exp(\beta(t - t_s)), & (t \geq t_s) \end{cases} \quad (1)$$

with $b_2 = [-b \sin \alpha(t_s - t_d)] / \beta$ and $b_1 = a + b \cos \alpha(t_s - t_d) - b_2$,

where a and b are the unknown coefficients, α is the angular frequency, t_d is the time at which temperature reaches its maximum ($a+b$), t_s is the starting time of attenuation, and β is the decay coefficient.

Table 1 Eight parameters defined from LST diurnal cycle for sensitivity analysis: dt is change of time, dT is change of LST, dS is the change of surface absorbed solar radiation in dt

Eight defined parameters	Short name and definition
LST rising rate in the mid-morning (1.5h to 4.5h after sunrise)	TRR= dT/dt
LST rising rate normalized by the change of the absorbed shortwave radiation in dt (1.5h to 4.5h after sunrise)	NTS= dT/dS
Daily maximum temperature	$T_{max}=a+b$
Daily minimum temperature	T_{min}
Mean LST in daytime	T_{mean}
LST diurnal range	$DT=T_{max}-T_{min}$
Time of daily maximum temperature	$MaxTime=t_d$
LST nocturnal attenuation coefficient	$Beta=\beta$

To explore the possibilities of retrieving SSM from geostationary satellite data, on the basis of the LST diurnal cycle model described in equation (1), we define eight parameters (see table 1) which are

intuitively thought to be sensitive to SSM and subsequently analyze the sensitivity of these parameters to environmental factors.

2.2 NOAH LSM

Noah LSM version 3.2 was used to simulate LST diurnal cycle under different environmental conditions for bare soil (<http://www.ral.ucar.edu/research/land/technology/lsm.php>). It also simulates soil moisture (both liquid and frozen), soil temperature, skin temperature, canopy water content, and the energy fluxes and water fluxes in the surface energy balance and surface water balance.

SSM and albedo have been proved to be highly related to LST and its temporal variation. Some modifications were carried out to the original NOAH LSM. Idso et al. (1975) indicated that thermal infrared data responded to soil moisture to a depth of 4-5 cm. The soil layer under canopy cover was then reformed, and divided into six layers with each depth 5, 10, 15, 30, 40, 100 cm. The top soil layer represents surface soil moisture. Additionally, land surface albedo is a function of soil moisture and soil color, but in NOAH LSM, surface albedo as a model input can not reflect the influence of SSM. Consequently, the mechanism of surface albedo calculation in the Biosphere-Atmosphere Transfer Scheme (BATS) (Dickinson et al., 1993) was incorporated into NOAH LSM

2.3 Sensitivity analysis method

A Bayesian Analysis of Computer Code Output (BACCO) Sensitivity Analysis (SA) method was chosen in this study to analyze the sensitivity of 8 defined parameters to environmental factors. BACCO is a global sensitivity analysis which can not only capture the major sensitivity of model outputs to input parameters, but also the interactions of model inputs. It has been implemented in a freely available software tool (GEM SA, V1.1) (<http://www.tonyohagan.co.uk/academic/GEM/index.html>). A recent application of this method to SimSphere SVAT model by Petropoulos et al.(2009) aimed to analyze the sensitivity of daily average net radiation, latent and sensible heat fluxes, air temperature, and surface moisture availability to 30 model input parameters. They found that topography parameters (slope, aspect), vegetation fraction cover and soil surface moisture availability were the most sensitive model inputs.

3. DATA----EXPERIMENT DESIGN

3.1 Soil types

Generally, the difference of soil types induces the difference of LST variation. Twelve soil types in NOAH LSM were selected in this study. For the soil

thermodynamic and hydrology parameterization, eight soil physical parameters were assigned to different value with different soil texture. These parameters are listed in the eight first lines of table 2 (labeling No.1 to No.8). These eight parameters control soil thermal and hydraulic characteristics including soil thermal conductivity, density, heat capacity, hydraulic conductivity, and hydraulic diffusivity.

3.2 Atmospheric data

In addition to SSM, soil albedo and soil physical parameters, the variation of atmospheric forcing data was also considered in the model simulation. It is evident that near surface air temperature, relative humidity, wind speed and downward solar radiation plays an important role in LST evolution for cloud free days. Downward long wave radiation is highly connected with near surface air temperature. All these four atmospheric parameters strongly control land surface energy incidence and energy exchange in land-atmosphere interface, which affect LST indirectly.

Level 2 Data in Santa Rita Mesquite Savanna site in 2007 from AmeriFlux was chosen as atmospheric forcing data to drive NOAH LSM (<http://public.ornl.gov/ameriflux/index.html>). Twenty cloud free days from the whole year with different wind speed, air temperature, global radiation and relative humidity were selected to investigate their impacts on LST evolution.

3.3 Data simulation and SA design

Two series simulations were conducted for two SA in this study. Due to the limitation number of SA in GEM SA tool, 400 cases were simulated in each simulation. In the first simulation, LST was simulated for different SSM, soil albedo, soil types and 20 days atmospheric forcing data described earlier. For the second simulation, model was executed only with one day atmospheric forcing data (DOY 74), and the different SSM, soil albedo and different soil types. The LP-tau sampling method integrated in GEM SA tool was used to generate model driver file involving all the parameter changing range.

In the model initialization, time step for model integration was set to 15 minutes (half of the time interval in forcing data), surface initial temperature was dependent on the air temperature, vegetation fraction cover and vegetation water content were set to zero. For soil moisture initialization, the soil moisture content of the deepest two soil level was set to the same value (0.25), and an interpolation method was used to calculate the mid-level soil moisture with initial SSM and deepest soil moisture. A batch program was built in NOAH LSM to execute 400 model runs for each SA. The flow chat of two model simulation is showed in figure 1.

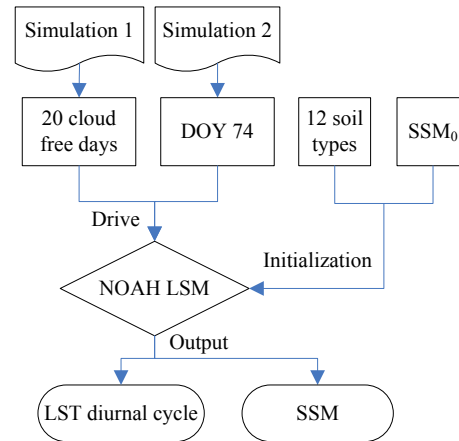


Fig. 1. Flow chart of two model simulations with NOAH LSM

On the basis of the model initialization and simulated LST evolution, model inputs and outputs were prepared for two SA. The model inputs and their value range for these two SA are showed in Table 2. All the parameters in table 2 were chosen as model inputs in the first SA and in the second SA, the ten first parameters (No.1 to No.10) in table 2 are involved only. Model outputs for SA are the eight parameters defined in table 1.

4. RESULTS

Two SA were then performed with two model inputs and model outputs. Tables 3 and 4 summarize the main effect of each model input to model output for these two SA, respectively. Theoretically, main effect of model input represents the expected amount of variance that would be removed from the total output variance if we are able to learn its true value, or in other words, it represents the contribution of model inputs to the total variance of model outputs.

4.1. Parameter sensitivity of TRR, NTS

Second column in Table 3 shows the sensitivity of the LST rising rate in the mid-morning (TRR) to each model input parameter. 93% of variance in TRR can be explained by the main effect of 14 model inputs, and the inputs with largest percent variance contribution are SSM, WS and SMC MAX. These three parameters together control 71% of the total variance. In table 4, the sum of main effect of total 10 model inputs occupies nearly 100%, and the most dominant ones are SSM, Alb and SMC MAX.

Table 2, Summary of model inputs for SA

No.	Model input parameters	Short name
1	Max soil moisture content (porosity) [m3/m3]	SMCMAX
2	Saturated soil potential	SATPSI
3	Saturated soil hydraulic conductivity [m/s]	SATDK
4	The 'b' parameter [-]	BEXP
5	Soil quartz content [m3/m3]	QUARTZ
6	Reference soil moisture (onset of soil moisture stress in transpiration) [m3/m3]	SMCREF
7	Wilting soil moisture contents [m3/m3]	SMCWLT
8	Saturated soil diffusivity [m2/s]	SATDW
9	Surface albedo [-]	Alb
10	Daily mean surface soil moisture [m3/m3]	SSM
11	Daily mean wind speed [m/s]	WS
12	Daily mean relative humidity [%]	RH
13	Daily mean air temperature [K]	Ta
14	Daily max global radiation [W/m2]	Rg

Table 3, Main effects of model inputs to model outputs in first SA with consideration of atmospheric factors

Model Inputs	Main Effects(%)							
	TRR	NTS	Tmax	Tmin	Tmean	DT	MaxTime	Beta
SMCMAX	7.04	5.98	2.06	0.36	1.38	5.56	5.05	3.57
SATPSI	0.12	0.04	0.03	0.09	0.03	0.02	0.78	0.59
SATDK	0.11	0.02	0.01	0.04	0.02	0.02	0.21	0.51
BEXP	0.93	0.39	0.02	0.33	0.03	0.06	2.8	4.15
QUARTZ	1.25	2.06	0.28	0.35	0.12	1.61	2.33	0.93
SMCREF	0.19	0.17	0.05	0.05	0.08	0.01	0.48	1.21
SMCWLT	1.97	1.46	0.04	0.55	0.02	0.25	4.86	8.12
SATDW	0.17	0.1	0.01	0.03	0.03	0.04	1.67	0.4
SSM	52.46	52.91	13.98	0.89	8.39	56.94	36	3.79
Alb	6.32	4.5	2.96	0.1	2.16	7.7	9.01	1.36
WS	12.46	18.53	2.54	0.05	0.91	4.97	0.4	7.37
RH	0.94	0.82	0.13	1.47	0.08	0.31	0.84	27.3
Ta	4.06	3.59	69.6	93.72	82.36	0.78	12.36	14.44
Rg	5.47	1.33	7.67	0.02	3.85	18.96	7.44	1.73
Total	93.49	91.89	99.39	98.04	99.45	97.21	84.23	75.47

Table 4, Main effects of top three model inputs to model outputs in second SA with only consideration of soil texture and surface soil moisture effects

Model outputs	Main effects of Top three model inputs (%)	Sum
TRR	SSM(76.2), Alb(9.58), SMCMA(9.23)	95.01
NTS	SSM(80.78), SMCMA(11.21), Alb(2.91)	94.9
T _{max}	SSM(75.61), Alb(14.17), SMCMA(7.22)	97
T _{min}	SSM(54.32), QUARTZ(8.55), SMCMA(7.93)	71.8
T _{mean}	SSM(75.02), Alb(15.59), SMCMA(6.64)	97.25
DT	SSM(76.99), Alb(9.25), SMCMA(8.92)	95.16
MaxTime	SSM(67.72), SMCMA(14.73), QUARTZ(5.88)	88.33
Beta	SSM(58.56), SMCWLT(14.5), BEXP(6.94)	90

From the main effect value of these three inputs in two SA, the impacts of SSM are the greatest no matter considering the atmospheric factors or not. The SSM influences thermal properties of soil, which then controls the surface temperature rising rate. This effect

is much more dominant under the same atmospheric condition. Wind speed has the second impact on TRR, and it is in agreement with the results of Wetzel et al. (1984). With increase in surface wind speed, water vapor from land surface diffuses quickly, and surface evapotranspiration and energy exchange rate were

accelerated inducing less energy for surface heating process. Surface soil max water content (soil porosity) in NOAH LSM determines the soil density and thermal conductivity at dry/saturated condition, has some influence on the surface temperature rising rate. The impact of surface albedo on TRR is reasonable too, since albedo affects the amount of surface absorbed shortwave radiation.

LST rising rate normalized by absorbed shortwave radiation (NTS) has the same sensitivity results as TRR under different atmospheric conditions. However, NTS exhibits a little change in the second SA. After normalized by absorbed shortwave radiation, NTS is less sensitive to surface albedo, and is influenced mainly by SSM and SMCMAX.

4.2. Parameter sensitivity of T_{max} , T_{min} , T_{mean}

Seen from Table 3, it is clear that T_{max} , T_{min} , and T_{mean} are highly sensitive to air temperature. Especially for T_{min} , the main effect of T_a reaches up to 93%. It could be partly explained by the soil thermodynamics parameterization in NOAH LSM. The surface skin temperature is determined following Mahrt and Ek (1984) by applying a single linearized surface energy balance equation where T_a is an additional term. Therefore, T_a plays a more important role on T_{max} , T_{min} and T_{mean} than other parameters like SSM, Rg and WS.

But from the second SA results shown in Table 4, due to the absence of atmospheric variation, T_{max} , T_{min} and T_{mean} all have a strong sensitivity to SSM. Because T_{max} and T_{mean} both depict the characteristic of LST in daytime, they have almost the same performance to environmental changes. SSM, Alb and SMCMAX are the top three main affecters. However, the performance of T_{min} is different. T_{min} happens at night-time and is dependent on the characteristic of soil. Consequently, besides the effect of SSM, contributions of soil texture parameters (SMCMAX and QUARTZ) also dominate a large part of its variation. The influence of SMCMAX has mentioned earlier. The quartz content affects soil solids' thermal conductivity which controls soil thermal conductivity directly. After sunset, there is a cooling process in land surface temperature, and it reaches the minimum value after a few hours. This process is controlled by the soil thermal properties determined by soil texture parameters. Therefore, the fact that T_{min} showed high sensitive to soil parameters is rational.

4.3. Parameter sensitivity of DT

DT is a good indication of surface soil moisture condition. As shown in Tables 3 and 4, DT is highly related to SSM. But in Table 3, the main effect of SSM to DT is only 56% compared with the value of 77% in Table 4. Rg, Alb, SSM and WS have somewhat

contributions on DT. The values of Rg and Alb determine how much shortwave radiation can be absorbed by land surface, and then they control the surface warming process. In addition to Rg and Alb, soil texture parameters like SMCMAX and QUARTZ also show an unnegligible effect.

4.4. Parameter sensitivity of MaxTime

MaxTime is a parameter less considered in recent studies. Usually the maximum intensity of global radiation occurs at local solar noon, land surface is warming throughout the morning, but its temperature can not catch up to the increasingly greater amount of energy that the Sun is providing. After noon, the Sun continues to raise the surface temperature until more energy is lost to space than the ground can take in from the Sun. As shown in Table 3, air temperature and shortwave radiation affect MaxTime to some degree, but soil physical parameters, albedo, and SSM are the main factor for MaxTime changes, which is in consistence with the SA results shown in Table 4. Besides the effect of SSM, SMCMAX and QUARTZ contribute 20% variation of MaxTime. These parameters control soil thermal and hydraulic conduction, which influence the soil warming process at daytime. Soil type difference influences MaxTime much more against other model outputs.

4.5. Parameter sensitivity of Beta

The sensitivity analysis results of Beta under different external condition are represented in Table 3. It was found that the total main effect of all inputs on Beta is only 75.47%, soil physical parameters (SMCWLT, BEXP and SMCMAX) and atmospheric parameters (WS, RH, and T_a) capture the main variation of Beta. Meanwhile, interaction effects between model inputs also play an important role on Beta. Taking SSM as an example, the main effect of SSM is low in Table 3, but the sum effect of interaction with other inputs on Beta reaches 18.9%, and total effect related to WS, RH and T_a are 18.2%, 48.68% and 27.06% respectively. Beta is the most complex one compared with the other seven outputs. Both atmospheric parameters and soil parameters strongly affect its value, and it behaves great uncertainty under different atmospheric conditions with different soil types.

6. SUMMARY AND CONCLUSIONS

On the basis of NOAH LSM and GEM SA tool, a systematic sensitivity analysis was conducted in the present study to analyze the influence of surface soil moisture, soil texture parameters and atmospheric variables on land surface temperature evolution.

As shown in Tables 3 and 4, it is clear that atmospheric parameters and soil parameters have strong impact on LST evolution. TRR and NTS are

both highly sensitive to surface soil moisture, and NTS is more sensitive to SSM than TRR. T_{\max} , T_{\min} and T_{mean} change greatly with air temperature. T_{\max} and T_{mean} have good relationships with SSM for a given atmospheric forcing data, but the sensitivity of T_{\min} seems more complex. Both SSM and soil texture parameters showed strong effect on T_{\min} . It was also proved that DT is a good variable to retrieve surface soil moisture. In addition, it was found that MaxTime is insensitive to atmospheric condition. For the parameter Beta, it was difficult to separate the influence of soil texture, soil moisture and atmosphere under different atmospheric conditions. However, it showed a strong correlation with surface soil moisture for a given atmospheric forcing data. Soil texture difference plays an important role in all the variables. Because of the high sensitivity of T_{\min} and MaxTime to soil texture difference, they provide a potential to eliminate the impacts of soil texture parameters combined with other parameters to derive SSM.

Land surface soil moisture retrieval from LST temporal change is possible and feasible. It will promote us to develop practical method to derive surface soil moisture with the LST evolution. This will be the part of our ongoing work. However, all the simulations in this study are implemented for bare soil condition, land surface with vegetation cover are not discussed in this study, and this also will be a direction in future work.

ACKNOWLEDGMENT

The work described in this publication has been partly supported by the European Commission (Call FP7-ENV-2007-1 Grant nr. 212921) as part of the CEOP-AEGIS project (<http://www.ceop-aegis.org/>) coordinated by the Université de Strasbourg, by the National Natural Science Foundation of China under Grant 40971199, by China international Science and Technology Cooperation project (0819).

REFERENCES

- Dickinson, R. E., A. Henderson-Sellers, and P. J. Kennedy, 1993, Biosphere-atmosphere transfer scheme (bats) version 1e as coupled to the near community climate model, Tech. rep., National Center for Atmospheric Research
- Idso, S.B., Jackson, R.D., Reginato, R.J., Kimball, B.A. and Nakayama, F.S., 1975, The dependence of bare soil albedo on soil water content. *Journal of Applied Meteorology*, 14, 109-13
- Jiang, Geng-Ming., Li, Zhao-Liang, and Nerry, F., 2006, Land surface emissivity retrieval from combined mid-infrared and thermal infrared data of MSG-SEVERI, *Remote Sensing of Environment*, 105, 326-340.
- Mahrt, L., and M. Ek, 1984, The influence of atmospheric stability on potential evaporation. *Journal of Climate and Applied Meteorology*, 23, 222-234.
- O'Hagan, A., 2006, Bayesian analysis of computer code outputs: a tutorial. *Reliability Engineering & System Safety*, 91, 1290-1300.
- Petropoulos, G. T., Wooster, M. J., Carlson, T. N., Kennedy, M. C. and Scholze, M. 2009, A global Bayesian sensitivity analysis of the 1-d SimSphere soil, vegetation, atmosphere transfer (SVAT) model using Gaussian model emulation. *Ecological Modeling*, 220, 2427-2440.
- Wetzel, P.J., D. Atlas and R.H. Woodward, 1984, Determining soil moisture from geosynchronous satellite infrared data: A feasibility study. *Journal of Climate and Applied Meteorology*, 23, 375-391.
- Verstraeten, W.W., Veroustraete, F., Van Der Sande, C.J., Grootaers I., and Feyen J., 2006, Soil moisture retrieval using thermal inertia, determined with visible and thermal spaceborne data, validated for European forests, *Remote Sensing of Environment*, 101 (3), 299-314.

Assimilation of CYCLOPES LAI product within the SURFEX platform over France

A. L. Barbu, J-C. Calvet and S. Lafont
CNRM-GAME, Météo-France, Toulouse
alina.barbu@cnrm.meteo.fr

ABSTRACT: *The GEOLAND2 European project is a major step of the evolution of the Land Monitoring Core Service (LMCS), the vegetation/land component of GMES. The development of a Land Data Assimilation System (LDAS) that takes into account carbon fluxes and biomass produced through photosynthesis processes is considered of high importance for monitoring the impact of weather and climate variability on terrestrial carbon fluxes. Within this context, a version of the Extended Kalman Filter scheme is used for the assimilation of the CYCLOPES Leaf Area Index (LAI) product derived from the SPOT4/VEGETATION sensor within the ISBA-A-gs model, a CO₂ responsive land surface model. In this study we demonstrate that the assimilation scheme works effectively within the multi-patch version of our model. An important reduction of the LAI bias between the model simulations and measurements is achieved.*

1 INTRODUCTION

Despite the increased modeling capabilities in land surface models (LSMs), they still show significant differences when compared with observations. The causes of this bias are highly complex and only partly understood. Reducing this discrepancies by merging optimally the model predictions with measurements is the objective of data assimilation. The quality of its performance depends on a realistic description of model parameters, an accurate specification of uncertainties associated with an increased number of processes that should be taken into account, as well as on the quality of the data to be assimilated.

In the framework of the Land Carbon Core Information Service of GEOLAND2, the C-TESSEL and SURFEX modeling platforms of ECMWF and Météo-France, respectively, are used for describing the continental vegetation state, surface fluxes and soil moisture. Gradually, EO data are integrated in the modeling platforms in order to improve the analysis of soil moisture and vegetation biomass and have a positive impact on carbon fluxes.

Several studies (Jarlan et al., 2008, Rüdiger et al., 2010) have shown the potential of assimilating LAI to estimate the vegetation characteristics and to reduce the model uncertainties.

The objective of this study is twofold:

First, it aims to demonstrate that our LDAS incorporates successfully remote sensing LAI data

within the multi-patch version of ISBA-A-gs at a regional scale. Second, it investigates to what extent our data assimilation approach is able to reduce a large bias between the model simulations and observations.

2 METHODOLOGY

2.1 ISBA-A-gs model

In this study the SURFEX modeling platform is used in the off-line mode. The meteorological forcing data required for simulations over France are provided hourly at a resolution of 8 km by SAFRAN, an atmospheric analysis system. Our focus is on the vegetation component of this platform: the ISBA-A-gs model, a CO₂ responsive land surface model able to simulate photosynthesis and plant growth. The vegetation biomass and Leaf Area Index (LAI) evolve dynamically in response to weather and climate conditions (Calvet et al., 1998, Calvet et al., 2004, Gibelin et al., 2006).

In a number of studies the performance of the model has been evaluated at global or regional scale showing that ISBA-A-gs is able to capture the general patterns observed from space.

In SURFEX the soil and vegetation parameters used by the land surface model are provided by the ECOCLIMAP II database (Faroux et al., 2009) that describes about 300 ecosystems and contains rules to aggregate these ecosystem types in twelve covers (patches). Over the France domain, the most present ecosystem types are grasslands (32%), C3 crop lands (24%), deciduous forest (20%), bare soil (11%), and C4 crop lands (8%). ISBA-A-gs simulates the aggregation of the different patches in the vegetation

tile providing the modeled LAI as an average LAI of vegetation types weighted with their cover fraction.

2.2 CYCLOPES product

Version 3 of CYCLOPES LAI product derived from VEGETATION sensor on-board SPOT-4 satellite is used in this study. The sensor provides a daily global coverage with a spatial resolution of 1 km. Details on the retrieval algorithm can be found in Baret et al., 2007. The temporal sampling interval of CYCLOPES LAI data is of 10 days.

Several sources of uncertainties in the satellite products may cause large errors that are difficult to estimate (Garrigues et al. 2008). In our study the error standard deviation of the observed LAI is rather empirically set to a constant ($0.4 \text{ m}^2\text{m}^{-2}$) for LAI values less than $2 \text{ m}^2\text{m}^{-2}$ and proportional with the observed LAI for larger values.

2.3 Data assimilation

Development of a land data assimilation system dedicated to carbon and water cycles is considered as a key aspect for monitoring activities of terrestrial carbon fluxes. The Leaf Area Index is an important variable of the sensible and latent heat partitioning, as it impacts the exchange of water vapor and CO_2 between the vegetation canopy and the atmosphere.

Therefore, a version of the Extended Kalman Filter scheme (Mahfouf et al., 2009) was adapted to the assimilation of satellite LAI products within the ISBA-A-gs model. The LAI data are incorporated into the model every 10 days to analyze its impact on vegetation biomass. The study period ranges from April to July 2007. The experiment is performed over France at a spatial resolution of 8 km. The LAI background error was set in the same way as for the observation error. A model grid box is divided in a number of patches, each having its own LAI prognostic variable. With 12 patches, the dimension of the control vector is increased, but the number of observations is the same. The filter algorithm is designed to provide the analysis for each patch, independently, by using one observation per grid box. Therefore the model counterpart of the observation is assumed to be the average of the corresponding simulated observation for each patch, weighted by the fraction occupied by each patch. The finite differences method is used to linearize the forecast model, as well as the observation operator by perturbing each model integration. Values of 0.001 corresponding to LAI perturbations of about $0.003 \text{ m}^2\text{m}^{-2}$ have been used to compute the Jacobian terms following the sensitivity

study performed by Rüdiger et al., 2010. The simulated observations over one patch depend only upon the control vector over the same patch. This approach reduces the number of perturbed runs needed to compute the Jacobian matrix.

We assume a static behavior of the background error matrix that is considered constant at the beginning of each analysis step. It results in a Simplified Extended Kalman Filter (SEKF) algorithm.

The Kalman gain is computed independently for each patch. A new LAI value that represents the analysis is obtained as an optimal combination of the observation and background. Finally, the updated LAI is aggregated from the weighted contribution of each patch over the vegetation tile.

3 ASSIMILATION RESULTS

The comparison between simulated and retrieved LAI reveals large discrepancies both in their intensity and in the timing of the leaf onset. The difference may be attributed to the shortcomings of both model and satellite (Brut et al., 2009) LAI estimates. Generally, the model exhibits larger values than CYCLOPES at the end of the growing season.

Figure 1 illustrates the simulated, observed and assimilated LAI over France for two days in 2007 that represent growing and senescence periods. The top row shows that the assimilation is able to reduce the bias caused by the delay at the start of the growing season. The senescence phase benefits also from the assimilation (see bottom row of Figure 1). At the end of July the model largely overestimates LAI. The assimilation reduces the bias by more than half.

An important difference between the model climatology (2000-2007) and LAI satellite observations can be noticed in Figure 2, especially in the second part of the annual cycle. This discrepancy is mainly caused by the bias in the LAI seasonal cycle for grassland and C3 crops. The errors are large for managed ecosystems where the local practices (choice of species, sowing date, harvest) have a strong impact on the vegetation development. On these ecosystems, data assimilation is an important tool to correct the model deficiencies.

Figure 3 shows time series of simulated, observed and assimilated LAI averaged over a number of grid cells that contain a large fraction of C3 crops (60%), and grasslands (70%). The analysis corrects the model towards the observations in June and July, but is not very effective in April and May.

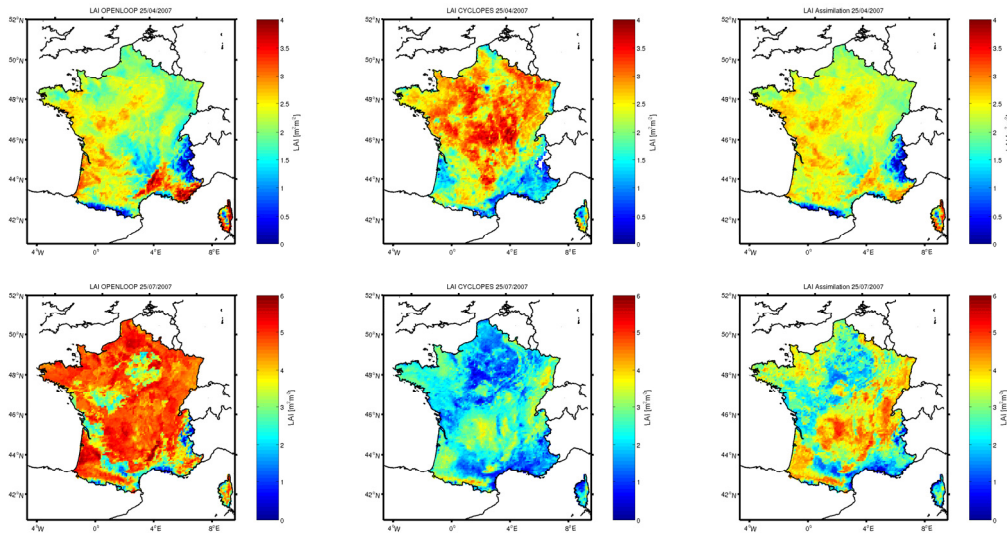


Figure 1: Simulated (left), observed (middle) and assimilated (right) LAI on 25.04.2007 (top row) and on 25.07.2007 (bottom row), respectively.

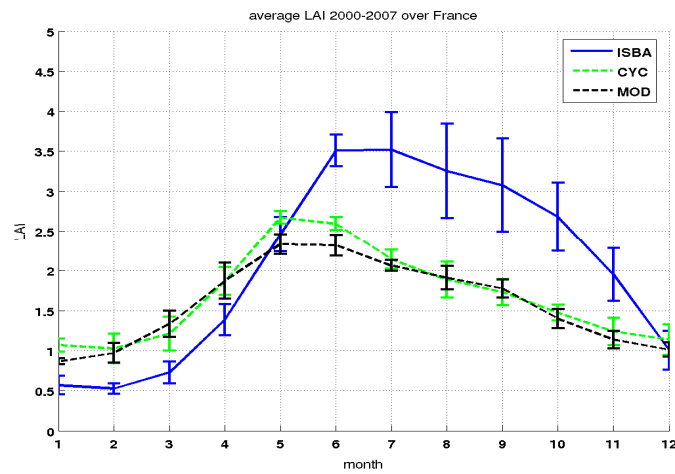


Figure 2: Monthly LAI climatology from 2000 to 2007 and inter-annual variability over France: (blue) ISBA model, (dashed green) CYCLOPES, (dashed black) MODIS.

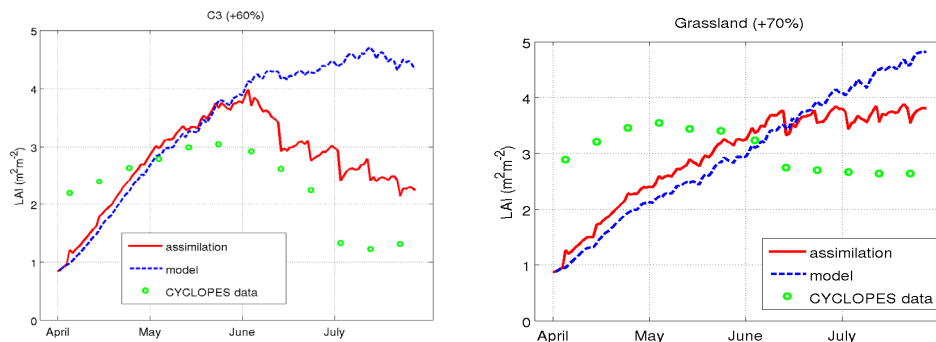


Figure 3: Simulated (dashed line), observed (circles) and assimilated (solid line) LAI time series for two ecosystems: (left) C3 crops (60%), (right) grasslands (70%).

3 CONCLUSIONS AND PERSPECTIVES

The SEKF system was adapted for the assimilation of remote sensing LAI by using the multi-patch ISBA-A-gs model. The evaluation of the system is performed over France from April to July 2007. This preliminary study shows a significant impact of the assimilation scheme on the LAI component of the system. The analysis corrects for a number of deficiencies in the model, in particular the delay on the leaf onset. The bias between the satellite-derived LAI and the model simulations is reduced, especially in the senescence phase.

At Météo-France, the SURFEX modelling system is intended to provide the surface fluxes. To accomplish this task, biomass and soil moisture should be analysed together as they are mutually dependent (Albergel et al., 2010, Sabater et al. 2008). Therefore the future experiments will include both the assimilation of soil moisture and LAI, instead of LAI only, as was presented in this study.

Also, future work will concern the use of different GEOLAND2 data sets for soil moisture and LAI. A Soil Wetness Index (SWI) product defined as the soil moisture content in the soil profile will be used. Regarding the Leaf Area Index, a new product based on pre-existing LAI algorithms will be provided as a fused product that is expected to give globally a better performance.

For data assimilation purposes, a better description of model and observation errors, as well as a bias correction scheme should be taken into account to improve the performance of our assimilation algorithm.

4 REFERENCES

- Albergel, C., Calvet, J.-C., Mahfouf, J.-F., Rüdiger, C., Barbu, A. L., Lafont, S., Roujean, J.-L., Walker, J. P., Crapeau, M. and Wigneron, J.-P., 2010, Monitoring of water and carbon fluxes using a land data assimilation system: a case study for southwestern France. *Hydrol. Earth Syst. Sci. Discuss.*, **7**, 1705–1744.
- Baret, F., Hagolle, O., Geiger, B., Bicheron, P., Miras, B., Huc, M., et al., 2007, LAI, fAPAR, fCOVERCYCLOPES global products derived from VEGETATION: Part1: Principles of the algorithm *Remote Sensing of Environment.*, **110**, 275–286.
- Brut, A., Rüdiger, C., Lafont, S., Roujean, J.-L., Calvet, J.-C., Jarlan, L., Gibelin, A.-L., Albergel, C., Le Moigne, P., Soussana, J.-F., Klumpp, K., Guyon, D., Wigneron, J.-P., and Ceschia, E., 2009, Modelling LAI at a regional scale with ISBA-A-gs: comparison with satellite-derived LAI over southwestern France, *Biogeosciences*, **6**, 1389–1404.
- Calvet, J.-C., Noilhan, J., Roujean, J.-L., Bessemoulin, P., Cabelguenne, M., Olioso, A., and Wigneron, J.-P., 1998, An interactive vegetation SVAT model tested against data from six contrasting sites, *Agr. Forest Meteorol.*, **92**, 73–95.
- Calvet, J.-C., Rivalland, V., Picon-Cochard, C., and Guehl, J.-M., 2004, Modelling forest transpiration and CO₂ fluxes – response to soil moisture stress, *Agr. Forest Meteorol.*, **124** (3–4), 143–156.

- Faroux, S. et al., 2009, La base de données de paramètres de surface Ecoclimap-II sur l'Europe, *Internal report*, CNRM, Météo-France.
- Garrigues S., Lacaze, R., Baret, F., Morisette J., Weiss, M., Nickeson, J. E., Fernandes, R., Plummer, S., Shabanov, N. V., Myneni, R. B., Knyazikhin, Y., and Yang, W., 2008, Validation and intercomparison of global LAI derived from remote sensing data, *J. Geophys. Res.* **113**, G022028.
- Gibelin, A.-L., Calvet, J.-C., Roujean, J.-L., Jarlan, L., and Los, S. O., 2006, Ability of the land surface model ISBA-A-gs to simulate leaf area index at the global scale: Comparison with satellites products, *J. Geophys. Res.*, **111**(D18), D18102.
- Jarlan, L., Balsamo, G., Lafont, S., Bejaars, A., Calvet, J.-C., and Mougin, E., 2008, Analysis of leaf area index in the ECMWF land surface model and impact on latent and carbon fluxes. Application to west Africa, *J. Geophys. Res.*, **113**, D24117.
- Mahfouf, J.-F., Bergaoui, K., Draper, C., Bouyssel, F., Taillefer, F., and Taseva, L., 2009, A comparison of two off-line soil analysis schemes for assimilation of screen level observations, *J. Geophys. Res.*, **114**, D08105.
- Sabater, J. M., Rüdiger, C., Calvet, J.-C., Fritz, N., Jarlan, L., and Kerr, Y., 2008, Joint assimilation of surface soil moisture and LAI observations into a land surface model, *Agric. For. Meteorol.*, **148** (8-9), 1362-1373.
- Rüdiger, C., Albergel, C., Mahfouf, J.-F., Calvet, J.-C., and Walker, J. P., 2010, Evaluation of Jacobians for Leaf Area Index data assimilation with an extended Kalman filter, *J. Geophys. Res.*, **115**, D09111.

Application of remote sensing and GIS techniques on QUICKBIRD images to locate and distinguish wild pear (*Pyrus bourgeana*) in Sierra Morena (Cordoba, Andalusia, Spain)

S. Arenas¹, G. Sòria², C. Mattar², V. Hidalgo², R. Oltra-Carrió², B. Franch², Y. Julien², J. C. Jiménez-Muñoz², J. A. Sobrino², J. F. Haeger¹, D. Jordano¹

1 Universidad de Córdoba (ESPAÑA) - Dpto. de Botánica, Ecología y F. Vegetal (Área de Ecología)

2 Universidad de Valencia (ESPAÑA) - Unidad de Cambio Global (UCG)

b62arcas@uco.es, s.arenascastro@hotmail.com

ABSTRACT - Recent advances in spatial and spectral resolution of satellite imagery as well as in processing techniques are opening new possibilities of fine scale vegetation analysis that might have interesting applications in natural resources management. We present the main results of a study carried out in Sierra Morena, province of Córdoba (Andalusia, southern Spain) in order to assess the potential of remote sensing techniques to discriminating and mapping individual wild pear trees (*Pyrus bourgeana*) in Mediterranean open woodland dominated by *Quercus ilex*. We used high spatial resolution (2.4 m MS/0.6 m Pan) QUICKBIRD satellite imagery obtained during the summer of 2008. Given the size and features of wild pear tree crowns, we applied 2 atmospheric correction methods (Dark Object Subtraction and FLAASH) and 4 different fusion "Pan-Sharpening" methods (HIS, Principal Components, Brovey and Gram-Schmidt Spectral Sharpening) to determine which procedure can provide the best results. Finally we assessed the potential of supervised classification techniques (Maximum Likelihood) to discriminating and mapping individual wild pear trees scattered over the Mediterranean open woodland.

1 INTRODUCTION

1.1 Environment and Remote Sensing

High spatial resolution images (2.4 to 4 m) generated by digital multi-spectral sensors aboard satellites such as IKONOS and QUICKBIRD, allow detailed observations of natural resources at wavelengths of visible and near infrared bands (Everitt *et al.* 2007). Remote sensing is very useful in this regard as it allows obtaining spatially explicit, statistically representative information of ecosystem variables (Coppin *et al.* 2004). Remote sensing from satellite or aerial imagery also provides the possibility of describing some structural and functional aspects of ecological systems at different scales (Cabello, J. & Paruelo, J.M. (2008). The spatial resolution of these systems offers new opportunities to discriminate vegetation units, forest types or even individual species in mixed forest from space platforms, being therefore an important tool for the management and conservation of biodiversity. In this regard, several studies have shown that many grassland plant species

have different spectral characteristics of crown and can be distinguished on infrared color aerial photographs (Anderson, Prosser, Haggard, & Foster, 1999; Everitt, Pettit, and Alaniz, 1987; Gausman, Menges, Escobar, Everitt, & Bowen, 1977; Tueller, 1982). High spatial resolution images have also allowed the identification and mapping of individual trees or groups of trees (Gougeon *et al.*, 1999; Wulder *et al.* 2000a; Culvenor, 2002).

1.2 Atmospheric Correction

Many atmospheric correction algorithms have been developed. We can distinguish several categories, *pixel darkness subtraction*, *radiance to reflectance conversion*, *linear regression* or *atmospheric modelling*. The choice of one or another method depends in part on the quality of available data.

1.3 Image Fusion

Image fusion is a tool whose main goal is to take advantage of the complementary nature of various

types of images (Vrabel 1996 cited by Vasantha *et al.*, 2000). According to Varshney (1997) and Lillo-Saavedra *et al.* (2006), the concept of image fusion can be seen as the synergistic combination of information from several sensors or by the same sensor in different scenarios (spatial, spectral and temporal). At present there is a large number of methods and algorithms for image fusion, color changes (*HSI*), statistical methods (*Principal Component*), numerical methods (*Brovey*, *CN Spectral Sharpening*, *Gram-Schmidt Spectral Sharpening*, *Wavelet Fusion*), combined methods (*Ehlers Fusion*),...

1.4 Classification

A method commonly used in remote sensing is based on classifications, automated processes to extract information used to synthesize the information contained in spectral bands of an image in discrete classes that share a common characteristic, such as water, soil, vegetation, etc. In these processes we used a learning mechanism on spectral characteristics of a pixels group, to extend the same information to the entire image. For this study, we chose a supervised parametric classification algorithm using the Maximum Likelihood algorithm (Fisher (1912-1922)), in which the user chooses a pixels group representing each of the classes being used in the training process of image classification. In this case there is a choice of a priori interest classes. The accuracy of the resulting maps was measured by means of the *Kappa* coefficient "K", of widespread usage. This index calculates the degree of fit between the classified image and the reality observed in the field.

1.5 Study species

Pyrus bourgaeana was first described by Joseph Decaisne (Decne) in 1871-72 (Jard. Fruit. 1: 318, pl. 2. It is a small deciduous tree up to 10 m with broad, irregular crown. This species is restricted to the southern half of the Iberian Peninsula and North Africa (Aldasoro *et al.*, 1996). In the study area trees start producing new leaves in mid March, shedding most of them in early June. They remain almost leafless during the summer. A complete description can be found in Flora Iberica (1989).

Wild pears produce valuable trophic resources in the form of palatable leaves and, more important, large fruit crops during the summer drought that are consumed by a wide array of mammals (deer, wild boar, fox, badger, genet, etc.) as well as bird species (jay, wood pigeon, etc.) Wild pear play an important role in the ecosystem and therefore it might be considered as a "keystone" species. In spite of this, almost nothing is known about the biology and ecology of this interesting tree, with just one paper published in the last decades (Fedriani, 2009).

Thus, the aims of this study were: (1) to test and compare the applicability of different methods of atmospheric correction (*Dark Object Subtraction* and *FLAASH* method) and image fusion or "Pan-Sharpening" (*HIS*, *Principal Components*, *Brovey* and *Gram-Schmidt Spectral Sharpening*) to QUICKBIRD satellite imagery in order to maximize both their spatial and spectral resolution for further analysis, and (2) to assess the potential of these techniques through supervised classification (*Maximum Likelihood*) for discriminating and mapping wild pear trees (*Pyrus bourgaeana*) in the study area, comparing the classification accuracy achieved with each method.

2 MATERIAL AND METHODS

2.1 Study plot

The study plot is located at Sierra Morena (37°53'53.53" N and 4°58'49.61" W), province of Cordoba (Andalusia, southern Spain). The plot stretches over approximately 230 ha (Figure 1).

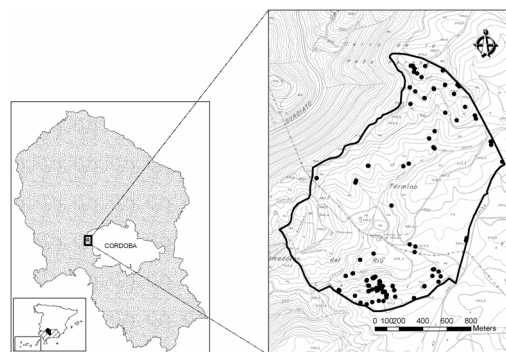


Figure 1. Location of study plot.

The vegetation is Mediterranean open woodland dominated by holm oak (*Quercus ilex*) with understory evergreen shrubs belonging to several plant families (*Cistaceae*, *Labiatae*, *Rosaceae*, *Ericaceae*, *Anacardiaceae*, *Aristolochiaceae*) scattered over a species rich, dry grassland. A section of the study plot is an old abandoned olive grove. The main land use here is sheep grazing and big hunting (deer and wild boar).

2.2 Sampling and data collection

A detailed GIS of the study plot was built with ArcView 3.2 and subsequently ArcGis 9.3. Different available layers were added, especially georeferenced aerial photographs of 0.5 x 0.5 m resolution and a 50 x 50 m grid. Detailed, large scale layouts were printed and used during the field work to carry out a complete census of wild pear trees in the study plot. Every tree with a trunk diameter at the base ≥ 5 cm was censused and given a unique code, and its height, as well as its trunk and crown diameters were measured. Besides, two wood cores were taken using an incremental core borer (HAGLÖF, Sweden), and its spatial position was recorded using a Trimble Pathfinder Pro XRS GPS.

2.3 QUICKBIRD imagery

We choose QUICKBIRD satellite imagery because it is probably the best suited to our needs. We obtained an BUNDLE Imagery product (MS 2.4m / PAN 0.6 m) of 25 km² obtained on July, the 15th, 2008. The multispectral imagery has 16-bit radiometric resolution, 2.4 m spatial resolution and four spectral bands (blue, 450-520 nm, green 520-600 nm, red 630-690 nm, near infrared, 760-900 nm). Panchromatic imagery has a 16-bit radiometric resolution channel and 0.6 m spatial resolution, comprises one spectral band in the range of 450-900 nm. We used ENVI V.4.5 (2007) - V.4.6 (2009) software package for image processing and analysis.

2.4 Atmospheric effect correction

Radiometric Correction

To QUICKBIRD satellite imagery we transformed the digital values of each pixel in the TOA (Top of Atmosphere) to spectral radiance values (W/m².sr).

We subsequently obtained spectral radiance values in the upper half of the atmosphere. For these purposes we used the algorithms provided in DigitalGlobe, Inc. (2003). Then, we transformed radiance values to apparent reflectance that are comparable over time, even under different weather conditions (Chuvieco, 1996). Finally, surface reflectance was obtained using the following expression,

$$R_{Pixel, Band} = L_{Pixel, Band} d^2 \pi / E \cos \Phi \quad (1)$$

Where $L_{Pixel, Band}$ spectral radiance calculated before, d is the distance between Earth and the Sun in astronomical units, E is the spectral solar irradiance and Φ is 90 less the solar elevation angle at the time of image acquisition.

Atmospheric correction

ENVI, V4.6, offers different atmospheric correction models. We chose 2, *Dark Object Subtract* (DOS) and *FLAASH* (atmospheric modelling) to determine which procedure can provide the best results. The first model (DOS) was chosen due to its simplicity and applicability, with some available modifications which have improved the algorithm. However, when all weather parameters for image are available, it is possible to apply the Fast Line-of-Sight Atmospheric Analysis technique of Spectral Hypercube (ENVI FLAASH, Atmospheric Correction Module, 2009) which incorporates the MODTRAN4 radiation transfer code.

2.5 Evaluation of image fusion methods

We carried out a study assess the adequacy of different fusion methods implemented in ENVI V4.6. QUICKBIRD multispectral imagery (2.4 m) was merged with panchromatic imagery (0.6 m) by a process called "Pan-Sharpning." We obtained multispectral imagery with increased spatial resolution (0.60 meters), preserving the original spectral resolution. We applied four different processing methods, namely: *Brovey Method* (Vrabel, J., 1996), *Gram-Schmidt Multiplicative Method* (Laben et al, 2000), *HSI Processing Method* (Kruse and Raines, 1994) *Principal Component Method* (Welch, R. and W. Ahlers, 1987).

2.6 Regions of interest (ROIs: training and checking

We selected 11 regions of interest, corresponding to either different vegetation units or some individual species in mixed forest. Besides, bare soil, shade and pool were considered as additional ROI's. Data from these ROIs were used for supervised classification through the training and checking phase

2.7 Digital grading process by Maximum Likelihood

Supervised classification was performed using the Maximum Likelihood algorithm on fused imagery. To validate the classification, we used the *Kappa coefficient* and *Overall Accuracy* of the imagery obtained. According to Congalton (1991), the Kappa coefficient can be calculated as follows:

$$K = \frac{N \sum_{i=1}^r (x_{ii}) - \sum_{i=1}^r (x_{i+} \cdot x_{+i})}{N^2 - \sum_{i=1}^r (x_{i+} \cdot x_{+i})} \quad (2)$$

Where N is the total number of reference pixels, X_{ij} number of observations in row i column j , x_{i+} marginal totals of row i , x_{+i} marginal totals of column i and r number of rows in the matrix. K values near 1 show a good agreement between observed reality and the map obtained. Conversely, values close to 0 suggests that the observed agreement is only due to chance.

3 RESULTS

3.1 Atmospheric effect correction

Before chose the fusion method, we proceeded to make a radiometric and atmospheric correction on the image. Several spectral profiles were compared for different coverages (vegetation, saturated soil, soil and shade), for original image at ND, radiance image at TOA and image atmospherically corrected for both methods, DOS and FLAASH.

3.2 Evaluation of different image fusion methods

To assess the quality of results achieved with different fusion methods, we selected a region of interest corresponding to the study plot, and extracted data for each band. The spatial quality evaluation was performed using visual analysis, which involves some

subjectivity. Figure 2 illustrates the image Sharpening process corresponding to the image fusion methods in false color-infrared. Concerning the spectral quality of results, we have studied the spectral similarity between the original and fused imagery. In this sense, each fused image has been degraded to the spatial resolution of the original QUICKBIRD image (2.4 meters). Table 1 shows average wavelength by band and correlation coefficients (table 2) between the original bands and the fusion process bands.

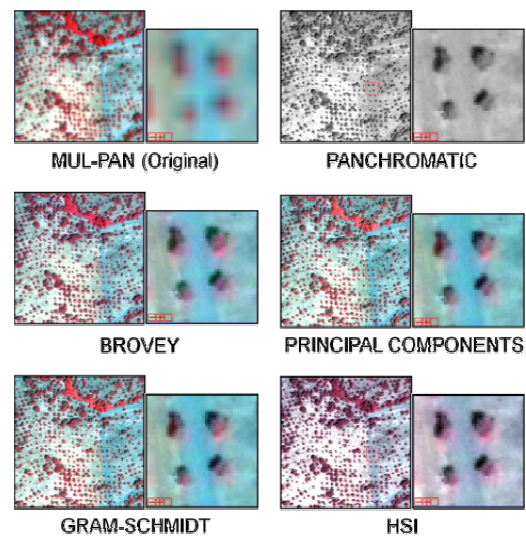


Figure 2. Fusion methods and original image for false-color infrared 2008 image.

Table 1. Average wavelength \pm sd, by band and fusion method.

N=397918 pixels	BLUE	GREEN	RED	NIR
Original	276,3 $\pm 32,1$	408 $\pm 73,3$	315,3 $\pm 96,3$	577,5 $\pm 80,3$
Brovey	122,8 $\pm 17,3$	181,4 $\pm 33,2$	139,3 $\pm 40,7$	196,9 $\pm 33,6$
G-S	272,7 $\pm 33,5$	400,7 $\pm 76,8$	305,9 $\pm 101,9$	571,3 $\pm 81,9$
HSI	149,4 $\pm 59,1$	134,1 $\pm 59,5$	113,6 $\pm 61,7$	144 $\pm 55,6$
PC	272,6 ± 33	400,4 $\pm 75,7$	305,3 $\pm 100,1$	571,5 ± 84

Table 2. Correlation Coefficients, $p < 0.05$ in all cases.

N=397918 pixels	BLUE	GREEN	RED	NIR
Brovey	0,5331	0,7737	0,9265	0,7764
G-S	0,8616	0,8660	0,8686	0,9157
HSI	0,7812	0,8629	0,9217	0,5998
PC	0,8529	0,8583	0,8578	0,9281

3.3 Digital grading process by Maximum Likelihood

Table 3 shows Kappa coefficient and overall accuracy data of supervised classification using the maximum likelihood algorithm, applied on fused imagery by the Gram-Schmidt method, atmospherically uncorrected (GS), corrected by the DOS method and corrected by FLAASH method.

Table 3. *Kappa Coefficient (K) and Overall Accuracy (A).*

	A (%)	K
DOS	78,76	0,764
FLAASH	80,06	0,778
G-S	52,25	0,466

The user's accuracy for all classes for the QUICKBIRD false color satellite image corrected by *Gram-Schmidt* and *FLAASH* methods, ranged from 72.31% to 100%, except for *Pyrus* and *Olea* class with a 31.06% and 12.16% respectively. The producer's accuracy ranged between 70.25% and 99.83% for all classes with 42.53% and 22.16% for *Pyrus* and *Olea*.

4 CONCLUSIONS

Concerning the atmospheric correction methods, the results show a slight improvement in the FLAASH corrected image. This is not surprising, since MODTRAN requires input of atmospheric data to model a transfer function allowing to obtain an image with lower atmospheric noise. All the fusion methods applied here provided satisfactory results. Assuming that during the fusion process there is a slight loss of spectral or spatial information, the Gram-Schmidt method provided better results. In terms of data of classification as reported by Kappa and Global indices for the three types of images analyzed, we can conclude that it is possible to discriminate categories in the study area. During the summer, the spectral response of vegetation and mainly deciduous trees

such as wild pears is highly influenced by the process of shedding leaves and senescence. The application of the already described procedures for classification of wild pear trees yielded poor results, as indicated by the data producer and user accuracy values obtained for wild pear: DOS (44.99% Producer / User 34.86%); FLAASH (42.53%/31.06%) and uncorrected (33.03% / 24.43 %). These poor results might be at least in part explained by the late date –mid July- of the QUICKBIRD image available for our study plot. Regrettably, by this date many wild pear trees in the study area had already shed a proportion of their leaves. Therefore, we believe that a better selection of imagery products by date might significantly improve the results. Besides, further refinement of the methods may deliver more accurate and applicable results.

5 REFERENCES

- Aldasoro *et al.*, 1996, The genus *Pyrus* L. (Rosaceae) in south-west Europe and North Africa. *Botanical Journal of the Linnean Society*. Volume 121, Issue 2. Pages 143 – 158.
- Anderson, G. L., Prosser, C. W., Haggart, S., & Foster, B., 1999, Change detection of leafy spurge infestations using aerial photography and geographic information systems. In: Proceedings of the 17th Biennial Workshop Color Aerial Photography and Videography in Resource Assessment. Bethesda, MD: American Society of Photogrammetry and Remote Sensing. p. 223–230.
- ArcGIS 9.3 package, 2008, Environmental Systems Research Institute (ESRI).
- Cabello, J. & Paruelo, J. M., 2008, La teledetección en estudios ecológicos. *Ecosistemas* 17(3):1-3.
- Chávez, P. S., 1996, Image-based atmospheric corrections, revisited and improved. *Photogrammetric Engineering and Remote Sensing*, **62**, pp. 1025-1036.
- Chuvieco, E., 1996, “Fundamentos de Teledetección especial”. Ediciones RIALP, Madrid, España.
- Congalton, R.G., 1991, A review of assessing the accuracy of classifications of remotely sensed data, *Remote Sensing of Environment*, **37**:35-46.

- Coppin, P., Jonckheere, I., Nackaerts K., Muys, B., & Lambin, E., 2004, Digital change detection methods in ecosystem monitoring: a review. *Internacional Journal of Remote Sensing* **25**(9):1565-1596.
- Culvenor, D., 2002. TIDA: an algorithm for the delineation of tree crowns in high spatial resolution remotely sensed imagery. *Computers and Geosciences* **28**, 33–44.
- Decne, J., 1871-72. *Jard. Fruit.* 1: 318, pl. 2
- DigitalGlobe, Inc. 2003, Radiometric Radiance Conversion for QB Data. Technical Note, RS_TN_radiometric_radiance_4002. Longmont, Colorado.
- ENVI (The Environment for Visualizing Images). V.4.5 (2007)-V.4.6 (2009).
- Everitt, J. H., Pettit, R. D., & Alaniz, M. A., 1987, Remote sensing of broom snakeweed (*Gutierrezia sarothrae*) and spiny aster (*Aster spinosus*). *Weed Science*, **35**, 295–302.
- Everitt, J. H., Yang, C. & Johnson, H. B., 2007, Canopy Spectra and Remote Sensing of Ashe Juniper and Associated Vegetation. *Environ. Monit. Assess.* **130**: 403–413.
- Fedriani, J. M., Wiegand T. & Delibes M., 2009, Spatial pattern of adult trees and the mammal-generated seed rain in the Iberian pear. *Ecography* **33**(3): 545-555.
- Flora ibérica, 1989, Plantas vasculares de la Península Ibérica e Islas Baleares.
- Gausman, H. W., Menges, R. M., Escobar, D. E., Everitt, J. H., & Bowen, R. L., 1977, Pubescence affects spectra and imagery of silverleaf sunflower (*Helianthus argophyllus*). *Weed Science*, **25**, 437–440.
- Gougeon, F., Leckie, D., Paradine, D. & Scott, I., 1999, Individual tree crown species recognition: the Nahmint study. *International Forum on Automated Interpretation of High Spatial Resolution Digital Imagery for Forestry*. Pacific Forestry Centre, Vic., Canada, pp. 209–223.
- Kruse, F. A. & Raines, G. L., 1994, A technique for enhancing digital color images by contrast stretching in Munsell color space. Proceedings of the ERIM Third Thematic Conference. Environmental Research Institute of Michigan, Ann Arbor, MI, pp. 755-760.
- Laben *et al.*, 2000, Process for Enhancing the Spatial Resolution of Multispectral Imagery Using Pan-Sharpning. US Patent 6,011,875.
- Lillo-Saavedra M. & Gonzalo C., 2006, Spectral or Spatial Quality for Fused Satellite Imagery? A Trade-Off Solution Using Wavelet à trous Algorithm. *International Journal of Remote Sensing*: **27**(7), 1453-1464.
- Tueller, P. T., 1982, Remote sensing for range management. In C. J. Johannsen & J. L. Sanders (Eds.). *Remote sensing for resource management* (pp. 125–140). Ankeny, IA: Soil Conservation Society of America.
- Varshney, P.K., 1997, Multisensor data fusion. *Electronics and Communication Engineering Journal*, **9**(6): 245-253.
- Vasanth, *et al.*, 2000, Land Cover Mapping: Performance Analysis of Image-Fusion Methods. www.gisdevelopment.net/application/environment/overview/envo0011.htm
- Vrabel, J., 1996, Multispectral Imagery Band Sharpning Study. *Photogrammetric Engineering & Remote Sensing*, Vol. 62, No. 9, pp. 1075-1083.
- Welch, R. & Ahlers, W., 1987, Merging Multiresolution SPOT HRV and Landsat TM Data. *Photogrammetric Engineering & Remote Sensing*, **53** (3), pp. 301-303.
- Wulder, M., Niemann, O. & Goodenough, D., 2000a, Local maximum filtering for the extraction of tree location and basal area from high spatial resolution imagery. *Remote Sensing of Environment* **73**, 103–114.

Analysing wildfires in Valencia with the Haines Index and monitoring the natural regeneration with MODIS data

M. J. Barberà ⁽¹⁾, R. Niclòs ⁽¹⁾, M. J. Estrela ⁽²⁾ and J. A. Valiente ⁽¹⁾

⁽¹⁾ *Unidad Mixta CEAM-UVEG. Instituto Universitario Centro de Estudios Ambientales del Mediterráneo CEAM - UMH*

Charles Darwin, 14. Parque Tecnológico. 46980 Paterna (Valencia)

Tel: 961 318 227, Fax: 961 318 190

⁽²⁾ *Unidad Mixta CEAM-UVEG. Facultat de Geografia i Història de la Universitat de Valencia. Blasco Ibáñez, 28. 46010 València*

barbera@ceam.es, niclos@ceam.es, majoesna@uv.es, josean@ceam.es

ABSTRACT - *This work studies two plume-dominated forest fires that took place in Valencia (Xàtiva and Simat) in 2005 by analyzing both the evolution of the Haines Index during the fires and the subsequent temporal evolution of the NDVI and EVI vegetation indexes. The latter were used to evaluate the fire impact and monitor the natural regeneration in the burnt areas. The Haines Index was calculated on both sites using the MOD07 and MYD07 products provided by the MODIS sensor onboard Terra and Aqua EOS satellites, with a 5 km spatial resolution. The temperatures used to compute the Haines Index are compared with those obtained from the NOAA-ARL (Air Resources Laboratory) GDAS1 model, and the results of calculating the Haines Index from GDAS1 data are also shown. In addition, the temporal evolution of the vegetation indexes for each area is analyzed by using the MOD13Q1 product from EOSTerra-MODIS, which consists of a 16-day data composition with a 250 m spatial resolution. The results of this study have led us to conclude that the methodology presented is useful both to evaluate the risk of plume-dominated fires and their effects on vegetation and to monitor the subsequent natural regeneration.*

1 INTRODUCTION

Wildfire risk forecasting to evaluate the probability of fire propagation and damage is essential because of the crucial role played by meteorological conditions in fire behaviour and dynamics. The meteorological variables used to calculate conventional fire risk indexes are usually related to the surface layer; however, these are not the only variables that can affect fire growth. Even when fuel content, topography and meteorological conditions remain constant, instability and dry air can increase the fire growth potential, originating the development of a convective plume and promoting strong streams, which will increase fire intensity. This type of fire, the so-called plume-dominated fire, can generate high-risk situations with catastrophic results for firefighters due to its virulence and erratic behaviour.

To analyze two fires that took place in Valencia (Xàtiva and Simat) in 2005, we have used the Haines Index (HI), which indicates the potential risk of forest fires in which the convective plume is more important

than the horizontal winds. We compute HI from MOD07/MYD07 and GDAS data and we also evaluate and monitor the natural regeneration in the burnt areas by using NDVI and EVI indexes from MOD13Q1.

2 METHODOLOGY

The HI (Haines, 1988) is calculated as the sum of two terms, A and B:

$$HI = A + B \quad (1)$$

where $A = (TP1 - TP2)$ is the stability term, and $B = (TP3 - TdP3)$ is the humidity term. TP_i and TdP_i are the air temperature and the dew point temperature at pressure level P_i .

Surface Elevations	Pressure Level	Stability (TP1 – TP2)	A	Humidity (TP3 – TdP3)	B	HI=A+B
< 305 m (low)	P1=950 hPa (925 hPa) P2=850 hPa P3=850 hPa	< 4°C (2,7°C)	1	< 6°C	1	Potential for large fires 2-3: very low 4: low 5: mid 6: high
		≥ 4°C (2,7°C)	2	≥ 6°C	2	
		< 8°C (6,7°C)	3	< 10°C	3	
		≥ 8°C (6,7°C)	3	≥ 10°C	3	
305 – 914 m (mid)	P1=850 hPa P2=700 hPa P3=850 hPa	< 6°C	1	< 6°C	1	
		≥ 6°C	2	≥ 6 °C	2	
		< 11 °C	3	< 13°C	3	
> 914 m (high)	P1=700 hPa P2=500 hPa P3=700 hPa	≥ 11°C	3	≥ 13°C	3	
		< 18°C	1	< 15°C	1	
		≥ 18 °C	2	≥ 15°C	2	
		< 22°C	3	< 21°C	3	
		≥ 22°C	3	≥ 21°C	3	

Table 1: Variables and scales for calculating the HI according to the terrain elevation (Haines, 1988, Choi et al., 2006 and Potter et al., 2008)

Values from 1 to 3 are assigned to each of these terms (A and B) depending on the magnitude of their differences with respect to predefined levels for each region. The more unstable the lower atmosphere is, higher the A term will be and the higher the probability of convective plume-dominated wildfires. Analogously, drier atmospheric conditions imply larger B values, which are favourable for the spread of wildfires. Thus, the HI varies between 2 and 6, and values equal to or greater than 5 indicate that conditions are critical for the formation of plume-dominated wildfires.

Depending on the surface elevation of the region of interest, there are three possible atmospheric layers used for computing the HI, and they provide what are known as the low, mid and high elevation HI variants (Table 1, Haines, 1988, Choi et al., 2006, Potter et al., 2008). The low elevation variant was originally developed for the P1=950hPa pressure level; however, the fact that this atmospheric level is not included in numerous atmospheric profile databases led Potter et al., (2008) to suggest using P1=925hPa as the standard pressure level. The thresholds for this level are the values shown in parentheses in Table 1 (Choi et al., 2006).

2.1 Selected Sites

The study areas selected were Xàtiva and Simat, both located in the province of Valencia (Figure 1). On June 21, 2005, a wildfire destroyed 78 ha. in Xàtiva. On the next day, a new fire in the same area burned over 400

ha., according to data from the “Conselleria de Territori i Habitatge de la Generalitat Valenciana” (Figure 2a). The altitude of the area burned varies between 140 and 550 meters, and the daily average wind speed was 2.8 m/s according to the CEAM network meteorological stations. In this area the vegetation after fire was composed of a *Pinus halepensis* mosaic and calcic thermophile shrubland with heterogeneous densities.

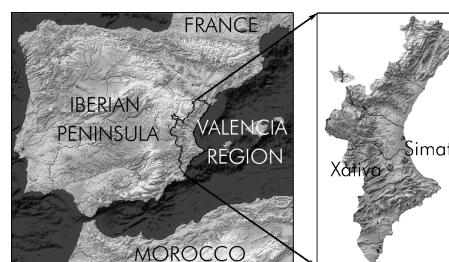


Figure 1: Location of the study area

On the other site selected, Simat de la Valldigna (Figure 2b), the wildfire started on July 12, 2005, affecting 641.95 ha. The average wind speed that day was 2.3 m/s. Most of the altitudes in the area affected by the fire ranged between 250 and 550 m, with the maximum altitude being 606.1 m. Before the fire, the predominant vegetation had been shrubland although there was an Aleppo pine area (*Pinus halepensis*) with variable densities and a small area of cork oak (*Quercus suber*) in the north.

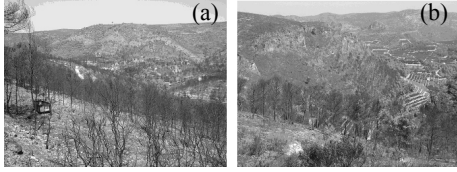


Figure 2: Burnt areas: (a) Xàtiva, (b) Simat.

2.2 Data

After characterizing the study areas and examining the fire-occurrence conditions, including burnt area, vegetation class, altitude and wind velocity, the HI was calculated during the period when the fires took place at both locations (see Table 1). According to the “Consortio Provincial de Bomberos de Valencia” a fire is considered wind-driven when the wind speed is greater than 8.3 m/s. We note that wind speeds were low at both sites and, therefore, the fires were non-wind driven.

The HI was computed from two sources:

- MOD07L2 and MYD07L2 products from EOSTerra-MODIS and EOSAqua-MODIS, respectively, with a 5 km spatial resolution and an approximately 12 hour temporal resolution for each product.
- Atmospheric profiles provided by NOAA’s Air Resources Laboratory (ARL), selecting the model GDAS1 (Global Data Assimilation System) whose data have 1°x1° spatial resolution and 3 hours temporal resolution (<http://www.arl.noaa.gov/READYamet.php>).

The next step was to monitor the natural regeneration in the burnt areas by using the MOD13Q1 product from the EOSTerra-MODIS sensor. This product provides vegetation indexes, like NDVI and EVI, every 16 days at 250 m resolution. We recall that the NDVI (Normalized Difference Vegetation Index) is defined as (Rousse et al., 1974):

$$NDVI = \frac{\rho_{NIR} - \rho_R}{\rho_{NIR} + \rho_R} \quad (2)$$

and the EVI (Enhanced Vegetation Index) is (Huete et al., 2002):

$$EVI = G * \frac{\rho_{NIR} - \rho_R}{\rho_{NIR} + c_1 * \rho_R - c_2 * \rho_B + L} \quad (3)$$

where ρ are atmospherically-corrected surface reflectances, L is the canopy background adjustment term, $c1$ and $c2$ are the coefficients of the aerosol resistance term, which uses the blue band to correct for aerosol influences in the red band and G is the gain factor.

3 RESULTS AND DATA ANALYSIS

3.1 GDAS and MODIS data comparison

The temperature comparison in the two selected areas shows a good correlation between GDAS and MODIS data (Figure 3). Nevertheless, we can see some differences in the values probably due to the different spatial and temporal resolutions.

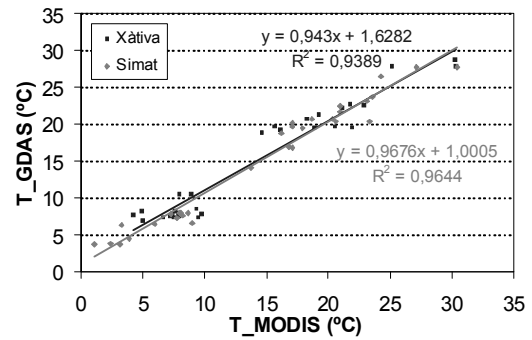


Figure 3: GDAS and MODIS data comparison

3.2 HI computation

The results of the HI evolution and the terms A and B during the fires are shown in Figure 4 from MODIS data and in Figure 5 from GDAS data (Barberà et al., 2009).

In both figures we can observe that the HI takes moderate (HI=5) or high (HI=6) values at the time of the fires. The observed differences in the two figures are mainly due to the different spatial and temporal resolution of the data used to plot them.

3.3 Monitoring vegetation

Figures 6 and 7 show the NDVI and EVI dynamics in Xàtiva and Simat. They represent the means (Mean), the standard deviations (Stdev) and the maximum (Max) and minimum (Min) values obtained for the pixels contained within the regions of interest created for each fire.

Although the NDVI is more related to the photosynthetic activity of forest stands and the EVI to the canopy structure, at both locations the indexes show a marked decrease on the fire date and recover their values progressively in the course of time. By two years after the fires, both indexes have approximately recovered pre-fire values. Figure 8 shows an example of some MODIS processed images in the area of Xàtiva, where the impact of the fire can be observed in the EVI index on that location.

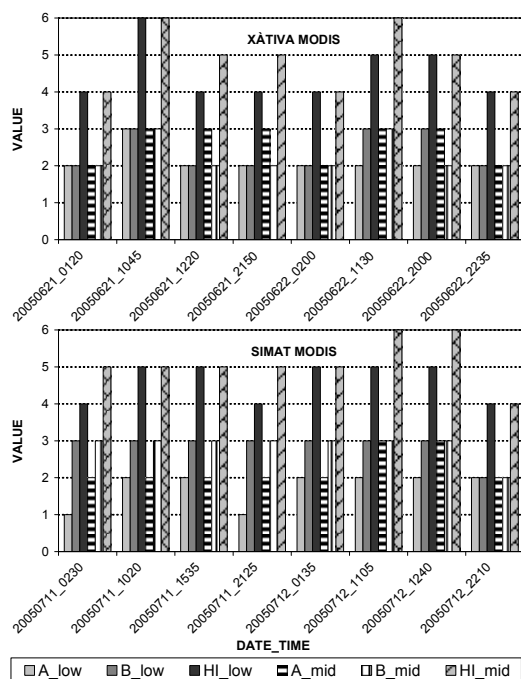


Figure 4: HI evolution in Xàtiva and Simat wildfires from MODIS data

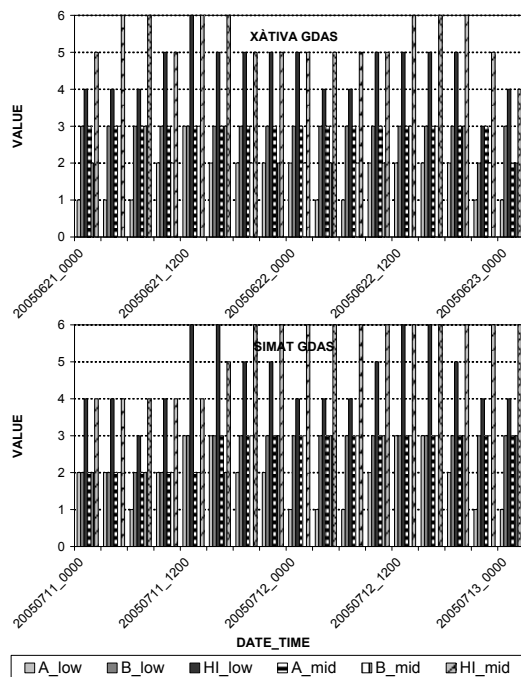


Figure 5: HI evolution in Xàtiva and Simat wildfires from GDAS data

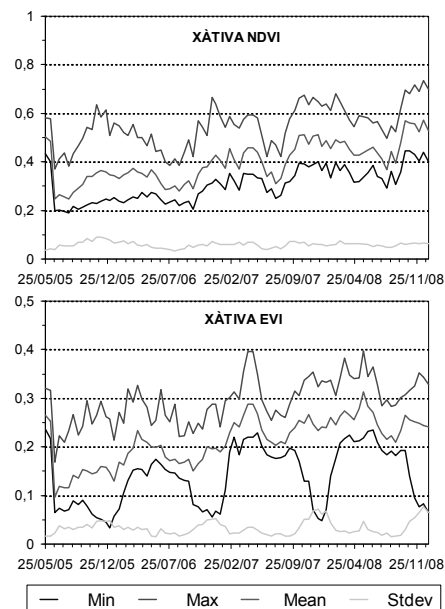


Figure 6: NDVI and EVI dynamics in Xàtiva

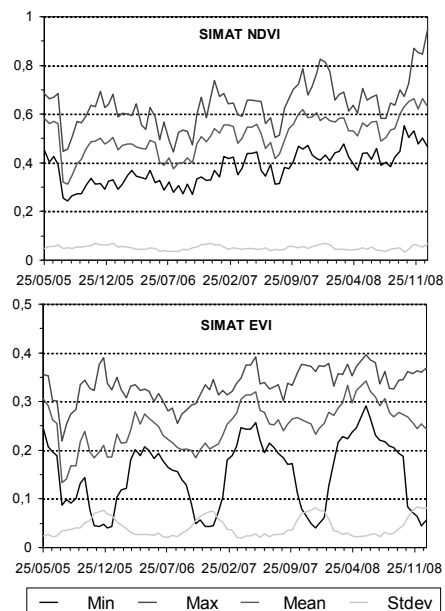


Figure 7: NDVI and EVI dynamics in Simat

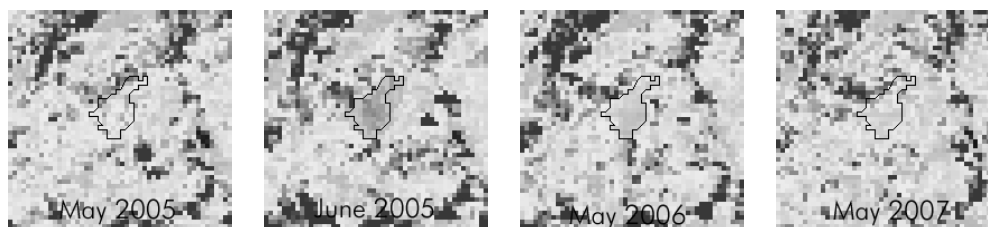


Figure 8: EVI dynamics in Xàtiva

4 CONCLUSIONS

In this study we analyzed the HI during two plume-dominated, non-wind driven, fires that occurred in the Valencia region in 2005. MOD07, MYD07 and GDAS1 data were used for the analysis after proving the good correlation between GDAS and MODIS data. The results show that the index takes quite high values during the both fires.

Moreover, the vegetation index dynamics studied with the MOD13Q1 product shows that this is a useful tool to evaluate the impact of fire in vegetation and to monitor the subsequent natural regeneration

5 REFERENCES

- Barberà, M. J., Niclòs, R., Estrela, M. J. & Valiente, J. A., 2009. Análisis del Índice de Haines durante los incendios de Xàtiva y Simat (Valencia) y monitorización de la regeneración natural mediante el uso de imágenes MODIS. XIII Congreso de la Asociación Española de Teledetección. Teledetección. Agua y desarrollo sostenible, 293-296. ISBN: 978-84-613-4257-0. Calatayud, 22-25 Septiembre, 2009
- Choi G., Kim J. & Won M.-S., 2006. Spatial Patterns and Temporal variability of the Haines Index related to the Wildland Fire Growth Potential over the Korean Peninsula. *Journal of the Korean Geographical Society*, Vol 41, nº 2
- Haines, D. A., 1988. A lower atmosphere severity index for wildlife fires. *National Weather Digest*, **13**(2), 23-27

Huete, A., Didan, K., Miura, T., Rodriguez, E., Gao, X. & Ferreira, L., 2002. Overview of the radiometric and biophysical performance of the MODIS vegetation indices. *Remote Sens. Environ.* **83**:195-213

Potter, B. E., Winkler, J. A., Wilhelm, D. F., Shadbolt, R. P. and Bian, X., 2008. Computing the low-elevation variant of the Haines Index for fire weather forecasts. *Weather and Forecasting*, **23**(1), 159-167.

Rousse, J. W., Haas, R. H., Schell, J. A. & Deering, D. W., 1974. Monitoring vegetation systems in the Great Plains with ERTS. Proceedings Third Earth Resources Technology Satellite-1 Symposium, Greenbelt: NASA SP-351, 3010-317

ACKNOWLEDGEMENTS

This work was supported by the Spanish Ministerio de Ciencia e Innovación under Projects CGL2007-65774/CLI and CGL2008-04550/CLI, by CONSOLIDER-INGENIO 2010 CSD2007-00067, by the AQ2 European Social Fund, and by the European Union (Project CIRCE N.036961). Instituto Universitario CEAM – UMH is supported by the Generalitat Valenciana and Fundación BANCAJA. Moreover, we thank Jackie Scheiding for the revision and the Forest Research Department of the Fundación CEAM and the “Consorcio Provincial de Bomberos de Valencia” for their collaboration.

A New Tool for Information Extraction and Mining from Satellite Imagery Available from Google Maps Engine

Sergio Bernabé and Antonio Plaza

Hyperspectral Computing Laboratory

Department of Technology of Computers & Communications

University of Extremadura, Avda. de la Universidad s/n, 10071 Cáceres, Spain

Emails: sbernabe@alumnos.unex.es, aplaza@unex.es

ABSTRACT- *The wealth of satellite imagery available in web mapping service applications such as Google Maps, which now provides high-resolution satellite images from many locations around the Earth, has opened the appealing perspective of performing information extraction and mining tasks via the Google Maps application programming interface (API). In fact, the introduction of Google's mapping engine (the Google Maps service is free for non-commercial use) has prompted a worldwide interest in satellite imagery exploitation. In this paper, we present a new tool for information extraction and mining from satellite images available Google Maps. Our main focus in this work will be on describing the interface and how the user can interact with the tool. The functionalities included in the tool comprise the possibility to perform unsupervised classification of image portions selected by the user (at the maximum zoom level) using ISODATA and K-Means classifiers, followed by spatial post-processing based on majority voting. Selected regions in the classified portion can then be used to train a more sophisticated classifier able to map larger image areas in a manner transparent to the user. Several examples of use, focused on the analysis of different locations around the Iberian Peninsula and comprising different types of information extraction case studies (vegetation, semi-arid environments, urban areas, etc.) are illustrated and thoroughly described.*

1 INTRODUCTION

The wealth of satellite imagery (Landgrebe, 2003) available in web mapping service applications such as Google Maps, which now provides high-resolution satellite images from many locations around the Earth, has opened the appealing perspective of performing classification and retrieval tasks via the Google Maps application programming interface (API) and other external libraries such as SwingX-WS. In fact, the introduction of Google's mapping engine prompted a worldwide interest in satellite imagery exploitation. The combination of an easily pannable and searchable mapping and satellite imagery tool such as Google Maps with advanced image classification and retrieval features has the potential to significantly expand the functionalities of the tool and also to allow end-users to extract relevant information from a massive and widely available database of satellite images (the Google Maps service is free for non-commercial use).

By using the Google Maps API or external libraries such as SwingX-WS, it is possible to embed the full Google Maps site into an external website application. Other similar services currently available comprise Yahoo Maps and OpenStreetMap. The characteristics of Yahoo Maps are similar to those available in Google Maps (although the spatial resolution of the satellite imagery available in Yahoo Maps is generally lower than the resolution of the

image data available from Google Maps). On the other hand, the OpenStreetMap follows a different approach. It is a collaborative project aimed at creating a free editable map of the world. Its design was inspired by sites such as Wikipedia. As shown by Fig. 1, the Google Maps service offers important competitive advantages, such as the availability of high resolution satellite imagery, the smoothness in the navigation and interaction with the system, the availability of a hybrid satellite view which can be integrated with other views (maps, etc.) and adequate adaptivity for general-purpose desktop applications. Despite its competitive advantages, the possibility to perform unsupervised or supervised classification of satellite images (Richards, 2005) is not available in Google Maps, despite image classification is widely recognized as one of the most powerful approaches in order to extract information from satellite imagery (Soille, 2003; Benediktsson et al., 2005; Bruzzone et al., 2006).

The remainder of the paper is organized as follows. Section 2 describes the programming libraries used to develop the proposed system and the integration of the different modules. Section 3 presents the unsupervised and supervised classification techniques considered in its implementation. Section 4 describes the integration of the different software modules. Section 5 presents an experimental evaluation of the proposed system which has been conducted by comparing the obtained classification

results with those provided by commercial software, such as the popular Research Systems ENVI package. Finally, section 6 concludes with some remarks and hints at plausible future research.

	Google maps	YAHOO! LOCAL	Openstreetmap
No Restrictions of use	No, up to certain limit	Yes	Yes
Hybrid satellite view	Yes	Yes, low visibility	No
High resolution imagery	Yes	No	No
Zooming levels	Very high quality	High quality	Medium quality
Error correction	Low	Low	Very high
Smoothness in navigation	Very high	High	High
Adaptivity for desktop applications	High	High	High

Figure 1. Comparison between the main functionalities of Google Maps, Yahoo Maps and OpenStreetMap.

2 LIBRARIES

In this section we describe the different steps that we followed for the integration of different software components in libraries towards the design of our proposed classification system for Google Maps satellite imagery. Our first approach to the design of such system was directed towards the exploitation of the Google Maps API in order to access the satellite imagery. However, we realized that the Google Maps API is mainly intended for exploitation in web-based applications and our goal was to develop an executable application in the PC. Another approach was to use Google Web Toolkit (GWT), an open source set of tools that allows web developers to create and maintain complex JavaScript front-end applications in Java. However, the fact that GWT is also intended for web-based applications led us to further discard this toolkit as the baseline package for the development of our tool. Finally, our approach to address the aforementioned issues was to resort to the SwingX-WS library. SwingX-WS attempts to simplify the use of web services (in the broad sense) by providing APIs that sit on top of existing libraries. It contains a set of JavaBeans for interacting with web services, but it allows embedding of those services into a standard application (this feature fit very well our desired functionality). The initial beans included in SwingX-WS comprise support for several Google web services such as searching news, video, images, and financial data, as well as a generic tile based mapping component. The SwingX-WS beans have been designed with graphical configuration in mind and work very well inside of a JavaBeans aware editor

such as NetBeans. The bean that we particularly exploited in the development of our application is JXMapView, a generic viewer for tile based map servers. For illustrative purposes, Fig. 2 shows a flowchart of our interaction with different libraries for accessing the satellite data available in Google Maps and our final choice, given by the use of SwingX-WS library with the JXMapView component.

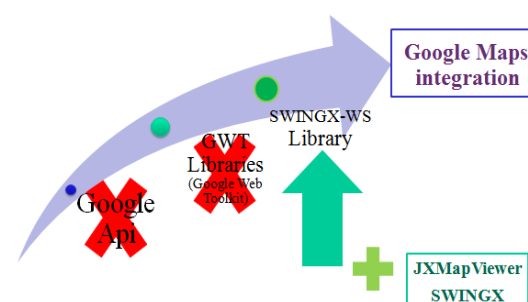


Figure 2. Flowchart describing our interaction with different libraries for accessing the satellite data available in Google Maps and our final choice (SwingX-WS library with the JXMapView component).

In addition to JXMapView, other additional SwingX-WS and SwingX modules were used in the development of our application. In the following, we provide a brief overview of these additional modules:

- **JXMapKit.** The JXMapKit is a pair of JXMapViewers preconfigured to be easy to use with common features built in. This includes zoom buttons, a zoom slider, and a mini-map in the lower right corner showing an overview of the map.
- **TileFactoryInfo.** This component encapsulates all information specific to a map server and is needed for the considered development.
- **GeoPosition.** Provides the geographical latitude and longitude and allows centering of the satellite image in a certain geographic location, thus allowing us to access such locations from our application.
- **Painter.** This API allows developers to be able to customize the background painting of a JPanel. Since many components within SwingX extend JPanel, the developer can implement custom painting on many parts of SwingX.
- **CompoundPainter.** Painters can be combined together by using the CompoundPainter, which uses an array to store several Painters, and the order in which these items should be painted in the application.

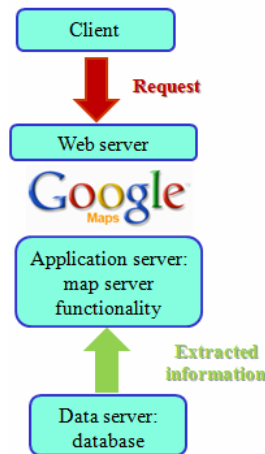


Figure 3. Flowchart describing the interaction procedure with Google Maps to obtain the satellite data.

Fig. 3 describes the overall procedure for interacting with Google Maps via the SwingX-WS library to obtain the satellite data. As shown by Fig. 3, a client (user) sends a request to a web server via SwingX-WS. The web server interacts with an application server that provides the map server functionality. Finally, the application server interacts directly with a database from which the extracted information is provided.

3 CLASSIFIERS

The proposed system incorporates functionalities of unsupervised clustering and supervised classification, all followed by spatial post-processing based on majority voting (Gamba et al., 2004).

Unsupervised clustering aims at grouping pixels if feature space, so that pixels belonging to the same cluster are spectrally similar (Richards, 2005). In our implementation, we have used the well-known ISODATA (Ball and Hall, 1965) and k-means (Hartigan and Wong, 1979) algorithms for this purpose. For instance, the ISODATA is a squared-error clustering method. The algorithm starts with a random initial partition of the available pixel vectors in the original image into c candidate clusters. It then iteratively optimizes this initial partition so that, at each iteration, a partition of the original set into c clusters is computed. A relevant issue for the ISODATA algorithm is how to set the number of clusters in advance.

In our work, the aforementioned choice is left to the end-user, who can adjust the quality of the clustering by interactively setting this parameter. Once a preliminary segmentation of the original image has been achieved via unsupervised clustering, a supervised procedure can be applied to classify other

different areas based on the training sites selected in a different spatial location. In our tool, this can be accomplished using the minimum distance and maximum likelihood classifiers (Richards, 2005). Conventional maximum likelihood classification is based on the assumption that the probability distribution for each spectral (color) class is of the form of a multivariate normal model with dimensions which equal the number of color bands. A spatial post-processing module can be applied to refine the outcome of the segmentation by simply sliding a square neighborhood window (with sizes ranging from 3×3 to 7×7 pixels) centered in each classified pixel and applying a majority voting procedure in which the central pixel is assigned to the most predominant class in the neighborhood window.

4 INTEGRATION

The final implementation of our system consists of the integration of the different software modules developed (unsupervised and supervised classifiers) with the functionalities provided by the SwingX-WS libraries (provided by the SwingX libraries), in the form of a general-purpose desktop application. For this purpose, we have resorted to the Java programming language (see Fig. 4), which is a multi-platform environment that simplifies porting of our tool to different environments. Specifically, we have resorted to the NetBeans platform, which allows applications to be developed from a set of modular software components called modules. In this framework, applications can install modules dynamically and any application can include the update center module to allow users of the application to download digitally-signed upgrades and new features directly into the running application. Reinstalling an upgrade or a new release does not force users to download the entire application again. The platform offers reusable services common to desktop applications, allowing developers to focus on the logic specific to their application.

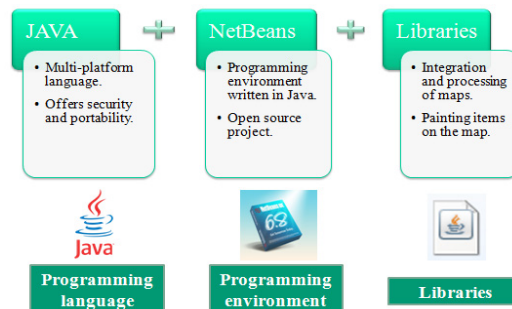


Figure 4. Different software modules used for the development of our application.

5 EXPERIMENTAL VALIDATION

In this section, we perform an experimental validation of the unsupervised and supervised classification features of our tool tested using satellite images obtained from Google Maps across different locations. The experimental validation of unsupervised (ISODATA, k-Means) and supervised (minimum distance, maximum likelihood) classification algorithms has been conducted by comparing the results provided by our implementations with those available in a well-known commercial software package: the Environment for Visualizing Images (ENVI) package distributed by ITT Visual Information Solutions. In our tests, conducted across four different locations around the world, we adopt exactly the same parameters when running our implementations and those available in the ENVI package, comparing the results in terms of the overall accuracy (OA) resulting from the confusion matrix between the classification maps provided by ENVI and by our tool.

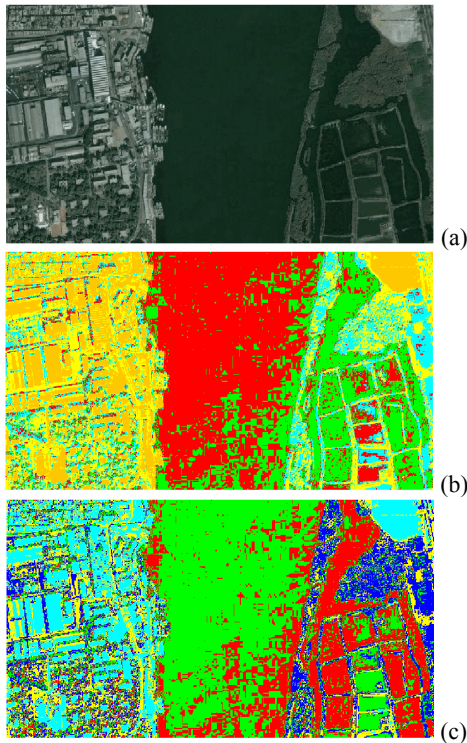


Figure 5. (a) Satellite image collected over a stretch of the Nile river in Egypt (the image is available online through Google Maps engine). (b) Unsupervised classification result provided by our implementation of ISODATA. (c) Unsupervised classification result provided by ENVI's implementation of ISODATA.

In the following, we present the obtained results in a specific case study focused on classification of satellite images available from the Nile river in the north of Cairo (Egypt) (see Fig. 5). The resolution of the image is quite high, with approximately 5 meters per pixel. As shown by Fig. 5, the color labels for our implementation and the one available in ENVI are different, but the classification maps are very similar. In both cases, the parameters for both algorithms have been set to exactly the same values, with the number of clusters set to 5. For illustrative purposes, Table 1 reports the OA (in percentage) measured after comparing our ISODATA classification map with the one obtained by ENVI. The similarity between both classification maps is very high, achieving an OA close to 90% assuming the ENVI ISODATA map as the ground reference.

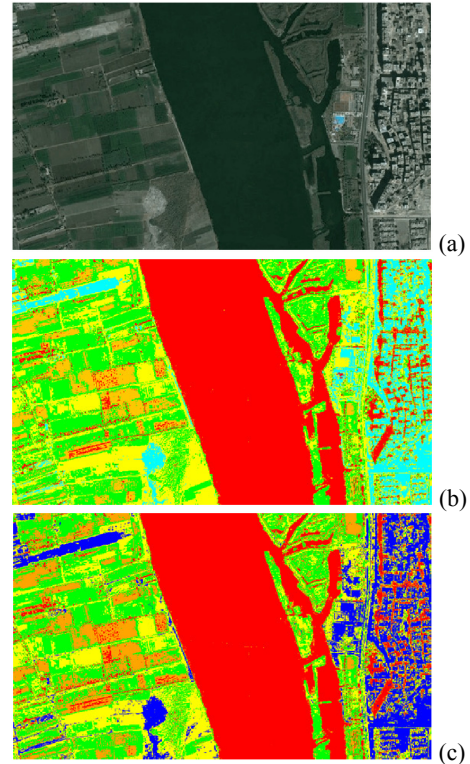


Figure 6. (a) Satellite image over a different location in the Nile river. (b) Supervised classification result provided by our implementation of maximum likelihood (trained with the areas derived from other zone by ISODATA). (c) Supervised classification result provided by ENVI's implementation of maximum likelihood (trained with the areas derived from other zone by ISODATA).

In a second experiment, we select a larger image over a different location centered over the Nile river in Egypt (see Fig. 6). The spatial resolution of this image is approximately 5 meters per pixel. In order to

classify this scene in supervised fashion, we have selected the areas resulting from an unsupervised classification (using ISODATA) and used those areas to train our maximum likelihood classifier using 5 clusters. In order to obtain this map, the maximum likelihood algorithm in ENVI was trained using exactly the same areas and with the same parameters as those used in our implementation.

Table 1. Overall (OA) and individual accuracies (percentage) after comparing our ISODATA classification map with the one obtained by ENVI for the scene in Fig. 5(a).

Soil #1 (blue)	Water#1 (green)	Urban #1 (orange)	Water (red)	Soil #2 (yellow)	Overall accuracy
63.89%	96.98%	99.74%	89.01%	94.59%	88.47%

Table 2. Overall (OA) and individual accuracies (in percentage) after comparing our maximum likelihood classification map with the one obtained by ENVI for the image in Fig. 6(a).

Urban areas (blue)	Vegeta- tion #3 (green)	Vegeta- tion #1 (orange)	Water (red)	Vegeta- tion #2 (yellow)	Overall accuracy
79.19%	99.68%	75.58%	99.99%	98.18%	90.52%

For illustrative purposes, Table 2 reports the OA (in percentage) measured after comparing our maximum likelihood classification map with the one obtained by ENVI. The similarity between both classification maps is very high, achieving on OA above 90% assuming the ENVI maximum likelihood map as the ground reference. These results indicate a high degree of similarity between our implementations of available classification algorithms and those available in ENVI. The main contribution of this work is the possibility of integrating these classifiers with the satellite images derived from Google Maps via the developed tool.

To conclude this section, Fig. 7 shows different views of the developed tool. As shown by the figure, the tool allows selecting an area to be classified, obtaining classification results both in unsupervised and supervised fashion, retaining the classified area at different zoom levels (although the classification is obtained at the maximum zoom level), and other functionalities not illustrated in Fig. 7 such as spatial post-processing of obtained results for increased spatial consistency, managing of the resulting classification and extracted satellite images, loading/storing of results via file logs which can be saved in a database, automatic positioning in any latitude and longitude coordinates in the entire Google Maps database, overlaying of classification results

with different views (satellite, map, hybrid), etc. Overall, we feel that the developed tool incorporates interesting additional functionalities to the Google Maps engine (particularly in the possibility of better exploiting the satellite images available from this tool in different application domains).

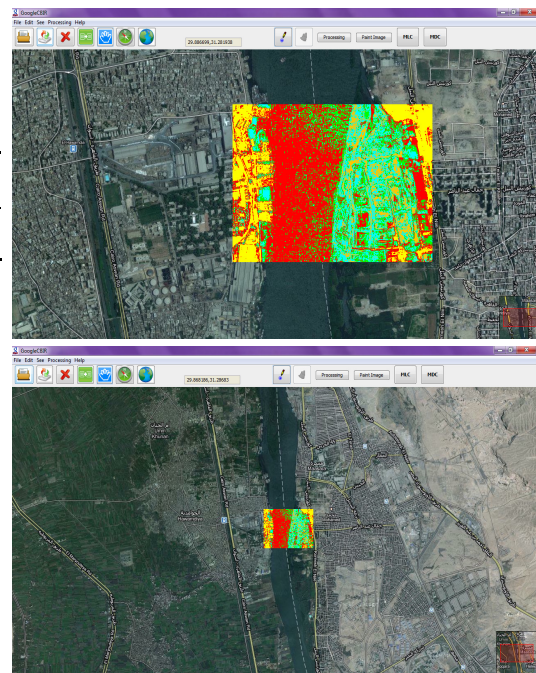


Figure 7. Different views of the developed tool. Unsupervised classification result provided by our implementation of ISODATA superimposed on the tool (top). Zoom reduction retaining the classified area (bottom).

6 CONCLUSION AND FUTURE LINES

This paper has described a new application for unsupervised and supervised classification of satellite images from Google Maps. The system has been developed using the SwingX-WS library, and incorporates functionalities such as unsupervised classification of image portions selected by the user (at the desired zoom level) using ISODATA and k-Means, and supervised classification using the Minimum Distance and Maximum Likelihood, followed by spatial post-processing based on majority voting. Our experimental results reveal that the proposed tool provides classification maps of high similarity with regards to those provided by ENVI for the same satellite imagery, but with the possibility to perform classification of any image portion available in Google Maps engine, both in unsupervised and supervised fashion.

In future developments, we plan to extend the developed tool with the incorporation of content-based

image retrieval functionalities. For that purpose, the strategy will be based on a query system linked to feature extraction from an image repository (Google Maps). The retrieved features (which will comprise shape descriptors, texture features, etc.) will be stored in a database of features and used to compare the feature vector of the input query with those recorded in the database by means of a similarity function, which will provide a result to the end-user in the form of image portions (across different locations) with sufficient similarity with regards to the features in the input query.

Finally, another drawback of the proposed tool is the high computational cost of extracting and processing large images (especially at the highest zoom level, which results in large image sizes). To address this issue, we are currently experimenting with different forms of high performance computing architectures (Plaza et al., 2006; Plaza and Chang, 2007; Plaza and Chang, 2008). The most promising strategy seems to be the parallelization of the different software modules for efficient processing in multiple cores (generally available in modern desktop PCs) as well as in graphics processing units (GPUs) of NVidia type (Setoain et al., 2008; Tarabalka et al., 2009). Both mechanisms allow incorporation of high performance computing capabilities at relatively low cost in order to speed-up the computations performed by the developed tool, which mainly comprise regular image processing-type computations which are quite appealing for parallel implementation.

ACKNOWLEDGEMENT

This work has been supported by the European Community's Marie Curie Research Training Networks Programme under reference MRTN-CT-2006-035927 (HYPER-I-NET). Funding from the Spanish Ministry of Science and Innovation (HYPERCOMP/EODIX project, reference AYA2008-05965-C04-02) is gratefully acknowledged.

REFERENCES

- Ball, G., and Hall, D., 1965, ISODATA, a novel method of data analysis and classification. *Technical Report AD-699616*, Stanford University.
- Benediktsson, J. A., Palmason, J. A., and Sveinsson, J. R., 2005, Classification of hyperspectral data from urban areas based on extended morphological profiles. *IEEE Transactions on Geoscience and Remote Sensing*, **42**, 480–491.
- Bruzzone, L., Chi, M., and Marconcini, M., 2006, A novel transductive SVM for the semisupervised classification of remote sensing images. *IEEE Transactions on Geoscience and Remote Sensing*, **44**, 3363–3373.
- Gamba, P., Dell'Acqua, F., Ferrari, A., Palmason, J. A., and Benediktsson, J. A., 2004, Exploiting spectral and spatial information in hyperspectral urban data with high resolution. *IEEE Geoscience and Remote Sensing Letters*, **1**, 322–326.
- Hartigan, J. A., and Wong, M. A., 1979, Algorithm AS 136: A k-means clustering algorithm. *Journal of the Royal Statistical Society, Series C*, **28**, 100–108.
- Landgrebe, D. A., 2003, *Signal Theory Methods in Multispectral Remote Sensing* (Hoboken, NJ: Wiley).
- Plaza, A., and Chang, C.-I., 2007, *High Performance Computing in Remote Sensing* (Boca Raton, FL: CRC Press).
- Plaza, A., and Chang, C.-I., 2008, Clusters versus FPGA for parallel processing of hyperspectral imagery. *International Journal of High Performance Computing Applications*, **22**, 366–385.
- Plaza, A., Valencia, D., Plaza, J., and Martinez, P., 2006, Commodity cluster-based parallel processing of hyperspectral imagery. *Journal of Parallel and Distributed Computing*, **66**, 345–358.
- Richards, J. A., 2005, Analysis of remotely sensed data: the formative decades and the future. *IEEE Transactions on Geoscience and Remote Sensing*, **43**, 422–432.
- Setoain, J., Prieto, M., Tenllado, C., and Tirado, F., 2008, GPU for parallel on-board hyperspectral image processing. *International Journal of High Performance Computing Applications*, **22**, 424–437.
- Soille, P., 2003, *Morphological Image Analysis: Principles and Applications* (Berlin, Germany: Springer-Verlag).
- Tarabalka, Y., Haavardsholm, T. V., Kasen, I., and Skauli, T., 2009, "Real-time anomaly detection in hyperspectral images using multivariate normal mixture models and GPU processing. *Journal of Real-Time Image Processing*, **4**, 1–14.

MODIS-based remote sensing monitoring of the spatiotemporal patterns of China's grassland vegetation growth

Xu Bin^{1,2}, Yang Xiuchun¹, Tao Weiguo³, Miao Jianming², Yang Zhi³, Liu Haiqi², Qin Zhihao¹, Lv Haiyan¹, Jin Yunxiang¹, Li Jinya¹, Zhu Xiaohua⁴, Li Zhaoliang⁴

1. Institute of Agricultural Resources and Regional Planning, Chinese Academy of Agricultural Sciences, Beijing 100081, China.

2. Comprehensive Operation Division, Remote Sensing Center, Ministry of Agriculture, Beijing 100026, China.

3. Grassland Monitoring and Supervision Center, Ministry of Agriculture, Beijing 100026, China.

4. Institute of Geographic Sciences and Natural Resources Research, Chinese Academy of Sciences, Beijing 100101, China.

xubin@mail.caas.net.cn; yangxc@caas.net.cn

ABSTRACT - Grasslands are an important base for boosting the development of China's livestock husbandry economy and maintaining China's ecological safety. Using moderate-resolution imaging spectroradiometer (MODIS) remote sensing data, this study developed a grassland vegetation growth index GI based on the normalised difference vegetation index (NDVI), and ranked the magnitude of grassland vegetation growth indices across a wide variety of field experiments. This study applied the grassland vegetation growth index to conduct remote sensing monitoring of the spatiotemporal status of China's grassland vegetation growth in 2008. We found that the vegetation growth of China's grassland was classified as "good" in 2008. Additionally, the good vegetation growth was stable within each 10-day study period in 2008. The vegetation growth reached a balance in early June. After early September, the proportion of grasslands with desirable vegetation growth declined, and the proportion of grasslands with balanced and less desirable growth increased. The regions with less desirable vegetation growth mainly included the middle and eastern regions of Inner Mongolia, the north region of Xinjiang, etc. The regions with desirable vegetation growth were mainly distributed in the north of Tibet, the southwest of Qinghai, etc. Furthermore, Inner Mongolia generally had better vegetation growth in 2008 than the multi-year average.

1 INTRODUCTION

China has approximately 400,000,000 hectares of various natural grasslands, which account for 41.7% of China's total land area. Understanding the status of grassland vegetation growth (i.e., the general growth and trends of grassland vegetation) is important for managing and regulating grassland livestock husbandry in real time. Ground monitoring and remote-sensing monitoring are the two primary ways to monitor grassland vegetation growth. Ground monitoring is used to determine the vegetation growth indices for sample plots or areas, and these indices are compared to previous results to illustrate the current status of grassland vegetation growth. Remote-sensing monitoring uses the close relationship between moderate-resolution imaging spectroradiometer (MODIS) data and the status of grassland vegetation to directly reflect grassland vegetation growth. Remote-sensing information from different periods can then be processed and compared. Remote-sensing

grassland vegetation growth monitoring, which is characterised by its rapid and broad coverage, has the potential for wide application.

2 MATERIALS AND METHODS

We used MODIS remote-sensing data from May 2003 to September 2008. These data had nationwide coverage at 250 m spatial resolution. The NDVI value for each day was calculated by geometric corrections, atmospheric corrections or other processes. This also allowed for the generation of the Maximum Value Composite of each ten-day period and the establishment of a MODIS-based. Next, we developed a grassland vegetation growth index model and a remote-sensing grassland vegetation growth monitoring system. The NDVI values were used to calculate and obtain the spatial distribution map of China's grassland vegetation growth. The detailed calculation processes are described below.

2.1 Calculation of vegetation indices

A vegetation index is often calculated by using the reflectance spectrum characteristics of green vegetation in different wavebands. In the present study, we used the NDVI, which was determined with the following equation:

$$NDVI = (B_2 - B_1) / (B_2 + B_1) \quad (1)$$

where B_1 refers to the MODIS reflectance in the first waveband (red waveband), and B_2 refers to the MODIS reflectance in the second waveband (near infrared waveband).

Generally, bigger NDVI values represent more dense vegetation growth, and smaller NDVI values suggest more sparse vegetation growth. When the NDVI value is less than 0.1 the area is usually bare land. When the NDVI value exceeds 0.8 the area has very dense vegetation.

The 10-day Maximum Value Composite method can mitigate the impact of damping factors, such as sun angle, water vapour, aerosol, observed angle, and clouds, on the vegetation index. The Maximum Value Composite method is defined by the following equation:

$$VI(X, Y) = \max[NDVI(X, Y)] \quad (2)$$

where X and Y represent coordinates and $VI(X, Y)$ is the maximum NDVI value of the (X, Y) position at different time phases during the composite period. In this study, the time series of ten-day period maximum NDVI value composites were used to build the database.

The maximum NDVI values of each ten-day period from May-September of each year from 2003-2007 were averaged to obtain the multi-year average value:

$$\overline{VI}(X, Y) = \text{Average}[NDVI(X, Y)] \quad (3)$$

where X and Y represent coordinates and $\overline{VI}(X, Y)$ is the maximum NDVI value of the (X, Y) position at different time phases during the composite period. The same ten-day period across five years was considered to be the composite period (e.g., “early May” includes the NDVI values from early May of each year from 2003 to 2007). This process allowed for the establishment of the ten-day period standard NDVI average value time-series database from 2003 to 2007.

2.2 Classification of grassland vegetation growth

After calculating the NDVI values, a comparison was made between the NDVI vegetation index charts of two periods to reflect the grassland vegetation growth. The following vegetation growth index model was built, and classifications were established based on the magnitude of corresponding index values from the equation:

$$GI = (NDVI_m - NDVI_n) / (NDVI_m + NDVI_n) \quad (4)$$

where GI is the grassland growth index and $NDVI_m$ and $NDVI_n$ represent the vegetation index values of different times. The NDVI value of each ten-day period, month or growing season from May to September of 2008 was considered to be $NDVI_m$. The average NDVI value from May to September 2003-2007 was considered to be $NDVI_n$.

To make a scientific and reasonable evaluation of nationwide grassland vegetation growth, the grassland vegetation growth of effectively monitored areas was classified into five grades (excellent, good, balanced, poor and very poor) based on the magnitude of GI values. The areas with remote-sensing data quality problems or cloud interference, as well as the non-grassland areas, were considered to be non-monitored areas. A thematic map was developed with different colours representing 1-6(excellent, good, balanced, poor, very poor and non-monitored areas), and statistics of proportion of grasslands were conducted across different grades.

2.3 Statistics and analyses of image data

To obtain a spatial distribution map of grassland vegetation growth at different time scales, statistics were conducted using GIS software. The grassland vegetation growth statistics were conducted using provincial administration units for each ten-day period, month and growing season from May to September. This allowed for the generation of a dynamic change diagram of nationwide and provincial grassland vegetation growth status and an analysis of the dynamic spatiotemporal changes of China's grassland vegetation growth.

3 RESULTS

3.1 China generally experienced grassland vegetation growth that was classified as “good” in 2008.

Compared to the average status of the same period across multiple years, the nationwide grassland vegetation growth of China was good from May 2008 to September 2008. The areas where the vegetation

growth was excellent, good, balanced, poor and very poor from early May to mid-September accounted for 9.97%, 28.50%, 38.67%, 14.69% and 8.16% of China's total grassland area, respectively. Thus, 2008 was a satisfactory year (Figure 1).

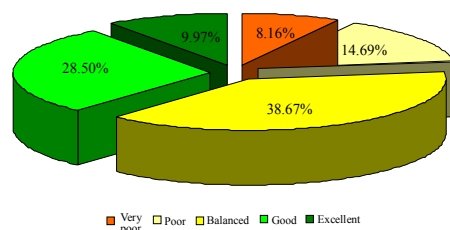


Figure 1. Remote-sensing monitoring results of nationwide grassland vegetation growth from May to September of 2008 compared with the average value of the same period across multiple years.

3.2 China had steady grassland vegetation growth in each ten-day period of 2008.

The grassland vegetation growth status of each ten-day period between May 2008 and September 2008 is shown in Figure 2 and Table 1. Compared with the multi-year average, China had good grassland vegetation growth in each ten-day period of the growing season throughout 2008. Although the vegetation growth was near balance in early June, around early September the proportion of areas with good growth declined.

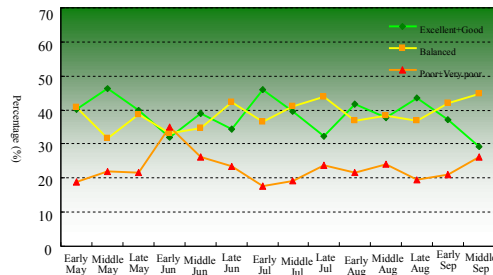


Figure 2. The dynamic change of China's grassland vegetation growth in 2008 compared with the same period over multiple years.

On average, 38.67% of China's grassland had balanced grassland vegetation growth in each ten-day period of 2008. The differences between various ten-day periods were between 32% and 45%. The grassland with good growth averaged 28.5%, and the differences between various ten-day periods ranged from 24% to 33%. Early June only showed a change of 20.10%, which was the lowest. The proportion of areas with excellent growth averaged 10%, and the changes between ten-day periods ranged from 5% to

15%. Chinese grassland with poor growth accounted for about 14.69% on average, and the changes between ten-day periods ranged from 12% to 18%. Early June showed a 20.63% change, which was the highest. The grassland with very poor growth accounted for about 8.16% of the total grassland, and the changes between ten-day periods ranged from 5% to 10%. Early June showed a 14.32% change, which was the highest. In general, China had good grassland vegetation growth during the 2008 growing season, and the growth was near balance in early June.

Table 1. Dynamic changes of China's grassland vegetation growth from May 2008 to September 2008 (10-day periods) compared with the average value of the same period during the previous five years.

Time	Percentage (%)				
	Very poor	Poor	Balanced	Good	Excellent
Early May	6.56	12.35	40.84	32.32	7.93
Mid-May	9.63	12.34	31.75	33.07	13.21
Late May	7.88	13.67	38.62	31.25	8.57
Early June	14.32	20.63	33.03	20.10	11.93
Mid-June	10.17	16.08	34.81	26.78	12.15
Late June	7.38	15.98	42.39	26.44	7.80
Early July	5.31	12.40	36.41	30.95	14.93
Mid-July	6.57	12.74	41.09	29.62	9.98
Late July	7.54	16.27	43.93	24.16	8.10
Early August	8.49	13.27	36.69	32.55	9.01
Mid-August	9.97	13.92	38.31	29.37	8.43
Late August	6.41	13.09	36.85	29.20	14.45
Early September	6.65	14.26	41.92	29.06	8.10
Mid-September	7.36	18.73	44.78	24.17	4.96
Average	8.16	14.69	38.67	28.50	9.97

3.3 Spatial patterns of China's grassland vegetation growth

In 2008, the areas with poor and very poor grassland vegetation growth in China mainly included middle and east Inner Mongolia, north Xinjiang, and most parts of Heilongjiang, etc (Figure 3). The areas with good vegetation growth were mainly distributed in north Tibet, southwest Qinghai, west Inner Mongolia, Gansu, Ningxia, Shanxi, etc (Figure 3).

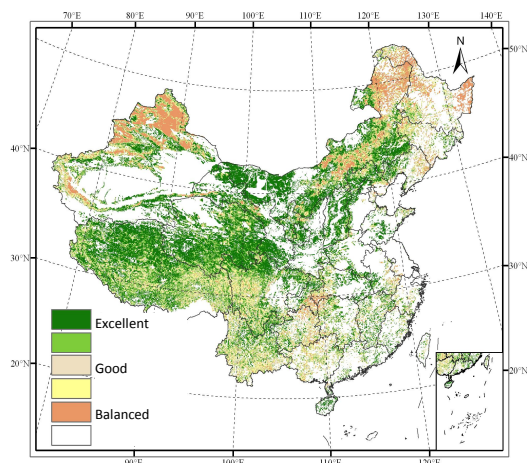


Figure 3. Spatial distribution map of China's grassland vegetation growth during the growing season of 2008 compared with the average of the same period across multiple years.

3.4 Dynamic changes in the spatial patterns of China's grassland vegetation growth

The remote-sensing monitoring results of all ten-day periods from early May to mid-May 2008 show that the areas with good vegetation growth extended further south and the areas with balanced growth decreased. In late May, the areas with balanced growth increased, and the grassland area with good vegetation growth decreased. From early June to mid-June, the grassland area with good vegetation growth continuously expanded, but the areas with balanced growth increased in late June. The areas with good vegetation growth became concentrated in middle and east Inner Mongolia, north Shanxi, east Guizhou and east Yunnan. The areas with poor vegetation growth were distributed in middle and west Heilongjiang, east Qinghai and north Xinjiang.

In early July 2008, the nationwide grassland growth was better than the multi-year average. In middle and late July, the areas with good vegetation growth decreased, and the areas with poor growth increased. In late July, the grassland vegetation growth in west Hulunbeier, north Xilinguole, Tibet, west Sichuan, and most parts of Guangxi was better than the multi-year average.

In early August 2008, China's grassland vegetation growth was better than the multi-year average. In mid-August, the areas with good vegetation growth decreased, and the areas with poor growth increased. In late August, the areas with good growth significantly increased, and the areas with poor growth decreased.

In early September 2008, China's grassland vegetation growth was slightly better than the multi-year average.

In mid-September, the grassland area with balanced growth increased, and the area with good growth decreased.

3.5 Monitoring the results of grassland vegetation growth in key provinces (municipalities)

Inner Mongolia, Tibet, Xinjiang, Gansu, Qinghai and Sichuan are the important pastoral areas of China. The change in grassland vegetation growth in these key provinces (municipalities) reflected the dynamic change of nationwide grassland vegetation growth. Due to space restrictions, only the monitoring results of Inner Mongolia are discussed in detail.

3.5.1 Inner Mongolia

In Inner Mongolia, the general vegetation growth was better than the multi-year average. Compared with the average status of the same period in previous years, the areas with excellent, good, balanced, poor and very poor vegetation growth in Inner Mongolia accounted for 10.22%, 32.36%, 37.68%, 14.08% and 5.66% of the region's total grassland area, respectively, in 2008. The monthly dynamic data (Table 2) show that the grassland vegetation growth of Inner Mongolia in May was higher than the multi-year average, the status in June was almost the same as the multi-year average, and the proportion of grassland with poor growth was larger than the area with good growth. During July to September, the vegetation growth was also better than the multi-year average. The dynamic data of the ten-day periods (Table 3) show that the grassland vegetation growth of Inner Mongolia during early May to late May 2008 was better than the previous multi-year average. Although early June had poor vegetation growth, middle and late June had balanced growth. The growth status from early July to mid-September was better than the multi-year average.

Table 2. Monthly dynamic data of Inner Mongolia's grassland vegetation growth in 2008 compared with the same period across multiple years.

Average for month	Percentage (%)					Monitored area
	Very poor	Poor	Balanced	Good	Excellent	
May	7.78	9.41	31.59	40.29	10.93	85.78
June	9.57	24.06	40.74	19.91	5.73	96.17
July	4.96	14.99	38.87	27.09	14.07	97.19
August	2.96	10.81	38.25	37.79	10.20	98.94
September	1.71	9.67	39.57	38.90	10.14	99.24

Table 3. Ten-day-period dynamic data of Inner Mongolia's grassland vegetation growth in 2008 compared with the same period across multiple years.

Time	Percentage (%)					
	Very poor	Poor	Balanced	Good	Excellent	Monitored area
Early May	1.31	3.67	31.96	49.87	13.19	64.90
Mid-May	14.65	11.27	24.99	35.35	13.74	94.44
Late May	7.39	13.28	37.82	35.64	5.87	97.99
Early June	11.19	29.88	40.56	14.63	3.74	96.90
Mid-June	9.71	21.20	38.82	24.67	5.61	98.94
Late June	7.80	21.09	42.83	20.43	7.85	92.67
Early July	5.72	17.44	37.96	23.31	15.56	95.01
Mid-July	3.15	9.97	36.16	35.66	15.05	97.86
Late July	6.01	17.57	42.50	22.31	11.60	98.69
Early August	4.80	11.00	37.04	38.18	8.97	99.73
Mid-August	1.12	8.86	42.39	38.20	9.42	99.92
Late August	2.96	12.55	35.30	36.97	12.21	97.16
Early September	1.97	10.70	41.06	36.60	9.68	98.72
Mid-September	1.45	8.65	38.09	41.21	10.61	99.76
Average	5.66	14.08	37.68	32.36	10.22	95.19

4 CONCLUSIONS

This study applied the grassland vegetation growth index to conduct remote sensing monitoring of the spatiotemporal status of China's grassland vegetation growth in 2008. The following conclusions were derived from the data of the present study:

- i) In general, 2008 was a year during which China's grasslands experienced good vegetation growth. The areas of grassland with desirable vegetation growth accounted for 38.47% of China's monitored grassland area, whereas the areas with less desirable vegetation growth accounted for 22.85%.
- ii) In 2008, the grassland throughout China exhibited good vegetation growth, which was stable over multiple ten-day periods. The vegetation growth almost became balanced in early June. After early September, the proportion of grasslands with desirable

vegetation growth declined, and the proportion of balance and less desirable parts increased.

iii) The regions with less desirable vegetation growth mainly included the middle and east regions of Inner Mongolia, the north region of Xinjiang and most parts of Heilongjiang. The regions with desirable vegetation growth were mainly distributed in the north region of Tibet, the southwest region of Qinghai, the west region of Inner Mongolia, Gansu, Ningxia, Shanxi and the northwest region of Liaoning, etc.

iv) Inner Mongolia generally had better vegetation growth in 2008 than the multi-year average.

The remote sensing monitoring conducted in this study on the spatiotemporal patterns of China's grassland vegetation growth revealed the overall vegetation growth status of China's grasslands on a broad scale. These results could provide a helpful scientific basis for understanding China's grassland vegetation conditions and for managing and regulating the grassland livestock husbandry.

REFERENCES

- Chen, J., Gu, S., Shen, M. G., Tang, Y. H., and Matsushita, B., 2009, Estimating aboveground biomass of grassland having a high canopy cover: an exploratory analysis of in situ hyperspectral data. *International Journal of Remote Sensing*, **30**, 6497-6517.
- Edwards, M. C., Wellens, J., and Eisawi, D., 1999, Monitoring the grazing resources of the Badia region, Jordan, using remote sensing. *Applied Geography*, **19**, 385-398.
- Liu, Y. J., and Yang, Z. D., 2001, Principle and algorithm of remote sensing processing based MODIS. (Beijing: Science Press), 232-240.
- Reeves, M. C., Zhao, M. S., and Running, S. W., 2006, Applying improved estimates of MODIS productivity to characterize grassland vegetation dynamics. *Rangeland Ecol Manage*, **59**, 1-10.
- Robert, A. W., Neil, E. W., Ramsey, R. D., and Rebecca, A. E., 2006, A protocol for retrospective remote sensing-based ecological monitoring of rangelands. *Rangeland Ecol Manage*, **59**, 19-29.
- Yang, B. J., and Pei, Z. Y., 1999, Definition of crop condition and crop monitoring using remote sensing. *Transactions of the Chinese Society of Agricultural Engineering*, **15**, 214-218.
- Zha, Y., Gao, J., and Ni, S. X., 2003, Most recent progress of international research on remote sensing of grassland resources. *Progress In Geography*, **1122**, 607-617.

Application of Artificial Neural Networks to the Prediction of Forest Fire Danger Using MODIS Data

Bisquert M.(*), Caselles E.(*), Sánchez J. M.(**), Caselles V.(*), Rubio E.(**, ***)

(*) *Earth Physics and Thermodynamics Department, University of Valencia, 46100, Burjassot, Valencia, Spain.*

(**) *Applied Physics Department, University of Castilla-La Mancha, 02071 Albacete, Spain.*

(***) *Regional Development Institute, University of Castilla-La Mancha, 02071 Albacete, Spain.*

Maria.Mar.Bisquert@uv.es

ABSTRACT: Remote sensing has been used in relation to forest fires with different purposes: mapping burned areas, detection of active fires, and obtaining parameters to be included in fire danger models. In this paper we focus on the prediction task. Fire danger models are a very useful tool for the prevention and extinction of forest fires. Inputs of these models are meteorological and topographic parameters, fire history, proximity to roads and towns, fuel models, vegetation status, etc. Some of these parameters can be obtained from remote sensing images, which offer higher spatial and temporal resolution than direct ground measures. In this paper, we focus on the Galicia region (northwest of Spain), and MODIS (MODerate resolution Imaging Spectroradiometer) images are used to monitor vegetation status as an essential input in forest fire danger models in this region. A six-year period (2001-2006) was selected, and images from the products MOD13Q1 (vegetation indices) and MOD11A1 (land surface temperature) were used. Fire data for this same period was used in order to obtain the relation between these parameters and fire frequency. A variety of techniques of analysis have been applied in recent literature to relate fire danger to different input parameters (linear regression, logistic regression, etc.). Artificial neural networks (ANN) can be also used with this aim. This technique is particularly attractive in applications where the complexity of the data makes other methods useless. In this work, we have tested the potential of ANN to estimate forest fires danger from remote sensing data and from fire history data, remote sensing input used are the land surface temperature and the EVI (Enhanced Vegetation Index) variation in a two-week period prior to the study date. Results obtained by ANN are compared to those using other techniques of analysis. A classification in three levels of fire danger was established. Fire danger maps, based on this classification, will facilitate fire prevention and extinction tasks.

1 INTRODUCTION

Forest fires are a dangerous threat for environment. In the last years, the number of fires in Spain has grown with terrible effects not only on environment, but also on economy, and even human lives. For these reasons the investigation in forest fires prevention has become essential. In particular, fire danger indices are very useful in forest fire fighting since they inform of regions and time of major fire danger. At this point some models have already been developed, integrating different inputs and using different techniques. For example, many authors have used logistic regression (Verbesselt et al. 2006; Lozano et al., 2007; Chuvieco et al., 2009; Chuvieco et al., 2010; Bisquert et al., 2010) to estimate fire danger from different input

parameters. Neural networks have been widely used too. Artificial neural networks are predictive models loosely based on the action of biological neurons. The original model was developed by Frank Rosenblatt (Rosenblatt, 1958). Rosenblatt's model consisted of three layers, (1) a "retina" that distributed inputs to the second layer, (2) "association units" that combine the inputs with weights and trigger a threshold step function which feeds to the output layer, (3) the output layer which combines the values. From that first model, a lot of progress has been made in the field of neural networks and their range of applications has been covering more and more disciplines. Specifically, artificial neural networks have been used in numerous studies for classification of fire danger from remote sensing data (Vasconcelos et al., 2001; Alonso-

Betanzos et al., 2003; Vasilakos et al., 2009; Maeda et al., 2009).

Some papers have shown that neural networks offer better results than logistic regression. Vasconcenlos et al. (2001) carried out a comparative study between logistic regression and neural networks for fire ignition probabilities. These authors concluded that both techniques produce models with good levels of concordance and achieve acceptable classification error rates, and that logistic models have better concordance in the training phase, but worse in the validation set, than the neural networks. It is evident that the neural networks have stronger generalization ability.

Fire danger indices use a variety of inputs. Remote sensing inputs are usually LST (Land Surface Temperature) and vegetation indices, both related to the vegetation stress and fire ignition probability. Additional parameters are fire history, proximity to roads/towns, week-in-year, meteorological variables, etc.

In this paper artificial neural networks have been used for estimating fire danger from remote sensing data and collections of fire data. Different combinations of the input variables have been trained and tested in order to select the best one. Logistic regression has been also applied, and results from the two methodologies have been compared.

2 STUDY SITE AND DATA USED

The study site in this work is the Galicia region placed at the Northwest of Spain (Figure 1). About 70% of the Galician territory is occupied by forest areas. Despite its humid and rainy climate, Galicia is the Spanish region with the largest number of forest fires.

The organisms for the management of fire prediction and extinction tasks use a grid as a basis dividing Galicia in 360 10-km side squares (UTM 29). Also, historic fire data are provided at the same spatial resolution.

Two different MODIS products were used to monitor the vegetation status, the vegetation indices MOD13Q1 product, which provides 16 day compositions images with 250 m spatial resolution, and the Land Surface Temperature (LST) MOD11A1 product, which provides daily images with 1 km spatial resolution. In particular the Enhanced Vegetation Index (EVI) was used in the present study, since in Bisquert et al. (2010) it was shown that there exist a relationship between the fire frequency and the variation of this index in the Galicia region.



Figure 1. Location of the Galicia region in Spain.

3 METODOLOGY

3.1. Pre-processing of MODIS data

Images from both products needed to be pre-processed in order to eliminate wrong values due to clouds, problems with the sensors, etc. MOD13Q1 pre-processing (figure 2) was carried out as described in Bisquert et al. (2010), including a filtering process (figure 2b) based on the quality band, a filling process (figure 2c) and an averaging process (figure 2d).

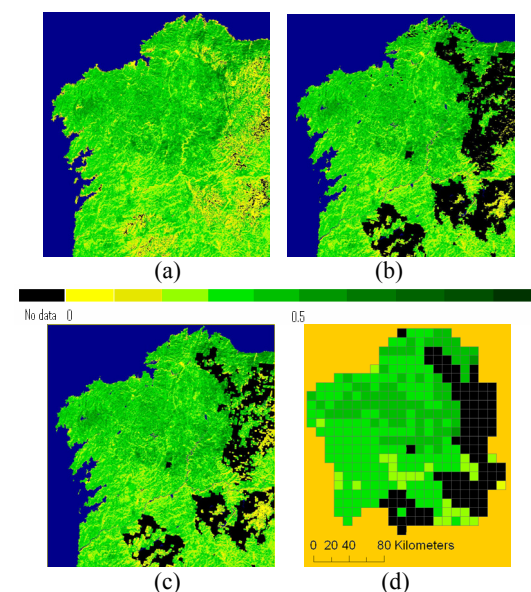


Figure 2. Processing of EVI images: a) original image, b) filtered image, c) filled image, d) average EVI per cell (10x10 km).

MOD11A1 images also needed a filtering process, in this case to ensure temporal homogeneity in the LST values avoiding combination of different satellite overpasses within the same image. Since these differences would be a problem for the study, only pixels with data obtained between 10 and 12 am were considered, and pixels that differed more than 36 minutes from the average hour were discarded. Also a filtering process based on the quality band was carried out. A filling process and a process for assigning a value of LST to each cell were carried out as described for MOD13Q1 in Bisquert et al. (2010). Finally, LST

compositions of 8 and 16 day were performed, using the same periods of 16 days as in the MOD13Q1 images.

16 day EVI composition, 16 day EVI variations (ΔEVI) composition (difference between two consecutive EVI images), 8 day LST composition, 16 day LST composition, as well as period of year and fire history in each cell were used as input variables for the different techniques used for fire danger estimation.

3.2 Artificial Neural Network (ANN)

In this work, a Multilayer Perceptron Neural Network was used since it best met the needs of our problem. The diagram shown in figure 3 illustrates a perceptron network with three layers as the one used in the present work.

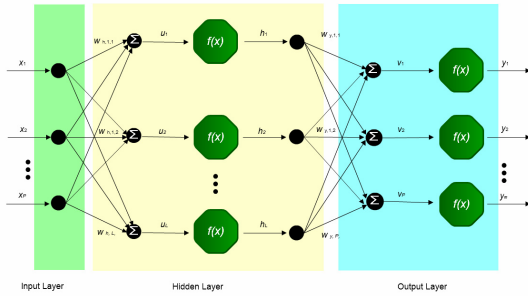


Figure 3. Perceptron network diagram.

This network has three different layers, each one with different number of neurons:

- **Input Layer:** input data is represented as a vector of variable values ($x_1...x_p$). These values are distributed to each of the neurons in the next layer (the hidden layer).
- **Hidden Layer:** the value from each input neuron is multiplied by a weight (w_{ji}), and the resulting weighted values are added together producing a combined value u_j . The weighted sum (u_j) is fed into a transfer function, $f(x)$, which outputs a value h_j . The outputs from this layer are distributed to the output layer.
- **Output Layer:** each hidden neuron value is multiplied by a weight (w_{kj}), and the resulting weighted values are added together producing a combined value v_j . The weighted sum (v_j) is fed into a transfer function, σ , which outputs a value y_k . The y values are the outputs of the network.

We used a network topology similar to the network presented in the above diagram: a full-connected (output from each neuron is distributed to every neuron in the following layer), three layer, feed-

forward (values only move from input to output layers, not back), perceptron neural network.

3.2.1 Neural Network Training Methodology

As explained in the beginning of this document, the aim of this study was to build a classifier to predict the fire danger, based on data from the state of vegetation (EVI, ΔEVI), the average temperature of the previous days (LST) and other parameters. We could solve the problem as a normal classification problem with output levels, (high fire danger and low fire danger) and some numerical input variables (land surface temperature, variation of the enhanced vegetation index, fire history, etc.). In other words, artificial neural networks were trained to work as fire danger level classifiers.

For the design of the experiments, data (about 50,000) were divided into three different disjoint data sets:

1. Training: around 70% of the data (approximately 35,000 samples). It was used to train the models of each experiment.
2. Validation: 10% of the data (approximately 5,000 samples). It was used to validate each trained model and to compare them.
3. Test: the remaining 20% (10,000 samples). It was used to test the best models and show their real performance.

For that purpose, a study was done to evaluate which was the best combination of input parameters (land surface temperature, variation of the enhanced vegetation index, fire history, etc.) to obtain the best classification results. To do this, we tried to combine the parameters set at the beginning of the document and analyze the behavior of each resulting network trained with each combination.

3.2.2 Data pre-processing and normalization

In order to train the classifier, a C++ script was made to read the samples and generate patterns in the format required by the Neural Network. Therefore, the samples were processed to create the different sets.

For this work, the high fire danger class was coded with a +1 value and low fire danger with a -1 value. As the data had already been processed to create patterns in a particular format, it was decided to normalize the data too. For this purpose a C++ function was implemented to calculate the maximum and minimum value of each variable and based on them, normalize all values between 0 and 1. This was done as a prelude to writing samples in each data file.

The reason for performing this operation is to accelerate the training process, to avoid using large

numbers in the calculations and to control the possible range of weights. Also, putting all the variables in the same range of values can avoid favoritism (not to give more weight, a priori) for some of them in all, it is trying to improve the efficiency of the classifier, both in performance and speed process (time to converge to the solution).

3.3.3 Training procedure

For the training of each neural network, the following process was designed, although for some specific experiment it was slightly modified.

1) The first step was to set the parameters of the network and the learning function (BackPropagation, QuickPropagation, BP Momentum, etc.), and then train the network with the training set.

2) In each training cycle, the validation MSE (Mean Square Error) was checked, if it was less than best value obtained so far, that value was updated and the current network was stored.

3) The previous step was repeated until the MSE of validation set did not improve in fixed number of consecutive training cycles.

4) Once we have the best trained networks, they were evaluated by classifying the Test Set, in order to be able to analyze and compare the error and success rates later.

3.4 Logistic regression

Logistic regression is usually applied when working with binary independent variables, like the presence or absence of fire. The algorithm obtained by logistic regression calculates the conditional probability of an event occurring from one or more input variables (equation 1).

$$P_{fire} = \frac{1}{1 + \exp(-\alpha - \beta_1 x_1 - \dots - \beta_k x_k)} \quad (1)$$

where α and β are the parameters of the equation, and x_k are the input variables.

Logistic regression can be used for estimating the contribution and significance of each variable. This technique is then useful to decide which variables or combination of variables should be introduced in a more complex model, such as ANN, in order to reduce the working time of these techniques.

4 RESULTS

Logistic regression was applied to 20 different combinations of the input variables. The combinations of variables that offered better results were then introduced in the ANN (12 combinations). The precision (percent of fires correctly predicted) and accuracy (percent of events correctly predicted) obtained using both techniques for those combinations that showed accuracies greater than 60% are presented in table 1.

Neural networks offer better accuracy in all cases, and better precision in the case were fire history, period of year and 8 day LST composition are put together (table 1). This combination was selected as the best one for obtaining fire danger in Galicia since it showed the best accuracy in both cases and the best precision of all cases when using neural network.

From the output values obtained by neural network (ONN) using this combination, a danger level classification was defined in order to simplify the fire fighting. The best classification was:

Low danger: $ONN \leq -1$

Medium danger: $-1 < ONN \leq -0.5$

High danger: $ONN > -0.5$

Table 2 shows the percent of cells classified in each fire danger level and the percent of fires observed in each level. By using this classification we obtain three levels perfectly separated.

This classification can be used for mapping the fire danger. An example corresponding to the period 12-19 of July of 2006 is shown in figure 4.

Table 1. Precision and accuracy obtained using ANN and logistic regression for different input combinations.

Input combinations	Neural network		Logistic regression	
	Precision	Accuracy	Precision	Accuracy
History + LST8+ V.EVI	60	74	66	69
History + LST16 + V.EVI	63	75	65	69
History + LST8 + V.EVI + EVI	62	75	66	69
History + LST16 + V.EVI + EVI	63	76	66	69
History + LST8 + Period	66	76	65	70

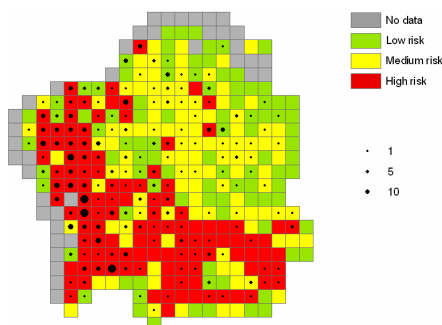


Figure 4. Example of fire danger map for the period 12-19 of July of 2006. Number of fires occurred in the same period is superposed.

Table 2. Percent of cells classified in each danger level and percent of fires observed.

Danger level	Percent of fires	Percent of cells
Low	14	43
Medium	25	36
High	65	21

5 CONCLUSIONS

Artificial neural networks were used for obtaining a fire danger model. Remote sensing variables (EVI and LST) were used as input variables for monitoring the vegetation status, together with fire history variables. Different combinations of input variables were checked (16 day EVI combination, 16 day EVI variation, 16 day LST combination, 8 day LST combination, fire history and period of year). Results obtained from artificial neural network were compared to results from logistic regressions with the same input parameters. The best combination of input parameters found was: 8 day LST, fire history and period of year. Artificial neural network showed better accuracy and precision (76.4% and 66.4%, respectively) than logistic regression. Finally, a classification in three fire danger levels was defined from results of the neural network, with 14% fire probability in the low danger level, 25% in the medium level and 65% in the high level. This classification is useful for obtaining fire danger maps which facilitate the prevention and extinction tasks.

REFERENCES

Alonso-Betanzos, A., Fontenla-Romero, O., Guijarro-Berdiñas, B., Hernández-Pereira, E., Paz

- Andrade, M. I., Jiménez, E., Legido Soto, J. L., Carballas, T., 2003, *Expert Systems with Applications*, **25**, 545-554.
- Bisquert, M. M., Sánchez J. M., Caselles, V., 2010, Fire danger estimation from MODIS Enhanced Vegetation Index data. Application to Galicia region (Northwest Spain). *International Journal of Wildland Fire*, In press.
- Chuvieco, E., Aguado, I., Yebra, M., Nieto, H., Salas, J., Martín, M. P., Vilar, L., Martínez, J., Martín, S., Ibarra, P., de la Riva, J., Baeza, J., Rodríguez, F., Molina J.R., Herrera, M.A., Zamora, R., 2010, Development of a framework for fire risk assessment using remote sensing and geographic information system technologies. *Ecological Modelling*, **221**, 46-58.
- Chuvieco, E., González, I., Verdú, F., Aguado, I., Yebra, M., 2009, Prediction of fire occurrence from live fuel moisture content measurements in a Mediterranean ecosystem. *International Journal of Wildland Fire*, **18**, 430-441.
- Lozano, F. J., Suárez-Seoane, S., de Luis, E., 2007, Assessment of several spectral indices derived from multi-temporal Landsat data for fire occurrence probability modelling. *Remote Sensing of Environment*, **107**, 533-544.
- Maeda, E. E., Formaggio A. R., Shimabukuro, Y. E., Arcoverde, F. B., Hansen, M. C., 2009, Predicting forest fire in the Brazilian Amazon using MODIS imagery and artificial neural networks. *International Journal of Applied Earth Observation and Geoinformation*, **11**, 265-272.
- Rosenblatt, F., 1958, The Perceptron: A Probabilistic Model for Information Storage and Organization in the Brain. In *Psychological Review*, **65**, 6, 386-408.
- Vasconcelos, M. J. P., Silva, S., Tomé, M., Alvim, M., Cardoso Pereira, J. M., 2001, Spatial Prediction of Fire Ignition Probabilities: Comparing Logistic Regression and Neural Networks. *Photogrammetric Engineering & Remote Sensing*, **67**, 1, 73-81.
- Vasilakos, C., Kalabokidis, K., Hatzopoulos, J., Matsinos, I., 2009, Identifying wildland fire ignition factors through sensitivity analysis of a neural network. *Natural Hazards*, **50**, 125-143.
- Verbesselt, J., Jönsson, P., Lhermitte, S., van Aardt, J., Coppin, P., 2006, Evaluating Satellite and Climate Data-Derived Indices as Fire Risk Indicators in Savanna Ecosystems. *IEEE Transactions on Geoscience and Remote Sensing*, **44**, 6, 1622-1632.

Monitoring natural and anthropized vegetation trends using remotely sensed LAI MODIS in semi-arid region. Study case of agricultural systems of northwest Senegal.

C. Bobée⁽¹⁾, C. Ottlé⁽¹⁾, F. Maignan⁽¹⁾, M. Ndiaye⁽²⁾

(1) LSCE-IPSL, Orme des Merisiers, 91191, Gif-sur-Yvette, France

(2) Agence Nationale de la Météorologie Sénégal, BP8257, Dakar Yoff, Sénégal

cecilia.bobee@gmail.com, catherine.ottle@lsce.ipsl.fr

ABSTRACT -Vegetation dynamics in anthropized semi-arid environments are assessed at local and regional scales, through the joint analysis of MODIS LAI, daily rainfall, morphopedological and land cover datasets for the period 2000-2008. The study area is located in northwest Senegal. Significant correlations between variation coefficient of LAI and mean annual precipitation for both herbaceous crops and natural vegetation are highlighted. The latter is reinforced using a rainfall distribution factor, which preferentially controls natural herbs behavior. LAI data was also used for modeling the greenness period and for deriving the timing of phenological onset and offset dates. The results show that rainfall thresholds allowing the green-up onset can be defined for each type of vegetation. Moreover, median maps of onset dates, suggest an increase of the phenological cycle length from Saint-Louis to Dakar, in accordance with both the North-South rainfall gradient and the intensification of agricultural practices around Dakar. In this study, a meteorological indicator is proposed for estimating green-up onsets for natural and anthropized vegetation.

1 INTRODUCTION

Estimate of land cover changes may be assessed using remotely sensed data. Among those, the Leaf Area Index (LAI) proved to be a significant biophysical parameter for crop yield assessment (Doraiswamy et al., 2005) and for hydrological modeling at regional scale (Andersen et al., 2002). In semi-arid environments, Privette et al. (2002) reported a good correlation between in situ LAI measurements and MODIS (MODerate resolution Imaging Spectroradiometer) LAI for woodland and savanna. Similarly, Fensholt et al. (2004) indicated that MODIS LAI data correctly reproduce the “real-world LAI” in Senegalese savanna.

The aim of this study is to assess the present-day vegetation dynamics under anthropized semi-arid environments through the joint analysis of MODIS LAI, daily rainfall, geomorphological and land cover datasets for the period 2000-2008. The study area is located in northwest Senegal. Phenological and climatic predicting indicators are proposed for determining green-up onset dates and vegetation biomass.

2 STUDY AREA

The study area is located in northwest Senegal, in a narrow strip of land along the north coast stretching over the cities of Dakar and Saint-Louis (Fig. 1).

Precipitations are concentrated in the core of the monsoon season, which last from June to October.

The landscape consists in a succession of live, semi-fixed and continental sand dunes, from West to East. The two studied ecoregions are the “Niayes” and the “Peanut Basin” ecoregions (Tappan et al., 2004). Niayes are wet micro-environments in interdunal depressions characterized both by intensive market gardening activities and the presence of subguinean forest relics. Vegetation in the Peanut Basin essentially consists of a mosaic of rainfed crops (essentially millet, peanut and sorghum) and sparse shrublands.

3 DATASETS AND METHODS

3.1 Datasets

Datasets used in this study are daily rainfall data, MODIS LAI products and land cover data.

Daily rainfall data were provided by the “Direction Nationale de la Météorologie” (DNM, Dakar, Senegal) for four synoptic rain gauge stations, located at Dakar, Saint-Louis, Thies and Louga (Fig. 1). Precipitation data are available for the period 2000-2008 (Table 1). During this period, the spatial distribution of rainfall is influenced both by the latitudinal gradient (mean annual precipitation (MAP) of 282.5 ± 60.0 mm and 296.2 ± 150.6 mm for the stations of Saint-Louis and

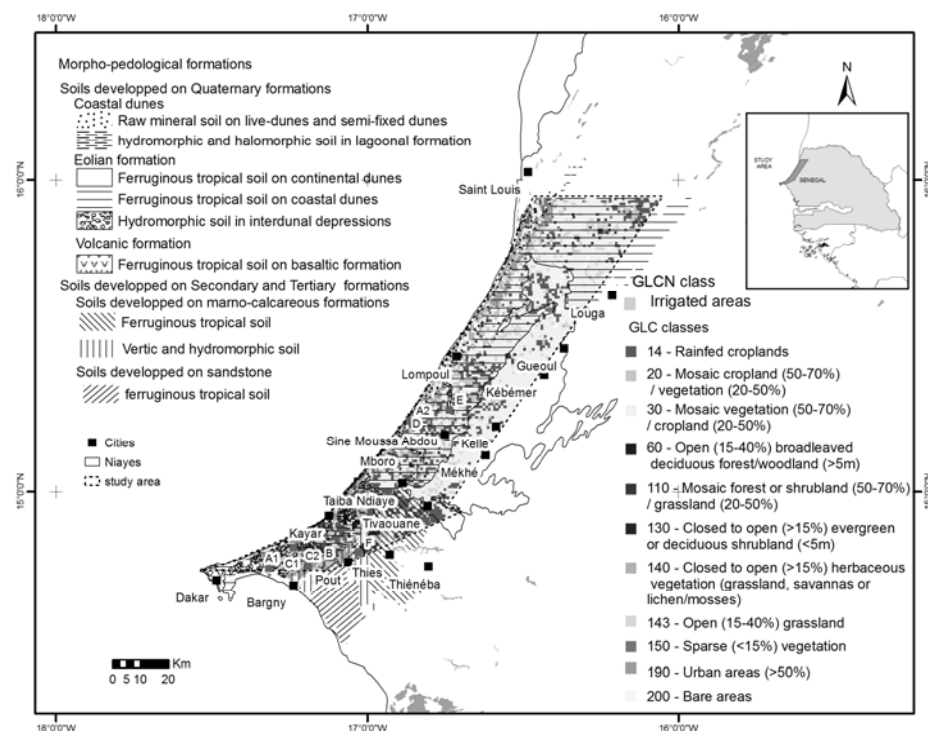


Figure 1: Vegetation land cover (GLC legend) aggregated to 1km² resolution. Morphopedological setting (from Stancioff et al., 1986, modified map) is superimposed to the land cover map.

Dakar, respectively) and by the topography (plateau of Thies).

Table 1: Rainfall distribution during rainy seasons for the period 2000-2008 (AP: annual precipitation (mm); RD: number of rainy events; BR: beginning of the rainy season (DOY); ER: end of the rainy season (DOY); RS: duration of the rainy season; (σ : standard deviation).

		Mean \pm 1 σ			Mean \pm 1 σ
Dakar	AP	296.2 \pm 150.6	Louga	AP	288.2 \pm 58.7
	RD	26.8 \pm 7.5		RD	26.7 \pm 6.3
	BR	172.9 \pm 13.0		BR	178.3 \pm 10.4
	ER	291.8 \pm 14.4		ER	280.7 \pm 11.3
	RS	118.9 \pm 10.9		RS	102.3 \pm 19.2
Thies	AP	511.1 \pm 212.1	Saint-Louis	AP	282.5 \pm 60.0
	RD	35.4 \pm 6.9		RD	29.2 \pm 6.0
	BR	176.1 \pm 15.6		BR	187.0 \pm 14.8
	ER	288.6 \pm 4.5		ER	285.4 \pm 14.9
	RS	112.5 \pm 18.1		RS	98.4 \pm 27.1

The MOD15A2 LAI used (MODIS TERRA sensor, collection 4) is a 8-day composite product provided at a 1km² spatial resolution (Knyazikhlin et al., 1999; Myneni et al., 2002). The LAI product is based on biome specific algorithms and is obtained by inversion of the 3-dimensional radiative transfer problem (Myneni et al., 1997). In this work, LAI time series were smoothed using a five-point moving window for reducing noise.

The analysis of LAI data was performed between DOY – day-of-year- 57 in 2000 and DOY 361 in 2008.

The land cover data used is the regional Globcover Land Cover (GLC) map. The GLC is a 300m resolution map (Bicheron et al., 2004) derived from the European MERIS/ENVISAT sensor full resolution images. Vegetation classes are reported in Fig. 1.

3.2 Methodology

The methodological approach is to identify specific phenological dates (green-up onset and offset) from LAI and to compare these ones with precipitation trends, types of vegetations and soils.

For estimating phenological dates, LAI values were fitted using the model of Zhang et al. (2003). This model is based on two 4-parameter sigmoidal functions for modeling separately the greenness and the senescence periods. The standard deviations between datasets and models exceeding 5% were removed from the modeled dataset. The green-up onset and offset dates are respectively defined as the ones for which the greenness and the senescence sigmoids equal 10% of amplitude of the signal.

Correlations between LAI signals and daily rainfall have been achieved around the four rain gauge stations (10km radius for Thies and Louga, 20 km radius for Saint-Louis and 25km radius for Dakar). The regions defined are a compromise between the outlying position

of the meteorological stations and the spatial distribution of Sahelian rain fields (Ali et al., 2003).

Moreover, a correspondence was defined for merging LAI pixels, soil and land cover maps: each LAI pixel was given the GLC code of the nearest vegetation pixel. The resulting land cover map is thus degraded to 1km² resolution, but still reflects the spatial distribution of the observed vegetation (Fig. 1).

The biomass vegetation was assessed through the calculation of the coefficient of variation (CV) of the LAI signals (CV_{LAI}). The CV is defined by the ratio of the standard deviation to the mean. It gives information about the relative spread in the LAI dataset and allows the different vegetation biomasses to be compared.

4 RESULTS

4.1 LAI dynamics at local and regional scales

Smoothed LAI pixels were extracted within a 25km radius from Dakar for the period 2000-2008. The LAI temporal profiles are analyzed according to soil and vegetation types (Fig. 2).

The four soil types which have been identified in the selected regions are hydromorphic soils, raw mineral soils, halomorphic soils and tropical ferruginous soils. Except for raw mineral soils, soil types are characterized by mixed vegetation comprising both natural vegetation (GLC110, GLC130 and GLC150 classes) and croplands (GLC14, GLC20 and GLC30, regrouped in a “crops” class in Fig. 1).

Three main results can be presented:

1/ LAI signals revealed to be in strong relation with soil type. Crops developed on ferruginous tropical soils, are indeed characterized by a higher LAI signal (averaged maximum LAI of $1.10 \pm 0.19 \text{ m}^2.\text{m}^{-2}$) than those developed on halomorphic ($0.68 \pm 0.06 \text{ m}^2.\text{m}^{-2}$) and hydromorphic soils ($0.77 \pm 0.10 \text{ m}^2.\text{m}^{-2}$). The low LAI signals recorded for raw mineral soils are the result of the easily erodible property of soils and their inherent low fertility.

2/ This result is reinforced at regional scale through the spatial analysis of CV_{LAI} (MCV_{LAI}) (median value for the period 2000-2008) (Fig. 3). The MCV_{LAI} is ranged between 7 and 71%. Distinct MCV_{LAI} signatures characterize raw mineral soils and ferruginous tropical soils. Raw mineral soils developed on live- and semi-fixed dunes are correlated to low MCV_{LAI} (7-37 %) when MCV_{LAI} for ferruginous tropical soils are higher (32-71 %). A clear MCV_{LAI} signature also appears south of Tivaouane between ferruginous tropical soils developed on marno-calcareous formations (50-71%) and those developed on eolian formations (38-49 %).

3/ The link between MAP and vegetation biomass is not *a priori* straightforward in Fig. 2. If for some years green-up and rainy season onsets are synchronous (years 2001, 2005, 2006), rain interruptions occurring at the beginning of the rainy season may delay the emergence phase of the vegetation (2002 and 2004).

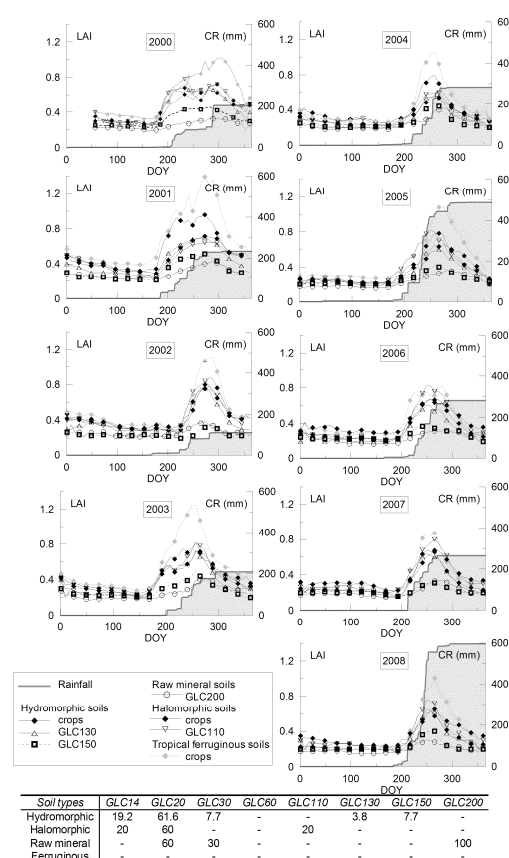


Figure 2: Comparison of MODIS LAI and cumulative rainfall (CR) around Dakar for different types of soils and vegetations. The associated table expresses the percentages of vegetation cover characterized by soil types

4.2 Correlations between precipitation behaviors and vegetation greenness index

The derived phenological parameter used is the annual CV_{LAI} . Significant correlations (R values, table 2) are observed between MAP and CV_{LAI} (0.58-0.70 for crops and 0.62-0.72 for natural vegetation). Slopes for crop and GLC110 classes are similar, revealing the same

vegetation response to MAP. The slope for the GLC140 class is twice larger and thus demonstrates the larger

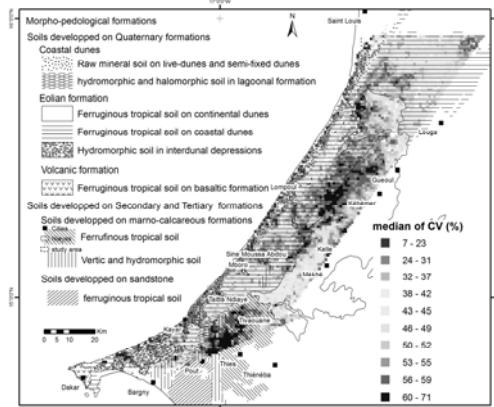


Figure 3: Map of median variation coefficient for the period 2000-2008.

Table 2: Correlation coefficients (R) between CV_{LAI} of LAI, MAP, K and I; P-values and slopes of linear fits are labeled P and d, respectively.

		MAP- CV_{LAI}	K- CV_{LAI}	I- CV_{LAI}
GLC14	R	0.67	0.48	0.65
	P	$<10^{-3}$	0.015	$<10^{-3}$
	d	0.050	70.4	0.108
GLC20	R	0.70	0.54	0.70
	P	$<10^{-3}$	0.005	$<10^{-3}$
	d	0.063	93.5	0.138
GLC30	R	0.58	0.42	0.58
	P	$<10^{-3}$	0.014	$<10^{-3}$
	d	0.043	58.3	0.096
GLC110	R	0.72	0.39	0.67
	P	$<10^{-2}$	0.145	$<10^{-2}$
	d	0.057	65.6	0.121
GLC130	R	0.06	0.19	0.13
	P	0.905	0.683	0.784
	d	0.004	30.6	0.019
GLC140	R	0.62	0.56	0.77
	P	0.077	0.115	0.015
	d	0.081	52.6	0.218
GLC150	R	0.29	0.56	0.41
	P	0.232	0.016	0.093
	d	0.023	66.9	0.085
GLC	R	0.64	0.51	0.70
	P	$<<10^{-3}$	$<<10^{-3}$	$<<10^{-3}$

Moreover, we propose to introduce two climatic parameters. The former, labeled K, is defined as the RD/RS ratio (Table 1). Moderate but significant K- CV_{LAI} (R: 0.51) relationships are shown: the more regular is the rainfall distribution, the higher is the LAI signal. The second parameter, I, defined as the product of MAP by K improves correlations: the R-value increases from 0.51 to 0.70 using the I- CV_{LAI} couple on the whole region. In addition, different vegetation responses, or sensitivities, to rainfall distribution can be identified: similar R-values for crops using CV_{LAI} -MAP or CV_{LAI} -I couples are observed when these ones are highly enhanced for natural herbs (GLC140) using the parameter I.

4.3 Dynamics of the vegetation

The green-up onset-rainfall relationship

We follow the Zhang et al. (2005)'s methodology for defining rainfall indicator: we have defined a number of cumulative rainfall thresholds, ranging from 5 to 100mm, and compared the dates at which those thresholds (RTD) are reached with the ones of green-up onset (OD) for the period 2000-2008. The beginning of the rainy season is considered in this study as the first rainy event from DOY 150 (Heug rains are not taken into account). R-values between OD and RTDs (Table 3) are used to derive the optimal rainfall thresholds ensuring the emergence phase for the different vegetation types.

Several vegetation behaviors emerge:

1/ Significant OD-RTD correlations for rainfed crops (GLC14, GLC20 and GLC30) occur once the cumulated rainfall reaches 20mm.

2/ Moderate correlation for the GLC110 class is observed for a 5mm RTD (R: 0.41), which tends to increase till a 40mm RTD (R: 0.86). Such a wide window of significant response probably results from the specific nature of this class which is composed of both grassland and mixed shrub/forest vegetation: herbaceous vegetation quickly responds to rainfall, while shrubs/trees are more sensitive to the amount of moisture available in a greater depth of soil.

3/ High R-values (R: 0.68) characterizing shrub class (GLC130) appear for a 40mm RTD while significant R-values are observed for open to closed grassland (GLC140 and GLC143) from the start of the rainy season.

4/ Significant OD-RTD correlations are observed for a 10-20mm threshold for sparse vegetation (GLC150).

Table 3: Correlation coefficients between RTDs and OD for different GLC classes. BR and ER are the start and the end of the rainy season, respectively.

<i>R</i>	<i>GLC</i> <i>14</i>	<i>GLC</i> <i>20</i>	<i>GLC</i> <i>30</i>	<i>GLC</i> <i>110</i>	<i>GLC</i> <i>130</i>	<i>GLC</i> <i>140</i>	<i>GLC</i> <i>150</i>
BR	-0.36	-0.29	-0.08	-0.19	0.15	0.21	0.09
5	-0.07	-0.03	-0.14	0.41	0.25	-0.09	0.35
10	-0.01	0.01	0.26	0.52	0.26	-0.11	0.45
20	0.43	0.43	0.49	0.66	0.18	0.05	0.23
30	0.46	0.45	0.48	0.79	0.39	0.10	-0.01
40	0.35	0.34	0.42	0.86	0.68	0.09	-0.14
50	0.41	0.40	0.35	0.81	0.58	0.20	-0.25
60	0.48	0.47	0.32	0.79	0.47	0.16	-0.12
70	0.43	0.43	0.29	0.78	0.44	0.19	-0.16
80	0.46	0.48	0.30	0.84	0.48	0.52	-0.05
90	0.28	0.25	0.23	0.84	0.47	0.54	-0.34
100	0.22	0.25	0.20	0.55	0.29	0.51	-0.09
ER	-0.42	-0.46	-0.10	-0.36	0.58	-0.59	-0.27

Growing season length

Maps of median OD (M_{on}), median offset dates (M_{off}) and median growing season length (M_{gsi}) are shown in Fig. 4.

The growing season length is defined as the period between the green-up onset and offset for the period 2000-2008. The M_{on} and M_{off} data ranged from DOY 169-225 and DOY 284-347, respectively. Contrary to what was expected, M_{on} does not always follow the latitudinal rainfall gradient: local areas, such as those observed West of Guéoul and Kébemer or, southwards, between Mékhé and Mboro and near Dakar, are characterized by early OD (DOY 169-197). North of the study area, phenological events (late onset and early offset) appear to be in better agreement with Monsoon variability while temporal shifts in onset and offset dates are locally observed near the Thies plateau and within the Lompoul-Kéllé-Kébemer area. The M_{off} spatial variations are in agreement with the rain front, which progressively moves southwards at the end of the monsoon season. The M_{off} are indeed estimated at about DOY 284-300 and DOY 314-347 respectively in the northern and southern parts of the study area. Moreover, the M_{gsi} respectively varies between 74 days and 130 days in the regions of Saint-Louis and Dakar.

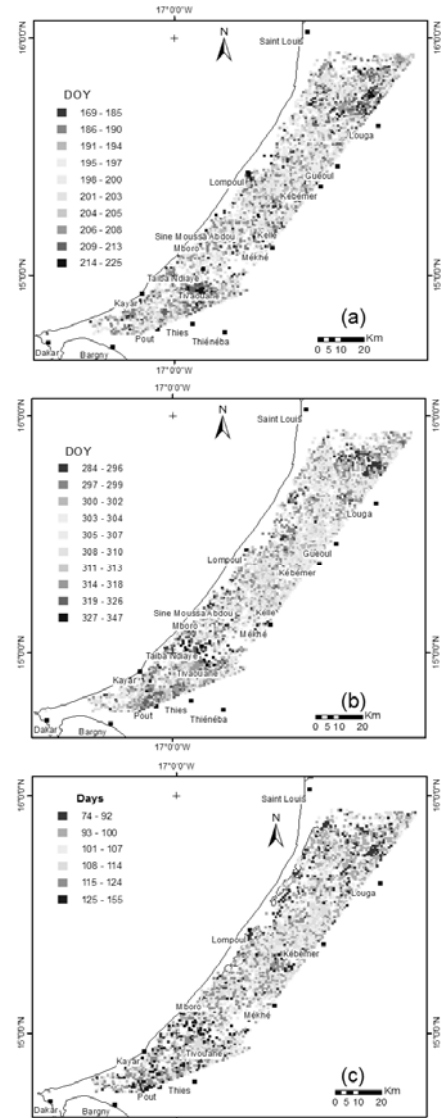


Figure 4: Maps of median (a) OD, (b) offset dates and, (c) growing season length considering the period 2000-2008.

5 CONCLUSION

The agricultural ecoregions of “Peanut basin” and “Long Coast”, located in northwestern Senegal, are subject to erratic rainfall and to an extension of human land-use practices which lead to vegetation biomass decrease. A mean to assess recent changes in vegetation biomass and

to understand these changes at regional scale is to use MODIS LAI time series. The derivation of phenological parameters from LAI data, through the calculation of the CV_{LAI} and the modeling of the phenological metric (green-up onset and offset dates), and their coupling with daily rainfall, geomorphological and land cover data are a useful tool for characterizing and monitoring the response of vegetation in high anthropized Sahelian ecosystems. Using correlations between RTDs and OD from LAI data reveals to be helpful for predicting sowing periods and vegetation biomass. Such indices could be helpful for modeling future vegetation growth using climatic scenarios.

ACKNOWLEDGEMENTS

This study was performed with financial support of GIS (Climat-Environnement-Société) and SAHELP (Sahara and SAHEL vulnerability: lessons from the Past) projects. We are grateful to the Senegalese "Direction Nationale de la Météorologie" for the facilities that have contributed to the achievement of this work. The authors acknowledge GES DAAC MODIS Data Support Team for making MODIS data available to the user community.

REFERENCES

- Ali, A., Lebel, T., Amani, A., 2003, Invariance in the spatial structure of sahelian rain fields at climatological scales. *Journal of Hydrometeorology*, **4**(6), 996-1011.
- Andersen, J., Dybkjaer, G., Jensen, K. H., Refsgaard, J. C., Rasmussen, K., 2002, Use of remotely sensed precipitation and leaf area index in a distributed hydrological model. *Journal of Hydrology*, **30**, 34-50.
- Bicheron, P., Leroy, M., Brockmann, C., Krämer, U., Miras, B., Huc, M., Nino, F., Defourny, P., Vancutsem, Ch., Arino, O., Ranéra, F., Petit, D., Amberg, V., Berthelot, B., Gross, D., 2006, GLOBCOVER: A 300 m global land cover product for 2005 using ENVISAT/MERIS time series. International Symposium on Recent Advances in Quantitative Remote Sensing, Torrent, Spain.
- Doraiswamy, P. C., Sinclair, T. R., Hollinger, S., Akhmedov, B., Stern, A., Prueger, J., 2005, Application of MODIS derived parameters for regional crop yield assessment. *Remote Sensing of Environment*, **97**, 192-202.
- Fensholt, R., Sandholt, I., Rasmussen, M. S., 2004, Evaluation of MODIS LAI, fAPAR and the relation between fAPAR and NDVI in a semi-arid environment using in situ measurements. *Remote Sensing of Environment*, **91**, 490-507.
- Knyazikhin, Y., Glassy, J., Privette, J. L., Tian, P., Lotsch, A., Zhang, Y., Wang, Y., Morisette, J. T., Votava, P., Myneni, R. B., Nemani, R. R., Running, S. W., 1999, MODIS Leaf Area Index (LAI) and fraction of photosynthetically active radiation absorbed by vegetation (fPAR). Product (MOD15) Algorithm Theoretical Basis Document.
- Myneni, R. B., Nemani, R. R., Running, S. W., 1997, Estimation of global leaf area index and absorbed PAR using radiative transfer model. *IEEE Transactions on Geoscience and Remote Sensing*, **35**, 1380-1393.
- Myneni, R. B., Knyazikhin, Y., Privette, J. L., Glassy, J., Tian, Y., Wang, Y., Hoffman, S., Song, X., Zhang, Y., Smith, G. R., Lotsch, A., Friedl, M., Morisette, J. T., Votava, P., Nemani, R. R., Running, S. W., 2002, Global products of vegetation leaf area and fraction absorbed PAR from year one of MODIS data. *Remote Sensing of Environment*, **83**, 214-231.
- Privette, J. L., Myneni, R. B., Knyazikhin, Y., Mukelabai, M., Roberts, G., Tian, Y., Wang, Y., Leblanc, S. G., 2002, Early spatial and temporal validation of MODIS LAI product in the Southern Africa Kalahari. *Remote Sensing of Environment*, **83**, 232-243.
- Tappan, G. G., Sall, M., Wood, E. C., Cushing, M., 2004, Ecoregions and land cover trends in Senegal. *Journal of Arid Environments*, **59**, 427-462.
- Zhang, X., Friedl, M.A., Schaaf, C.B., Strahler, A.H., Hodges, J.C.F., Gao, F., Reed, B.C., Huete, A., 2003, Monitoring vegetation phenology using MODIS. *Remote Sensing of Environment*, **84**, 471-475.
- Zhang, X., Friedl, M. A., Schaaf, C. B., Strahler, A. H., Liu, Z., 2005, Monitoring the response of vegetation phenology to precipitation in Africa by coupling MODIS and TRMM instruments. *Journal of geophysical research*, **110**, D12103, doi:10.1029/2004JD005263.

Discrimination of olive groves through object-based hierarchy classifications

I.L. Castillejo-González¹, A. García-Ferrer Porras¹, F.J. Mesas-Carrascosa¹, M. Sánchez de la Orden¹, F. López-Granados²

(1) *Department of Graphic Engineering and Geomatic, University of Córdoba. Campus Universitario de Rabanales. Ctra. N IV-A, Km. 396, 14071 Córdoba (Spain)*

(2) *Institute for Sustainable Agriculture, CSIC. Apdo.4048, 14080 Córdoba (Spain)*
ilcasti@uco.es

ABSTRACT- *One of the most widespread applications of remote sensing is the land use discrimination. Usually remote sensing offers very good results in homogeneous land uses, but the accuracy decrease significantly with covers that present high intraclass spectral variability (e.g. olive orchard, vineyard or urban soil). For an accurate discrimination of these mixed covers, an analysis based on objects at different levels can be proposed. The aim of this work is to develop an object-based hierarchy study for the identification and mapping of olive orchard using QuickBird imagery. Multilevel data segmentation had been made in order to isolate each olive tree by the data mining algorithm C4.5 to, subsequently detect the olive grove plots in a super-object level. The results showed that this methodology obtained an overall accuracy higher than 95% in olive grove plots discrimination with panchromatic data, a much better result than other pixel or object-based classifications tested.*

1 INTRODUCTION

Many of the land use studies based on remote sensing techniques consider each pixel of the image as a basic and independent work unit. These analyses provide very good results in homogeneous land uses, although many of the real land uses present high intraclass spectral variability. The olive grove is a very difficult crop to classify because the plots of these trees reflect the radiometric signals from the canopy of trees, soil and, in some cases, another kind of vegetable cover as well, what mix the signal even more. In this case, the classification could be improved by an analysis that takes into account the pixel data and also the information contained in the relationship between adjacent pixels. This information can be obtained by the image segmentation.

Image segmentation is a technique that allows the creation of objects by algorithms that determine the growth around some seed pixel based on certain criteria of homogeneity (Yu et al., 2006). The objects create by a segmentation are characterized not only by their spectral characteristics, but also by shape, textural and hierarchical characteristics. After segmentation, any further processing of the image is not based on pixel as minimum unit of information, but on objects. The segmentation is used to produce

image object primitives as a first step for further classification and other processing procedures (Batz and Shäpe, 2000).

The aim of this work is to develop an object-based hierarchy study for the identification and mapping of olive orchard using QuickBird imagery. Multilevel data segmentation had been made in order to isolate each olive tree to, subsequently detect the olive grove plots in a super-object level.

2 DATA

2.1 Study area

The study area is about 1190 ha (3.6 x 3.3 km) located near Montilla, province of Córdoba (Andalusia, Spain). This agricultural area is representative of Andalusian dryland crops, where the main land use is olive (*Olea europea* L.) orchards. In this image also can be observed vineyards (*Vitis vinifera* L.), winter cereal stubble, burnt crop stubble, river side tree areas, agricultural bare soil and urban soil (Fig. 1). The study area was visited to determine land uses. Ground-truth land use was randomly defined to substantiate and validate the classification procedures.

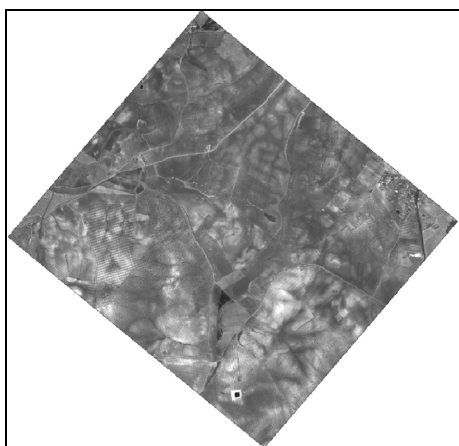


Figure 1: Panchromatic band of the study area

2.2 Remotely sensed data

Digital image data were acquired for the study area by QuickBird satellite on July 10th, 2004. The analysis was performed on a single-band panchromatic image with a spatial resolution of 0.7 m. An earlier study tested the ability to discriminate olive trees canopies with QuickBird products, and showed that panchromatic information was the most accurate of all analyzed bands. Multispectral and pansharpened with the AWLP method (Otazu et al., 2005) imagery were tested but both presented lower accuracies than panchromatic band (Castillejo-González et al., 2009).

3 METHOD

3.1 Multiresolution segmentation: 1st level

QuickBird panchromatic image was partitioned into image objects using the Fractal Net Evolution Approach (FNEA) segmentation algorithm carried out by the eCognition Developer 8 software (Definiens AG, 2009). Segmentation subdivides an image into homogeneous multi-pixel regions based on several user-defined parameters such as scale (control size parameter), color (spectral information) and shape (smoothness and compactness information). The user can influence the output of the segmentation process through specifications and weighting of input data and controlling these parameters.

For the first segmentation level, a set of parameters were defined to delimit properly the canopies of olive trees compared to other land uses. These settings of segmentation parameters were determined from a study where different scenarios with different input parameters were tested to evaluate the ability to discriminate olive trees canopies with QuickBird imagery (Castillejo-González et al., 2009). Based on

that study, the values used for this segmentation were a scale parameter of 10, a color weight of 1, a shape weight of 0 and therefore, a smoothness and compactness values of 0 (Fig. 2).

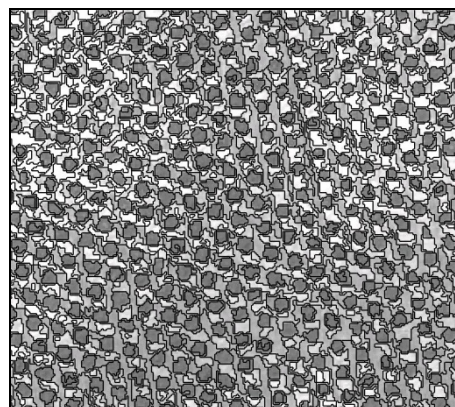


Figure 2: Example of 1st level segmentation (canopies)

3.2 Olive trees object-based classification

The olive trees canopies were isolated in two steps. In the first step all land uses observed in the image were classified with a decision tree method. The sequencing of discrimination was performed using the algorithm C4.5 (Quinlan, 1993), implemented in the Weka 3.6.1 software (University of Waikato (New Zealand), 2009). This algorithm generates a decision tree with a set of rules that will be used in the classification. Castillejo-González et al. (2009) analyzed the effect of different combinations of spectral and morphological variables in the discrimination of olive trees, showing that the collection of both types of variables were the most accurate. Therefore, to perform this analysis 19 bands (object-based features) were included (Table 1). These object-based features showed spectral and morphological information of the objects created in the first level segmentation, but only 3 of the 19 variables were spectral variables due to this study is based in only one original band (panchromatic band).

Once all land uses were classified, the second step was to isolate the olive trees canopies. To do that, the land use classification was re-classified again in two categories: olive trees canopy-Non olive tree.

3.3 Multiresolution segmentation: 2nd level

The Multiresolution segmentation approach allows, for different scales of segmentation, the simultaneous representation of image information at different resolutions (scales) by a hierarchical network. Information about adjacent objects on the same level (horizontal neighbours) and objects on different scales

resolutions by a hierarchical network. Information about adjacent objects on the same level (horizontal neighbours) and objects on different hierarchical levels (vertical neighbours) are allowed in this network.

From the first segmented image (first segmentation level), a new segmentation were carried out. In this

segmentation, a set of parameters were defined to delimit precisely each plot present in the image. To outperform this objective, cadastre ancillary data were included in the segmentation process; being this information band the only band considered in the process (no weight was assigned to the panchromatic band) (Fig. 3).

Table 1: Object-based features

Categories	Features	Description
Spectral	Mean	Layer mean value calculated from the layer values of all pixels forming an image object
	Brightness	Mean value of the spectral mean values of an image object
	Standard Deviation	Standard deviation calculated from the layer values of all n pixels forming an image object
Shape	Area	Area value calculated from the number of pixel in an image object and the area of them.
	Asymmetry	Ratio of the lengths o the minor and the major axis of an ellipse approximated to the object
	Border index	Ratio of the border length of the image object to the border of the smallest rectangle enclosing the image object
	Border length	Sum of edges of the image object that are shared with other image objects.
	Compactness	Ratio of the area of the image object to the area of the smallest rectangle enclosing the image object
	Density	The area covered by the image object divided by its radius
	Elliptic fit	Comparison between the area of a object and the area of an ellipse with the same area of this object
	Length	Calculation using the length-to-width ratio derived from a bounding box approximation of the object
	Length/Width	Ratio length/width of a bounding box approximation of the object
	Main direction	Direction of the eigenvector belonging to the larger of the two eigenvalues derived from the covariance matrix of the spatial distribution of the image object
	Radius of largest enclosed ellipse	Ratio of the radius of a ellipse with the same area as the object scaled down until being totally enclosed by the object to the radius of the original ellipse
	Radius of smallest enclosing ellipse	Ratio of the radius of a ellipse with the same area as the object enlarged until being totally enclosing the object in total to the radius of the original ellipse
	Rectangular fit	Comparison of the area of the object outside a rectangle with the same area as the object with the area inside the rectangle
	Roundness	Difference of the largest enclosed ellipse and the smallest enclosing ellipse
	Shape index	Comparison of the border length of an object and the border length of a n equivalent rectangle
	Width	Calculation using the length-to-width ratio derived from a bounding box approximation of the object

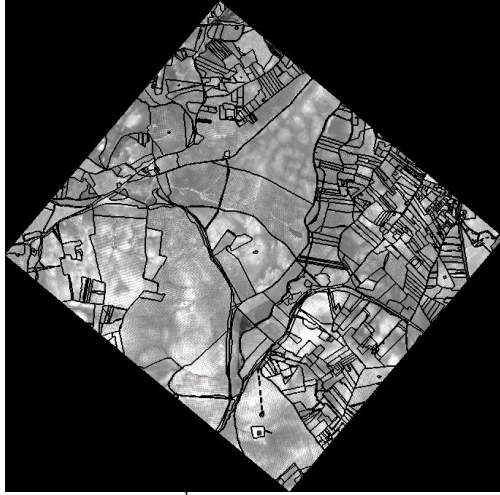


Figure 3: 2nd level segmentation (plots)

3.4 Hierarchical analysis

The information used in the hierarchical analysis was: a) the classified olive trees canopies (sub-objects) and b) the limits of the plots (super-objects). This information at different levels can be connected in various ways. This study was based on the calculation of the Related Area to Olive trees Canopies (RAOC). This relationship between the two levels of objects was the most satisfactory within the group of variables “*Related Area to Super-objects*”, which calculates for each top-level, the proportion of area classified in a given category at sub-objects. The RAOC was calculated as (1):

$$RAOC = \#P_v / \#P_{Uv(d)} \quad (1)$$

Where $\#P_v$ is the area of the pixels belonging to a v category and $\#P_{Uv(d)}$ is the area of the super-object.

The data obtained for this variable were exported to ENVI 4.5 software (ITT Visual Information Solutions, 2008), where an analysis of different proportions of olive trees canopies areas in the objects equivalent to plots was performed. The scenarios analyzed proportions ranged from more than 4% ($RAOC = 0.04$) of area classified as olive tree canopy in sub-object to more than 15% ($RAOC = 0.15$). The choice of the RAOC that better accuracy presented in the obtaining of olive trees plots was carried out by a supervised classification based in the Maximum Likelihood algorithm.

4 RESULTS

4.1 Olive trees object-based classification

Table 2 shows the reliability obtained in the discrimination of the olive trees canopies and the overall accuracy of the classification in the panchromatic image. Analyzing the ability to discriminate olive trees canopies, it is observed that the classification presented a high accuracy with a value above 88% (Fig. 4). However, the analysis of the overall accuracy of the classification (taking into account the area occupied by the olive trees canopies and the other land uses), showed higher values with almost a 95% of accuracy. As shown in Figure 4, the base of the tree canopy is well characterized, but there are some errors in the edges of the canopies and in very closed trees.

Table 2: Accuracy results of olive trees canopies classifications

	Olive trees accuracy (%)	Overall accuracy (%)
Pan image	88.34	94.72

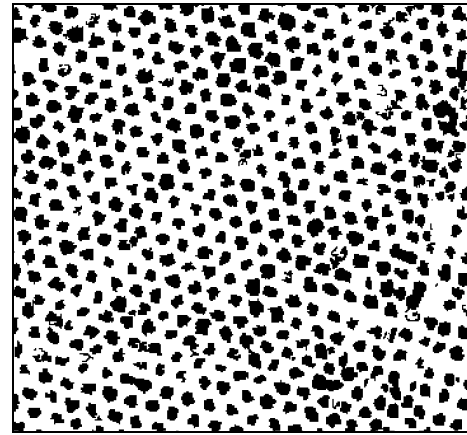


Figure 4: Example of classified olive trees canopies (black)

4.2 Hierarchical analysis

Table 3 shows the results of the analysis taking into account different proportions of areas of olive trees canopies (RAOC) on the object equivalent to plots for a QuickBird panchromatic image. As can be observed in the table, all RAOC proportions obtained an overall accuracy in the olive groves plots classifications very high with values higher than 90%. The RAOC proportion of 0.10 (more than 10% of the area of the plot (super-object) presented olive tree canopy

classification (sub-object)) showed the best result with an overall accuracy of 96.80% of the olive groves plots correctly classified (Fig. 5).

Table 3: Accuracy results of the plots classifications

Related Area of sub-object "RAOC"	Overall Accuracy (%)	
0.04		92.43
0.05		93.36
0.06		94.68
0.07		96.02
0.08		96.11
0.09		96.49
0.10		96.80
0.11		94.05
0.12		93.71
0.13		91.48
0.14		91.22
0.15		90.53



Figure 5: Olive groves plots classified (black) with a RAOC value of 0.10

The best olive groves classification (RAOC = 0.1) was used to create a mask to isolate the olive groves land use from the rest of the land uses present in the image (Fig. 6).

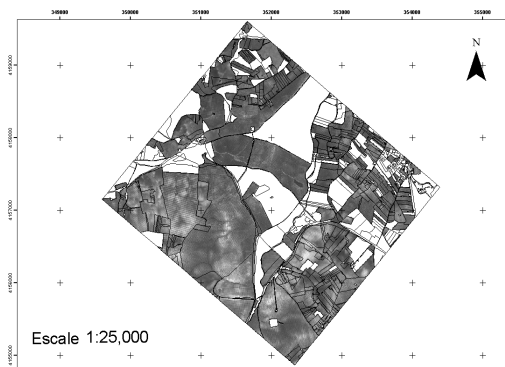


Figure 6: Olive groves plots isolated from other land uses

5 CONCLUSIONS

The main conclusions of this study are:

To classify olive trees canopies it is necessary to acquire a high spatial resolution image but it is not necessary a lot of spectral information. This study has concluded that the olive trees canopies can be classified very accurately with an object-based classification of a QuickBird single-band panchromatic image. This band must be segmented (1st level) with a low Scale Parameter and with the weight of the spectral variable (color) higher than 50%.

From the different types of variables (object-based features) that can be obtained in a segmentation, a mixture of spectral and morphological variables are the best choice to classify olive trees canopies. Due the original classification information is a single-band panchromatic image, few object-based features showed spectral information.

An object layer where each object is equivalent to a plot can be obtained with a segmentation (2nd level) where the image layer (panchromatic band) has no weight and all the weight is for the thematic layer (cadastre layer).

A hierarchical analysis with *the related area of olive trees (subobject) in each plot (superobject)* showed an overall accuracy higher than 95% in olive groves plots discrimination.

6 REFERENCES

- Baatz, M., Schäpe, A., 2000. Multiresolution segmentation: an optimization approach for high quality multi-scale image segmentation. Proceedings of the 12th Symposium for Applied Geographic Information Processing (Angewandte Geographische Informationsverarbeitung XII. AGIT 2000). Symposium held in Salzburg, Austria, pp. 12-23.
- Castillejo-González, I.L., García-Castillo, R., García-Ferrer, A., Sánchez de la Orden, M, and López-Granados, F. 2009. Grado de influencia de las variables espectrales y de forma en la detección de olivos mediante técnicas basadas en objetos. Proceedings of the 13th Symposium of the Spanish Remote Sensing Association (Teledetección: Agua y Desarrollo Sostenible). Symposium held in Calatayud, Spain, pp. 573-576
- Otazu, X., González-Audicana, M., Fors, O. and Núñez, J. 2005. Introduction of sensor spectral response into image fusion methods. Application to Wavelet-based methods. *IEEE Transactions on Geoscience and Remote Sensing*, 43, 2376-2385.
- Quinlan, J. R., 1993. C4.5 programs for machine learning (San Mateo, CA: Morgan Kaufmann)
- Yu, Q., Gong, P., Clinton, N., Biging, G., Kelly, M., and Schirokauer, D., 2006. Object-based detailed vegetation classification with airborne high spatial resolution remote sensing imagery. *Photogrammetric Engineering & Remote Sensing* 72, 799-811.

Monitoring water bodies over whole Africa in near real time: detection algorithms and preliminary results

Raphaël D'Andrimont¹, Jean-François Pekel², Eric van Bogaert¹, Pierre Defourny¹

¹Université Catholique de Louvain, Earth and Life Institute, Croix du Sud, 2, bte 16, 1348 Louvain-la-Neuve

²Joint Research Centre, Institute for Environment and Sustainability, Ispra, Italy

raphael.dandrimont@uclouvain.be, jean-francois.pekel@jrc.ec.europa.eu,

eric.vanbogaert@uclouvain.be, pierre.defourny@uclouvain.be

ABSTRACT - Detecting water bodies in nearly real time over the whole Africa is a challenge addressed by the Geoland-2 project (GMES). This information was found critical by end-users for natural resource management as well as for environmental monitoring. Non-permanent water bodies dynamic is also expected to be affected by climate change and requires appropriate system development for operational monitoring. In the framework of Geoland-2 project, a water bodies detection algorithm has been developed in two version. The Version1 (1km of spatial resolution) is the result of combination of three existing products in order to have the best information available. The Version2 (250m of spatial resolution) is the detection result of a method based on a standardized multispectral transformation (developed by Pekel et al., 2010), the new algorithm is suited to detect the water occurrence in various ecological conditions and appears to be more generic than classification approaches. Implementation of this algorithm allowed processing multi-year 250 m surface reflectance time series acquired by the MODIS instruments. Both versions are designed to be operational in nearly real time and to be externally validated.

1 INTRODUCTION

According to the users needs, monitoring the water bodies, especially the temporaries, is of major interest for environment protection (Gond et al., 2004). Moreover, it is a capital issue for economic purpose because they have a large amount of functions, in particular for agriculture, livestock and fishing. At continental scale it is difficult to expect a water body to have sufficiently specific properties for it to be recognized easily, everywhere and in any condition from space. Indeed, from an ecological point of view, the only thing that is sure is that a water body is characterized by permanent or seasonal water logging. Due to the large geographical context, a large range of vegetation conditions may be expected over these surfaces. Moreover the spectral behaviour of water may vary according to sediment load and the development of micro-organisms. Therefore there is no particular spectral signature to confidently rely on for water body identification.

The Version 1 of the waterbodies algorithm is the result of the fusion of one permanent water layer mask (based on SRTM) and two existing algorithms (working on SPOT-VGT data) in order to take advantage of existing methodologies. The two

algorithms are: VGT4AFRICA (referred here as Version 0) and GWW. This Version 1 is being implemented by VITO and validated by TU-WIEN.

The first existing algorithm (Gond et al., 2004) was developed in the framework of VGT4AFRICA by the Joint Research Centre (JRC) (see User Manual by Bartholomé et al., 2006) and is suited to arid and semi arid condition. The study region was centred over the Burkina Faso, i.e. from 9° to 16° North and 6° West to 3° East.

The second algorithm was first developed for GlobalWatch project (Pekel et al., 2005) and was optimized for the following window: from Senegal (17.7° West) to India (85° East) and from the equator to the Mediterranean Sea (37.4° North). The product is here referred as "Global Watch Water" (GWW).

Version	Extent	Data	Implementation year
0	West Africa	SPOT-VGT S10	2006
1	Whole Africa	SPOT-VGT DAILY	2010
2	Whole Africa	MODIS DAILY	2011

Table 1 : versioning summary of the water bodies algorithms

The Version 2 of the waterbodies algorithm uses a method based on a standardized multispectral transformation (developed by Pekel et al., 2010). Transforming RGB-like to HSV-like colorimetric space allows to determine a set of thresholds able to detect water in various eco-climatic conditions.

Other available water bodies maps and products were reviewed and their characteristics were assessed in order to determine if they fit with the user's requirements.

Until now the version 0 (SWB product of VGT4AFRICA) is widely used and available online (<http://www.vgt4africa.com>) every 10 days for whole Africa, by countries and by regions. However the algorithm used to produce the SWB product is suited only for a limited region of Africa centred over the Burkina Faso.

Three other products "not Nearly Real Time" are also currently available: GLWD, SRTM and MOD44W.

First alternative for the users is to use database as Global Lakes and Wetlands Database (GLWD) (Lhener et al., 2004, 2008). This compilation of most existing database is a precious information for lots of applications. However, according to Haas (2009), due to the wide difference of quality in the various dataset, the use of this data base as standard is limited. Furthermore the GLWD database contains data from a long period and thus inappropriate to monitor water in NRT.

The Shuttle Radar Topography Mission (SRTM by NGA and NASA) obtained elevation data on a near-global scale to generate a high-resolution digital topographic database of Earth. SRTM consisted of a specially modified radar system that flew onboard the Space Shuttle Endeavour during an 11-day mission in February of 2000. Despite the fact that SRTM data has a very high spatial resolution (30m), it corresponds to the situation observed during 11 days beginning of February (dry season in Sahel). Therefore it could only be used to validate methodology but is not appropriate for nearly real time monitoring.

The MOD44W product available on Global Land Cover Facility (GLCF) website since end of 2009 (GLCF, 2009) corresponds to a mix of SRTM data and MODIS data covering the years 2000-2002. Although the spatial resolution is 250 m, the time coverage of the data is not suited for monitoring water bodies over Africa (10 years old data). For further information

over the method used to perform this product, see Carroll et al. (2009).

2 DATA AND EXTENT

As summarized in Table 1, the source data used for Version 1 algorithm is SPOT VGT daily reflectance S1. Note that for the Version 0 algorithm, the compositing is processed by the VITO to obtain S10 composite whereas the Mean Compositing (Vancustem et al., 2007) algorithm is used for the Version 1.

The Version 2 algorithm is designed for MODIS Aqua and Terra daily Reflectance data (MYD09 and MOD09). This data are available on the WIST system (<https://wist.echo.nasa.gov/api/>). This data were acquired for the Africa extent from 2003 to 2010.

2 METHODOLOGY

2.1 Version 1 – Fusion algorithm

As shown in Figure 1, after the processing of SPOT-VGT daily reflectance in 10-days composite data, the variable used in both algorithm need to be computed.

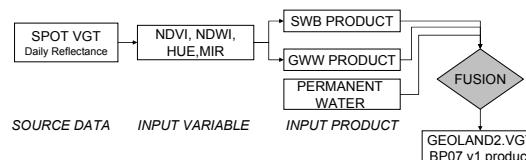


Figure 1 : Version 1 – general design

The input variables used by the algorithms are the NDVI, the NDWI, the HUE and the MIR.

NDVI- Normalised Difference Vegetation Index

NDVI is a ratio used to characterize the vegetation amount ($NDVI = (NIR - Red) / (NIR + Red)$) where NIR corresponds to the reflectance in the near infrared band, and Red to the reflectance in the red band. Obviously, this definition will depend on the specifications of the bands (Steven et al., 2003). In our case, NDVI will correspond to VEGETATION sensor characteristics for its Red (B2) and NIR (B3) bands.

NDWI-Normalised Difference Water Index

NDWI is a ratio used to characterize the water amount of the pixel. It is defined by Gao (1996) as:

$$NDWI = (NIR - MIR) / (NIR + MIR)$$

where NIR corresponds to the reflectance in the near infrared band, and MIR to the reflectance in the middle infrared band. In our case NIR will correspond to VEGETATION sensor characteristics for its NIR (B3) bands and MIR bands (B4).

HUE

The Hue of the HSV (Hue, Saturation, Value) color space is calculated by a nonlinear transformation of the RGB color space using 3 equations as describe by Pekel et al. (2010).

MIR-Middle Infra Red

The MIR variable corresponds to the reflectance in the middle infra-red, i.e. in our case to the MIR band of VEGETATION (B4).

The last step is a combination of the detections in order to have detection flagged if a product detects water. The output of the detection is a 2 bands file. The first band is a binary file corresponding to “water”/“no water” and the second one corresponding to the origin of the detection.

2.2 Version 2 – MODIS algorithm

The MODIS surface reflectance daily data are first cloud screened and composited using the Mean Compositing method (Vancustem et al., 2007). Afterwards band 1 (620-670 nm at 250 m of resolution), band 2 (841-876 nm at 250 m of resolution) and band 7 (2105-2155 nm at 500 m of resolution resampled at 250 m) are transformed using a standardized multispectral transformation (developed by Pekel et al., 2010). After the transformation, we obtain a HSV-like color space in which applying specific thresholds allows detecting waterbodies over heterogenous conditions. Depending of the cloud free data available, and thus of the number of observation used to make the compositing, a temporal filter is then applied resulting in different confidence interval of presence of water.

3 RESULTS

3.1. Version 1

Version 1 corresponds to the the need defined by the users to have the best available information. As Version 1 corresponds to the combination of three existing products, the major limitations of the algorithm correspond to the limitations of each merged product. It has to be reminded that these different products were designed for specific purposes and/or conditions. Each product’s limitation will be briefly described.

The Version 0 algorithm was validated over a large area in Sahel (Gond et al., 2004). Key conclusions of the authors are that commission errors

are in the order of 10%, whereas omission errors can be higher, due to the low resolution of the instrument used. Three other limitations described by the authors are: atmospheric contamination, cloud’s shadow confusion with water bodies and the extent of the zone for which is was designed.

Despite of the more generic results of the GWW method, no systematic accuracy study was carried out in order to evaluate the precision of the detection. However a qualitative investigation permits to outline major errors of the detection, i.e. , a lack of spatial consistency

Concerning the permanent water mask used (SRTM data), despite of the high spatial resolution and consistency, the acquisition period (2000) remains the major cause of omission errors. Furthermore, the mission was carried out during the dry season in the Sahelian region increasing the number of omission errors.

3.2 Version 2

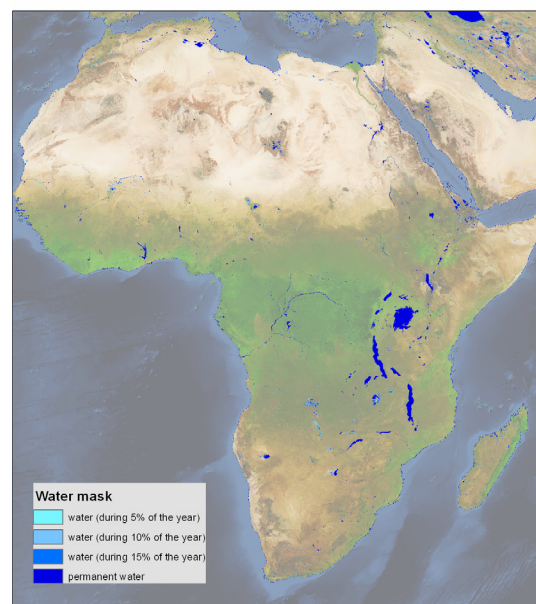


Figure 2 : African Water mask generated with reflectance MODIS daily data from 2004 to 2009 at 250 m of resolution. The classes show the seasonality information. The background image is a synthesis color composite of 10 years of spot-vgt images.



Figure 3 : following decades of 2009 in a zone located at East-South of Mali (centred at lat. 13°11'7.5 and long. -5°28'32.17'') shows the results of Version 2 near real time monitoring for water bodies seasonality

The Version 2 algorithm was used to create a water mask over Africa using 6 years of data (Figure 2). It was then possible to discriminate the permanent water bodies from the temporaries appearing a limited time in the year (during 15%, 10% and 5% of the year). This mask was compared with the MOD44W product and showed encouraging results.

As it is designed to run operationally, time series of water logging zone were also investigated (example in Figure 3). The Figure 3 represent following decades of 2009 in a zone located at East-South of Mali (centred at lat. 13°11'7.5 and long. -5°28'32.17'').

Comparison of both versions (Figure 4) allows to see the major interest to use finer resolution data to detect water bodies.

Both versions are being validated by Technische Universität, Wien.

4 REFERENCES

- Bartholomé, E., Combal, B., 2006, Small water bodies. In: E. Bartholomé, Editor, VGT4Africa User Manual (first ed.), Office for Official Publication of the European Communities, Luxembourg (2006).
- Carroll, M., Townshend, J., DiMiceli, C., Noojipady, P., Sohlberg, R. 2009, A New Global Raster Water Mask at 250 Meter Resolution. *International Journal of Digital Earth*. (in press)
- Pekel, J. F., Bogaert, P., Adans, S., Rasson, J. P., Defourny, P. 2005, STEREO: GlobalWatch - Traitement automatique de séries temporelles optiques pour la cartographie et la détection de changement. Intermediary report n°2 (2005)
- GAO, B. G., 1996, NDWI — a normalized difference water index for remote sensing of vegetation liquid water from space. *Remote Sensing of Environment*, **58**, 257–266.

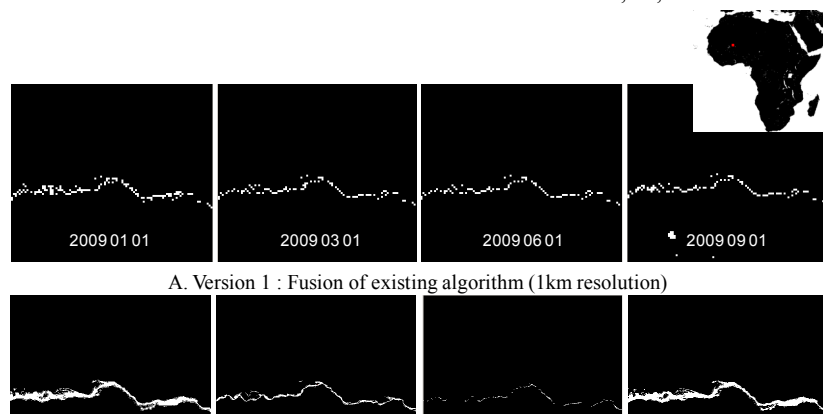


Figure 4 : comparison of Version 1 (A) and Version 2 (B) for 4 dates in 2009

- GLCF – Global Land Cover Facility web site. 2009. Website <http://landcover.org/data/>
- Gond, V., Bartholomé, E., Ouattara, F., Nonguierna, A., Bado, I., 2004, Surveillance et cartographie des plans d'eau et des zones humides et inondables en régions arides avec l'instrument VEGETATION embarqué sur SPOT-4, *Int. J. Remote Sens.* **25** (5), pp. 987–1004.
- Haas E. M., Bartholomé E., Combal B., 2009, Time series analysis of optical remote sensing data for the mapping of temporary surface water bodies in sub-Saharan western Africa. *Journal of Hydrology*, **370**, pp. 52 – 63.
- Lehner, B., Verdin, K., Jarvis, A., 2008, New global hydrography derived from spaceborne elevation data, *Eos, Trans. AGU* **89** (10), pp. 93–94.
- Lehner B., Döll, P., 2008, Development and validation of a global database of lakes, reservoirs and wetlands, *J. Hydrol.*, **296** (1–4), pp. 1–22.
- LP DAAC – LAND PROCESSES DISTRIBUTED ACTIVE ARCHIVE CENTER (<https://lpdaac.usgs.gov/>).
- Pekel, J.-F., Cressman, K., Ceccato, P., Vancutsem, C., Vanbogaert, E., Defourny, P., 2009, Development and application of multi-temporal colorimetric transformation to monitor vegetation in the desert locust habitat. *Proceeding MultiTemp 2009 – The Fifth International Workshop on the Analysis of Multi-temporal Remote Sensing Images - July 28-30, 2009 - Groton, Connecticut*.
- Pekel J.-F., Cressman K., Ceccato P., Vancutsem C., Van Bogaert E., Defourny P., 2010, Development and application of multi-temporal colorimetric transformation to monitor vegetation in the desert locust habitat. *IEEE Journal Of Selected topics In Applied Earth Observations & Remote Sensing*. Issue 99. pp 1-9.
- Steven, M.D., Malthus, T.J., Baret, F., Xud, H. and Chopping, M.J., 2003. Intercalibration of vegetation indices from different sensor systems. *Remote Sensing of Environment*, **88**(4): 412-422.
- SRTM Water Body Data Product Specific Guidance (v.2.0, March 12, 2003) - SWBD documentation (http://dds.cr.usgs.gov/srtm/version2_1/SWBD/SWBD_Documentation/)
- Vancutsem, C., Pekel, J.-F., Bogaert P., Defourny, P., 2007, Mean Compositing, an alternative strategy for producing temporal syntheses. Concepts and performance assessment for SPOT VEGETATION time series, *International Journal of Remote Sensing*, **28** (22), pp. 5123–5141

Land cover classification in Spain from seasonal trajectories of MODIS data

F. J. García-Haro and A. Pérez-Hoyos

Remote Sensing Unit, Facultat de Física, Universitat de València, Dr. Moliner, 50. 46100-Burjassot, Spain

e-mail: j.garcia.haro@uv.es; Ana.Perez-Hoyos@uv.es

ABSTRACT - This work presents a methodology to fully exploit remote sensing capabilities provided by modern-borne sensors (e.g. MODIS, VEGETATION, MERIS) to extract complex land cover type information at regional scale. The feasibility of this methodology is demonstrated for land cover mapping in Spain using as a reference time series of MODIS reflectance data covering a 10-year (2000-2009) period. The land cover classes were characterized by temporal features of fractional vegetation cover (FVC) annual cycle, along with derived phenological parameters (e.g. amplitude, start and duration of the annual and semi-annual cycles), reflectance composite corresponding to the period of maximum/minimum canopy closure and textural variables. This dataset offers a means for obtaining direct indicators of vegetation biomass, structure and condition, allowing discriminating between different land cover classes from the differences in the growth cycle of vegetation and other relevant features. SIOSE (Sistema de Información de Ocupación del Suelo en España) database provided a spatially detailed (1:25.000) reference for determination of a suitable classification system, selection of training samples, and accuracy assessment. A classification system was then developed to generate different land cover maps, each characterized by a varying level of hierarchy and detail. A critical step to improve classification accuracy was to identify the best appropriate variables that are most useful in separating land-cover classes. Different classification techniques, including both parametric and non parametric methods, were applied. A method based on Artificial Neural networks (ANN) provided a reliable thematic map with a hierarchy level of 14 major classes. The overall accuracy was 80.0%, with balanced values of user's accuracy and producer's accuracy for individual classes.

1 INTRODUCTION

Remote sensing is a useful and adequate tool for producing reproducible and reliable information on land cover at different scales, which is mandatory for a wide range of climate and land surface process models. One advantage in monitoring land cover with remotely sensed data is that temporal sequences of images can accurately characterize surface categories based on variation of geo-biophysical properties. Multitemporal remotely sensed data can be used to identify and update land cover classification over a large geographic region in a consistent, continuous and cost-effective manner. However, classification of land cover from remotely sensed data at national to global scales remains a challenge because many factors, such as the complexity of the landscape, spatial resolution, remotely sensed variables, selection of training samples, image-processing and classification approaches, may affect the success of a classification.

Using time series of vegetation indices, numerous researchers have explored large scale patterns in vegetation, and by extension, land cover type (e.g., Friedl et al. 1999; Dash et al. 2007; Wardlow and Egbert, 2008). These studies have demonstrated that a

wealth of information related to vegetation phenology can be extracted at regional to global scales from time series of coarse resolution satellite measurements.

A number of algorithms have been applied for land cover classification, including decision trees (Friedl et al. 1999), minimum distance classifier (Clevers et al. 2004), Hierarchical classification schemes (Wardlow and Egbert, 2008), Artificial Neural Networks (Ji. 2000, Carrao et al. 2006) and Support Vector Machines (Gonçalves et al. 2006). In addition, bagging and boosting have been used to improve classification performance in decision trees (Friedl et al. 1999, DeFries and Chan 2000) and Support Vector Machines (Kim et al. 2003).

This work presents a methodology to fully exploit remote sensing capabilities provided by modern-borne sensors (e.g. MODIS, VEGETATION, MERIS) to extract complex land cover type information at regional scale. The feasibility of this methodology is demonstrated using as a reference time series of MODIS reflectance data covering a 10-year (2000-2009) period. The study area is the entire Spanish mainland territory. Spain has a remarkable landscape diversity which makes it a challenging region for land cover characterization.

Biophysical variables such as fractional vegetation cover (FVC) and leaf area index (LAI) have proven to be appropriate for modeling terrestrial ecosystems on the global, continental, and regional scales. They allowed discriminating between different land cover classes from the differences in the growth cycle of vegetation types and retrieving key phenological parameters. Different classification techniques, including both parametric and non parametric methods, were applied.

2. SELECTION OF DATASETS

2.1 Multitemporal remotely sensed data

First, spatial and temporally consistent estimates of fractional vegetation cover (FVC) were obtained using a probabilistic spectral mixture analysis method (García-Haro et al. 2005). Adapted variants of the algorithm which is currently used operationally in the context of the EUMETSAT/LSA SAF mission (Trigo et al. 2010), have been used. Discrimination of the major land cover types was determined according to the temporal pattern of the FVC, key phenological parameters, spectral reflectance and texture variables. The use of multitemporal remotely sensed data has proven useful for improving classification accuracy, especially for crop and vegetation classification (e.g. Liu et al. 2002) because of different phenologies of vegetations formations and crops. Phenological metrics designed to summarize dynamics in vegetation -such as amplitude, maximum and minimum values, timing of phenological stages (onset of greenness, maximum development, senescence) and growing season length- were considered as additional features to the classification algorithm. They were obtained by applying Fourier analysis to decompose time series of FVC.

To improve mapping of coniferous forest, we placed emphasis on the photosynthetic efficiency of the forest canopy resulting in low visible reflectances. The timing of annual maximum/minimum of FVC was used to construct two synthetic MODIS spectral reflectance at three wavebands (red, near-infrared and middle-infrared) corresponding to the most-vegetated (e.g. representing maturity or maximum canopy closure) and least- vegetated (e.g. coinciding with harvest or falling of leaves in deciduous species) periods, respectively.

Compared to the obtained result based solely on temporal and spectral features, the addition of textures measures has been increasingly employed for improving classification results in different applications (e.g. Franklin and Peddle 1989). In this study different texture measures corresponding to first order (e.g. standard deviation, entropy) and second order (e.g. contrast, homogeneity, variance) statistics

in the spectral domain were computed. Different sizes of moving windows (i.e. 3×3, 5×5, 7×7 and 9×9) were considered.

2.2 Reference data

The selection of training data is the most difficult and critical part of the supervised classification process. A crucial assumption for classification accuracy assessment (i.e. that the sampling units are representative of the entire mapping domain) is often violated since producers are often constrained by data availability. A sufficient number of training samples with good representative for each class is critical for image classification. When the landscape of a study area is complex and heterogeneous, selecting sufficient training samples becomes difficult. This problem is complicated for classifications with coarse spatial resolution imagery, because a large volume of mixed pixels may occur.

The SIOSE geodatabase, provided by the IGN (Instituto Geográfico Nacional), was used as reference data for selecting training data and evaluating the accuracy of the map. SIOSE was produced between 2006-2009, in a decentralized and cooperative manner by Spanish National and Regional administrations (Valcarcel et al., 2008).

The preparation of the validation dataset is based on a five-step procedure (see Figure 1). The first step was to co-register the dataset in common frames with the land cover data, then we re-projected the data onto a WGS-84 geographic system. The second step consisted of rasterizing the vectorial layer to a 100 m resolution. Step 3 consists of breaking down the SIOSE legend into a more schematic one composed by 18 classes. The final result consisted of an eighteen multi-layer composed of each land cover and its percentage of occupation within the pixel. Although SIOSE lacks in its nomenclature two mixed classes, Sparse Vegetation and Mixed Forest, these complex areas can be delimited based on subpixel information provided by SIOSE. Reference data was then aggregated in step 5 into blocks that match the footprint of the classification data, and the distribution of land cover within each reference block was computed.

We choose the most representative training samples in the sense that they occupy more than a purity-based threshold, typically ranging from 75 to 95% according to the overall abundance of the class in the image. A small percentage of additional samples was allocated to improve precision for rare classes that have a very limited spatial extend.

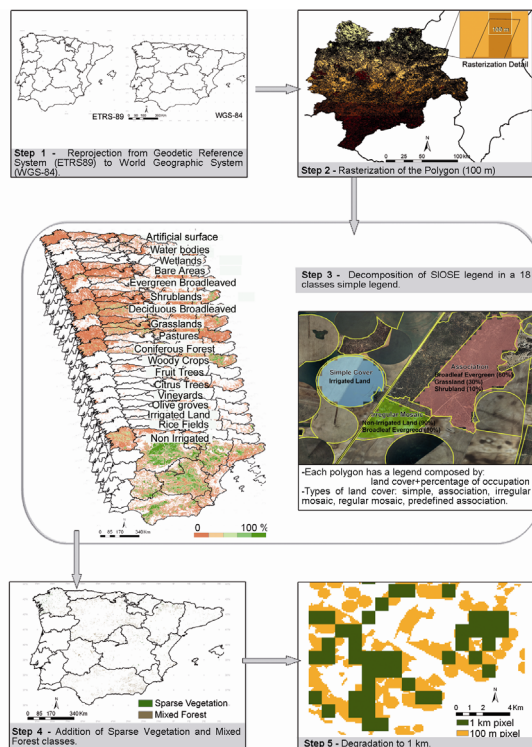


Figure 1. Flowchart of the methodology used for deriving a representative training dataset

3. METHODOLOGY

Differences in the annual cycle trajectories provides very valuable information for land cover discrimination. The seasonal trajectories of FVC present a large spatial variability in the Iberian Peninsula and allowed discriminating between different land cover classes from the differences in the growth cycle of vegetation types (see figure 2). The highest base-level (FVC~0.6) are found in pastures followed by evergreen broadleaved forest (FVC~0.5). Oppositely, vineyards have a very low coverage most part of the year (FVC~0.05). Deciduous and evergreen broadleaved forest revealed different well-separated patterns with distinct annual cycle.

Nevertheless, this figure illustrates that substantial overlap exists in the mean value of annual temporal profiles of FVC. Certain classes, such as shrub and coniferous, presented similar behaviour, and could be grouped together. Sophisticated classification algorithms and the use of additional features are thus required to discriminate certain classes. Complimentary information contained within spectral

reflectance and texture were helpful to discriminate classes with similar annual cycles of FVC (e.g. sparsely vegetated areas and artificial surfaces).

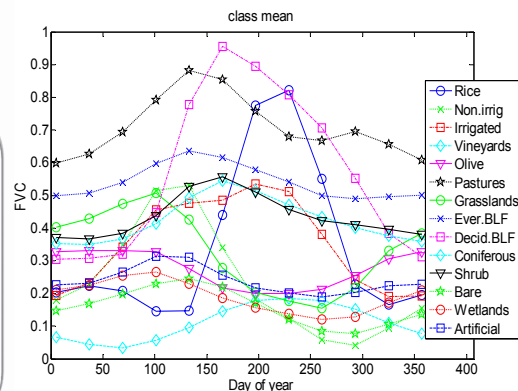


Figure 2. Mean value of annual cycle for 14 major land cover classes.

3.1 Classification methods

In this study, different classification techniques, including both parametric and non parametric methods, were applied several times, with random initial partitions of the training data, in order to assess quantitative and qualitative the derived thematic map. Since the training sample data are drawn randomly from the image population, the prior probabilities can be estimated by the fraction of each class in the pooled sample.

Moderate performance was achieved with the parametric maximum likelihood classifier, partly because the assumption of normal spectral distribution is often violated, especially in complex landscapes. For example, the climatic conditions can be highly variable at local scale and may lead to locally different behaviours within the same type of vegetation. In fact, multimode distributed training samples were obtained for several broad classes.

Non parametric methods are preferable since they no strong prior assumptions about the form of the probability distributions and can be adjusted flexibly to the different types of data and input structures. Among the most commonly used non-parametric classification approaches are neural networks, decision trees, support vector machines, and expert systems.

An Artificial Neural network (ANN) method – the classical Multilayer Perceptron (MLP) with two hidden-layers trained with the Levenberg-Marquardt (LM) algorithm- was selected since it outperformed other techniques such as classification trees, the Parzen density estimator and k-nearest neighbour classifier (with k optimized using the five-fold cross-validation method). The neural network has several

advantages, including easy adaptation to different types of data and input structures, fuzzy output values, and generalization for use with multiple images. We applied the multilayer perceptron, which is the most popular type of neural network in image classification (Atkinson and Tatnall 1997). In order to avoid overfitting, the training was stopped when the validation cost function starts to rise.

When multiple remotely sensed variables are used for input into a classification procedure, selecting the appropriate variables that are most useful in separating land-cover classes is an effective way to improve classification accuracy. In order to assess the importance of the involved variables, a sensitivity analysis over the MLP's was carried out. This technique assumes that after a MLP has been successfully trained to model a data set, the weights between the neurons are so adjusted that removing irrelevant features does not influence the output of the neural network in a great extent (Pal, 1999). A representative sample of the networks that best model the training data set was taken. Then the difference between the outputs of these models when excluding a given variable was calculated. This methodology sorts the importance of variables in order to reject those that do not significantly contribute to the predictive model.

The sensitivity analysis has revealed that temporal evolution FVC plays a key role on the discrimination of major land cover types (see figure 3). Using derived phenological metrics produces little improvement in classification accuracy relative to using an annual time series of FVC data. Further, the use of reflectance composites and texture variables position provided a more significant relative improvement.

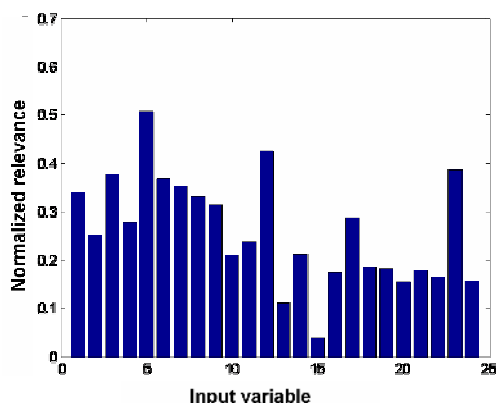


Figure 3. Relative importance of the involved variables, as assessed from difference between the outputs of ANN models when excluding a given variable. Variables 1-12 is a sequence of FVC (January to December), 13-15 are seasonal metrics (amplitude of annual cycle, mean FVC and phase), 16-18 (and 19-21) are MODIS reflectance composite at three

wavebands (red, near-infrared and middle-infrared) corresponding to the period of maximum (and minimum) canopy closure, respectively, and 22-24 are three first order texture measures (range, entropy and standard deviation).

4. RESULTS

Figure 4 shows the results of a ANN classification for the entire Spanish territory. Error matrices resulting from the cross validated accuracy assessments provided overall accuracy, omission errors, and commission errors for each class. The overall accuracy for the 14-class map was of 80.0%, with generally high and balanced values of user's accuracy and producer's accuracy for individual classes (see figure 5). The highest classification accuracies were produced for classes with higher pixel homogeneity and good spectral discrimination such as 'Deciduous broadleaved forest' and most cultivated classes. The lowest accuracy is observed for 'Evergreen broadleaved forest' and 'Bare areas', which are probably overestimated. Commission errors are partly due to the spectral confusion with other classes. In general, the classes 'Artificial surface', 'Bare areas', 'Shrublands' are difficult to classify as many of the training pixels corresponding to such classes were mixed pixels with a relatively low abundance of the dominant class (~75%). This evidences the well-known limits in accuracy of hard classification methods in heterogeneous regions.

Despite this encouraging result, visual inspection of this map (figure 4) reveals minor problems with certain classes. In particular, some patches in the south-east area were erroneously labeled as 'Artificial surface'. As previous research has indicated the combination of multiple classification results may improve the accuracy of the map to combine multiple classification results (e.g. Benediktsson and Kanellopoulos 1999; Huang and Lees 2004). To perform this task, different techniques can be applied in future work, such as confidence-based rules or Boosting techniques.

The classification was also assessed by comparing it with global and continental land cover mapping currently available, CORINE, GLC2000 and GLOBCOVER. The derived land cover presented closer agreement to reference data and an overall good consistency with existent products.

The classification was also assessed by comparing it with global and continental land cover mapping currently available, CORINE, GLC2000 and GLOBCOVER. The derived land cover presented closer agreement to reference data and an overall good consistency with existent products.

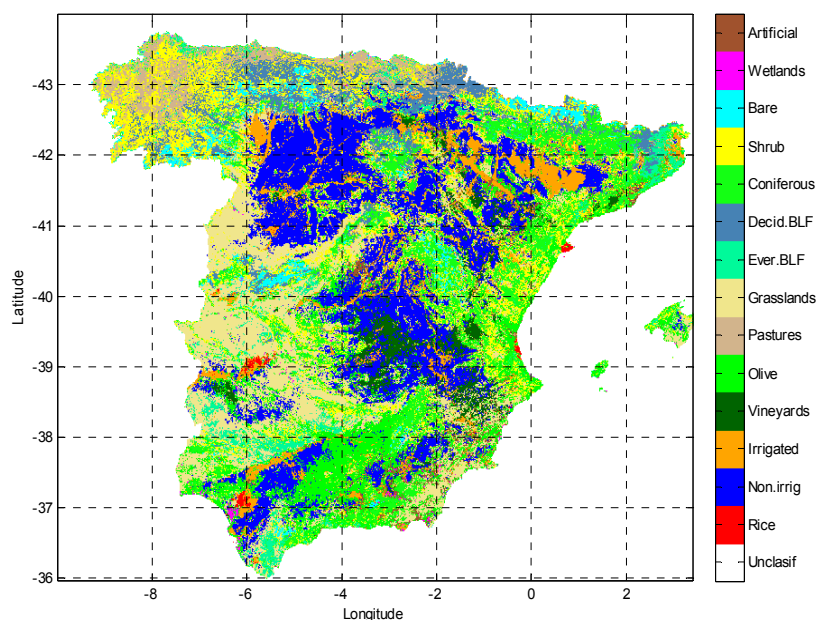


Figure 4. Derived land cover map with a hierarchy level of 14 major classes.

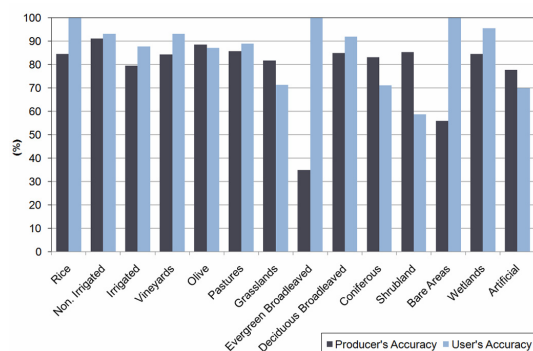


Figure 5. User's and producer's accuracy of individual classes for the obtained 14-class map.

5 CONCLUSIONS AND FUTURE WORK

The general objective of this work is to assess a strategy designed to maximize land cover classification accuracies derived from multitemporal MODIS data. Temporal trajectories of satellite-based biophysical parameters such as fractional vegetation cover provide a viable option for regional-scale land cover mapping in Spain. The sensitivity analysis has revealed that temporal evolution FVC plays a key role on the discrimination of major land cover types.

Further, the use of reflectance composites and texture variables provided a significant relative improvement.

The steps used to select appropriate variables that are most useful in separating land-cover classes and the selection of samples for algorithm training, are among the many factors that can strongly influence the resulting classification accuracy. A spatially detailed reference database allowed us maximize the representativity of training samples (i.e. evenly distributed in geographic space) of land cover across Spain, offering thus an optimal reference for map evaluation. A proper statistical characterization of classes was achieved by a stratified random sampling design, where a minimum number of samples are selected from each category according their overall abundance in the image.

An overall accuracy of 80.0% has been obtained with a hierarchy level of 14 major classes. The derived land cover presented closer agreement to reference data than global and continental land cover mapping currently available. One major limitation is due to the presence of mixtures within the pixel caused by landscape heterogeneity due to spatial and thematic resolution.

ACKNOWLEDGEMENTS

This work has been supported by DULCINEA (CGL2005-04202) and ARTEMIS (CGL2008-00381) projects. Special thanks are due to our colleagues of the

IGN (Instituto Geográfico Nacional) for granting us the access to SIOSE database.

REFERENCES

- Benediktsson, J. A. and Kanellopoulos, I., 1999, Classification of multisource and hyperspectral data based on decision fusion. *IEEE Transactions on Geoscience and Remote Sensing*, **37**, 1367–1377.
- Carrão, H., Capão, L., Bação, F., and Caetano, M., 2006, Meris Based Land Cover Classification With Self-Organizing Maps: Preliminary Results. Proceedings of the 2nd EARSeL SIG Workshop on Land Use & Land Cover, 28 - 30 September 2006, Bonn, Germany, unpaginated CD-ROM.
- Clevers, J. G. P. W., Bartholomeus, H. M. et al., 2005, Land covers classification with the Medium Resolution Imaging Spectrometer (MERIS). In: New Strategies for European Remote Sensing, Oluic (ed.) Millpress, Rotterdam, ISBN 90 5966 003 X, pp.687-694.
- Dash, J., Mathur, A., Foody, G. M., Curran, P. J., Chipman, J. and Lillesand, T. M., 2007, Landcover classification using multi-temporal MERIS vegetation indices. *International Journal of Remote Sensing*, **28**, 1137-1159.
- Defries, R. S. and Chan, J. C., 2000, Multiple criteria for evaluating machine learning algorithms for land cover classification from satellite data. *Remote Sensing of Environment*, **74**, 503–515.
- Franklin, S. E. and Peddle, D. R., 1989, Spectral texture for improved class discrimination in complex terrain. *International Journal of Remote Sensing*, **10**, 1437–1443.
- Friedl, M. A., C. E. Brodley, and A. H. Strahler, 1999, Maximizing Land Cover Classification Accuracies Produced by Decision Trees at Continental to Global Scales, *IEEE Transactions on Geoscience and Remote Sensing*, **37**, 969-977.
- García-Haro, F. J., S. Sommer, T. Kemper, 2005, Variable multiple endmember spectral mixture analysis (VMESMA). *International Journal of Remote Sensing*, **26**, 2135-2162.
- Gonçalves P., Carrão, H., Pinheiro, A. and Caetano, M., 2006, Land cover classification with Support Vector Machine Applied to MODIS imagery. In: Global Developments in Environmental Earth Observation from Space, edited by A Marçal (Rotterdam: Millpress), pp. 517-526.
- Huang, Z. and Lees, B. G., 2004, Combining non parametric models for multisource predictive forest mapping. *Photogrammetric Engineering and Remote Sensing*, **70**, 415–425.
- Ji, C. Y., 2000, Land-use classification of remotely sensed data using Kohonen Selforganizing feature map neural networks. *Photogrammetric Engineering and Remote Sensing*, **66**, 1451-1460.
- Kim, H., Pang, S., Je, H., Kim, D. and Bang, S. Y., 2003, Constructing support vector machine ensemble. *Pattern Recognition*, **36**, 2757–2767.
- Liu, Q. J., Takamura, T. and Takeuchi, N., 2002, Mapping of boreal vegetation of a temperate mountain in China by multitemporal Landsat TM imagery. *International Journal of Remote Sensing*, **23**, 3385–3405.
- Trigo, I. F., DaCamara, C., Viterbo, P., Roujean, J. L., Olesen, F., Siljamo, N., Meliá, J., Camacho-de Coca, F., García-Haro, F. J., Gellens-Meulenberghs, F., Geiger, B., 2010, The Satellite Application Facility on Land Surface Analysis, *International Journal of Remote Sensing*, in press.
- Valcarcel, N., Villa, G., Arozarena, A., Garcia-Asensio, L., Caballero, M. E., Porcuna, A., Domenech, E., Peces, J. J., 2008, SIOSE, A successful test bench towards harmonization and integration of land cover/use information as environmental reference data, The International Archives of the Photogrammetry, Remote Sensing and Spatial Information Sciences. Vol. XXXVII. Part B8. Beijing 2008.
- Wardlow, B. D., Egbert, L. D., 2008, Large-area crop mapping using time-series MODIS 250 m NDVI data: An assessment for the U.S. Central Great Plains, *Remote Sensing of Environment*, **112**, 1096–1116.

Assessment of vegetation response to climate variability in Spain

F. J. García-Haro(1), A. Moreno(1), A. Perez-Hoyos(1), M. A. Gilabert(1), J. Meliá(1), F. Belda(2), D. Poquet(2), B. Martínez(1), A. Verger(1)

(1) Remote Sensing Unit, Departament de Física de la Terra i Termodinàmica, Universitat de València. C/ Dr Moliner, 50. 46100 Burjassot, València (Spain)

(2) Delegación Territorial en Murcia. AEMET (Agencia Estatal de Meteorología), Libertad 11, 30107, Guadalupe, Murcia, Spain.

Email addresses: J.Garcia.Haro@uv.es; alvaro.moreno@uv.es; Ana.Perez-Hoyos@uv.es; m.amparo.gilabert@uv.es; joaquin.melia@uv.es; fbelda@inm.es; dpoquet@inm.es; Beatriz.Martinez@uv.es; aleixandre.verger@uv.es

ABSTRACT- Ecological and climate models require high-quality biophysical parameters as input. In this study, coherent estimates of biophysical variables parameters such fractional vegetation cover (FVC) have been derived in the Iberian Peninsula. The proposed methodology was applied on time series of MODIS reflectance covering a 10-year (2000-2010) period to obtain direct indicators of vegetation biomass and condition in the Iberian Peninsula. Monthly climatic maps of precipitation and temperature were obtained to build simple climatic indices, such as the Standard Precipitation Index (SPI) at different time scales and the Thornthwaite moisture index. The spatial and temporal dynamics of satellite-derived vegetation products and climatic indices enabled spatially explicit comparisons of vegetation condition in response to precipitation. Spatially, derived maps were used to tracking the current effect of climate variability on ecosystem functioning. In particular, the influence of the severe drought in Spain during 2004-2006 on vegetation cover dynamics was assessed. Strong temporal correlations were also found between water drought indices which employ cumulative rainfall summed over the preceding months (e.g. SPI-3) and satellite-derived vegetation products. They were particularly significant in semi-arid regions. A Self-Organizing Map (SOM) was built to determine the typical patterns of co-variation between vegetation activity and rainfall in Spain. FVC anomaly showed meaningful relationships with inter-annual climate variability. This implies that the anomaly of vegetation cover is a good indicator of moisture condition and can be an important data source when used for detecting and monitoring drought in the Iberian Peninsula.

1 INTRODUCTION

Monitoring the vegetation activity over long time-scales is necessary to discern ecosystem responses to climate variability. The importance of the relationships between water availability and vegetation has been traditionally recognised in Mediterranean and other regions and is a subject of growing interest (Lobo and Maisongrande, 2006). For example, recent climatic changes have enhanced plant growth in northern mid-latitudes and high latitudes (Nemani et al. 2003).

Vegetation has been traditionally monitored using time series of satellite based vegetation indices such as the NDVI. However, the advent of modern satellites (e.g. MODIS, MERIS, SEVIRI, VEGETATION) has improved the possibilities to retrieve new vegetation properties thanks to a better radiometric, spectral and angular performance of imaging instruments. Biophysical variables such as fractional vegetation cover (FVC) and leaf area index (LAI) have proven to be appropriate for modeling terrestrial ecosystems on the global, continental, and regional scales.

In this study, coherent estimates of these variables in the Iberian Peninsula have been derived. The algorithm for retrieving FVC relies on optimised SMA approaches (García-Haro et al. 2005). Adapted variants of a probabilistic spectral mixture analysis algorithm, which is currently used operationally in the context of the EUMETSAT/LSA SAF mission (Trigo et al. 2010), have been used. The proposed methodology was applied on time series of MODIS reflectance (MOD13A2) product at three spectral wavebands: red, near infrared and middle infrared.

The potential of derived biophysical variables in the field of drought conditions monitoring has been assessed. The study evaluates time series of both climatic data and satellite observations of FVC. The aim is to analyse the vulnerability of natural ecosystems against the effects of climate fluctuations like drought and extreme events in the Iberian Peninsula, from the relationship between the retrieved parameters and drought indices such as the Standardized Precipitation Index (SPI).

2 DATA SETS

2.1 Vegetation characterization

Figure 1 shows several examples of derived FVC maps at different time periods comprising the annual cycle of vegetation. The seasonal trajectories of vegetation abundance present a large spatial variability in the Iberian Peninsula. The potential of these data for land cover classification has been recently demonstrated (García-Haro and Pérez-Hoyos, 2010, this issue). It is observed a strong north-south gradient shift in the timing of greenup onset. This complex spatio-temporal variation comes about not only through climatic variability but also through variations in community composition, soils and land management (e.g. irrigation practices). For example, the greenup in some north-eastern and southern areas at the end of the year is explained by agricultural practices (irrigation and cereal crops) (Peñuelas et al. 2004).

2.2 Climatic data

Climatological data such as precipitation and temperature control differences in the Earth's vegetation cover, affecting growth rate, plant reproduction, and frost damage. In this study, monthly climatic maps of precipitation and temperature in Spain were derived during the 1950-2010 period at a 2-km spatial resolution using Geostatistical approaches for interpolation (García-Haro et al. 2008). The accurate estimation of the spatial distribution of precipitation requires a very dense network of measuring gaugement. The climatic data used in the study were obtained from the AEMET (Agencia Estatal de Meteorología) and correspond to between 2500 and 4800 (depending on the period) recording stations evenly distributed over Spain. From the monthly maps, annual and monthly averages for the analyzed period were computed.

2.3 Drought indices

Both the soil moisture conditions and the vegetation activity respond to precipitation anomalies on a relatively short scale (Ji and Peters, 2003). A 3-month rainless period may have an impact on vegetation activity because of the dependence of vegetation growth on soil water storage. The Standard Precipitation Index (SPI) expresses the number of standard deviations that the precipitation values - transformed to follow a normal distribution- would deviate from the long-term mean (McKee et al, 1993). The SPI was selected because of its flexibility to measure drought at different time scales. Since the impact of water deficits on vegetation is cumulative,

cero to six months of preceding rainfall amounts were used for linking drought severity and duration with the vegetation cover. The precipitation total of the current month and previous i months ($i=1, 3, 6, 12$ and 24) was used to compute the i -month scale of the SPI.

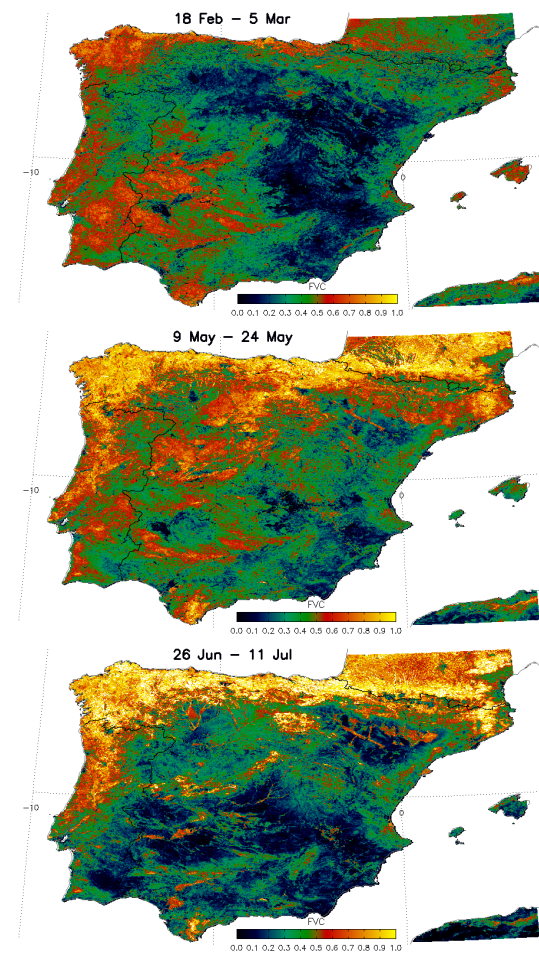


Figure 1. Monthly average (2000–2010) fractional vegetation cover for the Iberian Peninsula at three different time periods.

An illustrative example is shown in figure 2. The 12-month SPI in December 2005 reflects long-term precipitation patterns, corresponding to the severe drought suffered by the Iberian Peninsula during 2005, one of the worst drought in decades.

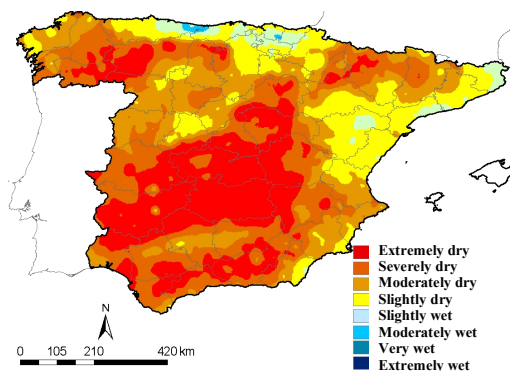


Figure 2. 12-month SPI values for Spain in December 2005 stratified into 8 intervals: extremely wet (>2.0), very wet (1.5 to 1.99), moderately wet (1.0 to 1.49), slightly wet (-0.99 to 0.0), slightly dry (0 to 0.99), moderately dry (-1.49 to 1.0), severely dry (-1.99 to 1.5), and extremely dry (<-2.0).

2.4 Climatic characterization

We calculated potential evapotranspiration (PET) from the monthly temperature maps according to Thornwaite (Thornwaite and Mather, 1957). The Thornthwaite moisture index was then computed using the difference between monthly precipitation and evapotranspiration (P-PET). This climate index is a useful indicator of the supply of water in an area relative to the demand for water (P) under prevailing climatic conditions (PET). It reflects the portion of total precipitation used to nourish vegetation over a certain area. Using average values over a 60 year period (1950-2009) the moisture index was computed. By stratifying this map into 9 intervals (see table 1) the nine-category classification Spain into nine climatic regions was obtained (figure 3).

Table 1. Legend of the climatic classification based on the moisture index.

<i>Climatic Type</i>		<i>Moisture Index</i>
A	Very humid	≥ 100
B ₄	Humid	80 to 100
B ₃	Humid	60 to 80
B ₂	Humid	40 to 60
B ₁	Humid	20 to 40
C ₂	Moist subhumid	0 to 20
C ₁	Dry subhumid	-20 to 0
D	Semiarid	-40 to -20
E	Arid	-60 to -40

Spain, the most arid country in Europe, presents a high contrast between humid and very humid regions in the North (moisture index values from 80 to 160) and the desertic South-eastern (SE) region (values below -40). A total of 15 percent of the Spain landmass is considered either arid or semi-arid, including the semi-arid ecosystems in SE Spain (provinces of Almería and Murcia), the semi-arid regions situated in the Ebro Basin and most of the La Mancha elevated plains of central Spain. A strong linear trend was observed between the values of mean fractional vegetation cover and moisture index.

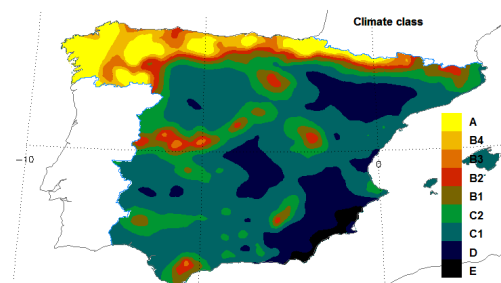


Figure 3. Nine-category climatic classification based on the moisture index. It corresponds to average values of climatic parameters over a 60 year period (1950-2009).

3. RELATIONSHIP BETWEEN VEGETATION AND PRECIPITATION

The spatial and temporal dynamics of FVC and SPI enabled spatially explicit comparisons of vegetation condition in response to precipitation. Significant positive correlations have been found between anomalies in cumulative rainfall summed over the preceding months and anomalies of vegetation cover.

3.1. Spatial relationships

Figure 4a illustrates the influence of the severe drought in Spain during the 2004-2006 period on vegetation cover. A severe disturbance in vegetation cover can be observed across Spain during the growing season (e.g. during May).

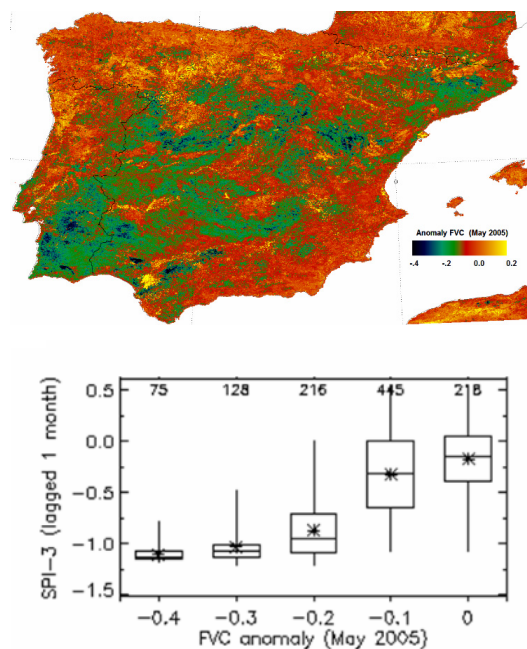


Figure 4. Top: FVC Anomaly (May 2005). Bottom: Whisker plot of SPI-3 lagged 1-month (i.e. using the precipitation of February, March and April) as a function of the FVC anomaly (May 2005). Data correspond to broadleaved deciduous forest. The number of valid pixels is printed on top of each box.

3.2. Temporal relationships

Figure 5 shows several examples of long-term series of monthly drought indices (SPI) and anomalies of vegetation cover. In addition to the severe drought of 2004-2005, moderate droughts in years 2001 and 2003 appeared also to be related with disturbance in the growing cycle of vegetation. In general, the relationship is more significant in semi-arid regions, as water is the most limiting resource in these environments. Multi-year drought affects these environments, influencing plant community composition, physiology, and growth (Weiss et al. 2004). Results suggest that while herbaceous cover and sclerophyllous vegetation appear to be very sensitive to rainfall, drought has a less influencing effect on woodland structures such as olive groves and coniferous forest.

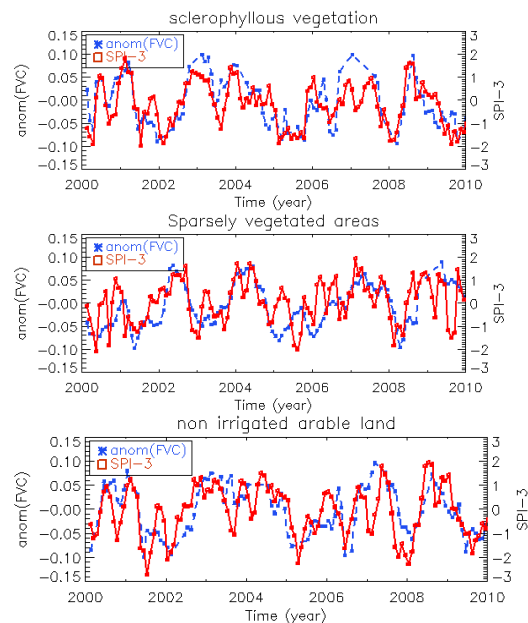


Figure 5. Temporal patterns of SPI and FVC anomaly over a 10-year period, at a 16 day time step, for three different vegetation types.

A regression model with seasonal dummy variables was used to build relationships between the disturbance of FVC and SPI at different time scales. When monitoring the vulnerability of natural ecosystems against drought conditions, both the seasonal timing and the time lag in the vegetation response to precipitation were taken into consideration. In general, the 3-month SPI lagged 1 month was found to have the best correlation, indicating lag and cumulative effects of precipitation on vegetation. In order to simplify the regression model and assess the effect of seasonal timing, different temporal windows covering a 4 month period were considered. A stepwise multiple regression was applied to determine a minimum number of regressors which explained the largest amount of variation in the anomaly of FVC.

Statistically significant correlations have been found between SPI and satellite-derived anomalies of vegetation activity, although they are highly dependent on the regional climate and vegetation community. Such influences are documented in Figure 6, which reveals a negative linear trend of R^2 against moisture index level. It is represented the April-July period, which covers the growing season in most of the area. This figure provides an immediate interpretation of the causality between water availability and vegetation cover anomaly.

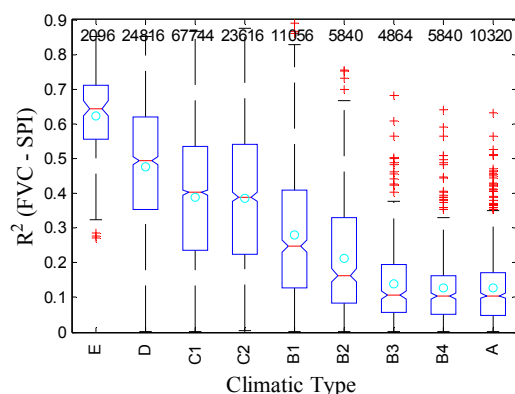


Figure 6. Boxplots of coefficient of determination (R^2) of the regression model with seasonal dummy variables between SPI-1month (1 month lagged) and anomaly of fractional vegetation cover, for the main moisture regions. It is represented the April-July period, which covers the growing season in most of the area. The data covers a ten-year (2000-2010) period.

The most important correlations ($R^2=0.4-0.7$) were found in the arid and semiarid areas. This reveals the notorious impact of water availability on vegetation activity for the summer period in these environments. This implies that the anomaly of vegetation cover provides a meaningful description of moisture condition and can be an important data source when used for detecting and monitoring drought in these areas. By contrast, rain has a low impact on summer vegetation activity over humid regions, presenting moderate to weak correlations.

3.3. Association between variables

In order to gain a deeper insight into the relationship between vegetation activity and rainfall in Spain, a Self-Organizing Map (SOM) has been built (Kohonen et al. 2006). The SOM is a nonlinear projection of the probability density function of the high-dimensional input data (e.g. the pixels of multi-band image) onto a 2-D codebook map of vectors or neurons. The SOM can be thought of as a net which is spread to the data cloud. The SOM training algorithm moves the weight vectors so that they span across the data cloud and so that the map is organized: neighboring neurons on the grid get similar weight vectors ().

Component planes (see figure 7) allowed us to visualize the relationship between time series of SPI and vegetation anomalies in the Iberian Peninsula. The figure reveals as anomaly of vegetation cover and SPI are very closely related to each other (e.g. a strong correlation between the planes associated to both variables). The moisture index shows a dominance of intermediate values in agreement with the mild

conditions in most parts of the peninsula. The strongest negative anomalies of vegetation cover (< -0.06) are found around August ($t \sim -0.7-0.8$) in dry regions, and around early spring ($t \sim -0.3$) in sub-humid areas. In both cases, they were coincidently to the anomalous dry period, in agreement with expectations.

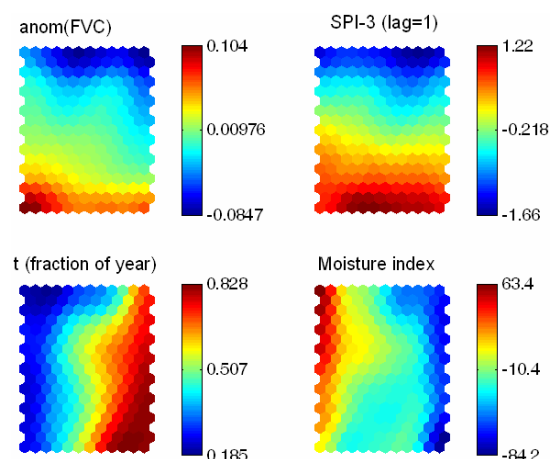


Figure 7. Visualization of the SOM trained from time series of vegetation and climatic data of the study area. The four figures are linked by position: in each figure, the hexagon in a certain position corresponds to the same map unit.

5 CONCLUSIONS

Time series of remotely-sensed vegetation products have provided spatial and temporally consistent parameters such FVC in the Iberian Peninsula. These products provide high-quality-data sources for climate, weather forecast and ecological models. We used long-term monthly climate statistics to build simple climatic indices at different time scales. The spatial and temporal dynamics of satellite-derived vegetation products and climatic indices enabled spatially explicit comparisons of vegetation condition in response to precipitation.

FVC has shown meaningful relationships with inter-annual climate variability. Significant positive correlations have been found between anomalies of the vegetation cover and SPI at different time scales. This implies that the anomaly of vegetation cover is a good indicator of moisture condition and can be an important data source when used for detecting and monitoring drought in the Iberian Peninsula. Correlations are more significant in arid and semiarid areas, since water availability most strongly limits vegetation growth in these environments.

A Self-Organizing Map (SOM), allowed us to find associations between anomalies of vegetation cover

and other relevant variables such as climatic type, water availability and period of year.

ACKNOWLEDGEMENTS

This work has been supported by DULCINEA (CGL2005-04202) and ARTEMIS (CGL2008-00381) projects. The climatic data used in the study were supplied by the Spanish AEMET.

REFERENCES

- García-Haro, F. J., Sommer, S., Kemper, T., 2005, Variable multiple endmember spectral mixture analysis (VMESMA). *International Journal of Remote Sensing*, **26**, 2135-2162.
- García-Haro, F. J., Belda, F. and Poquet, D., 2008, Estimation of climatological variables in Spain during the 1950-2008 period using geostatistical techniques, 8th Annual Meeting of the EMS / 7th ECAC EMS8/ECAC7 Abstracts, Vol. 5, EMS2008-A-00319.
- García-Haro, F. J. and Pérez-Hoyos, A., 2010, Land cover classification in Spain from seasonal trajectories of MODIS data, Proceedings of the RAQRS2010, 3rd International Symposium on Recent Advances in Quantitative Remote Sensing, Torrent (Valencia), Spain, 27 Sept-1 Oct. 2010.
- Ji, L., Peters, A. J., 2003, Assessing vegetation response to drought in the northern Great Plains using vegetation and drought indices, *Remote Sensing of Environment*, **87**: 85-98.
- Kohonen, T., Hynninen J., Kangas J., Laaksonen J., 1996, SOM_PAK: The Self-Organizing Map Program Package, Technical Report A31, Helsinki University of Technology, <http://www.cis.hut.fi/nnrc/nnrc-programs.html>
- Lobo, A. and Maisongrande, P., 2006, Stratified analysis of satellite imagery of SW Europe during summer 2003: the differential response of vegetation classes to increased water deficit, *Hydrol. Earth Syst. Sci.*, **10**:151-164.
- McKee, T. B., Doesken, N. J., and Kliest, J., 1993, The relationship of drought frequency and duration to time scales. In Proceedings of the 8th Conference of Applied Climatology, 17-22 January, Anaheim, CA. American Meteorological Society, Boston, MA. pp. 179-184.
- Nemani, R. R., Keeling, C. D., Hashimoto, H., Jolly, W.M., Piper, S. C., Tucker, C. J., Myneni, R. B. and Running, S. W., 2003, Climate-driven increases in global terrestrial net primary production from 1982 to 1999. *Science*, **300**: 1560-1563.
- Peñuelas, J., Filella, I., Zhang, X. Llorens, L., Ogaya, R. Lloret, F. Comas, P., Estiarte, M., Terradas, J., 2004, Complex spatiotemporal phenological shifts as a response to rainfall changes, *New Phytologist*, **161**: 837-846.
- Thornwaite, C. W. and Mather, J. R., 1957, Instructions and tables for computing potential evapotranspiration and water balance, Drexel Institute of Technology, Laboratory of Climatology, *Publications in Climatology*, **17**, 231-615.
- Trigo, I. F., DaCamara, C., Viterbo, P., Roujean, J. L., Olesen, F., Siljamo, N., Meliá, J., Camacho-de Coca, F., García-Haro, F. J., Gellens-Meulenberghs, F., Geiger, B., 2010, The Satellite Application Facility on Land Surface Analysis, *International Journal of Remote Sensing*, in press.
- Weiss, J. L., Gutzler, D. S., Coonrod, J. E. A. and Dahm, C. N., 2004, Long-term vegetation monitoring with NDVI in a diverse semi-arid setting, central New Mexico, USA, *Journal of Arid Environments*, **58**: 249-272.

Synergy of ECOCLIMAP land cover and LSA SAF vegetation parameters

F. J. García-Haro(1), A. Verger(1), J. L. Roujean(2), F. Camacho(3) and J. Meliá(1)

(1) Departament de Física de la Terra i Termodinàmica, Universitat de València. C/ Dr Moliner, 50. 46100 Burjassot, València (Spain)

(2) CNRM-GAME/ METEO-FRANCE 42, Av. Coriolis 31057 Toulouse Cedex 1 (France)

(3) EOLAB. Parc Científic Universitat de València. C/ Catedràtic José Beltrán, 2. 46980 Paterna, València (Spain)

Email addresses: j.garcia.haro@uv.es; aleixandre.verger@uv.es; jean-louis.roujean@meteo.fr; fernando.camacho@eolab.es; joaquin.melia@uv.es

ABSTRACT- Vegetation variables and land cover maps are essential input information required for modeling surface processes in meteorology, climate and environmental applications. The EUMETSAT/LSA SAF operationally delivers estimates of vegetation fields, including fractional vegetation cover (FVC) and leaf area index (LAI), on a daily basis from SEVIRI/MSG data. But their coarse spatial resolution results inappropriate for many applications. ECOCLIMAP provides a detailed 1-km land cover classification and a class specific coherent set of biophysical variables, amongst which are the surface albedo, FVC and LAI, based on historical series. This database represents adequately the ecosystem typical annual cycle but cannot capture inter-annual and intra-class variability. The aim of this paper is to develop a synergic approach for combining ECOCLIMAP with LSA SAF SEVIRI-vegetation products to take advantage of their complementary spatial and temporal characteristics. An unsupervised fuzzy k-means clustering of the LSA SAF LAI annual cycle was applied to identify substructures within the original set of within ECOCLIMAP classes. The approach has been automated for its application on near real-time SEVIRI LAI products for analysis of African continent. It offers daily estimates of LAI at the original ECOCLIMAP resolution. This generic approach can be applied to other land surface variables and regions providing an extended database for climate, weather forecast and ecological modeling.

1 INTRODUCTION

Global estimates of land surface properties such as land cover classification, fractional vegetation cover (FVC), leaf area index (LAI) and Fraction of Absorbed Photosynthetically Active Radiation (FAPAR) are increasingly necessary for Numerical Weather Prediction (NWP), regional and global climate modeling, weather forecasting and global change monitoring. Météo-France developed a global surface parameter database at 1km spatial resolution for meteorological and climate modeling (ECOCLIMAP) (Masson et al., 2003). This database includes a land cover map derived from NDVI profiles constrained by the SPOT/VEGETATION information, climate maps and auxiliary data by a classification process. In general, an average representation of phenology is represented within the major homogeneous classes, capturing well the seasonal cycle in LAI and showing realistic variations in start of the growing season as a function of latitude.

One underlying assumption of ECOCLIMAP is that the LAI ecosystem variability is generally quite large compared to the intra-ecosystem variability.

However, most ECOCLIMAP classes may occupy a large extension, particularly over African continent, and may thus present a large intra-class variability.

Since ECOCLIMAP surface parameters are based on climatological estimates, limitations caused by interannual variability of vegetation -such as time shift in phenology and changes of amplitude of annual cycle- in response to interannual climatic variations need to be considered (Lobo and Maisongrande, 2006).

The EUMETSAT Satellite Application Facility for Land Surface Analysis (LSA SAF) operationally delivers daily estimates of vegetation variables (FVC, LAI and FAPAR) on a pixel-by pixel basis at the SEVIRI/MSG resolution on a near real time. The LSA SAF products provide an accepted added-value with regard to similar existing products; in particular the products offer important improvements on the temporal continuity. Clearly, the best performance of the FVC and LAI products corresponds to the African continent, with nearly 100% coverage through the whole year, optimal quality retrievals in about 80% of the regions and a negligible percentage of poor quality or unprocessed pixels (Trigo et al. 2010). Nevertheless the coarse spatial resolution of SEVIRI hampers their

applicability for regional climate modeling studies, NWP and meso-scale models. The aim of this paper is to develop a synergic approach for combining ECOCLIMAP and LSA SAF products in order to provide an improved description of land surface. The methodology has been automated in order to produce near-real time products surface parameters.

2 SATELLITE VEGETATION PRODUCTS

2.1 ECOCLIMAP

The large variability of the vegetation does not permit a straightforward derivation of the land surface parameters based uniquely on a general land surface inventory. ECOCLIMAP stratify areas of the same land cover type into homogeneous zones using climate information (Masson et al., 2003). ECOCLIMAP provides, per ecosystem and in a tabular form, the annual cycle of a set of surface parameters including FVC and LAI. ECOCLIMAP version 2 relies on GLC2000 and CORINE land covers and an analysis of time series of NDVI from seven years (1999-2005) of SPOT/VEGETATION observations. LAI is derived from ground measured values extracted from the literature and scaled over the growth cycle of vegetation using remotely sensed data. ECOCLIMAP has been mainly validated over Europe (Faroux et al 2008). An improved database for Western Africa based on MODIS products has been recently developed (Tchuente et al., 2010)

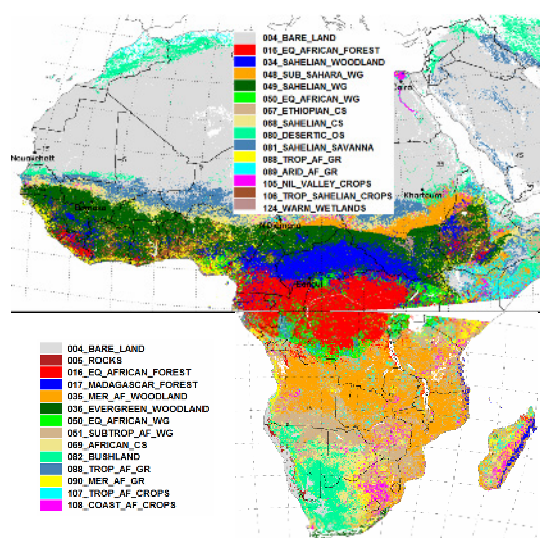


Figure 1: SEVIRI/MSG vegetation products SAF

FVC is estimated through the application of a spectral mixture analysis methodology, developed taking into

account the spectral variability of vegetation in different ecosystems (García-Haro et al 2005), to visible and near infrared reflectance values. LAI is estimated from FVC following the methodology developed by Roujean and Lacaze (2002). The high rate of acquisition provided by the SEVIRI instrument guarantees the availability of spatially consistent cloud-free data for adequately monitoring both the seasonality of vegetation and the long-term trends in the state of vegetation

3 ANALYSIS OF VARIANCE

The goal here is to evaluate if ECOCLIMAP stratification captures the large variability of the vegetation. A decomposition approach has been used to describe the spatial and temporal variability of LAI in Africa from time series of MODIS and SEVIRI products. The decomposition of the total variance is a commonly used technique in climate sciences (Von Storch and Zwiers, 1999). A decomposition approach has been used to describe the variability of LAI African continent. This approach is a variant of the technique proposed by Lindau (2003) to analyse heat fluxes at different timescales. The underlying idea is that the total variance of a dataset can be decomposed into two different kinds components, the external variance and the internal variance. The separation is performed by subdividing the complete dataset into several sub-samples. The complete dataset consisted of 4-year time profiles of two operational LAI products derived from SEVIRI/MSG and MODIS/TERRA (August 2005 to July 2009). Two different kinds of sub-division are performed in order to separate. In the spatial subdivision internal and external components correspond to the inter- and intra-ecosystem variance, respectively, as assessed from the ECOCLIMAP classification. The temporal counterparts correspond to the intra- and inter-annual variance. A separate analysis was performed for the two SEVIRI continental regions, NAfr – Northern Africa encompassing the Sahara and Sahel regions, and part of equatorial Africa, and SAfr – Southern Africa covering the African continent south of the Equator.

Table 1. Decomposition of the SEVIRI/MSG LAI spatial and temporal variance into the internal and external components for the NAfr continental region.

	Spatial	Temporal
External	1.39	0.32
Internal	0.31	0.06
Relative external in %	82.1	85.0

The total variance of the spatial subdivision is roughly five times higher than the temporal variance (Table 1), proving that the spatial component strongly dominates the overall LAI variability in Africa. The spatial subdivision into 21-28 main ECOCLIMAP classes retained the 82.1% and 72.0% of the total variance for NAfr and SAfr (the remaining is due to intra-ecosystem variability unaddressed by ECOCLIMAP). Results show that the subdivision of the entire region into the main ECOCLIMAP classes retains the major part of the overall variance. This means that the ECOCLIMAP representation of African continent is adequate for the capture of main LAI variability in this region. The temporal variance is clearly dominated by the annual cycle (~85% relative variance). The remaining variance due to the interannual variation is 0.06 (0.08) corresponding to a standard deviation of 0.25 (0.29) for NAfr (SAfr).

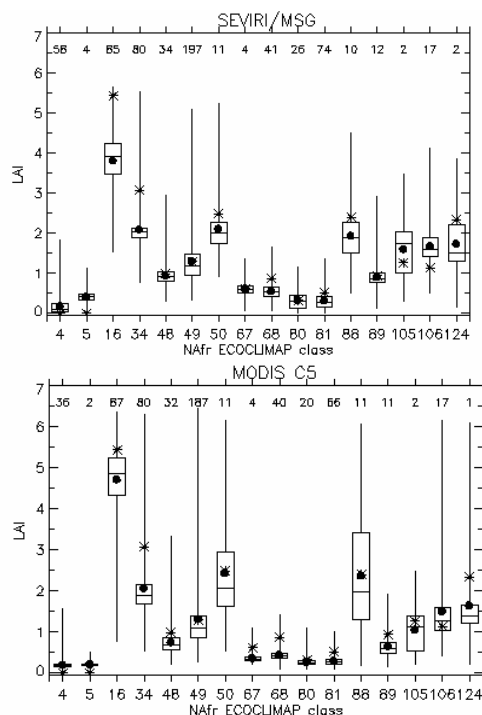


Figure 2. Boxplots of mean LAI during 2007 for the main ECOCLIMAP classes; left, SEVIRI/MSG, right MODIS/TERRA. The central segment in each box marks the median. A black filled circle denotes the mean value. The number of valid pixels (expressed in thousands) is printed on top of each box. The asterisk symbols correspond to the mean LAI provided by ECOCLIMAP for each class.

The procedure outlined above was also applied to describe the variance of MODIS collection 5 LAI data over the same period. The subdivision of MODIS LAI variance shows a high consistency with the results

obtained with SEVIRI, with slightly higher values of the total variability, but with similar partition of the variance between the external and the internal parts.

Rank statistics of the LAI for the main ECOCLIMAP classes are shown in figure 2. They correspond to the mean annual cycle of LAI for three different products: ECOCLIMAP, MODIS and SEVIRI. A noticeably high correspondence between MODIS and SEVIRI products is observed. ECOCLIMAP shows also a good correspondence although with an overall positive bias in certain classes, in particular 16_EQ_AFRICAN_FOREST and 034_SAHELIAN_WOODLAND.

4 MODELLING ECOCLIMAP CLASSES

The aim of this section is the construction of a proper description of the intra-ecosystem variability. The LSA SAF LAI annual cycle was explored to identify substructures within the original set of ECOCLIMAP classes.

4.1 Density estimation

Different parametric and non-parametric density estimation methods were considered. Figure 3 shows the discriminant boundaries/regions as given by the Maximum Likelihood and the Mixture of Gaussian classifiers, for a 4 class 2 band problem. It shows that the density of ECOCLIMAP is typically non-Gaussian although it can be appropriately modeled as a sum of multivariate spherical components.

4.2 Splitting ECOCLIMAP classes

The aim is now to split the classes into distinct substructures representing regions of similarity while reducing the within-ecosystem variability to the desired level of error. A fuzzy K-means (FKM) clustering approach (Bezdek et al. 1984) has been applied to search for substructures in a multidimensional data space of the individual ECOCLIMAP classes.

A challenging task consists in estimating the optimal number of substructures present in the data, which is not known a priori. Many criteria are applicable for validation of partitions generated by the FKM model. After convergence of the FKM algorithm, three validity criteria were calculated: Average Partition density (PD) (Gath and Geva, 1989), Xie-Beni index (XB) (Xie and Beni, 1991) and Fukuyama-Sugeno index (FS) (Fukuyama and Sugeno, 1989). They have been applied in the literature with varying degree of success (e.g. Hammah and Curran 2000; Duda and Canty, 2002).

The determination the optimal number of clusters relied on the combined analysis of the validity plots. Assuming that the data consists of well-separated clusters of approximately multivariate normally distributed pixels, the optimal number of clusters should maximize the PD measure and maximize the XB and FS indices. The validity criteria emphasized different properties: minimal volume, maximal concentration of data points around the centroids of resulting clusters and maximal separability between clusters.

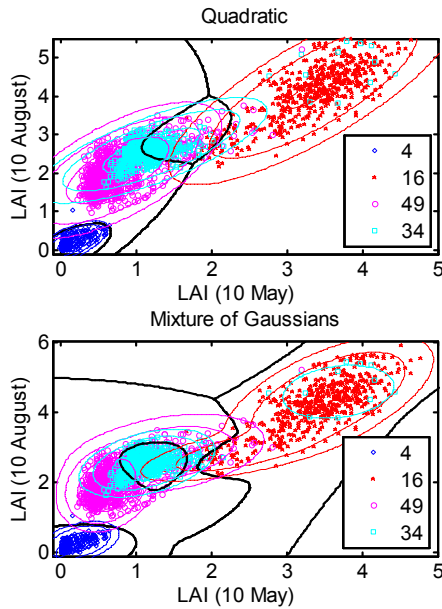


Figure 3. Bayes classification of four major ECOCLIMAP cover types in northern Africa from SEVIRI/MSG LAI estimations, for two algorithms: quadratic (top); Mixture of Gaussians, with two Gaussian components per class (bottom). Points are randomly drawn from the ECOCLIMAP database. 4: Bare land, 16: Equatorial African Forest, 34: Sahelian woodland, 49: Sahelian WG.

Figure 4 illustrates the performance of the proposed approach for the '48_Sub Sahara Wg.' class, in which two well separated clusters can be recognised. The small one shows low LAI value through the year and the broad one presents important seasonal variations: very low LAI values (<0.5) during the dry season and high LAI values (1-3) during the rainy season. The analysis of the validity plots evidences the limitation of the PD index to identify well-separated but scarcely populated components. In this example, the behaviour of the XB and FS indices was more consistent, reaching a minimum at about $k=4$. The 4-cluster subdivision reduced the within-group variance to 0.17 (59% reduction).

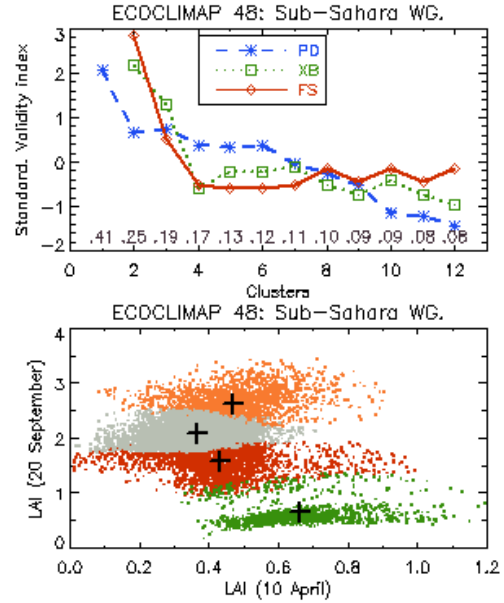


Figure 4. Clusters obtained with the FKM algorithm for a ECOCLIMAP class. Top: Validity index values for PD, XB and FS (transformed into standardized units) as a function of the number of cluster ranging from $k=1$ to 12. Note that XB and FS are defined only for $k>2$. The within-scatter variance as a function of the number of clusters is printed on bottom of the plot. Bottom: Optimal partition obtained for $k=4$ clusters, as represented in the features space of two dates, 10 April and 20 September. Cluster centroids are represented by plus symbols.

5. SYNERGY OF ECOCLIMAP AND LSA SAF PRODUCTS

The main objective is deriving maps of vegetation products (LAI, FVC) with the original spatial characteristics of ECOCLIMAP but offering a more accurate description of the spatial and temporal variance of SEVIRI products.

Each ECOCLIMAP pixel was associated with a weighted sum of SEVIRI temporal signatures of the the closest clusters:

$$\hat{y} = \sum_{k \in \Omega} f_k V_k, \quad \Omega = \{k \mid u_{ik} > 0.05\} \quad (1)$$

where u_{ik} is the degree of membership of ECOCLIMAP pixel k to the i -th cluster. Pixel membership values (as derived in the FKM partition) exceeding 0.05 were considered. V_k is the mean of cluster k . f_k denotes a vector with the unknown proportions of the closest clusters the ECOCLIMAP pixel. It was estimated by applying the classical mixing equation with two constraints: (1) the

proportions should add up to unity (2) no component of a mixed pixel can make a negative proportion. An example of the application of the proposed methodology for deriving LAI maps is shown in figure 5.

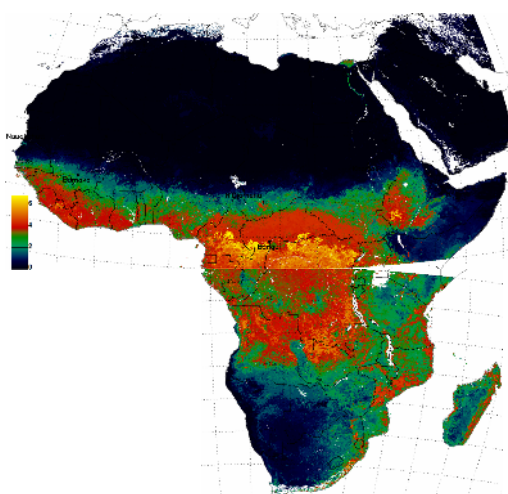


Figure 5. Example of LAI field based on the synergy of ECOCLIMAP and LSA SAF products.

5 CONCLUSIONS

A synergic approach for combining ECOCLIMAP with coarser resolution LSA SAF SEVIRI-vegetation products was here developed. The aim was to take advantage of the high temporal resolution and continuity of SEVIRI products to provide an improved ecosystem classification and land surface parameters database on a daily basis at the original ECOCLIMAP 1-km spatial resolution. The proposed synergic approach was here implemented for Africa and LAI parameter although it may be generalised for the other continents or other land surface parameters.

A decomposition approach has been used to describe the spatial and temporal variability of LAI in Africa from time series of SEVIRI products. The subdivision of the entire region into the main ECOCLIMAP classes retains the major part of the overall variance. This means that the ECOCLIMAP representation of African continent is adequate for the capture of main LAI variability in this region. The temporal variance is clearly dominated by the annual cycle (~85% relative variance), while the remaining variance is due to the interannual variation.

Part of the intra-ecosystem variability unaddressed by ECOCLIMAP is modeled through a mixing

approach that incorporates vegetation information provided by SEVIRI products.

The developed LAI fields capture the inter-annual variability, show temporal stability (gradual variations), temporal continuity (no missing data) and partly address the intra-class variability of the main cover types, leading to an important improvement for climate and environmental applications.

ACKNOWLEDGEMENTS

This work has been supported by LSA SAF/EUMETSAT, DULCINEA (CGL2005-04202) and ARTEMIS (CGL2008-00381) projects.

REFERENCES

- Bezdek, J. C., Ehrlich, R. and Full, C., 1984, The fuzzy c-means clustering algorithm. *Computers and Geosciences*, **10**: 191-203.
- Duda, T. and Canty, M. J., 2002, Unsupervised classification of satellite imagery: choosing a good algorithm, *International Journal of Remote Sensing*, **23**, 2193–2212.
- Faroux, S., Masson, V., and Roujean, J.-L., 2008, ECOCLIMAP-II: a climatologic global data base of ecosystems and land surface parameters at 1 km based on the analysis of time series of VEGETATION data, 3rd Land Surface Analysis SAF Workshop, Lisbon 4-6 June.
- Fukuyama, Y. and Sugeno, M., 1989, A new method of choosing the number of clusters for the fuzzy c-means method, in Proc. 5th Fuzzy Symp., 1989, pp. 247-250 (in Japanese).
- García-Haro, F. J., Sommer, S., and Kemper, T., 2005, Variable multiple endmember spectral mixture analysis (VMESMA). *International Journal of Remote Sensing*, **26**, 2135-2162.
- Gath, I. and Geva, A. B., 1989, Unsupervised optimal fuzzy clustering. *IEEE Transactions on Pattern Analysis and Machine Intelligence*, **7**: 773-781.
- Hammah, R.E. and Curran, J. H., 2000, Validity Measures for the Fuzzy Cluster Analysis of Orientations, *IEEE Transactions on pattern analysis and machine intelligence*, **22**, 1467-1472.
- Lindau R., 2003, Errors of Atlantic Air-Sea Fluxes Derived from Ship Observations. *Journal of Climate*, **16**, 783-788.

- Lobo, A. and Maisongrande, P., 2006, Stratified analysis of satellite imagery of SW Europe during summer 2003: the differential response of vegetation classes to increased water deficit, *Hydrol. Earth Syst. Sci.*, **10**, 151–164.
- Masson, V., Champeaux, J. L., Chauvin, F., Mérieux, C., and Lacaze, R., 2003, A global database of land surface parameters at 1-km resolution in meteorological and climate models, *Journal of Climate*, **16**, 1261–1282.
- Roujean, J. L. and Lacaze, R., 2002, Global mapping of vegetation parameters from POLDER multiangular measurements for studies of surface-atmosphere interactions: A pragmatic method and its validation. *Journal of Geophysical Research*, **107D**, 10129–10145.
- Tchuente, K., A. T., Roujean, J. L., and Faroux, S., 2010, ECOCLIMAP-II: An ecosystem classification and land surface parameters database of Western Africa at 1 km resolution for the African Monsoon Multidisciplinary Analysis (AMMA) project. *Remote Sensing of Environment*, **114**, 961–976.
- Trigo, I. F., DaCamara, C., Viterbo, P., Roujean, J. L., Olesen, F., Siljamo, N., Meliá, J., Camacho-de Coca, F., García-Haro, F. J., Gellens-Meulenberghs, F., Geiger, B., 2010, The Satellite Application Facility on Land Surface Analysis, *International Journal of Remote Sensing*, in press.
- Von Storch, H., and Zwiers, F. W., 1999, Statistical Analysis in Climate Research. Cambridge University Press, 484.
- Xie, X., L. and Beni, G., 1991, A Validity Measure for Fuzzy Clustering, *IEEE Trans. Pattern Analysis and Machine Intelligence*, **13**: 841–847.

Global vegetation monitoring with NOAA-AVHRR data between 1981 and 2001

Y. Julien¹, J. A. Sobrino¹, F. Gonzalez-Alonso², C. Mattar¹, J.-C. Jiménez-Muñoz¹, G. Soria¹, V. Hidalgo¹, B. Franch¹, R. Oltra-Carrió¹, J. Cuenca¹,

¹ *Global Change Unit, Image Processing Laboratory, Parque Científico, Universidad de Valencia, C/ Catedrático Agustín Escardino n°9, 46980 Paterna, Spain.*

² *Remote-Sensing Laboratory CIFOR-INIA, Crta. de La Coruña km 7,28035-Madrid, Spain.*
yves.julien@uv.es, sobrino@uv.es

ABSTRACT- *Vegetation is a key factor for climate change and climate modelling, and remote sensing provides the easiest way to observe vegetation at global scale. Normalized Difference Vegetation Index (NDVI) has been widely used to monitor vegetation health and evolution worldwide, thanks to its mathematical simplicity. In this work, we have used data from the GIMMS (Global Inventory Modeling and Mapping Studies) and Pathfinder AVHRR (Advanced Very High Resolution Radiometer) Land (PAL) dataset to retrieve NDVI when possible to monitor changes in vegetation between 1981 and 2001. The obtained time series of NDVI have been analyzed statistically on a pixel by pixel basis to retrieve anomalies and trends, which have been compared to the existing literature on vegetation change. This method allows to evidence vegetation change hotspots such as the deforested areas in South America, Central Africa and Indonesia.*

1 INTRODUCTION

Several studies have used NDVI (Normalized Difference Vegetation Index – Tucker, 1979) for the analysis of vegetation. This index is based on the difference in absorption at red and near infrared wavelengths for chlorophyllic vegetation, and has been used widely to monitor vegetation at regional and global scale (Myneni *et al.*, 1997; Tucker *et al.*, 2001; Zhou *et al.*, 2001; Bogaert *et al.*, 2002; Zhou *et al.*, 2003; Julien and Sobrino, 2009).

To this end, NOAA (National Oceanic and Atmospheric Administration)'s AVHRR (Advanced Very High Resolution Radiometer) data provide one of the longest satellite record for the analysis of the evolution of the vegetation, through the use of several databases. Such databases as the PAL (Pathfinder AVHRR Land) and GIMMS (Global Inventory Modeling and Mapping Studies) datasets allow for this vegetation monitoring, although the processing of the raw AVHRR data differs between both approaches.

The differences in processing of the same raw data may result in differences in the time series, propagating then in the statistics retrieved from these time series. Therefore, intercomparison of the different databases is needed, and has been carried out in the past for some specific locations. In the present work, we retrieved both PAL and GIMMS NDVI datasets long-term statistics to be analyzed and intercompared. Then, the obtained statistics are compared with independent data in order to identify the best dataset

for vegetation dynamics study. Such dataset is finally used to identify areas for which photosynthetically active vegetation has been changing during the 80s and 90s.

2 DATA

Two databases have been used in this work: Pathfinder AVHRR Land (PAL) and Global Inventory Modeling and Mapping Studies (GIMMS).

2.1 PAL database

PAL database (Smith *et al.*, 1997) has been compiled by the National Aeronautics and Space Administration (NASA) and was available free of charge from their website until 2008. This database consists of images acquired by the AVHRR sensor, onboard NOAA satellites. In spite of a daily acquisition frequency of the sensor, the dataset has a temporal resolution of 10 days, because of the image compositing (accordingly to the Maximum Value Compositing or MVC method), which diminishes the contamination of the images by clouds or aerosols (Holben, 1986). The dataset extends from July 1981 to September 2001, and for each 10-day period, 5 images are available: red reflectance (channel 1), infrared reflectance (channel 2), infrared radiometric temperatures (channels 4 and 5), and NDVI image. Images are available at 0.1 degree and eight kilometer resolution, at continental and global scale. In this work, global 10-day composites at 0.1 degree from July 1981 to September 2001 are used.

2.2 GIMMS database

The GIMMS dataset (Pinzon, 2002; Pinzon et al., 2005; Tucker et al., 2005) compiles NDVI images acquired by AVHRR sensor aboard NOAA satellites. The database is composed of quasi 15-day composites from July 1981 to December 2006. The composite images were also obtained by using the MVC (Maximum Value Compositing) technique. The spatial resolution of the data is 8 km at the Equator. The more than 22 years of data have been covered by 5 different satellites: NOAA-7, 9, 11, 14 and 16. NDVI images are obtained from AVHRR channel 1 and 2 images, which correspond respectively to red (0.58 to 0.68 μm) and near infra-red wavelengths (0.73 to 1.1 μm).

This dataset, in spite of its limitation to NDVI data (no other channel information is available), presents several improvements regarding its predecessor, the PAL (Pathfinder AVHRR Land) dataset (Smith et al., 1997). The first improvement consists of a better data process, including navigation, sensor calibration and atmospheric correction for stratospheric aerosols. Another main improvement regards the correction of NOAA's orbital drift (Price, 1991), through the empirical mode decomposition (EMD) technique (Pinzon et al., 2005).

In this work, global 15-day composites at 0.07 degree from July 1981 to September 2001 are used.

3 METHODOLOGY

NDVI data have been downloaded from PAL and GIMMS websites. Then, since cloud contamination may still affect the data in spite of the MVC composition technique, a data reconstruction technique (IDR – Julien & Sobrino, 2010) has been used for the GIMMS dataset, in order to stress out the importance of residual atmospheric contamination on trend retrieval. Then, monthly anomalies are retrieved from PAL, raw GIMMS and IDR corrected GIMMS time series, and finally changes are retrieved through the use of robust statistical techniques.

3.1 Data reconstruction

The IDR (Iterative Data Reconstruction) technique has been applied to the GIMMS database. This technique aims at identifying atmospherically contaminated pixels through the analysis of their time series. Since atmospheric effects (aerosols, clouds) tend to decrease NDVI values, each pixel time series shows slight to sharp decreases for cloudy dates. For these dates, NDVI data are linearly interpolated from adjacent dates. This correction is then iterated in order to account for enduring cloud contamination, until a convergence criterion (NDVI change lower than 0.02) is met. For more details, see Julien & Sobrino (2010).

3.2 Anomaly estimation

Anomalies are estimated from the whole dataset for each of the 3 cases: PAL raw data, GIMMS raw data, and IDR corrected GIMMS data. To this end, monthly NDVI averaged are estimated for all 3 datasets, which are then averaged over all years in order to obtain an average year of NDVI data. This average year is then rested from the time series of monthly averages.

In addition to the anomalies, yearly statistics are retrieved from the time series of monthly averages, which characterize the NDVI yearly curve. These statistics are NDVI yearly average, NDVI yearly standard deviation, and NDVI minimum and maximum yearly value.

3.3 Change detection

Monthly anomalies and yearly statistics are tested for trends using the Mann-Kendall statistical framework (Hirsch and Slack, 1984; Libiseller and Grimwall, 2002). For all 3 datasets, for all monthly anomalies and yearly statistics, each pixel time series is tested for trend presence using the Mann-Kendall trend test (Hirsch and Slack, 1984) corrected for ties, and the trend values for the pixels passing the Mann-Kendall trend test at a significance level of 0.90 are retrieved using Sen's slope (Sen, 1968).

4 RESULTS

Trends for monthly anomalies are presented in figure 1. The first observation is that the trends present in PAL dataset have higher absolute values than for both GIMMS datasets, with a lesser number of pixels exhibiting a significant trend (at 90% confidence level). As regards the difference between raw GIMMS and IDR corrected GIMMS datasets, anomaly trend general patterns are similar, although absolute trend values tend to be lower for the latter. This is easily explained by the fact that atmospheric contamination tends to decrease NDVI values, thus increasing the signal amplitude and as a consequence, increasing the retrieved trends. Monthly anomalies show a general increasing trend at global scale, except for a few subtropical locations for the last months of the year.

Figure 2 shows the trends retrieved for yearly statistics from all 3 datasets. As was the case with monthly anomalies, PAL dataset exhibits a lesser number of pixels with significant trend. On the opposite, IDR corrected GIMMS dataset shows the highest number of pixels with significant trend (at 90% confidence level), in that case with rather different values than raw GIMMS dataset, which was expected since atmospheric contamination influences all the retrieved statistics.

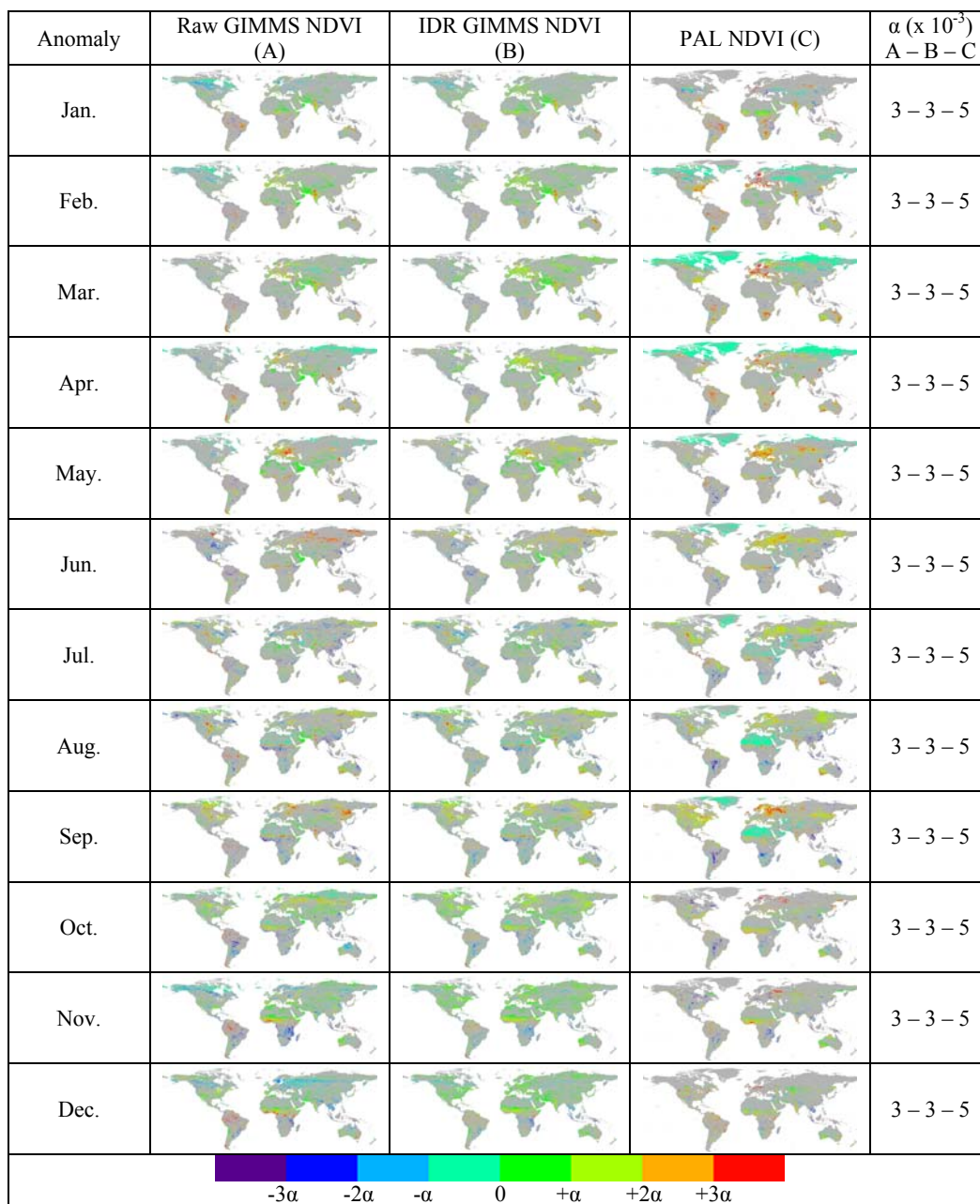


Figure 1: Comparison of anomaly trends for different global datasets of AVHRR derived NDVI. PAL dataset tends to overestimate trends, as is the case of GIMMS raw NDVI, although in a lesser way (non-significant trends – at 90% confidence level – in grey).

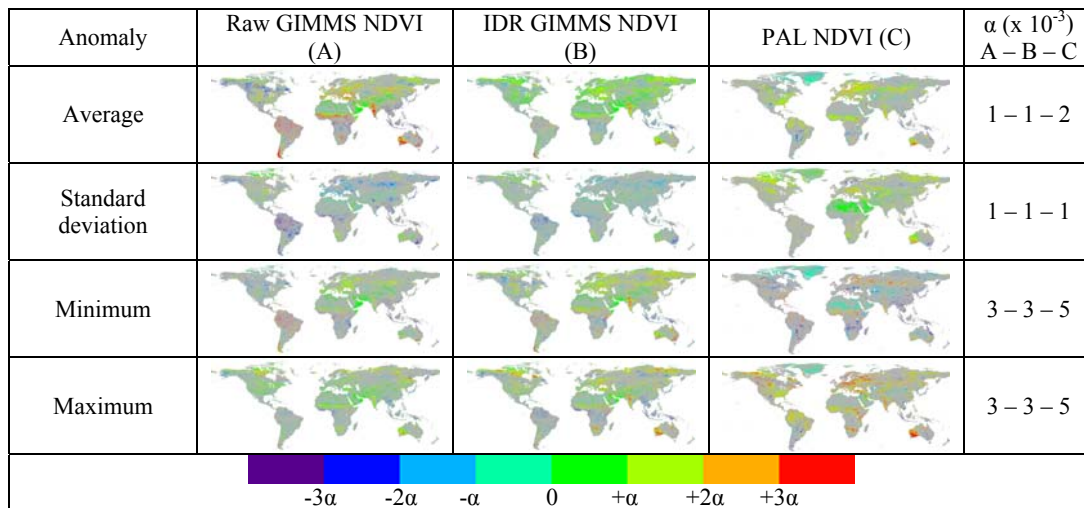


Figure 2: Comparison of yearly statistics trends for different global datasets of AVHRR derived NDVI. PAL dataset tends to overestimate trends, as is the case of GIMMS raw NDVI, although in a lesser way (non-significant trends – at 90% confidence level – in grey).

Yearly average tend to increase at global scale for all three datasets, especially for IDR corrected GIMMS dataset. Yearly standard deviation decreases for polewards areas as well as for the tropics, except for the PAL dataset which exhibit only positive trends. Yearly minimum and maximum values show an overall positive trend for all datasets over most of the globe, except for PAL dataset once again, especially as regards yearly minimum.

Such changes would imply an overall increase in vegetation at global scale, except in the tropics where decreasing trends are prevailing, except for raw GIMMS dataset, which present a noisy pattern of strong positive and negative trends, most probably due to residual cloud contamination.

5 DISCUSSION

The results presented above show that the three studied datasets exhibit different trend patterns, which mean that both data processing and residual atmospheric contamination influence the trends retrieved for monthly anomalies as well as for yearly statistics, which is confirmed by previous studies (De Beurs *et al.*, 2005; Moreno-Ruiz *et al.*, 2009; Stow *et al.*, 2007) at regional scales. However, these studies do not assess which dataset is more reliable as regards trend retrieval.

To this end, trends retrieved for yearly statistics have been compared with independent data, such as FAO (2005) and UNEP (2005). The areas identified by FAO (2005) as gaining forest cover should present an increasing trend in average NDVI for all datasets,

while decrease in forest cover should appear as a negative trend in this same parameter. This especially is the case for IDR corrected GIMMS dataset, for which the tropics show a general decrease in vegetation (negative yearly NDVI average trend), while Eastern Asia and Northern Mediterranean coast show an increase in vegetation (positive trend). Additionally, UNEP (2005) has identified and documented 125 change hotspots around the globe. These hotspots have been used in Sobrino and Julien (2010) to validate trends retrieved in yearly NDVI statistics retrieved from a double logistic fit of raw GIMMS data. However, this validation is only qualitative, although it shows that expected changes in NDVI yearly statistics are evidenced for the pixels corresponding to UNEP (2005) hotspots (Sobrino and Julien, 2010). Raw and IDR corrected GIMMS statistics also show these expected changes for most of the UNEP (2005) change hotspots (not showed).

On the whole, IDR corrected GIMMS is the closest dataset to the validation data, and therefore should be used for multitemporal vegetation monitoring, and the trends described in this work for this dataset (and this dataset only) should be considered as reliable.

Other datasets have been compiled from NOAA AVHRR NDVI, for which such validation as the one carried out in this work is still needed, and will be carried out by the authors in a near future.

6 CONCLUSIONS

NDVI anomalies have been retrieved from 3 different datasets (PAL, GIMMS, and IDR corrected GIMMS),

along with yearly NDVI statistics. From these different parameters, a robust trend analysis has been carried out, allowing for the characterization of areas undergoing vegetation change. These changes differ from one dataset to the other, which indicates that data processing and residual atmospheric effects have to be taken into account when monitoring vegetation from satellite. This confirms previous results at regional scale. In order to identify the best dataset for this application, the trends retrieved from all 3 datasets have been compared to independent data retrieved from intergovernmental agencies. This comparison has shown that IDR corrected GIMMS is the dataset which is closest to the validation data, and therefore the trends retrieved from this dataset should be preferred for vegetation monitoring.

ACKNOWLEDGEMENTS

The authors wish to thank the TERMASAT project (Ministerio de Educación y Ciencia, project ESP2005-07724-C05-04), the European Union (CEOPAEGIS, project FP7-ENV-2007-1 Proposal No. 212921; WATCH, project 036946) and the Ministerio de Ciencia y Tecnología (EODIX, project AYA2008-0595-C04-01) for their financial support. Source for the PAL dataset was the Goddard Earth Sciences Distributed Active Archive Center in 2004 (data unavailable in 2008), and the Global Land Cover Facility for the GIMMS dataset.

REFERENCES

- Bogaert, J., Zhou, L., Tucker, C. J., Myneni, R. B. & Ceulemans, R., 2002, Evidence for a persistent and extensive greening trend in Eurasia inferred from satellite vegetation index data. *Journal of Geophysical Research*, Vol. 107 (D11), 10.1029/2001JD001075.
- De Beurs, K. M., Henebry, G. M. & Gitelson, A. A., 2005, A comparative analysis to understand the influence of dataset choice for land surface phenology research in the northern latitudes, *Pecora-16 Conference Proceedings*, paper 23:1-11.
- FAO, 2005, *Global Forest Resources Assessment 2005: Progress Towards Sustainable Forest Management* (Rome: Food and Agriculture Organization of the United Nations).
- Hirsch, R. M. & Slack, J. R., 1984, A nonparametric trend test for seasonal data with serial dependence, *Water Resources Research*, 20, 727-732.
- Holben, B. N., 1986, Characteristics of maximum values composite images from temporal AVHRR data. *International Journal of Remote Sensing*, 1986, Vol. 7, 1417-1434.
- Julien, Y. & Sobrino, J. A., 2009, Global land surface phenology trends from GIMMS database, *International Journal of Remote Sensing*, Vol. 30, No. 13, 3495-3513.
- Julien, Y. & Sobrino, J. A., 2010, Comparison of cloud-reconstruction methods for time series of composite NDVI data, *Remote Sensing of Environment*, 114 (2010) 618-625.
- Libiseller, C. & Grimvall, A., 2002, Performance of partial Mann-Kendall test for trend detection in the presence of covariates, *Environmetrics*, 13: 71-84.
- Moreno-Ruiz, J. A., Riaño, D., García-Lázaro, J. R. & Ustin, S. L., 2009, Intercomparison of AVHRR PAL and LTDR Version 2 long-term data sets for Africa from 1982 to 2000 and its impact on mapping burned area, *IEEE Geoscience and Remote Sensing Letters*, Vol. 6, No. 4, October 2009, 738-742.
- Myneni, R. B., Keeling, C. D., Tucker, C. J., Asrar, G. & Nemani, R. R., 1997, Increased plant growth in the northern high latitudes from 1981 to 1991. *Nature*, Vol. 386, 17 april 1997.
- Pinzon, J., 2002, Using HHT to successfully uncouple seasonal and interannual components in remotely sensed data, *SCI 2002 Conference Proceedings*, July 14-18. Orlando, Florida.
- Pinzón, J. E., Brown, M. E. & Tucker, C. J., 2005, EMD correction of orbital drift artifacts in satellite data stream. In: *The Hilbert-Huang Transform and its Applications* (eds Huang NE, Shen SSP), World Scientific, Singapore.
- Price, J. C., 1991, Timing of NOAA afternoon passes, *International Journal of Remote Sensing*, vol. 12, no. 1, pp. 193-198, Jan. 1991.
- Sen, P. K., 1968, Estimates of the regression coefficient based on Kendall's tau, *Journal of the American Statistical Association*, 63:1379-1389.
- Smith, P. M., Kalluri, S. N. V., Prince, S. D. & Defries, R., 1997, The NOAA/NASA pathfinder AVHRR 8-km land data set, *Photogrammetric Engineering and Remote Sensing*, 63 (1): 12-31 jan 1997.
- Sobrino, J. A. & Julien, Y., 2010, Global trends in NDVI derived parameters obtained from GIMMS data, *International Journal of Remote Sensing*, in press.

- Stow, D., Petersen, A., Hope, A., Engstrom, R. & Coulter, L., 2007, Greenness trends of Arctic tundra vegetation in the 1990s: comparison of two NDVI data sets from NOAA AVHRR systems, *International Journal of Remote Sensing*, Vol. 28, No. 21, 10 November 2007, 4807-4822.
- Tucker, C. J., 1979, Red and Photographic Infrared Linear Combinations for Monitoring Vegetation, *Remote Sensing of Environment*, 8 (2), 127-150.
- Tucker, C. J., Slayback, D. A., Pinzon, J. E., Los, S. O., Myneni, R. B. & Taylor, M.G., 2001, Higher northern latitude NDVI and growing season trends from 1982 to 1999, *International Journal of Biometeorology*, 45:184-190.
- Tucker, C. J., Pinzon, J. E., Brown, M. E., Slayback, D. A., Pak, E. W., Mahoney, R., Vermote, E. F. and El Saleous, N., 2005, An extended AVHRR 8-km NDVI dataset compatible with MODIS and SPOT vegetation NDVI data, *International Journal of Remote Sensing*, Vol. 26, No. 20, 4485-4498.
- UNEP, 2005, *One Planet Many People: Atlas of Our Changing Environment*, Division of Early Warning and Assessment (DEWA), United Nations Environment Programme, P.O. Box 30552, Nairobi, Kenya, <http://na.unep.net/OnePlanetManyPeople/index.php>.
- Zhou, L., Tucker, C. J., Kaufmann, R. K., Slayback, D., Shabanov, N. V. & Myneni, R. B., 2001, Variations in northern vegetation activity inferred from satellite data of vegetation index during 1981 to 1999, *Journal of Geophysical Research*, 106(D17):20069-20083.
- Zhou, L., Kaufmann, R. K., Tian, Y., Myneni, R. B. & Tucker, C. J., 2003, Relation between interannual variations in satellite measures of vegetation greenness and climate between 1982 and 1999, *Journal of Geophysical Research* 108 (D1), doi: 10.1029/2002JD002510.

Pastoruri glacier cover mapping from Landsat and ASTER imagery

José J. Pasapera-Gonzales¹, Carmen Villon-Reinoso¹, Rodolfo D. Moreno¹, David Pareja-Quispe¹, Juan C. Jiménez-Muñoz², Cristian Mattar², José A. Sobrino²

¹Comisión Nacional de Investigación y Desarrollo Aeroespacial (CONIDA), Agencia Espacial del Perú, Av. Luís Felipe Villarán 1069 – San Isidro, Lima 27 (Perú)

²Global Change Unit, Image Processing Laboratory, University of Valencia (Spain)

Email: josephjesus79@gmail.com

ABSTRACT- *The Pastoruri glacier is a cirque glacier located in the southern part of the Cordillera Blanca, in Northern Peru in the Andes (Department of Ancash, Huascarán National Park). It is one of the few glaciers left in the tropical areas of South America, with an altitude of around 5,250 meters above sea level. The glacier was retreating slowly in the past, but it is currently retreating quickly due to global warming. Total loss of the glacier can lead not only to environmental damages but also to loss of water supply to surrounding agricultural areas, as well to economic losses due to a decrease in tourism. This work analyses the Pastoruri glacier cover change using Landsat ETM imagery acquired between May and September, since this period shows low rainfall. Landsat images were orthorectified using Digital Elevation Model (DEM) generated by the ASTER project. The glacierized area was estimated by using B3/B5 ratio and the Normalized Difference Snow Index (NDSI). Other parameters such as Land Surface Temperature (LST) retrieved from Landsat band 6 or climatic variables such as air temperature and total atmospheric water vapor extracted from reanalysis data were also analysed. The anomalous “El Niño” episodes according to the National Oceanic and Atmospheric Administration (NOAA) were also considered. Results presented in this work refer to the Pachacoto sub-basin, providing areas of 18.5 km² in 1999, 13.95 km² in 2001, 13.02 km² in 2002 and 12.92 km² in 2008. Therefore, the glacier area included in the Pachacoto sub-basin retreated 30% from 1999 to 2008, with a significant decrease of around 7% between 2000 and 2001.*

1 INTRODUCCIÓN

En los últimos años tanto la comunidad científica como la opinión pública han mostrado un interés creciente por conocer la influencia presentada por los cambios en el clima y su impacto sobre los glaciares del mundo, lo que trae consigo consecuencias de abastecimiento del recurso hídrico y del incremento del nivel medio de los océanos. La serie de recientes informes del Panel Inter-gubernamental de Cambio Climático (IPCC) ha puesto claramente de manifiesto este interés y la importancia de emprender políticas orientadas a disminuir las causas antropogénicas del calentamiento recientemente observado, así como a facilitar la adaptación a ciertos cambios ya considerados como irreversibles a corto y medio plazo (García, 2008; Moreno and Pasapera-Gonzales, 2010). Por lo tanto, la gran parte de las poblaciones del mundo que viven en regiones influenciadas por la presencia de estos glaciares han sido alertadas por los grandes cambios que se producirían y que traerían consigo la variación de disponibilidad de agua dulce, motivo creciente de preocupación en muchas regiones de bajas latitudes (Kaser et al., 2001). También, a partir del derretimiento de nevados, se observaron

riesgo de deslizamientos de grandes masas de hielo (Hinkler et al., 2002; Kaab et al., 2003). Estos problemas permiten proyectar planes de gestión social y políticos que se ven limitados por la ubicación de las regiones donde se ubican los glaciares, que representa difícil accesibilidad y temperaturas extremas. Un ejemplo claro es el deslizamiento de Yungay (Provincia del departamento de Ancash-Perú), el cual trajo consigo un aluvión de 50 a 100 millones de m³ de masa morrénica lo que ocasionó la muerte de 22,000 habitantes (Figura 1). Estos aspectos demuestran la importancia de la teledetección para el seguimiento de los glaciares.

En Perú se localizan un 70% de los glaciares tropicales del mundo, los cuales se encuentran regulados por las variaciones de precipitación de temporada, regulada por las variaciones de la escorrentía (Kaser et al., 2001). Según análisis presentados por el IPCC la tendencia global del clima en los glaciares tropicales presenta un fuerte retroceso durante los años 1980 y 1990, provocando que en algunas partes de las altas montañas tropicales puedan desaparecer (Kaser et al., 2001; IPCC, 2007). Esto es debido a la interacción clima-glaciár, que viene representada por el balance de masa de los glaciares, donde la atmósfera tropical, en general, se caracteriza

por las altas condiciones térmicas homogéneas con muy pequeñas variaciones de temperatura anual. Tenemos como ejemplo la estación Querococha en la cordillera blanca a 3980 m.s.n.m, donde se muestra particularmente una variación pequeña de solo 0.8 °C (Figura 2).

Cuando hablamos de la humedad la variación está gobernada por la Oscilación de la zona de convergencia intertropical (ITCZ) que se aproxima a la cordillera blanca desde el Este, entre los meses de octubre y abril, acercando alrededor del 70 a 80% de la precipitación anual. De mayo a setiembre, a su vez, el ITCZ se da muy al Norte y se presenta un sistema de vientos que hace que las condiciones climáticas sean secas. Por lo tanto, el régimen climático tropical es alterado entre un tropical y uno subtropical. Esto es debido a la cadena montañosa Cordillera de los Andes, con una longitud de 180 km de largo y alturas de hasta unos 7000 m que divide la selva peruana de la costa, provocando en ésta una zona extremadamente seca sin precipitaciones. Por lo tanto, en función de las mejores condiciones meteorológicas con el fin de disponer de la mayor cantidad de datos con imágenes de satélite, se han seleccionado los meses de mayo a setiembre (Kaser et al., 2001).

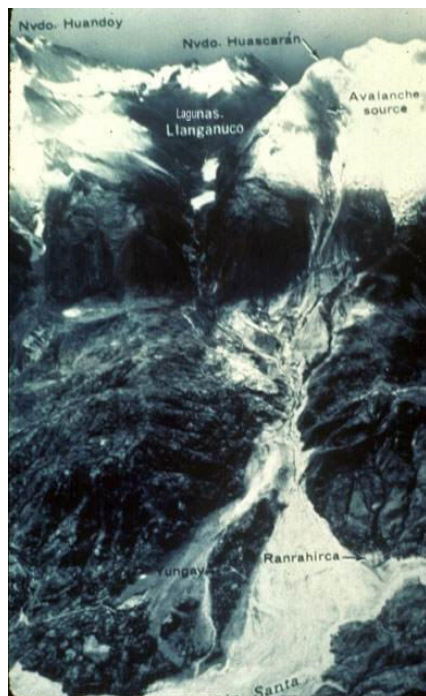


Figura 1. Deslizamiento en Yungay.

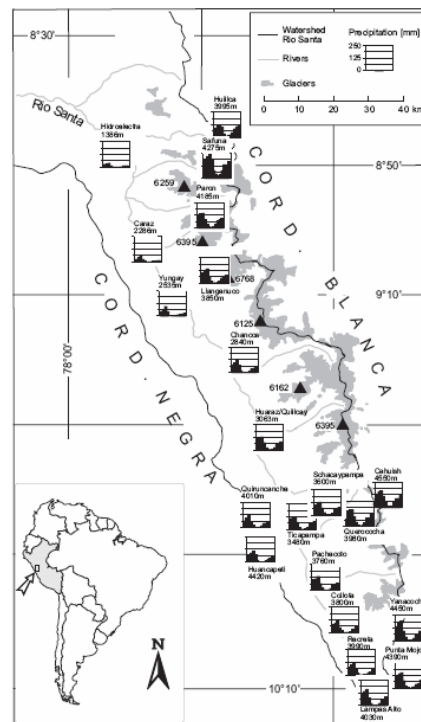


Figura 2. La cordillera blanca (extraída de Kaser et al., 2001).

En este trabajo se ha elegido el área glaciaria perteneciente al Nevado de Pastoruri como área de estudio, ubicado a 5250 m.s.n.m en la cordillera blanca (Figura 3). También es un nevado emblemático para la zona de Recuay-Huaraz-Perú, por representar una fuente de ingresos para el turismo y para las actividades agrícolas y mineras. El periodo seco, mayo a setiembre, también se ve influenciado por precipitaciones fuera de temporada, que repercuten en la variabilidad de la cobertura glaciaria, ya que la imagen puede estar estimando nieve temporal en vez de hielo glaciario. También existen investigaciones de investigadores peruanos que utilizan las variables meteorológicas y que las relacionaron con la presencia del índice de oscilación sur "ENSO. La metodología propuesta usa 53 imágenes del satélite Landsat TM, corregidas y orthorectificadas a partir de un modelo de elevación digital GDEM, el preprocesamiento considero la transformación de ND a radiancia, reflectancia, las cuales incluye la corrección atmosférica por Chavez, y la topográficamente por Minnaert. Para estimar el área glaciaria, se utilizó el Índice de nieve normalizado (NDSI) y el ratio, que utilizan las bandas 2, 3,5 del sensor TM, satélite Landsat.

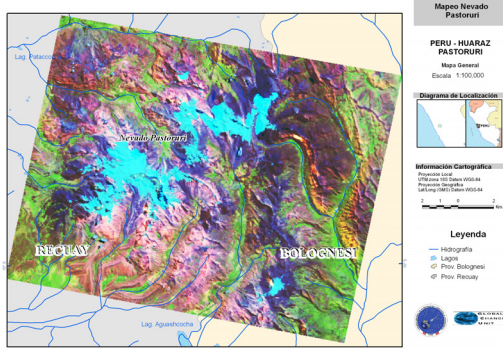


Figura 3. El nevado de Pastoruri.

2 METODOLOGÍA

2.1 Área de estudio

El área de estudio utiliza 53 escenas del satélite Landsat de path y rows 008/067, de las cuales se sustrajo el área geográfica perteneciente al Nevado Pastoruri (Figura 3), cuyas coordenadas (lat, lon) son: esquina superior izquierda: (-9.872775,-77.3140694) esquina superior derecha: (-9.87410278,-77.1117361) esquina inferior izquierda: (-10.0392389,-77.3152417) esquina inferior derecha: (-10.0405917,-77.1128083)

2.2 Orthorectificación y co-registro

Este proceso se inició seleccionando una imagen maestra (*master*) dentro del grupo de las 53 imágenes Landsat disponibles, luego se procedió a orthorectificar con puntos de control, y un modelo de elevación digital (DEM) del proyecto G-DEM ASTER de la zona de estudio. Para el co-registro se ha utilizado el Algoritmo de Sub Sección de Matriz de Nodos (SSMN) desarrollado en CONIDA (Xie et al., 2003). Esta metodología ha permitido tener una precisión RMS de 1 píxel.

2.3 Conversión ND a radiancia

La radiancia espectral se obtiene mediante la conversión de los Números Digitales (ND) a partir de las constantes de calibración “gain” y “bias” del satélite Landsat, tal y como se detalla en Chander et al. (2009).

2.4 Reflectividad aparente y de superficie

La reflectancia aparente (ρ^{TOA}) se calcula a partir de la ecuación:

$$\rho_{\lambda}^{TOA} = \frac{\pi L_{\lambda} d^2}{ESUN_{\lambda} \cos \theta_z} \quad (1)$$

siendo L la radiancia medida por el sensor, d la distancia Tierra-Sol, $ESUN_{\lambda}$ la irradiancia exoatmosférica y θ_z el ángulo solar cenital.

La corrección atmosférica necesaria para convertir la reflectividad aparente a reflectividad de superficie se ha realizado mediante el método de Chavez (1996):

$$\rho_{\lambda}^{sup} = \frac{\pi (L_{\lambda} - L_{ca \min o, \lambda}) d^2}{ESUN_{\lambda} \cos \theta_z \tau_{\lambda}}$$

$$L_{ca \min o, \lambda} = L_{\min, \lambda} - L_{1\%} \quad (2)$$

$$L_{1\%} = 0.01 \frac{\cos \theta_z \tau_{\lambda}}{\pi d^2} ESUN_{\lambda}$$

siendo τ la transmisividad, con los siguientes valores para las distintas bandas: b01 es 0.7, b02 es 0.78, b03 es 0.85, b04 es 0.91, b05 y b07 tiene el valor de 1.0.

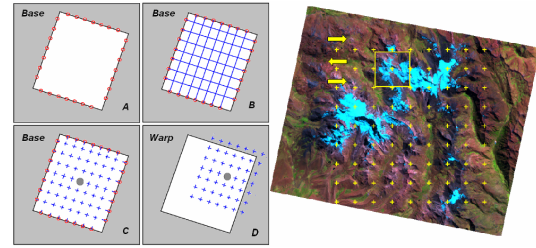


Figura 4. Algoritmo SSMN: (A) Generaron automática de puntos equidistantes en cada borde de la imagen base, (B) Unión de cada punto con el correspondiente lado opuesto, (C) Elaboración de ecuaciones de rectas, cuyas soluciones son las coordenadas de intersección que son usadas como puntos de coordenada base, (D) Punto de referencia entre imagen base y warp, (3) Puntos estimados en la imagen warp.

2.6 Corrección por iluminación

La corrección de una imagen por iluminación tiene como objetivo solucionar en parte el problema de la hipótesis de superficies lambertianas (Figura 5). En este trabajo se ha aplicado el método de Minnaert (Gao and Zhang, 2009), basado en la estimación del parámetro k . Para lograr una mejor estimación del parámetro k se ha recurrido a utilizar un “Subset” móvil donde se obtiene una constante k para cada píxel (Pasapera-Gonzales et al., 2010). La ecuación que permite hallar el ángulo de iluminación es:

$$\cos \gamma_i = \cos \theta_p \cos \theta_z + \sin \theta_p \sin \theta_z \cos (\phi_a - \phi_0) \quad (3)$$

siendo θ_z el ángulo cenital, θ_p el ángulo de la pendiente, γ_i el ángulo de iluminación, ϕ_a el ángulo azimut solar y ϕ_0 el ángulo de orientación. La ecuación de Minnaert viene dada por:

$$L_{\lambda} = L \left(\frac{\cos \theta_p}{\cos \gamma^k \cos^k \theta_p} \right) \quad (4)$$

donde el parámetro k viene dado por:

$$\begin{aligned} \ln(L \cos \theta_p) &= \ln(L_{\lambda}) + \\ &+ k \ln(\cos \gamma \cos \theta_p) + b \end{aligned} \quad (5)$$

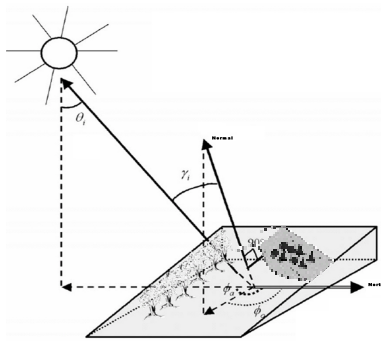


Figura 5. Esquema de la corrección por iluminación.

2.7 Estimación de área glaciar

Para delimitar y estimar la superficie de nieve y hielo en el área de pastoruri se utilizó las bandas visibles e infrarrojas del sensor Landsat, para obtener el índice de nieve normalizado y un ratio que permiten identificar áreas del nevado pastoruri de una forma correcta (Villon et al., 2010). A continuación se muestran las ecuaciones utilizadas:

$$\begin{aligned} NDSI &= \frac{B02 - B05}{B02 + B05} \\ RATIO &= \frac{B03}{B05} \end{aligned} \quad (6)$$

La estimación del área glaciar se realizó a partir del NDSI, con un umbral que oscila de 0.18 a 0.20, y a partir del RATIO con un umbral que oscila entre 1.8 a 2.0. Los índices NDSI y RATIO se calcularon una vez realizada la corrección por iluminación, así como la corrección atmosférica según lo indicado en los apartados anteriores.

3 RESULTADOS

De una lista de 53 imágenes del satélite Landsat, del periodo de mayo a setiembre de 1988 al 2010, se seleccionaron finalmente 32, por ser consideradas de condiciones climáticas secas. La selección ha tenido en cuenta la presencia de eventos del EL NIÑO y la NIÑA. Estos eventos produjeron un pequeño

incremento en el área glaciar en las imágenes del 2008, la cual se vio influenciada por la precipitación temporal reportada en el 2008 como una NIÑA (Figura 6). En la Figura 7 se representa el área mensual del Nevado Pastoruri para los años 1988 al 2010. En el año 1993 se observa un área mayor a 60 km², en comparación con el descenso abrupto en los años 1988 y 1995. Debido a la falta de información en los años 1989, 1990, 1991 y 1992 por lo que respecta a la precipitación obtenida por estaciones meteorológicas, resulta difícil de interpretar este repentino crecimiento del área glaciar.

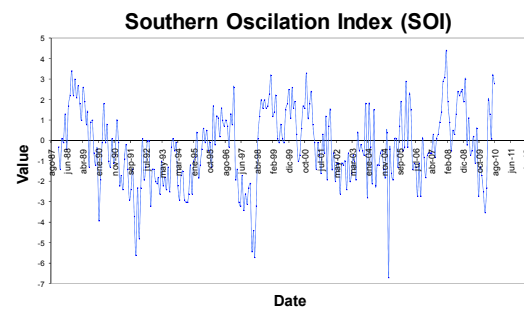


Figura 6. Índice de Oscilación Sur. Los valores positivos representan episodios de NIÑA mientras que los valores negativos episodios de NIÑO.

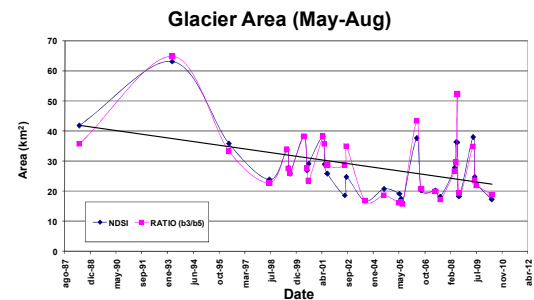


Figura 7. Retroceso glaciar del Nevado Pastoruri desde los años 1987 a 2010.

4 CONCLUSIONES

Los datos de área glaciar obtenidos a partir de los índices NDSI y RATIO muestran una disminución y por lo tanto una tendencia negativa. Esta disminución se encuentra afectada directamente por los eventos EL NIÑO/LA NIÑA.

5 REFERENCIAS

Otero García Jaime., 2008, Generación automática de malla de elementos finitos en modelos evolutivos de dinámica de glaciares., Tesis doctoral., pp 149.

- Kaser Georg., Juen Irmgard, Georges Christian, Gomez Jesús, Tamayo William, 2001, The impact of glaciers on the runoff and the reconstruction of mass balance history from hydrological data in the tropical Cordillera Blanca, Perú, *Glacier & Hydrology Peru-IAHS*, pp 25.
- Hinkler J., Pedersen, S., Rasch, M., Hansen, B., 2002, Automatic snow cover monitoring at high temporal and spatial resolution, using images taken by a standard digital camera., *International Journal Remote Sensing*, **23** N° **21**, pp 4669-4689.
- Kaab, Andy., Wessels Rick., Haeberli, Wilfried., Huggei Christian., Kargel J. S., Jcoha Siri., 2003, Rapid Aster Imaging Facilitates timely assessment of glacier hazards and disasters., *Eos, Transactions, America Geophysical Union*, **84-13**, pp. 117-124.
- Gyanesh Chander , Brian L. Markham b, Dennis L. Helder, 2009, "Summary of current radiometric calibration coefficients for Landsat MSS, TM, ETM+, and EO-1 ALI sensors, *Remote Sensing of Environment* **113**, pp. 893–903.
- Sobrino, J. A., Jiménez-Muñoz., J. C., Paolini L., 2009, "Land surface temperature retrieval from LANDSAT TM 5", *Remote Sensing of Environment* **90**, pp. 434–440.
- Moreno, Rodolfo, Pasapera-Gonzales, J. J., 2010, "Algoritmo de sub sección de matriz de nodos (SSMN) para la búsqueda de patrones (Pearson vs. Fourier), Simposio Latinoamericano de Percepción Remota SELPER., p. 8.
- Pasapera-Gonzales, J. J., Moreno, Rodolfo., Villon Carmen., 2010, Análisis de métodos de corrección topográfica usando imágenes de satélite", I Simposio Peruano de Teledetección.
- Villon Carmen, Vargas Christian, Pasapera-Gonzales J. J., Análisis multitemporal del retroceso glaciar con imágenes Landsat y Aster., el XIII Congreso Latinoamericano de Geología y XIV Congreso Peruano de Geología.
- Xie, Hongjie., Hicks, Nigel., Keller G. R., Huang, Haitao., Kreinovich, Vladik, 2003, *Computer & Geosciences*, pp. 1045-1055.
- IPCC. Summary for policymakers. In S. Solomon, D. Qin, M. Manning, Z. Chen, M. Marquis, K.B. Averyt, M. Tignor, and H. L. Miller, editors, *Climate Change 2007: The Physical Science Basis*. Cambridge University Press, Cambridge, United Kingdom and New York, NY, USA, 2007a.
- Gao, Yongnian, Zhang, Wanchang, 2009, A Simple empirical topographic correction method for ETM+imagery, *International Journal of Remote Sensing*, **30** N° **9**, pp. 2259-2275.

Ecosystem Functional Characterization in the Iberian Peninsula

A. Pérez-Hoyos, F.J. García-Haro, B. Martínez, M.A. Gilabert

Remote Sensing Unit, Facultat de Física, Universitat de València, Dr. Moliner, 50. 46100-Burjassot, Spain

e-mail: Ana.Perez-Hoyos@uv.es

ABSTRACT - Monitoring ecosystems is regarded as an essential element of many conservation plans or resource assessments. Analysis and management of landscapes requires the development of spatial frameworks that stratify landscapes into relatively homogeneous regions. In this study, a classification based on the Ecosystem Functional Types (EFTs) -i.e. units that group similarly functioning ecosystems- is proposed for the Iberian Peninsula. EFTs are mainly based on functional attributes, such as productivity or fluxes of matter and energy, which have a faster response to changing environmental conditions. In order to achieve a more accurate characterisation of EFTs, different satellite-based parameters directly related with the status and condition of vegetation were derived from MODIS multitemporal data over a 10 year (2000-2009) period. They include annual average biophysical variables, such as fractional vegetation cover (FVC), retrieved phenological parameters, spectral albedo and climatic parameters. An algorithm based on Self-organizing maps (SOM) combined with a modified k-means was used to derive the functional diversity of the main and most representative ecosystems in the Iberian Peninsula. The association between the functional ecosystem and structural maps (i.e. CORINE land cover) reveals that land cover only have partial importance in explaining the functioning of particular ecosystems

1 INTRODUCTION

Functional diversity, the extent of the functional differences among the species in community, is an important determinant of ecosystem processes (Petchey *et al.*, 2002). In this context, the importance of characterizing ecosystem heterogeneity attending the composition, structure and functioning is well recognized in both management and conservation.

Traditionally, the description and characterization of ecosystem relies only on structural attributes of the vegetation such as physiognomy, landform, dominant species, plant functional types proportions or total cover. Nevertheless, the structural attributes of ecosystems may not be sensitive enough to assess the impact of current environmental changes since vegetation structure might delay the perception of disturbances and stress.

Ecosystem functioning, the exchange of matter and energy of ecosystem between the biota and the environment, clearly complements traditional studies (Alcaraz *et al.*, 2009), since functional attributes have a faster response to disturbances than structural ones. These attributes allow the quantitative and qualitative characterization of ecosystem services. Additionally, they can easily be monitored by using remote sensing at different spatial scales, over large extents, which is a particularly useful to detect ecosystem response to environmental changes and analyze the vegetation dynamics.

Based on the functional classification of ecosystems, different approaches and nomenclatures have been applied. Azzali *et al.* (1999) described vegetation units in terms of homogeneous foliar phenology (maps of isogrowth). Previous approaches based on a similar concept were introduced to delineate biozones (Soriano *et al.* 1992) or ecoregions (Baily, 1983) representing association of similarly functioning groups geographically linked.

In this work, Ecosystem Functional Types (EFTs) are defined as a group of ecosystems sharing functional characteristics that include the amount and timing of matter and energy exchanged between the biotic community and the environment (Shugart, 1997). Synoptic patterns of such variables have been mainly retrieved from remote sensing observations. The variables used to characterize the EFTs include temporal features of fractional vegetation cover (FVC) annual cycle, along with derived phenological parameters (e.g. amplitude, start and duration of the annual and semi-annual cycles), spectral albedo at periods of maximum (and minimum) canopy closure and climatic parameters.

The annual amplitude indicated the variability of productivity over the year, while the phase summarized the timing of green-up. Other measures of ecosystem functioning are used, such as Land Surface Temperature (LST) as an indicator of energy partition into sensible and latent heat flux and albedo as a key component of the radiation balance (Fernandez *et al.*,

2010). The Thornthwaite moisture index was used, which reflects the portion of total precipitation used to nourish vegetation over a certain area. Climatic data such as precipitation and temperature control differences in the Earth's vegetation cover, affecting growth rate, plant reproduction, and frost damage.

Different strategies have been used previously to delineate EFTs. Non-supervised classification methods are generally preferable to automatically categorize the EFTs, with absolutely no requirements for any a priori class related structural data information. They provide principled methods to find the best choice for the natural (inherent) number of classes.

There are several popular algorithms that have been applied in the literature with this aim, such as ISODATA (Paruelo *et al.* 2001) and CLARA (Fernandez *et al.* 2010). Different classification algorithms generate different results even at the same data sets.

In this paper, Self-organizing maps (SOM) were applied with the ambition to explore the inherent distribution, dependence structure, and generalization ability in the automatic classification. We take advantage of SOM together with a modified k-means algorithm. The SOM allows a visual analysis of data by establishing relationships among variables that would not be possible to find out otherwise (Carrasco *et al.*, 2009). After training the SOM a set of prototypes are obtained. The clustering process is performed directly over this reduced dataset reducing the complexity of the analysis.

2. DATA SETS

2.1 MODIS/TERRA reflectances

Time series of MODIS 1 km 16-day collection 5 reflectance (MOD13A2) were used over the period 2000-2009 at three spectral wavebands: red, near infrared (NIR) and middle infrared (MIR).

2.2 FVC

FVC have been derived using MODIS reflectance (MOD13A2) time series (2000-2009) at 1 km resolution. Spatial and temporally consistent estimates of fractional vegetation cover (FVC) were obtained using a probabilistic spectral mixture analysis method (García-Haro *et al.* 2005). Adapted variants of the algorithm which is currently used operationally in the context of the EUMETSAT/LSA SAF mission, have been used.

2.3. Precipitation data

The climatic data used in the study were obtained from the AEMET (Agencia Estatal de Meteorología) and

correspond to between 2500 and 4800 (depending on the period) recording stations distributed over Spain. Monthly precipitation maps in Spain were derived during the 1950-2009 period at 2-km spatial resolution. Geostatistical approaches were chosen to derive the monthly maps, annual and monthly averages for the analyzed period. These maps reveal a strong north-south gradient. The Thornthwaite moisture index was computed using the difference between monthly precipitation and evapotranspiration (P-PET).

2.4 Geographical coordinates

Two new variables, the latitude and longitude geographical coordinates, were added to the features space for the purposes of improving the spatial consistency of the clustering.

3. METHODOLOGY

Figure 1 shows a simplified version of the proposed method, the main steps of which are presented here:

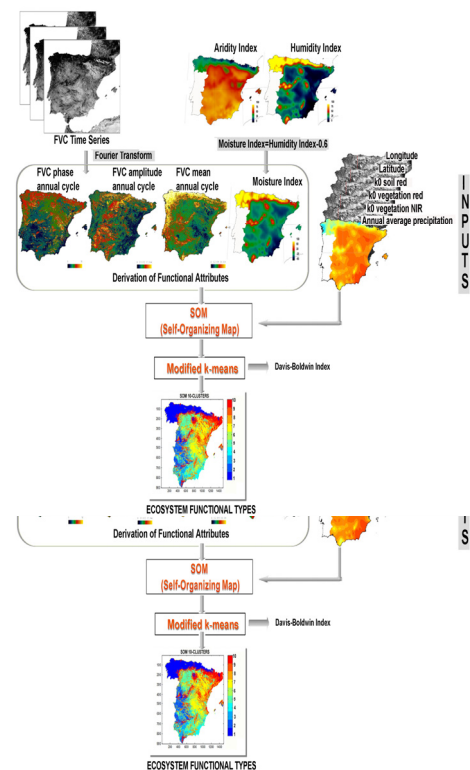


Figure 1. Methodology proposed to derive the EFTs in Spain.

First, several functional attributes were derived based on FVC imagery series and climatic data. Fourier analysis have been applied to derived several functional attributes of the ecosystem from the seasonal curves of FVC (mean, phase, amplitude). These attributes represent fundamental aspects of the carbon gain dynamics of the ecosystem (Paruelo *et al.*, 2001). The annual amplitude represents the variability in productivity over the year. The annual phase indicates the date of maximum greenness and the mean of the FVC is a good estimator of the primary production. Other functional variables were derived, such as the Moisture index that indicates how humid or how arid a climate is.

Previously to apply the SOM algorithm, variables were standardized in order to ensure that all variables had the same a priori relevance for the model. The second step consists in the application of the SOM algorithm introduced in Kohonen (1984). SOM consists of a set of neurons usually arranged in a one or two-dimensional grid. Every neuron has a fixed position in the grid, and is represented by an n -dimensional weight vector $w=[w_1, w_2, \dots, w_n]$, where n is the dimensionality of the input space. A user pattern x is randomly chosen from the data set on each training step. Then, the neuron whose weight vector is the most similar to the user pattern is searched, being this neuron the so-called Best Matching Unit (BMU). The weight vectors of the BMU and its neighborhood are updated as follows:

$$w^{t+1} = w^t + \alpha(t)h(t)(x - w^t) \quad (2)$$

where t stands for the iteration number, $\alpha(t)$ is the learning rate, and $h(t)$ the neighbourhood kernel, whose center is located at the BMU. The neighbourhood kernel determines which neurons around the BMU are updated, and how this update affects each neuron.

After the training with the SOM, a modified k-means clustering was applied on the prototypes of the SOM to derive the EFTs. One critical issue was deciding the optimal number of clusters. With the aim of avoid subjectivity in delimiting the EFTs we use the Davis-Bouldin Index for this purpose (Davies and Bouldin, 1979).

4. RESULTS

4.1 Phenological parameters

Using the annual averaged FVC curve as input and the FFT, three relevant functional attributes (mean, phase, and amplitude) were computed (Figure 2). A clear and contrasting pattern across Spain is observed. The phase of the annual cycle is related to the phenological cycle of each vegetation type. Two peaks of vegetation

are recorded in the figure, one in April located in the central plateau and mainly covered by non-irrigated crops. The other peak correspond to July (red colours in the figure), mainly located in the north of Spain and occupied by forest classes.

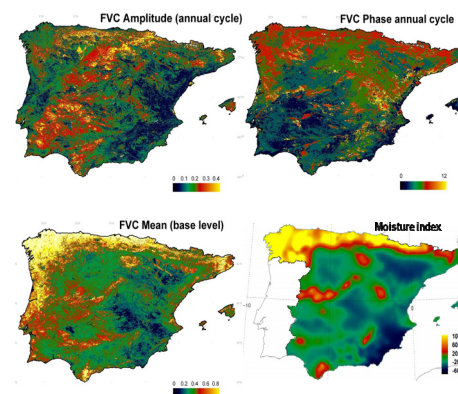


Figure 2. Annual magnitude of the FVC obtained from Fourier analysis of the time profiles for the 2000-2009 period and moisture index.

The mean FVC decreases gradually from the north-western to the southeast, with the exception of the broadleaved forest located in the south of Spain. Forested areas have the largest FVC values (near 0.8) indicating the high volume of green biomass. Extreme values about 0.2 correspond to areas of sparse vegetation such as the desert of Tabernas in the southeast and rugged areas. The FVC amplitude shows an opposite pattern to mean FVC. Northwest forested areas with abundant vegetation through the year have a low intra-annual variation. In contrast, areas with low FVC mean as the rice fields located in the Albufera and the annual crops of the center plateau have the higher amplitude values.

According to the moisture index, the north of Spain corresponds to a perhumid climatic type reaching values higher than 100. Lowest values are located in the southeast of the peninsula, corresponding to an arid climate type.

4.2 Training of a SOM

Component planes (see Figure 3) allowed us to visualize the relationship between the variables considered in the SOM analysis. It is easy to see that the amplitude and the near infrared reflectance are very closely related to each other, a strong correlation exists between both planes. Also some correlation exists between the FVC in September and the moisture index.

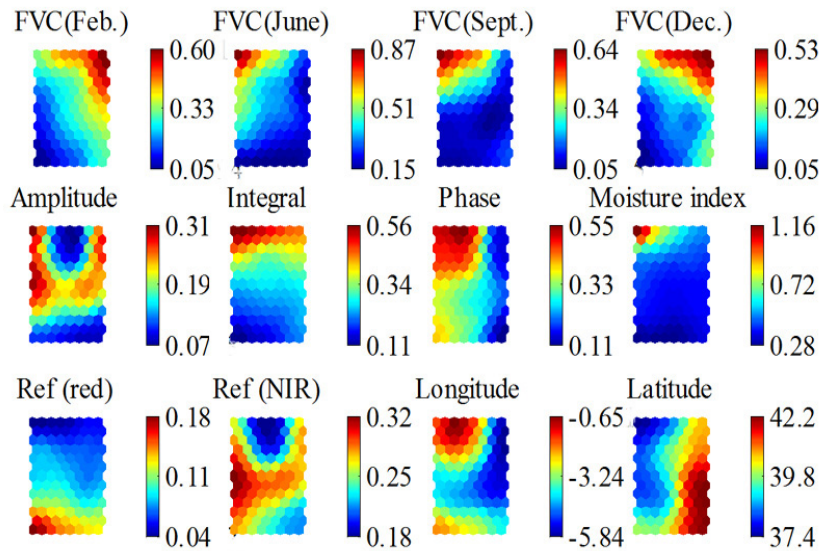


Figure 3. Visualization of the SOM trained from time series of vegetation and climatic data of the study area. The four figures are linked by position: in each figure, the hexagon in a certain position corresponds to the same map unit.

A challenging task consists in estimating the optimal number, k , of substructures representing the EFTs, which is not known a priori. In this study, we assume that k should minimize the Davies-Bouldin index (Davies and Bouldin, 1979), which is a function of the ratio of the sum of within-cluster difference to between-cluster separation. The minimum was reached at $k=10$ clusters (see figure 4b). The obtained clustering of prototypes is depicted in Figure 4a.

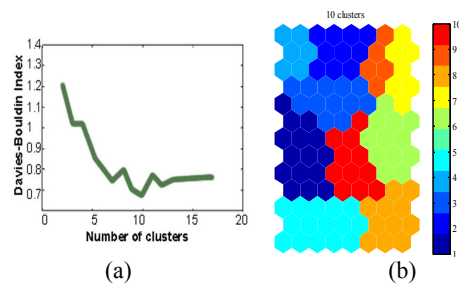


Figure 4. a) Clusters obtained with the modified k-means b) Validity index values for Davies-Bouldin as a function of the number of clusters ranging from 2 to 17.

4.3 Ecosystem Functional Types (EFTs).

Figure 5 shows the EFTs derived from the functional variables considered above. EFTs 8 is largely contiguous and located in the north of Spain. This EFT is mainly occupied by forest areas, which present low

values of amplitude and high values of red reflectance. Conversely, the EFT 1, which is located in the central plateau of the Peninsula and occupies non-irrigated crops, shows the highest amplitude values (around 0.31), with a well-defined bell-shaped phenological signature.

EFT1 and EFT5 are mainly occupied by non-irrigated crops, and present a similar pattern. Nevertheless, the values of intra-annual variation (amplitude) and NIR reflectance of the EFT1 are slightly higher than those observed in the EFT5.

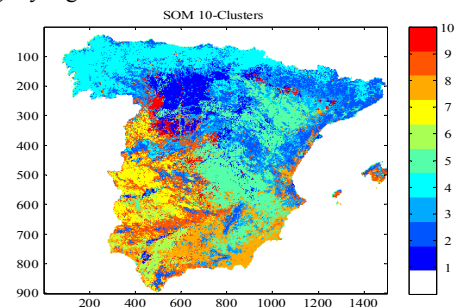


Figure 5. Ecosystem Functional Types (EFTs) in Spain.

4.4 Correspondence analysis between functional and structural classifications.

We explored the association between EFTs and Land cover units through a Correspondence analysis (CA).

For this purpose, we firstly have aggregated the CORINE legend in the ten most representative classes in the study area.

The relative agreement between ecosystem functional types and structural classes was evaluated exploring the amount of inertia accounted for in each dimension of the CA, a measure of the sum of eigenvalues that reflects the spread of class points around the centroid. The combined ordination of EFTs and structural classes into the first two axes explained 79.4% of the total inertia.

We did not find a clear correspondence between EFTs and land cover datasets. It is likely that different land cover units have similar functioning, mixed and needleleaf forest, which are close to EFT2. Nevertheless, several association between some EFTs and specific land cover types have been found, such as Herbaceous land cover and EFT7.

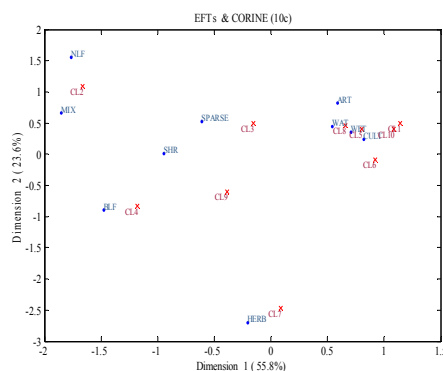


Figure 6. Correspondence analysis between ecosystem functional types (EFTs) and land cover classes of the CORINE land cover resampled to 10 classes (NLF: Needleleaf, MIX: Mixed Forest, BLF: Broadleaved, SHR: Shrubland, CULT: Cultivated, ART: Artificial, WET: Wetland, WAT: Water, HERB: Herbaceous, SPARSE: Sparse Vegetation).

4.5 Seasonal characterization of EFTs

Figure 7 shows the mean annual curve of Land Surface Temperature (LST), Gross Primary Production (GPP) and precipitation for the EFTs. There is a direct relationship between the magnitudes of annual precipitation and GPP. Thus EFTs characterized by very humid conditions present higher GPP values, (EFT4 and EFT2), and are mainly located in the north of the Peninsula. Conversely, EFT5 and EFT8, mainly located in the southeast or the Iberian Peninsula, correspond to dry conditions and low GPP values. In general, the EFTs with high values of precipitation and GPP present the lowest values of LST.

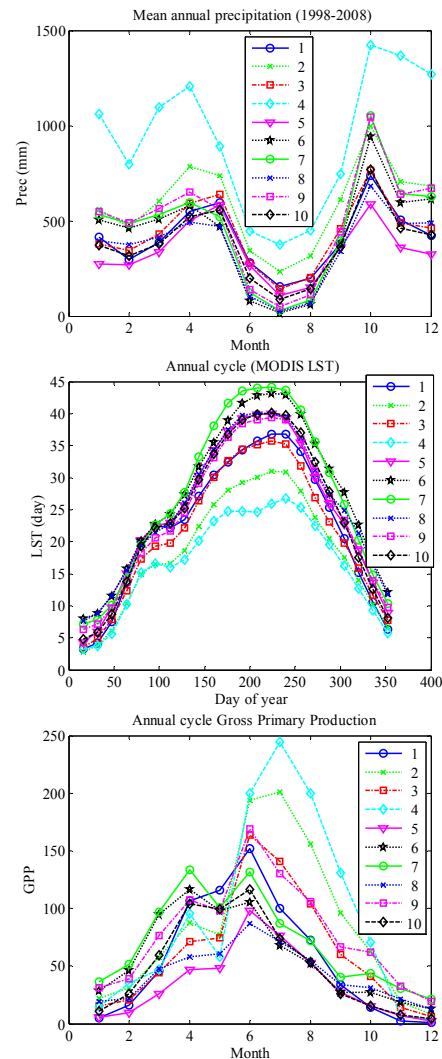


Figure 7. Mean seasonal profile of the precipitation, Land Surface Temperature (LST) and GPP (Gross Primary Production) for the ecosystem functional types (EFTs).

5. CONCLUSIONS

In this study, we characterized the functional heterogeneity of Spain. We described, classified, and mapped the EFTs through different parameters derived from the seasonal dynamics of the FVC and other functional variables such as spectral albedo, climatic parameters and geographical coordinates.

The preliminary results obtained show that methodology proposed is suitable to explore structural as well as functional attributes, such as productivity or fluxes of matter and energy, which have a faster response to changing environmental conditions.

Secondly, the correspondence analysis between the functional (EFTs) and structural (CORINE land cover) classification reveals that land cover only have partial importance in explaining the functioning of particular ecosystems. Marked differences among ecosystem functional types were obtained in terms of magnitude and timing of GPP cycle.

ACKNOWLEDGEMENTS

This work has been supported by DULCINEA (CGL2005-04202) and ARTEMIS (CGL2008-00381) projects, which provided us with climate data and biophysical variables such as vegetation production (GPP).

References

- Alcaraz, D., Cabello, J.M., Paruelo, J.M., Delibes, M., 2009, Baseline characterization of major Iberian vegetation types based on NDVI dynamics, *Plant Ecology*, 202,13-19.
- Azzali, S., Menenti, M., 1999, Mapping isogrowth zones on continental scale using temporal Fourier analysis of AVHRR-NDVI data, *International Journal of Applied Earth Observation and Geoinformation*, 1, 9-20.
- Bailey, R.G., 1983, Delineation of ecosystem regions, *Environmental Management*, 7, 365-373.
- Carrasco Fernández, J.J., Soria Olivas, E., Gómez Sanchis, J., Serrano, A.J., Soriano-Asensi, A., Guerrero Martínez, J.F., 2009, MATLAB-Based Educational Software for Exploratory Data Analysis (EDA Toolkit), Computer Applications in Engineering Education.
- Davies, D.L., Bouldin, D.W., 1979, A cluster separation measure, *IEEE Transactions on Pattern Analysis and Machine Intelligence*, 1, 224-227.
- Fernandez, N., Paruelo, J.M., Delibes, M., 2010. Ecosystem functioning of protected and altered Mediterranean environments: A remote sensing classification in Doñana, Spain, *Remote Sensing of Environment*, 114, 211-220.
- García-Haro, F.J., Sommer, S., Kemper, T., 2005, Variable multiple endmember spectral mixture analysis (VMESMA), *International Journal of Remote Sensing*, 26, 2135-2162.
- Kohonen, T., 1984., Self-Organization and Associative Memory, 3rd edition, Springer, Berlin.
- Paruelo, J.M., Jobbágy, E.G., Sala, O.E., 2001, Current Distribution of Ecosystem Functional Types in Temperate South America, *Ecosystems*, 4, 683-698.
- Petchey, O.L., Kevin, J.G., 2002, Functional diversity (FD), species richness and community composition, *Ecology Letters*, 5, 402-411.
- Soriano, A., Paruelo, J.M., 1992, Biozones- Vegetation units defined by functional characters identifiable with the aid of satellite sensor images, *Global Ecology and Biogeography Letter*, 2, 82-89.
- Shugart, H.H., 1997, Plant and Ecosystem Functional Types. In Plant Functional Types. Their relevance to ecosystem properties and global change, edited by T.M. Smith and J.J. Shugart and F.I. Woodward (Cambridge, Cambridge University Press), pp. 20-45.

Spatiotemporal Dynamic of French Forest Phenology from *MODIS* and *GLOBCARBON* products

J.-C. Samalens¹, D. Guyon¹, N. Bories^{1,2}, C. Moisy¹, J.-P. Wigneron¹

1. INRA, UR 1263 EPHYSE, 33140 Villenave d'Ornon, France

2. MAAP-DSF, Forest Health Department, 33000 Bordeaux, France

Corresponding author: jean-charles.samalens@bordeaux.inra.fr

ABSTRACT : Phenological trends studies based on remote sensing data appear to be a realistic and cost-effective way to monitor forest ecosystems over time. Although such vegetation trends have been widely investigated at the global scale, still little is known on pheno-phases anomalies at regional scales. Remote sensing time series at medium spatial resolution ($\leq 1\text{km}$) are now available to fill this gap but the derived phenological products still need to be validated. Our retrospective analysis is based on remotely sensed phenological metrics delivered over 10 years (1998-2007) through the GLOBCARBON project (VGCP product) and from MODIS sensors (MCD12Q2 product). For validation, we took advantage of tree canopy phenological observations of the French Permanent Plot Networks for Forest Monitoring (RENECOFOR) carried out at the ground on the same period. Focusing on two emblematic deciduous broadleaf tree species (beech and oaks) we also investigated phenological responses at the tree species level on a national extent. In-situ comparison of broadleaf forests leaf-on date shows a prediction uncertainty of 8 and 13.8 days and systematics errors of 2.2 and 9.8 days for MODIS and GLOBCARBON. Considering only pure beech forests reduce bias to 1.6 and 5.5 days respectively but no significant relationship could be retrieved for oaks forests. On the France extent, cross-product comparison remain stable against tree species. Neither early leaf-on nor senescence stages could accurately be depicted by satellite based metrics. Inter-annual leaf-on trends are consistent with ground observations and spatial patterns of green-up dates are related to latitudinal gradients for oaks forests and altitudinal gradients for beech forests.

1 INTRODUCTION

Tree phenology reflects their adaptive responses to climate variability and therefore constitutes an efficient bio-indicator of forest condition and productivity. Because warming climate has led to phenological timing shifts over the past half century (Chmielewski & Rotzer, 2001; Menzel et al., 2006), tracking the rhythm of the seasons is still challenging (Morissette et al., 2009) and remote sensing is a key tool for measuring and monitoring forest phenology on a large extent. Vegetation indices derived from satellite data are commonly used for this purpose essentially at global or continental scale. Finer spatial scale studies of vegetation trends can now be retrospectively be performed as medium spatial resolution ($\leq 1\text{km}$) data time series become available over the last decade. Those satellite data are regularly reprocessed to improve information quality (snow, clouds, aerosols correction) or combined via multiple sensors acquisition to get a higher temporal frequency. However, the remote sensing community regularly emphasizes the need for ground validation and multiple sensor comparisons to validate the accuracy of those products (Morissette et al., 2009).

Based on long-term in-situ forest phenological observations, the aim of this study was to evaluate the ability of high-level remote sensing products in monitoring forest foliar dynamics both in time and space. We report here the evaluation of the MODIS and GLOBCARBON “phenological” products (Cf. 2.1). For ground validation, we focus on two major deciduous broadleaf tree species: Beech (*Fagus sylvatica*) and Oaks (*Quercus sp.*) because there is significant seasonal trends differences between those two species (Davi et al., 2006; Vitasse et al., 2009a) but consistent within each one (Vitasse et al. 2009b).

2 MATERIALS & METHODS

To explore spatio-temporal trends at a national scale we look at long term remote sensing data time series, corrected for atmospheric and bidirectional effects, and for which phenological indicators were already computed.

2.1 Remote sensing data

First, we investigate the latest version of the MODIS “land Cover Dynamics” product available on the LPDAAC server, namely MCD12Q2 (V5), which combines the “Terra” and “Aqua” sensors reflectance

measurements over the period 2001 to 2006 (see Ganguly et al., 2010 for complete description). The interest of this recent version lies in both a high spatial and temporal resolution (500m and 8 days respectively). Ensuing yearly products gather several land surface phenology indicators derived from Enhanced Vegetation Index (EVI) annuals curves extended to ± 6 months. Those metrics characterize vegetation growth cycle using transition dates namely, Onset Greenness Increase (OGI), Maximum (OGMax), decrease (OGD), minimum (OGMin) and the annual integral of the vegetation index curve (EVI area). We also computed $(OGMax-OGI)/2$ as an indicator of the date of the growing season inflexion point (hereafter referred as OG).

On another hand, GLOBCARBON v2 “Vegetation Growth Cycle Parameters” product at 1km was used for the years 1998 to 2007. The baseline input combine satellite data from the ESA Earth Observations (ATSR-2, AATSR, MERIS) and SPOT VEGETATION sensors. Complete description of the GLOBCARBON initiative can be found in Plummer et al. (2007). The generation of annual growth cycle parameters is based on derived LAI profiles smoothed over 54 decades. Authors argue that LAI should be less sensitive to extraneous effects which are often seen on vegetation index time series (e.g. NDVI, EVI). Similarly to the MODIS product, several phenological metrics are provided (n=8) such as the day before the highest first derivative of LAI curve reach 90% of its maximum (hereafter referred as Dbefore).

2.2 In-situ phenological observations

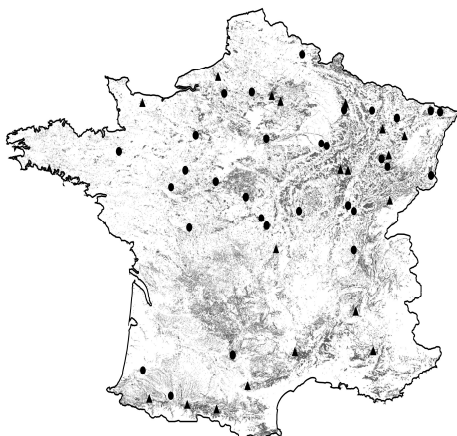


Figure 1: RENECOFOR forest network: location of the deciduous broadleaf forest stands (dots=oaks stands, triangles=beech stands. Grey area represents the Corine Land Cover 2006 broadleaf forest class.

Forest phenological observations are carried out annually since 1997 over the whole French Permanent Plot of the European Network for the Monitoring of Forest Ecosystems (RENECOFOR, see Figure 1).

Table 1: Detailed geographic characteristics of the 46 RENECOFOR deciduous broadleaf forest plots (O=oak, B=beech).

Plot	Tree Age (year)	Long. (°)	Lat. (°)	Elevation (m)	Slope (%)
O1	149	4°18'E	48°20'N	115	0
O2	61	0°50'W	43°44'N	20	5
O3	85	0°01'W	47°27'N	57	0
O4	115	5°46'E	49°01'N	220	0
O5	85	3°45'E	50°10'N	149	3
O6	69	0°02'W	43°12'N	370	12
O7	50	6°12'E	47°52'N	240	0
O8	82	5°14'E	46°58'N	190	0
O9	103	5°14'E	46°10'N	260	3
O10	130	2°43'E	46°40'N	260	0
O11	98	4°27'E	48°17'N	160	0
O12	93	2°07'E	47°15'N	176	1
O13	102	5°04'E	47°04'N	220	0
O14	70	1°30'E	49°21'N	175	0
O15	116	1°32'W	48°10'N	80	0
O16	107	1°15'E	47°34'N	127	0
O17	154	4°57'E	49°02'N	180	2
O18	100	6°29'E	48°52'N	315	4
O19	143	7°27'E	49°00'N	320	15
O20	76	3°39'E	46°58'N	270	7
O21	75	2°18'E	49°23'N	55	1
O22	103	0°40'E	48°31'N	220	5
O23	152	7°28'E	47°41'N	256	0
O24	79	0°22'E	47°47'N	170	0
O25	113	1°44'E	44°02'N	300	18
O26	97	0°29'E	46°37'N	116	4
O27	144	6°02'E	48°01'N	330	0
O28	91	7°43'E	48°59'N	350	10
O29	128	2°43'E	48°27'N	80	0
B1	68	3°07'E	49°12'N	145	0
B2	102	2°59'E	46°11'N	590	15
B3	103	5°48'E	44°07'N	1300	50
B4	167	1°16'E	42°55'N	1250	32
B5	98	0°51'W	49°10'N	90	4
B6	143	4°51'E	47°48'N	400	3
B7	56	6°16'E	47°11'N	570	2
B8	173	5°17'E	44°55'N	1320	12
B9	158	3°32'E	44°06'N	1400	25
B10	121	5°04'E	47°47'N	440	0
B11	104	5°00'E	49°10'N	250	0
B12	77	2°52'E	49°19'N	138	0
B13	82	0°39'W	43°09'N	400	44
B14	175	0°26'E	43°01'N	850	25
B15	102	1°19'E	49°42'N	210	0
B16	123	2°10'E	43°24'N	700	0
B17	83	6°14'E	48°06'N	400	3

This network encompasses a wide range of bioclimatic conditions of France, from oceanic to Mediterranean and from continental to high elevation mountain context. A subset of this network is composed by 49 stands of 0.5 ha of pure deciduous broadleaved forests. Stands are mostly managed as even-aged high forests (106 years on average, Table 1). *Quercus sp.* stands are mainly sampled in the northern part of France and homogeneously regarding to longitude. *Fagus sylvatica* stands are located in north-eastern plains and in southern French mountains. Average elevation is 200 m [20-370 m] for oak plots and 615 m [90-1400 m] for beech plots (Table 1).

Each year, the same 36 trees/plot are monitored and phenological key stages are recorded weekly in Julian days by local foresters. In spring (March-June), the onset and the end of the green-up phase are defined when leaf-unfolding occurred on 10% and 90% of the trees (hereafter reported as LU10% and LU90%). The same approach is achieved during the autumn season (September-November) for the leaf colouring stages (LC10% and LC90%). For consistent analysis, we selected the 46 stands (17 beech stands and 29 oaks stands, see Table 1) where at least 7 years were effectively observed during the decade 1998-2007 (63% were observed every year of the whole period). Inter-annual average of ground observations dates were plotted against each phenological metrics given by both remote sensing products and simple linear regression was computed. Difference between ground and remotely sensed data was reported as bias and the RMSE was used to evaluate the average satellite records uncertainty relative to in-situ observations.

2.3 Forest Cover

Cross-sensor validation was investigated at the national scale for all broadleaf forests and for each studied tree species. To this end, comparative analysis was conducted on image subsets to avoid mixture of

landcover classes in a same pixel. As no accurate tree species map was available on this spatial extent, we first used the latest version of Corine Land Cover 2006 to identify pixels covered by a majority of broadleaved forests. Then, we took advantage of the National Forest Inventory database over the period 2005-2008 (9080 NFI plots network based on a systematic sampling design) to locate pure beech or oaks forests. Finally, we combined those data for each tree species to select pixels covered by at least 95% of broadleaved forest (Broadleaf) and for which the NFI observations where pure tree species (Oaks and Beech). Because of different spatial resolution pixels selection was repeated for each remote sensing product.

3 RESULTS AND DISCUSSION

3.1 In-situ comparison

All phenological indicators of both products were compared with ground measurements. For the leaf unfolding phase, significant relationships could only be retrieved using OGa and Dbefore indicators for MODIS and GLOBCARBON respectively (Table 2). The earlier stage of leaf unfolding (LU10%) is overestimated by both indicators with a systematic error greater than 10 days. At the end of this phenological stage (LU90%) bias is reduced by 10 days, ranging from 1.6 to 12.6 days. Bias and RMSE are always lower for OGa as compared to Dbefore. Soudani et al. (2008) also found that OGa is a good marker of leaf unfolding stage with the earlier version of the product (MOD12Q2, bias = 7.5 days as compared to LU90%). Improved result reported here on the same plots (bias= 2.2 days for LU90%) can be due to the longer time series but also the higher spatial and temporal resolution of the MCD12Q2 product.

Better predictions of the LU90% stage are reached if beech stands are considered separately. Bias is then better for beech (1.6 and 5.4 days) than for

Table 2: Regression analysis in mean Julian days between in-situ observations of leaf unfolding dates (LU10% and LU90%) and satellite-based phenological dates (OGa for Modis and Dbefore for GLOBCARBON). Values shown in bold are Pearson's coefficients of correlation statistically significant at 5% probability level.

		Oaks (n=29)		Beech (n=17)		Broadleaf (n=46)	
		Modis*	GlobCarbon**	Modis*	GlobCarbon**	Modis*	GlobCarbon**
In-situ LU10%	r ²	0.08	0.01	0.58	0.21	0.41	0.03
	Bias	13.8	23.8	10.05	13.8	12.4	20.0
	RMSE	15.2	26.3	12.75	15.0	14.6	22.3
In-situ LU90%	r ²	0.01	0.05	0.47	0.27	0.23	0.10
	Bias	2.6	12.6	1.6	5.4	2.2	9.8
	RMSE	8.0	17.0	6.9	8.0	8.0	13.8

* OGa : Average date of Modis Onset Greenness Increase and Onset Greenness Maximum

** Dbefore: Day before the highest first derivative of LAI curve reach 90% of its maximum.

oaks (2.6 and 12.6 days) for OGa and Dbefore respectively. Those tree species discrepancies can be related to the potential mixture of different oaks species (and/or understory species) which may affect the spatial phenological variability within a pixel considered her as “monospecific”.

Neither MODIS nor GLOBCARBON products can reflect dates of foliar discoloration of tree senescence phase (no correlations with ground data). However, we find that MODIS EVI area can be used as a proxy of the annual length of the growing season (computed as LC90%-LU10%, $n=46$, $R^2=0.35$, $p=1.6 \times 10^{-5}$).

Overall, in-situ comparison shows higher estimations accuracy for MODIS product than GLOBCARBON and for beech forests as compared to oaks ones. Difference in spatial and temporal resolution can be invoked to explain lower accuracy level of the GLOBCARBON estimates as compared to MODIS. Another uncertainty source affecting the GLOBCARBON product might concern the LAI estimation which is based on the GLC2000 land cover map. Nevertheless, both of the satellite-based LU90% estimation accuracy are of the same order of magnitude than in-situ observations which are carried out on a weekly basis.

3.2 Spatiotemporal trends

On a wider dataset (NFI plots, Table 3), the correlation between the two satellite-based average leaf unfolding dates (OGa vs Dbefore) are low even if they are highly significative. As previously observed (Cf. Table 2), OGa indicates leaf unfolding dates of about 5 days earlier than Dbefore. Nevertheless, cross-product comparison shows a similar bias and accuracy level irrespective to tree species.

Table 3: Cross-comparison on specific NFI plots of the average leaf-unfolding date from MODIS OGa and GLOBCARBON Dbefore (see Table 2). Correlations are statistically significant ($p<0.0001$).

	Oaks	Beech	Broadleaf
n	816	349	17684
r^2	0.01	0.20	0.12
bias	5.4	5.8	5.4
RMSE	8.3	8.9	8.9

In spite of those differences, similar spatial trends can be retrieved. Leaf-unfolding maps reveal spatially consistent results, even for high elevation forests such as beech ones (Figure 2A). This altitudinal trend is quantitatively in accordance with ground observations of Vitasse et al. (2009) and further with satellite-based study of Guyon et al. (2010) on the French Pyrénées

Mountains. They report a similar trend of 1 day / 100m, just as the slope of Dbefore against elevation (Figure 2A right). This also confirms analysis of Lebourgeois et al. (2010) who found on the RENECOFOR network that elevation is the first spatial component driving unfolding trait. Because of a wider distribution range, a latitudinal variation of spring phenology (1.2 day/°) can also be retrieved within oaks forests ($n=621$, $r^2=0.03$, $p<0.0001$), also reported by Ducousso et al. (1996). Figure 2B shows that both satellite products correctly depict interannual phenology variability except for the year 2006 for which Dbefore reach peculiarly high values. As compared to in-situ annual observations, the best prediction is achieved for beech forests using the MODIS OGa indicator.

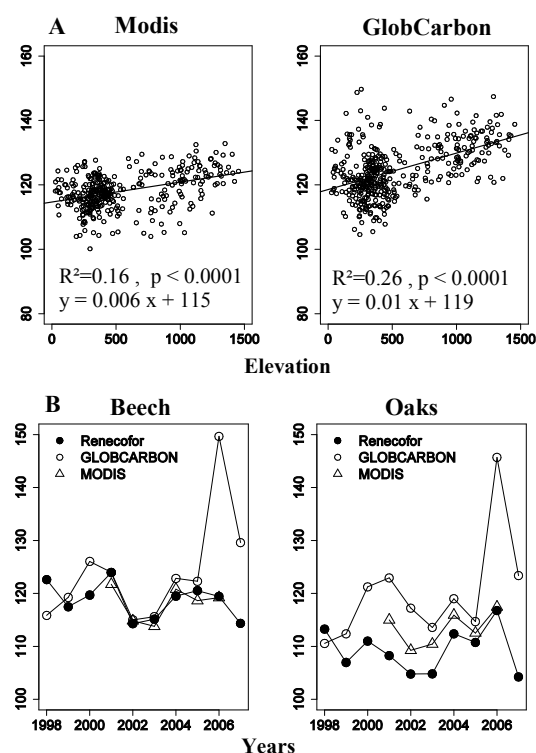


Figure 2: Satellite-based average leaf-unfolding dates (OGa, Dbefore) over specific NFI plots. A: regression analysis for beech forests against elevation (m). B: specific interannual variations. RENECOFOR LU90% records by species are also plotted.

4 CONCLUSION

Because of high variability of landscape feature but also because of the heterogeneity of climate change throughout France (Planton 2008), there is a clear expectation for different regional phenological

responses. Those first results are promising and show the relevance and the spatial consistency of the medium spatial resolution for tracking regional trends in forest phenology. MODIS tends to provide more accurate estimates of leaf unfolding dates than GLOBCARBON but these conclusions are closely dependant of ground data observations at the plot level. Discrepancies between phenological responses of tree species emphasize the need for accurate forest type mapping. Further sub-pixels analyses have to be performed to better take into account for tree species composition in forest landscapes.

5 ACKNOWLEDGMENTS

This study was supported by the CNES through a postdoctoral fellowship. We would like to thank the National Forest Inventory and the RENECOFOR network team of the National Forest Office for providing ground observations. Data from the GLOBCARBON project of European Space Agency are distributed by the VITO on the GEOSUCCESS web portal (<http://geofront.vgt.vito.be/geosuccess>). MODIS data are distributed by the Land Processes Distributed Active Archive Center (LP DAAC), located at the U.S. Geological Survey (USGS) Earth Resources Observation and Science (EROS) Center (lpdaac.usgs.gov).

6 REFERENCES

- Chmielewski, F.-M. & Rotzer, T., 2001, Response of tree phenology to climate change across Europe. *Agricultural and Forest Meteorology*, **108**: 101-112.
- Davi, H.; Duffrène, E.; Francois, C.; Maire, G. L.; Loustau, D.; Bosc, A.; Rambal, S.; Granier, A. & Moors, E., 2006, Sensitivity of water and carbon fluxes to climate changes from 1960 to 2100 in European forest ecosystems *Agricultural and Forest Meteorology*, **141**: 35-56.
- Ducousso, A., Guyon, J. P., Krémer, A., 1996, Latitudinal and altitudinal variation of bud burst in western population of sessile oak (*Quercus petraea* (Matt) Liebl). *Annales des sciences forestières*, **53**: 775-782.
- Ganguly, S., Friedl, M. A., Tan, B., Zhang, X. Verma, M., 2010, Land surface phenology from MODIS: Characterization of the Collection 5 global land cover dynamics product. *Remote Sensing of Environment*, **114**: 1805-1816.
- Guyon, D., Guillot, M., Vitasse, Y., Delzon, S., Wigneron, J. P., 2010, Monitoring elevation variations in leaf phenology of deciduous broadleaf forests from SPOT/VEGETATION time-series. *Remote Sensing of Environment*, RSE-D-10-00010R2.
- Lebourgeois, F., Pierrat, J.-C., Perez, V., Piedallu, C., Cecchini, S., Ulrich, E., 2010, Simulating phenological shifts in French temperate forests under two climatic change scenarios and four driving global circulation models. *International Journal of Biometeorology*, **54**(5): 563-81.
- Menzel, A.; Sparks, T. H.; Estrella, N.; Koch, E.; Aasa, A.; Ahas, R.; Alm-Kubler, K.; Bissolli, P.; Braslavská, O.; Briede, A.; Chmielewski, F.M.; Crepinsek, Z.; Curnel, Y.; Dahl, A.; Defila, C.; Donnelly, A.; Filella, Y.; Jactzak, K.; Mage, F.; Mestres, A.; Nordli, O.; Penuelas, J.; Pirinen, P.; Remisova, V.; Scheffinger, H.; Striz, M.; Susnik, A.; Van Vleet, A.J.H.; Wielgolaski, F.-E.; Zach, S.; Züst, A., 2006, European phenological response to climate change matches the warming pattern. *Global Change Biology*, **12**(10): 1969-1976.
- Morisette, J. T.; Richardson, A. D.; Knapp, A. K.; Fisher, J. I.; Graham, E. A.; Abatzoglou, J.; Wilson, B. E.; Breshears, D. D.; Henebry, G. M.; Hanes, J. M. & Liang, L., 2009, Tracking the rhythm of the seasons in the face of global change: phenological research in the 21st century. *Frontiers in Ecology and the Environment*, **7**, 253-260.
- Planton, S.; Déqué, M.; Chauvin, F. & Terray, L., 2008. Expected impacts of climate change on extreme climate events. *Comptes Rendus Geosciences*, **340**: 564-574.
- Plummer, S., Arino, O., Ranera, F., Tansey, K., Chen, J., Dedieu, G., Eva, H., Piccolini, I., Leigh, R., Borstlap, G., Beusen, B., Fierens, F., Heyns, W., Benedetti, R., Lacaze, R., Garrigues, S., Quaife, T., De Kauwe, M., Quegan, S., Raupach, M., Briggs, P., Poulter, B., Bondeau, A., Rayner, P., Schultz, M., McCallum, I., 2007, An Update on the GlobCarbon Initiative: Multi-Sensor Estimation of Global Biophysical Products for Global Terrestrial Carbon Studies, Plummer et al, *ENVISAT Symposium Proceedings, Montreux, Switzerland*, 23-27 April 2007.
- Soudani, K., le Maire, G., Duffrène, E., François, C., Delpierre, N., Ulrich, E., Cecchini, S., 2008, Evaluation of the onset of green-up in temperate deciduous broadleaf forests derived from Moderate Resolution Imaging Spectroradiometer

(MODIS) data. *Remote Sensing of Environment*, **112**(5): 2643-2655.

Vitasse, Y, Porté, A. J., Kremer, A, Michalet, R., Delzon, S., 2009(a), Responses of canopy duration to temperature changes in four temperate tree species: relative contribution of spring and autumn leaf phenology. *Oecologia* **161**: 187-198.

Vitasse, Y, Delzon, S, Dufrêne, E, Pontailier, J.-Y., Louvet, J.-M., Kremer, A., Michalet, R., 2009(b), Leaf phenology sensitivity to temperature in European trees: Do within-species populations exhibit similar responses? *Agricultural Forest and Meteorology* **149**: 735-744.

Dynamic mapping of cropland areas in sub-saharan africa using modis time series

C. Vancutsem¹, J.-F. Pekel², F. Kayitakire¹

Joint Research Centre of the European Commission,

¹ Monitoring Agricultural ResourceS Unit

² Global Environment Monitoring Unit

TP266 Via Enrico Fermi 2749, I-21027 Ispra (VA), Italy

Tel: +39 0332 78 9846, Fax: +39 0332 78 9028

Christelle.Vancutsem@jrc.ec.europa.eu,

Jean-Francois.Pekel@jrc.ec.europa.eu,

Francois.Kayitakire@jrc.ec.europa.eu

ABSTRACT - Mapping cropland areas in a dynamic way is of great interest to successfully monitor agricultural areas and food security. Existing cropland masks are commonly derived from global/continental land use/land cover datasets. However, these products are either too coarse and does not account correctly for the specificities of some regions or not adapted to map cropland extent or are limited in spatial coverage. This study aims at developing a method for dynamic mapping of cropland areas in Sub-Saharan Africa and at producing a multi-annual map of cropland extent at 250m using MODIS time series. The originality of the approach consists of (i) including a dynamic and automatic stratification that allows tuning the classification parameters according to the inter-annual variability, and (ii) exploiting the local differences of spectral signatures between natural vegetation and crops during the green-up season. The methodology has been applied to the data of 2009 and will be applied to 3 other years (2006-2008). Then the cropland masks of each year will be combined to produce a map of the potential cropland areas. The four annual products will be compared and the inter-annual variability will be analysed. The accuracy of the product will be assessed using a large sample of points interpreted on high resolution images and will be compared to the accuracy of two global data sets at a similar spatial resolution: the global cropland extent product (Pittman *et al.* 2010) and Globcover.

1 INTRODUCTION

Mapping cropland areas in a dynamic way is of great interest to successfully monitor agricultural areas and food security. In particular, the Monitoring Agricultural ResourceS Unit (MARS) of the European Commission Joint Research Centre (JRC), the global Information and Early Warning System on food and agriculture (GIEWS) of the Food and Agriculture Organization of the United Nations (FAO) and the Famine Early Warning Systems Network (FEWS NET) of the USAID are highly interested in crop extent maps to provide timely and rigorous early warning and vulnerability information on emerging and evolving food security issues.

Estimating cropland extent is generally difficult because of the heterogeneity, the different crop cycles, the spectral similarity with grassland mainly in dry areas, and the inter-annual variability due to climatic events such as drought and fallow periods.

Existing cropland masks are commonly derived from global/continental land use/land cover datasets. Two global land cover products have been produced at

1km spatial resolution: (i) the Global land cover Classification based on SPOT VEGETATION time series and referred to as GLC2000 (Bartholome *et al.* 2005, Mayaux *et al.* 2004), and (ii) the Boston University's Global Land Cover product based on Moderate Resolution Imaging Spectroradiometer (MODIS) and referred to as MOD12V1 (Friedl *et al.* 2002). Recently a global land cover map has been produced at 300m using MERIS time series in the framework of the Globcover project (Defourny *et al.* 2008). In spite of this improvement in term of spatial resolution, these maps are not dedicated for agriculture areas and the data and methods used are not fine-tuned for detecting croplands. A comparison between GLC2000, the MODIS land cover map, and national statistics show that uncertainties in African countries are high (Fritz *et al.* 2010). Other global maps specifically dedicated for croplands were produced by the International Water Management Institute's (IWMI): (i) the global map of rainfed cropland areas (GMRCa, Biradar *et al.*, 2009) and the global irrigated area mapping (GIAM, Thenkabail *et al.*, 2009). However those products are still spatially too coarse (10 km) for national and regional applications

and present a large number of uncertainties (Portmann *et al.* 2010). Very recently a global map of cropland extent was produced at 250m spatial resolution using MODIS time series (Pittman *et al.*, 2010). Although it represents a major improvement in term of data used and resolution, the approach does not account correctly for the specificities of some regions of the globe.

Landsat-derived maps such as the Cropland-Use Intensity (CUI) dataset (USGS) and the AFRICOVER dataset from the FAO (1998), are more detailed spatially and generally more comparable with national statistics (Fritz *et al.*, 2010) but they are limited in spatial coverage. Moreover, these dataset are quite outdated and the methodology used (visual interpretation of Landsat images) cannot be easily applied at the continental scale for regular updates.

MODIS data offer a unique combination of spectral, temporal, and spatial resolution compared to previous global sensors, making it a good candidate for cropland detection. The advantages of using high temporal resolution data are (i) increased ability to monitor the phenological change of crop plants, (ii) the possibility of generating consistent large area crop cover maps, and (iii) higher update frequency than the high spatial resolution data.

The objective of this study is twofold: (i) to develop a method for dynamic mapping of cropland areas in Sub-Saharan Africa and (ii) to produce a multi-annual map of cropland extent at 250m using MODIS time series. The legend will include two classes: (i) the rainfed croplands, and (ii) the post-flooding or irrigated croplands.

The selected study area covers the sub-Saharan countries above the equator, i.e. from Senegal (18° West) to Somalia (52° East) and from the equator to the North of Eritrea (19° North). This window is of particular interest for food-security monitoring as it includes wide agriculture areas mainly based on subsistence farming and therefore quite vulnerable to climate variability.

2 DATA

Four MODIS daily products (version 5, L2G) were used: (i) Aqua Surface Reflectance at 250m (MYD09GQ), (ii) Terra Surface Reflectance at 250m (MOD09GQ), (iii) Aqua Surface Reflectance at 500m (MYD09GA), and (iv) Terra Surface Reflectance at 500m (MOD09GA). These data have been downloaded from the Land Processes Distributed Active Archive Center: (<https://lpdaac.usgs.gov/>). Three wavelengths were used: the Red and the near-infrared (NIR) from the 250m product and the middle infrared (MIR) from the 500m product. The MIR channel was resampled to 250m.

Four years of data were processed, i.e. from 2006 to 2009.

High resolutions images provided by Google Earth were used as reference for the spatio-temporal analysis, and the interpretation.

3 METHOD

3.1. Data processing

The daily MODIS images are composited on a 10-day and 2-month basis using the Mean Compositing strategy that averages reflectance values after a quality control (Vancutsem *et al.*, 2007). This approach presents three main advantages compared to other compositing methods: (i) it reduces both the BRDF effects and the possible remaining perturbations after atmospheric correction and cloud removal, (ii) it requires few cloud free observations, and (iii) consumes little computing time.

Two vegetation indices are computed: the NDVI and the Hue index (Pekel *et al.*, 2010). The latter is derived from the colour transformation of the RGB colour space to HSV using the three reflectance bands, i.e. MIR, NIR, and Red.

3.2. Mapping methodology

The mapping approach aims to exploit local differences of spectral signatures between natural vegetation and crops during the green-up season due to a lag in vegetation start. The main reason for this lag (from 1 to 4 decades) is that crops are generally sown after the first rains whereas the natural vegetation starts growing at the first rain.

To achieve this objective, four steps are proposed: (i) mask the “no vegetation” areas, (ii) a latitudinal and longitudinal stratification of the sub-Saharan window, (iii) a spatio-temporal analysis to identify the best discrimination parameters for each region, and (iv) a classification per region.

3.2.1. Mask “no vegetation”

Two land cover types are masked during this step: (1) the permanent bare soils, and (2) the permanent waterbodies.

The permanent bare soils are identified combining the maximum Hue and the maximum NDVI computed over 4 years. From the following criteria, the pixels corresponding to permanent bare soils are selected.

$$\text{Max NDVI (4 years)} < 0.2 \quad (1)$$

$$\begin{aligned} \text{Max Hue (4 years)} &< 40 \quad \text{AND} \\ \text{Max NDVI (4 years)} &< 0.25 \end{aligned} \quad (2)$$

$$\text{Max Hue (4 years)} < 30 \quad (3)$$

The permanent waterbodies mask is provided by Pekel *et al.* (in preparation). They were detected by analysing the Hue, the Value, and the Land Surface Temperature over 7 years (2004-2010) of MODIS data at 250m resolution.

3.2.2. Stratification

The objective of the stratification is twofold: (i) to allow optimizing the input data used in the classification to the seasonality of each region, and (ii) to reduce the size of the classification window and therefore increase the performances of the classification algorithm.

The latitudinal stratification is dynamic in order to follow the inter-annual variability mainly due to the rise of the inter-tropical front. The strata are derived from the dates of the first vegetation detection during the growing season. These detections are based on the same approach that has been developed for the monitoring of the desert locust habitat (Pekel *et al.*, 2010), i.e. a combination of the Hue index and the NDVI every 10 days. It presents two main advantages compared to existing approaches based only on the NDVI: (i) avoids usual confusions between bare soils and vegetation as it exploits the multi-spectral information, and (ii) reduces the noise due to observation conditions. An additional stratum containing areas with a permanent vegetation cover was defined wherever the minimum NDVI during 4 consecutive years is always greater than 0.25.

The longitudinal stratification is based on natural breaks in the latitudinal stratification and on natural limits identified thanks to the mask of permanent bare soils.

3.2.3. Spatio-temporal analysis

The objective of the spatio-temporal analysis is to identify the best discriminant parameters that will be used in the classification.

This analysis includes four steps: (i) cropland areas are identified on high resolution images (from Google Earth), (ii) the extraction of NDVI time series for these croplands and the surrounding natural vegetation, (iii) the identification of the best period to discriminate croplands from natural vegetation, and (iv) the computation of seasonal composites for this period.

3.2.4. Classification

The classification is run independently for each region using specific parameters that have been initially defined in the spatio-temporal analysis. For each region, an isodata algorithm is applied to produce a classification with a number of classes varying from 40 to 80. The result is visually interpreted using high resolution images as a reference. The “pure” cropland classes are then integrated into the final product whereas the “non cropland” classes are masked on the input data. Finally, a second classification is applied on the “non pure” cropland classes possibly with new input data better adapted to avoid the confusions observed. A second interpretation is realised for these classes.

3.3. Validation

The validation is realised on the multi-annual mask (4 years). It includes a visual comparison of the mask with high resolution images and with two land cover data sets at a similar spatial resolution: the Pittman *et al.* (2010) product and Globcover. The accuracy of the 3 products is also assessed; a large sample of points is interpreted using high resolution images as well as external validation points coming from the geo-wiki tool (<http://www.geo-wiki.org>). A confusion matrix is provided for the 3 products.

The estimated areas are compared with national and sub-national statistics.

4. RESULTS

The methodology proposed in this paper has already been applied on the MODIS images for the year 2009. However, the interpretation of the classification results is still in progress. The mask and the stratification have already been finalised for the year 2009 and are presented in the following paragraphs.

4.1. Spatio-temporal analysis

The spatio-temporal analysis emphasized the following points:

- the latitudinal stratification is highly required due to the seasonality lag observed from North to South.
- the green-up period is a key parameter to discriminate crops from natural vegetation.
- the NDVI peak is an important parameter for the North of the study area in order to avoid confusions with the steppic savannas that can start at the same time as the croplands.

4.1. Mask “no vegetation”

The mask combining the permanent waterbodies and the permanent bare soils is presented at the Figure 1.

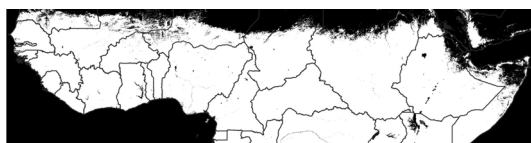


Figure 1. Mask of permanent bare soils and waterbodies (in black)

4.2. Stratification

The stratification has been realized for the year 2009.

Figure 2 and

Figure 3 present respectively the results for the latitudinal and longitudinal stratifications.

For three strata, the latitudinal stratification is based on the vegetation detections at different dates: (1) 1st decade of August, (2) 1st decade of July, and (3) first decade of May. The fourth stratum is based on an NDVI threshold.



Figure 2. Latitudinal stratification: (1) August, (2) July, (3) May-June, (4) NDVI > 0.25 (over 4 years)

The longitudinal stratification includes 4 regions per each stratum of the latitudinal stratification, i.e. a total of 16 strata.



Figure 3. Longitudinal stratification

4.3. Classification

The interpretation of the classification results is in progress. The first results already confirm the relevance of the MODIS data in term of spatial and temporal resolutions. The two-step classification is mandatory in order to adapt the input data according to the specificities of each region, i.e. the seasonality but

also the number of cloud-free observations. Indeed in some areas as the number of cloud-free observations is too low during the green-up season, it is necessary to use another period as input of the classification.

5. CONCLUSION

A methodology for mapping cropland areas in a dynamic way using MODIS time series has been developed. The originality of the approach consists of (i) including a dynamic and automatic stratification that allows tuning the classification parameters according to the inter-annual variability, and (ii) exploiting the local differences of spectral signatures between natural vegetation and crops during the green-up season using multi-spectral composites at this period.

The methodology has been already applied to one year of data and will be applied to 3 other years (2006-2008) in the coming months. Then the cropland masks of each year will be combined to produce a mask of the potential cropland areas. The four annual products will be compared and the inter-annual variability will be analysed.

Further work could also consider to extent the period to 10 years in order to better characterise the regional agricultural dynamics and the risk of food insecurity.

6. REFERENCES

- Bartholome, E. and Belward, A. S., 2005, GLC2000: a new approach to global land cover mapping from Earth Observation data. *International Journal of Remote Sensing*, **26**, 1959–1977.
- Biradar, C. M., Thenkabail, P. S., Noojipady, P., Li, Y., Dheeravath, V., *et al.*, 2009. A global map of rainfed cropland areas (GMRCA) at the end of last millennium using remote sensing, *International Journal of Applied Earth Observation and Geoinformation*, **11**, 114-129.
- Defourny, P., Vancutsem, C., Pekel, J. F., Bicheron, P., Brockmann, C., Niño, F., Schouten, L. and Leroy, M., 2006, Towards a 300 m global land cover product – the Globcover initiative. In: Braun, M. (ed.)
- Second Workshop of the EARSeL Special Interest Group on Land Use and Land Cover: Application & Development, Universitätsclub Bonn, Bonn (Germany).

- FAO, 1998. Land cover and land use: The FAO AFRICOVER Programme. Available online at: <http://www.africover.org/>.
- Friedl, M. A., Mciver, D. K., Hodges, J.C.F., Zhang, X. Y., Muchoney, D., Strahler, A.H., Woodcock, C.E., Gopal, S., Schneider, A., Cooper, A., Bacini, A., Gao, F. and Schaaf, C., 2002, Global land cover mapping from MODIS: algorithms and early results. *Remote Sensing of Environment*, **83**, 287–302.
- Fritz, S., Seeb, L., and Rembold, F., 2010, Comparison of global and regional land cover maps with statistical information for the agricultural domain in Africa, *International Journal of Remote Sensing*, **31**, 2237 -2256.
- Mayaux, P., Bartholome, E., Fritz, S. and Belward, A., 2004, A new land-cover map of Africa for the year 2000, *Journal of Biogeography*, **31**, 861–877.
- Pekel, J.-F., Ceccato, P., Vancutsem, C., Cressman, K., Vanbogaert, E., and Defourny, P., 2010, Development and Application of Multi-Temporal Colorimetric Transformation to Monitor Vegetation in the Desert Locust Habitat, *IEEE Journal of Selected Topics in Applied Earth Observations and Remote Sensing*, **99**, 1-9.
- Pittman, K., Hansen, M. C., Becker-Reshef, I., Potapov, P. V., Justice, C.O., 2010, Estimating Global Cropland Extent with Multi-year MODIS Data. *Remote Sensing*, **2**, 1844-1863.
- Portmann, F. T., Siebert, S., and Doll, P., 2010, MIRCA2000 – Global monthly irrigated and rainfed crop areas around the year 2000: a new high-resolution data set for agricultural and hydrological modelling, *Global biogeochemical Cycles*, **24**, GB1011, DOI:10.1029/2008GB003435.
- Thenkabail, P. S ., Biradar C. M., Noojipady, P., Dheeravath, V., Li, Y. J., Velpuri, M., Gumma, M., Reddy, G. P. O., Turrall, H., Cai, X. L., Vithanage, J., Schull, M., and Dutta, R. 2009. Global irrigated area map (GIAM), derived from remote sensing, for the end of the last millennium. Global Irrigated Area Map (GIAM) for the End of the Last Millennium Derived from Remote Sensing. *International Journal of Remote Sensing*, **30**, 3679-3733.
- Vancutsem, C., Pekel, J.-F., Bogaert, P., Defourny, P., 2007, Mean Compositing, an alternative strategy for producing temporal syntheses. Concepts and performance assessment for SPOT VEGETATION time series. *International Journal of Remote Sensing*, **28**, 5123 -5141.

A new 300 m vegetation map for Central Africa based on multi-sensor times series

A. Verhegghen, P. Defourny,
Earth and Life Institute, Université Catholique de Louvain, Louvain-la-Neuve, Belgium
astrid.verhegghen@uclouvain.be, pierre.defourny@uclouvain.be

ABSTRACT- *An operational characterization of the extend and location of vegetation types of the humid tropics is essential for studies concerning habitat and biodiversity monitoring, forest resources management, Carbon accounting, biogeochemical and climatic cycles. Central Africa contains the second largest and the least degraded area of contiguous tropical forest of the world. Estimating vegetation cover in this remote region would be a major challenge without the use of satellite imagery. However, in spite of recent progress in earth observation, vegetation mapping in tropical areas still represent an outstanding challenge owing to high cloud coverage and the extent and limited accessibility of the territory.*

In the present study, the vegetation types of 8 countries in Central Africa have been mapped thanks to a semi-automatic processing method based on temporal and spectral information from 19 months of ENVISAT MERIS FRS observation and 8 years of SPOT VEGETATION time series. The approach is based on a previous 1-km mapping effort for the Democratic Republic of Congo and on the lessons learnt from the ESA-GlobCover project. A land cover map with 20 vegetation classes was produced in five major steps: data compositing, seasonal stratification of the study zone, unsupervised classifications, automatic labelling and manual editing. The floristic composition and physiognomy of each vegetation type are described using the Land Cover Classification System developed by the FAO. This mapping exercise will be a reference document to deliver area estimates of the different forest types in a consistent way for DR Congo, Gabon, Cameroon, Equatorial Guinea, Central African Republic, Congo, Rwanda and Burundi.

1. INTRODUCTION

An operational characterization of the state and evolution of vegetation types is well recognized as essential for studies concerning habitat and biodiversity monitoring, forest resources management, Carbon accounting, biogeochemical and climatic cycles. This is especially true in tropical areas, where land cover change has occurred at unprecedented rates in recent decades (Hansen et al., 2008, Mayaux et al., 2004). The Congo Basin contains the second largest area and the least degraded of contiguous moist tropical forest of the world, covering about 2 millions km² (de Wasseige et al., 2009). Central Africa also contains a large diversity of habitats. Satellite images are a powerful tool to map the extend and the location of the vegetation cover in these remote areas. However, vegetation mapping in tropical regions still represent an outstanding challenge in spite of recent progress in earth observation. The primary data limitations for humid tropical forest monitoring is persistent cloud cover and the extent and limited accessibility of the territory (Hansen et al., 2008, Vancutsem et al., 2009). On one hand, the use of coarse resolution optical data is constrained by the lack of data, the limited performance of cloud screening, and by the noise arising from the necessary

compositing process, which limits the spatial consistency of the composite and the temporal resolution. On the other hand, the use of high-resolution data suffers from heterogeneity of atmospheric effects and from number of years between images to combine for a wall-to-wall coverage (Vancutsem et al., 2009)

In the last ten years, most vegetation maps of central Africa have been derived from satellite images (Mayaux et al., 2003). Land cover products are available at different scale and resolution. Among them, the GLOBCOVER initiative has produce a global land cover map using the 300 m resolution mode from the MERIS sensor onboard the ENVISAT satellite based on an automatic method (Defourny et al., 2006). In the framework of the Global Land Cover 2000 (GLC 2000), a land-cover map of Africa has been produced at a spatial resolution of 1 km using data from the VEGETATION sensor for the year 2000, capitalizing on image processing and local expert knowledge (Mayaux et al., 2004). (Vancutsem et al., 2009) presented a 1 km resolution map of the vegetation types of the Democratic Republic of Congo produced with a semi-automatic method applied on one year of SPOT VEGETATION data. (Hansen et al., 2008) developed a multi-resolution (MODIS and Landsat) methodology for a binary forest/non forest mapping of the Congo Basin. As land cover mapping

provides a static depiction of land cover (Achard et al., 2007), the products need to be often updated.

This paper presents a semi-automatic processing method for the production of a new vegetation map for 8 countries in Central Africa. The methodology developed is combining 19 months of ENVISAT MERIS FRS observation and 8 years of SPOT VEGETATION time series data. The research will take advantage of the spatial resolution of MERIS for a better spatial discrimination and take advantage of the temporal consistency of 8 years of SPOT VEGETATION to achieve a better spatial discrimination for cloudy areas. The approach is based on a previous 1-km mapping effort for the Democratic Republic of Congo with one year of VEGETATION data (Vancutsem et al., 2009) and of the ESA-Globcover global automatic land cover mapping (Defourny et al., 2006). Three main objectives are addressed: (i) achieving an improved spatial discrimination of the vegetation types by using 300 m resolution satellite images, (ii) describing the Central Africa regions with the most complete land cover legend as possible with the resolution used, (iii) using manual editing of the product to improve the quality of the map.

2. DATA AND STUDY AREA

The vegetation cover of 8 countries in Central African, i.e. Cameroon, Congo, Gabon, Burundi, Central African Republic, Equatorial Guinea, Republic Democratic of Congo and Rwanda has been mapped (Figure 1).

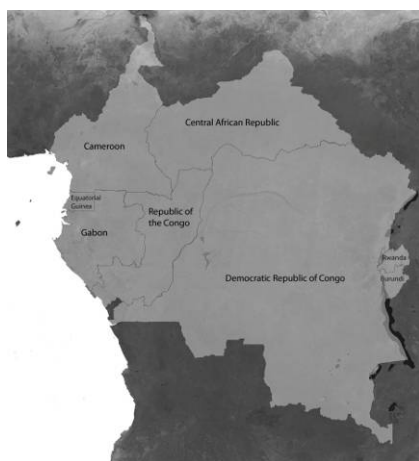


Figure 1 : Location of the eight countries of the study area - Spot VGT mosaic in the background

The mapping is based on the spatial and spectral information of 19 months, December 2004 to June

2006, of ENVISAT MERIS FRS at a 300 meter spatial resolution composited in 15 days and on the spectral and temporal information of 8 years of daily (S1 products) SPOT VEGETATION data, 2000 to 2007, at a spatial resolution of 1 km. The number of valid observation is available for the 15 days composites of MERIS. These data are available through the Globcover project.

MERIS was launched in March 2002 by the ESA on ENVISAT, a polar-orbit satellite. It measures reflected solar radiation in 15 spectral bands, from the visible to the near infrared (NIR). The MERIS swath is 1150 km wide, so global coverage is obtained in 3 days. The VGT instrument was launched on board SPOT-4 in March 1998 and delivers measurements that are specifically tailored to monitor land surface parameters on a global basis (<http://www.spot-vegetation.com/>). The four spectral bands of the sensor allow characterization of the main features of the plant canopy: (i) the red band centered on the absorption peak of chlorophyll (0.61–0.68 μm); (ii) the near-infrared (NIR) band (0.78–0.89 μm) corresponding to maximum vegetation spectral reflectance; and (iii) the shortwave infrared (SWIR) band centered around 1.65 μm for reflectance related to the water content of canopy components and to its structure. An additional band in the blue region (0.4 and 0.50 μm) is provided for characterizing the atmospheric state.

Moreover, other types of data were used as a support for interpretation of the clusters: the Landsat Geocover 2000 ETM+ data set (30-m spatial resolution) (MDA Federal, 2004) and reference vegetation maps and documents of the region, i.e. Globcover (

Arino), GLC 2000 on Africa (Mayaux et al., 2004), a vegetation map of the Republic Democratic of Congo (Vancutsem et al., 2009), a vegetation map of the Republic of Congo (Laudet), of Cameroon (WRI), of the Central African Republic (Boulvert). The Shuttle Radar Topography Mission (SRTM) data (www.srtm.usgs.gov) was used to discriminate the altitudinal land cover classes and Global Insight database for the urban sprawls. Finally, vectorial data for rivers from the geographical database of the FORAF project were superimposed on the classification result.

3. LEGEND

The land cover legend is derived from the legend of the map realized by (Vancutsem et al., 2009). As the Republic Democratic of Congo do not contain all the ecosystems of Central Africa, the legend had to be completed. Consultation of existing maps and notifications of experts on the study region helped modifying and completing the legend. The

result is a twenty land cover classes legend, presented in Table 1. The composition of each vegetation type is described using the standardized Land Cover Classification System developed by the FAO (Di Gregorio & Jansen, 2000).

4. METHODOLOGY

The land cover mapping methodology involves five steps: (i) Data processing in temporal composites (ii) Stratification of the study area in seasonal and "cloudy" zones, (iii) Unsupervised classification of the stratified zones, (iv) Automatic labelling and (v) Manual editing of the product.

4.1. Data compositing

A main challenge in land cover mapping of a large equatorial area is the production of cloud-free and spatially consistent images, called temporal syntheses or composites. The methodology selected is the mean compositing (MC) which improves the quality of temporal syntheses by reducing atmospheric and directional variations. The MC method involves averaging for each pixel and in each spectral band all the valid reflectance values acquired during the period chosen (Vancutsem et al., 2009). Three syntheses have been generated from each of the temporal SPOT VGT and MERIS FRS series acquired: (i) a seasonal composite for December–January corresponding to the dry season in the north of the country (above the

equator); (ii) an annual composite; and (iii) a seasonal composite for May–June corresponding to the dry season in the south (below the equator) as done in Vancutsem et al.(2009). All the information available at the time of interest for the compositing is taken into account (8 years for SPOT VGT, 19 months for MERIS). Compositing of MERIS is weighted considering the number of valid observation for each 15 syntheses.

Moreover, 10 days composites were produced with SPOT VGT daily data to characterize the seasonality of all vegetation types. The normalized difference vegetation index (NDVI) is computed on the basis of these reflectance averages. NDVI (Tucker, 1979) is well recognized for characterization of the chlorophyll activity of vegetation cover over time.

4.2. Seasonal and cloud stratification

Central Africa experiences an inversion of seasonality between the northern and southern part of the equator (White, 1983). This makes the classification step particularly complex, as the same land cover types in the north and south of the country do not present the same phenological stage at the same time, and thus it is impossible to classify the whole country in a single way. To consider this particularity of the study area, the region has been stratified in three zones (Figure 2) as it was done for the Democratic Republic of Congo map (Vancutsem et al., 2009).

Table 1 : User and LCCS legends for the land cover map of Central Africa

No.	User's label	LCCS label
1	Dense moist forest	Broadleaved Evergreen High Trees with Closed High Shrubs / Broadleaved Semi-Deciduous High Trees with Closed High Shrubs
2	Submontane Forest	Closed (>65%) broadleaved semi-deciduous (>14m) forest, altitude: 1100-1750 m
3	Mountain Forest	Closed(>65%) broadleaved semi-deciduous (>14m) forest, altitude >1750
4	Edaphic Forest	Semi-Deciduous High Trees On Permanently Flooded Land Water Quality: Fresh Water/ Semi-Deciduous High Trees On Temporarily Flooded Land Water Quality: Fresh Water.
5	Mangrove	Closed to Open (100-40)% Semi-Deciduous High Trees On Permanently Flooded Land Water Quality: Saline Water.
6	Forest/savanna mosaic	Mosaic closed (>65%) semi-deciduous high (>14m) forest-closed grassland with sparse trees
7	Rural complex (forest area)	Cultivated and Managed Terrestrial Area(s) / Broadleaved Semi-Deciduous Woodland With Closed Shrubs And Closed Herbaceous Layer
8	Closed to Open Deciduous Woodland	Broadleaved Deciduous High Trees
9	Savanna woodland-Tree Savanna	Broadleaved Deciduous Woodland with Closed Medium to Tall Herbaceous Layer
10	Shrubland and shrubland with sparse trees	Broadleaved Deciduous (40 - (20-10)%) High Shrubland with Closed Herbaceous
11	Grassland	Closed Tall Herbaceous Vegetation with Medium Sparse Trees
12	Aquatic grassland	Closed Tall Herbaceous Vegetation On Permanently Flooded Land// Closed Tall Herbaceous Vegetation On Temporarily Flooded Land.
13	Swamp grassland	Closed Tall Herbaceous Vegetation On Waterlogged Soil
14	Sparse (<15%) vegetation	Sparse Trees // Sparse Shrubs // Herbaceous Sparse Vegetation
15	Mosaic cultivated areas/vegetation (herbaceous or shrubs)	Cultivated and Managed Terrestrial Area(s) // Closed to Open Shrubland (Thicket) // Herbaceous Closed to Open Vegetation
16	Agriculture (> 70%)	Rainfed Herbaceous Crop(s)
17	Irrigated agriculture (> 70%)	Irrigated Herbaceous Crop(s)
18	Bare areas	Bare Area(s)
19	Artificial surfaces and associated areas (Urban areas> 50%)	Artificial Surfaces and Associated Area(s)
20	Waterbodies	Natural Waterbodies // Artificial Waterbodies



Figure 2 : Seasonal zones

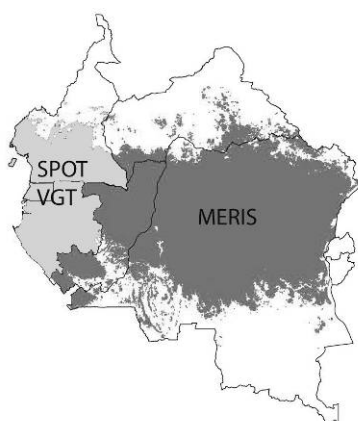


Figure 3 : The two “clouds” zone dividing the central strata

The first zone corresponds to the dry forest and savanna of the north, the second zones to the dense tropical forests of the center and the last to the open dry forests and savanna of the south. The stratification in tree seasonal zones was based on vegetation limits identified using the NDVI vegetation index values in two ways, the first is an unsupervised classification based on the NDVI annual temporal profile of ten days composite averaged for 8 years of SPOT Vegetation data. This allow to discriminate pixels which presents no or low seasonal variation, i.e. in the central dense tropical forest from pixels showing a stronger seasonal variation, i.e. tree savanna. In cloudy areas, ten days temporal syntheses, even averaged on 8 years, still present some pixels without valid observations. An unsupervised classification of NDVI annual SPOT VGT values was used to fill the gaps. A 3 km (10 pixels of Meris) buffer has been added to each

seasonal zone to avoid sharp limits when the 3 zones will be put together.

High cloud coverage is an important issue in a tropical area. Nineteen months of MERIS data was not enough to build consistent temporal syntheses for some area near the Atlantic coast, where the cloud coverage is the most important. Spot VGT data were used instead to map the central seasonal zone in Gabon, Cameroon and Equatorial Guinea. Figure 3 shows the two sub-strata dividing the central zone.

4.3. clustering for each seasonal and cloud zone

A specific unsupervised classification is performed for each of the four zones. For each stratum that present seasonality, a specific temporal syntheses of Red and NIR bands of MERIS is used in addition of a classic annual composite of MERIS for the unsupervised classification. The compositing period of the seasonal temporal syntheses is chosen according to the seasonality specificity of each zone. For the centre, an annual composite is the more relevant information, as tropical forest variation during the year is very low. For the north and the south on the other side, the clearer information is available during the period going from one month after the last rainfall to the beginning of the savanna fires. For each stratum, the MIR reflectance band of SPOT VEGETATION is added, MERIS not possessing a MIR band. The MIR is resample to 300m. For the “cloudy” stratum, only Spot VGT data is used.

4.4. clustering for each seasonal and cloud zone

A specific unsupervised classification is performed for each of the four zones. For each stratum that present seasonality, a specific temporal syntheses of Red and NIR bands of MERIS is used in addition of a classic annual composite of MERIS for the unsupervised classification. The compositing period of the seasonal temporal syntheses is chosen according to the seasonality specificity of each zone. For the centre, an annual composite is the more relevant information, as tropical forest variation during the year is very low. For the north and the south on the other side, the clearer information is available during the period going from one month after the last rainfall to the beginning of the savanna fires. For each stratum, the MIR reflectance band of SPOT VEGETATION is added, MERIS not possessing a MIR band. The MIR is resample to 300m. For the “cloudy” stratum, only Spot VGT data is used.

4.5. automatic labelling

The clusters produced by the classification are labelled with reference existing maps. The legend of these maps are aggregated to correspond to the legend of the new map. The clusters are superimposed to the reference maps and a label will be specified according to the proportions (in term of area) covered by the classes of the reference maps. A threshold is fixed to 50 % to inherit a label.

4.6. Manual editing

Unlabelled clusters, after the automatic step, are manually labelled by visual interpretation of the different composites with help of the NDVI season profile and Landsat images. NDVI value of the classes is useful to discriminate e.g. the rural complex from the non forest. It is indeed expected to find a low NDVI value for non forest and a higher NDVI value for rural complex. The seasonal profile of NDVI are used as well to take into account the seasonal profile of the ecosystem.

Specific classes such as mangroves are directly superimposed from the GLC 2000 map or the Cameroun WRI map. Land cover labels such as urban areas, aquatic grassland are reedited by hand.

5. RESULTS AND DISCUSSION

The final map product is presented in Figure 4. The spatial resolution of MERIS (300 m) better discriminate details in forest/savanna zones or rural complex. For the forest area of the Atlantic countries (Cameroon, Gabon and Equatorial Guinea) where SPOT VEGETATION data only was used, the spatial resolution is lower but the consistency of the signal is improved allowing to better map the state of degradation of the tropical forest there. The manual editing is time consuming but makes the difference in term of precision between a map like that and an automatic land cover mapping method.

The validation of this map, allowing to assess its accuracy, has been partially realized based on high resolution Landsat images extract by national experts during a workshop in Septembre 2009 and should be continued.

6. CONCLUSION AND PERSPECTIVES

A new 300 m map of the vegetation types of Central Africa has been achieved. This product is not only providing a precise mapping of vegetation types in Central Africa but could moreover be used to compute statistics of the vegetation types, useful for the monitoring of these ecosystems. By taking into account the seasonal and cloud coverage specificity of the region for the choice of the period of the compositing or the sensor used, an improvement from global automatic maps is observed.

Although this vegetation map wanted to be as exhaustive as possible, there is still a limitation due to the extractible information from optical remote sensing. Other types of data, typically radar data could be used to map the Edaphic forests. As other perspectives, the validation should be continued and the vegetation types should be described by their NDVI and NDWI temporal profiles.

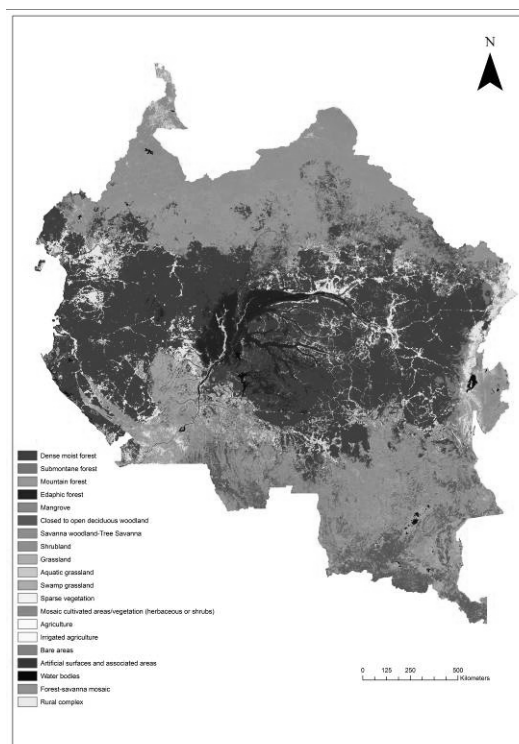


Figure 4: Vegetation map for Central Africa

REFERENCES

- Achard, F., DeFries, R., Eva, H., Hansen, M., Mayaux, P. & Stibig, H. J. (2007), 'Pan-tropical monitoring of deforestation', *Environmental Research Letters* 2(4), 045022.
- Arino, O., Gross, D., Ranera, F., Bourg, L., Leroy, M., Bicheron, P., Latham, J., Di Gregorio, A., Brockman, C., Witt, R., Defourny, P., Vancutsem, C., Herold, M., Sambale, J., Achard, F., Durieux, L., Plummer, S. & Weber, J. .L. (2008), 'Globcover. esa service for global land cover from meris', *2007 IEEE International Geoscience and Remote Sensing Symposium, IGARSS 2007* pp. 2412–15.

- de Wasseige, C., Devers, D., de Marcken, P., Eba'a Atyi, R., Nas, i. R. & Mayaux, P., eds (2009), *Les Forêts du Bassin du Congo, Etat des Forêts 2008*, Office des publications de l'Union européenne.
- Defourny, P., Vancutsem, C., Bicheron, P., Brockmann, C., Nino, F., Schouten, L., & Leroy, M. (2006), Globcover : A 300 m global land cover product for 2005 using envisat meris time series, in 'ISPRS Commission VII Mid-term Symposium "Remote Sensing: From Pixels to Processes"'.
- Di Gregorio, A. & Jansen, L. (2000), *Land cover classification system, classification concepts and user manual*, Food and Agriculture Organisation of the United Nations, Rome.
- Hansen, M. C., Roy, D. P., Lindquist, E., Adusei, B., Justice, C. O. & Altstatt, A. (2008), 'A method for integrating modis and landsat data for systematic monitoring of forest cover and change in the congo basin', *Remote Sensing Of Environment* **112**(5), 2495–2513.
- Mayaux, P., Bartholome, E., Fritz, S. & Belward, A. (2004), 'A new land-cover map of africa for the year 2000', *Journal Of Biogeography* **31**(6), 861–877.
- Mayaux, P., Gond, V., Massart, M., Pain-Orcet, M. & Achard, F. (2003), 'Évolution du couvert forestier du bassin du congo mesurée par télédétection spatiale', *Bois et forêts des tropiques* **277**, 47–52.
- MDA Federal (2004), Landsat GeoCover ETM+ 2000 Edition Mosaics, 1.0, USGS, Sioux Falls, South Dakota, 2000.
- Vancutsem, C., Pekel, J. F., Bogaert, P. & Defourny, P. (2007), 'Mean compositing, an alternative strategy for producing temporal syntheses. concepts and performance assessment for spot vegetation time series', *International Journal of Remote Sensing* **28**, 5123–5141.
- Vancutsem, C., Pekel, J. F., Evrard, C., Malaisse, F. & Defourny, P. (2009), 'Mapping and characterizing the vegetation types of the democratic republic of congo using spot vegetation time series', *International Journal Of Applied Earth Observation And Geoinformation* **11**(1), 62–76.
- White, F. (1983), *The vegetation of Africa. A descriptive memoir to accompany the Unesco/AEFTFAT/UNSO vegetation map of Africa*, Unesco.

Size matters: the effect of urban vegetation patch size on surface temperature patterns along a urban-to- rural gradient in NW Argentina

Antonela Gioia^(1,a), Leonardo Paolini⁽¹⁾, Agustina Malizia⁽¹⁾, Rosa Oltra-Carrio⁽²⁾ and José A. Sobrino⁽²⁾

⁽¹⁾ Instituto de Ecología Regional, Universidad Nacional de Tucumán. CC 34 , 4107, Tucumán, Argentina

⁽²⁾ Global Change Unit Image Processing Laboratory Universitat de València P.O. Box 22085 46071 Valencia, SPAIN

^(a) antonelagioia@yahoo.com.ar

ABSTRACT. Urbanization is one of the most extreme forms of land use change. The changes in vegetation cover and the increase of impervious caused by urbanization can contribute to an increase in surface temperature, leading to a phenomenon known as Surface Urban Heat Island (SUHI). The reforestation of public places can account of part of the overheating caused by concrete and asphalt construction. The main goal of this project is to analyze the relationship between different urban vegetation patches size and the spatial patterns of surface temperature (TS), in cities of Northwestern Argentina. We measure vegetation index NDVI and TS (based on Landsat TM satellite images) on 41 vegetation patches of different sizes. The results shows that while small patches (1 ha or less) show no effect on reducing TS, bigger patches show a decrease of 1 to 2.5 °C in comparison to the surrounding area dominated by human construction.

1. INTRODUCTION

Urban sprawl is associated with processes that lead to a loss of natural vegetation, with subsequent recovery of the same but modified in its composition (Grimm *et al.*, 2008). Built patches such as urban forests, parks, gardens, orchards and other built green areas are the most influential factors in the densely built-up and populated city regions (Aminzadeh & Khansefid, 2010). The main goal of this project is to analyze the relationship between different urban vegetation patches size and the spatial patterns of surface temperature (TS), in cities of Northwestern Argentina. Additionally, we want to explore the relationship between spatial patterns of TS and patch characteristics in different contexts and urbanization morphology.

2. METHODOLOGY

The study area includes four cities in the north of Argentina, located in the eastern foothills of mountain ranges: Yerba Buena, San Miguel de Tucuman, Salta and San Salvador de Jujuy (figure 1).

For data collection were selected 41 vegetation patches of different sizes. For each patch we calculated the percentage of surface vegetation from high-resolution images of Google Earth.

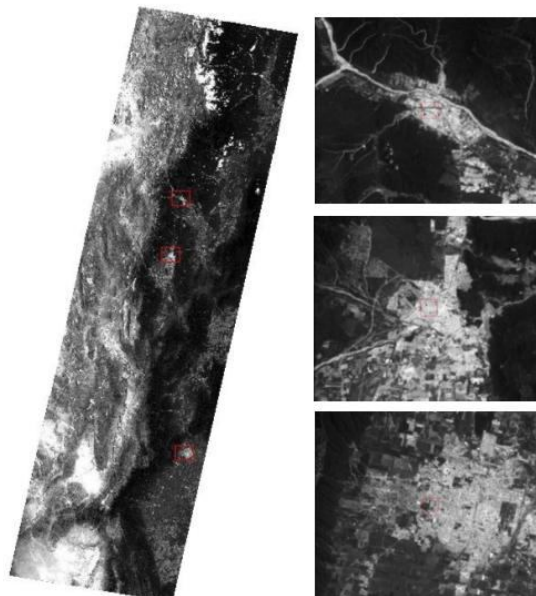


Figure 1. Landsat TM satellite images of the study area.

We used Landsat TM satellite images to calculate surface temperature (TS) and the normalized difference vegetation index (NDVI). CBERS satellite images were used (high spatial resolution) to accurately delineate the area corresponding to each patch and then applied the resulting polygons to Landsat TM images.

To relate spatial patterns of TS of the patch and its surroundings with characteristics of the patch in different contexts and urban morphology, we performed a multiple regression between the dependent variable (TS difference between green space and surrounding ΔTS) and the independent variables (vegetation patch size VPS, NDVI difference between green space and its surroundings $\Delta NDVI$, distance to the mountains DM).

3. RESULTS

The multiple regression results indicate a positive relationship ($r = 0.58$, $r^2 = 0.34$, $p = 0.002$) between the variables analyzed. That is, these variables explained 34% of ΔTS . Both VPS and DM are predictors of the ΔTS (VPS Beta = 0.51, $p = 0.001$; DM Beta = -0.34, $p = 0.04$) (figure 2).

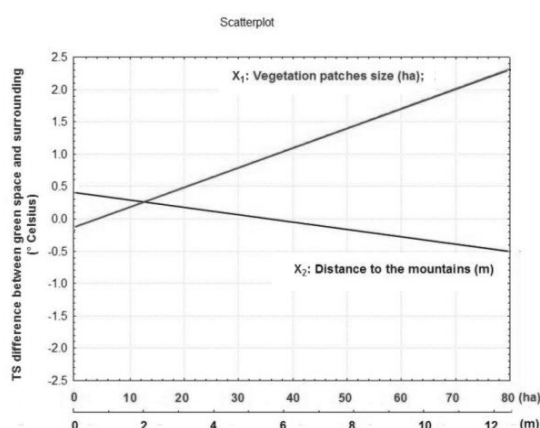


Figure 2. Regression graph between the surface temperature difference between green space and surrounding (ΔTS), vegetation patch size (VPS) and distance to the mountains (DM).

4. CONCLUSION

Vegetation patch size has an effect on the TS of the patch, which differs from the temperature of contiguous urban buildings. So, as the area increases the TS difference between green space (colder) and its surroundings (warmer) is higher. There is also a negative relationship between the TS difference and the distance to the mountains, so that as we move away from the mountains, the ΔTS is decreasing. Urban trees can modify the effect of environmental variables such as solar radiation, surface temperature, air temperature, humidity and wind speed, by reducing solar radiation from heating the surfaces, cooling the air by evapotranspiration, and reducing wind speed (Akbari *et al.*, 2001). These results may contribute to a better understanding of the effects of vegetation in urban areas in relation to its size and context.

5. REFERENCES

- Akbari, H., Pomerantz, M. and H. Taha. 2001. Cool surface and shade trees to reduce energy use and improve air quality in urban areas. *Solar Energy* 70: 259–310.
- Aminzadeh, B. and M. Khansefid. 2010. A case study of urban ecological networks and a sustainable city: Tehran's metropolitan area. *Urban Ecosyst* 13: 23–36.
- Grimm, N. B., Faeth, S. H., Golubiewski, N. E., Redman, C. L., Wu, J., Bai, X. and J. M. Briggs. 2008. Global Change and the Ecology of Cities. *Science* 319: 756-760.

Large-scale climatic influence on Sahelian vegetation dynamics

S. Huber and R. Fensholt

Dept. of Geography and Geology, University of Copenhagen, Øster Voldgade 10, DK-1350 Copenhagen, Denmark

Email: sh@geo.ku.dk

ABSTRACT *The greening of the Sahel during recent decades has been shown by several studies. Rainfall variability explains a significant part of this greening due to the close coupling between rainfall fluctuations and vegetation growth in the semi-arid Sahel. Many modelling and some satellite-based studies have revealed the association between Sahelian rainfall variability and a range of global sea surface temperature (SST) patterns. In this study we used the Normalized Difference Vegetation Index (NDVI) to study relationships between global SST and vegetation dynamics. If interannual variations in global SST patterns are found to cause interannual variations in the Sahelian vegetation productivity this will have important implications for (1) the ongoing debate of whether the observed greening of the Sahel is driven by anthropogenic or climatic change and (2) timely predictions of the Sahelian vegetation resource base. The analysis was performed using satellite-based SST and NDVI time series for the period 1982-2007. Prior to statistical analyses, the time series were smoothed and anomalies calculated. Spatial correlations were finally computed between the two time series of anomalies for different time lags in order to find ocean regions explaining most of the Sahelian vegetation dynamics. This study has shown that anomalies of Labrador Sea and Mediterranean SSTs have a significant impact on vegetation dynamics over the Sahel. Years with warmer than average SSTs in these two basins are often wetter over the Sahel leading to enhanced vegetation growth.*

1 INTRODUCTION

The development and prosperity of the African Sahel, a semi-arid transition zone between the Sahara desert to the north and the humid tropical savanna to the south, largely depends on the rainfall regime. Vegetation growth is limited to the short rainy season (3-4 months) with July to September being the months of highest rainfall over the Sahel and with August being the wettest month. The vegetation phenology thereby closely responds to the seasonal cycle of rain with biomass production taking place mainly during the rainy season. Precipitation in the region is characterized by large annual and decadal variability. Since the mid 1960's for instance, the Sahel underwent a severe rainfall decline culminating in a widespread drought in 1982-1985. But since then, rainfall has steadily increased and a greening trend has been observed for the region based on analyses of satellite NDVI time series (Eklundh and Olsson 2003; Anyamba and Tucker 2005; Herrmann, Anyamba et al. 2005). Rainfall variability explains a significant part of this greening (Nicholson, Davenport et al. 1990; Hickler, Eklundh et al. 2005) due to the close coupling between rainfall and vegetation growth in the semi-arid Sahel. Previous research suggested that these interannual to decadal variations of summer rainfall over the Sahel are related to global sea surface temperature (SST) patterns due to large scale and coherent changes in anomaly patterns (i.e.,

teleconnection) (Giannini, Saravanan et al. 2003; Raicich, Pinardi et al. 2003; Rowell 2003; Jarlan, Tourre et al. 2005; Caminade and Terray 2009).

Most of these studies were either purely modelling-based or they investigated the influence of SST on rainfall directly. In this study we used the Normalized Difference Vegetation Index (NDVI) to study relationships between global SST and vegetation dynamics. In the semi-arid Sahel, with the close coupling between rainfall and biomass production, NDVI is an attractive proxy of rainfall on small spatial scales (Philippon, Jarlan et al. 2007). If interannual variations in global SST patterns are found to cause fluctuations in the Sahelian vegetation productivity this will have important implications for (1) the ongoing debate of whether the observed greening of the Sahel is driven by anthropogenic or climatic change and (2) timely predictions of the Sahelian vegetation resource base.

The following research questions were investigated: a) is there a statistically significant relation between global SST and NDVI in the Sahel; b) which ocean regions explain most of the NDVI dynamics in the Sahel; c) which time lags are involved in the inter-relations between SST and NDVI and d) are certain regions in the Sahel more influenced than others.

2 DATASETS

2.1 Normalized Difference Vegetation Index (NDVI)

We used AVHRR (Advanced Very High Resolution Radiometer) GIMMS (Global Inventory Modelling and Mapping Studies) NDVI data as a proxy for vegetation greenness. GIMMS NDVI is currently available from 1982 to 2007 (full year coverage). This time period thus determines the temporal extent of analyses performed.

Monthly maximum NDVI composites with an 8 km spatial resolution used in this study were processed by the GIMMS Group at NASA's Goddard Space Flight Center, as described by Tucker et al. (2005) and Pinzon et al. (2005). More details about the binning and band calibration can be found in James and Kalluri (1994) and Vermote and Kaufman (1995). The original 8-bit GIMMS NDVI was converted into real NDVI values (range -1 to 1) for further analysis. NDVI was only analyzed for the Sahel region in sub-Saharan Africa. The boundaries of the Sahel used in this paper (indicated on the maps) is defined by Le Houérou (1989) using the 150 (to the north) and 700 mm (to the south) annual rainfall isohyets as borders of the Sahelian area based on rainfall average values for 1996-2007. All NDVI statistics and profiles presented in this paper refer to the area within this delimitation.

2.2 Sea surface temperature (SST)

NOAA Optimum Interpolation (OI) SST v2 data were used in this paper, provided by the NOAA-CIRES Climate Diagnostics Center, Boulder, USA (<http://www.esrl.noaa.gov/psd/data/gridded/data.noaa.oisst.v2.html>). The NOAA SST OIv2 product integrates both in situ and satellite data from November 1981 to the present at 1.0 degree spatial resolution globally in degrees Celsius (Reynolds, Rayner et al. 2002).

3 METHODS

3.1 Preprocessing

Prior to the statistical analysis, anomalies were calculated for both time series (NDVI and SST). All further calculations were performed on anomalies rather than the original data. Monthly anomalies for each 26-year data record (1982-2007 = 312 images) were obtained by computing the median value for each pixel for each month (=climatology value). This value was then subtracted from each image. For example, each January image would have the long-term January median value subtracted from it etc. Median values rather than mean values were used because the time series of this study are shorter than the typically 30

year data records used to calculate climatology values. The SST time series was smoothed using a moving average filter over a 3-month period (Jan-March, Feb-April, March-May etc.). From the NDVI time series mean values for the period July-September (termed JAS hereafter) were calculated for the Sahel, reflecting the rainy season. Finally, a Sahel NDVI Anomaly Index (SANAI) was obtained by taking the area-average of the mean JAS NDVI for the Sahel (Fig. 1).

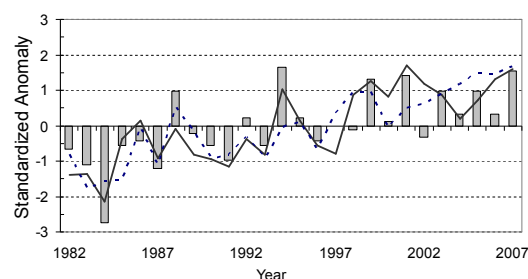


Fig. 1 Standardized anomalies of Sahel NDVI (SANAI) (bars), SE Mediterranean SST (SEMI) averaged for July-Sept. (solid line) and Labrador Sea SST (LSI) averaged for March-May (dashed line) for the period 1982-2007.

3.2 Teleconnections

Pixel-wise correlation coefficients were calculated, first between global SST anomalies (3-month means) and SANAI values for 1982-2007. Changes in SST can have an effect on the climate in the Sahel with a delay of several months therefore lagged correlation was also used, with SST observed at steps 0 to 6 months prior to the observations in the Sahel. Once the spatial correlations were retrieved, the two oceanic regions with highest correlations were selected and indices of SST anomalies extracted (Fig. 1) (Labrador Sea Index –LSI, and SE Mediterranean Index –SEMI; see section 4.2). Next, pixel-wise correlation coefficients between these SST anomaly indices and the NDVI anomaly time series for the Sahel were calculated to determine more specifically the geographical patterns and strength of impact throughout the Sahel region.

4 RESULTS AND DISCUSSION

4.1 Oceanic regions influencing Sahelian NDVI

The pixel-wise correlation analysis revealed several oceanic regions with significant correlations between SST anomalies and the area-averaged Sahel NDVI anomaly index (SANAI). Highest r values were obtained for the Labrador Sea and the southeastern (SE) Mediterranean (Fig. 2) yet for different time steps. SST anomalies in the Labrador Sea measured during March-May (MAM) achieved highest r values

(0.76) whereas July-September SST anomalies measured in the Eastern Mediterranean corresponded best with SANAI ($r = 0.82$). The spring SSTs of the northern Atlantic in general seems to influence summer vegetation dynamics in the Sahel, in contrast to the southern Atlantic, where no significant linkages were discovered neither for spring (MAM) nor for summer (JAS) SSTs. Also an influence of the Indian Ocean on Sahelian NDVI this study has not been able to show. These results differ somewhat from some published studies, where relationships between SSTs and Sahelian rainfall were investigated (Giannini, Saravanan et al. 2003; Lu 2009).

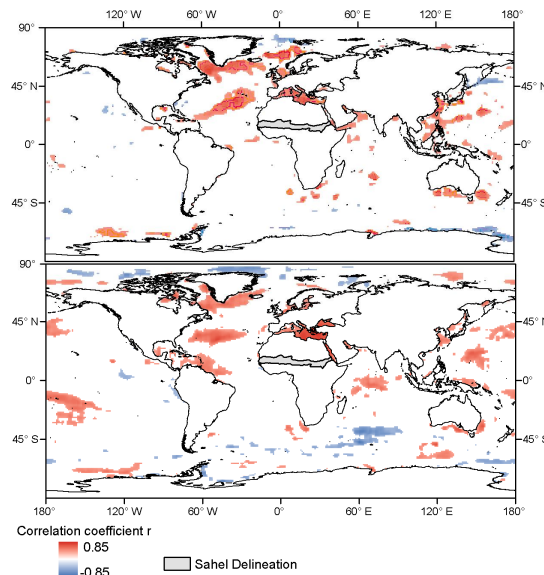


Fig. 2 Maps of correlation coefficients (r) between Sahel NDVI anomaly index (SANAI) and SST anomalies for (top) March-May and (bottom) July-Sept. for 1982-2007. Only correlations at the 95 % confidence level are shown.

The findings that the Mediterranean plays an important role in the Sahelian climate are consistent with those of other studies and suggest that a warming of the Mediterranean is often associated with enhanced Sahelian rainfall and hence increased NDVI values due to vegetation growth (Raicich, Pinardi et al. 2003; Rowell 2003). The main reason for the regional teleconnection leading to additional moisture over the Sahel in warm Mediterranean years is increased evaporation over the sea surface leading to an enhanced moisture content of the air that is advected southwards across the eastern Sahara into the Sahel (Rowell 2003).

4.2 Sahelian regions influenced by SST changes

When looking at the spatial correlations in the Sahel obtained by regressing the Labrador Sea Index (LSI) and the SE Mediterranean Index (SEMI), respectively, on the NDVI anomaly time series, we obtained for large parts of the Sahel significant r values and for both indices approximately the same spatial pattern (Fig. 3). Both maps show highest r values in Chad and the Darfur region of West Sudan. Winds originating in the Mediterranean region bringing moisture southwards (see section 4.1) (Raicich, Pinardi et al. 2003) and hitting the Sahel in this region. Moreover, the Chad-Sudan border region incl. Darfur has a mountainous topography, forcing the humid air to raise and rain off. A second region strongly influenced by SST patterns is the Mali-Burkina Faso border area.

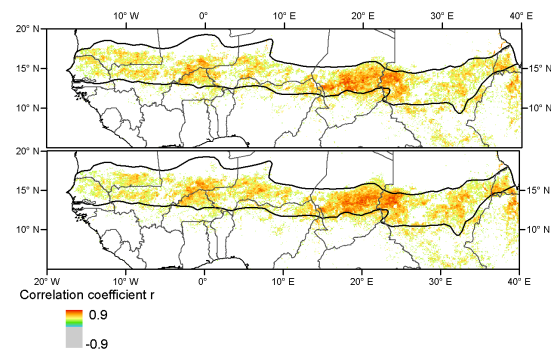


Fig. 3 Maps of correlation coefficients (r) between NDVI anomalies averaged over the period July-Sept. for 1982-2007 and (top) the Labrador Sea index (mean MAM) and (bottom) the SE Mediterranean index (mean JAS). Only correlations at the 95 % confidence level are shown.

The close match of the two maps suggests an interlinking of the Mediterranean basin with the Labrador Sea. Correlating the LSI with the SEMI resulted in an r value of 0.82. The influence of the North Atlantic Ocean on the European climate is known and reflected in the North Atlantic Oscillation (NAO) index. NAO displays fluctuations in the difference of atmospheric pressure at sea level between the Icelandic low and the Azores high. During its positive index phase, increased pressure generates more and stronger winter storms crossing the Atlantic Ocean on a more northerly track with Europe generally experiencing warm and wet winter conditions. During the negative NAO phase, fewer and weaker winter storms cross the Atlantic on a more west-east pathway resulting in cold air in northern Europe and moist air to the Mediterranean. However, when directly relating NAO to the Sahelian NDVI time series, no significant correlations were found.

6 CONCLUSIONS

This study has found significant relationships between global SST patterns and Sahelian NDVI, in particular in the North Atlantic Ocean and the Mediterranean Sea. The results show that the SSTs of the Labrador Sea and the Mediterranean have strongest influence on the vegetation dynamics in the Sahel. Warmer than average SSTs throughout these two oceanic basins seem to be associated with enhanced rainfall over the Sahel. In particular the relationship found for the Labrador Sea is interesting because strongest association was found for a time lag of 4 months between SST anomalies observed in the Labrador Sea and the NDVI in the Sahel. This time difference could be used for timely predictions of the Sahelian vegetation resource base.

ACKNOWLEDGEMENT

The authors thank the NASA Global Inventory Modelling and Mapping Studies (GIMMS) group for producing and sharing the AVHRR GIMMS NDVI data set as well as the NOAA-CIRES Climate Diagnostics Center, Boulder, USA, for providing the NOAA Optimum Interpolation (OI) SST v2 data.

REFERENCES

- Anyamba, A. and C. J. Tucker (2005). "Analysis of Sahelian vegetation dynamics using NOAA-AVHRR NDVI data from 1981-2003." *Journal of Arid Environments* **63**(3): 596-614.
- Caminade, C. and L. Terray (2009). "Twentieth century Sahel rainfall variability as simulated by the ARPEGE AGCM, and future changes." *Climate Dynamics*: 1-20.
- Eklundh, L. and L. Olsson (2003). "Vegetation index trends for the African Sahel 1982-1999." *Geophysical Research Letters* **30**(8).
- Giannini, A., R. Saravanan, et al. (2003). "Oceanic forcing of Sahel rainfall on interannual to interdecadal time scales." *Science* **302**(5647): 1027-1030.
- Herrmann, S. M., A. Anyamba, et al. (2005). "Recent trends in vegetation dynamics in the African Sahel and their relationship to climate." *Global Environmental Change-Human and Policy Dimensions* **15**(4): 394-404.
- Hickler, T., L. Eklundh, et al. (2005). "Precipitation controls Sahel greening trend." *Geophysical Research Letters* **32**(L21415).
- James, M. E. and S. N. V. Kalluri (1994). "The Pathfinder AVHRR Land Data Set - an Improved Coarse Resolution Data Set for Terrestrial Monitoring." *International Journal of Remote Sensing* **15**(17): 3347-3363.
- Jarlan, L., Y. M. Tourre, et al. (2005). "Dominant patterns of AVHRR NDVI interannual variability over the Sahel and linkages with key climate signals (1982-2003)." *Geophysical Research Letters* **32**(4).
- Le Houérou, H. N. (1989). *The grazing land ecosystems of the African Sahel*. Berlin ; New York, Springer-Verlag.
- Lu, J. (2009). "The dynamics of the Indian Ocean sea surface temperature forcing of Sahel drought." *Climate Dynamics* **33**(4): 445-460.
- Nicholson, S. E., M. L. Davenport, et al. (1990). "A Comparison of the Vegetation Response to Rainfall in the Sahel and East-Africa, Using Normalized Difference Vegetation Index from NOAA AVHRR." *Climatic Change* **17**(2-3): 209-241.
- Philippon, N., L. Jarlan, et al. (2007). "Characterization of the interannual and intraseasonal variability of West African vegetation between 1982 and 2002 by means of NOAA AVHRR NDVI data." *Journal of Climate* **20**(7): 1202-1218.
- Pinzon, J. E., M. E. Brown, et al. (2005). Hilbert-Huang transform and its applications. *Interdisciplinary mathematical sciences v. 5*. N. E. Huang. Singapore ; Hackensack, NJ ; London, World Scientific: xii, 311 p.
- Raichich, F., N. Pinardi, et al. (2003). "Teleconnections between Indian monsoon and Sahel rainfall and the Mediterranean." *International Journal of Climatology* **23**(2): 173-186.
- Reynolds, R. W., N. A. Rayner, et al. (2002). "An improved in situ and satellite SST analysis for climate." *Journal of Climate* **15**(13): 1609-1625.
- Rowell, D. P. (2003). "The impact of Mediterranean SSTs on the Sahelian rainfall season." *Journal of Climate* **16**(5): 849-862.
- Tucker, C. J., J. E. Pinzon, et al. (2005). "An extended AVHRR 8-km NDVI dataset compatible with MODIS and SPOT vegetation NDVI data." *International Journal of Remote Sensing* **26**(20): 4485-4498.
- Vermote, E. and Y. J. Kaufman (1995). "Absolute Calibration of Avhrr Visible and near-Infrared Channels Using Ocean and Cloud Views." *International Journal of Remote Sensing* **16**(13): 2317-2340.

Monitoring and forecasting the Urban Heat Island phenomenon in ten european cities: the UHI project

Paolo Manunta ^a, Monique Viel ^a, Giulio Ceriola ^a, Ioannis A. Daglis ^b, Koen de Ridder ^c, Theodoros Giannaros^d, Iphigenia Keramitsoglou ^b, Bino Maiheu ^c, Dimitrios Melas ^d, Enrique Montero Herrero ^e, Marc Paganini ^h, Marino Palacios ^e, Andrea Radius ^f, Tania Sapage ^f, Maria Tamame ^e, Han Tambuyzer ^g

(a) Planetek Italia Srl (Italy) (manunta @ planetek.it), (b) National Observatory of Athens - Institute for Space Applications and Remote Sensing – NOA-ISARS, Athens (Greece), (c) VITO, Flemish Institute for Technological Research, Mol (Belgium), (d) LAP_AUTH Aristotle University of Thessaloniki - Laboratory of Atmospheric Physics, Thessaloniki (Greece), (e) INDRA ESPACIO, S.A., Madrid (Spain), (f) EDISOFT S.A , Lisbon (Portugal), (g) EUROSENSE, Wemmel (Belgium), (h) European Space Agency - ESA

ABSTRACT Over the last decade, increasing morbidity and mortality of (mostly) elderly people is associated with extreme heat in cities particularly in southern Europe. Prolonged periods of high temperatures also put a strain on medical resources and place an additional financial cost to society as a whole. Another consequence is that energy consumption rises with the increased use of air conditioners and refrigeration appliance. In this context ESA is funding the Urban Heat Islands and Urban Thermography (UHI) project under the DUE – Data User Element – program. The project started on 1st November 2008 and will last 2.5 years. The project is analysing the UHI trends over 10 European cities (Athens, Bari, Brussels, Budapest, Lisbon, London, Madrid, Paris, Seville, Thessaloniki) over the last 10 years, using a multi-sensor approach and aims at establishing an operational EO based service for UHI monitoring and assessment. The project is relying on all satellite missions that embark TIR sensors with different spatial resolution (SEVIRI, AVHRR, AATSR, MODIS, LANDSAT, ASTER) to analyse the temporal and spatial variability of the UHIs in metropolitan areas. The available methodologies for extracting Land Surface Temperature and Air Temperature from space-borne sensors were reviewed and the most appropriate ones for monitoring the UHI, in 10 European cities of different climate, topology and size, were identified and applied. A demonstration of Near Real Time (NRT) and Forecasting service was performed in summer 2010 to show the potentiality of EO products for managing the UHI phenomenon.

1 INTRODUCTION

1.1 The UHI phenomenon

Over the last decade, heat waves have claimed an increasing number of casualties among the elderly – particularly in southern Europe that place an additional financial cost to society as a whole.. High densely built-up areas trap the heat, especially at night, causing what is called Urban Heat Islands in which city centres can be up to 10° C warmer than surrounding rural areas. Another consequence of UHIs is that energy consumption rises with the increased use of air conditioners and refrigeration appliance.

1.2 Urban climatology and remote sensing

The urban climatology is a complex phenomenon, due to the presence of many processes that influence the thermal parameters; mainly, the man-made structures of the cities modify the evapotranspiration

capacity of the terrain and the air fluxes, causing the changing of the absorption-reflectivity-emissivity processes of the solar radiation.

The thermal remote sensors can observe the Surface Urban Heat Island (SUHI), or, more specifically they ‘see’ the spatial patterns of up welling thermal radiance received by the sensor (most often radiometric or brightness temperatures corrected only for atmospheric transmission). The integration of the low, medium or high resolution thermal remote sensing observations with ground-based measurement and of the knowledge of the urban surface morphology allows to characterize the directional effects inherent in directional radiometric temperature observations made over urban areas; moreover, the integration with urban atmosphere models improves the analysis of the study surface–air temperature relations.

2. OBJECTIVES OF THE URBAN HEAT ISLANDS AND THERMOGRAPHY PROJECT.

ESA is funding the Urban Heat Island Urban Thermography project – so called UHI project - under the DUE – Data User Element – program as a contribution 1) to the study of urban climatology and 2) to help decision and policy makers in mitigating the effects of UHIs through appropriate alert systems and, in terms of reducing risk, through improved urban planning. The project started on 1st November 2008 and will last 2.5 years.

The main objectives of the project are:

1. Integration/assimilation of satellite remote sensing observations and ground weather stations data into urban meteorological and climate models, to facilitate mitigating the impact of UHI and to reduce the risk of a heat wave effects;
2. Study of the mission requirements for a high resolution TIR satellite sensor;
3. Study of how TIR observations from space can support the implementation of urban energy efficiency policies embracing typical issues from Southern (i.e. energy demand for air conditioning) as well as Northern (i.e. energy demand for domestic heating) Europe.

The prediction and mitigation of UHI spatial and temporal variability in metropolitan areas is the ultimate goal. For this reason the project is analysing the UHI trends over 10 European cities (Athens, Bari, Brussels, Budapest, Lisbon, Madrid, Paris, Seville, Thessaloniki) during the last 10 years, using a multi-sensor approach, making the best use of all satellite missions that embark TIR sensors (SEVIRI, AVHRR, (A)ATSR, MODIS, LANDSAT, ASTER). Thermography mapping using airborne data will be performed for three cities.

In detail, the project consists in:

- monitoring Land Surface Temperature and Air (1.5 to 2m height) Temperature (respectively LST and AT) variability with different temporal and spatial resolutions. LST retrievals – derived from remote sensing observations – will be assimilated into urban climate models. Long time series of data will be acquired to study the historical trends of surface and air temperatures in metropolitan and surrounding rural areas of the cities.
- producing bio-climatic indicators (e.g. thermal stress indices) which can be exploited for estimating the well-being of the population in relation to the current meteorological conditions
- identifying in Near Real Time and forecast the location and magnitude of urban heat islands in particular during heat waves. That entails to integrate LST retrievals derived from remote

sensing observations into Numerical Weather Prediction (NWP) models.

- analysing and interpreting the observed LST and AT as a function of land use/land cover, surface albedo, surface emissivity, surface roughness.
- producing thermographic maps at high and very high resolution to understand the energy efficiency of city surfaces and to monitor the impact of energy efficiency policies.

Seventeen (17) public organizations from the 10 European cities are involved in the project as users with different institutional roles, tasks and needs. The users are from Environmental institutes, planning authorities & urban engineering departments, Civil Protection, Meteorological services and broadcasting channels, Health Institute. Involvement of the users along the project enabled a better definition of the needs of each user category and an evaluation of the services and products delivered regarding usefulness and appropriateness to support their institutional tasks.

The UHI consortium is composed by six (6) organizations from Italy (Planetek Italia, Coordinator), Belgium (VITO & EUROSENSE), Greece (NOA-ISARS & LAP-AUTH), Portugal (Edisoft) and Spain (INDRA Espacio).

This article is focused on the approach followed by the project:

- to set up a standard methodology applicable to different European regions to exploits Earth Observation (EO) technology for supporting local authorities to assess, monitor and forecast heat waves and heat islands;
- to contribute to advanced research fields such as the retrieval of air temperature from observed LST imagery and its ‘direct’ assimilation into numerical models.

3 METHODOLOGY AND APPROACH

In order to select the most appropriate algorithms and methodology for satellite/airborne image processing, an accurate analysis of advantage and disadvantage of the algorithms and climatology proposed in literature followed by a trade-off analysis have been achieved for each of the UHI products, taking also into consideration criteria such as: 1) ancillary data needed in terms of quantity and characteristics 2) algorithms easy to translate into an operational implementation chain.

3.1 Implementation and production

All the selected algorithms and methodologies described in Tab.1 have been defined and developed into working processing chains.

Products	Sensor/model/algorithms
LST and Emissivity (3-5 km)	Seviri (GSW Freitas et al. 2010, Trigo et al., 2008a and 2008b)
AT (3-5 km)	LST (3-5km) + Surface energy balance + objective hysteresis model
LST and Emissivity (1 km)	AVHRR, ASTRR, MODIS (SWT Jiménez-Muñoz and Sobrino 2008)
AT (1km)	LST (1km) + Surface energy balance + objective hysteresis model
LST and Emissivity (~100m)	<ul style="list-style-type: none"> • ASTER (TES Gillespie et al. 1998; Dash et al. 2002) • Landsat (Single channel Jiménez-Muñoz and Sobrino 2003 and Jiménez-Muñoz and Sobrino Nichol et al., 2009)
AT (~100 m)	LST + Aerodynamic resistance model (test phase)
LST and Emissivity (5-30 m)	Airborne sensor (AHS) (Hybrid method Peres et al., 2008; SWT Jiménez-Muñoz et al. (2006), Single Channel; Sobrino et al. (2008)
AT (5-30) m)	LST (5-30m) + Aerodynamic resistance model (test phase)
NRT and forecast of AT (1km)	<ul style="list-style-type: none"> • HRES-SEB algorithm (NRT) (Homscheidt, 2008) • Forecasting Model (WRF) (LST assimilation is in development)
NRT and forecast of Discomfort Indexes	<ul style="list-style-type: none"> • Discomfort Index (DI); • Thermal Stress Index (TSI); • Predicted Mean Vote (PMV); • Predicted Percentage of Dissatisfied (PPD) • Universal Thermal Climate Index (UTCI)
Heat wave hazard and risk. NRT, forecasting and monthly	Evaluation of vulnerability from statistical and wealth information. Evaluation of hazard from the Discomfort Indexes
Thermographic mapping above 5m	Surface energy budget estimation by flux modelling approach from Grimmond and Oke (1999)
Thermographic mapping airborne	Based on the TES algorithm as per product LST at 100m.
Surface roughness	use of a LUT table which retrieves surface roughness from the CLC classes of Wieringa, J. (1993).
Surface Albedo	<ul style="list-style-type: none"> • Seviri (LandSAF AL product) • MODIS L3 product (500m)

Table 1. Algorithms and methodologies chosen for the UHI products

Taking into account the complexity of the matter and the number of UHI products, the delivery to the users is distributed along the 2.5 years of the project, as follows:

- 2010 (January): Athens, Lisbon, Madrid
- 2010 (June): Brussels. Bari, Seville
- 2011 (January): London, Paris, Thessaloniki, Budapest.

4 INNOVATIONS: modelling AT via assimilation of satellite derived surface temperature

One of the goals of the UHI project is to produce historic air temperature maps based upon satellite derived land surface temperature data for multiple years and urban agglomerations. At the start of the project no readily available model exists which is both accurate and fast enough to produce such a historic dataset, so a new approach was devised, which on the one hand tries to capture the essential physics behind the urban heat island phenomenon and on the other hand does not require the computing time a full mesoscale meteorological model would need.

The model implemented by VITO is split up into 2 parts, namely a flux model which computes the sensible heat flux H , and an atmospheric part calculating the effects of advection & vertical diffusion due to the large scale meteorological conditions (Fig.1). The flux model consists out of 4 main components, being the surface energy balance, a simple prognostic model for the surface and deep soil temperature and the objective hysteresis (OHM) model (Grimmond and Oke, 2002), which expresses the storage heat flux G as a function of the net radiation R_N at the surface, these 3 components are run in a sequential Monte Carlo data assimilation scheme, which integrates the remote sensing LST observations into the model evolution and at the same time produces dynamical estimates for the OHM model coefficients $a_{1,2,3}$. The resulting sensible heat fluxes are subsequently used as surface boundary conditions by a simplified atmospheric heat dispersion model. enabling the model to simulate heat transport downwind of urban agglomerations

5 TECHNOLOGICAL ADVANCEMENTS

To establish an operational chain to generate all UHI products, different technical solutions were developed, several algorithms and models improved contributing as such to put in place an advanced monitoring system of urban heat island phenomena.

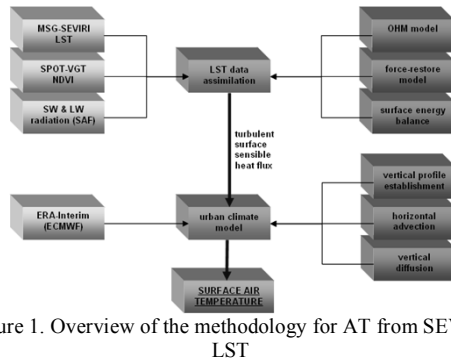


Figure 1. Overview of the methodology for AT from SEVIRI LST

5.1 Forecasting Air Temperature

The core of the retrieval of the AT for the UHI Forecasting Service (UHI-FS) is the prognostic meteorological model WRF (Weather Research and Forecasting). The general flow chart is shown in Fig.2.

The UHI-FS is characterized by a variety of innovative features that can be summarized as follows:

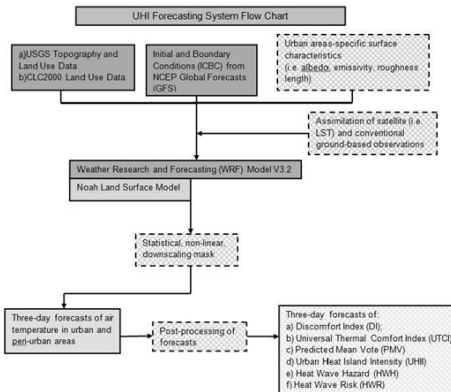


Figure 2. Flow chart of the UHI-FS

- *Exploitation of the CORINE-2000 (12/2009) land use database:* the CORINE-2000 land use (CLC) database is characterized by high spatial resolution, equal to 250m and is considered to be one of the most updated and reliable source of land use data for Europe. In the context of the UHI-FS by means of ingesting the CLC data into the model, it becomes possible to represent urban areas with a higher level of accuracy. Furthermore, the exploitation of these data enables the definition of three different “urban” land use classes, which is a critical fact for accounting for the great spatial variability of surface characteristics within urban areas.
- *Exploitation of satellite-derived data for defining surface characteristics of urban areas:* given the option of representing urban areas by three land use classes, satellite imagery was exploited in order to define values of albedo, emissivity and roughness

length for each of the considered land use classes. These particular surface characteristics are considered to play a key role in the configuration of the energy budget of urban areas, thus having a direct influence on the simulation of AT.

- *Statistical downscaling mask:* the primary forecasts that are provided by the service have a rather moderate spatial resolution (2km). A statistical, non-linear, downscaling mask was developed in order to improve the spatial resolution of the forecasts. The development of this mask was carried out in the context of designing and training an artificial neural network (ANN), whose aim is to predict AT at 250m spatial resolution (i.e. the resolution of CLC data). In order to accomplish this task, the ANN is trained given the inputs (patterns) of (i) model forecasted AT at the nearest CLC point; (ii) hour of the day for which the forecast is valid and; (iii) land use class at the considered CLC points. Observed AT at the considered land use points is also used during the training phase for verifying the learning ability of the ANN and adapting accordingly the whole learning (training) process.

5.2 NRT Air Temperature

The NRT Air Temperature is based on an empirical algorithm reported in Tab.1 which requires several inputs, as shown in Fig.3. Apart from DEM and Slope, all input data have to be obtained daily, just before the processing.

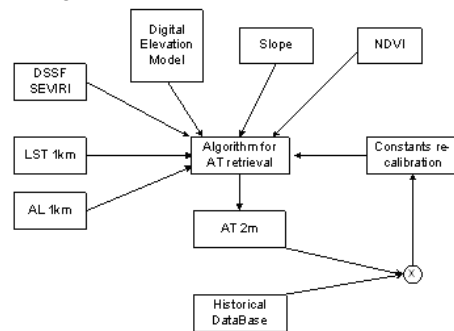


Figure 3. Flow chart of the NRT AT retrieval

This requirement implies the fast procurement of data from very different sources followed by a fast processing to be able to deliver the AT and the other derived products within few hours after the EO data acquisition. The adopted solution was semi-automatic: currently the only manual operation is the procurement of EO data at 1km (AVHRR, MODIS or AATSR) as soon as are made available from the respective agencies. Then they are automatically processed and transformed in LST by using the procedures implemented within the UHI project (see next paragraph).

5.3 LST products from multiple sensors

Different LST products have been implemented, classified according to their ground resolution. In the case of LST at 3-5km (from SEVIRI) the products have been taken from the LSA SAF project and then re-elaborated to meet the format requirement of the UHI Information System. In the case of LST at Very High Resolution from airborne sensor, it has been obtained within the DESIREX project framework and re-elaborated in the adequate format.

Solutions put in place to produce LST at 1 km took into consideration the following requirements:

- processing images from 4 different sensors (AVHRR, MODIS AQUA/TERRA and (A)ATSR)
- covering 10 cities with very different characteristics (size, latitude, topography, etc.)
- covering a large period of time (10 years).

To satisfy the first two points a great care has been put into the choice of a single algorithm (see Tab.1) calibrated for each sensor. For the third point a fully automatic procedure has been implemented, able to process data from all the four sensors and to process rapidly and automatically a large amount of images. The same procedure is used also into the NRT processing chain.

Finally for the LST at ~100m, a fully automatic procedure has been implemented for ASTER and a semi automatic one for Landsat TM.

6 VERIFICATION OF PRODUCTS

The verification of all the products in respect to their usefulness both as a contribution for the UHI phenomenon study and as a valid tool for the Users' institutional tasks is one of the central activities of the project and a verification protocol has been established for each of them which defines a quantitative and a qualitative approach.

For the quantitative one of the major issue is to find a suitable ground truth data to be compared with. This aspect is critical for LST and in this case, to overcome such difficulty, the comparison is against official level 2 products from the same sensors (for example the LST product at 1km from MODIS is compared with the MODIS L2 LST product from NASA). In this framework the ground data measurements from two in field campaign financed by ESA – DESIREX (summer 2008 over Madrid) and THERMOPOLIS (summer 2009 over Athens) – were available and have been used in particular for the verification of the AT products.

For the qualitative approach various techniques have been adopted:

- time series analysis
- spatial pattern recognition of temperature

- multi-resolutions and multi-sensors characterisation of UHI or heat wave events
 - those analysis for each city with its peculiarities
 - presentation of the products and feedbacks from the local users
- making fully use of the 10 years of historical products for each city.

7 NRT/FORECASTING DEMONSTRATION

During summer 2010, a two months NRT and Forecast service (FS) demonstration has been performed over six cities (Athens, Bari, Madrid, Lisbon, Seville and Thessaloniki) to make an assessment of the methodologies and algorithms adopted and check with the users the usefulness of the service.

The NRT/FS products are the following ones

- 2-m Air Temperature (°C)
- Discomfort Indexes: Predicted Mean Vote (PMV), Thermal Stress Index (TSI), Discomfort Index (DI), Universal Thermal Climate Index (UTCI) which can be exploited for estimating the well-being of the population in relation to the current meteorological conditions.
- Heat Island Intensity
- Heat Wave Risk

The NRT service demonstration has been carried out operationally by Edisoft, 5 days per week, in the months of July (Madrid and Lisbon) and August (Athens and Bari) 2010 and an alert system via email has been implemented.

The Forecast System demonstration has been carried out on a daily basis in July-August 2010 for the 6 cities using the computational infrastructure of LAP and HellasGrid. An example is shown in Fig.4.

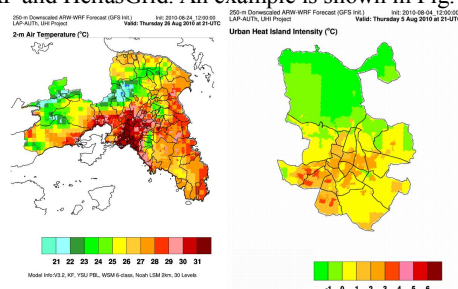


Figure 4. Example forecast maps at 21.00 UTC. Left: AT (°C) map over Athens: 24th August 2010 (right). Right UHI (°C) map over Madrid: 4th August 2010

Verification of the services with the users and validation of the results are on-going.

8 UHI INFORMATION SYSTEM

An Informative System (IS) has been designed to host all the products and to allow consultation and

downloading from a WebGIS interface, as a common tool for supporting local authorities of different European regions. All the products ingested into the system are converted in a common format and geographic projection complemented by metadata information compliant with the ISO 19115-2 standard.

9 CONCLUSIONS

The UHI project has been created with the ambitious goal of investigating the phenomenon of the Urban Heat Islands, by a synergy of EO data and in situ data combined into innovative meteorological and climatologic algorithms and models. This study is being conducted together with users belonging to 10 European cities, to make them able to understand the meaning and the use of the UHI products in their risk prevention or energy saving policies implementation.

The project has been conceived with a strong innovative drive, in particular for the use of the current TIS sensors and the development of models and methodologies to set up a standard methodology applicable to different European regions to exploits Earth Observation (EO) technology and to contribute to the thematic of retrieval of AT from observed LST imagery and its 'direct' assimilation into numerical models. This from one side lead to the development of a dedicated model able to retrieve AT by assimilating (among other parameters) LST maps from EO data, and based on the essential physics behind the UHI phenomenon. On the other side it lead to the implementation of operational procedures for processing a large number of data from multiple TIR sensors and to the realisation of a NRT and Forecasting service, both for the planning and emergency management related to the UHI effects.

Finally the users had and will have an important role, together with the verification activities, for assessing the reliability and usefulness of the UHI products for their use in risk management, prevention and planning activities related to the urban heat island phenomena and its consequences over the citizens

9 REFERENCES

- Dash P, Gottsche F.M., Olesen F.S. and Fischer H., 2002. Land surface temperature and emissivity estimation from passive sensor data: theory and practice-current trends. *Int. J. Remote Sens.*, 23, 2563-2594.
- DESIREX campaign at <http://www.uv.es/desirex/>
- Gillespie A., Rokugawa S., Matsunaga T., Cothorn J. S., Hook S. and Kahle A. B., 1998. A temperature and emissivity separation algorithm for advanced spaceborne thermal emission and reflection radiometer (ASTER) images *IEEE Transactions on Geoscience and Remote Sensing*, 36, 1113-1126.

Homscheidt M.S., Zaksek K, 2008 . Air temperature in high temporal and spatial resolution from a combination of the SEVIRI and MODIS instruments. *EUMETSAT Meteorological Satellite Conference*, 8-12 Sept. 2008

Grimmond C. S. B. and Oke, T. R. 1999. Aerodynamic properties of urban areas derived from analysis of surface form. *Journal of Applied Meteorology*, 38, 1262-1292.

Jiménez-Muñoz, J. C. and Sobrino, J. A., 2008. Split-Window Coefficients for Land Surface Temperature Retrieval From Low-Resolution Thermal Infrared Sensors. *IEEE Geoscience and Remote Sensing Letters*, 5, No. 4, 806 – 809.

Jimenez-Munoz, J.C. Cristobal, J. Sobrino, J.A. Soria, G. Ninyerola, M. Pons, X. , 2009. Revision of the Single-Channel Algorithm for Land Surface Temperature Retrieval From Landsat Thermal-Infrared Data *IEEE Transactions on Geoscience and Remote Sensing*, vol. 47, issue 1, pp. 339-34.

Peres L. F., Sobrino J. A., Libonati R., Jiménez-Muñoz J. C., Dacamara C. C. and Romaguera M.(2008), Validation of a temperature emissivity separation hybrid method from airborne hyperspectral scanner data and ground measurements in the SEN2FLEX field campaign, *International Journal of Remote Sensing*, 29:24,7251- 7268.

Trigo, I. F., I. T. Monteiro, F. Olesen, and E. Kabsch, 2008a: An assessment of remotely sensed land surface temperature. *J. Geophys. Res.*, 113, D17108, doi:10.1029/2008JD010035.

Trigo, I. F., L. F. Peres, C. C. DaCarnara, and S. C. Freitas, 2008b: Thermal land surface emissivity retrieved from SEVIRI/meteosat. *IEEE Trans. Geosci. Remote Sens.*, 46, 307-315.

Urban Heat Island and Thermography project website: <http://www.urbanheatisland.info/>

Wieringa, J., 1993: Representative roughness parameters for homogenous terrain. *Boundary-Layer Meteorology*, 63, 323-363

10 ACKNOWLEDGMENTS

We would like to warmly thank:

- ESA that fully support the implementation of the project (under contract number 21913/08/I-LG)
- SEVIRI/MSG LST was provided by the EUMETSAT Satellite Application Facility on Land Surface Analysis (LSA SAF)
- the UHI users for their guidance through the project, the provision of in-situ data and their efforts in validating the UHI services
- Luís Pessanha (Instituto de Meteorologia,Lisbon) for fruitful discussions on the LSA SAF LST.

Characterization of marine benthic habitats located at the Puerto Morelos Reef National Park, México incorporating remote sensing data

Zapata –Ramírez P.A.¹, H. Hernández – Nuñez², P. Blanchon¹ and J.A. Sobrino³

¹ *Coral Reef Unit. Inst. Marine Science and Limnology – UNAM. México*

² *Remote Sensing and GIS Laboratory. CINVESTAV Unidad Mérida – México*

³ *Global Change Unit –Image processing Laboratory, University of Valencia SPAIN*
paula.zapata.r@gmail.com

1 INTRODUCTION

Marine benthic habitats are being threatened by global warming, natural disasters and the increased pressure of the global population. As such perturbations may reduce diversity in marine environments; marine benthic habitats are increasingly seen as refuges for conserving biodiversity (Mellin et al., 2010). Global warming and human pollution are causing declines in the health and productivity of coastal ecosystems and have led to a significant decline in biodiversity. Although in the past, coastal ecosystems recovered from natural disturbances such as tropical cyclones, today these ecosystems are becoming more fragile and their recovering is more difficult. Natural disasters such as hurricanes and heavy storms are inevitable and it is almost impossible to fully recoup their damages. However, it is possible to minimize the potential risk by developing disaster early warning strategies, prepare and implement plans to favour resilience to such disasters and to help in post disaster rehabilitation (Scopéltis et al., 2010). These habitats are in urgent need of efficient monitoring and management programs to sustain their biological, economic and cultural values for the global community.

Coastal marine environments remain poorly characterized because they have not been mapped with sufficient accuracy and at spatial resolutions high enough to support their efficient management (Costa et al., 2009). Most of the considered *hot spots* for marine biodiversity around the world lack of information or resources to obtain such a comprehensive inventories. Thus, management decisions have too often to be based on limited information. Published marine benthic applications often still focus on spatially limited pilot sites which are investigated for research purposes, while synoptic, reliable and thematically rich habitat maps are in growing demand everywhere around the Planet for a variety of applications (Andréfouet, 2008).

Usually, available information is based on traditional in situ surveys which are time- and labour-intensive and generally lack the spatial resolution and precision required to detect subtle changes before they become catastrophic (Scopéltis et al., 2010). Accurate mapping at a scale at which conservation network sites are designated and managed, is essential to measure and consider biodiversity representation (Sarkar and Margules 2002, Mellin et al. 2010). As conservation efforts develop, repeated habitat mapping will become increasingly necessary in order to monitor habitat evolution as a result of protection measures. Remotely sensed data can provide broad-scale synoptic views of benthic environments and can also provide temporal data that may be used to assess change events and community dynamics in marine environments (Lim et al., 2009).

This study presents the integration of high-spatial resolution satellite images and *in situ* data for implementing a new spatial information tool for marine benthic habitats assessment at Puerto Morelos National Park (~9000 ha). Previous assessment of habitat changes in the area relied on the CARICOMP (CARibbean COastal Marine Productivity Program, 1998) program which was based on the monitoring of five 10 meters transects at two locations (Rodríguez-Martínez et al. 2010). To evaluate the occurrences of the marine benthic habitat locations, we classified and delineated benthic habitats along the north-east coast of Quintana Roo (Yucatan) from the shore to the 30 m isobath using a combination of a satellite images and scuba video transects. These data were assembled into a geographical information system to generate maps that will allow the evaluation of spatial and temporal changes following environmental disturbances, such as hurricanes, or as a result of climate change.

2 MATERIALS AND METHODS

2.1 Puerto Morelos National Park and recent history of disturbances

Puerto Morelos NP is located between the 21°00'00" - 20°48'33" N and 86°53'14.40" - 86°46'38.94" W (Instituto Nacional de Ecología, 2000), in the northeastern Yucatan Peninsula, in the state of Quintana Roo, México. The park was declared marine protected area (MPA) in 1998 and has an area of 9 066 ha that extends for 21 km along the NE side of the Yucatan Peninsula (Fig. 1).

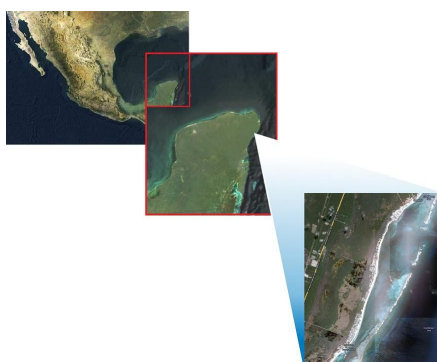


Figure 1. Study area

The MPA contains a reef system that is close to shore (0.1–2.5km) making it easily accessible to visitors (Rodríguez-Martínez, 2008). The marine benthic habitats located at the Yucatan coasts has been affected for several category 5 hurricanes, Gilberto in 1998, Mitch in 1998 and Wilma in 2005. On the other hand since the 1980s, the corals of this reef have been affected by pan-Caribbean infectious diseases and by relatively widespread non-lethal bleaching episodes (mild: 1997, 2002, 2003, 2006; moderate: 1998, and 2005). However the effects at large scale have not been monitored and to the best of our knowledge no quantitative data exist to assess any subsequent mortalities. *A. palmata* mortality on corals has also been observed in the past (Jordan-Dahlgren and Rodríguez-Martínez, 2003).

2.2 Remote sensing and in situ measurements

This project acquired IKONOS imagery (March 2006), which has a 4x4 m pixel size and four multispectral bands: Blue 0.45 – 0.52 μm ; Green 0.52 – 0.60 μm ; Red 0.63–0.69 μm and Near Infrared (NIR) 0.76 – 0.90 μm . This sensor has been already used to differentiate benthic community types up to at least 5 m depth (depending on water clarity) (Mumby and Edwards 2002, Andréfouët et al. 2003, Purkis 2004). The high spatial resolution provides details of the benthos at benthic community scales of 2 to 5 m

(Mumby and Edwards 2002). The image was geometrically corrected by the image provider (GEOEYE). Sun – glint corrections were applied following the methodology proposed by Hedley et al., (2005). Atmospheric corrections were also applied following the method proposed for (Aronoff, 2005). Land mask were manually delineated using expert knowledge of the coastal zone to differentiate between inter-tidal areas and land in the imagery.

Substrata, habitats and communities were examined using a combination of field trip campaigns and satellite information. We evaluated the marine benthic habitat between October 2008 and February 2009 over 289 sites using a rapid-survey technique based on check points (Roesfelmán, 2009) and video. Ground-truth variables were recorded such as sediment types (sand, hard-ground, coral rubbles...), biotopes components of the benthic habitat (algae, sea-grass, corals, sponges...)... The field trip (Figure 2) was designed by -1) stratifying the area by visual assessment of the spatial pattern of benthic structures evident in the IKONOS image combined to an unsupervised ISODATA classification using ENVI 4.5, and -2) by randomly choosing transect location, direction and length, inside of each stratified area.

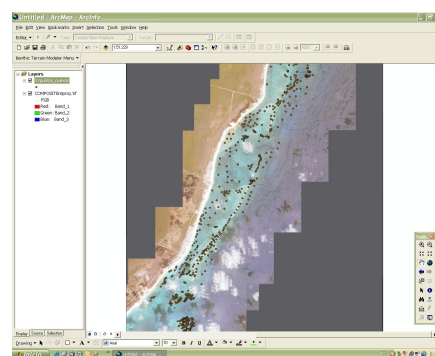


Figure 2. Field trip points

Video and photo surveys are a very valuable tool in habitat mapping, as they often give a first appreciation of the seabed in terms of physical substrate and biota (Mienis et al., 2006). In the same way, underwater video is well-suited to field survey because large areas can be covered fairly quickly and the method can be used without extensive training. For this survey, a snorkeler or diver swam over the bottom while recording the benthos using a standard camera. The video was pointed directly at the seabed and held between 1 m and 1.5 m from the substratum. Substrate coverage was recorded to the lowest possible taxonomic level. All benthic habitat and sample data, where located using GPS to facilitate the mapping of the habitat distribution using ArcGIS (ESRI).

2.3. Supervised classification and accuracy assessment

Ground – truth Areas Of Interest (AOI) in each benthic class were used to train a supervised maximum likelihood classifier (MLC) with ENVI 4.5 using the 3 first spectral bands (blue, green, red). This classification algorithm is based on image statistics derived from training pixels, representative for each benthic community type that have been determined from the data collected on the field trip. We used the standard classification scheme developed by Mumby (2000) and used in the frame of the Coral Millennium Project by Andréfouët et al. (2003). The supervised classification would ensure that the minimum unit mapped was at pixel scale, since each image pixel would be assigned a thematic class (Mumby and Edwards 2002). The number of training pixels attributed to each benthic community type also depended on the heterogeneity of the class. Spectrally homogeneous classes like deep sand and shallow sand just needed a minimal number of training pixels to determine reliable training statistics. Conversely, heterogeneous classes, like for instance sparse corals and dense live corals, required a larger training set in order to incorporate their characteristic variance. The selection of the training pixels was also therefore based on circumstantial evidence like, the position in the reef structure or the spectral characteristics of the benthic community type.

Formal accuracy assessment was summarized in a standard error matrix (Congalton, 1991). This matrix results from the comparison of the pixel values of the ground-truth AOI with the corresponding pixel values in the classification result. The matrix tabulated the level of agreement between the thematic class at a location in the image based map, and the same location in the reference data (Congalton, 1991), tabulations along the diagonal represent cases where the mapped category matched the true values. Off diagonal tabulations represent errors and are tabulated

as total in the margins. The error marginal represent the proportional error by category while error of omission was used as a basis for judging the adequacy of the mapping, and the error of commission as a means of determining how to fix the map to increase the accuracy (Eastman, 2003).

A global accuracy of the whole classified map was obtained by calculating the Tau accuracy (Ma and Redmond 1995; Purkis 2004; Roesfelman 2009) which has the ability to statistically represent the accuracy on the map in relation to the true environment by calculating the chance agreement between the reference and the results of a random classification. This parameter not only represents the overall accuracy but also takes into account the number of missclassifications.

3 RESULTS

From field measurements, twelve substrate classes were sufficient to encompass the sedimentary and biotic diversity on the area. However, a supervised classification trial with these 12 classes was not giving a good accuracy: Tau = 48%, while an overall accuracy of 80% is required for management purpose (Mumby and Green, 2000). This criterium was reached after the twelve original classes were collapsed into six broader classes: Tau = 79%. For instance, a reduction was made by merging seagrass and algae into a single class. It was deemed logical to merge the two classes, as they were both spectrally very similar and coded similar substrate assemblages on the lagoon. A typical view of each of the 6 final classes is presented in Figure 3.

The map that was obtained from the supervised classification is presented in Figure 4 and the standard error matrix in Table 1.

CLASS	1	2	3	4	5	6	Total	Error Comission
1 Sparse coral;	21	1	0	8	0	2	32	0.344
2 Seagrass and algae	1	64	1	1	2	0	69	0.073
3 Shallow sand	0	1	29	0	0	0	30	0.033
4 Dense live coral	13	6	0	28	1	4	52	0.462
5 Dead coral and hardground	0	1	0	0	58	0	59	0.017
6 Deep sand	3	0	0	5	1	38	47	0.192
Total	38	73	30	42	62	44	289	
Error Omission	0.447	0.123	0.033	0.333	0.065	0.136		0.177

Table 1. The error matrix contains a tabulation of the number of sample points found in each possible combination of true and mapped categories. As can be seen, tabulations along the diagonal represent cases where the mapped category matched the true value.

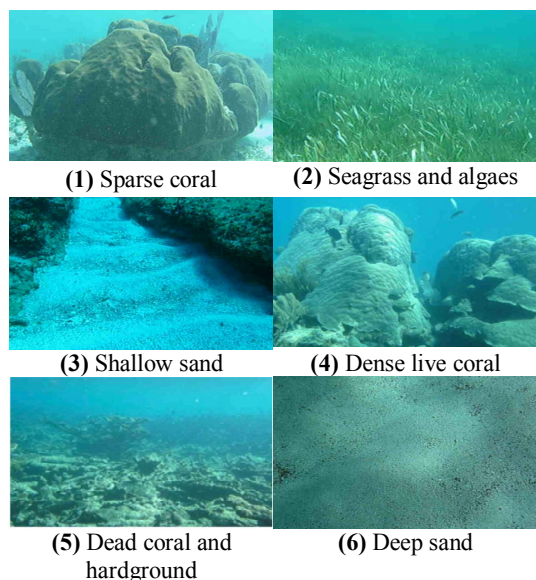


Figure 3: the different marine benthic habitat located at Puerto Morelos Reef Park.

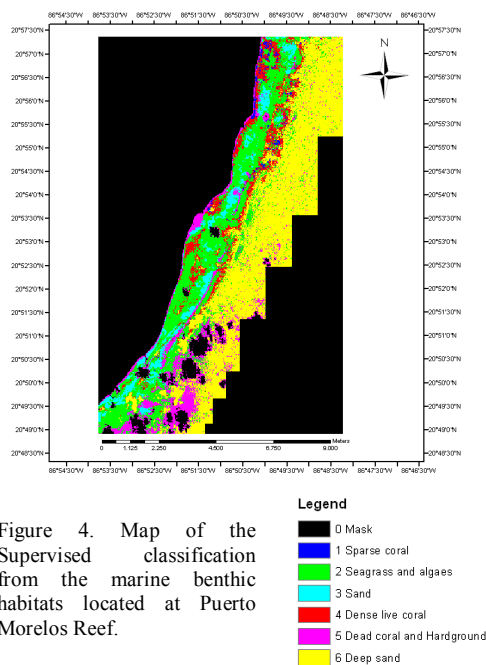


Figure 4. Map of the Supervised classification from the marine benthic habitats located at Puerto Morelos Reef.

Inspection of accuracy results revealed that IKONOS data allowed sand (class 3) and dead coral - hard ground (class 5) to be mapped very accurately (97% and 92% user accuracy respectively), seagrass and algae beds (class 2) to be mapped with a good

accuracy (85%), but that the user accuracies for corals, dense live coral and sparse coral (classes 1 and 4), were lower at 61 % and 56 % respectively. This low accuracy was also proved by the percentage of the omission error (0.447) in the sparse coral class and by the mayor commission error (0.462) of the dense live coral class.

This result was related to a low spectral separability using the 3 IKONOS visible bands. Other misclassifications occurred for instance when hardground was erroneously classified as seagrass along the high energy area at the fore reef (Figure 4). This is not a preferred seagrass growth habitat since seagrass requires low wave energy and unconsolidated substrate such as sand, which is just present at the lagoon.

In general, the Park is characterized by a great diversity of carbonate benthos such as live and dead corals, hardground and carbonate sand; the lagoon zone is dominated by seagrass and algae with minimal areas of unconsolidated carbonate sand; a zone near to the crest is dominated by aggregated coral rubble of the reef edge, postulated to be a storm deposit and the remains of the *Acropora* mortality. Habitat distribution in the area showed that the benthic community is present within areas characterized by rather abrupt morphological changes, hard substratum, low sedimentation rates and relatively shallow depths. The habitats are associated with seabed features that are indicative of vigorous bottom currents.

4. DISCUSSION

It seems evident from the observations that the present occurrence of marine benthic habitats are related to high current velocities within a limited water depth interval. These findings were supported by previous studies in other marine benthic habitats around the world, where overall mapping accuracy decreased with and increase in spatial complexity of or richness of benthic communities found on the benthic environments (Purkis, 2004; Roelfsema, 2009; Lim et al., 2009).

In this study it was possible to increase the overall accuracy by aggregating some of the mapping classes. In the error matrix, the off-diagonal element arises through confusion between sand and dead coral and hardground, and between sparse coral and dense live coral. Such confusions reflect in part, the weakness of the accuracy assessment rather than the potential of the classification algorithm. Areas of dead coral are frequently wrongly assigned to the deep sand class because the dead coral areas consist of dense and interlocking growths of *Acropora* tables in which depressions of the remaining framework, being sheltered from the prevailing currents, rapidly fill with

unconsolidated sand and branch fragments (Purkis, 2004). Even bare substrates are often covered with a thin layer of algae, transforming their otherwise clearly distinguishable spectral signature (Roelfsema, 2009). In agreement with Riegl et al., (2003), the difficult spectral separation of the bottom types was also complicated by the effects of the intervening atmosphere and water column.

The results indicate that the degree to which ecologically determined spatial factors influence accuracy is dependent on the amount of coral cover on the marine benthic habitat (the spatial resolution of the image that is classified may also be a factor, but it was not addressed in this study). These may be contributing factors to the differences in the accuracies obtained for mapping reefs in different geographical locations (Lim et al., 2009). Results also showed that qualitative categories (coral community structure) are recommended until affordable hyperspectral images with greater potential become easily available (Scopélitis et al., 2010).

Our results showed that the check point method was an interesting procedure which could be used in a range of marine benthic environments to map communities accurately. It is a fast and low cost approach suitable to map benthic communities. This shows that single field campaigns can be used to collect calibration and validation data, reducing field time and costs (Andréfouet, 2008). On the other hand, the demonstration that high map thematic resolution can be achieved is significant for many spatially explicit ecological studies. Precise benthic descriptions are valuable for studying reef process more realistically and to develop improved management strategies (Scopélitis et al., 2010).

This mapping database will allow analysis of before and after hurricane impacts and allow repetitive sampling to assess future environmental and ecological change as a result of climate change. All these features were mapped at a scale that is most useful to resource managers and urban planners.

5. REFERENCES

- Andréfouet, S. 2008. Coral reef Habitat Mapping Using Remote Sensing: A user Vs Producer Perspective. Implications for Research, Management and Capacity Building. *Journal of Spatial Science*, 53 (1): p113-129.
- Andréfouët, S., Kramer, P., Torres-Pulliza, D., Joyce K.E., Hochberg, E.J., Garza-Pérez, R., Mumby, P.J., Riegl, B., Yamano, H., White, W.H., Zubia, M., Brock, J. C., Phinn, S.R., Naseer, A., Hatcher, B.G. and Muller-Karger, F.E., 2003, Multi-site evaluation of IKONOS data for classification of tropical coral reef environments. *Remote Sensing of Environment*, 88, 128–143.
- Aronoff S., 2005, Remote sensing for GIS managers. New York, USA. ESRI Press. 487 p.
- CARIBBEAN COASTAL MARINE PRODUCTIVITY (CARICOMP), 1998, Caribbean coral reef, seagrass and mangrove sites. Edited by Byorn Kjerfve, UNESCO, Paris. 374 p.
- Congalton, R.G. 1991. A review of Assessing the accuracy of classifications of remotely sensed data. *Remote Sensing of Environment*, 37: p35-46.
- Costa, B.M., T.A. Battista and S.J. Pittman. 2009. Comparative evaluation of airborne LiDAR and ship-based multibeam SoNAR bathymetry and intensity for mapping coral reef ecosystem. *Remote Sensing of Environment* 113 pages 1082–1100.
- Eastman, J.R. 2003. IDRISI Kilimanjaro. Guide to GIS and Image Processing. Manual Version 14. IDRISI Production. 305p.
- Hedley, J. D., Harborne, A. R., and Mumby, P. J., 2005, Simple and robust removal of sun glint for mapping shallow-water benthos. *International Journal of Remote Sensing*. 26, 2017–2112.
- Instituto Nacional de Ecología, Comisión Nacional de Áreas Naturales Protegidas, 2000, Programa de Manejo del Parque Nacional Arrecife de Puerto Morelos. México. Primera Edición.
- Jensen, 2005. Introductory Digital Image Processing: A Remote Sensing Perspective. Third Edition, Prentice Hall: p316.
- Jordan-Dahlgren, E. and R.E. Rodriguez-Martinez, 2003, The Atlantic coral reefs of Mexico, in *Latin American Coral Reefs*. J. Cortes, ed. (Amsterdam: Elsevier Press, 2003), 149p.
- Lim, A., Hedley, J.D., LeDrew, E., Mumby, P.J. and C, Roelfsema, 2009, The effects of ecologically determined spatial complexity on the classification accuracy of simulated coral reef images. *Remote Sensing of Environment*, 113, 965–978.
- Ma, Z. and Redmond, R.L., 1995, Tau coefficients for accuracy assessment of classification of remote sensing data. *Photogrammetric Engineering & Remote Sensing*, 61, 435-439.

- Mellin, C., Cresswell, I.D and L.C. Radke, 2010, On the use of abiotic surrogates to describe marine benthic biodiversity. *Estuarine Coastal and Shelf Science*, 88, 21-32.
- Mienis, F; van Weering, t; de Hass, H; de Stigter, H; Huvenne V.A.I and A.J, Wheeler. 2006. Carbonate mound development at the SW Rockall Trough margin based on high resolution TOBI and seismic recording. *Marine Geology*, 233(1-4): 1-19.
- Mumby, P.J., 2000, Methodologies for defining habitats. In: Green, E.P., Mumby, P.J., Edwards, A.J. and Clark, C.D. (Eds.), *Remote Sensing Handbook of Tropical Coastal Management*. Coastal. Management Sourcebooks, 3, UNESCO (Paris: France), pp. 131-140.
- Mumby, P.J and A.J, Edwards, 2002, Mapping marine environments with IKONOS imagery: enhanced spatial resolution can deliver greater thematic accuracy. *Remote Sensing of Environment*, 82, 248–257.
- Purkis, S.J., 2004, Calibration of satellite images of reef environments. PhD Thesis, Universiteit Amsterdam. Faculty of Earth and Life Science. Department of Sedimentology and Marine Geology. The Netherlands. ISBN 90-9017043-5. 205p.
- Rodríguez-Martínez, R., 2008, Community involvement in marine protected areas: The case of Puerto Morelos reef, Mexico. *Journal of Environmental Management*, 88, 1151–1160.
- Rodríguez-Martínez, R.E; Ruíz-Rentería, F; van Tussenbroek, B; Barba-Santos, G; Escalante-Mancera, E; Jordán-Garza, G and E. Jordán – Dahlegren. 2010. State and environmental tendencies of the Puerto Morelos CARICOMP site, México. In Press: *Revista Biología Tropical*. 32p.
- Roelfsema, C.M., 2009, Integrating field and remotely sensed data for assessment of coral reef and seagrass habitats. PhD Thesis. The University of Queensland. School of Geography, Planning and Environmental Management. Australia. 251p.
- Sarkar, S. and C. Margules, 2002, Operationalizing biodiversity for conservation planning. *Journal Bioscience*, 27(Suppl. 2), 299–308.
- Scopélitis, J; Andréfouët, S; Phinn, S; Arroyo, L Dellau, M; Cros, A and P, Chabanet. (In press). The next step in shallow coral reef monitoring: Combining remote sensing and in situ approaches. *Mar. Pollut. Bull.* (2010) doi:10.1016/j.marpolbul.2010.07.033

Wheat yield monitoring in southern Spain using a series of satellite images

F. Muñoz-Padilla^{1*}; M.P. González Dugo¹, F. Mansilla¹, J. Domínguez¹; P. Gavilán¹,
I. IFAPA. Centro Alameda del Obispo, Córdoba (Spain)

* franciscol.munoz@juntadeandalucia.es

ABSTRACT. Recent studies show that the global demand for food will increase for at least another 40 years. This increase in demand and the limited resources available to produce food make it necessary to develop tools that allow estimations of crop production. These kind of tools should help to manage the way food is produced, stored and distributed. The aim of this study was to develop a methodology to estimate wheat yield at field scale. Information from weather stations and TM and ETM+ sensors onboard LANDSAT 5 and 7, respectively, were used during 2008 and 2009 growing seasons to that end. The Monteith biomass model was fitted in combination with an average harvest index (H_{la}) in the Genil-Cabra Irrigation Scheme (Córdoba, Southern Spain). The model parameters, light use efficiency (ϵ) and H_{la} were calibrated using information from 31 durum and soft wheat experimental plots. Field radiometer measurements were taken over every plot throughout the growing season to obtain experimental relationships between the Normalized Differential Vegetation Index (NDVI) and the Absorbed Photosynthetically Active Radiation (APAR). Fifty-three wheat fields, large enough to be describe by the satellite remote sensor and avoid edge effects, were chosen each year in order to evaluate the model, with yield data for each field being supplied by farmers. **A 12.5 % of error was obtained in seasonal yield estimation when compared with observations over the experimental plots with a root mean squared difference (RMSD) of 518 kg/ha. This error increased by 5% when yield estimation was performed at larger scale using information from a series of satellite images, but average yield for the area could be assessed with a 6% of error.** Since the experimental plots had the same treatments, the maximum estimation ability was achieved for them. However, at field scale the error was higher due to changes in the crop management (planting date, irrigation, fertilization etc). The H_{la} was different each year due to the different weather conditions. The H_{la} used in 2008 and 2009 was 0.31 and 0.37, respectively. The lack of rain in March 2008 probably affected the development of the inflorescence, resulting in a lower H_{la} for this year. Both H_{la} values are within the range referred by most authors. This methodology shows acceptable results but requires an annual calibration to adapt H_{la} to the changing weather.

1 TITLE OF SECTION (E.G. INTRODUCTION)

Regional estimates of crop yield are desirable for managing large agricultural lands and determining food pricing and trading policies (Macdonald and Hall, 1980). On the other hand, the growing world population needs to be fed, but with less water available for agriculture (Serageldin, 1999). All this arguments lead to think that it would be recommended to develop models to accurately estimate crop yield at field and regional scales.

An important cooperative research effort has been conducted during the last 4 decades over the world to develop models enabling to simulate crop growth and yield. In the past, the utility of combining in models remotely sensed data and crop growth has been evaluated and verified using different sensors.

One of the first applications of space-based sensors in the late 70s and early 80s was the land and crop

inventory and the estimation of crop yields. Programs such as LACIE (Large Area Crop Inventory Experiment) and AgRISTARS, conducted by the U.S. administration, demonstrated the potential of multispectral sensors to estimate large-scale agricultural production and laid down the foundations of the physical relationship between spectral measurements and the biophysical properties of soil and vegetation. At present, the number of available sensors has greatly increased, improving the quality of the information they provide.

Remote sensors are often used to obtain data which will be used as input variables on crop models that estimate or predict crop yield. Previous studies (Maas 1988 a, b) showed that it is possible to improve the performance of a crop model by using input variables derived from remote sensing. Doraiswamy (2004) estimated corn and soybean yield with errors of 3 and 7%, respectively, using a crop growth model

developed by the ARS-USDA and modified to use satellite-derived LAI as input.

The use of vegetation indices (VI) obtained from remote sensing measurement, has demonstrated a reduced ability to predict crop yield at plot scale through direct relationships between VI and yield. On the other hand, a healthy development (without biotic stresses) is required to obtain satisfactory results (Ma et al. 2001). There are many research results with prediction based on the relationships between VI obtained from radiometer measurements and yield of cotton (Zhao et al. 2007), rainfed and irrigated wheat (Aparicio et al. 2000) and soybean (Ma et al. 2001).

This predictions can be up-scaled using sensors onboard satellites. Thus, the annual average crop yield can be related to VI obtained from satellite images. As good examples, the average yield of large areas in maize (Mkhabela 2005) and wheat (Labus 2002) have been estimated with good results, however, poorer results have been obtained in cotton (Dalezios 2001). To improve the model's estimation ability, various authors included into their models information from other sources such as rainfall, soil temperature and/or moisture, achieving good predictions in wheat (Balaghi et al. 2008, Wall 2007), corn and soybeans (Prasad 2006). These empirical relationships cannot be extrapolated to other crops or areas, being this fact an important drawback.

This problem was partially solved by models with more physical basis, such as the Monteith biomass estimation model (1972,) which includes a harvest index that can be used for estimating yield (Lobell et al 2003; Zwart and Bastiaanssen 2007). This model allows the estimation of accumulated biomass by a crop in a given period by estimating the accumulation of APAR (absorbed photosynthetically active radiation) in that period and the light-use efficiency, that is, the amount of biomass that can be produced per unit of absorbed PAR. Subsequently, Asrar et al (1989) modified this model by introducing a stress index, as the initial model did not consider the possibility of a water shortage during the growing season.

The parameter FPAR (fraction of absorbed PAR) is needed for computing APAR. The ability to estimate FPAR from remotely sensed spectral measurements has been repeatedly demonstrated (Asrar et al 1984). Thus, the Monteith biomass estimation model has been applied over large areas. (Bastiaanssen et al.2003; Lobell et al 2003; Zwart and Bastiaanssen 2007).

The aim of this study was to evaluate the performance of a semi-empirical simple approach to estimate wheat yield at field and regional scale using remotely sensed data.

Several aspects of the model, as the inter-annual variability of field calibrated harvest index for wheat in this area and the estimation of the fraction of Absorbed Photo-synthetically Active Radiation (FPAR) from several Vegetation indexes (VI) were also addressed.

2 MATERIALS AND METHODS

2.1 Model description

The biomass estimation model of Monteith (Monteith, 1972; Monteith and Unsworth, 1990) in combination with an average harvest index was used in this study to estimate wheat yield using remote sensed data at the field scale.

The wheat yield is calculated as follows,

$$Yield = \int_0^t fPAR \cdot PAR \cdot \epsilon \cdot Hla \cdot dt \quad (1)$$

where fPAR is the fraction of absorbed PAR, PAR is the photosynthetically active radiation, ϵ is the light-use efficiency and Hla is the average harvest index.

2.2 Experimental plot and field data

Experimental plot data

Two experimental sites planted to wheat were monitored during the 2009 growing season (Fig. 1). The first site was located near Cañete de las Torres (Córdoba, Southern Spain). Sixteen durum and fiveteen bread wheat cultivars were sown on December 23, 2008, in 12-m² experimental plots (six rows, 20 cm apart). Measurements of the following factors were made every 15 days during the growing season: crop height, PAR, LAI and spectral reflectance. Daily values were obtained by averaging three point measurements made at three different locations in each plot. An AccuPAR Model LP-80 ceptometer was used to estimate PAR at each site and field canopy reflectance measurements were made using a hand-held field spectroradiometer (ASD FieldSpec). Table 2 shows the days on which measurements were made. The spectral range of the instrument was between 325 and 1075 nm with a sampling interval of 1 nm, which included the visible and near-infrared (NIR) portions of the spectrum used in computing vegetation indices. The measurements were taken at midday under cloudless conditions. Reflectance was calculated as the ratio of the reflected and the incident irradiance, where the incident irradiance was periodically measured using a white Spectralon reference panel (Labsphere, North Sutton, NH). The Normalized Difference Vegetation Index (NDVI), Soil Adjusted Vegetation Index (SAVI), and

the Enhanced Vegetation Index (EVI) were calculated from the reflectance measurements in the blue, red and NIR spectral bands. An average value of each vegetation index was obtained for each measurement day and cultivar. At the end of the growing season (July 2, 2009), the plots were manually harvested and grain yield (kg ha^{-1}) was determined for each plot.

The second experimental site consisted of a rainfed wheat field with an area of 2 ha located at the IFAPA Alameda del Obispo experimental farm in Córdoba. It was sown on December 19, 2008, with the wheat cultivar 'Lubrican'. Field information similar to that described above was collected twice a month, but in this case 20 measurements distributed across the field were made to produce field-representative average values for each parameter. In addition, above-ground biomass was measured by swathings three representative 0.25 m^2 areas. Dry weights of these samples were obtained by drying the samples in an oven at 80°C for 2 days. Finally, the remainder of each plot was mechanically harvested on July 3, 2009. In order to evaluate PAR from remote sensing data, relationships were developed based on measurements made on the experimental plots. The spectral radiometry measurements taken on each experimental plot over the course of the growing season were used to determine empirical relationships between PAR and the three vegetation indices. The ability of these indices to estimate PAR was evaluated based on the data in this study.

Daily total solar irradiance, were obtained from two weather stations belonging to the Andalusian regional weather station network (RIA). The first one was near Cañete de las Torres and the second was located 100 m from the wheat experimental plots located inside the IFAPA Alameda del Obispo experimental farm.

Commercial field data

Fifty-three commercial wheat fields, large enough to be clearly observed by the Landsat satellite sensor avoiding edge effects, were selected in 2008 and 2009 in semiarid Southern Spain (Genil-Cabra Irrigation District). All 2008 and 2009 cloudless Landsat-5 and Landsat-7 images for the study period (a total of 10) were acquired and processed. Moreover one 2008 IRS image was also processed to complete the data set. Geometric and atmospheric corrections were applied to the image data. Geometric correction was performed using ground control points extracted from a high-resolution orthophotography taken in 2004 as a reference. Each image was corrected for atmospheric transmittance to obtain surface reflectance values using the MODTRAN 4 radiative transfer model. NDVI maps were constructed using the red and NIR reflectance data for each Landsat image. Average values were computed from each NDVI map for each study field to obtain the change over time of NDVI for each field. Empirical relationships between FPAR and NDVI developed from the experimental plot data were used to estimate FPAR for each commercial field from the satellite data. Table 1 lists the images used in the study for both years. Yield data for each field were supplied by the farmers

2.3 Model parameter evaluation

The average harvest index was evaluated using information from the durum and bread wheat experimental plots. Light-use efficiency was evaluated using the biomass data collected from the experimental farm.

2.4 Model application

Once the performance of the model had been verified against the experimental plot data, yield estimations for 2008 and 2009 were made calculated for the commercial wheat fields.

Farmer's Fields				Experimental plots			
Santaella (2008)		Santaella (2009)		Cañete de las Torres (2009)		Córdoba (2009)	
DOY	Sensor	DOY	Sensor	DOY	Sensor	DOY	Sensor
350	ETM+	345	TM	49	Field radiometer	43	Field radiometer
65	ETM+	11	TM	72	Field radiometer	56	Field radiometer
105	TM	43	TM	85	Field radiometer	71	Field radiometer
122	Awifs	67	ETM+	98	Field radiometer	78	Field radiometer
177	ETM+	123	TM	112	Field radiometer	96	Field radiometer
		147	ETM+	124	Field radiometer	113	Field radiometer
				138	Field radiometer	125	Field radiometer
				168	Field radiometer	139	Field radiometer
					Field radiometer	175	Field radiometer

3 RESULTS

3.1 FPAR

Fig. 1 shows the relationship between the three VIs (NDVI, SAVI and EVI) used in this study and the field measurements of FPAR. The estimation ability was assessed using the coefficient of determination and root mean square difference (RMSD between estimated and measured FPAR values. RMSD values of 7, 8 and 8% were obtained for NDVI, SAVI and EVI, respectively.

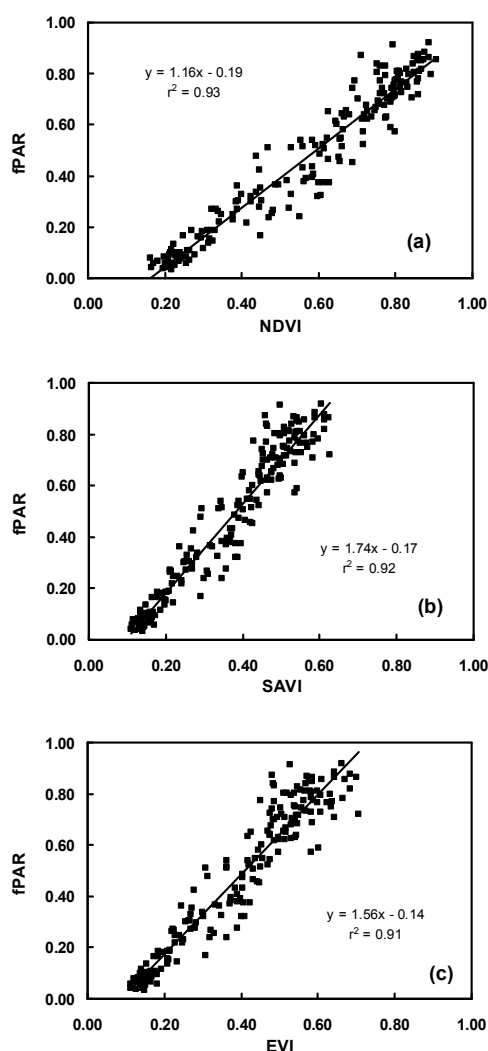


Fig.1. Relationship between (a) Normalized Difference Vegetation Index (NDVI), (b) Soil Adjusted Vegetation Index and (c) Enhanced Vegetation Index (EVI) and FPAR data from the 31 wheat cultivars.

3.2 light-use efficiency

The light-use efficiency was calibrated by minimizing the error in the above ground dry mass, reached for 2 g/MJ PAR with a RMSD = 125.72 g/m²

3.3. Average harvest index

This parameter was also estimated minimizing the differences between observed and simulated yield for several HI values, in an interval previously selected according to the crop and region of application. Average harvest indices of 0.31 and 0.37 were obtained for 2008 and 2009, respectively. Fig. 2 shows the result of simulating wheat yield in 2009 compared with observations.

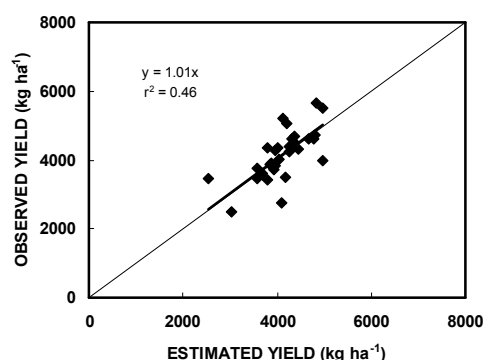


Fig.2. Wheat yield estimation of 31 cultivars using the biomass model of Monteith at the Cañete de las Torres experiment. The solid diagonal line represents the 1:1 line.

3.4. Local scale yield assessment.

The model estimation ability decreased (RMSD=850kg/ha) with commercial fields data. However, the average yield estimate for each year exhibited an error of approximately 6 %. Results of simulating wheat yields in 2008 and 2009 are presented in Figs. 3a and 3b, respectively.

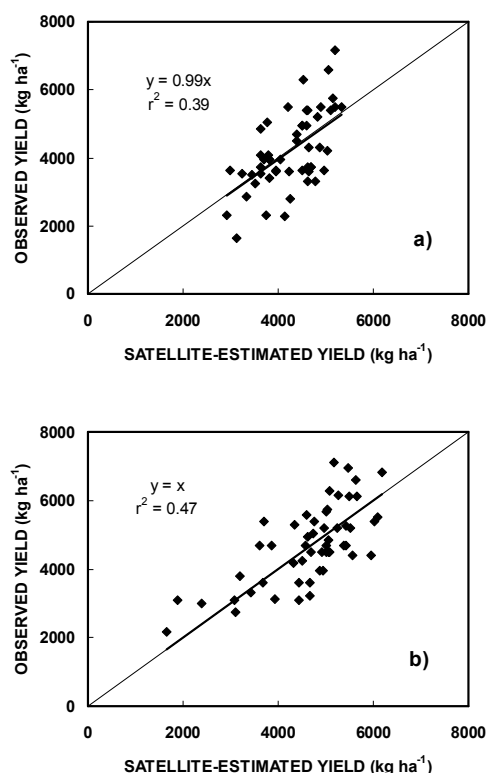


Fig.3. Wheat yield estimation for 53 fields in 2008 (a) and 2009 (b) using the biomass model of Monteith and satellite imagery. The thin solid diagonal line represents the 1:1 line.

4 CONCLUSIONS

The results support the ability of the model to estimate average crop yield at local scale, with an error of 6% in both years. Even when the variability on field crop management tasks and dates (planting date, irrigation, fertilization) hindered its application on a field by field basis, average results encourage a regional application to obtain accurate yield statistics at this scale. The three VIs provided a good estimation of FPAR, with NDVI presenting a slightly superior correlation under these experimental conditions. Even though the limited number of analyzed years, the dependence found of the H1a on weather conditions may hinder an operational application of this methodology at field scale. Further research is required to better quantify this variability and determine whether its effect is significant at regional scales.

5 ACKNOWLEDGMENT

The authors appreciate the support of CICE-Junta de Andalucía through the project P06-AGR-2317. We also would like to acknowledge the availability of IFAPA (Instituto Andaluz de Investigación y Formación Agraria, Pesquera, Alimentaria y de la Producción Ecológica) experimental fields, designed and maintained by personnel of the RAEA network.

6 REFERENCES

- Aparicio N., D. Villegas, J. Casadesús, J.L. Araus and C. Royo. 2000. Spectral vegetation indices as nondestructive tools for determining durum wheat yield. *Agronomy Journal*, 92, 83:91.
- Asrar, G., M. Fuchs, E.T. Kanemasu, and J.L. Hatfield. 1984. Estimating absorbed photosynthetically active radiation and leaf area index from spectral reflectance in wheat. *Agronomy Journal* 76, 300:306.
- Bastiaanssen, W.G.M., and S. Ali. 2003. A new crop yield forecasting model based on satellite measurement applied across the Indus Basing. *Agriculture, Ecosystems and Environment*, 97, 321-340.
- Dalezios, N. R., C. Domenikiotis, A. Loukas, S.T. Tzortzios and C. Kalaitzidis. 2001. Cotton yield estimation based on NOAA/AVHRR produced NDVI. *Physics and Chemistry of the Earth (B)* 26(3), 247-251.
- Doraiswamy, P.C., J.L., Hatfield, T.J. Jackson, B. Akhmedov, J. Prueger, A. Stern. 2004. Crop condition and yield simulation using Landsat and MODIS. *Remote Sensing of Environment*. 92, 548-559.
- Labus, M.P., G.A. Nielsen, R.L. Lawrence, R. Engel and D.S. Long. 2002. Wheat yield estimates using multi-temporal NDVI satellite imagery. *Int. Journal of Remote Sensing*. 23, 4169-4180.
- Lobell, D.B., G.P. Asner, J.I. Ortiz-Monasterio, T.L. Benning. 2003. Remote Sensing of regional crop production in the Yaqui Valley, Mexico: estimates and uncertainties. *Agriculture, Ecosystems and Environment*, 94, 205-220.

- Ma, B.L., L.M. Dwyer, C. Costa, E.R. Cober and M.J. Morrison. 2001. Early Prediction of soybean yield from canopy reflectance measurements. *Agronomy Journal*, 93, 1227-1234.
- Maas, S.J. 1988a. Use of remotely-sensed information in agricultural crop growth models. *Ecological Modelling*, 41,247-268.
- Maas, S.J. 1988b. Using satellite data to improve model estimates of crop yield. *Agronomy Journal*, 80, 655-662.
- Mkhabela, M. S., and N.N. Mashinini. 2005. Early maize yield forecasting in the four agro-ecological regions of Swaziland using NDVI data derived from NOAA's-AVHRR. *Agricultural and Forest Meteorology*, 129, 1-9.
- Monteith, J.L. 1972. Solar radiation and productivity in tropical ecosystems. *J. Appl. Ecol.* 9:747-766.
- Monteith, J.L., and M.H. Unsworth. 1990. *Principles of environmental physics*. 2nd ed Edward Arnold, New York.
- Prasad, A.K., L. Chai, R.P. Singh, and M. Kafatos. 2006. Crop yield estimation model for Iowa using remote sensing and surface parameters. *International Journal of Applied Earth Observation and Geoinformation*. 8,26-33.
- Serageldin, I. 1999. Biotechnology and food security in the 21st century. *Science* (Washington, DC). 285,387-389.
- Wall, L., D. Larocque, and P.M. Léger. 2007. The early explanatory power of NDVI in crop yield modelling. *International Journal of Remote Sensing*, 1, 1-15.
- Zhao, D., K.R. Reddy, V.G. Kakani, J.J. Read, and S. Koti. 2007. Canopy reflectance in cotton for growth assessment and lint yield prediction. *European Journal of Agronomy*. 26, 335-344.
- Zwart, S.J., and W.G.M. Bastiaanssen. 2007. SEBAL for detecting spatial variation of water productivity and scope for improvement in eight irrigated wheat systems. *Agricultural Water Management*, 89: 287-296.

Surface urban heat island monitoring. The case study of Madrid (Spain), Athens (Greece) and San Miguel de Tucumán (Argentina).

R. Oltra-Carrió, J. A. Sobrino, G. Sòria, J. C. Jiménez-Muñoz, C. Mattar, V. Hidalgo, B. Franch, Y. Julien, J. Cuenca.
Global Change Unit, Image Processing Laboratory, Universitat de València.
rosa.oltra@uv.es

ABSTRACT- *The Urban Heat Island (UHI) effect is the phenomenon produced due to the warmth of urban areas compared with their surrounding not urbanized areas. When remote sensing data is used, the measured and monitored parameter is the Surface Urban Heat Island (SUHI). This work analyzes the SUHI effect over three different cities, Madrid (Spain), Athens (Greece) and Gran San Miguel de Tucumán (GSMT) (Argentina). The study from Madrid and Athens is based on the data obtained during different experimental field campaigns of the European Space Agency (ESA). The results from Madrid correspond to the DESIREX 2008 experimental campaign carried out on June and July 2008. The ones from Athens correspond to the THERMOPOLIS 2009 experimental campaign that took place on July 2009. In both campaigns, in situ data was measured simultaneously with space borne and airborne imagery acquisition. For San Miguel de Tucumán, the SUHI monitoring has been performed using Landsat TM 5 images during the period from February 2008 to March 2009. Madrid and Athens have both a Mediterranean climate although Madrid is an inland city and presents a high level of continentality while Athens is a coastal city influenced by the sea. In the other hand, San Miguel de Tucumán is a subtropical city next to a high woodland zone. The study of such different cities permits to observe the behaviour of the SUHI effect taking into account the different urban structure and geographical location of each city. This work studies the SUHI phenomenon using different spatial resolution, from 4 m spatial resolution of the airborne imagery to the 120 m spatial resolution of the Landsat TM 5 images.*

1. INTRODUCTION

The urban heat island forms because of the differences in the rates of warming and cooling of cities relative to their surroundings. In cities with high density of tall buildings a cool island can be registered during daytime due to the presence of shadows, while in cities with higher sky view factor, there will be less shadowed areas. In the other hand, for cities surrounded by agricultural areas with changing crops depending on the season of the year, the UHI intensity will be hardly influenced by these changes.

In the literature we can find several examples of cities with negative islands during daytime and strong positive SUHI during night time, this is the example of Athens (Stathopoulou et al., 2009). There are other works that study the seasonal variability of the SUHI, is the example of the case of Houston, where, when night images are used, the SUHI is found positive during all year (Streutker, 2003)

In this work we are going to observe the diurnal cycle and the annual or seasonal cycle of the SUHI of three different cities: Madrid, Athens and San Miguel de Tucuman.

2. METHODS FOR LST RETRIEVAL

The LST is an important factor for the study of urban climates. It modulates the air temperature of the lowest layers of the urban atmosphere, is central to the energy balance of the surface, helps to determine the internal climates of buildings and affect the comfort of city dwellers (Voogt and Oke, 2003).

We are going to explain the methodology to obtain the LST maps used in this study.

2.1 Single-channel method

The single-channel (SC) method retrieves the LST product using only one thermal band. The LST is retrieved by inversion of the Planck's law.

There are different references about this methodology in the literature, in this work we follow the approximation explained by (Jiménez-Muñoz et al., 2009). for atmospheres with high water vapour content they are defined by equation.

2.3 TES algorithm

The TES (Temperature and emissivity separation) method solves the problem of coupling between LST and LSE that appears when the radiative transfer equation is applied to each thermal band of a multispectral sensor. Therefore, the TES estimates land surface emissivity and temperature from multispectral thermal data. This method is described

by (Gillespie et al., 1998), and a detailed description can be found in that work. The algorithm is divided into three modules (NEM, RATIO and MMD). It uses as input atmospherically corrected data: land-leaving radiance and down-welling atmospheric irradiance.

3. IMAGERY AND FIELD DATA

3.1 AHS sensor.

The airborne hyperspectral scanner (AHS) was developed by SensyTech Inc. and it is operated by the Spanish Institute of Aeronautics (INTA) onboard the aircraft CASA 212-200 Paternina. It has 80 spectral bands in four ports covering the VNIR (20 bands), SWIR (1+42 bands), MIR (7 bands) and TIR (10 bands). Other technical characteristics are: FOV of 90° ($\pm 45^\circ$), IFOV of 2.5 mrad.

3.2 Landsat 5 TM imagery and Gran San Miguel de Tucumán

The region of Tucumán is placed on the Northwest of Argentina. The study is centred on the GSMT, which is the urban agglomeration formed around the city of San Miguel de Tucumán. The GSMT is at the west of the San Javier Mountains (SJM). Nowadays the agricultural land is being transformed into urban area due to the population growth. At present there are 1.5 million of people living at the GSMT.

The analysis of the SUHI of the GSMT has been developed using Landsat 5 TM images. The overpass time over the GSMT is at 14:00 UTC. Six images have been processed, corresponding to the following dates: 28th of February 2008, 7th of September 2008, 9th of October 2008, 26th of November 2008, 13th of January 2009 and 2nd of March 2009.

To apply the SC algorithm, the atmospheric parameters required have been obtained from MODIS products.

3.3 Madrid: DESIREX 2008 experimental campaign

Madrid is the biggest city of the Iberian Peninsula. According to the National Institute of Statistics of Spain (www.ine.es) on January 2008 Madrid had a population of 3.2 million. The city is located in a relatively flat area about 50 km south of the Spanish Central Ridge. The main topographic feature is river Manzanares, which crosses the city from west to east. The city has a maximum height of about 700 m and a minimum of 550 m. Madrid has Mediterranean climates whose driest seasons are cool winters and hot summers and with most rainfall in Autumn and Spring.

During DESIREX 2008 campaign, in situ measurements consisted of atmospheric measurements, calibration of AHS and validation of products, mobile and fixed measurements of air

temperature and humidity and ground radiometric temperature, spectral characterization of urban surfaces, radiation balance and urban thermography. Airborne data was acquired with the AHS sensor. Ten flights were carried out in a 11h, 21h and 4h UTC scheme, from June 25th to July 4th, which means a total of thirty flight lines, divided into two different patterns, North-South and East-West. These give a total length of roughly 1000 Km along track recorded data, at different flight altitudes (2 m, 4 m and 6 m of spatial resolution). In this work we are going to analyze the 4 m spatial resolution images.

3.4 Athens: THERMOPOLIS 2009 experimental campaign

The chosen area for THERMOPOLIS 2009 campaign is Athens, the largest city of Greece. The urban area of Athens extends beyond the administrative city limits with a population of 3,130,841 (National Statistical Service of Greece, 2001) and a land area of 412 km² basin (Hellenic Interior Ministry). Athens sprawls across the central plain of Attica and bound by Mount Egaleo to the west, Mount Parnitha in the north, Mount Penteli in the northeast, Mount Hymettus in the east, and the Saronic Gulf in the southwest. Athens enjoys a typical Mediterranean climate. Summers can be particularly hot.

The THERMOPOLIS 2009 campaign combines the collection of quality and coordinated airborne hyper-spectral, spaceborne and in-situ measurements to generate spectrally, geometrically and radiometrically representative dataset to address observational requirements of UHI for the assessment of an operational system. The period chosen to develop the campaign was from 15th July to 2nd August 2009. Seven flights of the AHS were performed during the THERMOPOLIS campaign between the 18th of July and 24th of July. The flights were divided into 4 different overpasses, covering almost the entire city. The monitoring times were around noon, around midnight and in the morning, before sun rising. The spatial resolution of each image is 4 m.

4. RESULTS

4.1 San Miguel de Tucumán

Six maps of LST have been retrieved with the Landsat images. In Fig. 1 two of them are shown, one corresponding to the spring season and the other one to the summer. We can see that the LST of the city can change near to 15 K from one season to the other, at the same hour (14:00 UTC). In spring the city appears cooler than most of the surrounding fields, while in summer it happens at the other way.

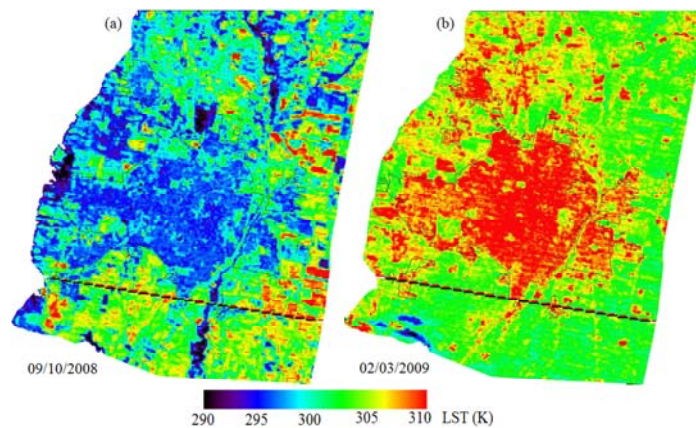


Fig. 1 LST maps from GSMT for (a) a spring image from 9th October 2008 and (b) a summer image from 2nd March 2009.

This difference between urban and rural is showed in Fig. 2., where the SUHI effect is plotted. The SUHI has been obtained as the difference between the urban zone LST and the rural LST. While during summer we obtain a positive SUHI, during winter and spring, the SUHI is negative. This can be due to the phenology of the crops surrounding the city, as the sugar cane, that changes the thermal properties of the rural surfaces during the year.

4.2 DESIREX 2008

The calibration of the AHS sensor using in situ measurement showed the good performance of all the thermal bands of the sensor. The results of the comparison between the radiometric temperature

obtained from the airborne sensor and the radiometric temperature simulated from in situ measurements to the sensor height level give a Bias of 0.1 K and a RMSE of 1.0 K.

The TES algorithm has been applied using 7 of the 10 bands of the AHS (bands 72, 73, 75, 76, 77, 78 and 79). This configuration has already showed good performance in previous campaigns and studies (Sobrino et al., 2006).

The semiempirical relation between ϵ_{\min} and the MMD for the TES algorithm is done by Eq. (1).

$$\epsilon_{\min} = 0.999 + 0.777 \cdot \text{MMD}^{0.815} \quad (1)$$

with a correlation coefficient of $R = 0.997$ and $\sigma = 0.005$.

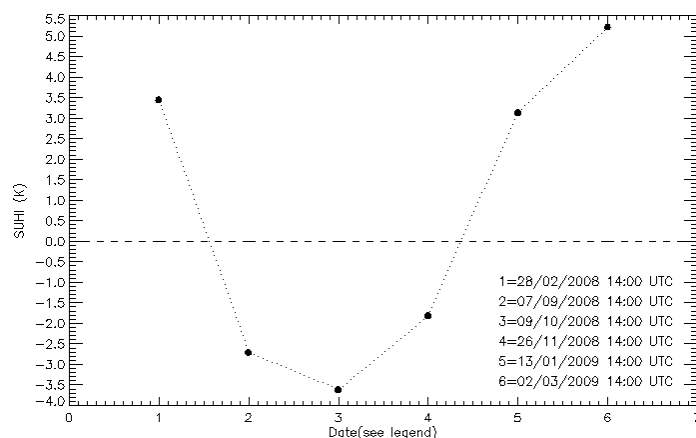


Fig. 2 SUHI effect obtained using LST images from Landsat TM over GSMT

The validation of the LST products obtained, using in situ values of urban and rural surfaces, gives a Bias of 0.7 K and a RMSE of 1.4 K, which are good statistical values and demonstrate the reliability of our LST products.

Figure 3 shows two examples of LST maps obtained, one at noon and the other at night. The images are a composition of both AHS overpasses, the North-South one and the Eat-West one.

At noon, the map is shown with an interval of temperatures of 27 degrees, between 301 K and 328 K. The maximum temperatures are achieved at rural sites. However, for the night image, the interval of

temperatures is of 14 degrees, between 290 K and 304 K. In this case, maximum temperatures appear in urban zones while the lower in rural ones. This is a clear case of UHI effect.

The SUHI has been measured from the LST maps. Limits between urban and rural zones are established according to urban contours and neighbourhood limits. Results are shown in Fig. 4. The SUHI obtained is positive at night and morning and negative at noon. This is an example of cool island, because of the surroundings that are warmer than the city, where a lot of shadowed areas can be found.

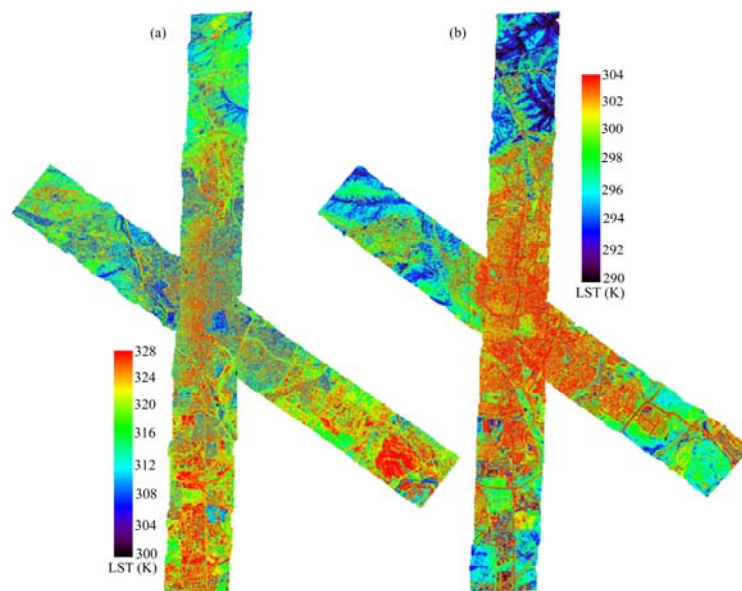


Fig. 3 Map of LST applying TES algorithm to AHS images in the framework of the DESIREX 2008 campaign. (a) AHS image from June 28 at noon. (b) AHS image from June 28 at night.

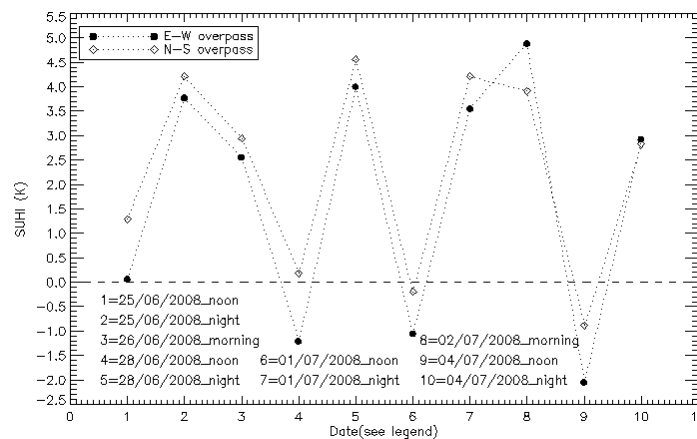


Fig. 4 SUHI effect obtained using LST images from both AHS overpasses over Madrid

4.3 THERMOPOLIS 2009

In this campaign the calibration of the AHS sensor give good results for all bands, only some noisy signal has been detected for band 78. The statistical results for the calibration are Bias = 0.6 K and RMSE = 1.36 K.

The semi empirical relation between ε_{\min} and the MMD for the TES algorithm, when all thermal bands, less band 78, are used, is done by Eq. (2)

$$\varepsilon_{\min} = 1.000 + 0.790 \cdot MMD^{0.821} \quad (2)$$

with a correlation coefficient of $R = 0.997$ and $\sigma = 0.004$.

All the LST maps have been retrieved, in Fig. 5 we are showing both of them. They correspond to a composition of the four overpasses.

Only the east-west overpass has been taken into account to retrieve the SUHI of Athens, as the surroundings of the city, for this image, do not involve the sea. The SUHI for Athens reproduce the pattern of the SUHI for Madrid. Positive at night time and negative at daytime (Fig. 6).

5. CONCLUSIONS

For Madrid and Athens summer high spatial resolution images have been analyzed. The SUHI obtained is higher at night time. While at noon time the SUHI is negative. This is characteristic of inner-city urban areas (Voogt, 2002), such as Madrid. But also of cities surrounded by dry rural areas, like Athens, that is surrounded by sparse low vegetation (particularly olive trees and vineyards) and bare soil, that become warm faster than urban

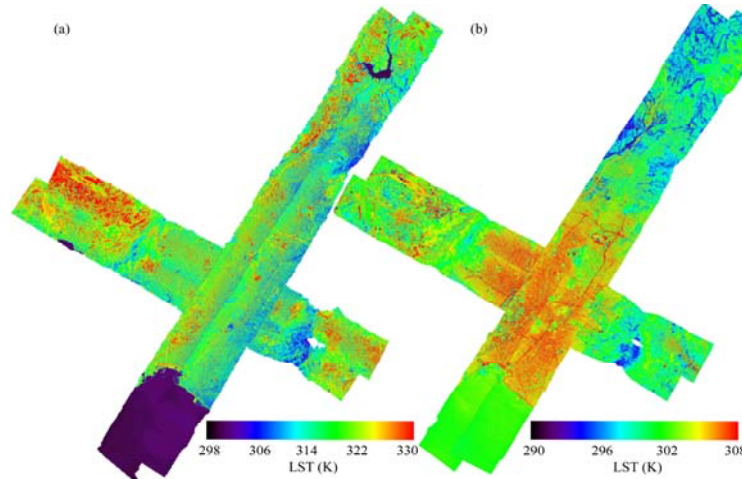


Fig. 5 Map of LST applying TES algorithm to AHS images in the framework of the Thermopolis 2009 campaign. (a) AHS image from July 18 at noon. (b) AHS image from July 18 at night.

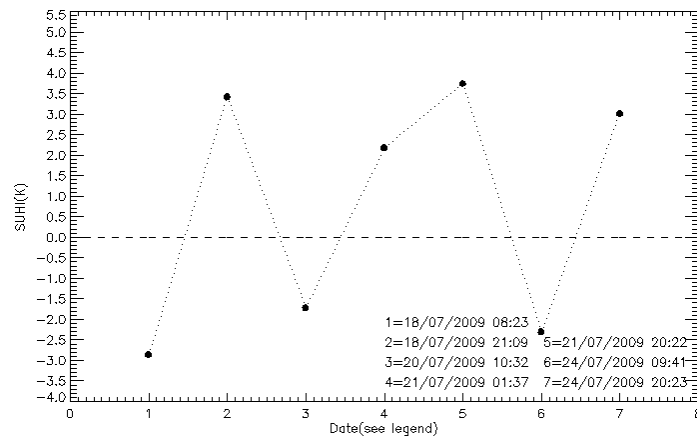


Fig. 6 SUHI effect obtained using LST images from AHS overpasses over Athens

surface areas which are extensively covered by building materials of high thermal capacity (Stathopoulou et al., 2009). Six low resolution daytime images have been processed from GSMT. We have measured a cool island during winter and spring but a warm SUHI during summer. This change of the magnitude of the SUHI can be done by a change of the thermal properties of the rural areas. GSMT is surrounded by sugar cane crops, which mean that the proportion of bare soil is lower at summer, growing the thermal admittance of the agricultural surface.

6 ACKNOWLEDGMENTS

We wish to thank the European Space Agency (ESA) for the DESIREX 2008 project (21717/08/I-LG). And for the THERMOPOLIS 2009 Experimental Campaign (22693/09/I-EC). And also all the people and groups that participate on both experimental campaigns.

We also wish to thank the AECID for the project *Efectos de la dinámica urbana sobre la estructura de la vegetación y la temperatura de superficie del GSMT*. (A/018766/08).

This work has been carried out while R. Oltra-Carrió was in receipt of a grant V Segles from the University of València.

7 REFERENCES

Gillespie, A., Rokugawa, S., Matsunaga, T., Cothorn, J. S., Hook, S. & Kahle, A. B. 1998. A temperature and emissivity separation algorithm for Advanced Spaceborne Thermal Emission and Reflection Radiometer (ASTER) images. *Ieee Transactions on*

Geoscience and Remote Sensing, 36, 1113-1126.

Jiménez-Muñoz, J. C., Cristóbal, J., Sobrino, J., Sòria, G., Ninyerola, M. & Pons, X. 2009. Revision of the Single-Channel Algorithm for Land Surface Temperature Retrieval From Landsat Thermal-Infrared Data. *IEE Transactions on Geoscience and Remote Sensing*, 47, 339-349.

Sobrino, J. A., Jiménez-Muñoz, J. C., Zarco-Tejada, P. J., Sepulcre-Cantó, G. & Miguel, E. 2006. Land surface temperature derived from airborne hyperspectral scanner thermal infrared data. *Remote Sensing of Environment*, 102, 99-115.

Stathopoulou, M., Synnefa, A., Caralis, C., Sanamouris, M., Karless, T. & Akbari, H. 2009. A surface heat island study of Athens using high-resolution satellite imagery and measurements of the optical and thermal properties of commonly used building and paving materials. *International Journal of Sustainable Energy*, 28, 59-76.

Streutker, D. R. 2003. Satellite-measured growth of the urban heat island of Houston, Texas. *Remote Sensing of Environment*, 85, 282-289.

Voogt, J. A. 2002. Urban Heat Island. In: MUNN, T. (ed.) *Encyclopedia of Global Environmental Change*.

Voogt, J. A. & Oke, T. R. 2003. Thermal remote sensing of urban climates. *Remote Sensing of Environment*, 86, 370-384.

Spatial distribution of air temperature measured from car transects along the cities of Madrid and Athens in the framework of the DESIREX 2008 and Thermopolis 2009 Urban Heat Island campaigns

G. Sòria, J.A. Sobrino, R. Oltra-Carrió, C. Mattar, J.C. Jiménez-Muñoz, V. Hidalgo, B. Franch, Y. Julien and J. Cuenca

Global Change Unit (GCU), Image Processing Laboratory (IPL), Parc Científic, University of Valencia, Catedrático Agustín Escardino nº9, E-46980, Paterna, Spain.

guillem.soria@uv.es, sobrino@uv.es

ABSTRACT - During the last two years an experimental field campaign was carried out in European cities with the main objective of UHI (Urban Heat Island) studies. From June 23rd to July 6th of 2008, the DESIREX 2008 (Dual-use European Security IR Experiment 2008) experimental campaign was developed in Madrid in support of the proposed activities for the Reorientation of the Fuegosat Consolidation Phase of the Earth Watch Programme. From July 15th to 31st of 2009, The THERMOPOLIS 2009 campaign was carried out in Athens, serving the Data User Element (DUE) “Urban Heat islands (UHI) and Urban Thermography (UT) Project” and also being part of the Reorientation of Fuegosat. The campaigns were funded by the European Space Agency (ESA) and different European groups were working on them acquiring different kind of data. The Global Change Unit (GCU) from the Image Processing Laboratory (IPL - University of València) carried out a set of measurements in both campaigns retrieving ground and atmospheric parameters (like air temperature, surface temperature, wind speed and direction, emissivity and reflectivity of urban and rural surfaces) measured daily using fixed masts, car transects and calibration/validation points. Airborne data were acquired by the Instituto Nacional de Técnica Aeroespacial (INTA) using the Airborne Hyperspectral Scanner (AHS).

The main objective of this work was to analyze the air temperature and surface radiometric temperature data obtained from the more than 100 transects on a car in the DESIREX 2008 campaign and also the obtained from the THERMOPOLIS 2009 campaign. In the case of DESIREX 2008 four different routes were defined in order to make transects driving cars along the city of Madrid and surroundings with the purpose of characterizing the Urban Heat Island. In THERMOPOLIS 2009 one route was defined along the city of Athens and surroundings to the Marathonos Lake. All the car transects were carried out simultaneously with the AHS overpass. A comparison has been carried out between the air temperature retrieved from the car transects and the AHS images of Land Surface Temperature (LST) taking into account their dependence with different atmospheric parameters.

1. INTRODUCTION

The DESIREX 2008 campaign over the city of Madrid, Spain, was coordinated by the Global Change Unit (Sobrino et al 2009), who carried out ground measurement activities in collaboration with the project partners. Airborne acquisitions over Madrid were carried out by INTA in two flight lines (N-S and E-W, Fig1). There were two kinds of in situ data: Atmospheric and ground measurements. All in situ data were distributed along the flight lines.

The THERMOPOLIS 2009 campaign was carried out in the city of Athens, Greece in the summer of 2009 and coordinated by the Centre for Research and Technology Hellas (CERTH – Rapsomanikis et al, 2010), who carried out ground measurement activities in collaboration with the project partners. Airborne acquisitions over Athens were carried out by INTA in a scheme of four flight lines (NE-SW and E-W, Fig2). The ground based experimental sites were distributed along the city of Athens.

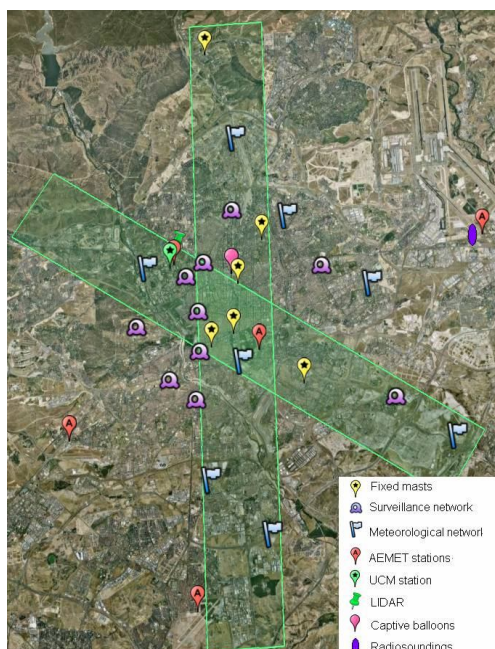


Figure 1. DESIREX 2008 – Flight lines and measurements

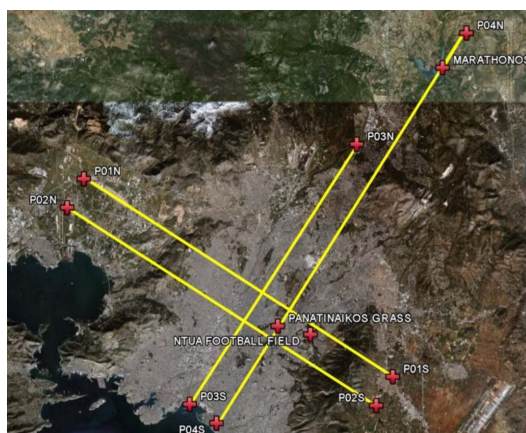


Figure 2. THERMOPOLIS 2009 Flight lines

Both DESIREX and THERMOPOLIS campaigns retrieve thermal parameters as temperature and emissivity by the GCU using multi and single band radiometers. Thermal cameras acquired urban imagery. Reflectivity was measured with spectroradiometers in the solar range. Atmospheric data was acquired in Madrid using soundings, lidar and different meteorological stations from the Meteorological and Surveillance Network (Fig. 3). In Athens, greek partners of the campaign measured atmospheric data with stations and instrumentation.



Figure 3. Sensors for ground measurements

In DESIREX, four different routes (Fig 4) were defined in order to make transects driving cars along the city of Madrid and surroundings with the purpose of characterizing the Urban Heat Island. The transects were carried out daily and three times per day at 4h, 11h and 22h UTC. Measurements of Air Temperature, Air Humidity, Radiometric Temperature, with simultaneous GPS acquisition, were carried out. The morphology and structure of the streets and buildings in each route were not homogeneous, in order to better characterize the thermal variation due to the Urban Heat Island effect. Transect 1 runs along the North-South vertical axis of Madrid, with wide avenues and high buildings. Transect 2 runs in Madrid old center, an urban dense area with narrow streets and high altitude variations. Transect 3 runs in wide spaces, close by vegetated areas, but also medium dense urban and rural areas. Transect 4 runs in wide streets and also along the highway.

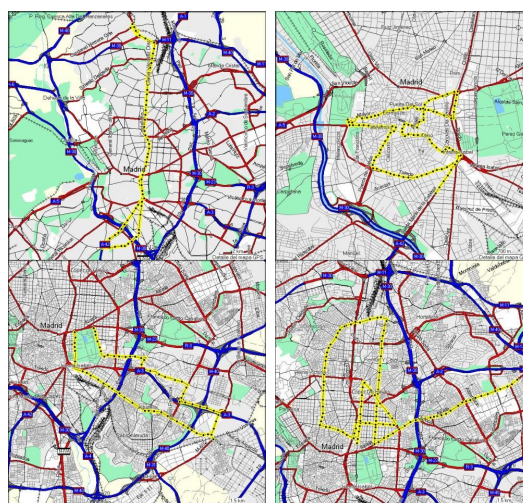


Figure 4. Routes for car transects used in the DESIREX 2008 campaign in Madrid

In THERMOPOLIS one route was defined by the GCU to make transects driving a car along the city of Athens and surroundings to help to characterize the UHI effect (fig 5). The transect run along the North-South AHS overpass. It starts near the city centre and goes by wide streets. Outside the city it goes through suburban, rural and even forest zones until the Marathonos Lake.



Figure 5. Route in Athens, THERMOPOLIS 2009

The analysis of DESIREX data showed that air temperature from car transects was higher for noon data than midnight and morning measurements (Fig 6). Differences between radiometric and air temperature were higher in noon data than both night and morning ones (Fig 7)

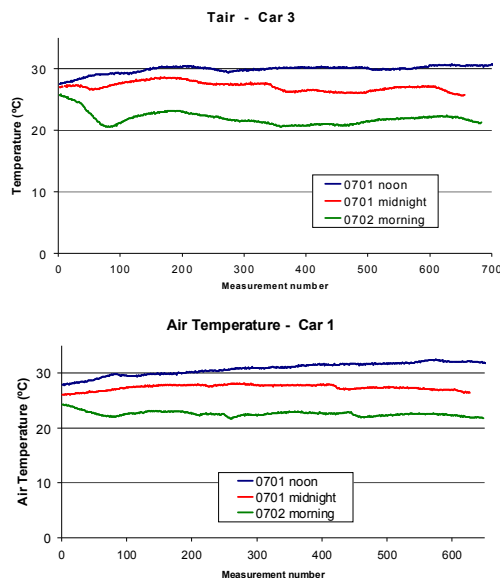


Figure 6. Air temperature in different transects for Route 1 and 3

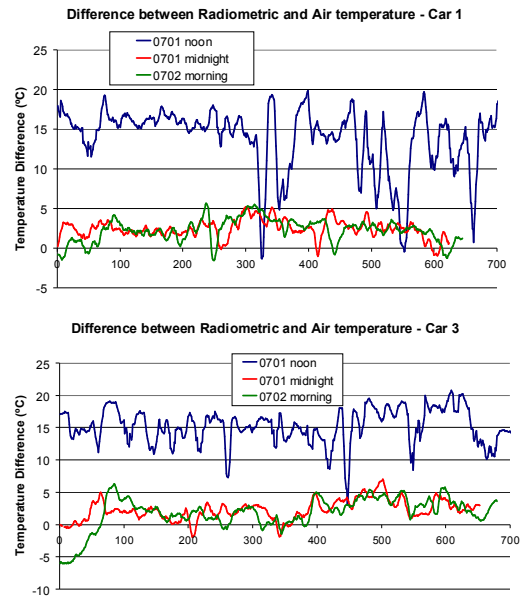


Figure 7. Difference between radiometric and air temperature in day and nighttime transects of Routes 1 and 3

Table 1 summarizes these differences for all the DESIREX Car Transects. These air temperature data has been also compared with meteorological stations data in moments and places where they coincide, showing a good agreement between data (Table 2). Fig 8 shows the effect of altitude and the presence of a water body (Marathonos Lake) in the air temperature data from THERMOPOLIS and the correlation with LST from AHS data along a car transect, respectively.

Table 1. Mean values of the differences between radiometric and air temperatures

	Mean Temperature Difference (°C)			
	Car 1	Car 2	Car 3	Car 4
1st July Noon	15 ± 4	11 ± 6	15 ± 3	15 ± 5
1st July Midnight	2.5 ± 1.1	3.0 ± 1.3	2.3 ± 1.6	3.0 ± 1.3
2n July Morning	2.3 ± 1.5	4 ± 3	2 ± 3	2.9 ± 1.5

Table 2. DESIREX 2008 air temperature data compared between Car transects and Met.Stations

CAR 1:

Comparison with Surveillance Station: E15 Pza Castilla					
Date	Car Time	Car Tair (°C)	Station Time	Station Tair (°C)	Difference (°C)
26/06/2008	11:10	29.4	11	29.8	-0.4
28/06/2008	4:01	21.1	4	21.9	-0.8
01/07/2008	11:01	29.6	11	29.8	-0.2
Comparison with Surveillance Station: E14 Pz Fdez Labreda					
Date	Car Time	Car Tair (°C)	Station Time	Station Tair (°C)	Difference (°C)
03/07/2008	22:23	21.7	22	22.1	-0.4

CAR 2:

Comparison with Car 1 Intersection					
Date	Car 2 Time	Car 2 Tair (°C)	Car 1 Time	Car 1 Tair (°C)	Difference (°C)
27/06/2008	11:48	30.7	11:23	30.0	0.7
03/07/2008	22:41	20.9	22:31	21.5	-0.6

CAR 3:

Comparison with Car 4 Intersection					
Date	Car 3 Time	Car 3 Tair (°C)	Car 4 Time	Car 4 Tair (°C)	Difference (°C)
29/06/2008	4:50	23.1	4:41	23.3	-0.2
02/07/2008	22:43	25.8	22:53	25.4	0.4

CAR 4:

Comparison with Surveillance Station: E15 Pza Castilla					
Date	Car Time	Car Tair (°C)	Station Time	Station Tair (°C)	Difference (°C)
02/07/2008	11:10	25.1	11	25.7	-0.6
02/07/2008	4:10	22.6	4	23.1	-0.5
Comparison with Surveillance Station: E10 Cuatro Caminos					
Date	Car Time	Car Tair (°C)	Station Time	Station Tair (°C)	Difference (°C)
28/06/2008	4:19	21.5	4	22.1	-0.6
03/07/2008	4:16	15.4	4	15.2	0.2
03/07/2008	11:18	22.0	11	22.4	-0.4

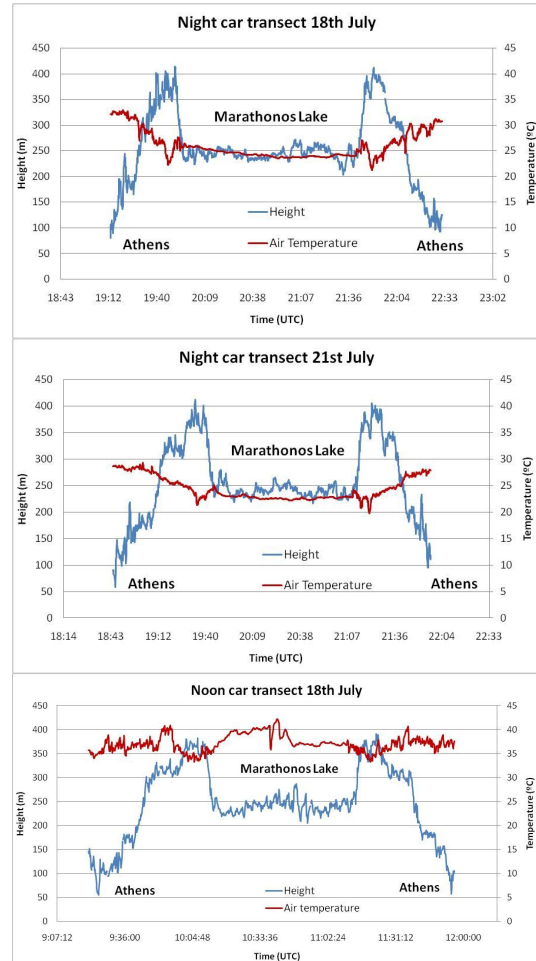


Figure 8. THERMOPOLIS transect in night and daytime compared with variation of altitude, showing a higher effect during nighttime data

In DESIREX, a linear correlation between LST and Tair was tested using the fixed masts data, considering every hour independently in order to obtain a better discrimination between daytime and night time measurements. Figure 9 shows the differences between surface and air temperature for every fixed mast in the DESIREX campaign, with a mean lowest value observed between 19h and 6h UTC.

Figure 10 shows the correlation coefficient and the error in the determination of Tair. Analyzing both parameters, we can conclude that night time fits provide better results than day time fits. The best results are found for 0h and 5h UTC (Table3), considered as the suitable moments for UHI studies in order to retrieve air temperature from LST data

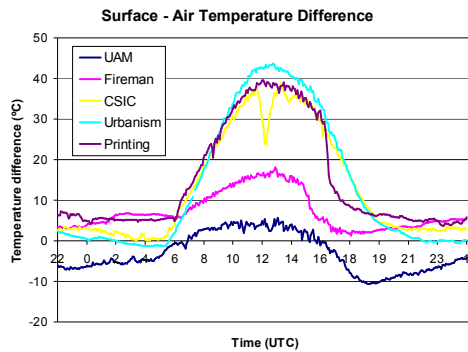


Figure 9. DESIREX 2008 correlation analysis between Surface and air temperature from fixed stations.

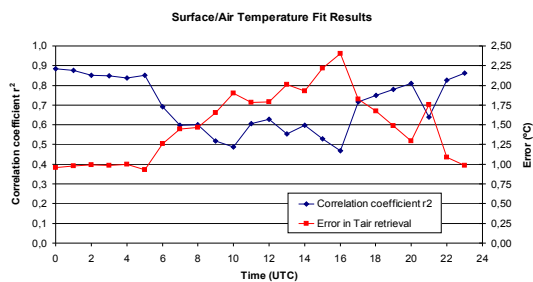


Figure 10. Mean values for all the fixed masts of the correlation coefficient and error in the determination of Tair for every hourly fit between Surface and Air Temperature.

Table 3. LST and Tair correlation using the linear fit $T_{air}(^{\circ}C) = m \cdot LST(^{\circ}C) + n$ for 0h and 5h UTC data that provides better results to retrieve Air temperature from satellite LST data.

0h UTC Fit

SITE	$m \pm \varepsilon(m)$	$n \pm \varepsilon(n)(^{\circ}C)$	r^2	error($^{\circ}C$)
Fireman	$1,25 \pm 0,04$	$-12,0 \pm 1,1$	0.90	0.92
CSIC	$0,84 \pm 0,02$	$2,6 \pm 0,5$	0.94	0.76
UAM	$0,42 \pm 0,02$	$12,4 \pm 0,4$	0.74	1.54
Urbanism	$0,68 \pm 0,02$	$7,9 \pm 0,4$	0.92	0.77
Printing	$1,08 \pm 0,02$	$-7,6 \pm 0,7$	0.94	0.80

5h UTC Fit

SITE	$m \pm \varepsilon(m)$	$n \pm \varepsilon(n) (^{\circ}C)$	r^2	error($^{\circ}C$)
Fireman	1.33 ± 0.04	-14.3 ± 1.0	0.91	0.77
CSIC	0.60 ± 0.03	6.9 ± 0.6	0.77	1.07
UAM	0.60 ± 0.03	7.6 ± 0.4	0.83	1.03
Urbanism	0.59 ± 0.02	8.7 ± 0.4	0.83	0.97
Printing	0.91 ± 0.02	-3.8 ± 0.6	0.92	0.80

DISCUSSION AND CONCLUSIONS

Two experimental field campaigns (DESIREX 2008 and THERMOPOLIS 2009) have been carried out to study the Urban Heat Island effect. Four routes for car transects for DESIREX and one route for THERMOPOLIS were defined to study the UHI effect along the cities of Madrid and Athens, respectively. Car transects show air temperature values higher in noon transects than in midnight and morning transects and always in this order for all the routes and days. High differences between surface and air temperatures are found in the noon transect, and quite low and stable in midnight and morning ones.

A good agreement of air temperature between car transects and meteorological stations has been observed, allowing a correlation analysis between surface and air temperature. A linear fit with good results has been obtained for 0h and 5h UTC, suggesting the best time periods for satellite observation in order to study UHI effect.

ACKNOWLEDGEMENTS

We wish to thank the European Space Agency ESA for its financial support in the Dual-use European Security IR Experiment 2008 (DESIREX 2008) project (21717/08/I-LG), and the Technical Assistance for Airborne, Satellite and Ground Based Measurements during THERMOPOLIS Campaign (THERMOPOLIS 2009) project (22693/09/I-EC).

REFERENCES

- J. A. Sobrino; R. Oltra-Carrio; G. Soria; R. Bianchi; M. Paganini; J.C. Jiménez-Muñoz; B. Franch; V. Hidalgo; C. Mattar; Y. Julien; J. Cuenca; J. A. Gómez; E. De Miguel; A. Fernandez-Renau; F. Nerry; G. Najard; M. Pujadas; F. Molero. The Dual-use European Security IR Experiment (Desirex 2008) a Study of the Urban Heat Island in Madrid. ESA Living Planet Symposium , 2010.
- S. Rapsomanikis; K. Konstantinos; I. Daglis; I. Keramitsoglou; V. Amiridis; G. Petropoulos; A. Papayannis; J.A.Gomez-Sanchez; E. de Miguel; J.A. Sobrino; J. Groebner; R. Bianchi. Thermopolis 2009, an Airborne Campaign over Athens, Greece, for the Study of the Urban Heat Island. ESA Living Planet Symposium, 2010.

Generation of continuous rasters of climatological variables using geographic weighted regression.

Luis Morales¹, Juan C. Parra² and Juan Espinosa¹

¹ Department of Environmental Sciences and Natural Renewable Resources. Faculty of Agricultural Sciences. University of Chile. PO-BOX 1004, Santiago, Chile.

² Department of Physical Sciences. Faculty of Ingeniering, Sciences and Administration. University of La Frontera. Av. Francisco Salazar 01145. Casilla 54-D. Temuco, Chile.

ABSTRACT One of the most widely used approaches to determine the spatial distribution of climatological data is through spatial interpolation methods, in order to obtain matrices (rasters) in Geographic Information System format. One of the used method is multiple linear regression with the help of remote sensing data, although regression coefficients are unique for the whole territory. This work presents a simple method for integrating geomorphological and remote sensing variables using multiple linear regressions with geographical weights in order to obtain the spatial distribution of climatological variables. The results show that this method for estimating the fields of climatic variables and reduce the error between observed and estimated values compared well with other methods. Finally, by incorporating remote sensing data, spatial estimation of climatic variables has been improved.

RESUMEN Una de las aproximaciones más utilizadas para conocer la distribución espacial de datos climatológicos es mediante métodos de interpolación espacial con el fin de obtener matrices (rasters) en un formato de un Sistema de Información Geográfico. Uno de los métodos usados es el de regresiones lineales múltiples con la incorporación de datos de teledetección, sin embargo los coeficientes de la regresión son únicos para todo el territorio. Este trabajo presenta un método de integración de variables fisiográficas y de teledetección usando regresiones lineales múltiples con pesos geográficos con el objetivo de obtener la distribución espacial de variables climatológicas. Los resultados muestran que este método permite estimar los campos de variables climatológicas y reducir el error entre los valores observados y estimados en comparación a otros métodos. Finalmente, al incorporar datos de sensores remotos, se ha mejorado la estimación espacial de las variables climatológicas.

INTRODUCTION

Different regression techniques have been used widely in different applications in remote sensing. These regression methods have been used to describe the relationship between an environmental variable measured over the Earth's surface and other parameters associated with remotely sensed data (e.g. a vegetation index). Often, the regression analysis is used with the aim of developing a model to make spatial predictions of the environmental variable by using remotely sensed data. Although a variety of approaches related to regression modelling have used remote sensing data and multiple linear regression analysis (MLRA) to obtain climatic cartography (Pesquer *et al*, 2007), this approximation has important limitations and is not always appropriate (Cohen *et al*, 2003).

One aspect frequently observed in predictive models to estimate spatial distribution of environmental

variables is the use of global techniques, with a single and unique set of parameters taken to apply uniformly in space. Previous works show that it is possible to improve MLRA for spatial modelling of environmental variables using remote sensing data (Cohen *et al*. 2003; Fotheringham *et al*, 2000). Such global analyses are based on the assumption that the relationship is spatially stationary, but this hypothesis may often be untenable, particularly when the study area is too extended.

The aim of this article is to apply a simple method to model a spatial distribution of a climatological variable using meteorological and remote sensing data. We made a spatial prediction through a geographical weighted regression since it is a local technique that allows the regression model parameters to vary in space (Fotheringham *et al*, 2002).

MATERIALS AND METHODS

This study was carried out in the Region del Maule (Figure 1), central zone of Chile, located between $-34^{\circ} 41'$ and $36^{\circ} 33'$ of latitude and represents a total area of 30469.1 km². The area has a temperate mesothermal estenothermic semiarid Mediterranean climate (Santibáñez and Uribe, 1992). The thermal regime is characterized by hot dry summers and cold winters with temperatures varying between a maximum mean of 26.9 °C in January and a minimum mean of 3.9 °C in July, and mean yearly precipitation is 1245.82 mm.

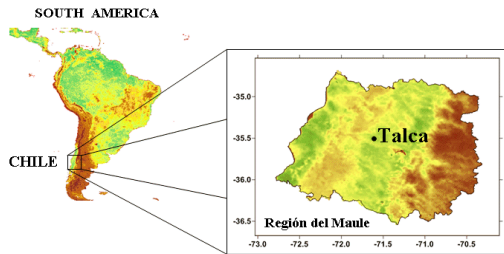


Figure 1.- Study area.

Geographic Weigthed Regression (GWR)

Recognizing that spatial data are not generally independent, so that statistical inference in ordinary regression models applied to spatial data is suspect, a number of attempts have been made to provide a regression framework in which spatial dependency is taken into account. The most popular technique for this purpose is regression analysis (Draper and Smith, 1981; Berry and Feldman, 1985; Grabill and Iyer, 1994; Fotheringham et al., 2000; Fotheringham et al., 2002).

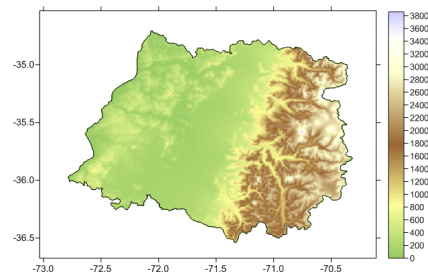
In the spatial climate data analysis, global regressions are used to estimate and describe a unique equation that describe the spatial behavior of a variable. This means, under topoclimatic concept, that the relationships between different topographical parameters and a climatic variable are considered spatially stationary (Morales *et al.*, 2006). Therefore, every non stationary climatic relation will not be modelled particularly well by a unique stationary parameter and the global estimation issued for the Global Spatial Regression can be misleded or definitely erroneous. In other complementary way, since this study is centered in the determination of topoclimatic or microclimatic zones at the study area, the Global Spatial Regression estimate the general spatial characteristics of the behavior of a given climate variable, indeed in contrast, the Local Weighted Regression model analyze the local particularities in the behavior of a climatic variable,

being useful in the topoclimate detection and classification process.

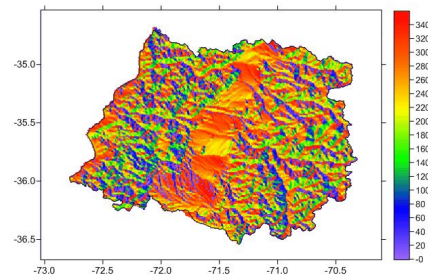
Mathematically, GWR is a technique that extend the traditional regression framework by allowing local rather than global parameters to be estimated so that the model is (Fotheringham et al., 2002):

$$y_i = a_0(u_i, v_i) + \sum_k a_k(u_i, v_i)x_{ik} + \varepsilon_i \quad (1)$$

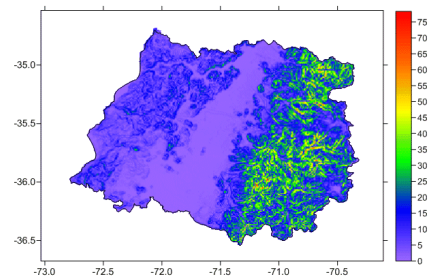
Where (u_i, v_i) denotes coordinates of the i^{th} point in space, y_i is the value of dependent variable, x_{ik} is an independent variable at the i point, $a_k(u_i, v_i)$ is a parameter of GWR regression at point i for each independent variable, and ε_i is the error in point i .



(a)



(b)



(c)

Figure 2.- Fisiographic independents variables used in the geographic weigthed regression method.

GWR method was used with adaptive kernel and a Cross Validation (CV) process to determine the number of local stations to consider in the weighting distribution function. GWR is designed to interpolate climatic variables starting from punctual data (meteorological stations) with the purpose of obtaining a non stationary distribution of the linear regression parameters. We have also used ordinary kriging (OK) for interpolation linear regression parameters and calculate the spatial distribution of climatic variables to the proposed resolution (GWR-OK).

RESULTS AND DISCUSSION

The independent variables used to carry out the method are geographic position (LAT, LON), altitude (ALT), slope (PEND), aspect (EXPO), distance to hydrologic network and distance to the ocean (DIL) of each point in area. Figure 2 shows some of the independent variables in matrix format, and figure 3 shows NDVI maps obtained from NOAA-AVHRR satellite for the months of January and July, also used as independent variables in GWR-OK.

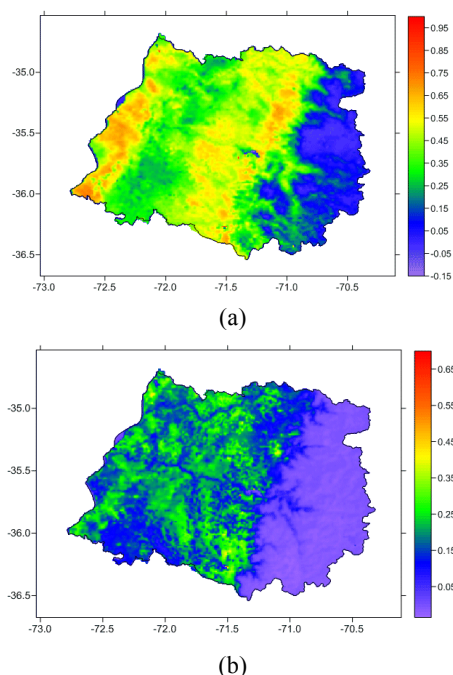


Figure 3.- Normalized difference vegetation index used as independent variable in geographic weighted regression method: a) January NDVI, b) July NDVI.

This factor combination describes the spatial characteristics of a climatic variable, making possible a spatialization or interpolation of the variable by a mathematical topoclimatical model based in GWR-OK (Fotheringham *et al.*, 2000; Fotheringham *et al.*, 2002;

Morales *et al.*, 2007). The statistical model is shown in equation (1). To calculate the spatial distribution of climatological variables using GWR (Eq. 1), we used the statistical software R (R Development Core Team, 2009). The climatological variables used to obtain spatial interpolation were January and July minimum (TNE-TNJ) and maximum (TXE-TXJ) mean temperature, January and July mean relative humidity (HRE - HRJ) and mean annual rainfall (PPA). Table 1 shows ANOVA statistic parameters, regression parameters (R^2 and p-value), root mean square error (RMSE) and Akaike information criterion (AIC) for each climatological estimated variable. Monthly average solar radiation was estimated from the PINSOL model (Seyfried M., 2003).

Table 1. Statistical results for GWR-OK, MAE and Akaike information criterion and ANOVA comparison.

Variable	$R^2(\%)$	P-Value(95%)	RMSE	AIC
TXE	97.4	0.0000	1.17	888.4
TXJ	98.3	0.0000	0.41	452.2
TNE	94.1	0.0000	0.61	625.0
TNJ	87.5	0.0000	0.92	787.9
HRE	97.9	0.0000	1.35	1016.7
HRJ	98.4	0.0000	1.71	1174.4
PPA	98.5	0.0000	79.30	3106.1

The results in Table 1 show the fitting with a GWR model to describe the relationship between specific climatic variable and independent variables. The coefficient of determination (R^2) statistic indicates that the model as fitted explains between 87.5 and 98.5 of the variability in each climatological variables. The corresponding p-value is less than 0.05, so this term is statistically significant at the 95.0% confidence level for each model. The root mean square error (RMSE) of the estimate shows the standard deviation of the residuals was 0.41 for TXJ and 79.3 for PPA as extreme values.

The results of statistical analysis shows that the models found for each variable are significant, making it possible to estimate the spatial distribution for each climatic variable. The model equation for each climate variable is the following:

$$y_i = a_0 + a_1 LAT + a_2 LON + a_3 ALT + a_4 DIL + a_5 NDVI \quad (2)$$

where a_0 , a_1 , a_2 , a_3 , a_4 and a_5 are specific coefficient matrices. The coefficients are found for each weather station used by GWR, so it is very easy to find the spatial distribution of each of them through interpolation, which in our case was ordinary kriging. The matrices of the coefficients should have the same dimensions as the matrices of independent variables, ie the same number of rows and columns. Using a geographic information system it is possible to build arrays of each climatological variable.

The figure 4 shows the results of the spatialized variables for the mean annual temperature, mean annual evapotranspiration calculated with Jensen Heise method (Allen *et al*, 1998) and the mean annual precipitation.

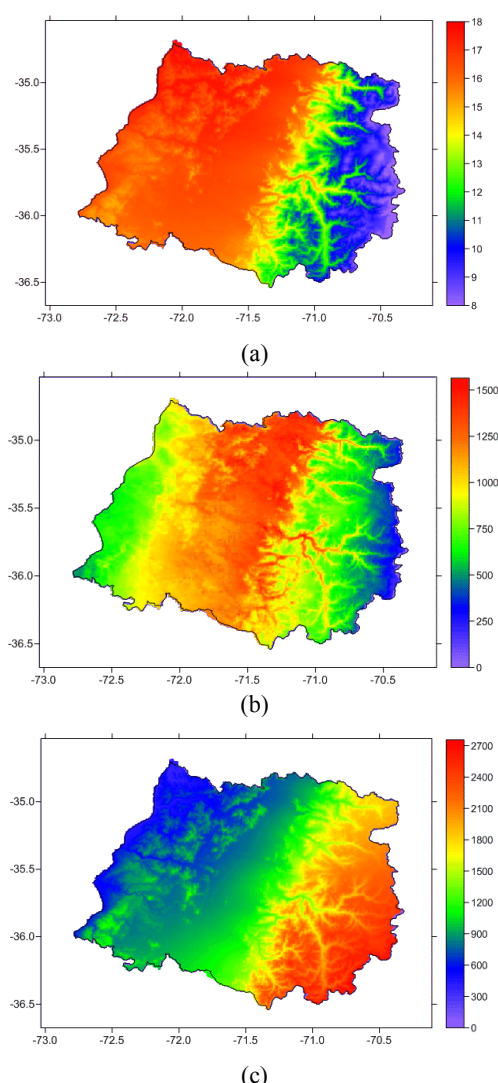


Figure 4.-. Images of mean annual (a) temperature, (b) evapotranspiration and (c) rainfall.

The results are satisfactory and show an improvement when compared with previous studies for this same study area (Novoa *et al*, 1989; Santibañez & Uribe, 1992). In Chile the methods previously used are based on interpolating isolines, usually drawn freehand by an expert climatologist. However, this method has errors when you want to interpolate linearly between isolines (Declercq, 1986). Another important aspect is that most

of the weather maps in Chile are in analogic format or paper. In this work, the maps are in digital format, which facilitates access to any data in the study area. All weather variables are in digital format and can be viewed with a GIS or be easily incorporated into other databases.

CONCLUSIONS

In this paper we have presented an implementation of a combined method to interpolate and extrapolate climate data. The described method, in spite of its simplicity, includes spatial statistical analysis, and has proven to be useful to know the spatial distribution of a climatic variable. Current literature presents several methods of interpolation and extrapolation data, although with some degree of error in the estimate, whereas the method presented allows a simple way to obtain continuous maps of climatic variables and minimize the error of estimation.

We believe that the proposed method can estimate spatial distribution of meteorological variables, on a daily basis, however some modifications may be needed for global application.

Finally, by incorporating remote sensing data in GWR-OK, the spatial estimation of climatic variables has been improved.

ACKNOWLEDGEMENTS

Funding for this study was provided by a grant from the Fundación para la Innovación Agraria (FIA), Chilean Ministry of Agriculture (grant N° FIA-ES-L-2005-1-A-003).

REFERENCES

- Allen, R.G.; L. S. Pereira y D. Raes (1998). Crop evapotranspiration - Guidelines for computing crop water requirements - FAO Irrigation and drainage paper 56. Available in: <http://www.fao.org/docrep/X0490E/X0490E00.htm#Contents>.
- Berry, W., Feldman, S., 1985. Multiple Regression in practice, quantitative applications in the social science. SAGE. London.
- Cohen, W.B., T.K. Maier, S.T. Gower, and D.P. Turner. 2003. An improved strategy for regression of biophysical variables and Landsat ETM+ data. Remote Sensing of Environment. 84: 561-571.

- Declercq, F.A.N., 1986. "Interpolation methods for scattered sample data: accuracy, spatial patterns, processing time". *Cartography and Geographic Information Systems*, 23(3):128-144.
- Draper, N., Smith, H., 1981. *Applied regression analysis*. WILEY. New York.
- Fotheringham, S., Brunsdaon, Ch., Charlton, M., 2000. *Quantitative Geography, Perspectives on spatial data analysis*. SAGE publications, London.
- Fotheringham, S., Brundson, Ch., Charlton, M., 2002. *Geographically Weighted Regression: the analysis of spatially varying relationships*, WILEY, West Sussex.
- Graybill, F., Iyer., H., 1994. *Regression Analysis: Concepts and applications*. Buxburry. Belmont.
- Morales Luis, Fabricio Canessa, Cristian Mattar, Raúl Orrego y Francisco Matus. 2006. Characterization and edafic and climatic zonification in the region of coquimbo, chile. *Journal Soil Sc. and Plant Nutrition*, Vol 6(3), pp. 52-74.
- Morales Luis, Fabricio Canessa, Cristian Mattar and Raúl Orrego. 2007. Comparison of stochastic and regression geostatistics interpolation methods for detection of microclimatic areas. 5th International Symposium on Spatial Data Quality, ISSDQ 2007, 13 – 15 June 2007, ITC Enschede, The Netherlands (www.itc.nl/ISSDQ2007/proceedings/).
- Novoa R., Villaseca S. Del Canto P.; Rouanet J. L.; Sierra C.; Del Pozo L. A. , 1989. *Mapa Agroclimático de Chile*. 60 pp.
- Pesquer L., Masó J. y Pons X., 2007. Integración S.I.G. de regresión multivariante, interpolación de residuos y validación para la generación de rásters continuos de variables meteorológicas. *Revista de Teledetección* 28:69-76.
- Santibañez F. and Urbie J., 1993. *Atlas agroclimático de Chile: Regiones IV a IX*. Universidad de Chile, Santiago, Chile. 64 pp.
- R Development Core Team (2009). *R: A language and environment for statistical computing*. R Foundation for Statistical Computing, Vienna, Austria. ISBN 3-900051-07-0, URL <http://www.R-project.org>.
- Seyfried Mark. 2003. Computational solar radiation subroutine PINSOL. Agricultural Research Service (ARS), USDA. Northwest Watershed Research Center (NWRC), personal communication.

STRS (Spectro-Temporal Reflectance Surfaces): a new conceptual framework for the integration of remote sensing data from multiple different sensors

Guillermo Villa¹, José Moreno², Alfonso Calera³, Julia Amorós², Gustavo Camps², Emilio Domenech¹, Purificación Escobar¹, Jesús Garrido³, Javier González-Matesanz¹, Luis Gómez-Chova², Silvia Luaces¹, Jose-Ángel Martínez¹, Sergio Molina⁴, Juan Carlos Ojeda¹, Juan-José Peces¹, Nuria Plaza¹, Ana Porcuna⁴, José-Antonio Tejeiro¹, Nuria Valcarcel¹
¹ Instituto Geográfico Nacional IGN Spain, ² University of Valencia (IPL), ³ University of Castilla-La Mancha (IDR), ⁴ Tragsatec

gmvilla@fomento.es, jose.moreno@uv.es, alfonso.calera@uclm.es, julia.amoros@uv.es, gustavo.camps@uv.es, edomenech@fomento.es, pescobar@fomento.es, jgarridorubio@gmail.com, fjgmatesanz@fomento.es, luis.gomez-chova@uv.es, sluaces@fomento.es, jmperez@fomento.es, smolina@tragsa.es, jcojeda@fomento.es, jjpeces@fomento.es, nplaza@fomento.es, aporcuna@tragsa.es, jatejeiro@fomento.es, nvalcarcel@fomento.es

ABSTRACT - *The conflict between spatial and temporal resolution of satellite systems, as well as the frequent presence of clouds in the images, have been the traditional limitations of remote sensing in the optical domain. The most obvious solution, which would have been designing, building and launching constellations of satellites with identical sensors, allowing to obtain cloud-free images with spatial and temporal resolution required by the different applications, has been rarely put in practice (at least in medium/high resolution), due to different economic, political or commercial reasons, or a combination of them. On the other hand, most of the conceptual tools and algorithms developed classically in remote sensing are based on the input of cloudless image series of identical sensors.*

In this study we propose a new conceptual framework, able to ingest data from several different sensors, make them homogeneous, eliminate clouds (virtually) and make them usable in a flexible, efficient and transparent way. The methodology is based on previous developments as: spatial “downscaling”, temporal interpolation and spectral transformations, but adds a conceptual framework able to integrate all of them and facilitate synergies between all these techniques. Developments made in this direction are being tested with the archive of Landsat images and other sensors of Spanish National Remote Sensing Program, in which all Landsat 5 images over Spanish territory, regardless of their cloud coverage, are received and processed.

1. MOTIVATION

More and more Earth Observation satellites are launched each year, responding to an increasing demand of better spatial, spectral and temporal resolution of data for a widening range of potential applications. But technological limitations of optical observation systems (mainly the impossibility to attain high spatial resolution and high temporal frequency with one sensor) have led so far to a “dual approach”:

- Sensors like MODIS and MERIS (we will call them “Low Resolution” -LR- from now on), with high temporal frequency, to monitor rapidly varying phenomena, with low spatial detail. E.g.: meteorology, oceanography, etc.

- Sensors like Landsat TM, IRS LISS,... (we will call them “Medium Resolution” -MR- from now on), with low temporal frequency, to monitor slowly varying phenomena, with good spatial detail. E.g: Land Cover, geology, etc.

Nevertheless, many of the most interesting applications (present and potential) require at the same time good spatial and good temporal resolution; e.g: precision agriculture, irrigation advisory services, real time change detection and updating of cartography, etc.

If we look, for example, at all Landsat 5 TM images available for one year over certain point of the South of Spain we find that, despite it is a “sunny region”, most of the images are covered with clouds in a big percentage. If we are only interested in a “pilot

project" of a small area, we will probably be able to find several images of more or less adequate dates, in which this small area is cloud-free (especially if we are allowed to choose the place of the pilot area, which is usually the case in research projects). But if we want an application to become "operational", it has to work always with available data, and across a whole large area, such as a complete region or country. In most cases, it becomes impossible to find an image series with enough "temporal density", that is cloud-free in this entire region. This is also true, or even worse, for all other MR sensors available today. European Union Land Monitoring Programs are based in the production of cloud-free "snapshot" mosaics (Image 2000-2006-2009) of the whole Europe of one or two "fixed dates": this objective has proved impossible to achieve, even using 2 or 3 different sensors.

However, the majority of algorithms developed to date in Earth Observation (classifications, indexes, biophysical parameters, model inversions...) need a sequence of images of the same sensor and cloud-free in its entire surface as input.

So the main problem of MR optical remote sensing, which makes it very difficult to transform "potential applications" into "operational", continues to be the availability of cloud-free image series.

We could try to generate "cloud-free composites" and to apply our algorithms to them; these composites are routinely generated for LR sensors such as MODIS, since its daily temporal frequency makes it possible to infer quite accurately the reflectance of the pixels that are covered by clouds. However, for applications requiring MR images, we find that temporal frequency of each sensor alone is insufficient to apply this method.

This makes us to consider the option of using all available images, even if they are covered by clouds in great part of the surface and even if they come from different sensors, and therefore have:

- different resolutions (spatial, temporal, spectral, radiometric)
- different bands: number, wavelength limits and "spectral response curves"

To do so, we must develop a methodology that allows us to "integrate" radiometric information of all images available, regardless of the sensor they are from. With such integration, we could take profit of "strong points" of each sensor (temporal frequency, spectral resolution, spatial resolution,...) and minimize the effects of the weaknesses of each. All sensors would be complementary and "cooperative".

This work proposes a "conceptual framework", to integrate and take advantage of the huge mass of seemingly "inconsistent" radiometric data. This

framework should ease the development of algorithms and techniques able to deal with this data, both for historical studies (with archived images of different satellites), and for "real-time applications".

2. THE CONCEPT OF STRS

Traditional Remote Sensing theory states that a "Ground Cell" (GC from now on) is characterized by its Spectral Signature curve:

$$\rho = \rho(\lambda) \quad (1)$$

But terrain is constantly changing over time, and so is the reflectance of each GC, so the real characterization of a GC is a surface:

$$\rho = \rho(\lambda, t) \quad (2)$$

This is the "Spectro-Temporal Reflectance Surface" (STRS) (Vieira et al, 2000). Each "appearance" of the GC in any image provides one point of the STRS for each spectral band of the image. Different images at different times should provide different points of the same surface, even if they come from different sensors.

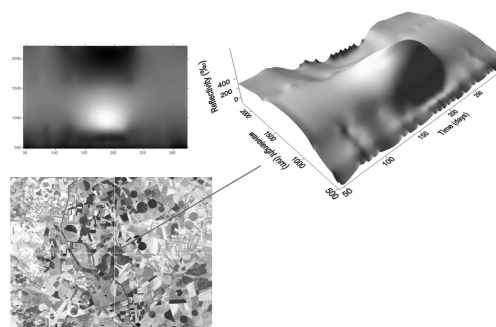


Figure 1: Visualization of the STRS of a Ground Cell inside a corn parcel: a) as an image; b) as a surface.

Our goal is to calculate or "reconstruct" such surface, as exactly as possible, for each GC in our area of study. Each available image becomes an "input" to feed a "single database" representing the radiometric reality of an area and its evolution over time. We change the vision of "multiple different images" as "unconnected" views of a changing reality, to a "single representation" of the "radiometric history" of an area.

3. PROCESS FOR THE RECONSTRUCTION OF THE STRS

To reconstruct the STRS of each GC we must use any available time series of LR and MR images. The general outline of a theoretical process for STRS reconstruction and use is showed in Figure 2, for the case in which we have two LR sensors and two MR sensors.

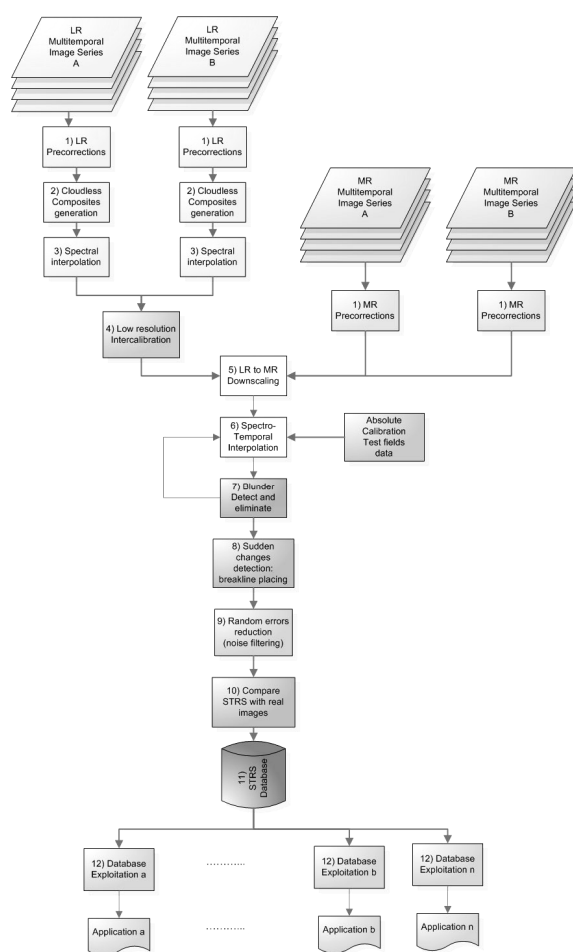


Figure 2: Schema of the process for the reconstruction of the STRS of each GC

The different phases, briefly described, could be:

1) Pre-correction of each LR and MR image series: this includes all the processes required to obtain "standardized" reflectances:

- TOA Radiance determination
- Geometric correction and resampling
- Atmospheric correction
- Topographic correction, terrain shadows removal
- BRDF and hot spot correction, possibly using a polynomial approach (see Villa, 1988 and Molina et al, 2010).
- Detection and masking of: clouds, cloud shadows, haze, snow, temporary water (eg: puddles,...), aberrant pixels, flares,...

2) Generation of cloud-free composites of each LR series. The temporal interval between composites can be 1 day, for example.

3) Spectral interpolation of each LR series: to be able to compare data of different sensors, we need to reconstruct the whole spectral curve (discretized in 10nm intervals, for example) for the wavelength interval of interest. This process is fairly easy and accurate with sensors having many narrow bands, like MODIS and MERIS. We can use splines interpolation, minimum curvature, etc. In some cases, if necessary, we can "stabilize" the solution applying spectral unmixing techniques.

4) Intercalibration of all the LR series: applying an appropriate gain and bias to each reflectance value. These parameters are determined comparing reflectance values for the same area, wavelength and time. (Villa and Fernández-Montoro, 1993; J.A. Tejeiro, 2000). Systematic errors committed with each sensor should be mitigated through this process.

5) LR to MR downscaling: as LR sensors give information with high frequency but only about "large" GC, we need a method to "transfer" the temporal information from LR to HR images. The method we propose for this task is "spatial downscaling": this process allows obtaining a composite image with the spectral and temporal characteristics of the LR instrument along with the spatial resolution of the MR images (Zhukov et al, 2008; Zurita-Milla et al, 2008). The processing scheme is described in Amorós-López, et al, 2010, and is summarized as follows (Figure 3):

First, a soft clustering is carried out over the MR image in order to obtain the land cover map at high spatial resolution, and the membership of each MR pixel to the clusters is also calculated. Next, these posterior probabilities at MR resolution are used to get the abundance or proportion matrix for each LR pixel.

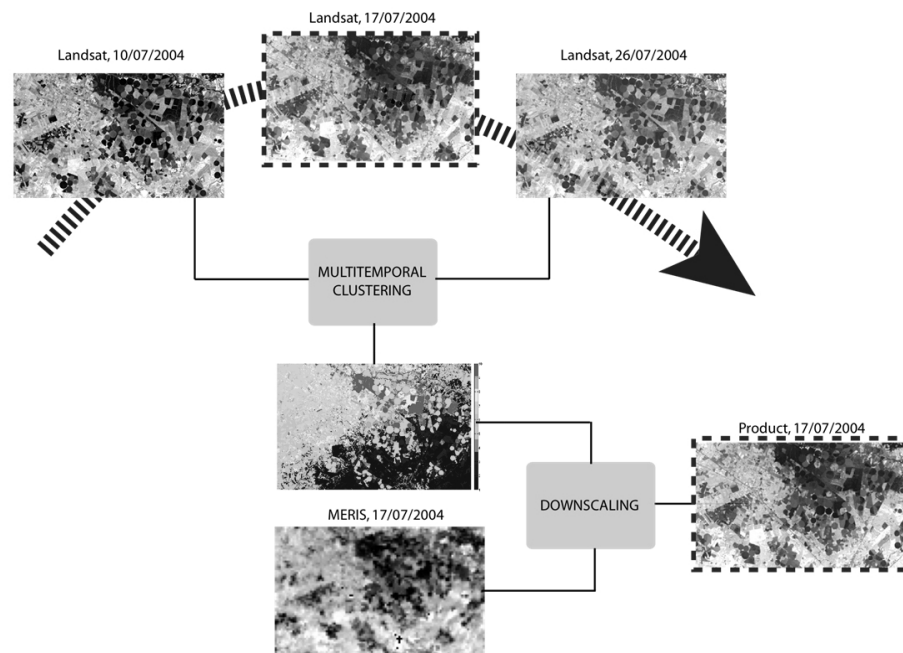


Figure 3: Schema of spatial downscaling process

Then, a sliding-window spatial unmixing is carried out over the LR image. In this step, the proportions of the MR pixels within the window are used to obtain a set of endmembers for each class through the inversion of a system of linear mixture equations. Finally, the fused pixels at high spatial resolution are obtained as a linear combination of the estimated LR endmembers of each class weighted by the corresponding MR membership. The use of these membership values from the MR image guarantees the spectral variability of the land cover classes within each LR pixel in the fused image.

6) Spectro-temporal interpolation: all reflectance data obtained for each GC through the previous phases are introduced in a process of “bundle adjustment” to generate the STRS surface that best fits the input data. This surface can be calculated using 2D interpolation methods such as: splines, minimum curvature, etc. (see González-Matesanz, 2007). In figure 1 we can see the calculated STRS for a GC inside a corn parcel, derived from a Landsat 5 TM series.

If available, absolute calibration information could be added in this phase by introducing radiometric field measurements over calibration fields (natural or artificial) in the same “block adjustment” process.

7) Detection and elimination of “outlayer data” (blunder –gross errors- elimination): reflectance data that differ too much of their surroundings, can be supposed to be gross errors that have not been detected in the precorrection phase. These outliers must be eliminated from the final adjustment of the surface.

8) Sudden changes breaklines: sudden changes in the GC should be detected; a sudden change should appear as a “vertical step” in the STRS, and a “breakline” should be introduced in the calculations.

9) Random errors filtering: STRS surface should be “smooth” in wavelength direction, and normally also in the time direction (except sudden changes). So random errors committed during precedent phases have now an opportunity to be reduced by “noise filtering” techniques, such as low-pass, median, de-speckle, etc. applied to the STRS surface. The filtering technique can be different in the wavelength and time directions.

10) Comparison of STRS with real images: Once the STRS is calculated, we can use it to synthesize the same images we started from, and compare the “real” version with the synthetic version. This comparison should allow to assess the precision we obtained, and maybe to “iterate” the calculations readjusting some parameters.

11) **Storing the STRS of each GC:** STRS can be stored in different schemas:

- Store one hyperspectral image for each day of the time interval of our study.
- Store one surface for each GC of the study area (in TIN or Grid format, or by storing polynomial or splines parameters,...)
- Store one “image tile” representing the STRS of each GC. (In TIFF or JP2 formats for example).
- Store one single relational database, with the appropriate data model and tables and fields structure.

Each of these schemas has its own advantages; e.g: storing in “image tiles” allows us to apply to STRS digital image processing techniques, such as: Fourier domain filtering, compression (lossless or lossy), etc.

In order to facilitate the use of this database, it should be “multiresolution”, and include “pyramids” in a self-consistent way: STRS of large GCs should be the exact averages of STRS of all smaller GCs inside it.

Storage space for 30 m pixel size, 1 day interval, from 350 to 2400 nm wavelengths, 2 bytes per reflectance value, for a country like Spain (about 500,000 Km²) would be 76 Tbytes/year of uncompressed data. Computation effort will be of course very big, but it should be possible to “parallelize” the calculations, which would allow using parallel computing.

12) **Exploitation of the Database:** from this STRS database, different exploitation schemas for different applications are possible. Each one will require the generation of specific products or services. For this exploitation, existing algorithms designed to work with multitemporal image series, or with hyperspectral images, should be adapted to work with this hyperspectral & hypertemporal database.

4. APPLICATIONS OF THE STRS

Some applications related to the spectro-temporal surface reflectance reconstruction can be identified, such as:

- Detection of clouds, cloud shadows, haze, snow, temporary water (eg: puddles,...), aberrant pixels, flares,...
- Removing of: clouds, cloud shadows,... through interpolation (see figure 4).
- Generation of cloud free mosaics of large areas of any exact date chosen.

But the most relevant applications will be those related to:

- Dynamic Biophysical parameters
- Sensor intercalibration
- Land cover classifications using different sensor multitemporal “cloudy” images
- “Dynamic” classifications (classes variation along time in one terrain cell); e.g: from crop to bare soil, to a new crop,...
- LR sensor calibration (through upscaling) from MR data.
- Pansharpening is a “particular case” of spatial downscaling, and should benefit of STRS approach.
- Generation of “Films” or interactive “time browsing” of image series. See:

<http://www.youtube.com/watch?v=Lm6A61A2Z4w>

<http://www.youtube.com/watch?v=YBtSnbvojtE>

This films show daily evolution of Landsat 5 TM bands 3, 4 and 5 reflectances over an agricultural area near Barrax, Spain, with a mixture of irrigated and non- irrigated parcels.

Many more applications can become available as such spectro-temporal series become the common database for the users community.

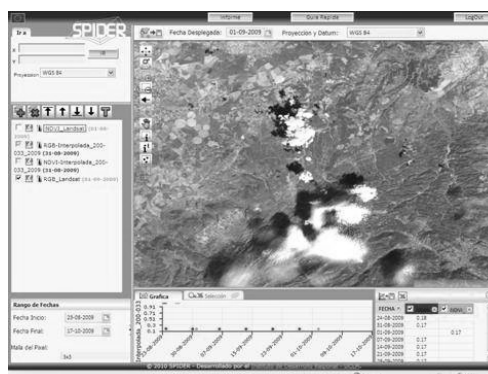


Figure 4a: cloudy image



Figure 4.b: clouds removed through temporal interpolation

5. CONCLUSIONS AND FUTURE WORK

The lack of coordinated satellite constellations with the same spectral bands, intercalibrated, and covering the whole range of temporal / spatial resolutions forces us to try a different approach to “integrate” all the available data.

In the next future, this situation will get better due to the launch of high performance satellite constellations, such as Sentinel 2, and others. Nevertheless, the increase in track width of these sensors will make it even more difficult to find cloud-free images. Also, more and more demanding applications, some of them “real time” such as precision agriculture support, will demand almost daily information about land surface. For this reasons, we will still need to use a “mixture” of different sensors (Sentinel 2, Sentinel 3, Landsat 8, CBERS, IRS,...). And maybe even mix them with high resolution sensors (SPOT 6-7,.. or Seosat/Ingenio next Spanish 2.5 m resolution satellite).

On the other hand, for historical studies as important as climate change assessing, deforestation monitoring, etc., we must face the fact that all available data in image archives has been captured by many different sensors, each one with its particular spectral bands, spatial and temporal resolution, etc. Many of these archived images are never used due to their high cloudiness percentage. With STRS approach we could “recycle” all this information, and make it usable. For this reason, long term data archives should keep every image regardless their cloud percentage.

The concept proposed should allow us to go from N different multispectral sensors (different bands, different resolutions,...) to one single integrated “datacube”.

So far, we have developed separately many of the different phases of the process described in point 3. The next task is to put them together in an integrated workflow, and test it “in the real world”. For example: trying to generate Landsat 5 “cloud free” daily composites of acceptable quality, for PNT (Spanish National Remote Sensing Program), with the help of MODIS/MERIS images.

7. REFERENCES

- B. Zhukov, D. Oertel, F. Lanzl, and G. Reinhackel. "Unmixing-based multisensor multiresolution image fusion", *Geoscience and Remote Sensing, IEEE Transactions on*, vol. 37, no. 3, pp. 1212–1226, May 1999.
- R. Zurita-Milla, J. Clevers, and M.E. Schaepman. "Unmixing-based landsat TM and MERIS FR data fusion", *Geoscience and Remote Sensing Letters, IEEE*, vol. 5, no. 3, pp. 453–457, July 2008.
- J. Amorós-López, L. Gómez-Chova, L. Guanter, L. Alonso, J. Moreno and G. Camps-Valls. "Multi-resolution Spatial Unmixing for MERIS and Landsat Image Fusion", *IEEE Geoscience and Remote Sensing Symposium (IGARSS'10)*, Hawaii, USA, July 2010.
- J. Amorós-López, L. Gómez-Chova, L. Guanter, L. Alonso, J. Moreno and G. Camps-Valls. "Regularized multi-resolution spatial unmixing for MERIS and Landsat image fusion", *Geoscience and Remote Sensing Letters, IEEE*, submitted in 2010.
- J., González.-Matesanz. "Aportaciones al estudio de los modelos de distorsión para el cambio de datum entre ED50 y ETRS89". Departamento de matemáticas. España, Universidad de Alcalá, 2007.
- J.A. Tejeiro. "Procedimiento Operativo Estándar. Plan Nacional de Teledetección. Procesado Básico Alta Resolución". IGN Spain, June 2010.
- S. Molina, G. Villa, C. Serrano, M. Valdepérez and, E. Domenech. "A polynomial approach for radiometric aerial triangulation", *International Calibration and Orientation Workshop (EuroCOW)*, Castelldefels, Spain, 2010.
- Vieira, C. A. O., Mather, P. M., and McCullagh, M., 2000, "The Spectral-Temporal Response Surface and its use in the multi-sensor, multi-temporal classification of agricultural crops". In *ISPRS: IAPRS*, v. 33, Amsterdam, The Netherlands, Part B2 (Amsterdam, International Society for Photogrammetry and Remote Sensing) Pp. 582-589.
- G. Villa, 1988. *Corrections radiométriques de photographies aériennes N & B numérisées en vue de la réalisation de mosaïques d'orthophotos: une méthode polynomiale*. Mémoire de stage D.E.S.S. de Télédétection, Méthodes et Applications, Université Pierre et Marie Curie (Paris VI), Paris, France.
- G. Villa and M.A. Fernandez-Montoro, "Ajuste radiométrico conjunto de varias imágenes de satélite para la realización de mosaicos de ortoimágenes", paper presented in "V Reunión Científica de la Asociación Española de Teledetección, Las Palmas, 1993.

Quality assessment of the first version of Geoland-2 biophysical variables produced at global scale

F. Camacho¹, J. Cernicharo¹, F. Baret³, R. Lacaze³, M. Weiss³

1 EOLAB. Parc Científic Universitat de València. C/ Catedrático José Beltrán, 2 46980 Paterna (Valencia). Spain.

2 HYGEOS, Cesbio Bpi 2108, 18 avenue E. Belin, 31401 Toulouse Cedex 9, France

3 INRA, EMMAH, site Agroparc, 84914 Avignon, France

fernando.camacho@eolab.es

ABSTRACT – *This study investigates the scientific quality of the first version of global biophysical products (FCover, LAI, FAPAR) developed in the Geoland-2 /BioPar Core Mapping Service, namely GEOV1. These products based on SPOT/VEGETATION data were built on MODIS and CYCLOPES products while reconciling their differences. The quality assessment strategy follows the CEOS/WGCV Land Product Validation guidelines. The spatial and temporal consistency of GEOV1 products is assessed by intercomparison with existing global products (MODIS C5, CYCLOPES V3.1, GLOBCARBON V2, JRC FAPAR) over a global network of homogeneous sites (BELMANIP-2) over two years period (2003-2005). The accuracy of GEOV1 is evaluated against a number of available ground truth maps. Several criteria of performance were evaluated, including spatial distribution, missing values, magnitude of retrievals, temporal variations, smoothness, precision and accuracy. Our results show that GEOV1 products present reliable spatial distribution, smooth temporal profiles, stable from year to year, reliable magnitude for bare areas and dense forest, and the best performance with ground-based maps. GEOV1 outperforms the quality of existing global products in most of the examined criteria, and constitutes a step forward in the development of global biophysical variables in the framework of Geoland-2.*

1 INTRODUCTION

The FP7 Geoland-2 project constitutes a major step forward in the implementation of the GMES Land Monitoring Core Service (LMCS), and addresses the local, continental and global components of the LMCS. Within geoland-2 the BioPar Core Mapping Service is in charge of developing key biophysical variables at global scale. Accurate and stable biophysical variables (LAI, FAPAR, FCOVER) are requested from users involved in climate change research, forestry, global crop monitoring and environmental applications.

Current operational global products (MODIS, GLOBCARBON, CYCLOPES) present significant discrepancies, which are larger than users' requirements, partly due to the sensors and preprocessing steps but mainly coming from the assumptions embedded in the retrieval algorithms. These products mainly differ in term of magnitude, temporal continuity and smoothness, while consistent seasonality is generally observed. Based on these results, a consensus product based on SPOT/VEGETATION data is proposed in Geoland-2/BioPar, building on MODIS and CYCLOPES products while reconciling their differences. The resulting algorithm will be implemented at VITO to

generate in near-real time the first collection of Geoland-2 biophysical variables over the globe at 1 km spatial resolution and 10 day frequency.

This paper describes the main results of the scientific quality assessment of the first version of geoland-2 biophysical parameters at global scale, named GEOV1. The quality assessment has been performed in agreement with standards of the GEO/CEOS WGCV LPV group. Two years (2003-2004) of global products was analysed. The overall accuracy of retrievals was determined based on existing ground reference maps. The product spatial and temporal consistency (precision) was assessed with emphasis on spatial distribution of values, missing values and temporal smoothness. Finally, an inter-comparison with existing satellite products (MODIS, GLOBCARBON, CYCLOPES, JRC-FAPAR) is performed.

2 REMOTE SENSING VEGETATION PRODUCTS

Below, the main characteristics of the global remote sensing vegetation products investigated here are described.

2.1 CYCLOPES

The Cyclopes Version 3.1, distributed by <http://postel.mediasfrance.org>, is produced from the

SPOT/VEGETATION sensor at 1/112° (about 1 km at equator) spatial resolution and a 10 days temporal sampling, in a Plate Carrée projection, for the period 1999-2005 (Baret et al., 2007). Products are estimated using a neural network trained from one-dimensional radiative transfer model simulations (PROSAIL model) without using any parameterisation as a function of the biome. Thus, the LAI corresponds with an effective LAI. The FAPAR corresponds with the instantaneous black-sky FAPAR at 10:00h.

2.2 MODIS

Terra MODIS LAI/FPAR (MOD15A2) collection 5, available from lpdaac.usgs.gov/lpdaac/products/ since 2000 is produced based on TERRA at 1 km spatial resolution and 8 days step over a sinusoidal grid (Yang et al., 2006). The main algorithm is based on LUTs simulated from a three-dimensional radiative transfer model. The model takes into account the clumping at plant and canopy level, thus the LAI corresponds with a true LAI. The FAPAR corresponds with the instantaneous black-sky at the time of the TERRA overpass (10:30 h). When the main algorithm fails, a backup algorithm based on LAI-NDVI relationships is used. In this work, only retrievals from the main algorithm were used.

2.3 GLOBCARBON

The Globcarbon LAI Version 2, distributed by <http://geofront.vgt.vito.be/geosuccess/>, is estimated for the period 1998-2007 from the combination of observations from two sensors: SPOT/VEGETATION and ENVISAT/AATSR (ATSR-2 for the 1998–2002 period). Individual estimates of LAI are produced for all the valid pixels from each sensor (atmospherically corrected, cloud-free and snow-free) and then the median is computed at a 10-day time step from all the available values from all the sensors. The 10-d values are subjected to a smoothing and interpolation procedure (Chen et al., 2006). The smoothed LAI observations are then averaged over one month period and aggregated to a 1 km at equator in a Plate Carrée projection.

2.4 JRC SeaWiFS FAPAR

The JRC FAPAR product, distributed by <http://fapar.jrc.ec.europa.eu/>, is estimated for the period 1997-2006 from the SeaWiFS sensor onboard Orbview-2. The products have been remapped into a global sinusoidal projection at 2.17 km and are produced on a daily basis. The FAPAR algorithm is based on an optimized vegetation index to estimate instantaneous FAPAR at the time of acquisition. The mathematical index optimization can be found in Gobron et al., (2002). An evaluation of the SeaWiFS FAPAR product can be found in Gobron et al., (2006).

2.5 BIOPAR GEOV1

Geoland-2 BioPar version 1 (GEOV1) is derived from the SPOT/VEGETATION sensor at 1/112° (about 1 km at equator) spatial resolution and a 10 days temporal sampling, in a Plate Carrée projection. The algorithm is a neuronal network trained over a fused product based on CYCLOPES for low to medium LAI and MODIS for medium to high LAI values (for details see Baret et al., *this issue*). Thus, the LAI is close to an actual value for high values, but closer to an effective LAI for low values. The FAPAR corresponds to the instantaneous black-sky around 10:15h, which is a close approximation of the daily integrated black-sky FAPAR value. These products will be produced and delivered by VITO in near real time. Here, the original version is analysed; A smoothed and gap filled version will be also produced in Geoland-2/BioPar.

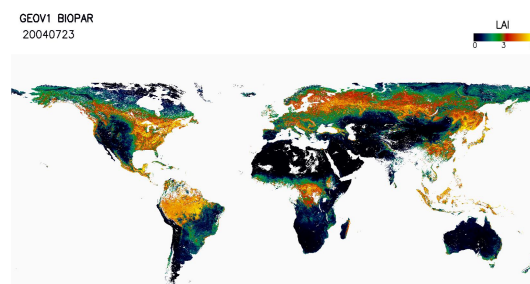


Figure 1. GEOV1 LAI global map corresponding to the 23 of July of 2004.

The version zero of Geoland-2 BioPar LAI is derived from the CYCLOPES algorithm, whereas the FCover is based on a linear relationship between FCover and NDVI. The analysed data corresponds to a test dataset over Europe and Africa produced for the period 2003-2005.

3 METHODOLOGY

This validation exercise was defined to be consistent with the best practices proposed by CEOS WGCV LPV subgroup (Morissette et al., 2006). First, an intercomparison with the existing global products was performed to examine the spatial and temporal consistency of GEOV1. Second, a direct validation approach was conducted using ground reference maps to quantify the overall performance of the products.

3.1 Intercomparison Approach

The products were intercompared over the BELMANIP-2 network of sites that was designed to represent globally the variability of land surface types. The land surface type is defined here using generic

classes derived from the GLC-2000 classification. In this paper, the products are analysed for 5 generic classes, namely: Evergreen Broadleaf Forest, Evergreen Deciduous Forest, Needle-leaf Forest, Crops-Grasslands, Shrubs-savannas-bare.

The products must be compared over a similar spatial support area and temporal support period. They were thus resampled over Plate Carrée projection at 1/112° (about 1 km at equator) spatial resolution. The intercomparison was conducted using an average value over 3x3 pixels to reduce coregistration errors between products and differences in their sensor Point Spread Function (PSF) which determines the actual footprint of the data. The temporal support period for the quantitative assessment is monthly as it is the lower temporal resolution. The original temporal sampling was used for compute missing values, histograms and the smoothness.

Product	Temporal window	Temporal Frequency	product date
GEOV1	30	10	j+17
GEOV0	30	10	j+30
CYCV31	30	10	j+15
MODC5	8	8	j
GLOB	30	30	j+15
JRC	1	1	j

Table 1. Temporal information, j: first day of the temporal window.

Intercomparison made at a monthly temporal support period was achieved selecting the central image of the month for GEOV1 and CYCV31, whereas for GEOV0 the first one was used (see table 1). In the case of MODIS products, with an 8 days temporal window, an average between the closest image to the reference date and the previous one is used for the scattering. Regarding JRC/FAPAR product, a monthly average was computed.

The smoothness of products is evaluated by taking three consecutive observations and computing the absolute value of the difference delta between the centre $P(d_{n+1})$ and the corresponding linear interpolation between the two extremes $P(d_n)$ and $P(d_{n+2})$.

$$\delta = \left| P(d_{n+1}) - P(d_n) - \frac{P(d_n) - P(d_{n+2})}{d_n - d_{n+2}} (d_n - d_{n+1}) \right|$$

The quantitative performance of the products was evaluated against ground truth data. In-situ data processed according with CEOS/WGCV LPV guidelines accounting for up-scaling effects was compiled by Garrigues et al., (2008) coming from international initiatives such as VALERI, BIGFOOT, CRSS and others. Ground truth data is affected by different sources of uncertainties: (i) Foliage clumping

is not characterised in many cases, leading to an underestimation of LAI (LAI_{eff}). (ii) Optical measurements usually do not distinguish between photosynthetic active issues and other plant elements, leading to a positive bias in vegetation parameters, (iii) Understory is not always characterised in forest sites.

Only those forest sites where the understory was measured have been selected for the quantitative analysis. Those LAI maps where foliar clumping was not measured have been corrected using the clumping index values proposed by Chen et al., (2005) as a function of the biome type, these points are labelled as LAI_{eff}/clumping. In addition, a few maps showing differences between the FAPAR and FCover greater than 0.15 are discarded. The scattering is carried out by comparing the field data with the closer product reference date. In-situ values for natural vegetation sites measured outside the period 2003-2004 are compared with satellite product estimates for the year in which the agreement is better.

3 RESULTS

3.1 Missing values

Figure 2 shows the global distribution of missing values over land as a function of the latitude and period. GEOV1 and CYCV31 have very similar results as both are based on SPOT/VGT observations.

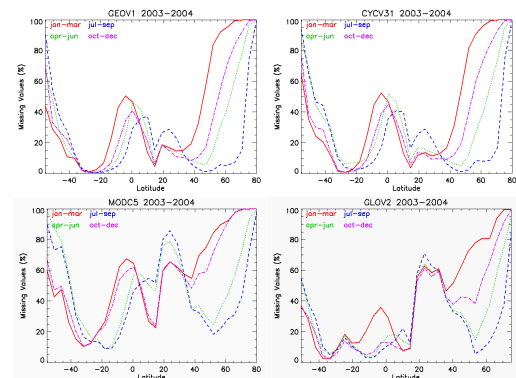


Figure 2. Percentage of missing values over land pixels as a function of latitude and period.

The missing values are very significant in January to March in northern latitudes. The equatorial region is another area in which missing values are very important (up to 50%).

3.2 Distribution of retrievals

Figure 3 shows the distributions of LAI retrieved values per biomes. Similar results for the different biomes were found with the exception of evergreen

broadleaf forests where GEOV1 products present a distribution of values with its mode between CYCLOPES mode and MODIS mode. A positive bias for MODIS over shrublands and bare areas was found, as well as a negative bias of CYCLOPES for forest sites.

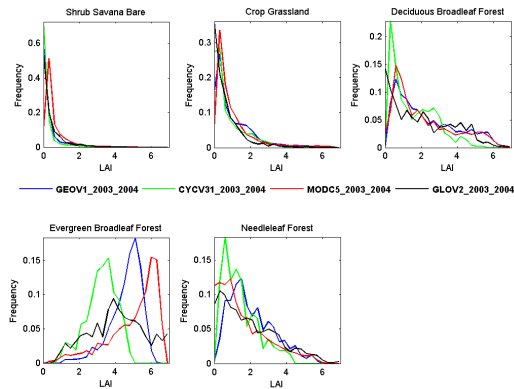


Figure 3. LAI histograms over BELMANIP-2 sites during 2003-2004 period.

Figure 4 shows the FAPAR histograms. A good agreement is found between MODIS and GEOV1 distributions for evergreen and deciduous forests. MODIS shows a clear positive bias over shrubs, savannas and bare areas. JRC FAPAR product shows a generalized underestimation as compared with other products.

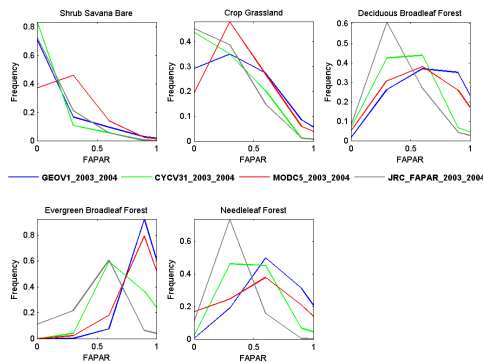


Figure 4. FAPAR histograms over BELMANIP-2 sites during 2003-2004 period.

Figure 5 shows the FCover histograms for CYC and GEOV1. The GEOV1 provides reliable distributions for forest, whereas CYCV31 shows a systematic underestimation.

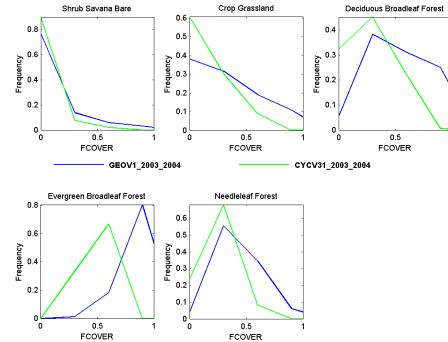


Figure 5. FCover histograms over BELMANIP-2 sites during 2003-2004 period.

3.3 Performance with global products

The performance with global products was evaluated over BELMANIP-2 sites and 24 dates. Overall performance (RMSE), systematic deviations (bias) and correlations (R^2) are shown in table 2. GEOV1 is highly correlated with CYCV31 and GEOV0 for LAI (RMS<0.5, R^2 >0.9), the performance with MODIS products is also good. Lower performances are found between GEOV1 and JRC FAPAR, GEOV1 and GLOBV2 LAI, and GEOV1 and CYCV31 FCover.

	LAI			FAPAR			FCOVER	
	R^2	RMS	bias	R^2	RMS	bias	RMS	bias
GEOV1-CYC	.95	0.43	.15	.97	.07	.04	.15	0.11
GEOV1-MODIS	.84	0.62	.02	.90	.09	-.05		
GEOV1-GEOV0	.93	0.38	.10				.10	-0.03
GEOV1-JRC				.64	.23	.13		
GEOV1-GLOB	.80	0.81	.34					

Table 2. Intercomparison exercise: Performance of GEOV1 among the different global products.

3.4 Temporal profiles

Temporal profiles of different products were displayed in order to evaluate their temporal consistency. Figure 6 shows an example over open woodland site in Mongu (Zambia). Field data symbols correspond to a different year (2000), acquired during SAFARI 2000 campaign. GEOV1 profiles show a good agreement with field measurements and a smooth trend over the period. GLOV2 present lower values and MODIS noisier profiles. For FAPAR, in-situ values were measured from two different instruments: TRAC and AccuPAR. The TRAC instrument estimates FAPAR from the gap fraction (FIPAR at SZ), whereas AccuPAR estimates FAPAR based on incident, reflected and transmitted PAR. As can be observed in Figure 6, ground estimates are within the error budget of the GEOV1 FAPAR.

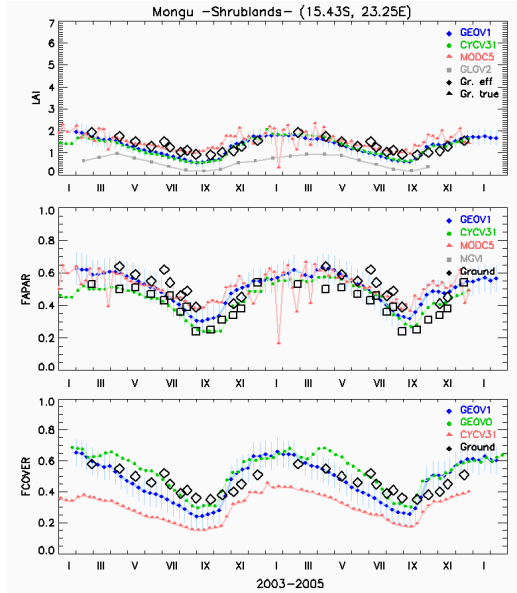


Figure 6. LAI, FAPAR and FCOVER temporal profiles at Mongu site in Africa.

3.1 Temporal smoothness

Figure 7 shows the cumulative histograms of the δ FAPAR (smoothness). CYCV31 and GEOV1 present the lower delta values. The higher delta values for JRC FAPAR are due to daily product is more unstable.

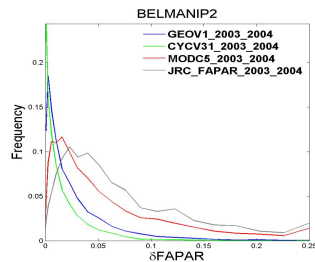


Figure 7. Temporal smoothness for the different FAPAR products. Note that the temporal sampling of JRC FAPAR is daily.

3.4 Direct validation

Figure 8 shows the scatter-plots of the comparisons of GEOV1 with in situ-based maps. For FAPAR and FCOVER correlation are better than 0.8, with an overall accuracy better than 0.1, and no systematic trends, which means that the target accuracy is achieved. For the LAI, overall performance is of 1 if only true LAI is used, and 0.85 when effective LAI corrected of clumping in-situ data is added. Correlation is better than 0.7, and minor systematic differences are found (bias<0.3).

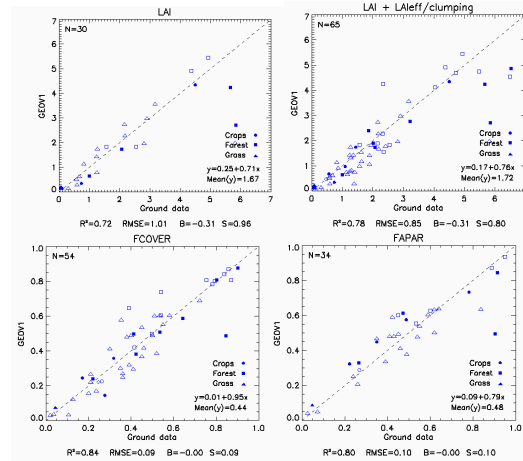


Figure 8. Comparison of GEOV1 products with ground-based estimates for LAI, LAI+LAIeff/clum, FAPAR and FCOVER. Filled symbols refers to coincident years, unfilled symbols refers to a different year.

For the other analysed products, the metrics are shown in table 3. In conclusion, GEOV1 presents the lowest RMSE with ground based data. The improvement is significant for the LAI (RMSE<1, lower bias, higher correlation), and for the FCOVER (RMSE<0.1, no bias). For the FAPAR the performance indicators of GEOV1 are identical to that of MODIS. The JRC FAPAR product presents systematic differences with the ground data, which should be partly explained by the different assumptions involved in the derivation of ground maps (i.e., black-leaves, daily integrated FAPAR) and satellite JRC product (i.e., instantaneous FAPAR at the time of acquisition).

Metric	CYCV31	MODC5	GLOBV2	GEOV0	JRC
LAI (+LAIeff/clumping)					
R²	0.72	0.59	0.74		
RMSE	1.08	1.13	1.17		
BIAS	-0.54	-0.27	-0.80		
FAPAR					
R²	0.78	0.80			0.89
RMSE	0.12	0.10			0.18
BIAS	-0.05	0			-0.14
FCOVER					
R²	0.82			0.80	
RMSE	0.19			0.13	
BIAS	-0.16			0.07	

Table 3. Direct validation results of global products.

4 CONCLUSIONS

In this study, a quality assessment of the first version of global biophysical products (LAI, FAPAR, FCOVER) developed in the framework of Geoland-2/BioPar, GEOV1, based on CYCLOPES and MODIS products,

was performed. The methodology used follows the guidelines proposed by the CEOS LPV group for validation of remote sensing vegetation products. First, an intercomparison with current existing global products (MODIS C5, GLOBCARBON V2, CYCLOPES V3.1, JRC- SeaWiFS FAPAR) was performed over the BELMANIP-2 sites distributed around the world. Second, the uncertainties were quantified by direct comparison with ground-based reference maps. Several criteria of performance were evaluated, including spatial distribution, missing values, magnitude of retrievals, temporal variations, smoothness, accuracy and precision. The main conclusions are:

GEOV1 present reliable and consistent global spatial distribution of retrievals. The intercomparison with global products shows that GEOV1 LAI and FAPAR products present similar values than CYCV31 for sparse vegetation and crops, and is much closer to MODIS for forest sites. GEOV1 overcomes the positive bias of MODIS for low LAI/FAPAR values, and the negative bias of CYCV31 for forest sites. For the FCover, the GEOV1 overcomes the important underestimation of CYCV31, and improves also the quality of GEOV0. The magnitude of retrievals is reliable for low and high vegetation abundance.

The analysis of temporal consistency showed that GEOV1 present reliable inter-annual and seasonal variations, showing very smooth profiles. GEOV1 clearly outperforms the quality of MODIS or GLOBCARBON temporal profiles.

The comparison with ground truth shows that GEOV1 is the most similar product to the reference maps, reaching an overall performance (RMSE) better than 0.1 for FCover and FAPAR with no bias, and better than 0.8 for LAI with a slight negative bias. GEOV1 products reach the target accuracy required by users.

The main limitation is the lack of continuity at high latitudes and equatorial regions as in the other global products. This limitation will be solved with the smoothed and gap filled version of GEOV1 products which is currently under evaluation.

In summary, GEOV1 products have a good quality, showing a spatial consistent global distribution of retrievals. Temporal profiles are very smooth and are highly consistent from year to year. Comparison with ground data shows that target accuracy is achieved, and no bias was detected.

5 REFERENCES

- Baret, F., et al. (2007). LAI, fAPAR and fCover CYCLOPES global products derived from VEGETATION: Part 1: Principles of the algorithm, *Remote Sensing of Environment*, 110, 275–286.
- Baret, F., M. Weiss, R. Lacaze, F. Camacho, P. Pacholczyk and B. Smets (this issue). Consistent and accurate LAI, FAPAR and FCOVER global products: principles and evaluation of GEOLAND2 products.
- Chen, J. M., F. Deng, and M. Chen (2006), Locally adjusted cubic-spline capping for reconstructing seasonal trajectories of a satellite-derived surface parameter, *IEEE Trans. Geosci. Remote Sens.*, 44(12), 3725–3736.
- Chen, J. M., C. H. Menges, S. G. Leblanc, (2005), Global mapping of foliage clumping index using multi-angular satellite data, *Remote Sensing of Environment*, 97: 447 – 457.
- Gobron, N., B. Pinty, F. Mélin, M. Taberner, and M. M. Verstraete (2002). Sea Wide Field of View Sensor (SeaWiFS) – Level 2 land surfaces products – ATBD. EUR Rep. 20144 En, Inst. for Environ. And Sustainability, Ispra, Italy.
- Garrigues, S., Lacaze, F. Baret, J. T. Morisette, M. Weiss, J. E. Nickeson, R. Fernandes, S. Plummer, N. V. Shabanov, R. B. Myneni, Y. Knyazikhin, and W. Yang (2008). Validation and intercomparison of global Leaf Area Index products derived from remote sensing data. *Journal of Geophysical Research*, Vol. 113, G02028, doi:10.1029/2007JG000635.
- Gobron, N. et al. (2006). Evaluation of fraction of absorbed photosynthetically active radiation products for different canopy radiation transfer regimes: Methodology and results using Joint Research Center products derived from SeaWiFS against ground based estimations. *Journal of Geophysical Research*, 111, D13110, doi:10.1029/2005JD006511.
- Morisette, Jeffrey T. et al. (2008). Validation of Global Moderate-Resolution LAI Products: A Framework Proposed Within the CEOS Land Product Validation Subgroup. *IEEE*, Vol. 44, No. 7, 1-14.
- Yang, W., D. Huang, B. Tan, J. C. Stroeve, N. V. Shabanov, Y. Knyazikhin, R. R. Nemani, and R. B. Myneni (2006), Analysis of leaf area index and fraction vegetation absorbed PAR products from the Terra MODIS sensor: 2000– 2005, *IEEE Trans. Geosci. Remote Sens.*, 44(7), 1829– 1842.

The GlobCorine land cover map – A joint EEA-ESA initiative for operational land cover mapping at pan-European scale

Sophie Bontemps¹, Pierre Defourny¹, Eric van Bogaert¹, Jean-Louis Weber², Olivier Arino³,

¹ *Earth and Life Institute, Université catholique de Louvain, Belgium*

² *European Environment Agency, Denmark*

³ *European Space Agency, European Space Research Institute, Italy*

Sophie.Bontemps@uclouvain.be, Pierre.Defourny@uclouvain.be,

Eric.VanBogaert@uclouvain.be, Jean-Louis.Weber@eea.europa.eu, Olivier.Arino@esa.int

ABSTRACT - Regular and global land cover mapping contributes to evaluating the impact of human activities on the environment. Jointly supported by the European Space Agency and the European Environmental Agency, the GlobCorine project builds on the GlobCover findings and aims at making the full use of the MERIS time series for frequent land cover monitoring. The GlobCover automated classification approach has been tuned to the pan-European continent and adjusted towards a classification compatible with the Corine typology. The GlobCorine 2005 land cover map has been achieved, validated and made available to a broadlevel stakeholder community from the ESA website. A GlobCorine land cover map for the year 2009 has also been produced and will be delivered by the end of 2010. This second land cover mapping exercise demonstrates the possibility for an operational and regular production of updated global land cover maps.

1 INTRODUCTION

Thanks to an efficient partnership led by the European Space Agency (ESA) and the GlobCover consortium, the GlobCover project successfully delivered the very first 300m global land cover map thanks to ENVISAT MERIS time series (Arino et al., 2008). Following the success of the GlobCover project, the European Space Agency has decided to launch the GlobCorine project, in a joint initiative with the European Environment Agency (EEA).

Land use studies allow coupling the social and ecological systems and so, linking land cover changes with human activities and economic drivers (GLP, 2005; EEA, 2006). EEA has acquired a unique experience in land use database through the Corine Land Cover (CLC) project and the derived information. However, two major concerns need to be faced: the update frequency and the spatial extent of the CLC products.

The CLC project currently covers the European Union countries and is updated on a 5-year basis with a delivery time of more than 2 years between the image acquisition and the derived results. Using MERIS time series would be highly complementary, allowing a more frequent monitoring of some major land dynamics. This would also result in a consistent mapping of the pan-European continent (i.e. the European Union countries extended to the European Russia and the whole Mediterranean basin), thus

improving land monitoring and decision making on regional environmental issues.

The GlobCorine project attempts to address these EEA concerns building on the GlobCover findings. It aims at making the full use of the MERIS time series through an operational land cover mapping activity dedicated to the pan-European continent. The GlobCover classification module has been adjusted to provide a land cover product dedicated to the pan-European continent as compatible as possible with the CLC aggregated typology (EEA, 2006). In addition, a twofold validation exercise has been performed, based on the GlobCover validation dataset and on the CLC 2006 database.

2 DATA AND STUDY AREA

The main source of data for the GlobCorine project is the MERIS Full Resolution Full Swath (FRS) composites as produced and delivered by the GlobCover processing chain (Vancutsem et al., 2007; Bicheron et al., 2009; Defourny et al., 2009). In the framework of the GlobCover 2005 and 2009 projects, MERIS FRS data were collected by ESA over the world between 85° N and 56° S.

The GlobCorine project only focuses on the pan-European area, which corresponds to the 27 EU (European Union) countries extended to the Mediterranean basin and to the Western Russia. It approximately extends from 20°N to 75°N and from 15°W to 65°E, as illustrated in Figure 1.

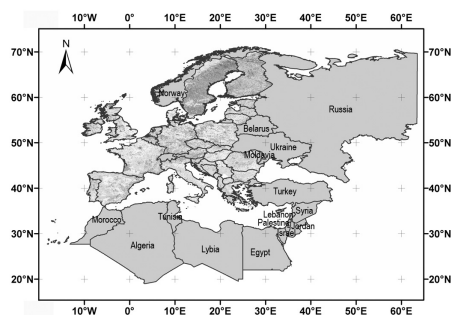


Figure 1. Pan-European extent of the GlobCorine land cover map.

The very first challenge of GlobCover was the global acquisition of a MERIS time series while the instrument was not initially designed to do so. As shown in Figure 2a for the year 2005, the data coverage was uneven due to programmatic constraints (Arino et al., 2007). As expected, the number of valid observations after the pre-processing steps, in particular that of cloud screening, was also rather variable (Figure 2b). Nevertheless, the dataset available over most of Europe was significantly better than in many places of the world both in 2005 and in 2009, allowing further investigating this continent.

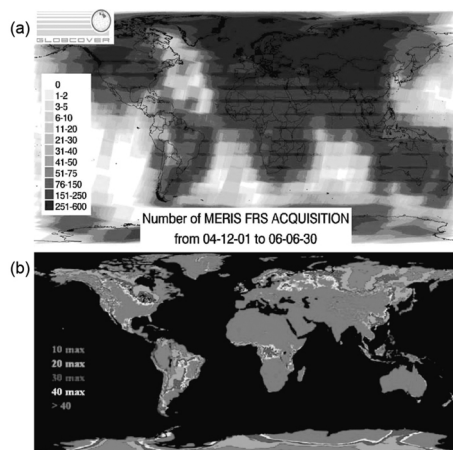


Figure 2. (a) Density of MERIS FRS acquisitions from 1st December 2004 to 30th June 2006, (b) Number of valid observations obtained after 19 months of MERIS FRS acquisitions. Magenta areas are defined as well covered (>40 observations)

3 CLASSIFICATION METHODOLOGY

The GlobCorine classification chain consists in transforming the MERIS multispectral mosaics produced by the GlobCover pre-processing modules into a meaningful pan-European land cover map. As explicitly requested by ESA and EEA, it should be based on the GlobCover classification module and

allow producing, in an automatic, repeatable and global way, a pan-European land cover map at 300-m spatial resolution.

The GlobCover classification module was designed to automatically interpret the MERIS surface reflectance composites into land cover classes at global scale. It aimed at combining both the spectral and temporal range of the MERIS FR time series and to be globally consistent while regionally tuned (Arino et al., 2007; Defourny et al., 2009).

Some technical choices, which were made in GlobCover to deal with the global scale, limit the quality of the output for a given region. Working at the smaller pan-European scale may remove some constraints, thus improving the quality of the GlobCorine land cover map. Improvements are expected to come from three distinct areas. First, the classification algorithm should take advantage of the MERIS spectral resolution (15 bands). Only few spectral channels were used for GlobCover and thus, enhancing the spectral content of the signal should improve the discrimination between specific classes of interest for EEA. Second, the temporal information should be more specifically used to discriminate particular land cover classes. Third, the reference dataset used to label the spectro-temporal classes could be enhanced to specifically address the EEA concerns, making the GlobCorine land cover map as compatible as possible with the CLC-aggregated typology.

The GlobCorine classification process is organized in five main steps (Figure 3) and is preceded by a stratification process. The stratification and classification processes are detailed hereafter.

3.1 Stratification

An a priori stratification is performed to split the pan-European continent in five equal-reasoning areas from an ecological and a remote sensing point of view. The objective is twofold: (1) reducing the land surface reflectance variability in the dataset in order to improve the classification efficiency and (2) allowing a regional tuning of the classification parameters to take into account the regional characteristics (vegetation seasonality, cloud coverage...).

3.2 Step 1: spectral classification

The spectral classification consists of a supervised and an unsupervised classification. The supervised classification aims at identifying land cover classes that are not well represented, i.e. urban and wetland areas. The pixels classified through this process are masked and an unsupervised classification is then applied on the remaining pixels with the aim of creating clusters of spectrally similar pixels.

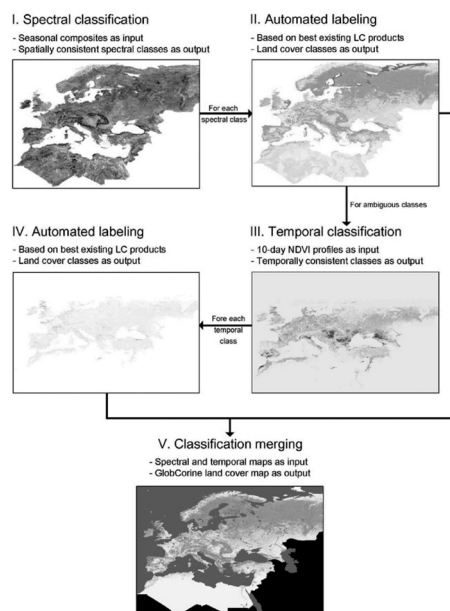


Figure 3. Classification principles starting with seasonal mosaics

3.3 Step 2: automated labeling procedure

The labeling procedure merges and transforms the spectral classes into land cover classes. The labeling procedure is automated and based on a pan-European reference land cover database compiled from CLC maps from 2000 and 2006 over Europe and from GlobCover 2005 map over North Africa and Western Russia. These maps were selected as the most accurate map available for a given region, with the highest spatial resolution and with a GlobCorine-compatible legend.

The GlobCorine land cover label is decided according to the correspondence between both set of classes, i.e. the spectral classes and the reference land cover classes. Several decision rules have been defined to derive a unique label for each spectral class.

3.4 Step 3: temporal classification

The third step focuses on pixels classified as cropland and mosaic classes after the step 2. An unsupervised classification is applied on MERIS 10-day NDVI profiles to create clusters of pixels similar in the temporal space.

3.5 Step 4: automated labeling procedure

A second labeling procedure is performed in order to transform the temporal classes into land cover classes. The fourth step is based on the same procedure than step 2 but using different labeling rules.

3.6 Step 5: classification merging

The land cover classes obtained from steps 2 and 4 are merged in order to produce the GlobCorine land cover map.

4 GLOBCORINE TYPOLOGY

As seen from the sky, land cover is a single image of both ecosystem and land use. Classification of land cover may address different purposes: importance can be given either to vegetation features, which are more related to habitats characteristics, or to landscape patterns, which reflect more land use. Typically, the GlobCover legend is of the first type, CLC of the second type.

There is no straightforward opposition between the two approaches as shown by several comparative analyses (Huettich et al., 2007; Herold et al., 2009). However, there are differences in purpose, enhanced by the classification methodologies. While GlobCover follows the UN Land Cover Classification System (LCCS) and automatically classifies 300-m pixels, CLC labels landscape objects that are visually identified from high spatial resolution images. At the end, there are significant differences between the two maps and, more important, different visions of what land cover changes are. For instance, land and ecosystem accounts can hardly be derived from the current GlobCover product. To this end, a specific request of EEA is a land use oriented typology, as compatible as possible with the CLC typology.

The GlobCorine typology focuses on the CLC aggregated typology which has demonstrated its capacity to capture the most important land cover changes (EEA, 2006).

The GlobCorine land cover product has been designed to be a consistent continental land cover map. Therefore, the legend is determined by the level of information that is available and that makes sense at the scale of the pan-European continent. The GlobCorine legend counts 14 classes and meets this requirement. It is presented in Table 1.

5 GLOBCORINE 2005

5.1 The land cover map

Figure 4 presents the GlobCorine 2005 land cover map, which is the second 300-m land cover map – after the GlobCover land cover map – produced for the pan-European continent for the period December 2004 – June 2006. The GlobCorine product and documentation are available at: <http://dup.esrin.esa.int/ionia/globcorine/products.asp>.

Table 1. 14 classes of the GlobCorine nomenclature

Class	Color
Urban and associated areas	Red
Rainfed cropland	Yellow
Irrigated cropland	Cyan
Forest	Green
Heathland and sclerophyllous vegetation	Brown
Grassland	Olive
Sparsely vegetated area	Light yellow
Vegetated low-lying areas on regularly flooded soil	Light green
Bare areas	Orange
Complex cropland	Orange
Mosaic cropland / natural vegetation	Light green
Mosaic of natural (herbaceous, shrub, tree) vegetation	Brown
Water bodies	Blue
Permanent snow and ice	White



Figure 4. GlobCorine 2005 land cover map

With regards to GlobCover, three major improvements have been achieved, which concern the urban areas, the mosaic classes and the sparsely vegetated areas. In addition, the high spatial consistency of the GlobCorine product has to be pointed out. Indeed, areas not covered by CLC2000 (i.e. by the European reference dataset) are coherently classified.

5.2 Validation

The quantitative validation of the GlobCorine 2005 land cover product aims at assessing the accuracy of the 14 classes of the land cover map from an independent reference dataset. A twofold validation has been achieved, based on two different reference dataset: the GlobCover validation dataset and the CLC 2006 map. The validation results allow a potential user determining the map's "fitness for use" for his or her application.

• GlobCover validation dataset

The first validation of the GlobCorine 2005 land cover map makes use of the validation dataset that has been constituted in the GlobCover project. First, 403 validation samples related to the GlobCorine area were extracted. Second, the set of LCCS classifiers and attributes that was collected in order to characterize the land cover of a particular site were transformed to the legend of the GlobCorine product. These 403 interpreted validation samples are then matched to the GlobCorine map and a confusion matrix is built.

The overall accuracy is found to be 79.9%. This figure is derived with equal weighting for each of the stratified randomly sampled reference points. Classes that cover only small surfaces are overrepresented in the sample set and conversely, classes that cover large surfaces may have been underrepresented in the set. As recommended by the CEOS, the overall accuracy value has to be weighted by the area proportions of the various land cover classes, resulting in an accuracy of 89.25%. The weighting factor corresponding to the area proportion of the given class has been derived from the GlobCorine product that has been projected in an equal area projection.

These final accuracy results are quite acceptable for a pan-continental product. Nevertheless, these figures have to be used cautiously. First, there is a clear contribution of the mosaic classes in the high global accuracy figure. Indeed, their agreement with several classes increases the global accuracy. However, these classes are not easily interpretable and they should thus be avoided as much as possible. Second, the number of validation points highly varies between classes. The stratified sampling that generated the validation dataset was indeed achieved on a global scale, based on the GlobCover product. The stratification, which ensures that each class is representatively sampled, is thus not necessarily valid at the GlobCorine pan-European scale. This slight bias has an influence on the overall accuracy value weighted by the class area, which is artificially increased. Accordingly, it is strongly recommended to also account for user's and producer's accuracies – which are provided in the product documentation available on the ESA website – to have a clear idea of the GlobCorine map accuracy.

• CLC2006 database

A quantitative evaluation of the GlobCorine 2005 product has also been achieved on the pan-European level by the European Topic Centre on Land use and Spatial Information (ETC-LUSI), using the CLC2006 data as reference dataset. It has to be stated that large countries like Finland, Germany, Greece, Italy, Norway, Spain, Sweden and United Kingdom were missing in this reference dataset.

The CLC2006 dataset has been re-mapped into the GlobCorine legend and GlobCorine reference grid. No sampling was defined, thus considering all pixels with valid GlobCorine product. On overall accuracy of 52.39% has been found.

This low figure is mainly due to the mosaic classes present in the GlobCorine legend (classes 100, 110 and 120). Mosaic/non-mosaic classes share and the mosaic class structure are indeed quite distinct between the GlobCorine product and the re-mapped CLC2006 dataset.

When the mosaic classes are not considered, the global agreement between the GlobCorine product and the remapped CLC2006 dataset increases up to 79.73%. In this case, overall class share is similar, except the grassland and urban areas which are clearly underestimated in the GlobCorine product. Water and wetland areas are represented quite similarly.

6 GLOBCORINE 2009

Figure 5 presents the GlobCorine 2009 land cover map, based on MERIS FRS time series for 2009.

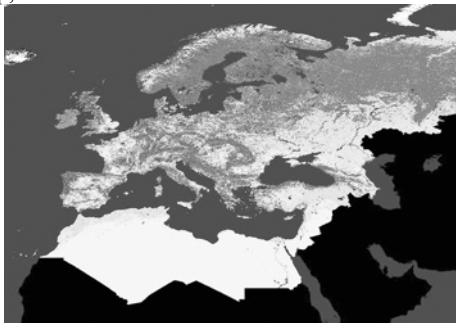


Figure 5. GlobCorine 2009 land cover map

The validation of the map is under progress and the product and documentation will be soon available at the ESA website.

7 CONCLUSION

The concept of a global Land Cover service operational at global scale requested by ESA was successfully developed through the GlobCover project. Based on the GlobCover findings, the GlobCorine project made the full use of the MERIS time series to produce a pan-European land cover map as compatible as possible with the CLC aggregated typology.

The overall accuracy of the GlobCorine 2009 land cover map is close to 80%. Significant improvements were made with regard the GlobCover land cover map, related to the urban areas, the mosaic classes and the sparsely vegetated areas. In addition, a land cover map for 2009 has been produced, thus demonstrating the possibility for an operational delivery of frequent and updated global land cover maps.

8 REFERENCES

- Arino, O., Leroy, M., Ranera, F., Gross, D., Bicheron, P., Niño, F., Brockmann, C., Defourny, P., Vancutsem, C., Achard, F., Durieux, L., Bourg, L., Latham, J., Di Gregorio, A., Witt, R., Herold, M., Sambale, J., Plummer, S., Weber, J.L., Goryl P., and Houghton, N., 2007, GlobCover – A global land cover service with MERIS. Proceedings of the ESA Envisat Symposium held in Montreux, Switzerland in April 2007.
- Arino, O., Bicheron, P., Achard, F., Latham, J., Witt, R., and Weber, J.L., 2008, GlobCover: the most detailed portrait of Earth. *ESA Bulletin*, **136** (http://www.esa.int/esapub/bulletin/bulletin136/bul136d_arino.pdf)
- Bicheron, P., Amberg, V., Bourg, L., Petit, D., Huc, M., Miras, B., Brockmann, C., Hagolle, O., Delwart, S., Ranera, F., Leroy, M., and O. Arino, 2009, Geo-location assessment of MERIS Globcover ortho-rectified products. *IEEE Transactions on Geoscience and Remote Sensing*, In press.
- Defourny, P., Bicheron, P., Brockman, C., Bontemps, S., van Bogaert, E., Vancutsem, C., Pekel, J.-F., Huc, M., Henry, C.C., Ranera, F., Achard, F., Di Gregorio, A., Herold, M., Leroy, M., and Arino, O., 2009, The first 300-m global land cover map for 2005 using ENVISAT MERIS time series: a product of the GlobCover system. Proceedings of the 33rd International Symposium on Remote Sensing of Environment - Sustaining the Millenium Development Goals held in Stresa, Italy, on 4-8 May 2009.
- EEA, 2006, Land accounts for Europe 1990 – 2000: towards integrated land and ecosystem accounting. *EEA Report*, **11** (http://www.eea.europa.eu/publications/eea_report_2006_11)
- GLP, 2005, Science Plan and Implementation Strategy. *IGBP Report*, **53**, *IHDP Report*, **19**.
- Herold, M., Hubald, R., and Di Gregorio, A., 2009, Translating and evaluating land cover legends using the UN Land Cover Classification Systems (LCCS), *GOFC-GOLD report*, **43**. Available at: http://nofc.cfs.nrcan.gc.ca/gofc-gold/Report%20Series/GOLD_43.pdf
- Huettich, C., Herold, M., Schmullius, C., Egorov, V., and Bartalev, S., 2007, Comparative assessment of CORINE2000 and GLC2000: spatial analysis of land cover data for Europe. *Journal of Applied Earth Observation and Geoinformation*, **9**, 425-437.

Vancutsem, C., Bicheron, P., Cayrol P. and Defourny, P., 2007, Performance assessment of three compositing strategies to process global ENVISAT MERIS time series. *Canadian Journal of Remote Sensing*, **33**, 492-502.

9 ACKNOWLEDGEMENT

The authors are grateful to ESA for his technical and financial support, to the GlobCover consortium for the availability of the MERIS dataset of the classification processing chain and to EEA for the scientific advices.

European Space Agency campaign activities in support of Earth Observation Projects

Remo Bianchi¹, Malcolm W. J. Davidson², Catherine Bouzinac², Dirk Schuettemeyer²
(1) European Space Agency (ESA), ESRIN, Via G. Galilei, CP 64, 00044 Frascati, Italy,
(2) European Space Agency (ESA), ESTEC, Keplerlaan 1, Postbus 299, 2200 AG Noordwijk, The Netherlands
Remo.Bianchi@esa.int, Malcolm.Davidson@esa.int, Catherine.Bouzinac@esa.int, Dirk.Schuettemeyer@esa.int

ABSTRACT - The European Space Agency (ESA) carries out campaigns, to provide support for the preparation of future Earth Observation space programmes and their users. Campaigns in support of future mission development have technological, geophysical and simulation objectives while exploitation projects need validation for the assessment of the quality of the earth observation products and of the service provision. Broad ranges of active and passive instrumentation in both the optical and microwave regions of the electromagnetic spectrum are deployed during campaigns supporting current missions in orbit as well as future missions. Since 1981 ESA has been running airborne campaigns over different locations inside and outside Europe in collaboration with national research organisations in the ESA member states as well as with international organisations harmonising European campaign activities. Thus, duplication of effort between international organisations and national research programmes is avoided. Campaigns and external/internal research studies are an important means of supporting Earth Observation projects. At present, recently deployed and ongoing scientific campaigns produce high value datasets and analyses to support for the Living Planet Programme (Earth Explorers Core and Opportunity missions), the GMES and Earth Watch missions as well as other ESA Earth Observation projects in the fields of Atmosphere, Ocean and Ice, Land Surface Processes and Solid Earth.

1 INTRODUCTION

ESA has been conducting airborne and ground measurements campaigns since 1981 and has recorded a rich variety of datasets with different instruments. The campaigns are conducted to aid in the development of mission concepts, to verify observation and performance requirements, and to simulate data products and evaluate retrieval methods. ESA campaigns are deployed during all phases (from Pre-Phase A to Phase E) of a typical ESA space mission and various types of campaigns are performed during the lifecycle of a space mission.

Furthermore exploitation projects need validation for the assessment of the quality of the Earth Observation (EO) products and of the service provision. For this, similar techniques are required as for satellite commissioning including in-situ measurements, data assimilation and satellite intercomparison using sensors with higher resolution than current operational satellites.

Campaign activities include experiments related to atmospheric dynamics, atmospheric chemistry, oceans, ice, coastal regions and land surfaces by deploying a broad range of active and passive instrumentation in both the optical and microwave regions of the

electromagnetic spectrum such as lidars, limb/nadir sounding interferometers/spectrometers, high-resolution spectral imagers, advanced synthetic aperture radars, altimeters and radiometers.

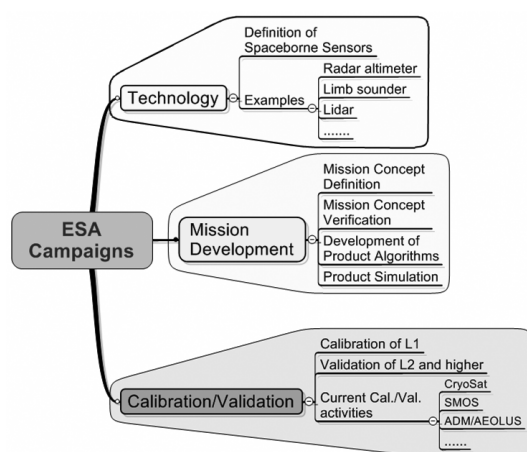
The Agency does not normally conduct ground-based, air-borne, balloon-borne, ship-borne and small satellite experiments in isolation but seeks collaboration with national research organizations in the ESA member states as well as with international organizations. There are two main reasons for this. Firstly it has always a strategic objective to harmonize European campaign activities and avoid duplication of effort between international organizations and national research programmes. Secondly, the financial constraints of ESA's campaign activity have imposed collaboration, taking advantage of projects initiated and funded by external partners.

2 CAMPAIGN REQUIREMENTS

Before embarking on a large Earth observation mission in space it is necessary to verify that the instrument being considered is capable of providing the remotely sensed information with required accuracy. This cannot always be achieved by scientific studies alone. Real data acquired by airborne sensors, ground-based equipment and/or laboratory

instruments are required. During the development phase of a typical mission, campaign data are needed for the development of interpretation methods, calibration concepts and the refinement of processing algorithms. During the operational phase when the satellite is in orbit, campaigns are needed for the validation of the satellite data products.

The related campaign requirements are thus associated with different objectives for technology, geophysical modelling, simulation and validation (see diagram below).



Technological campaigns: The main technological requirements for campaigns are testing new technologies to find answers to important questions related to technical parameters of new missions that satisfy user requirements such as choice of orbit, wavelength, spatial resolution, spectral resolution, temporal resolution and sensitivity. During technological campaigns calibration and validation methods can be investigated and new (sub) systems can be tested in an airborne environment prior to application in space.

Geophysical campaigns: These campaigns provide data and analysis to find answers to develop operational algorithms for the conversion from calibrated EO space sensor outputs (Level-1 products), in terms of physical variables (e.g. radiance, reflectance, transmittance, polarisation, radar backscattering coefficient, radar echo-time delay), to target geophysical characteristics (Level-2 products: e.g. atmospheric temperature and pressure, aerosol and cloud parameters, ocean surface wind and waves, ocean colour and salinity, sea and land surface temperatures, sea-ice thickness, biomass, vegetation index, soil moisture).

Simulation campaigns: Simulation is aimed at providing data sets to ESA engineers and the scientific and applications user community for training and

testing purposes. In many applications the end user can only be satisfied with higher than Level-2 products, whereby the Level-2 product is merged (assimilated) with other, non-satellite data. Campaigns have proven to be the ideal vehicle for involving the end-user community in the early development of these assimilation schemes.

Calibration and Validation campaigns: Earth Observation campaigns for calibration and validation (cal/val) are aimed at engineering calibration and geophysical validation of satellite data products. Typical engineering calibration campaigns arrange field deployment of reference devices (e.g. radar transponders) and/or make in-situ measurements to characterise natural reference surfaces in order to ensure instrument stability in orbit. Following internationally agreed definitions, instrument and data calibration involves pre-launch and post-launch measurements to fully characterise the payload instruments and subsequent activities to configure the ground processors to provide calibrated (Level 1b) data products.

Geophysical validation is a process whereby geophysical data products (Level 2) are derived from the Level 1 data products and checked against independent (in-situ, ground-based, airborne) measurements of the relevant geophysical variables.

The above objectives constitute the overall requirement for the ESA campaigns activities as defined in the various Earth Observation programmes. For individual campaigns specific requirements need to be established taking inputs from internal as well as external entities. Many of the requirements for campaigns come from ESA Advisory Groups supporting current missions in orbit as well as future missions but, depending upon the nature and purpose of the campaign, there are other sources for the campaign requirements definition (e.g. Mission scientists responsible for compliance of the different EO missions with mission requirements, technical officers responsible for mission preparatory activities, application development teams responsible for product/service validation).

3 RECENT CAMPAIGNS

Campaigns are an important means of supporting Earth Observation projects. Recently deployed and ongoing scientific campaigns produce high value datasets to support for the Living Planet Programme [1] (Earth Explorers Core and Opportunity missions), the GMES and Earth Watch missions.

In addition, cal/val campaigns are being prepared and conducted as part of the current missions, in orbit or under development.

Application development campaigns are also being pursued based on the requirements for campaign data for EO services (e.g. Data User Element - DUE).

3.1 Earth Explorer-7 mission definition campaigns

Twenty-four proposals were received within the 2005 call for Earth Explorer Core Mission Ideas with the aim to select a 7th Earth Explorer mission.

Three of them were selected as candidate mission concepts [2] for feasibility phase (phase A) investigation for further down-selection in 2011/12, with a projected launch of EE7 in the 2016/17 timeframe. The selected candidate missions for phase A are:

- **BIOMASS** - Global measurements of forest biomass and extent
- **CoReH2O** (Cold Regions Hydrology High-resolution Observatory) – Detailed observations of key snow, ice and water cycle characteristics
- **PREMIER** (PRocess Exploration through Measurements of Infrared and millimetre-wave Emitted Radiation) – Understanding the processes that link trace gases, radiation, chemistry and climate in the atmosphere

Past, ongoing and future campaigns are devoted to the above three candidate missions to support development of mission concepts, to verify observation and performance requirements, and to simulate data products and evaluate retrieval methods.

3.1.1 BIOMASS mission related campaigns

The BIOMASS mission objectives are to improve estimates of carbon stocks and fluxes over land through global measurements of forest biomass and biomass changes with time. The mission concept is based on a novel spaceborne P-band synthetic aperture polarimetric radar operating at 435 MHz with 6 MHz bandwidth.

The following campaigns have been started to provide feedback to ESA on important specific programmatic needs for the mission definition.

BIOSAR-2 campaign, deployed in 2008 over a boreal forest (6700 ha) in the Krycklan River catchment (Northern Sweden), collected in-situ and airborne SAR to support the evaluation of forest biomass retrieval and forest height retrieval performance. The campaign addressed the following important objectives:

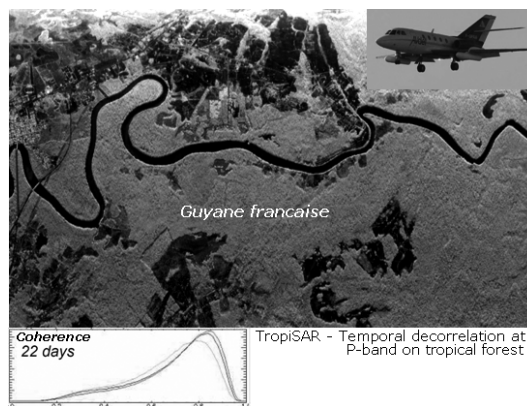
- Assess BIOMASS mission potential for biomass estimation in boreal forests
- Investigate temporal and spatial decorrelation at L- and P-band
- Explore the effects of topography and incidence angles at L- and P-band

- Investigate mitigation strategies applicable to the Level-2 processing algorithms

The campaign data package is now available for the scientific community and is expected to play a major role in science support studies for the BIOMASS mission. In addition it provides an important database for the study of longer term mission concepts.

TropiSAR2009 campaign have been deployed in August and September 2009 over a tropical forest in French Guiana to provide feedbacks on the performances of a P-band SAR to measure biomass and canopy height of a tropical forest with high biomass density. The campaign has been designed to address the following objectives:

- Provide measurements of temporal coherence at P- and L-band over tropical forests for time intervals compatible with spaceborne missions (typically 20-30 days)
- Assess performances of methods transforming P-Band SAR intensity and interferometric measurements into forest biomass and forest height
- Assess uncertainties in in-situ methods for biomass estimates and tree allometry



After data acquisition all collected data was reviewed confirming the excellent quality of the airborne data and the suitability of the processing and calibration approach. Preliminary results indicate only moderate temporal decorrelation at P-band over tropical forests.

3.1.2 CoReH2O mission related campaigns

The CoReH2O mission concept aims to improve the forecasting of water supply from snow cover and glaciers and, in general, supports the modelling of water and energy cycles at high latitudes. The mission concept employs twin frequency SARs (9.6 and 17.2 GHz) in two consecutive mission phases to deliver all-

weather, year-round information on regional and continental-scale snow-water equivalent.

To support Phase-A of CoreH2O mission the following campaigns have been recently started.

NoSREx (Nordic Snow Radar Experiment) campaign is currently on-going at Sodankyla (Northern Finland) for a long-term (2009 and 2010 winter periods) deployment of the ground-based ESA's SnowScat instrument. The campaign is dedicated to the study of the feasibility of snow parameter retrieval by combined passive/active remote sensing observations together with in-situ measurements addressing the following objectives:

- Validation of theoretical backscattering models of snow at Ku- and X-band frequencies
- Study the effects of snow accumulation (SWE - Snow Water Equivalent) and temporal evolution of snow morphology on backscatter signatures
- Sensitivity studies for Ku- and X-band backscattering in regard to physical parameters of the snow pack (SWE, grain size, stratification)
- Validation of SWE retrieval algorithms

Ku-band mini-SAR campaign is a planned activity aiming at the adaptation (by Jan 2011) of an existing small cost-efficient airborne X-band system to incorporate Ku-band capabilities and deploy the adapted airborne instrument for winter 2010/2011 to address the following objectives in support for the CoreH2O mission:

- Address data gap in airborne imagery at X- & Ku-band for CoReH2O Phase-A activities
- Document the backscattering signatures of snow and other terrain types
- Validate theoretical scattering models/retrievals
- Provide input for end-to-end simulation activity

3.1.3 PREMIER mission related campaign

The PREMIER mission aims to advance our understanding of the processes that control trace gases, radiation and chemistry in the upper troposphere and lower stratosphere. The radiative effects of water and clouds on weather and clouds are at a maximum in this region. It is also a region characterised by small-scale processes that have not been studied by previous missions.

The instrumentation will consist of an infrared limb-imaging spectrometer and a millimetre-wave limb-sounder. By linking with MetOp and the National Polar-orbiting Operational Environmental Satellite System (NPOESS) data, PREMIER also aims to provide insights into processes occurring in the lower troposphere.

PremierEx campaign objectives are derived from the scientific objectives of PREMIER. Two innovative limb sounding instruments that operate in the infrared and microwave region of the electromagnetic spectrum have been built. The campaign supports the in-flight testing of these instruments, and the preparation and execution of flights to support the definition of PREMIER capabilities to quantify:

- Horizontal transport and mixing processes in the mid to upper troposphere / lower stratosphere
- Cirrus formation processes in the Arctic upper troposphere

3.2 Campaigns supporting GMES Space Component

For its part in the Global Monitoring for Environment and Security (GMES) programme, ESA is undertaking the development of the Space Component with a series of five new satellite missions, called Sentinels, specifically designed for the needs of the joint European Commission-ESA programme [<http://www.esa.int/esaLP/LPgmes.html>].

The different Sentinels comprise radar and super-spectral imaging for land, ocean and atmospheric monitoring. The first three Sentinels are currently under industrial development, with Sentinel-1 planned to launch in 2012. The following campaigns have been recently started to provide support for Sentinel-1 (AgriSAR2009 campaign) and Sentinel-3 (SEN3EXP campaign) missions and for future campaigns, requirements for Sentinels products development and validation are being investigated.

AgriSAR2009 campaign has been initiated to define and quantify the performance of Sentinel SAR imagery in providing important agricultural information products. Particular emphasis has been given to multi-temporal algorithms utilising a dense temporal dataset acquiring multi-temporal, quad-polarisation SAR and optical images (RADARSAT-2 and RapidEye satellites) throughout the 2009 growing season over three different sites (Flevoland, NL - Barrax, E - Indian Head, CAN).

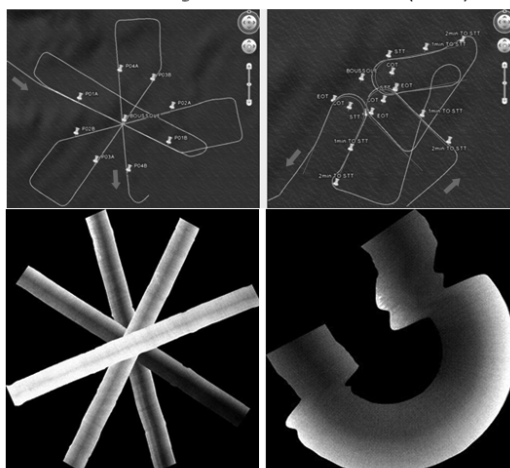
The objectives of the AgriSAR2009 campaign are:

- Simulation of Sentinel-1 data products in terms of repeat observation, resolution and polarisation
- Evaluation of the performance of Sentinel-1 for agricultural and land cover products based on dense time series of radar data
- Evaluate of the added value of multi-polarimetry for the same information products
- Development of methodology for the generation and validation of agricultural information and land cover map products based on C-band data.
- Assessment of the potential of Sentinel-1(radar)/Sentinel-2(optical) synergy for generation of prototype land cover products

During the period Apr-Sep 2009 there were 225 satellite acquisitions in total and fully polarimetric Radarsat-2, RapidEye and in-situ data were distributed to campaign PIs. Data analysis is on-going and a final workshop is planned for Feb./March 2011.

SEN3EXP campaign was deployed in the period Jun/Jul 2009 over different landscape types in Spain (agricultural crops), Italy (forest and coastal zone) and France (open water) combining airborne, satellite and coincident ground activities in support of the Sentinel-3 providing feedback on key issues related to the definition, performance and product quality of the OLCI and SLSTR instruments on Sentinel-3.

SEN3EXP Ocean Flight Patterns over Boussole (Jul 26)



CASI-077 Ls mosaic (star pattern)

CASI-077 Ls (racetrack pattern)

The campaign aims to generate spectrally, geometrically and radiometrically representative imagery from airborne and satellite (MERIS was reprogrammed for 8 orbits to simulate S-3 bands) data to be fed into the Level 1b/c Ground Prototype Processor (GPP) and the System Performance Simulator (SPS) that are currently under development. The output data will also support the Level 2 product development contract through the provision of suitable scenes and test data sets.

The campaign acquired a dataset at the necessary quality level to generate the input to the L1b/c ground segment simulation tools and to the L2 processor.

3.3 Campaigns supporting in Orbit Missions

Within a period a little over 1 year, starting in March 2009 with the launch of the Gravity field and steady-state Ocean Circulation Explorer (GOCE) mission, three Earth Explorer satellites were placed in orbit. Following GOCE launch, the Soil Moisture and Ocean Salinity (SMOS) mission has been launched in November 2009 and CryoSat-2 last April 2010. The

on-going Cal/Val campaign activities related to SMOS and CryoSat missions are shortly described in the following sections.

3.3.1 SMOS Cal/Val campaigns

As an important part of the mission, a number of intensive field campaigns are planned all over the world to make sure the mission is delivering true information on soil moisture and ocean salinity. These field campaigns involve measurements on the ground, from aircraft, ships, oceans buoys and platforms. The first such campaign to validate soil moisture data was recently (beginning 2010) completed in Southeast Australia and other two campaigns (both in Spring 2010) respectively over two sites in Germany and one site in Spain are going on.

AACES2010 campaign was successfully performed in January/February 2010 over a test site with a wide range of topographic, climatic and land-cover characteristics in Southeast Australia, deploying an airborne dual polarisation L-band (1.4 GHz) microwave radiometer, an airborne thermal imager and collecting ground measurements with the following objectives:

- First validation opportunity for SMOS Level-2 soil moisture products
- Product validation using measurements at ground and airborne level

During the validation campaign a significant rainfall event occurred in the middle of the campaign providing the opportunity to capture both extreme hot dry and cool wet conditions. The obtained extensive validation dataset, free of Radio Frequency Interferences, played a key role in benchmarking the performance of SMOS during its six-month commissioning phase.

Spring 2010 SMOS Cal/Val campaigns were deployed last May/June 2010. One over two well-modelled and instrumented Soil Moisture validation sites for match-up with SMOS pixels (the Rur-Erft and the Upper Danube Catchments in Germany) deploying a Skyvan aircraft equipped with the EMIRAD (from the Technical University of Denmark) and the HUT2D (from Helsinki University of Technology) instruments. The other covered the Valencia Anchor Site in Spain deploying the CAROLS (from IPSL, France) equipment on board the ATR42 aircraft of SAFIRE/CNES/CNRS. Both campaigns had the main objective to validate Level-1 brightness temperature and Level-2 soil moisture retrieval.

Future SMOS Cal/Val campaigns to continue the process of validating soil moisture, and also including the validation of ocean salinity data, are in the planning phase by ESA.

3.3.2 CryoSat Cal/Val campaigns

Following the launch of ESA's CryoSat-2 ice mission 8 April 2010 a six-month commissioning phase started together with implementation of Cal/Val campaigns plan before delivery of calibrated and validated data to the scientific community. The Cal/Val campaigns plan is presently based on two airborne platforms, one hosting airborne radar altimeter/laser altimeters and the other electromagnetic ice thickness measurement devices. The Cal/Val activity started with the

CryoVex2010 campaign, the first ESA CryoSat campaign with coincident satellite datatakes, deployed during summer 2010 with the following objectives:

- Verify performance of upgraded ASIRAS airborne radar altimeter in campaign conditions
- Continuity of data time series over a core validation test site
- CryoSat-2 verification flight along sub-track East coast of Greenland

The CryoSat Cal/Val campaigns implementation plan includes future campaign activities for 2010/2011 winter both in Arctic and Antarctic areas and some of them in coordination with NASA IceBridge activity.

3.4 Campaigns supporting Exploitation Projects

The Data User Element (DUE) is a programmatic component of the Earth Observation Envelope Programme, an optional programme of ESA, aiming to raise awareness with respect to the applicability of Earth Observation in day-to-day operations [<http://dup.esrin.esa.it>]. Within this framework in the past years a number of campaigns were organised to support DUE exploitation projects for validation and assessment of the quality of the application products and of the service provision.

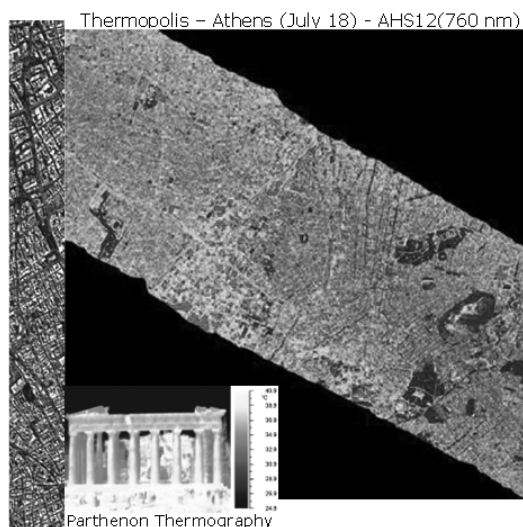
Recently campaign activities have been started in the framework of the DUE “Urban Heat Islands (UHI) and Urban Thermography (UT) Project” to support both the UHI project and the proposed activities for the Reorientation of the Fuegosat (TIR sensor) mission Consolidation Phase of the Earth Watch Programme.

Thermopolis2009 campaign represents the second experimental activity (the first was DESIREX2008 campaign over the city of Madrid) in support of the UHI project and Fuegosat reorientation.

The campaign has been deployed during summer 2009 over the city of Athens combining airborne, satellite and coincident ground activities to provide a full high resolution thermal dataset suitable for:

- Assessment of optimum spatial resolution and revisiting time for Land Surface Temperature (LST) retrievals in a maritime metropolitan areas

- LST and Air Temperatures (AT) retrieval of urban areas, at high spatial resolution (10 to 30m) to characterise the spatial UHI variability
- Generation and quality assessment of the UHI information products



The UHI project is finalising a TIR report that will be delivered to the Fuegosat Consolidation team at the completion of both DESIREX2008 and Thermopolis2009 campaigns data analysis devoted to refine the impact assessment of an operational system for European metropolitan areas. The two datasets will be also available for mission requirements trade-off studies for a dedicated future spaceborne TIR sensor.

4 ESA CAMPAIGN DATABASE

ESA campaign datasets are archived and users can access campaign data through the EOPI web portal [<http://eopi.esa.int>]. Formatted and documented datasets (including Final Reports) are directly accessible through web and PIs can request data submitting a Category 1 use proposal (data delivered over the internet or off-line via a physical support).

References

- [1] European Space Agency (2006) The Changing Earth: New scientific challenges for ESA's Living Planet Programme. ESA SP1304, see also <http://www.esa.int/esaLP>
- [2] European Space Agency (2008) Candidate Earth Explorer Core Missions – Reports for Assessment, ESA SP-1313(3), ISSN 0379-6566, 104pp, available at <http://www.congrex.nl/09c01>

First evaluation of SMOS observations and Level-2 products over agricultural sites in temperate regions

J-P Wigneron¹, Y. Kerr², A. Mialon², N. Novello¹, F. Cabot², S. Delwart³, F. Demontoux⁴, M. J. Escorihuela⁵, P. Ferrazzoli⁶, A. Govind¹, J. P. Grant⁷, D. Guyon¹, E. Jacquette², H. Lawrence^{1,4}, E. Lopez-Baeza⁸, A. Mahmoodi⁹, C. Mattar⁸, S. Mecklenburg³, C. Moisy¹, S. Monerris¹⁰, R. Rahmoune⁶, P. Richaume², P. de Rosnay¹¹, C. Rüdiger¹², K. Saleh¹³, M. Schwank¹⁴, J. Sobrino⁷, P. Waldteufel¹⁵

¹INRA, EPHYSE, Bordeaux France, wigneron@bordeaux.inra.fr ²CESBIO, Toulouse, France ³ESA, ESRI, Frascati, Italy ⁴IMS, Bordeaux, France ⁵isardSAT, Barcelona, Spain ⁶University of Tor Vergata, Roma, ⁷ESTEC, Noordwijk, The Netherlands, ⁸University of Valencia, Spain ⁹ARRAY, Toronto, Canada ¹⁰BEC, Barcelona, Spain ¹¹ECMWF, Reading, UK, ¹²Monash University VIC, Australia ¹³CDTI, Madrid, Spain, ¹⁴University of Zurich, Switzerland ¹⁵IPSL, Paris, France.

Abstract- The SMOS (Soil Moisture and Ocean Salinity) mission was launched on November 2, 2009. Over the land surfaces, simultaneous retrievals of several surface parameters including surface soil moisture (SM) and vegetation characteristics are made from the multi-angular and dual polarization SMOS observations by inverting the L-MEB (L-band Microwave Emission of the Biosphere) model. Preliminary analyses evaluating the SMOS observations in terms of Brightness Temperatures and Level-2 products (mainly soil moisture SM and vegetation optical depth TAU) were carried out over several sites at global scale. Here, we illustrate these studies over two sites where perturbations by RFI effects are low or negligible. It was found that there is a very good agreement between time series of retrieved SM and in situ SM measurements and rainfall estimations, as measured by local meteorological stations. Moreover, time series of retrieved TAU are consistent with our expectations in terms of magnitude of retrieved values and trends: slow increasing trends in TAU were generally retrieved at large scale (the SMOS pixel ~40 x 40 km) over the growing season.

1. INTRODUCTION

SMOS is the second Earth Explorer Opportunity mission to be developed as part of ESA's Living Planet Programme (Kerr et al., 2001, 2010). It aims to improve our understanding of the Earth's water cycle by making global observations of soil moisture over land and salinity over oceans. Over the land surfaces, SMOS will advance our understanding of the exchange processes between the Earth's surface and atmosphere, and will have many applications to improve weather and climate models and in areas such as agriculture and water resource management. Over the terrestrial ecosystems, the principle of the SMOS Level 2 retrieval algorithm is to exploit multi-angular data in order to simultaneously retrieve several surface parameters including surface soil moisture (SM) and vegetation characteristics (in particular the optical depth TAU). The L-MEB forward model was selected to simulate the microwave signatures of the various soil and vegetation types which are present in the mixed SMOS pixel, which is larger than about 30 x 30 km generally. Retrievals are based on the L-MEB inversion using a minimization procedure of a cost function evaluating the difference between the L-MEB simulations and the SMOS TB (Brightness Temperature) observations (Wigneron et al., 2000, 2007).

Ever since the launch of SMOS, the commissioning phase (November - end of April 2010) included testing of the Proteus platform – a generic 'satellite bus' developed by CNES and Thales Alenia Space and the MIRAS instrument developed by EADS-CASA in Spain. During this phase (after which the mission will be considered to be operational), and throughout the lifetime of the mission, the science team has been assessing the quality of the data products. The study presented in this paper was carried out in this assessment framework, specifically over the land surfaces. Preliminary analyses evaluating the SMOS observations in terms of Brightness Temperatures and L2 products (mainly soil moisture SM and vegetation optical depth TAU) were carried out over several sites globally. Preliminary evaluations were based on comparisons between the time series of TB and the L2 products, over several months, with in-situ micro-meteorological data (precipitations, SM, etc.) and remotely-sensed index of the vegetation development, biomass and water status estimated in the optical domain. This evaluation was carried out over several sites representative of the most widespread biomes of the globe (rainfall, boreal and temperate (coniferous or deciduous) forests, agricultural in temperate regions, arid and semi arid regions, etc.).

Preliminary results of this assessment are presented in this communication. Firstly, we present a synthesis of the main results concerning the calibration of the soil and vegetation parameters of L-MEB over a variety of vegetation covers. Secondly, we illustrate studies carried out to evaluate the SMOS L2 products over two sites, by (i) comparing time-series of SM retrievals against time-series of *in situ* estimations of SM and rainfalls and (ii) analysing time-series of the retrieved values of TAU.

2. L-MEB MODELING AND INVERSION

Illustrations of the first results of the Level 2 retrievals of SM and TAU from the SMOS observations are presented in this communication. The results were obtained from the inversion of the L-MEB model based on multi-angular, dual polarization and full polarization TB measurements. As the satellite orbits over the Earth, a given point within the Field Of View (FOV) is observed from different view angles by the 2-D interferometer. The series of dual-polarized or full-polarized multi-angular measurements allow simultaneous retrievals of several surface parameters including soil moisture (SM) and vegetation opacity (TAU) (Wigneron et al., 2000). In the Level-2 algorithm which has been developed, the different cover types (vegetated area (including crops, prairies, forests, etc.), open water, urban area, land use, etc.) present within the SMOS footprint are estimated from high resolution land use maps (30"x30" aggregated to 4 kmx4km). The surface microwave emission is simulated with L-MEB using land cover specific calibrations and parameterizations. Considering this, we present here a synthesis of the main results concerning the calibration of the soil and vegetation parameters of L-MEB over a variety of vegetation covers. Then we will briefly present the sites used for a very first evaluation of the Level 2 products (SM and TAU) against *in situ* measurements.

2.1 L-MEB calibration

A synthesis of results concerning the calibration of the soil and vegetation parameters of L-MEB is given in Table 1 over a variety of vegetation covers. As for soil parameters, the H_R parameter was found to vary between about 0.1 (for very smooth soils such as those of some crop fields) to about 1 or 1.5 for ploughed fields. If we consider that H_R depends on SM, improved retrievals results have been obtained in some studies over grassland mainly (Saleh et al., 2007; Panciera et al., 2009). This dependence will not be considered here. The Q_R parameter could be set equal to zero in most of the studies. The NR_V and NR_H values vary between $[-2, 0]$ and $[0, 2]$ respectively (typical values are $NR_V = 0$ and $NR_H = 2$, or $NR_V = -1$ and $NR_H = 1$, as in Escorihuela et al., 2007). Recently, Wigneron et al. (2010) demonstrated that the

difference $NR_H - NR_V$ decrease from about two for smooth soil up to about zero for very rough soils (Wigneron et al., 2010)

As for the vegetation parameters, the tt_p ($p=v$ or $p=h$) parameters were found to be close to unity except for some crops with a vertical structure (such as cereals for instance: wheat, corn fields, etc.) and for forests. The single scattering albedo ω_p ($p=v$ or $p=h$) was found to be close to zero over most of the non-forested vegetation covers (values distinct from zero were obtained only over corn and grassland while over forests the value of ω_p is generally found to vary between 0.05 and 0.1. The values of the b parameter (the parameter that relates TAU to the vegetation water content VWC, kg/m^2) were found to vary from 0.05 to ~ 0.2 over low vegetation. However, typical values over crop fields are ~ 0.12 . Few studies have evaluated the values of b' and b'' (relating TAU to the Leaf Area Index, LAI). However, the rare studies which have done so, tend to converge towards a value of b' close to 0.06 ($b' = 0.06$ is the default value considered to date in the ATBD, Kerr et al., 2010).

Over forests, tests of the forward model are in progress (Ferrazzoli et al., 2010). Preliminary results based on actual SMOS observations indicate that for tropical and subtropical broadleaf forests of different biomass, a good fit was obtained using the following parameters: $H_R = 0.3$, $\omega = 0.08$ (for both polarizations), $TAU = 0.29 LAI_{FMAX} + 0.06 LAI_V$ (for both polarizations) where LAI_{FMAX} is the maximum yearly value of the LAI of trees and LAI_V is the LAI of herbaceous vegetation.

2.2 Evaluation of the Level 2 products (SM and TAU)

The Level 2 products including the simultaneous retrievals of soil moisture (SM) and vegetation opacity (TAU) have been investigated over several sites since the SMOS launch. In this short communication we illustrate these evaluations over two sites enjoying a temperate climate: the SMOSREX site, in an agricultural region close to Toulouse in the South Western region of France (Lat = 43.4, Long = 1.3) and the "Ballarat" site, West of Melbourne, in the South Eastern region of Australia (Lat = -37.5, Long = 143.75). The SMOSREX site include a low fraction of open water and urban surfaces. It corresponds to an agricultural region (mostly grassland, corn) including a few forested areas (forest fraction < 3%). The second site corresponds also to an agricultural region (mainly heterogeneous grassland fields), including a larger fraction of forest ($\sim 35\%$) and a medium-size urban area (the town of Ballarat). The SMOSREX site is equipped with a meteorological station providing estimates of classical meteorological variables (air temperature, wind humidity), energy fluxes (latent heat, sensible heat, etc.) and profiles of the soil

moisture and soil temperature within soil (De Rosnay et al., 2006). In particular, estimates of the surface soil moisture over the 0-6cm soil layer were obtained from several theta probes installed at the site. These theta probes were installed in two main spots: a natural fallow including a litter layer (referred to as "Fallow"), and an area which was regularly ploughed and artificially maintained as a sparsely vegetated or bare soil surface without litter (referred to as "Bare soil"). Over the Ballarat site, rainfall data were obtained from a weather station of the Bureau of Meteorology, Australian Government

In this study, the 2-Parameter retrievals were based on a simple calibration of L-MEB using default parameters for soil and vegetation ($HR \approx 0.1$, $N_{RV} = 0$, $N_{RH} = 2$, $tt_p = 1$, $\omega_p = 1$, etc., Cf Table 1). The SMOS TB data were analysed from the beginning of January to the end of August-September 2010. This period corresponds mainly to spring and summer over the SMOSREX site and to autumn-winter conditions over the Ballarat site. During the August-September period, heavy rainfall events were recorded over the Ballarat site (precipitations exceeded 300 mm, while the average ~ 180 mm), leading to small flooded surface areas in September. Note that several versions of the Level-1 and -2 algorithms, which are regularly improved, were used in the data processing to obtain these first results. In particular, first versions of the algorithms used up to April-May have been significantly modified and improved and strong cautions should be taken in the analysis of the retrieval results obtained in the early period of the year 2010.

3. RESULTS

Illustrations of the evaluation of the SMOS Level 2 products (SM and TAU) are given over the SMOSREX and Ballarat sites in Figure 1a-b and 2a-b, respectively. In the upper panels of Figure 1 and 2, time series of the retrieved values of SM are compared with measured values of SM over the Fallow and Bare Soil plots (higher and lower curves corresponds to SM over the Fallow and Bare Soil plots respectively) over the SMOSREX site and with estimates of precipitation over both sites. Lower panel of both figures present the retrieved time variations of TAU parameter.

It appears that the SM and TAU retrievals are generally consistent with our expectations based on the *in situ* observations. Over both sites, large time changes in the retrieved SM could be associated to dry periods or to rainfall events. In terms of magnitude, measured SM seemed to be underestimated by the retrieved SM over the SMOSREX site (no measurements of SM were available over the Ballarat site). Even if the retrieved TAU values are a bit noisier than those of SM, it can be noted that slow time variations and trends in TAU were generally retrieved.

4. DISCUSSION AND CONCLUSION

SMOS was successfully launched and is currently in operation. Some illustrations of the first results obtained from the Level-2 retrievals are shown in this communication over two temperate sites in the South Western region of France and in the South Eastern region of Australia. In these sites, low to moderate levels of perturbations due to RFI have been detected (moderate over SMOSREX and very low in Australia). This is in contrast with some other regions in Eastern Europe and Asia, in particular, where high levels of RFI hamper, for the time being, significant use of the SMOS observations unless some mitigation is carried out. Time series of L2 retrievals of SM were found to be in good agreement with *in situ* estimates of SM over a ~ 5 cm depth obtained from local meteorological stations. Clear drying out trends or steep increase in the retrieved SM could be associated to dry periods or to rainfall events, respectively, over both sites. Over the SMOSREX site, the *in situ* measured values of SM over the two "Fallow" and "Bare soil" plots are underestimated by the retrieved values of SM. This fact also occurred over many other sites studied to date (results not shown here). In some cases, this could partly be due to the fact the retrieved SM corresponds to a very shallow soil layer (~ 0 to 2 to 3 cm, at L-band), while the probes used in the fields provided an estimate of SM over a thicker soil layer (0 to ~ 6 cm generally). This underestimation could also be due to a bias in the soil and vegetation parameters used in the retrievals. For instance, increasing the value stipulated for the roughness parameter H_R would lead to an increase in the retrieved values of SM. Presently, default values are used and H_R is set to a value close to 0.1 over agricultural fields in temperate regions. Over the Ballarat site, in spite of the significant forest and urban fractions included in the SMOS footprint, the very wet soil conditions that occurred in winter could be retrieved from the SMOS observations: a regular increase in SM can be seen from June to September. Moreover, high values of SM, close to saturation ($\sim 50\%$), are concurrent with the flooding of some agricultural surfaces that occurred in September.

Time series of the retrieved optical depth (TAU) were also consistent with our expectations concerning the time changes in the vegetation water content (VWC) of low vegetation at a rather large spatial scale ($\sim 40 \times 40$ km) in an agricultural area. Slow time variations in TAU were generally retrieved and a slight increasing trend in TAU could be noted in spring over the SMOSREX site. Over this latter site, TAU values close to zero were retrieved in winter (when most of the agricultural fields were bare soils), while values close to 0.25 (corresponding to an average VWC of 2.0 kg/m², using $b = 0.12$ and a LAI of 4, using $b' =$

0.06) were retrieved at the end of spring over a crop vegetation at a stage of full vegetation development. Over the Ballarat site, a value of TAU close to 0.1-0.2 was retrieved (~a VWC of 1 to 2 kg/m²), which may underestimate the rather dense vegetation cover (mainly grassland) present in this agricultural region in autumn and winter. As mentioned before, several versions of the Level-1 and -2 algorithms were used in the data processing and cautions should be taken in the analysis/interpretation of the retrieval results obtained in the early period of the year 2010. Future improvements in the Level-2 products and data processing will deal with many aspects of the L1 and L2 algorithms: better detection and filtering of RFI, parameterization of the soil and vegetation as a function of the ECOCLIMAP vegetation types (based on results of Table 1 for instance), test of the Mironov routine for soil permittivity, etc. Reprocessing of the whole 2010 SMOS data is scheduled for the end of this year.

ACKNOWLEDGEMENT: This study received financial support by TOSCA (CNES, Centre National d'Etudes Spatiales, France) and ESA (European Space Agency) in the framework of the cal/val activities of the SMOS mission.

REFERENCES

- Cano A., K. Saleh, J.-P. Wigneron, C. Antolín, J. E. Balling, Y. H. Kerr, A. Kruszwski, C. Millán-Scheiding, S. Schmidl Søbjaerg, N. Skou, E. López-Baeza, 2010, *Remote Sensing of Environment*, vol. 114, 15, 844-853.
- Escorihuela M. J., Y. Kerr, P. de Rosnay, J.-P. Wigneron, J.-C. Calvet, and F. Lemaître, 2007, 'A Simple model of the bare soil microwave emission at L-Band', *IEEE Trans. Geosc. Remote Sens.*, vol. 45., No. 7, July, pp. 1978-1987.
- Ferrazzoli P., L. Guerriero, and J.-P. Wigneron, 2002, 'Simulating L-band emission of forests in view of future satellite applications', *IEEE Trans. Geosc. Remote Sens.*, vol. 40, no. 12, pp. 2700-2708.
- Ferrazzoli P., R. Rahmoune, F. Grings, V. Douina, M. Salvia, H. Karszenbaum, 2010, 'Investigating the sensitivity to soil moisture variations of microwave radiometric signatures over the Argentinian Chaco Forest', *Proceedings of ESA Living Planet Symposium*, Bergen (Norway), June.
- Grant J. P., J.-P. Wigneron, A.A. Van de Griend, A. Kruszwski, S. Schmidl Søbjaerg, N. Skou, J. Balling, 2007, 'A Field Experiment on Microwave Forest Radiometry - L-band signal behaviour for varying conditions of surface wetness', *Remote Sens. Env.*, vol. 109, pp. 10-19.
- Grant J. P., K. Saleh, A. J.-P. Wigneron, M. Guglielmetti, Y. Kerr, M. Schwank, N. Skou, A. Van de Griend, 2008, 'Calibration of the L-MEB model over a coniferous and a deciduous forest', *IEEE Trans. Geosc. Remote Sens.*, vol. 46, 808-818.
- Grant J.P., A.A. Van de Griend, J.-P. Wigneron, K. Saleh, R. Panciera and J.P. Walker, 2010, 'Influence of forest cover fraction on L-band soil moisture retrievals from heterogeneous pixels using multi-angular observations', *Remote Sens. Env.*, vol. 114, 7, May, 1026-1037.
- Kerr Y. H., P. Waldteufel, J.-P. Wigneron, J. Font, M. Berger, 2001, 'Soil Moisture Retrieval from Space: The Soil Moisture and Ocean Salinity (SMOS) Mission', *IEEE Trans. Geosc. Remote Sens.*, 39(8):1729-1735.
- Kerr Y. H., P. Waldteufel, J.-P. Wigneron, F. Cabot, J. Boutin, M.-J. Escorihuela, N. Reul, C. Gruhier, S. Juglea, J. Font, S. Delwart, M. Drinkwater, A. Hahne, M. Martin-Neira, S. Mecklenburg, 2010, 'The SMOS mission: new tool for monitoring key elements of the global water cycle', *ieee-tgrs*.
- Kerr Y. H., P. Waldteufel, P. Richaume, P. Ferrazzoli, and J. P. Wigneron, 2008, 'SMOS level 2 processor soil moisture algorithm theoretical basis document (ATBD)', Prepared by the Expert Support Laboratories, CESBIO, IPSL-Service d'Aéronomie, INRA-EPHYSE, Tor Vergata University For Array Systems Computing Inc., CESBIO, Toulouse, France, ATBD SO-TN-ESL-SM-GS-0001, V3.a, Oct. 15.
- Panciera R., J. P. Walker, J. D. Kalma, E. J. Kim, K. Saleh and J.-P. Wigneron, 2009, 'Evaluation of the SMOS L-MEB passive microwave soil moisture retrieval algorithm', *Remote Sens. Env.*, 113, 435-444.
- P. de Rosnay, J.-C. Calvet, Y. Kerr, J.-P. Wigneron, F. Lemaître, M. J. Escorihuela, J. Muñoz Sabater, K. Saleh, J. Barrié, G. Bouhours, L. Coret, G. Cherel, G. Dedieu, R. Durbe, N. E. D. Fritz, F. Froissard, J. Hoedjes, A. Kruszwski, F. Lavenue, D. Suquia, and P. Waldteufel, 2006, 'SMOSREX: A Long Term Field Campaign Experiment for Soil Moisture and Land Surface Processes Remote Sensing', *Remote Sens. Env.*, vol. 102, 377-389.
- Saleh, K., Wigneron, J.-P., Waldteufel, P., de Rosnay, P., Schwank, M., Calvet, J.-C., Kerr, Y., 2007, 'Estimates of surface soil moisture over grass covers using L-band radiometry', *Remote Sens. Env.*, 109, 42-53.
- Saleh K., Kerr Y., Richaume P., Escorihuela M., R. Panciera, S. Delwart, G. Boulet, P. Maisongrande, J.P. Walker, P. Wursteisen, J.P. Wigneron, 2009, 'Soil moisture retrievals at L-band using a two-step inversion approach (COSMOS/NAFE'05 Experiment)', *Remote Sens. Env.*, 113, 1304-1312.
- Wigneron J.-P., Waldteufel P., Chanzy A., Calvet J.-C., Kerr Y., 2000, 'Two-D microwave interferometer retrieval capabilities of over land surfaces (SMOS Mission)', *Remote Sens. Environ.*, 73:270-282.
- Wigneron J.-P., Y. Kerr, P. Waldteufel, K. Saleh, M.-J. Escorihuela, P. Richaume, P. Ferrazzoli, P. de Rosnay, R. Gurney, J.-C. Calvet, J.P. Grant, M. Guglielmetti, B. Hornbuckle, C. Mätzler, T. Pellarin, M. Schwank, 'L-band Microwave Emission of the Biosphere (L-MEB) Model: Description and calibration against experimental data sets over crop fields', 2007, *Remote Sens. Env.*, 107, 639-655.
- Wigneron J.-P., A. Chanzy, Y. Kerr, H. Lawrence, J.-C. Shi, M.-J. Escorihuela, V. Mironov, A. Mialon, F. Demontoux, P. de Rosnay, K. Saleh, 2010, 'Evaluating an improved parameterization of the soil emission in L-MEB', *IEEE-GE*, in press

Table 1: Calibrated L-MEB parameters

	HR	NR _H	NR _V	tt _H	tt _V	ω _H	ω _V	b	b' _s (b'' _s =0)
Bare soil (Wig., 2007, 2010; Esc., 2007)	0.1 – 1.5 (plowed field) Q _R = 0	[0, 2]	[-2, 0]						
Crops general (Wig., 2007, 2010, Esc. et al., 2007)	0.1 – 1 Q _R = 0	[0, 2]	[0, -2]	1	1	0	0		0.06
Crops C3 Wheat (Wig., 2007)	0.1	0	-1	1	8	0	0	0.08	0.035
Wheat NAFE'05: Panciera et al., 2009, (average calibration 3)	1.5 – SM							0.08	
Sal., 2009	1	1	0	1	1	0	0		0.06
Crops C3 Soybean (Wig., 2007)	0.1-0.2	0	-1	1	1	0	0	0.17	0.09
Corn with rows at soil surface (Wig., 2007)	0.6	0	-1	2	1	0.05	0.05	0.05	0.05
GRASSLAND									
Grassland with litter, Smosrex (Sal., 2007)	1.3-1.13 SM	1	0	1	1	0	0.05	0.12	0.04 (N1)
Grassland with litter, general (Sal., 2007)	1.3-1.13 SM	1	0	1	1	0	0.05	0.12	0.04 (N1)
Grassland, no litter (BARC, Sal. 2007)	0.5	0	0	1	1	0	0.05	0.15	0.05
Grassland, NAFE'05 (Sal., 2009); Pan. used values from Sal. 2007	0.4	1	0	1	1	0	0		0.06
FOREST									
Fer., 2002-2010 Grant et al., 2008-2010									
Coniferous forest Les Landes	1.2	1.8	2	0.9	0.8	0.07	0.07		τ _{NAD} =0.67
Deciduous, FOSMEX	1.	1	2	0.5	0.4	0.07	0.07		τ _{NAD} =1.
Mixed forest	1.	1	2	0.75	0.65	0.07	0.07		τ _{NAD} =0.8
Eucalyptus forest	0.5	1	1	1	1	0.04	0.04		τ _{NAD} =0.52
Matorral (low shrubs in Mediterranean area) Cano et al., 2009	0.34 Q _R = 0.2	1.1	-0.8	1	1	0	0		0.07 τ _{NAD} =0.1, LAI=1.4

Esc. = Escorihuela et al.; Fer.= Ferrazzoli et al.; Pan. = Panciera et al.; Sal. = Saleh et al.; Wig. =Wigner et al.
(N1) another solution would be b'_s = 0.04 and b''_s = 0.03 if the effect of litter is included both in TAU and HR.

Default values given in ATBD (Kerr et al., 2010): a moderate amount of vegetation corresponds to a LAI of 4 (the order of magnitude of LAI/VWC is roughly ≈ 2). Using a value of 0.06 for the b' parameter and a value of b of 0.12 (typical for crops) and b''=0, the default value of TAU is about 0.24.

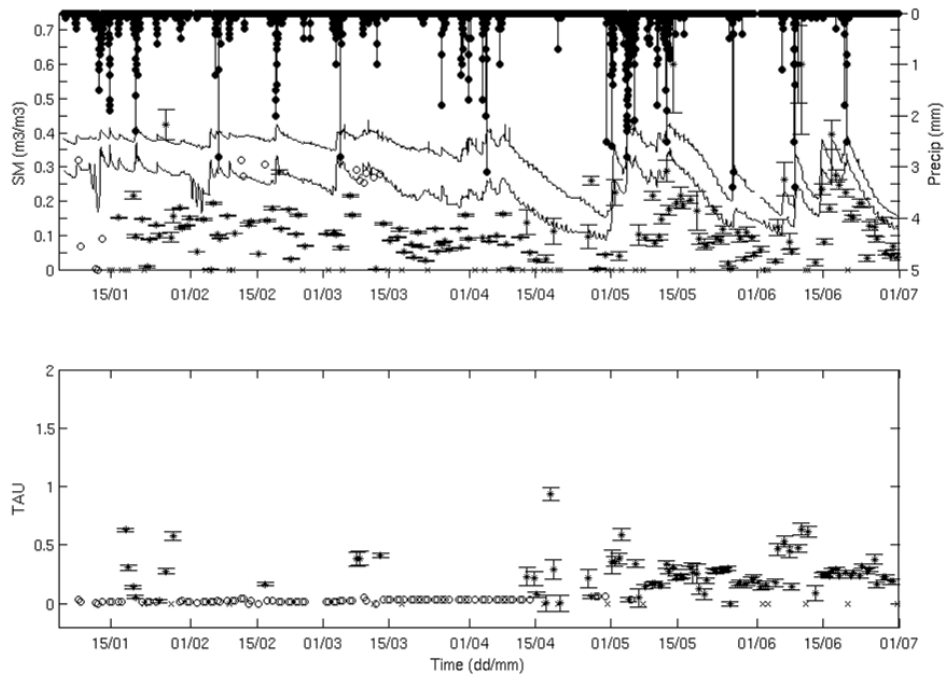


Fig. 1 Time variations in the retrieved SM (upper panel) and TAU (lower panel) from the Level 2 algorithm over the SMOSREX site. The upper plot includes measurements of SM (m^3/m^3) over both spots ("Fallow", upper curve, and "Bare soil", lower curve) & precipitations (mm, vertical lines) over the site.

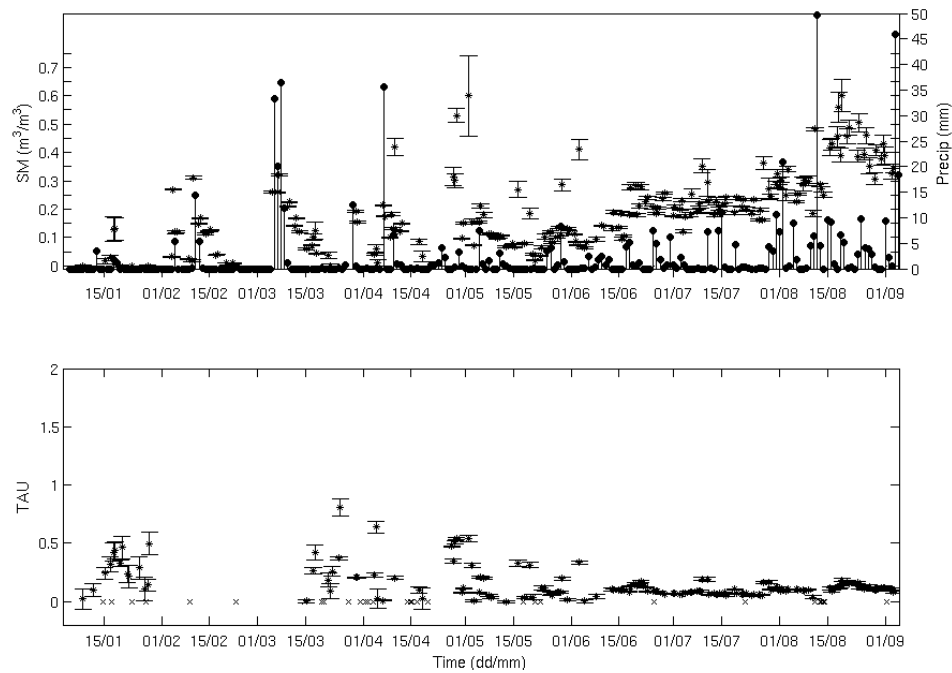


Fig. 2 Idem over the Ballarat site. The upper plot includes only measured precipitations (mm) over the site.

Satellite (MODIS) against ground-based (AERONET) AOD-Ångström for various aerosol case studies over southwestern Spain: A complement to the previous evaluation of climatologies

Y.S. Bennouna¹, V.E. Cachorro¹, C. Toledano¹, A. Berjón^{1,2}, D. Fuertes¹, R. Gonzalez¹, R. Rodrigo¹, B. Torres¹, A. de Frutos¹

1 Atmospheric Optics Group (GOA), University of Valladolid (UVA), 47071 Valladolid, Spain

2 Laboratory of Atmospheric Optics (LOA), University of Science and Technology (UST) of Lille, F-59655 Villeneuve d'Ascq Cedex, France

yasmine@goa.uva.es

ABSTRACT – *This work comes to complete a previous study on the evaluation of aerosol climatologies inferred from satellite (MODIS, OMI) observations. This evaluation was carried out by means of comparison with a ground truth reference provided by the long-term time series of the RIMA-AERONET site of El Arenosillo (37.1N, 6.7W), which is representative of the Spanish southwestern area. To explain the general agreement and differences between satellite and ground-based (AERONET) on a climatological basis, it appears necessary to carry out a detailed analysis of short time series under different atmospheric aerosol scenarios. As a preliminary study, the results presented here focus on two particular aerosol episodes: a strong desert dust intrusion in September 2007, and the smoke from forest in August 2003. Here the time series of MODIS and AERONET are compared for several parameters: the Aerosol Optical Depth (AOD), the Ångström exponent and the fine mode AOD fraction.*

1 INTRODUCTION

The Spanish Gulf of Cadiz is principally characterized by the influence of Atlantic air masses, and by frequent intrusions of African desert dust (Toledano et al, 2007a). This specificity makes it thus a region of great interest to investigate atmospheric aerosol properties and related climate and air quality issues.

Previous studies of Toledano et al. (2007b) and Bennouna et al. (2010) focused on two key columnar aerosol properties: the Aerosol Optical Depth (AOD) and Ångström exponent (Alpha), as measured using ground-based remote-sensing measurements from AERONET at the site of El Arenosillo (37.1N, 6.7W). These studies showed that in this region the annual seasonal patterns of these two parameters is modulated by the two major dust periods (late-winter/early-spring and summer/early autumn), where the transition is represented by a local AOD minimum in spring. Thus the seasonal patterns typically correspond to an increase of the AOD associated to a decrease of Alpha during the months which are affected by frequent intrusions of Saharan dust.

As demonstrated in the work of Bennouna et al. (2010), these overall variations of the climatology are in general satisfactorily reproduced by satellite data from MODIS (Moderate Resolution Imaging

Radiometer), and mean monthly climatological values from satellite differ mainly from ground-based during the spring season. On average, monthly values are overestimated by about 30%, and are higher in spring and summer (40-60%).

In the continuation of the above mentioned study, and with the aim to better explain the general agreement and differences between satellite (MODIS) and ground-based (AERONET) climatologies, it was decided to carry out a detailed analysis of various short time series. With this respect, the following result constitutes a preliminary study. Two particular events are presented: the desert dust event of September 2007, and the smokes from forest fires is also explored based on data of August 2003.

2 DATA DESCRIPTION

The ground-based data employed in this study were taken from the AERONET global sunphotometer network (Holben et al., 1998) (<http://aeronet.gsfc.nasa.gov>). The AERONET site of El Arenosillo, which was established and maintained by the Group of Atmospheric Optics (GOA) is also part of the RIMA (Iberian Network for Aerosol Measurements) network, a subnetwork within AERONET. Following AERONET protocols, the standardized sun photometer instruments routinely

performs direct sun measurements at the wavelengths of 440, 670, 870 and 1020 nm, at least every 15 minutes. The ground-based time series presented in this study use all available Level 2.0 data (i.e. cloud cleared, and quality assured) from AERONET-RIMA site of El Arenosillo: direct sun for the AOD, and O'Neill inversions for the fine-mode AOD fraction.

To represent the MODIS aerosol data over the AERONET site, the standard Terra-MODIS level 2 aerosol product MOD04 (collection 5) provided by NASA GSFC (<http://modis.gsfc.nasa.gov>) was used (Remer et al., 2006). This product provides the aerosol optical depth over land and ocean at the spatial resolution of 10x10 km². Spatial subsets of these MODIS data were extracted to select all pixels falling within a distance of 25 km from the AERONET location, and spatially averaged to obtain the data time series for MODIS.

The results also show the MODIS RGB images and the backward backtrajectories from the HYSPLIT (HYbrid Single-Particle Lagrangian Integrated Trajectoryback trajectories) model (Draxler and Rolph, 2003) which confirm the nature of the events studied.

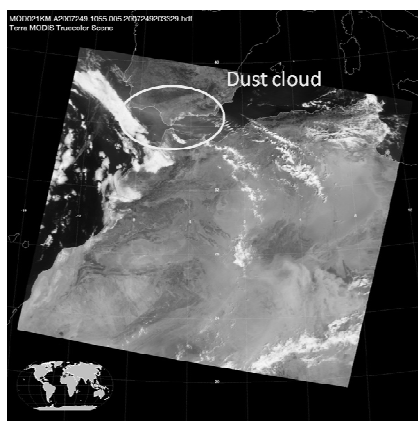


Figure 1: RGB true color image of Terra/MODIS over Spain on 6 September 2007 10:55 UTC.

3 RESULTS. CASE STUDY: Desert dust event of 6 September 2007

3.1 Satellite image and air mass analysis

As shown in Figure 1, on the RGB true color image of MODIS for the 6 September 2007 at 10:55 UTC, a dust cloud was observed above the north of Africa and the southwest of Spain. Besides, the 5-hour backward trajectories of the air masses arriving over el Arenosillo at 12:00 UTC as obtained with the HYSPLIT model for 3 levels (500, 1500, 3000 meters)

of altitude AGL (Above Ground Level), also supports the presence of desert dust aerosols from Africa over the Iberian Peninsula (figure not shown here). The three days preceding the 6 of September, some air masses crossed the Saharan desert westward from southern Lybia to southern Algeria at altitudes close to the surface, and reached El Arenosillo at the altitude of 3000 m.

3.2 Aerosol retrievals and comparison between AERONET and MODIS

To give an overall view on spatial extent and variations associated with this aerosol event, different information derived from MODIS observations are mapped in Figure 2 for the same scene as that presented in the RGB image. The maps a,b and c are relative to different aerosol parameter: AOD (Figure 2a) at 470 nm, Ångström exponent calculated from the AOD data at the wavelengths of 470 and 660 nm (Figure 2b), and the fine mode AOD fraction at 550 nm (Figure 2c). Figure 2d gives an indication on the corresponding cloud cover fraction data. To have a better representation of the spatial variations, it should be mentioned that the initial MOD04 data have been remapped onto a regular spatial grid with a resolution of 0.5 deg latitude by 0.5 deg longitude.

According to Figure 2a, the AOD reached values above 0.8 on the southern coast of Spain and Portugal. These high AODs are correlated with low Angstrom exponent both over ocean and land (see Figure 2b) with values below 0.4 and between 0.4-0.6, respectively. The contribution of the fine mode to the AOD fraction is found to be lower than 0.1 above land and slightly higher over ocean with 0.2 (see Figure 2c). These results and those of the Angstrom exponent confirm the dominance of large particles in the region on that date. The map of the cloud cover fraction (see Figure 2d) allows to further check the absence of possible remaining cloud contamination in the dataset, and in particular for the region of interest.

The time series of the aforementioned parameters retrieved from the satellite together with those measured by AERONET for the site of El Arenosillo are shown in Figure 3, from top to bottom: the 470 nm AOD, the 470-660 nm Angstrom exponent (noted as Alpha), and 550 nm fine mode AOD fraction (noted as FF). The graph at the very bottom is obviously only for MODIS data. As MODIS aerosol observations are based on two distinct algorithms over ocean and land, the left panel is associated exclusively to retrievals over ocean, and the right panel to retrievals over land.

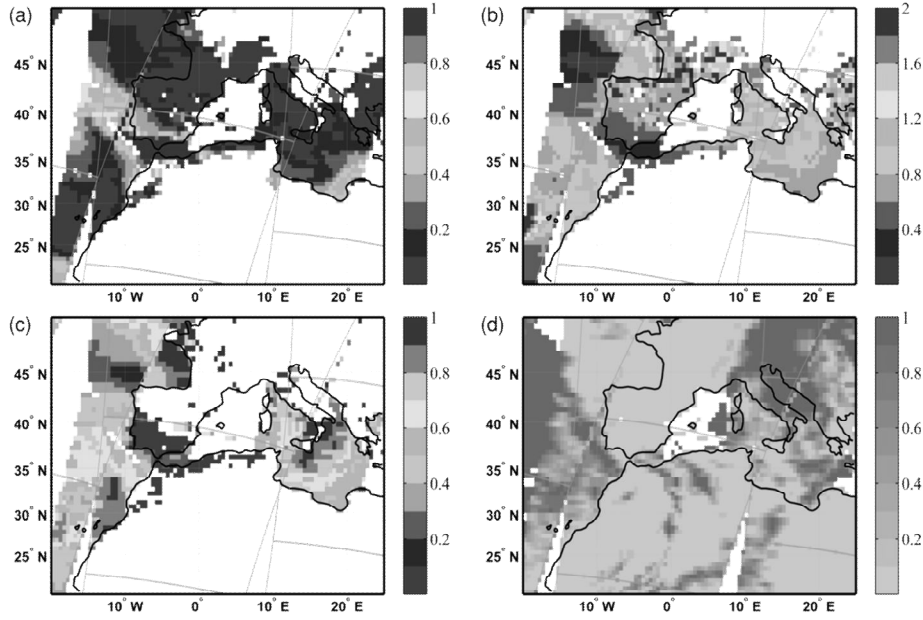


Figure 2: Daily maps from Terra/MODIS MOD04 (resampled to a regular 0.5 deg grid) for the 6 September 2007 representing (a) the AOD (470 nm), (b) the Ångström exponent (470-660 nm), (c) the fine mode AOD fraction (550 nm) and (d) the cloud cover fraction.

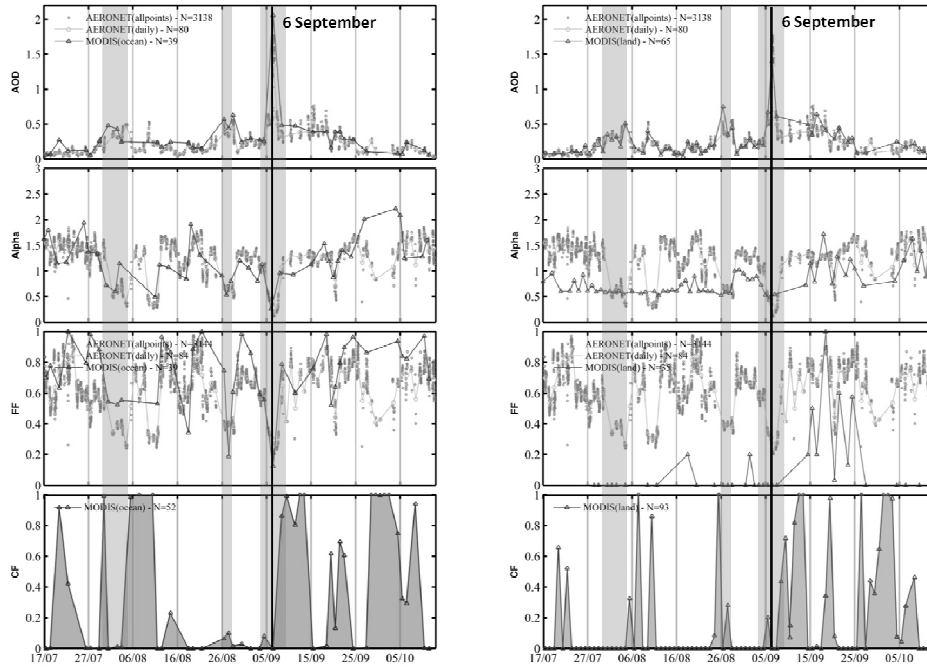


Figure 3: Time series over El Arenosillo between 17 July and 14 October 2007, from top to bottom: AOD, Ångström exponent (Alpha), Fine-mode AOD Fraction (FF), and Cloud Fraction (CF). The left and right panels correspond to the results obtained with the retrieval algorithm over ocean and over land respectively.

here). Before reaching El Arenosillo the biomass burning aerosols which appear confined in the first 2 km of the atmosphere, were transported mostly near the surface from Galicia and northern Portugal to the southwest of the Iberian Peninsula.

Smoke plume

This satellite image shows a massive, dark, swirling smoke plume rising from the Amazon rainforest, indicating a large-scale fire event. A white arrow points to the plume, and the text 'Smoke plume' is written below it. A small inset map in the bottom left corner shows the location of the Amazon basin within South America.

Figure 5: Same as Figure 1 for the 14 August 2003 12:05 UTC



Figure 4: Global 10-day fire map from MODIS Rapid Response showing the fire locations for the period 9-18 August 2003 (<http://rapidfire.sci.gsfc.nasa.gov>).

4 RESULTS. CASE STUDY: Forest fire smoke event of 14 August 2003

4.1 Satellite image and air mass analysis

In summer 2003, severe forest fires occurred across Spain and Portugal. Figure 4 presents all the fire locations detected by MODIS during the 10-day period between 9 and 18 August 2003 over the Iberian Peninsula. These data are based on the fire detection algorithm of (Giglio *et al.*, 2004).

On the MODIS RGB for the 14 August 2003 at 12:05 UT in Figure 5, it can be seen that the smoke plume (identified by an arrow on the figure) which is advected over the Atlantic Ocean is passing the site of El Arenosillo.

The HYSPLIT backward trajectories at 12:00 UTC for the 14 August 2003 clearly show that the site of El Arenosillo is mainly affected by local air masses from the surrounding land areas (figure not shown

4.2 Aerosol retrievals and comparison between AERONET and MODIS

The smoke plume is also clearly exhibited by the map of the AOD in Figure 6a. The AOD over the plume reach values above 0.7. Figure 6b reveals a discontinuity between the Alpha over ocean and that of over land over the southwest and the eastern part of the Iberian Peninsula. Over the plume, for ocean retrievals Alpha ranges between 1. and 1.4, whereas for land retrievals its values are much lower and more heterogeneous in the range of 0.4-1. As shown on Figure 6c, FF data are not available over land, however according to ocean retrievals the contribution of the fine mode to the total AOD is significant with FF values between 0.8 and 1 in the Gulf of Cadiz.

On the time series displayed in Figure 7, the 14 of August corresponds to a peak both in the daily AOD (0.79) and daily Alpha (1.6) as observed by AERONET. For this day, the 25 km average does not provide a data value from MODIS retrievals over ocean (i.e. missing), however over land the occurrence of smoke is well detected by the MODIS sensor, with a value of 0.92 at the satellite overpass. This peak also coincides with a peak in the MODIS Alpha of 1.01. As expected for such events, the FF product from AERONET is found to be very high with a value of 0.90 on average. In this case, MODIS is able to discriminate the contribution of the AOD due to the fine mode which is estimated in term of fraction to 0.45.

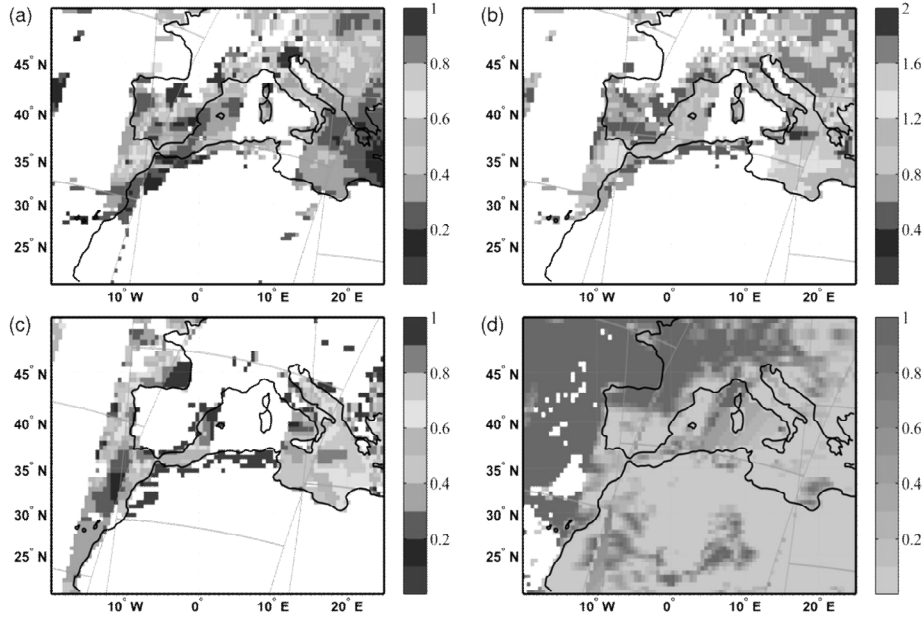


Figure 6: Same as Figure 2 for the 14 August 2003.

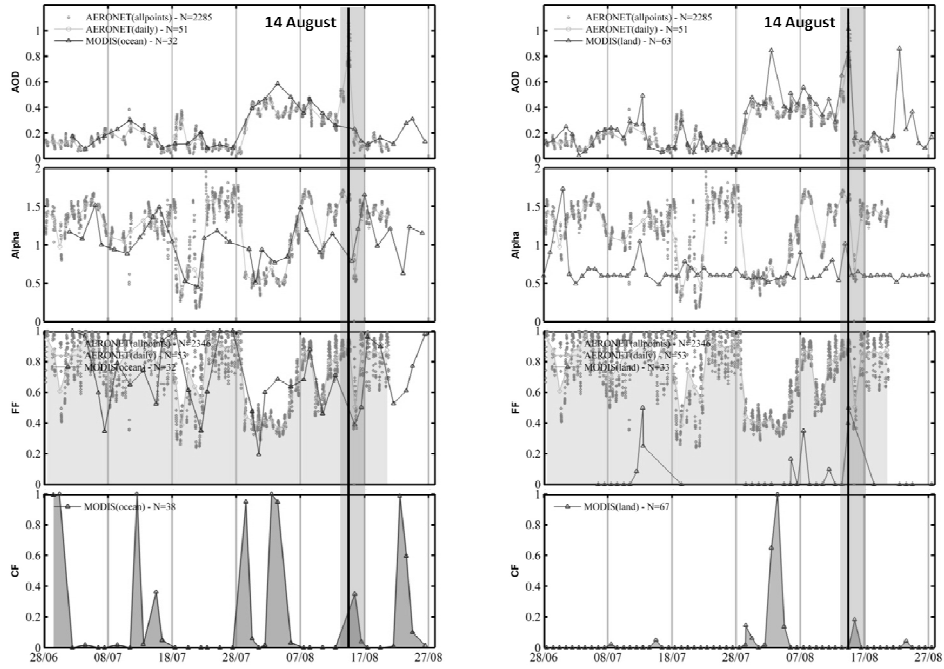


Figure 7: Same as Figure 3 for the period between 28 June 2003 and 27 August 2003.

5 CONCLUSIONS

In general the variations of the AERONET AOD are well captured by MODIS observations. The values and variations of the Ångström exponent are better reproduced by MODIS over ocean than MODIS over land.

Although the MODIS data for these punctual events are in reasonable agreement with those of AERONET, it should be noted when looking at the overall behavior of extended time series, that the variability of Alpha is very low for MODIS over land data as compared to over ocean. The same behaviour can be seen for the fine-mode contribution to the AOD. Besides the values of this parameter appear unexpectedly very low over land, and this is observed in most cases.

ACKNOWLEDGEMENTS

The authors would like to thank the teams of INTA-ESAT, AERONET and PHOTONS. We are also grateful to the members of the NASA MODIS science teams for providing the data used for this study. The authors gratefully acknowledge the NOAA Air Resources Laboratory (ARL) for the provision of the HYSPLIT transport and dispersion model used in this publication. Financial supports from the Spanish MICIIN (ref. CGL2008-05939-CO3-00/CLI and CGL2009-09740) and from the GR-220 Project of the "Junta de Castilla y León" are gratefully acknowledged.

REFERENCES

- Bennouna, Y.S., V.E. Cachorro, C. Toledano, A. Berjón, N. Prats, D. Fuertes, R. Gonzalez, R. Rodrigo, B. Torres, A.M. de Frutos, Comparison of atmospheric aerosol climatologies over southwestern Spain derived from AERONET, MODIS and OMI, Submitted for possible publication in *Remote Sensing of Environment*, April 2010.
- Draxler, R.R. and G.D. Rolph, 2010, HYSPLIT (HYbrid Single-Particle Lagrangian Integrated Trajectory) Model access via NOAA ARL READY <http://ready.arl.noaa.gov/HYSPLIT.php>. NOAA Air Resources Laboratory, Silver Spring, MD.
- Giglio, L., J. Descloitres, C. O. Justice and Y.J. Kaufman, 2003, An Enhanced Contextual Fire Detection Algorithm for MODIS, *Remote Sensing of Environment*, **87**(2-3), 273-282.
- Holben, B., T. Eck, I. Slutsker, D. Tanré, J. Buis, A. Setzer, E. Vermote, J. Reagan, Y. Kaufman, T. Nakajima, *et al.*, 1998, AERONET—A federated instrument network and data archive for aerosol characterization, *Remote Sensing of Environment*, **66**(1), 1-16.
- Toledano, C., V. Cachorro, A. De Frutos, M. Sorribas, N. Prats, B. De la Morena, 2007a, Inventory of African desert dust events over the southwestern Iberian Peninsula in 2000-2005 with an AERONET Cimel Sun photometer. *Journal of Geophysical Research-Atmospheres*, **112**(D21), D21201.
- Toledano, C., V. Cachorro, A. Berjón, A. de Frutos, M. Sorribas, B. de la Morena and P. Goloub, 2007b, Aerosol optical depth and Ångström exponent climatology at El Arenosillo AERONET site (Huelva, Spain), *Quarterly Journal of the Royal Meteorological Society*, **133**(624), 795-807.
- Torres, O., A. Tanskanen, B. Veihelmann, C. Ahn, R. Braak, P. Bhartia, P. Veefkind and P. Levelt, Aerosols and surface UV products from Ozone Monitoring Instrument observations: An overview, 2007, *Journal of Geophysical Research*, **112**(D24), D24S47.
- Remer, L., D. Tanré, Y. Kaufman, R. Levy and S. Mattoo, 2009, Algorithm for Remote Sensing of Tropospheric Aerosol from MODIS for Collection 005: Revision 2, http://modis-atmos.gsfc.nasa.gov/_docs/ATBD_MOD04_C005_rev2.pdf.

Calibration of thermal infrared radiometer by optimization of spectral filter function

Brogniez Gérard*, Philippe François*, and Bahaidin Damiri**

*Laboratoire d'Optique Atmosphérique, USTL 59655 Villeneuve d'Ascq Cedex, France

**CIMEL, 172 rue de Charonne, 75011 Paris, France

Email address : gerard.brogniez@univ-lille1.fr

ABSTRACT - Thermal infrared radiometers achieve measurements in several narrow spectral bands in the atmospheric window between 8 and 14 μm . The principle of CLIMAT instrument built by CIMEL is based on a differential method using a concealable mirror. This mirror allows the radiance coming from a target and from the thermopile cavity to be compared. Numerical counts difference between opened and closed mirror positions is linearly related with the corresponding difference radiances. The calibration of the instrument needs the spectral transmittance of the instrument in each spectral channel. As the instrument optics contains five elements, the transmittance of this optics is badly determined, because each of these elements is separately measured. Especially lenses transmittance are very badly measured. This fact leads to errors in brightness temperature retrieval. A method of radiometer calibration has been developed: it is based on an iterative method, which only requires several blackbody temperatures and corresponding output counts for opened and closed mirror positions. This method allows, in each channel of the instrument, to retrieve a correct spectral band-pass in order to obtain target brightness temperatures within the radiometric noise of the instrument, in a very large temperature range.

1 INTRODUCTION

The use of multi-channel infrared radiometers is manifold in atmospheric research. Airborne version have been used for cirrus cloud study – see French/Dirac campaign (Brogniez et al., 2004) –, atmospheric dust study (Pancrati, 2003). Infrared radiometers are also used in agronomy, geology, and for the determination of sea surface temperature using a split window method (Brogniez et al., 2003). They are also helpful for the determination of surface emissivity. Derivation of accurate brightness temperatures are very important, but difficult to obtain with a high precision with infrared radiometers, composed with multi narrow bands. For such instruments, it is not easy to obtain correct calibration in a large temperature range. In this paper, we describe a new calibration method based on an optimal estimation method.

2 RADIOMETER DESCRIPTIONS

The radiometer uses a thermopile situated into a cavity. A filter wheel allows the successive selection of the radiance incident into the thermopile in narrow bands centred at 8.7 μm , 10.5 μm , and 12.0 μm , with a FWHM = 1- μm . This kind of radiometer is also installed, downward looking, on-board the two French atmospheric research aircrafts (Falcon 20 and ATR-42).

This radiometer optics contains Ge lenses with a non-reflective treatment. Dimensions and shapes of the objective (convex-plane lens), and of the condenser (meniscus lens), have been designed to minimize the geometrical aberrations. The condenser is located in the focal plane of the objective following the Köhler design. Then, the optical field of view is well delimited, with values of 10° and 3° at half maximum, for ground-based, and airborne versions, respectively. The main advantages of thermopiles (thermal detectors) are the ambient temperature of operation, and a high level of detectivity, independent of the wavelength. Detectors are equipped with a germanium window (between 8 and 14 μm). Above 15 μm , the radiation is blocked by a ZnSe window. Spectral transmittances of the objective $F_L(\nu)$, of the condenser $F_C(\nu)$, of the ZnSe filter $F_Z(\nu)$, of the detector window $F_D(\nu)$, and of the three narrow band-pass filters $F_f(\nu)$ have been measured. They are presented on the Figure 1. The global transmittance of the optics is given, for each channel, by the transmittance product of each element:

$$F(\nu) = F_f(\nu) \times F_L(\nu) \times F_C(\nu) \times F_Z(\nu) \times F_D(\nu) \quad (1)$$

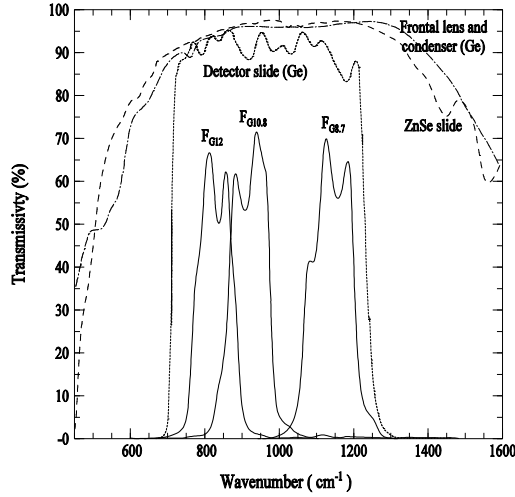


Figure 1. Spectral transmittance of each optic element of the radiometer.

The cavities are not thermostatically controlled but accurately monitored by a platinum probe with a temperature sensor. Each cavity is used as a reference of radiance (Legrand et al., 2000). A gilded concealable mirror with a high reflection coefficient (99.74%) over the spectral domain 8-14 μm is located in front of the optical head. This mirror allows the radiance originating from the target (opened position) and from the thermopile cavity (closed position) to be compared. The noise N (expressed in term of standard deviation of brightness temperature for a cavity temperature $T_C = 280$ K) is about 0.07 K in each channel.

The main characteristics and principles of radiometers are essentially:

- Digital radiometer with very good linearity.
- Very low noise, fast response, high stability over long term.
- Very weak change of sensitivity with the temperature, which permits its utilization in extreme thermal conditions, as at high altitudes.
- Only one sensitivity range whatever the incoming radiance.

3 MEASUREMENT PRINCIPLES

The principle of the instrument is based on a differential method using the concealable mirror.

In each channel, the difference between the counts (ΔC) obtained with opened (s) and closed (m) positions of the mirror is linearly related with the corresponding radiances, in each channel i . The energetic budget of the radiometer, for each channel is

given by:

$$\int_{\Delta v} B_v(T_s) f(v) dv = \int_{\Delta v} B_v(T_c) f(v) dv + \frac{\Delta C}{\sigma}, \quad (2)$$

where σ is the sensitivity of the radiometer in the channel i . T_c is the cavity temperature of the radiometer behaves like a blackbody, T_s is the brightness temperature of the source, and $f(v)$ is the normalized spectral transmittance of the optics obtained from a spectrometer. Note that $f(v)$ is badly determined, due to the great number of optics element, this implies a bad determination of the sensitivity σ , and then a bad determination of the brightness temperature of the source.

4 CLASSICAL CALIBRATIONS

The 'classical' calibration of the radiometer consists to determine σ using a high precision blackbody at varying temperature and plotting linear calibration

$$\text{curve: } \sigma = \frac{C_{BB} - C_m}{L_{BB} - L_m}.$$

Then, the radiance L_s coming from the target (over the spectral band pass i) is given by:

$$L_s = \frac{\Delta C}{\sigma} + L_m, \quad (3)$$

where L_m^i is the radiance emitted by the thermopile cavity whose the temperature T_C is monitored.

5 DESCRIPTION OF THE NEW CALIBRATION METHOD

In front of a blackbody at varying temperature T_{BB} , from a set of data $\{\Delta C, T_C, T_{BB}\}$ obtained during a calibration process, sensitivity σ , and normalised transmittance $f(v)$ can be properly determined.

5.1 Iterative method

a - From an initial guess of $f(v)$ obtained by spectroscopic measurements, we calculate the whole set of the values

$$S(T_{BB}, T_c) = \int_{\Delta v} [B_v(T_{BB}) - B_v(T_c)] f(v) dv, \quad (4)$$

obtained from calibration measurements.

b - We determine a sensitivity σ associated to $f(v)$ from the N measurements of $\Delta C(T_{BB}^j, T_c^j)$, and the N calculated values of $S(T_{BB}^j, T_c^j)$:

$$\sigma = \frac{\sum_{j=1}^N \Delta C(T_{BB}^j, T_c^j)}{\sum_{j=1}^N S(T_{BB}^j, T_c^j)}. \quad (5)$$

c - We calculate the quadratic bias:

$$\varepsilon^2 = \sum_{j=1}^N \left[\sigma S(T_{BB}^j, T_c^j) - \Delta C(T_{BB}^j, T_c^j) \right]^2. \quad (6)$$

Using a constrained method of steepest descent, we proceed to an iterative adjustment of $f(v)$ in order to minimize ε^2 . During the process $f(n)$ is constrained to remain positive.

d - After k iterations (to be adjustable):

(i) $f^k(v)$ is re-normalised.

(ii) Radiative temperatures $(T_{BB}^j)^k$ are re-calculated and compared to the measured one.

The best compromise is obtained when:

ε^2 has enough decreased, and when T_{BB}^j and $(T_{BB}^j)^k$ is minimum.

Note that the calculation of the radiative temperature is

obtained from the measurements of ΔC^j and T_c , and with the determination of σ and $f(v)$. Indeed, calculations of $\sigma S(T_{BB}^j, T_c)$ for $T_{BB}^j \in [T_{BB}^{\min}, T_{BB}^{\max}]$

allows to $(T_{BB}^j)^k$ by linear interpolation between

$\Delta C^j - c$, and $\Delta C^j + c$, where c can be as small as the precision need.

e - The process re-starts from the step b until convergence.

6 RESULTS

Hereafter, we present the results obtained for the channel of the radiometer centered at $12 \mu m$.

For the N measurements obtained during the calibration, Figure 2 shows the evolution of ε^2 with the iterations.

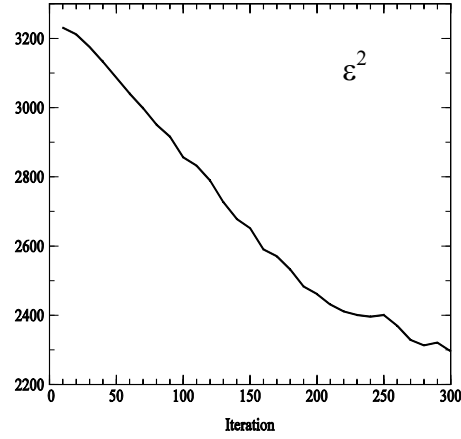


Figure 2. Variation of the quadratic bias ε^2 as function of the iteration number.

Figure 3 shows the corresponding standard deviation, $\text{Std}[T_{BB}^j, (T_{BB}^j)^k]$ expressed in Kelvin, between measured values of blackbody temperature T_{BB} , and radiative values of T_{BB} obtained from our iterative procedure.

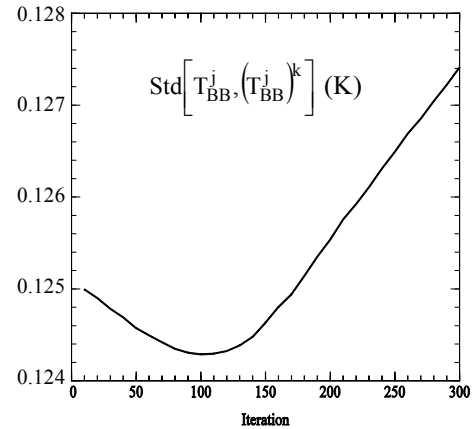


Figure 3. Variation of the standard deviation between the set of all the blackbody temperature measurements and the corresponding radiative values given from our iterative method, as function of the iteration number.

The best compromise is obtained when the standard deviation between the set of all the N blackbody temperatures T_{BB} , and N corresponding radiative values of T_{BB} is minimum.

For each channel, this best compromise corresponds to

corrected normalised spectral transmittance $f^*(\nu)$, and corrected sensitivity σ^* of the radiometer.

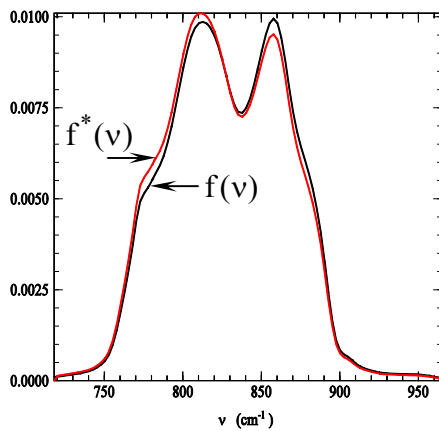


Figure 4. Corrected normalised spectral transmittance of the radiometer. The figure shows an example obtained with the channel 12, where the corrected spectral transmittance $f^*(n)$ is compared with the spectral transmittance $f(n)$ obtained from spectrometer measurements.

Moreover, the initial and final values of standard deviation between measured and retrieved blackbody temperatures, and the corresponding sensitivity of the radiometer in channel 12, are reported in Table 1.

Channel 12	Initial value	Final value
$\text{Std}(T_{BB}, (T_{BB})^k)$, K	0.621	0.124
σ , $\text{cnt}/(\text{Wm}^{-2}\text{sr}^{-1})$	66171.64	66631.55

Table 1. Initial and final values of sensitivity in channel 12, and corresponding standard deviation calculated from blackbody measured and retrieved temperatures during a calibration process.

7 CONCLUSION

The determination of spectral band pass characteristics is very difficult to obtain for infrared radiometer. This bad determination implies bad sensitivity retrieval, and thus bad determination of brightness temperatures. We have set up an iterative method of calibration. This original calibration method permit to obtain an optimal estimation of both the sensitivity and the spectral band pass simultaneously, for each spectral band pass of the radiometer. This method permit, in each channel of the radiometer, to derive brightness temperature of a given target, within about the noise equivalent temperature of the instrument.

REFERENCES

- Brogniez, G., Pietras, C., Legrand, M., Dubuisson, P., Haeffelin, M., 2003, A high-accuracy multiwavelength radiometer for in situ measurements in the thermal infrared. Part II: Behavior in field experiments. *J. Atmos. Oceanic Technol.*, **20**, 1023-1033.
- Brogniez, G., Parol, F., Bécu, L., Pelon, J., Jourdan, O., Gayet, J-F., Auriol, F., Verwaerde, C., Balois, J-Y., Damiri, B., 2004, Determination of cirrus radiative parameters from combination between active and passive remote sensing measurements during FRENCH/DIRAC 2001. *Atmos. Res.*, **72**, 425-452.
- Legrand, M., Pietras, C., Brogniez, G., Haeffelin, M., Abuhassan, N., Sicard, M., 2000, A high-accuracy multiwavelength radiometer for in situ measurements in the thermal infrared. Part1: Characterisation of the instrument. *J. Atmos. Ocean. Technol.*, **17**, 1203-1214.
- Pancrati, O., Télédétection de l'aérosol désertique depuis le sol par radiométrie infrarouge thermique multibande. *Thèse de l'Université des Sciences et Technologies de Lille*, 203 pp, 2003.

Consistency assessment of FVC and LAI operational products over Africa

F. Camacho¹, J. Cernicharo¹, J. García Haro², A. Verger², J. Meliá²

1- EOLAB. Parc Científic Universitat de València. C/ Catedrático José Beltrán, 2 46980 Paterna (Valencia). Spain.

2- Departament de Física de la Terra i Termodinàmica. Universitat de Valencia. C/Dr. Moliner, 50. 46100 Burjassot (Valencia). Spain.

fernando.camacho@eolab.es

ABSTRACT - This study investigates the consistency of three different operational (FVC and LAI) products over Africa. The VGT4Africa products derived from SPOT/VEGETATION data, the Land-SAF products derived from MSG/SEVIRI observations, and the NASA products based on MODIS/Terra observations. The spatial and temporal consistency was assessed by intercomparison over a global network of homogeneous sites (BELMANIP-2) for the period 2007-2010, following the CEOS/WGCV Land Product Validation guidelines. Several criteria of performance were evaluated, including spatial distribution, missing values, magnitude of retrievals, temporal variations, smoothness and precision. Our results shows that the products are quite consistent in spatial distribution and temporal variations, but important differences are found in terms of magnitude and product assumptions. The spatiotemporal continuity in geostationary sensor products (MSG) along with the high sampling (daily) over Africa opens avenues for its use in complementing the information provided by polar-orbiting sensor products.

1 INTRODUCTION

Fraction of Vegetation Cover (FVC) and Leaf Area Index (LAI) are key biophysical parameters for a wide range of environmental applications such as agriculture, forestry, environment management, food security, etc.

Operational distribution of vegetation parameters in near real time over Africa are of wide interest for developing the AMESD (African Monitoring of the Environment for Sustainable Development) program and for developing European environmental geo-information services focused on Africa such as the geoland-2 NARMA (Natural Resource Management of Africa) Core Information Service.

Different operational programs are currently delivering vegetation parameters over Africa. The EC VGT4Africa project (<http://www.vgt4africa.org>) delivers geo-biophysical products based on SPOT/VEGETATION data, which is the main option for users working in Africa. The Geoland-2/BioPar Core Mapping Services, a major step forward in the implementation of the GMES Land Monitoring Core Service (LMCS), provides temporal continuity to VGT4Africa products extending the production over the globe. In addition, the LSA SAF (Land-SAF) program (<http://landsaf.meteo.pt/>) of EUMETSAT provides geo-biophysical variables based on

geostationary SEVIRI/MSG data (Trigo et al., 2010), delivered via EUMETCast to African users. Furthermore, NASA provides global fields of geo-biophysical parameters based on MODIS/Terra through MODIS Land (<http://modis-land.gsfc.nasa.gov/index.htm>).

The goal of this paper is to assess the consistency between VGT4Africa/Geoland-2 v0, Land-SAF MSG, and MODIS C5 vegetation products. The assessment was performed in agreement with standards of the GEO/CEOS WGCV LPV group. The analysis was mainly focused on key points from the user perspective: product assumptions, spatial and temporal continuity, smoothness, statistical consistency, product availability and packaging.

2 REMOTE SENSING VEGETATION PRODUCTS

Below, the main characteristics of the remote sensing vegetation products investigated here are described.

2.1 VGT4Africa/Geoland-2 v0

VGT4Africa (V4A) products, distributed by VITO through DevCoCast (The GEONETCast for and by Developing Countries) (<http://www.vgt4africa.org>) and EUMETCast, are produced in near real time from the SPOT/VEGETATION sensor at 1/112° (about 1

km at equator) spatial resolution and a 10 days temporal sampling, in a Plate Carrée projection. VGT4Africa products are available since August of 2007. They are packaged in HDF format. Figure 1 shows an example of VGT4Africa FVC and LAI products.

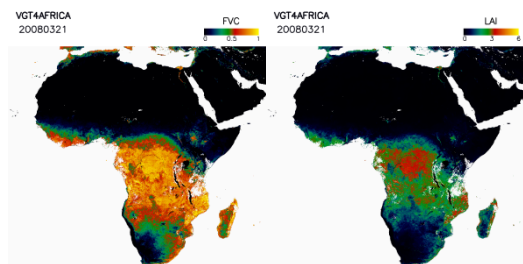


Figure 1. VGT4Africa FVC and LAI maps dated on March 21, 2008.

The LAI is estimated using a neural network approach trained from one-dimensional radiative transfer model simulations (PROSAIL model) without using any parameterisation as a function of the biome, as in the CYCLOPES v3.1 algorithm (Baret et al., 2007). Thus, the LAI corresponds with an effective LAI. The FVC is named here FCOVER; the processing line corresponds to that of CYCLOPES v3.1 up to Level 2 (BRDF), and then an optimization of the (Carlson and Ripley, 1997) NDVI-based method is applied (Camacho et al., 2006). VGT4Africa processing lines were later implemented in Geoland-2/BioPar for producing the version zero of FVC and LAI global products.

2.2 Land-SAF

Land-SAF MSG vegetation (FVC and LAI) VEGA products, distributed by EUMTETCast (NRT) and off-line by FTP (landsaf.meteo.pt), are produced in near real time from the MSG/SEVIRI observations a spatial resolution of 3 km at equator (~5 km over central Europe) on a daily basis, in the geostationary grid. VEGA products are available since mid 2005. Monthly composites produced on a 10-days basis will be available in 2011. They are packaged in HDF5 format. Figure 2 shows an example of Land-SAF MSG FVC and LAI daily products.

The FVC is estimated using an optimised spectral mixture analysis (Land-SAF, 2008a) using as input the k_0 parameter of the BRDF model. The LAI is derived from the FVC using a pragmatic approach. A correction of foliar clumping is performed applying the clumping index values derived by Chen et al., (2005). Validation results can be found at (Land-SAF, 2008b).

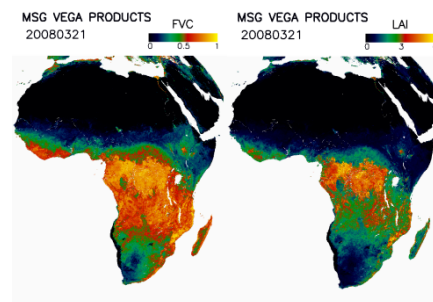


Figure 2. Land-SAF MSG LAI and FVC maps over Africa dated on March 21, 2008.

2.2 MODIS

Terra MODIS LAI/FPAR (MOD15A2) collection 5, available since 2000 from <https://lpdaac.usgs.gov/lpdaac/products/> is produced based on TERRA at 1 km spatial resolution and 8 days step over a sinusoidal grid (Yang et al., 2006). MOD15A2 are packaged in HDF format. Figure 3 shows an example of the MODIS product over Africa.

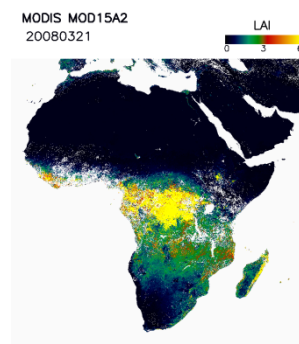


Figure 3. MODIS LAI map over Africa dated on March 21, 2008.

The main algorithm is based on LUTs simulated from a three-dimensional radiative transfer model (Knyazikhin et al., 1998). The model takes into account the clumping at plant and canopy level, thus the LAI corresponds with a true LAI. When the main algorithm fails, a backup algorithm based on LAI-NDVI relationships is used.

3 METHODOLOGY

This study was defined to be consistent with the best practices proposed by CEOS WGCV LPV subgroup for the validation of remote sensing land products.

The products were intercompared over the BELMANIP-2 network of sites that was designed to represent globally the variability of land surface types. The land surface type is defined here using generic classes derived from the GLC-2000 classification. In this paper, the products are analysed in overall and for 5 generic classes, namely: Broadleaf Evergreen (BE) Forest, Deciduous Evergreen (DE) Forest, Croplands/Mosaic, Herbaceous, and Shrublands.

The products must be compared over a similar spatial support area and temporal support period. MODIS and VGT4Africa products were remapped over the MSG grid (i.e., lower spatial resolution). The temporal support period for the quantitative assessment is 10-days (VGT4Africa dates) during the year 2008. The corresponding daily image of MSG was selected, and MODIS value (main algorithm) was interpolated using the closest 8-days images. The original spatial and temporal sampling was used for computing the missing values.

3 RESULTS

3.1 Missing values

Figure 4 shows the distribution of missing values over land as a function of the latitude and period of the year. MODIS and VGT4Africa (V4A) introduce an important number of gaps over central latitudes. This percentage is lower for V4A products over northern and southern areas, due to the largest compositing period. On the contrary, Land-SAF MSG FVC and LAI presented no missing values over Africa thanks to the high frequency of the MSG sampling (1 image each 15').

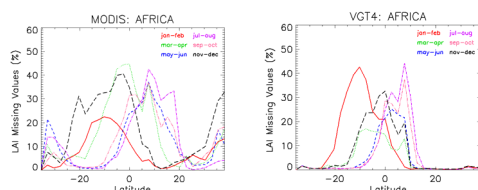


Figure 4. Percentage of missing values over Africa as a function of latitude and period for MODIS and V4A LAI products.

3.2 Spatial Consistency

Figure 5 shows maps of mean bias computed over the 2008 year. For the FVC, V4A and MSG present low systematic differences ($< \pm 0.1$) over the continent, with the exception of some areas with sparse vegetation. In those areas, MSG overestimates up to 0.2 V4A FVC retrievals. Similar results are

found between V4A and MSG for the LAI, where MSG slightly overestimates V4A. For equatorial forest mean differences goes up to 2. Differences between MSG and MODIS LAI products present a better defined spatial pattern-; MODIS overestimates MSG LAI in the equatorial forest and slightly over the Sahel region, whereas MSG slightly overestimates MODIS LAI in the other regions, especially in areas of Zambia and Mozambique. The strongest differences appear between V4A and MODIS in the forest areas.

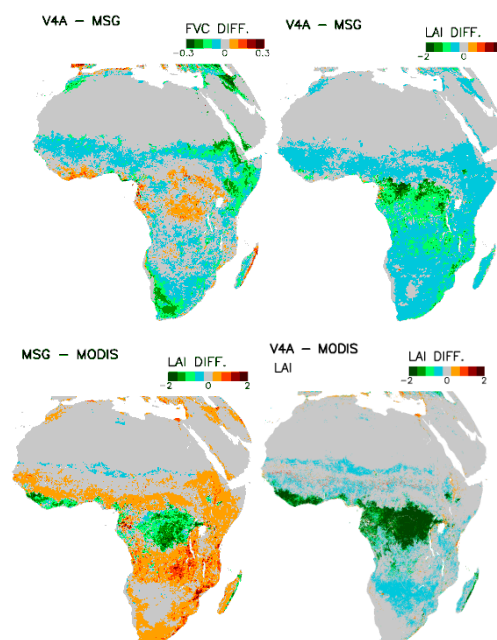


Figure 5. Mean annual bias for the year 2008 between V4A and MSG FVC (top left), V4A and MSG LAI (top right), MSG and MODIS LAI (bottom left), V4A and MODIS LAI (bottom right) products.

3.3 Consistency per vegetation type

To assess the discrepancies between the FVC and LAI products, product versus product scatterplots were generated over the BELMANIP-2 sites, using the FVC/LAI values from the 36 decades of 2008, for each vegetation class under study. Figure 6 shows the V4A versus MSG FVC scatterplots along with the computed metrics. The overall performance is quite good ($RMSE < 0.1$), showing systematic differences for low values. For vegetation type, the consistency is quite good in forest, but for Cultivated, Herbaceous and Shrubland areas systematic overestimation of MSG FVC regarding V4A FVC appears for low values. Discrepancies are really important when V4A FVC is lower than 0.1 where MSG FVC goes up to 0.4. This is a very important discrepancy to be explained for the simple parameterization of the NDVI-based method.

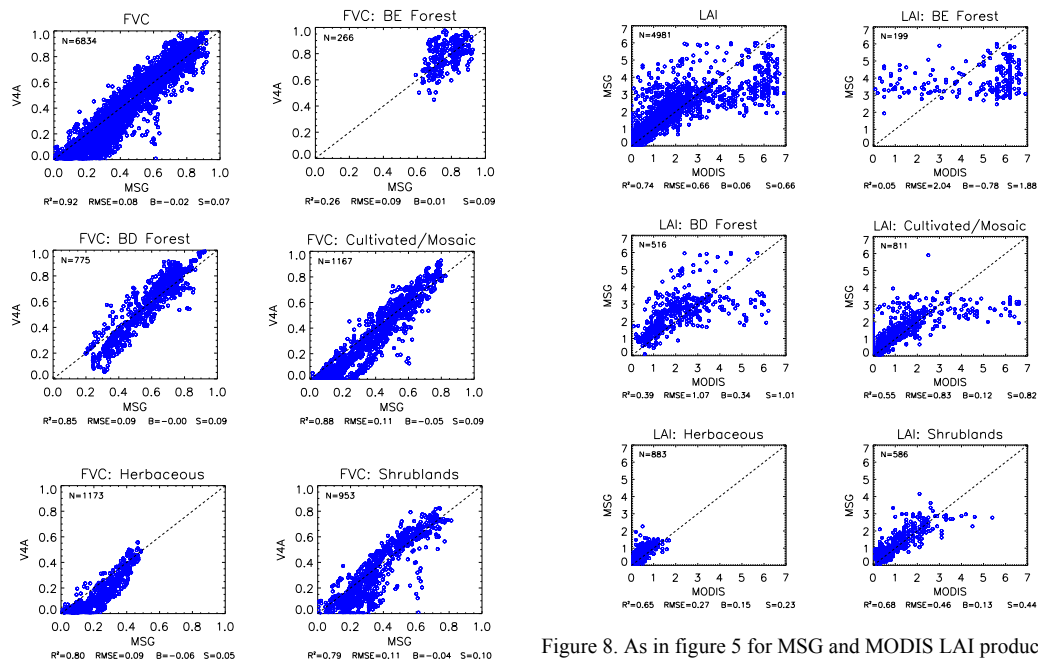


Figure 6. VGT4Africa and Land-SAF FVC scatter-plots over BELMANIP-2 sites for 2008. Correlation (R^2), Root Mean Square Error (RMSE), Bias (B) and random error (S) is shown.

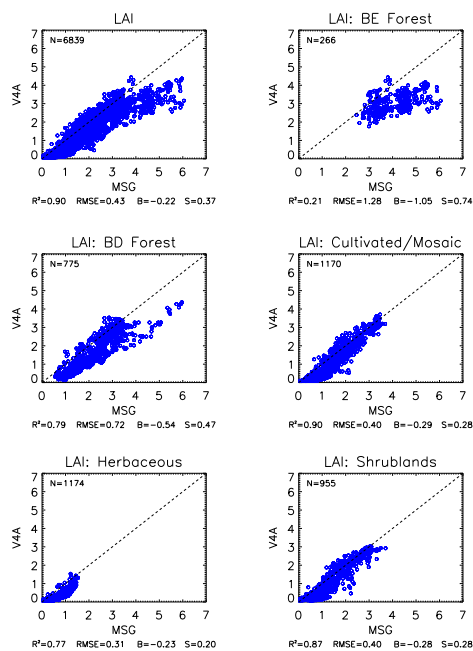


Figure 7. As in figure 5 for V4A and MSG LAI products.

Figure 8. As in figure 5 for MSG and MODIS LAI products.

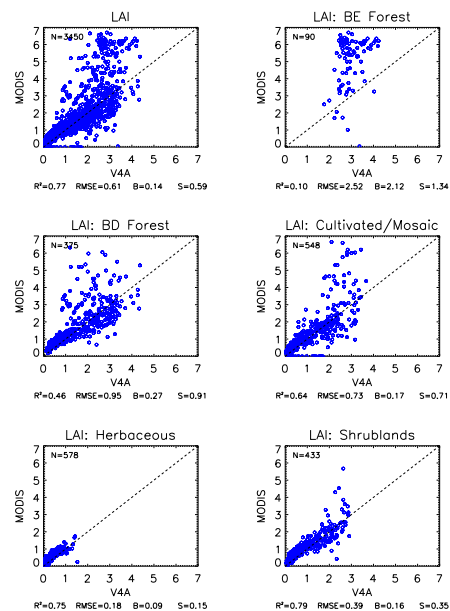


Figure 9. As in figure 5 for MODIS and V4A LAI products.

Figure 7 shows the scatterplots between V4A and MSG LAI. There is a systematic overestimation of MSG regarding V4A for all vegetation types, but both products are well correlated with the exception of Evergreen Broadleaf Forest. Part of these differences can be explained as V4A is providing an effective LAI

whereas MSG LAI is corrected of foliar clumping. In addition to that, we can observe that the highest deviations appear for very low values (where the clumping effect should be less important). Taking into account that V4A LAI and V4A FVC are based on different algorithms (PROSAIL and NDVI respectively), and that MSG LAI is based on MSG FVC, we infer that MSG FVC and MSG LAI might be overestimating FVC and LAI for low values ($LAI < 1$).

Figure 8 shows the scatters between MODIS and MSG LAI. In general, MSG is also overestimating MODIS LAI retrievals, with the exception of high values where MSG underestimates MODIS LAI values. As can be observed, the random component of the error is the main contribution to the total error. This is evident in the Evergreen Broadleaf forest, where MODIS presents very large variations from 1 to 7.

Similar results can be found regarding MODIS and V4A LAI values (figure 9). MODIS overestimates V4A LAI, which is very important in forest areas due to the saturation of the V4A LAI around 4. The scattering is also very important due to the noise in MODIS product.

3.4 Seasonal and inter-annual variations

Figures 10 and 11 show the temporal profiles for sites with different vegetation type. The three investigated products present similar seasonal and inter-annual variations, displaying some differences in magnitude. In Broadleaved Evergreen Forest, MSG presents no missing values. MODIS displays inconsistent retrievals when changes to the backup algorithm. For the shrublands Mongu site, ground truth data coming from the SAFARI 2000 campaign has been also displayed (ground data was acquired in 2000). MSG products show the best agreement with the ground data for this level of vegetation amount.

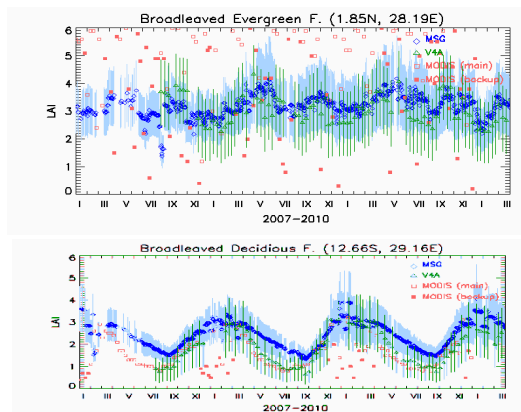


Figure 10. LAI temporal profiles for different sites in Africa.

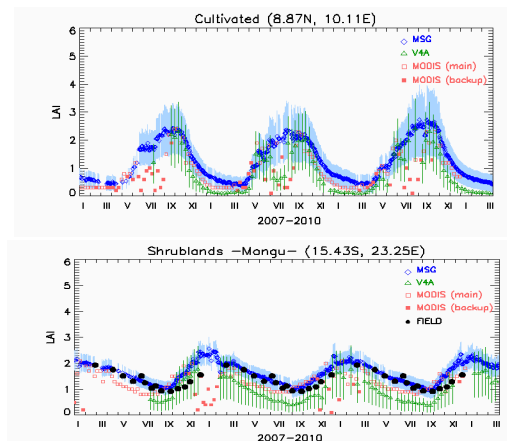


Figure 10 (cont). LAI temporal profiles for different sites in Africa.

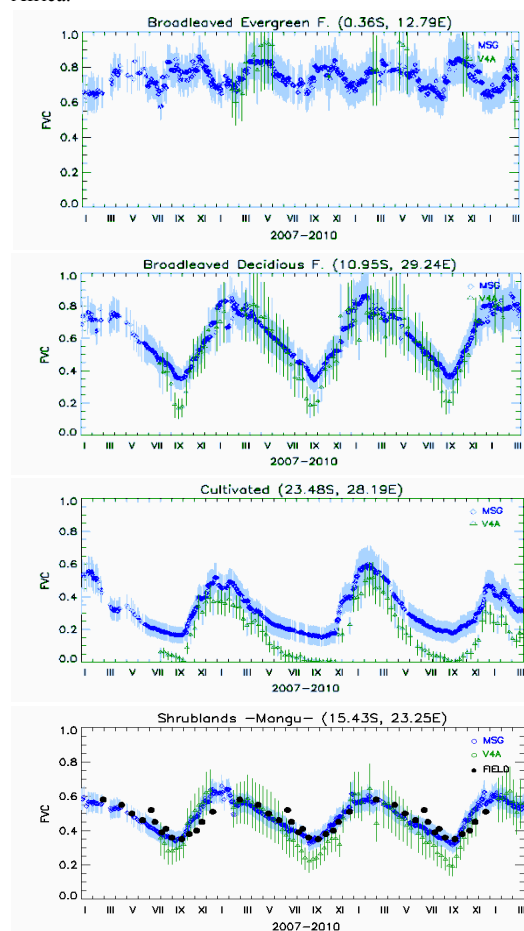


Figure 11. FVC temporal profiles over different biomes in Africa.

4 CONCLUSIONS

In this study, the spatiotemporal consistency of two FVC products (Land-SAF and VGT4Africa) and three LAI products (Land-SAF, VGT4Africa and MODIS) were assessed at the MSG grid for the period 2007-2010 using the BELMANIP-2 network of sites. Scatter-plots and metrics were computed using data from 2008. The comparisons were made according to several criteria of interest from the user's point of view. The following are the main conclusions.

All the products present reliable spatiotemporal distribution of retrievals, showing similar seasonality and inter-annual variations, but with some differences in their magnitude. The Evergreen Broadleaved forest is the biome where important discrepancies were found.

LSA SAF MSG products are the only that present spatiotemporal continuity (no missing values) over Africa, which is the main advantage of using geostationary satellites. On the contrary, MODIS and VGT4Africa present large percentage of missing values (up to 40%) in equatorial regions.

Concerning the magnitude of low values, LSA SAF MSG products tend to overestimate VGT4Africa and MODIS retrievals. This effect is quite important in the case of FVC. Concerning the magnitude of high values, MODIS present the highest values for forest, and VGT4Africa present a saturation around 4, which corresponds to an effective LAI.

The smoothness of temporal profiles was also evaluated; LSA SAF MSG presents the smoothest profiles at a daily basis, VGT4Africa present also very smooth profiles at 10-days basis. However, MODIS present noisy profiles and important inconsistencies between main and backup solutions.

The accuracy of the estimates was not properly analysed due to the lack of ground truth measurements in Africa, however MSG Land-SAF present the best agreement with ground data acquired at Mongu site (LAI ranging between 1 and 2).

In summary, this work shows the generally good spatiotemporal agreement of the different products, and the potential of geostationary sensor products to complement polar orbiting sensor products in regions of high cloud occurrence. There are, however, important discrepancies in terms of magnitude and product definition (true LAI, effective LAI) that hampers the synergy of remote sensing products.

5 ACKNOWLEDGEMENTS

This work was supported by LSA SAF/ EUMETSAT.

6 REFERENCES

- Baret, F., Hagolle, O., Geiger, B., Bicheron, P., Miras, B., Huc, M., et al. (2007). LAI, fAPAR and fCover CYCLOPES global products derived from VEGETATION. Part 1: Principles of the algorithm. *Remote Sensing of Environment*, 110, 275–286.
- Camacho -de Coca, F., J. C. Jiménez-Muñoz, B. Martínez, P. Bicheron, R. Lacaze and M. Leroy (2006). Prototyping of fCover product over Africa based on existing CYCLOPES and JRC products for VGT4Africa. *Proceedings of the 2nd RAQRS symposium: 722-727*. Torrent, 22-25 September 2006.
- Carlson, T. N., and Ripley, D. A. 1997. On the relation between NDVI, fractional vegetation cover, and leaf area index. *Remote Sensing of Environment*, 62, 241-252.
- Chen , J. M., C. H. Menges, S. G. Leblanc, (2005), Global mapping of foliage clumping index using multi-angular satellite data, *Remote Sensing of Environment*, 97: 447 – 457.
- LSA SAF. (2008a). Product user manual (PUM) vegetation parameters (FVC, LAI, FAPAR). SAF/LAND/UV/PUM-VEGA/2.1. 53pp. (Document online at <http://landsaf.meteo.pt>).
- LSA SAF. (2008b). Validation Report vegetation parameters (FVC, LAI, FAPAR). SAF/LAND/UV/VR-VEGA/2.1. 100pp. (Document online at <http://landsaf.meteo.pt>).
- Knyazikhin, Y., J. V. Martonchik, R. B. Myneni, D. J. Diner, and S. W. Running (1998), Synergistic algorithm for estimating vegetation canopy leaf area index and fraction of absorbed photosynthetically active radiation from MODIS and MISR data, *J. Geophys. Res.*, 103(D24), 32,257–32,275.
- Trigo, I. F., C. C. DaCamara, P. Viterbo, J.-L. Roujean, F. Olesen, C. Barroso, F. Camacho-de Coca, D. Carrer, S. C. Freitas, J. García-Haro, B. Geiger, F. Gellens-Meulenberghs, N. Ghilain, J. Meliá, L. Pessanha, N. Siljamo, and A. Arboleda, (2010). The Satellite Application Facility on Land Surface Analysis. *Int. J. Remote Sens.*, in press
- Yang, W., D. Huang, B. Tan, J. C. Stroeve, N. V. Shabanov, Y. Knyazikhin, R. R. Nemani, and R. B. Myneni, 2006. Analysis of leaf area index and fraction vegetation absorbed PAR products from the Terra MODIS sensor: 2000– 2005, *IEEE Transaction on Geoscience and Remote Sensing*, 44(7), 1829– 1842.

Integration of MSG-derived solar radiation maps with ground observations with a statistical copula model

Lorenzo Campo, Fabio Castelli

Dipartimento di Ingegneria Civile e Ambientale, Università degli Studi di Firenze, Via S. Marta 3, 50139 Firenze, Italy

lcampo1@dicea.unifi.it, Fabio@dicea.unifi.it

ABSTRACT - *The incident solar radiation constitutes the main forcing for the energy budget at the soil surface and it is an essential input for several applications, like hydrological balance models, agricultural planning and SVAT (Soil-Vegetation-ATmosphere) models. An accurate estimation of this variable on a large area needs a dense network of ground sensors and information on the cloud cover, that are rarely available. A valid alternative is constituted by remote sensing, that can provide reliable measures of the cloud cover with high spatial and temporal resolutions. In this work a simple algorithm has been used in order to integrate the LSA-SAF products of shortwave incident radiation obtained from MSG-SEVIRI imagery with ground radiometers observations. A statistical approach that utilizes a copula function was followed in order to define a criterion for accept or reject the ground sensors observations. In this approach both the mean daily error between the ground measure and a theoretical radiation time series and the cloud cover measures from MSG imagery were modeled with probability distribution functions. The theoretical time series was obtained from astronomical radiation values with a simple cloud cover correction formula. Through the use of the Frank's Copula, a conditional probability distribution function of the radiation error given the cloud cover was built and used for the accepting criterion. A dataset of corrected solar radiation maps were produced on the whole Italian territory in a period of 6 months in 2007.*

1 INTRODUCTION

An accurate estimate of this variable on large areas requires a particularly dense sensors network and continuous information about the cloud cover, that are rarely available (Fitzgibbon and Facundo, 2003, Bower and Fitzgibbon, 2004). A valid alternative is constituted by the remote sensing, that can provide reliable measures of the cloud cover at high spatial and temporal resolutions.

In this work a simple algorithm is proposed in order to integrate the Land Surface Analysis Satellite Applications Facility (LSA-SAF) product of surface shortwave incident radiation from MSG-SEVIRI imagery (LSA-SAF, 2006) with ground measures of incident radiation. The need of such correction is particularly important in the light of the presence of considerable errors in the LSA-SAF maps. Comparing the available ground measures with the satellite image data in corresponding pixels, significant differences are observed in both clear sky and cloud cover conditions, with errors, for what concern the Italian territory, up to hundreds of W/m^2 .

At the purpose to increase the reliability of the maps produced by the analysis it was necessary to define an acceptance criterion for the ground measures that allow to eliminate automatically the not reliable time series. In fact, observations performed on the

Italian Civil Protection national network highlighted several anomalies in the measures. The approach proposed in this work is constituted by the construction of a statistical model based on a conditional probability distribution of the radiation error with respect to the cloud cover. In this sense, in last years a number of hydrological applications have been developed with the use of the copulas (Favre et al, 2004; Grimaldi and Serinaldi, 2006; Renard and Lang, 2007), that allow to obtain joint probability distributions given the marginal ones and their correlation.

On the basis of this statistical model, a criterion for accepting or reject the ground measures of each single radiometer was defined. The radiation error was defined as a measure of the match between the observed series of the radiometer and a synthetic series produced applying a simple cloud cover correction formula to the daily-averaged astronomical radiation.

Given the selected radiometers for a day, hourly maps of solar radiation were produced on the Italian territory, basing on the LSA-SAF produced maps that were corrected with ground measures, interpolating errors separately for the different cloud cover zones.

The results of the algorithm applied on a nationwide sensors network are presented for a period of 6 months in 2007.

2 GROUND MEASURES ANALYSIS

The ground observations used in this work came from the Italian civil Protection sensors network. The available data were observed by a total of 161 gauges in the period 1 January – 31 December 2007. A number of anomalies was observed in these measures, like excessively low values also in condition of clear sky or values above the solar constant.

In figure 1 the location of the sensors are shown, together with the various observed anomalies, probably caused by errors in the transmission of the data, by malfunctioning sensors or by observations of other variables (diffuse radiation, global radiation, snow reflection, etc.).

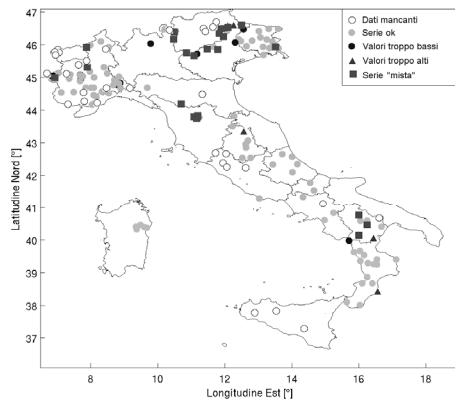


Figure 1. Location of the radiometers in the Italian territory and quality of the time series.

The network comprehended a total of 161 radiometers, of which:

- 89 with values in the expected range (up to about 1100 W/m^2)
- 5 with excessively high values (above the astronomical radiation)
- 5 with excessively low values (always below 250 W/m^2 , also in summer sunny days at the diurnal peak)
- 23 that presented both too high and too low values
- 39 not working sensors

In figures 2 and 3 examples of such anomalies are shown for what concern measured radiation above the astronomical radiation and values persistently below 200 W/m^2 . In Figure the observed time series is shown, together with the LSA-SAF estimate and the astronomical correction (without taking account of the cloud cover, if present). The instants in which cloud are present or in which the MSG data were not available are also shown.

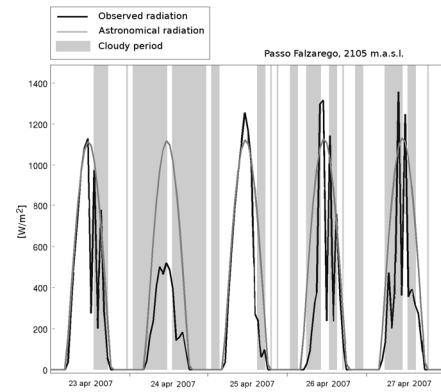


Figure 2. Example of anomalies in the ground observations: values above the astronomical radiation.

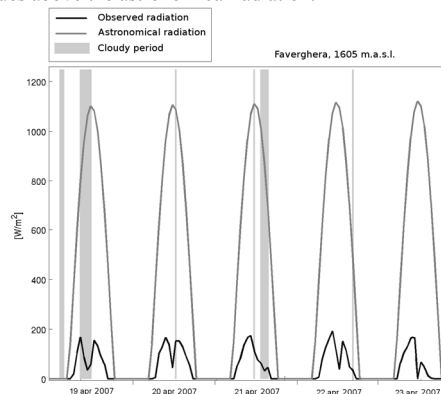


Figure 3. Example of anomalies in the ground observations: values always below 200 W/m^2 also at the diurnal peak in sunny days.

3 CRITERION FOR THE SELECTION OF THE RADIOMETERS

In order to obtain an operational algorithm for the production of solar radiation maps it is necessary to select reliable data between the ground observations, that will be used for the correction of the LSA-SAF satellite maps (see section 4). Thus a criterion of accepting or reject radiometers is needed.

A statistical approach was chosen, based on the comparison between the measures with a time series that was considered reliable and that was adopted as reference. The reference radiometer was chosen basing on the following requirements:

- reliability of the measures (absence of anomalies)
- availability of a large number of observations
- low height above the sea level, in order to avoid the risk of snow reflection effects on the measured values
- wide range of cloud cover conditions

The selected station was Florence University (Gauss-Boaga coordinates: 1681349 East, 4851823 North; height: 96 m a.s.l.). The observed time series was compared with the corresponding astronomical radiation time series, corrected with the following, daily-based, formula in order to take account of the presence of clouds:

$$R = R_a (1 - 0.65 N^2) (0.3 + 0.5 N_{ld} / N_l) \quad (1)$$

where R is the daily averaged incident solar radiation [W/m^2], R_a is the daily averaged astronomical solar radiation (at the atmosphere top) [W/m^2], N is the daily averaged cloud cover percentage [-], N_{ld} is the direct light period [hours] and N_l is the number of hours of light [hours]. In figure 4 a comparison is shown between the daily average radiation observed at the reference station and the corresponding synthetic time series.

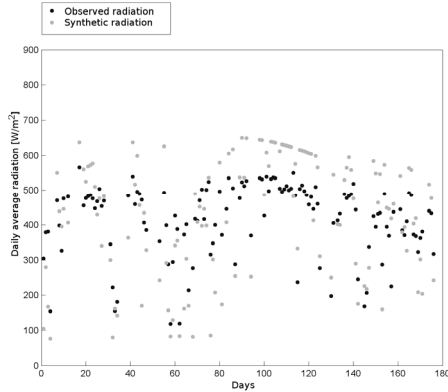


Figure 4. Comparison between observed daily average radiation and the corresponding synthetic time series obtained with equation (1). The station is Florence University.

The cloud cover was estimated by the MSG cloud data provided by LSA-SAF for the study period considering only two possible values: complete cloud cover and clear sky. A percent error between the observed and the synthetic series was computed, that resulted unbiased. It was also observed a strong correlation between this error and the fraction of cloud hours in the diurnal period, as shown in figure 5.

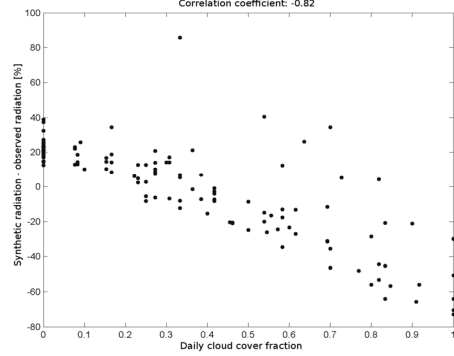


Figure 5. Scatterplot of the radiation percent errors with the fraction of cloud cover in the diurnal period.

Basing on these results, two probability distributions were chosen in order to describe the radiation error (random variable X) and the cloud cover percentage (random variable Y). The sample distribution of the errors showed a consistent left tail, so a modified version of the Gumbel distribution was chosen, in order to assure a better fitting on the sample data:

$$f_X(x) = \frac{\gamma}{\alpha} e^{\frac{\gamma x + u}{\alpha}} e^{-e^{\frac{\gamma x + u}{\alpha}}} \quad (2)$$

For what concern the cloud cover daily percentage an uniform distribution with two Delta of Dirac for the extreme cases (always cloudy sky and always free sky) was adopted:

$$f_Y(y) = \begin{cases} p_{fs} \delta(y) & y = 0 \\ 1 - p_{fs} - p_{cs} & 0 < y < 1 \\ p_{cs} \delta(y - 1) & y = 1 \end{cases} \quad (3)$$

where p_{fs} is the always free sky days percentage and p_{cs} is the always cloudy sky days percentage.

In figures 6 and 7 the fit of the two Cumulate Distribution Function on data for the reference station are shown for the radiation error and the cloud cover fraction, respectively.

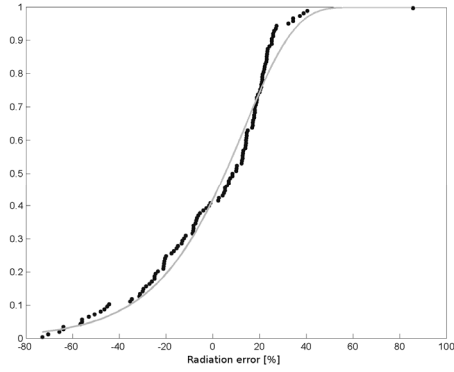


Figure 6. Cumulate Distribution Function for the radiation error (data are from the reference station).

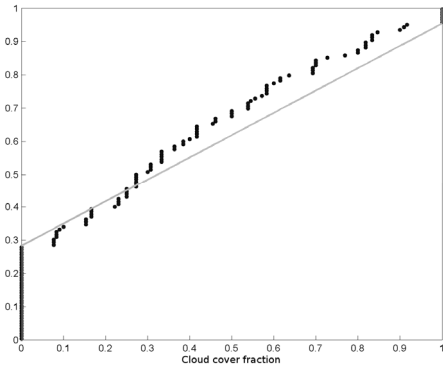


Figure 7. Cumulate Distribution Function for the cloud cover fraction (data are from the cloud cover over the reference station).

In order to obtain the conditional distribution of the radiation error given the cloud cover, the joint distribution function of the two random variables was computed by use of the bivariate Frank Copula:

$$F_{X|Y}(x|y) = \frac{e^{-\delta F_Y(y)}(1 - e^{-\delta F_X(x)})}{1 - e^{-\delta} - (1 - e^{-\delta F_X(x)})(1 - e^{-\delta F_Y(y)})} \quad (4)$$

where d is a parameter that describes the correlation between the two random variables. A representation of this function is shown in figure 8.

Given the expression of $F_{X|Y}(x|y)$, the base of the criterion for the selection of each radiometer for each day was the computation of the error between the daily-averaged observation and the corresponding synthetic radiation value (computed with (1)).

The selection algorithm was, for each day and for each radiometer, the following:

- computation of the daily cloud cover fraction
- computation of the daily averaged observed radiation
- generation of the synthetic radiation time series for that day and that location
- computation of the percent error between the observed and the synthetic daily averaged radiation
- comparison of the error computed at step d) with the α and $1-\alpha$ percentile of the conditional distribution of the radiation error given the cloud cover fraction: if the value is inside the interval the radiometer is accepted, otherwise it is excluded from the analysis.

4 INTEGRATION OF THE SATELLITE DATA WITH GROUND OBSERVATIONS

The integration of the observations of the radiometers selected with the algorithm described in section 3 with the LSA-SAF maps of incident radiation was realized by mean of a comparison between the instantaneous ground measured values with the corresponding cells of the map. For each instant of a given day, the differences between these values are computed and an interpolation is performed in order to produce an error map. The interpolation, realized with the inverse distance method, is performed separately for the three sub-area in which the domain is subdivided by the LSA-SAF cloud cover classes (clear sky, partially cloudy, complete cloud cover). Thus, this correction map is summed to the original LSA-SAF radiation map: in this way the actual cloud pattern is maintained, and the map matches exactly the ground observations that have been considered reliable.

5 INTEGRATION OF THE SATELLITE DATA WITH GROUND OBSERVATIONS

The algorithm was applied on the whole Italian territory for a period of 6 months in 2007, producing a dataset of solar incident radiation at MSG resolution (approximately 4 km) and at hourly time step. This dataset has both the accuracy of the satellite-derived cloud cover patterns and the reliability of the ground sensors observations. Applying the procedure described in Section 3, about the 25% of radiometers was rejected and excluded from the analysis.

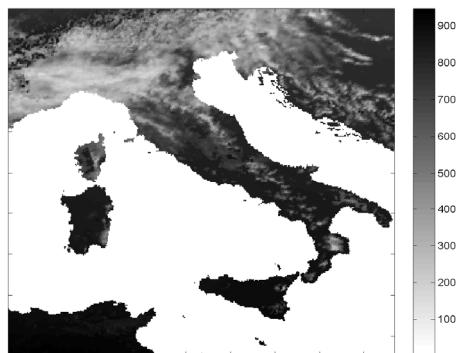


Figure 9. Map of solar incident radiation produced from LSA-SAF for 15 June 2007, at 12:00.

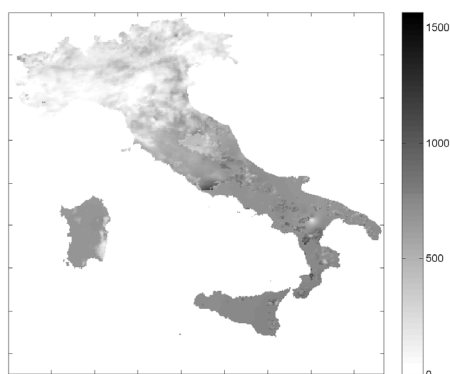


Figure 10. Map obtained by applying the correction procedure described in Section 4 but without the pre-selection of the radiometers described in Section 3. Values out of range are present in center-southern part of the country.

In figure 9 a LSA-SAF radiation map is shown: no correction are performed, the radiation values range from 0 to about 900 W/m². In figure 10 the map obtained by the correction procedure described in Section 4 is shown. In this case, however, the selection algorithm described in Section 3 was not applied. As a result, anomalous values are present in the center-southern part of the domain, in which values over 1500 W/m² are present. In figure 11, the correction is performed also pre-selecting the radiometers with the statistical procedure. As it is possible to see the pre-selection of the radiometers resulted to be essential: the application of the algorithm allowed to reject the sensors that measured the values out of range and produce the corrected map.

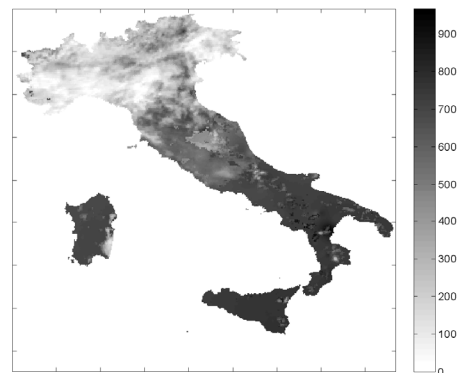


Figure 11. Map obtained by applying the complete correction algorithm. The map maintains the correct cloud cover pattern and matches the ground observations where these are available.

6 CONCLUSIONS

The estimation of the solar radiation by remote sensing can constitute a valid tool to map such variable in ungauged regions with temporal and spatial resolution sufficient for the hydrological modelling and for surface energy budget estimation. However, the LSA-SAF solar radiation product used in this work presents, in comparison with ground truth, considerable errors either in cloudy conditions or free sky.

A simple algorithm was proposed for correcting maps of solar radiation from satellite data elaboration, in order to match with the ground observations of the radiometers network. Due to the fact that a number of anomalies was observed also in ground measures, a statistical model based on a copula was employed in order to define criteria for accepting or rejecting the radiometers measure for a given day.

The method was applied on the whole Italian territory for a period of 6 months and allowed the production of solar radiation maps at MSG spatial resolution. All the anomalies observed in radiometers measures were eliminated.

In conclusion, the proposed algorithm allows to produce operationally reliable maps of incident solar radiation that require only satellite maps and ground observations.

REFERENCES

- Bower, C. A. Jr, and Fitzgibbon, J. J., 2004, National Weather Service In-situ Radiation Temperature Correction for Radiosonde Replacement System GPS Radiosondes. Proceedings of Eighth Symposium on Integrated Observing and Assimilation systems for Atmosphere, Oceans, and Land Surface held in Seattle, on 10-16 January 2004, 3.1.
- Dingman, S., 1994, Physical Hydrology (Macmillan Publishing Company).
- Favre, A. C., El Adlouni, S., Perreault, L., Thiemonge, N., Bobee, B., 2004, Multivariate hydrological frequency analysis using copulas. *Water Resources Research*, 2004:40, W01101, doi:10.1029/2003WR002456.
- Fitzgibbon, J., and Facundo, J., 2003, Technique for verifying radiosonde solar radiation correction algorithm. Preprints. Proceedings of 12th Symposium on Meteorological Observations and Instrumentation held in Long Beach, CA, American Meteorological Society, CD-ROM, JP8.2.
- Grimaldi, S. and Serinaldi, F., 2006, Asymmetric copula in multivariate flood frequency analysis. *Advanced Water Resources*, 29, pp. 1155–67.
- LSA-SAF Engineering Team, Product User Manual Down-welling Surface Short-Wave Radiation Flux, Document Version 1.4, 2006, SAF/LAND/MF/PUM_DSSF/1.4, <http://LSA-SAF.meteo.pt>.
- Renard, B. and Lang, M., 2007, Use of a Gaussian copula for multivariate extreme value analysis: Some case studies in hydrology. *Advances in Water Resources*, Volume 30, Issue 4, Pages 897-912.

LAND SURFACE TEMPERATURE: TOWARDS THE IDEAL DATASET

Edward Comyn-Platt¹, J.J. Remedios¹, E.J. Good², R. Saunders²

¹. Department of Physics and Astronomy, University of Leicester, Leicester, UK

². Met Office Hadley Centre, Exeter, UK

e-mail: emc19@le.ac.uk

ABSTRACT- *Land Surface Temperature (LST) is a vital parameter in Earth climate science, driving long-wave radiation exchanges that control surface energy fluxes. Satellites offer a convenient way to observe LST consistently and regularly over large areas. Here, we present a comparison of LST retrievals employed by two sensors over selected sites in Europe and Africa: the Advanced Along Track Scanning Radiometer (AATSR), which is in polar-orbit on board ENVISAT, and the Spinning Enhanced Visible and InfraRed Imager (SEVIRI), which is in geostationary orbit on board Meteosat Second Generation (MSG). The AATSR offers high precision, 1 km² measurements globally whereas the SEVIRI provides the high-temporal resolution (every 15 minutes) required for observing diurnal variability of surface temperatures. Regions of investigation were chosen such that retrieval response to view-angle and surface type and phenology could be examined acting as a preliminary step in constructing a combined retrieval which should provide optimal performance. These early results show that there is a seasonal cycle of discrepancy likely a result of differing classification of fractional vegetation and a strong correlation of discrepancy with individual surfaces classes. Secondly there is a correlation with the AATSR view-angle, possibly a result of the satellites “seeing” different scenes, i.e. SEVIRI seeing the sunlit side of topographical features where AATSR sees the sun-shade side for morning match-ups in the northern hemisphere. Essentially this research highlights some key areas of consideration in the goal of constructing a combined algorithm.*

1 INTRODUCTION

Land Surface Temperature (LST) is the primary driver for surface-atmosphere processes and energy fluxes; hence its measurement is required for a number of climatic, ecological, hydrological and biogeochemical applications as well as being a key identifier of climate change. Satellites offer a convenient way to observe LST consistently and regularly over large areas. The last couple of decades have witnessed significant progress in the art of retrieving LST from remotely sensed infrared satellite measurements culminating in a number of passive infrared instruments making such measurements. In the broadest sense, this plethora can be divided in to two distinct types, Geostationary and Polar Orbiting, both of which have their own strengths and weaknesses. Geostationary platforms provide excellent temporal resolution, for example the Spinning Enhanced Visible and InfraRed Imager (SEVIRI) on board Meteosat Second Generation (MSG) produces 3712x3712 pixel images covering a field of view (FOV) of ~1.6steradians of the Earth's surface (~40%) every 15 minutes. However, they lack global coverage and have relatively poor spatial resolution, 3.1km at nadir degrading to 12.0km at the rim of the FOV where there is the added problem of a greater path length. Polar orbiting satellites are generally sun-synchronous giving vast amounts of global data for the overpass times specific to the satellite. The lower altitude allows for a much greater

spatial resolution which, as well as providing a more accurate and detailed dataset, reduces the difficulties of validating such measurements. An example being the Advanced Along Track Scanning Radiometer (AATSR) onboard the ENVIRONMENTAL SATellite (ENVISAT) which has a descending node at 10:00a.m. (±20mins), a pixel resolution of ~1km² and with a swath width of 512km and an orbital period of 100mins, it takes ~3days to achieve global coverage.

The most common method of calculating LST from satellite data is to use a coefficient based Generalised Split Window (GSW) algorithm. Essentially this is the result of a simultaneously solved Radiative Transfer Equations (RTEs) for two (or more) spectrally close channels where the remaining unknowns have been replaced by context based coefficients. The term ‘*context based coefficients*’ refers to the method of selecting and weighting coefficients from look-up tables dependant on the measurements context, i.e. surface emissivity and atmospheric transmittance.

When considering the application of LST measurements it is often found that the important information lies in the diurnal cycle and daily temperature extremes for example, estimating the depth of permafrost thawing or the extent of crop damage due to frost. Ironically this measurement has tended to slip under the radar with prior LST research, where more of an emphasis has been on monthly averages which tell little of the finer effects of a

changing climate. It is not possible to make such measurements with the more accurate polar orbiting satellites which only observe at two specific local times. Thus, the ideal satellite LST dataset would use a combination of both types of observations, with the diurnal information from the geostationary sensors and the accuracy and spatial advantages of the polar-orbiting data sets.

This work presents a preliminary comparison between LST products of the two aforementioned space-born instruments such that a baseline understanding of the problem can be obtained. The LST products were compared over two $10^6 \times 10^0$ regions and correlated with a number of factors to identify sources of error. In short it was expected that the LST products would differ for one of two broad reasons, firstly the algorithmic differences such as the formulation and any auxiliary data used, secondly the physical differences between the two measurements such as the differing pixel sizes or the viewing geometry.

2 THE AATSR AND SEVIRI LST ALGORITHMS AND THEIR DIFFERENCES

2.1 The AATSR LST Algorithm

AATSR LST product used in this research is the proposed replacement to the operational product (Zeller 2010, submitted; Zeller, et al. 2010)¹ which, in short, simply uses higher resolution auxiliary data with the formulation remaining as first proposed by Prata (2002). The formulation is based on a Split-Window (SW) algorithm using the brightness temperature from AATSRs two thermal infrared (TIR) channels and pre-derived coefficients which are dependent on auxiliary data, that is:

$$LST = a_{f,i,p,w} + b_{f,i}(T_{11} - T_{12})^{p(\theta)} + (b_{f,i} + c_{f,i})T_{12} \quad (1)$$

where T_{11} and T_{12} are the AATSR nadir brightness temperatures (BT) for the 11 and 12 micron channels respectively; $a_{f,i,p,w}$, $b_{f,i}$, $c_{f,i}$ are retrieval coefficients depending on: surface type (i), fractional vegetation cover (f), precipitable water (pw), and time of day (currently for lakes only); and $p(\theta)$ is the satellite zenith view pointing angle which for the new retrieval has been set to unity as little is understood of its effect.

What is interesting about this method is that the emissivity and atmospheric transmission terms have been eradicated from its working form. Instead the impact of these variables has been wrapped up in the coefficients which, for the original and currently operational form of the algorithm, were derived from a

regression analysis for the varying scenarios of biome classification, FV, PW and whether the image was a daytime or night-time scene (Prata 2002). These coefficients have had to be recalculated to correspond to the land classes identified in the new dataset. As of yet these have not been calculated using a regression analysis, instead the land class maps were correlated. Where there was a strong correlation between one of the new surface types and one of the old surface types the coefficients were mimicked. For some cases it the new classes had strong correlations with 2 of the old classes, here the coefficients were averaged with weight if necessary. There were no cases where the new classes showed strong correlation with more than 2 old classes. It has been recognised that this method is not scientifically sound, but it has been shown to improve retrievals and until regression analysis is complete they have been deemed sufficient for investigation.

2.2 The SEVIRI LST Algorithm

The SEVIRI-LST product under consideration is that provided by the Land Surface Analysis- Satellite Application Facility (LSA-SAF) operational LST product (Trigo, et al. 2009), that is:

$$LST = \left(A_1 + A_2 \frac{1 - \varepsilon}{\varepsilon} + A_3 \frac{\Delta \varepsilon}{\varepsilon^2} \right) \frac{T_{10.8} + T_{12.0}}{2} + \left(B_1 + B_2 \frac{1 - \varepsilon}{\varepsilon} + B_3 \frac{\Delta \varepsilon}{\varepsilon} \right) \frac{T_{10.8} - T_{12.0}}{2} + C + \Delta LST \quad (2)$$

where $T_{10.8}$ and $T_{12.0}$ are the TOA-BTs for SEVIRI channels 10.8 μ m and 12 μ m respectively, ε is the average of the two channels surface emissivity, $\Delta \varepsilon$ the difference between them, A_j , B_j ($j = 1, 2, 3$) and C are the GSW coefficients dependant on water vapour and view angle and ΔLST is the model error of the algorithm. Although this looks quite different to the previous formulation the principle components are the same. The algorithm is dependent on a linearization of the TOA-BTs with the surface temperature and the controlling factors are the surface emissivity, atmosphere and satellite view-angle.

As with the AATSR algorithm the coefficients were calculated using a regressive analysis technique. Synthetic $T_{10.8}$ and $T_{12.0}$ were obtained from radiative transfer simulations performed over 90 atmospheric profiles covering a wide variety of atmospheric conditions. When compared with an independent dataset of radiative transfer simulations the algorithm and it's coefficients were found to be bias free, although random errors tended to increase with increasing water vapour content and at high view-angles (Trigo, et al. 2008). For the operational LST

¹ Also presented in these proceedings

product the water vapour database used is that provided by the European Centre for Medium-Range Weather Forecasts (ECMWF) (Andersson, et al. 2005).

The channel surface emissivity is calculated from an average of bare-ground and fully vegetated emissivity's weighted by the fractional vegetation cover (FVC²) and by the fraction of water within the pixel. In a similar fashion to the AATSR algorithm, the emissivity extremes are selected from a look-up-table (Peres and DaCamara 2005) in accordance to a land-classification map, in this case it is the International Geosphere-Biosphere Programme land cover map (Belward 1996). The FVC data used is another product produced by Land-SAF from SEVIRI/Meteosat and corresponds to a 5-day composite updated daily (Garcia-Haro and Sommer 2005). Hence, the input emissivities, ε_{eff_IRn} , are calculated using equations

$$\varepsilon_{LAND_IRn} = \varepsilon_{veg_IRn} FVC + \varepsilon_{bg_IRn} (1 - FVC) \quad (3)$$

$$\varepsilon_{eff_IRn} = \varepsilon_{LAND_IRn} F_{Land} + \varepsilon_{WATER_IRn} (1 - F_{Land}) \quad (4)$$

where, ε_{veg_IRn} and ε_{bg_IRn} are the previously assigned emissivity values for fully vegetated (FVC=1) and bare-ground (FVC=0), ε_{WATER_IRn} is the emissivity value for water and F_{Land} is the fraction of land within the pixel.

2.2 Key Differences

There are two fundamental differences between the LST retrievals which should be addressed. The first is the physical differences resulting from the difference in orbit between the two instruments. The geostationary SEVIRI LST measurements have a larger pixel size, 9km² at nadir up to ~20-30m² towards the rim of the disc compared to the 1km² resolution of the AATSR measurement. This is made more complicated still when one considers the spatial distribution of the radiance density that makes up each pixel which is not uniform. The difference in viewing geometry will also play a role in differing measurements, essentially the instruments "see" different surfaces which could explain discrepancies in data, highlighted later in this document.

Secondly there are obvious algorithmic differences both in terms of formulation and in the choice of auxiliary data. The formulations are not as different as they appear when comparing the equations. Essentially they have both used a regression analysis to derive coefficients to drive a linear fit of the differences in

BT between two spectrally close TIR channels, thus should have equally justified results. The choice in auxiliary data will play a significant role, as will be shown later in this document the auxiliary data drives the retrieval, thus misrepresentation of a surface can drastically effect the accuracy of the retrieval.

3 METHOD OF INVESTIGATION

3.1 Regions Investigated

This research has been carried out over two 10⁰x10⁰ regions within the SEVIRI footprint, namely Spain and Portugal (latitude range 35N-45N, longitude range 9W-1E) and Namibia (latitude range 30S-20S, longitude range 14E-24E). Spain and Portugal offers a diverse region of study where the effects of varying topography and surface type and a strong seasonal cycle of vegetation can be assessed. It is also beneficial that this region, the Iberian Peninsula in particular, has been of interest to a number of environmental scientists and is home to many ground stations where in-situ data is available for future analysis. In contrast, Namibia offers a highly homogeneous flat region with virtually no seasonal cycle of vegetation and near constant surface type, bare soil. This gives the ideal situation for LST retrieval and will act as a superb region to assess the problems faced with the differing pixel sizes. Namibia is also home to several ground truth stations for future analysis. This choice also allows for a good inter-comparison of results given that they both have similar SEVIRI view-angles but in opposite directions.

3.2 Construction of a Common Grid

The immediate problem when comparing LST data from SEVIRI and AATSR is the fact that the pixel sizes are different. To overcome this, the data was regridded to a common 0.05°x0.05° grid. This was done by averaging the satellite LST pixels whose centre lay within the 0.05°x0.05° grid box. This allows for much easier comparison of the two datasets however, it does have its weaknesses. For SEVIRI pixels at the view angles being investigated are of the order 10-20km², thus each new pixel is likely made up of 2-3 original pixel, it is very possible that the new pixel is not as spatially representative of the original data as desired. Even in this generous example it can be seen that the SEVIRI LST's actually correspond to a region translated ~2km northwest of the new pixel. It has been identified that as an improvement for future comparisons a weighting corresponding to the fraction of satellite pixel within the new pixel be used.

A second issue to face is the time difference between the AATSR and SEVIRI measurements. This issue has been overlooked in a number of prior works

² This is the same as FV for the AATSR algorithm, but to keep in line with the documentation provided for the SEVIRI algorithm it will take the acronym FVC

of this nature (Trigo, et al. 2008) where they common method has been to choose the closest SEVIRI image which could be out by as much as 10 minutes. Given that the morning AATSR overpass is at ~ 10 a.m. when the surface is heating most rapidly (Gottsche and Olesen 2009), it is quite possible that the LST could change by several degrees, adding an inherent inaccuracy which would skew results. This work used a time interpolation of the SEVIRI LST; a second order LST against time equation for each pixel was created using between three and six SEVIRI LST images. The SEVIRI LST pixel was then calculated to correspond to the AATSR LST time.

4 RESULTS

4.1 General Comments

The overview of this comparison is quite promising, with the vast majority of data within 5K for daytime matchups and within 2K for night-time matchups. As there is no direct dependence on day or night³ in either algorithm this significant difference seems quite irregular. The source of this effect is under debate, one argument is that the lower variation of LST at night removes some of the errors introduced through the spatially averaging the pixels into a common grid. Another argument is that in general, for both LSTs and Sea Surface Temperatures (SSTs), night-time measurements are more accurate, possibly because the lower air temperature lowers the impact of the atmospheric downwelling component in the radiative transfer equation.

4.2 Seasonality

Both locations investigated had strong indications of seasonal dependence upon the difference in retrieval between the two datasets (Figure 1). The effect of the seasonal dependence was consistent for both regions, that is: during the summer months of the relevant hemisphere the AATSR-LST is relatively warmer than the SEVIRI-LST with a sinusoidal progression to the reverse effect in the winter months. This is quite possibly a direct result of differing seasonal cycles in the auxiliary datasets, namely the fractional vegetation data which has the strongest seasonal effect on the retrieval response. This is further supported by the fact that the seasonal cycle is significantly stronger in Spain and Portugal where there is a much greater extent to seasonal vegetation. More investigation into this is required, namely an isolation of the different land classes identified by the auxiliary data as the effect of the fractional vegetation varies for different land classes.

³ Other than for lake LSTs measured by AATSR

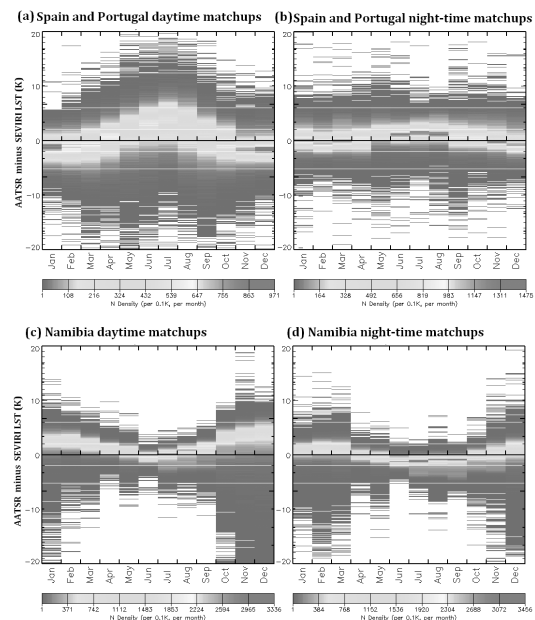


Figure 1 The 2008 seasonal cycle of difference in AATSR-LSTs and SEVIRI-LSTs for (a) Spain and Portugal daytime matchups, (b) Spain and Portugal night-time matchups, (c) Namibia daytime matchups and (d) Namibia night-time matchups

4.3 Viewing Geometry

Figure 2 shows plots of AATSR View angle against the difference in LST retrievals for both daytime and night-time matchups over Spain and Portugal averaged for the months of January and July, respectively. The view-angles have been collated into 2.5° bins and have been represented on the plots such that angles for AATSR looking to the left are to the left of the graph, nadir in the middle and right to the right. In terms of geographical orientation, for daytime matchups AATSR looking to the right is approximately southeast and looking to the left is approximately northwest, and for night-time matchups right is northeast and left is southwest.

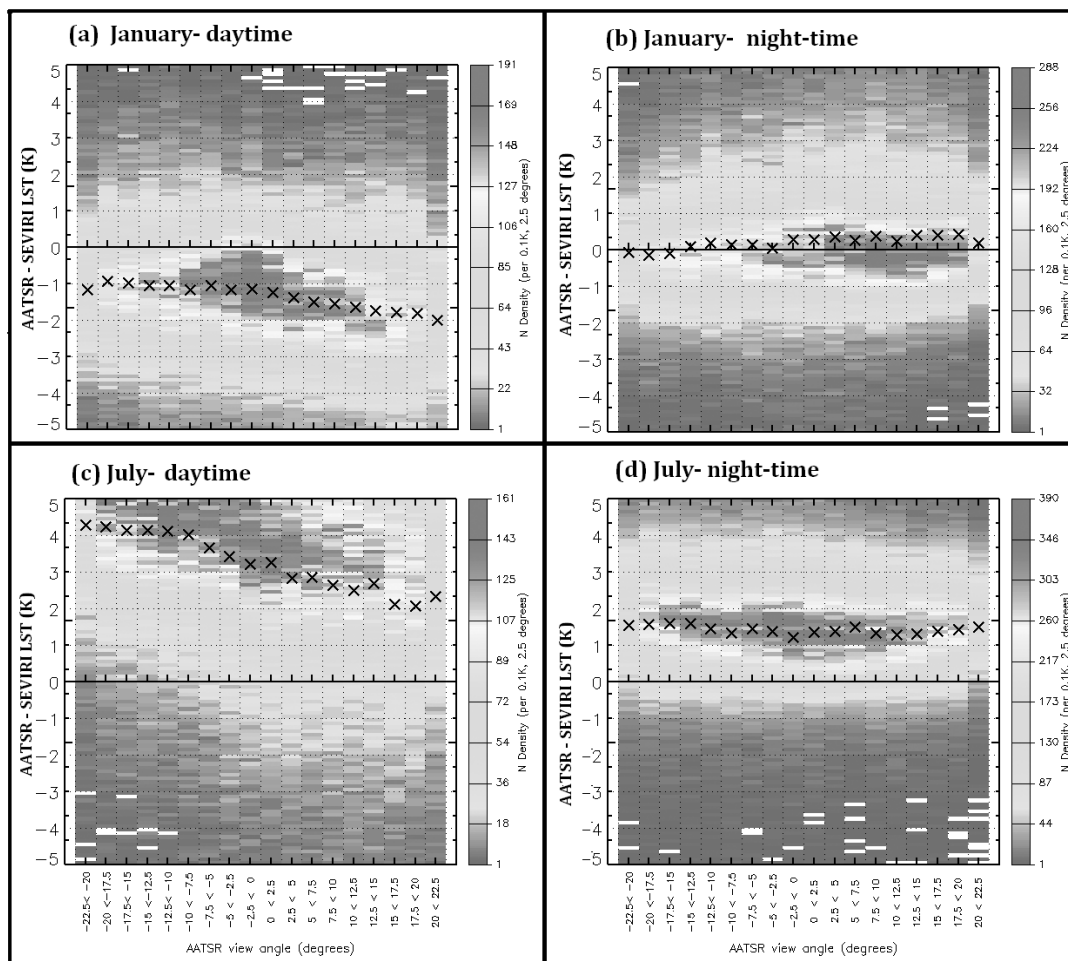


Figure 2 Plots of difference in LST against AATSR view-angle for the labelled months and matchup time. The crosses represent the mean and the greyscaled colourbar gives an indication of the distribution.

An interesting pattern is notable on these plots. For daytime matchups when AATSR is looking to the right, i.e. northwest, the difference in LST retrieval is constant. However, when AATSR is looking to the left, i.e. southeast, there is a gradient such that greater the extent of view angle the lower the relative AATSR temperature. This pattern is absent from the night-time plots.

There is a logical explanation for this effect, for this region SEVIRI is always looking to the north, thus will see the southern facing side of topographical features. In the morning, as the sunrises, these southern facing sides of topographical features warm up quicker due to the greater exposure to sunlight. Thus, when AATSR is looking northwest, like SEVIRI, it sees the warmer southern face of

topographical features, but when it is looking southeast it sees the cooler northern face. This is a prime example of the physical differences in the LST retrievals, it is not that either instrument has a flaw, but rather the instruments are actually seeing different surfaces, thus different LSTs. This is an important point to consider when constructing a common algorithm and will require much deeper investigation. A first step will be to isolate bins of topographical variance and see how the effect varies in order to put some sort of quantitative fit to the difference.

5 SUMMARY AND OUTLOOK

For the most part, AATSR and SEVIRI data are very similar for night-time retrievals, and with encouraging agreement for daytime retrievals, indicating that coefficient based algorithms perform reasonably well. However, there were disagreements exceeding 10K, thus there is still much progression to be made until they sufficiently precise for applications such as data assimilation.

Several sources of disagreement have been identified, and with further investigation could be solved. With regards to differences in the fractional vegetation there is an additional problem to face. It may be possible to attribute the seasonal error to systematic differences in the auxiliary data but to decide which is more reliable is a problem within itself. These fractional vegetation datasets are also satellite products which have only been validated for a limited number of situations, thus it is as hard to justify these as it is the LST products.

Future work will be to incorporate some ground truth data into the comparison. This will not only act as a good baseline but the method of investigation, i.e. looking at the exact satellite pixel footprint, will allow for an interesting investigation into sub-pixel make up. That is, looking at the AATSR pixels which are enclosed within a SEVIRI pixel in the hope that the effects of spatially up-scaling/down-scaling these LST measurements can be better understood. An ideal region for this will be the Namibian ground truth site which is located on highly homogeneous terrain such that there will be very little variation in all aspects of the retrieval.

REFERENCES

- Andersson, E., et al. "Assimilation and Modelling of the Atmospheric hydrological cycle in the ECMWF forecasting system." *Bulletin American Meteorological Society*, Vol. 86, 2005: 387-402.
- Belward, A. "The IGBP-DIS Global 1km Land Cover Data Set. Proposal and Implementation plans." International Geosphere-Biosphere Programme-Data and Information System working paper, Toulouse, 1996.
- Garcia-Haro, F.J., and T.K. Sommer. "Simultaneous land surface temperature-emissivity retrieval in the infrared split window." *International Journal of Remote Sensing*, vol. 26, 2005: 2135-2162.
- Gottsche, F., and F. Olesen. "A simple Physically Based Model of the Diurnal Cycles of Land Surface Temperature." 2009.
- Peres, L.F., and C.C. DaCamara. "Emissivity maps to retrieve land-surface temperature from MSG/SEVIRI." *IEEE transaction in Geoscience and Remote Sensing*, 43, 2005: 1824-1844.
- Prata, A. J. *Land Surface Temperature Measurement from Space: AATSR Algorithm Theoretical Basis Document*. CSIRO report, 2002.
- Trigo, I.F., I.T. Monteiro, F. Olesen, and E. Kabsch. "An assessment of remotely sensed land surface temperature." *Journal of Geophysical Research*, 2008.

Cross-calibration of CBERS-02B/CCD with Terra/MODIS

Caixia Gao¹, Xiaoguang Jiang^{2*}, Xianbin Li³, Xiaohui Li²

¹Graduate University of Chinese Academy of Sciences, Beijing 100049, China

²Academy of Opto-Electronics, Chinese Academy of Sciences, Beijing 100190, China

³Chengdu Guoheng Space Technique Engineering Co., LTD, Chengdu, 610041, China

Email: xgjiang@aoe.ac.cn

ABSTRACT - Radiometric calibration of remote sensing sensor is a prerequisite to quantitative remote sensing. Its precision has a direct impact on the reliability and precision of quantitative application of remote sensing data.

Chinese remote sensing satellite CBERS-02B was launched on September 19, 2007. Its data is an important source for remote sensing application in China, and can be widely used if the CCD instrument is well calibrated. Unfortunately, the CBERS-02B/CCD instrument does not have onboard calibration system and it degrades over time. Furthermore, vicarious calibration could not update radiometric calibration coefficients frequently, because it needs substantial material resources and manpower, and the proper time for vicarious calibration is very limited in a year allowing for climate and weather conditions. Cross-calibration is an effective approach to handle those problems successfully.

Terra/MODIS instrument has stable onboard calibration system whose calibration precision is up to 2%. Besides, there are significant bands correlation between CBERS-02B/CCD and Terra/MODIS. This paper attempts to calibrate the visible and near-infrared channel 1(450-520 nm), channel 2 (520-590 nm), channel 3 (630-690 nm) and channel 4 (770-890 nm) of CBERS-02B/CCD against the channel 3(459-479 nm), channel 4 (545-565 nm), channel 1 (620-670 nm) and channel 2 (841-876 nm) of Terra/MODIS respectively. The radiative transfer model (RTM) method is implemented by using the CBERS-02B/CCD and Terra/MODIS measurements in Dunhuang radiometric calibration test site in October, 2008. Top-of-atmosphere (TOA) reflectance is derived from the well-calibrated MODIS data, and then TOA radiance of CCD data is computed using the TOA reflectance from MODIS data in consideration of the differences in spectral band, solar zenith angle and view angles between the two sensors. The TOA radiance, which is correlated with the sensor digital number (DN) output, determines the in-flight calibration coefficients of CCD. At last, the precision of cross-calibration coefficients of CBERS-02B/CCD is evaluated through detailed analysis. The result of precision analysis shows that the calibration uncertainty is within 4%, and the calibration coefficients of CBERS-02B/CCD are compatible to that obtained synchronously by the more expensive and complicated vicarious calibration approach in Dunhuang radiometric calibration test site in October, 2008.

1 INTRODUCTION

With the development of quantitative application of remote sensing, the accurate characterization of the conversion of image digital counts to radiance values, or absolute calibration, is important for remote sensing as it enables to compare the responses of different satellite sensors, to monitor their changes over time and to provide users with data which do not depend on the sensor. Slater proposed a calibration method using a large homogeneous surface target, which has been proved promising and has been applied to many sensors, such as TM, ETM+, HRVIR (Li Xiaoying, *et al*, 2005). The China-Brazil Earth Resources Satellite (CBERS-02B) was launched by China and Brazil on September 19, 2007. It contains a multi-sensor payload with different spatial resolutions and data collecting frequencies, including a multi-spectral CCD sensor that has five bands: blue, green, red, near-infrared, and short wave near-infrared. However, it is known that there is no accurate in-flight calibrator

based on solar diffuser onboard CBERS-02B (Sheng Chen, *et al*, 2010). Therefore, to improve quantitative application of CBERS-02B/CCD data, in 2007, 2008 and 2009, China Center for Resources Satellite Data and Application (CRESDA) has conducted three vicarious calibration campaigns at test site in Dunhuang, Gansu province in northwest of China.

Although vicarious calibration has been proven successful, it has many limitations for test site, field measurements, and climate and weather conditions, and it is costly and time consuming. Cross-calibration among sensors is one of the alternative methods to acquire post-launch calibration coefficients much easier. It is the process of transferring the calibration of one sensor to other uncalibrated sensors. In comparison with vicarious calibration, cross-calibration can circumvent the rigid requirement of acquiring simultaneous observations of many atmospheric and surface variables. It is thus more feasible to regularly update the calibration coefficients with low cost, as long as a high calibration standard of

the reference sensor is maintained (J.-J.LIU, *et al*, 2004). In recent years, a lot of work on cross-calibration has been conducted. Cabot *et al*. used the Polarization and Directionality of the Earth's Reflectances (POLDER) sensor to cross-calibrate sensors such as AVHRR, SeaStar Sea-viewing Wide Field-of-view Sensor (SeaWiFS), and SPOT-4/Vegetation (VGT) over desert sites in Africa. O'Brien and Mitchell examined the calibration of AVHRR with respect to the well-calibrated Along Track Scanning Radiometer (ATSR-2) onboard the European Remote Sensing satellite (ERS-2) by comparing reflectances over a bright target in a semi-arid environment. Trishchenko *et al*. focused on moderate resolution satellite sensors, including the AVHRRs onboard the NOAA-6,-7,-8,-10,-11,-12,-14,-15,-16 spacecraft, Moderate Resolution Imaging Spectroradiometer (MODIS), VGT, and Global Imager (GLI) on the second Advanced Earth Observing Satellite (ADEOS-2), all with respect to NOAA-9/AVHRR. Rao *et al*. presented results on the cross-calibration of Terra/MODIS and ERS-2/ATSR-2 based on desert sites as common targets (P.M. Teillet, *et al*, 2006).

MODIS is a payload onboard the Terra (EOS AM) Satellite launched into Earth orbit by NASA in 1999, and onboard the Aqua (EOS PM) satellite launched in 2002. The instruments capture data in 36 spectral bands ranging in wavelength from 0.4 μm to 14.4 μm and at varying spatial resolutions (2 bands at 250 m, 5 bands at 500 m and 29 bands at 1 km). Together, the instruments image the entire Earth every 1 to 2 days, also three on-board calibrators (a solar diffuser combined with a solar diffuser stability monitor, a spectral radiometric calibration assembly, and a blackbody) provide in-flight calibration, whose precision is about 2%. Therefore, it had been used as reference to cross-calibrate the AVHRR, ATSR-2, SZ-3/CMODIS, and CBERS-02/CCD. In this paper, CBERS-02B/CCD is cross-calibrated against Terra/MODIS based on Radiative Transfer Modeling (RTM) method to make up for the deficiencies in vicarious calibration and promote quantitative applications of CBERS-02B/CCD data. The four spectral bands of MODIS corresponding to four multi-spectral bands of CBERS-02B/CCD are showed in table 1.

Table 1 CBERS-02B/CCD spectral bands corresponding to Terra/MODIS

CCD bands	Spectral bands/nm	Center wave-length/nm	Resolution /m	MODIS band	Spectral bands/nm	Center wave-length/nm	Resolution /m
1	450-520	490.48	19.5	3	459-479	465.74	500
2	520-590	581.7	19.5	4	545-565	553.74	500
3	630-690	662.4	19.5	1	620-670	646.5	250
4	770-890	830.3	19.5	2	841-876	856.7	250

2 RADIOMETRIC CROSS-CALIBRATION OF CBERS-02B/CCD AGAINST MODIS

In this paper, the cross-calibration is conducted with RTM method (E. F. Vermote and N. Z. Saleous, 2006, G.-M. JIANG and Z.-L. LI, 2009) based on reflectance. Fig. 1 illustrates the approach. For a given CCD spectral band, its top-of-atmosphere (TOA) reflectance is computed by adjusting the observed reflectance from the well-calibrated MODIS data using the radiative transfer theory. This is so called spectral matching process. According to the TOA reflectance of CCD, the corresponding TOA radiance is computed, and then the calibration coefficient for the CCD spectral band is derived.

There are three advantages to using RTM method based on reflectance instead of radiances. The first one is to reduce the difference in spectral responses between reference spectral band and the uncalibrated spectral band. The second one is to remove the cosine

effect of differences solar zenith angles due to time difference between data acquisitions. The last one is to compensate for different values of exo-atmospheric solar irradiance arising from spectral band differences (C.R.N.Rao, *et al*, 2003). Therefore, the method has been widely used, for example, the well-characterized ATSR-2 was used as a reference to determine the calibration of Visible and Infrared Spin Scan Radiometer (VISSR) onboard Geostationary Meteorological Satellite 5 (GMS-5) via RTM. The Multi-channel Visible and Infra-Red Scanning radiometer (MVIRS) onboard China's polar-orbiting meteorological satellite (FY-1D) was cross-calibrated against MODIS using the Second Simulation of Satellite Signal in the Solar Spectrum model (6S) and a Bidirectional Reflectance Distribution Function (BRDF) model, and a calibration accuracy of 5% was obtained (Geng-Ming Jiang, *et al*, 2009).

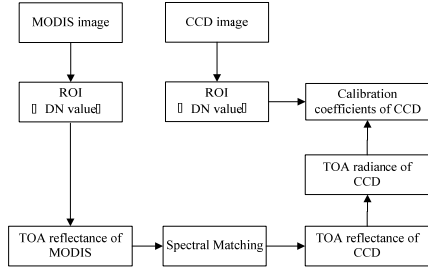


Figure 1. Flow chart of RTM method based on reflectance

2.1 Data Sets

The Dunhuang test site is located in the Gobi desert in northwest China, about 35 km west of the city of Dunhuang (Gansu Province). The calibration area is situated on a stabilised alluvial fan approximate 1.16 km above sea level with clear weather and typically low levels of aerosol loading. The surface comprises cemented gravels, no vegetation, and has preferable stability of surface reflectance. Thus, it is very suitable for conducting cross-calibration.

The data sets used in the paper are the paired images acquired on October 22, 2008 from MODIS and CBERS-02B/CCD in Dunhuang test site. The image of MODIS channel 1 and the image of CCD channel 3 in Dunhuang test site are showed as Fig.2.

2.2 Formulations for Cross-calibration

For CCD spectral band i , the relationship between the TOA radiance L_{ic} and the image digital number Q_{ic} is showed as Eq.1.

$$Q_{ic} = G_{ic} * L_{ic} + Q_{ic0} \quad (1)$$

Where G_{ic} is the gain of spectral band i , Q_{ic0} is the offset. Thus, the TOA radiance L_{ic} can be expressed as Eq. 2 according to Eq. 1.

$$L_{ic} = \Delta Q_{ic} / G_{ic} \quad (2)$$

The TOA reflectance ρ_i related to the TOA radiance L_i is expressed as Eq.3 (Li Xiaoying, *et al*, 2005).

$$\rho_i = \pi L_i d^2 / E_{0i} \cos(\theta) \quad (3)$$

Where d is the earth-sun factor, E_{0i} is extra atmospheric equivalent solar irradiance at the mean distance of the earth and sun, θ is solar zenith.

For CCD spectral band i , Eq. 4 can be acquired according to Eq. 3 and Eq. 2.

$$\Delta Q_{ic} = G_{ic} \rho_{ic} (E_{0i} \cos(\theta))_c / (\pi d^2) \quad (4)$$

For MODIS spectral band i , the TOA reflectance ρ_{im} is expressed as Eq.5 (Li Xiaoying, *et al*, 2005).

$$\rho_{im} * \cos \theta_m = (Q_{im} - m_{i0}) * m_i \quad (5)$$

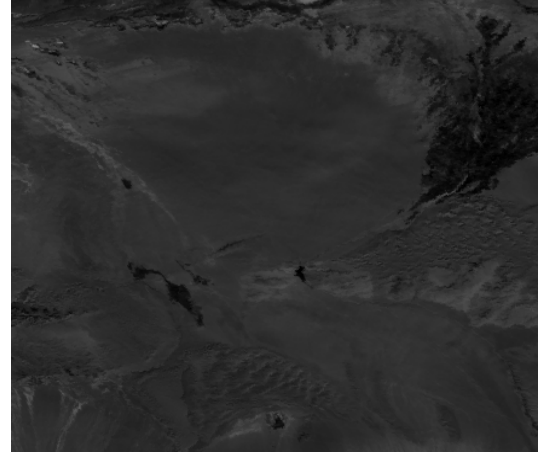
Where θ_m is solar zenith angle, Q_{im} is the digital number of MODIS image, m_i , m_{i0} are the reflectance calibration coefficients, and are available in the MODIS header file ($m_{i0} = 0$).

The cross-calibration formulation (Eq.6) for CCD spectral band i based on reflectance can be obtained via dividing Eq. 4 by Eq. 5.

$$Q_{ic} = \frac{\rho_{ic}}{\rho_{im}} * \frac{(E_{0i} \cos \theta)_c}{\pi d^2 \cos \theta_m} * m_i * Q_{im} * G_{ic} + Q_{ic0} \quad (6)$$

Where ρ_{ic}/ρ_{im} is the spectral matching factor of band i for CCD and MODIS.

(a)



(b)

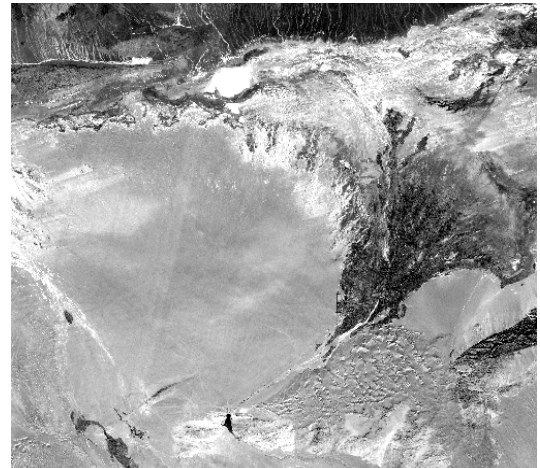


Figure 2. The paired images of MODIS (a) and CBERS-02B CCD (b)

2.3 Computation of Spectral Matching Factor

As showed in Fig. 3, there are significant difference in the spectral response functions between MODIS and CCD. A study by Teillet (2001) shows that the differences in relative spectral response profiles between the reference spectral band and that of uncalibrated sensor have effects on measured TOA reflectance. In order to solve the problem, spectral band matching factor should be computed, which is defined as the ratio of TOA reflectance of the reference spectral band to that of the uncalibrated spectral band in Eq. 6.

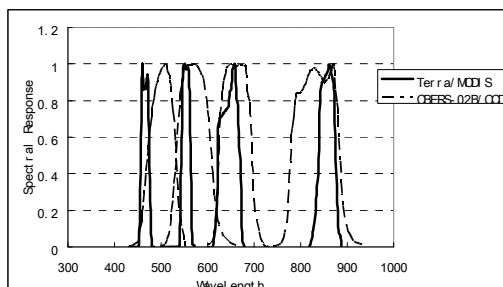


Figure 3. Spectral response profiles

In most researches, spectral band matching factor was calculated with synchro surface data. In this paper, a new method independent of synchro surface data is put forward to compute spectral band matching factor. For the paired images used for cross-calibration, it is assumed that the surface and atmospheric condition did not change during the imaging time span. The spectral band matching factor is generated by simulating targets spectrum via 6S. During the simulation, the reflectance varies from 0.14 to 0.30 with 0.02 as the simulation step, and the standard mid-latitude summer model atmosphere is adopted with a continental aerosol model and visibility of 23 km. Thus, for a paired spectral band i , a serial of TOA reflectances of CCD and MODIS are simulated via 6S model under the viewing geometry showed in tab. 2. Furthermore, the TOA reflectances of CCD are fitted against those of MODIS by linear regression, and the slope of fitted line is the matching factor for spectral band i . The extra atmospheric equivalent solar irradiances and the spectral band matching factors are showed in tab. 3 and tab. 4.

Table 2 Viewing geometry

	MODIS	CCD
Solar zenith	52.41°	52.26°
Solar azimuth	106.46°	347.43°
Sensor zenith	5.38°	-0.49°
Sensor azimuth	-78.76°	170.08°

Table 3 The extra atmospheric equivalent solar irradiances/
 $W \cdot m^{-2} \cdot \mu m^{-1}$

	MODIS	CCD
Blue band	2035.6	1919
Green band	1886.9	1812
Red band	1602.1	1523
Near infrared band	973.88	1042

Table 4 Spectral band matching factors

	Spectral matching factor
Blue band	1.062
Green band	1.036
Red band	1.032
Near infrared band	0.932

2.4 Cross-calibration Results

In order to derive the cross-calibration coefficients, a common calibration area is selected, with a coverage of 6*6 pixels in MODIS image at 250 m spatial resolution, and 75*75 pixels in CCD image, respectively (Fig.4), and the top left corner of the area is located at 40.25° N, 94.25° E. Its mean DN values are showed in tab. 5.

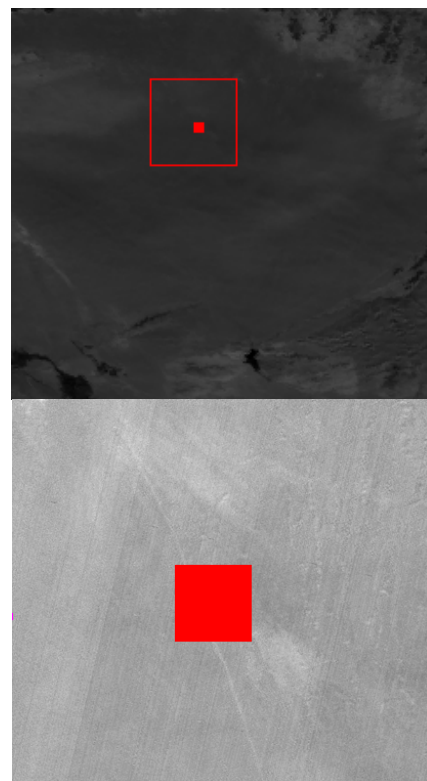


Figure 4. Calibration area in MODIS image of channel 1 and CCD image of channel 3

Table 5 The mean *DN* values of calibration site

	Blue band	Green band	Red band	Near infrared band
MODIS	2872.44	3513.67	2610.47	4521.03
CCD	73.41	59.39	101.57	85.01

Based on the mean *DN* values of the calibration site, spectral band matching factors, and reflectance calibration coefficients of MODIS in tab.6, the calibration coefficients of CCD spectral bands (tab.7) can be derived according to Eq. 6.

Table 6 Calibration coefficients of MODIS

Band	Gain	Bias
Blue band	0.00004081	0.0
Green band	0.00003502	0.0
Red band	0.00005078	0.0
Near infrared band	0.00003102	0.0

Table 7 The derived calibration coefficients of CCD

	Blue band	Green band	Red band	Near infrared band
Gain	0.9620	0.8050	1.5263	1.9543

3 UNCERTAINTY ANALYSIS

There are many factors affecting the precision of cross-calibration, but it is difficult to rigorously quantify them. In this paper, a rough estimation of potential of errors is listed as follows:

1. The uncertainty of MODIS calibration: The uncertainty of MODIS calibration is about 2% (Andrew K, *et al*).

2. The BRDF correction: The BRDF correction which is neglected in the paper, is one of the most critical steps in cross-calibration process. Generally, its error is about 2% when viewing zenith angle is less than 30°.

3. The uncertainty of 6S model: Generally speaking, the error of 6S model is estimated about 2%.

4. Atmospheric condition (Gao Hailiang, *et al*): Continental aerosol model is used when spectral matching factors are derived via 6S model in this paper. However, it could incur error in calibration coefficients because the aerosol type of Dunhuang test site is situated between continental model and desert model. Thus, in order to analyze the effect of aerosol type, new calibration coefficients for CCD spectral bands are derived with desert aerosols model, and the relative errors are also computed (tab.8). Similarly, change the visibility ± 10 km to analyze the effect on calibration coefficients (tab.9). The results demonstrate that relative errors caused by aerosol type and visibility are all within 1%.

5. Image co-registration error: Any inaccurate registration between the images acquired by the two sensors introduces error to the calibration. Given the exceptional uniformity of the surface in the central region of the Gobi desert, the maximum deviation of digital numbers from the two sensors is less than 1%.

From the detailed analysis above, the total uncertainty for the calibration method is within 4%, which is calculated with square root method.

4 VALIDATION

The cross-calibration procedure involves several steps, each of which may incur errors. To validate the results, the gains of the cross-calibration are compared with those of vicarious calibration on October, 2008 released by CRESDA in Dunhuang (tab.10). It is demonstrated that the gains of cross-calibration are quite consistent with those of vicarious calibration, and the relative error between them is within 4% except that of near infrared band, which may be caused by the uncertainty of spectral matching factor due to the limited band coincidence.

Table 8 The variations caused by aerosol type

	Blue band	Green band	Red band	Near infrared band
Gain of CCD	0.9694	0.8034	1.5293	1.9488
Relative error	0.77%	-0.20%	0.20%	-0.28%

Table 9 The variations caused by visibility

		Blue band	Green band	Red band	Near infrared band
Visibility decreasing by 10 km	Gain of CCD	0.9594	0.8058	1.5338	1.9587
	Relative error	0.27%	0.10%	0.49%	0.23%
Visibility increasing by 10 km	Gain of CCD	0.9639	0.8081	1.5278	1.9555
	Relative error	0.20%	0.39%	0.1%	0.06%

Table 10 Relative error of calibration coefficients between cross-calibration and vicarious calibration

	Blue band	Green band	Red band	Near Infrared band
Cross-calibration	0.9620	0.8050	1.5263	1.9543
Vicarious calibration	0.9282	0.8230	1.5066	1.7484
Relative error	3.64%	2.19%	1.31%	11.78%

5 SUMMARY

In this paper, MODIS is selected as a reference sensor to cross-calibrate CBERS-02B/CCD with RTM method. To account for discrepancies in spectral coverage and viewing geometries between the two sensors, spectral matching factors are computed by regression method, instead of using synchro measurements. Furthermore, through detailed error analysis, it is found that the total uncertainty for the cross-calibration coefficients are all within 4%, and among the various influencing factors, aerosol type and visibility have little effect on calibration coefficients. Therefore, it is demonstrated that cross-calibration doesn't need accurate atmospheric observations. At last, validation results demonstrate that our cross-calibration method performs well and the calibration coefficients are reliable except that of near infrared band. Our study indicates that the cross-calibration approach can provide a valuable "contemporary" calibration for CBERS-02B/CCD in visible spectral bands based on the excellent radiometric performance of MODIS.

In order to further improve cross-calibration precision, following strategies should be taken into consideration :

(1) Because atmospheric condition is essential for cross-calibration, proper data source should be used to reduce the error caused by the difference in atmospheric condition.

(2) In order to reduce the error caused by BRDF correction, the calibration area should have preferable stability of surface reflectance.

(3) Cross-calibration should be performed with as many calibration sites as possible by linear fitting if conditions permitted.

ACKNOWLEDGEMENTS

This work was supported by The National High Technology Research and Development Program of China (no. 2008AA121800)

REFERENCES

Andrew K. Heidinger, Changyong Cao and Jerry T. Sullivan, 2002, Using moderate resolution imaging spectrometer (MODIS) to calibrate advanced very high resolution radiometer reflectance channels. *Journal of Geophysical*

Research, 107 (D23), 4702.

C.R.N.Rao, C.Cao, and N.Zhang, 2003, Inter-calibration of the moderate-resolution imaging spectroradiometer and the along-track scanning radiometer-2. *International Journal of Remote Sensing*, 24(9), 1913-1924.

E. F.Vermote and N. Z. Saleous, 2006, Calibration of NOAA16 AVHRR over a desert site using MODIS data. *Remote Sensing of Environment*, 105(3), 214-220.

Geng-Ming Jiang, Hao Yan, and Ling-Ling Ma, 2009, Intercalibration of S_VISSR/FY-2C infrared channels against MODIS/Terra and AIRS/Aqua channels. *IEEE Transactions on Geoscience and Remote Sensing*, 47(5), 1548-1558.

G.-M. JIANG and Z.-L. LI, 2009, Cross-calibration of MSG1-SEVIRI infrared channels with Terra-MODIS channels. *International Journal of Remote Sensing*, 30(30), 753-769.

Gao Hailiang, Gu Xingga, Yu Tao, Li Xiaoying, Cheng Tianhai, Gong Hui, and Li Jiaguo, 2009, Radiometric Calibration for HJ-1A Hyper-Spectrum Imager and Uncertainty Analysis. *Acta Photonica Sinica*, 38(11), 2826-2833.

J.-J.LIU, Z.LI, Y.-L.QIAO, Y.-J. LIU, and Y.-X. ZHANG, 2004, A new method for cross-calibration of two satellite sensors. *International Journal of Remote Sensing*, 25(23), 5267-5281.

Li Xiaoying, Gu Xingfa, Min Xiangjun, Yu Tao, Fu Qiaoyan, Zhang Yong, and LI Xiaowen, 2005, Radiometric cross-calibration of the CBERS-02 CCD camera with the TERRA MODIS. *Science in China Ser. E Engineering and Materials Science*, 48(S2), 44-60.

P.M. Teillet, B.L. Markham, and Richard R. Irish, 2006, Landsat cross-calibration based on near simultaneous imaging of common ground targets. *Remote Sensing of Environment*, 102(2), 264-270.

P.M. Teillet, J.L. Barkerb, 2001, Radiometric cross-calibration of the Landsat-7 ETM+ and Landsat-5 TM sensors based on tandem data sets. *Remote Sensing of Environment*, 78(1-2), 39-54.

Sheng Chen, Chiu Long, Hui Lin, Yang Hong, Kin Yeung, and Junjun Hu, 2010, Cross-calibration of Landsat-5 TM and Multi-Spectral CBERS-02B CCD Sensors based on Tandem Data Sets for Southern China. Available online at: http://hydro.ou.edu/Publications_all.html.

Study of Remote Sensing Validation System

Xiaoguang Jiang¹, Xianfeng Song^{2*}, Zhao-Liang Li^{3,4}, Xianbin Li⁵, Xiaohuan Xi¹,
Ziyang Li¹, Xiaohui Li¹

¹Academy of Opto-Electronics, Chinese Academy of Sciences, Beijing 100190, China

²Graduate University of Chinese Academy of Sciences, Beijing 100049, China

³Institute of Geographic Sciences and Natural Resources Research, Chinese Academy of Sciences, Beijing, 100101, China.

⁴TRIO/LSIIT(UMR7005 CNRS)/ENSPS, Bld Sebastien Brant, BP10413, 67412 Illkirch, France

⁵Chengdu Guoheng Space Technique Engineering Co., LTD, Chengdu, 610041, China

Email : song.osgeo@gmail.com

ABSTRACT This paper focuses on the study of the remote sensing validation and validation system. First of all, the category of remote sensing validation is defined in this paper. Validation is to validate the authenticity and accuracy of remote sensing products in independent way. Remote sensing validation includes not only the data products validation which includes the validation of radiant feature, spectral feature and geometrical feature, but also the retrieval products validation and application products validation. Second, the new concept, remote sensing validation system, is proposed. The remote sensing validation is a very complicated system, and should be considered in the systematic viewpoint. Then, the general framework, software structure and functions of validation system are studied and put forward. The validation system is composed of validation fields module, synchronous data acquirement module, synchronous data processing module, data storage and management module, data scaling module, validation modules of remote sensing data products, retrieval products and application products. And finally the exterior and interior interfaces of remote sensing validation system are presented. The main functions of remote sensing validation system are the synchronous data (synchronous field measurement and remote sensing data and products) acquirement; synchronous data processing; data storage and management; scaling of field measurement data, remote sensing data and products; accuracy validation and analysis of remote sensing data, remote sensing retrieval products and remote sensing application products.

1 INTRODUCTION

Remote sensing is a very complicated course. It is influenced by many factors, such as feature of remote sensing sensor, radiant transmission characteristic of atmosphere, work environment of remote sensing platform, data transmission, data reception, data processing, and property of observed object etc. Whether the received data is consistent with the design specifications? Can the received data meet the demands of remote sensing applications? How about the accuracy of the data products, retrieval products and application products of remote sensing? It is essential to carry out the remote sensing validation to assess the data quality and application potential.

Validation is an indispensable and effective approach to value remote sensing products. It is the significant link between remote sensing data and information. Research on remote sensing validation is very important for sensor development, data quality analysis and remote sensing products verification. This paper focuses on the study of remote sensing validation and validation system. Different from the

previous work done by other researchers, we study the validation from the viewpoint of systematic engineering considering that validation is involved with many aspects as talked about. Validation is not just a single and simple course. It is complicated system. Validation system is the important part of whole earth observation system. It has close relationship with other systems of earth observation system (Zhao-Liang Li, *et al*, 2006). Therefore, the study of validation and validation system is of great importance.

2 RESEARCH CONTENTS OF REMOTE SENSING VALIDATION

As talked above, remote sensing validation is a comprehensive course, it deals with many aspects. As a whole, the main research contents of remote sensing validation include following aspects:

- (1) General design of validation system: according to the needs of earth observation, the relationships among the sub-systems in remote sensing ground system from the viewpoint of system, carry out

the research of top level design of remote sensing validation system, form general framework of remote sensing validation system, and lay a good foundation for the establishment of remote sensing validation system.

- (2) Study of validation field: according to the characteristics of sensors (scope of wavelength, resolution etc.) and remote sensing products (data products, retrieval products and application products to be validated), study the conditions, requirement and standard of remote sensing validation fields, set up validation field net (Frederic Baret *et al.*, 2006).
- (3) Carry out the research on theory, method and technology of validation, establish the systematic theory and technical methods, form the criterion and standard of remote sensing validation.
- (4) Research of true value acquirement in pixel scale: study on field measurement point arrangement and sampling strategy, scale effect and scale transformation theory and method of remote sensing products, and the method obtaining the true value of remote sensing products in pixel scale.

3 REMOTE SENSING VALIDATION SYSTEM

3.1 Technical Workflow of Remote Sensing Validation System

Remote sensing validation is to obtain synchronous data from validation fields, process and scale the synchronous data, validate and assess the accuracy of the remote sensing data products in radiance, geometry and spectrum, validate and evaluate the accuracy of remote sensing retrieval products and application products by direct and/or indirect approaches.

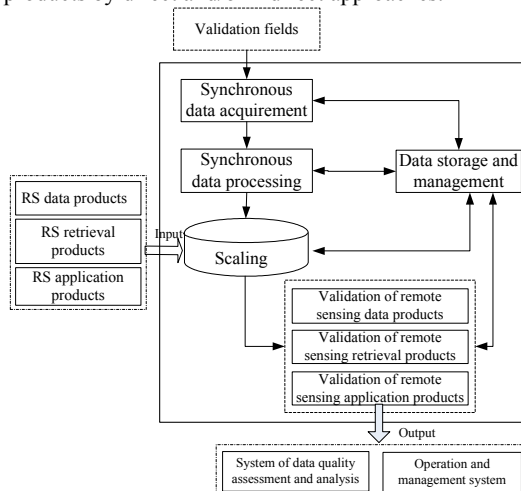


Fig. 1 Workflow of remote sensing validation system

3.2 Framework of remote sensing validation system

Remote sensing validation system is composed of seven modules, i.e. synchronous data acquirement module, synchronous data processing module, data storage and management module, scaling module, module of remote sensing data products validation, module of remote sensing retrieval products validation, and module of remote sensing application products validation.

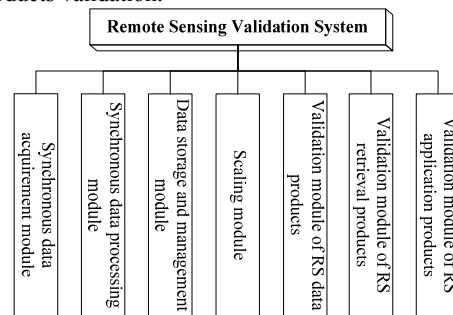


Fig. 2 Framework of remote sensing validation system

3.3 Functions of Remote Sensing Validation System

The functions of remote sensing validation system include synchronous data acquirement and processing, data storage and management, scaling of remote sensing data and products, validation of remote sensing data and products.

3.3.1 Synchronous Data Acquirement

Synchronous data acquirement includes two parts, one is the synchronous field measurement data acquirement which is used for direct validation of remote sensing data and products, the other is synchronous and validated remote sensing data and products which is used for indirect or cross validation of remote sensing data and products.

3.3.2 Synchronous Data Processing

Synchronous data processing includes processing of synchronous field measurement data and various synchronous remote sensing data and products. This function performs data form conversion, data radiant and geometric correction etc. so as to get corresponding data and products to those to be validated.

3.3.3 Data Storage and Management

Data storage and management module is used to save, inquire, search, update and manage all the data in validation system, including synchronous data and products (raw data and products, processed data and products), scaled data and products, to be validated data and products, validation results, and the fundamental geographical data necessary for validation, such as the information of weather,

hydrology, soil, vegetation, geology, relief and spectral database of ground objects etc.

3.3.4 Scaling of Remote Sensing Data and Products

The scales of synchronous field measurement data, synchronous remote sensing data and products, to be validated remote sensing data and products are different and they can't be compared each other. Therefore it is essential to scale all the data to the same scale level. Scaling plays two roles. One is assessing and analyzing the scale effect which occurs when the scale level of data and product is different, scale transformation law, and establishing the models of scale transformation. The other is transforming the synchronous field measurement data, synchronous remote sensing data and products, to be validated remote sensing data and products into identical level so as to compare them each other (Zhao-Liang Li *et al* , 2007, Wu Hua *et al* , 2008).

3.3.5 Validation of Remote Sensing Data Products

Validation of remote sensing data products module perform the validation of remote sensing data products (such as radiance resolution, SNR, dynamic scope, spatial resolution, spatial orientation accuracy, geometrical distortion of image, MTF, central band-length, band width, spectral response function etc.) in radiance, geometry and spectrum accuracy.

3.3.6 Validation of Remote Sensing Retrieval Products

Validation of remote sensing retrieval products perform the accuracy valuation of remote sensing retrieval products, such as object radiance, object reflectance, soil moisture, land surface temperature, vegetation index, LAI, aerosol concentration, ground evaporation etc (Jeffery T. Morisette *et al* , 2006).

3.3.7 Validation of Remote Sensing Application Products

Validation of remote sensing application products perform the accuracy valuation and analysis of remote sensing application products in natural resource investigation and management, environment and disaster monitoring and management, such as landuse/cover investigation, estimate of crop growth and crop yield, forest resource survey, grass degeneration monitoring, forest fire monitoring, flood monitoring, drought monitoring, and various geological disaster monitoring etc (Ivan A. Csiszar *et al* , 2006).

3.4 INTERFACES of REMOTE SENSING VALIDATION SYSTEM

3.4.1 Exterior Interfaces

As one part of Remote Sensing Ground System, the remote sensing validation system has interfaces with other systems of Remote Sensing Ground System (as shown in fig. 3)

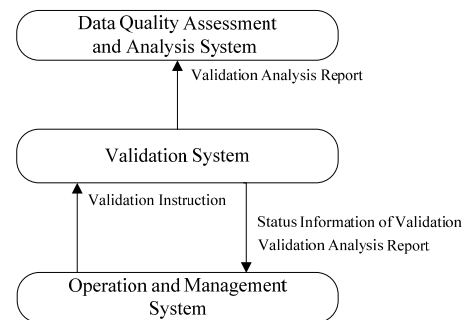


Fig. 3 The exterior interfaces of remote sensing validation system

(1) Interface between validation system and operation and management system

- Receiving the instruction of starting validation task from operation and management system
- Feeding back the status information of validation to operation and management system
- Submitting the validation result report to operation and management system

(2) Interface between validation system and data quality assessment and analysis system

- Submitting the validation result report to data quality assessment and analysis system

3.4.2 Interior Interfaces

There is close relationship among the different modules in remote sensing validation system. The interior interfaces of validation system are shown in fig. 4.

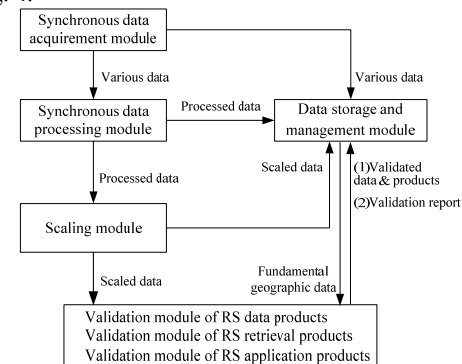


Fig. 4 The interior interfaces of remote sensing validation system

(1) Interface between synchronous data acquirement module and synchronous data processing module

Synchronous data acquirement module transfers all the obtained data (including synchronous field measurement data, synchronous remote sensing data and products) to synchronous data processing module.

(2) Interface between synchronous data acquirement module and data storage and management module
Synchronous data acquirement module transfers all the obtained data (including synchronous field measurement data, synchronous remote sensing data and products) to data storage and management module.

(3) Interface between synchronous data processing module and data storage and management module
Synchronous data processing module transfers the processed synchronous field measurement data, synchronous remote sensing data and products to data storage and management module.

(4) Interface between synchronous data processing module and scaling module
Synchronous data processing module transfers the processed synchronous field measurement data, synchronous remote sensing data and products to scaling module.

(5) Interface between scaling module and validation modules of RS data products, retrieval products, application products

Scaling module transfers the scaled remote sensing data products, remote sensing retrieval products and remote sensing application products to corresponding validation modules.

(6) Interface between scaling module and data storage and management module

Scaling module transfers the scaled remote sensing data products, remote sensing retrieval products and remote sensing application products to data storage and management module.

(7) Interfaces between data storage and management module and validation modules

- Data storage and management module provides fundamental geographical information to validation modules.
- Validation modules submit validation result reports to data storage and management module.
- Validation modules transfer the validated remote sensing data and products to data storage and management module.
-

4 CONCLUSION

Remote sensing validation and validation system are studied in this paper. First, a more comprehensive definition of remote sensing validation is given. Second, the new concept, remote sensing validation system, is proposed. Then, the general framework, software structure and functions of remote sensing validation system are studied and put forward. And finally the exterior and interior interfaces of remote sensing validation system are presented.

Validation system is the important part of whole earth observation system. Research on remote sensing validation system is very essential for sensor development, data quality analysis and remote sensing products verification.

Remote sensing validation system is very complicated. Only a primary study is carried out and a general framework is given in our paper. In validation key technology and validation system construction there are still a lot of further work needed to be done so that the remote sensing validation system of region and world can be established and improved gradually.

ACKNOWLEDGEMENTS

This work was supported by The National High Technology Research and Development Program of China (no. 2008AA121800) and Knowledge Innovation Project of Chinese Academy of Sciences (KGCX3 - SYW - 401) .

REFERENCES

- Frederic Baret et al. Evaluation of the Representativeness of Networks of Sites for the Global Validation and Intercomparison of Land Biophysical Products: Proposition of the CEOS-BELMANIP. IEEE TRANSACTIONS ON GEOSCIENCE AND REMOTE SENSING, VOL. 44, NO.7, 2006.
- Ivan A. Csizar et al. Validation of Active Fire Detection from Moderate-Resolution Satellite Sensors: The MODIS Example in Northern Eurasia. IEEE TRANSACTIONS ON GEOSCIENCE AND REMOTE SENSING, VOL. 44, NO.7, 2006.
- Jeffery T. Morisette et al. Validation of Global Moderate-Resolution LAI Products: A Framework Proposed Within the CEOS Land Product Validation Subgroup. IEEE TRANSACTIONS ON GEOSCIENCE AND REMOTE SENSING, VOL. 44, NO.7, 2006.
- Li Zhaoliang, Jiang Xiaoguang et al. Research on Remote Sensing Validation System. Feasibility Report, 2006.
- Li Zhaoliang, Wu Hua et al. Surface Temperature and Emissivity Scaling. Final Research Report, 2007.
- Wu Hua, Jiang Xiaoguang, Xi Xiaohuan, Tang Lingli, Li Zhaoliang. Research on Scale Effect and Transformation of Remote Sensing Information [J]. Journal of Remote Sensing (Chinese). NO.2, 2009.

Cross-calibration of HJ-1 CCD with Terra MODIS on Dunhuang Observations

Lingling Ma^{1,*}, Shi Qiu², Xinhong Wang¹, Lingli Tang¹

1. Academy of Opto-Electronics, Chinese Academy of Sciences, Beijing, China

* Email: llma@aoe.ac.cn

2. Laboratoire des Sciences de l'Image, de l'Informatique et de la Télédétection (UMR7005), Boulevard Sébastien Brant, BP10413, 67412 Illkirch, France

ABSTRACT -This paper deals with the cross-calibration of the visible and near-infrared spectral channels of the CCD onboard the Small Satellite Constellation for Environment and Disaster Monitoring (HJ-1) against the channels of MODerate resolution Imaging Spectroradiometer (MODIS) onboard Terra. Two types of cross-calibration method, including Ray-Matching (RM) method and Radiative Transfer Modelling (RTM) method, are introduced and tested using the HJ-1/CCD and Terra/MODIS images acquired on Dunhuang Gobi desert area on August 28th 2009. The top-of-atmosphere (TOA) reflectance of MODIS channels and CCD correspondences are assumed to be the same in RM method. While in the RTM method, TOA radiances of two sensors are both simulated by using radiative transfer model. The ratio of the two simulated radiances acts as the spectral matching factor which contains the differences induced by observing geometry and instrumental spectral response. Results of four bands were compared between the two cross-calibration methods based on vicarious calibration experiment data obtained at the same day. The calibration results for band 1, 3 and 4 of CCD using RTM method is closer to vicarious calibration results, which is because the RTM method has considered the observing geometry difference and spectral response difference. The opposite result for band 2 of CCD may indicate that the uncertainty of 6S model itself and the uncertainties of input parameters to 6S model exceed the influences due to the observing geometry and spectral response differences.

1 INTRODUCTION

The Small Satellite Constellation for Environment and Disaster Monitoring (HJ-1), designed by China, was launched on September 6, 2008. It contains a multi-spectral CCD sensor that has four bands within the range of visible to infrared: band 1 (B1, blue, 0.43-0.52 μm), band 2 (B2, green, 0.52-0.60 μm), band 3 (B3, red, 0.63-0.69 μm), band 4 (B4, near-infrared, 0.76-0.90 μm). The CCD sensor has spatial resolution 30m (<http://www.cresda.com>). For lack of onboard calibration instrument, the updates of calibration coefficients are provided by using vicarious calibration method to HJ-1 merely once a year, which is difficult to satisfy the requirement of quantitative remote sensing. Cross-calibration has been developed since recent years, with which a dedicated sensor can be calibrated on a certain spectral channel to another sensor which has high accuracy calibration coefficients. The advantage of cross-calibration method against vicarious calibration is its high economy since radiometrically stable site and simultaneous ground measurements are no longer necessary. Most of the methods used for cross-calibration can be categorized into two types: the Ray-Matching (RM) method and the Radiative Transfer Modelling (RTM) method (Jiang et al., 2008).

As we know, the Moderate Resolution Imaging Spectroradiometer (MODIS) onboard the polar-orbit satellite Terra/Aqua is a well calibrated multi-spectral sensor, containing four visible/near-infrared channels ranging from 0.4 μm to 1.0 μm . The radiance data product is accurate to better than 2%. E.F. Vermote et al. (2006) and Heidinger et al. calibrated AVHRR sensor with MODIS reflectance channels. Li et al.(2005) used the MODIS data to cross-calibrate the CCD sensor on board CBERS-02; Tong et al.(2005) used the MODIS data to cross-calibrate the VIRR sensor on board FY-1D[2]; Chen et al.(2008) used five pairs near simultaneous images, which were taken by SPOT4/HRVIR2, Landsat5/TM and Terra/MODIS, to cross-calibrate the Beijing-1 multispectral sensor. The uncertainty of the cross-calibration is between 8% and 9%. As demonstrated in Fig. 1, the CCD1 channels B1, B2, B3 and B4 are overlapped by the MODIS channels. So MODIS data can be used to cross-calibrate the corresponding channels of the CCD onboard HJ-1B. Certainly it should be noted that the spectral gaps over the MODIS spectral range will definitely affect the cross-calibration accuracy.

Table. 1 Spectral band characteristics of the HJ-1B/CCD1 and corresponding channels of Terra/MODIS

CCD1 channel	Spectral Bands /nm	Center wavelength /nm	MODIS channel	Spectral Bands/nm	Center Wave-Length /nm
B1	430-520	495	CH3	459-479	465.74
B2	520-600	564	CH4	545-565	553.74
B3	630-690	658	CH1	620-670	646.5
B4	760-890	827	CH2	841-876	856.7

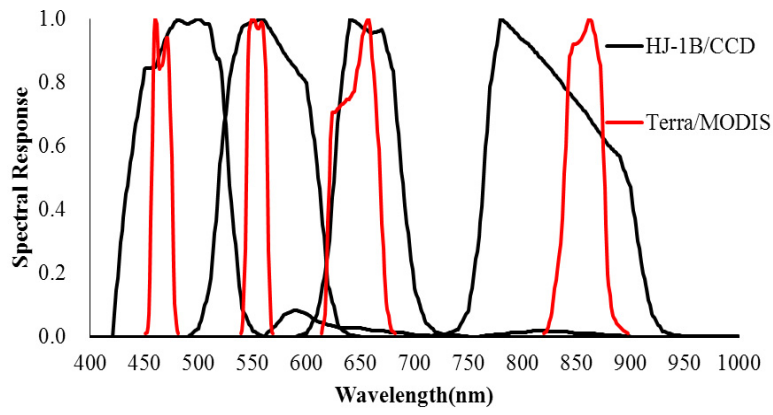


Fig. 1. Spectral responses of the HJ-1B/CCD1 channels and corresponding channels of Terra/MODIS

In this paper, HJ-1B/CCD1 channels (B1, B2, B3, B4) were cross-calibrated against the corresponding channels (CH3, CH4, CH1, CH2) of Terra/MODIS at similar passing time. Two types of cross-calibration method, including Ray-Matching (RM) method and Radiative Transfer Modeling (RTM) method, were introduced and tested using the HJ-1/CCD1 and Terra/MODIS images acquired on Dunhuang Gobi desert area on August, 2009. The results were validated with vicarious calibration coefficients, and the uncertainties in cross-calibration were analyzed.

2 METHODS

2.1 RM method

The RM (Ray-Matching) method simply uses the coincident, co-angled and co-located measurements to transfer the calibration of one well-calibrated instrument to another one. The scheme of cross-calibration of HJ-1B/CCD1 against Terra/MODIS using RM method is displayed on Fig. 2.

The apparent reflectance of reference sensor Terra/MODIS and undetermined sensor HJ-1B/CCD1 are respectively denoted as ρ_{MODIS} and ρ_{CCD} ,

$$\rho_{MODIS} = \frac{\pi L_{MODIS} d^2}{E_{MODIS} \cos \theta_{MODIS}} \quad (1)$$

$$\rho_{CCD} = \frac{\pi L_{CCD} d^2}{E_{CCD} \cos \theta_{CCD}} \quad (2)$$

where L is observing radiance of sensor, θ is the zenith angle of incident beam, d is the distance of the earth from the sun which is related to the date, subscript MODIS or CCD denote the name of sensor. The gain G of CCD1 is computed by,

$$G_{RM} = \frac{DN}{L_{CCD} - B} \quad (3)$$

Here, B is the bias of CCD1 which is assumed invariable. The apparent reflectance of reference sensor and undetermined sensor are assumed to be same in RM method, therefore letting eq. 1 equal to eq. 2, observing radiance of CCD1 is deduced as eq.4,

$$L_{CCD} = \frac{L_{MODIS} E_{CCD} \cos \theta_{CCD}}{E_{MODIS} \cos \theta_{MODIS}} \quad (4)$$

inserting Eq. 4 into Eq. 3, the gain G of CCD1 is acquired:

$$G = \frac{DN}{\frac{L_{MODIS} E_{CCD} \cos \theta_{CCD}}{E_{MODIS} \cos \theta_{MODIS}} - B} \quad (5)$$

with E_{CCD} and E_{MODIS} are in-band solar irradiance at the top of atmosphere within the spectral range.

The RM method does not take into account the spectral differences between two sensors, and the assumption of coincident, co-angled and co-located measurements are hard to acquired, so sometimes it leads to unacceptable errors.

2.2 RTM Method

Observed geometry and spectral response differences of various sensors are considered in the RTM (Radiative Transfer Modeling) method, observing radiances of reference sensor and undetermined sensor are simulated by using Radiative Transfer Model, respectively. The ratio of two simulated radiances is spectral matching factor, denoted as k , when the simulations are based on the same observed area,

$$k = \frac{L_{CCD}}{L_{MODIS}} \quad (6)$$

the differences induced by observed geometry and spectral response are contains in k . Then the gain G of CCD1 is therefore obtained,

$$G_{RTM} = \frac{DN}{k * L_{MODIS} - B} \quad (7)$$

The scheme of cross-calibration of HJ-1B/CCD1 against Terra/MODIS by using RTM method is displayed on Fig.3.

Although the RTM method can account for the spectral differences, the algorithm development is much more complicated, and it is also easily affected by the profile accuracy and the radiative transfer model.

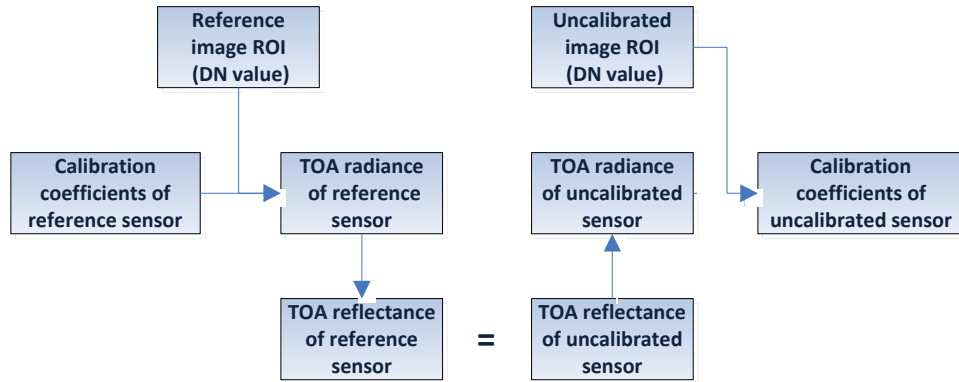


Fig.2. Scheme of cross-calibration of RM method

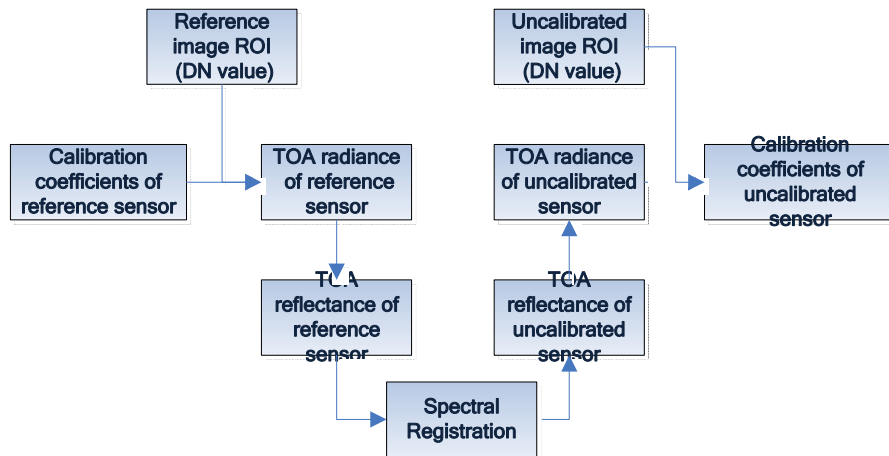


Fig. 3. Scheme of cross-calibration of RTM method

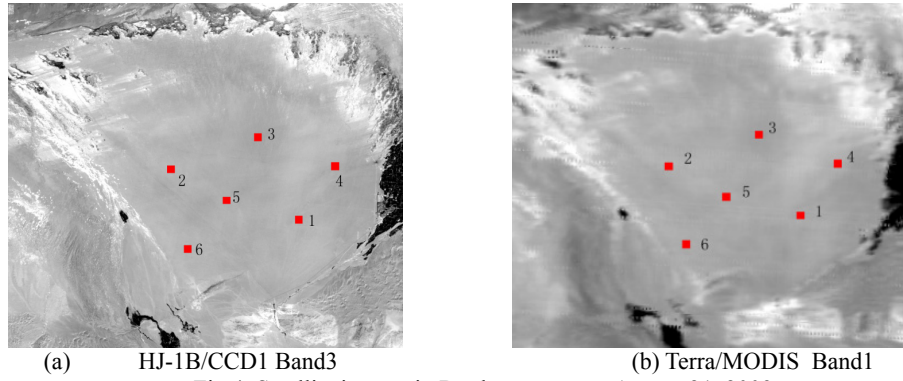


Fig.4. Satellite images in Dunhuang area at August 21, 2009

3 DATA DESCRIPTION AND DATA PROCESSING

3.1 Image description

The remote sensing data used in the paper include a HJ-1B/CCD1 image and corresponding Terra/MODIS image acquired on August 21, 2009, which covers Dunhuang Gobi desert in China. The overall size of the playa is approximately 20 km×30 km, and it is located at an elevation of approximately 1.19 km in a geographical region with reasonably high expectations of clear weather and typically low levels of aerosol loading. The test site has preferable stability of surface reflectance because very homogeneous of surface, therefore it has been in use for vicarious calibration since the mid-1990s (Li, 2005). Fig. 4 illustrates the registered pair of images of HJ-1B/CCD1 and Terra/MODIS. Six corresponding regions are selected in the two images to process, each of which covers about 1.4km×1.4km. The observed geometrical parameters are listed in Table 2, the difference of passing time for two sensors is less than one hour. Geometric correction and relative radiometric correction have been done with the images used in this work.

Table2. Geometrical parameters of HJ-1B/CCD1 and Terra/MODIS

	Passing Time (UTM)	Solar zenith	Solar azimuth	Observed zenith	Observed azimuth
CCD1	4:52	31.51	335.99	21.78	-76.96
MODIS	4:00	33.18	139.51	33.36	98.03

3.2 Data processing using RM method

Considering eq.5, in-band solar irradiance of CCD1 and MODIS at the top of atmosphere are needed, which is expressed as eq. 8,

$$E = \frac{\int_{\lambda_1}^{\lambda_2} E(\lambda) f(\lambda) d\lambda}{\int_{\lambda_1}^{\lambda_2} f(\lambda) d\lambda} \quad (8)$$

where λ is wavelength, λ_1 and λ_2 are the wavelength limits for the band, $f(\lambda)$ is the spectral response function (normalized to 1 at peak) of a given band, $E(\lambda)$ is the solar spectral irradiance, a popular solar model Thuillier (2004) is used here.

Solar spectral irradiances at top of atmosphere within the spectral range of HJ-1B/CCD1 and corresponding Terra/MODIS bands are listed as Table 3.

Table3. TOA Solar spectral irradiances of HJ-1B/CCD1 and corresponding Terra/MODIS bands ($Wm^{-2}um^{-1}$)

	Band 1	Band 2	Band 3	Band 4
CCD1	2035.6	1886.9	1602.1	973.88
MODIS	1902.2	1833.6	1566.7	1077.1

The gain G of CCD1 is easily obtained after introducing TOA Solar spectral irradiances of CCD1 and corresponding MODIS bands, with the assumption of known bias of CCD1.

2.3 Data processing using RTM method

As far as RTM method is concerned, land surface reflectance are synchronously measured and displayed as Fig.5.

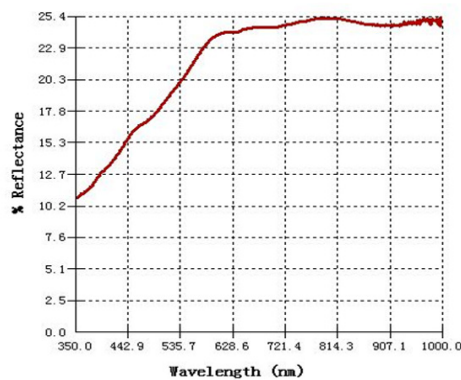


Fig.5. Surface reflectance measured on Aug 28, 2008

The observing radiances of CCD1 and MODIS are respectively simulated based on the same surface and particular responses of each sensor, “mid-latitude summer” is chosen as standard atmosphere in Radiative Transfer Model 6S (second simulation of satellite signal in the solar spectrum). Then spectral matching factors for each channel are calculated and displayed in Table 4. Following the scheme showed in Fig. 2, the calibration coefficients for each channel are calculated using Eq.7.

Table 4. Spectral matching factors (k) of HJ-1B/CCD1 against Terra/MODIS

CCD1	Band 1	Band 2	Band 3	Band 4
MODIS	Band 3	Band 4	Band 1	Band 2
k	0.948	0.999	0.995	1.063

4 RESULTS

Results of calibration coefficients for each channel using RM/RTM methods are displayed in Table 5. To validate the results, the gains of cross-calibration were compared with those of vicarious calibration on August, 2009, released by CRESDA (China Center for Resource Satellite Data and Applications). (<http://www.cresda.com/n16/n1100/n1370/n65245.files/n77968.doc>). The relative errors of spectral bands between cross-calibration and vicarious calibration are also shown as following.

It is demonstrated that the cross-calibration coefficients are close to that of vicarious calibration and the percentages of the difference are mostly less than 10% except for blue band 1, which proves the validity of the cross-calibration methods. The results also demonstrate that the precision for most of the spectral bands based on RTM method are higher than that based on RM method. The sources of uncertainties of RM method include: 1) the differences of spectral responses and observing geometry; 2) atmospheric change for 52 minutes' passing time difference; 3) the uncertainty of reference Terra/MODIS calibration coefficients; 4) the uncertainty of vicarious calibration results. As far as RTM method is concerned, the first uncertain factor is replaced by the uncertainties of 6S model itself and the uncertainties of input parameters to 6S model.

The calibration results for band 1, 3 and 4 of CCD1 using RTM method is closer to vicarious calibration results, which is because the RTM method has considered the observing geometry and spectral differences. The opposite results for band 2 of CCD1 can be explained by the uncertainties of 6S model and its input parameters have been greater than the observing geometry and spectral differences.

Table 5. Results of cross-calibration using RM/RTM methods

CCD1 bands	1	2	3	4
RM method	0.64 (17.2%)	0.736 (9.0%)	1.033 (7.5%)	1.006 (11.2%)
RTM method	0.646 (16.4%)	0.736 (9.1%)	1.041 (6.8%)	1.056 (6.9%)
Vicarious method	0.772	0.8092	1.1170	1.1337

5 CONCLUSIONS

In this paper, the four bands of HJ-1B/CCD1 are cross-calibrated based on the corresponding bands of EOS/MODIS, respectively by the Ray-Matching (RM) method, and the Radiative Transfer Modelling (RTM) method. Through the comparisons to vicarious calibration, results of RTM method are better than RM method, for having considered the observing geometry and spectral differences between the two sensors. But new uncertainties are induced by the radiative transfer model itself and the uncertainties of input parameters, which have caused the worse results for the band 2 of CCD1 using RTM method.

6 REFERENCES

- Vermote, E. F. and Saleous, N. Z., 2006, Calibration of NOAA16 AVHRR over a desert site using MODIS data [J]. Remote Sensing of Environment, 2006, 105, 214-220.
- Heidinger A. K., Cao C., and Sullivan J. T.. 2002, Using Moderate Resolution Imaging Spectrometer (MODIS) to calibrate advanced very high resolution radiometer reflectance channels. Journal of Geophysical Research, 2002, 107 (D23), 4702,.
- Li Xiao-ying, Gu Xing-fa, 2005, Radiometric Cross-calibration of the CBERS-02/CCD and MODIS , Science In China Ser.E Information Sciences, 2005,35, 41-58
- Tong Jin-jun, Qiu Kang-mu, 2005, Radiometric Cross-calibration of the FY1D/VIRR and EOS/MODIS in the Visible and Near-infrared Spectral Bands , Journal of Remote Sensing, 2005.9(4),349-356.
- Jiang, G.M., Yan, H., Ma L.L., 2008, Cross-calibration of MSGI-SEVIRI infrared channels with Terra-MODIS channels, International Journal of Remote Sensing, 2008, Vol.46, No.12, 1-17.
- Chen Zheng-chao, 2008, The Cross Calibration of Beijing-1 Microsatellite Multispectral Sensors, Journal of Astronautics, 2008, 29(3), 637-643.
- Xuan Li, Zhifeng Guo, 2005, Radiometric Cross-calibration of MODIS and CMODIS Based on Dunhuang Test Site, Progress In Electromagnetics Research Symposium , 2005, Hangzhou, China, August 22-26, 642-645
- G. Thuillier, L. Floyd, T. N. Woods, R. Cebula, E. Hilsenrath, M. Hersé and D. Labs, 2004, Solar irradiance reference spectra for two solar active levels, Advances in Space Research V34, Issue 2, 2004, 256-261

Evaluation of land surface temperature and emissivities retrieved from MSG-SEVIRI data with MODIS land surface temperature and emissivity products

Yong-Gang Qian¹, Zhao-Liang Li^{1,2,*}

1 State Key Laboratory of Resources and Environmental Information System, Institute of Geographical Sciences and Natural Resources Research, Beijing, 100101, China

2 LSIT, UdS, CNRS, Bld Sebastien Brant, BP10413, 67412 Illkirch, France

** Corresponding author: Zhao-Liang Li (e-mail: lizl@igsnrr.ac.cn)*

ABSTRACT Land surface temperature (LST) and land surface emissivity (LSE) are two key parameters in global climate study. This paper aims to cross-validate MSG/SEVIRI-derived LST/LSE proposed by Jiang (2007) using the MODIS (MOD11B1 and MOD11_L2) LST/LSE products in two regions (Iberian Peninsula, Egypt and Middle East areas). An area-weighted aggregation algorithm was used to aggregate SEVIRI and MODIS LST/LSE products. According to the quality control (QC) criterion and view angle, the cross-validation was carried out under clear sky conditions. The results showed that the SEVIRI LST/LSE are consistent with MODIS LST/LSE products and have the same trend in the daytime and night-time over two study areas. SEVIRI LST overestimates $\sim 1.0\text{K}$ in the night-time and $\sim 1.5\text{K}$ in the daytime compared with MOD11B1 and MOD11_L2 products over these two study areas. As for the comparison of LSE with MOD11B1 and MOD11_L2 products, SEVIRI LSE underestimates ~ 0.015 in $11\mu\text{m}$ and ~ 0.02 in $12\mu\text{m}$ over Iberian Peninsula, but two LSEs are in good agreement with the difference less than 0.01 over the Egypt and Middle East area. It is obvious that the comparison results of LST in the night-time are better than that in the daytime. The results showed that the retrieval algorithm proposed by Jiang (2007) for MSG-SEVIRI can produce the LST within 1.5K in comparison with MODIS/Terra LST product.

1 INTRODUCTION

Land surface temperature (LST) is one of the key parameters in the physics of land-surface processes on regional and global scales, combining the results of all surface-atmosphere interactions and energy fluxes between the atmosphere and the ground. The LST products retrieved from the data of the spinning enhanced visible and infra-red imager (SEVIRI) on board the first geostationary satellite Meteosat second generation (MSG-1) are available. The LST products were retrieved with the generalized split-window algorithm by Jiang and Li (2006). The retrieval of LST from satellite data involves the atmospheric correction of the satellite-observed radiances and nonunity of land surface emissivity correction. Therefore, it is necessary to assess the accuracy of the retrievals to provide the reliable information on the quality of the LST product.

In principle, land surface temperature and emissivity derived from satellite measurements can be validated with the ground-truth measurements concurrently with the satellite overpass, which is referred to as the temperature-based method (Wan and Li, 2008). However, it is a complex and hard task to perform such field measurements, because satellite pixels are usually many times the size of the ground-truth sensor's footprint and natural land covers and the

corresponding land surface temperatures and emissivities are quite spatially and temporally varied. Wan and Li (2008) proposed an alternative method, i.e., the radiance-based method, for validation of MODIS LST products. This method does not rely on the ground measured LST. The cross-validation is another method using the reliable product to validate the unknown product. Comparison between LST products estimated from different satellites has been completed (Trigo, et al., 2008; Jiang and Li, 2006; Noyes, et al., 2006; Cristina et al., 2005). However, the disadvantage of cross-validation method is that the difference of view angle of different satellite data has not been considered.

In this paper, we focus on the cross-validation between the LST/LSE derived from MSG-SEVIRI data (Jiang and Li, 2006) and the LST/LSE extracted from MOD11B1 and MOD11_L2 products under clear sky conditions. Section 2 describes the retrieval method of LST/LSE from MSG/SEVIRI data, the products of MODIS LST/LSE (MOD11B1 and MOD11_L2), and the study areas. Section 3 presents the cross-validation method including the area-weighted aggregation algorithm and the emissivity relationships between SEVIRI and MODIS channels. Section 4 is devoted to the results and analysis, and the summary and conclusion are given in the last section.

2 DATA AND STUDY AREAS

2.1 MSG/SEVIRI Land Surface Temperature and Emissivity

SEVIRI on board the MSG-1, is a 12-channel imager with 15min repeat cycle and about 3km spatial resolution at-nadir, except for the high-resolution visible channel of 1km spatial resolution

LST is estimated from the MSG/SEVIRI data using the generalized split-window algorithm which expresses LST as a linear function of the top of the atmosphere (TOA) brightness temperatures measured by SEVIRI atmospheric window channels centered at 10.8 μ m and 12.0 μ m.

$$LST = (A_1 + A_2 \frac{1-\varepsilon}{\varepsilon} + A_3 \frac{\Delta\varepsilon}{\varepsilon}) \frac{T_{10.8} + T_{12.0}}{2} + (B_1 + B_2 \frac{1-\varepsilon}{\varepsilon} + B_3 \frac{\Delta\varepsilon}{\varepsilon}) \frac{T_{10.8} - T_{12.0}}{2} + C \quad (1)$$

where the parameters A_1 , A_2 , A_3 , B_1 , B_2 , B_3 and C are the coefficients, which depend on the mean surface emissivity for the two channels and on the difference of emissivities between channel 10.8 μ m and 12.0 μ m. $T_{10.8}$ and $T_{12.0}$ are the TOA brightness temperature of SEVIRI data.

The coefficients A-C of the split-window algorithm were proposed by Jiang and Li (2008a). The generalized split-window algorithm was developed for eight view zenith angles (VZAs) by dividing LST, average emissivity (ε) and column water vapor (W) into several sub-ranges to improve LST estimating accuracy.

Jiang and Li (2006) proposed a LES retrieval method from combined mid-infrared and thermal infrared data of MSG/SEVIRI. A new atmospheric correction method was developed for both mid-infrared (MIR) and thermal infrared (TIR) data. For the MIR channel, because it is less sensitive to the change of water vapor content, the clear-sky and time-nearest European Centre for Median-range Weather Forecast (ECMWF) atmospheric data were used for the images where no atmospheric profile data are available. Diurnal temperature cycle (DTC) with 6 unknown parameters was used to perform the atmospheric correct for TIR channels. The LSE of MIR channel was retrieved on the basis of the concept of the temperature independent spectral indices (TISI) (Becker and Li, 1990) and kernel-driven RossThick-LiSparse-R model (Jiang and Li, 2008b). The LSE of TIR channel was therefore retrieved using the TISI and LSE in the MIR channel.

2.2 MODIS Land Surface Temperature and Emissivity Products

The MODIS/Terra MOD11_L2 LST product (version 5) is a LST product at 1 km spatial resolution, which is the result of the generalized split-window LST algorithm. The corresponding latitude and longitude data for each pixel is stored in the MODIS geolocation product (MOD03). The emissivities of band 31 and 32 in LSE product are estimated by the classification-based emissivity method according to land cover types.

The MODIS/Terra MOD11B1 product (version 5) is tile-based and gridded in the Sinusoidal projection, and is produced daily at 6 km spatial resolution. The exact grid size at the 6km spatial resolution is 5.56km by 5.56km. The MOD11B1 LST/LSE product is produced by the day/night LST algorithm (Wan and Li, 1997) from pairs of daytime and nighttime observations in seven MODIS TIR bands (bands 20, 22, 23, 29, and 31-33). This method yields the accuracies of 1K for LST and 0.01 for LSE in channels 31 and 32 for most situations. MOD11B1 product also contains the quality control file for LST and LSE. It should be noted that the zenith view and solar angles are also stored in MOD11_L2 and MOD11B1 product.

2.3 Study Areas

Two regions were selected as study areas in the LST/LSE cross-validation: the Iberian Peninsula area covered by Spain and Portugal (Longitude: 12.87W – 4.15E; Latitude: 35.86N – 44.98N) and an area covering Egypt and Middle East (Longitude: 27.65E – 37.59E; Latitude: 27.53N – 35.82N). The Iberian Peninsula area is a vegetated region, and the main land cover types are cultivated and managed areas, tree cover and herbaceous cover. While for the Egypt and Middle East area, the bare area is dominated. Most of Egypt is covered by the low-lying sand dunes and depressions of the Western and Libyan Deserts.

MODIS/Terra is a sun-synchronous and polar satellite, and the MODIS instrument onboard is a cross-track scanner. It descends across the equator from north-east to south-west at local time 10:30am, and ascends over the equator from south-east to north-west at night. Data acquisition time can be easily determined with orbit tracks for each pixel in the two study areas.

MODIS/Terra MOD11B1 LST/LSE product is a composite data from several neighboring orbits in different acquisition times. According to the sinusoidal grid, the Iberian Peninsula area can be covered by tile h17v04 and h17v05, and the Egypt and Middle East area can be covered by tile h20v05, h20v06, h21v05 and h21v06.

3 METHOD

3.1 Aggregation method of LST and LSE

The coordinate matching is a key factor for the LST/LSE cross-validation. The SEVIRI LST/LSE and MOD11_L2 products must be aggregated to the MOD11B1 spatial resolution using the area-weighted pixel aggregation algorithm. The aggregated SEVIRI and MOD11_L2 data are then accurately matched with the MOD11B1 data in terms of the minimum RMSE principle. In this work, the area-weighted algorithm, in which all satellite data are aggregated into the same spatial resolutions, is based on the following equation.

$$L_i = \sum_{j=1}^N \omega_j L_j / \sum_{j=1}^N L_j \quad \omega_j = A_{j,p} / A_j \quad (2)$$

In which L_i is the aggregated radiance and emissivity of the target pixel i . L_j is the radiance and emissivity of the pixel j . N is the total aggregated pixel count, ω_j is the area weight of pixel j , $A_{j,p}$ is the partial area of pixel j fallen into the target pixel i , A_j is the total area of pixel j . The coordinates actually represent the central location of one pixel. Therefore, the corner coordinates of a pixel are easily calculated by four neighboring pixels' coordinates. Based on the spatial relationship, the weights ω_j of the small pixels are calculated using polygon intersection algorithm, and then the aggregated value of the large pixel is obtained.

3.2 Emissivity relationship between MODIS and SEVIRI data

In order to compare the LSE between MODIS and SEVIRI data, the relationship of emissivity between TIR channels of SEVIRI and MODIS should be considered. The spectral emissivities, including water, ice, snow, vegetation, soil and mineral, were extracted from the MODIS UCSB emissivity library to build this relationship. The channel emissivities in TIR bands of the SEVIRI and MODIS were calculated firstly, and then the emissivity relationship between SEVIRI and MODIS channels was built using a linear fit (Figure 1). The relationship is:

$$\begin{aligned} \varepsilon_{31} &= 0.9492 \times \varepsilon_9 + 0.04916 \\ \varepsilon_{32} &= 0.9279 \times \varepsilon_{10} + 0.02757 \end{aligned} \quad (3)$$

where, ε_9 and ε_{10} are the emissivities of the SEVIRI channels 9 and 10, respectively. ε_{31} and ε_{32} are the emissivities of the MODIS channels 31 and 32, respectively. The fitting correlation coefficients are both greater than 0.99 and standard deviations are less than 0.0015.

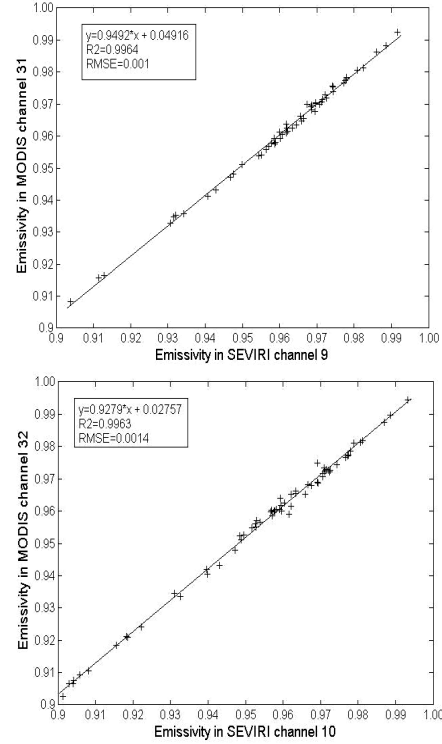


Figure 1. Relationships between the emissivities in the two split-window channels of SEVIRI and MODIS using the MODIS UCSB emissivity library.

3.3 Data processing

Considering the difference of spatial resolution, the MOD11_L2 product (1 km) is aggregated to the same resolution with the SEVIRI LST product using the coordinate matching method (equation 2). But the SEVIRI LST product should be aggregated to the same spatial resolution as MOD11B1 product (6 km) using the method described in section 3.1 (equation 3).

Besides the coordinate matching, the time matching is another requirement for the LST/LSE cross-validation. The cross-validation might be carried out in a good accuracy, if the observation time is accurately determined. It should be noted that, the data in MOD11B1 are composite data from several neighboring orbits with a difference in the acquisition UTC time of about 90min according to the Terra's orbit tracks. The observation time (local time) is divided into small strips with a width of 12min besides for the neighboring orbit passing time. The approximate UTC time in terms of the longitude of each pixel can be calculated. The UTC observation time of MOD11_L2 product can be accurately determined from the corresponding MOD11_L2 file name.

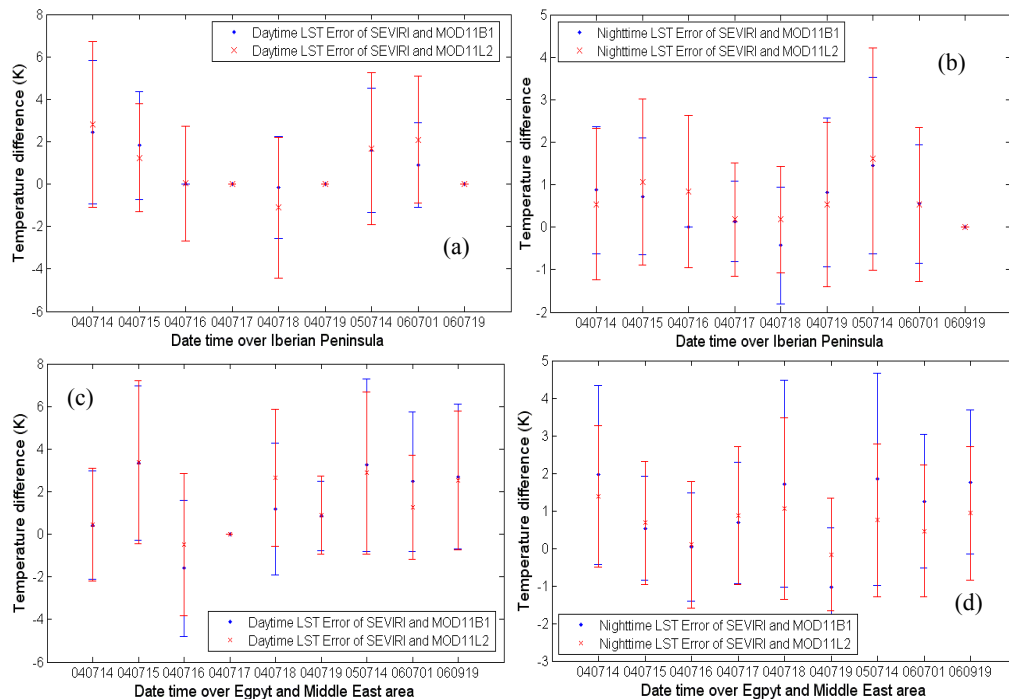


Figure 2. Mean and RMSE of temperature differences between SEVIRI LST and MOD11B1 and MOD11_L2 LST products.

View zenith angle (VZA) is the key parameter in cross-validation. SEVIRI VZAs in Iberian Peninsula vary from 43° to 50° , while SEVIRI VZAs vary from 45° to 55° in Egypt and Middle East area. In this work, the differences between SEVIRI VZAs and MODIS product VZAs are less than 5° to reduce the validation errors caused by the difference of view angle. Solar zenith angle (SZA) is another important parameter to be considered. However, according to the same observation time, longitude and latitude, the different products have the same SZAs in the same site.

Finally, according to the QC criterion of MODIS LST product, the cross-validation is carried out.

4 RESULTS AND ANALYSIS

Three time spans covering the year of 2004, 2005 and 2006 were used in the LST/LSE cross-validation.

Figure 2 shows the mean and RMSE of LSTs differences between SEVIRI LST and MODIS/Terra LST over the Iberian Peninsula and Egypt and Middle East areas. There is only one point in the figure if the pixels are cloud-contaminated or no matching pixels are available according to the view angle and QC files.

The results (Figure 2 and Table 1) show that, over the vegetated Iberian Peninsula area, when SEVIRI derived-LST is compared with LST extracted from MOD11B1. The average of the temperature differences (mean) in the daytime varies from -0.15 K to 2.4 K and the RMSE varies from 2.3 K to 3.3 K, while in the nighttime, the mean and RMSE varies from -0.4 K to 1.4 K and from 0.9 K to 3.3 K, respectively. When compared with LST extracted from MOD11_L2, the mean of temperature difference is ~ 2.0 K and RMSE varies between 1.0 K and 3.8 K in the daytime, while the mean and RMSE is less than 0.8 K and 1.5 K at night. Over the Egypt and Middle East area, the SEVIRI derived-LST is 2.5 K lower than the MOD11B1 LST in the daytime. At night, the SEVIRI derived-LST is averagely 1.7 K higher than the LST extracted from MOD11B1 and the average RMSE varies from 1.5 K to 2.3 K. When SEVIRI derived-LST is compared with LST extracted from MOD11_L2, it is ~ 2.5 K higher than the LST extracted from MOD11_L2 and the average higher than the LST extracted from MOD11_L2 and the RMSE varies from 1.4 K to 2.4 K. RMSE varies from 2.0 K to 3.5 K. For night-time image, the SEVIRI derived-LST is averagely 1.3 K

Area	ΔT	D/N	LST	
			Mean	RMSE
Iberia	ΔT_1	Day	1.32	2.65
		Night	0.59	1.49
	ΔT_2	Day	1.12	3.17
		Night	0.68	1.81
Egypt	ΔT_1	Day	1.58	3.10
	ΔT_2	Night	0.97	1.97
		Day	1.54	2.96
		Night	0.67	1.84

Table 1. The statistical values of temperature difference for all days. ΔT_1 and ΔT_2 denotes $T_{s,SEVIRI} - T_{s,MOD11B1}$ and $T_{s,SEVIRI} - T_{s,MOD11_L2}$.

Area	$\epsilon_9 - \epsilon_{31,MOD11B1}$		$\epsilon_{10} - \epsilon_{32,MOD11B1}$	
	Mean	RMSE	Mean	RMSE
Iberia	-0.013	0.017	-0.023	0.027
Egypt	-0.006	0.014	-0.006	0.016
Area	$\epsilon_9 - \epsilon_{31,MOD11_L2}$		$\epsilon_{10} - \epsilon_{32,MOD11_L2}$	
	Mean	RMSE	Mean	RMSE
Iberia	-0.012	0.019	-0.022	0.028
Egypt	-0.006	0.014	-0.006	0.017

Table 2. The statistical values of emissivities difference for all days.

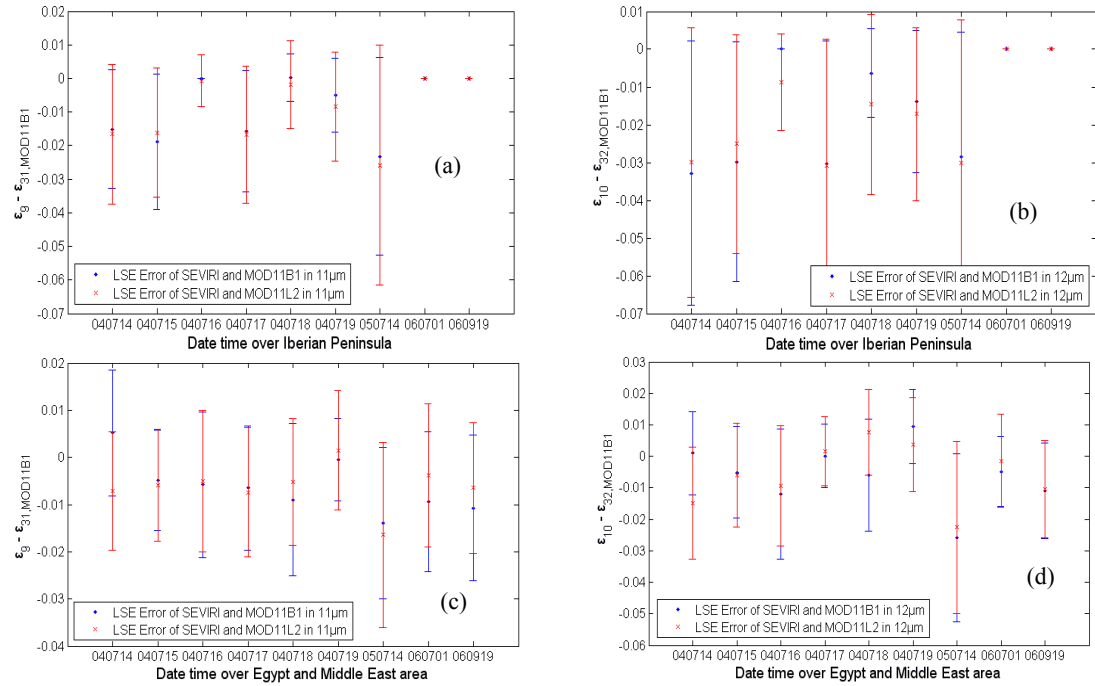


Figure 3. Mean and RMSE of emissivity differences between SEVIRI LSE and MOD11B1 and MOD11_L2 LSE products.

Figure 3 shows that the results of mean and RMSE of LSEs differences between SEVIRI LSE and MODIS/Terra LSE over the Iberian Peninsula and Egypt and Middle East areas.

The results (Figure 3 and Table 2) show that over the vegetated Iberian Peninsula area, when SEVIRI derived-LSE is compared with LSEs extracted from MOD11B1 and MOD11_L2, the average of the emissivity differences in 11μm varies from -0.02 to 0.005, and the RMSE varies from 0.007 to 0.029 (Figure 3a). In the channel at 12μm, it varies from -0.03 to -0.01, and the RMSE varies from 0.012 to

0.035 (Figure 3b). Over the Egypt and Middle East area, when SEVIRI LSE is compared with MOD11B1 and MOD11_L2 LSE, both averages of emissivity difference in 11μm are less than 0.01 and the averages RMSE are ~0.01 (Figure 3c), while in 12μm it is less than 0.02 and the average RMSE is less than 0.015 (Figure 3d). The reason of large LSE difference between SEVIRI and MODIS product might be that the Iberian Peninsula was covered by cloud for a long time in one day, which can affect the retrieval of LST/LSE from SEVIRI data.

5 CONCLUSIONS

The LSTs/LSEs retrieval from SEVIRI and the LSTs/LSEs extracted from MOD11B1 and MOD11_L2 are consistent and have the same trend in the daytime and nighttime over the Iberian Peninsula. However, the SEVIRI LST is ~1.5 K larger than MOD11B1 or MOD11_L2 products in the daytime, and SEVIRI LST is ~1.0 K than MOD11B1 or MOD11_L2 products in the nighttime. While the SEVIRI derived-LSE is compared with LSE extracted from MOD11B1 and MOD11_L2, both averages of emissivity difference in 11 μ m and 12 μ m underestimate ~0.013 and ~0.022 over the Iberian Peninsula, and underestimate ~0.006 and ~0.017 over the Egypt and Middle East area, respectively.

Land surface temperature and emissivity retrieved from satellite data must be validated with the temperature-based method or the radiance-based method or the cross-validation method concurrently with the satellite overpass. However, the temperature-based method is a complex and hard task to perform such field measurements. The radiance-based method must obtain the atmospheric profiles and land surface emissivity. The cross-validation method is the economical method for LST/LSE products, but the view angle of different satellite data must be considered. The comparison and validation of product retrieved from remotely sensed data is a hard work for quantitative remote sensing, further analysis must be carried out.

ACKNOWLEDGMENT

The research described in this paper was partly supported by the Hi-Tech Research and Development Program of China (863 Plan Program) under Grant 2008AA121805 and the Key Laboratory of Spatial Data Mining & Information Sharing, Ministry of Education, Fuzhou University.

REFERENCES

- Becker, F., and Li, Z.L., 1990. Temperature independent spectral indices in Thermal infrared bands. *Remote Sensing of Environment*, 32: 17–33.
- Coll, C., Wan, Z., and Galve, J. M., 2009. Temperature-based and radiance-based validations of the V5 MODIS land surface temperature product. *Journal of Geophysical Research*, 114, D20102, doi: 10.1029/2009JD012038.
- Cristina, M., Dash, P., Olesen F.S., and Trigo, I., 2005. Intercomparison of Meteosat-8 derived LST with MODIS and AATSR similar products. *LandSAF (Land- Satellite Application Facility) report in The 2005 EUMETSAT Met. Sat. Conf*, 19-23.
- Hulley, C.C., Hook, S.J., 2009. Intercomparison of versions 4, 4.1 and 5 of the MODIS Land Surface Temperature and Emissivity products and validation with laboratory measurements of sand samples from the Namib desert, Namibia. *Remote Sensing of Environment*, 113: 1313-1318.
- Li, Z. L., Petitcolin, F., Zhang, R. H., 2000. A physically based algorithm for land surface emissivity retrieval from combined mid-infrared and thermal infrared data. *Science in China Series: E-Technological Sciences*, 43: 23-33.
- Jiang, G. M. 2007. Retrievals of land surface emissivity and land surface temperature from MSG1-SEVIRI data. *Dissertation*.
- Jiang, G. M., Li, Z. L., 2008. Split-window algorithm for land surface temperature estimation from MSG1-SEVIRI data. *International Journal of Remote Sensing*, 29(20): 6067-6074.
- Jiang, G. M., Li, Z. L., Nerry, F., 2006. Land surface emissivity retrieval from combined mid-infrared and thermal infrared data of MSG-SEVIRI. *Remote Sensing of Environment*, 105(4): 326-340.
- Noyes, E.J., Corlett, G.K., Kong, X., Remedios J.J., Llewellyn-Jones, D.T., 2006. The AATSR land surface temperature (LST) product: comparison with LSTs from SEVIRI. *SAF 2nd User Training Workshop*.
- Trigo, I.F., Monteiro, I.F., Olesen, F., Kabsch, E., 2008. An assessment of remotely sensed land surface temperature. *Journal of geophysical research*, 113: 1-12.
- Wan, Z., 2007. MODIS Land Surface Temperature Products Users' Guide V-5.
- Wan, Z., and Li, Z.-L., 2008. Radiance-based validation for the V5 MODIS land-surface temperature product. *International Journal of Remote Sensing*, 29, 5373-5395.

First results towards building up a reliable in-situ measurements database for LST algorithms validations using modular WSN: Northern Morocco campaigns case study.

N. Raissouni^{1,*}, J. A. Sobrino², A. Chahboun^{1,3}, N. Ben Achhab^{1,3}, M. Lahraoua^{1,3}, and A. Azyat^{1,3},

¹ Remote Sensing & Mobile GIS Unit. Innovation & Telecoms Engineering Research Group. National School for Applied Sciences of Tetuan (ENSA-Tetuan). University Abdelmalek Essaadi (UAE). Morocco.

² Global Change Unit (GCU). Imaging Processing Laboratory (IPL). University of Valencia (UV). Spain.

³ Faculty of Sciences of Tetuan. University Abdelmalek Essaadi (UAE). Morocco.

* Corresponding author: nraissouni@uae.ma

ABSTRACT - Climate has changed throughout the 4.5 billion year history of the globe. In a vice-versa approach, the natural and human activities are affected directly by the global change of earth system attributes, such as temperature arising. Land Surface Temperature (LST) is an important but highly variable climate parameter. Its spatial distribution and the characteristic of its diurnal change over wide areas can only be determined with remote sensing methods. The power of Wireless Sensor Network (WSN) technology has provided the capability of developing large scale systems for remote sensing algorithms and sensors validation.

This paper presents a new method (sensitivity ~ 0.1 °C) for in-situ LST measurements. Results of a wide in-situ LST campaigns carried out during 2009 in four distant and different sites located in northern Morocco are shown: i) Kasr-Seghir ($+35^{\circ} 51' 28.08''$, $-5^{\circ} 32' 1.35''$) on the 16th of May, ii) Tangier ($+35^{\circ} 44' 56.43''$, $-5^{\circ} 50' 48.12''$) from the 17th to 18th August, iii) Targha ($+35^{\circ} 24' 4.49''$, $-5^{\circ} 1' 0.05''$) from the 4th to 10th of July, and iv) Chefchaouen ($+35^{\circ} 10' 0.07''$, $-5^{\circ} 16' 5.02''$) on 28th - 29th August. To this purpose, we have used two calibrated radiometers with Thermal Infra-Red (TIR) bands, OSM101 and TESTO845. Finally, during these campaigns, a total of 28886 measurements were made with the proposed Wireless-LST (Wi-LST) system. As expected, the maximum of diurnal thermal amplitude ($\Delta T = LST_{MAX} - LST_{MIN}$) with a value of 55.2 °C has been shown for Targha2-Site3-Target3 corresponding to bare soil sample during July, 2009. The preliminary results show a wide variability of the measurements which is in total accordance with the heterogeneity of the targets nature. This is encouraging in the way we are interested in building up a reliable and consistent standard in-situ LST measurements database for LST algorithms validations.

1 INTRODUCTION

Sensors on board satellites (e.g. Moderate Resolution Imaging Spectro-radiometer (MODIS), Advanced Spaceborne Thermal Emission and Reflection Radiometer (ASTER), Advanced Very High Resolution Radiometer (AVHRR), Spinning Enhanced Visible and InfraRed Imager (SEVIRI), etc.) provide multiple Land Surface Temperature (LST) daily products. However, these products have to be adequately validated (Moreno et al., 2001; Prata, 2003).

European Space Agency (ESA) and National Aeronautics and Space Administration (NASA) among other space agencies, have conducted several campaigns for satellite algorithm validations (e.g. DAISEX, SIFLEX, SEN2FLEX, S2K, SMEX05, etc.). For instance, scientists have used radiometers for the long-term ground measurements from one fixed point

in each validation site (Rasnaya et al., 2006; Sepulcre et al., 2006; Wenhui et al., 2008), and others have assessed LST in points uniformly distributed on the target field. All these temperatures were taken around the over flights time or satellite passes (García et al., 2001; Alonso et al., 2001; Sobrino et al., 2005; Sobrino et al., 2008).

The paper presents preliminary results using a new method (sensitivity ~ 0.1 °C) for in-situ LST measurements. The method provides long-term ground measurements in points uniformly distributed on different targets sites. During the year of 2009, a wide in-situ LST campaigns were carried out using the proposed Wireless-LST (Wi-LST) system; based on Wireless Sensor Network (WSN) technology, in four distant and different sites located in northern Morocco.

2 IN-SITU CAMPAIGNS OVERVIEW

During the last 25 years, about 50 Earth Observation (EO) campaigns have been conducted including ground-based, airborne, balloon-borne, ship-borne and small satellite experiments. These were initiated in support of future mission development and validation of missions in orbit. It is now well established that these activities constitute essential elements of EO missions. EO campaigns, in support of future mission development, have technological, geophysical and simulation objectives. They include data acquisition

using a broad range of active and passive instrumentation in the optical, infrared and microwave portion of the electromagnetic spectrum, synthetic aperture radar, limb sounding spectrometers, imaging spectrometers and radiometers.

In (Sobrino et al., 2001; Sobrino et al., 2005), transects were taken over several targets/samples surfaces. They were performed concurrently to the satellites and airborne flights over the studied samples. The measurements were taken with field radiometers, at regular steps (~ 2-3 meters) along a walk performed

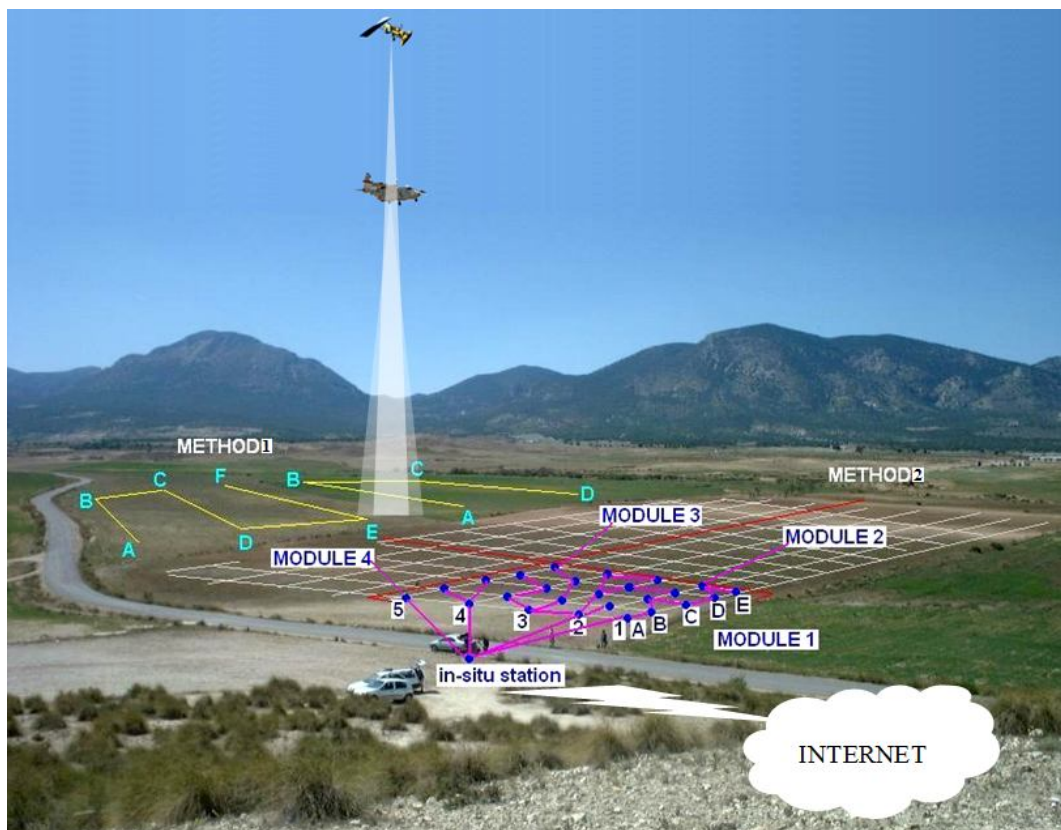


Figure 1: Transects (Method 1) vs Wi-LST (Method 2) based on modular system and Wireless Sensor Network (WSN) (12345/ABCDE array). Sensors detect temperature at nodes (blue dot) and communicate the data over a multi-hop network



Figure 2: Wi-LST base station

within a well defined area (example of transects A-B-C-D and A-B-C-D-E-F in Method 1, see Figure 1). These measurements were made half an hour before the scheduled satellite overpasses and ended half an hour later. Other thermal measurements were continuously recorded with radiometers located on fixed masts over determined areas in coincidence with the airborne/satellite over passes.

In (Wenhui et al., 2008), the FLUXNET sites in the U.S. were equipped with TIR sensors to continuously measure surface temperature at fixed points. In (Rasnaya et al., 2006) campaign,

continuously measurements of surface temperature at fixed points, with continuous ground measurements of meteorological variables, soil-moisture and temperature profiles have been taken.

3 PROPOSED IN-SITU VALIDATION METHOD

The proposed method (METHOD 2 as in Figure 1), using the Wireless-LST (Wi-LST) system, represents the modular in-situ LST measurements system based on WSN. The system is constituted by modules of node arrays (Module 1, Module 2...) (Chahboun et al., 2005). Each of which is constituted by 25 nodes scattered throughout a field by established routing topology. Information and processed LST data is broadcasted over WSN into the gateway node which is connected to the Wi-LST base station for the data parsing, storage and analysis (Figure 2). Modules 2, 3 and 4 are carrying out similar task and are connected through corresponding nodes defined in Module 1. Developed software is used for a real time monitoring, failure sensor detection, results visualization and all process control. The application demands for robust, scalable, low-cost and easy to deploy networks are perfectly met by a WSN. If one of the nodes should fail, a new topology would be selected and the overall network would continue to deliver data. If more nodes

shows the radiometers and blackbody characteristics used with the Wi-LST system.

5 RESULTS AND DISCUSSIONS

During these in-situ LST measurements campaigns, a total of 28886 measurements were made (see Table 3) with the Wi-LST system. As expected, a maximum of diurnal thermal amplitude ($\Delta T = LST^{MAX} - LST^{MIN}$) with a value of 55.2 °C has been shown for Targha-2-S3-Target8 corresponding to bare-soil sample during the month of July, 2009.

Figure 4 shows the results corresponding to Kasr-Seghir site (S1) LST measurements (in °C). For Targets 1 to 6, the values of LST(Wi-LST) measured by the calibrated OSM101 using the WSN radiometers are represented in function of LST(TESTO845) measured by the TESTO845 radiometer. Thus, Target3 exhibits the highest temperature (42.6 °C), followed by Target1 with a temperature of about 36.4 °C. The lowest temperature (14.8 °C) was observed in Target4 corresponding as expected to water, followed by vegetation (Target2) with a temperature of about 18.4 °C and mineral-soil (Target6) with 19.9 °C. The RMSE value is larger for Target6 of about 2.08 °C, indicating a wide variability in LST, probably, due to its heterogeneous nature. In contrast, the RMSE value

Table 1: Summary of validation sites characteristics

Site	Latitude Longitude	Target#(Sample)	Time Period
Kasr-Seghir (S1)	+35°51'28.08" -5°32'1.35"	Target1(Bare-Soil-1)	16 th of May 2009
		Target2(Vegetation)	
		Target3(Bare-soil-2)	
		Target4(Water)	
		Target5(Gravels)	
		Target6(Mineral-Soil)	
Tangier (S2)	+35°44'56.43" -5°50'48.12"	Target7(Water)	17 th to 18 th August 2009
Targha-1 (S3)	+35°24'4.49" -5°1'0.05"	Target8(Bare-Soil)	4 th to 5 th July 2009
Targha-2 (S3)	+35°24'4.49" -5°1'0.05"	Target8(Bare-Soil)	8 th to 10 th July 2009
Chefchaouen (S4)	+35°10'0.07" -5°16'5.02"	Target10(Water)	28 th to 29 th August 2009

are placed in the field, they only create more potential routing opportunities.

4 IN-SITU MEASUREMENTS AND STUDY AREA

The LST in-situ measurements campaigns were performed during the months of May, July, and August 2009, in four distant and different sites located in northern Morocco (see Figure 3 and Table 1). The corresponding land cover types are: bare soils, vegetation, water, gravels and mineral soil. Table 2



Figure 3: In-situ measurement sites (S1, S2, S3, S4) in northern Morocco.

Table 2: Campaign radiometers and blackbody characteristics




OSM101	TESTO 845	BB701
6-14μm ε: adjustable -18 to 538 °C ±3% of Rdg FOV : 10°	8-14μm ε: adjustable -35 to 950 °C ±0.75 °C FOV : 15°	18 to 149°C ±0.8°C
		

Table 3: In-situ Wi-LST measurements campaigns results and statistics. $\delta^{Modis} = LST(Wi-LST) - LST(MODIS)$.

Site	Target#(Sample)	# Data	LST (°C)				$\Delta T = (LST^{MAX} - LST^{MIN})$	δ^{Modis}
			Min	Max	Mean	Stdv		
Kasr-Seghir (S1)	Target1 (Bare-Soil1)	187	20.6	36.4	29.6	4.8	15.9	±0.9
	Target2 (Vegetation)	175	18.4	33.1	27.8	3.7	14.7	±0.8
	Target3 (Bare-Soil2)	171	26.6	42.6	36.2	4.4	16.0	±1.0
	Target4 (Water)	177	14.8	23.6	20.4	2.0	8.8	±0.8
	Target5 (Gravels)	175	22.4	32.6	28.3	2.5	10.3	±1.2
	Target6 (Mineral-Soil)	177	19.9	30.3	27.0	2.6	10.4	±0.8
Tangier (S2)	Target7 (Water)	7546	21.1	32.4	24.6	2.2	11.4	±0.8
Targha-1 (S3)	Target8 (Bare-Soil)	486	16.5	66.2	34.8	16.1	49.7	±1.1
	Target9 (Water)	393	14.0	34.8	24.4	4.8	20.8	±0.8
Targha-2 (S3)	Target8 (Bare-Soil)	14539	13.5	68.8	31.6	15.7	55.2	±1.1
Chefchaouen (S4)	Target10 (Water)	4860	19.7	31.6	23.7	3.1	11.9	±0.8
TOTAL		28886						
General Statistic		Min	13.5	23.6	20.4	2.0	8.8	
		Max	26.6	68.8	36.2	16.1	55.2	
		Mean	18.9	39.6	28.0	5.6	20.7	
		Stdv	3.9	14.5	4.8	5.2	16.1	

is relatively small for water (0.76 °C) owing to its homogeneity. Furthermore, Target5 possessed the smallest slope maybe due to the sample cavity effect.

Figure 5 shows the diurnal cycles for Target7 (water, #data=7546, August), Targha2-S3-Target8 (bare-soil, #data=4860, July) and Target10 (water, #data=14539, August) with their corresponding LST(Wi-LST) versus LST(TESTO845) in (°C). As expected the highest thermal amplitude ΔT (55.2 °C)

corresponds to bare-soil sample and the lowest ones to water samples with values of ΔT (11.4 °C) for Target7 and ΔT (11.9 °C) for Target10.

In order to have an idea about the thermal discrepancies in terms of thermal amplitude and response time, Figure 6, projects both diurnal cycles for Targha1 site (S3) LST measurements by Wi-LST calibrated system in (°C) for Target8 (bare-soil) and Target9 (water). Thus, minimum values of LST equal

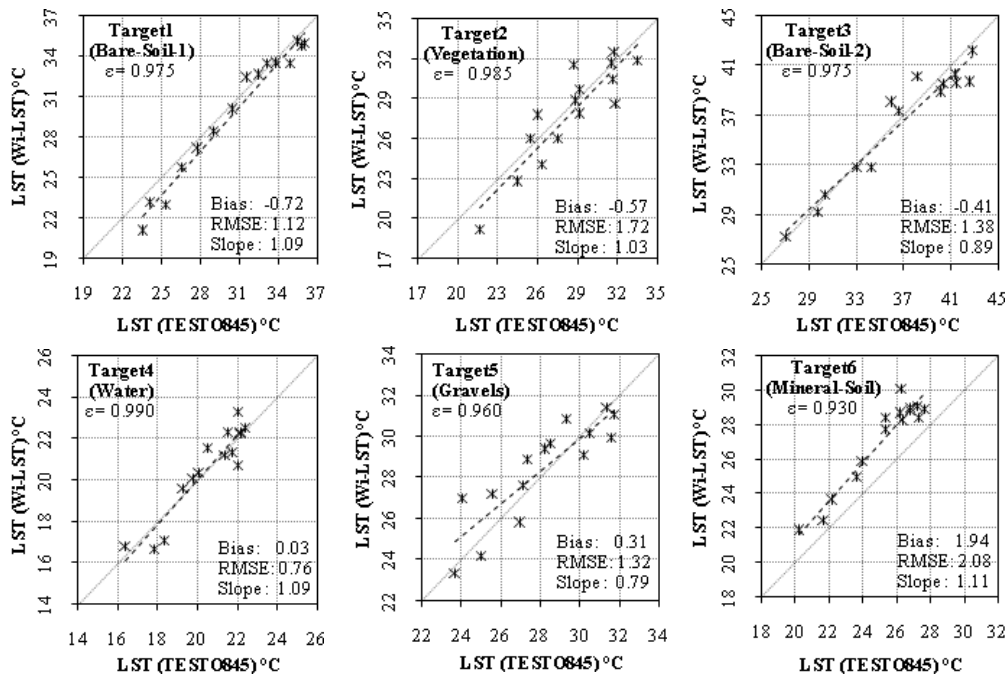


Figure 4: Kasr-Seghir site (S1) LST measurements. LST(Wi-LST) represents the LST measured by the calibrated OSM101 WSN radiometers vs LST(TESTO845) in (°C). Bias, RMSE and Slope are shown for the different targets.

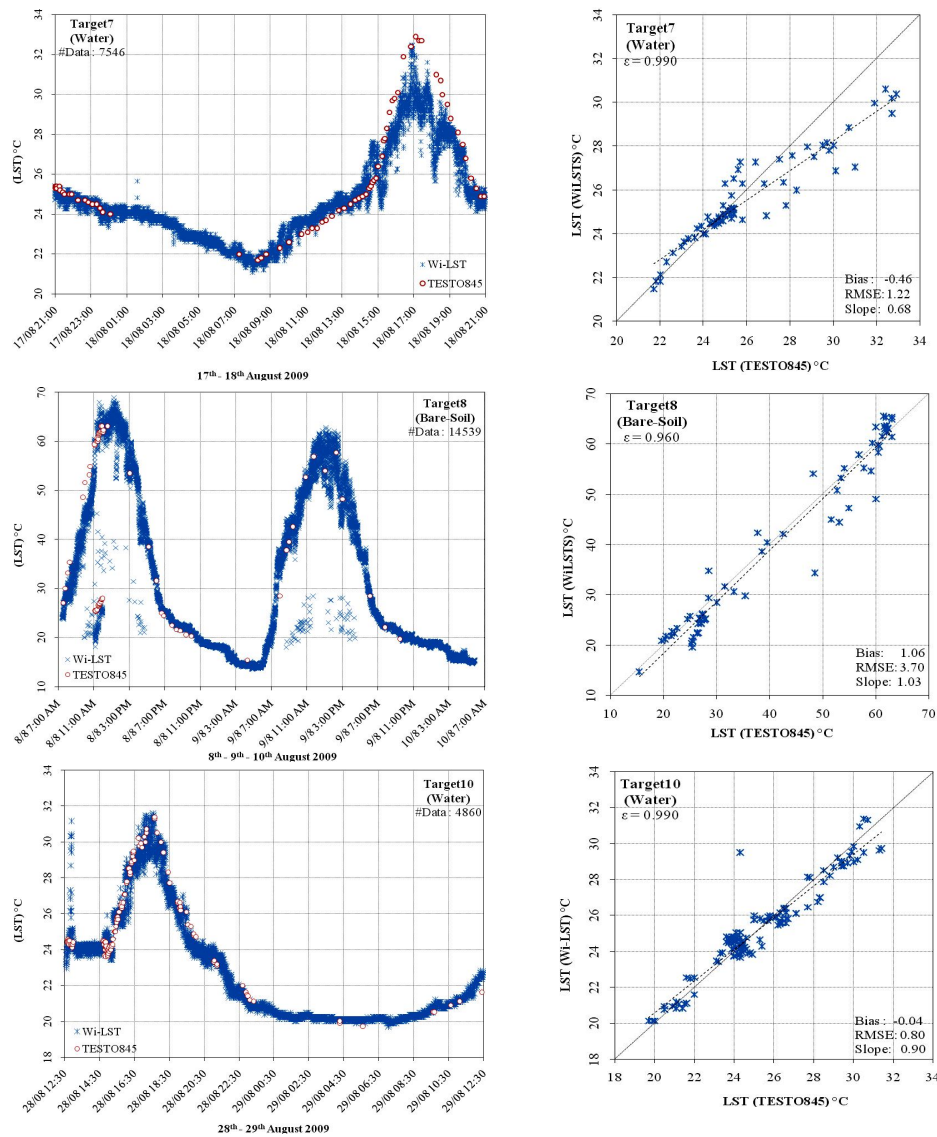


Figure 5: Diurnal cycles for Targets 7, 8 and 10 with corresponding LST(Wi-LST) vs LST(TESTO845) in (°C). Bias, RMSE and Slope are shown for the different targets.

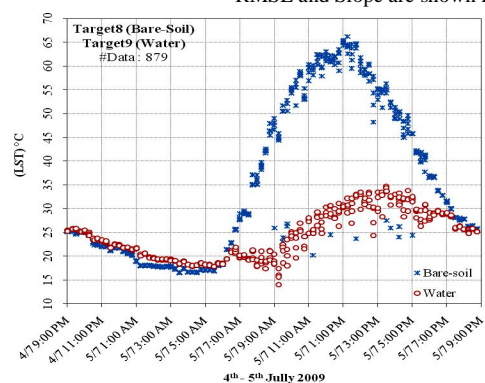


Figure 6: Targha1 site (S3) LST measurements by Wi-LST calibrated system in (°C) for Targets 8 and 9.

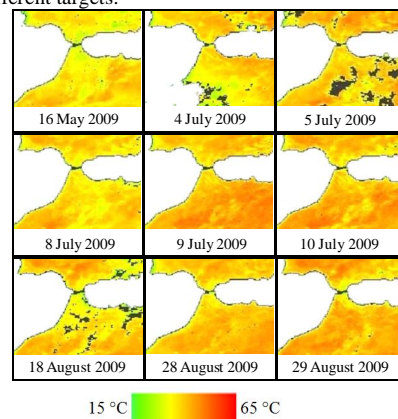


Figure 7: LST MODIS images corresponding to campaigns dates.

to 16.5 °C (with $\Delta T=49.7$ °C) and 17.2 °C (with $\Delta T=20.8$ °C) are researched during close hour for Target8 and Target9, consecutively. Nevertheless, the maximum values of LST (66.2 °C, Target8) and (34.8 °C, Target9) are researched during shifted times, 13:15GMT and 15:30GMT, consecutively. This is maybe due to the difference in the corresponding thermal inertia properties.

Finally, the mean values of LST(Wi-LST) in each site (S1, S2, S3, S4) have been compared with LST product obtained from MODIS data project (Figure 7). The results in Table 3 show a mean difference ($\delta^{Modis} = LST(Wi-LST) - LST(MODIS)$) of about ± 1 °C.

6 CONCLUSIONS

The paper presents a new modular method (Wi-LST) for in-situ LST measurements based on WSNs platforms, for remote sensing algorithms validations. Results and discussions of wide campaigns performed during the months of May, July, and August 2009 in northern Morocco are provided. Finally, a total of 28886 LST measurements were recorded along these campaigns. Thus, Wi-LST system can be highly recommended as support platform for in-situ intensive measurements to the purpose of building up a reliable LST database for remote sensing applications.

ACKNOWLEDGEMENTS

This work was supported in part by Morocco Ministry for Higher Education, Management Training and Scientific Research under CSPT Grants for “Ad hoc wireless sensor network validations for remote sensing algorithms” and “Integration and application of GIS and GPS on mobile systems” projects. Many thanks to anonymous referees.

REFERENCES

- Alonso L., Camacho-de Coca F., Caselles V., Coll C., Cuenca J., Cuñat C., Dempere L., El Kharraz H., El Kharraz J., Fernández G., García J. C., Gilabert M. A., González M. C., Hurtado E., Martí J. M., Martínez B., Meliá J., Moreno J., Palacios A., Raissouni N., Rubio E., Sobrino J. A., Sospedra F., Valor E., Younis M. T., González J., Scheer G., Ustin S. L., and Zomer R. J., Surface Radiometric Measurements at Barrax. The Digital Airborne Spectrometer Experiment (DAISEX), Proceedings of the Workshop, 71-77. 2001. M. Wooding and R.A. Harris. ESA SP-499.
- Chahboun A., Raissouni N., Essaïdi M., Towards an operative land surface temperature in-situ measurements system for remote sensing models validation. IEEE IGARS, Korea, 2005, pp. 2496-2499.
- García J. C., Cuñat C., Alonso L., González M. C., Palacios A., Moreno J., Montero F., Brasa A., Ruiz J. R., Martínez C., Vegetation & Soil Measurements at Barrax. ESA SP-499, 2001, p.79.
- Moreno J., Caselles V., Martínez-Lozano J. A., Meliá J., Sobrino J. A., Calera A., Montero F., Cisneros J. M., The measurement programme at barrax. The Digital Airborne Spectrometer Experiment (DAISEX), Proceedings of the Workshop, ESA SP-499, Noordwijk, Netherlands, 2001, pp. 43-51.
- Prata A. J., Land surface temperature measurement from space: Validation of the AATSR land surface temperature product. 40 pp. 2003. CSIRO.
- Rosnaya P., Calvetb J. C., Kerra Y., Wigneronc J. P., Lemaître F., Escorihuelaa M. J., Sabaterb J. M., Salehc K., Barriéb J., Bouhoursb G., Coreta L., Cherelb G., Dedieua G., Durbeb R., Fritz N. D., Froissardb F., Hoedjesa J., Kruszewskic A., Lavenua F., Suquiab D. and Waldteufele P., SMOSREX: A long term field campaign experiment for soil moisture and land surface processes remote sensing. RSE 102[3-4], 377-389. 2006.
- Sepulcre C. G., Zarco-Tejada P. J., Jiménez-Muñoz J. C., Sobrino J. A., Miguel E. and Villalobos F. J., Detection of water stress in an olive orchard with thermal remote sensing imagery. JAFM 136[1-2], 31-44. 2006.
- Sobrino J. A., Jiménez Muñoz J. C., Soria G., Gómez M., Barella Ortiz A., Romaguera M., Zaragoza M., Julien Y., Cuenca J., Atitar M., Hidalgo V., Franch B., Mattar A., Ruescas A., Morales L., Gillespie A., Balick L., Su Z., Nerry F., Peres L., and Libonati R., Thermal remote sensing in the framework of the SEN2FLEX project : field measurements, airborne data and applications. 4961-4991. 2008. IJRS.
- Sobrino J. A., Romaguera M., Soria G., Zaragoza-Ivorra M., Gómez M., Cuenca J., Julien Y., Jiménez Muñoz J., Su B., Jia L., Gieske A., Timmermans W., Van der Kwast H., Oliosio A., Nerry F., Sabol R., Moreno J., Thermal measurements in the framework of SPARC. ESA proceedings WPP-250: SPARC final workshop, Enschede : ESA, 6 p., 2005.
- Sobrino J. A., Raissouni N., Oliosio A., Hasager C. B., Ait Belaid M., Abdel Rahman S. and Chehbouni A., WATERMED WATER use Efficiency in natural Vegetation and agricultural areas by Remote Sensing in the MEDiterranean Basin, IGARSS, IEEE IGARS. Australia 9-13 July, 2001.
- Wenhui W., Shunlin L., and Tilden M., Validating MODIS land surface temperature products using long-term nighttime ground measurements. RSE 112[3], 623-635. 2008.

Using several water vapor MODIS-NIR algorithms for retrieval of the surface water vapor pressure in the Iberian Peninsula. *First results.*

C. Recondo, E. Pendás and R. Aguirre

INDUROT & Area of Cartographic, Geodesic and Photogrammetric Engineering.
University of Oviedo. Campus de Mieres. C/ Gonzalo Gutierrez Quirós, s/n. 33600 Mieres
(Asturias, España).

Email addresses: mdrecondo@uniovi.es

ABSTRACT: *In this work, we present the first results of using several water vapor MODIS-NIR algorithms for retrieval of the surface water vapor pressure in the Iberian Peninsula. Although these global MODIS-NIR algorithms obtain the atmospheric water vapor content or total precipitable water (W), it has already been proven in the past (using ground observations; Smith, 1966) that a linear relationship exists between these two variables (e_0 and W) and, in this study, we try to check it for W obtained from satellite data (MODIS) and for the Iberian Peninsula. The global W algorithms used are those by Gao and Kaufman (2003)-NASA's standard product MOD05, Sobrino et al. (2003) and Albert et al. (2005)-IMAPP product. Recondo's algorithm (Recondo et al., in revision), which was elaborated specifically for the north of Spain and that obtains directly e_0 from the water vapor MODIS-NIR channels, has also been tested for the rest of Spain. In situ data are relative humidity (mean, maximum and minimum) and temperature (mean, maximum and minimum) for twelve days of 2008 and they are from 276 ground meteorological stations spread across the Iberian Peninsula. From these data several water vapor pressures were derived: mean, maximum, minimum and average pressure. The comparison between e_0 versus W shows that the best linear fit is with the average e_0 ($R^2=0.6-0.7$) and with the IMAPP product, while MOD05 and Sobrino's algorithm give similar results. However, the slope of linear fit found for the three cases (3-4) is lower than the slope proposed by Smith for the latitudes of the Iberian Peninsula (6). Recondo's algorithm shows a fit similar to MOD05 and Sobrino ($R^2=0.60$), but the e_0 values obtained from the stations are lower than those estimated by the algorithm, indicating that this algorithm needs to be fitted for the rest of Spain.*

1 INTRODUCTION

In the fire risk models are fundamental two variables: Temperature (T) and Relative Humidity (RH) (or surface water vapor pressure, e_0). In the project FireGlobe (*Analysis of the fire risk scenarios at national and global scales*) we need an operational method to obtain these variables daily for the Iberian Peninsula. So, the faster method will be to obtain them from satellite data, in this case, from MODIS data.

Although global MODIS-NIR algorithms obtain the atmospheric water vapour content or total precipitable water (W), it has already been proven in the past (using ground observations; Smith, 1966) that a linear relationship exists between these two variables (e_0 and W) and, in this study, we try to check it for W obtained from satellite data (MODIS) and for the Iberian Peninsula.

So, in this study, we present the first results of the correlations found between e_0 y W for the Iberian

Peninsula. e_0 is obtained from the data from 276 ground meteorological stations spread across the Iberian Peninsula. W is obtained using the algorithms of the following authors: Gao and Kaufman (2003), Sobrino et al. (2003) and Albert et al. (2005). With Gao and Kaufman's algorithm is elaborated the NASA's standard product MOD05 (Total Precipitable Water (Water Vapor)) and with Albert's algorithm is produced the Near Infrared Water Vapor product (IMAPP product).

Recondo's algorithm has also been tested (Recondo et al., in revision). It was elaborated specifically for the north of Spain and it obtains directly e_0 from the water vapor MODIS-NIR channels. It will be tested if it can be extrapolated to the rest of Spain.

2 DATA

Two types of data for 12 days of the year 2008 (one per month) have been used in this work:

- Data from 276 ground meteorological stations spread across the Iberian Peninsula with information via web page (Table 1 and Figure 1). The daily variables taken from the stations for the selected dates are the Relative Humidity (RH) and the Temperature (T). The data taken are the Mean and the Maximum and the Minimum values of both variables (Tables 2 and 3). The hours taken were between 00:00 and 24:00 GMT.

Stations (N°)	Institution	Web page
196	SIAR	http://www.mapa.es/siar
24	RuralCat	http://www.ruralcat.net
17	MeteoGalicia	http://www2.meteogalicia.es
16	La Rioja	http://www.larioja.org
10	Junta Extremadura	http://agralia.juntaex.es
6	MeteoNavarra	http://meteo.navarra.es
3	Junta Andalucía	http://www.juntadeandalucia.es/agriculturaypesca
2	Oficina Regante (Aragón)	http://oficinaregante.aragon.es
2	SIARCastilla-La Mancha	http://crea.uclm.es/siar/
276	TOTAL	

Table 1: Ground meteorological stations used in this study, with the institutions and the websites that provided the data.

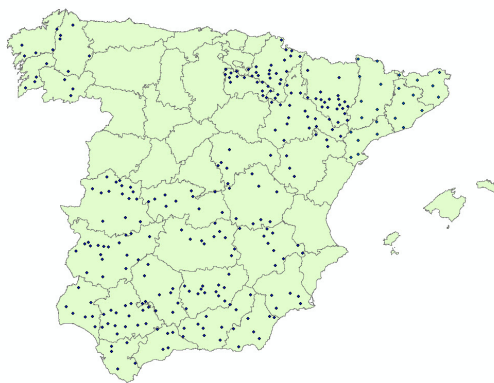


Figure 1: Location of the 276 ground meteorological stations spread across the Iberian Peninsula used in this study.

Dates in 2008
27 January
14 February
29 March
25 April
12 May
20 June
14 July
9 August
16 September
19 October
14 November
12 December

Table 2: Dates in 2008 (one per month) used in this study.

Variable	Value
Relative Humidity (RH)	Mean
	Maximum
	Minimum
Temperature (T)	Mean
	Maximum
	Minimum

Table 3: Variables and values taken in the stations.

- Terra-MODIS diurnal data (Figure 2 and Table 2). The hours taken were between 10:20 and 12:00 GMT. All the data are free of clouds and there are three type of data:
 - MOD021km data (Guenther *et al.*, 1996; 1998), which have calibrated and geolocated (WGS84) radiances (L) of the 36 spectral channels with a spatial resolution of 1 km. However, only six channels radiances (1, 2, 17, 18 and 19; see Table 4) are necessary in this work. These data were provided free of charge by NASA from Goddard's LAADS (Level 1 and Atmosphere Archive and Distribution System; from the web page: <http://ladsweb.nascom.nasa.gov>).
 - MOD05 (Total Precipitable Water (Water Vapor)). Gao and Kaufman (2003). NASA's standard product that can also be download from Goddard's LAADS.
 - Near Infrared Water Vapor product (IMAPP product). Albert *et al.* (2005). IMAPP (International MODIS/AIRS Processing Package; Huang *et al.*, 2004; see the website: <http://cimss.ssec.wisc.edu/imapp/>). MODIS Level 2 software, which was developed by the Space Science and Engineering Center at the University of Wisconsin. It is a freely distributed software.

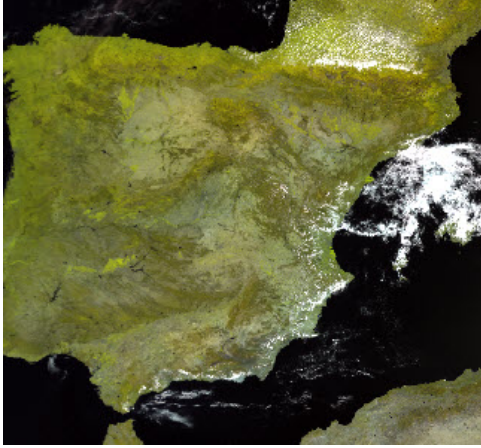


Figure 2: Example of Terra-MODIS diurnal data used. MOD021km product for 9 August at 10:40 GMT.

Channel number	Band centre (µm)-Spectral range	Original spatial resolution (m)
1	0.659 - Red	250
2	0.865 - NIR	250
17	0.905 - NIR	1000
18	0.936 - NIR	1000
19	0.940 - NIR	1000

Table 4: Spectral characteristics of MODIS channels used in this work.

3 METHOD

Our method is based on the possibility to obtain directly the surface water vapor pressure (e_0) from global MODIS-NIR algorithms for retrieval of the total atmospheric water vapour content or total precipitable water (W). It has already been proven in the past (using ground observations; *Smith, 1966*) that a more or less linear relationship exists between these two variables (e_0 and W) and, in this study, we try to check it for W obtained from satellite data (MODIS) and for the Iberian Peninsula.

So, e_0 (mean, maximum, minimum and average) has been obtained from the stations data (Figure 3) and W has been elaborated (or obtained directly) using three methods (Figure 4): Sobrino's algorithm (*Sobrino et al., 2003*); MOD05 product (*Gao and Kaufman, 2003*) and IMAPP product (*Albert et al., 2005*). The three algorithms use the relationships (usually the ratios) between the MODIS NIR water vapor absorbing channels (17, 18 and 19) and some of the transparent channels (2).

Recondo's algorithm has also been tested (*Recondo et al., in revision*). It is also based on water vapour MODIS NIR channels (Figure 4), but it estimates directly e_0 from these channels. The problem is that this algorithm has been specifically calculated for the north of Spain and not for the entire Iberian Peninsula.

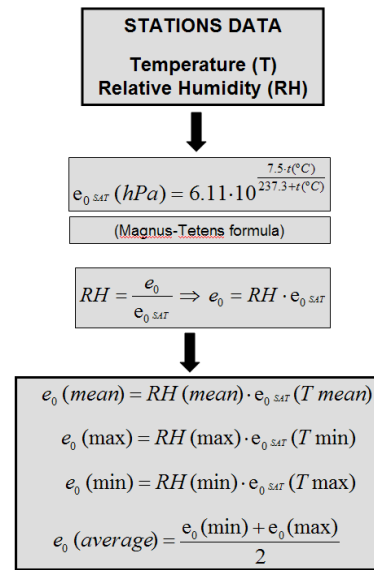


Figure 3: Process to obtain e_0 from the ground stations.

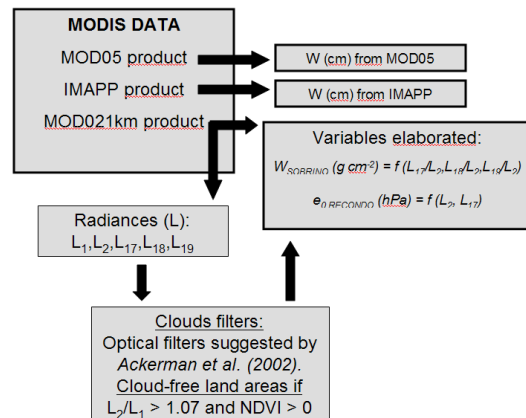


Figure 4: Process to obtain W (and MODIS- e_0 for Recondo's algorithm) in this study.

4 RESULTS

The comparison between e_0 and W shows that:

- For the three global MODIS algorithms, the best correlation is with the average e_0 ($R^2=0.6-0.7$), followed by the maximum ($R^2=0.5-0.7$), mean ($R^2=0.5-0.6$) and minimum e_0 ($R^2=0.4$). The results for the average e_0 are shown in Figure 5.
- The best correlation is with the IMAPP product. The results for MOD05 and Sobrino's algorithm are similar. See Figure 5.

Smith (1966) proposed the following linear relationship between e_0 and W :

$$e_0 = \frac{g(\lambda + 1)}{0.622} W \quad (1)$$

with λ depending on latitude and season. The annual average value for latitudes of 30°-40° N proposed by Smith is 3.00, while for latitudes of 40°-50° N is 2.78. The Iberian Peninsula is between 36°-44°, so that the annual average value for λ will be 2.89. So, following Smith, the relationship for the Iberian Peninsula will be:

$$e_0(\text{hPa}) = 6.13 W(\text{cm}) \quad (2)$$

However, our results show that:

- The slopes of the linear fits between e_0 and W found with our data (2.88-4.16; see Figure 5) are lower than the value proposed by Smith, indicating that $\lambda < 2.89$. The lower slope is for MOD05.

Using Recondo's algorithm, that estimates directly e_0 from MODIS-NIR channels (e_0 by Recondo's algorithm), the results are (Figure 6):

- This algorithm is a bit better than MOD05 and Sobrino's algorithm in R^2 and RSE, but worse than IMAPP one.
- The e_0 values of the Iberian Peninsula are lower than those estimated by the algorithm. This algorithm was obtained by empirical methods in the north of Spain and it has to be fitted for the rest of Spain.

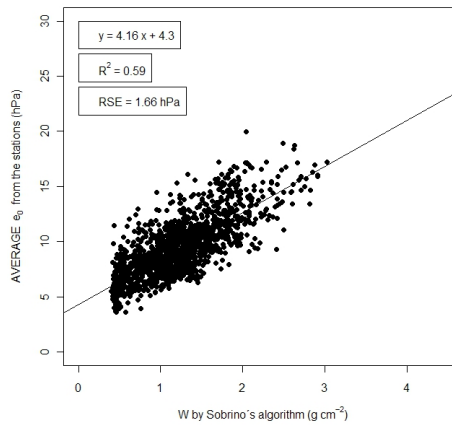
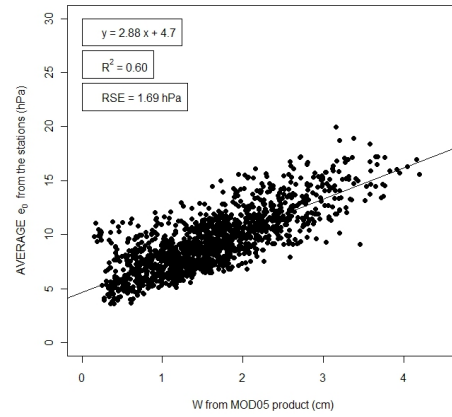
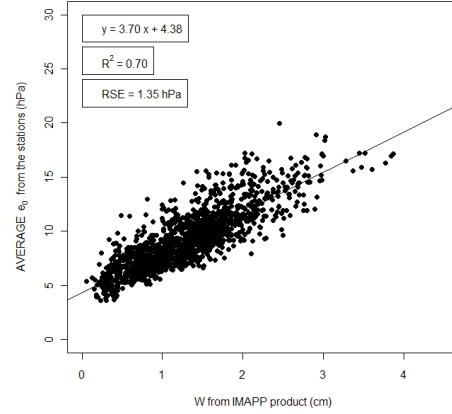


Figure 5: Average surface water vapor pressure (AVERAGE e_0) versus the total atmospheric water vapour content or total precipitable water (W) obtained from three global MODIS-NIR algorithms.

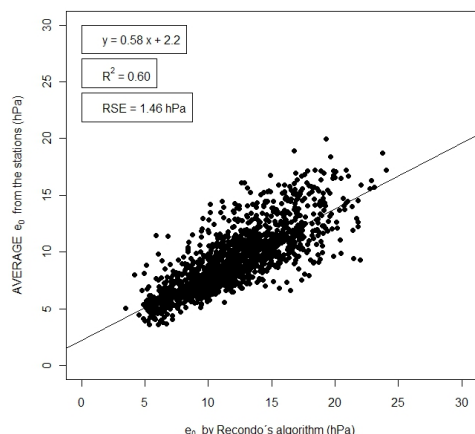


Figure 6: Average e_0 from the stations versus e_0 obtained from Recondo's algorithm, specifically elaborated for the north of Spain.

4 CONCLUSIONS

- A linear relationship between e_0 (from the ground stations) and W (from MODIS data) exists for the Iberian Peninsula. The best correlation ($R^2=0.70$) is obtained with the average e_0 and the water vapor IMAPP product. The RSE obtained ($RSE=1.35$ hPa) could be improved with simultaneous observations.
- The e_0 - W relationships (slopes between 2.88 and 4.16) found in this study don't coincide with the expected ones (slope=6.13) according to Smith for the latitudes of the Iberian Peninsula.
- Recondo's algorithm shows a fit similar to MOD05 and Sobrino's products ($R^2=0.60$), but the e_0 values of the Iberian Peninsula obtained from the stations are lower than those estimated by the algorithm. Maybe, as the algorithm was specifically obtained for the north of Spain, it needs to be fitted for the rest of Spain.

References

- Ackerman, S., Strabala, K., Menzel, P., Frey, R., Moeller, C., Gumley, L., Baum, B., Wetzel Seeman, S. and Zhang, H. (2002). Discriminating clear-sky from cloud with MODIS. Algorithm theoretical basis document (MOD35). Available online at http://modis.gsfc.nasa.gov/data/atbd/atbd_mod06.pdf (accessed 6 August 2009).
- Albert, P., Bennartz, R., Preusker, R., Leinweber, R. and Fischer, J. (2005). Remote sensing of atmospheric water vapor using the Moderate Resolution Imaging Spectroradiometer. *Journal of Atmospheric and Oceanic Technology*, 22, 309-314.
- Gao, B.-C. and Kaufman, Y. J. (2003). Water vapor retrievals using Moderate Resolution Imaging Spectroradiometer (MODIS) near-infrared channels. *Journal of Geophysical Research*, 108 (D13), 4389-4398.
- Recondo et al. (*in revision*). A simple empirical method for estimating surface water vapor pressure on a regional scale using MODIS. Applications to Northern Spain's Asturias Region.
- Smith, W.L. (1966). Note on the Relationship Between Total Precipitable Water and Surface Dew Point. *Journal of Applied Meteorology*, 5, 726-727.
- Sobrino, J. A., El Kharraz, J., and Li, Z.-L. (2003). Surface temperature and water vapour retrieval from MODIS data. *Int. J. Remote Sensing*, 20, 5161-5182.

Validation of Imaging Infrared Radiometer (IIR) onboard CALIPSO during the CIRCLE-2 and VALIDATION-CALIPSO campaigns.

O. Sourdeval* (1), G. Brogniez*, P. Dubuisson*, F. Parol*, L. Labonnote* and J. Pelon**

* LOA, Université Lille1, Villeneuve d'Ascq, FRANCE

** LATMOS, Université Pierre et Marie Curie, Paris, FRANCE

(1) odran@loa.univ-lille1.fr

ABSTRACT - Because of their important spatial and temporal coverage, cirrus clouds are considered of having a major but still badly determined influence on global climate and radiative phenomena in the atmosphere. Numerous studies have been performed during the last decades in order to enhance our knowledge of their global impact on the Earth-ocean-atmosphere energy balance. However, due to their high altitude precise observations are still seldom, especially using aircrafts. Consequently, the use of spatial data from instruments dedicated to climate studies such as IIR/CALIPSO occurs to be of primal importance. During May 2007 and October 2008, the "CIRCLE-2" and "Validation CALIPSO" campaigns were conducted with the intention to study cirrus clouds microphysical properties (optical thickness, ice crystal shape and effective diameter), but they also took place as the first validation campaigns of IIR. In this study, we compare radiative measurements performed by the CLIMAT-AV infrared radiometer onboard a FALCON-20 aircraft to those of IIR. The aircraft was also equipped with the LEANDRE lidar and in situ measurements instruments. The spectral ranges of the channels of CLIMAT-AV radiometer are highly similar to the ones of IIR in order to make data comparable. Good correlations are found between IIR and CLIMAT-AV measurements. Afterwards, inversions of cirrus optical thickness and crystals effective diameters are attempted, using the FASDOM radiative transfer code and an optimal estimation method. These inversions are then compared to in situ observations and also to IIR operational products. We retrieve optical thickness and crystal effective diameter values close from in situ observations and CALIOP operational products.

1 INTRODUCTION

The satellite CALIPSO took part of the A-Train constellation (Nasa Facts, March 2003) in April 2006 in order to provide new knowledge on the impact of clouds and atmospheric aerosols on weather and climate. CALIPSO carries the infrared radiometer IIR, the lidar CALIOP (1024 nm and 532 nm) and the visible Wide Field Camera (620-670 nm). IIR is a three channels radiometer measuring in the thermal infrared window region (filters centered at 8.65 μm , 10.6 μm and 12.05 μm , figure 1). The measurements are made nadir viewing with a 64 km by 64 km swath, and its spatial resolution at ground level is of 1km per pixel. This instrument has been developed by CNES in cooperation with the Pierre Simon Laplace Institute but has yet never been validated.

In May 2007 the CIRCLE-2 (CIRrus CLOUD Experiment) airborne campaign took place to study cirrus clouds but also in order to effectuate the first validation IIR. This campaign is followed in October 2008 by VALIDATION-CALIPSO. Both campaigns use two aircrafts flying at different altitudes simultaneously right under the track of CALIPSO in order to effectuate similar measurements. One aircraft

(a French Safire F-20, "FF-20") flies over the cirrus layer and is equipped with the thermal infrared radiometer CLIMAT-AV (Brogniez *et al*, 2004), which has characteristics very similar to IIR (channels centered at 8.7 μm , 10.8 μm and 12.0 μm , figure 1), and with the lidar LEANDRE (532nm). The second aircraft (a German DLR F-20, "GF20") flies inside the cirrus in order to measure *in situ* size distribution of ice crystals.

The first part of this paper is dedicated to the description of direct comparisons of radiances measurements, transposed in brightness temperatures, made by IIR and CLIMAT-AV along the same track simultaneously during several campaign days. In the second part computation will be used to explain differences between the measurements. Finally, in a third part, radiances from both instruments are used in order to inverse cirrus cloud microphysical properties (crystals effective diameters and cloud optical thickness). Results are then compared to *in situ* measurements and to CALIPSO operational algorithm.

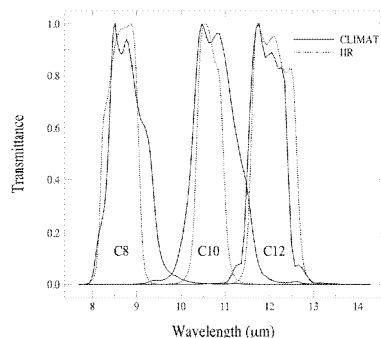


Fig 1: CLIMAT-AV and IIR filter transmittance for in each spectral channel

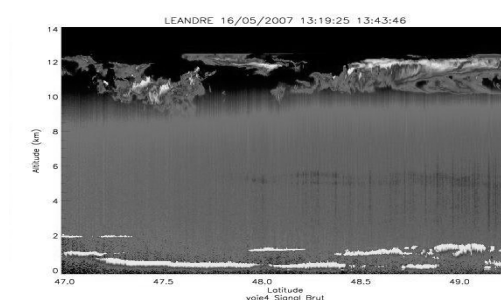


Fig 3: LEANDRE image during made during the flight of the CIRCLE-2 for May the 16th of 2007

2 OBSERVATIONS

Many flights took place during the CIRCLE-2 and VALIDATION-CALIPSO campaigns. However strict conditions on the simultaneity of the airplanes with CALIPSO, on a good correlation of the tracks, and of course on a well parameterization of instruments have been applied to restrict the effective flights that can be used for a good validation study to three (two days during CIRCLE-2 and one during VALIDATION-CALIPSO). For space convenience, only one day for each campaign is exposed here. The results of the last campaign day are nevertheless very similar.

2.1 CIRCLE-2, 16 May 2007

This flight takes place near Brittany coast over the Atlantic Ocean (fig. 2). Different legs were effectuated to measure cirrus properties considering a Lagrangian shift. However only the leg in exact coordination with CALIPSO track is kept for radiance comparisons.

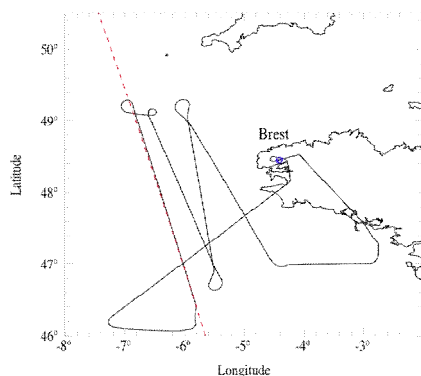


Fig 2: Flight tracks during the CIRCLE-2 campaign for May the 16th of 2007. Plain line represents the airplane track and dashes CALIPSO track.

The LEANDRE image (Figure 3) shows the presence of a thin cirrus layer between 10 km and 12.5 km. A constant layer of water cloud can as well be observed between 0 km and 2 km.

Figures 4 show the brightness temperatures measured by CLIMAT-AV and IIR for each channel (8 μ m, 10 μ m and 12 μ m respectively, noted as C8, C10 and C12). Several considerations had to be taken to ensure good comparisons:

- The uncertainties bars on IIR measurements show the deviation from the average measure of the 3 central pixels (IIR swath being much wider than the plane track only the 3 central pixels have been considered).
- A spatial shift has as well been performed considering the speed of winds at clouds altitude in order to make comparisons more readable.
- Finally, a spatial average has been effectuated on CLIMAT-AV measurement due to the difference of resolution at ground level for both instruments (1 km for IIR compared to 300 m for CLIMAT)

Comparisons of brightness temperatures (Figures 4) show strong correlations between IIR and CLIMAT-AV for each channel. However differences in the value of brightness temperature can still be observed, especially between 48.2° and 48.4° (corresponding to the clearest area). These differences will be treated in the simulation section of this paper.

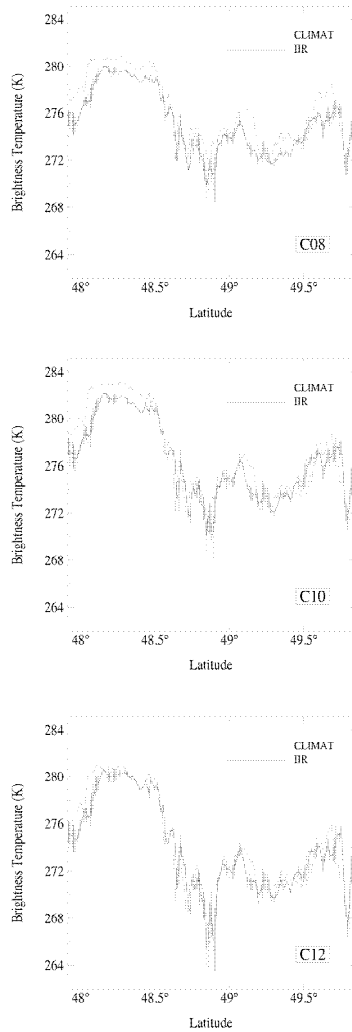


Fig 4: Brightness temperatures measured by CLIMAT-AV and IIR during the CIRCLE-2 campaign for May the 16th of 2007. Each channel is represented.

2.2 VALIDATION-CALIPSO, 18 October 2008

As for the case of May the 16th, the flight during this campaign day takes place over the Atlantic Ocean but also over Spain. (Figure 5). The flight track of the plane has been deviated in order to follow the global movement of the cloud.

The LEANDRE image (Figure 6) shows the presence of one very thick cirrus layer between 6km and 11km, but also a very clear zone between 48.2° and 45.2°. The same considerations have been taken to compare brightness temperatures.

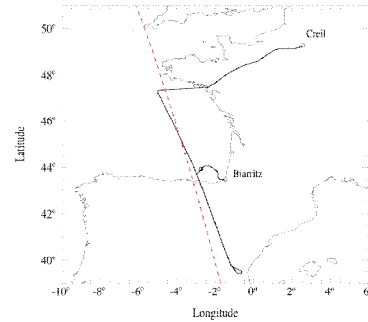


Fig 5: Flight tracks during the VALIDATION-CALIPSO campaign. Plain line represents the airplane track and dashes CALIPSO track.

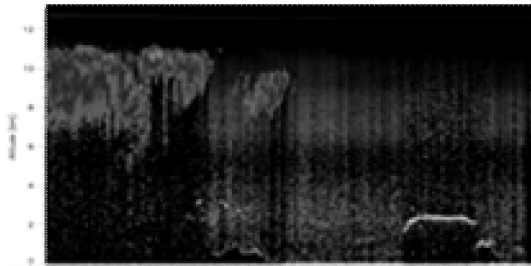
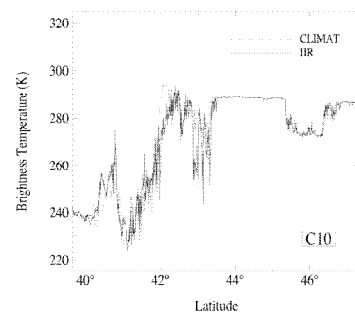
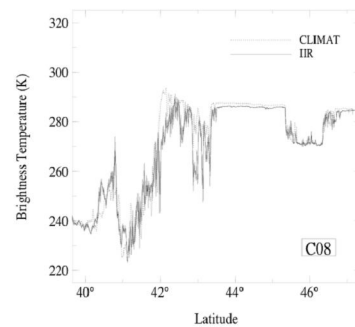


Fig 6: LEANDRE image during made during the flight of the VALIDATION-CALIPSO campaign.



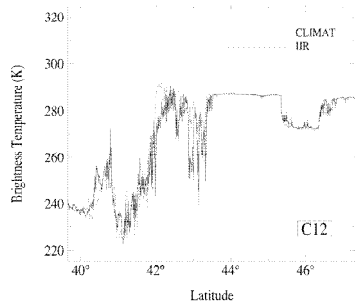


Fig 7: Brightness temperatures measured by CLIMAT-AV and IIR during the VALIDATION-CALIPSO campaign. Each channel is represented.

Brightness temperatures (Figures 7) show very good correlations as found for the case of May the 16th. Several recurrent differences in their value are still observed and will also be quantified and studied in the simulation section.

3 SIMULATIONS

Comparisons of brightness temperature in the previous section showed recurrent differences in their values. These differences are expected to be due to two factors: Firstly the spectral filters of both radiometers are very close but not strictly identical, and secondly CLIMAT-AV being inside a plane located around 12.5km, it ignored an important part of the atmosphere above seen by IIR.

In order to explain these differences simulations have been effectuated using a radiative transfer code (Dubuisson *et al*, 2005) to compute brightness temperatures in clear and cloudy atmospheres for both instruments, taking into account their spectral differences. To this purpose, atmospheric profiles measured by FF-20 during its ascent have been used and cloud properties were taken from P. Yang crystal models (P. Yang *et al*, 2001). However due to the lack of knowledge on clouds exact position and microphysical properties, best comparisons are expected in perfectly clear atmosphere areas (VALIDATION-CALIPSO). We nevertheless show simulations effectuated for CIRCLE-2 campaign in an almost clear atmosphere to prove the impact of even a very thin cirrus layer and to show the difficulty to simulate in these conditions.

3.1 VALIDATION-CALIPSO

Brightness temperatures have here been simulated in the perfectly clear area between 43.6° and 45.2° (with the presence of a thin water cloud around 44.8°). The horizontal plain lines in figures 8 represent these

simulations. Inputs in the radiative transfer code are reduced mostly to surface temperature and gas profiles, which minimize the errors. Inherent code uncertainties are nevertheless indicated by vertical bar in the graphs.

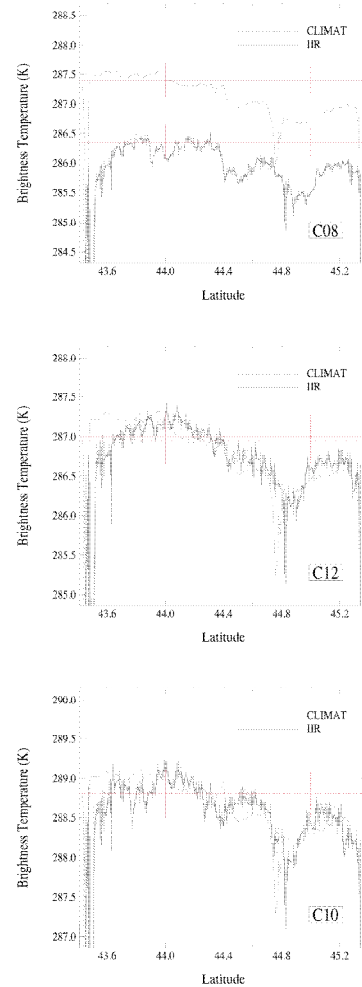


Fig 8: Brightness temperatures measured by CLIMAT-AV and IIR during the VALIDATION-CALIPSO campaign. For each channel corresponding simulations are represented in horizontal plain lines with their uncertainties.

Simulation show a very good correlations with measured brightness temperatures, and show that it is possible to retrieve the differences between the measurements of both instruments by taking into account the atmosphere above the plane, and their spectral differences.

3.2 CIRCLE-2

In the case of the CIRCLE-2 campaign no absolutely clear areas could be observed. The closest would correspond to the presence of a very thin cirrus layer, with often a water cloud underneath. In table 1 are shown the average differences between brightness temperatures measured by CLIMAT-AV and IIR along the clearest area that could be found ($48.2^\circ - 48.4^\circ$). In the following columns are presented the results of simulations effectuated in the case of different atmospheric situations.

TCLIMAT - TIR (K)	Averaged measurement May 16, 2007 ($48.2^\circ - 48.4^\circ$)	Simulation [plane altitude : 12.5 km]					
		Clear atmosphere	Position of water cloud $\tau=1.0$ (km)		Position of cirrus cloud $\tau=0.05$ (km)		
			0.5-1.0	1.5-2.0	10.0-10.5	11.5-12.0	12.5-13.0
Channel C8	1.05	0.80	0.78	0.74	0.74	0.78	1.15
Channel C10	1.15	0.04	0.05	0.06	0.01	0.03	0.55
Channel C12	0.56	-0.07	-0.07	-0.06	-0.08	-0.07	0.68

Table 1: Summary of simulations and measurements effectuated for the case of CIRCLE-2 (May the 16th of 2007)

What can be observed is that almost none of these situations can represent correctly the observations. The presence of a cloud would change the value of the brightness temperature but not the difference between the two instruments. Nevertheless it can be observed in the last column that the presence of one object unseen by one of the two instruments (here a very thin cirrus above the cloud) impacts the measurements in a way that could explain observations. But the contrary situation is also possible: a cloud seen by the airplane and not the satellite due to the resolution difference would impact in the same way. We can here observe that simulations in the presence of even thin clouds are complicated to effectuate to retrieve closely measurements. But we trust that our simulations effectuated in a perfectly clear sky for the VALIDATION-CALIPSO campaign allow explaining the difference observed.

4 INVERSIONS

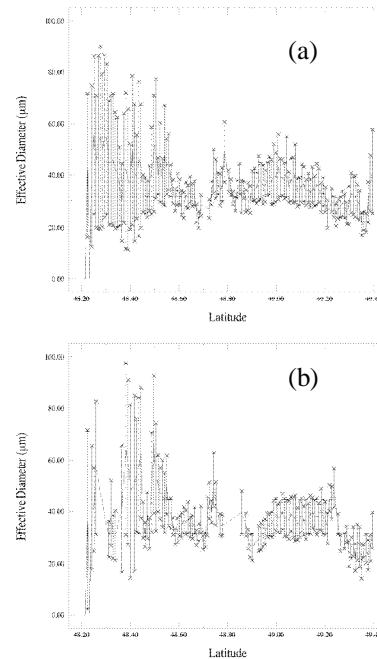
In the last part of this paper we effectuate inversions using only radiative data given by both radiometer respectively. The results of inversions using an optimal estimation method are shown here, even though a LUT method has also been used and gives very similar results. The optimal estimation method (Rodgers, 2000) uses Bayes theorem to determine – here with the help of a Gauss-Newton method – the most probable state vector (composed with the crystal effective diameter and cloud optical thickness) to fit a measurement vector (measured radiances) through the use of a radiative transfer code. The code used here is similar to the one described previously. Cirrus clouds are also computed using P. Yang crystal models. The

crystal shape has been set as an aggregate but we observe no real variations in the results by using another crystal model since the impact of shape is not of primal importance in thermal infrared measurements. The same remark holds for the size distribution which is here set as monomodal. The choice to present the results from the optimal estimation method over LUT allows retributions of measurements and model uncertainties on the inversions.

Only the case of CIRCLE-2 for May the 16th is shown here because it shows the most constant thin cirrus layer, best to inverse. The cirrus layer in the case of VALIDATION-CALIPSO is harder to treat due to its high optical thickness.

4.1 Effective Diameters

Ice crystal effective diameters (Figures 9) are very similar for inversions made using IIR and CLIMAT-AV radiometric measurements. Good correlations can also be found with CALIOP operational product on the same area. *In situ* observations also show crystal sizes retrieved in this range.



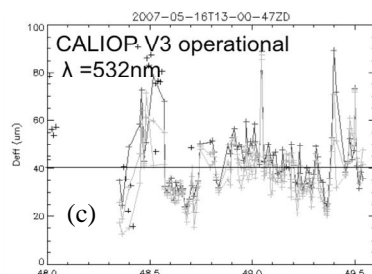


Fig 9: Inversion of effective diameters for CLIMAT-AV (a), IIR (b) and results of CALIOP operational products (c)

4.2 Optical Thickness

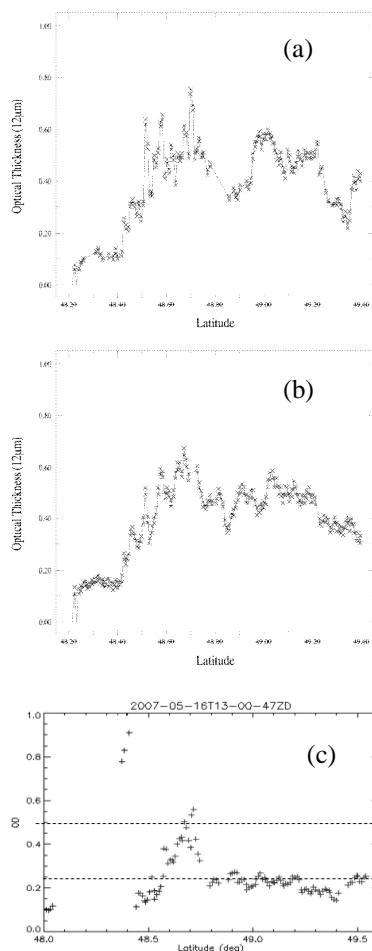


Fig 10: Inversion of optical thickness for CLIMAT-AV (a), IIR (b) and results of CALIOP operational products (c)

As for effective diameters, the results of inversions of optical thickness (figures 10) are quite similar using the radiometric measurements of IIR and CLIMAT-AV. A good concordance can be also found with CALIPSO operational products considering that these correspond for an optical thickness at 532 nm instead of 12 μm for our inversions. A factor close to 2 is then expected. *In situ* observations also give an optical thickness situated in the range 0.4 – 0.5.

5 CONCLUSION

As conclusion it is possible to say that IIR measurements seem very accurate after the two campaigns CIRCLE-2 and VALIDATION-CALIPSO. The use of the CLIMAT-AV radiometer onboard an aircraft and following the track of IIR shows very similar measurements. Some recurrent differences in the brightness temperature difference values are observed but well explained by simulations considering inherent differences between the radiometers and their measurements conditions. Also, inversions made purely using radiances from IIR show very good correlations with similar inversions made from CLIMAT-AV measurements, but also with CALIPSO operational products and with *in situ* observations.

6 REFERENCES

- Nasa Facts, March 2003 (FS-2003-1-053-GSFC)
- Brogniez G. *et al*, 2004, Determination of cirrus radiative parameters from combination between active and passive remote sensing measurements during FRENCH/DIRAC 2001, *Atmos. Res.*, **72**, 425-452.
- Yang P. *et al*, 2001, Radiative properties of cirrus clouds in the infrared (8-13 μm) spectral region, *Journal of Quantitative Spectroscopy & Radiative Transfer*, **70**, 473-504
- Dubuisson P. *et al*, 2005, Fast radiative transfer modeling for infrared imaging radiometry, *Journal of Quantitative Spectroscopy & Radiative Transfer*, **95**, 201-220
- Rodgers C. D., 2000, Inverse Methods For Atmospheric Sounding, Theory and Practice (World Scientific Publishing)

Subsidence determination in the city of Valencia and its surroundings using RADAR interferometry

J. Manuel Delgado¹, Fabio Cian², Ana B. Ruescas³, Francesco Sarti³, Mihai Datcu² and Raquel Capilla⁴

¹ Delft University of Technology (TU Delft),

² Deutschen Zentrums für Luft- und Raumfahrt (DLR),

³ European Space Agency/European Space Research Institute (ESA/ESRIN),

⁴ Institut Cartogràfic Valencià (ICV)

Correspondent author : J.M.DelgadoBlasco@tudelft.nl

ABSTRACT - Construction works in the city of Valencia are changing continuously the appearance of the city: new metro lines, the construction of the high speed railway lines, for the train between Madrid and Valencia, the renewal of the districts of El Grao, Cabanyal and Campanar, and some other works for the extension of the harbor area including commercial docks, the facilities for the America's Cup and the Formula 1 circuit. All these changes could affect the city of Valencia, for example with subsidence, landslides, uplift, since it is located over a quaternary alluvial plane with a complex hydro-geological system. Due to its proximity to the sea, the phreatic surface is at only seven meters depth. Construction works are always affected by this fact and the special characteristics of an unstable but very fertile soil. Interferometric studies have been done in order to estimate possible cases of subsidence over the city and its surroundings. Our work covers a period of 7 years, from 2003 to the present, and it is focused mainly over the port area, where we could detect the most significant results. Our dataset includes ENVISAT ASAR and TerraSAR-X, the German radar satellite, Stripmap images. The collaboration with the Port of Valencia allowed us to have access to the study area and documents that helped us to explain our results.

1 INTRODUCTION

The objective of this work is the detection and mapping of ground subsidence related to human activities using Differential Interferometric Synthetic Aperture Radar techniques (DInSAR) over a period of seven years (2003-2010) using a small perpendicular baseline (< 500 m) interferogram approach (Masonnet and Feigl, 1998).



Figure 1. Left: the port of Valencia in 1980 Right: the port in 2009

In this work, the attention is put on the harbour area, the part of the city that has suffered more changes in the last 25 years, as it can be noted in figure 1. The results we present were obtained mainly using data coming from TerraSAR-X, the German radar satellite.

2 METHODOLOGY AND DATA

2.1 Methodology

We used the Delft Object-oriented Radar Interferometric Software (DORIS) of the Delft Institute of Earth Observation and Space Systems (DEOS, 2008) to build the differential interferograms and unwrap them. Precise orbits provided by the European Space Agency and the Delft University of Technology have been used to process Advance Synthetic Aperture Radar (ASAR) data to remove orbital errors. The topographic contribution is removed using a 30 m spatial resolution digital elevation model (DEM) provided by the Advance Spaceborne Thermal Emission and Reflection radiometer (ASTER) by the Jet Propulsion Laboratory (JPL). Multilooking by a factor of 5 is applied to the ASAR interferograms along the azimuth (100 m x 100 m final pixel resolution), and by a factor of 2 to

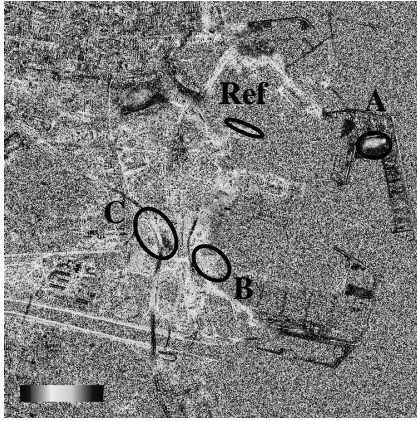


Figure 2.A – 10Oct2009-3Nov2009 Baseline: 337.3 m

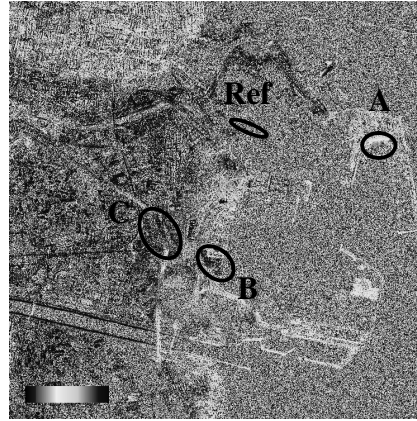


Figure 2.D – 8Jan2010-10Feb2010 Baseline: 259.7 m

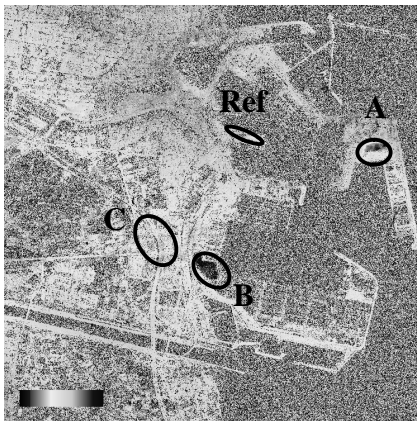


Figure 2.B – 3Nov2009-6Dic2009 Baseline: 3.7 m

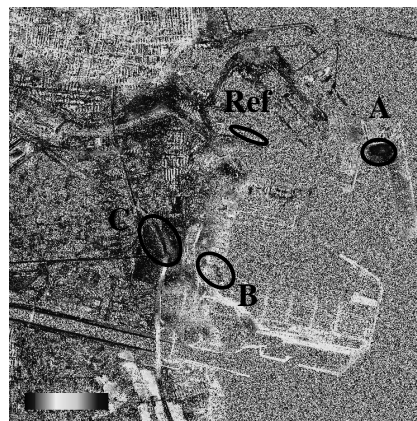


Figure 2.E – 10Feb2010-15Mar2010 Baseline: 202 m

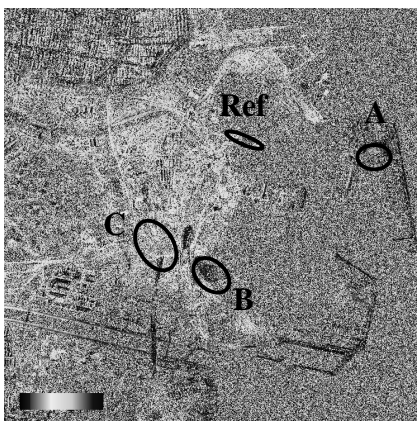


Figure 2.C – 6Dic2009-8Jan2010 Baseline: 143 m

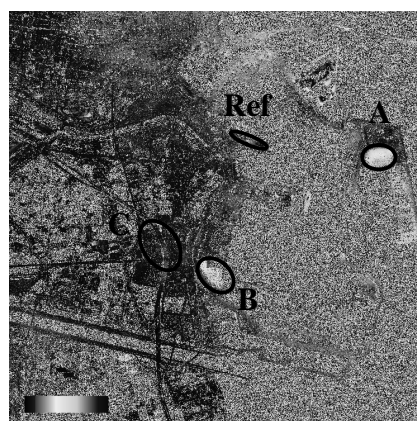


Figure 2.F – 15Mar2010-17Apr2010 Baseline: 31.5 m

Figure 2..A-F: Wrapped interferograms (phase) over Valencia city computed from TerraSAR-X stripmap images from October 2009 to May 2010 showing the subsidence in the port area. The color wheel goes from $-\pi$ to $+\pi$.

the TerraSAR-X interferogram along the azimuth and range (8m x 8m final pixel resolution). The unwrapping process is made using the Statistical-Cost, Network-Flow Algorithm for Phase Unwrapping (SNAPHU) by Chen & Zebker (2002).

We analyzed mainly three areas in the vicinity of the port, indicated in Fig. 2.A-E with A, B and C showing interesting behaviour. The displacement d , extracted from the phase of the unwrapped interferogram ϕ , ($d = \phi\lambda / (-4\pi)$), has been referred to an area of the old part of the port indicated in Fig. 2.A-E with Ref..

2.2 Data

We used an ENVISAT dataset that covers a seven year period, in particular, 21 Advanced Synthetic Aperture Radar images, 8 from ascending track 330 and 13 from descending track 466 from 2003 to the present. We found a total of 9 valid interferograms: 4 in the ascending orbit and 5 in the descending.

Furthermore, we used a TerraSAR-X stripmap dataset of eight months, from October 2009 to may 2010: 8 images in the descending orbit. We found 7 valid interferograms in total.

Our dataset has been complemented by GPS measurements in the harbour area, provided by the Port of Valencia, which will be used for a future validation process.

3 RESULTS & DISCUSSION

3.1 Analysis of the results for the selected areas

The results we obtained with the ASAR dataset (not shown in this paper) were not good enough to help us to make an analysis over the city, due to the low resolution of this sensor. Hence, we decided to keep this dataset for future work, probably using the PS technique (Lopez-Quiroz *et al.*, 2009).

Due to the high resolution of the TerraSAR-X stripmap dataset, we could obtain much more detailed results (Wegmuller *et al.*, 2008) and thus, we could perform a careful analysis over some areas of the city, and from this point our discussion will be only about this dataset. The results we obtained show three evident areas of subsidence and uplift (areas A, B and C in Fig. 2.A-E). Thus, our work, at this stage, will focus on the analysis of these parts of the port that present interesting behaviour. Moreover, for these areas we have accurate information about the activities that happened in recent years that allow us to give a reliable conclusion.

The results we present, especially the one in figure 3, are not to be considered as precise, but they rather represent a qualitative analysis since we did not

perform an atmospheric correction and we could not use the GPS data in order to compare the values we obtained.

Figure 2.A-E shows some interferograms we obtained with various TerraSAR-X image pairs from October 2009 to May 2010. The subsidences are clearly visible in almost every interferogram.

In figure 3 the evolution of the subsidence over time in the studied areas can be seen (red, green and blue lines for area A, B and C respectively). In every interferogram we computed the mean elevation of the reference area (indicated as Ref. in figure 2.A-E) and we related to this value the mean displacement in the areas A, B and C. As it can be easily noted, Zone A is affected by a much bigger subsidence with respect to the other considered areas. The lower graph in figure 3 represents the coherence over time for the considered areas (red, green and blue lines for area A, B and C respectively) and the respective

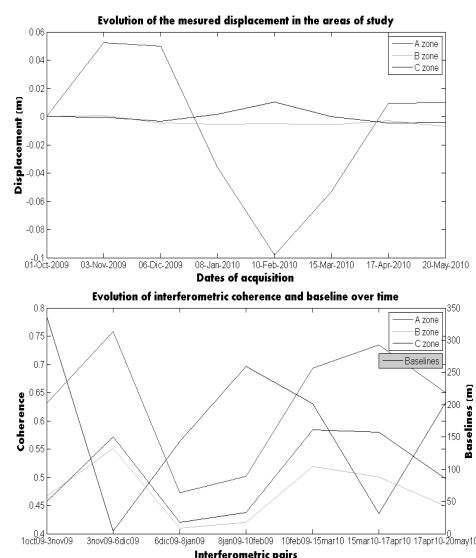


Figure 3: In the upper graph we can see the evolution over time of the subsidence in the studied areas. In the lower one, the coherence values over time of the studied areas can be noted

baseline (black line) for every interferometric pair. It can be easily noted how the coherence increases with smaller baselines.

The first area, indicated as “Zone A” in the pictures, shows movements of subsidence and uplift in all of the 7 interferograms of the TerraSAR-X dataset. These changes are probably due to the use of this area as a loading dock of material used for the expansion of the harbour to the North. The subsidence could be caused by the packing of material that has been there for a long time, caused by humidity or water

infiltration. The information coming from the Port Authority confirms our analysis.

The second area indicated as “Zone B” in the pictures, shows clear and localized displacement in more than one interferogram. The area covers a zone of the port where cars for the import/export market were stored. Since last year (late summer 2009), this area has been filled with more earth in order to enforce it. This area will be used to store containers in the future, which are much heavier than cars. From a recent picture of the port, we can see very clearly this area. The subsidence we detect could be due to growth of vegetation or very small packing of the soil.

The last area we analysed indicated as “Zone C” in the pictures, is crossed by one of the main roads that exist in the south of the city. It is an area with intense traffic and very near the channel of the Turia River. The entrance of sea water or the swelling of the river that packs the dirt and provokes a rise in the phreatic levels could be the caused of the subsidence here.

3.2 Discussion

The qualitative results shown are deemed to be reliable, but still more precise quantitative analysis is needed. The atmospheric correction of the images has to be improved as well as the use of a more accurate DEM in the interferogram extraction process. New acquisitions and hopefully the use of very high resolution TerraSAR-X spotlight images will help in the understanding of some subsidence cases. Furthermore GPS data, provided by the *Autoridad Portuaria de Valencia*, that are now being processed at the *Institut Cartogràfic Valencià* (ICV) will provide a proper quantitative validation of the work.

4 FUTURE RESEARCH

The research will continue and make use of the Stanford Method for Persistent Scatterers. A more accurate DEM provided by the *Instituto Geográfico Nacional* (IGN) will be used in order to improve the topographic correction (10 m spatial resolution), Figure 4. The temporal baseline of the study needs also to be extended, integrating previous dates using ASAR and new acquisitions of Stripmap and Spotlight TerraSAR-X. The extension of the study area to the whole city could provide very useful information about the areas affected by terrain movements due to natural or artificial causes (for example the construction of the new metro line) in order to establish the necessary protocols. Furthermore, in-situ data provided by the Port of Valencia, in particular GPS measurements and information about the evolution of the works in the port area, will have to be

used to validate the results and give a more precise evaluation.

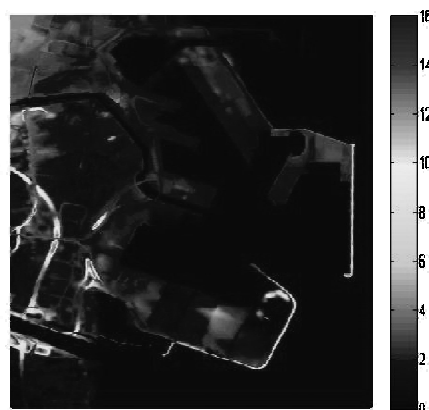


Figure 4. DEM 10 m spatial resolution provided by *Instituto Geográfico Nacional* (IGN) of Spain.

5 ACKNOWLEDGEMENTS

We would like to thank ESA/ESRIN, DLR, Delft University of Technology, the Valencia Port Authority, the Cartographic Institute of Valencia and the National Geographic Institute of Spain, with special mention to Carmen García Vilar, Raquel Capilla and E. G. Alonso respectively.

6 REFERENCES

- Massonnet D., Feigl K. L., 1998, RADAR Interferometry and its application to changes in the Earth's surface. *Reviews of Geophysics*, 36 ,4, 441-500.
- Delft Institute of Earth Observation and Space Systems (DEOS). Delft University of Technology, December 2008, Delft Object-oriented Radar Interferometry Software. User's manual and technical documentation. Version 4.02.
- Chen C.W and Zebker H.A., 2002, Phase unwrapping for large SAR interferograms: Statistical segmentation and generalized network models, *IEEE Transactions on Geoscience and Remote Sensing*, vol. 40, pp. 1709-1719 .
- López-Quiroz P., Doin M.P., Tupin F., Briole P. and Nicolas J.M., 2009, Time series analysis of Mexico City subsidence constrained by radar

interferometry, *Journal of Applied Geophysics*
falta el numero y paginas

Wegmüller, U., D. Walter, V. Spreckels, and C. Werner, 2008. Evaluation of TerraSAR-X DINSAR and IPTA for ground-motion monitoring. *Proc. of The 3rd TerraSAR-X Science Team Meeting*, 25-26 Nov 2008, DLR, Oberpfaffenhofen, Germany.

Numerical modeling of the L-Band emission and scattering of a rough soil layer covered with a grass litter layer- consideration of Moisture and Temperature gradients

F. Demontoux¹, H. Lawrence^{1,2}, J.-P. Wigneron², A. Mialon³, C. Duffour^{1,2}, A. Kruszwski², V. L. Mironov⁴, L. G. Kosolapova⁴, Y. Kerr³

¹University of Bordeaux 1 – Laboratory IMS UMR 5218 – MCM department, Bordeaux, France

²INRA-EPHYSE, Villenave d'Ornon, France

³Centre d'Etudes Spatiales de la Biosphère (CESBIO), Toulouse, France

⁴Kirensky Institute of Physics, Siberian Branch, Russian Academy of Sciences, Russia
françois.demontoux@ims-bordeaux.fr

ABSTRACT - We have developed a new approach for the calculation of rough surface scattering and emission at L-band. It has recently been validated for the case of scattering from a single layer rough surface of Gaussian autocorrelation function. This approach relies on the use of ANSOFT's numerical computation software HFSS (High Frequency Structure Simulator), which in turn solves Maxwell's equations using the Finite Element Method (FEM). The interest of this approach is that it can be extended to calculate the emission of complicated multilayer media, including features such as volume effects, gradients effects and inclusions, as well as rough surfaces. This is therefore especially useful for the problem of the emission from soil-litter systems in forests. In this paper we present the work we done to use FEM method to compute thermal effects and water infiltration effects in ground. Coupling electromagnetic and thermal computation we will be able to study scattering of media such as permafrost or effects of rapid changes in temperature condition. It can be very useful for global observations with a frequent repeat coverage (future NASA Soil Moisture Active/Passive mission SMAP). In the present study we present water infiltration in ground effects (as moisture gradients) on the emissivity and bi-static coefficient of soil.

1. INTRODUCTION

In the context of the European Space Agency's (ESA) Soil Moisture and Ocean Salinity (SMOS) mission, we present a study of the emission of rough surfaces at 1.4 GHz and the effects on this emission of a grass litter layer covering the surface. Surface roughness has been studied in some depth in the literature as it is a key influencing parameter on ground emission. A litter layer has also been shown to greatly affect the L-band emission of forests, making it difficult to retrieve soil moisture from space-based radiometer measurements over forests, [1] - [2], but the effects of this layer on the overall forest emission have been little investigated and are not yet well understood.

A new approach for the calculation of rough surface scattering and emission at L-band has recently been validated for the case of scattering from a single layer rough surface of Gaussian autocorrelation function [3], [4]. This approach relies on the use of ANSOFT's numerical computation software HFSS (High Frequency Structure Simulator), which in turn solves

Maxwell's equations using the Finite Element Method (FEM). The interest of this approach is that it can be extended to calculate the emission of complicated multilayer media, including features such as volume effects, gradients effects and inclusions, as well as rough surfaces. This is therefore especially useful for the problem of the emission from soil-litter systems in forests.

We have validated this numerical approach and demonstrated its capability of calculating the L-band emission of the soil-litter forest system [5]. To do this we have compared results of the approach with experimental emissivity data, firstly for the case of the emissivity of a bare soil with a rough surface

In this paper we present the work we done to use FEM method to compute thermal effects and water infiltration effects in ground. Coupling electromagnetic and thermal computation we will be able to study scattering of media such as permafrost or effects of rapid changes in temperature condition. It can be very useful for global observations with a frequent repeat coverage (future NASA Soil Moisture

Active/Passive mission SMAP). In the present study we present water infiltration in ground effects (as moisture gradients) on the emissivity and bi-static coefficient of soil.

2.METHOD

In the context of active and passive remote sensing analysis of soil, the moisture and temperature gradients must be taken into account.

In order to complete our model we have worked to take into account these gradients in our multi layer model of soil.

Our electromagnetic model solves Maxwell's equations using the finite element method (FEM). We also use this method to solve other equations. It enables the creation of moisture or thermal profiles in our structures.

The process can be divided into three steps. Initially, applying boundary conditions to our structures, we solve the equations related to thermal phenomena or diffusion of water in our layers. This resolution achieves to the creation of a 3D numerical meshing of the multilayer structure profiles (temperature or moisture).

The second step deals with the replacement the moisture and temperature variables in each cell of the system by the permittivity of the material according to the temperature or moisture value. This is possible using the curves of permittivities (Figure 1 and 2) measured in the laboratory using the wave guide experimental set-up presented in [2] or computed with estimating soil permittivity model (Mironov) [6] [7].

The last step deals with the integration of these permittivity profiles (Figure 3 and 4) in our model to solve Maxwell's equations. This allows us to calculate the emissivity or the bi-static coefficients of the structures.

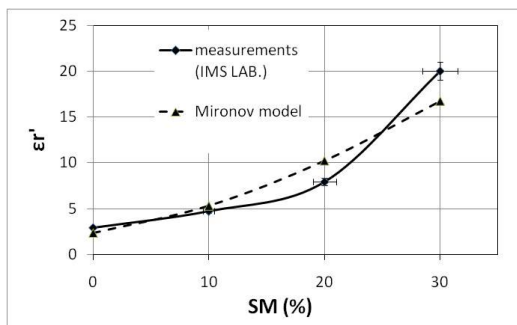


Fig 1 : Real part of the permittivity vs SM(%)
Measurement and Mironov model computation

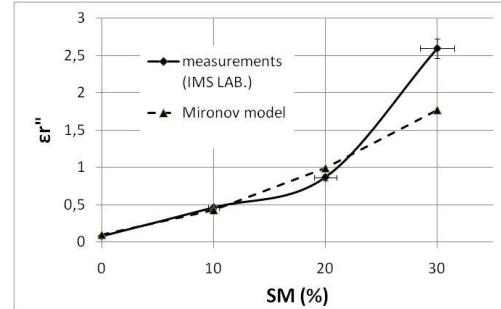


Fig 2 : Imaginary part of the permittivity vs SM(%)
Measurement and Mironov model computation

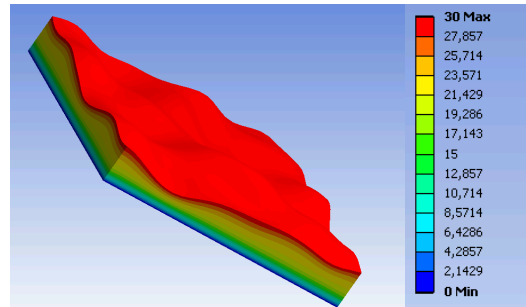


Fig 3 : Soil moisture profile 1 introduced in the model.
Surface soil moisture = 30 % - Deep soil moisture [15cm] = 0%

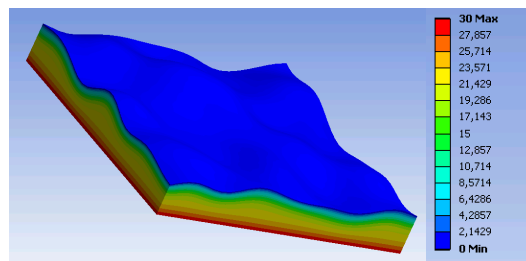


Fig 4 : Soil moisture profile 2 introduced in the model.
Surface soil moisture = 0 % - Deep soil moisture [15cm] = 30%

3.RESULTS

To present the first results of our approach we focus in this paper with the study of the moisture gradients. These were created by applying moisture gradients between the soil surface and in depth of the layer (15cm). A diffusion equation yielded profiles of Figures 1 and 2. Note that these gradients are not realistic but will allow us to highlight the inclusion of profiles in our model.

Soil moisture was initially regarded as homogeneous. We calculated the bistatic coefficient and emissivity of soil from the site SMOSREX on which we had already performed validation of our model (soil

texture = [17% Clay 36% Sand] Roughness [$k\sigma = 1$, $kLc = 6$]). The results are shown in figures 5 and 6.

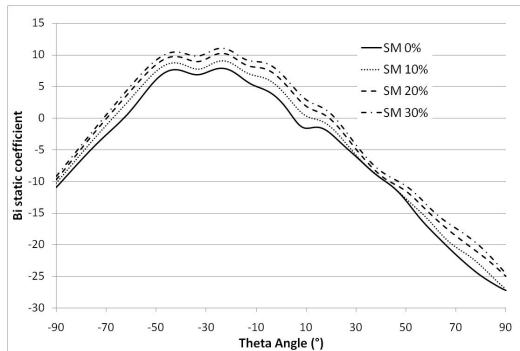


Fig 5 : Bi-static coeff. of soil layer with rough surface
Frequency=1.4GHz, Incident angle $\phi=0^\circ$ Theta= 30° ,
Observation angle $\phi=0^\circ$, HH polarization, soil texture =
[17% Clay, 36% Sand], Roughness [$k\sigma=1$, $kLc=6$],
Homogeneous soil temperature= 25°C , Homogeneous soil
moisture profile [0%,10%,20%,30%].

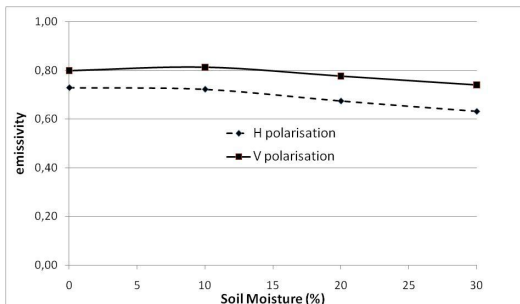


Fig 6 : Emissivity of soil layer with rough surface
Frequency=1.4GHz, Observation angle $\phi=0^\circ$, H and V
polarization, soil texture = [17% Clay, 36% Sand],
Roughness [$k\sigma=1$, $kLc=6$], Homogeneous soil
temperature= 25°C , Homogeneous soil moisture profile
[0%,10%,20%,30%].

In a second step, the inhomogeneous soil moisture profiles were incorporated into our model. To focus on the effect of the presence of moisture gradients we have chosen to present the difference between the bi-static coefficient at moisture treated and bi-static coefficient at 0% moisture (see Figure 7). In this figure we observe the effects of moisture gradients. For profile 1 (30% for the surface moisture and 0% at 15 cm depth) the value of the bi-static coefficient computed fluctuates between the coefficients calculated for 30% and 20% moisture. The effect is more pronounced for the profile 2 (0% for surface moisture and 30% at 15 cm depth).

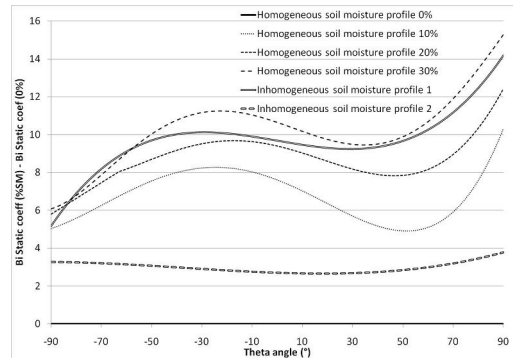


Fig 7 :Bi-static coefficient (%SM) - Bi-static coefficient (0%)

Frequency=1.4GHz, Incident angle $\phi=0^\circ$ Theta= 30° ,
Observation angle $\phi=0^\circ$, HH polarization, soil texture =
[17% Clay, 36% Sand], Roughness [$k\sigma=1$, $kLc=6$],
Homogeneous soil temperature= 25°C , Inhomogeneous
[profile 1 & 2] and Homogeneous soil moisture profile
[0%,10%,20%,30%].

4.CONCLUSION

These studies on unrealistic moisture profiles were designed to ensure correct inclusion of profiles into our model. These promising results will be followed by a validation stage. To do that, we have experimental data sets. We have moisture measurements (with the presence of gradients) and emissivities from the site of SMOSREX (nearly no temperature gradients). On the other hand, we have measurements of high temperature gradients, moisture, emissivity and bi coefficients from a measurement site in Siberian [8].

The profiles of humidity and temperature will be integrated into our model and results will be compared with experimental data to validate the introduction of moisture and temperature gradients into our model.

REFERENCES

- [1] J. P. Grant, J.-P. Wigneron, A. A. Van de Griend, A. Kruszewski, S. Schmidl Søjbjerg, and N. Skou, "A field experiment on microwave forest radiometry: L-band signal behaviour for varying conditions of surface wetness," *Remote Sens. Environ.*, vol. 109, no. 1, pp. 10–19, Jul. 2007.
- [2] F. Demontoux, B. Le Crom, G. Ruffié, J.P. Wigneron, J.P. Grant, V.L. Mironov and H. Lawrence, "Electromagnetic characterisation of soil-litter media: Application to the simulation of the microwave emissivity of the ground surface in forests," *EPJ Applied Physics*, vol. 44, no. 3, pp. 303-315, Dec. 2008

[3] H. Lawrence, F. Demontoux, J.-P. Wigneron, P. Paillou, T.-D. Wu and Y. H. Kerr, "A New Numerical Approach for Modeling the 3-Dimensional Scattering and Emission of a Rough Surface," *submitted IEEE Trans. Geosci. Remote Sensing Lett.*, Oct. 2009

[4] H. Lawrence, F. Demontoux, J.-P. Wigneron, Y. Kerr, T.-D. Wu, P. Borderies, P. Paillou, L. Chen and J.-C. Shi, "Modeling the Effect of surface roughness on the back-scattering coefficient and emissivity of a soil-litter medium using a numerical model," *proc. Igarss 2009*

[5] H. Lawrence, F. Demontoux, J.-P. Wigneron, A. Mialon, Y. Kerr, T.D. Wu, V.L. Mironov, L. Chen, J.-C. Shi "L-Band emission of rough surfaces: comparison between experimental data and different modeling approaches" *proc. Microrad 2010*

[6] V.L. Mironov, L.G.Kosolapova, and S.V. Fomin, "Physically and Mineralogically Based Spectroscopic Dielectric Model for Moist Soils," *IEEE Trans. Geosci. Remote Sens.*, vol.47, no.7, pp.2059-2070, July 2009.

[7] V.L. Mironov, Fomin S.V "Temperature and mineralogy dependable model for microwave dielectric spectra of moist soils" in *PIERS Proceedings*, 938 - 942, August 18-21, Moscow Russia, 2009.

[8] P.P. Bobrov, V.L. Mironov, A.S. Yashchenko, Diurnal Dynamics Radiobrightness Temperature of Soil on the Frequency 1.4 and 6.9 GHz in the Processes of Freezing/Thawing. Abstracts of IGARSS'2010, July 25-30, Honolulu, USA.

Comparison between SMOS and VUA soil moisture products

Leroux Delphine ⁽¹⁾⁽²⁾, Kerr Yann ⁽¹⁾, de Jeu Richard ⁽³⁾, Wood Eric ⁽⁴⁾, Berthelot Beatrice ⁽²⁾

⁽¹⁾ Centre d'Etudes Spatiales de la Biosphère (CESBIO), Toulouse, France

⁽²⁾ Vega Technologies, Toulouse, France

⁽³⁾ Vrije Universiteit Amsterdam, Netherlands

⁽⁴⁾ Princeton University, USA

delphine.leroux@cesbio.cnes.fr

ABSTRACT - Soil moisture is one of the most important variables regarding climate evolution. It is now an Essential Climate Variable (ECV). Long time series of soil moisture are necessary in order to be able to capture long term evolution and trends. For more than 30 years, many satellites have been providing moisture information at global scale but acquired at different frequencies, incidence angles, crossing times. These technical differences may lead to significant discrepancies in the retrieved information. It has been demonstrated that L-band (1.4 GHz) is the most suitable frequency to retrieve soil moisture from a microwave signal. However, algorithms operating at higher frequencies have been developed in the absence of L-band sensors. The most used are at C and X bands (6 and 10 GHz). Richard de Jeu developed an algorithm to retrieve soil moisture from C and X bands taking into account the vegetation that plays an important role in the signal at those frequencies. In this study, soil moisture derived from SMOS and ASMR-E (with de Jeu's algorithm: VUA product) are compared and analyzed over the region of San Pedro, Arizona, USA. Two statistic methods are tested: the CDF matching and the copulas method. Both are based on the comparison between the distributions of the two datasets. The main goal of this paper is to simulate SMOS soil moisture from the VUA product so as to be able to generate a homogeneous time series over a long time period.

1 INTRODUCTION

1.1 Soil moisture

Soil moisture is a key variable in the water and has an important role in climate monitoring, weather forecasting and many radiative transfer models. In this paper, soil moisture refers to the amount of water contained in the first centimeters of the ground. Soil moisture interacts with the atmosphere from the top through evapotranspiration and with the root zone from the bottom through infiltration.

One way to monitor soil moisture at a global scale is to use passive microwave radiometers on satellites. It has been proved that L-band is the most suitable frequency to retrieve soil moisture because the signal is more sensitive to the water (Schmugge, 1988). SMOS is the first satellite that has been launched with a passive microwave radiometer working at this frequency.

Other satellites have been launched before but with different frequencies (SMMR in 1978 or AMSR-E in 2002 for ex.), so the evolution of the signal does not only correspond to the evolution of the soil moisture but also to the evolution of the biomass, cloud water or surface roughness (Kerr, 1996).

Moreover, this difference in frequency represents a difference in the penetration depth of the signal and soil moisture value is not the same in the first 5 cm as in the 1st cm, especially after a rainfall event.

The goal of this study is to create a homogeneous time series of soil moisture by generating SMOS soil moisture from AMSR-E dataset with statistical methods (CDF matching and the copulas method).

1.2 The region of interest

Six months of SMOS data are now available (January-June 2010) but this is a too short time period to draw any conclusion on the evolution of the soil moisture of a particular point. However studying a homogeneous area allows us to have more points and statistics can then be applied.

One region of 1°x1° in latitude and longitude has been selected: San Pedro, Arizona, USA. This region is a low vegetated mountainous area extending from 31° to 32° N in latitude and from 111° to 110° W in longitude (see Figure 1). Ground data are available from July 2007 until February 2010 (hourly and 12-hour average) from a monitoring station located at 31.56 N, 110.14 W.

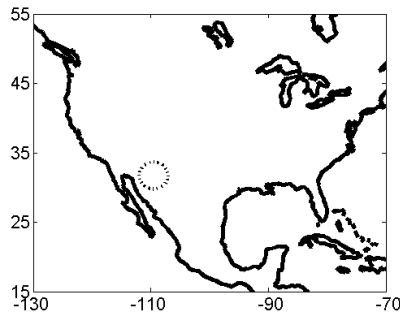


Figure 1 - San Pedro region in the circle, USA

2 THE DATA

2.1 SMOS

2.1.1 The mission

Soil Moisture and Ocean Salinity (SMOS) is a space mission of the European Space Agency (Kerr, 2001). The satellite has been successfully launched on 2, November 2009. The embedded passive microwave radiometer is operating at L-band (1.4 GHz) and is providing multi-angular brightness temperatures. This mission has been specially designed to retrieve surface soil moisture over land and salinity over sea. SMOS soil moisture represents the water content of the first 3 to 5 cm of the soil and has an accuracy of $0.04 \text{ m}^3/\text{m}^3$. The ascending and descending crossing times are 6 a.m. and 6 p.m. respectively (local time).

The algorithm to retrieve soil moisture uses this angular information to fit a model based on the L-MEB model (Wigneron, 2007) to the acquired brightness temperatures. It gives the value of the soil moisture (and of other parameters such as the vegetation optical thickness) that minimizes the difference between the model and the data.

2.1.2 The grid

The data are available on the Icosahedral Snyder Equal Area (ISEA) grid with an inter-cell distance of about 15 km (Snyder, 1992).

2.2 VUA product

2.2.1 AMSR-E

The Advanced Microwave Scanning Radiometer - Earth observation (AMSR-E) has been launched on Aqua satellite in May 2002. AMSR-E is a six-frequency passive microwave radiometer and measures brightness temperatures with an angle of 55° at 6.9, 10.7, 18.7, 23.8, 36.5 and 89.0 GHz. The

ascending and descending crossing times are 1.30 p.m. and 1.30 a.m. respectively.

The algorithm from the Vrije Universiteit Amsterdam (VUA) in Netherlands is retrieving soil moisture from AMSR-E brightness temperatures at 6 and 10 GHz and uses the 36 GHz channel (vertical polarization) to retrieve soil temperature (Owe, 2008). The optical thickness is analytically calculated from the polarization ratio (Meesters, 2005) and the value of the soil moisture is the one that minimizes the best a cost function between the forward model and the data. AMSR-E signal represents only the very first centimeters of the soil (0.5-1 cm).

2.2.2 The grid

Before using the brightness temperatures from AMSR-E, they have been resampled on a $0.25^\circ \times 0.25^\circ$ grid (Knowles, 2006). The retrieved soil moisture data (VUA products) are available on this grid.

2.3 Interpolation of the VUA product on the SMOS grid

VUA products are interpolated from the $0.25^\circ \times 0.25^\circ$ grid to the ISEA grid with the cubic method (see Figure 2).

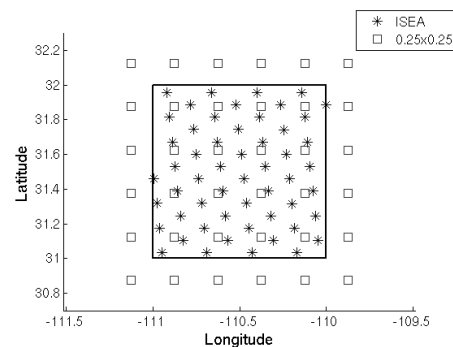


Figure 2 - Positions of the nodes of both grids in San Pedro region (the square in thick line)

3 TWO STATISTIC METHODS

The CDF matching and copulas method are presented in this section. They are based on the same theory but are different in the way they are applied to the data. Moreover, the copulas method needs further definitions.

3.1 Basic statistic theory

The probability density function (PDF) gives the probability that a random variable takes values in a given interval:

$$\Pr[a \leq x \leq b] = \int_a^b f(x)dx \quad (1)$$

where $f(x)$ is the density function of the random variable X .

The cumulative density function (CDF) is the probability that the random variable takes a value less than or equal to a given value:

$$F_X(x) = \Pr[X \leq x] \quad (2)$$

The joint distribution function of 2 random variables is the probability that the first variable is less than or equal to a first real number and that the second variable is less than or equal to a second real number:

$$H_{XY}(x, y) = \Pr[X \leq x, Y \leq y] \quad (3)$$

In statistics, a rank correlation coefficient measures the correspondence between two rankings. Two of the most popular rank correlation coefficients are:

- Spearman's rho: used to measure how well the relationship between two variables can be described by a monotonic function,
- Kendall's tau: used to measure the similarity of the ordering of the data ($\text{tau} = (\text{number of concordant pairs} - \text{number of discordant pairs}) / \text{total number of pairs}$).

Over San Pedro region, rho and tau have been computed: rho = 0.62 and tau = 0.43. It can be assumed there exists a monotonic function describing the relationship between soil moisture from SMOS and VUA products. However, tau is not high enough to say that the two datasets are ordered similarly.

3.2 CDF matching

In remote sensing CDF matching is often used to correct a bias of a dataset when it is compared to another one (Drusch, 2005).

Let X and Y be two random variables, for example X can be the soil moisture from AMSR-E and Y the soil moisture from SMOS over San Pedro region. Their CDF can be computed and then compared. The algorithm is as follows (see Figure 3):

- 1) Compute CDF of both dataset: F_X and G_Y
- 2) Given a value x of the variable X , compute the corresponding u such that $u = F_X(x)$
- 3) Set $v = u$ and compute the corresponding y such that $y = G_Y^{-1}(v)$

When CDF matching is used, one assumption is made: the two datasets have the same ranking.

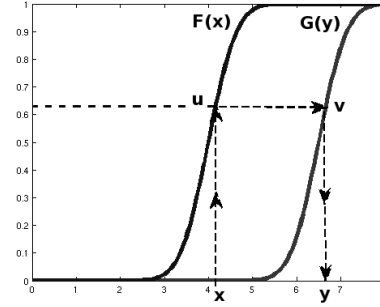


Figure 3 - CDF matching approach with $u=v$

3.3 Copulas method

The copulas theory is a very useful and powerful tool to model the dependence structure between two sets of random variables (Arnold, 2006). Instead of comparing the data directly (X and Y) the cumulative density functions are compared and analyzed. This comparison is the difference with the CDF matching where v is set equal to u .

3.3.1 General theory

The proper definition for a copula is a function joining multivariate distribution functions to their marginal distribution function (Nelsen, 2005). The most important theorem of the copulas theory is Sklar's theorem. It translates this link into a mathematic function named copula.

Sklar's theorem:

Let X and Y be two random variables with distribution function F and G , and joint distribution H . Then there exists a copula C such that:

$$H(x, y) = C_{XY}(F(x), G(y)) = \Pr[X \leq x, Y \leq y] \quad (4)$$

where C_{XY} is the copula of X and Y .

If a function C joining the two CDF can be found, the joint distribution H can be defined. But the most interesting is to be able to simulate Y knowing X ($Y|X$). That means that SMOS soil moisture could be simulated from VUA products. In statistics, it is called a conditional probability.

$$C_{Y|U}(u, v) = \frac{\partial C(u, v)}{\partial u} \quad (5)$$

One family of copulas is mostly used: the Archimedean family. It has the advantage to have different formulations to take into account the tail

dependence and one parameter to fit the data and the strength of the tail. The method to choose a copula is described in Genest, 2003 and is based on ranking correlation and generators.

The Gumbel copula fits the best the data over the San Pedro region. It takes the following form:

$$C_{\theta}(u, v) = \exp(-((-\ln u)^{\theta} + (-\ln v)^{\theta})^{1/\theta}) \quad (6)$$

The dependence parameter θ is restricted to $[1, \infty)$. For $\theta=1$, it is independence. This copula does not allow negative dependence and it has strong right tail dependence and weak left tail dependence (see Figure 4).

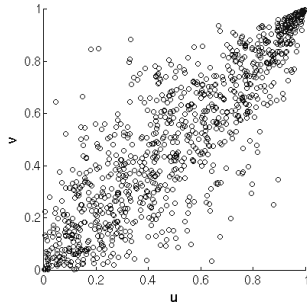


Figure 4 - Gumbel copula for $\theta=3$

3.3.2 How to use the copulas method

The method to use the copulas approach is as follows:

- 1) Compute the CDF of both datasets X and Y (F and G) and choose the appropriate copula by fitting the parameter of the copula to the data
- 3) Compute $u = F(x)$ and derive the conditional copula $C_{V|U}$
- 4) Generate a random variable t following a uniform law between 0 and 1
- 5) Compute v such that $v = C_{V|U}^{-1}(t)$ and y such that $y = G^{-1}(v)$

4. RESULTS

4.1 General results

Over San Pedro region, soil moisture products from SMOS and from AMSR-E (VUA products) have been compared (see Figure 5). VUA products have a bigger amplitude than SMOS soil moisture. The signal from SMOS looks flatter.

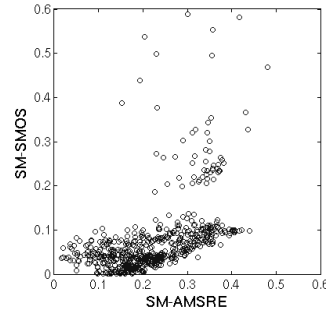


Figure 5 - Soil moisture products from SMOS vs. AMSR-E (m^3/m^3)

The CDFs (cumulative density function) of each dataset have been computed and compared (see Figure 6). The shape of the scatter plot is thinner on the top right corner than on the bottom left corner. This shape is characteristic of a Gumbel copula. By fitting the tail dependence parameter θ to the data, we get $\theta = 1.71$.

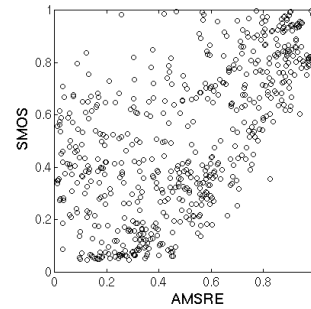


Figure 6 - CDF VUA vs. CDF SMOS

Now that the copula is chosen and the parameter is fitted, data simulation can be performed. Thus we are able to simulate SMOS data from VUA products and calculate the mean and the variance of these simulations (see Figure 7).

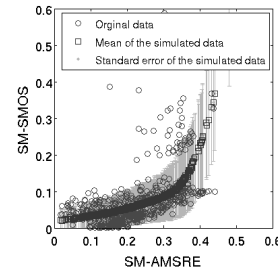


Figure 7 - Simulation of SMOS data from VUA products (m^3/m^3)

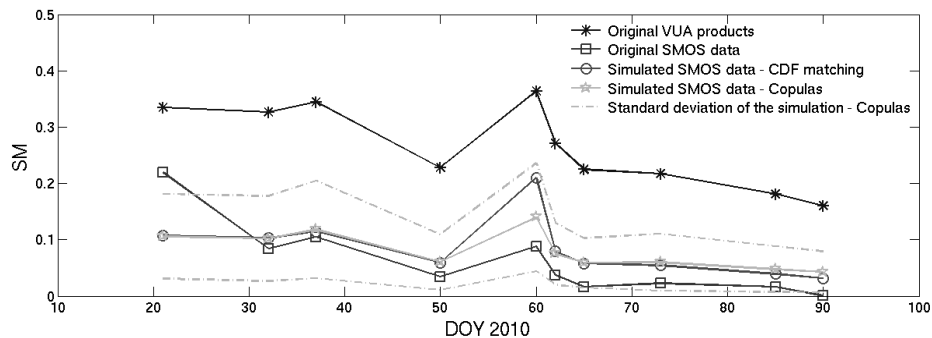


Figure 8 – Original VUA, original SMOS and simulated SMOS soil moisture (m^3/m^3) - 2010

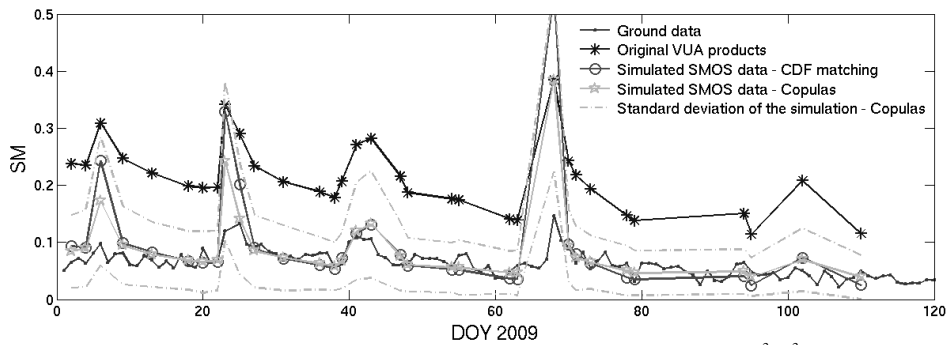


Figure 9 – Ground data, original VUA and simulated SMOS soil moisture (m^3/m^3) - 2009

4.2 Comparison between the CDF matching and the copulas method

Two statistic methods have been presented. Simulated SMOS data can be produced from the CDF matching and the copulas method. The data used to compute the cumulative density functions have been retrieved for the period January-June 2010. Correlation coefficients are computed to see which method gives the best simulations (closest to the SMOS products).

Figure 8 presents the time series of soil moisture from AMSR-E (VUA products), SMOS and the simulations with the CDF matching and the copulas from January to April 2010. The first thing to see is that VUA gives higher values of soil moisture than SMOS. Except the first point, these two datasets behave in the same way: when one is increasing, the other is decreasing as well. There exists a bias between them. The simulations have been computed over the entire region and only the closest node to the San Pedro station is showed here.

The simulations from the two statistic methods give results close to the real SMOS data. The main difference can be seen when an extreme event occurs: the simulated data from CDF matching takes a higher value than the one from the copulas method.

Otherwise, during calm periods, the two methods are equivalent.

	Correlation (SMOS/simulations) 2010
CDF matching	0.56
Copulas	0.71

Over San Pedro region, the simulations from copulas give better results than CDF matching.

4.3 Time series of soil moisture between January and April 2009

The copula fitted to data of 2010 can be used to simulate soil moisture data from VUA products of 2009 for the same months (January-April). Ground data are available at this period and can be compared to the simulations (see Figure 9).

	Correlation (simulations/ground) 2009
CDF matching	0.81
Copulas	0.82

The simulations from CDF matching and from copulas give comparable results when compared to the

ground data. Generally both follow the same evolution and they are quite close to the ground data. The main difference can be seen when an extreme event occurs. For example, around day 25, one can assume a rain event: ground measurements take higher values and retrieved soil moisture from AMSR-E and simulated data as well. However, simulated data by CDF matching and by copulas are reacting differently. Both give too high results but CDF matching reacts too strongly to the rain event. Around day 65, the simulated soil moisture is even higher than the VUA product.

VUA product overestimates the soil moisture. Compared to the ground measurements, VUA soil moisture takes higher values.

4 CONCLUSION

The main goal of this study was to generate a homogeneous time series of soil moisture. By using statistic methods, we have been able to learn how SMOS soil moisture products behave with the VUA products from January to April 2010. Simulations have then been performed: knowing a VUA product value, a simulated SMOS value can be computed. Thus, a time series of SMOS soil moisture has been simulated over the same period of 2009.

The CDF matching is a statistic technique with a starting assumption (the same ranking for the two datasets) whereas the copulas method does not assume anything about the ranking because it is studied through the comparison between the two cumulative density functions. Using copulas to simulate data is the best option if the two dataset are not ranked in the same way.

The two statistic methods have been performed over the region of San Pedro. The simulations have been compared to real SMOS data in 2010 and to the ground data in 2009. The simulations with copulas give a better performance than with CDF matching, especially during rain events. Rank correlations for this dataset are not very good ($\rho=0.62$, $\tau=0.43$) showing that working with copulas is adapted to this situation.

This study has been done over only one region with special climate conditions: arid and low vegetated. All the presented results are then only valid for this particular region but the statistic methods can be applied to other types of area. This work represents a first step to a homogeneous global soil moisture product.

REFERENCES

Arnold, H., 2006, Dependence modeling via the copula method, Master's thesis, CSIRO Mathematical and Information Sciences.

Drusch, M., Wood, E.F., and Gao, H., 2005, Observation operators for the direct assimilation of TRMM microwave imager retrieved soil moisture, *Geophysical Research Letters*, **32**, 1-4.

Genest, C., and Rivest, L., 1993, Statistical inference procedure for bivariate Archimedean copulas, *Journal of the American Statistical Association*, **88**, 1034-1043.

Kerr Y., 1996, Optimal choice for MIRAS frequencies scientific requirements, CESBIO.

Kerr, Y., Waldteufel, P., Wigneron, J.-P., Martinuzzi, J.-M., Font, J., and Berger, M., 2001, Soil moisture retrieval from space: the soil moisture and ocean salinity (smos) mission, *IEEE Transactions on Geoscience and Remote Sensing*, **39**, 1729-1735.

Knowles, K.W., Savoie, M.H., Armstrong, R.L., and Brodzik, M.J., 2006, AMSR-E/Aqua daily global quarter-degree gridded brightness temperatures, January 2009 to June 2010, Boulder, Colorado, USA, National Snow and Ice Data Center, Digital Media.

Meesters, A., de Jeu, R., and Owe, M., 2005, Analytical derivation of the vegetation optical depth from the microwave polarization difference index, *IEEE Geoscience and Remote Sensing Letters*, **2**, 121-123.

Nelsen, R., 2005, An introduction to copulas, *Springer Series in Statistic*, Second Edition.

Owe, M., de Jeu, R., and Holmes, T., 2008, Multisensor historical climatology of satellite-derived global land surface moisture, *Journal of Geophysical Research*, **113**, doi: 10.1029/2007JF000769

Snyder, J.P., 1992, An equal-area map projection for polyhedral globes, *Cartographica*, **29**, 10-21.

Schmugge, T.J., Wang, J.R., and Asrar, G., 1988, Results from the push broom microwave radiometer flights over the Konza Prairie in 1985, *IEEE Transactions on Geoscience and Remote Sensing*, **26**, 590-597.

Wigneron, J.-P., Kerr, Y.H., Waldteufel, et al., 2007, L-band microwave emission of the biosphere (L-MEB) model: description and calibration against experimental data sets over crop fields, *Remote Sensing of Environment*, **107**, 639-655.

Synergy of SMOS Microwave Radiometer, Thermal data and Vegetation Index for monitoring the water status of forest and natural vegetation

C. Mattar^a, J.A. Sobrino^a, J.P. Wigneron^b, Y. Kerr^c, A. Al-Bitar^c, N. Novello^b, Y. Julien^a, J.C. Jiménez-Muñoz^a, G. Sòria^a, V. Hidalgo^a, B. Franch^a, R. Oltra-Carrió^a and J. Cuenca^a

^a*Global Change Unit, Image Processing Laboratory, Parc Científic-University of Valencia, P.O. Box 22085, E-46071 Valencia, Spain..*

cristian.mattar@uv.es

^b*EPHYSE, INRA, Centre Bordeaux-Aquitaine, 33883, Villenave D'Ordon, France.*

^c*Centre d'Etudes Spatiales de la Biosphère (CESBIO), CESBIO, 18 avenue. Edouard Belin, bpi 2801, 31401 Toulouse cedex 9,, France*

ABSTRACT.- Soil moisture is the water held in the soil generally within reach of plant roots and is one of the most important land environmental variables, relevant for land surface climatology, hydrology, and ecology. In fact, variations in soil moisture have a strong impact on surface energy balance, regional runoff, and vegetation productivity (potential crop yield). In this framework, the Soil Moisture and Ocean Salinity (SMOS) mission was recently launched to observe soil moisture over the Earth's land surfaces and salinity over the oceans. The baseline SMOS payload is an L-band (1.4 GHz) two dimensional interferometric radiometer that aims at providing global maps of soil moisture with an accuracy better than $0.04 \text{ m}^3 \text{ m}^{-3}$ every 3 days and with a resolution better than 50 Km. SMOS operations make use of the so called 'SMOS L2' processor to retrieve soil moisture and other surface parameters (e.g. vegetation optical thickness and roughness) taking advantage of the dual-polarised multi angular brightness temperatures that this sensor provides. These temperatures, in addition to nominal parameters and physical algorithms, are used to deliver the SMOS level-2 products following the established user requirements. Soil moisture is a very important index to monitor the ecosystem functioning and mass and energy exchanges at the soil- vegetation-atmosphere interface. However it cannot provide by itself an accurate information about the vegetation water status, that depends also on key parameters such as the vegetation root system and soil depth, among others. In this study, improvements in monitoring the vegetation water status consider the use of the synergy between passive microwave and visible/thermal remote sensing data. This work establishes some semi-empirical relationships between both land surface temperature and vegetation index products provided by Moderate Resolution Imaging Spectroradiometer (MODIS) and passive microwave data, in addition to the monitoring of water status using Meteosat Second Generation-Spinning Enhanced Visible and Infra-red Imager (MSG SEVIRI) and Reanalysis information. While redacting this work, SMOS Level-2 products were still under commissioning phase, therefore results presented here will be improved continuously to establish clear patterns for the synergy between passive microwave and other remote sensing data when SMOS Level-2 products are available for scientific community.

Keywords: Soil Moisture, Land Surface Temperature, SMOS, MODIS, MSG2-SEVIRI, synergy

1. INTRODUCTION

Soil moisture has been widely recognized as one of the most important variable for live development. It is a key parameter in describing water and energy exchanges, which establishes the basic conditions for crop growth and hydrology/climate modeling (Zhang et al., 2007).

Soil moisture is widely referred to as the water content in the root zone (0.00 to 1.0 m depth) and it constitutes an indispensable variable to take into account in environmental studies. Typically, soil moisture has

been estimated by conventional point measurements, which are scarce, complex and expensive (Mallick et al., 2009). However, one way to improve the spatial soil moisture measurements is throughout remote sensing techniques which fulfil an important role for generating soil moisture maps at different spatial scales. In this context, the Soil Moisture Ocean Salinity (SMOS) space mission is the first satellite to make specific observation in the L-band (1.4 GHz) and providing global soil moisture maps with an accuracy better than 4%v/v every 3 days with a resolution better than 50 km (Kerr et al., 2001).

This satellite was launched in November 2009 and is currently in the commissioning phase. However, the coarse spatial resolution retrieved by SMOS is a challenge that is being carried out. In fact, in order to improve the spatial resolution of the soil moisture estimated by SMOS, there are some attempts in using downscaling methods and surrogate Optical/Infrared variables such as land surface temperature or vegetation indexes (Merlin et al., 2008; 2009). These techniques which relate optical/IR and microwave frequency enhance the ability of extracting information on soil moisture conditions. A thorough analysis of advantages/drawbacks of these remote sensing techniques is presented in Moran et al. (2004), where the strong relation between soil moisture surface temperature and vegetation index is one of the most important advantages when using TIR emittance.

The aim of this work is to analyze some biophysical interactions between the SMOS soil moisture data and optical/IR data provide by Moderate Resolution Imaging Spectroradiometer (MODIS) using a non-parametric equation basically constituted by the land surface temperature (LST) and vegetation index (NDVI, a definir). Additionally, the relation between the precipitation and soil moisture has also been assessed with Meteosat Second Generation-Spinning Enhanced Visible and Infra-red Imager geostationary data (MSG-SEVIRI) and Reanalysis products.

2. DATA

2.1 Study Area

In this work, two study areas have been used. One is located in eastern Australia, where several SMOS calibration/validation field campaigns were carried out (Panciera et al. 2008). The other area is located in south of Africa where the images provided by the MSG geostationary satellite match with SMOS. Both study areas are shown in figure 1.

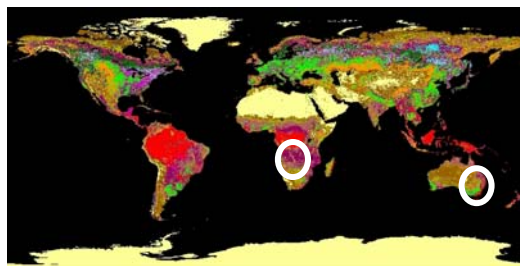


Figure 1. Global land cover map. White circles indicate the study area of Africa and Australia.

2.2 SMOS data

Soil moisture data from SMOS level-2 products were used for the two study area (Africa and Australia). These two products were filtered by the quality flags presented in the products (DQX and RFI). However, at the moment of this work, the SMOS data was finishing the commissioning phase, so the results presented here are not definitive and necessary deserve further analysis.

2.3 MODIS data

Daily MODIS LST (MOD11L2) and NDVI (MOD13C1) products were acquired for the 9th February 2010 over the study area located in the east part of Australia. These were processed using the quality flags images and georeferenced. LST and NDVI were separated for each cover type described in the next section.

2.5 Cover Map

The Global Land Cover 2000 (GLC2000) has been used to link the data obtained from MODIS products and the land cover classification for Australia (Bartholomé & Belward). The cover map presents tree main classes: forest 6%, shrublands 72%, grasslands 13% and bare soil 9%.

2.4 METEOSAT Data

The METEOSAT SEVIRI data were acquired for the 7th July 2010 between 03 and 06 UTC every 15 min. These images were acquired by the Global Change Unit antenna station and were georeferenced using the provided metadata file.

2.5 NCEP-1 data

The National Center of Environmental Prediction (NCEP) and the National Center of Atmospheric Results (NCAR) founded the Reanalysis project which generate several meteorological and climatological variables at global scale (2,5° x 2,5° latitude – longitude) since January 1948 (Kalnay et al., 1996). In this work, the precipitation rate and the soil moisture for 3 March 2010 and 7 March 2010 have been used to compare the synoptic information retrieved by Numerical Prediction Model with the Information retrieved by SEVIRI and SMOS. The NCEP-1 information was processed every 6 hours for the African continent.

3. METHODOLOGY

In this work, LST and NDVI were compared to obtain the wet and dry zones using the universal triangle (Carlson et al. 1994). Then, simple non-linear equations were generated to estimate the soil moisture for each land cover class following equation 1.

$$SM = \sum_{i=0}^2 \sum_{j=0}^2 a_{ij} T^{*(i)} NDVI^{*(j)} \quad (1)$$

where SM is the soil moisture, T^* and $NDVI^*$ is the modified surface temperature and vegetation index respectively (see Chauhan et al. 2003). This procedure was applied for both Africa and Australia study areas. The obtained soil moisture was directly compared with SMOS soil moisture estimation. It is important to keep in mind that this work was carried out during the SMOS commissioning phase, therefore the obtained results will have to be deeply analyzed when SMOS data are definitive.

On the other hand, SEVIRI data were used to analyse a strong rainfall event. To this end, the NCEP-1 precipitation rate and soil moisture (0 -10 cm) data were used to compare the strong rainfall event with SEVIRI total liquid clouds and soil moisture from SMOS Level-2. The land surface temperature (LST) of each Seviri images was obtained using the algorithm proposed by Sobrino and Romaguera (2004). Then, LST and SEVIRI visible bands were combined with a simplification of the method proposed by Roebing et al (2006) to estimate the total liquid clouds. The obtained results were combined with SMOS and Reanalysis data to analyze the rainfall and the soil moisture during that event.

4. RESULTS

Figure 2 shows the universal Triangle generated by LST and NDVI values over the Australian study area. This figure also shows the low and high level of soil moisture presented in the Australia Study Area. Most pixels present a low content of soil moisture in agreement with the date of the analysis (February-Summer-Dry season) and the land cover types provided by the GLC2000 for this area (shrublands: 70%). However, the empirical relationship obtained for this zone is non-significant. Despite this fact, the empirical relationship is significant for grasslands and

bare soil types, which was expected since the method applied here was established and validated for low NDVI values (Table 1).

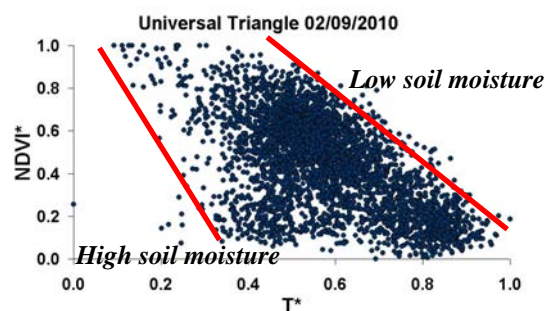


Figure 2. Universal triangle over Australia study area for 9th February 2010.

On the other hand, for the Africa study area, Figure 3a,b shows the precipitation rate and soil moisture retrieved by NCEP-1. It presents the intrusion, at synoptic scale, of high water amounts into the continent, which generates high levels of soil moisture. In coincidence, figure 3c presents a short temporal evolution of the calculated liquid clouds from Seviri in the study area. These results coincide with high soil moisture values in the same region (white rectangle) retrieved by SMOS (figure 3d). The same case was observed for 3rd March 2010. A high rate of convective precipitation and soil moisture is retrieved by NCEP-1 in the south-east part of Africa (Figure 4a,b). Using SEVIRI data (Figure 4c), the liquid clouds are identified in the same area with high level of soil moisture showed in SMOS products (Figure 4d). These results present an illustration to assess the hydrological status of a given region using the synergy between optical, thermal and passive microwave data.

Table I. Retrieved empirical equation based on MODIS and SMOS data. Significant relationships appear in bold.

GLC 2000 Class type	Equation	R2	Number of points
Forest	$SM = 1.08814 - 0.830718 * LST^* - 2.29676 * NDVI^* + 0.0338988 * LST^{*2} + 1.59529 * NDVI^{*2} + 0.821799 * NDVI^* * LST^*$	0.18	190
Shrublands	$SM = 0.41874 - 0.623923 * LST^* - 0.346135 * NDVI^* + 0.2513 * LST^{*2} + 0.422697 * NDVI^{*2} + 0.120616 * LST^* * NDVI^*$	0.27	2225
Grasslands	$SM = 0.305739 - 0.328528 * T^* + 0.109447 * NDVI + 0.033086 * LST^{*2} - 0.0375956 * NDVI^{*2} - 0.265069 * NDVI^* * LST^*$	0.78	393
Bare soil	$SM = 1.26109 - 2.8222 * LST^* - 2.60481 * NDVI^* + 1.61762 * LST^{*2} + 2.35666 * NDVI^{*2} + 2.88995 * NDVI^* * LST^*$	0.84	290

5. GENERAL CONCLUSIONS

The synergy between visible, thermal infrared and passive microwave data presents several advantages to assess meteorological and climate variables. In this work the soil moisture was analyzed to establish empirical equations over several land cover types in Australia, where MODIS data products (NDVI and LST) have been used in addition to soil moisture retrieved by SMOS. On the other hand, SEVIRI geostationary data (visible and thermal infrared data) have been used to retrieve liquid clouds, which properties are correlated with the precipitation rate and

soil moisture from NCEP-1 and soil moisture retrieved by SMOS.

As a first step, soil moisture retrieved by passive microwave data like SMOS can be useful to generate more accurate results in the assessment of water status over natural vegetation. This new data can be combined with other data source (visible and thermal infrared) using the synergy presented here. However, the results presented here have to be validated with additional SMOS level-2 products during more observed time and using other study areas with different cover types.

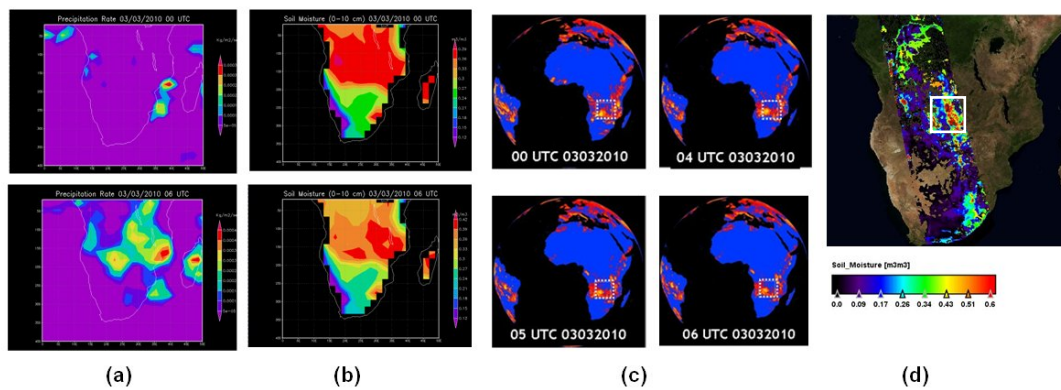


Figure 3. Precipitation rate (a) and Soil Moisture (b) retrieved by NCEP-1, Total liquid clouds estimated from SEVIRI (c) and SMOS Soil Moisture (d) on 3rd March 2010

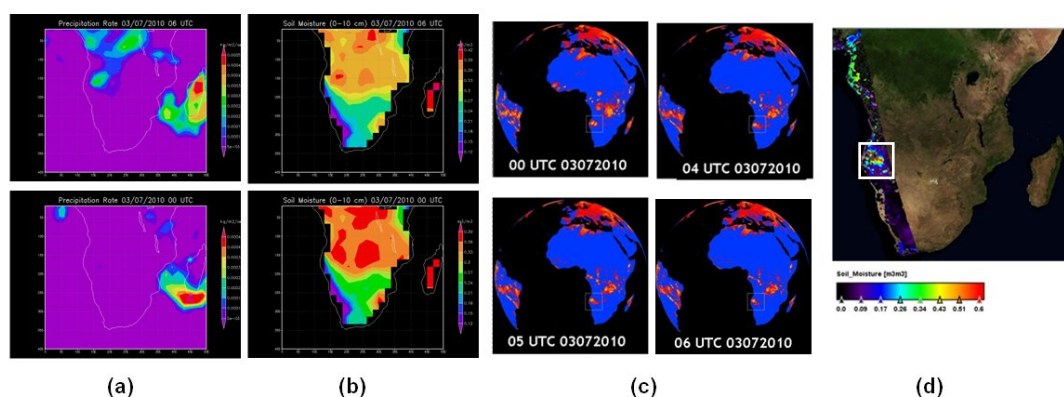


Figure 4. Precipitation rate (a) and Soil Moisture (b) retrieved by NCEP-1, Total liquid clouds estimated from SEVIRI (c) and SMOS Soil Moisture (d) on 7th March 2010

5 ACKNOWLEDGMENTS

The authors would like to thank the Spanish Ministerio de Ciencia y Tecnología (TERMASAT, project ESP2005-07724-C05-04; EODIS, project AYA2008-0595-C04-01), and the European Union (CEOP-AEGIS, project FP7-ENV-2007-1 proposal No. 212921; WATCH, project 036946) for supporting the work presented in this paper. Finally, we also thank the NCEP NCAR Reanalysis project which provided the data by the NOAA/OAR/ESRL PSD, Boulder, Colorado, USA, from their website at <http://www.esrl.noaa.gov/psd/>.

6 REFERENCES

- Bartholomé, E. & Belward, A.S. 2005. GLC2000: a new approach to global land cover mapping from Earth observation data. *International Journal of Remote Sensing*, Vol 26 (9), 1959–1977.
- Carlson, T., Gillies, R., and Perry, E. 1994. A method to make use of thermal infrared temperature and NDVI measurements to infer surface soil water content and fractional vegetation cover. *Remote Sensing Review*, 9, 161 – 173.
- Chauhan, N.S., Miller, S. and Ardanuy, P., 2003. Spaceborne soil moisture estimation at high resolution: a microwave optical/IR synergistic approach. *International Journal of Remote Sensing*, 24, pp. 4599–4622
- Mallick, K., Bhattacharya, B.K. and Patel, N.K. 2009. Estimating volumetric surface moisture content for cropped soils using a soil wetness index based on surface temperature and NDVI. *Agricultural and Forest Meteorology*, 149, 1327 – 1342.
- Kalnay and Co-Authors. 1996. The NCEP/NCAR 40-year reanalysis project, *Bull. Amer. Meteor. Soc.*, 77, 437-470.
- Kerr, Y., Waldteufel, P., Wigneron, J.P., Martinuzzi, J.M., Font, J. & Berger, M. (2001). Soil moisture retrieval from space. The soil Moisture and Ocean Salinity (SMOS) mission. *IEEE Transaction on Geoscience and Remote Sensing*, 39(8), 1729 -1735.
- Merlin, O., Al-Bitar, A., Walker, J.P. and Kerr, Y. 2009. A sequential model for disaggregating near-surface soil moisture observations using multi-resolution thermal sensors. *Remote Sensing of Environment*, 113, 2275 – 2284.
- Merlin, O., Walker, J.P., Chehbouni, A. and Kerr, Y. 2008. Towards deterministic downscaling of SMOS soil moisture using MODIS derived soil evaporative efficiency. *Remote Sensing of Environment*, 112, 3935 – 3946.

- Moran, S., Peters-Lidard, C.D., Watts, J. and McElroy, S. 2004. Estimating soil moisture at the watershed scale with satellite-based radar and land surface models. *Canadian Journal of Remote Sensing*, 30(5), 805 – 826.
- Panciera, R., Walker, J. P., Kalma, J. D., Kim, E. J., Hacker, J., Merlin, O. and Berger, M., 2008. The NAFE'05 Dataset: Towards SMOS Calibration, Downscaling and Assimilation. *IEEE Transactions on Geoscience and Remote Sensing*, 46(3), doi:10.1109/TGRS.2007.915403.
- Roebeling, R.A., Feijt, A.J. and Stammes, P. 2006. Cloud Property retrieval for climate monitoring. Implications of differences between SEVIRI and AVHRR. *JGR*. Vol. 111. D20210.
- Sobrino, J.A. & Romaguera, M. 2004. Land surface temperature retrieval from MSG1-SEVIRI data. *Remote Sensing of Environment*, 92, 247–254.
- Zhang, X., Tang, B., Jia, Y., and Li, Z.-L., 2007, Estimation of Bare Surface Soil Moisture using Geostationary Satellite Data. *IGARSS'07*, 23-28 July, Barcelona, Spain.

Sampling strategy for the validation of SMOS surface soil moisture at the Valencia Anchor station. Campaigns of 2008, 2009, 2010.

C¹. Millán-Scheiding; M. C. Antolín¹; E. Carbó¹; E. López-Baeza²

¹ Dept. of Land Use Planning. Centre for Desertification Research (CIDE);

² Dept. of Physics of the Earth and Thermodynamics. University of Valencia

Cristina.Millan@uv.es

M.Carmen.Antolin@uv.es

Ernesto.Lopez@uv.es

ABSTRACT The objective of the SMOS (Soil Moisture and Ocean Salinity) space mission is to observe soil moisture and ocean salinity from the surface of the earth. The calibration and validation of the data from SMOS requires a realistic estimation of the surface soil moisture in different areas within a SMOS footprint. At the Valencia Anchor Station three campaigns were carried out. In the Campaigns of 2008 (ESA SMOS Validation Rehearsal Campaign), 2009, and 2010 (CNES Cooperative Airborne Radiometer for Ocean and Land Studies), three different, but complementary sample strategies were followed with a double objective, namely to optimize the work of acquisition of necessary ground measurements for the validation of the airborne sensors and for the establishment of relations between the environmental factors, and the soil moisture. The ultimate objective of all the information obtained is to maximize resources and time in the elaboration of soil moisture maps for the validation of SMOS data.

1 INTRODUCTION

The objective of the SMOS (Soil Moisture and Ocean Salinity) space mission is to observe soil moisture and ocean salinity with enough resolution to be used in global climate studies (ESA). The calibration and validation of the data from SMOS require a realistic estimation of the surface soil moisture in different areas within a SMOS footprint. Knowledge of the distribution of the soil moisture (SM) in semi-arid Mediterranean ecosystems, and of the environmental factors influencing it will enable the acquisition of in situ data simultaneous to the observations from SMOS in the area of the Valencia Anchor Station (VAS). Variability of soil moisture depends on soil factors intrinsic and extrinsic (López-Baeza, *et al* 2008). It is necessary to have a sampling strategy that integrates the relationships between hydrological variables, SM in particular and the parameters of the landscape at different spatial scales. The strategy used in the Valencia Anchor Station is to subdivide the landscape into hydrological units with well-known parameters in relation to soil moisture. As these units respond in the same hydrological way to climate, soil type, topography, vegetation cover conditions, lithology, and elevation, they are considered to have similar soil moisture levels (López-Baeza, *et al* 2008, and Saleh, *et al* 2008).

In the Campaigns of 2008 (ESA SMOS Validation Rehearsal Campaign), 2009, and 2010 (CNES and

ESA-CNES Cooperative Airborne Radiometer for Ocean and Land Studies), three different, but complementary sample strategies were followed with a double objective, namely to optimize the work of acquisition of necessary ground measurements for the validation of the airborne sensors and for the establishment of relations between the environmental factors, and the units (fig. 1). The ultimate objective of all the information obtained is to maximize resources and time in the elaboration of soil moisture maps for the validation of SMOS data.

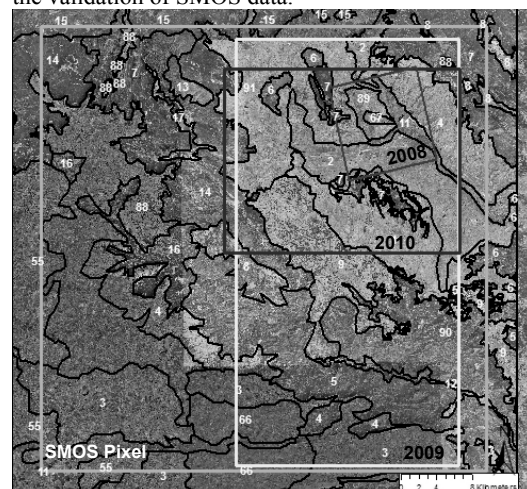


Figure 1. Valencia Anchor Station Reference Pixel, and campaign areas of 2008, 2009 and 2010.

2 METHODS

2.1. Between April and May 2008, the "*Experimental Plan for the SMOS Validation Rehearsal Campaign at the VAS Site*" was performed to obtain ground SM and compare it to the data acquired from the different airborne radiometers. A control area of $10 \times 10 \text{ km}^2$ inside the SMOS reference pixel was delimited. The area was then divided in environmental units attending to soil types, topography, geological material, use and vegetation covers, etc. The sampling intensity was carried out at two scales, depending on the flight height of the aircraft which transported the sensors, and covered all of the area in a stratified random way (fig. 2).

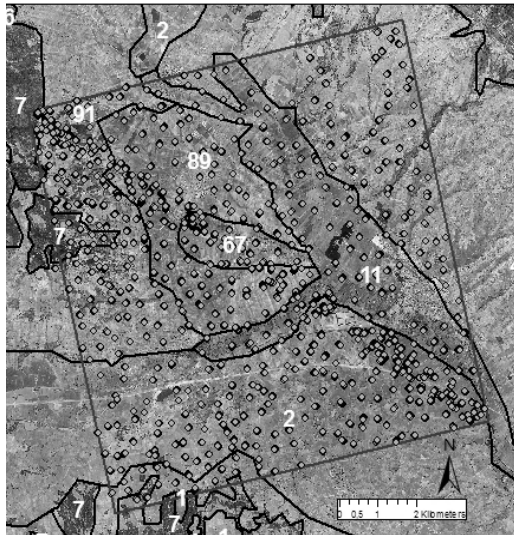


Figure 2. Sampling design of the 2008 rehearsal campaign. Delimitation of the units in black and unit Id in white.

2.2 In the CAROLS campaign (April-May 2009) a mapping of the units was conducted in an area of $25 \times 37 \text{ km}^2$ inside the SMOS reference pixel that previously stratified the classes (fig. 3). The strategies developed on these units were:

- A selection of 10 stationary points, close to 10 meteorological stations representative of the different units of the area. The aim of these stations was to reflect the variability of all types of vegetation and of the different roughness parameters.

- A simple random sampling in areas of $1 \times 1 \text{ km}^2$ selected inside the environmental units most representative of the area covered.

- A transecting sample strategy in the control area of $10 \times 10 \text{ km}^2$ from the previous 2008 rehearsal campaign, naturally included in the CAROLS study area.

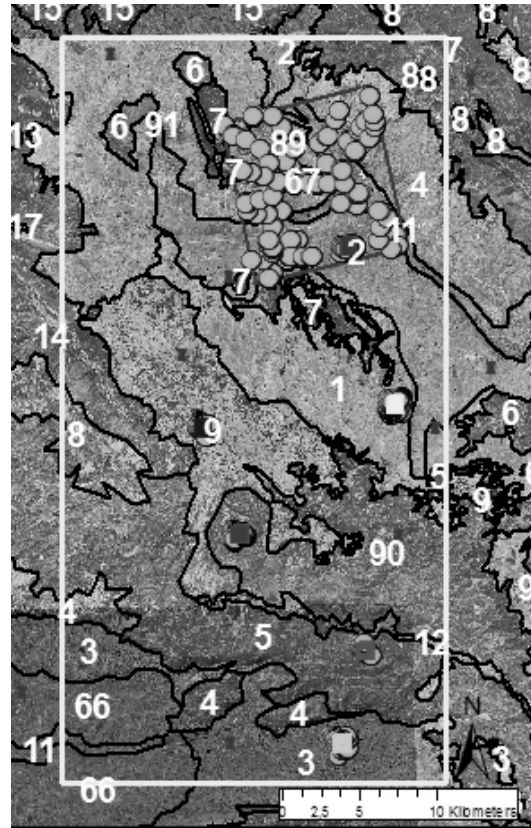


Figure 3. Sampling design of the CAROLS campaign of 2009. Big squares are $1 \times 1 \text{ km}^2$ study areas, small squares are stationary points and dots are transecting sample plots repeated from the 2008 campaign.

2.3 The CAROLS campaign (May-June 2010) had a combination of both sampling strategies carried out in the 2008, and 2009 campaigns. The units found in the studied area were sampled extensively throughout the campaign with stationary and mobile teams, taking into account the differences in soil moisture found in the previous campaigns within each unit due to geomorphological and vegetation cover (fig. 4).

- A selection of 11 stationary points, close to 10 meteorological stations representative of the different units of the area.

- A transecting sample strategy in plots representative of different geomorphological aspects and land uses of each unit of the area.

- A transecting sample strategy in the control area of 10 x 10 km² from the previous 2008 rehearsal campaign, included in the CAROLS study area.

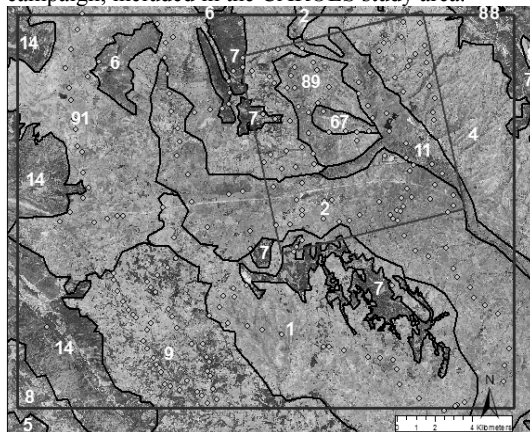


Figure 4. Sampling design of the CAROLS campaign 2010.

3 RESULTS

The variation in the water content at any given point of the soil will partially depend on the degree of variability of the intrinsic edaphic properties that most influence the water retention capacity (López-Baeza, et al 2008, Saleh, et al 2008, Millán-Scheiding, et al 2007 and 2009, Cano, et al 2007).

In 2008, maps of SM have been obtained assigning an average value of θ/km^2 (fig. 5) contrasting and confirming its similarity with the data obtained from using values from each unit delimited. The result was a good correlation with those obtained from the airborne sensors (Saleh, et al 2008)

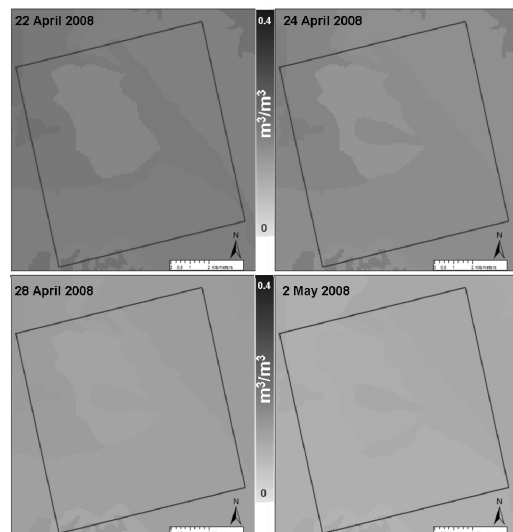


Figure 5. Soil moisture maps of each day of the 2008 rehearsal campaign.

In the 2009 CAROLS campaign, soil moisture data corresponding to each km², representative of the environmental units, showed certain homogeneity in relation to the inner variability of each unit. This suggests the possibility of extending the measurements to the whole unit (fig. 6). In each unit, vegetation cover has been found to predominate over soil texture with respect to the soil moisture content. Therefore, it is necessary to separate vegetation covers and geomorphological aspects within each unit for a better soil moisture estimation.

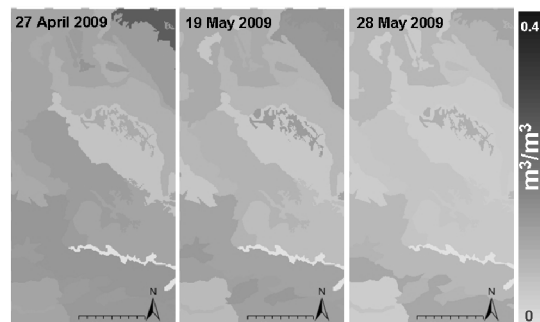


Figure 6. Soil moisture (m³/m³) maps of the three days of the CAROLS campaign of 2009.

The CAROLS campaign of 2010 shows maps of soil moisture for each unit (fig. 7). Including the conclusions extracted from the campaign of 2009 into the sampling design, the separation of vegetation covers and geomorphological aspects used in 2010 gave a more correct soil moisture average for each unit.

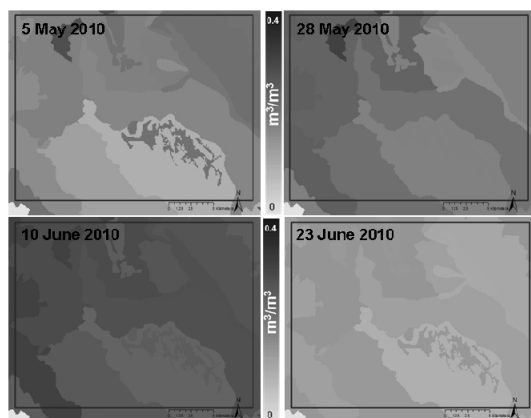


Figure 7. Soil moisture maps of each day of the Carols 2010 campaign.

In both CAROLS campaigns, the SM data from transects of the control area of 10 x 10 km², corroborates their similarity to the units were they are located. Also, the stationary measurements are representative of the situations they typify.

4 CONCLUSIONS

The combined sampling designs used have enabled the estimation of SM values in larger areas, and the resulting SM maps are correlated with those produced from the airborne sensors. This confirms the use of these strategies for the validation of SMOS at the Valencia Anchor Station.

5 BIBLIOGRAPHY

Cano, A., Anon, J.L., Reig, C., Millán-Scheiding, C., López-Baeza, E., 2007, Wireless Sensor Network for Soil Moisture Applications. International Conference on Sensor Technologies and Applications, 14-20 Oct. 2007 - Valencia, Spain

European Space Agency:
<http://www.esa.int/esaLP/LPsmos.html>

López-Baeza, E. & SMOS Cal/Val AO Project no.3252 Team., 2008, Valencia Site Data Processing & Model Results. Workshop SMOS Validation Rehearsal Campaign. NH Conf. Centre Leeuwenhorst, Netherlands, 18-19 Nov.2008

Millán-Scheiding, C., Antolin, C., Cano, A., Lopez-Baeza E., 2007, Uso de Unidades Fisi-Hidrologicas en la Monitorizacion de la Humedad del Suelo con SMOS. III Simp Nacional sobre Control de la Degradacion de Suelos y Desertificacion. Fuerteventura, 16-20 Sep. 2007

Millán-Scheiding, C., Antolín, C., Marco, J., Soriano, M.P., E. Torre, E., Requena, F., E. Carbó, E., Cano, A., López-Baeza, E. 2009, Use of physio-hydrological units for SMOS validation at the Valencia Anchor Station study area. Geophysical Research Abstracts. EGU General Assembly

Saleh, K., López-Baeza, E., Cano, A., Millán-Scheiding, C., Antolín C. & SMOS Validation Rehearsal Team, 2008, SMOS Validation Rehearsal Flights (EMIRAD) VALENCIA. SMOS Meeting, Bordeaux. INRA, 30-31 Oct. 2008

Application of GNSS-R Data Over the Valencia Anchor Station Site During the SMOS Validation Rehearsal Campaign 2008

Buil, A.⁽¹⁾, V. Gomez Rubio⁽²⁾, F. Fabra⁽³⁾, E. Cardellach⁽³⁾, A. Rius⁽³⁾, C. Millan⁽⁴⁾, E. Lopez-Baeza⁽¹⁾

(1) *University of Valencia. Dept. of Physics of the Earth & Thermodynamics. Climatology from Satellites Group*

(2) *University of Castilla-La Mancha, Dept. of Mathematics*

(3) *Spanish Advanced Council for Research, Institute of Space Sciences*

(4) *Center for Desertification Research, University of Valencia*

Alejandro.Buil@uv.es Ernesto.Lopez@uv.es

ABSTRACT *The objective of this work is to gain more knowledge to relate the Global Navigation Satellite Systems (GNSS) signals reflected by the land surface to soil moisture. During the ESA SMOS Validation Rehearsal Campaign (April-May, 2008), the Short SC.7 Skyvan 3A-100 from the Technical University of Helsinki included the GOLD-RTR (GPS open-loop differential real-time receiver) receptor as part of the payload, acquiring the signals proceeding from the GPS constellation. At the same time, a comprehensive volumetric soil moisture sampling was performed in the 10 x 10 km² Valencia Anchor Station control area by means of volumetric soil cylinder samples and Delta-TetaProbe sensors. We have firstly analyzed the raw data over homogeneous areas (crop types, texture,...). Once we achieved acceptable relationships, geo-statistical models (Universal Kriging) were used and validated, taking advantage of the maximum possible quantity of data. We also used the Environmental Unit map used by our research group in SMOS validation activities where we could compare soil moisture for each Environmental Unit to GOLD-RTR data, thus determining the units that offered better results.*

1 INTRODUCTION

Soil moisture is a variable that plays a crucial role in various processes that occur in the soil-atmosphere interface. It determines the distribution of solar radiation and the distribution of rainfall into surface runoff and infiltration. It is also a factor in the growth and development of crops and plants in general, since it determines the available water content in top soil where they develop the roots of most crops in the early stages. As seen, soil moisture is a determining parameter in many processes, but really hard to get operationally. GPS signals will be increasingly operational when GPS sensors will be installed onboard future missions for Earth observation. This paper intends to use data from test campaigns for the validation of SMOS at the Valencia Anchor Station to study the relationship between soil moisture and the GPS signal.

1.1 Study Area

The study area includes the reference area of the Valencia Anchor Station in the Natural Region of *La Plana de Utiel-Requena*, located west of the province of Valencia. It represents an area of about 2500 km² (The area is fairly homogeneous and is mainly dedicated to the cultivation of vineyards). The coordinates of the study area the following:

Latitude: 39.838°- 39.199 ° N

Longitude: 1.541°-0.884°W.

The area has a dry continental climate. Within this area, a control area 10 x 10 km² was established, heavily equipped with soil moisture measuring instruments and other meteorological sensors.

2 METHODOLOGY

2.1 GNNS-R

Observation of soil moisture from satellite has always been predominantly performed in the microwave electromagnetic region, mainly in the range between 1-3 GHz. This is because in that range, atmospheric attenuation is largely reduced and better penetration of vegetation is achieved at longer wavelengths. Njoku and O'Neill (1982) showed that P-band (0.775 GHz) and L-band (1.4 GHz) frequencies are optimal for sensing soil moisture in the top 0-4 and 0-2 cm surface layers, respectively.

Bistatic radar using L-band signals transmitted by the Global Positioning System (GPS) was first proposed by the *European Space Agency* (ESA) and addressed by Hall and Cordey (1988) as an ocean scatterometer. ESA researcher Martin-Neira (1993) later proposed an altimeter system using ocean GPS reflections to measure sea surface height.

The GPS constellation consists of 24 satellites orbiting the Earth at an altitude of about 20,126.61 km over the Ecuador. These satellites are designed so that at any point on Earth at least 4 satellites are available for three-dimensional navigation. Each satellite transmits a PRN (*Pseudo Random Noise*), a random code which is always the same for each satellite and orthonormal with respect to the other).

GPS signals reflected from the surface of the Earth are a function of the dielectric constant so that a component associated with that signal will be a function of soil moisture.

Figure 1 shows the geometry of a bistatic radar (GPS satellite) and a receiver on an airplane or over a tower. The receiver simultaneously measures the direct signal from the GPS (CPR mode right-hand circularly polarized) and the reflected one from the surface (usually LCP mode is usually left-hand circularly polarized).

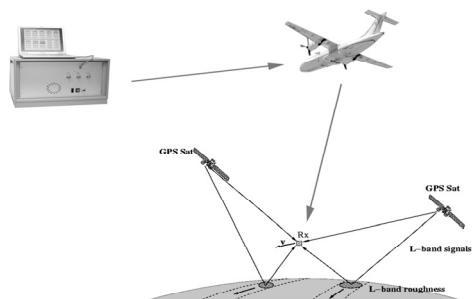


Figure 1 :Gold-RTR (Nogues, 2007) and PAssive Reflectometry and Interferometry System (PARIS) (Neira,2001)

Our receiver onboard the aircraft was the GOLD-RTR. This has 10 channels but they are reduced to 5 and the other remaining 5 are dedicated to the direct signal from the satellite. The resolution can be obtained using the equations:

$$a = \sqrt{2\rho H \cos\theta / \cos^2\theta} \quad b = \sqrt{2\rho H \cos\theta / \cos\theta} \quad (1)$$

where H is the height of the receiver from the surface, ρ is the delay and θ the angle of incidence. In our case, the resolution was about 30 meters.

2.2 Geostatistics Model

Geostatistics is a branch of statistics focusing on spatial or spatiotemporal datasets. Developed originally to predict probability distributions of ore grades for mining operations, it is currently applied in different disciplines including petroleum geology, hydrogeology, hydrology, meteorology, etc....

Kriging is a group of geostatistical techniques to interpolate the value of a random field at an unobserved location from observations of its value at nearby locations.

We have chosen universal kriging since it had additional information (covariates) such as clay and sand contents that are associated with soil moisture content obtained from maps of soil moisture. In the appendix we show the kriging map for one of the days, 22/04/2008 (Figure 2).

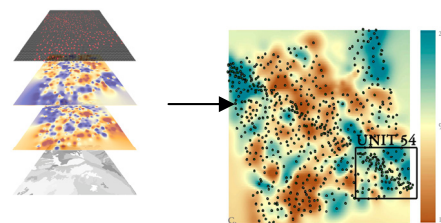


Figure 2: Multilayer sampling point and grid+ sand content+clay content+unit environment units .

Validation (cross validation) of the model was performed giving a value of R between observed and predicted values of 0.56. This is mainly due to the low sampling density that exists in some areas. However there were areas where sampling was sufficiently dense so that the variance in that area was very low (for example along the diagonal flight line) and we took advantage of such data for the analysis.

3 RESULTS

3.1 Ground Data

First we compare data from a wet day (22/04/2008) and a dry day (02/5/2008) to see the signal variation as shown in Figure 3.

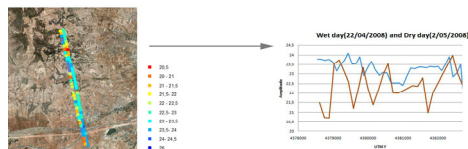


Figure 3: Variation of amplitude on dry day and wet day.

We chose two areas which had similar angle of elevation because, as we will see, this parameter produces a big influence on the signal. The graphs do not show an exact similarity in form, but it decreases the average signal in the drier surface.

Once we saw that there was some relationship between the signal and soil moisture a comparison was made between aircraft raw data and ground measurements obtained by means of volumetric cylinder soil samples. As mentioned above, the footprint was approximately 30 m and there was rarely a coincidence of GPS and in situ data. Then we established a threshold of 100 meters in diameter (see figure 8) to consider both type of measurements. Figure 4 shows the data from the plane vs the in situ data ($R=0,69$).

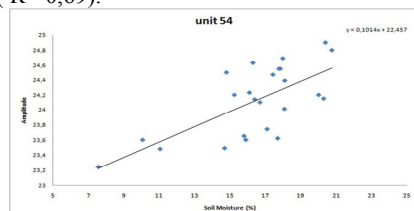


Figure 4: Relationship between airborne data and in situ data 22,24,28 April 2008.

With this comparison we note that the signals from the plane were strongly influenced by the angle of elevation, so we decided to parameterize the correlation for the observation angle (figure 5).

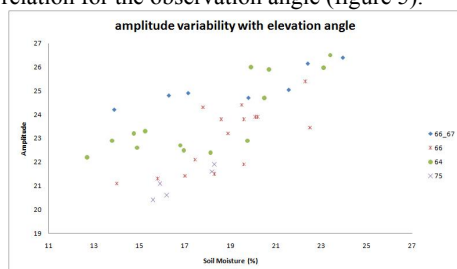


Figure 5: Different correlation between the amplitude and the soil moisture data at different angle of observation.

3.2 Geo-statistical Data

Due to the sparsity of the data at our disposal to analyze the relationship between the signal and soil moisture, we decided to use geostatistics to construct a map of soil moisture throughout the study area of 10x10 km² from in situ data measurements.

In our case, besides soil moisture, we also used clay and sand contents as covariates of the model, together with the definition of environmental units in each sampling point.

The geostatistical validation of our model is not very good, but there are areas where the variance is low enough to make this comparison (those areas from the diagonal flight line).

We chose unit 54 as shown in Figure 2. This area is predominantly composed of vineyards. During the time of the measurements, the area could be considered as bare soil so we did not have to consider the disturbance of the leaves (Figure 6).



Figure 6: Unit 54 during the camping SMOS Validation 2008.

Below we show the signal in Figure 7 (with a unique elevation angle) with the generated map in the environmental unit 54 ($R=0,84$).

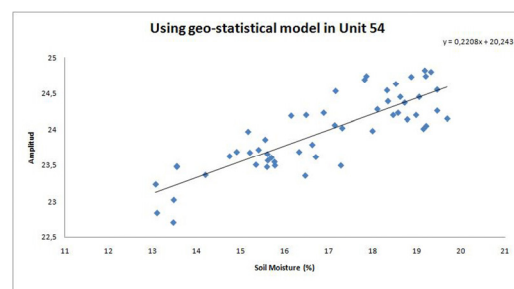


Figure 7: Relationship between geo-statistical model and airborne data 22,24,28 April 2008.

4 CONCLUSION

For the study area of the Valencia Anchor Station, the amplitude of the waveform is closely related to soil moisture, and this relationship strongly depends on the elevation angle. We also found that the best results correspond to bare soil areas.

The geostatistical model (universal kriging) used for the prediction of soil moisture from sampling points was not as satisfactory as expected ($r = 0.56$), although the results could be used in areas where the sampling density is relatively high.

Thus, we could get good relationships between model (kriging) and airborne data for the conditions mentioned above, namely, bare soil, high sampling density and a specific elevation angle, always above 60 deg.

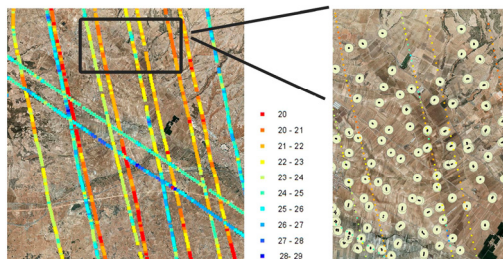


Figure 8: Buffer between in situ data and airborne data (22/04/2008).

5 REFERENCES

- Masters, D., Axelrad, A., & Katzberg, S. J. 2004: Initial results of land reflected GPS bistatic radar measurements in SMEX02. *Remote Sensing of Environment*.
- M. Martín-Neira, M. Caparrini, J. Font-Rosselló, S. Lannelongue, and C. S. Vallmitjana, 2001: "The PARIS concept: An experimental demonstration of sea surface altimetry using GPS reflected signals," *IEEE Trans. Geosci. Remote Sens.*, vol. 39, no. 1, pp. 142–149, Jan. 2001.
- O. Nogués-Correig, E. Cardellach, J. Sanz & A. Rius 2007: "A GPS-Reflections Receiver That Computes Doppler/Delay Maps in Real Time", *IEEE Trans. Geosci. Remote Sens.*, vol. 45, no. 1, pp. 156–174, Jan. 2007.
- Chanzy, A., 2003. Evaporation from soils. In: *Encyclopedia of water science*, Editores: B.A. Stewart y T.A. Howell Editors, Marcel Dekker Ed., USA.
- Njoku, E., & O'Neill, P. (1982). Multifrequency radiometer measurements of soil moisture. *IEEE Trans. Geosci. Remote Sens.*, 20, 468– 475.
- Hall, C., & Cordey, R. (1988). Multistatic scatterometry. *Proc. IEEE Int.Geosci. Remote Sens. Symp. (IGARSS '88)*, Edinburgh, Scotland.

Estimation of TVDI (*Temperature Vegetation Dryness Index*) and its relation to soil moisture in the framework of the SMOS validation campaigns in the Valencia Anchor Station

M.A.Coll, E.López-Baeza

University of Valencia. Dept. of Physics of the Earth & Thermodynamics. Climatology from Satellites Group

M.Amparo.Coll@uv.es, Ernesto.Lopez@uv.es

ABSTRACT- TVDI (*Temperature Vegetation Dryness Index*) can be used as an indicator of drought, desertification monitoring, validation of hydrological models, fire risk assessment, estimation of surface water condition and evapotranspiration, etc. A study of the Temperature Vegetation Dryness Index (TVDI) is being carried out using MODIS (Moderate Resolution Imaging Spectroradiometer) data over the SMOS (Soil Moisture and Ocean Salinity) validation area at the Valencia Anchor Station (Natural Region of the Utiel-Requena Plateau), west of the province of Valencia. We intend to relate TVDI with soil moisture content from the network of stations that the Climatology from Satellites Group has distributed in the area. In this study we use MODIS instantaneous products for LST (surface temperature) and 16-day cumulative products for NDVI (Normalized Difference Vegetation Index).

1 INTRODUCTION

Soil moisture content is an important variable in both hydrological, meteorological and climatic modelling but is also highly variable in both time and space which makes it very difficult to characterize. Improving the predictive capability of these models requires consideration of this variability. TVDI can be used as an indicator of drought, desertification monitoring, validation of hydrological models, fire risk assessment and assessment of surface water status and evapotranspiration. TVDI turns out to be very useful in supporting distributed hydrological models in terms of providing valuable information about the spatial pattern of soil moisture.

Soil moisture content is a variable difficult to determine by remote sensing. Most measurement methods are limited to the outermost layer on the bare ground, i.e. in the first uppermost five centimeters. Current indirect methods to estimate soil moisture by remote sensing are based on measurements of surface brightness temperature or through a combination of this and a vegetation index, for example, NDVI.

A simple method using MODIS data utilizes surface temperature (LST) and the normalized difference vegetation index (NDVI) to derive the temperature vegetation dryness index (TVDI) (Sandholt et al., 2002). The method is a simplification of the approach described by Moran et al. (1994). The main advantage of the method is that it is valid for vegetated as well as for bare surfaces and only relies on remotely sensed information. In Andersen et al.

(1998), it was demonstrated that TVDI correlates well with distributed model simulations of surface soil moisture.

1.1 Study Area

The TVDI study area includes the reference area of the Valencia Anchor Station in Spain representing an area of about 125 x 125 km² delimited between the following geographic coordinates:

Latitude: 39,783° - 38,672°N

Longitud: 2,572° - 1,105°W

The area is reasonably homogeneous and is mainly dedicated to vineyard crops. There are also relatively large areas of Mediterranean shrubs, together with other areas of olive-, almond-trees, etc. The climate is of a dry continental type.

2 METHODOLOGY

The signal measured by a satellite, normally is combined with ground-truth measurements of the physical variable of interest in order to calibrate the algorithm for transforming the signal measured to the value for the variable considered.

This study attempts to see the evolution of TVDI based on satellite data only versus in situ measurements of soil moisture.

2.1 TVDI Estimation

TVDI quantifies soil moisture indirectly. The measurement of this index is by the relationship between the state of vegetation (NDVI) and Land

Surface Temperature (LST). Both parameters are obtained from satellite data and images.

NDVI is not a very appropriate indicator for water stress because vegetation remains green after passing the threshold of water stress. The NDVI is a good indicator of green biomass, the state of vegetation, but there is no direct relationship with the water content in the soil. By contrast, soil surface temperature (LST) increases rapidly with water stress.

The amount of vegetation present is an important factor in estimating surface temperature. When soil moisture increases, thermal inertia increases and the surface temperature changes as well, because the absorption of solar energy decreases.

This sensitivity to temperature changes with soil moisture is higher in bare soil, i.e. NDVI decreases, so the ratio LST / NDVI may be an indicator of soil moisture.

TVDI provides a relationship between LST and NDVI through the equation:

$$TVDI = \frac{LST - LST_{MIN}}{LST_{MAX} - LST_{MIN}} \quad (1)$$

TVDI appears to be sensitive to rainfall amounts. In particular, TVDI values appear higher during periods with less or no precipitation amounts while they tend to be lower during days with higher precipitation amounts. Given that soil moisture is conditioned amongst other by precipitation, we can assume that the temporal evolution of TVDI can potentially be used to capture the temporal variation of soil moisture.

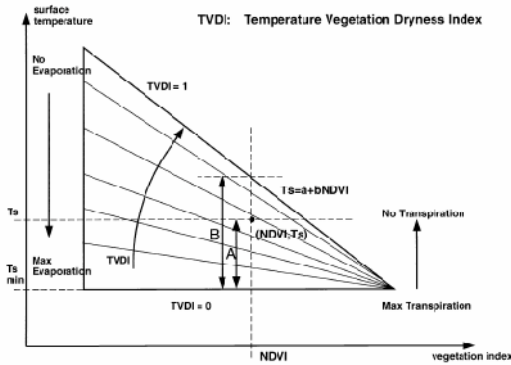


Figure 1: Definition of the triangle and boundary dry (Sandholt et al. 2002)

The regression line is:

$$LST_{MAX} = a + b \cdot NDVI \quad (2)$$

This regression line corresponds to that formed from the maximum ground surface temperature (LST_{MAX})

that is achieved for each of the NDVI values of the study area. This line defines the dry edge of each image. The maximum values of T_s for a given NDVI are represented by the upper limit "dry edge" ($TVDI = 1$) is, when water availability is limited, while the minimum values are limited by the lower limit "wet edge" ($TVDI = 0$) where there is maximum evapotranspiration and therefore access to unlimited water.

The index is defined by the ratio between the distance from the a point to the wet edge and the distance between edges for a given value of NDVI.

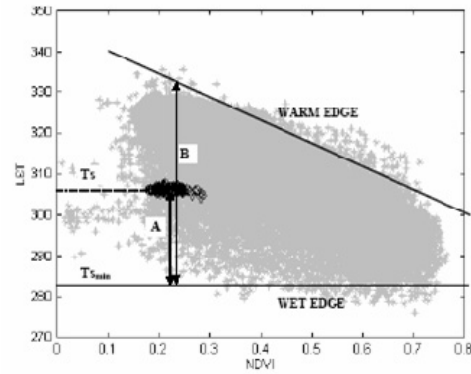


Figure 2: Scatter plot for example of ratio A/B.(Sandholt et al. 2002)

The TVDI for a given pixel (NDVI, LST) is the result of the ratio of the distance from of point to wet edge and the distance between wet edge and dry edge.

2.2 Soil Moisture Estimation

The Climatology from Satellites Group of the University of Valencia has soil moisture stations in the SMOS validation area at the Valencia Anchor Station. These stations have ThetaProbe sensors to measure soil moisture.

The ThetaProbe sonde was used to measure the water content in soil. Through changes in dielectric constant, values in soil moisture, which are proportional to moisture contents, the absolute water content can be measured.

The probe is an impermeable device that contains board electronic and 4 sensors and can be fixed in the soil. When running, it generates a signal of 100 MHz that can be attenuated by means of two components: a dielectric apparent constant and an ionic conductivity.

It measures soil moisture in the first 5 cm of the soil and collects the information every 10 minutes.

For this study we use three stations, station V1 and MELBEX_III are intalled under the vineyards, but the

station M4 is intalled under scrub. Coordinates of stations are:

-V1 (39,548°, -1,277°)
 -M4 (39,573°, -1,251°)
 -MELBEX_III (39,522°, -1,292°)

3 RESULTS

The study of TVDI and soil moisture at the three stations allows us to observe the evolution of both throughout the year 2009.

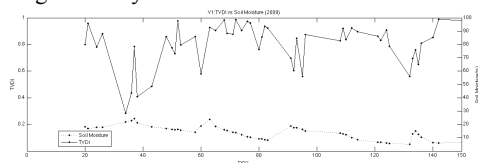


Figure 3: TVDI vs Soil Moisture in V1

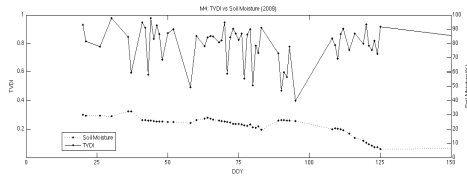


Figure 4: TVDI vs Soil Moisture in M4

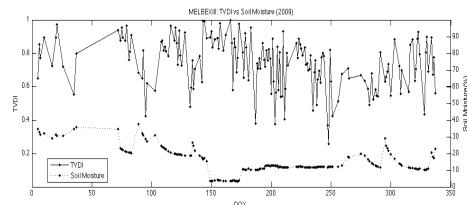


Figure 5: TVDI vs Soil Moisture in Melbex_III

Figures 6, 7, 8, 9 are an example of the calculation of TVDI for the day 25/09/2009.

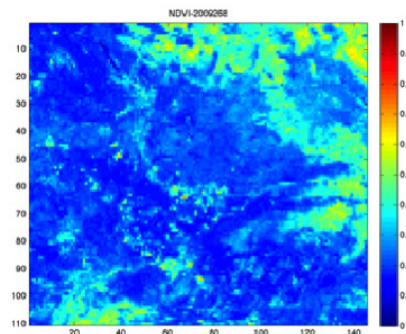


Figure 6: LST (28/09/2009)

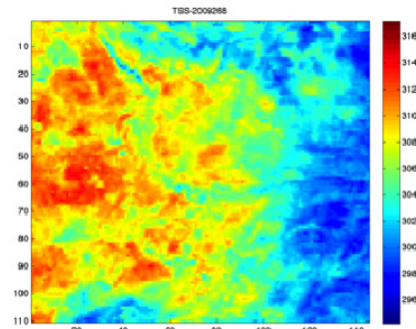


Figure 7: NDVI (28/09/2009)

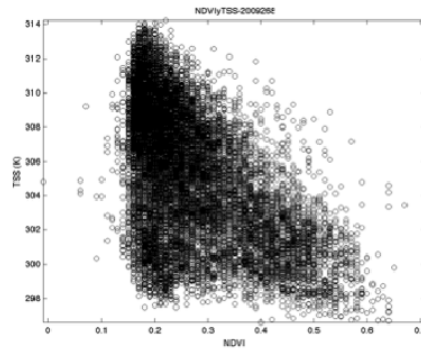


Figure 8: Scatterplot NDVI vs LST (28/09/2009)

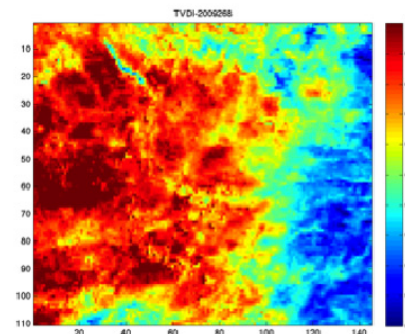


Figure 9: TVDI (28/09/2009)

4 DISCUSSION AND CONCLUSIONS

TVDI is sensitive to rainfall amounts. In particular, the highest values of TVDI appear during periods with little or no precipitation, while they tend to be lower on days with higher amounts of precipitation. For high values of TVDI we are dealing with dry conditions and low values of TVDI in wet conditions. Since soil moisture is conditioned inter alia by precipitation, one can assume that the temporal evolution of TVDI can potentially be used to capture the temporal variation of soil moisture. A complicating

factor is that the estimate of TVDI satellite data is very sensitive to cloud cover. The TVDI is very sensitive to changes in LST for high values of NDVI. The uncertainty increases for high NDVI values, ie, when the contours of TVDI tend to congregate. The main advantage of this method is that it can be obtained both for vegetation and bare surfaces and that is entirely based on remote sensing information.

REFERENCES

- Andersen, J., Sandholt, I., Jensen, K. H., Refsgaard, J. C. y Gupta, H. (2002): Perspectives in using a remotely sensed dryness index in distributed models at the river-basin scale. *Hydrological Processes*, 16, 2973-2987
- Sandholt, I. y Pedersen, M.W. (2004): Relation between field measurements of soil moisture and information derived from satellite observations of vegetation and surface temperature. *Geophysical Research Abstracts*, Vol. 6, 10-2-2004, 1607-7962/gra/EGU04-A-05490
- Sandholt, I., Ramussen, y Andersen, J. (2002): A simple interpretation of the surface temperature/vegetation index space for assessment of surface moisture status. *Remote Sensing of Environment*, 79, 213-224.
- Paul J. Pinter Jr., M.Susan Moran (1994): Remote sensing of soil and vegetation. *Remote Sensing of Environment*, Vol. 49, Issue 3, 167-168.
- Ruiz Calaforra, C. (2005): Verificación y aplicación del Índice de Sequedad del Suelo Temperature-Vegetation Difference Index con datos de Teledetección del sensor MODIS, en la comarca de la Plana Utiel-Requena Trabajo Fin de Carrera, Universidad Politécnica de Valencia, Escuela Técnica Superior de Ingenieros Agrónomos, Ingeniería de Montes. Director: Dr. Ernesto López Baeza, Tutor: Dr. Antonio Luis Lidón Cerezuela, Valencia, Noviembre de 2005
- Hung, T., Yoshifumi, Y. (2005): MODIS Applications in Environmental Change Researches in the Indochina Region. *International Journal of Geoinformatics*, Vol. 1, No. 1, 117-123, March 2005
- López- Baeza, E. &SMOS Cal/Val AO Project no. 3252 Team. (2009): *SMOS Validation Rehearsal Campaign at the VAS site*. SMOS Validation & Retrieval Team. Readiness Review Workshop, Lisboa, Portugal, 11-13 March 2009
- Chaouch N., Leconte R., Magagi R. (2007): Downscaling surface soil moisture status over the Mackenzie River Basin using a Temperature/Vegetation index. *Proceedings IEEE International Geoscience and Remote Sensing Symposium*, Barcelona, Spain, July 2007

Impact of atmospheric effects on the land surface brightness retrieval from AMSR-E data over the China continent

Shi Qiu^a, Zenglin Liu^{b,c}, Zhao-Liang Li^{a,*},

a. LSIT, Uds, CNRS, Bld Sebastien Brant, BP10413, 67412 Illkrich, France

b. State Key Laboratory of Resources and Environment Information System, IGSNRR, Beijing, 100101, China

c. Graduate University of Chinese Academy of Sciences, Beijing, 100049, China

* Corresponding author: Zhao-Liang Li (e-mail: lizl@igsnrr.ac.cn)

ABSTRACT - Land surface temperature (LST) variation over Qinghai-Tibet Plateau in response to the increase in greenhouse gases is challenging, while the land surface brightness temperature (TBS) retrieval is an important step for estimating LST from satellite data. In this study, a microwave atmospheric transfer model (MWMOD) was used with atmospheric profiles to estimate the atmospheric quantities involved in the Radiative Transfer Equation (RTE) in the microwave bands, and subsequently the TBS was retrieved by the inversion of the RTE with at-satellite data and atmospheric quantities estimated earlier. With two polarized six bands (89.0, 36.5, 23.8, 18.76, 10.65, 6.935GHz) of Advanced Microwave Scanning Radiometer for EOS (AMSR-E) data, we have estimated both the TBS from satellite data measured at 18.7, and 36.5 GHz for two polarization modes and the atmospheric effects. The results showed that the atmospheric effects at both H and V polarization of 18.7GHz and 36.5GHz were small and in most cases within 4K over land surfaces, but they were as large as 16K for water surfaces, implying that the atmospheric corrections are not necessary for most places of Qinghai-Tibet Plateau.

1 INTRODUCTION

Land surface temperature (LST) is of considerable importance for many applications, notably global climatic, hydrological, ecological and biogeochemical studies. It is a key issue in the earth science for a long time. With the development of remote sensing technology, it becomes possible to retrieve and monitor LST in a large scale. Two steps are generally needed for accurate estimation of LST from remotely sensed data: that is, (1) the surface brightness temperature (TBS) needs to be firstly retrieved from the original data with atmospheric corrections, and (2) the surface emissivity correction which is needed to obtain LST from TBS.

Qinghai-Tibet Plateau of China is a maximal highland of the world located in the Asian central region, the average altitude of the plateau is above 4000 meters; it has name of "the third pole". It is expected to respond more strongly to global change.

Many studies have been performed on the determination of LST from Thermal InfraRed (TIR) data. However, TIR can not capture the land surfaces information underneath the cloud and consequently can not be used to get LST under cloudy conditions. Compared with TIR, microwave (MV) remote sensing provides a unique capability for sensing land surfaces for all weather conditions because it can penetrate

cloud to capture the land surface information. On the other hand, since the passive MV data has a low spatial resolution and contains mainly the information of soil moisture, vegetation, surface roughness and secondarily LST, fewer efforts have been focused on the LST retrieval from passive microwave radiometry data. To produce long-term LST for all weather conditions required for many applications, it is therefore necessary to combine LST retrieved from TIR data with that retrieved from MV data (Fily et al., 2003; Nioku et al., 1999; Picard et al., 2009; Armstrong et al., 2001). As stated earlier, LST retrieval from MV data needs to perform both atmospheric corrections and emissivity correction. In this paper, we will focus on the first step of LST retrieval, i.e. TBS estimation from passive MV data, and intend to investigate the atmospheric impacts on the multi-channel and multi-polarization AMSR-E data. Section 2 introduces the study area, the atmospheric profile data and AMSR-E microwave data; Section 3 describes the microwave transfer mode and algorithm to retrieve TBS; the results are shown and discussed in the fourth section. Finally, the conclusion is given in the fifth section.

2 DATA AND STUDY AREA

2.1 Satellite Data

Brightness temperatures (TBsat) at satellite level are distributed by National Snow and Ice Data Center of Boulder, Colorado (Jones et al. 2010). Microwave passive AMSR-E instrument is deployed on the Aqua satellite. Aqua is polar orbiting satellite with 1:30A.M. (descending pass) and 1h30P.M. (ascending pass) local time equatorial crossings. AMSR-E measures Vertical (V) and Horizontal (H) polarized TBsat at six frequencies (6.9, 10.7, 18.7, 23.8, 36.5, 89.0GHz), scanning conically in the forward direction at a constant incidence angle of 55° from nadir. The native resolution is about 0.25° (≈27km) (Kawanishi et al., 2003).

2.2 Atmospheric Profile Data and Elevation Data

The synchronous atmospheric quantities will be estimated from atmospheric profile data provided by European Centre for Medium-Range Weather Forecasts (ECMWF) at 00:00, 06:00, 12:00 and 18:00 Coordinated Universal Time (UTC) at a spatial resolution of 1X1°. ECMWF provides the atmospheric profile data including wind speed, temperature, humidity and geopotential at 21 levels in vertical and covers spatially from -20°N to 160°N and -10°E to 60°E. As an example, AMSR-E data acquired over the entire China continent in April, June, August and September 2006 were used.

To take into account the topographic effects in the atmospheric correction, the 30 arc-second digital elevation model (DEM) of the world (GTOPO30) from the USGS EROS Data Center was employed to modify the atmospheric profile provided by the ECMWF.

Since the spatial resolution of DEM is about 1KM, to match with the ECMWF spatial resolution of 1x 1°, DEM of 1KM was resized to a horizontal resolution of 1° using ENVI software.

2.3 Study Area

AMSR-E data acquired in four months of 2006 (April, June, August and September) over whole China area (Lon E71.875° to E134.875°, Lat N4.125° to N54.125°) were selected to derive TBS using the method described below with the atmospheric profiles provided by ECMWF.

3 METHOD

Estimation of atmospheric quantities involved in the atmospheric correction of MV data was performed using the microwave radiation simulation model

MWMOD. This model was designed to simulate TBsat measured by MV sensors at different frequencies and different polarizations provided that the land surface parameters, sensor configuration and atmospheric profiles are known as model input. In addition, the model output generates bypass the atmospheric transmittances, the upward and downward atmospheric brightness temperatures for 6 channels of AMSR-E at V and H polarized modes (Fuhrhop et al., 1998).

Because the spatial resolution of atmospheric quantities estimated by the MWMOD with ECMWF is different from that of AMSR-E satellite data (0.25X0.25°), a bilinear interpolation scheme in the latitude and longitude directions was used to interpolate the atmospheric quantities of 1degree into 0.25degree. To process AMSR-E descending pass data (1:30AM), the atmospheric profiles provided by the ECMWF for UTC time 0600 was input to the MWMOD, while the atmospheric profiles for UTC time 2400 was used to process the satellite data at 1:30PM.

Provided that the atmospheric quantities for each pixel of AMSR-E data are known, TBS is retrieved straightforward from TBsat using equation 1.

$$TBS = (TBsat - \tau) / trans \quad (1)$$

where τ is the upward atmospheric brightness temperature, and $trans$ is the atmospheric transmittance.

Figure 1 depicts the general scheme used in this study to derive TBS from TBsat. In this study, MWMOD was used with atmospheric profiles to compute the atmospheric quantities involved in the Radiative Transfer Equation (RTE), the land surface brightness temperature was then obtained by inversion of the RTE from at-satellite data with calculated atmospheric quantities. After the atmospheric correction, the TBS had been retrieved for each band of AMSR-E.

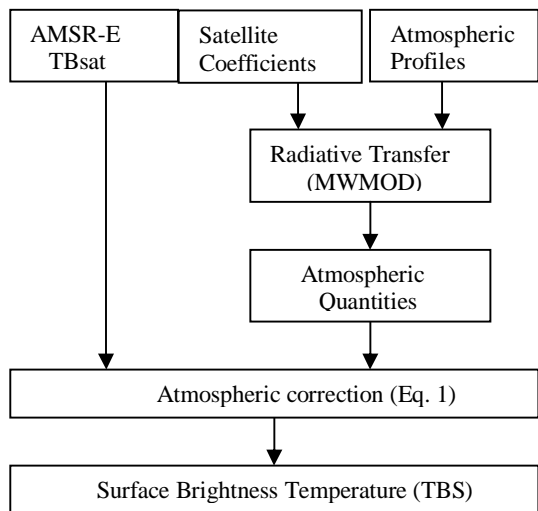


Fig. 1 A flowchart of the retrieval of surface brightness temperature from AMSR-E brightness temperature.

4 RESULTS AND DISCUSSIONS

To study the atmospheric effects in estimating TBS from TBsat, the differences (D) between TBsat and TBS (see equation 2) were calculated for our whole study period. Figures 2, 3, 4 and 5 show the histogram of these differences for 18GHz and 37GHz channels at V and H polarizations, respectively.

$$D = TB_{sat} - TBS \quad (2)$$

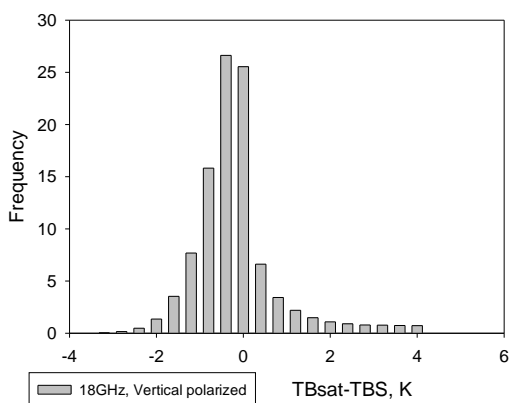


Fig.2 Histogram of difference between satellite measured brightness temperature and retrieved land surface brightness temperature after atmospheric corrections from data acquired in April, June, August and September, 2006 for Vertical polarization at 18GHz.

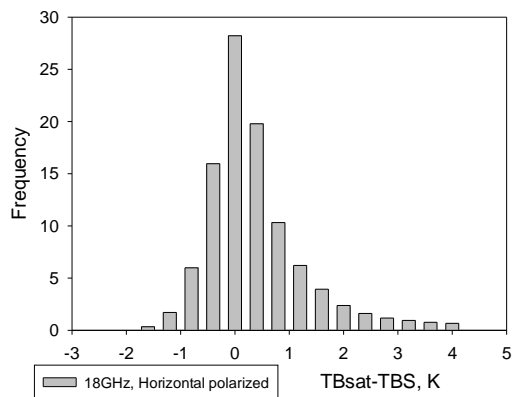


Fig.3 Same as figure 2, but for Horizontal polarization

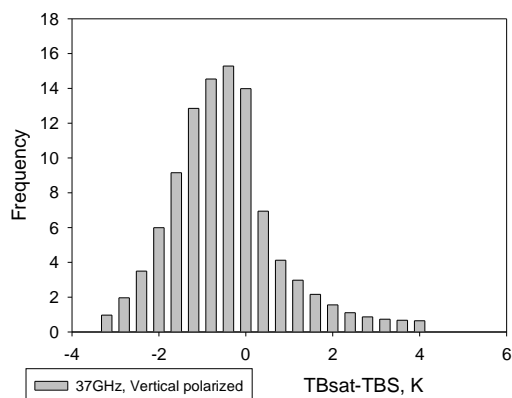


Fig.4 Same as figure 2, but for Vertical polarization at, 37GHz

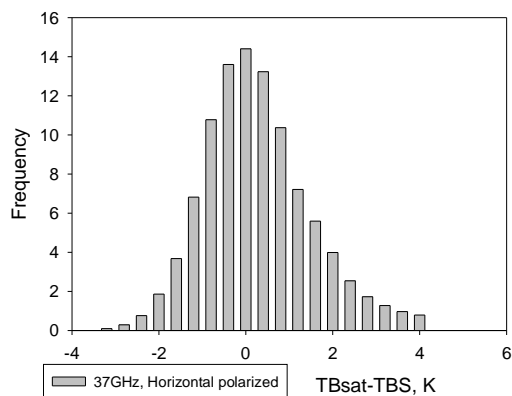


Fig.5 Same as figure 2, but Horizontal polarization at 37GHz,

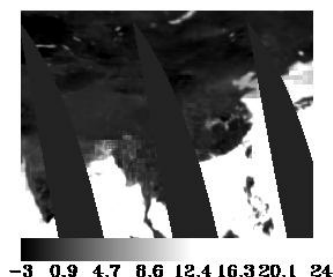


Fig.6 Map of the different between TBSat and TBS for Julian day 234 in 2006 at Horizontal polarization of 18GHz, (Unit, K).

From these figures, one can note that the difference D is within 4 K over the land, but the difference D over the sea can reach 16K as shown in figure 6. That is due to the much lower at-sensor brightness temperature over sea compared with that over land surface, implying that the emissivity of sea surfaces is much lower than that of land surfaces in microwave bands.

To demonstrate clearly the results, we took three typical pixels in China, pixel A (33°N, 89°E) in Tibet, B (42°N, 108°E) in Mongolia province, and wet pixel C (26°N, 116°E) in the south of China. The plot of the difference (D) between TBS and TBSat is displayed in Fig.7 and Fig.8. This shows that the difference is more obvious when the land cover has higher water content (the place C locates in the south of China); the difference at place A is within 2 K and can be ignored in most cases.

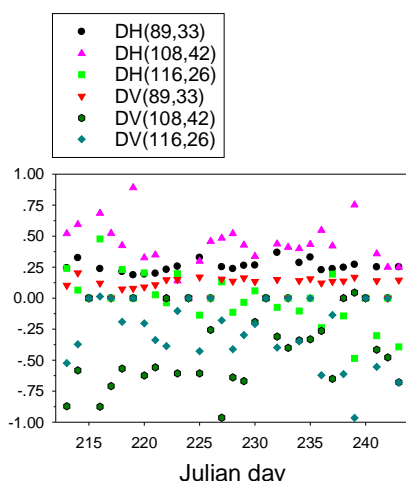


Fig.7 The difference (D) between Tbsat and TBS for Julian day 234 in 2006, at 18GHz (H: Horizontal; V: Vertical polarization)

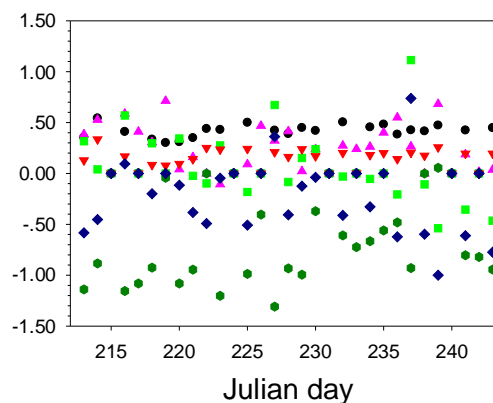


Fig.8 Same as fig. 7, but for 37GHz

5 CONCLUSION

This paper demonstrated that the atmospheric effects at both H and V polarization of 18.7GHz and 36.5GHz were small and in most cases within 4K over land surfaces, but they were as large as 16K for water surfaces. The results show that the atmospheric corrections are not necessary for most places of Qinghai-Tibet Plateau. This provides a directive for the future work.

ACKNOWLEDGMENT

The work described in this publication has been partly supported by the European Commission (Call FP7-ENV-2007-1 Grant nr. 212921) as part of the CEOP-AEGIS project (<http://www.ceop-aegis.org/>) coordinated by the Université de Strasbourg.

REFERENCES

- Armstrong, R.L. and M.J. Brodzik, 2001, Recent Northern Hemisphere snow extent: A comparison of data derived from visible and microwave satellite sensors, *Geophysical Research Letters*, **28**, 3673-3676.
- Fily, M., A. Royer, K. Goita, and C. Prigent, 2003, A simple retrieval method for land surface temperature and fraction water surface determination from satellite microwave brightness temperatures in sub-arctic areas, *Remote Sensing of Environment*, **85**, 328-338.
- Fuhrhop, R., and C. Simmer, 1998, MWMOD User Manual, (Kiel, Germany: Insitutut für Meereskunde).

- Jones, L. A., C. R. Ferguson, J. S. Kimball, Ke Zhang, S. T. K. Chan, K. C. McDonald, Eni G. Njoku and Eric F. Wood, 2010, Satellite microwave remote sensing of daily land surface air temperature minima and maxima from AMSR-E, *IEEE Transactions on Applied Earth Observations and Remote sensing*, **3**, 111-123
- Kawanishi, T. J., T. Sezai, Y. Ito, K. Imaoka, T. Takeshima, Y. Ishido, A. Shibata, M. Miura, H. Inahata and Roy W. Spencer., 2003, The Advanced Scanning Microwave Radiometer for the Earth Observing System (AMSR-E): NASDA's contribution to the EOS for global energy and water cycle studies, *IEEE Transactions on Geoscience and Remote Sensing*, **41**, 184-194.
- Nioku, Eni G., and Li Li, 1999, Retrieval of land surface parameters using passive microwave measurements at 6 to 18 GHz, *IEEE Transactions on Geoscience and Remote Sensing*, **37**, 79-93.
- Picard, G., L. Brucker, M. Fily, H. Gallée and G. Krinner, 2009, Modeling time series of microwave brightness temperature in Antarctica, *Journal of Glaciology*, **55**, 537-551.

Characterization of sunflower, cotton and maize through aerial lidar data

E. Aguirre-Lora, I.L. Castillejo-González, A. García-Ferrer, F.J. Mesas-Carrascosa, J.E. Meroño de Larriva, M. Sánchez de la Orden.

Department of Graphic Engineering and Geomatic, University of Córdoba, Campus Universitario de Rabanales. Ctra. N IV-A, Km. 396, 14071 Córdoba (Spain)
g32agloe@uco.es

ABSTRACT - Remote sensing conventional techniques, which are based on multispectral or hyperspectral sensors, have significant limitations for agricultural applications, owing to including problems to distinguish crops with similar spectral behaviour. To overcome this problem, it could be useful the incorporation of active LIDAR sensor data as source of information. Therefore, the aim of this study is to characterize sunflower, cotton and maize, three crops with a similar spectral response in the middle of July, period in which they must be distinguished by the Spanish Administration. Several testing fields were analyzed and these three crops were characterized based on LIDAR variables, which provided information such as height of the crop, intensity response and number and type of returns of every beam. The results showed that the remarkable characteristics of the plant structure in this phenological stage, such as number, size and distribution of leaves and brains and average height of the crops are different enough to improve the discrimination between these crops. The inclusion of LIDAR data in the analyses clearly outperformed multispectral analyses based on a DMC digital camera, yielding overall accuracies higher than 86% in most of the classifications, with an average of 20% improvement in performance relative to use only multispectral data.

1 INTRODUCTION

The Spanish agricultural area amounts to about half of the total geographical surface, likewise, around 42% (3.67 M ha) of the whole Andalusia (Andalusia, southern Spain) surface is devoted to intensive agricultural production. Specifically, in the agricultural production, the herbaceous crops take on a higher relevance in the Spanish and Andalusian agriculture, taking into notable consideration some crops such as the cotton, being almost all Spanish production (99,8%), the sunflower and its high extension in the national surface (35,5%), and lastly the maize, showing a deficit in the European fields.

Another important fact is the intensive institutional support by the European Union (E.U.) Common Agricultural Policy in terms of modernization of its structures and diversification of its activity. These changes have been carried out by agricultural subsidies, whose control requires a precise follow-up of crop inventories and cropping systems by the E.U. and local administrations.

The follow-up of cropping systems by the E.U. administrations has been achieved by sampling and ground visits to selected farms. However, this procedure is time-consuming and very expensive, delivering inconsistent results owing to the fact that it is covering relatively small areas or only target fields, and it does not sample inaccessible areas. Remotely

sensed data may offer the ability to efficiently identify and map crops and cropping methods over large areas (South et al., 2004). These techniques can signify lower costs, faster work and better reliability than ground visits.

In this way, different methodologies based on remote sensing like aerial photography and satellite images have been used making an important improvement and a better control possible. However, current methodologies can still improve by means of new techniques incorporation or new resources that enable an advance in the crops identification.

To get this purpose, the incorporation of the LIDAR technology (Light Detection and Ranging) could be really useful, since it can measure distances from the sensor position to the selected object in a quick and precise way, just as the capture of multiple reflexes of a same beam or the reflectance of a sign, so-called intensity. Therefore, the inclusion of LIDAR technology for the agricultural subsidies control expects to be a new source of information, contributing details about the crop height, intensity or the number of the returns of each pulse with the obtained information from multispectral images to identify crops more easily.

Most of the studies had been focused on the creation and optimization of models for understanding the geometric reality of the territory. More recently, some works have been exploring other variables provided by

the LIDAR sensor, such as intensity or number of returns, as well as its behavior under varying field conditions (Pesci et Teza, 2008), environment (Baltsavias, 1999) or certain features of the flight (Mao et al, 2008). As for the characterization of crops, in recent years there are some publications that refer to the usefulness of LIDAR data, which include improved monitoring of forest/trees characteristics (Antonarakis et al., 2008; Dubayah et al, 2000; Holmgren and Persson, 2003; Solberg et al, 2006). Other research shows that the incorporation of LIDAR technology for passive remote sensing methods lead to notable improvements in the discrimination of land uses with the combination of LIDAR data and multispectral images (Bork and Su, 2007)

In this context, the aim of this study is the advance and the progress in the use of LIDAR technology for identification of herbaceous crops. More specifically, the objective is the characterization of sunflower, cotton and corn, crops with similar spectral behavior, using LIDAR data for a subsequent integration with multispectral information and thus to facilitate the discrimination of these crops

2 DATA

2.1 Study Area

The study area is located in Lora del Río municipality (Seville, Spain). The field studied is a rectangle defined by UTM ED50 zone 30 coordinates (280119, 4171188) and (283092, 4168226), respectively. The 900 ha zone consists of 38 m above sea level flat relief, where typical Mediterranean crops are grown. The major vegetation types found and their phenological stage at the time of the study are described below:

- (a) Sunflower (*Helianthus annuus L.*), the second most important dry-farmed crop next to cereals group. At the time of the study, this crop was at phenological stage of senescence, next to harvest, therefore the photosynthetic efficiency was limited and the average height of sunflower was maximum, around 125 cm.
- (b) Maize (*Zea Mays L.*) is a typical irrigated crop of this area, which was in the middle of vegetative development, reaching an average height of 200 cm and high photosynthetic efficiency.
- (c) Cotton (*Gossypium Hirsitium L.*) is an irrigated plant. This crop was at the first phase of growth, thus the average height was around 50 cm and the photosynthesis rate was low.

2.2 LIDAR data acquisition

Airborne scanning laser data were collected, as commissioned by Andalucía Government for this study. The laser system was flown 900 m above sea level (average above ground elevation 810 m) on July 15, 2008. Flight lines were approximately 450 m apart, with a total of 10 lines covering the study area and the maximum off-nadir scanning angle was 30°. Thus, there is a great degree of overlapping between adjacent scan paths, which were ranged from 950 to 1100 m. The frequency and wavelength of the laser pulse were respectively 120 kHz and 1550 nm. Final LIDAR data sampling density across the area averaged was 3.5points/m².

2.3 Digital image acquisition

Multispectral images were collected for the study at the same time (in the same flight) as the LIDAR data on July 15, 2008. Therefore, the flight height and scan path had the same characteristics as for LIDAR sampling. The resultant images were taken with a digital camera DigiCam H39, which had three spectral bands: green (0.52-0.60 µm), red (0.63-0.69 µm) and infra-red (0.78-1 µm). These images were clipped from a mosaic of 9, 1 by 1 km images with a spatial resolution of 0.4 m

3. METHODOLOGY

3.1 LIDAR data processing

Before any LIDAR data processing to discriminate crops, the possibility of deleting overlapped points was arisen to reduce distortion on LIDAR response intensity produced by off-nadir angle (Mao et Al., 2008). However, the loss of information caused by these points elimination due to the irregular relief of the study area was checked to know how affected in the results, keeping overlapping points.

The first step of mapping LIDAR data was to classify point cloud into different categories, which facilitate subsequent processes. This classification was automatically executed according to a height criterion plus an assisted visual analysis.

3.2 Acquisition of images from LIDAR data

To integrate LIDAR and multispectral data, LIDAR point cloud was processed and rasterized in order to obtain resultant images, whose digital levels assigned represent values of interesting LIDAR features.

Three LIDAR features were identified to be used for reaching the purpose of this study: height of crop, LIDAR intensity and number of returns. The different

methods used to acquire those images from LIDAR data are described below.

3.2.1 Height of crop image

Height is a characteristic feature of every crop, which depends on the phenological stage for similar environmental condition. The maximum height of crop could identify crops in a precise way in the concluded study area. To obtain height of crop image from elevation values of points provided by LIDAR sensor, two methods were propounded.

(a) Minimum Distance method

Height of crop (or height of the highest points of every plant) was estimated from elevation values of LIDAR point cloud. Every vegetation point was associated with the nearest ground point in order to calculate the difference between their elevation values. Afterwards, a 1 by 1 m maximum filter was used to guarantee that height of the points classified as vegetation showed the maximum height of crop, avoiding distortions caused by the effect of intermediate vegetation points (Fig. 1).

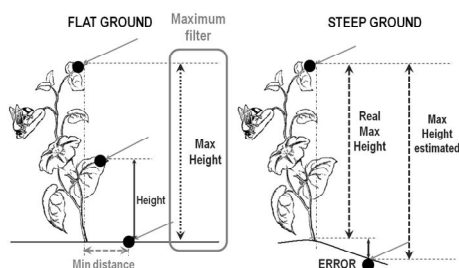


Figure 1. Determination of height of crops correctly and with errors

However, minimum distance method had some limitations in case that ground was on a slope. The steeper ground is the most important committed error in height calculation where minimum distance between point is high (Fig.1). Hence this method was eventually rejected.

(b) Triangulated Irregular Network method

Height of crop was determined by means of Triangulated Irregular Networks (TIN) previously acquired from LIDAR point cloud.

Triangles were built adjusting a plane to three non-collinear points and creating a mosaic which adapts to the surface. Two triangulated irregular networks were developed, a Digital Terrain Model (DTM) from ground points and a Digital Surface Model (DSM) from the highest points in the surface (eg. vegetation) to calculate height of crops for each

laser point as the difference between both networks (Fig.2). In this method, a maximum filter had been applied to remove the distorting effect that vegetation middle point could cause.

This Triangulated Irregular Network method obtained more accurate heights of crops than Minimum Distance procedure.

3.2.2 LIDAR intensity image

Intensity is defined as the ratio of strength of reflected light to that of emitted light, and is influenced mainly by the reflectance of the surface object. Reflectance depends on material characteristics and the light used, showing that different materials have different reflectance.

Song et al., (2002) studied this variable to provide extra information about reflective surfaces obtaining good results at land-cover classification. Since the laser scanner uses light in the near infrared spectrum, the intensity could provide complementary information to multispectral response.

3.2.3 Number of returns image

LIDAR scanners can usually record more than one return signals for a single transmitted pulse. If the transmitted laser signal hits a hard surface such as terrain or dense vegetation, there is only one return. However, if the laser pulse hits the leaves or branches of trees, there are at least two recorded returns, one from the top of the tree and the others from other parts of the plant or from the ground. That allowed authors to estimate the canopy structural characteristics such as the compactness degree of vegetation from returns per pulse captured and enable better discrimination among studied crops.

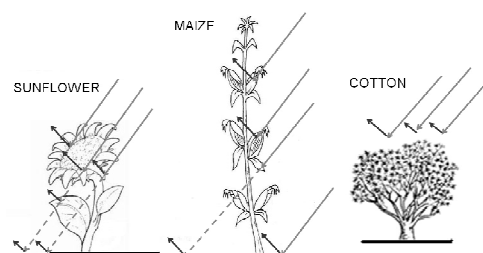


Figure 3. Degree of compactness of studied crops

Number of returns obtained from each beam depends on physical structure of vegetation (degree of compactness) and its typical plantation pattern. Sunflower is characterized by an open structure with few leaves, whereas maize with fair amount of narrow

leaves and, especially, cotton with a lot of small leaves is more compact (Fig.3)

3.3 Development of the classifications

Different digital classifications were carried out to check that information provided by LIDAR sensor was really useful to characterize sunflower, cotton and maize. As LIDAR data were given in the form of point data, it was necessary to convert the data to grid form for its integration with the rest of information provided.

In maximum likelihood classifications, pixel categorization is controlled by some numerical descriptions of the several present classes. This process requires that all features (height of crop, LIDAR intensity, number of returns, and spectral response in multispectral bands) be adequately represented in the training statistics.

Maximum likelihood classifications were performed with different combinations and the full set of the features to analyse the effect of information provided by LIDAR sensor on crops discrimination. Accuracy assessment was performed by determining the overall classification accuracy and kappa coefficient for the global. Furthermore, a 7 by 7 pixel majority filter was used on the classification to remove salt and pepper noise and thus, improve slightly assessment parameters.

4 RESULTS AND DISCUSSION

Once LIDAR images were acquired, a statistical study of its features and spectral behavior was carried out for each crop: cotton, maize and sunflower (Table 1). To illustrate the results, in figure 5 class/feature histograms are shown. It should be noted that these are marginal histograms and therefore do not show inter-feature correlation. However, looking at the histograms, they indicate some sense of relative complexity within the features and their differences, which would allow the discrimination. The aim of this analysis was to characterize the crops and according to that, evaluate the suitability of LIDAR information for improving the discrimination of crops.

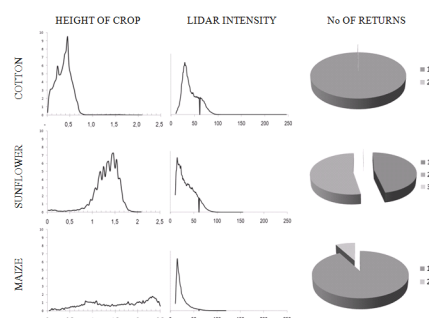


Figure.5. Statistics charts for LIDAR data: a) Height of crop histogram; b) LIDAR intensity marginal histogram c) Pie charts of number of returns

Statistics and graphics show that height of crop and number of returns is variables, whose values are quite different among crops, as we would have expected (Table 1). Therefore, height of crop could be useful to distinguish cotton and sunflower, whereas a worse result would be expected in the identification of maize due to the wide range of height values. The number of returns would allow improving global discrimination because every crop presents quite different number of returns values within its narrow range of data. On the other hand, although LIDAR intensity mean is slightly different in every crop, the range and distribution of these data is similar for all the crops, as well as multispectral response is.

In relation to the assessment of classifications, it is observed that the inclusion of more features usually produces better results and, in any case, the use of a final majority filter contributes to improve overall accuracy (Table 2).

1. *NIR-R-H**: Just using multispectral information, the overall accuracy is low, hence discriminating crops was not possible due to a misclassification of classes.
2. *NIR-R-G-H**: Adding just height of crop to multispectral data distinguishing crops is quite effective (94.87%)
3. *NIR-R-G-L**: Incorporating LIDAR to *NIR-R-H* worsens the results marginally. This is primarily due to the repetition of information, which creates confusion.
4. *NIR-R-G-N**: Adding number of returns to *NIR-R-H*, improves results yielding overall accuracy around 15%, but it is not as high as *NIR-R-G-L*.
5. *NIR-R-G-H-L-N**: Finally, adding all the available information, overall results improvement is only marginal respect to *NIR-R-G-H*.

Table 2: Accuracy results of the classifications

BANDS	C.		C + F	
	OA	K	OA	K
NIR-R-G	62.80	0.2668	69.54	0.3609
NIR-R-G-H	91.08	0.7638	94.87	0.8580
NIR-R-G-L	62.72	0.2661	69.44	0.3601
NIR-R-G-N	83.02	0.5811	86.29	0.6535
NIR-R-G-H-L-N	94.15	0.8351	96.30	0.8942

G: Green; R: Red; NIR: Near InfraRed; H: Height; N: No of returns and L: Intensity; C: classification; C+F: Classification + Filter; OA: Overall Accuracy; K: Kappa coefficient

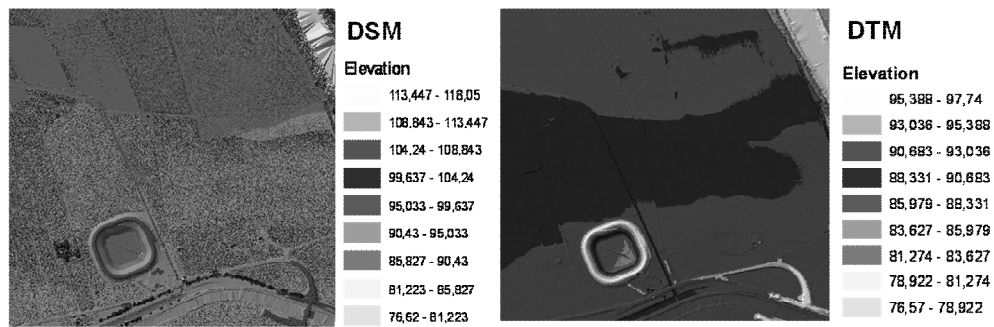


Figure.2. Digital Surface Model (right) and Digital Terrain Model (left), showed by TIN from LIDAR point cloud



Figure.4: Best classification with multispectral image (right) and best classification with multispectral and LIDAR information (left)

Table 1: Analysis of LIDAR features and spectral behaviour in green, red and infrared spectrum of crops: cotton, maize and sunflower

BANDS	COTTON			MAIZE			SUNFLOWER		
	RANGE	MEAN	STAND. DESV.	RANGE	MEAN	STAND. DESV	RANGE	MEAN	STAND. DESV
IR	2-255	161.52	51.33	12-255	189.55	35.34	0-255	121.94	37.87
R	0-255	163.45	52.49	0-255	120.41	30.85	0-255	109.94	35.70
G	0-255	149.11	42.81	0-255	133.53	23.52	0-255	121.65	29.34
HEIGHT (cm)	4-1190	55	26	9-9350	205	33	2-1214	130	43
No OF RETURNS	1-2	1.003	0.06	1-2	1.07	0.26	1-3	1.48	0.50
INTENSITY	10-130	42.06	42.06	10-138	18.97	7.74	10-155	40.42	21.22

5 CONCLUSIONS

This study is intended to evaluate the suitability of LIDAR data for cotton, maize and sunflower discrimination. We converted LIDAR point data to image and assessed the improvement of identification of these crops using a supervised classification. The conclusions are as follows:

With regard to multispectral image classification, cotton generates confusion owing to the fact that its behaviour is a mixture between maize and sunflower spectral signal.

Multispectral information is not enough to discriminate accurately sunflower, cotton and maize, obtaining an overall accuracy lower than 70%. However, LIDAR information, since showing phenological differences of crops, makes their distinction possible with higher overall accuracies (96% with the best combination of bands).

More importantly, results achieved identified what features may be appropriate for the identification. The Height of crop is the variable which characterizes crops best and consequently, contributes to the discrimination of crops most. Whereas, LIDAR intensity is the least useful information in the classification, since the laser scanner uses light of a portion of the near infra-red spectrum, which is included in the spectrum captured by aerial

6 ACKNOWLEDGEMENTS

The acquisition of LIDAR data and multispectral images were financed by Department of Agriculture and Fishery, Andalucía Government. Furthermore, the authors would like to thank them for their helpful information about ground truth of the study area.

7 REFERENCES

- Antonarakis, A.S., Richards K.S., Brasington J. "Object-based land cover classification using airborne LIDAR" *Remote sensing of environment* 102, pp 2988-2998, 2008.
- Baltsavias, E.P., 1999: "A comparison between Photogrammetry and Laser Scanning" *ISPRS Journal of Photogrammetry and Remote Sensing*, 54 (2-3), 83-94
- Bork E.W., Su J.G., 2007. Integrating LIDAR data and multispectral imagery for enhanced classification of rangeland vegetation: A meta analysis. *Remote Sensing of Environment* 111, pp. 11-24, 2007.
- Dubayah, R.O., Knox, R., Hofton, M., Blair, J.B., Drake, J., 2000: "Land Surface Characterization Using Lidar Remote Sensing". Editorial M Hill and R. Aspinall. Spatial information for Land Use Management, International Publisher Direct, Singapore.
- Holmgren, J., Persson A., 2004. "Identifying species of individual trees using airborne laser scanner" *Remote Sensing of Environment* 90, pp 415-423.
- Lim, K., Treitz, P., Wulder, M., St-Onge, B., Flood, M., 2003: "Lidar Remote Sensing of Forest Structure". *Progress in Physical geography*, 27(1), 88-106.
- Mao, J. H., Zeng, Q.H., Liu, X. F., Lai, J. Z., 2008: "Filtering Lidar Points by fusions of intensity measures and aerial images". *The International Archives of the Photogrammetry, Remote Sensing and Spatial Information Sciences*. Vol. XXXVII. Part B3b, Beijing 2008, pp. 25-31.
- Pesci A., Teza G., 2008: "Effects of surface irregularities on intensity data from laser scanning: an experimental approach". *Annals of Geophysics*, vol. 51, pp. 839-848.
- Peucker, T. K., Fowler, R. J., Little, J. J., Mark, D. M., 1978: "The triangulated irregular network". *Proceedings of the ASP Digital Terrain Models (DTM) Symposium*, American Society of Photogrammetry. Falls Church, Virginia, pp. 516-540.
- Song J.H., Han, S.H., Yu, K., Kim Yong-Il, 2002: "Assesing the possibility of land-cover classification using Lidar intensity data". *Proceeding of the ISPRS Technical Commission III Symposium 2002 XXXIV PCV'02*, from September 9 to 13, 2002 at Graz (Austria).
- Solberg, S., Næsset, E., Hanssen, K.H., and Christiansen, E., 2006: "Mapping defoliation during a severe insect attack on Scots pine using airborne laser scanning". *Remote Sensing of Environment*, 102, 364-376.
- South, S.; Qi, J., Lusch, D.P., 2004: "Optimal classification methods for mapping agricultural tillage practices". *Remote Sensing of Environment* 91, pp 90-97.

Atmospheric aerosol characterization by lidar depolarization profiles

J.A. Bravo-Aranda, F. Navas-Guzmán, M.J. Granados and L. Alados-Arboledas
Applied Physic Department. Science Faculty. University of Granada. Fuentenueva s/n, 18071, Granada. Spain
Andalusian Center for Environmental Research. Autonomous Government of Andalusia- University of Granada. Av. del Mediterráneo s/n. 18006. Granada. Spain
jabravo@ugr.es, fguzman@ugr.es, mjgranados@.ugr.es, alados@ugr.es

ABSTRACT – We have used a Raman lidar system to monitor the aerosol depolarization at the Andalusian Center for Environmental Research (CEAMA), in Granada, Southeastern of Spain. The lidar system has recently been upgraded in order to enable the application of the $\pm 45^\circ$ -calibration method which does not require any external optical device. We analyze the method and classify the atmospheric aerosols following criteria based on the depolarization and backscattering ratios. Backscatter coefficient, backscatter-related Angström exponent ($\hat{\alpha}_p$), linear volume depolarization (δ^v) and particle volume depolarization (δ^p) profiles are studied in Saharan dust and biomass-burning aerosol events occurred during summer 2010.

1 INTRODUCTION

It is well known that the laser light is linearly polarized and its interaction with gases, droplets and aerosols induces some depolarization which depends on the shape and size of the scatterer. The depolarization lidar technique makes use of this phenomenon by different approaches (Cairo, 1999). Different depolarization definitions are issued by the lidar community, where the linear volume depolarization ratio (δ^v , ratio of the total perpendicular- to the total parallel-polarized backscattered signals) one of the most frequently used.

Various phenomena have been studied by polarization lidar, such as hydrometeors, clouds, and polar stratospheric clouds (Schofield, 1971; Cho, 2008; Ansmann, 2009). On the other hand, the different degrees of depolarization in combination with the observed backscattering ratios (ratio of the total backscatter coefficient to the molecular component) allow for classifying aerosols such as Saharan dust and biomass-burning aerosols. However, the linear volume depolarization ratio takes into account the induced depolarization both by molecules and particles. The study of the atmospheric aerosol requires a parameter that depends exclusively on the aerosol shape and size, i.e. the particle volume depolarization (δ^p). This parameter is derived from the combination of the linear volume depolarization ratio and the aerosol and molecular backscatter coefficients. These coefficients are estimated through the Klett-Fernald-Sasano's algorithm (Fernald, 1972; Klett, 1981; Fernald, 1984; Klett, 1985; Sasano, 1985).

In order to obtain good depolarization measurements it is necessary a careful calibration of the instrument. Along the time different calibration methods have been proposed. Some of them use the theoretical value of the molecular depolarization (Cairo, 1999). Others are designed to determine the instrumental gain factor between the perpendicular and parallel polarization channels. Some of these methods are based on the use of optical components like half-wave plates or polarization filters (Alvarez, 2006; Snels, 2009). However, there is a calibration procedure which allows determine the relative amplification factor between parallel and perpendicular photodetectors without an external optical device. This calibration method is the $\pm 45^\circ$ -calibration method (Freudenthaler, 2009) implemented recently in the Raman lidar operated at Granada's station.

In this paper, we describe the Raman lidar system operated routinely at the Andalusian Center for Environmental Research (CEAMA), located at Granada (Spain, 37.16°N, 3.58°W, 680 m above sea level, asl) in the section 2. In section 3, we explain the recent upgrade to calibrate the depolarization as well as we describe the methodology to determine the relative amplification factor. In section 4, the analysis of the depolarization calibration is presented and an atmospheric aerosol event is discussed in terms of depolarization, backscatter coefficient and backscatter-related Angström exponent profiles. Finally, the conclusions are given in section 5.

2 INSTRUMENTATION

The Raman lidar model LR321D400 (Raymetrics S.A, Greece) is a system with emissions at 355, 532 and 1064 nm. The Nd:YAG laser fundamental wavelength is frequency doubled and tripled and the 532 nm is assumed to be perfectly linear polarized. The receiving system consists of a Cassegrain telescope, 40 cm diameter. The collected radiation is split into seven channels allowing for the detection of elastic signals at 355, 532 (in parallel and perpendicular components) and 1064 nm, and three Raman signals at 387, 408 and 607 nm. The station is included in the SPALINET (Spanish and Portuguese Aerosol Lidar NETwork) and EARLINET (European Aerosol Research Lidar NETwork) networks.

3 METHODOLOGY

The Raman lidar system has been upgraded in order to allow for the depolarization calibration by means of the $\pm 45^\circ$ -calibration method. This calibration procedure allows for determining the relative amplification factor between the parallel and perpendicular photodetectors without an external optical device.

In the $\pm 45^\circ$ -calibration method, the polarizing beamsplitter cube (PBC) and 532nm-photomultipliers (532PMTs) are rotated jointly to $+45^\circ$ and -45° from the normal measuring position. Using these configurations the optical dependence can be separated and the relative amplification factor (V^*) determined. This procedure has been described by Freudenthaler *et al.* (2009), where it is shown that V^* is given by:

$$V^* = \frac{T_p + T_s}{R_p + R_s} \sqrt{\delta^*(+45^\circ) \cdot \delta^*(-45^\circ)} \quad (1)$$

where T_p , T_s , R_p y R_s are the transmissivity (T) and reflectivity (R) for linearly polarized light parallel (p) and perpendicular (s) to the incident plane of the PBC; $\delta^*(+45^\circ)$ and $\delta^*(-45^\circ)$ are the signal ratio measured with the $+45^\circ$ and -45° from the normal measuring position.

Once the calibration parameter is determined, the depolarization analysis can be carried out with the linear volume depolarization (δ^v) and the particle volume depolarization (δ^p). The δ^v is determined using the relative amplification factor as follows:

$$\delta^v = \frac{R_s - \frac{\delta^*}{V^*} \cdot T_s}{\frac{\delta^*}{V^*} \cdot T_p - R_p} \quad (2)$$

and the δ^p is calculated from (Biele, 2000):

$$\delta^p = \frac{(1 + \delta^m) \delta^v R - (1 + \delta^v) \delta^m}{(1 + \delta^m) R - (1 + \delta^v)} \quad (3)$$

where δ^m is the linear depolarization ratio of air molecules and the backscattering ratio (R) are given by:

$$\delta^m = \frac{\beta_{\perp}^m}{\beta_{\parallel}^m} \quad (4)$$

$$R = \frac{\beta_{\perp}^m + \beta_{\perp}^a}{\beta_{\parallel}^m} \quad (5)$$

The δ^m can be determined with high accuracy (Behrendt and Nakamura, 2002) and the backscattering ratio (R) is computed here using the aerosol backscatter profiles retrieved by the Klett-Fernald-Sasano algorithm. Thus, aerosol backscatter profiles have been retrieved using this algorithm. The lidar ratio (extinction-to-backscatter ratio) values have been selected using the bibliography depending on the aerosol type (De Tomasi, 2003; Mattis, 2004; Murayama, 2004; Amiridis, 2005; Papayannis, 2005; Muller, 2007).

4 RESULTS AND DISCUSSION

4.1 Methodological results

As it is shown in the previous section, V^* depends strongly on the ratio of the measured signals. Thus, V^* must be determined under stable atmospheric conditions in order to avoid differences between $+45^\circ$ and -45° signal ratios. Therefore, the night time calibration provides a better accuracy due to the stable atmospheric conditions and lower background signal than daytime, specially in the photon counting mode detection, where the mean standard deviation of V^* is increased in 50% from daytime to night time.

V^* depends on the lidar setup and the gain factor of each 532PMT. Therefore, V^* changes with the 532PMTs applied voltages. In Figure 1, the V^* profiles measured under different voltage combinations are shown.

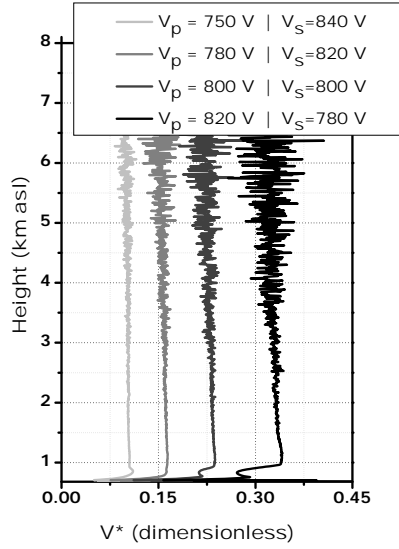


Figure 1: V^* profiles measured with different voltage combinations

A data range must be selected to compute a mean V^* from the corresponding profile (Figure 1). In order to avoid the saturation of 532PMTs and the incomplete overlap for the analog mode detection, the analyzed range was 1.75-8 km asl. As it can be seen in Figure 2, the average value of V^* depends on the total range and minimum height of the data used. In this way, using a constant value for the total range the averaged V^* decreases as the minimum height increases. Furthermore, changing the range from 1.75-3 km asl to 7-8 km asl implies a decrease of about 7.5% in V^* . Taking account all this facts and considering that the coefficient of variation of the relative amplification factor must be sufficiently low, we propose that the mean value of V^* should be computed using the range 1.75-4 km asl (range 2 in Figure 2). In this way we can guarantee the coefficient of variation of V^* is around 1%.

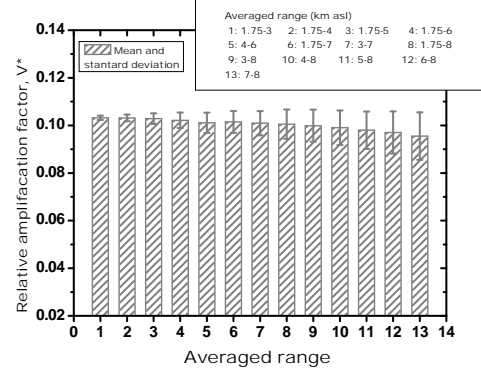


Figure 2: Mean and standard deviation of relative amplification factor (V^*) averaged in different ranges.

Due to the relationship between V^* and the applied voltages, the calibration parameter should be determined every time if the PMT voltages are modified. In order to simplify the calibration method, the voltage dependence of V^* has been determined. The relative amplification factor and the 532PMTs voltages show a potential dependence (Figure 3) which can be fitted by:

$$V^* = \xi \cdot \left(\frac{V_p}{V_s} \right)^k \quad (6)$$

$$\ln V^* = \ln \xi + k \cdot \ln \left(\frac{V_p}{V_s} \right) \quad (7)$$

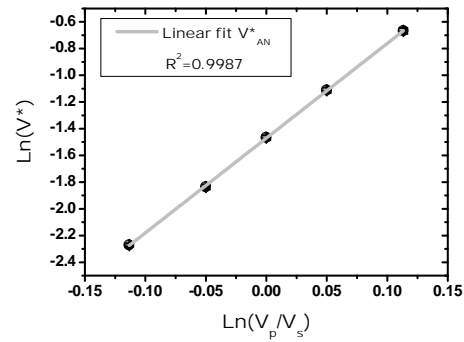


Figure 3: Linear fit using Equation (3) with different applied voltages to 532PMTs.

4.2 Application

During summer 2010, several episodes with high loads (in terms of backscatter coefficient) of aerosol particles occurred over the Iberian Peninsula. In fact, the study area usually experiences some episodes of high turbidity (Alados-Arboledas, 2003), especially during Saharan dust outbreaks (Lyamani, 2005). In particular, the backward trajectories from HYSPLIT model (Draxler and Rolph, 2003) show Saharan air masses outbreak over our station on 23th July 2010 (Figure 4). Likewise, NAAPS model (www.nrlmry.navy.mil/aersol/) predicted the Saharan dust aerosol on 23th July 2010 (not shown) and it was monitored by the lidar system in our station in the planetary boundary layer (PBL) and free troposphere (FT).

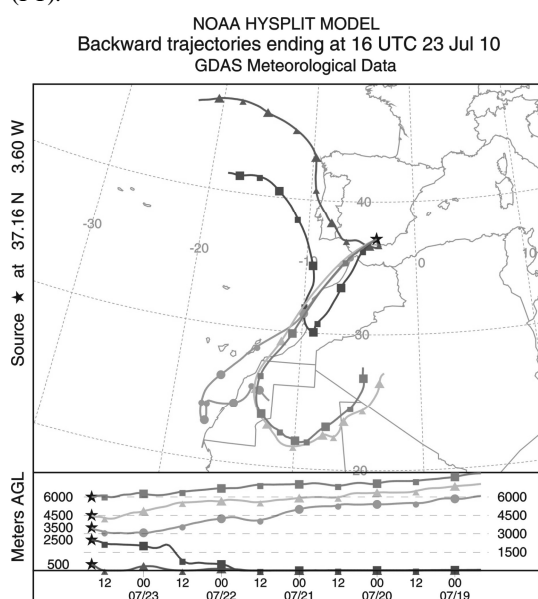


Figure 4: 5-day backward trajectories ending at Granada at 16:00 GMT for 23rd July 2010 (500, 2500, 3500, 4500 and 6000 m agl).

In the Figure 4, the averaged vertical profiles for 16:30-17:00 UTC of 23rd July 2010 are shown. Only profile segments not corrupted by overlap or misalignment effects are considered. In the case of δ^p , data with $R < 1.4$ was removed due to the instability of equation (2) (Biele, 2000). Also, the error bars presented in the profiles consider the effect of the signal noise in the final retrieval. For this purpose, Monte Carlo techniques have been used as was established in EARLINET network (Pappalardo, 2004; Guerrero-Rascado, 2008).

The averaged vertical profiles show the aerosol load distributed in the PBL and one layer (layer A)

located at 3.7-7 km asl in the FT (Figure 5). The $\hat{\alpha}_\beta$ is similar for both layers suggesting that the coarse particles are predominant on fine particles. However, depolarization parameters are different in each layer with mean and standard deviation of 0.09 ± 0.05 and 0.16 ± 0.2 , at the PBL and Layer A, respectively. The particle volume depolarization values in the layer A are according to the bibliography depolarization values which correspond to aged dust after long-range transport (Freudenthaler, 2009). However, the δ^p are not comparable in the PBL due to the potential mixing of anthropogenic and local dust aerosols.

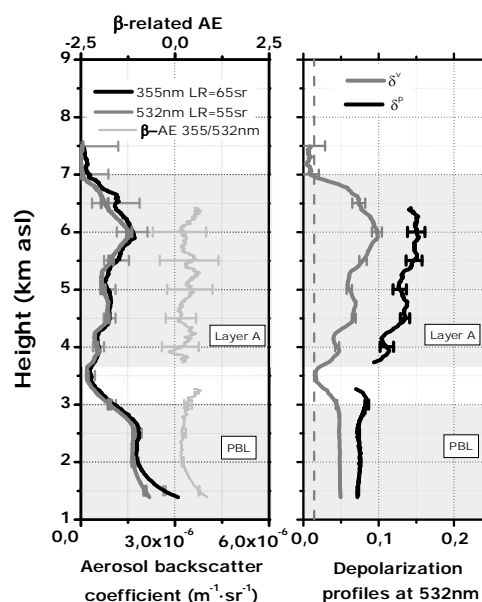


Figure 5: Vertical profiles of several optical properties on 23rd July 2010 (profiles averaged 16:30-17:00 UTC). The grey dash line marks the molecular depolarization value (right panel).

5 CONCLUSIONS

In this work the $\pm 45^\circ$ -calibration method for lidar depolarization have been analyzed. The analysis shows that V^* must be measured during stable atmospheric aerosol conditions in order to reduce the differences between $+45^\circ$ and -45° signal ratios. In the same manner, it is strongly recommended to calibrate the depolarization at night time reducing the background signal. In addition, V^* depends on the applied voltages of each 532-photodetector. Therefore, a potential dependence between V^* and the applied voltages has been fitted.

The independent-height behaviour of V^* requires a data range in order to determine an averaged V^* . Therefore, the range of 1.75-4 km asl has been

selected with a coefficient of variation of 1% and 2km-thickness.

The analyzed event indicated the requirement of introducing the depolarization parameters to improve the aerosol typing and to accurately characterize the processes that take place in the atmosphere.

6 ACKNOWLEDGEMENTS

This work is supported by Spanish Ministry of Science through grant CGL2007-28871-E/CLI and projects CGL2007-66477-C02-01 and CSD2007-00067 and the Acciones Complementarias CGL2008-01330-E/CLI (Spanish and Portuguese Lidar Network); by Autonomous Government of Andalusia through the projects P08-RNM-3568 and P06-RNM-01503, and by EARLINET-ASOS project (EU-CA.,025991 ,RICA). Thanks to NASA/University of Maryland. 2002. MODIS Hotspot / Active Fire Detections. Data set. MODIS Rapid Response Project, NASA/GSFC [producer], University of Maryland, Fire Information for Resource Management System [distributors]. Available on-line [<http://maps.geog.umd.edu>]

7 REFERENCES

- Alados-Arboledas, L., Lyamani, H. and Olmo, F. J., 2003, Aerosol size properties at Armilla, Granada (Spain). Quarterly Journal of the Royal Meteorological Society, 129, 1395-1413
- Alvarez, J. M., Vaughan, M. A., Hostetler, C. A., Hunt, W. H. and Winker, D. M., 2006, Calibration technique for Polarization-Sensitive Lidars. Journal of Atmospheric and Oceanic Technology, 23, 683-699
- Amiridis, V., Balis, D. S., Kazadzis, S., Bais, A., Giannakaki, E., Papayannis, A. and Zerefos, C., 2005, Four-year aerosol observations with a Raman lidar at Thessaloniki, Greece, in the framework of European Aerosol Research Lidar Network (EARLINET). Journal of Geophysical Research-Atmospheres, 110,
- Ansmann, A., Tesche, M., Seifert, P., Althausen, D., Engelmann, R., Fruntke, J., Wandinger, U., Mattis, I. and Muller, D., 2009, Evolution of the ice phase in tropical altocumulus: SAMUM lidar observations over Cape Verde. Journal of Geophysical Research-Atmospheres, 114,
- Behrendt, A. and Nakamura, T., 2002, Calculation of the calibration constant of polarization lidar and its dependency on atmospheric temperature. Optics Express, 10, 805-817
- Biele, J., Beyerle, G. and Baumgarten, G., 2000, Polarization Lidar: Corrections of instrumental effects. Optics Express, 7, 427-435
- Cairo, F., Di Donfrancesco, G., Adriani, A., Pulvirenti, L. and Fierli, F., 1999, Comparison of various linear depolarization parameters measured by lidar. Applied Optics, 38, 4425-4432
- Cho, H. M., Yang, P., Kattawar, G. W., Nasiri, S. L., Hu, Y. X., Minnis, P., Trepte, C. and Winker, D., 2008, Depolarization ratio and attenuated backscatter for nine cloud types: Analyses based on collocated CALIPSO lidar and MODIS measurements. Optics Express, 16, 3931-3948
- De Tomasi, F., Blanco, A. and Perrone, M. R., 2003, Raman lidar monitoring of extinction and backscattering of African dust layers and dust characterization. Applied Optics, 42, 1699-1709
- Draxler, R. R. and Rolph, G. D., 2003, HYSPLIT (HYbrid Single-Particle Lagrangian Integrated Trajectory) Model access via NOAA ARL READY Website <www.arl.noaa.gov/ready/hysplit4.html>. NOAA Air Resources Laboratory, Silver Spring, MD.,
- Fernald, F. G., Herman, M. B. and Reagan, J. A., 1972, Determination of aerosol height distributions by lidar. Journal of applied meteorology, 11, 482-489
- Fernald, F. G., 1984, Analysis of atmospheric lidar observations: some comments. Applied Optics, 23, 652-653
- Freudenthaler, V., Esselborn, M., Wiegner, M., Heese, B., Tesche, M., Ansmann, A., Muller, D., Althausen, D., Wirth, M., Fix, A., Ehret, G., Knippertz, P., Toledano, C., Gasteiger, J., Garhammer, M. and Seefeldner, M., 2009, Depolarization ratio profiling at several wavelengths in pure Saharan dust during SAMUM 2006. Tellus Series B-Chemical and Physical Meteorology, 61, 165-179
- Guerrero-Rascado, J. L., Ruiz, B. and Alados-Arboledas, L., 2008, Multi-spectral lidar characterization of the vertical structure of Saharan dust aerosol over southern Spain. Atmospheric Environment, 42, 2668-2681
- Klett, J. D., 1981, Stable analytical inversion solution for precessing lidar returns. Applied Optics, 20, 211-220

- Klett, J. D., 1985, Lidar inversion with variable backscatter/extinction ratios. *Applied Optics*, 24, 1638-1643
- Lyamani, H., Olmo, F. J. and Alados-Arboledas, L., 2005, Saharan dust outbreak over southeastern Spain as detected by sun photometer. *Atmospheric Environment*, 39, 7276-7284
- Mattis, I., Ansmann, A., Müller, D., Wandinger, U. and Althausen, D., 2004, Multiyear aerosol observations with dual-wavelength Raman lidar in the framework of EARLINET. *Journal of Geophysical Research-Atmospheres*, 109,
- Müller, D., Mattis, I., Ansmann, A., Wandinger, U., Ritter, C. and Kaiser, D., 2007, Multiwavelength Raman lidar observations of particle growth during long-range transport of forest-fire smoke in the free troposphere. *Geophysical Research Letters*, 34,
- Murayama, T., Müller, D., Wada, K., Shimizu, A., Sekiguchi, M. and Tsukamoto, T., 2004, Characterization of Asian dust and Siberian smoke with multiwavelength Raman lidar over Tokyo, Japan in spring 2003. *Geophysical Research Letters*, 31,
- Papayannis, A., Balis, D., Amiridis, V., Chourdakis, G., Tsaknakis, G., Zerefos, C., Castanho, A. D. A., Nickovic, S., Kazadzis, S. and Grabowski, J., 2005, Measurements of Saharan dust aerosols over the Eastern Mediterranean using elastic backscatter-Raman lidar, spectrophotometric and satellite observations in the frame of the EARLINET project. *Atmospheric Chemistry and Physics*, 5, 2065-2079
- Pappalardo, G., Amodeo, A., Pandolfi, M., Wandinger, U., Ansmann, A., Bösenberg, J., Matthias, V., Amiridis, V., De Tomasi, F., Frioud, M., Iarlori, M., Komguem, L., Papayannis, A., Rocadenbosch, F. and Wang, X., 2004, Aerosol lidar intercomparison in the framework of the EARLINET project. 3. Raman lidar algorithm for aerosol extinction, backscatter, and lidar ratio. *Applied Optics*, 43, 5370-5385
- Sasano, Y., Browell, E. V. and Ismail, S., 1985, Error caused by using a constant extinction/backscattering ratio in the lidar solution. *Applied Optics*, 24, 3929-3932
- Schotland, R. M., Sassen, K. and Stone, R., 1971, Observations by lidar of linear depolarization ratios for hydrometeors. *Journal of applied meteorology*, 1011-1017
- Snels, M., Cairo, F., Colao, F. and Di Donfrancesco, G., 2009, Calibration method for depolarization lidar measurements. *International Journal of Remote Sensing*, 30, 5725-5736

Evaluation of fluorescence estimation using different methodologies at airborne and in situ level

B. Franch, J. A. Sobrino, V. Hidalgo, J. C. Jiménez-Muñoz, G. Sòria, Y. Julien, R. Oltra-Carrió, C. Mattar and J. Cuenca

Global Change Unit, Image Processing Laboratory (UCG-IPL)

Parque Científico, Universitat de Valencia (Spain)

belen.franch@uv.es

ABSTRACT - In this work three different methods to measure chlorophyll fluorescence (ChF) from remote sensing are evaluated: the FLD (Fraunhofer Line Discrimination), the FRM (Fluorescence Radiative Method) and the iFLD (improved Fraunhofer Line Discrimination). The three methods have been applied to data acquired in the framework of the CEFLES2 (CarboEurope, FLEX and Sentinel-2) campaign in Les Landes (France) in April, June and September 2007. The airborne data considered in this work were retrieved by the Airflex sensor. We have centred the attention in the oxygen-A absorption band and in the September campaign as this month presented more heterogeneity of crops. Comparing airborne estimations with in situ measurements, the results indicate that the methods that provide best results are the FLD and the iFLD with a RMSE (Root Mean Square Error) of 0.4 and 0.5 ($\text{mW m}^{-2} \text{sr}^{-1} \text{nm}^{-1}$) respectively, while the FRM provides an error of 0.8 ($\text{mW m}^{-2} \text{sr}^{-1} \text{nm}^{-1}$).

1 INTRODUCTION

The chlorophyll fluorescence (ChF) consists of low intensity radiation placed in the red and near infrared spectral regions (approximately between 650 and 800 nm), which is emitted by the chlorophyll a when it is excited by the solar irradiance. ChF can provide an early and more direct approach for detecting sub-optimal conditions before significant reductions in chlorophyll content or leaf area index (LAI) have occurred (Meroni et al., 2009). In fact, a more accurate assessment of the terrestrial vegetation's carbon budget can be obtained directly by measuring ChF emissions (Entcheva Campbell et al., 2008). Additionally, ChF is a pre-visual indicator of water stress, i.e. before the onset of stress (Zarco-Tejada et al., 2009).

Under natural illumination, the low intensity of the ChF compared to the solar radiation reflected by the plant in the same spectral range makes its detection with remote sensing sensors a challenging problem. As a consequence it is necessary to make use of some absorption bands of the solar spectrum where the ChF radiation is placed, the line H α at 656 nm and the bands situated at 687 (oxygen-B) and 760 nm (oxygen-A). In concrete, this work is centred in the analysis of the fluorescence in the oxygen-A absorption band.

There are several methods to measure fluorescence from remote sensing (Meroni et al.,

2009). In this paper, we investigate three of them: the FLD (Fraunhofer Line Discrimination), the FRM (Fluorescence Radiative Method) and the iFLD (improved Fraunhofer Line Discrimination).

2 THEORETICAL BACKGROUND

In this section, three different methods to estimate fluorescence through remote sensing are described. The main difference between them is the approximation considered on the surface reflectance and fluorescence spectral dependence inside and outside the absorption band. The FLD method considers that these parameters are constant within the nearby wavelengths. However, the FRM and the iFLD consider a lineal approach of the surface reflectance and fluorescence. In the first case, the coefficients of proportionality are constant through every pixel of the image and in the second the coefficients are estimated for each pixel.

2.1 FLD method

The FLD is based on the use of the Fraunhofer lines or their immediacy for the fluorescence estimation and it is applied to atmospherically corrected data. In this way, it is compared the radiance reflected by a reference panel with the radiance reflected by a vegetation into equal illumination conditions. The FLD method considers that both the reflectance and the fluorescence remain constant inside and outside the

absorption band (Plascyk, 1975; Plascyk & Gabriel, 1975), i.e. $R_{in} = R_{out}$ and $F_{in} = F_{out}$.

2.2 FRM method

The FRM is based on the estimation of fluorescence by including it into the radiative transfer equations as an emission term so in this case the atmospheric correction is included into the equations and they are applied to raw data. Considering the surface as uniform and Lambertian, the radiative transfer equations for the atmosphere can be written as (Verhoef and Bach, 2003):

$$E_s(b) = \tau_{ss} E_s(t) \quad (1)$$

$$E^-(b) = \tau_{sd} E_s(t) + \rho_{dd} E^+(b) \quad (2)$$

$$E_o(t) = \rho_{so} E_s(t) + \tau_{do} E^+(b) + \tau_{oo} E_o(b) \quad (3)$$

$$E^+(b) = \rho_{surf} [E_s(b) + E^-(b)] + \pi F \quad (4)$$

where (b) and (t) indicate the bottom and the top of the atmosphere irradiance respectively. In eq. (1), it is described the attenuation of direct sunlight by direct transmittance τ_{ss} through the whole atmospheric layer, Eq. (2) reflects the generation of diffuse downward flux (sky irradiance) by diffusely transmitted direct solar flux and upwelling diffuse flux from the surface that is reflected back by the atmosphere. Here, the term ρ_{dd} is the atmospheric spherical albedo. Eq. (3) describes how the top-of-atmosphere radiance that reaches the sensor (E_o) is generated from atmospherically scattered direct sunlight via the term ρ_{so} (which can be considered a bi-directional reflectance of the atmospheric layer), diffuse upwelling flux that is scattered into the direction of view via the transmittance term τ_{do} , and directly transmitted radiance from the target via the direct transmittance τ_{oo} . Finally, Eq. (4) describes the reflection of radiance by a Lambertian surface.

In this case, in order to estimate the fluorescence it is considered a lineal approach of the reflectance and fluorescence inside and outside the absorption band.

$$\rho_{surf}^{in} = \beta_R \rho_{surf}^{out} \quad (5)$$

$$F^{in} = \beta_F F^{out} \quad (6)$$

Therefore, we can estimate the fluorescence from this equation:

$$F^{in} = \frac{A^{in} \left(\frac{E_s^{out}}{\beta_R \pi} + \frac{A^{out} \rho_{dd}^{out}}{\beta_R} \right) - A^{out} \left(\frac{E_s^{in}}{\pi} + A^{in} \rho_{dd}^{in} \right)}{C^{in} \left(\frac{E_s^{out}}{\beta_R \pi} + \frac{A^{out} \rho_{dd}^{out}}{\beta_R} \right) - \frac{C^{out}}{\beta_F} \left(\frac{E_s^{in}}{\pi} + A^{in} \rho_{dd}^{in} \right)} \quad (7)$$

$$\text{where } A^{in/out} = \frac{L_{sensor}^{in/out} - L_o^{in/out}}{T^{in/out}} \text{ and } C^{in/out} = \frac{(\tau_{do}^{in/out} + \tau_{oo}^{in/out})}{T^{in/out}}.$$

Regarding the fluorescence it is assumed that β_F is constant and equal to 0.8 (Moya et al., 2004). However, to estimate the reflectance slope it has been considered that it shouldn't include the fluorescence emission, that is, the case of bare soils. Forcing fluorescence equal to 0 in the fluorescence equation, β_R can be estimated as:

$$\beta_R = \frac{A^{in} \left(\frac{E_s^{out}}{\pi} + A^{out} \rho_{dd}^{out} \right)}{A^{out} \left(\frac{E_s^{in}}{\pi} + A^{in} \rho_{dd}^{in} \right)} \quad (8)$$

The methodology proposed considers the pixels where the NDVI is less than 0.2. There, the fluorescence should be equal to zero as they correspond to bare soils. In application to real data, β_R will be the average through the pixels of bare soil.

2.3 iFLD method

The iFLD method (Alonso et al., 2008) allows avoiding the limitations of considering the reflectance and fluorescence constant inside and outside of the oxygen absorption band. It is based on the FLD method and also it is applied to atmospherically corrected data. This method considers the variation of these parameters describing it by two coefficients α_R and α_F defined as:

$$R_{out} = \alpha_R R_{in} \quad (9)$$

$$F_{out} = \alpha_F F_{in} \quad (10)$$

It should be noted the difficulty in obtaining the coefficients α_R and α_F from spectrometric measurements in natural conditions. This is due to the fact that the measured radiance also includes the fluorescence contribution. Therefore, only the apparent reflectance (\hat{R}), contaminated by fluorescence (see Eq. 11), can be estimated from direct measurements.

$$\hat{R} = \frac{L}{I} = R + \frac{F}{I} \quad (11)$$

As a result, it is defined the apparent coefficient as:

$$\hat{\alpha}_R = \frac{\hat{R}_{out}}{\hat{R}_{in}} \quad (12)$$

where $\hat{R}_{out} = L_{out} / I_{out}$ and \tilde{R}_{in} are obtained using splines interpolation to estimate the apparent reflectance in λ_{in} (wavelength of the absorption band). \tilde{R}_{in} is equivalent to the reflectance that would be retrieved in the absence of the atmospheric absorption on the radiance and irradiance but still affected by fluorescence.

With these elements the fluorescence can be expressed in terms of measurable quantities:

$$\hat{F}_{in} = \frac{\alpha_R I_{out} L_{in} - L_{out} I_{in}}{\alpha_R I_{out} - \alpha_F I_{in}} \quad (13)$$

where $\hat{\alpha}_F$ is determined considering $\hat{F}_{in} = F_{in}$ (Alonso et al., 2008):

$$\alpha_F \approx \frac{I_{out}}{\tilde{I}_{in}} \alpha_R \quad (14)$$

with \tilde{I}_{in} determined interpolating the irradiance in λ_{in} to remove the atmospheric absorption in the same way as \tilde{R}_{in} .

3 EXPERIMENTAL DEVELOPMENT

3.1 Field campaign

CEFLES2 (CarboEurope, FLEX and Sentinel-2) was a multi-objective campaign that exploited the synergies between several airborne and ground measurements performed in coordination with CERES (CarboEurope Regional Experiment Strategy). Airborne and ground measurements were acquired in the Les Landes region of France in April, June and September of 2007 to capture different growth stages of vegetation. Airborne measurements taken covered the visible, near-, shortwave- and thermal-infrared wavelengths. Ground measurements included rates of photosynthetic carbon dioxide uptake, efficiency of light reaction, evapotranspiration, leaf area index, leaf chlorophyll content, emissivity and temperature (Rascher et al., 2009).

3.2 Airborne data: Airflex

AIRFLEX is an interference-filter based airborne sensor (Moya et al., 2006). Basically, it is a six channel photometer aimed to measure the in-filling of the atmospheric O₂ bands. A set of 3 different channels (each with a specific interference filter) is used to characterize each absorption band: one at the absorption peak and two others immediately before and after the O₂ absorption feature (Table 1).

Table 1. Filters position of the Airflex sensor.

Band	Outside band (nm)	Inside band (nm)	Outside band (nm)	FWHM (nm)
O2 B	685.541	687.137	694.114	0.5
O2 A	757.191	760.39	770.142	1.0

The FWHM (Full Width Half Maximum) are 0.5 nm and 1.0 nm for the O₂B and O₂A band respectively. During the CEFLES2 campaign, the Airflex sensor was fixed on the floor of the Pippin Seneca airplane of the IBIMET (Istituto di Biometeorologia of the CNR).

The data considered in this work were acquired in straight line at an altitude of 465m with a resulting ground spatial resolution of 16m.

3.3 In situ data

In situ measurements retrieved by an OceanOptics HR4000 spectrometer at nadir have been considered to estimate in situ fluorescence. These measurements were performed by the group from UNIMIB (University of Milano – Bicocca). Two crops have been considered: a corn field and a bean field. Measurements were retrieved the 13th and the 15th of September respectively.

In case of the corn field, the spectrometer was installed on top of a two floors scaffolding tower of 3.2 m height, resulting in an observed circular area of 49 cm radius. However, the bean field was observed from a height (above ground) of 150 cm and its mean height was 45 cm, resulting in an observed circular area of 23 cm radius (CEFLES2 Data Acquisition Report).

4 RESULTS

Airflex data have been calibrated considering the in situ measurements simultaneous to the airborne overpasses of two kinds of surfaces, bare soil and vegetation (corn). With this aim, atmospheric correction has been inverted over in situ data estimating the reflectance that would be measured by the sensor using the radiative transfer code MODTRAN 4.3 (Berk et al., 1998). A lineal regression has been performed for each band representing the value measured by the sensor versus the one estimated from the atmospheric correction inversion over in situ data, where the slope and the intercept are the calibration coefficients. In Table 2, it is summed up the calibration coefficients corresponding to the three Airflex bands centred in the oxygen-A absorption band.

Table 2. Calibration factors of the Airflex sensor
where $R(\text{in situ}) = a \cdot R(\text{Airflex}) + b$

Airflex Bands	a	b
B760 (757 nm)	0.39	0.03
F760 (760 nm)	0.55	0.01
R770 (770 nm)	0.42	0.03

atmospheric correction with MODTRAN 4.3 following Verhoef and Bach (2003) methodology.

The three different methods described in the methodology section have been considered: FLD, FRM and iFLD. Figure 4 shows the fluorescence estimated with the different methods and the NDVI through one Airflex flight line over the study area.

The surface reflectance is then obtained applying these coefficients to every raw data and performing the

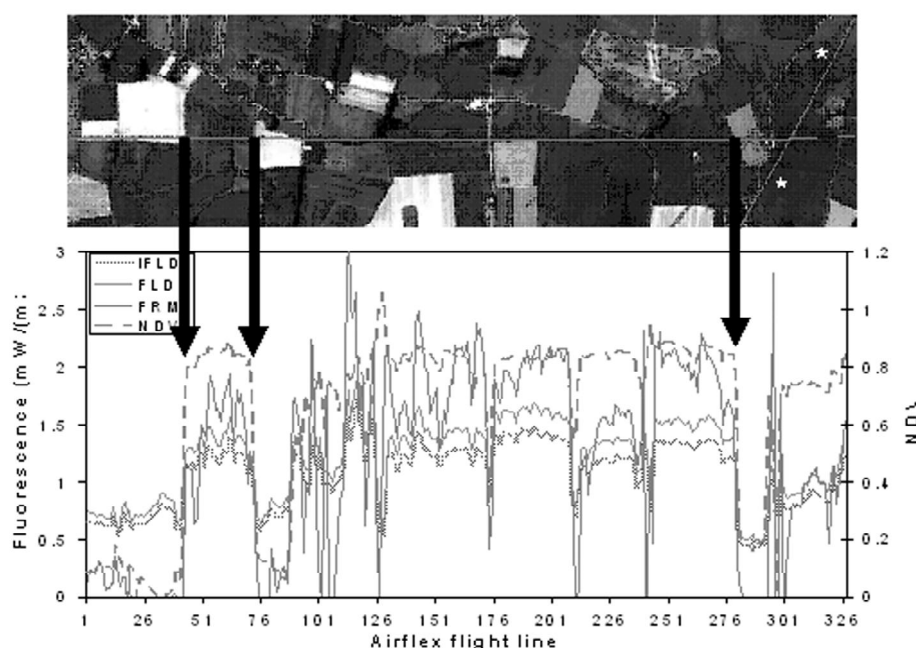


Figure 1. Airflex flight line (the stars point to the place where in situ measurements were performed) (up) and NDVI and fluorescence estimated considering the FLD method, using the radiative transfer equation and iFLD method through the Airflex flight line 1 (down).

As a general view, the fluorescence profile is similar to the NDVI. Comparing the different results of fluorescence obtained, it can be observed that the FRM involved the higher values, and the profile seems to be noisier. Intermediate values of fluorescence are estimated considering the FLD method, obtaining with the iFLD method the lowest values.

With the aim of evaluating the method closest to the real values the results have been compared to in situ measurements. These ones were centred in a corn field (in Figure 4 the left star) and a bean field (right star). The measurements were performed by the group from UNIMIB (University of Milano – Bicocca) using an OceanOptics HR4000 spectrometer as explained in the previous section.

Fluorescence in situ measurements were performed in the corn field on 13th of September and

in the bean field on 15th. Therefore, only measurements acquired in the bean field were simultaneous to the Airflex overpass, which was performed on 15th of September. However, we also consider the 13th of September in situ measurements in the test since data were atmospherically corrected and also both days were very clear.

The band position, width and depth of the oxygen absorption bands strongly depend on the spectral resolution with which they are observed (Meroni et al., 2009). Therefore, in order to compare in situ and airborne measurements, spectra measured in situ were band averaged using Airflex spectral response functions. Then we applied the FLD and iFLD methods to these data. The FRM method can't be applied to in situ measurements as it includes the atmospheric correction. Table 3 shows the comparison

of in situ and airborne fluorescence estimated with the same method. The airborne fluorescence estimated with the FRM method has been compared to in situ fluorescence estimated with the FLD. The errors in the table refer to the standard deviation of the value due to its spatial variation.

Table 3. Fluorescence values (in $\text{mW m}^{-2} \text{sr}^{-1} \text{nm}^{-1}$) estimated with the different methods from Airflex data, and compared to in situ measurements.

		Time (UTC)	NDVI	Airflex	In situ		
FLD	Bean	9:17	0.84 ± 0.02	1.16 ± 0.06	1.37 ± 0.12	Bias: -0.3 Std. Dev.: 0.3 RMSE: 0.4	Bias: -0.2 Std. Dev.: 0.3 RMSE: 0.4
		9:28	0.85 ± 0.02	1.45 ± 0.07	2.15 ± 0.05		
		11:40	0.84 ± 0.06	2.7 ± 0.3	2.92 ± 0.13		
		11:49	0.83 ± 0.05	2.6 ± 0.3	2.5 ± 0.5		
	Corn	9:53	0.55 ± 0.04	1.02 ± 0.13	1.12 ± 0.01	Bias: -0.2 Std. Dev.: 0.3 RMSE: 0.4	
		11:24	0.44 ± 0.08	1.1 ± 0.2	1.8 ± 0.2		
		11:40	0.50 ± 0.08	1.46 ± 0.2	1.63 ± 0.02		
		11:49	0.49 ± 0.08	1.44 ± 0.2	1.32 ± 0.12		
iFLD	Bean	9:17	0.84 ± 0.02	1.04 ± 0.05	0.81 ± 0.14	Bias: 0.5 Std. Dev.: 0.4 RMSE: 0.6	Bias: 0.4 Std. Dev.: 0.3 RMSE: 0.5
		9:28	0.85 ± 0.02	1.25 ± 0.06	0.93 ± 0.01		
		11:40	0.84 ± 0.06	2.4 ± 0.3	1.61 ± 0.07		
		11:49	0.83 ± 0.05	2.3 ± 0.3	1.4 ± 0.3		
	Corn	9:53	0.55 ± 0.04	0.89 ± 0.11	0.64 ± 0.01	Bias: 0.2 Std. Dev.: 0.3 RMSE: 0.3	
		11:24	0.44 ± 0.08	0.97 ± 0.18	1.06 ± 0.17		
		11:40	0.50 ± 0.08	1.25 ± 0.19	1.00 ± 0.05		
		11:49	0.49 ± 0.08	1.25 ± 0.17	0.72 ± 0.09		
FRM	Bean	9:28	0.85 ± 0.02	1.4 ± 0.4	2.15 ± 0.05	Bias: 0.3 Std. Dev.: 0.9 RMSE: 0.9	Bias: 0.4 Std. Dev.: 0.7 RMSE: 0.8
		11:40	0.84 ± 0.06	3.6 ± 0.5	2.92 ± 0.13		
		11:49	0.83 ± 0.05	3.5 ± 0.6	2.5 ± 0.5		
	Corn	9:53	0.55 ± 0.04	2.1 ± 0.3	1.12 ± 0.01	Bias: 0.5 Std. Dev.: 0.6 RMSE: 0.8	
		11:24	0.44 ± 0.08	1.4 ± 0.4	1.8 ± 0.2		
		11:40	0.50 ± 0.08	1.9 ± 0.2	1.63 ± 0.02		
		11:49	0.49 ± 0.08	2.2 ± 0.5	1.32 ± 0.12		

From Table 3, at first we can observe that the standard deviations of the in situ measurements in the bean field are (in most cases) higher than the corn field independently of the method. This can be a consequence of the lower observed circular area in the bean field measurements, affecting more the structural effects and the shadows. We can also remark that the fluorescence values in the bean field are higher than in the corn field, which agree with the NDVI values.

Centring the attention in the comparison between in situ and airborne fluorescence, the FLD subestimates and the iFLD and FRM overestimates the fluorescence value. The lowest RMSE (Root Mean Square Error) in case of the bean field is reached considering the FLD method. However, in the corn field (which presents less standard deviation) the RMSE is lowest with the iFLD. The FRM presents the worst error. On the one hand, it could be due to it is compared with in situ fluorescence estimated with

another methodology (the FLD). On the other hand, the FRM method overestimates significantly the fluorescence, which is caused by the assumption of β_R (equation 17) constant and equal to the corresponding value of bare soils. Consequently, as soils' spectrum slope is lower than vegetation's (in the oxygen-A absorption band spectral range) β_R is lower than it should be and, according to equation (16), the fluorescence values are overestimated.

Therefore, the methods that provide better results when compared to in situ fluorescence are the FLD and iFLD with a RMSE of 0.4 and 0.5 ($\text{mW m}^{-2} \text{sr}^{-1} \text{nm}^{-1}$) respectively, while the error committed with the FRM is 0.8 ($\text{mW m}^{-2} \text{sr}^{-1} \text{nm}^{-1}$). These errors could be associated to the structural effects of the vegetation, which are less important in airborne data than in situ measurements due to the different spatial resolution.

Comparing the fluorescence at airborne level obtained with the different methods we can see in

Table 3 that the FRM estimates the highest values while the iFLD estimates the lowest ones. The overestimation of the FRM method has been already discussed. However, the difference between the FLD and iFLD fluorescence values is due to the assumption of considering the reflectance and fluorescence constant (in case of the FLD) or variable (in case of the iFLD) inside and outside of the oxygen absorption band. The results agree with Alonso et al. (2008), who demonstrate that the assumption of spectrally-constant fluorescence and reflectance of FLD actually leads to fluorescence overestimation at the oxygen-A absorption band.

5 CONCLUSIONS

In this paper, three different methods of estimating the fluorescence have been investigated: the FLD, the FRM and the iFLD. They have been applied to Airflex airborne data in the framework of the CEFLES2 campaign, and have been evaluated through its comparison with in situ measurements. In the comparison with in situ measurements, the methods that provide the best results are the FLD and the iFLD with a RMSE of 0.4 and 0.5 ($\text{mW m}^{-2} \text{sr}^{-1} \text{nm}^{-1}$) respectively, while the FRM provides an error of 0.8. Further data is needed, both in situ and airborne, in order to develop a more extensive study. In June of 2009 it has been performed the SEN3EXP (Sentinel-3 Experiment) campaign over different zones of Spain and Italy providing more in situ and airborne data.

6 ACKNOWLEDGEMENTS

The authors will like to thank for supporting this paper in part by the European Spatial Agency (CEFLES2, project 20801/07/I-LG), in part by Ministerio de Ciencia y Tecnología (EODIX, project AYA2008-0595-C04-01) and in part by the European Union (CEOP-AEGIS, project FP7-ENV-2007-1 proposal No. 212921; WATCH, project 036946). We also will like to thank the groups that provided us the data: the LMD (Laboratoire de Météorologie Dynamique) that provided us the Airflex data and the group from UNIMIB (University of Milano – Bicocca) that provided us the in situ measurements.

7 REFERENCES

- Alonso L., Gomez-Chova L., Vila-Frances J., Amorós-Lopez J., Guanter L., Calpe J. and Moreno J., 2008, Improved Fraunhofer Line Discrimination Method for Vegetation Fluorescence Quantification. *IEEE Geoscience and Remote Sensing Letters*, 5, No. 4, 620-624.
- Berk A., Bernstein L. S., Anderson G. P., Acharya P. K., Robertson D. C., Chetwynd J. H. and Adler-Golden S. M., 1998, MODTRAN cloud and multiple scattering upgrades with application to AVIRIS. *Remote Sensing of Environment*, 65, 367-375.
- Entcheva Campbell P.K., Middleton E.M., Corp L.A. and Kim M.S., 2008, Contribution of chlorophyll fluorescence to the apparent vegetation reflectance. *Science of the total environment*, 404, 433-439.
- Meroni M., Rossini M., Guanter L., Alonso L., Rascher U., Colombo R. and Moreno J., 2009, Remote sensing of solar-induced chlorophyll fluorescence: review of methods and applications. *Remote sensing of environment*, 113, 2037-2051.
- Moya I., N. Moise, A. Ounis, Y. Goulas, J. Louis and R. Pedros, 2004, Passive Remote Sensing of the Vegetation Fluorescence Using The Fraunhofer Line Discrimination Method. *2nd International Workshop on Remote Sensing of Vegetation Fluorescence*. ESA publications, WPP-242
- Moya, I., Daumard, F., Moise, N., Ounis, A. and Goulas, Y., 2006, First airborne multiwavelength passive chlorophyll fluorescence measurements over La Mancha (Spain) fields. *The 2nd International Symposium on Recent Advances in Quantitative Remote Sensing: RAQRS'II 25-29 September 2006*. Torrent (Valencia)-Spain
- Plascyk, J., 1975, The MKII Fraunhofer Line Discriminator (FLD-II) for airborne and orbital remote sensing of solar stimulated luminescence. *Optical Engineering*, 14(4), 339-346.
- Plascyk, J. and Gabriel, F., 1975, The Fraunhofer Line Discriminator MKII - an airborne instrument for precise and standardized ecological luminescence measurements. *IEEE Transactions on Instrumentation and Measurement*, 24, 306-313.
- Rascher U., Agati G., Alonso L., Cecchi G., Champagne S., Colombo R., Damm A., Daumard, et al. 2009, CEFLES2: The remote sensing component to quantify photosynthetic efficiency from the leaf to the region by measuring sun-induced fluorescence in the oxygen absorption bands. *Biogeosciences*, 6, 1181-1198.
- Verhoef W. and Bach H., 2003, Simulation of hyperspectral and directional radiance images using coupled biophysical and atmospheric radiative transfer models, *Remote Sensing of Environment*, 87, 23-41
- Zarco-Tejada P.J., Berni J.A.J., Suarez L., Sepulcre-Canto G., Morales F. and Miller J.R., 2009, Imaging chlorophyll fluorescence with an airborne narrow-band multispectral camera for vegetation stress detection. *Remote Sensing of Environment*, 113, 1262

Characterization of middle- and high-altitude clouds over Évora (Portugal)

Juan L. Guerrero-Rascado¹⁻³, Maria J. Costa^{1,4}, Jana Preißler¹, Frank Wagner¹, Ana M. Silva^{1,4}

¹ Évora Geophysics Centre (CGE), University of Évora, Rua Romão Ramalho 59, 7000 Évora, Portugal

² Andalusian Centre for Environmental Research (CEAMA), University of Granada – Autonomous Government of Andalusia, Av. del Mediterráneo s/n, 18071 Granada, Spain

³ Department of Applied Physics, University of Granada, Fuentenueva s/n, 18071 Granada, Spain

⁴ Department of Physics, University of Évora, Rua Romão Ramalho 59, 7000 Évora, Portugal

Email: jrascado@uevora.pt

ABSTRACT - This study is based on a systematic application of the lidar techniques in the westernmost EARLINET (European Aerosol Research Lidar NETwork) station located in Évora, Portugal (38.6°N, 7.9°W, 293 asl) to investigate cloud properties. A cloud property database is being developed since September 2009, based on lidar profiles averaged over 10 minutes. In this work the optical and geometrical properties of middle- and high-altitude clouds have been analyzed in order to perform a first attempt of seasonal analysis for improving the knowledge about clouds. A simple method based on the comparison of the lidar signal just below and above the cloud has been used to derive the cloud optical depth from the uncalibrated lidar signals. Additionally, geometrical properties as cloud base and top height, as well as geometrical thickness are obtained using derivative methods. Modelled radiosonde data from NOAA has been used to obtain relevant thermodynamic properties of the clouds.

1 INTRODUCTION

The interest in cloud research arises from the important effects that clouds have on Earth's radiation budget. Water, ice crystals, and mixed-phase clouds play a significant role in the energy budget of the earth-atmosphere system by their effects on the transfer of radiant energy through the atmosphere [Liou, 2004] as they are the major regulators of solar fluxes in the terrestrial atmosphere [Kokhanovsky, 2004], and they are critical to understand feedback processes that modulate the climate response to forcing. Concretely, clouds reflect a portion of short-wave incoming solar radiation back to outer space, and have an important role acting as a blanket to protect the Earth's surface against cooling during the night. This is due to the fact that clouds emit long-wave radiation back to Earth after the absorption of terrestrial infrared radiation by highly absorbing water droplets. In particular, cirrus clouds are one of the most important and yet uncertain components in weather and climate studies [Lin and Zhang, 2004, Li et al., 2005]. High thin cirrus clouds scatter and absorb only a small amount of solar radiation, allowing it to

reach the Earth's surface; conversely these clouds highly absorb terrestrial infrared radiation therefore preventing a large quantity of long-wave radiation from leaving the Earth-atmosphere system. In addition, cloudy media (including clouds, mists and fogs) reduce the visibility of objects in the atmosphere, and thus, capabilities of atmospheric vision, remote sensing, and detection systems become limited. Therefore, it is of great importance to understand the peculiarities of light interaction with cloudy media. Accordingly, considerable effort has been done, and continues to be done, to accurately characterize the spatial and temporal distribution of cloud properties over the globe.

Lidars are one of the leading techniques to remotely study the characteristics and properties of clouds. Regarding clouds, elastic backscatter and Raman lidar systems have been used to provide information on geometrical and optical properties of clouds, mainly cirrus, since the 1970's (e.g. Platt, 1973; Platt et al., 1987; Ansmann et al., 1992; Chen et al., 2002; Giannakaki et al., 2007). Some cloud related key optical parameters that can be measured using a lidar are the cloud optical depth, the depolarization

and lidar ratios. Besides those, the lidar can also provide the cloud top and base heights. Concretely, depolarization ratio, which allows for the distinction between water drops and ice crystals, and lidar ratio, defined as the extinction-to-backscatter ratio, are considered to be related to microphysical properties of ice crystals and water droplets contained in the clouds; the top and base heights and the mean cloud temperature are necessary to determine cloud radiative properties. Because the optical depth of clouds is a key parameter in radiative transfer computations, considerable effort has been put in its retrieval.

In this study, we systematically apply the lidar technique to investigate cloud properties in one of the westernmost European lidar station. After a brief description of the lidar system used, a short description of the data analysis methods is presented. The statistical analysis of high- and middle-altitude clouds created from lidar data collected in Évora between September 2009 and February 2010 is presented and discussed. Finally, the conclusions are given.

2 EXPERIMENTAL SYSTEM

PAOLI (Portable Aerosol and cLOUD LIdar) is a Raman lidar system of type PollyXT [Althausen et al., 2009] routinely operated at the Centro de Geofísica de Évora (CGE) in Évora (Portugal, 38.6°N, 7.9°W, 293 m asl). The lidar system PAOLI operates with a Nd:YAG laser at the fundamental wavelength of 1064 nm, and second and third harmonics at 532 and 355 nm, respectively. The radiation is transmitted into the atmosphere after two directing prisms and a beam expansion telescope. The receiver telescope is of Newtonian type, with a primary mirror of 300-mm diameter, an obscuration aperture of 66 mm, and a focal length of 0.9 m. The field of view is 1 mrad. The elastic backscattered signals at those three wavelengths as well as inelastic backscattered signals at 387 and 607 nm (corresponding to the Raman shift on nitrogen molecules) are detected simultaneously. To protect the photomultiplier tubes from overloading, neutral density filters are placed in front of them. These neutral density filters are adjusted at the beginning of each measurement because the intensity of the backscattered light may vary much due to different aerosol loads and/or clouds. The laser beam of PAOLI and the detection optics are tilted by about 5° in order to avoid specular reflections on ice crystals, and it has enough energy to penetrate medium size clouds allowing for characterizing several properties of interest for different types of clouds.

The vertical resolution of the data acquisition is 30 m and temporal resolution is 30 s. However, due to the cloud variability in space and time, the lidar signals

were averaged over 10 minutes to improve the signal-to-noise ratio, and a sliding average function (window of 240 m) was applied in order to filter (smooth) the fluctuations for all the cases studied.

PAOLI has been included recently as member of the European Aerosol Research Lidar Network (EARLINET) [Boesenberg et al., 2001] and of the Spanish and Portuguese Aerosol Lidar NETwork (SPALINET) [Sicard et al., 2009], in order to contribute to the networks' objectives and to benefit from their expertise and support, which assures a high quality of the measurements and subsequent data analysis.

3 METHODOLOGY

In this work the evaluation of optical depth of middle- and high-altitude clouds has been done through the application of the transmittance method using the standard lidar equation [Platt, 1973; Young, 1995; Chen et al., 2002]. The procedure is based on the comparison of the backscattered lidar signals just below and above the cloud, assuming that the lidar signals correctly represent the scattering medium. For clouds with optical depth larger than 1, the multiple scattering effect should be considered, and it was corrected through the multiple scattering factor according to Chen et al. (2002). A detailed description is given by Guerrero-Rascado et al. (2010).

The presence of clouds in a lidar profile implies an abrupt increase in the signal values, such that around the cloud base and cloud top the sign of this derivative changes. The localization of cloud boundaries is performed here by using the zero-crossing behaviour for the logarithmic derivative of the range corrected signal. If different cloud layers are present, they are interpreted as different clouds only when they are separated by more than 150 m.

To investigate the cloud temperature and pressure, radio-sounding data are needed. Because of the lack of a radio-sounding station nearby Évora, data from model radio-sounding from NOAA are used (available in <http://ready.arl.noaa.gov/READYamet.php>). This model provides radio-sounding values every three hours on a global scale using GDAS data.

4 RESULTS AND DISCUSSION

As an attempt to understand the cloud climatology over Évora, PAOLI has been operated since September 2009, and until the end of February 2010, 531 profiles averaged over 10 minutes containing cloud layers have been obtained. We focus on the seasonal differences of cloud properties between autumn (September–November 2009) and winter

(December 2009–February 2010), considering middle-altitude clouds as those with base height between 2 and 5 km agl, and high-altitude clouds as those with base height above 5 km. Sometimes, the presence of low clouds inhibits the laser to reach possible middle- and high-altitude clouds, especially during winter. Moreover, to avoid a potential impact of aerosols in our data, we only consider clouds with base height above 3.0 km from November to March, and above 4.0 km from April to October.

Considering the limitations mentioned previously, our database is biased towards a predominance of high-altitude clouds which can be penetrated by the laser beam completely. Thus, the frequency of high-altitude clouds (cirrus, cirrocumulus and cirrostratus) is 96% in autumn and 72% in winter. Although the frequency of middle-altitude clouds (mainly altocumulus and altostratus) is considerably lower (4% in autumn and 28% in winter), it is still enough to obtain some statistical features, especially in winter. Figure 1 shows the distribution of cloud optical depth at 532 nm in autumn and winter. Around 78% of the cases in autumn and ~54% in winter correspond to cloud optical depth <1 that agrees with the presence of a large number of high-altitude clouds, which typically exhibit low cloud optical depths.

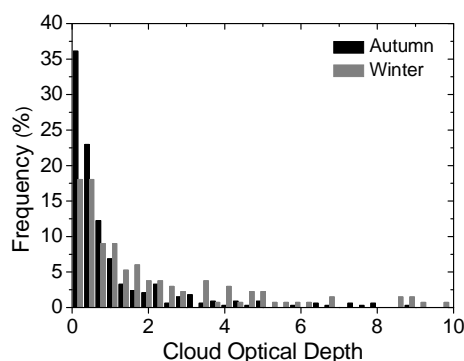


Figure 1. Histogram of cloud optical depths at 532 nm during autumn and winter.

Figure 2 shows the vertical distribution of the frequency of cloud top and base heights and frequency of geometrical thickness measured by PAOLI for high- and middle-altitude clouds during autumn and winter. Each type of cloud is analyzed separately.

4.1 High-altitude clouds

In general, we observe a bimodal behaviour for the vertical distribution of high-altitude cloud top and base heights. The distribution for high-altitude cloud top heights shows a marked bimodal signature with a cut-

off height ~9.5 km in autumn and winter (minimum of frequency ~6% and ~4%, respectively). The maximum for the upper mode is located ~12.5 km (23.1%) in autumn and ~10.5 km (30.2%) in winter. Similarly, the maximum for the lower mode is located ~8.5 km (12.4%) in autumn and ~8.5 km (15.5%) in winter. This decrease in the height for the maximum frequencies in winter respect to autumn is related to a decrease in temperatures, allowing for the formation of ice crystals (that are the predominant constituents in cirrus clouds) at lower heights. Similar distributions are observed for the base heights, although the upper mode is not clearly defined in winter. Thus, the maximum frequencies for the lower mode of base heights are placed ~6.5 km (15.8%) in autumn and ~5.5 km (27.6%) in winter. These large frequencies at low heights (~5–6 km) agree with the presence of cirrus at low heights reported in previous studies such as the global characterization of cirrus clouds using CALIPSO data, performed by Nazaryan et al. (2008).

The geometrical thickness of the high-altitude clouds varies from 0.57–6.10 km in autumn and 0.87–6.72 km in winter. Similar variability of geometrical thickness (0.24–6.65 km) was found for cirrus clouds over Taiwan by Das et al. (2009). The distributions show differences between autumn and winter (both fittings with correlation coefficient, R , larger than 0.93). The geometrical thickness distribution is centred at $2.47 (\pm 0.15)$ km with a width of $2.4 (\pm 0.3)$ km in autumn, and centred at $2.64 (\pm 0.23)$ km with a width of $3.1 (\pm 0.5)$ km in winter. Therefore, the high-altitude clouds are thicker and with more variable geometrical thickness in winter than in autumn.

In order to analyze the thickness variability, Figure 3 presents the dependence of the geometrical thickness of high-altitude clouds with their formation height. We observe a strong anti-correlation between these parameters and no difference is found for the slopes in autumn and winter (-0.14 ± 0.12). The standard deviations indicate that, in general, the clouds at lower heights show very wide geometrical thicknesses. When the base heights are at higher altitudes the geometrical thickness decreases as the heights increase. This behaviour was expected and has been reported by several authors. The instrument LITE (Lidar In space Technology Experiment) showed that the laminar cirrus occur in the vicinity of the tropopause while the denser cirrus appear at lower heights and have mixed structure [Winker and Trepte, 1998]. Das et al. (2009) found that nearly 24% of the observed cirrus are found in the vicinity of the tropopause and mostly with laminar structure. They also attributed the wider thickness at lower heights to anvil cirrus that are formed from cumulonimbus clouds due to deep convection.

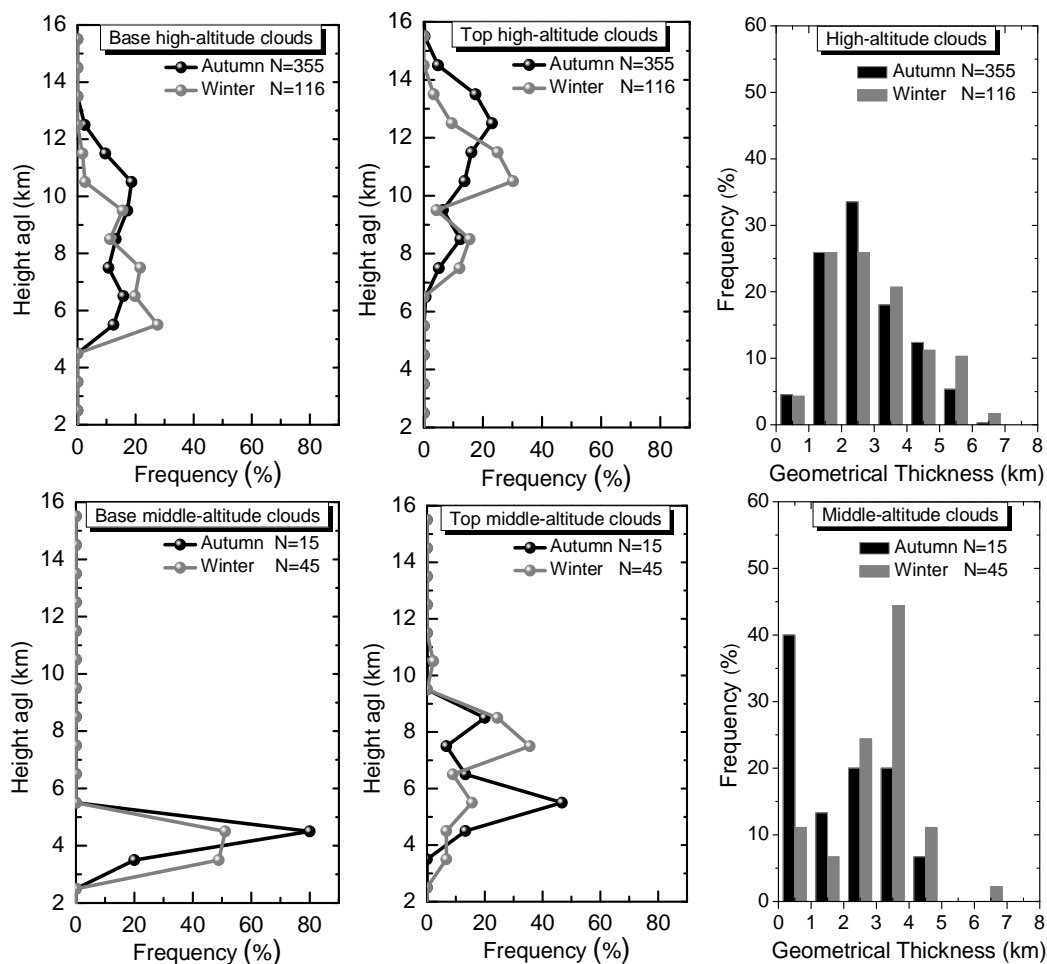


Figure 2. Vertical distribution of the base and top heights and histogram of geometrical thickness for high- (upper) and middle- (lower) altitude clouds.

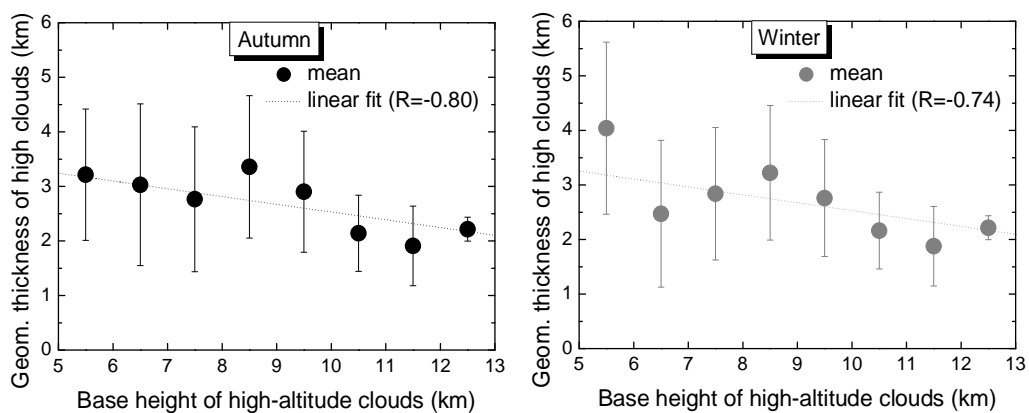


Figure 3. Dependence of the geometrical thickness of high-altitude clouds with the base height (intervals of 1 km). The error bars correspond to the standard deviation.

4.2 Middle-altitude clouds

The vertical distribution of middle-altitude cloud top heights shows a non-balanced bimodal behaviour. The predominant mode appears at ~5.5 km (46.7%, lower mode) in autumn and ~7.5 km (35.6%, upper mode) in winter. The middle-altitude clouds are mainly mixed-phase clouds, and thus containing both water drops (supercooled at temperatures below 0°C) and ice crystals (Glossary of Meteorology of the American Meteorological Society, <http://amsglossary.allenpress.com/glossary>).

The prevalence of the lower mode in autumn and the upper mode in winter may be related to a different crystals-to-drops ratio of the clouds in each season. In this sense, the middle-altitude clouds may be constituted predominantly by water drops in autumn and therefore are located at heights with warmer temperatures. In winter these clouds may be predominantly formed by ice crystals that require lower temperatures and thus are more frequent at higher heights. This hypothesis will be checked in the future on the basis of statistical analyses performed with lidar depolarization measurements.

In contrast, the middle-altitude cloud base heights show a monomodal distribution in altitude, with maximum frequencies located ~4.5 km (80.0% and 51.1% in autumn and winter, respectively). The absence of a second mode (lower mode) can be related to the bias introduced in order to avoid the potential contamination of aerosols in the cloud data.

The analysis of the geometrical thickness indicates that the middle-altitude clouds are thinner in autumn than in winter. In particular, the geometrical thickness varies from 0.57–4.24 km in autumn and 0.60–6.28 km in winter. Such large values are due to some high-altitude clouds at the lowest heights, which can be coupled to the middle-altitude clouds and cannot be distinguished as individual clouds. The distribution of frequencies reveals a higher predominance of clouds with geometrical thickness lower than 2 km in autumn (53.3%), and larger than 2 km in winter (82.1%), when the coupling effect may be more important. The dependence of the geometrical thickness of middle-altitude clouds with their formation height has been analyzed, similarly to what was done for the high-altitude clouds. However, an opposite behaviour was observed. The geometrical thickness of middle-altitude clouds increases with increasing base height and seasonal differences are found for the slopes (1.35 and 0.85 in autumn and winter, respectively).

5 CONCLUSIONS

This study provides a first attempt to understand the seasonal variability of middle- and high-altitude cloud

properties over Évora. However, it is necessary to extend the database in the future to complete the seasonal analysis.

Our results show that ~78% of the cloud analyzed in autumn and ~54% in winter has cloud optical depth <1 that agrees with the presence of a large number of high-altitude clouds in our database, which typically exhibit low cloud optical depths. Concretely, the frequency of high-altitude clouds (cirrus, cirrocumulus and cirrostratus) is 96% in autumn and 72% in winter (the remaining ones correspond to middle-altitude clouds).

In general, we observe a bimodal behaviour for the vertical distribution of high-altitude cloud top and base heights and a decrease in the height of the both modes in winter with respect to autumn, which is related to a decrease in temperatures, allowing for the formation of ice crystals at lower heights. On the other hand, our analyses indicate that the vertical distribution of middle-altitude cloud top heights shows a non-balanced bimodal behaviour with a prevalence of the lower mode in autumn and the upper mode in winter. This may be explained in terms of a different crystals-to-drops ratio of these mixed-phase clouds in each season, but this hypothesis must be checked in the future on the basis of lidar depolarization measurements.

The analyses of the geometrical thickness shows, that the high-altitude clouds are thicker and with more variable geometrical thickness in winter than in autumn. In general, the clouds at lower heights show high values of the geometrical thickness. When the base heights are at higher altitudes the geometrical thickness decreases as the heights increase. No seasonal differences were found for the geometrical thickness decrease with the height in autumn and winter. Furthermore, the middle-altitude clouds are thinner in autumn than in winter. A wide variability range was found for the geometrical thickness of middle-altitude clouds that may be due to some high-altitude clouds at the lowest heights, which can be coupled to the middle-altitude clouds and cannot be distinguished as individual clouds. The geometrical thickness of middle-altitude clouds increases with increasing base height and seasonal differences are found for the slopes.

6 ACKNOWLEDGMENTS

This work has been supported by the National Reequiment Programme Rede Nacional de Geofísica REDE/1527/RNG/2007, by the FCT project PTDC/CTE-ATM/65307/2006. Dr. Guerrero-Rascado was partially funded by FCT under grant SFRH/BPD/63090/2009 and by the Spanish Ministry of Education under the grant EX2009-0700. J. Preißler

was funded by FCT under grant SFRH/BD/47521/2008. The authors want to thank the lidar team of the Leibniz- Institute for Tropospheric Research (IFT) in Leipzig, Germany. This work has benefitted from EARLINET and SPALINET networks.

7 REFERENCES

- Althausen, D., R. Engelmann, H. Baars, B. Heese, A. Ansmann, D. Müller and M. Komppula, 2009, Portable Raman Lidar PollyXT for Automated Profiling of Aerosol Backscatter, Extinction, and Depolarization, *J. Atmos. Ocean. Technol.*, **26**, 2366-2378.
- Ansmann, A., U. Wandinger, M. Riebesell, C. Weitkamp, and W. Michaelis, 1992, Independent measurement of extinction and backscatter profiles in cirrus clouds by using a combined Raman elastic-backscatter lidar, *Appl. Opt.*, **31**, 7113-7131.
- Boesenberg, J., A. Ansmann, J. M. Baldasano, D. Balis, C. Böckmann, B. Calpini, A. Chaikovsky, P. Flamant, A. Hagard, V. Mitev, A. Papayannis, J. Pelon, D. Resendes, J. Schneider, N. Spinelli, T. Trickl, G. Vaughan, G. Visconti, M. Wiegner, 2001, EARLINET: a European aerosol research lidar network, laser remote sensing of the atmosphere, in: Selected Papers of the 20th International Laser Radar Conference, 2001, edited by Dabas, A., Loth, C., and Pelon, J., Edition Ecole Polytechnique, Palaiseau, France, pp. 155-158.
- Chen, W. N., C. W. Chiang, and J. B. Nee, 2002, Lidar ratio and depolarization ratio for cirrus clouds, *Appl. Opt.*, **41**, 6470-6476.
- Das, S. K., C.-W. Chiang, and J.-B. Nee, 2009, Characteristics of cirrus clouds and its radiative properties based on lidar observation over Chung-Li, Taiwan, *Atmos. Res.*, **93**, 723-735.
- Giannakaki, E., D. S. Balis, V. Amiridis, and S. Kazadzis, 2007, Optical and geometrical characteristics of cirrus clouds over a Southern European lidar station, *Atmos. Chem. Phys.*, **7**, 5519-5530.
- Guerrero-Rascado, J. L., M. J. Costa, J. Preißler, F. Wagner and A. M. Silva, 2010, First results about cloud properties obtained by lidar over Évora (Portugal), Book of extended abstracts of "Cuarta Reunión Española de Ciencia y Tecnología de Aerosoles", C8-1-6.
- Kokhanovsky, A., 2004, Optical properties of terrestrial clouds, *Earth-Science Reviews*, **64**, 189-241.
- Li, J.-L., D. E. Waliser, J. H. Jiang, D. L. Wu, W. Read, J. W. Waters, A. M. Tompkins, L. J. Donner, J.-D. Chern, W.-K. Tao, R. Atlas, Y. Gu, K. N. Liou, A. Del Genio, M. Khairoutdinov, and A. Gettelman, 2005, Comparisons of EOS MLS cloud ice measurements with ECMWF analyses and GCM simulations: Initial results, *Geophys. Res. Lett.*, **32**, L18710, doi:10.1029/2005GL023788.
- Lin, W. Y., and M. H. Zhang, 2004, Evaluation of clouds and their radiative effects simulated by the NCAR Community Atmospheric Model against satellite observations, *J. Clim.*, **17**, 3302-3318.
- Liou, K. N., 2002, Introduction to Atmospheric Radiation, Academic Press, NY.
- Nararyan, H., M. P. McCormick, and W. P. Menzel, 2008, Global characterization of cirrus clouds using CALIPSO data, *J. Geophys. Res.*, **113**, D16211, doi:10.1029/2007JD009481.
- Platt, C. M. R., 1973, Lidar and radiometric observations of cirrus clouds, *J. Atmos. Sci.*, **30**, 1191-1204.
- Platt, C. M. R., J. C. Scott, and A. C. Dilley, 1987, Remote sounding of high clouds. Part VI: Optical properties of mid-latitude and tropical cirrus, *J. Atmos. Sci.*, **44**, 729-747.
- Sicard, M., F. Molero, J. L. Guerrero-Rascado, R. Pedrós, F. J. Expósito, C. Córdoba-Jabonero, F. Rocadenbosch, A. Comerón, M. Pujadas, L. Alados-Arboledas, J. A. Martinez-Lozano, J. P. Díaz, F. Navas-Guzmán, M. Gil, 2009, Aerosol Lidar intercomparison in the framework of SPALINET – the SPANish Lidar NETwork: methodology and results, *IEEE Trans. Geosci. Remote Sens.*, doi: 10.1109/TGRS.2009.2021525.
- Winker, D. M., and C. R. Trepte, 1998, Laminar cirrus observed near the tropical tropopause by LITE, *Geophys. Res. Lett.*, **25**, 3351-3354.
- Young, S., 1995, Analysis of lidar backscatter profiles in optically thin cirrus, *Appl. Opt.*, **34**, 7019-7031.

Global Climatology of the of the Aerosol Extinction-to-Backscatter Ratio from Direct Irradiance Values of the AERONET Network

R, Pedrós, V. Estellés, J. L. Gómez-Amo, M. P. Utrillas, J. A. Martínez-Lozano

Earth Physics Department, University of Valencia

E-mail: pedrose@uv.es

ABSTRACT - *The elastic lidar equation contains two unknown atmospheric parameters, namely, the particulate optical extinction and backscatter coefficients, which are related through the lidar ratio (i.e., the particulate-extinction-to-backscatter ratio). So far, independent inversion of the lidar signal has been carried out by means of Raman lidars (usually limited to nighttime measurements), high-spectral-resolution lidars, or scanning elastic lidars under the assumption of a homogeneously vertically stratified atmosphere. We use instead a procedure to obtain the lidar ratio at 532 nm by a combined sun photometer – aerosol-model inversion, where the viability of the solution is largely reinforced by assimilating categorized air-mass back-trajectory information. The retrieved lidar ratios have been validated with inversions of lidar data based on the Klett–Fernald–Sasano algorithm and with the Aerosol Robotic Network (AERONET)- retrieved lidar ratios. The method is applied to extract climatological values of the lidar ratio using measurements of direct solar irradiance (more numerous than those of sky radiance) for several AERONET sites. We also explore a climatology of the lidar ratio only based on back trajectories. This knowledge of the lidar ratio would benefit satellite lidars GLAS and CALIPSO when ancillary data such as the aerosol optical depth are not available, yet air-mass back trajectories are.*

1 INTRODUCTION

Active lidar systems contribute to the global climate effort through their ability to determine the vertical profiles of aerosol extinction and backscattering, which must be known to reduce uncertainty in the aerosol forcing of climate. Therefore, both elastic–Raman lidars (i.e., the combination of, at least, one elastic channel and one Raman channel) and HSRL (High Spectral Resolution Lidars) enable independent inversion of the particulate extinction and backscatter (and hence, of their quotient, the so-called lidar ratio). Scanning elastic lidars can serve the purpose under the assumption of a homogeneously vertically stratified atmosphere. In contrast, (single-wavelength) elastic lidars using the well-known Klett–Fernald–Sasano (KFS) inversion method (see also Klett, 1985; Fernald, 1984; Sasano, 1984) depends on two hypotheses: (1) A relationship between the particulate extinction and the backscatter: the lidar ratio; (2) A far-range lidar molecular calibration. This calibration is usually computed by assuming that the total atmospheric backscatter coefficient at the far-end reference range equals the molecular atmospheric backscatter level (Rayleigh's scattering) at that reference range. Therefore, the backscatter profiles obtained from KFS inversion strongly depend on the variability of the lidar ratio. The a priori value of the lidar ratio is usually the largest source of systematic errors.

On the other hand, the retrieval of vertical profiles of aerosol extinction and backscatter coefficients from down-looking instruments, such as LEANDRE, Cloud Physics Lidar, GLAS or CALIPSO, also necessitates the prescription of the lidar ratio. The accuracy of this prescribed ratio determines the accuracy of the retrieved profiles. In this paper we present a procedure to obtain the lidar ratio at 532 nm by a combined sun photometer – aerosol model inversion, with the purpose of establishing a climatology of the lidar ratio.

2 INSTRUMENTATION

The measurements of the direct solar irradiance were made by a CIMEL CE318 photometer. This is a sun photometer designed for automatic measurements of direct solar irradiance and sky radiance. It measures in five non polarized channels nominally centered at 440, 670, 870, 940 and 1020 nm. The 940 nm channel is dedicated to obtaining the atmospheric columnar water vapor. The nominal full width at half maximum of each channel is 10 nm and the sensor head is equipped with a double collimator with a 1.2° Field of View (FOV). In this paper we use data from The CE318 unit installed in Burjassot (Spain) to derive the aerosol optical depth (AOD) and aerosol data from the CE318 unit maintained in Barcelona. The calibrations and the uncertainty of the measurements are described in Estellés et al. (2007). An AERONET-recommended automatic procedure for cloud screening was implemented.

The lidar ratio output of the algorithm is validated using simultaneous lidar measurements. The lidar instrument was developed by the Polytechnic University of Catalonia (Spain). It is based on a frequency-doubled Nd:YAG laser delivering simultaneously pulses of approximately 160 mJ and 7-nanoseconds duration at 1064 and 532 nanometers (Rocadenbosch et al., 2002). The lidar ratios computed from the lidar inversion are retrieved with an iterative method based on the KFS algorithm and constraining the integral over height of the aerosol extinction coefficient profile (the lidar-derived AOD) to the sun photometric AOD. This method requires a first-guess lidar ratio fixed to 60 sr and by iteration on the lidar ratio it looks for the value that allows the lidar-derived AOD to match the sun photometric AOD to a given uncertainty fixed by the user, 0.001 here.

3 METHOD

First, the AOD is determined by measuring the extinction of the solar direct flux with the CIMEL CE318 sun photometer, as described in section 3.1. Next, an initial combination of basic aerosol components is selected based on the 120-hour air mass back trajectories (Draxler & Hess, 1998), the so-called first-guess solution. The modeled AOD of such combination of aerosol components is calculated according to the procedure described in section 3.2. The choice of the first-guess solution and the particle densities of each basic component are related to the air-mass classification is discussed in section 3.4. Then, the particles densities are changed iteratively by simplex minimization of an objective function defined from the measured AOD and the modeled AOD. Section 3.3 details the minimization procedure. Finally, the lidar ratio of the combination of basic components is calculated using the Mie scattering model.

Section 4.2 presents the validation of the retrieved lidar ratios with inversions of lidar data based on the Klett–Fernald–Sasano (KFS) algorithm and with AERONET–retrieved lidar ratios. In section 4.3 the described procedure is used to extract climatological values of the lidar ratio.

3.1 AOD measured values

The AOD calculation is based on the Bouguer–Lambert–Beer law, which relates the direct flux incident at ground level with the extraterrestrial flux for the aerosol channels (440, 670, 870 and 1020 nm)

More details concerning the calculation of the optical depths can be found in Estellés et al. (2007). The uncertainty associated to the measurement of the

AOD was calculated by using the well-known error propagation method. The calculated uncertainty is of the same order as the nominal uncertainty of the Aerosol Robotic Network, AERONET (0.01–0.02).

3.2 AOD modeled values

The AOD is calculated by integrating the extinction coefficient of a composite aerosol model over the whole atmospheric column. The composite aerosol model is a combination of several basic components, whose optical properties have been computed using OPAC (Optical Properties of Aerosols and Clouds) package (Hess et al., 1998) by means of the Mie scattering theory. These properties include for each basic aerosol component the refractive index as well as the following aerosol distribution parameters: the mode radii for several relative humidity values, and the standard deviation of the lognormal size distribution. The above mentioned basic aerosol components used in our approach are water-insoluble particles, water-soluble particles, soot, sea salt and transported mineral dust. As a simplification we assume that the aerosols are in external mixture, i.e. there is no physical or chemical interaction between particles of different components that constitute the aerosol composite (Hess et al., 1998). The extinction coefficient of the aerosol composite is calculated as the linear combination of the extinction coefficient of the basic components (using for water-soluble and sea salt the mode radii at the measured relative humidity) weighted by their respective particle densities. Finally, the AOD is calculated by integrating the extinction coefficient over the whole atmospheric column.

3.3 AOD inversion and lidar ratio determination

The determination of the lidar ratio is based on iteratively reconstructing the AOD determined from sun photometric measurements, from now on combined sun photometer – aerosol model inversion. For a chosen combination of basic aerosol components, i.e. a linear combination of lognormal size distributions the particle densities are changed iteratively until the AOD modeled values and the AOD measured values match within $\pm 5\%$ at the most. The selection of the appropriate basic components is discussed in section 3.4. The objective function F that is minimized is the norm of the resulting vector of subtracting the measured AOD and the modeled AOD vectors

$$F = \left\| \overline{AOD}_{measured} - \overline{AOD}_{modeled} \right\|, \quad (1)$$

where the vector components correspond to the wavelengths of the sun photometric measurement. The F function is minimized by varying iteratively the

particle densities of the chosen basic aerosol components using the Nelder–Mead simplex minimization method. Nevertheless, the solution is not necessarily unique as several combinations of basic aerosol components and particle densities might lead to the same AOD. A priori information on the origin and type of air mass reaching the study zone can provide a reasonable first-guess solution. This solution is an initial combination of basic aerosol components selected according to the 120-hour air mass back trajectories (Draxler & Hess, 1998). The first-guess solution constrains the inversion by selecting only one or occasionally two combinations of basic aerosol components and excluding the remaining possibilities. Thus, the use of back trajectories synergetically contributes in finding a unique combination of components closer to reality.

The lidar ratio is calculated by using the composite aerosol model using as input parameters the combination of basic aerosol components and their corresponding particle densities that minimized the objective function.

3.4 AOD Air mass classification

The HYSPLIT model (Hybrid Single-Particle Lagrangian Integrated Trajectory Model) developed by NOAA (Draxler and Hess, 1998) allows the possibility to obtain the air mass trajectory quantitatively. Thus, a simple classification model was implemented by us that would permit the back trajectories to be described using simple basic indices, and to assign to them the primary and secondary characteristics of the air masses. By performing this classification automatically it would be possible to apply objective criteria and also to study the sensitivity of the classification to different input parameters of the HYSPLIT model.

Figure 1 shows the meshing of the Northern Hemisphere, with cells of 5° of longitude by 5° of latitude. The aim is to characterize the air masses based on the trajectories of the air.

We assign to each cell a characteristic aerosol type depending on the source region, by using two basic parameters: temperature and surface type. The types were defined as follows:

European (EU) type is defined by continental polar air masses and included the northern Mediterranean coast. Given its basically continental character it was expected that these air masses would transport mineral particles - originating in the soil - but actually its differential characteristic is the urban type aerosol load. The first-guess associated to this sector is the

continental combination of basic components: water-insoluble particles, water-soluble particles and soot.

African (AF) type is characterized by tropical continental air masses, with a significant load of mineral dust due to the Sahara desert. For this sector, the first-guess would be the mineral dust combination of components: water-soluble particles and transported mineral.

For the tropical (TR) type, the Atlantic Ocean was subdivided into three different regions. The first of these was the region of tropical maritime air masses located to the west of Africa. Due to the global easterly circulation below 30° the air masses were predicted to possess a certain mineral footprint due to aerosols transported from the desert.

Polar (PO) type was the region of the Atlantic located between average latitudes (between 30° and 60°) which would have an intermediate character between the maritime air masses of the tropics and the artic. These were polar maritime air masses generated by the movement of continental air masses from North America perhaps with an occasional residue of anthropogenic aerosols.

Arctic (AR) type was defined by the back trajectories originating in Canada or in the Arctic basin. Given the time taken to cross the ocean the continental memory would be very vague. For the three sectors TR, PO and AR the first-guess would be the maritime typified distribution (water-soluble particles, soot and sea salt, both in accumulation mode and in coarse mode), or a mixture of continental and maritime (adding the insoluble component to the maritime combination).

To complement these definitions another regional class was defined (O type), characterized by those trajectories whose maximum distance travelled was less than 600 km from the measurement station. For this sector a first-guess is not possible, so all the above mentioned combinations of basic components are examined.

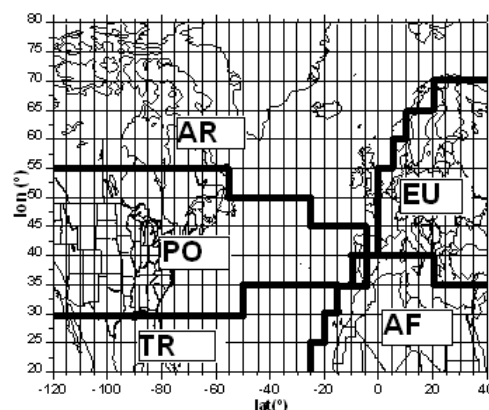


Figure 1. Meshing of the Northern Hemisphere with the different classification.

4 RESULTS

A two-year database has been used to validate the combined sun photometer – aerosol model inversion with lidar ratios based on the KFS lidar inversion and with AERONET retrieved lidar ratios. The AOD inversion is then applied to obtain a climatology of the lidar ratio in a Mediterranean coastal site.

4.1 Uncertainty estimates of the retrieved lidar ratios

For the combined sun photometer – aerosol model inversion the uncertainty of the lidar ratio is computed by using the well known error propagation method. Specifically this is the quadratic sum of two terms: (1) the uncertainty which arises from the inversion in the form of the root mean square value of the residuals after minimizing the objective function; and (2) the uncertainty associated with the AOD retrieval from sun photometric data, in the range 0.01–0.02 (Estellés et al, 2007). For the set of data used, a worst case estimate of the uncertainty is 20%.

For the AERONET–inversion, the possible errors in instrument and inversion cannot be computed analytically to furnish an uncertainty estimate in the retrieved lidar ratios. Nevertheless, Catrall et al., (2005) state that the uncertainties are not high, though they rather use the standard deviation of a Gaussian fit as an indicator.

The uncertainty of the KFS–retrieved lidar ratio is the quadratic sum of two terms: (1) the uncertainty resulting from the natural variability associated with the data, which is calculated as the standard deviation of the lidar ratio computed for each individual profiles, and (2) the uncertainty associated with the uncertainty on the AOD, i.e. 0.01–0.02. For the set of data considered in this study, a worst case estimate of the uncertainty associated with the lidar ratio is 10%.

4.2 Validation

We have compared the lidar ratio outputs of the combined sun photometer – aerosol model inversion at 532 nm with the lidar ratios computed from the lidar inversion based on the Klett–Fernald–Sasano (KFS) algorithm considering a constant lidar ratio. The AOD-inverted lidar ratios have also been compared with those obtained from AERONET aerosol inversions. The database covers the years 2007 and 2008 and has been selected so that measurements of direct solar irradiance, sky radiance and lidar profiles are made with less than an hour difference. The simultaneity is very demanding and has reduced the two-year database to 26 days of measurement. The AERONET aerosol inversions (level 1.5) provide the single scattering albedo and the phase function at 180°, which are used to calculate the

lidar ratio at 532 nm (from now on AERONET–inverted lidar ratio).

Although the combined aerosol model–sun photometer inversion considers that aerosols are spherical, in some cases with Saharan dust intrusion, mineral dust is the composite that minimizes the objective function in equation (1). The reason for the agreement is the low Ångström coefficient α i.e. the smaller slope in the curve of AOD as a function of wavelength of the mineral dust composite. Nevertheless, the fact that the OPAC model uses spherical particles may lead to underestimate the lidar ratio for mineral dust. Thus, when mineral dust is the combination of aerosol basic components that minimizes the objective function in equation (1), we suggest using the latest state-of-the-art computation values for spheroid-like particle shapes by Dubovik et al. (2006) for several radius values, rather than sticking to the Mie output lidar ratio values. These computed lidar ratios are about 70 sr (for a radius r_v of 5 μm), 55 sr (for 2 μm), and 45 sr (for 1 μm). The AERONET aerosol inversions will provide the radius of the size distribution to select the appropriate lidar ratio for each dust situation.

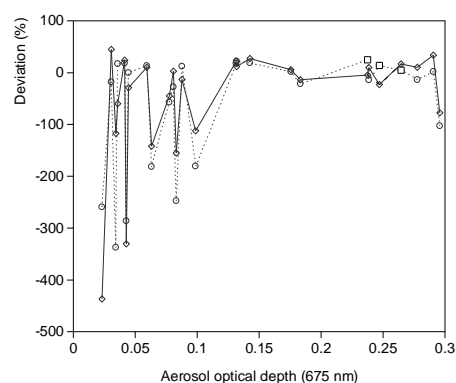


Figure 2. Deviation of the lidar ratio at 532 nm derived from the AOD inversion (straight line) and from the AERONET inversion (dotted line) with respect to KFS lidar inversion.

Figure 2 shows the results of the deviations of the lidar ratios of the AOD inversion and the AERONET inversion with respect to the KFS lidar inversion. For the AOD at 675 nm below 0.1 the deviations are large. One cause is that low AOD values make the AERONET inversion less reliable. Also, many low AOD cases appear in winter when boundary layer heights are of about 1 km. In these cases the fact that the full overlap of the lidar is 0.5 km leads to errors in the lidar inversion. On the contrary, for larger AOD values the deviations with respect to the KFS-inverted lidar ratios are smaller, with an average deviation for both procedures of $\pm 21\%$ and similar tendencies.

We have also analyzed the deviations of the AOD-inverted lidar ratios with respect to AERONET-inverted lidar ratios for the whole 2007–2008 AERONET database, i.e. without the restriction of temporal coincidence with lidar measurements. The differences of the combined sun photometer – aerosol model inversion with respect to the AERONET-inverted lidar ratios are of $\pm 21\%$ for AOD at 675 nm above 0.1. This value is consistent with the uncertainty estimate of the lidar ratio for the proposed method.

4.2 Multi-annual climatology of the lidar ratio

We have applied the procedure described in section 3 to a database of continuous measurements carried out with a CIMEL sun photometer from 6th June 2003 to 30th July 2005. The site of measurements is Burjassot, which is located in the metropolitan area of Valencia (39.5°N, 0.4°W), a Mediterranean coastal site. After filtering cloudy days and only selecting the data with available relative humidity, the database was reduced to 545 days of measurement. HYSPLIT air mass back trajectories were obtained for the entire database.

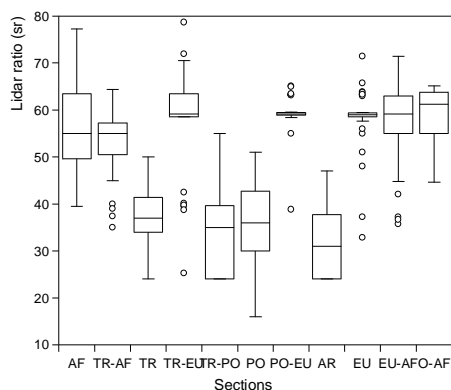


Figure 3. Lidar ratio at 532 nm as derived from the AOD inversion for each relevant air mass section (abscissa). AF: African; TR: Tropical; EU: European; PO: Polar; AR: Arctic; O: auxiliary regional class.

Figure 3 shows a climatology of the lidar ratios according to the air mass sector, or combination of two sectors.

The EU sector is dominated by continental aerosols with 88% of the cases, and thus the median lidar ratio is 59 ± 11 sr. The AF sector has an equal occurrence of 44% for both continental and mineral dust outbreak, and 12% of maritime and a mixture of continental and maritime aerosols. This accounts for the median value of 55 ± 5 sr: on 44% of the days aerosols are dust, 56% of which have a radius for the coarse mode of $2 \mu\text{m}$; and on 12% of the days aerosols are maritime pure or mixture with a median lidar ratio of 41 ± 4 sr. On the other hand, the three Atlantic sectors PO, AR and TR

exhibit similar features. Maritime aerosols constitute the more typical situation occurring in more than 80% of the cases. Thus, the median values are 36 ± 11 sr for PO, 31 ± 11 sr for AR, and 37 ± 9 sr for TR.

With regard to the mixed sectors, TR-AF has a median lidar ratio of 55 ± 7 sr. This value corresponds to 30% of days with maritime pure and mixture with continental aerosols, and 43% of days with mineral dust, 80% of which have a particle radius of $2 \mu\text{m}$. Sector TR-EU has a lidar ratio of 59 ± 13 sr as it is dominated by continental aerosols on nearly 80% of the days. Similarly, section PO-EU is also dominated by continental aerosols leading to a lidar ratio of 59 ± 11 sr. On the contrary, the TR-PO sector exhibits a lidar ratio of 35 ± 11 sr, which corresponds to more than 80% of maritime pure aerosols. With regard to section O-AF, continental aerosols account for 71% of the days, as opposed to 21% of mineral dust leading to a median lidar ratio of 61 ± 6 sr.

5 CONCLUSIONS

We have obtained the lidar ratio at 532 nm for a multi-annual database of continuous sun photometric measurements of the direct irradiance at a Mediterranean coastal site.

The results show that the proposed method yields lidar ratios which agree within the uncertainty range with both the values resulting from KFS lidar inversion and with the AERONET inversion. However, the Mie theory considers that the aerosols are spherical, which in the case of mineral dust may lead to underestimating the lidar ratio. In the longer term we will devise a spheroid-based scattering model to replace the spherical model currently used in OPAC.

We have obtained a climatology of the lidar ratio according to the air mass classification. We plan to apply the methodology to other AERONET stations.

The advantage of the proposed technique to retrieve the lidar ratio is that is based on direct sunlight measurements. AERONET-retrieved lidar ratios are only available when no clouds are present at all. Moreover, the radiance inversion requirements (high aerosol loading and large elevation angle) reduce further the data that can be used. Thus, the proposed method will be more applicable to the practical use.

Next, a climatology of the lidar ratio only based on back trajectories will be explored. This knowledge of the lidar ratio would benefit satellite lidars GLAS and CALIPSO when ancillary data such as the AOD is not available, yet air mass back trajectories are.

6 REFERENCES

Catrrall C., Reagan J., 2005, Variability of aerosol and spectral lidar and backscatter and extinction ratios of key aerosol types derived from selected

- Aerosol Robotic Network locations, *Journal Geophysical Research*, **110**, D10S11, doi:10.1029/2004JD005124.
- Draxler, R.R., and G.D. Hess, 1998, An overview of the HYSPLIT_4 modeling system of trajectories, dispersion, and deposition. *Australian Meteorological Magazine*, **47**, 295-308.
- Dubovik O., A. Sinyuk, et al., 2006, Application of spheroid models to account for aerosol particle nonsphericity in remote sensing of desert dust. *Journal Geophysical Research*, **111**, doi: 10.1029/2005JD006619.
- Estellés V., Martínez-Lozano J. A., et al., 2007 Columnar aerosol properties in Valencia (Spain) by ground-based Sun photometry. *Journal of Geophysical Research*, **112**, doi:10.1029/2006JD008167.
- Hess M., Koepke P. and Schult I., 1998, Optical properties of aerosols and clouds: The software package OPAC, *Bulletin of the American Meteorological Society*, **79**, 831–844.
- Klett J. D., 1985, Lidar inversion with variable backscatter extinction ratios. *Applied Optics*, **24**, 1638–1643.
- Fernald F. G., 1984, Analysis of atmospheric lidar observation—some comments. *Applied Optics*, **23**, 652–653.
- Rocadenbosch F., Sicard M., et al., 2002, The UPC scanning Raman lidar: an engineering overview, *Proceedings of the 21st International Laser Radar Conference*, vol. 1, pp. 69–70, 2002.
- Sasano Y., and H. Nakane, 1981, Significance of the extinction/backscatter ratio and the boundary value term in the solution for the two-component lidar equation. *Applied Optics*, **23**, 11–13.

7 ACKNOWLEDGEMENTS

This work was financed by the Spanish Ministry of Science and Innovation through the Projects CGL2007-60648, CGL2009-07790, PROMETEO/2010/064.

Technological solutions of ScanEx company for remote sensing data acquisition and processing

D.Fedotkin¹ and I.Farutin²

¹Head of Software Development and Marketing Department, ScanEx R&D Center

Email: fedotkin@scanex.ru

²Product Manager, Software Development and Marketing Department, ScanEx R&D Center

Email: farutin@scanex.ru

ABSTRACT - ScanEx RDC is currently the leading company on the Russian market, offering a complete set of integrated solutions on remote sensing data reception and processing. The core of technology by ScanEx is the UniScan multi-mission ground stations for X-band data reception from over 15 different satellites. There are more than 50 such receiving ground stations currently operating worldwide.

Three networks of ministerial level are now equipped with UniScan ground stations on the Russian territory: at the Ministry of Natural Resources, Emercom of Russia and Russian Federal Service for Hydrometeorology and Environmental Monitoring. Based on the UniScan ground stations a proprietary network of receiving centers of ScanEx has been also deployed in four cities covering the entire territory of Russia. This network comprising a dozen of antenna systems provides for the data reception of over hundred daily passes, thus enabling to get up to 20 terabytes of information through a month.

The software developed and supplied by ScanEx Center enables to exert ground receiving stations control; to perform preliminary processing of acquired data; to create remote sensing data catalogs; to automate geospatial data batch processing; to carry out thematic processing of optical and radar imagery data, etc. The most popular among the specialists in Remote Sensing and GIS are ScanMagic® and ScanEx Image Processor® software. Such software solutions have high functionality and enable to do image cataloging, radiometric calibration, geolocation, ortho-rectification, creation of mosaics, processing of multispectral and SAR data, image fusion, image classification, DEM generation, 3D visualization, and many more.

1 ABOUT THE COMPANY

ScanEx Research and Development Center (ScanEx R&D Center) is the leading Russian company on the remote sensing market that offers a complete set of services ranging from acquisition to thematic processing of Earth observation images from space. Today, ScanEx is the only Russian company that has signed license agreements with the top world remote sensing Operators for direct data acquisition from IRS, SPOT, EROS, RADARSAT and ENVISAT satellites series to UniScan™ ground stations, enabling regular near real-time monitoring of territories of Russia and the CIS countries with spatial resolution from hundreds to less than one meter.

ScanEx has been building, maintaining and updating networks of receiving ground stations that belong to such Russian governmental agencies as Emergencies Ministry, Service of hydrometeorology and environmental monitoring (Roshydromet), Ministry of Natural Resources as well as regional space monitoring centers under educational and scientific institutions. Remote sensing centers in Spain, UAE, Vietnam, Iran, Nigeria and Kazakhstan are among the users of ScanEx technologies. Having signed license agreements with Earth observing missions operators, ScanEx is entitled to grant sub-

licenses for data reception to UniScan™ ground stations owners within Russia and the CIS countries and to supply UniScan ground stations abroad. Geography of ScanEx receiving stations is shown at Figure 1.



Figure 1. Geography of ScanEx stations

2 ABOUT THE STATIONS

State-of-the-art computer technologies make it possible to receive Earth imagery from space at

personal computers. These images are a source of independent real-time information about natural sites and the infrastructure status. Thus this remotely sensed data becomes an indispensable tool to increase reliability of the decision support system.

2.1 UniScan™

The UniScan™ technology is the best solution if the time factor is the most crucial issue for decision making and the situation analysis requires timely data. Such data acquisition at the station is the only way to get remotely sensed data from space in real time mode.

Today the UniScan™ stations (Figure 2.) developed at the R&D Center ScanEx provide for receiving both optical and all-weather round-the-clock radar images with a spatial resolution from 1 km to 0.7 m. One UniScan™ station covers area of about 12 million sq. km. This provides for the most efficient routine monitoring of the coverage zone without leaving the place of work. In addition the expenses for in-situ and aerial observations could be significantly reduced. The UniScan™ station is not only the tool for data acquisition but also a set of software products for this data storage, processing and thematic analysis.



Figure 2. UniScan-36™ antenna system

At present time the UniScan™ station provides for reception and processing of data from Terra, Aqua, IRS-P5, IRS-P6, CARTOSAT-2, SPOT 4, EROS A, EROS B, RADARSAT-1, ENVISAT satellites. UniScan™ hardware is universal and programmable. Station parameters enable to receive data from wide range of Earth observing satellites. Besides mentioned above satellites UniScan™ can acquire data from existing or prospective SPOT 5, FORMOSAT-2, RADARSAT-2, NPOESS satellites and many other.

The wide range of the data received by the UniScan™ station in terms of spatial resolution, swath width and spectral range, the frequent overall survey repeat period and the all-weather day-and-night capability of the radar imaging provide opportunities to apply these data in all kinds of practical tasks. The main application areas include:

- update of topographic maps (up to the scale of 1:10 000);
- operational detection and monitoring of oil spills on land and at sea;
- control over compliance with the licensing agreements in natural resources development;
- operational monitoring of the ice and snow cover;
- monitoring the state of agricultural lands, including the control over crop rotation and over the use of lands;
- rapid assessment of the status and the degree of degradation of crop and pasture lands;
- monitoring of hydraulic structures, such as river dams
- creation of up-to-date thematic maps (e.g. vegetation, soil cover condition, potential hazards in an area, etc.);
- creation of digital elevation models;
- environmental impact assessment;
- glacier monitoring;
- control over illegal fishing;
- land cadastre;
- update of forestry maps;
- early detection and monitoring of forest and grassland fires;
- rapid and objective damage assessment after natural disasters

2.2 Alice-SC™

Universal Alice-SC™ ground station (Figure 3.) is intended for receiving and processing of the imagery transmitted from polar-orbital satellites in 1.7GHz frequency.

The station provides for the RS data reception and processing from the following satellites:

- NOAA (POES)

- MetOp
- FengYun
- NPOESS (to be launched in 2013)
- Main applications of data received to Alice-SC™ ground station:
 - hydrology, meteorology and weather forecast;
 - agriculture;
 - monitoring of forest fires and floods;
 - monitoring of sea ice and dynamics of snow cover;
 - education.



Figure 3. Alice-SC™ antenna system

3 ABOUT THE SOFTWARE

ScanEx has developed a number of software for reception planning and station control as well as software for preliminary processing of data from different satellites. And every ScanEx station is completed with the set of software intended to generate data in generic formats from raw data (ScanEx SPOT Processor, ScanEx RADARSAT Processor, ScanEx ENVISAT Processor etc.).

Besides mentioned above, ScanEx develops applications for operational processing and in-depth image analysis. The most popular among the specialists in Remote Sensing and GIS are ScanEx Image Processor® and ScanMagic® software applications.

3.1 ScanEx Image Processor®

The application is intended for extended analysis and in-depth thematic processing of optical and radar imagery data and is an efficient tool to resolve a wide range of applied tasks.

Application features cover almost all key tasks of RS data processing, which makes ScanEx Image Processor® an effective tool for solution of multiple applied tasks.

The application has modular structure and consists of Base Module and six add-on modules:

- “ThematicPro Module” – innovative system for image classification, segmentation and interpretation;
- “3D Module” allows to create 3D landscapes based on satellite images;
- “DEM Module” allows to generate digital elevation models from stereo pairs or from vector maps;
- “SAR Module” allows to do SAR data filtration, segmentation, has in-built oil spill detection and ship detection algorithms and many more;
- “Modelling Module” allows to calculate Solar radiation balance, to simulate flooding, overflow and many more;
- “SDK Module” allows to create own scripts and GUI for scripts option.

3.2 ThematicPro

The Thematic Pro module of ScanEx Image Processor is intended for in-depth thematic processing of space images and their interpretation. The functionality of the application enables to use both conventional (visualization, filtration, obtaining new images by computation) and up-to-date methods, using adaptive algorithms based on topographic mapping during the source remote sensing data processing. The latter are used for more comprehensive (from the viewpoint of thematic interpretation) classification and segmentation of satellite images. Application of algorithms based on topographic mapping enables to achieve better results when selecting thematic information.

The Thematic Pro module allows the user to process vector and raster data simultaneously by applying vector maps for thematic interpretation process control and to vectorize the classification results in the best way.

The application runs all know pixel-by-pixel and object-oriented algorithms of space images, i.e.:

- Unsupervised (automatic) classification based on cluster analysis using ISODATA algorithm (Iterative Self-Organizing Data Analysis Technique).

- Supervised classification based on Topographic Mapping (*Figure 4*).
- Supervised classification of multispectral and radar data based on segmentation algorithms (object-oriented interpretation)

The possibility of using both pixel-by-pixel algorithms based on topographic mapping and segmentation ones is a unique feature of the Thematic Pro module, ensuring wide possibilities of RS data thematic interpretation, missing in similar software products.

3.3 ScanMagic

The application is built based on modern image processing technology and is a user-friendly standalone multifunctional software solution for preview, analysis and processing of Earth observation data, as well as for cataloguing the imagery results.

The application features include support of more than 70 generic/GIS/RS formats, geometric correction, vector editor, universal tools for RS data cataloguing (*Figure 5*), access to web-map services, integrated tools for batch processing of raster and vector data, image enhancement algorithms and many more.

ScanMagic® utilizes efficient innovative techniques of image processing. On-the-fly spooling enables the user to open images of up to 4 GB in size instantly and to analyze large data volumes in real-time viewing mode. On-the-fly processing (for example, image re-projection on-the-fly) enables to

repeatedly change the data processing parameters and make an immediate visual assessment of the results.

4 GEOPORTALS

Geoportal services (*Figure 6*), enabling to create different web-mapping solution, complete this technological cycle. As of today, ScanEx technology is used as the backbone of several special departmental geoportals that have been built and are successfully functioning: at the Russian Ministry of Emergencies, at the Lukoil petroleum company, at the Russian Railways, etc.

5 CONCLUSION

ScanEx has always provided technically competent and financially feasible solutions for each of its clients and partners, whether commercial or non-commercial. The company serves a wide range of requests from an order of a satellite sub-scene up to establishment of the client's own center for remote sensing data reception, archiving and processing.

With future in mind, ScanEx continuously designs and implements new technological and IT solutions: from universal small-aperture ground stations programmable for new Earth observing satellites to the state-of-the-art neural classification software for satellite image interpretation.

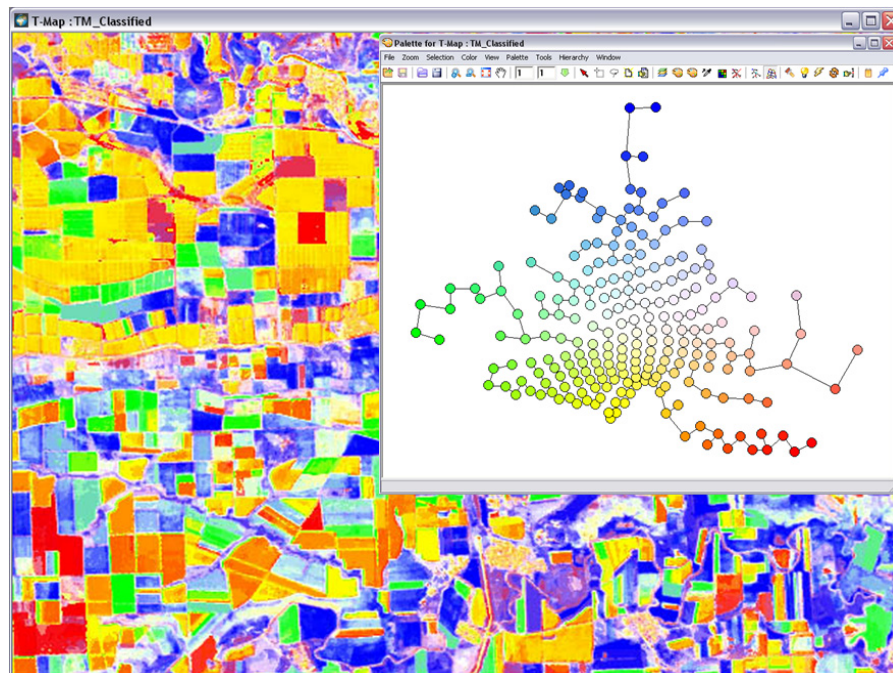


Figure 4. Classification based on Topographic Mapping

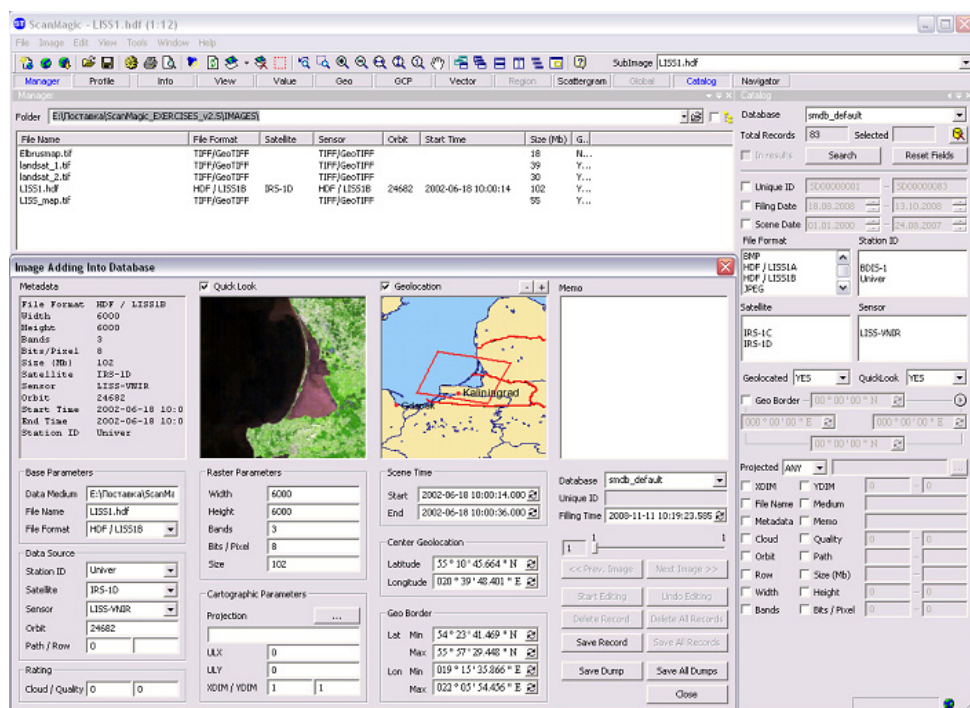


Figure 5. Cataloguing tools of ScanMagic

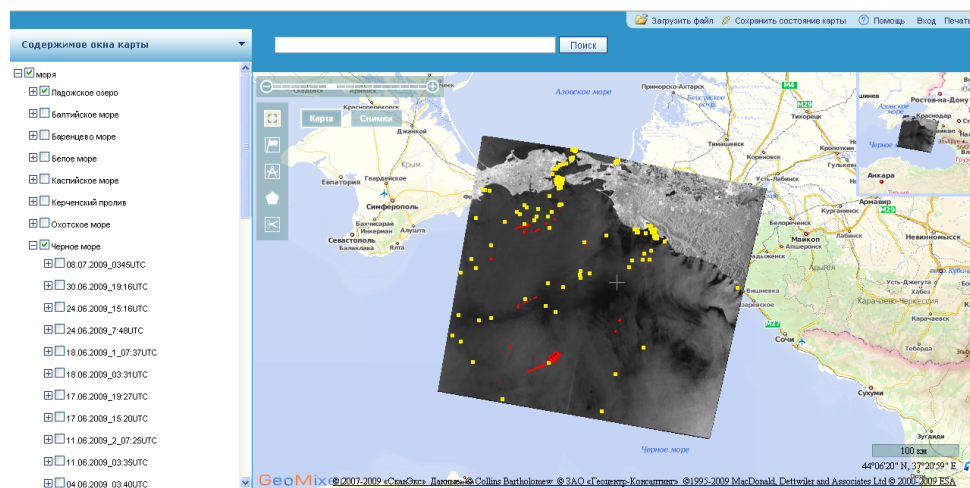


Figure 6. ScanEx Geoportal

Defining the revisit frequency for the MISTIGRI project of a satellite mission in the thermal infrared

J.-P. Lagouarde ⁽¹⁾, A. Oliso ⁽²⁾, G. Boulet ⁽³⁾, B. Coudert ⁽⁴⁾, S. Dayau ⁽¹⁾, S. Castillo ⁽²⁾, M. Weiss ⁽²⁾, J.-L. Roujean ⁽⁵⁾, E. Delogu ⁽⁴⁾, N. Puche ⁽⁴⁾

⁽¹⁾ UR 1263 EPHYSE, INRA, 71 av. E. Bourlaux, F-33140 Villenave d'Ornon, France

⁽²⁾ INRA-EMMAH UMR 1114, Domaine St Paul, Site Agroparc, F-84 914 Avignon Cedex 9

⁽³⁾ IRD, CESBIO, 18 av. E. Belin, F-31401 Toulouse cedex 9, France

⁽⁴⁾ CESBIO, 18 av. E. Belin, F-31401 Toulouse cedex 9, France

⁽⁵⁾ CNRM-GAME, Météo-France, 42, av. G. Coriolis, F-31057 Toulouse, France

Email corresponding author: lagouarde@bordeaux.inra.fr

ABSTRACT. *Both for scientific (monitoring of rapid temporal changes in the water status of surfaces) and for technical reasons (choice of the orbit height), the revisit is a crucial specification in the definition of the recent projects of microsatellites (such as MISTIGRI and TIREX) combining high spatial resolution and revisit capacities in the thermal infrared. The revisit must be adapted to cope with cloud frequency constraints and with the accuracy requirements on derived surface fluxes. The paper first presents a study of cloud frequency and of potential satellite data availability based on the analysis of a long meteorological dataset on France and on MODIS cloud masks on Europe. The impact of the revisit on the accuracy of derived evapotranspiration is then evaluated using long term series of surface fluxes either directly obtained from measurements or from simulations. The impact of the overpass time is simultaneously studied. Even though they have to be confirmed to other locations and climates in the world, the results clearly reveal the need of a 1 day revisit in the TIR.*

1 INTRODUCTION

This study aims at defining the revisit of the MISTIGRI and TIREX missions. MISTIGRI is a project of a microsatellite in the thermal infrared conducted by CNES in cooperation with Spain, and currently in A phase (Lagouarde et al., 2011, in this issue). TIREX (Sobrino et al., 2011, in this issue) is a proposal made at ESA to the recent call for Earth Explorer Opportunity Missions. The originality of MISTIGRI and TIREX is to combine a high spatial resolution (~50m) with high revisit capabilities of 1 or 2 days compatible with water budget monitoring objectives. The revisit must be defined carefully both for scientific reasons (ability to retrieve accurate fluxes) and technical constraints (orbit altitude). It must cope with cloudiness for acquiring a sufficient number of images with the required quality, and at the same time allow one to monitor rapid changes in surface water status and fluxes during short time scale events such as drying after rainfall or irrigation. One must finally make sure it is compatible with the specified accuracy on fluxes retrieval. These different constraints are examined in the paper. The complementary question of the overpass time is simultaneously addressed.

2 ANALYSIS OF CLOUD FREQUENCY AND POTENTIAL AVAILABILITY OF DATA

The combination of cloud occurrence and of revisit first governs the potential number of available cloud free data. Two methods have been used to evaluate it.

2.1 Method 1: evaluation of the data availability from a statistical analysis of a meteorological data base

This method was based on the analysis of an 18 year-dataset (INRA AGROCLIM, 1992-2009) of hourly solar incoming radiation. Eight French stations located all over the country and corresponding to different climates were considered. The principle for discriminating cloud free conditions considered a threshold criterion in the solar radiation. For a given location, the maximum observed radiation in the 18 values available at any given date and time of the year was first assumed to correspond to clear sky conditions at that moment. In fact the data set was not long enough and this was not always the case, resulting in a remaining noise on the evolution of the maximum radiation throughout the year, which required a final smoothing using an empirical solar radiation model to be done (Figure 1). For a given

location and time we generated a typical yearly curve of the evolution of the solar incoming radiation to be compared with. A realistic value of 90% was chosen - and justified afterwards- to identify cloud free conditions all along the 18 year-dataset.

We based our study on a criterion of 1 clear day by 5 day-periods, often considered as a good requirement for monitoring water budgets, which is the first objective of the MISTIGRI mission. The average number of clear days by 5 days-periods estimated on the whole dataset directly provided the potential availability of data with a one day revisit. By sampling the 18 year-dataset, we could similarly study the impact of the revisit.

The results obtained for 3 of the studied locations in France, Avignon, Bordeaux and Rennes are presented in Figure 2. They revealed that the 1/5 day-availability criterion can be fulfilled all year long only with a 1 day-revisit. It can also be seen that, as expected, the frequency of cloud free conditions decreased from Avignon to Rennes corresponding to

Mediterranean and oceanic climates respectively, and that the 2 day-revisit is quite insufficient for Rennes. Five days revisit never matched the requirements.

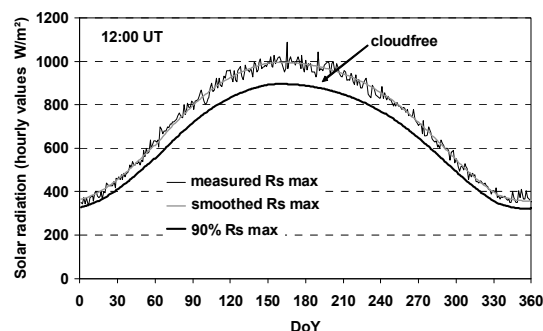


Figure 1. Principle of selection of cloudfree conditions on the AGROCLIM database.

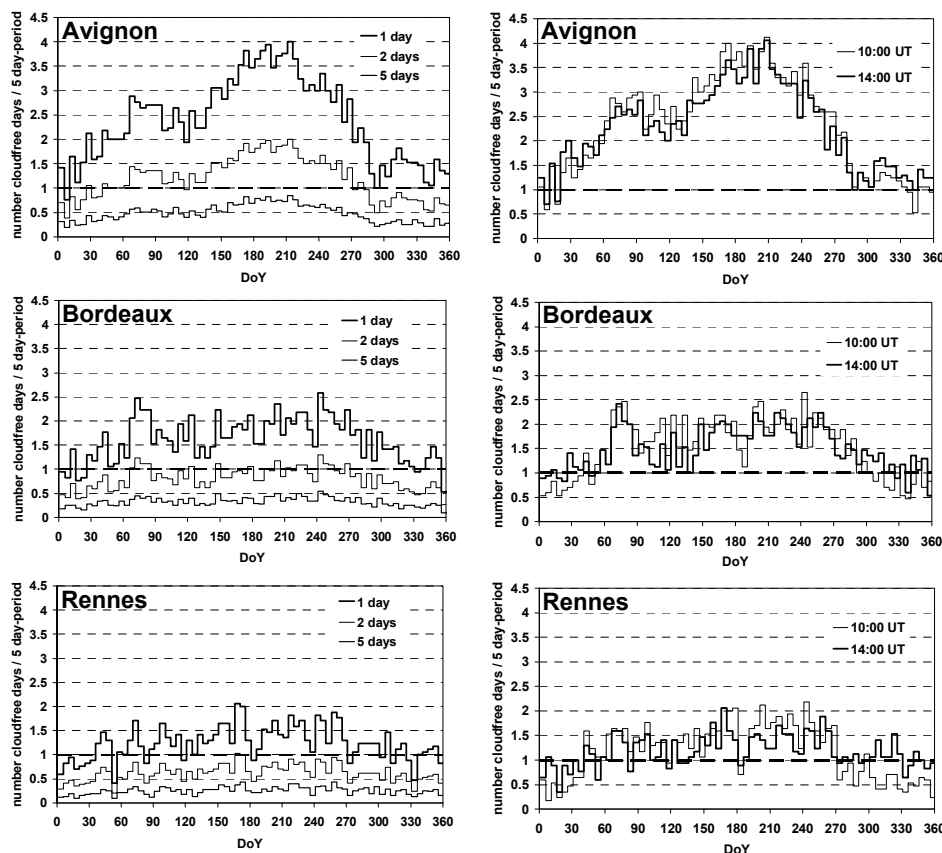


Figure 2. Availability of cloudfree days per 5 day-periods along the year for 3 revisit frequencies (1, 2 and 5 days) (left) and impact of the overpass time (right) for 3 French locations.

We could simultaneously study the impact of the time acquisition. For clarity only the potential data availability for 10 and 14 UT acquisition times for a 1 day-revisit are presented in Fig. 2. Morning haze or fog are likely to explain the data deficit observed in winter for 10 UT. On the opposite, the slight decrease

appearing in summer for 14 UT could possibly be related to convective clouds development phenomena. In this idea, the 12 UT acquisition time (not presented in figure 2) seems to be best suited, but this remains to be confirmed on a large panel of locations and climates.

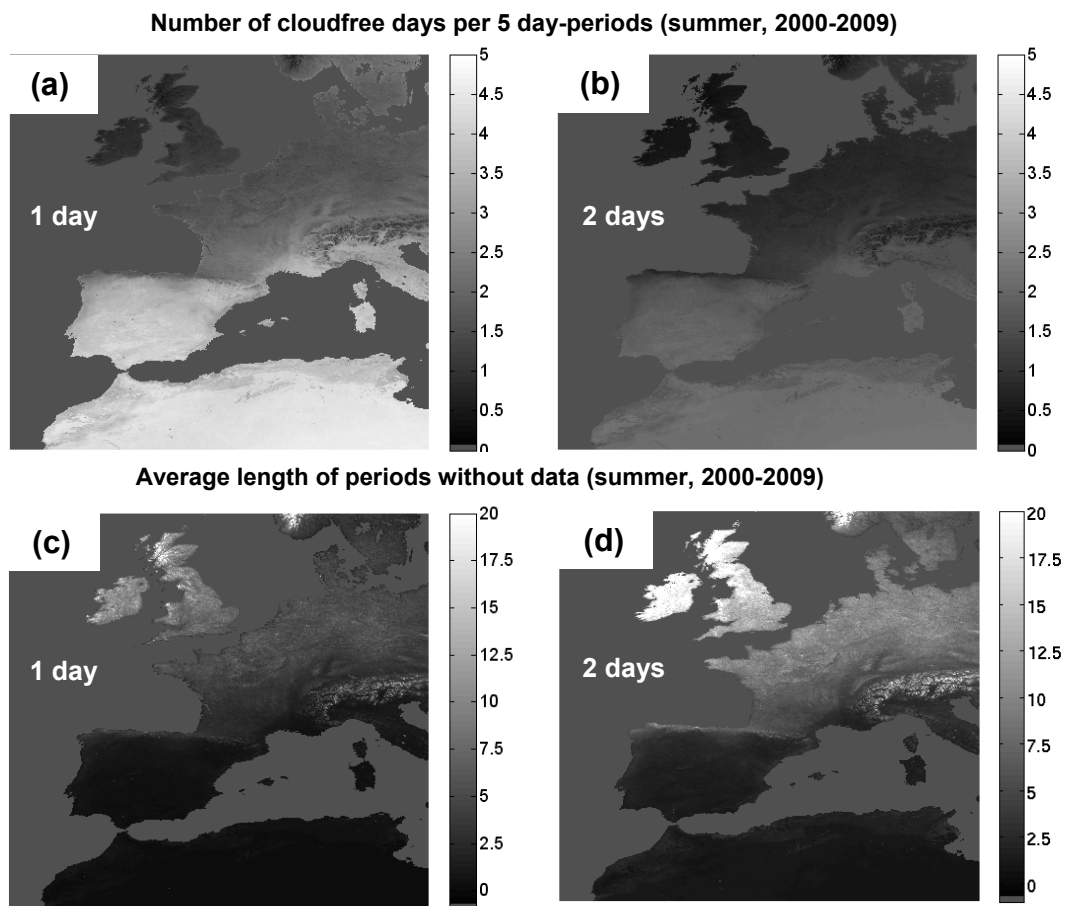


Figure 3. Average number of cloudfree days per 5 day-periods on the years 2000-2009 over Europe for summer (June 1st - August 31st) for 1 day- [up left] and 2 day-revisit [up right]. Down: average corresponding length of periods without data (expressed in days).

2.2 Method 2: analysis of MODIS cloud masks

The number of cloudfree days per 5 day-periods over Europe was also estimated directly using the standard MODIS Terra Surface Reflectance MOD09GA products (<https://wist.echo.nasa.gov/api/>). A retrospective analysis of actual MODIS cloud masks was performed at the European scale on the period 2000-2009 (Figure 3). Despite some artifacts over mountainous regions due to difficulties to discriminate clouds from snow, it emphasized the previous results

quite well and the need of a 1 day-revisit was confirmed at least for all northern Europe. Another interesting indicator was the average length of periods without data: it brought complementary information as it allowed one to reduce the weight of partly redundant information available in the case of consecutive clear days. The analysis on western Europe for spring and summer (Fig. 3 c and d) showed that, excepted for southern Europe countries, the average length of periods without data varied on a range between 5 and 10 days for a 1 day-revisit, but may reach up to 20

days for a 2 day revisit. Other case studies should obviously be examined on other climates and regions of the World to generalize these results and confirm the need of daily revisit. Data from geostationary satellites could also be used for that purpose.

3 IMPACT OF THE REVISIT ON THE ESTIMATION OF EVAPOTRANSPIRATION

3.1 Modelling approach

The impact of the revisit on the accuracy of satellite-estimated annual evapotranspiration was tested using a simulation approach. Continuous reference series of evapotranspiration (ET) were first generated based on simulations by the ISBA-A-gs model (Calvet et al. 1998, 2008). Simulations of vegetation growth and daily ET were performed for 3 sites in France (Avignon, Bordeaux and Versailles close to Paris), 3 vegetation types (irrigated corn, deciduous and coniferous forests) and 3 soils (differing in water holding capacity). Climate forcing corresponded to ARPEGE climate models simulations between 1950 and 2100 (scenario A1B from the last IPCC exercise).

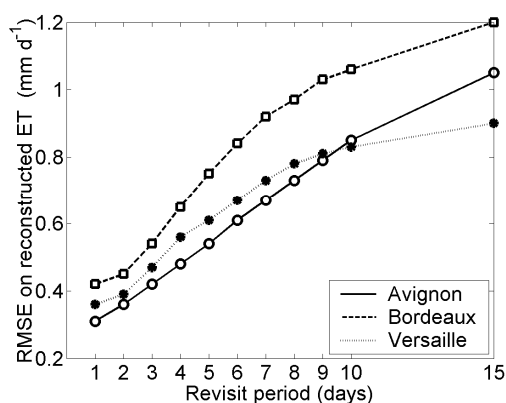


Figure 4. Influence of revisit on the RMSE of reconstructed time series of daily evapotranspiration ET for 3 sites.

Series of daily ET as derived from satellite were then simulated by combining a revisit frequency with a selection of cloudfree conditions. Several thresholds on solar radiation R_s were successively considered (80 %, 90 % or 95 %), in order to generate different cloud frequencies. In total, 12150 years were simulated (3 sites x 3 plant types x 3 soil types x 3 threshold values x 150 years). An error (RMSE 0.8 mm d⁻¹) was then given to the selected ET estimates in order to account for the errors in daily ET satellite mapping algorithms. Continuous series of daily ET were finally

reconstructed using a linear interpolation of the ratio ET/ R_s between the discrete satellite ET estimates available for clear days. They were compared against the continuous original simulations (without added errors) using a simple RMSE criteria. Revisit frequencies between 1 and 15 days were tested.

Figure 4 displays the variation of RMSE with the revisit. It can be seen that the RMSE increased rapidly with the revisit. The rather smooth aspect of the curves was explained by the fact that the RMSE were estimated at year scale on the whole 150 years-datasets (combining years, thresholds, plants and soils). The impact of the revisit may be even much more critical for shorter periods or periods with particular meteorological conditions. For example, revisit and cloud frequencies may combine in generating rather long periods without available data, preventing to catch drying periods between water supplies by rain or irrigation.

3.2 Experimental approach

The previous results were confirmed by a similar approach applied on experimental datasets. Meteorological and micrometeorological observations acquired for whole cultural seasons at 4 sites (France: Avignon, Auradé, Lamasquère, Morocco: Sidi Rahal/R3) were used to produce available energy ($R_n - G$) and latent heat flux (LE) data in a large range of conditions varying from stressed to nearly potential. The identification of cloudfree sky days were based on in-situ solar radiation and clear sky solar radiation according to the Meeus model (Anneer and Wells, 2007). This model displayed a Nash Efficiency between computed and observed solar radiation of 0.75 and a bias less than 60 W/m². Daily values of evapotranspiration on days without image acquisition were obtained by interpolating linearly either the observed evaporative fraction $EF = LE / (R_n - G)$ or a stress factor $SF = LE / LE_{pot}$ between two successive satellite acquisitions (LE was the latent heat flux and LE_{pot} its value in potential conditions).

Figure 5 shows the impact of the revisit frequency on the performance of reconstructed daily LE if SF was linearly interpolated between two acquisitions. The error significantly increased for the Moroccan site whereas it remained low for Auradé. This was explained by the absence of water stress over this site contrarily to Marrakech where water stress occurred several times during the growing season.

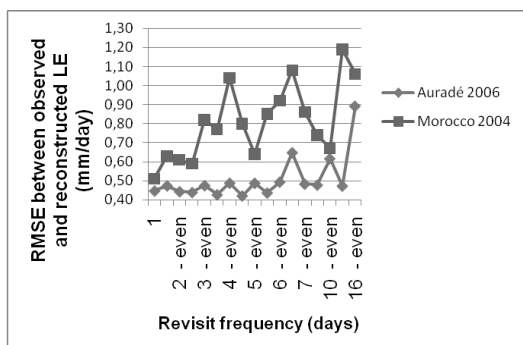


Figure 5. Evolution of the RMSE in reconstructed LE as a function of revisit frequency.

The analysis of the same datasets additionally allowed investigating the impact of the time of overpass on the accuracy of retrieved LE fluxes. One assumed that instantaneous R_n-G , LE and LE_{pot} were perfectly known when an image was acquired; LE was then extrapolated from this instantaneous value to a daily estimate assuming either the evaporative fraction EF or the stress factor SF constant throughout the day or assuming a known course of EF throughout the day (Hoedjes et al., 2008). We can see in figure 6 that acquisition times between 12:00 and 13:00 provided the best estimates of daily actual latent heat flux.

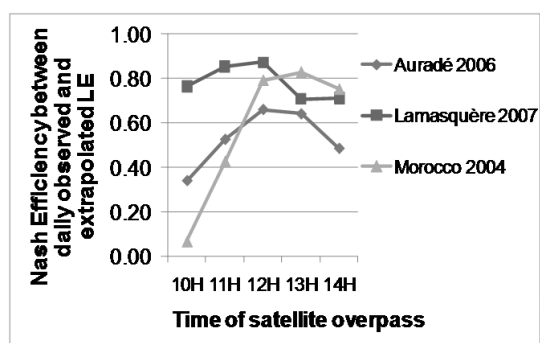


Figure 6. Evolution of the Nash efficiency for the extrapolation of LE according to time of satellite overpass from 10AM to 2PM.

3.2 Statistical analysis of the potential data availability per stress periods (from experimental data)

The analysis of the data availability for 1 day-revisit on stress periods on the South-West of France (Auradé 2005-2007 and Lamasquère 2006-2007) and Morocco (SudMed project, 2004) sites showed that the

threshold of at least 1 data per stress period is not always reached for this sample of 6 years in real conditions. As an example, on Lamasquère, there were 4 stress periods 4 to 5 days long between 2005 and 2007 and only 1.5 day (statistically) with a data available (clear sky conditions and stress). The criterion of having at least 1 TIR observation per stress period is particularly important for regions with extensive irrigation. Together with the criteria of having at least 1 data per 5 day-period, it emphasizes the recommendation of a daily revisit for MISTIGRI and TIREX missions.

4 CONCLUSIONS

In this study, several approaches have been followed and several criteria used to determine the revisit specification for the MISTIGRI and TIREX missions. The cloud frequency analysis performed using hourly solar radiation meteorological datasets on French locations and MODIS cloud masks over Europe clearly revealed that a 1 day revisit was necessary to get at least 1 clear day observation per 5 day-periods on most of northern Europe. For southern countries, and considering only the same criteria, one could imagine that a 2 day revisit could be enough. However, such regions often suffer from dry and sometimes semi-arid conditions and include a number of irrigated areas for which it was demonstrated on some case studies that only the 1 day revisit was adapted -and even not always- to provide at least one data per stress period: for example for Morocco, a 2 days revisit hardly met this requirement and for Lamasquère this requirement was already not fulfilled with a 1 day revisit. This revisit frequency was also shown to provide the best accuracy on retrieved evapotranspiration estimates: the differences were not very important between 1 and 2 day revisits (but for the particular examples of temperate areas considered), but they provided very strong improvement compared to ~7 or ~15 days revisits (the latter being obtained with Landsat satellites). Our study additionally revealed that simple methods based on a linear interpolation of EF or LE/R_g performed well when there was a lack of data (cloudy day, or no visit from satellite) to derive the seasonal evapotranspiration.

Moreover it was also shown that an overpass time around 12:00 would be more suited.

Further work is needed to analyze in details specific temporal sequences during which the water supply is not known (for precision irrigation management applications for instance) and to generalize the results by considering other climates.

5 REFERENCES

- Annear, R.L., Wells, S.A., 2007. A comparison of five models for estimating clear-sky solar radiation. *Water Resources Research*, 43(10).
- Calvet, J.-C., J. Noilhan, J.-L. Roujean, P. Bessemoulin, M. Cabelguenne, A. Olioso and J.-P. Wigneron, 1998, An interactive vegetation SVAT model tested against data from six contrasting sites, *Agric. For. Meteorol.*, 92, 73–95
- Calvet, J.-C., Gibelin, A.-L., Roujean, J.-L., Martin, E., Le Moigne, P., Douville, H., Noilhan, J., 2007, Past and future scenarios of the effect of carbon dioxide on plant growth and transpiration for three vegetation types of south-western France. *Atmos. Chem. Phys.*, 8, 397-406.
- Hoedjes, J.C.B., Chehbouni, A., Jacob, F., Ezzahar, J., Boulet, G., 2008. Deriving daily evapotranspiration from remotely sensed instantaneous evaporative fraction over olive orchard in semi-arid Morocco. *Journal of Hydrology*, 354(1-4): 53-64.
- Lagouarde J.-P., Bach M., Boulet G., Briottet X., Cherchali S., Coudert B., Dadou I., Dedieu G., Gamet Ph., Hagolle O., Jacob F., Nerry F., Olioso A., Ottlé C., Pascal V., Roujean J.-L., Sobrino J. A., Tintó Garcia-Moreno F., 2010. MISTIGRI, a microsatellite project associating high spatial resolution and high revisit frequency in the Thermal InfraRed. 3rd Int Symp RAQRS'III, Valencia, sept 27th - oct 1st 2010, in this issue.
- Sobrino J. A., Lagouarde J.-P., Boulet G., Briottet X., Cherchali S., Coudert B., Dadou I., Dedieu G., Gillespie A., Hagolle O., Jacob F., Jiménez-Muñoz, Manunta P., Mueller M., Nerry F., Olioso A., Ottlé C., Price K., Roujean J.-L., Royer A., Stefanov W.L., Voogt J., Wattson I.M., Zarco-Tejada P.J., 2010. Overview of the Thermal InfraRed Explorer (TIREX) mission. 3rd Int Symp RAQRS'III, Valencia, sept 27th - oct 1st 2010, in this issue.

Challenges and Solutions on the Development of the Ingenio/SEOSAT Mission Primary Payload

Demetrio Zorita, Jose Ignacio Bueno, Carlos Miravet, Luis Pascual, Gonzalo Taubmann, Jaime Azcona, Jose María Arroyo, Iker Monasterio, Unai García, Julio Martín, Jacinto Muñoz, Alfonso López, Javier Eguía, Santiago Jarabo; *SENER Ingeniería y Sistemas (E)*. Rocío García, Rafael Navarro; *Thales Alenia Space España (E)*. Tomás Belenguer, Luis Miguel González, Carmen Pastor, David Arrazola, *INTA (E)*. Isabel Cabeza, *EADS CASA Espacio (E)*. Andrea Marini, *ESA/ESTEC (NL)*.
demetrio.zorita@sener.es

ABSTRACT - *The Ingenio/SEOSAT mission is the flagship mission for the Spanish Space Plan 2007-2011 elaborated by CDTI in 2006. It is also part of the Spanish Earth Observation Satellite System". This system comprises two spacecrafts with imagery capabilities within the optical and radar ranges. SEOSAT/Ingenio and SEOSAR/Paz respectively. SEOSAT/Ingenio is a Programme funded by the Ministry of Industry, Tourism and Trade, who has delegated in the Centro para el Desarrollo Tecnológico Industrial (CDTI) the overall programmatic and financial responsibility. Following approval by ESA Council on 13-14 June 2007 an Agreement has been signed between the CDTI and the European Space Agency (ESA) concerning the technical and managerial assistance that ESA will provide to the Implementation phase of the SEOSAT/Ingenio Space and Ground Segment activities.*

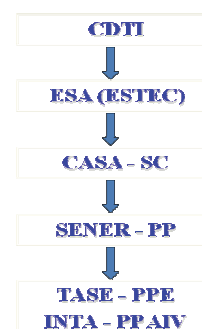
Ingenio/SEOSAT is a high performance satellite for Earth Remote Sensing, designed to provide imagery for applications in land zoning, urban and rural planning, cartography, emergency support, water resources management, agriculture, environment, etc. This is a novel scenario, as for first time an industrial Spanish consortium is fully responsible of the design, development and in-orbit operation of a satellite of this characteristics.

The primary users, composed of several Spanish Governmental Organizations and Scientific Institutions, have defined the requirements of the mission, encompassing state-of-the-art image quality and radiometric performances. In order to fulfill these requirements, it has been defined a high performance instrument, facing several challenges on the design and manufacturing from the engineering point of view.

1 INTRODUCTION

This mission is devoted to providing high resolution multi-spectral land optical images to different Spanish civil, institutional and government users, and potentially to other European users in the frame of GMES and GEOSS.

SEOSAT/Ingenio is a Low Earth Orbiting mission. It features a Primary Payload (PP) with one broadband 2.5 meter resolution panchromatic channel and four visible/near infrared 10 meter resolution spectral channels. The PP swath close to 55 km ensures a frequent revisit period, and offers quick accessibility to any point on Earth in emergency situations.



User Requirements:

- Two channels: Panchromatic (PAN) and Multispectral (MS)
- Four bands in the MS: Blue, Green, Red and Near Infrared (NIR)
- High resolution in PAN: 2.5m
- Medium resolution in MS: 10m

- Swath 55Km (Field of View: circa 4.75 deg; frequent revisiting period)
- MTF: 0.115 in PAN and 0.300 in MS @ Nyquist (along and across)
- SNR @ Lref: 110 PAN, 125 Blue, 200 Red/Green/NIR (Lref 74 PAN, 82 Blue, 77 Green, 70 Red, 114 NIR [W/m²/sr/um])
- No single point failure (SPF) allowed



2 OPTICAL DESIGN

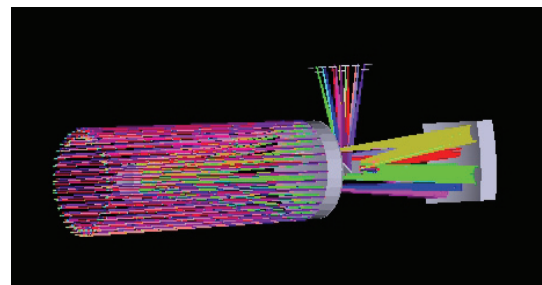
The SEOSAT telescopes are of the Korsch type. The Korsch optical system uses three powered anastigmatic mirrors plus one flat folding mirror used to extract the focal plane and compact the whole structure. The primary and tertiary mirrors are concave ellipsoids while the secondary mirror is a convex hyperboloid. It works on-axis in pupil and field. This design embodies a large Cassegrain focal field and a comparatively small exit pupil. Some significant benefits of this telescope design are:

- Capability of operating with focal planes of large dimensions
- Efficient and compact stray-light baffling, due to the presence of an intermediate image, and the possibility of placing a Lyot stop at the exit pupil of the system, which in this design lies close to the folding mirror
- Pure catoptrical system (but for the marginal effect of filter and detector windows), and hence free of chromatic aberrations, which was a priori serious concern given the large spectral ranges of operation of the instrument. Also, the instrument will not suffer typical glass ageing effects due to incoming gamma-ray radiation
- On-axis tertiary mirror, in contrast to other solutions based on the basic Korsch telescope design. This feature provides substantially advantages in terms of

lower manufacturing and alignment complexities. Also, it enables the use of a small folding mirror without central hole

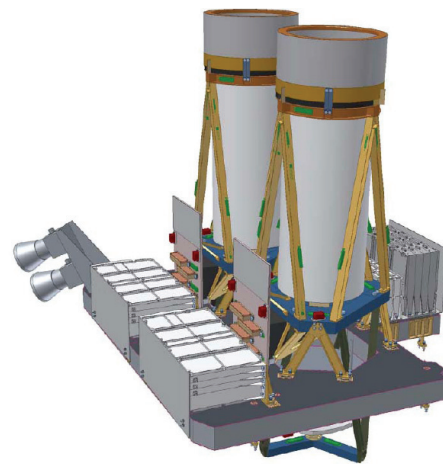
- Focal length of the primary-secondary group of mirrors close to the effective focal length of the complete system. This enables the use of a tertiary mirror with magnification close to unity, making this element relatively tolerant to misalignment

SEOSAT PP mirrors are manufactured by SAGEM.



3 STRUCTURAL DESIGN

All the elements constituting the PP are located over a High Stability Support Panel (HSSP). This concept was proven to be the most convenient in terms of stiffness and integration in comparison with a decouple structure for optics and electronics.

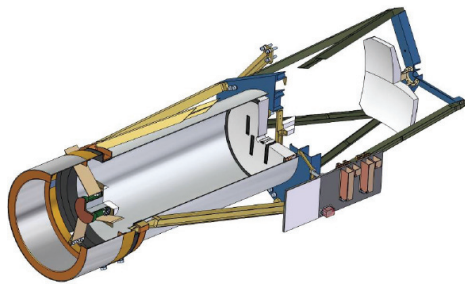


The HSSP is a high thermo-mechanical stability plate that is attached to the S/C I/F Platform iso-statically with the IMD (Isos-static Mounting Device).

The Cameras are approximately 1.5m large and are mounted in perpendicular direction to the HSSP. The attachment between the Camera and the HSSP is through the Optical Bench with 3 Bipods providing Iso-

static support. The Optical Bench is in the central area of the camera and the HSSP need a hole (one per Camera) to allow penetration of the Camera through it. In fact, part of the Camera penetrates inside the S/C below the Platform I/F plane.

Both telescopes are identical with the exception of the legs that are symmetric due to the angular deviation of 1.17° .



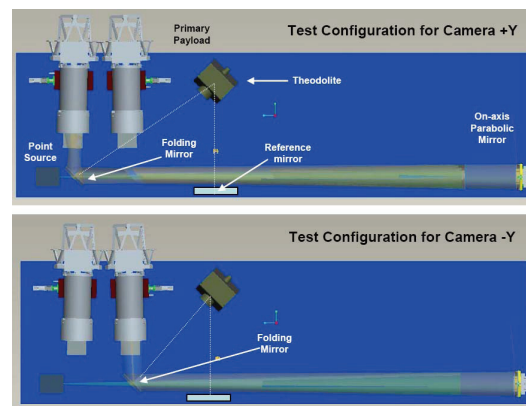
The table below outlines the materials used in the different optomechanical parts:

- Zerodur: Very high thermal stability but poor mechanical properties. Mirrors (Shott).
- SiC: Good thermal stability and high stiffness but heavy. Focal Plane with radiator and Detector Shims.
- CFRP: Good thermal stability and excellent stiffness-density ratio, but cannot be machined and can be used only in simple geometry elements. The baseline of fibre is the M55J and the Cyanate Ester matrix EX-1515. HSSP skins (BTS).
- Invar: Good stiffness and thermal stability and it is feasible to be machined, but high density. M2 supporting bipods (SENER) & Partial mirrors IMD's (SAGEM).
- Ti-6Al-4V: Medium thermal stability and stiffness. Telescope tube legs, Optical Bench, Optical bench legs, focal plane support (SENER) & HSSP IMD's (BTS) & Partial mirrors IMD's (SAGEM).
- AA 7075: Poor stiffness and thermal stability but very light for no critical components. Fittings and inserts (BTS).
- AA 6082: Poor stiffness and thermal stability but very light for no critical components and good thermal conductivity. Baffles, covers, radiators, MLI supports (SENER).
- FR4: Very low thermal conductivity. Thermal washers (SENER).

4 ASSEMBLY, INTEGRATION and VERIFICATION (AIV)

Three models will be built for the SEOSAT PP: Structural Model (SM), Engineering Qualification Model (EQM), and Flight Model (FM). The EQM will consist of one full camera, being the other dummy. This is adequate because the two cameras are functionally, mechanically, thermally and electromagnetically decoupled from each other. In addition, one of the cameras of the FM will be made by refurbishment of the EQM, adding flight electronics but maintaining the structural elements and mirrors.

The AIV of the SEOSAT Primary Payload will be carried out in INTA facilities by INTA personnel in close cooperation with SENER personnel. This includes the mirror alignment in each camera, the focal plane integration in each camera, the alignment of the two cameras in the HSSP, and all the qualification and acceptance verification activities, i.e. functional tests, image quality tests, radiometric performances tests, and environmental tests.



5 FOCAL PLANE (Detectors and Filters)

Detectors: Each SEOSAT PP camera Focal Plane includes two PAN detectors and two MS detectors, making a total of four and four in the overall PP. All detectors are manufactured by E2V (E2V/ATMEL). The PAN detector is a TDI mode back-illuminated CCD, with photoMOS type pixels with lateral anti-blooming structure. The image section has 6000 columns of active pixels each $13\ \mu\text{m}$ square and is clocked continuously to give a time-delay-and-integrate (TDI) function. The transfer of charge along the CCD is made synchronous with the velocity of the scan image.

The MS detector is a quadrilinear CCD. The spacing between the centres of adjacent lines is $936\ \mu\text{m}$, allowing the necessary area for the readout registers and associated bus structures for each line. The photo-sensing element of the pixel is a photodiode. Each line of pixels has 1500 photo-elements with $52\ \mu\text{m}$ pitch and the size of each photo-element is $52\ \mu\text{m}$ square.



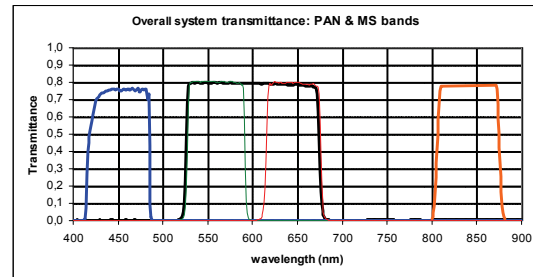
MS detector front view

Filters: SEOSAT PP demands compact and robust designs including both, single and multispectral channels, and simplicity and high accuracy are design drivers factors. It is widely accepted that the most cost/effective solution for filtering the incoming light is to use a strip filters windows located just in front of the CCD detector lines.

The PP implements the following filters:

- PAN filter consisting of a window of glass with one high performance filter patterned on its surface.
- MS micro stripe filter, consisting of a window of glass with four parallel high performance micro strip filters patterned on its surface.

SEOSAT PP filters are supplied by JENA Optronik



6 RESULTS and CONCLUSIONS

SEOSAT Primary Payload implements the following features:

Optical parameters:

Focal length = 3.5m

Pupil diameter = 250mm

Mechanical parameters:

Overall mass = 130Kg

Maximum instantaneous power = 270W

Image quality:

MTF	PAN	Blue	Green	Red	NIR
Across track	0,12	0,38	0,38	0,35	0,33
Along track	0,11	0,25	0,25	0,24	0,24

Radiometric performances:

Table of Signal to Noise ratio (SNR) at End of Life (7 years in orbit), and at the centre of the FoV of each camera:

SNR	PAN	Blue	Green	Red	NIR
@ Lref	103	142	181	183	326
@ Lmin	39	87	78	59	33

(Lref = 74 PAN, 82 Blue, 77 Green, 70 Red, 114 NIR [W/m²/sr/um])

(Lmin = 23 PAN, 43 Blue, 28 Green, 18 Red, 6 NIR [W/m²/sr/um])

Spanish National Remote Sensing Program, a way to achieve massive use of remote sensing data.

J.J. Peces (*), G. Villa (*), A. Arozarena (*), J.A. Tejeiro (*), E. Domenech (*), N. Plaza (*).

* Instituto Geográfico Nacional, C/ General Ibáñez Íbero, 3, 28003 Madrid

gmvilla@fomento.es, jjpeces@fomento.es,

ABSTRACT - Spanish National Remote Sensing Program (PNT) provides regular coverage of the Spanish territory with current and historical satellite imagery. This imagery is acquired with multi-user licenses for all Spanish Public Institutions, and processed once with geometric and radiometric processing agreed by experts of Spanish scientific community. Spanish imagery is structured in three levels of spatial and temporal resolution:

High resolution: Images from 2 to 10m of spatial resolution in panchromatic mode and from 10 to 30m in multispectral mode. It is planned to acquire a complete coverage every year with summer images. From 2005 to nowadays SPOT5 HRG (Simultaneous panchromatic 2,5m and multispectral 10m) satellite is selected to provide that type of resolution.

Medium resolution: Images from 10 to 15 m of spatial resolution in panchromatic mode and from 20 to 50 m in multispectral mode. It was planned to acquire at least four coverage every year, but since January 2008 all Landsat5 imagery (Thematic Mapper, multispectral 30 m) captured over Spain is acquired.

Low resolution: Multispectral images from 50 to 1000 m of spatial resolution, with a periodicity of 1 or 2 days. MODIS and MERIS sensors are the main source of this type of resolution.

To reduce the time between the collection of data and the moment the information is available, PNT has designed a processing system, achieving an online spreading using servers and networks. There are some important aspects such as designing a storage infrastructure suitable to the volume of information, an appropriate workflow, distribution control and an efficient spreading.

1 INTRODUCTION

In this century, XXI, Spain has posed two challenges, both of them very important for its sustainable development, besides the intention of modernization, the impulse of the infrastructure and the concern about the environment. The recently dynamism of the Spanish society as well as the development of the whole country cause a great impact over our territory. All of these aspects demand the availability of accurate information about the territory constantly updated and adapted to the geographical data standards (ISO, INSPIRE, IDEE...). The images of the satellite give the possibility to answer about the dynamic changes that are taking place in our territory. These images are also an important part of the geographical and environmental information. Therefore, the applications and the uses are increasing. The Remote Sensing is a mature technique with even more applications than it used to have, some of them have reached such a development that makes them being in "operational phase". However, most of the techniques and their required processing are complex, so a great specialization and hard work is needed to apply them in the correct and efficient way. This drives us to the necessity to implement systematic production lines, properly designed and constantly improved.

2 DESCRIPTION OF SPANISH NATIONAL REMOTE SENSING PROGRAM

2.1. Legal and Administrative framework

The "Consejo Superior Geográfico" (CSG) is the advisory and planning agency of the Spanish State dealing with the geographical information. It depends on the Ministry of Public Works, being regulated by the Royal Decree 1792/1999, November, 26th. Its aim is the coordination of geographic information of Spain. Specifically, the CEOT (special commission of land monitoring) coordinates the photogrammetric flights and territory mapping from satellite.

Under the CEOT, it is created the group of general coordination of the project, formed by the Ministry of Public Works (through the IGN, CNIG), the Ministry of Environment, Rural and Marine Environment and the Defence Ministry (through INTA). Likewise, it has been named a Coordinator in every Ministry involved and every Autonomous Community, to deal with the agreement and negotiate economic transfers needed to the development of the project.

2.2. Organization

Inside the PNT, different work groups by experts and users have been created in order to consolidate the

requirements and identify solutions. The groups created until now are:

a) Technology Groups: High Resolution, Medium resolution, Low resolution, Radar, Biophysical parameters and spectro-radiometry and Architecture computing, data and metadata.

b) Application Groups : Agriculture, Forest and fires, agrienvironment index and other applications.

The technology groups have as the mission to define technical specifications of the products to be generated from the original images and productive processes to be implemented in the PNT.

The mission of the application groups is to write technical recommendations about complete processes to facilitate the hiring by the Public Administration of products and services of an added value from the images and basic data generated.

2.3. Imagery acquisition

The coverage considered on the Spanish National Remote Sensing Program are structured in three levels of spatial and temporal resolution: high, medium and low

a) High Resolution

PNT considers that high resolution is an image from 0,5 m pixel size to 10m in panchromatic and from 2m to 30m in a multispectral. The acquisition forecast of this type of images is a complete coverage a year at least, preferably between June, 15th and September, 15th.

The main applications of these images are: to obtain land cover cartography (project SIOSE and project CORINE land cover of the European Union), updating cartographic database of medium and small scales, to obtain environmental and agricultural information, etc. It also may be obtained "Image Cartography" (Orthoimagery and Carthoimagery).

From 2005 to 2009, the high resolution sensor chosen has been the HRG on board of the satellite SPOT5. Images that this sensor captures are from 2,5m pixel size in the panchromatic (1 band) and 10m in the multispectral (4 bands). Other alternatives are Formosat or the Spanish satellite INGENIO (in a near future).

b) Medium resolution

PNT considers that medium resolution is an image from 10m to 15m pixel size in the panchromatic and from 20m to 50m in multispectral. The regular recurrence initially planned were at least of 4 coverage a year, but all the images taken from Spain by the satellite Landsat5 sensor have been acquired since May 2008.

The repetitive captured of information of the same zone is carried out with the aim to allow the

multitemporal monitoring (intra and inter-annual) of environment and territory evolution, It is also useful for environmental management, design of plans and policies of prevention and emergency according to natural catastrophe, risky places, control of environmental quality, etc, in which remote sensing is combined with tools like Geographical Information Systems. Other applications are land cover automatic classification, crop identification, irrigated land detection, forest information, biophysical parameters, etc.

Other additional alternatives to Landsat5 are CBERS2 and DEIMOS1(private initiative Spanish satellite). In the future Sentinel2 will also be available.

c) Low Resolution

PNT considers as low resolution coverage with multispectral images from 100m to 1000m, of spatial resolution and periodicity from 1 to 30 days.

Low resolution data are used mainly to analyze the evolution of phenomena which change quickly along time, through the creation of biophysical parameters. The daily availability of the images of these sensors and of derivate parameters of them, facilitate the monitoring in nearly real Earth time, directed to the analysis of environmental variables.

So, main applications of the low resolution images are the extraction of the biophysical and environmental parameters (indexes of vegetation, temperatures, quantity of combustible materials, and risk of fire...) theses parameters can facilitate the obtaining of standard environmental index by different world organizations.

The suggested sensors are AQUA/TERRA Modis and ENVISAT Meris (with 250m and 300m of maximum resolution respectively) Other complementary alternatives of very low resolution are: NOAA, AVHRR, SPOT Vegetation. In the future it will also be available Sentinel 3.

2.4. Image processing and derivate products

Each type of territory coverage: high, medium and low resolution, counts with its own set of data, work flow and products.

a) High resolution

SPOT5 images are received with a processing level 1A. All the subsequent geometric processing, such as the radiometric treatments, is carried out at the National Geographic Institute.

a.1. Ground control points measurement and block adjustment.

The unit LPS from software ERDAS is required. Blocks are formed with the panchromatic images and with the multispectral images: one for the whole peninsula and one for each island.

-Block preparation: definition of the geodetic reference system, type of images to be corrected, mathematical model which is going to be used and charge images in the block.

- Ground control points measuring: Around 13 control points are taken per image measuring their terrain coordinates from aerial orthophotographies with 0.5m of pixel size.

-block adjustment and mathematical model parameters calculation: One only adjustment is required on the block getting a unique set of parameters of the model for each image.

-Block images orthorectification. Finally, the calculated parameters are applied to every image to be transformed into the desired geodetic reference system.

a.2. Geometric correction

Including ground control points coordinates and tie points coordinates in one only block adjustment, images are georeferenced. The geodetic reference system used is ETRS89, projection UTM.

An exhaustive visual quality control is carried out to make sure there are no geometric deformations in the generation process of corrected images. Besides, a geometric control of the mentioned images is made through the measurement of 10 check points in each image. Check points are measured over panchromatic image and distributed regularly over a mesh defined by technical direction; they are different from ground control points. The check point medium error obtained should be smaller than 1,5 pixels and maximum error in any point, smaller than 2 pixels.

The panchromatic and multispectral images are resampling by bicubic interpolation method, and also by nearest neighbour with multispectral images.

a.3. Pansharpen.

Trough pansharpening it is obtained an image with the same spatial resolution as panchromatic image and same spectral resolution as multispectral image.

To make pansharpening is used "Fast SRF" method created by María González de Audicana, from Navarra University. This method has the best relation quality-processing time.

a.4. Radiometric balance.

Radiometric balance is used to homogenize the radiometry of images to obtain a continuous mosaic. All radiometric values of all spot5 images are transformed into radiometric values of a reference image through a lineal mathematical transformation: $y = a \cdot x + b$. This equation is applied band to band. Formulas to obtain "a" and "b" parameters are:

$$a = s1 / s2$$

$$b = \mu1 - \mu2 (s1/s2)$$

s1: Standard deviation of reference image

s2: Standard deviation of image to balance.

$\mu1$: Average of reference image.

$\mu2$: Average of image to balance.

A MODIS image has been used as reference image to make balance in 2005. Later date, mosaic generated in 2005 with all spot5 images has been used as referenced image to make new balance.

a.5. Band combination.

Four band combinations are generated: classic false color, assigning bands 321 to RGB colour mode, Corine false colour, assigning bands 342 to RGB colour mode, natural pseudocolor, assigning bands 432 to RGB colour mode and SIOSE natural pseudocolor which is a mixture of 50% from SIOSE natural pseudocolor and a natural color that is derived from a synthetic blue.

a.6. Enhancement

It is used to obtain an easy image to interpret and consist of a contrast lineal expansion for red, green and blue bands. After that, a gamma function is applied for getting brightness. Enhancement is determined for each separate portion of land. Only one enhancement is calculated for the peninsula mosaic and it is applied to all mosaic images. As well, different enhancements are calculated for each Spanish island and they are applied to all images of each island. These enhancements were determined in 2005. From 2006, balance and enhancement are applied to images at the same time because the reference image which is used is mosaic generated in 2005 (which is already enhanced).

a.7. Mosaics

One mosaic is obtained for Spanish peninsula and Balearic Island and another one for Canary Island. Mosaics are made in different band combinations: natural pseudo-colour and false colour. Break lines are calculated for repairing big radiometric differences that balance could not save. In 2005 and 2008, Spanish territory was completely covered with high spatial resolution images, so there are two hold mosaics for these years. There is another Spanish coverage within 2006 and 2007, so one mosaic was made for these two

years. From 2009 to future an “incremental mosaic” is generated adding new images to most current mosaic for the moment, so users could see the most recent data for each surface point.

b) Medium resolution

Landsat images are received with a level processing called 1G (only sensor deformations). All geometric and radiometric processing subsequent is carried out within Spanish National Remote Sensing Program. The main steps of processing are:

a.1. Geometric processing:

- Ground control points measurement and block adjustment: it is a process similar to that made with high-resolution images but measuring 33 control points per image.
- Geometric correction: project image to ETRS89 geodetic reference system.

a.2. Radiometric processing for optical wavelength:

- Radiance calculation: Radiances are calculated from sensor calibrations coefficients through next mathematical equation:

$$L_{\lambda} = G \cdot ND + B$$

L_{λ} : radiance obtained by sensor ($W \cdot m^{-2} \cdot sr^{-1} \cdot \mu m^{-1}$),
 ND: image digital levels,
 G: gain,
 B: bias.

- TOA Reflectivity calculation: next mathematical formula it is used:

$$\rho_{TOA} = \frac{\pi \cdot L_{\lambda} \cdot d^2}{E_{0,\lambda} \cos \theta_s}$$

d: land-sun distance at the moment of image capture, expressed in astronomical units (ua).
 L_{λ} : spectral radiance, calculated as in the previous case.
 $E_{0,\lambda}$: spectral solar exoatmospheric irradiance.
 θ_s : solar zenith angle.

- Atmospheric correction. It is used “dark object model”, developing by Chavez (1988; 1996).

$$\rho = \frac{\pi * [L - L_a] * d^2}{\cos \theta * E_0 * \tau_1 * \tau_2}$$

ρ : reflectivity, E_0 : spectral solar exoatmospheric irradiance ($W \cdot m^{-2} \cdot \mu m^{-1}$), τ_1 : atmospherically transmission coefficient on the road Sun-Land, τ_2 : atmospherically transmission coefficient on the road Land-Sensor, L_a : radiance which is received by the

sensor in an area where there is only atmospheric contribution (area of shadow or water according to the spectral region), L : radiance of the pixel to correct, θ : solar zenith angle and d : land-sun distance, in astronomical units.

- Topographical correction. The empirical-statistical method is used. This is the mathematical algorithm:

$$\rho_{\lambda,h,i} = \rho_{\lambda,i} \cos \gamma_i m_{\lambda} - b_{\lambda} + \bar{\rho}_{\lambda,i}$$

$\rho_{\lambda,h,i}$: pixel reflectivity in horizontal land.

$\rho_{\lambda,i}$: pixel reflectivity in steep land.

$\bar{\rho}_{\lambda,i}$: Reflectivity average of all $\rho_{\lambda,i}$

γ_i : incidence angle in a pixel i

b_{λ} : la ordenada en el origen de la regresión lineal en entre γ_i y $\rho_{\lambda,i}$

m_{λ} : la pendiente de la regresión lineal entre γ_i y $\rho_{\lambda,i}$

c) Low resolution

Images will be acquired in real time using Spanish receiving antennas. Raw data (.pds format) will be transforming into level 1b which are radiance and reflectance at sensor, TOA radiance, TOA reflectivity and observation and illumination angle and georeferenced data. So next values will be calculated:

- TOA radiances and TOA reflectance, RAD-TOA and REF- TOA.
- Latitude and longitude, observation and illumination angles.
- TOA radiances and TOA reflectance for georeferenced images.

TOA radiance will be transform into radiometric temperature (Trad-TOA) for infrared channels according to Planck law. Finally, georeferenced images will be projected to geographic coordinates.

Derivate products will be:

- Radiative products: radiance at sensor, temperature at earth's surface and normalized reflectance at earth's surface.
- Biophysical products: Normalized Difference Vegetation Index (NDVI), Fraction of Vegetation Cover (FVC), Leaf Area Index (LAI) and Fraction of Absorbed Photosynthetically Active Radiation (FAPAR).

2.5. Dissemination of images and derivate products.

There is a working Group in PNT called “architecture and data” aimed at defining and establishing all items in storage and distribution in PNT project. Storage and distribution must satisfy those requirements:

- a. Organized and accessible storage for all generated information.
- b. Efficient distribution according to the priorities of access.
- c. Control of the information distribution as data policy says.
- d. Normalization.

a. Needs of hard drive for all generated information in PNT Project reach the amount of 9 Terabytes each year for more than 17.000 images. This disk volume will be increase with the images of "Historic PNT Project" (to acquire all the images captured by different sensors of Landsat constellation from their launch), whose estimated needs of hard drive are about 40 Terabytes. Moreover, it must be remembered the possibility to incorporate coverage from other satellites to PNT project.

To meet the first requirement, it has an EVA array formed by a disk array with enough capacity for storing all current information and possible to expand the storage volume in future. By implementing a document manager for the Project provides a tool for managing information: definition of metadata-based searches and data organization, allowing the possibility of incorporating a process Management system.

b. We must have a bandwidth appropriate to the size of the files and the Lumber of users connected so that the response time is acceptable. Currently, data and derived products are distributed via FTP.

c. The medium and high spatial resolution images are acquired with a multi-user license restricted for Spanish Public Administration, Universities, Public Investigation Agencies and Companies working for Public Administration.

d. To meet the last requirement of the PNT Project in storage and information distribution are considered, among other regulatory issues, the implementation rules of the INSPIRE Directive, International Standard ISO and OGC specifications. Derived products in PNT project have their ISO metadata in order to comply with INSPIRE Directive.

3 CURRENT PROBLEMS, SOLUTIONS AND FUTURE WORK.

3.1. Description of the problem.

The big drawback that satellite images users can find when working with them is the subject of the clouds. According to the International Satellite Cloud Climatology Project (ISCCP) estimates that our planet is permanently covered by clouds more than 60%.

From an operational standpoint, clouds are the most significant source of error to calculate the land surface reflectivity and have an adverse effect on most remote

sensing applications, making useless many of the images acquired by different satellites.

Therefore, the ideal thing to do it would be to eliminate the clouds of any image while preserving the land information.

Until now, the research has been focused on automatic clouds detection. Some detection algorithms have been developed for different sensors but what they get is a mask of clouds, leaving useless that part of the image.

3.1. Solutions and future Works.

The National Geographical Institute (PNT coordinator agency), Regional Development Institute of Albacete (IDR), Image Processing Laboratory U. Valencia (IPL), and Center for Ecological Research and Forestry Applications in Barcelona (CREAF), are working on a research project to obtain cloudless images from temporal series of images from different sensors with different spatial and temporal resolutions which are available for the same point on earth.

The idea is: using images from multiple sensors to determine the spectro-temporal reflectance surface (STRS) for each point of Earth surface and to make a surface model. After creating the model this surface, the reflectivity of any point of surface can be obtained, for any date and wavelength, where there is no baseline data (image).

Therefore, it may remove the cloud of an image by replacing the radiometric values of affected pixels with the reflectance values corresponding to each pixel. To achieve this purpose it is necessary to deal with two concepts:

- Downscaling or Upscaling, is to transform an image pixel size to another to compare images with different spatial resolution. It allows to homogenize radiometric information from images with different pixel size.

- Temporal interpolation is to obtain information from the earth's surface of a date which there is no image captured, interpolating between the images captured before and after dates.

It is also necessary to introduce a new concept: the spectro-temporal reflectance surface (STRS) for each point of an image.

From the beginning, in remote sensing each point of image (or Earth surface point) was characterized by its spectral signature, i.e. by the reflectance value for each wavelength.

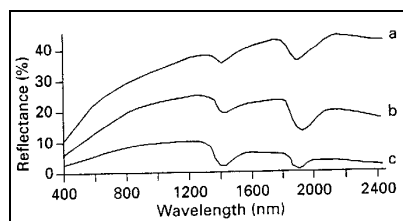


Figure 1: spectral signature example

If time is added, this figure becomes a surface where reflectivity values are represented according to the corresponding wavelength and date.

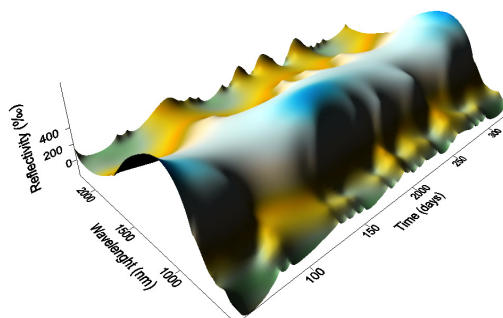


Figure 2: spectro-temporal reflectance surface example

Once know the STRS for each point on Earth, it would be possible to calculate reflectance values for this pixel of every date, including date where there is no images taken.

This way it is possible to replace radiometric values of pixels with clouds of an image with reflectance values which represent the existing land below the cloud. As well, it is possible to generate synthetic images free of clouds of a desired date where there is any image capture by a satellite.

Future work will include improved methods of merging images of different resolutions (downscaling and upscaling) and methods of interpolation to achieve better spectro-temporal reflectance surfaces, i.e., surfaces which represent much better the real values.

4 CONCLUSIONS

Thanks to Spanish Remote Sensing National Program (PNT), it has been promoted the massive use of satellite images on multiple projects and jobs. PNT Project is responsible for coordinating the acquisition of satellite imagery, performing basic geometric and radiometric treatments on the images and distributing them to all the Spanish Public Administration, Universities and Public Investigation Agencies.

Now, one more step is intended by solving the major problem that all users of satellite images have for most applications in remote sensing: the clouds. Several Spanish public agencies are collaborating on a research project, where cloudless images of a desired date are obtained by removing radiometric values of pixels with clouds and replacing with reflectance values that represent the existing land below the cloud. As well, it is possible to generate synthetic cloudless images of a desired date where there is any image capture by a satellite.

5 REFERENCES

- Arozarena, A., García Asensio, L., Villa, G., Domenech, E., Conama 2008. Plan Nacional de Observación del Territorio en España.
- Instituto Geográfico Nacional. 2009. Documento PNT version 2.4. Madrid.
- Equipo Técnico Nacional. 2005. Especificaciones Técnicas para el Plan Nacional de Teledetección (PNT). Madrid.
- Calera, A., Amoros, J., Garrido, J., Gómez, L., Saiz, J., Camps, G., Villa, G., Peces, JJ. 2009. Interpolación Normalizada de Imágenes procedentes de múltiples sensores.
- Camacho, F., Sobrino, J.A., Romaguera M., y Jiménez-Muñoz, J.C., E. 2009. Estudio de los tratamientos a realizar sobre las imágenes de satélite de baja resolución adquiridas para el PNT. Valencia.
- Chuvieco, E., Hantson, S., Moré, G., Cea, C. et al. 2008. Propuesta de procesamiento de imágenes Landsat y evaluación de algunos aspectos en zonas piloto para el PNT. Barcelona.
- J. Amorós-López, L. Gómez-Chova, L. Guanter, L. Alonso, J. Moreno and G. Camps-Valls, "Multi-resolution Spatial. Unmixing for MERIS and Landsat Image Fusion, IEEE Geoscience and Remote Sensing Symposium (IGARSS'10)Hawaii,USA, July 2010.
- Gómez, L., Calpe, J., Camps i Valls, G. PhD Thesis: Cloud screening algorithm for MERIS and CHRIS multispectral sensors. Valencia 2008.

Thermal Airborne Spectrographic Imager for Temperature and Emissivity Retrieval

L. Pipia, F. Pérez, A. Tardà, L. Martínez, V. Pala and R. Arbiol

Institut Cartogràfic de Catalunya (ICC) Remote Sensing Department, Barcelona, Spain

luca.pipia,fernandop.anna.tarda,vicenc.pala,lucas.martinez,arbiol@icc.cat

ABSTRACT *The Thermal Airborne Spectrographic Imager 600 (TASI-600) is a hyperspectral infrared sensor manufactured by the Canadian company ITRES© which started being operated by the Institut Cartogràfic de Catalunya (ICC) at the end of 2009. The system works in a pushbroom configuration and provides the user with 32-band hyperspectral data obtained through a spectral alignment operation in the nominal 8-11.5 μm range. In this work, the effects of spectral interpolation on pixels' radiance balance are shown to yield pixels' absolute temperature uncertainties proportional to emissivity if nominal atmosphere compensation is carried out. Accordingly, an alternative processing chain to cope with this issue is put forward. The estimation of absolute temperature is carried out using ARTEMIS technique (Borel, 2008). Results are finally assessed using ground-truth measurements obtained with multiband field radiometers.*

1 The TASI Sensor

The Thermal Airborne Spectrographic Imager (TASI) by ITRES© is a pushbroom hyperspectral sensor with a 40° Field-Of-View (FOV) operating in the thermal infrared (TIR) spectral region. It nominally acquires 32 bands to provide continuous spectral coverage in the wavelength range of 8-11.5 μm (Itres, 2010). Thermal IR photons emitted from the scene are focused on a plane through two curved slits, generating hyperspectral images with 640 across-track pixels with 6% overlapping.

TASI actually acquires radiance information in 55-bands ranging from 6.5 μm up to 12 μm approximately. Bands at the shorter wavelengths are employed to estimate pixels' spectral shift induced by temperature variation within airborne platform. Remaining bands are radiometrically calibrated (Radcorr block), spectrally aligned (Specorr block) and filtered in space or frequency by user as needed for blinking pixels removal. At the end of the ITRES traceable processing chain, 32-band hyperspectral data at the system nominal wavelengths are provided.

2 Spectral Interpolation Drawbacks

Spectral Interpolation carried out at radiance level might lead to temperature miscalculation due to the difference between nominal and real central wavelength of TASI's filters and, consequently, to an incorrect MODTRAN-based atmospheric contribution removal. This is stressed in the example of Fig. 1, where it can be seen that the transmissivity τ characterizing the interpolated radiance (red filter) from real measurements (blue filters) differs appreciably from the value estimated by MODTRAN5.0 (Berk A. et al., 2005).

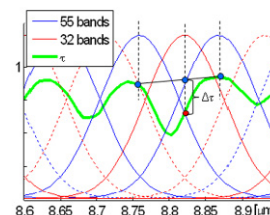


Fig.1: Incorrect atmospheric compensation due to radiance spectral interpolation.

Accordingly, an atmospheric compensation based on the nominal position of sensor's bands might turn out to be incorrect. The error in terms of temperature is proportional to scene's emissivity itself, in a way that, the lower the emissivity, the higher the temperature uncertainty. This is shown in Fig. 2 for emissivity ϵ values spanning within the [0.2, 0.7] interval.

3 TASI Processing Chain

A novel processing chain was developed by ICC for an accurate retrieval of absolute temperature and emissivity information from TASI acquisitions. Hyperspectral energy is sampled by TASI at a fixed frequency equal to 200 Hz. Energy frames are then grouped and time-normalized in order to provide squared-pixel radiance information. A first radiometric calibration is carried out using the ITRES© procedure.

An additional calibration block called *RadCapp* developed by ICC is then applied. Essentially, calibration polynomials are used in a pixel-by-pixel approach to make up for hyperspectral radiance systematic underestimation caused by calibration blackbody emissivity uncertainties (Quattrochi, 2000).

Afterwards, the problem of atmosphere contribution is tackled. Geometrical parameters characterizing each pixel are first estimated.

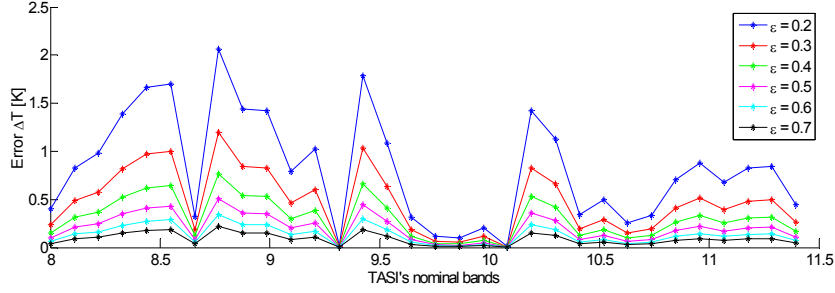


Fig. 2 : Absolute temperature error due to radiance spectral interpolation for ε spanning from 0.2 to 0.7.

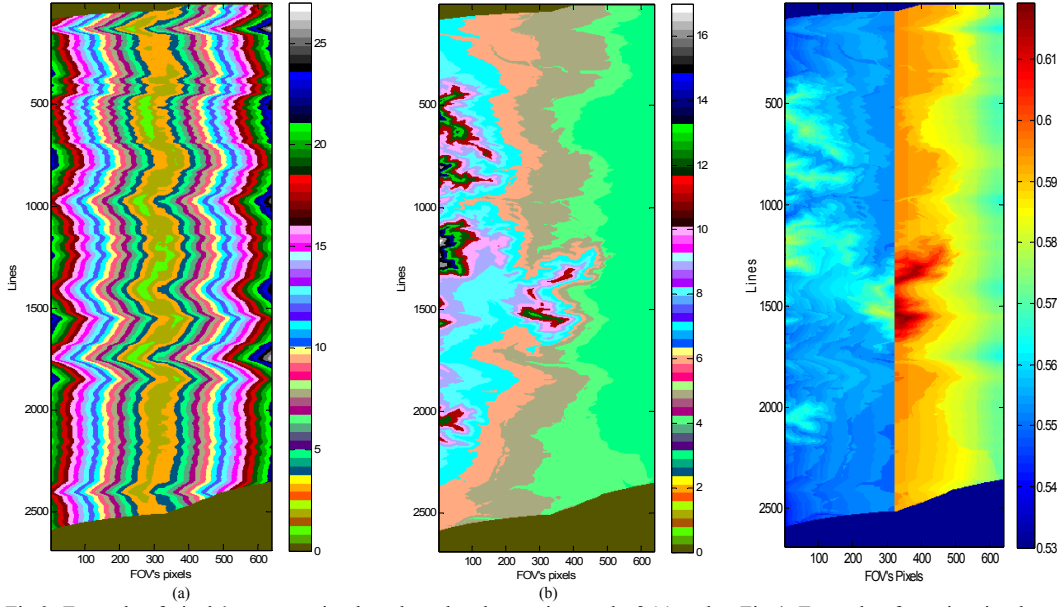


Fig.3: Example of pixels' segmentation based on the observation angle θ (a) and vertical distance to the sensor h (b) with $\Delta\theta=1.5^\circ$ and $\Delta h=30\text{m}$ (Vandellós).

Fig.4: Example of τ estimation based on segmentation of Fig. 3a-b (Vandellós).

Denoting with l and p the image line and FOV's pixel indices, the observation angle $\theta(l,p)$ and the vertical distance to the sensor $h(l,p)$ are calculated for each point of the hyperspectral image in the sensor reference system. Then, height minimum increment Δh and angular step $\Delta\theta$ are fixed to group pixels into subsets, as it is shown in Fig. 3a and Fig. 3b. The number of angular sectors and height intervals are equal to

$$N_\theta = \theta_{\max} / \Delta\theta \quad (1)$$

$$N_h = h_{\max} / \Delta h \quad (2)$$

where θ_{\max} is fixed to 30° ($>\text{FOV}/2$) to take into account turbulence effects.

At this point, MODTRAN5.0 (Berk A. et al, 2005) is employed to estimate atmospheric downwelling radiance $L^\downarrow(\lambda)$, upwelling radiance $L^\uparrow(\lambda)$ and transmissivity $\tau(\lambda)$ profiles for the $N_\theta \times N_h$ possible

geometries in the $[6\mu\text{m}, 12\mu\text{m}]$ spectral range. Note that a wavelength range wider than the nominal $[8\mu\text{m}, 11.5\mu\text{m}]$ span is required to deal with possible spectral shifts of the 55 bands actually acquired by TASI.

The last step is to match the spectral properties of FOV's pixels to the corresponding observation geometry, which slightly changes at each line of the hyperspectral image. The hyperspectral filter f imaging pixel p of the FOV in a specific band b is Gaussian-shaped. Then, it is fully-characterized by the central wavelength $\lambda_0(p)$ and the spectral bandwidth $\Delta\lambda(p)$ and can be expressed as

$$f(p,b) = G(\lambda_0(p), \Delta\lambda(p)). \quad (3)$$

where G stands for the normalized Gaussian function.

It follows that the three atmospheric contributions affecting the radiance information provided by pixel p of TASI images at line l in the band b can be modeled as

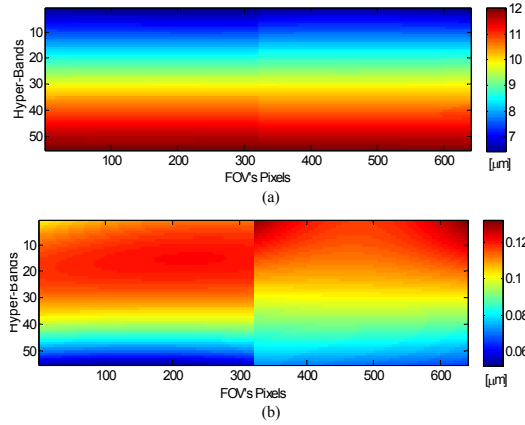


Fig. 5: Example of the distribution of central wavelength λ_0 (a) and bandwidth $\Delta\lambda$ (b) of FOV's pixels among the 55 bands acquired by TASI.

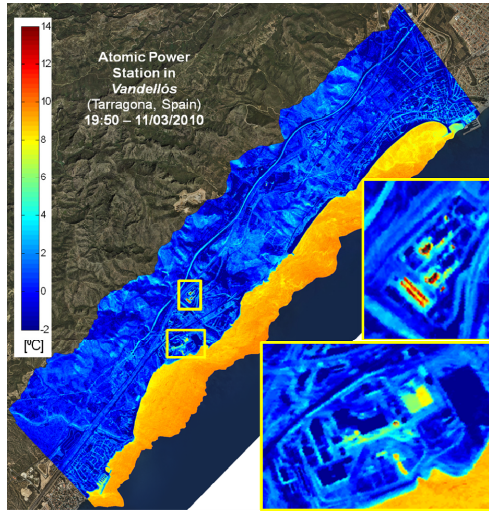


Fig.6: Temperature map of Vandellós retrieved from TASI hyperspectral data using MODTRAN5.0 atmosphere standard model and ARTEMIS technique.

$$\begin{aligned}\underline{L}^{\downarrow}(l,p,b) &= L^{\downarrow}\left(\left[\frac{\theta(l,p)}{\Delta\theta}\right], \left[\frac{h(l,p)}{\Delta h}\right], b\right) \cdot G(\lambda_0(p,b), \Delta\lambda(p,b)) \\ \underline{L}^{\uparrow}(l,p,b) &= L^{\uparrow}\left(\left[\frac{\theta(l,p)}{\Delta\theta}\right], \left[\frac{h(l,p)}{\Delta h}\right], b\right) \cdot G(\lambda_0(p,b), \Delta\lambda(p,b)) \\ \underline{\tau}(l,p,b) &= \tau\left(\left[\frac{\theta(l,p)}{\Delta\theta}\right], \left[\frac{h(l,p)}{\Delta h}\right], b\right) \cdot G(\lambda_0(p,b), \Delta\lambda(p,b))\end{aligned}\quad (4)$$

where $[\dots]$ denotes the floor function and defines the subset pixel p at the specific line l belongs to. Fig.4 shows an example of the spatial distribution the transmissivity τ corresponding to a TASI acquisition in Vandellós (south Catalonia) when $b=25$. Note that differences in filters' spectral properties as well as in pixels' observation geometry turn into changes in the estimation of the atmospheric attenuation to be

compensated for. The discontinuity between left and right halves of τ in Fig.4 is due to spectral differences between the two slits imaging the incoming radiance. This is shown in Fig.5a and Fig. 5b, where an example of the distribution of $\lambda_0(p)$ and $\Delta\lambda(p)$ among the 55 bands acquired by TASI is given.

The last step of the processing chain is the separation of emissivity $\varepsilon(\lambda)$ and temperature T information. Among the alternative techniques available in the literature (Borel, 2008) (Borel, 2003) (Gillespie, 1998), the *Automatic Retrieval of Temperature and Emissivity* using *Spectral Smoothness* (ARTEMIS) algorithm is used.

In contrast to the first version of the ARTEMIS technique proposed in (Borel, 2003), which essentially finds T_{opt} by maximizing the smoothness of emissivity profile $\varepsilon(b)$, the radiance fitting-based approach described in (Borel, 2008) is more suitable for TASI acquisitions. According to simulations, this minimization approach needs a lower number of hyperspectral bands to converge to the correct temperature information. Then, it better deals with the 32-band data provided by TASI for quantitative parameters estimation.

It is acknowledged that $\varepsilon(\lambda)$ and T are coupled in the equation describing the radiation measured by a hyperspectral TIR sensor $L^S(\lambda)$, which is generally expressed as

$$L^S(\lambda) = [\underline{L}^{\downarrow}(\lambda) (1 - \varepsilon(\lambda)) + \varepsilon(\lambda) B(T, \lambda)] \tau(\lambda) + \underline{L}^{\uparrow}(\lambda), \quad (5)$$

where B is the Planck's function. The rationale of ARTEMIS is that thermal-infrared spectra of solids are much smoother than gases'.

By defining a reference emissivity (usually $\varepsilon_{\text{ref}}=0.95$), a reference temperature T_{ref} is first obtained at pixel level as

$$\begin{aligned}T_{\text{ref}}(l,p) &= \\ &= B^{-1} \{ [\underline{L}^G(l,p,b_0) - \underline{L}^{\downarrow}(l,p,b_0) (1 - \varepsilon_{\text{ref}})] / \varepsilon_{\text{ref}}, \lambda_0(p,b_0) \} \quad (7)\end{aligned}$$

where B^{-1} is the inverse Planck's function and b_0 is a TASI spectral band where atmosphere is highly transmissive. Then, T_{ref} is used as input seed to an iterative function fitting the measured and estimated radiances. The optimum temperature is finally given, pixel-by-pixel, by

$$T_{\text{opt}} = \min[\sigma \{ L^S(l,p,b) - \underline{L}^S(l,p,b, T_{\text{opt}}, \varepsilon_{\text{opt}}) \}] \quad (8)$$

where

$$\begin{aligned}\underline{L}^S(\dots) &= [\underline{L}^{\downarrow}(l,p,b) (1 - \varepsilon_{\text{opt}}(b)) - \varepsilon_{\text{opt}}(b) B(T_{\text{opt}}, b)] \cdot \\ &\cdot [\underline{\tau}(l,p,b) + \underline{L}^{\uparrow}(l,p,b)]\end{aligned}, \quad (9)$$

and ε_{opt} is the low-pass filtered emissivity profile calculated from T_{opt} .

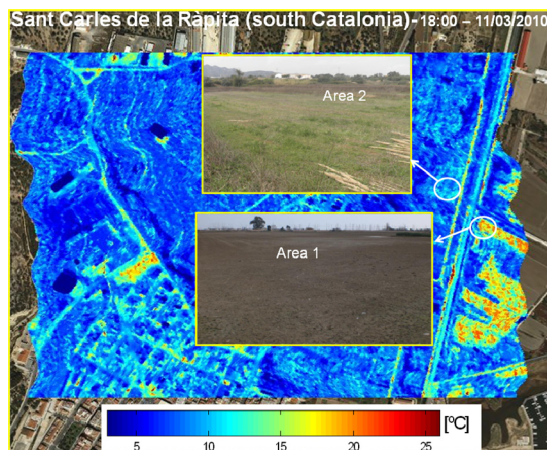


Fig. 6: Temperature map estimated from TASI data of the area close to Sant Carles de la Ràpita.

4 TASI Real Measurements

First flights with TASI sensor were carried out by ICC in the areas of Vandellòs and Ebre delta, in south Catalonia (Spain). Datasets were acquired on 11/03/2010 at two different heights - 1600m and 3200m- providing images with a pixel size about 2m×2m and 4m×4m, respectively. For the estimation of the atmospheric parameters in the TIR region, the mid-latitude winter model was used. Hyperspectral data were processed as explained in Section 2. The geocoded temperature map retrieved by ARTEMIS for the area of Vandellòs is shown as an example in Fig. 5. The two zoomed subareas correspond to the facilities of a power station over which the TASI sensor was flown.

In order to perform a first assessment of TASI hyperspectral acquisitions, in-situ measurements were also carried out in the framework of a collaboration between the Institut Cartogràfic de Catalunya (ICC) and the Universitat de València Estudi General (UEG). For this purpose, two test-areas were selected close to Sant Carles de la Ràpita village, one corresponding to bare soil and another one to meadows. In-situ measurements were acquired during TASI passage using two multiband field radiometers, CIMEL CE 312-1 and CIMEL CE312-2. Absolute ground temperature information was obtained by averaging the values retrieved by inverting the Planck's equation from each band with the emissivity values given by the TES technique (Gillespie, 1998). The temperature map estimated from TASI data over the test-areas is shown in Fig. 6 whereas the time-evolution of in-situ temperature mean-value and standard deviation is displayed in Figs. 7a and 7b, respectively.

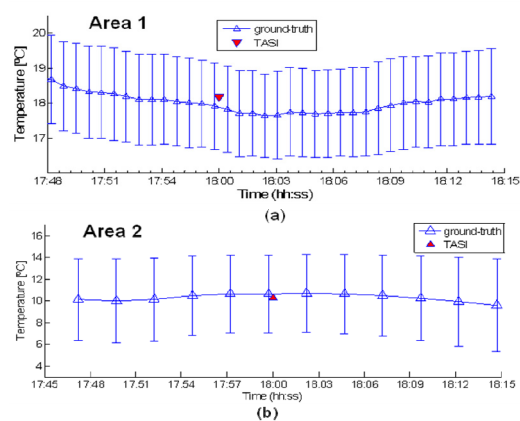


Fig.7: Time evolution of in-situ mean temperature and standard deviation versus TASI estimation concerning the bare soil (a) and low-vegetated (b) areas selected for TASI assessment.

In order to match TASI and in-situ measurements, a 5×5 boxcar around UVEG field-GPS coordinates was used to average the temperature retrieved by TASI data. The outcome is represented by the red triangle in Fig. 7a and Fig. 7b. It can be observed a very good matching between the TASI-based and in-situ temperature information, with an error of 0.4K and 0.3K for bare soil and low-vegetation, respectively. The results constitute a first assessment of the quality of hyperspectral data acquired by the TASI sensor as well as of the accuracy of the processing chain implemented by ICC for absolute temperature retrieval.

5 Conclusions

A novel processing chain for TASI hyperspectral data has been proposed and assessed using ground-truth measurements. Absolute temperature information was retrieved with an error of 0.3K/0.4K using standard atmospheric profile available in MODTRAN5.0 software. In the near future, improvements provided by in-situ radio-sounding will be assessed and comparisons between retrieved and ASTER-based emissivity profiles will be also performed.

References

- Berk A. et al., 2005, MODTRAN 5: A Reformulated Atmospheric Band Model with Auxiliary Species and Practical Multiple Scattering Options: Update, *Proceedings of the SPIE*, Vol. **5806**, pp. 662-667.
- Borel, C. 2003, ARTEMIS-an Algorithm to Retrieve Temperature and Emissivity from Hyper-Spectral

- Thermal Image Data, 28th Annual GOMACTTech Conference, Mar. 31-Apr.3, Tampa, Florida.
- Borel, C. 2008, Error analysis for a temperature and emissivity retrieval algorithm for hyperspectral imaging data, *International Journal of Remote Sensing*, No. **17-18**, Vol. **29**, 239-246.
- Gillespie, A.R., S. Rokugawa, T. Matsunaga, J.S. Cothren, S. Hook, and A.B. Kahle, Temperature and Emissivity Separation from Advanced Spaceborne Thermal Emission and Reflection Radiometer (ASTER) images, *Transaction of Geoscience and Remote Sensing*, Vol. 35, No. 4, 1113-1126.
- ITRES 2010, <http://www.itres.com/products/imagers/tasi600>.
- Quattrochi D.A. and Luvall J.C., 2000, *Thermal Remote Sensing in Land Surface Process* (Boca Raton, London, New York, Washington D.C: CRC Press)

Spectral Measurements of Photosynthetic Efficiency

Elizabeth M. Middleton^{1*}, Yen-Ben Cheng², Karl F. Huemmrich³, Qingyuan Zhang³, Petya K.E. Campbell³, Lawrence A. Corp⁴, William P. Kustas⁵, Hank A. Margolis⁶

¹NASA/Goddard Space Flight Center, Greenbelt, MD, USA

²Earth Resources Technology, Inc., Laurel, MD, USA

³University of Maryland, Baltimore County, Baltimore, MD, USA

⁴Sigma Space Corp., Lanham, MD, USA

⁵Beltsville Agricultural Research Center, Beltsville, MD, USA

⁶Laval University, Quebec, Canada

*Elizabeth.M.Middleton@nasa.gov

ABSTRACT- The photosynthetic efficiency of plants was examined for plants in two very different canopies, a USDA cornfield having an instrumented flux tower in Beltsville, MD, USA and a coniferous forest in British Columbia, Canada, included in the tower network of the Canadian Carbon Program. Basic field studies were conducted at both sites with high spectral resolution radiometers to determine spectral indices that were well-correlated to leaf and canopy-level photosynthetic light use efficiency (LUE). LUE is the ratio of gross primary production (GPP) and the photosynthetically active radiation absorbed by the canopy (APAR), or GPP/APAR. We focus here on the Photosynthetic Reflectance Index (PRI), a normalized difference index that uses two narrow green spectral bands. We present diurnal, seasonal, and directional results for the PRI in both vegetated systems.

1 INTRODUCTION

The terrestrial ecosystem and remote sensing science communities have a common goal: to employ hyperspectral information on a global scale to improve assessments of ecosystem productivity and down-regulation of photosynthesis in vegetation due to environmental stresses. Direct retrieval of the functional carbon uptake status of vegetation has not been highly successful with broad band spectral indices acquired by ground or satellite-based radiometers at any spatial scale. However, continuous high spectral resolution (i.e., hyperspectral) reflectance sensors, or those having well-chosen physiologically responsive narrow bands, offer this exciting possibility (Grace et al., 2007).

Our Spectral Bio-Indicator Team at NASA/Goddard Space Flight Center is investigating various remote sensing approaches for retrieving and monitoring vegetation photosynthetic parameters, including light use efficiency (LUE), at leaf, canopy, tower, and

satellite levels. The traditional LUE model (Monteith 1972, 1977) expresses the ability of vegetation to capture atmospheric carbon dioxide (CO₂) and convert it into biomass using solar energy. LUE (or ϵ) is defined as the ratio of gross primary production (GPP) to the amount of incident photosynthetically active radiation (PAR, 400-700 nm) absorbed (APAR) over a given time period:

$$\epsilon = \frac{GPP}{PAR \times f_{APAR}} \quad (1)$$

The denominator provides APAR, as the product of PAR and the fraction of APAR (f_{APAR}), the quantity potentially available for photosynthesis. GPP, PAR, and APAR are flux densities often expressed in units of $\mu\text{mol m}^{-2} \text{s}^{-1}$; f_{APAR} is dimensionless, ranging between 0-1. LUE can be expressed in several

different units (e.g., $\mu\text{mol CO}_2 \mu\text{mol}^{-1} \text{ PAR}$; $\text{g C MJ}^{-1} \text{ PAR}$; or $\mu\text{mol C } \mu\text{mol}^{-1} \text{ PPFD}$, the photosynthetic photon flux density).

The Photochemical Reflectance Index (PRI) (Gamon et al., 1990; 1992; 1997) has been used in many studies to as a bio-indicator to track LUE. The original formulation of the PRI is a normalized difference spectral index using the physiologically active 531 nm wavelength and a reference wavelength (REF λ) at 570 nm, or PRI₅₇₀. Several other REF λ , such as 551 nm and 488 nm, have been used to yield PRI₅₅₁ or PRI₄₈₈ and applied to available satellite bands (Drolet et al., 2005; 2008). The general form of the PRI equation is:

$$PRI_{\text{REF } \lambda} = \frac{\rho(531) - \rho(\text{REF } \lambda)}{\rho(531) + \rho(\text{REF } \lambda)} \quad (2)$$

The physiological responses captured by the PRI are linked to the xanthophyll cycle, a biochemical inter-conversion of specialized carotenoid pigments bound to the photosystem II (PSII) light harvesting complexes of chloroplasts. With PRI₅₇₀, short term responses to high light conditions (i.e., high light-induced stress) are indicated by relatively lower negative values (e.g., those that fall below approximately -0.02), and greater photosynthetic down-regulation is indicated by the lowest observed values (e.g., the most negative values, ≤ -0.08). This is also the case for PRI₅₅₁ (but with a shift to more negative values), while the reverse situation occurs with PRI₄₈₈, for which increasingly greater down-regulation is indicated with larger positive values.

The use of the PRI for LUE monitoring was first documented at the leaf level by Gamon et al. (1990; 1993; 1992; 1997) and substantiated by many others (Filella et al., 1996; Trotter et al., 2002; Guo and Trotter, 2006; Inoue et al., 2008; Peñuelas et al., 1994; 1995; 1997). Although the PRI signal is relatively weak compared with red edge spectral indices, it has successfully been observed remotely over forests from aircraft and towers (Nichol et al., 2000; 2002; Rahmen et al., 2001; Hilker et al., 2008; Hall et al., 2008; Middleton et al., 2009; Cheng et al., 2009) and from satellites (Drolet et al., 2005; 2008). In this paper, we present our efforts to investigate spatial and temporal variation of PRI and its capability to track LUE from

leaf, canopy, tower to satellite level for a coniferous forest and a cornfield.

2 METHODS

2.1 USDA Cornfield

The cornfield experiments were conducted on corn canopies and plants (*Zea mays* L.; variety, Pioneer 33A14) at the research cornfield managed by the USDA/Agriculture Research Service (ARS) in Beltsville, MD, USA. An instrumented tower was installed (39.03°N, 76.85°W) for continuous carbon flux and environmental measurements during the growing season. We conducted intensive diurnal measurements weekly from June-August (6 dates) in 2007 during a drought period, and from mid-July through early October 2008 (14 dates) when precipitation was normal. Canopy-level reflectance observations were collected one meter above the vegetation with a nadir view from pole-mounted fiber optic probes. These were linked to spectroradiometers carried in body-packs by investigators who traversed along 100 m transects at multiple times (4-11) per day (~hourly), sampling at ~1 m intervals, on cornrows selected to be representative of the flux tower footprint. A transect collection for canopy reflectance typically was completed in ~15 min.

On field days in 2007 (June 21; July 2, 9, 31; and August 9, 14), we collected observations with a spectroradiometer (ASD-FR FieldSpec Pro, Analytical Spectral Devices, Inc., Boulder, CO, USA) having a spectral resolution of ~3 nm (sampled at 1 nm). On field days in 2008 (July 25; August 1, 6, 12, 19, 26; September 2, 8, 18, 24; and October 2, 7, 10, 11), we collected canopy-level reflectance spectra along two parallel transects ~20 m apart using two different field spectroradiometers, an ASD and an USB4000 Miniature Fiber Optic Spectrometer (Ocean Optics Inc., Dunedin, Florida, USA), having a spectral resolution of ~1.5 nm (sampled at 0.2 nm). Approximately ~60-100 spectral observations were acquired along transects at the canopy level during each hourly measurement period, which generated between 240 and 1,100 spectra per day for each instrument.

Along a third transect located between the two used for canopy reflectance, we tagged 20 leaves each day for *in situ* measurements on either the 3rd or 4th leaf from terminal (leaf #13/14). On all field days,

supporting plant information and leaf level data were acquired (e.g., CO₂ gas exchange) as well as biophysical field data, including leaf area index (LAI), mid-day canopy PAR transmission, soil reflectivity, and soil moisture. On the morning following a field day, the tagged leaves were excised for laboratory measurements (e.g., leaf optical properties).

BRDF measurements were conducted in 2008 (July 25 and Aug 1) from a pole-mount using ASD FieldSpec pro. Directional reflectances were collected at canopy level at various view geometry. Leaf optical properties were taken simultaneously at the adaxial leaf surfaces. Leaf level observations were later utilized as input for radiative transfer modeling exercise while canopy level measurements were used as “true values” for validation (Cheng et al., 2010).

Half-hourly averages of Net Ecosystem Production (NEP, mg CO₂ m⁻²s⁻¹) were determined using eddy covariance techniques. Midday measurements of the fraction of absorbed PAR (*f*APAR) were collected along the transect using a Ceptometer (Decagon Devices, Inc., Pullman, WA, USA) on several of the observation days. For each transect, *f*APAR was estimated using the difference between the Normalized Difference Vegetation Index (NDVI) values for the vegetation (calculated from the average transect canopy reflectance) and bare soil reflectance. Light use efficiency (LUE, mol C/mol Qa) was computed as the ratio, NEP/APAR (where APAR = Qa = incident PAR x *f*APAR).

2.2 British Columbia, DF49

The study site is located in the coastal temperate region of Vancouver Island, British Columbia, Canada, approximately 10 km southwest of the city of Campbell River. The data were collected from a research tower (49°52'7.8"N, 125°20'6.3"W) and the surrounding second-growth forest at ~300 m above sea level. The forest is dominated by Douglas-fir stands planted in 1949 after harvesting of the original stand, and therefore is referred to as DF49. It consists of 80% Douglas-fir (*Pseudotsuga menziesii* (Mirbel) Franco), 17% western red cedar (*Thuja plicata* Donn ex D. Don) and 3% western hemlock (*Tsuga heterophylla* (Raf.) Sarg.). Half-hour average values have been available year-round since 1997 for eddy covariance flux measurements of CO₂, and sensible and latent heat, from a 45 m tall, 51-cm triangular open-lattice type tower. Net ecosystem exchange

(NEE) values were obtained by correcting CO₂ flux measurements for changes in air column storage. Net ecosystem productivity (NEP) values were calculated as -NEE. GPP values were obtained by adding measured daytime NEP values to values of daytime ecosystem respiration (R).

Spectral data were acquired continuously through the 2006 growing season (April through November) with the Automated Multi-angular Spectroradiometer for Estimation of Canopy (AMSPEC) reflectance system. AMSPEC is a fully automated tower based platform which was installed at a height of 45 m, or ~10 m above the tree canopy. This system obtained hyperspectral visible/near-infrared (VIS/NIR) reflectance observations (350 – 1200 nm) using upward and downward pointing probes from a Unispec-DC spectroradiometer (PP Systems, Amesbury, MA, USA) featuring 256 contiguous bands, although we limited our examination to the 400-900 nm region. Spectra were produced using a 3.5 nm sampling interval, although the actual spectral resolution was ~8 nm at full width half maximum.

AMSPEC was pointed off-nadir at 62° to optimize observations for canopy clumping effects and measurements were made in the near-360° azimuth plane at 11.5° increments, completing one cycle every 15 minutes during daylight hours. We extracted the data along the solar principal plane at the hot-spot (the sunlit foliage sector) and the dark spot (the shaded foliage sector), and midway between along the cross-plane (the sunlit/shaded sector).

3 RESULTS

3.1 Canopy AMSPEC Measurements: seasonal PRI averages per foliage sector

Comparisons among the canopy sectors (**Figure 1**) were made for daily averages on both sunny and overcast days across the season (**Fig. 1A,B**) and for seasonal averages at three times of day (**Fig. 1C,D**). Significant PRI₅₇₀ differences were observed for sunlit vs. shaded foliage on sunny days (shaded > sunlit/shaded > sunlit). Even when averaged over the growing season (**Fig. 1C**), this trend on sunny days was maintained ($\bar{X} \pm \text{SE}$: shaded, -0.04 ± 0.001 > shaded/sunlit, -0.06 ± 0.0004 > sunlit, -0.075 ± 0.001). However, these distinctions among foliage groups disappeared on overcast days (**Fig. 1B**) when excess light conditions did not occur and which yielded

higher, and relatively constant PRI_{570} values seasonally (-0.032 ± 0.0003 , **Fig. 1D**) across all three canopy foliage sectors. In fact, this average PRI_{570} on highly diffuse radiation days is approximately twice the average value observed on sunny days (-0.06 ± 0.03). Further examination of **Fig. 1C,D** reveals that sunlit leaves generally exhibited recovery in the late afternoons from light-induced photosynthetic down-regulation, as captured by higher late afternoon PRI_{570} values on both sunny and overcast days (Middleton et al., 2009).

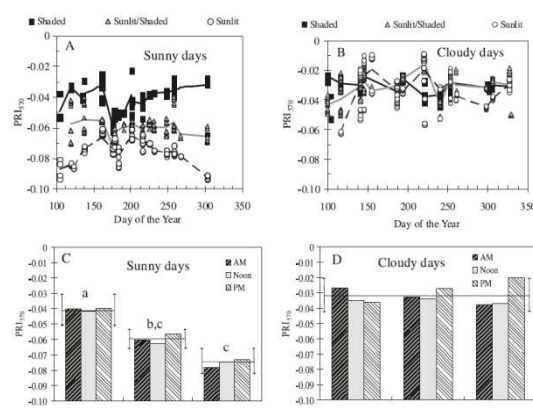


Figure 1. The seasonal courses (April–November) for daily PRI_{570} averages are shown for three foliage groups at the Douglas fir stand-- shaded foliage (■), sunlit foliage (○), and the intermediate sunlit/shaded foliage (▲): [A] sunny days; and [B] cloudy days. For each foliage group, the seasonal PRI_{570} averages at three times of day are shown [morning (■), noon (□), and afternoon (■)]: [C] sunny days, where the mean and SD per group is indicated with horizontal and vertical bars; and [D] cloudy days, where a single mean and SD is given for all foliage. On sunny days [C], the seasonally averaged PRI_{570} values for the three foliage groups displayed significant diurnal differences. Statistics given are the mean \pm SE (n, SD, COV): shaded foliage, -0.04 ± 0.001 (n = 294, SD = 0.010, COV = 24.8%); sunlit foliage, -0.075 ± 0.001 (n = 262, SD = 0.008, COV = 11.0%); and shaded/sunlit foliage, -0.060 ± 0.000 (n = 266, SD = 0.007, COV = 11.6%). On cloudy days [D], no foliage group differences for PRI_{570} were significant across the season (mean \pm SE: -0.0315 ± 0.00034 ; n = 926, SD = 0.010, COV = 32.8%).

3.2 USDA Cornfield: Spectral Bio-Indicators

The PRI and fluorescence parameter values (solar induced fluorescence, SIF, and fluorescence yield, Fyiel), determined with measurements acquired at 1 nm spectral resolution (with an Ocean Optics spectroradiometer, tracked daily as well as seasonal changes in canopy level physiological stress. SIF and

fluorescence yield presented here were derived using the original two-band Fraunhofer Line Depth (FLD) algorithm. The values remain preliminary and advanced algorithms will be utilized to improve the estimates. Nevertheless, diurnal and seasonal dynamics are expected to be similar regardless the algorithm. All of the physiologically active spectral indicators (PRI, SIF, and Fyiel) showed seasonal declines over the entire 2008 field campaign (**Figure 2**). The greatest seasonal change was captured by SIF expressed as Fyiel: F688yiel ($r^2 = 0.93$) and F760yiel ($r^2 = 0.87$). SIF expressed in energy units ($W m^{-2} sr^{-1} nm^{-1}$) also showed significant, but less strongly expressed, seasonal change: the O_2 -B band, F@Red ($r^2 = 0.89$); and F@Far-red for the O_2 -A band ($r^2 = 0.81$). Over the season, Fyiel dropped from $\sim 11\%$ to 2% , while SIF (F@Red and F@Far-red) decreased from 0.025 to $0.0095 W m^{-2} sr^{-1} um^{-1}$. The PRI also exhibited a strong linear decline across the season ($r^2 = 0.88$), from -0.02 to -0.06 . For PRI and fluorescence, the higher values that occurred early in the growing season indicate less stressful conditions, whereas the progressively lower values seen later in the season occurred during the physiological changes for reproductive stages and senescence. However, the Normalized Difference Vegetation Index (NDVI) was almost constant seasonally, $\sim 0.73 \pm 0.02$ (**Fig. 2**).

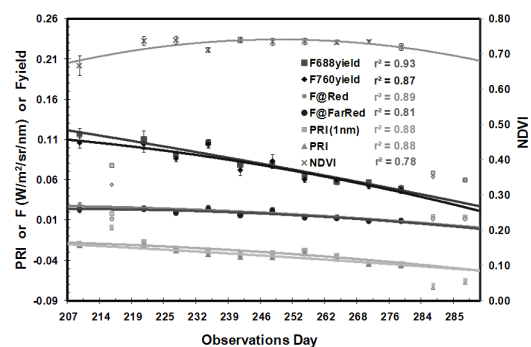


Figure 2. Daily average values for PRI, SIF, and fluorescence yield, Fyiel (F688yiel, F760yiel), and NDVI are plotted against day of the year. Fyiel exhibits the strongest seasonal change for F688yiel ($r^2 = 0.93$) and for F760yiel ($r^2 = 0.87$). The original SIF values (F@Red, F@FarRed) changed less seasonally. PRI values also showed strong seasonal declines over the season ($r^2 = 0.88$).

The relationship of PRI to corn canopy LUE is shown in **Figures 3 and 4**. PRI values determined with the ASD-FR (at ~ 3 nm resolution) were combined for measurements made in 2007 and 2008 ($r^2 = 0.67$), and

yielded similar trends in both years (Fig. 3). The relatively high, positive PRI values (+0.02) in the early growth stage indicate low environmental stress, whereas late stage values of -0.075 indicate substantial stress effects, associated with LUE values that declined from 0.048 mol C/mol Qa to near zero LUE. A nearly identical result for the PRI:LUE relationship was obtained with the observations acquired at 1 nm spectral resolution (with the Ocean Optics) in 2008 ($r^2 = 0.61$), but the narrower resolution enabled detection of a slightly greater range in LUE (zero to +0.65 mol C/mol Qa) (Fig. 4). Although the linear pattern of change in PRI with LUE was apparent over the growing season, there was considerable variation within each day (Figs. 3, 4).

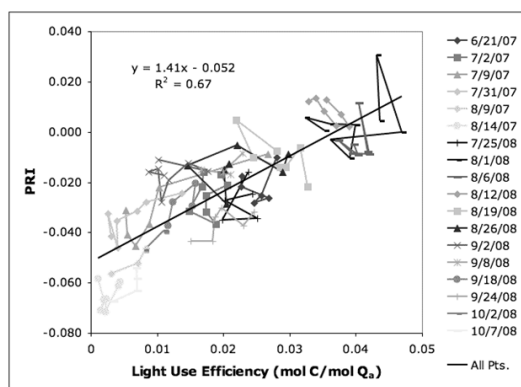


Figure 3. The PRI was determined from average transect reflectance measured with the ASD (~3 nm resolution) versus LUE (mol C/mol Qa) from observations at the UDASA/ARS cornfield in 2007 and 2008. Separate lines connect observations collected over the same day. Regression line ($r^2 = 0.67$, $n = 109$).

3.3 Canopy Structure – Sunlit & Shaded Foliage

In a further study in the cornfield, where *in situ* spectrometer measurements were made in 45° increments around the full azimuth range with off-nadir view angles, the PRI values exhibited the expected stress effects in sunlit foliage as compared to shaded foliage, in agreement with simulations with a radiative transfer model, the Markov-Chain Canopy Reflectance Model (MCRM), adequately showing the effects and viewing geometry and illumination conditions on PRI values (Fig. 5) (Cheng et al., 2010).

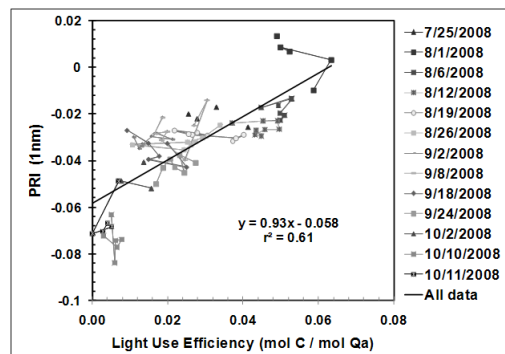


Figure 4. The PRI was determined from average transect reflectance measured with the Ocean Optics (1 nm resolution) versus LUE (mol C/mol Qa) from observations at the UDASA/ARS cornfield in 2008. Different lines/symbols connect observations collected over the same day. Regression line ($r^2 = 0.61$, $n = 81$).

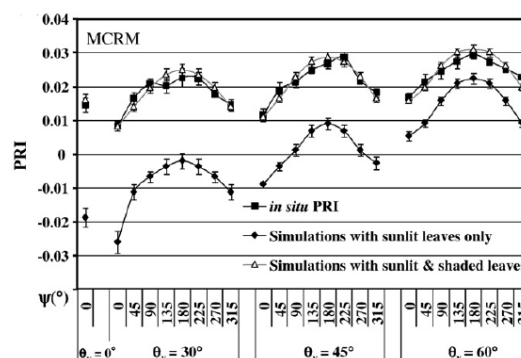


Figure 5. Comparisons between *in situ* PRI and simulated PRI with the MCRM model. Values are shown as mean \pm SE. Simulations were conducted using sunlit leaves only (\square) and using both sunlit and shaded leaves (Δ).

4 SUMMARY

We provided clear evidence for the capability of PRI to track LUE at various scales in two very different vegetation canopies. Moreover, we show the importance of knowing whether the observed canopy sector is dominated by sunlit or shaded leaves, and taking this into account in interpreting the canopy LUE. These findings demonstrated an opportunity to monitor and model carbon exchange between terrestrial ecosystems and the atmosphere with remote sensing technology and future satellite missions.

5 REFERENCES

Cheng, Y.-B., Middleton, E.M., Huemmrich, K.F., Zhang, Q., Campbell, P.K.E., Corp, L.A., Russ, A.L., & Kustas, W.P., 2010, Utilizing *in situ* directional

- hyperspectral measurements to validate bio-indicator simulations for a corn crop canopy. *Ecological Informatics*, 5 (5), 330-338.
- Drolet, G.G., Huemmrich, K.F., Hall, F.G., Middleton, E.M., Black, T.A., Barr, A.G., & Margolis, H.A., 2005, A MODIS-derived photochemical reflectance index to detect inter-annual variations in the photosynthetic light-use efficiency of a boreal deciduous forest. *Remote Sensing of Environment*, 98 (2-3), 212-224.
- Drolet, G.G., Middleton, E.M., Huemmrich, K.F., Hall, F.G., Amiro, B.D., Barr, A.G., Black, T.A., McCaughey, J.H., & Margolis, H.A. ,2008, Regional mapping of gross light-use efficiency using MODIS spectral indices. *Remote Sensing of Environment*, 112 (6), 3064-3078.
- Filella, I., Amaro, T., Araus, J.L., & Peñuelas, J. ,1996, Relationship between photosynthetic radiation-use efficiency of barley canopies and the photochemical reflectance index (PRI). *Physiologia Plantarum*, 96 (2), 211-216.
- Gamon, J.A., Field, C.B., Bilger, W., Björkman, O., Fredeen, A.L., & Peñuelas, J. ,1990, Remote sensing of the xanthophyll cycle and chlorophyll fluorescence in sunflower leaves and canopies. *Oecologia*, 85 (1), 1-7.
- Gamon, J.A., Field, C.B., Roberts, D.A., Ustin, S.L., & Valentini, R. ,1993, Functional patterns in an annual grassland during an AVIRIS overflight. *Remote Sensing of Environment*, 44 (2/3), 239-253.
- Gamon, J.A., Penuelas, J., & Field, C.B. ,1992, A narrow-waveband spectral index that tracks diurnal changes in photosynthetic efficiency. *Remote Sensing of Environment*, 41 (1), 35-44.
- Gamon, J.A., Serrano, L., & Surfus, J.S. ,1997, The photochemical reflectance index: an optical indicator of photosynthetic radiation use efficiency across species, functional types, and nutrient levels. *Oecologia*, 112 (4), 492-501.
- Grace, J., Disney, C.J.N.M., Lewis, P., Quaife, T., & Bowyer, P. ,2007, Can we measure terrestrial photosynthesis from space directly, using spectral reflectance and fluorescence? *Global Change Biology*, 13 (7), 1484-1497.
- Guo, J.M., & Trotter, C.M. ,2006, Estimating photosynthetic light-use efficiency using the photochemical reflectance index: the effects of short-term exposure to elevated CO₂ and low temperature. *International Journal of Remote Sensing*, 27 (20), 4677 - 4684.
- Hall, F.G., Hilker, T., Coops, N.C., Lyapustin, A., Huemmrich, K.F., Middleton, E., Margolis, H., Drolet, G., & Black, T.A. ,2008, Multi-angle remote sensing of forest light use efficiency by observing PRI variation with canopy shadow fraction. *Remote Sensing of Environment*, 112 (7), 3201-3211.
- Hilker, T., Coops, N.C., Hall, F.G., Black, T.A., Wulder, M.A., Nesic, Z., & Krishnan, P. ,2008, Separating physiologically and directionally induced changes in PRI using BRDF models. *Remote Sensing of Environment*, 112 (6), 2777-2788.
- Inoue, Y., Peñuelas, J., Miyata, A., & Mano, M. ,2008, Normalized difference spectral indices for estimating photosynthetic efficiency and capacity at a canopy scale derived from hyperspectral and CO₂ flux measurements in rice. *Remote Sensing of Environment*, 112 (1), 156-172.
- Middleton, E.M., Cheng, Y.-B., Hilker, T., Black, T.A., Krishnan, P., Coops, N.C., & Huemmrich, K.F. ,2009, Linking Foliage Spectral Responses to Canopy Level Ecosystem Photosynthetic Light Use Efficiency at a Douglas-fir Forest in Canada. *Canadian Journal of Remote Sensing*, 35 (2), 166-188.
- Nichol, C.J., Huemmrich, K.F., Black, T.A., Jarvis, P.G., Walthall, C.L., Grace, J., & Hall, F.G. ,2000, Remote sensing of photosynthetic-light-use efficiency of boreal forest. *Agricultural and Forest Meteorology*, 101 (2-3), 131-142.
- Nichol, C.J., LLOYD, J., SHIBISTOVA, O., ARNETH, A., RÖSER, C., KNOHL, A., MATSUBARA, S., & GRACE, J. ,2002, Remote sensing of photosynthetic-light-use efficiency of a Siberian boreal forest. *Tellus B*, 54 (5), 677-687.
- Peñuelas, J., Filella, I., & Gamon, J.A. ,1995, Assessment of photosynthetic radiation-use efficiency with spectral reflectance. *New Phytologist*, 131 (3), 291-296.
- Peñuelas, J., Gamon, J.A., Fredeen, A.L., Merino, J., & Field, C.B. ,1994, Reflectance indices associated with physiological changes in nitrogen- and water-limited sunflower leaves. In, *Remote Sensing of Environment* (pp. 135-146)
- Peñuelas, J., Llusia, J., Pinol, J., & Filella, I. ,1997, Photochemical reflectance index and leaf photosynthetic radiation-use-efficiency assessment in Mediterranean trees. *International Journal of Remote Sensing*, 18 (13), 2863-2868.
- Rahman, A.F., Gamon, J.A., Fuentes, D.A., Roberts, D.A., & Prentiss, D. ,2001, Modeling spatially distributed ecosystem flux of boreal forest using hyperspectral indices from AVIRIS imagery. *J. Geophys. Res.*, 106 (D24), 33579-33591.
- Trotter, G.M., Whitehead, D., & Pinkney, E.J. ,2002, The photochemical reflectance index as a measure of photosynthetic light use efficiency for plants with varying foliar nitrogen contents. *International Journal of Remote Sensing*, 23 (6), 1207 - 1212.

Estimation of gross ecosystem production by hyperspectral measurements in terrestrial ecosystems

Micol Rossini^{1,*}, Michele Meroni¹, Mirco Migliavacca¹, Sergio Cogliati¹, Lorenzo Busetto¹, Edoardo Cremonese², Marta Galvagno², Beniamino Gioli³, Federico Magnani⁴, Franco Miglietta³, Umberto Morra di Cella², Consolata Siniscalco⁵, Roberto Colombo¹

¹ Remote Sensing of Environmental Dynamics Lab., DISAT, University of Milano-Bicocca, piazza della Scienza 1, 20126 Milano, Italy. Ph: +390264482848; Fax +390264482895; email: micol.rossini@unimib.it

² ARPA Valle d'Aosta, Aosta, Italy

³ IBIMET CNR, Firenze, Italy

⁴ Department of Fruit Tree and Woody Plant Science, University of Bologna, Bologna, Italy

⁵ Plant Biology Department, University of Torino, Torino, Italy

* micol.rossini@unimib.it

ABSTRACT - This study investigates the possibility of monitoring carbon fixation of terrestrial ecosystems from field spectroscopy measurements collected using unattended spectral systems. These systems allow high temporal frequency acquisitions of high spectral resolution radiometric measurements which make it possible to estimate sun-induced chlorophyll fluorescence at 760 nm (F_{760}) as well as spectral vegetation indexes. Spectral observations were collected during 2009 in two terrestrial ecosystems (a mountain grassland and an alfalfa crop field) monitored with eddy covariance flux towers providing half-hourly measurements of gross ecosystem productivity (GEP). Estimation of GEP from remotely sensed data was based on the light-use efficiency model (LUE). Models investigated in this study rely on different assumptions concerning light-use efficiency (ϵ) and the photosynthetically active radiation absorbed by vegetation (APAR) used as input of the LUE model. GEP estimation accuracy of different models was then compared. Results show that the use of the apparent fluorescence yield and the Photochemical Reflectance Index to model ϵ instead of holding ϵ constant improves the estimation of GEP. Furthermore, we successfully investigate the use of F_{760} to model the APAR. This latter model is very attractive because it is entirely based on remotely sensed quantities without requiring any ancillary measurement, like other LUE model formulations which require ancillary measurements of the incident PAR to estimate APAR, and it is very interesting in the perspective of a spatial estimation of GEP.

1 INTRODUCTION

Assessment and modeling of photosynthetic functioning of terrestrial ecosystems are critical issues in climate change research and crucial in predicting carbon dynamics. Over the last few decades, eddy covariance (EC) measurements (Baldocchi et al., 1996) of carbon and water fluxes between the atmosphere and terrestrial ecosystems have greatly improved our understanding of carbon cycling at the stand-level. Remote sensing (RS) observations can provide spatial and temporal variability of ecosystem parameters driving carbon fluxes which can be integrated with EC measurements to scale up carbon estimates to regional and global level.

One way to better understand the relationships between RS data and photosynthesis is the installation of RS devices at EC sites to measure near-surface spectra at time and space scales similar to those of the

flux towers. For these reasons, network approaches (e.g., the SpecNet initiative (Gamon et al., 2006) and the COST action ES0903 'Spectral Sampling Tools for Vegetation Biophysical Parameters and Flux Measurements in Europe') have been established to analyze the relationship between plant physiological processes and canopy spectral properties acquired nearly continuously at the stand level (e.g., Hilker et al., 2007; Leuning et al., 2006). Such networking approaches may greatly improve our knowledge on the relationships between RS and EC measurements at the stand-level that may be used to upscale these findings to regional and global scales.

Most models aimed at the estimation of GEP from RS data are based on the light use efficiency model (LUE) (Monteith, 1972; Monteith, 1977), which states that carbon uptake is a function of the light energy absorbed by vegetation and the efficiency with which it is used to fix carbon.

$$GEP = \varepsilon \times fAPAR \times PAR_i = \varepsilon \times APAR \quad (1)$$

where ε is the photosynthetic radiation-use efficiency (i.e. the efficiency with which absorbed radiation is converted to biomass) and APAR is the photosynthetically active radiation (PAR) absorbed by the canopy, determined as the product of the fraction of PAR absorbed by the canopy ($fAPAR$) and the incident PAR (PAR_i). LUE models are attractive because RS measurements can provide some key input parameters (for a review see Hilker et al., 2008).

Rossini et al. (2010) compared the accuracy of several versions of LUE model to monitor carbon fixation of rice from high spectral resolution field spectroscopy measurements, including sun-induced chlorophyll fluorescence. Spectral measurements collected using high resolution spectrometers were used to derive both the APAR and the ε term. Results showed that the inclusion of a variable, instead of constant, ε derived from RS data improved midday GEP estimation. In this study we test this approach to assess GEP from hyperspectral data acquired with automatic spectral systems during 2009 in two terrestrial ecosystems monitored with EC flux towers. Several versions of LUE models have been tested in order to understand the most effective formulation to estimate EC derived GEP. The different models analysed differ with respect to the methods selected for ε and APAR estimation based on RS techniques.

2 MATERIALS AND METHODS

2.1 Experimental sites

Spectral observations were collected during 2009 in two terrestrial ecosystems monitored with EC flux towers measuring the net ecosystem exchange of the ecosystems. The first study site was a semi-abandoned pasture of the subalpine belt composed mainly by matgrass (*Nardus stricta*, *Arnica Montana*, *Trifolium alpinum* and *Carex sempervirens* as dominant species), located at 2160 m a.s.l. in the municipality of Torgnon (45.84 N 7.58 E), in the North-Western side of Alps in Italy (Valle d'Aosta Region). The second one was an alfalfa (*Medicago sativa* L.) crop field near Pisa (43.67 N 10.30 E, 4 m a.s.l.), in Central Italy (Toscana Region). This latter experiment was conducted in the context of the ESA campaign 'Sen3Exp', an activity in support of the future ESA Sentinel-3 Earth observation mission.

2.2 Eddy covariance data

The turbulent vertical fluxes of CO₂, latent and sensible heat, were measured using the EC technique. Eddy fluxes were calculated with a time step of 30 minutes according to EUROFLUX methodology

(Aubinet et al., 2000). Half-hourly measurements of net ecosystem exchange were partitioned to derive gross ecosystem productivity (GEP). Along with EC fluxes, the main meteorological variables (in particular the incident photosynthetically active radiation, PAR_i) are available with a time step of 30 minutes.

2.3 Radiometric measurements

Canopy radiance spectra were collected using unattended spectral data collection systems designed for high temporal frequency acquisition of high spectral resolution radiometric measurements. Two different spectral systems were used. Both systems host a couple of HR4000 spectrometers (OceanOptics, USA). The first one covers the visible and near-infrared range (400-1000 nm) with a full width at half maximum (FWHM) of 1 nm and allows the computation of vegetation indexes (VIs) including the Photochemical Reflectance Index (PRI, Gamon et al., 1992). The second one covers with a finer resolution (FWHM = 0.1 nm) a restricted spectral range (700-800 nm). This spectrometer is specifically intended for sun-induced fluorescence measurements in the oxygen absorption band O₂-A (see Meroni et al., 2009) positioned at 760 nm (F_{760}).

Both spectral systems are operated automatically through a dedicated software (Meroni and Colombo, 2009). We employed the field spectroscopy technique referred to as 'single beam' (Milton and Rollin, 2006). The target measurement is 'sandwiched' between two downwelling irradiance measurements made a few seconds apart. For every acquisition, 10 and 4 scans (for Spectrometer 1 and 2, respectively) are averaged and stored as a single file. Additionally, a dark current measurement was collected for every set of acquisitions.

In the subalpine pasture the optical system named HyperSpectral Irradiometer (HSI) was used (Meroni et al., 2010b). Briefly, HSI employs a rotating arm to observe alternately the sky and the target surface with a cosine-response optic, allowing the computation of the BHR (Bi-Hemispherical Reflectance factor).

In the alfalfa crop field the Multiplexer-based Radiometer Irradiometer (MRI) (Meroni et al., 2010b) was used. MRI employs a commercial optical multiplexer (MPM-2000, OceanOptics, USA) that switches the input of the spectrometers between a channel measuring the incident irradiance (through a fiber connected to an up-looking cosine-response optic) and a channel measuring the radiance upwelling from the surface through a down-looking bare fiber with a 25° field of view. MRI thus allows the measurement of the HCRF (Hemispherical-Conical Reflectance Factor).

Spectral indexes were computed from the canopy reflectance spectra acquired with the automatic

systems with a five/three minutes step for HSI/MRI, respectively. Spectral indexes were successively averaged for each half-hourly period, in order to obtain data comparable to those acquired at the EC tower. Spectral indexes investigated in this study are reported in Table 1.

Among various VIs proposed in the literature as a proxy of $fAPAR$, we selected the well-known normalized difference vegetation index (NDVI, Rouse et al., 1974). The selection of the best index for $fAPAR$ estimation is beyond the aim of this study, but we are aware that other VIs can perform better (or worse). To estimate ϵ by RS indices we compute a scaled value of PRI according to Rahman et al. (2004) and the apparent fluorescence yield at 760 nm (F_{760}), computed as the ratio between F_{760} and PAR_i . F_{760} was estimated by exploiting the spectral fitting method described in Meroni and Colombo (2006) and Meroni et al. (2010a), assuming a linear variation of reflectance and fluorescence in the O_2-A absorption band region. The spectral interval used for F_{760} estimation was set to 759.00 - 767.76 nm for a total of 439 spectral channels used.

Since fluorescence is driven by the intensity of PAR_i and by the amount of canopy biomass and structure and considering that at 760 nm it is not influenced by reabsorption (Louis et al., 2005), F_{760} is used in this study as a proxy of photosynthetic canopy APAR (Rossini et al., 2010).

Index	Formulation	References
<i>fAPAR</i>		
NDVI	$(R_{800}-R_{680})/(R_{800}+R_{680})$	Rouse et al., 1974
<i>APAR</i>		
F_{760}		Meroni and Colombo, 2006
ϵ (E indexes)		
SPRI	$[(R_{531}-R_{570})/(R_{531}+R_{570}) + 1]/2$	Gamon et al., 1992
F_{y760}	F_{760}/PAR_i	Meroni and Colombo, 2006

Table 1. Spectral vegetation indices investigated in this study. R is the reflectance at the specified wavelength (nm). Spectral indices are grouped in three classes according to their suitability in inferring $fAPAR$, $APAR$ and ϵ (E indexes).

Model code	ϵ	APAR	Model formulation
1	Const.	$f(NDVI, PAR_i)$	$GEP = \epsilon \cdot (a_0NDVI + a_1) \cdot PAR_i = (b_0NDVI + b_1) \cdot PAR_i$
2	$f(E)$	$f(NDVI, PAR_i)$	$GEP = (a_0E + a_1) \cdot (a_2NDVI + a_3) \cdot PAR_i = (b_0E + b_1NDVI + b_2NDVI \cdot E + b_3) \cdot PAR_i$
3	$f(E)$	$f(F_{760})$	$GEP = (a_0E + a_1) \cdot (a_2F_{760} + a_3) = b_0E + b_1F_{760} + b_2F_{760} \cdot E + b_3$

Table 2. Formulation of LUE models used in this study for the estimation of GEP.

2.4 GEP modeling

Estimation of GEP from remotely sensed data was based on the LUE model (Eq. 1). Half-hourly values of spectral indices and GEP measured around midday (solar noon ± 1 hour) were used to test several versions of the basic LUE model in order to select the most effective formulation for the description of GEP. Linearity is always assumed between the spectral index and its target variable.

Models investigated in this study rely on different assumptions concerning APAR estimation and ϵ , which can be considered constant or estimated from RS data. GEP estimation accuracy of different models, including sun-induced fluorescence were then compared. Different model formulations together with their underlying assumptions are reported in Table 2.

3 RESULTS

3.1 Seasonal variations of reflectance spectra

As an example, Figure 1 shows temporal changes of the average monthly canopy reflectance spectra collected around solar noon during 2009 with HSI in the subalpine pasture.

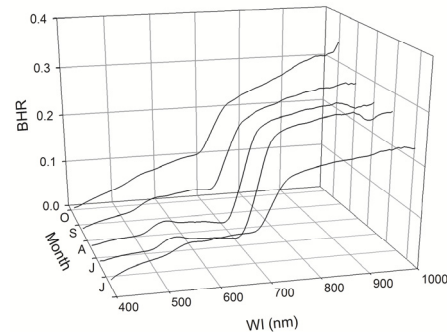


Figure 1. Temporal changes of the average monthly canopy reflectance spectra collected with Spectrometer 1 (400 - 1000 nm spectral range).

3.2 Seasonal variations of spectral indexes

As an example of optical signal derived from MRI data, Figure 2 (upper panel) shows the evolution of sun-induced chlorophyll fluorescence computed using the ultra-fine resolution spectrometer.

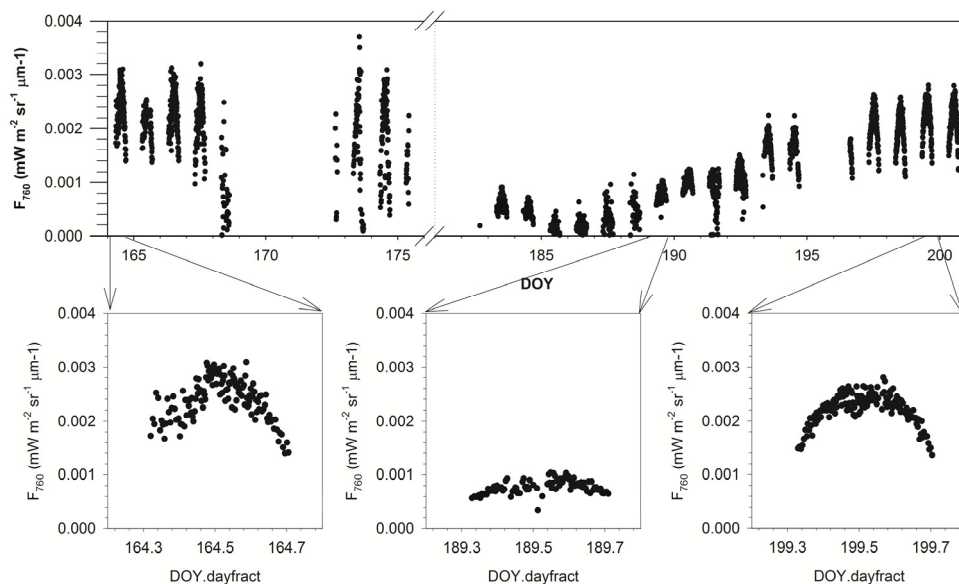


Figure 2. Example of F_{760} time series acquired with MRI (Spectrometer 2) at alfalfa eddy flux site.

The two gaps in the time series are due to crop management operations that required to shut down the spectral system. Lower panels of Figure 2 show that the intensity of F_{760} is due to the interaction of the incident photosynthetic photon flux density (PPFD), being maximum at solar noon, and the presence/efficiency of chlorophyll photosystems, being low at the beginning of the growing cycle (e.g., DOY 189) and maximum at the end of it (e.g., DOY 199).

Reliable fluorescence estimate at the subalpine pasture was often hampered by instable meteorological conditions and by the presence of low clouds. In these conditions, the incident irradiance is changing fast and a large fraction of fluorescence data was rejected during quality control.

3.3 Estimation of GEP through EC-LUE models

The statistics of different models tested in this study are reported in Table 3.

Model 1 showed a RMSE in GEP estimation of 2.71 and 4.79 $\mu\text{mol CO}_2 \text{ m}^{-2} \text{ s}^{-1}$ for the pasture and the alfalfa field, respectively, corresponding to a rRMSE of about 22% for both sites.

To overcome the assumption of constant ϵ , model 2 in which ϵ is estimated with physiologically based vegetation indices was considered. The use of sPRI and/or F_{y760} to describe ϵ improves GEP estimation up to a rRMSE of 17.8 and 19.3% for the pasture and the alfalfa field, respectively, demonstrating that besides sPRI also F_{y760} is a promising candidate powerful RS parameter that can be used to directly quantify light use efficiency.

Finally, model 3 estimating APAR as a function of F_{760} and ϵ as a function of sPRI showed the best performances (RMSE of 1.92 and 2.69 $\mu\text{mol CO}_2 \text{ m}^{-2} \text{ s}^{-1}$ for the pasture and the alfalfa field, respectively, corresponding to a rRMSE of 16 and 12.8%).

Model code		r^2	RMSE ($\mu\text{mol CO}_2 \text{ m}^{-2} \text{ s}^{-1}$)	rRMSE (%)
<i>Subalpine pasture</i>				
1		0.52	2.71	22.6
2	sPRI	0.71	2.13	17.8
	F_{y760}	0.56	2.59	21.6
3	sPRI	0.76	1.92	16.0
	F_{y760}	0.48	2.84	23.7
<i>Alfalfa field</i>				
1		0.77	4.79	22.7
2	sPRI	0.80	4.51	21.4
	F_{y760}	0.83	4.08	19.3
3	sPRI	0.93	2.69	12.8
	F_{y760}	0.80	4.48	21.2

Table 3. Statistics of the models used in this study for the estimation of midday GEP. r^2 is the determination coefficient of the model, RMSE is the root mean square error ($\mu\text{mol CO}_2 \text{ m}^{-2} \text{ s}^{-1}$) and rRMSE the relative RMSE (%).

4 CONCLUSIONS

Results show that the use of the apparent fluorescence yield and the Photochemical Reflectance Index to model ϵ instead of holding ϵ constant improves the estimation of GEP.

Furthermore, we successfully test the use of F_{760} to model the photosynthetically active radiation absorbed

by the photosynthetic components of vegetation. This latter model is very attractive because it is entirely based on remotely sensed quantities without requiring any ancillary measurement, like other LUE model formulations which require ancillary measurements of the incident PAR to estimate APAR, and it is very interesting in the perspective of a spatial estimation of GEP. The approach proposed in this study find application within the framework of the established SpecNet (Spectral Network) and recent activities related to the 'Spectral Sampling Tools for Vegetation Biophysical Parameters and Flux Measurements in Europe' COST action that are aimed to collect spectral data continuously, regularly and from a worldwide network in connection to the well-established network of flux tower (FLUXNET).

Furthermore, the use of remote as opposed to proximal spectral sensors for GEP estimation based on models developed in this study may become a powerful tool in better understanding the spatio-temporal variations of productivity on a broader scale.

5 ACKNOWLEDGMENTS

Spectral data collection has been performed within the framework of the PhenoAlp EU-Interreg Project and ESA Sen3EXP 2009 campaign. The participation in this conference was supported by the COST ESSEM Conference Grant in the framework of the Action ES0903.

6 REFERENCES

- Aubinet, M., Grelle, A., Ibrom, A., Rannik, U., Moncrieff, J., Foken, T., Kowalski, A.S., Martin, P.H., Berbigier, P., Bernhofer, C., Clement, R., Elbers, J., Granier, A., Grunwald, T., Morgenstern, K., Pilegaard, K., Rebmann, C., Snijders, W., Valentini, R., and Vesala, T., 2000, Estimates of the annual net carbon and water exchange of forests: The EUROFLUX methodology. *Advances in Ecological Research*, **30**, 113-175.
- Baldocchi, D., Valentini, R., Running, S., Oechel, W., and Dahlen, R., 1996, Strategies for measuring and modelling carbon dioxide and water vapour fluxes over terrestrial ecosystems. *Global Change Biology*, **2**, 159-168.
- Gamon, J.A., Penuelas, J., and Field, C.B., 1992, A Narrow-Waveband Spectral Index That Tracks Diurnal Changes in Photosynthetic Efficiency. *Remote Sensing of Environment*, **41**, 35-44.
- Gamon, J.A., Rahman, A.F., Dungan, J.L., Schildhauer, M., and Huemmrich, K.F., 2006, Spectral Network (SpecNet) - What is it and why do we need it? *Remote Sensing of Environment*, **103**, 227-235.
- Hilker, T., Coops, N.C., Nesic, Z., Wulder, M.A., and Black, A.T., 2007, Instrumentation and approach for unattended year round tower based measurements of spectral reflectance. *Computers and Electronics in Agriculture*, **56**, 72-84.
- Hilker, T., Coops, N.C., Wulder, M.A., Black, T.A., and Guy, R.D., 2008, The use of remote sensing in light use efficiency based models of gross primary production: A review of current status and future requirements. *Science of the Total Environment*, **404**, 411-423.
- Leuning, R., Hughes, D., Daniel, P., Coops, N.C., and Newnham, G., 2006, A multi-angle spectrometer for automatic measurement of plant canopy reflectance spectra. *Remote Sensing of Environment*, **103**, 236-245.
- Louis, J., Ounis, A., Ducruet, J.-M., Evain, S., Laurila, T., Thum, T., Aurela, M., Wingsle, G., Alonso, L., Pedros, R., and Moya, I., 2005, Remote sensing of sunlight-induced chlorophyll fluorescence and reflectance of Scots pine in the boreal forest during spring recovery. *Remote Sensing of Environment*, **96**, 37-48.
- Meroni, M., Busetto, L., Colombo, R., Guanter, L., Moreno, J., and Verhoef, W., 2010a, Performance of Spectral Fitting Methods for vegetation fluorescence quantification. *Remote Sensing of Environment*, **114**, 363-374.
- Meroni, M., Cogliati, S., Rossini, M., Barducci, A., Castagnoli, F., Panigada, C., Migliavacca, M., and Colombo, R., 2010b, Ground-based long-term unattended hyperspectral measurements of vegetated surface: instrumentation and collected data. Proceedings of the 'Hyperspectral Workshop 2010' held at ESA-ESRIN, in Frascati, Italy on 17- 19 March 2010, ESA SP-683 (H. Lacoste-Francis ESA Communications; ESTEC, Noordwijk, The Netherlands: ESA Communications).
- Meroni, M., and Colombo, R., 2006, Leaf level detection of solar induced chlorophyll fluorescence by means of a subnanometer resolution spectroradiometer. *Remote Sensing of Environment*, **103**, 438-448.
- Meroni, M., and Colombo, R., 2009, A novel program for field Spectrometry at Subnanometer Spectral resolution. *Computers & Geosciences*, **35**, 1491-1496.

- Meroni, M., Rossini, M., Guanter, L., Alonso, L., Rascher, U., Colombo, R., and Moreno, J., 2009, Remote sensing of solar induced chlorophyll fluorescence: review of methods and applications. *Remote Sensing of Environment*, **113**, 2037-2051.
- Monteith, J.L., 1972, Solar radiation and productivity in tropical ecosystems. *Journal of Applied Ecology*, **9**, 747-766.
- Monteith, J.L., 1977, Climate and efficiency of crop production in Britain. *Philosophical Transactions of the Royal Society of London Series B-Biological Sciences*, **281**, 271-294.
- Milton, E.J., and Rollin, E.M., 2006, Estimating the irradiance spectrum from measurements in a limited number of spectral bands. *Remote Sensing of Environment*, **100**, 348-355.
- Rahman, A.F., Cordova, V.D., Gamon, J.A., Schmid, H.P., and Sims, D.A., 2004, Potential of MODIS ocean bands for estimating CO₂ flux from terrestrial vegetation: A novel approach. *Geophysical Research Letters*, **31**.
- Rossini, M., Meroni, M., Migliavacca, M., Manca, G., Cogliati, S., Busetto, L., Picchi, V., Cescatti, A., Seufert, G., and Colombo, R., 2010, High resolution field spectroscopy measurements for estimating gross ecosystem production in a rice field. *Agricultural and Forest Meteorology*, **150**, 1283-1296.
- Rouse, J.W., Haas, R.H., Schell, J.A., Deering, D.W., and Harlan, J.C., 1974, Monitoring the Vernal Advancements and Retro Gradation of Natural Vegetation, Greenbelt, MD, USA.

Modelling vegetation fluorescence from single leaves and the canopy, observed on the ground and from space

Wout Verhoef

Faculty of Geo-Information Science and Earth Observation (ITC), University of Twente,
The Netherlands
e-mail: verhoef@itc.nl

ABSTRACT – In support of the candidate ESA mission FLEX, models have been developed to simulate vegetation chlorophyll fluorescence and its observation on the level of single leaves, the canopy and from space. The Fluspect model is based on the PROSPECT leaf model and includes an additional module which calculates the excitation-fluorescence matrix for both sides of the leaf by means of an efficient doubling algorithm. Fluorescence spectra for white incident light, and of course the spectra of reflectance and transmittance, are computed as well. The FluorSAIL model is a numerical variant of SAIL which calculates top-of-canopy fluorescent radiance in the direction of viewing for given incident radiation spectra from the sun and the sky, obtained from the MODTRAN radiative transfer code. In a recent version called FluorSAIL3, high spectral resolution data (0.1 nm) from MODTRAN5 (beta) are used by the model to simulate observations by the candidate FLEX mission. The model computes the directional canopy reflectance with and without fluorescence for the given incident radiation spectra obtained from MODTRAN and the results have been used to evaluate several algorithms for the retrieval of fluorescence from the apparent reflectance signal.

In this contribution emphasis will be on the detection of the fluorescence signal, the dependence of fluorescence observations on leaf chlorophyll content and other PROSPECT parameters, canopy structure, and observational conditions, including the properties of the atmosphere. In addition, some attention is paid to the definition of fluorescence quantum efficiencies at photosystem level, leaf level, and canopy level. This is important for the study of the relation between canopy fluorescence and actual photosynthesis. From the simulations it can be concluded that the interpretation of the fluorescence signal is complex, and probably the comparison of actual observations of spectra of fluorescence and reflectance with spectra simulated by a coupled chain of models such as Fluspect-FluorSAIL-MODTRAN will be of great help in drawing the correct conclusions from observations by a mission like FLEX.

1 INTRODUCTION

During photosynthesis a small part of the radiation absorbed by leaf chlorophyll can be re-emitted as fluorescence at a longer wavelength. This may provide information about the functioning of the photosynthetic apparatus, and through this, about the actual sequestration of carbon in the green vegetation on the land territory. Fluorescence by chlorophyll depends on many different factors, amongst which stress factors and the light level are the most important ones. In the present contribution we will only assume that there is a factor which expresses the efficiency of fluorescence emission as a percentage of the radiation absorbed by the chlorophyll. This factor is called the fluorescence quantum efficiency, FQE. There are two photosystems capable of producing fluorescence, and these are called photosystems I and II, respectively. Both have their own characteristic fluorescence spectrum, and the ratio of the weights applied to photosystems I and II determines the final fluorescence spectrum. It has been reported in the literature that photosystem I is relatively stable, and that especially photosystem II is

sensitive to stress factors, in negative as well as positive sense. Fluorescence by photosystem II may increase with light stress and decrease when photosynthesis is limited by other factors. In this paper the emphasis is put on the modelling of the fluorescence signal on the photosystem level, the leaf level, the canopy level and finally its observation from space.

2 PHOTOSYSTEM LEVEL

At the photosystem level the following assumptions are made:

- A sigmoid function is applied to suppress anti-Stokes fluorescence; this is fluorescence at a shorter wavelength than the one of excitation. Although quantum-mechanically this is not forbidden, its probability is reduced by applying the sigmoid function

$$\text{sig}(\lambda_e, \lambda_f) = \frac{1}{1 + \exp[(\lambda_e - \lambda_f)/10]}$$

where the subscripts *f* and *e* indicate the wavelengths of fluorescence and excitation, respectively.

- The inputs are FQE (fluorescence quantum efficiency), and the peak ratio PS I / PS II
- The spectral distributions for PS I and PS II are given (literature data). See Fig. 1.
- F is proportional to the absorption by Chlorophyll
- Forward and backward F are equal

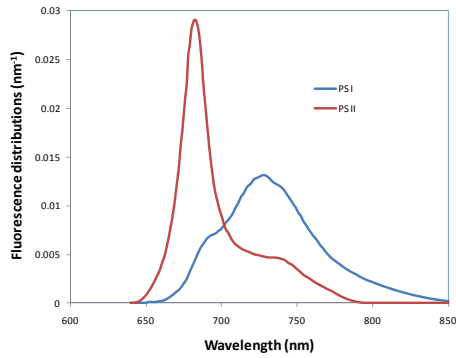


Fig. 1 Spectral distributions of the fluorescence from photosystems I and II

The spectral distribution functions for PS I and PS II are symbolized by Φ_I and Φ_{II} , respectively, and the production of fluorescence at photosystem level is described by

$$f = g = 0.5 Q [w_1 \Phi_I(\lambda_f) + w_2 \Phi_{II}(\lambda_f)] k_C(\lambda_e) \mathcal{E} \times \text{sig}(\lambda_e, \lambda_f) \quad (1)$$

where f and g are the forward and backward fluorescence, Q is the fluorescence quantum efficiency, w_1 and w_2 are weighting factors applied to photosystems I and II, $k_C(\lambda_e)$ is the chlorophyll absorption coefficient at the excitation wavelength, and \mathcal{E} is a small number expressing a fraction of the optical thickness of the leaf. In the present implementation of the applied doubling algorithm 15 doubling steps are executed, and in this case \mathcal{E} is equal to 2^{-15} . The peak ratio p is used to calculate the weights applied to PS I and PS II by $w_1 = p/(1+p)$, and $w_2 = 1/(1+p)$, respectively.

3 LEAF LEVEL

At the leaf level the PROSPECT model (Jacquemoud & Baret, 1990) is used to determine single leaf reflectance and transmittance (ρ and τ). The version of PROSPECT with 5 input parameters is used, namely C_{ab} , C_w , C_{dm} , C_s and N , which stand for the concentrations of chlorophyll (a and b), leaf water, dry matter, senescent material (brown pigments) and the internal scattering parameter, respectively.

Contrary to Pedrós et al. (2005), in Fluspect fluorescence is included by applying a doubling algorithm. The absorption and backscattering coefficients (k and s) are derived from ρ and τ , and next a Kubelka-Munk type of model is applied in forward direction, which is implemented as a very efficient doubling routine, whereby ρ and τ are reconstituted to their input values, and the forward and backward fluorescence matrices F_f and F_b are computed as new output products. The matrices are computed at a spectral resolution of 1 nm, and comprise the regions 400 – 750 nm for the excitation wavelength, and 640 – 850 nm for the fluorescence wavelength. For each combination of excitation and fluorescence wavelength the following piece of code is executed:

Initialisation

$$t_e = 1 - (k_e + s_e) \mathcal{E}; \quad r_e = s_e \mathcal{E};$$

$$t_f = 1 - (k_f + s_f) \mathcal{E}; \quad r_f = s_f \mathcal{E};$$

Do 15 times:

$$x_e = t_e / (1 - r_e^2); \quad t_e' = x_e t_e; \quad r_e' = r_e (1 + t_e');$$

$$x_f = t_f / (1 - r_f^2); \quad t_f' = x_f t_f; \quad r_f' = r_f (1 + t_f');$$

$$f' = f(x_e + x_f) + g x_e x_f (r_e + r_f);$$

$$g' = g [1 + x_e x_f (1 + r_e r_f)] + f(x_e r_e + x_f r_f);$$

$$t_e = t_e'; \quad r_e = r_e'; \quad t_f = t_f'; \quad r_f = r_f';$$

$$f = f'; \quad g = g';$$

End do

Here, f and g are the forward and backward fluorescence, and each primed quantity is the updated result after a doubling step. Note that f and g have been initialised according to Eq. (1) given in section 2. A graphical user interface (Fig. 2) has been written in the Visual Basic 5 language in order to demonstrate the leaf level model as a function of the input parameters and to save spectra of reflectance, transmittance and both fluorescence matrices as output files. This version provides additional outputs related to the fluorescence quantum efficiencies (FQE) at the photosystem and leaf levels, and information about the total forward and backward fluorescence produced for white incident light. Also total leaf absorption in the PAR range as well as the absorption by chlorophyll only are presented. At the photosystem level, and for white incident light, FQE can be defined by

$$\text{FQE} = \frac{\int_{400}^{750} \int_{640}^{850} [f_b(\lambda_f, \lambda_e) + f_f(\lambda_f, \lambda_e)] d\lambda_f d\lambda_e}{\int_{400}^{750} k_C(\lambda_e) d\lambda_e} \quad (2)$$

With this definition the actually obtained FQE is a little less than the target one, which is given by Q in Eq. (1). This is because the suppression of anti-Stokes fluorescence by the sigmoid function introduces a slight loss of radiation. The example in Fig. 2 shows that a target FQE of 0.02 produces an actual FQE at photosystem level of 0.0191.

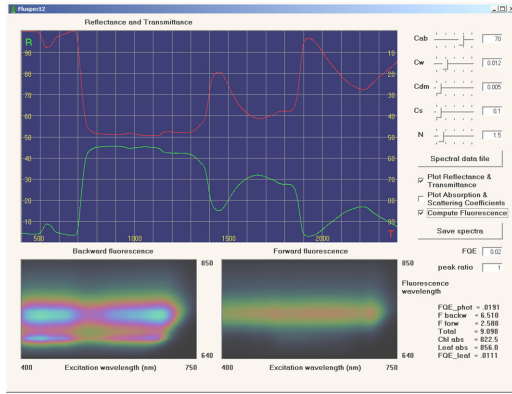


Fig. 2 Graphical user interface written in Visual Basic 5

At the leaf level one can also define a fluorescence quantum efficiency (for white incident light), which is defined by

$$FQE = \frac{\int_{400}^{750} \int_{640}^{850} [F_f(\lambda_e, \lambda_f) + F_b(\lambda_e, \lambda_f)] d\lambda_f d\lambda_e}{\int_{400}^{750} [1 - \rho(\lambda_e) - \tau(\lambda_e)] \frac{k_C(\lambda_e)}{k_{TOT}(\lambda_e)} d\lambda_e}$$

Here, the normalisation is done by means of an estimate of the radiation absorbed by chlorophyll, in which total leaf absorption is corrected by the ratio of the absorption coefficient of chlorophyll and that of all absorbers together. In the example it appears that, mainly due to re-absorption effects, the FQE for the leaf is reduced in magnitude to a value of 0.0111. The other quantities (backward and forward F, total F, chlorophyll absorption, and total leaf absorption) are given in pro-mille of the (white) incident radiation. Fig. 3 shows the effect of an increasing chlorophyll concentration on leaf absorption and fluorescence in cases when also the N parameter and the amount of brown pigments were varied. It appears that in all cases there is a strong relationship between backward fluorescence and leaf absorption when chlorophyll is increased.

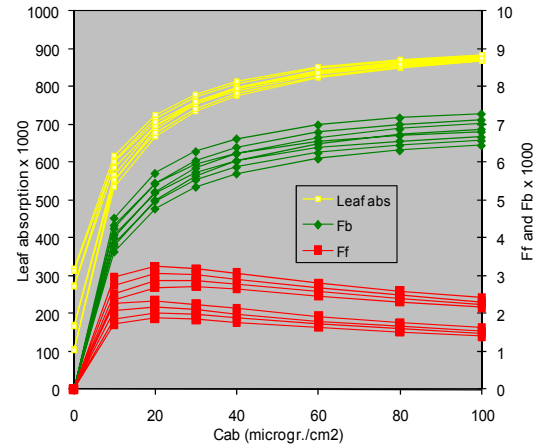


Fig. 3 Effects of chlorophyll concentration on total leaf absorption, backward and forward fluorescence (all in pro-mille of the incident radiation) according to the Fluspect model

Both tend to saturate at high chlorophyll concentrations, whereas forward fluorescence reaches a maximum at around 20 micrograms/cm². However, the spectral effects of a chlorophyll are more pronounced, as can be seen in Fig. 4 a and b. The backward fluorescence increases all over with chlorophyll concentration, but at the first peak at 685 nm saturation is reached quite soon, whereas around the second peak at 740 nm fluorescence keeps increasing with chlorophyll concentration. The second peak finally becomes higher than the first peak. For the forward fluorescence the spectral effects are even stronger.

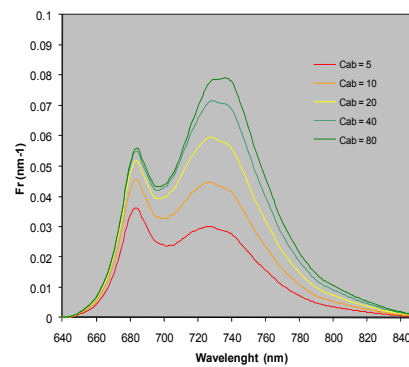


Fig. 4a Backward fluorescence spectra for an increasing chlorophyll concentration

In this case the first peak at 685 nm is only high at low concentrations, and then rapidly disappears due to an increasing re-absorption effect

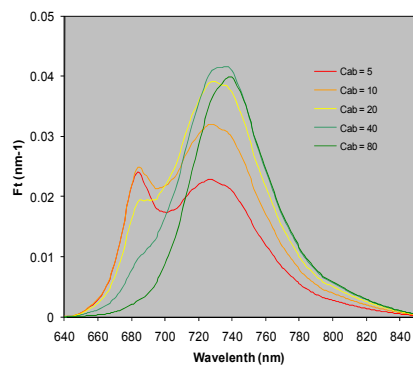


Fig. 4b Forward fluorescence spectra for an increasing chlorophyll concentration

In the examples so far the peak ratio for PS I and II was equal to one. The effects of a changing peak ratio are shown in Fig. 5 for the backward fluorescence and a chlorophyll concentration of 80 micrograms/cm². It appears that both FQE and the peak ratio have an effect on the magnitude and the shape of the fluorescence spectra. In this respect it should be noted that these parameters are still of a semi-empirical nature, and that the relationships with leaf physiology still have to be established.

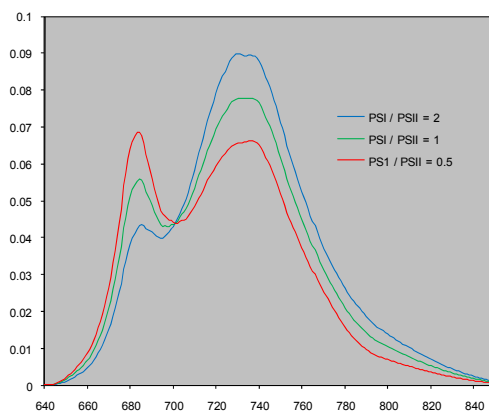


Fig. 5 Effects of changing the PS I / PS II peak ratio

4 CANOPY LEVEL

The canopy level model FluorSAIL has been developed in an ESA study in the period 2002-2005 (Verhoef, 2004; Miller et al., 2005). The model is based on the SAIL model (Verhoef, 1984), but canopy fluorescence is computed numerically by dividing the canopy into 60 optically thin layers. Also, a light level dependence according to Rosema et al. (1998) has been included to take account of photochemical quenching. In the recent version FluorSAIL3.0 the 1 nm spectral resolution output of the model is used together with

high spectral resolution (0.1 nm) atmospheric data obtained from MODTRAN5 beta (Berk et al., 2005) in order to provide realistic simulation of TOA (top-of-atmosphere) radiance spectra as obtained by the future fluorescence mission FLEX. Fig. 6 shows a diagram of the modular set-up of the FluorSAIL model, which uses ASCII text inputs from the leaf level model and the MODTRAN 4 and 5 atmospheric models.

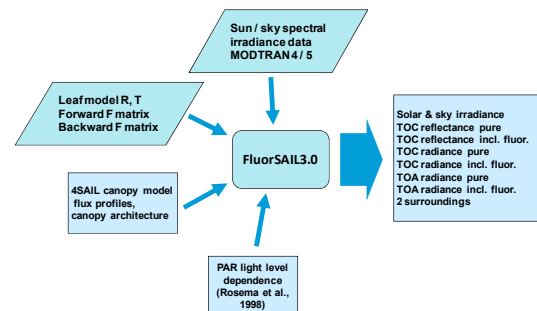


Fig. 6 Modular set-up of the FluorSAIL program

For the retrieval of fluorescence from TOA or TOC (top-of-canopy) radiance data it is important to separate surface reflectance from fluorescence. Fig. 7a and 7b show surface reflectance and the fluorescent radiance at TOC level for a series of simulations with increasing chlorophyll concentration.

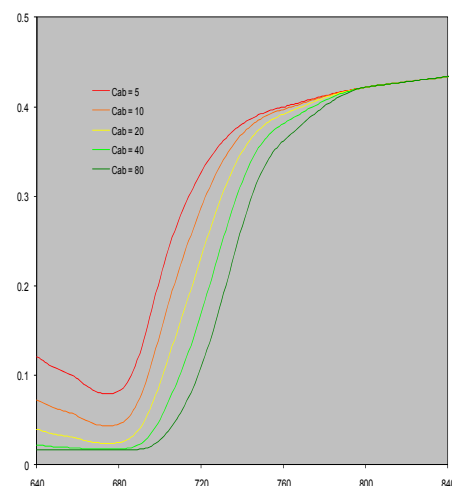


Fig. 7a Surface reflectance spectra for increasing chlorophyll contents

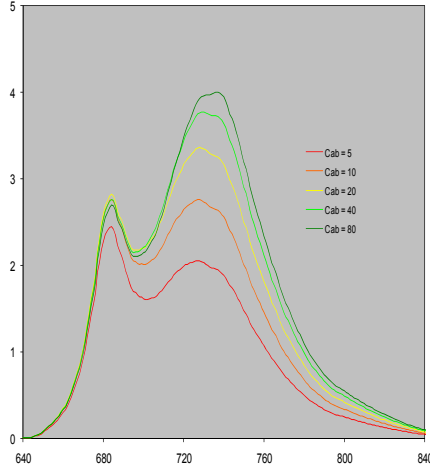


Fig. 7b Fluorescent radiance spectra (mW/m² sr nm) at TOC level for increasing chlorophyll contents

From these results it appears that especially the first peak at 685 nm is little affected by the leaf chlorophyll concentration, but the second peak clearly is. In the spectral regions corresponding to the oxygen A and B bands (761 and 684 nm) the fluorescence level is of the order of 2 - 3 mW/m² sr nm, which is fairly in agreement with results obtained during measurement campaigns in the field (Meroni et al., 2010).

The fluorescent radiance signal is also direction-dependent, as illustrated in Fig. 8, which shows its variation in the principal plane of the sun for a solar zenith angle of 30 degrees. A clear hot spot effect is visible and a decreasing trend in the forward scattering direction, followed by an increase again at larger viewing zenith angles.

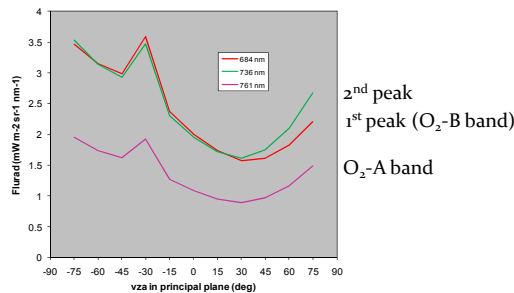


Fig. 8 Directional effects on fluorescent radiances at a few selected wavelengths

The Fraunhofer Line Detection (FLD) method makes use of the difference between apparent and pure reflectance, which is amplified in absorption bands of the solar and terrestrial atmospheres. Fig. 9 shows this difference in three spectral windows. The first is located around the H-alpha line in the solar spectrum,

and the other two are the oxygen regions of atmospheric absorption. The solar H-alpha line at 656 nm is very weak and produces only a faint peak in the apparent reflectance spectrum, too small to be detectable. The O₂-B region at 686 nm gives a higher response, but the O₂-A region at 761 nm produces the most pronounced peak in the apparent reflectance curve.

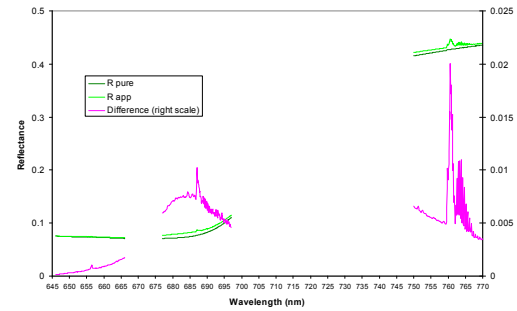


Fig. 9 Pure and apparent reflectances in 3 windows at 0.1 nm spectral sampling distance: i) H-alpha, ii) O₂-B, iii) O₂-A. The purple lines show the differences (right scale)

4 ATMOSPHERIC EFFECTS

The FLD method is complicated by the fact that the elevated radiance levels found in atmospheric absorption bands and caused by fluorescence are reduced in magnitude again by the same absorption features in the atmosphere on the way back from target to sensor. The TOA radiance signal is a complicated function of atmospheric and surface optical properties, which can be described by means of four-stream radiative transfer theory by

$$L_o^{TOA} = L_0 + F_s \tau_{oo} + E_s^o \frac{\cos \theta_s}{\pi} \left[\left(\tau_{ss} r_{so} + \frac{\tau_{sd} + \tau_{ss} \overline{r_{sd} \rho_{dd}}}{1 - r_{dd} \rho_{dd}} r_{do} \right) \tau_{oo} + \frac{\tau_{ss} \overline{r_{sd}} + \tau_{sd} \overline{r_{dd}}}{1 - r_{dd} \rho_{dd}} \tau_{do} \right] \quad (3)$$

where L_0 is the atmospheric path radiance, F_s is the solar-induced fluorescent radiance at ground level, E_s^o is the extraterrestrial solar irradiance and θ_s is the solar zenith angle. The τ -quantities are various atmospheric direct and diffuse transmittances, the r -quantities are directional reflectances of the target and the surroundings (with over bar), and ρ_{dd} is the spherical albedo of the atmosphere at the bottom of the atmosphere for upwelling radiation from below. Strictly, Eq. (3) applies only to monochromatic radiation. For finite spectral intervals one has to consider the fact that atmospheric transmittances may have a high covariance over

the interval, so that the products of transmittances are much higher than the products of their average values over the interval. So it is better to calculate the products before the spectral integration over intervals. In that case an effective formula which holds for finite spectral intervals is given by

$$\begin{aligned} \langle L_o^{TOA} \rangle = & \overline{t_1 + t_2 F_s + t_4 r_{so}} \\ & + \frac{t_5 + t_6 r_{sd}}{1 - t_3 r_{dd}} r_{do} + \frac{t_7 r_{sd} + t_8 r_{dd}}{1 - t_3 r_{dd}} \end{aligned}$$

where the terms $t_1 - t_8$ are all atmospheric variables.

Fig. 10 shows how these variables behave as a function of wavelength for the interval 750 - 770 nm of the O₂-A region. For the Y-axis a log scale was used to capture the large dynamic ranges and to facilitate the comparability.

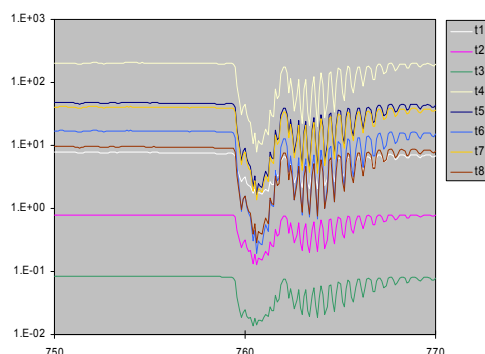


Fig. 10 Plot of $t_1 - t_8$ for the O₂-A region at 0.1 nm resolution on a log scale

From this plot it is clear that the spectral curves are highly similar due to the common absorption features of oxygen gas in the atmosphere. However, the depth of the spectral absorptions varies over the terms $t_1 - t_8$, and this property might be used to discriminate fluorescence from surface reflectance effects in high-resolution TOA radiance spectra.

5 CONCLUSIONS

A consistent chain of vegetation fluorescence models from photosystem scale, leaf scale and canopy scale to observations from space is available for numerical experiments and validation. A fluorescence quantum efficiency of 0.02 explains recent TOC and TOA fluorescent radiance observations of a magnitude of ~2 mW/m² sr nm.

Results indicate that the retrieval of F and R from TOA data is still a challenge and that the above models can support the interpretation of the F signal.

TOA observations are influenced by BRDF-effects, adjacency effects and many atmospheric parameters, and these effects should be considered in the design of algorithms for the retrieval of fluorescence from TOA radiance spectra.

6 REFERENCES

- Berk, A., Anderson, G.P., Acharya, P.K., Bernstein, L.S., Muratov, L. and Lee, J., et al., 2005, MODTRAN5: A reformulated atmospheric band model with auxiliary species and practical multiple scattering options, *Proceedings of SPIE, the International Society for Optical Engineering* **5655**, p. 88 10.1117/12.578758
- Jacquemoud, S., Baret, F., 1990, PROSPECT: a model of leaf optical properties spectra, *Remote Sensing of Environment* **34**: 75-91.
- Meroni, M., Busetto, L., Colombo, R., Guanter, L., Moreno, J. and Verhoef, W., 2010, Performance of spectral fitting methods for vegetation fluorescence quantification. *Remote Sensing of Environment* **114** (2), 363-374.
- Miller, J.R., Berger, M., Goulas, Y., Jacquemoud, S., Louis, J., Mohammed, G., Moise, N., Moreno, J., Moya, I., Pédros, R., Verhoef, W. and Zarco-Tejada, P., 2005, Development of a Vegetation Fluorescence Canopy Model, Final report, ESTEC Contract No. 16365/02/NL/FF, 138 pp.
- Pedrós, R., Goulas, Y., Jacquemoud, S., Louis, J. and Moya, I., 2010, FluorMODleaf: A new fluorescence emission model based on the PROSPECT model, *Remote Sensing of Environment* **114**: 155-167.
- Rosema, A., Snel, J.F.H., Zahn, H., Buurmeijer, W.F., Van Hove, L.W.A., 1998, The Relation between Laser-Induced Chlorophyll Fluorescence and Photosynthesis - 2. Physiological significance of fluorescence signal in response to environmental stress, *Remote Sensing of Environment* **65**(2): 143-154.
- Verhoef, W., 1984, Light scattering by leaf layers with application to canopy reflectance modeling: the SAIL model, *Remote Sensing of Environment* **16**: 125-141.
- Verhoef, W., 2004, Extension of SAIL to model solar-induced canopy fluorescence spectra, 2nd International Workshop on Remote Sensing of Vegetation Fluorescence, Nov. 2004, Montreal, Canada.

AUTHOR INDEX

A

Abaoui, J., 434
Abbott, E. A., 27, 117
Aguirre, R., 740
Aguirre-Lora, E., 789
Alados, I., 16
Alados-Arboledas, L., 16, 83, 795
Albergel, C., 405
Al-Bitar, A., 766
Alchanatis, V., 243
Allen, R. G., 495
Alonso, L., 225
Amici, S., 123
Amorós, J., 654
Antolín, M. C., 772
Arbiol, R., 840
Arenas, S., 518
Arino, O., 666
Arozarena, A., 834
Arrazola, D., 830
Arroyo, J. M., 830
Aslett, Z., 178
Ayash, T., 77
Azcona, J., 830
Azyat, A., 734

B

Bach, H., 1
Bach, M., 444
Baldwin, D., 286
Balick, L., 196, 220
Balsamo, G., 405, 416
Balzarolo, M., 405
Barberá, M. J., 321, 187, 524

Barbu, A., 405, 513
Baret, F., 6, 67, 99, 208, 326, 343, 416, 428, 660,
Barroso, C., 298
Barsi, J. A., 456
Baup, F., 251, 292
Beget, M. E., 6
Beguet, B., 251
Belayev, V., 310
Belda, F., 568
Belenguer, T., 830
Ben Achhab, N., 734
Bennouna, Y. S., 684
Berjón, A., 684
Bernabé, S., 529
Berni, J. A. J., 355
Berthelot, B., 760
Béziat, P., 364, 388
Bianchi, R., 672
Bin, X., 535
Bisquert, M., 540
Blanchard, Y., 77
Blanchet, J.-P., 77
Blanchon, P., 626
Blumberg, D., 196
Bobée, C., 545
Bonfil, D. J., 243
Bontemps, S., 666
Bories, N., 597
Boulet, G., 364, 388, 444, 824
Boussetta, S., 405
Bouzinac, C., 672
Bravo-Aranda, J. A., 795
Briottet, X., 444
Brogniez, G., 690, 745
Bueno, J. I., 830

Buil, A., 776
Buongiorno, M. F., 123, 440
Busetto, L., 851

C

Caballero-Novella, J. J., 133
Cabeza I., 830
Cabot, F., 678
Cacciani, M., 33
Cachorro, V. E., 684
Calera, A., 237, 495, 654
Calle, A., 149, 370
Calvet, J.-C., 405, 411, 416, 513
Camacho, F., 99, 208, 399, 416, 471, 574, 660, 694
Campbell, P. K. E., 845
Campo, L., 280, 700
Campos, I., 237
Camps, G., 654
Caparrini, F., 280
Capilla, R., 751
Carbó, E., 772
Cardellach, E., 776
Casanova, J. L., 370
Caselles, E., 540
Caselles, V., 21, 72, 495, 540
Castañeda, C., 143
Castellanos, P., 286
Castelli, F., 280, 700
Castillejo-González, I. L., 158, 551, 789
Castillo, S., 824
Caycho, M., 138
Ceriola, G., 620
Cernicharo, J., 399, 660, 694
Cescatti, A., 405
Ceschia, E., 364
Chahboun, A., 734
Chakroun, H., 376
Châteauneuf, F., 77
Chehbouni, G., 364, 388, 434
Chen, L., 382
Chen, M., 450
Cheng, Y.-B., 845
Cherchali, S., 444
Chevallier, F., 405
Chiesi, M., 471
Chirouze, J., 364, 388
Ciais, P., 411
Cian, F., 751
Cierniewski, J., 10
Cirujano, S., 181
Clevers, J. G. P. W., 56
Cogliati, S., 851
Cohen, Y., 243
Colin, J., 495
Coll, C., 21
Coll, M. A., 780
Colombo, R., 851
Comyn-Platt, E., 706
Corbari, C., 393
Corp, L. A., 845
Costa, M. J., 807
Coudert, B., 444, 824
Courault, D., 214
Cremonese, E., 851
Cristo, A., 127
Cuenca, J., 422, 477, 580, 638, 644, 801
Cuevas, J. M., 149
Curnel, Y., 256

D

D'Andrimont, R., 416, 557
Dadou, I., 444
Daglis, I. A., 620
Damiri, B., 690
Danilina, I., 196
Datcu, M., 751

Davidson, M. W. J., 672
 Dayau, S., 824
 De Castro, A. I., 133
 de Frutos, A., 684
 de Jeu, R., 760
 de Miguel, E., 169, 461
 De Ridder, K., 620
 de Rosnay, P., 678
 de Vries, J., 405
 de Wit, A., 256, 343
 Dedieu, G., 214, 247, 251, 444
 Defourny, P., 256, 343, 557, 608, 666
 Dejoux, J.-F., 251, 292
 Delbart, N., 405
 Delgado, J. M., 751
 Delibes, M., 466
 Delogu, E., 824
 Delwart, S., 678
 Demontoux, F., 678, 756
 Despini, F., 338
 Di Bella, C. M., 6
 di Sarra, A., 33
 Díaz Núñez, M. Y., 138
 Djaby, B., 256
 Domenech, E., 654, 834
 Domínguez, J., 632
 Domínguez, M., 143
 Dópido, I., 315
 Driouech, F., 434
 Dubuisson, P., 745
 Duchemin, B., 214, 434
 Ducrot, D., 251, 292
 Duffour, C., 756
 Duveiller, G., 256, 343

E

Eerens, H., 428
 Eguía, J., 830
 Emery, W. J., 286

Entekhabi, D., 280
 Er-raki, S., 388
 Escobar, P., 654
 Escorihuela, M. J., 678
 Espinosa, J., 649
 Estellés, V., 89, 813
 Esteve, A. R., 89
 Estrela, M. J., 187, 321, 524
 Evrard, O., 310
 Ezzahar, J., 388

F

Fabra, F., 776
 Farutin, I., 819
 Faude, U., 181
 Federes, E., 355
 Fedotkin, D., 819
 Feilhauer, H., 181
 Fensholt, R., 616
 Fernández, N., 466
 Ferrazzoli, P., 678
 Fieuzal, R., 388
 Foyo-Moreno, I., 16
 Franch, B., 39, 422, 477, 518, 580, 638, 644, 801
 François, P., 690
 Freitas, S. C., 298, 416
 Fuertes, D., 684

G

Galvagno, M., 851
 Galve, J. M., 21
 Gamet, P., 444
 Gao, C., 712
 Gao, Y., 382
 Garand, L., 77
 Garatuza-Payan, J., 388
 García, M., 466

García, R., 830
 García, U., 830
 García-Ferrer Porras, A., 158
 García-Ferrer Porras, A., 551
 García-Ferrer, A., 789
 García-Haro, F. J., 99, 471, 562, 568, 574, 591, 694
 García-Santos, V., 21, 72
 Garrido, J., 654
 Gavilán, P., 632
 Giannaros, T., 620
 Gilabert, M. A., 471, 489, 568, 591
 Gillespie, A. R., 27, 117, 154, 196, 220
 Gilson, L., 27
 Gioia, A., 614
 Gioli, B., 851
 Goldhamer, D., 355
 Gómez Rubio, V., 776
 Gómez Sánchez, J. A., 169
 Gómez-Amo, J. L., 33, 813
 Gómez-Candón, D., 133
 Gómez-Casero, M. T., 133
 Gómez-Chova, L., 654
 González Dugo, M. P., 632
 González, L. M., 830
 González, R., 684
 González-Alonso, F., 149, 370, 580
 González-Dugo, V., 355,
 González-Matesanz, J., 654
 González-Piqueras, J., 237
 Good, E. J., 706
 Götsche, F.-M., 202
 Govind, A., 678
 Granados, M. J., 795
 Grant, J. P., 678
 Guerrero-Rascado, J. L., 807
 Gutiérrez de la Cámara, O., 461
 Guyon, D.,
 Guyon, D.,

Guyon, D., 274, 597, 678

H

Hadria, R., 214
 Haeger, J. F., 518
 Hagolle, O., 214, 247, 251, 444
 Haiqi, L., 535
 Haiyan, L., 535
 Hanocq, J.-F., 6
 Hernández, L., 127
 Hernández-Guerra, A., 286
 Hernández-Núñez, H., 626
 Herrmann, I., 10, 243
 Hidalgo, V., 39, 393, 422, 477, 518, 580, 638, 644, 801
 Hook, S. J., 456
 Huber, S., 616
 Huc, M., 251
 Huemrich, K. F., 845
 Huesca, M., 149
 Hulley, G., 27

I

Inglada, J., 247, 251
 Iordache, M.-D., 315

J

Jacob, F., 444
 Jacquette, E., 678
 Jarabo, S., 830
 Jarlan, L.,
 Jarlan, L., 388, 434
 Jia, Y., 501
 Jiang, X.,
 Jiang, X., 712, 718
 Jianming, M., 535
 Jiménez-Muñoz, J.-C., 27, 39, 154, 220, 422, 477, 518, 580, 586, 638, 644, 801

Jinya, L., 535
 Jordano, D., 518
 Julien, Y., 39, 422, 477, 518, 580,
 638, 644, 801
 Jurado-Expósito, M., 133

K

Kahle, A. B., 117
 Kallel, A., 44, 50
 Kang, G., 163
 Karnieli, A., 10, 243
 Kayitakire, F., 603
 Keramitsoglou, I., 620
 Kerr, Y., 678, 756, 760, 766
 Kharrou, H., 434
 Kirchgaessner, U., 262
 Koch, M., 127
 Kooistra, L., 225
 Kosolapova, L. G., 756
 Kouadio, L., 256
 Koukal, T., 268
 Kratt, Ch., 178
 Kruse, F. A., 178
 Kruszewski, A., 756
 Kullman, L., 405
 Kurz, B., 274
 Kuśnierek, K., 10
 Kustas, W. P., 845

L

Labonnote, L., 745
 Lacaze, R., 208, 416, 660
 Lafont, S., 405, 411, 513
 Lagouarde, J.-P., 274, 444, 824
 Lahraoua, M., 734
 Laurent, V. C. E., 56
 Lawrence, H., 678, 756
 Le Hégarat-Masclé, S., 50, 304, 310

Le Page, M., 434
 Lebon, E., 67
 Leng, P., 94
 Leroux, D., 760
 Li, C., 349
 Li, J., 62
 Li, X. H., 94
 Li, X. T., 94
 Li, X., 712, 718
 Li, Z., 718
 Li, Z.-L., 94, 111, 163, 231, 332, 358, 501,
 507, 718, 728, 784
 Lio Soon Shun, N., 310
 Liu, Q., 62
 Liu, Z., 784
 Loaiza, Y., 138
 López, A., 830
 López-Baeza, E., 399, 678, 772, 776, 780
 López-Granados, F., 133, 551
 López-Lozano, R., 67
 Lou, J., 501
 Luaces, S., 654
 Lyamani, H., 16, 83

M

Ma, L., 349, 722
 Macedo, J., 298
 Magnani, F., 851
 Mahfouf, J.-F., 405
 Mahmoodi, A., 678
 Maignan, F., 405, 545
 Maiheu, B., 620
 Makhmara, H., 208
 Malizia, A., 614
 Mansilla, F., 632
 Manunta, P., 620
 Manzini, M., 393
 Marais-Sicre, C., 251, 292
 Margolis, H. A., 845

Marini, A., 830
 Markham, B. L., 456
 Martín, G., 315
 Martín, J., 830
 Martín, M. P., 483
 Martínez, B., 471, 489, 568, 591
 Martínez, F. J., 483
 Martínez, J. A., 654
 Martínez, L., 21, 72, 840
 Martínez, P., 127
 Martínez, S., 149
 Martínez-Beltrán, C., 237
 Martínez-Lozano, J. A., 33, 89, 813
 Maselli, F., 471
 Masse, A., 292
 Mattar, C., 39, 422, 477, 518, 580, 586, 638, 644, 678, 766, 801
 Mecklenburg, S., 678
 Melas, D., 620
 Meliá, J., 99, 471, 568, 574, 694,
 Meloni, D., 33
 Mendiguren, G., 483
 Menenti, M., 495
 Merino de Miguel, S., 149
 Merino, J., 127
 Meroni, M., 851
 Meroño de Larriva, J. E., 789
 Mesas-Carrascosa, F. J., 158, 551, 789
 Mialon, A., 678, 756
 Middleton, E. M., 845
 Migliavacca, M., 851
 Miglietta, F., 851
 Millán, C., 776
 Millán-Scheiding, C., 772
 Minor, T., 178
 Mira, M., 21, 274
 Miranda Peña, M. A., 138
 Miravet, C., 830
 Miró, J., 321

Mironov, V. L., 756
 Mizzon, H., 220
 Moisy, C., 274, 597, 678
 Mokssit, A., 434
 Molina, S., 654
 Monasterio, I., 830
 Monerris, S., 678
 Montero Herrero, E., 620
 Morales, L., 193, 649
 Moreau, P., 274
 Moreno, A., 471, 489, 568
 Moreno, J., 225, 654
 Moreno, R. D., 586
 Morkin, T., 178
 Morra di Cella, U., 851
 Mougnot, B., 143
 Mouillot, F., 376
 Muñoz, J., 830
 Muñoz-Padilla, F., 632
 Mushkin, A., 196

N

Navarro, R., 830
 Navas-Guzmán, F., 83, 795
 Ndiaye, M., 545
 Nerry, F., 444
 Niclòs, R., 187, 321, 524
 Nouri, M., 376
 Novello, N., 678, 766

O

Odi, M., 237
 Ogée, J., 274
 Ojeda, J. C., 654
 Olesen, F.-S., 202
 Olioso, A., 214, 364, 444, 824
 Olmo, F. J., 16, 83

Oltra-Carrió, R., 39, 422, 477, 518, 580, 614, 638, 644, 801
 Osann, A., 495
 Otlé, C., 50, 304, 310, 444, 545
 Ou Yang, X., 163
 Ouldbba, A., 434

P

Pacheco, J., 483
 Pacholczyk, P., 208, 416
 Paganini, M., 620
 Pala, V., 840
 Palacios, M., 620
 Pancrati, O., 77
 Paolini, L., 614
 Papale, D., 405
 Pareja-Quispe, D., 586
 Parol, F., 745
 Parra, J. C., 193, 649
 Pasapera-Gonzales, J. J., 586
 Pascal, V., 444
 Pascual, L., 830
 Pastor, C., 830
 Peces, J. J., 654, 834
 Pedrós, R., 813
 Pekel, J.-F., 557, 603
 Pelegrí, J. L., 286
 Pelon, J., 745
 Pendás, E., 740
 Pérez González, I., 169
 Pérez, F., 72, 840
 Pérez, R., 127
 Perez-Hoyos, A., 568, 471, 562, 591
 Pérez-Ramírez, D., 83
 Peylin, P., 411
 Pieri, D., 123, 440
 Pimstein, A., 243
 Pipia, L., 840
 Piscini, A., 123

Plaza, A., 315, 529
 Plaza, J., 315
 Plaza, N., 654, 834
 Poilvé, H., 67, 416
 Poquet, D., 568
 Porcuna, A., 654
 Prata, A. J., 105
 Preißler, J., 807
 Privette, J. L., 450
 Puche, N., 824
 Putze, U., 262

Q

Qian, Y.-G., 728
 Qiu, S., 349, 722, 784

R

Radius, A., 620
 Rahmoune, R., 678
 Raissouni, N., 734
 Raqueno, N. G., 456
 Recondo, C., 740
 Remedios, J. J., 105, 706
 Riaño, D., 483
 Richaume, P., 678
 Rius, A., 776
 Rivalland, V., 364
 Rivera, J. P., 225
 Robles González, C., 169
 Rodrigo, R., 684
 Rodríguez, J. C., 388
 Rodríguez, M., 181
 Rodríguez, R., 461
 Romero, J., 193
 Romijn, E., 225
 Rossini, M., 851
 Roujean, J. L., 444, 574, 824
 Rousseau, J., 67
 Royer, A., 77

Rubio, E., 495, 540
Rüdiger, C., 678
Ruescas, A. B., 751
Ruget, F., 214

S

Sabol, D., 178
Saleh, K., 678
Salvador, P., 370
Samalens, J.-C., 597
Sánchez de la Orden, M., 158, 551, 789
Sánchez, J. M., 495, 540
Sánchez, R., 181
Sánchez, S., 181, 315
Sanz, J., 370
Sapage, T., 620
Sarti, F., 751
Saunders, R., 706
Schaepman, M. E., 56
Schmid, T., 127, 181
Schneider, W., 268
Schott, J. R., 456
Schuettmeyer, D., 672
Schwank, M., 678
Segura, S., 89
Sierra, M. J., 181
Silva, A. M., 807
Silva, R., 298
Siniscalco, C., 851
Smets, B., 208, 416
Smith, M. R., 220
Smith, M., 196
Sobrinho, J. A., 27, 39, 154, 193, 220, 393, 422, 444, 477, 518, 580, 586, 614, 626, 638, 644, 678, 734, 766, 801
Song, X. N., 94
Song, X., 718

Sòria, G., 39, 422, 477, 518, 580, 638, 644, 801
Sourdeval, O., 745
Suárez, L., 355
Sun, X., 501
Swinnen, E., 428
Szczpta, C., 405

T

Tamame, M., 620
Tambuyzer, H., 620
Tang, B.-H., 231, 358
Tang, L., 722
Tang, R., 332, 501
Tansey, K., 416
Tao, H., 382
Taranik, J., 178
Tardà, A., 840
Tasumi, M., 495
Taubmann, G., 830
Teggi, S., 338
Tejeiro, J. A., 654, 834
Tintó García-Moreno, F., 444
Tisseyre, B., 67
Toledano, C., 684
Torres B., 684
Torres, E., 495
Tourre, Y. M., 434
Trezza, R., 495
Trigo, I. F., 298
Tychon, B., 256

U

Unkelbach, A. B., 202
Utrillas, M. P., 33, 89, 813

V

Valcarcel, N., 654
Valiente, J. A., 187, 321, 524
Valor, E., 21, 72
van Bogaert, E., 557, 666
Vancutsem, C., 603
Vergier, A., 99, 326, 399, 471, 568, 574, 694
Verhegghen, A., 608
Verhoef, W., 56, 857
Verrelst, J., 225
Viel, M., 620
Vilar, L., 483
Villa, G., 654, 834
Villon-Reinoso, C., 586
von Schoenermark, M., 262

W

Wagner, F., 807
Wagner, W., 416
Waldteufel, P., 678
Wang, J., 111
Wang, K., 332
Wang, N., 231
Wang, X., 349, 722
Watts, C., 388
Weber, J.-L., 666
Weiguo, T., 535
Weiss, M., 208, 326, 343, 411, 428, 660, 824
Wigner, J.-P., 597, 678, 756, 766
Wood, E., 760
Wu, H., 358

X

Xi, X., 718
Xiaohua, Z., 535
Xiuchun, Y., 535

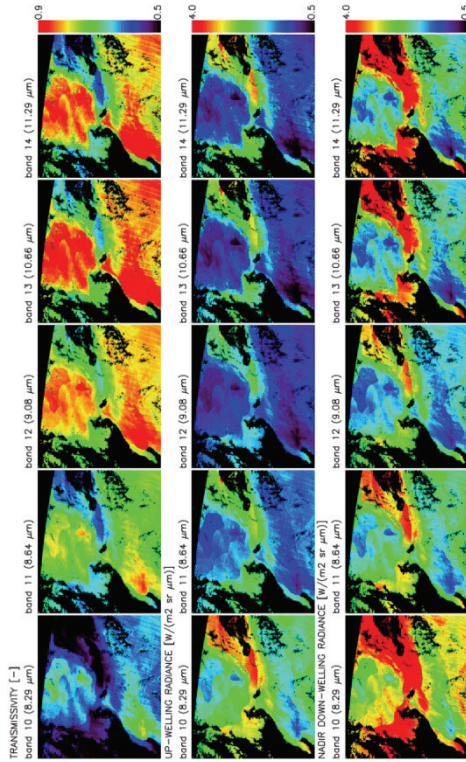
Y

Yan, J., 382
Yu, Y., 450
Yunxiang, J., 535

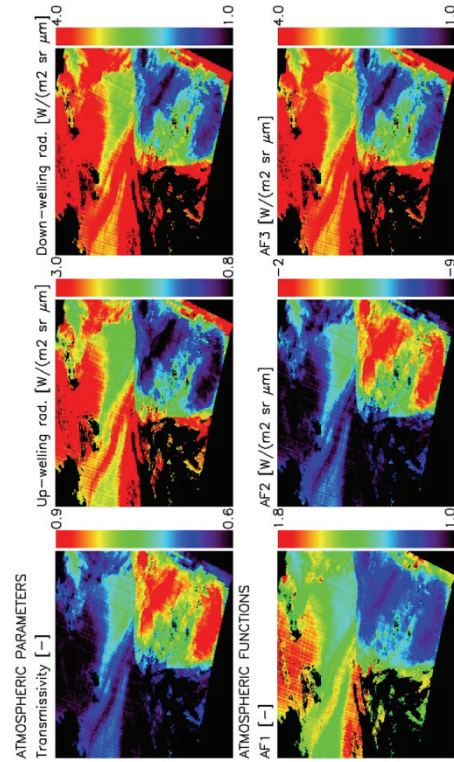
Z

Zapata-Ramírez, P. A., 626
Zarco-Tejada, P. J., 355
Zeller, O., 105
Zeng, F., 163, 231
Zhang, Q., 845
Zhang, X., 111
Zhao, W., 507
Zhao, Y., 411
Zhaoliang, L., 535
Zhi, Y., 535
Zhihao, Q., 535
Zorita, D., 830

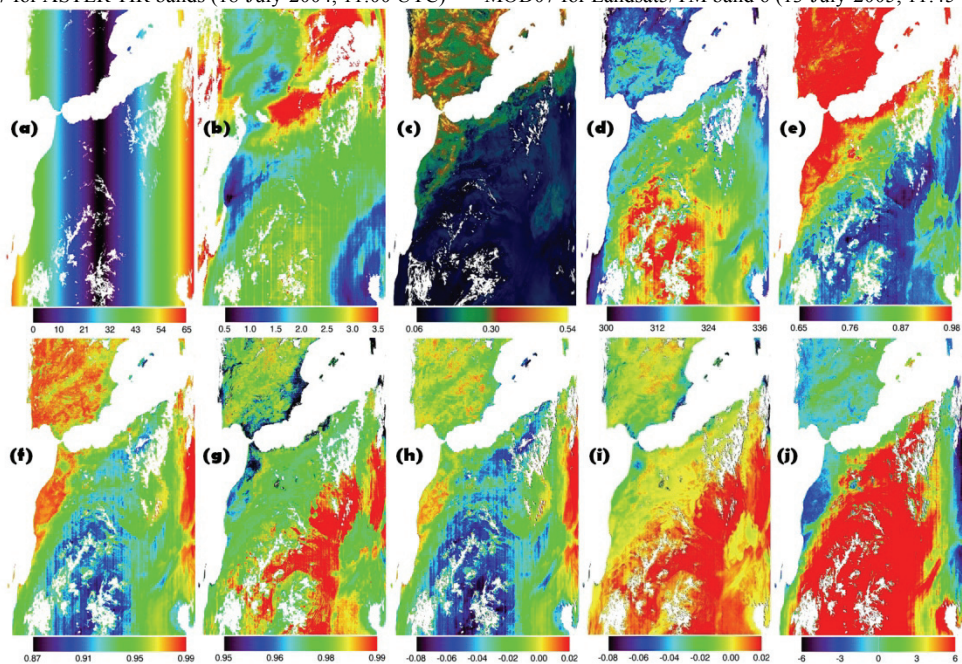
FIGURES IN COLOUR



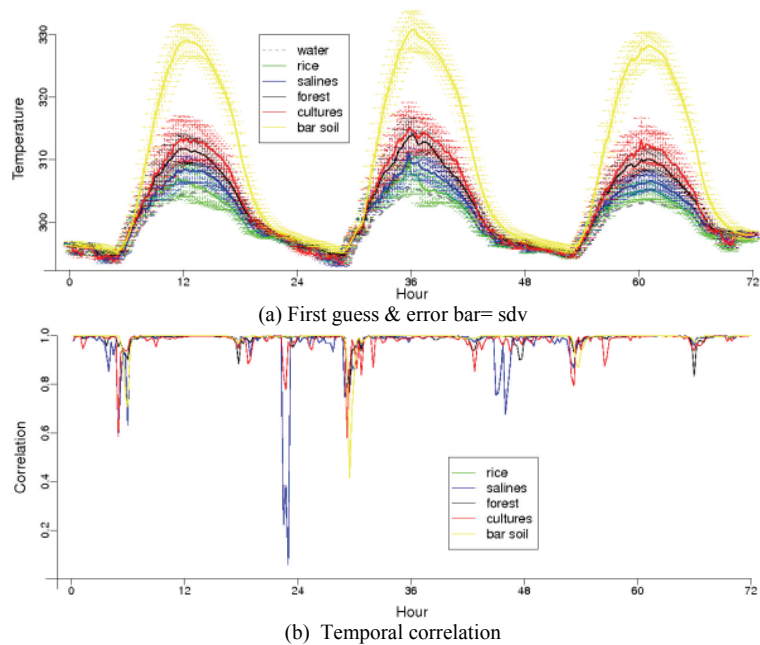
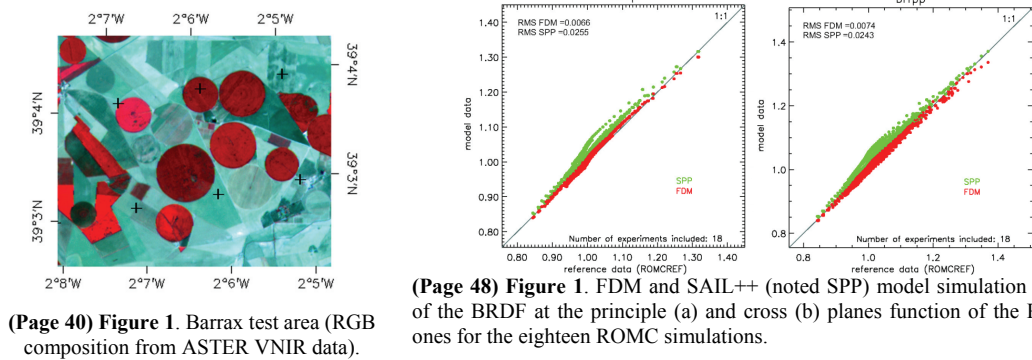
(Page 41) **Figure 5.** Atmospheric parameters obtained from MOD07 for ASTER TIR bands (18-July-2004, 11:00 UTC)



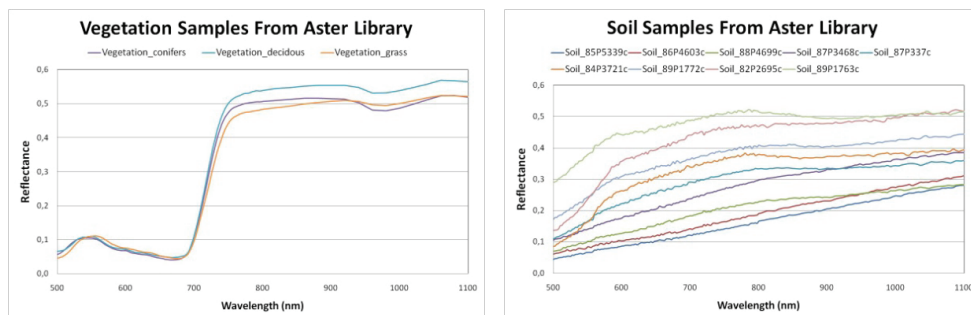
(Page 41) **Figure 6.** Atmospheric parameters obtained from MOD07 for Landsat5/TM band 6 (13-July-2005, 11:45 UTC).



(Page 42) **Figure 7.** Retrievals from MODIS data acquired on 18 July 2004 (1km): a) view angle in degrees, b) water vapor in cm (MOD05), c) NDVI from TOA reflectances (MOD021KM), d) TES-LST e) TES- ϵ at b29 (8.5 μ m), f) TES- ϵ at b31 (11 μ m), g) TES- ϵ at b32 (12 μ m), h) TES minus MOD11 ϵ at b31, i) TES minus MOD11 ϵ at b32, j) TES minus MOD11 LST.

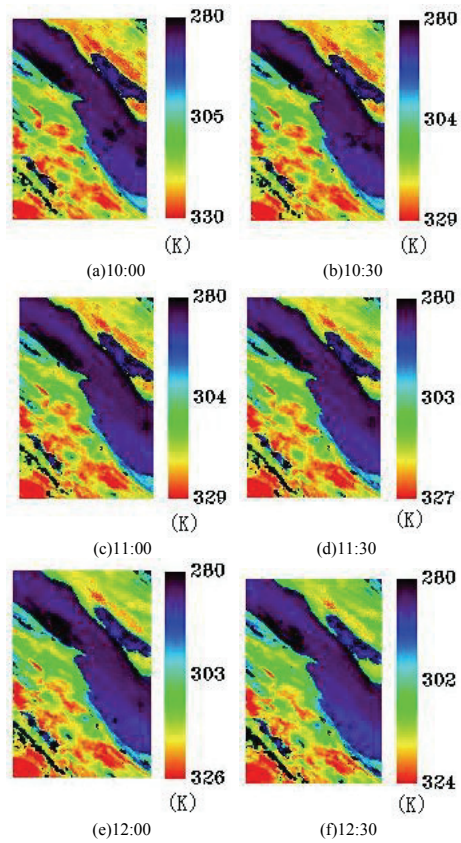


(Page 53) Figure 2. Temperature statistics for the six vegetation classes. In the first subfigure the first guess variation is plotted as well as an error bar corresponding to the std value. In the second subplot, the temporal correlation is between times t and $t+1$.

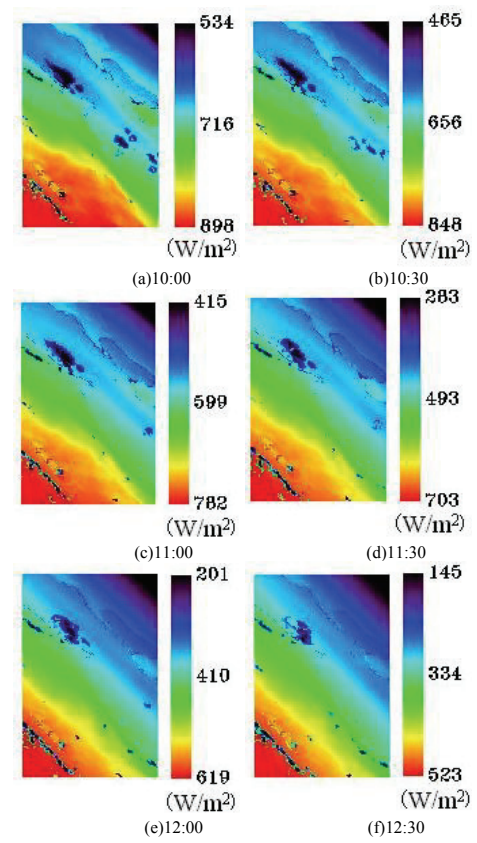


(Page 74) Figure 1 Vegetation samples from Aster spectral library used to characterize the vegetation covers.

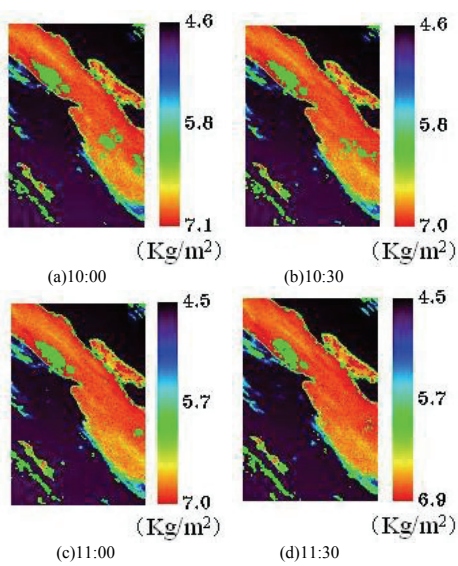
(Page 74) Figure 2 Soil samples from Aster spectral library used to characterize the soil covers.



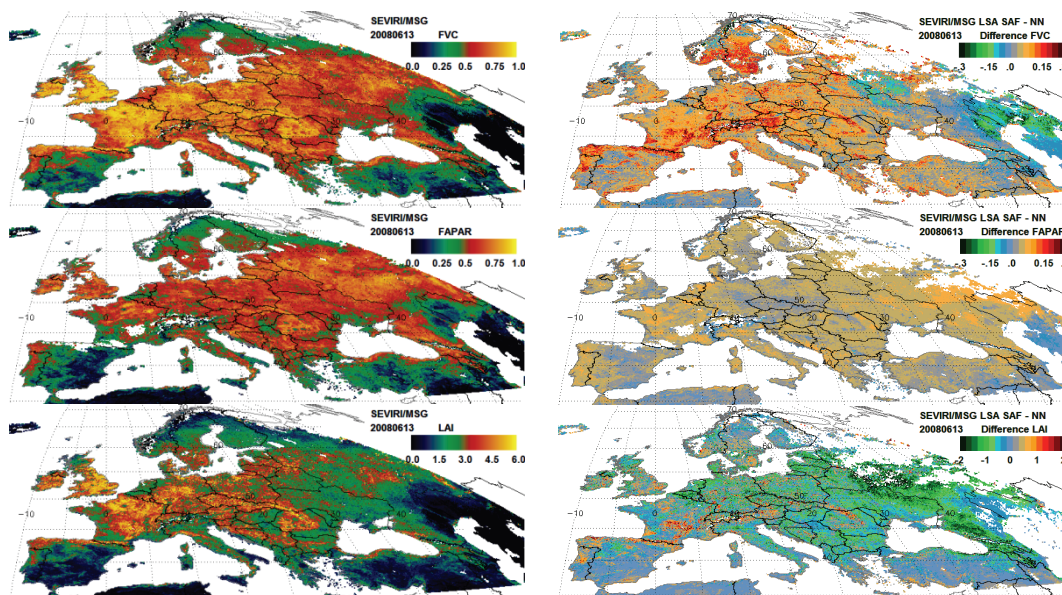
(Page 97) Figure 2 Time serial land surface temperature



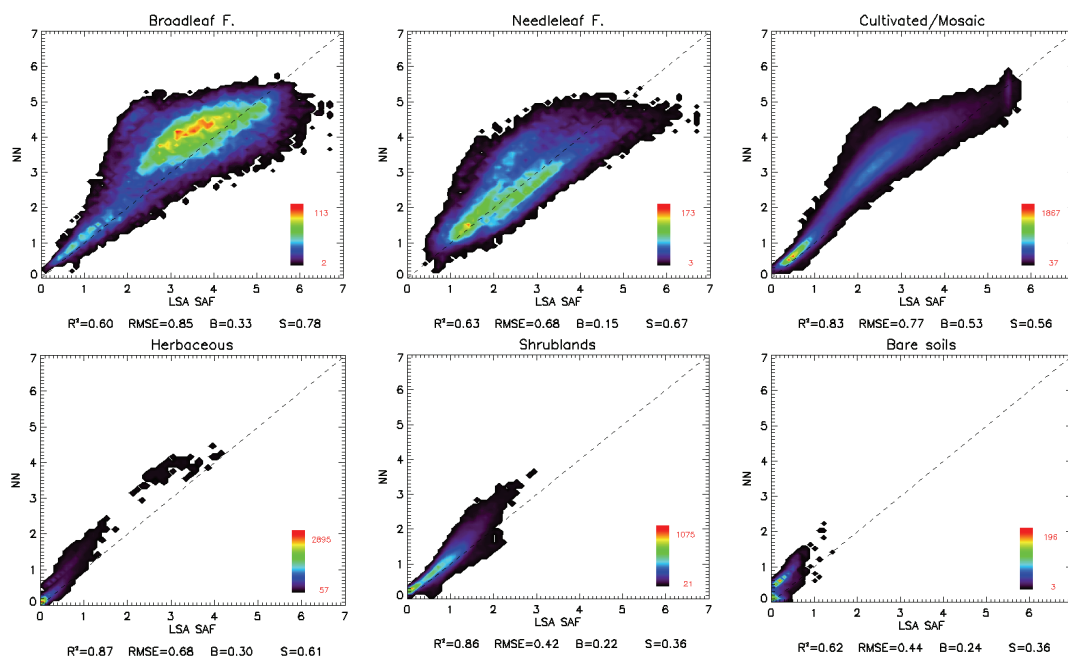
(Page 97) Figure 3 Time serial surface shortwave radiation



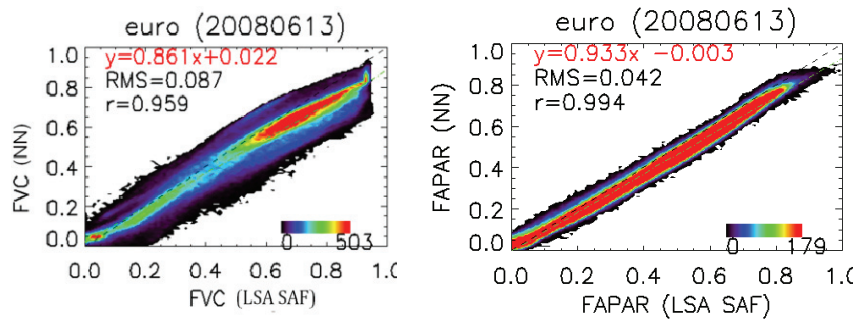
(Page 98) Figure 4. Soil moisture inverted



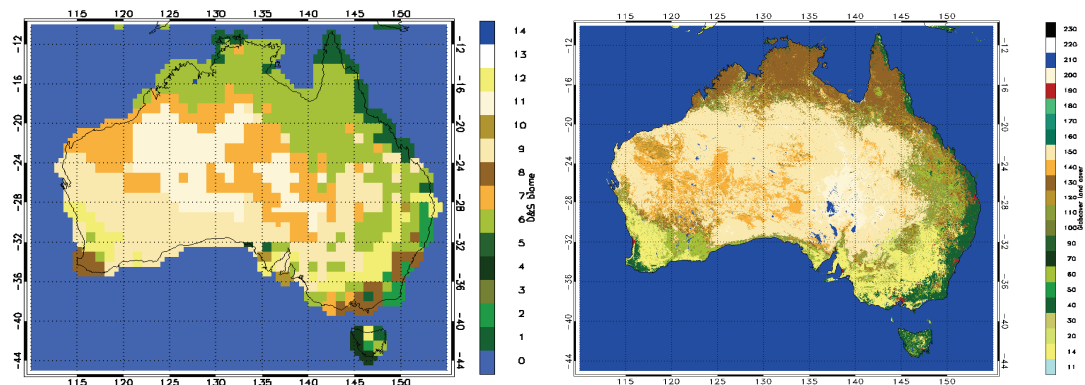
(Page 101) Figure 1. Left: LSA SAF FVC, FAPAR and LAI maps of Europe for the date 2008/06/13. Right: maps of differences of the comparison of LSA SAF and neural network (NN) FVC, FAPAR and LAI estimates.



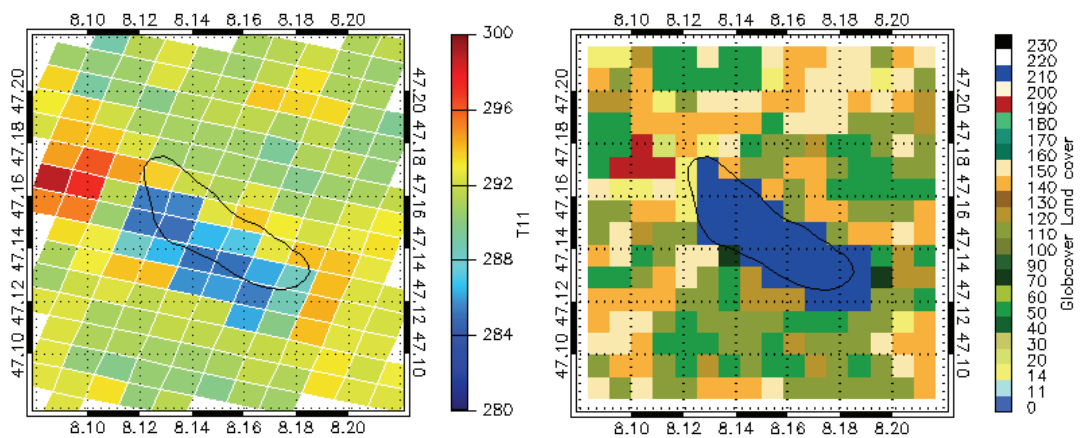
(Page 102) Figure 3. Density scatter plots of the biome class comparison of NN and LSA SAF LAI estimates of Europe for the date 2008/06/13.



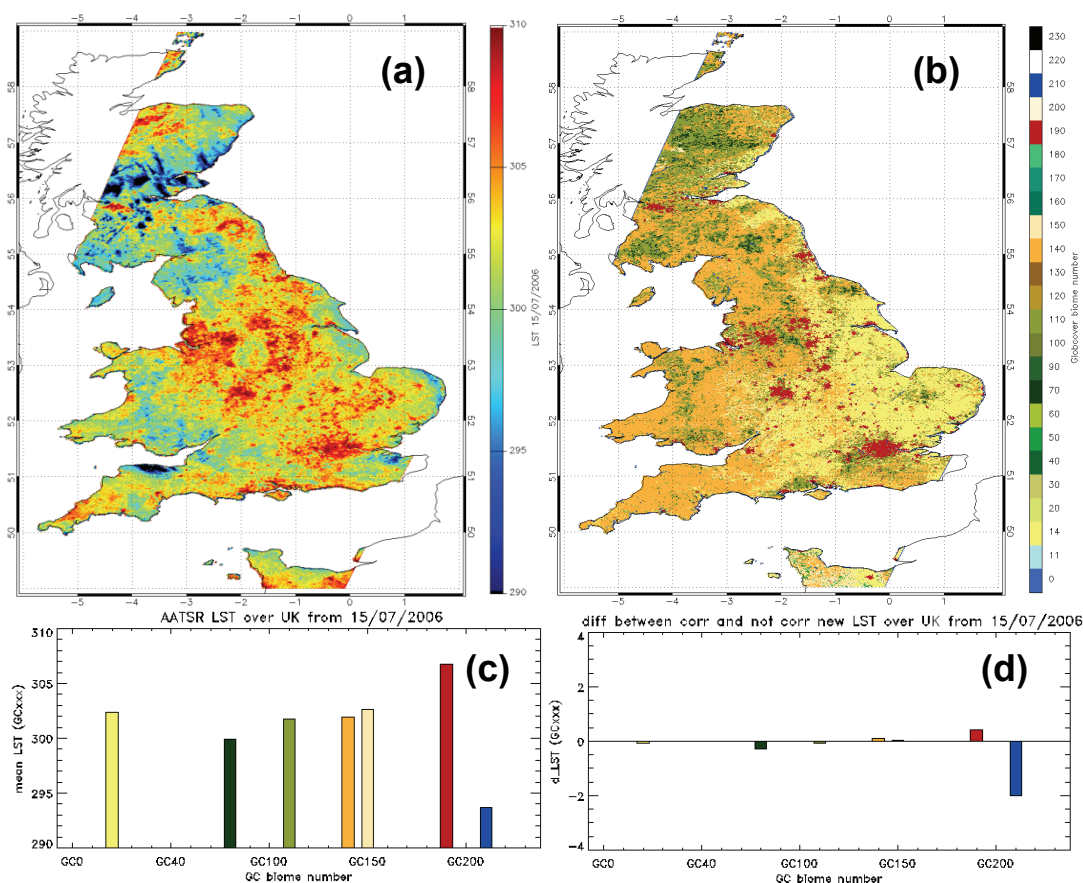
(Page 101) **Figure 2**
Density scatter plots of
neural network (NN)
and LSA SAF FVC and
FAPAR estimates of
Europe for the date
2008/06/13.



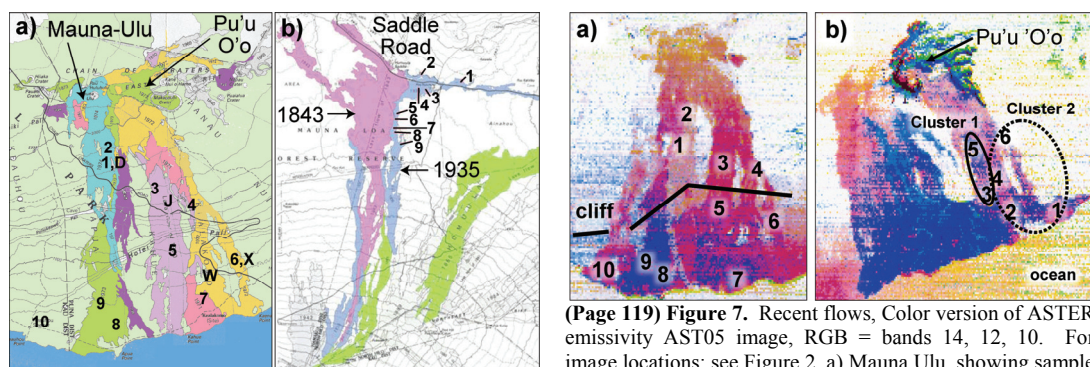
(Page 106) **Figure 2** left: Global auxiliary biome map for the operational AATSR LST retrieval from based on (Dorman, et al., 1989); right: Globcover biome map for Australia as the new biome map for the LST retrieval.



(Page 107) **Figure 3** left: Pixels of the day-time AATSR brightness temperature at 11 μ m for Lake Sempachersee from 5th May 2008; black solid line show the coast line from NGDC NOAA. Right: associated Globcover map.

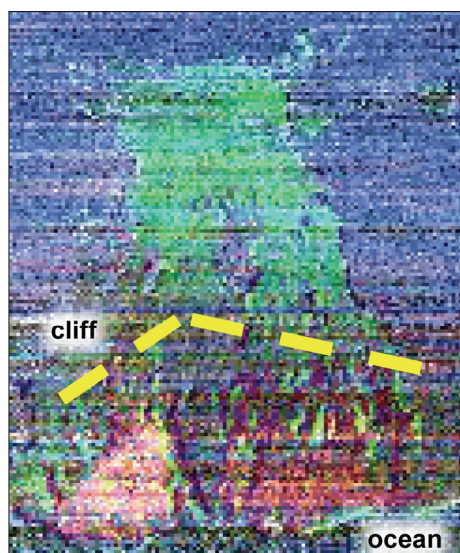


(Page 109) **Figure 4** (a) New AATSR LST over UK from 15th July after shift correction of the Globcover biome map of 1 AATSR pixel forward and 1 pixel right to the swath direction; (b) associated GC biome map after mentioned shift correction; (c) Mean LST for UK in dependence on the GC biome type, in order to avoid cloud contamination, only LST ≥ 290 K have been taken account for the mean calculation; (d) Difference of the mean LST with and without shift correction.

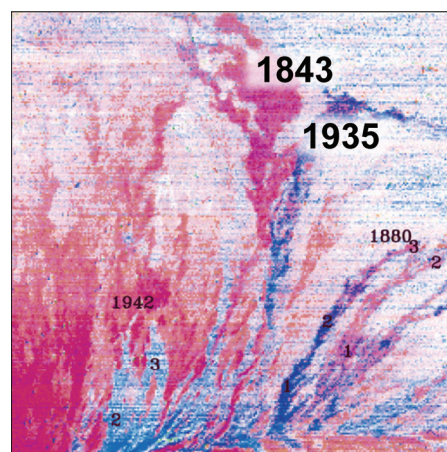


(Page 118) **Figure 3.** Color version of detailed flow maps at sample sites. a) Mauna Ulu study area showing sample sites #1-10 and D, J, W, X and Pu'u 'O'o. b) Mauna Loa-Mauna Kea saddle area showing sample sites (#1 - 9) on the 1935 and 1843 flows. After U.S. Geologic Survey (1986).

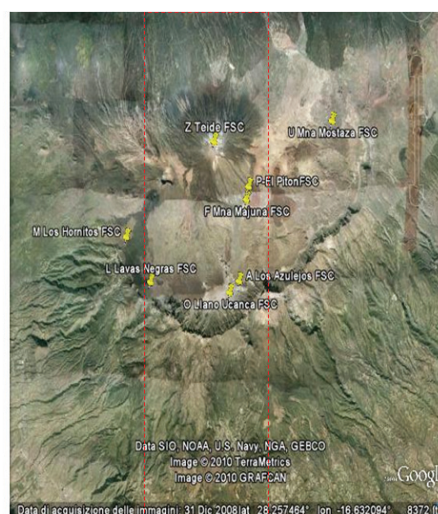
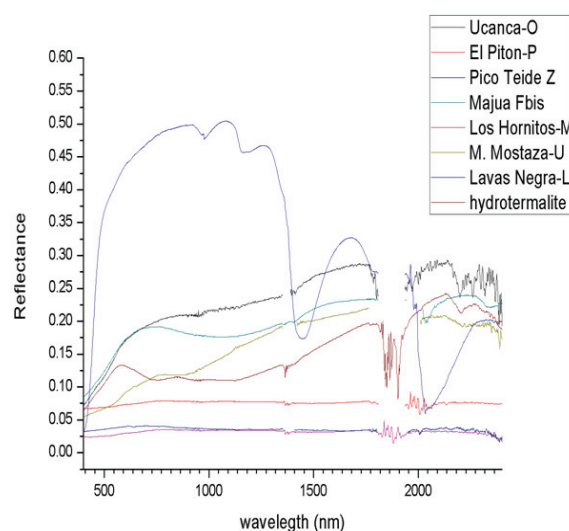
(Page 119) **Figure 7.** Recent flows, Color version of ASTER emissivity AST05 image, RGB = bands 14, 12, 10. For image locations: see Figure 2. a) Mauna Ulu, showing sample sites above and below the cliff or pali. b) Pu'u 'O'o, showing sample sites from two spectral groups of lava - Cluster 1 (red) and Cluster 2 (blue).



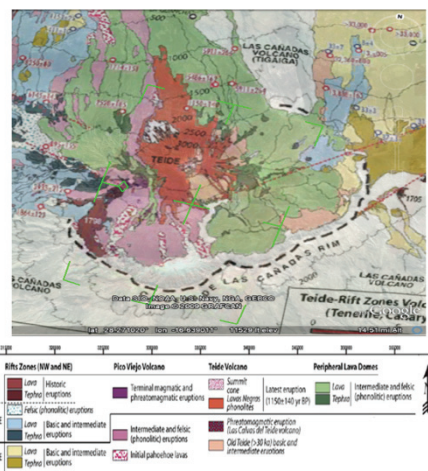
(Page 120) **Figure 9.** Color version of temporal ratio image, Mauna Ulu, 2008 ÷ 2000 RGB=bands 14, 12, 10. Blue, no change; green near Mauna Ulu and red near coast change.



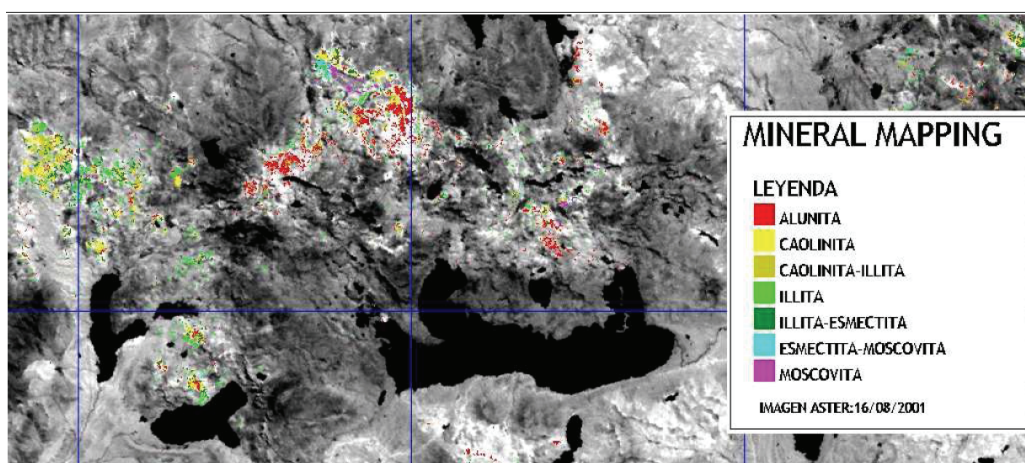
(Page 121) **Figure 10.** Color version of AST05 image showing saddle flows, Mauna Loa. RGB=bands 14,12,10. Red 1843 flow; blue 1935 flow. Numbers show sample sites.



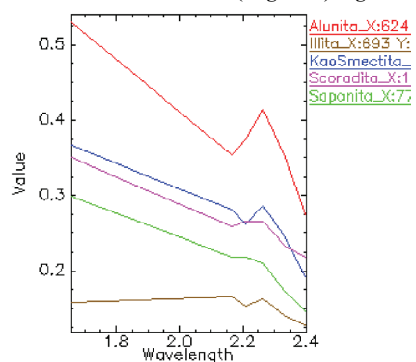
(Page 123) **Figure 1.** Ground truth reflectance spectra acquired by ASD FieldSpec® (left). The positions of the indicated points were found using latitude and longitude coordinates within Google Earth™



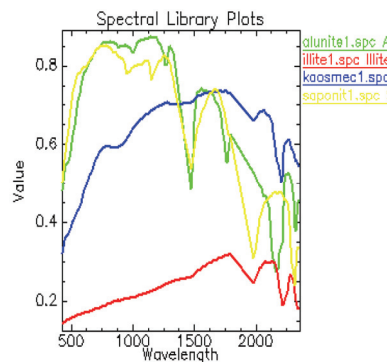
(Page 125) Figure 6. Teide Volcano geological map.



(Page 141) **Fig.3.** Imagen Aster, clasificada con el método SAM



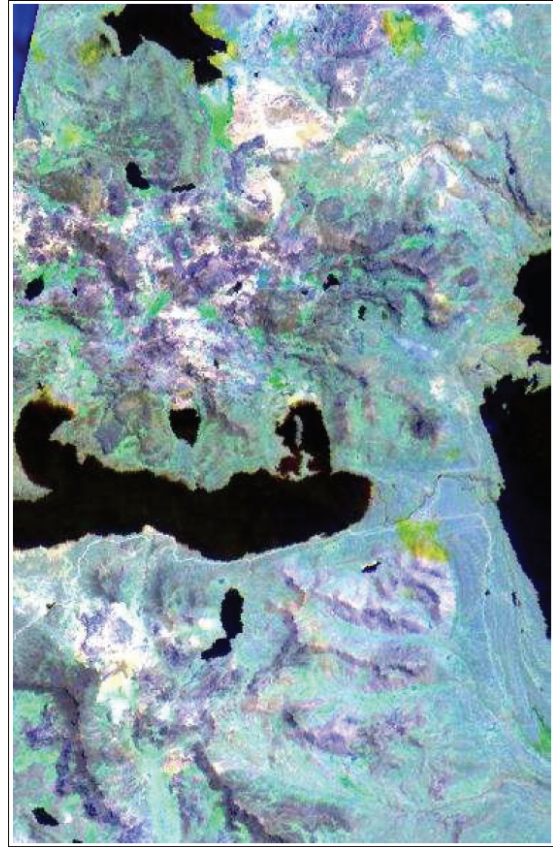
(Page 142) Fig.6 a. Firms espectral determinadas.



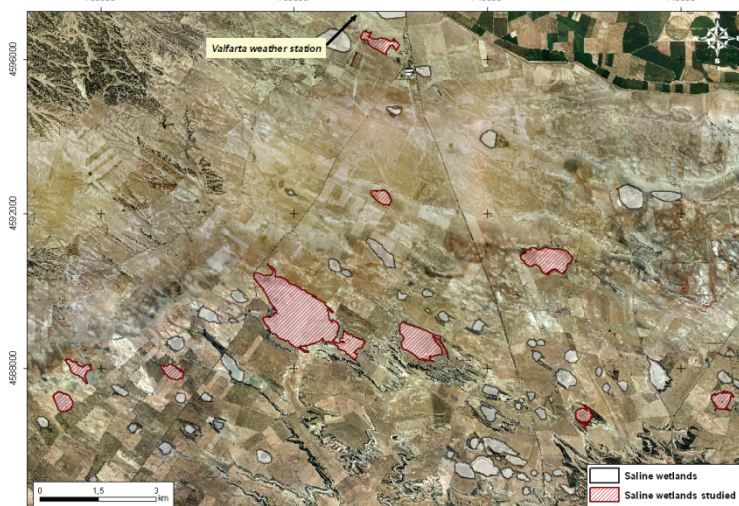
(Page 142)Fig.6b. Firma espectrales



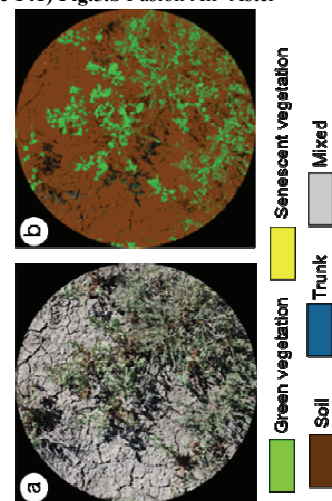
(Page 141) Fig.5.a Imagen Aster



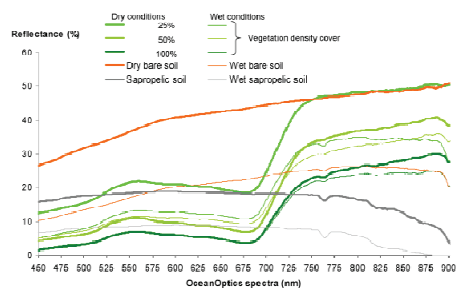
(Page 141) Fig.5.b Fusión Ali>Aster



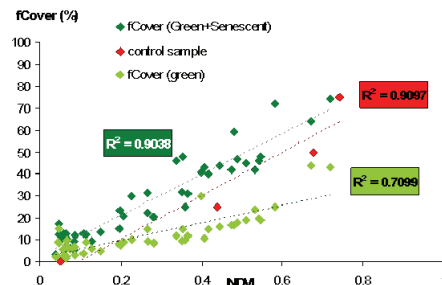
(Page 144) Figure 1. The saline wetlands studied in 2007 (blue striped filling), in 2008 (green striped filling), and in both years (red striped filling)



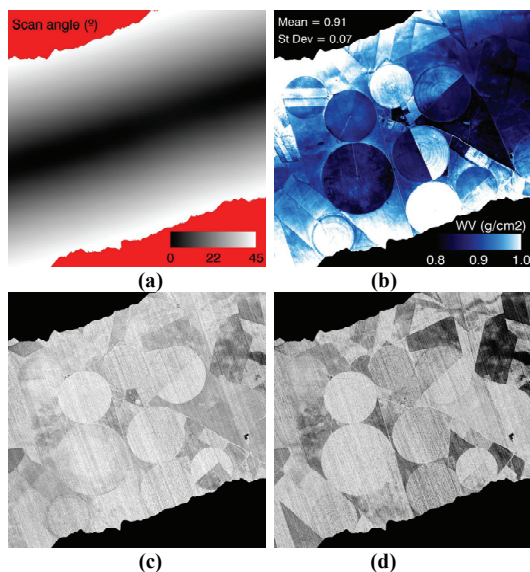
(Page 145) Figure 2. (a): Photograph of a sampled point (field of vision adjusted). (b): CanEye classification in five classes.



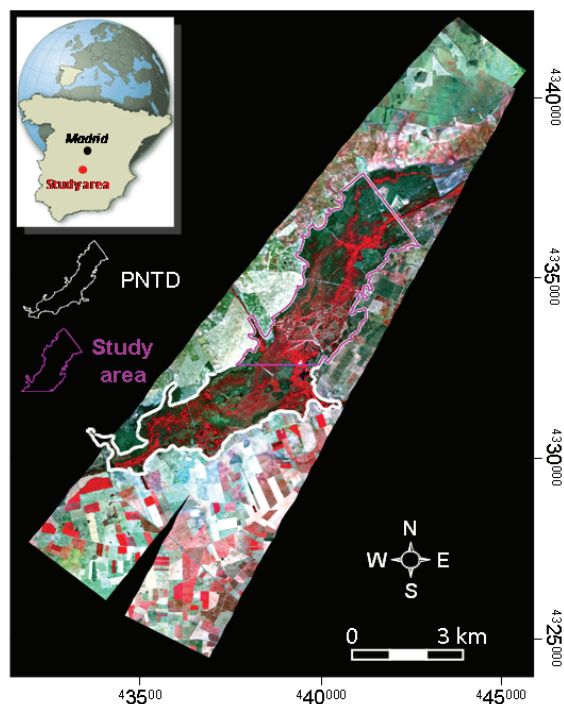
(Page 145) Figure 3. Reflectance of soil and vegetation (different density cover) under dry and moist conditions.



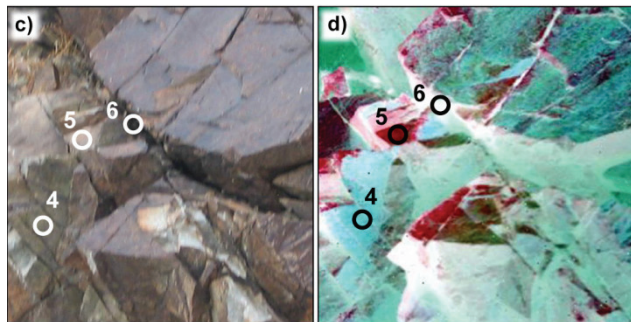
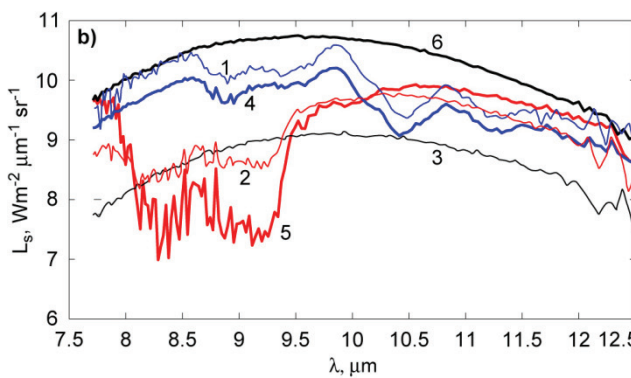
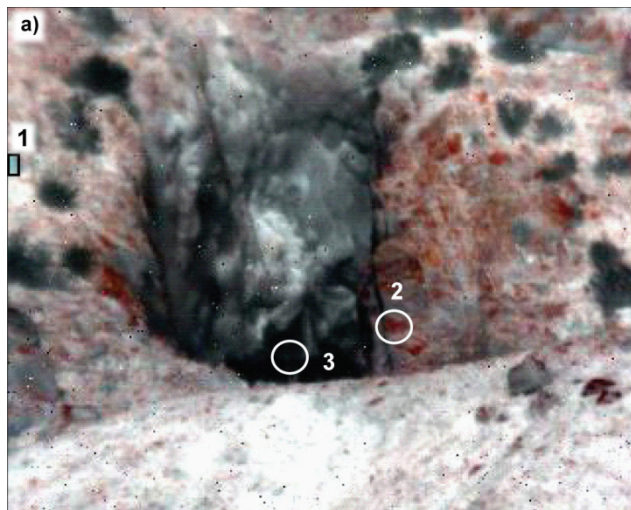
(Page 146) Figure 4. Regressions of $fCover$ on NDVI, for control sample (in red), green (in light green) and green plus yellow-green (in dark green) fraction cover.



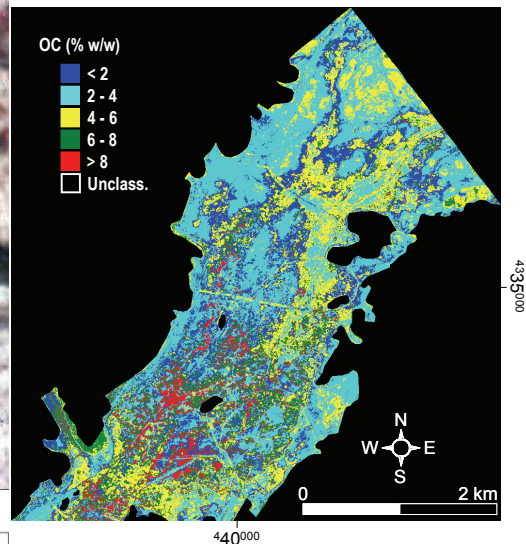
(page 156) Figure 3. a) AHS scan angle, b) atmospheric water vapor content at pixel level for the flight altitude, c) LSE obtained with TES algorithm after atm corr using one single value for atmospheric parameters over the whole image and d) LSE/TES image obtained after atm corr in a pixel-by-pixel basis.



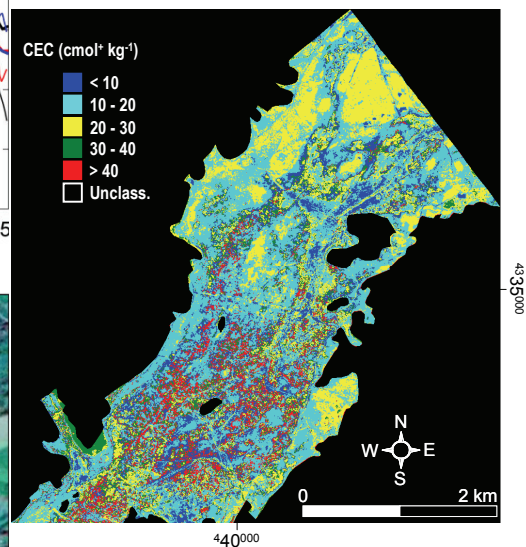
(page 182) Figure 1. Study area of the Las Tablas de Daimiel wetland National Park acquired with HyMap on 12th August 2009 (false color composite using bands at wavelengths of 0.833, 0.661 and 0.558 μm in the red, green and blue channels).



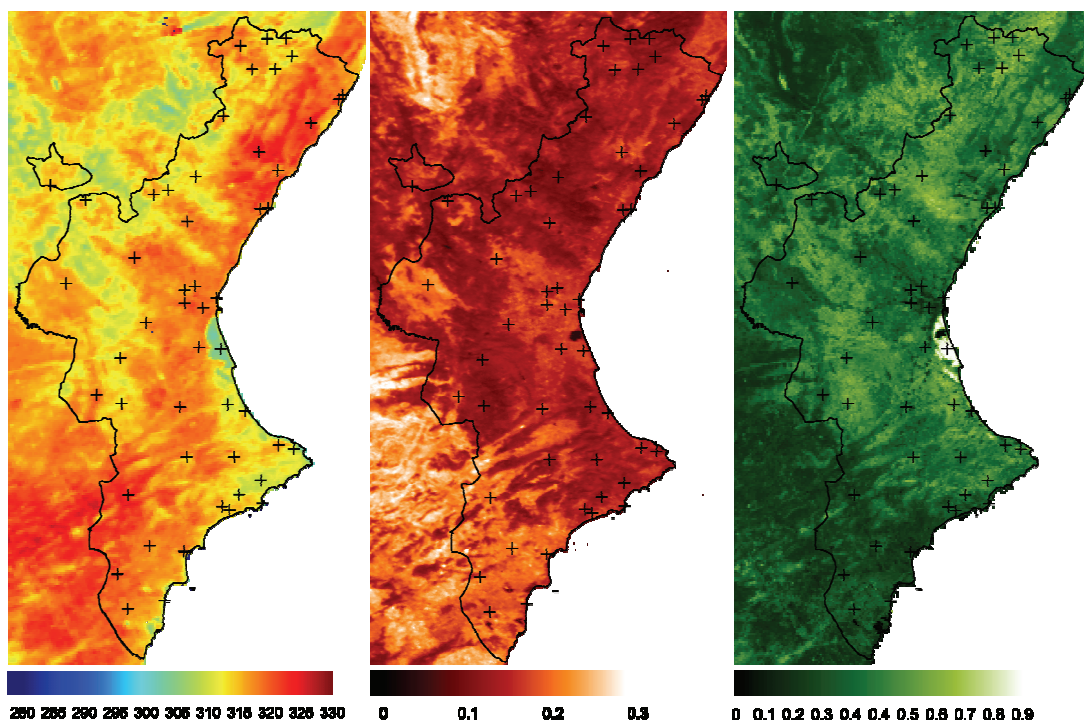
(Page 197) **Figure 1.** Telops, Inc., Hyper-Cam TIR data, Owens Valley, CA, USA (range: ~25 m). a) False-color image ~10 m across (RGB= 10.87, 8.59, 8.26 μm). b) Radiance spectra of schistose (1) and quartzite (2) wall rocks, the adit (3), schistose (4) and quartzite (5) parts of a 1 m rock fallen from the cliff, and deep cracks in the rock c) Photo of the rock (range: ~9 m; image is ~80 cm across). d) False-color TIR image of the same rock (RGB same as in a).



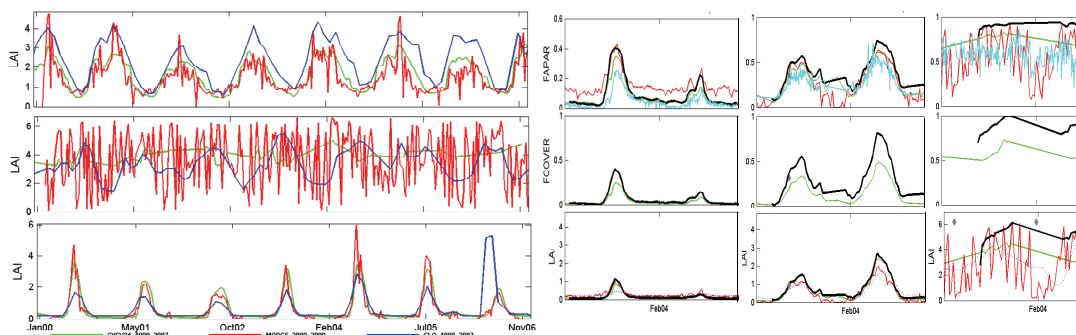
(Page 184) **Figure 5.** Spatial distribution of OC in the study area.



(Page 185) **Figure 7.** Spatial distribution of CEC in the study area.

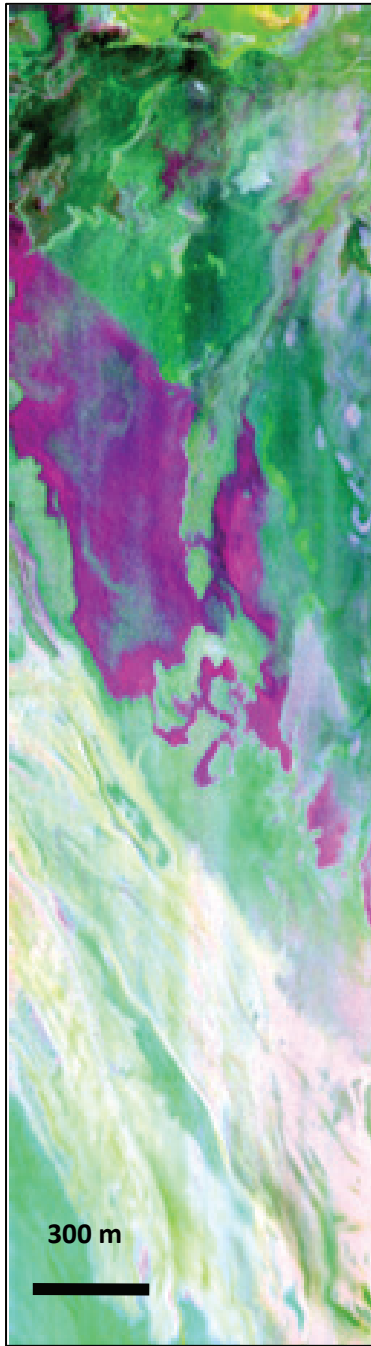


(Page 188) **Figure 1.-** From left to right, examples of: daytime LSTs (in K) retrieved from the daily 1-km MYD11A1 product (2009/07/24, 13:30-13:36UTC), albedo obtained from the 16-day 500-m MCD43A3 product (2009/07/28-2009/08/12), and NDVI obtained from the 16-day 1-km MYD13A2 product (2009/07/20-2009/08/04). The locations of the CEAM ground meteorological stations are shown with +.

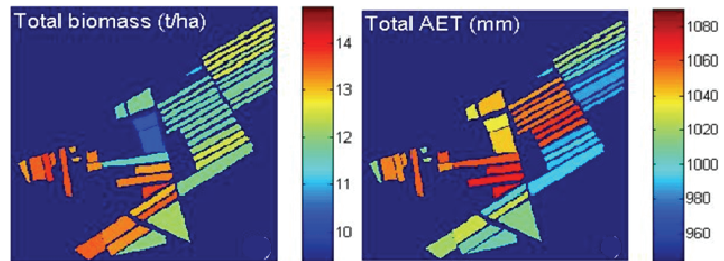


(Page 210) **Figure 4.** Example of *LAI* dynamics of CYCLOPES, MODIS and GLOBACARBON products for 3 typical sites.

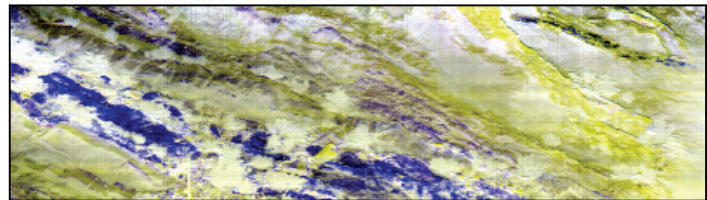
(Page 213) **Figure 12.** Temporal profiles of *LAI* (bottom), *FAPAR* (top) and *FCOVER* (middle) products: MODIS (red), CYCLOPES (green), GLOBACARBON (dashed blue), JRC-FAPAR (cyan) and GEOVI (black). Gourma grassland (left 15.32°; -1.55°), Fundulea crop land (centre 44.41°; 26.58°) and Tapa evergreen broadleaf forest (right 2.87°; -54.95°) sites are presented for years 2003-2004.



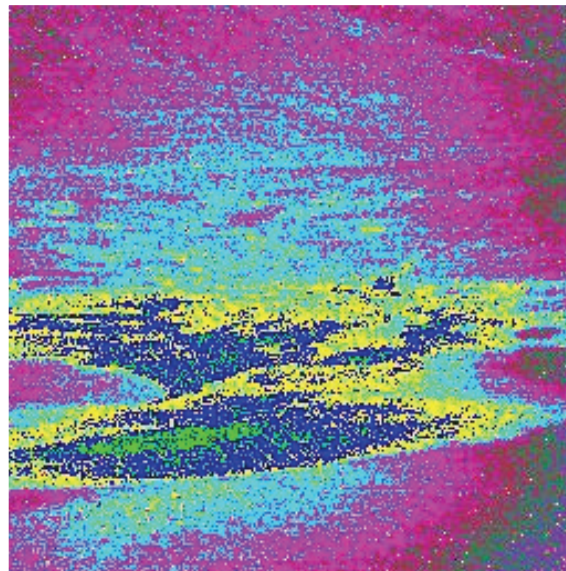
(Page 221) **Figure 1.** False-color image using SEBASS of Badwater Basin, Death Valley, CA [R: 8.28 μm , G: 9.55 μm , B: 8.59 μm]



(Page 217) **Figure 4.** Total biomass and evapotranspiration simulated by STICS from 1/1 to 30/9/2006 at farm scale over 47 grassland fields ($\sim 4\text{km}^2$). (Figure 4_S5.3)



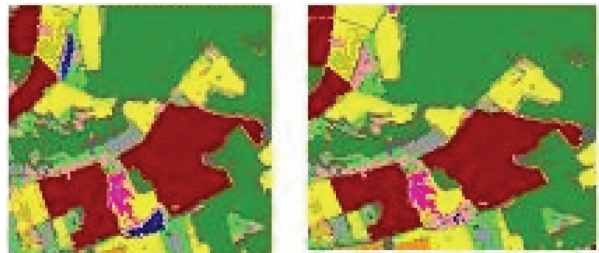
(Page 222) **Figure 3.** False color image using SEBASS of Hell's Gate, Death Valley, CA [R: 8.3 μm , G: 9.18 μm , B: 11.15 μm]



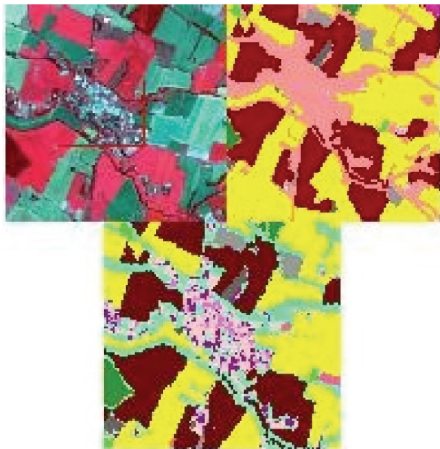
(Page 224) **Figure 10.** Ratio of 10 to 8 μm in uncorrected TELOPS radiance data. White circle indicates that radial pattern is not strictly circular, indicating some additional path length or mineralogic effects on spectra.



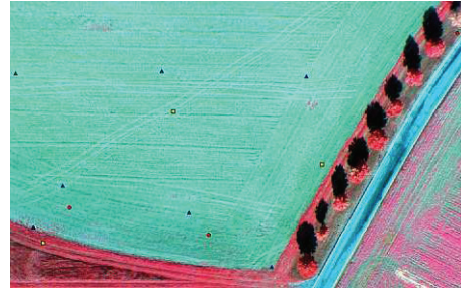
(Page 295) **Figure 1:** right, 9 date classification (grey frame: cloud corresponds to Built), left this classification merged without February classification → cloud is removed



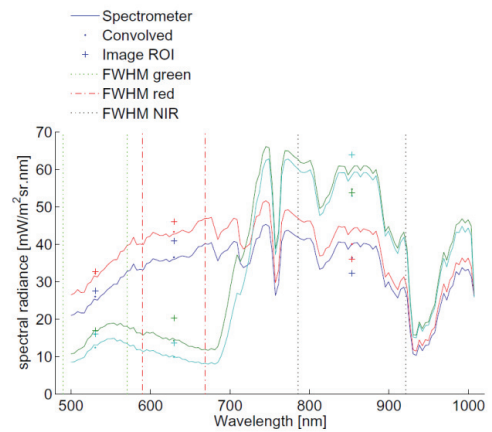
(Page 295) **Figure 2:** right, previous fusion (figure 1), left, fusion with NDVI classification; small lakes appear (dark blue), previously classified as mineral surfaces



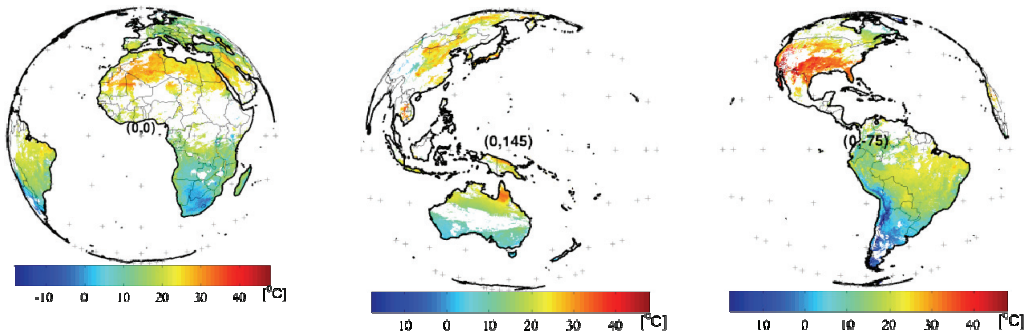
(Page 295) **Figure 3:** (a) Colored composition 08/07/10 Formosat (b) final classification (c) fusion with unsupervised classification to distinguish hedges and different stage of Built



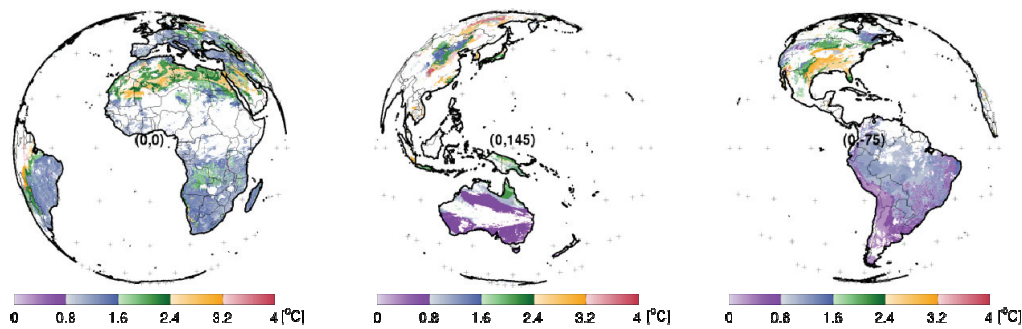
(Page 266) **Figure 4** Example of georeferenced colored infrared mosaic (NIR-Red-Green).



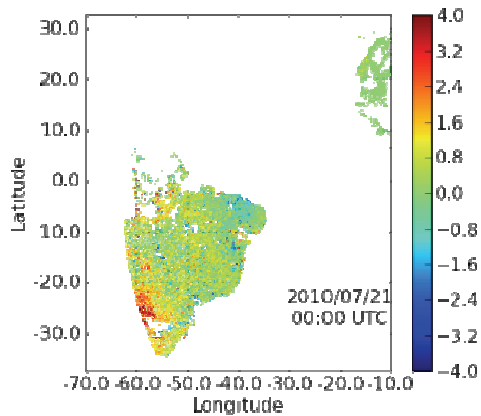
(Page 267) **Figure 5** Example of spectrometer data with corresponding image data.



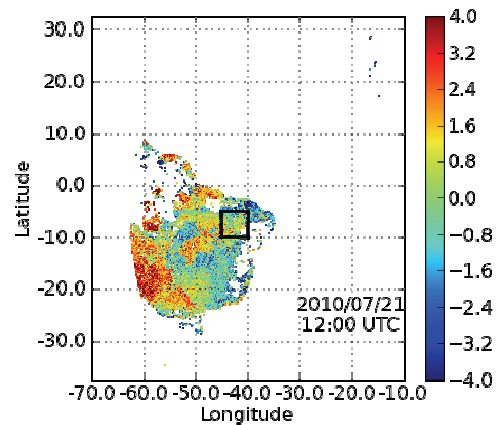
(Page 300) **Figure 2** – LST Estimated for 21st July 2010 at 12UTC.



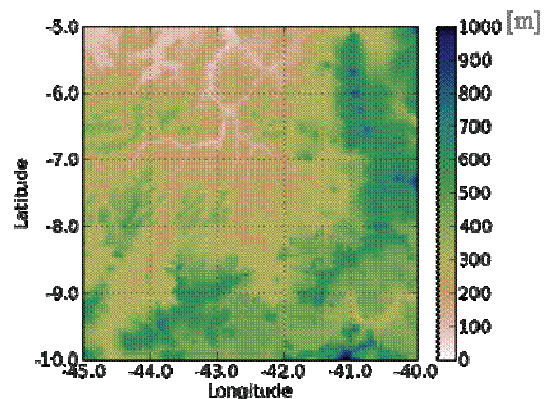
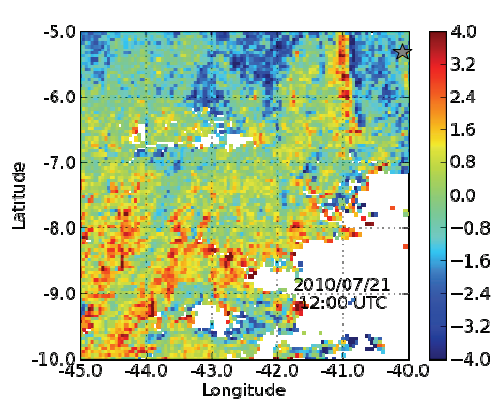
(Page 301) Figure 3 – Map of LST error bar [°C] for the 21st July 2010 at 12UTC.



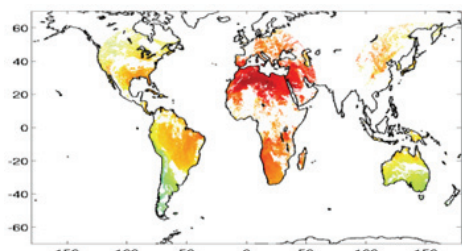
(Page 301) Figure 4 – Difference between LST from MSG and GOES [°C] for 21st July 2010 at 00UTC.



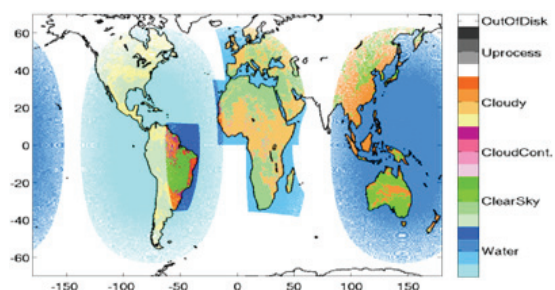
(Page 301) Figure 5 – Same as Figure 4 but at 12UTC.



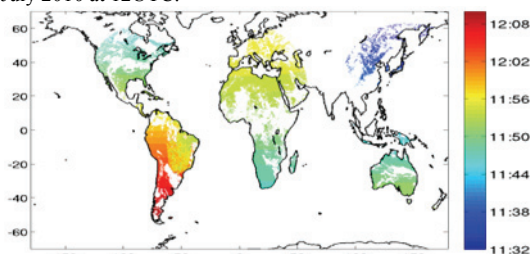
(Page 302) Figure 6 – Zoom over the field of differences between LST from and MSG and GOES [°C] for 21st July 2010 at 12UTC (left panel) and the Elevation Map for the same geographical region (right panel).



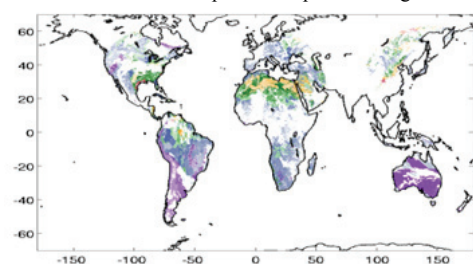
(Page 302) **Figure 9a** - Global LST product [°C] 21st July 2010 at 12UTC.



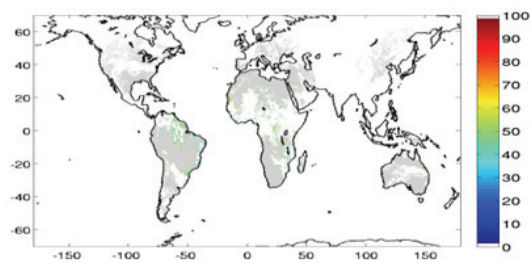
(Page 302) **Figure 9b** Quality Flag corresponding to the LST estimate depicted in Figure 9a. Blues correspond to water pixels; greens correspond to clear sky regions; pinks correspond to could contaminated pixels; oranges correspond to cloudy areas; greys are the unprocessed pixels and white represent the out of disk areas. The 4 graded colours in each main class give information about the satellite(s). From light to dark: GOES, MSG, MTSAT and Multi-Mission.



(Page 302) **Figure 9c** - Time of sensed data (HH:MM) used to retrieve the LST product depicted in Figure 9a.



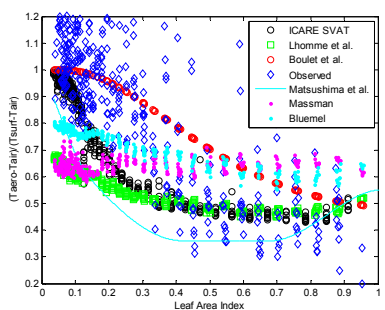
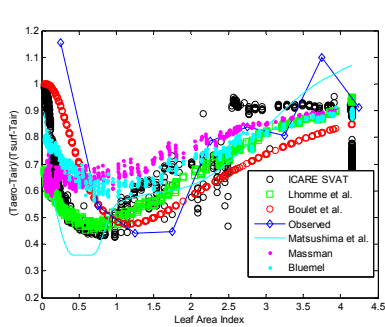
(Page 303) **Figure 9d** - Error Bars [°C] associated to the LST product depicted in Figure 9a.



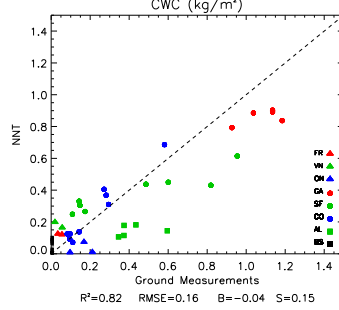
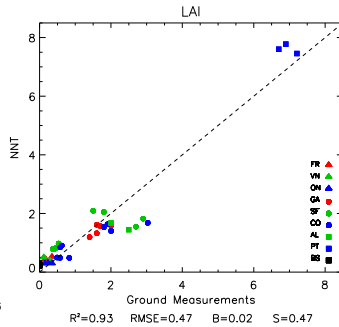
(Page 303) **Figure 9e** - Fraction of processed pixels used to retrieve the LST product depicted in Figure 9a.



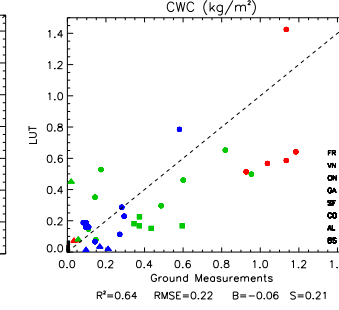
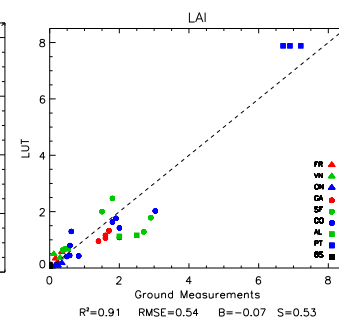
(Page 347) **Figure 4.** Visual assessment of the spatial correlation between the high spatial resolution GAI maps and the GAI estimations from MODIS for DoY: 94, 123 and 144 (from left to right). All GAI values use the same colour scale the goes from dark purple (GAI=0) to dark green (GAI=6) passing by a range of yellows. The images in the background are the respective Red channel of the original SPOT imagery used to derive the GAI maps.



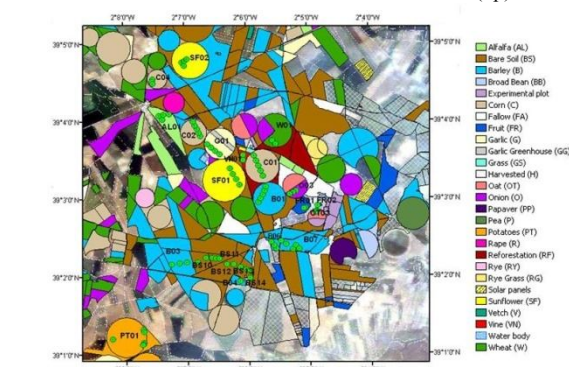
(Page 366) Figure 1a: β (LAI) relationships for the R3 B124 site; 1b: idem for LAI between 0 and 1.



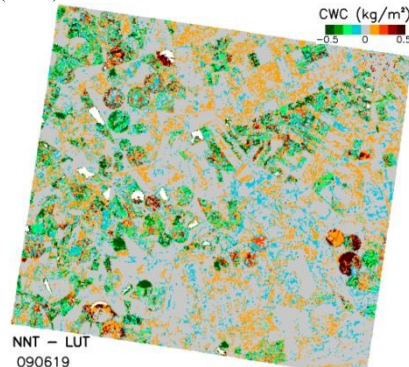
(Page 402) Figure 4. Comparison of NNT estimates with ground data for LAI (up) and for CWC (down)



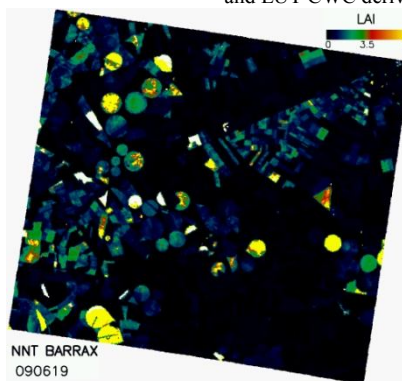
(Page 402) Figure 6. Comparison for classes between in-situ and LUT derived data



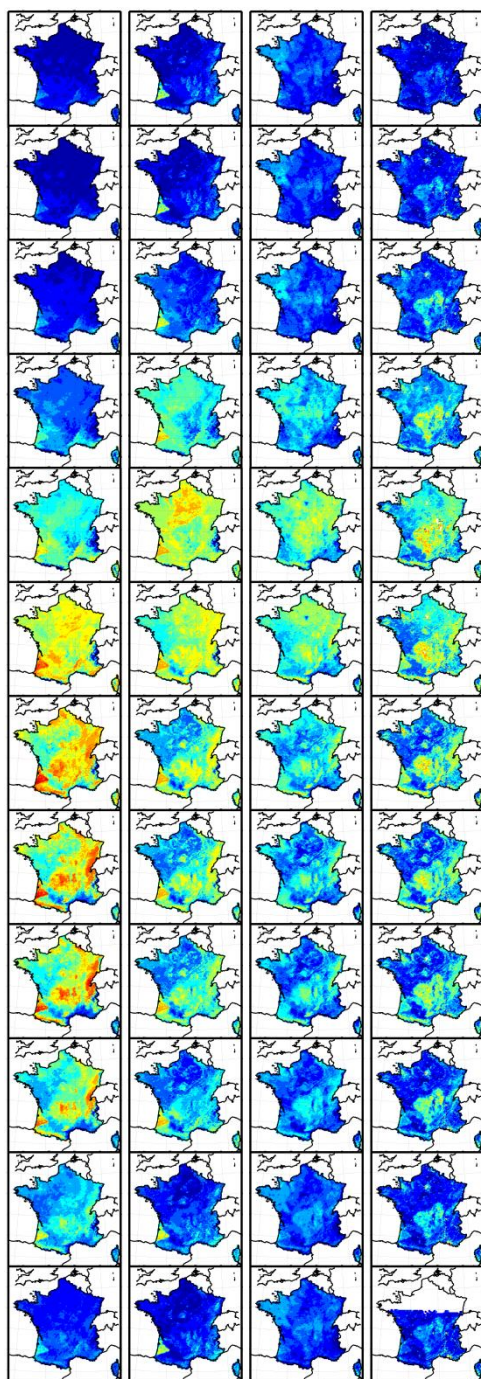
(Page 399) Figure 1. Land uses at Barrax area and ESUs location



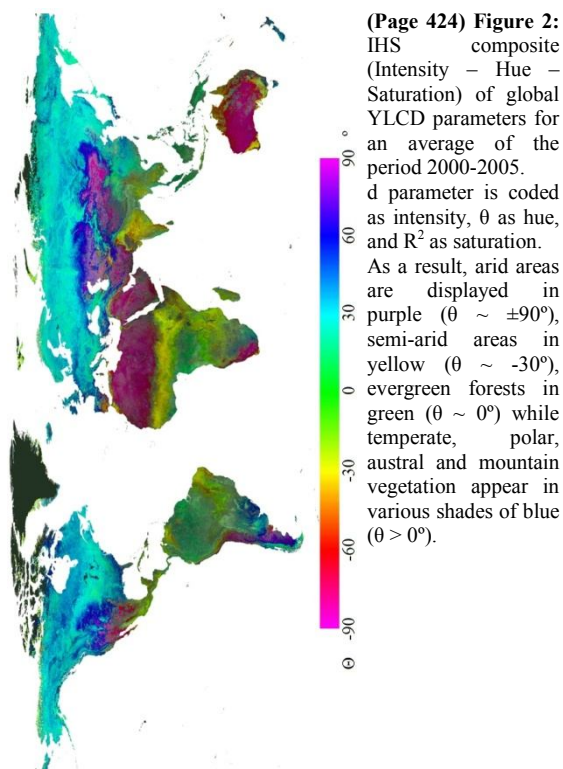
(Page 404) Figure 7. Differences between NNT and LUT CWC derived maps.



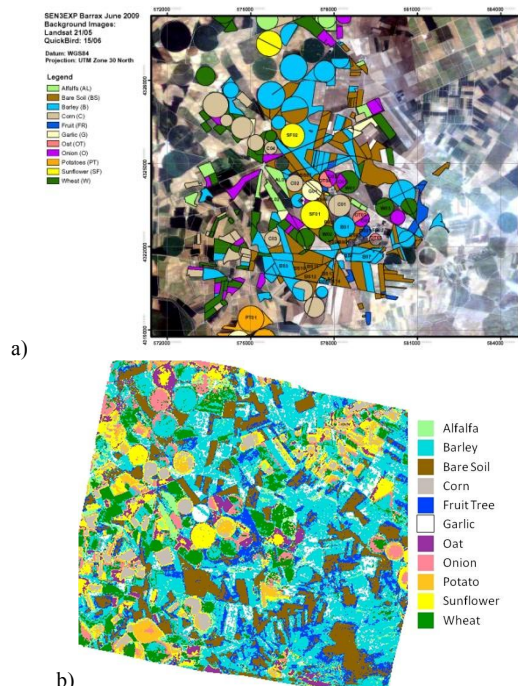
(Page 402) Figure 5. CWC (left) and LAI (right) derived map from neural network training and CHRIS data.



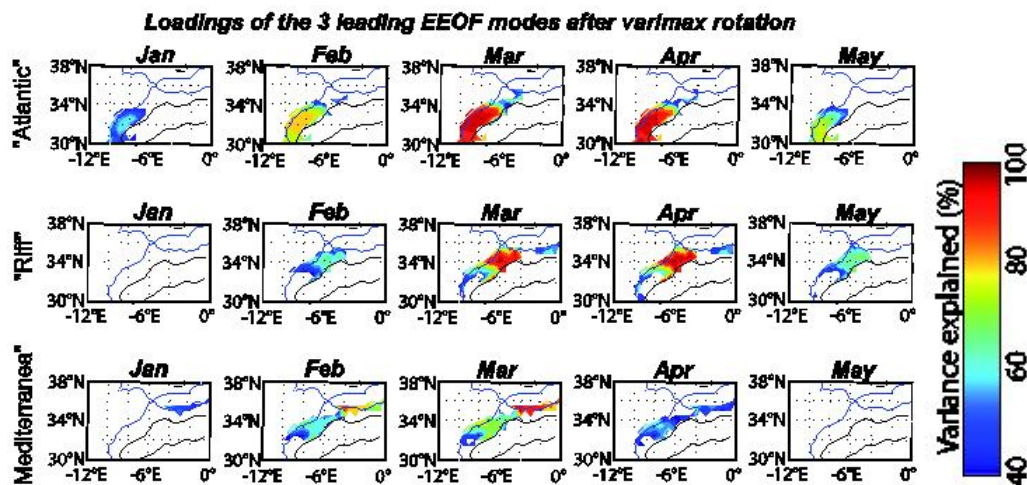
(Page 413) **Figure 1:** Monthly LAI climatology (2000-2007) derived from (from left to right) ISBA-A-gs, ORCHIDEE, CYCLOPES, MODIS. (Top) January to (bottom) December.



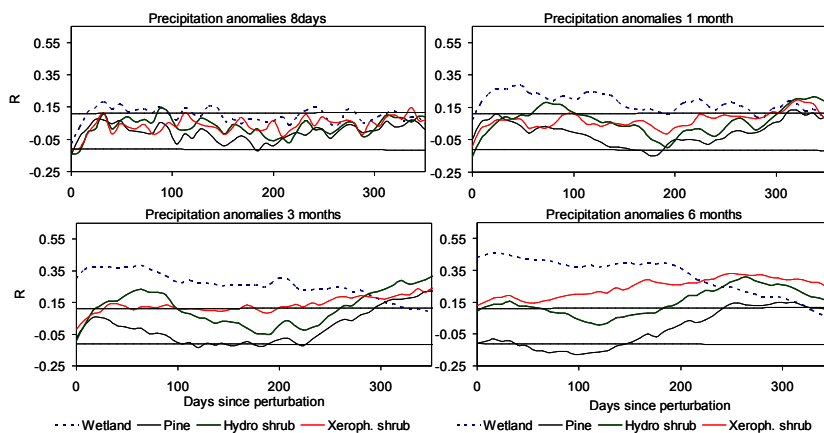
(Page 424) **Figure 2:** IHS composite (Intensity - Hue - Saturation) of global YLCD parameters for an average of the period 2000-2005. d parameter is coded as intensity, θ as hue, and R^2 as saturation. As a result, arid areas are displayed in purple ($\theta \sim \pm 90^\circ$), semi-arid areas in yellow ($\theta \sim -30^\circ$), evergreen forests in green ($\theta \sim 0^\circ$) while temperate, polar, austral and mountain vegetation appear in various shades of blue ($\theta > 0^\circ$).



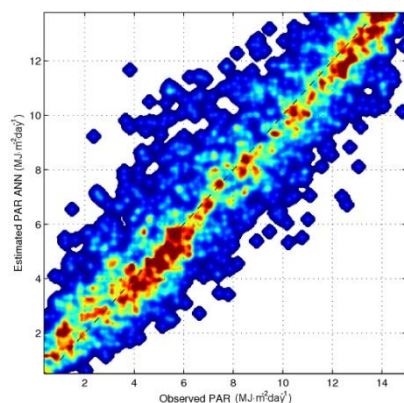
(Page 424) **Figure 3:** Nomenclature (a) and classification (b) of the Barrax (Albacete, Spain) area. The classification has been obtained by carrying out the YLCD method on one year of Landsat data from 2009.



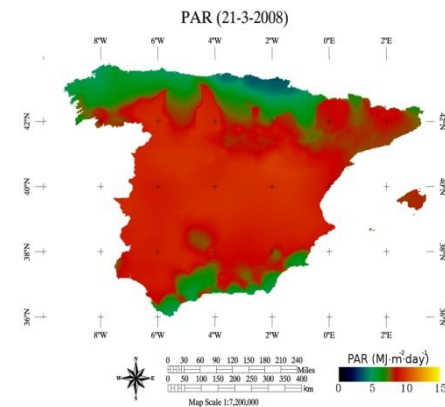
(Page 436) Fig.1 Loadings of rotated extended EOFs from the AVHRR/NDVI datasets over the 'Moroccan window' (30°N-36°N and 12°W-0°) during the 1982-2008 period for the three first modes in term of variance explained (12.1, 11.9 and 9.8 % of total variance, respectively). Mode 1 is located along the atlantic coast to the South West of the country, mode 2 occupy the Rif mountains near the Gibraltar channel and mode 3 is located along the mediterranean sea to the East. The maximum of variance explained for the three modes is around the peak of vegetation (March for mode 1 and 3 and April for mode 2).



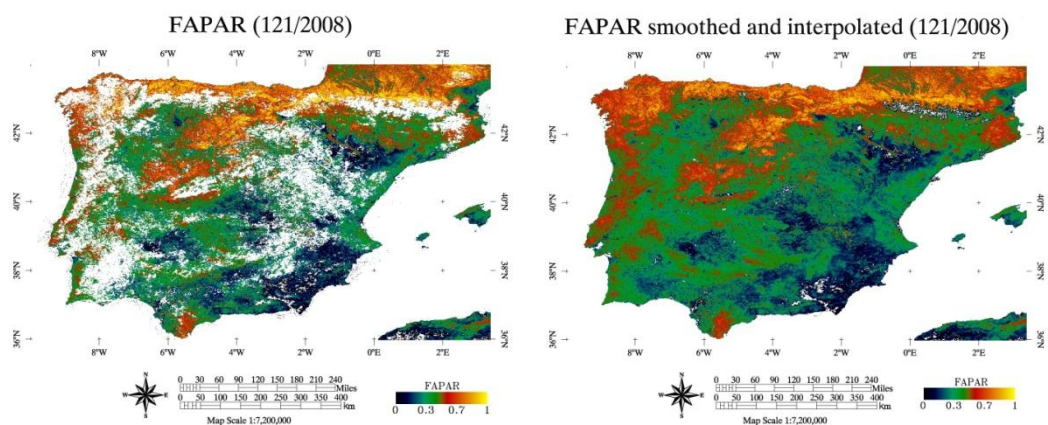
(Page 469) Figure 4: Cross-correlations between precipitation anomalies occurring at different time-scales and evapotranspiration anomalies. Lagged time since the beginning of the perturbation is shown in X axis. The value of R is significant ($p < 0.05$) above and below the horizontal lines.



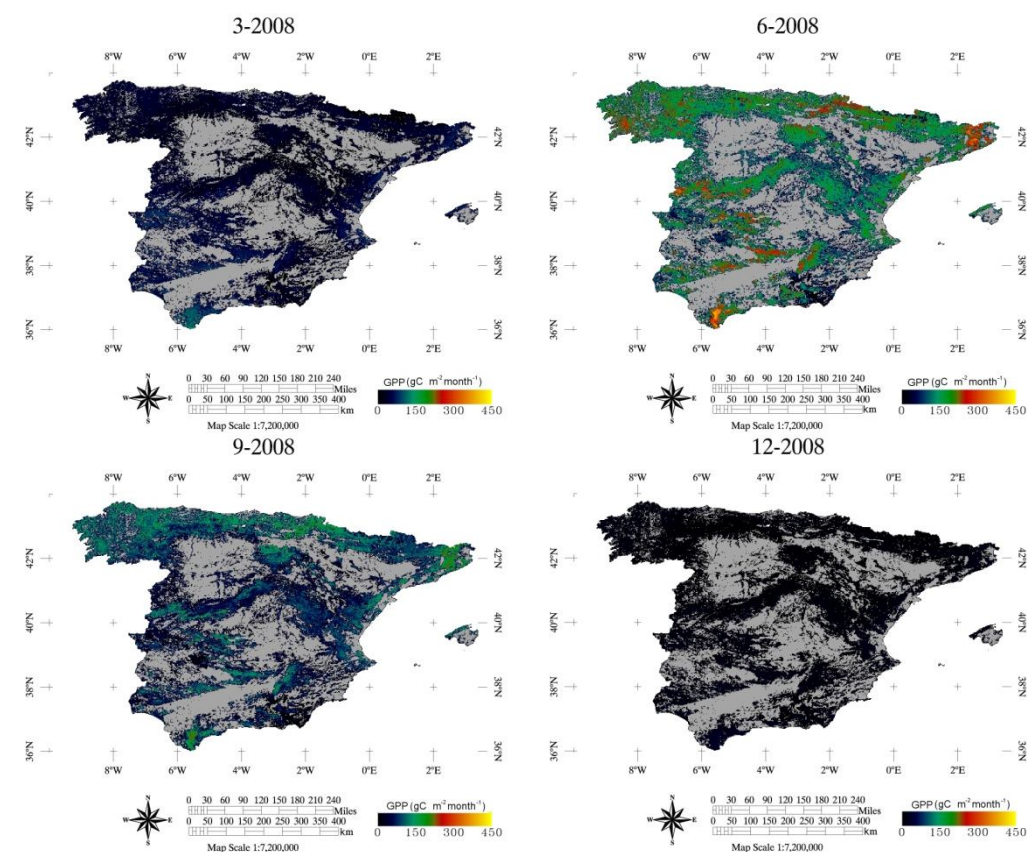
(Page 473) Figure 3. Scatterplot of the estimated vs. observed PAR with the ANN method.



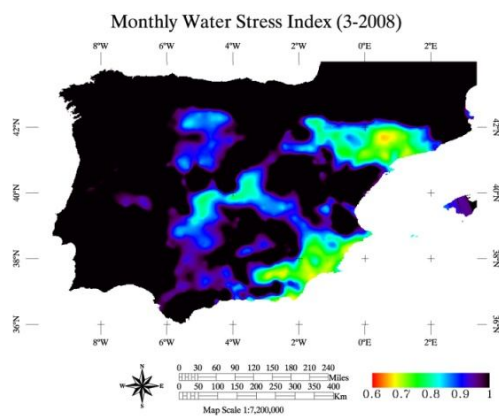
(Page 473) Figure 4. Example of the daily estimated PAR map at 1 km spatial resolution over Spain from the ANN method for 21th of March.



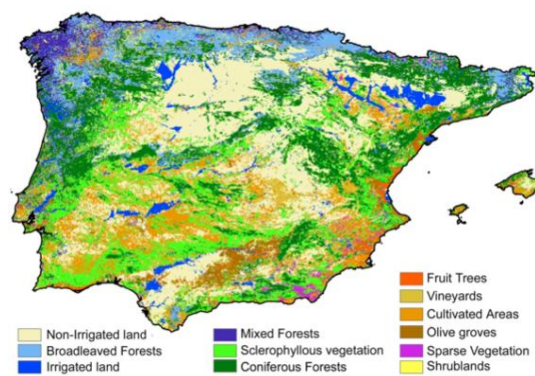
(Page 474) **Figure 5.** Original fAPAR estimates (top) for a day of spring, and filtered fAPAR (bottom) product from the LOESS approach.



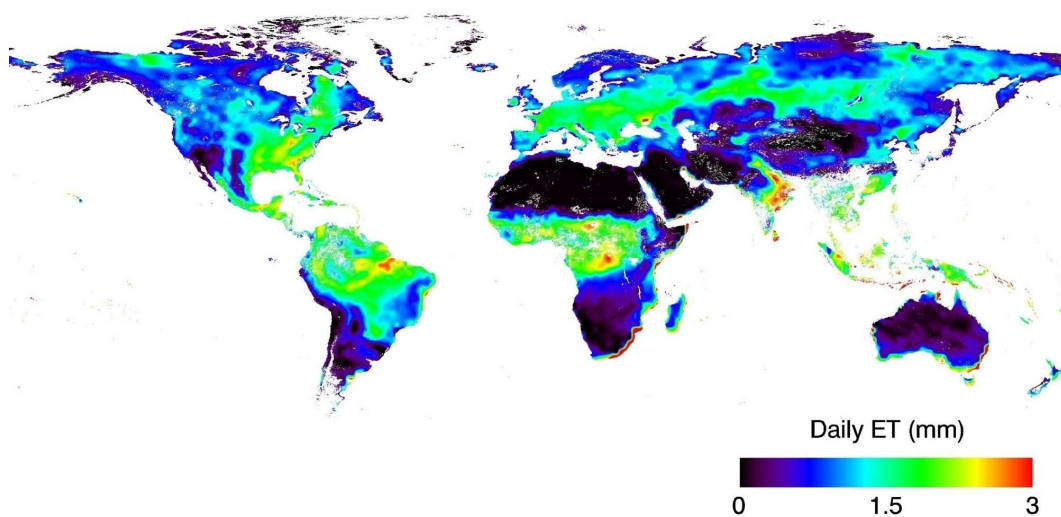
(Page 476) **Figure 9.** Examples of monthly GPP estimated for the different seasons. Grey: non-forestal areas, excluded from the study.



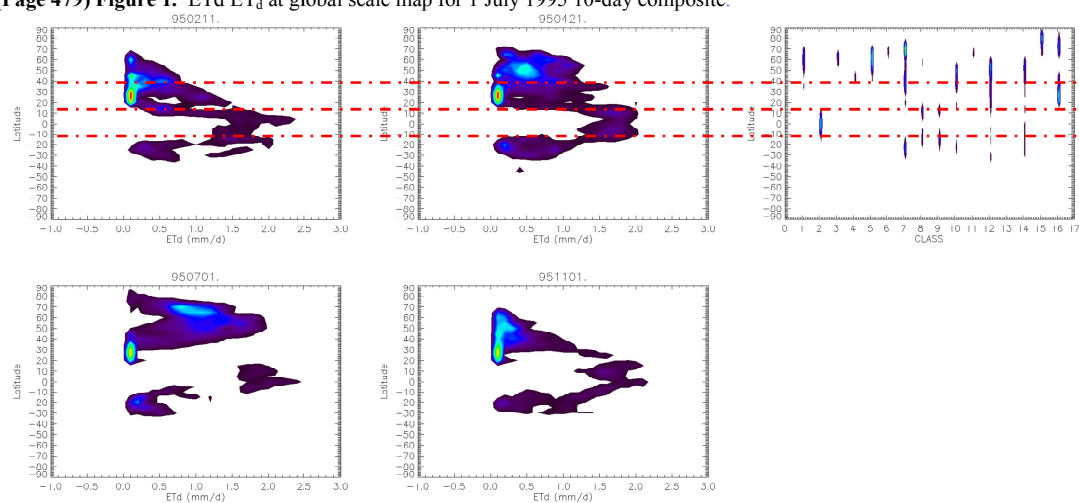
(Page 474) Figure 7. Monthly water stress index derived from temperature and precipitation data.



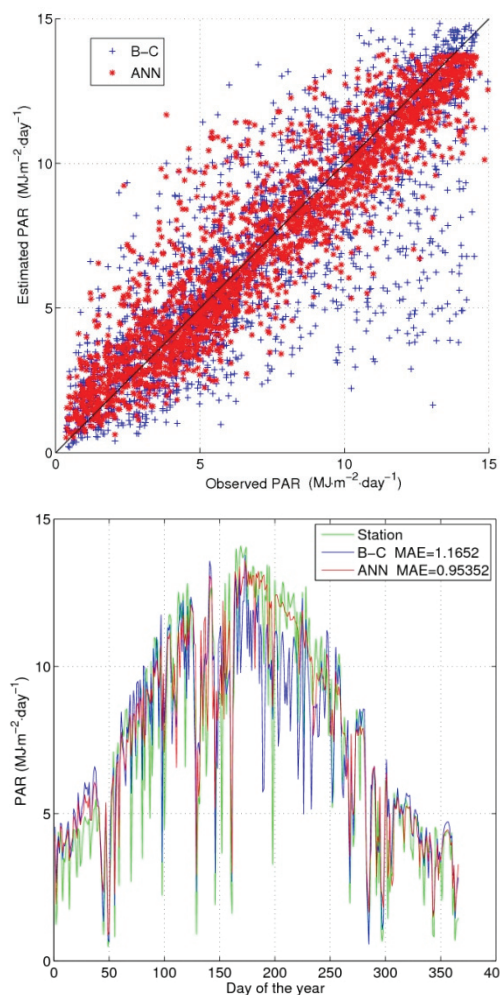
(Page 475) Figure 8. Optimized land cover proposed by Pérez-Hoyos and García-Haro (2009).



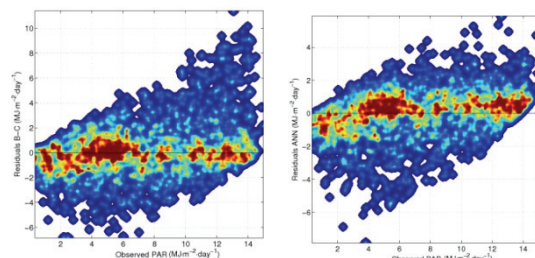
(Page 479) Figure 1. ET_d at global scale map for 1 July 1995 10-day composite.



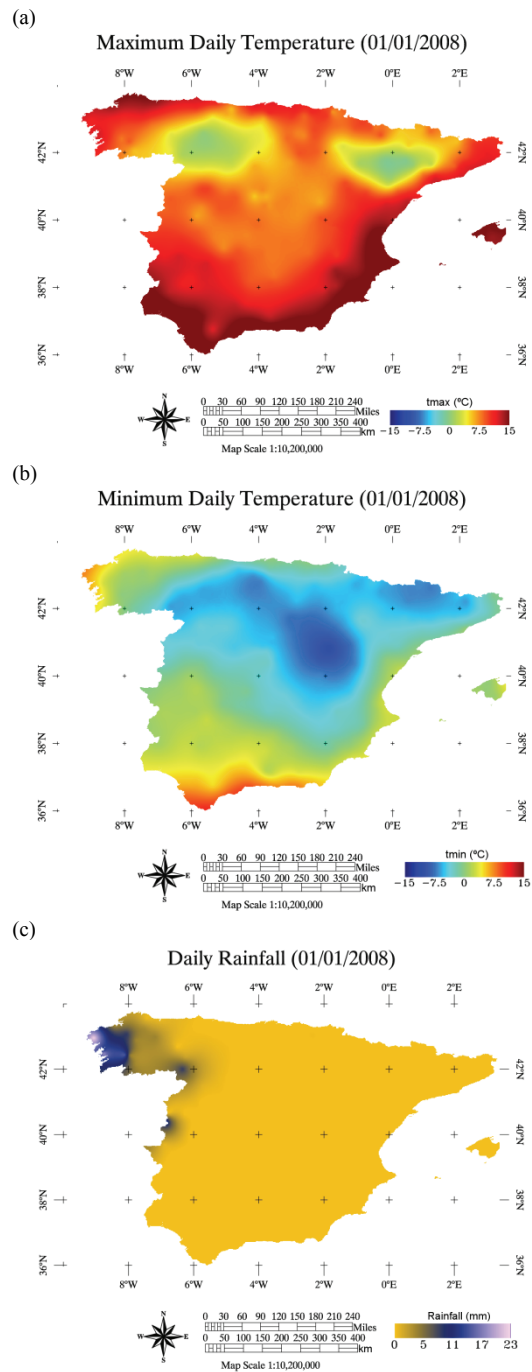
(Page 481) Figure 5. Relationship between ET_d density and latitude for February, April, July and November of 1995.



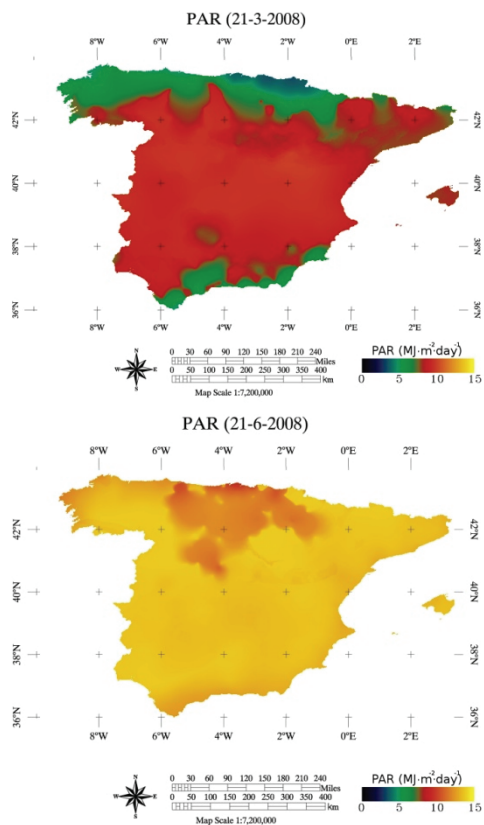
(Page 492) **Figure 3.** Performance of the models over the complete test data set from 2008 (top). Performance of the models over train and test data in the Manises ground station (bottom).



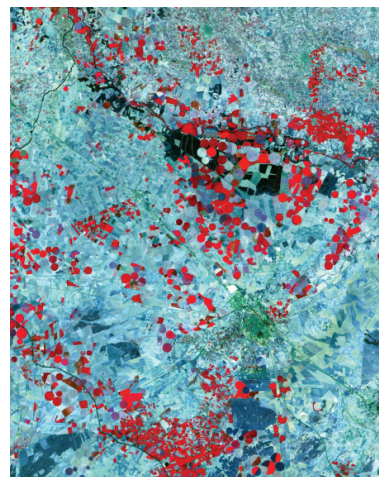
(Page 492) **Figure 4.** Observed vs. residuals for the BC (top) and ANN (bottom) approaches.



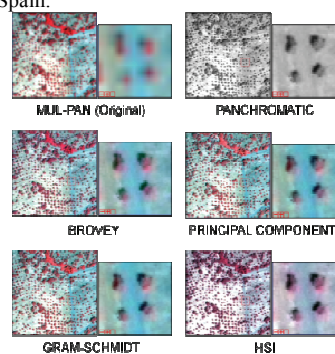
(Page 490) **Figure 2.** Example of images obtained by kriging from the meteorological stations' data obtained on 1 January 2008: (a) Maximum temperature, (b) Minimum temperature, (c) Precipitation.



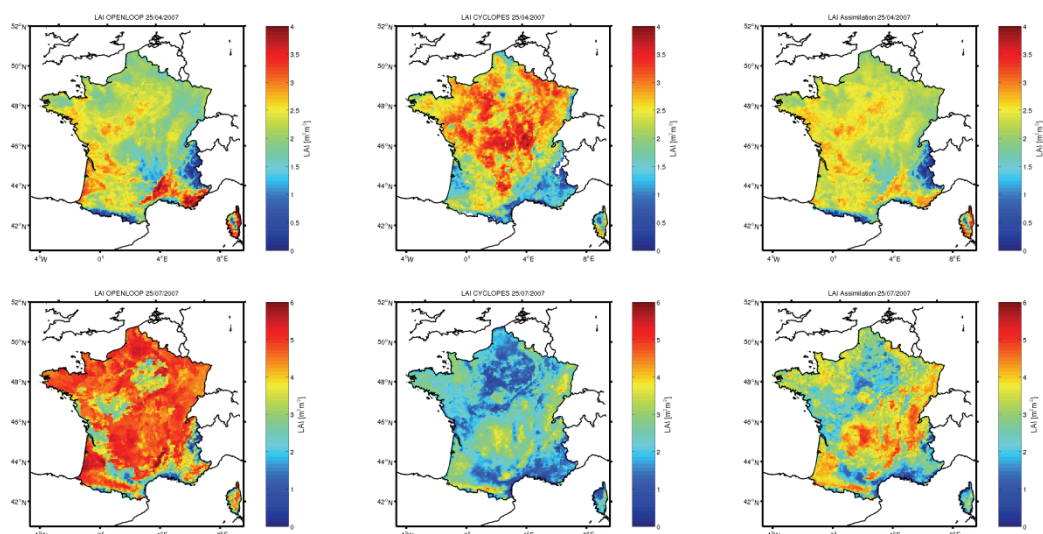
(Page 493) **Figure 6.** Example of the daily estimated PAR map at 1 km spatial resolution over Spain from the ANN method for two days: 21 March (top) and 21 June (bottom).



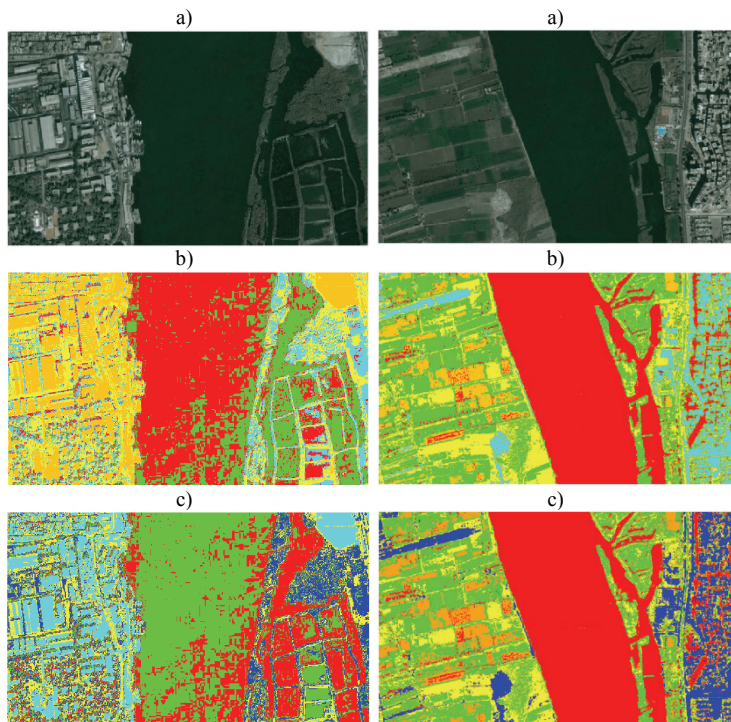
(Page 496) **Figure 1.-** False color composite of the Landsat TM-5 image (July 15, 2003) of the study area at Barrax, La-Mancha, Spain.



(Page 521) **Figure 2.** Fusion methods and original image for false-color infrared 2008 image.

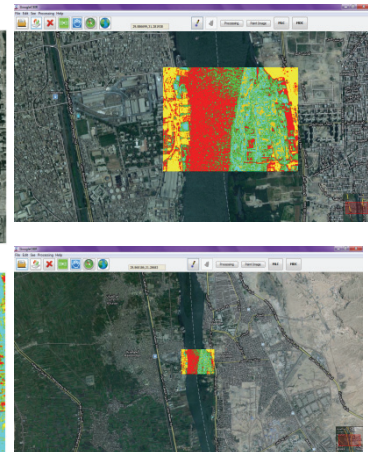


(Page 515) **Figure 1:** Simulated (left), observed (middle) and assimilated (right) LAI on 25.04.2007 (top row) and on 25.07.2007 (bottom row), respectively.

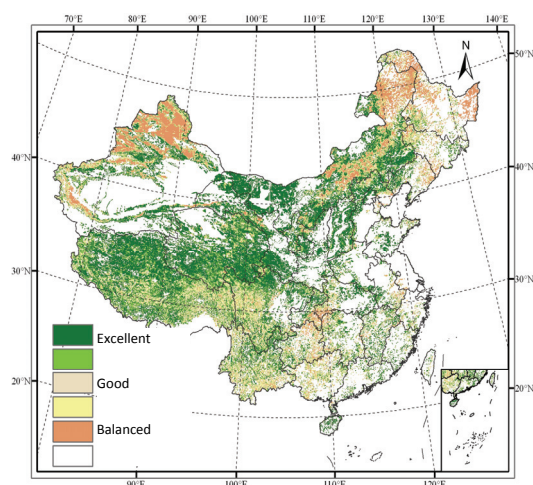


(Page 532) **Figure 5.** (a) Satellite image collected over a stretch of the Nilo river in Egypt (the image is available online through Google Maps engine). (b) Unsupervised classification result provided by our implementation of ISODATA. (c) Unsupervised classification result provided by ENVI's implementation of ISODATA.

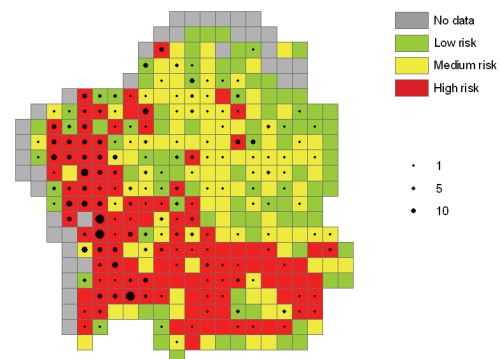
(Page 532) **Figure 6.** (a) Satellite image over a different location in the Nilo river. (b) Supervised classification result provided by our implementation of maximum likelihood (trained with the areas derived from other zone by ISODATA). (c) Supervised classification result provided by ENVI's implementation of maximum likelihood (trained with the areas derived from other zone by ISODATA).



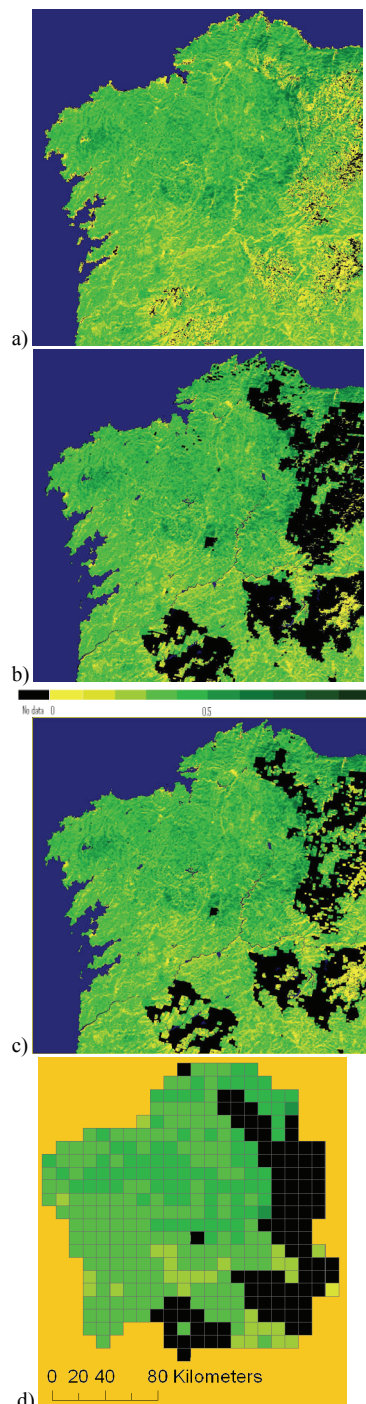
(Page 533) **Figure 7.** Different views of the developed tool. Unsupervised classification result provided by our implementation of ISODATA superimposed on the tool (top). Zoom reduction retaining the classified area (bottom)



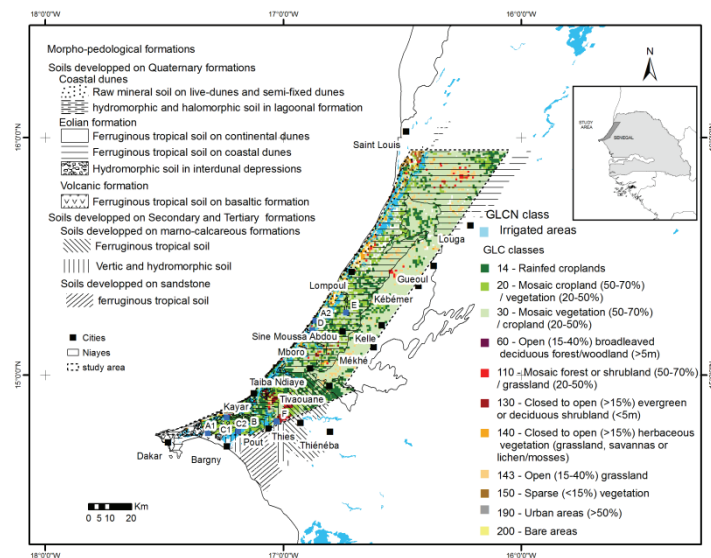
(Page 538) **Figure 3** Spatial distribution map of China's grassland vegetation growth during the growing season of 2008 compared with the average of the same period across multiple years.



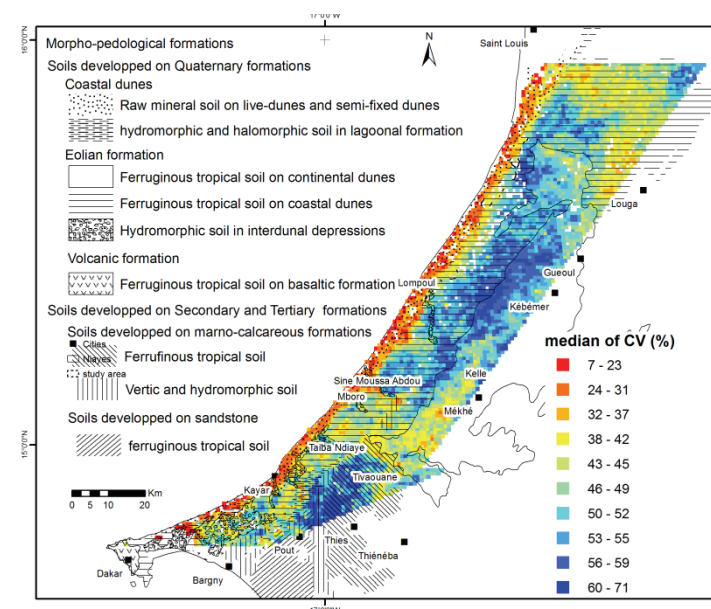
(Page 544) **Figure 4.** Example of fire danger map for the period 12-19 of July of 2006. Number of fires occurred in the same period is superposed.



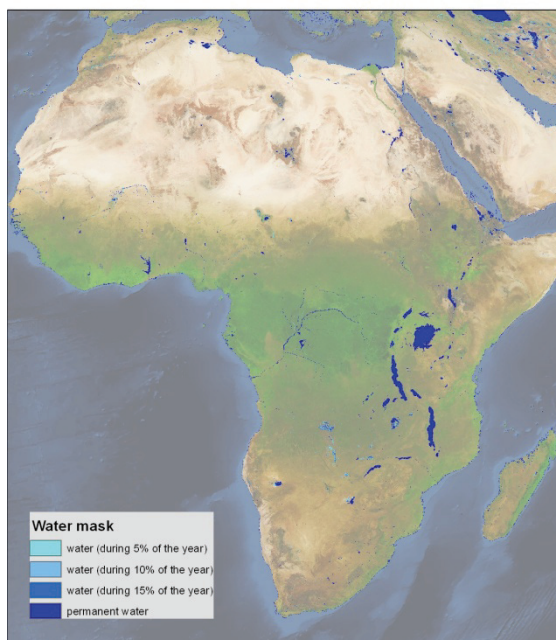
(Page 541) **Figure 2.** Processing of EVI images: a) original image, b) filtered image, c) filled image, d) average EVI per cell (10x10 km).



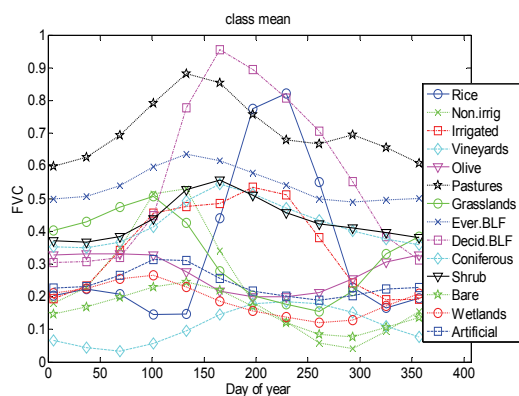
(Page 546) **Figure 1:** Vegetation land cover (GLC legend) aggregated to 1km² resolution. Morphopedological setting (from Stancioff et al., 1986, modified map) is superimposed to the land cover map.



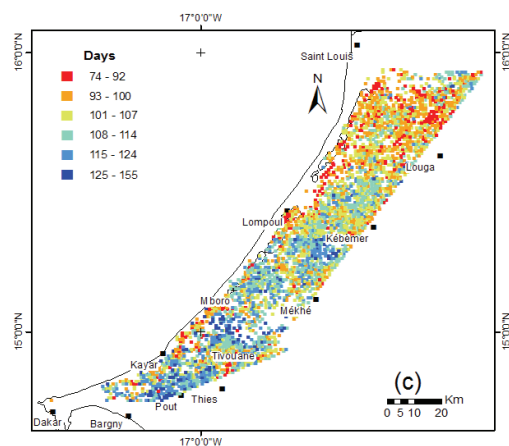
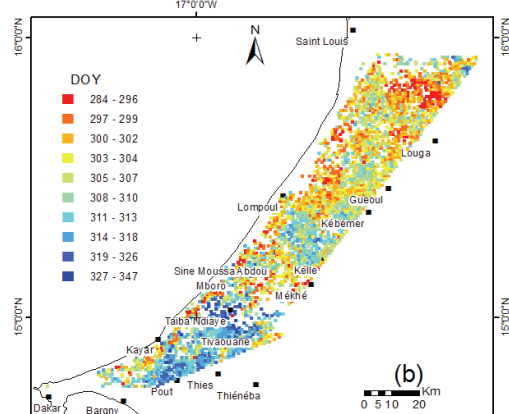
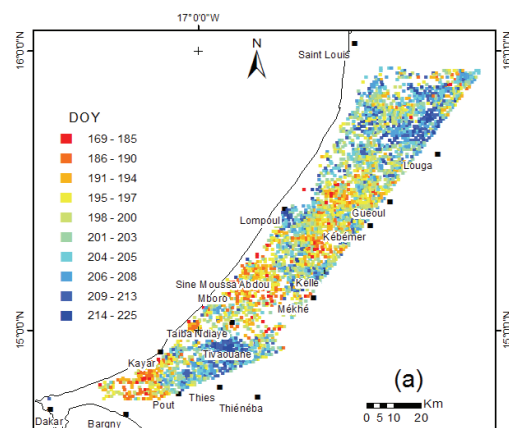
(Page 548) **Figure 3:** Map of median variation coefficient for the period 2000-2008.



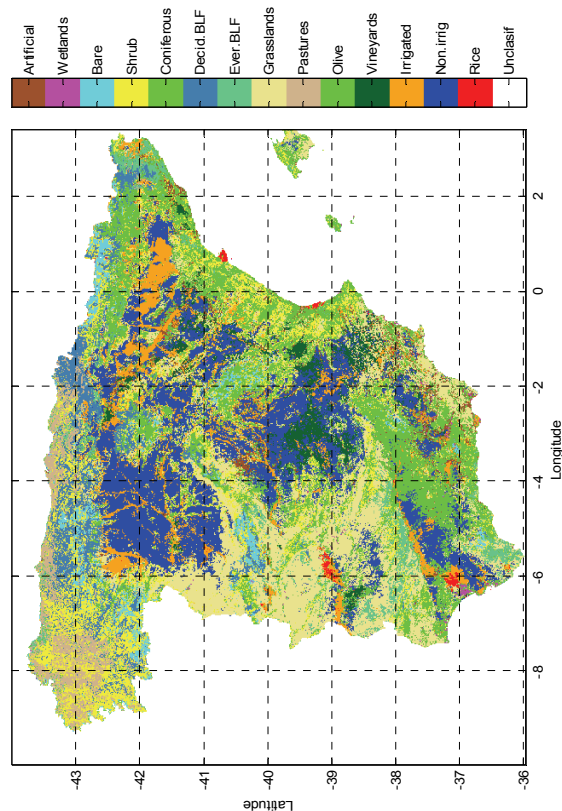
(Page 559) **Figure 1.** African Water mask generated with reflectance MODIS daily data from 2004 to 2009 at 250 m of resolution. The classes show the seasonality information. The background image is a synthesis color composite of 10 years of spot-vgt images.



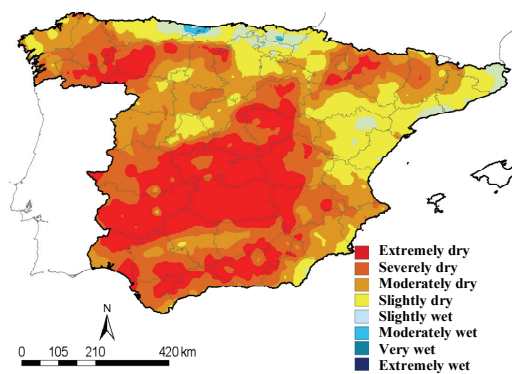
(Page 564) **Figure 2.** Mean value of annual cycle for 14 major land cover classes.



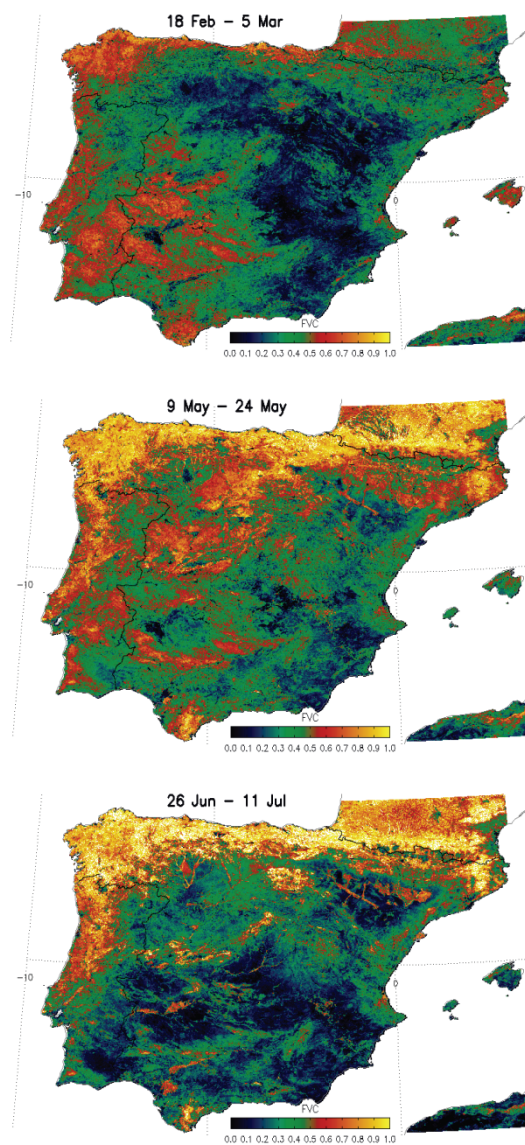
(Page 549) **Figure 4:** Maps of median (a) OD, (b) offset dates and, (c) growing season length considering the period 2000-2008.



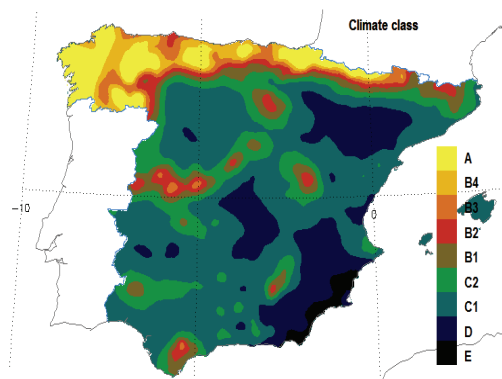
(Page 566) Figure 4. Derived land cover map with a hierarchy level of 14 major classes.



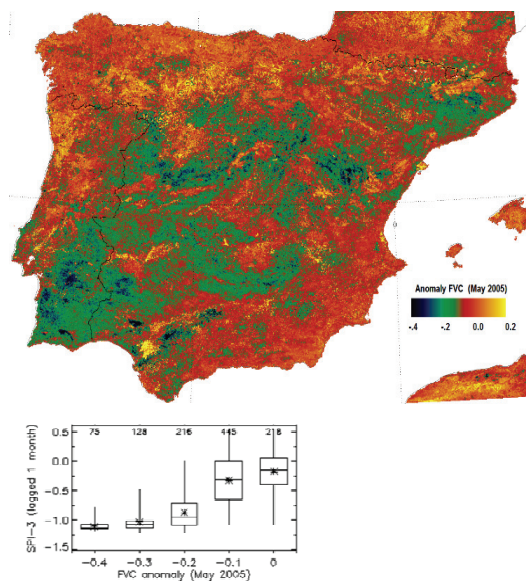
(Page 570) Figure 2. 12-month SPI values for Spain in December 2005 stratified into 8 intervals: extremely wet (>2.0), very wet (1.5 to 1.99), moderately wet (1.0 to 1.49), slightly wet (-0.99 to 0.0), slightly dry (0 to 0.99), moderately dry (-1.49 to 1.0), severely dry (-1.99 to 1.5), and extremely dry (<-2.0).



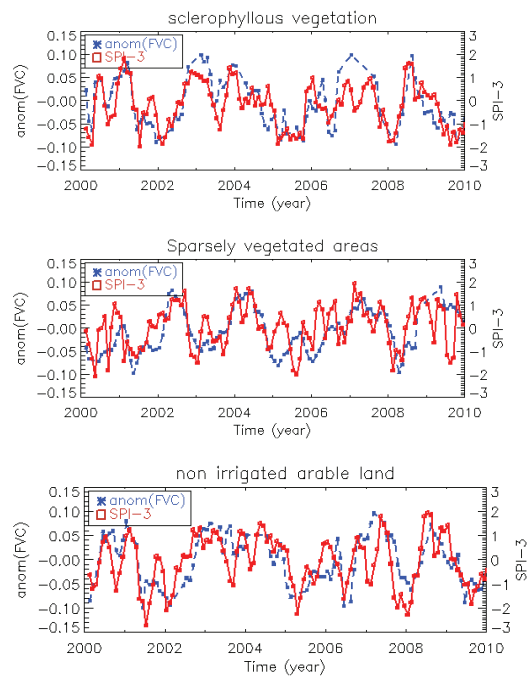
(Page 569) Figure 1. Monthly average (2000–2010) fractional vegetation cover for the Iberian Peninsula at three different time periods.



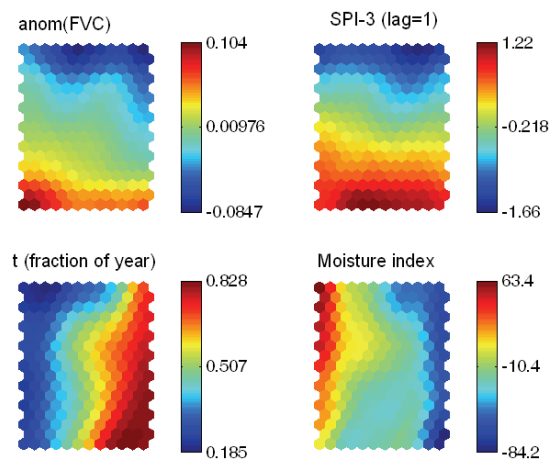
(Page 570) **Figure 3.** Nine-category climatic classification based on the moisture index. It corresponds to average values of climatic parameters over a 60 year period (1950-2009).



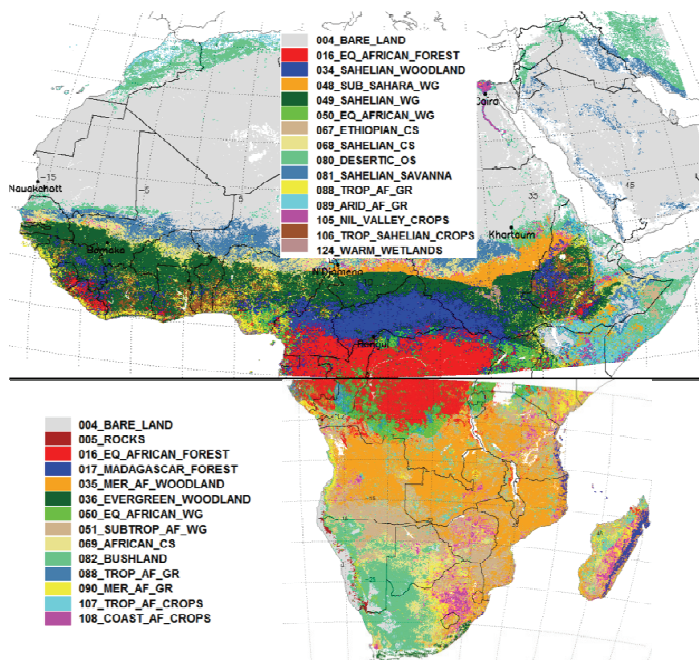
(Page 571) **Figure 4.** Top: FVC Anomaly (May 2005). Bottom: Whisker plot of SPI-3 lagged 1-month (i.e. using the precipitation of February, March and April) as a function of the FVC anomaly (May 2005). Data correspond to broadleaved deciduous forest. The number of valid pixels is printed on top of each box.



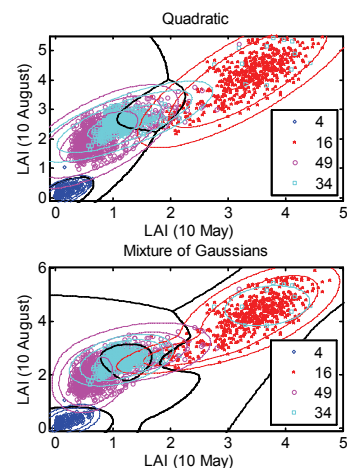
((Page 571) **Figure 5.** Temporal patterns of SPI and FVC anomaly over a 10-year period, at a 16 day time step, for three different vegetation types.



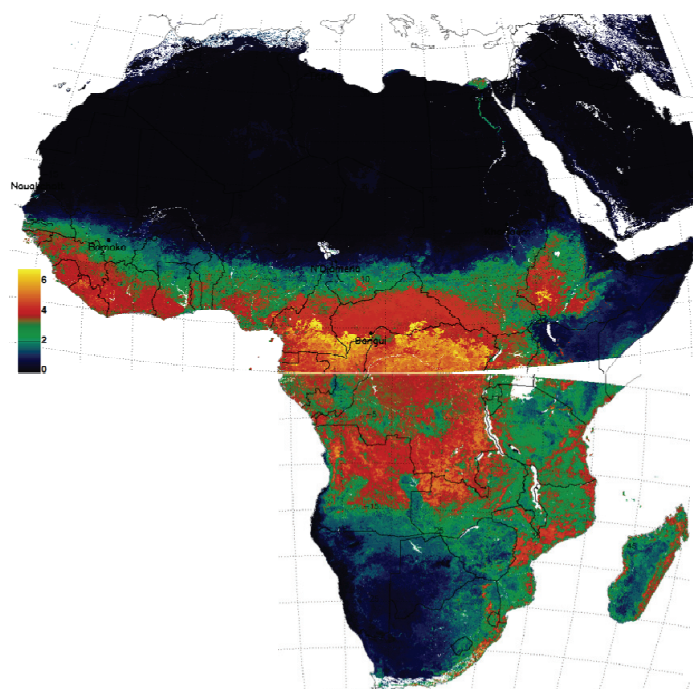
(Page 572) **Figure 7.** Visualization of the SOM trained from time series of vegetation and climatic data of the study area. The four figures are linked by position: in each figure, the hexagon in a certain position corresponds to the same map unit.



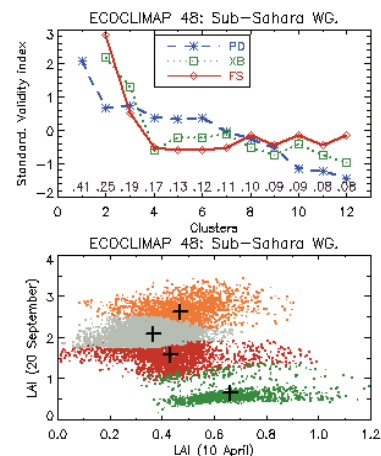
(Page 575) Figure 1: SEVIRI/MSG vegetation products SAF



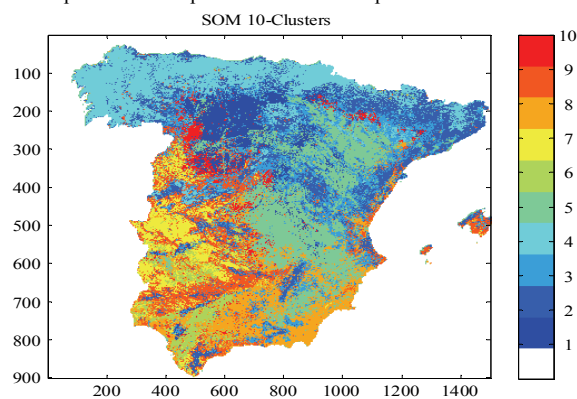
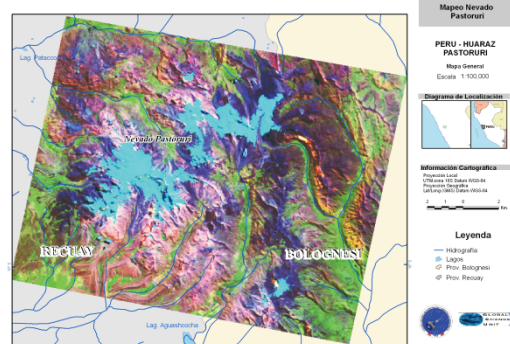
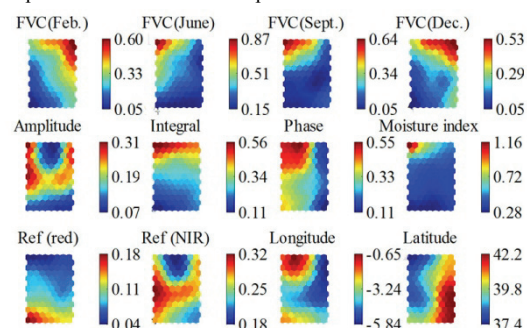
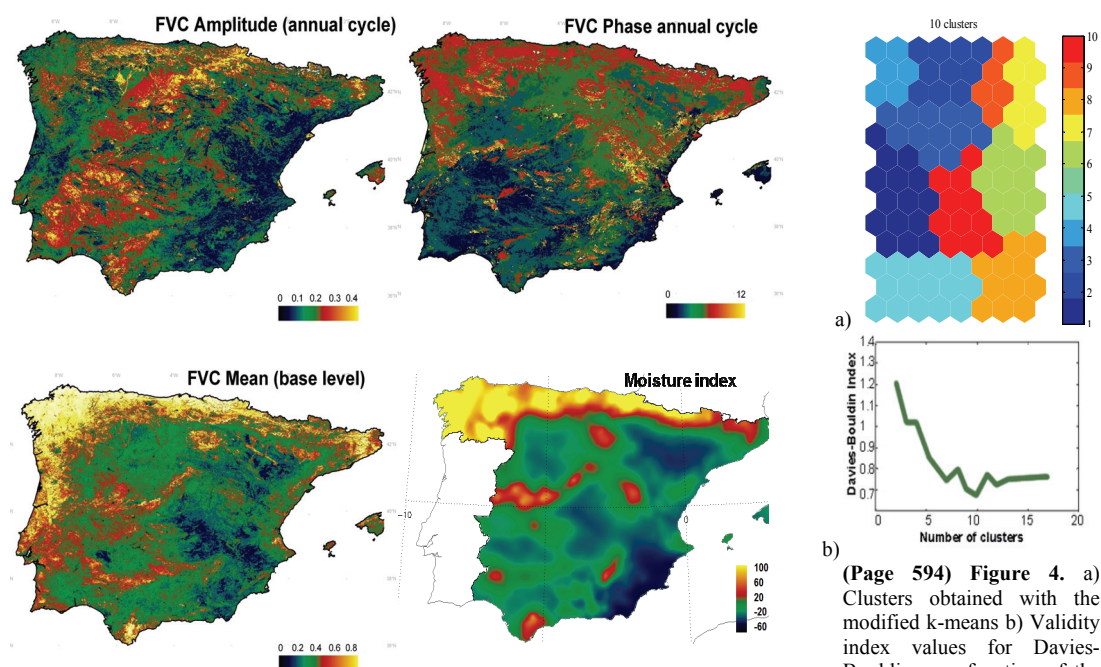
(Page 577) Figure 3. Bayes classification of four major ECOCLIMAP cover types in northern Africa from SEVIRI/MSG LAI estimations, for two algorithms: quadratic (top); Mixture of Gaussians, with two Gaussian components per class (bottom). Points are randomly drawn from the ECOCLIMAP database. 4: Bare land, 16 Equatorial African Forest, 34: Sahelian woodland, 49: Sahelian WG.

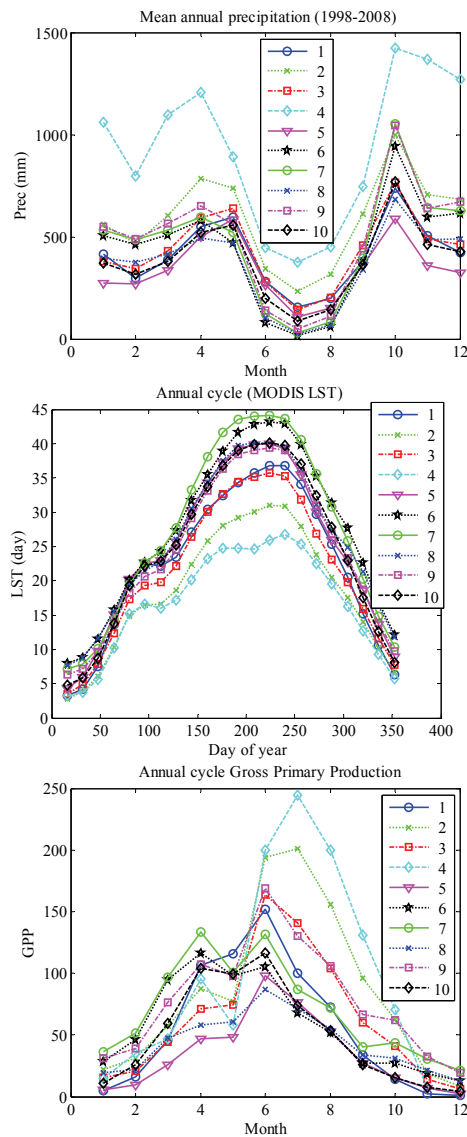


(Page 578) Figure 5. Example of LAI field based on the synergy of ECOCLIMAP and LSA SAF products.

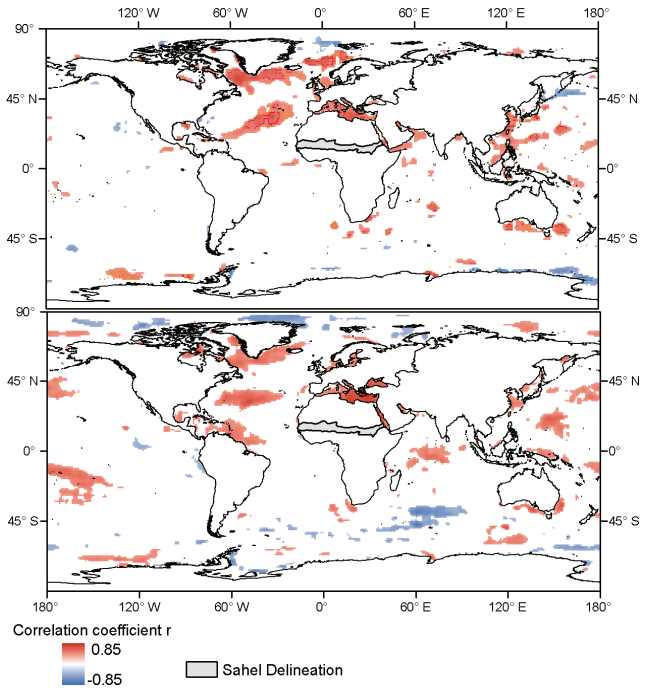


(Page 577) Figure 4. Clusters obtained with the FKM algorithm for an ECOCLIMAP class. Top: Validity index values for PD, XB and FS (transformed into standardized units) as a function of the number of cluster ranging from $k=1$ to 12. Note that XB and FS are defined only for $k>2$. The within-scatter variance as a function of the number of clusters is printed on bottom of the plot. Bottom: Optimal partition obtained for $k=4$ clusters, as represented in the features space of two dates, 10 April and 20 September. Cluster centroids are represented by plus symbols.

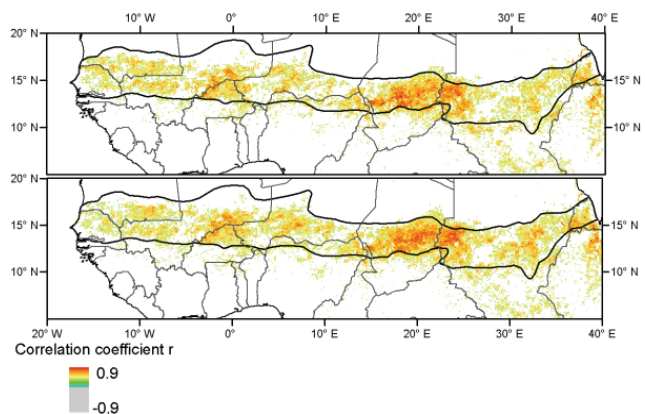




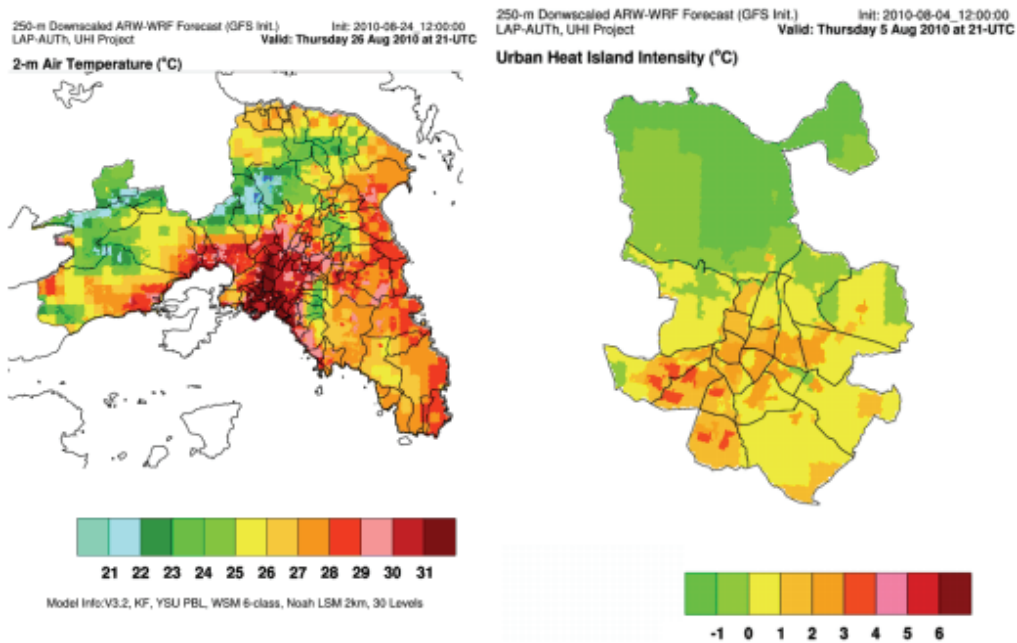
(Page 595) **Figure 7.** Mean seasonal profile of the precipitation, Land Surface Temperature (LST) and GPP (Gross Primary Precipitation) for the ecosystem functional types (EFTs).



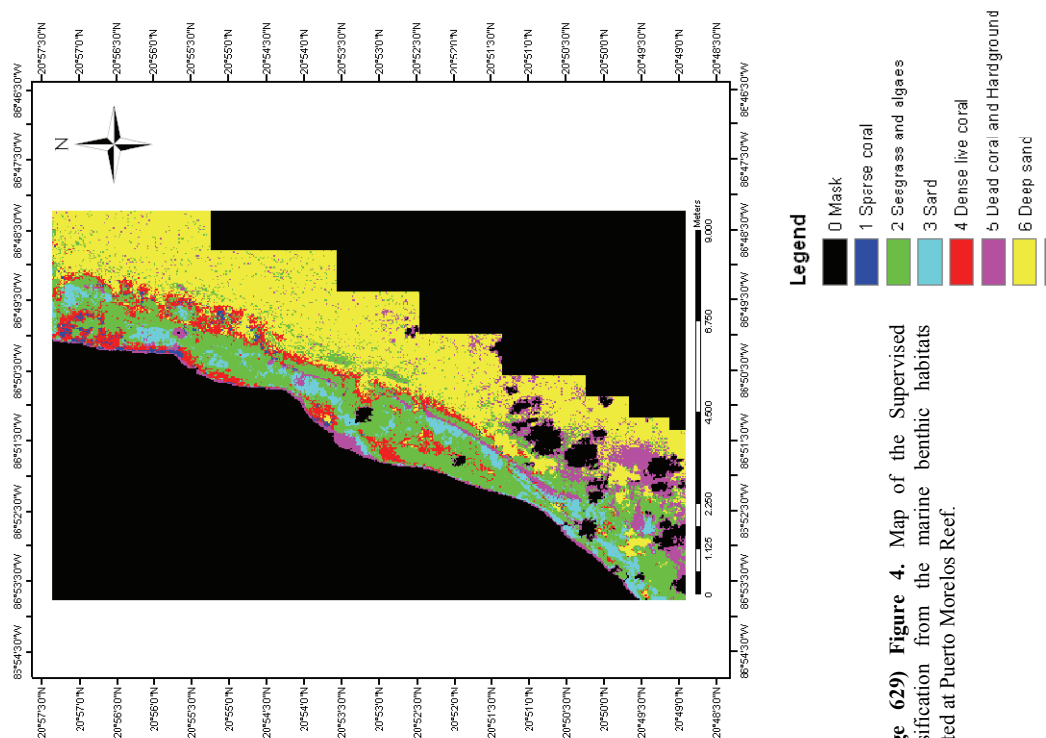
(Page 618) **Fig. 1** Maps of correlation coefficients (r) between Sahel NDVI anomaly index (SANAI) and SST anomalies for (top) March-May and (bottom) July-Sept. for 1982-2007. Only correlations at the 95 % confidence level are shown.



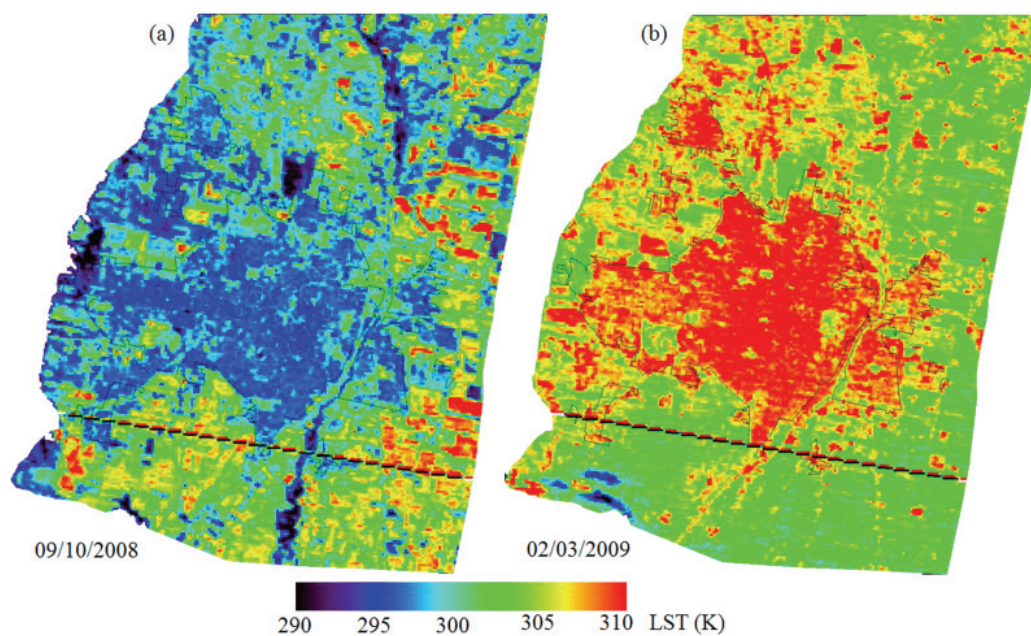
(Page 618) **Fig. 2** Maps of correlation coefficients (r) between NDVI anomalies averaged over the period July-Sept. for 1982-2007 and (top) the Labrador Sea index (mean MAM) and (bottom) the SE Mediterranean index (mean JAS). Only correlations at the 95 % confidence level are shown.



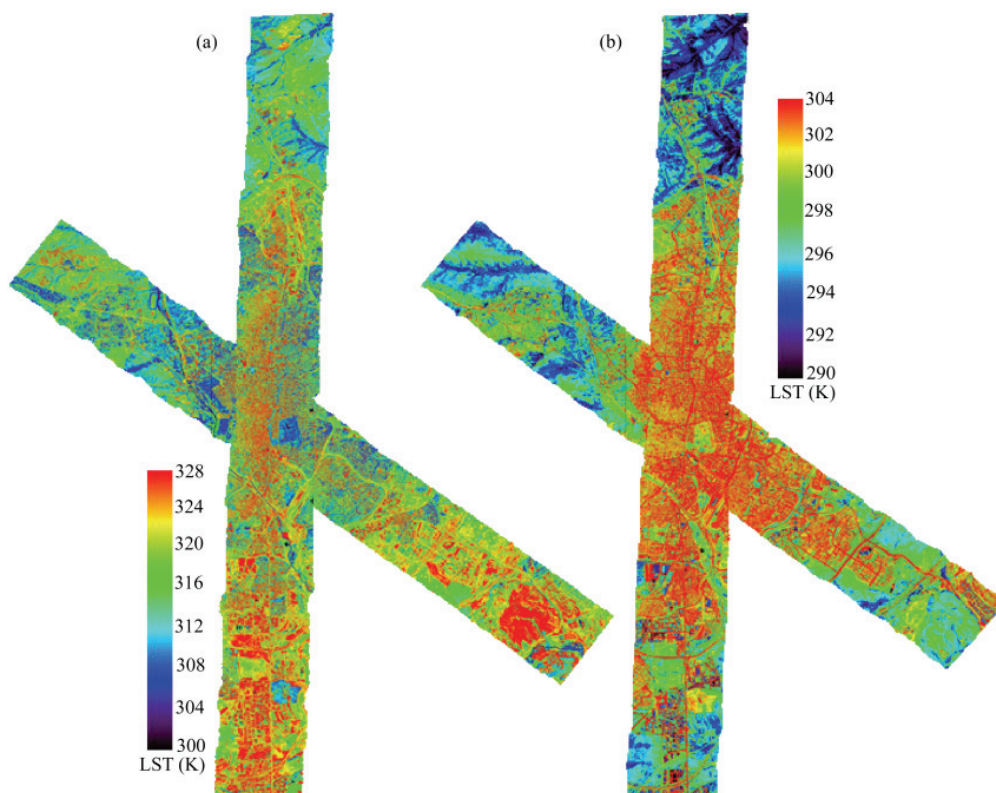
(Page 624) Figure 4. Example forecast maps at 21.00 UTC. Left: AT (°C) map over Athens: 24th August 2010. Right UHI (°C) map over Madrid: 4th August 2010



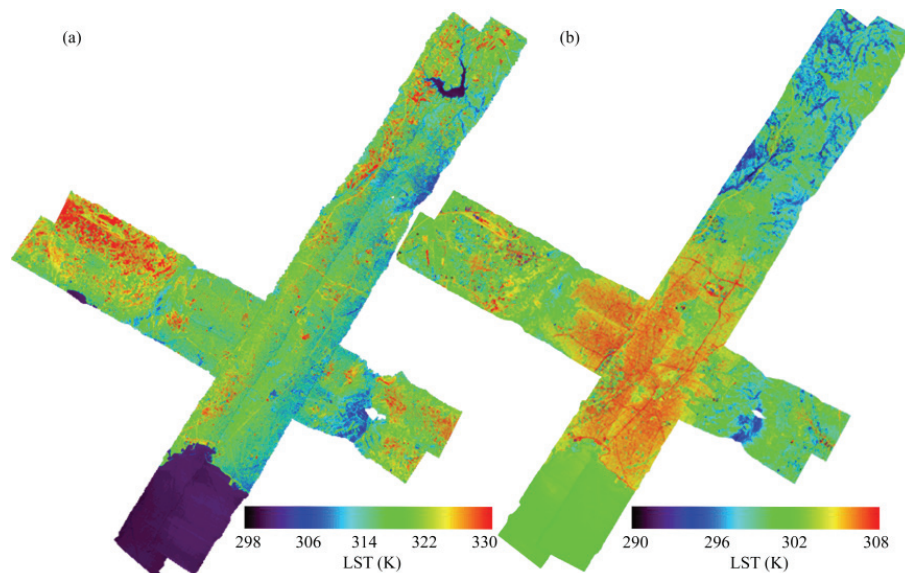
(Page 629) Figure 4. Map of the Supervised classification from the marine benthic habitats located at Puerto Morelos Reef.



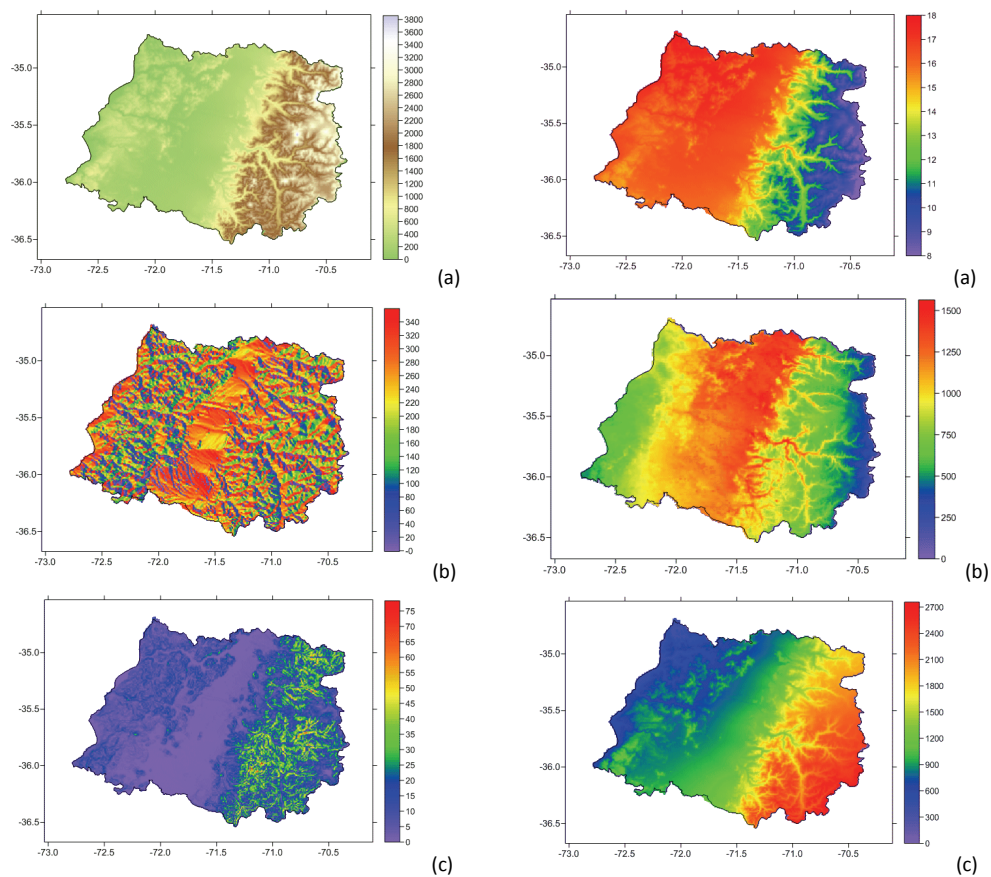
(Page 640) **Fig. 1** LST maps from GSMT for (a) a spring image from 9th October 2008 and (b) a summer image from 2nd March 2009.



(Page 641) **Fig. 3** Map of LST applying TES algorithm to AHS images in the framework of the DESIREX 2008 campaign. (a) AHS image from June 28 at noon. (b) AHS image from June 28 at night.

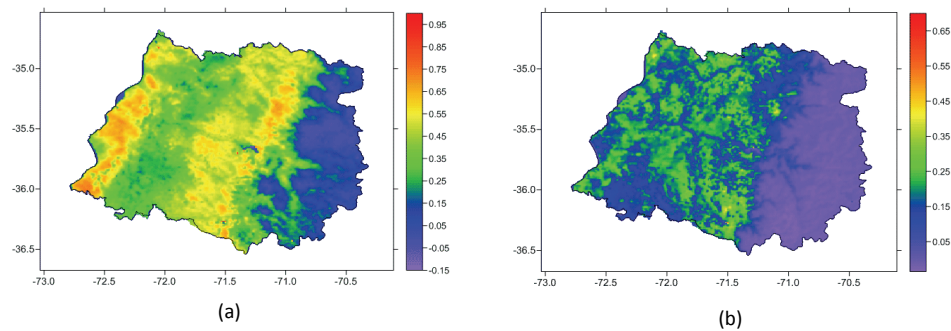


(Page 642) **Fig. 5** Map of LST applying TES algorithm to AHS images in the framework of the Thermopolis 2009 campaign. (a) AHS image from July 18 at noon. (b) AHS image from July 18 at night.

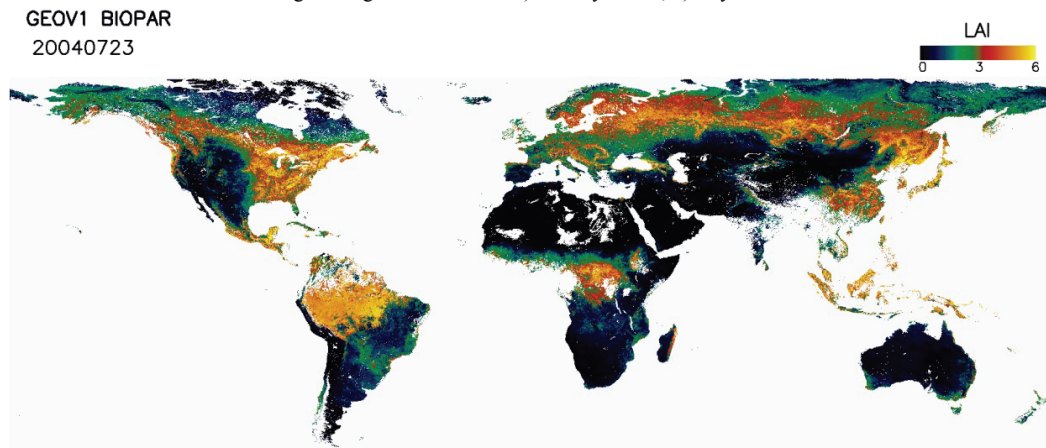


(Page 650) **Figure 2.-** Physiographic independent variables used in the geographic weighted regression method.

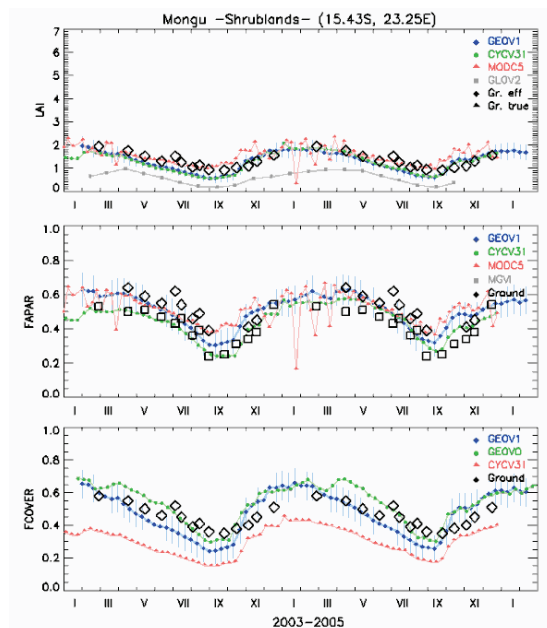
(Page 652) **Figure 4.-** Images of mean annual (a) temperature, (b) evapotranspiration and (c) rainfall.



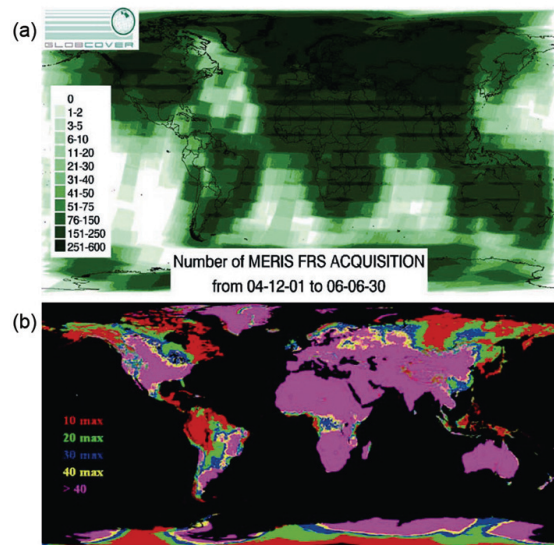
(Page 653) **Figure 3.-** Normalized difference vegetation index used as independent variable in geographic weighted regression method: a) January NDVI, b) July NDVI.



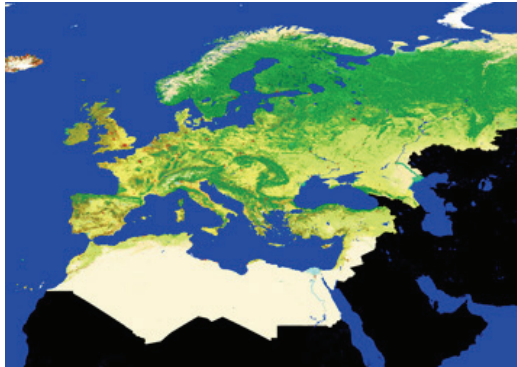
(Page 661) **Figure 1.** GEOV1 LAI global map corresponding to the 23 of July of 2004.



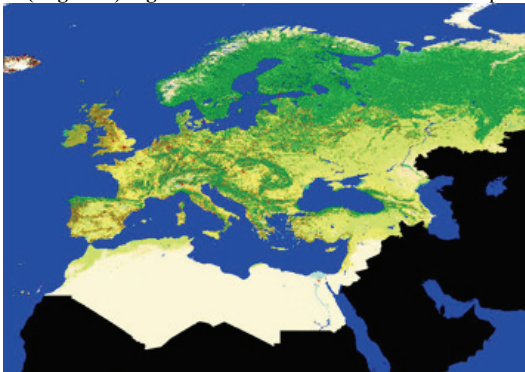
(Page 664) **Figure 6.** LAI, FAPAR and FCOVER temporal profiles at Mongu site in Africa.



(Page 667) **Figure 2.** (a) Density of MERIS FRS acquisitions from 1st December 2004 to 30th June 2006, (b) Number of valid observations obtained after 19 months of MERIS FRS acquisitions. Magenta areas are defined as well covered (>40 observations)



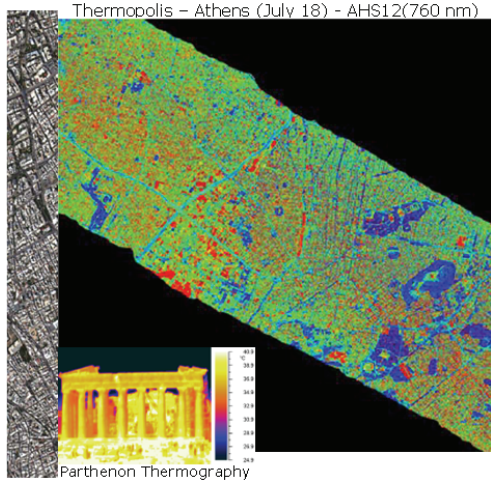
(Page 669) Figure 4. GlobCorine 2005 land cover map



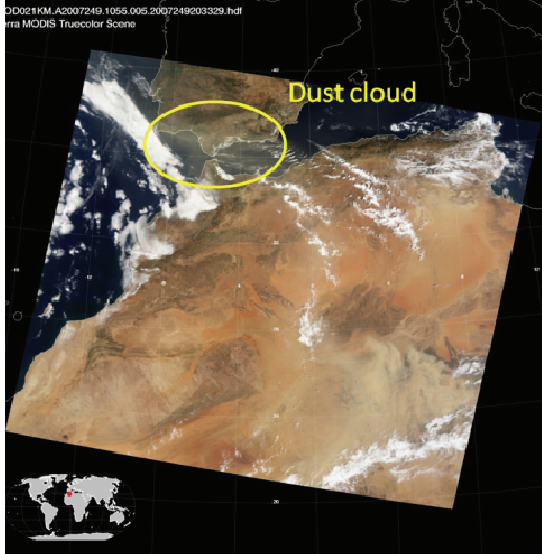
(Page 670) Figure 5. GlobCorine 2005 land cover map

(Page 669) Table 1. 14 classes of the GlobCorine nomenclature

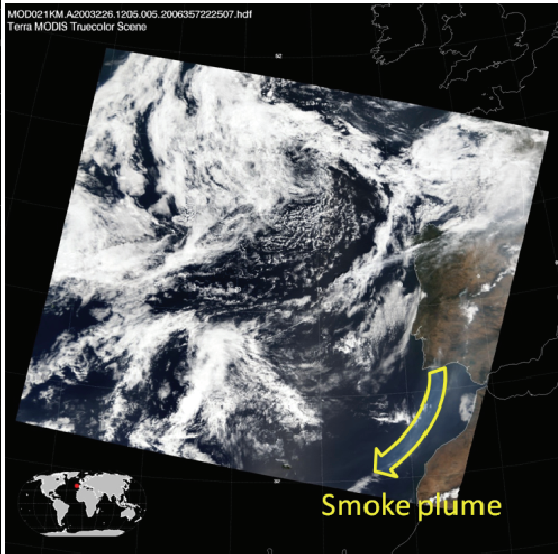
Class	Color
Urban and associated areas	Dark blue
Rainfed cropland	Yellow
Irrigated cropland	Light green
Forest	Green
Heathland and sclerophyllous vegetation	Brown
Grassland	Olive green
Sparsely vegetated area	Light yellow
Vegetated low-lying areas on regularly flooded soil	Dark green
Bare areas	White
Complex cropland	Orange
Mosaic cropland / natural vegetation	Light yellow-green
Mosaic of natural (herbaceous, shrub, tree) vegetation	Dark brown
Water bodies	Blue
Permanent snow and ice	White



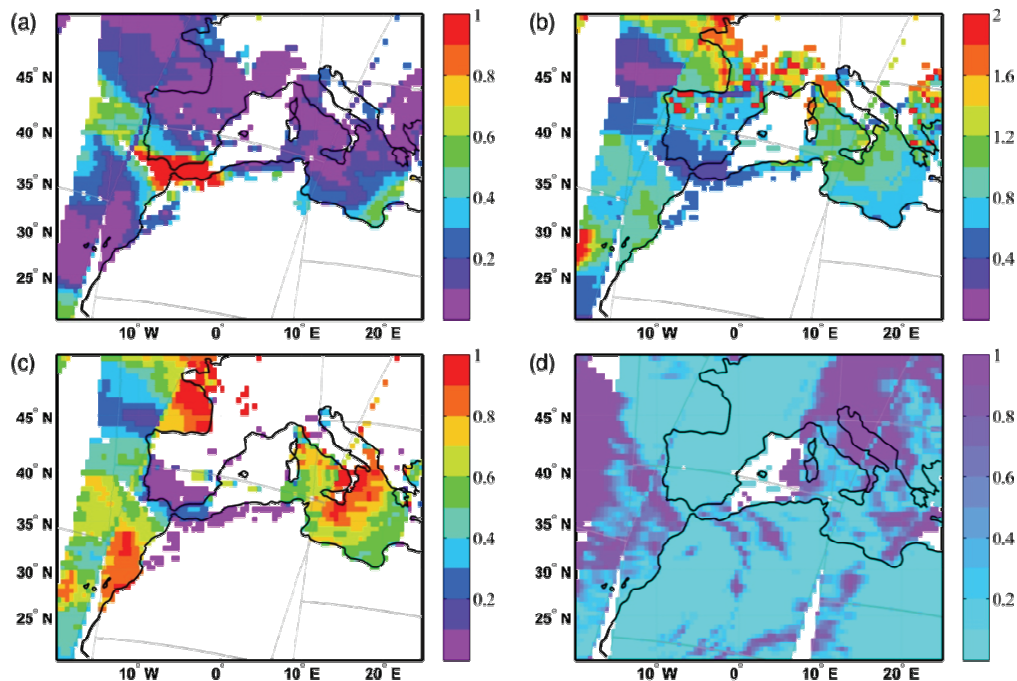
(Page 677)



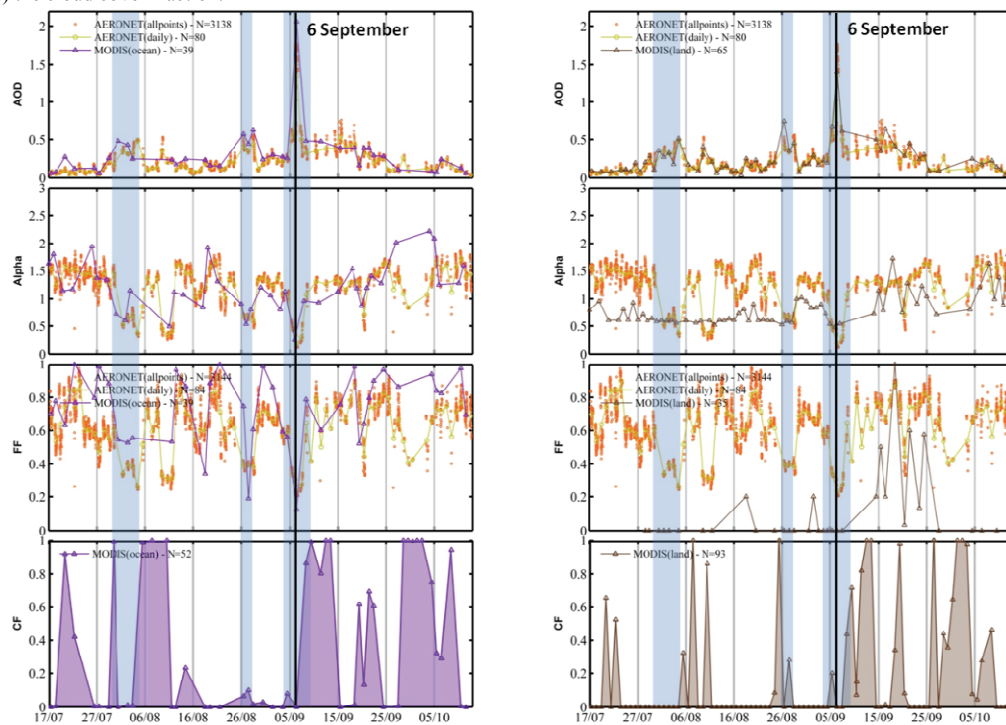
(Page 685) Figure 1: RGB true color image of Terra/MODIS over Spain on 6 September 2007 10:55 UTC.



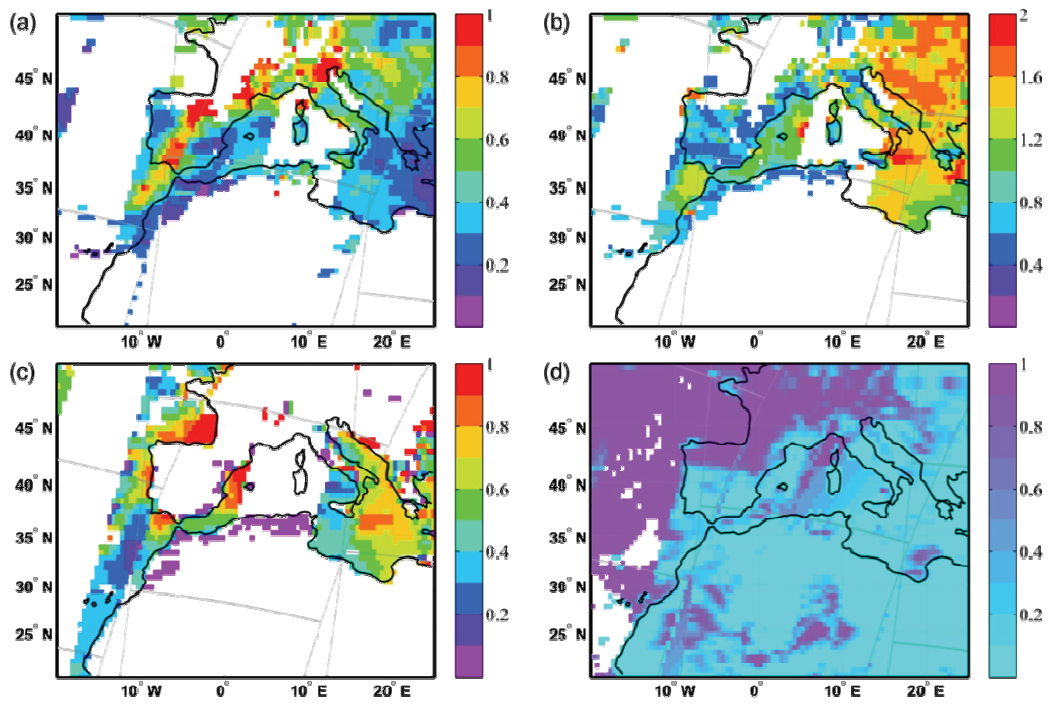
(Page 687) Figure 5 Same as Figure 1 for the 14 August 2003 12:05 UTC.



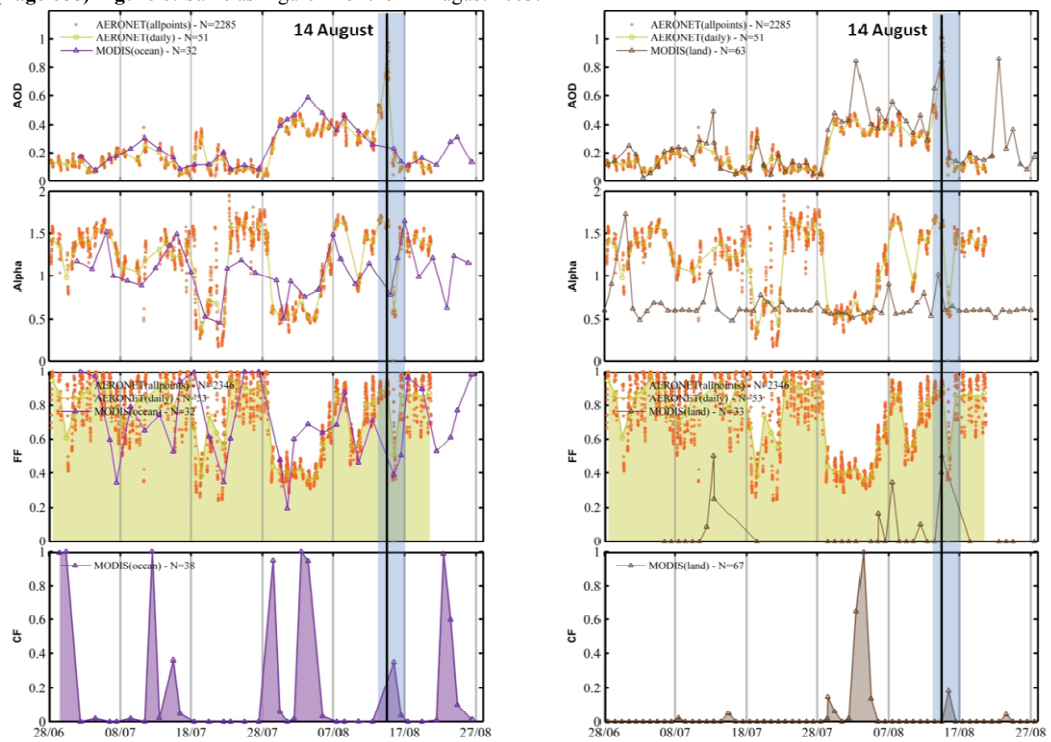
(Page 686) **Figure 2:** Daily maps from Terra/MODIS MOD04 (resampled to a regular 0.5 deg grid) for the 6 September 2007 representing (a) the AOD (470 nm), (b) the Ångström exponent (470-660 nm), (c) the fine mode AOD fraction (550 nm) and (d) the cloud cover fraction.



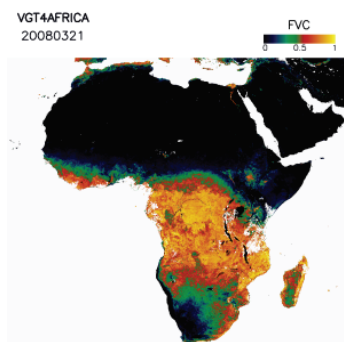
(Page 686) **Figure 3:** Time series over El Arenosillo between 17 July and 14 October 2007, from top to bottom: AOD, Ångström exponent (Alpha), Fine-mode AOD Fraction (FF), and Cloud Fraction (CF). The left and right panels correspond to the results obtained with the retrieval algorithm over ocean and over land respectively.



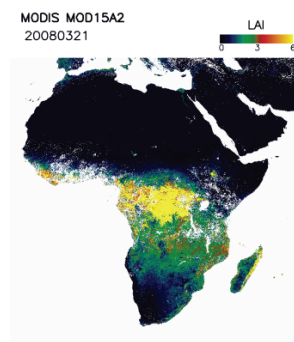
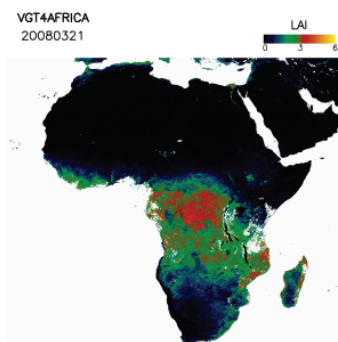
(Page 688) Figure 6: Same as Figure 2 for the 14 August 2003.



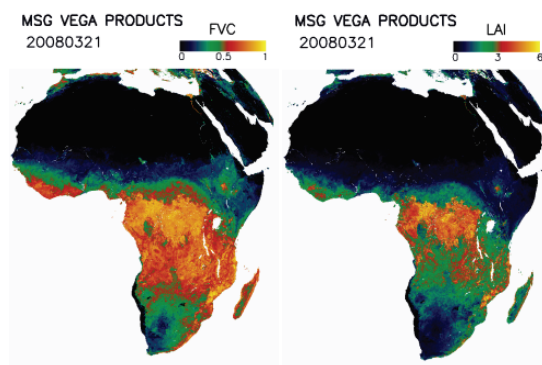
(Page 688) Figure 7: Same as Figure 3 for the period between 28 June 2003 and 27 August 2003.



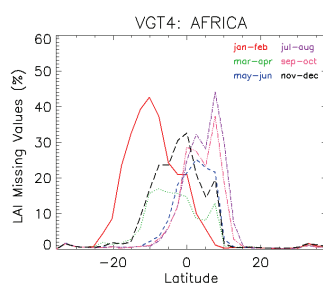
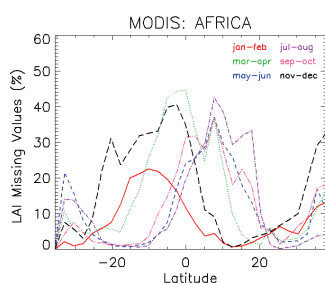
(Page 695) Figure 1. VGT4Africa FVC and LAI maps dated on March 21, 2008



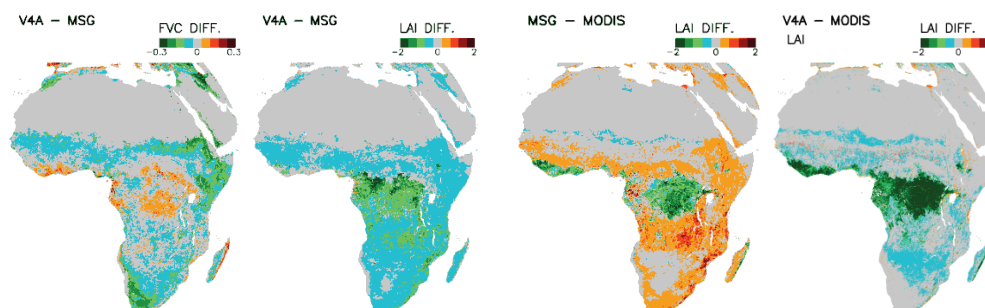
(Page 695) Figure 3. MODIS LAI map over Africa dated on March 21, 2008.



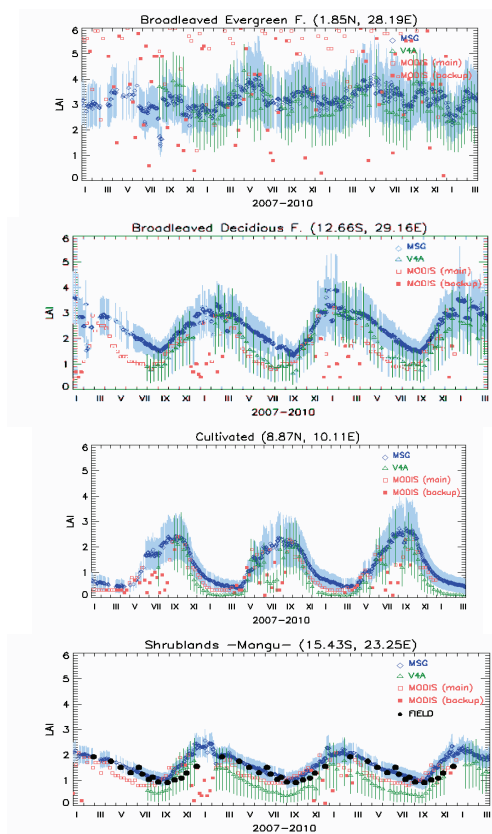
(Page 695) Figure 2. Land-SAF MSG LAI and FVC maps over Africa dated on March 21, 2008.



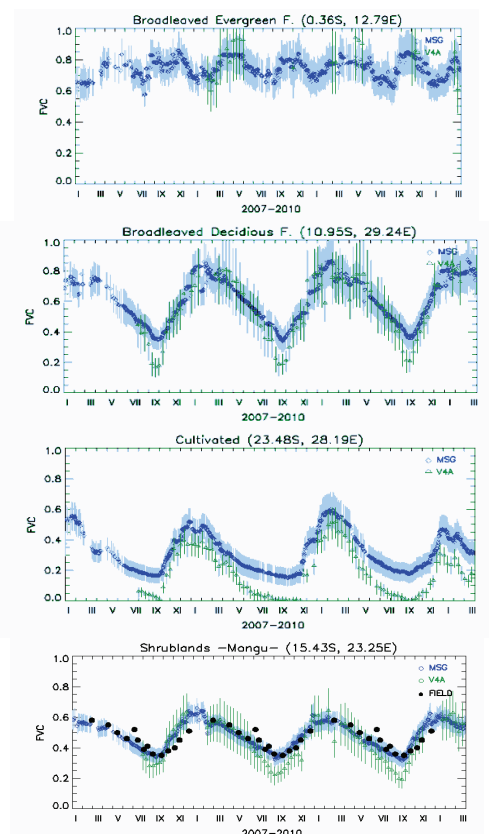
(Page 696) Figure 4. Percentage of missing values over Africa as a function of latitude and period for MODIS and V4A LAI products.



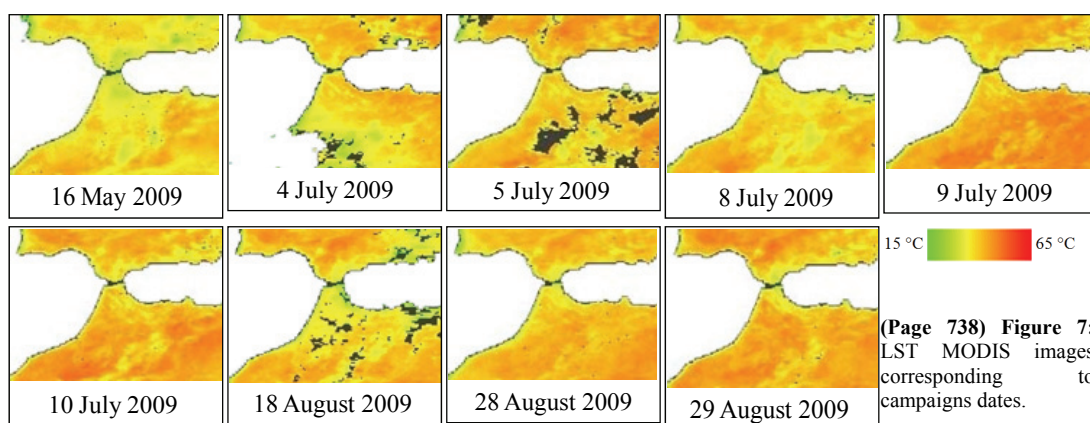
(Page 696) Figure 5. Mean annual bias for the year 2008 between V4A and MSG FVC (top left), V4A and MSG LAI (top right), MSG and MODIS LAI (bottom left), V4A and MODIS LAI (bottom right) products.



(Page 698) Figure 10. LAI temporal profiles for different sites in Africa.



(Page 698) Figure 11. FVC temporal profiles over different biomes in Africa.



(Page 738) Figure 7: LST MODIS images corresponding to campaigns dates.

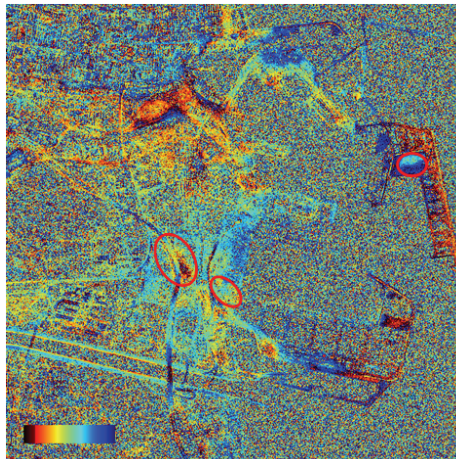


Figure 2.A

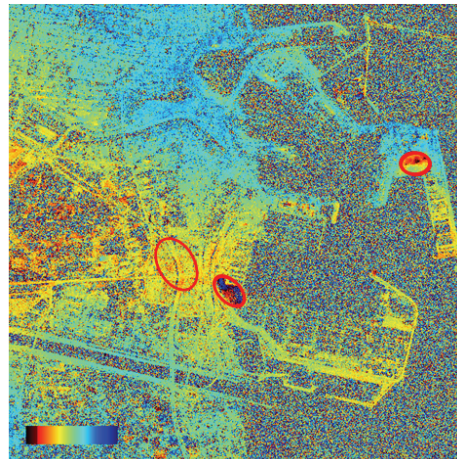


Figure 2.B

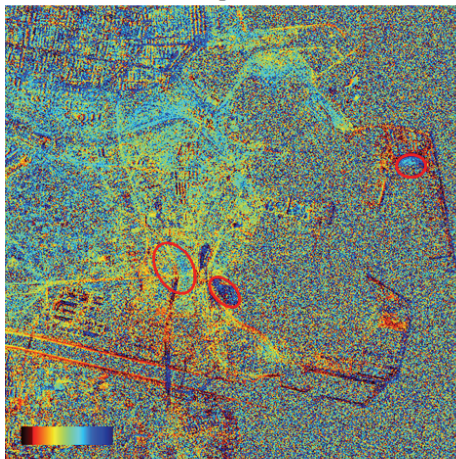


Figure 2.C

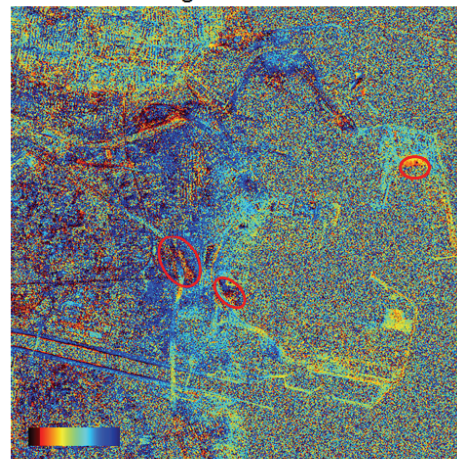


Figure 2.D

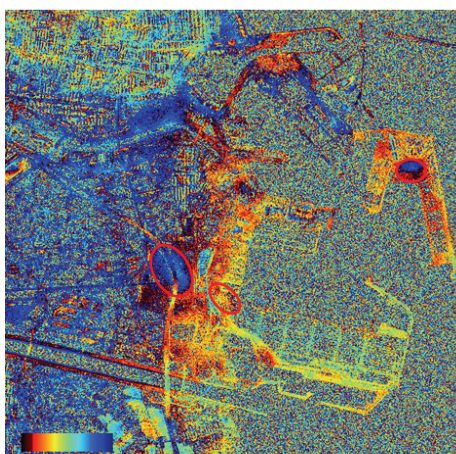


Figure 2.E

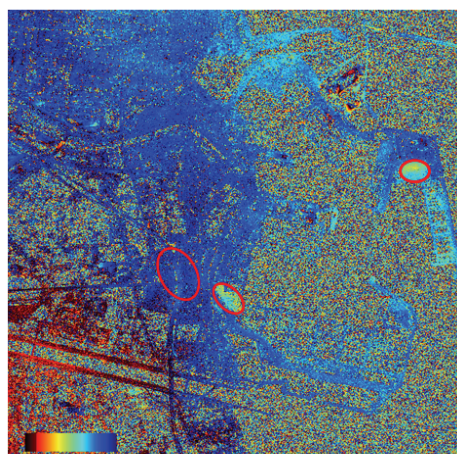
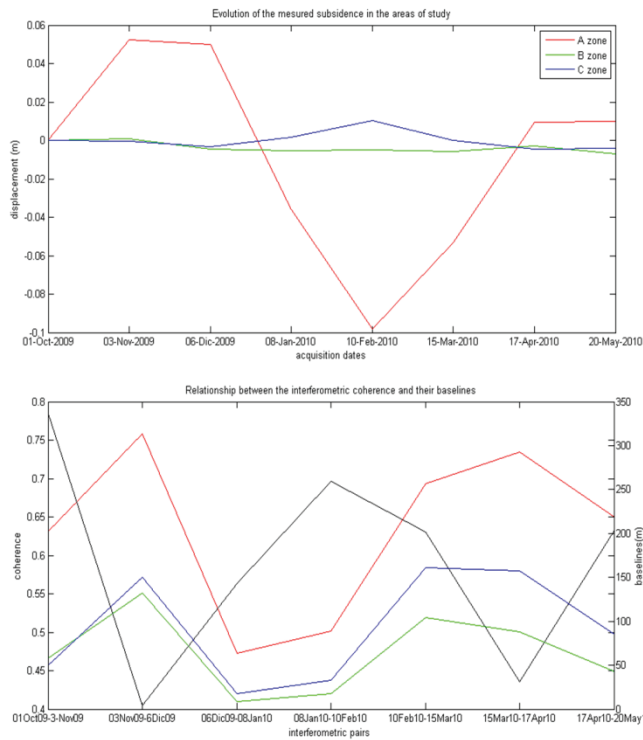
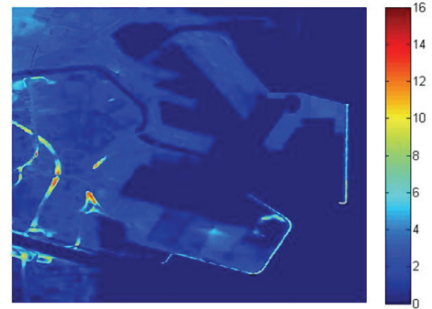


Figure 2.F

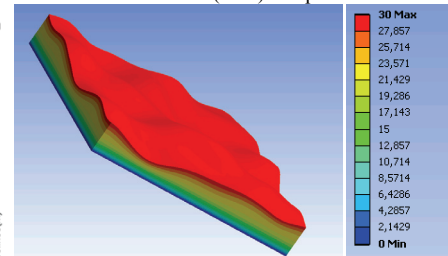
(Page 752) **Figure 2..A-F:** Wrapped interferograms (phase) over Valencia city computed from TerraSAR-X stripmap images from October 2009 to May 2010 showing the subsidence in the port area. The color wheel goes from $-\pi$ to $+\pi$.



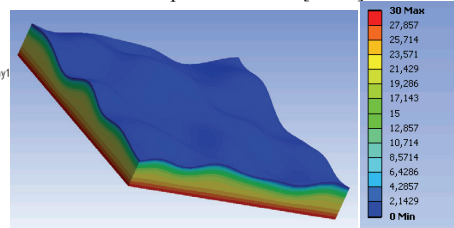
(Page 753) Figure 3: In the upper graph we can see the evolution over time of the subsidence in the studied areas. In the lower one, the coherence values over time of the studied areas can be noted



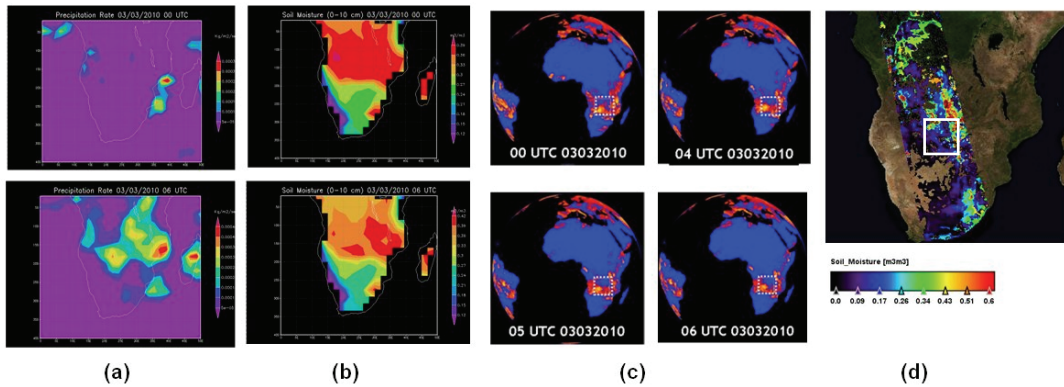
(Page 754) Figure 4. DEM 10 m spatial resolution provided by Instituto Geografico Nacional (IGN) of Spain.



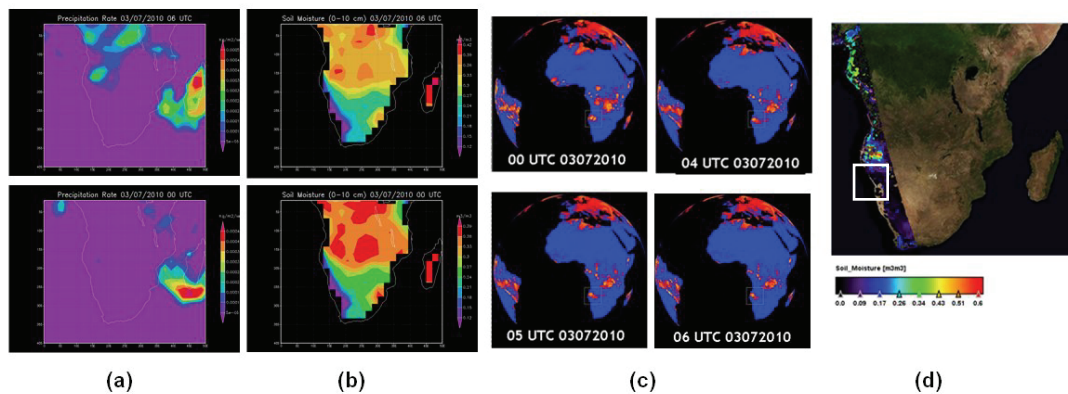
(Page 757) Fig 3 : Soil moisture profile 1 introduced in the model. Surface soil moisture = 30 % - Deep soil moisture [15cm] = 0%



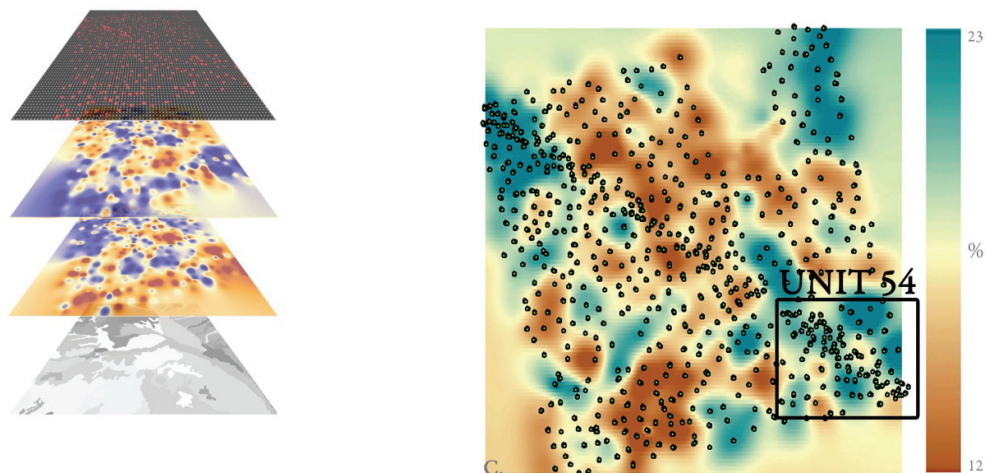
(Page 757) Fig 4 : Soil moisture profile 2 introduced in the model. Surface soil moisture = 0 % - Deep soil moisture [15cm] = 30%



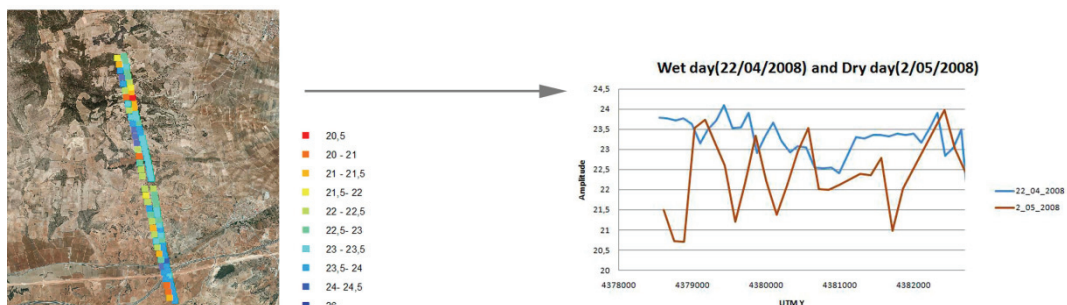
(Page 769) Figure 3. Precipitation rate (a) and Soil Moisture (b) retrieved by NCEP-1, Total liquid clouds estimated from SEVIRI (c) and SMOS Soil Moisture (d) on 3rd March 2010



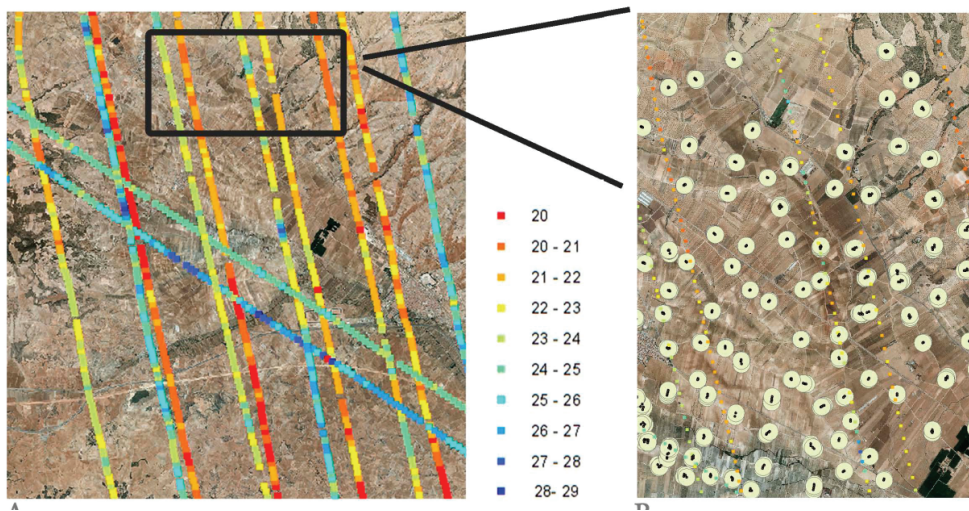
(Page 770) **Figure 4.** Precipitation rate (a) and Soil Moisture (b) retrieved by NCEP-1, Total liquid clouds estimated from SEVIRI (c) and SMOS Soil Moisture (d) on 7th March 2010



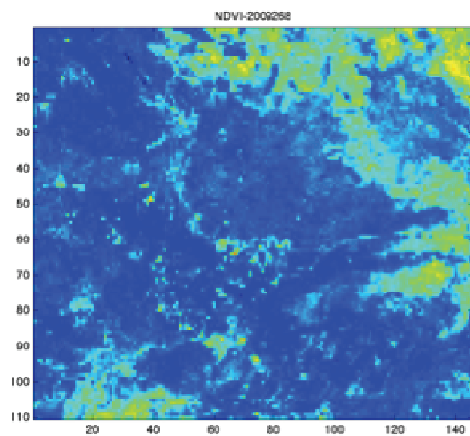
(Page 777) **Figure 2** Multilayer sampling point and grid+ sand content+clay content+unit environment units .



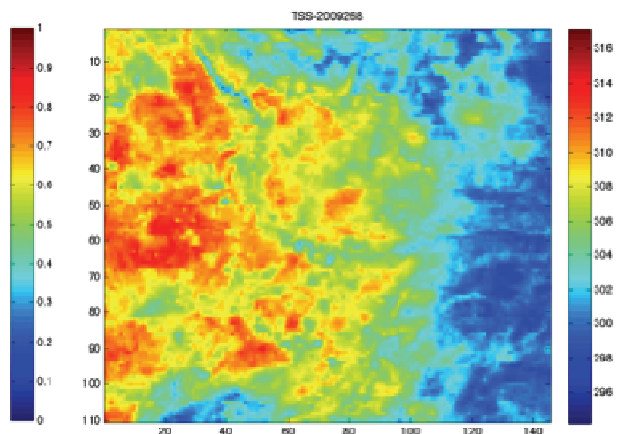
(Page 778) **Figure 3** Variation of amplitude on dry day and wet day.



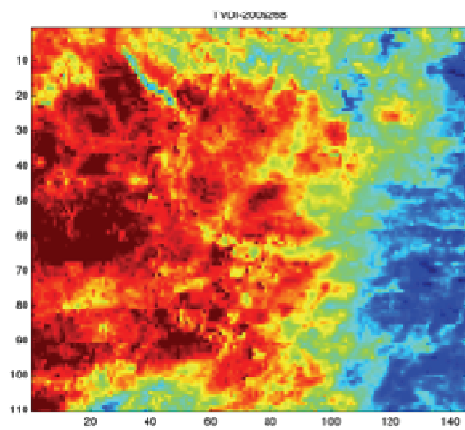
(Page 779) Figure 8 Buffer between in situ data and airborne data (22/04/2008).



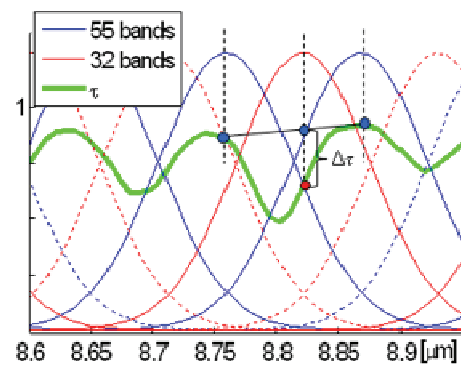
(Page 782) Figure 6: LST (28/09/2009)



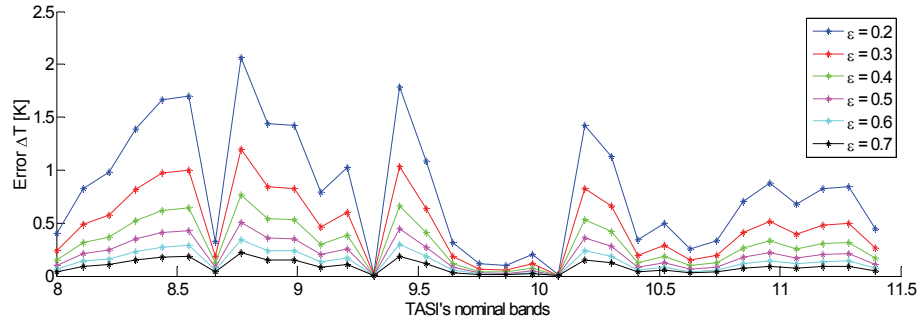
(Page 782) Figure 7: NDVI (28/09/2009)



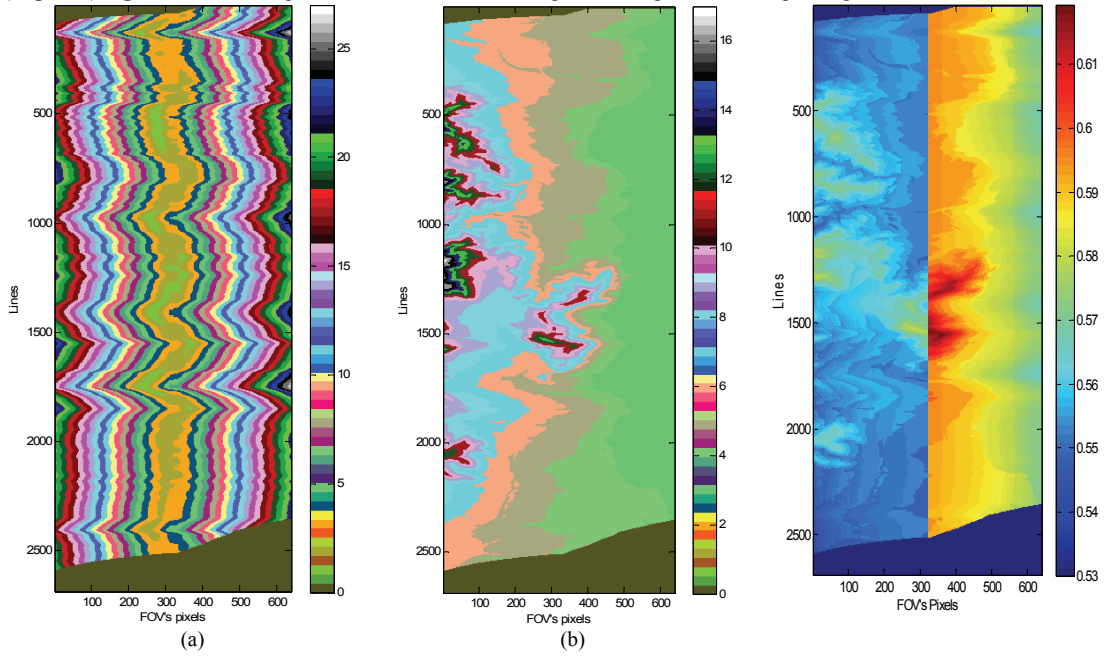
(Page 782) Figure 9: TVDI (28/09/2009)



(Page 840) Fig.1: Incorrect atmospheric compensation due to radiance spectral interpolation.

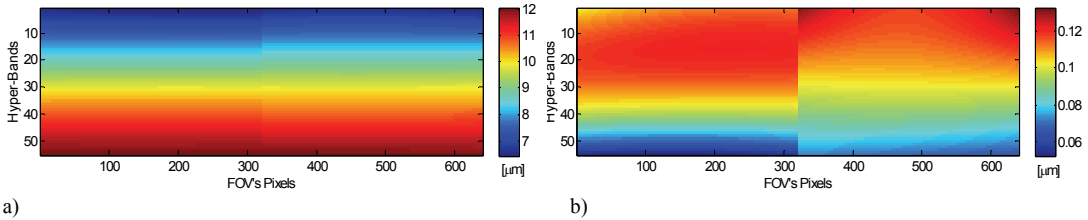


(Page 841) Fig. 2 : Absolute temperature error due to radiance spectral interpolation for ϵ spanning from 0.2 to 0.7.

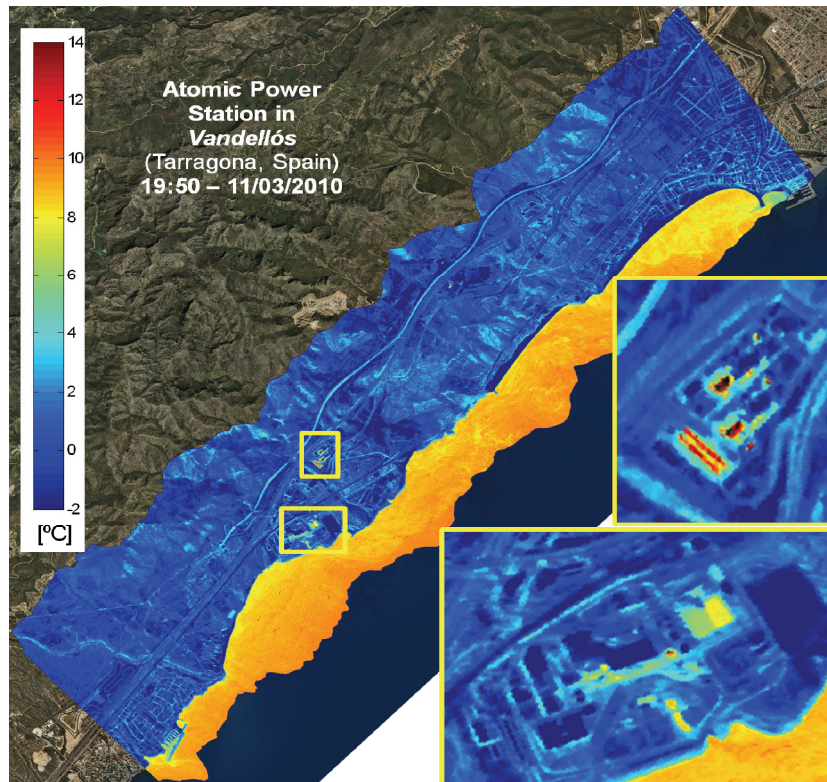


(Page 842) Fig.3: Example of pixels' segmentation based on the observation angle θ (a) and vertical distance to the sensor h (b) with $\Delta\theta=1.5^\circ$ and $\Delta h=30\text{m}$ (Vandellós).

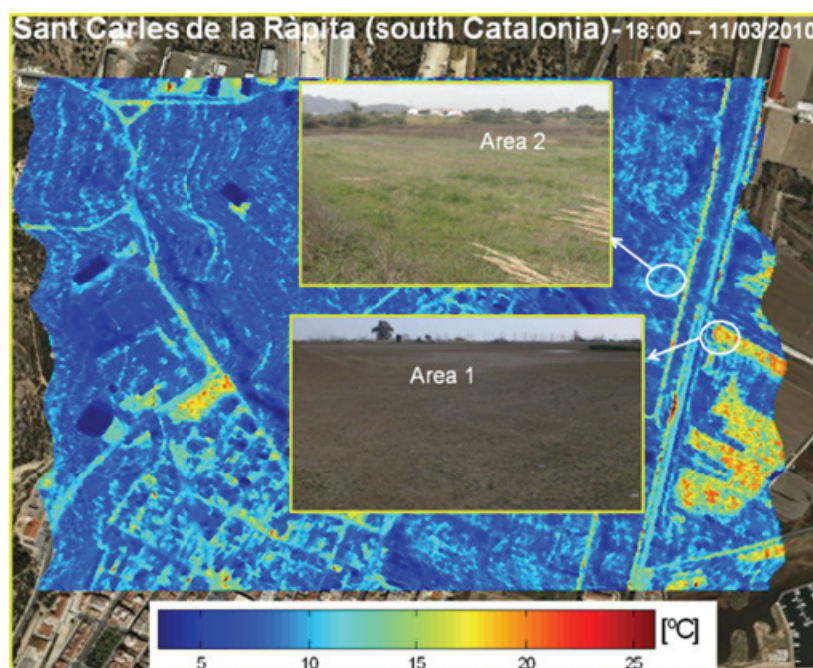
(Page 842) Fig.4: Example of τ estimation based on segmentation of Fig. 3a-b (Vandellós).



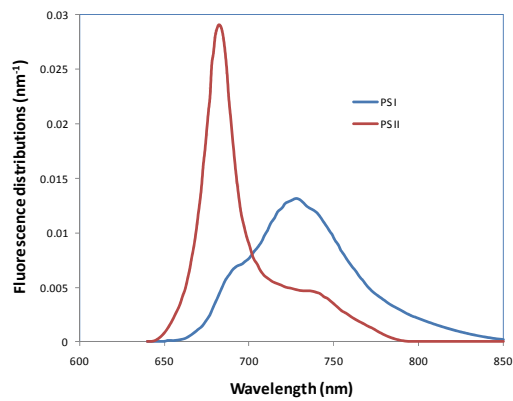
(Page 842) Fig. 5: Example of the distribution of central wavelength λ_0 (a) and bandwidth $\Delta\lambda$ (b) of FOV's pixels among the 55 bands acquired by TASI.



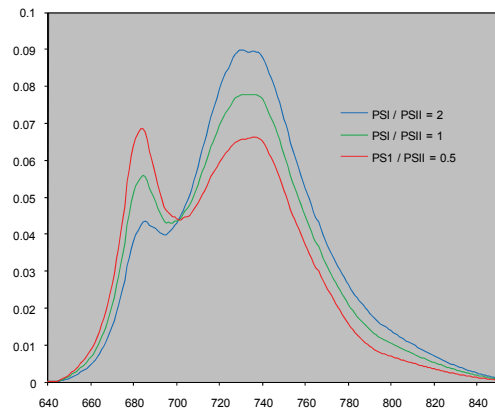
(Page 842) Fig.6: Temperature map of Vandellós retrieved from TASI hyperspectral data using MODTRAN5.0 atmosphere standard model and ARTEMIS technique.



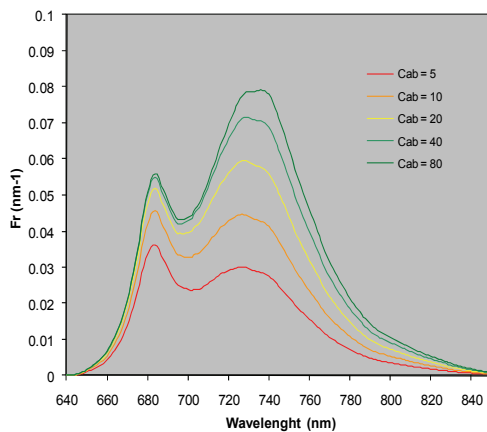
(Page 843) Fig. 6: Temperature map estimated from TASI data of the area close to Sant Carles de la Ràpita.



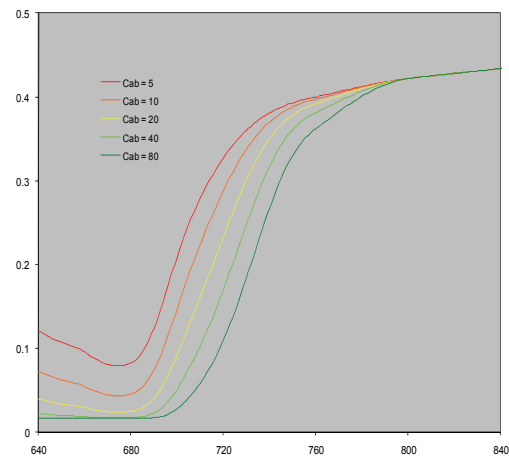
(Page 858) **Fig. 1** Spectral distributions of the fluorescence from photosystems I and II



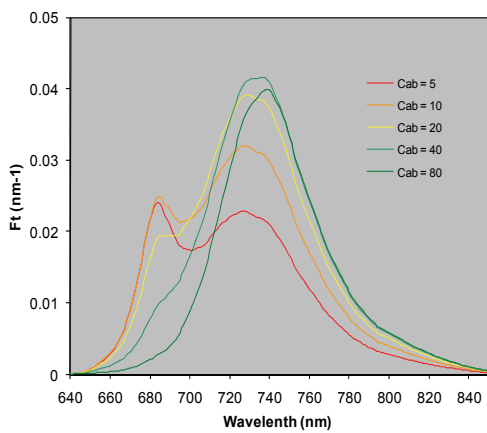
(Page 860) **Fig. 5** Effects of changing the PS I / PS II peak ratio



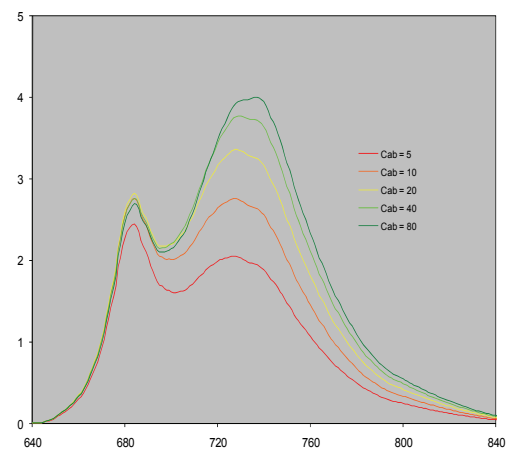
(Page 859) **Fig. 4a** Backward fluorescence spectra for an increasing chlorophyll concentration



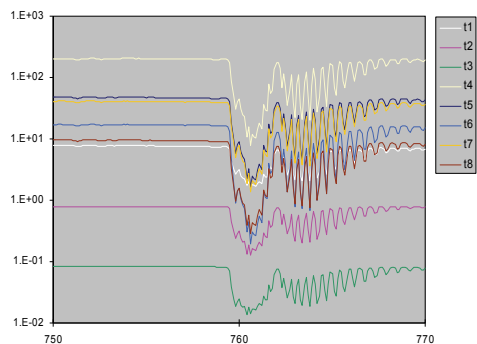
(Page 860) **Fig. 7a** Surface reflectance spectra for increasing chlorophyll contents



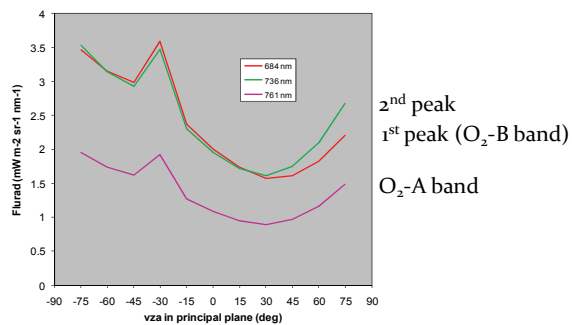
(Page 860) **Fig. 4b** Forward fluorescence spectra for an increasing chlorophyll concentration



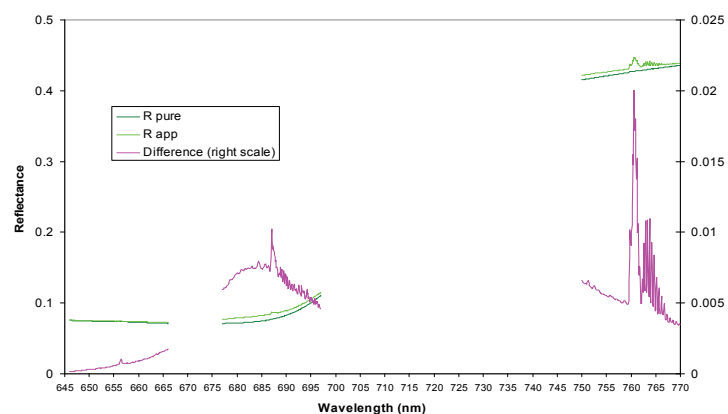
(Page 861) **Fig. 7b** Fluorescent radiance spectra ($\text{mW/m}^2 \text{ sr nm}$) at TOC level for increasing chlorophyll contents



(Page 862) Fig. 10 Plot of $t_1 - t_8$ for the O_2 -A region at 0.1 nm resolution on a log scale



(Page 861) Fig. 8 Directional effects on fluorescent radiances at a few selected wavelengths



(Page 861) Fig. 9 Pure and apparent reflectances in 3 windows at 0.1 nm spectral sampling distance: i) H-alpha, ii) O_2 -B, iii) O_2 -A. The purple lines show the differences (right scale)

